Bioconjugate Chemistry

COMMENT

pubs.acs.org/bc

Remembering Professor Tae Gwan Park (1957−2011)

Haeshin Lee, Ph.D.*

Department of Chemistry, The Graduate School of Nanoscience and Technology, Korea Advanced Institute of Science & Technology (KAIST), Republic of Korea

Ji Hoon Jeong, Ph.D.

School of Pharmacy, Sungkyunkwan University, Republic of Korea

Allan S. Hoffman, Sc.D.

Emeritus Professor, Bioengineering Department, University of Washington, Seattle, Washington, United States

Professor Tae Gwan Park (1957−2011) was an outstanding, innovative biomaterial scientist, and was highly admired and respected around the world. He was personally a warm-hearted, exceptionally honest, and modest person. His profound intellectual curiosity and his strong desire for excellence in research inspired many of his colleagues, his students, and his postdocs. He will be deeply missed by many people around the world.

Dr. Park obtained his B.S. degree from Department Chemical Technology at Seoul National University in 1980 and got his Ph.D. in Bioengineering at the University of Washington, Seattle, in 1990 (under Professor Allan Hoffman). His dissertation involved groundbreaking, seminal research on the immobilization of drugs, enzymes, and cells within "smart" hydrogels.[1,2] He showed how enzymes and cells in such hydrogels could be turned on and off by cyclic changes in temperature. In addition, Dr. Park revealed how a packed bed enzyme-hydrogel system could convert substrate to product with increased efficiency due to enhanced mass transport of substrate in and product out. He also developed a temperature gradient column of smart hydrogel beads as a molecular size separation chromatographic system.

After receiving his Ph.D., Dr. Park did postdoctoral work on PLGA drug delivery systems at MIT, under Professor Bob Langer. Following that, he began his professional academic carrier as an Assistant Professor at Temple University, School of Pharmacy (1992−1995). In 1996, he joined the Department of Biological Sciences at the Korea Advanced Institute of Science and Technology (KAIST) where he remained until his death.

Dr. Park published 252 peer-reviewed papers spanning many areas involving polymer chemistry, nanotechnology, and bioconjugation chemistry. His research interests were in three areas: (1) delivery of proteins, peptides, and nucleic acid-based drugs such as siRNA, (2) tissue engineering, and (3) intelligent or "smart" polymers and hydrogels. At KAIST, he developed novel methods for preparation of biodegradable porous scaffolds for tissue engineering, utilizing gas forming reagents[3] and thermally induced phase separation to form the pores.[4] He also dedicated himself to the development of polymeric micelles for anticancer drug delivery,[5] microspheres for peptide/protein delivery,[6] protein PEGylation techniques,[7] and nonviral gene delivery systems.[8−10] His recent research interests included PEG-assisted solubilization of DNA in organic solvents (cover article *Bioconjugate Chemistry*[11]), molecular imaging,[12−14] and mussel-inspired tissue adhesives[15]

Dr. Park received a number of awards, including the Clemson award (2009) from the Society for Biomaterials. The Korean Ministry of Education, Science, and Technology selected him as one of six of the most highly cited Korean scientists for the past ten years (Creative Knowledge Award, 2009). He was invited to speak at many international meetings.

The impact that Dr. Park had as a world-class scientist, an outstanding mentor, and one of the pioneers of biotechnology in Korea was significant around the world. We are saddened from his death and will miss him greatly.

AUTHOR INFORMATION

Corresponding Author

*Haeshin Lee, Ph.D. E-mail: haeshin@kaist.ac.kr.

REFERENCES

(1) Park, T. G., and Hoffman, A. S. (1988) Effect of temperature cycling on the activity and productivity of immobilized β-galactosidase in a thermally reversible hydrogel bead reactor. *Appl. Biochem. Biotechnol. 19*, 1–9.

Published: June 13, 2011

ACS Publications © 2011 American Chemical Society

(2) Park, T. G., and Hoffman, A. S. (1994) Estimation of temperature-dependent pore sizes in poly(NIPAAm) hydrogel beads. *Biotechnol. Prog. 10*, 82–86.

(3) Nam, Y. S., Yoon, J. J., and Park, T. G. (2000) A novel fabrication method for macroporous scaffolds using gas foaming salt as porogen additive. *J. Biomed. Mater. Res. 53*, 1–7.

(4) Nam, Y. S., and Park, T. G. (1999) Porous biodegradable polymeric scaffolds prepared by thermally induced phase separation method. *Biomaterials 47*, 8–17.

(5) Yoo, H. S., and Park., T. G. (2001) Biodegradable polymeric micelles composed of doxorubicin conjugated PLGA-PEG block copolymer. *J. Controlled Release 70*, 63–70.

(6) Kim, H. K., Chung, H. J., and Park., T. G. (2006) Biodegradable polymeric microspheres with "open/close" pores for sustained release of human growth hormone. *J. Controlled Release 112*, 167–174.

(7) Lee, H., and Park, T. G. (2002) Preparation and characterization of mono-PEGylated epidermal growth factor: Evaluation of in vitro biologic activity. *Pharm. Res. 19*, 845–851.

(8) Park, T. G., Jeong, J. H., and Kim, S. W. (2006) Current status of polymeric gene delivery systems. *Adv. Drug Delivery Rev. 58*, 467–486.

(9) Kim, S. H., Jeong, J. H., Lee, S. H., Kim, S. W., and Park, T. G. (2006) PEG conjugated VEGF siRNA for anti-angiogenic gene therapy. *J. Controlled Release 116*, 123–129.

(10) Mok, H., Lee, S. H., Park, J. W., and Park, T. G. (2010) Multimeric small interfering ribonucleic acid for highly efficient sequence-specific gene silencing. *Nat. Mater. 9*, 272–278.

(11) Mok, H., and Park, T. G. (2006) PEG-assisted DNA solubilization in organic solvents for preparing cytosol specifically degradable PEG/DNA nanogels. *Bioconjugate Chem. 17*, 1369–1372.

(12) Lee, Y., Lee, H., Kim, Y. B., Hyeon, T., Park, H., Messersmith, P. B., and Park, T. G. (2008) Bioinspired surface immobilization of hyaluronic acid on monodisperse magnetite nanocrystals for targeted cancer imaging. *Adv. Mater. 20*, 4154–4157.

(13) Lee, H., Lee, K., Lee, I. K., and Park, T. G. (2009) Gold nanoprobe sensitive to intracellular reactive oxygen species. *Adv. Funct. Mater. 19*, 1884–1890.

(14) Bae, K. H., Kim, Y. B., Lee, Y., Hwang, J. Y., Park, H. W., and Park, T. G. (2010) Bio-inspired synthesis and characterization of gadolinium-labeled magnetite nanoparticles for dual contrast T1- and T2-weighted magnetic resonance imaging. *Bioconjugate Chem. 21*, 505–512.

(15) Lee, Y., Chung, H. J., Yeo, S., Ahn, C.-H., Lee, H., Messersmith, P. B., and Park, T. G. (2010) Thermo-sensitive, injectable, and tissue adhesive sol-gel transition hyaluronic acid/pluronic composite hydrogels prepared from bio-inspired catechol-thiol reaction. *Soft Matter 6*, 977–983.

Bioconjugate Chemistry

COMMUNICATION

pubs.acs.org/bc

Strain-Promoted "Click" Chemistry for Terminal Labeling of DNA

Isaac S. Marks, Jun Sung Kang, Brady T. Jones, Kevin J. Landmark, Andrew J. Cleland, and T. Andrew Taton*

Department of Chemistry, University of Minnesota, 207 Pleasant Street SE, Minneapolis, Minnesota 55455, United States

Supporting Information

ABSTRACT: 1,3-Dipolar [3 + 2] cycloaddition between azides and alkynes—an archetypal "click" chemistry—has been used increasingly for the functionalization of nucleic acids. Copper(I)-catalyzed 1,3-dipolar cycloaddition reactions between alkyne-tagged DNA molecules and azides work well, but they require optimization of multiple reagents, and Cu ions are known to mediate DNA cleavage. For many applications, it would be preferable to eliminate the Cu(I) catalyst from these reactions. Here, we describe the solid-phase synthesis and characterization of 5′-dibenzocyclooctyne (DIBO)-modified oligonucleotides, using a new DIBO phosphoramidite, which react with azides via copper-free, strain-promoted alkyne−azide cycloaddition (SPAAC). We found that the DIBO group not only survived the standard acidic and oxidative reactions of solid-phase oligonucleotide synthesis (SPOS), but that it also survived the thermal cycling and standard conditions of the polymerase chain reaction (PCR). As a result, PCR with DIBO-modified primers yielded "clickable" amplicons that could be tagged with azide-modified fluorophores or immobilized on azide-modified surfaces. Given its simplicity, SPAAC on DNA could streamline the bioconjugate chemistry of nucleic acids in a number of modern biotechnologies.

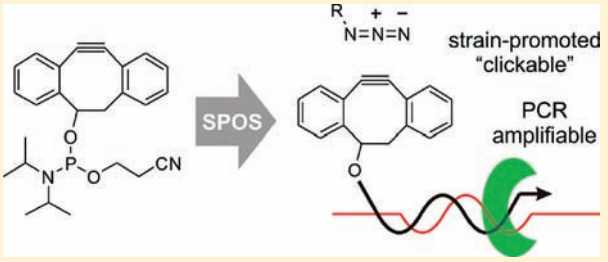

The recent, rapid development of new DNA sequencing and sequence detection technologies[1−3] has created a demand for new bioconjugate chemistries for oligodeoxynucleotides (ODNs) and DNA.[4] In the case of ODNs, synthetic modifications are typically introduced during solid-phase oligonucleotide synthesis (SPOS) via modifier phosphoramidites or appropriately derivatized solid supports.[5] A great many synthetic modifiers have been developed for ODN functionalization, with the only critical requirement being that the modifier survives the conditions of SPOS. When these modified ODNs are used as primers in PCR, the functional groups must also be compatible with the thermal cycling and chemistry of PCR.[6] 5′-Terminal modifiers intended for PCR are typically appended to primers via SPOS prior to PCR amplification, and 5′-fluorophore-, -biotin-, -digoxigenin-, -amine-, -thiol-, and -acrylate-tagged PCR products are commonly made in this way. Some of these functional groups can subsequently be used for post-PCR reactions, including attachment of the DNA to microarrays, beads, or other surfaces.[7,8]

Despite this assortment of techniques for modifying DNA, there is still a need for new covalent DNA functionalization methods with improved kinetics, selectivity, and simplicity. Toward this end, a number of research groups have investigated 1,3-dipolar cycloaddition—a prototypical "click" reaction[9]—as a means of functionalizing ODNs and PCR-amplified DNA.[10] In particular, the copper-catalyzed azide−alkyne cycloaddition (CuAAC)[11] has been used to fluorescently tag ODNs[12−16] and PCR amplicons,[17] to attach DNA to surfaces,[18−21] to cross-link,[22] ligate[23,24] and circularize[25,26] DNA, and to conjugate ODNs to carbohydrates,[27,28] peptides,[29] and proteins.[30] These reactions give high yields, and the bio-orthogonality of the azide−alkyne reaction ensures selectivity. However, CuAAC requires multiple reagents in addition to the azide−alkyne pair, and Cu(II) is known to mediate oxidative cleavage of DNA,[31,32] although Cu-mediated DNA cleavage can be minimized by optimizing click reaction conditions and by appropriate choice of ligand.[23] As an alternative to copper-catalyzed click chemistry, various copper-free click reactions have been developed for bioconjugate applications.[33] Heaney and co-workers have recently applied copper-free alkyne-nitrone cycloadditions, in which nitrones are used in place of azides, to ODN chemistry,[34,35] and Carell and co-workers have used similar nitrone-alkene cycloadditions for modification of modified nucleosides.[36,37] These reactions are fast, but limited by the instability of many nitrones to hydrolysis and dimerization.[38] Bertozzi and co-workers[39−42] and others[43,44] have developed a catalyst-free, strain-promoted alkyne−azide cycloaddition (SPAAC) reaction between azides and cyclooctynes[45] for bioconjugate chemistry. However, strain-promoted click chemistry has not yet been applied to bioconjugation of DNA.

In this report, we describe the solid-phase synthesis, purification, and characterization of cyclooctyne-modified ODNs that react with azides via SPAAC. The ODN modifications were introduced via SPOS using the new dibenzocyclooctyne (DIBO) phosphoramidite **2**, which was synthesized from the strained hydroxydibenzocyclooctyne **1** reported by Boons and co-workers

Received: August 11, 2010
Revised: April 16, 2011
Published: May 03, 2011

ACS Publications © 2011 American Chemical Society

Scheme 1

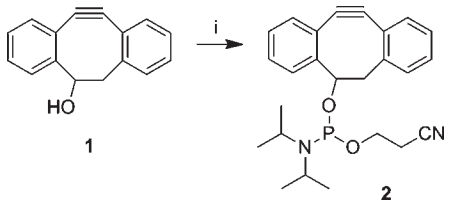

i. ClP[N(*i*Pr)$_2$](OEtCN), DIPEA, rt, CH_2Cl_2, 1 h.

Scheme 2

a 5′ X-T_{10}
b 5′ X-T_8CGTGATCCCACCTCATTTTC

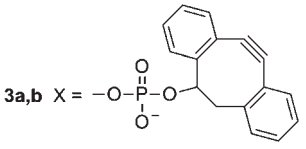

3a,b X = −O−P(=O)(O$^-$)−O−

4a,b X = −OH

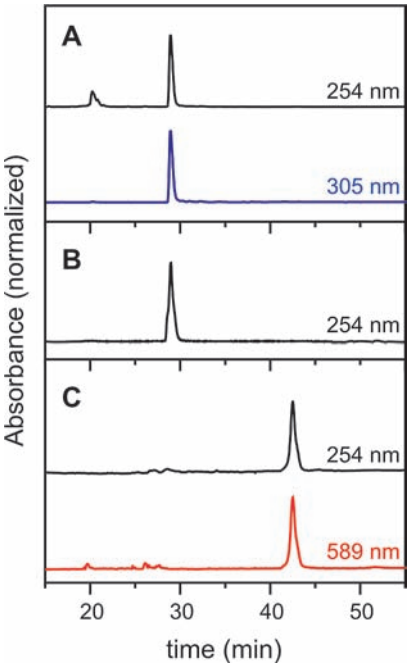

Figure 1. HPLC chromatograms of 5′-DIBO-modified ODN **3a** (A) before purification, (B) after HPLC purification, and (C) after reaction with azide **5** to form ODN **7a**.

(Scheme 1).[43] This phosphoramidite was then used in SPOS, using standard chemistries for synthesis, base deprotection, and cleavage from solid support, to generate 5′-DIBO-modified ODNs **3a**/**b** (Scheme 2). These ODNs were purified by reverse-phase (RP) gradient HPLC, where the hydrophobic 5′-cyclooctyne resulted in longer retention times on C18 RP media (Figure 1A, B). The attachment of the DIBO group to each purified ODN was confirmed by ESI-MS. The 5′-DIBO group was also characterized by UV−vis absorbance spectroscopy (Figure 2A). By

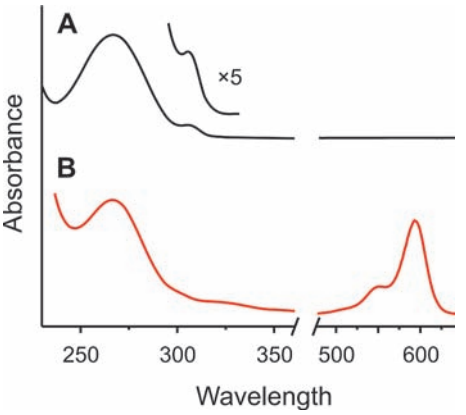

Figure 2. UV−vis spectra of ODN **3a** (A) and clicked Texas Red-ODN **7a** (B).

Scheme 3

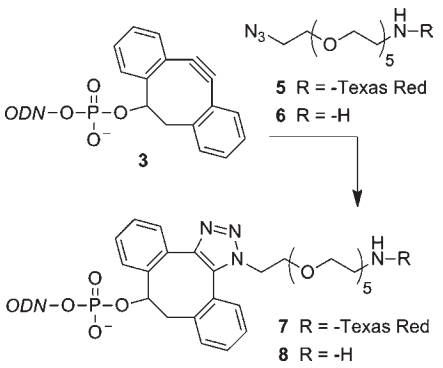

itself, hydroxy-dibenzocyclooctyne **1** absorbs UV light in the λ = 305 nm region of the UV−vis spectrum, with extinction coefficient $\varepsilon_{305} = 9.97 \times 10^3\ M^{-1}\ cm^{-1}$ in $CHCl_3$. When attached to an ODN, the cyclooctyne group adds a peak in the same λ = 305 nm region to the typical λ = 260 nm absorbance peak of the ssDNA, with $\varepsilon_{305} = 2 \times 10^4\ M^{-1}\ cm^{-1}$ in H_2O—larger than, but comparable to, the extinction coefficient of **1** in $CHCl_3$. These data indicate that the strained DIBO group survives reaction conditions in SPOS that we imagined might alter a strained alkyne,[46] including phosphorus oxidation with I_2, exposure to acidic tetrazole in the coupling step, and incubation in concentrated NH_4OH at 60 °C during deprotection and cleavage from solid support.

As expected, DIBO-modified ODNs **3a**/**b** reacted quantitatively with organic azides to produce clicked bioconjugates (Scheme 3). These reactions could be conducted either on solid support at the end of SPOS or in aqueous solution after the cyclooctyne-modified oligonucleotide is released from support. To evaluate the efficiency and rate of the solution-phase reaction, we combined the sulforhodamine azide **5** with ODNs **3a**/**b** at room temperature in H_2O to generate clicked oligonucleotide products **6a**/**b** that were readily identified and purified by HPLC (Figure 1C). The identities of the purified products were confirmed by ESI-MS, which showed the added mass of the azide. UV−vis spectroscopy of **6a**/**b** indicated that the characteristic UV absorbance peak at λ = 305 nm from the starting DIBO group had disappeared, and that a new absorbance at λ = 595 nm appeared corresponding to the newly attached fluorophore (Figure 2B). Polyacrylamide gel electrophoresis

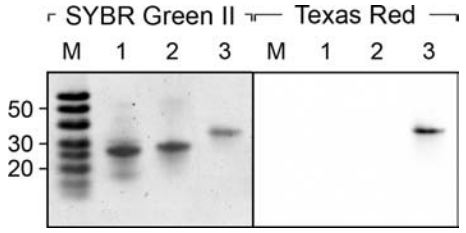

Figure 3. Gel electrophoresis (16% denaturing PAGE) of unmodified ODN **4b** (lane 1), DIBO-modified ODN **3b** (lane 2), and clicked Texas Red-ODN **7b** (lane 3). After electrophoresis, the gel was scanned in the Texas Red channel to generate the image on the right, stained with SYBR Green II, and then scanned in the SYBR Green channel to generate the image on the left.

(PAGE) of **3a**/**b**, **6a**/**b**, and unmodified ODNs **4a**/**b** (Figure 3) showed that both the 5′-DIBO group and the clicked fluorophore retarded the electrophoretic mobility of each ODN slightly, and confirmed the purity of the products.

Kinetic analysis of the reaction between **3a** and **6** in phosphate-buffered saline yielded a second-order rate constant k = 0.9 M^{-1} s^{-1}, which is comparable to the value of 2.3 M^{-1} s^{-1} previously measured by Ning et al. for the reaction between **1** and benzyl azide.[43] Consistent with this result, solution-phase click reactions between even dilute (μM) concentrations of DIBO-modified ODNs and excess azides were quantitatively complete in minutes to hours. The same reaction could be conducted during SPOS, before the ODN was deprotected or cleaved from the controlled-pore glass (CPG) support. Incubation of **CPG-3a** with 270 mM **5** in H_2O overnight, followed by standard deprotection, cleavage from the CPG, and purification via RP HPLC, yielded the same clicked ODN **7a** as synthesized in solution. Morvan and co-workers previously reported that copper-catalyzed azide−alkyne click chemistry of ODNs on solid support required the use of microwaves to drive the reaction to completion;[26] we find that strain-promoted, copper-free click reactions on solid support go to completion without the need for microwave irradiation. Despite this reactivity, we found that cyclooctyne ODNs **3a**/**b** were indefinitely stable under typical solution and storage conditions used for DNA (and in the absence of azides).

An important goal of this research was to use 5′-DIBO-modified ODNs as primers in PCR reactions, such that the resulting cyclooctyne-modified amplicons could be tagged with fluorophores or attached to surfaces via SPAAC. In the specific case of surface attachment, PCR products are often attached to streptavidin-conjugated surfaces noncovalently via a 5′-biotin group;[47] a simple, covalent alternative to the biotin-streptavidin pair could be useful for applications in which the surface-bound DNA is exposed to conditions (e.g., heat or organic cosolvents) that would release biotin.[48] To test the stability of the 5′-DIBO group to the conditions of PCR, we amplified a 500 base-pair sequence from bacteriophage λ DNA using ODN **3b** as a primer. The crude PCR reaction mixture was then incubated with Texas Red azide **5** to fluorescently label the 5′-terminus of the DNA. Agarose gel electrophoresis of the PCR product (Figure 4) demonstrated that amplification with primer **3b** had been successful, and that the DIBO group remained reactive to fluorescent azide **5** after 30 cycles of PCR, as indicated by the observation of Texas Red-labeled product bands in the gel (Figure 4, lanes 4,5). Control experiments, also monitored by gel electrophoresis, showed

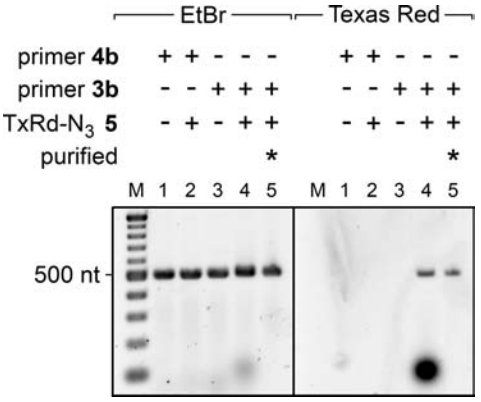

Figure 4. Gel electrophoresis (1.5% agarose, 1× TBE) of PCR products formed from either unmodified (lanes 1−2) or DIBO-modified (lanes 3−5) upstream primers. Primers were designed to amplify nucleotides 7131−7630 (500 bp total) of the bacteriophage λ genome. Crude PCR reaction mixtures were then either loaded directly onto the gel (lanes 1,3), or incubated with 33 μM Texas Red (TxRd)-azide **5** (lanes 2,4,5) before loading onto the gel. The sample in lane 5 was also purified using a PCR purification kit (Qiagen QiaQuick) to remove excess primers and reagents prior to loading. After electrophoresis, the gel was scanned in the Texas Red channel to generate the image on the right, stained with ethidium bromide (EtBr), and then scanned in the EtBr channel to generate the image on the left.

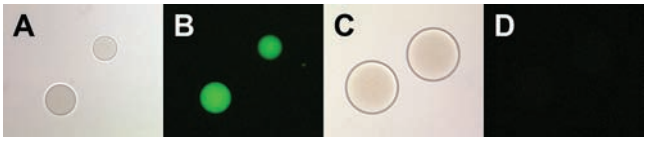

Figure 5. Brightfield (A,C) and fluorescence (B,D) microscopy of Sepharose beads incubated successively with DIBO-modified PCR amplicon and SYBR Green I dye. The beads were either functionalized with azide groups (A,B) or not (C,D).

that no nonspecific labeling occurred in the absence of the cycloalkyne group (Figure 4, lane 2). Similarly, DIBO-modified PCR products were attached to azide-functionalized Sepharose gel by simply combining the two in Tris·HCl (pH 8) buffer overnight (Figure 5A,B). Control experiments showed no attachment for unmodified DNA or for ordinary Sepharose (Figure 5C,D). From these observations, we conclude that post-PCR, strain-promoted click reactions between DIBO-modified DNA and both solution- and solid-phase azides were efficient, selective, and simple, and serve as a potential alternative to terminal biotin−streptavidin association for surface attachment of ODNs.

As cyclooctyne reagents like **1** become commercially available, we anticipate that they will find increasing use in a variety of bioconjugate chemistries. The stability of cyclooctynes under storage, the specificity of their reactions with azides, and the overall ease of SPAAC reactions make them ideal for biomolecule tagging. In this communication, we have demonstrated the broad utility of SPAAC in the bioconjugate chemistry of nucleic acids. Our hope is that this chemistry could be useful for DNA biotechnologies—such as solid-phase and emulsion PCR, in situ PCR labeling, or bioconjugation of extremely dilute or complex samples—where selectivity, simplicity, and speed are at a premium.

■ ASSOCIATED CONTENT

Supporting Information. Synthesis, purification, and characterization of organic compounds and oligonucleotides; kinetics data; details of PCR and post-PCR modification. This material is available free of charge via the Internet at http://pubs.acs.org.

■ AUTHOR INFORMATION

Corresponding Author

*E-mail: taton@umn.edu. Tel: (612) 626-4681, fax: (612) 626-7541.

■ ACKNOWLEDGMENT

This work was supported by the NIH (CA122603).

■ REFERENCES

(1) Metzker, M. L. (2010) Sequencing technologies—the next generation. *Nat. Rev. Genet. 11*, 31–46.

(2) Shendure, J., and Ji, H. (2008) Next-generation DNA sequencing. *Nat. Biotechnol. 26*, 1135–1145.

(3) Zwolak, M., and Di Ventra, M. (2008) Colloquium: Physical approaches to DNA sequencing and detection. *Rev. Mod. Phys. 80*, 141.

(4) Weisbrod, S. H., and Marx, A. (2008) Novel strategies for the site-specific covalent labelling of nucleic acids. *Chem. Commun.* 5675–5685.

(5) Beaucage, S. L., and Iyer, R. P. (1993) The synthesis of modified oligonucleotides by the phosphoramidite approach and their applications. *Tetrahedron 49*, 6123–6194.

(6) Kricka, L. J. (1999) Nucleic acid detection technologies — labels, strategies, and formats. *Clin. Chem. 45*, 453–458.

(7) Pirrung, M. C. (2002) How to make a DNA chip. *Angew. Chem., Int. Ed. 41*, 1276–1289.

(8) Di Giusto, D. A., and King, G. C. (2005) Special-purpose modifications and immobilized functional nucleic acids for biomolecular interactions. *Top. Curr. Chem. 261*, 131–168.

(9) Kolb, H. C., Finn, M. G., and Sharpless, K. B. (2001) Click chemistry: Diverse chemical function from a few good reactions. *Angew. Chem., Int. Ed. 40*, 2004–2021.

(10) Gramlich, P. M. E., Wirges, C. T., Manetto, A., and Carell, T. (2008) Postsynthetic DNA modification through the copper-catalyzed azide-alkyne cycloaddition reaction. *Angew. Chem., Int. Ed. 47*, 8350–8358.

(11) Meldal, M., and Tornøe, C. W. (2008) Cu-catalyzed azide−alkyne cycloaddition. *Chem. Rev. 108*, 2952–3015.

(12) Berndl, S., Herzig, N., Kele, P., Lachmann, D., Li, X., Wolfbeis, O. S., and Wagenknecht, H.-A. (2009) Comparison of a nucleosidic vs non-nucleosidic postsynthetic "click" modification of DNA with base-labile fluorescent probes. *Bioconjugate Chem. 20*, 558–564.

(13) Gramlich, P. M. E., Warncke, S., Gierlich, J., and Carell, T. (2008) Click-click-click: Single to triple modification of DNA. *Angew. Chem., Int. Ed. 47*, 3442–3444.

(14) Seo, T. S., Li, Z., Ruparel, H., and Ju, J. (2002) Click chemistry to construct fluorescent oligonucleotides for DNA sequencing. *J. Org. Chem. 68*, 609–612.

(15) Seela, F., Sirivolu, V. R., and Chittepu, P. (2007) Modification of DNA with octadiynyl side chains: Synthesis, base pairing, and formation of fluorescent coumarin dye conjugates of four nucleobases by the alkyne−azide "click" reaction. *Bioconjugate Chem. 19*, 211–224.

(16) Seela, F., and Ingale, S. A. (2009) Double click" reaction on 7-deazaguanine DNA: Synthesis and excimer fluorescence of nucleosides and oligonucleotides with branched side chains decorated with proximal pyrenes. *J. Org. Chem. 75*, 284–295.

(17) Gierlich, J., Burley, G. A., Gramlich, P. M. E., Hammond, D. M., and Carell, T. (2006) Click chemistry as a reliable method for the high-density postsynthetic functionalization of alkyne-modified DNA. *Org. Lett. 8*, 3639–3642.

(18) Rozkiewicz, D. I., Gierlich, J., Burley, G. A., Gutsmiedl, K., Carell, T., Ravoo, B. J., and Reinhoudt, D. N. (2007) Transfer printing of DNA by "click" chemistry. *ChemBioChem 8*, 1997–2002.

(19) Devaraj, N. K., Miller, G. P., Ebina, W., Kakaradov, B., Collman, J. P., Kool, E. T., and Chidsey, C. E. D. (2005) Chemoselective covalent coupling of oligonucleotide probes to self-assembled monolayers. *J. Am. Chem. Soc. 127*, 8600–8601.

(20) Seo, T. S., Bai, X., Ruparel, H., Li, Z., Turro, N. J., and Ju, J. (2004) Photocleavable fluorescent nucleotides for DNA sequencing on a chip constructed by site-specific coupling chemistry. *Proc. Natl. Acad. Sci. U.S.A. 101*, 5488–5493.

(21) Fischler, M., Sologubenko, A., Mayer, J., Clever, G., Burley, G., Gierlich, J., Carell, T., and Simon, U. (2008) Chain-like assembly of gold nanoparticles on artificial DNA templates via 'click chemistry'. *Chem. Commun.* 169–171.

(22) Kočalka, P., El-Sagheer, A. H., and Brown, T. (2008) Rapid and efficient DNA strand cross-linking by click chemistry. *ChemBioChem 9*, 1280–1285.

(23) Kumar, R., El-Sagheer, A., Tumpane, J., Lincoln, P., Wilhelmsson, L. M., and Brown, T. (2007) Template-directed oligonucleotide strand ligation, covalent intramolecular DNA circularization and catenation using click chemistry. *J. Am. Chem. Soc. 129*, 6859–6864.

(24) El-Sagheer, A. H., and Brown, T. (2009) Synthesis and polymerase chain reaction amplification of DNA strands containing an unnatural triazole linkage. *J. Am. Chem. Soc. 131*, 3958–3964.

(25) Grajkowski, A., Cieślak, J., Kauffman, J. S., Duff, R. J., Norris, S., Freedberg, D. I., and Beaucage, S. L. (2008) Thermolytic release of covalently linked DNA oligonucleotides and their conjugates from controlled-pore glass at near neutral pH. *Bioconjugate Chem. 19*, 1696–-1706.

(26) Lietard, J., Meyer, A., Vasseur, J.-J., and Morvan, F. (2007) New strategies for cyclization and bicyclization of oligonucleotides by click chemistry assisted by microwaves. *J. Org. Chem. 73*, 191–200.

(27) Jawalekar, A. M., Meeuwenoord, N., Cremers, J. G. O., Overkleeft, H. S., van der Marel, G. A., Rutjes, F. P. J. T., and van Delft, F. L. (2007) Conjugation of nucleosides and oligonucleotides by [3 + 2] cycloaddition. *J. Org. Chem. 73*, 287–290.

(28) Bouillon, C., Meyer, A., Vidal, S., Jochum, A., Chevolot, Y., Cloarec, J.-P., Praly, J.-P., Vasseur, J.-J., and Morvan, F. (2006) Microwave assisted "click" chemistry for the synthesis of multiple labeled-carbohydrate oligonucleotides on solid support. *J. Org. Chem. 71*, 4700–4702.

(29) Chao, J., Huang, W.-Y., Wang, J., Xiao, S.-J., Tang, Y.-C., and Liu, J.-N. (2009) Click-chemistry-conjugated oligo-angiomax in the two-dimensional DNA lattice and its interaction with thrombin. *Biomacromolecules 10*, 877–883.

(30) Duckworth, B. P., Chen, Y., Wollack, J. W., Sham, Y., Mueller, J. D., Taton, T. A., and Distefano, M. D. (2007) A universal method for the preparation of covalent protein-DNA conjugates for use in creating protein nanostructures. *Angew. Chem., Int. Ed. 46*, 8819–8822.

(31) Burrows, C. J., and Muller, J. G. (1998) Oxidative nucleobase modifications leading to strand scission. *Chem. Rev. 98*, 1109–1152.

(32) Sigman, D. S., Mazumder, A., and Perrin, D. M. (1993) Chemical nucleases. *Chem. Rev. 93*, 2295–2316.

(33) Jewett, J. C., and Bertozzi, C. R. (2010) Cu-free click cycloaddition reactions in chemical biology. *Chem. Soc. Rev. 39*, 1272–1279.

(34) Singh, I., Vyle, J. S., and Heaney, F. (2009) Fast, copper-free click chemistry: A convenient solid-phase approach to oligonucleotide conjugation. *Chem. Commun.* 3276–3278.

(35) Singh, I., and Heaney, F. (2010) Metal free, "click and click-click" conjugation of ribonucleosides and 2′-OMe oligoribonucleotides on the solid phase. *Org. Biomol. Chem. 8*, 451–456.

(36) Gutsmiedl, K., Fazio, D., and Carell, T. (2010) High-density DNA functionalization by a combination of Cu-catalyzed and Cu-free click chemistry. *Chem.—Eur. J. 16*, 6877–6883.

(37) Gutsmiedl, K., Wirges, C. T., Ehmke, V., and Carell, T. (2009) Copper-free "click" modification of DNA via nitrile oxide−norbornene 1,3-dipolar cycloaddition. *Org. Lett. 11*, 2405–2408.

(38) Corsaro, A., Chiacchio, U., and Pistarà, V. (2001) Regeneration of carbonyl compounds from the corresponding oximes. *Synthesis 2001*, 1903–1931.

(39) Agard, N. J., Prescher, J. A., and Bertozzi, C. R. (2004) A strain-promoted [3 + 2] azide−alkyne cycloaddition for covalent modification of biomolecules in living systems. *J. Am. Chem. Soc. 126*, 15046–15047.

(40) Codelli, J. A., Baskin, J. M., Agard, N. J., and Bertozzi, C. R. (2008) Second-generation difluorinated cyclooctynes for copper-free click chemistry. *J. Am. Chem. Soc. 130*, 11486–11493.

(41) Sletten, E. M., and Bertozzi, C. R. (2008) A hydrophilic azacyclooctyne for Cu-free click chemistry. *Org. Lett. 10*, 3097–3099.

(42) Baskin, J. M., Prescher, J. A., Laughlin, S. T., Agard, N. J., Chang, P. V., Miller, I. A., Lo, A., Codelli, J. A., and Bertozzi, C. R. (2007) Copper-free click chemistry for dynamic in vivo imaging. *Proc. Natl. Acad. Sci. U.S.A. 104*, 16793–16797.

(43) Ning, X., Guo, J., Wolfert, M. A., and Boons, G.-J. (2008) Visualizing metabolically labeled glycoconjugates of living cells by copper-free and fast Huisgen cycloadditions. *Angew. Chem., Int. Ed. 47*, 2253–2255.

(44) Debets, M. F., van Berkel, S. S., Schoffelen, S., Rutjes, F. P. J. T., van Hest, J. C. M., and van Delft, F. L. (2010) Aza-dibenzocyclooctynes for fast and efficient enzyme PEGylation via copper-free [3 + 2] cycloaddition. *Chem. Commun. 46*, 97–99.

(45) Wittig, G., and Krebs, A. (1961) Zur Existenz niedergliedriger Cycloalkine, I. *Chem. Ber. 94*, 3260–3275.

(46) Wittig, G., and Dorsch, H.-L. (1968) Zur Existenz niedergliedriger Cycloalkine, VIII. Zur Bildung und Reaktivität von Cyclooctin. *Justus Liebigs Ann. Chem. 711*, 46–54.

(47) Misiura, K., Durrant, I., Evans, M. R., and Gait, M. J. (1990) Biotinyl and phosphotyrosinyl phosphoramidite derivatives useful in the incorporation of multiple reporter groups on synthetic oligonucleotides. *Nucleic Acids Res. 18*, 4345–4354.

(48) Diehl, F., Li, M., He, Y., Kinzler, K. W., Vogelstein, B., and Dressman, D. (2006) BEAMing: single-molecule PCR on microparticles in water-in-oil emulsions. *Nat. Methods 3*, 551–559.

Supporting Information

Strain-promoted "click" chemistry for terminal labeling of DNA

Isaac S. Marks, Jun Sung Kang, Brady T. Jones, Kevin J. Landmark, Andrew J. Cleland, and T. Andrew Taton*

Department of Chemistry, University of Minnesota
207 Pleasant Street SE, Minneapolis, MN 55455, USA

General methods for organic synthesis

Chemicals were obtained from commercial suppliers and used as received unless otherwise specified. Glassware was oven-dried overnight, cooled under vacuum, and backfilled with nitrogen before use. Progress of organic reactions was monitored by thin-layer chromatography (TLC) on Baker-flex TLC sheets (IB-F, 200 μm analytical layer) using 254 nm UV illumination. Flash chromatography was performed using 50 μm silica gel (Luknova, Mansfield, MA) and eluted using nitrogen pressure. UV-visible spectra were acquired on a Beckman Coulter DU 720 (Chaska, MN) or an Agilent 8453 (Santa Clara, CA) UV-Vis spectrophotometer. ^{1}H, ^{13}C, and ^{31}P NMR spectra were acquired in $CDCl_3$ on either a Varian Unity VAC-300 or a Varian INOVA VI-500 spectrometer. Chemical shifts (δ) are given in ppm relative to reference peaks (^{1}H, $CDCl_3$, δ 7.26; ^{13}C, $CDCl_3$, δ 77.16; ^{31}P, $P(CH_3)_3$, δ 3.1); coupling constants (*J*) are reported in Hz.

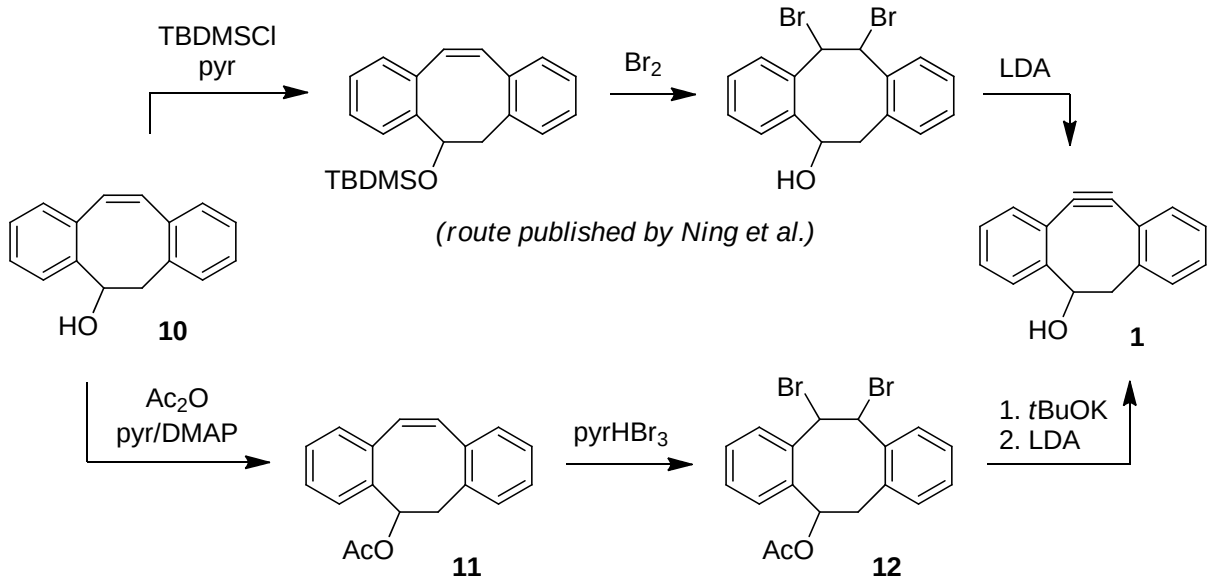

3-hydroxy-1,2:5,6-dibenzocyclooct-7-yne (**1**), the synthetic precursor to phosphoramidite **2**, was prepared via two synthetic routes: either the original route described by Ning et al. (*1*), or via an alternate route illustrated on the previous page.

Synthesis of 1,2:5,6-dibenzocyclooct-7-en-3-yl acetate (11)

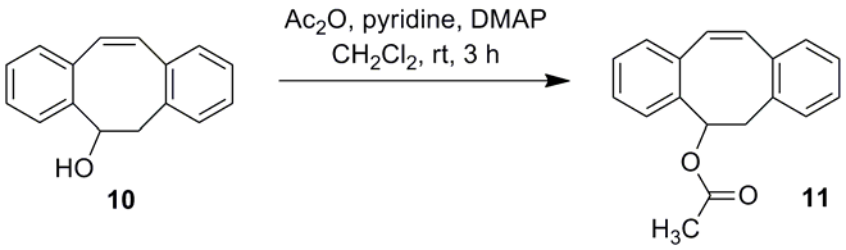

To 3-hydroxy-1,2:5,6-dibenzocyclooct-7-ene **10** (*1*) (2.00 g, 9.00 mmol) in 45 mL of CH_2Cl_2 was added 4-dimethylaminopyridine (0.110 g, 0.900 mmol) with stirring. After the solids dissolved, pyridine (1.30 mL, 16.21 mmol) and acetic anhydride (1.27 mL, 13.5 mmol) were added sequentially via syringe. After 3 h, the reaction mixture was poured into water (60 mL). The aqueous layer was extracted with CH_2Cl_2 (2 × 30 mL), and the organic layers were combined and washed with 50 mL 10% HCl, 50 mL water, and 50 mL brine. The organic layer was dried over $MgSO_4$ and filtered. Solvents were removed under reduced pressure to yield crude **11** as a yellow-brown oil (2.28 g, 96% crude). This material could be further purified by flash chromatography (15:1 hexanes/EtOAc, R_f = 0.29), but crude **11** was typically used directly in the next synthetic step without purification. ^{1}H NMR (Figure S1, 300 MHz, $CDCl_3$; only majority peaks listed) δ 7.26-7.10 (8H, m), 6.90 (2H, dd, J_1 = 12, J_2 = 9), 6.425 (1H, dd, J_1 = 9, J_2 = 6), 3.41 (2H, m), 2.09 (3H, m). ^{13}C NMR (Figure S2, 75 MHz, $CDCl_3$) δ 170.91, 137.50, 137.21, 136.25, 135.98, 132.55, 132.26, 130.73, 130.56, 130.38, 129.23, 128.06, 127.96, 126.79, 76.27, 40.16, 22.15. HR-MS (ESI, positive-ion mode) *m/z* 205.1018 $[M - OAc]^+$, expected 205.1017.

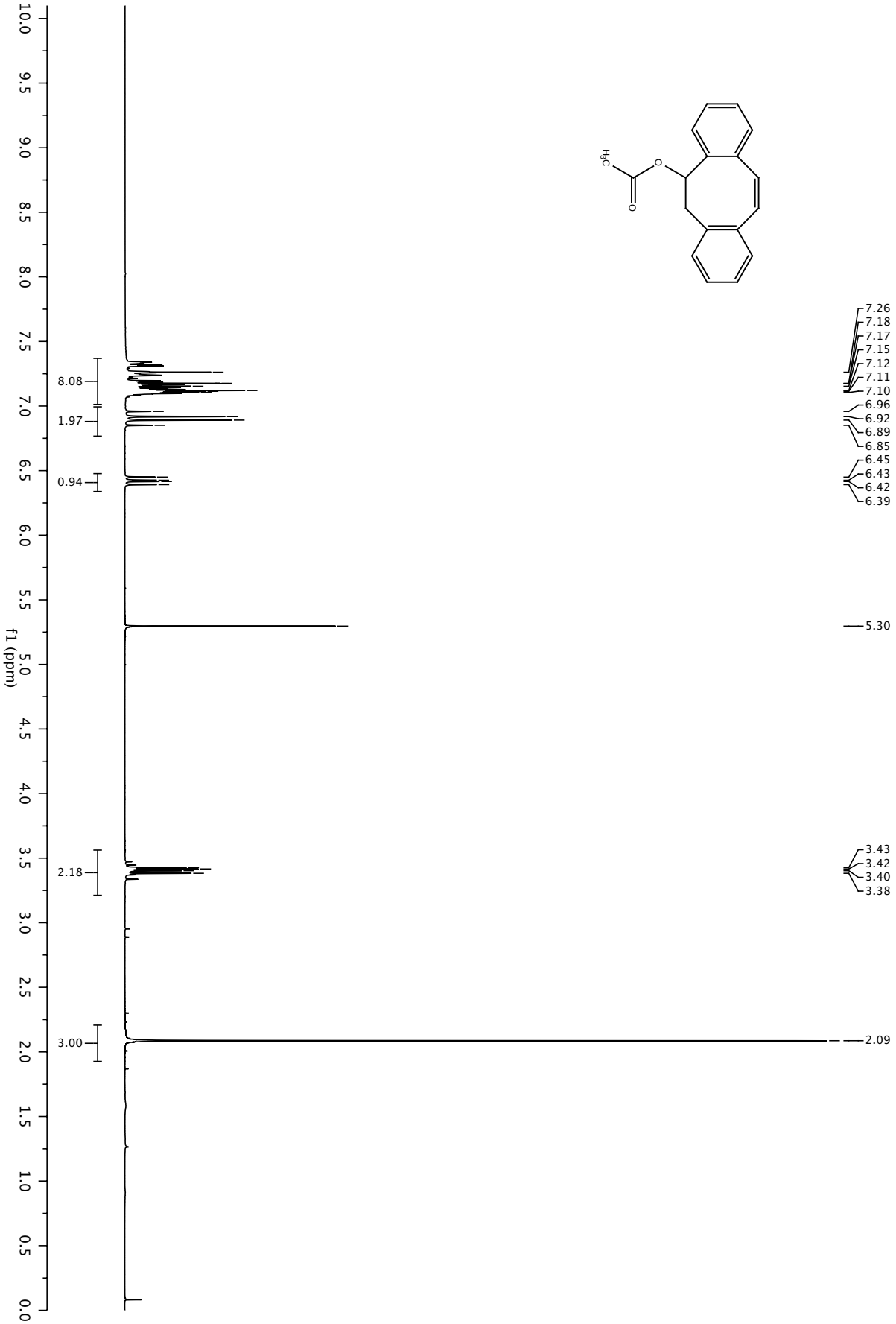

Figure S1. ^{1}H NMR (300 MHz, $CDCl_3$) of **11**.

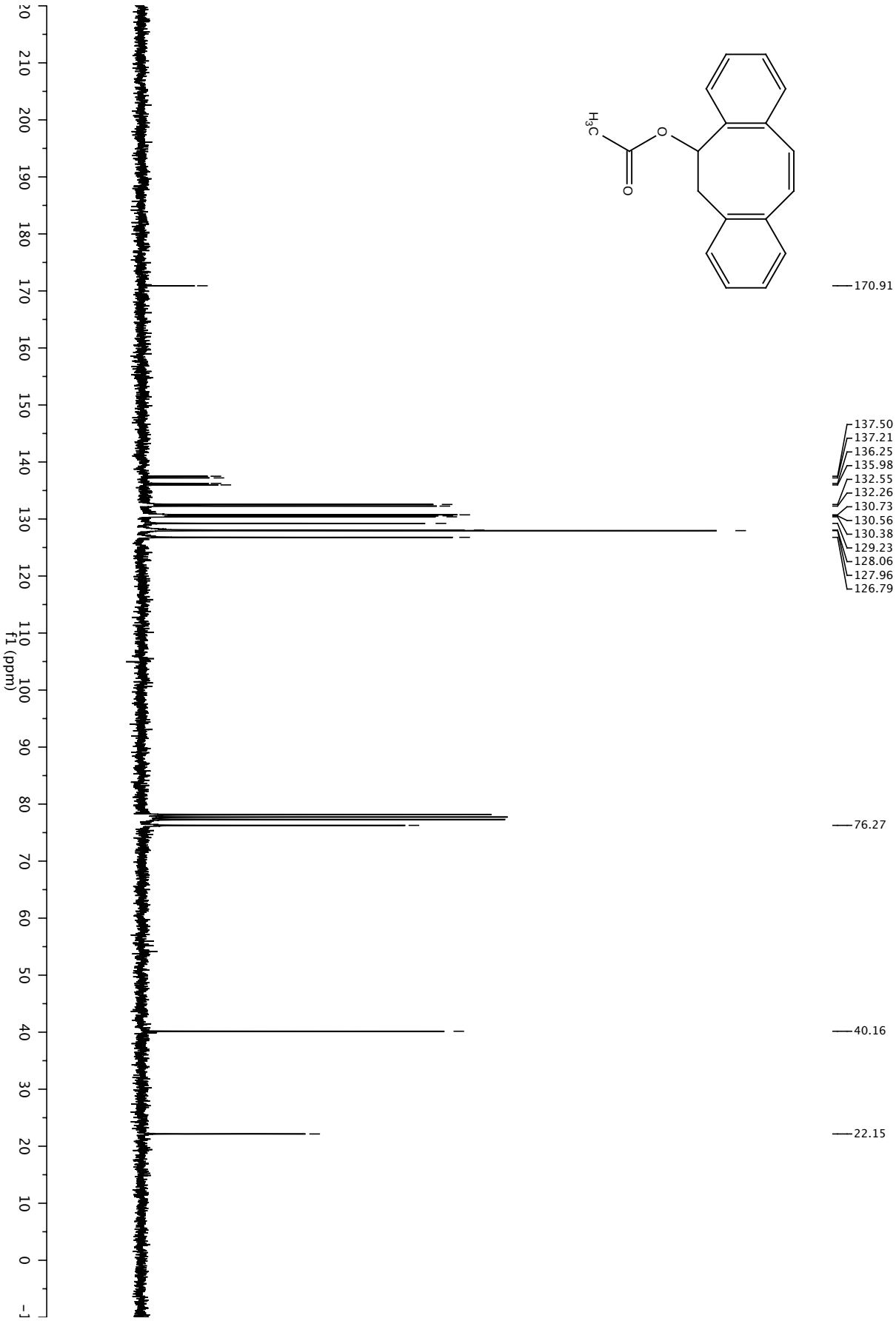

Figure S2. ^{13}C NMR (75 MHz, $CDCl_3$) of **11**.

Synthesis of 7,8-dibromo-1,2:5,6-dibenzocyclooct-3-yl acetate (12)

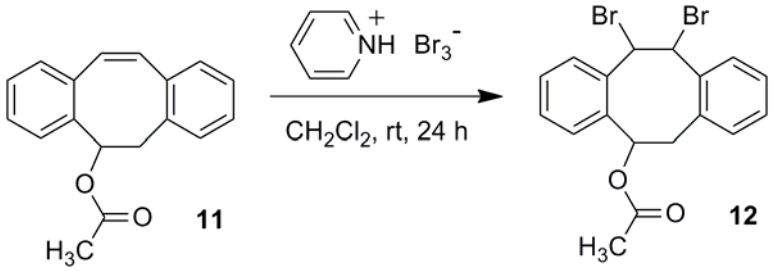

To compound **11** (2.01 g, 7.61 mmol) dissolved in 76.1 mL of CH_2Cl_2 was added pyridinum tribromide (3.62 g, 11.42 mmol) with stirring. The color of the solution changed rapidly from yellow to deep red-orange. The reaction vessel was immediately covered with aluminum foil. After 24 h (when TLC indicated that starting material was completely consumed), the reaction mixture was combined with 100 mL of saturated $Na_2S_2O_3$. The aqueous layer was then extracted with CH_2Cl_2 (2 × 20 mL). The organic layers were combined and then washed with 50 mL 10% HCl, 75 mL water, and 75 mL brine. The organic layer was then dried over $MgSO_4$ and filtered. Solvents were removed under reduced pressure to yield a yellow oil that was purified via flash chromatography (2:1 hexanes/CH_2Cl_2, R_f = 0.17) to yield **12** (2.32 g, 72%) as a yellow-white powder. This material appeared to be predominantly one diastereomer by ^{1}H NMR analysis, but still contained other diastereomers as evidenced by minority peaks in the ^{1}H NMR spectrum; we were unable to separate these diastereomers by flash chromatography or HPLC. Nevertheless, this material could be used directly in subsequent synthesis. ^{1}H NMR (Figure S3, 300 MHz, $CDCl_3$) δ 7.08-6.90 (8H, m), 6.12 (1H, t, J = 9), 5.33-5.24 (2H, m), 3.62 (2H, dd, J_1 = 12, J_2 = 3), 2.14 (3H, s). ^{13}C NMR (Figure S4, 75 MHz, $CDCl_3$) δ 171.05, 139.41, 137.54, 135.59, 134.83, 132.34, 132.24, 130.68, 130.22, 129.94, 129.87, 129.70, 128.27, 71.51, 63.46, 57.77, 42.40, 39.97, 22.13. MS (ESI, positive-ion mode) *m/z* 449 [M(^{81}Br^{81}Br) + Na]$^+$, 447 [M(^{79}Br^{81}Br) + Na]$^+$, 445 [M(^{79}Br^{79}Br) + Na]$^+$.

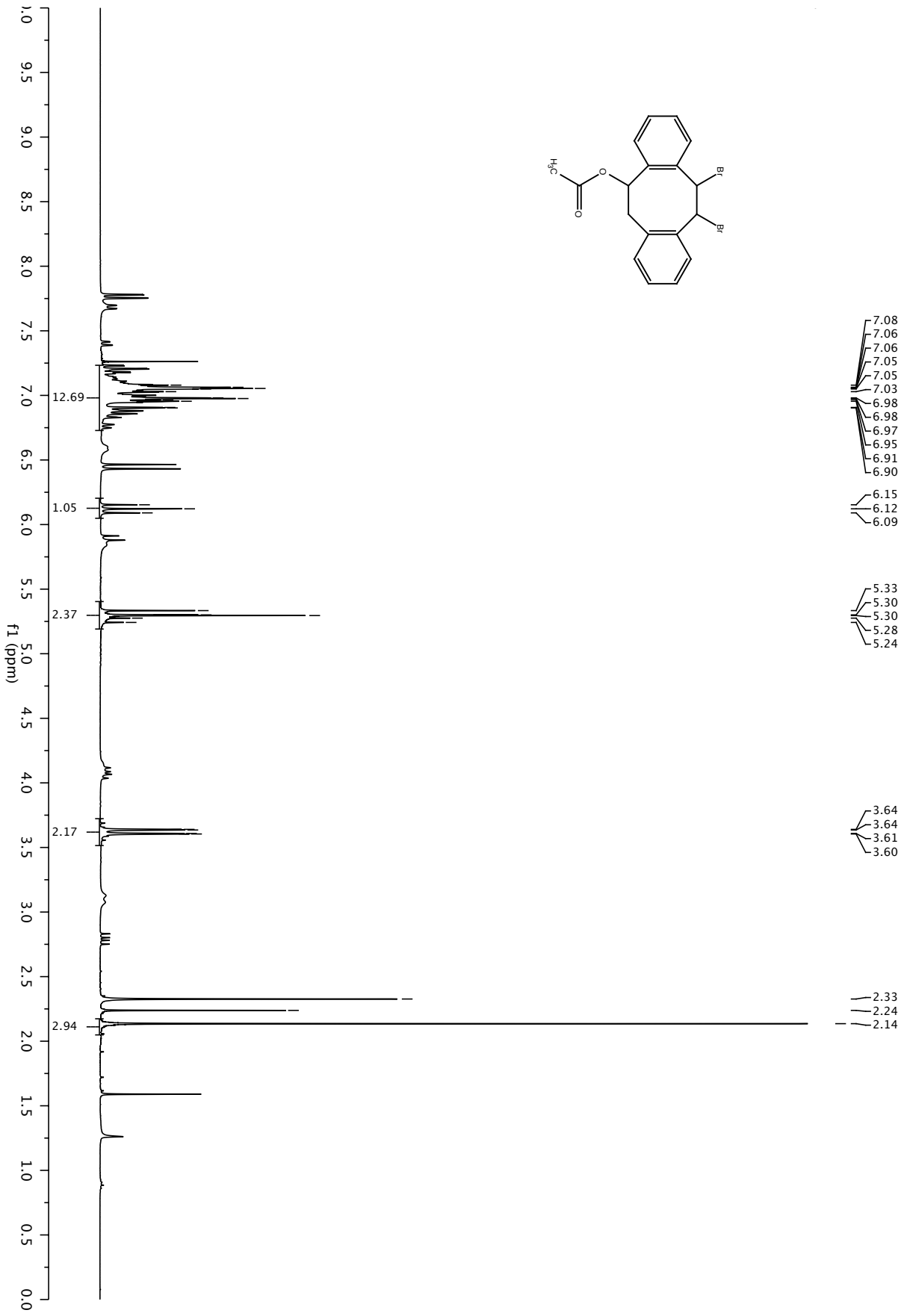

Figure S3. ^{1}H NMR (300 MHz, $CDCl_3$) of **12**.

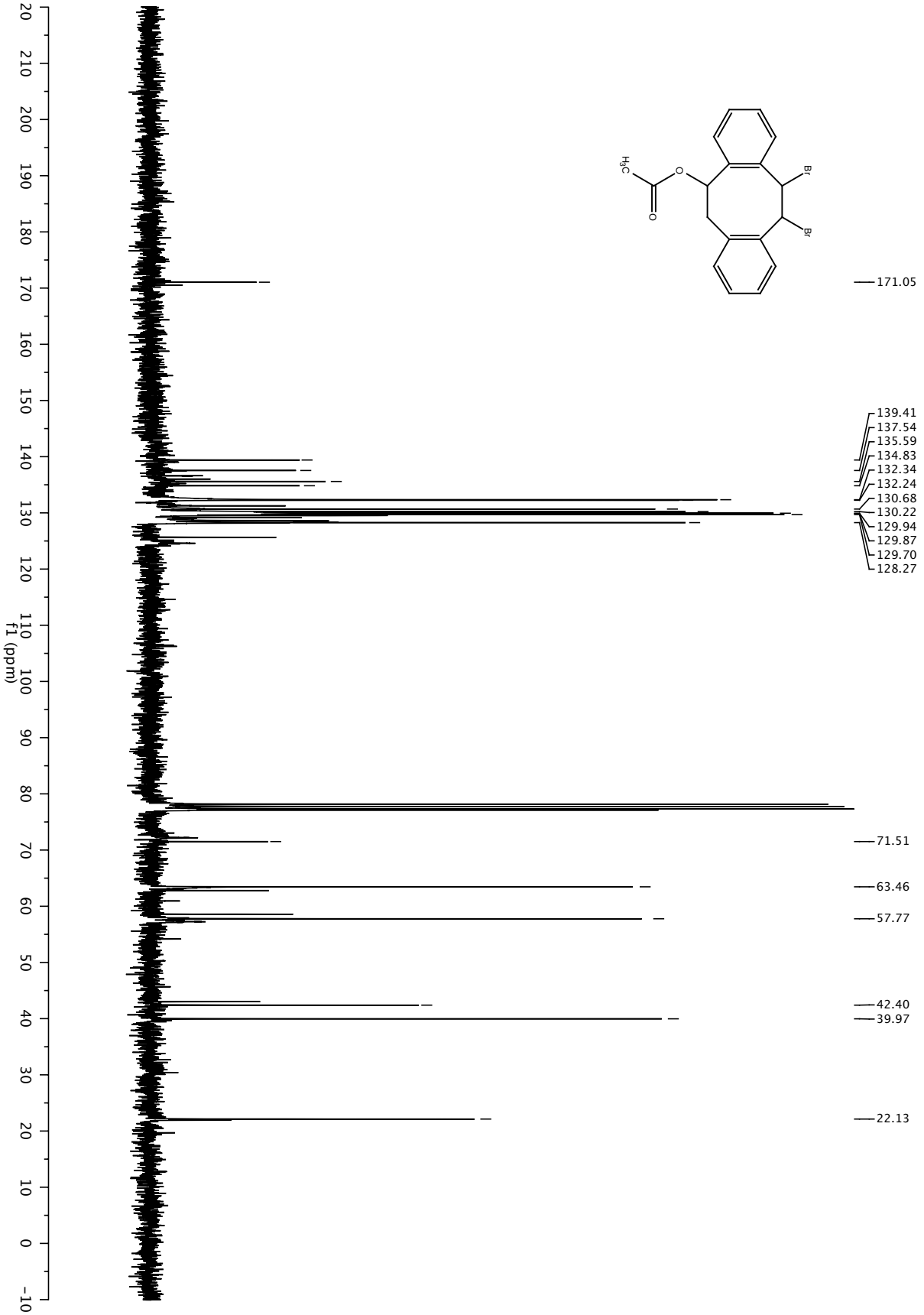

Figure S4. ^{13}C NMR (75 MHz, $CDCl_3$) of **12**.

Synthesis of 3-hydroxy-1,2:5,6-dibenzocyclooct-7-yne (1)

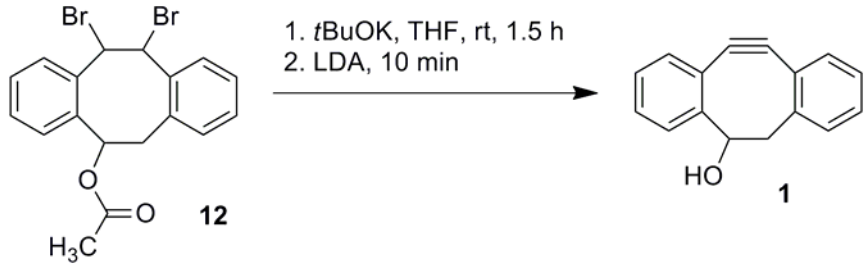

To compound **12** (2.10 g, 4.98 mmol) dissolved in 59.7 mL of THF was added 7.50 mL of a solution of potassium *tert*-butoxide (1.0 M in THF, 7.50 mmol). This was allowed to stir for 1.5 h, until TLC analysis indicated that all starting material was consumed. During this time, lithium diisopropylamide (LDA) was prepared in a separate flask. Diisopropylamine (5.2 mL, 38.3 mmol) was added to 10 mL of THF at 0 °C with stirring. Then, 11.4 mL of a solution of *N*-butyllithium in hexanes (2.5 M, 28.5 mmol) was then added dropwise at 10 mL/h via syringe pump to yield a yellow, slightly turbid solution of LDA. This solution was then added via syringe pump to the reaction vessel at a rate of 0.15 mL/sec. Once addition was complete, an aliquot was removed from the reaction every 10 min and analyzed by UV-vis spectroscopy; the appearance of peaks at λ = 285 nm and 305 nm indicated that the reaction was proceeding, and once these peaks reached their maximum intensity, the reaction was judged to be complete (~10 min.) The reaction was then quenched with 100 mL water, and extracted with CH_2Cl_2 (100 mL, then 2 × 40 mL). The organic layers were combined, washed with 50 mL water and 50 mL brine, and dried over $MgSO_4$. The organics were filtered and concentrated under reduced pressure to give an orange-brown solid. This solid was purified using flash chromatography (2:1 CH_2Cl_2/ hexanes v/v, R_f = 0.19) to yield **1** (0.90 g, 82%) as a white solid. The spectroscopic properties of purified **1** (^{1}H NMR, ^{13}C NMR) were identical to those previously published (*1*).

Synthesis of *O*-(1,2:5,6-dibenzocyclooct-7-yn-3-yl)-*O*-(2-cyanoethyl)-*N*,*N*-diisopropylphosphoramidite (2)

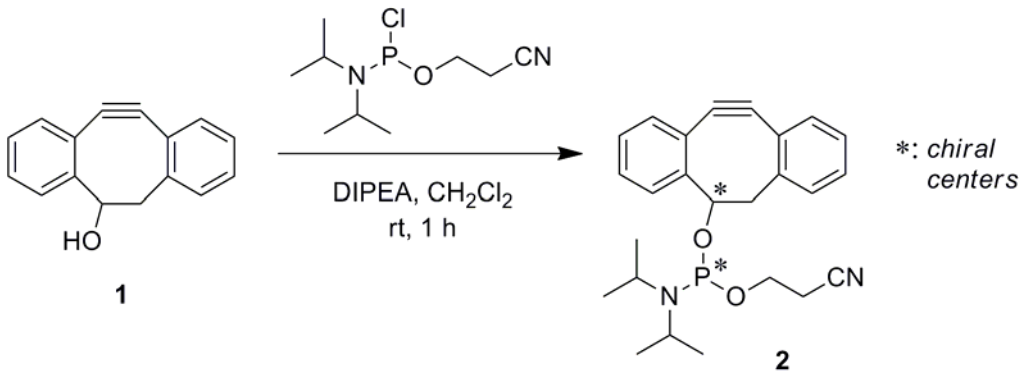

To a solution of 3-hydroxy-1,2:5,6-dibenzocyclooct-7-yne **1** (10.6 mg, 0.0481 mmol) in anhydrous CH_2Cl_2 (0.7 mL) was added *N*,*N*-diisopropylethylamine (20 μL, 0.115 mmol) and 2-cyanoethyl *N*,*N*-diisopropylchlorophosphoramidite (27 μL, 0.121 mmol), dropwise, using oven-dried glassware. The solution was stirred at room temperature for one hour under a nitrogen atmosphere. After monitoring for reaction completion by TLC, the mixture was washed with 5% aqueous $NaHCO_3$ (1 × 0.5 mL) and extracted with CH_2Cl_2 (2 × 0.5 mL) and dried over anhydrous Na_2SO_4. The CH_2Cl_2 layers were combined, filtered, and concentrated by rotary evaporation. The resulting yellow oil was purified by silica gel column chromatography (1:1 ethyl acetate: hexanes, v/v) to grant **2** as a clear oil (12.3 mg, 61%, R_f = 0.6). The product **3** was used immediately in oligonucleotide synthesis to minimize hydrolysis on storage.

^{1}H-^{1}H COSY NMR (Figure S8, 300 MHz, $CDCl_3$) analysis indicated that product **2** was a nearly equal mixture of two (racemic) diastereomers. Attempts to separate the diastereomers via flash chromatography on silica and via reverse-phase HPLC failed. As a result, the diastereomeric phosphoramidite mixture was used for subsequent oligonucleotide synthesis. ^{1}H/^{13}C NMR spectra were obtained at both 500/126 MHz and 300/75 MHz; because of extensive coupling, the lower frequency spectra were clearer and are shown here. Pairs of resonances in the ^{1}H and ^{31}P NMR spectra could be assigned to distinct diastereomers, but resonances in the ^{13}C NMR spectrum could not be. ^{13}C-^{31}P coupling constants J_{CP} were observed in the ^{1}H-decoupled ^{13}C NMR spectrum, and were confirmed by recording the NMR at two different instrument frequencies.

^{1}H NMR (Figure S5, 300 MHz, $CDCl_3$): δ 7.79 (1H, d, J = 4.8, ArH, one diastereomer), 7.75 (1H, d, J = 4.8, ArH, other diastereomer), 7.48-7.42 (7H+7H, m, ArH, both diastereomers), 4.70 (1H, dt, J_1 = 1.5, J_2 = 13, C[3]*H*OP, one diastereomer), 4.60 (1H, dt, J_1 = 1.5, J_2 = 13, C[3]*H*OP,

other diastereomer), 3.81-3.58 (4H+4H, m, OCH_2CH$_2$CN and NCH(CH$_3$)$_2$, both diastereomers), 3.29 (1H, t, J = 2.4, C[4]H_α, one diastereomer), 3.28 (1H, t, J = 2.4, C[4]H_α, other diastereomer), 2.94 (1H, dd, J_1 = 3.5, J_2 = 11, C[4]H_β, one diastereomer), 2.89 (1H, dd, J_1 = 3.5, J_2 = 11, C[4]H_β, other diastereomer), 2.47 (2H, m, OCH$_2$CH_2CN, one diastereomer), 2.39 (2H, m, OCH$_2$CH_2CN, other diastereomer), 1.18 (3H, d, J = 6.6, NC$_\alpha H_3$, one diastereomer), 1.15 (3H, d, J = 6.6, NC$_\alpha H_3$, other diastereomer), 1.13 (3H, d, J = 6.6, NC$_\beta H_3$, one diastereomer), 0.97 (3H, d, J = 6.6, NC$_\beta H_3$, other diastereomer).

^{13}C NMR (Figure S6, 75 MHz, CDCl$_3$): δ 154.62 (d, J_{CP} = 5.2), 154.47 (d, J_{CP} = 2.4), 151.64, 151.57, 130.43, 129.90. 128.01, 127.96, 127.84, 127.81, 127.02, 126.88 (×2), 126.14, 125.96 (×2), 125.38, 125.00, 124.16, 124.04, 121.15, 121.14, 117.67, 117.45, 113.05, 112.95, 110.81, 110.66, 77.64 (d, J_{CP} = 16.9), 77.62 (d, J_{CP} = 16.9), 76.68 (d, J_{CP} = 15.5), 76.66 (d, J_{CP} = 15.5), 58.45 (d, J_{CP} = 22.1), 58.33 (d, J_{CP} = 20.7), 48.85, 48.60 (d, J_{CP} = 3.6), 43.43, 43.33, 43.28, 43.18, 24.75, 24.72, 24.69, 24.66, 24.57 (d, J_{CP} = 7.7), 24.35 (d, J_{CP} = 7.3), 20.26 (d, J_{CP} = 7.2), 20.12 (d, J_{CP} = 7.5).

^{31}P NMR (Figure S7, 121 MHz, CDCl$_3$): 149.4 (s, one diastereomer), 149.3 (s, other diastereomer).

HR-MS (ESI, positive ion mode) *m/z* 443.1848 $[M + Na]^+$, expected 443.1859.

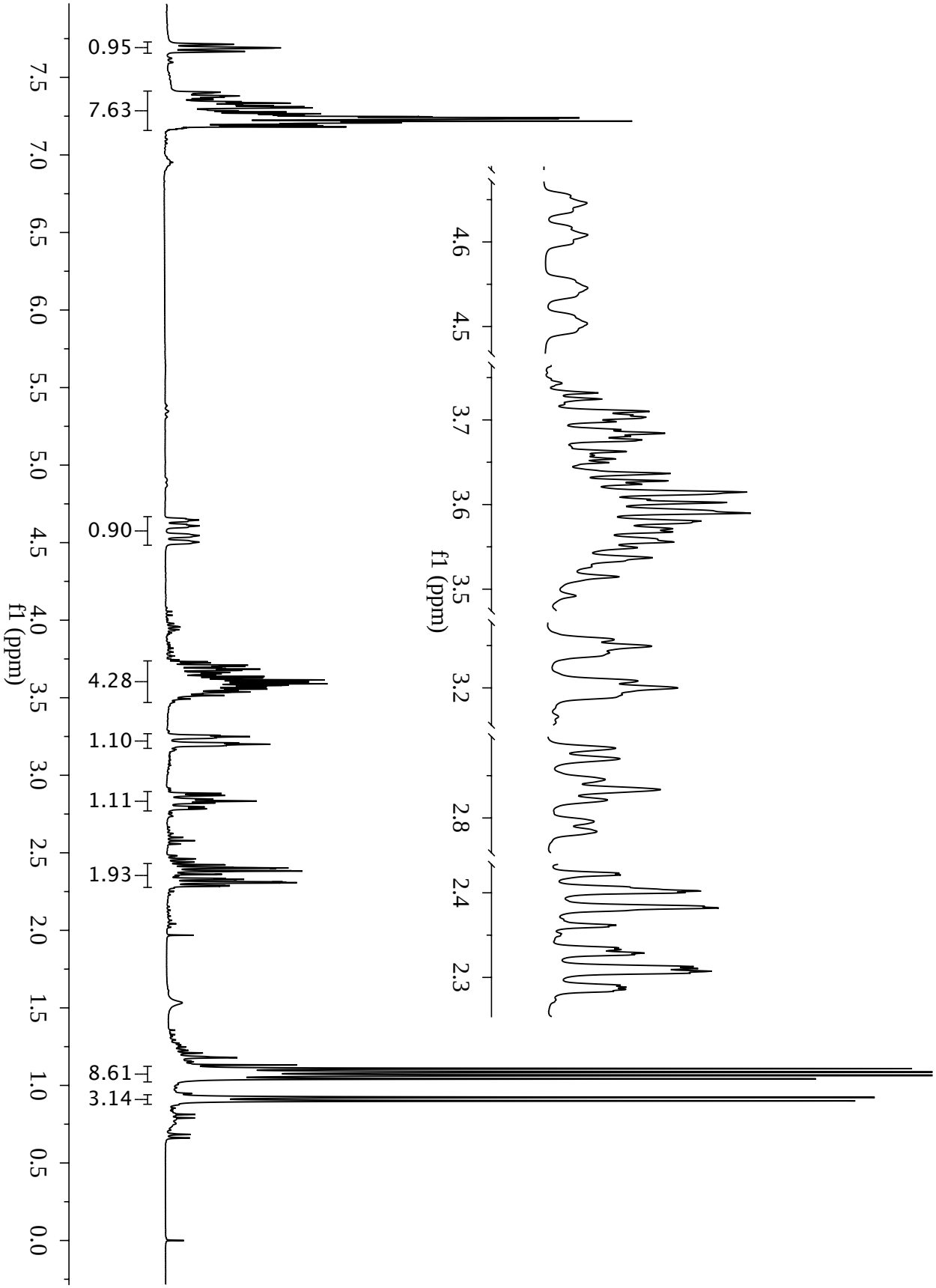

Figure S5. ^{1}H NMR (300 MHz, $CDCl_3$) of **2**.

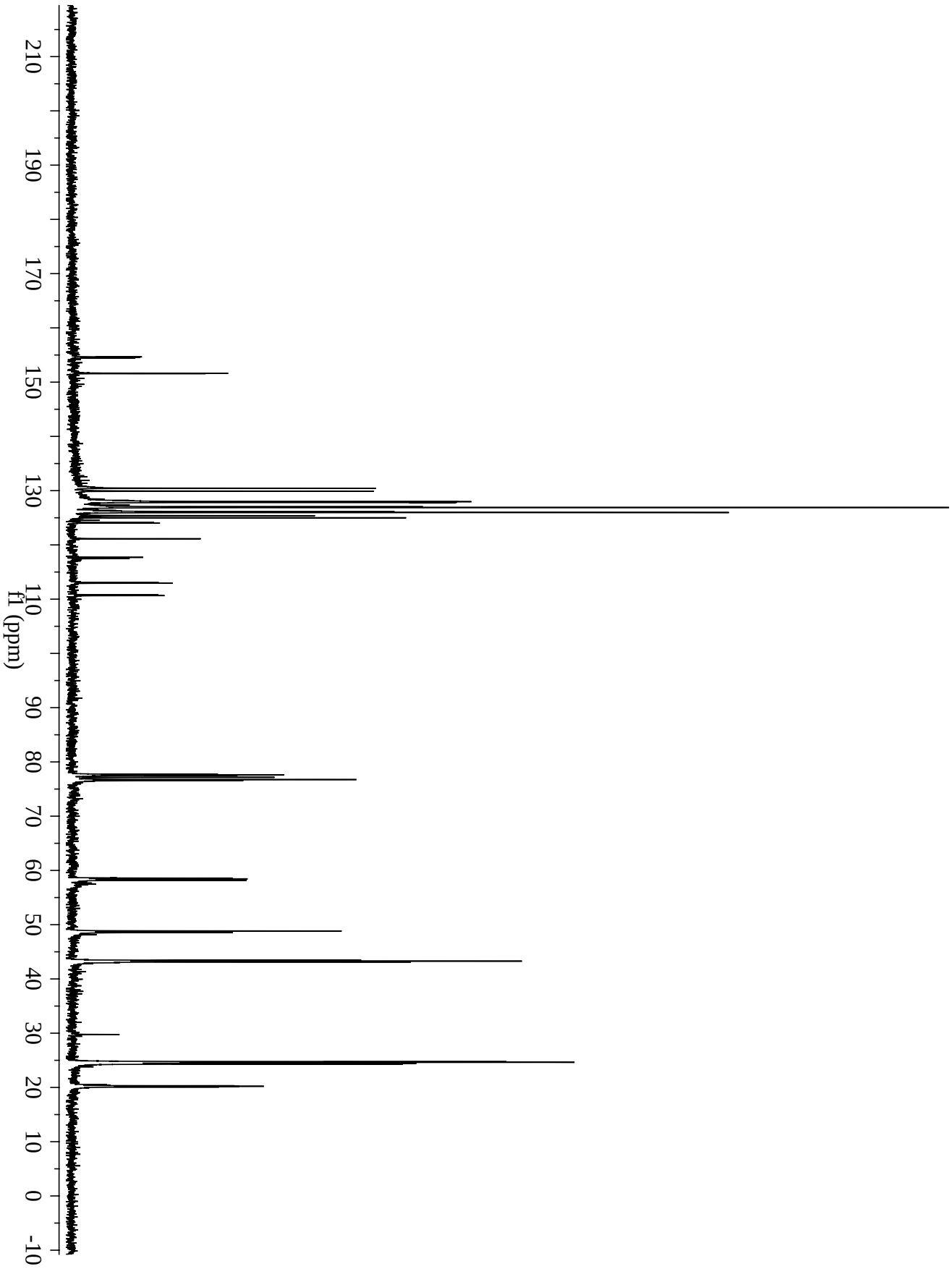

Figure S6. ^{13}C NMR (75 MHz, $CDCl_3$) of **2**.

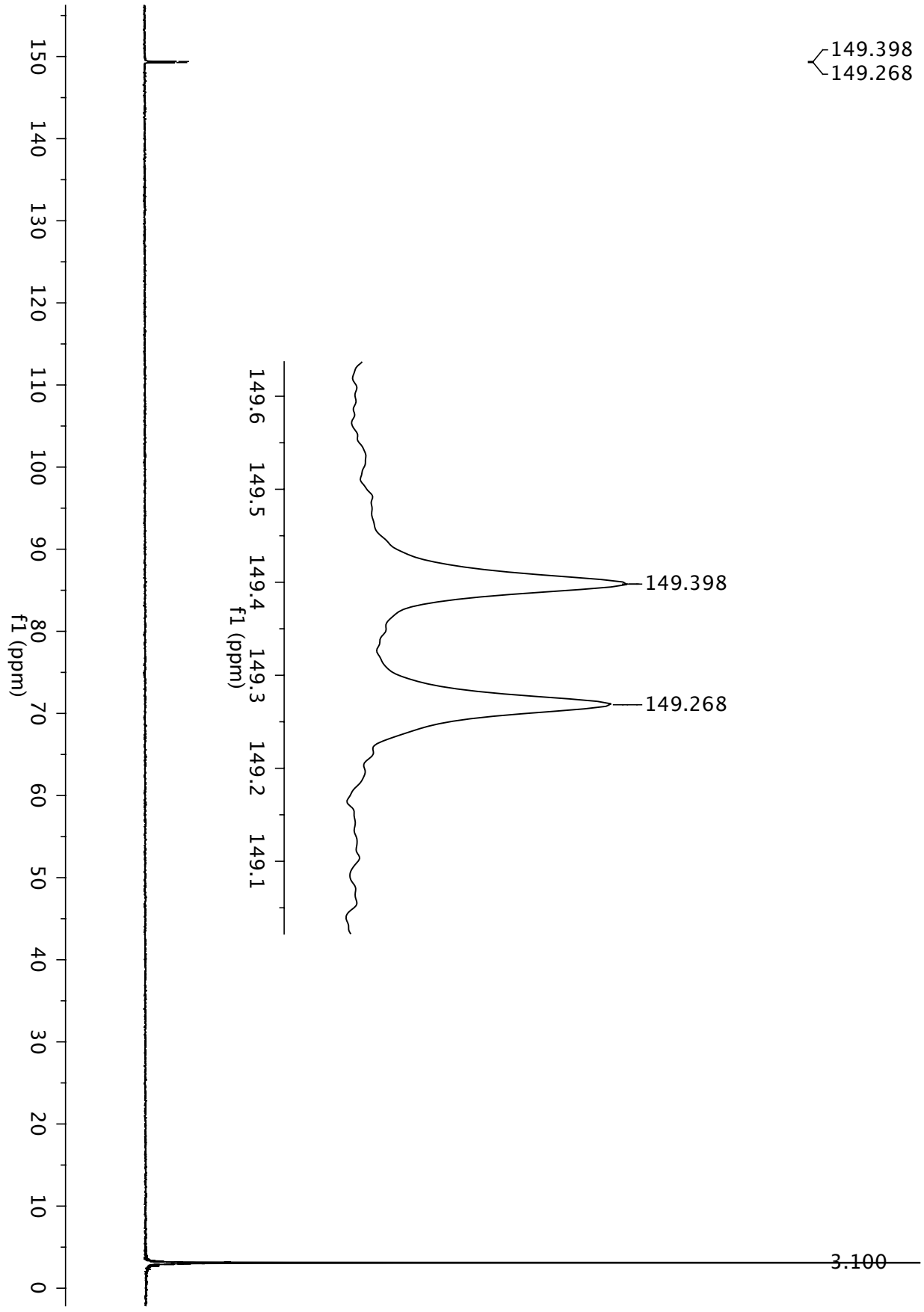

Figure S7. ^{31}P NMR (124 MHz, $CDCl_3$) of **2**.

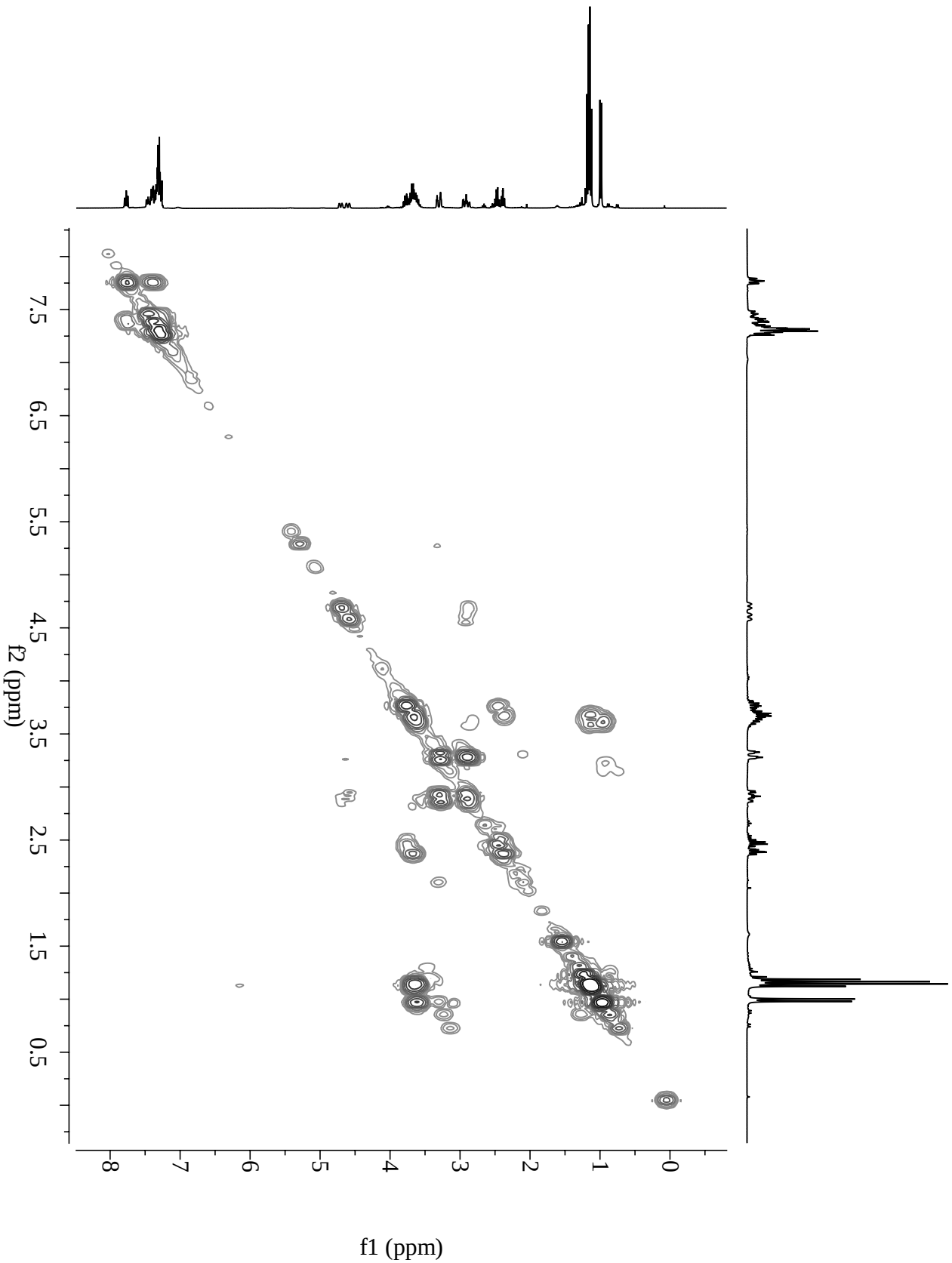

Figure S8. ^{1}H-^{1}H COSY NMR (500 MHz, $CDCl_3$) of **2**.

Synthesis of Texas Red-(pentaethylene glycol)-azide (5)

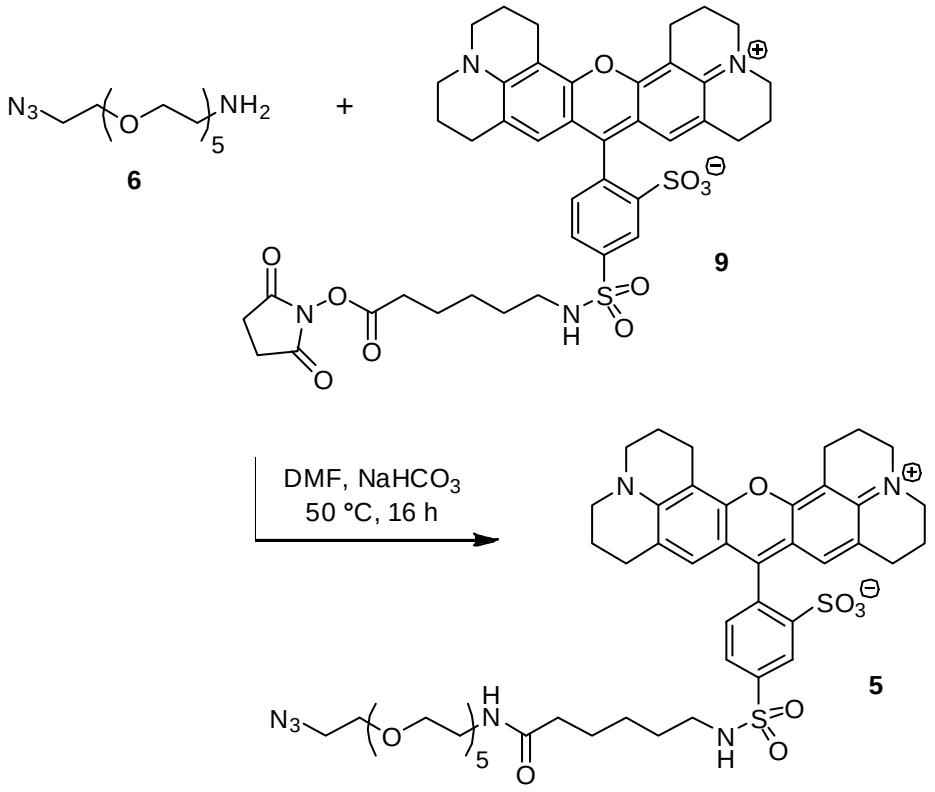

To a solution of Texas Red–X succinimidyl ester **9** (2 mg, 2.45 μmoles; single isomer, Molecular Probes, Inc.) in DMF (1.25 mL) was added *O*-(2-aminoethyl)-*O′*-(2-azidoethyl)pentaethylene glycol **6** (0.75 mg, 2.45 μmoles) and $NaHCO_3$ (0.5 mg, 6.2 μmoles). The solution was heated to 50 °C and gently shaken overnight. The DMF was decanted away from solids, and the remaining solid material was rinsed with CH_3CN (3 × 1.5 mL). This material was purified by reverse-phase HPLC. The HPLC system (Agilent 1100) was fitted with a semi-preparative column (Varian Dynamax Microsorb 300 C_{18}, 10 μm particle size, 250 × 10 mm) and a diode array UV-vis detector and a fluorescence detector. Samples were run with a two-solvent gradient of 0.03 M triethylammonium acetate (TEAA) buffered H_2O (solvent A) and 95:5 acetonitrile:0.03 M TEAA-buffered H_2O (solvent B) as the mobile phase, with a flow rate of 3.5 mL/min and a gradient of 0-60% solvent B over 60 min (after an initial 2 min at 0% B). Chromatograms from this separation are shown in Figure S9. Fractions were collected from the product peak at t = 57 min and concentrated under reduced pressure. The product yield and concentration of **5** were determined by optical absorbance at λ = 589 nm, assuming an extinction coefficient $\varepsilon_{589} = 1.1 \times 10^5\ M^{-1}\ cm^{-1}$, based on that of Texas Red.

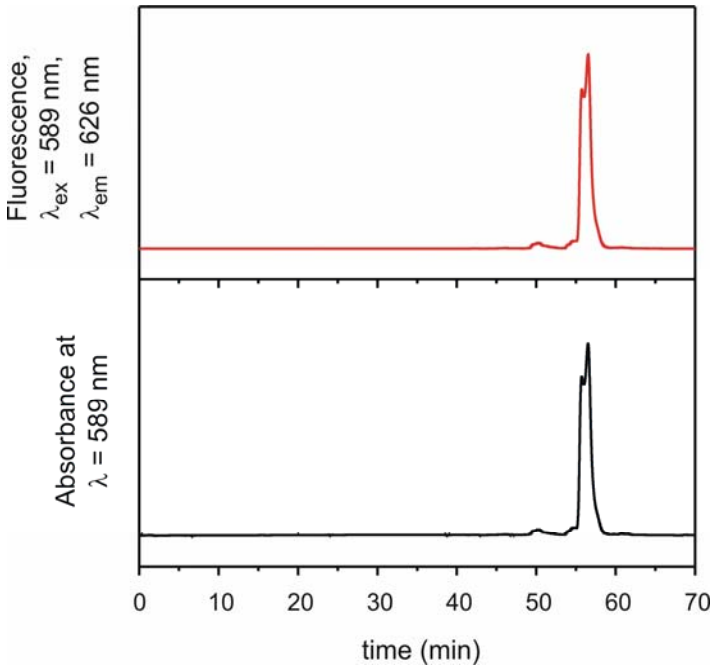

Figure S9. HPLC chromatograms of crude **5**, measured by fluorescence (top) and absorbance (bottom).

Synthesis of unmodified and 5'-dibenzocyclooctyne (DIBO)-modified oligodeoxynucleotides (ODNs)

The unmodified portion of ODNs were synthesized on solid phase using an Expedite 8909 DNA Synthesizer (Perseptive Biosystems, Framingham, MA) and standard phosphoramidite (3'→5') methodology (*2*). All reagents and solvents for DNA synthesis were purchased from Glen Research (Sterling, VA) and used as received or diluted according to accompanying instructions. ODN syntheses began on nucleoside-functionalized controlled-pore glass (CPG), and were extended using standard protected nucleoside phosphoramidites. In the case of unmodified ODNs, the final 5'-dimethoxytrityl (DMT) group was retained at the end of synthesis and only removed after HPLC purification.

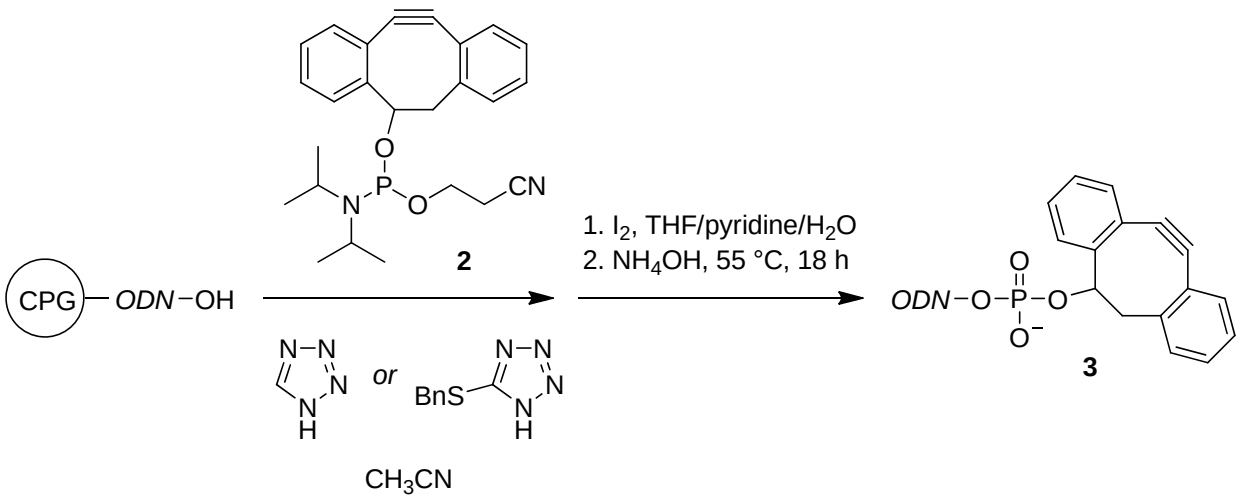

In the case of 5'-DIBO-modified ODNs, the final 5'-DMT group was removed on the instrument, and then the synthesis column was removed from the instrument for manual coupling (*3*) of the final 5'-DIBO group. Phosphoramidite **2** was dissolved in anhydrous CH_3CN to a concentration of 0.1 M. This solution (250 μL), as well as either 1*H*-tetrazole or 5-benzylthio-1*H*-tetrazole (0.45 M in CH_3CN, 250 μL), were forced through the ODN synthesis column by alternately expelling two syringes oriented on opposite ends of the column over a period of 10 minutes. The column contents were then washed with anhydrous CH_3CN (2 × 1 mL), treated with oxidizing solution (0.75 mL of 0.02 M I_2 in THF/pyridine/H_2O), and then washed with 1:1 (v/v) pyridine/CH_3CN (2 × 1 mL) and CH_3CN (2 × 1 mL). The CPG was dried under a stream of N_2.

Deprotection and cleavage of ODNs from CPG were achieved by incubating the CPG in concentrated aqueous NH_4OH (2 mL, 28-30%) at 55 °C overnight. The solution was concentrated to 200 μL under a stream of N_2. The remaining liquid was removed from the CPG and filtered through a syringe filter (0.45 μm nylon w/ 10 μm glass pre-filter). The CPG was further washed with ddH_2O (2 × 250 μL), and the washes were filtered and combined with the first filtrate.

The resulting solution, containing both full-length ODNs as well as failure strands, was purified by reverse-phase HPLC, using the same system and gradient described above for the purification of **5**. Fractions were collected from the desired product peak and concentrated under reduced pressure. Product concentrations and yields were determined by UV absorbance (Beckman Coulter DU720), using extinction coefficients at λ = 260 nm (ε_{260}) estimated by summing the ε_{260} for the oligonucleotide sequence (calculated by the nearest-neighbor method) (*4*) with, when appropriate, the measured extinction coefficient of the DIBO group ($\varepsilon_{260} = 2.65 \times 10^3$ M^{-1} cm^{-1} in $CHCl_3$ for molecule **1**). UV absorbance at λ = 305 nm was also measured for 5'-DIBO-functionalized ODNs. ODNs were also characterized by RP-HPLC-ESI-MS, performed on a

Agilent MSD SL Ion Trap with a Zorbax SB-C_{18} column (150 x 0.5 mm, 5 μm particle size). A two-solvent gradient of 15 mM NH_4OH (solvent A) and CH_3CN (solvent B), with a 3% increase of solvent B per minute starting with 5% solvent B, was used to introduce sample to the ESI-MS.

Data for the 5'-DIBO-functionalized ODNs prepared in this study are shown in Table S1.

Table S1. 5'-DIBO-modified ODN data.

oligonucleotide	sequence	yield (HPLC)[a]
3a	5'-DIBO–TTT TTT TTT T-3'	73%
3b	5'-DIBO–T_8 CGT GAT CCC ACC TCA TTT TC-3'	43%

[a]Yield calculated as the percentage of total oligonucleotide products, determined by the sum of success and failure strand peak areas in the HPLC A_{254} trace.

oligonucleotide	ε_{260} (calculated, M^{-1} cm^{-1})	ε_{305} (calculated, M^{-1} cm^{-1})[b]	ε_{305} (UV, M^{-1} cm^{-1})[c]	MW (calculated, Da)	MW (ESI-MS, Da)
3a	8.42×10^4	9.97×10^3	1.63×10^4	3262.2333	3262.3
3b	2.43×10^5	9.97×10^3	2.04×10^4	8700.8310[d]	8701.2

[b]Taken from ε_{305} of 3-hydroxy-1,2:5,6-dibenzocyclooct-7-yne (**1**) in $CHCl_3$.
[c]From UV absorbance spectrum, assuming ε_{260} (calculated) is correct.
[d]Monopotassium adduct.

When 1*H*-tetrazole was used as the phosphoramidite activator in the manual synthesis, yields of 5'-dibenzocyclooctyne-modified **3a** were low, though increasing the number of sequential coupling attempts did increase yield. We attributed the lower coupling efficiency of phosphoramidite **2** to steric hindrance by the dibenzocyclooctyne group. Similar decreases in coupling efficiency have been noted for sterically hindered, 2'-*O*-[(triisopropylsilyl)oxy]methyl-protected ribonucleoside phosphoramidites used in solid-phase RNA synthesis (*5*). Replacing 1*H*-tetrazole with 5-benzylthio-1*H*-tetrazole (BTT) as the phosphoramidite activator has been used to address this problem (*6*), and in our hands, using BTT as the activator gave excellent yields of ODNs **3a-d** in only one manual coupling step.

Click reactions of 5'-DIBO-modified ODNs (3) with azides (5/6)

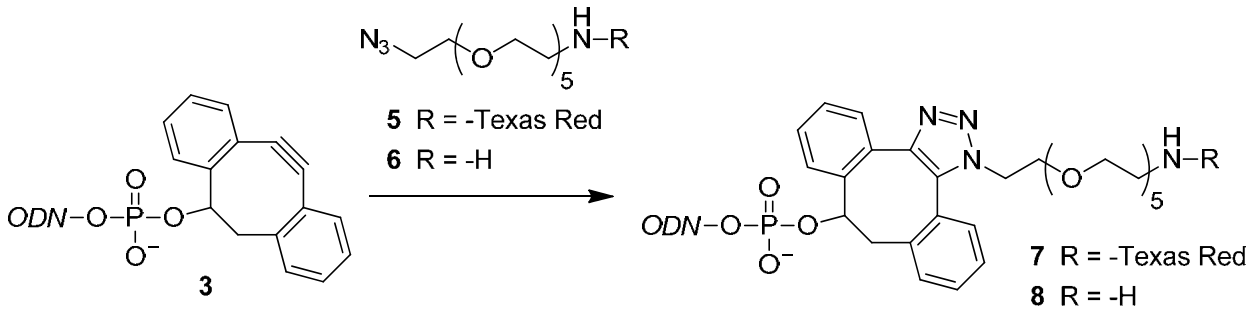

To perform solution-phase preparative click reactions, ODN **3a** and Texas Red azide **5** were combined in a 1:1 mole ratio to a final concentration of 0.45 μM of each reactant in water, and the reaction mixture was left at room temperature overnight. Clicked ODN product was then purified either by RP-HPLC or by size exclusion chromatography (NAP-5, GE Healthcare).

Kinetics experiments on the reaction between ODN **3a** and azide **6** were performed under pseudo-first-order conditions, assuming $-d[\mathbf{3a}]/dt = k[\mathbf{3a}][\mathbf{6}]$, using 18 μM **3a** and (excess) concentrations of **6** ranging from 183 μM to 546 μM in phosphate-buffered saline (1X PBS; 150 mM NaCl, 10 mM KH_2PO_4/K_2HPO_4, pH 7). Reaction progress was monitored by UV-vis absorbance at λ = 305 nm (Figure S10A,B). Each decay in absorbance was fit to the first-order integrated rate law to obtain values for $k_{obs} = k[\mathbf{6}]$ at different concentrations of **6**. These k_{obs} values were then plotted against [**6**], and fitted to a line passing through the origin, to obtain the second-order rate constant $k = 0.9\ M^{-1}\ sec^{-1}$ as the slope (Figure S10C).

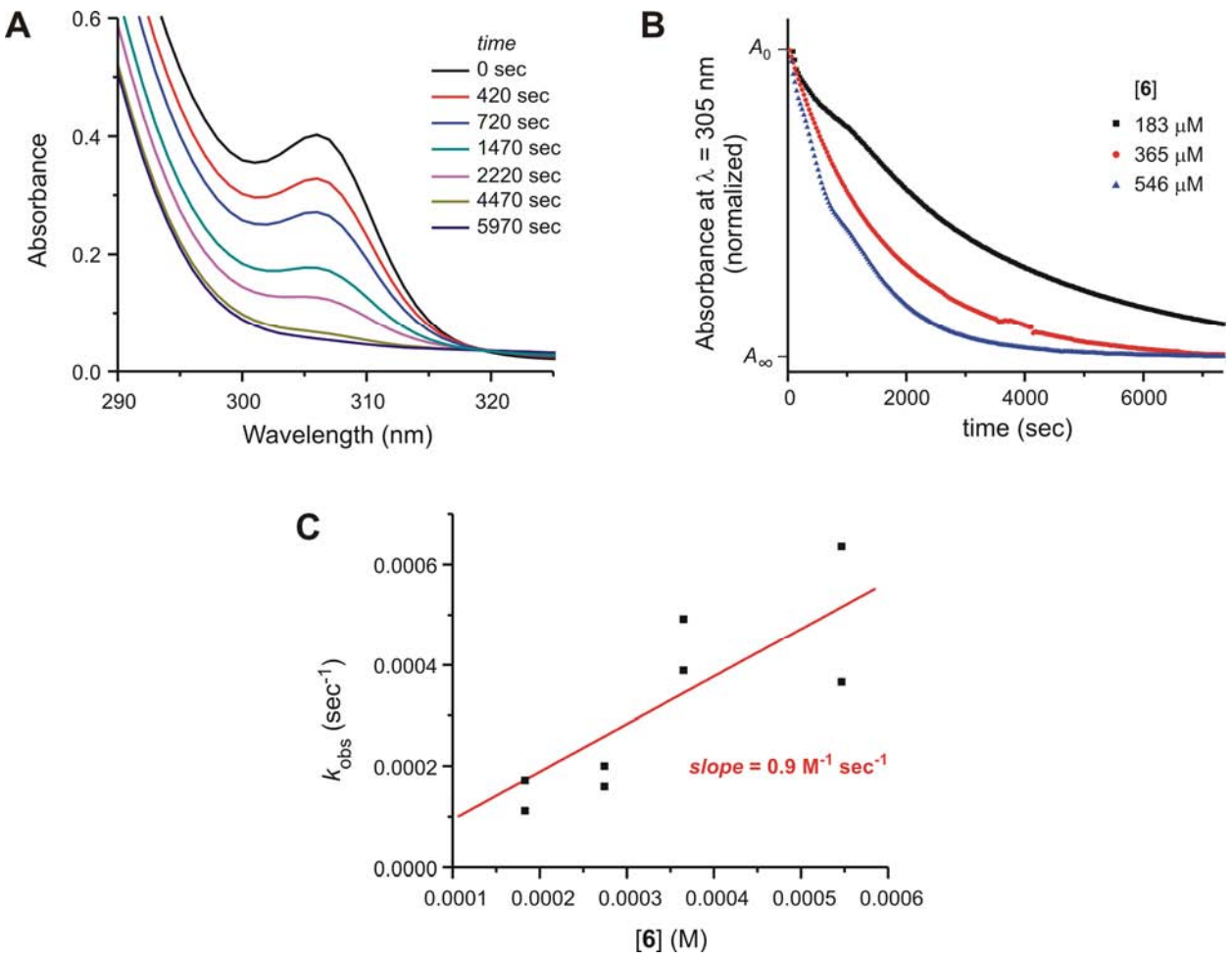

Figure S10. Kinetics experiments on the reaction between 18 mM ODN **3a** and azide **6** in 1X PBS buffer. (A) Representative time-dependent UV absorbance spectra of the reaction between **3a** and 365 mM **6**. The characteristic absorbance peak at λ_{max} = 305 nm for **3a** decreases as the starting material reacts. (B) Absorbance at λ_{max} = 305 nm vs. time for representative reactions between **3a** and different concentrations of **6**. (C) Pseudo first-order rate constants k_{obs}—obtained by fitting curves like those in (B) to the first-order integrated rate law—vs. azide concentration [**6**]. The slope of the linear fit to this data is equal to the second-order rate constant for the reaction between **3a** and **6**.

Solid-phase click reaction of 5'-DIBO-modified ODNs (3) with Texas Red azide (6)

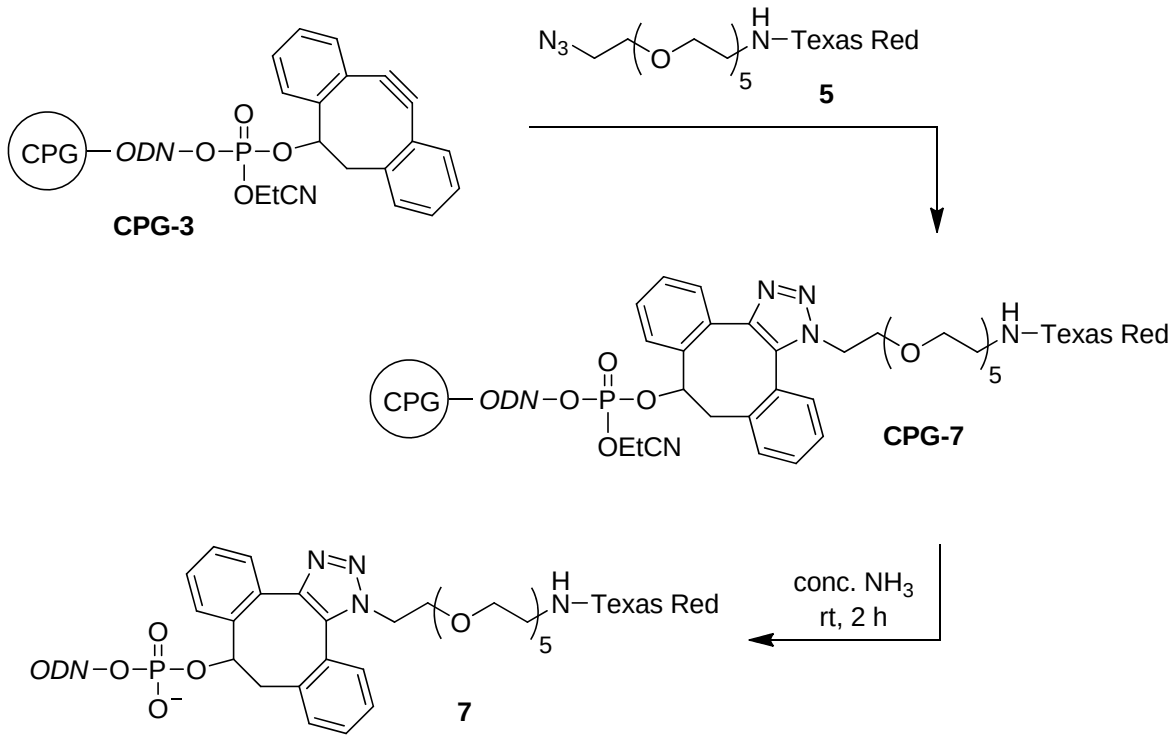

To perform click reactions on solid phase, a 5'-DIBO-modified ODN was synthesized on CPG as described above. One portion of this CPG was reserved as a control, and the other portion was incubated with 270 mM Texas Red azide **5** in H_2O for 18 h in an Eppendorf tube at room temperature, with gentle vortexing. Both the clicked and the unclicked CPG were then washed with H_2O, and then each was combined with 1 mL conc. NH_4OH in H_2O for 2 h at rt. The solution over the CPG was concentrated to 200 μL under a N_2 stream, removed from the CPG, and filtered through a 0.45 μm-pore nylon filter. The CPG was further washed with ddH_2O (2 × 150 μL) and DMSO (2 × 150 μL). The washes were filtered, combined with the first filtrate, concentrated *in vacuo* to dryness, and resuspended in ddH_2O. The clicked ODNs in this solution were then analyzed and purified by HPLC (Figure S11) as described above for other ODNs.

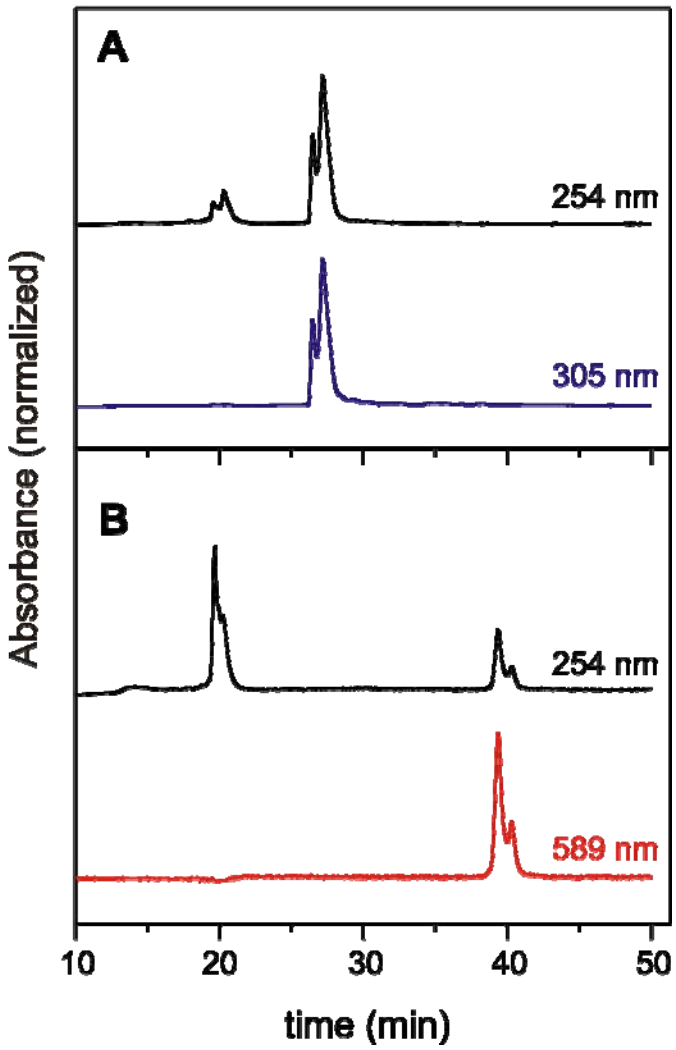

Figure S11. HPLC chromatograms of (A) crude 5'-DIBO-modified ODN **3a** and (B) crude click product **7a**. Based on retention times and spectral signatures, we assign peaks in these chromatograms to acetyl-capped failure strands from the solid-phase oligonucleotide synthesis (*t* = 20 min, with absorbance from nucleic acid at λ = 254 nm only), 5'-DIBO-modified ODN **3a** (*t* = 27 min, with absorbance from nucleic acid at λ = 254 nm and from DIBO at λ = 305 nm), and clicked, Texas Red ODN **7a** (*t* = 40 min, with absorbance from nucleic acid at λ = 254 nm and from Texas Red at λ = 589 nm). Peaks in these traces consistently appear as doublets because of the degraded performance of the reverse-phase column used in this experiment, which was different from the column used in Figure 1.

Clicked ODNs were also analysed by polyacrylamide gel electrophoresis (PAGE) in 16% TBE-Urea gels. Samples were electrophoresed for 1 h at 180 V, using TBE buffer (0.089 M Tris Base, 0.089 M Boric Acid, 0.002 M EDTA, pH 8.3) as the running buffer. Gels were then imaged for fluorescence in the Texas Red channel with a Bio-Rad Molecular Imager FX. The gel was subsequently dyed with SYBR Green II Gel Stain (Molecular Probes, S-7568) for 20 minutes, according to the manufacturer's protocol. The stained gel was then imaged for green fluorescence (Molecular Dynamics STORM 840, 450 ± 30 nm excitation, 500 nm longpass).

PCR reactions

PCR reactions were conducted using GeneAmp PCR reagent kit with AmpliTaq DNA polymerase (Applied Biosystems Inc.), according to the instructions included in the kit. Primers were designed to amplify nucleotides 7131-7630 of the bacteriophage λ genome (*7*). Reagents were combined in 1X PCR buffer to target concentrations (AmpliTaq DNA polymerase, 2.5 U/100 μL; ODNs **3b** and **4c** as primers, 0.2 μM; each dNTP, 200 μM; bacteriophage λ DNA template, 1 ng/ 100 μL). The thermal cycling protocol involved initial heating at 94 °C for 3 min; then 30 cycles of 94 °C for 30 sec, 40 °C for 1 min, and 72 °C for 1 min; and finally 72 °C for 6 min.

Conjugation of 5'-DIBO-modified PCR amplicons to Texas Red azide (5)

In a 1.5 mL tube, 40 μL of the completed PCR reaction mixture was mixed with 0.4 μL Texas Red-azide **5** (33.4 μM). This mixture was gently shaken overnight. PCR amplicons were then isolated from primers, PCR reaction components and unreacted **5** using a QiaQuick PCR Purification Kit (Qiagen) according to the manufacturer's instructions.

PCR reactions (before and after click modification) were characterized by gel electrophoresis in 1.5% agarose in 1X TBE. Wells were loaded with either 4 μL (unpurified) or 8 μL (kit-purified) of each PCR reaction, and the gel was electrophoresed for 1 h at 100 V. Gels were then imaged for Texas Red fluorescence using a Bio-Rad Molecular Imager FX. Gels were then stained with 50 μg/mL ethidium bromide (EtBr) for 10 min, washed with ddH_2O for 10 min, and imaged for EtBr fluorescence.

Immobilization of 5'-DIBO-modified PCR amplicons on Sepharose beads

A 1-mL suspension of *N*-hydroxysuccinimide-activated Sepharose 4 Fast Flow beads (GE Healthcare) was washed with cold 1 mM aqueous HCl (4 × 5 mL). Immediately, the beads were washed with 2 × 4 mL coupling solution (1:1 dioxane/0.1 M aqueous $NaHCO_3$) and then resuspended in 660 μL fresh coupling solution. To this suspension were added 100 mg of *O*-(2-aminoethyl)-*O′*-(2-azidoethyl)pentaethylene glycol **6** (0.29 mmol) and 330 μL of methanol. The mixture was gently swirled overnight. Then, the suspension was transferred into a 100 kDa

centrifugal filter device and centrifuged for 30 sec at 3,000 RCF × *g*. The beads were rinsed with coupling solution (2 × 4 mL) in the filter device. Next, the beads were reacted with 1 mM ethanolamine in 1 mL of Tris·HCl (0.1 M, pH 8.0) for 2 h. Finally, the beads were washed with Tris·HCl (2 × 4 mL), ddH_2O (2 × 4 mL), and 20 % ethanol (4 mL), isolating the beads after each wash by centrifugation. Azide-modified beads (Sepharose-N_3) were stored in 20 % ethanol.

Sepharose-N_3 bead suspension (100 µL) was washed with 3 × 400 µL of 1X binding and washing buffer (B&W buffer; 10 mM Tris·HCl, pH 8.0, 2 M NaCl, and 1 mM EDTA). Then, 30 µL of purified PCR amplicon and 30 µL of 2X B&W buffer containing 0.02% Tween 20 were added to the solution of the beads. The suspension was gently shaken overnight. Then, the suspension was centrifuged for 15 sec at 3,000 RCF × *g*. After the supernatant was removed, the beads were re-dispersed into 1.5 mL of 1X B&W buffer containing 0.01% Tween 20. This suspension was centrifuged again for 15 sec at 3,000 RCF × *g*, and the supernatant removed. Then, 50 µL of 2X TBE buffer (pH 8.0) and 50 µL of 2X SYBR Green I were added to the beads. This suspension was incubated at 4 °C prior to microscopy. Finally, green fluorescence and brightfield microscope images of the bead suspension were obtained on a Zeiss Axiovert 2 upright microscope.

References

(1) Ning, X., Guo, J., Wolfert, M. A., and Boons, G.-J. (2008) Visualizing metabolically labeled glycoconjugates of living cells by copper-free and fast Huisgen cycloadditions. *Angew. Chem. Int. Ed. 47*, 2253-2255.

(2) Brown, T., and Brown, D. J. S. (1991) Modern machine-aided methods of oligodeoxyribonucleotide synthesis, in *Oligonucleotides and Analogues: A Practical Approach* (Eckstein, F., Ed.) pp 1-24, Oxford University Press, New York.

(3) Tanaka, T., and Letsinger, R. L. (1982) Syringe method for stepwise chemical synthesis of oligonucleotides. *Nucleic Acids Res. 10*, 3249-3259.

(4) Tataurov, A. V., You, Y., and Owczarzy, R. (2008) Predicting ultraviolet spectrum of single stranded and double stranded deoxyribonucleic acids. *Biophys. Chem. 133*, 66-70.

(5) Pitsch, S., Weiss, P. A., Wu, X., Ackermann, D., and Honegger, T. (1999) Fast and reliable automated synthesis of RNA and partially 2'-*O*- protected precursors (`caged RNA') based on two novel, orthogonal 2'-*O*-protecting groups, preliminary communication. *Helv. Chim. Acta 82*, 1753-1761.

(6) Pitsch, S., Weiss, P. A., Jenny, L., Stutz, A., and Wu, X. (2001) Reliable chemical synthesis of oligoribonucleotides (RNA) with 2'-*O*-[(triisopropylsilyl)oxy]methyl(2'-*O*-TOM)-protected phosphoramidites. *Helv. Chim. Acta 84*, 3773-3795.

(7) Sanger, F., Coulson, A. R., Hong, G. F., Hill, D. F., and Petersen, G. B. (1982) Nucleotide sequence of bacteriophage λ DNA. *J. Mol. Biol. 162*, 729-773.

Bioconjugate Chemistry

COMMUNICATION

pubs.acs.org/bc

Enhancement of Blood Compatibility of Poly(urethane) Substrates by Mussel-Inspired Adhesive Heparin Coating

Inseong You,[†,¶] Sung Min Kang,[†,‡,¶] Youngro Byun,[§] and Haeshin Lee*[,†,‡]

[†]Graduate School of Nanoscience and Technology (WCU) and [‡]Department of Chemistry, 335 Science Rd., KAIST, Daejeon 305-701, South Korea

[§]WCU Department of Molecular Medicine and Biopharmaceutical Sciences, College of Pharmacy, Seoul National University, Seoul 151-742, South Korea

Supporting Information

ABSTRACT: Heparin immobilization on surfaces has drawn a great deal of attention because of its potential application in enhancing blood compatibility of various biomedical devices such as catheters, grafts, and stents. Existing methods for the heparin immobilization are based on covalent linkage formation and electrostatic interaction between substrates and heparin molecules. However, complicated multistep procedures and uncontrolled desorption of heparin are limitations of these methods. In this work, we report a new heparin derivative that exhibits robust adhesion on surfaces. The derivative, called hepamine, was prepared via conjugation of dopamine, a mussel-inspired adhesive moiety, onto a heparin backbone. Immersion of poly(urethane) substrates into an aqueous solution of hepamine resulted in robust heparin coating of the poly(urethane), the most widely used polymeric material for blood-contacting medical devices. The hepamine-coated poly(urethane) substrate showed significant inhibition of blood coagulation and platelet adhesion. The use of hepamine for surface modification is advantageous for several reasons: for example, no chemical pretreatment of the substrates is necessary, and surface functionalization is a simple, one-step procedure. Thus, the heparin immobilization method described herein is an excellent alternative approach for the introduction of heparin molecules onto surfaces.

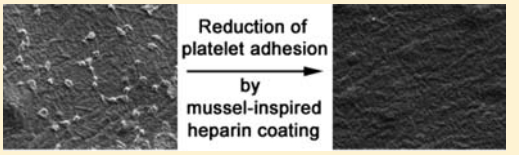

INTRODUCTION

Heparin has been widely used in various blood-contacting materials because of its ability to inactivate blood coagulation pathways.[1,2] Therefore, stable immobilization of heparin molecules onto surfaces is of great importance in the development of blood-contacting medical devices, such as catheters, grafts, implants, and stents.[3−6] There are two common approaches for the surface immobilization of heparin: methods involving covalent linkage and those involving electrostatic interactions.[7−16] Approaches to the formation of covalent bonds require chemical derivatization of both the substrates and the heparin molecules—procedures that are often time-consuming and complicated. For example, heparin was chemically activated with 1-ethyl-3-(3-dimethylaminopropyl) carbodiimide, and the substrate was modified to contain amine groups.[9] On the other hand, methods for utilizing an electrostatic interaction involve binding between anionic heparin molecules and cationic substrates. Examples in this category include a direct heparin deposition onto a cationic polyurethane surface.[10−12] Barbucci et al. prepared a cationic, poly(amidoamine)-immobilized polyurethane material to which heparin was immobilized by electrostatic interactions. Although the heparin immobilization was successful, uncontrolled desorption of immobilized heparin in media with a high ionic strength was a significant drawback. Furthermore, additional procedures to prepare cationic substrates are necessary for most substrates. Thus, the development of a simple and robust heparin immobilization method has remained an important goal.

Mussels are promiscuous underwater fouling organisms that attach to virtually any material, whether natural or synthetic. Studies of the fouling mechanisms have revealed that the unusual amino acid 3,4-dihydroxy-L-phenylalanine (DOPA) plays a critical role in mussel adhesion.[17−21] Single-molecule atomic force microscopy (AFM) studies showed that DOPA exhibits multifunctional, surface-dependent adhesion mechanisms in which it forms reversible coordination bonds to metal oxide surfaces and establishes irreversible covalent bonds to organic surfaces.[22,23] Thus, the introduction of DOPA or catechol (a side chain of DOPA) onto biopolymers has been a meaningful avenue for researchers seeking to enhance the adhesive properties of biopolymers.[24−28] For example, catechol-grafted poly(ethyleneimine) and poly(ethylene glycol) backbone showed successful adhesion onto various substrates including poly(tetrafluoroethylene) and poly(carbonate).[25,27] Recently, Park et al. reported the conjugation of heparin with dopamine, a small adhesive molecule inspired by mussel adhesive proteins.[29,30] They used dopamine-conjugated heparin as a stable platform for layer-by-layer coating of a mitotic inhibitor for cancer chemotherapy. Furthermore, the dopamine-conjugated heparin showed promise as a surface-modifying agent of gold nanoparticles (AuNPs) for computed tomography imaging. Despite the successful use of dopamine-conjugated heparin, the

Received: January 27, 2011
Revised: June 14, 2011
Published: June 16, 2011

ACS Publications © 2011 American Chemical Society

surfaces used in these studies were only metal surfaces: cobalt−chromium alloy and Au. We hypothesized that dopamine-conjugated heparin can modify other types of substrates, including synthetic polymers, because of dopamine's ability to adhere to versatile substrates.[17,22] Although the immobilization of heparin onto synthetic polymers used to manufacture blood-contacting medical devices is of great practical importance, studies for this purpose utilizing dopamine-conjugated heparin have not been completed.

In the present study, we used dopamine-conjugated heparin, termed hepamine, to coat the surface of a poly(urethane) (PU) substrate. PU has been extensively investigated for use in biomedical devices because of its unique mechanical property and biocompatibility.[31,32] However, PU's level of thromboresistance has been reported to be insufficient for long-term use in medical settings.[33,34] Thus, we chose to use hepamine-coated PU to evaluate thromboresistance at the interface. The hepamine-coated PU exhibited a significant reduction in platelet adhesion and blood coagulation, demonstrating enhancement of blood compatibility.

EXPERIMENTAL SECTION

Materials. Heparin sodium salt (unfractured heparin, avg. MW 12 000 Da) was purchased from Nanjing King-Friend Biochemical Pharmaceutical Co., Ltd. 2-Morpholinoethanesulfonic acid (MES), *N*-hydroxysuccinimide (NHS), 3-hydroxytyramine hydrochloride (dopamine hydrochloride), formaldehyde (37 wt % solution in water), and phosphate-buffered saline (PBS) were purchased from Sigma-Aldrich. Dialysis membranes (MWCO = 3500 Da) were obtained from Spectrum Laboratories (Canada) and 1-ethyl-3-(3-dimethylaminopropyl)-carbodiimide (EDC) was bought from Tokyo Chemical Industry. The gold (Au) and titanium (Ti) substrates were prepared by thermal evaporation onto silicon wafers (thickness = 100 nm). Poly(urethane) (PU), poly(carbonate) (PC), and silicon rubber (Si rubber) sheets were purchased from Hanmi Inc. (South Korea). For ellipsometric analysis, PU-coated Ti substrates were prepared by spin-casting of PU onto Ti substrates. PU (15 mg/mL in DMF) was spin-casted onto Ti substrates at 3000 rpm, and PU substrates were dried at 70 °C for 3 h. A concentrated platelet solution (1.4×10^6 cells/μL) was obtained from Redcross blood center (Daejeon, Korea), and the platelet was used to all assays as received.

Preparation of Dopamine-Conjugated Heparin: Hepamine. Heparin (200 mg) was dissolved in 0.05 M MES buffer (pH 5.5, 20 mL). NHS (0.05 M, 0.115 g) and EDC (0.1 M, 0.383 g) were subsequently added to the heparin solution to activate the carboxylic acid groups of heparin molecules. The solution was stirred at room temperature for 2 h, and dopamine (0.015 M, 0.06 g) was added to the solution. The resulting mixture was stirred at room temperature for additional 8 h. The solution was transferred to a dialysis membrane (MWCO = 3500 Da) and dialyzed for 12 h to remove unreacted coupling reagents and dopamine. Acidified water (1 mL addition of 5 M HCl per 1 L of deionized distilled water) was used for a dialysis procedure. The final product was obtained by lyophilization of the solution.

The number of conjugated dopamine per heparin was obtained from the intensity of dopamine peak in the UV−vis spectrum. From the molecular weight of heparin (12 kDa), the authors assume that each disaccharide repeating unit (M_w = 624 Da) has one carboxylic acid. The concentration of carboxylic groups of heparin can therefore be calculated by dividing the concentration of heparin (mg/mL) by 625 (mg/mmol). On the basis of the A_{280} intensity of hepamine, the catechol concentration of hepamine can be calculated, and the degree of dopamine conjugation can be determined by A280 intensity from a dopamine standard curve.

Hepamine Coating onto PU Substrates. Hepamine was dissolved in a 10 mM of Tris buffer solution (5 mg/mL, pH 8.5), and PU substrates were immersed into the hepamine solution. The PU substrate was cleaned by ultrasonication in an ethanol solvent for 10 min before use. After 10 h, the substrates were taken out, rinsed with water, and dried with N_2 gas. The hepamine-coated substrates were characterized by contact angle goniometer and X-ray photoelectron spectroscopy (XPS).

Platelet Adhesion and Serum Protein Adsorption onto Hepamine-Coated PU Substrates. Unmodified and hepamine-coated PU substrates were immersed in a PBS solution (pH 7.4) for 24 h, and then, each substrate was immersed into a 5 mL of platelet media (1.4×10^6 cells/μL). After 4 h incubation at 37 °C, the substrates were rinsed by PBS and immediately immersed into a formaldehyde solution (2%) for 24 h to fix the adhered platelets and were dehydrated by utilizing a series of ethanol solutions (50%, 60%, 70%, 80%, 90%, and 100%). Finally, the platelet adhesion onto the substrates was analyzed by scanning electron microscopy (SEM).

For investigation of blood component adsorption, PU-coated Ti substrates were used. PU substrates were modified by hepamine in alkali solution (pH 8.5) overnight. Subsequently, unmodified and hepamine-coated substrates were immersed in 50% EtOH for 10 min and incubated in human blood for two and seven days. Resulting substrates were taken out and sufficiently rinsed with water. The thickness of adsorbed blood component on the surface was measured by ellipsometer.

Characterization. UV−vis spectra were obtained using an UV−vis spectrophotometer (8453, Hewlett-Packard). Fourier transform infrared (FT-IR) spectra were obtained in a single-reflection mode using a dry N_2-purged Thermo Nexus FT-IR spectrophotometer. We averaged 1000 scans to yield the spectra at a resolution of 4 cm^{-1}. The contact angle measurements were performed with a Phoenix 300 goniometer (Surface Electro Optics Co., Ltd., Korea). Static water contact angles were measured at three different locations on each sample, and the average values are reported. Platelet-adhered substrates were studied by Field Emission SEM (S-4800, Hitachi). XPS was performed with a ESCA 2000 (Thermo VG Scientific, England) with a monochromatic twin X-ray source (Mg/Al target). Emitted photoelectrons were detected by a multichannel detector at a takeoff angle of 45° relative to the surface. During the measurements, ultralow vacuum (10^{-9} to 10^{-10} Torr) at an analysis chamber pressure was maintained. The thickness of adsorbed serum protein was measured with a Gaertner L116s ellipsometer (Gaertner Scientific Corporation, IL) equipped with a He−Ne laser (632.8 nm) at a 70° angle of incidence. A refractive index of 1.46 was used for all samples. The bioactivity of heparin, hepamine, and surface-immobilized hepamine was analyzed using Coatest heparin kit (Chromogenix, USA) (1 IU of heparin corresponded to 7.05 μg).

RESULTS AND DISCUSSION

The hepamine was prepared using carbodiimide chemistry as described in the methods section (Figure 1). The reaction mixture was dialyzed (MWCO = 3500 Da) to remove unreacted reactants and then lyophilized. Acidified water was used during

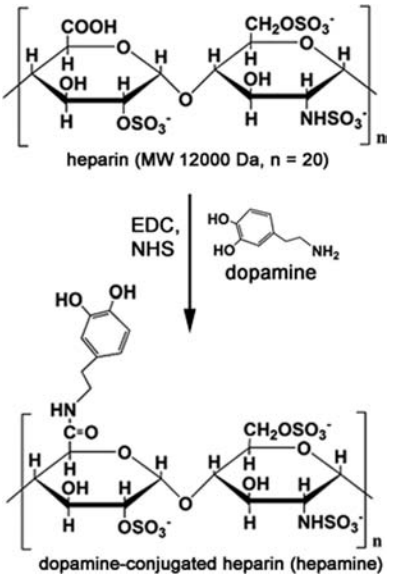

Figure 1. Reaction scheme to prepare hepamine.

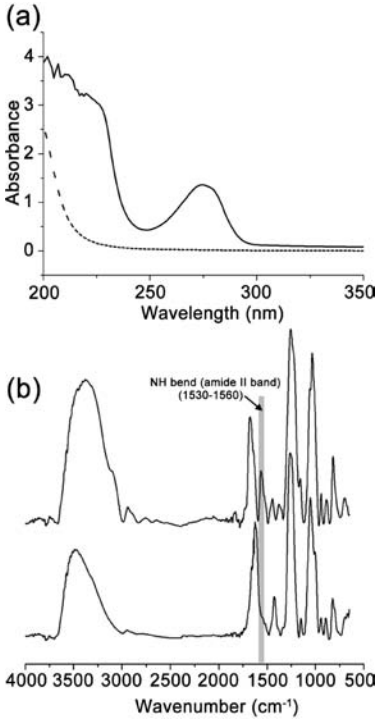

Figure 2. (a) UV−vis spectra of hepamine (1 mg/mL, solid) and heparin (1 mg/mL, dash). (b) FT-IR spectra of hepamine (upper) and heparin (lower).

dialysis to avoid catechol oxidation. UV−vis spectroscopy results showed that dopamine was successfully conjugated to heparin, as indicated by the presence of a peak at 280 nm (Figure 2a, solid line). The intensity at 280 nm was used to quantify the extent of dopamine conjugation to the carboxylic groups of heparin. Utilizing a dopamine standard curve, we found that 27 ± 8% of the carboxylic groups in heparin were conjugated with dopamine. Furthermore, FT-IR spectroscopy results confirmed the amide bond formation (1530−1560 cm^{-1}) (Figure 2b, upper line); this

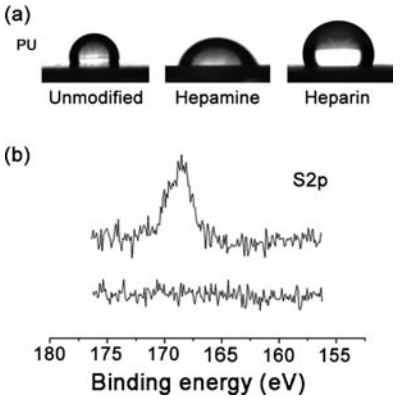

Figure 3. (a) Static water contact angle images for the unmodified PU surface (left), hepamine-coated PU surface (middle), and PU surface incubated in heparin solution for 10 h (right). (b) High-resolution S2p spectra of hepamine-coated (upper) and unmodified (lower) PU surfaces.

bond was absent in unconjugated heparin (lower line). The activity determined by Coatest heparin kit showed that there was little effect by dopamine conjugation under the same concentration (2 μg/mL): 0.38 IU/mL for heparin and 0.34 IU/mL for hepamine.

We hypothesized that hepamine can be immobilized onto various substrates as the conjugated catechol moiety demonstrated robust surface immobilization. PU was chosen as a model substrate because it has been a widely used material for manufacturing blood-contacting medical devices.[31,32] Also, the presence of phenyl groups in PU chains might enable the catechol moiety in hepamine to interact with PU substrates by $\pi-\pi$ interactions.[22] PU substrates were functionalized through immersion into the hepamine solution, and the functionalized PU surface was characterized by water contact angle measurement and XPS analysis (Figure 3). The unmodified PU substrate was hydrophobic, with a contact angle value of 103.3°, which was reduced to 62.0° after hepamine immobilization for 10 h. The decrease in the water contact angle originated from the hydrophilic nature of heparin,[35] and this result clearly indicated successful hepamine coating (Figure 3a, left and center). The presence of catechol moieties in hepamine was critical in surface functionalization; the PU substrate that was incubated in a solution of heparin alone showed a negligible change in the contact angle, indicating that unmodified heparin was not able to modify the PU substrate (Figure 3a, right). The hepamine-coated surface was further characterized by XPS. After hepamine coating onto the PU surface, a new peak for sulfur (S) 2p (168.5 eV) was observed (Figure 3b, upper curve), whereas no S 2p peak was detected for the unmodified PU surface (Figure 3b, lower curve). The S 2p peak originated from the sulfate groups of hepamine, and the presence of the peak clearly demonstrates successful hepamine coating. We also applied hepamine coating to other substrates to demonstrate the versatility of its coating ability (Supporting Information Figure S1). Significant changes of the contact angle values indicated successful hepamine coating: poly(carbonate) (PC) (85.4° → 48.1°), Au (81.9° → 45.4°), and elastic Si rubber (97.9° → 57.8°). This result indicates that the use of hepamine is an efficient approach to immobilize heparin molecules onto surfaces without the need for chemical pretreatment of substrates.

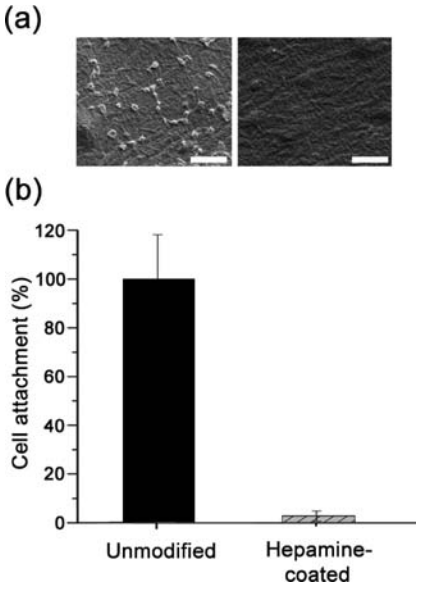

Figure 4. (a) SEM images of unmodified (left) and hepamine-coated (right) PU surfaces after 2 h platelet adhesion. (The scale bar is 10 μm.) (b) Quantitative analysis of platelet adhesion results shown above. Adhered platelets were counted at five different locations on each sample, and the average values are reported.

Quantitative analysis of the surface-immobilized hepamine onto PU substrates (1 cm^2) was achieved by a chromogenic anti-FXa assay. The amount of immobilized hepamine was 22.25 $\pm$ 2.75 ng/cm^2, which corresponded to 3.15 $\times$ 10^{-3} IU/cm^2. To investigate the blood compatibility of hepamine-coated PU substrates in a more detailed manner, we carried out a platelet adhesion experiment on the hepamine-coated PU substrate. Heparin is a well-known polysaccharide that inhibits platelet adhesion onto surfaces, and thus, we expected that the hepamine-coated substrate could prevent blood coagulation on surfaces.[36,37] Platelets (1.4 $\times$ 10^6 cells/μL) were seeded onto unmodified and hepamine-coated PU surfaces, and after 4 h of incubation, the substrates were examined by scanning electron microscopy (SEM) (Figure 4a). The hepamine-coated PU surface showed excellent resistance against platelet adhesion, whereas the unmodified surface exhibited significant adhesion of platelets. The average platelet densities adhered onto the unmodified and functionalized PU surfaces were 32 000 and 650 cells/mm^2, respectively. Quantitatively, the adhered platelet density was reduced by 98% after hepamine coating (Figure 4b). The result indicates that the hepamine remains stably immobilized on PU surfaces, markedly enhancing blood compatibility of the most widely used catheter material, PU. Although the detailed mechanisms of platelet interactions with heparin molecules are unclear, there are a number of studies demonstrating a significant reduction of platelet adhesion onto heparin-immobilized substrates.[6,36,37] A proposed mechanism is probably due to electrostatic repulsion between heparins and platelets.[38] The anticoagulation effect of hepamine-coated substrates was also evaluated by measuring the thickness of the adsorbed blood component layers by ellipsometry. PU-coated Ti substrate was used, and hepamine functionalized the substrate. Hepamine coating thickness determined by an ellipsometer was 26.46 $\pm$ 4.1 Å. Subsequently, human blood (2 mL) taken from a human volunteer was applied directly to the substrate (Supporting Information Figure S2, inset). After 2 and 7 days of blood contact, the substrates were rinsed with water, and then, the amount of adsorbed blood components was measured. The hepamine-coated PU substrates exhibited a significant reduction in blood component adsorption; the thickness was 100 Å (2 days) for the unmodified PU substrate, which was greatly increased to 307 Å (7 days). However, the hepamine-coated substrates showed reduced adsorption 32 Å and 150 Å for 2- and 7-day exposure, respectively (Supporting Information Figure S2). These results suggest that hepamine-coated PU substrates showed improved resistance against adsorption of blood components.

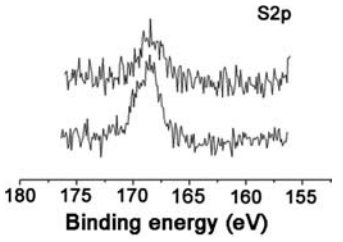

Figure 5. High-resolution S2p spectra of hepamine-coated PU (lower) and hepamine-coated PU immersed in 50% EtOH for 2 h (upper).

Stability of the hepamine layer upon exposure of a sterilizing solution is an important factor for practical utility of the hepamine coating approach. A popular sterilizing solution, 50% (v/v) ethanol, was prepared to which the hepamine-coated PU substrate was immersed for 2 h. XPS was used to monitor delamination of the coated hepamine layer (Figure 5). XPS surface analysis revealed that the hepamine-coated PU substrate exhibited a clear S2p signal, which still remained after incubation in 50% ethanol solution. This result demonstrated that the stability of hepamine coating was suitable in practical medical settings.

CONCLUSIONS

In this study, a new adhesive heparin derivative called hepamine was introduced. Hepamine was prepared by conjugation of dopamine, a mussel-inspired adhesive compound, and showed excellent surface coating capability on various substrates particularly on PU substrates. Unlike existing approaches that require multistep, complicated heparin immobilization, one-step immersion of a substrate into the hepamine solution was shown to be sufficient for the coating without chemical treatment of PU. The resulting hepamine immobilized surfaces showed significantly improved blood compatibility, preventing blood coagulation and platelet adhesion. The coating was stable in a typical disinfectant solution (50% ethanol), and the anticoagulant activity of the hepamine-coated surface remained for 7 days. These results suggest that the use of hepamine can be an effective alternative approach for stable surface immobilization of heparin. Thus, we believe that the strategy described herein can be generally applied in a variety of biomedical devices such as catheters, grafts, and stents to achieve a thromboresistance property.

ASSOCIATED CONTENT

Supporting Information. Supporting Figures S1, S2. This material is available free of charge via the Internet at http://pubs.acs.org.

AUTHOR INFORMATION

Corresponding Author

*E-mail: haeshin@kaist.ac.kr. Tel: +82-42-350-2849. Fax: +82-42-350-2810.

Author Contributions

¶These authors equally contributed to this work.

ACKNOWLEDGMENT

The authors are grateful to financial supports from National Research Foundation (NRF) of Korea: Korea Biotech R&D Program (2010K001356), WCU Program (R31-10071-0), and Molecular-Level Interface Research Center (2010-0001954). National Cancer Control R&D Program from the Ministry of Health and Welfare also supports to this work (920340).

REFERENCES

(1) Andersson, J., Sanchez, J., Ekdahl, K. N., Elgue, G., Nilsson, B., and Larsson, R. (2003) Optimal heparin surface concentration and antithrombin binding capacity as evaluated with human non-anticoagulated blood *in vitro*. *J. Biomed. Mater. Res. A 67A*, 458–466.

(2) Jeon, O., Yang, H. S., Lee, T. J., and Kim, B. S. (2008) Heparin-conjugated polyethylenimine for gene delivery. *J. Controlled Rel. 132*, 236–242.

(3) Du, Y. J., Brash, J. L., McClung, G., Berry, L. R., Klement, P., and Chan, A. K. (2006) Protein adsorption on polyurethane catheters modified with a novel antithrombin-heparin covalent complex. *J. Biomed. Mater. Res. A 80*, 216–225.

(4) Christensen, K., Larsson, R., Emanuelsson, H., Elgue, G., and Larsson, A. (2005) Improved blood compatibility of a stent graft by combining heparin coating and abciximab. *Thromb. Res. 115*, 245–253.

(5) Wang, A. F., McAllister, J. P., Finlayson, P., Brabant, K., Tang, H. Y., Black, C., Cao, T., Liang, X. M., Salley, S. O., Auner, G. W., and Ng, K. Y. S. (2007) Short-and long-term neural biocompatibility of heparin coated sapphire implants. *Mater. Sci. Eng., C 27*, 237–243.

(6) Lee, Y. K., Park, J. H., Moon, H. T., Lee, D. Y., Yun, J. H., and Byun, Y. (2007) The short-term effects on restenosis and thrombosis of echinomycin-eluting stents topcoated with a hydrophobic heparin-containing polymer. *Biomaterials 28*, 1523–1530.

(7) Park, K. D., Okano, T., Nojiri, C., and Kim, S. W. (1988) Heparin immobilized onto segmented polyurethaneureas surfaces: effects of hydrophilic spacers. *J. Biomed. Mater. Res. 22*, 977.

(8) Weng, Y., Hou, R., Xie, D., Wang, J., and Huang, N. (2007) Covalent immobilization of heparin on anatase TiO_2 films via chemical adsorbent phosphoric acid interface. *Key Eng. Mater. 330−332*, 865.

(9) Heyman, P. W., Cho, C. S., Mcrea, J. C., Olsen, D. B., and Kim, S. W. (1985) Heparinized polyurethanes: *in vitro* and *in vivo* studies. *J. Biomed. Mater. Res. 19*, 419–436.

(10) Barbucci, R., Magnani, A., Albanese, A., and Tempesti, F. (1991) Heparinized polyurethane surface through ionic bonding of heparin. *Int. J. Artif. Organs 14*, 499–507.

(11) Albanese, A., Barbucci, R., Belleville, J., Bowry, S., Eloy, R., Lemke, H. D., and Sabatini, L. (1994) *In vitro* biocompatibility evaluation of a heparinizable material (PUPA), based on polyurethane and poly(amido-amine) components. *Biomaterials 15*, 129–136.

(12) Barbucci, R., and Magnani, A. (1994) Conformation of human plasma proteins at polymer surfaces: the effectiveness of surface heparinization. *Biomaterials 15*, 955–962.

(13) Arnander, C., Baggersjoback, D., Frebelius, S., Larsson, R., and Swedenborg, J. (1987) Long-term stability *in vivo* of a thromboresistant heparinized surface. *Biomaterials 8*, 496–499.

(14) Bindslev, L., Eklund, J., Norlander, O., Swedenborg, J., Olsson, P., Nilsson, E., Larm, O., Gouda, I., Malmberg, A., and Scholander, E. (1987) Treatment of acute respiratory-failure by extracorporeal carbon-dioxide elimination performed with a surface heparinized artificial lung. *Anesthesiology 67*, 117–120.

(15) VanDelden, C. J., Engbers, G. H. M., and Feijen, J. (1996) The effect of protein adsorption on the anticoagulant activity of surface immobilized heparin. *J. Biomat. Sci.-Polym. E. 7*, 727–740.

(16) Wang, A. F., Cao, T., Tang, H. Y., Liang, X. M., Salley, S. O., and Ng, K. Y. S. (2005) *In vitro* haemocompatibility and stability of two types of heparin-immobilized silicon surfaces. *Colloid Surf., B 43*, 245–255.

(17) Waite, J. H. (1999) Reverse engineering of bioadhesion in marine mussels. *Ann. N.Y. Acad. Sci. 875*, 301–309.

(18) Papov, V. V., Diamond, T. V., Biemann, K., and Waite, J. H. (1995) Hydroxyarginine-containing polyphenolic proteins in the adhesive plaques of the marine mussel *Mytilus edulis*. *J. Biol. Chem. 270*, 20183–20192.

(19) Waite, J. H., and Qin, X. X. (2001) Polyphenolic phosphoprotein from the adhesive pads of the common mussel. *Biochemistry 40*, 2887–2893.

(20) Waite, J. H. (2002) Adhesion á la moule. *Integr. Comp. Biol. 42*, 1172–1180.

(21) Harrington, M. J., Masic, A., Holten-Andersen, N., Waite, J. H., and Fratzl, P. (2010) Iron-clad fibers: a metal-based biological strategy for hard flexible coatings. *Science 328*, 216–220.

(22) Lee, H., Scherer, N. F., and Messersmith, P. B. (2006) Single-molecule mechanics of mussel adhesion. *Proc. Natl. Acad. Sci. U. S. A. 103*, 12999–13003.

(23) Zeng, H., Hwang, D. S., Israelachvili, J. N., and Waite, J. H. (2010) Strong reversible Fe^{3+} mediated bridging between Dopa-containing protein films in water. *Proc. Natl. Acad. Sci. U. S. A. 107*, 12850–12853.

(24) Lee, H., Dellatore, S. M., Miller, W. M., and Messersmith, P. B. (2007) Mussel-inspired surface chemistry for multifunctional coatings. *Science 318*, 426–430.

(25) Lee, H., Lee, Y., Statz, A. R., Rho, J., Park, T. G., and Messersmith, P. B. (2008) Surface-independent Layer-by-Layer assembly using mussel adhesive inspired polymers. *Adv. Mater. 20*, 1619–1623.

(26) Kang, S. M., Rho, J., Choi, I. S., Messersmith, P. B., and Lee, H. (2009) Norepinephrine: material-independent, multifunctional surface modification reagent. *J. Am. Chem. Soc. 131*, 13224–13225.

(27) Lee, H., Lee, K. D., Pyo, K. B., Park, S. Y., and Lee, H. (2010) Catechol-grafted poly(ethylene glycol) for PEGylation on versatile substrates. *Langmuir 26*, 3790–3793.

(28) Holowka, E. P., and Deming, T. J. (2010) Synthesis and cross linking of L-DOPA containing polypeptide vesicles. *Macromol. Biosci. 10*, 496–502.

(29) Sun, I. C., Eun, D. K., Na, J. H., Lee, S., Kim, I. J., Youn, I. C., Ko, C. Y., Kim, H. S., Lim, D., Choi, K., Messersmith, P. B., Park, T. G., Kim, S. Y., Kwon, I. C., Kim, K., and Ahn, C. H. (2009) Heparin-coated gold nanoparticles for liver-specific CT imaging. *Chem.—Eur. J. 15*, 13341–13347.

(30) Kim, T. G., Lee, H. J., Jang, Y. S., and Park, T. G. (2009) Controlled release of paclitaxel from heparinized metal stent fabricated by layer-by-layer assembly of polylysine and hyaluronic acid-g-poly-(lactic-co-glycolic acid) micelles encapsulating paclitaxel. *Biomacromolecules 10*, 1532–1539.

(31) Lelah, M. D., and Cooper, S. L. (1986) *Polyurethanes in medicine*, CRC Press, Boca Raton, FL.

(32) Planck, H., Syré, I., Dauner, M., and Egbers, G. (1987) *Polyurethane in Biomedical Engineering II. Progress in Biomedical Engineering*, Elsevier Science, Amsterdam.

(33) Coleman, D. L., Meuxelaar, H. L. C., Kessler, T. R., Mclennan, W. H., Richards, J. M., and Gregonis, D. E. (1986) Retrieval and analysis of a clinical total artificial heart. *J. Biomed. Mater. Res. 20*, 417–431.

(34) Stokes, K. (1988) Polyether polyurethanes: biostable or not? *J. Biomater. Appl. 3*, 228–259.

(35) Jaques, L. B. (1979) Heparin: an old drug with a new paradigm. *Science 206*, 528–533.

(36) Yoon, Y. S., and Kim, S. C. (1999) Blood compatibility of sulfonated poly(ethylene oxide)-grafted polyurethane/polystyrene

IPN (II): surface properties and *in vitro* platelet adhesion test. *Polym.-Korea 23*, 926–935.

(37) Lee, H. J., Park, K. D., Han, D. K., Kim, Y. H., and Cho, I. (1997) Synthesis and characteristics of thromboresistant copolymers having PEG/PEG-SO_3. *Polym.-Korea 21*, 1045–1052.

(38) Lin, W. C., Liu, T. Y., and Yang, M. C. (2004) Hemocompatibility of polyacrylonitrile dialysis membrane immobilized with chitosan and heparin conjugate. *Biomaterials 25*, 1947–1957.

Supporting Information

Enhancement of Blood Compatibility of Poly(urethane) Substrates by Mussel-Inspired Adhesive Heparin Coating

Inseong You[a,#], Sung Min Kang[a,b,#], Youngro Byun[c], Haeshin Lee[a,b]*

[a]Graduate School of Nanoscience and Technology and [b]Department of Chemistry, 335 Science Rd. KAIST, Daejeon 305-701, South Korea
[c]WCU Department of Molecular Medicine and Biopharmaceutical Sciences, College of Pharmacy, Seoul National University, Seoul 151-742, South Korea

Email: haeshin@kaist.ac.kr

* To whom correspond should be addressed
[#] These authors equally contributed to this work.

Contents

Figure S1. Static water contact angle images on various substrates (Au, PC, and silicon rubber).
Figure S2. Thickness of the adsorbed blood components on substrates after 2- and 7-day exposure to human blood: bare PU (black) and hepamine-coated PU (gray).

Figure S1. Static water contact angle images on various substrates (Au, PC, and silicon rubber).

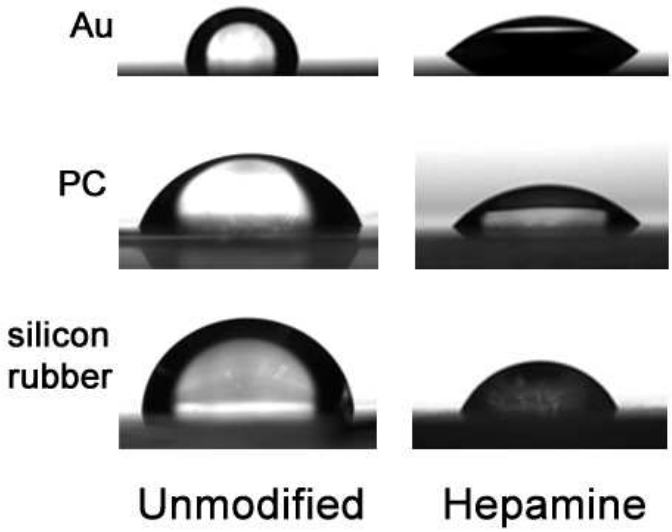

Figure S2. Thickness of the adsorbed blood components on substrates after 2- and 7-day exposure to human blood: bare PU (black) and hepamine-coated PU (gray).

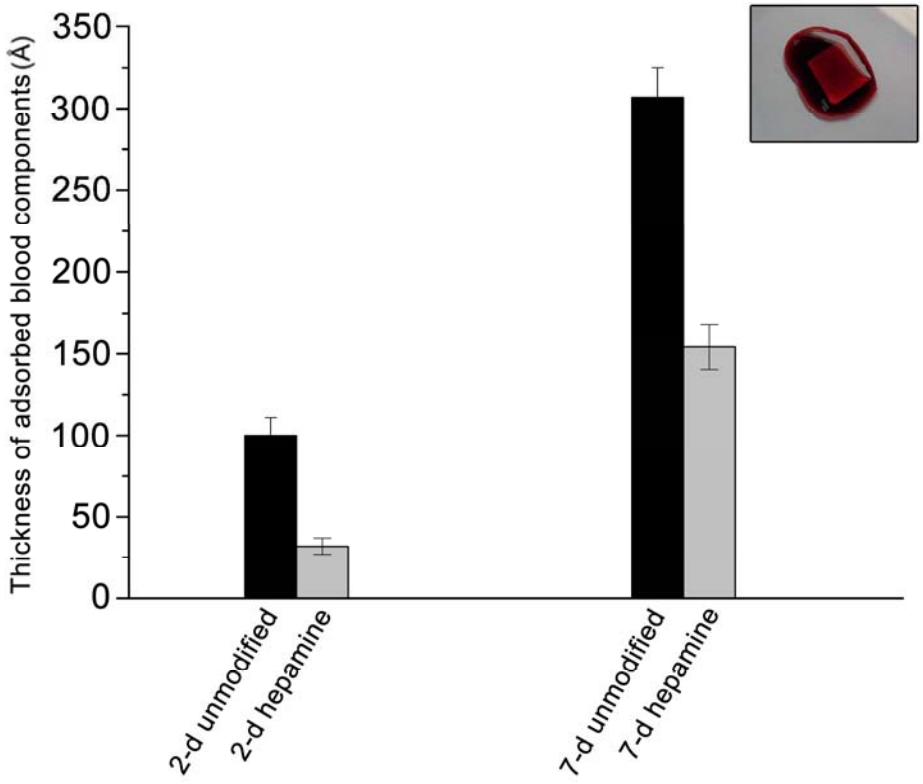

Bioconjugate Chemistry

ARTICLE

pubs.acs.org/bc

Cell-Specific Targeting by Heterobivalent Ligands

Jatinder S. Josan,[†] Heather L. Handl,[†] Rajesh Sankaranarayanan,[†] Liping Xu,[§] Ronald M. Lynch,[∥] Josef Vagner,[∥] Eugene A. Mash,[†] Victor J. Hruby,[†,∥] and Robert J. Gillies*[,§]

[†]Department of Chemistry & Biochemistry, 1306 E. University Blvd., The University of Arizona, Tucson, Arizona 85721, United States

[§]Department of Radiology, H. Lee Moffitt Cancer Center, 12902 Magnolia Drive, Tampa, FL 33612, United States

[∥]BIO5 Institute, 1657 E. Helen Street, The University of Arizona, Tucson, Arizona 85719, United States

Supporting Information

ABSTRACT: Current cancer therapies exploit either differential metabolism or targeting to specific individual gene products that are overexpressed in aberrant cells. The work described herein proposes an alternative approach—to specifically target combinations of cell-surface receptors using heteromultivalent ligands ("receptor combination approach"). As a proof-of-concept that functionally unrelated receptors can be noncovalently cross-linked with high avidity and specificity, a series of heterobivalent ligands (htBVLs) were constructed from analogues of the melanocortin peptide ligand ([Nle^4, D-Phe^7]-α-MSH) and the cholecystokinin peptide ligand (CCK-8). Binding of these ligands to cells expressing the human Melanocortin-4 receptor and the Cholecystokinin-2 receptor was analyzed. The MSH(7) and CCK(6) were tethered with linkers of varying rigidity and length, constructed from natural and/or synthetic building blocks. Modeling data suggest that a linker length of 20−50 Å is needed to simultaneously bind these two different G-protein coupled receptors (GPCRs). These ligands exhibited up to 24-fold enhancement in binding affinity to cells that expressed both (bivalent binding), compared to cells with only one (monovalent binding) of the cognate receptors. The htBVLs had up to 50-fold higher affinity than that of a monomeric CCK ligand, i.e., Ac-CCK(6)-NH_2. Cell-surface targeting of these two cell types with labeled heteromultivalent ligand demonstrated high avidity and specificity, thereby validating the receptor combination approach. This ability to noncovalently cross-link heterologous receptors and target individual cells using a receptor combination approach opens up new possibilities for specific cell targeting *in vivo* for therapy or imaging.

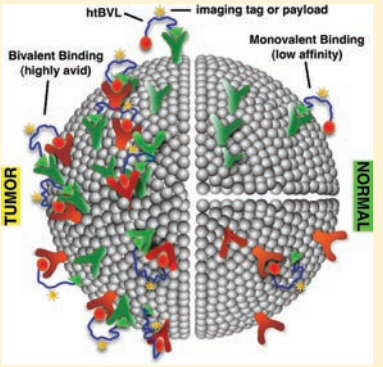

INTRODUCTION

Multivalent ligands (MVLs) are characterized by the simultaneous binding of an entity that displays multiple molecular recognition elements to multiple receptors/epitopes. Such multiple interactions significantly enhance the affinity (avidity) of an agent whose constituent ligands may otherwise exhibit weak binding.[1,2] For example, we demonstrated earlier that linear homobivalent and trivalent ligands of the MSH pharmacophore bound with higher affinities than the corresponding monovalent ligands to the human melanocortin-4 receptor (hMC4R).[3,4] Simultaneous targeting of multiple cell-surface receptors with homomultivalent ligands (hmMVLs) has been the subject of intensive research in recent years.[2,5−7] However, hmMVLs cannot differentiate among different binding modes, such as the *chelation effect*, the *receptor clustering effect*, or the *statistical effect*.[8] Further, although homomultivalent binding can give rise to tissue-level specificity, there is no inherent specificity at the molecular binding event. Thus, its utility in tumor-specific targeting can be limited.[7,9,10] The *clustering effect* is the only binding paradigm that takes advantage of protein expression combinations. A multivalent construct with at least two distinct binding pharmacophores spaced adequately apart is needed to demonstrate noncovalent cross-linking (i.e., clustering) of receptors.

We hypothesize that, by combining one or more copies of different binding moieties into a heteromultivalent ligand (htMVL), it should be possible to create compounds that will specifically and selectively bind to cells bearing the appropriate combination of complementary cell-surface receptors (Figure 1A).[11,12] Further, we have manually curated the Agilent whole genome array and have identified 2408 genes encoding for cell-surface proteins (Morse et al., unpublished) that can potentially be targeted. The number of possible combinations of n genes organized into sets of x is $[n!/(n-x)!] \div x!$, indicating that there are $\sim 2.9 \times 10^6$ potential two-gene combinations and $\sim 2.3 \times 10^9$ potential three-gene combinations (and thus potential targets). Thus, it is increasingly likely that specific combinations of cell-surface proteins can be found that are expressed on a target (cancer) cell but not on any healthy cell (e.g., see ref 13 for gene expression profiling-based identification of receptor

Received: September 28, 2010
Revised: June 3, 2011
Published: June 03, 2011

ACS Publications © 2011 American Chemical Society

combination targets in pancreatic cancer). To exploit this potential, these combinations will have to be targeted with heteromultivalent ligands carrying imaging and/or therapeutic payloads (Figure 1A). Such constructs could also be used to investigate ligand−receptor or cell−cell interactions, investigate cellular signaling complexes such as "immune synapse", mimic the multivalent binding of antibodies to antigens, and use them for combined *in vivo* imaging and therapeutic targeting.[5]

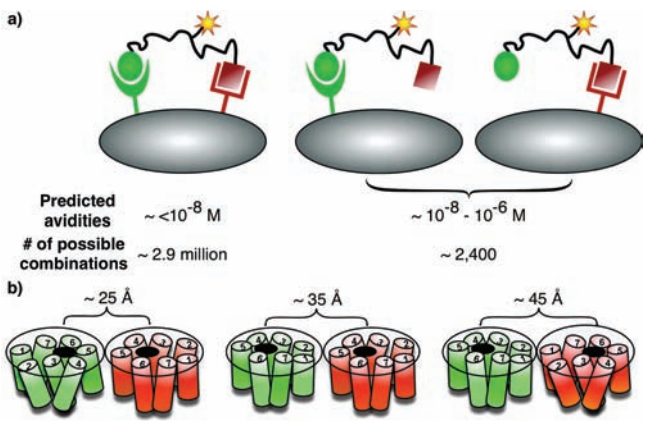

Figure 1. (A) **Receptor combination approach:** predicted avidities of an htBVL binding to cells expressing one or two complementary receptors, and the number of possible combinations for potential targeting. High avidity and specificity can be expected for heterobivalent binding. (B) **GPCR modeling.** The two receptors can pack in any number of orientations, and the distance span between the two binding pockets could be up to 100 Å long depending on the dimer packing, domain swapping, or lipid rafts involvement (also see refs 3, 14, 18, 22, and 23).

In this report, we provide proof-of-principle studies, i.e., htMVL-directed noncovalent cross-linking of desired cell-surface proteins with high avidity and specificity. Further, we unambiguously prove the utility of this "receptor combination approach" in specific targeting with *in vitro* imaging of a fluorescently tagged htBVL. We present here the design, synthesis, and biological evaluation of a set of synthetic htBVLs composed of ligand motifs that target the human melanocortin-4 receptor (hMC4R) and the cholecystokinin-2 receptor (CCK-2R). For this purpose, MSH(7), a seven residue fragment of NDP-α-MSH ([Nle^4, DPhe^7]-α-MSH) and CCK(6), a six residue fragment of [Nle^{28}, Nle^{31}]CCK-8, respectively, were used (Scheme 1, inset). These ligands were conjoined with linkers of varying rigidity and length, which ranged from 18 to 148 atoms and spanned a distance of up to ca. 100 Å.[3,4,14] The htBVLs were tested for their ability to compete against europium-labeled "lanthaligands"[15] (Eu-DTPA-NDP-α-MSH and Eu-DTPA-CCK-8) for binding to cells that expressed one or both complementary receptors.

Scheme 1. Synthetic Route for Heterobivalent Ligands (htBVLs)[a]

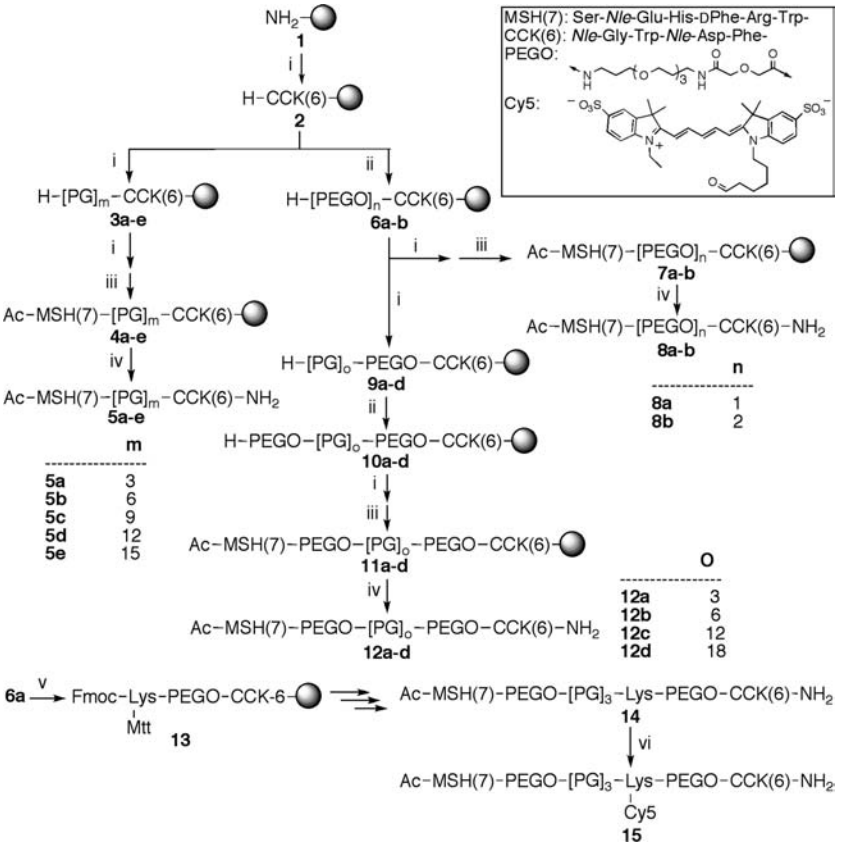

[a] The inset shows the sequence of MSH(7) and CCK(6) ligands and the structure of the PEGO linker (20 atoms). The reagents for each step are as follows: (i) Fmoc-amino acid-OH (3 equiv), HOCt (3 equiv), diisopropylcarbodiimide (3 equiv); (ii) 50% Ac_2O in pyridine; (iii) 20% piperidine/DMF; (iv) (a) diglycolic anhydride (10 equiv) in DMF, (b) CDI (20 equiv) in anhyd. DMF, (c) 4,7,10-trioxa-1,13-tridecaneamine (20 equiv) in anhyd. DMF; (v) TFA/H_2O/Thioanisole/Triisopropylsilane/Ethanedithiol 82.5:5:5:5:2.5; *m* is 3, 6, 9, 12, or 15; *n* is 1 or 2; *o* is 3, 6, 12, or 18.

EXPERIMENTAL PROCEDURES

General. All solvents and reagents were purchased from commercial sources and used without further purification. Peptides were synthesized on Tentagel Rink amide resin (initial loading: 0.2 mmol/g) using N^{α}-Fmoc protecting groups and a standard DIC/HOCt or HBTU/HOBt activation strategy, as published previously.[4,16] The purity of final products was analyzed using Waters high-performance liquid chromatography (HPLC) apparatus and with a Vydac C18 reverse-phase column (diam × length, 4.6 mm × 150 mm; pore size: 3 μm). Purification of compounds was achieved using a Waters 600 HPLC apparatus equipped with a Vydac C18 reverse phase column (22 × 250 mm, 5 μm) under optimized gradients and flow rates, and monitored at 230 and 280 nm. Size exclusion chromatography was performed on a borosilicate glass column (2.6 × 250 mm, Sigma, St. Louis, MO) filled with medium-sized Sephadex G-25 or G-10. Solid-phase extraction (SPE) was employed where simple isolation of final compound was needed from excess salts and buffers, using C-18 Sep-Pak cartridges. Mass spectra of positive ions were recorded either with a single stage reflectron MALDI-TOF mass spectrometer (Bruker Rexlex III, Bruker Daltonics, Billerica, MA; α-cyanocinnamic acid as a matrix) in reflectron mode or with a low-resolution ESI mass spectrometer (Finnigan, Thermoquest LCQ ion trap instrument, Lake Forrest, CA) and/or using high-resolution Fourier transform mass spectrometer (FT-ICR MS, Bruker Apex Qh, Bremen, Germany) equipped with an ESI source. The peptide concentrations were determined by monitoring absorbance of peptides against 0.5 mM solution of tryptophan (D or L) in DMSO at 280 nm. (See Supporting Information for details.)

Molecular Modeling and Circular Dichroism of Linkers. The computation experiments were carried out using *MacroModel 9.1* implemented under *Maestro 7.5* interface on a Linux Dell workstation, and with MacroModel implementations of AMBER*, MMFF, and OPLS all-atom force fields and GB/SA continuum model for water.[17] GPCR intra- and inter-receptor distance estimations were carried out using PDB file 1GZM[18] loaded in PyMOL program. CD measurements were carried out on a Jasco model J-710 spectropolarimeter using thermostatted quartz cuvettes (0.1 cm path length) (see ref 3 and Supporting Information).

Cloning, Transfection, and Cell Culture. HEK293 cells overexpressing either or both of the human melanocortin-4 receptor (hMC4R) and the cholecystokinin-2 (CCK-2) receptor were used to assess the binding. HEK293/hMC4R cells were grown in Dulbecco's Modified Eagle Medium (DMEM) with 10% FBS. Monovalent CCK binding was tested on HEK293 cells with stable expression of CCK-2 receptor. These cells were grown in DMEM supplemented with 10% FBS and were maintained under selection with 100 μg/mL Zeocin. Evaluation of bivalent ligand binding was completed on HEK293/hMC4R cells with transient expression of CCK-2R (referred to as HEK293/hMC4R/tCCK cells). For transient receptor expression, cells were plated at a density of 10 000 cells/well in Wallac B&W Isoplate TC (Wallac/PerkinElmer, 1450−583) 96-well plates. The day after plating, cells were transfected with CCK-2R using FuGENE 6 Transfection Reagent (Roche, 1814−443). A 3:1 ratio of FuGENE to DNA was used, as per reagent protocol. Reagents (30 μL media, 0.15 μL FuGENE 6, and 0.05 μg CCK-2R DNA per well) were added to a sterile microtube and incubated at room temp for 15 min. The media used during the incubation was antibiotic-free, serum-free DMEM. After the 15 min incubation, the reaction mixture (30 μL) was added to the cells in their normal media. It was determined that 72 h post-transfection was optimal for high surface expression of CCK-2R; thus, all binding assays were performed 72 h post-transfection. The presence of both receptors on a dual-expressing cell line was ascertained with antibody staining (nearly 100% coverage of cells with both receptors was observed). (See ref 19 on more details of various cell lines generated and protocols.)

Receptor Number Determination. The number of receptors present on the cell surface was determined with saturation binding analysis followed by correlation of fluorescent signal achieved at B_{max}. Increasing amounts of Eu-labeled ligand were added to cells until saturation was achieved. For hMC4R, the B_{max} was determined to be 95 200 ± 2500 AFU (Figure 2A). A standard curve relating the fluorescent signal to the concentration of Eu-labeled ligand present in the well was produced and used to determine the concentration of Eu-ligand present at saturation (Figure 2B). In case of hMC4R, a signal of 95 200 AFU correlates with 380 fmol/well. Assuming that during the saturation study that each receptor is bound by a single Eu-labeled ligand, this correlates with 2.3×10^{11} receptors/well. The average number of cells/well was obtained via counting with a hemocytometer and this number (61 800 cells/well, $n = 10$) was then used to determine the number of hMC4R receptors per cell. The same process was followed for determining the number of CCK-2R per cell (also see Supporting Information Figure S6 for more details).

Lanthanide-Based Binding Assays. Lanthanide-based competitive binding assays were conducted according to the method which has been previously described.[19−21] (See Supporting Information for detailed protocols and Figure 2 and S7 for representative binding curves.)

Digital Imaging Microscopy. Cells were grown on #1 coverslips harbored in individual wells of six-well culture dishes. Individual slides were mounted in a chamber maintained at 37 °C on the stage of an inverted Olympus IX70 microscope equipped with a 40× 1.35 NA objective. For excitation of Cy5 fluorescence, white light emitted from a 150 W Xe lamp was passed through a 10 nm band-pass filter centered at 640 nm. The emitted light was selected using a band-pass filter centered at 680 nm, and subsequently imaged onto a CCD camera (Photometrics CH-350; TEK-512 chip). Baseline control images were acquired at 5 min intervals prior to addition of the labeled htBVL to incubation medium. Following 3 min of ligand addition, the medium was replaced with ligand-free medium prior to further image acquisition. Control images were subtracted from images acquired from the same ligand bound cells. Image analysis was performed on a SGI Indy-2 workstation using customized software.

RESULTS AND DISCUSSION

Ligand Design. In order to test the proof-of-hypothesis that heteromultivalent ligands (htMVL) will specifically and selectively bind (noncovalently) to cells bearing the appropriate combination of complementary heterologous cell-surface receptors (Figure 1A), two model receptors—hMC4R and CCK-2R—were chosen. To estimate the linker length required to engage the two proof-of-principle receptors used in this study, G-protein coupled receptors (GPCRs) were modeled as dimers, based on the crystal structure of rhodopsin in a trigonal crystal form with

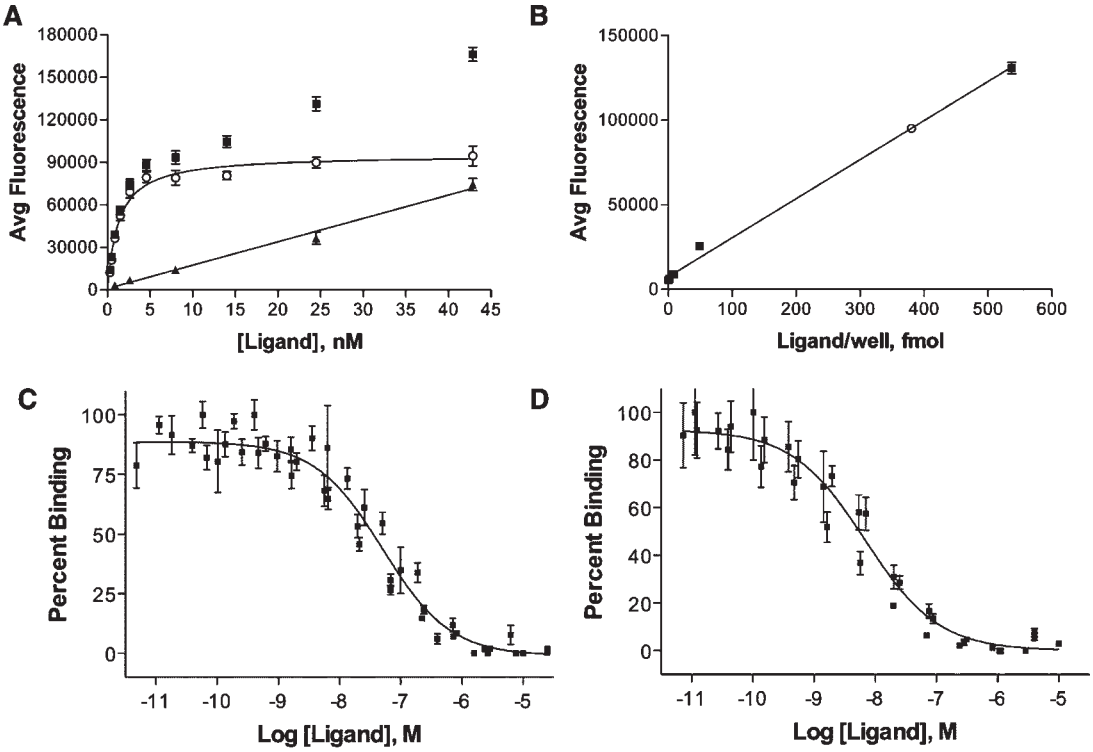

Figure 2. Receptor number determination and representative binding curves. (A) Saturation binding analysis of Eu-DTPA-NDP-α-MSH binding to HEK293/hMC4R/tCCK cells where (■), (○), and (▲) indicate total, specific, and nonspecific binding, respectively. From these data, K_d = 1.30 ± 0.14 nM and B_{max} = 95 200 ± 2500 AFU. (B) Standard curve relating [Eu-DTPA-NDP-α-MSH] to fluorescent signal. For binding to the hMC4R, the B_{max} was determined to be 95 200 ± 2500 AFU, which correlates to 380 fmol/well. (C) The ligands were evaluated for their monovalent and bivalent binding by comparing them against Eu-labeled lanthaligands. Single plot IC_{50} values were determined where data from all *n* measurements were pooled first and nonlinear regression analysis performed. Binding of ligand **12c** compared with 0.1 nM Eu-DTPA-CCK8 in HEK293/CCK cells, with an IC_{50} of 130 nM. (D) Binding of ligand **12c** compared with 0.1 nM Eu-DTPA-CCK8 in HEK293/hMC4R/CCK cells, with an IC_{50} of 38 nM.

two protein molecules per asymmetric unit.[18] The width of a GPCR dimer was estimated to be 70 Å along the longer elliptical axis in a closely packed form. The centers of the binding pockets in each case were located approximately 10−15 Å from the nearest edge of the elliptical seven-membrane bundle (off-center). Thus, depending upon the orientation of binding pockets, the inter-receptor distance could span 20−50 Å (Figure 1B; also see Supporting Information Figure S3 for details). Any association of annular lipids with GPCRs may add 8 Å per layer of lipid molecules.[22] Thus, in the case of loosely packed dimers, the inter-receptor distance could extend up to 100 Å or more (also see refs 3 and 14 for discussion on GPCR dimer modeling). These estimations assume that, upon dimerization, the two receptors do not participate in domain swapping.[23] Upon the basis of these estimates, three families of htBVLs were designed composed of semirigid Pro-Gly linkers and/or flexible PEGO linkers (see Scheme 1 and Table 1). The design of these htBVLs required placement of the α-MSH peptide at the N-termini and the CCK peptide at the C-termini of the linkers because the CCK peptide requires the free amide form of the carboxyl terminus for optimal binding.[24] Moderately weak ligands, namely, MSH(7) and CCK(6) (Scheme 1, inset), were used in place of more potent analogues, as it was anticipated that a more pronounced enhancement might be achieved with weaker ligands in a bivalent binding mode.[25,26] The binding affinities of monovalent Ac-MSH(7)-NH_2 [Ac-Ser-Nle-Glu-His-DPhe-Arg-Trp-NH_2] and Ac-CCK(6)-NH_2 [Ac-Gly-Nle-Trp-Nle-Asp-Phe-NH_2] ligands, in terms of IC_{50}, are 39 ± 4 nM and 26 ± 4 nM, respectively.

Linker Design and Structural Features. In our search for an ideal linker, we designed one based on polyproline helices that were modified appropriately for desirable characteristics. The polyproline helix type II (PPII) forms a highly rigid rod-like structure. Although the pitch/residue ratio of this helix may be appropriate for building a linker, ligand presentation may be conformation-dependent. The poly(Pro-Gly) linker presented here lacks residues with bulky aliphatic side chains and eliminates any functional groups to render it inert. Further, glycine at alternate positions provides flexibility in the linker backbone, compared to PPII. Remarkably, these two residues have opposing rigidity/flexibility characteristics giving the linker a semirigid structure. A representative set of computational analyses on the poly(Pro-Gly) linker and experimental confirmation is shown in Figure 3 (and Supporting Information Figure S4). Briefly, conformational analysis and molecular dynamic (MD) simulation studies on this linker predicted that the alternating Pro-Gly sequence would assume a relaxed helical conformation (Figure 3A) with a characteristic triangular shape (viewed down the radial axis) similar to PPII. However, the helix is much broader than PPII and, thus, takes a shorter pitch of 5−12 Å per turn of six residues with an average of 8 Å in the sampled MD set. As expected, the range of excursions is higher for smaller linker length. Circular dichroic (CD) analyses of 100 μM of Ac-$[PG]_6$-NH_2 in water exhibited a characteristic negative absorption band around 202 nm.[27] This is slightly blue-shifted. Notably, the slight

Table 1. Binding Data of Heterobivalent Ligands Tested for Cross-Linking in HEK293/hMC4R/tCCK-2R (hMC4R > CCK-2R)[a]

				IC_{50} (nM) of CCK(6)[b]			IC_{50} (nM) of MSH(7) [b]		
no.	linker	linker length (atoms)	estimated linker length (Å)	CCK-2R[c]	dual expression[e]	fold increase	hMC4R[d]	dual expression[e]	fold increase
5a	-$[PG]_3$-	18	≤13	**11** (8.3−15)	**1.4** (1.0−2.0)	8	**11** (8.9−12)	**1300** (880−1900)	0
5b	-$[PG]_6$-	36	≤25	**46** (40−52)	**2.3** (1.8−2.9)	20	**110** (85−140)	**1000** (690−1500)	0.1
5c	-$[PG]_9$-	54	≤35	**320** (240−420)	**170** (130−240)	2	**460** (250−850)	**530** (180−1500)	0.9
5d	-$[PG]_{12}$-	72	≤45	**50** (43−58)	**6.9** (5.6−8.6)	7	**28** (23−33)	**980** (250−3900)	0
5e	-$[PG]_{15}$	90	≤55	**230** (190−290)	**55** (43−70)	4	**680** (310−1500)	**3500** (1300−9500)	0.2
8a	-PEGO-	20	≤18	**11** (9.0−13)	**0.50** (0.31−0.82)	22	**28** (22−34)	**250** (210−300)	0.1
8b	-PEGO-PEGO-	40	≤36	**50** (41−62)	**4.5** (3.4−5.8)	11	**60** (49−75)	**320** (260−400)	0.2
12a	-PEGO-$[PG]_3$-PEGO-	58	≤46	**150** (120−180)	**6.3** (5.0−7.9)	24	**390** (89−1700)	**1600** (560−4700)	0.2
12b	-PEGO-$[PG]_6$-PEGO-	76	≤56	**72** (56−94)	**20** (15−26)	4	**230** (160−340)	**21** (17−27)	11
12c	-PEGO-$[PG]_{12}$-PEGO-	112	≤76	**130** (110−150)	**38** (29−50)	3	**10** (6.7−16)	**32** (25−39)	0.3
12d	-PEGO-$[PG]_{18}$-PEGO-	148	≤96	**160** (130−200)	**93** (78−110)	2	**35** (26−47)	**28** (21−40)	1.3

[a] The IC_{50} values of Ac-MSH(7)-NH_2 and Ac-CCK(6)-NH_2 are 39 ± 4 nM and 26 ± 4 nM, respectively. "Fold Increase" is the ratio of IC_{50} values between single- and dual-expressing cell lines. [b] IC_{50} concentration in nM from at least 4 independent experiments reported. Values in parentheses represent the 95% confidence intervals of the IC_{50} values. [c] Binding data from competition with Eu-DTPA-CCK-8 (unsulfated) against CCK-2R expressing cells. [d] Binding data from competition with Eu-DTPA-NDP-α-MSH against hMC4R expressing cells. [e] Binding data from competition with either Eu-DTPA-CCK-8 (unsulfated) or Eu-DTPA-NDP-α-MSH against cells expressing both CCK-2R and hMC4R.

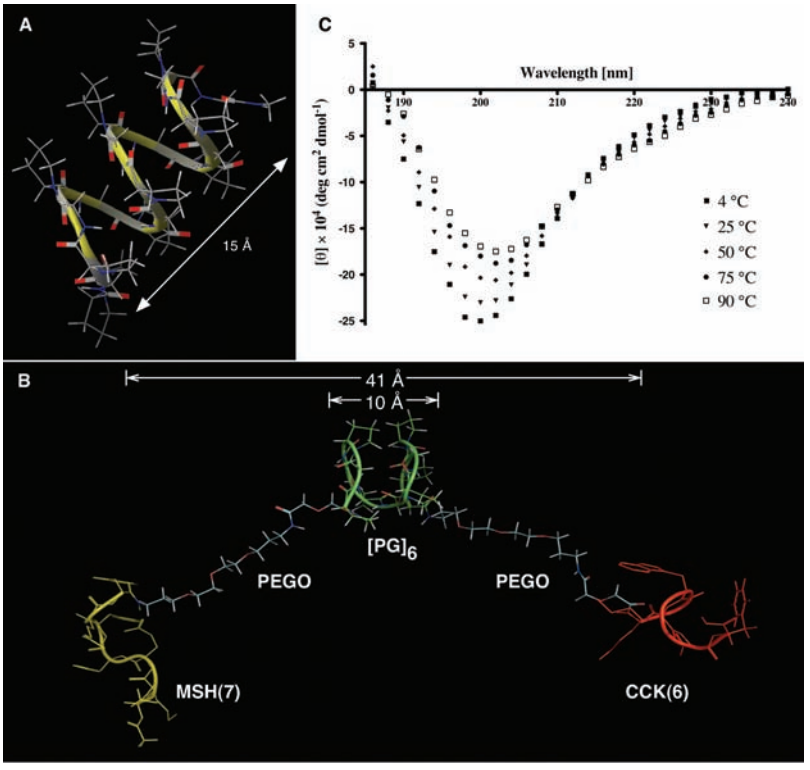

Figure 3. Studies on linkers and heterobivalent ligand **12b**. (A) Computationally generated structure of $[PG]_9$ linker. (B) One of the conformations of htBVL **12b** during MD simulation indicating the semirigid Pro-Gly backbone, the flexible PEGO ends, and β-turn features of MSH(7) and CCK(6) ligands with appropriate distances. (C) CD spectra of 100 μM of Ac-$[PG]_6$-NH_2 in water (pH 7) at different temperatures. The spectra reproduce a typical polyproline type II spectrum,[27] albeit the positive band is not prominent.

positive band at 225 nm usually seen in PPII is barely noticeable here (Figure 3C; also see Supporting Information Figure S5). This indicates that the poly(Pro-Gly) sequence does not have a predominantly rigid PPII helical conformation (about ~40% content; data not shown) but may acquire some random or other secondary structure components as well, thus, highlighting a semirigid backbone structure. This study was used as a guide to estimate the maximum linker lengths in each BVL (see Figure 3B for htBVL **12b** and Table 1 for the complete set).

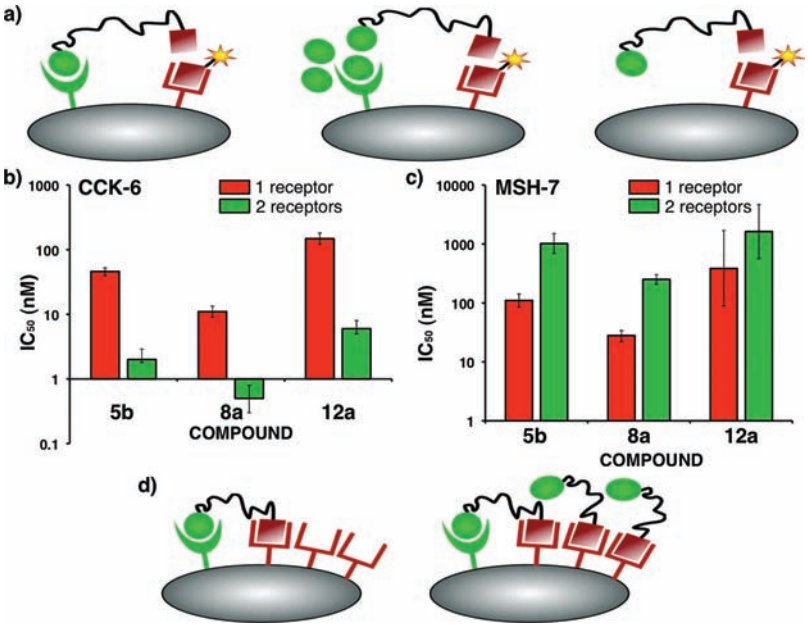

Figure 4. Binding analysis of htBVLs. (A) The ligands are tested for bivalent binding on cells expressing both complementary receptors (*left*), and for monovalent binding by either saturating (blocking) one of the receptors on dual-expressing cells (*middle*), or on cells expressing single complementary receptor (*right*). A cross-linking event would result in higher affinity for each ligand. (B) Plot of monovalent and bivalent IC_{50} of CCK(6) ligand for the htBVLs **5b**, **8a**, and **12a** displaying up to 24-fold higher bivalent affinity. (C) Plot of monovalent and bivalent IC_{50} values of MSH(7) ligand for the same htBVLs revealing decrease in bivalent affinity. (D) The lack of enhancement at the more abundant receptor could be explained on the basis that (left) at low concentrations, all the high affinity cross-linked sites are occupied corresponding to the less abundant receptor; (right) any subsequent binding event for the more abundant receptor is, therefore, monovalent resulting in no significant binding enhancement.

Synthetic Strategy. The synthesis of htBVLs **5a**−**15** consisting of MSH(7) and CCK(6) ligands connected in a head-to-tail fashion by PEGO and/or Pro-Gly linkers are depicted in Scheme 1. The htBVLs were synthesized using a modular strategy based on parallel solid-phase synthesis.[14,16] This stepwise strategy allows easy modification at any step with functional handles for further incorporation of imaging and therapeutic tags (e.g., dyes, lanthanide chelates, toxins, etc.). (See Supporting Information Experimental Procedure for details.)

Parallel Library Synthesis. Following hexapeptide CCK(6) assembly on resin, resin **2** was split into two portions. To one portion, a PEGO linker was coupled on the N-terminus following published procedures.[4] The resin **6a** containing a PEGO unit was again proportionally split for the synthesis of compounds **8a**−**b** and **12a**−**d**. At this stage, proline and glycine residues were added alternatively for resins **3a**−**e** and **9a**−**d**. After the final proline addition for these compounds, the N^{α}-Fmoc protecting group was removed. A second PEGO unit was coupled to the resins **6a** and **9a**−**d** for **6b** and **10a**−**d**, respectively. The free amine terminals of all resins were coupled with Fmoc-Trp(Boc)-OH and syntheses continued to complete the MSH(7) sequence, the N^{α}-terminus deprotected, then acetylated to give **4a**−**e**, **7a**−**b**, and **11a**−**d**. Following cleavage with TFA cocktail, the crude peptides **5a**−**e**, **8a**−**b**, and **12a**−**d** were isolated from the resin by filtration, the filtrate was reduced to low volume by evaporation using a stream of nitrogen, and the peptides were precipitated in ice-cold diethyl ether, centrifuged, washed several times with ether, dried, dissolved in water, and lyophilized to give off-white solid powders that were stored at −20 °C until purified. The final compounds were purified by size-exclusion chromatography and RP-HPLC, and characterized by ESI-MS and/or MALDI-TOF and/or FT-ICR. The yields of the crude peptides were 50−80% based on the resin weight gain, and overall, the purified yields for the syntheses were 5−30% based on the loading of the resin.

Labeled Ligands. The Cy5 label was introduced using lysine as a functional handle. After the first PEGO linker incorporation in resin **6a**, an N^{α}-Fmoc-N^{ε}-Mtt protected lysine was incorporated into the sequence (**13**) and the peptide synthesis continued to the end as above; the peptide was then cleaved from the resin and purified using preparative HPLC to give **14**. For Cy5 labeling, the purified peptide was dissolved in DMSO, Cy5-NHS ester was added, and the reaction was monitored using analytical HPLC at 280 nm. The labeled peptide **15** was separated using size exclusion chromatography and lyophilized to yield a blue amorphous product. Finally, lanthaligands (Eu-DTPA labeled NDP-α-MSH and CCK-8) were synthesized for competition binding assays as described previously.[20,28]

Receptor Binding Assay in Cells Co-Expressing hMC4R and CCK-2R. In order to assess the binding of htBVLs, a series of three cell lines was established. All cell lines originated from a human embryonic kidney, HEK293, parental cell line and were transfected to express either hMC4R or CCK-2R. Stable surface expression was selected and maintained by growing cells in appropriate selection media. Cell surface expression was validated with immunocytochemistry (data not shown). In order to assess htBVL binding at both receptors simultaneously, HEK293/hMC4R cells were transiently transfected with CCK-2R (referred to here as HEK293/hMC4R/tCCK-2R). High surface expression of CCK-2R was observed 72 h post-transfection, and at this time, the receptor ratio for hMC4R and CCK-2R was approximately 11:1. This time point was used to assess ligand binding to cells with dual expression using a time-resolved fluorescence (TRF) based competitive lanthaligand binding assay.[19,20,29]

The htBVLs were evaluated for monovalent binding in cell lines stably expressing only one of the complementary receptors

(HEK293/hMC4R and HEK293/CCK-2R) and compared to bivalent binding in HEK293/hMC4R/tCCK-2R cells (see Figure 4A for assay scheme, Table 1 for cumulative data, and Figure 2C,D Supporting Information Figure S7 for representative binding curves). The htBVLs **5b**, **8a**, and **12a** with a semirigid Pro-Gly linker, a flexible PEGO linker, and a combination of both, respectively, showed over 20−24-fold enhancement in bivalent binding affinity as compared to monovalent binding (Figure 4B). Enhancement decreased when the length of linker was increased as evident from the series of compounds **5c**−**e**, **8b**, and **12b**−**d**. As expected, when only one receptor was available for binding (i.e., monovalent binding), the IC_{50} values of CCK-(6) and MSH(7) binding motifs in the htBVLs were higher than the parent ligands, Ac-CCK(6)-NH_2 and Ac-MSH(7)-NH_2. This is presumably due to the entropic cost of the linker region. However, once bivalent constructs were able to bind through both ends simultaneously, the IC_{50}'s of CCK ligand decreased, and thus, the binding affinity increased nearly 50-fold, when compared to Ac-CCK(6)-NH_2 peptide (cf. bivalent IC_{50} of 0.5 nM for htBVL **8a** vs 26 nM for Ac-CCK(6)-NH_2). We hypothesize that this was due to a slower off-rate of the htBVL construct in the bivalent binding mode and the enthalpic gain provided by the apparent cooperativity effect from simultaneous binding of the MSH ligand.

Of particular note is the consistent lack of affinity enhancement at the hMC4R (Table 1 and Figure 4C). This phenomenon of enhancement at one receptor but not at the other appears to be related to the receptor expression ratio where only the less abundant receptor shows enhanced binding. At low nM concentration of htBVLs, the lower-abundant CCK-2 receptors get saturated with bound htBVLs and yet occupy only a small fraction of the hMC4R pool (Figure 4D, left). At higher concentrations, only hMC4R remains available for binding (as monovalent); thus, htBVLs exhibit a lack of binding enhancement (Figure 4D, right). Further, the phenomenon here may reflect the ligands' binding to "low affinity states" of the more abundantly expressed receptor, once all the high affinity states have been occupied in these overexpressed systems.[30] The results display a similar trend as was seen earlier with the δ-opioid receptor (δ-OR)/hMC4R co-expression system (6:1 receptor ratio), where a 50-fold maximum enhancement was noticed again only at the lower-abundant receptor (hMC4R in this case).[14] Therefore, irrespective of the receptor pairs investigated in our studies, the reversal of the MSH(7) binding pattern in these two systems clearly shows that the effect was not linked to a particular receptor, nor was it ligand-dependent. Similarly, in our latest studies with the hMC4R/CCK-2R system with opposite receptor ratio (CCK-2R/hMC4R = 2:1), no binding enhancement was observed on CCK-2R, but up to 80-fold enhancement was seen for the hMC4R, the lower-abundant receptor in this case (data not shown).

The aim of systematically studying linker lengths in this and our previous study on hMC4R/δOR[14] was twofold: (a) to estimate a general length requirement for cross-linking any two receptors with the type of linkers used here and (b) to test the broad applicability of rigid, flexible, or semirigid linkers when different receptor pairs are considered. Notably, the estimated inter-receptor distance of 25 ± 10 Å from GPCR modeling studies generally fits well with predicted linker lengths in the three best compounds here and is in agreement with reports in the literature[31] (although slightly longer linker requirement was noticed with hMC4R/δOR system). Though PEGO-[PG]*n*-PEGO linker provided no additional gain in affinity enhancement than the [PG] or PEGO linkers alone, it was observed to cross-link the receptors at shorter [PG] lengths in both hMC4R/CCK-2R and hMC4R/δOR systems. Thus, from our studies conducted so far, PEGO-[PG]*n*-PEGO, where n = 3 or 6, seems to be adequate for initial investigation of optimized linkers for any cell-surface receptor pair. Further, the use of shorter [PG] sequences and flexible PEGO chains aid in synthetic ease and solubility of compounds.

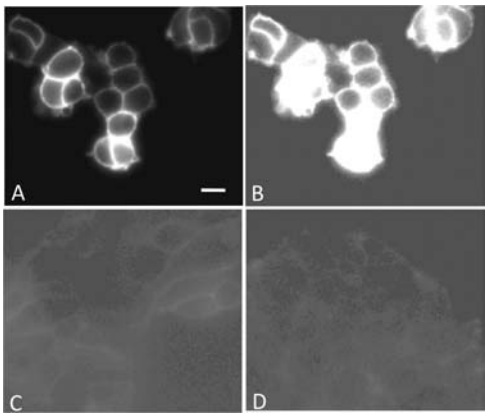

Figure 5. Cell-surface labeling with the Cy5 conjugated htBVL **15**. (A,B) Binding of Cy5-labeled htBVL **15** (0.2 nM) to cells expressing both hMC4R and CCK-2R. (C) Binding of **15** (0.2 nM) to cells expressing CCK-2R only. (D) Binding of **15** (0.8 nM) to cells expressing hMC4R only. Image (B) is the same as (A) with contrast and background set to levels shown in (C) and (D) to highlight and compare absolute levels of binding between dual receptor-expressing cells and monoreceptor expressing cells. The intensity differential underscores the utility of targeting receptor combinations to enhance specificity of binding of the imaging/therapeutic agent to tumor cells. Scale bar = 25 μM.

It must be emphasized here that whereas enhancement through cross-linking two subsites on a protein (*subsite effect*) or through *chelate effect* (e.g., vancomycin model) can be three or more orders of magnitude,[32,33] synthetic multivalent effectors binding multiple cell-surface proteins have exhibited much smaller improvements. The enhancement through (homo)bivalency has been reported to be generally 1−2 orders of magnitude.[3,4,31,34] This is presumably due to the different on-/off-rates of the individual binding events relative to the limiting diffusion rates of receptors across the membrane. Also, it is notable that the lack of affinity enhancement on the more abundant receptor does not invalidate our model to achieve specificity using receptor combinations. The goal of increased affinity was shown by the CCK(6) binding data for hMC4R > CCK-2R expression system, and by MSH(7) binding data for δ-OR > hMC4R.[14] Nonetheless, the results are mechanistically revealing, i.e., since the avidity changes were inferred from the measurement of affinity changes at each ligand motif by competition assays, the observed effect is an attribute of the assay scheme used. Labeled ligands, on the other hand, should display enhanced bivalent avidity on both receptor sites, as demonstrated below.

Microscopic Observation of Cell-Surface Labeling using the Cy5 Conjugated htBVL 15. In order to confirm the bivalent binding of these multivalent constructs and test the targeting specificity, a fluorescently labeled htBVL **15** was synthesized and evaluated for differential labeling of cells expressing one or two receptor types. The htBVL **12a**, the most promising compound

in the series, was modified in the linker region to incorporate a Cy5 dye (far-red emission profile) yielding htBVL **15**. This ligand was chosen as a template since the attachment of label in between the PEGO and [PG] linker units provides necessary spacing of the label from the ligands, thus minimizing any influence on ligand binding. Figure 5A,B shows cell-surface labeling of cells expressing both hMC4R and CCK-2R at a ligand concentration of 0.2 nM. Figure 5C shows labeling of cells expressing CCK-2R only (at 0.2 nM). Figure 5D shows labeling of cells expressing hMC4R only (at 0.8 nM). The labeled ligand bound to the dual-expressing cells with high avidity, as demonstrated by the high fluorescence intensity even at subnanomolar concentrations (Figure 5A). Moreover, the ligand displayed weak binding to the cell lines expressing only single receptor at these concentrations (compare Figure 5C,D with B with same contrast scale). Since only cells that expressed both receptors bound the multivalent ligand with high affinity (Table 1), the enhanced labeling must be characteristic of dual receptor expression and bivalent cross-linking. These imaging data provide a direct visualization of the binding results and a clear demonstration that the labeled htBVL bound rapidly with relatively high avidity and with enhanced specificity to target cells that expressed the complementary receptor combination.

CONCLUSION

In summary, this study demonstrated that htBVLs targeted to two heterologous receptors—MSH and CCK receptors—were able to simultaneously bind them resulting in avidity enhancement. The optimized heterobivalent constructs exhibited higher "apparent" affinities (20−24-fold increase and low nanomolar range affinities, 0.5−10 nM) on cells expressing both receptors, when compared to their binding on cells with only one of the receptor. It is our contention that htBVL will specifically target cells expressing the two-receptor combination when applied at low (nM) concentrations. This is clearly borne out from studies with the Cy5 labeled htBVL **15**, which showed high avidity and specificity to dual-expressing cells at subnanomolar concentrations (0.2−0.8 nM). The observed affinity gain is most likely the result of clustering of receptors (*cluster effect*).[35] Note that the concept presented here is fundamentally different in nature and purpose from the bispecific (or bifunctional) ligands reported in literature,[31] which are often overlapping pharmacophores or two pharmacophore units connected via very short linkers. Using a "receptor combination approach", payloads attached to multivalent ligands could be targeted to cell surface receptor combinations that are expressed in cancer but are absent in normal cells.[13] These payloads could be cell-specific toxins ("magic bullets") or could have more regional effects ("smart bombs"). We believe this approach can provide novel targets and agents for various malignancies that are currently not feasible with single-receptor approaches. This may also address some of the serious concerns with conventional approaches, e.g., it is rare that the target protein is expressed only in the aberrant cells, few good single protein targets have been identified, and the fact that the expression of a single target is heterogeneous in many cancers.[12] Although much remains to be studied regarding the behavior of these ligands and receptor combinations in terms of bioavailability, immunogenicity (albeit the ligands are relatively smaller in size as compared to antibodies), internalization properties, receptor densities, lateral diffusion of receptors, etc., the present data indicate that these combinations should provide a remarkably higher degree of cell-surface differentiation, and must be further explored. To this end, our current studies are directed toward the *in vivo* potential of this approach with the receptor systems described here.

ASSOCIATED CONTENT

Supporting Information. Additional experimental data and details can be found in Table S1 and Figures S1−S7. This material is available free of charge via the Internet at http://pubs.acs.org.

AUTHOR INFORMATION

Corresponding Author

*Prof. Robert J. Gillies, Departments of Radiology, H. Lee Moffitt Cancer Center, 12902 Magnolia Drive, Tampa, FL 33612, USA. Phone: (813) 451-4594; Fax: (813) 745-6855; E-mail: robert.gillies@moffitt.org.

ACKNOWLEDGMENT

We thank Ms. Lucinda Begay, Mrs. Renata Patek, and Ms. Tiffany Bialis for HPLC and technical assistance. This work was supported by grants R33 CA 95944 and RO1 CA 97360 from the National Cancer Institute.

ABBREVIATIONS

AFU, Arbitrary Fluorescence Units; AMBER, Assisted Model Building Energy Refinement; CCK-2R, Cholecystokinin Receptor subtype 2; CCK-6, Nle-Gly-Trp-Nle-Asp-Phe-NH_2; CCK-8, Asp-Tyr-Nle-Gly-Trp-Nle-Asp-Phe-NH_2; CD, Circular Dichroism; CDI, N,N′-carbonyldiimidazolide; Cy5, Cyanine 5 dye; δ-OR, delta-opioid receptor; DCM, dichloromethane; DIC, N,N′-diisopropylcarbodiimide; DIEA, diisopropylethylamine; DMF, N,N′-dimethylformamide; DMSO, dimethylsulfoxide; DTPA, diethylenetriamine-N^1,N^2,N^3,N^4-pentaacetic acid; ESI-MS, Electrospray ionization - mass spectrometry; FT-ICR, Fourier Transform - Ion Cyclotron Resonance; HBTU, 2-(1H-benzotriazol-1-yl)-1,1,3,3-tetramethyluronium hexafluoro-phosphate; HEK, human embryonic kidney; hMC4R, human melanocortin-4-receptor; HOBt, N-hydroxybenzotriazole; HOCt, 6-chloro-1H-hydroxybenzotriazole; htBVL, heterobivalent ligands; htMVL, heteromultivalent ligand; MALDI, Matrix Assisted Laser Desorption Ionization - Time of Flight; MD, Molecular Dynamics; MMFF, Merck Molecular Force Field; MSH, melanocyte-stimulating hormone; MSH-7, Ser-Nle-Glu-His-DPhe-Arg-Trp; Mtt, N-methyltrityl; NDP-α-MSH, Ac-Ser-Tyr-Ser-Nle-Glu-His-DPhe-Arg-Trp-Gly-Lys-Pro-Val-NH_2; NHS, N-hydroxysuccinimide; OPLS, Optimized Potentials for Liquid Simulations; PEGO, 19-amino-5-oxo-3,10,13,16-tetraoxa-6-azanonadecan-1-oic acid; RP-HPLC, reverse-phase high performance liquid chromatography; SPPS, solid-phase peptide synthesis; SD, stochastic dynamics; THF, tetrahydrofuran; TFA, trifluoroacetic acid; TRF, time-resolved fluorescence

REFERENCES

(1) Hornick, C. L., and Karush, F. (1972) Antibody affinity. III. The role of multivalance. *Immunochemistry 9*, 325–340.

(2) Mammen, M., Choi, S.-K., and Whitesides, G. M. (1998) Polyvalent interactions in biological systems: Implications for design and use of multivalent ligands and inhibitors. *Angew. Chem., Int. Ed. 37*, 2754–2794.

(3) Handl, H. L., Sankaranarayanan, R., Josan, J. S., Vagner, J., Mash, E. A., Gillies, R. J., and Hruby, V. J. (2007) Synthesis and evaluation of bivalent NDP-alpha-MSH(7) peptide ligands for binding to the human melanocortin receptor 4 (hMC4R). *Bioconjugate Chem. 18*, 1101–9.

(4) Vagner, J., Handl, H. L., Gillies, R. J., and Hruby, V. J. (2004) Novel targeting strategy based on multimeric ligands for drug delivery and molecular imaging: homooligomers of alpha-MSH. *Bioorg. Med. Chem. Lett. 14*, 211–5.

(5) Kiessling, L. L., Gestwicki, J. E., and Strong, L. E. (2006) Synthetic multivalent ligands as probes of signal transduction. *Angew. Chem., Int. Ed. 45*, 2348–2368.

(6) Sharma, S. D., Granberry, M. E., Jiang, J., Leong, S. P., Hadley, M. E., and Hruby, V. J. (1994) Multivalent melanotropic peptide and fluorescent macromolecular conjugates: new reagents for characterization of melanotropin receptors. *Bioconjugate Chem. 5*, 591–601.

(7) Sharma, S. D., Jiang, J., Hadley, M. E., Bentley, D. L., and Hruby, V. J. (1996) Melanotropic peptide-conjugated beads for microscopic visualization and characterization of melanoma melanotropin receptors. *Proc. Natl. Acad. Sci. U. S. A. 93*, 13715–20.

(8) Kiessling, L. L., Gestwicki, J. E., and Strong, L. E. (2000) Synthetic multivalent ligands in the exploration of cell-surface interactions. *Curr. Opin. Chem. Biol. 4*, 696–703.

(9) Ghaghada, K. B., Saul, J., Natarajan, J. V., Bellamkonda, R. V., and Annapragada, A. V. (2005) Folate targeting of drug carriers: a mathematical model. *J. Controlled Release 104*, 113–28.

(10) Saul, J. M., Annapragada, A., Natarajan, J. V., and Bellamkonda, R. V. (2003) Controlled targeting of liposomal doxorubicin via the folate receptor *in vitro*. *J. Controlled Release 92*, 49–67.

(11) Caplan, M. R., and Rosca, E. V. (2005) Targeting drugs to combinations of receptors: a modeling analysis of potential specificity. *Ann. Biomed. Eng. 33*, 1113–24.

(12) Gillies, R. J., and Hruby, V. J. (2003) Expression-driven reverse engineering of targeted imaging and therapeutic agents. *Expert Opin. Ther. Targets 7*, 137–9.

(13) Balagurunathan, Y., Morse, D. L., Hostetter, G., Shanmugam, V., Stafford, P., Shack, S., Pearson, J., Trissal, M., Demeure, M. J., Von Hoff, D. D., Hruby, V. J., Gillies, R. J., and Han, H. (2008) Gene expression profiling-based identification of cell-surface targets for developing multimeric ligands in pancreatic cancer. *Mol. Cancer. Ther. 7*, 3071–80.

(14) Vagner, J., Xu, L., Handl, H. L., Josan, J. S., Morse, D. L., Mash, E. A., Gillies, R. J., and Hruby, V. J. (2008) Heterobivalent ligands crosslink multiple cell-surface receptors: the human melanocortin-4 and delta-opioid receptors. *Angew. Chem., Int. Ed. 47*, 1685–8.

(15) We have coined the term "lanthaligand" to denote a lanthanide chelate labeled ligand. See Josan, J. S. (2008) Heteromultivalent ligands directed targeting of cell-surface receptors - Implications in cancer diagnostics & therapeutics, Ph.D. Thesis, The University of Arizona, Tucson.

(16) Josan, J. S., Vagner, J., Handl, H. L., Sankaranarayanan, R., Gillies, R. J., and Hruby, V. J. (2008) Solid-phase synthesis of heterobivalent ligands targeted to melanocortin and cholecystokinin receptors. *Int. J. Pept. Res. Ther. 14*, 293–300.

(17) Mohamadi, F., Richards, N. G. J., Guida, W. C., Liskamp, R., Lipton, M., Caufield, C., Chang, G., Hendrickson, T., and Still, W. C. (1990) Macromodel - an integrated software system for modeling organic and bioorganic molecules using molecular mechanics. *J. Comput. Chem. 11*, 440–467.

(18) Li, J., Edwards, P., Burghammer, M., Villa, C., and Schertler, G. (2004) Structure of bovine rhodopsin in a trigonal crystal form. *J. Mol. Biol. 343*, 1409–1438.

(19) Xu, L., Vagner, J., Josan, J. S., Lynch, R. M., Morse, D. L., Baggett, B., Han, H., Mash, E. A., Hruby, V. J., and Gillies, R. J. (2009) Enhanced targeting with heterobivalent ligands. *Mol. Cancer Ther. 8*, 2356–2365.

(20) Handl, H. L., Vagner, J., Yamamura, H. I., Hruby, V. J., and Gillies, R. J. (2004) Lanthanide-based time-resolved fluorescence of *in cyto* ligand−receptor interactions. *Anal. Biochem. 330*, 242–250.

(21) Handl, H. L., and Gillies, R. J. (2005) Lanthanide-based luminescent assays for ligand-receptor interactions. *Life Sci. 77*, 361–371.

(22) Carnie, S., Israelachvili, J. N., and Pailthorpe, B. A. (1979) Lipid packing and transbilayer asymmetries of mixed lipid vesicles. *Biochim. Biophys. Acta 554*, 340–57.

(23) Hadac, E. M., Ji, Z., Pinon, D. I., Henne, R. M., Lybrand, T. P., and Miller, L. J. (1999) A peptide agonist acts by occupation of a monomeric G protein-coupled receptor: dual sites of covalent attachment to domains near TM1 and TM7 of the same molecule make biologically significant domain-swapped dimerization unlikely. *J. Med. Chem. 42*, 2105–11.

(24) Fourmy, D., Escrieut, C., Archer, E., Galès, C., Gigoux, V., Maigret, B., Moroder, L., Silvente-Poirot, S., Martinez, J., Fehrentz, J. A., and Pradayrol, L. (2002) Structure of cholecystokinin receptor binding sites and mechanism of activation/inactivation by agonists/antagonists. *Pharmacol. Toxicol. 91*, 313–20.

(25) Handl, H. L., Vagner, J., Han, H., Mash, E. A., Hruby, V. J., and Gillies, R. J. (2004) Hitting multiple targets with multimeric ligands. *Expert Opin. Ther. Targets 8*, 565–86.

(26) Vagner, J., Handl, H. L., Monguchi, Y., Jana, U., Begay, L. J., Mash, E. A., Hruby, V. J., and Gillies, R. J. (2006) Rigid linkers for bioactive peptides. *Bioconjugate Chem. 17*, 1545–50.

(27) Ladokhin, A. S., Selsted, M. E., and White, S. H. (1999) CD spectra of indolicidin antimicrobial peptides suggest turns, not polyproline helix. *Biochemistry 38*, 12313–12319.

(28) Reubi, J. C., Waser, B., Schaer, J. C., Laederach, U., Erion, J., Srinivasan, A., Schmidt, M. A., and Bugaj, J. E. (1998) Unsulfated DTPA- and DOTA-CCK analogs as specific high-affinity ligands for CCK-B receptor-expressing human and rat tissues *in vitro* and *in vivo*. *Eur. J. Nucl. Med. 25*, 481–490.

(29) Handl, H. L., Vagner, J., Yamamura, H. I., Hruby, V. J., and Gillies, R. J. (2005) Development of a lanthanide-based assay for detection of receptor−ligand interactions at the δ-opioid receptor. *Anal. Biochem. 343*, 299–307.

(30) Huang, J., Dong, L., and Lebreton, G. (2006) Mass-dependent signaling between G protein coupled receptors. *Cell. Signal 18*, 564–576.

(31) Portoghese, P. S. (2001) From models to molecules: opioid receptor dimers, bivalent ligands, and selective opioid receptor probes. *J. Med. Chem. 44*, 2259–69.

(32) Rao, J., Lahiri, J., Isaacs, L., Weis, R. M., and Whitesides, G. M. (1998) A trivalent system from vancomycin. DAla-DAla with higher affinity than avidin.biotin. *Science 280*, 708–11.

(33) Shrivastava, A., Von Wronski, M., Sato, A., Dransfield, D., Sexton, D., Bogdan, N., Pillai, R., Nanjappan, P., Song, B., Marinelli, E., Deoliveira, D., Luneau, C., Devlin, M., Muruganandam, A., Abujoub, A., Connelly, G., Wu, Q., Conley, G., Chang, Q., Tweedle, M., Ladner, R., Swenson, R., and Nunn, A. (2005) A distinct strategy to generate high-affinity peptide binders to receptor tyrosine kinases. *Protein Eng. Des. Sel. 18*, 417–424.

(34) Carrithers, M. D., and Lerner, M. R. (1996) Synthesis and characterization of bivalent peptide ligands targeted to G-protein-coupled receptors. *Chem. Biol. 3*, 537–42.

(35) Zheng, Y., Akgün, E., Harikumar, K. G., Hopson, J., Powers, M. D., Lunzer, M. M., Miller, L. J., and Portoghese, P. S. (2009) Induced Association of μ Opioid (MOP) and Type 2 Cholecystokinin (CCK 2) Receptors by Novel Bivalent Ligands. *J. Med. Chem. 52*, 247–258.

Supporting information

Cell-Specific Targeting by Heteromultivalent Ligands

Jatinder S. Josan, Heather L. Handl, Rajesh Sankaranarayanan, Liping Xu, Ronald M. Lynch, Josef Vagner, Eugene A. Mash, Victor J. Hruby and Robert J. Gillies

CONTENTS

Abbreviations S2
Materials S2
Solid-phase peptide synthesis S2
HPLC analysis, size exclusion chromatography, solid phase extraction, and peptide conc. determination S4
Mass spectrometry S4
Molecular modeling S4
Circular dichroism S5
Cloning, transfection and cell culture S5
Receptor number determination S5
Lanthanide based binding assays S5
Cell-surface labeling S6
Table S1. HPLC & MS data S7
Figure S1. HPLC profile of htBVL **8a** S8
Figure S2. ESI-MS of compound **8a** S9
Figure S3. GPCR modeling S12
Figure S4. Molecular modeling S10
Figure S5. CD study on poly(Pro-Gly) linker S11
Figure S6. Receptor number determination S13
Figure S7. Representative binding curves S14
References S15

EXPERIMENTAL SECTION

Abbreviations:

Abbreviations used for amino acids and designation of peptides follow the rules of the IUPAC-IUB Commission of Biochemical Nomenclature in *J. Biol. Chem.* **1972**, *247*, 977-983. The following additional abbreviations are used: AMBER, Asisted Model Building Energy Refinement; Boc, tert-butyloxycarbonyl; *t*Bu, tert-butyl; CCK-2R, Cholecystokinin Receptor subtype 2; CCK-6, Nle-Gly-Trp-Nle-Asp-Phe-NH_2; CCK-8, Asp-Tyr-Nle-Gly-Trp-Nle-Asp-Phe-NH_2; CD, Circular Dichroism; CDI, N,N'-carbonyldiimidazolide; CH_3CN, acetonitrile; Cy5, Cyanine 5 dye; δ-OR, delta-opioid receptor; DCM, dichloromethane; DIC, N,N'-diisopropylcarbodiimide; DIEA, diisopropylethylamine; DMEM, Dulbecco's Modified Eagle Medium; DMF, N,N'-dimethylformamide; DMSO, dimethylsulfoxide; DTPA, diethylenetriamine-N^1,N^2,N^3,N^4-pentaacetic acid; ESI-MS, Electrospray ionization - mass spectrometry; Et_2O, Diethyl ether; Fmoc, (9H-fluoren-9-ylmethoxy)carbonyl; FT-ICR, Fourier Transform - Ion Cyclotron Resonance; HBTU, 2-(1H-benzotriazol-1-yl)-1,1,3,3-tetramethyluronium hexafluoro-phosphate; hMC4R, human melanocortin-4 receptor; HOBt, N-hydroxybenzotriazole; HOCt, 6-chloro-1H-hydroxybenzotriazole; htBVL, heterobivalent ligands; htMVL, heteromultivalent ligand; MALDI, Matrix Assisted Laser Desorption Ionization - Time of Flight; MD, Molecular Dynamics; MMFF, Merck Molecular Force Field; MSH, melanocyte-stimulating hormone; MSH-7, Ser-Nle-Glu-His-DPhe-Arg-Trp; NDP-α-MSH, Ac-Ser-Tyr-Ser-Nle-Glu-His-DPhe-Arg-Trp-Gly-Lys-Pro-Val-NH_2; Mtt, 4-methyltrityl; NHS, N-hydroxysuccinimide; Pbf, 2,2,4,6,7-pentamethyl-dihydrobenzofuran-5-sulfonyl; PEG, Polyethyleneglycol; PEGO, 19-amino-5-oxo-3,10,13,16-tetraoxa-6-azanonadecan-1-oic acid; RP-HPLC, reverse-phase high performance liquid chromatography; SPPS, solid-phase peptide synthesis; SD, stochastic dynamics; THF, Tetrahydrofuran; TFA, trifluoroacetic acid; TRF, time-resolved fluorescence; Trt, triphenylmethyl (trityl).

Materials:

N^{α}-Fmoc protected amino acids, HBTU, and HOBt were purchased from SynPep (Dublin, CA) or from Novabiochem (San Diego, CA). Rink amide Tentagel S resin was acquired from Rapp Polymere (Tubingen, Germany). HOCt, DIC and DIEA were purchased from IRIS Biotech (Marktredwitz, Germany). The following side chain protecting groups were used for the amino acids: Arg(N^g-Pbf); Asp(O-*t*Bu); Glu(O-*t*Bu); His(N^{im}-Trt); Ser(*t*Bu), Trp(N^i-Boc); Lys(N^{ε}-Mtt). Cy5-NHS ester was acquired from Amersham Biosciences (Piscataway, NJ). Diglycolic anhydride and 4,7,10-trioxa-1,13-tridecandediamine were acquired from TCI America (Portland, OR). Peptide synthesis solvents, dry solvents, and solvents for HPLC were reagent grade, were acquired from VWR (West Chester, PA) or Sigma-Aldrich (Milwaukee, WI), and were used without further purification unless otherwise noted. All the peptides were manually assembled using 5 to 50 mL plastic syringe reactors equipped with a frit, and Domino manual synthesizer obtained from Torviq (Niles, MI). The C-18 Sep-Pak™ Vac RC cartdridges for solid phase extraction were purcahsed from Waters (Milford, MA).

Solid-Phase Peptide Synthesis

Peptides were synthesized on Tentagel Rink amide resin (initial loading: 0.2 mmol/g) using N^{α}-Fmoc protecting groups and a standard DIC/HOCt or HBTU/HOBt activation strategy. The resin was swollen in THF for an hour, washed with DMF, and Fmoc protecting group removed with 20% piperidine in DMF (2 min, washing, then 20 min). The resin was washed with DMF (3X), DCM (3X), 0.2 M HOBt in DMF (2X), and finally with DMF (2X) and the first amino acid coupled using pre-activated 0.3 M HOCt ester in DMF (3 eq. of N^{α}-Fmoc amino acid, 3 eq. of HOCt and 6 eq. of DIC). An on-resin test using Bromophenol Blue was used for qualitative and continuous monitoring of reaction progress.[1,2] To avoid deletion sequences and slower coupling rate in longer sequences, the double coupling was performed at all steps with 3 eq. of amino acid, 3 eq. of HBTU and 6 eq. of DIEA in DMF. A third coupling was performed with symmetric anhydride method (2 eq. of amino acid and 1 eq. of DIC in dichloromethane) wherever beads still tested Kaiser positive. Any unreacted NH_2 groups on the resin thereafter were capped using an excess of 50% acetic anhydride in pyridine for 5 min. When the coupling reaction was finished, the resin was washed with DMF, and the same procedure was repeated for the next amino acid until all amino acids were coupled. The PEGO spacers were introduced as described before.[1,3], Briefly, the N-terminal of the peptide on resin was coupled with the glycolic acid spacer using 10 eq. of diglycolic anhydride in DMF for 5 min. The resin was washed with DMF (3X), with the last washing with dry DMF, and the free carboxylic groups were activated using 10 eq. of carbonyldiimidazole in dry DMF for 30 min. The resin was washed with dry DMF (3X), and the PEG diamine coupled using 20 eq. of 4,7,10-trioxa-1,13-tridecanediamine in dry DMF for 30 min (vigorous vortexing for first 5 minutes).

Parallel Library Synthesis: The syntheses of htBVLs **5a** – **12d** consisting of MSH-7 and CCK-6 ligands connected in a head-to-tail fashion by PEGO and/or Pro-Gly linkers are depicted in Scheme S1. Starting with Tentagel Rink amide polystyrene resin (initial loading 0.2 mmol/g), the hexapeptide CCK-6 was constructed and the resin **2** split into two portions. To one portion, a PEGO linker was coupled on the N-terminus. The resin **6a** containing PEGO unit was again proportionally split for the synthesis of compounds **8a-b** and **12a-d**. At this stage, proline and glycine residues were added alternatively for resins **3a-e** and **9a-d**. After the final proline addition for these compounds, the N^{α}-Fmoc protecting group was removed. A second PEGO unit was coupled to the resins for **6b** and **10a-d**. The free amine terminals of all resins were coupled with Fmoc-Trp(Boc)-OH and syntheses continued to complete the MSH-7 sequence, the N^{α}-terminus deprotected, then acetylated to give **4a-e**, **7a-b**, and **11a-d**.

Frequently during the synthetic steps, a small amount of peptide was cleaved and analyzed by HPLC to monitor the

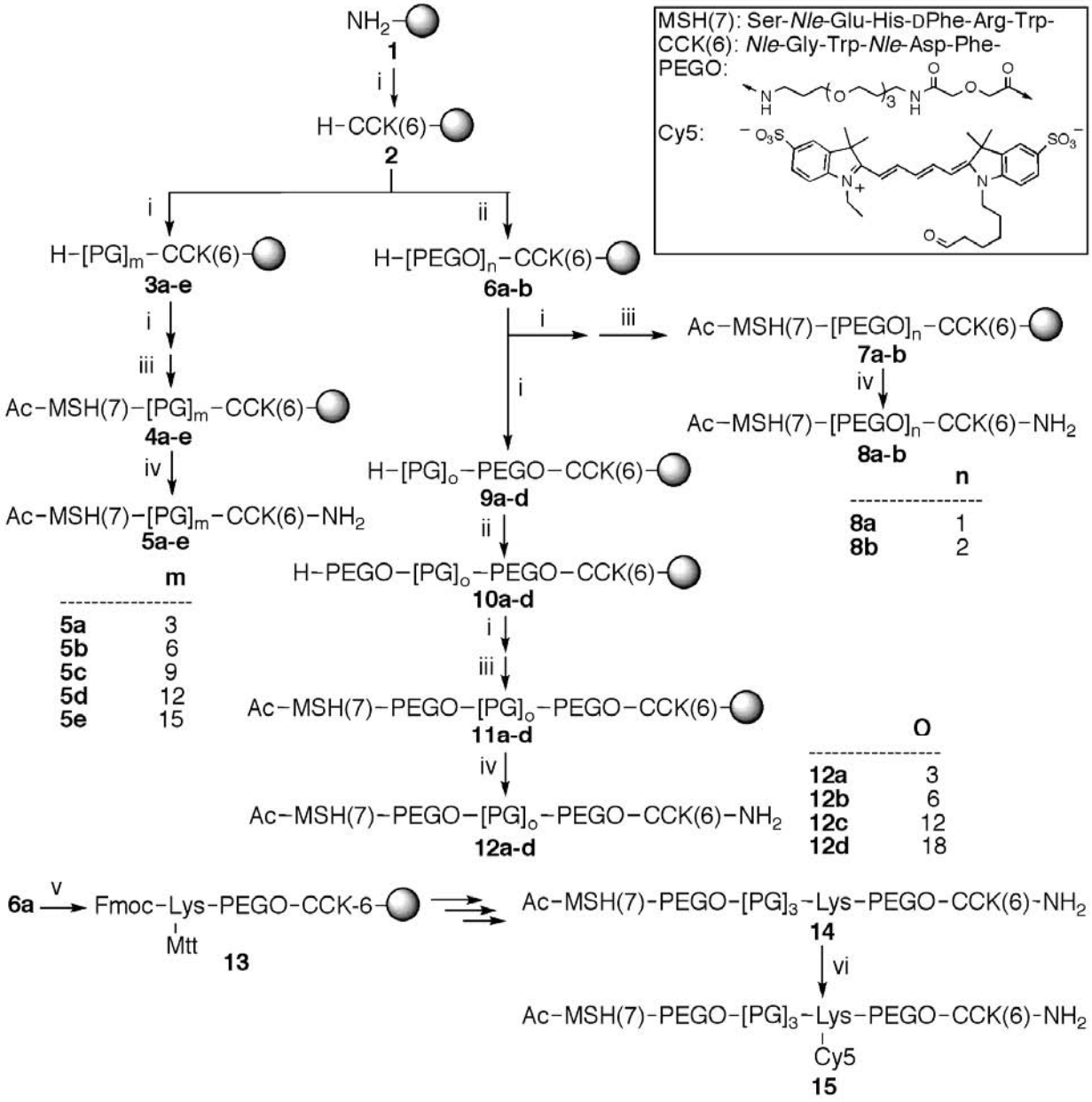

SCHEME S1. Synthetic route for heterobivalent ligands (htBVLs). The inset shows sequence of MSH-7 and CCK-6 ligands, structure of the PEGO linker (20 atoms), and the Cy5 dye with a hexanoyl linker. i. Fmoc/*t*Bu synthesis continued as follows: a) Fmoc-AA-OH (3eq), HOCt (3eq), and DIC (6eq) in DMF (10 mL / 1g of resin) for amino acid couplings; b) Piperidine/DMF (1:4) for Fmoc deprotection; ii. The PEGO linker was assembled as follows: a) Diglycolic anhydride (10eq) in DMF for 5 min, b) CDI (20eq) in anhyd. DMF for 30 min, c) 4,7,10-trioxa-1,13-tridecaneamine (20eq) in anhyd. DMF for 30 min; iii. Ac_2O/Pyridine (1:1) for acetylation (or N-capping); iv. TFA-scavengers cocktail (82.5% trifluoroacetic acid, 5% water, 5% triisopropylsilane, 5% thioanisole, 2.5% ethanedithiol); v. Fmoc-Lys(Mtt)-OH (3eq.), HOCt (3eq.), DIC (6eq.) in DMF; vi. Cy5-NHS ester (1.2 eq.) in DMSO. AA = amino acid.

synthesis and purity of the peptide. The resin was washed with DMF, DCM and THF and dried. A cleavage cocktail (10 mL per 1 g of resin) of TFA (82.5%), water (5%), triisopropylsilane (5%), thioanisole (5%), and ethanedithiol (2.5%) was injected into the resin and stirred for 3 h at room temperature. The crude peptides **5a-e**, **8a-b**, and **12a-d** were isolated from the resin by filtration, the filtrate was reduced to low volume by evaporation using a stream of nitrogen, and the peptides were precipitated in ice-cold diethyl ether, washed several times with ether, dried, dissolved in water and lyophilized to give off-white solid powders that were stored at -20°C until purified. The final compounds were purified by size-exclusion chromatography and RP-HPLC, and characterized by ESI-MS and/or MALDI-TOF and/or FT-ICR. The yields of the crude peptides were 50-80% based on the resin weight gain, and overall, the purified

yields for the syntheses were 5-30% based on the loading of the resin.

The Cy5 label was introduced in the bivalent ligand construct using lysine as a functional handle. After, the first PEGO linker incorporation in resin **6a**, an N^{α}-Fmoc-N^{ε}-Mtt protected lysine was incorporated into the sequence (**13**) and the peptide synthesis continued to the end as above, the peptide was then cleaved from the resin and purified using preparative HPLC to give **14**. For Cy5 labeling, the purified peptide **14** was dissolved in DMSO, 1.2 eq. of commercially available Cy5-NHS ester was added and the reaction was monitored using analytical HPLC at 280 nm. Finally, the labeled peptide was separated using size exclusion chromatography and lyophilized to yield a blue amorphous final product.

The lanthaligands (Eu-DTPA labeled NDP-α-MSH and CCK-8) for screening were synthesized using Fmoc/*t*Bu synthesis as described previously.[4,5] Briefly, the NDP-α-MSH and CCK-8 ligands were synthesized on Tentagel Rink amide resin. After the final amino acid addition, the N-terminal was deprotected and the DTPA chelator was attached to the N-terminus of the peptide using an ε-aminocaproic spacer. Using an *in situ* HOBt ester method, DTPA dianhydride was treated with HOBt for 20 min to obtain di-HOBt ester, which was coupled to the free ε-amino groups on resin. After cleavage, the peptides were purified by reverse-phase HPLC and chelate labeled with Eu(III) chloride in neutral pH buffer. The excess of metal salt was removed by solid-phase extraction (SPE). The purified products were characterized using high resolution ESI-MS and/or MALDI-TOF and/or FT-ICR.

HPLC Analysis, Size Exclusion Chromatography, Solid Phase Extraction and Peptide Conc. Determination:

The purity of final products was analyzed using Waters high-performance liquid chromatography (HPLC) apparatus and with a Vydac C18 reverse phase column (dia × length: 4.6 mm × 150 mm, pore size: 3 μm). Buffer A was with 0.1% TFA in water and buffer B was 0.1% TFA in acetonitrile. Peptides were analyzed using a linear gradient of buffer B under various gradient conditions at a flow rate of 0.3 - 1 mL/min and the separations monitored at 220 and 280 nm. Purification of compounds was achieved using a Waters 600 HPLC apparatus equipped with a Vydac C18 reverse phase column (22 × 250 mm, 5μm) with similar buffers and under optimized gradients and 3 - 10 mL/min flow rate, and monitored at 230 and 280 nm (see Table S1 for characterization data and Figure S1a for an example).

Size exclusion chromatography was performed on a borosilicate glass column (2.6 × 250 mm, Sigma, St. Louis, MO) filled with medium sized Sephadex G-25 or G-10. The compounds were eluted with an isocratic flow of 1.0 M aqueous acetic acid.

Solid-Phase Extraction (SPE) was employed where simple isolation of final compound was needed from excess salts and buffers for e.g., lanthaligand synthesis. For this purpose, C-18 Sep-Pak™ cartridges (100 mg or 500 mg) were used and pre-conditioned initially with 5 column volumes (5 times the volume of packed column bed) each of acetonitrile, methanol, and water, in that order. After loading the compound, the column was washed several times with water, and then gradually with 5, 10, 20, 30, 50, and 70% of aqueous acetonitrile to elute the peptide.

The peptide concentrations were determined by monitoring absorbance of peptides against 0.5 mM solution of Tryptophan (D or L) in DMSO at 280 nm. The peptides were initially dissolved in DMSO at approximately 1-5 mM concentration. Co-injections of peptide and Trp were made on analytical HPLC with a number of different volumes and peptide concentration calculated from area under the peaks (see Figure S1b for an example) using the formula given here:

$$\text{Peptide Conc.} = \frac{[\text{Abs. of Comp.}]}{[\text{Abs. of Trp}]} \times \frac{0.5}{\frac{\sum \varepsilon_{280}(\text{Trp} + \text{Tyr} + \text{Cys} + \text{Cy5} + \ldots)}{\varepsilon_{280}(\text{Trp})}} \times \frac{\text{Vol. of Trp}}{\text{Vol. of Comp.}}$$

where ε_{280} of compounds were determined by summation of tryptophans (ε_{280} = 5500), Cy5 dye (ε_{280} = 5800), and normalized to extinction coefficient of one tryptophan. Other amino acids in these peptides do not absorb significantly at this wavelength. For Cy5 dye, ε_{280} was determined in a similar manner by comparing the absorbances of 0.5 mM of both Trp and Cy5-NHS ester in DMSO at 280 nm wavelength.

Mass Spectrometry:

Mass spectra of positive ions were recorded either with a single stage reflectron MALDI-TOF mass spectrometer (Bruker Rexlex III, Bruker Daltonics, Billerica, MA; α-cyanocinnamic acid as a matrix) in reflectron mode or with a low resolution ESI mass spectrometer (Finnigan, Thermoquest LCQ ion trap instrument, Lake Forrest, CA) and/or using high resolution Fourier transform mass spectrometer (FT-ICR MS, Bruker Apex Qh, Bremen, Germany) equipped with an ESI source. For internal calibration, an appropriate mixture of standard peptides was used with an average resolution of *ca.* 10,000 on the Reflex III and 60,000 on the FT-ICR instrument (see Figure S2 for an example).

Molecular Modeling:

Conformational searches and molecular dynamics were performed with Macromodel version 9.1 implemented under Maestro 7.5 interface on a Linux workstation. The MacroModel implementations of Merck Molecular Force Field (MMFF), AMBER* and OPLS all-atom force fields were used.[6] AMBER* is a reparametrized AMBER force field containing a new set of torsional parameters that more closely reproduces *ab initio* calculations on the conformational preferences of simple peptides.[7] For solution phase calculations, the GB/SA continuum model for water was used. Amide bonds were required to be *trans* except in case of prolines whose imide bonds were intentionally sampled and accepted with either *cis* or *trans* geometry in the conformational searches. Conformational searches were performed with systematic Monte Carlo method of Goodman and Still.[8] For each search, 5000 starting structures were generated and minimized until the gradient was less than 0.05 kJ/mol/Å, using the truncated Newton-Raphson method implemented in MacroModel. Duplicate conformations and

those with energy greater than 50 kJ/mol above the global minimum were discarded.

All molecular dynamic simulations were performed at 310°K with Monte Carlo/Stochastic Dynamics (MC/SD) hybrid simulation algorithm[9] with either the AMBER* all-atom force field or the new OPLS-2005 force field in MacroModel 9.1. A time step of 1.5 fs was used for the stochastic dynamics (SD) part of the algorithm. The MC part of the algorithm used random torsional rotations between ± 60° and ± 180° that were applied to all rotatable bonds except the proline imide C-N bond where the random rotations between ± 90° and ± 180° were applied. No torsion rotations were applied to bonds in the pyrrolidine ring of proline as the barriers are low enough to permit adequate sampling from the SD part of the simulation. The total simulation time was up to 20,000 ps and samples were taken at 1 ps interval, yielding appropriate number of conformations for analysis. This analysis is represented in Figure S4.

For G-Protein Coupled Receptor size estimations, the PDB file of a recently described bovine rhodopsin protein in a trigonal crystal form (1GZM)[10] was loaded into PyMOL program (www.pymol.org). Several residues on the outer edges of the transmembrane domain were chosen and distances across the GPCR were measured. The "width" of the GPCR was taken as the average of 8 of these measured distances. Similarly, the homology modeled GPCR structures of hMC4R and CCK-2R were downloaded from www.gpcr.org and the distance of the binding pocket from the edge of the receptor and the depth of the binding pocket were determined. The residues forming the binding pocket were taken as available from the literature. This analysis is represented in Figure S3.

Circular Dichroism:

CD measurements were carried out using a JASCO J-720 spectrometer equipped with a water-jacketed cuvette holder. Data were collected with a quartz cuvette of 2 mm path length, from 300 to 185 nm, at 0.5 nm intervals, and with a scan rate of 1 nm per second. The spectra were recorded as an average of at least 3 scans and were corrected by subtracting the solvent/buffer base line contributions. No curve-smoothing procedure was applied. The solvent conditions included water, 95% TFE v/v in water, 95% nPrOH v/v in water, and PBS (phosphate buffered saline) buffer (pH 7.4). The concentration dependence was studied initially for Ac-$[PG]_6$-NH_2 peptide from 1 mM to 10 μM range, and was then kept constant at 100 μM for the rest of the studies. For melting temperature scan in water, a heating rate of 1°C/minute was used and the full CD spectra were collected at 5°C intervals from -10°C to 90°C. Data are presented in molar ellipticities ([θ], deg•cm^2•$dmol^{-1}$) (see Figure S5 for results).

Cloning, Transfection and Cell Culture:

HEK293 cells overexpressing the human melanocortin-4 receptor (hMC4R) were used to assess the binding at the hMC4R. The hMC4R vector was originally received from Dr. Ira Gantz, University of Michigan.[11] The coding region of the hMC4R gene was expressed in pcDNA3.1 (Invitrogen, V790-20). HEK293/hMC4R cells were grown in Dulbecco's Modified Eagle Medium (DMEM) supplemented with 10% FBS. Monovalent CCK binding was tested on HEK293 cells with stable expression of CCK-2 receptor. These cells were grown in DMEM supplemented with 10% FBS and were maintained under selection with 100 μg/mL Zeocin. Evaluation of bivalent ligand binding was completed on HEK293/hMC4R cells with transient expression of CCK-2R (referred to as HEK293/hMC4R/tCCK cells). For transient receptor expression, cells were plated at a density of 10,000 cells/ well in Wallac B&W Isoplate TC (Wallac/PerkinElmer, 1450-583) 96-well plates. The day after plating, cells were transfected with CCK-2R using FuGENE 6 Transfection Reagent (Roche, 1814-443). A 3:1 ratio of FuGENE to DNA was used, as per reagent protocol. Reagents (30 μL media, 0.15 μL FuGENE 6, and 0.05 μg CCK-2R DNA per well) were added to a sterile microtube and incubated at room temp for 15 min. The media used during the incubation was antibiotic free, serum free DMEM. After the 15 min incubation, the reaction mixture (30 μL) was added to the cells in their normal media. It was determined that 72 hours post-transfection was optimal for high surface expression of CCK-2R, thus all binding assays were performed 72-hours post-transfection.

Receptor Number Determination:

The number of receptors present on the cell surface was determined through saturation binding analysis followed by correlation of the fluorescent signal achieved at B_{max}. Increasing amounts of Eu-labeled ligand were added to cells until saturation was achieved. For hMC4R, the B_{max} was determined to be 95, 244 ± 2480 AFU (Figure S6a). A standard curve relating fluorescent signal to the concentration of Eu-labeled ligand present in the well was produced (Figure S6b) and used to determine the concentration of Eu-labeled ligand present at saturation. In the case of hMC4R, a signal of 95, 244 AFU correlates with 380 fmol/well. Assuming that during the saturation study that each receptor is bound by a single Eu-labeled ligand, this correlates with 2.29×10^{11} receptors/well. The average number of cells/well was obtained via counting with a hemocytometer and this number (61,840 cells/well, average of 10 determinations) was then used to determine the number of hMC4R receptors per cell. The same process was followed for determining the number of CCK-2R per cell.

Lanthanide Based Binding Assays:

Lanthanide based competitive binding assays were conducted according to the method which has been previously described.[12] As an example, HEK293/hMC4R cells were plated in black and white 96-well isoplates (Wallac, 1450-584) at a density of 12,000 cells/well and were allowed to grow for 3 days. On the day of the experiment, media was aspirated from all wells. 50 μL of non-labeled ligand and 50 μL of Eu-labeled lanthaligand (final concentration of 10 nM for Eu-NDP-α-MSH) were added to each well. Ligands were diluted in binding media (DMEM, 1mM 1,10-Phenanthroline, 200 mg/L Bacitracin, 0.5 mg/L Leupeptin, 0.3% BSA) and samples were tested in quadruplicate, unless otherwise noted. Cells were incubated in the presence of ligands for 1 hr at 37°C. Following

the incubation, cells were washed 3× with 250 μL Wash Buffer (50 mM Tris-HCl, 0.2%BSA, 30 mM NaCl). Enhancement solution (Perkin Elmer; 1244-105) was added (100 μL/well) and the plate was incubated for at least 30 min at 37°C prior to reading. The plates were read on a Wallac VICTOR instrument using the standard Eu TRF measurement (340 nm excitation, 400 μsec delay, and emission collection for 400 μsec at 615 nm). Competition curves were analyzed with GraphPad Prism Software using the sigmoidal dose-response (variable slope) classical equation for non-linear regression analysis. See Figure 2 & S7 for representative binding curves.

Cell-Surface Labeling:

Cells were grown on #1 coverslips harbored in individual wells of six well plates. Individual slides were mounted in a chamber maintained at 37^{o}C on the stage of an inverted Olympus IX70 microscope equipped with a 40X 1.35 NA objective. For excitation of Cy5 fluorescence, white light emitted from a 150W Xe lamp was passed through a 10 nm band pass filter centered at 640 nm. The emitted light was selected using a band pass filter centered at 680 nm, and subsequently imaged onto a CCD camera (Photometrics CH-350; TEK-512 chip). Three control images were acquired at 5 min intervals prior to addition of the labeled htBVL to incubation medium. Immediately following addition of the ligand, images were acquired within 30 sec, 1 min and 3 min, then the media was then replaced with ligand-free medium prior to further image acquisition. Image analysis was performed on a SGI Indy-2 workstation using customized software. See Figure 5 for illustration of specific cell-surface labeling with htBVL **15**.

TABLE S1. HPLC & MS data of Ac-MSH(7)-NH_2, Ac-CCK(6)-NH_2 and heterobivalent ligands **5a** – **15**.

Compound	Mass Calculated[a]	Mass Found	t_R (Purity %)	K'
Ac-MSH(7)-NH_2	1015.5035 $(M+1)^{1+}$	1015.4881[b] $(M+1)^{1+}$	17.0[e] (96)	9.2
Ac-CCK(6)-NH_2	791.4014 $(M+1)^{1+}$	791.1[b] $(M+1)^{1+}$	15.4[f] (96)	7.7
5a ($C_{107}H_{145}N_{27}O_{25}$)	1105.0452 $(M+2)^{2+}$	1105.2[b] $(M+2)^{2+}$	20.3[g] (99)	11.9
5b ($C_{128}H_{175}N_{33}O_{31}$)	1336.1566 $(M+2)^{2+}$	1336.3[b] $(M+2)^{2+}$	19.2[g] (100)	11.3
5c ($C_{149}H_{205}N_{39}O_{37}$)	1045.1786 $(M+3)^{3+}$	1045.1891[c] $(M+3)^{3+}$	18.3[g] (98)	10.8
5d ($C_{170}H_{235}N_{45}O_{43}$)	1199.2529 $(M+3)^{3+}$	1199.2559[c] $(M+3)^{3+}$	18.0[g] (99)	10.6
5e ($C_{191}H_{265}N_{51}O_{49}$)	4059.9942* $(M+1)^{1+}$	4060.5121*[d] $(M+1)^{1+}$	17.7[g] (87)	10.4
8a ($C_{100}H_{141}N_{23}O_{25}$)	1033.0235 $(M+2)^{2+}$	1032.9[b] $(M+2)^{2+}$	21.5[g] (100)	12.7
8b ($C_{114}H_{167}N_{25}O_{31}$)	1192.1129 $(M+2)^{2+}$	1192.0[b] $(M+2)^{2+}$	21.2[g] (100)	12.5
12a ($C_{135}H_{197}N_{31}O_{37}$)	949.1496 $(M+3)^{3+}$	949.2[b] $(M+3)^{3+}$	20.1[g] (100)	11.8
12b ($C_{156}H_{227}N_{37}O_{43}$)	827.6678 $(M+4)^{4+}$	827.6797[c] $(M+4)^{4+}$	26.1[h] (98)	11.4
12c ($C_{198}H_{287}N_{49}O_{55}$)	1058.7792 $(M+4)^{4+}$	1058.7916[c] $(M+4)^{4+}$	25.4[h] (98)	11.0
12d ($C_{240}H_{347}N_{61}O_{67}$)	5156.5621 $(M+1)^{1+}$	5156.5889[d] $(M+1)^{1+}$	24.7[h] (93)	10.7
15 ($C_{174}H_{246}N_{35}O_{45}S_2$)	3610.7478 $(M+1)^{1+}$	903.6916[c] $(M+4)^{4+}$	14.6[f] (96)	5.1

[a] Exact Mass calculated based on the most abundant isotope of the element; * This compound is shown with the exact mass of most abundant peak in the monoisotopic peak pattern; [b] ESI-MS; [c] FT-ICR MS; [d] MALDI-MS; [e] 10-40% B gradient in 30 min; [f] 10-90% B gradient in 30 min; [g] 20-60% B gradient in 50 min; [h] 10-40% B gradient in 50 min; HPLC eluents: Phase A is 0.1% TFA in water; Phase B is 0.1% TFA in acetonitrile; t_R is the retention time of compound peak in HPLC; (purity of final product in percentage is given in parenthesis); K' is retention time of compound peak/retention time of solvent peak.

FIGURE S1. HPLC profile of htBVL 8a. A) HPLC profile of crude compound **8a** at 220 and 280 nm, (B) Peptide concentration determination of compound **8a** using 0.5 mM D-Tryptophan standard (Retention time of 2.4 min) co-injected in analytical HPLC and monitored at 280 nm.

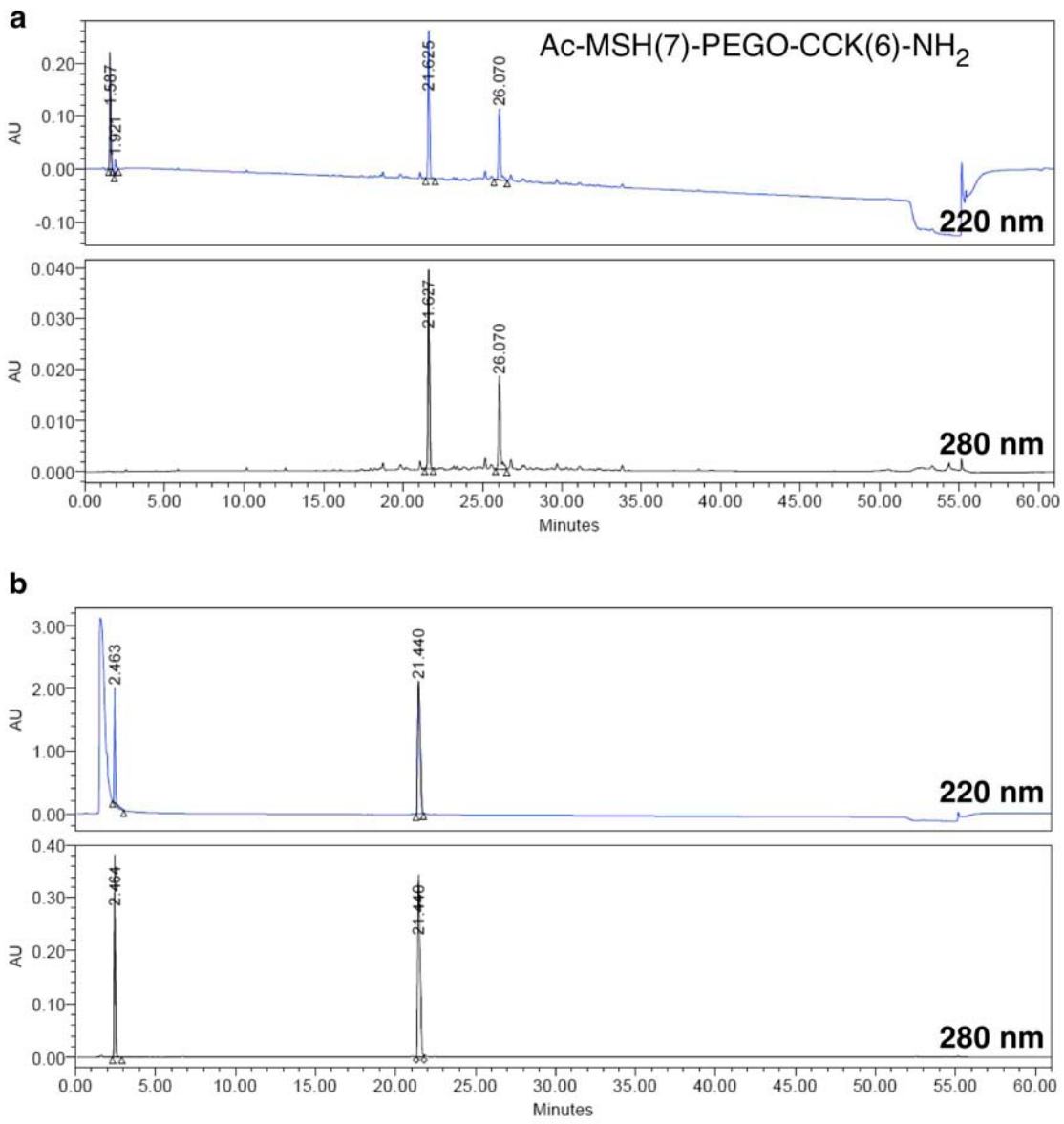

FIGURE S2. ESI-MS of compound **8a**

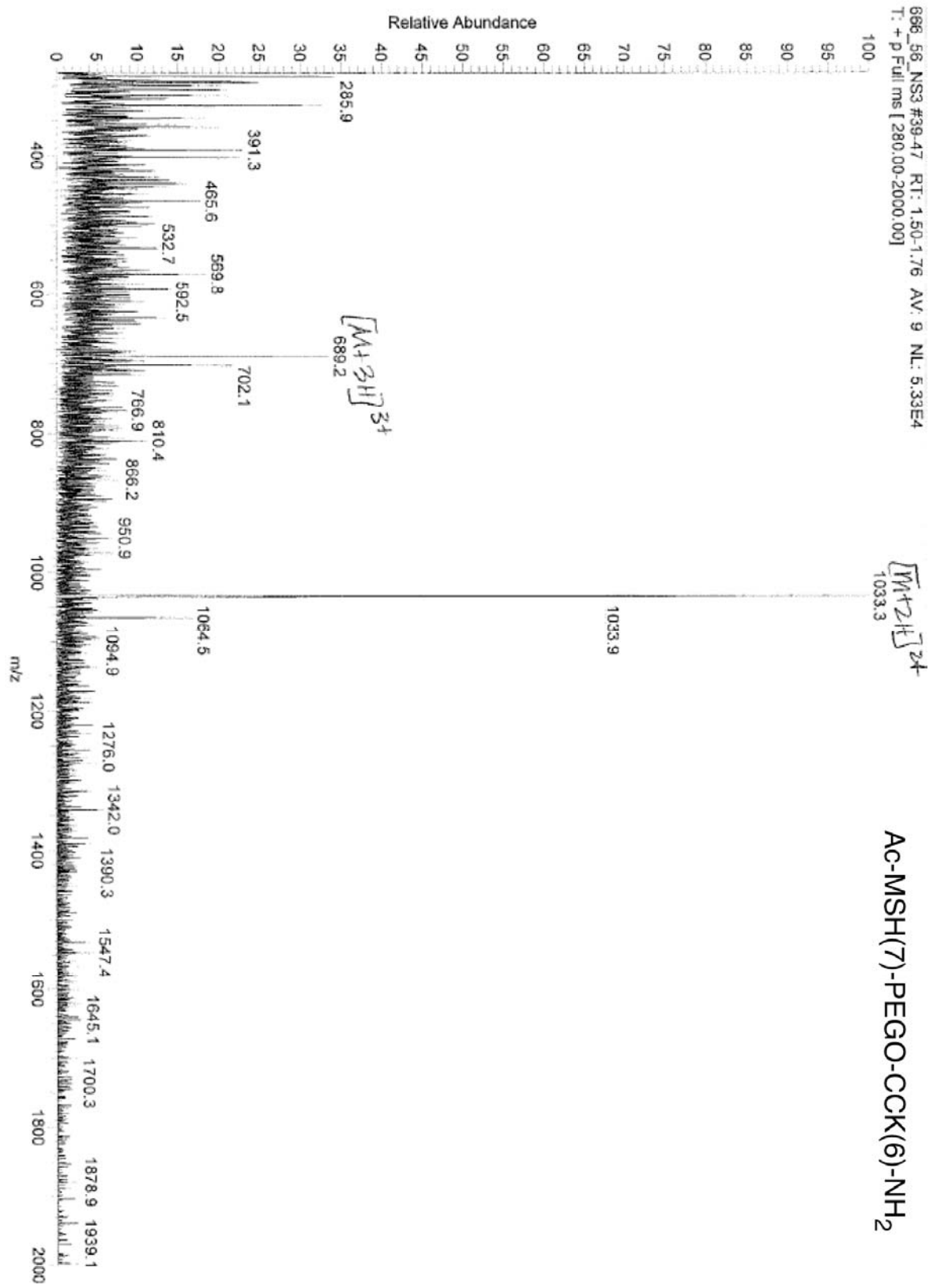

FIGURE S3. GPCR modeling a) PDB file 1GZM loaded in PyMOL software and shows the two GPCR molecules per each asymmetric crystal unit. The end-to-end distance along the longer elliptical axis is ~ 70 □.[10] b) The distance between two adjacent TM4 helices is shown in the picture. Note that this distance is not between the binding pockets as the two GPCRs are oriented head-to-tail, and merely suggests an approximate distance that would be between two off-center binding pockets arranged head-to-head. c) The homology modeled GPCR structure of hMC4R with off-center binding pocket (green surface) and measured distances. d) GPCR dimer orientations. The two receptors can pack in a (*top*) head-to-head, (*middle*) head-to-tail or (*bottom*) tail-to-tail or any number of intermediate orientations. The distance span between the two binding pockets could be up to 50 □ long in a tightly packed dimer. The possibility of domain swapping or involvement of lipid rafts could shorten or lengthen this distance span.

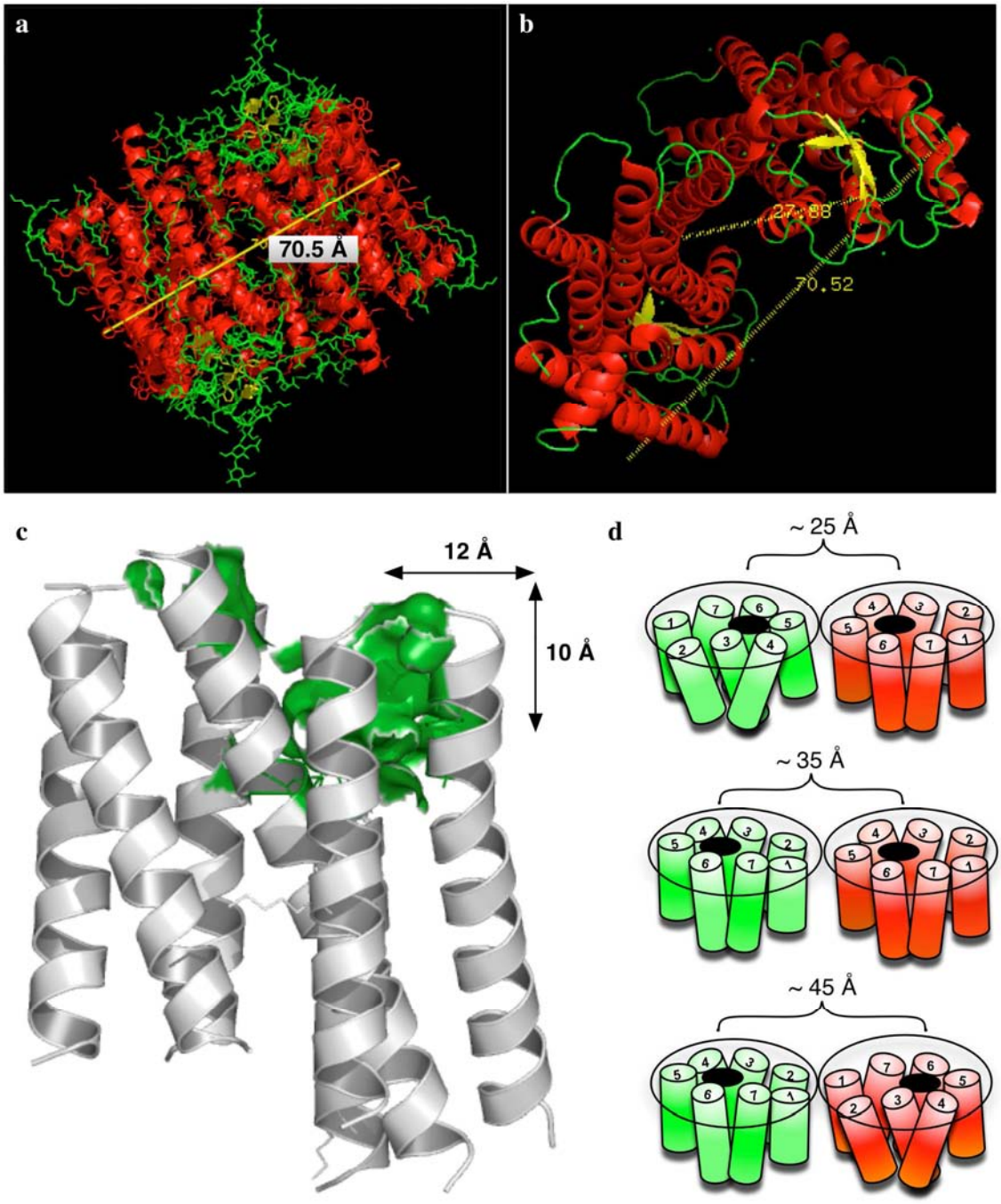

FIGURE S4. Molecular modeling. Computational studies were carried out on Ac-PEGO-NH_2, Ac-$[PG]_n$-NH_2, where n = 3, 6, or 9, htBVL **12b**, and were used to estimate the linker length in each htBVL given in Table 1. Representative cases of linkers are described here. a,b) One of the low energy conformers of modeled Ac-PEGO-NH_2 linker with a bent conformation. The MD simulations indicated that this linker could extend up to 18 Å length (distance between atoms labeled 1 and 50); c) One of the low energy conformers of Ac-$[PG]_9$-NH_2 linker highlighting the helical secondary structure. The modeling studies indicated the presence of PolyProline Type II (PPII) structure in this proline-rich sequence (also see CD studies in Figure S4). d,e) MD simulations carried on the htBVL **12b** depicting the excursion of linker region $[PG]_6$ and PEGO-$[PG]_6$-PEGO in the sampled MD simulation of 20,000 ps. The PEGO-$[PG]_6$-PEGO linker could extend up to 53 Å in this simulation. The $[PG]_6$ part of the linker exhibited some random conformations that could extend up to nearly 30 Å but most conformations retained a certain degree of helicity with linker length less than 20 Å. More detailed studies on $[PG]_n$ linker will be published elsewhere.

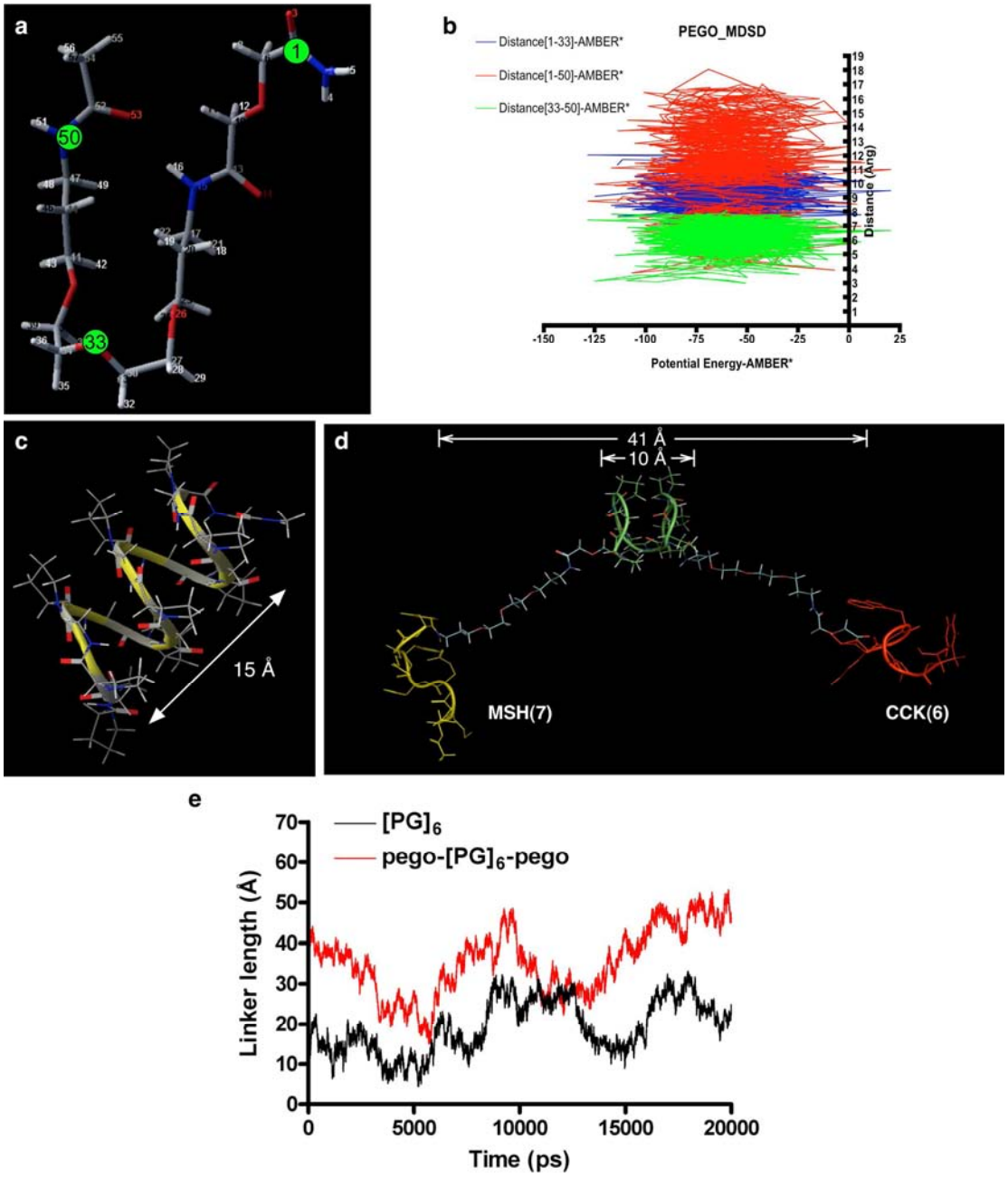

FIGURE S5. CD study on poly(Pro-Gly) linker. a) CD spectrum of Ac-$[PG]_6$-NH_2 in different solvent at 100 μM concentration and 25 °C temperature. The peptide was synthesized on solid-phase using procedures described earlier in the supporting text. This linker shows negative absorption band at 205 nm, which is characteristic of polyproline type II (PPII) secondary structure. However, the weak the postive band usually centered at 225 nm in PPII is absent in this linker, and may reflect the presence of some other structural element. b) Temperature scan of Ac-$[PG]_6$-NH_2 linker in water at 100 μM concentration, highlighting the trace similar to other polyproline sequences and the presence of an isodichroic point at 213 nm that suggests the presence of two equilibrating structures. Further deconvolution analysis of these linkers with different peptide lengths revealed a mixture of PPII (~ 40% content), β-turn, and random coils, reinforcing our design consideration of a semi-rigid linker. More experimental details on poly(Pro-Gly) linkers will be published elsewhere.

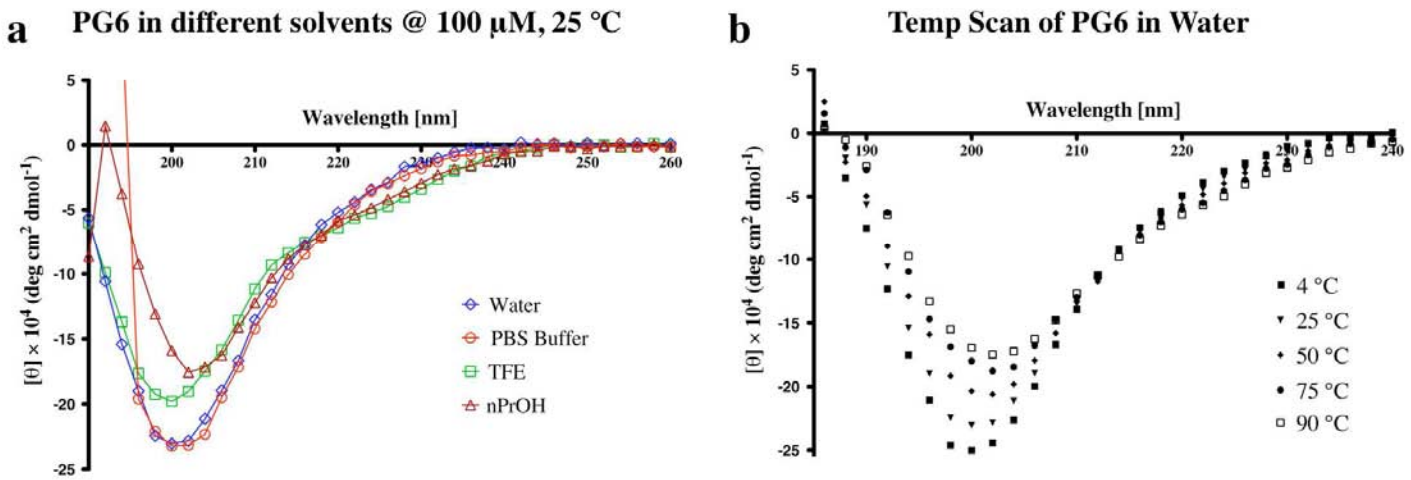

FIGURE S6. Receptor number determination. a) Saturation binding analysis of Eu-NDP-α-MSH binding to HEK293/hMC4R/tCCK cells where (■), (o) and (▲) indicate total, specific and non-specific binding, respectively. Increasing amounts of Eu-NDP-α-MSH were added to cells and incubated for 1 hr at 37ºC. Non-specific binding was determined in the presence of 100 μM NDP-α-MSH. From these data, the K_d = 1.30 ± 0.14 nM, and B_{max} = 95,244 ± 2480 AFU. The data were fit using GraphPad Prism software using the non-linear regression, one site-binding equation, with a R^2 value of 0.93. Each data point indicates the average of 4 samples, with error bars indicating the standard error mean. b) Standard curve relating [Eu-NDP-α-MSH] to fluorescent signal. Increasing amounts of Eu-NDP-α-MSH were added to wells of a 96-well plate. Each data point indicates the average of 4 replicates with error bars indicating the standard error mean. The standard curve allowed for the determination of the amount of ligand present at the B_{max} value obtained from the saturation binding curve. For binding to the hMC4R, the B_{max} was determined to be 95,244 ± 2480 AFU which correlates to 380 fmol/well.

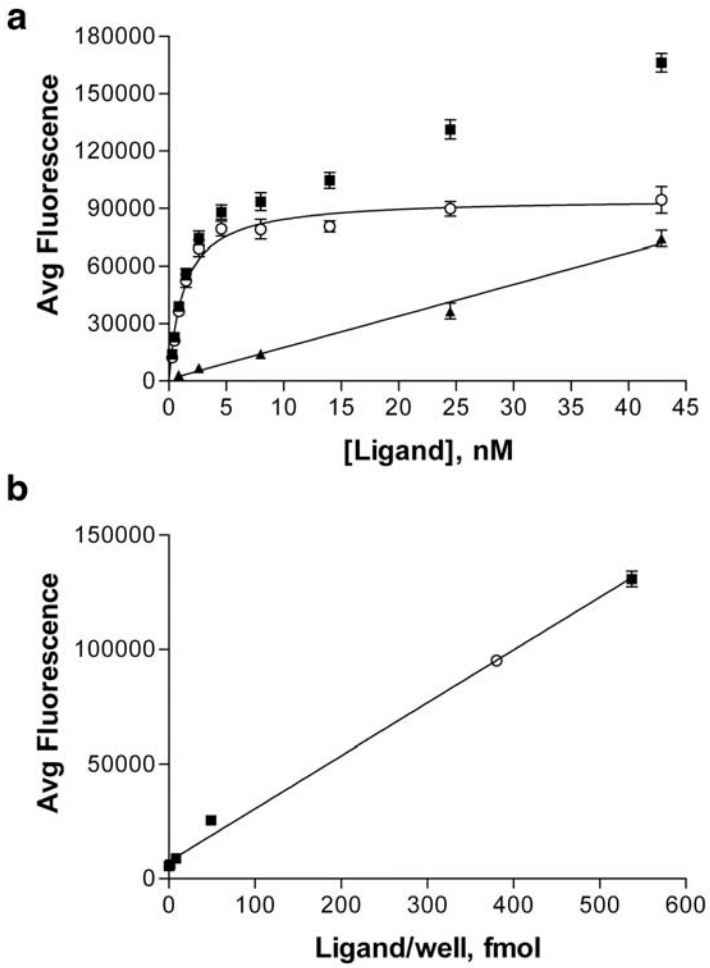

FIGURE S7. Representative curves from the competitive binding assay of heterobivalent ligands. The ligands were evaluated for their monovalent and bivalent binding by competing them against Eu-labeled NDP-α-MSH and CCK-8 lanthaligands. Single plot IC_{50} values were determined where data from all n measurements were pooled first and non-linear regression analysis performed. a) Binding of Ligand **5b** competed with 0.1 nM Eu-CCK8 in HEK293/CCK cells, with an IC_{50} of 46 nM (R^2 = 0.90). b) Binding of Ligand **5b** competed with 0.1 nM Eu-CCK8 in HEK293/MC4R/CCK cells, with an IC_{50} of 2.3 nM (R^2 = 0.89). c) Binding of Ligand **5b** competed with 0.1 nM Eu-NDP-α-MSH in HEK293/MC4R cells, with an IC_{50} of 110 nM (R^2 = 0.81) d) Binding of Ligand **5b** competed with 0.1 nM Eu-NDP-α-MSH in HEK293/MC4R/CCK cells, with an IC_{50} of 1000 nM (R^2 = 0.86).

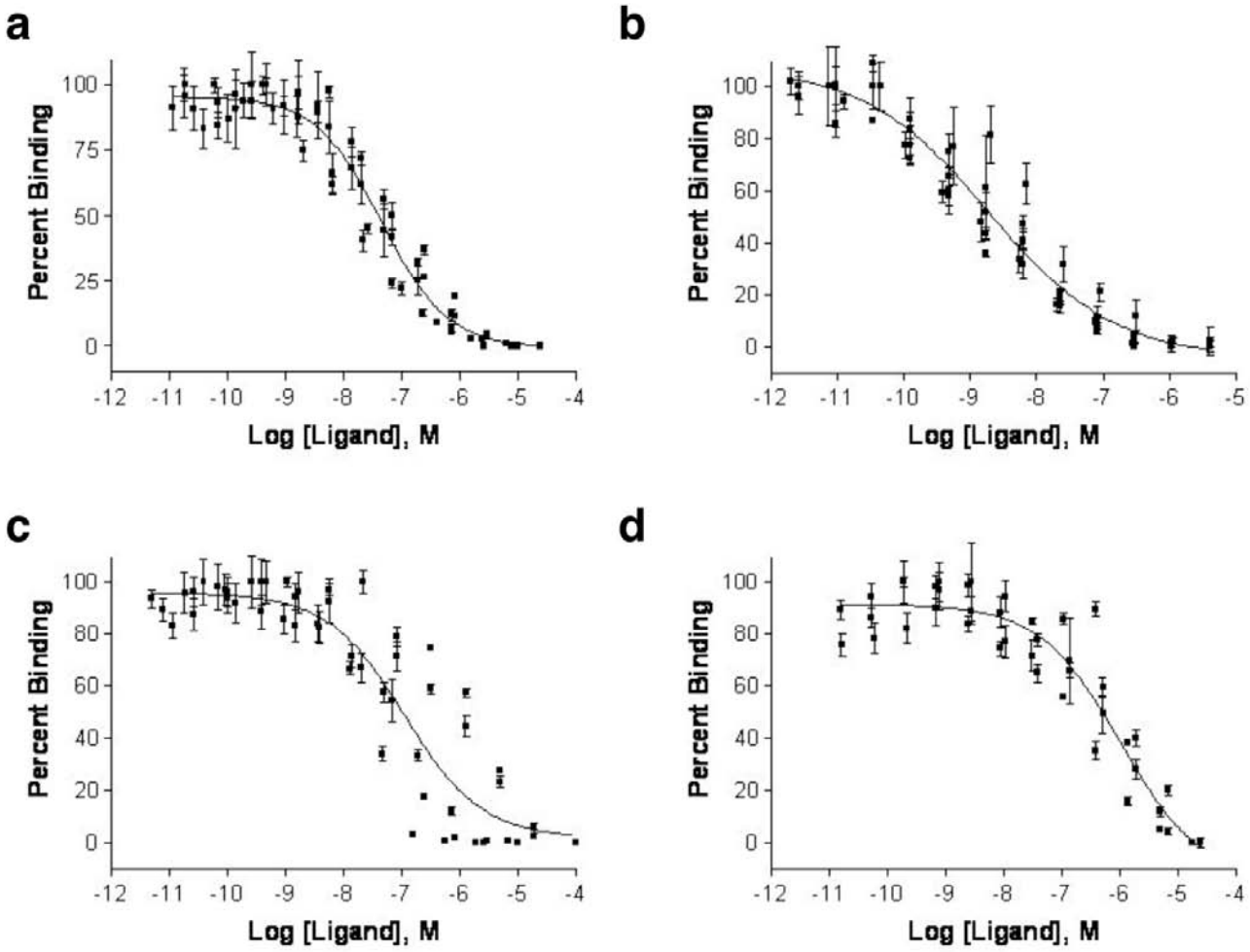

REFERENCES:

[1] V. Krchnák, J. Vágner, M. Lebl, *Int. J. Pept. Prot. Res.* **1988**, *32*, 415.
[2] J. S. Josan, J. Vagner, H. L. Handl, R. Sankaranarayanan, R. J. Gillies, V. J. Hruby, *Int. J. Pep. Res. Ther.* **2008**, *14*, 293.
[3] J. Vagner, H. L. Handl, R. J. Gillies, V. J. Hruby, *Bioorg. Med. Chem. Lett.* **2004**, *2004*, 211.
[4] H. L. Handl, J. Vagner, H. I. Yamamura, V. J. Hruby, R. J. Gillies, *Anal. Biochem.* **2005**, *343*, 299.
[5] J. Reubi, B. Waser, J. C. Schaer, U. Laederach, J. Erion, A. Srinivasan, M. A. Schmidt, J. E. Bugaj, *Eu. J. Nucl. Med.* **1998**, *25*, 481.
[6] F. Mohmadi, N. G. J. Richards, W. C. Guida, R. Lizkamp, M. Lipton, C. Caulfield, G. Chang, T. Hendickson, W. C. Still, *J. Comput. Chem.* **1990**, *11*, 440.
[7] D. Q. McDonald, W. C. Still, *Tet. Lett.* **1992**, *33*, 7743.
[8] J. M. Goodman, W. C. Still, *J. Comput. Chem.* **1991**, *12*, 1110.
[9] F. Guarnieri, W. C. Still, *J. Comput. Chem.* **1994**, *15*, 1302.
[10] J. Li, P. C. Edwards, M. Burghammer, C. Villa, G. F. X. Schertler, *J. Mol. Biol.* **2004**, *343*, 1409.
[11] I. Gantz, H. Miwa, Y. Konda, Y. Shimoto, T. Tashiro, S. J. Watson, J. Delvalle, T. Yamada, *J. Biol. Chem.* **1993**, *268*, 15174.
[12] H. L. Handl, J. Vagner, H. I. Yamamura, V. J. Hruby, R. J. Gillies, *Anal. Biochem.* **2004**, *330*, 242.

Bioconjugate Chemistry

ARTICLE

pubs.acs.org/bc

Conjugation of Lipid and CpG-Containing Oligonucleotide Yields an Efficient Method for Liposome Incorporation

Chasity D. Andrews,[†] Chester J. Provoda,[†] Gary Ott,[‡] and Kyung-Dall Lee*[,†]

[†]Department of Pharmaceutical Sciences, University of Michigan, Ann Arbor, Michigan 48109, United States

[‡]Dynavax Technologies, Berkeley, California 94710, United States

ABSTRACT: For optimal stimulation of T cells, protein-based vaccines must deliver protein antigens to antigen-presenting cells while simultaneously providing immunostimulatory signals. Listeriolysin O (LLO)-containing liposomes have been utilized to efficiently deliver protein antigens to the cytosolic pathway for antigen processing and major histocompatibility complex class I-dependent presentation while codelivering immunostimulatory CpG-oligodeoxyribonuceotides (ODNs). In this report, we describe the synthesis of lipid-CpG-ODN conjugates utilizing maleimide-phosphatidylethanolamine (PE) lipids and 5′-sulfhydryl-containing CpG-ODNs as a method for facile incorporation of CpG-ODNs in liposomal vaccine carriers, an alternative to co-encapsulation inside liposomes and as a means to enhance delivery of CpG-ODNs to their major receptor, Toll-like receptor 9 (TLR9), in the endosome. The characterization and biological evaluation of the vaccine delivery system made of liposomes, which contain the lipid-CpG-ODN conjugates inserted in the liposomal membrane, is described. We demonstrate in vitro in bone marrow derived macrophages that the lipid-CpG-ODN conjugates incorporated onto the liposome bilayers interact with their receptor TLR9 as readily as liposome-encapsulated ODNs and exert their immunostimulatory capabilities. The liposomal vaccine delivery systems were evaluated in mice using ovalbumin (OVA) as a model antigen, and the results indicate equally robust OVA-specific cytotoxic T lymphocyte responses and similar Th1 immune skewing capabilities between liposomes containing lipid-conjugated or encapsulated CpG-ODNs. Overall, this work indicates that conjugating PE lipids and CpG-ODNs results in an efficient method that allows facile incorporation of CpG-ODNs into a liposome-based delivery platform while retaining the immune-stimulating capabilities of CpG-ODNs.

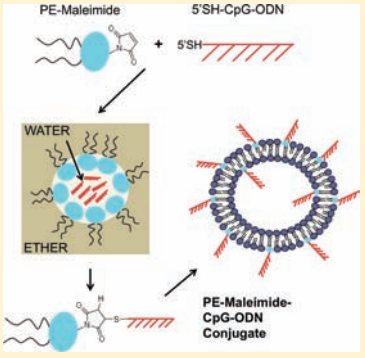

INTRODUCTION

The immune system generates humoral and cellular immune responses to viruses and bacteria by recognizing a variety of the components of the pathogen. Traditional vaccination strategies have successfully exploited these responses by utilizing whole live attenuated or inactivated pathogens for the treatment and prevention of a large number of diseases; however, both safety and production concerns have led to the development of protein antigen or subunit vaccines.[1] Compared to whole pathogens, protein-based vaccines are inherently limited in (i) their ability to stimulate a robust immune response and (ii) their ability to deliver antigen(s) to the cytosolic pathway of antigen presentation. Hence, adjuvants have been utilized in protein vaccines as an effective means for enhancing the immunogenicity of the antigens and modulating the types of immune responses. Classical adjuvants such as aluminum hydroxide (alum) and oil/water emulsions enhance the humoral response to protein antigens but not the cellular response, thus limiting their utility.[1,2] A cellular immune response, particularly the T helper (Th)1-type that is associated with interferon (IFN)-γ production and cytotoxic T lymphocytes (CTLs), is desirable in a number of cases and is often needed to clear tumors or intracellular pathogens such as viruses.[3] Traditional vaccines rely on the molecular composition of the whole pathogen to stimulate the innate immune system through an array of pathogen-associated molecular patterns (PAMPs) such as unmethylated cytosine-phosphate-guanine (CpG)-containing DNA, lipopolysaccharides, lipoproteins, flagellin, and double-stranded RNA.[4] Recognition of one or more PAMPs induces antigen-presenting cell (APC) maturation resulting in cytokine secretion, costimulatory molecule expression, and enhanced antigen presentation, ultimately stimulating both the humoral and cellular arms of the immune system. The ability of some PAMPs to stimulate cellular immune responses has led to an increased interest in their utilization in vaccines as adjuvants that target innate immune receptors.[5] Our current approach is to generate a vaccine delivery system emulating traditional whole pathogen-based vaccines to stimulate both humoral and cellular immune responses, while reducing the relative toxicity by including in the protein-based vaccine only essential, well-defined components for eliciting an antigen-specific immune response.

Synthetic CpG-oligodeoxyribonuceotides (ODNs) that mimic bacterial CpG-containing unmethylated DNA have been shown to activate monocytes/macrophages, dendritic cells, natural killer cells, and B cells; induce the production of proinflammatory cytokines (interleukin (IL)-6, IL-12, IFNs, TNF-α);

Received: October 4, 2010
Revised: April 1, 2011
Published: May 25, 2011

ACS Publications © 2011 American Chemical Society

dx.doi.org/10.1021/bc100436y | *Bioconjugate Chem.* 2011, 22, 1279–1286

and upregulate the expression of major histocompatibility complex (MHC) class I, MHC class II, and costimulatory molecules.[6] CpG-ODNs may be coadministered with antigens to enhance the immune response (reviewed by Krieg[6]). When APCs receive antigen without concomitant costimulation, however, T cell anergy, rather than the development of a memory T cell response, may occur.[7] To address this issue, various methods of codelivering CpG-ODNs and antigens are being explored, including, but not limited to, antigen-CpG-ODN conjugates,[8,9] liposomal encapsulation,[10−12] and microparticle loading.[13,14]

Liposomes, which are internalized via endocytosis and disrupted inside the endosomal compartment,[15] have tremendous potential for delivering co-encapsulated CpG-ODNs to facilitate their interaction with Toll-like receptor 9 (TLR9) in the endosome.[16] We have previously explored and demonstrated the ability of listeriolysin O (LLO)-containing pH-sensitive liposomes to efficiently deliver antigen into the cytosol of APCs to enhance MHC class I processing and presentation as a means to augment CTL activity.[17−19] LLO, the pore-forming cytolysin of the facultative intracellular bacterium *Listeria monocytogenes* (*Lm*), exerts optimal activity at pH 5.5 to temporarily disrupt endosome membranes and promote *Lm*'s escape from the endolysosome uptake pathway into the cytosol.[20] LLO can thus be exploited to mimic the cytosol-invading aspect of *Lm*'s infectivity to efficiently deliver macromolecules to the cytosol. We have also shown that co-encapsulating ovalbumin (OVA) and CpG-ODNs within LLO-containing pH-sensitive liposomes significantly enhances the CTL response, while also skewing the immunity toward the Th1-type, as compared with OVA and CpG-ODN administered in solution (C. D. Andrews and M. S. Huh; unpublished results).

Although the previous results obtained from LLO-liposomes with co-encapsulated antigen and CpG-ODN were promising, the encapsulation efficiency of CpG-ODN was relatively low, resulting in a significant loss of material during the removal of unencapsulated ODNs. Furthermore, because of its encapsulation within the liposomes, the access of CpG-ODN to TLR9 in the endosome may be limited both spatially and temporally, in effect reducing the overall targeting efficiency. Therefore, in order to increase the recovery of CpG-ODN and enhance the probability of CpG-ODN binding to TLR9, CpG-ODN was conjugated to lipid via an irreversible thioether bond and incorporated into the liposomal membrane. The hypothesis tested in this report is that lipid-conjugated CpG-ODNs on the surface of the liposomes will promote the interaction between CpG-ODN and TLR9, before the endosomal contents are released into the cytosol upon LLO-mediated perforation of the endosomal membrane. Here, we show that we can conjugate CpG-ODN to phosphatidylethanolamine (PE), yielding an efficient process for incorporating CpG-ODNs in liposome membranes. The lipid-CpG-ODN conjugates incorporated in the liposomal membrane of the vaccine delivery system exhibited robust immunostimulatory activity as tested in bone marrow derived macrophages (BMMs) and are capable of readily interacting with TLR9. In mice, we use the model antigen OVA and show that liposomes containing OVA and LLO with either encapsulated or conjugated CpG-ODN enhance CTL activity compared with liposomes containing only OVA and LLO. Both conjugated and encapsulated CpG-ODNs are capable of stimulating a Th1-type response as indicated by enhanced IFN-γ secretion and anti-OVA IgG2a antibody production.

EXPERIMENTAL PROCEDURES

Mice, Cell Culture, Media, and Reagents. C57BL/6 (female, 8−9 weeks old; Harlan, Indianapolis, IN) and C57BL/10ScNJ ($Tlr4^{Lps\text{-}del}$, $H\text{-}2K^{b}$, female, 6−8 weeks old; Jackson Laboratory, Bar Harbor, ME) were used in this study and were handled according to Institutional Guidelines. All tissue culture media and reagents were purchased from Invitrogen (Carlsbad, CA), and all cells were maintained and experimental incubations were conducted in a humidified incubator at 37 °C and 5% CO_2, unless otherwise noted. Bone marrow was harvested from the femurs and tibia of C57BL/10ScNJ mice and differentiated into bone marrow-derived macrophages (BMMs) in BMM media (DMEM with 20% heat-inactivated FBS (HI-FBS), 30% L-cell conditioned media, 2 mM glutamine, 100 μg/mL streptomycin, 100 U/mL penicillin, and 55 μM 2-mercaptoethanol) as described by Stier et al.[21] BMMs were harvested on day six and frozen in liquid nitrogen until the experiment. Unmodified and 5′-disulfide ODNs used in this study were composed of 22 bases with a phosphorothioate-modified backbone (Dynavax Technologies; Berkeley, CA). The positive control, CpG-ODN ISS 1018 (5′TGACTGTGAACGTTCGAGATGA), contains unmethylated CpG sequences, and the negative control, non-CpG-ODN ISS 1040 (5′TGACTGTGAACCTTAGAGATGA), lacks unmethylated CpG sequences.

Lipid-ODN Conjugate Synthesis. The disulfide precursors to 5′-sulfhydryl ISS 1018 CpG-ODN and 5′-sulfhydryl ISS 1040 non-CpG-ODN were a gift from Dynavax Technologies (Berkeley, CA). A 700 mM tris-(2-carboxyethyl) phosphine (TCEP; Pierce, Rockford, IL) solution was made in HBSE (140 mM NaCl buffered with 10 mM HEPES containing 1 mM EDTA) pH 7, and used at a five molar excess to reduce 5′-disulfide-ODN at 40 °C for 2 h. Residual TCEP was removed using either a PD-10 or a NAP-5 desalting column (GE Healthcare, Piscataway, NJ) and eluted in HBSE pH 6.5. Reduced 5′-SH-ODN was used immediately or stored at −80 °C until use. Chloroform was removed from 1,2-dioleoyol-*sn*-glycero-3-phosphoethanolamine-*N*-[4-(*p*-maleimidophenyl)butyramide] (MPB-PE; Avanti Polar Lipids, Alabaster, AL) using rotary evaporation at <10 mmHg pressure at room temperature (RT) followed by dissolving in ether, and a water-in-oil emulsion was formed by adding reduced 5′-SH-ODN in HBSE at a 2:1 organic/aqueous ratio. The optimal MPB-PE:5′-SH-ODN ratios were identified as 1:10 and 1:20 for 5′-SH-CpG-ODN and 5′-SH-non-CpG-ODN, respectively. The emulsion was formed by brief sonication, and the MPB-PE and 5′-SH-ODN reacted for 4−5 h while continuously vortexing at RT. Ether was removed using rotary evaporation; after which, water was removed by lyophilization. Two chloroform washes (25 mL) were performed to remove unreacted MPB-PE from the PE-ODN, and residual chloroform was removed by evaporation. Thin-layer chromatography was performed to verify the removal of unconjugated lipids. Both the reduced 5′-SH-ODN and the MPB-PE and 5′-SH-ODN reaction were resolved in a Tris-Borate-EDTA (TBE) polyacrylamide gel (BioRad, 15%) and stained with ethidium bromide. Conjugation efficiency was assessed by using known concentrations of ODNs resolved in the same gel. Unconjugated 5′-SH-ODN was removed from PE-ODN conjugates by Sepharose CL-4B size-exclusion chromatography (1 × 25 cm; GE Healthcare). A TBE polyacrylamide gel (15%) stained with ethidium bromide was used to identify fractions containing conjugated PE-ODN, which were then combined, lyophilized, and the dried solid dissolved in methanol/*N*-methyl-2-pyrrolidone

(MeOH/NMP; 3.3:1). The amount of PE-ODN recovered was determined by measuring phosphate as described by Bartlett.[22]

Preparation of LLO. The *hly* gene encoding for LLO was inserted into the plasmid pET-29b (EMD Chemicals, Gibbstown, NJ) for expression in bacteria with a C-terminal His6 tag. Recombinant LLO was purified from *E. coli* as described by Mandal et al.,[18] with the following exceptions. LLO expression was induced in bacterial culture for 4−6 h with 1 mM isopropyl β-D-thiogalactopyranoside; the cell pellet was collected and resuspended in wash buffer (50 mM sodium phosphate, 300 mM sodium chloride, 20 mM imidazole, pH 8) containing 2 mM PMSF and 1 mM 2-mercaptoethanol and then lysed using a French press. Lysate supernatant was incubated with to Ni-NTA agarose (Qiagen) for 2 h and the Ni-NTA extensively washed with 200 bed volumes of wash buffer. His6-tagged LLO was eluted in wash buffer containing 400 mM imidazole and extensively dialyzed against HBSE pH 8.4 at 4 °C. Protein purity and activity were assessed by SDS-PAGE and hemolysis assay, respectively, as previously described.[18]

Liposome Preparation. Lipid films containing a 2:1 (mol/mol) mixture of egg phosphatidylethanolamine/cholesteryl hemisuccinate (ePE/CHEMS; Avanti Polar Lipids, Alabaster, AL, and Sigma-Aldrich, respectively) were made by removing chloroform and methanol using rotary evaporation at <10 mmHg pressure at RT. PE-ODNs dissolved in MeOH/NMP were incorporated in the lipid film at 0.2 or 0.3 mol percent for in vivo or in vitro studies, respectively, and solvent was removed by rotary evaporation at 40 °C and <10 mmHg pressure. The films were rehydrated with HBSE pH 8.4 containing a combination of ovalbumin [OVA; 10 mg (in vitro studies) or 2 mg (in vivo studies), Sigma-Aldrich, grade VI], LLO (0.1 mg), and ODN (2 mg); and the resulting liposomes were subjected to five freeze−thaw cycles followed by 7 × 1 min bursts of bath sonication. Unencapsulated materials were separated from the liposomes in Sepharose CL-4B size-exclusion columns (1 × 25 cm). OVA and LLO encapsulation was determined by staining proteins resolved in SDS-PAGE with Krypton staining (Pierce) and measuring band intensities using a Molecular Dynamics Typhoon 9200 with ImageQuant (GE Healthcare). Calculations were based on known concentrations of proteins resolved in the same gel. ODN encapsulation was determined by generating a standard curve from free ODN or PE-ODN, depending on the type of ODN to be quantified. All samples and standards contained normalized lipid amounts and C12E8 (1%, Sigma-Aldrich). SYBR Green I (Invitrogen) was added to the plate at a final dilution of 1:15 000 and the fluorescence quantified in a Synergy HT plate reader (BioTek Instruments, Winooski, VT) using an excitation of 485 nm and emission of 528 nm.

IL-12p40 Secretion by ELISA. BMMs (2×10^5/well) from C57BL/10ScNJ mice were plated in 96-well tissue culture plates in complete DMEM one day prior to liposome treatment. BMMs (in triplicate) were pulsed with liposomes containing PE-ODN for 3 h in DMEM containing penicillin and streptomycin. BMMs were washed three times and incubated for 20 h in complete DMEM (DMEM + 10% HI-FBS, 100 μg/mL streptomycin, and 100 U/mL penicillin). Supernatants were collected and analyzed for IL-12 secretion by ELISA using IL-12p40 antibodies (R&D Systems, Minneapolis, MN) and IL-12p40 standard (Peprotech, Rocky Hill, NJ). Briefly, ELISA plates were coated with antimouse IL-12/IL-23p40 monoclonal antibody diluted in PBS, washed, and then blocked with 5% sucrose and 1% BSA in PBS prior to incubating with supernatant. Plates were then washed and incubated with biotinylated antimouse IL-12/IL-23p40 antibody, followed by avidin-horseradish peroxidase (HRP, eBioscience, San Diego, CA) and TMB SureBlue Substrate (KPL, Gaithersburg, MD). The reaction was stopped using 2 N sulfuric acid, and the absorbance at 450 nm was measured using a Molecular Devices (Sunnyvale, CA) Emax plate reader.

Immunization Protocol. C57BL/6 mice were primed with 8 μg of OVA on day 0 via the subcutaneous route at the base of the tail. Mice were euthanized on day 10, sera were collected via cardiac puncture, and spleens were isolated for assays.

In Vivo Cytotoxic T Lymphocyte Assay. RBC-lysed, single-cell spleen suspensions from naïve mice were pulsed at 1×10^7 cells/mL with either SIINFEKL or influenza nucleoprotein $(NP)_{147-155}$ peptide (1 μg/mL; Anaspec, Fremont, CA) for 1 h at 37 °C. The cells were washed and diluted to 1×10^8 cells/mL in PBS with 0.1% FBS. The SIINFEKL peptide-pulsed and $NP_{147-155}$ peptide-pulsed populations were labeled with 4 or 0.4 μM carboxyfluorescein diacetate succinimidyl ester (CFSE; Invitrogen), respectively, for 10 min at RT. CFSE labeling was stopped by adding an equal volume of FBS for 5 min on ice. Cells were washed thrice with PBS + 5% FBS, counted, and 1×10^7 cells of each peptide-pulsed population were mixed together and injected via tail vein into immunized or naïve mice. Mice were euthanized 8.5 h postadoptive transfer; spleens were harvested, and single cell suspensions were obtained by grinding spleens through a 70 μm mesh screen containing mouse media. Splenocytes were washed, RBCs were removed using Ficoll-Paque Premium (GE Healthcare), and purified splenocytes were analyzed by FACSCalibur. Ten thousand viable CFSE-labeled cells were analyzed for each mouse. The percentage of specific lysis for each mouse was calculated by 100 × [1 − (ratio of cells recovered from naïve mice/ratio of cells recovered from immunized mice)].

Antigen-Specific Cytokine Secretion. Splenocytes (5×10^5/well) were added to 96-well tissue culture plates in duplicate in 200 μL mouse media (RPMI 1640, 10% HI-FBS, 2 mM L-glutamine, 100 U/mL penicillin, 100 μg/mL streptomycin, 55 μM 2-mercaptoethanol (Sigma-Aldrich)) supplemented with media, $NP_{147-155}$ or MHC class I OVA peptide SIINFEKL, (5 μM; Anaspec), or concanavalin A (10 μg/mL, Sigma-Aldrich). After 76 h, splenocyte supernatants from a given mouse and treatment were combined and analyzed for IFN-γ secretion by ELISA as previously described.[23] Briefly, samples were assayed in duplicate using ELISA plates coated with purified rat antimouse IFN-γ capture antibody (BD Biosciences, San Jose, CA). Cytokines were detected in dilutions of the cell culture supernatants with biotinylated rat antimouse IFN-γ (BD Biosciences) followed by avidin-HRP, and absorbance values were obtained as described above.

Anti-OVA Ig ELISA. Postimmune sera were analyzed by ELISA as described[18] with the following modifications. Briefly, ELISA plates were coated with OVA (10 μg/mL), blocked, and incubated with serial dilutions of sera. Anti-OVA isotype-specific secondary antibodies (goat antimouse IgG2a-biotin or goat antimouse IgG1-biotin; Southern Biotechnology Associates, Birmingham, AL) were detected with avidin-HRP, and absorbance values were determined as described above. The titer was defined as the reciprocal of the serum dilution that produced an absorbance value of 0.3 using a four-parameter analysis (*Softmax Pro5.2*, Molecular Devices). If no titer was observed, the lowest dilution tested was reported.

Statistical Analyses. Grubb's test was used to analyze for outliers in animal studies. Data from liposome-treated animals were compared by ANOVA and Tukey's post-test for data with

homogeneous variance. In the case of nonhomogeneous variance, the data were compared using the Kruskal−Wallis test followed by the Dunn's multiple comparison test. A p-value of <0.05 was considered significant; * $p < 0.05$, ** $p < 0.01$, *** $p < 0.001$.

RESULTS AND DISCUSSION

Lipid-ODN Conjugate Synthesis and Liposome Incorporation. We recently investigated the co-encapsulation of CpG-ODN within LLO-containing pH-sensitive liposomes as a strategy for codelivery of a protein antigen and the adjuvant to the same APC (C. D. Andrews and M. S. Huh; unpublished results). CpG-ODN was chosen as an adjuvant in this system because its receptor, TLR9, is located in the endocytic pathway, the primary route of uptake of liposomes by cells.[15,24,25] However, the efficiency of co-encapsulation of CpG-ODNs in LLO-liposomes is relatively low (<10%). Furthermore, after the pH-sensitive LLO-liposomes are taken up by APCs and the liposomal contents are released in the acidic endosome, the perforation of the endosomal membrane by LLO leads to release of the contents, including CpG-ODN, into the cytosol where there is as yet no known CpG-ODN receptor. Therefore, we hypothesized that we could promote CpG-ODN interaction with TLR9, before endosomal rupture by LLO, using the strategy of incorporating lipid-CpG-ODN conjugates in the liposomal membrane (Figure 1).

CpG-ODNs with 5′-sulfhydryls were conjugated to maleimide-PE (sulfhydryl-reactive maleimide group conjugated to the lipid headgroup of PE) through the formation of a thioether bond; this typically resulted in 90−95% of the CpG-ODN being conjugated, as determined by ethidium bromide staining of ODN and its lipid-conjugate after separation in TBE gels (Figure 2). In order to ensure that the enhanced immunopharmacological effects were not due to contaminating free CpG-ODNs, the PE-CpG-ODN conjugates were purified using size-exclusion chromatography to remove unconjugated monomeric and/or homodimeric (disulfide-bonded) ODNs. Fractions from size-exclusion chromatography were resolved using TBE-PAGE to identify the fractions that contain PE-CpG-ODN conjugate. The overall CpG-ODN recovery after pooling all fractions with conjugates was approximately 50% (data not shown). After lyophilization and dissolving in methanol/NMP, PE-CpG-ODNs were found to be stable under argon at −20 °C for at least 26 days (data not shown).

The synthesized PE-CpG-ODNs were added at 0.2 to 0.3 mol % (see method section for details) to the lipid mixture and dried by rotary evaporation to make lipid films used for liposome preparation. After liposome rehydration, we then tested whether PE-CpG-ODNs were incorporated and remained associated with the liposomes; liposomes were resolved in a Ficoll step density gradient (0%, 10%, 20% Ficoll) and ODNs were identified in the gradient fractions by ethidium bromide staining of TBE gels. In this assay, liposomes floated to the interface of the 0% and 10% layers, whereas nonliposomal PE-CpG-ODNs remained in the 20% Ficoll fractions (data not shown); all of the liposomal PE-CpG-ODNs detected were in the 0% and 10% interface, indicating that all lipid-CpG-ODN conjugates were incorporated in the liposome membrane. In agreement with previous work reporting the asymmetric distribution of gangliosides in liposome bilayers,[26] using a nuclease protection assay[27] against nuclease P1 we found the membrane leaflet distribution of PE-CpG-ODN to be ∼80% extra-liposomal and ∼20% luminal (data not shown).

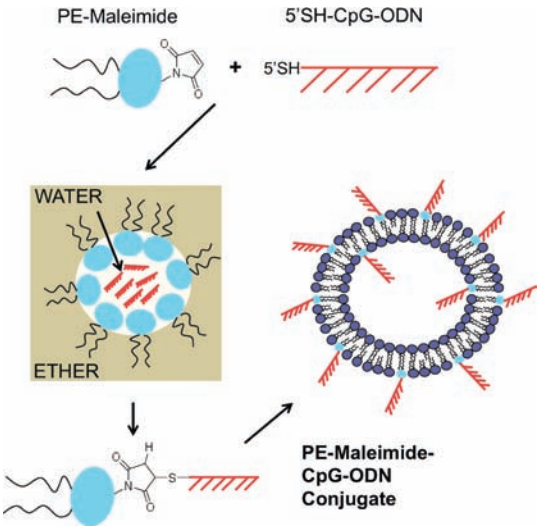

Figure 1. Schematic of PE-maleimide and 5′-SH-CpG-ODN conjugation procedure and liposome incorporation. Freshly reduced 5′-SH-CpG-ODN in aqueous buffer was added to ether containing PE-maleimide. A water-in-ether emulsion was formed by brief sonication and the conjugation reaction proceeded ∼4 h while vortexing at room temperature. The solution containing purified PE-maleimide-CpG-ODN conjugates was added to the lipid mixture, which was then dried to form lipid films. The rehydrated liposomes contained PE-maleimide-CpG-ODN conjugates in the membrane.

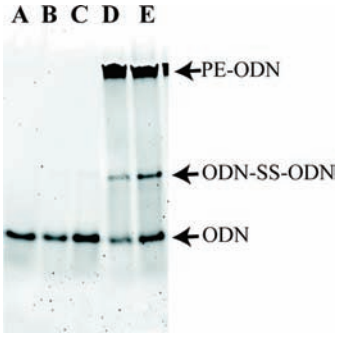

Figure 2. Representative PAGE gel of PE-CpG-ODN conjugation. Conjugation was assessed by resolving PE-CpG-ODNs from disulfide bonded (ODN-SS-ODN) and unconjugated 5′-SH-CpG-ODN in a 15% TBE/polyacrylamide gel stained with ethidium bromide. The amounts of disulfide-bonded and unconjugated ODN were calculated from a standard curve of known ODN amounts. (A) 176 ng CpG-ODN standard, (B,C) reduced 5′-SH-CpG-ODN added to MPB-PE (0.03, 0.06 μL, respectively), (D,E) PE-CpG-ODN conjugation reaction (5.25, 10.5 μL, respectively). These results indicate that >95% 5′-SH-CpG-ODN is conjugated.

Overall, these data indicate that PE-CpG-ODNs are efficiently synthesized with approximately 50% recovery after purification, and no loss of the conjugate was incurred during incorporation into the liposome membrane using the traditional method of liposome preparation. The majority of the loss of CpG-ODNs resulted from the size-exclusion chromatography step, which may not in fact be required as the efficiency of the conjugation process was so high (typically 90−95%). Overall, the process of lipid conjugation and incorporation into liposome bilayers is much more efficient than the more commonly employed passive

encapsulation technique, which typically results in less than 10% CpG-ODN encapsulated.

IL-12 Secretion is PE-CpG-ODN Dose-Dependent. Next, we asked whether CpG-ODN incorporated onto the liposomes in the form of PE-CpG-ODN conjugates retains the capacity of CpG-ODN to stimulate and modulate an immune response. The liposomes were evaluated for their ability to induce the secretion of the Th1-type proinflammatory cytokine IL-12 in BMMs in culture. It has been shown that the surface charge of liposomes affects their uptake by macrophages.[28] Therefore, to eliminate uptake differences the surface charge of the liposomes was held constant by maintaining the total percentage of conjugated ODNs in the liposome membrane (total PE-ODN kept at 0.3 mol % of total phospholipids) while varying the percentage of PE-ODNs that contain the CpG sequence at 0%, 25%, 50%, and 100%; the remaining PE-ODNs consisted of PE-non-CpG-ODN conjugates. Increasing the percent of PE-CpG-ODN in the liposomal membranes increased the amount of IL-12 secreted in a linear fashion (Figure 3). No IL-12 was detected when treated with the 0% PE-CpG-ODN sample (100% PE-non-CpG-ODN). As the fraction PE-CpG-ODN of the total PE-ODNs (PE-CpG-ODN plus PE-non-CpG-ODNs) was increased in these experiments, greater than 25% PE-CpG-ODN was required to stimulate detectable IL-12 secretion; this was shown by the lack of detectable IL-12 when cells were treated with 25% PE-CpG-ODN and by the presence of detectable IL-12 secretion at 50% PE-CpG-ODN. These data suggest that a certain threshold or minimum number of PE-CpG-ODN conjugates per liposome are required to achieve optimal BMM activation. It is noteworthy that a similar dose responsiveness phenomenon was observed when dendritic cells were treated with acid-degradable microparticles loaded with CpG-ODNs.[29]

Lipid-Conjugated ODNs Likely Interact with TLR9 before Encapsulated ODNs. We hypothesized and investigated that conjugating CpG-ODN to PE lipids would promote the interaction between CpG-ODN and its presumptive receptor TLR9 in the endosomal compartment, before the pH-sensitive liposomes are destabilized by the low pH of the endosome and release their LLO. Ultimately, the effects of LLO breaching the endosomal membrane may have negative implications for the binding of CpG-ODN and signaling by TLR9. First, it is established that protease inhibitors or inhibitors of endosomal acidification prevent the activation of TLR9,[30,31] and when LLO forms pores in the endosomal membrane, a transient rise in pH occurs.[32] Second, LLO-mediated membrane perforation results in the release of endosomal contents,[17] in this case CpG-ODNs, into the cytosol where there is no known receptor for single-stranded ODNs (reviewed by Ishii and Akira[33]). To test this hypothesis, we made PE-CpG-ODN-containing liposomes that contained either encapsulated CpG-ODN or encapsulated non-CpG-ODN; we also made PE-non-CpG-ODN-containing liposomes that encapsulated either CpG-ODN or non-CpG-ODN. Previous reports strongly suggest that phosphorothioate ODNs bind the ectodomain of TLR9 regardless of sequence composition (i.e., CpG-containing or not); however, activation of TLR9 is CpG-dependent,[34,35] indicating that non-CpG-ODNs do not stimulate IL-12 secretion despite their binding to TLR9. On the basis of these data, we predicted that there would be reduced IL-12 secretion with PE-non-CpG-ODNs if these ODNs were to bind TLR9 before release of encapsulated CpG-ODN, thus reducing both the interaction and the effect of encapsulated CpG-ODNs via TLR9. The results from Figure 4 support our hypothesis that the lipid-conjugated ODNs on the

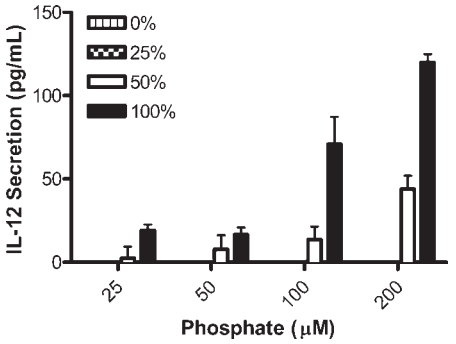

Figure 3. IL-12 secretion is PE-CpG-ODN dose-dependent. The percentage of PE-CpG-ODN incorporated in liposomes was varied while maintaining total PE-ODN (PE-CpG-ODN plus PE-non-CpG-ODN) fixed at 0.3 mol % of phospholipids. BMMs were treated in serum-free media with serial dilutions of liposomes for 3 h, washed, and incubated in complete media for 20 h. The supernatant was collected and analyzed for secreted IL-12p40 by ELISA.

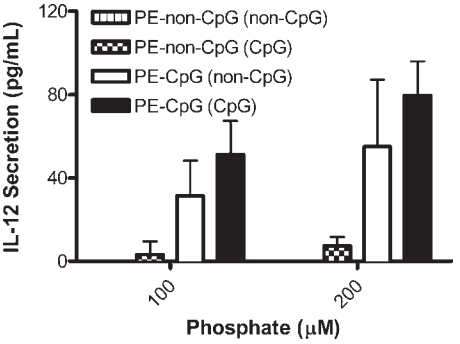

Figure 4. Lipid-conjugated ODNs interact with TLR9 before encapsulated ODNs. Liposomes encapsulating either CpG-ODN or non-CpG-ODN (encapsulation denoted by the ODN type in parentheses in the figure caption) were made containing 0.3 mol % PE-CpG-ODN or PE-non-CpG-ODN. BMMs were treated in serum-free media with serial dilutions of liposomes for 3 h, washed, and incubated in complete media for 20 h. The supernatant was collected and analyzed for secreted IL-12p40 by ELISA.

surface of the liposomes interact with TLR9 before encapsulated ODNs do, as we observed significantly attenuated IL-12 secretion with non-CpG-ODNs on the outside of liposomes encapsulating CpG-ODNs. Importantly, antigen presentation assays confirmed that the incorporation of conjugated ODNs did not affect the intracellular delivery of LLO-containing PE/CHEMS liposomes as shown by cytosolic delivery of the model antigen OVA (data not shown); therefore, we expected co-encapsulated ODNs to also have been efficiently released from the liposomes to interact with TLR9.

PE-CpG-ODNs Stimulate CTL Immune Responses Similar to Encapsulated CpG-ODNs. The in vitro studies indicated that lipid-conjugated CpG-ODNs on the liposome membrane exhibit immunostimulatory capabilities; to corroborate our results in vivo, we immunized mice to compare the two methods for including CpG-ODNs in the liposomes; incorporation of the CpG-ODN lipid conjugate onto liposome membranes versus incorporation via encapsulation. OVA and LLO were co-encapsulated in pH-sensitive liposomes with either lipid-conjugated or co-encapsulated CpG-ODNs as methods for simultaneously delivering antigen and costimulatory molecules to the same APC. These

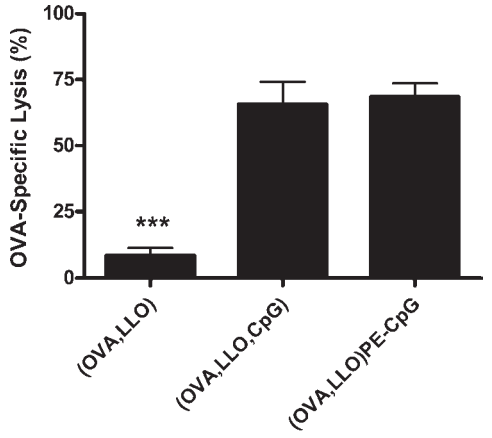

Figure 5. Encapsulated and lipid-conjugated CpG-ODNs induce an OVA-specific CTL response. Mice were immunized subcutaneously on day 0 with liposomes containing OVA and LLO (8 μg OVA) or OVA, LLO, and CpG-ODN (8 μg OVA and 3.8 μg CpG-ODN), or OVA and LLO with PE-CpG-ODN conjugates (8 μg OVA and 4.6 μg CpG-ODN). OVA-specific CTL activity was monitored in vivo on day 10 by lysis of intravenously injected $CFSE^{HIGH}$-labeled SIINFEKL-pulsed splenocytes in comparison to $CFSE^{LOW}$-labeled influenza NP peptide-pulsed splenocytes. The CFSE profiles were analyzed by FACS 8.5 h after adoptive transfer. The mean ± SEM is shown (n = 5−7 mice per group).

liposomes were tested for their capacity to stimulate OVA-specific CTL activity relative to that of OVA-containing LLO-liposomes without CpG-ODN. Mice were vaccinated subcutaneously with liposomes normalized for the amount of OVA (8 μg), and ten days later, equal populations of $CFSE^{HIGH}$- and $CFSE^{LOW}$-labeled splenocytes were injected intravenously. The $CFSE^{HIGH}$ target cells were pulsed with the $CD8^+$ T-cell epitope SIINFEKL ($OVA_{257-264}$ peptide), while $CFSE^{LOW}$ control cells were pulsed with a nonspecific influenza NP peptide. The CTL responses were comparable when mice were immunized with liposomes co-encapsulating CpG-ODN or with lipid-conjugated CpG-ODNs; specific lysis was 66% ± 22% or 69% ± 13%, respectively (Figure 5). The OVA-specific lysis was significantly enhanced (p < 0.001) when mice were immunized with either of the liposome formulations containing CpG-ODN compared with liposomes containing only OVA and LLO (specific lysis of 9% ± 6%). These results indicate that lipid-conjugated CpG-ODNs are capable of interacting with TLR9, providing T cells with the additional costimulation required for optimal activation in vivo.

PE-CpG-ODNs Stimulate a Th1-type Immune Response Similar to Encapsulated CpG-ODNs. In addition to antigen-specific CTL induction, we evaluated the ability of $CD8^+$ T cells from the splenocytes of immunized mice to secrete IFN-γ ex vivo upon antigen-specific CD8 peptide stimulation. Splenocytes were incubated with the OVA CD8 peptide SIINFEKL for 76 h in culture, and the supernatants were harvested and analyzed for the amount of secreted IFN-γ by ELISA. Splenocytes from mice immunized with liposomes co-encapsulating OVA and LLO secreted 2702 (±1401) pg/mL IFN-γ (Figure 6A). IFN-γ secretion was significantly enhanced when CpG-ODN was co-encapsulated or lipid-conjugated: 42 599 (±9460) and 25 848 (±8534) pg/mL, respectively. As negative controls, media alone or the irrelevant NP peptide generated no detectable IFN-γ in any of the groups, while the positive control mitogen concanavalin A stimulate splenocytes from all groups to secrete IFN-γ (data not shown).

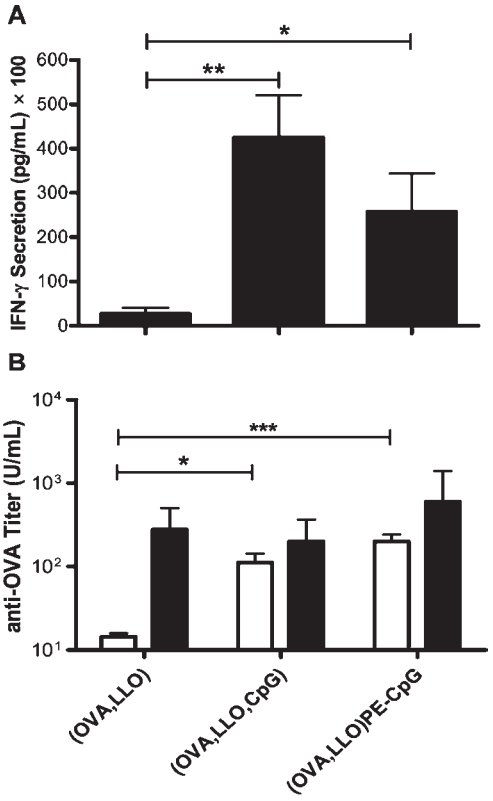

Figure 6. PE-CpG-ODNs stimulate a Th1-type immune response similar to that of encapsulated CpG-ODNs. (A) Mice were immunized with liposome formulations on day 0, and spleens were harvested on day 10. Isolated splenocytes were stimulated with SIINFEKL for 76 h and the resulting IFN-γ secretion was monitored by ELISA. The mean ± SEM is shown. (B) Sera were obtained from blood of immunized mice harvested by cardiac puncture on day 10. Anti-OVA IgG2a (open bars) and IgG1 (closed bars) were monitored using ELISA. The geometric mean titer ± SEM is shown (n = 7−8 mice per group).

The induction of anti-OVA Th1- and Th2-type antibodies in the immunized mice was monitored, in addition to investigating the cytokine milieus induced by the APCs. CpG-ODNs stimulate a Th1-type immune response mediated by the cytokine IFN-γ, which drives the production of Th1-type antibodies such as IgG2a. Mice immunized with (i) liposomal OVA and LLO only, (ii) liposomes encapsulating OVA and LLO with CpG-ODN, or (iii) liposomes encapsulating OVA and LLO with lipid-conjugated CpG-ODN all produced similar levels of anti-OVA IgG1 (Figure 6B). However, adding CpG-ODN, either encapsulated or conjugated, significantly enhanced the IgG2a antibody response: 80 (±31) U/mL or 158 (±43) U/mL, respectively, compared with mice immunized with liposomal OVA and LLO, 15 (±2) U/mL. Note that these antibody responses are relatively weak which is due to the fact that prime only, and not prime-boost, was employed; similar studies performed with prime-boost regimens resulted in stronger anti-OVA antibody responses with similar trends, confirming the results illustrated here by the prime-only study. These results are consistent with the IFN-γ secretion data, indicating that conjugating CpG-ODN to lipid and incorporating it onto the liposomal membrane does not alter the ability of the CpG-ODN to stimulate a Th1-type response as shown by the ex vivo IFN-γ secretion upon CD8 peptide stimulation and the Th1-type antibody induction.

Although reduced immunostimulatory activity of CpG-ODNs has been reported for some CpG-containing sequences after conjugation at the 5′-end,[29,36] the activity of the CpG-ODN ISS 1018 used in this study appears to be unaffected by the choice of terminus (5′ or 3′) used for coupling when conjugated to proteins (G. Ott, personal communication). Consistent with these findings, we observed similar CTL and Th1 responses when CpG-ODN were conjugated through the 5′-end or encapsulated. It is possible that the predicted reduction in immunostimulatory activity observed with 5′-conjugated CpG-ODNs was offset here by (i) the liposomal surface position of PE-CpG-ODN more readily allowing interactions with TLR9 vis-à-vis encapsulated CpG-ODN, or (ii) PE-CpG-ODNs on the liposome surface may enhance uptake by APCs, similar to that which has been observed with antigen-CpG-ODN-conjugates.[37] Regardless of any potential mechanistic implications, this study demonstrates that liposomes containing lipid-conjugated CpG-ODNs are capable of stimulating an immune response that is skewed toward the Th1-type, and future studies may include conjugation at the 3′-end, which typically results in a relatively smaller reduction in immunostimulatory activity.[29,36] The study reported here was performed solely to compare the effects of incorporating CpG-ODNs in the liposomal formulation through either lipid-conjugation or encapsulation; however, future studies are required to determine the optimal PE-CpG-ODN density in the liposome membrane for LLO-liposomes as well as the orientation of the conjugation.

CONCLUSION

We have evaluated two methods for including CpG-ODNs in an LLO-liposome vaccine carrier. Conjugating CpG-ODNs to lipid allows the design of a liposome-based delivery platform that results in greater recovery of CpG-ODNs than does passive encapsulation. Moreover, lipid-conjugated CpG-ODNs in the liposome membrane exhibit immunostimulatory activity both in vitro and in vivo. The results in this report strongly suggest that LLO-containing liposomes with lipid-conjugated CpG-ODN are a versatile and efficient delivery vehicle that may be used with a variety of antigens for vaccination. The strong CTL and Th1-type immune responses indicate the potential for this vaccine delivery system for a variety of vaccines against viruses or cancer.

AUTHOR INFORMATION

Corresponding Author

*Kyung-Dall Lee, University of Michigan, College of Pharmacy, Department of Pharmaceutical Sciences, 428 Church St., Ann Arbor, MI 48109-1065 Tel.: 734-647-4941; Fax: 734-764-6282; E-mail: kdl.cmdt@umich.edu.

ACKNOWLEDGMENT

The authors would like to thank Zachary F. Walls, Ph.D., for helpful discussions. This work was supported by NIH R01 AI047173 to K.D.L. C.D.A. was supported by NIH GM008353 and the American Foundation for Pharmaceutical Education.

REFERENCES

(1) Guy, B. (2007) The perfect mix: recent progress in adjuvant research. *Nat. Rev. Microbiol. 5*, 505–17.

(2) Ott, G., Barchfeld, G. L., and Van Nest, G. (1995) Enhancement of humoral response against human influenza vaccine with the simple submicron oil/water emulsion adjuvant MF59. *Vaccine 13*, 1557–62.

(3) O'Hagan, D. T., and Rappuoli, R. (2004) Novel approaches to vaccine delivery. *Pharm. Res. 21*, 1519–30.

(4) Medzhitov, R. (2001) Toll-like receptors and innate immunity. *Nat. Rev. Immunol. 1*, 135–45.

(5) Reed, S. G., Bertholet, S., Coler, R. N., and Friede, M. (2009) New horizons in adjuvants for vaccine development. *Trends Immunol. 30*, 23–32.

(6) Krieg, A. M. (2002) CpG motifs in bacterial DNA and their immune effects. *Annu. Rev. Immunol. 20*, 709–60.

(7) Schwartz, R. H. (2003) T cell anergy. *Annu. Rev. Immunol. 21*, 305–34.

(8) Cho, H. J., Takabayashi, K., Cheng, P. M., Nguyen, M. D., Corr, M., Tuck, S., and Raz, E. (2000) Immunostimulatory DNA-based vaccines induce cytotoxic lymphocyte activity by a T-helper cell-independent mechanism. *Nat. Biotechnol. 18*, 509–14.

(9) Tighe, H., Takabayashi, K., Schwartz, D., Marsden, R., Beck, L., Corbeil, J., Richman, D. D., Eiden, J. J., Jr., Spiegelberg, H. L., and Raz, E. (2000) Conjugation of protein to immunostimulatory DNA results in a rapid, long-lasting and potent induction of cell-mediated and humoral immunity. *Eur. J. Immunol. 30*, 1939–47.

(10) Li, W. M., Dragowska, W. H., Bally, M. B., and Schutze-Redelmeier, M. P. (2003) Effective induction of CD8+ T-cell response using CpG oligodeoxynucleotides and HER-2/neu-derived peptide co-encapsulated in liposomes. *Vaccine 21*, 3319–29.

(11) de Jong, S., Chikh, G., Sekirov, L., Raney, S., Semple, S., Klimuk, S., Yuan, N., Hope, M., Cullis, P., and Tam, Y. (2007) Encapsulation in liposomal nanoparticles enhances the immunostimulatory, adjuvant and anti-tumor activity of subcutaneously administered CpG ODN. *Cancer Immunol. Immunother. 56*, 1251–64.

(12) Gursel, I., Gursel, M., Ishii, K. J., and Klinman, D. M. (2001) Sterically stabilized cationic liposomes improve the uptake and immunostimulatory activity of CpG oligonucleotides. *J. Immunol. 167*, 3324–8.

(13) Standley, S. M., Mende, I., Goh, S. L., Kwon, Y. J., Beaudette, T. T., Engleman, E. G., and Frechet, J. M. (2007) Incorporation of CpG oligonucleotide ligand into protein-loaded particle vaccines promotes antigen-specific CD8 T-cell immunity. *Bioconjugate Chem. 18*, 77–83.

(14) Zwiorek, K., Bourquin, C., Battiany, J., Winter, G., Endres, S., Hartmann, G., and Coester, C. (2008) Delivery by cationic gelatin nanoparticles strongly increases the immunostimulatory effects of CpG oligonucleotides. *Pharm. Res. 25*, 551–62.

(15) Straubinger, R. M., Papahadjopoulos, D., and Hong, K. L. (1990) Endocytosis and intracellular fate of liposomes using pyranine as a probe. *Biochemistry 29*, 4929–39.

(16) Latz, E., Schoenemeyer, A., Visintin, A., Fitzgerald, K. A., Monks, B. G., Knetter, C. F., Lien, E., Nilsen, N. J., Espevik, T., and Golenbock, D. T. (2004) TLR9 signals after translocating from the ER to CpG DNA in the lysosome. *Nat. Immunol. 5*, 190–8.

(17) Lee, K. D., Oh, Y. K., Portnoy, D. A., and Swanson, J. A. (1996) Delivery of macromolecules into cytosol using liposomes containing hemolysin from Listeria monocytogenes. *J. Biol. Chem. 271*, 7249–52.

(18) Mandal, M., and Lee, K. D. (2002) Listeriolysin O-liposome-mediated cytosolic delivery of macromolecule antigen in vivo: enhancement of antigen-specific cytotoxic T lymphocyte frequency, activity, and tumor protection. *Biochim. Biophys. Acta 1563*, 7–17.

(19) Mandal, M., Kawamura, K. S., Wherry, E. J., Ahmed, R., and Lee, K. D. (2004) Cytosolic delivery of viral nucleoprotein by listeriolysin O-liposome induces enhanced specific cytotoxic T lymphocyte response and protective immunity. *Mol. Pharm. 1*, 2–8.

(20) Portnoy, D. A., and Jones, S. (1994) The cell biology of Listeria monocytogenes infection (escape from a vacuole). *Ann. N.Y. Acad. Sci. 730*, 15–25.

(21) Stier, E. M., Mandal, M., and Lee, K. D. (2005) Differential cytosolic delivery and presentation of antigen by listeriolysin O-liposomes to macrophages and dendritic cells. *Mol. Pharm. 2*, 74–82.

(22) Bartlett, G. R. (1958) Organization of red cell glycolytic enzymes; cell coat phosphorus transfer. *Ann. N.Y. Acad. Sci. 75*, 110–4.
(23) Sun, X., Provoda, C., and Lee, K. D. (2010) Enhanced in vivo gene expression mediated by listeriolysin o incorporated anionic LPDII: Its utility in cytotoxic T lymphocyte-inducing DNA vaccine. *J. Controlled Release 148*, 219–225.
(24) Barton, G. M., Kagan, J. C., and Medzhitov, R. (2006) Intracellular localization of Toll-like receptor 9 prevents recognition of self DNA but facilitates access to viral DNA. *Nat. Immunol. 7*, 49–56.
(25) Kumagai, Y., Takeuchi, O., and Akira, S. (2008) TLR9 as a key receptor for the recognition of DNA. *Adv. Drug Delivery Rev. 60*, 795–804.
(26) Thomas, P. D., and Poznansky, M. J. (1989) Curvature and composition-dependent lipid asymmetry in phosphatidylcholine vesicles containing phosphatidylethanolamine and gangliosides. *Biochim. Biophys. Acta 978*, 85–90.
(27) Semple, S. C., Klimuk, S. K., Harasym, T. O., Dos Santos, N., Ansell, S. M., Wong, K. F., Maurer, N., Stark, H., Cullis, P. R., Hope, M. J., and Scherrer, P. (2001) Efficient encapsulation of antisense oligonucleotides in lipid vesicles using ionizable aminolipids: formation of novel small multilamellar vesicle structures. *Biochim. Biophys. Acta 1510*, 152–66.
(28) Lee, K. D., Hong, K., and Papahadjopoulos, D. (1992) Recognition of liposomes by cells: in vitro binding and endocytosis mediated by specific lipid headgroups and surface charge density. *Biochim. Biophys. Acta 1103*, 185–97.
(29) Beaudette, T. T., Bachelder, E. M., Cohen, J. A., Obermeyer, A. C., Broaders, K. E., Frechet, J. M., Kang, E. S., Mende, I., Tseng, W. W., Davidson, M. G., and Engleman, E. G. (2009) In vivo studies on the effect of co-encapsulation of CpG DNA and antigen in acid-degradable microparticle vaccines. *Mol. Pharm. 6*, 1160–9.
(30) Ewald, S. E., Lee, B. L., Lau, L., Wickliffe, K. E., Shi, G. P., Chapman, H. A., and Barton, G. M. (2008) The ectodomain of Toll-like receptor 9 is cleaved to generate a functional receptor. *Nature 456*, 658–62.
(31) Park, B., Brinkmann, M. M., Spooner, E., Lee, C. C., Kim, Y. M., and Ploegh, H. L. (2008) Proteolytic cleavage in an endolysosomal compartment is required for activation of Toll-like receptor 9. *Nat. Immunol. 9*, 1407–14.
(32) Beauregard, K. E., Lee, K. D., Collier, R. J., and Swanson, J. A. (1997) pH-dependent perforation of macrophage phagosomes by listeriolysin O from Listeria monocytogenes. *J. Exp. Med. 186*, 1159–63.
(33) Ishii, K. J., and Akira, S. (2006) Innate immune recognition of, and regulation by, DNA. *Trends Immunol. 27*, 525–32.
(34) Latz, E., Verma, A., Visintin, A., Gong, M., Sirois, C. M., Klein, D. C., Monks, B. G., McKnight, C. J., Lamphier, M. S., Duprex, W. P., Espevik, T., and Golenbock, D. T. (2007) Ligand-induced conformational changes allosterically activate Toll-like receptor 9. *Nat. Immunol. 8*, 772–9.
(35) Haas, T., Metzger, J., Schmitz, F., Heit, A., Muller, T., Latz, E., and Wagner, H. (2008) The DNA sugar backbone 2′ deoxyribose determines toll-like receptor 9 activation. *Immunity 28*, 315–23.
(36) Kandimalla, E. R., Bhagat, L., Yu, D., Cong, Y., Tang, J., and Agrawal, S. (2002) Conjugation of ligands at the 5′-end of CpG DNA affects immunostimulatory activity. *Bioconjugate Chem. 13*, 966–74.
(37) Shirota, H., Sano, K., Hirasawa, N., Terui, T., Ohuchi, K., Hattori, T., Shirato, K., and Tamura, G. (2001) Novel roles of CpG oligodeoxynucleotides as a leader for the sampling and presentation of CpG-tagged antigen by dendritic cells. *J. Immunol. 167*, 66–74.

Bioconjugate Chemistry

ARTICLE

pubs.acs.org/bc

Synthesis, In Vitro Evaluation, and In Vivo Metabolism of Fluor/Quencher Compounds Containing IRDye 800CW and Black Hole Quencher-3 (BHQ-3)

Karen E. Linder,* Edmund Metcalfe, Palaniappa Nanjappan, Thangavel Arunachalam, Kimberly Ramos, Tina Marie Skedzielewski, Edmund R. Marinelli, Michael F. Tweedle,† Adrian D. Nunn, and Rolf E. Swenson

Ernst Felder Laboratories, Bracco Research USA, 305 College Road East, Princeton, New Jersey 08540, United States

Supporting Information

ABSTRACT: Protease-cleavable peptides containing a suitable fluor/quencher (Fl/Q) pair are optically dark until cleaved by their target protease, generating fluorescence. This approach has been used with many Fl/Q pairs, but little has been reported with IRDye 800CW, a popular near-infrared (NIR) fluor. We explored the use of the azo-bond-containing Black Hole Quencher 3 (BHQ-3) as a quencher for IRDye 800CW and found that IRDye 800CW/BHQ-3 is a suitable Fl/Q pair, despite the lack of proper spectral overlap for fluorescence resonance energy transfer (FRET) applications. Cleavage of IRDye 800CW-PLGLK(BHQ-3)AR-NH_2 (**8**) and its D-arginine (Darg) analogue (**9**) by matrix metalloproteinases (MMPs) in vitro yielded the expected cleavage fragments. In vivo, extensive metabolism was found. Significant decomposition of a "non-cleavable" control IRDye 800CW-(1,13-diamino-4,7,10-trioxatridecane)-BHQ-3 (**10**) was evident in plasma of normal mice by 3 min post injection. The major metabolite showed a m/z and UV/vis spectrum consistent with azo bond cleavage in the BHQ-3 moiety. Preparation of an authentic standard of this metabolite (**11**) confirmed the assignment. Although the IRDye 800CW/BHQ-3 constructs showed efficient contact quenching prior to enzymatic cleavage, BHQ-3 should be used with caution in vivo, due to instability of its azo bond.

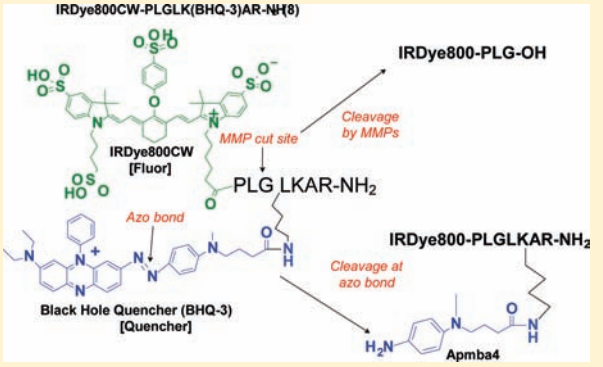

INTRODUCTION

In vivo optical imaging using compounds that fluoresce in the near-infrared (NIR) region ~750−900 nm is a useful research tool. This spectral region is marked by both low autofluorescence and absorbance minima for water, hemoglobin, and lipids. Use of NIR fluors such as Indocyanine Green (ICG) or IRDye 800CW facilitates both access of the excitation light to the fluorophore and escape of emitted fluorescence from the animal to the detector, due to the significant tissue penetration depths attainable.[1,2]

NIR fluorescent probes fall into three main classes. The first are nonspecific agents, often consisting of only a fluorophore itself. These have been used to visualize the lymphatic system[3] and to image pathology in areas where exit from the vasculature is enhanced due to leakage, such as tumors[4,5] or arthritis.[6,7] Here, contrast is obtained due to enhanced extravasation and/or delayed clearance from abnormal tissue. The second type of probe is a targeted agent labeled with a fluorophore. These agents are also permanently fluorescent and range in size from small molecules and peptides to antibodies and nanoparticles.[8] With such compounds, sufficient clearance from blood and nontarget tissues is required to detect localization in the target compounds.

Fluorophore-containing constructs of the third type are designed to become fluorescent only after proteolytic cleavage.[9,10] Such "smart probes" or "activatable probes" either contain a multiplicity of self-quenching fluors or contain a nonfluorescent quencher that "quenches" fluorescence in the intact construct (Figure 1). After cleavage, the fluorophore and quencher are separated, resulting in an increased fluorescent signal. Such compounds are optically dark before cleavage, so background signal from parent compound does not interfere with signal at the target. This is an obvious advantage that stands in contrast to typical fluorescently labeled compounds, where both the parent compound and its metabolites are fluorescent.

Many activatable probes are labeled with a fluor and quencher that allegedly undergo fluorescence resonance energy transfer (FRET), wherein the emission of the fluor falls within the absorbance envelope of the quencher. Such an approach has long been used for the detection of protease activity[11−13] in vitro. Enzyme activity in cells or biological fluids can be readily measured in a functional assay, based on the fluorescence generated following proteolytic cleavage of a synthetic fluor/quencher peptide that contains a substrate for the enzyme of interest.

Received: October 16, 2010
Revised: May 31, 2011
Published: June 04, 2011

ACS Publications © 2011 American Chemical Society

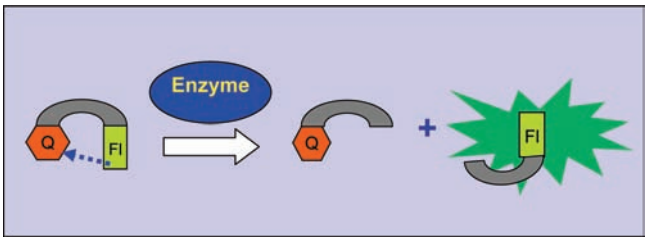

Figure 1. Schematic for protease-cleavable activatable probes. Fluorescence is quenched until proteolytic cleavage, which separates the fluor and quencher, generating fluorescence.

Several types of dual-labeled fluor/quencher oligonucleotide probes (e.g., "molecular beacons") have also been developed[14,15] for the in vitro or in vivo monitoring of DNA and RNA-related processes such as polymerase chain reactions hybridization, sequencing, and ligation.

Activatable fluor/quencher probes have been used successfully for imaging or in vitro studies with peptide-containing constructs cleaved by cathepsins,[16−20] MMPs,[21−24] and caspases.[9,25−27] The cyanine dye Cy5.5 [excitation/emission (Ex/Em), 660/710 nm] is frequently used as a fluor in such constructs. Reported studies on molecules labeled with IRDye 800CW[28] are somewhat limited,[3,29−34,36] and to our knowledge, no studies on FRET-based compounds containing IRDye 800CW (Ex/Em: 778/789 nm) have been reported to date. This is likely due to the fact that until recently[35] no commercial quenchers with the proper spectral characteristics to quench the dye via FRET have been available. An effective quencher for IRDye 800CW would be of significant interest, as it has been reported that an anti-EGF antibody labeled with IRDye 800CW showed significantly reduced background from autofluorescence relative to its Cy5.5 analogue, leading to an enhanced tumor to background ratio.[36]

On the basis of its effectiveness as a quencher in other systems, we decided to evaluate the effectiveness of the "dark" quencher known as Black Hole Quencher 3 (BHQ-3)[37] to quench IRDye 800CW, despite the fact that it does not show the spectral overlap needed for FRET (Figure 8a). BHQ-3 is widely used in DNA duplex probes, where a fluorescent emitter is on one strand and an acceptor is on the complementary one,[38] and in activatable probes to quench Cy5.5, Cy5, fluorescein, and pheophorbide.[26,39]

To probe the quenching capabilities of this combination, we have prepared an IRDye 800CW/BHQ-3 analogue of the well-known matrix metalloproteinase (MMP)-cleavable sequence Mca-Pro-Leu-Gly-Leu-Dap(Dnp)-Ala-Arg-NH_2, first identified by Knight et al.,[40] where Mca is 7-methoxycoumarin and Dnp is the quencher 2,4-dinitrophenyl. This compound is commercially available for the detection of MMPs in vitro, but does not have the proper spectral properties for in vivo imaging. An imaging agent for the detection of MMP activity in vivo would be of interest, as this family of highly homologous proteases collectively cleave most, if not all, of the constituents of the extracellular matrix (ECM) and have been implicated in the growth and metastasis of tumors[41,42] and in inflammatory processes such as arthritis.[43]

The studies described here show that IRDye 800CW-PLGLK-(BHQ-3)-AR-NH_2 (**8**) and its D-arginine analogue (**9**) are effective substrates for MMPs and that IRDye 800CW/BHQ-3 is a suitable Fl/Q pair, despite the lack of proper spectral overlap for FRET. This manuscript describes the synthesis, spectral characterization, in vitro cleavage by MMPs, and in vivo pharmacokinetics and metabolism of **8** and **9** and a "noncleavable" control with a PEG linker (IRDye 800CW-Ttda-(BHQ-3) (**10**), along with synthesis and characterization of selected analogues and metabolites.

EXPERIMENTAL PROCEDURES

Synthesis of Fluor-Quencher Constructs and Intermediates. Solvents were E. Merck Omni grade. *N*,*N*-Dimethylformamide (DMF) was purchased from Pharmco Products Inc. and was peptide synthesis grade or low water/amine-free Biotech grade quality. Piperidine (sequencing grade, redistilled 99+%) and trifluoroacetic acid (TFA, spectrophotometric grade or sequencing grade) were purchased from Sigma-Aldrich Corporation or Fluka. *N*,*N*′-Diisopropylcarbodiimide (DIC), *N*,*N*-diisopropylethylamine (DIEA), *O*-(*N*-succinimidyl)-*N*,*N*,*N*′,*N*′-bis-(tetramethylene) uronium hexafluorophosphate (HSPyU), and triisopropylsilane (TIPS) were purchased from Sigma-Aldrich. The 4,7,10-trioxatridecane-1,13-diamine (Ttda), Fmoc-protected amino acids, *O*-(benzotriazol-1-yl)-*N*,*N*,*N*′,*N*′-tetramethyluronium hexafluorophosphate (HBTU), and *N*-hydroxybenzotriazole (HOBt) were purchased from Novabiochem. Black hole quencher 3 carboxylic acid succinimidyl ester (BHQ3-OSu) was purchased from Biosearch Technologies, Inc. and IRDye 800CW-NHS ester (NHS = *N*-hydroxysuccinimide) was purchased from LI-COR Biosciences.

HPLC and MS. Analytical HPLC data were obtained using a Shimadzu LC-10AT VP dual-pump gradient system using a Waters XTerra MS-C18 column (4.6 × 50 mm, 5 μ, 120 Å, 3 mL/min flow rate) and linear gradient elution using H_2O/(0.1% TFA) and CH_3CN/(0.1% TFA) as solvents A and B, respectively. Compounds were detected at 220 and 254 nm (deuterium lamp) or at 701 and 790 nm (tungsten lamp). Preparative HPLC was conducted on a Shimadzu LC-8A dual-pump gradient system equipped with a SPD-10AV UV detector and a Waters XTerra Prep MS-C18 column (19 × 300 mm, 10 μ, 120 Å) using gradient elution with H_2O/(0.1% TFA) and CH_3CN/(0.1% TFA) as solvents A and B, respectively, and a flow rate of 40 mL/min unless otherwise stated. Generally, the crude peptide solution was loaded onto the column using a third pump. Reaction mixture solvents were eluted from the column at low organic phase composition, followed by linear gradient elution with increasing percentages of solvent B.

Mass spectral data were obtained in-house on an Agilent LC-MSD (1100) mass spectrometer using API-ES in ∓ ion mode. MS results and HPLC purity were used to monitor the completeness of reactions, and to select appropriate fractions during HPLC purification.

Solid-Phase Peptide Synthesis of Peptides 1 and 2. Fmoc-protected linear peptides Fmoc-Pro-Leu-Gly-Leu-Lys-Ala-X-NH_2, X = Arg (**1**) and D-arginine (**2**) were synthesized on a 0.25 mmol scale with an ABI 433A Peptide Synthesizer employing FastMoc protocols, Fmoc-Pal-Peg-PS, or NovaSyn TG Sieber resin (0.2 mmol/g), Fmoc-protected amino acids, and HBTU-mediated HOBt ester activation. The general methods used for preparation were described previously.[44] Compounds were analyzed using gradient elution from 20% to 65% B over 15 min. Detection: UV at 230 and 254 nm. Both **1** and **2** had a retention time t_R = 6.29 min. MS: m/z = 975.2 $[M+H]^+$; 487.5 $[M+2H]^{2+}/2$.

Preparation of BHQ3-Containing Peptides 3 and 4. (BHQ-3)-OSu (5 mg, 0.0063 mmol) was added to a solution of peptide

1 or **2** (10 mg, 0.0068 mmol) in dry DMF (0.3 mL), followed by DIEA (10 mg, 0.077 mmol). The mixture was stirred for 4 h at room temperature (r.t.) in a foil-covered flask to protect from light, then diluted to 10 mL with dry DMF. Piperidine (0.2 mL) was added, and the mixture was stirred for 30 min to remove the Fmoc group. The reaction mixture was diluted to 50 mL with water and loaded onto a preparative HPLC column. After the sample was applied to the column, the eluant was ramped to 20% B over 1 min, followed by a linear gradient to 45% B over 50 min. Fractions (15 mL) were manually collected using absorbance at 700 nm as an indicator of product elution. Product-containing fractions were combined and freeze−dried to afford 5 to 7 mg (40−50% yield) of the desired BHQ-3-containing peptide (>95% purity). Compounds were analyzed by HPLC using gradient elution from 25% to 55% B over 30 min. Detection: 701 and 790 nm. Both **3** and **4** had a t_R = 6.23 min. MS: m/z = 1282.7 $[M+H]^+$; 641.5 $[M+2H]^{2+}/2$.

Addition of IRDye 800CW to Form 8 and 9. IRDye 800CW-NHS ester (3 mg, 0.0026 mmol) was added to a solution of the peptide-(BHQ-3) conjugate **3** or **4** (3 mg, 0.0017 mmol) in dry DMF (0.3 mL), followed by DIEA (10 mg, 0.077 mmol). The solution was stirred for 8 h at r.t., protected from light. After completion of the coupling reaction with IRDye 800CW NHS ester, the reaction mixture was diluted to 20 mL with water, loaded onto the preparative HPLC column, purified, and freeze−dried. Isolated **8** and **9** were analyzed by HPLC using gradient elution from 15% to 45% B over 20 min. Detection: 701 and 790 nm. Yield: 2−3 mg (30−40%). Purity: >98%, t_R = 6.27 min, MS: m/z = 2268.8 $[M+H]^+$; 1134.0 $[M+2H]^{2+}/2$; 756.4 $[M+3H]^{3+}/3$.

1-*N*-(BHQ-3)-13-amino-4,7,10-trioxatridecane (H-Ttda-BHQ-3) (5). BHQ-3 NHS ester (17 mg, 0.026 mmol) was added to a solution of 1-*N*-trityl-4,7,10-trioxatridecane-13-amine (Ttda, 10 mg, 0.022 mmol) and DIEA (10 mg, 0.038 mmol) in CH_2Cl_2 (1 mL) and stirred for 3 h at r.t. Volatiles were removed on a rotary evaporator, and the paste obtained was treated with a mixture of CH_2Cl_2/TFA/TIPS (5 mL, 90:5:5) and stirred for 2 h to remove the trityl group. After evaporation of volatiles, the paste was redissolved in H_2O/CH_3CN (5 mL, 1:1), purified by preparative HPLC (flow rate = 40 mL/min) and freeze−dried. Isolated **5** eluted at 6.28 min using gradient elution from 25% to 55% B over 30 min. Detection: 701 and 790 nm. Yield: 9 mg (46%). Purity: >95%. MS: m/z = 750 $[M+H]^+$; 375.8 $[M+2H]/2$.

IRDye 800CW-Ttda-BHQ-3 (10). PEG-containing fluor/quencher construct **10** was prepared by coupling IRDye 800CW NHS ester (8 mg, 0.007 mmol) to **5** (5 mg, 0.007 mmol), following the general procedure described for **8** and **9** above. The resulting solid was analyzed using gradient elution from 25% to 65% B over 15 min. Detection: 701 and 790 nm. It was isolated as a fluffy dark blue−green solid in 40% yield (5 mg). Purity: >98%. t_R = 6.60 min, MS: m/z = 1733.2 $[M-H]^-$; 1155.2 $[2M-3H]/3$; 865.6 $[M-2H]/2$.

***N*-*t*-Butyloxycarbonyl-1,4-phenylenediamine (14).** Di-*t*-butyldicarbonate (6.2 g, 28 mmol) was added to a solution of 1,4-phenylenediamine·2HCl (**13**) (5 g, 28 mmol) and K_2CO_3 (8.0 g, 58 mmol) in dioxane−water (2:1, 100 mL). The mixture was stirred at r.t. for 4 h, volatiles were removed on a rotary evaporator, and the product was added to water (50 mL) to precipitate the product. The solid was filtered, washed with water (2 × 50 mL), and dried to yield **14** as a colorless solid (7.5 g, 78%). ^{1}H NMR (500 MHz, $CDCl_3$) δ 1.52 (s, 9H, C_4H_9), 6.22 (bs, 1H, N*H*) and 7.17, 7.34 (2 d, 4H, Ar*H*). MS: m/z = 208 $[M+H]^+$.

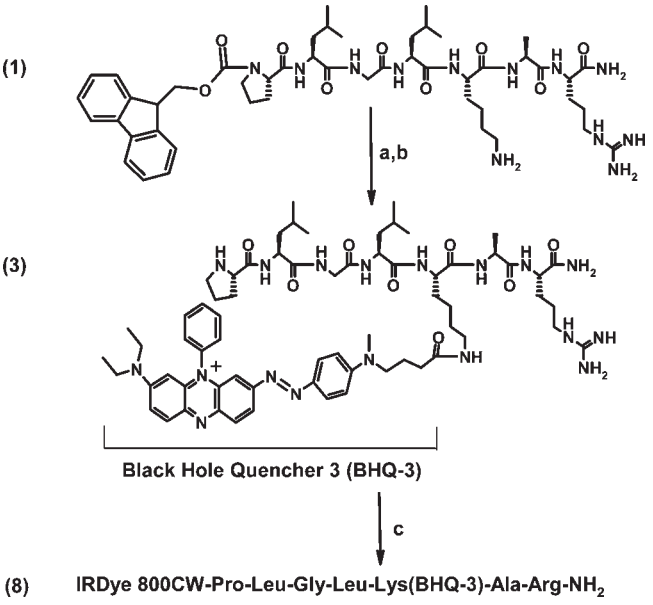

Figure 2. Synthesis of IRDye 800CW-PLGLK(BHQ-3)-AR-NH_2 (**8**). a) (BHQ-3)-OSu, DIEA, NMP, DMF, RT, 4 h; b) Piperidine, NMP, RT, 30 min; c) IRDye800CW NHS ester, DIEA, DMF, RT, 8 h.

Ethyl 4-*N*-(4-*t*-Boc-aminophenyl)-butyrate (15). Ethyl 4-bromobutyrate (2.25 g, 11.5 mmol) was added to a solution of **14** (2 g, 9.6 mmol) and powdered anhydrous K_2CO_3 (2.7 g, 19.3 mmol) in dry DMF (20 mL) and heated at 60 °C for 4 h. The reaction mixture was then poured into ice-cooled water (100 mL), stirred, and filtered. The collected ethyl 4-*N*-(4-*t*-Boc-aminophenyl)butyrate **15** (Boc = *tert*-Butyloxycarbonyl) was isolated as a colorless solid, washed with water (3 × 50 mL), and dried. Yield: 2.8 g (90%). MS: m/z = 323 $[M+H]^+$.

4-*N*-(4-*t*-Boc-aminophenyl)-4-*N*-methylbutyric Acid (16). NaH (60% dispersion in mineral oil, 0.08 g, 2.0 mmol) was added to a solution of **15** (0.5 g, 1.56 mmol) in dry DMF (2 mL) and the mixture was stirred at r.t. for 30 min under N_2. Methyl iodide (0.25 g, 1.76 mmol) was added and the mixture was stirred for 4 h. LiOH (0.2 g, 8.3 mmol) in water−methanol (1:1, 1 mL) was added, and the reaction mixture was stirred for 2 h. After completion of the hydrolysis, the reaction mixture was diluted with H_2O to 5 mL and loaded onto the preparative HPLC column. After the sample solution was applied to the column, the HPLC system was ramped to 10% B over 1 min, followed by a linear gradient from 10% to 35% B over 50 min. Fractions (15 mL) were collected using UV at 230 nm as an indicator of product elution. Product-containing fractions of >95% purity were combined and freeze−dried to afford 0.25 g (52% yield) of the desired 4-*N*-(4-*t*-Boc-aminophenyl)-4-*N*-methylbutyric acid **16**. ^{1}H NMR (500 MHz, $CDCl_3$) δ 1.53 (s, 9H, C_4H_9), 1.79 (m, 2H, $CH_2CH_2CH_2$), 2.38 (t, 2H, CH_2COOH), 3.18 (s, 3H, CH_3), 3.61 (t, 2H, NCH_2) and 7.25, 7.54 (2 d, 4H, Ar*H*). MS: m/z = 309 $[M+H]^+$.

1-*N*-(4-*N*-(4-*t*-Boc-aminophenyl)-4-*N*-methylbutyroyl)-13-amino-4,7,10-trioxatridecane (H-Ttda-BocApmba4) (Apmba = 4-*N*-(4-Aminophenyl)-4-*N*-methylbutyric acid) (6). HSPyU (150 mg, 0.36 mmol) was added to a solution of **16** (100 mg, 0.32 mmol) in CH_2Cl_2 (2 mL), followed by DIEA (100 mg, 0.77 mmol), and stirred for 30 min at r.t. 1-*N*-Trityl-4,7,10-trioxatridecane-13-amine (Ttda, 100 mg, 0.22 mmol) was added, and the reaction mixture was stirred for an additional 3 h. Volatiles

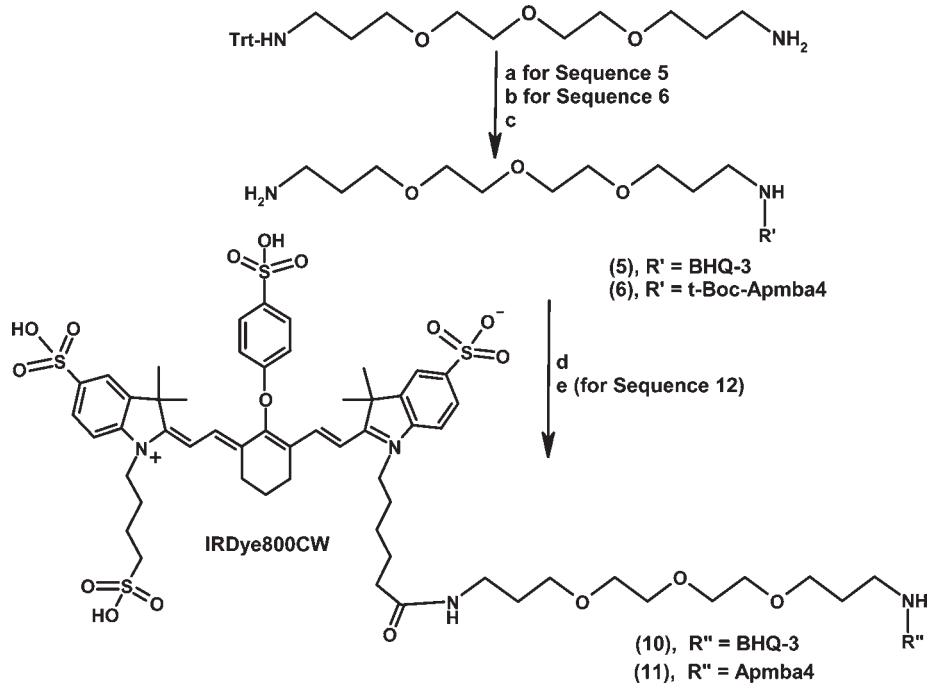

Figure 3. Synthesis of "noncleavable control" IRDye 800CW-Ttda-(BHQ-3) (**10**) and its azo-bond cleavage product IRDye 800CW-Ttda-Apmba4 (**11**). a) BHQ-3 NHS ester (1.2 eq.), NMP, DIEA, RT, 4 h; b) 4-*N*-(4-*t*-Boc-aminophenyl)-4-*N*-methylbutyric acid (1.2 eq.), HSPyU (1.2 eq.), DIEA (4 eq.), CH_2Cl_2, RT, 4 h; c) CH_2Cl_2:TFA:TIPS (95:2:3), RT, 30 min; d) IRDye800CW NHS ester (1 eq.), DIEA (3 eq.), CH_2Cl_2, RT. 4 h; e) CH_2Cl_2:TFA:TIPS (50:45:5), RT, 30 min.

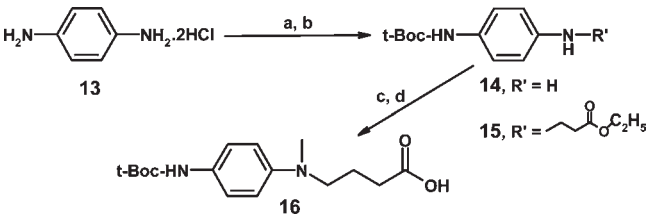

Figure 4. Synthesis of 4-*N*-(4-*t*-Boc-aminophenyl)-4-*N*-methylbutyric acid, 4-t-Boc Apmba4 (**16**). a) Di-t-butyldicarbonate (1.1 eq.), K_2CO_3 (2 eq.), Dioxane-water (1:1), RT, 4 h; b) Ethyl 4-bromobutyrate (1.2 eq.), K_2CO_3 (2 eq.), NMP, 60 °C, 6 h; c) CH_3I (1.2 eq.), NaH (1.1 eq.). NMP, RT, 6 h; d) LiOH (4 eq.), CH_3OH:H_2O (1:1), RT, 4 h.

were removed on a rotary evaporator, and the paste obtained was treated with a mixture of CH_2Cl_2/TFA/TIPS (5 mL, 95:2:3) and stirred for 2 h at r.t. to remove the trityl group. After evaporation of the volatiles, the paste was redissolved in H_2O/CH_3CN (5 mL, 1:1) and loaded onto a preparative HPLC column that had been pre-equilibrated with 5% B. After the sample was applied to the column, the eluant was ramped to 20% B over 1 min, followed by a linear gradient to 45% B over 50 min. Fractions of >95% purity were pooled and freeze−dried to afford **6** in 55% yield (62 mg). t_R = 6.47 min using gradient elution from 15% to 35% B over 20 min. MS: m/z = 510.8 $[M+H]^+$; 256.2 $[M+2H/2]$.

IRDye 800CW-Ttda-Apmba4 (11). IRDye 800CW-NHS ester (5 mg, 0.0045 mmol) was added to a solution of **6** (10 mg, 0.02 mmol) in CH_2Cl_2 (0.5 mL), followed by DIEA (10 mg, 0.077 mmol). The solution was stirred for 4 h at r.t., protected from light. After completion of the coupling reaction, volatiles were removed on a rotary evaporator and the paste obtained was treated with a mixture of CH_2Cl_2/TFA/TIPS (5 mL, 95:2:3) and stirred for 2 h to remove the trityl group. After evaporation of the volatiles, the paste was redissolved in H_2O/CH_3CN (5 mL, 1:1) and purified by preparative HPLC as described for **8** and **9**. Fractions of >95% purity were combined and freeze−dried to afford 2.8 mg (44%) of dark blue IRDye 800CW-Ttda-Apmba4 (**11**) (t_R = 6.98 min using a linear gradient of 20−60% B over 20 min). Detection: 701 and 790 nm. MS: 1396.7 $[M-H]^-$; 696.5 $[M-2H]/2$.

H-Pro-Leu-Gly-Leu-Lys(t-Boc-Apmba4)-Ala-D-arginine-NH_2 (7). HSPyU (40 mg, 0.10 mmol) was added to a solution of **16**

Table 1. Summary of Fluorogenic IRDye800CW/BHQ-3 Constructs, Intermediates, And Metabolites Synthesized

compound	peptide sequence	MW
1	Fmoc-Pro-Leu-Gly-Leu-Lys-Ala-Arg-NH_2	975
2	Fmoc-Pro-Leu-Gly-Leu-Lys-Ala-Darg-NH_2	975
3	H-Pro-Leu-Gly-Leu-Lys(BHQ-3)-Ala-Arg-NH_2	1283
4	H-Pro-Leu-Gly-Leu-Lys(BHQ-3)-Ala-Darg-NH_2	1283
5	H-Ttda-(BHQ-3)	750
6	H-Ttda-BocApmba4	511
7	H-Pro-Leu-Gly-Leu-Lys(Boc-Apmba4)-Darg-NH_2	1042
8	IRDye800CW-Pro-Leu-Gly-Leu-Lys (BHQ-3)-Ala-Arg-NH_2	2268
9	IRDye800CW-Pro-Leu-Gly-Leu-Lys (BHQ-3)-Ala-Darg-NH_2	2268
10	IRDye800CW-Ttda-(BHQ-3)	1735
11	IRDye800CW-Ttda-Apmba4	1397
12	IRDye800CW-Pro-Leu-Gly-Leu-Lys (Apmba4)-Ala-Darg-NH_2	1928

Table 2. Results from MMP Cleavage Assay[a]

	peptide without enzyme		MMP-1		MMP-2		MMP-3		MMP-9		MMP-13	
peptides	T = 0 (60) min	max RFU*	slope	*Y*-int.	slope	*Y*-int.	slope	*Y*-int.	slope	*Y*-int.	slope	*Y*-int.
IRDye800CW-PLGLK- (BHQ-3)-AR-NH_2 (**8**)	28 (22)	1755 ± 105	0.42	2.84	1.18	3.44	0.91	2.04	2.77	3.89	6.72	2.98
	28 (25)		0.28	3.47	1.60	3.51	0.76	2.33	2.41	2.85	6.66	4.84
	26 (23)		0.23	2.98	1.27	3.58	0.57	3.00	2.38	3.56	6.72	4.39
IRDye800CW-PLGLK- (BHQ-3)-A-r-NH_2 (**9**)	70 (63)	1574									6.70	5.65
IRDye800CW-Ttda-BHQ-3 (**10**)	119 (120)	121 (no cleavage									121 (no cleavage)	

[a] Int. = intercept. Max RFU = maximum fluorescence intensity (observed after 60 min at 37 °C in the presence of MMP-13).

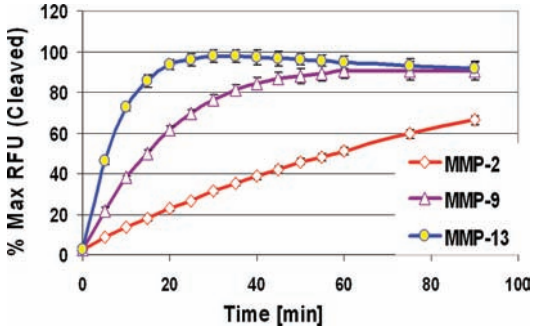

Figure 5. In vitro cleavage of IRDye 800CW-PLGLK(BHQ-3)AR-NH_2 (**8**) by MMP-2, -9, and -13 at r.t. (~23 °C). Cleavage is fastest with MMP-13.

(25 mg, 0.08 mmol) in CH_2Cl_2 (2 mL), followed by DIEA (50 mg, 0.38 mmol). The mixture was stirred for 30 min at r.t., Fmoc-Pro-Leu-Gly-Leu-Lys-Ala-D-arginine-NH_2 **2** (95 mg, 0.10 mmol) was added, and the reaction was stirred for an additional 3 h. The reaction mixture was diluted to 10 mL with dry DMF, piperidine (0.2 mL) was added, and the mixture was stirred for 30 min. After removal of the Fmoc group was completed, the reaction mixture was diluted with water to 50 mL and loaded onto the preparative HPLC column. Purification was performed as described for **3** and **4**, using UV at 230 nm as an indicator of product elution. Product-containing fractions of >95% purity were combined and freeze−dried. By HPLC using gradient elution from 15% to 35% B over 20, the isolated peptide **7** had a t_R = 9.98 min. MS: m/z = 1043.2 $[M+H]^+$; 522.4 $[M+2H]^{2+}/2$.

IRDye 800CW-Pro-Leu-Gly-Leu-Lys(Apmba4)-Ala-D-arginine-NH_2 (12). Compound **12**, an authentic standard for the azo-bond cleavage product of **9** was prepared by coupling the t-Boc-Apmba4-peptide containing compound **7** (5 mg, 0.005 mmol) with IRDye 800CW-NHS ester (5 mg, 0.0046 mmol), following the procedure described for **8** and **9**. **12** was isolated as a blue−green solid in 33% yield (3 mg). By HPLC using gradient elution from 20% to 60% B over 20 min, the compound had a t_R = 10.91 min. Detection: 701 and 790 nm. MS: m/z = 1926.4 $[M-H]^-$; 1283.8 $[2M-2H]^{2-}/3$; 962.4 $[M-3H]^{3-}/2$.

In Vitro Cleavage Studies with MMPs. Fluor/quencher-containing peptides were tested in an in vitro assay to determine their relative rates of cleavage by MMPs. MMPs (AnaSpec) were stored in 50 mM Tris-HCl, 150 mM NaCl, 10 mM $CaCl_2$ (pH 7.5) buffer at −80 °C until use. APMA (aminomethylphenyl mercuric acetate) was purchased from Sigma. The assay was performed in 96-well plates (NUNC MaxiSorb black plate) on a fluorescence plate reader (BioTek-Synergy2), using excitation and emission filters with 780 ± 20 and 820 ± 20 nm cutoff values, respectively. Peptide stock solutions (500 μM) in DMSO were diluted to 10 μM using assay buffer, just prior to assay. APMA solutions (10 mM) were prepared in water. MMPs (supplied at a concentration of 1 μg in 100 μL) were activated on the day of the study with 1 mM APMA just prior to assay, using incubation/activation times based on the manufacturer recommendations. As an example, MMP-13 (1 μg in 100 μL) was diluted to 450 μL in MMP assay buffer, mixed with APMA (10 mM, 50 μL), and incubated at 37 °C for 45 min. It was then cooled in ice (4 °C), diluted to 1.25 mL in assay buffer to give a final enzyme concentration of 0.8 μg/mL, and stored in ice until use. Each IRDye800-containing compound (50 μL of a 10 μM solution, ~500 pmol/well) was added to duplicate wells in a 96-well plate, followed by 50 μL of assay buffer. Various activated MMPs were added to the wells (50 μL, 0.8 μg/mL, 40 ng/well), providing a peptide to enzyme ratio of about 1000:1. The plate was incubated at r.t. (~23 °C) for up to 90 min. The progress of the enzymatic cleavage was determined by measuring the relative increase in fluorescence (RFU) using the plate reader. A parallel experiment was carried out at 37 °C to determine the maximum RFU emitted by the fully cleaved IRDye 800CW dye-containing fragment from each peptide tested. Data were normalized and plotted as % cleaved, rather than as relative fluorescence units (RFU), to allow comparison between different compounds with different final fluorescence values. The normalized data were plotted as % maximum vs time. From this, the initial slope and the *Y*-intercept were determined to obtain the rate of cleavage and the background fluorescence of the fluorogenic peptide under study.

LC/MS Analysis of In Vitro Cleavage Products. Following MMP cleavage studies with **8** or **9**, a 100 μL aliquot of the test well was analyzed by LC/MS to establish identity of the cleavage fragments formed.

In Vivo Metabolism Studies. Animal studies with **8**, **9**, and **10** were conducted in accordance with the U.S. Public Health Service Policy on Humane Care and Use of Laboratory Animals as well as institutional guidelines. Subjects (male Balb/cJ mice) were restrained in a Decapicone restrainer (Braintree Scientific). Test compound (40 nmol, 0.1 mL) was administered via the lateral tail vein. Retro-orbital or saphenous blood samples (15−50 μL) were collected from conscious animals at 3, 8, 20, 40, and 60 min into heparinized microvettes (Sarstedt Microvette CB300) and placed on ice immediately. Within 10 min of collection, each sample was centrifuged at 4 °C for 15 min at 1000 × *g* to remove the cellular fraction. Proteins were precipitated from a known

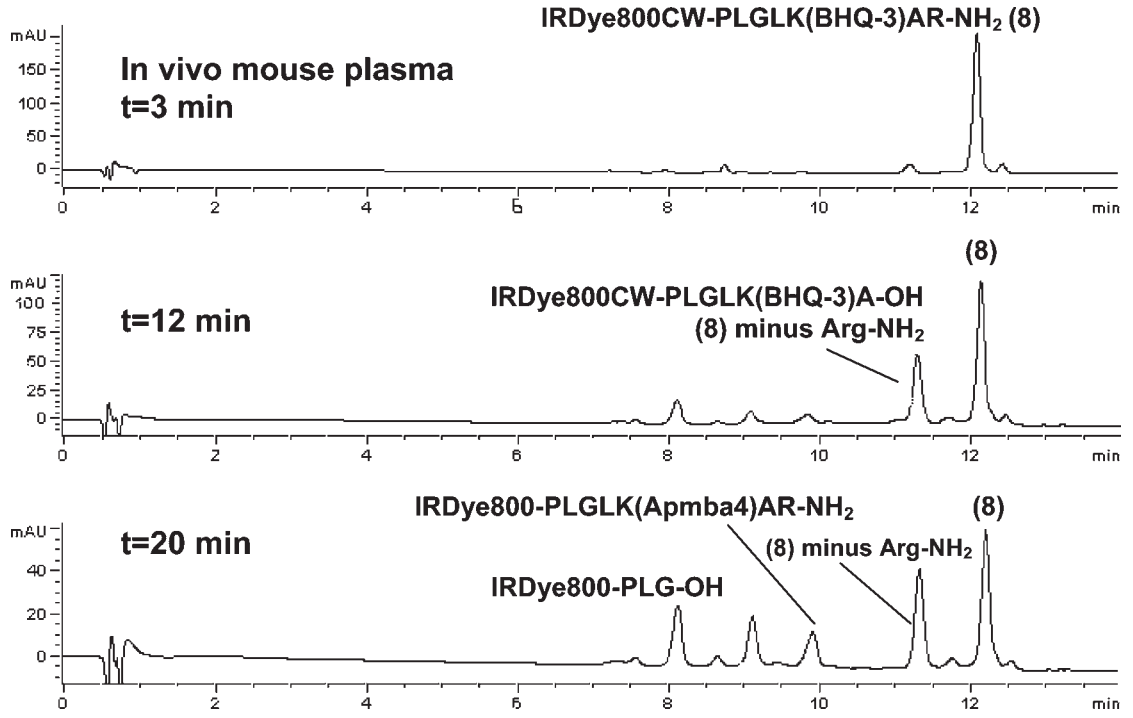

Figure 6. Time course for in vivo metabolism of IRDye 800CW-PLGLK(BHQ-3)AR-NH_2 (**8**) in mouse plasma. Over time, **8** is metabolized to a number of products. Peaks from t_R = 7−10 min contain spectral features for IRDye 800CW only; no BHQ-3 absorbance peak is observed.

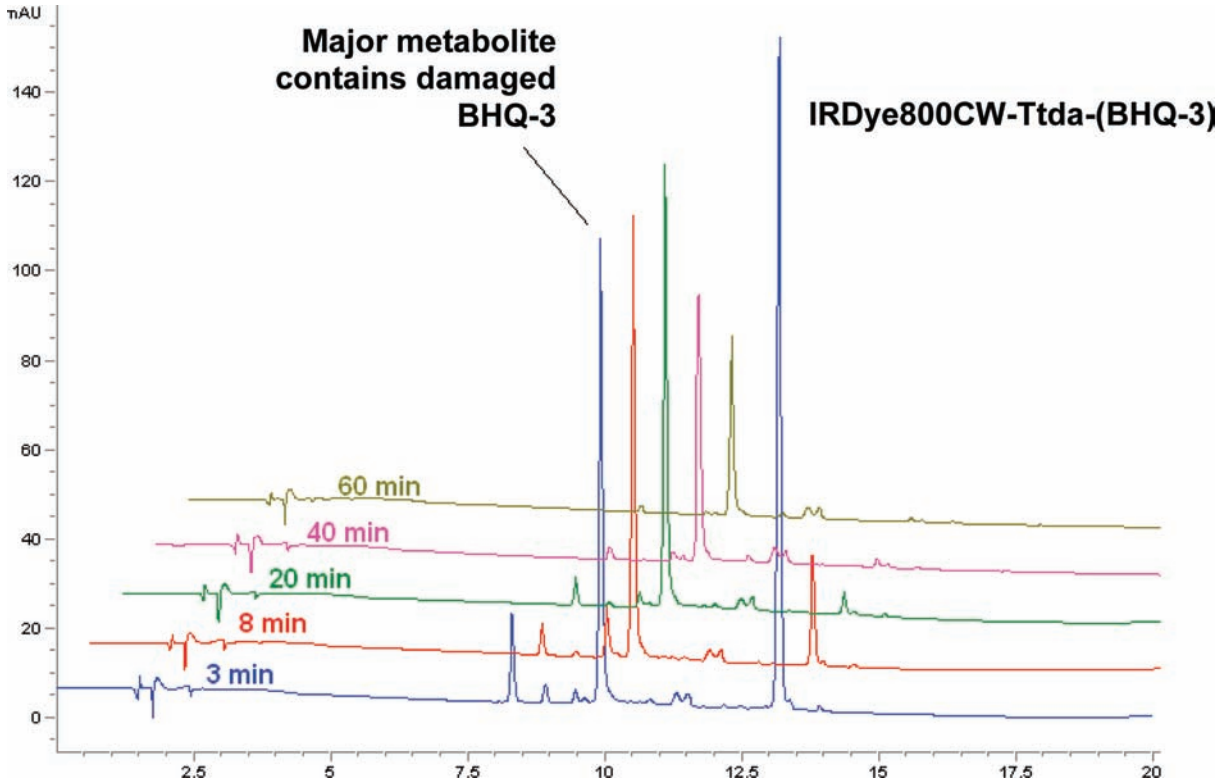

Figure 7. Time course for metabolism of IRDye 800CW-Ttda-(BHQ-3) in mouse plasma. Within 3 min, significant metabolism is evident, as shown by the rapid conversion of **10** at t_R of 12.65 min to a fluorescent metabolite with t_R of 10 min. By 20 min, almost no **10** remains. The primary metabolite coelutes with compound **11**.

volume of plasma using an equal volume of 50% EtOH, followed by a 3× volume of ice−cold CH_3CN, and centrifugation for 20 min at 20 000*g* at 4 °C. The supernates were taken to dryness (Speedvac), resuspended in 30% MeOH, and analyzed

dx.doi.org/10.1021/bc100457s |*Bioconjugate Chem.* 2011, 22, 1287–1297

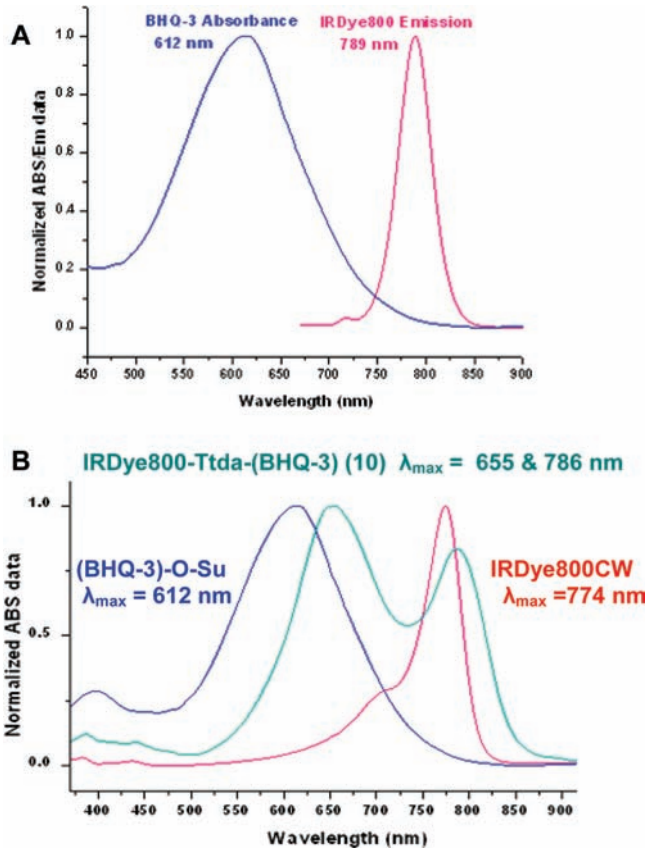

Figure 8. (A) Normalized absorbance spectrum of BHQ-3-O-succinimidyl ester (blue) and the fluorescence emission spectrum of IRDye 800CW in water (red). The spectral characteristics of the IRDye 800CW/BHQ-3 fluor/quencher pair are not suitable for quenching by FRET. (B) Normalized absorbance spectra of BHQ-3-O-succinimidyl ester (blue), IRDye 800CW (red), and IRDye 800CW-Ttda-(BHQ-3) **10** (green) in water. Conjugation of the quencher and fluor via a PEG-type linker causes a significant shift in the absorbance maxima associated with the quencher and fluor, suggestive of contact quenching.

by LC-MS at pH 6.8 on a Phenomenex Luna C8(2) column eluted with a gradient of 0−100% B over 20 min, where A = H_2O, and B = 1:1 CH_3CN/MeOH, both A and B containing 1 g/L NH_4OAc. Urine was collected from subjects following sacrifice by cervical dislocation, chilled on ice immediately, and treated as described for plasma.

In Vivo Metabolism Studies and Plasma Recovery. Compounds **8** and **10** were dissolved in DMSO to a concentration of 400 μM. For **10**, a second standard was prepared at 80 μM by diluting the 400 μM standard 1/5 in DMSO. These stock solutions were diluted to 1 μM, 20 μM, and 400 μM using mouse plasma (Lampire Biological Laboratories, Inc. or Innovative Research, Na Citrate anticoagulant). Samples were chilled on ice immediately, and then processed, extracted, resuspended, and HPLC analyzed in an identical fashion to that used for the in vivo metabolism samples above.

RESULTS

Synthesis of IRDye800/BHQ-3 Fluorogenic Constructs. IRDye 800CW-PLGLK(BHQ-3)AR-NH_2 (**8**) and a "noncleavable" control IRDye 800CW-(1,13-diamino-4,7,10-trioxatridecane [Ttda])-BHQ-3 (**10**) were prepared from the corresponding precursors, Fmoc-PLGLKAR-NH_2, and Trt-Ttda linker-NH_2 by coupling first with (BHQ-3)-O-Succinimide, followed by coupling to IRDye 800CW-NHS, after removal of the Fmoc/Trt protecting group. The synthesis of **8** is outlined in Figure 2. Its D-arginine analogue **9** and a des-Arg analogue (data not shown) were similarly prepared. The synthetic scheme used to prepare **10** is shown in Figure 3.

Synthesis of Azo-Bond-Cleaved Metabolites. Metabolism studies in mice (vide infra) demonstrated that the azo bond of the BHQ-3 quencher in **10** was readily cleaved in vivo. An authentic sample of metabolite IRDye 800CW-Ttda-Apmba4 (**11**) was prepared by the reaction of (H-Ttda-Boc-Apmba4) **6** [Apmba = 4-*N*-(4-Aminophenyl)-4-*N*-methylbutyric acid)] with IRDye 800CW-NHS ester, followed by removal of the trityl group. The synthesis of the Apmba4 precursor **16** used to prepare **6** is shown in Figure 4. **16** was also used in the preparation of IRDye 800CW-Pro-Leu-Gly-Leu-Lys(Apmba4)-Ala-D-arginine-NH_2 (**12**), an authentic standard of the azo-bond cleavage product of **9**. All compounds prepared had a purity of >95% by HPLC and displayed mass spectral and UV/vis data consistent with their proposed formulation. Table 1 summarizes the compounds prepared.

In Vitro MMP Cleavage Assay. Summary results from the fluorogenic cleavage assay with various matrix metalloproteases (MMPs) are shown in Table 2. Almost complete (>98%) self-quenching was found for **8** until it was cleaved by MMP-13, causing fluorescence to rise from 28 ± 1 relative fluorescence units (RFU) at t = 0 to 1755 ± 105 after 60 min (n = 3), a 56-fold increase in Fl with enzyme treatment. Similar results were observed for D-arginine analogue **9**. For **8**, slower cleavage was seen with other MMPs (Figure 5). Under similar conditions, **10** had values of 119 and 121 RFU in the absence of MMPs at t = 0 and 60 min, revealing less complete quenching; no cleavage was noted when treated with MMP-13 in vitro (Supporting Information Figure 1). Analysis of well contents by LC/MS after MMP cleavage revealed that the expected cleavage fragments IRDye 800CW-PLG-OH and NH_2-LK(BHQ-3)-AX (X = R, r) were formed from **8** and **9**.

In Vivo Metabolism. As shown in Figure 6, following administration of **8** to normal mice, rapid metabolism was observed in mouse plasma in vivo. A major metabolite at t_R = 11.5 min was identified as the dearginated compound IRDye 800CW-PLGLK-(BHQ-3)A-OH, by comparison to an authentic standard (data not shown). Administration of **9**, which contains D-arginine in the place of the N-terminus Arg of **8** prevented the formation of the dearginated metabolite, but polar metabolites eluting between 8 and 10 min were still formed. This finding indicates that these polar products did not form as a result of exopeptidase activity.

Using LC/MS, many of the metabolites were identified (Figure 9), based on their spectral characteristics (Supplementary Figure 2) and molecular weights, and/or by comparison to authentic standards. IRDye 800CW-PLG−OH, the same product formed in the in vitro MMP assay, was a major component found in vivo in both plasma and urine. This suggests that at least one of the MMPs found in normal mice can cleave **8** and **9**.

Surprisingly, "noncleavable" control **10**, which contains only a PEG spacer between IRDye 800CW and BHQ-3, was very rapidly metabolized (Figure 7). LC/MS analysis of mouse plasma extracts demonstrated that the key metabolite formed was **11**, the azo-bond cleavage product of the BHQ-3 moiety in **10**. HPLC traces comparing the retention times of authentic standards of **10** and **11** to those of the products found in mouse plasma at 3 min post administration (Supporting Information

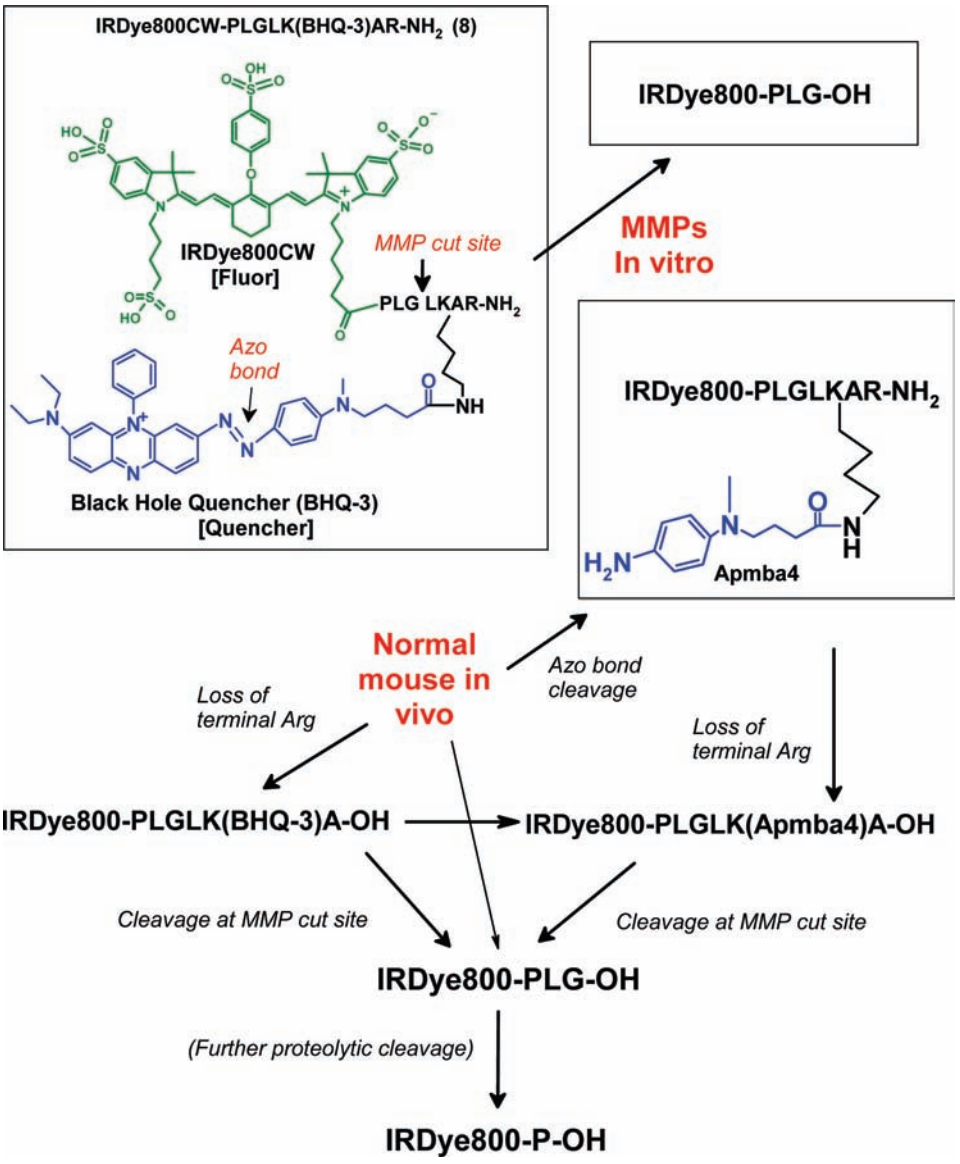

Figure 9. Metabolites formed from IRDye 800CW-PLGLK(BHQ-3)AR-NH_2 (**8**) in vitro and in vivo.

Figure 3) show excellent agreement between the retention time of the primary metabolite (t_R = 9.7 min) and authentic standard **11**. The azo bond in BHQ-3 is very rapidly cleaved in vivo. However, none of the metabolites observed contained any apparent damage to IRDye 800CW.

Recovery results for **8** and **10** from mouse plasma were >90% at all spike levels tested (Supporting Information Table 1), with little degradation observed due to workup. These results demonstrate that the peaks observed in metabolism samples are due to in vivo metabolism, and not to post collection decomposition.

■ DISCUSSION

The compounds described in this paper were prepared to determine how well BHQ-3 can quench fluorescence from the NIR fluorophore IRDye 800CW and whether such constructs are metabolized in normal mice. The data obtained indicate that BHQ-3 is an effective quencher for IRDye 800CW, but examination of the visible spectra of the compounds prepared indicates that quenching is not likely due to FRET,[45−47] wherein excitation is transferred from a donor fluor to an acceptor molecule through dipole−dipole interaction without the emission of a photon. Figure 8A shows an overlay of the fluorescence emission spectrum of IRDye 800CW and the absorption spectrum of (BHQ-3)-O-Su ester. The excitation and emission spectra show very poor overlap for the fluor and quencher, as the emission maximum for IRDye 800CW falls at 789 nm, whereas the absorption maximum for BHQ-3 is at a much shorter wavelength of 612 nm. As **8**, **9**, and **10** show relatively little florescence prior to cleavage, an alternate quenching mechanism to FRET must be proposed.

Figure 8B compares the absorbance spectrum of BHQ-3 and IRDye 800CW when tethered together by a PEG linker in **10**. The absorbance band for BHQ-3 has shifted 43 to 655 nm, and the absorbance maximum for IRDye 800CW has shifted 22 nm from 774 to 786 nm. Such shifts in absorbance maxima have been ascribed to the formation of an intramolecular ground state complex between the fluor and quencher, which leads to

suppression of fluorescence. Johansson et al. have reported that the azo-aromatic dark quencher BHQ-1 appears to quench the fluor Cy3.5 primarily via static quenching, also known as contact quenching, wherein the fluor and quencher form an intramolecular complex.[14,15,48,49] Such an intramolecular complex is likely to be operative in the compounds reported here.

No metabolism of the IRDye 800 fluor was observed during the in vitro or in vivo studies described here. However, the results obtained with **10** suggest that BHQ-3 is not an ideal quencher for use in vivo. The formation of the fluorescent aromatic amine-containing metabolite **11** via cleavage of the azo bond in the quencher was found to be facile. This should not be a surprising result, as there is a precedent for reductive cleavage of the azo linkage in vivo. Reductive enzymes in the liver and intestinal microbial azoreductases have long been known to catalyze the reductive cleavage of the azo linkage in dyes.[50]

In spite of our negative findings with the IRDye800CW-PEG-BHQ-3 constructs, where we observed rapid breakdown of the azo bond of BHQ-3 in the PEG-linked construct in vivo, we have had some success with MMP cleavable BHQ-3 containing constructs, both in vitro (in assays of MMP activity in samples of human synovial fluid) and in imaging studies in vivo with arthritic mice. However, imaging results in arthritic mice in vivo were modest, presumably due to nonspecific cleavage of the quencher. Signal increases in arthritic paws were observed, suggestive of enzymatic cleavage, but the resulting target to background ratios were lower than desired. These data will be reported elsewhere.

We hypothesize that, if BHQ-3 is used in vivo as a quencher in an enzyme-cleavable probe, the effectiveness of such a construct as a probe for protease activity will be affected by the rate at which such azo bond cleavage takes place, relative to probe activation of a fluor/quencher construct by cleavage at the desired cut site. In support of this hypothesis, we note that researchers who have used BHQ-3 as a quencher in vivo (using intratumoral injection or intracartilage injection, rather than systemic (tail vein) injection have had mixed results. With direct intertumoral injection, Lo et al.[51] found that the fluorescent signal in vector positive tumors was only twice that of the FAP vector negative tumor line control. In contrast, Lee et al.[52] found that injection of Cy5.5-GPLGMRGLGK-(BHQ-3) into osteoarthritis-induced cartilage produced a strong fluorescent signal (up to 7.4 ± 1.4-fold increase relative to the normal joints.

However, recent results indicate that use of FRET type fluor/quencher constructs containing BHQ-3 under hypoxic conditions in vitro might prove problematical, based on the recent work of Kiyose et al.[53] They surmised that a cyanine dye-containing (Cy5, Cy5.25, or Cy5.5)/BHQ-3 construct was reduced under hypoxic conditions, generating fluorescence. No characterization of the product was reported, but as the linker between the fluor and quencher was noncleavable, azo bond reduction of the BHQ-3 quencher was hypothesized, leading to generation of fluorescent signal due to the loss of FRET between the cyanine dye and the quencher. The group proposes use of this finding for the imaging of hypoxia. These varied results suggest that care should be taken to characterize metabolites if BHQ-3 is used in vivo.

CONCLUSIONS

Efficient quenching of the fluorescence emissions from IRDye 800CW by BHQ-3 was found for IRDye 800CW-PLGLK-(BHQ-3)-AR-NH_2 **8**, D-arginine analogue **9**, and IRDye 800CW-Ttda-BHQ-3 **10**. Since the spectral overlap for IRDye 800CW and BHQ-3 is not optimal for FRET quenching, contact quenching must be inferred, and appears to be a viable quenching approach for this fluor/quencher pair. The peptide backbone in **8** and **9** is readily cleaved by MMPs in vitro, generating the fluorescent IRDye 800CW-PLG-OH fragment expected, based on the known protease cut site in the starting peptide.

Following in vivo administration of **8** and **9**, many metabolites were observed in normal mouse plasma and urine. All observed metabolites in urine were fluorescent. Although the enzyme(s) responsible for cleavage in vivo are not known, one major fluorescent metabolite in plasma and urine corresponds to that formed by cleavage at the known MMP cut site for the peptides. A second (nonfluorescent) plasma metabolite corresponded to loss of the terminal Arg. Replacement of this residue with D-arginine halted deargination, but cleavage at the MMP cut site as well as cleavage of the azo bond in the BHQ-3 quencher were still observed. Most of the metabolites formed will contribute to background, thereby reducing the ability to specifically detect MMP activity in pathologies such as tumors or arthritis.

Metabolism studies with IRDye 800CW-Ttda-BHQ-3 **10** in normal mice clearly revealed the in vivo instability of the azo bond in BHQ-3 quencher. The primary metabolite observed had a molecular weight consistent with azo bond cleavage of the quencher, and coeluted with an authentic standard of the proposed metabolite. Thus, although IRDye 800CW and BHQ-3 appear to be a suitable Fl/Q pair, BHQ-3 should be used with caution in vivo.

ASSOCIATED CONTENT

Supporting Information. Results from fluorogenic MMP cleavage assay, UV/vis spectra of the major metabolites of **8**, and HPLC comparison of the metabolite of **10** in mouse plasma, and that of an authentic sample of azo-bond cleaved product **11**. This material is available free of charge via the Internet at http://pubs.acs.org.

AUTHOR INFORMATION

Corresponding Author

*Karen E. Linder, E-mail: karen.e.linder@gmail.com. Phone:609-683-0483.

Present Addresses

†Department of Radiology, The Ohio State University Medical School Biomedical Research Tower, Rm. 710, 460 W. 12th Ave, Columbus, Ohio 43210, United States.

REFERENCES

(1) Licha, K. (2002) Contrast agents for optical imaging. In *Topics of Current Chemistry*, Vol. 222, Springer-Verlag, Berlin Heidelberg.

(2) Ntziachristos, V., Bremer, C., and Weissleder, R. (2003) Fluorescence imaging with near-infrared light: new technological advances that enable in vivo molecular imaging. *Eur. Radiol. 13* (1), 195–208.

(3) Rasmussen, J. C., Tan, I. C., Marshall, M. V., Fife, C. E., and Sevick-Muraca, E. M. (2009) Lymphatic imaging in humans with near-infrared fluorescence. *Curr. Opin. Biotechnol. 20* (1), 74–82.

(4) Licha, K., Riefke, B., Ntziachristos, V., Becker, A., Chance, B, and Semmler, W. (2000) Hydrophilic cyanine dyes as contrast agents for near-infrared tumor imaging: synthesis, photophysical properties and spectroscopic in vivo characterization. *Photochem. Photobiol. 72* (3), 392–398.

(5) Li, X., Beauvoit, B., White, R., Nioka, S., Chance, B., and Yodh., G. (1995) Tumor localization using fluorescence of indocyanine green (ICG) in rat models. *SPIE 2389*, 789–798.

(6) Fischer, T., Gemeinhardt, I., Wagner, S., Stieglitz, D. V., Schnorr, J., Hermann, K. G., Ebert, B., Petzelt, D., Macdonald., R., Licha, K., Schirner, M., Krenn, V., Kamradt, T., and Taupitz, M. (2006) Assessment of unspecific near-infrared dyes in laser-induced fluorescence imaging of experimental arthritis. *Acad. Radiol. 13* (1), 4–13.

(7) Hansch, A., Hilger, I., Frey, O., Sauner, D., Gajda, M., Haas, M., Malich, A., Böttcher, J., Bräuer, R., and Kaiser, W. A. (2006) Near-infrared imaging of flare-up arthritis with native fluorochrome Cy5.5 and albumin-bound Cy5.5. *J. Exp. Anim. Sci. 43* (3), 129–139.

(8) Pierce, M. C., Javier, D. J., and Richards-Kortum, R. (2008) Optical contrast agents and imaging systems for detection and diagnosis of cancer. *Int. J. Cancer 123* (9), 1979–1990.

(9) Zhang, Z., Fan, J., Cheney, P. P., Berezin, M. Y., Edwards, W. B., Akers, W. J., Shen, D., Liang, K., Culver, J. P., and Achilefu, S. (2009) Activatable molecular systems using homologous near-infrared fluorescent probes for monitoring enzyme activities in vitro, in cellulo, and in vivo. *Mol. Pharmaceutics 6* (2), 416–427.

(10) Funovics, M., Weissleder, R., and Ching-Hsuan, T. (2003) Protease sensors for bioimaging. *Anal. Bioanal. Chem. 377*, 956–963.

(11) Fields, G. B. (2002) Using fluorogenic peptide substrates to assay matrix metalloproteinases. In *Methods of Molecular Biology*, Vol 151 Matrix Metalloproteinase Protocol, Clark, I. Ed., Humana Press Inc., Totowa, NJ.

(12) Yaron, A., Carmel, A., and Katchalski-Katzir, E. (1979) Intramolecularly quenched fluorogenic substrates for hydrolytic enzymes. *Anal. Biochem. 95*, 228–235.

(13) Ekici, O. D., Zhu, J., Wah Chung, I. Y., Paetzel, M., Dalbey, R. E., and Pei, D. (2009) Profiling the substrate specificity of viral protease VP4 by a FRET-based peptide library approach. *Biochemistry 48* (24), 5753–5759.

(14) Johansson, M. K. (2006) Choosing reporter-quencher pairs for efficient quenching through formation of intramolecular dimers. In *Methods of Molecular Biology*, Vol 335, Fluorescent Energy Transfer Nucleic Acid Probes: Designs and Protocols, Didenko, V.V., Ed., Humana Press Inc., Totowa, NJ.

(15) Didenko, V. V. (2001) DNA probes using fluorescence resonance energy transfer (FRET): designs and applications. *BioTechniques 31* (5), 1106−1116, 1118, 1120−1121.

(16) Tung, C.-H., Bredow, S., Mahmood, U., and Weissleder, R. (1999) Preparation of a Cathepsin D sensitive near-infrared fluorescence probe for imaging. *Bioconjugate Chem. 10* (5), 892–896.

(17) Tung, C.-H., Mahmood, U., Bredow, S, and Weissleder, R. (2000) In vivo imaging of proteolytic enzyme activity using a novel molecular reporter. *Cancer Res. 60* (17), 4953–4958.

(18) Mahmood, U., Tung, C.-H., Bogdanov, A., Jr., and Weissleder, R. (1999) Near-infrared optical imaging of protease activity for tumor detection. *Radiology 213* (3), 866–870.

(19) Blum, G., von Degenfeld, G., Merchant, M. J., Blau, H. M., and Bogyo, M. (2007) Noninvasive optical imaging of cysteine protease activity using fluorescently quenched activity-based probes. *Nat. Chem. Biol. 3* (10), 668–677.

(20) Melancon, M. P., Wang, W., Wang, Y., Shao, R., Ji, X., Gelovani, J. G., and Li, C. (2007) A novel method for imaging in vivo degradation of Poly(L-Glutamic Acid), a biodegradable drug carrier. *Pharm. Res. 24* (6), 1217–1224.

(21) Bremer, C., Bredow, S., Mahmood, U., Weissleder, R., and Tung, C.-H. (2001) Optical imaging of matrix metalloproteinase-2 activity in tumors: feasibility study in a mouse model. *Radiology 221* (2), 523–529.

(22) McIntyre, J. O., Fingleton, B., Wells, K. S., Piston, D. W., Lynch, C. C., Gautam, S., and Matrisian, L. M. (2004) Development of a novel fluorogenic proteolytic beacon for in vivo detection and imaging of tumour-associated matrix metalloproteinase-7 activity. *Biochem. J. 377* (3), 617–628.

(23) Scherer, R. L., VanSaun, M. N., McIntyre, J. O., and Matrisian, L. M. (2008) Optical imaging of matrix metalloproteinase-7 activity in vivo using a proteolytic nanobeacon. *Mol. Imaging 7* (3), 118–131.

(24) Lee, S., Park, K., Lee, S.-Y., Ryu, J. H., Park, J. W., Ahn, H. J., Choi, K., Kwon, I. C., Youn, I.-C., Kim, K., and Choi, K. (2008) Dark quenched matrix metalloproteinase fluorogenic probe for imaging osteoarthritis development in vivo. *Bioconjugate Chem. 19* (9), 1743–1747.

(25) Lee, H., Akers, W. J., Cheney, P. P., Edwards, W. B., Liang, K., Culver, J. P., and Achilefu, S. (2009) Complementary optical and nuclear imaging of caspase-3 activity using combined activatable and radiolabeled multimodality molecular probe. *J. Biomed. Optics 14* (4), 040507/1–040507/3.

(26) Stefflova, K., Chen, J., Marotta, D., Li, H., and Zheng, G. (2006) Photodynamic therapy agent with a built-in apoptosis sensor for evaluating its own therapeutic outcome in situ. *J. Med. Chem. 49* (13), 3850–3856.

(27) Maxwell, D., Chang, Q., Zhang, X., Barnett, E. M., and Piwnica-Worms, D. (2009) An improved cell-penetrating, caspase-activatable, near-infrared fluorescent peptide for apoptosis imaging. *Bioconjugate Chem. 20* (4), 702–709.

(28) Narayanan, N., Little, G., Raghavachari, R., Gibson, J., Lugade, A., Prescott, C., Reiman, K., Roemer, S., Steffens, D., Sutter, S., and Draney, D. (1998) New NIR dyes: synthesis, spectral properties and applications in DNA analyses. NATO ASI Series, Series 3: High Technology 52 (Near-Infrared Dyes for High Technology Applications), 141−158.

(29) Wang, W., Ke, S., Wu, Q., Charnsangavej, C., Gurfinkel, M., Gelovani, J. G., Abbruzzese, J. L., Sevick-Muraca, E. M., and Li, C. (2004) Near-infrared optical imaging of integrin alpha$_v$beta$_3$ in human tumor xenografts. *Mol. Imaging 3* (4), 343–351.

(30) Li, C., Wang, W., Wu, Q., Ke, S., Houston, J., Sevick-Muraca, E., Dong, L., Chow, D., Charnsangavej, C., and Gelovani, J. G. (2006) Dual optical and nuclear imaging in human melanoma xenografts using a single targeted imaging probe. *Nucl. Med. Biol. 33* (3), 349–358.

(31) Kovar, J. L., Johnson, M. A., Volcheck, W. M., Chen, J., and Simpson, M. A. (2006) Hyaluronidase expression induces prostate tumor metastasis in an orthotopic mouse model. *Am. J. Pathol. 169* (4), 1415–1426.

(32) Sampath, L., Kwon, S., Ke, S., Wang, W., Schiff, R., Mawad, M. E., and Sevick-Muraca, E. M. (2007) Dual-labeled trastuzumab-based imaging agent for the detection of human epidermal growth factor receptor 2 overexpression in breast cancer. *J. Nucl. Med. 48* (9), 1501–1510.

(33) Tanaka, E., Choi, H. S., Humblet, V., Ohnishi, S., Laurence, R. G., and Frangioni, J. V. (2008) Real-time intraoperative assessment of the extrahepatic bile ducts in rats and pigs using invisible near-infrared fluorescent light. *Surgery 144* (1), 39–48.

(34) Kovar, J. L., Volcheck, W., Sevick-Muraca, E., Simpson, M. A., and Olive, D. M. (2009) Characterization and performance of a near-infrared 2-deoxyglucose optical imaging agent for mouse cancer models. *Anal. Biochem. 384* (2), 254–262.

(35) Peng, X., Chen, H., Draney, D. R., Volcheck, W., Schutz-Geschwender, A., and Olive, D. M. (2009) A nonfluorescent, broad-range quencher dye for Förster resonance energy transfer assays. *Anal. Biochem. 388* (2), 220–228.

(36) Adams, K. E., Ke, S., Kwon, S., Liang, F., Fan, Z., Lu, Y., Hirschi, K., Mawad, M. E., Barry, M. A., and Sevick-Muraca, E. M. (2007) Comparison of visible and near-infrared wavelength-excitable fluorescent dyes for molecular imaging of cancer. *J. Biomed. Opt. 12* (2), 024017.

(37) Cook, R., Lyttle, M., and Daren, D. Dark quenchers for donor-acceptor energy transfer. U.S. Patent 7,019,129. Biosearch Technologies Inc., issued March 28, 2006.

(38) Liang, M., Liu, X., Cheng, D., Nakamura, K., Wang, Y., Dou, S., Liu, G., Rusckowski, M., and Hnatowich, D. J. (2009) Optical antisense tumor targeting in vivo with an improved fluorescent DNA duplex probe. *Bioconjugate Chem. 20* (6), 1223–1227.

(39) Mawn, T., Leung, D.-J., Beardsley, N. J., Popov, A. V., and Delikatny, E. J. (2008) Dual modality imaging of phosphatidylcholine-specific phospholipase C in DU145 prostate cancer cells and solid tumors. *Proc. Int. Soc. Mag. Reson. Med. 16*, 1702.

(40) Knight, C. G., Willenbrock, F., and Murphy, G. (1992) A novel coumarin-labelled peptide for sensitive continuous assays of the matrix metalloproteinases. *FEBS Lett. 296* (3), 263–266.

(41) Kim, J., Yu, W., Kovalski, K., and Ossowski, L. (1998) Requirement for specific proteases in cancer cell intravasation as revealed by a novel semiquantitative PCR-based assay. *Cell 94* (3), 353–362.

(42) Karakiulakis, G., Papanikolaou, C., Jankovic, S. M, Aletras, A., Papakonstantinou, E., Vretou, E., and Mirtsou-Fidani, V. (1997) Increased type IV collagen-degrading activity in metastases originating from primary tumors of the human colon. *Invasion and Metastasis 17* (3), 158–168.

(43) Murphy, G., Knäuper, V., Atkinson, S., Butler, G., English, W., Hutton, M., Stracke, J., and Clark, I. (2002) Matrix metalloproteinases in arthritic disease. *Arthritis Res. 4* (Suppl 3), S39–S49.

(44) Pillai, R., Marinelli, E. R., and Swenson, R. E. (2006) A flexible method for preparation of peptide homo- and heterodimers functionalized with affinity probes, chelating ligands, and latent conjugating groups. *Biopolymers 84*, 576–585.

(45) Clegg, R. M. (1995) Fluorescence resonance energy transfer. *Curr. Opin. Biotechnol. 6* (1), 103–110.

(46) Selvin, P. R. (1995) Fluorescence resonance energy transfer. *Methods Enzymol. 246*, 300–334.

(47) Lakowicz, J. R. (2006) Chapter 13: Energy transfer, pp 443−468, in *Principles of Fluorescence Spectroscopy*, 3rd ed., Springer, New York.

(48) Johansson, M. K., and Cook, R. M. (2003) Intramolecular dimers: a new design strategy for fluorescence-quenched probes. *Chem.—Eur. J. 9* (15), 3466–3471.

(49) Johansson, M. K., Fidder, H., Dick, D., and Cook, R. M. (2002) Intramolecular dimers: A new strategy to fluorescence quenching in dual-labeled oligonucleotide probes. *J. Am. Chem. Soc. 124*, 6950–6956.

(50) Chung, K. T., Stevens, S. E., Jr., and Cerniglia, C. E. (1992) The reduction of azo dyes by the intestinal microflora. *Crit. Rev. Microbiol. 18* (3), 175–190.

(51) Lo, P. C., Chen, J., Stefflova, K., Warren, M. S., Navab, R., Bandarchi, B., Mullins, S., Tsao, M., Cheng, J. D., and Zheng, G. (2009) Photodynamic molecular beacon triggered by fibroblast activation protein on cancer-associated fibroblasts for diagnosis and treatment of epithelial cancers. *J. Med. Chem. 52* (2), 358–368.

(52) Lee, S., Park, K., Lee, S. Y., Ryu, J. H., Park, J. W., Ahn, H. J., Kwon, I. C., Youn, I. C., Kim, K., and Choi, K. (2008) Dark quenched matrix metalloproteinase fluorogenic probe for imaging osteoarthritis development in vivo. *Bioconjugate Chem. 19*, 1743–1747.

(53) Kiyose, K., Hanaoka, K., Oushiki, D., Nakamura, T., Kajimura, M., Suematsu, M., Nishimatsu, H., Yamane, T., Terai, T., Hirata, Y., and Nagano, T. (2010) Hypoxia-sensitive fluorescent probes for *in vivo* real-time fluorescence imaging of acute ischemia. *J. Am. Chem. Soc. 132* (45), 15846–15848.

Supporting material for

Synthesis, In Vitro Evaluation and In Vivo Metabolism of Fluor/Quencher Compounds Containing IRDye 800CW and Black Hole Quencher-3 (BHQ-3)

Karen E. Linder*, Edmund Metcalfe, Palaniappa Nanjappan,
Thangavel Arunachalam, Kimberly Ramos, Tina Marie Skedzielewski,
Michael F. Tweedle[a], Adrian D. Nunn, Rolf E. Swenson

Ernst Felder Laboratories, Bracco Research USA,
305 College Road East, Princeton, New Jersey 08540

*Corresponding author: Karen E. Linder,
Email: karen.e.linder@gmail.com 609-683-0483

a) current address: Department of Radiology, The Ohio State University Medical School
Biomedical Research Tower, Rm. 710, 460 W. 12th Ave, Columbus, Ohio 43210

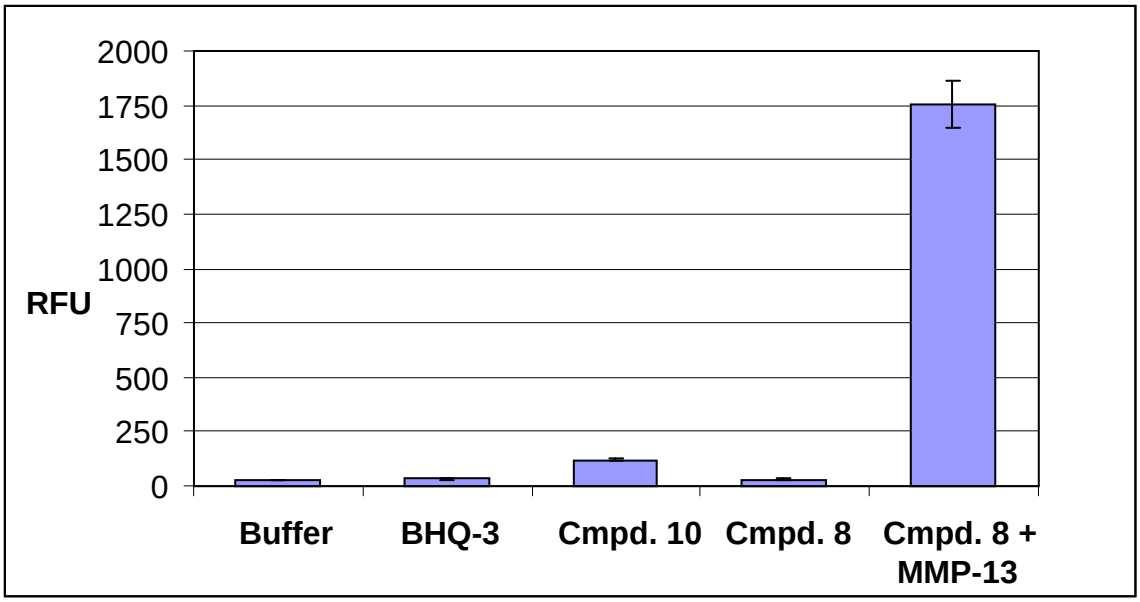

Supplementary Figure 1: Results from fluorogenic MMP cleavage assay for 8 and 10 in buffer and after cleavage by MMP-13. 10 is unaffected by MMPs (data not shown).

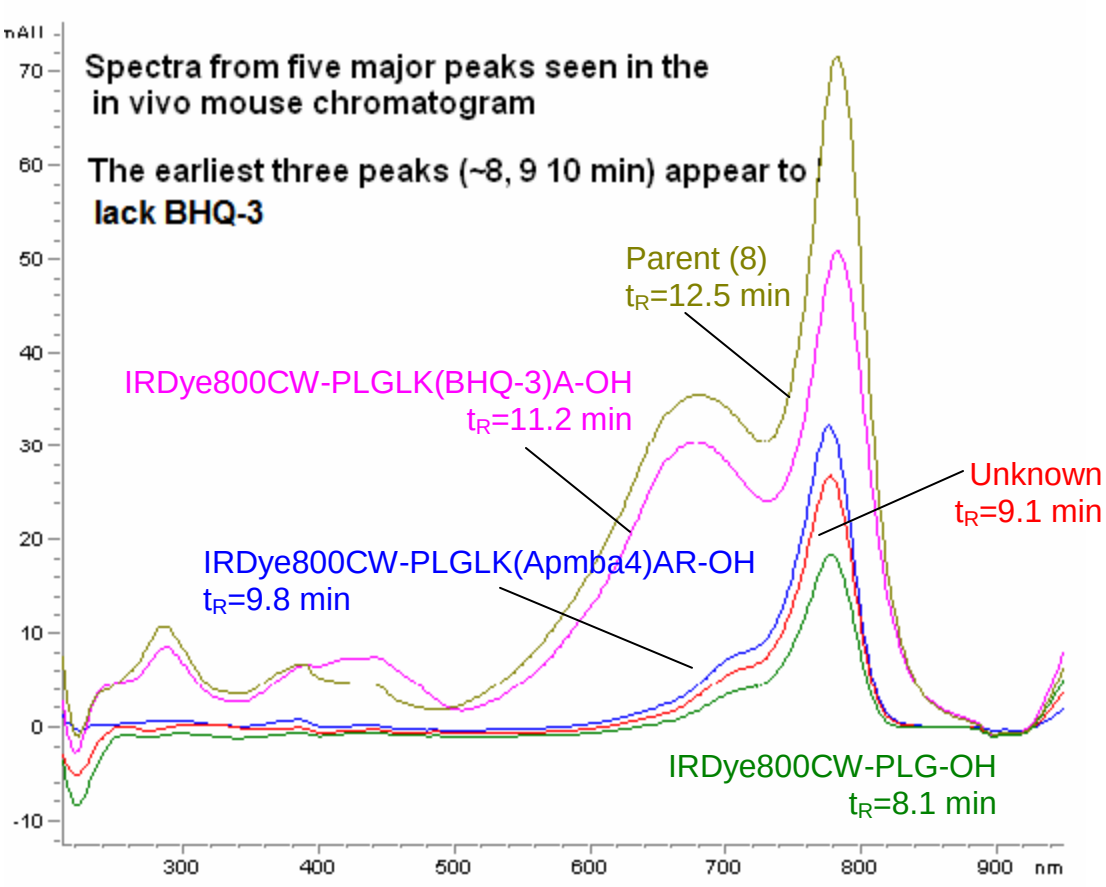

Supplementary Figure 2: Diode array UV/Vis spectra from the LC/MS analysis of IRDye 800CW-PLGLK(BHQ-3)-AR-NH_2 and key metabolites in mouse plasma. Retention times in the figure above refer to HPLC peaks shown in Fig 6.

Both parent 8 and its dearginated analog (peak at t_R=11.2 min in Figure 6) contain absorbance peaks characteristic of IRDye 800CW (λ_{max} ~790 nm) and BHQ-3 (λ_{max} ~670 nm). However, metabolites eluting at t_R = 8-10 min no longer contain the absorbance band for BHQ-3. For IRDye 800CW-PLGLK(Apmba4)AR-OH, the observed m/z corresponds to cleavage of the BHQ-3 quencher at its azo bond. For IRDye800CW-PLG-OH, peptide bond cleavage in normal animals gives rise to loss of the quencher.

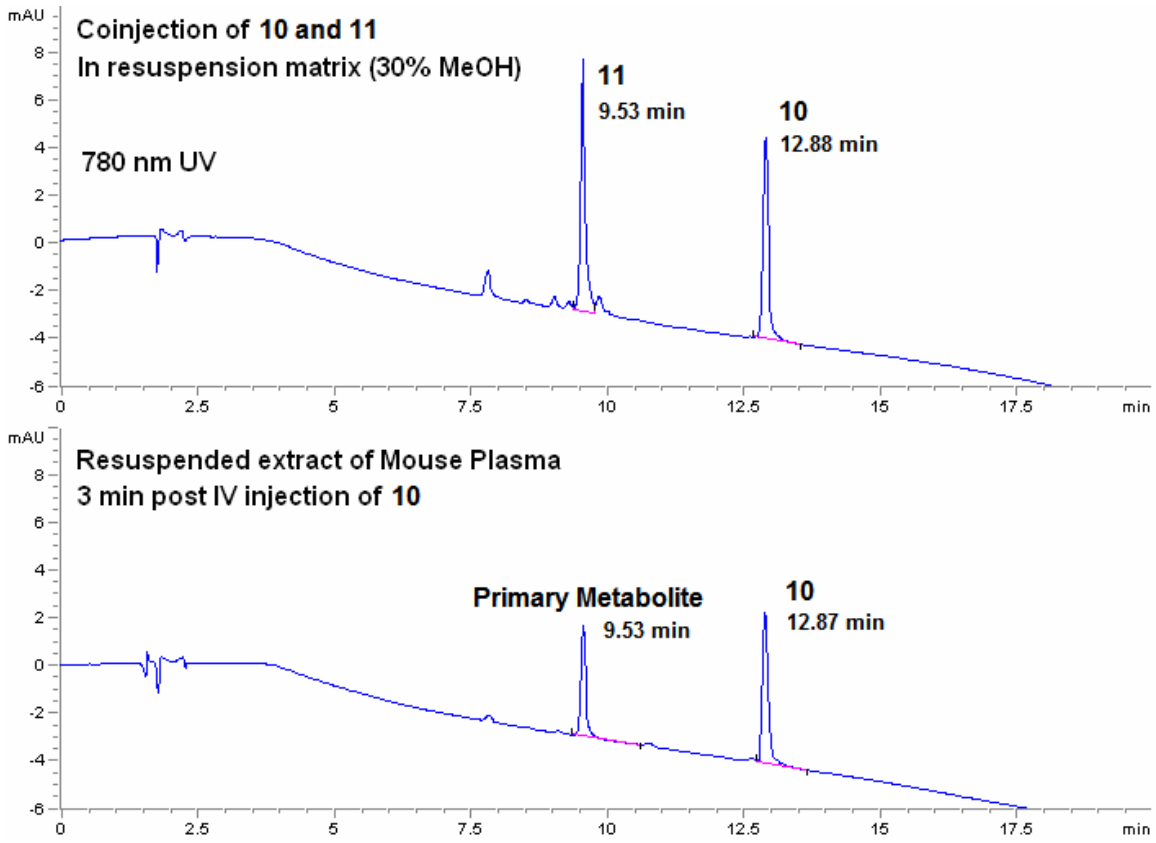

Supplementary Figure 3: Metabolism of IRDye800CW-Ttda-(BHQ-3) (**10**) in mouse plasma, and comparison to an authentic sample **10** and azo-bond cleaved product **11**.

The primary metabolite (t_R~9.5 min) co-elutes with an authentic standard of **11**.

Supplementary Table 1: Recovery of IRDye800CW-PLGLK(BHQ-3)-AR-NH_2 (8) and IRDye800CW-Ttda-(BHQ-3) (10) from mouse plasma

	Recovery from spiked Normal Mouse Plasma (%)		
Compound	**20 µM**	**4 µM**	**1 µM**
(8) (n=3)	98.5	91.6	92.1
(10) (n=2)	92.8	97.6	n.d.

n.d. = not determined

Bioconjugate Chemistry

ARTICLE

pubs.acs.org/bc

Suitable Labels for Molecular Imaging – Influence of Dye Structure and Hydrophilicity on the Spectroscopic Properties of IgG Conjugates

Jutta Pauli,[†] Markus Grabolle,[†] Robert Brehm,[†] Monika Spieles,[†] Franziska M. Hamann,[‡] Matthias Wenzel,[§] Ingrid Hilger,[‡] and Ute Resch-Genger*[,†]

[†]BAM Bundesanstalt für Materialforschung und -prüfung, OE I.5, Richard-Willstaetter-Str. 11, D-12489 Berlin, Germany

[‡]Institut für Diagnostische und Interventionelle Radiologie des Klinikums der Friedrich-Schiller-Universität Jena (IDIR), Forschungszentrum Lobeda, Erlanger Allee 101, D-07747 Jena, Germany

[§]DYOMICS GmbH, Otto-Schott-Str. 15, D-07745 Jena, Germany

Supporting Information

ABSTRACT: Aiming at the design of highly brilliant NIR emissive optical probes, e.g., for *in vivo* near-infrared fluorescence imaging (NIRF), we studied the absorption and fluorescence properties of the asymmetric cyanines Dy678, Dy681, Dy682, and Dy676 conjugated to the model antibody IgG. The ultimate goal was here to derive general structure–property relationships for suitable NIR fluorescent labels. These Dy dyes that spectrally match Cy5 and Cy5.5, respectively, were chosen to differ in chromophore structure, i.e., in the substitution pattern of the benzopyrylium end group and in the number of sulfonic acid groups. Spectroscopic studies of the free and IgG-bound fluorophores revealed a dependence of the obtained dye-to-protein ratios on dye hydrophilicity and control of the fluorescence quantum yields (Φ_f) of the IgG conjugates by the interplay of different fluorescence reduction pathways like dye aggregation and fluorescence resonance energy transfer (FRET). Based upon aggregation studies with these dyes, the amount of dye dimers in the IgG conjugates was determined pointing to dye hydrophilicity as major parameter controlling aggregation. To gain further insight into the exact mechanism of dye dimerization at the protein, labeling experiments at different reaction conditions but constant dye-to-protein ratios in the reaction solution were performed. With Dy682 that displays a Φ_f of 0.20 in PBS and 0.10 for moderate dye-to-protein ratio of 2.5, a low aggregation tendency, and a superior reactivity in IgG labeling, we identified a promising diagnostic tool for the design of NIR fluorescent probes and protein conjugates.

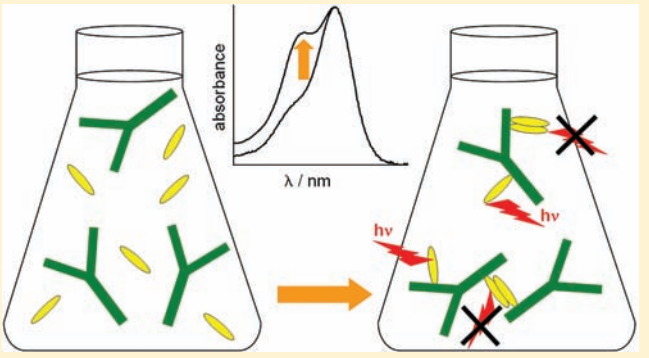

INTRODUCTION

Conjugation of biomolecules like proteins to fluorophores is of considerable importance for many fluorescence-based analytical techniques in the life sciences.[1−5] One of the most active research areas presents the design of optical probes for the detection of pathological changes and disease-related biomarkers employing molecular fluorescent reporters and, lately, also luminescent nanoparticles or combinations of different fluorophores.[6−15] This enables, e.g., the investigation of the molecular basis of cancer pathogenesis and the timely detection of metastases and provides a tool for therapy monitoring with comparatively inexpensive, easy-to use, and highly sensitive fluorescence techniques such as *in vivo* fluorescence reflectance imaging (FRI)[16] and fluorescence tomography.[17] Moreover, in contrast to all imaging modalities that rely on high-energy radiation and radioactive contrast agents like positron emission tomography (PET) and computer tomography (CT), optical techniques are not prone to rigid safety regulations. Advances in instrumentation and label and probe technologies have helped to continuously increase the sensitivity and detection capability of optical imaging techniques with some applications being meanwhile part of the clinical routine.[18−20]

Indispensable for optical imaging are highly specific and sensitive molecular probes that respond to or target molecular species or processes. Such probes typically consist of a target-specific ligand like an antibody or antibody fragment covalently bound to a fluorescent reporter (e.g., organic dye molecule(s), nanocrystalline label, or fluorophore-containing particle).[6,7,11] Although chromophores absorbing and emitting in the visible region can be used for certain applications in cell and small animal imaging,[21−23] near-infrared (NIR) fluorophores that absorb and emit between 650 and 900 nm, where hemoglobin and water absorption and autofluorescence are minimum, are mandatory to enhance the sensitivity of optical imaging and to enable deep tissue human imaging.[10,24−26] Suitable NIR reporters should display a

Received: October 31, 2010
Revised: May 5, 2011
Published: May 17, 2011

ACS Publications © 2011 American Chemical Society

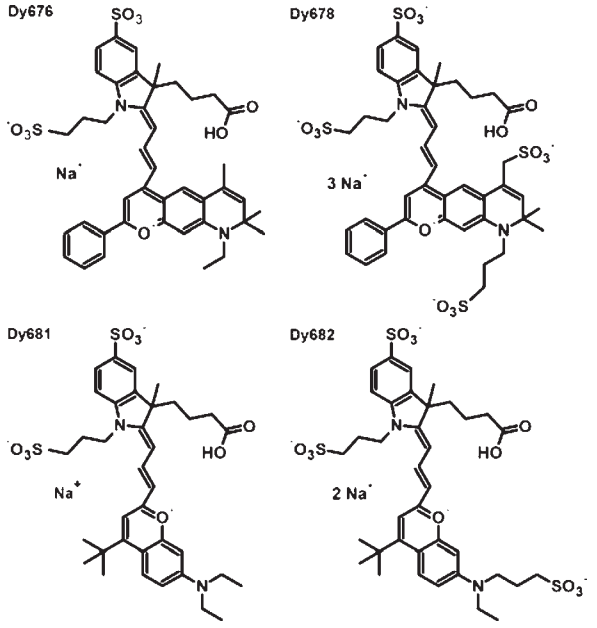

Figure 1. Chemical structures of the asymmetric cyanines Dy676, Dy678, Dy681, and Dy682.

high molar absorption coefficient at the excitation wavelength and a high fluorescence quantum yield in the nonconjugated state under application-relevant conditions, i.e., in aqueous solution and bound to a target-specific ligand, to realize the desired high sensitivity.[7,11,16,27−30] Other prerequisites are minimum nonspecific binding, sufficient thermal and photochemical stability, and low cytotoxicity.

Despite the intensive research dedicated to NIR chromophores and optical probes, challenges to overcome still include (i) problems arising from the low solubility of chromophores, especially in the case of NIR dyes, (ii) control of the labeling efficiency,[4,5] (iii) comparatively low fluorescence quantum yields of many NIR fluorophores in aqueous solution,[27,31,32] and (iv) dye- and biomolecule-specific fluorescence quenching of conjugated dye molecules that is typically also label-density dependent.[33−38] For all tailormade biological applications of fluorescent labels like fluorescence-based diagnostic assays or the design of improved fluorescent probes, the knowledge of these fluorescence quenching processes and the understanding of the fundamental molecular interactions between dye molecules and possible matrix components is crucial. This also includes the identification of application-relevant parameters that can be exploited for label and probe screening. This encouraged us to systematically study and evaluate the potential of different cyanine dyes for protein labeling and the preparation of highly fluorescent protein conjugates in comparison to our workhorse Dy676 that has been successfully exploited, e.g., for the design of a variety of target-specific probes like a contrast agent directed against carcinoembryonic antigen (CEA).[16,27,39,40] These dyes were chosen to differ in the substitution pattern of the benzopyrylium group and the number of sulfonic acids attached to the chromophore (see Figure 1). This affords the systematic study of the influence of dye hydrophilicity, charge, and steric effects on dye−dye interactions and on dye−protein interactions without affecting parameters like spectral overlap that controls the efficiency of fluorescence resonance energy transfer (FRET) between chemically identical chromophores (homo-FRET). Fluorophore-labeled immunoglobulins (IgG) were used as model systems for label comparison, thereby also enabling the comparison with other dye−IgG conjugates reported in the literature.[35,41,42] Moreover, IgG−dye conjugates present valuable model systems for the design of immunoassays,[42,43] play an important role as unspecific control or probe for the *in vitro* and *in vivo* evaluation and validation of the binding selectivity of target-specific optical probes,[16] and can be exploited, e.g., for the mapping of the lymphatic drainage pattern within axillary nodes.[44] The overall aim here was to identify screening strategies for the choice of NIR labels that maintain moderate to high fluorescence quantum yields upon bioconjugation for moderate dye-to-protein (D/P) ratios (D/P ca. 2−6).

Table 1. Photometrically Determined Dye-to-Protein (D/P) Ratios of the IgG-Dy67x and IgG-Dy68x Conjugates Prepared from Reaction Mixtures of the Dye and IgG using D/P Ratios of 3:1, 6:1, and 24:1, Respectively

dye	D/P (3:1)	D/P (6:1)	D/P (24:1)
Dy676	1.7	2.8	5.1
Dy678	3.2	5.6	16.0
Dy681	2.7	3.8	9.4
Dy682	2.5	4.2	10.0

EXPERIMENTAL PROCEDURES

Materials. Dy676, Dy678, Dy681, and Dy682 (Figure 1) were provided by Dyomics GmbH (Jena, Germany). Dye purity was at least 90% according to the manufacturer's specification. Oxazine 1 used as fluorescence quantum yield standard was obtained from Lambda Physik GmbH (Goettingen, Germany). Polyclonal IgG from rabbit serum for the preparation of the IgG-Dy67x and IgG-Dy68x conjugates was purchased from Sigma-Aldrich Chemie GmbH (Steinheim, Germany). DMF and ethanol were of spectroscopic grade and purchased from Sigma Aldrich. Phosphate buffer solution (PBS; Hanks balanced salt solution; Ca(II)- and Mg(II)-free without phenol red) was obtained from PAA Laboratories GmbH (Pasching, Austria). Sodium dodecyl sulfonate (SDS) was obtained from Sigma-Aldrich and used without further purification. Sephadex G25 medium employed for the preparation of the columns for the purification of the IgG−dye conjugates was purchased from GE Healthcare Amersham (Freiburg, Germany). Bovine serum albumin (BSA; fraction V) was purchased from Merck KgaA (Darmstadt, Germany).

Preparation of Dy dye−IgG Conjugates (IgG-Dy dye). The IgG conjugates of Dy676, Dy678, Dy681, and Dy682 were obtained by reacting IgG, dissolved in a carbonate buffer (bicarbonate (0.1 mol/L, sodium chloride (0.5 mol/L) solution, pH 8; IgG concentration of 1.5×10^{-5} mol/L), with the amine-reactive *N*-hydroxysuccinimidyl (NHS) esters of the dyes dissolved in DMF at room temperature using identical reaction conditions for all labels (e.g., solvent, pH, temperature, reaction time). To vary the labeling density or dye-to-protein (D/P) ratio (Table 1), we used dye NHS ester-to-IgG ratios of 3:1, 6:1, and 24:1 (starting materials; IgG concentration kept constant at 1.5×10^{-5} mol/L; dye concentrations between ca. 4.5×10^{-5} M (D/P = 3:1) and 3.6×10^{-4} M (D/P = 24:1)), respectively, for this statistical labeling procedure. The reaction mixtures were stirred for 3 h at 22 °C. The resulting IgG conjugates were

purified chromatographically using a Sephadex column and a phosphate buffer as eluent.

For the determination of the D/P ratio of each conjugate, the absorption spectrum of the nonconjugated dye and the respective IgG conjugate were measured in PBS. The D/P ratio was calculated from the absorbance of the conjugate at 280 nm (corrected for dye contribution) and the integral absorption of the dye's longest wavelength absorption band. Use of the integral absorption instead of the commonly employed molar absorption coefficient at the dye's absorption maximum is more appropriate for the calculation of D/P ratios of conjugates showing conjugation-induced changes in the shape of the fluorophore's absorption band.[42] We employed a molar absorption coefficient of IgG of 210 000 L mol^{-1} cm^{-1} (taken from the manufacturer's data sheet).

Absorption and Fluorescence Measurements. The absorption spectra were recorded on a CARY 5000 spectrometer (Varian Inc., Palo Alto, USA) using 1 cm quartz cells. The absorption spectra of the Dy dyes and their IgG conjugates were determined in duplicate in a PBS solution (1×10^{-6} mol/L, pH 7.4). For selected samples, measurements were also performed in PBS containing 5% (w/w) BSA (PBS/BSA) and in PBS containing 5% (w/w) SDS (PBS/SDS) using a dye concentration of 1×10^{-6} mol/L. For the aggregation studies, quartz cells with optical pathlengths varying from 0.01 to 1 cm were employed. Fluorescence measurements were performed with a calibrated Spectronics Instruments 8100 (Westbury, NY, USA) spectrofluorometer (T-type design; sole use of NIR emission channel here) equipped with Glan Thompson polarizers in the excitation and the emission channel (set to 0° and 54.7° if not otherwise stated).[45] Typically, the emission of the fluorophore and IgG−dye conjugate solutions in 1 cm quartz cells was excited at the vibronic shoulder of the longest wavelength absorption band (absorbances of 0.02 to 0.06 to minimize inner filter effects and reabsorption). The emission spectra of the Dy dyes and their bioconjugates were determined in duplicate, commonly at a dye concentration of 1×10^{-6} mol/L. For selected samples, excitation spectra were also measured that represent the absorption spectra of the emitting species.

For each compound−solvent pair, the fluorescence quantum yields (Φ_f) were determined in duplicate using dye and standard solutions freshly prepared upon dilution of stock solutions (typical dye concentration of 100×10^{-6} mol/L, stored in the refrigerator at 4 °C in the dark). The Φ_f values of the nonconjugated and the IgG-bound Dy dyes were calculated from integrated, blank, and spectrally corrected emission spectra (wavelength scale; prior to integration multiplication with λ)[1,45] relative to the standard Oxazine 1 dissolved in ethanol ($\Phi_f = 0.15$) using the following formula

$$\Phi_{f,x} = \Phi_{f,st} \times \frac{F_x}{F_{st}} \times \frac{f_{st}(\lambda_{ex})}{f_x(\lambda_{ex})} \times \frac{n_x^2}{n_{st}^2} \quad (1)$$

Here, $f(\lambda_{ex})$ is the absorption factor at the excitation wavelength λ_{ex}, F the integral emission intensity, i.e., the area under the blank and spectrally corrected emission spectrum on a wavelength scale, and n the refractive index of the solvent(s) used. The subscripts x and st denote sample and standard. Typical uncertainties (standard deviations) of fluorescence quantum yield measurements as derived from previous experiments (relative standard deviations derived from six independent measurements) are ±2% (for $\Phi_f > 0.5$), as well as ±5% (for $\Phi_f > 0.4$) and ±10% for weaker emitting dyes (for $0.2 > \Phi_f > 0.02$), and ±20% (for $0.02 > \Phi_f > 0.005$), respectively.[46,47] The procedures used for the correction of the measured absorption intensities at the excitation wavelengths for contributions from (absorbing) nonfluorescent dimers and the procedures employed for the consideration of the contribution of fluorescence resonance energy transfer (FRET) from fluorescent dye monomers to nonfluorescent dimers to a reduction in Φ_f are detailed in the Supporting Information (SI).

For steady-state measurements of the emission anisotropy r, the samples were excited with the excitation polarizer set to 0° and the resulting fluorescence intensities were measured for emission polarizer settings of 0° and 90°, respectively. The emission anisotropy was calculated from integrated blank and spectrally corrected emission spectra according to eq 2.[1]

$$r = \frac{F_{0°/0°} - F_{0°/90°}}{F_{0°/0°} + 2F_{0°/90°}} \quad (2)$$

Dye Hydrophilicity. As a measure of the hydrophilicity of the, we obtained the retention times of the fluorophores using high performance liquid chromatography (HPLC; comparison of retention times of the dyes measured under identical conditions, see SI, Figure 1S, as a relative measure for dye hydrophilicity) and the partition coefficients between octanol (O) and water (W) (K_{OW} values) (SI). In addition, the distribution coefficients (log D) of the fluorophores studied were calculated with the *MarvinSketch* software (ChemAxon Kft, Budapest, Hungary).

Data Evaluation. All data calculations and fitting routines were performed with the software *MATLAB* (see also SI).

RESULTS AND DISCUSSION

IgG conjugates of Dy67x and Dy68x. A comparative labeling study with Dy676, Dy678, Dy681, and Dy682 using different D/P ratios for conjugate preparation (Table 1) revealed that, in the case of Dy68x, the labeling density is only slightly affected by the number of sulfonic acid groups attached to the chromophore in contrast to the Dy67x series. For each dye-to-IgG concentration ratio employed, the highest labeling densities were always found for Dy678.

Absorption and Fluorescence Properties of IgG Conjugates of Dy67x and Dy68x. The spectroscopic properties of the Dy dyes and selected IgG conjugates in PBS are highlighted in Table 2 and Figure 2. The absorption and emission spectra of the nonconjugated and IgG-bound dyes display the typical narrow absorption and emission bands due to cyanine-type optical transitions delocalized over the whole π-conjugated system. The—for trimethine dyes—very red-shifted absorption and emission bands underline the strong electron accepting character of the benzopyrylium moiety (strong effective length) that provides the basis for spectral matching with the absorption and emission spectra of the pentamethine dyes Cy5 and Cy5.5.[27] The less structured absorption and emission bands of nonconjugated Dy681 and Dy682 are bathochromically shifted compared to Dy676 and Dy678 emphasizing the enhanced electron acceptor strength of the benzypyrylium entity in Dy68x. The molar decadic absorption coefficients ε (at the fluorophore's main absorption maximum; measured at $c(\text{dye}) = 2 \times 10^{-6}$ mol L to minimize dye aggregation) are on the order of 100 000 to 130 000 L mol^{-1} cm^{-1} in PBS (Dy676, ε = 114 470 L mol^{-1} cm^{-1}; Dy678, ε = 130 547 L mol^{-1} cm^{-1}; Dy681, ε = 98 127 L mol^{-1} cm^{-1}; Dy682, ε = 109 874 L mol^{-1} cm^{-1}). As follows from Table 2, the Φ_f values of the Dy68x series increase with increasing number of sulfonate groups, although

Table 2. Spectroscopic Properties of the IgG−Dye Conjugates and the Corresponding Nonconjugated Dyes in PBS[a]

	λ_{abs}[b]/nm		λ_{em}[c]/nm		Φ_f	
dye	free dye	IgG conjugate	free dye	IgG conjugate	free dye	IgG conjugate (D/P = 4)
Dy676	664	677	700	704	0.04	0.01
Dy678	662	671	696	700	0.04	0.05
Dy681	679	687	714	716	0.11	0.06
Dy682	679	684	708	712	0.20	0.07

[a] Maxima of the main absorption (λ_{abs}) and emission (λ_{em}) bands and fluorescence quantum yields (Φ_f) for an exemplary chosen dye-to-protein ratio of 4. [b] Longest wavelength absorption maximum. [c] Emission maximum; exemplary chosen dye-to-protein ratio of 4 for the comparison of the different fluorophores.

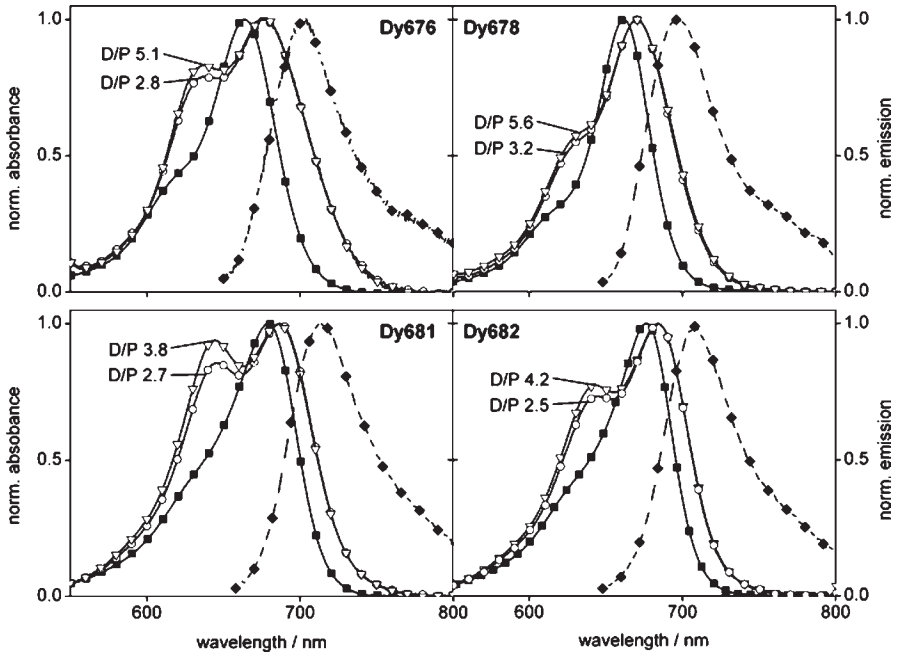

Figure 2. Absorption spectra of the free dyes (full squares) and their IgG conjugates (open symbols; two different D/P ratios) and emission spectra of the nonconjugated dyes (diamonds, dashed lines) in PBS.

the absorption spectra of Dy682 and Dy681 are very similar. Contrary, the Φ_f values of Dy67x, equipped with a more planar benzopyrylium moiety, are barely influenced by the number of sulfonate groups, even though the spectral shape of the absorption spectrum of Dy676 (Figure 2) suggests partial dye aggregation that is absent for Dy678. With a value of 0.20 in PBS, the fluorescence quantum yield of Dy682 is promisingly high. For comparison, the Cy5.5 displays a Φ_f of 0.29 in PBS.[32]

IgG conjugation leads to small red shifts of the absorption and emission bands of the Dy dyes (Table 2), pointing to a decrease in the polarity of the dye microenvironment, and an enhanced absorption within the region of the dye's vibronic shoulder. The intensity of this new absorption band (Figure 2) increases with advancing D/P ratios. The size of these effects increases in the order of IgG-Dy678 < IgG-Dy682 < IgG-Dy681 < IgG-Dy676. Solely in the latter case, solutions of the nonconjugated dye (dye concentration of 1×10^{-6} M and higher) also show this enhanced absorption peak that disappears upon dilution (see also following section, Figure 4). These new absorption bands, the occurrence of which has been reported for many other bioanalytically relevant labels including Cy3 and Cy5, is ascribed to the formation of aggregates, most likely H-type dimers.[33,35,38,41,43,48−50] The nonemissive nature of these species follows from the match of the fluorescence excitation spectra of the IgG conjugates (not shown here) and the free dyes.

IgG conjugation of the fluorophores results in a reduction in Φ_f with increasing D/P ratio (Figure 3; solvent PBS). We cannot exclude an initial increase in Φ_f upon IgG conjugation as reported, e.g., for Cy5 and a recently introduced squaraine label, due to, e.g., a restricted torsional motion about the central methane bridge or to a reduced polarity of the dye microenvironment.[41,51] For D/P ratios of ≤5, the Φ_f values display the following trend: IgG-Dy682> IgG-Dy681 > IgG-Dy678 > IgG-Dy676, paralleling the trend of the Φ_f values of the free dyes. Since the Φ_f values of the IgG conjugates in Figure 3 were always measured at excitation wavelengths, at which the nonfluorescent dimers also absorb,[41,43] these data present lower limits of the Φ_f values of the IgG-bound emissive dyes. Such a diminution in Φ_f with increasing D/P ratios has been reported, e.g., for xanthene dyes [4,52] as well as for NIR-emissive cyanines (including, e.g., Cy5, Cy5.5, Cy7, and several Alexa dyes), porphyrins, and squaraines.[33,35,37,38,41−43,48,53] The D/P ratio where such effects

dx.doi.org/10.1021/bc1004763 |Bioconjugate Chem. 2011, 22, 1298–1308

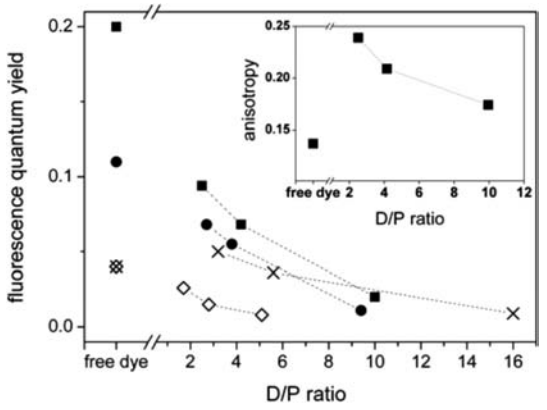

Figure 3. Fluorescence quantum yields of the IgG conjugates of Dy676 (open diamonds), Dy678 (crosses), Dy681 (full circles), and Dy682 (full squares) in PBS as a function of D/P ratio. The inset shows exemplary emission anisotropy r of IgG-Dy682 as a function of D/P ratio. For comparison, the corresponding properties of the free dyes are included as well.

occur and the extent of fluorescence quenching are dye- and biomolecule-specific.

Among the dyes studied, Dy682 is the most promising label for IgG and, most likely, for other immunoglobulines and proteins as well. Although its fluorescence quantum yield decreases with increasing labeling density (Figure 3), it should be, e.g., kept in mind that, for Cy5, likewise a ca. 95% drop in Φ_f per Cy5 label has been described for D/P $\geq$ 6[35] and a similar behavior was reported for Cy5.5. Moreover, for a D/P ratio of approximately 2, the fluorescence quantum yield of Cy5 reaches a value of 0.10[51] as found by us for Dy682.

The observed conjugation-induced dimution in fluorescence is attributed to a combination of effects with the main contributions arising from the formation of nonfluorescent aggregates (H-type homodimers) and from FRET from the fluorescent monomeric dyes to the increasing number of nonemissive dimers on the biomolecule.[41,43] The size of FRET-induced fluorescence quenching is expected to correlate, e.g., with the aggregation tendency of the label, the spectral overlap between monomer emission and dimer absorption, and the donor−acceptor distance, as well as with the fluorescence quantum yield of the emissive monomer and the relative orientation of the transition dipole moments of the interacting donor and acceptor molecules (orientational factor κ^2).[37,54−56] As FRET is known to result in a reduction in emission anisotropy r,[1,37] we determined this quantity for the different IgG conjugates as a function of D/P ratio. Exemplary Dy682 is shown in the inset of Figure 3. Conjugation of Dy682 leads to an initial increase in r for D/P = 2.5 as compared to the free dye, reflecting the binding-induced reduction in rotational freedom, followed by a continuous decrease with increasing labeling density. The latter underlines the contribution of FRET to the observed fluorescence quenching in the IgG−Dy dye conjugates.

To gain further insight into the fluorescence quenching mechanisms and the role of dye aggregation, we studied the aggregation behavior of the four cyanines in PBS. The concentration-dependent absorption spectra summarized in Figure 4 revealing isosbestic points indicate the exclusive formation of dimers in all cases. These data were subsequently exploited for the calculation of the absorption spectra of the dimers shown in Figure 4 (see also SI). The spectral shape of the dimer spectra is only slightly affected by the number of sulfonate groups for each family of dyes, yet differs among the Dy67x and Dy68x series suggesting a rather similar dimer structure for Dy676 and Dy678, as well as for Dy681 and Dy682.[57,58]

Dye Aggregation. The dimerization constants K_D of the Dy dyes in PBS were determined to 1.3 × 10^5 L/mol (Dy676; two SO_3^- groups) and 8 × 10^3 L/mol (Dy678; four SO_3^- groups) for the DY67x series and to 6 × 10^3 L/mol (Dy681; two SO_3^- groups) and 2 × 10^3 L/mol (Dy682; three SO_3^- groups), for Dy68x, respectively, from the data shown in Figure 4 (see also SI). These K_D values are on the same order of magnitude as found for other cyanine dyes.[58,59] To correlate the aggregation tendency with dye hydrophilicity, we determined the retention times of the dyes via with high-performance liquid chromatography (HPLC) using identical conditions (see SI, Figure 1S, and the partition coefficients between octanol (O) and water (W) (K_{OW} values or logK_{OW} values)). Furthermore, we calculated the distribution coefficients or ratios D (log D) with the program *MarvinSketch*. All three methods revealed the following trend in dye hydrophilicity: Dy678 > Dy682 > Dy681 > Dy676. This suggests control of the aggregation tendency of our dyes by both electrostatic effects (number of sulfonate groups) and steric effects governed by the substitution pattern of the benzopyrylium moieties. Obviously, the sterically demanding *tert*-butyl substituent of the benzopyrylium moiety of the Dy68x series diminishes dye−dye interactions compared to the Dy67x series with its planar benzopyrylium end group (Figure 1).

Correction of Measured Φ_f Values of the IgG-Conjugated Dyes for Dimer Absorption. The absorption spectra of the dye dimers (Figure 4) were subsequently used for the calculation of the fraction of dimerized dyes present in the different IgG conjugates (Figure 5). As follows from Figure 5, for all D/P ratios studied, the IgG conjugates of Dy682 contain the smallest amount of dimers and those of Dy676 the highest fraction. The IgG conjugates of Dy681 and Dy678 comprise a comparable fraction of dimerized dye molecules, especially for D/P $\geq$ 5. Accordingly, the fraction of IgG-conjugated dimers reflects the trends of the K_D values found for the Dy dyes.

Subsequently, the measured apparent Φ_f values of the IgG-Dy dye conjugates were corrected for the contribution of the nonemissive dimers to the measured absorption at the excitation wavelengths employed for the determination of the fluorescence quantum yields (see SI). The resulting dimer absorption-corrected Φ_f values that provide a measure for the fluorescence quantum yields of the IgG-attached emissive monomers are summarized in Figure 6 (open squares). As follows from this figure, for D/P $\leq$ 4, consideration of dimer absorption results in an increase in Φ_f of ca. 3 for IgG-bound Dy676 (IgG-Dy676) followed by a factor of ca. 2 for IgG-Dy678 and IgG-Dy681 and a factor of ca. 1.5 for IgG-Dy682, respectively.

Correction of Φ_f for Monomer−Dimer FRET. Despite the dimer absorption correction, all IgG conjugates still display a diminution in Φ_f with increasing labeling density. This is attributed to fluorescence quenching due to monomer−dimer FRET. The contribution of this fluorescence deactivation pathway was approximated using a procedure similar to that reported by Schobel et al. (see SI).[41,43,60] The relevant parameter for this quenching pathway, the Förster radius R_0, differs only slightly among the four dyes (R_0 of 5.71 nm, 5.75 nm, 5.50 nm, and 5.65 nm calculated for IgG-Dy676, IgG-Dy678, IgG-Dy681, and IgG-Dy682, respectively). As follows from Figure 6 (open triangles) and for

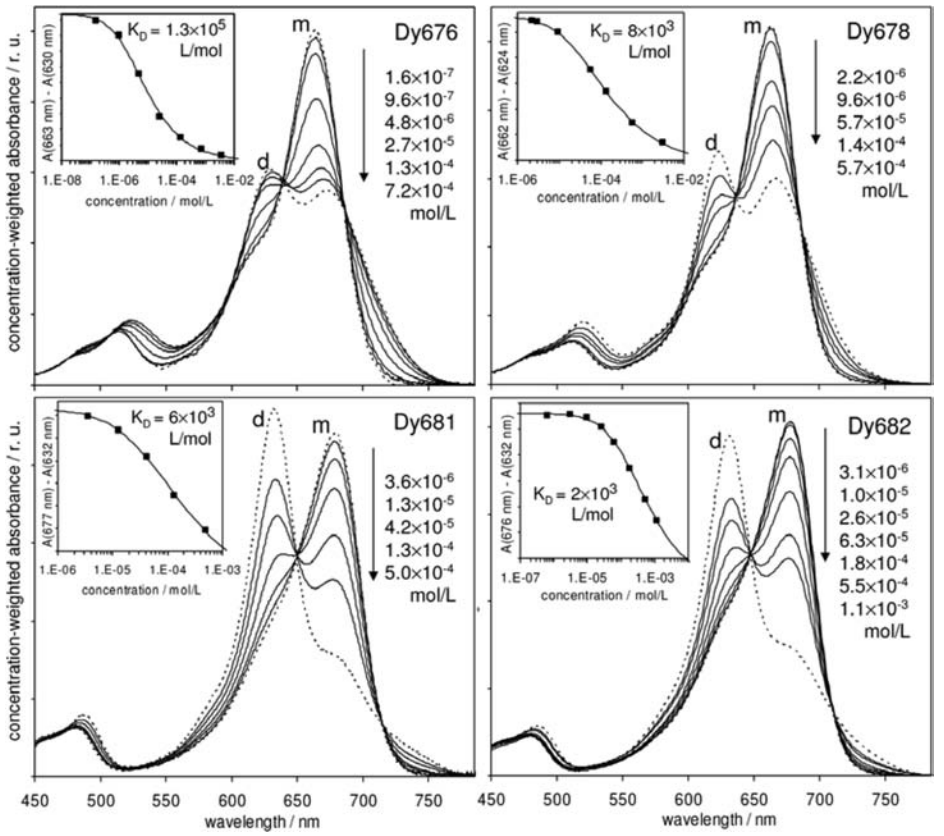

Figure 4. Concentration dependence of the absorption spectra of the Dy dyes: Concentration-weighted absorbances for the dye concentration range of 10^{-7} to 10^{-3} mol/L (solid lines) and the calculated spectra of the monomer (m) and dimer (d) (dotted lines), respectively. The insets show the differences in absorbance (squares) taken at the wavelengths of the monomer absorption maximum (at about 670 nm) and the dimer absorption maximum (at about 630 nm) together with the simulation (lines) and the resulting dimerization constants K_D. The data evaluation procedure is detailed in the Supporting Information.

selected IgG conjugates also from Table 2, consideration of monomer−dimer FRET leads to a further increase in Φ_f for all D/P ratios. With these corrections, i.e., in the absence of dimers, e.g., Φ_f values of ca. 0.1 should result for IgG-Dy682 even at D/P ratios of 10. The maximum accomplishable fluorescence quantum yields $\Phi_{f,max}$ of the IgG-bound dyes can be estimated from the extrapolation of the D/P dependence of the dimer absorption- and FRET-corrected Φ_f values to a D/P ratio of 0. This yields $\Phi_{f,max}$ values of the protein-bound monomeric fluorophores of 0.12 and 0.14 for Dy676 and Dy678 and 0.20 and 0.21 for Dy681 and Dy682. These values that are barely affected by the number of sulfonate groups within each series of fluorophores exceed the fluorescence quantum yields found for the free dyes in PBS solution with the exception of Dy682. The remaining reduction in the corrected Φ_f values with increasing label density observed for all conjugates is ascribed to our simplified model used for the FRET calculations, as well as to the presence of other fluorescence diminishing pathways like homo-FRET between emissive IgG-bound dye monomers in different microenvironments that accordingly display different fluorescence quantum yields.

For a better comparison of our IgG-conjugated fluorophores, we determined the ratios of the fluorescence quantum yields in the absence (interpolated values, taken from Figure 6) and presence of the discussed fluorescence reducing processes for an exemplary chosen D/P ratio of 4 (see Figure 7). As follows

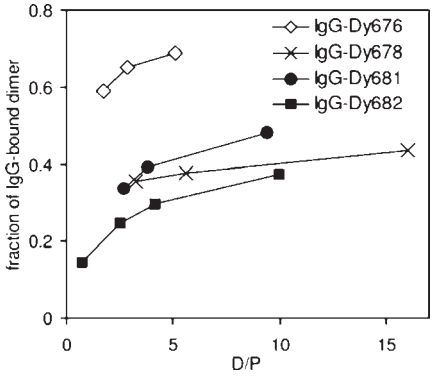

Figure 5. Fraction of IgG-bound dimers as a function of D/P ratio in PBS.

from this figure, comparable effects are observed for Dy678, Dy681, and Dy682. The minor differences among these fluorophores are mainly ascribed to the slightly different aggregation tendencies and different molar absorption coefficients of the dimers at the excitation wavelength (Figure 4). Obviously, for the preparation of highly emissive protein conjugates, the Dy68x family is a better choice than the Dy67x family, with Dy682 yielding the most promising results.

Origin of the IgG-Conjugated Dimers. The considerable extent of dimer formation observed for all IgG conjugates is

dx.doi.org/10.1021/bc1004763 |*Bioconjugate Chem.* 2011, 22, 1298–1308

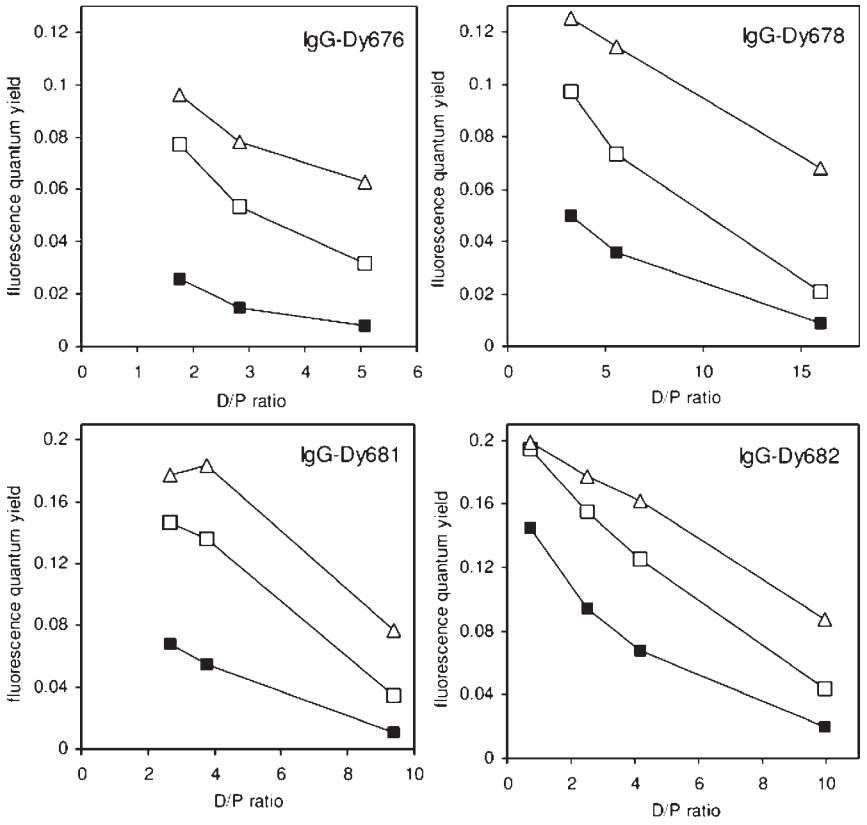

Figure 6. Correction of the measured fluorescence quantum yields of the different IgG-conjugated Dy dyes (full squares; solvent PBS) for the absorption of the nonfluorescent dimers at the excitation wavelengths (open squares) and additionally, for FRET from the emissive monomers to the nonfluorescent dimers (open triangles). Extrapolation of the corrected Φ_f values to a dye-to-protein ratio of 0 provides an estimate of the maximum accomplishable $\Phi_{f,max}$ of the IgG-bound fluorophores.

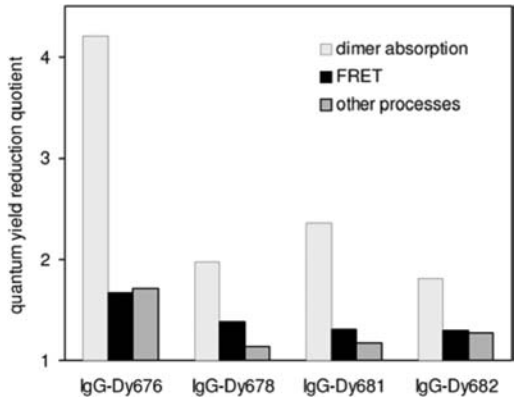

Figure 7. Quotients of the fluorescence quantum yields of the IgG-conjugated dyes corrected for dye aggregation and monomer−dimer FRET and the corresponding uncorrected fluorescence quantum yields exemplary for a D/P ratio of 4 (interpolated values, taken from Figure 6). This includes the ratios of the dimer absorption-corrected $\Phi_{f,Abs}$ values to the measured Φ_f values (dimer absorption), the ratios of the dimer absorption-corrected and FRET-corrected $\Phi_{f,Abs+FRET}$ values and the dimer absorption-corrected $\Phi_{f,Abs}$ values (FRET), and the ratios of the estimated maximum accomplishable $\Phi_{f,max}$ values of the IgG-conjugated dyes (extrapolated from Figure 6 to D/P = 0) and the dimer absorption-corrected and FRET-corrected $\Phi_{f,Abs+FRET}$ values (other processes). These ratios provide a clue for the contribution of each of these processes to the observed reduction in fluorescence. The correction procedure is detailed in the Supporting Information.

surprising, considering, e.g., the number of sulfonate groups (Dy678: 4 sulfonate groups) and the dimerization constants of ca. $(2-8) \times 10^{-3}$ L/mol found for Dy682, Dy681, and Dy678, respectively, that are comparable in size to K_D values obtained for other labels.[58,59] This encouraged us to study the absorption and fluorescence properties of selected IgG−Dy dye conjugates (selected D/P ratios) in the presence of deaggregating BSA and deaggregating and denaturating SDS[23,27,61,62] in comparison to the nonconjugated fluorophores. The overall goals were to exclude the presence of adsorbed dyes and to obtain a hint for the accessibility/location of the IgG-conjugated monomeric and dimeric fluorophores.

Influence of BSA. BSA presents a frequently employed model system to study dye−protein interactions and is known to enhance the emission of many fluorophores due to a combination of rigidization, reduction in the polarity of the dye's microenvironment (binding in hydrophobic BSA pocket), and deaggregation.[27,32,61] Moreover, PBS solutions containing 5% BSA (w/w; PBS/BSA) are often used as a model for body fluids.[16] As follows from Tables 2 and 3, the absorption and emission bands of the free dyes are red-shifted in the presence of BSA and their fluorescence quantum yields are considerably increased, especially for Dy676 and Dy678. Moreover, the absorption spectra do not show any signs of dye dimerization, even in the case of Dy676, and the absorption and fluorescence excitation spectra match. The spectral position and shape of the absorption and emission spectra of the IgG-conjugated Dy

Table 3. Spectroscopic Properties of Exemplary Chosen IgG Conjugates (dye-to-protein ratio of 4) in PBS/BSA (5% BSA, w/w) in Comparison to the Spectroscopic Properties of the Corresponding Nonconjugated Dyes in PBS/BSA[a]

	λ_{abs}[b]/nm		λ_{em}[c]/nm		Φ_f	
dye	free dye	IgG conjugate	free dye	IgG conjugate	free dye	IgG conjugate (D/P = 4)
Dy676	678	679	699	704	0.31	0.03
Dy678	675	672	710	702	0.31	0.08
Dy681	693	688	710	716	0.39	0.06
Dy682	691	686	710	712	0.42	0.10

[a] Maxima of the main absorption (λ_{abs}) and emission (λ_{em}) bands and fluorescence quantum yields (Φ_f). [b] Longest-wavelength absorption maximum. [c] Emission maximum; exemplary chosen dye-to-protein ratio of 4 for the comparison of the different fluorophores.

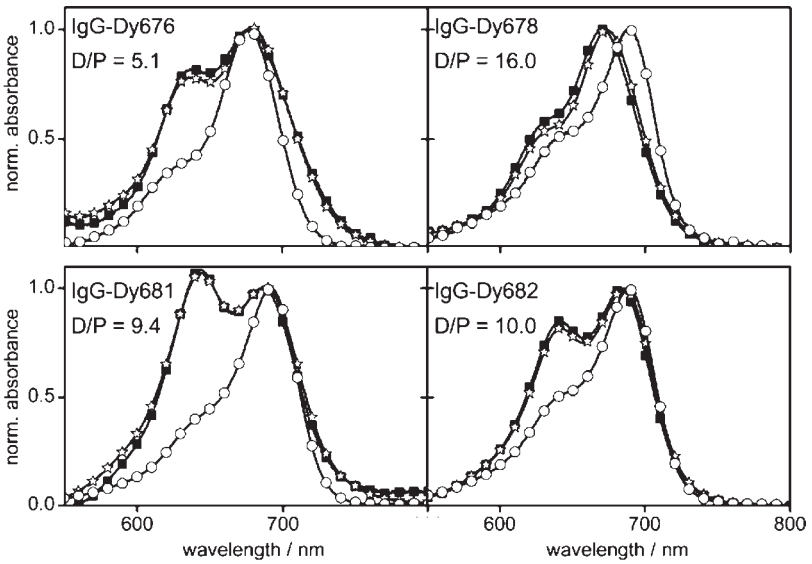

Figure 8. Spectral changes in absorption resulting for IgG−dye conjugates of high labeling density in PBS (full squares) upon addition of 5% BSA (w/w) (stars) and in the presence of 5% SDS (w/w) (open circles). The D/P ratios used for each fluorophore are given in the panels.

dyes, however, remain almost unaffected, with the absorption spectra in PBS/BSA still displaying clear hints for dimerization (Figure 8). In addition, the Φ_f values (experimental values) in PBS/BSA barely increase as compared to PBS. Thus, the unexpectedly high fraction of dimers in the IgG conjugates (Figure 5) cannot be ascribed to the interaction between IgG-conjugated (monomeric) dye molecules and adsorbed dyes.

Influence of SDS. Addition of SDS to the nonconjugated Dy dyes results in similar effects as observed for BSA: a strong fluorescence enhancement, especially for the Dy67x series, and bathochromic shifts in absorption and emission. In the presence of SDS, inducing protein unfolding and deaggregation, the IgG-conjugated dyes also undergo similar spectral shifts as their nonconjugated counterparts and, even at high D/P ratios, the dimer absorption bands disappear (Figure 8). Simultaneously, the fluorescence quantum yields of all IgG conjugates increase considerably, amounting to about 85−90% of the fluorescence quantum yields of the free labels even for the highest labeling densities used. Obviously, protein unfolding in conjunction with dye−SDS interactions are needed to break up already formed dye aggregates bound to the protein. In addition, these results underline the suitability of our Φ_f corrections assuming dimer absorption and monomer−dimer FRET as main fluorescence diminution channels.

At present, we can only speculate about the reason for the formation of H-dimers observed already at low D/P ratios. One possible explanation could be the existence of preferential reaction sites for each dye at the protein based upon physicochemical characteristics such as charge and hydrophilicity as has been discussed for other fluorescent labels[35] resulting in closely neighboring IgG-bound fluorophores, the interaction of which resulted in the previously discussed spectroscopic effects.[63] Alternatively, preformed reactive dimers in the reaction solution or IgG aggregation enabling the interaction between IgG-bound fluorophores from different antibodies may account for these observations. As follows from Figure 4, at the dye concentrations used for the labeling reaction (see Experimental Procedures) dye dimerization has already occurred to a considerable extent in PBS. For example, for a dye concentration of 1×10^{-4} M, the percentage of dimerized dye in PBS amounts to 82% for Dy676, 46% for Dy678, 41% for Dy681, and 24% for Dy682 and increases to 94%, 78%, 75%, and 61%, respectively, for a dye concentration of 1×10^{-3} M. In comparison, the fraction of dimers in IgG conjugates of D/P = 4 reaches 67% for Dy676, 38% for Dy678, 40% for Dy681, and 30% for Dy682, respectively (Figure 5). Possibly, both dye monomers and dye dimers can react with the lysines of IgG, although the reaction speed of the monomers is expected to exceed that of the dimers. This could

also explain the higher D/P ratios obtained for the most hydrophilic dye Dy678 followed by Dy682 (Table 1) where the reaction mixtures contained the smallest fraction of dimers. When comparing the labeling protocols of other dye manufacturers (e.g., Invitrogen/Amersham, ATTO-TEC, Seta Biomedicals), we found recommended dye concentrations of the reaction solutions on the order of ca. 1.2×10^{-4} M (Invitrogen/Amersham; calculated for Cy5, D/P = 4:1 to 12:1), 0.4×10^{-4} M to 3.0×10^{-4} M (ATTO-TEC; calculated for ATTO-647, D/P = 3:1 and 24:1), and 0.6×10^{-4} M to 4.8×10^{-4} M (Seta Biomedicals; calculated for Seta-1407, D/P = 3:1 and 24:1), respectively. Obviously, care has to be taken with respect to proper choice of fluorophore concentration and reaction conditions for the labeling reaction mixtures to minimize undesired dye dimerization.

To distinguish between the attachment of preformed dimers and the formation of dimers primarily on the protein, we systematically varied the reaction conditions of the IgG labeling reaction exemplary for Dy678 using a constant D/P ratio of 24:1 in the reaction mixture. Parameters varied included the dye concentration in the reaction mixture (c(dye) = 3.3×10^{-4} M and 3.3×10^{-5} M; c(IgG) = 1.4×10^{-5} and 1.4×10^{-6} M); see Experimental Procedures for typical reaction conditions. Using two different dye concentrations and, thus, different fractions of preformed dimers in the reaction mixture (c(dye) = 3.3×10^{-4} M, 65% dimers in the reaction solution; c(dye) = 3.3×10^{-4} M, 28% dimers in the reaction solution) resulted in more or less the same fraction of IgG-bound dimers of 44%. Apparently, the extent of dimerization of IgG-bound dye does not depend on the fraction of dimers in the reaction solution. Two possible mechanisms for dimer formation at the protein are (1) the enhanced probability for dye binding in close neighborhood of already attached dye molecules, and (2) dye-induced protein aggregation. The latter effect has been observed, e.g., by Villaraza et al.[64] These findings underline the need for reaction procedures that minimize fluorescence diminishing dye aggregation. One possible approach here could be the addition of aggregation-suppressing additives like nondenaturing surfactants to the dye−biomolecule reaction mixtures as indicated by first labeling studies. This is currently being systematically assessed by us.

CONCLUSION AND OUTLOOK

In summary, the assessed protein labels Dy681 and especially Dy682, spectrally matching Cy5.5, exhibit enhanced fluorescence quantum yields in PBS and attached to IgG in comparison to our workhorse Dy676 and its more hydrophilic analogue Dy678, spectrally matching Cy5. The fluorescence quantum yield of the Dy dyes in aqueous solution is primarily dependent on the substitution pattern of the benzopyrylium-type end group, which also notably determines the aggregation tendency. Sterically demanding substituents and negatively charged sulfonate groups reduce the aggregation tendency, thereby allowing for higher dye labeling densities without simultaneously enhancing fluorescence quenching. With Dy682, we identified a new attractive diagnostic tool for *in vitro* and *in vivo* fluorescence applications. Labeling experiments at different reaction conditions showed that simple reduction of the fraction of dimerized dye in the reaction solution is not sufficient to diminish the extent of dimerization in the IgG conjugates. One of the approaches currently studied by us is dye bioconjugation in the presence of surfactants. First results suggest that this strategy leads to conjugates containing a reduced fraction of dimers that accordingly reveal an increase in fluorescence quantum yield per label for higher labeling ratios. Although dye aggregation is commonly undesired for protein labeling and the preparation of optical probes, for certain applications, aggregation phenomena and high D/P ratios can be advantageous. This includes, e.g., the design of activatable fluorescent probes for *in vivo* imaging of tumors and metastasis as recently demonstrated by Ogawa and Kobayashi, and assays read out with single molecule spectroscopy, where photobleaching presents a serious limitation.

Our findings present an important advance toward new and comparatively less expensive tools of known stability and cytotoxicity for NIRF imaging. In addition, these results clearly reveal the importance of known structure−property relationships and suitable screening tests for the choice of optimum fluorophores. As derived here, such screening tests should include the determination of the fluorescence quantum yields of the nonconjugated fluorophores in PBS and PBS/BSA as a hint for the maximum achievable fluorescence output as well as aggregation studies and spectroscopic studies in the presence of deaggregating and denaturing SDS.

ASSOCIATED CONTENT

Supporting Information. HPLC analysis, determination and calculation of the distribution coefficients (log D values), determination of the dimerization constant K_D and calculation of the dimer and monomer spectra, determination of the fraction of dimerized dye bound to IgG and correction of Φ_f for dimer absorption, correction of Φ_f for monomer−dimer FRET and estimation of the maximum accomplishable fluorescence quantum yield of the IgG-bound monomeric dyes. This material is available free of charge via the Internet at http://pubs.acs.org.

AUTHOR INFORMATION

Corresponding Author

*Dr. Ute Resch-Genger, BAM Bundesanstalt für Materialforschung and -prüfung, Richard-Willstaetter-Str. 11, D-12489 Berlin, Germany. Phone: 0049-(0)30-8104 1134, Fax: 0049-30-8104 1157, e-mail: ute.resch@bam.de.

ACKNOWLEDGMENT

We are grateful to DYOMICS GmbH (Jena, Germany) for the generous supply of the dyes Dy676, Dy678, Dy681, and Dy682.

REFERENCES

(1) Lakowicz, J. R. (2006) *Principles of fluorescence spectroscopy*, 3rd ed., Springer Science+Business Media, LLC, New York.

(2) Demchenko, A. P. (2005) Optimization of fluorescence response in the design of molecular biosensors. *Anal. Biochem. 343*, 1–22.

(3) Borisov, S. M., and Wolfbeis, O. S. (2008) Optical biosensors. *Chem. Rev. 108*, 423–461.

(4) Resch-Genger, U., Grabolle, M., Cavaliere-Jaricot, S., Nitschke, R., and Nann, T. (2008) Quantum dots versus organic dyes as fluorescent labels. *Nat. Methods 5*, 763–775.

(5) Sapsford, K. E., Berti, L., and Medintz, I. L. (2006) Materials for fluorescence resonance energy transfer analysis: Beyond traditional donor-acceptor combinations. *Angew. Chem., Int. Ed. 45*, 4562–4588.

(6) Weissleder, R., and Pittet, M. J. (2008) Imaging in the era of molecular oncology. *Nature 452*, 580–589.

(7) Kobayashi, H., Ogawa, M., Alford, R., Choyke, P. L., and Urano, Y. (2010) New strategies for fluorescent probe design in medical diagnostic imaging. *Chem. Rev. 110*, 2620–2640.

(8) Lovell, J. F., Liu, T. W. B., Chen, J., and Zheng, G. (2010) Activatable photosensitizers for imaging and therapy. *Chem. Rev. 110*, 2839–2857.

(9) Louie, A. (2010) Multimodality imaging probes: design and challenges. *Chem. Rev. 110*, 3146–3195.

(10) Kovar, J. L., Simpson, M. A., Schutz-Geschwender, A., and Olive, D. M. (2007) A systematic approach to the development agents for optical imaging of mouse of fluorescent contrast cancer models. *Anal. Biochem. 367*, 1–12.

(11) Achilefu, S. (2004) Lighting up tumors with receptor-specific optical molecular probes. *Technol. Cancer Res. Treat. 3*, 393–409.

(12) Escobedo, J. O., Rusin, O., Lim, S., and Strongin, R. M. (2010) NIR dyes for bioimaging applications. *Curr. Opin. Chem. Biol. 14*, 64–70.

(13) Nahrendorf, M., Waterman, P., Thurber, G., Groves, K., Rajopadhye, M., Panizzi, P., Marinelli, B., Pittet, M., Swirski, F., and Weissleder, R. (2009) In vivo imaging of cathepsin activity in atherosclerosis with customized protease nanosensors. *Circulation 120*, S354–S355.

(14) Kobayashi, H., Koyama, Y., Barrett, T., Hama, Y., Regino, C. A. S., Shin, I. S., Jang, B. S., Le, N., Paik, C. H., Choyke, P. L., and Urano, Y. (2007) Multimodal nanoprobes for radionuclide and five-color near-infrared optical lymphatic imaging. *ACS Nano 1*, 258–264.

(15) Almutairi, A., Guillaudeu, S. J., Berezin, M. Y., Achilefu, S., and Frechet, J. M. J. (2008) Biodegradable pH-sensing dendritic nanoprobes for near-infrared fluorescence lifetime and intensity imaging. *J. Am. Chem. Soc. 130*, 444–445.

(16) Lisy, M. R., Goermar, A., Thomas, C., Pauli, J., Resch-Genger, U., Kaiser, W. A., and Hilger, I. (2008) In vivo near-infrared fluorescence imaging of carcinoembryonic antigen-expressing tumor cells in mice. *Radiology 247*, 779–787.

(17) von Wallbrunn, A., Holtke, C., Zuhlsdorf, M., Heindel, W., Schafers, M., and Bremer, C. (2007) In vivo imaging of integrin alpha vs. beta(3) expression using fluorescence-mediated tomography. *Eur. J. Nucl. Med. Mol. Imaging 34*, 745–754.

(18) Benson, R. C., and Kues, H. A. (1978) Fluorescence properties of indocyanine green as related to angiography. *Phys. Med. Biol. 23*, 159–163.

(19) Bradley, E. C., and Barr, J. W. (1968) Determination of blood volume using indocyanine green (Cardio-GreenR) dye. *Life Sci., Part 1 Physiol. Pharmacol. Part 2 Biochem. Gen. Mol. Biol. 7*, 1001–1006.

(20) Leevy, C. M., Smith, F., Longuevi., J, Paumgart., G, and Howard, M. M. (1967) Indocyanine green clearance as a test for hepatic function. *J. Am. Med. Assoc. 200*, 236–240.

(21) Hama, Y., Urano, Y., Koyama, Y., Bernardo, M., Choyke, P. L., and Kobayashi, H. (2006) A comparison of the emission efficiency of four common green fluorescence dyes after internalization into cancer cells. *Bioconjugate Chem. 17*, 1426–1431.

(22) Longmire, M. R., Ogawa, M., Hama, Y., Kosaka, N., Regino, C. A. S., Choyke, P. L., and Kobayashi, H. (2008) Determination of optimal rhodamine fluorophore for in vivo optical imaging. *Bioconjugate Chem. 19*, 1735–1742.

(23) Ogawa, M., Kosaka, N., Choyke, P. L., and Kobayashi, H. (2009) H-type dimer formation of fluorophores: a mechanism for activatable, in vivo optical molecular imaging. *ACS Chem. Biol. 4*, 535–546.

(24) Adams, K. E., Ke, S., Kwon, S., Liang, F., Fan, Z., Lu, Y., Hirschi, K., Mawad, M. E., Barry, M. A., and Sevick-Muraca, E. M. (2007) Comparison of visible and near-infrared wavelength-excitable fluorescent dyes for molecular imaging of cancer. *J. Biomed. Opt. 12*, 024017–1 - 024017−9.

(25) Ballou, B., Ernst, L. A., and Waggoner, A. S. (2005) Fluorescence imaging of tumors in vivo. *Curr. Med. Chem. 12*, 795–805.

(26) Mahmood, U., and Weissleder, R. (2003) Near-infrared optical imaging of proteases in cancer. *Mol. Cancer Ther. 2*, 489–496.

(27) Pauli, J., Vag, T., Haag, R., Spieles, M., Wenzel, M., Kaiser, W. A., Resch-Genger, U., and Hilger, I. (2009) An in vitro characterization study of new near infrared dyes for molecular imaging. *Eur. J. Med. Chem. 44*, 3496–3503.

(28) Lee, H., Mason, J. C., and Achilefu, S. (2008) Synthesis and spectral properties of near-infrared aminophenyl-, hydroxyphenyl-, and phenyl-substituted heptamethine cyanines. *J. Org. Chem. 73*, 723–725.

(29) Hilderbrand, S. A., Kelly, K. A., Weissleder, R., and Tung, C. H. (2005) Monofunctional near-infrared fluorochromes for imaging applications. *Bioconjugate Chem. 16*, 1275–1281.

(30) Hansch, A., Frey, O., Sauner, D., Hilger, I., Haas, M., Malich, A., Brauer, R., and Kaiser, W. A. (2004) In vivo imaging of experimental arthritis with near-infrared fluorescence. *Arthrit. Rheumatism 50*, 961–967.

(31) Soper, S. A., and Mattingly, Q. L. (1994) Steady -state and picosecond laser fluorescence studies of nonradiative pathways in tricarbocyanine dyes: implications to the design of near-IR fluorochromes with high fluorescence efficiencies. *J. Am. Chem. Soc. 116*, 3744–3752.

(32) Pauli, J., Brehm, R., Spieles, M., Kaiser, W. A., Hilger, I., and Resch-Genger, U. (2010) Novel fluorophores as building blocks for optical probes for in vivo near infrared fluorescence (NIRF) imaging. *J. Fluoresc. 20*, 681–693.

(33) Berlier, J. E., Rothe, A., Buller, G., Bradford, J., Gray, D. R., Filanoski, B. J., Telford, W. G., Yue, S., Liu, J. X., Cheung, C. Y., Chang, W., Hirsch, J. D., Beechem, J. M., Haugland, R. P., and Haugland, R. P. (2003) Quantitative comparison of long-wavelength Alexa Fluor dyes to Cy dyes: Fluorescence of the dyes and their bioconjugates. *J. Histochem. Cytochem. 51*, 1699–1712.

(34) Panchuk-Voloshina, N., Haugland, R. P., Bishop-Stewart, J., Bhalgat, M. K., Millard, P. J., Mao, F., Leung, W. Y., and Haugland, R. P. (1999) Alexa dyes, a series of new fluorescent dyes that yield exceptionally bright, photostable conjugates. *J. Histochem. Cytochem. 47*, 1179–1188.

(35) Gruber, H. J., Hahn, C. D., Kada, G., Riener, C. K., Harms, G. S., Ahrer, W., Dax, T. G., and Knaus, H. G. (2000) Anomalous fluorescence enhancement of Cy3 and Cy3.5 versus anomalous fluorescence loss of Cy5 and Cy7 upon covalent linking to IgG and noncovalent binding to avidin. *Bioconjugate Chem. 11*, 696–704.

(36) Buschmann, V., Weston, K. D., and Sauer, M. (2003) Spectroscopic study and evaluation of red-absorbing fluorescent dyes. *Bioconjugate Chem. 14*, 195–204.

(37) Luchowski, R., Matveeva, E. G., Gryczynski, I., Terpetschnig, E. A., Patsenker, L., Laczko, G., Borejdo, J., and Gryczynski, Z. (2008) Single molecule studies of multiple-fluorophore labeled antibodies. Effect of homo-FRET on the number of photons available before photobleaching. *Curr. Pharm. Biotechnol. 9*, 411–420.

(38) Luschtinetz, F., Dosche, C., and Kumke, M. U. (2009) Influence of streptavidin on the absorption and fluorescence properties of cyanine dyes. *Bioconjugate Chem. 20*, 576–582.

(39) Lisy, M.-R., Schuler, E., Lehmann, F., Czerney, P., Kaiser, W. A., and Hilger, I. (2006) Diagnosis of peritonitis using near-infrared optical imaging of in vivo labeled monocytes-macrophages. *J. Biomed. Opt. 11*, 064014.

(40) Deissler, V., Ruger, R., Frank, W., Fahr, A., Kaiser, W. A., and Hilger, I. (2008) Fluorescent liposomes as contrast agents for in vivo optical imaging of edemas in mice. *Small 4*, 1240–1246.

(41) Schobel, U., Egelhaaf, H.-J., Brecht, A., Oelkrug, D., and Gauglitz, G. (1999) New donor-acceptor pair for fluorescent immunoassays by energy transfer. *Bioconjugate Chem. 10*, 1107–1114.

(42) Matveeva, E. G., Terpetschnig, E. A., Stevens, M., Patsenker, L., Kolosova, O. S., Gryczynski, Z., and Gryczynski, I. (2009) Near-infrared squaraine dyes for fluorescence enhanced surface assay. *Dyes Pigm. 80*, 41–46.

(43) Schobel, U., Engelhaaf, H.-J., Fröhlich, D., Brecht, A., Oelkrug, D., and Gauglitz, G. (2000) Mechanism of fluorescence quenching in donor-acceptor labeled antibody conjugates. *J. Fluoresc. 10*, 147–154.

(44) Hama, Y., Koyama, Y., Urano, Y., Choyke, P. L., and Kobayashi, H. (2007) Two-color lymphatic mapping using Ig-conjugated near infrared optical probes. *J. Invest. Dermatol. 127*, 2351–2356.

(45) Resch-Genger, U., Pfeifer, D., Monte, C., Pilz, W., Hoffmann, A., Spieles, M., Rurack, K., Hollandt, J., Taubert, D., Schonenberger, B., and Nording, P. (2005) Traceability in fluorometry: Part II. Spectral fluorescence standards. *J. Fluoresc. 15*, 315–336.

(46) Grabolle, M., Spieles, M., Lesnyak, V., Gaponik, N., Eychmüller, A., and Resch-Genger, U. (2009) Determination of the fluorescence quantum yield of quantum dots: suitable procedures and achievable uncertainties. *Anal. Chem. 81*, 6285–6294.

(47) Wurth, C., Lochmann, C., Spieles, M., Pauli, J., Hoffmann, K., Schuttrigkeit, T., Franzl, T., and Resch-Genger, U. (2010) Evaluation of a commercial integrating sphere setup for the determination of absolute photoluminescence quantum yields of dilute dye solutions. *Appl. Spectrosc. 64*, 733–741.

(48) Cox, W. G., Beaudet, M. P., Agnew, J. Y., and Ruth, J. L. (2004) Possible sources of dye-related signal correlation bias in two-color DNA microarray assays. *Anal. Biochem. 331*, 243–254.

(49) Eisfeld, A., and Briggs, J. S. (2006) The J- and H-bands of organic dye aggregates. *Chem. Phys. 324*, 376–384.

(50) Mujumdar, R. B., Ernst, L. A., Mujumdar, S. R., Lewis, C. J., and Waggoner, A. S. (1993) Cyanine dye labeling reagents - sulfoindocyanine succinimidyl esters. *Bioconjugate Chem. 4*, 105–111.

(51) Povrozin, Y. A., Kolosova, O. S., Obukhova, O. M., Tatarets, A. L., Sidorov, V. I., Terpetschnig, E. A., and Patsenker, L. D. (2009) Seta-633-A NIR fluorescence lifetime label for low-molecular-weight analytes. *Bioconjugate Chem. 20*, 1807–1812.

(52) Ogawa, M., Kosaka, N., Longmire, M. R., Urano, Y., Choyke, P. L., and Kobayashi, H. (2009) Fluorophore-quencher based activatable targeted optical probes for detecting in vivo cancer metastases. *Mol. Pharmaceutics 6*, 386–395.

(53) Burke, M., O'Sullivan, P. J., Ponomarev, G. V., Yashunsky, D. V., and Papkovsky, D. B. (2007) Analysis of close proximity quenching of phosphorescent metalloporphyrin labels in oligonucleotide structures. *Anal. Chim. Acta 585*, 139–146.

(54) Johansson, M. K., and Cook, R. M. (2003) Intramolecular dimers: A new design strategy for fluorescence-quenched probes. *Chem.—Eur. J. 9*, 3466–3471.

(55) Packard, B. Z., Komoriya, A., Nanda, V., and Brand, L. (1998) Intramolecular excitonic dimers in protease substrates: modification of the backbone moiety to probe the H-dimer structure. *J. Phys. Chem. B 102*, 1820–1827.

(56) Takalo, H., Mukkala, V. M., Mikola, H., Liitti, P., and Hemmila, I. (1994) Synthesis of europium(III) chelates suitable for labeling of bioactive molecules. *Bioconjugate Chem. 5*, 278–282.

(57) Antonov, L., Gergov, G., Petrov, V., Kubista, M., and Nygren, J. (1999) UV-Vis spectroscopic and chemometric study on the aggregation of ionic dyes in water. *Talanta 49*, 99–106.

(58) Sarkar, D., Das, P., Girigoswami, A., and Chattopadhyay, N. (2008) Spectroscopic characterization of phenazinium dye aggregates in water and acetonitrile media: Effect of methyl substitution on the aggregation phenomenon. *J. Phys. Chem. A 112*, 9684–9691.

(59) Sabate, R., and Estelrich, J. (2008) Determination of the dimerization constant of pinacyanol: Role of the thermochromic effect. *Spectrochim. Acta, Part A 70*, 471–476.

(60) Gennis, R. B., and Cantor, C. R. (1972) Use of nonspecific dye labeling for singlet energy transfer measurements in complex systems. A simple model. *Biochemistry 11*, 2509–2512.

(61) Patonay, G., Kim, J. S., Kodagahally, R., and Strekowski, L. (2005) Spectroscopic study of a novel bis(heptamethine cyanine) dye and its interaction with human serum albumin. *Appl. Spectrosc. 59*, 682–690.

(62) Chibisov, A. K., Prokhorenko, V. I., and Gorner, H. (1999) Effects of surfactants on the aggregation behaviour of thiacarbocyanine dyes. *Chem. Phys. 250*, 47–60.

(63) Packard, B. Z., Komoriya, A., Nanda, V., and Brand, L. (1998) Intramolecular excitonic dimers in protease substrates: Modification of the backbone moiety to probe the H-dimer structure. *J. Phys. Chem. B 102*, 1820–1827.

(64) Villaraza, A. J. L., Milenic, D. E., and Brechbiel, M. W. (2010) Improved speciation characteristics of PEGylated indocyanine green-labeled panitumumab: revisiting the solution and spectroscopic properties of a near-infrared emitting anti-HER1 antibody for optical imaging of cancer. *Bioconjugate Chem. 21*, 2305–2312.

Supporting Information

Suitable Labels for Molecular Imaging – Influence of Dye Structure and Hydrophilicity on the Spectroscopic Properties of IgG Conjugates

Jutta Pauli, Markus Grabolle, Robert Brehm, Monika Spieles, Franziska Hamann, Matthias Wenzel, Ingrid Hilger, and Ute Resch-Genger*

Supporting Information Available:

1. HPLC analysis
2. Determination and calculation of the distribution coefficients (log *D* values)
3. Determination of the dimerization constants K_D and calculation of the dimer and monomer spectra
4. Determination of the fraction of dimerized dye bound to IgG and correction of Φ_f for dimer absorption
5. Correction of Φ_f for monomer-dimer FRET and estimation of the maximum accomplishable fluorescence quantum yields of the IgG-bound monomeric dyes

This material is available free of charge via the Internet at http://pubs.acs.org.

1. HPLC analysis

HPLC measurements with Dy676, Dy678, Dy681, and Dy682 were performed at T = 296 K and a pressure of 200 bar with a HPLC system from Knauer (WellChrom Solvent Organizer K-1500, WellChrom HPLC-Pumpe K-1001) equipped with a diode array detector (K-2800,

WellChrom; detection at 670 nm) and a EC 250/4 column from Machery-Nagel EC 250/4 packed with NUCLEODUR C-18 gravity (particle diameter 5 μm) to derive retention times as a measure for the relative dye hydrophilicity. The following solvents and eluent gradient were used: t = 0 min.: 90% H_2O with 0.1% trifluoroacetic acid (TFA) + 10% acetonitrile (ACN) with 0.1% TFA, 15 min.: 10% H_2O with 0.1% TFA + 90% ACN with 0.1% TFA, 27 min.: 10% H_2O with 0.1% TFA + 90% ACN with 0.1% TFA, 28 min.: 100% ACN with 0.1% TFA, 29 min:.00% ACN with 0.1% TFA, and 30min.: 90% H_2O with 0.1% trifluoroacetic acid (TFA) + 10% acetonitrile (ACN) with 0.1% TFA. The accordingly obtained retention times are summarized in Figure 1S.

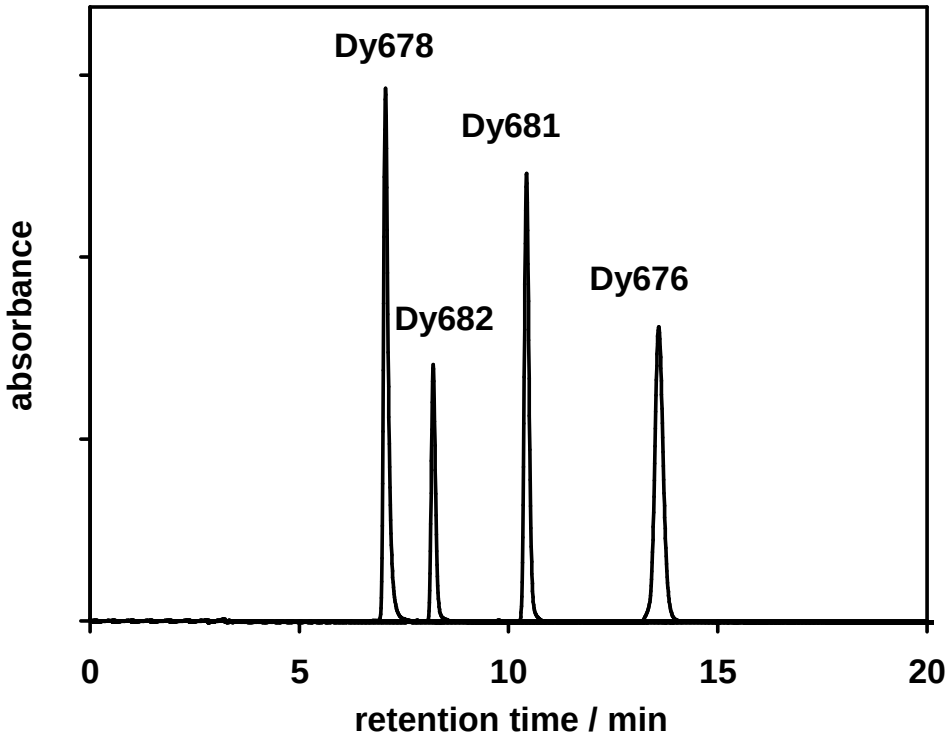

Figure 1S. HPLC diagram (diode array detector set to 670 nm) of a mixture of the four dyes studied. The retention times provide a relative measure for dye hydrophilicity with more hydrophilic dyes displaying shorter retention times under the measurement conditions used.

2. Determination and calculation of the distribution coefficients (log *D* values)

Partition coefficients between octanol (O) and water (W) ($K_{OW;}$ provided here as logK_{OW} values for comparison with the calculated distribution ratios given as log D values below) of Dy676, Dy681, and Dy682 were determined to K_{OW}(Dy676) = 1.8×10^{-2} (log*K*ow = -1.74), K_{OW}(Dy681) = 4.1×10^{-3} (log*K*ow = -2.39), and K_{OW}(Dy682) = 6.3×10^{-4} (log*K*ow = -3.20), respectively. For these measurements, 100 µl of the stock solution of the dyes Dy676, Dy681, and Dy682 (100×10^{-6} mol/L) were dissolved in 1 mL water and extracted with 5 mL octanol (Dy676, Dy681) or 10 mL (Dy678, Dy682) over night. The dye concentrations in both solvents were then determined photometrically using previously measured molar absorption coefficients of the fluorophores in the pure solvents. No attempts were made to determine the K_{OW} value of Dy678 due to its extremely low solubility in octanol.

The distribution ratios (log *D* values) of the Dy dyes were calculated with the MarvinSketch Software (ChemAxon Kft, Budapest, Hungary) to -0.95 (Dy676), -5.87 (Dy678), -2.08 (Dy681), and -5.38 (Dy682), respectively.

3. Determination of the dimerization constant K_D and calculation of the dimer and monomer spectrum

The dimerization constant K_D was obtained using the law of mass action (equations S1 and S2) and the mass balance for the total dye concentration (equation S3).

$$D + D \leftrightarrow D_2 \qquad \text{(eq. S1)}$$

$$K_D = \frac{[D_2]}{[D][D]} \qquad \text{(eq. S2)}$$

$$[D_0] = [D] + 2[D_2] \qquad \text{(eq. S3)}$$

This yields equation S4 for the fraction m of the dye molecules that exist as monomers.

$$m = \frac{[D]}{[D_0]} = -\frac{1}{4K_D[D_0]} + 2\sqrt{\left(\frac{1}{8K_D[D_0]} + \frac{1}{2}\right)^2 - \frac{1}{4}} \qquad \text{(eq. S4)}$$

The molar absorption coefficient ε (or the concentration-weighted absorbance) at a given wavelength is related the (wavelength-dependent) molar absorption coefficients of the monomer (ε_m) and the dimer (ε_d) and the fraction of monomers according to

$$\varepsilon(\lambda, m) = \varepsilon_m(\lambda)m + \tfrac{1}{2}\varepsilon_d(\lambda)(1-m) \qquad \text{(eq. S5)}$$

Insertion of equation S4 into equation S5 gives the molar absorption coefficient at a given wavelength in dependence of the total dye concentration [D_0]. Equation S5 is fitted to the measured molar absorption coefficient (or concentration-weighted absorbance) with the parameters varied being the dimerization constant K_D, and the molar absorption coefficients

of the monomer and the dimer $\varepsilon_m(\lambda)$ and $\varepsilon_d(\lambda)$, respectively. To improve the signal-to-noise ratio, instead of taking the values of the molar absorption coefficient at a single wavelength, we used the differences in $\varepsilon(\lambda)$ obtained at the wavelength of the maximum of the monomer spectrum and the maximum of the dimer spectrum ($\varepsilon_m(\lambda_{max})$ - ε_d (λ_{max})), respectively.

The absorption spectra (or wavelength-dependent molar absorption coefficients) of the dimer and the monomer can be calculated using equation S5. If $\varepsilon(\lambda)$ is given for two (or more) different D_0 and thus different m, this yields a set of equations $\varepsilon(D_0)$, that can be solved for $\varepsilon_m(\lambda)$ and $\varepsilon_d(\lambda)$.Doing this for each wavelength leads to the monomer and dimer spectrum of each dye.

4. Determination of the fraction of dimerized dye bound to IgG and correction of Φ_f for dimer absorption

Using the absorption spectrum of the dimeric and monomeric forms of the dyes (see Figure 4 in the manuscript), the fraction of dimers bound to the protein was calculated by fitting the measured absorption spectrum of each protein-conjugated fluorophore to a linear combination of the dimer and monomer absorption spectrum. This approach assumes that the monomer and dimer spectra have essentially the same spectral shape for the free and the protein-bound dye. Prior to this fitting procedure, both the monomer and dimer spectrum were shifted to longer wavelengths by about 10 nm to account for the bathochromic shift of the absorption of each fluorophore induced upon IgG binding. Subsequently, the measured fluorescence quantum yields were corrected for the absorption of the non-fluorescent dimers at the chosen

excitation wavelengths using equation S6. In this equation, Φ_f and $\Phi_{f,Abs}$ are the measured and the dimer absorption-corrected fluorescence quantum yields.

$$\Phi_{f,Abs} = \Phi_f \frac{\varepsilon_m m + \frac{1}{2}\varepsilon_d (1-m)}{\varepsilon_m m} \qquad \text{(eq. S6)}$$

5. Correction of Φ_f for monomer-dimer FRET and estimation of the maximum accomplishable quantum yield of the IgG-bound monomeric dyes

If more than a single dye molecule is bound to the protein, energy transfer can occur between these IgG-bound molecules. The efficiency of such processes depends on the distance between the dye molecules acting as donor and acceptor, the spectral overlap of the absorption spectrum of the acceptor and the emission spectrum of the donor, and the relative orientation of their transition dipole moments. In the presence of non-fluorescent dimers, that absorb at wavelengths where the fluorescent monomers emit, this can result in a decrease of the fluorescence quantum yields (Φ_f values as measured and dimer absorption-corrected fluorescence quantum yields), because the excitation energy transferred from the emissive monomer to the dimer is dissipated radiationlessly at the dimer. In contrast, if the energy is transferred between different monomeric dye molecules (classic homo-FRET), a decrease in fluorescence intensity is only expected to occur if the involved monomers have different fluorescence quantum yields, e.g. due to variations in their local environments. In this case, the dyes with the diminished fluorescence quantum yields act as “energy sinks”. For chemically and spectroscopically identical molecules, no change in fluorescence quantum yield is anticipated as is e.g. the case for monomeric dyes in solution. At the surface of a protein, however, the dyes, attached to different amino acids, are located at different sites and

can thus face different local environments. This can result in different fluorescence quantum yields. In our case of statistical labeling, it is difficult to estimate the sizes of these variations. We thus consider only energy transfer from emissive monomers to non-fluorescent dimers as fluorescence quenching pathway. To calculate the efficiency for monomer-dimer FRET, we followed the approaches of Gennis et al. [1] and Schobel et al. [2,3]. The fluorescence quantum yield of the monomers in the presence of N dimers, i.e., the dimer absorption-corrected fluorescence quantum yield Φ_{Abs}, is then given by equation S7

$$\Phi_{f,Abs} = \Phi_{f,Abs+FRET}(1-E) \qquad \text{(eq. S7)}$$

with $\Phi_{f,Abs+FRET}$ presenting the fluorescence quantum yield of the donor molecules in the absence of acceptor dimers. The efficiency of the energy transfer E follows from equation S8

$$E = \frac{\sum_{i=1}^{N}\left(\frac{R_0}{r_i}\right)^6}{1+\sum_{i=1}^{N}\left(\frac{R_0}{r_i}\right)^6} \qquad \text{(eq. S8)}$$

where r_i are the individual donor-acceptor distances. R_0 is the Förster-radius (see below). The the individual donor-acceptor distances r_i can be in principle calculated on the basis of statistical considerations and the geometry of the IgG antibody. For reasons of simplicity, we follow here the approach of Schobel et al. [2,3] and use a mean donor-acceptor distance of 5.9 nm which is given by the spatial separation between two arbitrary chosen points at the protein surface. The number of dimers N at the protein was assumed to follow a Poisson distribution $P(N,\langle N\rangle)$ with the mean number $\langle N\rangle$ being calculated from the D/P ratio and the fraction of dimerized dye. The average FRET efficiency $\langle E\rangle$ is then given by

$$< E >= \sum_{N=1}^{\infty} P(N, < N >) \cdot E(N) \qquad \text{(eq. S9)}$$

with

$$E(N) = \frac{N\left(\frac{R_0}{r}\right)^6}{1 + N\left(\frac{R_0}{r}\right)^6} \text{ and } P(N, < N >) = \frac{< N >^N}{N!} e^{-<N>} \qquad \text{(eq. S10)}$$

The R_0 values were then calculated from equation 11S

$$R_0^6 = \frac{9000(\ln 10)\kappa^2 \Phi_{f,\max}}{128\pi^5 N_A n^4} \int_{\lambda=0}^{\infty} F_D(\lambda)\varepsilon_d(\lambda)\lambda^4 d\lambda \qquad \text{(eq. S11)}$$

using the area-normalized fluorescence spectra of the IgG-conjugated dyes F_D and taking into account the IgG-binding induced red shift of the dimer absorption spectrum ($\varepsilon_d(\lambda)$). N_A in equation 11S is the Avogadro number. The orientation factor κ^2 was set to 2/3 (random orientation of donor and acceptor) and a refractive index n of 1.333 (water) was used. The maximum achievable fluorescence quantum yield of the monomeric protein-bound dye in the absence of dimers and fluorescence quenching processes induced by the presence of other dye molecules (dimers or monomers) $\Phi_{f,max}$ can be estimated from the extrapolation of the dimer absorption-corrected fluorescence quantum yield $\Phi_{f,Abs}$ to a D/P ratio of zero. Using this value of $\Phi_{f,max}$, R_0 was calculated and $\Phi_{f,Abs+FRET}$ was subsequently obtained for each D/P ratio. The extrapolation of the $\Phi_{f,Abs+FRET}$ values to a D/P of 0 should then yield the same $\Phi_{f,max}$ value as obtained by extrapolation of the solely dimer absorption-corrected data $\Phi_{f,Abs}$. Finally, $\Phi_{f,max}$ was optimized to match both extrapolated values.

References

(1) Gennis, R. B., and Cantor, C. R. (1972) Use of nonspecific dye labeling for singlet energy transfer measurements in complex systems. A simple model. *Biochemistry 11*, 2509-2512.

(2) Schobel, U., Egelhaaf, H.-J., Brecht, A., Oelkrug, D., and Gauglitz, G. (1999) New donor-acceptor pair for fluorescent immunoassays by energy transfer. *Bioconjugate Chemistry 10*, 1107-1114.

(3) Schobel, U., Engelhaaf, H.-J., Fröhlich, D., Brecht, A., Oelkrug, D., and Gauglitz, G. (2000) Mechanism of fluorescence quenching in donor-acceptor labeled antibody conjugates. *Journal of Fluorescence 10*, 147-154.

Bioconjugate Chemistry

ARTICLE

pubs.acs.org/bc

Synthesis of a Dibromoperylene Phosphoramidite Building Block and Its Incorporation at the 5′ End of a G-Quadruplex Forming Oligonucleotide: Spectroscopic Properties and Structural Studies of the Resulting Dibromoperylene Conjugate

Marco Franceschin,[‡,§] Nicola Borbone,[†,§] Giorgia Oliviero,[†] Valentina Casagrande,[‡] Maria Scuotto,[†] Teresa Coppola,[†] Silvia Borioni,[‡] Luciano Mayol,[†] Giancarlo Ortaggi,[‡] Armandodoriano Bianco,[‡] Jussara Amato,[†] and Michela Varra*[,†]

[†]Dipartimento di Chimica delle Sostanze Naturali, Facoltà di Farmacia, Università degli Studi di Napoli Federico II, via D. Montesano 49, 80131 Napoli, Italy

[‡]Dipartimento di Chimica, Sapienza Università di Roma, Piazzale A. Moro 5, 00185 Roma, Italy

Supporting Information

ABSTRACT: Previous studies indicate that some perylene bisimide derivatives can drive the assembly of DNA G-quadruplexes, thus suggesting the possible advantage in the adoption of perylene-conjugated G-rich oligonucleotides in biological and biotechnological applications. Nevertheless, the typical poor solubility of perylene bisimides strongly limits the number of suitable chemical strategies to prepare perylene-conjugated oligonucleotides. In order to overcome these difficulties, we employed the earlier described core twisted perylene derivatives possessing unique optical and electronic properties, besides good solubility in common solvents. As a first result, the large-scale synthesis of a new dibromoperylene derivative (PEOEBr) phosphoramidite building block is herein reported. Furthermore, the structural behavior of the conjugated PEOEBr-GGGTTAGGG (HTRp2) human telomeric repeat was investigated by using CD, UV, fluorescence, and gel electrophoresis techniques in desalted water and in K^+- and Na^+-containing buffers. We observed that the peculiar property of PEOEBr moieties to form dimers instead of extended aggregates drives the HTRp2 strands toward dimerization and mainly promotes the formation of quadruplex species having both the 5′-ends located at the same side of the structures. However, the counterions present in solutions (K^+ or Na^+) as well as the strand concentration, also contribute to influence the topology and the stoichiometry of formed structures. Furthermore, unlike the unmodified sequence GGGTTAGGG (HTR2), HTRp2 strands quickly associate into G-quadruplexes even in desalted water, as assessed by CD experiments.

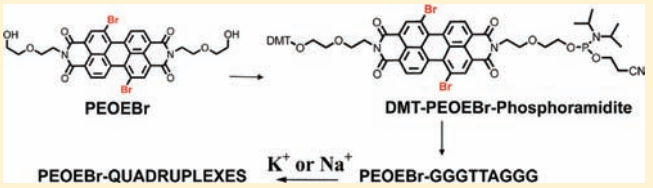

INTRODUCTION

G-rich oligonucleotides (GROs) are able to form higher-ordered noncanonical DNA structures, known as G-quadruplexes[1−3] (herein Qs), on the basis of reverse Hoogsteen-like pairing of four guanines (G-tetrad). Qs currently are among the most studied DNA structures since they are supposed to be involved in important biological functions[4,5] such as telomere maintenance,[6,7] DNA−protein recognition,[8] and protein inhibition.[9] Furthermore, they represent promising models in biotechnological applications[10,11] including biosensors[12,13] and nanomechanical devices.[14] The use of DNA Qs in nanomechanics is encouraged by the stability of Qs in a large variety of experimental conditions. GROs can be chemically modified by covalent linkage to suitable molecules[15−24] in order to investigate their structural and biological properties. The conjugation has a wide range of advantages, including the thermodynamic stabilization of derived structures[17,23] and the induction of fluorescence and/or electron transfer properties.[24] Typically, conjugated molecules are characterized by the presence of a large aromatic core, (e.g porphyrine, pyrene, acridine, and pyrene), capable of interacting with G-tetrads by $\pi-\pi$ forces.

Among the great number of molecules potentially suitable for conjugation to GROs, perylene bisimide and its derivatives are of particular interest because their presence could add desired features such as chemical resistance and the propensity to form higher-ordered aggregates, as well as favorable fluorescence and electronic properties.[25,29,30] Furthermore, a member of this family, PIPER (*N*,*N*′-bis-[2-(1-piperidino)ethyl]-3,4,9,10-perylenetetracarboxylic bisimide) demonstrated the ability to drive the association of G-rich strands into Qs.[27] This mechanism, known as "threading intercalation", has been extensively studied because of its potential involvement in the inhibition of human telomere elongation by telomerase.[26−28] Although a variety of DNA structures formed by linked perylene-oligonucleotides

Received: December 2, 2010
Revised: April 11, 2011
Published: June 20, 2011

ACS Publications © 2011 American Chemical Society

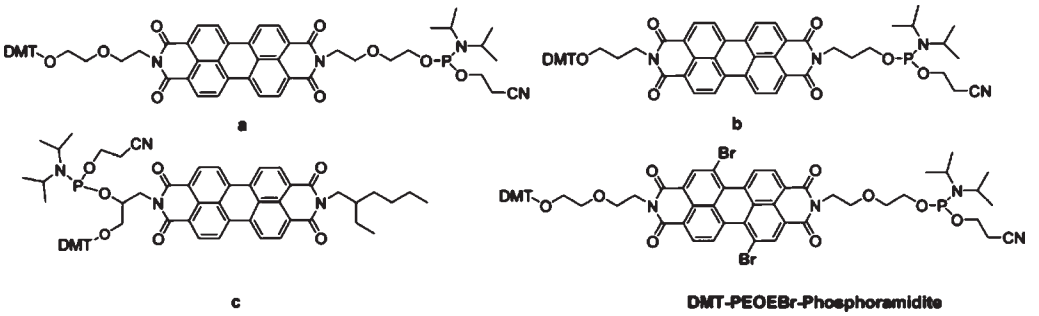

Figure 1. a, b, and c: some previously reported perylene derivative building blocks.[32,34,37] DMT-PEOEBr-Phosphoramidite: new building block synthesized starting from dibromo-perylene diimide derivative **3d**.

(-ONs), including duplexes,[31−33] triplexes,[34] hairpins, and capped hairpins,[35−38] have been discussed extensively in many papers, to the best of our knowledge only one perylene bisimide-conjugated GRO has been reported to date.[39] For this reason, in this work we explore the properties of DNA Qs formed by perylene-conjugated GROs. To achieve this goal, the synthesis of a perylene bisimide phosphoramidite building block, suitable for subsequent solid-phase functionalization, was required. Despite the poor water solubility of perylene derivatives, some successful conjugations of duplex-forming ONs have been reported in aqueous solutions,[32,34,37] as the water solubility of perylene moieties significantly improves after association with the target ON. This behavior could probably be ascribed to the presence of the negatively charged phosphate groups on the ON backbone.[31] However, we did not expect to observe a similar behavior for GROs conjugation, as even unmodified GRO(s) can result in insoluble aggregates,[40] hence, the importance of developing a new methodology for the synthesis of conjugated perylene-GROs.

The starting point of the synthesis was the formation of a new bromine-substituted perylene bisimide phosphoramidite building block (DMT-PEOEBr-Phoshoramidite, Figure 1), that was incorporated at the 5′-end of the selected GGGTTAGGG (HTR2) human telomeric repeat sequence. The choice of the PEOEBr moiety was due to our previous observation[41,42] that perylene bisimide derivatives containing suitable groups on the carbocyclic scaffold (known as "bay-area") exhibited greater solubility in aqueous solution. UV, CD, fluorescence, and gel electrophoresis techniques were used in order to investigate the self-assembly properties of the resulting molecule, in which two types of association forces, i.e., strand organization in Qs and perylene derivative aggregation, are potentially involved.

EXPERIMENTAL PROCEDURES

Reagents and Equipment. Chemicals and anhydrous solvents were purchased from Fluka-Sigma-Aldrich. TLCs were run on Merck silica gel 60 F254 plates. Silica gel chromatography was performed by using Merck silica gel 60 (0.063−0.200 mm). API 2000 (Applied Biosystem) and the Micromass Q-TOF MICRO electrospray mass spectrometers were used to acquire the mass data of the intermediates and the monomer. NMR experiments were recorded using Varian NMR spectrometers running at 400 (Mercury Plus) and 500 (^{Unity}INOVA) MHz. Elemental analyses (C, H, N) were carried out on a CE instrument EA1110 CHNS-O (Thermo-Fischer). Reagents and phosphoramidites for DNA synthesis were purchased from Glenn Research. ON syntheses were performed on a PerSeptive Biosystem Expedite DNA synthesizer. HPLC analyses and purifications were carried out using a JASCO PU-2089 Plus HPLC pump equipped with a JASCO BS-997-01 UV detector. A Purospher-STAR RP-18 end-capped (5-μm) HPLC column was used to purify the sequences. Both conjugated and unmodified ONs were dialyzed using Slide-A-Lyzer Dialysis Cassettes, with a 3500 molecular weight cutoff, manufactured by Thermo-Scientific. MALDI-TOF experiments were performed on a Bruker Autoflex I mass spectrometer using a picolinic/3-hydroxypicolinic acid mixture as the matrix. The UV thermal experiments were carried out using a JASCO 530 spectrophotometer equipped with ETC-505 T temperature controller. CD experiments were performed on a JASCO 715 spectropolarimeter equipped with a PTC-348 temperature controller. Fluorescence emission spectra were recorded using a Varian Cary Eclipse Fluorescence spectrophotometer (fluorescence data are reported in the Supporting Information). EMSA studies were performed at 4 °C in a Biorad apparatus equipped with Power Pack 3000.

General Procedures for 3a−d. Starting material **2** (500 mg, 0.91 mmol), synthesized as previously described[42] as a mixture of the two possible isomers, was dissolved in anhydrous *N,N*-dimethylacetamide (10 mL) and 1,4-dioxane (10 mL). The appropriate commercially available amino-alcohol (2 mmol) was added, and the reaction mixture was stirred at 120 °C under argon, for 2 h (2-aminoethanol and 3-amino-1-propanol), 30 min (5-amino-1-pentanol), or 15 min (2-(2-aminoethoxy)ethanol). Upon cooling and water addition, the red solid was washed repeatedly with water, separated by filtration, and dried. To remove the 1,6- from 1,7-dibromo-perylene derivatives, each product **3a−d** was first converted into the corresponding acetyl-derivative, by treatment with acetic anhydride in dry pyridine. The resulting mixtures were dried under vacuum, dissolved in DCM, and washed three times with water. Each organic layer was dried and the residue dissolved in DCM/MeOH (9:1; v/v), from which the 1,7-dibromo-perylene derivatives were selectively precipitated.[43,44] After three reprecipitations, the desired products were obtained as pure solids, as ascertained by ^{1}H and ^{13}C NMR (Figures 2 and S1−S2 (Supporting Information)). Finally, the acetyl groups were removed by treatment with a mixture of aqueous NH_3 (33%) and MeOH (1:1 v/v, 2 h, r.t.) to give the pure bisimides **3a−d** (Scheme 1).

***N,N′*-Bis(2-hydroxyethyl)-1,7-dibromoperylene-3,4:9,10-tetracarboxylic bisimide (3a).** Reaction yield was 82% (70% after purification of the 1,7 regioisomer). Anal. found C 52.6%, H 2.6%, N 4.3% (calcd for $C_{28}H_{16}Br_2N_2O_6$: C 52.8%, H 2.5%, N 4.4%). In order to achieve an affordable NMR characterization,

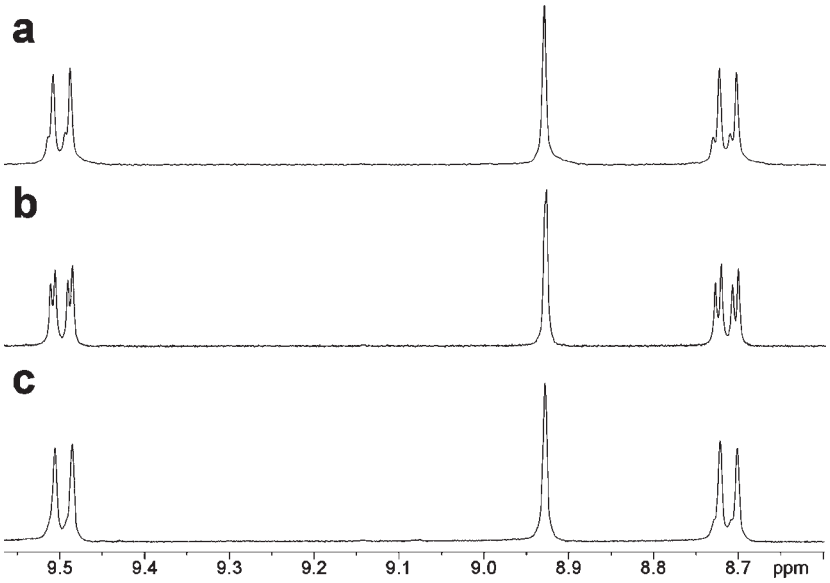

Figure 2. expanded aromatic regions of ^{1}H NMR spectra in $CDCl_3$ of (a) a mixture 6:1 of 1,7 and 1,6 regioisomers of acetylated **3d**; (b) mother liquor enriched with the 1,6 regioisomer after precipitation; (c) 1,7 regioisomer of acetylated **3d**. All spectra were registered after two precipitation steps.

Scheme 1. Synthesis of DMT-PEOEBr-Phosphoramidite[a]

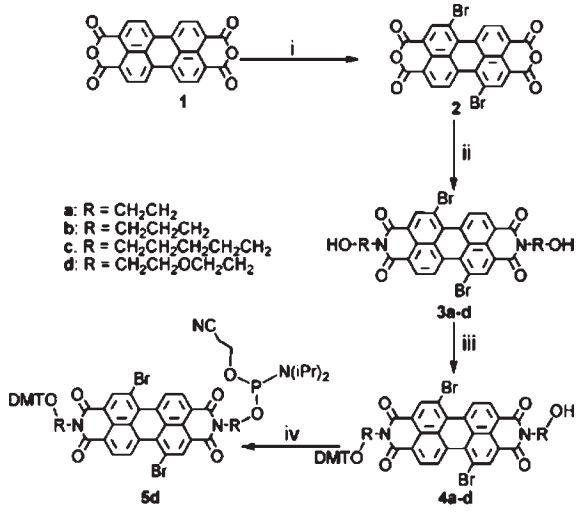

[a] Reagents and conditions: (i) **1** (1 mmol), H_2SO_4 conc. 2 h; I_2 80 °C; Br_2, 4 h, 100 °C; (ii) **2** (0.91 mmol), $HORNH_2$ (2 mmol), DMA (10 mL), dioxane (10 mL), under argon, using different reaction times (from 30′ up to 2 h) depending on the amine used (see Experimental Procedures section); (iii) **3a**−**d** (0.5 mmol, 1 equiv), DMT-Cl, (0.280 mmol, 0.6 equiv), DMAP, (0.024 mmol, 0.05 equiv) Py/ACN (3:1 V:V, 5 mL), 1 h 30′; (iv) **4d** (0.241 mmol), $(iPr)_2NP(OCH_2CH_2CN)Cl$ (0.380 mmol, 90 μL, 1.5 equiv), DIPEA (1 mmol, 180 μL, 4 equiv) in DCM (6 mL), 30′. Only substrate **3d** gave rise to satisfactory yields in DMT-O-derivative **4d**, which, in turn, was converted in the corresponding phosphoramidite building block **5d**.

acetylation of a portion of **3a** was performed (pyridine, 20 h, rt, acetic anhydride) with a yield of 100%. ^{1}H NMR (400 MHz, $CDCl_3$): δ 9.46 (d, J = 8.1 Hz, 2H, aromatic H), 8.91 (s, 2H, aromatic H), 8.69 (d, J = 8.1 Hz, 2H, aromatic H), 4.50 (m, 8H, N−CH_2-CH_2−O), 2.03 (s, 6H, acetyl) ppm. MS (ESI) m/z: 740.9466 $[M+Na]^+$ (Calcd for $C_{32}H_{20}{}^{79}Br_2N_2O_8$-Na: 740.9484).

***N,N′*-Bis(3-hydroxypropyl)-1,7-dibromoperylene-3,4:9,10-tetracarboxylic diimide (3b).** Reaction yield was 89% (75% after purification of 1,7 regioisomer). ^{1}H NMR (400 MHz, $CDCl_3/CD_3OD$ 9:1): δ 9.42 (d, J = 8.1 Hz, 2H, aromatic H), 8.83 (s, 2H, aromatic H), 8.61 (d, J = 8.1 Hz, 2H, aromatic H), 4.24 (t, J = 6.7 Hz, 4H, N_{imidic}-CH_2), 3.60 (t, J = 6.7 Hz, 4H, CH_2−OH), 1.90 (m, 4H, CH_2−CH_2-CH_2−OH) ppm. ^{13}C NMR (100 MHz, 8:2 $CDCl_3$:CD_3OD): δ (referred to $CDCl_3$) 163.2, 162.8, 138.3, 133.0, 132.8, 130.3, 129.1, 128.5, 127.1, 123.1, 122.0, 121.0, 59.5, 37.7, 30.8 ppm. MS (ESI) m/z: 684.9589 $[M+Na]^+$ (calcd for $C_{30}H_{20}Br_2N_2O_6Na$: 684.9586).

***N,N′*-Bis(5-hydroxypentyl)-1,7-dibromoperylene-3,4:9,10-tetracarboxylic diimide (3c).** Reaction yield was 92% (80% after purification of 1,7 regioisomer). ^{1}H NMR (400 MHz, $CDCl_3$): δ 9.47 (d, J = 8.1 Hz, 2H, aromatic H), 8.91 (s, 2H, aromatic H), 8.69 (d, J = 8.1 Hz, 2H, aromatic H), 4.23 (t, J = 7.4 Hz, 4H, N_{imidic}-CH_2), 3.69 (t, J = 6.3 Hz, 4H, CH_2−OH), 1.8−1.2 (m, 12H, CH_2−CH_2−CH_2) ppm. ^{13}C NMR (100 MHz, $CDCl_3$): δ 163.2, 162.5, 138.4, 133.2, 131.3, 130.9, 128.8, 128.5, 123.2, 122.4, 121.9, 121.0, 63.0, 40.5, 33.2, 28.0, 23.2. MS (ESI) m/z: 741.0234 $[M+Na]^+$ (calcd for $C_{34}H_{28}{}^{79}Br_2N_2O_6Na$: 741.0212).

***N,N′*-Bis(5-hydroxy-3-oxapentyl)-1,7-dibromoperylene-3,4:9,10-tetracarboxylic diimide (3d).** Reaction yield was 95% (75% after purification of 1,7 regioisomer). ^{1}H NMR (400 MHz, $CDCl_3$): δ 9.38 (d, J = 8.1 Hz, 2H, aromatic H), 8.84 (s, 2H, aromatic H), 8.62 (d, J = 8.1 Hz, 2H, aromatic H), 4.49 (t, J = 5.5 Hz, 4H, N−CH_2), 3.91 (t, J = 5.5 Hz, 4H, O−CH_2), 3.72 (m, 8H, O−CH_2) ppm. ^{13}C NMR (100 MHz, $CDCl_3$): δ 163.2, 162.8, 138.3, 133.0, 132.2, 130.3, 129.2, 128.6, 127.1, 123.1, 122.7, 121.0, 72.6, 68.5, 62.0, 40.2 ppm. MS (ESI) m/z: 744.9830 $[M+Na]^+$ (calcd for $C_{32}H_{24}{}^{79}Br_2N_2O_8Na$: 744.9797) . Anal. found C 53.3%, H 3.2%, N 3.8% (calcd for $C_{32}H_{24}Br_2N_2O_8$: C 53.1%, H 3.3%, N 3.9%). UV ($CHCl_3$) λ_{max}, nm ($\varepsilon \times 10^{-4}$, $M^{-1}cm^{-1}$): 492 (3.2), 528 (4.7); UV (DMSO) λ_{max}, nm ($\varepsilon \times 10^{-4}$, $M^{-1}cm^{-1}$): 492 (3.2), 527 (4.6).

General Procedures for 4a−d. Compounds **3a**−**d** were dried on anhydrous $MgCl_2$ under vacuum (three days). To each compound (0.5 mmol, 1 equiv), 0.280 mmol of 4,4′-dimethoxytrityl

chloride (0.6 equiv) and 0.024 mmol of 4-dimethylaminopyridine (0.05 equiv) were added. The corresponding 5 mL of the desired mixture of solvents (Py/ACN 3:1 v/v) was added and the solution stirred at room temperature under argon for 1 h. The residual of reactant was then disrupted by the addition of dry methanol. After 10 min, the solvents were removed by vacuum and the crude product dissolved in DCM/TEA (99:1, v/v) and chromatographed on a silica gel column eluted with DCM/MeOH/TEA (99:1:0.5, v/v/v). The resulting yields for each reaction are reported in Table S1 (Supporting Information).

*N-2-[(2-O-4,4-Dimethoxytrytilethoxy)ethyl]-N′-2-(2-ethoxy)-ethyl-1,7-dibromoperylene-3,4:9,10-tetracarboxylic Diimide (**4d**).* Yield = 48%. R_f = 0.4 (92:8 DCM/MeOH). ^{1}H NMR (400 MHz, $CDCl_3$): δ 9.43 (d, J = 8.0 Hz, 2H), 8.89 (s, 2H), 8,67 (d, J = 8.0 Hz, 2H), 7.27 (5H overlapped by solvent signal), 7.16 (d, J = 8.8 Hz, 4H), 6.82 (d, J = 8.8 Hz, 4H), 4.48 (t, J = 5.5 Hz, 4H), 3.89 (t, J = 5.5 Hz, 4H), 3.80 (s, 6H), 3.70 and 3.68 (m, 8H) ppm. ^{13}C NMR (100 MHz, $CDCl_3$): δ 163.0, 162.6, 158.5, 147.0, 139.4, 138.0, 133.0, 132.8, 130.2, 130.0, 129.1, 128.5, 128.0, 127.7, 127.0, 122.8, 122.4, 120.8, 113.1, 72.2, 68.2, 61.8, 55.2, 45.7, 39.9 ppm. ESI MS m/z: 1063.1 $[M+K]^+$ (calcd for $C_{53}H_{42}{}^{79}Br_2N_2O_{10}K$: 1063.1).

*N-2-[(2-O-4,4′-Dimethoxytrytilethoxy)ethyl]-N′-2-{[(2-cyanoethyldiisopropylphosphino)ethoxy]ethyl}-1,7-dibromoperylene-3,4:9,10-tetracarboxylic Diimide (**5d**).* Perylene derivative **4d** (0.270 g, 0.241 mmol) was dried *in vacuo* overnight before being dissolved in anhydrous CH_2Cl_2 (6 mL) and 180 μL of diisopropylethylamine (1 mmol, 4 equiv). To this solution, 90 μL (0.380 mmol, 1.5 equiv) of 2-cyanoethyl diisopropylchlorophosphoramidite was added. After 30 min, the reaction mixture was quenched by the addition of dry methanol, diluted with ethyl acetate (10 mL), and washed with 10% sodium carbonate solution (10 mL) and brine (10 mL). The organic layer was dried on magnesium sulfate and concentrated *in vacuo*. The residue was purified on a silica gel column eluted with 80:10:10 v/v/v CH_2Cl_2/ethyl acetate/TEA. Yield = 95%. R_f = 0.8 (80:10:10 in v/v/v CH_2Cl_2/ethyl acetate/triethylamine). The presence of two PEOEBr atropisomers leads the broadening of signals, principally in the aromatic region of ^{1}H NMR spectra and the splitting of some signals in the ^{13}C NMR spectra. ^{1}H NMR (400 MHz, $CDCl_3$) δ 9.47 (br. d, 2H), 8.90 (br. d, 2H), 8,69 (br. d, 2H), 7.31−7.27 (broad, 5H), 7.17 (4H), 6.83 (4H), 4.47 (4H), 4.33−4.23 (m, 2H, $OC\underline{H}_2CH_2CN$), 3.89 (m, 4H), 3.63 (s, 6H, $OC\underline{H}_3$), 3.62−3.58 (8H), 3.40 [m, J = 6.60 Hz, 1H, $C\underline{H}(CH_3)_2$], 3.12 (m, 1H, $CH_2C\underline{H}_2CN$), 2.80 (m, 1H, $CH_2C\underline{H}_2CN$), 1.28 (d, J = 6.60 Hz, 6H, $CH(C\underline{H}_3)_2$). ^{13}C NMR (100 MHz, $CDCl_3$): δ 162.9, 162.5, 158.5, 145.2, 144.9, 139.4, 138.1, 138.0, 137.7, 135.5, 135.4, 131.0, 130.2, 130.1, 129.6, 129.2, 129.1, 129.0, 128.5, 127.9, 127.8, 127.7, 127.6, 127.0, 126.9, 123.0, 122.5, 120.8, 116.1, 113.1, 112.9, 72.2, 69.5, 68.2, 67.9, 65.4, 63.5, 61.8, 59.6, 55.3, 55.2. 53.0, 45.8, 39.8, 39.5, 29.6, 22.5, 22.3, 20.0, ppm. ^{31}P NMR (200 MHz, $CDCl_3$, referenced toward H_3PO_4 85%) δ 147.56, 146.45 (two signals resulting from the splitting of the phosphite signal due to the presence of the dibromoperylene atropisomers[45,46] (Figure S8, Supporting Information). ESI MS m/z 1225.8 $[M+H]^+$ (calcd for $C_{62}H_{59}{}^{79}Br_2N_2O_{11}PH$: 1225.2).

Synthesis of Oligomers. The ON sequences were synthesized with the above cited automated DNA synthesizer using a controlled pore glass support (100 mg, IcaaCPG high loading, loaded with G nucleotide) following the standard β-cyanoethyl phosphoramidite method (DMT-on protocol). After the elongation of the sequence, the solid support was charged in a small column supplied with a stopcock and a glass filter on the bottom, washed with dry ACN, fluxed by argon (5 min), and finally treated with three cycles of deblock solution (a solution of dichloroacetic acid in ACN; 5 mL of each cycle) to detach the 4,4′-dimethoxytrityl groups. All of the acidic washing solutions were collected, and the quantitative spectrophotometric 4,4′-dimetoxytrityl cation test[47] was used to evaluate the yields of each conjugation step. The solid support was washed three times with anhydrous ACN, fluxed by argon (5 min), and then reacted for 20 min with a solution of **5d** in dry DCM, in the presence of the activator solution (5-ethylthio-1*H*-tetrazole in ACN). After five washing cycles with a 1:1 mixture of dry ACN/DCM, the solid support was dried by argon (5 min) and submitted to the second coupling cycle. The support was washed from the residual excess of reactants by using four swelling cycles in dry solvents under argon flow (2 mL each, for 2 min). The subsequent capping and oxidation cycles were performed manually by using the same conditions of a standard automated synthesis. Finally, the solid support was treated with the deblock solution (five cycles, 5 mL each) to detach the 4,4′-dimethoxytrityl groups. The solid support was then washed with ACN, dried under argon, charged in a vial supplied with a cap, and treated with aqueous ammonia (33%) at room temperature for 24 h to detach the ON. The combined filtrates and washings were concentrated under reduced pressure, dissolved in a basic aqueous solution (2% NH_3), and purified by HPLC by using a C18 reverse phase column [H_2O/ACN 98:2 v/v for 10 min and then by a gradient of ACN in H_2O (from 2 to 20% in 30 min)]. The peaks were identified by setting the UV detector at 260 and 540 nm in two different courses (the conjugated sequence produced a peak at 540 nm). To remove undesired ions, the ON aqueous solutions were subjected to three dialysis treatments (3500 MW cutoff). The concentration of samples used in CD, UV, fluorescence, and electrophoreses experiments were determined by measuring the UV absorbance (at 260 nm, 80 °C) of the aqueous ON solutions, using the extinction coefficient calculated according to the method of Gray et al..[48] The absorbance contribution of the dibromo-perylene moiety was calculated by using the molar extinction coefficient measured in $CHCl_3$ (29,500 for the band at 265 nm).

UV and CD Experiments. UV and CD experiments were carried out on DNA samples at concentrations of 2, 4, and/or 10 μM. The buffers used contained 100 mM NaCl and 10 mM NaH_2PO_4 at pH 7.4, or 100 mM KCl and 10 mM KH_2PO_4 at pH 7.4. The samples were annealed by heating at 90 °C for 5 min and then slow cooling at room temperature (12 h). The UV and CD spectra were registered at increasing temperatures, from 10 to 90 °C with heating steps of 10 °C, from 200 to 700 nm. Before each spectrum, the sample was equilibrated for 20 or 30 min, respectively, at the specific temperature. The samples used for the CD measurements of ONs in desalted water (HPLC-grade water, Merck) were not submitted to the annealing procedure. Each reported spectrum is the background-subtracted average of three scans. The spectra were collected with the following conditions: response, 16 s; bandwidth, 1 nm; speed, 100 nm/min.

CD melting curves were obtained by following the changes in the amplitude of CD bands at 263 nm as a function of temperature. ON solutions were heated from 10 to 90 °C, at the rate of 0.5 °C/min.

Electrophoretic Mobility Shift Assay (EMSA). Nondenaturing polyacrilamide gels were performed at 4 °C. The gels

(16%, 29:1 monomer/bis ratio, 10 × 7.2 × 0.1 in size) were run for 3 h at 150 V in 89 mM TBE buffer supplemented with 0.1 M KCl or NaCl. The samples, 0.10 mM of ONs dissolved in 10 mM phosphate buffer containing 100 mM of KCl or NaCl, were annealed by heating at 90 °C for 5 min, slow cooling at 25 °C, and finally storing at 25 °C for 10 days. All unmodified ONs were loaded on gels at the final concentration of 10 μM, whereas the conjugated HTRp2 sequence was loaded at higher concentrations (50−100 μM) because of difficulties in staining. The gels were visualized by Biorad Gel DOCXR after SYBR-green staining.

RESULTS

Preparation of Brominated Perylene Bisimide Phosphoramidite Building Block 5d. Dibromo-perylenetetracarboxylic dianhydride (**2**, Scheme 1), synthesized as previously described,[42,49] was reacted with a series of commercially available amino-alcohols to obtain the bisimides **3a**−**d**. No side products involving the reaction of hydroxyl groups with the cyclic anhydride were detected. However, the excess of reactants, the temperature, and the reaction times were strictly controlled to avoid bromine substitution with a primary amine (see the Experimental Procedures section).

Each compound **3a**−**d** was obtained as a mixture of 1,7 and 1,6 dibrominated regioisomers, which, similar to previous reports by Wurthner et al. and Rajasingh et al.,[46,47] were resolved by selective precipitation. The mixtures of regioisomers **3a**−**d** were first acetylated and then purified by repetitive precipitation from dichloromethane/methanol (9:1 v/v). The purity of the 1,7 regioisomers was ascertained by ^{1}H and ^{13}C NMR. The ^{1}H NMR signals of the aromatic portion of the acetylated **3a**−**d** before and after the purification steps (for an example, see Figures 2 and S1 (Supporting Information)) indicated that the mixtures were efficiently resolved. The acetyl groups were then removed by treatment with a mixture of aqueous NH_3 and MeOH to obtain the 1,7 dibrominated regioisomers **3a**−**d** (about 90% purity, ascertained by ^{1}H NMR).

The solubility of derivatives **3a**−**d** was properly related to the length of the side chains, and it was always higher than that for the corresponding nonbrominated bisimides. The selective introduction of a DMT group was performed by the reaction of **3a**−**d** with DMT-Cl in the presence of dimethylaminopyridine as a catalyst and a mixture of pyridine-acetonitrile as solvent. Compounds **4a**−**d** were isolated with yields from 15 to 45%. The reaction yields (Table S1, Supporting Information) were not particularly influenced by the length of the side chains of the perylene bisimides, whereas the presence of an intrachain oxygen significativelly affected the reactivity of the hydroxyl group, as suggested by the opposite behavior of **3c** and **3d**. On the basis of these results, **4d** was selected for the conversion in the corresponding phosphoramidite derivative **5d**. The synthesis was carried out by using the classical procedure (95% yields; see the Experimental Procedure section).[47] The stability of the new phosphoramidite in the standard chemical conditions found in each cycle of the automated solid-phase synthesis was verified prior to its incorporation onto the ON sequence.

Dibromo-Perylene Conjugated ONs. In order to select the best conditions for the coupling step in ON solid phase synthesis, building block **5d** was manually reacted with the commercially available IcaaCPG high-loading solid support functionalized with A, C, G, or T. Upgraded yields were obtained by increasing the time of each coupling cycle from 2 (standard condition) to 20 min (Table S2, Supporting Information). No further improvements were observed by extending the coupling time above 20 min.

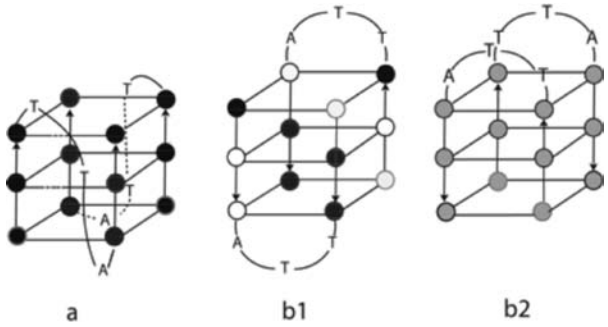

Figure 3. Schematic representation of parallel (a) and antiparallel (b1 and b2) Q structures formed by unmodified HTR2. Black and white balls are used to indicate *anti* and *syn* conformations of dG residues, respectively. The exact orientation of dG residues in the parallel structure has been attributed by X-ray[55] and NMR results,[54] whereas in the case of antiparallel b1, by NMR experiments.[54] The antiparallel form b2 has been determined by biochemical results.[53] The N-glycosidic orientation of dG residues has not been determined.

The selected sequence HTR2 was first synthesized by automated solid phase synthesis, then manually coupled with **5d** by using two 20 min coupling cycles (Table S2, Supporting Information), and finally detached from the solid support by treatment with 33% aqueous ammonia at room temperature for 48 h (see the Experimental Procedures section). After HPLC purification (Figure S3, Supporting Information), HTRp2 was checked for successful conjugation by MALDI-TOF analyses (Figure S4, Supporting Information).

CD and UV Experiments. The structural behavior of the truncated human telomeric sequence HTR2 has been previously well characterized by using UV, CD, gel electrophoresis, NMR, and X-ray techniques.[50−55] In K^+-containing buffer (hereafter in K^+), HTR2 can form both parallel and antiparallel G-quadruplex structures, which differ by the spatial arrangement of lateral TTA loops (Figure 3). NMR and CD studies[52−56] evidenced that the two structures can coexist and interconvert in solution. It was also demonstrated that the antiparallel Q arrangement is kinetically favored, while the parallel one corresponds to the thermodynamical one.[52−56] CD spectra of HTR2 in K^+ give rise to two positive dichroic bands centered at 263 and 295 nm, which can be ascribed to the formation of a mixture of both parallel and antiparallel Q structures.[52] Furthermore, in Na^+-containing solution (hereafter in Na^+), only antiparallel Q arrangements were observed (b1 and b2, Figure 3).[52,53] In the latter case, HTR2, possessing a run of guanines at both ends of the sequence, can form at high strand concentration the b2 antiparallel structure (Figure 3), in which the two lateral loops are located on the same side of the Q. Two of these arrangements can mutually interact by π-stacking, forming a dimer of dimers.[53] The two-repeat human telomeric sequence carrying additional bases at the ends of the sequence can form only the antiparallel Q in which the two lateral loops TTA are located at opposite sides of the Q structure (b1, Figure 3).[57] In both cases, CD spectra in Na^+ give rise to a positive dichroic band centered at 295 nm and a negative one at about 260 nm.

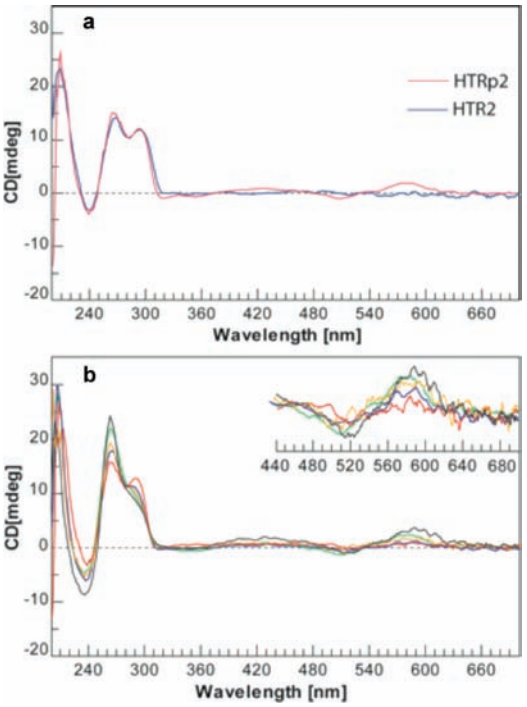

Figure 4. (a) CD profiles of HTRp2 (red, 2 μM) and HTR2 (blue, 2 μM) in 10 mM phosphate buffer (pH 7.4) containing 100 mM of KCl. Both spectra were registered after 12 h from the annealing. (b) Time dependence of CD spectra of HTRp2 (2 μM) in 10 mM phosphate buffer (pH 7.4) containing 100 mM KCl. The sample was heated at 90 °C for 5 min then slowly cooled (12 h) at room temperature, stored at 25 °C, and the CD spectra registered at 25 °C after 12 h (red), and 3 (blue), 5 (green), 7 (orange), and 10 (black) days.

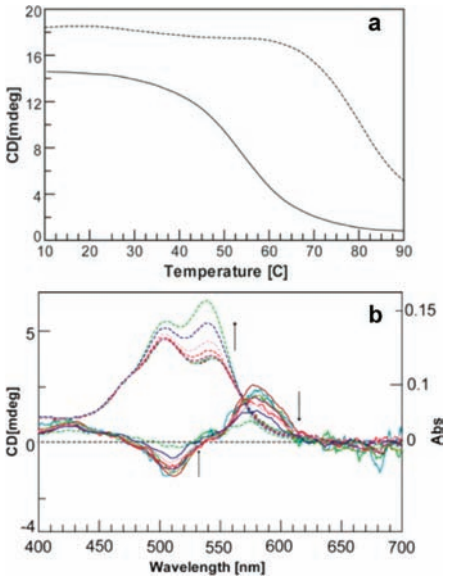

Figure 5. (a) CD melting profiles (at 263 nm) of structures formed by HTR2 (2 μM) (continuous) and HTRp2 (2 μM) (outlined) in 10 mM phosphate buffer (pH 7.4) containing 100 mM of KCl. (b) Temperature-dependent CD and UV profiles in the long wavelength region for HTRp2 in 10 mM phosphate buffer (pH 7.4) containing 100 mM KCl. The arrows indicate the changes in UV and CD bands by increases in the temperature from 10 up to 90 °C with steps of 10 °C.

In order to verify the effect of perylene conjugation on Q typologies formed by HTR2, CD analyses were performed both in K^+ and in Na^+. Figure 4 shows the CD profiles obtained from HTRp2 and HTR2 at 10 °C in K^+. Looking at the similarity of the shape and intensities of dichroic bands observed in the CD spectra of either HTR2 or HTRp2, it appears that the conjugation with the perylene moiety does not significantly affect the topology of resulting Qs. Similarly to HTR2,[52] the CD profiles of HTRp2 also showed different time-dependent contributions of the two dichroic bands at 262 and 295 nm (Figure 4b), with a constant increase of the first band associated with a constant decrease of the second one. However, according to CD melting experiments (Figure 5a), the conjugation provides a strong stabilizing effect on the parallel Q structure, allowing an increase of the melting temperature of about 30 °C.

Furthermore, in K^+, HTRp2 exhibits strong long-wavelength features in CD profiles (Figure 5b) with a Cotton effect centered at 542 nm (a negative band at 500 nm and a positive band at 565 nm). By increasing the temperature, these CD bands progressively decrease in intensity, completely disappearing at 90 °C, whereas the corresponding UV band at 542 nm (Figure 5b) undergoes a strong increase in intensity. The comparison between CD and UV data suggests the existence of exciton coupling between dibromo-perylene moieties.[56] Interestingly, the CD profile of HTRp2 in Na^+ changed significantly depending on the ON concentration (Figure 6a) and on the time elapsed from annealing (Figure 6b). At low (2 μM) strand concentration, the CD profile showed a positive band at 295 nm and a negative one at 260 nm (Figure 6a, blue line), the same as those for the unmodified HTR2.[52] By increasing the strand concentration, a new band at 263 nm appeared (Figure 6a, green and red lines). Furthermore, regardless of strand concentration, the band at 295 nm completely disappeared after two days from annealing (Figure 6b). However, in all cases, no significant visible CD bands were observed. The CD melting profile (Figure 6c) obtained by monitoring the intensity of the CD band at 263 nm (ΔT = 0.5 °C/min) showed a strong enhancement in the stability of quadruplex structures formed by HTRp2.

The long-wavelength region of UV profiles (Figure 6d) showed two UV−visible bands produced by the dibromo-perylene moieties. By increasing the temperature from 10 up to 90 °C, the band at 542 nm shifted to 538 nm, increasing its intensity. At the same time, its red-broadening disappeared producing an isosbestic point at 570 nm. These observations suggest the existence of exciton coupling between chromophores.[31−36,56]

Furthermore, the ability of HTRp2 to associate in Q structures in desalted water has also been evaluated. The CD spectra registered after heating at 80 °C and rapidly cooling at 10 °C displayed a positive band at 295 and a negative one at 246 nm (Figure 7a, blue line). At 25 °C, the two bands slowly converted, leading after 10 days to the disappearance of the band at 295 nm and to the formation of a new band at 263 nm (Figure 7a, continuous red line). By increasing the temperature, the intensity of the new CD band decreased, and CD profiles showed a mixture of folded and unfolded structures (Figure 7b). These data strongly suggest the formation of Q structures. It is noteworthy that HTR2 did not produce significant CD signals in desalted solution, in agreement with previously reported data (Figure S5, Supporting Information).[52]

Finally, the short wavelength UV profiles of HTRp2 (Figure S6, Supporting Information), in all explored experimental conditions, showed an isosbestic point at 285 nm according to the

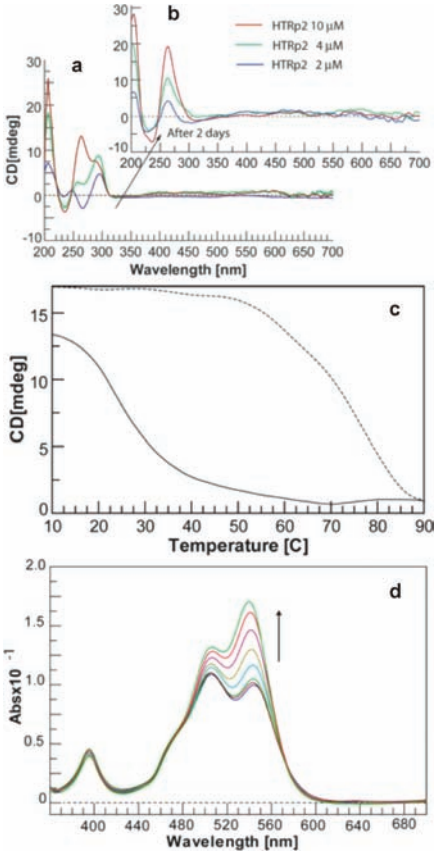

Figure 6. (a) CD spectra of HTRp2 in 10 mM phosphate buffer (pH 7.4) containing 100 mM of NaCl, registered by using different strand concentrations (2, 4, and 10 μM). (b) CD spectra registered by using the same samples after two days. (c) CD melting profiles of structures formed by HTR2 (10 μM) (continuous) and HTRp2 (10 μM) (outlined) in 10 mM phosphate buffer (pH 7.4) containing 100 mM NaCl, registered by positioning the wavelength at 295 and 263 nm, respectively. (d) Long wavelength portion of UV spectra at different temperatures (10−90 °C) produced by HTRp2 (4 μM) in 10 mM phosphate buffer (pH 7.4) containing 100 mM of NaCl. The arrow indicates the changes in UV bands by raising the temperature from 10 to 90 °C.

presence of Q structures in K^+, Na^+, and in water solutions, in agreement with previously reported studies.[57]

EMSA. Figure 8 shows the electrophoresis shift assay for HTRp2 obtained in K^+. The SYBR-green staining of the bands on these gels required a higher concentration of conjugated ONs than unmodified ones, which have been used as internal standards. This phenomenon could be due to interferences in the stain caused by conjugation with the perylene bisimide moiety. In agreement with CD data, in the presence of K^+ ions, both HTRp2 (lane 4) and HTR2 (lane 3) show a main band. The band corresponding to HTRp2 migrates faster than the tetramolecular Q $(TG_4T)_4$, used at two different concentrations as the internal standard (lanes 1 and 2), and slightly slower than the bimolecular Q formed from HTR2.[52] These results are in agreement with the association of HTRp2 in a bimolecular Q, which has a higher molecular weight than that formed from HTR2, according to the presence of two dibromoperylene moieties in the structure. Furthermore, HTRp2 also produced another weak band that migrates near the principal one, suggesting the presence of minor bimolecular Q species. The same study

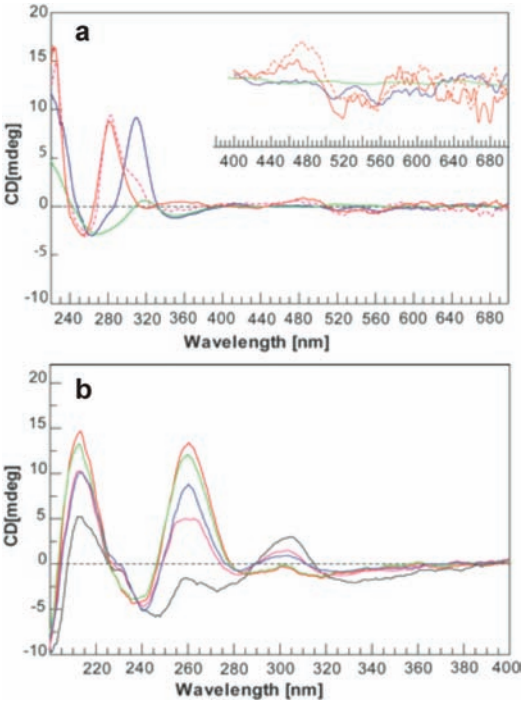

Figure 7. CD and UV spectra of HTRp2 in desalted water. (a) Time dependent CD spectra. The sample was heated at 80 °C, rapidly cooled at room temperature (10 min), and kept at 20 °C. The spectra were than registered after 1 h (blue line) and 3 days (dashed red line) and 10 days (red line). In green is reported the CD profile of the same sample heated at 80 °C. (b) Temperature dependent CD spectra of HTRp2 in water of a sample kept for 10 days at 10 °C. The spectra were registered at 10 (red), 20 (green), 40 (blue), 50 (violet), and 80 °C (black).

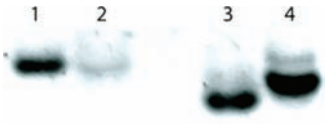

Figure 8. Page experiment on 16% acrylamide gel (acrylamide/bisacrylamide 29:1; running buffer, 89 mM TBE containing 0.1 M KCl). Time course 3 h; 150 V. All samples are annealed in 10 mM phosphate buffer containing 0.1 M KCl. Samples were loaded on gel 10 days after annealing. The gel was stained with Sybr-green for 30 min and visualized by Biorad Gel DOC-XR. Lanes 1 and 2, tetraplex $(TG_4T)_4$ at 10 and 4 μM, respectively; lane 3, HTR2 (5′GGGTTAGGG3′) at 10 μM; lane 4, HTRp2 (5′PEOEBr-GGGTTAGGG3′) at 50 μM. Prior to loading, all samples were annealed using an ON concentration of 0.1 mM.

did not give significant information in Na^+, due to the insolubility of the aggregates formed by HTRp2, at the high strand concentration required, that affected the results of PAGE experiments. However, some results (one of these is shown in Figure S7, Supporting Information) account for the formation of higher molecular weight structures, most likely involving four HTRp2 strands.

DISCUSSION AND CONCLUSIONS

Perylene bisimide derivatives show very interesting physical properties that render them useful for a high number of possible technical applications.[28−30] In order to explore their ability to interact with different DNA structures (duplex, triplex, and

quadruplex), a wide range of perylene conjugated ONs have been synthesized and studied for their physical properties and structural behaviors.[35−38] Considering the unique structural features of bay-substituted perylene bisimide derivatives,[41,42,58−60] we have performed the synthesis of a new dibromoperylene phosphoramidite building block, suitable for conjugation with quadruplex-forming GROs, to investigate the effect of such conjugation on the formation of Q species. For this purpose, the Q assembly properties of the 5′-conjugated PEOEBr-HTR2, namely, HTRp2, were evaluated in different conditions using UV, CD, EMSA, and fluorescence methods (discussed in Supporting Information).

The CD data in the short wavelength region showed that in K^+ HTR2 and HTRp2 give rise to similar profiles having two dichroic bands, which can be related to the formation of both parallel and antiparallel Q structures (Figure 4a). We also observed that in K^+ the antiparallel Q formed by HTRp2 slowly switched to the parallel one (Figure 4a), in agreement with previously reported data by Vorlikova and co-workers.[52] EMSA results (Figure 8) also confirmed the CD data. HTR2 and HTRp2 gave a main band attributable to a parallel dimeric Q structure, which is the predominant conformation present in solution after 10 days of annealing.[52] Furthermore, the CD-melting behavior in K^+ showed that the unfolding of the Q structures produced by HTRp2 is still incomplete at 90 °C (Figure 5a), thus suggesting a strong stabilizing effect due to PEOEBr conjugation. Conversely, in Na^+, the shape of CD profiles displayed strong changes by increasing the ON concentration and the time elapsed from annealing (Figure 6). CD spectra registered 3 h after annealing at 2 μM HTRp2 concentration showed profiles closely related to the unmodified HTR2, which could be ascribed to the formation of antiparallel dimeric species. By increasing the strand concentration, the CD profiles progressively changed, and the new profiles could be related to the presence in solution of a mixture of both parallel and antiparallel species. However, 2 days after annealing all of the CD spectra profiles, registered using different strand concentrations, showed only the positive band at 263 nm and the negative one at 243 nm. Furthermore, in desalted water, we observed that HTRp2 produced a time-dependent CD profile (Figure 7) very similar to that obtained in Na^+, suggesting the higher ability of HTRp2 to assemble into Q structures than the corresponding HTR2. The overall CD results obtained in the short wavelength region suggest that HTRp2 preferentially forms a parallel Q structure in solution, regardless of the presence of salts. Despite the fact that all the UV spectra have similar behaviors in the long wavelength regions, even in different conditions, the CD curves in the same regions were different, depending on the solvent. This aspect will be further investigated. Although it is not possible to explain the nature of these phenomena with only the use of spectroscopic data, it is possible to point out that core twisted perylene derivatives preferentially form dimers instead of extended aggregates.[25,58−60] Furthermore, the core twisted PEOEBr can generate two enantiomers[46] that become diastereoisomers when a nitrogen atom of the imide functions is substituted with the ON chain. The low energy of isomerization makes the diastereoisomers produced by the single strand HTRp2 indistinguishable so that the visible CD bands must be attributed to the environment of PEOEBr moieties in the Qs. On this basis, we could hypothesize that the interaction between PEOEBr moieties promotes the dimerization of strands and that the Q typologies formed in solution will be tightly dependent on

Figure 9. Schematic representation of the hypothesized mechanism of strand structuration into parallel Q in K^+-containing solution. Red circles are used to visualize the G residues carrying the perylene moiety.

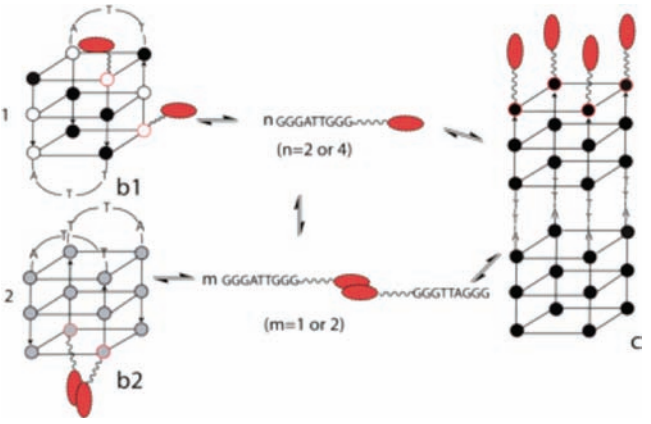

Figure 10. Schematic representation of the hypothesized mechanism of strand structuration into parallel Q in Na^+-containing solution. At low strand concentration, the kinetic antiparallel Q (b1) is the main structure present in the solution after the annealing; it formed from unstacked dibromoperylene conjugated strands. After reaching equilibrium, the thermodynamic structure c becomes the main Q structure in the solution. At high strand concentration, the Q structures b2 and c are probably formed by the reorganization of dimers of HTRp2. In the latter case, the kinetic antiparallel Q is most likely represented by b2, which in turn, evolves in the thermodynamic Q structure c. Red circles are used to visualize the G residues carrying the perylene moiety.

the association of PEOEBr cores, rather than on the association of two single strands. Consequently, the obtained data could be explained according to the formation of HTRp2 dimers in solution. In fact, in desalted water strand dimerization promotes the folding into Qs, and, due to the poor stability of Qs, there are no forces obstructing the complete conversion of antiparallel into parallel species.

In K^+, the presence of PEOEBr dimers determines a strong stabilization of Qs, particularly for the parallel bimolecular species, where the two 5′-ends arrange on the same side of the Q structure. The negative−positive signature of the Cotton effect observed in the visible region of CD spectra suggests the presence of a right-handed helical arrangement of PEOEBr units in the structure. It could be hypothesized that the right-handed nature of the helix forces the PEOEBr chromophores to interact with each other following the same helical sense (in Figure 9, a schematic representation of the hypothesized strand association for the HTRp2 parallel Q is reported). Conversely, in Na^+ the existence of HTRp2 dimers obstructs the folding into b1 Q topology (Figure 10), which can only be obtained in solutions containing low ON strand concentration. The HTRp2 association in antiparallel species is a kinetic process. The comparison of time dependent changes occurring in the amplitudes of the

two CD bands at 263 and 295 nm in the explored conditions (Na^+, K^+, and desalted water) evidenced that the highest rate of conversion occurs in Na^+, suggesting that the antiparallel association of HTRp2 in Qs is particularly unfavorable in the latter condition. The thermodynamically stable Q species is formed after about two days from annealing at room temperature, and it could be most likely based on a parallel tetramolecular Q arrangement, as previously reported by Hamilton and co-workers for a perylene-conjugated GRO.[39] Differently from K^+ containing solutions, in the presence of Na^+ ions the long wavelength region of CD profiles does not display any dichroic band. These results could be ascribed to compensative effects produced by the different stacking mode of four dibromoperylene moieties at the ends of tetramolecular parallel Q species. Interestingly, unlike the short wavelength region, the long wavelength region of CD spectra seems to be able to discriminate the two Q topologies formed from conjugated ON (Figures 9 and 10).

In conclusion, because of the increased solubility of intermediates in organic solvents, the synthetic transformation of the core twisted PEOEBr derivative into the corresponding phosphoramidite building block is a more efficient and simple process compared to other syntheses involving unsubstitued perylene derivatives. Furthermore, the structural behavior of HTR2 incorporating PEOEBr at its 5′-end seems to be responsible for both the accelerating effect on quadruplex assembly of the resulting molecule in desalted solution and for the strong stabilizing effect of Q structures formed both in Na^+ and in K^+. In the presence of Na^+ ions, as previously described by Hamilton and co-workers for a perylene-conjugated GRO, the presence of the dibromoperylene moiety promotes the structuration in parallel Qs. However, the decrease in the size of aggregates formed by dibromoperylene moieties, allows also the formation of antiparallel Q species, which have been found to convert into the parallel one in a time- and concentration-dependent manner. All of the phenomena are ascribed to the preference of PEOEBr to form dimers instead of extended aggregates, thus allowing the Q assembly from HTRp2 dimeric species. In our opinion, the introduction of tailored substitutions on the perylene bay area of perylene-conjugated GROs might be a useful tool for the control of the molecularity of resulting Qs since perylene substitution greatly influences the size of perylene aggregates. Moreover, the different CD features shown by PEOEBr moieties could be used as the starting point for the development of new CD methods for the discrimination of different Q structures displaying the same CD profile at short wavelengths. These new CD methods would be particularly suitable also considering that the NMR study of perylene-conjugated GROs in K^+ and in Na^+ is precluded by the formation of insoluble aggregates at the concentration required by the NMR technique (higher than 100 μM). Most likely, this drawback will be overcome by the introduction of tailored substitutions on the perylene bay-area. The synthesis of several PEOEBr-conjugated GROs is currently underway in our laboratories in order to verify the latter hypothesis.

■ ASSOCIATED CONTENT

Ⓢ Supporting Information. Yields of reaction between PEOEBr derivatives **3a**−**d** and DMT-Cl; yields of the coupling step of DMT-PEOEBr-phosphoramidite **5d** on functionalized solid supports; ^{1}H- and ^{13}C NMR spectra of the acetylated 1,7-dibromoperylene derivative **3d**; analytical HPLC chromatograms of HTRp2 and HTR2; MALDI-TOF mass spectrum of HTRp2; PAGE experiment on 16% acrylamide gel; ^{31}P NMR spectrum of DMT-PEOEBr-phosphoramidite **5d**; additional UV and CD spectra cited in the text; and fluorescence data (including Figures S9 and S10). This material is available free of charge via the Internet at http://pubs.acs.org.

■ AUTHOR INFORMATION

Corresponding Author

*Tel: +39 081 678540. Fax: +39 081 678746. E-mail: varra@unina.it.

Author Contributions

§These authors contributed equally to this work.

■ ACKNOWLEDGMENT

Funding was provided by Regione Campania (Legge 5), M.I.U.R. (PRIN), and Sapienza Università di Roma. We thank Luisa Cuorvo for technical assistance, Alina Ciammaichella for help in the synthesis of brominated perylene bisimides, Mario Barteri for support in fluorescence measurements, and Caterina Lombardo for precious help in manuscript revision.

■ REFERENCES

(1) Burge, S., Parkinson, G. N., Hazel, P., Todd, A. K., and Neidle, S. (2006) Quadruplex DNA: sequence, topology and structure. *Nucleic Acids Res. 34*, 5402–5415.

(2) Simonsson, T. (2001) G-Quadruplex DNA structures variations on a theme. *Biol. Chem. 382*, 621–628.

(3) Qin, Y., and Hurley, L. H. (2008) Structures, folding patterns, and functions of intramolecular DNA G-Quadruplexes found in eukaryotic promoter regions. *Biochimie 90*, 1149–1171.

(4) Huppert, J. L. (2008) Hunting G-Quadruplexes. *Biochimie 90*, 1140–1148.

(5) Maizels, N. (2006) Dynamic roles for G4 DNA in the biology of eucaryotic cells. *Nat. Struct. Mol. Biol. 13*, 1055–1059.

(6) Paeschke, K., Simonsson, T., Postberg, J., Rhodes, D., and Lipps, H. J. (2005) Telomere end-binding proteins control the formation of G-Quadruplex DNA structures *in vivo*. *Nat. Struct. Mol. Biol. 12*, 847–854.

(7) Xu, Y., Ishizuka, T., Kurabayashi, K., and Komiyama, M. (2009) Consecutive formation of G-Quadruplexes in human telomeric-overhang DNA: a protective capping structure for telomere ends. *Angew. Chem., Int. Ed. 48* (42), 7833–7836.

(8) Bryan, T. M., and Jarstfer, M. B. (2007) Interrogations of G-Quadruplex-protein interactions. *Methods 43*, 332–339.

(9) Rawal, P., Bhadra, V., Kummarasetti, R., Ravindran, J., Kumar, N., Halder, K., Sharma, R., Mukerji, M., Kumar Das, S., and Chowdhury, S. (2006) Genome wide prediction of G4 DNA as regulatory motifs: role of *Escherichia coli* global regulation. *Genome Res. 16*, 644–655.

(10) Alberti, P., Bourdoncle, A., Saccà, B., Lacroix, L., and Mergny, J. L. (2006) DNA nanomachines and nanostructures involving quadruplexes. *Org. Biomol. Chem. 4*, 3383–3391.

(11) Guo, A. -M., and Xiong, S. -J. (2009) Effects of contact and efficient charge transport in G4-DNA molecules. *Phys. Rev. 80*, 035115−1–5.

(12) Hong, Y., Häubler, M., Lam, J. W. Y., Li, Z., Sin, K. K., Dong, Y., Tong, H., Liu, J., Qin, A., Renneberg, R., and Tang, B. Z. (2008) Label-free fluorescent probing of G-Quadruplex formation and real-time monitoring of DNA folding by a quaternized tetraphenylethene salt with aggregation-induced emission characteristics. *Chem.—Eur. J. 14*, 6428–6437.

(13) Miranda-Castro, R., de-los-Santos-Alvarez, N., Lobo-Castañón, M. J., Miranda-Ordieres, A. J., and Tuñón-Blanco, P. (2009) Structured nucleic acid probes for electrochemical devices. *Electroanalysis 21*, 2077–2090.

(14) Deng, M., Zhang, D., Zhou, Y., and Zhou, X. (2008) Highly effective colorimetric and visual detection of nucleic acids using an asimmetrically split peroxidase DNAzyme. *J. Am. Chem. Soc. 130*, 13095–13102.

(15) Hayashida, H., Paczesny, J., Juskowiak, B., and Takenaka, S. (2008) Interactions of sodium and potassium ions with oligonucleotides carrying human telomeric sequence and pyrene moieties at both termini. *Bioorg. Med. Chem. 16*, 9871–9881.

(16) Jayawickramarajah, J., Tagore, D. M., Tsou, L. K., and Hamilton, A. D. (2007) Allosteric control of self-assembly: modulating the formation of guanine quadruplexes through orthogonal aromatic interactions. *Angew. Chem., Int. Ed. 46*, 7583–7586.

(17) Jena, P. V., Shirude, P. S., Okumus, B., Katta, L. -R., Godde, F., Huc, I., Balasubramanian, S., and Ha, T. (2009) G-Quadruplex DNA bound by a synthetic ligand is highly dynamic. *J. Am. Chem. Soc. 131*, 12522–12523.

(18) Margulies, D., and Hamilton, A. D. (2009) Digital analysis of protein properties by an ensemble of DNA quadruplexes. *J. Am. Chem. Soc. 131*, 9142–9143.

(19) Rosenzweig, B. A., and Hamilton, A. D. (2009) Self-assembly of a four-helix bundle on a DNA quadruplex. *Angew. Chem., Int. Ed. 48*, 2749–2751.

(20) Xu, Y., Suzuki, Y., Lonnberg, T., and Komiyama, M. (2009) Human telomeric DNA sequence-specific cleaving by G-Quadruplex formation. *J. Am. Chem. Soc. 131*, 2871–2874.

(21) Cai, J., Shapiro, E. M., and Hamilton, A. D. (2009) Self-assembling DNA quadruplex conjugated to MRI contrast agents. *Bioconjugate Chem. 20*, 205–208.

(22) Murat, P., Cressend, D., Spinelli, N., Van der Heyden, A., Labbe, P., Dumy, P., and Defranco, E. (2008) A novel conformationally constrained parallel G Quadruplex. *ChemBioChem. 9*, 2588–2591.

(23) Cogoi, S., Paramasivam, M., Filichev, V., Geci, I., Pedersen, E. B., and Xodo, L. E. (2009) Identification of a new G-quadruplex motif in the *KRAS* promoter and design of pyrene-modified G4-decoys with antiproliferative activity in pancreatic cancer cells. *J. Med. Chem. 52*, 564–568.

(24) Margulies, D., and Hamilton, A. D. (2009) Protein recognition by an ensemble of fluorescent DNA G-Quadruplexes. *Angew. Chem. 48*, 1771–1774.

(25) Würthner, F. (2004) Perylene bisimide dyes as versatile building blocks for functional supramolecular architectures. *Chem. Commun. 14*, 1564–1579.

(26) Franceschin, M. (2009) G-Quadruplex DNA structures and organic chemistry: More than one connection. *Eur. J. Org. Chem. 14*, 2225–2238and references therein reported.

(27) Han, H., Cliff, C. L., and Hurley, L. H. (1999) Accelerated assembly of G-quadruplex structures by a small molecule. *Biochemistry 38*, 6981–6986.

(28) Tuesuwan, B., Kern, J. T., Thomas, P. W., Rodriguez, M., Li, J., David, W. M., and Kerwin, S. M. (2008) Simian virus 40 large T-antigen G-quadruplex DNA helicase inhibition by G-quadruplex DNA-interactive agents. *Biochemistry 47*, 1896–1909.

(29) Imahori, H., Umeyama, T., and Ito, S. (2009) Large π-aromatic molecules as potential sensitizers for highly efficient dye-sensitized solar cells. *Acc. Chem. Res. 42*, 1809–1818.

(30) Chen, Z., Lohr, A., Saha-Möller, C. R., and Würthner, F. (2009) Self-assembled pi-stacks of functional dyes in solution: structural and thermodynamic features. *Chem. Soc. Rev. 38*, 564–584.

(31) Baumastark, D., and Wagenknecht, H. A. (2008) Perylene bisimide dimers as fluorescent "glue" for DNA and for base-mismatch detection. *Angew. Chem., Int. Ed. 47*, 2612–2614.

(32) Wagner, C., and Wagenknecht, H. -A. (2006) Perylene-3,4:9,10-tetracarboxylic acid bisimide dye as an artificial DNA base surrogate. *Org. lett. 8*, 4191–4194.

(33) Baumastark, D., and Wagenknecht, H. A. (2008) Fluorescent hydrophobic zippers inside duplex DNA: Interstrand stacking of perylene-3,4:9,10-tetracarboxylic acid bisimides as artificial DNA base dyes. *Chem.—Eur. J. 14*, 6640–6645.

(34) Bevers, S., Schutte, S., and McLaughlin, L. W (2000) Naphthalene- and perylene-based linkers for the stabilization of hairpin triplexes. *J. Am. Chem. Soc. 122*, 5905–5915.

(35) Lewis, F. D., Zhang, L., Kelley, R. F., McCamant, D., and Wasielewski, M. R. (2007) A perylenedicarboxamide linker for DNA hairpins. *Tetrahedron 63*, 3457–3464.

(36) Zheng, Y., Long, H., Schatz, G. C., and Lewis, F. D. (2006) A cooperative beads-on-a-string approach to exceptionally stable DNA triplexes. *Chem. Commun. 29*, 3830–3832.

(37) Rahe, N., Rinn, C., and Carell, T. (2003) Development of donor−acceptor modified DNA hairpins for the investigation of charge hopping kinetics in DNA. *Chem. Commun. 17*, 2120–2121.

(38) Hariharan, M., Zheng, Y., Long, H., Zeidan, T. A., Vura-Weiss, J., Wasielewski, M. R., Schatz, G. C., and Lewis, F. D. (2009) Hydrophobic dimerization and thermal dissociation of perylenediimide-linked DNA hairpins. *J. Am. Chem. Soc. 131*, 5920–5929and references reported therein.

(39) Saha, S., Cai, J., Eiler, D., and Hamilton, A. D. (2010) Programing the formation of DNA and PNA quadruplexes by $\pi-\pi$-stacking interactions. *Chem. Commun. 46*, 1685–1687.

(40) Mergny, J. L., De Cian, A., Ghelab, A., Saccà, B., and Lacroix, L. (2005) Kinetics of tetramolecular quadruplexes. *Nucleic Acids Res. 33*, 81–94and references reported therein.

(41) Alvino, A., Franceschin, M., Cefaro, C., Borioni, S., Ortaggi, G., and Bianco, A. (2007) Synthesis and spectroscopic properties of highly water-soluble perylene derivatives. *Tetrahedron 63*, 7858–7865.

(42) Franceschin, M., Alvino, A., Ortaggi, G., and Bianco, A. (2004) New hydrosoluble perylene and coronene derivatives. *Tetrahedron Lett. 45*, 9015–9020.

(43) Wurthner, F., Stepanenko, V., Chen, Z., Saha-Moller, C. R., Kocher, N., and Stalke, D. (2004) Preparation and characterization of regioisomerically pure 1,7-disubstituted perylene bisimide dyes. *J. Org. Chem. 69*, 7933–7939.

(44) Rajasingh, P., Cohen, R., Shirman, E., Shimon, L. J. W., and Rybtchinski, B. (2007) Selective bromination of perylene diimides under mild conditions. *J. Org. Chem. 72*, 5973–5979.

(45) Gryaznov, S. M., and Letsinger, R. L. (1992) Selective O-phosphitilation with nucleoside phosphoramidite reagents. *Nucleic Acids Res. 20*, 1879–1882.

(46) Osswald, P., and Würthner, F. (2007) Effects of bay substituents on the racemization barriers of perylene bisimides: Resolution of atropo-enantiomers. *J. Am. Chem. Soc. 129*, 14319–14326.

(47) Sinha, N. D., Biernat, J., McManus, J., and Koster, H. (1984) Polymer support oligonucleotide synthesis XVIII: Use of *ss*-cyanoethyl-N,N-dialkylamino-/N-morpholino phosphoramidite of deoxynucleosides for the synthesis of DNA fragments simplifying deprotection and isolation of the final product. *Nucleic Acids Res. 12*, 4539–4557.

(48) Gray, D. M., Hung, S. H., and Johnson, K. M. (1995) Absorption and circular dichroism spectroscopy of nucleic acid duplexes and triplexes. *Methods Enzymol. 246*, 19–34.

(49) Rohr, U., Schlichting, P., Böhm, A., Gross, M., Meerholz, K., Bräuchle, C., and Müllen, K. (1998) Liquid crystalline coronene derivatives with extraordinary fluorescence properties. *Angew. Chem., Int. Ed. 37*, 1434–1437.

(50) Mergny, J. L., Phan, A. T., and Lacroix, L. (1998) Following G-quartet formation by UV-spectroscopy. *FEBS Lett. 435*, 74–78.

(51) Mergny, J. L., and Lacroix, L. (2003) Analysis of thermal melting curves. *Oligonucleotides 13*, 515–537.

(52) Vorlíčková, M., Chládková, J., Kejnovská, I., Fialová, M., and Kypr, J. (2005) Guanine tetraplex topology of human telomere DNA is governed by the number of (TTAGGG) repeats. *Nucleic Acids Res. 33*, 5851–5860.

(53) Balagurumoorthy, P., and Brahmachari, S. K. (1994) Structure and stability of human telomeric sequence. *J. Biol. Chem. 34*, 21858–21869.

(54) Phan, A. T., and Patel, D. J. (2003) Two-repeat human telomeric d(TAGGGTTAGGGT) sequence forms interconverting

parallel and antiparallel G-quadruplexes in solution: Distinct topologies, thermodynamic properties, and folding/unfolding kinetics. *J. Am. Chem. Soc. 125*, 15021–15027.

(55) Parkinson, G. N., Lee, M. P. H., and Neidle, S. (2002) Crystal Structure of Parallel Quadruplexes from Human Telomeric DNA. *Nature 417*, 876–880.

(56) Zheng, Y., Long, H., Schatz, G. C., and Lewis, F. D. (2005) Duplex and hairpin dimer structures for perylene diimide−oligonucleotide conjugates. *Chem. Commun. 38*, 4795–4797.

(57) Mergny, J. L., Li, J., Lacroix, L., Amrane, S., and Chaires, J. B. (2005) Thermal difference spectra: a specific signature for nucleic acid structures. *Nucleic Acids Res. 33*, e138/1–6.

(58) Würthner, F. (2006) Bay-substituted perylene bisimides: Twisted fluorophores for supramolecular chemistry. *Pure Appl. Chem. 78*, 2341–2349.

(59) Kaiser, T. E., Stepanenko, V., and Wurthner, F. (2009) Fluorescent J-aggregates of core-substituted perylene bisimides: studies on structure-property relationship, nucleation-elongation mechanism, and sergeants-and-soldiers principle. *J. Am. Chem. Soc. 131*, 6719–6732.

(60) Zhang, X., Rehm, S., Safont-Sempere, M. M., and Würthner, F. (2009) Vesicular perylene dye nanocapsules as supramolecular fluorescent pH sensor systems. *Nat. Chem. 1*, 623–629.

Supplementary Information

Synthesis of a dibromoperylene phosphoramidite building block and its incorporation at 5' end of G-quadruplex forming oligonucleotide. Spectroscopic properties and structural studies of resulting dibromoperylene-conjugate

Marco Franceschin[§,‡] , Nicola Borbone[§,†], Giorgia Oliviero[†], Valentina Casagrande[‡], Maria Scuotto[†],Teresa Coppola[†], Silvia Borioni[‡], Luciano Mayol[†], Giancarlo Ortaggi[‡], Armandodoriano Bianco [‡], Jussara Amato[†], Michela Varra[†,*]

[†] Dipartimento di Chimica delle Sostanze Naturali, Facoltà di Farmacia, Università degli Studi di Napoli Federico II, via D. Montesano 49, 80131, Napoli, Italy

[‡]Dipartimento di Chimica, Sapienza Università di Roma, Piazzale A. Moro 5, 00185, Roma, Italy

[§]These authors contributed equally to this work.

*corresponding author, e-mail: varra@unina.it. Tel. +39 081 678540; Fax +39 081 678746

Running title: Synthesis and structural characterization of a dibromoperylene-oligonucleotide conjugate.

List of contents

Table S1 Yields of reactions of **3a-d** with DMT-Cl. **p.3**

Table S2 Yields of the coupling steps of DMT-PEOEBr-Phosphoramidite **5d** on functionalized solid supports. **p.3**

Figure S1 ^{1}H NMR spectrum of the 1,7-dibromo regioisomer of acetylated **3d**. **p. 4**

Figure S2 ^{13}C NMR spectrum of the 1,7-dibromo regioisomer of acetylated **3d**. **p. 5**

Figure S3 HPLC chromatograms of HTRp2 and HTR2. **p. 6**

Figure S4 MALDI-TOF mass spectrum of HTRp2. **p. 7**

Figure S5 CD spectra of 4 µM and 6 µM HTR2 in desalted water. **p. 8**

Figure S6 Temperature-dependent UV spectra of 2 µM HTRp2. **p. 9**

Figure S7 EMSA experiment on 16% polyacrylamide gel. **p. 10**

Figure S8 ^{31}P NMR spectrum of DMT-PEOEBr-Phosphoramidite **5d**. **p. 11**

Experimental details and discussion of fluorescence data. **p. 12**

Figure S9 .Fluorescence spectra of HTRp2 in water, Na^{+}- and K^{+}-containing buffer. **p. 13**

Figure S10. Absorption and fluorescence spectra of compound **3d** in chloroform. **p. 14**

Starting compound	Reaction with DMT-Cl	
	products	Yield (%)
3a	**4a**	<20
3b	**4b**	20
3c	**4c**	15
3d	**4d**	45

Table S1. Yields of reactions of **3a-d** with DMT-Cl. The yields reported are referred to reactions conducted in a mixture of pyridine-acetonitrile 3:1 v/v.

Sequence (5'→3')	1° coupling cycle		2° coupling cycle	
	Reaction time (min)	Yield (%)	Reaction time (min)	Yield (%)
IcaaCPG-X-PEOEBr (X=A, G, C or T)	2	15	2	17
	10	30	10	45-48
	20	40-45	20	65-70
	40	42-45	60	65-70
IcaaCPG-GGGATTGGG-PEOEBr (HTRp2)	20	52	20	73

Table S2: Yields of the coupling steps of DMT-PEOEBr-Phosphoramidite **5d** on functionalized solid supports. The yields were almost insensitive to the nature of the nucleotide linked to the solid support (A, G, C, or T).

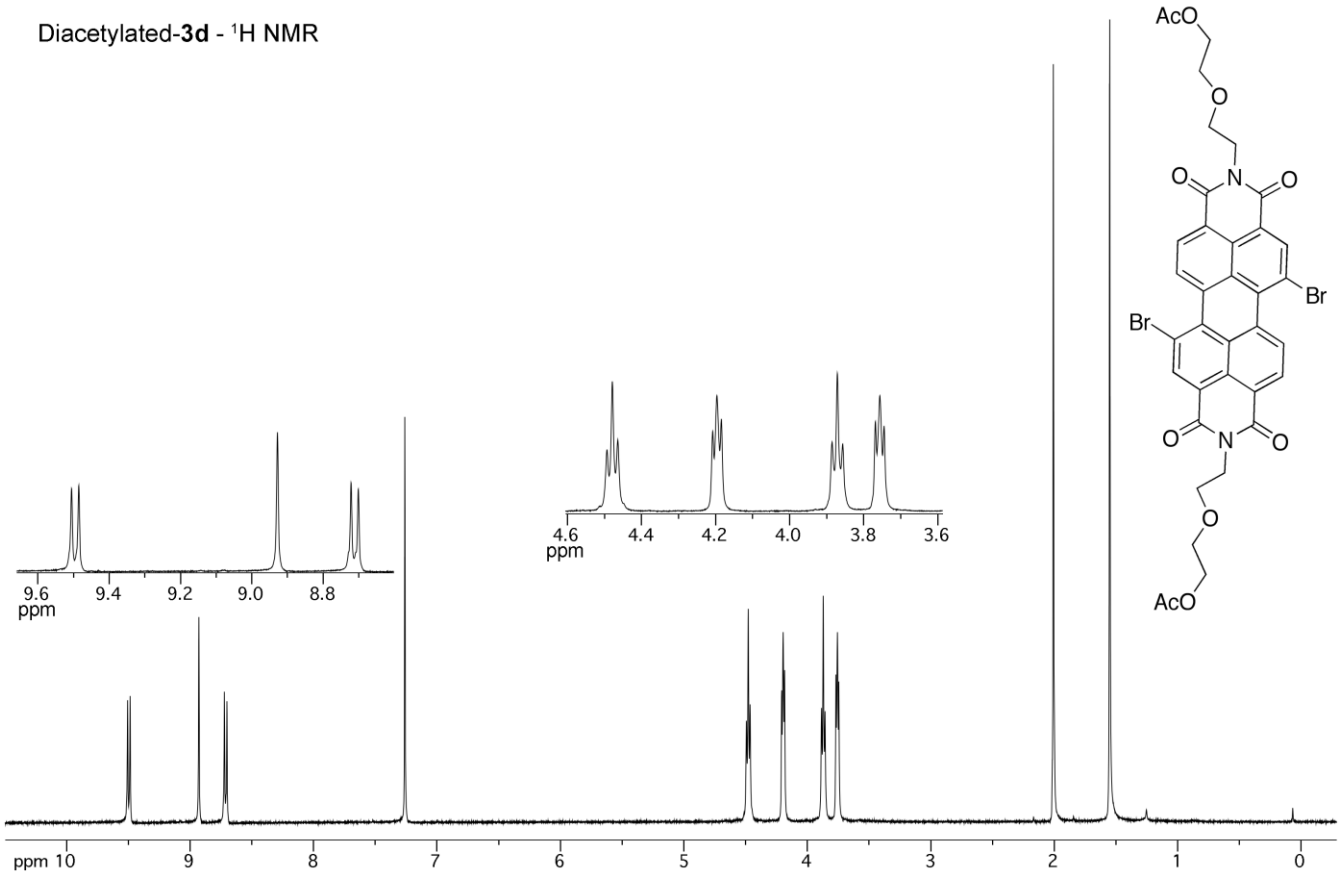

Figure S1. ^{1}H NMR (400 MHz, $CDCl_3$) spectrum of the 1,7-dibromo regioisomer of acetylated **3d**.

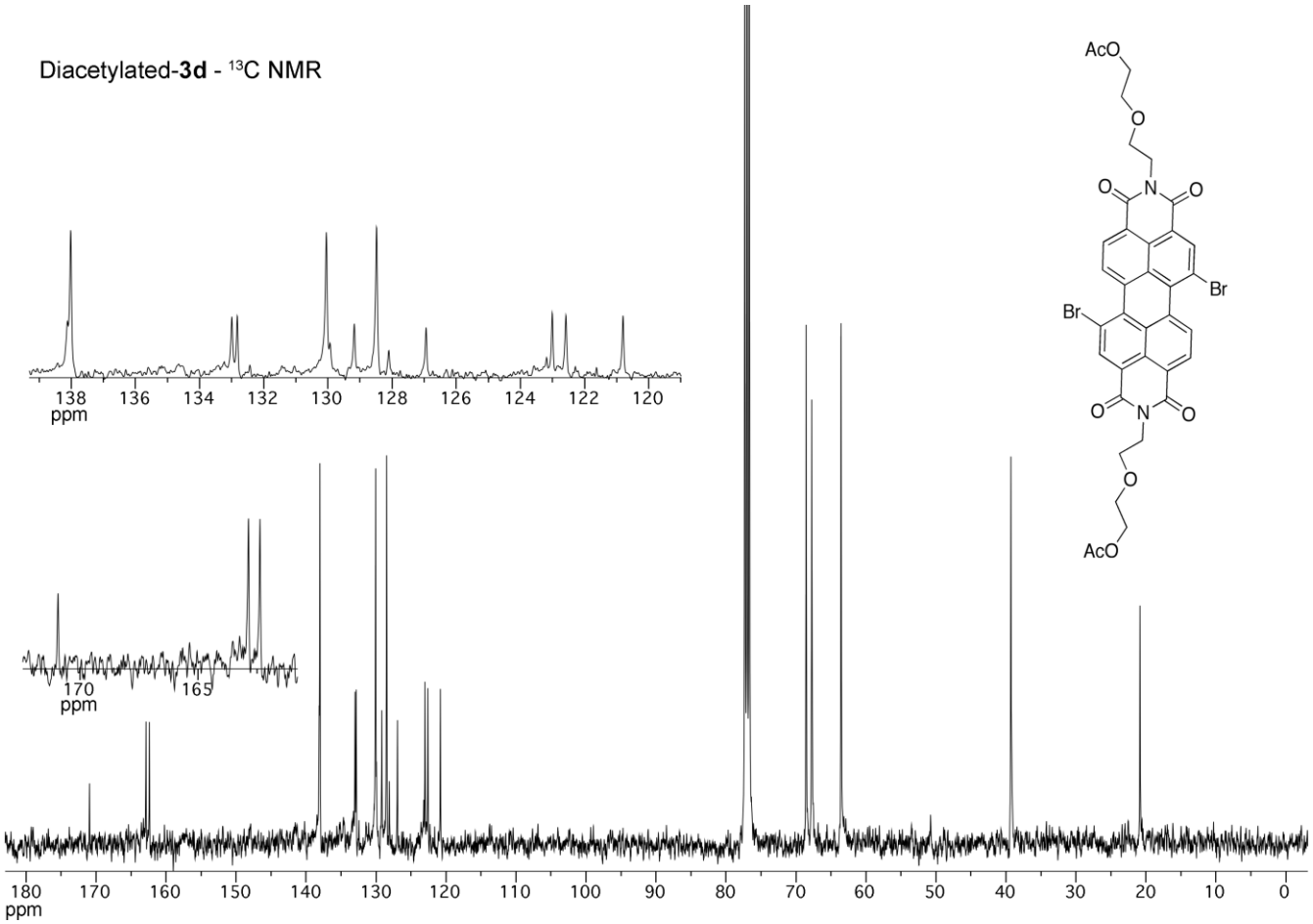

Figure S2. ^{13}C NMR (100 MHz, $CDCl_3$) of the 1,7-dibromo regioisomer of acetylated **3d**.

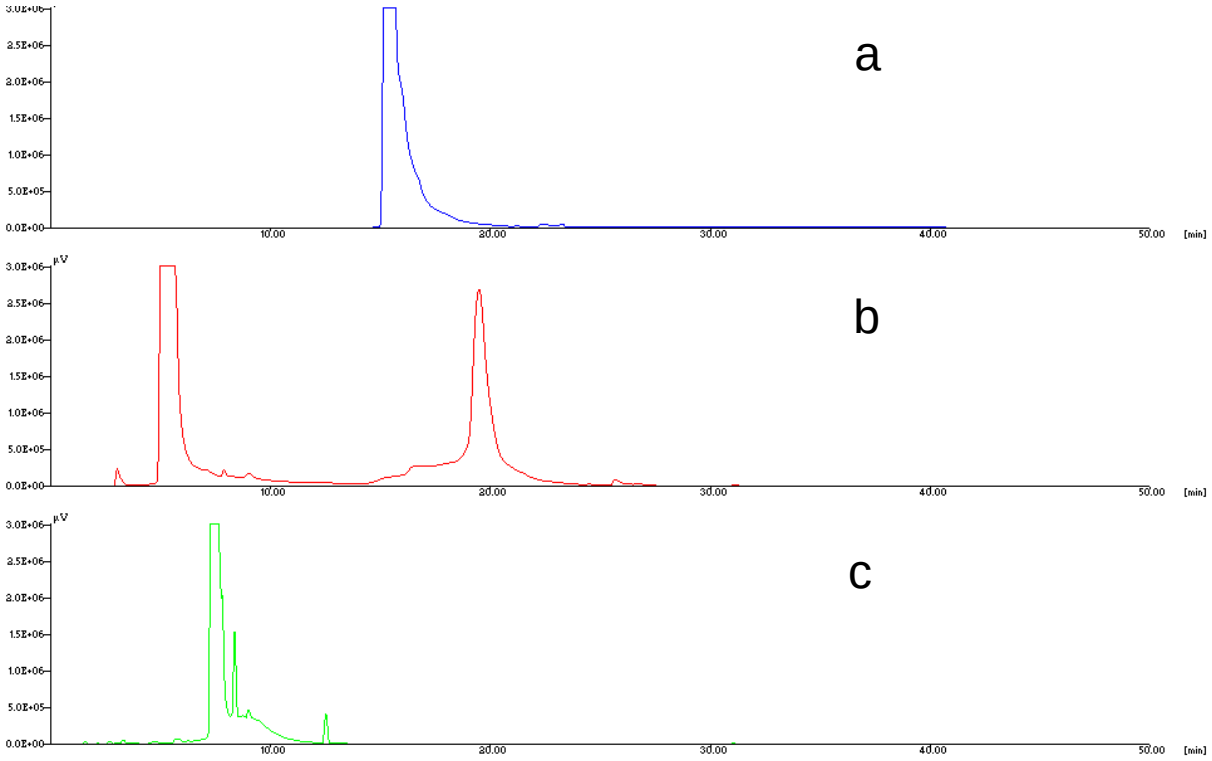

Figure S3. HPLC chromatograms of HTRp2 (**a** and **b**) and HTR2 (**c**) obtained on a C18 column, (Purosphere STAR®, MERCK, 4.6 mm x 250 mm) eluted with H_2O/ACN 98:2 v/v, for 10 min and then by a gradient of ACN in H_2O (30 min from 2 to 20 %). Flow rate 0.8 mL/min. The UV lamp of detector was positioned at 540 nm or 260 nm to obtain the chromatogram **a** or **b** and **c**, respectively.

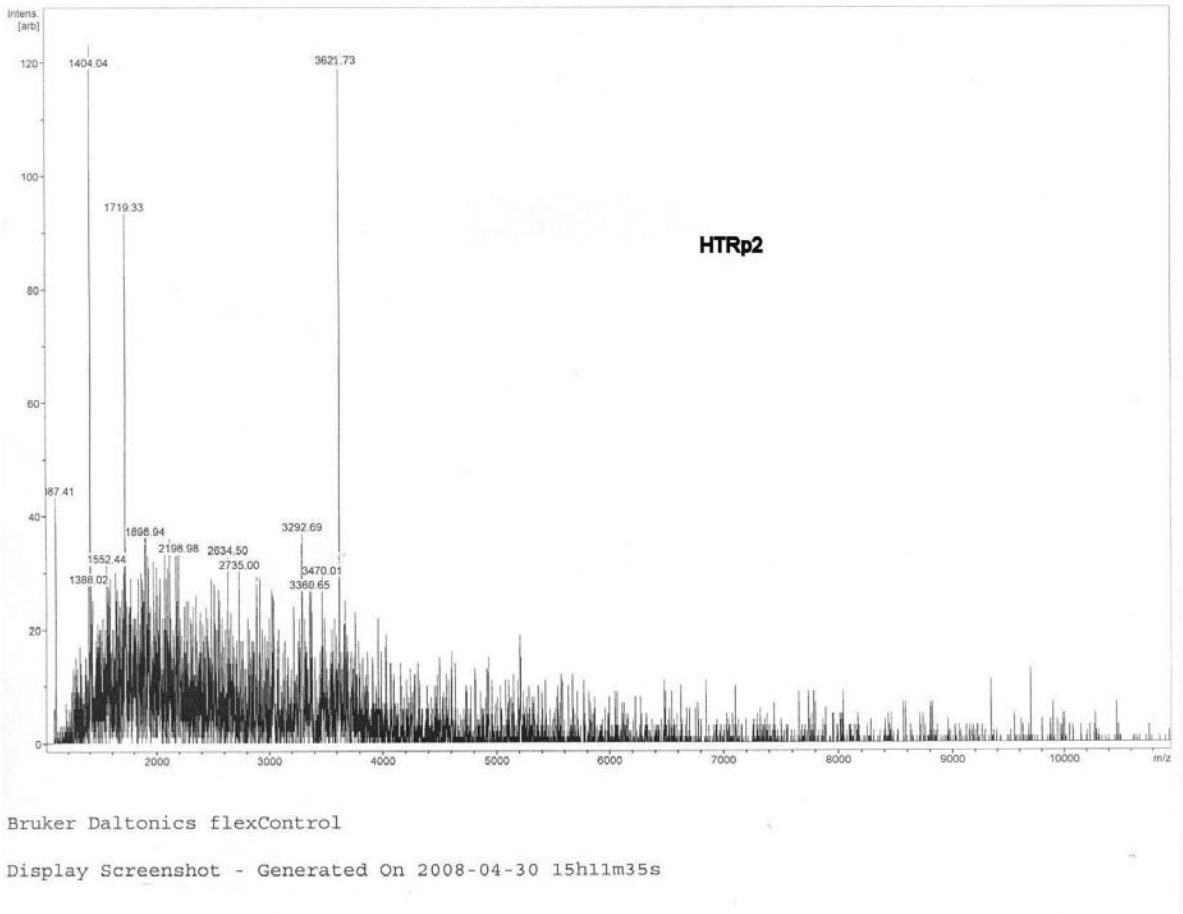

Figure S4. MALDI-TOF mass spectrum of HTRp2 (positive mode). The sample was prepared using a mixture of picolinic/3-hydroxypicolinic acids as the matrix.

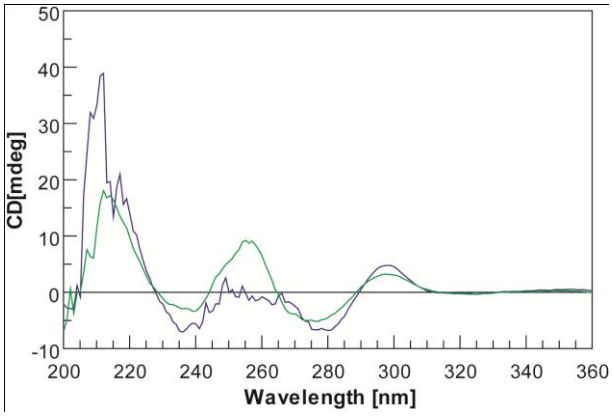

Figure S5. CD spectra of 4 μM (green line) and 6 μM (blue line) HTR2 in desalted water (HPLC grade). The spectra were registered after heating at 90 °C and rapid cooling at 10 °C.

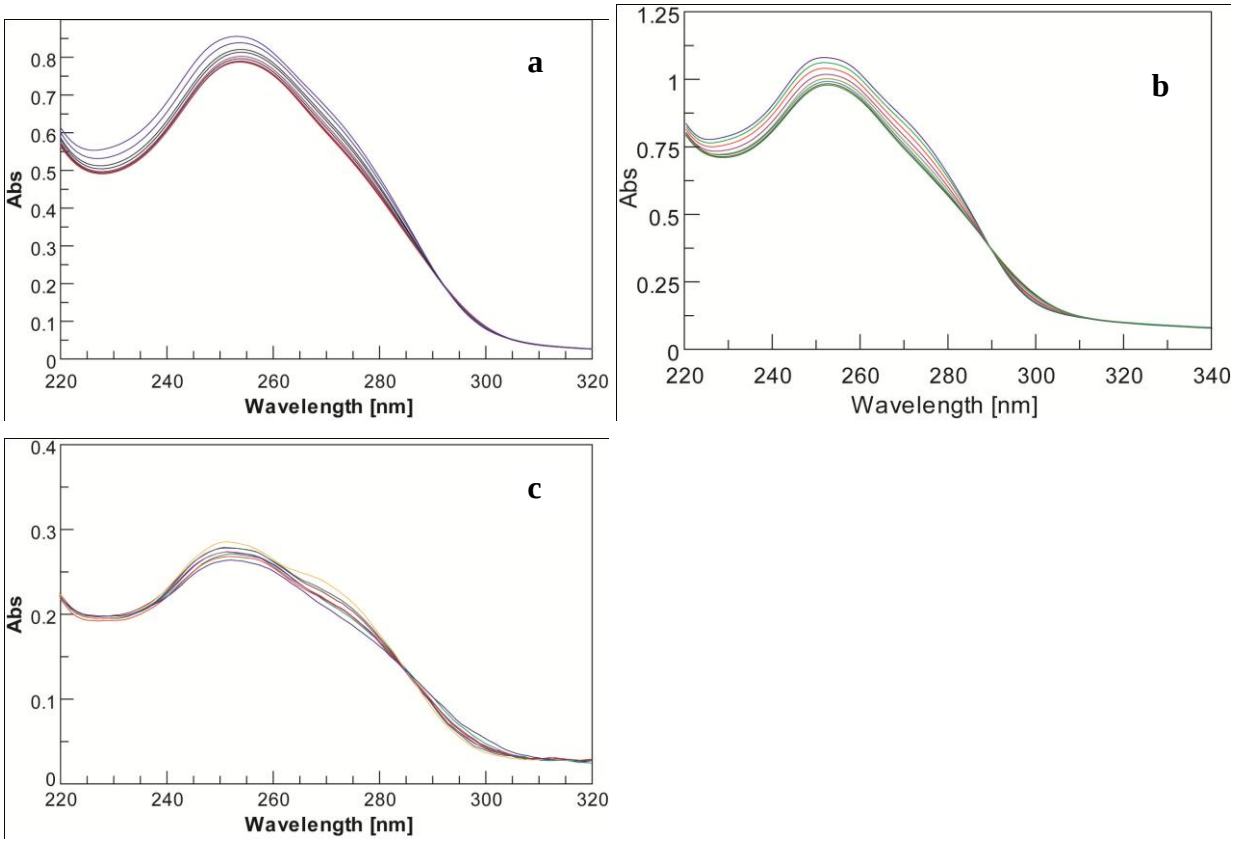

Figure S6. Short wavelength region of temperature-dependent UV spectra of HTRp2 (2 μM) in 10 mM phosphate buffer (pH = 7.4) containing 100 mM of KCl (**a**), 100 mM of NaCl (**b**), or in desalted water (HPLC grade) (**c**).

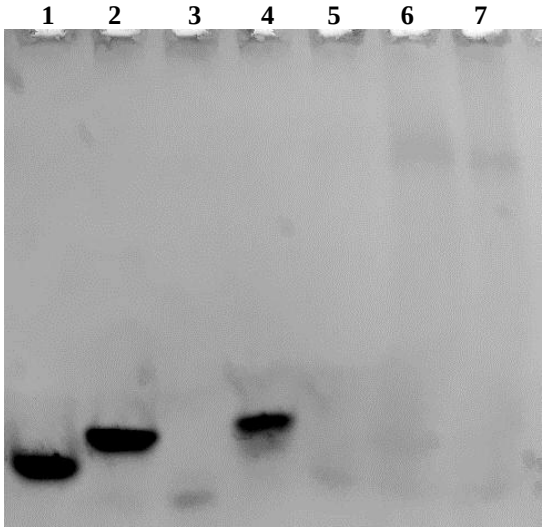

Figure S7. PAGE experiment on acrylamide gel 16% (acrylamide/bisacrylamide 29:1) using as running buffer TBE 89 mM containing 0.1 M NaCl. Time course was 3 h; voltage was 150 V. All samples were annealed in 10 mM phosphate buffer containing 0.1 M NaCl. The gel was stained with Sybr-green for 30 min and visualized on a Biorad Gel DOC-XR gel visualizer.

Lane 1: tetraplex $(TG_4T)_4$ at 10 μM; lane 2: duplex 5'TCAGTTAGCTCTGTT3'–5' AACAGAGCTAACTGA3' at 10 μM; lane 3: single stranded 5'AACAGAGCTAACTGA3' at 10 μM; lane 4: HTR2 (5'GGGTTAGGG3') at 10 μM; lanes 5, 6 and 7: HTRp2 (5'PEOEBr-GGGTTAGGG3') at 20, 40 and 100 μM, respectively. The lanes corresponding to the PEOEBr-conjugated sequence were charged with higher amount of sample because of difficulties in the stain with Sybr-green. Nevertheless in Na^+-containing solutions, HTRp2 gave rise to insoluble aggregates for concentration higher than 30-50 μM.

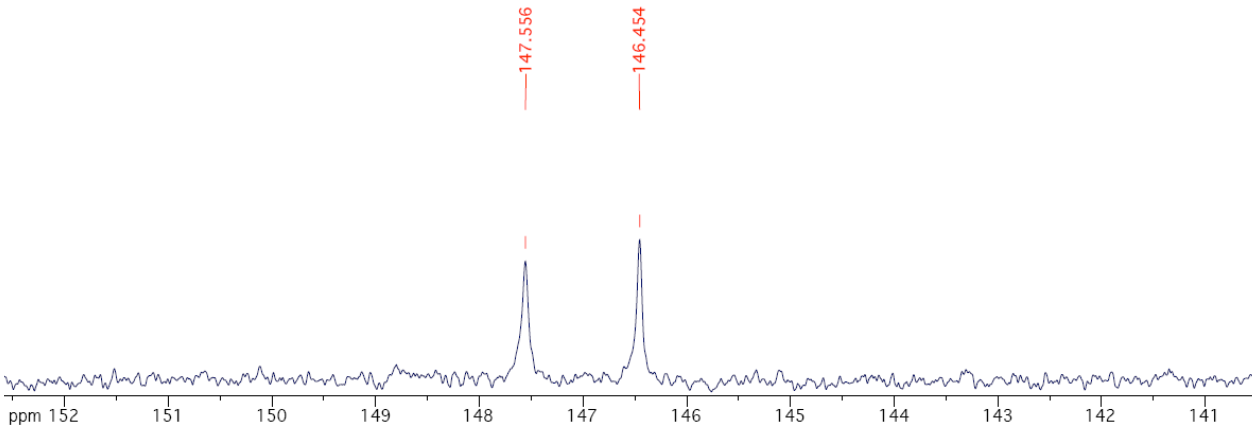

Figure S8. ^{31}P NMR data of **5d** registered on a Varian Unity INOVA 500 MHz spectrometer. The reported spectrum was acquired at 25 °C as 64,745 data points with a recycle delay of 1.0 s. Data were apodized with an exponential window function prior the Fourier transformation.

Fluorescence experiments

Fluorescence emission spectra were recorded using a Varian Cary Eclipse Fluorescence spectrophotometer. Fluorescence emission spectra were performed at 298 K, if not otherwise indicated. The fluorescence emission of compound **3d** in chloroform was recorded setting the excitation and emission slits width to 5 nm and the emission PMT (PhotoMultiplier Tubes) detector voltage to 600 V. Fluorescence spectra of the perylene-conjugated oligonucleotide HTRp2 at different temperatures, were recorded setting the excitation and emission slits widths to 20 and 10 nm, respectively, and the emission PMT detector voltage to 700 V; the emission range was set from 530 to 750 nm.

Despite, the dibromo-perylene derivative showed significant fluorescence in organic solvent (figure S10), in all explored conditions, the conjugated oligonucleotide, showed only a weak fluorescence with a maximum at 560 nm (figure S9), and the quantum yield greatly increased when arising the temperature. This effect is known for such systems, and it can be explained as a consequence of quenching by neighboring DNA bases which decreases with temperature increasing. (see Hariharan, M., Zheng, Y., Long, H., Zeidan, T. A., Vura-Weiss, J., Wasielewski, M. R., Schatz, G. C. and Lewis, F. D. (2009) Hydrophobic dimerization and thermal dissociation of perylenediimide-linked DNA hairpins. *J. Am. Chem. Soc*. *131*, 5920-5929 and references therein reported).

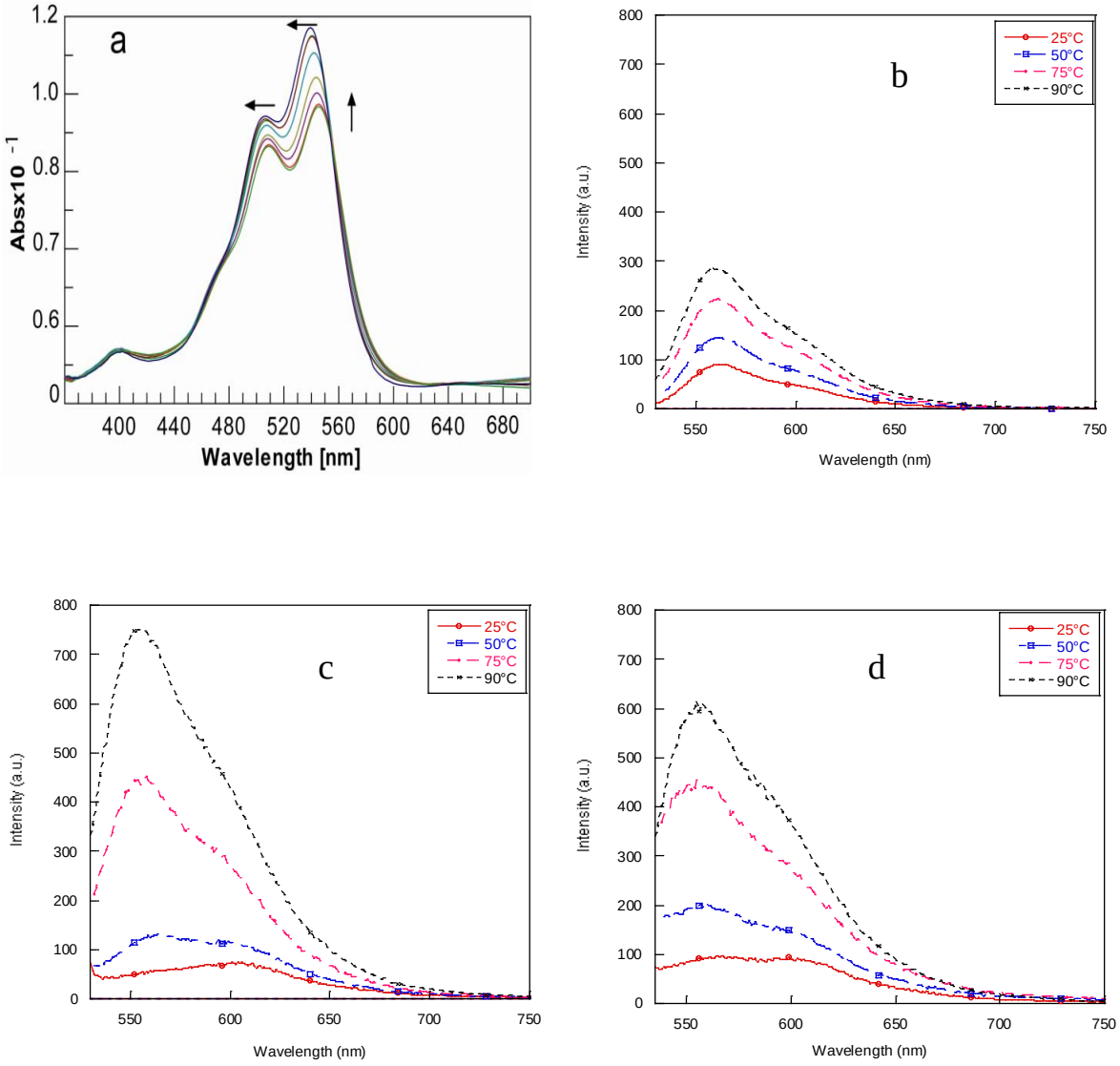

Figure S9. a) long wavelength region of UV spectra registered from 10 up to 80 °C in desalted water. The arrows indicate the changes in the UV bands by increasing the temperature. **b)**, **c)** and **d)** fluorescence spectra of HTRp2, respectively, in deionized water solution, in 10 mM phosphate buffer (pH 7.4) containing KCl 100 mM and in 10 mM phosphate buffer (pH 7.4) containing NaCl 100 mM. The spectra were acquired at different temperature by positioning ex.= 505 nm , ex. slit = 20, emission slit = 10, Voltage= 800 V, [HTRp2] = 3 μM.

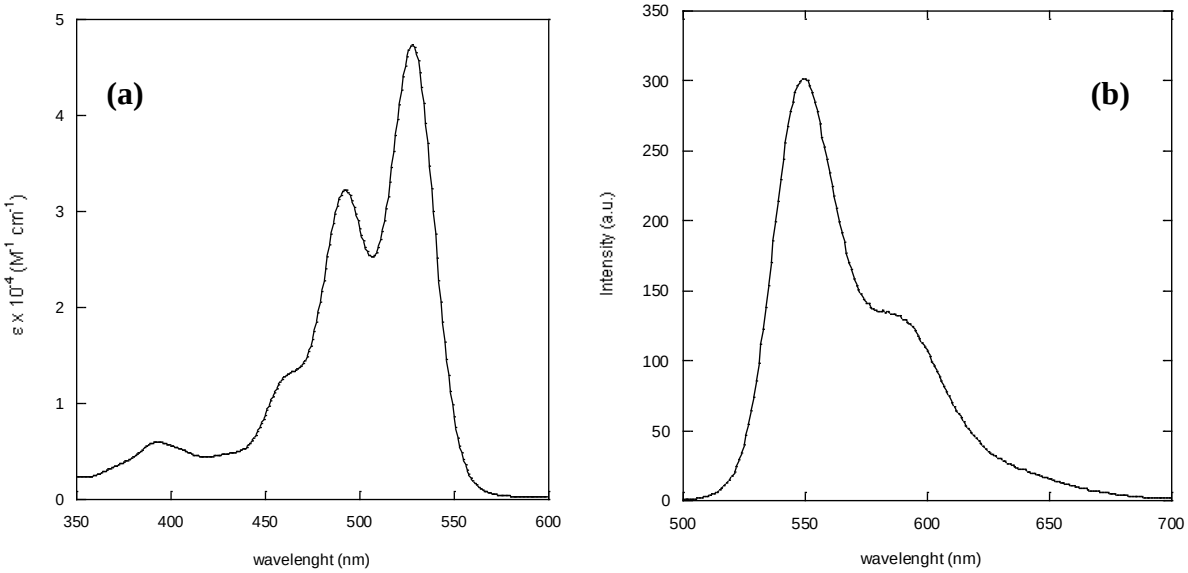

Figure S10. Absorption (**a**) and fluorescence spectra (**b**) of compound **3d** in chloroform. The excitation wavelength was 505 nm, the excitation and emission slits width were set to 5 nm and the emission PMT detector voltage to 600 V.

Bioconjugate Chemistry

ARTICLE

pubs.acs.org/bc

Enhanced Enzymatic Stability and Antitumor Activity of Daunorubicin-GnRH-III Bioconjugates Modified in Position 4

Marilena Manea,[*,§,†] Ulrike Leurs,[§] Erika Orbán,[‡] Zsuzsa Baranyai,[‡] Peter Öhlschläger,[▽,⊥] Andreas Marquardt,[∥] Ákos Schulcz,[#] Miguel Tejeda,[#] Bence Kapuvári,[#] József Tóvári,[#] and Gábor Mezö[″‡]

[§]Laboratory of Analytical Chemistry and Biopolymer Structure Analysis, Department of Chemistry

[†]Zukunftskolleg

[⊥]Laboratory of Immunology, Department of Biology

[∥]Proteomics Facility

University of Konstanz, 78457 Konstanz, Germany

[‡]Research Group of Peptide Chemistry, Hungarian Academy of Sciences, Eötvös Loránd University, 1117 Budapest, Hungary

[#]National Institute of Oncology, 1122 Budapest, Hungary

Supporting Information

ABSTRACT: Here, we report on the synthesis, enzymatic stability, and antitumor activity of novel bioconjugates containing the chemotherapeutic agent daunorubicin attached through an oxime bond to various gonadotropin-releasing hormone-III (GnRH-III) derivatives. In order to increase the enzymatic stability of the bioconjugates (in particular against chymotrypsin), ^{4}Ser was replaced by *N-Me*-Ser or Lys(Ac). A compound in which ^{4}Lys was not acetylated was also prepared, with the aim of investigating the influence of the free ε-amino group on the biochemical properties. The *in vitro* cytostatic effect of the bioconjugates was determined on MCF-7 human breast, HT-29 human colon, and LNCaP human prostate cancer cells by 3-(4,5-dimethylthiazol-2-yl)-2,5-diphenyltetrazolium bromide assay. Their stability/degradation (1) in human serum, (2) in the presence of rat liver lysosomal homogenate, and (3) in the presence of digestive enzymes (trypsin, chymotrypsin, and pepsin) was analyzed by liquid chromatography in combination with mass spectrometry. The results showed that (1) all synthesized bioconjugates had *in vitro* cytostatic effect, (2) they were stable in human serum at least for 24 h, and (3) they were hydrolyzed in the presence of lysosomal homogenate. All compounds were stable in the presence of (1) pepsin and (2) trypsin (except for the ^{4}Lys containing bioconjugate). In the presence of chymotrypsin, all bioconjugates were digested; the degradation rate strongly depending on their structure. The bioconjugates in which ^{4}Ser was replaced by *N-Me*-Ser or Lys(Ac) had the highest enzymatic stability, making them potential candidates for oral administration. *In vivo* tumor growth inhibitory effect of two selected bioconjugates was evaluated on orthotopically developed C26 murine colon carcinoma bearing mice. The results indicated that the compound containing Lys(Ac) in position 4 had significantly higher antitumor activity than the parent bioconjugate.

Glp-His-Trp-Xxx-His-Asp-Trp-Lys-Pro-Gly-NH_2

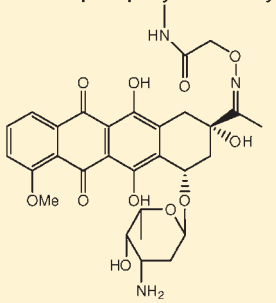

Xxx = Ser, *N-Me*-Ser, Lys, Lys(Ac)

INTRODUCTION

The hormonal decapeptide gonadotropin-releasing hormone-I (GnRH-I; Glp-His-Trp-Ser-Tyr-Gly-Leu-Arg-Pro-Gly-NH_2) plays a major role in the regulation of the reproduction by influencing the secretion of pituitary gonadotropin hormones.[1] Moreover, GnRH-I and many of its derivatives have an antiproliferative effect on various cancer cells,[2,3] which can be exerted by indirect or direct ways.[4,5] In the first case, the continuous exposure to GnRH-I results in the suppression of gonadotropin and sex-steroid secretion due to the desensitization of gonadotropic cells and the downregulation of pituitary GnRH receptors (GnRH-Rs). The observed chemical castration is a therapeutic approach of hormone-dependent tumors such as prostate and breast cancers. However, it has been shown that GnRH analogues also have direct antitumor activity on both hormone-dependent and -independent tumors, an effect which could be mediated through the GnRH receptors highly expressed on many types of tumors.

Thousands of synthetic peptide analogues of GnRH have been prepared since its discovery in order to increase, e.g., the antiproliferative effect. Interestingly, one of the less modified amino acids in the sequence is Ser in position 4. It seems that ^{4}Ser is not directly involved in the receptor binding;[6,7] however, the secondary structure is stabilized by a backbone hydrogen bond between $^{4}Ser_{NH}$ and $^{1}Glp_{CO}$ or by a side chain to backbone hydrogen bond

Received: December 3, 2010
Revised: May 7, 2011
Published: June 13, 2011

ACS Publications © 2011 American Chemical Society

of $^{4}Ser_{OH}$ and $^{1}Glp_{CO}$.[8] These interactions might influence the biologically active conformation of the *N*-terminal part of the peptide which is important for binding to the receptor. Moreover, it has been shown that in a GnRH-tandem-dimer peptide used as an antigen for immunocastration, Ser could be replaced by Ala without negatively affecting the efficacy.[9]

The stability of peptide-based drugs against enzyme-catalyzed hydrolysis is crucial for their therapeutic applications; for instance, in the case of oral administration, the compounds should be stable in the presence of digestive enzymes present in stomach and intestine. GnRH and its derivatives are highly susceptible to degradation by chymotrypsin, the main cleavage site being the -^{3}Trp-^{4}Ser- peptide bond. Slower degradation rates of GnRH derivatives were observed in the case of elastase, while most of them were stable to trypsin catalyzed hydrolysis. The -^{3}Trp-^{4}Ser- bond was also cleaved by angiotensin-converting enzyme. Furthermore, it was found that peptide bonds involving ^{4}Ser were cleaved in different cell homogenates.[10] Haviv et al. reported the complete stabilization of leuprolide against chymotrypsin and lumenal degradation by substituting the ^{4}Ser by *N-Me*-Ser.[11] Most recently, Pappa et al. indicated the incorporation of *N-Me*-Ser in position 4 in leuprolide analogues as a good strategy to enhance the stability against degradation by α-chymotrypsin and subtilisin, while maintaining their antiproliferative bioequivalence to leuprolide.[12]

In addition to human GnRH, intensive research is currently being conducted on GnRH-III (Glp-His-Trp-Ser-His-Asp-Trp-Lys-Pro-Gly-NH_2), a native GnRH analogue isolated from sea lamprey[13] which acts as a weak GnRH agonist in the pituitary. Compared to GnRH-I, GnRH-III causes 2−3 orders of magnitude lower release of luteinizing hormone (LH) and follicle stimulating hormone (FSH) in mammals.[14] Moreover, GnRH-III directly and specifically inhibits the growth of cancer cells expressing GnRH-Rs,[15] and it seems to be the most potent analogue containing only native amino acids on MDA-MB 231 human breast cancer cells.[16] Only a few GnRH-III analogues have been prepared so far. The *in vitro* evaluation of their antitumor activity indicated that slight modifications of the amino acid sequence did not result in a loss of the antitumor activity. It has been shown that two analogues containing either Lys or Lys(Ac) instead of Ser in position 4 were as active as GnRH-III on different tumor types.[17] However, tryptophane residues in positions 3 and 7 were essential for the biological activity. The modification of ^{8}Lys by cyclization with ^{6}Asp,[17] Ala-scan,[18] conjugation to a carrier,[19] or dimerization through disulfide bond[20] was also tolerated. The LH- and FSH-releasing activity of [^{4}Lys]-GnRH-III was slightly higher than that of GnRH-III, while the modification of the ε-amino group of ^{8}Lys by cyclization, conjugation, or dimerization decreased the endocrine effect of the peptide hormone.[20,21]

In our previous work, the side chain of ^{8}Lys was used for the attachment of anticancer drugs (e.g., anthracycline derivatives) leading to the formation of drug delivery systems for targeted cancer chemotherapy.[10] Some of the anthracycline derivative-GnRH-III bioconjugates had *in vitro* cytostatic activity with IC_{50} values in the low μM range. Moreover, two oxime bond-linked daunorubicin-GnRH-III bioconjugates had significant tumor growth inhibitory effect on colon carcinoma bearing mice.[22,23] Both bioconjugates were administered intraperitoneally.

Oral administration is considered to be the most convenient route for the delivery of drugs and might be very efficient in the case of colorectal cancer. In order to be orally administered, anticancer drug-GnRH-III derivative bioconjugates must have increased stability in the presence of digestive enzymes present in the gastrointestinal tract, such as trypsin, chymotrypsin, and pepsin. We have previously reported that GnRH-III and its dimer derivatives were not substrates for trypsin catalyzed hydrolysis; however, they were cleaved by chymotrypsin, the main cleavage site being the -^{3}Trp-^{4}Ser- peptide bond.[20] In the case of an oxime bond-linked daunorubicin-GFLG-GnRH-III bioconjugate (<EHWS-HDWK(Dau═Aoa-GFLG)PG-NH_2; where <E is pyroglutamic acid, and Aoa is aminooxyacetyl), besides -^{3}Trp-^{4}Ser-, two further cleavage sites were identified after longer incubation times (6−24 h), namely, -Phe-Leu- and -Leu-Gly- in the GFLG branch, and no digestion of -^{7}Trp-^{8}Lys- was observed (Manea, M. et al., unpublished results). One approach to increase the stability of the anticancer drug-GnRH-III derivative bioconjugates against enzymatic degradation, in particular, against chymotryptic digestion, could be the replacement of ^{4}Ser by *N-Me*-Ser or Lys(Ac), modifications that might also influence the biological properties of the bioconjugates, such as antitumor activity.

Here, we report on the synthesis, enzymatic stability, cellular uptake, and *in vitro* cytostatic effect of novel daunorubicin-GnRH-III bioconjugates in which ^{4}Ser was replaced by Lys, Lys(Ac), or *N-Me*-Ser. The stability/degradation of the bioconjugates in human serum, in the presence of rat liver lysosomal homogenate or digestive enzymes (trypsin, chymotrypsin, and pepsin) was determined by liquid chromatography in combination with mass spectrometry. Their *in vitro* cytostatic effect was evaluated on HT-29 human colon, MCF-7 human breast, and LNCaP human prostate cancer cells. The *in vivo* tumor growth inhibitory effect of the compound containing Lys(Ac) in position 4 and of the parent bioconjugate was determined on orthotopically developed C26 murine colon carcinoma bearing mice.

MATERIALS AND METHODS

Materials. All amino acid derivatives, benzotriazole-1-yloxytris-pyrrolidinophosphonium-hexafluoro-phosphate (PyBOP), bis-Boc-aminooxyacetic acid (bis-Boc-Aoa-OH), and Rink-Amide MBHA resin were purchased from NovaBiochem (Läufelfingen, Switzerland) and GL Biochem Shanghai Ltd. (Shanghai, China).

Scavengers, coupling agents, and cleavage reagents (triisopropylsilane (TIS), 4-methylmorpholine (NMM), piperidine, 1,8-diazabicyclo[5.4.0]undec-7-ene (DBU), trifluoroacetic acid (TFA)), as well as daunorubicin (Dau), diisopropylethylamine (DIPEA), acetic anhydride (Ac_2O), and 3-(4,5-dimethylthiazol-2-yl)-2, 5-diphenyltetrazolium bromide (MTT), were obtained from Sigma-Aldrich Ltd. (St. Louis, MO, USA). Dimethylformamide (DMF) and acetonitrile (MeCN) were purchased from Acros Organics (Geel, Belgium), while ethanol and diethyl ether were from Riedel de Häen (Seelze, Germany). All reagents and solvents were of analytical grade or highest available purity.

Synthesis of Oxime Bond-Linked Daunorubicin-GnRH-III Derivative Bioconjugates. Aminooxyacetylated (Aoa) derivatives of GnRH-III (<EHWSHDWK(Aoa)PG-NH_2, <EHW(*N-Me*)SHDWK(Aoa)PG-NH_2, <EHWK(Ac)HDWK(Aoa)PG-NH_2, and <EHWKDWK(Aoa)PG-NH_2, where <E is pyroglutamic acid) were prepared manually by solid-phase peptide synthesis according to Fmoc/tBu chemistry on a Rink-Amide MBHA resin (0.38 mmol/g coupling capacity). The following Fmoc-protected amino acid derivatives were used: Fmoc-Gly-OH, Fmoc-Pro-OH, Fmoc-Lys(Mtt)-OH, Fmoc-Lys(Dde)-OH, Fmoc-Lys(Boc)-OH, Fmoc-*N-Me*-Ser(tBu)-OH, Fmoc-Trp(Boc)-OH, Fmoc-Asp(OtBu)-OH, Fmoc-His(Trt)-OH, and Fmoc-Ser(tBu)-OH.

The protocol of the synthesis was as follows: (i) DMF washing (4 × 1 min), (ii) Fmoc deprotection with 2% DBU, 2% piperidine in DMF (2 + 2 + 5 + 10 min), (iii) DMF washing (10 × 1 min), (iv) coupling of 5 equiv α-Fmoc-protected amino acid/PyBOP/NMM (1:1:2) in DMF (60 min), (v) DMF washing (4 × 1 min).

In order to synthesize the GnRH-III derivatives <EHWSHDWK(Aoa)PG-NH_2, <EHWKDWK(Aoa)PG-NH_2, and <EHW(*N-Me*)SHDWK(Aoa)PG-NH_2, after completion of the synthesis of the protected decapeptides, the Mtt-protecting group was removed from the ε-NH_2 group of ^{8}Lys with 2% TFA in DCM (6 × 5 min). Afterward, bis-Boc-Aoa-OH was attached to the free ε-NH_2 group of ^{8}Lys after preactivation with PyBOP in the presence of NMM (5 and 10 equiv to the resin capacity; coupling time 45 min).

For the synthesis of <EHWK(Ac)HDWK(Aoa)PG-NH_2, the Dde-protecting group of the ε-NH_2 group of ^{4}Lys was removed by 2% hydrazine in DMF (2 × 15 min); subsequently, the acetylation of the ε-NH_2 group was achieved by treatment with Ac_2O/DIPEA/DMF (1:1:3, v/v/v) for 1 h. After removing the Mtt-protecting group from the ε-NH_2 group of ^{8}Lys, bis-Boc-Aoa-OH was coupled as described above.

Aminooxyacetylated peptides were cleaved from the resin using a mixture of 95% TFA, 2.5% TIS, and 2.5% water (v/v/v) for 2.5 h at room temperature and then precipitated with ice-cold diethyl ether, washed three times with diethyl ether, and solubilized in 100% acetic acid prior to freeze−drying. The crude products were purified by semipreparative RP-HPLC and analyzed by mass spectrometry.

The conjugation of daunorubicin to the aminooxyacetylated GnRH-III derivatives was carried out in 0.2 M sodium acetate buffer (pH 5.0), at a peptide concentration of 10 mg/mL. Daunorubicin was used in 30% excess compared to the aminooxyacetylated derivatives of GnRH-III. The reaction mixtures were stirred at room temperature for 24 h and then subjected to RP-HPLC purification. The purified bioconjugates, GnRH-III(^{4}Ser, ^{8}Lys(Dau═Aoa)) (**1**), GnRH-III(*N-Me*-^{4}Ser, ^{8}Lys(Dau═Aoa)) (**2**), GnRH-III(^{4}Lys(Ac), ^{8}Lys(Dau═Aoa)) (**3**), and GnRH-III(^{4}Lys, ^{8}Lys(Dau═Aoa)) (**4**) were characterized by analytical RP-HPLC and mass spectrometry.

High Performance Liquid Chromatography (HPLC). The crude products were purified on an UltiMate 3000 HPLC system (Dionex, Idstein, Germany) using a semipreparative Vydac C18 column (250 mm × 10 mm) with 10 μm silica (300 Å pore size). Linear gradient elution (0 min 20% B; 5 min 20% B; 55 min 70% B) with eluent A (0.1% TFA in water) and eluent B (0.1% TFA in MeCN-H_2O (80:20, v/v)) was used at a flow rate of 4 mL/min. Peaks were detected at 220 and 280 nm.

Analytical RP-HPLC was performed on an UltiMate 3000 system (Dionex, Idstein, Germany) using a Vydac C18 column (250 mm × 4.6 mm) with 5 μm silica (300 Å pore size) as a stationary phase. Linear gradient elution (0 min 0% B; 5 min 0% B; 50 min 90% B) with eluent A (0.1% TFA in water) and eluent B (0.1% TFA in MeCN-H_2O (80:20, v/v)) was used at a flow rate of 1 mL/min. Peaks were detected at 280 nm.

Mass Spectrometry (MS). Electrospray (ESI)-mass spectrometric analyses were carried out on an Esquire 3000+ ion trap mass spectrometer (Bruker Daltonics, Bremen, Germany). Spectra were acquired in the 50−2500 *m/z* range. Samples were dissolved in a mixture of 50% methanol, 48% water, and 2% acetic acid.

Liquid chromatography−mass spectrometry (LC-MS) was carried out on an Esquire 3000+ ion trap mass spectrometer (Bruker Daltonics, Bremen, Germany) equipped with an Agilent 1100 HPLC system and a diode array detector (Agilent, Waldbronn, Germany). Peptides were separated on a Vydac MS C18 column (150 mm × 1 mm; 300 Å, 3 μm) using a linear gradient from 90% solvent A (0.1% formic acid in water (v/v)) and 10% solvent B (0.1% formic acid in acetonitrile (v/v)) to 70% solvent B over 60 min and a flow rate of 50 μL/min. Spectra were recorded in positive ion mode in the 50−2500 *m/z* range.

Stability of Daunorubicin-GnRH-III Derivative Bioconjugates in 90% Human Serum. Bioconjugates **1**−**4** were first dissolved in water at a concentration of 100 μM and then human serum was added (final peptide concentration: 10 μM). The mixtures were incubated at 37 °C and aliquots of 100 μL were taken after 5 min, 8 h, and 24 h (the reactions were quenched by adding 10 μL of acetic acid). Prior to mass spectrometric analysis, the larger human serum proteins were removed using Microcon centrifugal devices, cutoff 10 kDa (Millipore Corporation, Bedford, MA, USA), and the lower molecular weight fraction was analyzed by LC-MS.

Two control experiments were performed: (1) compounds with molecular weight lower than 10000 from human serum were separated and analyzed by LC-MS and (2) aqueous solutions of bioconjugates (c = 10 μM) were incubated at 37 °C for 24 h and then analyzed by LC-MS.

Degradation of Daunorubicin-GnRH-III Derivative Bioconjugates in Rat Liver Lysosomal Homogenate. The rat liver lysosomal homogenate was prepared as previously described.[24] The protein concentration was determined by Pierce BCA protein assay (bicinchoninic acid) according to the manufacturer's protocol (ThermoFisher Scientific, Rockford, IL, USA) and it was 16.6 μg/μL.

The degradation of the bioconjugates in the rat liver lysosomal homogenate was determined as follows: bioconjugates were dissolved in 0.2 M NaOAc, pH 5.0, at a concentration of 0.1 μg/μL and then the rat liver lysosomal homogenate was added (bioconjugate/lysosomal homogenate ratio = 1:1, w/w). The reaction mixtures were incubated at 37 °C and aliquots of 50 μL were taken at 5 min, 1 h, 2 h, 4 h, 6 h, 8 h, and 24 h. The reactions were quenched by adding 5 μL of acetic acid, followed by LC-MS analysis.

Stability/Degradation of Daunorubicin-GnRH-III Derivative Bioconjugates in the Presence of Digestive Enzymes. Daunorubicin-GnRH-III derivative bioconjugates **1**−**4** were incubated with the three major enzymes of the intestinal tract: trypsin (Promega, Madison, WI, USA), α-chymotrypsin (Sigma, Saint Louis, MO, USA), and pepsin (Sigma, Saint Louis, MO, USA). In each case, the enzyme to substrate ratio was 1:50 (w/w). For tryptic digestion, bioconjugates were dissolved in 10 mM NH_4HCO_3, pH 8.0, at 37 °C, and then trypsin was added. The chymotryptic digestion was carried out in 100 mM Tris-HCl/10 mM $CaCl_2$, pH 7.8, at 25 °C, and the pepsin digestion was performed in 0.1% formic acid, pH 1.8, at 37 °C. Aliquots were taken after 5 min, 1 h, 2 h, 4 h, 6 h, and 24 h. Reactions were quenched by the addition of acetic acid in the case of tryptic and chymotryptic digestion and by the addition of NaOH in the case of pepsin digestion. All samples were analyzed by LC-MS.

Cells. MCF-7 human breast cancer cell line was maintained in DMEM GlutaMAX-I (Sigma Ltd., St. Louis, MO) medium containing 10% FCS (fetal calf serum, Sigma Ltd.) and gentamicine (160 μg/mL). HT-29 human colon cancer cells were maintained in RPMI-1640 (GIBCO Invitrogen, Germany) supplemented with 10% FCS and 1% penicillin/streptomycin. LNCaP human prostate cancer cell line was maintained in RPMI-1640 supplemented with

10% FCS, 1% penicillin/streptomycin, and 10 nM testosterone. Cell cultures were maintained at 37 °C in a humidified atmosphere with 5% CO_2.

***In Vitro* Cytostatic Effect of Bioconjugates 1−4 Determined by MTT Assay.** To study the *in vitro* cytostatic effect of the bioconjugates, 3-(4,5-dimethylthiazol-2-yl)-2,5-diphenyl-tetrazolium bromide assay (MTT assay) was carried out. One day before the treatment with the compounds, 5×10^3 cells per well were plated on 96-well plates. After 24 h incubation at 37 °C, cells were treated for 6 h with the bioconjugates dissolved in serum-free medium. The compounds were used in the 2.6×10^{-4} to 10^2 μM concentration range. Cells treated for 6 h with serum-free medium were used as a control. After treatment and incubation, cells were washed twice with serum-free medium and cultured in serum-containing medium for 72 h. On the fourth day, the MTT assay was performed. Therefore, MTT was added to each well (final concentration: 367 μg/mL), and during 3.5 h incubation at 37 °C, purple crystals were formed by mitochondrial dehydrogenase enzyme present in the living cells. After that, the cells were centrifuged for 5 min at 2500 rpm and the supernatant was removed. The crystals were dissolved in 100 μL DMSO and the optical density (OD) was determined at λ = 540 and 620 nm using an ELISA Reader (Labsystems MS reader, Helsinki, Finland). OD_{620} was subtracted from OD_{540} and the percentage of cytostasis was calculated using the following equation:

$$\text{Cytostasis}\% = [1 - (OD_{\text{treated}}/OD_{\text{control}})] \times 100$$

where OD_{treated} and OD_{control} correspond to the optical densities of treated and control cells, respectively.

Cytostasis % was plotted as a function of concentration, fitted to a sigmoidal curve, and the 50% inhibitory concentration (IC_{50}) value was determined on the basis of these curves.

Cellular Uptake of Daunorubicin-GnRH-III Derivative Bioconjugates. To examine the cellular uptake of the bioconjugates by MCF-7 human breast cancer cell line, cells were plated at a number of 1×10^5 cells per well on 24-well plates in 1 mL of complete medium. After 24 h incubation at 37 °C, the cells were centrifuged 5 min at 1000 rpm and the supernatant was removed. Thereafter, 250 μL of bioconjugate solutions (in serum-free medium) were added onto the cells, concentrations ranging from 0.16 μM to 100 μM. The control cells were treated with serum-free medium. The cells were incubated with the bioconjugate solutions at 37 °C for 6 h. After that, the solutions were removed from the cells, and 100 μL trypsin/EDTA was added per well and incubated for 10 min at 37 °C. After adding 700 μL of 10% FCS in HPMI, the cells were transferred to FACS tubes and centrifuged for 5 min at 1000 rpm. After removing the supernatant, the cells were resuspended in 500 μL FCS-free HPMI. The fluorescence intensity of the cells was determined by flow cytometry (BD LSR II, BD Bioscience, San Jose, California, USA). Data were analyzed with the *FACSDiVa* software and the daunorubicin positive cell percentage was calculated.

Circular Dichroism Spectroscopy. Circular dichroism (CD) spectra were recorded on a Jasco J-715 spectropolarimeter at 25 °C in quartz cells of 0.05 cm path length, under constant nitrogen flush. The instrument was calibrated with 0.06% (w/v) ammonium-D-camphor-10-sulfonate (Katayama Chemical, Japan) in water. The bioconjugates were dissolved in water at a concentration of 500 μM. The spectra were averages of six scans in the wavelength range 180−400 nm. The results were expressed in terms of mean molar ellipticity (deg cm^2 $dmol^{-1}$) after subtracting the solvent baseline.

Animals and Surgical Microprocedures. Female inbred Balb/c mice from a specified pathogen free (SPF) breeding of the Department of Experimental Pharmacology, National Institute of Oncology (Budapest, Hungary), weighing 22−24 g, were used in these experiments. Mice were maintained in a sterile environment in Macrolon cages at 22−24 °C (40−50% humidity), with a lighting regimen of 12/12 h light/dark. The animals had free access to tap water and were fed a sterilized standard diet (Charles River VRF1, autoclavable, Germany) ad libitum. They were cared for according to the "Guiding Principles for the Care and Use of Animals" based upon the Helsinki declaration and the experiments were approved by the local ethical committe.

For direct implantation, mice were anasthetized and the abdomen was sterilized with iodine and alcohol swabs. A small midline incision (0.5 cm) was made and the colorectal part of the intestine was exteriorized. Serosa of the site where the tumor pieces were to be implanted were removed. A piece of 2 mm^3 C26 murine colon tumor was implanted on the top of the animal intestine; an 8/0 surgical (polypropylene) suture was used to suture it on the wall of the intestine. The intestine was returned to the abdominal cavity, and the abdominal wall was closed with 4/0 surgical (polyglycolic acid) sutures. The wound was sterilized with iodine and alcohol swab again and the animals were kept in a sterile environment. For pain release and rehydation, mice were treated s.c. with 100 mg/kg algopyrine in Ringer solution that contained 5% glucose. On the next day, no sign of pain and/or stress of the mice was observed.

***In Vivo* Antitumor Effect of Daunorubicin and Dau-GnRH-III Derivative Bioconjugates on C26 Colon Carcinoma Bearing Mice.** Two treatments were applied on days 4 and 7 after tumor transplantation by i.p. administration of the compounds dissolved in d.i. water (250 μL/mouse). In this experiment, 7−7 mice/group were used for the treatment with the bioconjugates (GnRH-III(^{4}Ser, ^{8}Lys(Dau=Aoa)) and GnRH-III(^{4}Lys(Ac), ^{8}Lys(Dau=Aoa))) and 10 animals in the control group. The bioconjugates were administered a dose of 26.6 μmol/kg body weight (15 mg Dau content in the bioconjugate/kg), while the free Dau was used at a dose of 2 mg (3.55 μmol)/kg. The mice from all groups were sacrificed by cervical dislocation on day 13 after tumor transplantation, because some mice, in particular from the control group, were in bad physical condition (apathy, no movement, no eating, no drinking, no reaction, etc.) which would lead to their death in the following days. After that, the tumors were removed and the tumor weight was determined in all cases.

RESULTS AND DISCUSSION

Oxime Bond-Linked Daunorubicin-GnRH-III Derivative Bioconjugates. Recently, the application of hormone peptides (e.g., GnRH or somatostatin) for drug targeting or delivery of radiolabeled compounds as diagnostic tools have intensively been investigated.[25] So far, efficient anticancer drug−hormone peptide bioconjugates have been developed in A. V. Schally's laboratory. In these compounds, doxorubicin (Dox) or 2-pyrrolino-doxorubicin was attached through an ester bond by the aid of a glutaric acid linker to appropriate hormone peptide derivatives (GnRH, somatostatin, bombesin) that were used as targeting moieties.[5,26] The bioconjugates showed high selectivity and significant growth inhibition on many tumor types. One of them, AN-152 containing doxorubicin attached to [D-^{6}Lys]-GnRH-I is currently in

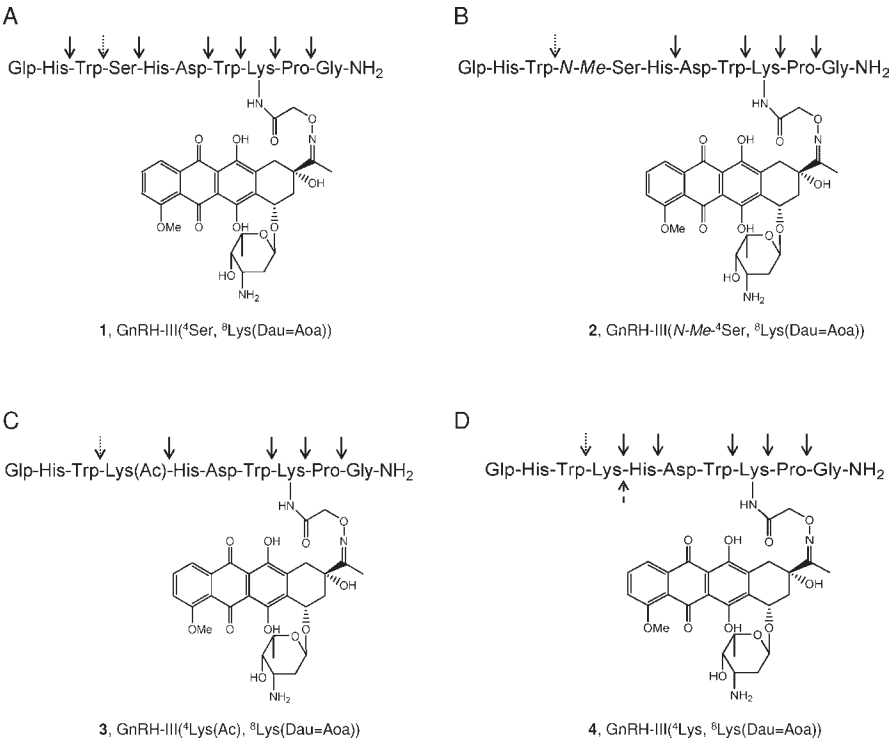

Figure 1. Cleavage sites produced by the proteolysis of Dau-GnRH-III derivative bioconjugates in the presence of rat liver lysosomal homogenate (full-line arrows), chymotrypsin (dotted-line arrows), and trypsin (dashed-line arrows): (A) GnRH-III(^{4}Ser, ^{8}Lys (Dau═Aoa)), (B) GnRH-III(*N-Me*-^{4}Ser, ^{8}Lys(Dau═Aoa)), (C) GnRH-III(^{4}Lys(Ac), ^{8}Lys(Dau═Aoa)), and (D) GnRH-III(^{4}Lys, ^{8}Lys(Dau═Aoa)).

phase II clinical trial on ovarian and endometrial cancer (http://clinicaltrials.gov).

We have previously reported that oxime bond-linked daunorubicin-GnRH-III derivative bioconjugates had significant *in vitro* and *in vivo* antitumor activity, even if no free drug release was detected in the presence of lysosomal homogenates (the *in vivo* antitumor activity was evaluated on colon carcinoma bearing mice).[22−24]

To increase the bioactivity of the compounds, several approaches could be employed such as (1) structural modifications of the targeting moiety to improve the binding to the receptors on cancer cells, (2) the attachment of more than one anticancer drug to the same carrier, or (3) the conjugation to the targeting moiety of drugs with increased antitumor activity. In the present work, we investigated GnRH-III analogues modified in position 4 as targeting moieties for drug delivery. It was indicated by several authors that slight modifications of the GnRH-III sequence were possible without resulting in the loss of receptor binding and antitumor activity.[16−18] The most potent GnRH-III derivatives were the [^{4}Lys]-GnRH-III and its acetylated version [^{4}Lys(Ac)]-GnRH-III.[17] Furthermore, the replacement of Ser in position 4 by *N-Me*-Ser did not significantly decrease the antitumor activity of leuprolide, a superagonist derivative of human GnRH, but it improved its enzymatic stability.[11,12]

These observations prompted us to develop daunorubicin-GnRH-III bioconjugates in which ^{4}Ser was replaced by Lys, Lys(Ac), or *N-Me*-Ser. All peptides were synthesized by solid-phase methodology using Fmoc-chemistry. Lys(Mtt) was incorporated in position 8, and the Mtt protecting group was removed under mild acidic conditions (2% TFA in DCM), followed by the attachment of an aminooxyacetic acid derivative. For the synthesis of ^{4}Lys(Ac) modified compound, an orthogonal protecting scheme for lysine residues was used (Dde-Mtt). The cleavage of the Dde protecting group and the acetylation of ^{4}Lys were carried out prior to the removal of Mtt, followed by the attachment of bis-Boc-Aoa-OH. All compounds were cleaved from the resin with TFA in the presence of appropriate scavengers. Daunorubicin was conjugated to the aminooxyacetylated GnRH-III derivatives by oxime ligation which was carried out under slightly acidic conditions (pH 5.0). The structures of the synthesized compounds are schematically represented in Figure 1.

All bioconjugates were purified by semipreparative RP-HPLC, and the purified compounds were analyzed by analytical RP-HPLC and mass spectrometry (Table 1 and Supporting Information, Figures S1−S4). The purity of the compounds was over 95%, and they were obtained with 65−70% yield. As previously reported,[24,27] it is important to note the fragmentation of the glycosidic bond under the ESI-mass spectrometric conditions resulting in the loss of daunosamine (−129, −147). These fragments were assigned in all mass spectra by an asterisk.

Enzymatic Stability/Degradation of Bioconjugates. The *in vitro* stability/degradation of the anticancer drug-GnRH-III derivative bioconjugates in human serum, in lysosomal homogenate, and in the presence of gastrointestinal enzymes is of remarkable importance for their therapeutic applications. The main principle of targeted cancer chemotherapy is the delivery of a chemotherapeutic agent solely to cancer cells, so as to prevent affectation of healthy cells. The chemical bond between GnRH-III and the anticancer drug should therefore exhibit high stability in human serum to prevent the decomposition of the anticancer drug from GnRH-III in the bloodstream. In contrast, the compounds should be degraded in lysosomes, so as to favor the release of the free chemotherapeutic agent or the formation of an active metabolite. Oral administration is considered to be the most convenient route for the delivery of drugs, and might be

Table 1. Chemical Characteristics of Daunorubicin-GnRH-III Derivative Bioconjugates

		RP-HPLC[a]	ESI-MS[b]
compound	code	R_t [min]	MW_{calc}/MW_{exp}
1	GnRH-III(^{4}Ser, ^{8}Lys(Dau=Aoa))	29.1	1841.91/1841.95
2	GnRH-III(*N-Me*-^{4}Ser, ^{8}Lys(Dau=Aoa))	29.3	1855.96/1855.70
3	GnRH-III(^{4}Lys(Ac), ^{8}Lys(Dau=Aoa))	29.9	1925.05/1924.83
4	GnRH-III(^{4}Lys, ^{8}Lys(Dau=Aoa))	28.4	1883.01/1882.50

[a] Column: Vydac C18 (250 mm × 4.6 mm) with 5 μm silica (300 Å pore size); gradient: 0 min 0% B, 5 min 0% B, 50 min 90% B; eluents: 0.1% TFA in water (A) and 0.1% TFA in acetonitrile−water (80:20, v/v) (B); flow rate: 1 mL/min; detection = 280 nm. [b] Bruker Daltonics Esquire 3000 + ion trap mass spectrometer.

very efficient in the case of colorectal cancer. In order to be orally administered, the peptide based drugs must possess increased stability in the presence of digestive enzymes present in the stomach and intestine, such as pepsin, trypsin, and chymotrypsin.

The stability of daunorubicin-GnRH-III derivative bioconjugates in 90% human serum was determined by LC-MS. All bioconjugates were stable in human serum for at least 24 h. LC-MS analysis of the compounds incubated for 24 h at 37 °C with human serum revealed the presence of intact compounds and did not result in the identification of degradation products. ESI-ion trap mass spectra averaged over the chromatographic window where compounds **2**−**4** eluted are shown in the Supporting Information, Figure S5. The stability in human serum of bioconjugate **1** which contains the native GnRH-III sequence has previously been reported.[24]

The degradation of the bioconjugates in the presence of rat liver lysosomal homogenate was also investigated by LC-MS. As shown in Figure 1 and Supporting Information Table S1, all daunorubicin-GnRH-III derivative bioconjugates were degraded in the presence of lysosomal homogenate, resulting in the formation of various peptide fragments (all cleavage sites were located within the GnRH-III derivative sequences). The ESI-mass spectra recorded after 4 and 24 h of incubation of the bioconjugates **2**−**4** with the lysosomal homogenate are shown in the Supporting Information, Figure S6 (the detailed analysis of bioconjugate **1** has previously been reported[24]). In all cases, the smallest drug-containing fragment was H-Lys(Dau=Aoa)-OH, indicating that no cleavage of the isopeptide bond occurred in the presence of lysosomal enzymes. Furthermore, no free daunorubicin could be detected by LC-MS analyses even if the samples were incubated with the lysosomal homogenate for 24 h. We have shown that the H-Lys(Dau=Aoa)-OH fragment detected in the mass spectra at m/z 729.5 (1+) was able to bind to DNA;[24] this is an important feature for the antitumor activity of the bioconjugates.

All bioconjugates showed high stability in the presence of pepsin even after 24 h of incubation, as no proteolytic fragments were identified by LC-MS. UV chromatograms and ESI-ion trap mass spectra are shown in the Supporting Information Figure S7. In the presence of trypsin, only bioconjugates **1**−**3** were stable (see Supporting Information Figure S8), whereas the GnRH-III(^{4}Lys, ^{8}Lys(Dau=Aoa)) was rapidly digested. After 5 min incubation with trypsin, fragments corresponding to the cleavage of the -^{4}Lys-^{5}His- peptide bond were detected by LC-MS. The cleavage was complete after 2 h, as no intact bioconjugate could be identified in the reaction mixture. Only the H-HDWK-(Dau=Aoa)PG-NH_2 tryptic fragment was detected by mass spectrometry (m/z 1321.2 (1+) and 661.6 (2+) — Supporting Information Figure S9). Trypsin is a serine protease known to specifically cleave peptide bonds between basic amino acid residues such as Lys and Arg and another amino acid. In the case of Dau-GnRH-III derivative bioconjugates, trypsin cleaved the peptide bond after the unmodified ^{4}Lys, but not after the modified ^{4}Lys and ^{8}Lys. Tryptic digestion of the bioconjugates could be prevented by the modification of the ε-amino group of lysine residues, either by acetylation or by attachment of daunorubicin.

In the presence of chymotrypsin, the -^{3}Trp-^{4}Xxx- peptide bond was cleaved in all four bioconjugates, the rate of degradation being strongly dependent on the structure of the compounds. As shown in the UV chromatograms depicted in Supporting Information Figure S10A, GnRH-III(^{4}Ser, ^{8}Lys(Dau=Aoa)) was degraded quite rapidly by chymotrypsin at an enzyme to substrate ratio of 1:50. After 2 h, approximately 60% of the bioconjugate was degraded and the degradation was almost complete after 6 h (only 8% of the compound was not cleaved). Mass spectrometric analysis of the reaction mixtures led to the identification of -^{3}Trp-^{4}Ser- cleavage site (the fragment H-SHDWK(Dau=Aoa)PG-NH_2 was detected at m/z 1407.9 (1+) and 704.8 (2+); see Supporting Information Figure S11).

The replacement of ^{4}Ser by *N-Me*-Ser provided increased stability of the bioconjugate against chymotryptic digestion. Even after 24 h, only 37% of the bioconjugate was degraded. The -^{3}Trp-*N-Me*-^{4}Ser- cleavage site was identified by mass spectrometry (H-(*N-Me*)SHDWK(Dau=Aoa)PG-NH_2 fragment detected at m/z 1421.9 (1+) and 711.8 (2+); Supporting Information Figures S10B and S12). Mutation of ^{4}Ser by Lys(Ac) led to an increased stability of the bioconjugate against chymotryptic degradation. Compared to the GnRH-III(^{4}Ser, ^{8}Lys(Dau=Aoa)), which was almost completely degraded after 6 h in the case of GnRH-III(^{4}Lys(Ac), ^{8}Lys(Dau=Aoa)), only 67% degradation was achieved after 6 h incubation time. The compound was completely degraded after 24 h, as only the H-K(Ac)HDWK-(Dau=Aoa)PG-NH_2 fragment was detected by mass spectrometry at m/z 1490.9 (1+) and 746.3 (2+) (Supporting Information Figures S10C and S13).

GnRH-III(^{4}Lys, ^{8}Lys(Dau=Aoa)) showed the quickest degradation in the presence of chymotrypsin. After 1 h, approximately 62% of bioconjugate was degraded, and after 4 h, the degradation was complete. After 4 h, only the H-KHDWK(Dau=Aoa)PG-NH_2 fragment was detected by mass spectrometry at m/z 1429.6 (1+) and 725.7 (2+) (Supporting Information Figures S6D and S14).

For all compounds, the cleavage by chymotrypsin occurred exclusively between ^{3}Trp and ^{4}Xxx. The increased stability of compound **3** seemed to correlate with the hydrophobicity of the ^{4}Lys modification. In compound **4**, the ε-amino group of ^{4}Lys

Table 2. *In Vitro* Cytostatic Effect of Daunorubicin-GnRH-III Derivative Bioconjugates on Various Human Cancer Cell Lines

	cytostasis (MCF-7)	cytostasis (HT-29)	cytostasis (LNCaP)
compound	IC_{50} (μM)	IC_{50} (μM)	IC_{50} (μM)
1, GnRH-III(^{4}Ser, ^{8}Lys(Dau=Aoa))	6.5 ± 1.8	27.8 ± 4.2	6.1 ± 2.1
2, GnRH-III(*N-Me*-^{4}Ser, ^{8}Lys(Dau=Aoa))	10.6 ± 2.1	>50	14.1 ± 1.3
3, GnRH-III(^{4}Lys(Ac), ^{8}Lys(Dau=Aoa))	3.1 ± 1.7	7.4 ± 2.6	3.6 ± 1.9
4, GnRH-III(^{4}Lys, ^{8}Lys(Dau=Aoa))	2.6 ± 0.8	8.1 ± 2.6	5.1 ± 0.4

was free, whereas it was acetylated in compound **3**. Interestingly, only the -^{3}Trp-^{4}Lys- peptide bond was cleaved by chymotrypsin, whereas the bond between ^{7}Trp and ^{8}Lys remained intact. Considering that both peptide bonds should have the same overall structure, the adjacent ^{2}His residue might facilitate the chymotryptic digestion by its ability to transfer protons.

Taking into consideration the stability of the bioconjugates in the presence of digestive enzymes, we can conclude that the *N-Me*-^{4}Ser and ^{4}Lys(Ac) containing bioconjugates might be good candidates for oral administration. Moreover, these findings can be used for the design of further optimized anticancer drug-GnRH-III derivative bioconjugates.

Secondary Structure Determination by Circular Dichroism Spectroscopy. To investigate whether the modification of GnRH-III in position 4 has an influence on the secondary structure of the bioconjugates, circular dichroism (CD) spectra were recorded in water. All CD spectra were characterized by a strong negative band around 200 nm and a positive band at 230 nm, indicating an unordered conformation (Supporting Information Figure S15). A negative band around 285 nm, most probably caused by interactions between aromatic residues (Trp and daunorubicin), was also present in all spectra.[28] The secondary structure of the bioconjugates was not influenced by the replacement of ^{4}Ser by Lys or Lys(Ac). However, the replacement of Ser by *N-Me*-Ser led to slight conformational changes. In the CD spectrum, an additional negative shoulder at around 215 nm was present, being characteristic for a more structured compound.

Cytostatic Effect of the Bioconjugates. The *in vitro* cytostatic effect of the bioconjugates was determined on MCF-7 human breast, HT-29 human colon, and LNCaP human prostate cancer cell lines by 3-(4,5-dimethylthiazol-2-yl)-2,5-diphenyltetrazolium bromide (MTT) assay. The IC_{50} values determined from the dose−response curves (Table 2) indicated that all investigated bioconjugates had *in vitro* cytostatic effect. The replacement of ^{4}Ser by Lys or Lys(Ac) led to an increased cytostatic effect on all tested human cancer cell lines, whereas the replacement by *N-Me*-Ser resulted in a decreased cytostatic effect. GnRH-III(^{4}Ser, ^{8}Lys(Dau=Aoa)), containing the native GnRH-III sequence, had overall higher IC_{50} values compared to GnRH-III(^{4}Lys(Ac), ^{8}Lys(Dau=Aoa)) and GnRH-III(^{4}Lys, ^{8}Lys(Dau=Aoa)). However, the acetylation of the ε-amino group of ^{4}Lys did not result in an alteration of the cytostatic effect, as there was no significant difference between the IC_{50} values of compounds **3** and **4**. On all three tested human cancer cell lines, the *N-Me*-Ser containing bioconjugate had lower cytostatic effect compared to the other compounds, probably due to some conformational differences that might lead to altered receptor binding and/or intracellular processing of the bioconjugate. All compounds had higher cytostatic effect on MCF-7 and LNCaP than on HT-29 cells. This is in agreement with our previously reported data[24] showing that Dau-GnRH-III bioconjugates had lower antitumor activity on

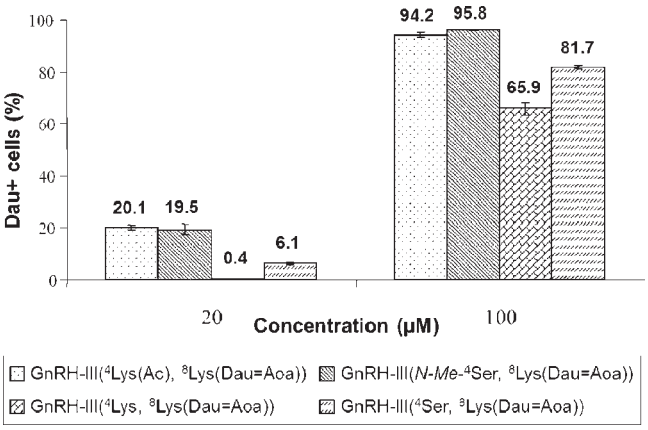

Figure 2. Cellular uptake of daunorubicin-GnRH-III derivative bioconjugates by MCF-7 human breast cancer cells.

HT-29 human colon cancer cell line. Possible explanations of these results might be the higher number of GnRH receptors on MCF-7 cells[20] and/or the different intracellular route of the compounds in HT-29 cells compared to MCF-7 cells.[16]

Taken together, our results indicate that the replacement of ^{4}Ser by Lys (either acetylated or unmodified) in the GnRH-III sequence leads to an increased cytostatic effect of daunorubicin containing bioconjugates.

Cellular Uptake of the Bioconjugates on MCF-7 Human Breast Cancer Cell Line. Cellular uptake of bioconjugates **1**−**4** was investigated by flow cytometry on MCF-7 human breast cancer cells. Taking into account that the compounds were more cytostatic on MCF-7 cells compared to the other investigated cell lines, the MCF-7 cell line was chosen for flow cytometry. Different concentrations between 0.16 and 100 μM were applied. In the lower concentration range (0.16, 0.8, and 4 μM), no significant cellular uptake could be observed. Therefore, the cellular uptake of the compounds was compared only in the case of 20 and 100 μM concentrations. The percentage of daunorubicin positive cells in the case of different bioconjugates is shown in Figure 2. There was no significant difference in the cellular uptake of GnRH-III(^{4}Lys(Ac), ^{8}Lys(Dau=Aoa)) and GnRH-III(*N-Me*-^{4}Ser, ^{8}Lys(Dau=Aoa)), neither at 20 nor at 100 μM. GnRH-III(^{4}Lys, ^{8}Lys(Dau=Aoa)) was taken up less effectively compared to the other compounds: only 0.4% of the cells were daunorubicin positive at 20 μM concentration and 65.9% at 100 μM concentration. The cellular uptake of GnRH-III(^{4}Ser, ^{8}Lys(Dau=Aoa)) was lower compared to GnRH-III(^{4}Lys(Ac), ^{8}Lys(Dau=Aoa)) and GnRH-III(*N-Me*-^{4}Ser, ^{8}Lys(Dau=Aoa)) bioconjugates; however, it could be taken up more effectively than GnRH-III(^{4}Lys, ^{8}Lys(Dau=Aoa)).

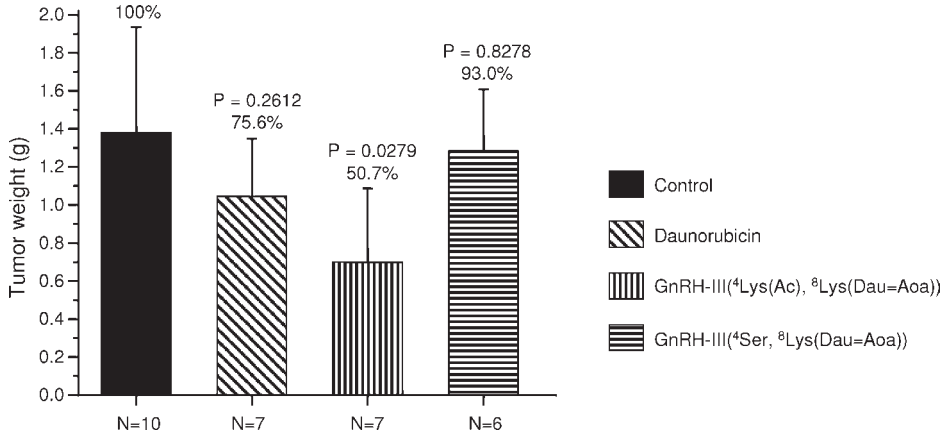

Figure 3. *In vivo* antitumor effect of free daunorubicin and Dau-GnRH-III derivative bioconjugates on C26 murine colon carcinoma bearing Balb/c female mice (mean ± SD, *P* values were calculated by Mann−Whitney test).

The cytostatic effect of all four investigated bioconjugates was comparable on MCF-7 cells, while their cellular uptake properties were different. Surprisingly, the cellular uptake of the most cytostatic bioconjugate, [GnRH-III(^{4}Lys, ^{8}Lys(Dau═Aoa))], was the lowest. This result might be explained by a different intracellular route or degradation pathway in the cells. Our data suggest that, besides the cellular uptake of the compounds, other intracellular processes could play an important role for their antitumor activity.

On the basis of its increased enzymatic stability, cellular uptake, and *in vitro* cytostatic effect, GnRH-III(^{4}Lys(Ac), ^{8}Lys(Dau═Aoa)) was selected for the evaluation of its antitumor activity *in vivo*.

***In Vivo* Antitumor Activity.** The results of previous acute toxicity studies indicated that free daunorubicin at a dose of 2 mg/kg body weight was well tolerated by BDF-1 healthy mice in the case of repeated treatments.[23] However, a higher dose of Dau was toxic.[22,23] Dau-GnRH-III bioconjugates containing an oxime linkage between the drug and the hormone peptide (e.g., GnRH-III(^{4}Ser, ^{8}Lys(Dau═Aoa))) did not exert toxic side effects. When mice were treated 4 times with a dose of 30 mg Dau content in the bioconjugate/kg, the body weight of mice increased similarly to that of the controls and none of the animals died during the experiments.[23] Taking into account that GnRH-III(^{4}Lys(Ac), ^{8}Lys(Dau═Aoa)) differs from GnRH-III(^{4}Ser, ^{8}Lys(Dau═Aoa)) only in position 4 of the peptide sequence (Lys(Ac) instead of Ser) and that the degradation in the presence of lysosomal homogenates results in the same Dau containing metabolite (H-Lys-(Dau═Aoa)-OH),[24] the acute toxicity of GnRH-III(^{4}Lys(Ac), ^{8}Lys(Dau═Aoa)) was not evaluated in the present study.

C26 murine colon carcinoma is an aggressive, fast-growing tumor containing GnRH receptors;[22] therefore, it is a good model for the evaluation of the antitumor activity of Dau-GnRH-III bioconjugates. In our previous work, C26 tumor xenograft was subcutaneously implanted into mice.[22,23] However, this model does not represent the native form of colon cancer. Thus, in the present study, orthotopically developed C26 murine colon carcinoma bearing Balb/c mice were used. A piece of 2 mm^3 C26 murine colon tumor was implanted on the top of the animal intestine. The treatments with free Dau (at a dose of 2 mg/kg), GnRH-III(^{4}Ser, ^{8}Lys(Dau═Aoa)), and GnRH-III(^{4}Lys(Ac), ^{8}Lys(Dau═Aoa)) bioconjugates (at a dose of 15 mg Dau content in bioconjugate/kg) started on day 4 after tumor transplantation and they were repeated on day 7. The experiment was terminated on day 13 because some mice from the control group were in bad physical condition (apathy, no movement, no eating, no drinking, no reaction, etc.) which would lead to their death in the following days (the results of the study would not be relevant in the absence of a suitable control group). This indicates that the orthotopically developed tumors are more aggressive than the s.c. implanted tumors. The results of the tumor growth inhibition study showed that GnRH-III(^{4}Ser, ^{8}Lys(Dau═Aoa)) did not have an inhibitory effect on this tumor model, while it was fairly effective (~30% inhibition) on s.c. C26 colon carcinoma bearing mice.[23] The administration of the free drug resulted in 24.4% tumor growth inhibition, while GnRH-III(^{4}Lys(Ac), ^{8}Lys(Dau═Aoa)) bioconjugate exerted the highest tumor growth inhibitory effect, 49.3% (Figure 3).

CONCLUSIONS

In the present work, gonadotropin releasing hormone-III and its derivatives containing *N-Me*-Ser, Lys, or Lys(Ac) instead of Ser in position 4 were employed as targeting moieties to which daunorubicin was attached via an oxime bond leading to the formation of drug delivery systems for targeted cancer chemotherapy.

All investigated bioconjugates were stable at least for 24 h in human serum, while they were degraded in the presence of rat liver lysosomal homogenate. In all cases, the smallest drug containing fragment identified by LC−MS was H-Lys(Dau═Aoa)-OH. We have previously found that this metabolite was able to bind to DNA, which is an important feature for the antitumor activity of the bioconjugates. However, no free daunorubicin release could be detected. The stability/degradation of the compounds was also investigated in the presence of the three main digestive enzymes of the intestinal tract, namely, trypsin, chymotrypsin, and pepsin. According to the LC-MS analyses of the digestion mixtures, all bioconjugates were stable in the presence of (1) pepsin and (2) trypsin (except for the ^{4}Lys containing compound in which the -^{4}Lys-^{5}His- peptide bond was very rapidly degraded by trypsin). In the presence of α-chymotrypsin, all bioconjugates were digested; the degradation rate strongly depending on their structure. The bioconjugates in which ^{4}Ser was replaced by *N-Me*-Ser or Lys(Ac) had the highest enzymatic stability, making them potential candidates for oral administration.

All bioconjugates had *in vitro* cytostatic effect on MCF-7 human breast, HT-29 human colon, and LNCaP human prostate

cancer cell lines. The replacement of ^{4}Ser by Lys or Lys(Ac) led to an increased cytostatic effect on all tested human cancer cell lines, whereas the replacement by *N-Me*-Ser resulted in a decreased cytostatic effect. However, the *N-Me*-Ser containing compound had the highest stability in the presence of α-chymotrypsin.

The *in vivo* tumor growth inhibitory effect of free daunorubicin and two selected bioconjugates, GnRH-III(^{4}Ser, ^{8}Lys(Dau═Aoa)) and GnRH-III(^{4}Lys(Ac), ^{8}Lys(Dau═Aoa)), was evaluated on orthotopically developed C26 colon carcinoma bearing mice. GnRH-III(^{4}Lys(Ac), ^{8}Lys(Dau═Aoa)) was more effective than the parent bioconjugate (GnRH-III(^{4}Ser, ^{8}Lys(Dau═Aoa)), exerting 49.3% tumor growth inhibition.

When considering all these data, we conclude that the modification of GnRH-III in position 4 can result in promising targeting moieties for the preparation of anticancer drug delivery systems.

■ ASSOCIATED CONTENT

Ⓢ Supporting Information. RP-HPLC profiles and ESI-ion trap mass spectra of the bioconjugates, stability/degradation of the bioconjugates in human serum, in the presence of rat liver lysosomal homogenate and digestive enzymes, circular dichroism spectra. This material is available free of charge via the Internet at http://pubs.acs.org.

■ AUTHOR INFORMATION

Corresponding Author

*Dr. Marilena Manea, University of Konstanz, Zukunftskolleg and Department of Chemistry, Laboratory of Analytical Chemistry and Biopolymer Structure Analysis, Universitätsstrasse 10, 78457 Konstanz, Germany. Phone: (+49)-7531-882285. Fax: (+49)-7531-883097. E-mail: marilena.manea@uni-konstanz.de.

Present Addresses

▽University of Applied Sciences Aachen, Chemisty and Biotechnology, Campus Jülich, 52428 Jülich, Germany.

■ ACKNOWLEDGMENT

This work was supported by grants from the University of Konstanz (Zukunftskolleg, Project 879/08; AFF and Young Scholar Fund, Projects 01/09 and 836/09), the Hungarian National Science Fund (OTKA NK 77485) and GVOP-3.2.1.-2004-04-0005/3.

■ REFERENCES

(1) Kastin, A. J., Coy, D. H., Schally, A. V., and Zadina, J. E. (1980) Dissociation of effects of LH-RH analogs on pituitary regulation and reproductive behavior. *Pharmacol., Biochem. Behav. 13*, 913–914.

(2) Engel, J. B., and Schally, A. V. (2007) Drug Insight: clinical use of agonists and antagonists of luteinizing-hormone-releasing hormone. *Nat. Clin. Pract. Endocrinol. Metab. 3*, 157–167.

(3) Mező, G., and Manea, M. (2009) Luteinizing hormone-releasing hormone antagonists. *Expert Opin. Ther. Pat. 19*, 1771–1785.

(4) Limonta, P., Moretti, R. M., Marelli, M. M., and Motta, M. (2003) The biology of gonadotropin hormone-releasing hormone: role in the control of tumor growth and progression in humans. *Front. Neuroendocrinol. 24*, 279–295.

(5) Schally, A. V., and Nagy, A. (2003) New approaches to treatment of various cancers based on cytotoxic analogs of LHRH, somatostatin and bombesin. *Life Sciences 72*, 2305–2320.

(6) Millar, R. P. (2005) GnRHs and GnRH receptors. *Anim. Reprod. Sci. 88*, 5–28.

(7) López de Maturana, R., Pawson, A. J., Lu, Z. L., Davidson, L., Maudsley, S., Morgan, K., Langdon, S. P., and Millar, R. P. (2008) Gonadotropin-releasing hormone analog structural determinants of selectivity for inhibition of cell growth: support for the concept of ligand-induced selective signaling. *Mol. Endocrinol. 22*, 1711–1722.

(8) Watts, C. R., Mezei, M., Murphy, R. F., and Lovas, S. (2001) Conformational space comparision of GnRH and lGnRH-III using molecular dynamics, cluster analysis and Monte Carlo thermodynamic integration. *J. Biomol. Struct. Dynam. 18*, 733–748.

(9) Turkstra, J. A., Oonk, H. B., Schaaper, W. M. M., and Meloen, R. H. (2002) The role of the individual amino acids of a GnRH-tandem-dimer peptide used as an antigen for immunocastration of male piglets determined with systematic alanine replacements. *Vaccine 20*, 406–412.

(10) Mező, G., Manea, M., Szabó, I., Vincze, B., and Kovács, M. (2008) New derivatives of GnRH as potential anticancer therapeutic agents. *Curr. Med. Chem. 15*, 2366–2379.

(11) Haviv, F., Fitzpatrick, T. D., Nichols, C. J., Swenson, R. E., Bush, E. N., Diaz, G., Nguyen, A., Nellans, H. N., Hoffman, D. J., Ghanbari, H., Johnson, E. S., Love, S., Cybulski, V., and Greer, J. (1992) Stabilization of the N-terminal residues of luteinizing hormone-releasing hormone agonists and the effect on pharmacokinetics. *J. Med. Chem. 35*, 3890–3894.

(12) Pappa, E. V., Zompra, A. A., Spyranti, Z., Diamantopoulou, Z., Pairas, G., Lamari, F. N., Katsoris, P., Spyroulias, G. A., and Cordopatis, P. (2011) Enzymatic stability, solution structure, and antiproliferative effect on prostate cancer cells of leuprolide and new GnRH peptide analogs. *Biopolymers (Pept. Sci.) 96*, 260–272.

(13) Sower, S. A., Chiang, Y.-C., Lovas, S., and Conlon, J. M. (1993) Primary structure and biological activity of a third gonadotropin-releasing hormone from lamprey brain. *Endocrinology 132*, 1125–1131.

(14) Kovács, M., Seprődi, J., Koppán, M., Horváth, J. E., Vincze, B., Teplán, I., and Flerkó, B. (2002) Lamprey gonadotropin hormone-releasing hormone-III has no selective follicle-stimulating hormone-releasing effect in rats. *J. Neuroendocrinol. 14*, 647–655.

(15) Lovas, S., Pályi, I., Vincze, B., Horváth, J., Kovács, M., Mező, I., Tóth, G., Teplán, I., and Murphy, R. F. (1998) Direct anticancer activity of gonadotropin-releasing hormone-III. *J. Pept. Res. 52*, 384–389.

(16) Herédi-Szabó, K., Murphy, R. F., and Lovas, S. (2006) Is lGnRH-III the most potent GnRH analog containing only natural amino acids that specifically inhibits the growth of human breast cancer cells. *J. Pept. Sci. 12*, 714–720.

(17) Mező, I., Lovas, S., Pályi, I., Vincze, B., Kálnai, A., Turi, G., Vadász, Zs., Seprődi, J., Idei, M., Tóth, G., Gulyás, É., Ötvös, F., Mák, M., Horváth, J. E., Teplán, I., and Murphy, R. F. (1997) Synthesis of gonadotropin-releasing hormone III analogs. Structure−antitumor activity relationships. *J. Med. Chem. 40*, 3353–3358.

(18) Herédi-Szabó, K., Lubke, J., Tóth, G., Murphy, R. F., and Lovas, S. (2005) Importance of the central region of lamprey gonadotropin-releasing hormone III in the inhibition of breast cancer cell growth. *Peptides 26*, 419–422.

(19) Pályi, I., Vincze, B., Lovas, S., Mező, I., Pató, J., Kálnai, A., Turi, G., Gaál, D., Mihalik, R., Péter, I., Teplán, I., and Murphy, R. F. (1999) Gonadotropin-releasing hormone analogue conjugates with strong selective antitumor activity. *Proc. Natl. Acad. Sci. U. S. A. 96*, 2361–2366.

(20) Mező, G., Czajlik, A., Manea, M., Jakab, A., Farkas, V., Majer, Zs., Vass, E., Bodor, A., Kapuvári, B., Boldizsár, M., Vincze, B., Csuka, O., Kovács, M., Przybylski, M., Perczel, A., and Hudecz, F. (2007) Structure, enzymatic stability and antitumor activity of sea lamprey GnRH-III and its dimer derivatives. *Peptides 28*, 806–820.

(21) Kovács, M., Vincze, B., Horváth, J. E., and Seprődi, J. (2007) Structure-activity study on the LH- and FSH-releasing and anticancer effects of gonadotropin-releasing hormone (GnRH)-III analogs. *Peptides 28*, 821–829.

(22) Szabó, I., Manea, M., Orbán, E., Csámpai, A., Bősze, S., Szabó, R., Tejeda, M., Gaál, D., Kapuvári, B., Przybylski, M., Hudecz, F., and Mező, G. (2009) Development of an oxime bond containing daunorubicin-gonadotropin-releasing hormone-III conjugate as a potential anticancer drug. *Bioconjugate Chem. 20*, 656–665.

(23) Manea, M., Tóvári, J., Tejeda, M., Schulcz, Á., Kapuvári, B., Vincze, B., and Mező, G. (2011) *In vivo* antitumor effect of daunorubicin − GnRH-III derivative conjugates on colon carcinoma bearing mice. *Anti-Cancer Drugs*, submitted.

(24) Orbán, E., Mező, G., Schlage, P., Csík, G., Kulić, Ž., Ansorge, P., Fellinger, E., Möller, H., and Manea, M. (2011) *In vitro* degradation and antitumor activity of oxime bond-linked daunorubicin-GnRH-III bioconjugates and DNA-binding properties of daunorubicin-amino acid metabolites. *Amino Acids 41*, 469–483.

(25) Mező, G., and Manea, M. (2010) Receptor-mediated tumor targeting based on peptide hormones. *Expert Opin. Drug Delivery 7*, 79–96.

(26) Schally, A. V., and Nagy, A. (2004) Chemotherapy targeted to cancers through tumoral hormone receptors. *Trends Endocrinol. Metab. 15*, 300–310.

(27) Sleno, L., Campagna-Slater, V., and Volmer, D. A. (2006) Dissociation reactions of protonated anthracycline antibiotics following electrospray ionization-tandem mass spectrometry. *Int. J. Mass Spectrom. 255−256*, 130–138.

(28) Gasymov, O. K., Abduragimov, A. R., and Glasgow, B. J. (2008) Site-directed circular dichroism of proteins: 1Lb bands of Trp resolve position-specific features in tear lipocalin. *Anal. Biochem. 374*, 386–395.

Bioconjugate Chemistry

Supporting Information

Enhanced enzymatic stability and antitumor activity of daunorubicin-GnRH-III bioconjugates modified in position 4

Marilena Manea[§,†,*], Ulrike Leurs[§], Erika Orbán[‡], Zsuzsa Baranyai[‡], Peter Öhlschläger[⊥,~], Andreas Marquardt[∫], Ákos Schulcz[#], Miguel Tejeda[#], Bence Kapuvári[#], József Tóvári[#] and Gábor Mező[‡]

[§]Laboratory of Analytical Chemistry and Biopolymer Structure Analysis, Department of Chemistry, University of Konstanz, 78457 Konstanz, Germany

[†]Zukunftskolleg, University of Konstanz, 78457 Konstanz, Germany

[‡]Research Group of Peptide Chemistry, Hungarian Academy of Sciences, Eötvös Loránd University, 1117 Budapest, Hungary

[⊥]Laboratory of Immunology, Department of Biology, University of Konstanz, 78457 Konstanz, Germany

[∫]Proteomics-Facility, University of Konstanz, 78457 Konstanz, Germany

[#]National Institute of Oncology, 1122 Budapest, Hungary

[~]Present address: University of Applied Sciences Aachen, Chemisty and Biotechnology, Campus Jülich, 52428 Jülich, Germany

[*]Correspondence to:

Dr. Marilena Manea

University of Konstanz, Zukunftskolleg and Department of Chemistry, Laboratory of Analytical Chemistry and Biopolymer Structure Analysis, Universitätsstrasse 10, 78457 Konstanz, Germany; Phone: (+49)-7531-882285; Fax: (+49)-7531-883097

E-mail: marilena.manea@uni-konstanz.de

Table of Contents

RP-HPLC profile and ESI-ion trap mass spectrum of GnRH-III(^{4}Ser, ^{8}Lys(Dau=Aoa)) 3

RP-HPLC profile and ESI-ion trap mass spectrum of GnRH-III(*N-Me*-^{4}Ser, ^{8}Lys(Dau=Aoa)) 3

RP-HPLC profile and ESI-ion trap mass spectrum of GnRH-III(^{4}Lys(Ac), ^{8}Lys(Dau=Aoa)) 4

RP-HPLC profile and ESI-ion trap mass spectrum of GnRH-III(^{4}Lys, ^{8}Lys(Dau=Aoa)) 4

Stability of bioconjugates **2** – **4** in human serum (24 h reaction time) 5

Degradation of bioconjugates **2** – **4** in rat liver lysosomal homogenate 6

Degradation of bioconjugates in the presence of pepsin (24 h reaction time) 7-8

Degradation of bioconjugates **1** - **3** in the presence of trypsin (24 h reaction time) 9-10

Degradation of bioconjugate **4** in the presence of trypsin (5 min and 2 h reaction time) 11

Degradation of bioconjugates by α-chymotrypsin 12

Degradation of GnRH-III(^{4}Ser, ^{8}Lys(Dau=Aoa)) in the presence of chymotrypsin 13

Degradation of GnRH-III(*N-Me*-^{4}Ser, ^{8}Lys(Dau=Aoa)) in the presence of chymotrypsin 13

Degradation of GnRH-III(^{4}Lys(Ac), ^{8}Lys(Dau=Aoa)) in the presence of chymotrypsin 14

Degradation of GnRH-III(^{4}Lys, ^{8}Lys(Dau=Aoa)) in the presence of chymotrypsin 14

Circular dichroism spectra of daunorubicin-GnRH-III derivative bioconjugates 15

Fragments produced by the cleavage of daunorubicin-GnRH-III derivative bioconjugates 16

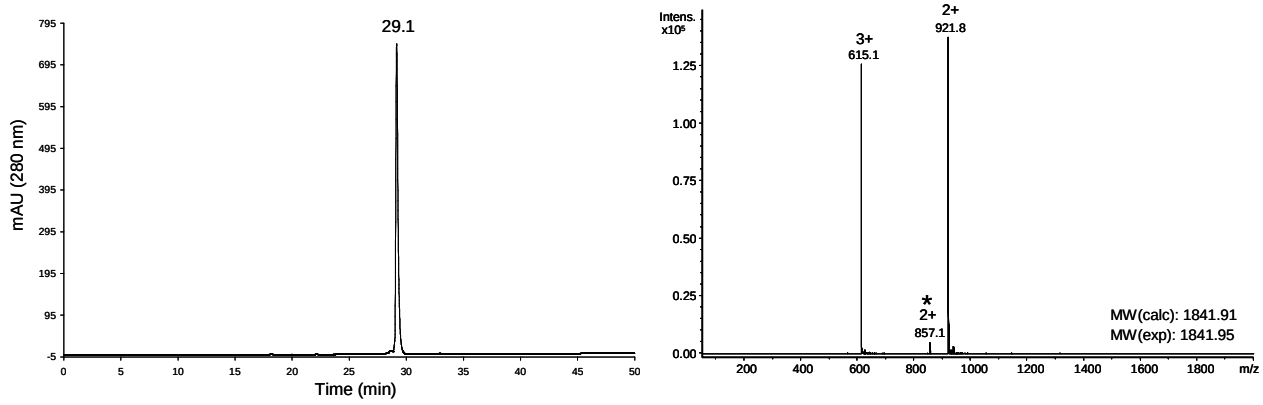

Figure S1. RP-HPLC profile and ESI-ion trap mass spectrum of GnRH-III(^{4}Ser, ^{8}Lys(Dau=Aoa)).

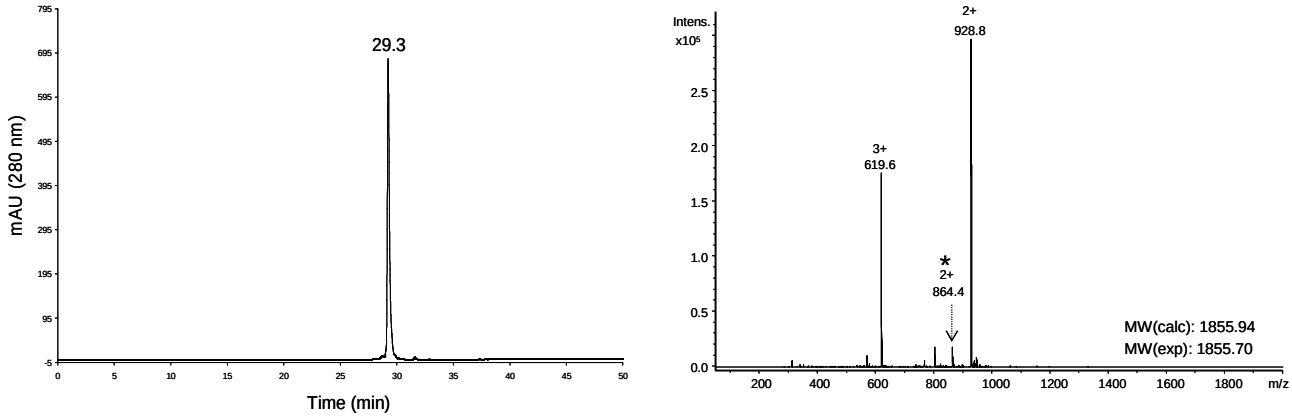

Figure S2. RP-HPLC profile and ESI-ion trap mass spectrum of GnRH-III(*N-Me*-^{4}Ser,^{8}Lys(Dau=Aoa))

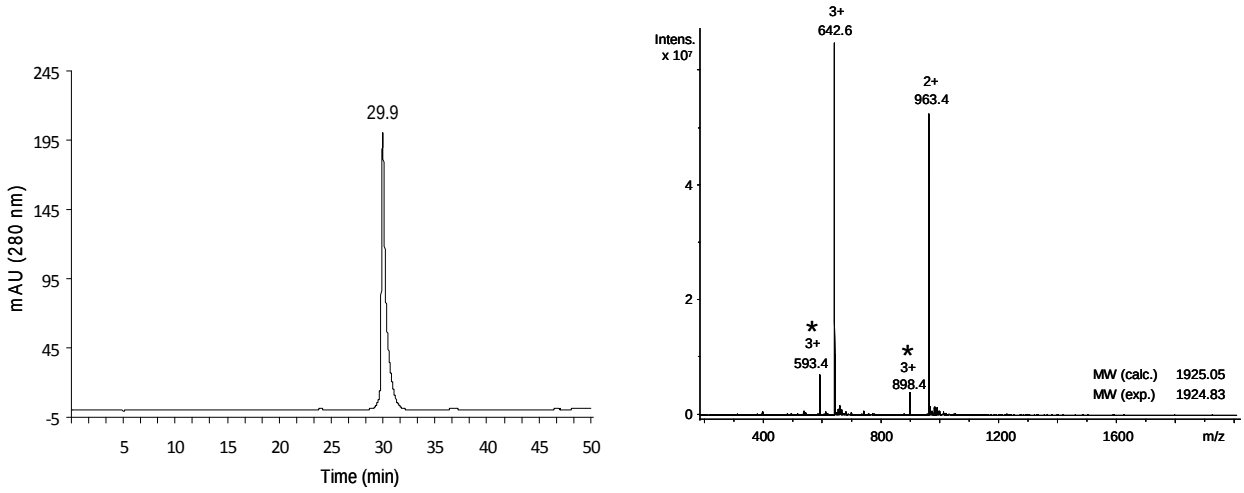

Figure S3. RP-HPLC profile and ESI-ion trap mass spectrum of GnRH-III(^{4}Lys(Ac), ^{8}Lys(Dau=Aoa))

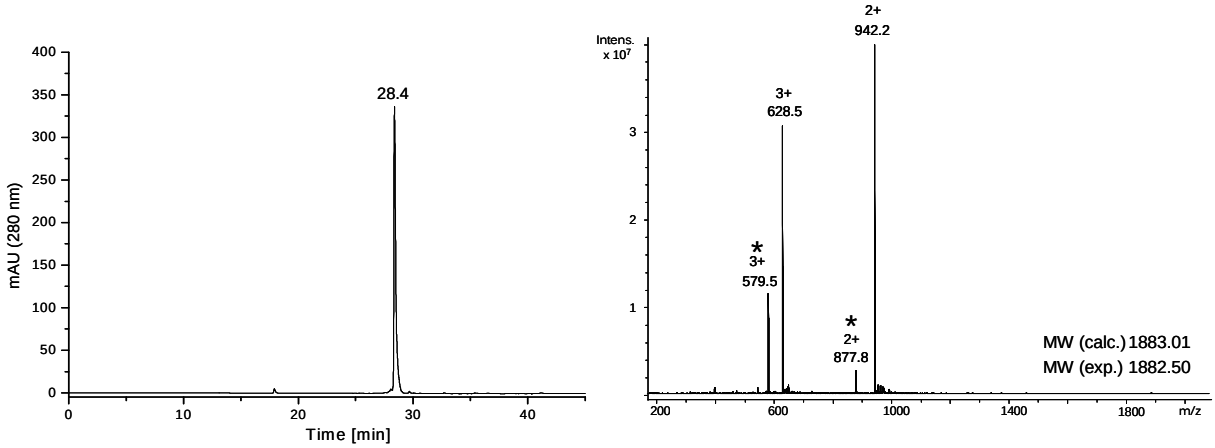

Figure S4. RP-HPLC profile and ESI-ion trap mass spectrum of GnRH-III(^{4}Lys, ^{8}Lys(Dau=Aoa))

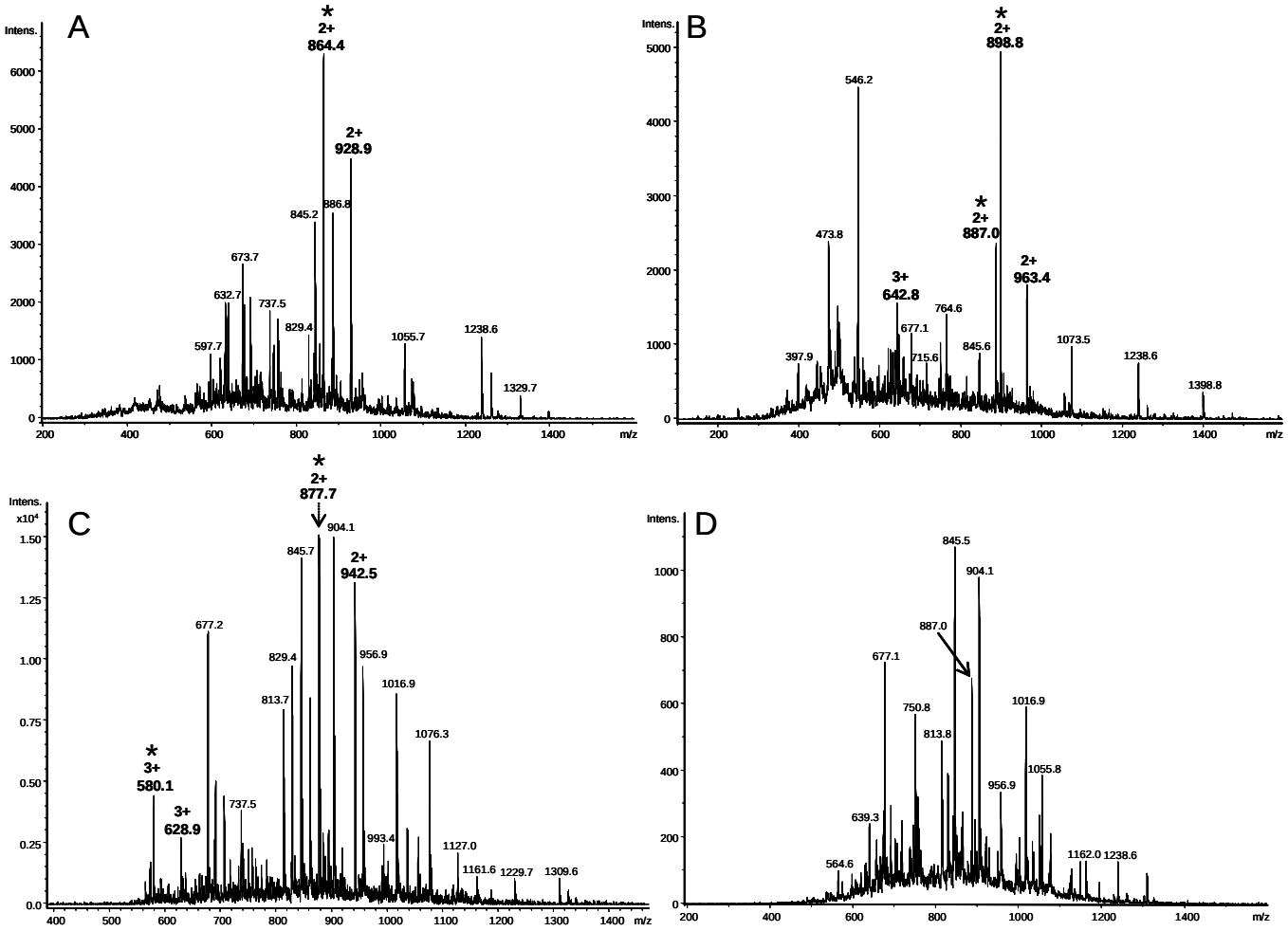

Figure S5. Stability of bioconjugates in human serum. ESI-ion trap mass spectra were recorded after incubating the bioconjugates in 90% human serum for 24 hours at 37°C. Spectra were averaged over the chromatographic window where the compounds eluted. The m/z values corresponding to the intact bioconjugates are marked bold. LC-MS analysis of the human serum prepared similarly to the bioconjugate samples was also performed.

(A) GnRH-III(*N-Me*-^{4}Ser, ^{8}Lys(Dau=Aoa))

(B) GnRH-III(^{4}Lys(Ac), ^{8}Lys(Dau=Aoa))

(C) GnRH-III(^{4}Lys, ^{8}Lys(Dau=Aoa))

(D) human serum

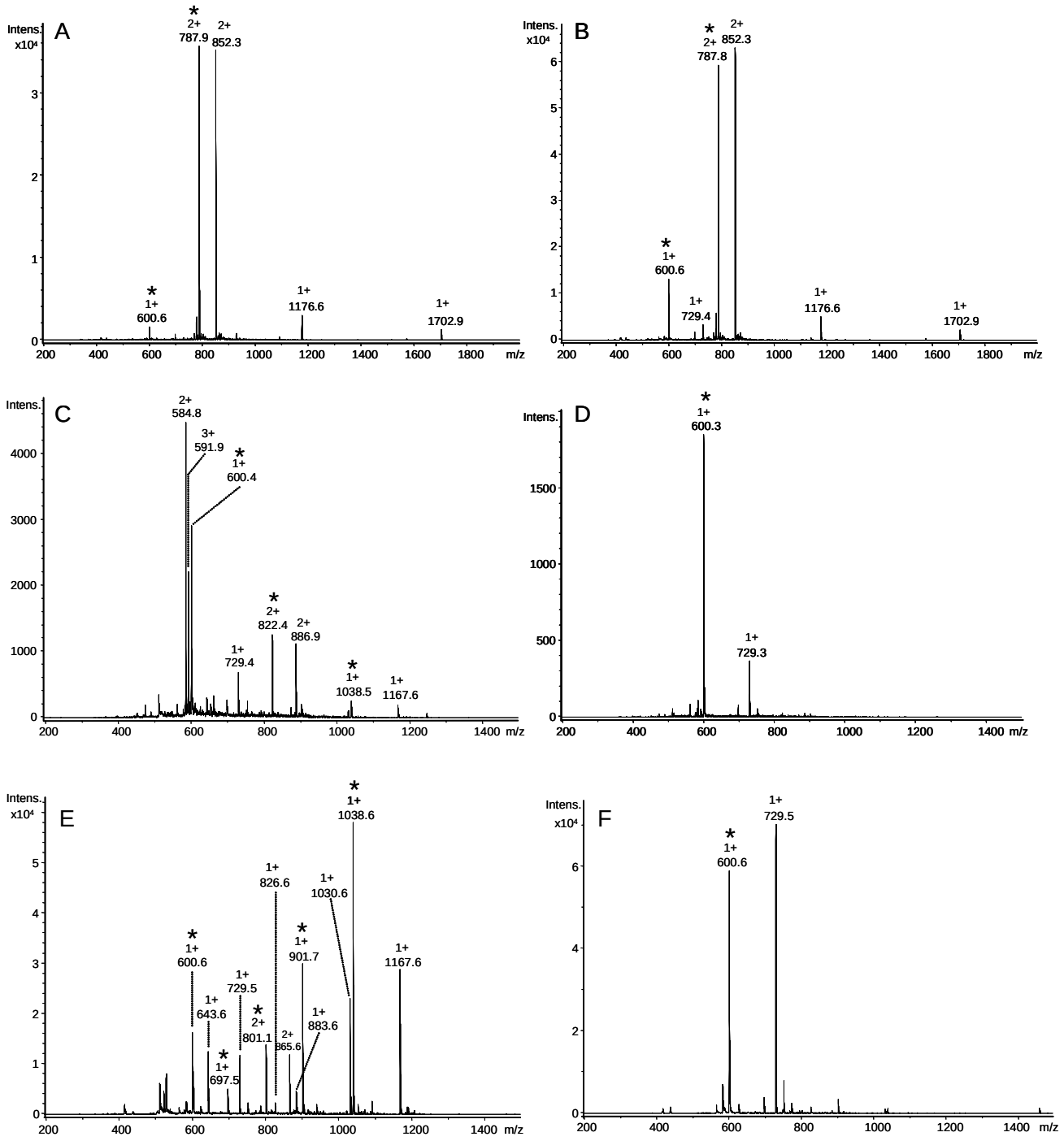

Figure S6. Degradation of bioconjugates **2 - 4** in the presence of rat liver lysosomal homogenate. ESI-ion trap mass spectra were recorded after incubating the bioconjugates with the rat liver lysosomal homogenate (1:1 ratio, w/w) at 37°C for 4 hours (A, C and E) and 24 h (B, D, F). Spectra were averaged over the chromatographic window where the compounds eluted.

(A) and (B) GnRH-III(*N-Me*-^{4}Ser, ^{8}Lys(Dau=Aoa))

(C) and (D) GnRH-III(^{4}Lys(Ac), ^{8}Lys(Dau=Aoa))

(E) and (F) GnRH-III(^{4}Lys, ^{8}Lys(Dau=Aoa))

A

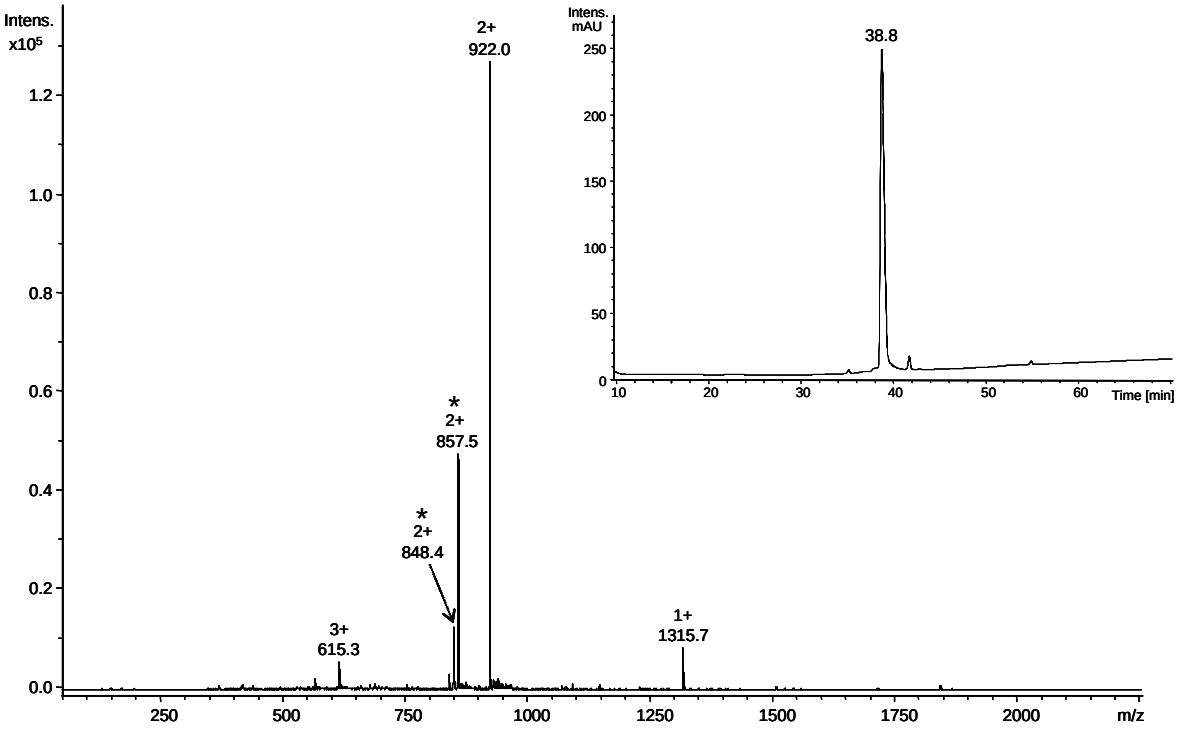
Intens.
x10^5
1.2
1.0
0.8
0.6
0.4
0.2
0.0
2+
922.0
*
2+
857.5
*
2+
848.4
3+
615.3
1+
1315.7
250
500
750
1000
1250
1500
1750
2000
m/z
Intens.
mAU
250
200
150
100
50
0
38.8
10
20
30
40
50
60
Time [min]

B

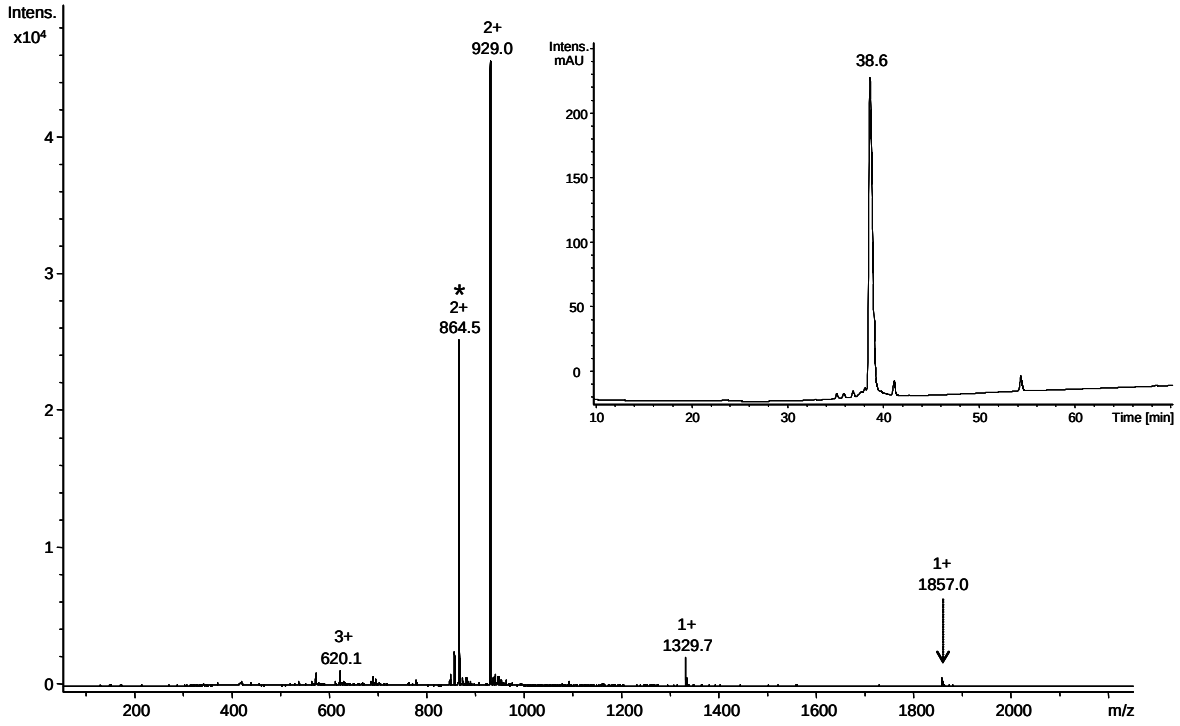
Intens.
x10^4
4
3
2
1
0
2+
929.0
*
2+
864.5
3+
620.1
1+
1329.7
1+
1857.0
200
400
600
800
1000
1200
1400
1600
1800
2000
m/z
Intens.
mAU
200
150
100
50
0
38.6
10
20
30
40
50
60
Time [min]

C

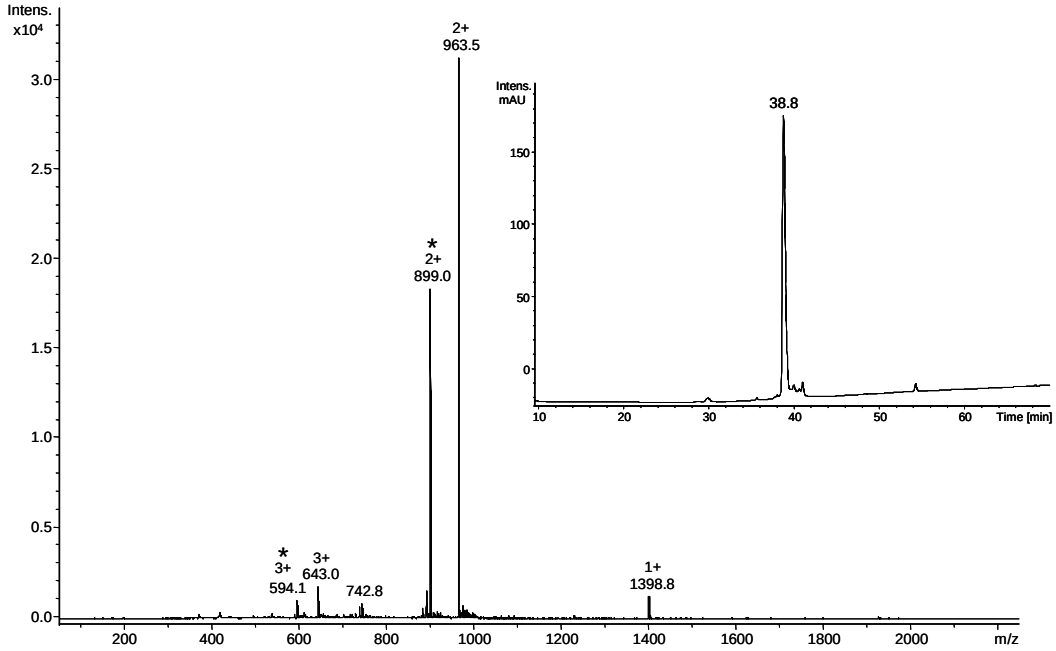

D

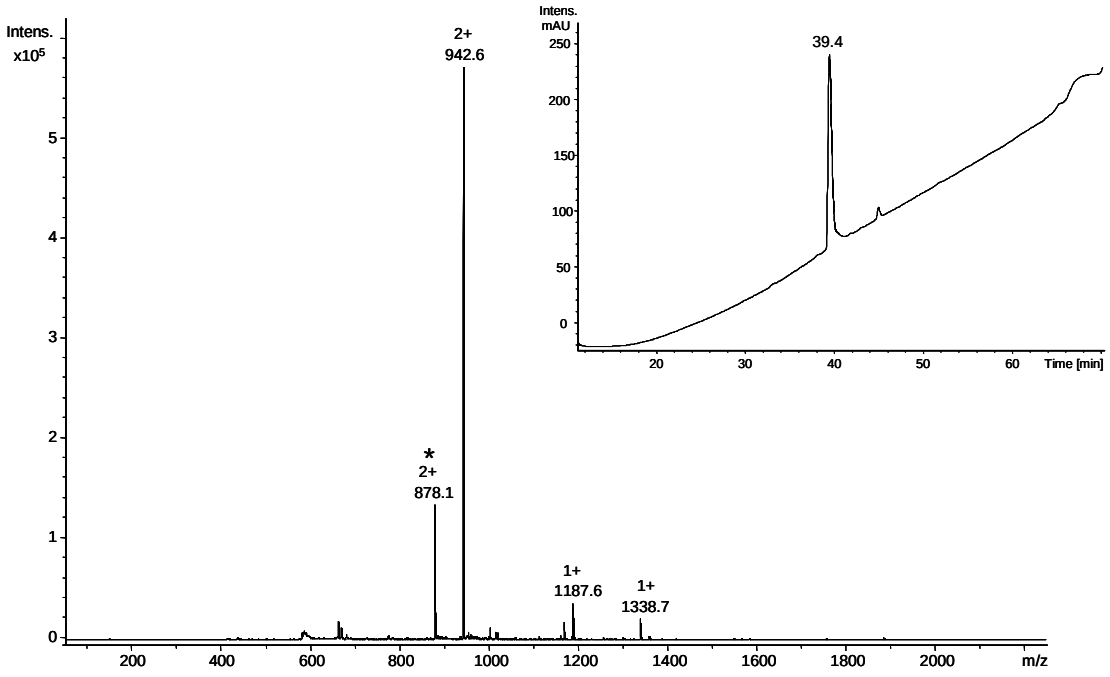

Figure S7. Degradation of bioconjugates in the presence of pepsin (E : S = 1: 50 w/w; 24 h incubation time at 37°C). UV chromatograms and ESI-ion trap mass spectra averaged over the chromatographic window where the compounds eluted are shown: (A) GnRH-III(^{4}Ser, ^{8}Lys(Dau=Aoa)), (B) GnRH-III(*N-Me*-^{4}Ser, ^{8}Lys(Dau=Aoa)), (C) GnRH-III(^{4}Lys(Ac), ^{8}Lys(Dau=Aoa)), (D) GnRH-III(^{4}Lys, ^{8}Lys(Dau=Aoa)).

A

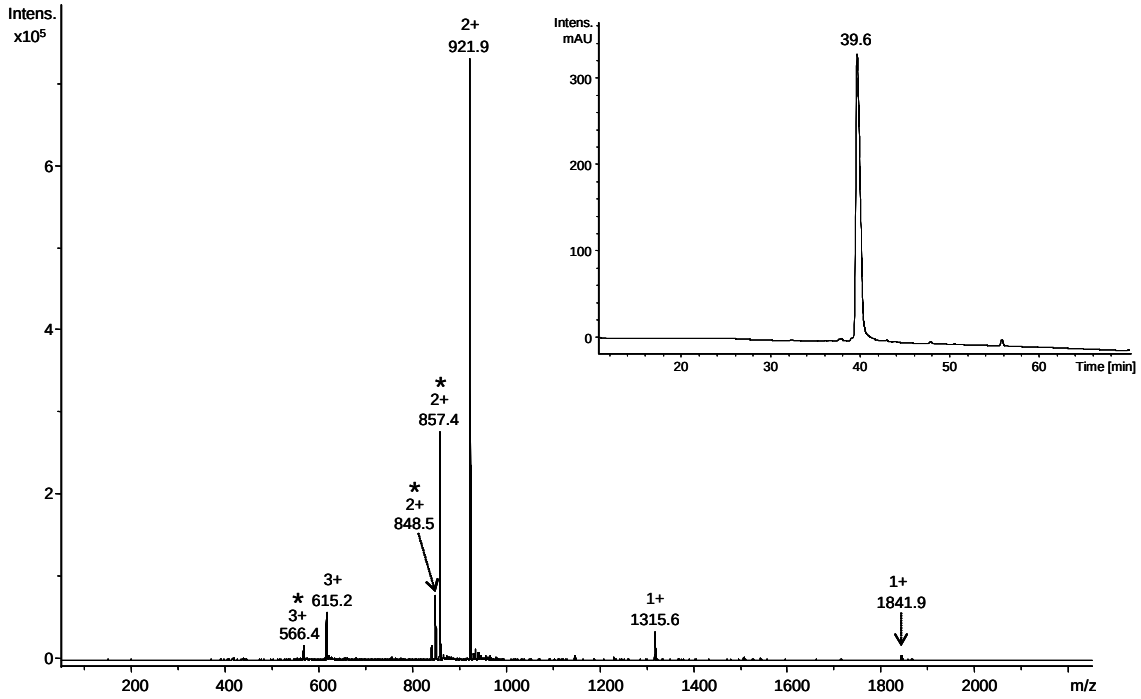
Intens.
x10^5
2+
921.9
Intens.
mAU
39.6
Time [min]
*
2+
857.4
*
2+
848.5
3+
615.2
*
3+
566.4
1+
1315.6
1+
1841.9
m/z

B

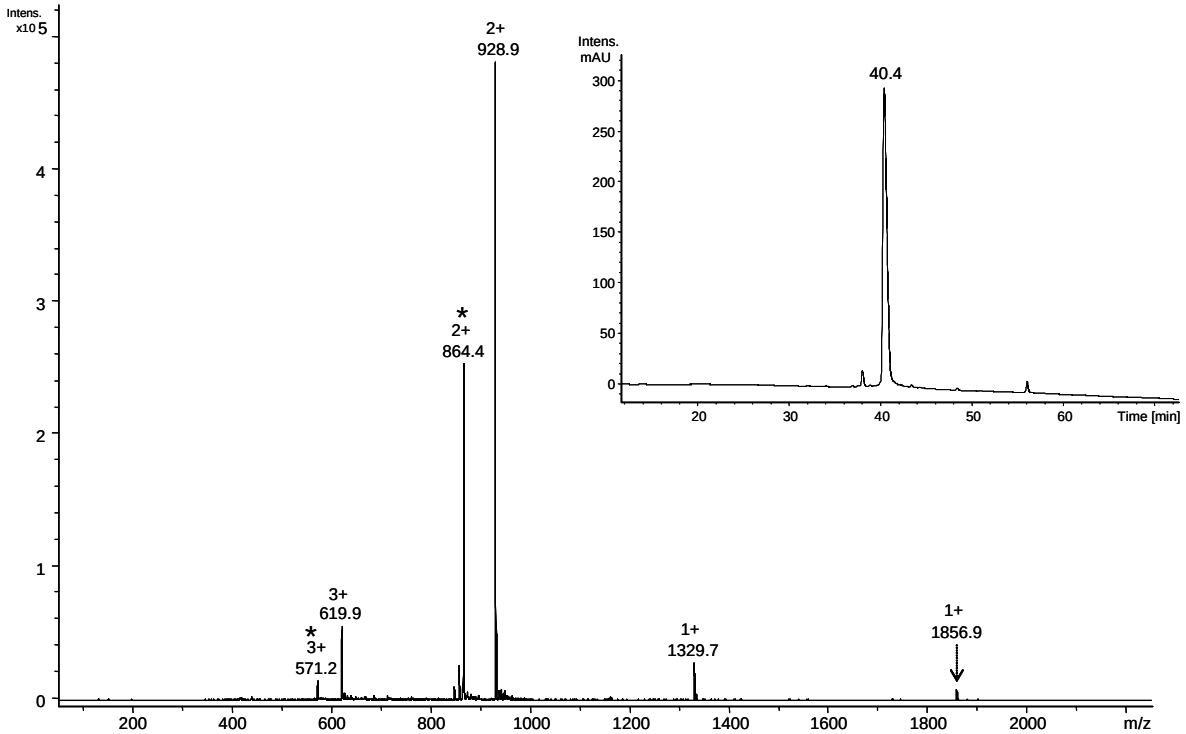
Intens.
x10^5
2+
928.9
Intens.
mAU
40.4
Time [min]
*
2+
864.4
3+
619.9
*
3+
571.2
1+
1329.7
1+
1856.9
m/z

C

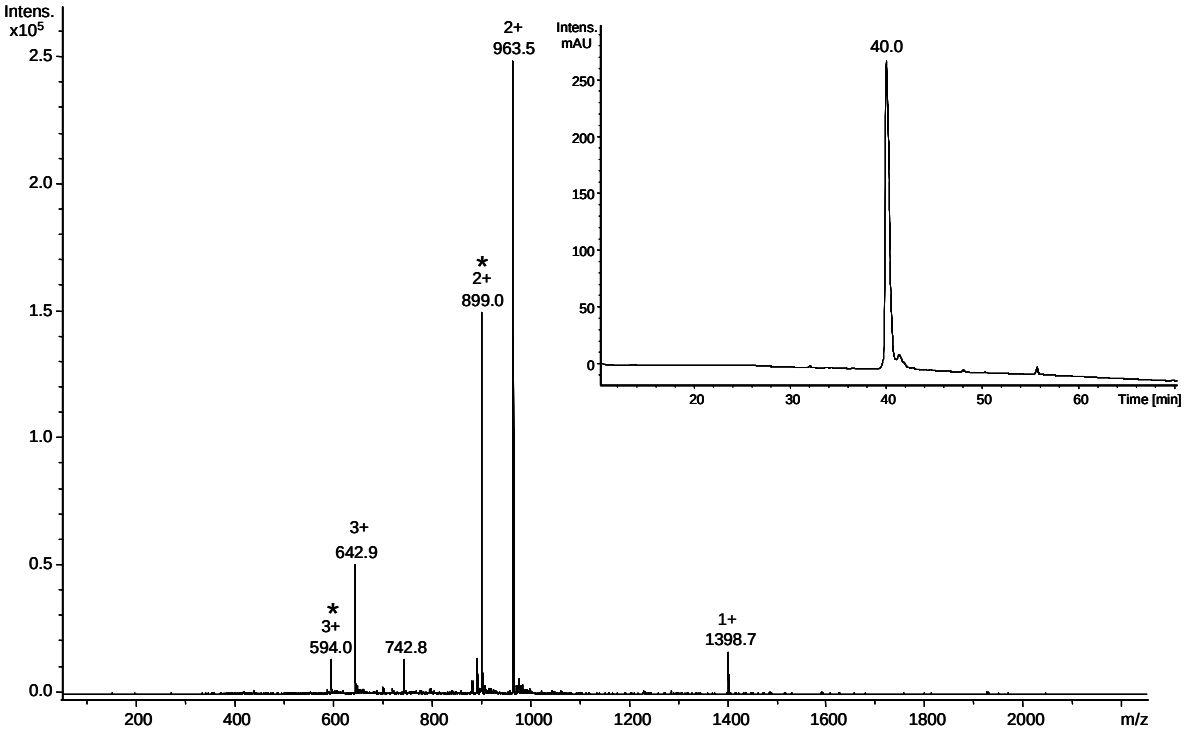

Figure S8. Degradation of bioconjugates **1** – **3** in the presence of trypsin (E : S = 1: 50, w/w; 24 h incubation time at 37°C). UV chromatograms and ESI-ion trap mass spectra averaged over the chromatographic window where the compounds eluted are shown:

(A) GnRH-III(^{4}Ser, ^{8}Lys(Dau=Aoa))

(B) GnRH-III(*N*-*Me*-^{4}Ser, ^{8}Lys(Dau=Aoa))

(C) GnRH-III(^{4}Lys(Ac), ^{8}Lys(Dau=Aoa)).

A

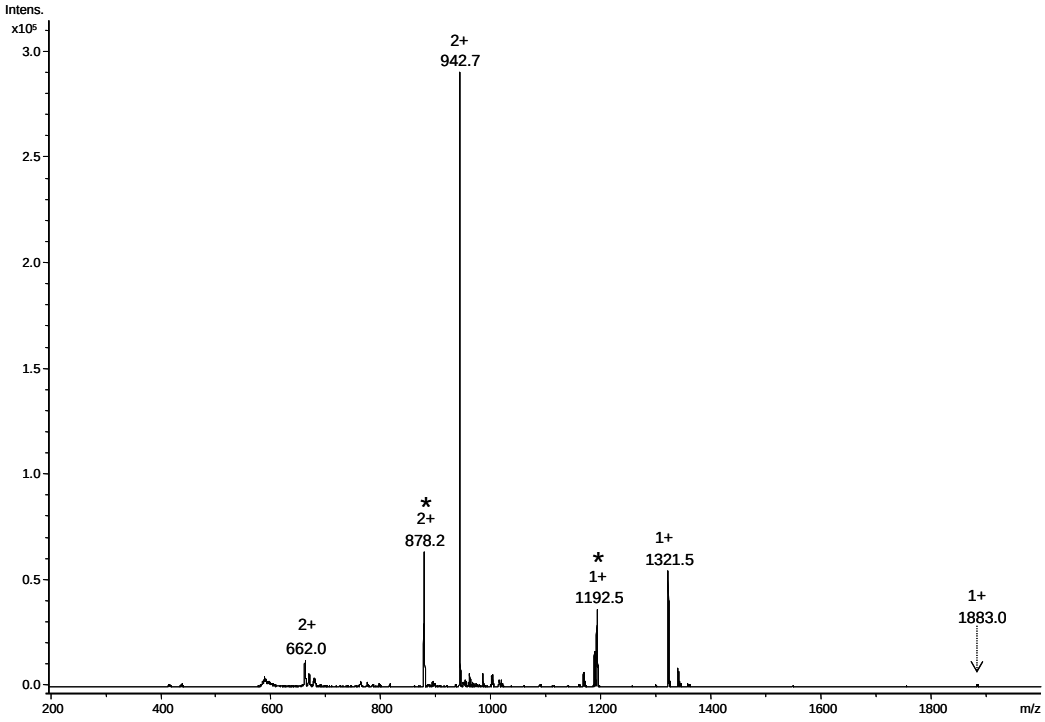

B

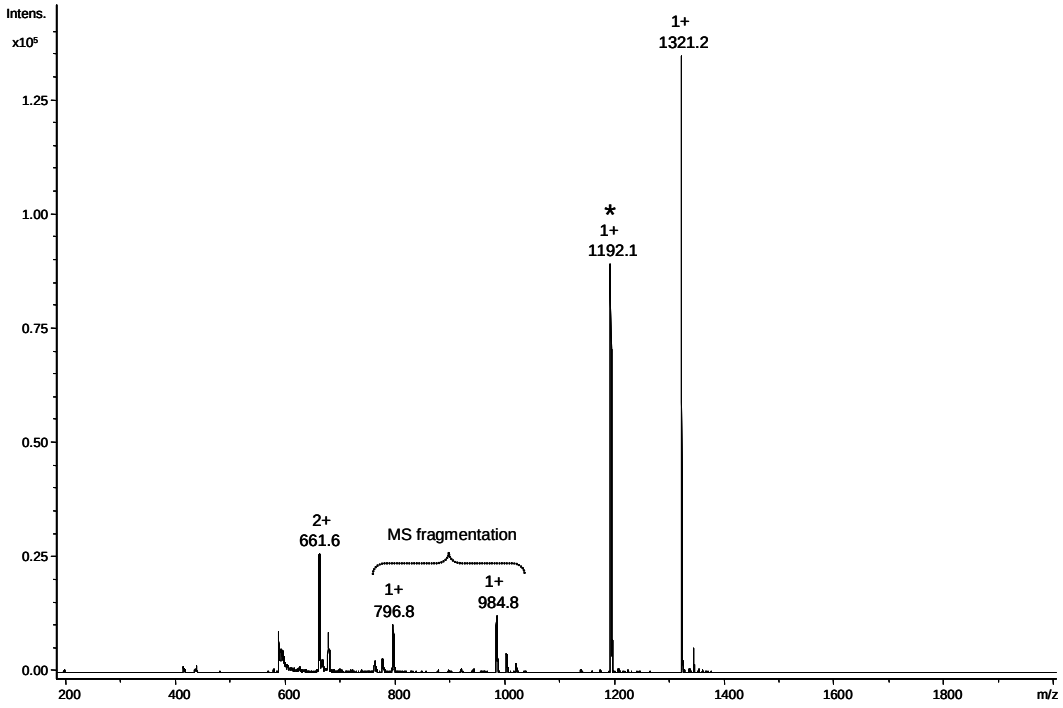

Figure S9. Degradation of bioconjugate **4** in the presence of trypsin. ESI-ion trap mass spectra averaged over the chromatographic window where the compounds eluted are shown: (A) 5 min and (B) 2 h reaction time.

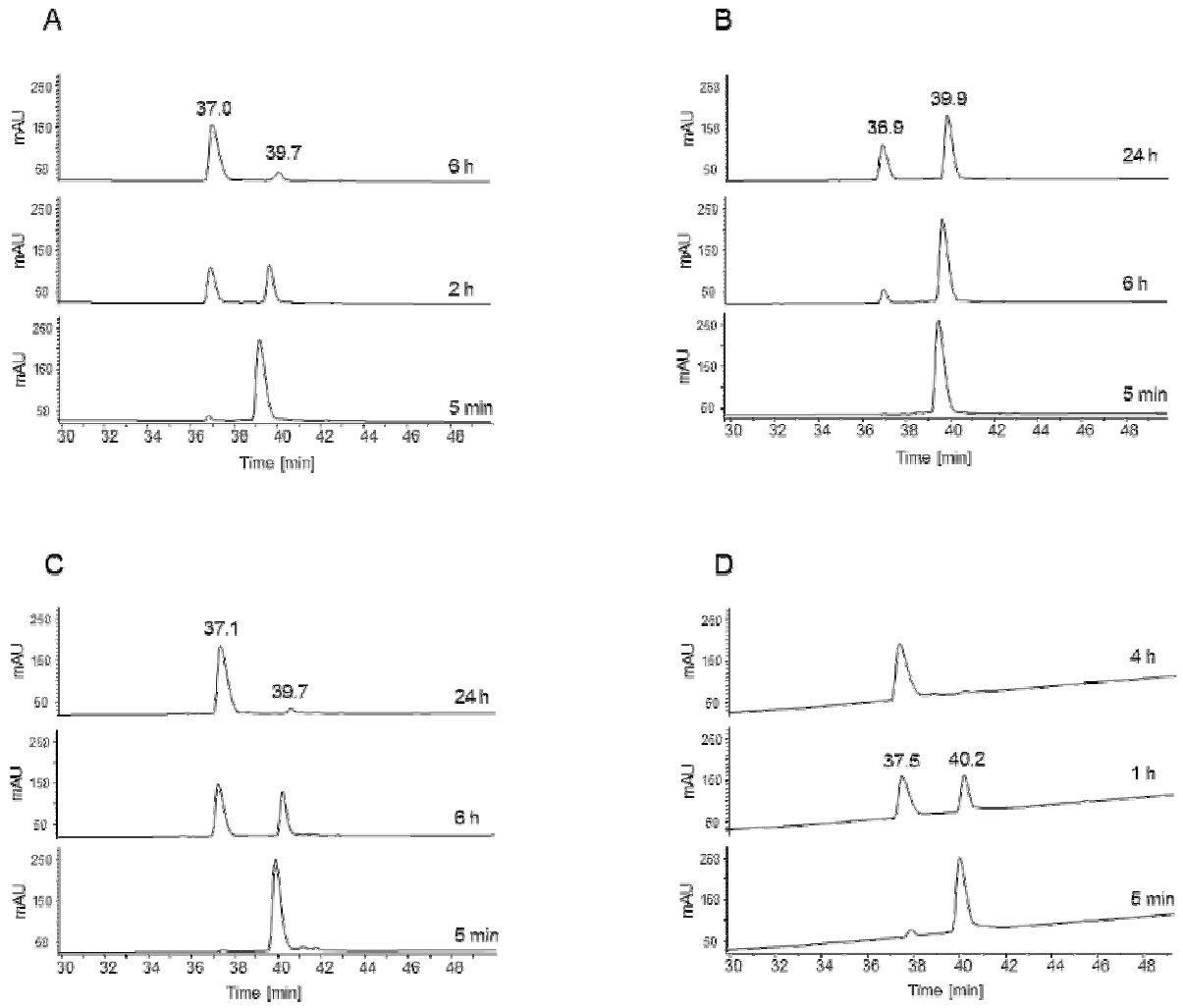

Figure S10. Degradation of bioconjugates by α-chymotrypsin: (A) GnRH-III(^{4}Ser, ^{8}Lys(Dau=Aoa)), (B) GnRH-III(*N-Me*-^{4}Ser, ^{8}Lys(Dau=Aoa)), (C) GnRH-III(^{4}Lys(Ac), ^{8}Lys(Dau=Aoa)) and (D) GnRH-III(^{4}Lys, ^{8}Lys(Dau=Aoa)).

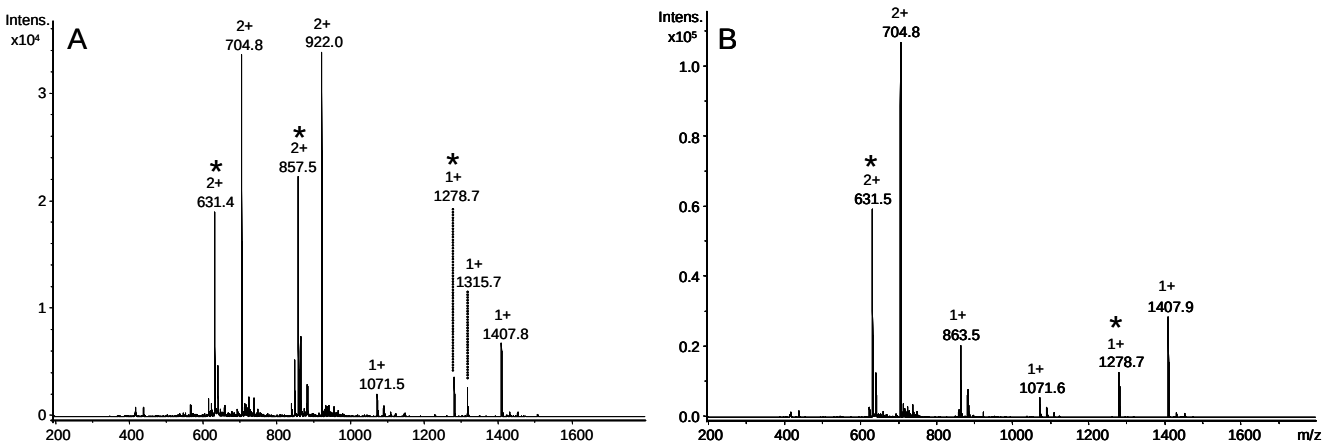

Figure S11. Degradation of GnRH-III(^{4}Ser, ^{8}Lys(Dau=Aoa)) in the presence of chymotrypsin. ESI-ion trap mass spectra averaged over the chromatographic window where the compounds eluted are shown: (A) 2 h and (B) 6 h reaction time.

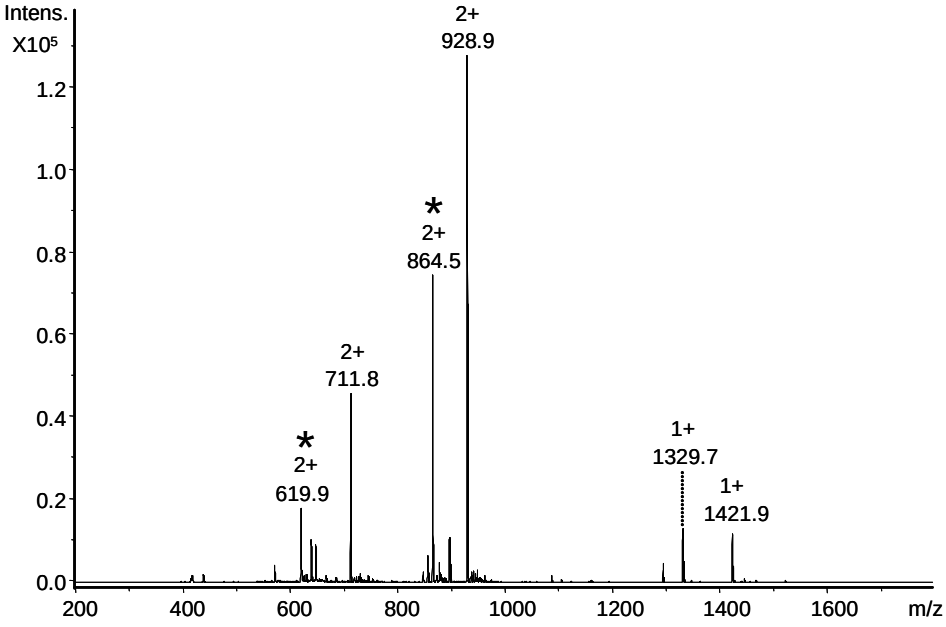

Figure S12. Degradation of GnRH-III(*N-Me*-^{4}Ser, ^{8}Lys(Dau=Aoa)) in the presence of chymotrypsin – 24 h incubation time. ESI-ion trap mass spectrum averaged over the chromatographic window where the compounds eluted is shown.

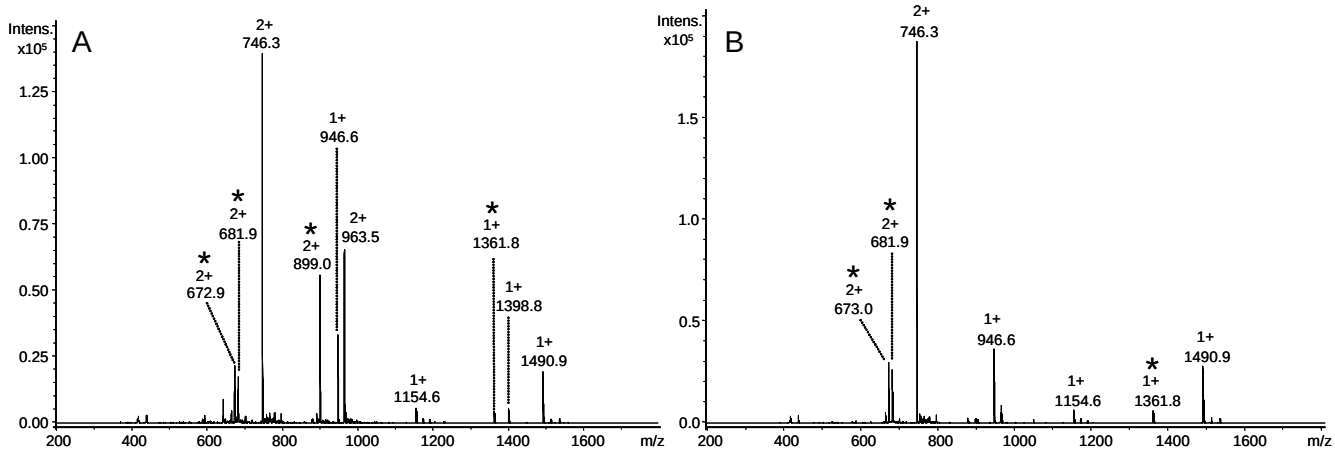

Figure S13. Degradation of GnRH-III(^{4}Lys(Ac), ^{8}Lys(Dau=Aoa)) in the presence of chymotrypsin. ESI-ion trap mass spectra averaged over the chromatographic window where the compounds eluted are shown: (A) 6 h and (B) 24 h reaction time.

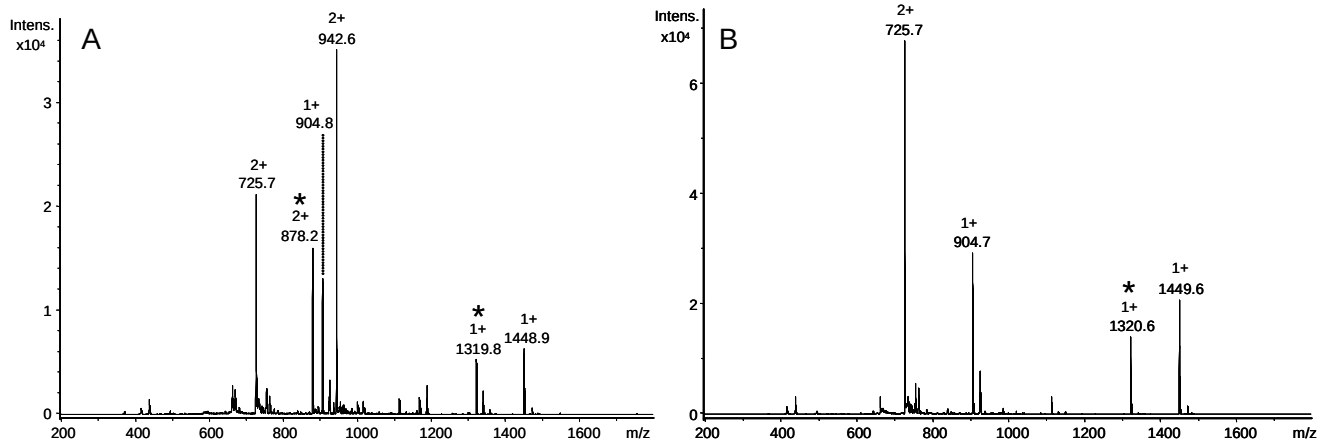

Figure S14. Degradation of GnRH-III(^{4}Lys, ^{8}Lys(Dau=Aoa)) in the presence of chymotrypsin. ESI-ion trap mass spectra averaged over the chromatographic window where the compounds eluted are shown: (A) 1 h and (B) 4 h reaction time.

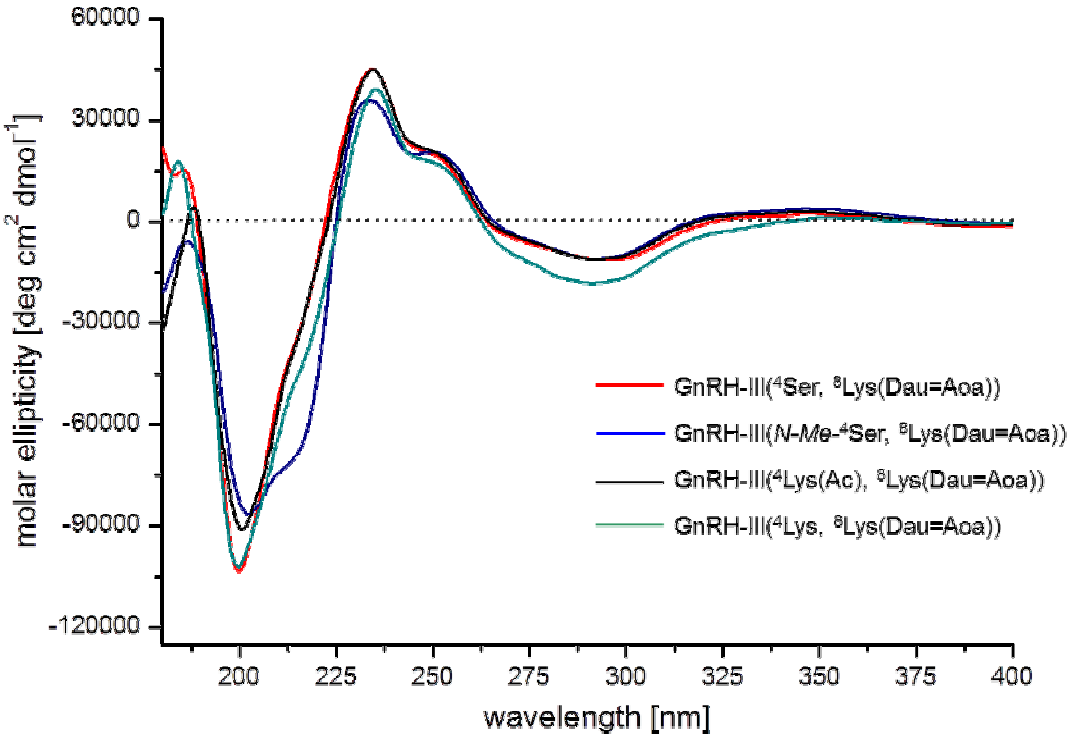

Figure S15. Circular dichroism spectra of daunorubicin-GnRH-III derivative bioconjugates recorded in water.

Table S1 Fragments produced by the cleavage of daunorubicin-GnRH-III derivative bioconjugates in the presence of rat liver lysosomal homogenate, chymotrypsin and trypsin

Compound	Fragment	MW_{calc} / MW_{exp}
1 GnRH-III(^{4}Ser, ^{8}Lys(Dau=Aoa))	H-SHDWK(Dau=Aoa)PG-NH_2	1407.46 / 1406.80
2 GnRH-III(*N-Me*-^{4}Ser,^{8}Lys(Dau=Aoa))	<EHW(N-Me)SHDWK(Dau=Aoa)PG-NH_2 <EHW(N-Me)SHDWK(Dau=Aoa)-OH H-(N-Me)SHDWK(Dau=Aoa)PG-NH_2 H-DWK(Dau=Aoa)-OH H-K(Dau=Aoa)P-OH H-K(Dau=Aoa)-OH	1855.94 / 1856.12 1702.76 / 1702.25 1421.49 / 1421.20 1029.40 / 1029.60 825.34 / 825.40 728.29 / 728.40
3 GnRH-III(^{4}Lys(Ac), ^{8}Lys(Dau=Aoa))	<EHWKHDWK(Dau=Aoa)PG-NH_2 <EHWKHDWK(Dau=Aoa)-OH H-KHDWK(Dau=Aoa)PG-NH_2 H-HDWK(Dau=Aoa)PG-NH_2 H-HDWK(Dau=Aoa)-OH H-DWK(Dau=Aoa)-OH H-K(Dau=Aoa)PG-NH_2 H-K(Dau=Aoa)P-OH H-K(Dau=Aoa)-OH	1883.01 / 1883.00 1729.82 / 1729.80 1448.55 / 1449.00 1319.55 / 1319.70 1166.46 / 1166.60 1029.40 / 1029.60 881.94 / 882.60 825.34 / 825.50 728.29 / 728.50
4 GnRH-III(^{4}Lys, ^{8}Lys(Dau=Aoa))	<EHWKHDWK(Dau=Aoa)PG-NH_2 <EHWKHDWK(Dau=Aoa)-OH H-KHDWK(Dau=Aoa)PG-NH_2 H-HDWK(Dau=Aoa)PG-NH_2 H-HDWK(Dau=Aoa)-OH H-DWK(Dau=Aoa)-OH H-K(Dau=Aoa)PG-NH_2 H-K(Dau=Aoa)P-OH H-K(Dau=Aoa)-OH	1883.01 / 1883.00 1729.82 / 1729.80 1448.55 / 1449.00 1319.55 / 1319.70 1166.46 / 1166.60 1029.40 / 1029.60 881.94 / 882.60 825.34 / 825.50 728.29 / 728.50

Bioconjugate Chemistry

ARTICLE

pubs.acs.org/bc

Rapid Identification of Fluorochrome Modification Sites in Proteins by LC ESI-Q-TOF Mass Spectrometry

Prakash Manikwar,[†] Tahl Zimmerman,[§] Francisco J. Blanco,[§,∥] Todd D. Williams,[‡] and Teruna J. Siahaan*[,†]

[†]Department of Pharmaceutical Chemistry, University of Kansas, Lawrence, Kansas 66047, United States

[§]Unidad de Biología Estructural, CIC bioGUNE, 48160 Derio, Bizkaia, Spain

[∥]IKERBASQUE, Basque Foundation for Science, 48011 Bilbao, Spain

[‡]Mass Spectrometry Laboratory, University of Kansas, Lawrence, Kansas 66045, United States

Supporting Information

ABSTRACT: Conjugation of either a fluorescent dye or a drug molecule to the ε-amino groups of lysine residues of proteins has many applications in biology and medicine. However, this type of conjugation produces a heterogeneous population of protein conjugates. Because conjugation of fluorochrome or drug molecule to a protein may have deleterious effects on protein function, the identification of conjugation sites is necessary. Unfortunately, the identification process can be time-consuming and laborious; therefore, there is a need to develop a rapid and reliable way to determine the conjugation sites of the fluorescent label or drug molecule. In this study, the sites of conjugation of fluorescein-5′-isothiocyanate and rhodamine-B-isothiocyanate to free amino groups on the insert-domain (I-domain) protein derived from the α-subunit of lymphocyte function-associated antigen-1 (LFA-1) were determined by electrospray ionization quadrupole time-of-flight mass spectrometry (ESI-Q-TOF MS) along with peptide mapping using trypsin digestion. A reporter fragment of the fluorochrome moiety that is generated in the collision cell of the Q-TOF without explicit MS/MS precursor selection was used to identify the conjugation site. Selected ion plots of the reporter ion readily mark modified peptides in chromatograms of the complex digest. Interrogation of theses spectra reveals a neutral loss/precursor pair that identifies the modified peptide. The results show that one to seven fluorescein molecules or one to four rhodamine molecules were attached to the lysine residue(s) of the I-domain protein. No modifications were found in the metal ion-dependent adhesion site (MIDAS), which is an important binding region of the I-domain.

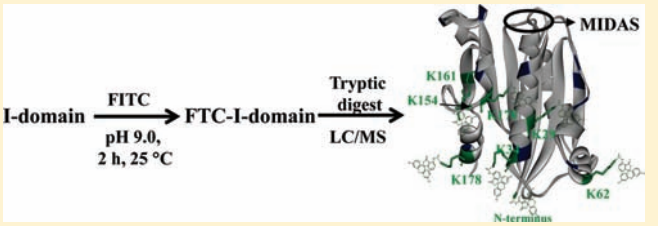

INTRODUCTION

Proteins (e.g., antibodies) have been modified with fluorochromes with high quantum yields such as fluorescein-5′-isothiocyanate (FITC) or rhodamine-B-isothiocyanate (RITC) to maximize the detection sensitivity in binding assay or cell imaging.[1] The isothiocyanate group on the fluorescent dye is reacted with the primary amines and thiol groups of proteins to yield thiourea or dithiourethane adducts.[2] Frequently, the reaction product is a heterogeneous mixture of conjugates with different number of fluorochromes attached to the protein. It may be worthwhile to determine the modification sites because the conjugation of fluorochrome on the protein-binding site may alter protein affinity to its receptors. Unfortunately, this task can be challenging and laborious because of sample heterogeneity and low abundance of the modified residues. In this study, a rapid and reliable method was evaluated to determine the site(s) of conjugation of FITC and RITC groups on the insert-domain (I-domain) protein derived from the α-subunit of lymphocyte function-associated antigen-1 (LFA-1) receptor.

T-cell adhesion to vascular endothelial cell is mediated by LFA-1 and intercellular adhesion molecule-1 (ICAM-1) interactions via the I-domain of LFA-1 to the domain-1 (D1) of ICAM-1. I-domain interacts via the metal ion-dependent adhesion site (MIDAS) to a glutamate residue of D1 of ICAM-1.[3−5] In autoimmune diseases such as multiple sclerosis,[6−8] rheumatoid arthritis,[9] type 1 diabetes,[10] and lupus,[11] the cell surface expression of ICAM-1 is upregulated on different types of cells. Thus, there is a possibility of conjugating drug molecules to the I-domain protein. The resulting drug-I-domain conjugate can be used to target cells with upregulated ICAM-1 expression to lower the side effects of the drugs. To evaluate the utility of the I-domain for targeting the upregulated ICAM-1, the I-domain was conjugated with FITC and RITC at lysine residues and the N-terminus (Figure 1 and Supporting Information Figure S2) to produce the FTC- and RTC-I-domains, respectively. FTC- and RTC-I-domains have been shown to bind ICAM-1 and are also transported into the intracellular space of leukocytes. Because the I-domain has 20 lysine residues and modification of certain lysine residues could influence the binding and cellular uptake of I-domain conjugates, it is important to determine the sites of

Received: December 9, 2010
Revised: May 18, 2011
Published: May 26, 2011

ACS Publications © 2011 American Chemical Society

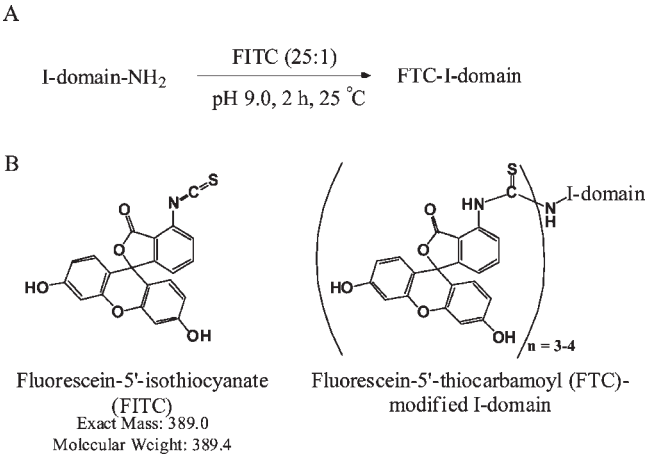

Figure 1. (A) Schematic representation of a single-step modification of I-domain protein with FITC. (B) Illustration of chemical structures of FITC and FTC-I-domain.

modification on the I-domain. The conjugation reaction was optimized to introduce an average of 3−4 fluorescein molecules per I-domain molecule or 2−3 rhodamine molecules per I-domain molecule.

A combination of tryptic digestion and mass spectrometry was used to identify the conjugation sites of the fluorophores because it is a sensitive and flexible method for the characterization of modified peptides. The thiocarbamoyl modification of proteins has been detected by mass spectrometry since the early use of soft ionization such as thermospray, or chemical ionization, to detect phenyl thiohydantoin (PTH) derivatives of amino acids, the result of phenyl isothiocyanate (PTC) coupling to amines.[12] While the focus of this early work was differentiating among the amino acids in the classic Edman degradation, the spectra also presented a "reporter ion" of the modifying group. The related reporter ion from isothiocyanate (ITC) dyes is readily generated in an electrospray ionization source with cone fragmentation or in the collision cell of quadrupole time-of-flight (ESI-Q-TOF) instrument. A strategy of using fragmentation in the collision cell of a Q-TOF without explicit MS/MS has been exploited in the fatty acid analysis of complex lipids[13] and provides the fundamental data used in so-called MSE, or high and low energy offsets of the collision cell on alternation scan cycles by WATERS for proteomics.[14] This data acquisition strategy for generating fragmentation information has expanded to metabolite identification[15] and quantitative proteomics.[16] A description of a data reduction algorithm for chromatographic time alignment to determine precursor/fragments relationship in MSE data[17] can be instructive in appreciating a MSE data set.

In this study, we initially employed high and low energy cycles on the collision cell of a Q-TOF, the usual MSE acquisition method, and observed that at a low to intermediate energy a reporter ion for the dye and corresponding neutral loss dominated fragmentation in spectra. The classic uses of reporter ions in structure determination include amino acid indicating from peptides,[18] neutral loss of hexose groups from glycopeptides,[19−21] and phosphate from phosphorylation.[22−25] All these aid rapid identification of modification sites. Previously, Schnaible and Przybylski demonstrated the possibility of the identification of fluorescent dye-modified sites by increasing the declustering potential (so-called "cone" fragmentation) in the electrospray ion (ESI) source to generate a reporter ion from the dye on a peptide.[26] This specific fragmentation was utilized for assigning the fluorescent dye modification sites in peptides obtained from enzymatic digestion of fluorescein-modified hen egg white lysozyme.[6] This work is an adaptation of emerging method of using a Q-TOF for improved information content during LC/MS with an MSE-like approach. We used ESI-Q-TOF MS to readily generate reporter ions in the collision cell of the Q-TOF and, along with LC/MS, expand the earlier observations of Schnaible and Przybylski to assess the fluorochrome distribution and determine the fluorescent dye conjugation sites in the modified I-domain after trypsin digestion.

EXPERIMENTAL PROCEDURES

Materials. FITC isomer I, RITC mixed isomers, solvents, and reagents of highest available purity were purchased from Sigma-Aldrich (St. Louis, MO). Sequence-grade modified trypsin was purchased from Promega (Madison, WI).

Peptide Synthesis and Purification. The model peptides cyclo(1,12)Pen-ITDGEATDSGC (cLABL) and cyclo(1,12)Pen-PRGGSVLVTGC (cIBR) were synthesized as linear peptides by standard Fmoc solid-phase peptide chemistry using the automated peptide synthesis system (Pioneer PerSpective Biosystems, Framingham, MA) as described elsewhere.[27] The sequences of cLABL (ITDGEATDSG) and cIBR (PRGGSVLVTG) peptides were derived from the LFA-1 I-domain and domain-1 (D1) of ICAM-1 proteins, respectively. LFA-1 I-domain serves as a ligand for ICAM-1 receptor. The model peptides also showed that the dye-modified peptides were hydrophobic. The product from synthesis was purified by HPLC followed by cyclization and purification as previously described.[27] The molecular weight of the peptide was confirmed by electrospray ionization mass spectrometry ($M + H^1$ = 1197.3 for cLABL and 1174.5 for cIBR).

Fluorochrome Modification of the Peptides. Conjugation of FITC with cLABL was carried out using the procedure previously published by our laboratory.[28] Briefly, pure peptide (0.04 mmol) was dissolved in 5 mL nanopure water followed by addition of FITC (0.08 mmol). The pH of the solution was adjusted to 10 with a 1.0 N NaOH solution, and it was stirred for 1 h. Then, the reaction mixture was neutralized by the addition of a 10% v/v acetic acid solution followed by lyophilization. The lyophilized crude peptide was then purified by semipreparative C_{18} reversed-phase HPLC. The pure fractions of the peptide were pooled and lyophilized. The lyophilized FITC-peptide was analyzed by analytical C_{18} reversed-phase HPLC for its purity, and its identity was confirmed by ESI-MS ($M + H^1$). Conjugation of rhodamine with cIBR was done in a manner identical to that described above with the exception that FITC was replaced by RITC.

LFA-1 I-Domain Protein Expression and Fluorochrome Modification. The LFA-1 I-domain protein (residues 128−307, with an addition of N-terminal methionine) was expressed, refolded, and purified as previously described.[29] The sequence of the I-domain protein is provided in the Supporting Information (Figure S1). Briefly, the expression vector pET-11d containing the gene of LFA-1 I-domain$_{128-307}$ was used in *E. coli* BL21 (Stratagene, La Jolla, CA) competent cells, where the protein was found in inclusion bodies, which were subsequently solubilized in guanidine-HCl and refolded by dilution.[29] The identity of the pure protein was confirmed by mass spectrometry.

The procedure for conjugation of fluorescent dyes (FITC/RITC) with the I-domain protein was adopted from the previously published method with some modifications.[1] To a total of 6.0 mg of the I-domain in PBS containing 10 mM $MgSO_4$, a one-fourth volume of 1.0 M $NaHCO_3$−Na_2CO_3 buffer at pH 9.0 was added. FITC (5 mg/mL in DMSO) was added to the protein solution to a 25-fold molar excess over the I-domain protein with a final concentration of 1.5 mg/mL. The reaction was carried out for 2 h at 25 °C in the dark with constant stirring. The reaction was quenched with addition of 0.1 N HCl. Separation of the free dye from dye-coupled protein was done using a Superdex 200 size-exclusion column. The fractions belonging to the conjugated protein were collected and concentrated using an ultrafiltration device. The concentrated protein was filtered using a 0.2 μm filter and stored at 4 °C. Modification of I-domain with rhodamine was done in a manner identical to that described above with the exception that a 25-fold molar excess FITC was replaced by a 20-fold molar excess of RITC. The number of FITC or RITC groups conjugated to the I-domain protein was determined by electrospray mass spectrometry.

In-Gel Tryptic Digestion and LC ESI-Q-TOF Mass Spectrometry Analysis. The protein (100 μg) was separated by SDS-PAGE and stained with Coomassie blue. The stained gel spot of interest was excised and cut into smaller pieces for better solvent penetration into the gel. Then, the gel pieces were transferred to a clean microcentrifuge tube, washed twice with a solution containing a 1:1 mixture of acetonitrile and 50 mM ammonium bicarbonate buffer at pH 8.0 for 45 min at 37 °C with gentle agitation. After discarding the washing solution, the gel pieces were shrunk with 250 μL of neat acetonitrile. After 10−15 min, the residual solvent was discarded, and the gel pieces were dried completely. The gel pieces were reswelled with 40 μL of digestion buffer A (0.2 M ammonium bicarbonate buffer at pH 8 and 5 mM $CaCl_2$) containing 2 μg trypsin. Then, 50 μL of the digestion buffer B (0.2 M ammonium bicarbonate buffer at pH 8 and 10% acetonitrile) was added to keep the gel pieces immersed throughout the digestion. The digestion was carried out overnight at 37 °C, and the reaction was stopped by the addition of 0.1% formic acid. The gel pieces were sonicated and the supernatant containing the digested peptides was collected as primary sample fraction and analyzed by LC ESI-Q-TOF MS.

All HPLC separations were performed with a Water Acquity solvent delivery system using a binary gradient of solvent A composed of 98.92:1:0.08 H_2O/acetonitrile/formic acid (vol/vol/vol) and solvent B containing 98.92:1:0.08 acetonitrile/H_2O/formic acid (vol/vol/vol). The primary sample fraction (20 μL) containing the digested peptides was separated on a C_4 (5 cm × 1 mm i.d.) reversed-phase HPLC column (VM5C4W, packed by Micro-Tech Scientific, Vista, CA) with a linear gradient from 10% to 70% B in 60 min with a flow rate of 100 μL/min followed by a wash and re-equilibration step. Furthermore, the HPLC system was coupled online to the electrospray source of a Q-TOF-2 mass spectrometer (Micromass UK Ltd., Manchester, U.K.). Mass spectra were acquired with instrument cone voltage 35 eV, collision energy 10 eV with Ar in the collision cell. The instrument was set up such that ESI-MS spectra were acquired in positive reflector mode with a scan time of 6 s and in the mass range 200−3000. The instrument was calibrated using NaI.

Analysis of the Peptide Fragments. The reporter ion chromatograms (m/z of 390.0 ± 0.1 Da for FITC and 500.2 ± 0.1 Da for RITC) were processed to obtain the molecular weights of the modified peptides using MaxEnt3 in the *MassLynx* v 4.1 software (Micromass UK Ltd.) to reduce the spectral complexity to single charge representation. A theoretical list of all the possible peptides (including missed cleavages) as products of tryptic digestion and their corresponding masses was generated using BioLynx. Under each peak of the reporter ion, we interrogated for the missed cleavage peptide that was in the theoretical list. To this we added the molecular weight of FITC (389.0) or RITC (500.2) to identify the modified peptide.

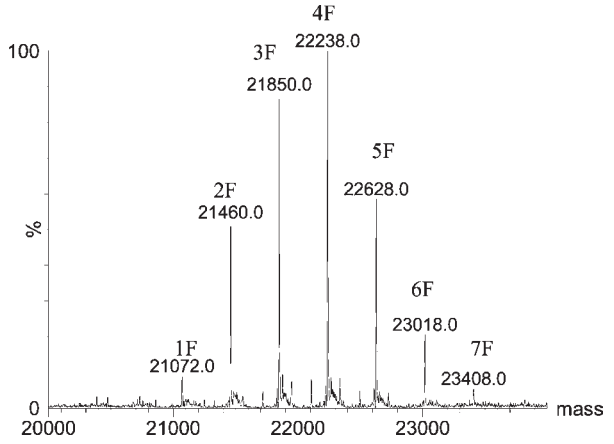

Figure 2. Deconvoluted mass spectrum of FTC-I-domain. The modification of one FITC molecule to either lysine or the N-terminus amino group increases the theoretical mass of the I-domain protein by 389.0 Da. F, is the number of FITC molecules conjugated.

RESULTS

Analysis of I-Domain Conjugates by ESI-MS. The I-domain protein was modified with fluorescent dye (FITC or RITC) in an aqueous buffer solution using a molar ratio of fluorescent dye/I-domain of 25:1 or 20:1, respectively, for 2 h at 25 °C at pH 9.0 as shown in Figure 1 (and Supporting Information Figure S2). Under such conditions, the isothiocyanate group of the fluorescent dye preferentially reacts with primary amino and thiol groups on proteins forming stable thiourea and dithiourethane adducts. Because the I-domain does not contain any cysteine residues, it is expected that only thiourea adducts are formed. After removal of the unreacted fluorescent dye by SEC, the number of conjugated FITC molecules was ascertained using ESI-Q-TOF MS. The deconvoluted spectrum shows seven prominent peaks (Figure 2). Each adjacent peak is separated by a mass difference of 388.0 to 390.0 Da with a mean of 389.0 Da. This consistent mass difference between the adjacent peaks in the spectra is due to the covalent link of the FITC group (molecular weight 389.0 Da) on the I-domain protein. The mass of the first peak in the series is 21 072.0 Da (1F, one fluorescein), which is associated with I-domain conjugated with one FITC molecule. The parent I-domain protein has a molecular weight of 20 682.0 Da (0F, no fluorescein). In this case, the associated error is less than 0.01%, which is typical for such mass measurements. The rest of the peaks can be assigned to the I-domain conjugated with two, three, four, five, six, and seven covalently linked FITC (2−7F) molecules, respectively. The spectrum also shows the disappearance of the peak for the parent I-domain (0F), indicating a complete conversion. A similar analysis done using RTC-I-domain

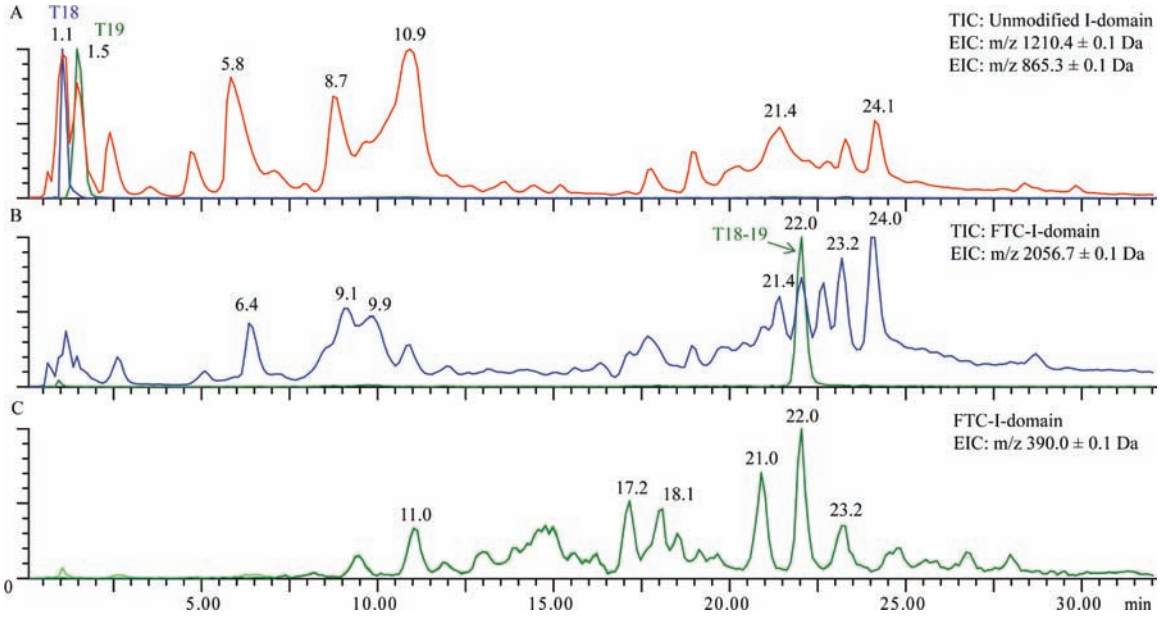

Figure 3. Ion chromatograms of tryptic digest of unmodified I-domain and FTC-I-domain. (A) Total ion chromatogram (TIC) of unmodified I-domain superimposed with the extracted ion chromatograms (EIC) of the peptide T18 (m/z 1210.4 ± 0.1 Da) in blue and T19 (m/z 865.3 ± 0.1 Da) in green. (B) TIC of FTC-I-domain superimposed with the EIC of the peptide fragment T18−19 (m/z 2056.7 ± 0.1 Da) in green. (C) EIC of the reporter ion, indicating all components whose spectra contain an ion of m/z 390.

shows 0−4 covalently linked RITC molecules (Supporting Information Figure S3).

Analysis of Model Peptide Conjugates by ESI-MS. Before analyzing the tryptic-digest products of I-domain conjugates, the fragmentation profile of model peptide-conjugated with fluorescent dye was first investigated using the Q-TOF. cLABL peptide was reacted with FITC at the free amino group to give FTC-cLABL and cIBR peptide was reacted with RITC to produce RTC-cIBR. After HPLC purification, pure FTC-cLABL or RTC-cIBR was used for ESI-MS analysis. Under the conditions employed, the presence of the reporter ion (i.e., free dye molecule) was detected. In this case, several fragments were detected, including the free dye (i.e., FTC, m/z = 390.0, or RTC, m/z = 500.3), the parent peptide fragment, and the modified peptide. The fluorescent dye demonstrated facile fragmentation at low energies readily generating reporter ions. Selected ion profiles of the dye reporter ions enabled the peptides to which the dyes are attached to be found chromatographically and the mass of the peptides was revealed in a fragment resulting from neutral loss of the dye. These results suggest the possibility of identifying the conjugation sites in the I-domain protein by tracking the modified and unmodified peptide fragments.

Determination of Conjugation Sites in the I-Domain. For determination of FITC conjugation sites, a classical peptide-mapping technique involving trypsin digestion and ESI-Q-TOF mass spectrometry followed by computer-facilitated data analysis of peptides was performed. It is well-known that trypsin cleaves the C-terminal Lys and Arg residues; however, the modified Lys residues in the I-domain cannot be clipped by trypsin. Thus, the total ion chromatograms (TIC) from the tryptic digest of FTC-I-domain and parent I-domain proteins were compared (Figure 3A,B). The TIC shows differences in the profiles, peak intensities, and retention times. For example, the increase in the retention time of the dye-modified peptides is due to the increase in hydrophobicity of the peptide fragment conjugate to the dye. Because of the large differences between the chromatograms of the tryptic digests of FTC-I-domain and I-domain, the identification of the conjugation sites using UV and/or fluorescence traces was laborious and time-consuming. Therefore, MS data were used to identify the modified peptides. During the analysis, the assumptions were that the modifications occurred at lysine residues and the expected mass of the uncleaved tryptic peptides increased by 390.0 Da for FTC-modified peptides and 500.2 Da for RTC-modified peptides. Interestingly, MS data of the dye-modified proteins showed a unique peak that could be assigned to the mass of the free fluorescent dye molecule (reporter ion with a mass of 390.0 or 500.3 Da), similar to that found in the model peptide analysis. Thus, the observed free dye molecule was derived from a specific peptide fragment upon cleaving the dye moiety (i.e., FTC or RTC) during collision-induced dissociation (CID).

Extracted ion chromatograms (EICs) of m/z 390.0 Da (FITC) or of 500.2 (RITC) were generated from the full scan data with an error tolerance of 0.1 Da. A similar extraction was also done from unmodified protein profile (data not shown). The EIC of the FTC-modified protein shows several peaks that appeared between 7.2 and 30.0 min (Figure 3C), indicating that the amino group of the lysine side chain and/or the N-terminus of methionine could be modified in these peptides. Each of the peaks from the reporter ion chromatogram was processed using MaxEnt3 charge state deconvolution algorithm. The processed spectra were then searched for three ions: reporter ion (FTC), peptide fragment ion, and its corresponding FTC-modified peptide.

The ESI-MS spectrum of a peak eluting at 22.0 min from the tryptic-digest of FTC-I-domain is shown in Figure 4A. The deconvoluted spectrum shows three prominent ions (Figure 4B), including m/z 390.0 Da (Figure 4A), which corresponded to the FTC moiety, m/z 2056.7 Da, which correlated with the peptide fragment ion (T18−19; ^{151}FAS···FE^{168}K; Cal: 2057.1 Da), and m/z 2445.7 Da, which corresponded to the modified

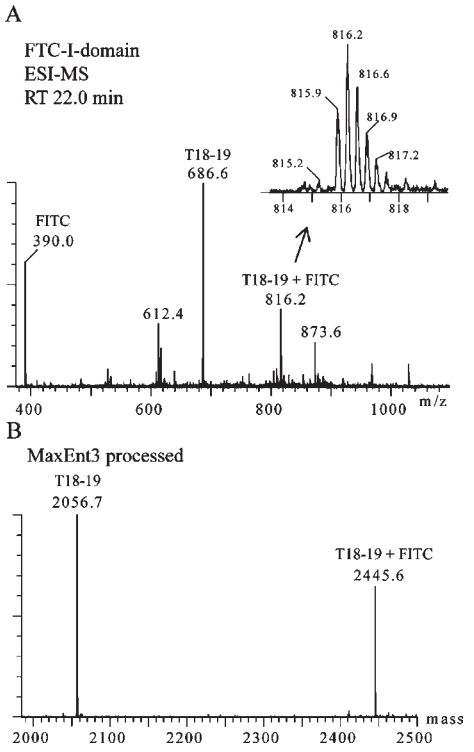

Figure 4. ESI-MS and MaxEnt3 processed spectra of the peak eluting at 22.0 min derived from the LC-MS analysis of the tryptic digests of FITC labeled I-domain showing the MW of the parent compound and the fragments representing the peptide and the fluorescent dye. (A) ESI-MS of the peak eluting at 22.0 min derived from the LC-MS analysis of the tryptic digests of FTC-I-domain, shows the reporter ion (FITC) and the inset shows the spectrum of FITC modified T18−19 peptide. (B) MaxEnt3 processed spectrum of peak eluting at 22.0 min derived from the ESI-MS spectra of the tryptic digests of FTC-I-domain showing the peptide fragment and the FITC labeled peptide.

FTC-peptide T18−19 (^{151}FAS...^{154}K...FE^{168}K or ^{151}FAS···^{161}K···FE^{168}K). The FTC-peptide T18−19 has modification either at ^{154}K or ^{161}K. In addition, the ESI-MS spectrum of another peak eluting at 28.0 min shows a fourth ion with m/z 2834.6 Da, which corresponds to an FTC-peptide with modification at both the ^{154}K and ^{161}K residues. Peaks corresponding to the mass of 2445.7 and 2834.6 Da were found in the modified-peptide mapping profile but not in that of the unmodified I-domain profile, suggesting that both ^{154}K and ^{161}K were indeed modification sites. Further, the ability to find the peptide T18−19 (Figure 3B) along with its FITC-peptide at the same retention time in the modified-peptide profile supports that the peak at 2056.7 Da is a result of fragmentation from its corresponding FTC-peptide. However, there are populations of protein that were not modified at both ^{154}K and ^{161}K residues. This is due to the observation of peptides T18 (m/z 1210.4) and T19 (m/z 865.3) derived from complete trypsin cleavage. We were not able to find the mass corresponding to the unmodified peptide (^{151}FAS···FE^{168}K), 2056.7 Da, in the LC/MS profile of the unmodified I-domain as a result of trypsin cleavage at ^{161}K; however, we were able to find the smaller portions of the peptide, T18 and T19 (Figure 3A). Similar conclusions were drawn from the analysis of a peak eluting at 24.0 min from the tryptic-digest of RTC-I-domain as shown in the Supporting Information Figures S4 and S5.

Table 1. FITC Modification Sites in the FTC-I-Domain Detected in Peptides from Trypsin Digestion

modified peptide	sequence	RT (min)	modified sites
T1	^{1}MGNVDLVFLFDGSMSLQPDEFQ^{23}K	28.0	1M (N-terminus)
T2−3	^{24}ILDFMKDVM^{33}K	21.0	29K
T4−5	^{34}KLSNTSYQFAAVQFSTSY^{52}K	17.5	34K
T6−7	^{53}TEFDFSDYVK^{63}R	18.1	62K
T18−19	^{151}FASKPASEFVKILDTFE^{168}K	22.0	154K, 161K
T20−21	^{169}LKDLFTELQ^{178}K	19.7	170K
T21−22	^{171}DLFTELQK^{179}K	17.2	178K

Table 2. RTC Modification Sites in the RTC-I-Domain Detected in Peptides from Trypsin Digestion

modified peptide	sequence	RT (min)	modified sites
T1	^{1}MGNVDLVFLFDGSMSLQPDEFQ^{23}K	29.2	1M (N-terminus)
T2−3	^{24}ILDFMKDVM^{33}K	22.2	29K
T4−5	^{34}KLSNTSYQFAAVQFSTSY^{52}K	18.9	34K
T15−16	^{131}YIIGIGKHFQT^{142}K	23.1	137K
T18−19	^{151}FASKPASEFVKILDTFE^{168}K	24.0	154K, 161K

In summary, a total of 8 and 6 modification sites were identified in the FTC-I-domain and RTC-I-domain, respectively. Tables 1 and 2 show a complete list of modified peptides obtained from the FTC-I-domain and RTC-I-domain. In all the identified peptides, the conjugation sites were assigned to the internal lysine residue except for peptide T1, where the conjugation site was assigned to the primary amino group or the N-terminus of the first amino acid residue, methionine. Interestingly, most of the conjugation sites found in the RTC-I-domain were similar to those found in the FTC-I-domain.

DISCUSSION

The conjugation method adopted for the preparation of the I-domain-fluorescent dye conjugates yields samples with a heterogeneous distribution of fluorochrome groups covalently linked to the lysine residues. However, the reaction conditions have been optimized to maintain batch-to-batch reproducibility. Each batch consistently showed the same number of fluorochrome modifications per molecule of protein as determined by whole protein MS analysis and UV. Also, as a quality control tool, CD spectroscopy results showed reproducibility of the spectra of modified proteins.

The FTC-I-domain preparation contained 1 to 7 linked FTC molecules (Figure 2), while the RTC-I-domain preparation contained 1 to 4 linked RTC molecules (Supporting Information Figure S3). Out of 21 modifiable residues (20 lysine + N-terminus methionine), there are 8 sites modified by FTC and 6 sites modified by RTC (Tables 1 and 2). In addition, all of the identified sites were partially modified. There are possibly low abundant modification sites that cannot be detected during LC-MS analysis. The MS data analysis using the reporter ion can identify almost all of the modified peptides in relatively short time. Also, such analysis can aid in identifying low-abundance modified peptides that fall within the detectable range of detecting either dye + peptide or the neutral loss peptide only ion. However, very low levels of modified peptides were flagged by

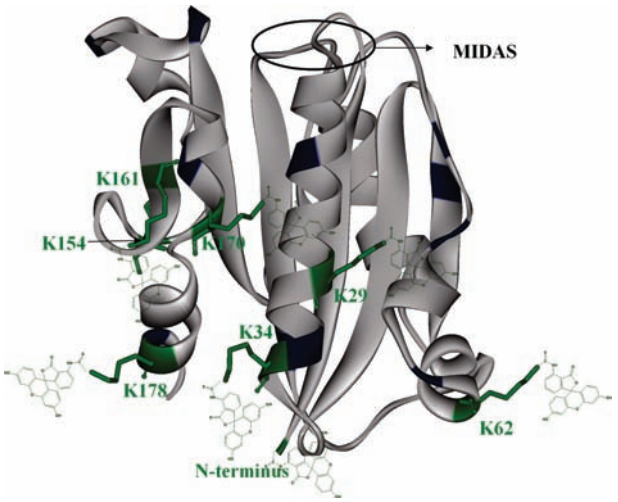

Figure 5. X-ray structure of I-domain (PDB code 1ZON). The residues in green are the FITC modification sites and the residues in blue are the unmodified lysine modification sites. The modified lysine residues and the N-terminus are labeled. The protein images were created using *Accelrys DS Visualizer 1.7*.

the presence of the reporter ion but precursor peptides mass were inconclusive. Using single intermediate collision energy, compared to the low/high energies used in MSE, simplified the data reduction such that only one set of spectra required interrogation. This study shows a combination of tryptic digest and LC ESI-MS with elevated collision energy in the cell of a Q-TOF analysis is proven to be a powerful and reasonably rapid technique in identifying the modification sites.

Fluorescent dye labeling of the I-domain protein serves two main purposes. The first purpose is that the labeling of I-domain increases the sensitivity of detection of the protein during in vitro binding studies. It is hoped that conjugation with the fluorescein and rhodamine does not alter the structure and binding site of the I-domain. Second, characterization of the modification sites provides an idea regarding the reactivity and availability of certain lysine residues for conjugation with drug molecules within the I-domain. Neither of these goals may be accomplished if the residues at the MIDAS region and the structure of I-domain have been altered to make the molecule inactive.

Our results indicate that FTC-moieties are found at lysine residues away from the MIDAS region (Figure 5). In a separate study, the FTC-I-domain has been shown to bind to ICAM-1 on Raji cells, indicating the conjugation of the I-domain with fluorochrome does not alter its binding properties to ICAM-1. The binding properties of FTC-I-domain to ICAM-1 on the cell surface are concentration and temperature dependent. Binding of FTC-I-domain to its receptor suggests structural competence. Recently, the I-domain has also been conjugated to antigenic peptides for targeting to antigen-presenting cells (APC) for controlling T-cell differentiation in autoimmune diseases. The antigen-I-domain conjugate can suppress the progress of experimental autoimmune encephalomyelitis (EAE) in the mouse model, a model for multiple sclerosis. The results from the biological studies suggest that I-domain can be used to target drug molecules to ICAM-1-expressing cells.

In conclusion, the reporter ion quickly allowed identification of peaks modified with peptides in a complex peptide chromatogram. While this approach may be similar to the cone fragmentation study,[26] the activation in the collision cell provided superior data quality. The observation of reporter ion and the peptide fragment observed as a neutral loss suggests ion trap instruments using a data-dependent neutral loss strategy can also rapidly screen digests for these types of dyes. This method can be extended to determine the sites of conjugation of drug molecules or antigenic peptides on the I-domain or other proteins.

■ ASSOCIATED CONTENT

Supporting Information. The sequence of LFA-1 I-domain protein, chemical structures of RITC and RTC-I-domain, deconvoluted mass spectrum of RTC-I-domain, ion chromatograms of tryptic digest of RTC-I-domain, and an example of a processed spectra. This material is available free of charge via the Internet at http://pubs.acs.org.

■ AUTHOR INFORMATION

Corresponding Author

*Dr. Teruna J. Siahaan, Department of Pharmaceutical Chemistry, The University of Kansas, Simons Research Laboratories, 2095 Constant Avenue, Lawrence, KS 66047, USA. Tel.: (785) 864-7327. Fax: (785) 864-5736. E-mail: siahaan@ku.edu.

■ ACKNOWLEDGMENT

This work is supported by the National Institutes of Health (R01-AI-063002 and R56 AI-063002), National Multiple Sclerosis Society, and Institute for Advancing Medical Innovation, University of Kansas Cancer Center. We thank Amgen Inc. Predoctoral Fellowships to Prakash Manikwar. The Q-Tof2 was purchased with support from KSTAR, Kansas administered NSF EPSCoR, and the University of Kansas. The Acquity UPLC was purchased with partial support from K-INBRE (www.kumc.edu/kinbre/) and Protein Lynx Global Server software was obtained with support from KCALSI (www.kclifesciences.org). We also thank Nancy Harmony for proofreading the manuscript.

■ REFERENCES

(1) Schreiber, A. B., and Haimovich, J. (1983) Quantitative fluorometric assay for detection and characterization of Fc receptors. *Methods Enzymol. 93*, 147–155.

(2) Swoboda, G., and Hasselbach, W. (1985) Reaction of fluorescein isothiocyanate with thiol and amino groups of sarcoplasmic ATPase. *Z. Naturforsch. C 40*, 863–875.

(3) Qu, A., and Leahy, D. J. (1995) Crystal structure of the I-domain from the CD11a/CD18 (LFA-1, alpha L beta 2) integrin. *Proc. Natl. Acad. Sci. U. S. A. 92*, 10277–10281.

(4) Shimaoka, M., Xiao, T., Liu, J. H., Yang, Y., Dong, Y., Jun, C. D., McCormack, A., Zhang, R., Joachimiak, A., Takagi, J., Wang, J. H., and Springer, T. A. (2003) Structures of the alpha L I domain and its complex with ICAM-1 reveal a shape-shifting pathway for integrin regulation. *Cell 112*, 99–111.

(5) Stanley, P., and Hogg, N. (1998) The I domain of integrin LFA-1 interacts with ICAM-1 domain 1 at residue Glu-34 but not Gln-73. *J. Biol. Chem. 273*, 3358–3362.

(6) Archelos, J. J., Previtali, S. C., and Hartung, H. P. (1999) The role of integrins in immune-mediated diseases of the nervous system. *Trends Neurosci. 22*, 30–38.

(7) Dietrich, J. B. (2002) The adhesion molecule ICAM-1 and its regulation in relation with the blood-brain barrier. *J. Neuroimmunol. 128*, 58–68.

(8) Lee, S. J., and Benveniste, E. N. (1999) Adhesion molecule expression and regulation on cells of the central nervous system. *J. Neuroimmunol. 98*, 77–88.

(9) Aoki, S., Imai, K., and Yachi, A. (1993) Soluble intercellular adhesion molecule-1 (ICAM-1) antigen in patients with rheumatoid arthritis. *Scand. J. Immunol. 38*, 485–490.

(10) Campbell, I. L., Cutri, A., Wilkinson, D., Boyd, A. W., and Harrison, L. C. (1989) Intercellular adhesion molecule 1 is induced on isolated endocrine islet cells by cytokines but not by reovirus infection. *Proc. Natl. Acad. Sci. U. S. A. 86*, 4282–4286.

(11) Wuthrich, R. P., Jevnikar, A. M., Takei, F., Glimcher, L. H., and Kelley, V. E. (1990) Intercellular adhesion molecule-1 (ICAM-1) expression is upregulated in autoimmune murine lupus nephritis. *Am. J. Pathol. 136*, 441–450.

(12) Fairwell, T. (1983) Chemical ionization mass spectral analysis of phenylthiohydantoin derivatives. *Methods Enzymol. 91*, 502–511.

(13) Esch, S. W., Tamura, P., Sparks, A. A., Roth, M. R., Devaiah, S. P., Heinz, E., Wang, X., Williams, T. D., and Welti, R. (2007) Rapid characterization of the fatty acyl composition of complex lipids by collision-induced dissociation time-of-flight mass spectrometry. *J. Lipid Res. 48*, 235–241.

(14) Chakraborty, A. B., Berger, S. J., and Gebler, J. C. (2007) Use of an integrated MS--multiplexed MS/MS data acquisition strategy for high-coverage peptide mapping studies. *Rapid Commun. Mass Spectrom. 21*, 730–744.

(15) Bateman, K. P., Castro-Perez, J., Wrona, M., Shockcor, J. P., Yu, K., Oballa, R., and Nicoll-Griffith, D. A. (2007) MSE with mass defect filtering for in vitro and in vivo metabolite identification. *Rapid Commun. Mass Spectrom. 21*, 1485–1496.

(16) Bostanci, N., Heywood, W., Mills, K., Parkar, M., Nibali, L., and Donos, N. (2010) Application of label-free absolute quantitative proteomics in human gingival crevicular fluid by LC/MS E (gingival exudatome). *J. Proteome Res. 9*, 2191–2199.

(17) Wong, J. W., Schwahn, A. B., and Downard, K. M. (2009) ETISEQ--an algorithm for automated elution time ion sequencing of concurrently fragmented peptides for mass spectrometry-based proteomics. *BMC Bioinformatics 10*, 244.

(18) Hunt, D. F., Yates, J. R., 3rd, Shabanowitz, J., Winston, S., and Hauer, C. R. (1986) Protein sequencing by tandem mass spectrometry. *Proc. Natl. Acad. Sci. U. S. A. 83*, 6233–6237.

(19) Carr, S. A., Hemling, M. E., Bean, M. F., and Roberts, G. D. (1991) Integration of mass spectrometry in analytical biotechnology. *Anal. Chem. 63*, 2802–2824.

(20) Carr, S. A., Huddleston, M. J., and Bean, M. F. (1993) Selective identification and differentiation of N- and O-linked oligosaccharides in glycoproteins by liquid chromatography-mass spectrometry. *Protein Sci. 2*, 183–196.

(21) Huddleston, M. J., Bean, M. F., and Carr, S. A. (1993) Collisional fragmentation of glycopeptides by electrospray ionization LC/MS and LC/MS/MS: methods for selective detection of glycopeptides in protein digests. *Anal. Chem. 65*, 877–884.

(22) Ohguro, H., Palczewski, K., Ericsson, L. H., Walsh, K. A., and Johnson, R. S. (1993) Sequential phosphorylation of rhodopsin at multiple sites. *Biochemistry 32*, 5718–5724.

(23) Papac, D. I., Oatis, J. E., Jr., Crouch, R. K., and Knapp, D. R. (1993) Mass spectrometric identification of phosphorylation sites in bleached bovine rhodopsin. *Biochemistry 32*, 5930–5934.

(24) Ding, J., Burkhart, W., and Kassel, D. B. (1994) Identification of phosphorylated peptides from complex mixtures using negative-ion orifice-potential stepping and capillary liquid chromatography/electrospray ionization mass spectrometry. *Rapid Commun. Mass Spectrom. 8*, 94–98.

(25) Hoffmann, R., Metzger, S., Spengler, B., and Otvos, L., Jr. (1999) Sequencing of peptides phosphorylated on serines and threonines by post-source decay in matrix-assisted laser desorption/ionization time-of-flight mass spectrometry. *J. Mass Spectrom. 34*, 1195–1204.

(26) Schnaible, V., and Przybylski, M. (1999) Identification of fluorescein-5′-isothiocyanate-modification sites in proteins by electrospray-ionization mass spectrometry. *Bioconjugate Chem. 10*, 861–866.

(27) Majumdar, S., Kobayashi, N., Krise, J. P., and Siahaan, T. J. (2007) Mechanism of internalization of an ICAM-1-derived peptide by human leukemic cell line HL-60: influence of physicochemical properties on targeted drug delivery. *Mol. Pharmaceutics 4*, 749–758.

(28) Gursoy, R. N., and Siahaan, T. J. (1999) Binding and internalization of an ICAM-1 peptide by the surface receptors of T cells. *J. Pept. Res. 53*, 414–421.

(29) Zimmerman, T., Oyarzabal, J., Sebastian, E. S., Majumdar, S., Tejo, B. A., Siahaan, T. J., and Blanco, F. J. (2007) ICAM-1 peptide inhibitors of T-cell adhesion bind to the allosteric site of LFA-1. An NMR characterization. *Chem. Biol. Drug Des. 70*, 347–353.

Supporting Information

Rapid Identification of Fluorochrome Modification Sites in Proteins by LC ESI-Q-TOF Mass Spectrometry

Prakash Manikwar,[†] Tahl Zimmerman,[§] Francisco Blanco,[§¥] Todd D. Williams,[‡] and Teruna J. Siahaan[†]*

List of contents:

Figure S1
Figure S2
Figure S3
Figure S4
Figure S5

```
        10          20          30          40          50          60
MGNVDLVFLF DGSMSLQPDE FQKILDFMKD VMKKLSNTSY QFAAVQFSTS YKTEFDFSDY
        70          80          90         100         110         120
VKRKDPDALL KHVKHMLLLT NTFGAINYVA TEVFREELGA RPDATKVLII ITDGEATDSG
       130         140         150         160         170         180
NIDAAKDIIR YIIGIGKHFQ TKESQETLHK FASKPASEFV KILDTFEKLK DLFTELQKKI

Y
```

Figure S1. The amino acid sequence of LFA-1 I-domain protein (residues 128–307) with an extra methionine residue at the N-terminus incorporated during protein expression. For the purpose of convenience the sequence is numbered from 1-181.

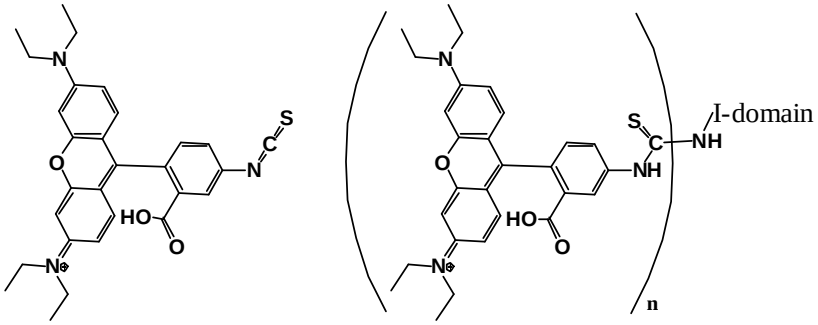

Rhodamine-B-isothiocyanate (RITC)
Exact Mass: 500.2
Molecular Weight: 500.6

Rhodamine-B-thiocarbamoyl (RTC) modified I-domain

Figure S2. Illustration of chemical structures of RITC and RTC-I-domain.

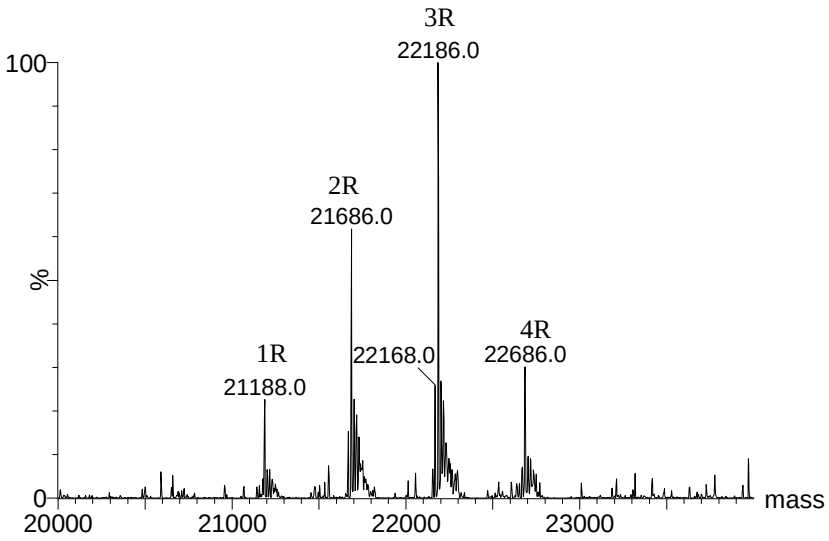

Figure S3. Deconvoluted mass spectrum of RTC-I-domain. The modification of one RITC molecule to either lysine or the N-terminus amino group increases the theoretical mass of the I-domain protein by 500.2 Da. R, is the number of RITC molecules conjugated.

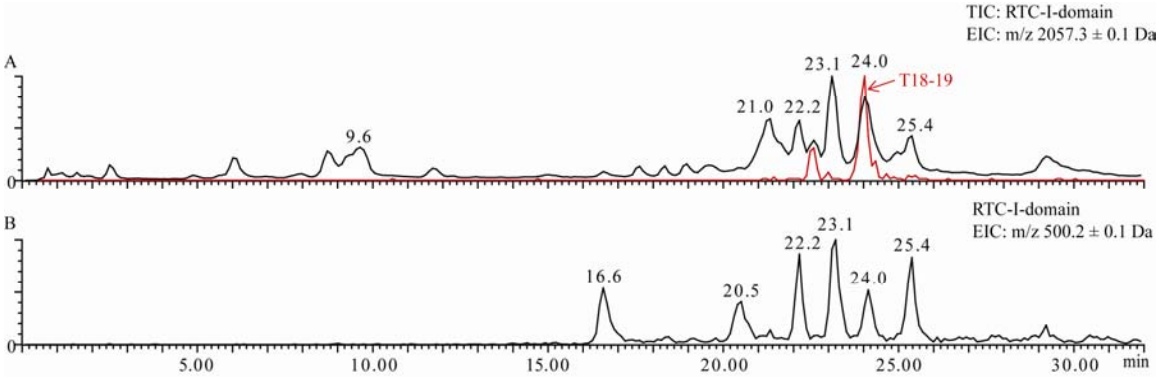

Figure S4. The ion chromatograms of tryptic digest of RTC-I-domain. **(A)** The total ion chromatogram (TIC) of RTC-I-domain superimposed with the EIC of the peptide fragment T18-19 (m/z 2057.3 ± 0.1 Da) in red. **(B)** The EIC of RTC-I-domain separating all the peaks containing the reporter ion (RITC; m/z 500.2 ± 0.1 Da) from the TIC.

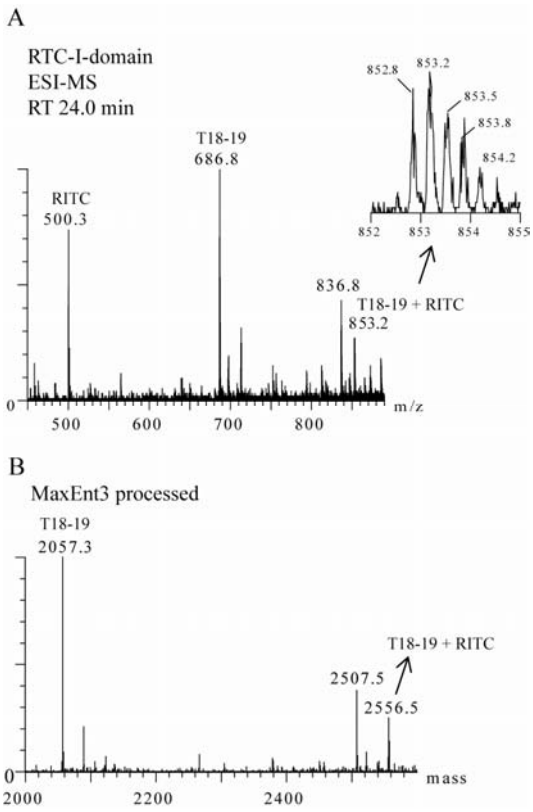

Figure S5. The ESI-MS and MaxEnt3 processed spectra of the peak eluting at 24.0 min derived from the LC-MS analysis of the tryptic digests of RITC labeled I-domain showing the MW of the parent compound and the fragments representing the peptide and the fluorescent dye. **(A)** The ESI-MS of the peak eluting at 24.0 min derived from the LC-MS analysis of the tryptic digests of RTC-I-domain, shows the reporter ion (RITC) and the inset shows the spectrum of RITC modified T18-19 peptide. **(B)** The MaxEnt3 processed spectrum of peak eluting at 24.0 min derived from the ESI-MS spectra of the tryptic digests of RTC-I-domain showing the peptide fragment and the RITC labeled peptide.

Bioconjugate Chemistry

ARTICLE

pubs.acs.org/bc

Comparative Study of the Phototoxicity of Long-Wavelength Photosensitizers Targeted by the MornigaG Lectin

Emi Evangelio,[†,‡] Guillaume Poiroux,[‡,§] Raphaël Culerrier,[§] Geneviève Pratviel,[†] Els J. M. Van Damme,[#] Willy J. Peumans,[#] Annick Barre,[‡] Pierre Rougé,[‡] Hervé Benoist,[§] and Marguerite Pitié*[,†]

[†]CNRS, LCC (Laboratoire de Chimie de Coordination), 205 route de Narbonne, 31077 Toulouse, France

[‡]UMR-CNRS 5546, 31326 Castanet-Tolosan, France

[§]INSERM U858, 31432 Toulouse, France

[#]Department of Molecular Biotechnology, Ghent University, Belgium

Supporting Information

ABSTRACT: Morniga G is a plant lectin selective for high density of tumor-associated carbohydrate T and Tn antigens on the surface of cells. The interaction of the protein with Tn induces its cell penetration. This property was used for targeting photosensitizers (consisting of the porphyrins TrMPyP and TPPS, the Al(III)-phthalocyanin $AlPcS_4$, and the chlorin e6) against leukemic Jurkat T cells after covalent coupling to the protein. The control of MornigaG/photosensitizer loading allowed the comparison of the toxicity of the different photosensitizer conjugates. Conjugate including a single $AlPcS_4$ per protein appeared promising, since it is poorly toxic when irradiated under white light, while it shows a strong phototoxicity (LD_{50} = 4 nM) when irradiated in the therapeutic window, it preferentially kills cancerous lymphocytes, and the sugar binding specificity of the lectin part of the molecule remains unaltered.

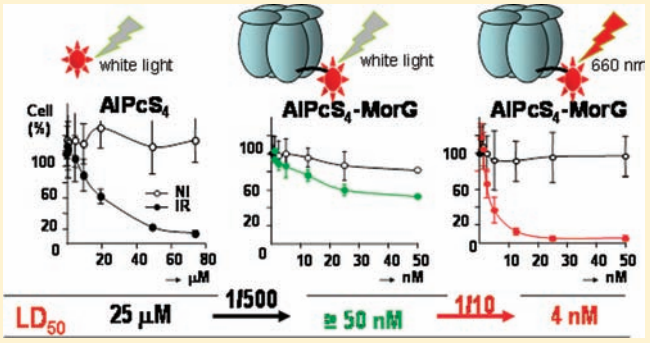

INTRODUCTION

Medicinal, i.e., photodynamic therapy (PDT), or biological uses of photosensitizers (PS) often suffer from a lack of cell selectivity.[1−7] The employment of carriers to enhance drug selectivity is one strategy to increase their efficiency and to reduce their side effects in antitumor therapy. Taking advantage of highly specific lectin/sugar epitope interaction to direct the PS in the desired tumor cell can be a solution to the selectivity problem.[8−12] Recently, we prepared a covalent conjugate between Morniga G (MorG), a plant lectin selective for clustered T and Tn antigens on the surface of cells, and a cationic porphyrin: TrMPyP.[13] Morniga G was isolated from the bark of black mulberry (Morus nigra) and belongs to the family of jacalin-related lectins. The native lectin is a homotetramer with a molecular mass of 72 kDa and 4 sites of sugar recognition.[14−16] Each monomer contains a short β (2.175 kDa) and a long (16 kDa) α-chain, both involved in the saccharide binding. Although Morniga G is specific for galactose pyranoside moiety at a monosaccharide level, it reacts better with glycoproteins presenting a high density of tumor-associated carbohydrate antigens Tn (GalNacα1-Ser/Thr) and Tα (Galβ1−3GalNAcα1-Ser/Thr).[14,17,18]

Preliminary experiments demonstrated that the TrMPyP-MorG conjugate was quickly and specifically internalized by leukemic Jurkat T cells (known to be Tn-positive cells) and exhibited a dramatically increased phototoxicity as compared to free (unconjugated) TrMPyP.[13] This phototoxicity was correlated to cell penetration and can be inhibited by suppressing the Tn/MornigaG interaction (by complementary carbohydrates). In addition, TrMPyP-MorG caused a selective leukemic cell death when compared to healthy T lymphocytes. These results are promising for the possible development of such conjugates for PDT and particularly for extracorporeal photochemotherapy that is developed to treat blood malignant leukocytes.[19,20]

These primary results validate the targeting strategy. However, TrMPyP is probably not the best adapted PS, since this dissymmetric porphyrin is difficult to synthesize,[21] and it is only efficiently activated by irradiation wavelength corresponding to its Soret band (∼420 nm) far away from the therapeutic window (600−800 nm) where biomolecules do not absorb.[1,2,5,6] In the present work, we intend to optimize this first generation of PS-MorG conjugates by modulating the photosensitizer part.

In the past, Al(III)-tetrasulfonatophthalocyanine ($AlPcS_4$)[4,6] and chlorin e_6 (ce_6)[2,4,6] derivatives have been used and even clinically tested in PDT. These compounds, that are commercially available or easy to prepare, have received particular attention due to the high molar absorption coefficient of their

Received: December 14, 2010
Revised: June 14, 2011
Published: June 14, 2011

ACS Publications © 2011 American Chemical Society

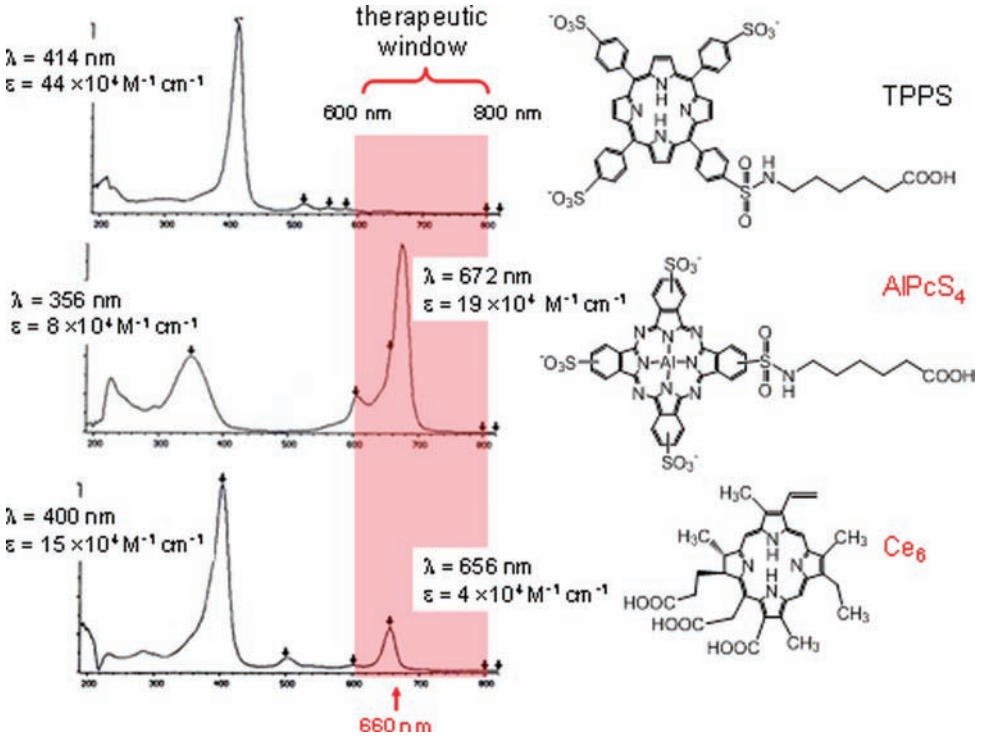

Figure 1. Spectrophotometric spectra of the used photosensitizers. TPPS **1** and AlPcS4 **2** derivatives are shown; axial ligand on aluminum was omitted. Significant absorbances are given.

Q bands in the clinically useful part of the visible spectrum (Figure 1). Therefore, these molecules were chosen here to prepare new conjugates to Morniga G. Conjugates with *meso*-tetra(4-sulfonatophenyl)porphyrin (TPPS) including four sulfonato groups as in $AlPcS_4$ were also prepared to compare the phthalocyanine conjugates with a porphyrin series. Care was taken to obtain the same number of PS per protein for a clear comparison of the conjugate efficiency regarding their phototoxicity on Jurkat cells. A clear effect of the excitation wavelength was observed. Since our previous results showed that the cell penetration is due to the Morniga G part of the conjugates, this study reports on a clear comparison of cell phototoxicity of classical PS under very similar penetration conditions.

EXPERIMENTAL PROCEDURES

General Procedures. Tetrasodium-*meso*-tetra(4-sulfonatophenyl)porphyrin dodecahydrate, chlorin e_6, and Al(III)-tetrasulfonatophthalocyanine chloride were purchased from Frontier Scientific Inc. Other commercially available reagents and solvents were purchased from standard chemical suppliers and used without further purification. Sep-Pak C18 cartridge (20 cc, 5 g, Waters) and Slide-A-Lyzer dialysis cassettes (10 000 MWCO, 0.5−3 mL, Pierce) were used for purification. Stirring was performed with a Thermomixer Comfort (Eppendorf) at 1200 and 500 rpm for carboxylic acid activation and coupling reaction, respectively. MALDI-TOF analyses were performed on a Voyager-DE PRO spectrometer (Applied Biosystems), a solution of sinapic acid in acetonitrile and TFA (30%/0.1%) was used as matrix. The protein concentration was determined by MicroBCA assay (Pierce); the quantification was done from bovine serum albumin standard curve.

*5-[4-(7-Carboxy-1-pentasulfonimide)-phenyl]-10,15,20-tris-(4-sulfonatophenyl)porphyrin (**1**).* A solution of TPPS (20 mg, 0.02 mmol) in 300 μL of chlorosulfonic acid was stirred for 2 h at 50 °C then carefully poured over ice to obtain a precipitate that was filtered and dried over P_2O_5. This product was added in small portions to an aqueous solution (1 mL) of 6-aminohexanoic acid (11.5 mg, 0.09 mmol) and sodium carbonate (37 mg, 0.35 mmol), and the mixture was stirred for 5 h at room temperature. Then, pH was adjusted to 6−7 with aqueous HCl and the reaction mixture was purified over a C18 cartridge with 0−33% CH_3OH in sodium phosphate buffer (10 mM pH 5.0). The collected product was desalted on C18 cartridge (H_2O washing followed by elution with a H_2O/CH_3OH (3/1) mixture) to give **1** (5 mg, 20%) as a red powder. ^{1}H NMR (300 MHz, DMSO-d_6): δ 8.89−8.87 (m, 6H), 8.82 (d, 2H, J = 5.0 Hz), 8.46 (d, 2H, J = 8.2 Hz), 8.23 (d, 2H, J = 8.2 Hz), 8.19 (d, 6H, J = 8.2 Hz), 8.05 (d, 6H, J = 8.2 Hz), 7.94 (t, 1H, J = 6.0 Hz, NH), 3.08 (m, 2H), 2.26 (m, 2H), 1.61−1.51 (m, 4H), 1.42 (m, 2H), −2.92 (s, 2H, NH-pyrrole). ^{13}C NMR (300 MHz, DMSO-d_6): δ 174.9, 148.3, 145.5, 141.6, 140.9, 135.3, 134.2, 132.1, 125.6, 124.7, 120.6, 120.9, 118.6, 43.2, 34.1, 29.4, 26.2, 24.7. ESI (<0) MS: m/z = 348.2 $[M]^{3-}$, 533.7 $[MNa]^{2-}$. HRMS (ESI > 0) obs 1048.1693 $[MH]^+$, calcd for $C_{50}H_{42}N_5O_{13}S_4$: 1048.1662.

*Carboxy-1-pentasulfonimide of Aluminum-tetrasulfophtalocyanine (**2**).* It was prepared as previously described,[22] with minor modifications concerning its purification step that was conducted on C18 cartridge as for compound **1**. Due to the presence of isomers, monosubstituted compounds were eluted as different fractions. They were selected by ES-MS analysis before being pooled.

TPPS-MorG Conjugates. To a solution of **1** (23 mM in dry DMSO, 1 equiv) were added 1 equiv of 4-dimethylaminopyridine (DMAP, dissolved at 50 mg/mL in DMSO), 2 equiv of

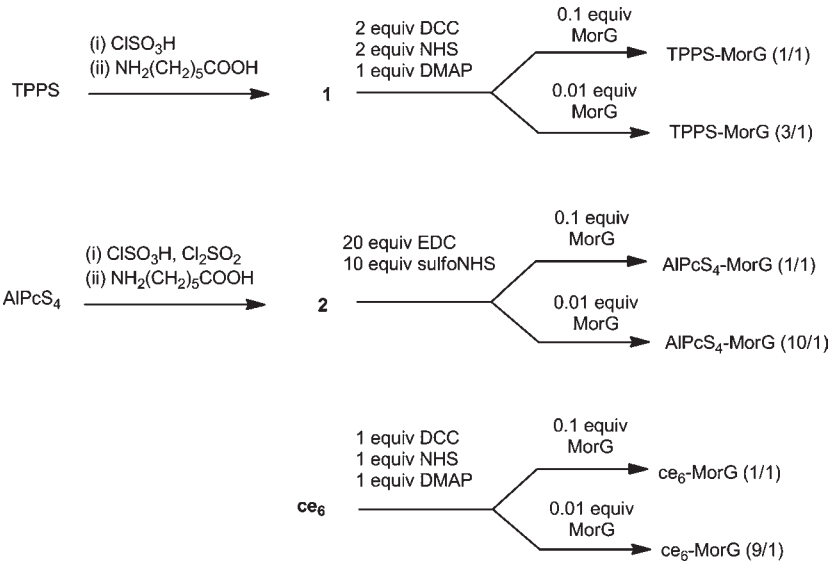

Figure 2. Synthesis of the PS-MorG conjugates.

dicyclohexylcarbodiimide (DCC, 100 mg/mL in DMSO), and 2 equiv of *N*-hydroxysuccinimide (NHS, 100 mg/mL in DMSO) and the mixture was stirred for 2 h at 50 °C in the dark. Activated ester was precipitated by adding 9 volumes of $CHCl_3$. Supernatant was removed after centrifugation (15 min, 15 °C, 9000 rpm) and the pellet was washed with $CHCl_3$, then dried under vacuum. The product was dissolved in dry DMSO (20 mM). Then, 2 μL (~10 equiv with respect to Morniga G) or 19 μL (~100 equiv) of this mixture was added to 300 μL of a solution of Morniga G (14 μM, 1 mg/mL) in sodium borate buffer 50 mM pH 8.8 where D-galactose (3 mg, 17 μmol) was added just before use. After stirring for 90 min at 37 °C in the dark, additional D-galactose (3 mg, 17 μmol) was added and the mixture was stirred for 15 h before purification (see the general method below).

$AlPcS_4$—MorG Conjugates. 1-(3-Dimethylaminopropyl)-3-ethylcarbodiimide-hydrochloride (4.6 mg, 24 μmol) and *N*-hydroxysulfosuccinimide sodium salt (1.6 mg, 12 μmol) were added to a solution of **2** (1.30 mg, 1.21 μmol) in 200 μL of sodium phosphate buffer (10 mM, pH 5.0). The mixture was stirred for 90 min at room temperature, purified over a Sep-Pak C18 1 cm^3 cartridge (Waters) by 20 mL phosphate buffer washing, followed by elution with 1 mL of phosphate buffer/CH_3OH (1/3, vol/vol). Aliquots corresponding to 10 or 100 equiv with respect to Morniga G were lyophilized. Then, these aliquots received 300 μL of a Morniga G solution (14 μM, 1 mg/mL) in sodium borate buffer 50 mM pH 8.8 where D-galactose (3 mg, 17 μmol) was added just before use. After stirring for 90 min at 37 °C in the dark, additional D-galactose (3 mg, 17 μmol) was added and the mixture was stirred for 15 h before purification (see the general method below).

Chlorin e_6-MorG Conjugates. To a solution of ce_6 (1.36 mg, 2.3 μmol, 26 mM, 1 equiv) in dry DMSO were added 1 equiv of DMAP (dissolved at 50 mg/mL in DMSO), 1 equiv of DCC (100 mg/mL in DMSO), and 1 equiv of NHS (100 mg/mL in DMSO), and the mixture was stirred for 2 h at 50 °C in the dark. Then, 2 μL (~10 equiv with respect to Morniga G) or 19 μL (~100 equiv) of this mixture was added to 300 μL of a solution of Morniga G (14 μM, 1 mg/mL) in sodium borate buffer 50 mM pH 8.8 where D-galactose (3 mg, 17 μmol) was added just before use. After stirring for 90 min at 37 °C in the dark, additional D-galactose (3 mg, 17 μmol) was added and the mixture was stirred for 15 h before purification (see the general method below).

General Method of Purification and Quantification of MorniGaG-Photosensitizer Conjugates. Conjugates were dialyzed (at 4 °C in the dark) against PBS buffer containing 50 mM D-galactose (2 times) then PBS (4 times). The mixture was then purified on NickSpin G25 column eluted with PBS. Conjugates were then quantified on aliquots by microBCA assay (for Morniga G) and UV—visible spectrophotometry (for the photosensitizer part) using published molar extinction coefficients of TPPS,[23,24] $AlPcS_4$,[22] and ce_6,[25−27] respectively (see Supporting Information Figure S3). The conjugate solutions in PBS were stored at 4 °C.

Photodynamic Treatment and Cell Death Evaluation. Parental Jurkat T leukemia cells (clone A3) were grown or maintained in RPMI 1640 medium containing glutamate, 10% FCS, and 1% penicillin/streptomycin. Cells (10^6 cells/mL) were exposed to photosensitizers for 15 min at 37 °C, then they were pelleted and washed in RPMI 1640 medium before being taken in RPMI 1640 medium with 10% FCS and 1% penicillin/streptomycin in 96-well plates (10^5 cells/well). Then, they were irradiated with a bank of four white fluorescent tubes (Philips master TL-D 18W/840) for 7.5 min (allowing a 1.7 J/cm^2 light dose) or with a bank of 96 red ($\lambda = 660 \pm 20$ nm) LEDs (one per well) for 2 min at 140 W/m^2 (1.7 J/cm^2 light dose). Then, cells were incubated for 24 h at 37 °C, 5% CO_2, before cell viability determination by the MTT reduction method.[28] All experiments were carried out in triplicate independent experiments.

Healthy blood samples were obtained from the hematology department (Rangueil Hospital, Toulouse). Normal T lymphocytes were separated from blood using the Rosette Sep human T cell enrichment cocktail (StemCell Technologies, Grenoble, France).[29] A mixture of freshly isolated healthy T lymphocytes and Jurkat T cells was treated by photochemotherapy. The percentage of each viable cell type was determined after PDT by flow cytometry, using the cell size and CD1d mAb staining (BD Pharmingen, San Diego, CA, USA). T lymphocytes were defined as CD1d-negative cells with low size and Jurkat T cells as CD1d-positive cells with a greater size. The cell size allowed an efficient discrimination between leukemic and normal T cells.

Statistical Analysis. Results are expressed as the means ± SD of data obtained from at least 3 independent experiments. Statistical significance, determined by means of Student's *t*-test, was considered when $P < 0.05$.

Hemagglutination Assays. They were carried out in 96-well plates in 0.9% NaCl as previously described.[30,31] Briefly, hemagglutination titers were determined using serial dilutions of Morniga G or PS-MorG (50 μL) mixed with equal volumes of a 1% rabbit erythrocytes suspension (bioMérieux) during 45 min at room temperature. This was scored as the minimum hemagglutination concentration (MHC) of the lectin. Inhibition of hemagglutination was performed using serial dilution of glucose, mannose, galactose or *N*-acetyl-α-D-galactosamine in Morniga G or PS-MorG solutions mixed with equal volumes of a 1% rabbit erythrocytes suspension. This was scored as the minimum inhibition concentration of sugar solution. All experiments were carried out in triplicate.

RESULTS AND DISCUSSION

Synthesis of PS-MorG Conjugates. Syntheses are depicted in Figure 2. The water solubility of PS allowed coupling with Morniga G in an aqueous medium which minimized protein denaturation.

For TPPS and $AlPcS_4$, a spacer arm including a carboxylic group was first added giving compounds **1** and **2**, respectively. Then, the carboxylic group was activated for the covalent attachment to Morniga G by amide linkage. Two major precautions were taken for this step (see Experimental Procedures): (i) activated esters were purified before their addition to the protein because we observed that excess of activating agents induced undesired cross-linkage between MornigaG α-chains (it appeared as a new band with an apparent molecular weight of ~50 kDa on SDS-PAGE control analysis of the coupling reaction; results not shown); (ii) docking experiments showed that a potential site of conjugation (NH_2-end of the protein) is located within the carbohydrate-binding site of Morniga G,[14,15] which is a major concern because it has been demonstrated for several lectins including Jacalin that porphyrins interact in the vicinity of this site.[12,32−34] Therefore, this site was protected from conjugation by addition of a large excess of galactose that is one of the most potent monosaccharides interacting with the carbohydrate-binding site of Morniga G.[14−16]

In the case of ce_6, carboxylic functions of the molecule were used to perform coupling. Unfortunately, we were unable to purify the activated ester. Therefore, activation was performed with only 1 equiv of activators per chlorin molecule. Since ce_6 contains three carboxylic groups, this consumed all the activators and undesired cross-links were not possible even though the coupling step was performed without intermediate purification of the activated ester.

The noncovalent binding of porphyrins and chlorins to proteins is well-documented, and hence, an effective cleanup procedure was optimized.[12,25,26,32,35] The process associated extensive dialysis and Sephadex chromatography to remove all the noncovalently linked PS. No major changes were observed in the PS-MorG absorption spectra measured in phosphate buffer when compared to those obtained for known quantities of free PS in the presence of a MorG (Supporting Information Figure S3). Consequently, simple spectroscopic analysis in association with microBCA dosage allowed quantification of the bound PS per protein.

Table 1. LD_{50} of the PS-MorG Conjugates on Jurkat Cells

PS	PS/MorG	LD_{50}[a] (nM) white light	LD_{50}[a] (nM) 660 ± 20 nm
TrMPyP		15 000[c]	n.d.[b]
TPPS derivative **1**		>75 000	>75 000
$AlPcS_4$ derivative **2**		25 000 ± 5000	12 000 ± 6000
ce_6		2000 ± 1800	750 ± 500
TrMPyP-MorG	1/1	<10[c]	n.d.[b]
TPPS-MorG	1/1	4 ± 0.3	25 ± 7
	3/1	2 ± 0.1[*]	12 ± 0.1[°]
$AlPcS_4$−MorG	1/1	≥50	4 ± 1.8
	10/1	35 ± 3	5 ± 0.8[°]
ce_6-MorG	1/1	16 ± 4	7 ± 1.2
	9/1	7 ± 1.2[*]	2 ± 0.8[*]

[a] LD_{50} is the concentration of studied molecule inducing 50% of cell death. [b] n.d. = not determined. [c] Value obtained in ref 13. Values are mean ± SD of three independent experiments. For each PS-MorG conjugate, statistical significance was determined between the conjugate with 1/1 PS/MorG ratio and the conjugate with higher PS/MorG ratio. [*] $P < 0.05$ was considered significant. [°] Unsignificant.

Optimization of the quantity of the activated ester used in the coupling reaction allowed the synthesis of 1/1 PS/MorG conjugates. They were obtained when MorG reacted with 10 equiv of the activated ester form of PS. MALDI-TOF MS revealed that, in the case of these 1/1 conjugates, the major product formed was always a monoadduct on the heavy chain. The light chain proved unmodified (see Figures S1 and S2 of the Supporting Information). This mass analysis showed also that all the noncovalently bound PS was efficiently removed during the purification step (unlinked PS are easy to observe in the m/z 500−1200 Da area of the mass spectra, which allowed a control of their elimination, not shown). This result was confirmed by SDS-PAGE analysis where unlinked PSs are also observable (when they are present). Other conjugates including higher PS/MorG ratio (in the 3/1, 10/1, and 9/1 ratio for TPPS-, $AlPcS_4$-, and ce_6-MorG conjugates, respectively) were also prepared by reaction of MorG with 100 equiv of the activated ester form of PS. They consisted of a mixture of 1−3 PS per heavy chain (Supporting Information Figure S2). In the case of ce_6 conjugate, multiadducts also showed some covalent attachment of the PS on the light chain (Supporting Information Figure S1).

Phototoxicity. The ability of PS-MorG conjugates to induce cell death after irradiation with white and red light was compared with that triggered by free PS (Table 1). The molecules were tested for cytotoxicity toward Jurkat T cells allowing the comparison with previous study with the TrMPyP/MorG conjugate. The latter compound showed >90% phototoxicity upon white-light irradiation at 10 nM concentration with no toxicity at 1 nM concentration.[13]

Under our experimental conditions, the free lectin was only weakly toxic since a LD_{50} of 5 μM was observed. This low toxicity of MorG was independent of light irradiation. Whereas no toxicity was noticed after incubation of free PS or conjugates in the absence of irradiation, a dose-dependent cell death was observed for all of them upon irradiation (Figures 3 and 4). However, free PS appeared poorly toxic (LD_{50} in the micromolar level) compared to the conjugates (LD_{50} in the nanomolar range).

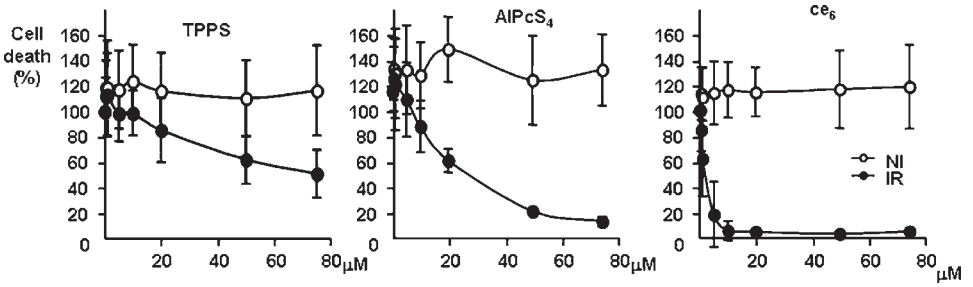

Figure 3. In vitro evaluation of PS-mediated cytotoxicity on Jurkat T cells. Cell viability was evaluated using MTT assay. Results are means ± SD from 3 independent experiments. NI: non-irradiated; IR irradiation with white light.

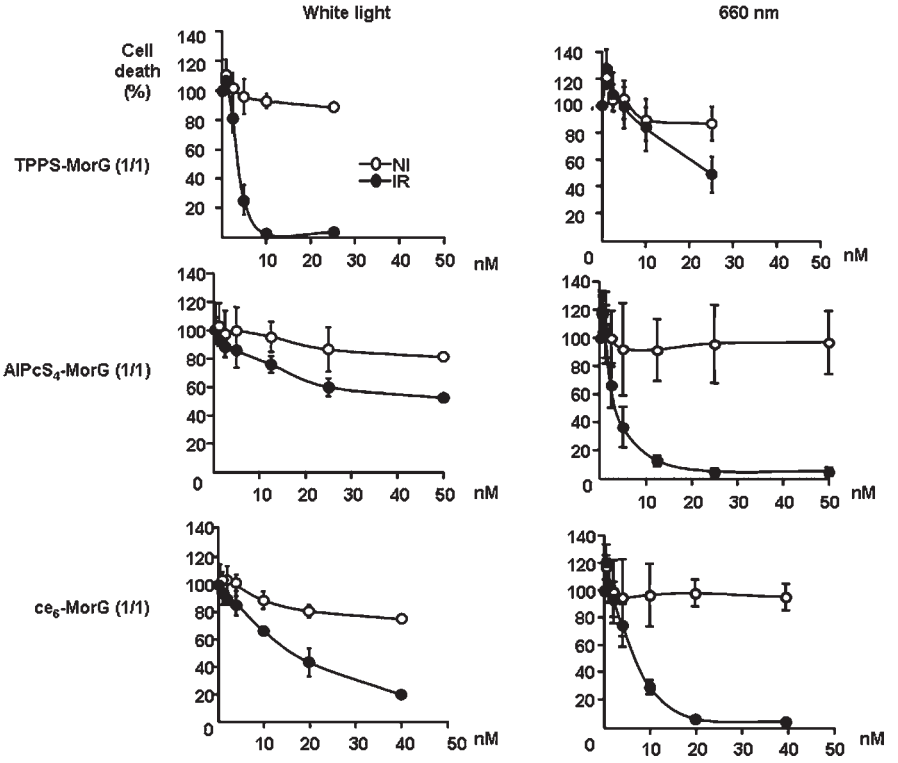

Figure 4. In vitro evaluation of PS-MorG conjugate-mediated cytotoxicity on Jurkat T cells. Cell viability was evaluated using MTT assay. Results are means ± SD from 3 independent experiments. NI: non irradiated; IR irradiation with white light or at 660 ± 20 nm.

Chlorin e6 appeared more toxic upon irradiation than the other free PS. This activity seems difficult to associate to best photochemical properties of the chlorin since ce_6 shows lower absorbance than TPPS for its Soret band (around 400 nm) and of $AlPcS_4$ for its Q-band (around 660 nm), respectively (Figure 1). After white light irradiation, ce_6 was more phototoxic than TPPS (Table 1); however, the absorbance of TPPS around 400 nm was 3 times higher, suggesting that TPPS might be the most efficient to induce cell death. This result on cell death can be explained by the complexity of interactions between PS and cells. Indeed, the PS phototoxicity involves photophysical properties of PS molecule, but also (i) its uptake by the cells (depending of PS solubility, molecule electric charges, etc.), (ii) its intracellular concentration, and (iii) its subcellular localization. Thus, recent data demonstrated that two derivatives of pheophorbide with similar photophysical properties and, a priori, potential favorable phototoxicity can demonstrate drastic differences in phototoxicity on cells, because they have strong differences of intracellular localization.[36] This also probably explains the higher activity of ce_6, upon red irradiation, when compared to $AlPcS_4$.

After the conjugation with MorG, regardless of the PS molecule the conjugation of 1 PS with 1 lectin strongly increased the PS phototoxicity, probably by enhancing the uptake of PS by the cells, as recently demonstrated using the TrMpyP-MorG conjugate.[13] The absorption properties of PS tested here do not change significantly with covalent coupling (Supporting Information Figure S3). However, the cell toxicity of conjugates correlate better with their UV−vis properties when compared to free PS (Table 1).

The nanomolar range of the LD_{50} of the 1/1 conjugates shows that the covalent attachment of the PS to MorG greatly increases the phototoxicity. However, major differences due to the nature of the PS linked to the lectin are observed.

For this 1/1 ratio, porphyrin conjugates TPPS-MorG (this work) and TrMPyP-MorG[13] have similar phototoxicity (white light irradiation) from 1 to 10 nM concentrations (Table 1,

dx.doi.org/10.1021/bc1005703 |*Bioconjugate Chem.* 2011, 22, 1337–1344

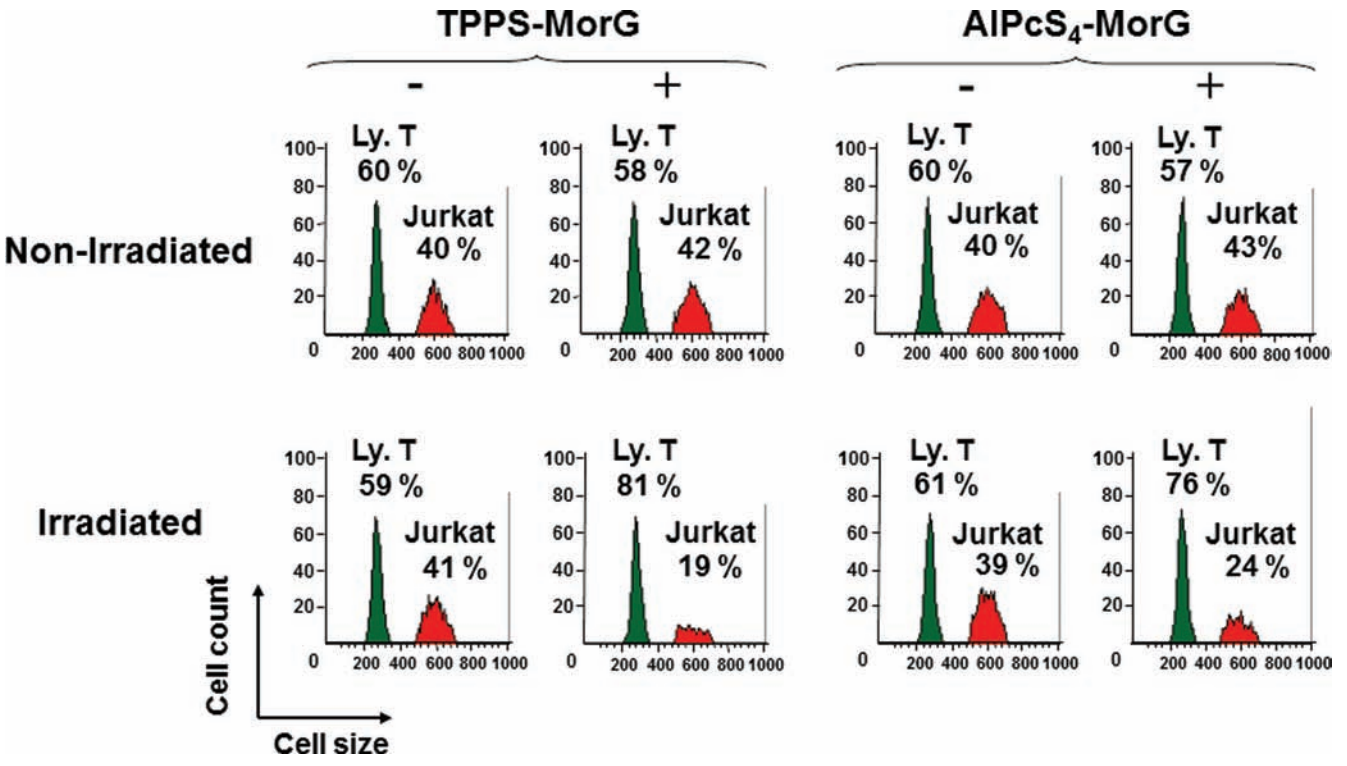

Figure 5. Phototoxic effect of PS-MorG on a mixture of Jurkat leukemia T cells and healthy T lymphocytes. T lymphocytes (10^6/mL) from healthy donors were mixed with Jurkat T cells (10^6/mL), then treated by PS-MorG using the 1/1 PS/MorG conjugates at the LD_{50} and white light (TPPS-MorG) or red light (AlPcS4-MorG), or left untreated, as indicated in the Experimental Procedures section. The cell mixture was analyzed by flow cytometry after 24 h culture. As compared to T lymphocytes, Jurkat T cells were characterized by a larger size. The percentage of the two cell types in the cell mixture was indicated. Results are representative of two independent experiments performed with T lymphocytes from two different donors. Ly. T: T lymphocytes (green); Jurkat: Jurkat T cells (red).

Figure 4, and ref 13), even though TrMPyP is cationic and TPPS is anionic indicating that the charge of the PS has no influence on the phototoxicity. This result is probably due to the lectin part of the conjugate that reaches the same cell area independently of the proper structure of the PS part (if porphyrin part had some influence, the cationic TrMPyP might have shown some difference in reactivity, when compared to TPPS, due to its capacity to interact with anionic biomolecules such as nucleic acids). When irradiation was performed at a more therapeutically useful wavelength of 660 nm, TPPS-MorG conjugate showed a clear decrease in phototoxicity (LD_{50} 25 nM) due to its low absorption at this wavelength (Figure 1).

On the opposite, $AlPcS_4$—MorG (1/1) conjugate which is only weakly toxic upon irradiation with white light ($LD_{50} \geq$ 50nM) shows good activity when red light irradiation was used (LD_{50} 4 nM) (Table 1 and Figure 4). These data are in accordance with the spectroscopic properties of $AlPcS_4$, which has a strong absorbance above 660 nm (Figure 1). Therefore, this latter conjugate appears as a promising reagent for development in PDT.

Ce_6-MorG (1/1) appeared more potent under red light compared to white light. However, the difference between its photoxicity under white and red light irradiations was lower than that of $AlPcS_4$-MorG. These data are also in agreement with the absorbance of ce_6 chromophore (Figure 1) since the Soret band of ce_6 is high in the visible region. Overall, ce_6-MorG conjugate also seems less interesting since (i) the phototoxicity of the free chlorin e_6 is higher than that of all the other tested PS, increasing the risk of side effects; (ii) the phototoxicity of the conjugate upon 660 nm irradiation is lower than for $AlPcS_4$-MorG; and (iii) the difference of phototoxicity between white and red light irradiation is small (LD_{50} of 16 and 7 nM, respectively).

Finally, the phototoxicity of TPPS-MorG and $AlPcS_4$-MorG conjugate was evaluated comparatively on Jurkat leukemic T lymphocytes and normal T lymphocytes from healthy donors (Figure 5). Irradiation was performed in the most efficient conditions previously observed for each photosensitizer: in white light and at 660 nm for the porphyrin and the phthalocyanin conjugate, respectively. Under the experimental conditions tested, and in accordance with previous results obtained with TrMPyP-MorG,[13] the normal T lymphocytes were clearly more resistant to PS-MorG conjugate-mediated phototoxicity.

Because the efficiency of the PS-MorG conjugates in the destruction of cells will depend on the amount of PS able to be delivered to the target, it seemed desirable to increase the number of bound PS molecules per lectin. Therefore, conjugates of $AlPcS_4$ and ce_6 including 9 and 10 PS/protein, respectively, were also tested. Their similar PS/protein ratio allowed comparison. However, in both cases, only a minor increase of phototoxicity was observed when compared to 1/1 conjugates (Table 1). A weak but significant increase of LD_{50} (2 to 3 times) can be observed by increasing the number of PS molecules per lectin with ce_6 but not with $AlPcS_4$-MorG conjugate (unsignificant). A similar conclusion can be drawn for a 3/1 TPPS/MorG molecule.

The binding of MorG to antigen clusters is probably due to the presence of several sugar-binding sites on the lectin. Therefore, this surprising result may be explained by a lower capacity of

Table 2. Hemagglutination Induced by PS-MorG Conjugates

PS	PS/MorG	MHC[a] (ng/mL)
Morniga G		31
$AlPcS_4$-MorG	1/1	27
	10/1	78
ce_6-MorG	1/1	31
	9/1	156

[a] MHC is the minimum concentration of PS-MorG conjugate that induced agglutination of rabbit erythrocytes.

conjugates with high PS/MorG ratio to interact with clusters of tumor-associated antigens because an excessive PS loading could mask some saccharide-binding sites of the lectin. In an attempt to test this hypothesis, the carbohydrate-binding activity of the conjugates was (semiquantitatively) checked by hemagglutination assays (Table 2). It consists of the determination of the quantity of lectin necessary to agglutinate red blood cells.[30,31,37] To summarize the method, the lectin interacts with carbohydrates on the surface of the erythrocytes, and because the protein has several sugar-binding sites, it can link the red blood cells together, which induces their agglutination. Hemagglutination of red blood cells requires the presence of at least two functional carbohydrate-binding sites per lectin molecule. Therefore, the specific agglutination activity of a lectin or a conjugate is particularly instructive concerning the activity of the whole of binbing sites, which is essential to obtain good reactivity against clusters of sugar epitopes on the cell surface.

$AlPcS_4$-MorG 1/1 and ce_6-MorG 1/1 conjugates exhibited the same hemagglutination activity (MHC ~ 30 ng/mL) as the free lectin indicating that the carbohydrate-binding activity of the lectin compound of these conjugates is not altered (Table 2). Hapten inhibition assays further confirmed that the covalent coupling of the PS did not alter the original specificity of the MornigaG toward monosaccharides. Indeed, we determined the minimal concentration of sugar allowing the inhibition of agglutination induced by 125 ng/mL of Morniga G, $AlPcS_4$-MorG 1/1, or ce_6-MorG 1/1 on 1% suspension of rabbit erythrocytes. For the free lectin and both conjugates, the same inhibiting concentrations were obtained: 3.1 and 12.5 mM for galactose and *N*-acetyl-α-D-galactosamine, respectively, when 25 mM of glucose or mannose has no inhibitory effect. This result showed that the original specificity of the Morniga G for *N*-acetyl-α-D-galactosamine and (to a lesser extend) for galactose was conserved for both conjugates.

When ce_6-MorG 9/1 and $AlPcS_4$-MorG 10/1 conjugates were used, a clear decrease of the hemagglutination capacity was observed (Table 2) that was not associated to a decrease of *N*-acetyl-α-D-galactosamine and galactose potential to inhibit hemmaglutination (not shown). Taken together, the data observed for the conjugates including 9 or 10 PS per Morniga G could be explained by the blocking of one or two saccharide recognition sites by the PS coupling. Therefore, the observation of a poor increase of phototoxicity when the PS/protein ratio increased can be correlated to a loss of the reactivity of the lectin on sugars that is nevertheless unmodified in the case of the 1/1 ratio.

However, a significant increase of LD_{50} (2 to 3 times) can be observed by increasing the number of PS molecules per lectin with TPPS and ce_6 (Table 1). Indeed, in spite of a decrease of MHC, the conjugate conserved a sufficient number of functional carbohydrate-binding sites to trigger hemmaglutination. When conjugates with a high level of PS were used in photodynamic treatment, the probable decrease of binding efficiency toward tumor cells could be compensated, at least partly, by the increase of number of PS molecules linked to the lectin.

CONCLUSIONS

Morniga G conjugate including one $AlPcS_4$ per protein appeared to be particularly promising to be developed as a PDT agent, since it is poorly toxic when irradiated by white light, although it shows a notable phototoxicity when irradiated in the therapeutic window, it kills preferentially cancerous lymphocytes and the sugar selectivity of the lectin part of the molecule is unaltered. Furthermore, the control of the MornigaG/PS ratio allowed the comparison of different photosensitizers targeted against tumoral cells expressing Tn antigen. Indeed, the precise 1/1 PS/lectin ratio obtained with conjugates avoided any misleading due to the different penetration levels of various PS.

ASSOCIATED CONTENT

Supporting Information. MALDI-TOF mass analysis of conjugates and UV−visible spectra of conjugates compared to free lectin and PS. This material is available free of charge via the Internet at http://pubs.acs.org.

AUTHOR INFORMATION

Corresponding Author
*E-mail: marguerite.pitie@lcc-toulouse.fr.

ACKNOWLEDGMENT

E. Evangelio and G. Poiroux contributed equally on this work.

REFERENCES

(1) Celli, J. P., Spring, B. Q., Rizvi, I., Evans, C. L., Samkoe, K. S., Verma, S., Pogue, B. W., and Hasan, T. (2010) Imaging and photodynamic therapy: mechanisms, monitoring, and optimization. *Chem. Rev. 110*, 2795–838.

(2) O'Connor, A. E., Gallagher, W. M., and Byrne, A. T. (2009) Porphyrin and nonporphyrin photosensitizers in oncology: preclinical and clinical advances in photodynamic therapy. *Photochem. Photobiol. 85*, 1053–74.

(3) Ribeiro, S. M., Serra, A. C., and Rocha Gonsalves, A. M. (2008) Immobilised porphyrins in monoterpene photooxidations. *J. Catal. 256*, 331–337.

(4) Juzeniene, A., Peng, Q., and Moan, J. (2007) Milestones in the development of photodynamic therapy and fluorescence diagnosis. *Photochem. Photobiol. Sci. 6*, 1234–45.

(5) Szacilowski, K., Macyk, W., Drzewiecka-Matuszek, A., Brindell, M., and Stochel, G. (2005) Bioinorganic photochemistry: frontiers and mechanisms. *Chem. Rev. 105*, 2647–94.

(6) Nyman, E. S., and Hynninen, P. H. (2004) Research advances in the use of tetrapyrrolic photosensitizers for photodynamic therapy. *J. Photochem. Photobiol. B 73*, 1–28.

(7) Soukos, N. S., Hamblin, M. R., and Hasan, T. (1997) The effect of charge on cellular uptake and phototoxicity of polylysine chlorin(e6) conjugates. *Photochem. Photobiol. 65*, 723–9.

(8) Liu, B., Bian, H. J., and Bao, J. K. (2010) Plant lectins: potential antineoplastic drugs from bench to clinic. *Cancer Lett. 287*, 1–12.

(9) Bies, C., Lehr, C. M., and Woodley, J. F. (2004) Lectin-mediated drug targeting: history and applications. *Adv. Drug Delivery Rev. 56*, 425–35.

(10) Gabius, H. J., Siebert, H. C., Andre, S., Jimenez-Barbero, J., and Rudiger, H. (2004) Chemical biology of the sugar code. *ChemBioChem 5*, 740–64.

(11) Lis, H., and Sharon, N. (1998) Lectins: carbohydrate-specific proteins that mediate cellular recognition. *Chem. Rev. 98*, 637–674.

(12) Komath, S. S., Kavitha, M., and Swamy, M. J. (2006) Beyond carbohydrate binding: new directions in plant lectin research. *Org. Biomol. Chem. 4*, 973–88.

(13) Poiroux, G., Pitié, M., Culerrier, R., Segui, B., Van Damme, E. J., Peumans, W. J., Bernadou, J., Levade, T., Rouge, P., Barre, A., and Benoist, H. (2011) Morniga g: a plant lectin as an endocytic ligand for photosensitizer molecule targeting toward tumor-associated T/Tn antigens. *Photochem. Photobiol. 87*, 370–7.

(14) Singh, T., Wu, J. H., Peumans, W. J., Rouge, P., Van Damme, E. J., and Wu, A. M. (2007) Recognition profile of Morus nigra agglutinin (Morniga G) expressed by monomeric ligands, simple clusters and mammalian polyvalent glycotopes. *Mol. Immunol. 44*, 451–62.

(15) Rouge, P., Peumans, W. J., Barre, A., and Van Damme, E. J. (2003) A structural basis for the difference in specificity between the two jacalin-related lectins from mulberry (Morus nigra) bark. *Biochem. Biophys. Res. Commun. 304*, 91–7.

(16) Van Damme, E. J., Hause, B., Hu, J., Barre, A., Rouge, P., Proost, P., and Peumans, W. J. (2002) Two distinct jacalin-related lectins with a different specificity and subcellular location are major vegetative storage proteins in the bark of the black mulberry tree. *Plant Physiol. 130*, 757–69.

(17) Ohtsubo, K., and Marth, J. D. (2006) Glycosylation in cellular mechanisms of health and disease. *Cell 126*, 855–67.

(18) Springer, G. F. (1997) Immunoreactive T and Tn epitopes in cancer diagnosis, prognosis, and immunotherapy. *J. Mol. Med. 75*, 594–602.

(19) Maeda, A. (2009) Extracorporeal photochemotherapy. *J. Dermatol. Sci. 54*, 150–156.

(20) Knobler, R., Barr, M. L., Couriel, D. R., Ferrara, J. L., French, L. E., Jaksch, P., Reinisch, W., Rook, A. H., Schwarz, T., and Greinix, H. (2009) Extracorporeal photopheresis: past, present, and future. *J. Am. Acad. Dermatol. 61*, 652–65.

(21) Casas, C., Saint-Jalmes, B., Loup, C., Lacey, C., and Meunier, B. (1993) Synthesis of cationic metalloporphyrin precursors related to the design of DNA cleavers. *J. Org. Chem. 58*, 2913–2917.

(22) Brasseur, N., Langlois, R., La Madeleine, C., Ouellet, R., and van Lier, J. E. (1999) Receptor-mediated targeting of phthalocyanines to macrophages via covalent coupling to native or maleylated bovine serum albumin. *Photochem. Photobiol. 69*, 345–52.

(23) Tniguchi, V. T. (1978) Ph.D. thesis.

(24) Khadish, K. M., Smith, K. M., Guilard, R. (2000) in *The Porphyrin Handbook* (Press., A., Ed.) p 198.

(25) Tarrago-Trani, M. T., Jiang, S., Harich, K. C., and Storrie, B. (2006) Shiga-like toxin subunit B (SLTB)-enhanced delivery of chlorin e6 (Ce6) improves cell killing. *Photochem. Photobiol. 82*, 527–37.

(26) Hamblin, M. R., Miller, J. L., and Ortel, B. (2000) Scavenger-receptor targeted photodynamic therapy. *Photochem. Photobiol. 72*, 533–40.

(27) Soukos, N. S., Hamblin, M. R., Keel, S., Fabian, R. L., Deutsch, T. F., and Hasan, T. (2001) Epidermal growth factor receptor-targeted immunophotodiagnosis and photoimmunotherapy of oral precancer in vivo. *Cancer Res. 61*, 4490–6.

(28) Milhas, D., Cuvillier, O., Therville, N., Clave, P., Thomsen, M., Levade, T., Benoist, H., and Segui, B. (2005) Caspase-10 triggers Bid cleavage and caspase cascade activation in FasL-induced apoptosis. *J. Biol. Chem. 280*, 19836–42.

(29) Benoist, H., Culerrier, R., Poiroux, G., Segui, B., Jauneau, A., Van Damme, E. J., Peumans, W. J., Barre, A., and Rouge, P. (2009) Two structurally identical mannose-specific jacalin-related lectins display different effects on human T lymphocyte activation and cell death. *J. Leukoc. Biol. 86*, 103–14.

(30) Zhang, W., Peumans, W. J., Barre, A., Astoul, C. H., Rovira, P., Rouge, P., Proost, P., Truffa-Bachi, P., Jalali, A. A., and Van Damme, E. J. (2000) Isolation and characterization of a jacalin-related mannose-binding lectin from salt-stressed rice (Oryza sativa) plants. *Planta 210*, 970–8.

(31) Nicolson, G. L., and Blaustein, J. (1972) The interaction of Ricinus communis agglutinin with normal and tumor cell surfaces. *Biochim. Biophys. Acta 266*, 543–7.

(32) Goel, M., Anuradha, P., Kaur, K. J., Maiya, B. G., Swamy, M. J., and Salunke, D. M. (2004) Porphyrin binding to jacalin is facilitated by the inherent plasticity of the carbohydrate-binding site: novel mode of lectin-ligand interaction. *Acta Crystallogr., Sect. D: Biol. Crystallogr. 60*, 281–8.

(33) Goel, M., Jain, D., Kaur, K. J., Kenoth, R., Maiya, B. G., Swamy, M. J., and Salunke, D. M. (2001) Functional equality in the absence of structural similarity: an added dimension to molecular mimicry. *J. Biol. Chem. 276*, 39277–81.

(34) Komath, S. S., Bhanu, K., Maiya, B. G., and Swamy, M. J. (2000) Binding of porphyrins by the tumor-specific lectin, jacalin [Jack fruit (Artocarpus integrifolia) agglutinin]. *Biosci. Rep. 20*, 265–76.

(35) Sutton, J. M., Clarke, O. J., Fernandez, N., and Boyle, R. W. (2002) Porphyrin, chlorin, and bacteriochlorin isothiocyanates: useful reagents for the synthesis of photoactive bioconjugates. *Bioconjugate Chem. 13*, 249–63.

(36) Stamati, I., Kuimova, M. K., Lion, M., Yahioglu, G., Phillips, D., and Deonarain, M. P. (2010) Novel photosensitisers derived from pyropheophorbide-a: uptake by cells and photodynamic efficiency in vitro. *Photochem. Photobiol. Sci. 9*, 1033–41.

(37) Lundquist, J. J., and Toone, E. J. (2002) The cluster glycoside effect. *Chem. Rev. 102*, 555–78.

Supporting Information for

Comparative Study of the Phototoxicity of Long-Wavelength Photosensitizers Targeted by the MornigaG Lectin.

Emi Evangelio,†‡ Guillaume Poiroux,‡§ Raphaël Culerrier,§ Geneviève Pratviel,† Els J. M. Van Damme,# Willy J. Peumans,# Annick Barre,‡ Pierre Rougé,‡ Hervé Benoist,§ Marguerite Pitié†*

† CNRS; LCC (Laboratoire de Chimie de Coordination), 205 route de Narbonne, 31077 Toulouse, France.

‡ UMR-CNRS 5546, 31326 Castanet-Tolosan, France

§ INSERM U858, 31432 Toulouse, France

Department of Molecular Biotechnology, Ghent University, Belgium

* Corresponding author: E-mail: marguerite.pitie@lcc-toulouse.fr

Figure S1: MALDI-TOF mass analysis of the β light chain of PS-MorG conjugates.

Figure S2: MALDI-TOF mass analysis of the α heavy chain of PS-MorG conjugates.

Figure S3: Spectroscopic characterization of PS-MorG conjugates and typical examples of the estimation of the PS/lectine ratio.

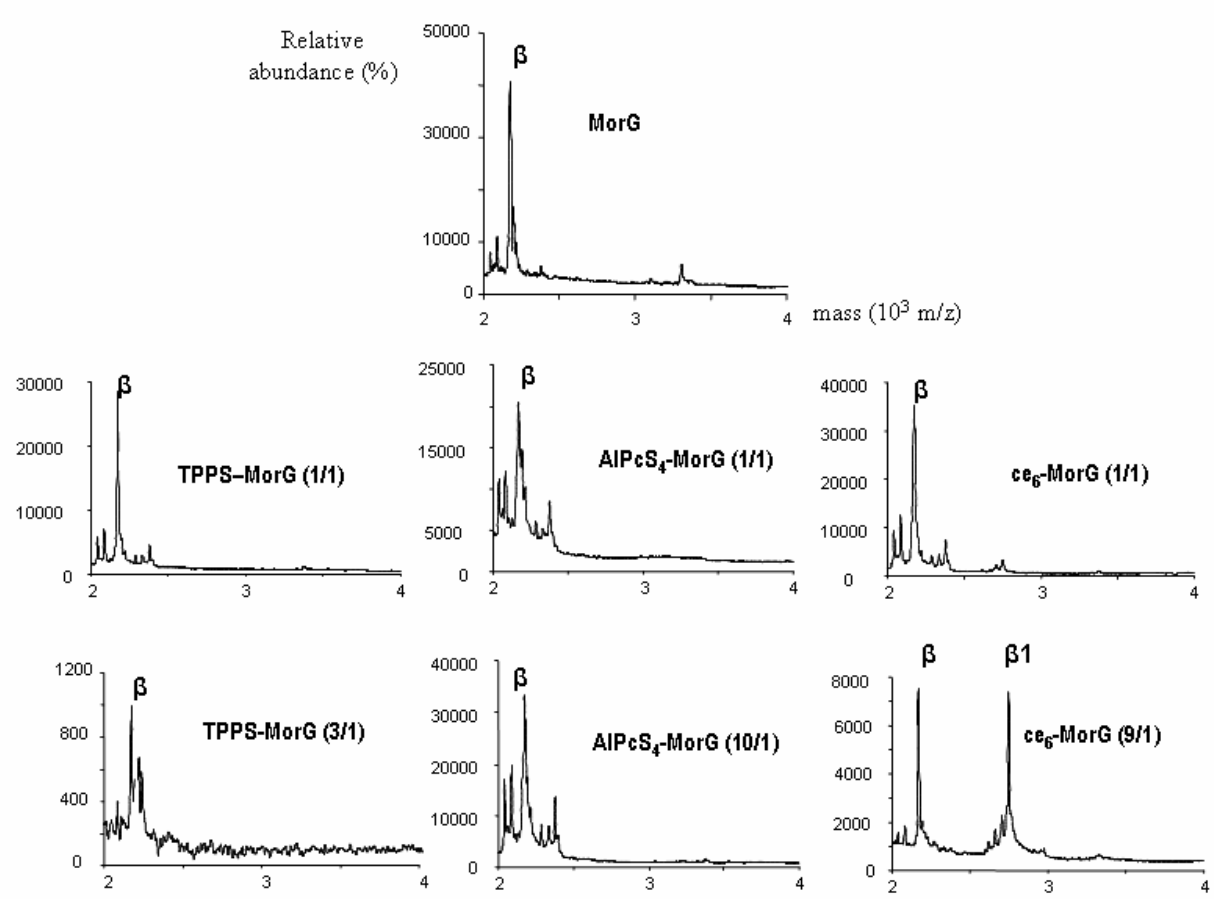

Figure S1: MALDI-TOF mass analysis of the β light chain of PS-MorG conjugates.

β unmodified subunit (MW = 2,179 Da); β1: β light chain covalently linked to one PS. The covalent linkage of ce6 on the β-subunit increased the MW of 578 Da.

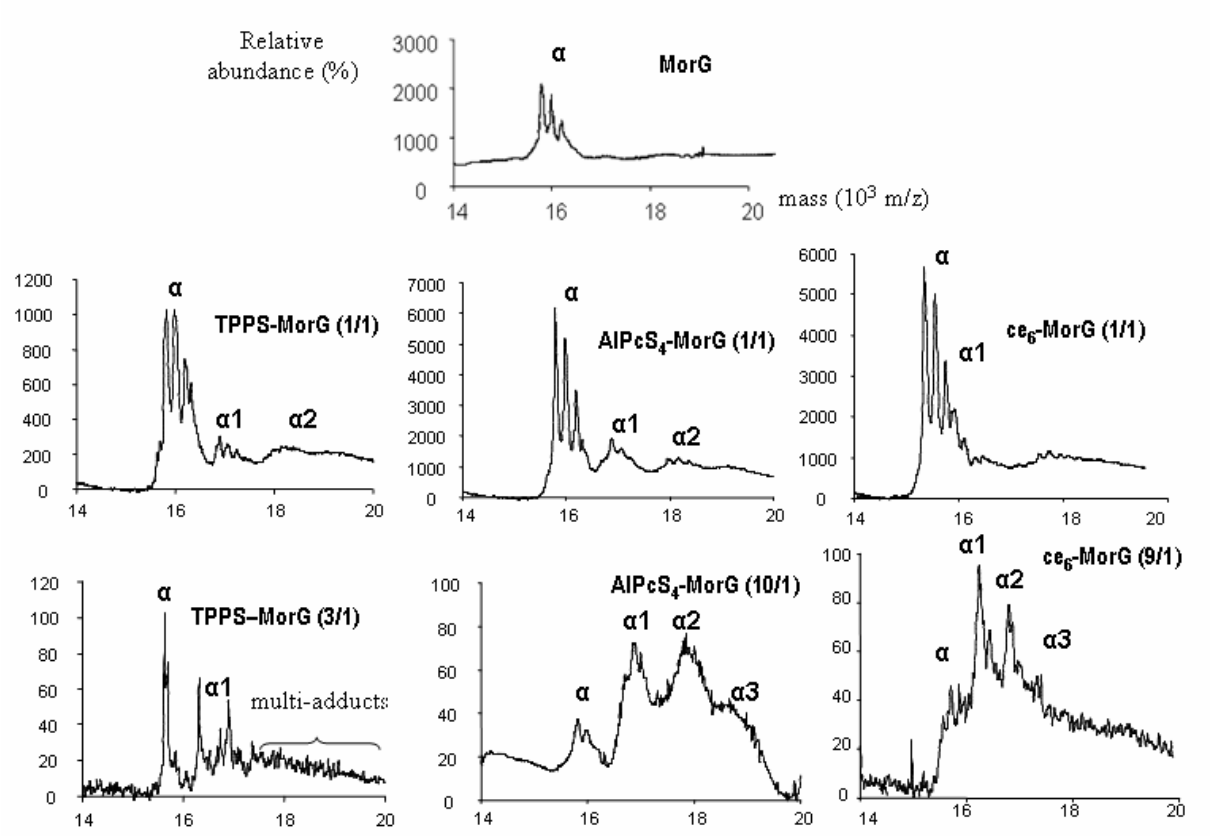

Figure S2: MALDI-TOF mass analysis of the α heavy chain of PS-MorG conjugates. The α chain appeared as a mixture of three polypeptides due to glycosylation of this Morniga G subunit.

α: unmodified subunit (MW = 15,800; 15,990 and 16,190 Da); α1: α heavy chain covalently linked to one PS; α2: α heavy chain covalently linked to Two PS; α3: α heavy chain covalently linked to three PS. The covalent linkage of one PS molecule increased the MW of the α-subunit of 1029, 1079 and 578 Da for TPPS derivative **1**, $AlPcS_4$ derivative **2** (with a TFA ligand on the Al atom) and ce6, respectively. The α1 conjugate appeared in the same mass massif than α in the case of the covalent linkage of one ce6 du to the weak MW of this ce6 chlorine.

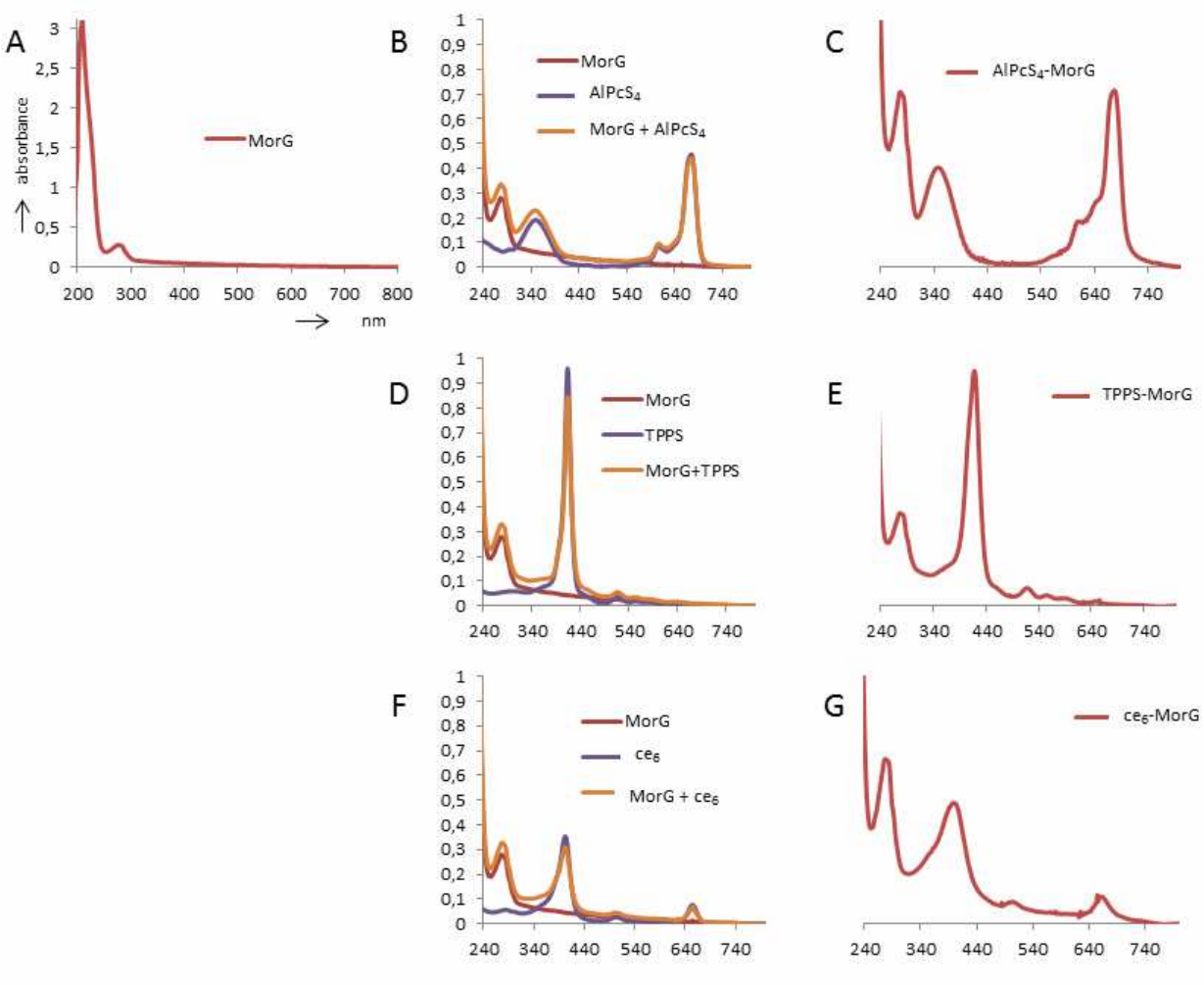

Figure S3: Spectroscopic characterization of PS-MorG conjugates and typical examples of the estimation of the PS/lectine ratio. All experiments were performed in PBS buffer.

A: MorG 2.4 μM. This spectrum was reproduced in red on part B, D and F. B: $AlPcS_4$ derivative **2** at the 2.4 μM concentration (blue) and mixture of MorG 2.4 μM with 2.4 μM of **2** (orange). The presence of MorG induces an increase of 20% of the absorbance at the Soret band of the phthalocyanine when its Q band remained unchanged. C: Typical spectrum of an $AlPcS_4$-MorG conjugate. After correction (increase of 20%) due to the presence of MorG on the absorbance of the phthalocyanine, the PS/lectine ratio was calculated to be 0.9 at the Soret band and a similar ratio of 0.85 was observed at the Q band. Therefore, the increase of 20% of the Soret band previously observed for the mixture of free $AlPcS_4$ and MorG was conserved

for the conjugate since same PS/lectine ratio was measured at the Soret and Q bands when this correction was included. Same argue was used for the estimation of PS/lectine ratios of the others conjugates. D: TPPS derivative **1** at the 2.2 μM concentration (blue) and mixture of MorG 2.4 μM with 2.2 μM of **1** (orange). The presence of MorG induces a decrease of 10% of the absorbance of the Soret band of the porphyrin. E: Typical spectrum of a TPPS-MorG conjugate. After correction due to the presence of MorG on the absorbance of the porphyrin, the PS/lectine ratio was calculated to be 0.9. F: Chlorin e6 at the 2.4 μM concentration (blue) and mixture of MorG 2.4 μM with 2.4 μM of ce6 (orange). The presence of MorG induces a decrease of 20% of the absorbance at the Soret band of the chlorin when its Q band remained unchanged. G: Typical spectrum of a ce6-MorG conjugate. After correction due to the presence of MorG on the absorbance of the chlorin, the PS/lectine ratio was calculated to be 0.7.

For cells experiments, other conjugates showing a PS/lectin ratio of 1 were used.

Bioconjugate Chemistry

ARTICLE

pubs.acs.org/bc

Design and Synthesis of ATP-Based Nucleotide Analogues and Profiling of Nucleotide-Binding Proteins

Justina. C. Wolters,[†] Gerard Roelfes,[‡] and Bert Poolman*[,†]

[†]Department of Biochemistry, Groningen Biomolecular Sciences and Biotechnology Institute, Netherlands Proteomics Centre & Zernike Institute for Advanced Materials

[‡]Department of Biomolecular Chemistry, Stratingh Institute for Chemistry

University of Groningen, Nijenborgh 4, 9747 AG Groningen, The Netherlands

Supporting Information

ABSTRACT: Two nucleotide-based probes were designed and synthesized in order to enrich samples for specific classes of proteins by affinity-based protein profiling. We focused on the profiling of adenine nucleotide-binding proteins. Two properties were considered in the design of the probes: the bait needs to bind adenine nucleotide-binding proteins with high affinity and carry a second functional group suitable and easily accessible for coupling to a chromatography resin. For this purpose, we synthesized *p*-biotinyl amidobenzoic acid-ATP (*p*-BABA-ATP) and *p*-biotinyl aminomethylbenzoic acid-ATP (*p*-BAMBA-ATP). *p*-BABA-ATP and *p*-BAMBA-ATP both bind to ATP-binding cassette (ABC) proteins with at least 10-fold higher affinity than ATP. Several ABC transporters could be enriched using *p*-BABA-ATP or *p*-BAMBA-ATP.

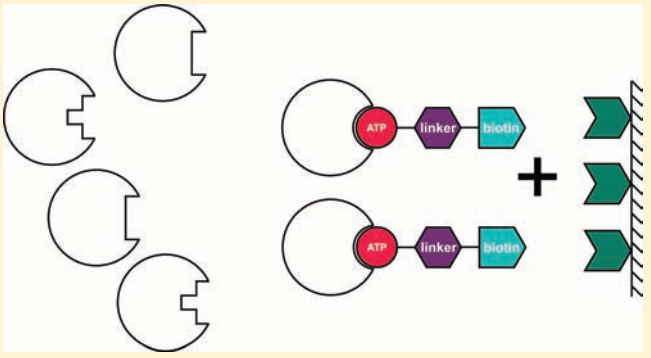

INTRODUCTION

In activity-based protein profiling, protein classes are enriched via a reactive probe that requires the protein or protein domain to be functional. The probe (bait) contains a reactive group and a reporter tag, usually connected via a linker moiety. The binding moiety is designed to react with a specific class of proteins, and the reporter tag of the probe enables their detection and/or enrichment (via fluorescent, affinity, antigen, or isotope-labeled reporter tags). The use of different binding moieties and reactive groups can help in the analysis of the active site of the proteins. The probes can be used to screen for inhibitors via competitive binding studies, with the clear advantage that experiments can be performed in complex mixtures without the requirement for prior enrichment steps (e.g., as used for the identification of drug targets.[1] This protein profiling is routinely done in cell homogenates rather than *in vivo*, because the size of the probes limits their uptake and distribution in the cells. This limitation can be overcome by splitting the label into two parts: a cross-linking group and a reporter tag (fluorescent probe or biotin tag). Both parts of the probe contain an extra reactive group to attach the two halves, using so-called click chemistry (see refs 2,3,4 for click chemistry implemented in activity-based probes). Numerous reviews about activity-based proteomics and their applications have been published in recent years.[5−11]

For the use of ATP analogues, modifications to all three moieties of ATP (the nucleobase, ribose ring, or phosphate groups) have been prepared, yielding nucleotide analogues with different functionalities. The reporter analogues can be divided in molecules with spectroscopic or radioactive moieties and probes that can bind to antibodies or column based materials (like a biotin moiety).[12−15] The features of ATP analogues in studies of nucleotide-binding proteins, in combination with their structures, have been exploited by us to find patterns for modifications. ATP analogues with small modifications at the nucleobase (like azido-ATP, εATP) and phosphate (AMP-PNP, AMP-PCP, and ATPγS) of ATP are tolerated by most adenine nucleotide-binding proteins. Bulkier groups are generally restricted to either the phosphate or ribose ring. The extents to which these modifications are tolerated vary for the different classes (adenine) nucleotide-binding proteins.

Adenine nucleotide-binding proteins cover a large range of protein classes. They can use ATP as source of metabolic energy in living cells, fueling of transport (via transport ATPases) or movement (via molecular motors), and phosphorylation of enzymes and small metabolites via kinases. Most often, ATP (binding and/or hydrolysis) is used in coupling reactions and drives the endergonic steps. Moreover, it is a substrate and/or cofactor involved in DNA/RNA modifying processes like transcription, DNA

Received: January 4, 2011
Revised: April 21, 2011
Published: June 21, 2011

ACS Publications © 2011 American Chemical Society

replication, recombination, and restriction. Besides its function as energy storage unit or substrate for the biosynthesis of DNA/RNA, ATP acts as a signaling molecule for proteins belonging to the class of purinergic receptors. The probes described in this paper were designed for screening of proteins from the ATP-binding cassette (ABC) superfamily but are likely to have broader uses.

Within the class of the adenine nucleotide-binding proteins, ABC proteins play an important role in a wide range of physiological functions, mostly involving translocation of compounds across the membrane (so-called ABC transporters).[16] At least eighteen of the human ABC genes are associated to diseases, including cystic fibrosis (ABCC7), Tangier disease (ABCA1), immune deficiency (ABCB2/3), and many others (listed in ref 17 and on http://nutrigene.4t.com/humanabc.htm).

ABC transporters share a conserved overall architecture with two conserved nucleotide-binding domains (NBDs) and two transmembrane domains (TMDs). The transmembrane domains form a pathway through the membrane for the translocation of the substrates. The energy needed for the translocation is provided by ATP that binds to the NBDs and is hydrolyzed at these sites. A limited number of ATP analogues have been exploited to probe functional and structural aspects of ABC proteins. The fluorescent ATP analogues trinitrophenyl-ATP (TNP-ATP), but also the cross-linking azido-derivatives,[18] have been used to determine binding constants for nucleotides.[19,20] The non- (or slowly) hydrolyzable analogues AMP-PNP[21−23] and ATPγS [24,25] have been used to dissect the effects of adenine nucleotide binding and hydrolysis. Profiling of ABC proteins has, to the best of our knowledge, not been reported.

Here, we describe the synthesis of two adenine nucleotide analogues, *p*-biotinyl amidobenzoic acid-ATP (*p*-BABA-ATP) and *p*-biotinyl aminomethylbenzoic acid-ATP (*p*-BAMBA-ATP), their structural characterization, and their binding to the ABC transporter OpuA. As a proof of principle for the profiling of ABC transporters, several ABC and non-ABC transporters were used for the characterization of the ATP analogues.

EXPERIMENTAL SECTION

Synthesis of Biotinylated Linkers. The synthesis of biotinylated linkers is based on a description of biotinylated amino acid precursors by Skander et al.[26] Briefly, biotin (2.1 mmol) was dissolved in DMF (40 mL) with tributylamine (0.64 mL, 2.7 mmol). isobutyl chloroformate (0.32 mL, 2.5 mmol) was added to the solution to activate the biotin, and the mixture was incubated at room temperature for about 15 min after which it was cooled on ice. Meanwhile, linker (4.1 mmol) was dissolved in DMF (40 mL) and cooled on ice. After cooling, the activated biotin mixture was slowly added to the linker dissolved in DMF, and the mixture was incubated for two hours at 5 °C. The solvent was removed under vacuum, the crude precipitate was recrystallized from 3:1 ethanol/H_2O, and the obtained crystals were washed extensively with water and ethanol. The reaction was performed with two different linkers: *p*-aminobenzoic acid (*p*-ABA) and *p*-aminomethylbenzoic acid (*p*-AMBA). Both biotinylated linkers recrystallized as a white solid, but the recrystallized solid of the biotinylated *p*-aminomethylbenzoic acid was more hygroscopic compared to the solid of the biotinylated *p*-aminobenzoic acid. The yield of pure biotinylated linker was about 40% and the purity of the products was analyzed by NMR:

p-Biotinyl-amidobenzoic Acid (p-BABA). ^{1}H NMR (300 MHz, CD_3SOCD_3): δ = 1.34−1.62 (m, 6H), 2.33 (t, J = 7.3 Hz, 2H), 2.56 (d, J = 12.5, 1H), 2.80 (dd, J = 12.5, 5.1 Hz, 1H), 3.07−3.13 (m, 1H), 4.12 (t, J = 5.1 Hz, 1H), 4.29 (t, J = 6.2 Hz, 1H), 6.39 (d, J = 23.4 Hz, 2H), 7.68 (d, J = 8.8 Hz, 2H), 7.85 (d, J = 8.8, 2H). ^{13}C NMR (200 MHz, CD_3SOCD_3): δ = 25.1, 28.3, 36.5, 55.5, 59.4, 61.3, 118.5, 125.1, 130.5, 143.4, 163.0, 167.2, 172.1. ESI-MS: calculated mass $C_{17}H_{21}N_3O_4S$ 363.44, found m/z $[M]^-$ 362.6.

p-Biotinyl-amidobenzoic Acid (p-BAMBA). ^{1}H NMR (300 MHz, CD_3SOCD_3): δ 1.31−1.57 (m, 6H), 2.14 (t, J = 7.1 Hz, 2H), 2.56 (d, J = 12.5 Hz, 1H), 2.81 (dd, J = 12.5, 5.1 1H), 3.06−3.09 (m, 1H), 4.11 (t, J = 5.1 Hz, 1H), 4.27−4.31 (m, 3H), 6.39 (d, J = 21.2 Hz, 2H), 7.33 (d, J = 8.4 Hz, 2H), 7.87 (d, J = 8.4 Hz, 2H), 8.41 (t, J = 5.5 Hz, 1H). ESI-MS: calculated mass $C_{18}H_{23}N_3O_4S$ 377.47, found m/z $[M]^-$ 376.2.

Synthesis Biotinyl-linker-ATP. The synthesis of the biotinyl-linker-ATP complex is adapted from the synthesis of 3′-*O*-(4′-benzoyl)benzoyl-ATP as described by Williams et al.[27] Glassware was dried at 160 °C prior to use. Biotinylated linker (0.5 mmol) was dissolved in dry DMF (3 mL) together with carbonyldiimidazole (CDI) (1.2 mmol), keeping the setup with the dried glassware under a flow of nitrogen. The reaction was monitored by the evaporation of CO_2 gas, which stopped after 1 h after addition of CDI. Then, ATP (0.5 mmol) in H_2O (12 mL) was added to the mixture, and the reaction was incubated for 6 h under constant stirring at room temperature.

The crude reaction mixture was purified in batches (5 mL) by RP-HPLC, using a preparative C18 column (prepared from Vydac218TPB_1015RPC column material; column dimensions 25/132) connected to an Äkta-purifier system. The column was run at a flow rate of 3 mL/min, using buffer A, triethylammoniumacetate (TEAA, 10 mM) pH 7, and buffer B, acetonitrile plus TEAA pH 7 (10 mM), and the following gradient: 35 min 5% buffer B, 75 min gradient 5−35% buffer B, 15 min 90% buffer B, 15 min 0% buffer B. Fifteen millliliter fractions were collected and analyzed by ESI-MS to determine the fractions containing the ATP analogue. ATP analogue peak fractions of multiple runs were pooled and freeze−dried, and the material was then resuspended in TEAA pH 7 (200 mM) and loaded onto a 1 mL monoQ sepharose column, pre-equilibrated with 20 column volumes TEAA pH 7 (200 mM). The column was washed with 2 × 10 column volumes TEAA pH 7 (200 mM) and eluted with 4 × 5 column volumes TEAA pH 7.0 (1M). Multiple rounds of freeze−drying (the solids were resuspended in Milli-Q) were done to remove the (volatile) TEAA pH 7 completely. The yield of pure product was about 20% based on the amount of the pure ATP analogues (dry weight). The final products were analyzed with ESI-MS:

p-Biotinyl-amidobenzoic Acid-ATP (p-BABA-ATP). (ESI-MS), calculated mass $C_{27}H_{35}N_8O_{16}P_3S$ 852,61, found m/z $[M]^-$ 851.71 (ACN (50%) plus formic acid (0.1%))/ 851.3 (methanol).

p-Biotinyl-amidobenzoic acid-ATP (p-BAMBA-ATP). (ESI-MS), calculated mass $C_{28}H_{37}N_8O_{16}P_3S$ 866.64, found m/z $[M]^-$ 865.6 (ACN (50%) plus formic acid (0.1%)).

Spectral Properties. UV spectra of *p*-BABA-ATP and *p*-BAMBA-ATP were measured on a Cary100 Bio UV−visible spectrophotometer (Varian) with samples of 400 μL (20 μM in a quartz cuvette, with maxima for *p*-BABA-ATP (264 nm), *p*-BABA (260 nm), ATP (258 nm), *p*-BAMBA-ATP (245 nm), and *p*-BAMBA (230 nm). The molar extinction coefficient was not altered upon modification of ATP, and under the experimental conditions, ATP, *p*-BABA-ATP, and *p*-BAMBA-ATP all

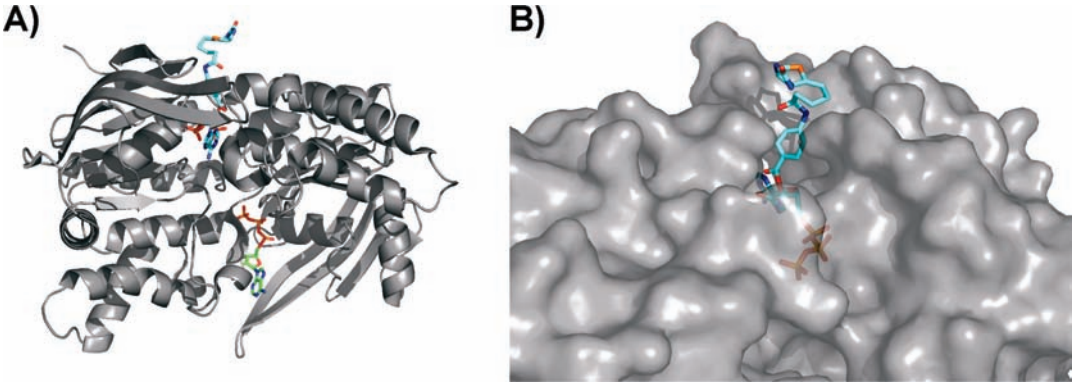

Figure 1. X-ray crystallography structure of the ATPase dimer of the ABC transporter MJ0796 (1L2T).[49] The structure was solved in the presence of ATP (panel A, ATP green/orange), showing the position of the nucleotides. One of the ATP molecules was overlaid with the ATP analogue *p*-BABA-ATP (in blue/orange). Panel B depicts an enlargement of a space-filling model of MJ0796 with the ATP analogue, showing the accessibility of the biotin group.

had molar extinction coefficients of around 15 000 M^{-1} cm^{-1} at their respective absorption maxima.

Partial Hydrolysis of *p*-BABA-ATP. A few milligrams of *p*-BABA-ATP was dissolved in methanol (250 μL). Sodium carbonate was added until the total volume was filled about halfway with powder, to ensure saturating conditions. The mixture was incubated for 1 h at 40 °C, under mixing (800 rpm). The mixture was shortly spun down and the supernatant was mixed 1:1 with ACN (50%) plus formic acid (0.1%). Formic acid was added for the ESI-MS analysis. For ESI-MS/MSMS analysis, the samples were diluted 10× in ACN (50%) plus formic acid (0.1%).

Analytical Methods. Nuclear magnetic resonance spectra were recorded with a 200/300 MHz (^{1}H NMR) or 50/75 MHz (^{13}C NMR) spectrometer. Chemical shifts are reported in delta (δ) units, parts per million (ppm), and as an average shift for split peaks. Coupling constants (J) are reported in Hz.

ESI-MS spectra were measured with a LCQ fleet mass spectrometer (Thermo scientific) via direct injection at a flow rate of 10 μL/min. Settings of the spectrometer were tuned with a standard solution of ATP both in positive and negative ion mode. Samples were diluted in ACN (50%) plus formic acid (0.1%) prior to the measurements. ESI-MS/MSMS mass spectra were recorded on an API3000 triple quadrupole mass spectrometer equipped with a TurboIonSpray source (MDS-Sciex, Concord, Ontario, Canada) in positive ion mode with nitrogen as collision gas, at a collision energy of 40 eV.

Analytical RP-HPLC was performed using a polystyrene/divenyl benzene column (Source 5RPC ST 4.6/150) connected to an Äkta-purifier system. Two buffers were used for the separation: Buffer A, TEAA (100 mM) pH 7.0, and Buffer B, acetonitrile plus TEAA (100 mM) pH 7.0. The settings for the separations were as follows: 200 μL loop, flow 1 mL/min, gradient: 5 min 17% buffer B, 10 min gradient 17−20% buffer B, 5 min 90% buffer B, 5 min 0% B.

TNP-ATP Binding. Purified OpuA (0.7 μM) was preincubated for 10 min with TNP-ATP (2 μM) in KP_i (50 mM) pH 7 plus glycerol (20%), KCl (200 mM), and DDM (0.04%). Fluorescence was measured in a total volume of 800 μL under constant stirring at 25 °C on a Fluorolog-3 spectrophotometer (Jobin Yvon, settings: excitation wavelength of 409 nm (slit 1 nm), emission wavelength of 540 nm (slit 5 nm), and data points were averaged from measurements of 20 s). Nucleotides to chase the TNP-ATP were added via a Hamilton syringe pump (Harvard apparatus) in steps of 4.5 μL ATP (2 mM) and for the ATP analogues (0.14 mM) using stock solutions of ATP (357 mM) and for the ATP analogues (25 mM), both dissolved in KP_i (50 mM) pH 7) and a mixing time of 15 s. Titration of protein solution with KP_i (50 mM) pH 7 were performed to correct for dilution and bleaching during the measurements.

Protein and DNA Constructs. The following ABC transporters were used: OpuA,[28] OpuAΔSBD,[29] GlnPQ,[30] Sav1866,[31] and the soluble nucleotide-binding domain (GlcV) of the ABC transporter GlcSTUV.[32] The following membrane proteins were used as controls (non-ABC transporters): LacS (C320A/A635C),[33] LacY,[34] IIC,[35] and RibU.[36] The Sav1866 gene construct was cloned into the N-Lic vector pNZnLIC as described by Geertsema et al.[37] The genes for GlcV and LacY were expressed in *E. coli,* and all other proteins were produced in *L. lactis* as described in the listed references. GlcV was obtained from M. Pretz and C. van der Does (University Groningen, The Netherlands). Actin (from bovine muscle, A3653), myosin (from rabbit muscle, M1636), and protein kinase A (from bovine heart, P5511) were purchased from Sigma Aldrich.

Profiling with ATP Analogues. Isolation of membrane vesicles and purification of the proteins was done as described.[38] Membrane vesicles were prepared in KP_i (50 mM) pH 7 at a concentration of ca. 20 mg/mL, unless indicated otherwise; for protein purifications, the membrane vesicles were diluted to 5 mg/mL in KP_i (50 mM) pH 7, KCl (200 mM) plus glycerol (20%) and, subsequently, solubilized with DDM (0.5%); purified protein was obtained in KP_i (50 mM) pH 7, KCl (200 mM), glycerol (20%), and DDM (0.05%) plus imidazole (200 mM). GlcV was purified in Na-MES (20 mM) pH 6.5 plus NaCl (100 mM) as described by Pretz and collegues[39] and stored in aliquots at −20 °C. For profiling with the ATP analogues, protein mixtures were incubated with streptactin column material (Streptactin Sepharose from IBA, binding capacity 300 nmol/mL) in the presence of the ATP analogue, using Biospin Poly-Prep columns (volume 1.2 mL, Biorad). The mixture was incubated for at least 1 h at 4 °C (under continuous mixing), before washing and elution of the proteins bound to the column material. The column material was washed in general, with 4 column volumes, prior to elution of the bounds proteins with 1 column volume of 2× SDS loading buffer, which is composed of Tris-HCl (100 mM) pH 6 plus glycerol (20%), bromophenol blue

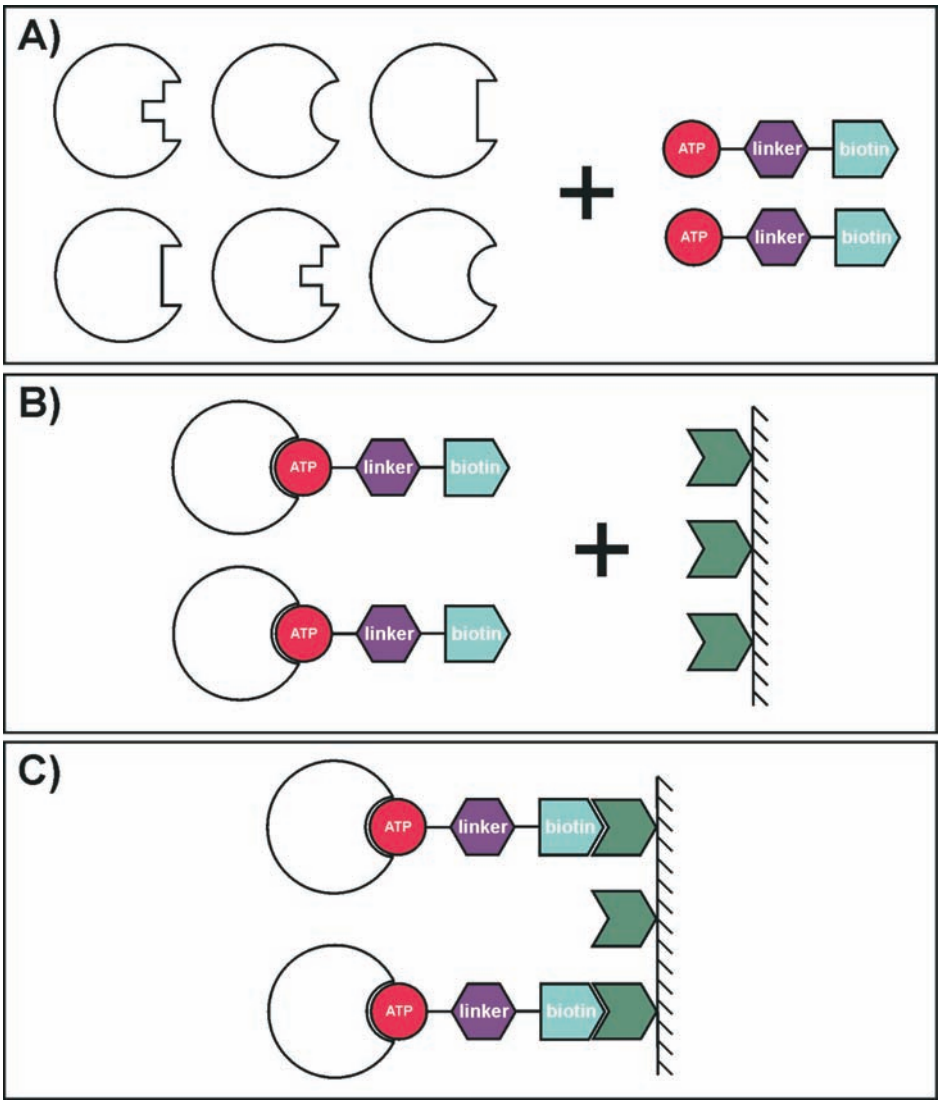

Figure 2. Schematic representation of activity based profiling using an ATP analogue as a probe. Panel A: The ATP (reactive group) moiety of the probe binds specifically to nucleotide-binding proteins within a complex sample. Panel B: The biotin (reporter group) moiety of the probe is used for enrichment of the proteins on streptactin column material. Panel C: The proteins enriched via this method can be analyzed after elution.

(0.002%), and SDS (4%) plus β-mercaptoethanol (1%). Analysis of the protein samples was done on SDS-PAGE gels (12.5%, stained with Coomassie brilliant blue) or subsequent immunoblotting on polyvinylidene difluoride (PVDF) membrane, using the semidry electroblotting technique (blotting for 35 min at 80 mA per blot). Immunodetection was done with an antibody (Amersham Pharmacia Biotech) against the His-tag of the various proteins. The signals were imaged with a CCD camera (Fujifilm, Las-3000 imaging system), using the Western light kit (Tropix Inc.), and quantification of the signals from the SDS-PAGE gels and immunoblots was done with the *AIDA* image analyzer software (version 4.15).

Analytical RP-HPLC. Analytical RP-HPLC was performed using a polystyrene/divenyl benzene column (Source 5RPC ST 4.6/150) connected to an Äkta-purifier system. Two buffers were used for the separation: Buffer A2, triethyl ammonium acetate (TEAA, 100 mM) pH 7.0, and Buffer B2, acetonitrile plus TEAA (100 mM) pH 7.0. The settings for the separations were as follows: 200 μL loop, flow rate 1 mL/min, gradient: 5 min 17% buffer B2, 10 min gradient 17−20% buffer B2, 5 min 90% buffer B2, 5 min 0% B.

RESULTS AND DISCUSSION

Design of the ATP Analogues. (+)-Biotin-hex-acyl-ATP (BHacATP) has been used for activity-based profiling of protein kinases.[40] Protein kinases have a conserved lysine in the binding pocket, i.e., near the phosphates of the nucleotide.[41,42] The electrophilic acyl-phosphate bond of the analogue couples with the ε-amine from this lysine, connecting the biotinylated linker to the protein and freeing it from the nucleotide. Using this analogue, 136 proteins, mostly ATP phosphohydrolases, (protein) kinases, and several heat shock proteins, were identified in lysates of breast cancer cells.[40] However, this probe is not suitable for ABC proteins, because the space for the hexyl-linker with the biotin moiety would be too limited. On the basis of the structures of ABC transporters, relatively large modifications are likely to be tolerated at the 2′- and 3′-OH of the ribose (Figure 1). The

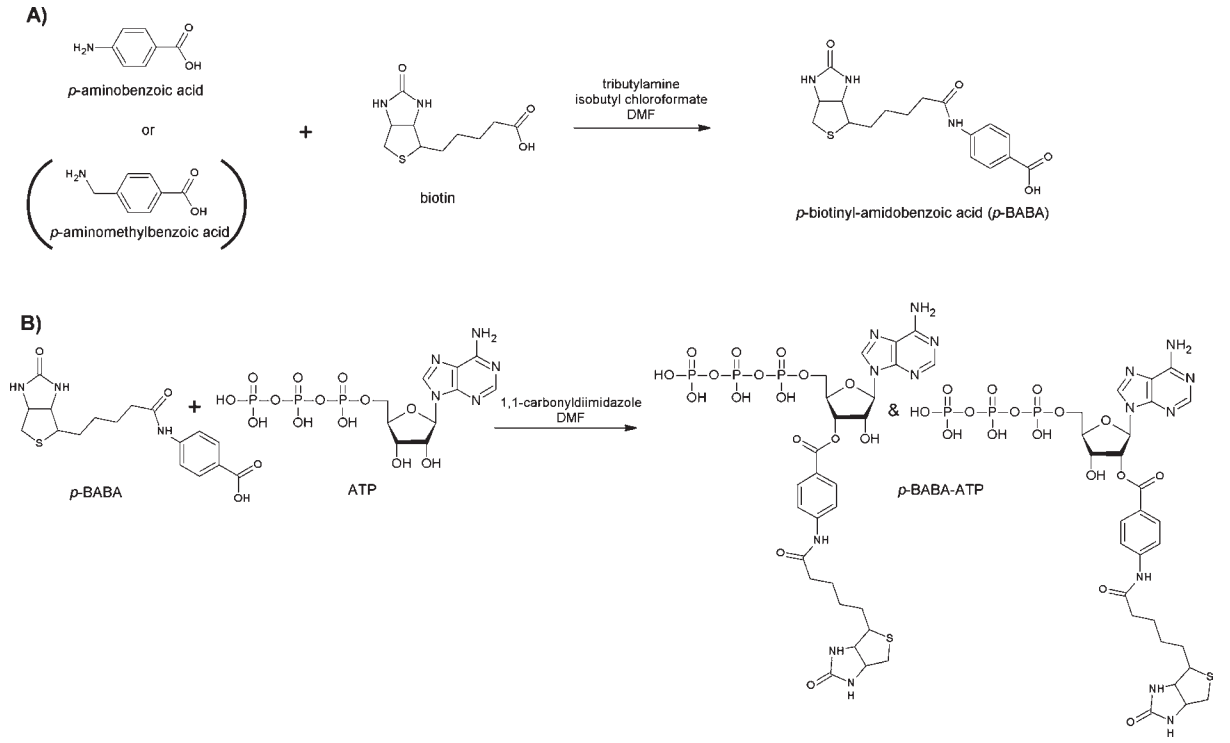

Figure 3. Chemical structures and reaction schemes for the synthesis of the two ATP analogues. Panel A: Synthesis of the biotinylated linkers *p*-biotinyl-amidobenzoic acid (*p*-BABA) and *p*-biotinyl-amidomethylbenzoic acid (*p*-BAMBA). Panel B: Synthesis of *p*-biotinyl-amidobenzoic acid-ATP, shown as two isoforms, from the biotinylated linker and ATP.

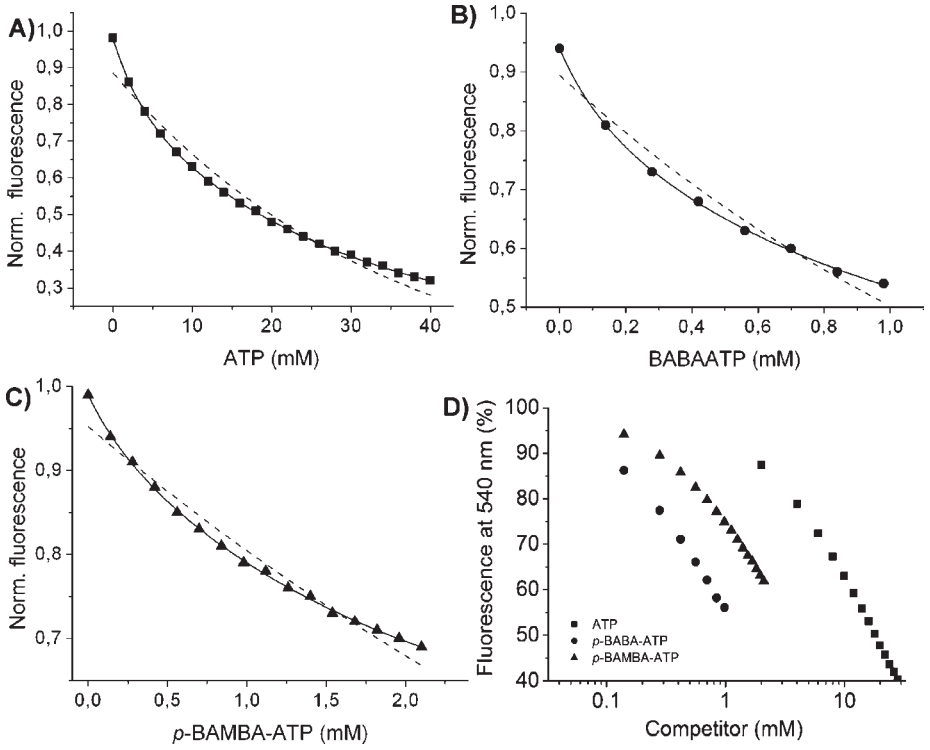

Figure 4. Nucleotide-binding properties of the ATP analogues *p*-BABA-ATP and *p*-BAMBA-ATP. Binding of ATP or the ATP analogues was measured by competition with the TNP-ATP bound to the purified ABC transporter OpuA. Panels A, B, and C show the fluorescence decay upon addition of ATP, *p*-BABA-ATP, and *p*-BAMBA-ATP, respectively, and fitting of the results with single (dashed lines) and double (solid lines) exponential decay fits. Panel D compiles the results collectively on a logarithmic scale.

dx.doi.org/10.1021/bc100592q |*Bioconjugate Chem.* 2011, 22, 1345–1353

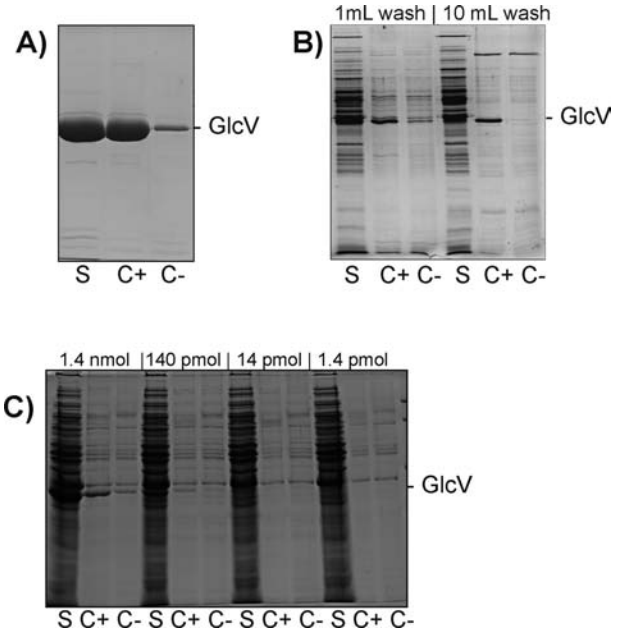

Figure 5. SDS-PAA gels of protein binding to streptactin columns (30 nmol binding sites) in the presence or absence of the ATP analogue *p*-BABA-ATP (30 nmol), using the nucleotide-binding protein GlcV of a glucose ABC transporter from *S. solfataricus* as test sample. Panel A shows the binding of GlcV in the presence or absence of *p*-BABA-ATP as a purified fraction of GlcV (3.4 nmol). Panel B shows the binding of purified GlcV (0.6 nmol) mixed in a *L. lactis* crude cell lysate (0.2 mg) after washing of the column fraction with 1 or 10 mL of washing buffer using 50 mM Na-MES pH 7. Panel C shows the profiling of GlcV present in *L. lactis* crude cell lysates (0.2 mg) at concentrations of 1.4 nmol to 140 pmol GlcV, corresponding to about 27−0.027% of GlcV protein in the lysate using 50 mM KP_i pH7 as buffer. Annotations are as follows: start material (S) and fractions eluted from the column (C); (+) means that proteins were incubated with the column material in the presence of *p*-BABA-ATP and (−) in the absence of ATP analogue. Equal volumes of each fraction were loaded on the gel.

structure of the nucleotide binding protein HlyB indicates that certain modifications may affect the interaction between the ribose of the nucleotide and a glutamine residue in the C-loop of the ABC proteins.[43] We thus designed two ATP analogues with a linker coupled to the ribose to keep the biotin group accessible for binding to a chromatography resin. We introduced an aromatic group in the linker, as previous studies had shown that an aromatic group like trinitrophenol linked to ATP (TNP-ATP) binds to ABC proteins with much higher affinity than genuine ATP.[19,44,45] In fact, ABC transporters have been reported to bind ATP with K_D values in the submillimolar to low millimolar range, which is too low for efficient profiling of the proteins. Guided by these observations, the aromatic ring-structure was used as the basis for the design of the linkers to couple the biotin moiety to ATP. For the activity-based protein profiling with these probes (as summarized in Figure 2), the ATP moiety is the bait to enrich for the ABC proteins, and the biotin moiety is the reporter tag for enrichment.

Synthesis of the ATP Analogues. The general synthetic approach was designed and optimized for biotinyl-amidobenzoic acid-ATP (*p*-BABA-ATP). The synthesis of biotinyl-amidobenzoic acid (Figure 3A) was achieved as described previously for biotinylated amino acid precursors, using isobutyl chloroformate to activate the biotin prior to reaction with the amine of the linker moiety.[26]

A second linker, that is, 4-aminomethylbenzoic acid, was used to synthesize 4-biotinylamidomethylbenzoic acid (*p*-BAMBA) (Figure 3A). The presence of an additional methylene group compared to *p*-BABA resulted in a significant decrease in the solubility of the biotintylated linker in DMF. The coupling of the biotinylated linker to adenosine triphosphate (ATP) was based on a method described for 3′-*O*-(4-benzoyl)benzoyl-ATP.[27] This involved the activation of the acid group from biotin with carbonyldiimidazole,[46] which subsequently reacted with a hydroxyl group on the ribose ring of ATP to form an ester linkage (Figure 3B).

The ratio between ATP and *p*-BABA was varied from 1:8 to 2:1. With an 8-fold excess of *p*-BABA, hardly any *p*-BABA-ATP was formed (data not shown). The optimal yield of *p*-BABA-ATP was found using equimolar amounts of ATP and *p*-BABA as judged by reversed-phase HPLC analysis. *p*-BABA-ATP always gave a double peak in the RP-HPLC analysis (Supporting Information Figure S5A-B). However, ESI MS analysis showed only a single peak at m/z 851. This can be explained by the formation of two isomeric products, resulting from the coupling of the biotinylated linker to the 2′- and 3′-OH group of the ribose ring of ATP.

The reaction time was varied from 1 to 25 h (Supporting Information Figure S5B) with the highest yield after 25 h. Notably, the *p*-BABA-ATP isomer of the first peak was formed first and the other isomer only after longer conversion times (>1 h).

Two purification steps were performed to obtain the pure ATP derivatives: after preparative RP-HPLC (pRP-HPLC) purification, the ATP-derivative containing fractions were pooled and further purified on a strong anion exchange resin (monoQ sepharose). *p*-BABA-ATP and *p*-BAMBA-ATP eluted at 1 M TEAA pH 7 and the ESI-MS analysis of the pooled elution fractions (elution fractions 1−3) showed a clean signal for the ATP analogue (Supporting Information Figure S5C-G).

Structural Properties. The ESI-MS spectra of the product proved that the coupling of *p*-BABA to ATP was successful but did not establish connectivity of the product, that is, the position of the coupling. Although literature reports suggest the present method to result at the 2′-OH or 3′-OH position of the ribose ring,[27] in principle, also, coupling to the γ-phosphate or the amine group of the adenine ring can occur. NMR analysis was complicated as a result of the formation of the two isomers (Supporting Information Figure S4). However, the appearance of new signals in the ^{1}H NMR spectra between 5 and 6 ppm with the expected multiplicity corresponds to what was reported for the ribose modified ATP-analogue BzATP,[27] indicating that the linker is coupled to the ribose hydroxy groups. Measurements with ^{13}C NMR (^{13}C NMR and HSQC) were limited by the low solubility of the ATP analogue. The spectra did not improve enough at higher temperatures or longer measurement times (up to 1 week).

A variety of other methods were used to demonstrate the coupling of the biotinylated linker to the hydroxyl groups of the ribose ring of ATP. Measurements of *p*-BABA-ATP and ATP with ^{31}P NMR showed equal spectra (both with shifts at 39.2 ppm (t) and 51.2 ppm (dd)), which excludes coupling of the *p*-BABA to the γ-phosphate of ATP. Partial hydrolysis and detection by ESI-MS (and MSMS) of *p*-BABA-ATP was used to distinguish between coupling of the biotinylated linker to the amine group of the adenine ring or the hydroxyl groups of the ribose ring. The ESI-MS spectrum of the ATP analogue after hydrolysis with sodium carbonate in methanol did show

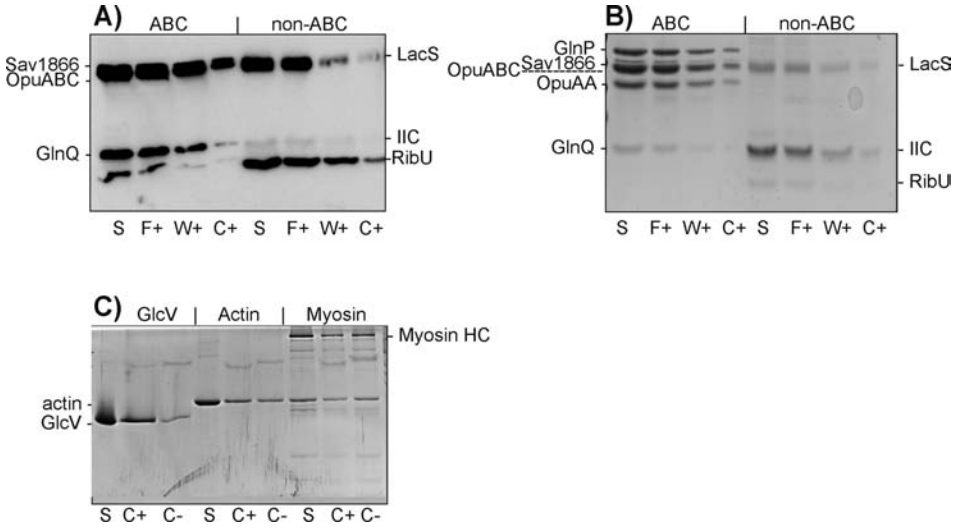

Figure 6. Immunoblot (panel A) and SDS-PAA gel (panels B and C) monitoring the binding of ABC transporters, non-ABC transporters, and other nucleotide-binding proteins from mixtures of purified proteins [15−30 μg purified protein (panel A and B) and 80 μg protein (panel C)] to streptactin [15 nmol (panel A and B) and 30 nmol (panel C) binding sites] in the presence of *p*-BABA-ATP [15 nmol (panel A and B) and 30 nmol (panel C)]. 50 mM KP_i pH 7 plus 200 mM KCl was used as buffer for these experiments, supplemented with 0.04% DDM for the samples with purified membrane proteins. The following ABC transporter proteins: OpuA, GlnPQ, and Sav1866 were used; RibU, LacS, and the IIC domain of the mannitol-PTS (panel A and B) served as controls, as these proteins do not contain a nucleotide-binding site; actin and myosin (myosin heavy chains (myosin HC) binds the ATP) (panel C) were used as a second set of controls as these are non-ABC type nucleotide-binding proteins. Annotations are as follows: start material (S), flowthrough (F), wash fraction (W), and fractions eluted from the column (C), (+) means that proteins were incubated with the column material in the presence of *p*-BABA-ATP and (−) in the absence of ATP analogue. Equal volumes of each fraction were loaded on the gel.

transesterification of *p*-BABA-ATP (Supporting Information Figure S6) and the methyl ester of *p*-BABA could be detected. Reaction of the amide bonds under these conditions is highly unlikely, as it is illustrated that the amide bond between the biotin and linker moiety remained intact under these conditions. In combination, these experiments demonstrate that *p*-BABA is indeed attached to the 2′/3′-OH group via an ester linkage.

Nucleotide-Binding Properties. A competition assay was used to determine the binding properties of *p*-BABA-ATP and *p*-BAMBA-ATP relative to that of ATP. The purified ABC transporter OpuA from *Lactococcus lactis*[47] was used as a model protein to assess the relative binding affinities. The nucleotide binding affinity of OpuA for ATP is in the millimolar range and cannot be probed directly. The fluorescent ATP analogue trinitrophenyl-adenosine triphosphate (TNP-ATP) binds to OpuA with micromolar affinity, and the relative affinity of ATP or other analogues can be accessed via competitive nucleotide-binding studies[48] (Figure 4). Figure 4A,B,C shows the decrease in TNP-ATP fluorescence with increasing concentration of ATP, *p*-BABA-ATP, and *p*-BAMBA-ATP, respectively. The data were fitted with single- and double-exponential decay functions, and only the latter yielded excellent fits. The data are indicative of low- and high-affinity binding of TNP-ATP, which most likely reflects the open (low-affinity) and closed (high-affinity) conformation of the nucleotide-binding domains. The data and interpretation are consistent with observations on the soluble nucleotide-binding protein OpuAA from *B. subtilis*: here, the low- and high-affinity binding correspond to the monomeric and dimeric nucleotide-binding domains.[19] In the concentration range used, the high-affinity component of TNP-ATP binding could not be fully chased with ATP, *p*-BABA-ATP, or *p*-BAMBA-ATP; for economic reasons, we did not titrate at higher concentrations as it would have taken an impractical amount of synthesized ATP (analogue) to chase all TNP-ATP. Despite the complex biphasic kinetics, the data clearly show that both *p*-BABA-ATP and *p*-BAMBA-ATP were at least 10-fold more efficient in competing with TNP-ATP from the binding pocket of OpuA than ATP; *p*-BABA-ATP displayed the highest affinity (Figure 4D). These measurements show that the linker does improve the binding affinity of the nucleotide analogues to the ABC transporter OpuA.

Binding of Nucleotide-Binding Proteins. Binding of the proteins via the ATP analogues was confirmed by SDS-PAGE analysis using the soluble nucleotide-binding domain (GlcV) of the glucose ABC transporter from *Sulfolobus solfataricus* (with a nanomolar affinity for ATP[39]). GlcV bound efficiently to streptactin column material in the presence of *p*-BABA-ATP as can be seen in Figure 5A. Spiking of GlcV to a crude cell free extract of *L. lactis* (0.2 mg total protein) at a protein concentration of 3 μM GlcV still yielded a highly significant binding in the presence of *p*-BABA-ATP (Figure 5B). Quantification of the signals on the SDS-PAGE gel showed that about 41% of the GlcV was bound to the column in the presence of *p*-BABA-ATP, which compares to 6% (unspecific binding) in the absence of the ATP analogue. Further dilution of GlcV into the crude cell free extract showed that specific binding could still be detected until a concentration of 0.7 μM (140 pmol) of GlcV (Figure 5C).

Next, mixtures of three purified ABC transporters (OpuA, GlnPQ, and Sav1866) and three non-ABC transporters (LacS, RibU, and IIC) were compared (Figure 6A,B), where the membrane proteins lacking a nucleotide-binding site (non-ABC transporters) are used as controls for the levels of nonspecific binding. Sav1866 and OpuA showed clear binding. The fact that OpuAA was detected by immunoblotting indicated that the whole complex of OpuA was bound since the His-tag is on OpuABC subunit and *p*-BABA-ATP is binding to the OpuAA

subunit. In the case of GlnPQ, the His-tag is on the ATPase subunit (GlnQ), but no binding of GlnQ was detected. However, GlnP (the transmembrane domain-substrate binding protein) was detected on SDS-PAGE gels, most likely reflecting aspecific binding. LacS and IIC did not significantly bind to the streptactin column. Experiments using detergent-solubilized membrane vesicles with overexpressed proteins yielded similar results (data not shown). The results show that ABC transporters can be enriched specifically with the ATP analogues, but the presence of residual protein in the flowthrough and wash fractions indicates that a further improvement in binding affinity would be desirable. We also assessed the binding of other types of nucleotide-binding proteins, namely, actin, myosin, and protein kinase A, for which the probes were not designed. No specific binding was observed for any of these proteins (Figure 6C; data for protein kinase A is not shown), confirming the specificity of the probes for ABC-type nucleotide-binding proteins.

CONCLUSION

Two ATP analogues with biotinylated linkers coupled to the hydroxyl groups of the ribose ring of ATP were synthesized successfully, namely, *p*-biotinyl amidobenzoic acid-ATP (*p*-BABA-ATP) and *p*-biotinyl aminomethylbenzoic acid-ATP (*p*-BAMBA-ATP). The coupling of biotin to the linker was demonstrated by ^{1}H and ^{13}C NMR, and the correct coupling of the biotinylated linker to the ATP was deduced from ESI-MS/MSMS analyses of partial digests of the ATP analogues and ^{31}P NMR. Ligand-binding experiments showed that the two ATP analogues bind to the ABC transporter OpuA with at least 1 order of magnitude higher affinity than genuine ATP. The presence of the biotin moiety on the analogues was exploited for the enrichment and profiling of nucleotide-binding proteins. Relatively specific binding was demonstrated for several ABC transporters.

ASSOCIATED CONTENT

Supporting Information. NMR spectra (Figure S1−4), RP-HPLC/MS spectra (Figure S5−6), and absorbance analyses (Figure S7) of the synthesis steps. This material is available free of charge via the Internet at http://pubs.acs.org.

AUTHOR INFORMATION

Corresponding Author

*Bert Poolman, Nijenborgh 4, 9747AG, Groningen, The Netherlands. Tel: +31 50 3634190. Fax: +31 50 3634195. E-mail: b.poolman@rug.nl.

ACKNOWLEDGMENT

We would like to thank Hjalmar Permentier for his help with the ESI-MS/MSMS measurements, and Ruud Scheek and Renee Otten for their help with the NMR measurements. We would like to thank the following people for providing purified proteins or membrane vesicles: Monika Pretz and Chris van der Does (purified GlcV), Gea Schuurman-Wolters (GlnPQ, IIC, Sav1866, LacY), Siva Ramadurai (LacS), Josy ter Beek (RibU), Guus Erkens (soluble cell free extracts) and Faizah Fulyani (soluble cell free extracts). We would like to thank Wim Huibers and Fabrizia Fusetti for their help with the LC-MS measurements. This work was supported by grants from The Netherlands Organisation for Scientific research (NWO, Chemical Sciences Top Subsidy to BP; grant number 700-56-302 and The Netherlands Proteomics Centre (NPC).

REFERENCES

(1) Heal, W. P., Wickramasinghe, S. R., and Tate, E. W. (2008) Activity based chemical proteomics: profiling proteases as drug targets. *Curr. Drug Discovery Technol. 5*, 200–212.

(2) Kolb, H. C., Finn, M. G., and Sharpless, K. B. (2001) Click chemistry: diverse chemical function from a few good reactions. *Angew. Chem., Int. Ed. Engl. 40*, 2004–2021.

(3) Speers, A. E., Adam, G. C., and Cravatt, B. F. (2003) Activity-based protein profiling in vivo using a copper(i)-catalyzed azide-alkyne [3 + 2] cycloaddition. *J. Am. Chem. Soc. 125*, 4686–4687.

(4) Speers, A. E., and Cravatt, B. F. (2004) Profiling enzyme activities in vivo using click chemistry methods. *Chem. Biol. 11*, 535–546.

(5) Barglow, K. T., and Cravatt, B. F. (2007) Activity-based protein profiling for the functional annotation of enzymes. *Nat. Methods 4*, 822–827.

(6) Cravatt, B. F., Wright, A. T., and Kozarich, J. W. (2008) Activity-based protein profiling: from enzyme chemistry to proteomic chemistry. *Annu. Rev. Biochem. 77*, 383–414.

(7) Evans, M. J., and Cravatt, B. F. (2006) Mechanism-based profiling of enzyme families. *Chem. Rev. 106*, 3279–3301.

(8) Hagenstein, M. C., and Sewald, N. (2006) Chemical tools for activity-based proteomics. *J. Biotechnol. 124*, 56–73.

(9) Schmidinger, H., Hermetter, A., and Birner-Gruenberger, R. (2006) Activity-based proteomics: enzymatic activity profiling in complex proteomes. *Amino Acids 30*, 333–350.

(10) Sieber, S. A., and Cravatt, B. F. (2006) Analytical platforms for activity-based protein profiling--exploiting the versatility of chemistry for functional proteomics. *Chem. Commun. (Camb.)* 2311–2319.

(11) Uttamchandani, M., Li, J., Sun, H., and Yao, S. Q. (2008) Activity-based protein profiling: new developments and directions in functional proteomics. *ChemBioChem 9*, 667–675.

(12) Bagshaw, C. R. (2001) ATP analogues at a glance. *J. Cell Sci. 114*, 459–460.

(13) Cremo, C. R. (2003) Fluorescent nucleotides: Synthesis and characterization. *Biophotonics, Part A 360*, 128–177.

(14) Jameson, D. M., and Eccleston, J. F. (1997) Fluorescent nucleotide analogs: Synthesis and applications. *Fluoresc. Spectrosc. 278*, 363–390.

(15) Yount, R. G. (1975) ATP analogs. *Adv. Enzymol. Relat. Areas Mol. Biol. 43*, 1–56.

(16) Davidson, A. L., Dassa, E., Orelle, C., and Chen, J. (2008) Structure, function, and evolution of bacterial ATP-binding cassette systems. *Microbiol. Mol. Biol. Rev. 72*, 317-64, table.

(17) Dean, M. (2005) The genetics of ATP-binding cassette transporters. *Methods Enzymol. 400*, 409–429.

(18) al Shawi, M. K., Urbatsch, I. L., and Senior, A. E. (1994) Covalent inhibitors of P-glycoprotein ATPase activity. *J. Biol. Chem. 269*, 8986–8992.

(19) Horn, C., Bremer, E., and Schmitt, L. (2003) Nucleotide dependent monomer/dimer equilibrium of OpuAA, the nucleotide-binding protein of the osmotically regulated ABC transporter OpuA from Bacillus subtilis. *J. Mol. Biol. 334*, 403–419.

(20) Liu, R. H., and Sharom, F. J. (1997) Fluorescence studies on the nucleotide binding domains of the P-glycoprotein multidrug transporter. *Biochemistry 36*, 2836–2843.

(21) Orelle, C., Ayvaz, T., Everly, R. M., Klug, C. S., and Davidson, A. L. (2008) Both maltose-binding protein and ATP are required for nucleotide-binding domain closure in the intact maltose ABC transporter. *Proc. Natl. Acad. Sci.U. S. A. 105*, 12837–12842.

(22) Shapiro, A. B., and Ling, V. (1995) Reconstitution of drug transport by purified P-glycoprotein. *J. Biol. Chem. 270*, 16167–16175.

(23) Verdon, G., Albers, S. V., Dijkstra, B. W., Driessen, A. J., and Thunnissen, A. M. (2003) Crystal structures of the ATPase subunit of

the glucose ABC transporter from Sulfolobus solfataricus: nucleotide-free and nucleotide-bound conformations. *J. Mol. Biol. 330*, 343–358.

(24) Morbach, S., Tebbe, S., and Schneider, E. (1993) The ATP-binding cassette (ABC) transporter for maltose/maltodextrins of Salmonella typhimurium. Characterization of the ATPase activity associated with the purified MalK subunit. *J. Biol. Chem. 268*, 18617–18621.

(25) Sauna, Z. E., Kim, I. W., Nandigama, K., Kopp, S., Chiba, P., and Ambudkar, S. V. (2007) Catalytic cycle of ATP hydrolysis by P-glycoprotein: evidence for formation of the E.S reaction intermediate with ATP-gamma-S, a nonhydrolyzable analogue of ATP. *Biochemistry 46*, 13787–13799.

(26) Skander, M., Humbert, N., Collot, J., Gradinaru, J., Klein, G., Loosli, A., Sauser, J., Zocchi, A., Gilardoni, F., and Ward, T. R. (2004) Artificial metalloenzymes: (Strept)avidin as host for enantioselective hydrogenation by achiral biotinylated rhodium-diphosphine complexes. *J. Am. Chem. Soc. 126*, 14411–14418.

(27) Williams, N., and Coleman, P. S. (1982) Exploring the adenine-nucleotide binding-sites on mitochondrial F1-ATPase with a new photoaffinity probe, 3′-O-(4-benzoyl)benzoyl adenosine 5′-triphosphate. *J. Biol. Chem. 257*, 2834–2841.

(28) van der, Heide, T., and Poolman, B. (2000) Osmoregulated ABC-transport system of Lactococcus lactis senses water stress via changes in the physical state of the membrane. *Proc. Natl. Acad. Sci. U. S. A. 97*, 7102–7106.

(29) Biemans-Oldehinkel, E., and Poolman, B. (2003) On the role of the two extracytoplasmic substrate-binding domains in the ABC transporter OpuA. *EMBO J. 22*, 5983–5993.

(30) Schuurman-Wolters, G. K., and Poolman, B. (2005) Substrate specificity and ionic regulation of GlnPQ from Lactococcus lactis. An ATP-binding cassette transporter with four extracytoplasmic substrate-binding domains. *J. Biol. Chem. 280*, 23785–23790.

(31) Dawson, R. J., and Locher, K. P. (2006) Structure of a bacterial multidrug ABC transporter. *Nature 443*, 180–185.

(32) Verdon, G., Albers, S. V., Dijkstra, B. W., Driessen, A. J., and Thunnissen, A. M. (2002) Purification, crystallization and preliminary X-ray diffraction analysis of an archaeal ABC-ATPase. *Acta Crystallogr., Sect. D: Biol. Crystallogr. 58*, 362–365.

(33) Doeven, M. K., Folgering, J. H., Krasnikov, V., Geertsma, E. R., van den, Bogaart, G., and Poolman, B. (2005) Distribution, lateral mobility and function of membrane proteins incorporated into giant unilamellar vesicles. *Biophys. J. 88*, 1134–1142.

(34) Teather, R. M., Bramhall, J., Riede, I., Wright, J. K., Furst, M., Aichele, G., Wilhelm, U., and Overath, P. (1980) Lactose carrier protein of Escherichia coli. Structure and expression of plasmids carrying the Y gene of the lac operon. *Eur. J. Biochem. 108*, 223–231.

(35) Boer, H., Hoeve-Duurkens, R. H., Schuurman-Wolters, G. K., Dijkstra, A., and Robillard, G. T. (1994) Expression, purification, and kinetic characterization of the mannitol transport domain of the phosphoenolpyruvate-dependent mannitol phosphotransferase system of Escherichia coli. Kinetic evidence that the E. coli mannitol transport protein is a functional dimer. *J. Biol. Chem. 269*, 17863–17871.

(36) Burgess, C. M., Slotboom, D. J., Geertsma, E. R., Duurkens, R. H., Poolman, B., and van Sinderen, D. (2006) The riboflavin transporter RibU in Lactococcus lactis: molecular characterization of gene expression and the transport mechanism. *J. Bacteriol. 188*, 2752–2760.

(37) Geertsma, E. R., and Poolman, B. (2007) High-throughput cloning and expression in recalcitrant bacteria. *Nat. Methods 4*, 705–707.

(38) Biemans-Oldehinkel, E., Mahmood, N. A., and Poolman, B. (2006) A sensor for intracellular ionic strength. *Proc. Natl. Acad. Sci. U. S. A. 103*, 10624–10629.

(39) Pretz, M. G., Albers, S. V., Schuurman-Wolters, G., Tampe, R., Driessen, A. J. M., and van der Does, C. (2006) Thermodynamics of the ATPase cycle of GlcV, the nucleotide-binding domain of the glucose ABC transporter of Sulfolobus solfataricus. *Biochemistry 45*, 15056–15067.

(40) Patricelli, M. P., Szardenings, A. K., Liyanage, M., Nomanbhoy, T. K., Wu, M., Weissig, H., Aban, A., Chun, D., Tanner, S., and Kozarich, J. W. (2007) Functional interrogation of the kinome using nucleotide acyl phosphates. *Biochemistry 46*, 350–358.

(41) Zheng, J., Knighton, D. R., Ten Eyck, L. F., Karlsson, R., Xuong, N., Taylor, S. S., and Sowadski, J. M. (1993) Crystal structure of the catalytic subunit of cAMP-dependent protein kinase complexed with MgATP and peptide inhibitor. *Biochemistry 32*, 2154–2161.

(42) Hanks, S. K., and Hunter, T. (1995) Protein kinases 6. The eukaryotic protein kinase superfamily: kinase (catalytic) domain structure and classification. *FASEB J. 9*, 576–596.

(43) Oswald, C., Holland, I. B., and Schmitt, L. (2006) The motor domains of ABC-transporters. What can structures tell us? *Naunyn Schmiedebergs Arch. Parmacol. 372*, 385–399.

(44) Qu, Q., Russell, P. L., and Sharom, F. J. (2003) Stoichiometry and affinity of nucleotide binding to P-glycoprotein during the catalytic cycle. *Biochemistry 42*, 1170–1177.

(45) Oswald, C., Jenewein, S., Smits, S. H., Holland, I. B., and Schmitt, L. (2008) Water-mediated protein-fluorophore interactions modulate the affinity of an ABC-ATPase/TNP-ADP complex. *J. Struct. Biol. 162*, 85–93.

(46) Gottikh, B. P., Krayevsky, A. A., Tarussova, N. B., Purygin, P. P., and Tsilevich, T. L. (1970) The general synthetic route to amino acid esters of nucleotides and nucleoside-5′-triphosphates and some properties of these compounds. *Tetrahedron 26*, 4419–4433.

(47) Patzlaff, J. S., van der Heide, T., and Poolman, B. (2003) The ATP/Substrate stoichiometry of the ATP-binding cassette (ABC) transporter OpuA. *J. Biol. Chem. 278*, 29546–29551.

(48) Wolters, J. C., Berntsson, R. P., Gul, N., Karasawa, A., Thunnissen, A. M., Slotboom, D. J., and Poolman, B. (2010) Ligand binding and crystal structures of the substrate-binding domain of the ABC transporter OpuA. *PLoS One 5*, e10361.

(49) Smith, P. C., Karpowich, N., Millen, L., Moody, J. E., Rosen, J., Thomas, P. J., and Hunt, J. F. (2002) ATP binding to the motor domain from an ABC transporter drives formation of a nucleotide sandwich dimer. *Mol. Cell 10*, 139–149.

SUPPORTING INFORMATION

Design and synthesis of ATP-based nucleotide analogues for the profiling of adenine-nucleotide binding proteins

Justina. C. Wolters [†], Gerard Roelfes [‡] and Bert Poolman *[†]

[†] Department of Biochemistry, Groningen Biomolecular Sciences and Biotechnology Institute, Netherlands Proteomics Centre & Zernike Institute for Advanced Materials University of Groningen, Nijenborgh 4, 9747 AG Groningen, The Netherlands
[‡] Department of Biomolecular Chemistry, Stratingh Institute for Chemistry, University of Groningen, Nijenborgh 4, 9747 AG Groningen, The Netherlands
*Corresponding author: Bert Poolman, Nijenborgh 4, 9747AG, Groningen, The Netherlands, Tel: +31 50 3634190. Fax: +31 50 3634195, E-mail: b.poolman@rug.nl

List of contents

Figure S1-4 NMR spectra
Figure S5-6 RP-HPLC/MS spectra
Figure S7 Absorbance analyses of the synthesis steps.

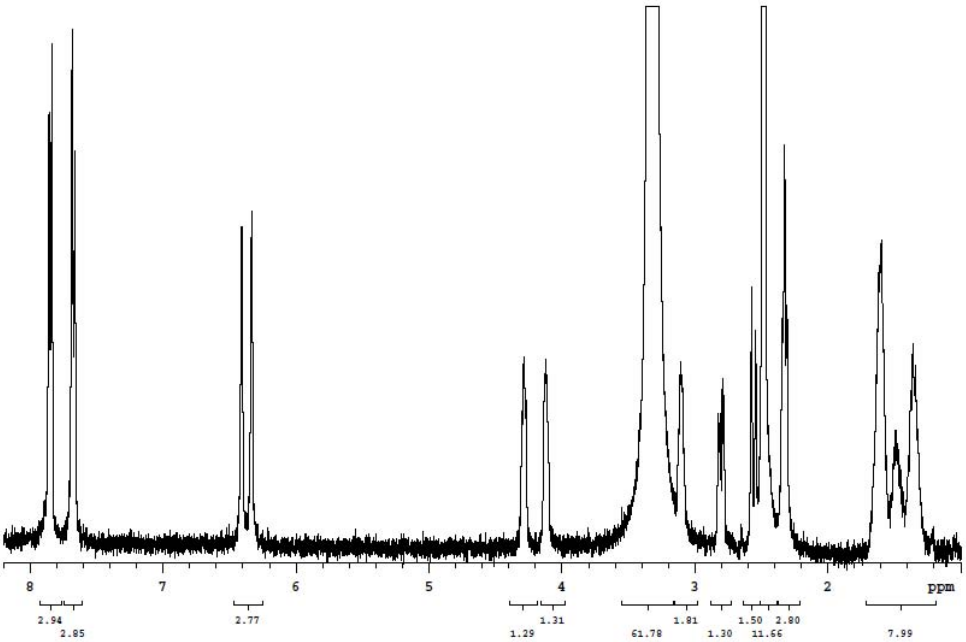

Figure S1. ^{1}H-NMR spectrum *4-[5-(2-Oxo-hexahydro-thieno[3,4-d]imidazol-4-yl)-pentanoylamino]-benzoic acid* (para-biotinyl-amidobenzoic acid, *p*-BABA): ^{1}H-NMR (300 MHz, CD_3SOCD_3): δ = 1.34-1.62 (m, 6H), 2.33 (t, *J* = 7.3 Hz, 2H), 2.56 (d, *J* = 12.5, 1H), 2.80 (dd, *J* = 12.5, 5.1 Hz, 1H), 3.07-3.13 (m, 1H), 4.12 (t, *J* = 5.1 Hz, 1H), 4.29 (t, *J* = 6.2 Hz, 1H), 6.39 (d, *J* = 23.4 Hz, 2H), 7.68 (d, *J* = 8.8 Hz, 2H), 7.85 (d, *J* = 8.8, 2H).

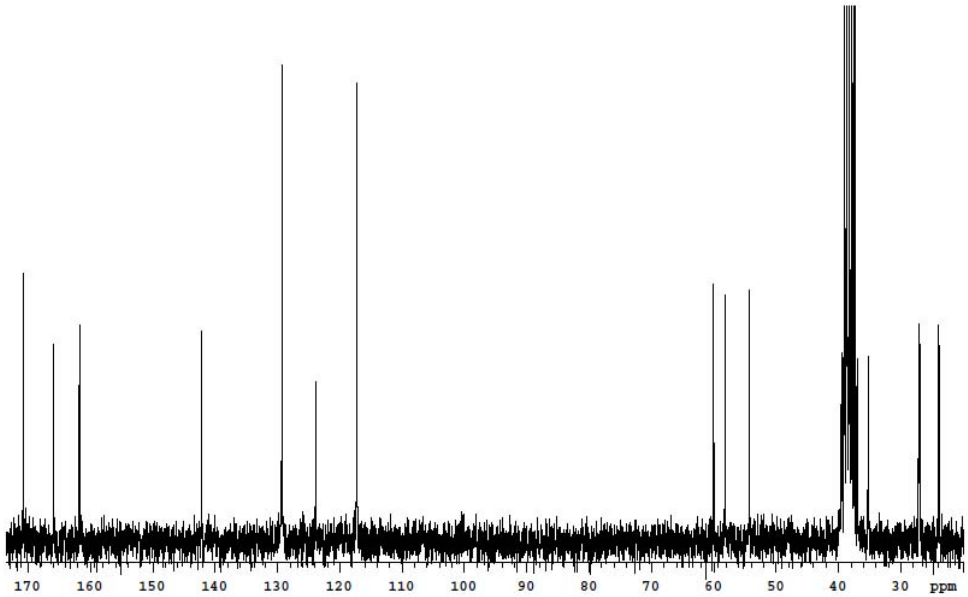

Figure S2. ^{13}C-NMR spectrum *4-[5-(2-Oxo-hexahydro-thieno[3,4-d]imidazol-4-yl)-pentanoylamino]-benzoic acid* (para-biotinyl-amidobenzoic acid, *p*-BABA): ^{13}C-NMR (200 MHz, CD_3SOCD_3): δ = 25.1, 28.3, 36.5, 55.5, 59.4, 61.3, 118.5, 125.1, 130.5, 143.4, 163.0, 167.2, 172.1.

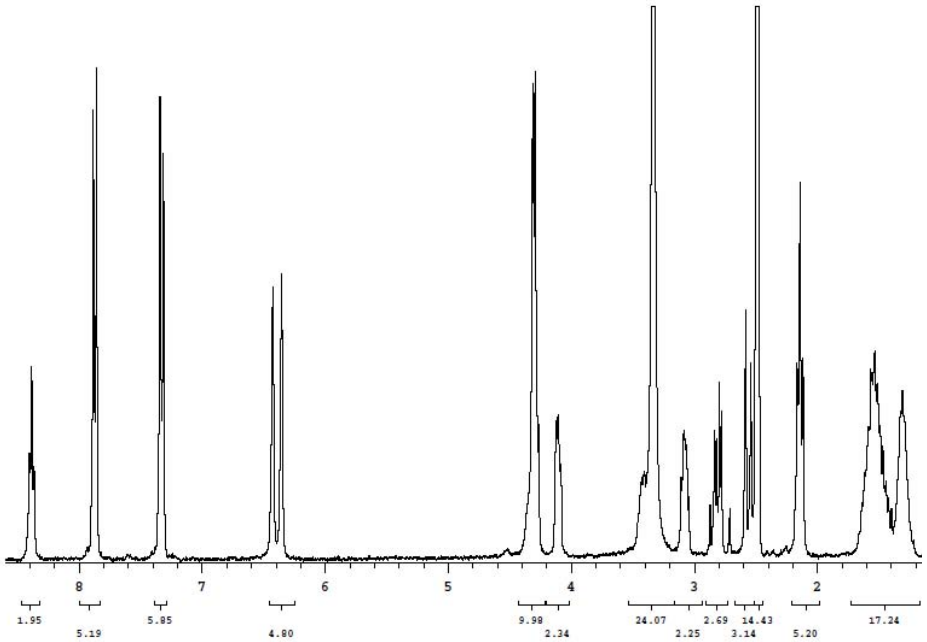

Figure S3. ^{1}H-NMR spectrum *4-{[5—(2-Oxo-hexahydro-thieno[3,4-d]imidazol-4-yl)-pentanoylamino]-methyl}-benzoic acid* (para-biotinyl-amidobenzoic acid, *p*-BAMBA): ^{1}H-NMR (300 MHz, CD_3SOCD_3): δ 1.31-1.57 (m, 6H), 2.14 (t, *J* = 7.1 Hz, 2H), 2.56 (d, *J* = 12.5 Hz, 1H), 2.81 (dd, *J* = 12.5, 5.1 1H), 3.06-3.09 (m, 1H), 4.11 (t, *J* = 5.1 Hz, 1H), 4.27-4.31 (m, 3H), 6.39 (d, *J* = 21.2 Hz, 2H), 7.33 (d, *J* =8.4 Hz, 2H), 7.87 (d, *J* = 8.4 Hz, 2H), 8.41 (t, *J* = 5.5 Hz, 1H).

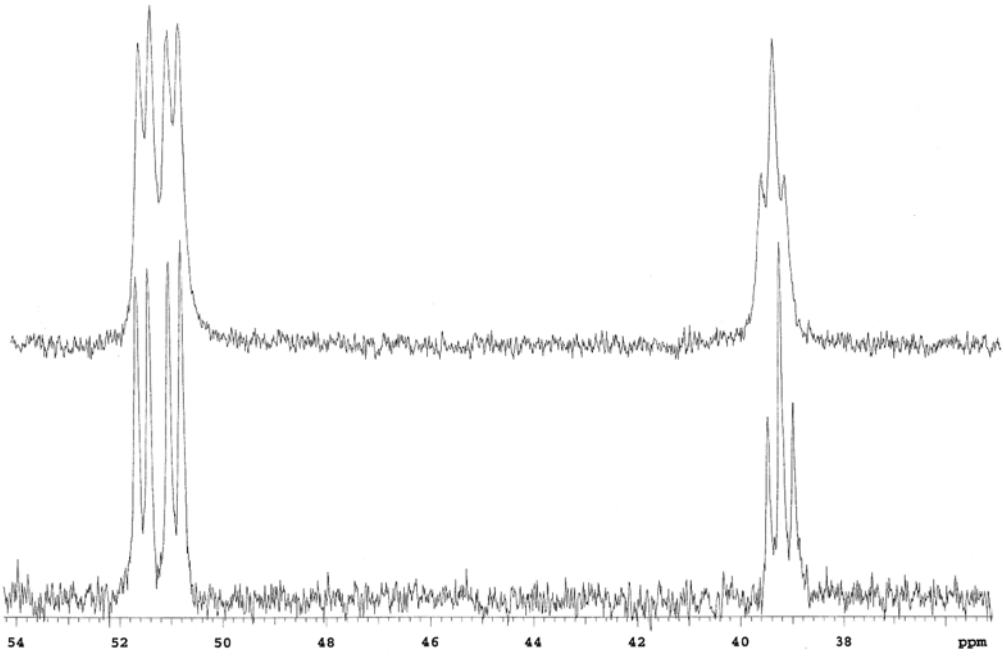

Figure S4. Overlay of the ^{31}P-NMR spectra of ATP (top spectrum) and *p*-BABA-ATP (bottom spectrum).

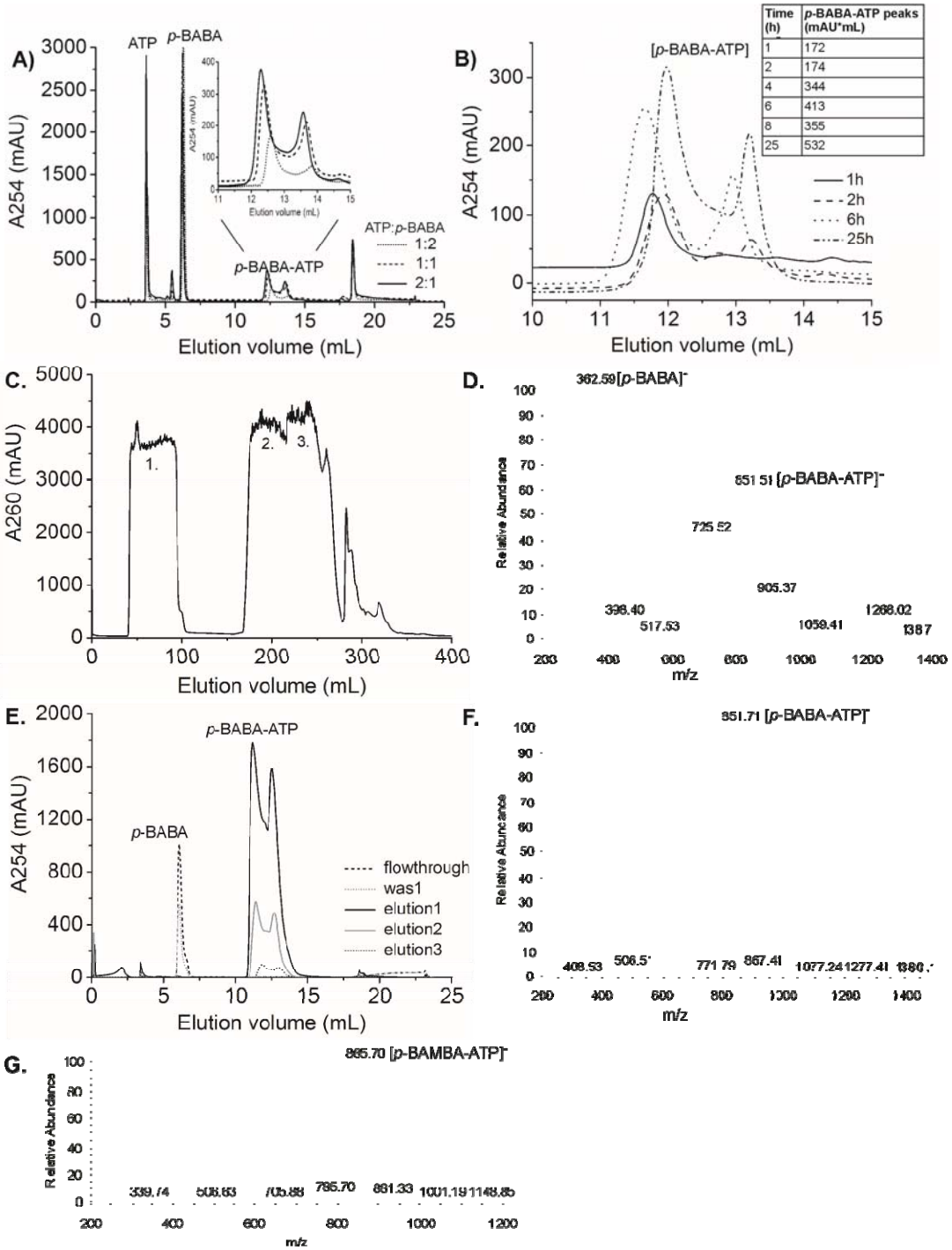

Figure S5. Characterization of the reaction products from the syntheses of the two ATP analogues. Annotation of the peaks in the HPLC measurements was based on standard runs with ATP and *p*-BABA and/or ESI-MS analysis of the peak fractions. Panel A: aRP-HPLC analysis of the *p*-BABA-ATP synthesis at different ratios of the starting materials, that are, ATP and *p*-BABA (inset: enlargement of the *p*-BABA-ATP double peaks); 20x diluted samples of the reaction mixtures are shown. Panel B: aRP-HPLC analysis of the *p*-BABA-ATP synthesis as a function of time; 100x diluted samples are shown (inset table: the summed values of the integral of both *p*-BABA-ATP peaks). Panel C: spectrum of a pRP-HPLC purification of the crude *p*-BABA-ATP reaction mixture. Peak 1 contains ATP, peak 2 contains *p*-BABA and peak 3 contains *p*-BABA-ATP, all based on ESI-MS analysis. Panel D: ESI-MS (negative mode) analysis of the pooled fractions of pRP-HPLC purified *p*-BABA-ATP (fractions from peak 3, panel C). Panel E: aRP-HPLC spectra from a monoQ purification of the pRP-HPLC purified *p*-BABA-ATP reaction mixture. Panel F: ESI-MS (negative mode) analysis of the pooled elution fractions of the *p*-BABA-ATP after monoQ purification (elution fractions from panel F after multiple rounds of freeze drying to remove the TEAA buffer). Panel G: ESI-MS (negative mode) analysis of monoQ-purified *p*-BAMBA-ATP

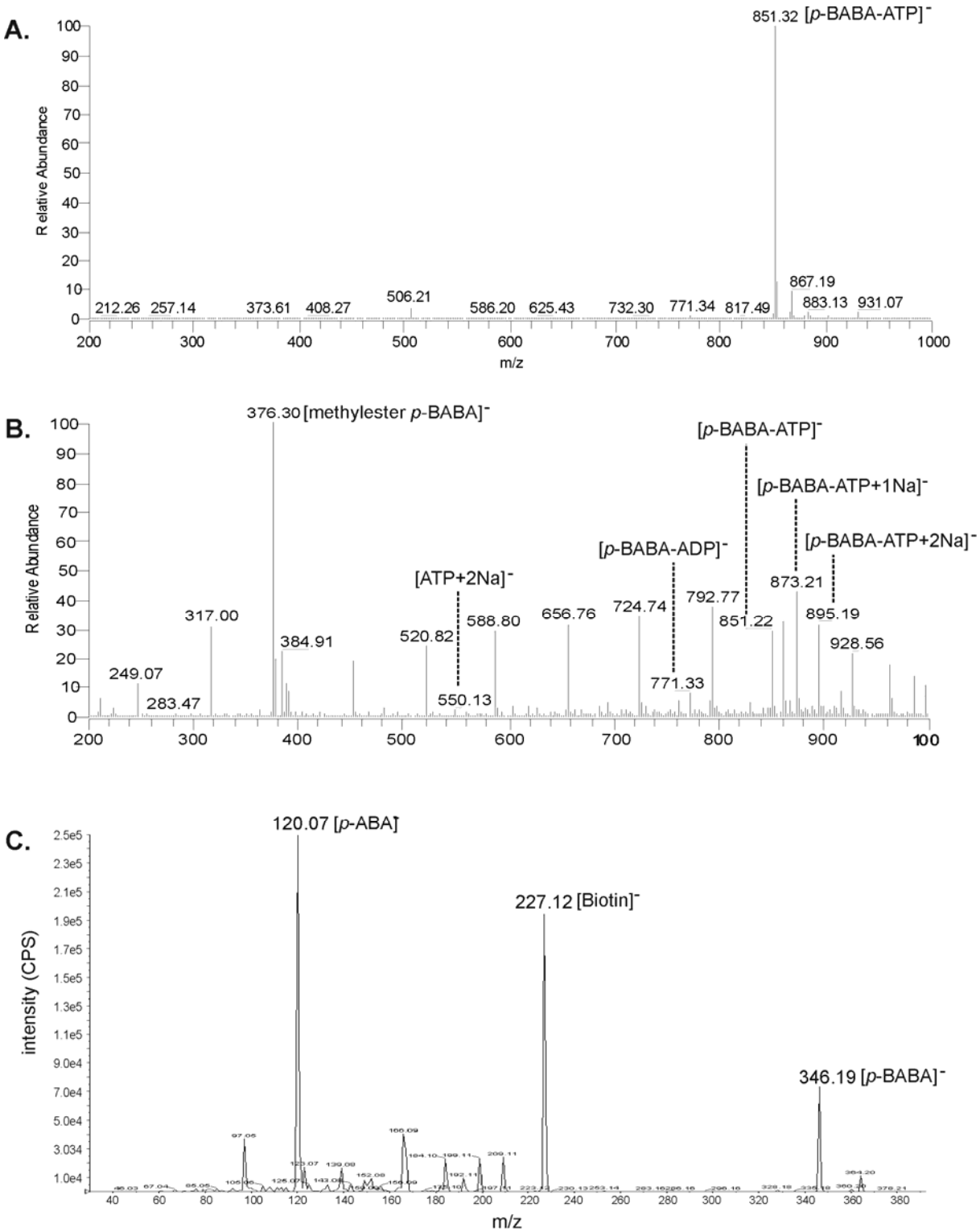

Figure S6. Analysis of the partial hydrolysis of *p*-BABA-ATP. Panel A: ESI-MS (negative mode) of *p*-BABA-ATP dissolved in methanol. Panel B: ESI-MS (negative mode) of *p*-BABA-ATP hydrolyzed in sodium-carbonate after 1h incubation at 40 °C. Panel C: ESI-MSMS (positive mode) peak analysis of the *p*-BABA methylester.

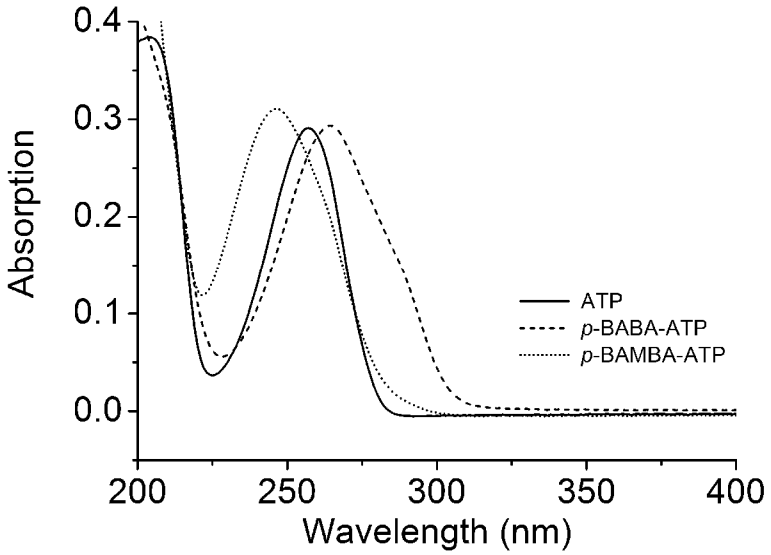

Figure S7. Spectral properties of ATP, *p*-BABA-ATP and *p*-BAMBA-ATP (20 µM). The absorption reached an optimum at 245 nm for *p*-BAMBA-ATP, 258 nm for ATP and 264 nm for *p*-BABA-ATP in 50 mM KP_i pH 7.

Bioconjugate Chemistry

ARTICLE

pubs.acs.org/bc

Pseudosaccharide Functionalized Dendrimers as Potent Inhibitors of DC-SIGN Dependent Ebola Pseudotyped Viral Infection

Joanna Luczkowiak,[§] Sara Sattin,[‡] Ieva Sutkevičiūtė,[∥,#] José Juan Reina,[‡] Macarena Sánchez-Navarro,[†] Michel Thépaut,[∥,⊥] Lorena Martínez-Prats,[§] Anna Daghetti,[‡] Franck Fieschi,[*,∥,#] Rafael Delgado,[*,§] Anna Bernardi,[*,‡,¶] and Javier Rojo[*,†]

[†]Glycosystems Laboratory, Instituto de Investigaciones Químicas, CSIC — Universidad de Sevilla, Américo Vespucio 49, 41092 Seville, Spain

[‡]Università degli Studi di Milano, Dipartimento di Chimica Organica e Industriale, and CISI, Milano, Italy

[§]Laboratorio de Microbiología Molecular, Instituto de Investigación Hospital 12 de Octubre (imas12), 28041 Madrid, Spain

[∥]Institut de Biologie Structurale, CNRS, UMR 5075, 41 rue Jules Horowitz, 38027 Grenoble France

[⊥]CEA, DSV, 38027 Grenoble France

[#]Université Joseph Fourier, Institut Universitaire de France, 38000 Grenoble, France

[¶]CNR-ISTM, Institute of Molecular Sciences and Technologies, Milano, Italy

S *Supporting Information*

ABSTRACT: The development of compounds with strong affinity for the receptor DC-SIGN is a topic of remarkable interest due to the role that this lectin plays in several pathogen infection processes and in the modulation of the immune response. DC-SIGN recognizes mannosylated and fucosylated oligosaccharides in a multivalent manner. Therefore, multivalent carbohydrate systems are required to interact in an efficient manner with this receptor and compete with the natural ligands. We have previously demonstrated that linear pseudodi- and pseudotrisaccharides are adequate ligands for DC-SIGN. In this work, we show that multivalent presentations of these glycomimetics based on polyester dendrons and dendrimers lead to very potent inhibitors (in the nanomolar range) of cell infection by Ebola pseudotyped viral particles by blocking DC-SIGN receptor. Furthermore, SPR model experiments confirm that the described multivalent glycomimetic compounds compete in a very efficient manner with polymannosylated ligands for binding to DC-SIGN.

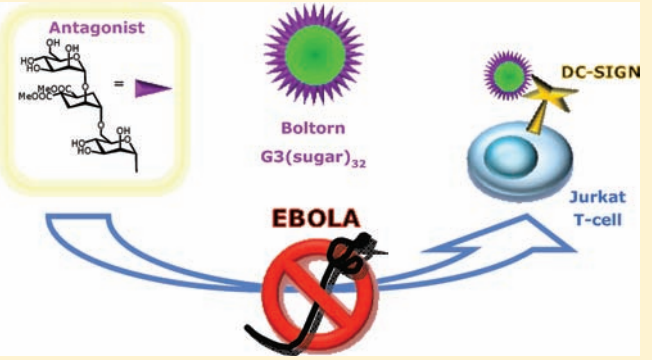

INTRODUCTION

Carbohydrates are involved in several biological processes including cell-differentiation, migration, tumor progression and metastasis, inflammation, pathogen infection, and so forth.[1] Carbohydrates participate in these events through complex and selective recognition processes triggered by interaction with receptors.

One of the processes that initialize immune response to pathogen invasion is the interaction of the pathogen surface glycans with C-type lectin receptors expressed on the antigen-presenting cells (APCs), such as dendritic cells (DCs). Although usually individual carbohydrate unit binding to lectin is weak (K_D in millimolar range), the clustered organization of these receptors as well as high glycosylation of their ligands create the conditions for more specific multivalent interactions, and thus overcome low affinity problems.[2−5] The use of scaffolds to prepare carbohydrate multivalent systems is nowadays a very useful and common approach to develop tools to understand and intervene in these biological processes where carbohydrates play a key role.[6,7]

The lack of design in these multivalent systems is partly a result of the often scarce information about the structural details of the multivalent presentation of the corresponding receptors at the cell surface. However, even if these details were known, topological design of large, multivalent molecules would still not be straightforward and the valency and 3D structures required to achieve a strong cluster effect on a given receptor cannot be estimated a priori. These facts explain the huge number of examples illustrating different strategies to target cellular receptors in a multivalent manner. In this context, our research is focused on the development of glycodendrimers to block a C-type lectin, DC-SIGN, which recognizes glycoconjugates present on the surfaces of several pathogens including viruses (HIV, Ebola, Cytomegalovirus, Dengue, SARS), bacteria (*M. tuberculosis, S. pneumoniae*) fungi (*C. albicans, A. fumigatus*), and

Received: January 21, 2011
Revised: March 31, 2011
Published: June 08, 2011

ACS Publications © 2011 American Chemical Society

parasites (*Leishmania, S. mansoni*).[8−14] It has been proven that this lectin plays a key role in the early stages of the infection processes caused by some of these pathogens. Therefore, DC-SIGN can be selected as a new therapeutic target for the design of antiviral drugs.[15−18] Previous results from our groups indicate that glycodendrimers based on Boltorn-type structures bearing mannoses exhibit a strong antiviral activity in a pseudotype Ebola viral particles infection model both for in *cis* and in *trans* infection.[19−21] Additionally, we have demonstrated that carbohydrate mimics such as a pseudomannobioside present an activity around 1 order of magnitude higher than mannose in such infection studies.[22,23] These new glycomimetics are more stable against enzymatic degradation than the corresponding natural counterparts, and therefore, they are more adequate compounds to be used in clinical applications.

In this study, we combined the improved binding properties of these new pseudomannoside ligands with the potency of multivalent presentation on Boltorn scaffolds. Indeed, nanomolar inhibition levels have been reached in a pseudotyped Ebola viral particles infection model. Binding properties between these compounds and their receptor, DC-SIGN, have been analyzed at the molecular level using biosensors with surface plasmon resonance (SPR) detection method. Altogether, this work opens road to new compounds in antiviral strategy.

MATERIALS AND METHODS

Reagents were purchased from Sigma-Aldrich, Senn Chemicals, Flucka and were used without purification. Solvents were dried by standard procedures. Reactions requiring anhydrous conditions were performed under nitrogen. Synthetic compounds were purified by flash chromatography using medium or fine silica gel or by Sephadex (LH20, G25). Thin layer chromatography (TLC) was carried out with precoated Merck F_{254} silica gel plates. Flash chromatography (FC) was carried out with Macherey-Nagel silica gel 60 (230−400 mesh). Reaction completion was observed by TLC using as development reagents phosphomolibdic acid, 10% sulfuric acid in methanol or anisaldehyde. ^{1}H and ^{13}C spectra were recorded at 400 MHz on Bruker Avance DPX 300, DRX 400, and DRX 500 MHz spectrometers. Chemical shifts (δ) for ^{1}H and ^{13}C spectra are expressed in ppm relative to internal TMS (tetramethylsilane) using manufacturer indirect referencing method. Signals were abbreviated as s, singlet; bs, broad singlet; d, doublet; t, triplet; q, quartet; and m, multiplet. Mass spectra were obtained with a Bruker ion-trap Esquire 3000 or 6000 apparatus (ESI ionization) and Microflex apparatus (MALDI ionization) from Bruker. HRMS (FT-ICR, ESI) were obtained with an Apex II instrument. Infrared spectra were recorded with a Bruker Vector 22 FT-IR spectrometer. Elemental analyses were obtained with a Leco CNHS instrument. All hydrogenation reactions were carried out under H_2 atmosphere at atmospheric pressure.

Synthesis of Compounds. Compounds **G1(Bn)$_4$**,[24] **G1-(OH)$_8$**,[25] **1**,[26] **2**,[27] **3**,[28] **6**,[29] **11**,[23] **13**,[22] and **14**−**15**[23] were prepared as described previously in the literature.

Synthesis of G2(Bn)$_8$. G1(OH)$_8$ (100 mg, 0.17 mmol) and DMAP (70 mg) were dissolved in dry pyridine (1 mL) and then diluted with CH_2Cl_2 (2 mL). Anhydride **1** (812 mg, 2.04 mmol) was added and the reaction mixture was stirred at room temperature for 15 h. Then, the excess of anhydride **1** was quenched by stirring the reaction mixture with 1 mL of pyridine/H_2O (1:1) solution overnight. The organic phase was diluted with CH_2Cl_2 (100 mL), and washed with $NaHSO_4$ 1 M (2 × 40 mL), Na_2CO_3 (10%) (2 × 40 mL), and NaCl sat. (40 mL). The organic phase was dried using $MgSO_4$ anh., and the solvent was evaporated under vacuum. The residue was recrystallized from CH_2Cl_2/hexane to give **G2(Bn)$_8$** (370 mg, 97%) as white crystals. ^{1}H NMR (300 MHz, $CDCl_3$): δ (ppm) 7.40−7.38 (m, 16 H, H_{Ar}), 7.32−7.26 (m, 30H, H_{Ar}), 5.36 (s, 8H, 8 × CH_{Bn}), 4.53 (d, 16H, J = 11.7 Hz, CH_{2G2}), 4.36 (d, 8H, J = 11.4 Hz, CH_{2G1}), 4.29 (d, 8H, J = 11.4 Hz, CH_{2G1}), 3.89 (s, 8H, $CH_{2Pentaerythritol}$), 3.52 (d, 16H, J = 11.7 Hz, CH_{2G2}), 1.15 (s, 12H, CH_{3G1}), 0.88 (s, 24H, CH_{3G1}); ^{13}C NMR (100 MHz, $CDCl_3$) δ (ppm) 175.9 (COO_{G2}), 174.1 (COO_{G1}), 140.2 (C_{Ph}), 131.2 (C_{Ph}), 130.4 (CH_{Ph}), 128.5 (CH_{Ph}), 104.0 (CH_{Bn}), 75.7, 75.7, 67.2, 63.6, 49.2, 44.8, 36.2, 20.0 (CH_{3G2}), 19.9 ($CH_{3\ G1}$); ESI-MS for $C_{121}H_{140}O_{40}$; calcd 2232.9 $[M]^+$; found 2256.7 $[M+Na]^+$ and 1139.8 $[M+2Na]^{2+}$; Elemental analysis calcd (%) for $C_{121}H_{140}O_{40}$: C, 65.04%; H, 6.32%; found: C, 65.32%; H, 6.31%.

Synthesis of G2(OH)$_{16}$. G2(Bn)$_8$ (3.8 g, 1.70 mmol) was dissolved in CH_2Cl_2 (50 mL) and diluted with MeOH (50 mL). A catalytic amount of Pd(C) was added to the solution and the reaction mixture was hydrogenated under vigorous stirring for 12 h. Then, the reaction mixture was filtered over a pad of Celite. The solvent was evaporated to give **G2(OH)$_{16}$** (860 mg, 95%) as a white solid. ^{1}H NMR (300 MHz, CD_3OD): δ (ppm) 4.39 (d, 8H, J = 11.1 Hz, CH_{2G1}), 4.30 (d, 8H, J = 11.1 Hz, CH_{2G1}), 4.29 (s, 8H, $CH_{2Pentaerythritol}$), 3.70 (d, 16H, J = 10.8 Hz, CH_{2G2}), 3.61 (d, 16H, J = 10.8 Hz, CH_{2G2}), 1.35 (s, 12H, CH_{3G1}), 1.17 (s, 24H, CH_{3G2}); ^{13}C NMR (75 MHz, CD_3OD): δ (ppm) 176.0 (COO_{G2}), 173.8 (COO_{G1}), 66.1 ($CH_{2Pentaerythritol}$), 65.9 (CH_{2G2}), 63.6 (C_{G2}), 51.8 (CH_{2G1}), 44.3 (C_{G1}), 18.3 (CH_{3G1}), 17.4 (CH_{3G2}); ESI-MS for $C_{65}H_{108}O_{40}$; calcd: 1528.6 $[M]^+$; found: 1551.4 $[M+Na]^+$.

Synthesis of G3(Bn)$_{16}$. G2)OH)$_{16}$ (1.00 g, 0.654 mmol) and DMAP (445 mg) were dissolved in dry pyridine (20 mL) and then diluted with CH_2Cl_2 (40 mL). Anhydride **1** (6.02 g, 14.13 mmol) was added, and the reaction mixture was stirred at room temperature for 15 h. Then, the excess of anhydride **1** was quenched by stirring the reaction mixture with 20 mL of pyridine/H_2O (1:1) solution overnight. The organic phase was diluted with CH_2Cl_2 (300 mL), and washed with $NaHSO_4$ 1 M (2 × 150 mL), Na_2CO_3 (10%) (2 × 150 mL), and NaCl sat. (150 mL). The organic phase was dried using $MgSO_4$ anh., and the solvent was evaporated under vacuum. The residue was recrystallized from CH_2Cl_2/MeOH to give **G3(Bn)$_{16}$** (2.7 g, 97%) as white crystals. ^{1}H NMR (500 MHz, $CDCl_3$): δ (ppm) 7.37−7.34 (m, 32H, CH_{Ph}), 7.27−7.21 (m, 48H, CH_{Ph}), 5.32 (s, 16H, CH_{Bn}), 4.49 (d, 32H, CH_{2G3}), 4.34−4.25 (m, 32H, 2 × 16 CH_{2G2}), 4.12 (d, 8H, CH2$_{G1}$), 4.11 (s, 8H, $CH_{2Pentaerythritol}$), 4.02 (d, 8H, CH_{2G1}), 3.55−3.51 (m, 32H, CH_{2G3}), 1.18 (s, 24H, CH_{3G2}), 1.08 (s, 12H, CH_{3G1}), 0.88 (s, 48H, CH_{3G3}); ^{13}C NMR (125 MHz, $CDCl_3$): δ (ppm) 173.2 (COO_{G3}), 171.9 (COO_{G2}), 171.5 (COO_{G1}), 138.0 (C_{Ph}), 128.8 (CH_{Ph}), 128.1 (CH_{Ph}), 126.2 (CH_{Ph}), 101.6 (CH_{Bn}), 73.4, 73.3, 64.9, 46.9, 46.6, 42.5 (CH_{2G3}), 34.0, 25.0, 17.7 (CH_{3G2}), 17.6 (CH_{3G3}), 17.2 (CH_{3G1}); ESI-MS for $C_{257}H_{300}O_{88}$; calcd: 4793.9 $[M]^+$; found: 2420.5 $[M+2Na]^{2+}$ and 1621.8 $[M+3Na]^{3+}$; Elemental analysis calcd (%) for $C_{257}H_{300}O_{88}$: C, 64.34%; H, 6.30%; found: C, 64.07%; H, 6.46%.

Synthesis of G3(OH)$_{32}$. G3(Bn)$_{16}$ (1.7 g, 0.354 mmol) was dissolved in CH_2Cl_2 (30 mL) and diluted with MeOH (30 mL). A catalytic amount of Pd(C) was added to the solution and the reaction mixture was hydrogenated under vigorous stirring for 12 h. Then, the reaction mixture was filtered over a pad of Celite. The solvent was evaporated to give **G3(OH)$_{32}$** (1.14 g, 95%) as a white solid. ^{1}H NMR (500 MHz, CD_3OD): δ (ppm) 4.36−4.22 (m, 56H, $CH_{2Pentaerythritol}$ + CH_{2G1} + CH_{2G2}), 3.68 (m, 32H, CH_{2G3}), 3.58 (d, 32H, J = 10.0 Hz, CH_{2G3}), 3.39 (s, 32H, CH_2OH), 1.34 (s, 12H,

CH_{3G1}), 1.30 (s, 24H, CH_{3G2}), 1.12 (s, 48H, CH_{3G3}); ^{13}C NMR (75 MHz, CD_3OD): δ (ppm) 176.0 (COO_{G2}), 173.8 (COO_{G1}), 66.1 ($CH_{2Pentaerythritol}$), 65.9 (CH_{2G2}), 63.6 (C_{G2}), 51.8 (CH_{2G1}), 44.3 (C_{G1}), 18.3 (CH_{3G1}), 17.8 (CH_{3G3}), 17.4 (CH_{3G2}); ESI-MS for $C_{65}H_{108}O_{40}$; calcd: 3385.4 $[M]^+$; found: 1716.0 $[M+2Na]^{2+}$ and 1151.0 $[M+3Na]^{3+}$.

Synthesis of G3(sucBn)$_{32}$. (460 mg, 1.36 mmol), succinic acid derivate **2** (1.086 g, 5.22 mmol) and DPTS (512 mg, 1.74 mmol) were disolved in CH_2Cl_2 (15 mL) under argon atmosphere. DCC (1.433 g, 6.96 mmol) was added and the reaction mixture was stirred for 24 h at room temperature. Then, the reaction mixture was diluted with (6 mL), filtered over a pad of Celite, and the solvent was evaporated. The residue was purified by flash chromatography on silica gel (Hex-AcOEt, 1:1.2), to afford **G3(sucBn)$_{32}$** (1.10 g, 81%) as an oil. ^{1}H NMR (500 MHz, $CDCl_3$): δ (ppm) 7.41−7.33 (m, 160H, CH_{Ar}), 5.13 (bs, 64H, $CH2_{Bn}$), 4.50−4.21 (m, 120H, $CH_{2dendrimer}$), 2.63 (bs, 128H, CH_{2suc}), 1.39 (bs, 12H, CH_{3G1}), 1.31 (bs, 24H, CH_{3G2}), 1.23 (bs, 48H, CH_{3G3}); ^{13}C NMR (125 MHz, $CDCl_3$) δ (ppm) 171.9 (COO_{G3}), 171.7 (COO_{G2}), 171.6 (COO_{G1}), 135.9 (C_{ArBn}), 128.5 (CH_{ArBn}), 128.4 (CH_{ArBn}), 128.2 (CH_{ArBn}), 66.4 (CH_{2Bn}), 65.1, 64.9 ($CH_{2dendrimer}$), 46.7 (C_{G1}), 46.6 (C_{G2}), 46.3 (C_{G3}), 28.9 (CH_{2suc}), 28.8 (CH_{2suc}), 17.7 (CH_{3G3}), 17.6 (CH_{3G2}), 17.4 (CH_{3G1}); ESI-MS for $C_{497}H_{556}O_{184}$; calcd: 9467.4 $[M]^+$; found: 4758.5 $[M+2Na]^{2+}$ and 3185.3 $[M+3Na]^{3+}$; Elemental analysis calcd (%) for $C_{497}H_{556}O_{184}$: C, 63.01%; H, 5.92%; found: C, 62.54%; H, 6.00%.

Synthesis of G3(suc)$_{32}$. **G3(sucBn)$_{32}$** (87 mg, 9.19×10^{-3} mmol) was dissolved in CH_2Cl_2 (3 mL) and diluted with MeOH (6 mL). A catalytic amount of Pd(C) was added to the solution and the reaction mixture was hydrogenated under vigorous stirring for 12 h. Then, the reaction mixture was filtered over a pad of Celite. The solvent was evaporated to give **G3(suc)$_{32}$** (79 mg, quant.) as a white solid. ^{1}H NMR (300 MHz, D_2O): δ (ppm) 4.50−4.20 (m, 120, 60 × CH_2OCO), 2.70−257 (m, 128H, 64 × CH_{2suc}), 1.42 (s, 12H, 4 × CH_{3G1}), 1.35 (s, 32H, 8 × CH_{3G2}), 1.28 (s, 52H, 16 × CH_{3G3}); ^{13}C NMR (125 MHz, CD_3CN): δ (ppm) 174.2 (COO), 173.0 (COO), 172.9 (COO), 66.3 (CH_2O), 47.4 (C), 29.1 (CH_{2suc}), 17.9 (CH_3).

G3(pseudodi)$_{32}$. To a solution of **G3(suc)$_{32}$** (3.5 mg, 5.31×10^{-4} mmol, 1 equiv) in dry DMA (100 μL) under nitrogen atmosphere, HATU (13 mg, 0.034 mmol, 64 equiv) and DIPEA (12 μL, 0.068 mmol, 128 equiv) were added. After 15 min a solution of **13** (16.0 mg, 0.037 mmol, 69 equiv) in dry DMA (170 μL) was added. The reaction was stirred at room temperature for 1 day. MALDI mass analysis of a sample of the reaction mixture showed the completion of the reaction. The reaction mixture was diluted in methanol and charged directly onto a Sephadex LH-20 column in methanol. Slow elution led to the purification of the product **G3(pseudodi)$_{32}$** that was isolated in good yield (9.2 mg, 88%). ^{1}H NMR (400 MHz, D_2O): δ (ppm) 5.00 (s, H_{1M}), 4.43−4.14 (m, CH_2O_{G1} + CH_2O_{G2} + CH_2O_{G3}), 4.02−3.95 (m, H_{D2} + H_{2M}), 3.92 (s, H_{2M}), 3.86 (d, J = 11.2 Hz, H_{6MB}), 3.81 (dd, J = 3.2 and 8.8 Hz, H_{3M}), 3.78−3.56 (m, H_{6MA} + H_{D1} + H_{4M} + H_{5M} + H_7), 3.69 (s, $COOCH_3$), 3.69 (s, $COOCH_3$), 3.42−3.32 (m, H_8), 2.97−2.81 (m, H_{D4} + H_{D5}), 2.72−2.61 (m, CH_2COO), 2.61−2.49 (m, CH_2CONH), 2.16−2.03 (m, H_{D6eq} + H_{D3eq}), 1.89−1.71 (m, H_{D6ax} + H_{D3ax}), 1.39−1.18 (m, CH_{3G1} + CH_{3G2} + CH_{3G3}); ^{13}C NMR (100 MHz, D_2O): 177.1, 176.8, 173.4 ($COOCH_3$, $COOCH_2$, CONH), 98.7 (C_{1M}), 73.9 (C_{D1}), 73.6 (C_{4M}), 71.1 (C_{D2}), 70.6 (C_{2M} + C_{3M}), 67.1 (C_7), 66.9 (C_{5M}), 65.5 (CH_2O_{G1} + CH_2O_{G2} + CH_2O_{G3}), 61.1 (C_{6M}), 52.5 (CH_3O), 46.5 (C_{quatG1} + C_{quatG2} + C_{quatG3}), 39.5 (C_8), 39.1 (C_{D4}, C_{D5}), 30.2 (CH_2CONH), 29.3 (CH_2COO), 27.3, 26.9 (C_{D6}, C_{D3}), 17.3 (CH_{3G1} + CH_{3G2} + CH_{3G3}); MALDI-ToF MS (matrix, SA): distribution centered on 31 sugar loaded, for 31 sugars $[M+Na]^+$ calculated: 19614.8, found: 19689.5.

G3(pseudotri)$_{32}$. To a solution of **G3(suc)$_{32}$** (7.6 mg, 1.15×10^{-3} mmol, 1 equiv) in 100 μL of dry DMA under nitrogen atmosphere, HATU (28.1 mg, 0.074 mmol, 64 equiv) and DIPEA (26 μL, 0.148 mmol, 128 equiv) were added. After 15 min, a solution of **15** (35.7 mg, 0.06 mmol, 52 equiv) in dry DMA (230 μL) was added. The reaction was stirred at room temperature for 2 days. MALDI mass analysis of a sample of the reaction mixture showed the completion of the reaction. The reaction mixture was diluted in methanol and charged directly onto a Sephadex LH-20 column in methanol. Slow elution led to the purification of the product **G3(pseudotri)$_{32}$** that was isolated in good yield (25.5 mg, 88% yield). ^{1}H NMR (400 MHz, D_2O): δ (ppm) 5.00 (s, $H_{1M'}$), 4.84 (s, H_{1M}), 4.40−4.10 (m, CH_2O_{G1} + CH_2O_{G2} + CH_2O_{G3}), 4.04 (s, H_{D2}), 3.97 (bs, $H_{2M'}$), 3.92 (s, H_{2M}), 3.89−3.53 (m, $H_{3M'}$ + $H_{6M'B}$ + H_{6MB} + H_{D1} + $H_{6M'A}$ + H_{6MA} + H_{3M} + H_{4M} + $H_{4M'}$ + H_7 + H_{5M} + $H_{5M'}$), 3.69 (s, $COOCH_3$), 3.68 (s, $COOCH_3$), 3.49−3.34 (m, H_8), 3.00−2.85 (m, H_{D4} + H_{D5}), 2.73−2.59 (m, CH_2COO), 2.59−2.46 (m, CH_2CONH), 2.27−2.03 (m, H_{D6eq} + H_{D3eq}), 1.89−1.71 (m, H_{D6ax} + H_{D3ax}), 1.40−1.15 (m, CH_{3G1} + CH_{3G2} + CH_{3G3}); ^{13}C NMR (100 MHz, D_2O): δ (ppm) 177.3, 177.0, 173.5, 173.0 ($COOCH_3$, $COOCH_2$, CONH), 99.9 (C_{1M}), 98.7 ($C_{1M'}$), 74.7 (C_{D1}), 73.5, 72.2 (C_{4M} + $C_{4M'}$), 71.0 (C_{D2}), 70.9, 70.7, 70.6 ($C_{2M'}$ + C_{3M} + $C_{3M'}$), 70.2 (C_{2M}), 68.2 (C_{6M}), 67.1, 66.9 (C_{5M} + $C_{5M'}$), 66.2 (C_7), 65.4 (CH_2O_{G1} + CH_2O_{G2} + CH_2O_{G3}); 61.1 ($C_{6M'}$), 52.6 (CH_3O), 46.4 (C_{quatG1} + C_{quatG2} + C_{quatG3}), 39.1, (C_{D4}, C_{D5}), 39.0 (C_8), 30.1 (CH_2CONH), 29.2 (CH_2COO), 27.2, 26.9 (C_{D6}, C_{D3}), 17.3 (CH_{3G1} + CH_{3G2} + CH_{3G3}). MALDI-ToF MS (matrix: SA): distribution centered on 31 sugar loaded, for 31 sugar $[C_{1041}H1_{612}N_{32}O_{664}Na]^+$ calcd: 25222.75, found: 25227.9.

2-Azidoethyl Isopropylidene-2,2-bis(oxymethyl)propionate (4). 2-Bromoethanol (1.2 mL, 17.0 mmol) and DMAP (0.325 g, 2.6 mmol) were dissolved in pyridine (25 mL), followed by the addition of CH_2Cl_2 (70 mL). The anhydride of isopropylidene-2,2-bis(oxymethyl)propionic acid **6** (7.4 g, 22.4 mmol) was added slowly. The solution was stirred at room temperature overnight and then was quenched with water (1 mL) under vigorous stirring, followed by dilution with of CH_2Cl_2 (200 mL), and the solution was washed with 10% of $NaHSO_4$ (3 × 40 mL), 10% of Na_2CO_3 (3 × 40 mL), and brine (20 mL). The organic phase was dried with $MgSO_4$, filtered, and concentrated. The crude product was purified by flash chromatography on silica gel, eluting with hexane (100 mL) and gradually increasing the polarity to EtOAc/hexane (9:1; 6:1) to give 2-bromoethyl isopropylidene-2,2-bis(oxymethyl)propionate as colorless oil (4.9 g, 86%). This bromo derivative (4.9 g, 14.6 mmol) and NaN_3 (2.6 g, 40.0 mmol) were dissolved in dry DMF (50 mL) and the reaction mixture was stirred at 50 °C for 15 h. The solvent was removed under high vacuum and AcOEt was added to the residue. The NaN_3 on excess was taken off by filtration, and the solvent was removed to obtain **4** as colorless oil (3.53 g, 99%). ^{1}H NMR (300 MHz, $CDCl_3$) δ: 4.30 (t, 2H, J = 5.1 Hz, $CH_2CH_2N_3$), 4.18 (d, 2H, J = 11.9 Hz, CH_2OCO), 3.64 (d, 2H, J = 11.9 Hz, CH_2OCO), 3.67 (t, 2H, J = 5.1 Hz, $CH_2CH_2N_3$), 1.41 (s, 3H, CH_3), 1.36 (s, 3H, CH_3), 1.19 (s, 6H, 2 × CH_3); ^{13}C NMR (100 MHz, $CDCl_3$) δ: 173.8 (COO), 98.0 (C_{ipr}), 65.8 (CH_2OCO), 63.5 ($CH_2CH_2N_3$), 49.7 ($CH_2CH_2N_3$), 41.9 (C), 24.8, 22.2 (CH_3), 17.7 (CH_3); ESI-MS for

$C_9H_{15}N_3O_4$; calcd: 243.1, $[M]^+$; found 266.1 $[M+Na]^+$. IR (υ, cm^{-1}): 3448 (bs), 2992, 2940, 2105, 1734, 1638.

2-Azidoethyl 2,2-Bis(hydroxymethyl)propionate (5). Azido derivative **4** (11.0 g, 45.2 mmol) was dissolved in MeOH (50 mL). One teaspoon of a Dowex, H+ resin was added, and the reaction mixture was stirred at 40 °C until complete disappearance of starting material. When the reaction was complete, the Dowex H+ resin was filtered off in a glass filter and carefully washed with methanol. The methanol was evaporated to give **5** as colorless oil (9.0 g, 98%). ^{1}H NMR ($CDCl_3$, 300 MHz) δ: 4.34 (t, 2H, J = 5.1 Hz, $CH_2CH_2N_3$), 3.92 (d, 2H, J = 11.2 Hz, CH_2OCO), 3.74 (d, 2H, J = 11.2 Hz, CH_2OCO), 3.52 (t, 2H, J = 5.1 Hz, $CH_2CH_2N_3$), 3.02 (bs, 2H, *OH*), 1.12 (s, 3H, CH_3); ^{13}C NMR ($CDCl_3$, 100 MHz) δ: 175.3 (COO), 67.8 (CH_2OCO), 63.5 ($CH_2CH_2N_3$), 49.8 ($CH_2CH_2N_3$), 49.4 (C), 17.0 (CH_3); ESI-MS for $C_7H_{13}N_3O_4$; calcd: 203.1 $[M]^+$; found: 226.0 $[M+Na]^+$. IR (υ, cm^{-1}): 3405 (bs), 2945, 2885, 2105, 1729, 1660, 1459. Elemental analysis calcd. (%) for $C_7H_{13}N_3O_4$: C, 41.38%, H, 6.45%; N, 20.68%; found: C, 41.83%; H, 6.79%; N, 20.50%.

Compound 7. Azido derivative **5** (2.4 g, 11.8 mmol) and DMAP (0.43 g, 3.54 mmol) were dissolved in pyridine (6 mL), followed by the addition of CH_2Cl_2 (12 mL). The anhydride of isopropylidene-2,2-bis(hydroxymethyl)propionic acid **6** (9.3 g, 30.7 mmol) was added slowly. The solution was stirred at room temperature until completion. The reaction was quenched with water (1 mL) under vigorous stirring, followed by dilution with CH_2Cl_2 (50 mL), and the solution was washed with 10% of $NaHSO_4$ (3 × 20 mL), 10% of Na_2CO_3 (3 × 20 mL), and brine (10 mL). The organic phase was dried with $MgSO_4$, filtered, and concentrated. The crude product was purified by flash chromatography on silica, eluting with hexane (100 mL) and gradually increasing the polarity to EtOAc/hexane (1:3) to give **7** as colorless oil (4.4 g, 73%). ^{1}H NMR ($CDCl_3$, 300 MHz) δ: 1.17 (s, 6H, CH_3), 1.34 (s, 3H, CH_3), 1.38 (s, 6H, CH_3), 1.43 (s, 6H, CH_3), 3.51 (t, J = 5.1 Hz, 2H, $CH_2CH_2N_3$), 3.64 (d, J = 11.9 Hz, 4H, CH_2OCO), 4.17 (d, J = 11.8 Hz, 4H, CH_2OCO), 4.34−4.28 (t, J = 5.1 Hz, 2H, $CH_2CH_2N_3$), 4.36 (s, 4H, CH_2OCO); ^{13}C NMR ($CDCl_3$, 75.5 MHz) δ: 173.5, 172.3 (COO), 98.1 (C^ipr), 66.0, 66.0, 65.3 (CH_2OCO), 63.9 ($CH_2CH_2N_3$), 49.6 ($CH_2CH_2N_3$), 46.9, 42.1 (C), 25.3, 22.0 (CH_3^ipr), 18.0, 17.0 (CH_3); ESI-EM calc for $C_{23}H_{37}N_3O_{10}$(m/z): 515.2; found 538.2 $[M+Na]^+$. IR (υ, cm^{-1}): 3453 (bs), 2991, 2940, 2876, 2106, 1738, 1643, 1455.

Compound 8. Azido derivative **7** (4.3 g, 8.4 mmol) was dissolved in MeOH (20 mL). One teaspoon of a Dowex H+ resin was added, and the reaction mixture was stirred at 40 °C until complete disappearance of starting material by TLC. When the reaction was complete, the Dowex H+ resin was filtered off in a glass filter and carefully washed with methanol. The methanol was evaporated to give **8** as colorless oil (3.5 g, 97%). ^{1}H NMR ($CDCl_3$, 300 MHz) δ: 4.46 (d, J = 11.1 Hz, 2H, CH_2OCO), 4.36−4.26 (m, 4H, CH_2OCO, $CH_2CH_2N_3$), 3.90−3.78 (m, 4H, CH_2OCO), 3.76−3.67 (m, 4H, CH_2OCO), 3.51 (t, J = 5.1 Hz, 2H, $CH_2CH_2N_3$), 3.19−2.87 (bs, 4H), 1.36 (s, 3H, CH_3), 1.08 (s, 6H, CH_3); ^{13}C NMR ($CDCl_3$, 75.5 MHz) δ: 175.0, 175.0, 172.8 (COO), 67.3, 67.2, 67.2, 64.8 (CH_2OCO), 64.0 ($CH_2CH_2N_3$), 49.8 ($CH_2CH_2N_3$), 49.8, 49.6 (C), 18.0, 17.0 (CH_3); ESI-EM calcd for $C_{17}H_{29}N_3O_{10}$ (m/z): 435.2; found 458.2 $[M+Na]^+$. IR (υ, cm^{-1}): 3405 (bs), 2943, 2886, 2108, 1731, 1469.

Compound 10. 4-Oxo-4-(2-(trimethylsilyl)ethoxy)butanoic acid (**9**) (1.43 g, 6.57 mmol), tetraol **8** (0.50 g, 1.09 mmol), and DPTS (0.65 g, 2.18 mmol) were mixed in CH_2Cl_2 anhydrous (10 mL). Then, the reaction flask was flushed with argon and DCC (1.35 g, 6.57 mmol) was added. Stirring at 40 °C was continued for 15 h under argon atmosphere. Once the reaction was complete, the formed urea was filtered off on a glass filter and washed with a small volume of CH_2Cl_2. The crude product was purified by liquid chromatography Sephadex LH20 (CH_2Cl_2/MeOH; 1:1) to give **10** as colorless viscous oil (1.11 g, 81%). ^{1}H NMR ($CDCl_3$, 300 MHz) δ: 4.43−3.97 (m, 14H, 4 CH_{2G1}, 8 CH_{2G2}, 2 $CH_2CH_2N_3$, 8 $CH_2CH_2COCH_2$), 3.53−3.43 (t, J = 5.1 Hz, 2H, $CH_2CH_2N_3$), 2.65−2.47 (m, 16H, CH_2suc), 1.26 (s, 3H, $CH_{3\ G1'}$), 1.20 (s, 6H, $CH_{3\ G2'}$), 1.00−0.88 (t, J = 8.5 Hz, 8H, CH_2-TMS), 0.00 (s, 36 H, CH_3TMS); ^{13}C NMR ($CDCl_3$, 75.5 MHz) δ: 172.1, 171.9, 171.9, 171.7 (COO), 65.6, 65.3, 64.0, 62.9 (CH_2OCO, $CH_2CH_2N_3$, $CH_2CH_2COCH_2$), 49.6 ($CH_2CH_2N_3$), 46.7, 46.4 (CCH_2O), 29.1, 28.8 (CH_2suc), 17.7, 17.4 (CH_2-TMS, CH_3), 17.2, −1.5, −1.9 (CH_3TMS); ESI-HRMS calcd for $C_{53}H_{93}N_3O_{22}Si_4Na$ (m/z): 1258.5291; found: 1258.5226. IR (υ, cm^{-1}): 2955, 2898, 2104, 1730, 1471.

Compound 11. TFA (5 mL) was added to a solution of **10** (142 mg, 0.115 mmol) in CH_2Cl_2 (5 mL). The mixture was stirred at room temperature for 2 h. After complete conversion, the solvent was evaporated and dried in high vacuum to afford **11** as pale yellow syrup (96 mg, 100%). The compound was used in the next step without purification. ^{1}H NMR (MeOH-d_4, 400 MHz) δ: 4.30 (m, 28H, 4$CH_{2\ G1}$ 8$CH_{2\ G2}$, 2$CH_2CH_2N_3$), 3.57 (t, J = 5.1 Hz, 2H, $CH_2CH_2N_3$), 2.62 (m, 16H, CH_2CONH, CH_2COO), 1.34 (s, 3H, $CH_{3G1'}$), 1.27 (s, 6H, $CH_{3G2'}$); ^{13}C NMR ($CDCl_3$, 100 MHz) δ: 174.4, 172.2, 172.2, 172.0 (COO), 65.5, 65.3, 65.2, 64.0 (CH_2OCO, $CH_2CH_2N_3$, $CH_2CH_2COCH_2$), 49.4 ($CH_2CH_2N_3$), 46.9, 46.5, 46.3 (CCH_2O), 28.6, 28.5, 28.3, 28.2 (CH_2CONH, CH_2COO), 16.7, 16.5 (CH_3); ESI-HRMS calcd for $[M+Na]$ $C_{33}H_{45}N_3O_{22}Na$ (m/z): 858.2392; found: 858.2435.

Compound 12. To a solution of the scaffold dendron **11** (6.0 mg, 0.00718 mmol, 1 equiv) in 150 μL of dry DMA under nitrogen atmosphere, HATU (22 mg, 0.0575 mmol, 8 equiv) and DIPEA (20 μL, 0.1157 mmol, 16 equiv) were added. After 15 min, a solution of **13** (23.4 mg, 0.05349 mmol, 8 equiv) in dry DMA (210 μL) was added. The reaction was stirred at room temperature for 3 days. MALDI mass analysis of a sample of the reaction mixture showed the completion of the reaction. The reaction mixture was diluted in methanol and charged directly onto a Sephadex LH-20 column (methanol). Slow elution led to the purification of the product **12** that was isolated in good yield (16.9 mg, 94%). ^{1}H NMR (400 MHz, D_2O): δ (ppm) 4.93 (s, 4H, H_1), 4.27 (bs, 6H, $OCH_2CH_2N_3$, CH_2O_{G1}), 4.18 (bs, 8H, CH_2O_{G2}), 3.91 (bs, 8H, D_2, H_2), 3.78 (d, 4H, H_6B, J = 12 Hz), 3.76−3.71 (m, 4H, H_3), 3.69−3.59 (m, 8H, H_{6A}, H_{D1}), 3.63 (s, 24H, OCH_3), 3.59−3.49 (m, 18H, H_4, H_5, H_7, CH_2N_3), 3.30 (bt, 8H, H_8), 2.91−2.72 (m, 8H, H_{D4}, H_{D5}), 2.65−2.56 (m, 8H, CH_2COO), 2.54−2.45 (m, 8H, CH_2CONH), 2.10−1.99 (m, 8H, H_{D6eq}, H_{D3eq}), 1.81−1.64 (m, 8H, H_{D6ax}, H_{D3ax}), 1.26 (s, 3H, $CH_{3G1'}$), 1.19 (s, 6H, CH_{3G2}); ^{13}C NMR (100 MHz, D_2O): 177.4, 177.2, 174.1, 174.0, 173.8, 173.7 ($COOCH_3$, $COOCH_2$, CONH), 98.6 (C_{1M}), 73.8 (C_{D1}), 73.5 (C_{4M}), 71.0, 70.5 (C_{D2}, C_{2M}, C_{3M}), 66.9 (C_7), 66.8 (C_{5M}), 65.9 (OCH_{2G1}, OCH_{2G2}), 64.8 ($OCH_2CH_2N_3$), 61.0 (C_{6M}); 52.6 (CH_3O); 49.4 (CH_2N_3); 46.6, 46.4 ($C_{quat\ G1,\ G2}$); 39.4 (C_8); 39.0 (C_{D4}, C_{D5}); 30.1 (CH_2CONH); 29.3 (CH_2COO); 27.0, 26.7 (C_{D6}, C_{D3}); 16.9 ($CH_{3G1,G2}$); ESI-MS calcd for $[C_{105}H_{161}N_7O_{62}Na_2]^{+2}$ 1279.7, found: 1279.2; MALDI-ToF MS (matrix DHB) $[C_{105}H_{161}N_7O_{62}Na]^+$ calcd: 2536.4, found: 2537.2.

Production of Recombinant Viruses. Recombinant viruses were produced in 293 T cells. The viral construction was pseudotyped with Ebola virus envelope glycoprotein (EboGP) and

Scheme 1. Synthesis of Compound G3(suc)$_{32}$ from Pentaerythritol

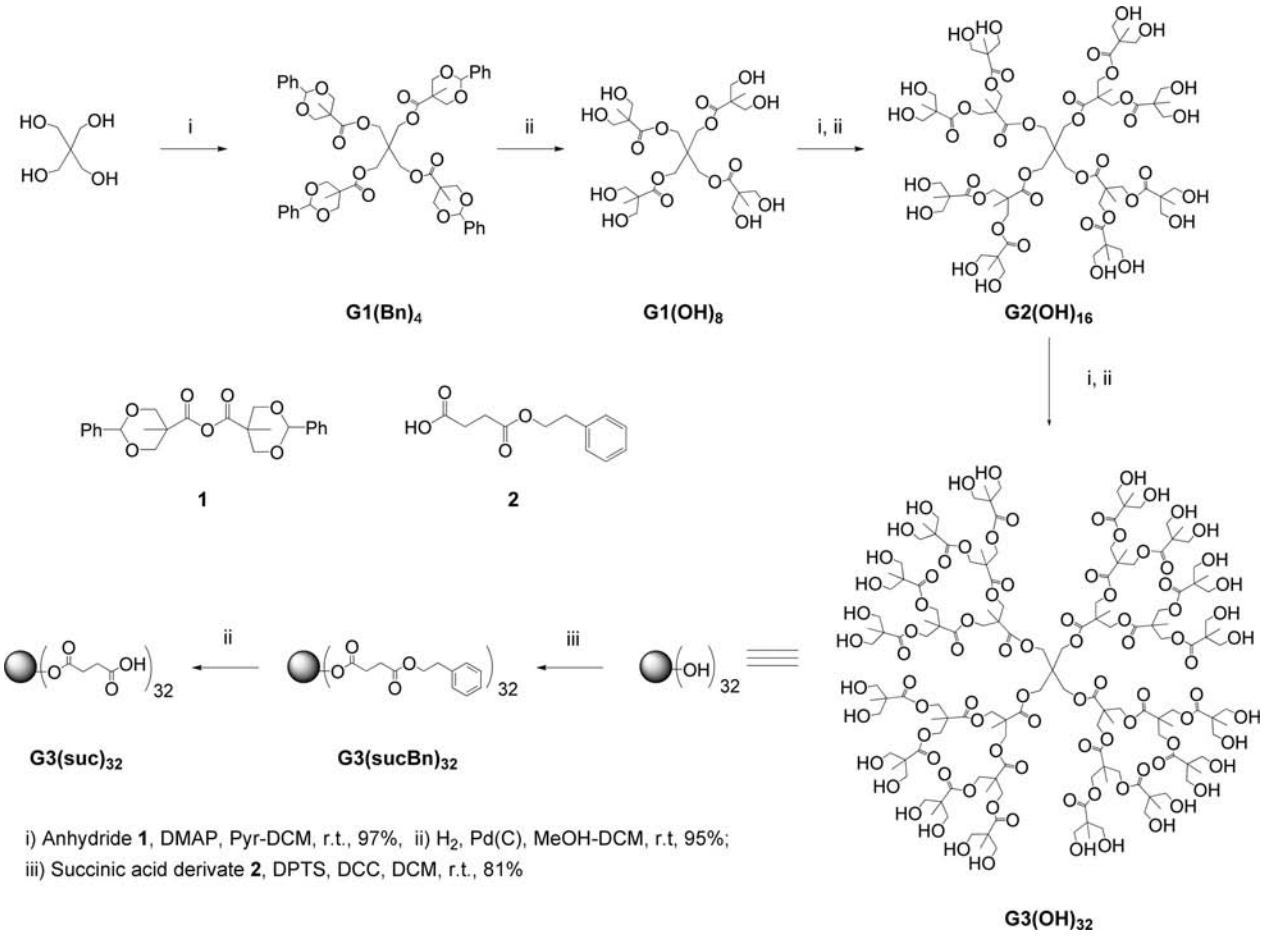

expressed luciferase as a reporter of the infection. The infection of Jurkat cells (a CD+ T-lymphocyte cell line) by EboGP is absolutely dependent on virus envelope interaction with DC-SIGN. As a control of DC-SIGN independent infection, we produced recombinant viruses pseudotyped with vesicular stomatitis virus envelope glycoprotein (VSV-G).

One day (18−24 h) before transfection, 6×10^6 293 T cells were seeded onto 10 cm plates. Cells were cultured in DMEM medium supplemented with 10% heat-inactivated FBS, 25 mg Gentamicin, and 2 mM L-glutamine. Few minutes before transfection, the medium on transfection plates was changed to 9 mL DMEM and 25 μM chloroquine. Transfection reaction with all reagents at room temperature (r.t.) was prepared in 15 mL tubes: 183 μL of 2 M $CaCl_2$, 450 ng of Ebola virus envelope, 21 μg of pNL4−3 luc, and 1200 μL of H_2O. Next, 1.5 mL of 2×HBS (Hepes Buffer Saline) pH 7.00 was added quickly to the tubes and bubbled for 30 s. HBS/DNA solution was dropwise added onto medium. After 8 h of incubation at 37 °C with 5% CO_2, medium on transfection plates was changed to 10 mL DMEM and once again one day after transfection to 7 mL DMEM. Transfection supernatants were harvested after 48 h, centrifuged at 1200 rpm for 10 min at r.t. to remove cell debris, and stored frozen at −80 °C.

Infection Assay. *Infection in cis.* Infection was performed on Jurkat cells expressing DC-SIGN. Since Ebola virus does not infect T-lymphocytes, its entry into Jurkat cells is absolutely dependent on the interaction with DC-SIGN.[30]

DC-SIGN$^+$ Jurkat cells (2.5×10^5) were incubated with carbohydrate multivalent compounds on 24-well suspension plates for 30 min at r.t. and then challenged with 10 000 tissue culture infective dose (TCID) of recombinant viruses. After 48 h of incubation, cells were washed twice with PBS and lysed with 100 μL of 1× Lysis Buffer for luciferase assay (Promega).

Infection control experiment was performed with VSV-G pseudoviruses under the same conditions.

Infection in trans. DC-SIGN$^+$ Jurkat cells (2.5×10^5) were preincubated for 20 min at r.t. with carbohydrate multivalent compounds. Then, they were challenged with 10 000 TCID of recombinant viruses and incubated for 2 h at r.t. with rotation. After 2 h, cells were centrifuged at 1000 rpm for 5 min and washed twice with 1 mL of PBS supplemented with 0.5% bovine serum albumin (BSA) and 1 mM $CaCl_2$. DC-SIGN$^+$ Jurkat cells were resuspended in 500 μL of RPMI medium and co-cultivated with adherent HeLa cells (10^5 cells/well) on 24-well plate. After 48 h, supernatant was removed and monolayer of HeLa was washed twice with 1 mL of PBS and lysed with 100 μL of 1× Lysis Buffer for luciferase assay.

As control experiment, *trans*-infection test with VSV-G pseudoviruses was performed.

Surface Plasmon Resonance. Extracellular domain (ECD) of DC-SIGN protein (residue 66−404) has been overexpressed and purified as described previously.[31] All experiments were performed on a Biacore 3000 using functionalized CM4 sensor chips and the corresponding reagents from BIAcore. Two flow

Scheme 2. Synthesis of Tetravalent Compounds 12 and 14

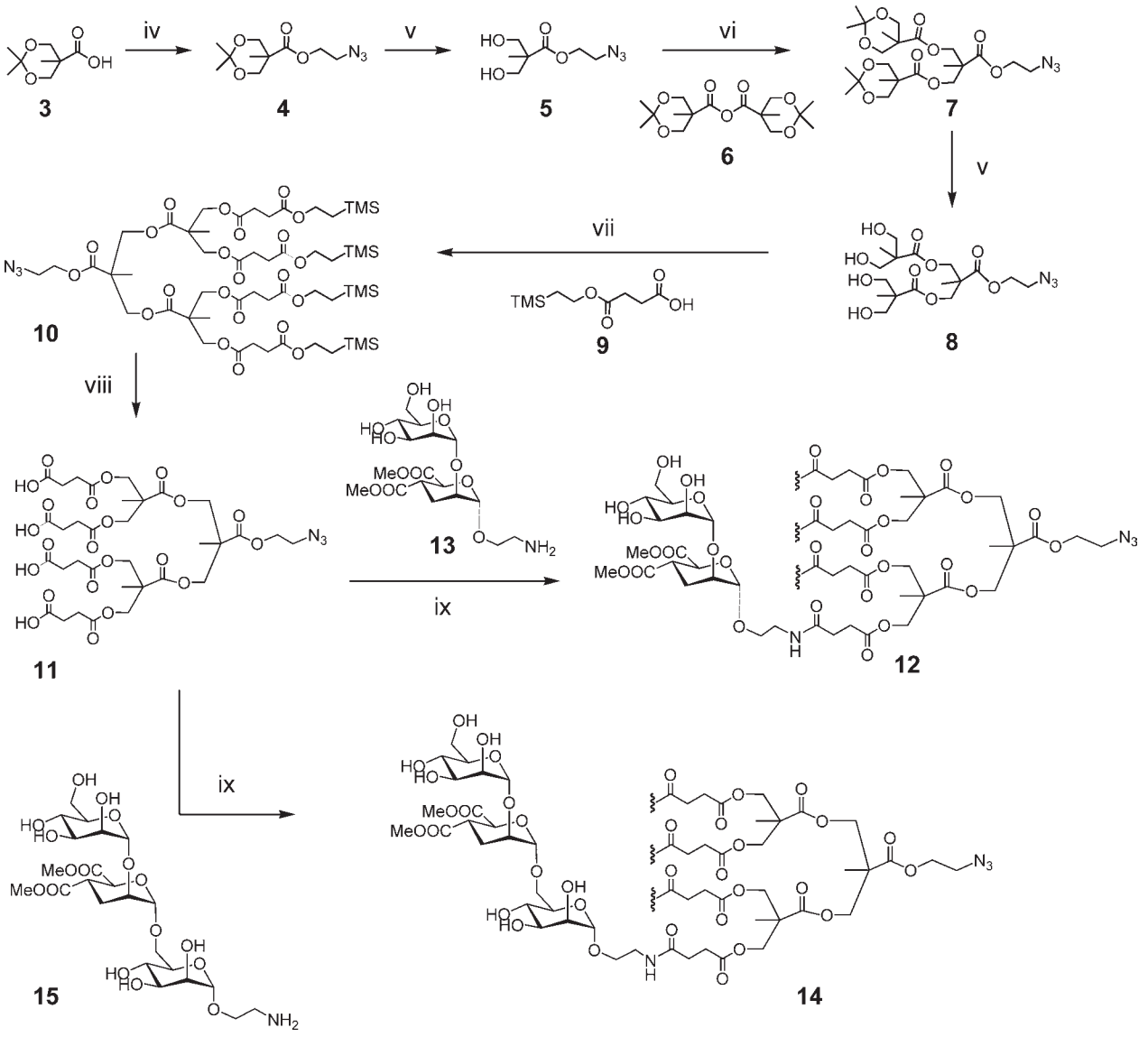

iv) a) 2-bromoethanol, DMAP, DCM, r.t.; b) NaN_3, DMF, 86%; v) Dowex, H+ resin, MeOH, r.t., 98%; vi) DMAP, Anhydride **6**, DCM, r.t., 73%, vii) Acid **9**, DPTS, DCC, DCM, 40ºC, 81%; viii) TFA, DCM, r.t., quant.; ix) pseudomannobioside **13** or pseudomannotrioside **15**, HATU, DIPEA, DMA, r.t., 94%

cells were activated as previously described.[32] Flow cell one was then blocked with 30 μL of 1 M ethanolamine and used as a control surface. The second one was treated with BSA-Manα1−3[Manα1−6]Man (BSA-Mannotriose, Dextra) (60 μg/mL) in 10 mM acetate buffer, pH 4. Remaining activated groups were blocked with 30 μL of 1 M ethanolamine. The final density immobilized on the surface of the second flow cell was 1200 RU. The BSA-Mannotriose used to functionalize CM4 chip harbors 12 glycosylation sites according to manufacturer. The affinity of the various sugars and mimics was then estimated through a DC-SIGN ECD binding inhibition assay. The ECD of DC-SIGN was injected onto the BSA-Mannotriose surface, at 20 μM alone or in presence of an increasing concentration of the sugar derivatives. Injections were performed at 20 μL/min using 25 mM Tris-HCl, pH 8, 150 mM NaCl, 4 mM $CaCl_2$, and 0.005% of P20 surfactant as running buffer. The original sensorgrams are reported as Supporting Information.

To determine IC_{50} values for sugar derivatives, the steady state binding responses of DC-SIGN ECD to BSA-Mannotriose surface were obtained from sensorgrams and converted to relative residual activity values. Relative IC_{50} values were determined from the plots of sugar derivative concentration vs relative residual DC-SIGN ECD activity by fitting four-parameter logistic model (see eq 1 in SI) to the experimental data.

RESULTS

In previous works, we have demonstrated that the commercially available and very cheap third generation of a Boltorn

dx.doi.org/10.1021/bc2000403 |*Bioconjugate Chem.* 2011, 22, 1354–1365

Scheme 3. Coupling of Glycomimetics 13 and 15 on G3(suc)$_{32}$

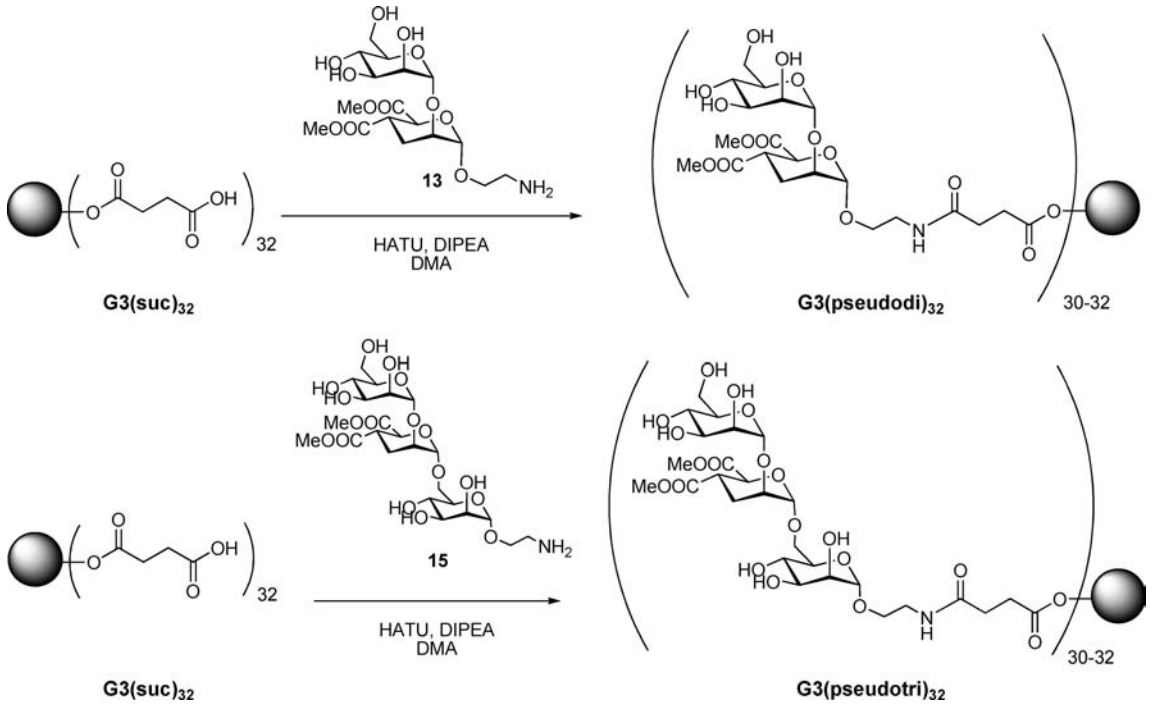

dendritic polymer was a very convenient platform for a multivalent presentation of carbohydrates.[19] This polydisperse dendritic polymer, bearing 32 copies of mannose, exhibited a high antiviral activity (IC_{50} = 0.3 μM) in an Ebola infection model.[20] The polydispersity of the commercial Boltorn scaffold is a major drawback of this strategy. On the basis of these preliminary results, we decided to prepare a Boltorn-type polyester dendrimer in a completely monodisperse manner. To approach this synthesis, we used a divergent strategy based on the anhydride **1** as a building block monomer and pentaerythritol as a central core, a strategy previously used to prepare polyester dendrons.[26] A sequential set of two reactions was employed as described in Scheme 1. A coupling reaction with anhydride **1** to grow to the next generation, followed by hydrogenolysis using palladium on carbon as catalyst to remove the benzylidene protecting groups, yielded the first (G1(OH)$_8$), second (G2(OH)$_{16}$), and third (G3(OH)$_{32}$) generations of the polyester dendrimers in a very efficient way and with complete monodispersity, as shown by mass spectrometry. These dendrimers were prepared in multigram-scale and purified by recrystallization in a very straightforward way.

Carboxylic acids were introduced as functional groups at the surface of the third-generation dendrimer G3(OH)$_{32}$ to allow coupling with conveniently functionalized ligands by the formation of amide bonds. In contrast to our previous experience, where the carboxylic acids were introduced by reaction of G3(OH)$_{32}$ with a large excess of succinic anhydride, succinic acid monobenzyl ester and DCC were used for the coupling reaction (Scheme 1). Using this strategy, the resulting compound G3(sucBn)$_{32}$ was soluble in organic solvents and very easy to purify by flash chromatography on silica gel. Again, a complete analysis of the compound, especially by MS, confirmed the monodispersity of the molecule. After a simple step of benzyl ester deprotection by hydrogenolysis at atmospheric pressure using Pd(C) (10%) at room temperature, the dendrimer G3(suc)$_{32}$ with 32 carboxylic acids was obtained almost quantitatively.

To evaluate the importance of the valency, a tetravalent system also based on 2,2′-bis(hydroxymethyl) propionic acid (bis-MPA) (Scheme 2) was considered as a scaffold for presentation of four copies of selected ligands.

Starting from the isopropylidene-2,2-bis(methoxy)propionic acid (**3**) prepared as reported in the literature[28] and following the experimental procedure described in Scheme 2, we obtained **4** in good yields with adequate functionalization. As a protecting group of the carboxylic acid, the azidoethanol was used. This terminal azide has been used in our laboratory in a convergent strategy to create higher valency compounds applying a click chemistry Cu catalyzed cycloaddition (unpublished results). Compound **4** was prepared in good yields by reaction of **3** with 2-bromoethanol in the presence of DCC and 4-(dimethylamino)pyridinum 4-toluenesulfonate (DPTS) followed by treatment with sodium azide in DMF at 40 °C. After deprotection of the hydroxyl groups using an acidic resin in methanol, the tetraol **8** was prepared using a two-step synthetic sequence reported in the literature to prepare similar polyester dendrons.[28,29,33] This synthetic sequence begun coupling **5** with 2 equiv of anhydride **6** which, in turn, was prepared in one step from acid **3** using DCC,[29] in pyridine and dimethylaminopyridine as catalyst. The second step was the deprotection of the isopropylidene acetals of **7** using Dowex H+. Tetraol **8** was obtained in good yield after chromatographic purification. The introduction of the carboxylic acid linkers on **8** was performed using the trimethylsilylethanol monosuccinate **9** prepared by ring-opening of succinic anhydride by trimethylsilylethanol as described in the literature.[34] In this way, the silyl protected compound was prepared in good yields and easily purified. After deprotection using trifluoroacetic acid at room temperature, the tetraacid **11** was obtained in very good yield and was used in the next step without any further purification.

Our previous studies have demonstrated that compounds **13** and **15**, linear glycomimetics of the disaccharide Manα1,2Man and of the trisaccharide Manα1,2Manα1,6Man, respectively, were

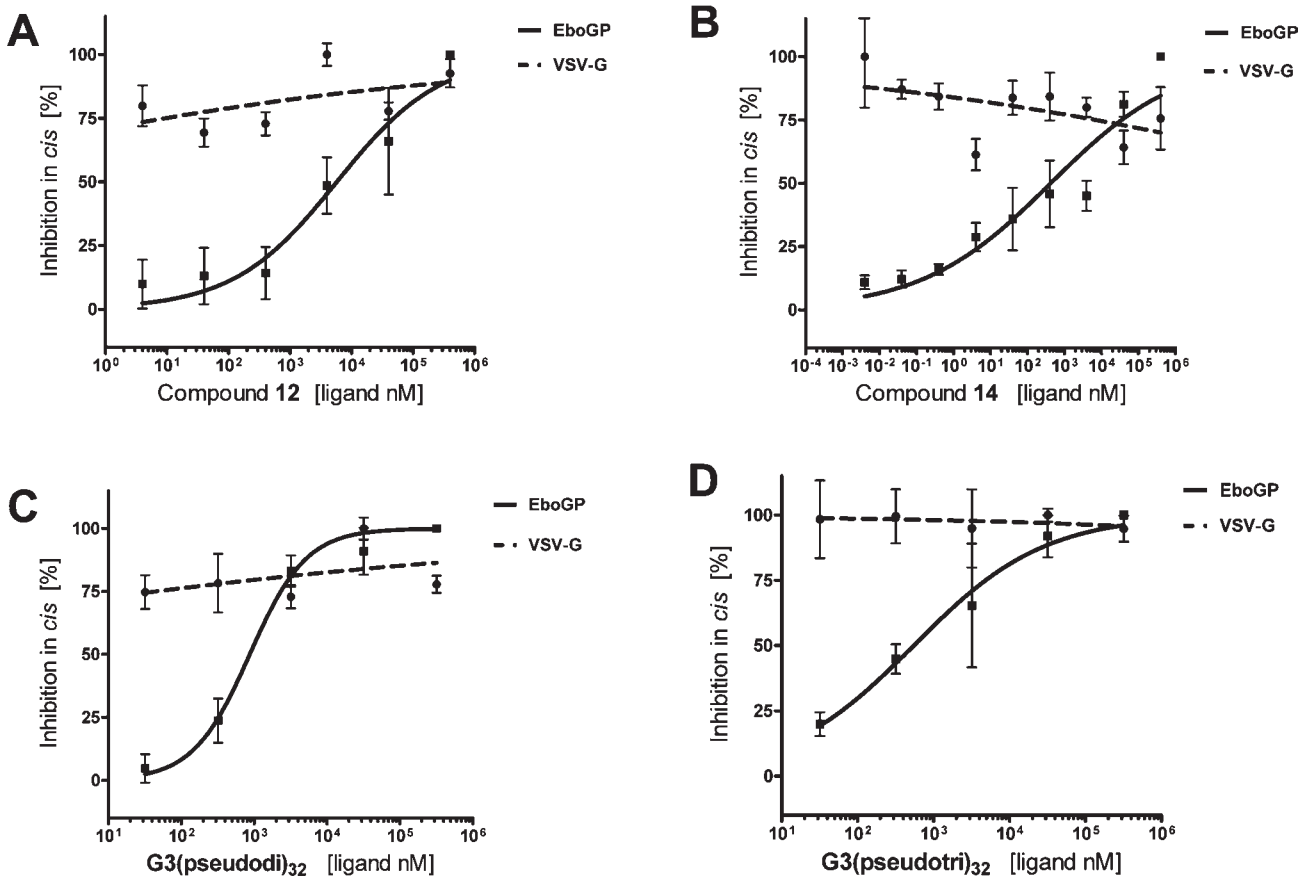

Figure 1. Infection results of the *cis*-experiments using **12**, **14**, G3(pseudodi)$_{32}$, and G3(pseudotri)$_{32}$ compounds as inhibitors. Concentrations are expressed based on ligand concentration.

very adequate ligands for DC-SIGN providing better stability against enzymatic degradation than the corresponding natural counterparts. The synthesis of these glycomimetics has been previously described.[22,23]

Conjugation of **13** and **15** on the tetra- and multivalent scaffolds was performed using HATU as an activating reagent in the presence of DIPEA at room temperature and afforded the corresponding multivalent systems with high yields after purification by size exclusion chromatography as described in Schemes 2 and 3.

The tetravalent compounds were fully characterized by NMR, IR, and MS analysis. MALDI-MS of the compounds G3(pseudodi)$_{32}$ and G3(pseudotri)$_{32}$ using sinapinic acid (SA) as matrix allowed to observe a complex signal centered on the molecular weight corresponding to the 31-loaded dendrimer both for pseudodi- and pseudotrimultivalent systems (see SI for MS spectra). This is consistent with the number of 30−32 ligands which could be estimated based on the integration of significant signals in the ^{1}H NMR spectrum (see SI). Although the MS spectra were not conclusive, we concluded that almost all the reactive sites of the scaffold were conjugated with ligands to obtain a high load narrowly disperse system.

Infection Studies. The antiviral activity of these tetra- and multivalent systems was tested using pseudotyped viral particles presenting the EboGP and Jurkat cell line expressing DC-SIGN on the surface. Two kinds of experiments were set up: a *cis*-infection assay of DC-SIGN+ Jurkat cells with this artificial Ebola virus, and a *trans*-infection experiment of HeLa cells using DC-SIGN+ Jurkat cells as viral particle transporters.

We have used these infection models previously to test the activity of mannosylated Boltorn-type hyperbranched dendritic polymers.[20] The DC-SIGN blocking efficiency has been evaluated as dependence of multivalency and of the different pseudomannoside ligands used in the compounds synthesized. The infection inhibition analysis has been done as a function of compound concentration. All compounds were used in at least 3 independent experiments. The results of the infection assays are represented as a percentage of infection inhibition compared with DC-SIGN+ Jurkat cells infected by pseudoviruses without addition of any compound (blank experiment). The IC_{50} values were calculated with the 95% confidence intervals. Control experiment with VSV-G pseudoviruses was performed with final concentrations of 10 nM and 10 μM (negative control).

The results obtained in the *cis* infection experiments indicate that the tetravalent systems presenting four copies of the pseudomannotrioside, **14**, show an IC_{50} 1 order of magnitude lower than the system with four pseudomannobiosides, **12** (Figure 1). In a previous publication, we have shown that the tetravalent system **14** bearing four copies of linear pseudomannotrioside **15** was an effective inhibitor of T-cell *trans* infection by HIV.[23]

Multivalent systems with an average of 30−32 copies of glycomimetic ligands were tested. In this case, no significant differences were found as a function of the pseudosaccharide presented. The IC_{50} values found for the multivalent systems were around 20 nM (around 0.5 μM, based on ligand concentration), which shows that their inhibitory potency is between

dx.doi.org/10.1021/bc2000403 |*Bioconjugate Chem.* 2011, 22, 1354–1365

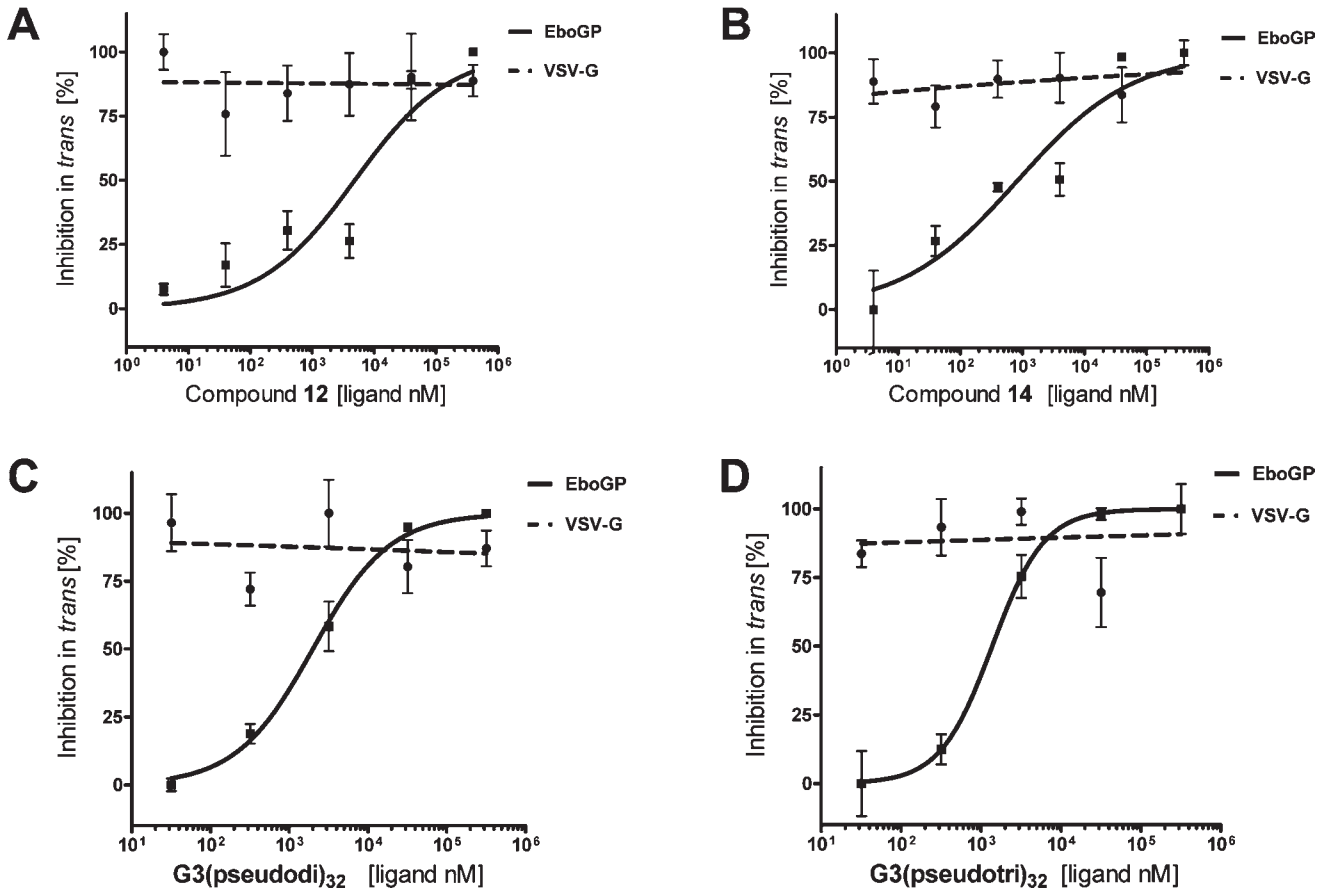

Figure 2. Infection results of the *trans* experiments using **12**, **14**, G3(pseudodi)$_{32}$, and G3(pseudotri)$_{32}$ compounds as inhibitors. Concentrations are expressed based on ligand concentration.

1 to 2 orders of magnitude higher than that of the corresponding tetravalent systems.

Similar results were obtained in the *trans* infection experiments (Figure 2). The IC_{50} of 32-valent systems bearing pseudomannobioside **13** or pseudomannotrioside **15** were 62 nM and 31.5 nM, respectively (2 and 1 μM, based on ligand concentration, respectively). The tetravalent dendron **14** with four copies of pseudomannotrioside showed an IC_{50} of 203 nM (0.8 μM, based on ligand concentration), and the tetravalent dendron **12** with four copies of pseudomannobioside was 1 order of magnitude less potent with an IC_{50} of 1.22 μM (4.9 μM, based on ligand concentration) (Figure 2).

SPR Studies. Competition experiments using Biacore SPR were performed to analyze the interaction of these glycomimetic tetra- and multivalent systems with the receptor DC-SIGN and to characterize the interaction at the molecular level.

For this aim, Biacore CM4 sensor chip was functionalized as described in the experimental section with BSA-Mannotriose. A fixed amount of DC-SIGN ECD was injected over the sensor chip flow cells in the presence or absence of different concentrations of the glycodendritic compounds to be evaluated. Analysis of the sensorgrams (see Supporting Information) allowed estimating IC_{50} for the monovalent, tetravalent, and multivalent compounds. At the monovalent level, strong differences were found (almost 1 order of magnitude) between the IC_{50} of monovalent pseudodi- and pseudotrisaccharides (IC_{50} 1.19 mM for the pseudodisaccharide **13** and 0.16 mM for the pseudotrisaccharide **15**). However, these differences decrease notably when the ligands are presented on the tetravalent scaffold (IC_{50} 227 μM for the tetravalent pseudodi **12** and 120 μM for the tetravalent pseudotri **14**) and are very similar when a dendrimer of third generation is used as multivalent platform (IC_{50} 2 μM for the multivalent pseudodi G3(pseudodi)$_{32}$ and 1.25 μM for the multivalent pseudotri G3(pseudotri)$_{32}$. (Figure 3)

These data show that tetravalent presentation of the pseudodisaccharide **13** on dendron **12** affords a very modest (1.3 per pseudosugar), if any, polyvalency effect (β), which improves significantly (18 per pseudosugar) in the full dendrimer G3-(pseudodi)$_{32}$. Strikingly, the tetravalent presentation of the pseudotrisaccharide **15** on dendron **14** does not afford any affinity increase (β = 0.3 per pseudosugar) and only a modest improvement (4 per pseudosugar) is observed for the full dendrimer G3(pseudotri)$_{32}$.

DISCUSSION

DC-SIGN is considered a very interesting therapeutic target for the design of new antiviral drugs. In addition, the ability of DC-SIGN to trigger signaling pathways that lead to a specific immune response has attracted attention on this lectin.[35−42] The development of specific tools to interact with and to understand the role and function of this lectin is of great interest. Furthermore, specific ligands designed to block the carbohydrate recognition domain of this lectin could be good candidates to be tested as antimicrobial agents.

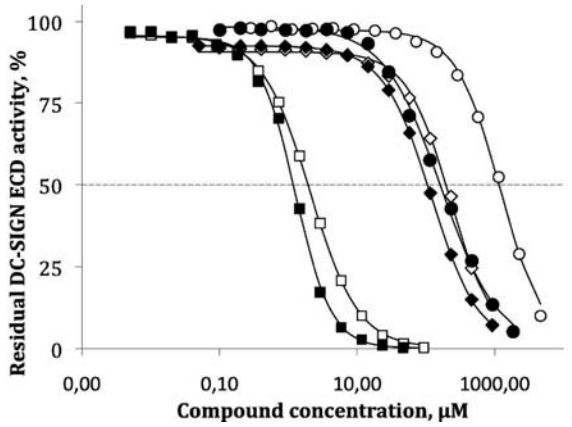

Figure 3. Inhibition of DC-SIGN ECD interaction with BSA-Mannotriose surface. DC-SIGN ECD (20 μM) was incubated with pseudomannobioside and pseudomannotrioside compounds at increasing concentrations: from 0 to 5000 μM and to 2000 μM for monovalent pseudomannobioside and pseudomannotrioside, respectively, from 0 to 1000 μM for compounds **12** and **14**, and from 0 to 100 μM for G3(pseudodi)$_{32}$, and G3(pseudotri)$_{32}$. The samples were coinjected over BSA-Mannotriose surface (1200 RU functionalization level). The steady state responses were extracted from the sensorgrams (see Supporting Information), converted to DC-SIGN ECD residual activity, and plotted against corresponding compound concentration. ○,● – monovalent, ◊,♦ – tetravalent, and □,■ – multivalent compounds; the empty and filled symbols represent pseudomannobioside and pseudomannotrioside compounds, respectively.

In this context, we have selected two linear pseudosaccharides **13** and **15** with good affinity for this receptor. The affinity has been remarkably enhanced *via* a multivalent presentation of these ligands. Tetra- and multivalent scaffolds based on bis-MPA as building block have been prepared with adequate functionalization on the surface for attachment of the selected ligands. The corresponding glycoconjugates with 4 and 32 copies of these ligands were prepared in good yields and were characterized using typical spectroscopic methods. MS analysis demonstrated the monodispersity of the tetravalent systems (compounds **12** and **14**). Higher valency systems obtained from monodisperse G3 Boltorn-type dendrimer G3(OH)$_{32}$ did not give good MS spectra and by analysis of the NMR spectra could only be described as systems with 30−32 ligands as an average loading; therefore, the monodispersity of these systems was not confirmed.

These tetra- and multivalent systems were tested *in vitro* as antiviral compounds in a well-established infection model based on pseudotyped viral particles with the Ebola virus envelope glycoprotein GP1. This infection system is a very efficient and "clean" model where the infection is exclusively dependent on DC-SIGN.[20] Cells that do not express the receptor and viruses able to infect the cells independently of DC-SIGN have been used as controls in these experiments. The results obtained have clearly demonstrated inhibition of the infection through blockage of the DC-SIGN receptor. The tetravalent systems **12** and **14** were very active in the low micromolar range, and the multivalent systems G3(pseudosugar)$_{32}$ showed a very strong inhibition effect with IC$_{50}$ in the nanomolar range. These systems could be considered as very potent inhibitors to be tested in further experiments. On the other hand, relatively small differences were observed between the two selected monovalent ligands the pseudodi **13** and the pseudotrisaccharide **15**.

In order to analyze this in more detail and to have additional molecular-level data on the interaction of these compounds with DC-SIGN, competition experiments using a biosensor with SPR detection were performed. A chip functionalized with mannosylated BSA was used to compete with our ligands for DC-SIGN. Analysis of the results obtained in these competition experiments demonstrates that the pseudosugars are good ligands for DC-SIGN, and that the pseudotrisaccharide **15** is 1 order of magnitude better than the pseudodisaccharide **13** when used as monovalent units. Surprisingly, this trend was not observed when the ligands are used in multivalent presentations: they both present a similar affinity when are exposed on the multivalent scaffolds. A plausible explanation for these facts could be the loss of different binding modes of the ligands when they are linked to a scaffold. In the particular case of DC-SIGN, it has been experimentally determined by X-ray[43] and also by NMR[44] that different binding modes are possible for carbohydrate ligands. These binding modes were observed for free ligands, but once they are conjugated to scaffolds, some or all of these alternative binding modes could become inaccessible; consequently, this could notably influence binding affinity. As a consequence, despite the improved affinity of the pseudomannotrioside at the monovalent level, our data suggest that the pseudomannobioside is the effective lead compound to use for further improvement of our multivalent pseudosaccharide compounds.

More structural experiments are currently being carried out in our laboratory at the monovalent level to obtain more detailed information and to investigate the factors that govern this phenomenon.

In summary, we present in this work the preparation of carbohydrate mimics on a tetra- and multivalent presentations and the analysis of their antiviral activity using a pseudotyped Ebola virus infection model. A strong inhibitory activity was found for the higher valency compounds with IC$_{50}$ in the nanomolar range. Competition experiments using SPR have also demonstrated the ability of these compounds to interact with DC-SIGN and compete for this receptor. Our results confirm pseudoglycosylated multivalent systems as very promising antiviral drugs with strong activities and encourage us to pursue more *in vitro* and *in vivo* studies concerning the potential biomedical applications.

■ ASSOCIATED CONTENT

Supporting Information. Additional information as described in the text. This material is available free of charge via the Internet at http://pubs.acs.org.

■ AUTHOR INFORMATION

Corresponding Author

*E-mail: franck.fieschi@ibs.fr (F.F); rdelgado.hdoc@salud.madrid.org (R.D.); anna.bernardi@unimi.it (A.B.); javier.rojo@iiq.csic.es (J.R.).

■ ACKNOWLEDGMENT

We would like to acknowledge the financial support by the MICINN of Spain CTQ2008-01694, the EU RTN CARMUSYS (PITN-GA-2008-213592), Comune di Milano (Convenzione 55/2008), Sidaction – Ensemble contre le Sida, Fundación Mutua Madrileña (FMM2007-700) and the European FEDER funds. The

expression plasmid for the glycoprotein of the Zaire strain of Ebola virus was kindly provided by Dr. A. Sanchez, Centers for Disease Control and Prevention, Atlanta, GA.

REFERENCES

(1) Varki, A. (1993) Biological roles of oligosaccharides: all of the theories are correct. *Glycobiology 2*, 97–130.

(2) Lundquist, J. J., and Toone, E. J. (2002) The cluster glycoside effect. *Chem. Rev. 102*, 555–578.

(3) Lee, R. T., and Lee, Y. C. (2000) Affinity enhacement by multivalent lectin-carbohydrate interaction. *Glycoconj. J. 17*, 543–551.

(4) Mammen, M., Choi, S.-K., and Whitesides, G. M. (1998) Polyvalent interactions in biological systems: implications for design and use of multivalent ligands and inhibitors. *Angew. Chem., Int. Ed. 37*, 2754–2794.

(5) Lee, Y. C., and Lee, R. T. (1995) Carbohydrate-protein interactions: basis of glycobiology. *Acc. Chem. Res. 28*, 321–327.

(6) Chabre, Y. M., and Roy, R. (2010) Designs and creativity in synthesis of multivalent neoglycoconjugates. *Adv. Carb. Chem. Biochem. 63*, 168–393.

(7) Lahmann, M. (2009) Architectures of multivalent glycomimetics for probing carbohydrate-lectin interactions. *Top. Curr. Chem. 288*, 17–65.

(8) Curtis, B. M., Scharnowske, S., and Watson, A. J. (1992) Sequence and expression of a membrane-associated C-type lectin that exhibits CD4-independent binding of human immunodeficiency virus envelope glycoprotein gp120. *Proc. Natl. Acad. Sci. U.S.A. 89*, 8356–8360.

(9) Geijtenbeek, T. B. H., Kwon, D. S., Torensma, R., Van Vliet, S. J., Van Duijnhoven, G. C. F., Middel, J., Cornelissen, I. L. M. H. A., Nottet, H. S. L. M., KewalRamani, V. N., Littman, D. R., Figdor, C. G., and Van Kooyk, Y. (2000) DC-SIGN, a dendritic cell-specific HIV-1-binding protein that enhances *trans*-infection of T Cells. *Cell 100*, 587–597.

(10) Geijtenbeek, T. B. H., Torensma, R., Van Vliet, S. J., Van Duijnhoven, G. C. F., Adema, G. J., Van Kooyk, Y., and Figdor, C. G. (2000) Identification of DC-SIGN, a novel dendritic cell−specific ICAM-3 receptor that supports primary immune responses. *Cell 100*, 575–585.

(11) Feinberg, H., Mitchell, D. A., Drickamer, K., and Weis, W. (2001) Structural basis for selective recognition of oligosaccharides by DC-SIGN and DC-SIGNR. *Science 294*, 2163–2166.

(12) Mitchell, D. A., Fadden, A. J., and Drickamer, K. (2001) A novel mechanism of carbohydrate recognition by the C-type lectins DC-SIGN and DC-SIGNR. *J. Biol. Chem. 276*, 28939–28945.

(13) van Kooyk, Y., Geijtenbeek, T. B. H. (2003) DC-SIGN: escape mechanism for pathogens. *Nat. Rev. Immunol. 3*, 697−709.

(14) Geijtenbeek, T. B. H., and van Kooyk, Y. (2003) Pathogens target DC-SIGN to influence their fate DC-SIGN functions as a pathogen receptor with broad specificity. *APMIS 111*, 698–714.

(15) Rojo, J., and Delgado, R. (2004) Glycodendritic structures: promising new antiviral drugs. *J. Antimicrob. Chemother. 54*, 579–581.

(16) Borrok, M. J., and Kiessling, L. L. (2007) Non-carbohydrate inhibitors of the lectin DC-SIGN. *J. Am. Chem. Soc. 129*, 12780–12785.

(17) Becer, C. R., Gibson, M. I., Geng, J., Ilyas, R., Wallis, R., Mitchell, D. A., and Haddleton, D. M. (2010) High-affinity glycopolymer binding to human DC-SIGN and disruption of DC-SIGN interactions with HIV envelope glycoprotein. *J. Am. Chem. Soc. 132*, 15130–15132.

(18) Sánchez-Navarro, M., and Rojo, J. (2010) Targeting DC-SIGN with multivalent systems. *Drug News and Perspectives 23*, 557–572.

(19) Arce, E., Nieto, P. M., Díaz, V., Castro, R. G., Bernad, A., and Rojo, J. (2003) Glycodendritic structures based on Boltorn hyperbranched polymers and their interactions with Lens Culinaris lectin. *Bioconjugate Chem. 14*, 817–823.

(20) Lasala, F., Arce, E., Otero, J. R., Rojo, J., and Delgado, R. (2003) Mannosyl glycodendritic structure inhibits DC-SIGN-mediated Ebola virus infection in cis and in trans. *Antimicrob. Agents Chemother. 47*, 3970–3972.

(21) Rojo, J., and Delgado, R. (2007) Dendrimers and dendritic polymers as anti-infective agents: new antimicrobial strategies for therapeutic drugs. *Anti-infect. Agents Med. Chem. 6*, 151–174.

(22) Reina, J. J., Sattin, S., Invernizzi, D., Mari, S., Martinez-Prats, L., Tabarani, G., Fieschi, F., Delgado, R., Nieto, P. M., Rojo, J., and Bernardi, A. (2007) 1,2-Mannobioside mimic: synthesis, DC-SIGN interaction by NMR and docking, and antiviral activity. *ChemMedChem 2*, 1030–1036.

(23) Sattin, S., Daghetti, A., Thépaut, M., Berzi, A., Sánchez-Navarro, M., Tabarani, G., Rojo, J., Fieschi, F., Clerici, M., and Bernardi, A. (2010) Inhibition of DC-SIGN-mediated HIV infection by a linear trimannoside mimic in a tetravalent presentation. *ACS Chem. Biol. 3*, 301–312.

(24) Annby, U., Malmberg, M., Pettersson, B., and Rehnberg, N. (1998) Benzylidene protected Bis-MPA A convenient dendrimer building block. *Tetrahedron Lett. 39*, 3217–3220.

(25) Goodwin, A. P., Lam, S. S., and Fréchet, J. M. J (2007) Rapid, efficient synthesis of heterobifunctional biodegradable dendrimers. *J. Am. Chem. Soc. 129*, 6994–6995.

(26) Ihre, H., Padilla de Jesús, O. L., and Fréchet, J. M. J. (2001) Fast and convenient divergent synthesis of aliphatic ester dendrimers by anhydride coupling. *J. Am. Chem. Soc. 123*, 5908–5917.

(27) Isomura, S., Wirsching, P., and Janda, K. D. (2001) An immunotherapeutic program for the treatment of nicotine addiction: hapten design and synthesis. *J. Org. Chem. 66*, 4115–4121.

(28) Ihre, H, Hult, A., Fréchet, J. M. J., and Gitsov, I. (1998) Double-stage convergent approach for the synthesis of functionalized dendritic aliphatic polyesters based on 2,2-Bis(hydroxymethyl)propionic acid. *Macromolecules 31*, 4061–4068.

(29) Malkoch, M., Malmström, E., and Hult, A. (2002) Rapid and efficient synthesis of aliphatic ester dendrons and dendrimers. *Macromolecules 35*, 8307–8314.

(30) Alvarez, C. P., Lasala, F., Carrillo, J., Muñiz, O., Corbí, A. L., and Delgado, R. (2002) C-Type lectins DC-SIGN and L-SIGN mediate cellular entry by ebola virus in *cis* and in *trans*. *J. Virol. 76*, 6841–6844.

(31) Tabarani, G., Thepaut, M., Stroebel, D., Ebel, C., Vives, C., Vachette, P., Durand, D., and Fieschi, F. (2009) DC-SIGN neck domain is a pH-sensor controlling oligomerization: SAXS and hydrodynamic studies of extracellular domain. *J. Biol. Chem. 284*, 21229–21240.

(32) Halary, F., Amara, A., Lortat-Jacob, H., Messerie, M., Delaunay, T., Houlès, C., Fieschi, F., Arenzana-Seisdedos, F., Moreaus, J.-F., and Déchanet-Merville, J. (2002) Human cytomegalovirus binding to DC-SIGN is required for dendritic cell infection and target cell *trans*-infection. *Immunity 17*, 653–664.

(33) Yim, S.-H., Huh, J., Ahn, C.-H., and Park, T. G. (2007) Development of a novel synthetic method for aliphatic ester dendrimers. *Macromolecules 40*, 205–210.

(34) Anderson, G. T., Alexander, M. D., Taylor, S. D., Smithrud, D. B., Benkovic, S. J., and Weinreb, S. M. (1996) Catalytic antibodies in synthesis: design and synthesis of a hapten for application to the preparation of a scalemic pyrrolidine ring synthon for Ptilomycalin A. *J. Org. Chem. 61*, 125–132.

(35) Zhou, T., Chen, Y., Hao, L., and Zhang, Y. (2006) DC-SIGN and immunoregulation. *Cell. Mol. Immunol. 3*, 279–283.

(36) Caparrós, E., Muñoz, P., Sierra-Filardi, E., Serrano-Gómez, D., Puig-Kröger, A., Rodríguez-Fernández, J. L., Mellado, M., Sancho, J., Zubiaur, M., and Corbí, A. L. (2006) DC-SIGN ligation on dendritic cells results in ERK and PI3K activation and modulates cytokine production. *Blood 107*, 3950–3958.

(37) Shan, M., Klasse, P. J., Banerjee, K., Dey, A. K., Iver, S. P., Dionisio, R., Charles, D., Campbell-Gardener, L., Olson, W. C., Sanders, R. W., and Moore, J. P. (2007) HIV-1 gp120 mannose induce immunosupresive responses from dendritic cells. *PLoS Pathogens 3*, e169.

(38) van Kooyk, Y. (2008) C-type lectins on dendritic cells: key modulators for the induction of immune responses. *Biochem. Soc. Trans. 36*, 1478–1481.

(39) den Dunnen, J., Gringhuis, S. I., and Geijtenbeek, T. B. H. (2009) Innate signaling by the C-type lectin DC-SIGN dictates immune responses. *Cancer Immunol. Immunother. 58*, 1149–1157.

(40) Geijtenbeek, T. B. H., den Dunnen, J., and Gringhuis, S. I. (2009) Pathogen recognition by DC-SIGN shapes adaptive immunity. *Future Microbiol. 4*, 879–890.

(41) Gringhuis, S. I., den Dunnen, J., Litjens, M., van der Vlist, M., and Geijtenbeek, T. B. H. (2010) Carbohydrate-specific signaling through the DC-SIGN signalosome tailors immunity to Mycobacterium tuberculosis, HIV-1 and Helicobacter pylori. *Nat. Immunol. 10*, 1081–1089.

(42) den Dunnen, J., Gringhuis, S. I., and Geijtenbeek, T. B. H. (2010) Dusting the sugar fingerprint: C-type lectin signaling in adaptive immunity. *Immunol. Lett. 128*, 12–16.

(43) Feinberg, H., Castelli, R., Drickamer, K., Seeberger, P. H., and Weis, W. I. (2007) Multiple modes of binding enhance the affinity of DC-SIGN for high mannose *N*-linked glycans found on viral glycoproteins. *J. Biol. Chem. 282*, 4202–4209.

(44) Angulo, J., Reina, J. J., Tabarani, G., Fieschi, F., Rojo, J., and Nieto., P. M. (2008) Saturation transfer difference (STD) NMR spectroscopy characterization of dual binding mode of a mannose disaccharide to DC-SIGN. *ChemBioChem 9*, 2225–2227.

■ NOTE ADDED AFTER ASAP PUBLICATION

This paper was published on the Web on June 20, 2011 with a production error, the omission of the reagent lists in Schemes 1 and 2. The corrected version was reposted on June 23, 2011.

Supplementary Information

Pseudosaccharide functionalized dendrimers as potent inhibitors of DC-SIGN dependent Ebola pseudotyped viral infection

Joanna Luczkowiak,[c] Sara Sattin,[b] Ieva Sutkevičiūtė,[d,f] José Juan Reina,[b] Macarena Sánchez-Navarro,[a] Michel Thépaut,[d,e] Lorena Martínez-Prats,[c] Anna Daghetti,[b] Franck Fieschi,[d,e,f,*] Rafael Delgado[c,*] Anna Bernardi,[b,*] Javier Rojo,[a,*]

[a] *Grupo Carbohidratos, Instituto de Investigaciones Químicas, CSIC – Universidad de Sevilla, Américo Vespucio 49, 41092 Seville, Spain. Tel: 954489568; Fax: 954460565*

[b] *Università degli Studi di Milano, Dipartimento di Chimica Organica e Industriale, Milano, Italy*

[c] *Laboratorio de Microbiología Molecular- Hospital Universitario 12 de Octubre, Madrid, Spain*

[d] *Institut de Biologie Structurale, CNRS, UMR 5075, 41 rue Jules Horowitz 38027 Grenoble France*

[e] *CEA, DSV, 38027 Grenoble France*

[f] *Université Joseph Fourier, 38000 Grenoble, France*

1. SPR sensorgrams for the inhibition curves reported in Figure 3. The arrows denote EDTA injections for BSA-Mannotriose surface regeneration between each cycle.

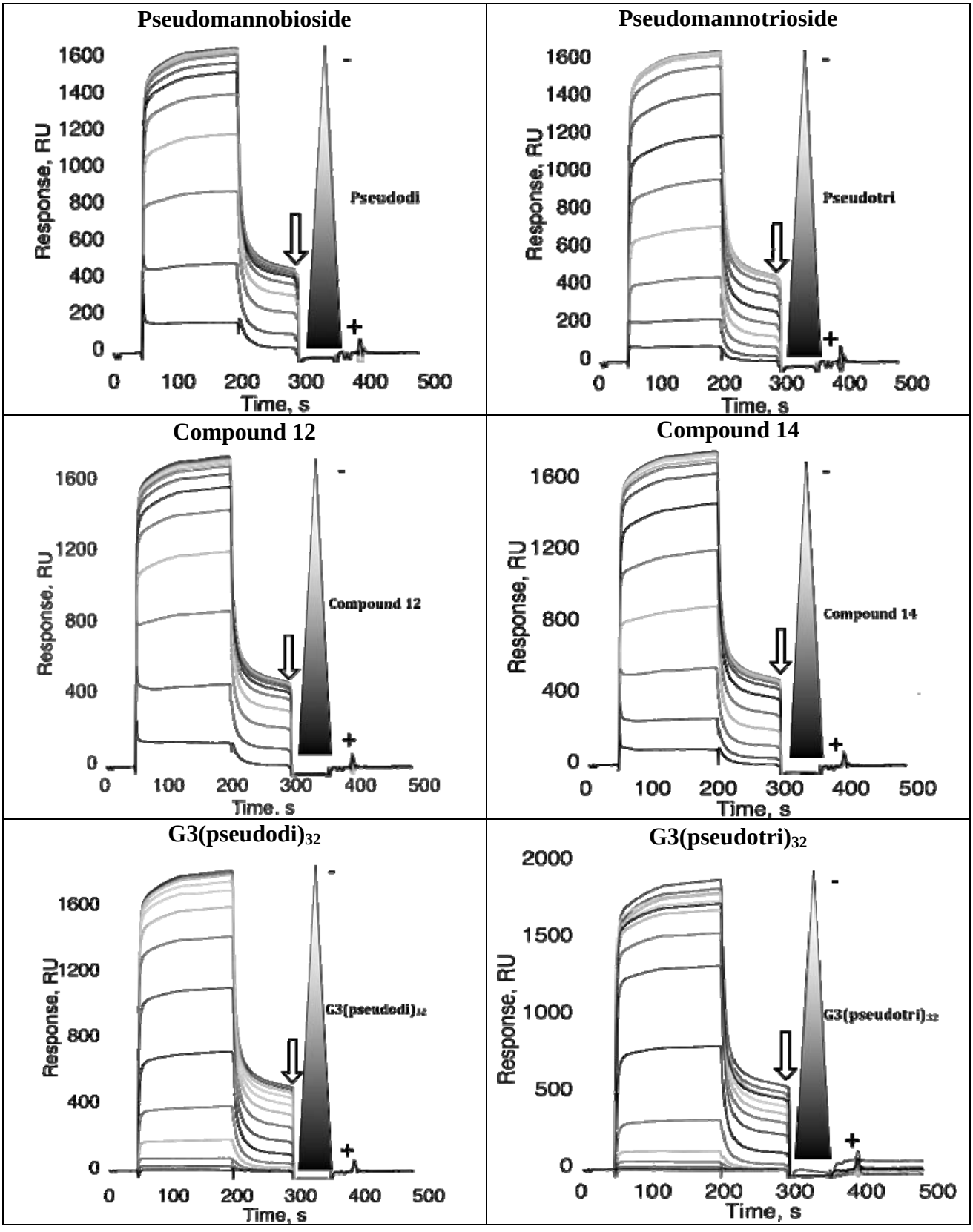

2. Mass spectra for multivalent compounds with glycomimetics **13** and **15**.

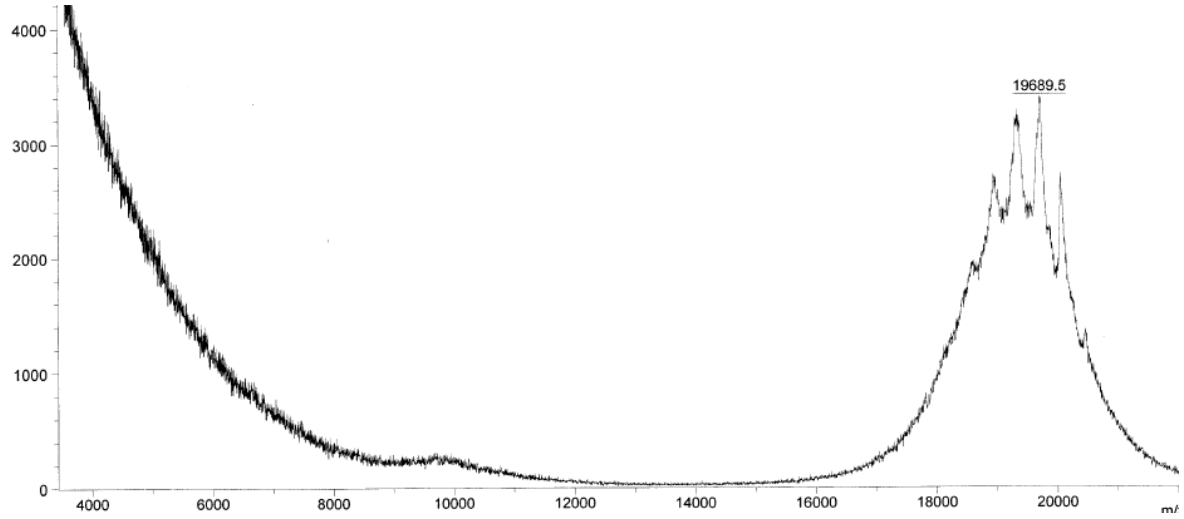

MALDI mass spectrum of 3G(pseudodi)$_{32}$. Matrix: SA.

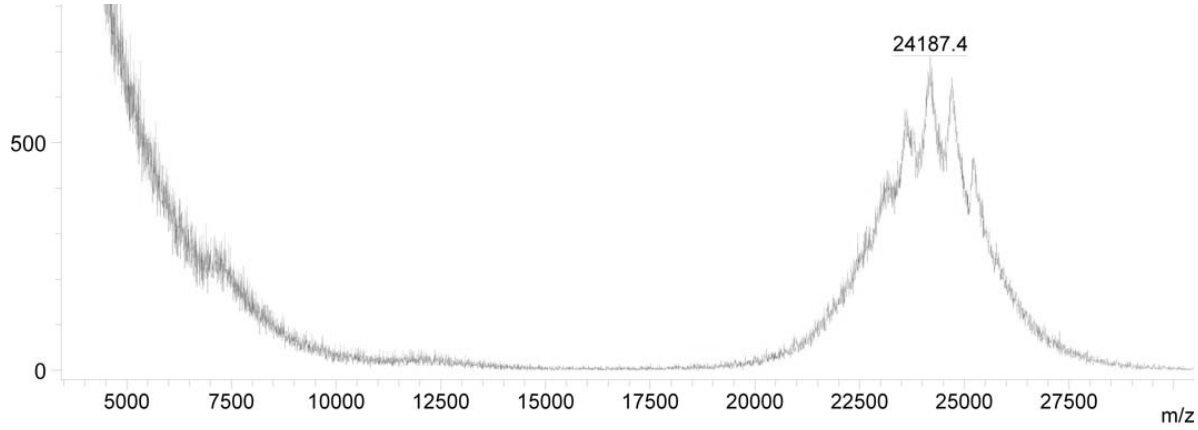

MALDI mass spectrum of 3G(pseudotri)$_{32}$. Matrix: SA.

Equation 1 (determination of relative IC_{50} values)

$$y = bot + \frac{top - bot}{1 + \left(\frac{x}{IC_{50}}\right)^{slope}}$$

where *y* is the percent activity, *x* is the corresponding concentration, *bot* and *top* are the lowest and the highest values of percent activity, respectively.

Bioconjugate Chemistry

ARTICLE

pubs.acs.org/bc

Restriction Endonuclease SsoII with Photoregulated Activity—a "Molecular Gate" Approach

Le Thi Hien,[†,∥] Timofei S. Zatsepin,[†,§] Benno Schierling,[#] Eugene M. Volkov,[†] Wolfgang Wende,[#] Alfred Pingoud,[#] Elena A. Kubareva,[‡] and Tatiana S. Oretskaya*[,†,‡]

[†]Department of Chemistry

[‡]Belozersky Institute of Physico-Chemical Biology

Lomonosov Moscow State University, Leninskie gory, Moscow 119991, Russia

[§]Central Research Institute of Epidemiology, Novogireevskaya street 3a, Moscow 111123, Russia

[#]Justus-Liebig-Universität, Institut für Biochemie, FB 08, Heinrich-Buff-Ring, Giessen, D-35392 Germany

Supporting Information

ABSTRACT: A novel method for regulating the activity of homodimeric proteins—"molecular gate" approach—was proposed and its usefulness illustrated for the type II restriction endonuclease SsoII (R.SsoII) as a model. The "molecular gate" approach is based on the modification of R.SsoII with azobenzene derivatives, which allows regulating DNA binding and cleavage via illumination with light. R. SsoII variants with single cysteine residues introduced at selected positions were obtained and modified with maleimidoazobenzene derivatives. A twofold change in the enzymatic activity after illumination with light of wavelengths of 365 and 470 nm, respectively, was demonstrated when one or two molecules of azobenzene derivatives were attached to the R.SsoII at the entrance of or within the DNA-binding site.

INTRODUCTION

In "genome surgery", a number of enzymes are used as molecular tools for cleaving defective genes—restriction and homing endonucleases, fusion of DNA cleavage domains (e.g., the nonspecific DNA cleavage domain of FokI) with DNA binding modules (e.g., "zinc fingers").[1,2] Specific DNA cleavage at the desired position and at the appropriate time is a key requirement for precise gene targeting. In the case of the human genome, only so-called meganucleases (sequence specific endonucleases with extended recognition sites) could be used to cleave a single unique site.[3] However, even such enzymes can show undesirable activity in the cell. There are numerous methods to regulate the protein activity on the level of gene expression[4,5] or through the reversible or irreversible interaction with different types of molecules including oligonucleotides.[6−9] Usually, attaching low molecular mass ligands to proteins allows the synthesis of bioconjugates with special properties—i.e., modified or novel activity.[10−12] One of the methods used is based on the photoregulation of the activity of a protein via an azobenzene "photoswitch".[13] Azobenzene can reversibly isomerize from the extended *trans*-configuration to the more compact *cis*-configuration by illumination with UV light (*trans* → *cis*) or vice versa by blue light (*cis* → *trans*). Thermal relaxation is also possible (*cis* → *trans*).[14] Rapid and effective *cis*−*trans* isomerization of azobenzene and its derivatives allows their application for in vivo studies.[15] The regulation of the activity of restriction endonucleases (RE) or homing endonucleases (HE) by light opens up new prospects for controlling DNA duplex cleavage and creating safer molecular tools for gene manipulations. Thus, the modified nuclease can be delivered to the cell nucleus in the less active state for the subsequent remote activation by an external signal (UV light) after binding to the DNA at a specific site. Undesirable DNA cleavage can be reduced by lowering the nuclease activity after hydrolysis of the target area by illumination with blue light. The primary requirement for production of a photoregulated protein is the selective attachment of appropriate light-sensitive compounds.

So far, there are only reports about two RE for which activity can be regulated by light, namely, for *Bam*HI (R.*Bam*HI)[16−18] and PvuII (R.PvuII).[19] R.*Bam*HI specifically hydrolyzes double-stranded DNA only after formation of the correct homodimeric form of the enzyme. Nakayama et al. introduced phenylazophenylalanine (AzoAla) into the dimer interface to regulate the activity of this enzyme by affecting the dimerization process.[20] The activity of the enzyme in the dark (*trans*-AzoAla-*Bam*HI) was suppressed, but after illumination with UV light, the activity of the enzyme (*cis*-AzoAla-*Bam*HI) was restored. However, this method is time-consuming and tedious.

Previously, we have demonstrated an efficient method, which one might call the "molecular spring" approach for regulating the

Received: January 31, 2011
Revised: May 4, 2011
Published: June 20, 2011

ACS Publications © 2011 American Chemical Society

Scheme 1. Photoregulation of Modified RE SsoII by "Molecular Gate" Approach

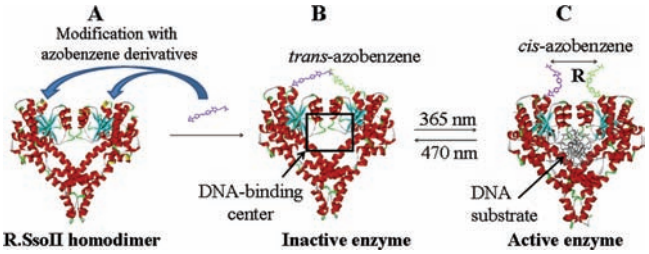

activity of R.PvuII.[19] A symmetric azobenzene derivative—bis(maleimido)azobenzene—was introduced as a cross-linker to connect two neighboring cysteine residues next to the active site of the protein. When the exciting light changes from UV to blue and vice versa, the isomerization of azobenzene works like a spring, altering the local conformation of the protein, which can lead to a change in the activity of the enzyme. The "molecular spring" method is better applied to proteins of small molecular mass. In this case, the isomerization of bis(maleimidoazobenzene) changes the local structure of the protein. In addition, linkage of the two subunits of the homodimer protein by a peptide spacer proved to be advantageous for achieving a high photoswitching effect. Here, the N- and C-termini of the two subunits of the wild-type R.PvuII are brought close to each other with the help of a four-amino-acid linker.

In this study, we propose a "molecular gate" approach to regulate the activity of a restriction endonuclease. This approach is based on the fact that most type II restriction endonucleases in the active state are homodimers with the DNA-binding center located in the interface between the two subunits. Modification of the protein with azobenzene derivatives (A) (Scheme 1) at the entrance of the DNA binding site might make the DNA binding site inaccessible due to steric hindrance in the case of the extended configuration of *trans*-azobenzene (B). When illuminated by UV, the extended *trans*-form of azobenzene isomerizes into the compact *cis*-form (C) that might increase the distance R between the ends of the two molecules of azobenzene (Scheme 1). Therefore, in the *cis*-form of azobenzene the DNA substrate could possibly reach the DNA-binding center of the protein.

The subject of our investigation was the homodimeric restriction endonuclease SsoII (R.SsoII). It recognizes and cleaves the double-stranded pentanucleotide sequence: 5′···↓CCNGG···3′/3′···GGNCC↑···5′ (N = A, G, C, T). A thiol group of a cysteine residue can be introduced into the protein by site-directed mutagenesis and this is the most convenient way for the specific modification of the protein by various reagents. Previously, we synthesized symmetrical bis(maleimido)azobenzene and asymmetrical azobenzene derivatives bearing a maleimide group in one of the benzene rings for binding to a cysteine of the protein and a hydroxyl or carboxyl group in the other ring. The optical properties of the azobenzene derivatives in free form and after its attachment to the R.SsoII variants were studied.[21]

The aim of the present investigation was to modify variants of R.SsoII by azobenzene derivatives, for the purpose of regulating the activity of the enzyme by light. The tasks of the work were as follows: (1) synthesis of azobenzene derivatives, confirmation of their structures, investigation of their chemical and optical properties; (2) selection of amino acid residues in R.SsoII on the basis of the X-ray structure analysis of its homologue—restriction endonuclease Ecl18kI (R.Ecl18kI)[22] in order to introduce Cys residues in appropriate positions; (3) production of mutant forms of R.SsoII, containing Cys residue(s) in the selected positions; (4) modification of R.SsoII variants by azobenzene derivatives and analysis of the DNA cleavage activity of modified R.SsoII when illuminated by UV and blue light, respectively.

EXPERIMENTAL SECTION

General. Materials and reagents were obtained from commercial suppliers and used without further purification unless otherwise noted. The following reagents were used in this study: monomaleimide derivative of 2.3 kDa poly(ethylene glycol) (Pierce, USA) and 5 kDa poly(ethylene glycol) (PEG-Mal) (Sigma, USA), Ni^{2+}-NTA-agarose (Qiagen, Germany), protein ladder PageRuler, DNA-marker pUC mix (Fermentas, Lithuania). Äkta FPLC (GE Heathcare, USA) was used with HiTrap G-25 Superfine Sephadex desalting 5 mL column (GE Healthcare, USA). Mass spectra were recorded on a system that consisted of an ACQUITY UPLC and a TQD tandem quadrupole mass-spectrometric detector (Waters, USA). NMR spectra were recorded on the Avance 400 spectrometer (Bruker, Germany) at 25 °C. $CHCl_3$ served as an internal standard.

*4-Maleimido-4′-[2-(2-hydroxyethylthio)succinimido]azobenzene (MAB−OH) (**1**).* MAB-OH was synthesized as described previously[21] with minor modifications (Scheme 2).

A solution of 2-mercaptoethanol (0.4 mmol) in dioxane (2 mL) was added to a solution of bis(maleimido)azobenzene (150 mg, 0.4 mmol) in dioxane (20 mL) within 30 min while stirring solution. The target product (R_f 0.23) was isolated by chromatography on a silica gel column with an ethanol gradient in chloroform (0−5%) with a yield of 45 mg (25%). ^{1}H NMR ($CDCl_3$, π, ppm): 8.0 (4 H, d), 7.7 (4 H, d), 7.3 (2 H, s), 4.2 (1 H, s), 3.7 (2 H, m), 3.0 (2 H, m), 2.7 (2 H, m); MS: $C_{22}H_{18}N_4O_5S$ $(MH)^+$ calcd/found: 450.10/451.24.

*4-Maleimido-4′-(2-(2-amino-2-carboxyethylthio)succinimido)-azobenzene (MAB-Cys) (**2**).* An aqueous solution of L-cysteine hydrochloride (10 mL, 63 mg, 0.4 mmol) was added to a solution of bis(maleimido)azobenzene (200 mg, 0.5 mmol) in dioxane (30 mL) within 30 min while stirring solution. The mixture obtained was extracted twice with 30 mL chloroform. The precipitate, containing products, was filtered and dried in air. The yield of a mixture of products with one **2** and two cysteine residues **2.1** (Scheme 2) was 111 mg (50%). MS: $C_{23}H_{19}N_5O_6S$ $(MH)^+$ calcd/found: 493.49/494.31.

Mutagenesis, Protein Expression, and Purification. Site-directed mutagenesis of the R.SsoII gene was performed using a PCR method.[23] The plasmids pQESso9 carrying the gene coding for the restriction endonuclease SsoII and pACMS7 containing the gene coding for the methyltransferase SsoII were a generous gift from Dr. V. Pingoud (Institute of Biochemistry, Justus-Liebig University, Giessen, Germany). The plasmid pQESso9 or plasmids carrying mutant forms of the R.SsoII gene were used to transform the *E. coli* strain JM109 which had previously been transformed with the plasmid pACMS7. All genetic constructs were confirmed by DNA sequencing over the entire coding region. Cultures were grown at 37 °C to $OD_{600} \approx 0.7$ and protein expression was induced by the addition of 1 mM IPTG. After 3 h of induction, cells were harvested by centrifugation for 15 min, 4000 g at 4 °C. The cell pellet was resuspended in 20 mM Tris-HCl buffer (pH 7.9), containing 500 mM NaCl, 20 mM imidazole,

Scheme 2. Synthesis of Monosubstituted Azobenzene Derivatives

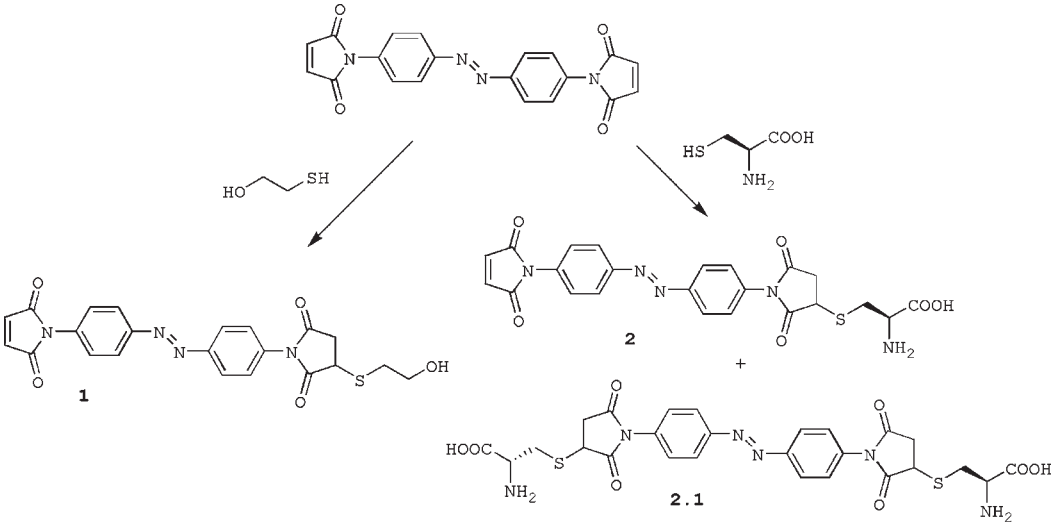

1 mM phenylmethanesulfonylfluoride, pH 7.9, and lysed by sonication. Cell debris was removed by centrifugation (17000 × g) for 30 min at 4 °C. The recombinant His-tagged proteins were purified by affinity chromatography over Ni-NTA agarose using 20 mM Tris-HCl (pH 7.9), 500 mM NaCl, 200 mM imidazole, 5 mM 1,4-dithiothreitol (DTT) for elution. Fractions containing pure protein were dialyzed overnight at 4 °C against 10 mM potassium phosphate buffer (pH 7.4), containing 200 mM KCl, 50% v/v glycerol, and stored at −20 °C. Protein purification was monitored by SDS-PAGE analysis, and protein concentration was determined by absorbance measurements at 280 nm. The molecular mass of the recombinant R.SsoII was determined as 37.2 kDa.

Protein Labeling with Azobenzene Derivatives. To confirm reactivity of cysteine residues introduced into R.SsoII mutants, 5 μM R.SsoII in 20 mM K-phosphate buffer (pH 7.4), containing 150 mM NaCl, was incubated with a 50-fold molar excess of PEG-Mal (5 kDa) (freshly dissolved in DMSO) for 10 min at RT. The conjugates were analyzed by SDS-PAGE. To synthesize azobenzene−protein conjugates, 5 μM R.SsoII variant in 20 mM K-phosphate buffer (pH 7.4), containing 150 mM NaCl, was incubated with a 5-fold molar excess (over the number of cysteine residues in the protein) of the azobenzene derivative **1** or **2** (freshly dissolved in DMSO) for 10 min at RT. The yield of the conjugate was estimated in the following way. A 50-fold molar excess of PEG-Mal was added to an aliquot of the reaction mixture and analyzed by SDS-PAGE. The reaction mixture was purified by Äkta FPLC gel filtration and dialyzed overnight at 4 °C against 10 mM K-phosphate buffer (pH 7.4), containing 200 mM KCl, 50% v/v glycerol. Purified protein was stored at −20 °C.

DNA Cleavage by Modified R.SsoII after Specific Illumination. Modified R.SsoII was pre-illuminated with light and then the cleavage reaction was started under continuous illumination. The "pre-illumination" of the R.SsoII variants was performed as follows: protein solution was illuminated with blue light (470 nm) for 2 min at a distance of 15 cm to transform azobenzene in the modified R.SsoII variants to the *trans*-state and was illuminated for 7 min with a UV lamp (365 nm) at a distance of 9 cm to transfer azobenzene in the modified R.SsoII variants to the *cis*-state. The pre-illuminated enzyme was incubated with the DNA substrate under continuous specific illumination. After every 1, 2, 3, 5, 7, and 10 min, an aliquot of the reaction mixture was taken and analyzed by SDS-PAGE.

DNA cleavage activity was analyzed by using an 873 base pair (bp) PCR fragment as substrate, which has a single R.SsoII site. The DNA substrate was incubated with R.SsoII for 15 min at 37 °C in 20 mL of 10 mM Tris-HCl buffer (pH 7.5), containing 10 mM $MgCl_2$, 5 mM NaCl, 1 mM DTT, and 0.1 mg/mL bovine serum albumin (BSA). The concentration of DNA substrate was 5−10 nM (for R.SsoII variants with low activity) or 20 nM (for R.SsoII variants with high activity). Concentration of wt and mutant forms of R.SsoII ranged from 20 to 500 nM. Reaction products (DNA fragments of 530 bp and 338 bp in length) were analyzed by electrophoresis in a 4−6% polyacrylamide gel under nondenaturing conditions. Gels were stained with ethidium bromide, and the fluorescence was measured with a BioDocAnalyze system (Biometra) and quantitated. Intensities of DNA-containing bands were determined by processing the gel image using the *ImageQuant* program (GE Healthcare). The amount of cleavage (%) was calculated as the ratio between the intensities of the product bands and the total intensities of all the bands (initial DNA substrate and products). WtR.SsoII was used as a control. When R.SsoII variants, modified with MAB-Cys (**2**) were used, the cleavage reaction was carried out in 10 mM Tris-HCl buffer (pH 7.5) without DTT, containing 10 mM $MgCl_2$, 5 mM NaCl, 0,1 mg/mL BSA and, in addition, 1 μM $NiCl_2$ or 10 μM $CoSO_4$ (for forming a complex between the Cys residue in MAB-Cys and metal ions) was used.

RESULTS AND DISCUSSION

Synthesis of Azobenzene Derivatives. Asymmetric azobenzene derivatives MAB-OH (**1**) and MAB-Cys (**2**) were obtained by the reaction of two different thiols with bis(maleimido)azobenzene (Scheme 2). However, compound **2** was quite hydrophilic and could not be isolated by silica gel column chromatography. Therefore, the reaction mixture was extracted with chloroform to remove bis(maleimido)azobenzene. Further, the mixture of **2** and **2.1** was

used for modification of protein, since only compound **2** is able to react with the cysteine residue of a protein.

Design of R.SsoII Variants and Their Properties. There are two native cysteine residues at positions 33 and 60 of wtR.SsoII. The variant without cysteine residues R.SsoII(C33S/C60S), Cys-free R.SsoII (cfR.SsoII or 2CS), was produced by site-directed mutagenesis. Other R.SsoII variants, in which some amino acids were changed for cysteine, were produced from the cfR.SsoII gene. Previously, the structure of R.Ecl18kI with a DNA substrate was determined.[22] This RE is an isoschizomer of R. SsoII and differs from it by one amino acid only (Val232 in R. Ecl18kI corresponds to Ile232 in R.SsoII). The amino acid residues to be substituted by mutagenesis were chosen based on the R.Ecl18kI structure (Figure 1). The homodimeric protein contains internal and external clamps that surround the DNA substrate. Two amino acid residues S171 and R174 on the external clamp and three amino acids R198, I220, and A224 on the internal clamps were selected and changed for cysteine residues for subsequent modification by azobenzene derivatives (Figure 1). Thus, 5 variants each with one cysteine residue at the positions listed above and 6 variants with 2, 3, or 4 cysteine residues in various combinations were produced. It was expected that the larger the number of molecules of azobenzene located near the entrance of the DNA-binding site of a protein, the greater the steric effect and the greater should be the influence of illumination on the activity of the protein.

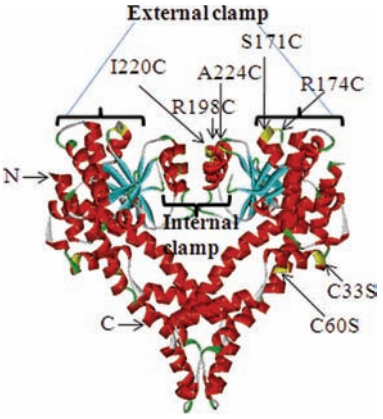

Figure 1. Structure model of the homodimer R.SsoII (based on the X-ray structure analysis for R.Ecl18kI[22]). Amino acid residues S171, R174, R198, I220, and A224 that were changed to cysteine are marked with arrows.

The enzymatic activity of R.SsoII was assessed by its ability to hydrolyze a 873 bp DNA substrate, having only one recognition site for this enzyme. It was shown that the enzymatic activity of variants of R.SsoII depends on the position and the number of cysteine residues introduced into the enzymes (Figure 2). The closer the Cys residue is to the DNA-binding center of the enzyme and the greater the number of cysteine residues introduced is, the less active the mutant form of R.SsoII is likely to be. Thus, the cleavage of a DNA substrate by the 2CS/S171C variant is 70% of the activity of wtR.SsoII, of the 2CS/S171C/R174C variant is about 40%, and of the 2CS/S171C/R174C/I220C/A224C variant is only 25% even with 3-fold higher concentration of this enzyme. This activity comparison is shown in Figure 2. For further studies, enzyme concentrations were selected so that the DNA cleavage ranged from 20% to 80%. In the variant 2CS/R198C, the replaced R198 residue is located next to E195, which takes part in catalysis; this explains the low enzymatic activity of this variant among the other ones that have only a single cysteine residue modified per subunit. Variants with two cysteine residues modified per subunit, one of which at position 198, show the lowest activity (2CS/R198C/A224C) or almost no activity (2CS/R174C/R198C).

Modification of Protein with Maleimide Derivatives. Poly-(ethylene glycol) containing a maleimide group (PEG-Mal) was used to assess the reactivity of cysteine residues in R.SsoII variants. The high molecular mass of PEG-Mal (2.3 or 5 kDa) allows one to measure the formation of its conjugate with mutant

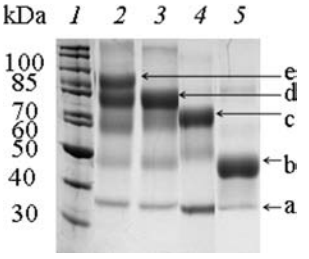

Figure 3. SDS-PAGE analysis of R.SsoII variants (5 μM) containing 1 (lane 5), 2 (lane 4), 3 (lane 3), or 4 (lane 2) cysteine residues per protein monomer modified with with PEG-Mal (500 μM). Lane 1 — Protein molecular mass marker. Gel was stained with a Coomassie solution. a - unmodified protein; b - conjugate of 2CS/I220C with PEG-Mal; c - conjugate of 2CS/S171C/R174C with PEG-Mal; d - conjugate of 2CS/S171C/R174C/I220C with PEG-Mal; e - conjugate of 2CS/S171C/R174C/I220C/A224C with PEG-Mal.

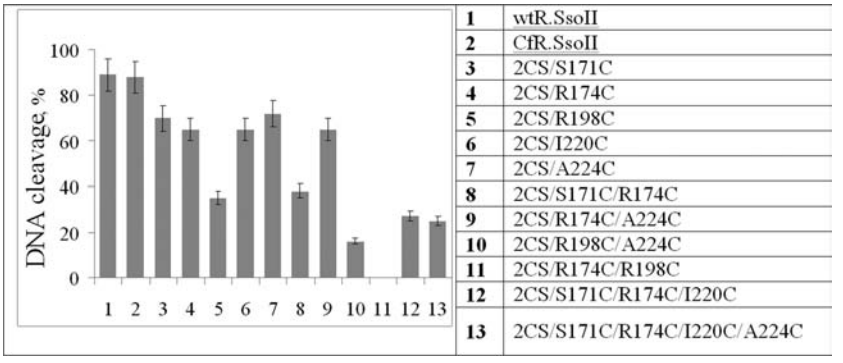

Figure 2. Histogram showing the amount of cleavage of a DNA substrate by R.SsoII variants. The degree of DNA cleavage was determined as the arithmetic mean of three independent experiments.

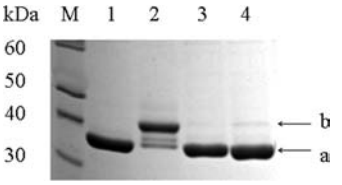

Figure 4. Analysis of R.SsoII(2CS/R174C) (5 μM) modified with PEG-Mal (2.3 kDa, 500 μM) and (or) MAB-OH (50 μM) by SDS gel electrophoresis. The gel was stained with a Coomassie solution. The protein was incubated with PEG-Mal (lane 2), with MAB-OH (lane 3), initially with MAB-OH, and then with PEG-Mal (lane 4). Lane M - protein molecular mass marker, lane 1 - protein control. a - R.SsoII-(2CS/R174C); b - conjugate of R.SsoII(2CS/R174C) with PEG-Mal.

forms of R.SsoII by SDS-PAGE. PEG-Mal reacted almost quantitatively with the majority of the R.SsoII variants with one and two cysteine residues per subunit, which indicated the high reactivity of cysteine residues toward the maleimide group (Figure 3). However, the yield of modification of the R.SsoII variants with three and four cystein residues per subunit was low due to steric hindrance, so we excluded these variants from further studies.

A 5-fold excess of a solution of one of the azobenzene derivatives (**1** or **2**) (over the number of cysteine residues) was added to the protein solution at room temperature in order to modify Cys residues of R.SsoII variants. The molecular mass of azobenzene derivatives (<0.5 kDa) is much smaller than the molecular mass of R.SsoII (37.4 kDa). Therefore, attachment of any of them to the protein has practically no effect on the mobility of the conjugates in the gel. To evaluate the effectiveness of the reaction between the R. SsoII variants and the azobenzene derivatives, 10 min after the start of incubation an excess of PEG-Mal was added to an aliquot of the reaction mixture. Formation of protein-PEG-Mal conjugate was monitored by SDS-PAGE and the yield was not more than 5% (Figure 4). It can be concluded, therefore, that the yield of protein−azobenzene derivative conjugates reached 95%. It was shown that the substitution of the azobenzene derivatives has practically no influence on the reactivity of the maleimide group with Cys residues. Thus, compounds **1** and **2** can be used for efficient and selective modification of proteins.

Optical Properties of R.SsoII Variants Modified with Azobenzene Derivatives. To clarify the ability of azobenzene derivatives to *cis*−*trans* isomerize after their attachment to the R.SsoII variants, conjugates were exposed to UV and blue light, respectively. UV absoption spectra are shown in Supporting Information. The absorption spectra of azobenzene derivatives are characterized by a peak with a maximum at 340 nm. Analysis of the optical properties of free azobenzene derivatives and azobenzene derivatives after attachment to the protein showed no significant differences. Consequently, the process of *cis*−*trans* isomerization of azobenzene proceeds in the same way as derivatives in free form or after their attachment to the proteins.

Hydrolysis of DNA Substrate by R.SsoII Variants Modified with Azobenzene Derivatives under Blue and UV Illumination. Enzymes modified by MAB-OH ((**1**), Scheme 2) were tested for DNA cleavage activity under specific illumination. The ratio between the initial rate of hydrolysis of a DNA substrate by a modified R.SsoII variant when illuminated by UV irradiation (azobenzene in the *cis*-form) and the initial rate of cleavage by the same enzyme when illuminated with blue light (azobenzene in the *trans*-form) was defined as the photoswitch effect. The final aim of the work was to identify the modified variant with the largest photoswitch effect.

Table 1. Comparison of the Enzymatic Activity of R.SsoII Variants Modified with the Azobenzene Derivative MAB-OH, under UV and Blue Light Illumination, Respectively

	enzyme	photoswitch effect
1	wtR.SsoII	1.00 ± 0.01
2	cfR.SsoII	1.1 ± 0.1
3	2CS/S171C-MAB−OH	1.00 ± 0.01
4	2CS/R174C-MAB−OH	1.10 ± 0.01
5	2CS/R198C-MAB−OH	1.2 ± 0.1
6	2CS/I220C-MAB−OH	1.3 ± 0.2
7	2CS/A224C-MAB−OH	1.4 ± 0.2
8	2CS/R174C/A224C-MAB−OH	2.4 ± 0.4
9	2CS/S171C/R174C-MAB−OH	1.3 ± 0.2

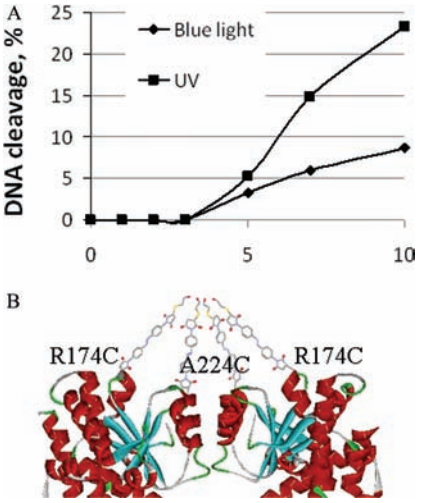

Figure 5. (A) Hydrolysis of a DNA substrate by the modified 2CS/R174C/A224C-MAB-OH variant under UV and blue light irradiation, respectively. Concentration of DNA substrate − 20 nM, concentration of enzyme − 500 nM. (B) Schematic image of a detail of the 2CS/R174C/A224C-MAB-OH variant.

Initially, the modified enzyme was illuminated by light of the appropriate wavelength ("pre-illumination"). Then, this pre-illuminated enzyme was added to the DNA substrate and continued to be exposed to light. After 1, 2, 3, 5, 7, and 10 min incubation, an aliquot of 10 μL was taken and analyzed by gel electrophoresis. The amount of cleavage (%) of the DNA substrate by R.SsoII variants was determined, the kinetics was measured, and the initial rate of DNA hydrolysis was calculated. The results are presented in Table 1.

Control experiments showed that the enzymatic activity of wtR.SsoII and cfR.SsoII by UV and blue light irradiation was comparable. The greatest difference in the hydrolysis rates (>2 times) by specific illumination was obtained for the modified 2CS/R174C/A224C-MAB-OH variant, in which one molecule of MAB-OH was attached per subunit to the Cys residue at the entrance of the DNA-binding site (C224) and the other one to the Cys residue on the outer surface of the protein (C174). We assume that hydrogen bonds could form between the hydroxyl groups of the azobenzene derivatives (MAB-OH) in the *trans*-form, which could interfere with DNA binding (Figure 5).

In the present work, maleimidoazobenzene that contains a cysteine residue in one of the benzene rings, MAB-Cys (**2**), was

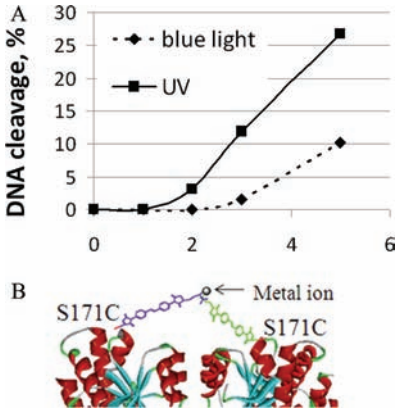

Figure 6. (A) DNA cleavage by the enzyme 2CS/R171C-MAB-Cys in the presence of Ni^{2+} ions (concentration 1 μM) under specific illumination. (B) Schematic detail of the 2CS/R171C-MAB-Cys variant with metal ions.

Table 2. Kinetic Parameters of 20 bp DNA Duplex Hydrolysis by wtR.SsoII and the 2CS/S171-MAB-Cys Variant

enzyme	V_{max}, nM/min	K_M, nM	V_{max}/K_m
wtR.SsoII	100 ± 13	4.07 ± 0.65	24.6
2CS/S171C-MAB-Cys	77 ± 5	17.03 ± 0.09	42.3

synthesized. A cysteine residue was selected as the substituent in one of the benzene rings of maleimidoazobenzene, because cysteine and its derivatives form complexes with many metal ions.[24] In the modified protein, the Cys residue of MAB-Cys might coordinate the metal ion when the MAB-Cys is in the *trans*-form. Such a "barrier" (one metal ion complexed by two opposite MAB-Cys residues) should prevent the entrance of the substrate into the DNA-binding site. Analysis of the R.Ecl18kI structure showed that the most preferred variant for attachment of the MAB-Cys was the 2CS/S171C variant (Figures 1, 6).

Kinetic parameters of DNA hydrolysis by wild-type R.SsoII and protein 2CS/S171C-MAB-Cys were determined without illumination and without adding any nickel or cobalt ions. Initial hydrolysis rates of a 20 bp DNA duplex, containing one recognition site of R.SsoII, by the enzymes were calculated. Different substrate concentrations were used. From the data, the values of the Michaelis constant (K_M) and the maximum rate of the enzymatic reaction (V_{max}) were determined (Table 2).

It was demonstrated that the K_M of 2CS/S171C-MAB-Cys was 4 times higher than that of wtR.SsoII, while the maximum hydrolysis rate V_{max} of both enzymes differed less significantly. Thus, a 20 bp duplex has lower affinity for the 2CS/S171C-MAB-Cys variant compared to the wild-type enzyme. This was consistent with our expectation, because azobenzene derivatives, which are next to the entrance to the DNA binding site, should impair substrate binding to the enzyme.

It was shown previously that Ni^{2+} and Co^{2+} ions form complexes with cysteine and its derivatives, and chelate stability constants of these complexes are higher in the case of Ni^{2+} ions.[24] However, Ni^{2+} ions show a higher inhibitory effect on the activity of RE.[25,26] Therefore, we determined the maximum concentration of the metal ions at which wtR.SsoII was still active. It was found that wtR.SsoII was able to hydrolyze the DNA substrate if the reaction mixture contains 1 to 10 mM $CoSO_4$ or 1 mM $NiCl_2$ in the presence of 10 mM $MgCl_2$ (data not shown). The cleavage rates of the DNA substrate by wtR.SsoII under specific illumination in the absence and in the presence of Co^{2+} or Ni^{2+} are comparable (Table 3). The same result was obtained for the 2CS/R171C-MAB-Cys variant in the absence of metal ions Co^{2+} or Ni^{2+} (Table 3), while in the presence of nickel ions (concentration 1 mM), the initial cleavage rate under UV light was 2-fold higher than that after irradiation with blue light (Figure 6). It can be concluded that the observed difference in the activity 2CS/R171C-MAB-Cys when illuminated by UV and blue light, respectively, was due to the formation of the complex with metal ions. In the presence of 10 mM $CoSO_4$, the photoswitch effect was 1.6 (Table 3).

Table 3. Comparison of the Enzymatic Activity of R.SsoII and Its Variants, Modified with the Azobenzene Derivative MAB-Cys, under UV and Blue Light Illumination, Respectively

	enzyme	photoswitch effect
1	wt	1.00 ± 0.01
2	wt +1 mM $NiCl_2$	1.00 ± 0.02
3	wt +1 mM $CoSO_4$	1.1 ± 0.1
4	2CS/S171C-MAB-Cys	1.1 ± 0.1
5	2CS/S171C-MAB-Cys +1 mM NiCl2	2.2 ± 0.2
6	2CS/S171C-MAB-Cys +1 mM CoSO4	1.2 ± 0.1
7	2CS/S171C-MAB-Cys +10 mM CoSO4	1.6 ± 0.1

It needs to be discussed whether DNA damage by UV illumination is more critical for the integrity of the genome than DNA cleavage by a nonspecific nuclease. We are fully convinced that a low-intensity UV-B illumination is much less toxic to the cell than uncontrolled nonspecific DNA cleavage. It is clear that UV-B light (290−320 nm) is much more harmful for the cell than UV-A light (320−400 nm). However, the dose (<∼10 J/cm^2) and wavelength (365 nm) that we have used in our study hardly lead to any increase in the mutation rate and do not signifcantly affect the viability of the cells.[27,28] Any—even minimal—effects on mutation rate and cell viability may be further decreased by using ortho-amino-substituted azobenzene derivatives, whose *trans*−*cis* isomerization is triggered by illumination at wavelength >400 nm.[29]

CONCLUSIONS

We developed a "molecular gate" approach for the regulation of the DNA cleavage activity of R.SsoII by light illumination. A number of R.SsoII mutants were produced that have cysteine residue(s) at selected positions, modified with maleimidoazobenzene derivatives and tested for DNA cleavage activity when illuminated by UV and blue light, respectively. A twofold change in the enzymatic activity of the modified R.SsoII by illumination with UV and blue light was demonstrated in the case of 2CS/R174C/A224C-MAB-OH and 2CS/S171C-MAB-Cys in the presence of Ni^{2+} ions.

The "molecular gate" approach developed in the present work might be most suitable for proteins with high molecular mass and a large surface area near the entrance of the substrate-binding center of the enzyme. The latter allows one to vary the position of modification by azobenzene derivatives in order to achieve the largest effect of "closure" and "opening" of the gate. To determine the optimal position for modification in the "molecular gate" approach is less tedious than in the "molecular spring"

method, because the site of modification should be next to the entrance of the DNA substrate into the DNA-binding center of the enzyme. A significant advantage of the "molecular gate" approach is that only one product is formed during attachment azobenzene derivatives to the protein.

The method of regulation of enzyme activity by light can be applied not only to restriction endonucleases, but also to any homodimeric DNA- or RNA-binding protein, and other proteins. Regulation of enzymatic activity of a RE by light opens up new prospects for controlling DNA duplex cleavage and creating safer molecular tools for manipulating genes for gene targeting, including gene therapy.

■ ASSOCIATED CONTENT

Supporting Information. Cartoon-style principle of the method, example of analysis of DNA cleavage activity of wtR.SsoII, and example of the absorption spectrum of the conjugate 2CS/S171C/R174C with the azobenzene derivative **1** and its changes during *trans* → *cis* and *cis* → *trans* isomerization. This material is available free of charge via the Internet at http://pubs.acs.org.

■ AUTHOR INFORMATION

Corresponding Author

*Department of Chemistry, Lomonosov Moscow State University, Leninskie gory, Moscow 119991, Russia. Tel.: +7-495-939-5411, Fax: +7-495-939-3181, e-mail: oretskaya@belozersky.msu.ru.

Present Addresses

‖Department of Engineering Physics and Nanotechnology, University of Engineering and Technology,144 Xuan Thuy, Hanoi, Vietnam

■ ACKNOWLEDGMENT

This work has been supported by the German Research Foundation and the Russian Foundation for Basic Research by the DFG-RFBR program "International Research Training Groups" (grants GRK 1384, 11-04-91338), Russian Foundation for Basic Research (grants 10-04-01578 and 09-04-93108), and grant for Leading Scientific Schools (3314.2010.4).

■ REFERENCES

(1) Pingoud, A., and Silva, G. H. (2007) Precision genome surgery. *Nat. Biotechnol. 25*, 743–744.

(2) Grizot, S., Smith, J., Daboussi, F., Prieto, J., Redondo, P., Merino, N., Villate, M., Thomas, S., Lemaire, L., Montoya, G., Blanco, F. J., Pâques, F., and Duchateau, P. (2009) Efficient targeting of a SCID gene by an engineered single-chain homing endonuclease. *Nucleic Acids Res. 37*, 5405–5419.

(3) Pingoud, A., Fuxreiter, M., Pingoud, V., and Wende, W. (2005) Type II restriction endonucleases: structure and mechanism. *Cell. Mol. Life Sci. 62*, 685–707.

(4) Bumcrot, D., Manoharan, M., Koteliansky, V., and Sah, D. W. (2006) RNAi therapeutics: a potential new class of pharmaceutical drugs. *Nat. Chem. Biol. 2*, 711–719.

(5) Li, C., Feng, Y., Coukos, G., and Zhang, L. (2009) Therapeutic microRNA strategies in human cancer. *AAPS J. 11*, 747–757.

(6) Sarkar, F. H., and Li, Y. (2008) NF-kappaB: a potential target for cancer chemoprevention and therapy. *Front. Biosci. 13*, 2950–2959.

(7) Dolinnaya, N. G., Kubareva, E. A., Kazanova, E. V., Zigangirova, N. A., Naroditsky, B. S., Gintsburg, A. L., and Oretskaya, T. S. (2008) Low-molecular-weight inhibitors of NF-κB signalling pathways. *Russ. Chem. Rev. 77*, 967–981.

(8) Zatsepin, T. S., Gait, M. J., and Oretskaya, T. S. (2004) 2′-Functionalized nucleic acids as structural tools in molecular biology. *IUBMB Life 56*, 209–214.

(9) Gryaznov, S. M. (2010) Oligonucleotide N3′→P5′ phosphoramidates and thio-phoshoramidates as potential therapeutic agents. *Chem. Biodivers. 7*, 477–493.

(10) Chattopadhaya, S., Abu Bakar, F. B., and Yao, S. Q. (2009) Expanding the chemical biologist's tool kit: chemical labelling strategies and its applications. *Curr. Med. Chem. 16*, 4527–4543.

(11) Algar, W. R., Tavares, A. J., and Krull, U. J. (2010) Beyond labels: a review of the application of quantum dots as integrated components of assays, bioprobes, and biosensors utilizing optical transduction. *Anal. Chim. Acta 673*, 1–25.

(12) Teicher, B. A. (2009) Antibody-drug conjugate targets. *Curr. Cancer Drug Targets 9*, 982–1004.

(13) Volgraf, M., Gorostiza, P., Numano, R., Kramer, R., Isacoff, E., and Trauner, D. (2006) Allosteric control of an ionotropic glutamate receptor with an optical switch. *Nat. Chem. Biol. 2*, 47–52.

(14) Kumar, G., and Neckers, D. (1989) Photochemistry of azobenzene-containing polymers. *Chem. Rev. 89*, 1915–1925.

(15) Harvey, J., and Trauner, D. (2008) Regulating enzymatic activity with a photoswitchable affinity label. *ChemBioChem 9*, 191–193.

(16) Nakayama, K., Endo, M., and Majima, T. (2004) Photochemical regulation of the activity of an endonuclease BamHI using an azobenzene moiety incorporated site-selectively into the dimer interface. *Chem. Commun. 21*, 2386–2387.

(17) Endo, M., Nakayama, K., and Majima, T. (2004) Design and synthesis of photochemically controllable restriction endonuclease BamHI by manipulating the salt-bridge network in the dimer interface. *J. Org. Chem. 69*, 4292–4298.

(18) Nakayama, K., Endo, M., and Majima, T. (2005) A hydrophilic azobenzene-bearing amino acid for photochemical control of a restriction enzyme BamHI. *Bioconjugate Chem. 16*, 1360–1366.

(19) Schierling, B., Noël, A. J., Wende, W., Le Thi Hien, Volkov, E., Kubareva, E., Oretskaya, T., Kokkinidis, M., Römpp, A., Spengler, B., and Pingoud, A. (2010) Controlling the enzymatic activity of a restriction enzyme by light. *Proc. Natl. Acad. Sci. U. S. A. 107*, 1361–1366.

(20) Hohsaka, T., Kajihara, D., Ashizuka, Y., Murakami, H., and Sisido, M. (1999) Efficient incorporation of nonnatural amino acids with large aromatic groups into streptavidin in vitro protein synthesizing systems. *J. Am. Chem. Soc. 121*, 34–40.

(21) Le Thi Hien, Schierling, B., Ryazanova, A., Zatsepin, T. S., Volkov, E. M., Kubareva, E. A., Velichko, T. I., Pingoud, A., and Oretskaya, T. S. (2009) New azobenzene derivatives for directed modification of proteins. *Russ. J. Bioorg. Chem. 35*, 549–555.

(22) Bochtler, M., Szczepanowski, R., Tamulaitis, G., Grazulis, S., Czapinska, H., Manakova, E., and Siksnys, V. (2006) Nucleotide flips determine the specificity of the Ecl18kI restriction endonuclease. *EMBO J. 25*, 2219–2229.

(23) Kirsch, R. D., and Joly, E. (1998) An improved PCR-mutagenesis strategy for two-site mutagenesis or sequence swapping between related genes. *Nucleic Acids Res. 26*, 1848–1850.

(24) Lenz, G., and Martell, A. (1964) Metal chelates of some sulfur-containing amino acids. *Biochemistry 3*, 745–750.

(25) Vipond, B., Baldwin, G., and Halford, S. (1995) Divalent metal ions at the active sites of the EcoRV and EcoRI restriction endonucleases. *Biochemistry 34*, 697–704.

(26) Baldwin, G., Sessions, R., Erskine, S., and Halford, S. (1999) DNA cleavage by the EcoRV restriction endonuclease: roles of divalent metal ions in specificity and catalysis. *J. Mol. Biol. 288*, 87–103.

(27) Robert, C., Muel, B., Benoit, A., Dubertret, L., Sarasin, A., and Stary, A. (1996) Cell survival and shuttle vector mutagenesis induced by ultraviolet A and ultraviolet B radiation in a human cell line. *J. Invest. Dermatol. 106*, 721–78.

(28) Schindl, A., Klosner, G., Hönigsmann, H., Jori, G., Calzavara-Pinton, P. C., and Trautinger, F. (2009) Flow cytometric quantification of UV-induced cell death in a human squamous cell carcinoma-derived cell line: dose and kinetic studies. *J. Photochem. Photobiol. B 44*, 97–106.

(29) Sadovski, O., Beharry, A. A., Zhang, F., and Woolley, G. A. (2009) Spectral tuning of azobenzene photoswitches for biological applications. *Angew. Chem., Int. Ed. Engl. 48*, 1484–1486.

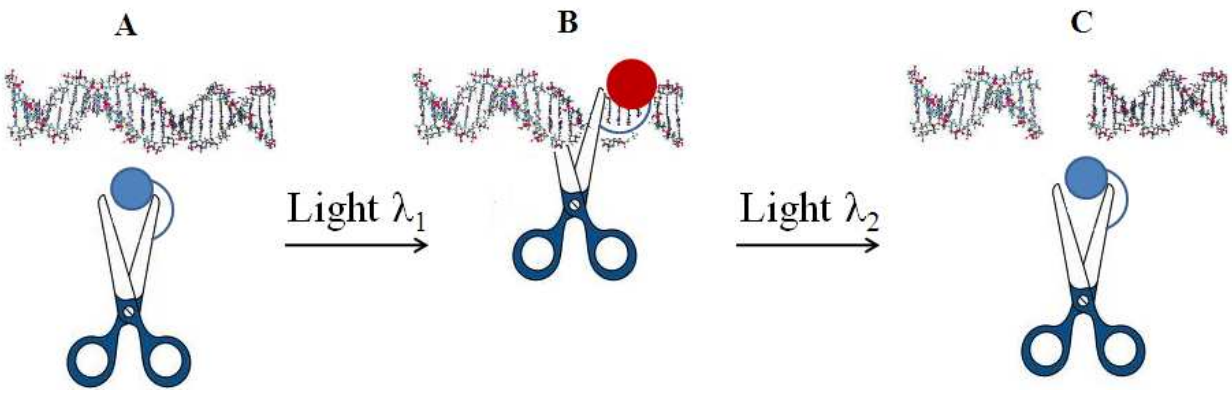

Figure 1. Principle of the method.

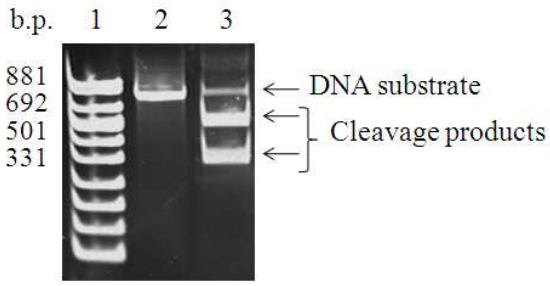

Figure 2. Analysis of DNA (20 nM) cleavage activity of wtR.SsoII (20 nM) by 6% native PAGE (lane 3). 1 – DNA-marker; 2 – 837 b.p. DNA substrate. Incubation condition: 37ºC, 10 min. Gel was stained with ethidium bromide.

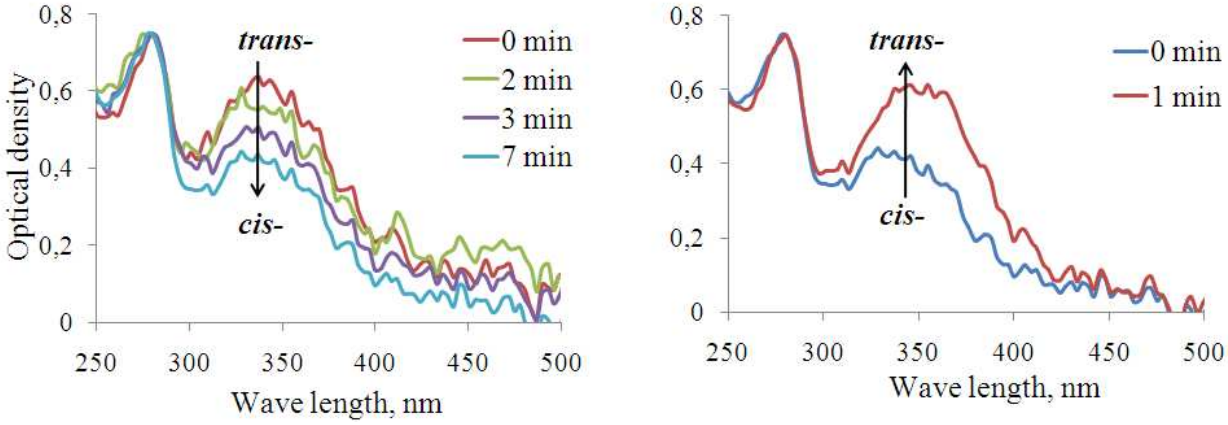

Figure 3. The absorption spectrum of the conjugate 2CS/S171C/R174C with the azobenzene derivative **1**: *trans* → *cis* isomerization under UV light (365 nm) and *cis* → *trans* isomerization under blue light (470 nm).

Bioconjugate Chemistry

ARTICLE

pubs.acs.org/bc

Novel DOTA-Neurotensin Analogues for ^{111}In Scintigraphy and ^{68}Ga PET Imaging of Neurotensin Receptor-Positive Tumors

Faisal Alshoukr,[†,‡,§,Δ] Aurélie Prignon,[∥,Δ] Luc Brans,[⊥] Abdelhak Jallane,[†,‡,§] Sandra Mendes,[†,‡,§] Jean-Noël Talbot,[∥] Dirk Tourwé,[⊥] Jacques Barbet,[#,§] and Anne Gruaz-Guyon*[,†,‡,§]

[†]Inserm, U773, Paris, F-75018, France

[‡]Université Denis Diderot-Paris 7, UMR S773 Paris, F-75018, France

[§]CNRS, GDR 3260 Antibodies and therapeutic targeting, Tours, F-37032, France

[∥]Plateforme LIMP, IFR 65, Université Pierre et Marie Curie, Paris, F-75020, France

[⊥]Department of Organic Chemistry, Vrije Universiteit Brussel, Pleinlaan 2, B-1050 Brussels, Belgium

[#]Centre de Recherche en Cancérologie de Nantes-Angers, Inserm, Université de Nantes, U892, Nantes, F-44000, France

ABSTRACT: Overexpression of the high affinity neurotensin receptor 1 (NTSR1), demonstrated in several human cancers, has been proposed as a new marker for human ductal pancreatic carcinoma and as an independent factor for poor prognosis for ductal breast cancer, head and neck squamous cell carcinoma, and non-small cell lung cancer. The aim of the present study was to develop new DOTA-neurotensin analogues for positron emission tomography (PET) imaging with ^{68}Ga and for targeted radiotherapy with ^{90}Y or ^{177}Lu. We synthesized a DOTA-neurotensin analogue series. Two of these peptides bear two sequence modifications for metabolic stability: DOTA-NT-20.3 shares the same peptide sequence as the previously described DTPA-NT-20.3. In the sequence of DOTA-NT-20.4, the Arg^8-Arg^9 bond was N-methylated instead of the Pro^7-Arg^8 bond in DOTA-NT-20.3. An additional sequence modification was introduced in DOTA-LB119 to increase stability. A spacer was added between DOTA and the peptide sequence to increase affinity. Binding to HT29 cells, which express NTSR1, *in vivo* stability, and biodistribution of the various analogues were compared, and the best candidate was used to image tumors of various sizes with the microPET in mice. ^{111}In-DOTA-NT-20.3, in spite of a relatively high uptake in kidneys, showed specific tumor uptake and elevated tumor to other organ uptake ratios. High contrast images were obtained at early time points after injection that allowed tumor detection at a time interval postinjection appropriate for imaging with the short-lived radionuclide ^{68}Ga. ^{111}In-DOTA-NT-20.4 displayed inferior binding to HT29 cells and reduced tumor uptake. ^{111}In-DOTA-LB119 displayed at early time points a significantly lower renal uptake but also a lower tumor uptake than ^{111}In-DOTA-NT-20.3, although binding to HT29 cells was similar. ^{68}Ga-DOTA-NT-20.3 displayed higher tumor uptake than ^{68}Ga-DOTA-LB119 and allowed the detection of very small tumors by PET. In conclusion, DOTA-NT-20.3 is a promising candidate for ^{68}Ga-PET imaging of neurotensin receptor-positive tumors. DOTA-NT-20.3 may also be considered for therapy, as the yttrium-labeled peptide has higher affinity than that of the indium-labeled one. A prerequisite for therapeutic application of this neurotensin analogue would be to lower kidney uptake, for example, by infusion of basic amino acids, gelofusin, or albumin fragments, to prevent nephrotoxicity, as with radiolabeled somatostatin analogues.

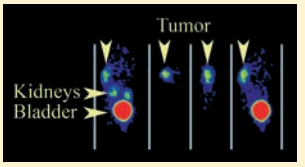

INTRODUCTION

During the past few years, several reports have pointed to the role of neurotensin and the high affinity neurotensin receptor 1 (NTSR1) in the progression of a variety of human cancers.[1] Neurotensin (NT) is a tridecapeptide which acts, in the central nervous system, as a neuromodulator involved in dopamine transmission, inhibition of food intake, hypothermia, and analgesia. In the periphery, neurotensin effects involve hypotension, decrease in gastric acid secretion, lipid digestion, gut motility, proinflammatory response, and also cell proliferation of a variety of normal or cancer cells such as pancreatic adenocarcinoma, colon, prostate, breast, and lung cancer cells.[1−4] Neurotensin exerts its trophic effects, in an endocrine, paracrine, or autocrine fashion, predominantly through NTSR1, but NTSR2 and particularly NTSR3 may also contribute to growth stimulation of normal and neoplastic tissues.[3] Overexpression of NTSR1 has been demonstrated in several human cancers such as pancreatic adenocarcinoma (75−88%),[5,6] invasive ductal breast cancer (91%),[7] non-small cell lung carcinoma (60%),[8] malignant mesothelioma (90%),[9] colon adenocarcinoma,[10] head and neck squamous cell carcinoma,[11] prostate cancer,[12] small cell lung carcinoma, Ewing's sarcoma, and meningioma.[13] Recent studies have suggested that increased NTSR1 expression contributes to the progression and aggressiveness of several tumors.[7,8,10,11] In addition, NTSR1 overexpression has been proposed as a new marker for human ductal pancreatic carcinoma [6] and as an independent factor for poor prognosis for ductal breast cancer,[14] head and neck squamous cell carcinoma,[11] and non-small cell lung cancer.[8]

Received: February 8, 2011
Revised: May 18, 2011
Published: June 12, 2011

ACS Publications © 2011 American Chemical Society

Table 1. Peptide Sequence and Analytical Data

peptide	sequence	% purity	M+H$^+$ MALDI-TOF	M+H$^+$ calculated
NT	pGlu-Leu-Tyr-Glu-Asn-Lys-Pro-Arg-Arg-Pro-Tyr-Ile-Leu-OH			
NT(8−13)	H-Arg-Arg-Pro-Tyr-Ile-Leu-OH			
NT-20.3	Ac-Lys-Pro-Me-Arg-Arg-Pro-Tyr-Tle-Leu-OH			
DTPA-NT-20.3[a]	Ac-Lys(DTPA)-Pro-Me-Arg-Arg-Pro-Tyr-Tle-Leu-OH	>99	1473.83	1473.80
DOTA-NT-20.3	Ac-Lys(DOTA)-Pro-Me-Arg-Arg-Pro-Tyr-Tle-Leu-OH	98	1484. 83	1484.85
DOTA-NT-20.4	Ac-Lys(DOTA)-Pro-Arg-Me-Arg-Pro-Tyr-Tle-Leu-OH	>97	1484. 84	1484.85
DOTA-LB119[b]	Ac-Lys(Ahx-DOTA)-Pro-Me-Arg-Arg-Pro-Dmt-Tle-Leu-OH	>95	1627.08	1626.98

[a] Previously published.[19] [b] Ahx: aminohexanoic acid; Dmt: 2′,6′-dimethyltyrosine.

Radiolabeled neurotensin analogues could be used with scintigraphy or positron emission tomography (PET) for staging and/or prognostication, treatment follow-up, and further for internal radiotherapy of tumors overexpressing neurotensin receptors. The potential of radiolabeled peptide receptor ligands has been demonstrated by the role of somatostatin receptor ^{111}In-scintigraphy, which is nowadays a routine imaging modality in the diagnosis and staging of gastroenteropancreatic neuroendocrine tumors (GEPNETs), and by the therapy results obtained with ^{90}Y- and ^{177}Lu-labeled somatostatin analogues.[15,16]

We have previously developed DTPA-conjugated analogues of NT(8−13), the minimal sequence that mimics the effects of full-length NT,[17] and of NT(6−13).[18,19] Since neurotensin is rapidly degraded *in vivo*, sequence modifications were introduced to stabilize these molecules. An NT(6−13) analogue, DTPA-(^{111}In)-NT-20.3, may be considered a promising candidate for ^{111}In imaging of neurotensin receptor-positive tumors. This tracer showed specific tumor uptake *in vivo* and yielded high contrast on planar and SPECT tumor imaging in nude mice. In spite of a relatively high uptake in kidneys, uptake ratios between tumors and other normal organs including stomach, small intestine, and colon were high. Tumor was detected at early time points postinjection (30−60 min) on images obtained with ^{111}In-DTPA-NT-20.3. Such a time interval is appropriate for imaging with the short-lived radionuclide ^{68}Ga (half-life of 68 min). Indeed, ^{68}Ge/^{68}Ga generators, with a relatively long half-life that permits use over more than one year, have been made available. They provide ^{68}Ga independently of an on-site cyclotron. The generators make the labeling of peptides with this positron emitting radionuclide relatively easy by simple chelation.[20] They prompted the development of several ^{68}Ga-labeled radiopharmaceuticals, particularly peptide receptor ligands such as somatostatin, α-MSH, or bombesin analogues.[15,21−23] The superiority of PET imaging of somatostatin receptors with ^{68}Ga-labeled somatostatin derivatives over SPECT with ^{111}In-labeled pentetreotide has been reported in a number of publications.[24−27]

DTPA provides easy and stable peptide labeling with indium-111. However, labeling stability has been shown to be less satisfactory with other radioactive metals, particularly for yttrium-90 for therapy. The macrocyclic chelator 1,4,7,10-tetraazacyclododecane-*N*,*N*′,*N*″,*N*‴-tetraacetic acid (DOTA) is suitable for labeling with numerous radionuclide and is much more efficient in preventing leakage and subsequent bone marrow toxicity in targeted radionuclide therapy with yttrium-90.[28] DOTA-substituted peptides have also been used successfully for labeling with lutetium-177 and gallium-68. The aim of the present study was thus to develop a new DOTA conjugated neurotensin analogue series that would allow PET imaging with ^{68}Ga of neurotensin receptor-positive tumors, using DTPA-NT-20.3 as lead molecule. These DOTA-neurotensin analogues should also be suitable for labeling with ^{90}Y or ^{177}Lu in the aim of internal radiotherapy. Binding to HT29 cells, which express NTSR1, *in vivo* stability, and biodistribution of the various analogues were compared, and the best candidate was used to image tumors of various sizes with the microPET in mice.

MATERIALS AND METHODS

Cells. Experiments were performed with the HT29 human colorectal carcinoma cell line (ATCC, Rockville, USA). Cells were grown in DMEM (Gibco, France) supplemented with 10% fetal calf serum, 2 mM glutamine, and 50 μg/mL gentamycin at 37 °C in 5% CO_2.

Synthesis of the DOTA-NT Analogues. All reagents used for the synthesis were obtained from Sigma-Aldrich (Saint Quentin Fallavier, France, or Bornem, Belgium), Macrocyclics (Dallas, USA), Novabiochem (Läufelfingen, Switzerland), Bachem (Bubendorf, Switzerland), and RSP (Shirley, USA).

Sodium acetate 2 M was obtained from Hospira (Lake Forest, USA), absolute ethanol from Prolabo (Briare, France), trifluoroacetic acid from Supelco (Bellefont, USA). Water purified on Chelex resin from Biorad (St. Louis, USA) was used in all reactions.

The purity of the compounds was checked by HPLC on a Nucleosil C_{18} (5 μm, 100 Å, Shandon, France) reverse-phase column or on a Discovery BIO SUPELCO Wide Pore (5 μm, 300 Å, Sigma-Aldrich) column with a gradient of A, water (0.05% TFA), and B, CH_3CN (0.05% TFA), at a flow rate of 1.5 mL/min on a Waters apparatus.

The acetylated NT(6−13) analogues NT-20.3 (Ac-Lys-Pro-Me-Arg-Arg-Pro-Tyr-Tle-Leu-OH) and NT-20.4 (Ac-Lys-Pro-Arg-Me-Arg-Pro-Tyr-Tle-Leu-OH) were synthesized by NeoMPS (Strasbourg, France). 1,4,7,10-Tetraazacyclododecane-1,4,7-tris-(acetic acid)-10-acetic acid mono(*N*-hydroxysuccinimidyl ester) (DOTA-NHS ester) (Macrocyclics, Dallas, TX, USA) (5 equiv) was coupled to the lysine ε-NH_2 of NT-20.3 or of NT-20.4 (1 equiv) as described.[29] These DOTA-NT-20.3 and DOTA-NT-20.4 were purified by C_{18} reverse phase chromatography (5 μm, 100 Å, Nucleosil, Shandon, France) using a linear 150 min gradient (flow rate, 2 mL/min; A, H_2O/TFA(0.05%); B, acetonitrile/TFA(0.05%)) from 0% to 37% B. Coupling yields were approximately 85% for DOTA-NT-20.3 and 64% for DOTA-NT-20.4.

DOTA-LB119 was obtained starting from Ac-Lys(Dde)-Pro-Me-Arg(Pbf)-Arg(Pbf)-Pro-Dmt(Trt)-Tle-Leu-OWang resin. After deprotection of the Dde protection using $NH_2OH.HCl$/imidazole,[30] Fmoc-Ahx was coupled to the free ε-NH_2 group of Lys (DIC/HOBt) followed by Fmoc deprotection and coupling

dx.doi.org/10.1021/bc200078p |*Bioconjugate Chem.* 2011, 22, 1374–1385

of DOTA($OtBu$)$_3$ using HATU. The peptide was cleaved from the resin using TFA/H_2O/thioanisole/phenol/ethanedithiol (82.5:5:5:5:2.5) and purified by HPLC.

All DOTA-peptides were purified to at least 95% purity and identified by mass spectrometry (Table 1).

Radiolabeling. *^{111}In Labeling.* DTPA-NT-20.3 was labeled with ^{111}In as already described.[19] The DOTA-NT analogues (1 nmol) were labeled with indium-111 ($^{111}InCl_3$, 10−20 MBq, Covidien imaging, France) in 270 mM acetate, 27 mM citrate, buffer pH 4.5 during 25 min at 95 °C. Excess free indium was removed on a Sep-Pak cartridge (Waters Milford, USA). Radiochemical purity was confirmed by reverse-phase HPLC.

^{68}Ga Labeling. A fully automatic, PC-controlled, radiopharmaceutical synthesis device (SynChrom R&D, Raytest, Germany) was used for all labeling steps. ^{68}Ga ($t_{1/2}$ 68 min) was eluted from a ^{68}Ge/^{68}Ga-generator-system (IGG100, Eckert Ziegler, Berlin) in which ^{68}Ge ($t_{1/2}$ 270.8 d) was attached to a borosilicate glass column containing a titanium dioxide bed. The ^{68}Ga was eluted with 5 mL of 0.1 M hydrochloric acid. DOTA-peptide (25 nmol) in 290 μL 0.8 M sodium acetate was added to 300 MBq of $^{68}GaCl_3$ in 2 mL 0.1 M HCl. The reaction mixture (pH 3.5) was incubated at 95 °C for 8 min. Excess free ^{68}Ga was removed on a Sep-Pak cartridge (Waters Milford, USA). Radiochemical purity was confirmed by reverse-phase HPLC.

Determination of the IC_{50} of the DOTA-NT Analogues for Binding to NTSR1 in Living HT29 Cells and Kinetics of Activity Associated to or Internalized into Cells. The chelate formed by the nonradioactive metal (Me) and the DOTA-peptides (Me-DOTA-peptides) was obtained by incubation (25 min at 95 °C) of the DOTA-peptide (150 nmol in 150 μL water) with solutions of $InCl_3$, YCl_3, or $GaCl_3$ (1.5 μmol in 150 μL acetate 100 mM, citrate 10 mM, buffer, pH 5). IC_{50} for the binding to living HT29 cells was determined by competition between ^{125}I-labeled neurotensin (Perkin-Elmer, France) and the Me-DOTA-peptide chelate. HT29 cells (1.5×10^6 cells) were rinsed with 500 μL DMEM 0.2% BSA and incubated for 60 min at 37 °C with ^{125}I-labeled neurotensin (40 pM, 300 μL DMEM, 0.2% BSA, 0.8 mM 1,10-phenanthroline) in the presence of increasing concentrations of nonradioactive Me-DOTA-NT analogue. After washing the wells twice with ice-cold DMEM 0.2% BSA, cells were lysed in 500 μL 0.1 N NaOH and radioactivity was counted. Nonspecific binding was evaluated in the presence of 10^{-6} M neurotensin. Competition curves were analyzed with the *Equilibrium Expert* software.[31] All experiments were performed three times in triplicate.

Kinetic studies were performed with 0.5×10^{-9} M ^{111}In-DOTA-NT-20.3 or ^{111}In-DOTA-LB119 or 5×10^{-9} M ^{111}In-DOTA-NT-20.4 as above, except for the use of twelve-well plates (600 μL, 1.5×10^6 cells). At selected times, total radioactivity associated to the cells was evaluated as above. To determine the amount of internalized radioactivity, wells were incubated in DMEM/0.2% BSA, pH 2.0, for 15 min at 4 °C, to dissociate the surface-bound ligand. Internalized activity was then counted after washing and cell lysis. Nonspecific binding and internalization was evaluated in the presence of 10^{-6} M neurotensin. Results are expressed as the percentage of acid washed resistant activity, corresponding to specific binding, related to the activity specifically associated with the cells (I/B, mean ± sem).

***In Vivo* Metabolic Stability.** Female BALB/c mice ($n = 3-4$) were injected in the tail vein with ^{111}In-labeled DOTA-NT analogues (50 pmol). Mice were sacrificed 15 min after injection. Plasma and urine samples (50 μL) were added to 200 μL methanol and filtered. Then, methanol was evaporated under vacuum and the sample was analyzed by C_{18} RP-HPLC. Detection was performed with a radioactivity detector (HERM LB 500, Berthold, France). Elution was performed using, after 5 min at 0% B, a linear 15 min gradient from 0% to 35% B and a linear 25 min gradient from 35% to 50%; flow rate: 1.5 mL/min. The sample was also coinjected with fresh radioactive peptide to identify the peak corresponding to intact peptide. Under these conditions, the retention times of the peptides were 34.0 min for ^{111}In-DOTA-NT-20.3 and ^{111}In-DOTA-LB119 and 33.1 min for ^{111}In-DOTA-NT-20.4.

Biodistribution and Imaging Studies. All *in vivo* experiments were performed in compliance with the French guidelines for experimental animal studies and fulfill the UKCCCR guidelines for the welfare of animals in experimental neoplasia.

HT29 cells (6.7×10^5 cells) were inoculated subcutaneously in the flank of 6−8 week old athymic nu/nu male mice (Harlan, France). Biodistribution and imaging studies were performed two weeks later except as mentioned otherwise.

Biodistribution and Imaging Studies of ^{111}In-Labeled DOTA-NT Analogues. Mice were injected in the tail vein with ^{111}In-labeled DTPA-NT-20.3 (25−45 pmol) or ^{111}In-labeled DOTA-NT analogues (40−65 pmol, 0.5−0.7 MBq in 100 μL PBS 0.01% mouse serum albumin, except for mice dissected 49 h postinjection which received 500−900 pmol, 7−12 MBq) and sacrificed at different times. Blood, organs, and tumors were collected and weighed and radioactivity was counted. Injected activity was corrected for losses by subtraction of noninjected and subcutaneously injected material remaining in the animal tail. In blocked control experiments, each mouse received a coinjection of the labeled peptide and of its unlabeled counterpart (180 nmol NT-20.3 for DOTA-NT-20.3, Ac-Lys-Pro-Arg-Me-Arg-Pro-Tyr-Tle-Leu-OH for DOTA-NT-20.4, and Ac-Lys(Ahx)-Pro-Me-Arg-Arg-Pro-Dmt-Tle-Leu-OH for DOTA-LB119).

To estimate the areas under the time concentration curves (AUC) of the various peptides, biodistribution data collected at various time after injection were fitted using *WinSAAM*[32] to a pharmacokinetic model with two compartments to describe the distribution and elimination kinetics. Specific uptake in tumors and kidneys was modeled using one additional compartment for each tissue. Uptake data in tumor and kidneys were then fitted as the sum of the content of these additional compartments plus a fraction of the content of the central compartment of the model. To reduce the number of adjustable parameters, the volume of the central compartment was set to that of blood calculated as 9.5% of mean mouse body weight,[33] and the fractions of rapidly exchangeable fluid (blood + interstitial fluid) were set to 0.25 and to 0.39 for tumor and kidneys, respectively, as determined by Sung and co-workers[34] and Covell and co-workers.[35] The same model was used for all peptides. Addition of more compartments or adjusting the central compartment volume or the fractions of rapidly exchangeable fluid did not significantly improve data fitting. AUC were then calculated for blood, tumor, and kidneys by adding an accumulation compartment and extrapolating to 12 000 min.

^{111}In scintigraphic imaging was performed at the imaging platform of CEFI (Institut Claude Bernard, IFR 2, Paris). Mice under pentobarbital anesthesia were i.v. injected with ^{111}In-DOTA-NT analogues (500−900 pmol, 7−12 MBq) using a dedicated small animal Gamma Imager-S/CT system (Biospace Mesures) equipped with a parallel collimator (matrix 128 × 128,

with 15% energy windows centered on both indium-111 peaks at 171 and 245 keV). Planar anterior acquisitions were performed from 0 to 1 h, 1 to 1.5 h, 4.5 to 5.5 h, 24 to 25 h, and 48 to 49 h postinjection. Tumor to kidney activity ratio was evaluated using ROI surrounding the tumor and the right kidney. Radioactivity excretion in urine was determined from activity collected in the bladder 1.5 h postinjection.

Biodistribution and Imaging Studies with ^{68}Ga-Labeled DOTA-NT Analogues. Animals were injected in the retro-orbital sinus, under general anesthesia by isoflurane inhalation, with ^{68}Ga-DOTA-NT-20.3 (420 ± 30 pmol, 0.96 ± 0.08 MBq) or ^{68}Ga-DOTA-LB119 (450 ± 50 pmol, 1.2 ± 0.1 MBq) in 0.1 mL saline, 8 and/or 14 days after graft PET acquisitions were performed at the LIMP imaging platform (Hôpital Tenon, IFR 65 of Université Pierre et Marie Curie, Paris) with the Mosaic animal PET machine (Philips Medical systems, Cleveland, OH, USA). Static acquisitions were performed 45 min later with an exposure time of 10 min except otherwise mentioned.

Data were standardized with SUV units (standardized uptake value, g/mL). It is a widely used, simple PET quantifier, calculated as the ratio of radioactive concentration in a ROI surrounding the organ (MBq/mL) to the injected activity per animal body weight corrected from decay (MBq/g). Data were analyzed using *PETView* and Syntegra−Philips software (PETView; Philips Medical Systems, Bothell, WA).

Mice were sacrificed by cervical dislocation while under anesthesia one hour after injection. Blood, organs, and tumors were collected and weighed and radioactivity was counted. Tissue activity was decay-corrected.

For comparison, 9 days after inoculation of tumor cells, after a fasting period of 12 h, mice were injected intravenously with 6 to 10 MBq fluorodeoxyglucose (^{18}F) (FDG). Images were recorded one hour later with a 10 min acquisition time.

Statistical Analysis. Statistical analysis of differences in tissue uptake values was performed using unpaired *t* test for comparison between two groups or ANOVA analysis followed by Newman-Keuls' test for multiple comparisons. Differences of $p < 0.05$ were considered significant.

RESULTS

Synthesis of DOTA-NT Analogues. A series of NT (6−13) analogues that bear DOTA on the Lys^6 lateral chain were synthesized. The N-terminal end was acetylated to protect against amino-peptidases and to neutralize the positive charge of the α-NH$_2$ that favors renal accumulation.[36,37] Changes were introduced in the peptide sequence to protect the bonds between Arg^8 and Arg^9, Pro^{10} and Tyr^{11}, or Tyr^{11} and Ile^{12} against enzymatic degradation (Table 1). DOTA-NT-20.3 is the DOTA analogue of DTPA-NT-20.3, which provided, in a previous study, very encouraging ^{111}In targeting to neurotensin receptor-positive tumors.[19] This peptide was doubly stabilized by N-methylation of the Pro^7-Arg^8 bond and a Tle^{12} substitution. In DOTA-NT-20.4, the N-methylation was introduced at the Arg^8-Arg^9 bond instead of the Pro^7-Arg^8 bond in DOTA-NT-20.3.

We previously demonstrated that coupling of polyaminopolycarboxylate chelators such as DTPA dramatically decreases the affinity, unless the distance between the chelating agent and the NT(8−13) sequence that binds to the NTSR1 receptor is increased.[19] Therefore, we introduced an aminohexanoic acid spacer between DOTA and the peptide sequence in DOTA-LB119, an analogue of DOTA-NT-20.3 in which Tyr^{11} was replaced by 2′,6′-dimethyltyrosine (Dmt) to further stabilize the molecule.

Table 2. Affinity of Peptides for Binding to HT29 Cells

peptide	IC_{50} (nM)
NT[a]	1.7 ± 0.4
NT-20.3[a]	2.2 ± 0.3
In-DTPA-NT-20.3[a]	16 ± 2
In-DOTA-NT-20.3	15 ± 1
Ga-DOTA-NT-20.3	14 ± 2
Y-DOTA-NT-20.3	5.6 ± 0.7
In-DOTA-NT-20.4	190 ± 20
In-DOTA-LB119	14.1 ± 0.7
Ga-DOTA-LB119	7.5 ± 0.7
Y-DOTA-LB119	9.9 ± 0.5

[a] For comparison, previously published.[19]

All DOTA-peptides were purified to at least 95% purity and identified by mass spectrometry (Table 1).

Radiolabeling. ^{111}In-labeling yields of the DOTA-NT analogues were 82 ± 3% for DOTA(^{111}In)-NT-20.3, 79 ± 6% for DOTA(^{111}In)-NT-20.4, and 87 ± 2% for DOTA(^{111}In)-LB119. Very similar specific activities of about 11 MBq/nmol were obtained for the three peptides.

The decay-corrected labeling yield of ^{68}Ga obtained was 67 ± 9% with a specific activity of 2.5−4.5 MBq/nmol at the end of the labeling. The overall preparation time was 30 min.

After purification of the labeled compound on a reverse phase C_{18} cartridge (Sep-Pak cartridge), the radiochemical purity of the ^{111}In- or ^{68}Ga-labeled analogues was checked by reverse-phase HPLC with a radioactivity detector: only one peak corresponding to the labeled peptide was detected on the chromatogram.

Binding Affinities. The IC_{50} of the Me-DOTA-peptide chelates for the binding of ^{125}I-labeled neurotensin to living HT29 cells was measured after 60 min incubation at 37 °C. Since the peptides are rapidly internalized by target cells (see below), the determination of affinity constants for NTSR1 at 37 °C is not straightforward, and IC_{50} values reflect the binding potential of the various peptides (Table 2). In-DOTA coupling had similar effects on affinity as In-DTPA, since In-DOTA-NT-20.3 IC_{50} was similar to that of its In-DTPA-counterpart. Conversely, N-methylation of the Arg^8-Arg^9 bond, instead of the Pro^7-Arg^8 bond of In-DOTA-NT-20.3, increased the IC_{50} by a factor of about 12 in In-DOTA-NT-20.4. This loss of affinity may be attributed to the importance of Arg^9 for binding to NTSR1, since replacement of this amino acid by citrulline decreases the affinity by about 100-fold.[38] In-DOTA-LB119 displayed an IC_{50} similar to that of In-DOTA-NT20.3 in spite of the substitution of Tyr^{11} by Dmt, which decreased the affinity by a factor of 5 in the In-DTPA-NT(8−13) analogue series.[19] Most probably, the expected loss of affinity was compensated for by the introduction of an aminohexanoic acid spacer, between DOTA and the ε-NH2 of Lys^6 in In-DOTA-LB119.

The chelated metal also had an influence on the affinity of the complex. The yttrium complexes of DOTA-NT-20.3 and of DOTA-LB119 displayed lower IC_{50} than the indium ones ($p < 0.01$). The IC_{50} of the gallium chelate of DOTA-NT-20.3 was not significantly different from that of the indium complex, in opposition to the IC_{50} decrease of the Ga-DOTA-LB119 as compared to In-DOTA-LB119 ($p < 0.001$).

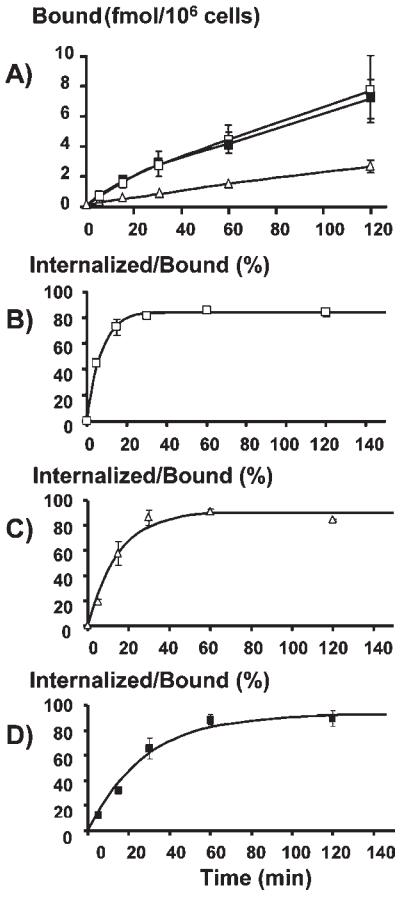

Figure 1. *In vitro* binding and internalization kinetics of ^{111}In-DOTA-peptides in HT29 cells. Panel A: Kinetics of specific radioactivity accretion to 1×10^6 HT29 cells at 37 °C (bound, fmol, mean ± sem) in the presence of 5×10^{-10} M labeled peptide. Each point is the average of four experiments performed in triplicate. Open squares: ^{111}In-DOTA-NT-20.3. Black squares: ^{111}In-DOTA-LB119. Triangles: ^{111}In-DOTA-NT-20.4. Panels B (^{111}In-DOTA-NT-20.3), C (^{111}In-DOTA-NT-20.4), and D (^{111}In-DOTA-LB119): Internalization kinetics. Results are expressed as the percentage of acid washed resistant activity, corresponding to specific binding, related to the activity associated with the cells (internalized/bound, mean ± SEM). Radioactivity, associated to cells or acid wash resistant, corresponding to nonspecific binding was evaluated in the presence of 10^{-6} M neurotensin. Solid line: results fitted with a monoexponential curve. Three experiments performed in triplicate.

Kinetics of *in Vitro* Radioactivity Binding and Internalization into HT29 Cells. As expected from their IC_{50}, the binding of ^{111}In-DOTA-NT-20.3 and of ^{111}In-DOTA-LB119 was not significantly different at every time point, and a significantly lower binding was observed for ^{111}In-DOTA-NT-20.4 after 15 min of incubation (Figure 1). The amount of ^{111}In-DOTA-peptide associated with cells that was internalized into cells increased rapidly with time reaching a 85 ± 2% plateau for ^{111}In-DOTA-NT-20.3, 91 ± 2% for ^{111}In-DOTA-NT-20.4, and 93 ± 2% for ^{111}In-DOTA-LB119 after less than 60 min.

***In Vivo* Peptide Catabolism.** The stability to enzymatic degradation was evaluated *in vivo*. The fraction of radioactivity associated to the intact ^{111}In-DOTA-peptides in plasma was determined 15 min after *iv* injection to BALB/c mice (Figure 2). Samples were analyzed by C_{18} RP-HPLC chromatography. Metabolites eluted at shorter retention times than the full-length radioactive peptide.

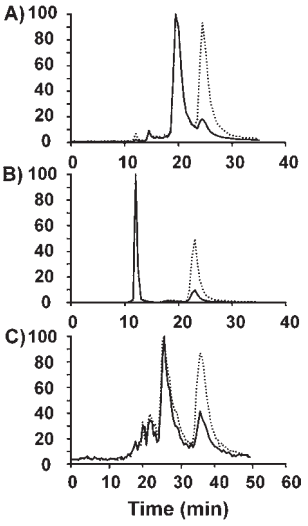

Figure 2. *In vivo* serum stability of ^{111}In-DOTA-peptides: representative C18 HPLC chromatograms of plasma samples collected 15 min postinjection to mice. (A) ^{111}In-DOTA-NT-20.3. (B) ^{111}In-DOTA-NT-20.4. (C) ^{111}In-DOTA-LB119. Solid line: plasma sample. Dotted line: coinjection of the sample with the radioactive control. Chromatograms were normalized to the highest metabolite peak.

There was no significant difference between the amount of intact peptide recovered in the plasma of mice injected with ^{111}In-DOTA-NT-20.3 (22 ± 1%) and ^{111}In-DOTA-LB119 (26 ± 3%), but ^{111}In-DOTA-NT-20.4 (16 ± 2%) was less stable than ^{111}In-DOTA-LB119 ($p < 0.05$). The fraction of activity (% ID/g) remaining in blood 15 min postinjection amounted to 6.1 ± 0.4%, 5.2 ± 0.2%, and 3.9 ± 0.8% for ^{111}In-DOTA-NT-20.3, ^{111}In-DOTA-NT-20.4, and ^{111}In-DOTA-LB119, respectively.

Biodistribution and Imaging Studies of the DOTA(^{111}In)-NT Peptides. Biodistribution studies of the neurotensin analogues ^{111}In-DTPA-NT-20.3 (Table 3), ^{111}In-DOTA-NT-20.3 (Table 4), ^{111}In-DOTA-NT-20.4 (Table 5), and ^{111}In-DOTA-LB119 (Table 6) were performed at various time points postinjection in male nude mice. Tumor accretion expressed as the percentage of injected dose per gram of tumor (%ID/g) showed no significant difference between ^{111}In-DTPA-NT-20.3 and ^{111}In-DOTA-NT-20.3 at any time postinjection, indicating similar tumor targeting efficacy of these two peptides. A slow tumor washout of both peptides was observed between 3 and 6 h, as already described for ^{111}In-DTPA-NT-20.3 in female nude mice. The renal uptake of these two peptides was not significantly different, except at 6 h postinjection ($P < 0.05$).

At early time points, ^{111}In-DOTA-NT-20.3 displayed a higher tumor uptake than ^{111}In-DOTA-LB119 (1 h $P < 0.001$ and 3 h $P < 0.05$), but ^{111}In-DOTA-LB119 tumor uptake decreased slowly with time and, from 6 to 24 h, no significant difference was observed between these two peptides. Renal accumulation of radioactivity was lower for ^{111}In-DOTA-LB119 than for ^{111}In-DOTA-NT-20.3 at early times postinjection ($P < 0.001$ at 1 h and $P < 0.05$ from 3 to 6 h). As a consequence, despite its lower tumor uptake, ^{111}In-DOTA-LB119 tumor to kidney uptake ratios were higher at 6 h ($P < 0.001$) postinjection than that of ^{111}In-DOTA-NT-20.3. ^{111}In-DOTA-NT-20.4 displayed a lower tumor uptake than ^{111}In-DOTA-NT-20.3 at every time point and than ^{111}In-DOTA-LB119 from 3 to 24 h, and a higher kidney uptake than these two peptides. As a consequence, the tumor to

Table 3. Tissue Distributions of ^{111}In-DTPA-NT-20.3 in Male Nude Mice Grafted with HT29 Cells

	^{111}In-DTPA-NT-20.3				
uptake (%ID/g)[a]	1 h $n = 4$	3 h $n = 4$	6 h $n = 6$	24 h $n = 4$	48 h $n = 3$
blood	0.13 ± 0.03	0.026 ± 0.004	0.023 ± 0.004	0.0076 ± 0.0008	0.0028 ± 0.0005
lungs	0.6 ± 0.3	0.11 ± 0.02	0.13 ± 0.04	0.044 ± 0.003	0.035 ± 0.003
liver	0.12 ± 0.01	0.093 ± 0.008	0.075 ± 0.009	0.049 ± 0.003	0.041 ± 0.002
spleen	0.13 ± 0.01	0.13 ± 0.02	0.10 ± 0.01	0.074 ± 0.005	0.064 ± 0.004
stomach[b]	0.14 ± 0.03	0.08 ± 0.02	0.15 ± 0.05	0.27 ± 0.08	0.033 ± 0.008
small intestine[b]	1.1 ± 0.4	0.5 ± 0.1	0.61 ± 0.09	0.38 ± 0.05	0.192 ± 0.005
large intestine[b]	0.5 ± 0.2	0.23 ± 0.02	1.4 ± 0.2	0.82 ± 0.13	0.15 ± 0.03
muscle	0.5 ± 0.4	0.14 ± 0.09	0.024 ± 0.005	0.023 ± 0.007	0.016 ± 0.004
bone	0.20 ± 0.06	0.10 ± 0.02	0.08 ± 0.01	0.044 ± 0.003	0.027 ± 0.004
kidney	7.8 ± 0.1	7 ± 2	2.8 ± 0.3	1.9 ± 0.3	1.5 ± 0.3
tumor	3.1 ± 0.4	2.0 ± 0.4	2.0 ± 0.2	0.86 ± 0.07	0.9 ± 0.1
			tumor(T)/organ		
T/blood	28 ± 7	75 ± 6	100 ± 20	110 ± 10	360 ± 90
T/kidney	0.40 ± 0.03	0.32 ± 0.03	0.72 ± 0.09	0.5 ± 0.1	0.64 ± 0.06
T/liver	26 ± 2	21 ± 3	27 ± 3	17.7 ± 0.5	23 ± 3
T/muscle	25 ± 9	40 ± 30	100 ± 10	50 ± 10	70 ± 10

[a] Uptake is expressed as the percentage of injected dose per gram of tissue (%ID/g). [b] Organs with their content.

Table 4. Tissue Distributions of ^{111}In-DOTA-NT-20.3 in Male Nude Mice Grafted with HT29 Cells

	^{111}In-DOTA-NT-20.3				
uptake (%ID/g)[a]	1 h $n = 7$	3 h $n = 11$	6 h $n = 7$	24 h $n = 4$	49 h $n = 3$
blood	0.36 ± 0.06	0.014 ± 0.002	0.006 ± 0.002	0.0028 ± 0.0003	0.0028 ± 0.0004
lungs	0.47 ± 0.04	0.14 ± 0.02	0.10 ± 0.01	0.062 ± 0.004	0.07 ± 0.01
liver	0.21 ± 0.02	0.13 ± 0.02	0.123 ± 0.008	0.085 ± 0.002	0.07 ± 0.01
spleen	0.19 ± 0.01	0.11 ± 0.01	0.113 ± 0.009	0.10 ± 0.01	0.16 ± 0.01
stomach[b]	0.13 ± 0.03	0.2 ± 0.1	0.09 ± 0.04	0.06 ± 0.01	0.020 ± 0.005
small intestine[b]	0.9 ± 0.1	0.52 ± 0.09	0.34 ± 0.06	0.32 ± 0.02	0.070 ± 0.003
large intestine[b]	0.39 ± 0.05	1.1 ± 0.3	1.5 ± 0.5	0.19 ± 0.02	0.058 ± 0.007
muscle	0.10 ± 0.02	0.027 ± 0.009	0.04 ± 0.01	0.0116 ± 0.0008	0.008 ± 0.001
bone	0.15 ± 0.02	0.10 ± 0.03	0.099 ± 0.007	0.030 ± 0.005	0.053 ± 0.002
kidney	7.6 ± 0.9	4.9 ± 0.4	5.2 ± 0.5	2.5 ± 0.1	0.86 ± 0.08
pancreas	0.095 ± 0.009	0.03 ± 0.01	0.030 ± 0.002	ND	ND
tumor	4.7 ± 0.8	2.5 ± 0.2	1.9 ± 0.2	1.3 ± 0.2	0.68 ± 0.09
			tumor(T)/organ		
T/blood	17 ± 5	170 ± 30	420 ± 90	500 ± 100	250 ± 30
T/kidney	0.63 ± 0.07	0.53 ± 0.05	0.35 ± 0.02	0.50 ± 0.04	0.78 ± 0.03
T/liver	22 ± 3	21 ± 2	17 ± 3	15 ± 1	11 ± 4
T/muscle	60 ± 20	130 ± 20	80 ± 20	110 ± 20	80 ± 20
T/pancreas	47 ± 8	90 ± 10	70 ± 10	ND	ND

[a] Uptake is expressed as the percentage of injected dose per gram of tissue (%ID/g). [b] Organs with their content.

kidney uptake ratio of this peptide was very low at every time postinjection.

Tumor uptake was receptor mediated, as shown by the dramatic decrease in tumor uptake when the radiolabeled ^{111}In-DOTA-peptides were coinjected with their unlabeled counterpart: 2.5 ± 0.2% vs 0.14 ± 0.02% ID/g for ^{111}In-DOTA-NT-20.3, 1.41 ± 0.05% vs 0.12 ± 0.03% for ^{111}In-DOTA-LB119, and 0.52 ± 0.07% vs 0.11 ± 0.01% for ^{111}In-DOTA-NT-20.4 ($p < 0.001$, 79−94% reduction, 3 h postinjection).

Radioactivity excretion in urine was fast, and more than 60% of the injected activity was recovered in the bladder 1.5 h after injection of ^{111}In-DOTA-NT-20.3 or ^{111}In-DOTA-LB119. Blood activity decreased rapidly for the three ^{111}In-DOTA-peptides, and low radioactivity uptake was observed in most nontumor organs, except in kidneys and, to some extent, in the gastrointestinal tract, particularly in small intestine and in colon. With the exception of kidneys, tumor to normal organ uptake ratios were high for ^{111}In-DOTA-NT-20.3 and, to a lesser extent,

Table 5. Tissue Distributions of ^{111}In-DOTA-NT-20.4 in Male Nude Mice Grafted with HT29 Cells

	^{111}In-DOTA-NT-20.4				
uptake (%ID/g)[a]	1 h $n = 4$	3 h $n = 4$	6 h $n = 4$	24 h $n = 4$	49 h $n = 3$
blood	0.27 ± 0.03	0.040 ± 0.003	0.037 ± 0.005	0.016 ± 0.005	0.0019 ± 0.0006
lungs	0.27 ± 0.02	0.10 ± 0.03	0.07 ± 0.01	0.06 ± 0.01	0.037 ± 0.001
liver	0.107 ± 0.007	0.076 ± 0.008	0.09 ± 0.01	0.071 ± 0.007	0.074 ± 0.007
spleen	0.097 ± 0.006	0.082 ± 0.006	0.070 ± 0.006	0.075 ± 0.009	0.08 ± 0.02
stomach[b]	0.18 ± 0.09	0.16 ± 0.09	0.062 ± 0.005	0.05 ± 0.02	0.0086 ± 0.0009
small intestine[b]	0.5 ± 0.3	0.12 ± 0.03	0.15 ± 0.05	0.090 ± 0.008	0.023 ± 0.003
large intestine[b]	0.20 ± 0.04	0.5 ± 0.3	0.36 ± 0.05	0.12 ± 0.02	0.033 ± 0.007
muscle	0.10 ± 0.02	0.04 ± 0.01	0.040 ± 0.008	0.023 ± 0.008	0.010 ± 0.002
bone	0.16 ± 0.05	0.09 ± 0.01	0.06 ± 0.01	0.035 ± 0.005	0.037 ± 0.008
kidney	9 ± 2	8 ± 1	9 ± 2	4.2 ± 0.8	1.7 ± 0.7
pancreas	0.044 ± 0.004	0.027 ± 0.002	0.022 ± 0.003	0.023 ± 0.003	ND
tumor	0.8 ± 0.1	0.52 ± 0.07	0.5 ± 0.1	0.33 ± 0.05	0.21 ± 0.08
			tumor(T)/organ		
T/blood	3.1 ± 0.8	13 ± 2	13 ± 3	40 ± 10	130 ± 80
T/kidney	0.095 ± 0.008	0.064 ± 0.005	0.053 ± 0.002	0.080 ± 0.007	0.2 ± 0.1
T/liver	7.2 ± 0.7	6.8 ± 0.7	5.4 ± 0.6	7 ± 2	2.8 ± 0.8
T/muscle	9 ± 1	14 ± 3	12 ± 3	26 ± 7	30 ± 10
T/pancreas	18 ± 4	20 ± 4	23 ± 5	21 ± 5	ND

[a] Uptake is expressed as the percentage of injected dose per gram of tissue (%ID/g). [b] Organs with their content.

Table 6. Tissue Distributions of ^{111}In-DOTA-LB119 in Male Nude Mice Grafted with HT29 Cells

	^{111}In-DOTA-LB119				
uptake (%ID/g)[a]	1 h $n = 7$	3 h $n = 4$	6 h $n = 4$	24 h $n = 3$	49 h $n = 3$
blood	0.38 ± 0.05	0.023 ± 0.002	0.0045 ± 0.0002	0.007 ± 0.002	0.0016 ± 0.0003
lungs	0.36 ± 0.03	0.106 ± 0.007	0.09 ± 0.01	0.06 ± 0.01	0.04 ± 0.01
liver	0.20 ± 0.01	0.151 ± 0.007	0.14 ± 0.02	0.080 ± 0.005	0.09 ± 0.03
spleen	0.153 ± 0.007	0.09 ± 0.01	0.076 ± 0.009	0.064 ± 0.003	0.10 ± 0.03
stomach[b]	0.28 ± 0.08	0.16 ± 0.04	0.5 ± 0.5	0.08 ± 0.01	0.024 ± 0.004
small intestine[b]	1.1 ± 0.1	0.67 ± 0.08	0.7 ± 0.1	0.35 ± 0.05	0.084 ± 0.005
large intestine[b]	0.4 ± 0.1	1.5 ± 0.5	1.2 ± 0.8	0.16 ± 0.03	0.101 ± 0.006
muscle	0.09 ± 0.01	0.021 ± 0.005	0.05 ± 0.02	0.010 ± 0.003	0.015 ± 0.007
bone	0.15 ± 0.04	0.05 ± 0.01	0.07 ± 0.02	0.05 ± 0.01	0.05 ± 0.02
kidney	3.4 ± 0.2	2.4 ± 0.2	2.2 ± 0.2	1.04 ± 0.07	0.6 ± 0.1
pancreas	0.081 ± 0.008	0.0217 ± 0.0008	0.018 ± 0.001	0.0180 ± 0.0006	0.013 ± 0.002
tumor	1.8 ± 0.1	1.41 ± 0.05	1.4 ± 0.2	1.0 ± 0.3	0.46 ± 0.06
			tumor(T)/organ		
T/blood	6 ± 1	63 ± 7	300 ± 40	160 ± 60	330 ± 90
T/kidney	0.55 ± 0.05	0.60 ± 0.05	0.63 ± 0.06	0.9 ± 0.2	0.74 ± 0.07
T/liver	9.0 ± 0.7	9.4 ± 0.4	10 ± 2	12 ± 3	6 ± 1
T/muscle	24 ± 7	80 ± 10	80 ± 40	130 ± 70	40 ± 10
T/pancreas	25 ± 4	65 ± 2	75 ± 7	50 ± 10	37 ± 3

[a] Uptake is expressed as the percentage of injected dose per gram of tissue (%ID/g). [b] Organs with their content.

for ^{111}In-DOTA-LB119. For example, tumor to blood amounted to 170 ± 30% and 63 ± 7%, respectively, tumor to muscle 130 ± 20% and 80 ± 20%, tumor to pancreas 90 ± 10% and 65 ± 2%, and tumor to liver 21 ± 2% and 9.4 ± 0.4% at three hours postinjection (Tables 4 and 6). Some excretion by the digestive route was also observed: 55 ± 8% and 60 ± 10% of the radioactivity in the stomach and 76 ± 8% and 79 ± 2% in the colon were associated to the organ content for ^{111}In-DOTA-NT-20.3 and ^{111}In-DOTA-LB119, respectively, at 3 h postinjection. Nevertheless, tumor to stomach (32 ± 8% at 3 h postinjection), to small intestine (7 ± 1%), and to colon (4 ± 1%) ratios were quite high for ^{111}In-DOTA-NT-20.3. They were somewhat

dx.doi.org/10.1021/bc200078p |*Bioconjugate Chem.* 2011, 22, 1374–1385

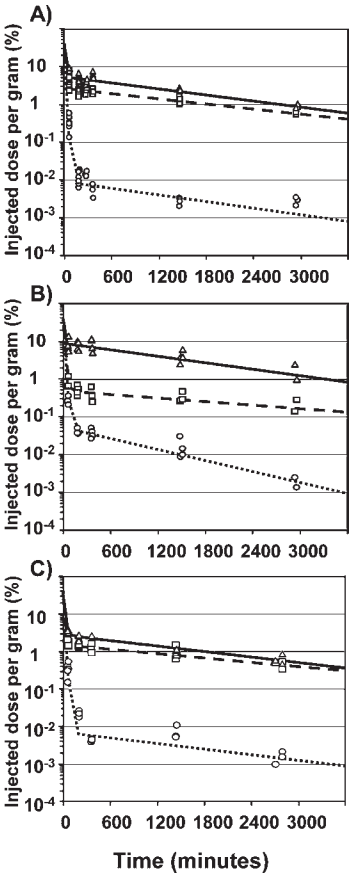

Figure 3. Biodistribution kinetics of ^{111}In-DOTA-peptides in tumor-bearing nude mice. Mice were injected with ^{111}In-DOTA-NT-20.3 (panel A), ^{111}In-DOTA-NT-20.4 (panel B), or ^{111}In-DOTA-LB119 (panel C) and sacrificed at selected time intervals. Blood sample (circles), tumors (squares), and right kidneys (triangles) were weighed and counted, and the activity was expressed as %ID/g. The three kinetics were fitted simultaneously using the same pharmacokinetic model as described in Materials and Methods, and the fitted curves for blood (dotted line), tumor (dashed line), and right kidney (solid line) are shown in the graphs as semilogarithmic plots.

lower for ^{111}In-DOTA-LB119: 10 ± 2%, 2.2 ± 0.3%, and 1.2 ± 0.3%, respectively. Some of the radioactivity accretion in the intestines was receptor-mediated, since after removal of their content, the radioactivity uptake was significantly reduced in small intestine (0.171 ± 0.008% vs 0.082 ± 0.007% ID/g for ^{111}In-DOTA-20.3 and 0.68 ± 0.01% vs 0.17 ± 0.04% ID/g for LB119, $p < 0.001$) and in colon (0.4 ± 0.1% vs 0.09 ± 0.02%, $p < 0.05$, and 0.7 ± 0.1% vs 0.16 ± 0.06% ID/g, $p < 0.01$, respectively), when the tracer was coinjected with an excess of unlabeled peptide.

Comparison between organ uptakes of different peptides at selected times postinjection hardly reflects irradiation doses delivered to these organs over time for a therapeutic injection of radiolabeled peptides. Then, for a preliminary evaluation of the potential of these peptides for targeted radiotherapy, areas under the time−activity curves (AUC expressed as %ID/g.min) were calculated after simultaneously fitting the activity biodistribution data for blood, tumor, and kidney to a multicompartmental model. The same, relatively simple model was used for all peptides with two compartments to describe the blood pharmacokinetic and one additional compartment to describe tumor and kidney uptake kinetics. The addition of a fraction of the central compartment, calculated on the basis of published data for the fractions of blood and interstitial fluid contained in tumors and normal organs,[34,35] to these tissues considerably improved data fitting. A total of seven parameters were thus adjusted to simultaneously fit the biodistribution data in blood, tumor, and kidneys. Good fitting was obtained in all cases (Figure 3, Table 7); however, it should be kept in mind that the kinetics reflect the total activity present in the tissues, responsible for tissue irradiation, and not the intact radiolabeled peptide, which is quickly catabolized. The estimated values for these parameters were rather similar for all peptides with subtle changes explaining the differences in pharmacokinetics.

Table 7. Area under Curves for Tumor, Kidneys, and Blood

peptide	tumor AUC[a]	kidney AUC[a]	blood AUC[a]
^{111}In-DTPA-NT-20.3	6743	10767	464
^{111}In-DOTA-NT-20.3	5463	9210	500
^{111}In-DOTA-LB-119	3687	5163	514
^{111}In-DOTA-NT-20.4	1618	13774	492

[a] Area under curve (AUC) are expressed as %ID/g.min.

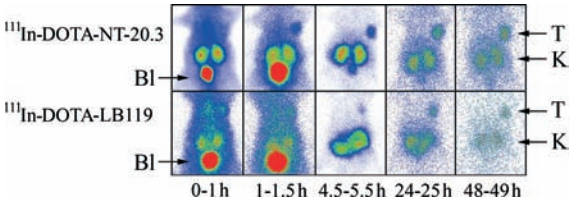

Figure 4. ^{111}In-DOTA-NT-20.3 and ^{111}In-DOTA-LB119 planar images of male nude mice grafted with HT29 cells. Planar anterior acquisitions were performed from 0 to 1 h, 1 to 1.5 h, 4.5 to 5.5 h, 24 to 25 h, and 48 to 49 h postinjection under anesthesia. Bl: bladder. K: kidney. T: tumor. Tumor weight: 167 mg for ^{111}In-DOTA-NT-20.3 and 196 mg for ^{111}In-DOTA-LB119.

Blood clearances were pretty close for all peptides; however, as judged by the AUC, tumor uptake was similar for ^{111}In-DTPA-NT-20.3 and ^{111}In-DOTA-NT-20.3, lower for ^{111}In-DOTA-LB119, and still lower for ^{111}In-DOTA-NT-20.4. Kidney uptake was lower for ^{111}In-DOTA-LB119, higher for ^{111}In-DTPA-NT-20.3 and ^{111}In-DOTA-NT-20.3, and even higher for ^{111}In-DOTA-NT-20.4. These resulted in similar tumor/kidney AUC ratios (0.6 to 0.7) for ^{111}In-DTPA-NT-20.3, ^{111}In-DOTA-NT-20.3, and ^{111}In-DOTA-LB119 and in a much lower value for ^{111}In-DOTA-NT-20.4 (0.1). The IC_{50} of the yttrium complex of DOTA-NT-20.3 is 2-fold lower than that of the indium one ($p < 0.01$).Then, one can expect that tumor AUC and so tumor to kidney AUC ratio may be higher with ^{90}Y- than ^{111}In-labeled DOTA-NT-20.3.

Planar images of mice grafted with HT29 cells were recorded from 1 to 48 h, after injection of ^{111}In-DOTA-NT-20.3 or ^{111}In-DOTA-LB 119 (Figure 4). There was a clear visualization of the tumor at early time points in mice injected with ^{111}In-DOTA-NT-20.3. At late time points, the tumor could be clearly detected with the two peptides. These results were consistent with biodistribution data and tumor to organ uptake ratios. Kidneys and bladder were the only other sites of visible activity accumulation. The activity ratio between tumor and kidneys was 0.47 ± 0.03% at 1 h and 0.69 ± 0.07% at 24 h for ^{111}In-DOTA-NT-20.3

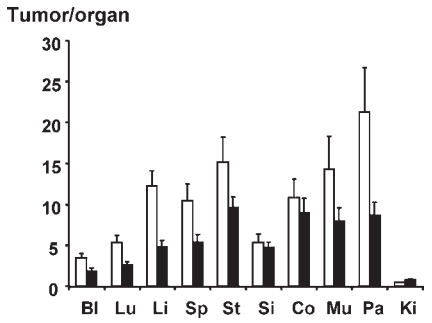

Figure 5. Tumor to normal organ uptake ratios obtained 1 h after injection of ^{68}Ga-DOTA-NT-20.3 (420 ± 30 pmol, 0.96 ± 0.08 MBq) or ^{68}Ga-DOTA-LB119 (450 ± 50 pmol, 1.2 ± 0.1 MBq) in male nude mice, grafted with HT29 cells. Bl: blood. Lu: lung. Li: liver. Sp: spleen. St: stomach. Si: small intestine. Co: colon. Mu: muscle. Pa: pancreas. Ki: kidney.

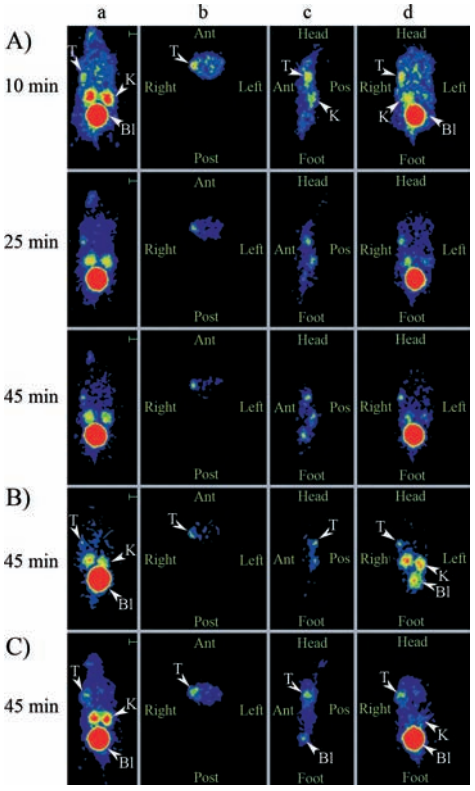

Figure 6. TEP imaging of male nude mice, grafted with HT29 cells in the right flank, injected with ^{68}Ga-DOTA-NT-20.3: (A) images were recorded at different time points after injection of ^{68}Ga-DOTANT-20.3; in the same mouse (tumor volume 40 mm^3), no tumor was detectable on ^{18}F-FDG PET images performed 24 h later; (B) and (C) images recorded 45 min after ^{68}Ga-DOTA-NT-20.3 injection (tumor volumes: 22 and 288 mm^3). Imaging was performed seven (A and B) or twelve days (C) after cell graft. The acquisition time was 10 min a = Maximum Intensity Projection (MIP), frames: b = axial, c = sagittal, and d = coronal. Bl: Bladder. K: Kidney. T: Tumor. ant: anterior. pos: posterior.

(tumor weight: 0.15 ± 0.04% g), 0.45 ± 0.05% and 0.50 ± 0.01% for ^{111}In-DOTA-LB119 (tumor weight: 0.20 ± 0.05% g).

Biodistribution and PET Imaging with ^{68}Ga-DOTA-NT-20.3 and ^{68}Ga-DOTA-LB119. Biodistribution studies were performed 1 h after injection of ^{68}Ga-DOTA-NT20.3 (420 ± 30 pmol, 0.96 ± 0.08 MBq) or ^{68}Ga-DOTA-LB119 (450 ± 50 pmol, 1.2 ± 0.1 MBq). No significant difference was observed between tumor uptake of ^{68}Ga-labeled and ^{111}In-labeled DOTA-NT-20.3, but, probably due to its higher affinity, ^{68}Ga-DOTA-LB119 tumor uptake was significantly increased as compared to ^{111}In-DOTA-LB119 (50% increase, $P < 0.05$). Nevertheless, the tumor uptake of ^{68}Ga-DOTA-NT20.3 was higher than that of ^{68}Ga-DOTA-LB119 ($P < 0.05$).

As observed for the ^{111}In complexes the renal accretion of ^{68}Ga-DOTA-LB119 was lower than that of ^{68}Ga-DOTA-NT20.3 ($P < 0.05$), and for both ^{68}Ga-labeled peptides, the renal uptake was similar to that of the ^{111}In-labeled ones. Tumor to normal tissue uptake ratios were similar or higher for ^{68}Ga-DOTA-NT20.3 as compared to ^{68}Ga-DOTA-LB119 except for kidneys (0.46 ± 0.06% vs 0.79 ± 0.07%) (Figure 5).

High contrast images were obtained with ^{68}Ga-DOTA-NT20.3, which allowed the visualization of very small tumors (Figure 6). As shown in Figure 6, 22 and 40 mm^3 tumor grafts could be easily detected as soon as 45 min after ^{68}Ga-DOTA-NT20.3 injection (10 min acquisition). The tumor SUV_{max} 45 min after ^{68}Ga-DOTA-NT-20.3 injection amounted to 0.9 ± 0.1 and the tumor to kidney SUV_{max} ratio was 0.6 ± 0.1. Tumor was not detectable on FDG PET images (not shown).

DISCUSSION

Since radiolabeled neurotensin analogues may be valuable tools for both imaging and therapy of neurotensin receptor-positive tumors, a number of radiolabeled neurotensin analogues, stabilized against enzymatic degradation *in vivo* by changes in the peptide sequence, has been described in the literature. In a series of peptides bearing (N^{α}His)Ac, a chelator of ^{99m}Tc and ^{188}Re, NT-XIX, an NT(8−13) analogue, displayed the most promising properties to target these radionuclides *in vivo*, with low kidney uptake, and reduction of tumor mass was observed after treatment with the rhenium-188-labeled peptide.[39,40] Nevertheless, some intestine uptake may be a source of background for imaging and of toxicity for therapeutic applications. Polyaminopolycarboxylate chelators, such as DTPA or DOTA, coupled to somatostatin analogues have been used with success to deliver various radiometals, including ^{111}In, ^{68}Ga, ^{90}Y, or ^{177}Lu, to somatostatin receptor-positive tumors, such as gastroenteropancreatic neuroendocrine tumors (GEPNETs). PET imaging with [^{68}Ga-DOTA^0,Tyr^3]octreotate or [^{68}Ga-DOTA^0,Tyr^3]octreotide has been reported to achieve higher diagnostic efficacy than SPECT with ^{111}In-labeled analogues.[24−27] In addition, therapy with [^{90}Y-DOTA^0,Tyr^3]octreotide and [^{177}Lu-DOTA^0,Tyr^3]octreotate provided symptomatic improvement, tumor regression, improved quality of life, and a benefit in overall survival.[15,16] Several DTPA and DOTA neurotensin analogues have been developed to target these radionuclides to tumors overexpressing neurotensin receptors.[18,41,42] However, these radiolabeled peptides showed moderate tumor uptake and comparably high kidney uptake. We recently reported the encouraging results obtained with a new DTPA-neurotensin(6−13) analogue, DTPA-NT-20.3, which displayed improved uptake ratio between tumor and kidneys, superior to previously published DTPA and DOTA neurotensin analogues.[19] High-quality planar scintigraphy and SPECT images were obtained after a short delay, compatible with the use of the short-lived radionuclide ^{68}Ga for PET imaging.

A macrocyclic chelator, such as DOTA, is necessary for targeted radionuclide therapy with ^{90}Y, since *in vivo* leakage of this radionuclide from DTPA complexes leads to bone marrow toxicity.[28] For PET imaging, the *in vivo* stability of ^{68}Ga-DTPA chelates remains a matter of controversy. Then, the aim of the present study was to design new DOTA-substituted neurotensin analogues suitable for ^{68}Ga PET imaging and possibly for ^{90}Y or ^{177}Lu targeted radiotherapy of neurotensin-receptor-positive tumors.

In the three synthesized DOTA-peptides, a Tle^{12} substitution was introduced to protect the bond between Tyr^{11} and Ile^{12}. Since positive charges increase renal uptake,[36,37] the α-NH_2 was neutralized by acetylation, which also protected the peptides against aminopeptidases. In DOTA-NT-20.3, which shares the same peptide sequence with DTPA-NT-20.3, an N-methylation of the Pro^7-Arg^8 bond was introduced for stability. In the triple-stabilized DOTA-LB119, Tyr^{11} was substituted with Dmt and a spacer was introduced between the peptide and the chelator in order to reduce the affinity loss induced by polyaminopolycarboxylate coupling, which we previously observed.[19] In DOTA-NT-20.4, the Arg^8-Arg^9 bond was protected by an N-methylation.

The properties of the ^{111}In labeled DOTA-peptides were evaluated and compared to those of ^{111}In-DTPA-NT-20.3. The affinity decrease induced by DOTA coupling is similar to that observed with DTPA, as indicated by the similar IC_{50} of these two peptides. As already observed for ^{111}In-DTPA-NT-20.3, the DOTA analogue rapidly internalizes *in vitro*. Biodistribution of both peptides was very similar in male nude mice grafted with HT29 cells. Circulating activity decreased rapidly, and high tumor to blood uptake ratios were obtained at early times postinjection. Tumor uptakes of both peptides were not significantly different at any time point and decreased quite slowly with time. Uptake in normal organs was low, leading to high tumor to organs ratio except in kidneys.

The three ^{111}In-DOTA-peptides exhibited receptor mediated tumor targeting, abolished by coinjection of their unlabeled counterpart. N-Methylation of the Pro^7-Arg^8 or of the Arg^8-Arg^9 bonds was similarly effective for *in vivo* stabilization, as shown by the stability results obtained with ^{111}In-DOTA-NT-20.3 and ^{111}In-DOTA-NT-20.4. Probably due to its lower affinity, tumor uptake of ^{111}In-DOTA-NT-20.4 was lower than the two other ^{111}In-DOTA-analogues. Unexpectedly, renal accumulation of this peptide was also higher. Although ^{111}In-DOTA-NT-20.3 and ^{111}In-DOTA-LB119 displayed similar stability and IC_{50}, the tumor uptake of this last peptide was significantly lower at early time points. Renal uptake was also lower at early time points for ^{111}In-DOTA-LB119, as already observed for Dmt^{11} substituted (N^{α}His)Ac-NT(8−13) analogues.[39] In agreement with the biodistribution studies, high contrast images were obtained with ^{111}In-DOTA-NT-20.3 with a clear detection of tumors at early time points.

Since tumor grafts were detected at early time points postinjection with ^{111}In-DOTA-LB119 and particularly ^{111}In-DOTA-NT-20.3, these peptides were further evaluated for ^{68}Ga targeting. Radiolabeling was obtained in good yields with ^{68}Ga, and no free ^{68}Ga was detected after purification. The specific activities obtained allowed the injection of less than 500 pmol per mouse for PET imaging, in order to minimize the saturation of tumor neurotensin receptors. For both peptides, uptake in normal organs, 1 h postinjection, was low except in kidneys. ^{68}Ga-DOTA-NT-20.3 provided reasonably high tumor uptake, higher than that of ^{68}Ga-DOTA-LB119. Very small tumor masses (20−40 mm^3) could be detected with ^{68}Ga-DOTA-NT-20.3 at 45 min after injection.

Metal complexation had an influence on the IC_{50} of the DOTA-peptides. Effects observed with gallium differed according to the peptide. No significant difference was observed with DOTA-NT-20.3, but it enhanced DOTA-LB119 affinity as compared to indium, and the tumor uptake of ^{68}Ga-DOTA-LB119 was significantly increased (by 50%). Yttrium significantly decreased the IC_{50} of both peptides. Such an affinity difference induced by the incorporated metal has already been described in the literature for DOTATOC[43] and bombesin analogues.[44]

CONCLUSION

In summary, in spite of a relatively high uptake in kidneys, ^{111}In-DOTA-NT-20.3 showed specific tumor uptake, provided elevated tumor to other organ uptake ratios, particularly tumor to intestine, and high contrast images at early time points after injection. A very low background in normal tissues, except kidneys, was obtained by PET imaging with ^{68}Ga-DOTA-NT-20.3 which allowed the detection of very small tumors. DOTA-NT-20.3 may be considered a promising candidate for ^{68}Ga-PET imaging of neurotensin receptor-positive tumors, such as pancreatic adenocarcinoma, invasive ductal breast cancer, and non-small cell lung carcinoma. The high affinity observed for the yttrium complex of DOTA-NT-20.3, higher than that of the indium one, suggests that targeting ^{90}Y with this peptide may ensure a higher tumor uptake than with ^{111}In. A prerequisite for therapeutic application of this neurotensin analogue would be to lower kidney uptake, for example, by infusion of basic amino acids, gelofusin, or albumin fragments, to prevent nephrotoxicity, as with radiolabeled somatostatin analogues.[45,46]

AUTHOR INFORMATION

Corresponding Author

*Anne Gruaz-Guyon, Inserm, U773, Faculté de Médecine Xavier Bichat, 16 rue Henri Huchard, BP 416, F-75018, France. E-mail: anne.gruaz-guyon@inserm.fr, Phone: (33) 1 57 27 75 55, Fax (33) 1 57 27 75 31.

Notes

[Δ]Faisal Alshoukr and Aurélie Prignon are to be considered as equal coauthors.

ACKNOWLEDGMENT

This work was supported by Inserm, by the Association pour la Recherche sur le Cancer (ARC), and by the Cancéropole Ile de France. We thank the Syrian government for awarding a research fellowship to F.A. We are grateful to Edouard Treca for IC_{50} determination of some peptides.

REFERENCES

(1) Myers, R. M., Shearman, J. W., Kitching, M. O., Ramos-Montoya, A., Neal, D. E., and Ley, S. V. (2009) Cancer, chemistry, and the cell: molecules that interact with the neurotensin receptors. *ACS Chem. Biol. 4*, 503–525.

(2) Vincent, J. P., Mazella, J., and Kitabgi, P. (1999) Neurotensin and neurotensin receptors. *Trends Pharmacol. Sci. 20*, 302–309.

(3) Evers, B. M. (2006) Neurotensin and growth of normal and neoplastic tissues. *Peptides 27*, 2424–2433.

(4) Thomas, R. P., Hellmich, M. R., Townsend, C. M., Jr., and Evers, B. M. (2003) Role of gastrointestinal hormones in the proliferation of normal and neoplastic tissues. *Endocr. Rev. 24*, 571–599.

(5) Ehlers, R. A., Kim, S., Zhang, Y., Ethridge, R. T., Murrilo, C., Hellmich, M. R., Evans, D. B., Townsend, C. M., Jr., and Mark Evers, B. (2000) Gut peptide receptor expression in human pancreatic cancers. *Ann. Surg. 231*, 838–848.

(6) Reubi, J. C., Waser, B., Friess, H., Buchler, M., and Laissue, J. (1998) Neurotensin receptors: a new marker for human ductal pancreatic adenocarcinoma. *Gut 42*, 546–550.

(7) Souaze, F., Dupouy, S., Viardot-Foucault, V., Bruyneel, E., Attoub, S., Gespach, C., Gompel, A., and Forgez, P. (2006) Expression of neurotensin and NT1 receptor in human breast cancer: a potential role in tumor progression. *Cancer Res. 66*, 6243–6249.

(8) Alifano, M., Souaze, F., Dupouy, S., Camilleri-Broet, S., Younes, M., Ahmed-Zaid, S. M., Takahashi, T., Cancellieri, A., Damiani, S., Boaron, M., Broet, P., Miller, L. D., Gespach, C., Regnard, J. F., and Forgez, P. (2010) Neurotensin receptor 1 determines the outcome of non-small cell lung cancer. *Clin. Cancer Res. 16*, 4401–4410.

(9) Alifano, M., Loi, M., Camilleri-Broet, S., Dupouy, S., Regnard, J. F., and Forgez, P. (2010) Neurotensin expression and outcome of malignant pleural mesothelioma. *Biochimie 92*, 164–170.

(10) Gui, X., Guzman, G., Dobner, P. R., and Kadkol, S. S. (2008) Increased neurotensin receptor-1 expression during progression of colonic adenocarcinoma. *Peptides 29*, 1609–1615.

(11) Shimizu, S., Tsukada, J., Sugimoto, T., Kikkawa, N., Sasaki, K., Chazono, H., Hanazawa, T., Okamoto, Y., and Seki, N. (2008) Identification of a novel therapeutic target for head and neck squamous cell carcinomas: a role for the neurotensin-neurotensin receptor 1 oncogenic signaling pathway. *Int. J. Cancer 123*, 1816–1823.

(12) Swift, S. L., Burns, J. E., and Maitland, N. J. (2010) Altered expression of neurotensin receptors is associated with the differentiation state of prostate cancer. *Cancer Res. 70*, 347–356.

(13) Reubi, J. C., Waser, B., Schaer, J. C., and Laissue, J. A. (1999) Neurotensin receptors in human neoplasms: high incidence in Ewing's sarcomas. *Int. J. Cancer 82*, 213–218.

(14) Dupouy, S., Viardot-Foucault, V., Alifano, M., Souaze, F., Plu-Bureau, G., Chaouat, M., Lavaur, A., Hugol, D., Gespach, C., Gompel, A., and Forgez, P. (2009) The neurotensin receptor-1 pathway contributes to human ductal breast cancer progression. *PLoS One 4*, e4223.

(15) Kwekkeboom, D. J., Kam, B. L., van Essen, M., Teunissen, J. J., van Eijck, C. H., Valkema, R., de Jong, M., de Herder, W. W., and Krenning, E. P. (2010) Somatostatin-receptor-based imaging and therapy of gastroenteropancreatic neuroendocrine tumors. *Endocr. Relat. Cancer 17*, R53–73.

(16) Krenning, E. P., Teunissen, J. J., Valkema, R., deHerder, W. W., deJong, M., and Kwekkeboom, D. J. (2005) Molecular radiotherapy with somatostatin analogs for (neuro-)endocrine tumors. *J. Endocrinol. Invest. 28*, 146–150.

(17) Granier, C., van Rietschoten, J., Kitabgi, P., Poustis, C., and Freychet, P. (1982) Synthesis and characterization of neurotensin analogues for structure/activity relationship studies. Acetyl-neurotensin-(8−13) is the shortest analogue with full binding and pharmacological activities. *Eur. J. Biochem. 124*, 117–124.

(18) Hillairet De Boisferon, M., Raguin, O., Thiercelin, C., Dussaillant, M., Rostene, W., Barbet, J., Pelegrin, A., and Gruaz-Guyon, A. (2002) Improved tumor selectivity of radiolabeled peptides by receptor and antigen dual targeting in the neurotensin receptor model. *Bioconjugate Chem. 13*, 654–662.

(19) Alshoukr, F., Rosant, C., Maes, V., Abdelhak, J., Raguin, O., Burg, S., Sarda, L., Barbet, J., Tourwe, D., Pelaprat, D., and Gruaz-Guyon, A. (2009) Novel neurotensin analogues for radioisotope targeting to neurotensin receptor-positive tumors. *Bioconjugate Chem. 20*, 1602–1610.

(20) Maecke, H. R., Hofmann, M., and Haberkorn, U. (2005) (68)Ga-labeled peptides in tumor imaging. *J. Nucl. Med. 46* (Suppl 1), 172S–178S.

(21) Wei, L., Zhang, X., Gallazzi, F., Miao, Y., Jin, X., Brechbiel, M. W., Xu, H., Clifford, T., Welch, M. J., Lewis, J. S., and Quinn, T. P. (2009) Melanoma imaging using (111)In-, (86)Y- and (68)Ga-labeled CHX-A″-Re(Arg11)CCMSH. *Nucl. Med. Biol. 36*, 345–354.

(22) Mansi, R., Wang, X., Forrer, F., Kneifel, S., Tamma, M. L., Waser, B., Cescato, R., Reubi, J. C., and Maecke, H. R. (2009) Evaluation of a 1,4,7,10-tetraazacyclododecane-1,4,7,10-tetraacetic acid-conjugated bombesin-based radioantagonist for the labeling with single-photon emission computed tomography, positron emission tomography, and therapeutic radionuclides. *Clin. Cancer Res. 15*, 5240–5249.

(23) Pagou, M., Zerizer, I., and Al-Nahhas, A. (2009) Can gallium-68 compounds partly replace (18)F-FDG in PET molecular imaging? *Hell. J. Nucl. Med. 12*, 102–105.

(24) Buchmann, I., Henze, M., Engelbrecht, S., Eisenhut, M., Runz, A., Schafer, M., Schilling, T., Haufe, S., Herrmann, T., and Haberkorn, U. (2007) Comparison of 68Ga-DOTATOC PET and 111In-DTPAOC (Octreoscan) SPECT in patients with neuroendocrine tumours. *Eur. J. Nucl. Med. Mol. Imaging 34*, 1617–1626.

(25) Hofmann, M., Maecke, H., Borner, R., Weckesser, E., Schoffski, P., Oei, L., Schumacher, J., Henze, M., Heppeler, A., Meyer, J., and Knapp, H. (2001) Biokinetics and imaging with the somatostatin receptor PET radioligand (68)Ga-DOTATOC: preliminary data. *Eur. J. Nucl. Med. 28*, 1751–1757.

(26) Gabriel, M., Decristoforo, C., Kendler, D., Dobrozemsky, G., Heute, D., Uprimny, C., Kovacs, P., Von Guggenberg, E., Bale, R., and Virgolini, I. J. (2007) 68Ga-DOTA-Tyr3-octreotide PET in neuroendocrine tumors: comparison with somatostatin receptor scintigraphy and CT. *J. Nucl. Med. 48*, 508–518.

(27) Kowalski, J., Henze, M., Schuhmacher, J., Macke, H. R., Hofmann, M., and Haberkorn, U. (2003) Evaluation of positron emission tomography imaging using [68Ga]-DOTA-D Phe(1)-Tyr(3)-Octreotide in comparison to [111In]-DTPAOC SPECT. First results in patients with neuroendocrine tumors. *Mol. Imaging Biol. 5*, 42–48.

(28) Liu, S. (2008) Bifunctional coupling agents for radiolabeling of biomolecules and target-specific delivery of metallic radionuclides. *Adv. Drug Delivery Rev. 60*, 1347–1370.

(29) Wang, D., Miller, S. C., Sima, M., Parker, D., Buswell, H., Goodrich, K. C., Kopeckova, P., and Kopecek, J. (2004) The arthrotropism of macromolecules in adjuvant-induced arthritis rat model: a preliminary study. *Pharm. Res. 21*, 1741–1749.

(30) Brans, L., Maes, V., Garcia-Garayoa, E., Schweinsberg, C., Daepp, S., Blauenstein, P., Schubiger, P. A., Schibli, R., and Tourwe, D. A. (2008) Glycation methods for bombesin analogs containing the (NalphaHis)Ac chelator for 99mTc(CO)3 radiolabeling. *Chem. Biol. Drug Des. 72*, 496–506.

(31) Raguin, O., Gruaz-Guyon, A., and Barbet, J. (2002) Equilibrium expert: an add-in to Microsoft Excel for multiple binding equilibrium simulations and parameter estimations. *Anal. Biochem. 310*, 1–14.

(32) Stefanovski, D., Moate, P. J., and Boston, R. C. (2003) WinSAAM: a windows-based compartmental modeling system. *Metabolism 52*, 1153–1166.

(33) Riches, A. C., Sharp, J. G., Thomas, D. B., and Smith, S. V. (1973) Blood volume determination in the mouse. *J. Physiol. 228*, 279–284.

(34) Sung, C., Youle, R. J., and Dedrick, R. L. (1990) Pharmacokinetic analysis of immunotoxin uptake in solid tumors: role of plasma kinetics, capillary permeability, and binding. *Cancer Res. 50*, 7382–7392.

(35) Covell, D. G., Barbet, J., Holton, O. D., Black, C. D., Parker, R. J., and Weinstein, J. N. (1986) Pharmacokinetics of monoclonal immunoglobulin G1, F(ab′)2, and Fab′ in mice. *Cancer Res. 46*, 3969–3978.

(36) Akizawa, H., Arano, Y., Mifune, M., Iwado, A., Saito, Y., Mukai, T., Uehara, T., Ono, M., Fujioka, Y., Ogawa, K., Kiso, Y., and Saji, H. (2001) Effect of molecular charges on renal uptake of 111In-DTPA-conjugated peptides. *Nucl. Med. Biol. 28*, 761–768.

(37) Froidevaux, S., Calame-Christe, M., Tanner, H., and Eberle, A. N. (2005) Melanoma targeting with DOTA-alpha-melanocyte-stimulating hormone analogs: structural parameters affecting tumor uptake and kidney uptake. *J. Nucl. Med. 46*, 887–895.

(38) Barroso, S., Richard, F., Nicolas-Etheve, D., Reversat, J. L., Bernassau, J. M., Kitabgi, P., and Labbe-Jullie, C. (2000) Identification of

residues involved in neurotensin binding and modeling of the agonist binding site in neurotensin receptor 1. *J. Biol. Chem. 275*, 328–336.

(39) Garcia-Garayoa, E., Blauenstein, P., Blanc, A., Maes, V., Tourwe, D., and Schubiger, P. A. (2009) A stable neurotensin-based radiopharmaceutical for targeted imaging and therapy of neurotensin receptor-positive tumours. *Eur. J. Nucl. Med. Mol. Imaging 36*, 37–47.

(40) Maes, V., Garcia-Garayoa, E., Blauenstein, P., and Tourwe, D. (2006) Novel 99mTc-labeled neurotensin analogues with optimized biodistribution properties. *J. Med. Chem. 49*, 1833–1836.

(41) Achilefu, S., Srinivasan, A., Schmidt, M. A., Jimenez, H. N., Bugaj, J. E., and Erion, J. L. (2003) Novel bioactive and stable neurotensin peptide analogues capable of delivering radiopharmaceuticals and molecular beacons to tumors. *J. Med. Chem. 46*, 3403–3411.

(42) de Visser, M., Janssen, P. J., Srinivasan, A., Reubi, J. C., Waser, B., Erion, J. L., Schmidt, M. A., Krenning, E. P., and de Jong, M. (2003) Stabilised 111In-labelled DTPA- and DOTA-conjugated neurotensin analogues for imaging and therapy of exocrine pancreatic cancer. *Eur. J. Nucl. Med. Mol. Imaging 30*, 1134–1139.

(43) Froidevaux, S., Eberle, A. N., Christe, M., Sumanovski, L., Heppeler, A., Schmitt, J. S., Eisenwiener, K., Beglinger, C., and Macke, H. R. (2002) Neuroendocrine tumor targeting: study of novel gallium-labeled somatostatin radiopeptides in a rat pancreatic tumor model. *Int. J. Cancer 98*, 930–937.

(44) Koumarianou, E., Mikolajczak, R., Pawlak, D., Zikos, X., Bouziotis, P., Garnuszek, P., Karczmarczyk, U., Maurin, M., and Archimandritis, S. C. (2009) Comparative study on DOTA-derivatized bombesin analog labeled with 90Y and 177Lu: in vitro and in vivo evaluation. *Nucl. Med. Biol. 36*, 591–603.

(45) de Jong, M., Rolleman, E. J., Bernard, B. F., Visser, T. J., Bakker, W. H., Breeman, W. A., and Krenning, E. P. (1996) Inhibition of renal uptake of indium-111-DTPA-octreotide in vivo. *J. Nucl. Med. 37*, 1388–1392.

(46) Vegt, E., van Eerd, J. E., Eek, A., Oyen, W. J., Wetzels, J. F., de Jong, M., Russel, F. G., Masereeuw, R., Gotthardt, M., and Boerman, O. C. (2008) Reducing renal uptake of radiolabeled peptides using albumin fragments. *J. Nucl. Med. 49*, 1506–1511.

Bioconjugate Chemistry

ARTICLE

pubs.acs.org/bc

RGD-Modified Angiogenesis Inhibitor HM-3 Dose: Dual Function during Cancer Treatment

Hanmei Xu,*[,†] Li Pan,[†] Yinling Ren,[†] Yongjing Yang,[†] Xiaofeng Huang,[‡] and Zhendong Liu[†]

[†]State Key Laboratory of Natural Medicines, China Pharmaceutical University, Nanjing, 210009, P. R. China

[‡]Department of Oral Pathology, Nanjing Stamotology Hospital, Affiliated Medical School, Nanjing University, 210008, P. R. China

ABSTRACT: In the present study, we have undertaken pharmacodynamic studies of HM-3 *in vitro* and *in vivo*. A dual function of HM-3 with various doses was observed. HM-3 at low dose revealed obvious anticancer activity. In contrast, HM-3 at high dose had a tendency to promote tumorigenesis and tumor metastasis. Microarray analysis demonstrated that HM-3 at high dose could up-regulate the transcription of AKT1 and MEK1, which resulted in the promotion of tumorigenesis and metastasis. Therefore, the dose of angiogenesis inhibitors plays a critical role in cancer treatment. In order to achieve the ideal effect of angiogenesis inhibitor drugs on cancer treatment, a ful exploration of administration dose, frequency, and period for this kind of drugs is highly desired.

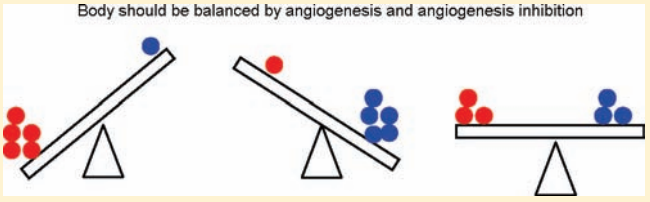

INTRODUCTION

Since Judah Folkman proposed the theory of tumor angiogenesis in 1971, the inhibition of tumor angiogenesis has become an attractive strategy for cancer therapy and has received tremendous attention by scientists. This cancer treatment strategy can effectively inhibit tumor angiogenesis, reduce the supply of nutrients and oxygen, and arrest tumor growth and metastasis. The angiogenesis inhibitors are characteristics of few side effects and less drug resistance. Currently, several angiogenesis inhibitor drugs have been developed for the clinical application, which include monoclonal anti-VEGF antibody drugs such as bevacizumab[1,2] and the second-generation multitargeted receptor tyrosine kinase inhibitor drugs such as sunitinib[3,4] and sorafenib.[5] These investigations suggested that angiostatic therapies have been recognized and accepted. However, compared with traditional cancer treatments, angiogenesis inhibitor drugs still have unclear pharmacological mechanisms, undefined treatment efficacy, and debated views due to their short history in clinical application. In 2009, Ebos and Paez-Ribes[6,7] reported that angiogenesis inhibitors could promote tumor metastasis. In previous experiments from Ebos' research group,[8] the mice treated with sunitinib at the doses of 60 and 120 mg/kg exhibited an increased trend for host (mouse) and tumor (human) VEGF levels. In contrast, plasma levels in mice treated with sunitinib at the doses of 15 and 30 mg/kg did not exhibit the obvious increase. However, based on clinical application, the effective dose in mice should be 10−12 mg/kg, which suggested that higher than effective dose could promote the development of tumors.

Therefore, the administration dose, frequency, and period of angiogenesis inhibitor drugs can result in significant impact on treatment efficacy. The high dose of angiogenesis inhibitors may interrupt the antitumor effect and induce the generation of tumor metastasis factors.

In our laboratory, we found that if a comprehensive investigation of the dosage of angiogenesis inhibitors such as HM-3 was not undertaken, an objective evaluation of angiogenesis inhibitors could not be achieved.

We synthesized HM-3 and explored its anticancer activity *in vitro* and *in vivo*. The HM-3,[9] a polypeptide containing 18 amino acids, was designed and synthesized in our laboratory. During the design process of HM-3, RGD integrin ligand sequence was added to improve its target capability to tumor cells with highly expressed integrin $\alpha v\beta 3$. On the basis of the experimental results *in vitro*, HM-3 had no inhibitory effect on tumor cells, but significantly inhibited the migration of endothelial cells. Matrigel and aortic ring tests in rats demonstrated that HM-3 effectively inhibited angiogenesis, indicating that its antitumor effect was accomplished by inhibiting the migration of endothelial cells and angiogenesis. Meanwhile, the antitumor activity was dose-dependent in the range 0.75−3 mg/kg. No obvious antitumor activity was observed when the dose of HM-3 was lower than 0.75 mg/kg or higher than 6 mg/kg. On the other hand, HM-3 at the dose higher than 6 mg/kg could promote the migration of endothelial cells and result in the overexpression of genes related to tumor metastasis. We hope that our investigations will provide a reference for further research of angiogenesis inhibitors: preclinical and clinical applications should consider administration dose, frequency, and period of angiogenesis inhibitors to achieve an objective evaluation.

EXPERIMENTAL PROCEDURES

Drugs. HM-3 (synthesized by GL Biochem (Shanghai) Ltd.) was kept at −20 °C. Recombinant Human Endostar Injection

Received: February 19, 2011
Revised: June 12, 2011
Published: June 13, 2011

ACS Publications © 2011 American Chemical Society

(obtained from Simcere) was kept at 4 °C. Both of them were diluted to desired concentration using serum-free endothelial cell medium.

Cell Lines. Human umbilical vein endothelial cells (HUVECs, obtained from American ScienCell Research Laboratory) were maintained in endothelial cell medium (ECM) with 5% fetal bovine serum (FBS) and 1% endothelial cell growth supplement (ECGS). Cells were incubated at 37 °C in 5% CO_2 in a humidified incubator.

HUVECs Migration Assay. Diluted matrigel (purchased from BD Biosciences) 1:3 using serum-free medium, mixed sufficiently, was coated evenly on the surface of the transwell bottom. HUVECs were detached with 0.2% EDTA and resuspended in serum free ECM at a density of 1×10^5 cells/mL, and then added to the matrigel-coated transwell (1×10^4 cells/well). HM-3 and Endostar were diluted to the indicated concentrations using serum-free ECM and added to the transwell to incubate HUVEC cells. An appropriate amount of ECM was added, which contained 5% FBS and 1% ECGS to a 24-well flat-bottom polyviny1 chloride plate (COSTAR). The transwells were then put to the 24-well plate, and cells were incubated at 37 °C in 5% CO_2 in the humidified incubator for 24 h. After that, the medium was aspirated, and the migrated cells were fixed with ethanol for 30 min and then stained with 0.1% crystal violet for 10 min. Clear cells were migrated by cotton swab and photos taken under a microscope.

Matrigel Experiment. 50 μL melting matrigel was applied to 96-well cell plates and incubated with synthetic rubber and polyethylene at 37 °C for 1 h. 1×10^4 cells per well were seeded in the gel, then HM-3 was administered at concentrations of 4 μg/mL, 8 μg/mL, 16 μg/mL, and 32 μg/mL, and the positive drug endostar 20 μg/mL, respectively. Cells were incubated at 37 °C, 5% CO_2 for 6 h. The effects of HM-3 on the differentiation of HUVECs stimulated by ECGS were observed with microscope (Olympus).

Culture of Murine Aortic Rings. Young (4−5 months old) female mice were obtained from the Shanghai Laboratory Animal Center of Chinese Academy of Sciences. To prepare aortic segments, mice were sacrificed by isoflurane inhalation, and thoracic aortae were removed and rinsed in PBS with 100 U/mL penicillin and 100 μg/mL streptomycin. The isolated aortae were cleaned of perivascular adipose tissue and cut into segments 1 mm in length. Fibrinogen was dissolved in serum-free culture medium DMEM; final concentration was 3 g/L. 20 μL of 50 U/mL of bovine thrombin solution was added into 1 mL solution of the fibrinogen. Then, the fibrinogen can form fibrin glue at room temperature in 30 s. After dispensing the collagen solution, the preparations were incubated at 37 °C for 30 min for collagen to gel. Subsequently, one aortic segment was placed onto the center of each collagen gel and each segment was then overlaid with 20 μL of collagen solution. After polymerization of the overlaid collagen, 96-well plates filled with 100 μL of DMEM, then administered with 0, 4, 8, 16, and 32 μg/mL of HM-3, and 20 μg/mL of Endostar. After 7−8 days of culture, the microvessel-like structures were observed by inverted microscope.

Tumor Implantation. Tumor cells were grown in culture medium. Cell lines were washed with phoshate buffered saline (PBS), dispersed in a 0.05% trypsin solution, and resuspended. After centrifugation at 1000 rpm for 5 min, the cell pellets were resuspended in PBS and adjusted to a concentration of 5×10^6 cells/mL. C57BL/6 female mice or nude mice (5 to 6 weeks old) were implanted subcutaneously (s.c.) on the mid-right side with 5×10^5 B16F10 cells in 0.1 mL PBS or 1×10^6 human SMMC-7721 hepatic carcinoma cells.

C57BL/6 Female Mice Treatment. After the average tumor volume of B16F10 mouse melanoma had reached 50−100 mm^3, mice were randomly divided into different groups with eight mice per group. Group 1 received PBS. Group 2 was injected with Paclitaxel (Taxol, provided by Taiji Pharmaceutical Co. Ltd., Chendu in Sichuan province of China) once daily at a dose of 10 mg/kg in PBS. Groups 3 to 7 received HM-3 twice a day at doses of 1.5, 3, 6, 12, and 24 mg/kg/day, respectively. All of the mice were injected subcutaneously far from the tumor sites.

BALB/c Nude Mouse Treatment. After the mean SMMC-7721 tumor volume reached 50−100 mm^3, mice were randomly divided into two groups with three mice per treatment group. Group 1 received PBS. Group 2 was injected with HM-3, twice a day at a dose of 48 mg/kg/day. All nude mice were injected intravenously with 0.2 mL.

Measurement of Tumor Growth. Tumors were measured individually with a vernier caliper. Volumes were determined using the formula: tumor volume = length × width^2 × 0.52. Therapeutic effects on tumor growth were expressed as mean tumor volume versus time, calculated as $(1 - T/C) \times 100\%$, where T = treated tumor volume and C = control tumor volume. For example, if the volume of the treated tumor was 40% that of the control on a given day, tumor suppression in the treated group was regarded as 60%.

Immunohistochemistry. Mice were euthanized 2 weeks post-treatment, and tumor tissue was collected, fixed with 4% formaldehyde, embedded in paraffin, and sectioned for hematoxylin and eosin (H&E) staining and immunohistochemical staining for CD31. Vascular structures in tumors were evaluated by immunohistochemical staining of CD31 with rabbit anti-CD31 polyclonal antibody (Boster Biological Company). Briefly, staining for CD31 was performed on sections using their specific primary antibodies and biotinylated goat antirabbit secondary antibody, incubated with horseradish peroxidase-labeled streptavidin, visualized with diaminobenzidine (DAB) chromogen, counterstained with hematoxylin, and observed with a microscope. The microvessel density (MVD) was determined as follows, and the most highly vascularized areas in the sections were identified and viewed at 40× original magnification; then, the number of microvessels was assessed in fifteen randomly selected fields in this area viewed at 200× magnification. The MVD of this section was obtained by counting the average number of the fifteen fields. Three different sections were selected per group.

Human Tumor Metastasis PCR Array. Human tumor metastasis gene array (SABiosciences http://www.sabiosciences.com) containing 84 genes was performed. Cultured HUVECs in ECM with 5% FBS and 1% ECGS. Cells were then incubated with HM-3 at the concentration of 0 μg/mL (as control), 8 μg/mL, and 32 μg/mL at 37 °C for 24 h when reached 80% confluent. RNA was isolated and purified under the instruction of RNA extraction kit (OMEGA). After synthesizing the first strand of cDNA, Real-Time PCR was performed. The cycle duration temperature was set as follows: 95 °C for 10 min, 95 °C for 15 s, and 60 °C for 1 min, respectively; and the melting curve was analyzed through the $\Delta\Delta Ct$ method. First, ΔCt was calculated for each pathway-focused gene in each treatment group. Then, $\Delta\Delta Ct$ was calculated for each gene across two PCR arrays (or groups). Finally, change was calculated for each gene from group 1 to group 2 as $2^{-\Delta\Delta Ct}$.

Western Blot Analysis. HUVECs were seeded at 3×10^5 per well in 6-well culture plates and incubated for 24 h, treated by HM-3 for 24 h, harvested with 0.05% trysin (Hyclone, UT, USA)/0.53 mM EDTA (Hyclone, UT, USA), washed with PBS, and resuspended in 100 μL of Mammalian Protein Extraction Reagent (Shanghai Generay Biotech Co. Ltd., Shanghai, China). Concentrated protein were separated on 12% SDS-polyacrylamide gel (SDS-PAGE) for VEGF, PDGD-A, Akt1, Bcl-2, ERK1/2, MEK1, and 8% for integrin $\alpha v\beta 3$ and integrin $\alpha 5\beta 1$ SDS-polyacrylamide gel (SDS-PAGE), respectively, and then the gel was transferred to polyvinylidene difluoride (PVDF) membrane (Millipore, MIT, USA). Briefly, PVDF membrane was incubated with a 1:1000 dilution of VEGF, PDGD-A, Akt1, Bcl-2, ERK1/2, MEK1, integrin $\alpha v\beta 3$, integrin $\alpha 5\beta 1$, and β-actin antibodies (Cell Signaling Technology, USA). After incubation with the appropriate secondary antibodies, blots were incubated with the ECL reagents (Beyetime, Jiangsu province, China) and exposed to photographic film to detect protein expression.

RESULTS

HM-3 at Low Dose Inhibited Endothelial Cell Migration and Angiogenesis. In this study, the effects of HM-3 at various doses on the migration of endothelial cells were explored. Compared with the negative control, antitumor peptide HM-3 exhibited an obvious inhibitory effect on the migration of ECGS-induced human umbilical vein endothelial cells (HUVECs) in a dose-dependent manner in the concentration range 0.5−8 μg/mL, as shown in Figure 1a,b. Meanwhile, the peptide HM-3 at the dose of 8 μg/mL revealed the best inhibitory effect on cell migration. However, the further increased dose of HM-3 resulted in the gradual decrease in inhibitory activity of HM-3 on cell migration. HM-3 at the dose of 32 μg/mL or higher resulted in the loss of inhibitory activity on cell migration.

During the evaluation of matrigel experiments, the ECGS-induced HUVECs differentiated into branched capillary-like division structures during the treatment of HM-3 for 6−48 h. HM-3 at low concentrations (4 μg/mL) began to reveal the inhibitory activity on cell differentiation. The most obvious blocking effect on the differentiation of HUVECs into tube-like structures *in vitro* was observed when the concentration of HM-3 was 8 μg/mL. Meanwhile, HM-3 at this dose level could significantly reduce the number of small tubes and attenuate the lumen formation during the differentiation of HUVECs ($P < 0.01$). Furthermore, most HUVECs exhibited a messy arrangement due to cell aggregation. In contrast, at the concentration up to 32 μg/mL, HM-3 did not exhibit a significant effect on the formation of small tubes, as shown in Table 1 and Figure 2a,b.

During the aortic ring experiments in rats, after the third day of the experiment, the migration and proliferation of a large number of endothelial cells around arterial rings were observed, and vascular buds from the arterial wall sprouted. The growth phase was the first 6−13 days. A peak with 114 newly generated microvessels was observed at the 14th day; however, no increase in microvessel growth was observed at the 15th day or later. HM-3 at the dose of 4 μg/mL exhibited the initial inhibition effect on angiogenesis with blood vessel number of 32; the most obvious effect on angiogenesis inhibition was observed at HM-3

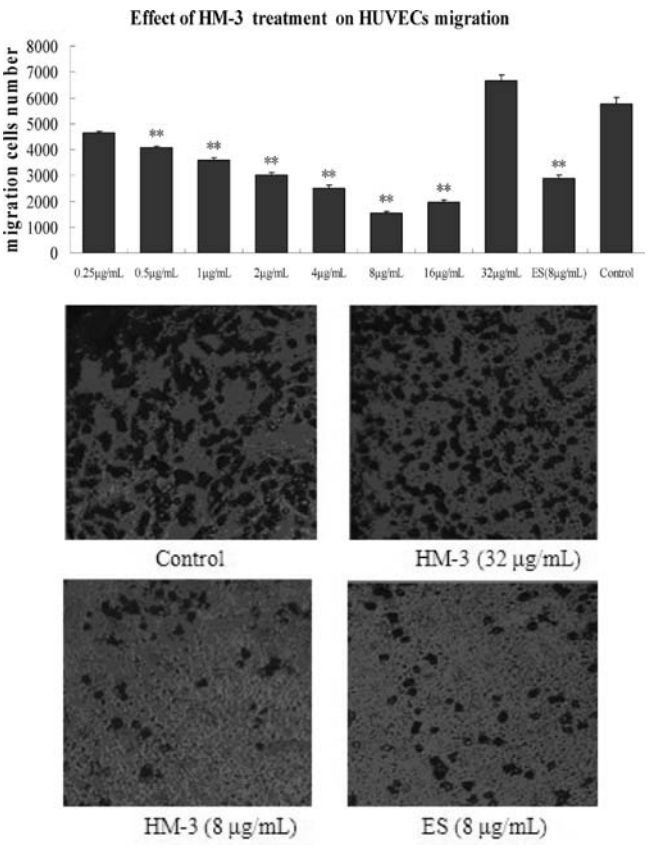

Figure 1. Effects of HM-3 on the migration of endothelial cells. HM-3 exhibited an obvious inhibitory effect on the migration of ECGS-induced human umbilical vein endothelial cells (HUVECs) in a dose-dependent manner in the concentration range 0.5−8 μg/mL (a). The further increased dose of HM-3 (32 μg/mL) resulted in the gradual decrease in inhibitory activity of HM-3 on cell migration. The migrated cells of positive drug ES (endostar, 8 μg/mL), control, HM-3 (8 μg/mL), and HM-3 (32 μg/mL) are shown in (b). ($n = 5$, $^*P < 0.05$, $^{**}P < 0.01$).

Table 1. Results of Antitumor Peptide HM-3 Inhibiting HUVEC Differentiation[a]

times	control	4 μg/mL	8 μg/mL	16 μg/mL	32 μg/mL	endostar
6 h	37.80 ± 11.8	11.00 ± 3.4**	13.00 ± 3.2**	19.60 ± 7.2*	25.80 ± 4.6	18.40 ± 5.8
12 h	29.00 ± 8.68	8.00 ± 2.0*	8.60 ± 2.3**	19.00 ± 5.2	23.00 ± 4.8	15.00 ± 4.7*
24 h	18.40 ± 2.4	4.33 ± 1.2*	7.40 ± 2.3**	12.50 ± 2.0*	15.80 ± 2.8*	13.00 ± 3.8
48 h	11.33 ± 4.1	1.33 ± 0.6*	2.00 ± 0.5*	9.50 ± 1.3	10.50 ± 1.8	6.75 ± 1.7
72 h	9.00 ± 2.9	0.66 ± 0.2	1.33 ± 0.2*	6.50 ± 1.3	8.50 ± 1.2	2.33 ± 0.2
96 h	5.00 ± 1.5	0.66 ± 0.1	0.66 ± 0.2	3.00 ± 0.5	6.66 ± 0.6	1.00 ± 0.2
120 h	2.66 ± 0.5	0.66 ± 0.1	0.33 ± 0.1	2.00 ± 0.2	3.00 ± 0.3	0.66 ± 0.1
144 h	0	0	0	0	0	0

[a] ($\bar{x} \pm$ SD) × 40 (OHP), ($n = 5$, $^*P < 0.05$, $^{**}P < 0.01$).

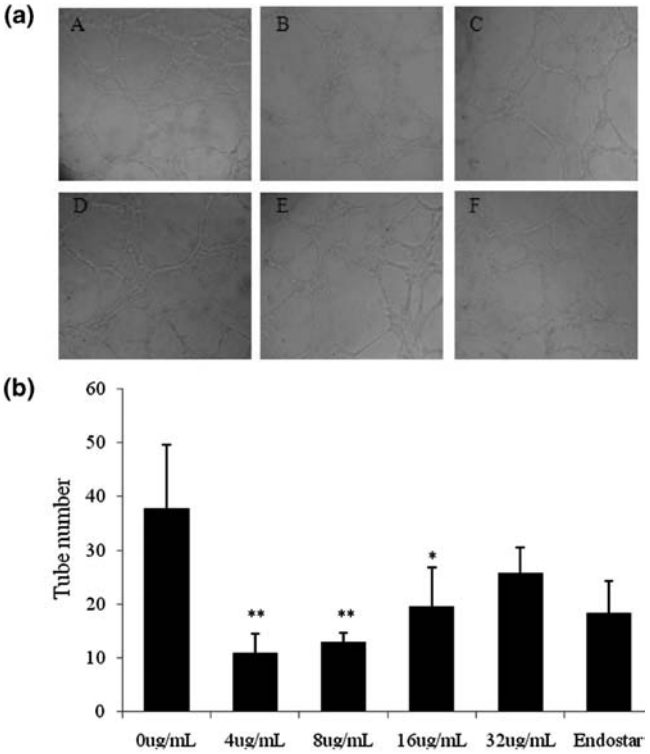

Figure 2. (a) Antitumor peptide HM-3 could inhibit HUVEC differentiation. A and F display the control and the positive drug of endostar (20 μg/mL). B, C, D, and E display HM-3 at doses of 4, 8, 16, and 32 μg/mL. (b) The effects of HM-3 inhibiting HUVEC differentiation at 6 h. The HM-3 at low concentrations (4 μg/mL) began to reveal the inhibitory activity on cell differentiation. The most obvious blocking effect on the differentiation of HUVECs into tube-like structures *in vitro* was observed when the concentration of HM-3 was 8 μg/mL. At the concentration up to 32 μg/mL, HM-3 did not exhibit a significant effect on the formation of small tubes. Columns represented $\bar{x} \pm$ SD of experiments, $n = 5$, $^{*}P < 0.05$, $^{**}P < 0.01$ vs control.

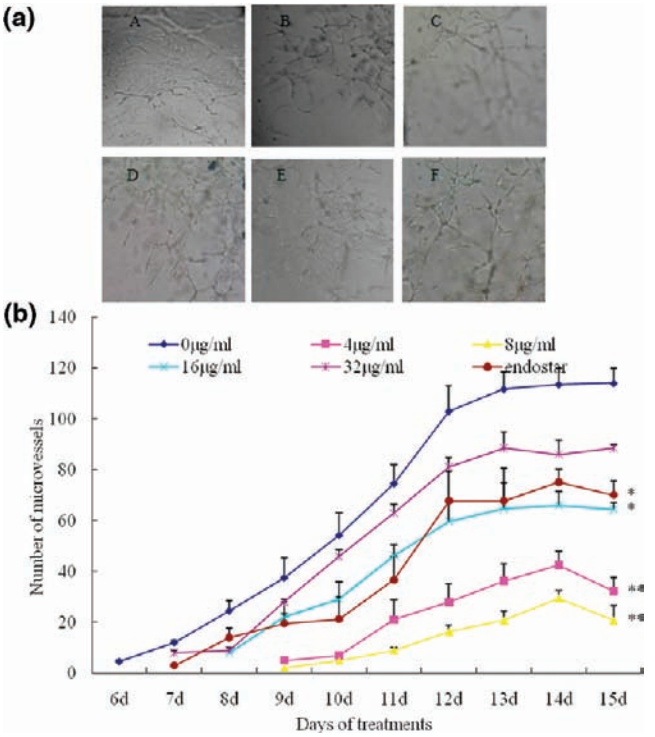

Figure 3. (a) Fourteenth day of microvessel growth under different treatments. A represents control, and F displays the positive drug of endostar, 20 μg/mL. B, C, D, and E display HM-3 at the doses of 4, 8, 16, and 32 μg/mL. (b) Microvascular growth curves of aortic ring-fibrin gel cultues in serum-free DMEM. HM-3 at the dose of 4 μg/mL exhibited the initial inhibition effect on angiogenesis with blood vessel number of 32; the most obvious effect on angiogenesis inhibition was observed at dose of 8 μg/mL and 20 blood vessels were detected at this condition. However, when the concentration of HM-3 was up to 32 μg/mL, the total loss of angiogenesis inhibition effect was observed, which exhibited a similar number of blood vessels as the negative control group with 88 blood vessels. ($n = 5$, $^{*}P < 0.05$, $^{**}P < 0.01$).

dose of 8 μg/mL, and 20 blood vessels were detected at this condition. However, when the concentration of HM-3 was up to 32 μg/mL, the total loss of angiogenesis inhibition effect was observed, which exhibited a similar number of blood vessels as the negative control group with 88 blood vessels, as shown in Figure 3a,b.

HM-3 at Low Dose Significantly Inhibited Tumor Growth. As shown in Figure 4a, HM-3 with various doses exhibited an obvious tumor inhibition effect. Compared with the negative control, HM-3 revealed a clear inhibition effect on tumor growth after 9 days treatment, and the inhibition rates of tumor volume subjected to HM-3 treatments at the doses of 1.5, 3, 6, 12, and 24 mg/kg were 57.37%, 53.04%, 23.82%, 15.88%, and 9.47%, respectively. This result suggested that the inhibitory effect of HM-3 treatment on tumor growth was not dose-dependent. HM-3 at low dose exhibited an excellent antitumor effect; in contrast, the antitumor activity was decreased or lost at the dose higher than 6 mg/kg.

Moreover, previous experiments also demonstrated that HM-3 at the dose of 3 mg/kg could effectively inhibit the growth of SMMC-7721 cell in liver cancer.[9] However, when administrated at the dose of 48 mg/kg for 10 days, there was no significant difference in the tumor anatomical detection between the treatment and the control groups, as shown in Figure 4b.

HM-3 at High Dose Promoted the Formation of Tumor Blood Vessels. In order to further confirm the effect of HM-3 at different doses on angiogenesis, tumor tissues from nude mice treated with HM-3 at two doses (3 and 48 mg/kg) were immunohistochemically analyzed for CD31 antibody. The average of 5.8 capillaries was detected in the tumor tissues treated with HM-3 at an effective dose of 3 mg/kg, which was much lower than that (16.8 capillaries) in the group treated with HM-3 at a high dose of 48 mg/kg. Interestingly, HM-3 at the high dose did not inhibit tumor growth; however, the amount of blood vessels within tumor tissues treated with HM-3 at high dose was higher than that in the group at the effective dose. These results suggested that HM-3 at the high dose could not inhibit the growth of blood vessels; in contrast, it exhibited a promotional role in angiogenesis (Figure 5).

HM-3 at High Dose Was Associated with the Regulation Genes of Tumor Metastasis. In order to explore the effect of HM-3 at various doses on tumor metastasis, 84 tumor metastasis-related genes were analyzed by using human tumor metastasis PCR array. Genes selected for this array encoded several classes of protein factors including cell adhesion, ECM components, cell cycle, cell growth and proliferation, apoptosis, transcription factors and regulators, and other genes related to tumor metastasis. After HM-3 at both doses (8 and 32 μg/mL) had been used

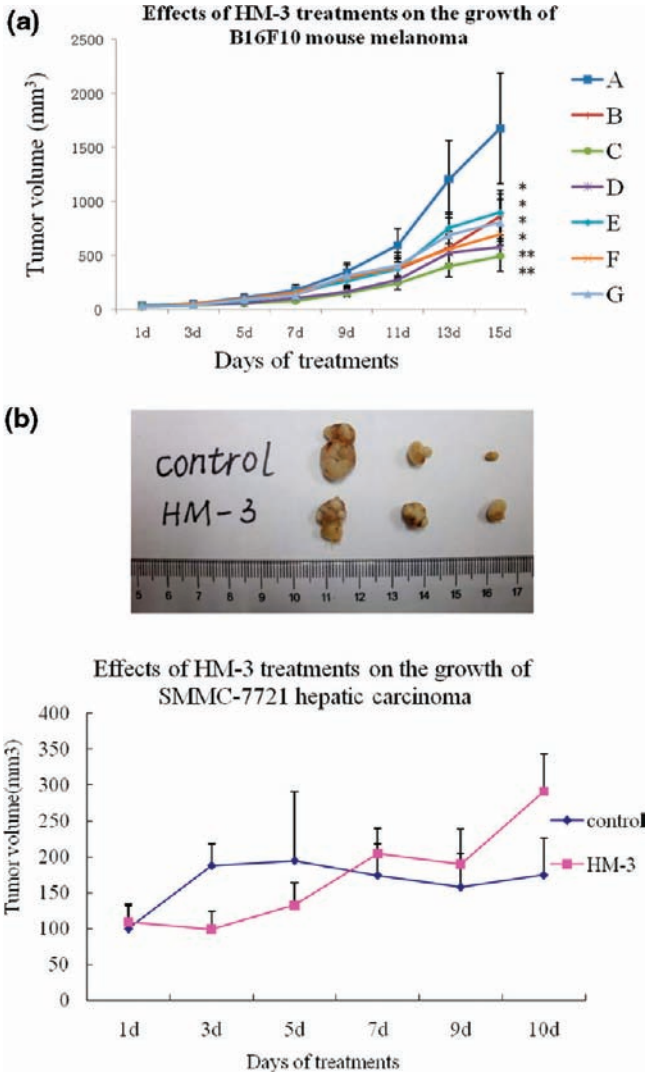

Figure 4. (a) Therapeutic effects of peptides on the growth of B16F10 mouse melanoma tumor. A represents control, and B displays the positive drug Taxol, 10 mg/kg, once a day. C, D, E, F, and G display HM-3 at the dose of 1.5, 3, 6, 12, and 24 mg/kg twice a day, and the inhibition rates of tumor volume were 57.37%, 53.04%, 23.82%, 15.88%, and 9.47%, respectively. Each point represents $\bar{x} \pm$ SD of each group (n = 8, $^{**}P < 0.01$, $^{*}P < 0.05$ vs control). (b) Therapeutic effects of peptides at the dose of 48 mg/kg for 10 days on the growth of SMMC-7721 hepatic carcinoma. Tumor could not be inhibited by 48 mg/kg HM-3 twice a day. Each point represents mean (SD of each group (n = 3, $^{*}P < 0.05$, $^{**}P < 0.01$ vs control).

to treat the HUVECs, HM-3 treatment at the dose of 8 μg/mL exhibited an obvious enhancement on gene transcription of CTSL1, KiSS-1, Syk, and SSTR2, while revealing an inhibition effect on gene transcription of ETV4 and Myc. On the other hand, HM-3 at the dose of 32 μg/mL exhibited a great impact on the genes of tumor metastasis, which included the increase of Hras, MMP10, SSTR2, and TCF20 and the reduction of NR4A3 (Nor1). These results indicated that HM-3 at a higher dose might promote tumor development and metastasis, as shown in Figure 6.

HM-3 Down-Regulated AKT and ERK1/2 Pathway Activity by Integrin αvβ3. During the design of the peptide HM-3, the RGD sequence was included in HM-3 for targeting integrin receptor. Previous studies verified that HM-3 could bind to

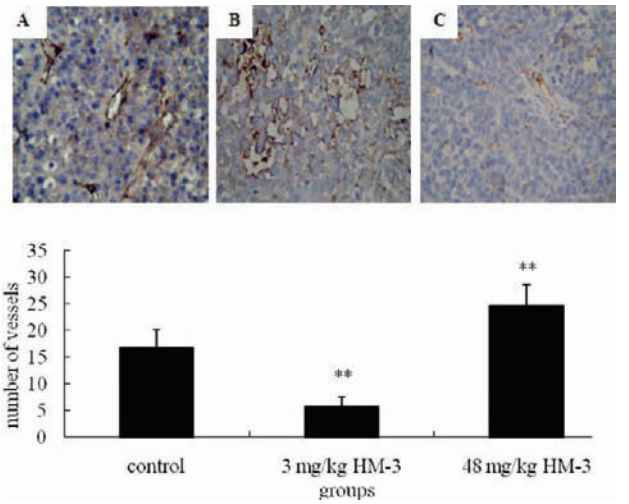

Figure 5. Blood vessel density within tumor tissue. A, B, and C represent tumor tissues from nude mice treated with PBS, HM-3 (48 mg/kg), and HM-3 (3 mg/kg), that have been immunohistochemically analyzed for CD31 antibody (top), the staining observed with light microscope (40× original magnifications). The blood vessels were counted (bottom graph), HM-3 at dose of 3 mg/kg with average of 5.8 capillaries, 16.8 capillaries were detected in the group treated with HM-3 at a high dose of 48 mg/kg. Results were expressed as mean (SD of 15 regions of three sections per group, $^{*}P < 0.05$; $^{**}P < 0.01$ vs control).

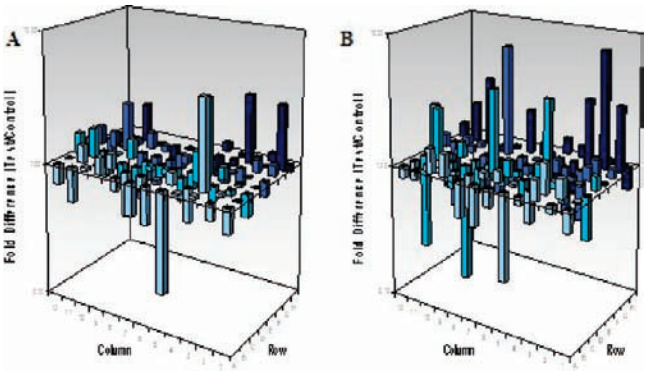

Figure 6. HM-3 at the dose of 32 μg/mL exhibited a great impact on the genes of tumor metastasis. A and B represent tumor metastasis genes of HUVEC impacted by HM-3 (3 mg/kg) and HM-3 (32 mg/kg) treatments.

overexpressed integrin αvβ3 in tumor cells.[9] In the present study, the roles in intracellular signaling were further explored. Western blot results showed that HUVECs treated with HM-3 revealed a reduced expression level of VEGF, PDGF-A, Bcl-2, and AKT1 as well as the MEK1 in a dose-dependent mode, as shown in Figure 7a. Meanwhile, although HM-3 did not exhibit an obvious impact on integrin α5β1, it revealed a significant impact on the expression of integrin αvβ3, indicating that HM-3 executed its biological activity through integrin αvβ3.

On one hand, HM-3 can regulate the transduction pathway through integrin αvβ3 to result in the down-regulation of MEK1 and AKT1, thus inhibiting the migration of tumor vascular endothelial cells to accomplish its antitumor activity. On the other hand, HM-3 can directly induce endothelial cells to decrease the expression of VEGF and PDGF-A, thus in turn accomplishing

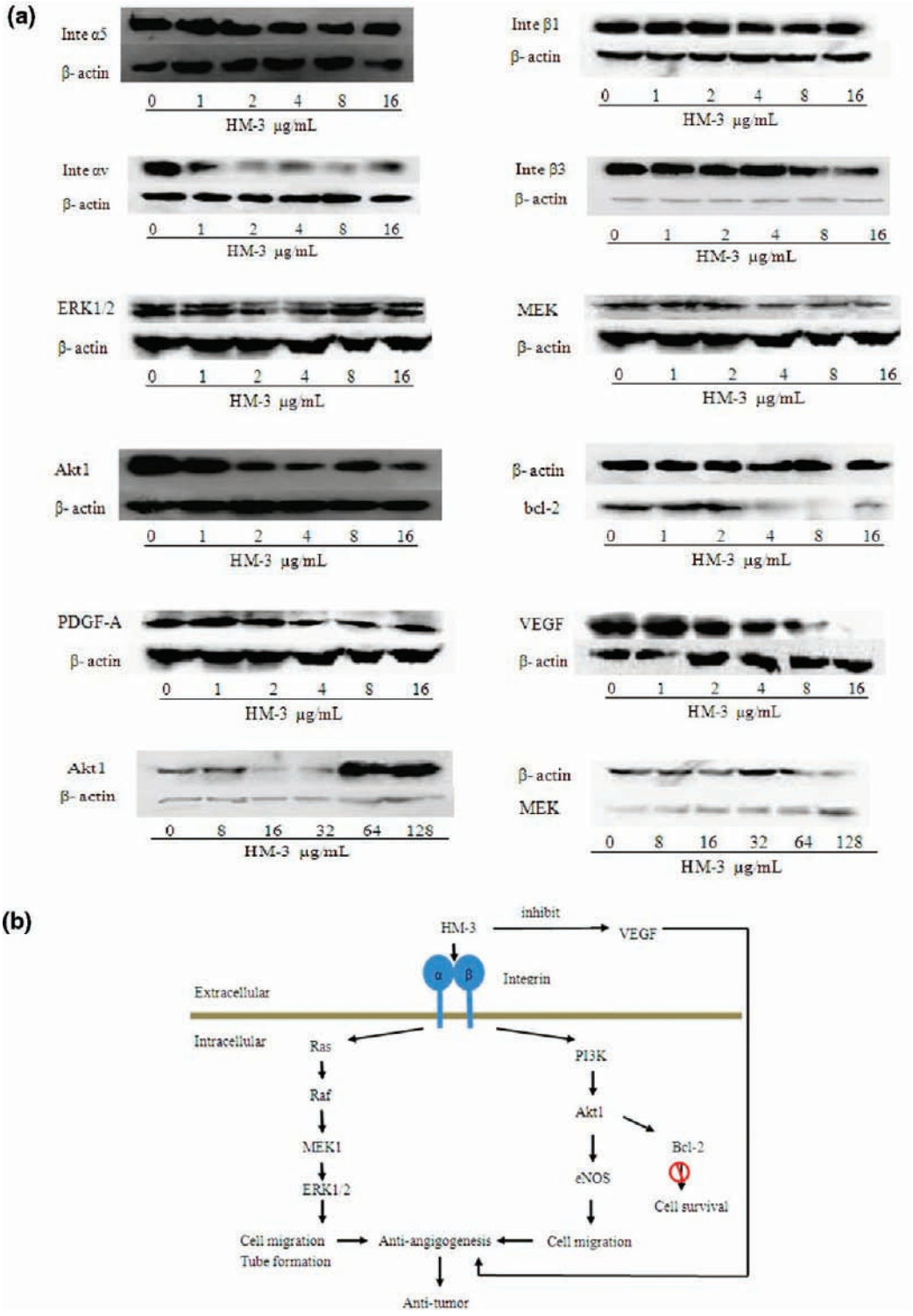

Figure 7. (a) Western blot analysis of the expression level of VEGF, PDGF-A, Bcl-2, AKT1, ERK1/2, MEK1, and integrin. Significant impact on the expression of VEGF, PDGF-A, Akt1, Bcl-2, MEK1, and integrin $\alpha v\beta 3$ was revealed in HUVECs after HM-3 treatments. (b) HM-3 may execute its biological activity through integrin $\alpha v\beta 3$.

tumor angiogenesis inhibition and executing antitumor activity, as shown in Figure 7b.

Similarly, the dose of HM-3 plays a critical role in its antitumor activity. A possible explanation is that HM-3 at the high dose condition has the function of regulating two key proteins, which is due to the dramatically increased expression of AKT1 and enhanced expression of MEK1 to some extent when treated with HM-3 at the dose of 64 μg/mL, as shown in Figure 7a.

DISCUSSION

Human cancer is a disease that is difficult to eradicate. Due to the complex pathological mechanisms, a single treatment

dx.doi.org/10.1021/bc2000929 |*Bioconjugate Chem.* 2011, 22, 1386–1393

method is still unable to achieve good results for cancer. Thus, a number of different strategies and means for cancer treatment have been developed in clinical applications. Angiogenesis inhibitors are newly developed anticancer drugs entering the market in recent years. Unlike traditional chemotherapy and radiation therapy, angiogenesis inhibitor drugs have the characteristic of high safety, and promote less suffering for patients during the treatment.

Some angiogenesis inhibitors are endogenous inhibitors such as tumstatin and endostatin. Tumstatin and endostain as angiogenesis inhibitors have been derived from precursor human collagen molecules known as the α3 chain of type IV collagen and α1 chain of type XVIII collagen, respectively. In a normal person, there is a balanced state between the angiogenesis signal output and angiogenesis inhibition. Angiogenic signals can be provided by growth factor alkaline FGF, VEGF, IL-8, and PDGF as available. Endogenous angiogenesis inhibitors were distributed in different tissues or blood. These angiogenesis inhibitors include thrombosis contractile protein, tumstatin, canstatin, endostatin, angiostatin, and interferon.[10] Some drugs such as avastin can inhibit angiogenesis factor VEGF to reduce the output signal of tumor angiogenesis and delay the onset of cancer. Another strategy is to improve the angiogenesis defense system, thus providing a natural angiogenesis inhibitor as part of the cancer treatment.

In our laboratory, peptide HM-3 was designed and synthesized on the basis of adhesion molecule integrin receptor $\alpha v\beta 3$. Its antitumor activity was accomplished by improving the angiogenesis defense system, which was validated by pharmacodynamic and pharmacological tests *in vitro* and *in vivo*. During the pharmacodynamic study *in vivo*, peptide HM-3 at low dosage conditions (1.5 and 3 mg/kg) exhibited a significant tumor inhibition effect. Similarly, HM-3 at too high or too low dose proved to have no inhibitory effect on the cell migration or vascular activity *in vitro*. Through gene chip analysis, HM-3 at effective dosage can be seen to increase CTSL1, KiSS-1, Syk, and SSTR2 gene transcription and inhibit ETV4 and Myc gene transcription. TSLC1 as a tumor suppressor gene was detected in lung cancer. KISS1 as a metastasis suppressor gene plays an important role in a variety of tumor invasion and metastasis. Somatostatin or its analogues can inhibit the proliferation of tumor cells via the regulation of SSTR2. In addition, the c-Myc gene is highly associated with the development of many kinds of tumors. Whereas ETV4, ETV1, and ERG genes belonging to ETS gene family are correlated with normal division of cells, their integration with other genes can result in overexpression and abnormal activity. HM-3 at the condition of effective dose can inhibit tumor-related genes, whereas HM-3 treatment at high dose greatly impacts tumor metastasis genes. Interestingly, HM-3 at the dose of 32 μg/mL results in an increased number of transcription genes including FN1, IL1B, CXCR2, IGF1, KISS1, PLAUR, RORB, SRC, SYK, TIMP4, TRPM1, and TSHR. Moreover, the increased transcription of genes such as Hras, MMP10, SSTR2, and TCF20, as well as the reduced NR4A3 (Nor1), was related to tumor metastasis. For example, Nor1 is a tumor suppressor gene of myeloid leukemia. The transcriptional regulation activity of NR4A3 (Nor1) is dependent on cell-specific and stimulus-specific gene induction and protein phosphorylation, not the ligands. Overdose of HM-3 can result in excessive stimulation on cells, thus correspondingly leading to the decreased expression of the NR4A3 (Nor1) gene and interrupt the balance among cell proliferation, apoptosis, and

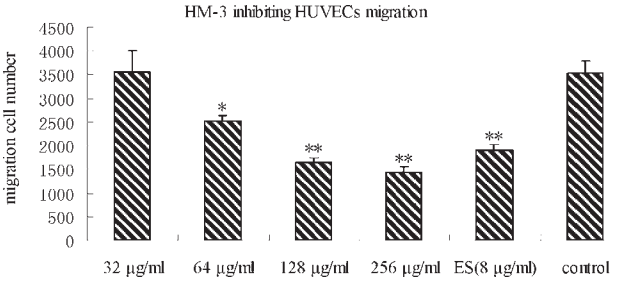

Figure 8. Effects of HM-3 on the migration of endothelial cells at the dose range 64−256 μg/mL.

differentiation. At the considered protein level, HM-3 at the effective dose can result in a dramatic decrease in expression of AKT1 as well as MEK1. These results remind us of a cancer treatment strategy of "supporting righteousness and dispelling evil" using Chinese medicine. It is well-known that the human body is a balanced system with its own operation laws. Tumorigenesis results from damaged balance, less righteousness, or too much evil. The principle of "supporting righteousness and dispelling evil" is to restore the balance in the body and achieve coordination of the internal organs. Therefore, the cancer treatment should use drugs reasonably; overkill is also a taboo, which is consistent with the phrase, "overkill can not achieve the expectation" from Confucius, a Chinese ancient thinker and philosopher.

Angiogenesis and angiogenesis inhibition remain a balanced process in normal organisms including animals and people. The process of tumorigenesis is due to the loss of balance. Therefore, the application of angiogenesis inhibitors for cancer treatment is to restore balance. Then, inadequate dose or administration of HM-3 is not enough to achieve the desired results; similarly, excessive dose of HM-3 can further result in the interruption of the balance and no expected treatment efficacy. Interestingly, based on the HUVEC migration, with HM-3 at the dose of 32 μg/mL, no inhibitory effect on cell migration was observed; however, with the increased HM-3 at the dose range 64−256 μg/mL, a new dose−effect relationship was apparent, as shown in Figure 8. All of these investigations suggested that cells or the human body have the capability to adjust their own signal change according to external stimulation.

In this study, HM-3 executes the antitumor effect through increasing angiogenesis as a defense system. In contrast, some drugs complete the antitumor effect by inhibiting angiogenesis factor VEGF to reduce the output signal of tumor angiogenesis. Regardless of the cancer treatment strategy, the appropriate treatment dose is important. In 2009, Ebos, Paez-Ribes, and their co-workers reported that the VEGF-target treatment could inhibit tumor growth and improve the survival period of patients. However, the promotion effect of angiogenesis inhibitors on tumor metastasis was also described. On the basis of our analysis of Ebos' investigation, the treatment with sunitinib at high dose (120 mg/kg) increased tumor metastatsis and reduced the animal survival period. We found that, in previous studies,[11] the optimal dose range of sunitinib was 40 mg/kg/day for HT-29 or 80 mg/kg/day (Colo205) with treatment duration of 100 days. Also, according to the calculation of clinical dose (60 mg daily), the effective dose of sunitinib was 10−12 mg/kg for mice. However, the cancer treatments with angiogenesis inhibitors at high doses and short treatment period promoted the metastasis of tumors and shortened the survival time. These trials include

sorafenib at the dose of 150 mg/kg/day and SU10944 at the dose of 225 mg/kg/day. For example, the recommended daily dose of sorafenib for human is 400 mg (2 × 200 mg tablets). According to the recommended daily dose and human body weight (400 mg/60−70 kg), the dose of sorafenib should be 75−85 mg/kg for mice; similarly, the appropriate dose of SU10944 should be 100 mg/kg/day in mice.[12] Therefore, we believe that excessive angiogenesis inhibitors did not reduce the output signal of angiogenesis; in contrast, they could lead to the interruption of body balance and stimulate other signaling pathways under the body stress to produce more angiogenesis factors and express more tumor metastasis-associated genes. This hypothesis is consistent with previous experimental results in which the mice administered with sunitinib at doses of 60 and 120 mg/kg exhibited increased VEGF levels, while the plasma VEGF levels remained intact when treated with sunitinib at the doses of 15 or 30 mg/kg.[8]

Because angiogenesis and angiogenesis inhibition in the human body is a very delicate process, patient status, symptoms, and pathological mechanisms must be fully considered while using angiogenesis inhibitors. It is really necessary to understand the tumor mechanisms (whether the tumor is derived from increased tumor angiogenesis factor such as VEGF or decreased angiogenesis defense system); drug type, administration dose, treatment frequency, and period are the determinants for cancer treatments.

AUTHOR INFORMATION

Corresponding Author

*Hanmei Xu, State Key Laboratory of Natural Medicines, China Pharmaceutical University, Nanjing, 210009, China. Tel: 86-25-83271007. Fax: 86-25-83271007. E-mail: xuhanmei@cpu.edu.cn.

ACKNOWLEDGMENT

We would like to thank Wenhui Jiang (Department of immunity analyze, Nanjing oral medical hospital, P. R. China) for critical assistance on histochemistry and immunohistochemistry analysis. The authors thank Chunyan Pu, Chi Zhang, and Yongbing Li for assisting in implanting tumors. Funding was provided by China scientific and technological major special project — 'significant creation of new drugs' (Grant No. 2009ZX09102) and National Science Foundation of China (NSFC, No. 30873073).

REFERENCES

(1) Hurwitz, H., Fehrenbacher, L., Novotny, W., Cartwright, T., Hainsworth, J., Heim, W., Berlin, J., Baron, A., Griffing, S., Holmgren, E., Ferrara, N., Fyfe, G., Rogers, B., Ross, R., and Kabbinavar, F. (2004) Bevacizumab plus irinotecan, fluorouracil, and leucovorin for metastatic colorectal cancer. *N. Engl. J. Med. 350*, 2335–42.

(2) Miller, K., Wang, M., Gralow, J., Dickler, M., Cobleigh, M., Perez, E. A., Shenkier, T., Cella, D., and Davidson, N. E. (2007) Paclitaxel plus bevacizumab versus paclitaxel alone for metastatic breast cancer. *N. Engl. J. Med. 357*, 2666–76.

(3) Demetri, G. D., Van Oosterom, A. T., Garrett, C. R., Blackstein, M. E., Shah, M. H., Verweij, J., McArthur, G., Judson, I. R., Heinrich, M. C., Morgan, J. A., Desai, J., Fletcher, C. D., George, S., Bello, C. L., Huang, X., Baum, C. M., and Casali, P. G. (2006) Efficacy and safety of sunitinib in patients with advanced gastrointestinal stromal tumor after failure of imatinib: a randomised controlled trial. *Lancet 368*, 1329–38.

(4) Motzer, R. J., Michaelson, M. D., Redman, B. G., Hudes, G. R., Wilding, G., Figlin, R. A., Ginsberg, M. S., Kim, S. T., Baum, C. M., DePrimo, S. E., Li, J. Z., Bello, C. L., Theuer, C. P., George, D. J., and Rini, B. I. (2006) Activity of SU11248, a multitargeted inhibitor of vascular endothelial growth factor receptor and platelet-derived growth factor receptor, in patients with metastatic renal cell carcinoma. *J. Clin. Oncol. 24*, 16–24.

(5) Abou-Alfa, G. K., Schwartz, L., Ricci, S., Amadori, D., Santoro, A., Figer, A., De Greve, J., Douillard, J. Y., Lathia, C., Schwartz, B., Taylor, I., Moscovici, M., and Saltz, L. B. (2006) Phase II study of sorafenib in patients with advanced hepatocellular carcinoma. *J. Clin. Oncol. 24*, 4293–300.

(6) Ebos, J. M., Lee, C. R., Cruz-Munoz, W., Bjarnason, G. A., Christensen, J. G., and Kerbel, R. S. (2009) Accelerated metastasis after short-term treatment with a potent inhibitor of tumor angiogenesis. *Cancer Cell. 15*, 232–9.

(7) Pàez-Ribes, M., Allen, E., Hudock, J., Takeda, T., Okuyama, H., Viñals, F., Inoue, M., Bergers, G., Hanahan, D., and Casanovas, O. (2009) Antiangiogenic therapy elicits malignant progression of tumors to increased local invasion and distant metastasis. *Cancer Cell. 15*, 220–31.

(8) Bocci, G., Man, S., Green, S. K., Francia, G., Ebos, J. M., du Manoir, J. M., Weinerman, A., Emmenegger, U., Ma, L., Thorpe, P., Davidoff, A., Huber, J., Hicklin, D. J., and Kerbel, R. S. (2004) Increased plasma vascular endothelial growth factor (VEGF) as a surrogate marker for optimal therapeutic dosing of VEGF receptor-2 monoclonal antibodies. *Cancer Res. 64*, 6616–25.

(9) Xu, H. M., Yin, R. T., Chen, L. Sh., Sami, S., Huang, X. F., Wang, M., Fang, H. Sh., and Wang, Y. (2008) An RGD-modified endostatin-derived synthetic peptide shows antitumor activity *in vivo*. *Bioconjugate Chem. 19*, 1980–6.

(10) Folkman, J., and Kalluri, R. (2004) Cancer without disease. *Nature 427*, 787.

(11) Christensen, J. G. (2007) A preclinical review of sunitinib, a multitargeted receptor tyrosine kinase inhibitor with anti-angiogenic and antitumour activities. *Ann. Oncol. 18*, x3–x10.

(12) Pietras, K., and Hanahan, D. (2005) A multitargeted, metronomic, and maximum-tolerated dose "chemo-switch" regimen is antiangiogenic, producing objective responses and survival benefit in a mouse model of cancer. *J. Clin. Oncol. 23*, 939–52.

Bioconjugate Chemistry

ARTICLE

pubs.acs.org/bc

Direct Synthesis of Rev Peptide-Conjugated Gold Nanoparticles and Their Application in Cancer Therapeutics

Ngoc Thi Thanh Tran,[†] Tzu-Hao Wang,[‡,§] Chiao-Yun Lin,[‡] Yi-Chun Tsai,[†] Chyong-Huey Lai,[‡] Yian Tai,[*,†] and Benjamin, Y. M. Yung[∥]

[†]Department of Chemical Engineering, National Taiwan University of Science and Technology, Taipei, Taiwan

[‡]Department of Obstetrics and Gynecology, Chang Gung Memorial Hospital and Chang Gung University, Taoyuan, Taiwan

[§]Genomic Medicine Research Core Laboratory, Chang Gung Memorial Hospital, Taoyuan, Taiwan

[∥]Department of Health Technology and Informatics, The Hong Kong Polytechnic University, Hong Kong, China

S *Supporting Information*

ABSTRACT: We have developed a simple approach for generating peptide-conjugated gold nanoparticles (AuNPs) from the Rev peptide and gold aqueous solution. The peptide functions as both a reducing agent and a capping molecule. AuNPs of various sizes (20−300 nm) and shapes (spheres, triangular plates, and polygons) can be obtained upon modulating the ratio of gold ions to the Rev peptide. Transmission electron microscopy, X-ray diffraction, and UV−vis spectroscopy were utilized to characterize these nanoparticles. Fourier-transform infrared and X-ray photoelectron spectroscopy measurements were performed to investigate chemical interactions between the Rev peptide and AuNPs. Lactate dehydrogenase and 3-(4,5-dimethylthiazol-2-yl)-2,5-diphenyltetrazolium bromide assays revealed that the Rev peptide−AuNP nanocomposites exhibited exceptionally high cytotoxic effects toward mouse ovarian surface epithelial cell lines, relative to the effects of equal doses of the free Rev peptide. Our study suggests a new way of utilizing biomolecule-conjugated AuNPs as potentially effective anticancer drugs.

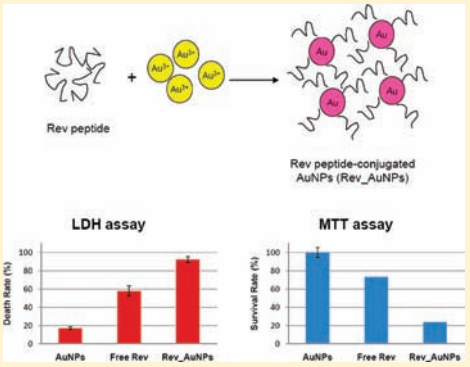

INTRODUCTION

Metal nanoparticles possess many properties that are useful in biomedical applications.[1,2] In particular, gold nanoparticles (AuNPs) are of tremendous interest due to their unique optical and photothermal properties,[1−4] which are due in large part to their localized surface plasmon resonance (LSPR) properties that can be modulated by varying particle size and shape.[5] AuNPs are good candidates for medical processes such as labeling,[6] sensing and imaging,[7] drug delivery,[8] and cancer therapeutics.[6,9] Among their versatile biomedical applications, cancer therapeutics that utilize AuNPs have attracted much attention since they can provide both localized and targeted therapies, minimizing invasion, thus reducing the severity of side effects[10,11] and improving a patient's quality of life. With thiol-derivatized PEG and recombinant human tumor necrosis factor (TNF) directly bound to the AuNP surface, Paciotti et al. demonstrated that a less toxic and more effective reduction in tumor burden can be realized by using AuNPs in preference over native TNF since maximal antitumor response is achievable at lower drug doses.[12] The most promising cancer therapy that utilizes AuNPs is hyperthermic tumor cell ablation by optical heating. In AuNP-mediated hyperthermia, nanoparticles are delivered to cancer cells where they agglomerate into larger clusters that form bubbles under laser irradiation, providing effective tumor cell elimination.[13,14] Such improvements benefit from the high photon-energy absorption profile of AuNPs for which minimal irradiation energy is required. Additionally, selective targeting of AuNPs to biomarkers on cancer cells is a promising cancer therapy technique. By binding HER2, a protein often overexpressed in breast cancer cells, with gold nanoshell conjugated antibodies, Halas et al. successfully performed precision photodamage of cancer cells *in vitro* using a NIR laser.[15] Moreover, a method using AuNPs has been applied in a noninvasive radio wave cancer treatment. Tumor ablation using a variable power RF signal, after direct injection of citrate-AuNPs into a target tumor to focus the radio wave for selective heating, has been reported for both *in vitro* and *in vivo* investigations [16]

One of the prerequisites for AuNPs in cancer therapy applications is their biocompatibility. These nanoparticles are typically functionalized with biomolecules post-synthesis to avoid any undesired effects on live cells.[17,18] Efforts have been made for direct synthesis of AuNPs using various biological entities, such as plant extracts,[19] fruit extracts,[20] fungi,[21] and peptides.[22,23] In each case, the biospecies functioned as both reducing agent and capping molecule.[22] Among the list of biological entities, peptides have attracted significant attention due to their versatility in

Received: March 10, 2011
Revised: June 7, 2011
Published: June 14, 2011

ACS Publications © 2011 American Chemical Society

cancer therapy.[24−26] For example, the Rev peptide has been reported as a promising candidate as an anticancer drug;[27] Nucleophosmin/B23, which is often overexpressed in proliferating cells,[28] has been implicated as a marker for ovarian,[29] gastric,[30] colon,[31] prostate,[32] and bladder [33] cancers. Using small molecules to bind to cancer-specific targets is a potentially powerful anticancer strategy. Since the Rev peptide exhibits high binding affinity toward nucleophosmin/B23, it might prove useful as a powerful anticancer technology.

Herein, we report a simple, direct, and reproducible method for fabricating water-dispersible Rev peptide-conjugated AuNPs (Rev_AuNPs) for cancer therapy applications. Various sizes and shapes of Rev_AuNPs can be generated by manipulation of the concentration of Au ion solution or the temperature during the synthetic process. Lactate dehydrogenase (LDH) and 3-(4,5-dimethylthiazol-2-yl)- 2,5-diphenyltetrazolium bromide (MTT) assays revealed that Rev_AuNPs exhibited remarkably higher *in vitro* cytotoxic effects on mouse ovarian surface epithelial cell (MOSEC) lines relative to the effect of an equal dose of the pure Rev peptide.

EXPERIMENTAL SECTION

Materials. The Rev peptide, $C_{17}H_{128}N_{36}O_{18}S$ (Figure S1, Supporting Information), was provided by Kelowna International Scientific Inc. Hydrogen tetrachloroaurate hydrate ($HAuCl_4 \cdot 3H_2O$), sodium hydroxide (NaOH), and potassium bromide (KBr, IR grade) were purchased from Acros Organics (USA). Deionized (DI) water (18 MΩ) was obtained from a Milli Q reagent water system. The colorimetric MTT assay was acquired from Roche Applied Science (Mannheim, Germany); the LDH assay was purchased from Roche Applied Science (Indianapolis, IN, USA).

Synthesis of Rev_AuNPs. In a standard experiment, aqueous $HAuCl_4$ (0.001 M, 2 mL) was added dropwise into a solution of Rev (5 mM, 1 mL) and NaOH (0.01 M, 1 mL), and then the mixture was stirred (500 rpm) for 4 h at room temperature. After the addition of DI water (4 mL), the mixture was left undisturbed, for one day to complete of the reaction. The mixture was centrifuged (24,000 rpm, 30 min) and the precipitate collected and redispersed in DI water (4 mL) using an ultrasonic bath to form a solution; the supernatant was collected separately. Both solutions were passed through a membrane filter (mesh size: 400 nm) and quantified (UV−vis spectrometry) prior to *in vitro* testing.

The shape-modulation experiments of the peptide-conjugated AuNPs were performed by varying the ratio of Au^{3+} ions to Rev peptide or by altering the temperature during synthesis, while maintaining other conditions constant.

Synthesis of Reference AuNPs. Reference AuNPs for the *in vitro* tests were fabricated using a previously reported standard procedure.[34] Aqueous sodium citrate solution (3.88×10^{-2} M, 10 mL) was added to boiling $HAuCl_4$ solution (1×10^{-3} M, 100 mL), and the mixture was boiled for a further 10 min. As the AuNPs formed, the solution color changed from light yellow to wine red.

Characterization. Rev_AuNPs UV−vis absorbances were measured using UV−vis−NIR spectroscopy (Jasco V-670). The sizes and shapes of the fabricated AuNPs were determined using a Philips Tecnai F30 field-emission-gun transmission electron microscope, equipped with selected area electron diffraction (SAED) attachment. FTIR spectra were recorded in transmittance mode, on a Nicolet iS10 instrument using KBr plates. The synthesized AuNP crystallinity was determined by X-ray diffraction (XRD, Rigaku D/MAX-B) with CuKα radiation (λ = 1.54 Å). X-ray photoelectron spectroscopy (XPS) was performed in an analysis chamber equipped with an X-ray photoelectron spectrometer (VG ESCA Scientific Theta Probe; takeoff angle, 53°) and an aluminum Kα (1486.5 eV) anode, operated at a power of 200 W (20 kV). XPS spectra were recorded using a hemispherical energy analyzer operated at a pass energy of 50.0 eV for survey scans. For practical XPS data analyses, spectral calibration was performed by employing Au 4f peaks at either 83.9 or 84.1 eV as internal standards.

Quantification. Two calibration plots were constructed to quantify the amount of Rev peptide bonded to the AuNPs prior to conducting *in vitro* tests. One plot was based on UV−vis absorbance measurements of the reaction solutions to quantify the concentration of excess Rev peptide after the synthetic reaction. The plot (Figure S2a, Supporting Information) was constructed using the pure Rev peptide absorption band at 276 nm, the absorbance of which changed with concentration of the peptide solution (Figure S2b, Supporting Information). Rev_AuNP exhibits a characteristic absorption at 550 nm, and its intensity changes according to its concentration, thus providing the basis for a calibration graph. Figure S3a (Supporting Information) presents the calibration plot monitored at three wavelengths: the band at 550 nm, the first base wavelength at 490 nm, and the second at 620 nm, respectively; Figure S3b (Supporting Information) shows variation in absorbance with changes in Rev_AuNP concentration.

Cytotoxicity and Viability Assays. The MOSEC line was cultured in RPMI 1640, supplemented with 10% fetal bovine serum and antibiotics, at 37 °C with 5% CO_2. Approximately 5000 cells (200 μL of a suspension of 2.5×10^4 cells/mL) were placed in each well of a 96-well culture plate for 24 h. For the cytotoxicity and viability experiments, cancer cells in serum-free medium were treated with the AuNPs, the Rev peptide, or Rev_AuNPs for various periods. After gentle agitation, the culture medium (100 μL) was transferred into fresh wells in a 96-well plate for the LDH assay, performed according to the manufacturer's protocol. For the colorimetric MTT assay, MTT (5 mg/mL, 25 μL) was added into each well containing treated cells; after 4 h, the supernatant was discarded, and DMSO (100 μL) was added to each well; the mixture was shaken and measured at 570 nm using an ELISA reader scanning multiwell spectrophotometer (PerkinElmer VICTOR 2, GMI, Minnesota, USA).

Transmission Electron Microscopy Images of Cells. Cells were fixed in phosphate buffer containing 3% glutaraldehyde, postfixed in 1% OsO_4, dehydrated in graded alcohol, and finally embedded in Epon 812. Ultrathin (80 nm) sections were stained with 4% uranyl acetate and lead citrate, then examined using transmission electron microscopy (TEM) (H-7500, Hitachi, Tokyo, Japan).

RESULTS AND DISCUSSION

AuNPs with an average size of 25 nm (Figure 1a) were fabricated by the dropwise addition of 0.001 M aqueous $HAuCl_4$ into 5 mM Rev peptide solution under constant stirring at room temperature. The nanostructures exhibited characteristic UV−vis absorption centered at 550 nm (Figure 1b), which can be assigned to the surface plasmon resonance (SPR) band of AuNPs.[2,5] The dispersion of these AuNPs in water produced a light-purple color (Figure 1b, inset). The presence of −C═O, $-NH_x$, and −SH functional groups within the Rev peptide molecular

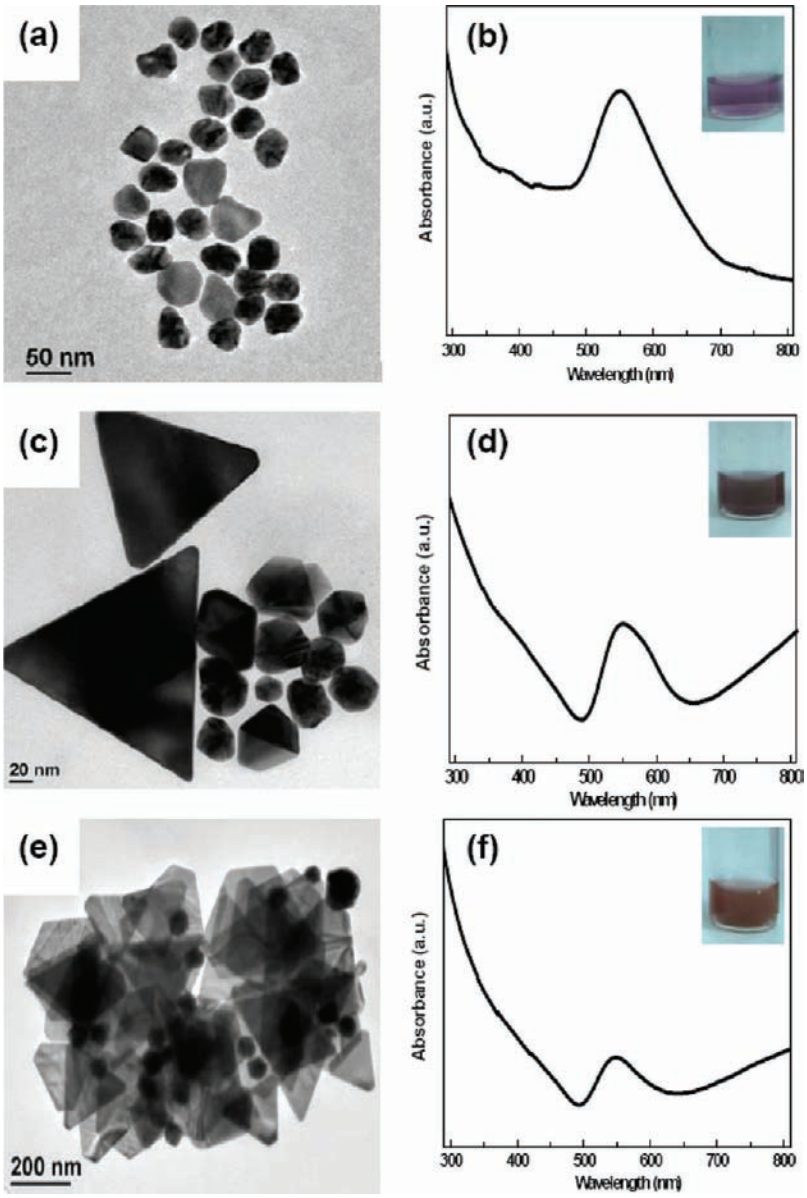

Figure 1. (a, c, and e) TEM images and (b, d, and f) UV−vis spectra (the insets are photographs of aqueous dispersions) of the Rev_AuNPs synthesized from $HAuCl_4$ at concentrations of (a,b) 0.001 M, (c,d) 0.002 M, and (e,f) 0.005 M.

structure presumably caused it to act as a mild reductant, reducing Au^{3+} ions to metal Au, thereby forming the AuNPs.[35] Moreover, the AuNPs were protected and stabilized by the conjugated Rev peptide backbones.[22,35] Larger triangular plate (100−200 nm) AuNPs can be prepared by increasing the aqueous $HAuCl_4$ concentration to 0.002 M (Figure 1c). The UV−vis absorption spectrum of this sample features an absorption band at around 550 nm, and a broad band appeared in the higher wavelength region (Figure 1d). The band centered at 550 nm possibly results from a mixture of the SPR band of small AuNPs as shown in Figure 1b and an out-of-plane quadrupole resonance of the triangular plates.[36] The Figure 1d inset shows a photograph of an aqueous dispersion of these nanostructures, which is dark red in color. We suspect that variation in Rev_AuNPs size and shape occurs upon varying the ratio of the Rev peptide to $HAuCl_4$. Our explanation for this is that strong relationships exist between the capping agent to metal−ion concentration ratio, and the sizes and shapes of metal NPs.[37,38] Indeed, a large abundance of anisotropic Rev_AuNPs nanoplates, including triangular, hexagonal, and truncated polygonal plates form upon increasing the concentration of Au ions to 0.005 M (Figure 1e), possibly due to the increased $HAuCl_4$ concentration which provided more Au ions for further growth and led to larger nanoplates. The aqueous dispersion of these Rev peptide-conjugated nanoplates was colored brown (Figure 1f, inset). The UV−vis absorption of these particles (Figure 1f) is similar to the spectrum shown in Figure 1d. In addition to manipulation of the ratio between Au ions and Rev peptide, Rev_AuNPs of various sizes and shapes can be generated by carrying out the reaction at elevated temperatures (Figure S4, Supporting Information).

With the purpose of application in cancer therapeutics, we selected the 25-nm Rev_AuNPs, as shown in Figure 1a, for further investigation since the most suitable particle size for biomedical applications is 20−70 nm.[8]

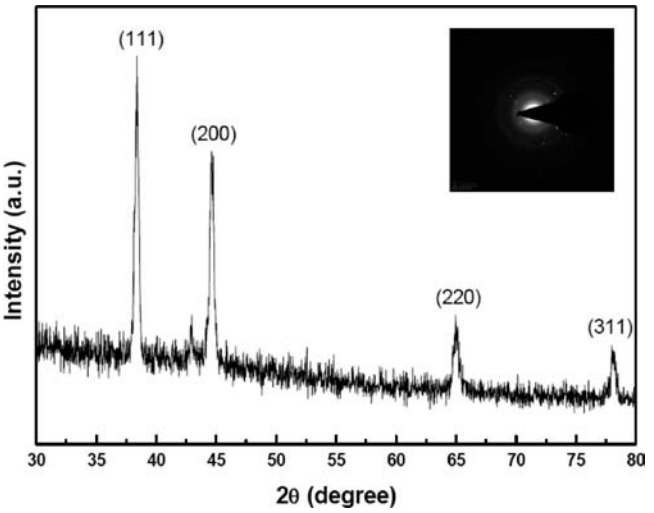

Figure 2. XRD and SAED patterns of AuNPs synthesized using the Rev peptide.

XRD analysis revealed that these AuNPs were polycrystalline (Figure 2), with characteristic peaks at 38.3, 44.6, 64.9, and 77.8° that correspond to the (111), (200), (220), and (311) crystal planes, respectively, implying a face-centered cubic crystal structure.[39] Moreover, selected area electron diffraction (SAED) (Figure 2, inset) reveals a random distribution of bright spots together with ring patterns, further confirming the polycrystalline structure of Au atoms in Rev_AuNPs.

The Rev_AuNPs FTIR spectra were recorded to verify that the Rev peptide had conjugated to AuNP as a capping agent. Figure 3a and b shows FTIR spectra of the pure Rev peptide and the Rev_AuNPs, respectively. The intense broad bands in the region between 3308 and 3401 cm^{-1} in Figure 3a represent N−H stretching vibrations, indicating the presence of amino groups.[40] We assign two sharp absorption bands at 1536 and 1669 cm^{-1} to the amide II and amide I groups of the Rev peptide, respectively.[40] By contrast, the Rev_AuNPs absorption bands for amide II and amide I groups appeared at 1544 and 1676 cm^{-1}, respectively (Figure 3b). The shifts of these two amide absorption bands to the higher wavenumber suggest that conformational changes occurred to the Rev peptide upon binding to the Au surface.[40] The major vibrational absorption bands corresponding to the C═O groups were not identifiable, possibly because of overlap with the amide I bands.[41] Nevertheless, the signals at 1436 cm^{-1} in Figure 3a and 1451 cm^{-1} in Figure 3b correspond to the symmetrical stretching vibrations of carboxylate groups, indicating the presence of C═O units in the free Rev peptide and in Rev_AuNPs.[40] Again, this shift to a higher wavenumber suggests that a conformational change occurred to the Rev peptide upon binding to AuNPs.[41,42]

To further understand the nature of the chemical interactions between the Rev peptide and the AuNP, XPS has been carried out. The signals in the Rev_AuNPs Au 4f spectrum (Figure 4a) indicate the presence of Au atoms.[20]The low intensity of the signal seen for the Au 4f energy level resulted from attenuation caused by an abundance of Rev peptide units on the AuNP surfaces. We attribute the slight shift in the Au 4f signal toward higher binding energy to the Au atoms attached to organic molecules (i.e., the Rev peptide).[20] Moreover, the presence of C 1s, O 1s, and N 1s photoelectron signals confirmed the existence

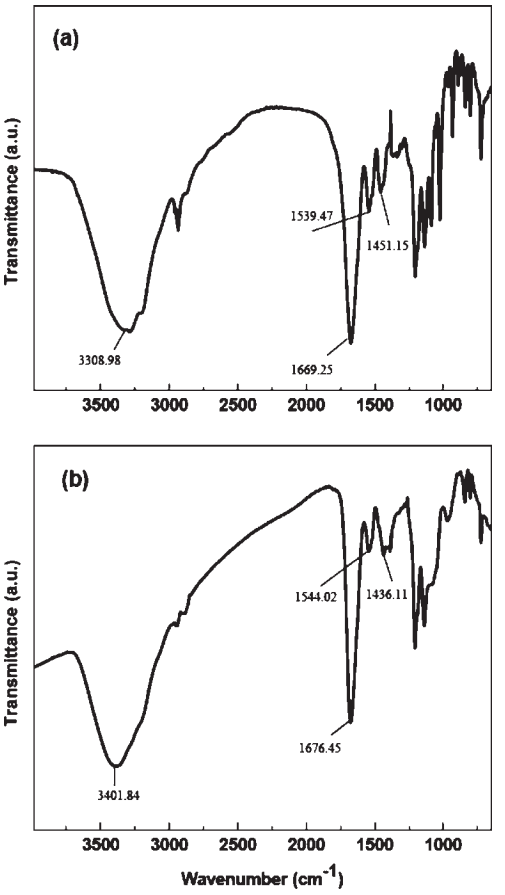

Figure 3. FTIR spectra of the (a) free Rev peptide and (b) Rev_AuNPs.

of Rev peptide units anchored to the AuNP surfaces. Figure 4b presents the C 1s spectra of both the free Rev peptide and the Rev_AuNPs. The XPS signals in both spectra are represented by three individual peaks, 284.9−285.1, 286.0−286.2, and 288.6−288.8 eV, which we assign to aliphatic and aromatic hydrocarbon species, −$\underline{C}NH_x$ and −$\underline{C}$═O groups, respectively.[20] Notably, the relative intensity of the high binding energy peak in the range 288.6−288.8 eV to the hydrocarbon signal (284.9−285.1 eV) in the spectrum of the Rev_AuNPs [Figure 4b(ii)] was lower than that of the free Rev peptide [Figure 4b(i)]. This possibly arose through conversion of a carbonyl (C═O) functional group in the free Rev peptide to a C−O−Au moiety when the Rev peptide bound to the AuNPs surface. Since AuNPs are electron reach species, they donate electrons to the oxygen atom via the O−Au bond, thus decreasing oxygen's inductive electron withdrawing effect toward the attached carbon atoms. As a consequence, the signal of these carbon atoms move to lower binding energy and overlap with that for the hydrocarbon units, leading to the observed decrease in high binding energy signal and increase in the low binding energy intensity. The oxygen spectra shown in Figure 4c further confirm our proposed mechanism. The O 1s peak of the free Rev peptide [Figure 4c(i)] shifts to lower binding energy for Rev_AuNP [Figure 4c(ii)]), presumably because of the conversion of the oxygen atoms from C═O units to C−O−Au moieties upon binding of the Rev peptide to the Au surface. The signal for the N 1s energy level remains unchanged in the spectra of the free Rev peptide [Figure 4d(i)] and Rev_AuNPs [Figure 4d(ii)], suggesting that no (or very few)

dx.doi.org/10.1021/bc2001215 |*Bioconjugate Chem.* 2011, 22, 1394–1401

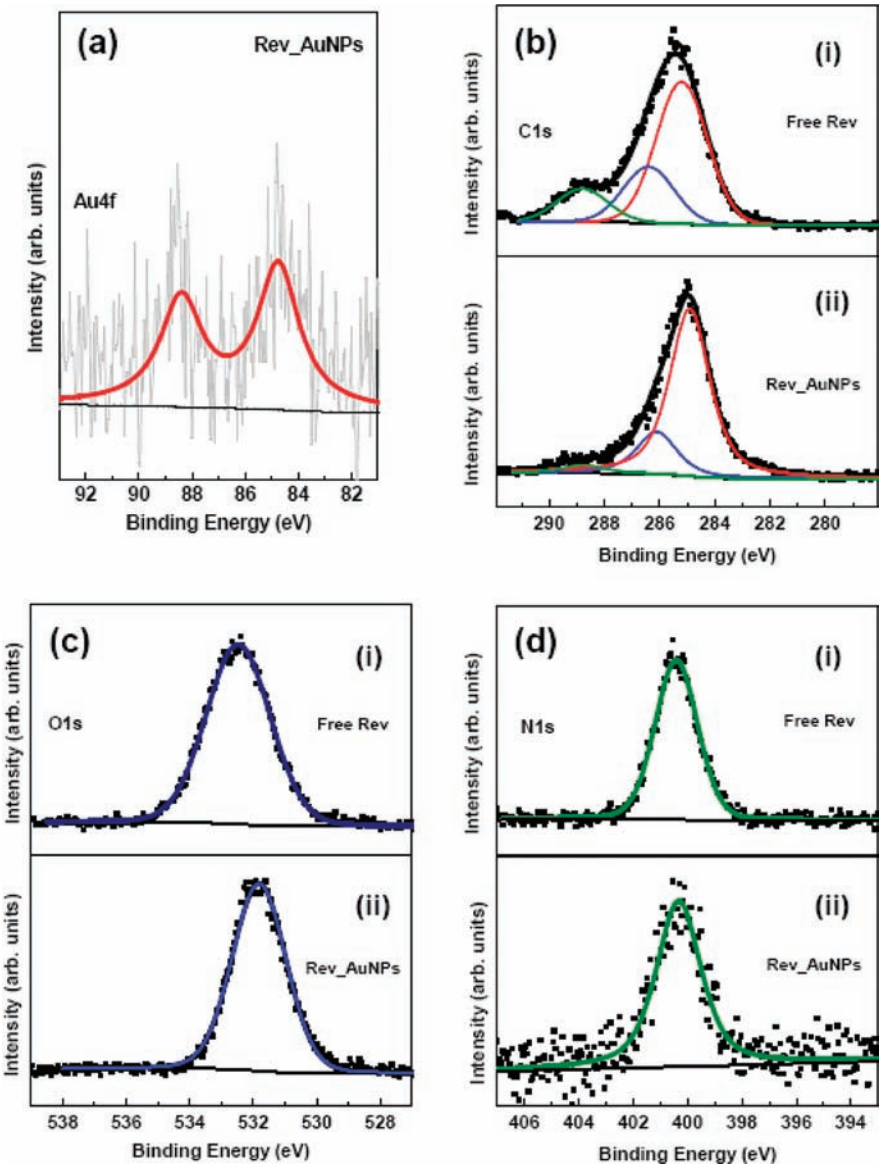

Figure 4. XPS spectra of (a) the Au 4f energy level of the Rev_AuNPs and (b−d) the (b) C 1s, (c) O 1s, and (d) N 1s energy levels for the (i) free Rev peptide and (ii) Rev_AuNPs.

CNH_x groups were involved in the formation of Rev_AuNPs. Moreover, the full-width-at-half-maximum height (fwhm) of the XPS peaks for Rev_AuNPs were noticeably narrower than those of the free Rev peptide, implying that the Rev peptide molecules possessed higher configurational order when bound to the AuNPs' surfaces compared to that in their free form.

The Rev peptide (primary sequence: ARRNRRRRWREYC) has a high binding affinity for nucleophosmin/B23 within tumor cells.[27] In principle, conjugation to AuNP should result in the Rev peptide being retained for longer durations with improved stability within a cellular environment.[43,44] Therefore, we employed the MOSEC line to test the Rev_AuNPs as Rev peptide carriers *in vitro*.[45] The cells were incubated individually with both Rev_AuNPs and free Rev peptide at the same dose for comparison. Additionally, AuNPs of similar size and shape to Rev_AuNPs, but lacking the bound Rev peptide (Figure S5, Supporting Information), were incubate separately as a reference. For all samples, cell incubation was performed for 24 or 48 h, and then cell viability and toxicity were determined using MTT and LDH assays. The results, summarized in Figure 5, are presented as mean viability ± standard deviation (SD) from three independent experiments, each of which were performed in triplicate. Figure 5a shows that both the reference AuNPs and free Rev peptide exhibited MOSEC survival rates close to 100% after incubation for 24 h (MTT assay), suggesting no cytotoxic effects. By contrast, the survival rate (MTT assay) decreased significantly to 56.1% for MOSEC incubated with Rev_AuNPs. Moreover, Figure 5b reveals that LDH release from this cell line reached 76.5%, nearly twice that from the cell line incubated with the free Rev peptide (39.0%). Furthermore, the incubated MOSEC death rate for the reference AuNPs was only 15.9%, implying a very low cytotoxic effect by AuNP itself. Notably, a significantly lower MOSEC survival rate (24.2%, MTT assay) occurred when the Rev_AuNPs incubation time was increased to 48 h (Figure 5c). Similar results from the LDH assay were obtained. A remarkably high death rate of 92.3% is seen (Figure 5d). Once more, the free

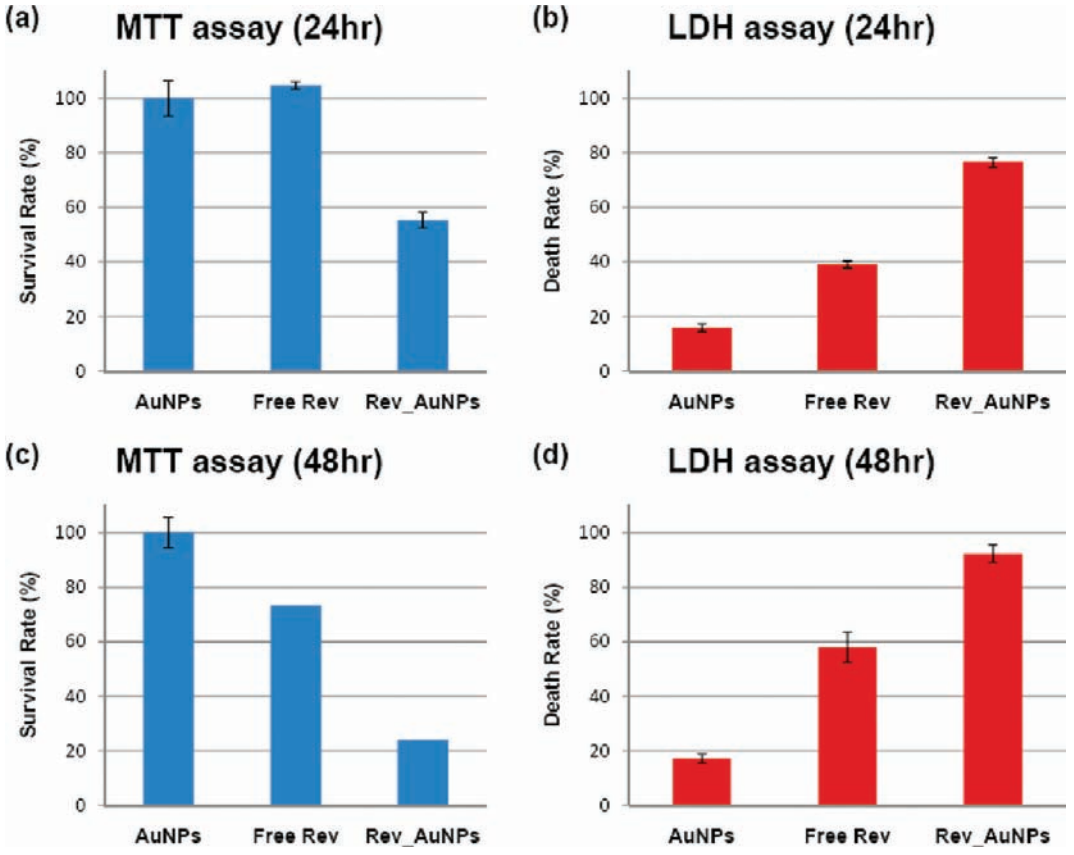

Figure 5. Cytotoxicity data after MOSEC exposure to the reference AuNPs, the free Rev peptide, and the Rev_AuNPs for (a, b) 24 and (c, d) 48 h. (a, c) MTT assays; (b, d) LDH assays.

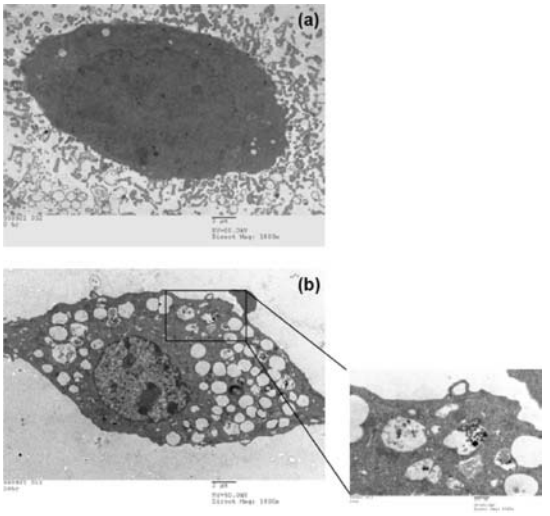

Figure 6. TEM images of MOSEC internalization of Rev_AuNPs after (a) 0 h and (b) 24 h.

Rev peptide and the reference AuNPs had no dramatic effect on the MOSECs after 48 h of incubation, suggesting that Rev_AuNPs had a significantly greater cytotoxic effect on the MOSEC cell line than equal doses of either the free Rev peptide or the reference AuNPs did.

To investigate whether the enhanced Rev_AuNP cytotoxicity was due to internalization of Rev_AuNPs by the cells, we incubated a confluent MOSEC monolayer with the Rev_AuNPs. After 24 h of exposure, the cells were fixed and examined by TEM. Figure 6 compares the degree of Rev_AuNPs internalization at different periods. Initially (0 h), no Rev_AuNPs were present within the cells (Figure 6a). After 24 h, however, AuNP internalization occurred in the cells (Figure 6b). Notably, Rev_AuNPs were localized in the intracellular membrane-bound vesicles and were not freely dispersed in the cytoplasm. These results are consistent with those of previous investigations performed with HeLa cells.[46] By using TEM, Chithrani et al. found that AuNPs having diameters between 14 and 74 nm entered cultured HeLa tumor cells where they became trapped in vesicles of the cytoplasm. Thus, we suspect that Rev_AuNP's enhanced cytotoxicity might be mediated through internalization of the particles into the mouse ovarian cells.

SUMMARY

In summary, we have developed a simple, one-pot method for the direct synthesis of AuNPs in the presence of the Rev peptide in aqueous solution. Varying either the concentration of auric ions or the reaction temperature influenced the sizes and shapes of the synthesized Rev_AuNPs. *In vitro* testing (LDH and MTT assays) using 25-nm size Rev_AuNPs produced significantly greater cytotoxicity toward the MOSEC line than the pure Rev peptide exhibited. These results suggest that Rev_AuNP might be more effective than the free Rev peptide when used in cancer therapies. We anticipate that our new route toward the direct synthesis of biomolecule-conjugated Au nanocomposites will pave the way toward new effective therapeutic applications.

■ ASSOCIATED CONTENT

Supporting Information. Chemical structure of the Rev peptide, UV−vis calibration curve for the Rev peptide and Rev_AuNPs, TEM images of Rev_AuNPs synthesized at elevated temperature, and TEM image of reference AuNPs. This material is available free of charge via the Internet at http://pubs.acs.org.

■ AUTHOR INFORMATION

Corresponding Author

*Dr. Yian Tai, Department of Chemical Engineering, National Taiwan University of Science and Technology, 43 Keelung Road, Sec. 4, Taipei 106, Taiwan. Phone: +886-2-2737-6620. Fax: +886-2-2737-6644. E-mail: ytai@mail.ntust.edu.tw.

■ ACKNOWLEDGMENT

We are grateful to Mr. Tsung-Ching Wu for technical assistance, Taiwan Tech (NTUST) for providing support of the TEM and XPS instruments, and Professor Thomas C.-K. Yang (NTUT) for providing support of the XRD instrument. This study was partially funded by the National Science Council (NSC98-2113-M-011-002-MY2).

■ REFERENCES

(1) Giljohann, D. A., Seferos, D. S., Daniel, W. L., Massich, M. D., Patel, P. C., and Mirkin, C. A. (2010) Gold nanoparticles for biology and medicine. *Angew. Chem., Int. Ed. 49*, 3280–3294.

(2) Jain, P. K., Huang, X., El-Sayed, I. H., and El-Sayed, M. A. (2008) Noble metals on the nanoscale: Optical and photothermal properties and some applications in imaging, sensing, biology, and medicine. *Acc. Chem. Res. 41*, 1578–1586.

(3) Cao, Y. C., Jin, R., and Mirkin, C. A. (2002) Nanoparticles with Raman spectroscopic fingerprints for DNA and RNA detection. *Science 297*, 1536–1540.

(4) Skrabalak, S. E., Chen, J., Sun, Y., Lu, X., Au, L., Cobley, C. M., and Xia, Y. (2008) Gold nanocages: Synthesis, properties, and applications. *Acc. Chem. Res. 41*, 1587–1595.

(5) Orendorff, C. J., Sau, T. K., and Murphy, C. J. (2006) Shape-dependent plasmon-resonant gold nanoparticles. *Small 2*, 636–639.

(6) Stoeva, S. I., Lee, J. S., Smith, J. E., Rosen, S. T., and Mirkin, C. A. (2006) Multiplexed detection of protein cancer markers with biobarcoded nanoparticle probes. *J. Am. Chem. Soc. 128*, 8378–8379.

(7) Chuang, Y. C., Li, J. C., Chen, S. H., Liu, T. Y., Kuo, C. H., Huang, W. T., and Lin, C. S. (2010) An optical biosensing platform for proteinase activity using gold nanoparticles. *Biomaterials 31*, 6087–6095.

(8) Han, G., Ghosh, P., and Rotello, V. M. (2007) Functionalized gold nanoparticles for drug delivery. *Nanomedicine 2*, 113–123.

(9) Huang, X., El-Sayed, I. H., Qian, W., and El-Sayed, M. A. (2006) Cancer cell imaging and photothermal therapy in the near-infrared region by using gold nanorods. *J. Am. Chem. Soc. 128*, 2115–2120.

(10) Bhattacharyya, S., Kudgus, R. A., Bhattacharya, R., and Mukherjee, P. (2011) Inorganic nanoparticles in cancer therapy. *Pharm. Res. 28*, 237–259.

(11) Kennedy, L. C., Bickford, L. R., Lewinski, N. A., Coughlin, A. J., Hu, Y., Day, E. S., West, J. L., and Drezek, R. A. (2011) A new era for cancer treatment: Gold-nanoparticle-mediated thermal therapies. *Small 7*, 169–183.

(12) Paciotti, G. F., Myer, L., Weinreich, D., Goia, D., Pavel, N., McLaughlin, R. E., and Tamarkin, L. (2004) Colloidal gold: A novel nanoparticle vector for tumor directed drug delivery. *Drug Delivery: J. Delivery Targeting Ther. Agents 11*, 169–183.

(13) Brigger, I., Dubernet, C., and Couvreur, P. (2002) Nanoparticles in cancer therapy and diagnosis. *Adv. Drug Delivery Rev. 54*, 631–651.

(14) Zharov, V. P., Galitovskaya, E. N., Johnson, C., and Kelly, T. (2005) Synergistic enhancement of selective nanophotothermolysis with gold nanoclusters: Potential for cancer therapy. *Lasers Surg. Med. 37*, 219–226.

(15) Loo, C., Lowery, A., Halas, N., West, J., and Drezek, R. (2005) Immunotargeted nanoshells for integrated cancer imaging and therapy. *Nano Lett. 5*, 709–711.

(16) Cardinal, J., Klune, J. R., Chory, E., Jeyabalan, G., Kanzius, J. S., Nalesnik, M., and Geller, D. A. (2008) Noninvasive radiofrequency ablation of cancer targeted by gold nanoparticles. *Surgery 144*, 125–132.

(17) Katz, E., and Willner, I. (2004) Integrated nanoparticle-biomolecule hybrid systems: Synthesis, properties, and applications. *Angew. Chem., Int. Ed. 43*, 6042–6108.

(18) Niemeyer, C. M. (2003) Functional hybrid devices of proteins and inorganic nanoparticles. *Angew. Chem., Int. Ed. 42*, 5796–5800.

(19) Shankar, S. S., Rai, A., Ankamwar, B., Singh, A., Ahmad, A., and Sastry, M. (2004) Biological synthesis of triangular gold nanoprisms. *Nat. Mater. 3*, 482–488.

(20) Sharma, J., Tai, Y., and Imae, T. (2010) Biomodulation approach for gold nanoparticles: Synthesis of anisotropic to luminescent particles. *Chem.—Asian J. 5*, 70–73.

(21) Mukherjee, P., Senapati, S., Mandal, D., Ahmad, A., Khan, M. I., Kumar, R., and Sastry, M. (2002) Extracellular synthesis of gold nanoparticles by the fungus Fusarium oxysporum. *ChemBioChem 3*, 461–463.

(22) Dickerson, M. B., Sandhage, K. H., and Naik, R. R. (2008) Protein- and peptide-directed syntheses of inorganic materials. *Chem. Rev. 108*, 4935–4978.

(23) Tan, Y. N., Lee, J. Y., and Wang, D. I. C. (2010) Uncovering the design rules for peptide synthesis of metal nanoparticles. *J. Am. Chem. Soc. 132*, 5677–5686.

(24) Aina, O. H., Liu, R., Sutcliffe, J. L., Marik, J., Pan, C. X., and Lam, K. S. (2007) From combinatorial chemistry to cancer-targeting peptides. *Mol. Pharmaceutics 4*, 631–651.

(25) McDonnell, L. A., Corthals, G. L., Willems, S. M., van Remoorter-eA., van Zeijl, R. J. M., and Deelder, A. M. (2010) Peptide and protein imaging mass spectrometry in cancer research. *J. Proteomics 73*, 1921–1944.

(26) Reubi, J. C. (2003) Peptide receptors as molecular targets for cancer diagnosis and therapy. *Endocr. Rev. 24*, 389–427.

(27) Chan, H. J., Weng, J. J., and Yung, B. Y. M. (2005) Nucleophosmin/B23-binding peptide inhibits tumor growth and up-regulates transcriptional activity of p53. *Biochem. Biophys. Res. Commun. 333*, 396–403.

(28) Lin, C. Y., Liang, Y. C., and Yung, B. Y. M. (2006) Nucleophosmin/B23 regulates transcriptional activation of E2F1 via modulating the promoter binding of NF-κB, E2F1 and pRB. *Cell. Signalling 18*, 2041–2048.

(29) Shields, L. B. E., Gerçel-Taylor, C., Yashar, C. M., Wan, T. C., Katsanis, W. A., Spinnato, J. A., and Taylor, D. D. (1997) Induction of immune responses to ovarian tumor antigens by multiparity. *J. Soc. Gynecol. Invest. 4*, 298–304.

(30) Tanaka, M., Sasaki, H., Kino, I., Sugimura, T., and Terada, M. (1992) Genes preferentially expressed in embryo stomach are predominantly expressed in gastric cancer. *Cancer Res. 52*, 3372–3377.

(31) Nozawa, Y., Van Belzen, N., Van der Made, A. C. J., Dinjens, W. N. M., and Bosman, F. T. (1996) Expression of nucleophosmin/B23 in normal and neoplastic colorectal mucosa. *J. Pathol. 178*, 48–52.

(32) Subong, E. N. P., Shue, M. J., Epstein, J. I., Briggman, J. V., Chan, P. K., and Partin, A. W. (1999) Monoclonal antibody to prostate cancer nuclear matrix protein (PRO:4- 216) recognizes nucleophosmin/B23. *Prostate 39*, 298–304.

(33) Tsui, K. H., Cheng, A. J., Chang, P. L., Pan, T. L., and Yung, B. Y. M. (2004) Association of nucleophosmin/B23 mRNA expression with clinical outcome in patients with bladder carcinoma. *Urology 64*, 839–844.

(34) Polavarapu, L., and Xu, Q. H. (2009) A simple method for large scale synthesis of highly monodisperse gold nanoparticles at room temperature and their electron relaxation properties. *Nanotechnology 20*, 185606.

(35) Au, L., Lim, B., Colletti, P., Jun, Y. S., and Xia, Y. (2010) Synthesis of gold microplates using bovine serum albumin as a reductant and a stabilizer. *Chem.—Asian J. 5*, 123–129.

(36) Millstone, J. E., Park, S., Shuford, K. L., Qin, L., Schatz, G. C., and Mirkin, C. A. (2005) Observation of a quadrupole plasmon mode for a colloidal solution of gold nanoprisms. *J. Am. Chem. Soc. 127*, 5312–5313.

(37) Carotenuto, G., and Nicolais, L. (2003) Size-controlled synthesis of thiol-derivatized gold clusters. *J. Mater. Chem. 13*, 1038–1041.

(38) Zhou, M., Chen, S., and Zhao, S. (2006) Synthesis of icosahedral gold nanocrystals: A thermal process strategy. *J. Phys. Chem. B 110*, 4510–4513.

(39) Kawamura, G., Yang, Y., Fukuda, K., and Nogami, M. (2009) Shape control synthesis of multi-branched gold nanoparticles. *Mater. Chem. Phys. 115*, 229–234.

(40) Palui, G., Ray, S., and Banerjee, A. (2009) Synthesis of multiple shaped gold nanoparticles using wet chemical method by different dendritic peptides at room temperature. *J. Mater. Chem. 19*, 3457–3468.

(41) Philip, D. (2009) Honey mediated green synthesis of gold nanoparticles. *Spectrochim. Acta, Part A 73*, 650–653.

(42) Ankamwar, B., Chaudhary, M., and Sastry, M. (2005) Gold nanotriangles biologically synthesized using tamarind leaf extract and potential application in vapor sensing. *Synth. React. Inorg., Met.-Org. Nano-Met. Chem. 35*, 19–26.

(43) Chen, Y. H., Tsai, C. Y., Huang, P. Y., Chang, M. Y., Cheng, P. C., Chou, C. H., Chen, D. H., Wang, C. R., Shiau, A. L., and Wu, C. L. (2007) Methotrexate conjugated to gold nanoparticles inhibits tumor growth in a syngeneic lung tumor model. *Mol. Pharmaceutics 4*, 713–722.

(44) Ghosh, P., Han, G., De, M., Kim, C. K., and Rotello, V. M. (2008) Gold nanoparticles in delivery applications. *Adv. Drug Delivery Rev. 60*, 1307–1315.

(45) Chang, C. L., Tsai, Y. C., He, L., Wu, T. C., and Hung, C. F. (2007) Cancer immunotherapy using irradiated tumor cells secreting heat shock protein 70. *Cancer Res. 67*, 10047–10057.

(46) Chithrani, B. D., Ghazani, A. A., and Chan, W. C. W. (2006) Determining the size and shape dependence of gold nanoparticle uptake into mammalian cells. *Nano Lett. 6*, 662–668.

Supporting Information (SI)

Direct Synthesis of Rev Peptide–Conjugated Gold Nanoparticles and the Application in Cancer Therapeutics

Ngoc Thi Thanh Tran[a], Tzu-Hao Wang[b,c], Chiao-Yun Lin[b], Yi-Chun Tsai[a], Chyong-Huey Lai[b], Yian Tai*[a], and Benjamin, Y. M. Yung[d]

[a]Department of Chemical Engineering, National Taiwan University of Science and Technology, Taipei, Taiwan.

[b]Department of Obstetrics and Gynecology, Chang Gung Memorial Hospital and Chang Gung University, Taiwan, Taoyuan, Taiwan.

[c]Genomic Medicine Research Core Laboratory, Chang Gung Memorial Hospital, Taoyuan, Taiwan.

[d]Department of Health Technology and Informatics, The Hong Kong Polytechnic University, Hong Kong, China.

*Corresponding Author:

Prof. Yian Tai

Department of Chemical Engineering, National Taiwan University of Science and Technology, 43 Keelung Road, Sec.4, Taipei 106, Taiwan

Phone: +886-2-2737-6620; Fax: +886-2-2737-6644

E-mail: ytai@mail.ntust.edu.tw

Figure S1. Chemical structure of Rev peptide.

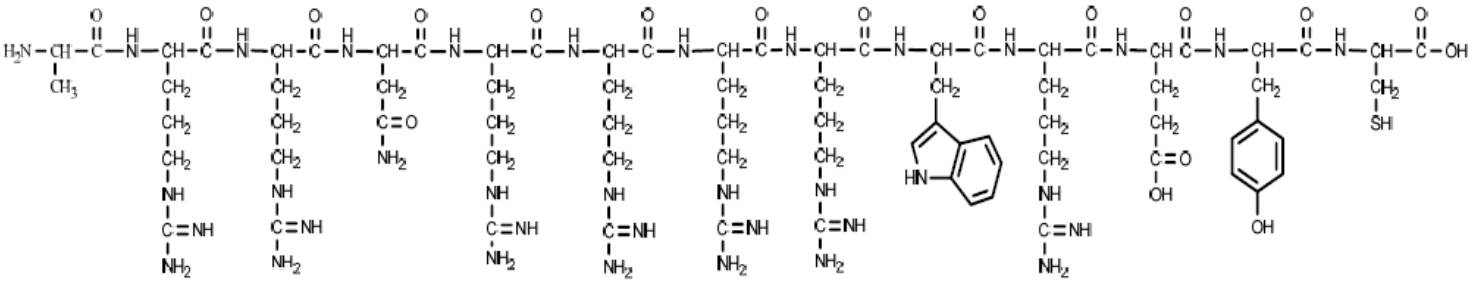

Figure S2. a) UV-Vis spectra for Rev peptide solution with different concentrations and b) UV-Vis calibration curve for Rev peptide aqueous solution.

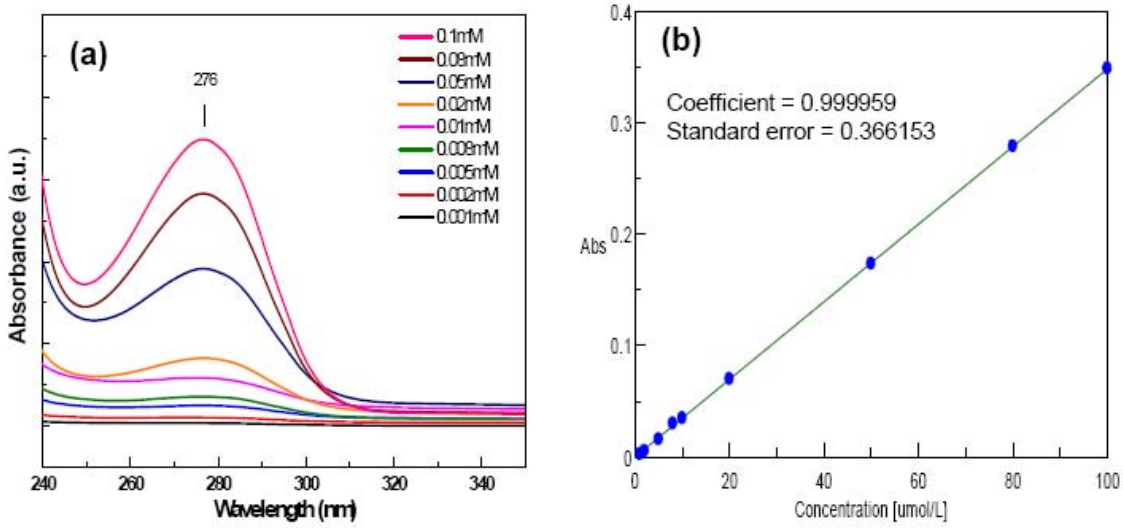

Figure S3. a) UV-Vis spectra for Rev_AuNPs aqueous solution with different concentrations and b) UV-Vis calibration curve for Rev_AuNPs aqueous solution.

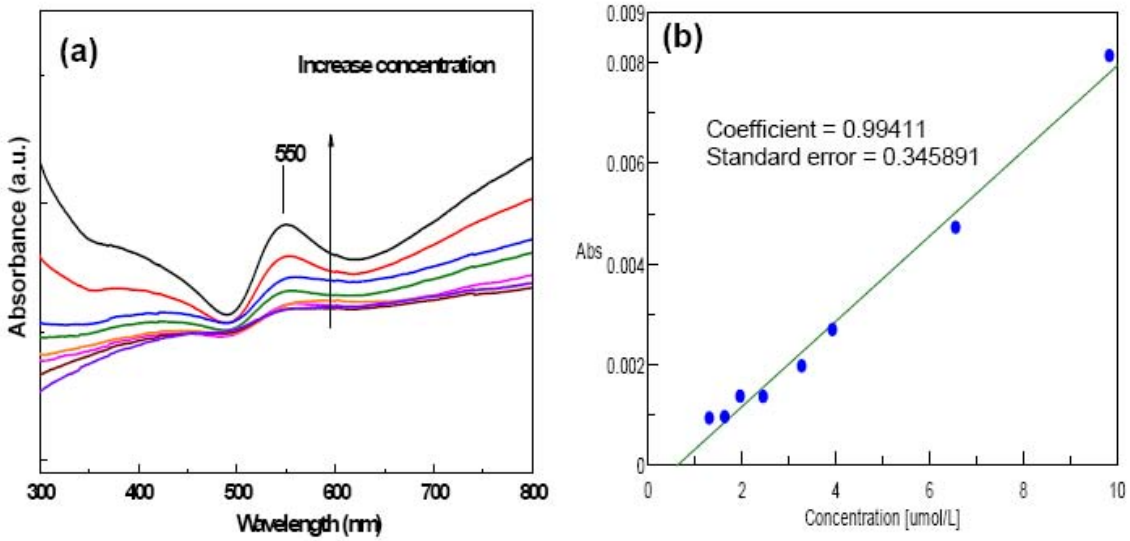

Figure S4. TEM images of the Rev_AuNPs synthesized at 120 °C.

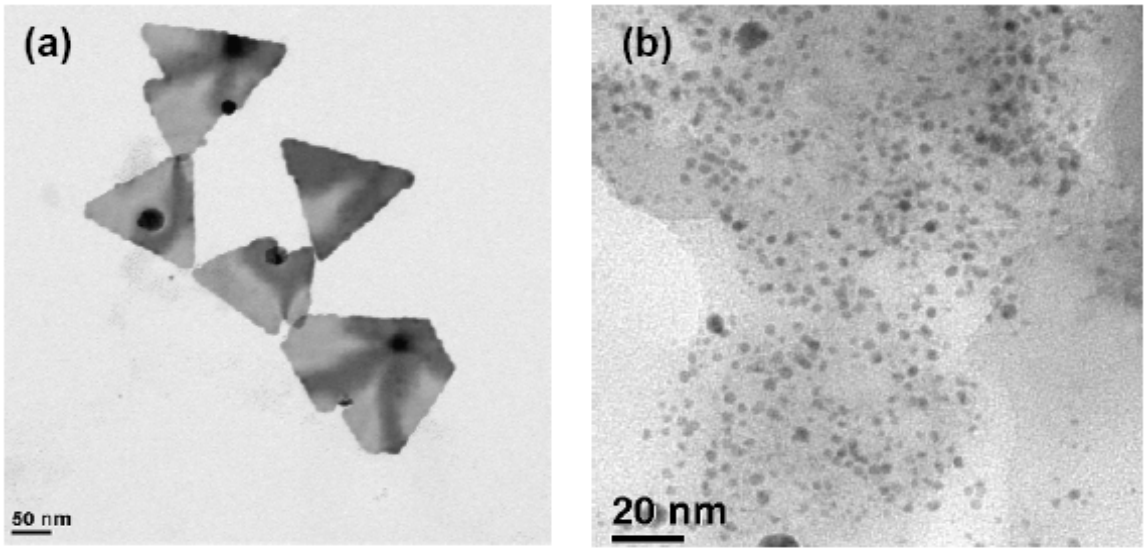

Figure S5. TEM image of reference gold nanoparticles

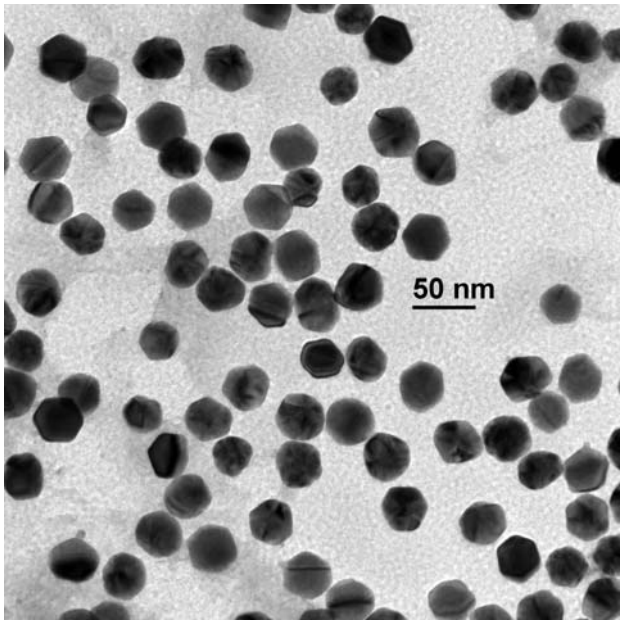

Bioconjugate Chemistry

ARTICLE

pubs.acs.org/bc

Luminescent Trimethoprim−Polyaminocarboxylate Lanthanide Complex Conjugates for Selective Protein Labeling and Time-Resolved Bioassays

D. Rajasekhar Reddy, Laura E. Pedró Rosa, and Lawrence W. Miller*

University of Illinois at Chicago, Department of Chemistry, 845 W. Taylor Street, MC 111, Chicago, Illinois 60607, United States

ABSTRACT: Labeling proteins with long-lifetime emitting lanthanide (III) chelate reporters enables sensitive, time-resolved luminescence bioaffinity assays. Heterodimers of trimethoprim (TMP) covalently linked to various cs124-sensitized, polyaminocarboxylate chelates stably retain lanthanide ions and exhibit quantum yields of europium emission up to 20% in water. A time-resolved, luminescence resonance energy transfer (LRET) assay showed that TMP-polyaminocarboxylates bind to *Escherichia coli* dihydrofolate reductase (eDHFR) fusion proteins with nanomolar affinity in purified solutions and in bacterial lysates. The ability to selectively impart terbium or europium luminescence to fusion proteins in complex physiological mixtures bypasses the need for specific antibodies and simplifies sample preparation.

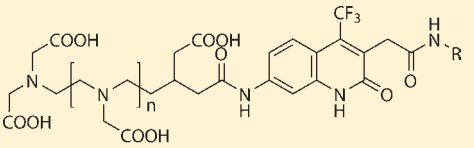

R: Trimethoprim
n = 1: DTPA
n = 2: TTHA

INTRODUCTION

Ligand-sensitized complexes of lanthanide cations have unique photophysical properties, including large Stokes shifts (>150 nm), multiple, narrow emission bands (<10 nm at half-maximum), and long emission lifetimes (μs−ms). These properties offer distinct advantages for luminescence-based biological assays and microscopy, most notably high signal-to-background ratios that are obtained by temporally discriminating lanthanide luminescence from short-lifetime (<10 ns) scattering and autofluorescence background.[1,2] Direct conjugation of terbium or europium complexes to oligonucleotides, antibodies, and proteins has enabled the development of sensitive luminescence resonance energy transfer (LRET1, also known as time-resolved fluorescence resonance energy transfer, or TR-FRET) assays of biomolecular interactions in purified biochemical preparations, cellular extracts, and on cell surfaces.[3−5] Recently, we showed that interactions between a terbium complex-labeled protein and a green fluorescent protein (GFP) fusion could be microscopically imaged in living cells by detecting long-lived, terbium-to-GFP LRET in time-resolved mode.[6]

Because lanthanide absorption transitions are parity-forbidden, direct excitation is inefficient, and Tb^{3+} or Eu^{3+} complexes typically incorporate the metal ion into an organic chelating ligand that contains a sensitizing chromophore. When excited with ultraviolet (UV) light in the absorption band, the chromophore undergoes intersystem crossing to its triplet excited state followed by intramolecular energy transfer to the emissive level of the chelated metal.[1] In general, lanthanide complexes used in time-resolved screening or cellular imaging applications must meet several requirements: (i) the molecule must be kinetically stable; (ii) the molecule must have a high extinction coefficient and quantum yield of emission (i.e., good brightness); (iii) the excitation wavelength should be as long as possible; (iv) the molecule must be resistant to photobleaching; and (v) bioconjugates of the molecule must be easy to prepare. Kinetic stability is particular important for cellular imaging or screening applications in cell lysates where endogenous chelators could scavenge metal from the complex.[2] For microscopy, near-UV (>340 nm) absorption is preferred because typical optics will not transmit below this limit.[7] While hundreds of luminescent lanthanide chelates have been prepared over the past decades, relatively few meet most or all of the aforementioned criteria.[1,2]

Polyaminocarboxylates, diethylene triamine pentaacetic acid (DTPA), and triethylene tetraamine hexaacetic acid (TTHA) have proven to be robust scaffolds for developing bright and photostable luminescent chelates of Tb^{3+} and Eu^{3+}. Selvin and co-workers have developed various DTPA and TTHA chelates that utilize 7-aminoquinolinone (carbostyril 124, or cs124) as the sensitizing chromophore.[5,8−13] Conjugable analogues include an amide-linked, amine-reactive, or thiol-reactive moiety at one end of the polyaminocarboxylate chain, opposite the sensitizer (Figure 1). The cs124-sensitized chelates have reasonable extinction coefficients ($\varepsilon = \sim 10\,500\ M^{-1}\ cm^{-1}$ at $\lambda_{max} = 341$ nm) and overall quantum yields of emission up to 40% for Tb^{3+} and up to 28% for Eu^{3+}.[12,14] Variants that incorporate 7-amino-4-trifluoromethyl-2-(1*H*)-quinolinone (cs124CF_3) were shown to be effective Eu^{3+} luminophores, being 2- to 4-fold brighter than their analogous cs124-sensitized DTPA and TTHA analogues with ∼15 nm red-shifted excitation maxima.[15] However, cross-linkable DTPA-cs124 analogues are 8-dentate chelates and therefore suffer reduced brightness and higher kinetic instability, because one or more water molecules are coordinated with the metal. This is not the case with TTHA-cs124 conjugates.[11] Mustaev and co-workers addressed this issue by developing

Received: March 14, 2011
Revised: May 11, 2011
Published: May 29, 2011

ACS Publications © 2011 American Chemical Society

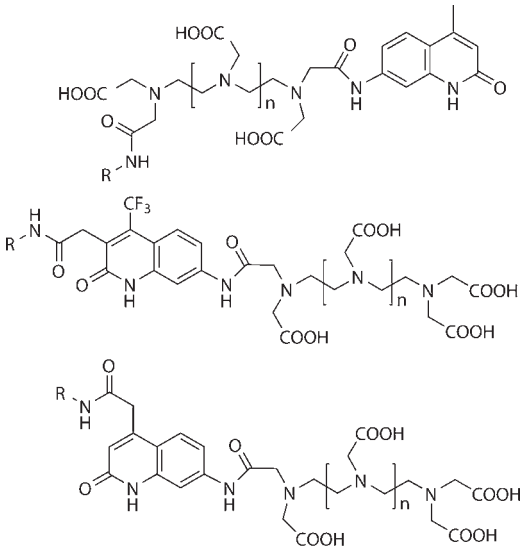

Figure 1. Variants of carbostyril 124-polyaminocarboxylates and their modes of attachment to biomolecules.

DTPA-cs124 analogues that could be conjugated to biomolecules via modification of the chromophore moiety (Figure 1).[16] Chromophore-linked DTPA-cs124 conjugates were shown to be highly luminescent and exhibited greater resistance to EDTA challenge than Selvin-type DTPA-cs124 analogues. Analogous thiol-reactive, coumarin-sensitized DTPA and TTHA chelates were reported by Heyduk and Heyduk, but these molecules only supported Eu^{3+} luminescence and were less bright than cs124-sensitized chelates.[17]

In this article, we present results of our continued efforts to develop luminescent lanthanide protein labels for time-resolved LRET microscopy and screening applications. We previously showed that conjugates of the common antibiotic, trimethoprim (TMP), linked to Tb^{3+}-complexed cs124-polyaminocarboxylates or a 2-hydroxyisophthalamide-based macrocycle (Lumi4-Tb) bound to *Escherichia coli* dihydrofolate reductase (eDHFR) with high affinity, thereby offering an effective means of selectively imparting Tb^{3+} luminescence to fusion proteins.[18] Here, our original goal was to develop a TMP-linked, Eu^{3+} chelate that exhibited good brightness, high kinetic stability, and appreciable absorption at 365 nm (for eventual microscopy applications). We prepared conjugates of TMP coupled to 3- and 4-acetic acid derivatives of $cs124CF_3$ and cs124, respectively (Scheme 1), and linked these moieties to DTPA and TTHA (Scheme 2). We then assessed the photophysical properties of these chelates as well as our previously reported, Selvin-type, cs124-TTHA-TMP conjugate by measuring the relative quantum yields of Eu^{3+} and Tb^{3+} luminescence using DTPA-cs124 as a reference compound. We assessed comparative kinetic stability by measuring the time-dependent decrease in lanthanide luminescence in the presence of a large excess of EDTA.

The previously developed cs124-TTHA-TMP (**10**) and the novel TTHA-$cs124CF_3$-TMP (**7**) were the most efficient Eu^{3+} complexes with estimated overall quantum yields of ~20%, and they exhibited relatively high resistance to EDTA challenge. Affinity for eDHFR (K_D = ~1.5 nM) was measured directly in purified biochemical preparations and in bacterial lysates by titrating a GFP-eDHFR fusion protein against a fixed concentration (20 nM) of selected, TMP-Tb^{3+} chelates and measuring the protein concentration-dependent increase in Tb^{3+}-to-GFP LRET. The ability to selectively impart Tb^{3+} or Eu^{3+} luminescence to fusion proteins and to quantitatively measure binding events in cellular extracts simplifies LRET-based bioassays and eliminates the need for lanthanide chelate-conjugated antibodies. Moreover, the good brightness, kinetic stability, and long-wavelength absorption of the Eu^{3+} complex of TTHA-$cs124CF_3$-TMP (**7**) make it a potentially useful reporter label for live-cell microscopy.

EXPERIMENTAL PROCEDURES

Chemicals and Instrumentation. The following chemicals were purchased from Sigma-Aldrich: TTHA, DTPA dianhydride, diaminobenzene, methyl bromoacetate, TMP, hydrobromic acid (HBr, 48%), 1,8-diazabicyclo[5.4.0]undec-7-ene (DBU), 2,2′-(ethylenedioxy)bis(ethylamine), diethyl-1,3-acetonedicarboxylate, ethyl bromovalerate, di-*tert*-butyl dicarbonate, dichloromethane, trifluoroacetic acid (TFA), citric acid, *O*-benzotriazole-*N*,*N*,*N*′,*N*′-tetramethyluronium hexafluorophosphate (HBTU), *N*-hydroxybenzotriazole (HOBt), benzotriazol-1-yl-oxytripyrrolidinophosphonium hexafluorophosphate (PyBOP), ethyl acetoacetate, ethyl 4,4,4-trifluoroacetoacetate, anhydrous dimethylformamide (DMF, in sure seal bottle), anhydrous dimethyl sulfoxide (DMSO, in sure seal bottle), $EuCl_3 \cdot 6H_2O$, $TbCl_3 \cdot 6H_2O$, $ZnCl_2$, diisopropyl ethylamine (DIPEA), pyridine, acetic anhydride, triethylamine (TEA), and β-nicotinamide adenine dinucleotide phosphate (β-NADPH). glacial acetic acid, NaOH, KOH, NaCl, $NaHCO_3$, H_2SO_4, anhydrous Na_2SO_4, ethylenediaminetetracetic acid (EDTA) disodium salt dihydrate, acetonitrile, methanol, hexane, ethyl acetate, diethyl ether, BugBuster, DNase, Halt protease inhibitor cocktail, PMSF, and imidazole were purchased from Thermo Fisher Scientific. Tris(hydroxymethyl) aminomethane hydrochloride (Tris·HCl) was purchased from Acros Organics. Distilled and deionized (18 MΩ cm^{-1}) water was used throughout. All glassware was washed with a 10% nitric acid solution and thoroughly rinsed with deionized, distilled water. ^1H NMR and ^{13}C NMR spectra were recorded at the UIC Research Resources Center (RRC) in the deuterated solvents stated. ^1H and ^{13}C chemical shifts were referenced to internal solvent resonances and reported relative to $SiMe_4$. Low-resolution and high-resolution electrospray (ESI) mass spectra were obtained at the UIC RRC. UV−visible (UV−vis) absorption spectra were recorded using a Cary 3000 spectrophotometer (Varian, Inc.). Fluorescence emission spectra were recorded using a Fluoromax 3 fluorimeter (Horiba−Jobin Yvon, Inc.). Time-resolved luminescence intensity was measured using a 96-well plate reader (Perkin-Elmer, Victor 3 V) with 340 nm excitation (60 nm bandpass) and indicated emission filters (10 nm bandpass).

Purification. Reverse-phase high-performance liquid chromatography (HPLC) was performed using a Beckman System Gold instrument equipped with an analytical-scale pump (model 128), a UV−vis detector (model 168), and a C18 analytical column (GraceVydac, cat. no. 218TP54, 5 μm, 4.6 mm i.d. × 250 mm). A 20 min linear gradient, from 0% to 30%, 3−33%, or 5−25% solvent B (solvent A = 0.1 M triethylammonium acetate (pH 6.5), solvent B = CH_3CN) was used (Table 1). An initial hold of 3 min was applied for all runs.

Scheme 1. Synthesis of TMP Conjugated to (A) cs124-CF3 (3) and (B) cs124 (5)

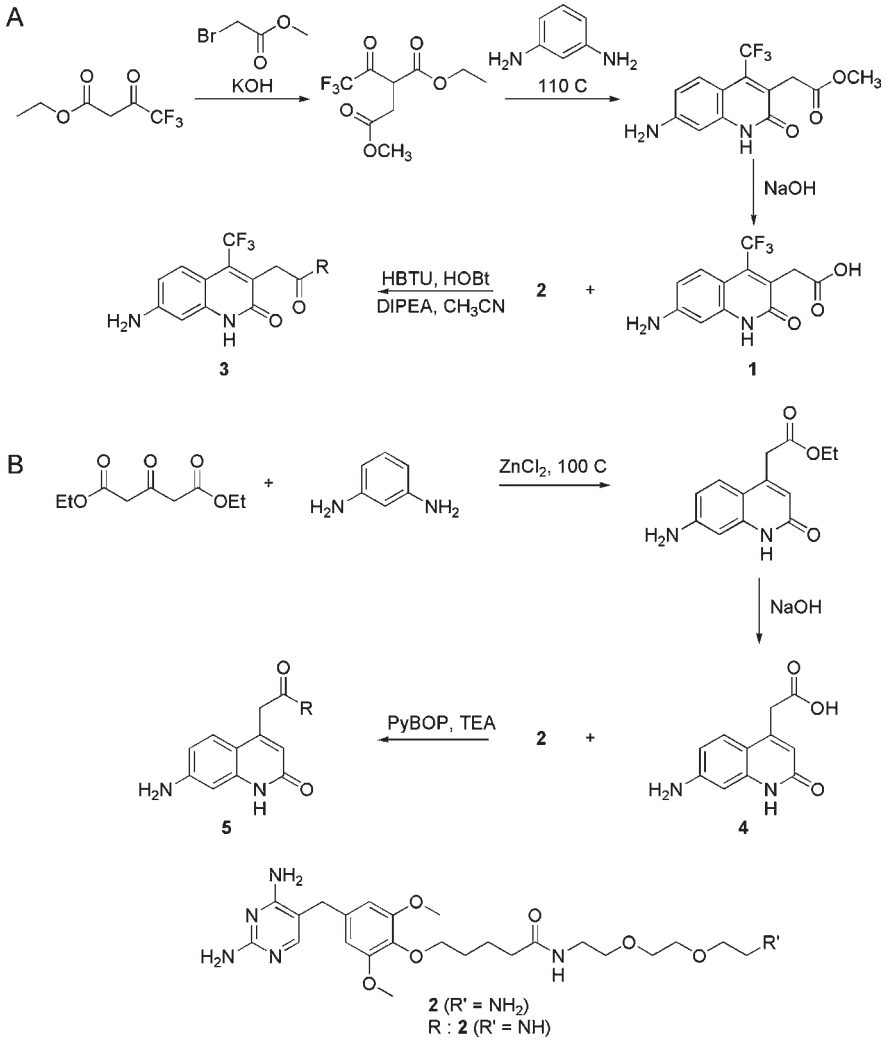

Synthesis. *Compound* ***1*** *(Scheme 1A).* Ethyl-4,4,4-trifluoroacetoacetate (2.2 mL, 15 mmol) and KOH (0.86 g, 15 mmol) were mixed in 7 mL of DMF and stirred at 40 °C for 20 min. To this mixture, 1.5 mL of methylbromoacetate was added and the solution was stirred overnight at room temperature under nitrogen. 300 mg (5.2 mmol) of KOH was then added and stirred at 60 °C for 1 h. This mixture was diluted by the addition of 20 mL of water and was then extracted with chloroform. The organic layer was collected, dried over anhydrous sodium sulfate, and then evaporated *in vacuo*, first at 30 °C, and then at 75 °C for 45 min. The residue obtained was dissolved in 3.5 mL of DMSO, and then 0.76 g (7 mmol) of diaminobenzene was added and the solution stirred at 110 °C for 6 h. This solution was cooled overnight and diluted with 30 mL of 0.05 M aqueous NaOH and extracted with ether (2 × 50 mL). The aqueous phase obtained after ether extraction containing product **1**, was acidified by the addition of citric acid to pH 3−3.5; the precipitate was collected by centrifugation, washed with water, and dried. Recrystallization from ethyl acetate resulted in the isolation of pure compound **1**. Yield 3%. ESIMS (m/z) 287 $[M+H]^+$, 309 $[M+Na]^+$, 285 $[M-H]^-$. ^{1}H NMR (500 MHz, DMF-d_7, ppm): δ = 7.65 (d, 1H), 6.87 (d, 2H), 6.36 (s, br, 2H), 4.10 (s, 2H). ^{13}C NMR (125 MHz, DMF-d_7, ppm): δ = 171.99, 161.81, 152.07, 141.07, 134.82, 126.16, 124.85, 122.00, 112.05, 105.40, 97.18, 31.99.

Compound 2 was prepared as previously reported.[18]

Compound ***3*** *(Scheme 1A).* To a stirred solution of compound **1** (11.44 mg, 0.04 mmol) in CH_3CN (7 mL) was added HBTU (18.2 mg, 0.05 mmol), HOBt (6.5 mg, 0.05 mmol), and DIPEA (0.02 mL, 0.12 mmol) and the mixture was stirred for 30 min at room temperature under nitrogen. Then, compound **2** (20 mg, 0.04 mmol) in CH_3CN (3 mL) was added to the reaction mixture and stirred for 3 h. After evaporation of CH_3CN, 15 mL water was added and the mixture was extracted with ethyl acetate (4 × 50 mL). The organic extracts were washed with saturated $NaHCO_3$ solution, dried over anhydrous Na_2SO_4, and evaporated under reduced pressure. The crude reaction mixture was purified on reverse-phase HPLC to obtain the pure compound **3**. ESIMS (m/z) 775 $[M+H]^+$, 797 $[M+Na]^+$, 773 $[M-H]^-$. HRMS: Pred. m/z for $C_{36}H_{45}N_8F_3O_8$ 775.3385; meas. m/z 775.3382 $[M+H]^+$.

Compound ***4*** *(Scheme 1B).* A suspension of 1.36 g (10 mmol) of $ZnCl_2$ in 5 mL of DMSO was supplemented with 1.08 g (10 mmol) of diaminobenzene and 2.02 g (10 mmol) of

dx.doi.org/10.1021/bc200131k |*Bioconjugate Chem.* 2011, 22, 1402–1409

Scheme 2. Synthesis of Sensitized TMP-Polyaminocarboxylate Conjugates

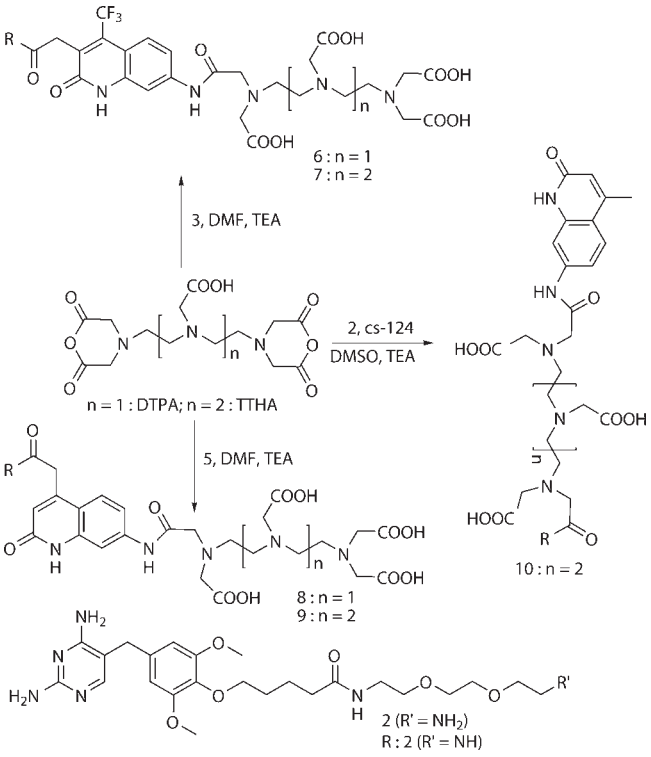

diethyl-1,3-acetonedicarboxylate. The reaction mixture was stirred at 100 °C for 24 h. This mixture was diluted with 8 mL of ethanol, poured into 150 mL of ice-cold 0.1 M citric acid, and left for 3−5 h at 4 °C. The residue was filtered and successively washed with water (4 × 15 mL) and with hot CH_3CN (2 × 10 mL), and then dried in vacuo. Yield 53%. From this, 200 mg was taken and dissolved in 3 mL dioxane. To this, 4 mL of aqueous 2 M NaOH was added and stirred at 50 °C for 5 h, and then 15 mL water was added and extracted with ether (2 × 40 mL). The product (**4**) was precipitated from the aqueous phase by the addition of 10% H_2SO_4 to pH 2.5, collected by centrifugation, washed a few times with water, and dried in vacuo. Yield 37%. ESIMS (*m/z*) 219 $[M+H]^+$. ^1H NMR (500 MHz, DMSO-d_6, ppm): δ = 11.24 (s, 1H), 7.26 (d, 1H), 6.41 (d, 1H), 6.35 (s, 1H), 5.98 (s, 1H), 5.77 (s, br, 2H), 3.65 (s, 2H). ^{13}C NMR (125 MHz, DMSO-d_6, ppm): δ = 171.97, 162.65, 151.27, 145.40, 141.39, 125.95, 116.60, 111.07, 110.33, 97.42, 38.28.

Compound ***5*** *(Scheme 1B).* To a stirred solution of compound **4** (19 mg, 0.09 mmol) in DMF (1 mL) was added PyBop (45.24 mg, 0.09 mmol), and TEA (0.08 mL, 0.58 mmol) and allowed to stir for 30 min at room temperature under nitrogen. Then, compound **2** (15 mg, 0.03 mmol) in DMF (0.5 mL) was added to the reaction mixture and stirred for 12 h. The reaction mixture was purified on reverse-phase HPLC to obtain the pure compound **5**. ESIMS (*m/z*) 707 $[M+H]^+$, 705 $[M-H]^-$. HRMS: Pred. *m/z* for $C_{35}H_{46}N_8O_8$ 354.1792; meas. *m/z* 354.1797 $[M+2H]^{2+}$.

General Procedure for the Synthesis of Compounds 6, 7, 8, and 9 (Scheme 2). Five equivalents of DTPA dianhydride/TTHA dianhydride was dissolved in DMF and 20 equiv of TEA under nitrogen. One equivalent of compound **3**/compound **5** in DMF was added and stirred at room temperature for 8−10 h. A few drops of water were added to quench the reaction. The products were purified by reverse-phase HPLC.

Table 1. HPLC Purification Solvents, Retention Times, and Detected *m/z* Ratios for Chelates Prepared in This Study

compound	linear gradient	retention time (min)	ESI MS $[M+H]^+$
cs124CF_3-TMP (**3**)	3−33% CH_3CN/TEAA	22	775
cs124-TMP (**5**)	5−25% CH_3CN/TEAA	18	707
DTPA-cs124CF_3-TMP (**6**)	0−30% CH_3CN/TEAA	22	1151
TTHA-cs124CF_3-TMP (**7**)	0−30% CH_3CN/TEAA	20	1252
DTPA-cs124-TMP (**8**)	0−30% CH_3CN/TEAA	18	1083
TTHA-cs124-TMP (**9**)	0−30% CH_3CN/TEAA	17	1184
cs124-TTHA-TMP (**10**)	0−30% CH_3CN/TEAA	18	1140

Table 2. Relative Quantum Yields of Emission for Prepared Chelates of Tb^{3+} and Eu^{3+}

lanthanide	compound	quantum yield
Tb^{3+}	DTPA-cs-124[a]	1.00
	DTPA-cs-124-TMP (**8**)	0.23
	TTHA-cs-124-TMP (**9**)	0.20
	cs-124-TTHA-TMP (**10**)	0.90
Eu^{3+}	DTPA-cs-124[a]	1.00
	DTPA-cs-124-CF_3-TMP (**6**)	0.56
	TTHA-cs-124-CF_3-TMP (**7**)	2.02
	DTPA-cs-124-TMP (**8**)	0.77
	TTHA-cs-124-TMP (**9**)	1.56
	cs-124-TTHA-TMP (**10**)	1.98

[a] Reference compound.

Compound ***10*** *(Scheme 2).* Two equivalents of TTHA dianhydride was dissolved in DMSO and 20 equiv of TEA under nitrogen. 0.7 equivalents of cs-124 was added and stirred at room temperature for 10 min. One equivalent of compound **2** in DMSO was added and stirred for 3−8 h. A few drops of water were added to quench the reaction. The product was purified by reverse-phase HPLC.

Addition of Metals. Compound concentration was obtained using measured absorptions and reported extinction coefficients for the fluorophores (cs124, ε = 10 500 M^{-1} cm^{-1} at λ = 341 nm; cs124CF_3, ε = 21 000 M^{-1} cm^{-1} at λ = 341 nm).[12,15] $EuCl_3 \cdot 6H_2O$ or $TbCl_3 \cdot 6H_2O$ was added to the chelate in a 1:1.3 molar ratio at typically >5 μM concentration in TBS buffer (50 mM Tris·HCl, 150 mM NaCl, pH 7.6) and allowed to stand for 30 min at room temperature before use.

Quantum Yield Measurements. The luminescence quantum yield of lanthanide chelates in TBS (pH = 7.6) was determined by standard methods using DTPA-cs124 as a reference from the equation

$$\Phi_S = \Phi_R \left(\frac{Grad_S}{Grad_R}\right)\left(\frac{\eta_S}{\eta_R}\right) \quad (1)$$

where Φ_S and Φ_R equal the quantum yields of the sample and reference, respectively. $Grad_S$ and $Grad_R$ equal the slopes of plots of integrated luminescence intensity vs absorption (0.02 < Abs < 0.1) for either the sample or the reference, and η_S and η_R equal the refractive indices of the respective sample and reference solutions.[19] The excitation wavelength was 330 nm in all cases. The results were reported as relative to cs124

(Table 2), so Φ_R was taken to equal 1. The quantum yield of Tb^{3+} emission for DTPA-cs124 was measured using quinine sulfate as a reference (Φ = 0.54 in 0.1 M H_2SO_4). Each sample was measured at least twice, and results did not vary by more than ±15%.

EDTA Challenge Assay. In order to measure the stability of the TMP-lanthanide complex conjugates, each metalated compound was diluted to 50 nM in TBS, pH = 7.4, in a 1.5 mL centrifuge tube. EDTA was added from a 0.02 M stock solution (H_2O/NaOH, pH = 8.0) to a final concentration of 10 mM, and the samples were vortexed for 1 min. The samples were then aliquotted (100 μL) into 96-well plates, and the Tb^{3+} or Eu^{3+} emission was measured over time using a time-resolved luminescence plate reader (time delay = 100 μs; measurement window = 1400 μs; λ_{ex} = 340/60 nm; Tb^{3+}, λ_{em} = 545/10 nm; Eu^{3+}, λ_{em} = 615/10 nm). Lanthanide luminescence was normalized to the value measured at the first time point (10 min) and plotted vs time using *Kaleidagraph* (Synergy Software).

Protein Expression and Purification. GFP-eDHFR was purified from the *E. coli* strain BL21 DE3 (pLysS) transformed with pRSETb-EGFP-eDHFR.[18] A 5 mL luria broth (LB) overnight culture was used to inoculate 500 mL of LB (Ampicillin, 100 mg/mL; chloramphenicol, 34 mg/mL). The 500 mL culture was grown at 37 °C, shaking at 200 rpm, to an OD_{600} of ~0.6, at which time expression of the protein was induced by the addition of IPTG to a final concentration of 1 mM. After growth for another 4 h, the cells were harvested by centrifugation. The pellet was lysed in 30 mL of lysis buffer (1× BugBuster Protein Extraction Reagent (Novagen), 10 μg/mL DNase, 1 mM PMSF, 100 mM HEPES, 10 mM imidazole, pH 7.5). Samples were placed on an orbital shaker for 30 min, then centrifuged (15 000 rpm, 15 min, 4 °C) and applied to a column containing 2.0 mL of HisLink Protein Purification Resin (Promega). Following purification, the protein was concentrated (to ~10 μM), dialyzed with phosphate buffer (10 mM K_2HPO_4, KH_2PO_4, pH 7.4), and stored at −80 °C.

Cell Lysate Preparation. Cell lysates containing GFP-eDHFR were obtained from 5.0 mL LB cultures of *E. coli* strain BL21 DE3 (pLysS) transformed with pRSETb-EGFP-eDHFR and treated to induce protein expression as described above. After growth and expression, the cells were harvested by centrifugation. The cell pellets were resuspended in 10 mM phosphate buffer (pH 7.4, with Halt Protease and Phosphatase Inhibitor, Thermo Scientific, Inc.) to a final concentration of 0.1 mg/μL. The cells were then lysed by sonicating for 1 min (2, 15 s on/off cycles) and recentrifuged (15 000 rpm, 15 min, 4 °C). The GFP-eDHFR concentration in the cell supernatant was determined by measuring the absorption of GFP at 484 nm (ε_{484} = 56 000 M^{-1} cm^{-1}).

Binding Affinity Assay. The binding affinity of compounds **9** and **10** complexed with Tb^{3+} for eDHFR was determined by measuring Tb^{3+}-to-GFP LRET in time-resolved mode. TMP conjugates (20 nM) were titrated in 96-well plates with either bacterial cell lysates containing GFP-eDHFR or purified protein at concentrations ranging from ~0.5 nM to 1000 nM in assay buffer (50 mM K_2HPO_4, KH_2PO_4, 18 mM β-mercaptoethanol, 20 μM β-NADPH, pH 7.2). Titrations were done in triplicate for each sample. Time-resolved luminescence (time delay = 100 μs; measurement window = 1400 μs, λ_{ex} = 340/60 nm) was measured at λ_{em} = 520/10 nm (LRET-sensitized GFP emission signal) and at λ_{em} = 615/10 nm (Tb^{3+} donor signal). For each well, the percent change in the donor-normalized LRET signal was calculated from the following equation

$$\Delta\mathrm{LRETN\%} = \left(\frac{\left(\frac{520}{615}\right)_S - \left(\frac{520}{615}\right)_{-\mathrm{ctrl}}}{\left(\frac{520}{615}\right)_{-\mathrm{ctrl}}} \right) \times 100 \qquad (2)$$

where $(520/615)_S$ represents the ratios of the emission signals at the indicated wavelengths for the sample well and $(520/615)_{-ctrl}$ represents the average emission ratio for three wells containing TMP-conjugate (20 nM) and no GFP-eDHFR. Using *Kaleidagraph* (Synergy Software), ΔLRETN% was plotted against protein concentration and dissociation constants were obtained by fitting the data to the following equation

$$L = L_{\min} - (L_{\min} - L_{\max}) \times \frac{[\mathrm{L}]_T + K_D + [\mathrm{P}]_T - \sqrt{\left([\mathrm{L}]_T + K_D + [\mathrm{P}]_T\right)^2 - \left(4[\mathrm{L}]_T[\mathrm{P}]_T\right)}}{2[\mathrm{L}]_T} \qquad (3)$$

where L_{min} is the ΔLRETN% of the TMP-Tb^{3+} complex with no receptor, L_{max} is the maximum ΔLRETN% signal observed at saturating receptor concentration, $[L]_T$ is the total amount of lanthanide complex used, and $[P]_T$ is the total amount of protein used.

RESULTS AND DISCUSSION

Syntheses. The compounds cs124,[20] DTPA-cs124,[12] TTHA dianhydride,[21] and an amine-derivatized TMP (**2**)[18] were prepared according to previously reported procedures. Compounds **1** and **4** were obtained by condensing diaminobenzene with ethyl-4,4,4-trifluoroacetoacetate and diethyl-1,3-acetonedicarboxylate, respectively.[16] Compounds **3** and **5** were prepared by peptide coupling between compounds **1** or **4** and **2** (Scheme 1). DTPA-based chelates (**6**, **8**) were prepared by reacting an excess of commercially available DTPA dianhydride with **3** or **5** in DMF at room temperature. TTHA dianhydride was similarly reacted with **3** or **5** to form compounds **7** and **9**. Compound **10** was synthesized in a three-component reaction by treating TTHA dianhydride (2 equiv) with 0.7 equiv of cs-124, followed by the addition of 1 equiv of compound **2** in DMSO (Scheme 2). All of the polyaminocarboxylate compounds were purified by reverse-phase HPLC and identified by mass spectrometry (Table 1), UV−vis absorption spectroscopy, and lanthanide luminescence properties.

Absorption Spectra. The absorption spectra of representative TMP conjugates of cs124- and cs124CF_3-polyaminocarboxylates complexed with Eu^{3+} are shown in Figure 2 and compared to DTPA-cs124. The compounds were assumed to retain the molar absorptivities of the sensitizing chromophores (10 500 M^{-1} cm^{-1} @ 341 nm for cs124, 21 000 M^{-1} cm^{-1} @ 341 nm for cs124CF_3).[12,15] This assumption was supported by the observation that ~1.3 equiv of Tb^{3+} or Eu^{3+} was sufficient to saturate lanthanide luminescence emission of all the chelates. The absorption spectrum of cs124-TTHA-TMP (**10**) is nearly identical to that of DTPA-cs124, but with a slight red shift of 2 nm. Consistent with previous studies by Mustaev and coworkers, we observed a red shift of 6 nm for the chromophore-linked cs124 and cs124CF_3 analogues.[16] Thus, TTHA-cs124CF_3-TMP (**7**) has a long-wavelength absorption maximum at 348 nm

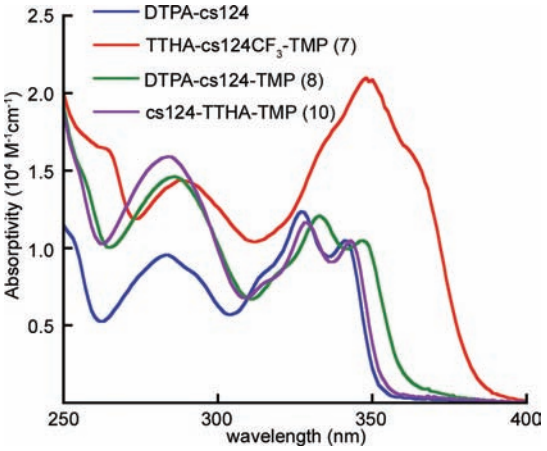

Figure 2. UV absorption spectra of representative trimethoprim-polyaminocarboxylate Eu^{3+} complexes and the reference compound (DTPA-cs124) described in this study.

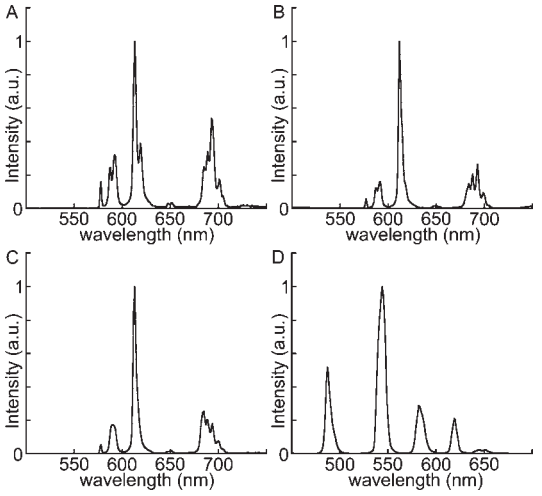

Figure 3. Normalized emission spectra (λ_{ex} = 330 nm) of Eu^{3+} complexes of (A) DTPA-cs124$_{CF3-}$ TMP (**6**); (B) TTHA-cs124$_{CF3-}$TMP (**7**); (C) cs124-TTHA-TMP (**10**); and (D) Tb^{3+} complex of **10**.

with a shoulder at 366 nm and DTPA-cs124-TMP (**8**) has a long-wavelength maximum at 348 nm. The analogous compounds DTPA-cs124CF_3-TMP (**6**) and TTHA-cs124-TMP (**9**) exhibited identically shaped spectra to those of compounds **7** and **8**, respectively (not shown). The 2-fold greater absorptivity and longer-wavelength maxima of compounds **6** and **7** allow for efficient excitation with high-power UV LED sources that emit at 365 nm, an important aspect for microscopy.[7]

Emission Spectra. All compounds displayed the narrow emission spectra typical of luminescent lanthanide chelates (Figure 3). The emission spectra and relative peak heights of Tb^{3+} emission with all compounds were essentially the same, matching the spectrum shown for **10** (Figure 3D). However, the relative intensities of the different Eu^{3+} emission lines are dependent on the chelate (DTPA or TTHA) but are independent of the sensitizer (cs124 or cs124CF_3).[12,15] The Eu^{3+} complexes of the TTHA conjugates, **7** (Figure 3B), **9** (not shown, identical to **7**), and **10** (Figure 3C) have a greater fraction of their luminescence in the sharply spiked peak at 613 nm, whereas the DTPA compounds all have relatively higher emission intensity in the peaks centered around 580 and 700 nm, as seen in the emission spectrum for **6** (Figure 3A). The Eu^{3+} emission pattern of **10** varies slightly from that of **7** or **9**, reflecting a different coordination environment resulting from amide bonds at both ends of TTHA. For spectroscopic or microscopic detection of Eu^{3+} luminescence through a narrow-pass emission filter at 613 nm, TTHA chelates are more detectable, as a lesser proportion of the emission intensity is excluded.

Relative Quantum Yields of Emission. We measured overall luminescent quantum yields for both Tb^{3+} and Eu^{3+} complexes of our heterodimeric TMP-linked chelates using appropriately metalated DTPA-cs124 as a reference standard (Table 2). We chose DTPA-cs124 as the reference because its quantum yields for Tb^{3+} and Eu^{3+} luminescence were reported previously (0.32 and 0.10, respectively),[14] and it offered a similar spectral profile and intensity for comparison. We also measured the overall quantum yield of DTPA-cs124(Tb^{3+}) using quinine sulfate as a reference and obtained a similar result (0.29) to the reported literature value (0.32).

The quantum yield data revealed some unexpected trends based on prior literature and the molecular architecture of the chelates. For Tb^{3+} luminescence, both chromophore-linked TMP conjugates, **8** and **9**, exhibited quantum yields of only

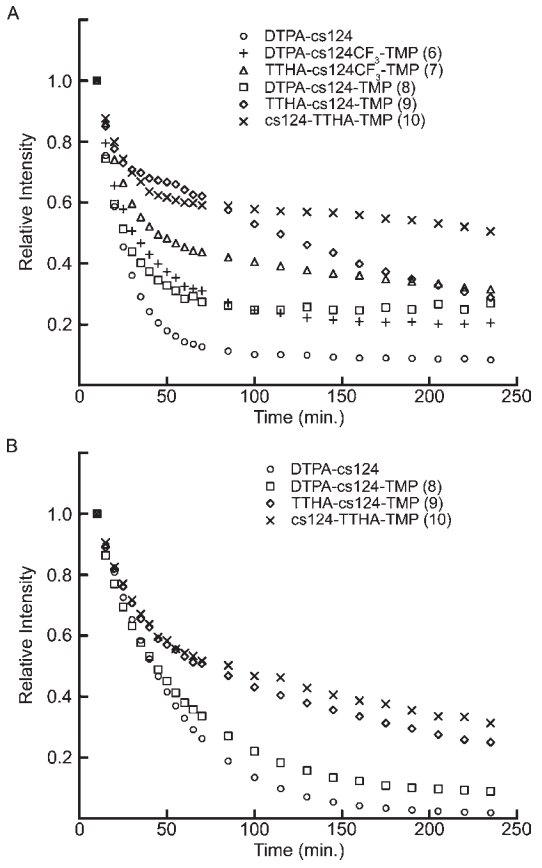

Figure 4. Relative emission intensity over time in the presence of EDTA for trimethoprimpolyaminocarboxylate conjugates and DTPA-cs124. (A) Eu^{3+} complexes. (B) Tb^{3+} complexes.

~20% relative to DTPA-cs124, whereas a similarly structured DTPA-cs124-isothiocyanate was reported by Mustaev and coworkers to be ~80% as bright as DTPA-cs124.[16] Similarly, for Eu^{3+} luminescence, **8** and **6** had relative quantum yields of 0.77 and 0.56, respectively; substantially lower than the 1.4-fold greater Eu^{3+} luminescence reported for DTPA-cs124-isothiocyanate

dx.doi.org/10.1021/bc200131k |*Bioconjugate Chem.* 2011, 22, 1402–1409

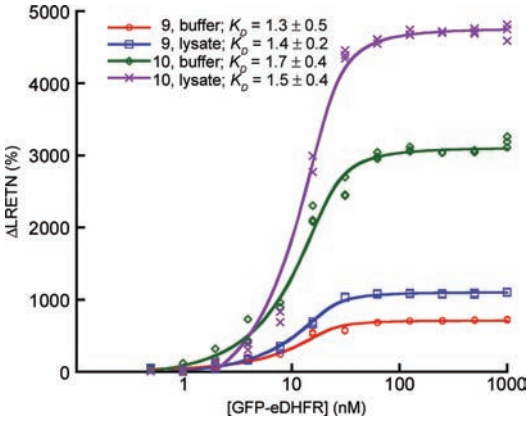

Figure 5. Intramolecular, luminescence resonance energy transfer (LRET) between eDHFR-bound Tb^{3+} complexes of TTHA-cs124-TMP (**9**) or cs124-TTHA-TMP (**10**) and GFP. Increasing concentrations of either purified eDHFR-GFP or a bacterial lysate containing the protein were titrated against a constant concentration (20 nM) of each compound. Sensitized GFP emission (520 nm) and Tb^{3+} emission (615 nm) was detected after a time delay of 100 μs, upon pulsed excitation with near-UV light (~340 nm). The *y*-axis represents the percent change in the 520/615 emission ratio. Lines represent nonlinear least-squares fit to the data.

relative to that of DTPA-cs124.[16] While the previous study did not directly measure quantum yields, the identical absorptivities observed for chromophore-linked vs conventional cs124 analogues allow for direct comparison. While the aforementioned compounds showed low quantum yields relative to DTPA-cs124 (and thus lower brightness), the Eu^{3+} complexes of **7** and **10** emitted with twice the efficiency of DTPA-cs124 (Table 2). Thus, assuming a ~10% overall Eu^{3+} quantum yield for DTPA-cs124,[14] we estimate a ~20% Eu^{3+} quantum yield for compounds **7** and **10**. The higher quantum yield, greater absorptivity, and longer wavelength absorption make compound **7** a potentially useful label for cell-based microscopy.

Relative Stability of the Lanthanide Chelates. Besides photophysical characteristics, stable retention of the metal ion is an important property for studies in living cells or cell extracts where endogenous chelators could scavenge metal from the lanthanide probes. To compare relative stability, we measured Tb^{3+} and Eu^{3+} emission intensity over a period of 3 h in the presence of EDTA for the metal complexes of the TMP-polyaminocarboxylate conjugates and of DTPA-cs124 (Figure 4). In the presence of 10 mM of EDTA, the Eu^{3+} emission intensity for nearly all compounds rapidly decreases and stabilizes after ~75 min, suggesting equilibrium was achieved (compound **9** did not appear to equilibrate within 3 h). The Eu^{3+} complex of **10** was the most stable, retaining ~55% of its initial intensity after 3 h, while DTPA-cs124(Eu^{3+}) was the least stable (~9% initial intensity). A similar pattern was seen for Tb^{3+} complexes, with TTHA analogues exhibiting greater stability than DTPA chelates, although neither of the TTHA compounds achieved equilibrium with EDTA within the 3 h observation period.

Protein Binding Affinity Measurements. For both *in vitro* and cell-based applications, TMP conjugates must necessarily bind with high affinity to eDHFR fusion proteins. To determine the dissociation constants for binding of select TMP-polyaminocarboxylate Tb^{3+} complex conjugates to eDHFR, we performed a time-resolved LRET assay that detected binding to a GFP-eDHFR fusion protein as Tb^{3+}-sensitized, GFP emission. The assay was performed in two formats: (1) purified GFP-eDHFR was titrated against a fixed concentration (20 nM) of either **9** or **10** in assay buffer; and (2) a lysate of *E. coli* expressing GFP-eDHFR was diluted directly into assay buffer without purification and titrated against 20 nM of each compound. Using a time-resolved luminescence plate reader, we measured sensitized, long-lifetime (>100 μs) GFP emission at 520 nm (the LRET signal) and the Tb^{3+} donor emission signal (615 nm). The percent change in the 520 nm/615 nm emission ratio was plotted vs GFP-eDHFR concentration, revealing characteristic binding isotherms (Figure 5). Nonlinear, least-squares fits of the data showed that the dissociation constants for binding to GFP-eDHFR equaled ~1.5 nM for both compounds under each assay condition. The ability to quantitatively measure binding events in a complex mixture, coupled with the large dynamic range of the LRET signal (~5000% for compound **10** in lysate/buffer), suggests that TMP-lanthanide complex conjugates could be used for high-throughput screening or quantification of biomolecular interactions, especially in cases where highly pure biochemical preparations cannot be obtained.

CONCLUSIONS

Currently, homogeneous, LRET-based assays of protein−protein or protein−DNA/RNA interactions require direct conjugation of lanthanide reporters to purified proteins or to specific antibodies. However, antibodies are not always available for a particular target, and many proteins cannot be purified. In such cases, and especially for specific protein labeling in living cells, the high-affinity interaction between TMP and eDHFR provides an effective means for imparting lanthanide luminescence to recombinant fusion proteins. Of the TMP-polyaminocarboxylate conjugates described here, the Tb^{3+} and Eu^{3+} complexes of cs124-TTHA-TMP (**10**) and the Eu^{3+} complex of TTHA-cs124CF_3-TMP (**7**) have the requisite brightness and kinetic stability to be effective reporters for time-resolved bioassays. Compound **7** is particularly promising as an Eu^{3+} reporter for cell-based microscopy because of its relatively long-wavelength absorption and high molar extinction coefficient. Paired with a suitable Tb^{3+} complex, **7** (Eu^{3+}) could be used for multiplexed lanthanide luminescence imaging.

AUTHOR INFORMATION

Corresponding Author

*E-mail: lwm2006@uic.edu; Phone: 312 996 8542; Fax: 312 996 0431.

ACKNOWLEDGMENT

This study was supported by the National Institutes of Health (National Institute of General Medical Sciences Grant R01-GM081030).

ABBREVIATIONS

(DTPA), diethylenetriaminepentaacetic acid; (eDHFR), *Escherichia coli* dihydrofolate reductase; (GFP), green fluorescent protein; (LRET), luminescence resonance energy transfer; (TMP), trimethoprim; (TTHA), triethylenetetraaminehexaacetic acid

REFERENCES

(1) Bunzli, J. C. (2010) Lanthanide luminescence for biomedical analyses and imaging. *Chem. Rev. 110*, 2729–55.

(2) Hovinen, J., and Guy, P. M. (2009) Bioconjugation with stable luminescent lanthanide(III) chelates comprising pyridine subunits. *Bioconjugate Chem. 20*, 404–21.

(3) Leblanc, V., Delaunay, V., Claude Lelong, J., Gas, F., Mathis, G., Grassi, J., and May, E. (2002) Homogeneous time-resolved fluorescence assay for identifying p53 interactions with its protein partners, directly in a cellular extract. *Anal. Biochem. 308*, 247–54.

(4) Maurel, D., Comps-Agrar, L., Brock, C., Rives, M. L., Bourrier, E., Ayoub, M. A., Bazin, H., Tinel, N., Durroux, T., Prezeau, L., Trinquet, E., and Pin, J. P. (2008) Cell-surface protein-protein interaction analysis with time-resolved FRET and snap-tag technologies: application to GPCR oligomerization. *Nat. Methods 5*, 561–7.

(5) Selvin, P. R., and Hearst, J. E. (1994) Luminescence energy transfer using a terbium chelate: improvements on fluorescence energy transfer. *Proc. Natl. Acad. Sci. U. S. A. 91*, 10024–8.

(6) Rajapakse, H. E., Gahlaut, N., Mohandessi, S., Yu, D., Turner, J. R., and Miller, L. W. (2010) Time-resolved luminescence resonance energy transfer imaging of protein-protein interactions in living cells. *Proc. Natl. Acad. Sci. U. S. A. 107*, 13582–7.

(7) Gahlaut, N., and Miller, L. W. (2010) Time-resolved microscopy for imaging lanthanide luminescence in living cells. *Cytometry A 77*, 1113–25.

(8) Chen, J., and Selvin, P. R. (1999) Thiol-reactive luminescent chelates of terbium and europium. *Bioconjugate Chem. 10*, 311–5.

(9) Ge, P., and Selvin, P. R. (2003) Thiol-reactive luminescent lanthanide chelates: part 2. *Bioconjugate Chem. 14*, 870–6.

(10) Ge, P., and Selvin, P. R. (2004) Carbostyril derivatives as antenna molecules for luminescent lanthanide chelates. *Bioconjugate Chem. 15*, 1088–94.

(11) Ge, P., and Selvin, P. R. (2008) New 9- or 10-dentate luminescent lanthanide chelates. *Bioconjugate Chem. 19*, 1105–11.

(12) Li, M., and Selvin, P. R. (1995) Luminescent polyaminocarboxylate chelates of terbium and europium: the effect of chelate structure. *J. Am. Chem. Soc. 117*, 8132–8138.

(13) Li, M., and Selvin, P. R. (1997) Amine-reactive forms of a luminescent diethylenetriaminepentaacetic acid chelate of terbium and europium: Attachment to DNA and energy transfer measurements. *Bioconjugate Chem. 8*, 127–132.

(14) Xiao, M., and Selvin, P. R. (2001) Quantum yields of luminescent lanthanide chelates and far-red dyes measured by resonance energy transfer. *J. Am. Chem. Soc. 123*, 7067–73.

(15) Chen, J., and Selvin, P. R. (2000) Synthesis of 7-amino-4-trifluoromethyl-2-(1H)-quinolinone and its use as an antenna molecule for luminescent europium polyaminocarboxylates chelates. *J. Photochem. Photobiol., A 135*, 27–32.

(16) Krasnoperov, L. N., Marras, S. A., Kozlov, M., Wirpsza, L., and Mustaev, A. (2010) Luminescent probes for ultrasensitive detection of nucleic acids. *Bioconjugate Chem. 21*, 319–27.

(17) Heyduk, E., and Heyduk, T. (1997) Thiol-reactive, luminescent europium chelates: luminescence probes for resonance energy transfer distance measurements in biomolecules. *Anal. Biochem. 248*, 216–27.

(18) Rajapakse, H. E., Reddy, D. R., Mohandessi, S., Butlin, N. G., and Miller, L. W. (2009) Luminescent terbium protein labels for time-resolved microscopy and screening. *Angew. Chem., Int. Ed. Engl. 48*, 4990–2.

(19) Demas, J. N., and Crosby, G. A. (1971) The measurement of photoluminescence quantum yields. A review. *J. Phys. Chem. 75*, 991–1024.

(20) Barraja, P., Diana, P., Montalbano, A., Dattolo, G., Cirrincione, G., Viola, G., Vedaldi, D., and Dall'Acqua, F. (2006) Pyrrolo[2,3-h]quinolinones: a new ring system with potent photoantiproliferative activity. *Bioorg. Med. Chem. 14*, 8712–28.

(21) sZitha-Bovens, E., Muller, R. N., Laurent, S., Elst, L. V., Geraldes, C. F. G. C., Bekkum, H. v., and Peters, J. A. (2005) Structure and dynamics of lanthanide complexes of triethylenetetramine-N,N,N′,N″,N‴,N‴-hexaacetic acid (H6ttha) and of diamides H4ttha(NHR) derived from H6ttha as studied by NMR, NMRD, and EPR. *Helv. Chim. Acta 88*.

Bioconjugate Chemistry

ARTICLE

pubs.acs.org/bc

Design of Acid-Activated Cell Penetrating Peptide for Delivery of Active Molecules into Cancer Cells

Wei Zhang,[▽,†] Jingjing Song,[▽,†] Bangzhi Zhang,[†] Liwei Liu,[†] Kairong Wang,[†] and Rui Wang*[,†,‡]

[†]Key Laboratory of Preclinical Study for New Drugs of Gansu Province, Institute of Biochemistry and Molecular Biology, School of Basic Medical Sciences, Lanzhou University, China

[‡]State Key Laboratory of Chiroscience, Department of Applied Biology and Chemical Technology, The Hong Kong Polytechnic University, Kowloon, Hong Kong

ABSTRACT: TP10−5 (TK) was screened as the most promising candidate among the designed analogues of transportan 10 (TP10), a cell penetrating peptide (CPP) with remarkable capacity for membrane translocation. However, low levels of specificity and high toxicity limit its successful use for drug delivery applications. Here, we developed a new type of acid-activated CPP (TH) by replacement of all lysines of TK with histidines. As expected, histidine-containing TH can be activated and subsequently enter cells at pH 6.0, whereas it is less active at pH 7.4. In contrast, the uptake of TK has no significant difference for both pH values. Importantly, the toxicity of TH is significantly lower than that of TK under physiological conditions. After attachment of camptothecin (CPT) to TH, this conjugate exhibited remarkable cytotoxicity to cancer cells in a pH-dependent manner compared with free CPT and TK-CPT. This study opens a new avenue to design CPPs that preferentially enter cells in acidic solid tumors, with minimal cellular uptake in normal tissues.

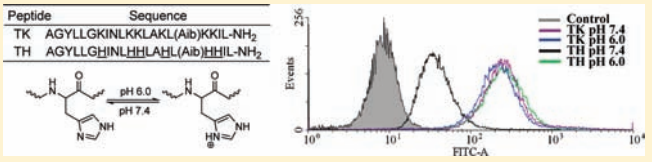

INTRODUCTION

A long-standing problem in cancer chemotherapy is the lack of tumor-specific treatments. Targeted therapy can improve the therapeutic index by using specific cell surface markers.[1,2] However, these approaches have achieved limited success against solid tumors, most likely because of heterogeneity in both tumor cell types and cell surface markers.[3,4] Thus, it is necessary to develop new therapeutic strategies that exploit other features of tumor physiology that are different from normal tissues. One major difference between many solid tumors and normal tissues is that tumor tissues have a more acidic extracellular environment.[5,6] The pH targeting approach is regarded as a more general strategy than conventional specific tumor cell surface targeting approaches, because the acidic extracellular environment is most common in solid tumors.[7] In recent years, several attempts have been made to use the solid tumor acidity to develop new pH-dependent approaches to cancer therapy[8,9] or drug delivery.[7,10,11]

The ability to cross the lipid bilayer of cells and access the cell interior is still one of the major obstacles to overcome in order to progress current drug development. Cell-penetrating peptides (CPPs) have become one of the most popular and efficient techniques for taking a wide variety of therapeutic cargos directly into cells without entrapment in the lysosome.[12,13] However, the lack of cell specificity restricts their successful utilization.[12−14] Several targeting strategies, based on selective unleashing of CPP activity, were used to enhance the applications of CPPs.[15−19] In all cases, the CPPs domain is first somehow shielded prior to reaching the targeted area to avoid nonspecific uptake. After reaching targeted tissues, CPPs are then fully deshielded to promote an efficient internalization.

Tp10, a 21-residue cell penetrating peptide with a remarkable capacity for membrane translocation, has been employed for the intracellular delivery of a wide variety of therapeutic cargos, such as oligonucleotides, peptide nucleic acid, peptides and proteins.[20] In our previous study, TP10−5 (TK) was screened as the most promising candidate among the designed analogues of transportan 10 (TP10). Because cancer cell membranes carry a more negative charge than normal cells, TP10 and TK preferentially bind to cancer cell membranes by electrostatic attraction and subsequently enter cells. However, a relatively large amount of peptides can still enter normal cells. In addition, they showed toxicity to normal cells. Therefore, the low level of specificity and the toxicity remain the major drawbacks for their drug delivery applications.

To develop new CPPs for drug delivery with high specificity and low toxicity, we hope to design a new type of CPP that can be activated by tumor acidity; otherwise, it is not active under physiological conditions. To this goal, we used TK as a template and replaced all of lysines by histidines, a change that should make the peptide positively charged and active primarily at acidic pH values.

EXPERIMENTAL PROCEDURES

Synthesis of Peptides. All peptides were synthesized on an MBHA resin using the standard Fmoc-chemistry-based strategy. The fluorescein moiety (FITC) was attached to the N-terminus

Received: March 17, 2011
Revised: May 20, 2011
Published: June 13, 2011

ACS Publications © 2011 American Chemical Society

via an aminohexanoic acid spacer by treating a resin-bound peptide (0.1 mmol) with FITC (0.1 mmol) and diisopropyl ethyl amine (0.5 mmol) in DMF for 12 h. All crude peptides were purified and analyzed by reversed-phase high performance liquid chromatography (RP-HPLC) on a C18 column, and then characterized by electrospray ionization mass spectrometry (ESI-MS).

Synthesis of Conjugates. All peptides with cysteine to serve as N-terminus were synthesized, where the thiol group was to serve as the attachment site for the cleavable linker. Following a procedure reported in previous literature,[21] camptothecin (CPT) was attached to the cysteine of peptides with a disulfide carbonate releasable linker.

Cell Cultures. HeLa cell lines were cultured in RPMI1640 medium (Gibco BRL) supplemented with 10% heat-inactivated neonatal bovine serum (NBS) (Sijiqing Biotech, PR China). MDA-MB-231 cell line was grown in DMEM (Gibco BRL) supplemented with 10% FBS (Sijiqing Biotech, PR China). All cell lines were cultured in a 5% CO_2 humidified atmosphere at 37 °C.

Quantitative Cellular Uptake Assays. HeLa cells were plated into 6 well microplates and cultured for 24 h. After incubation with serum-free medium adjusted to pH 7.4 or 6.0 containing 2 μM FITC labeled peptides for 30 min, the cells were washed twice with PBS and then incubated with 0.02% trypsin for 10 min. The cells were harvested and centrifuged at 1000 rpm for 5 min. The cell pellet was suspended and washed twice with PBS and finally resuspended in PBS for fluorescence analysis with a BD FACS Caliber Flow Cytometer using a 488 nm laser excitation.

Confocal Fluorescence Microscopy. HeLa cells were cultured on coverslips 24 h before treatment. The cells were incubated with the FITC labeled peptides or CPP-CPT conjugates using conditions and concentrations described above. The cells were then washed three times with PBS. Images were taken with an inverted Zeiss LSM 710 confocal microscope. Differential interference contrast (DIC) images were taken along with both fluorescence channels, and no bleedthrough was observed during colocalization studies with these parameters.

Cytotoxicity Assays. The antiproliferative effects of all peptides were determined by MTT assay. Cells were seeded at 8×10^3 cells/well in 96-well plates 24 h before treatment. After being washed, cells were treated with serum-free medium adjusted to pH 7.4 or 6.0 containing various concentrations of peptides. After 2 h incubation, 10 μL of MTT (5 mg/mL) was added to each well and incubated for 4 h. The absorbance was determined using a microplate reader (Bio-Rad 680) at 570 nm.

The antiproliferative effects of all conjugates were also determined by MTT assay. Cells were seeded in 96-well plates at a density of 4×10^3 cells per well. After incubation with serum-free medium adjusted to pH 7.4 or 6.0 containing various concentrations of agents for 30 min, the remaining agents that did not enter cells were washed to remove. Then, the cytotoxicity of the relevant agents was determined by the MTT assay after 72 h.

LDH (lactate dehydrogenase) Leakage Assays. Membrane integrity was measured using the CytoTox-ONE assay (Promega). Cells were seeded at 8×10^3 cells/well in 96-well plate 24 h before treatment. After incubation with 100 μL serum-free medium adjusted to pH 7.4 or 6.0 containing various concentrations of peptides for 2 h, 40 μL of medium was transferred to a black fluorescence plate and incubated for 10 min with 40 μL of CytoTox-ONE reagent, followed by 20 μL of stop solution.

(A)

Peptide	Sequence
TK	AGYLLGKINLKKLAKL(Aib)KKIL-NH_2
TH	AGYLLGHINLHHLAHL(Aib)HHIL-NH_2

(B)

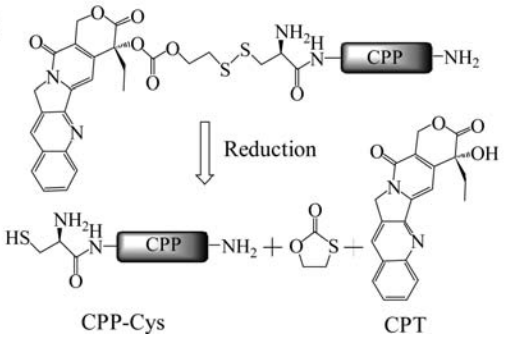

Figure 1. Sequences of peptides and structure of CPP-CPT conjugations. (A) Sequences of TK and TH. (B) Disulfide mediated release of CPT from CPPs.

Fluorescence was measured at 560/590 nm. Untreated cells were defined as no leakage and 100% leakage was defined as total LDH release by lysing cells in 0.2% Triton X-100.

Hemolysis Assays. Freshly collected mouse blood with heparin was centrifuged to remove the buffy coat, and the obtained erythrocytes were washed three times with phosphate buffered saline (PBS), centrifuged for 10 min at 1000 × *g*, and resuspended in PBS to 4% (v/v). 100 μL of peptide solution with various concentrations and 100 μL of the erythrocyte suspension were added to the wells of a 96-well plate. PBS and 0.1% Triton X-100 were used as agents for 0% and 100% hemolysis, respectively. Plates were incubated for 1 h at 37 °C and centrifuged at 1000 × *g* for 10 min. 100 μL of supernatants were transferred to a 96-well plate, and the release of hemoglobin was determined using a microplate reader at 450 nm.

Acute Toxicity Assays. Acute toxicity was examined after injection of the peptides to six Swiss mice. The doses of peptides administered per mouse were 100 mg/kg of body weight for i.p., or 25 mg/kg of body weight for i.v. Animal behavior and survival were monitored over a 14 day period.

RESULTS AND DISCUSSION

Design and Synthesis of Acid-Activated CPPs and CPP-CPT Conjugates. It was reported that the permeation of TP10 is attributed to creating a mass imbalance that disturbs the membrane after binding to the outer leaflet.[22] Likewise, TK, derived from TP10, has the same mechanism of permeation. In all processes of permeation, the electrostatic attraction of peptides to membrane is the first and critical step. Thus, weakening the electrostatic attraction will decrease the peptide internalization, concomitant with decreased toxicity. Compared with lysine, which is protonated at pH 7.4, histidine has a pK_a of approximately 6.5. Consequently, histidine-containing peptides have a net positive charge below pH 6.5 but are predominantly uncharged at pH 7.4. This feature of histidine has been used to design new pH-dependent membranolytic peptides.[9,23−25] After the lysines of TK were replaced with histidines (Figure 1A shows the sequences of peptides), TH cannot bind to the cell membrane and subsequently enter cells because of the loss of positive

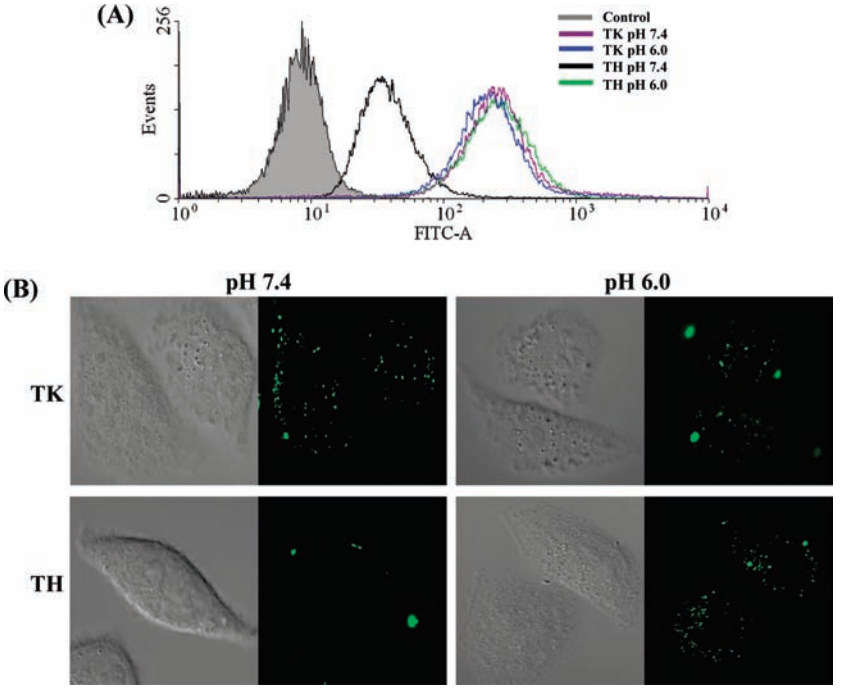

Figure 2. Uptake of TK and TH in HeLa cells. Cells were incubated with serum-free medium adjusted to pH 7.4 or 6.0 containing 2 μM FITC labeled peptides for 30 min. (A) Flow cytometry histograms of TK and TH internalized into HeLa cells. (B) Confocal images of HeLa cells treated with TK and TH.

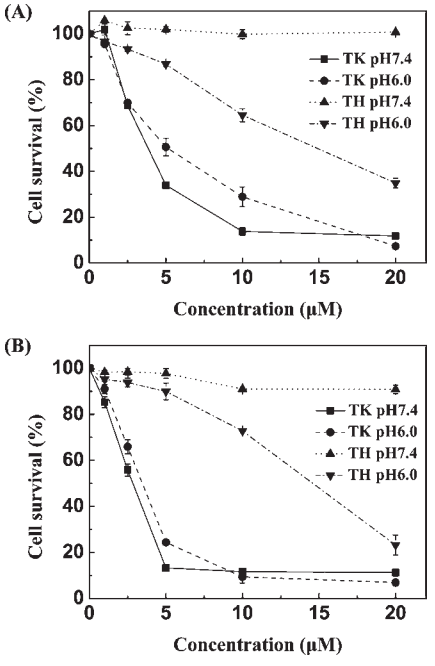

Figure 3. Cytotoxity of TK and TH. Cells were incubated with serum-free medium adjusted to pH 7.4 or 6.0 containing various concentrations of peptides for 2 h, and then measured by MTT assay. (A) HeLa cells. (B) MDA-MB-231 cells.

charge at physiological pH. In contrast, TH becomes protonated and cationic under tumor acidic environment, and then binds to the cell membrane by electrostatic attraction, resulting in membrane perturbation and internalization.

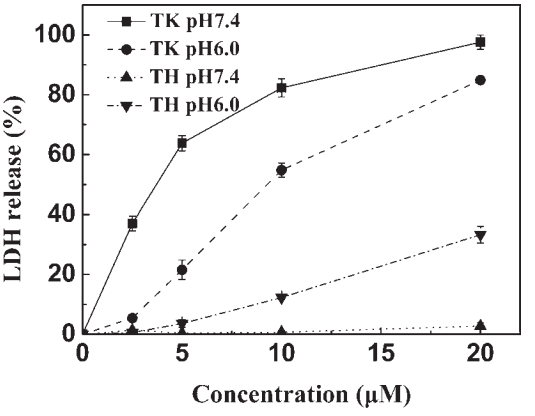

Figure 4. LDH leakage in HeLa cells treated with TK and TH. Cells were incubated with serum-free medium adjusted to pH 7.4 or 6.0 containing various concentrations of peptides for 2 h.

To evaluate the applications of TK and TH in drug delivery, we attached the CPPs to the 20-OH position of camptothecin (CPT) by using a disulfide releasable carbonate linker (Figure 1B). We selected CPT in this study for the following reasons. Fist, it possess potent anticancer properties that derive from its inhibition of topoisomerase I.[26] Second, major limitations of the drug, including selectivity, solubility, and instability of its lactone ring under physiological conditions, prevent full clinical utilization.[26] Attachment of CPT to the N-terminus of CPPs may contribute to overcoming these limitations. Preference was also given to a disulfide linker, because its cleavage would occur only after cellular entry of the conjugates after encountering a high glutathione concentration.[27] The thiol resulting from glutathione cleavage was expected to cyclize into

the proximate carbonyl group of the linker, leading subsequently to the release of free CPT, as shown in Figure 1B.

Cellular Uptake of CPPs at Different pH. Although highly efficient in mediating cell uptake of various active molecules, the lack of specificity limits extensive applications of CPPs. To determine whether the internalization of TK and TH is in a pH-dependent manner, the uptake of FITC labeled TK and TH at pH 7.4 and pH 6.0 was quantified by flow cytometry in HeLa cells. As expected, the results presented in Figure 2A showed that the fluorescence intensity of the internalized TH at pH 6.0 was remarkably higher than that at pH 7.4. However, lysine-containing TK showed similar histograms for both pH 7.4 and pH 6.0, indicating that the pH does not affect its internalization. Importantly, despite less activity at pH 7.4, the internalization ability of TH at pH 6.0 is comparable to that of TK.

Confocal fluorescence microscopy was further used to evaluate the cell uptake of TK and TH at different pH. Figure 2B showed fluorescent images of HeLa cells that have been incubated with TK and TH at pH 7.4 and pH 6.0 for 30 min. Confocal images revealed that TH has strong uptake in HeLa cells at pH 6.0, but poor translocation into cells at pH 7.4. In contrast, TK showed similar fluorescence intensity for both pH 7.4 and pH 6.0. These data strongly support the results indicated by the flow cytometry experiments.

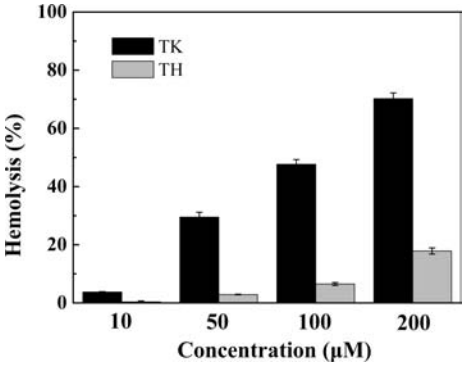

Figure 5. Hemolytic activity of TK and TH on mice red blood cells.

Table 1. Acute Toxicity of TK and TH

peptide	dose (mg/kg)	death of mice
TK	25[a]	6/6
	100[b]	4/6
TH	25[a]	0/6
	100[b]	0/6

[a] Peptides were administered i.v. [b] Peptides were administered i.p.

In Vitro Toxicity of CPPs. To get a general view of the toxic profile displayed by TK and TH, the cytotoxic properties of peptides were evaluated at different pH by MTT and LDH leakage assay. Since TK are able to kill cells within a very short period of time, we have kept the exposure time of cells to peptides for only 2 h in our study. As shown in Figure 3, TK showed similar cytotoxicity for both pH 7.4 and pH 6.0 in the MTT assay. However, TH killed cancer cells in a dose-dependent manner at pH 6.0, whereas it had no cytotoxicity at pH 7.4, indicating that the killing activity of TH is pH-dependent. The LDH leakage assay, used to measure acute membrane disturbance, supported the results indicated by the MTT assay (Figure 4). Furthermore, we also used the hemolysis assay to evaluate the toxicity of TK and TH to normal cells. As shown in Figure 5, TH showed remarkably low cytotoxicity to red blood cells compared with TK. Taken together, due to the loss of cationic charge at physiological pH, histidine-containing TH exhibited little cytotoxicity to cancer cells and normal cells, which is very useful for decreasing its in vivo toxicity.

In Vivo Toxicity of CPPs. Concomitant with peptide translocation, our results showed that TK exhibits remarkable membranolytic toxicity. Although the lytic activity of TK to cancer cells is useful, the damage to normal cells is one of major problems that

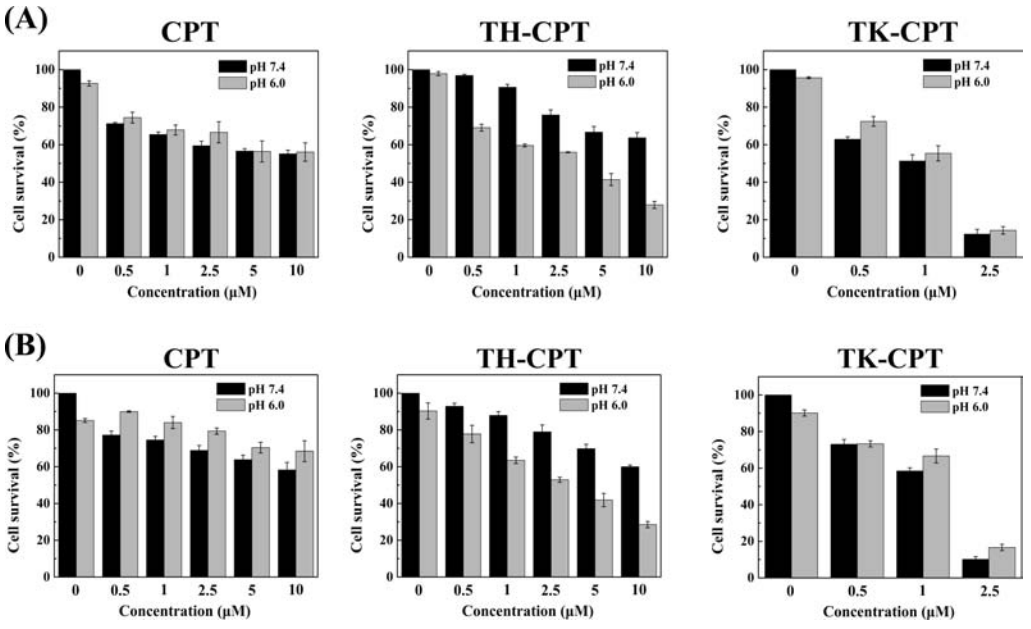

Figure 6. Cytotoxicity of free CPT, TK-CPT, and TH-CPT to different cancer cells. Cells were incubated with serum-free medium adjusted to pH 7.4 or 6.0 containing various concentrations of agents for 30 min, and then measured by MTT assay after 72 h. (A) HeLa cells. (B) MDA-MB-231 cells.

dx.doi.org/10.1021/bc200138d |*Bioconjugate Chem.* 2011, 22, 1410–1415

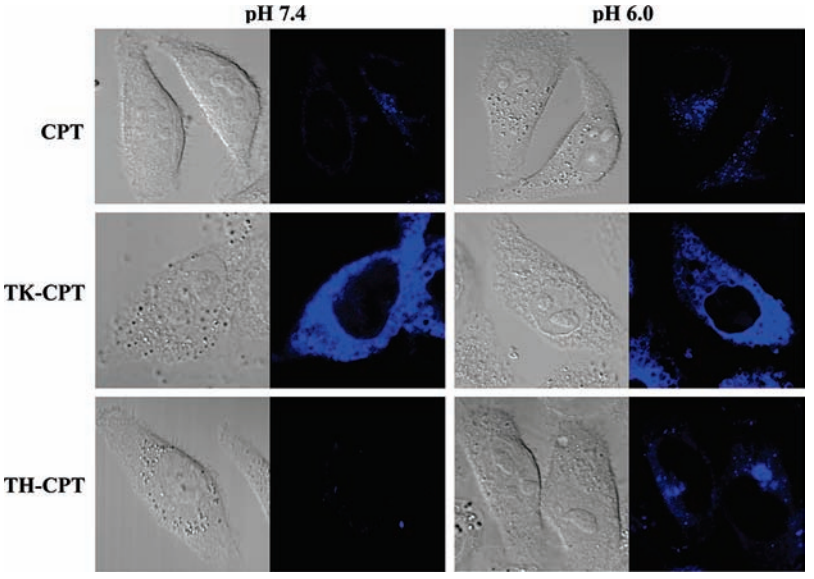

Figure 7. Uptake of free CPT, TK-CPT, and TH-CPT in HeLa cells. Cells were incubated with serum-free medium adjusted to pH 7.4 or 6.0 containing 2 μM agents for 30 min. Cell observation was done with a confocal microscopy.

restrict its successful utilization. In this study, the acute toxicity assay confirmed that TK has significantly higher in vivo toxicity than TH (Table 1). The high toxicity is attributed not only to the lytic activity of TK to normal cells, but also maybe to its highly cationic nature.[28] Substitution of lysines for histidines greatly decreases the affinity of the cells and cationic charge of TH at physiological pH, eventually resulting in reduced in vivo toxicity. The low toxicity of TH could expand its concentration used in cancer therapy, where TH can deliver more therapeutic agents to the targeted tissues.

Antiproliferative Effects of CPP-CPT Conjugates at Different pH. The majority of clinically approved anticancer drugs have very little or no specificity, which leads to systemic toxicity, causing undesirable severe side effects. It has been shown that drug therapy can be improved if the drug is targeted to tumor cells.[29,30] The translocation of TH in a pH-dependent manner suggests that this acid-activated CPP could be used for this purpose. The cytotoxicity of CPT, TK-CPT, and TH-CPT at pH 7.4 and pH 6.0 was evaluated in HeLa and MDA-MB-231 cells. As shown in Figure 6, TH-CPT showed significantly pH-dependent cytotoxicity, whereas the antiproliferative effects of CPT and TK-CPT had no significant difference between pH 7.4 and pH 6.0. As compared with free CPT, TH-CPT showed remarkably high cytotoxicity and selectivity to cancer cells in a pH-dependent manner.

To further study the pH-selectivity of the conjugates, the uptake of the conjugates and CPT in HeLa cells were analyzed by confocal fluorescence microscopy. Excitation was performed by a 405 nm line, blue fluorescence of CPT was observed. As shown in Figure 7, the images showed that CPT and TK-CPT could translocate into HeLa cells, and their fluorescence intensity was not significantly different between pH 7.4 and pH 6.0. In contrast, the fluorescence intensity of TH-CPT in HeLa cells at pH 6.0 was remarkably stronger than at pH 7.4. These results confirmed that the cytotoxicity of TH-CPT was pH-dependent compared with CPT and TK-CPT.

Although TH-CPT exhibited remarkable cytotoxicity in a pH-dependent manner, it slightly inhibited growth of cancer cells at pH 7.4. This is because TH has not completely lost the internalization activity at pH 7.4 (as shown in Figure 2). Figure 7 also confirmed that TH could deliver a small amount of CPT into cells at pH 7.4. As compared with CPT and TK-CPT, TH-CPT showed remarkable pH-selectivity to cancer cells. Thus, this pH-dependent cytotoxicity makes TH-CPT a potent anticancer drug that is targeted to the tumor tissues with an acidic extracellular environment.

CONCLUSIONS

In this study, we developed a new type of acid-activated CPP with low toxicity under physiological conditions by replacement of all lysines of TK with histidines. This work opens a new avenue to designing CPPs that preferentially enter cells in acidic solid tumors, with minimal cellular uptake in normal tissues. The histidine-containing TH with pH-selectivity and low toxicity will meet the needs of various applications. For example, this acid-activated TH can be used to selectively deliver a wide variety of cargo, such as nanoparticles, micelles, polymers, oligonucleotides, proteins, and small molecules, into the tumor cells with an acidic extracellular environment. In addtion, based on the lytic activity under acidic condition, TH can be used as an endosomolytic peptide to enhance endosomal escape of macromolecules and highly hydrophilic molecules. This is a preliminary work; further studies on applications of this acid-activated CPP are underway in our laboratory.

AUTHOR INFORMATION

Corresponding Author

*Rui Wang, School of Basic Medical Sciences, Lanzhou University, Lan zhou 730000, China, E-mail address: wangrui@lzu.edu.cn. Tel.:+86 931 8912567, fax: +86 931 8911255.

Author Contributions

▽These authors contributed equally to this work.

■ ACKNOWLEDGMENT

This study was supported by the grants from the National Natural Science Foundation of China (nos. 20932003 and 90813012), the Ministry of Science and Technology of China (nos. 2009ZX09503-017 and 2007AA02Z321).

■ REFERENCES

(1) Ojima, I. (2008) Guided molecular missiles for tumor-targeting chemotherapy-case studies using the second-generation taxoids as warheads. *Acc. Chem. Res. 41*, 108–119.

(2) Low, P. S., Henne, W. A., and Doorneweerd, D. D. (2008) Discovery and development of folic-acid-based receptor targeting for imaging and therapy of cancer and inflammatory diseases. *Acc. Chem. Res. 41*, 120–129.

(3) Scholler, N., Fu, N., Yang, Y., Ye, Z., Goodman, G. E., Hellström, K. E., and Hellström, I. (1999) Soluble member(s) of the mesothelin/megakaryocyte potentiating factor family are detectable in sera from patients with ovarian carcinoma. *Proc. Natl. Acad. Sci. U. S. A. 96*, 11531–11536.

(4) Fox, E. J., Salk, J. J., and Loeb, L. A. (2009) Cancer genome sequencing-an interim analysis. *Cancer Res. 69*, 4948–4950.

(5) Vaupel, P., Kallinowski, F., and Okunieff, P. (1989) Blood flow, oxygen and nutrient supply, and metabolic microenvironment of human tumors: a review. *Cancer Res. 49*, 6449–6465.

(6) Gerweck, L. E., and Seetharaman, K. (1996) Cellular pH gradient in tumor versus normal tissue: potential exploitation for the treatment of cancer. *Cancer Res. 56*, 1194–1198.

(7) Lee, E. S., Gao, Z., and Bae, Y. H. (2008) Recent progress in tumor pH targeting nanotechnology. *J. Controlled Release 132*, 164–170.

(8) Tannock, I. F., and Rotin, D. (1989) Acid pH in tumors and its potential for therapeutic exploitation. *Cancer Res. 49*, 4373–4384.

(9) Makovitzki, A., Fink, A., and Shai, Y. (2009) Suppression of human solid tumor growth in mice by intratumor and systemic inoculation of histidine-rich and pH-dependent host defense-like lytic peptides. *Cancer Res. 69*, 3458–3463.

(10) An, M., Wijesinghe, D., Andreev, O. A., Reshetnyak, Y. K., and Engelman, D. M. (2010) pH-(low)-insertion-peptide (pHLIP) translocation of membrane impermeable phalloidin toxin inhibits cancer cell proliferation. *Proc. Natl. Acad. Sci. U. S. A. 107*, 20246–20250.

(11) Na, K., Lee, E. S., and Bae, Y. H. (2007) Self-organized nanogels responding to tumor extracellular pH: pH-dependent drug release and in vitro cytotoxicity against MCF-7 cells. *Bioconjugate Chem. 18*, 1568–1574.

(12) Vivès, E., Schmidt, J., and Pèlegrin, A. (2008) Cell-penetrating and cell-targeting peptides in drug delivery. *Biochim. Biophys. Acta 1786*, 126–138.

(13) Fonseca, S. B., Pereira, M. P., and Kelley, S. O. (2009) Recent advances in the use of cell-penetrating peptides for medical and biological applications. *Adv. Drug Delivery Rev. 61*, 953–964.

(14) Myrberg, H., Zhang, L., Mäe, M., and Langel, U. (2008) Design of a tumor-homing cell-penetrating peptide. *Bioconjugate Chem. 19*, 70–75.

(15) Jiang, T., Olson, E. S., Nguyen, Q. T., Roy, M., Jennings, P. A., and Tsien, R. Y. (2004) Tumor imaging by means of proteolytic activation of cell-penetrating peptides. *Proc. Natl. Acad. Sci. U. S. A. 101*, 17867–17872.

(16) Sethuraman, V. A., and Bae, Y. H. (2007) TAT peptide-based micelle system for potential active targeting of anti-cancer agents to acidic solid tumors. *J. Controlled Release 118*, 216–224.

(17) Olson, E. S., Aguilera, T. A., Jiang, T., Ellies, L. G., Nguyen, Q. T., Wong, E. H., Gross, L. A., and Tsien, R. Y. (2009) In vivo characterization of activatable cell penetrating peptides for targeting protease activity in cancer. *Integr. Biol. (Camb.) 1*, 382–393.

(18) Nguyen, Q. T., Olson, E. S., Aguilera, T. A., Jiang, T., Scadeng, M., Ellies, L. G., and Tsien, R. Y. (2010) Surgery with molecular fluorescence imaging using activatable cell-penetrating peptides decreases residual cancer and improves survival. *Proc. Natl. Acad. Sci. U. S. A. 107*, 4317–4322.

(19) Shamay, Y., Adar, L., Ashkenasy, G., and David, A. (2011) Light induced drug delivery into cancer cells. *Biomaterials 32*, 1377–1386.

(20) El-Andaloussi, S., Järver, P., Johansson, H. J., and Langel, U. (2007) Cargo-dependent cytotoxicity and delivery efficacy of cell-penetrating peptides: a comparative study. *Biochem. J. 407*, 285–292.

(21) Henne, W. A., Doorneweerd, D. D., Hilgenbrink, A. R., Kularatne, S. A., and Low, P. S. (2006) Synthesis and activity of a folate peptide camptothecin prodrug. *Bioorg. Med. Chem. Lett. 16*, 5350–5355.

(22) Yandek, L. E., Pokorny, A., Florén, A., Knoelke, K., Langel, U., and Almeida, P. F. (2007) Mechanism of the cell-penetrating peptide transportan 10 permeation of lipid bilayers. *Biophys. J. 92*, 2434–2444.

(23) Midoux, P., Kichler, A., Boutin, V., Maurizot, J. C., and Monsigny, M. (1998) Membrane permeabilization and efficient gene transfer by a peptide containing several histidines. *Bioconjugate Chem. 9*, 260–267.

(24) Tu, Z., Volk, M., Shah, K., Clerkin, K., and Liang, J. F. (2009) Constructing bioactive peptides with pH-dependent activities. *Peptides 30*, 1523–1528.

(25) Li, L., He, J., Eckert, R., Yarbrough, D., Lux, R., Anderson, M., and Shi, W. (2010) Design and characterization of an acid-activated antimicrobial peptide. *Chem. Biol. Drug Des. 75*, 127–132.

(26) Venditto, V. J., and Simanek, E. E. (2010) Cancer therapies utilizing the camptothecins: a review of the in vivo literature. *Mol. Pharmaceutics 7*, 307–349.

(27) Saito, G., Swanson, J. A., and Lee, K. D. (2003) Drug delivery strategy utilizing conjugation via reversible disulfide linkages: role and site of cellular reducing activities. *Adv. Drug Delivery Rev. 55*, 199–215.

(28) El-Aneed, A. (2004) An overview of current delivery systems in cancer gene therapy. *J. Controlled Release 94*, 1–14.

(29) Burke, P. J., Senter, P. D., Meyer, D. W., Miyamoto, J. B., Anderson, M., Toki, B. E., Manikumar, G., Wani, M. C., Kroll, D. J., and Jeffrey, S. C. (2009) Design, synthesis, and biological evaluation of antibody-drug conjugates comprised of potent camptothecin analogues. *Bioconjugate Chem. 20*, 1242–1250.

(30) Dal Pozzo, A., Esposito, E., Ni, M., Muzi, L., Pisano, C., Bucci, F., Vesci, L., Castorina, M., and Penco, S. (2010) Conjugates of a novel 7-substituted camptothecin with RGD-peptides as $\alpha_v\beta_3$ integrin ligands: An approach to tumor-targeted therapy. *Bioconjugate Chem. 21*, 1956–1967.

Bioconjugate Chemistry

ARTICLE

pubs.acs.org/bc

Inflammation Responsive Logic Gate Nanoparticles for the Delivery of Proteins

Enas A. Mahmoud,[†] Jagadis Sankaranarayanan,[†] José M. Morachis,[†] Gloria Kim,[†] and Adah Almutairi*[,†,‡,§]

[†]Skaggs School of Pharmacy and Pharmaceutical Sciences, [‡]Materials Science and Engineering, and [§]NanoEngineering, University of California at San Diego, La Jolla, California 92093-0657, United States

Supporting Information

ABSTRACT: Oxidative stress and reduced pH are important stimuli targets for intracellular delivery and for delivery to diseased tissue. However, there is a dearth of materials able to deliver bioactive agents selectively under these conditions. We employed our recently developed dual response strategy to build a polymeric nanoparticle that degrades upon exposure to two stimuli in tandem. Our polythioether ketal based nanoparticles undergo two chemical transformations; the first is the oxidation of the thioether groups along the polymer backbone of the nanoparticles upon exposure to reactive oxygen species (ROS). This transformation switches the polymeric backbone from hydrophobic to hydrophilic and thus allows, in mildly acidic environments, the rapid acid-catalyzed degradation of the ketal groups also along the polymer backbone. Dynamic light scattering and payload release studies showed full particle degradation only in conditions that combined both oxidative stress and acidity, and these conditions led to higher release of encapsulated protein within 24 h. Nanoparticles in neutral pH and under oxidative conditions showed small molecule release and swelling of otherwise intact nanparticles. Notably, cellular studies show absence of toxicity and efficient uptake of nanoparticles by macrophages followed by cytoplasmic release of ovalbumin. Future work will apply this system to inflammatory diseases.

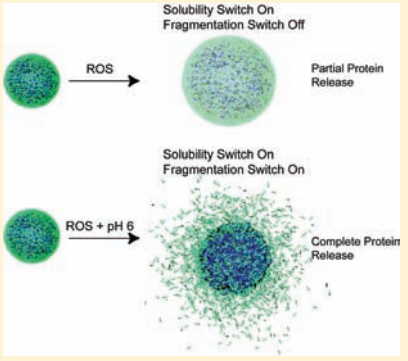

INTRODUCTION

Inflammation, especially chronic, relates to various diseases including cancerous and cardiovascular. Although there are numerous reports of "smart" nanoparticles that rapidly and selectively respond to different disease-specific stimuli, there is a dearth of nanoparticles capable of specifically targeting inflammation.[1,2] Furthermore, nanoparticles capable of cytoplasmic delivery are particularly challenging and this remains a major hurdle for effective therapeutic delivery.[3,4] In achieving increased cytoplasmic delivery, burst, fragmenting nanoparticles hold promise, as they can lead to elevated osmotic pressure within the endosome leading to endosomal escape of the nanoparticles payload.[5−7] Important biomarkers of diseased tissue that have been successfully used to trigger nanoparticle degradation include reduced extracellular pH,[8] thermal responsiveness,[9] reductive microenvironments,[10] and oxidative stress.[11] These nanoparticles respond to a single disease stimulus. Furthermore, control over the degradation kinetics, and thus, the ON/OFF state of the system has been difficult to achieve. For example, polyketals have gained prominence as the choice of drug delivery nanoparticles owing to their rapid pH response.[12,13] Nanoparticles formulated from these polyketals degrade at acidic pH into acetone and other benign molecules, rapidly releasing the payload within to the cytoplasm.[14] However, a key drawback of these systems is that as hydrophobic polymeric nanoparticles their degradation rates are very slow (many days)[12,13,15] in acidic pH (pH 6−5) because of reduced water influx. Although a hydrophobic backbone is advantageous in formulating stable nanoparticles at physiological conditions, a hydrophilic backbone is needed to produce fast release in targeted tissue. On the other hand, a hydrophilic backbone often results in nanoparticles that are not stable in pH 7.4 for longer than a few hours.[16] Recently, we introduced logic gate nanoparticles that use dual response mechanisms to impart stability to the "OFF" state while maintaining a rapid degradation or a sharp "ON" state.[6] We demonstrated the ability of such particles to deliver their payload to the cytoplasm because of the rapid fragmentation of the nanoparticle.[14] Here, we apply this strategy to physiological cues of inflammatory diseases.[17−19] Our new nanoparticles composed of a dual stimuli and response polymeric backbone are stable in healthy physiological conditions, yet they are able to rapidly fragment in subcellular and diseased conditions. Rapid fragmentation is important for cytoplasmic release of the bioactive payload.

It is known that polyketals degrade via surface hydrolysis while polysuflides degrade via bulk erosion.[28,29] Herein, we designed a novel polythioether ketal by incorporating a thioether moiety in our polymer backbone; the thioether acts as a solubility switch that turns the polymer more hydrophilic when it becomes oxidized from a thioether into a sulfone. Sulfones are inherently

Received: March 18, 2011
Revised: June 17, 2011
Published: June 21, 2011

ACS Publications © 2011 American Chemical Society

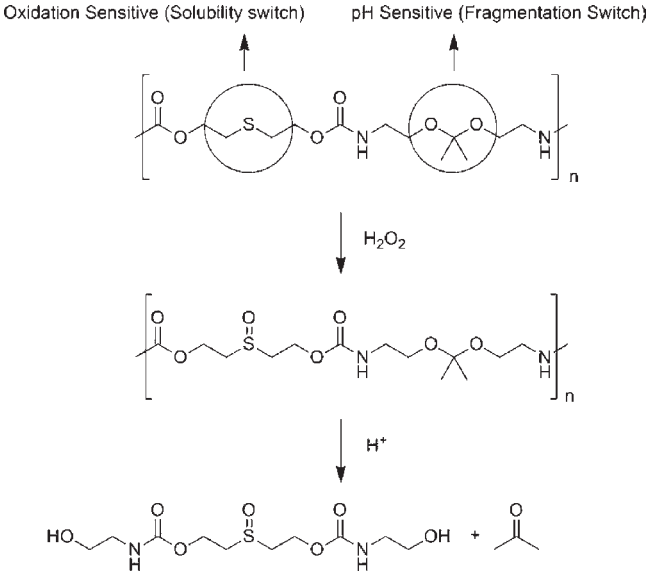

Figure 1. Degradation mechanism of polythioether ketal. Hydrogen peroxide and acidic pH stimulate the degradation of the polymeric nanoparticles in tandem.

more hydrophilic because of a strong dipole due to the presence of the sulfur oxygen double bond; this strong dipole leads to an increased affinity for water, resulting in an accelerated rate of hydrolysis of the ketal groups along the backbone. This allowed our polymers sharper, more rapid degradation kinetics in comparison to conventional polyketals (Figure 1). Various other polysulfides have been used to successfully formulate oxidation sensitive vesicles[1] and nanoparticles,[20] with such nanoparticles also being used to selectively target dendritic cells in vivo.[21]

The synthesized polythioether ketal nanoparticles were prepared to target the oxidative stress areas of many diseases including tumors,[22] atherosclerosis,[23] and causes of aging due to mitochondrial damage.[24] During these abnormalities, reactive oxygen species (ROS) are formed when oxygen undergoes a partial one-electron reduction to super oxide anion and subsequently forms hydrogen peroxide, hypochlorite peroxynitrite, and other oxidants.[25] Herein, the formulated nanoparticles that are triggered by both ROS and low pH (typical of inflamed tissue), function akin to an "AND" logic gate in circuits. We hope that our design will lead to nanoparticles that will better target diseased tissue for drug delivery or diagnostics.

MATERIALS AND METHODS

Materials. Potassium monohydrogen phosphate (K_2HPO_4) and potassium dihydrogen phosphate (KH_2PO_4) were purchased from Alfa Aesar Organics (Ward Hill, MA). Dichloromethane (DCM, methylene chloride) was purchased from Fisher Scientific (Hampton, NH). Nile red and poly(vinyl alcohol) (PVA) (MW 30−70k) were purchased from Sigma Chemical Co. (St. Louis, MO). 2,2′-Thiodiethanol was purchased Sigma Chemical Co. (St. Louis, MO). 4-Nitrophenylchloroformate was purchased from Acros organics (Belgium). PLGA (Resomer RG 502H) was purchased from Boehringer Ingelheim (Germany). Ovalbumin Alexa Fluor 594 was purchased from Invitrogen. All reagents were purchased from commercial sources and were used without further purification unless otherwise stated.

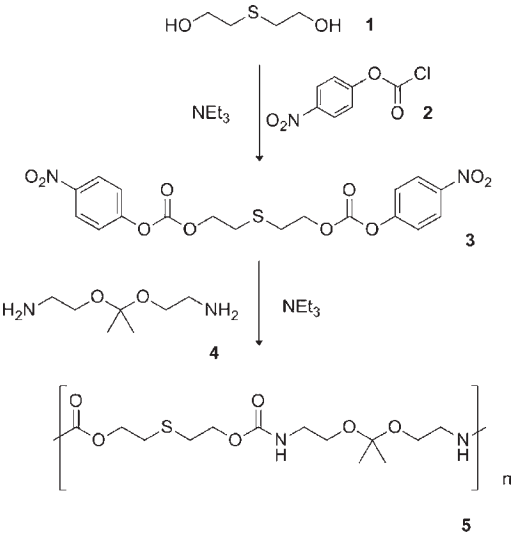

Figure 2. Synthesis of polythioether ketal.

Synthesis of the Polymer. As shown in Figure 2, 2,2′-thiodiethanol (compound **1**, 3.66 g, 0.03 mol) was taken with 4-nitrophenylchloroformate (compound **2**, 13.3 g, 0.064 mol) in a dry, round-bottom flask with 125 mL of dry dichloromethane and stirred under a nitrogen atmosphere. To this, triethylamine (30 mL, 0.21 mol) in 25 mL of dry dichloromethane was added dropwise over 30 min at room temperature. The reaction was subsequently stirred for 4 h. At the end of the reaction, the reaction mixture was rotavaped, diluted with 250 mL of dichloromethane, and extracted from 2 × 100 mL of 1% HCl. The organic layer was dried over $MgSO_4$ and rotavaped. The resulting crude solid was recrystallized from ethyl acetate three times to yield 8.0 g (0.017 mol, 60% yield) of a white solid (MP 138.6−140.1 °C).

^{1}H NMR (500 MHz, chloroform-*d*) δ 8.28 (d, J = 7.5 Hz, 1H), 7.38 (d, J = 7.5 Hz, 1H), 4.47 (dd, J = 6.3, 5.3 Hz, 1H), 2.97 (dd, J = 6.4, 5.2 Hz, 1H). ^{13}C NMR (126 MHz, chloroform-*d*) δ 155.46, 152.52, 145.61, 125.48, 121.91, 67.84, 30.79. HR-ESI-FT-MS (Orbit-Trap-MS) C18 H16 N2 O10 S Na. Mass Measured: 475.0420, Theo. Mass: 475.0418 δ (ppm) 0.4.

Polymer synthesis was completed by preparing diamine (compound **4**, Figure 2) as per the literature.[12] Diamine (0.518 g, 3.2 mmol) and carbonate (compound **3**, Figure 2) (1.446 g, 3.2 mmol) were taken with 2 mL of dry dichloromethane in an 8 mL vial with a Teflon cap and purged with nitrogen. To this, 1 mL of triethylamine was added via syringe, and the contents were stirred for 4 days at room temperature. The contents were precipitated into diethyl ether and the waxy yellow solid obtained was subsequently purified on a gel column packed with lipophilic sephadex (LH-20) using dichloromethane as the eluent, to obtain a pale yellow solid in 70% yield.

^{1}H NMR (500 MHz, chloroform-*d*) δ 5.42 (s, 1H), 4.21 (t, J = 6.4 Hz, 2H), 3.45 (t, J = 5.2 Hz, 2H), 3.30 (d, J = 5.3 Hz, 2H), 2.77 (t, J = 6.5 Hz, 2H), 1.32 (s, 3H). ^{13}C NMR (126 MHz, chloroform-*d*) δ 156.42, 100.32, 64.24, 64.21, 59.93, 41.20, 31.34, 24.93, 24.90. Molecular weight: Obtained via GPC against polystyrene standards using DMF(0.01% LiBr) as the eluent. M_w = 59 800 Da, M_n = 34 100, PDI = 1.75.

Nanoparticle Formulation. In o/w procedure, 25 mg of the synthesized polymer was dissolved in 2.5 mL DCM. Then,

500 μg Nile red were added, for preparing Nile red containing particles. DCM was added to 50 mL of phosphate buffer (pH 8) containing 1% PVA, and the mixture was stirred at 1000 rpm for 5 min to prepare an emulsion. Further emulsification was achieved using a high-pressure homogenizer (Microfluidic 110PS, USA) at 23 000 psi for three cycles. The nanoparticle suspension was stirred at 1000 rpm using a magnetic stirrer to evaporate the DCM. Nile red containing nanoparticles were filtered through 1 μm filter to remove the insoluble Nile red aggregate, and a concentrated mode tangential flow filtration system with 500 kDa Pellicon XL cassettes (Millipore, USA) was used to remove the PVA and any unencapsulated material. The nanoparticle suspension was concentrated to 10 mL and washed twice.[26] Protein was encapsulated into the nanoparticles using the w/o/w emulsion method. Briefly, 2 mg Ovalbumin Alexa Fluor 594 was dissolved in 0.2 mL of PBS buffer and subsequently emulsified with 5 mL of DCM containing 100 mg polymer using probe sonication (stabilized using 2% Span 80) at amplitude of 40% for 5 min (1/8 inch tip, Misonix S-4000, USA). The primary emulsion was added to 50 mL of 1% PVA in buffer (pH 8) under stirring at 1000 rpm, and the secondary emulsion was produced. Additional emulsification was achieved using the high-pressure homogenizer at 23 000 Psi for two cycles and tangential flow filtration was accomplished as previously described. Finally, 5% Trehalose was added to the particles before lyophilization. The lyophilized particles were suspended in aqueous media at different pHs and H_2O_2 levels for further evaluation of stability or release.

The encapsulation efficiencies of the particles were determined by incubating them at acidic pH in presence of 100 mM H_2O_2 until no further particles are detected by the DLS and the detected fluorescence reaches its maximum.

Dynamic Light Scattering Measurements of the Nanoparticles. Nanoparticles were suspended in a phosphate buffer pH 7.4 or 5 in the presence or absence 100 mM H_2O_2, with stability determined by monitoring their size for 24 h via dynamic light scattering (DLS) using a Zetasizer-ZS (fixed attenuator of 7, Malvern Worcestershire, UK).

Effect of pH and H_2O_2 on Nile Red Release. Nile red was encapsulated into the nanoparticles as a sensor of changes in the hydrophobic−hydrophilic character of the surrounding environment. Nile red fluoresces in the hydrophobic environment inside the nanoparticles and quenches once released into the aqueous release media; this quenching was measured as an indicator of Nile red release into an aqueous media. Nanoparticle powder was dispersed in PB pH 7.4 or 5 in the presence or absence 100 mM H_2O_2. The pH was checked in the presence of H_2O_2 to confirm the pH. Samples were taken and Nile red fluorescence was determined at different time intervals. Decrease in the nanoparticles fluorescent was an indication of Nile red release to the aqueous media.

Effect of pH and H_2O_2 on Ovalbumin Release. Nanoparticle powder was dispersed in PB pH 7.4 or 6.5 in presence or absence 100 mM H_2O_2. PB pH 6.5 was chosen for ovalbumin release study to prevent its precipitation upon release into PB having pH near ovalbumin isoelectric point (pH ∼5).[27] Samples were taken at different time intervals and spun down at 20K *g* for 10 min at 4 °C. The supernatant was analyzed for released ovalbumin Alexa Fluor 594 after appropriate dilution.

Degradation of the Polythioether Ketal by ^{1}H NMR. Ten milligrams of the polymer were taken with deuterated (a) 1:1 acetonitrile−water (pH = 5, phosphate buffer); (b) 1:1 acetonitrile−water (pH = 5, phosphate buffer) with 20 μL of H_2O_2; the ^{1}H NMR was obtained at regular intervals.

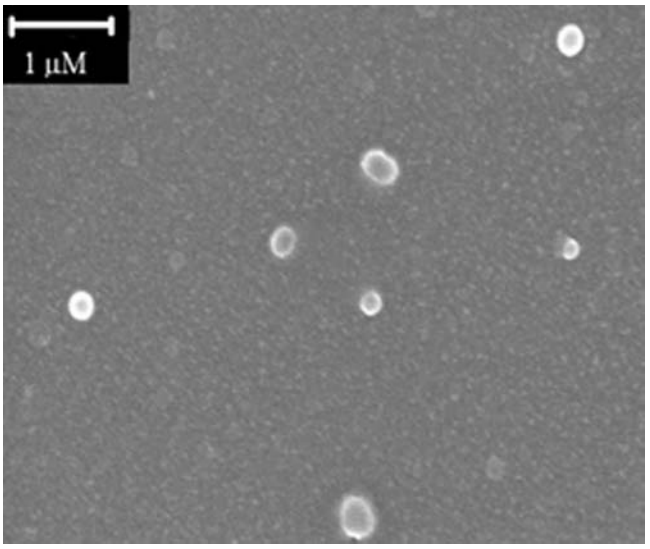

Figure 3. SEM image of the nanoparticles showing a particle diameter of <1 μm.

Cell Toxicity of Nanoparticles. The cytotoxicity of nanoparticles was investigated using a 3-(4,5-dimethylthiazol-2-yl)-2,5-diphenyltetrazolium bromide (MTT) reduction assay. RAW 264.7 macrophage cells were seeded at a density of 15 000 cells/well in a 96-well plate and incubated for 24 h to reach 60% confluency. Cells were treated with various amounts of nanoparticles that corresponded to the varying amounts of polymer contained in them (0−300 μg/mL) and incubated for 20 h. To each well was added 10 μL of MTT solution, and the wells were incubated for 3 h. Dimethyl sulfoxide (DMSO, 100 μL) was added to cells to dissolve the resulting formazan crystals. After 20 min of incubation, the absorbance at 570 nm was measured using a FlexStation microplate reader (Molecular Devices, Inc., Sunnyvale, CA, USA). Cell viability was obtained by comparing the absorbance of nanoparticle-treated cells to that of control cells not treated with particles.

Cellular Internalization of Ovalbumin-Containing Nanoparticles. The uptake of ovalbumin Alexa Fluor 594-loaded nanoparticles was studied in RAW264.7 cells using a fluorescent microscope. Cells were plated on CultureWell Chambered Coverglass slides (Invitrogen Corporation, Carlsbad, CA, USA) at a density of 10 000 cells per well for 24 h followed by treatment with polythioketal or PLGA nanoparticles. The nanoparticle payload contained a final concentration of approximately 10 μg/mL ovalbumin Alexa Fluor594. After 8 h at 37 °C, the cells were washed with PBS before mounting and staining with DAPI.

RESULTS AND DISCUSSION

Infected tissues are frequently characterized by a decreased pH and the presence of reactive oxygen species (ROS).[17−19] In order to simulate these conditions, particle behavior was tested at acidic pH and in the presence of H_2O_2, which is a prevalent reactive oxygen species. Accordingly, nanoparticles were subjected to different physiologically relevant conditions: pH 7.4 (pH of healthy tissue), pH 7.4/100 mM H_2O_2 (presence of ROS), acidic pH, and acidic pH/100 mM H_2O_2. Their behavior was

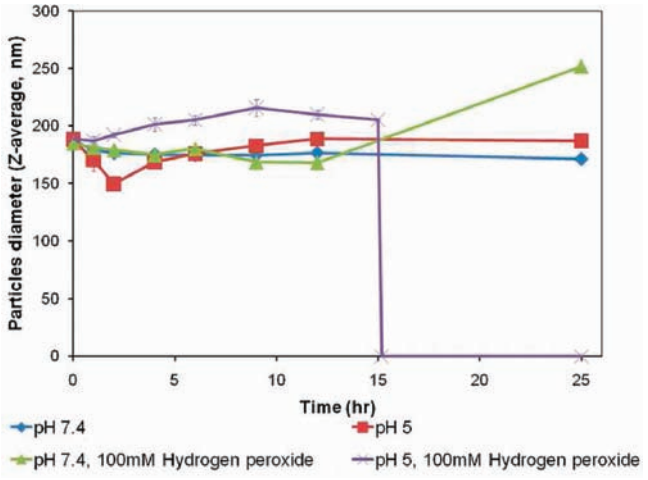

Figure 4. Effect of pH and H_2O_2 on the *Z*-average of the nanoparticles. Triplicate measurements were taken using the DLS at a fixed attenuator of 7.

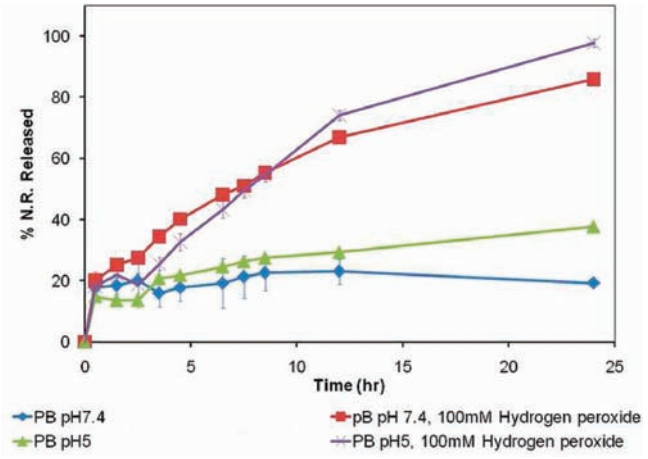

Figure 5. Release of Nile red from polythioether ketal nanoparticles. Decrease in nanoparticle suspension fluorescence was correlated to Nile red release in different conditions.

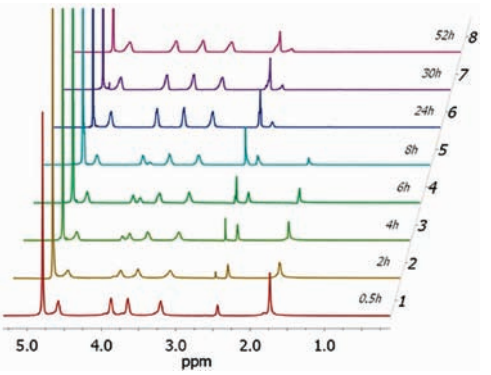

Figure 6. Degradation of polymer 5 at pH 5 in 1:1 deuterated acetonitrile and water by ^{1}H NMR. Hydrolysis of ketal is evidenced by the appearance of acetone peak (at δ 2.6 ppm) and disappearance of the ketal peak (at δ 1.6 ppm). There is also a concomitant change in the peak at δ 3.8 ppm to δ 3.9 ppm due to the formation of alcohol upon degradation of the ketal.

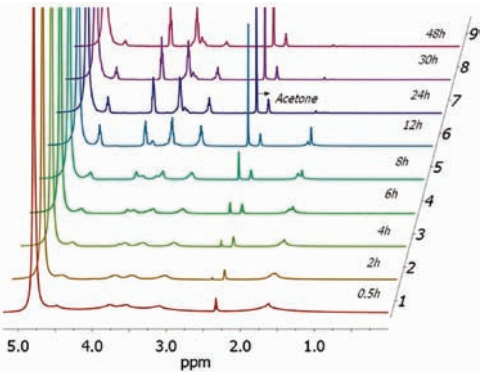

Figure 7. Degradation of polymer 5 at pH 5 in 1:1 deuterated acetonitrile and water with addition of 20 μL of 30% H_2O_2 by ^{1}H NMR. In addition to the changes noted in the Figure 6, upon addition of H_2O_2 we see that the peak at δ 3.6 ppm shifts to δ 3.7 ppm. This is consistent with the oxidation of sulfur in the backbone to a sulfoxide. These NMR studies establish that the sulfur moiety undergoes oxidation when subjected to H_2O_2.

monitored via DLS and by measuring the release of Nile red and ovalbumin.

The hydrophobic nature of the polymer permitted the formulation of the nanoparticles using single- or double-emulsion techniques. This in turn allowed the encapsulation of different payloads with different hydrophobic−hydrophilic characteristics like Nile red and ovalbumin (Figure 3).

Monitoring the behavior of the nanoparticles using DLS (Figure 4) showed that only nanoparticles dispersed in pH 5 in the presence of H_2O_2 degraded within 24 h, while the particles dispersed in pH 5 alone remained detectable throughout this time period. Thus, the presence of both stimuli caused an accelerated degradation of the nanoparticles. This is further evidenced by the observed increase in particle size upon incubation in H_2O_2 at pH 7.4. This swelling is due to the backbone becoming oxidized, resulting in the hydration of the particles.

When Nile Red is encapsulated in the particles, it acts as a fluorescent probe of hydrophobicity and release. In the presence of H_2O_2, oxidation of the polymer backbone occurs, rendering the nanoparticles more hydrophilic. This causes quenching of encapsulated Nile red upon its release from the nanoparticles (*Z*-average = 200 nm). This hydrophilic change occurred in both neutral and acidic conditions and depended entirely on whether the particles were incubated in hydrogen peroxide or not (Figure 5). Also, Nile red was minimally quenched at pH 5 due to the slow degradation of the particle via surface erosion. However, more quenching is observed when both conditions are operational. Finally, in order to confirm that our polymer degrades under the said conditions, we performed degradation and analyzed via ^{1}H NMR (Figure 6 and Figure 7). Here, as expected, we did not see a difference in polyketal hydrolysis rates because the polymer is completely dissolved without the need of oxidation. The control that we observed in the rates of particle degradation is due to the nanoparticle architecture, which is lost when the polymer is dissolved. We subsequently tested this systemic control in releasing ovalbumin as a model protein.

Figure 8 shows that ovalbumin release was initiated by oxidation of the polymer, or more accurately due to *swelling* of the nanoparticles. Meanwhile, higher release was observed at acidic pH in the presence of hydrogen peroxide due to

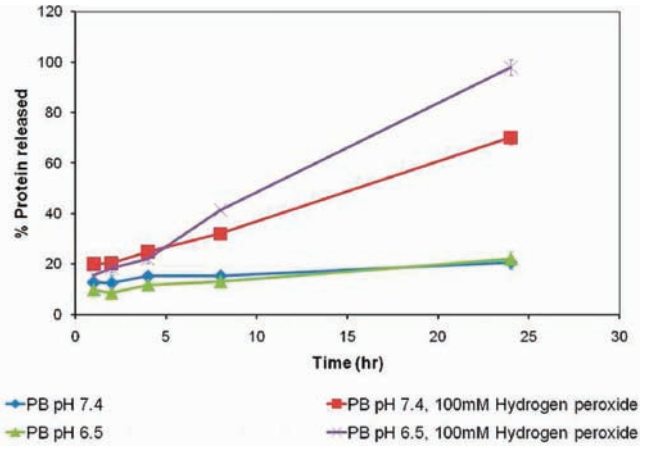

Figure 8. Release of ovalbumin AlexaFluor 488 from polythioketal nanoparticles. Nanoparticle supernatants were tested for fluorescence to determine ovalbumin release profile over time (n = 3).

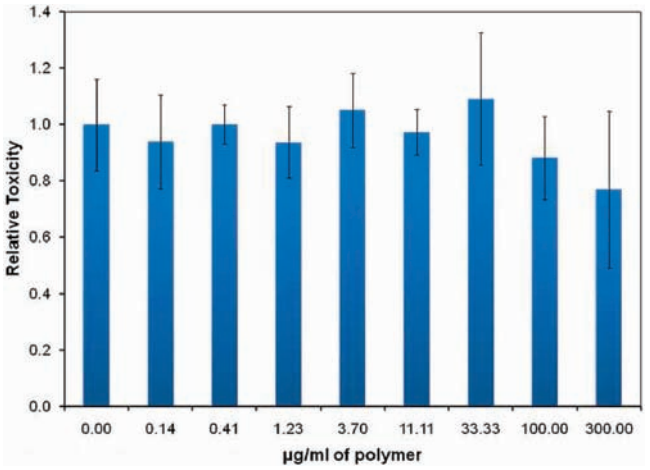

Figure 9. Cytotoxicity of polythioether ketal nanoparticles at different concentrations in RAW 264.7 macrophage cells. The cells were incubated with the nanoparticles for 20 h before performing the MTT assay.

degradation of the nanoparticles. Importantly, the nanoparticles showed excellent stability at pH 7.4. Furthermore, the full degradation of our new nanoparticles system is important as small fragments are more readily excreted.[30−32]

We evaluated the cytotoxicity of polythioketal nanoparticles in cells using the MTT assay using RAW264.7 cell line. The RAW264.7 macrophage cell line is a great model system for studying immune response and can produce relatively higher levels of endogenous ROS. Additionally, these cells are able to take up cells very readily without the need of cell penetrating peptides.

RAW 264.7 cells were incubated with various amounts of nanoparticles for 20 h. Figure 9 illustrates the comparison of cytotoxicity between cells treated with increasing concentrations of polythioether ketal polymer. There was no significant cytotoxicity observed with the cells incubated with up 300 μg/mL of polymer (p = 0.294).

Finally, we analyzed the cellular uptake of nanoparticles and release of cargo within cells by comparing polythioether ketal and PLGA nanoparticles containing equal amounts of fluorescently

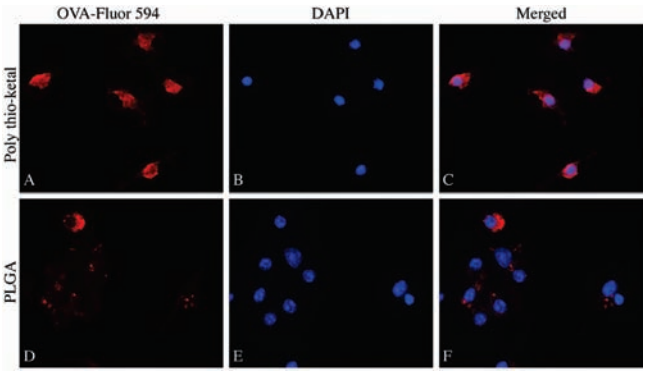

Figure 10. Uptake of nanoparticles loaded with fluorescent ovalbumin. Raw 264.7 macrophage cells were treated for 8 h with polythioether ketal or PLGA nanoparticles containing ovalbumin Alexa Fluor 594 (red) and stained with DAPI (blue).

labeled ovalbumin (Figure 10). Nanoparticles were added to RAW 264.7 cells and evaluated by fluorescence microscopy. Polythioether ketal nanoparticles were able to efficiently deliver protein within RAW264.7 macrophage cells that have an H_2O_2 concentration of 2 μM.[33]

Cells treated with polythioether ketal nanoparticles show thorough diffusion of ovalbumin throughout the cytoplasm and the nucleus, indicating that labeled ovalbumin was released within the cell. This is in contrast to slow-degrading PLGA nanoparticles that show punctuated spots and less diffused ovalbumin throughout the cell.

CONCLUSION

We designed a polymeric nanoparticle with two stimuli responsive moieties in its backbone, and which undergoes programmed degradation when stimulated by inflammatory cues, ROS, and acidic pH, respectively. This system functions akin to an "AND" Logic Gate. Upon stimulation by ROS, the polymer becomes hydrophilic, followed by ketal hydrolysis promoted at an acidic pH. We observed release of small hydrophobic molecules, Nile red, in acidic pH and an increase in polymer hydrophilicity upon oxidation. Higher release of encapsulated ovalbumin was observed in the presence of both hydrogen peroxide and acidic pH. We found that the nanoparticles were readily taken up by macrophage cells and that ovalbumin release from the nanoparticles into the cytoplasm was in agreement with the degradation behavior of the nanoparticles as shown in the DLS measurements. We hypothesize that these nanoparticles can differentiate among the conditions of our target areas from others. This should ensure the release of the payload in specific diseased regions such as inflammatory or tumor sites and allows for intracellular delivery. These studies suggest that our nanoparticles can be applied to the delivery of diagnostics and therapeutics to sites of inflammation. Thus, our current work focuses on the application of these nanoparticles in targeting theranostics to vulnerable plague versus stable plaque.

ASSOCIATED CONTENT

Supporting Information. ^{1}H NMR of compound **3**, ^{13}C NMR of compound **3**, HR-ESI-FT-MS (Orbit-Trap-MS) of compound **3**, ^{1}H NMR of *poly* 5, ^{13}C NMR of *poly* 5, GPC trace

of Poly 5 calibrated against Polystyrene standards. This material is available free of charge via the Internet at http://pubs.acs.org.

AUTHOR INFORMATION

Corresponding Author
*Prof. Adah Almutairi, aalmutairi@ucsd.edu.

ACKNOWLEDGMENT

The research described in this paper was sponsored in part by the UCSD IRACDA Fellowship NIH Grant GM06852 (JM), the NIH New Innovator Award (1 DP2 OD006499-01), and the King Abdulaziz City for Science and Technology (KACST). We thank Dr. Eric Schopf for his help with SEM imaging.

REFERENCES

(1) Napoli, A., Valentini, M., Tirelli, N., Mueller, M., and Hubbell, J. A. (2004) Oxidation-responsive polymeric vesicles. *Nat. Mater. 3*, 183–189.

(2) Wilson, D. S., Dalmasso, G., Wang, L. X., Sitaraman, S. V., Merlin, D., and Murthy, N. (2010) Orally delivered thioketal nanoparticles loaded with TNF-alpha-siRNA target inflammation and inhibit gene expression in the intestines. *Nat. Mater. 9*, 923–928.

(3) Vasir, J. K., and Labhasetwar, V. (2007) Biodegradable nanoparticles for cytosolic delivery of therapeutics. *Adv. Drug Delivery Rev. 59*, 718–728.

(4) Mescalchin, A., Detzer, A., Wecke, M., Overhoff, M., Wuensche, W., and Sczakiel, G. (2007) Cellular uptake and intracellular release are major obstacles to the therapeutic application of siRNA: novel options by phosphorothioate-stimulated delivery. *Expert Opin. Biol. Ther. 7*, 1531–1538.

(5) Hu, Y., Litwin, T., Nagaraja, A. R., Kwong, B., Katz, J., Watson, N., and Irvine, D. J. (2007) Cytosolic delivery of membrane-impermeable molecules in dendritic cells using pH-responsive core-shell nanoparticles. *Nano Lett. 7*, 3056–3064.

(6) Sankaranarayanan, J., Mahmoud, E. A., Kim, G., Morachis, J. M., and Almutairi, A. (2010) Multiresponse strategies to modulate burst degradation and release from nanoparticles. *ACS Nano 4*, 5930–5936.

(7) Sonawane, N. D., Szoka, F. C., Jr., and Verkman, A. S. (2003) Chloride accumulation and swelling in endosomes enhances DNA transfer by polyamine-DNA polyplexes. *J. Biol. Chem. 278*, 44826–44831.

(8) Vaupel, P., Kallinowski, F., and Okunieff, P. (1989) Blood flow, oxygen and nutrient supply, and metabolic microenvironment of human tumors: a review. *Cancer Res. 49*, 6449–65.

(9) Meyer, D. E., Shin, B. C., Kong, G. A., Dewhirst, M. W., and Chilkoti, A. (2001) Drug targeting using thermally responsive polymers and local hyperthermia. *J. Controlled Release 74*, 213–224.

(10) Saito, G., Swanson, J. A., and Lee, K.-D. (2003) Drug delivery strategy utilizing conjugation via reversible disulfide linkages: role and site of cellular reducing activities. *Adv. Drug Delivery Rev. 55*, 199–215.

(11) Vo, C. D., Kilcher, G., and Tirelli, N. (2009) Polymers and sulfur: what are organic polysulfides good for? Preparative strategies and biological applications. *Macromol. Rapid Commun. 30*, 299–315.

(12) Paramonov, S. E., Bachelder, E. M., Beaudette, T. T., Standley, S. M., Lee, C. C., Dashe, J., and Frechet, J. M. J. (2008) Fully acid-degradable biocompatible polyacetal microparticles for drug delivery. *Bioconjugate Chem. 19*, 911–919.

(13) Heffernan Michael, J., and Murthy, N. (2005) Polyketal nanoparticles: a new pH-sensitive biodegradable drug delivery vehicle. *Bioconjugate Chem. 16*, 1340–2.

(14) Broaders, K. E., Cohen, J. A., Beaudette, T. T., Bachelder, E. M., and Frechet, J. M. J. (2009) Acetalated dextran is a chemically and biologically tunable material for particulate immunotherapy. *Proc. Natl. Acad. Sci. U. S. A. 106*, 5497–5502.

(15) Jain, R., Standley, S. M., and Frechet, J. M. J. (2007) Synthesis and degradation of pH-sensitive linear poly(amidoamine)s. *Macromolecules 40*, 452–457.

(16) Murthy, N., Thng, Y. X., Schuck, S., Xu, M. C., and Frechet, J. M. J. (2002) A novel strategy for encapsulation and release of proteins: Hydrogels and microgels with acid-labile acetal cross-linkers. *J. Am. Chem. Soc. 124*, 12398–12399.

(17) Punnia-Moorthy, A. (1987) Evaluation of pH changes in inflammation of the subcutaneous air pouch lining in the rat, induced by carrageenan, dextran and staphylococcus aureus. *J. Oral Pathol. Med. 16*, 36–44.

(18) Ródenas, J., Mitjavila, M. T., and Carbonell, T. (1995) Simultaneous generation of nitric oxide and superoxide by inflammatory cells in rats. *Free Radical Biol. Med. 18*, 869–875.

(19) Greenwald, R. A. (1991) Oxygen radicals, inflammation, and arthritis: Pathophysiological considerations and implications for treatment. *Seminars in Arthritis and Rheumatism 20*, 219–240.

(20) Rehor, A., Hubbell, J. A., and Tirelli, N. (2005) Oxidation-sensitive polymeric nanoparticles. *Langmuir 21*, 411–417.

(21) Reddy, S. T., Rehor, A., Schmoekel, H. G., Hubbell, J. A., and Swartz, M. A. (2006) In vivo targeting of dendritic cells in lymph nodes with poly(propylene sulfide) nanoparticles. *J. Controlled Release 112*, 26–34.

(22) Giles, G. I. (2006) The redox regulation of thiol dependent signaling pathways in cancer. *Curr. Pharm. Des. 12*, 4427–4443.

(23) Navab, M., Ananthramaiah, G. M., Reddy, S. T., Van Lenten, B. J., Ansell, B. J., Fonarow, G. C., Vahabzadeh, K., Hama, S., Hough, G., Kamranpour, N., Berliner, J. A., Lusis, A. J., and Fogelman, A. M. (2004) Thematic review series: The pathogenesis of atherosclerosis: The oxidation hypothesis of atherogenesis: The role of oxidized phospholipids and HDL. *J. Lipid Res. 45*, 993–1007.

(24) Shigenaga, M. K., Hagen, T. M., and Ames, B. N. (1994) Oxidative damage and mitochondrial decay in aging. *Proc. Natl. Acad. Sci. U. S. A. 91*, 10771–8.

(25) Szatrowski, T. P., and Nathan, C. F. (1991) Production of large amounts of hydrogen peroxide by human tumor cells. *Cancer Res. 51*, 794–798.

(26) Dalwadi, G., Benson, H. A., and Chen, Y. (2005) Comparison of diafiltration and tangential flow filtration for purification of nanoparticle suspensions. *Pharm. Res. 22*, 2152–62.

(27) Smith, E. R. B. (1935) The effect of variations in ionic strength on the apparent isoelectric point of egg albumin. *J. Biol. Chem. 108*, 187–194.

(28) Khutoryanskiy, V. V., and Tirelli, N. (2008) Oxidation-responsiveness of nanomaterials for targeting inflammatory reactions. *Pure Appl. Chem. 80*, 1703–1718.

(29) Burkersroda, F. v., and Goepferich, A. M. (1999) An approach to classify degradable polymers. *Mater. Res. Soc. Symp. Proc. 550*, 17–22.

(30) Greish, K., Fang, J., Inutsuka, T., Nagamitsu, A., and Maeda, H. (2003) Macromolecular therapeutics - Advantages and prospects with special emphasis on solid tumour targeting. *Clin. Pharmacokinetics 42*, 1089–1105.

(31) Kwon, G. S., Yokoyama, M., Okano, T., Sakurai, Y., and Kataoka, K. (1993) Biodistribution of micelle-forming polymer drug conjugates. *Pharm. Res. 10*, 970–974.

(32) Lu, Z. R., Parker, D. L., Goodrich, K. C., Wang, X. H., Dalle, J. G., and Buswell, H. R. (2004) Extracellular biodegradable macromolecular gadolinium(III) complexes for MRI. *Magn. Reson. Med. 51*, 27–34.

(33) Gong, X., Li, Q., Xu, K., Liu, X., Li, H., Chen, Z., Tong, L., Tang, B., and Zhong, H. (2009) A new route for simple and rapid determination of hydrogen peroxide in RAW264.7 macrophages by microchip electrophoresis. *Electrophoresis 30*, 1983–1990.

Inflammation responsive logic gate nanoparticles for the delivery of proteins

Enas A. Mahmoud[†], Jagadis Sankaranarayanan[†], Jose´ M. Morachis[†], Gloria Kim[†], and Adah Almutairi[†, ‡, §]*

[†]Skaggs School of Pharmacy and Pharmaceutical Sciences, [‡]Materials Science and Engineering, and [§]NanoEngineering, University of California at San Diego, La Jolla, California 92093-0657

*Correspoding author: Prof. Adah Almutairi, aalmutairi@ucsd.edu

Content:

1. ^{1}HNMR of compound 3.
2. ^{13}CNMR of compound 3.
3. HR-ESI-FT-MS (Orbit-Trap-MS) of compound 3.
4. ^{1}HNMR of *poly* 5.
5. ^{13}CNMR of *poly* 5.
6. GPC trace of Poly 5 calibrated against Polystyrene standards.

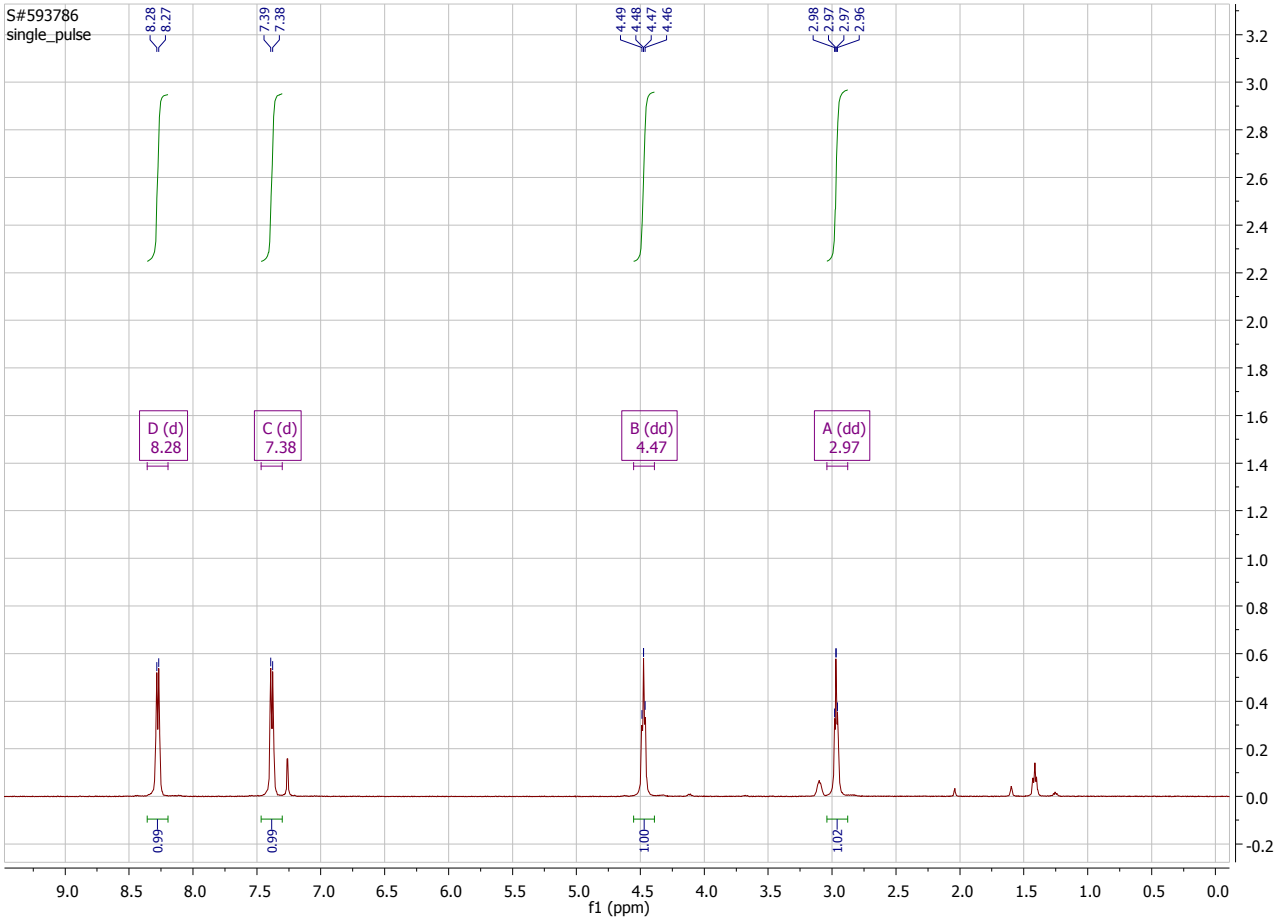

Sl-figure 1: ^{1}HNMR of compound 3.

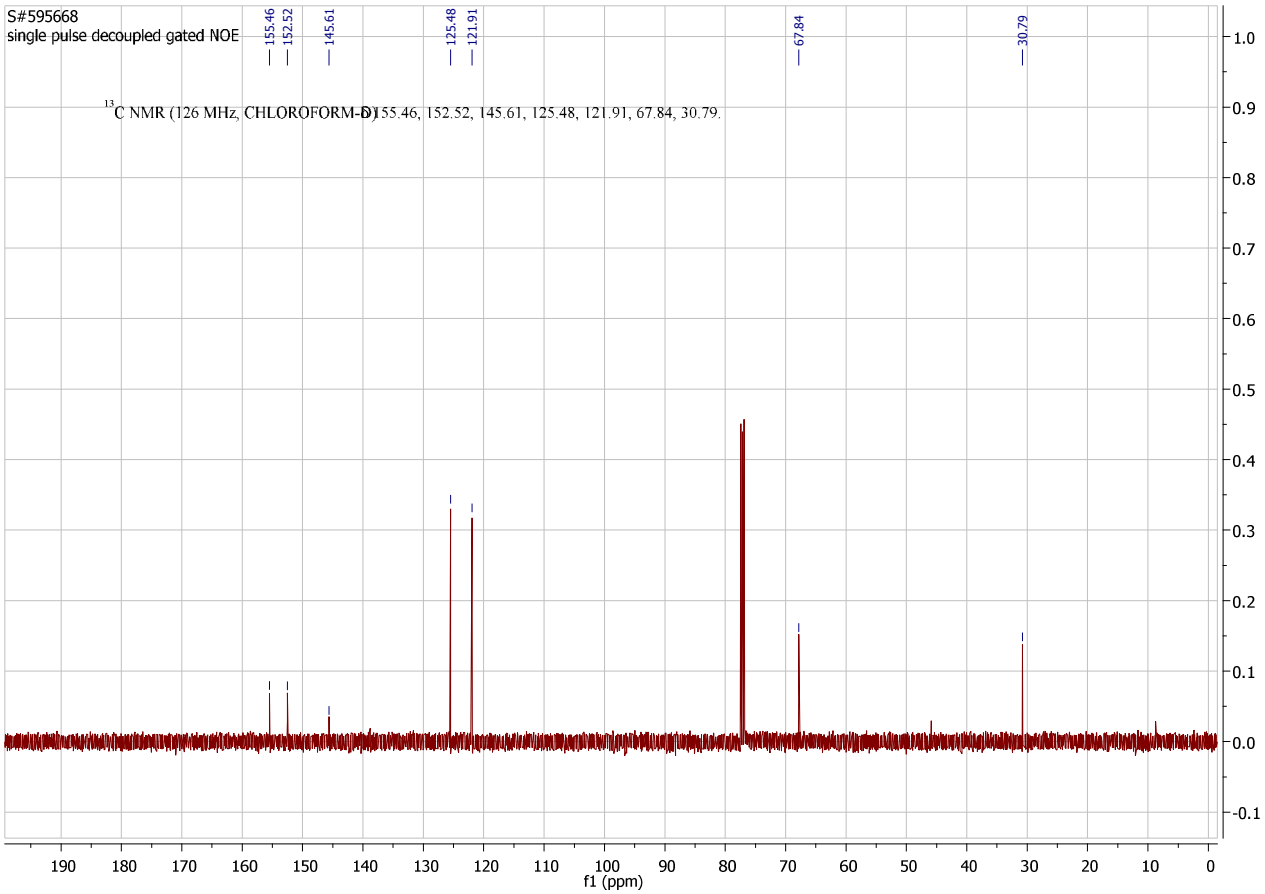

Sl-figure 2: ^{13}CNMR of compound 3.

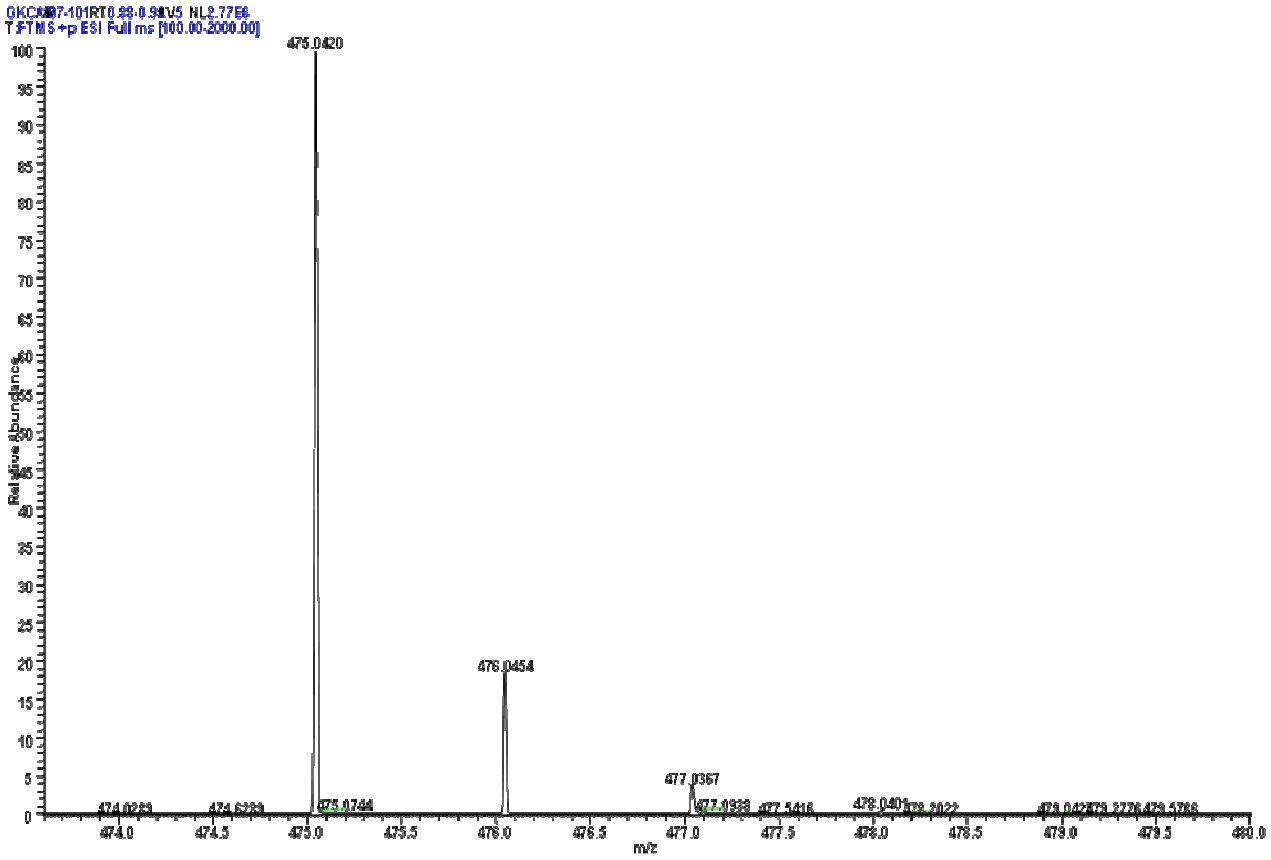

Sl-figure 3: HR-ESI-FT-MS (Orbit-Trap-MS) of compound 3.

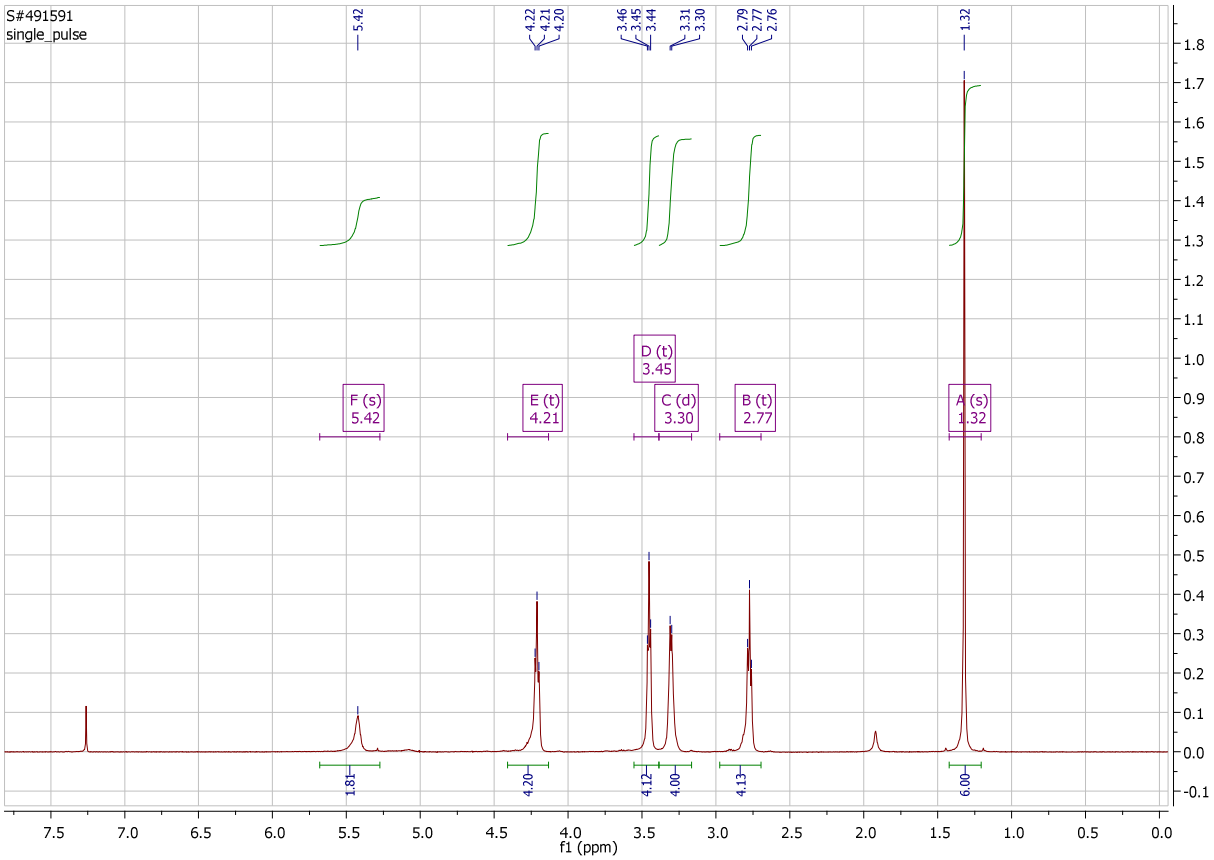

Sl-figure 4: ^{1}HNMR of *poly* 5

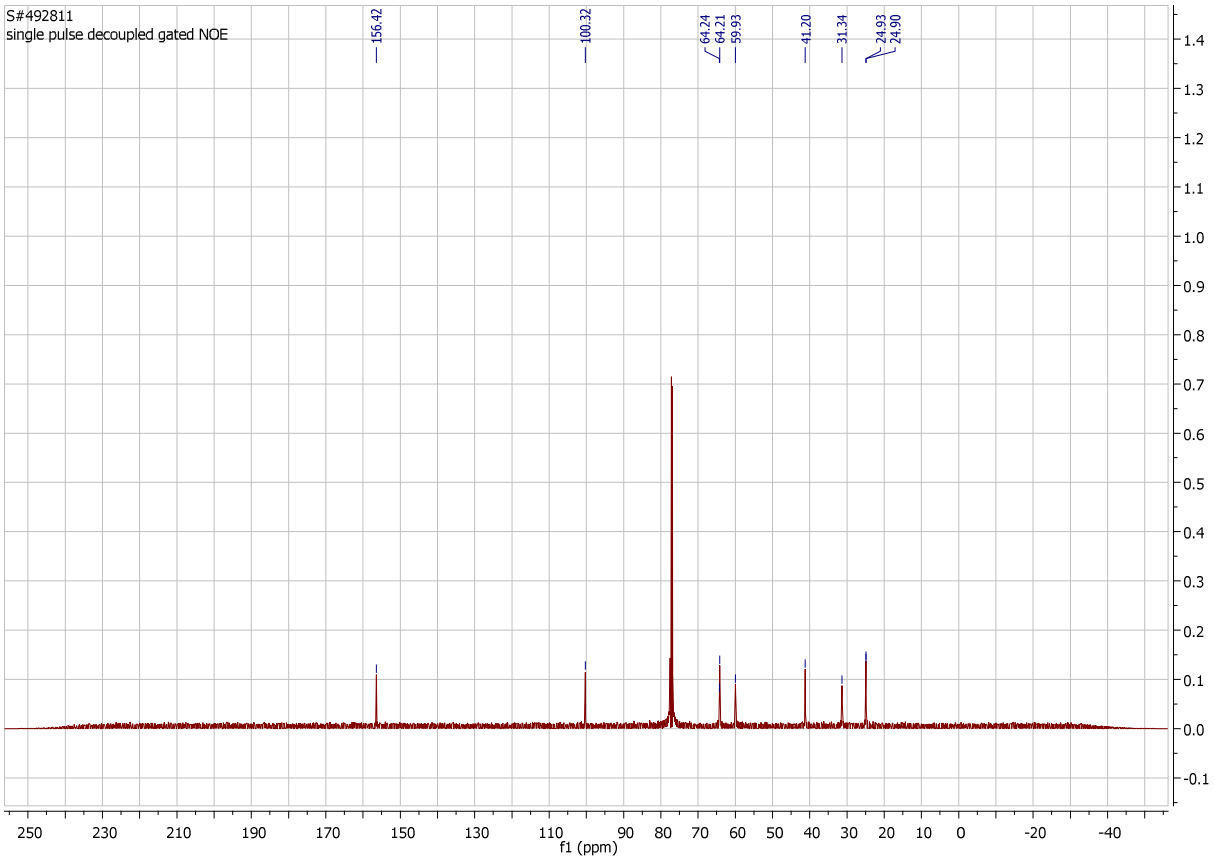

Sl-figure 5: ^{13}CNMR of *poly* 5.

GPC-DMF:

(1) 2 Columns: Viscotek I-MBHMW-3078, I-Series Mixed Bed High Molecular Weight, GPC/SEC Columns; Seperation Range 100-20 k(30cm x 7.8mm id.), and (2) 2 Columns Viscotek IMBLMW-3078, I-Series Mixed Bed Low Molecular Weight GPC/SEC Columns, Separation Range: 100-20k (30cm x 7.8mm id).

DMF: One of the most commonly employed solvents for studying solution properties of polar molecules. The addition of the electrolytic salt, LiBr (0.01%), stabilizes the effects whether associated with the polymer or the columns, enabling normal fractionation to occur.

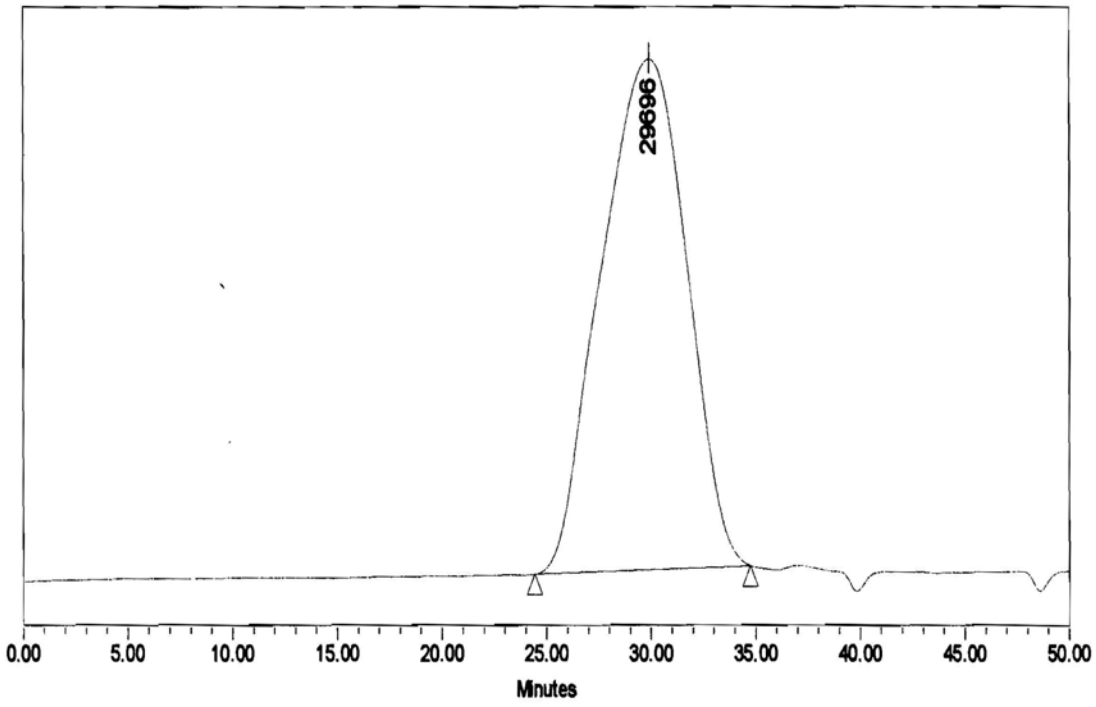

GPC Results

	Dist Name	Mn	Mw	MP	Mz	Mz+1	Mv	Poly dispersity	MW Marker 1	MW Marker 2
1		27623	49775	29696	98764	172877		1.801988		

Sl-figure 6: GPC trace of Poly 5 calibrated against Polystyrene standards

Bioconjugate Chemistry

ARTICLE

pubs.acs.org/bc

Covalent Cell Surface Functionalization of Human Fetal Osteoblasts for Tissue Engineering

Françoise Borcard,[§] Aurélien Godinat,[§] Davide Staedler,[§] Horacio Comas Blanco,[§] Anne-Laure Dumont,[§] Catherine Chapuis-Bernasconi,[†] Corinne Scaletta,[‡] Lee Ann Applegate,[‡] Franziska Krauss Juillerat,[∥] Urs T. Gonzenbach,[∥] Sandrine Gerber-Lemaire,[*,§] and Lucienne Juillerat-Jeanneret[*,†]

[§]Institute of Chemical Sciences and Engineering, EPFL, CH-1015, Lausanne, Switzerland

[†]University Institute of Pathology

[‡]Department of Musculoskeletal Medicine, Cellular Therapy Unit CHUV-UNIL, CH-1011 Lausanne, Switzerland

[∥]Nonmetallic Inorganic Materials, ETHZ, CH-8093 Zürich, Switzerland

Supporting Information

ABSTRACT: The chemical functionalization of cell-surface proteins of human primary fetal bone cells with hydrophilic bioorthogonal intermediates was investigated. Toward this goal, chemical pathways were developed for click reaction-mediated coupling of alkyne derivatives with cellular azido-expressing proteins. The incorporation via a tetraethylene glycol linker of a dipeptide and a reporter biotin allowed the proof of concept for the introduction of cell-specific peptide ligands and allowed us to follow the reaction in living cells. Tuning the conditions of the click reaction resulted in chemical functionalization of living human fetal osteoblasts with excellent cell survival.

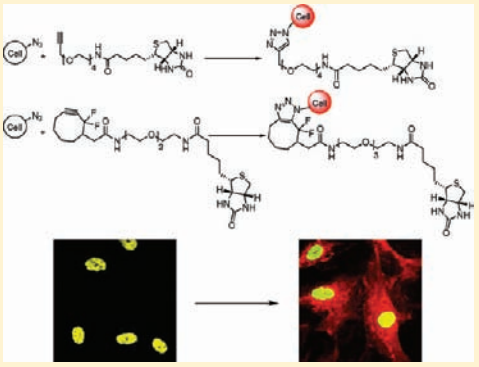

INTRODUCTION

During the past decade, bioorthogonal chemical reactions have been developed to probe biomolecules in living systems.[1−5] The chemical motifs involved in these reactions include peptide sequence with specific side chain combinations, carbonyl moieties for condensation with aminooxy or hydrazides probes, and azides for Staudinger ligation with triarylphosphines and cycloadditions to alkynes.[6,7] The biocompatibility of these reactions provides efficient tools for the modification of proteins, the labeling of enzymes, and the metabolic labeling of cell-surface glycans and lipids within their native cellular environment and thus allows us to study the biological processes in which these biomolecules are involved. Further development of highly reactive bioorthogonal reagents, avoiding the use of metal promoters,[8−14] extended the application of these probing methodologies to living cells and animals.

A promising approach in tissue engineering is to seed implants with the cells of interest prior to implantation. Such an approach may require chemical functionalization of the cell surface. Human fetal cells have an interesting potential for therapeutic use in tissue engineering and regeneration, including bone tissue engineering, due to their rapid growth rate and their ability to differentiate *in vitro* into mature osteoblasts, as well as their histocompatibility,[15−17] eliminating the need for antigraft rejection medication of the patients.

For further development of bone implants, we aimed to develop means to chemically functionalize human fetal osteoblasts toward future application of these modified cells in implant biomaterials. As small peptides[18,19] can promote cell adhesion and proliferation, we have focused on the development of hydrophilic ligands containing amino acid residues. Here, the use of copper-mediated and copper-free catalyzed azide−alkyne [3 + 2] dipolar cycloaddition was investigated for the covalent functionalization of cell-surface proteins of human primary fetal osteoblasts. Chemical ligands containing amino acid residues, a terminal alkyne for functionalization of cell surface proteins through copper-mediated and copper-free [3 + 2] dipolar cycloadditions, and a biotin label for probing cell functionalization were designed and synthesized. Then, their potential to covalently functionalize human fetal osteoblasts was evaluated. The efficiency of the coupling reaction was determined using the reporter biotin conjugate, as previously used in a different cellular model,[20,21]

Received: March 24, 2011
Revised: May 13, 2011
Published: June 13, 2011

ACS Publications © 2011 American Chemical Society

and the long-term survival of the functionalized cells following the click reactions was optimized.

EXPERIMENTAL PROCEDURES

General Methods. Commercial reagents (Fluka, Aldrich, Bachem) were used without purification. Anhydrous solvents were obtained by filtration. Liquid/solid flash chromatography (FC): columns of silica gel (0.040−0.63 mm, Merck no. 9385 silica gel 60, 240−400 mesh). Eluent: mixture of light petroleum ether (PE) and ethyl acetate (EtOAc) or mixture of dichloromethane (DCM) and methanol (MeOH). TLC for reaction monitoring: Merck silica gel 60 F_{254} plates; detection by UV light; Pancaldi reagent, $KMnO_4$, ninhydrine or phosphomolybdic acid. IR spectra: Perkin-Elmer-1420 spectrometer. ^{1}H NMR spectra: Bruker-ARX-400 spectrometer (400 MHz); δ(H) in ppm relative to the solvent's residual ^{1}H signal [$CHCl_3$, δ(H) 7.27, MeOD, δ(H) 3.31] as internal reference. ^{13}C NMR spectra: same instrument as above (100.6 MHz); δ(C) in ppm relative to solvent's C-signal [$CDCl_3$, δ(C) 77.1, MeOD, δ(C) 49.0] as internal reference. GC-MS spectrometer (Nermag R-10-10C, chemical ionization (NH_3) mode m/z); MALTI-TOF spectrometer (Axima-CFR+, Kratos, Manchester); ESI-Q spectrometer (Finnigan SSQ 710C, Thermoquest, UK); ESI-QT spectrometer (Ultima spectrometer, Micromass, Manchester).

Syntheses. *tert-Butyl N^2-[9A fluoren-9-ylmethoxy)carbonyl]-N-3,6,9,12-tetraoxa-pentadec-14-yn-1-yl-L-α-glutaminate (**5**).* Fmoc-glu-(O*t*Bu)-OH (360 mg, 0.9 mmol, 1 equiv) and PyBOP (540 mg, 1.0 mmol, 1.2 equiv) were dissolved in DCM (8 mL). DIPEA (0.3 mL, 1.7 mmol, 2 equiv) was added, followed by a solution of **3**[22] (200 mg, 0.9 mmol, 1 equiv) in dichloromethane (4 mL) at 0 °C. After 15 min, the reaction mixture was warmed to 25 °C and stirred for 12 h. The solvent was removed under reduced pressure and the resulting mixture was dissolved in EtOAc. This solution was washed with saturated NH_4Cl, H_2O, 5% $NaHCO_3$, and finally with saturated NaCl. The organic phase was dried over anhydrous $MgSO_4$, filtered, and concentrated under reduced pressure. The product was purified by flash column chromatography (EtOAc/petroleum ether 2:1, then 3:1) (332 mg, 60%). IR (film): 3285, 2870, 1715, 1665, 1520, 1450, 1390, 1350, 1245, 1150, 1085, 1045, 950, 840, 760, 740, 645, 620, 555, 540, 515, 500 cm^{-1}. ^{1}H NMR (400 MHz, $CDCl_3$): δ = 7.76 (d, ^3J = 7.5 Hz, 1H, H_{arom}), 7.60 (d, ^3J = 7.4 Hz, 1H, H_{arom}), 7.40 (t, ^3J = 7.4 Hz, 1H, H_{arom}), 7.32 (t, ^3J = 7.4 Hz, 1H, H_{arom}), 6.75 (s, 1H, NH), 5.83 (s, 1H, NH), 4.41 (m, 2H, H-1″), 4.21 (m, 4H, H_2-13, H-9, H-2), 3.69−3.45 (m, 16H, $(CH_2$-$O)_8$), 2.36 (m, 2H, H-4, H_2-3), 2.01 (m, 3H, H-4, H_2-3, H-15), 1.46 (s, 9H, $(CH_3)_3$). ^{13}C NMR (100 MHz, $CDCl_3$): δ = 172.7, 171.9, 143.8, 141.3, 127.7, 127.1, 125.1, 119.9, 80.7, 74.7, 70.2, 70.1, 70.0, 69.9, 68.6, 67.0, 58.3, 54.4, 47.2, 39.3, 31.6, 28.1. HRMS (ESI): (m/z): calcd for $C_{35}H_{46}N_2O_9$+H: 639.3282, found: 639.3292. $[\alpha]_D^{25}$ = −22 (c = 0.085, CH_2Cl_2).

*tert-Butyl N^2-[4-Oxohexahydro-1H-thieno[3,4-d]imidazol-4-yl-pentanoyl]-N-(3,6,9,12-tetraoxapentadec-14-yne-1-yl)-L-α-glutaminyl-L-phenylalaninate (**9**).* N^2-[9A fluoren-9-ylmethoxy)-carbonyl]-*N*-3,6,9,12-tetraoxa-pentadec-14-yn-1-yl-L-α-glutaminate **5** (536 mg, 0.84 mmol, 1 equiv) was dissolved into a solution of 4 M HCl in dioxane (3.20 mL) at 25 °C. After stirring for 1 h, the solvent was removed and HCl was coevaporated in the presence of acetonitrile to afford acid **6** as a white solid (420 mg, 86%). *N*^{2}-[9A fluoren-9-ylmethoxy)carbonyl]-*N*-3,6,9,12-tetraoxa-pentadec-14-yn-1-yl-L-α-glutaminate **6** (100 mg, 0.17 mmol, 1 equiv) and PyBOP (107 mg, 0.21 mmol, 1.2 equiv) were dissolved in dry DCM (1.6 mL). Triethylamine (88 μL 0.51 mmol, 3 equiv) was added at −5 °C. A solution of L-Phe-O*t*Bu (44 mg, 0.17 mmol, 1 equiv) in DCM (1.2 mL) was added dropwise. The reaction mixture was stirred until total conversion of the starting material (monitored by TLC). The solvent was removed under reduced pressure and EtOAc was added. The organic phase was washed with saturated NH_4Cl, H_2O, and finally aqueous 5% $NaHCO_3$. The resulting mixture was dried over anhydrous $MgSO_4$, filtered, and concentrated. The product **7** was purified by flash column chromatography (CH_2Cl_2/MeOH 95:5) to afford a colorless oil (100 mg, yield 75%). *tert*-Butyl *N*^{2}-[9A fluoren-9-ylmethoxy)carbonyl]-*N*-(3,6,9,12-tetraoxa-pentadec-14-yn-1-yl)-L-α-glutaminyl-L-phenylalaninate **7** (100 mg, 0.13 mmol, 1 equiv) was dissolved into a solution of 20% piperidine in DMF (2.5 mL) at 25 °C. After stirring for 1 h, the solvent was evaporated and piperidine was removed by coevaporation with toluene. The product was purified by flash column chromatography (CH_2Cl_2/MeOH 95:5) to afford a colorless oil (17 mg, 18%). *tert*-Butyl *N*-(3,6,9,12-tetraoxa-pentadec-14-yn-1-yl)-L-α-glutaminyl-L-phenylalaninate (17 mg, 0.03 mmol, 1 equiv) and biotin-OSu (10 mg, 0.03 mol, 1 equiv) were dissolved in DMF (0.3 mL) at 25 °C. Triethylamine (6.3 μL, 0.05 mmol, 1.5 equiv) was added. The reaction mixture was stirred for 12 h at 25 °C. The solvent was removed, and the product was purified by HPLC (XTerra Prep RP C18, (19 × 150 mm Waters)) to afford **9** as a colorless oil (7 mg, 30%). IR (film): 3275, 2925, 2860, 2405, 1645, 1535, 1455, 1365, 1255, 1200, 1150, 1095, 1030, 840, 700, 605, 580, 570, 520 cm^{-1}. ^{1}H NMR (400 MHz, MeOD): δ = 7.25 (m, 5H, H_{arom}), 4.54 (dd, ^2J = 8.2, ^3J = 6.7 Hz, H-6a), 4.49 (dd, 1H, ^2J = 7.8, ^3J = 4.8 Hz, H-2, H-2′), 4.30 (dd, 1H, ^2J = 7.8, ^3J = 4.4 Hz, H-2, H-2′), 4.25 (dd, 1H, ^2J = 8.2, ^3J = 6.4 Hz, H-3a), 4.18 (d, 2H, ^4J = 2.4 Hz, H-13), 3.67−3.34 (m, 16H, $(CH_2$-$O)_8$, 3.20 (m, 1H, H-4‴), 3.07 (dd, 1H, ^2J = 13.8, ^3J = 6.7 Hz, H_2-3), 2.98 (dd, 1H, ^2J = 13.8, ^3J = 5.5 Hz, H_2-3), 2.92 (dd, 1H, ^2J = 12.7, ^3J = 5.0 Hz, H_2-6‴), 2.85 (t, 1H, ^3J = 2.4 Hz, H-15), 2.70 (d, 1H, ^3J = 12.7 Hz, H_2-6‴), 2.27 (m, 4H, $(CH_2)_2$), 1.99−1.44 (m, 8H, $(CH_2)_4$), 1.42 (s, 9H, $(CH_3)_3$). ^{13}C NMR (100 MHz, MeOD): δ = 176.0, 174.8, 173.9, 172.7, 166.2, 138.2, 130.4, 129.4, 127.9, 83.0, 76.0, 71.5, 71.5, 71.3, 71.2, 70.4, 70.1, 63.2, 61.6, 59.0, 56.9, 55.9, 54.2, 41.0, 40.4, 38.6, 36.4, 32.8, 29.6, 29.4, 29.0, 28.2, 26.6. HRMS (ESI): (m/z): calcd for $C_{39}H_{59}N_5O_{10}$S+H: 790.4061, found: 790.4073. $[\alpha]_D^{25}$ = −55 (c = 0.04, CH_2Cl_2).

*tert-Butyl N^2-[5-(2-oxohexahydro-1H-thieno[3,4-d]imidazol-4-yl)-pentanoyl]-N-(3,6,9,12-tetraoxapentadec-14-yne-1-yl)-L-α-glutaminyl-L-prolinate (**10**).* N^2-[9A fluoren-9-ylmethoxy)-carbonyl]-*N*-3,6,9,12-tetraoxa-pentadec-14-yn-1-yl-L-α-glutaminate **5** (100 mg, 0.17 mmol, 1 equiv) and PyBOP (107 mg, 0.21 mmol, 1.2 equiv) were dissolved in dry DCM (1.6 mL). Triethylamine (88 μL, 0.51 mmol, 3 equiv) was added at −5 °C. A solution of L-Pro-O^{t}Bu (36 mg, 0.17 mmol, 1 equiv) in DCM (1.2 mL) was added dropwise. The reaction mixture was stirred until total conversion of the starting material. The solvent was removed under reduced pressure and EtOAc was added. The organic phase was washed with saturated NH_4Cl, H_2O, and finally 5% $NaHCO_3$. The resulting mixture was dried over anhydrous $MgSO_4$, filtered, and concentrated. The product was purified by flash column chromatography (CH_2Cl_2/MeOH 95:5) to afford a colorless oil (81 mg, yield 65%). *tert*-Butyl *N*^{2}-[9A fluoren-9-ylmethoxy)carbonyl]-*N*-(3,6,9,12-tetraoxa-pentadec-14-yn-1-yl)-L-α-glutaminyl-L-prolinate **8** (81 mg, 0.11 mmol, 1 equiv) was dissolved into a solution of 20% piperidine in DMF (2.2 mL)

at 25 °C. After stirring for 1 h, the solvent was evaporated and piperidine was removed by coevaporation with toluene. The product was purified by flash column chromatography (CH_2Cl_2/MeOH 95:5 then 9:1) to afford a colorless oil (34 mg, 60%). *tert*-Butyl *N*-(3,6,9,12-tetraoxa-pentadec-14-yn-1-yl)-L-α-glutaminyl-L-prolinate (34 mg, 0.07 mmol, 1 equiv) and biotin-OSu (23 mg, 0.07 mol, 1 equiv) were dissolved in DMF (0.7 mL) at 25 °C. Triethylamine (13.8 μL, 0.99 mmol, 1.5 equiv) was added. The reaction mixture was stirred at 25 °C for 12 h. The solvent was removed and the product was purified by HPLC (XTerra Prep RP C18, (19 × 150 mm Waters)) to afford **10** as a colorless oil (12 mg, 25%). IR (film): 3270, 2870, 2475, 1640, 1535, 1445, 1345, 1245, 1200, 1090, 1035, 940, 840, 650, 605, 595, 530, 520 cm^{-1}. ^1H NMR (400 MHz, MeOD): δ = 4.48 (m, 1H, H-6a), 4.33 (m, 2H, H-3a, H-2), 4.19 (d, 2H, ^4J = 2.3 Hz, H_2-13), 3.68−3.54 (m, 16H, $(CH_2\text{-}O)_8$), 3.42 (m, 2H, H_2-5), 3.21 (m, 1H, H-4), 2.93 (dd, 1H, ^2J = 12.7, ^3J = 5.0 Hz, H_2-6) 2.86 (t, 1H, ^3J = 2.4 Hz, H-15), 2.71 (d, 1H, ^2J = 12.7 Hz, H_2-6), 2.48−1.56 (m, 16H, $(CH_2)_8$), 1.47, (s, 9H, $(CH_3)_3$).^{13}C NMR (100 MHz, MeOD): δ = 176.1, 173.3, 173.2, 82.7, 76.0, 71.6, 71.6, 71.3, 70.5, 70.1, 63.3, 61.7, 61.1, 59.1, 57.0, 54.3, 48.4, 41.1, 40.6, 40.4, 36.5, 31.6, 30.3, 29.6, 29.4, 29.3, 28.3, 26.7, 25.6. HRMS (ESI) (*m*/*z*) calcd for $C_{35}H_{57}N_5O_{10}S$+H: 740.3904, found: 740.3927. $[\alpha]_D^{25}$ = −31 (*c* = 0.035, CH_2Cl_2).

*N-(tert-Butoxycarbonyl)glycyl-N-(2-{2-[2-(2-hydroxyethoxy)-ethoxy]ethoxy}ethyl)prolinamide (**11**).* Triethylamine (2.3 mL, 16.5 mmol, 3 equiv) and PyBOP (3.2 g, 6.1 mmol, 1.1 equiv) were added to a solution of Boc-Gly-Pro (1.5 g, 5.5 mmol, 1 equiv) in DCM (26 mL). After 15 min, 2-(2-(2-(2-aminoethoxy)-ethoxy)ethoxy)ethanol (1.1 g, 5.5 mmol, 1 equiv) in DCM (26 mL) was added. The reaction mixture was stirred until total conversion of the starting material (monitored by TLC). The solvent was removed under reduced pressure and the product was purified by column chromatography (CH_2Cl_2/MeOH 95:5) to afford a colorless oil (2.34 g, 95%). IR (film): 3410, 2875, 2495, 1650, 1440, 1365, 1250, 1165, 1120, 980, 840, 630, 540, 505 cm^{-1}. ^1H NMR (400 MHz, MeOD): δ = 4.44 (dd, ^2J = 8.6, ^3J = 2.8 Hz, $1H_a$, H-2) 4.40 (dd, ^2J = 8.6, ^3J = 3.7 Hz, $1H_b$, H-2), 3.91 (m, H_2-2′), 3.68−3.35 (m, 18H, $(CH_2\text{-}O)_6$, CH_2-OH, H_2-5), 3.22 (q, $N^+H(CH_2CH_3)_3$), 2.35−1.86 (m, 4H, H_2-3, H_2-4), 1.45 (s, 9H, $(CH_3)_3$), 1.31 (t, $N^+H(CH_2CH_3)_3$).^{13}C NMR (100 MHz, MeOD): δ = 174.6, 170.5, 158.5, 80.6, 73.6, 71.6, 71.3, 71.2, 71.1, 70.4, 70.3, 62.2, 61.9, 61.4, 47.6, 43.8, 40.4, 40.5, 33.3, 30.7, 28.7, 25.6, 23.40. HRMS (ESI) (*m*/*z*) calcd for $C_{20}H_{37}N_3O_8$+H: 448.2659, found: 448.2658. $[\alpha]_D^{25}$ = −26 (*c* = 0.09, CH_2Cl_2).

*tert-Butyl N²-[5-(2-Oxohexahydro-1H-thieno[3,4-d]imidazol-4-yl)-pentanoyl]-N-(3,6,9,12-tetraoxa-pentadec-14-yn-1-yl)-L-α-glutaminylglycyl-N-(2-{2-[2-(2-hydroxyethoxy)ethoxy]-ethoxy}ethyl)-L-prolinamide (**12**).* N^2-[9A fluoren-9-ylmethoxy)-carbonyl]-*N*-3,6,9,12-tetraoxa-pentadec-14-yn-1-yl-L-α-glutaminate **6** (100 mg, 0.17 mmol, 1 equiv) and PyBOP (107 mg, 0.21 mmol, 1.2 equiv) were dissolved in dry DCM (1.6 mL). Triethylamine (88 μL, 0.51 mmol, 3 equiv) was added at −5 °C. A solution of glycyl-*N*-(2-{2-[2-(2-hydroxyethoxy)ethoxy]ethoxy}-ethyl)-L-prolinamide **11** (60 mg, 0.17 mmol, 1 equiv) in DCM (1.2 mL) was added dropwise. The reaction mixture was stirred until total conversion of the starting material (monitored by TLC). The solvent was removed under reduced pressure and EtOAc was added. The organic phase was washed with saturated NH_4Cl, H_2O, and finally 5% $NaHCO_3$. The resulting mixture was dried over anhydrous $MgSO_4$, filtered, and concentrated. The product was purified by flash column chromatography (CH_2Cl_2/MeOH 9:1) to afford a colorless oil (20 mg, yield 12%). *tert*-Butyl N^2-[9A fluoren-9-ylmethoxy)carbonyl]-*N*-(3,6,9,12-tetraoxa-pentadec-14-yn-1-yl)-L-α-glutaminylglycyl-*N*-(2-{2-[2-(2-hydroxyethoxy)ethoxy]ethoxy}ethyl)-L-prolinamide (20 mg, 0.02 mmol, 1 equiv) was dissolved into a solution of 20% piperidine in DMF (0.5 mL) at 25 °C. After stirring for 1 h, the solvent was evaporated and piperidine was removed by coevaporation with toluene. The product was purified by flash column chromatography (CH_2Cl_2/MeOH 9:1 then CH_3CN/NH_4 5:1) to afford a colorless oil (13 mg, 86%). *tert*-Butyl *N*-(3,6,9,12-tetraoxa-pentadec-14-yn-1-yl)-L-α-glutaminylglycyl-*N*-(2-{2-[2-(2-hydroxyethoxy)ethoxy]ethoxy}ethyl)-L-prolinamide (13 mg, 0.02 mmol, 1 equiv) and biotin-OSu (7 mg, 0.02 mol, 1 equiv) were dissolved in DMF (0.2 mL) at rt. Triethylamine (4.0 μL, 0.03 mmol, 1.5 equiv) was added. The reaction mixture was stirred at 25 °C for 12 h. The solvent was removed and the product was purified by HPLC (XTerra Prep RP C18, (19 × 150 mm Waters)) (to afford **12** as a colorless oil (6 mg, 33%). IR (film): 3265, 3075, 2920, 2865, 1780, 1640, 1535, 1445, 1345, 1330, 1245, 1200, 1090, 1030, 940, 830, 645, 600, 545, 540, 525, 510, 500 cm^{-1}.^1H NMR (400 MHz, MeOD): δ = 4.49 (dd, 1H, ^2J = 7.8, ^3J = 5.1 Hz, H-6a), 4.43 (dd, 1H, ^2J = 8.6, ^3J = 3.7 Hz, H-2, H-2″), 4.33 (m, 2H, H-3a, H-2, H-2″), 4.19 (d, 2H, ^4J = 2.4 Hz, H-13), 4.15 (dd, 1H, H-2′), 3.94 (dd, 1H, ^2J = 17.0, ^3J = 4.6 Hz, H-2′), 3.69−3.35 (m, 34H, $(CH_2\text{-}O)_{16}$, H_2-5), 3.21 (m, 1H, CH), 2.93 (dd, 1H, ^2J = 12.8, ^3J = 5.0 Hz, H_2-6), 2.86 (t, 1H, ^3J = 2.4 Hz, H-15), 2.71 (d, 1H, ^2J = 12.7 Hz, H_2-6), 2.40−1.45 (m, 16H, $(CH_2)_8$).^{13}C NMR (100 MHz, MeOD): δ = 176.0, 175.3, 174.0, 171.8, 169.9, 76.0, 73.7, 71.6, 71.55, 71.5, 71.4, 71.3, 71.2, 70.3, 70.1, 70.1, 63.2, 62.2, 61.9, 61.7, 59.0, 57.0, 54.1, 47.8, 42.8, 41.0, 40.6, 40.4, 36.4, 36.3, 32.9, 30.8, 29.6, 29.5, 29.4, 28.9, 26.7, 26.6, 25.7. HRMS (ESI) (*m*/*z*) calcd for $C_{41}H_{69}N_7O_{14}S$+H: 916.4702, found: 916.4717. $[\alpha]_D^{25}$ = −18 (*c* = 0.05, CH_2Cl_2).

*[5-[3a,4a,6a)-2-oxohexahydro-1H-thieno[3,4-d]imidazol-4-yl)-pentanoyl]-N-(3,6,9,12-tetraoxa-pentadec-14-yn-1-yl)pentanamide (**13**).* Biotin-OSu (0.83 g, 2.4 mmol, 1 equiv) followed by triethylamine (0.5 mL, 3.6 mmol, 1.5 equiv) were added to a solution of 3,6,9,12-tetraoxapentadec-14-yn-1-amine (0.56 g, 2.4 mmol, 1 equiv) in DMF (24 mL). The reaction mixture was stirred overnight at rt. The solvent was removed under reduced pressure and the desired product was purified by column chromatography (CH_2Cl_2/MeOH 95/5) to provide a colorless oil (560 mg, 51%). IR (film): 3245, 2925, 2865, 1810, 1780, 1700, 1645, 1550, 1460, 1350, 1325, 1305, 1265, 1245, 1210, 1090, 1035, 945, 860, 840, 760, 635, 600, 540, 530, 505 cm^{-1}.^1H NMR (400 MHz, MeOD): δ = 4.49 (dd, 1H, ^2J = 8.0, ^3J = 5.0 Hz, H-6a), 4.31 (dd, 1H, ^2J = 7.9, ^3J = 4.5 Hz, H-3a), 4.19 (d, 2H, ^4J = 2.5 Hz, H-13), 3.69−3.61 (m, 12H, $(CH_2\text{-}O)_6$, 3.56 (t, 2H, ^3J = 5.3 Hz, CH_2-O), 3.36 (m, 2H, CH_2-O), 3.20 (m, 1H, H-4a), 2.93 (dd, 1H, ^2J = 12.8, ^3J = 5.0 Hz, H_2-6), 2.85 (t, 1H, ^3J = 2.4 Hz, H-15), 2.71 (d, 1H, ^3J = 12.7 Hz, H_2-6), 2.23 (t, 2H, ^3J = 7.3 Hz, CH_2), 1.77−1.41 (m, 6H, $(CH_2)_3$). ^{13}C NMR (100 MHz, MeOD): δ = 176.22, 75.97, 71.55, 71.51, 71.50, 71.34, 71.23, 70.57, 70.11, 63.34, 61.60, 59.04, 56.98, 41.04, 40.38, 36.77, 29.74, 29.48, 26.83, 26.28. HRMS (ESI) (*m*/*z*) calcd for $C_{21}H_{35}N_3O_6S$+H: 458.2325, found: 458.2337. $[\alpha]_D^{25}$ = 22 (*c* = 0.195, CH_2Cl_2).

*N-[14-(2,2-Difluorocyclooct-3-yn-1-yl)-13-oxo-3,6,9-trioxa-12-azatetradec-1-yl]-5-(2-oxohexahydro-1H-thieno[3,4-d]imidazol-4-yl)pentanamide (**16**).* The (2,2-difluorocyclooct-3-yn-1-yl)acetic acid (10 mg, 0.05 mmol, 1 equiv) was dissolved with dry dichloromethane (0.38 mL) in a flame-dried round-bottom flask and put under an argon atmosphere. A solution of amino-PEG-biotin

(20.70 mg, 0.05 mmol, 1 equiv) and *N*-ethyldiisopropylamine (12.69 mg, 0.07 mmol, 1.5 equiv) in dry DCM (0.38 mL) was added to the reaction mixture. The system was stirred at rt for 5 h, and then purified by flash chromatography (9:1 to 8:2 EtOAc/MeOH) to afford a white solid (12.10 mg, 0.02 mmol, 41%). IR (film): 3265, 2930, 2870, 2220, 1705, 1645, 1555, 1460, 1385, 1280, 1240, 1130, 1030, 1010, 940, 750, 690, 665, 650, 605 cm^{-1}.^{1}H NMR (400 MHz, MeOD-d_4): δ= 4.50 (dd, 1H, ^2J = 7.7, ^3J = 5.0 Hz, H-34), 4.31(dd, 1H, ^2J = 7.7, ^3J = 4.5 Hz, H-30), 3.64 (app. d, 8H, ^3J = 5.6 Hz H_2-15, H_2-16, H_2-18, H_2-19), 3.55 (t, 4H, ^3J= 5.4 Hz, H_2-34, H_2-21), 3.37 (m, 4H, H_2-12, H_2-22), 3.21 (m, 1H, H-29), 2.93 (dd, 1H, ^2J = 12.8, ^3J = 4.9 Hz, H_2-35a), 2.83−2.74 (m, 1H, H-1), 2.71 (d, 1H, ^2J = 12.7 Hz, H_2-35b), 2.51 (dd, 1H, ^2J = 12.7, ^3J = 3.8 Hz, H_2-9a), 2.47−2.31 (m, 2H, H_2-5), 2.22 (app. t, 3H, ^3J = 6.9 Hz, H_2-25, H_2-9b), 2.17−2.08 (m, 2H, H_2-6), 1.86−1.51 (m, 6H, H_2-26, H_2-28, H_2-7), 1.48−1.29 (m, 4H, H_2-27, H_2-8) ppm. ^{13}C NMR (100 MHz, MeOD-d_4): δ = 176.1, 173.8, 166.1, 111.7, 111.5, 71.6, 71.27, 71.26, 70.6, 70.5, 63.3, 61.6, 57.0, 54.4, 41.0, 40.4, 40.3, 36.7, 35.9, 33.77, 33.75, 33.3, 33.2, 29.8, 29.5, 28.9, 26.8, 20.6 ppm. HRMS (ESI) (*m*/*z*) calcd for $C_{28}H_{44}F_2N_4O_6S$+H: 603.3028, found: 603.3027. $[\alpha]_D^{25}$ = 130 (*c* = 0.105, CH_2Cl_2).

Cellular Assays. *Cells and Cell Culture Reagents.* Human fetal osteoblasts were derived by the explant technique from the femoral bone of a 12-week-old fetus according to a protocol accepted by the Lausanne Hospital and University Ethics Committee and with the mother's oral and written approval (protocol no. 51/01, 2008). The cells were used at passage 6 of the initial culture. Cells were routinely grown in DMEM medium containing 4.5 g/L glucose, 10% heat-inactivated fetal calf serum (FCS), and penicillin/streptomycin (P/S). All cell culture reagents were obtained from Invitrogen, Basel, Switzerland. L-Azidohomoalanine (AHA) was purchased from Invitrogen, bovine serum albumin (BSA), copper sulfate and tris[(1-benzyl-1*H*-1,2,3-triazol-4-yl)methyl]amine (TBTA) from Sigma-Aldrich, Buchs, Switzerland, and the WST-1 reagent (2-(4-iodophenyl)-3-(4-nitrophenyl)-5-(2,4-disulfophenyl)-2*H*-tetrazolium) from Roche Diagnostics, Rotkreuz, Switzerland. The click reactions were performed in the BD Falcon CultureSlides (BD Biosciences, Belgium).

Experimental Conditions for the Click Reactions. Human fetal osteoblasts (80−90% confluent) were washed with warm (37 °C) PBS and incubated in methionine-free DMEM culture medium containing 4.5 g/L glucose, antibiotics (P/S), and 3% FCS for 30−60 min to deplete methionine reserves. Then, they were incubated for 4 h in the presence of AHA (50 μM) in fresh complete culture medium. The culture medium was removed, and the cell layer was washed twice with PBS. Then, the click reactions were performed and efficacy of the reaction was evaluated by fluorescence microscopy or fresh complete medium was added and culture continued for assessing cell survival using the WST-1 test.

Fluorescence Microscopy Experiments. Click Reaction (Scheme 5A). Stock solutions of compounds **9**, **10**, **12**, **13** (0.2 mM in PBS), TBTA (1.7 mM in 4:1 ^{t}butanol/DMSO), and $CuSO_4$ (20 mM in water) were prepared. For microscopy experiments, the click reaction was performed in a total volume of 500 μL, containing PBS (410 μL), compounds **9**, **10**, **12**, **13** (20 μM), TBTA (80 μM), and $CuSO_4$ (0.8 mM) sequentially added to the cells. Incubation was performed for 1 h at 37 °C. The reaction mixture was removed and two washings with PBS allowed the complete removal of the different reagents. Streptavidin-Cy3 (Sigma-Aldrich) (1:100) and DAPI (4′,6-diamidino-2-phenylindole, Roche Diagnostics) (1 μg/mL in PBS) were then added and incubated with the cells for 30 min in the dark. After two washings with PBS during 5 min in the dark, the cells were fixed using a 4% *p*-formaldehyde solution at 4 °C. Two additional washings with PBS were performed. The chamber was removed from the slide glass by using the chamber removal device, and the evaluation of the click reaction was performed by fluorescence microscopy and slides photographed under a fluorescence microscope (Zeiss Axioplan 2).

Click Reaction (Scheme 5B). Stock solutions of compounds **12** and **13** (1 mM in PBS), $CuSO_4$ (2 mM in water), THPTA (10 mM in PBS), aminoguanidine (50 mM in PBS), and sodium ascorbate (100 mM) were prepared. The reaction mixture containing compounds **12** or **13** (100 μM), aminoguanidine (1 mM), $CuSO_4$ (50 μM), THPTA (250 μM), and sodium ascorbate (2.5 mM) in PBS was preincubated for 1 h at 4 °C. The cell culture medium was removed and the cell layer was washed twice with HBSS. For microscopy experiments, the reaction mixture was added to the cells at 4 °C for 5 min. The reaction mixture was removed and two washings with PBS at 37 °C allowed the complete removal of the different reagents. The cells were then fixed using a 4% *p*-formaldehyde solution for 10 min at room temperature. After two washings with warm PBS, the cells were incubated with PBS containing 1% BSA for 1 h at room temperature, and then the labeling was performed as above.

Click Reaction (Scheme 5C). Stock solution of compound **16** (2.5 mM in PBS/DMF (7:3)) was prepared. For microscopy experiments, the click reaction was performed in a solution containing compound **16** (100 μM) in DMEM containing additional HEPES (20 μM). Incubation was performed for 1 h at 25 °C. The reaction mixture was removed and two washings with PBS at 37 °C allowed the complete removal of the reagents. The cells were then fixed using a 4% *p*-formaldehyde solution for 10 min at room temperature. After two washings with warm PBS, the cells were incubated with PBS containing 1% BSA for 1 h at room temperature and the labeling was performed as above.

Evaluation of the Conjugation of the Ligands to the Cells. The copper-free click reaction with compound **16** (100 μM), and the THPTA/copper-catalyzed click reaction with compounds **12** or **13** (100 μM) were performed on human fetal osteoblasts grown on histological slides and preincubated with AHA, and subsequently exposed to fluorescent streptavidin to label biotin according to the described procedures. To evaluate for nonspecific binding, human fetal osteoblasts without preincubation with AHA were exposed to compound **16** or **13** (100 μM) in the presence of the copper catalyst then to fluorescent streptavidin. The cell-associated fluorescence was determined by fluorescence microscopy (Zeiss Axioplan 2). For each treatment, a picture was taken under identical exposure conditions and the fluorescence of individual cells (20 cells per treatment) was quantified using *ImageJ* software. Results are the mean ± sd of the mean fluorescence intensity (MFI) per cell.

Alternatively, human fetal osteoblasts were grown in 96-wells plates (Costar) and either copper-free or THPTA/copper-catalyzed click reactions were performed with the compounds **16** (100 and 200 μM) or **13** (100 and 200 μM) or without AHA or the compounds for baseline controls. The cell layers were carefully washed and 100 μL/well of a 1:1000 dilution of HRP (horse radish peroxidase)-conjugated streptavidin (Dako, Baar, Switzerland, 0.83 mg/mL) in PBS containing 1% BSA were added for 30 min at 37 °C, then after washing with PBS containing 0.05% Tween, 100 μL/well of a 3,3,5,5′-tetramethylbenzidine (TMB)-H_2O_2 solution (R&D Systems, Abingdon, U.K.) were added and the

Scheme 1. Synthesis of the Glutamic Acid Derivative Containing Three Orthogonal Groups[a]

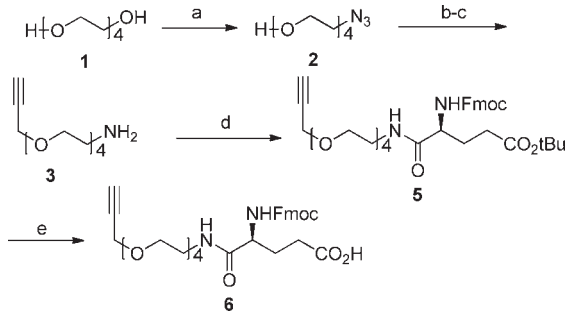

[a] Reagents and conditions: (a) Ref 18, (b) Propargylbromide, NaH, THF; (c) Triphenylphosphine, THF/H_2O, 62 % for 2 steps; (d) **4**, PyBOP, DIPEA, CH_2Cl_2 60 %; (e) 4 M HCl, dioxane, 86%.

increase of absorbance at 450 nm was recorded for 30 min at 37 °C in a thermostatted absorbance multiwell-plate reader (iEMS, LabSystems). Then, the liquid was aspirated and the cell layers were lyzed in 20 μL/well of lysis buffer (20 mM Tris-HCl, 137 mM NaCl, 10% v/v glycerol, 1% v/v NP40, 1% w/v CHAPS), 20 μL/well of PBS-0.1% Triton X-100 was added, and the protein content of the lyzed cells was quantified using the BCA kit (BCA Protein Assay Kit, Pierce, Rockford, USA) and bovine serum albumin as standard, according to the provider's protocol.

WST-1 Cell Viability Assay. Cytotoxicity of the Click Reagents. Cell cultures were treated in culture medium with various concentrations of the reagents for 1 h at 37 °C. The culture medium was removed and the cells were washed twice with HBSS, then cultures were continued in complete medium for 24 to 96 h. The culture medium was removed, and cells were rinsed with culture medium without phenol red (Invitrogen) and incubated with the WST-1 reagent (Roche Diagnostics), diluted 1:10 in culture medium without phenol red and without FCS for 3 h. Optical density of the supernatants was measured at 450 nm in a multiwell-plate reader (iEMS Reader MF, Labsystems, Bioconcept) against a blank containing culture medium and WST-1.

Copper-Catalyzed Click Reaction. Cell cultures were treated with the reaction mixture containing compound **13** (20 μM), $CuSO_4$ (0.8 mM), and TBTA (80 μM) in PBS at 37 °C for 1 h. The culture medium was removed and the cells were washed twice with HBSS, then cultures were continued in complete medium. Cell survival was evaluated after 24 to 96 h as above.

Modified Copper-Catalyzed Click Reaction. Cell cultures were treated with the reaction mixture containing compound **13** (100 μM), aminoguanidine (1 mM), $CuSO_4$ (50 μM), THPTA (250 μM), and sodium ascorbate (2.5 mM) in PBS at 4 °C for 5 min. Then, cell survival was evaluated after 24 to 96 h as above.

Copper-Free Click Reaction. Cell cultures were treated with compound **16** (100 μM) in DMEM containing 4.5 g/L glucose, antibiotics (P/S), and additional HEPES (20 μM) for 1 h at room temperature. Then, cell survival was evaluated after 24 to 96 h as above.

RESULTS

Synthesis of Chemical Ligands for Functionalization of Cell Proteins. Following the procedure of Svensson,[22] tetraethylene glycol was transformed into monoazide **2** in 61% yield (Scheme 1). The alkynyl functionality was introduced by alkylation

Scheme 2. Synthesis of Ligands for Cell Functionalization[a]

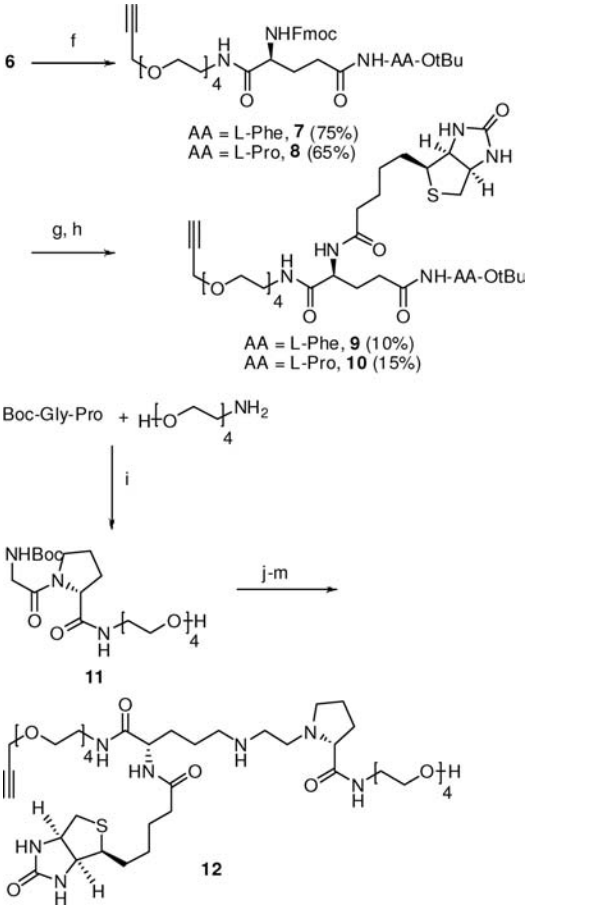

[a] Reagents and conditions: (f) AA-OtBu, PyBOP, NEt_3, CH_2Cl_2; (g) 20% piperidine, DMF; (h) Biotin-OSu, NEt_3, DMF; (i) PyBOP. NEt_3, CH_2Cl_2, 95%; (j) 4 M HCl, dioxane; (k) **6**, PyBOP, DIPEA, −5 °C, CH_2Cl_2, 12 %; (l) 20 % piperidine, DMF, 86%; (m) Biotin-OSu, NEt_3, DMF, 33%.

in the presence of propargyl bromide, followed by Staudinger reduction[23,24] to provide the amine **3** in good yield. Coupling with semiprotected L-glutamic acid **4** and subsequent acidic cleavage of the resulting *tert*-butyl ester afforded the intermediate derivative **6**, presenting three orthogonal groups for the successive introduction of amino acids or peptides, a labeling agent and a group for the attachment to cell surface glycoproteins. Further coupling with protected amino acids was performed in the presence of PyBOP, at −5 °C, to deliver the intermediates **7** and **8** in good yields (Scheme 2).

Cleavage of the carbamate under basic conditions, followed by conjugation with an activated biotin moiety afforded compounds **9** and **10**, ready to undergo copper catalyzed [3 + 2] cycloaddition to azido-modified cell surface glycoproteins. A similar route was applied to introduce a Gly-Pro dipeptide. Boc-Gly-Pro was functionalized in 95% yield with an amino-tetraethylene glycol chain to increase hydrophilicity. Further coupling with intermediate **6** at low temperature and derivatization with a biotin label afforded compound **12** as an alkynyl substrate for click reaction with azido-modified cellular proteins.

The simpler model molecule **13** was also prepared to determine the appropriate conditions for the copper-mediated click

reaction. The synthesis was performed starting from amine **3** which was coupled with an activated biotin in the presence of triethylamine (Scheme 3). The desired product **13** was provided in 51% yield.

To avoid the use of a metal catalyst, a chemical ligand suitable for copper-free click reaction was also synthesized. The difluorinated cyclooctyne (DIFO) moiety developed by Bertozzi and co-workers[11] which has demonstrated a high potential to bind to cell surface proteins via a copper-free click reaction was introduced in one of our conjugates for the functionalization of human fetal osteoblasts. The DIFO **14** was coupled with the tetraethylene glycol-biotin derivative **15** in the presence of PyBOP at room temperature to provide the model compound **16** (Scheme 4) which can react with azido-modifed cell proteins.

Biological Evaluation of the Synthesized Compounds Using Click Reactions. The cell experiments were designed to determine which experimental coupling conditions represent the best compromise between chemical reactivity and biocompatibility. The functionalization of the cell proteins of human primary fetal osteoblasts was performed under three different experimental conditions: two copper-catalyzed click reactions in the presence of different copper complexes and protective reagents and one copper-free click reaction performed in cell culture medium without fetal calf serum (FCS) (Scheme 5). The biocompatibility of the copper catalyst and of the synthesized compounds was determined using assessment of cell viability with the WST-1 assay up to 96 h after the click reactions.

In order to express azido-modified proteins, human fetal osteoblasts were cultured in the presence of the non-natural amino acid L-azidohomoalanine (AHA) which can replace methionine without cell alterations,[6] thus allowing the insertion of an azide moiety in cellular proteins. Proliferating primary human fetal osteoblasts were labeled for 4 h with AHA added to methionine-free cell culture medium before performing the click reactions. The model molecule **13** was used first to establish the optimal conditions for the copper-mediated click reaction with cells. Different ratios of copper sulfate to the copper-reducing agent tris[(1-benzyl-1*H*-1,2,3-triazol-4-yl)methyl]amine (TBTA) were evaluated at a fixed concentration (10 μM) of **13**. Reported standard conditions use 1 mM copper sulfate and 0.1 mM TBTA at 25 °C.[6] Here, the reaction was performed at 37 °C in phosphate buffered saline pH 7.4 (PBS) for 1 h in order to decrease the loading of copper catalyst. Cell nuclei labeling was performed with the fluorescent reporter 4′,6-diamidino-2-phenylindole (DAPI). Detection of cell surface ligation of **13**, as evidenced by the binding of fluorescent streptavidin-Cy3 to the reporter biotin moiety of the prepared conjugate, was demonstrated by fluorescence microscopy (Figure 1). The results showed that a ratio of copper to TBTA of 10 to 1 was optimal, confirming published information.[25] Therefore, for further experiments the concentrations used were 0.8 mM copper sulfate and 0.08 mM TBTA. Then, we determined the optimal concentration of the alkyne moiety for performing the click reaction with cells using increasing concentrations of **13**. The best results were obtained with a 20 μM concentration of **13** (Figure 1B), whereas in the absence of preincubation of cells with AHA no labeling was detected (Figure 1A). Thus, these conditions were applied for the functionalization of the fetal osteoblast with compounds **9**, **10**, and **12** (Figure 1C−E). The functionalization of cells, as evidenced by the binding of fluorescent streptavidin to cells, was observed for all compounds **9**, **10**, **12**, and **13**.

However, an important and very rapid cytotoxicity was observed under these experimental conditions (Figure 2A). While ligands **9**, **10**, **12**, and **13** did not show any cytotoxicity at concentrations up to 100 μM (Figure 2C), the catalytic system TBTA/$CuSO_4$ induced cell death after 1 h exposure at concentrations higher than 0.8 mM in copper (Figure 2B). This significant cytotoxicity of the copper catalytic promoter prompted us to explore alternative conditions for the functionalization of the fetal osteoblasts by click reaction.

Hong and co-workers have recently reported[26] a modified copper-catalyzed click reaction with decreased cytotoxicity that allows the labeling of living cells. In this modification, the use of the water-soluble tris-(hydroxypropyltriazolylmethyl)amine (THPTA) promoter in the catalytic system in the presence of sodium ascorbate increases the reaction rate allowing a lower copper concentration and captures the reactive oxygen species (ROS) generated by the metal, thus decreasing cytotoxicity. Aminoguanidine also added to the reaction mixture traps dehydroascorbate and its decomposition products before they can react with protein side chains.[26] These reaction conditions were applied for the functionalization of fetal osteoblasts with **12** and **13**. Aminoguanidine (1 mM), **12** or **13** (100 μM), copper sulfate (50 μM), THPTA (250 μM), and sodium ascorbate (2.5 mM) were

Scheme 3. Synthesis of the Model Molecule for the Copper Click Reaction[a]

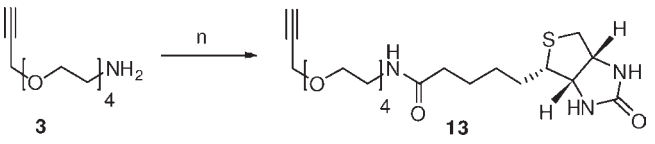

[a] Reagents and conditions: (n) Biotin-OSu, NEt_3, DMF, 51%.

Scheme 4. Synthesis of the Model Molecule for the Copper-Free Click Reaction[a]

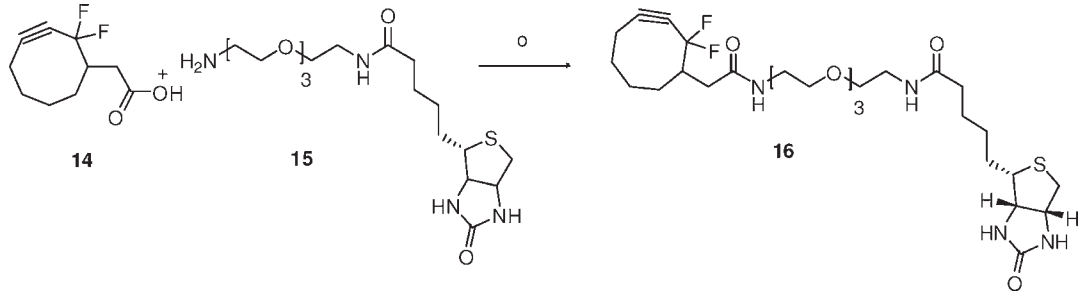

[a] Reagents and conditions: (o) PyBOP, DIPEA, CH_2Cl_2, 41 %.

Scheme 5. Experimental Conditions for the Functionalization of Human Primary Fetal Osteoblasts[a]

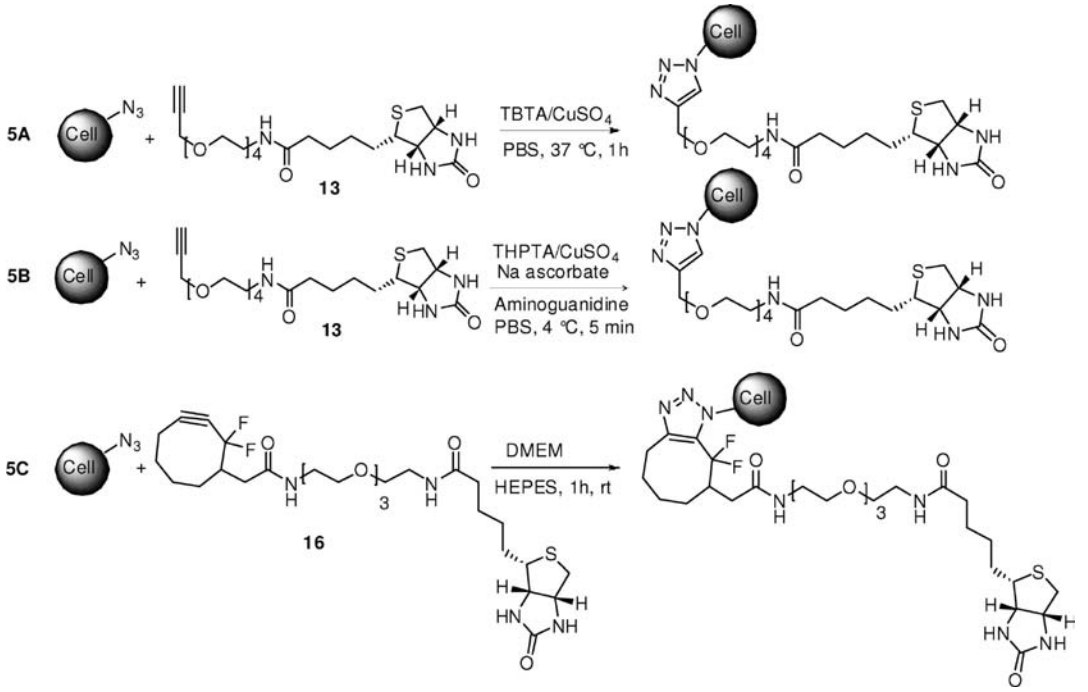

[a] 5A: copper-mediated click reaction using tris[(1-benzyl-1*H*-1,2,3-triazol-4-yl)methyl]amine (TBTA) as catalyst without copper-protective reagents 5B: copper-mediated click reaction using tris-(hydroxypropyltriazolylmethyl)amine (THPTA) as catalyst with ascorbate and aminoguanine as copper-protective reagents. 5C: copper-free click reaction in cell culture medium.

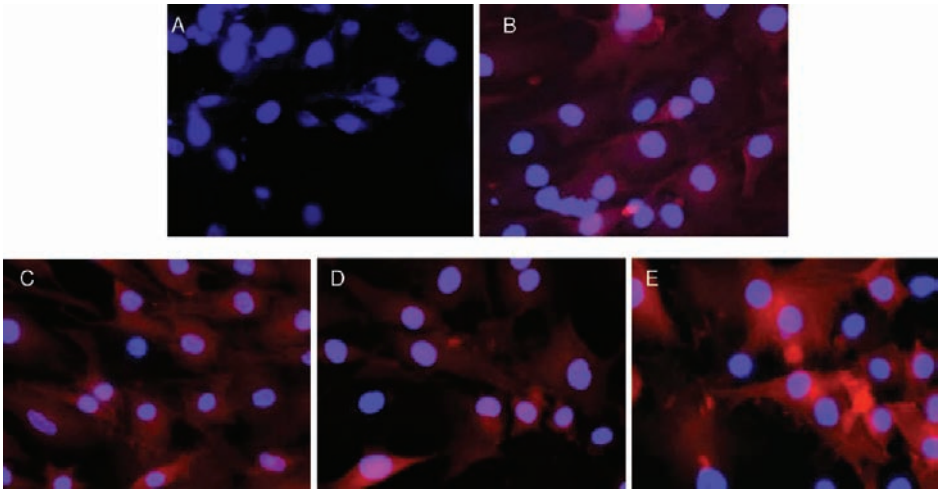

Figure 1. TBTA/copper-catalyzed click reaction performed on human fetal osteoblasts. (A) To evaluate for nonspecific binding, human fetal osteoblasts without preincubation with AHA were exposed to the TBTA/copper catalyst and biotin-containing compound **13**, then to fluorescent streptavidin to label biotin and DAPI to label nuclei. (B–E) Human fetal osteoblasts were preincubated with AHA and subsequently exposed for 1 h at 37 °C to compounds **13** (B), **9** (C), **10** (D), or **12** (E) using TBTA/copper-catalyzed click reaction, then to fluorescent streptavidin to label biotin and DAPI to label cell nuclei. Bound compounds fluoresce red and cell nuclei blue.

sequentially added to the cells. After 5 min at 4 °C, the reagents were removed and labeling of cell nuclei with DAPI and detection of streptavidin-Cy3 binding by fluorescence microscopy were performed. The functionalization of the cell surface was observed for both **12** and **13** (Figure 3B and C), whereas in the absence of preincubation of cells with AHA no labeling was detected (Figure 3A). After the reaction, the cells were washed free of the reagents and cultured in complete culture medium and the WST-1 assay was performed after 24, 48, 72, and 96 h (Figure 4A). The results demonstrated good cell survival since human fetal osteoblasts survived and proliferated for up to four days after the copper-catalyzed click reaction performed with the THPTA ligand in the presence of aminoguanidine.

Finally, the functionalization of the human fetal osteoblasts by copper-free click reaction with compound **16** was evaluated. Compounds presenting activated difluorinated cyclooctyne[11] can react

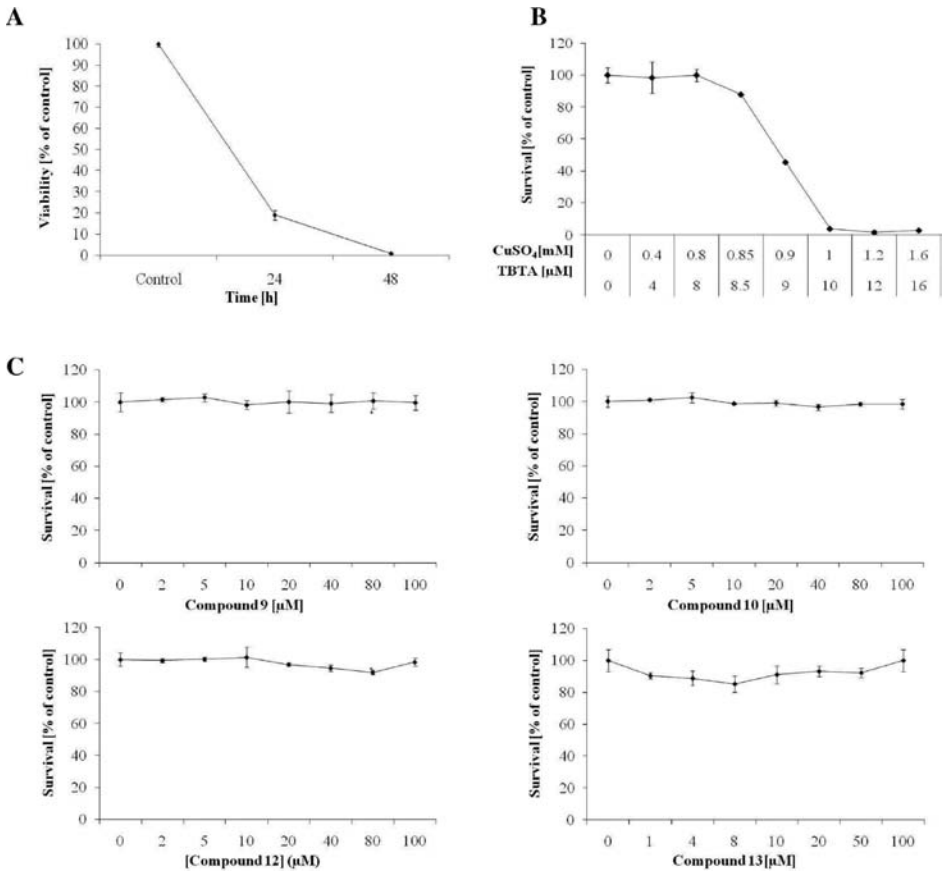

Figure 2. Evaluation of the biocompatibility of the TBTA/copper catalyst and of compounds **9**, **10**, **12**, and **13**. (A) TBTA/copper-catalyzed click reaction was performed for 1 h at 37 °C between compound **13** and human fetal osteoblasts preincubated with AHA, cell culture medium was changed, and culture was continued for 24 to 48 h. Then, the WST-1 assay was performed. (B) Human fetal osteoblasts without preincubation with AHA were exposed for 1 h at 37 °C to the TBTA/copper catalytic system at increasing concentrations of the catalysts, then the WST-1 assay was performed. (C) Human fetal osteoblasts without preincubation with AHA were exposed for 1 h at 37 °C to compound **9**, **10**, **12**, and **13** in the absence of TBTA/copper catalysts, cell culture medium was changed and culture was continued for 24 h, then the WST-1 was performed. Results are the means ± sd of triplicate wells of a representative experiment out of 3 independent experiments.

with azide moieties without copper catalyst since the loss of the ring strain (18 kcal/mol) and the decrease of the lowest unoccupied molecular orbital (LUMO) energy by the two fluoride atoms allow the decrease of the activation energy of the click reaction. The copper-free click reaction of compound **16** (100 μM) with human fetal osteoblasts was performed at room temperature for 1 h in culture medium without FCS containing additional HEPES (20 μM) for buffering. Cell nuclei were labeled with DAPI, and the cell functionalization was demonstrated by fluorescence microscopy using Cy3-streptavidin (Figure 3E), whereas in the absence of preincubation of cells with AHA no labeling was detected (Figure 3D). An excellent cell survival rate for up to 96 h after the cycloaddition process was evidenced (Figure 4B).

The level of conjugation of compounds **12**, **13**, and **16** or in the absence of AHA (for nonspecific binding) to human fetal osteoblasts was evaluated following click reactions performed under noncytotoxic conditions using two techniques. The cell-associated fluorescence of individual cells (20 cells per treatment) was quantified under identical exposure conditions using *Image J* software as the mean fluorescence intensity (MFI) per cell (Figure 5A), showing a slightly increased conjugation rate of compounds **16** under copper-free click reaction and **12** under copper-catalyzed click reaction compared to compound **13** under copper-catalyzed click reaction. Quantification was also performed using HRP-streptavidin and a cellular-ELISA assay. The increase in cell-bound HRP enzymatic activity per well was related to the amount of cell proteins per well (Figure 5B), showing a dose-dependent binding of both compounds **13** and **16**, without noticeable differences between both, suggesting that copper-free and protected copper-mediated click reactions performed with comparable efficacy.

DISCUSSION

Human fetal cells represent an appealing approach for the seeding of implant biomaterials for tissue engineering, including bone engineering, as these cells do not require the use of antigraft rejection treatment.[16] This study has demonstrated the possibility of functionalizing primary human fetal osteoblasts through click chemistry with amino acid containing chemical ligands able to maintain cell survival and proliferation. While ligands **9**, **10**, and **12** were easily conjugated to azido-modified surface proteins of fetal osteoblasts in the presence of a Cu(I) promoter, these reaction conditions induced a drastic loss of cell viability even with reduced reaction time. This major drawback was circumvented by the introduction of a highly reactive alkynyl

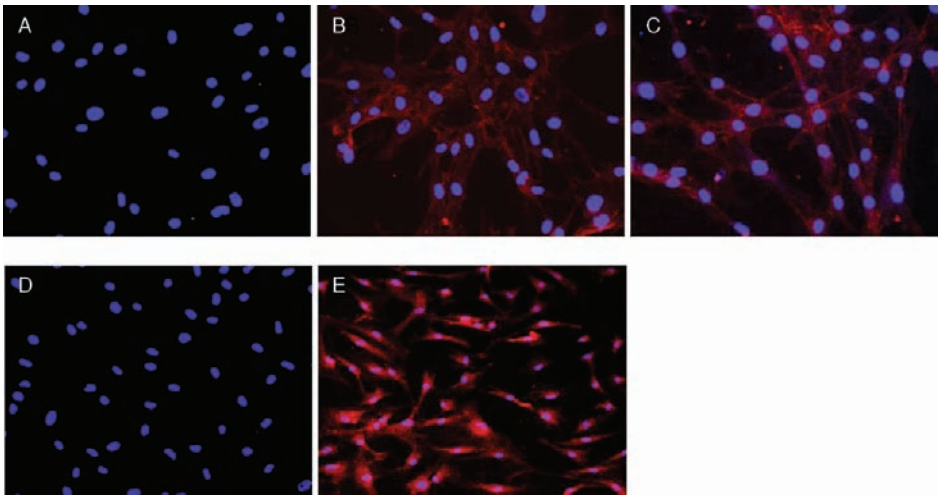

Figure 3. Modified THPTA/copper-catalyzed and copper-free click reactions performed on human fetal osteoblasts. (A) To evaluate for nonspecific binding, human fetal osteoblasts without preincubation with AHA were exposed to biotin-containing compound **13** in the presence of the modified THPTA/copper catalyst, then to fluorescent streptavidin to label biotin and DAPI to label cell nuclei. (B,C) Human fetal osteoblasts were preincubated with AHA and subsequently exposed for 5 min at 4 °C to compounds **13** (B) or **12** (C) using the THPTA/copper-catalyzed click reaction, then exposed to fluorescent streptavidin to label biotin and to DAPI to label cell nuclei. (D) To evaluate for nonspecific binding, human fetal osteoblasts without preincubation with AHA were exposed to biotin-containing compound **16**, then to fluorescent streptavidin to label biotin and DAPI to label cell nuclei. (E) Human fetal osteoblasts were preincubated with AHA and subsequently exposed to compound **16** for 1 h at 25 °C using copper-free click reaction, then to fluorescent streptavidin to label biotin and to DAPI to label cell nuclei. Bound compounds fluoresce red and cell nuclei blue.

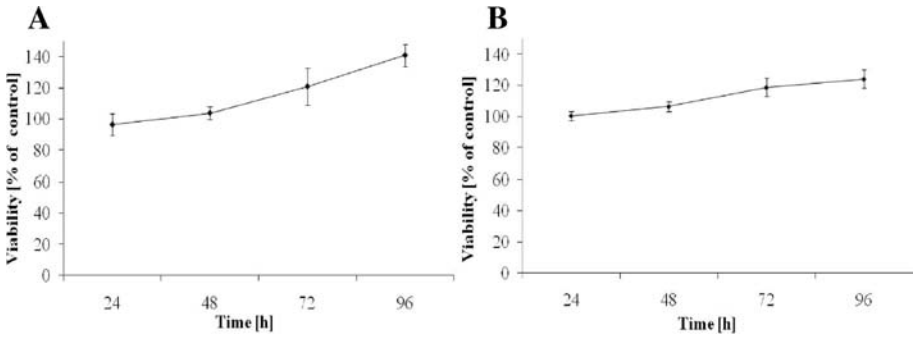

Figure 4. Evaluation of human fetal osteoblast viability after modified THPTA/copper-catalyzed and copper-free click reactions. (A) Modified THPTA/copper-click reaction was performed for 5 min at 4 °C between compound **13** and human fetal osteoblasts preincubated with AHA, cell culture medium was changed, and culture was continued for 24 to 96 h, and then the WST-1 assay was performed. (B) Copper-free click reaction was performed for 1 h at 25 °C between compound **16** and human fetal osteoblasts preincubated with AHA, cell culture medium was changed, and culture was continued for 24 to 96 h, and then the WST-1 assay was performed. Results are the means ± sd of triplicate wells of a representative experiment out of 3 independent experiments.

functionality in the ligands (compound **16**), thus avoiding the use of a copper catalyst in the cycloaddition process. Nevertheless, as the preparation of DIFO containing ligands[11] is more complex, requiring a much higher number of steps compared to a simple alkynyl containing ligand, we turned our attention to the protection of cells from the Cu(I) catalyst by the aminoguanidine-THPTA combination recently proposed by Hong et al.[26] In our hands, these experimental conditions applied to primary human fetal osteoblasts resulted in both efficient cell functionalization and excellent cell survival. In addition, all chemical ligands prepared to promote further cell adhesion and proliferation showed perfect biocompatibility with the studied cells.

In conclusion, we have shown that biocompatible biotin-containing ligands can be designed and synthesized for conjugation to cellular azido-modified proteins of primary human fetal osteoblasts. Using the click reaction, cell functionalization was probed with fluorescent streptavidin. Three methods of cell functionalization were explored allowing a comparison in term of efficiency and biocompatibility of different experimental conditions. The use of the classical TBTA/$CuSO_4$ catalytic system led to efficient conjugation but suffered from high cytotoxicity, which prevented further application for developing implant biomaterials. Protection of the cells from the copper catalyst through the use of the THPTA-ascorbate system in the presence of aminoguanidine led to a good reaction rate while maintaining a high level of cell viability. Similarly, good reaction rates and excellent cell viability were observed for the copper-free click reaction. Incorporation of peptidic components in the ligands was possible maintaining the efficacy and biocompatibility of functionalization and the survival of the primary human fetal

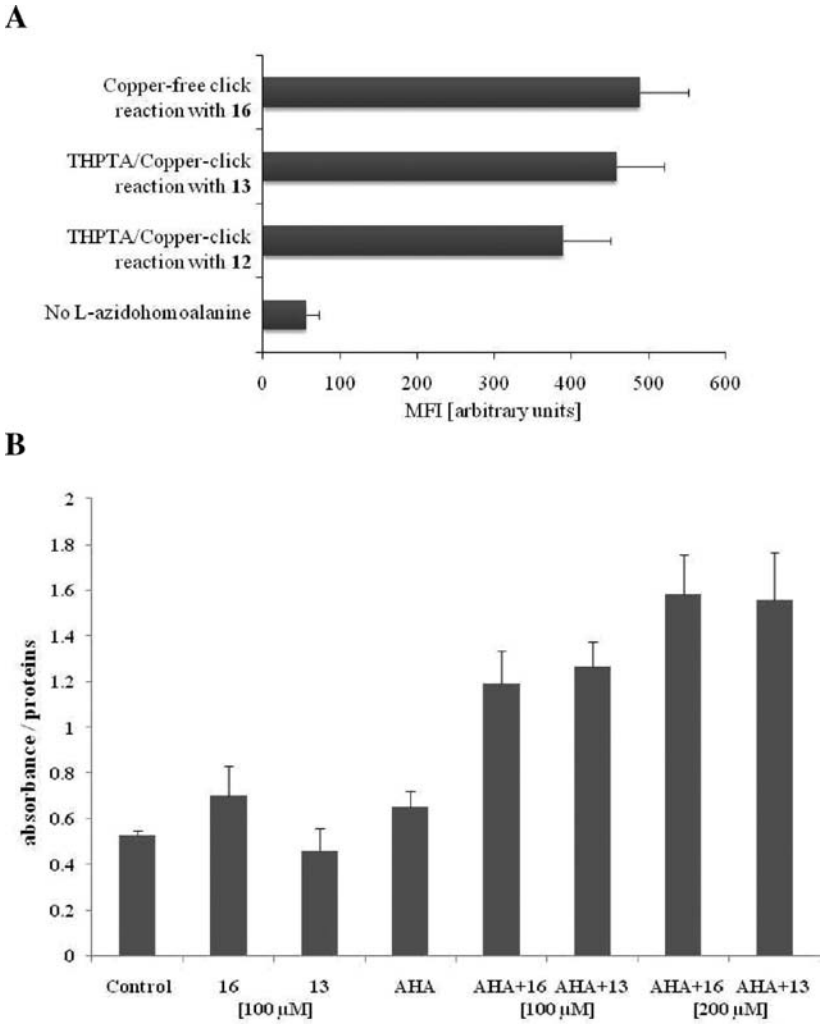

Figure 5. Evaluation of compound conjugation to the cells. Following click reactions performed on human fetal osteoblasts under noncytotoxic conditions with compound **12** or **13**, or **16** or in the absence of AHA or the compounds (for nonspecific binding): (A) Cell-associated fluorescence was quantified using 100 μM of compound **12**, **13**, or **16**. Results are expressed as the mean fluorescence intensity (MFI) per cell ± sd. (B) Enzymatic activity of cell-associated HRP-streptavidin was related to the protein content of the cells. Control: no compound or AHA added to the cells. **16** or **13**: cells exposed to the compounds in the absence of AHA. AHA: cells exposed to AHA in the absence of the compound. AHA+**16**/+**13**: cells exposed to AHA and the compounds. Results are expressed as the ratio of the cell-bound HRP activity to the protein content per well.

osteoblasts. These results open the route for the use of peptide-functionalized human fetal osteoblasts as seeding components for implant biomaterials.

■ ASSOCIATED CONTENT

Supporting Information. Detailed protocols for synthesis and analytical data for compounds **5**, **9**, **10**, **12**, **15**, and **16**. This material is available free of charge via the Internet at http://pubs.acs.org.

■ AUTHOR INFORMATION

Corresponding Author

*Dr. Lucienne Juillerat, Ph.D., Privat Docent, MER, Centre Hospitalier Universitaire Vaudois and University of Lausanne (CHUV-UNIL), University Institute of Pathology, rue du Bugnon 25, CH-1011 Lausanne; Switzerland. Phone: +41 21 314 71 73; Fax: +41 21 314 71 15; e-mail: lucienne.juillerat@chuv.ch.

Dr. Sandrine Gerber-Lemaire, Ph.D., HDR, MER, Laboratory of Synthesis and Natural Products, Ecole Polytechnique Fédérale de Lausanne (EPFL), ISIC, Batochime, CH-1015 Lausanne, Switzerland. Phone: +41 21 693 93 72, fax: +41 21 693 93 55, e-mail: Sandrine.Gerber@epfl.ch.

■ ACKNOWLEDGMENT

We thank the Swiss National Science Foundation (grant n° CR23I3-124753) for financial support. We also thank Mr. Martial Rey (NMR spectrometry service, ISIC, EPFL), Dr. Laure Menin, and Mr. Francisco Sepulveda (MS service, ISIC, EPFL) for technical help. We thank Mr Pascal Miéville for his advice on NMR experiments. The authors declare no conflicts of interest.

■ ABBREVIATIONS LIST

AHA	L-azidohomoalanine
BSA	bovine serum albumin

DAPI	4′,6-diamidino-2-phenylindole
DIFO	difluorinated cyclooctyne
DIPEA	*N*,*N*-diisopropylethylamine
DMEM	Dulbecco modified Eagle medium
FCS	fetal calf serum
HBSS	Hank's buffered salt solution
HEPES	4-(2-hydroxyethyl)-1-piperazineethanesulfonic acid
HRP	horseradish peroxidase
LUMO	lowest unoccupied molecular orbital
PBS	phosphate buffered saline
P/S	penicillin/streptomycin
PyBOP	benzotriazol-1-yl-oxytripyrrolidinophosphonium hexafluorophosphate
ROS	reactive oxygen species
TBTA	tris[(1-benzyl-1*H*-1,2,3-triazol-4-yl)methyl]amine
TMB	3,3,5,5′-tetramethylbenzidine
THPTA	tris-(hydroxypropyltriazolylmethyl)amine
WST-1	2-(4-iodophenyl)-3-(4-nitrophenyl)-5-(2,4-disulfophenyl)-2*H*-tetrazolium

REFERENCES

(1) Saxon, E, and Bertozzi, C. R. (2000) Cell surface engineering by a modified Staudinger reaction. *Science 287*, 2007–2010.

(2) Van Swieten, P. F., Leeuwenburgh, M. A., Kessler, B. M., and Overkleeft, H. S. (2005) Bioorthogonal organic chemistry in living cells: novel strategies for labeling biomolecules. *Org. Biomol. Chem. 3*, 20–27.

(3) Best, M. D. (2009) Click chemistry and bioorthogonal reactions: unprecedented selectivity in the labeling of biological molecules. *Biochemistry 48*, 6571–6584.

(4) Sletten, E. M., and Bertozzi, C. R. (2009) Bioorthogonal chemistry: fishing for selectivity in a sea of functionality. *Angew. Chem., Int. Ed. 48*, 6974–6998.

(5) Lim, R. K. V., and Lin, Q. (2010) Bioorthogonal chemistry: recent progress and future directions. *Chem. Commun. 46*, 1589–1600.

(6) Griffin, R. J. (1994) The medicinal chemistry of the azido group. *Prog. Med. Chem. 31*, 121–232.

(7) Koehn, M., and Breinbauer, R. (2004) The Staudinger ligation: a gift to chemical biology. *Angew. Chem., Int. Ed. 43*, 3106–3116.

(8) Ning, X. H., Guo, J., Wolfert, M. A., and Boons, G. J. (2008) Visualizing metabolically labeled glycoconjugates of living cells by copper-free and fast Huisgen cycloadditions. *Angew. Chem., Int. Ed. 47*, 2253–2255.

(9) Lutz, J. F. (2008) Copper-free azide-alkyne cycloadditions: new insights and perspectives. *Angew. Chem., Int. Ed. 47*, 2182–2184.

(10) Sletten, E. M., and Bertozzi, C. R. (2008) A hydrophilic azacyclooctyne for Cu-free click chemistry. *Org. Lett. 10*, 3097–3099.

(11) Codelli, J. A., Baskin, J. M., Agard, N. J., and Bertozzi, C. R. (2008) Second-generation difluorinated cyclooctynes for copper-free click chemistry. *J. Am. Chem. Soc. 130*, 11486–11493.

(12) Debets, M. F., van der Doelen, C. W. J., Rutjes, F. P. J. T., and van Delft, F. L. (2010) Azide: A unique dipole for metal-free bioorthogonal ligations. *ChemBioChem 11*, 1168–1184.

(13) Jewett, J. C., Sletten, E. M., and Bertozzi, C. R. (2010) Rapid Cu-free click chemistry with readily synthesized biarylazacyclooctynones. *J. Am. Chem. Soc. 132*, 3688–3690.

(14) Jewett, J. C., and Bertozzi, C. R. (2010) Cu-free click cycloaddition reactions in chemical biology. *Chem. Soc. Rev. 39*, 1272–1279.

(15) Quintin, A., Hirt-Burri, N., Scaletta, C., Schizas, C., Pioletti, D. P., and Applegate, L. A. (2007) Consistency and safety of cell banks for research and clinical use: preliminary analysis of fetal skin banks. *Cell Transplant. 16*, 675–684.

(16) Hohlfeld, J., de Buys Roessingh, A. D., Hirt-Burri, N., Chaubert, P., Gerber, S., Scaletta, C., Hohlfeld, P., and Applegate, L. A. (2005) Tissue engineered fetal skin constructs for paediatric burns. *Lancet 366*, 840–842.

(17) Montjovent, M. O., Mark, S., Mathieu, L., Scaletta, C., Scherberich, A., Delabarde, C., Zambelli, P. Y., Bourban, P. E., Applegate, L. A., and Pioletti, D. P. (2008) Human fetal bone cells associated with ceramic reinforced PLA scaffolds for tissue engineering. *Bone 42*, 554–564.

(18) Bellis, S. L. (2011) Advantage of RGD peptides for directing cell association with biomaterials. *Biomaterials 32*, 4205–44210.

(19) Barker, T. H. (2011) The role of ECM proteins and protein fragments in guiding cell behavior in regenerative medicine. *Biomaterials 32*, 4211–4214.

(20) Dieterich, D. C., Link, A. J., Graumann, J., Tirrell, D. A., and Schuman, E. M. (2006) Selective identification of newly synthesized proteins in mammalian cells using bioorthogonal noncanonical amino acid tagging (BONCAT). *Proc. Natl. Acad. Sci. U. S. A. 103*, 9482–9487.

(21) Dieterich, D. C., Hodas, J. J., Gouzer, G., Shadrin, I. Y., Ngo, J. T., Triller, A., Tirrell, D. A., and Schuman, E. M. (2010) In situ visualization and dynamics of newly synthesized proteins d proteins in rat hippocampal neurons. *Nat. Neurosci. 13*, 897–905.

(22) Svedhem, S., Hollander, C. A., Shi, J., Konradsson, P., Liedberg, B., and Svensson, S. C. T. (2001) Synthesis of a series of oligo(ethylene glycol)-terminated alkanethiol amides designed to address structure and stability of biosensing interfaces. *J. Org. Chem. 66*, 4494–4503.

(23) Staudinger, H., and Meyer, J. (1919) Ueber neue organische phosphorverbindungen. II. Phosphazine. *Helv. Chim. Acta 2*, 635–646.

(24) Gololobov, Y. G., and Kasukhin, L. F. (1992) Recent advances in the Staudinger reaction. *Tetrahedron 48*, 1353–1406.

(25) Baskin, J. M., and Bertozzi, C. R. (2007) Bioorthogonal click chemistry: covalent labeling in living systems. *QSAR Comb. Sci. 26*, 1211–1219.

(26) Hong, W., Steinmetz, N. F., Manchester, M., and Finn, M. G. (2010) Labeling live cells by copper-catalyzed alkyne-azide click chemistry. *Bioconjugate Chem. 21*, 1912–1916.

Covalent cell surface functionalization of human fetal osteoblasts for tissue engineering

Françoise Borcard, Aurélien Godinat, Davide Staedler, Horacio Comas, Catherine Chapuis-Bernasconi, Anne-Laure Dumont, Corinne Scaletta, Lee Ann Applegate, Franziska Krauss Juillerat, Urs T. Gonzenbach, Sandrine Gerber-Lemaire* and Lucienne Juillerat-Jeanneret*

Supporting Information

Detailed protocols and analytical data for compounds **5**, **9**, **10**, **12**, **15** and **16**

General methods

Commercial reagents (Fluka, Aldrich, Bachem) were used without purification. Anhydrous solvents were obtained by filtration. Liquid/solid flash chromatography (FC): columns of silica gel (0.040-0.63 mm, Merck No.9385 silica gel 60, 240-400 mesh). Eluent: mixture of light petroleum ether (PE) and ethyl acetate (EtOAc) or mixture of dichloromethane (DCM) and methanol (MeOH). TLC for reaction monitoring: Merck silica gel 60 F_{254} plates; detection by UV light; Pancaldi reagent, $KMnO_4$, ninhydrine or phosphomolybdic acid. IR spectra: Perkin-Elmer-1420 spectrometer. ^{1}H NMR spectra: Bruker-ARX-400 spectrometer (400 MHz); δ(H) in ppm relative to the solvent's residual ^{1}H signal [$CHCl_3$, δ(H) 7.27, MeOD, δ(H) 3.31] as internal reference; ^{13}C NMR spectra: same instrument as above (100.6 MHz); δ(C) in ppm relative to solvent's C-signal [$CDCl_3$, δ(C) 77.1, MeOD, δ(C) 49.0] as internal reference. MS: Nermag R-10-10C, chemical ionization (NH_3) mode m/z (amu) [% relative base peak (100%)]. GC-MS spectrometer (Nermag R-10-10C, chemical ionization (NH3) mode m/z); MALTI-TOF spectrometer (Axima-CFR+, Kratos, Manchester); ESI-Q spectrometer (Finnigan SSQ 710C, Thermoquest, UK); ESI-QT spectrometer (Ultima spectrometer, Micromass, Manchester).

***Tert*-butyl N^2-[9A fluoren-9-ylmethoxy)carbonyl]-N-3,6,9,12-tetraoxa-pentadec-14-yn-1-yl-L-α-glutaminate (5)**

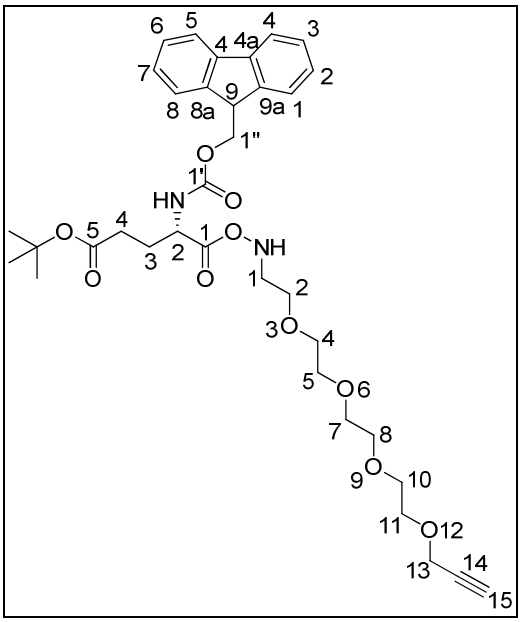

Fmoc-glu-(O^{t}Bu)-OH (360 mg, 0.9 mmol, 1 equiv) and PyBOP (540 mg, 1.0 mmol, 1.2 equiv) were dissolved in dichloromethane (8 mL). DIPEA (0.3 mL, 1.7 mmol, 2 equiv) was added followed by a solution of 3,6,9,12-tetraoxapentadec-14-yn-1-amine (200 mg, 0.9 mmol, 1 equiv) in dichloromethane (4 mL) at 0 °C. After 15 min the reaction mixture was warmed to 25 °C and stirred for 12 h. The solvent was removed under reduced pressure and the resulting mixture was dissolved in EtOAc. This solution was sequentially washed with saturated NH_4Cl, H_2O, 5 % $NaHCO_3$ and brine, dried over anhydrous $MgSO_4$, filtered and concentrated under reduced pressure. The product was purified by flash column chromatography (EtOAc/EP 2:1 then 3:1) (332 mg, 60 %).

IR (film): 3285, 2870, 1715, 1665, 1520, 1450, 1390, 1350, 1245, 1150, 1085, 1045, 950, 840, 760, 740, 645, 620, 555, 540, 515, 500 cm^{-1}.

^{1}H NMR (400 MHz, $CDCl_3$): δ= 7.76 (d, ^3J= 7.5 Hz, 1H, C**H** (aromatic)), 7.60 (d, ^3J= 7.4 Hz, 1H, C**H** (aromatic)), 7.40 (t, ^3J= 7.4 Hz, 1H, C**H** (aromatic)), 7.32 (t, ^3J= 7.4 Hz, 1H, C**H** (aromatic)), 6.75 (s, 1H, N**H**), 5.83 (s, 1H, N**H**), 4.41 (m, 2H, C(1'')**H$_2$**), 4.21 (m, 4H, C(13)**H$_2$**, C(9)**H**, C(2)**H**), 3.69-3.45 (m, 16H, (C**H$_2$**-O)$_8$), 2.36 (m, 2H, C(4), C(3)**H$_2$**), 2.01 (m, 3H, C(4), C(3)**H$_2$**, C(15)**H**), 1.46 (s, 9H, (C**H$_3$**)$_3$C).

^{13}C NMR (100 MHz, $CDCl_3$): δ= 172.7 (s, **C**q), 171.9 (s, **C**q), 143.8 (s, **C**q), 141.3 (s, **C**q), 127.7 (d, ^1J= 160 Hz, **C**H(aromatic)), 127.1 (d, ^1J= 160 Hz, **C**H(aromatic)), 125.1 (d, ^1J= 158 Hz, **C**H(aromatic)), 119.9 (d, ^1J= 159 Hz, **C**H(aromatic)), 80.7 (s, **C**q), 74.7 (d, **C**(15)H), 70.2 (t, **C**H$_2$-O) 70.1 (t, **C**H$_2$-O), 70.1 (t, **C**H$_2$-O), 70.0 (t, **C**H$_2$-O), 69.9 (t, **C**H$_2$-O), 68.6 (t, **C**H$_2$-O), 67.0 (t, **C**H$_2$-O), 58.3 (t, ^1J= 145 Hz, **C**(1'')H$_2$), 54.4 (d, ^1J= 144 Hz, **C**(2)H), 47.2 (d, ^1J= 130 Hz, **C**(9)H), 39.3 (t, ^1J= 139 Hz, **C**(4)H$_2$), 31.6 (t, ^1J= 129 Hz, **C**(3)H$_2$) , 28.1 (q, ^1J= 127 Hz, (**C**H$_3$)$_3$).

MS (ESI): calculated: 639.3282; found: 639.3292
Optical rotation (CH_2Cl_2, 25 °C, *c*= 0.085 g/100 mL): $[\alpha]_D^{25}$ = -22

^{1}H NMR:

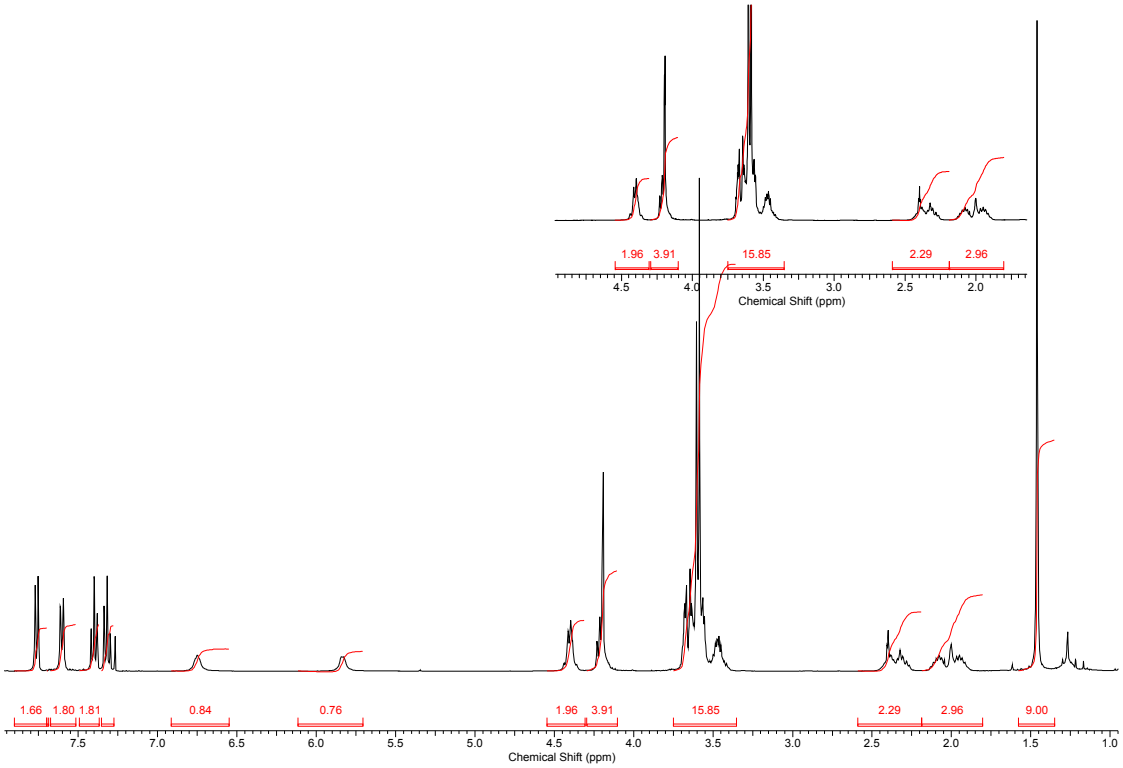

^{13}C NMR:

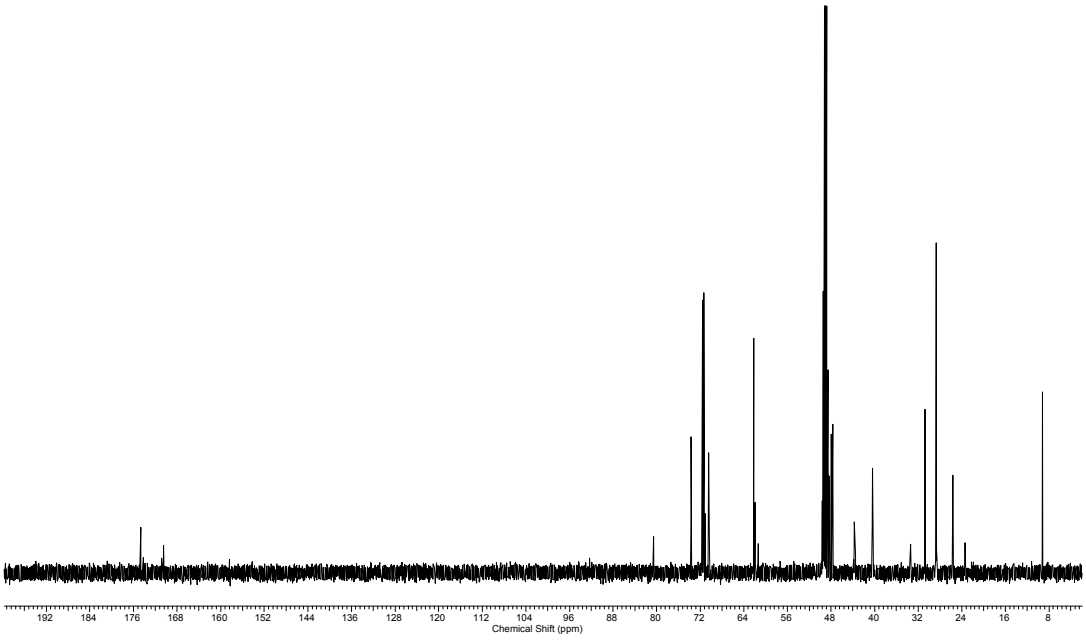

***Tert*-butyl N^2-[4-oxohexahydro-1H-thieno[3,4-d]imidazol-4-yl-pentanoyl]-N-(3,6,9,12-tetraoxapentadec-14-yne-1-yl)-L-α-glutaminyl-L-phenylalaninate (9)**

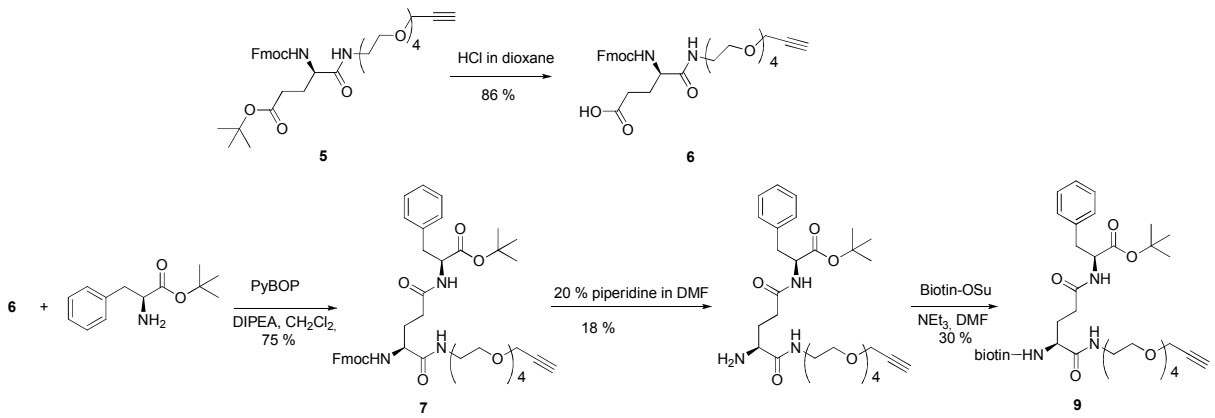

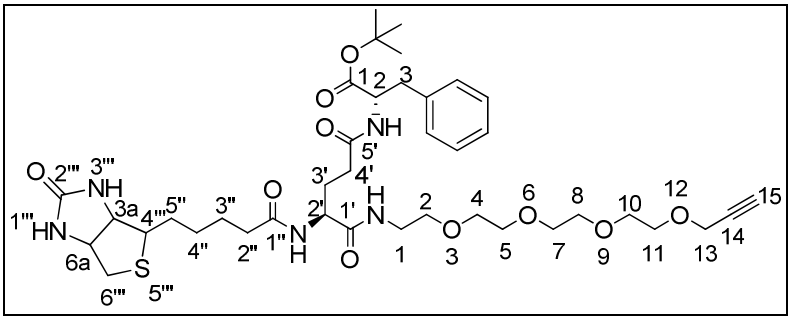

(**5**) (536 mg, 0.84 mmol, 1 equiv) was dissolved into a solution of 4 M HCl in dioxane (3.20 mL) at 25 °C. After stirring for 1h the solvent was removed and HCl was coevaporated in presence of acetonitrile to afford acid as a white solid (420 mg, 86 %).

(**6**) (100 mg, 0.17 mmol, 1 equiv) and PyBOP (107 mg, 0.21 mmol, 1.2 equiv) were dissolved in dry DCM (1.6 mL). Triethylamine (88 µL 0.51 mmol, 3 equiv) was added at -5 °C. A solution of L-Phe-OtBu (44 mg, 0.17 mmol, 1 equiv) in DCM (1.2 mL) was added dropwise. The reaction mixture was stirred until total conversion of the starting material (monitored by TLC). The solvent was removed under reduced pressure and EtOAc was added. The organic phase was sequentially washed with saturated NH_4Cl, H_2O, 5 % $NaHCO_3$ and brine, dried over anhydrous $MgSO_4$, filtered and concentrated under reduced pressure. The product was purified by flash column chromatography (CH_2Cl_2/MeOH: 95:5) to afford a colorless oil (100 mg, yield 75 %).

(**7**) (100 mg, 0.13 mmol, 1 equiv) was dissolved in a solution of 20 % piperidine in DMF (2.5 mL) at 25 °C. After stirring for 1 h the solvent was evaporated and piperidine was removed by coevaporation with toluene. The product was purified by flash column chromatography (CH_2Cl_2/MeOH: 95:5) to afford a colorless oil (17 mg, 18 %).

Tert-butyl N-(3,6,9,12-tetraoxa-pentadec-14-yn-1-yl)-L-α-glutaminyl-L-phenylalaninate (17 mg, 0.03 mmol, 1 equiv) and biotin-OSu (10 mg, 0.03 mol, 1 equiv) were dissolved in DMF (0.3 mL) at 25 °C. Triethylamine (6.3 µL, 0.05 mmol, 1.5 equiv) was added. The reaction mixture was stirred for 12 h at 25 °C. The solvent was removed and the product was purified by HPLC (XTerra Prep RP C18, (19x150 mm Waters)) to (**9**) as a colorless oil (7 mg, 30 %).

IR (film): 3275, 2925, 2860, 2405, 1645, 1535, 1455, 1365, 1255, 1200, 1150, 1095, 1030, 840, 700, 605, 580, 570, 520 cm^{-1}.

^{1}H NMR (400 MHz, MeOD): δ= 7.25 (m, 5H, C**H** (aromatics)), 4.54 (dd, ^{2}J= 8.2, ^{3}J= 6.7 Hz, C(6a)**H**)), 4.49 (dd, 1H, ^{2}J= 7.8, ^{3}J= 4.8 Hz, C(2)**H**, C(2')**H**), 4.30 (dd, 1H, ^{2}J= 7.8, ^{3}J= 4.4 Hz, C(2)**H**, C(2')**H**), 4.25 (dd, 1H, ^{2}J= 8.2, ^{3}J= 6.4 Hz, C(3a)**H**), 4.18 (d, 2H, ^{4}J= 2.4 Hz, C(13)**H**), 3.67-3.34 (m, 16H, (C$\mathbf{H_2}$-O)$_8$, 3.20 (m, 1H, C(4''')**H**), 3.07 (dd, 1H, ^{2}J= 13.8 Hz, ^{3}J= 6.7 Hz, C(3)$\mathbf{H}_2$), 2.98 (dd, 1H, ^{2}J= 13.8, ^{3}J= 5.5 Hz, C(3)$\mathbf{H}_2$), 2.92 (dd, 1H ^{2}J= 12.7, ^{3}J= 5.0 Hz, C(6'')$\mathbf{H}_2$), 2.85 (t, 1H, ^{3}J= 2.4 Hz, C(15)**H**), 2.70 (d, 1H, ^{3}J= 12.7 Hz, C(6''')$\mathbf{H}_2$), 2.27 (m, 4H, (C$\mathbf{H_2}$)$_2$), 199-1.44 (m, 8H, (C$\mathbf{H_2}$)$_4$), 1.42 (s, 9H, (C$\mathbf{H_3}$)$_3$).

^{13}C NMR (100 MHz, MeOD): δ= 176.0 (s, C**q**), 174.8 (s, C**q**), 173.9 (s, C**q**), 172.7 (s, C**q**), 166.2 (s, C**q**), 138.2 (s, C**q**), 130.4 (d, ^{1}J= 157 Hz, **C**H (aromatic)), 129.4 (d, ^{1}J= 159 Hz, **C**H (aromatic)), 127.9 (d, ^{1}J= 159 Hz, **C**H (aromatic)), 83.0 (s, C**q**(14)), 76.0 (d, **C**H), 71.5 (t, **C**H_2), 71.5 (t, **C**H_2), 71.3 (t, **C**H_2), 71.2 (t, **C**H_2), 70.4 (t, **C**H_2), 70.1 (t, **C**H_2), 63.2 (d, ^{1}J= 161 Hz, **C**H), 61.6 (d, ^{1}J= 149 Hz, **C**H), 59.0 (t, ^{1}J= 148 Hz, **C**H_2), 56.9 (d, ^{1}J= 135 Hz, **C**H), 55.9 (d, ^{1}J= 144 Hz, **C**H), 54.2 (d, ^{1}J= 141 Hz, **C**H), 41.0 (t, ^{1}J= 142 Hz, **C**H_2), 40.4 (t, ^{1}J= 139 Hz, **C**H_2), 38.6 (t, ^{1}J= 134 Hz, **C**H_2), 36.4 (t, ^{1}J= 127 Hz, **C**H_2), 32.8 (t, ^{1}J= 128 Hz, **C**H_2), 29.6 (t, **C**H_2), 29.4 (t, **C**H_2), 29.0 (t, **C**H_2), 28.2 (q, ^{1}J= 123 Hz, **C**H_3), 26.6 (t, ^{1}J= 129 Hz, **C**H_2).

MS (ESI): calculated: 790.4061; found: 790.4073
Optical rotation (CH_2Cl_2, 25 °C, *c*=0.04 g/100 mL): $[\alpha]_D^{25}$ = -55

^{1}H NMR:

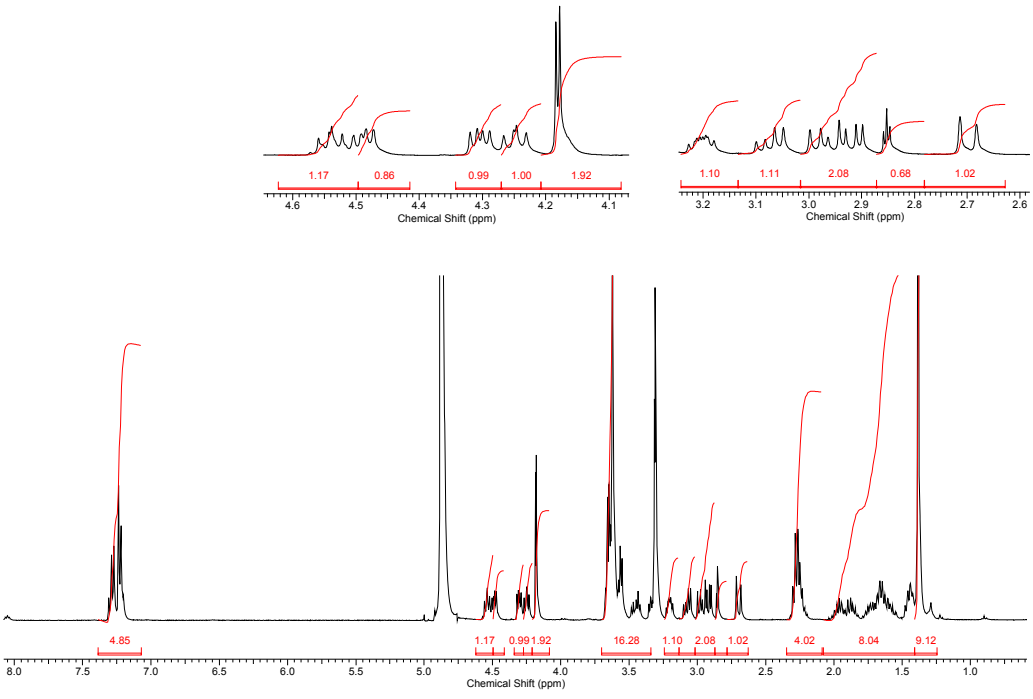

^{13}C NMR:

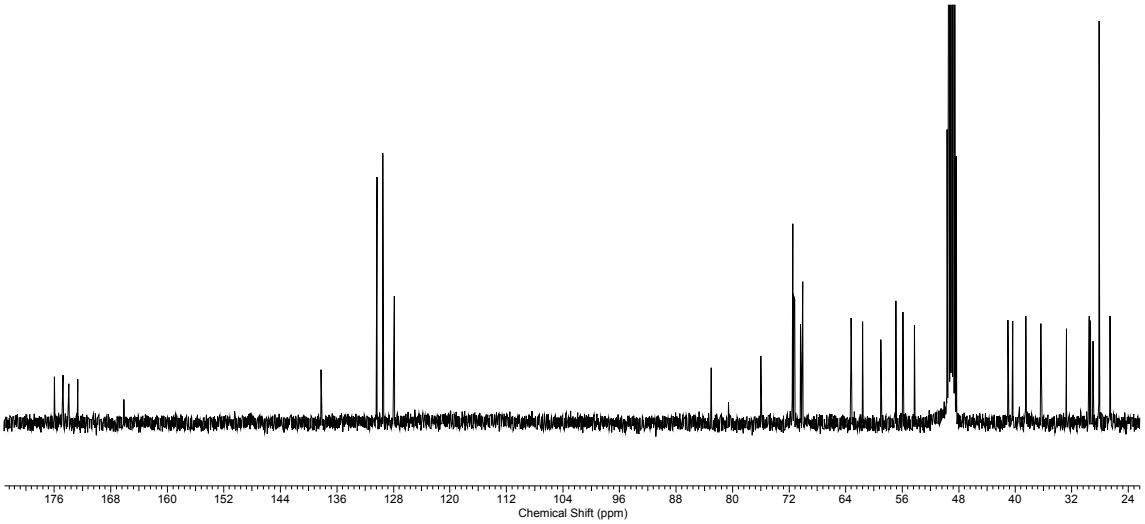

***Tert*-butyl N^2-[5-(2-oxohexahydro-1H-thieno[3,4-d]imidazol-4-yl)-pentanoyl]-N-(3,6,9,12-tetraoxapentadec-14-yne-1-yl)-L-α-glutaminyl-L-prolinate (10)**

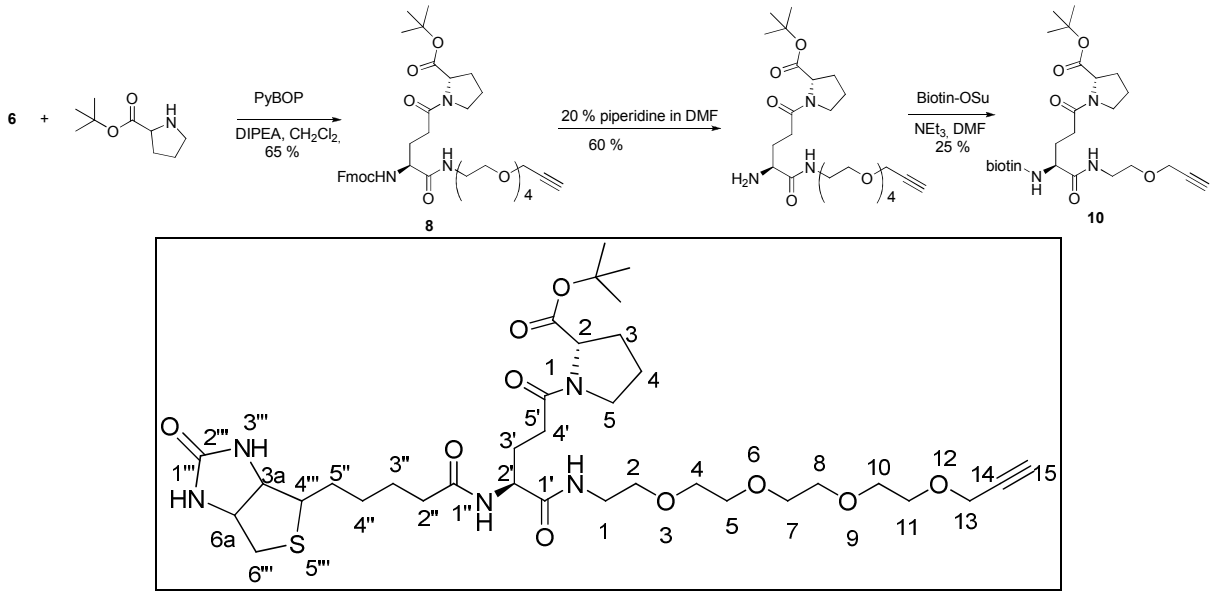

(**6**) (100 mg, 0.17 mmol, 1 equiv) and PyBOP (107 mg, 0.21 mmol, 1.2 equiv) were dissolved in dry DCM (1.6 mL). Triethylamine (88 µL, 0.51 mmol, 3 equiv) was added at -5 °C. A solution of L-Pro-O^{t}Bu (36 mg, 0.17 mmol, 1 equiv) in DCM (1.2 mL) was added dropwise. The reaction mixture was stirred until total conversion of the starting material. The solvent was removed under reduced pressure and EtOAc was added. The organic phase was sequentially washed with saturated NH_4Cl, H_2O, 5 % $NaHCO_3$ and brine, dried over anhydrous $MgSO_4$, filtered and concentrated under reduced pressure. The product was purified by flash column chromatography (CH_2Cl_2/MeOH: 95:5) to afford a colorless oil (81 mg, yield 65 %).

Tert-butyl N-(3,6,9,12-tetraoxa-pentadec-14-yn-1-yl)-L-α-glutaminyl-L-prolinate (**8**) (81 mg, 0.11 mmol, 1 equiv) was dissolved into a solution of 20 % piperidine in DMF (2.2 mL) at 25

°C. After stirring for 1 h the solvent was evaporated and piperidine was removed by coevaporation with toluene. The product was purified by flash column chromatography (CH_2Cl_2/MeOH: 95:5 then 9:1) to afford a colorless oil (34 mg, 60 %).

Tert-butyl N-(3,6,9,12-tetraoxa-pentadec-14-yn-1-yl)-L-α-glutaminyl-L-prolinate (34 mg, 0.07 mmol, 1 equiv) and biotin-OSu (23 mg, 0.07 mol, 1 equiv) were dissolved in DMF (0.7 mL) at 25 °C. Triethylamine (13.8 µL, 0.99 mmol, 1.5 equiv) was added. The reaction mixture was stirred at 25 °C four 12 h. The solvent was removed and the product was purified by HPLC (XTerra Prep RP C18, (19x150 mm Waters)) to afford (**10**) as a colorless oil (12 mg, 25 %).

IR (film): 3270, 2870, 2475, 1640, 1535, 1445, 1345, 1245, 1200, 1090, 1035, 940, 840, 650, 605, 595, 530, 520 cm^{-1}.

^{1}H NMR (400 MHz, MeOD): δ= 4.48 (m, 1H, C(6a)**H**), 4.33 (m, 2H, C(3a)**H**, C(2)**H**), 4.19 (d, 2H, ^4J= 2.3 Hz, C(13)$\mathbf{H_2}$), 3.68-3.54 (m, 16H, (C$\mathbf{H_2}$-O)$_8$), 3.42 (m, 2H, C(5)$\mathbf{H_2}$), 3.21 (m, 1H, C(4)**H**), 2.93 (dd, 1H, ^2J= 12.7, ^3J= 5.0 Hz, C(6)$\mathbf{H}_2$) 2.86 (t, 1H, 2.4 Hz, C(15)**H**), 2.71 (d, 1H, ^2J= 12.7 Hz, C(6)$\mathbf{H}_2$), 2.48-1.56 (m, 16H, (C$\mathbf{H_2}$)$_8$), 1.47, (s, 9H, (C$\mathbf{H_3}$)$_3$).

^{13}C NMR (100 MHz, MeOD): δ= 176.1 (s, C**q**), 173.3 (s, C**q**), 173.2 (s, C**q**), 82.7 (s, C**q**(14)), 76.0 (d, **C**H), 71.6 (t, ^1J= 144 Hz, **C**H_2), 71.6 (t, ^1J= 142 Hz, **C**H_2), 71.3 (t, **C**H_2), 70.5 (t, **C**H_2), 70.1 (t, **C**H_2), 63.3 (d, ^1J= 161 Hz, **C**H), 61.7 (d, ^1J= 168 Hz, **C**H), 61.1 (d, ^1J= 151 Hz, **C**H), 59.1 (t, ^1J= 147 Hz, **C**H_2), 57.0 (d, ^1J= 132 Hz, **C**H), 54.3 (d, ^1J= 141 Hz, **C**H), 48.4 (t, **C**H_2), 41.1 (t, ^1J= 142 Hz, **C**H_2), 40.6 (t, **C**H_2), 40.4 (t, ^1J= 139 Hz, **C**H_2), 36.5 (t, ^1J= 128 Hz, **C**H_2), 31.6 (t, ^1J= 133 Hz, **C**H_2), 30.3 (t **C**H_2), 29.6 (t, **C**H_2), 29.4 (t, **C**H_2), 29.3 (t, **C**H_2), 28.3 (q, ^1J= 127 Hz, **C**H_3), 26.7 (t, **C**H_2), 25.6 (t, **C**H_2).

MS (ESI): calculated: 740.3904; found: 740.3927
Optical rotation (CH_2Cl_2, 25 °C, *c*=0.035 g/100 mL): $[\alpha]_D^{25}$ = -31

^{1}H NMR:

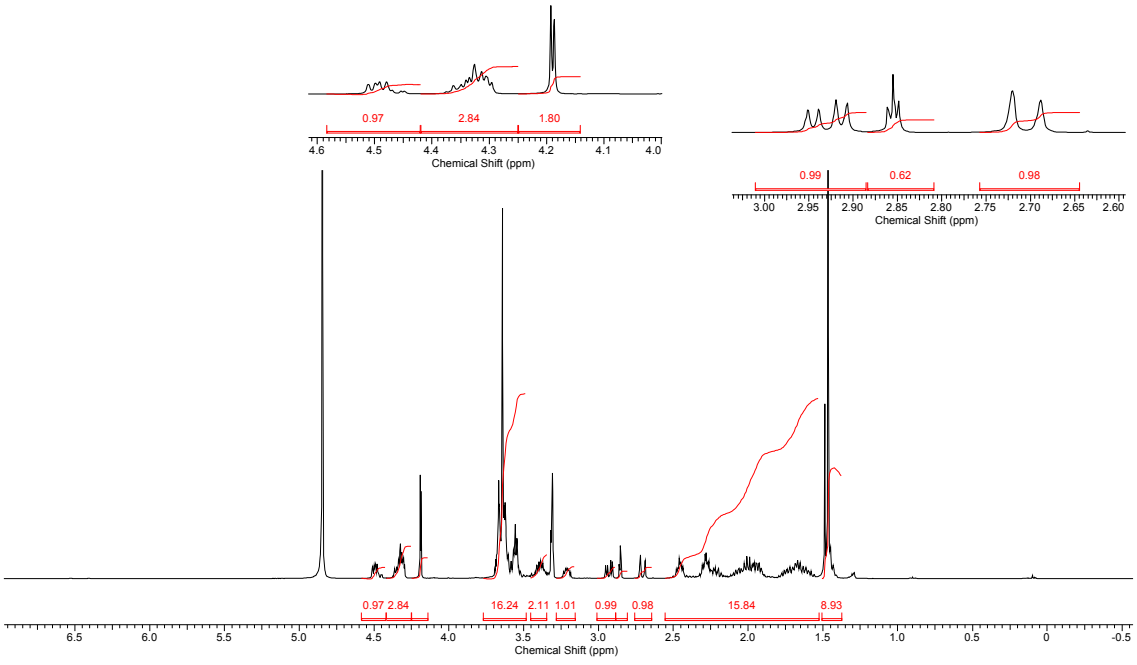

^{13}C NMR:

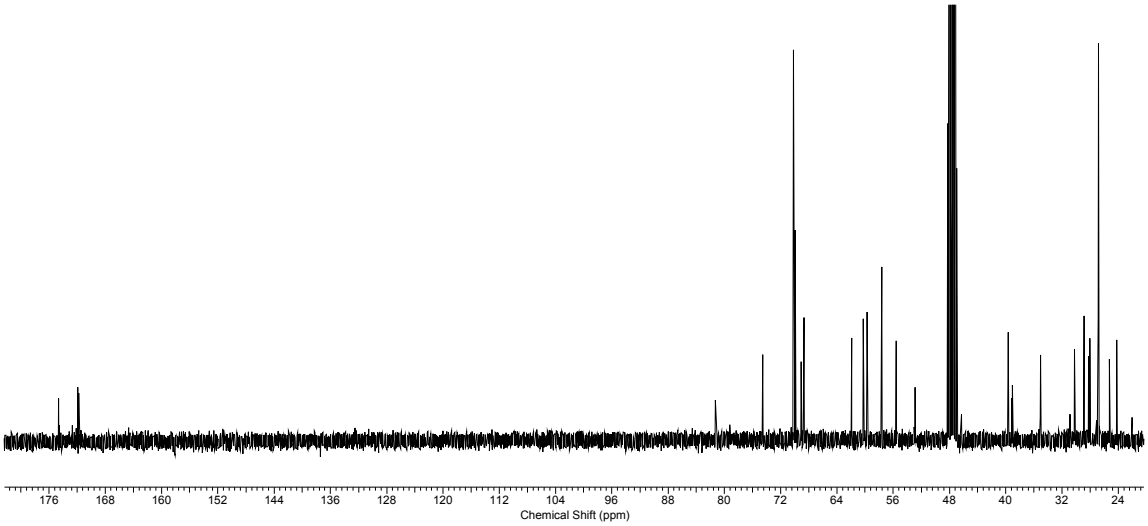

***Tert*-butyl N^2-[5-(2-oxohexahydro-1H-thieno[3,4-d]imidazol-4-yl)-pentanoyl]-N-(3,6,9,12-tetraoxa-pentadec-14-yn-1-yl)-L-α-glutaminylglycyl-N-(2-{2-[2-(2-hydroxyethoxy) ethoxy]ethoxy}ethyl)-L-prolinamide (12)**

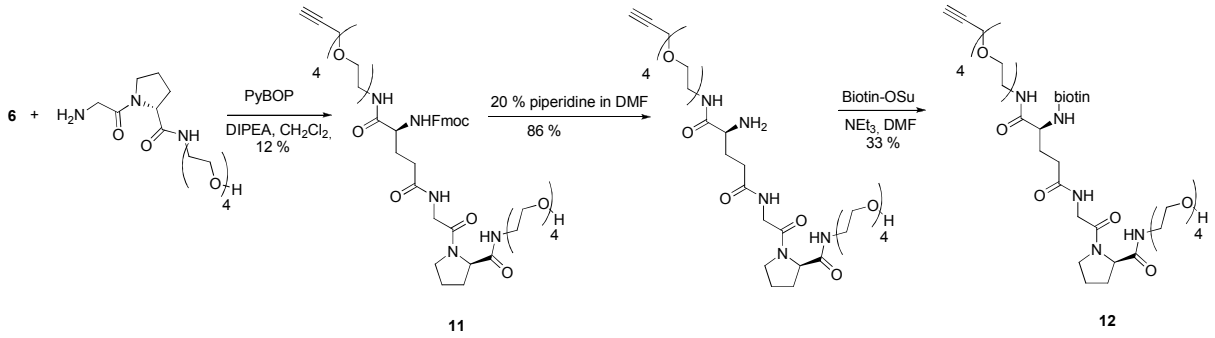

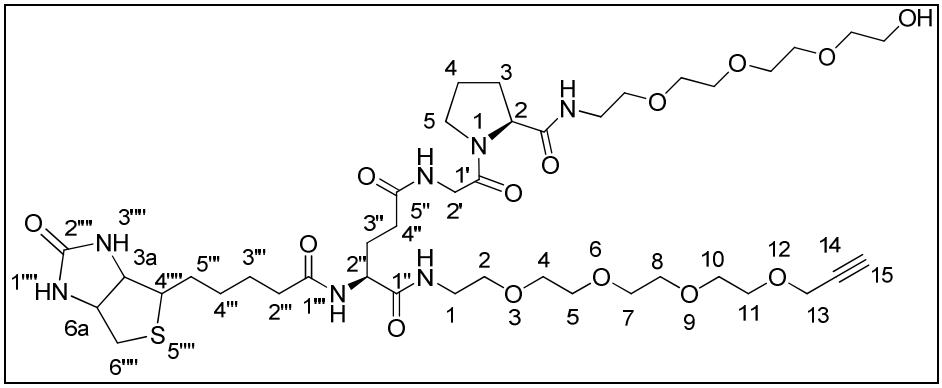

N^2-[9A fluoren-9-ylmethoxy)carbonyl]-N-3,6,9,12-tetraoxa-pentadec-14-yn-1-yl-L-α-glutaminate (**6**) (100 mg, 0.17 mmol, 1 equiv) and PyBOP (107 mg, 0.21 mmol, 1.2 equiv) were dissolved in dry DCM (1.6 mL). Triethylamine (88 µL, 0.51 mmol, 3 equiv) was added at -5 °C. A solution of glycyl-*N*-(2-{2-[2-(2-hydroxyethoxy)ethoxy]ethoxy}ethyl)-L-prolinamide (60 mg, 0.17 mmol, 1 equiv) in DCM (1.2 mL) was added dropwise. The

reaction mixture was stirred until total conversion of the starting material (monitored by TLC). The organic phase was sequentially washed with saturated NH_4Cl, H_2O, 5 % $NaHCO_3$ and brine, dried over anhydrous $MgSO_4$, filtered and concentrated under reduced pressure. The product was purified by flash column chromatography (CH_2Cl_2/MeOH: 9:1) to afford a colorless oil (20 mg, yield 12 %).

Tert-butyl N^2-[9A fluoren-9-ylmethoxy)carbonyl]-N-(3, 6, 9, 12-tetraoxa-pentadec-14-yn-1-yl)-L-α-glutaminylglycyl-N-(2-{2-[2-(2-hydroxyethoxy)ethoxy]ethoxy}ethyl)-L-prolinamide (20 mg, 0.02 mmol, 1 equiv) was dissolved into a solution of 20 % piperidine in DMF (0.5 mL) at 25 °C. After stirring for 1 h the solvent was evaporated and piperidine was removed by coevaporation with toluene. The product was purified by flash column chromatography (CH_2Cl_2/MeOH: 9:1 then CH_3CN/NH_4: 5:1) to afford a colorless oil (13 mg, 86 %).

Tert-butyl N-(3, 6, 9, 12-tetraoxa-pentadec-14-yn-1-yl)-L-α-glutaminylglycyl-N-(2-{2-[2-(2-hydroxyethoxy)ethoxy]ethoxy}ethyl)-L-prolinamide (13 mg, 0.02 mmol, 1 equiv) and biotin-OSu (7 mg, 0.02 mol, 1 equiv) were dissolved in DMF (0.2 mL) at rt. Triethylamine (4.0 µL, 0.03 mmol, 1.5 equiv) was added. The reaction mixture was stirred at 25 °C for 12 h. The solvent was removed and the product was purified by HPLC (XTerra Prep RP C18, (19x150 mm Waters)) (to afford **38** as a colorless oil (6 mg, 33 %).

IR (film): 3265, 3075, 2920, 2865, 1780, 1640, 1535, 1445, 1345, 1330, 1245, 1200, 1090, 1030, 940, 830, 645, 600, 545, 540, 525, 510, 500 cm^{-1}.

^{1}H NMR (400 MHz, MeOD): δ= 4.49 (dd, 1H, ^2J= 7.8, ^3J= 5.1 Hz, C(6a)**H**), 4.43 (dd, 1H, ^2J= 8.6, ^3J= 3.7 Hz, C(2)**H**, C(2'')**H**) 4.33 (m, 2H, C(3a)**H**, C(2)**H**, C(2'')**H**), 4.19 (d, 2H, ^4J= 2.4 Hz, C(13)$\mathbf{H_2}$), 4.15 (dd, 1H, C(2')$\mathbf{H}_2$), 3.94 (dd, 1H, ^2J= 17.0, ^3J= 4.6 Hz, C(2')$\mathbf{H}_2$), 3.69-3.35 (m, 34H, (C$\mathbf{H_2}$-O)$_{16}$, C(5)$\mathbf{H_2}$), 3.21 (m, 1H, C**H**), 2.93 (dd, 1H, ^2J= 12.8, ^3J= 5.0 Hz, C(6)$\mathbf{H}_2$) 2.86 (t, 1H, 2.4 Hz, C(15)**H**), 2.71 (d, 1H, ^2J= 12.7 Hz, C(6)$\mathbf{H}_2$), 2.40-1.45 (m, 16H, (C$\mathbf{H_2}$)$_8$).

^{13}C NMR (100 MHz, MeOD): δ= 176.0 (s, C**q**), 175.3 (s, C**q**), 174.0 (s, C**q**), 171.8 (s, C**q**), 169.9 (s, C**q**), 76.0 (d, **C**H), 73.7 (t, ^1J= 141 Hz, **C**H_2), 71.6 (t, **C**H_2) 71.55 (t, **C**H_2), 71.5 (t, **C**H_2), 71.4 (t, **C**H_2), 71.3 (t, **C**H_2), 71.2 (t, **C**H_2), 70.3 (t, **C**H_2), 70.1 (t, **C**H_2), 70.1 (t, **C**H_2), 63.2 (d, ^1J= 156 Hz, **C**H), 62.2 (d, **C**H), 61.9 (d, ^1J= 125 Hz, **C**H) 61.7 (d, ^1J= 134 Hz, **C**H), 59.0 (t, ^1J= 145 Hz, **C**H_2), 57.0 (d, ^1J= 131 Hz, **C**H), 54.1 (d, ^1J= 139 Hz, **C**H), 47.8 (t, **C**H_2), 42.8 (t, ^1J= 139 Hz, **C**H_2), 41.0 (t, **C**H_2), 40.6 (t, **C**H_2), 40.4 (t, **C**H_2), 36.4 (t, **C**H_2), 36.3 (t, **C**H_2), 32.9 (t, **C**H_2), 30.8 (t, **C**H_2), 29.6 (t, **C**H_2), 29.5 (t, **C**H_2), 29.4 (t, **C**H_2), 28.9 (t, **C**H_2), 26.7 (q, ^1J= 127 Hz, **C**H_3), 26.6. (t, **C**H_2), 25.7 (t, **C**H_2).

MS (ESI): calculated: 916.4702; found: 916.4717
Optical rotation (CH_2Cl_2, 25 °C, *c*=0.05 g/100 mL): $[\alpha]_D^{25}$ = -18

^{1}H NMR:

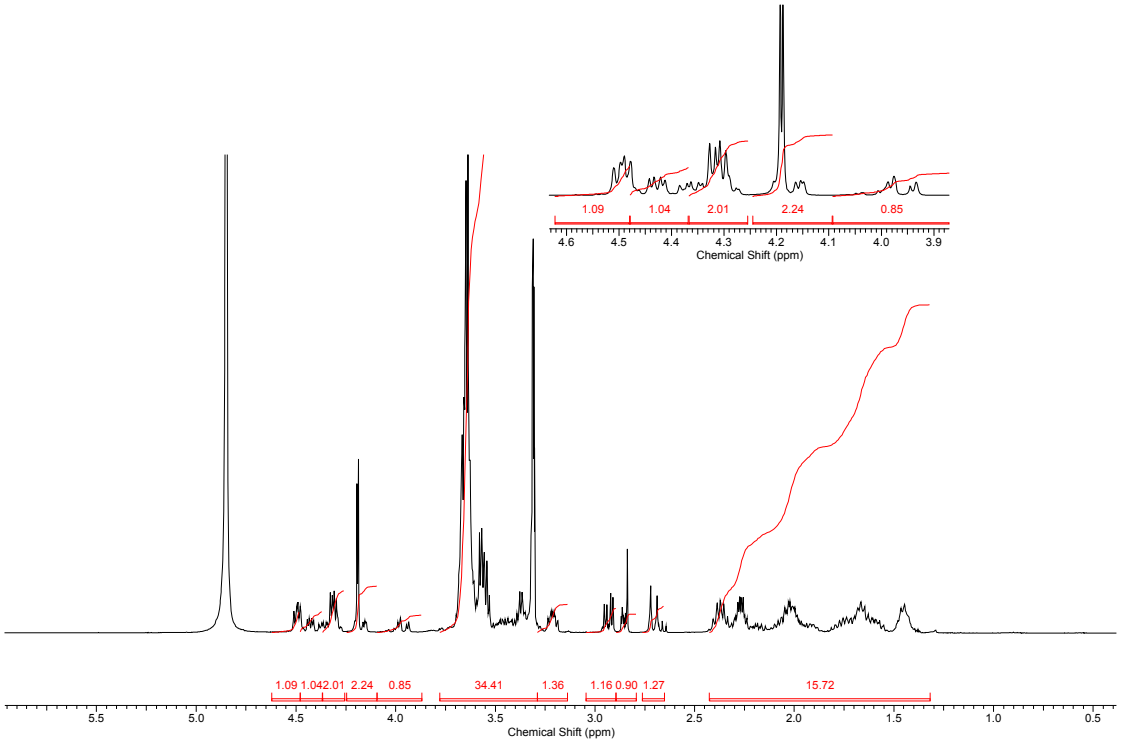

^{13}C NMR:

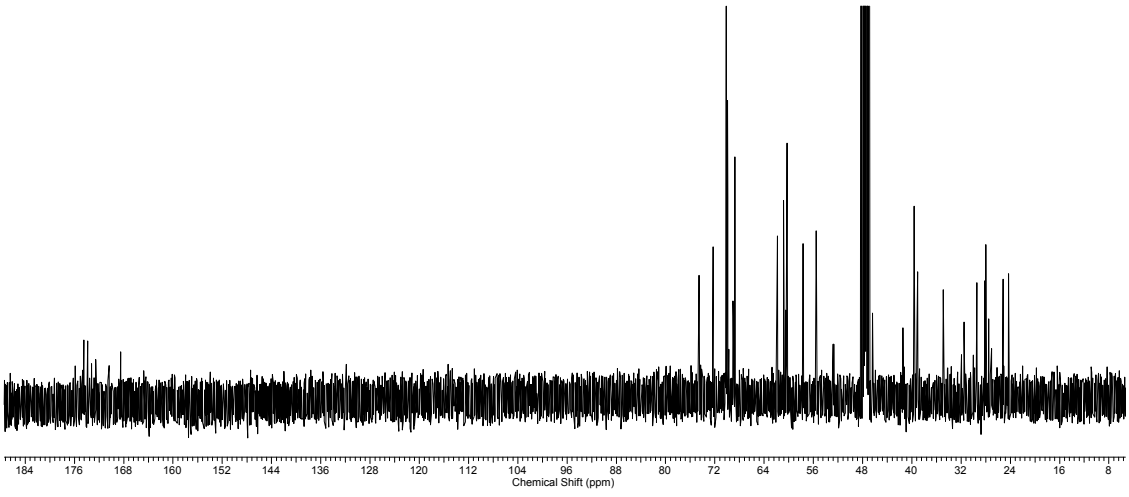

[5-[3a,4a,6a)-2-oxohexahydro-1H-thieno[3,4-d]imidazol-4-yl)-pentanoyl]-N-(3,6,9,12-tetraoxa-pentadec-14-yn-1-yl)pentanamide (13)

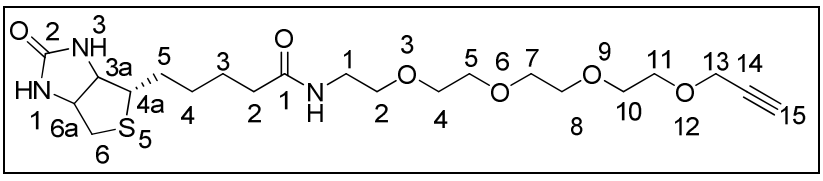

Biotin-OSu (0.83 g, 2.4 mmol, 1 equiv) followed by triethylamine (0.5 mL, 3.6 mmol, 1.5 equiv) were added to a solution of 3,6,9,12-tetraoxapentadec-14-yn-1-amine (**3**) (0.56 g, 2.4 mmol, 1 equiv) in DMF (24 mL). The reaction mixture was stirred overnight at rt. The solvent was removed under reduced pressure and the desired product was purified by column chromatography (CH_2Cl_2/MeOH 95/5) to provide a colorless oil (560 mg, 51 %).

IR (film): 3245, 2925, 2865, 1810, 1780, 1700, 1645, 1550, 1460, 1350, 1325, 1305, 1265, 1245, 1210, 1090, 1035, 945, 860, 840, 760, 635, 600, 540, 530, 505 cm^{-1}.

^{1}H NMR (400 MHz, MeOD): δ= 4.49 (dd, 1H, ^2J= 8.0, ^3J= 5.0 Hz, C(6a)**H**)), 4.31 (dd, 1H, ^2J= 7.9, ^3J= 4.5 Hz, C(3a)**H**), 4.19 (d, 2H, ^4J= 2.5 Hz, C(13)**H**), 3.69-3.61 (m, 12H, (C**H$_2$**-O)$_6$), 3.56 (t, 2H, ^3J= 5.3 Hz, C**H$_2$**-O), 3.36 (m, 2H, C**H$_2$**-O), 3.20 (m, 1H, C(4a)**H**), 2.93 (dd, 1H, ^2J= 12.8, ^3J= 5.0 Hz, C(6)**H**$_2$), 2.85 (t, 1H, ^3J= 2.4 Hz, C(15)**H**), 2.71 (d, 1H, ^3J= 12.7 Hz, C(6)**H**$_2$), 2.23 (t, 2H, ^3J= 7.3 Hz, C**H$_2$**), 1.77-1.41 (m, 6H, (C**H$_2$**)$_3$).

^{13}C NMR (100 MHz, MeOD): δ= 176.22 (s, C**q**), 75.97 (d, ^1J= 250.7 Hz, **C**H), 71.55 (t, **C**H$_2$), 71.51 (t, **C**H$_2$), 71.50 (t, **C**H$_2$), 71.34 (t, **C**H$_2$), 71.23 (t, **C**H$_2$), 70.57 (t, **C**H$_2$), 70.11 (t, **C**H$_2$), 63.34 (d, ^1J= 147.7 Hz, **C**H), 61.60 (d, ^1J= 149.8 Hz, **C**H), 59.04 (t, ^1J= 151.3 Hz, **C**H$_2$), 56.98 (d, ^1J= 133.0 Hz, **C**H), 41.04 (t, ^1J= 142.0 Hz, **C**H$_2$), 40.38 (t, ^1J= 137.8 Hz, **C**H$_2$), 36.77 (t, ^1J= 127.7 Hz, **C**H$_2$), 29.74 (t, ^1J= 123.7 Hz, **C**H$_2$), 29.48 (t, ^1J= 131.7 Hz, **C**H$_2$), 26.83 (t, ^1J= 126.2 Hz, **C**H$_2$), 26.28 (t, ^1J= 13.3 Hz, **C**H$_2$).

MS (ESI): calculated: 458.2325; found: 458.2337
Optical rotation (CH_2Cl_2, 25 °C, *c*=0.195 g/100 mL): $[\alpha]_D^{25}$ = -22

^{1}H NMR:

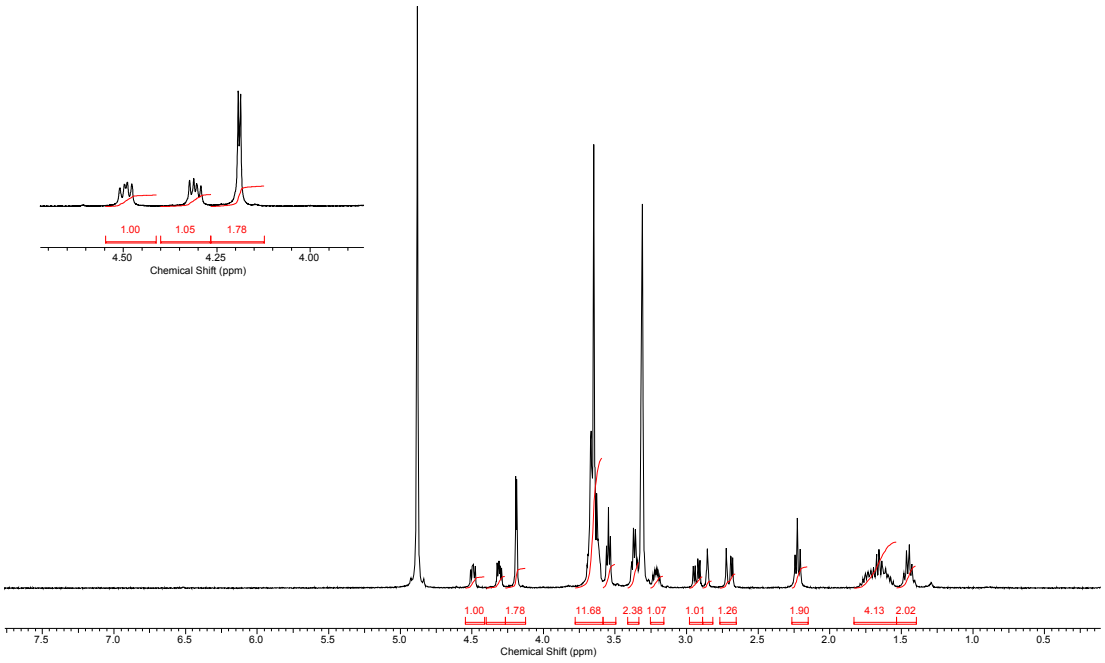

^{13}C NMR

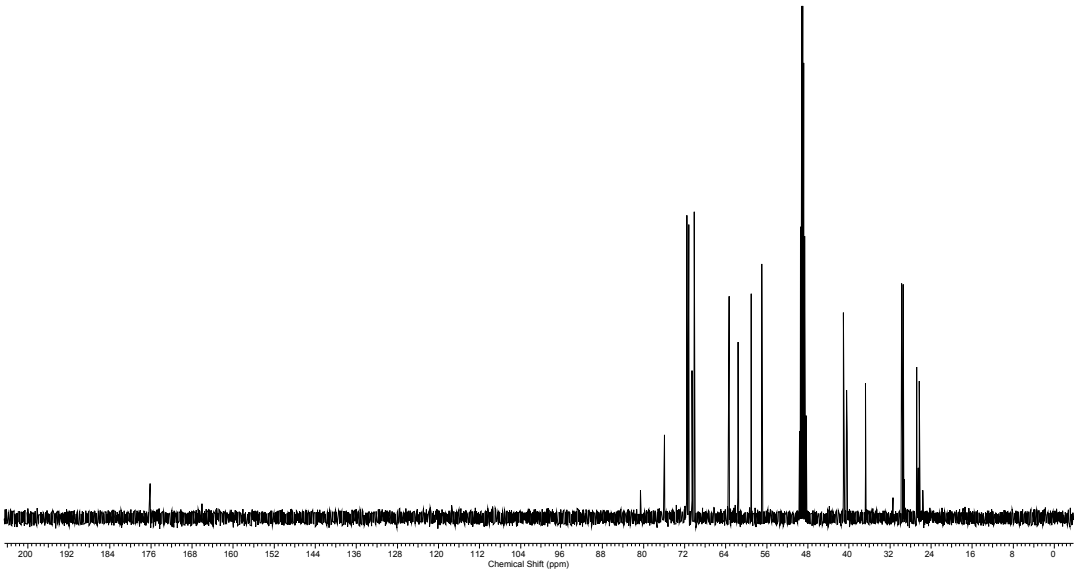

(Z)-1,2-Bis(trimethylsiloxy)cyclohept-1-ene

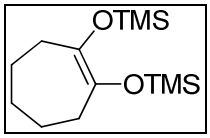

A suspension of sodium (2.76 g, 119.9 mmol, 4.7 equiv) in toluene (75 mL) was heated at reflux for 30 min. Then a solution of diethylpimelate (5.47 g, 25.3 mmol, 1 equiv) and trimethylsilylchloride (13.70 g, 126.5 mmol, 5 equiv) in toluene (25 mL) was added dropwise to the reaction mixture over 2.5 h under reflux. The reaction mixture was stirred for 4h at reflux before it was allowed to reach rt. The organic layer was removed via a syringe. Toluene was added and the system was stirred for 5 min, before that the organic layers was removed again via a syringe. This operation was repeated twice. The collected organic layers were combined and concentrated under reduced pressure to yield a pale yellow liquid (5.51 g, 20.24 mmol, 80 %).
The analytical data were in accordance with reported characterization.[1]

1,7-Bis(trimethylsiloxy)bicyclo[5.l.0]octane

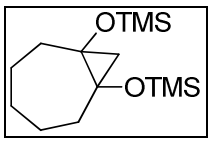

In a flame-dried two-neck round-bottom flask, 1,2-bis(trimethylsiloxy)cycloheptene (5.35 g, 19.7 mmol, 1 equiv) and diiodomethane (14.20 g, 53.2 mmol, 2.7 equiv) were dissolved in toluene (28 mL). The reaction mixture was cooled in an ice/salt bath. A 1.5 M solution of diethylzinc (18.23 mL, 27.3 mmol, 2.8 equiv) was added dropwise over 30 min. The system was stirred for 1 h at 0 °C and then 16 h at rt. The reaction was cooled again in an ice/salt bath and was quenched by adding water. A saturated solution of NH_4Cl (29 mL) was added and extracted three times with toluene (3 x 56 mL). The combined organic layers were washed with a saturated solution of NH_4Cl (56 mL) and brine (56 mL), dried over anhydrous $MgSO_4$ and filtered. The organic layer was concentrated under reduced pressure and diluted in

diethylether before being filtered and concentrated again under reduced pressure to yield a yellow oil (2.20 g, 7.7 mmol, 77 %).
The analytical data were in accordance with reported characterization.[1]

Cyclooctan-1,3-dione

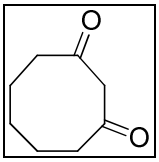

In a flame-dryed round-bottom flask, periodic acid (1.80 g, 7.9 mmol, 1.03 equiv) was dissolved in dry ethanol (14 mL) under argon atmosphere. The system was cooled to -10 °C. A 0.55 M solution of 1,7-bis(trimethylsiloxy)bicyclo[5.1.0]octane (14 mL, 7.7 mmol, 1 equiv) in dry ethanol was added. A dark orange colour formed immediately. The system was stirred for 45 min at -10 °C or until the colour has turned to pale yellow. The reaction mixture was allowed to reach rt and then diluted with chloroform (120 mL). The organic layer was washed with water (120 mL), 5 % aqueous Na_2SO_3 solution (120 mL) and brine (120 mL), The organic layer was dried over anhydrous $MgSO_4$, filtered and concentrated under reduced pressure. A Kugelrohr distillation was done to yield a light yellow oil (433 mg, 3.1 mmol, 40 %).
Alternative method: In a flame-dried two-neck round-bottom flask, 1,2-bis(trimethylsiloxy)cycloheptene (5.11 g, 18.7 mmol, 1 equiv) and bromoform (3.28 mL, 37.5 mmol, 2 equiv) were dissolved in toluene (30 mL). The system was cooled to 0 °C and diethyl zinc (27.50 mL, 41.3 mmol, 2.2 equiv) was added dropwise over 1.5 h. The reaction mixture was allowed to reach rt after 30 min and it was stirred overhight at rt. A saturated solution of ammonium chloride was added dropwise at 0 °C and the aqueous layer was extracted three times with AcOEt and then washed with brine. The organic phase was concentrated under reduced pressure and and purified by flash chromatography (6:1 hexanes/EtOAc), affording the desired product (1.05 g, 7.5 mmol, 40 %).
The analytical data were in accordance with reported characterization.[1]

^{1}H NMR:

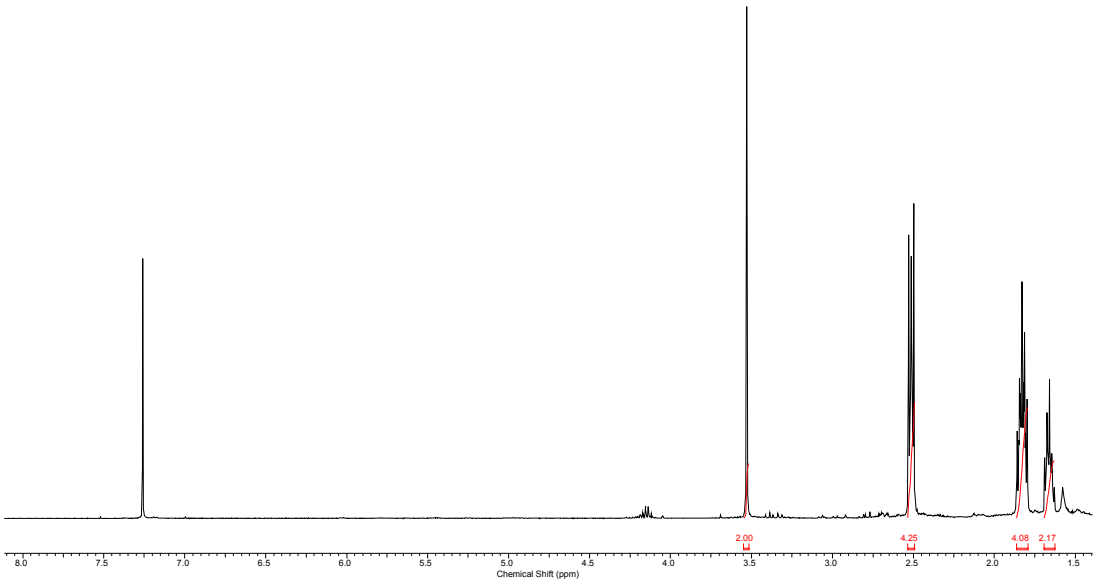

{2-[(3-methyloxetan-3-yl)methoxy]-2-oxoethyl}(triphenyl)phosphonium iodide

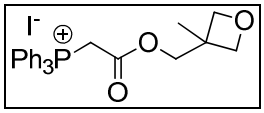

N,N'-Dicyclohexylcarbodimide (DCC) (3.66 g, 17.7 mmol, 1.1 equiv), 4-dimethylaminopyridine (DMAP) (98.6 mg, 0.8 mmol, 0.05 equiv) and 3-methyl-3-oxetanemethanol were dissolved in a flame-dried round-bottom flask in dichloromethane (20 mL) under argon atmosphere. The reaction mixture was stirred and cooled to 0 °C. A solution of iodoacetic acid in dichloromethane (30 mL) was then added. The reaction mixture was stirred at 0 °C for 1 h, and then at rt for an additional 1.5 h. The reaction was quenched with acetic acid (1 mL) and stirred for 30min. The reaction mixture was diluted with dichloromethane (250 mL) before filtering on a glass frit. The filtrate was washed with water (200 mL), twice with a saturated solution of sodium hydrogenocarbonate (sodium bicarbonate) (2 x 200 mL) and with brine (200 mL). The organic layer was dried over anhydrous $MgSO_4$, filtered and concentrated under reduced pressure. The crude product was dissolved again in dichloromethane, filtered again on a glass frit and concentrated under reduced pressure to afforded a yellow oil.
This material was dissolved in THF (100 mL) and triphenylphosphine (4.65 g, 17.7 mmol, 1.1 equiv) was added to the reaction mixture. The system was stirred under an argon atmosphere for 20 h at rt and then diluted with diethyl ether (100 mL). The reaction mixture was filtered on Büchner and the precipitate was dried under reduced pressure to yield a white solid (5.23 g, 9.8 mmol, 61 %).
The analytical data were in accordance with reported characterization.[2]

(3-methyloxetan-3-yl)methyl(2Z)-(2,2-difluoro-3-oxocyclooctylidene)ethanoate

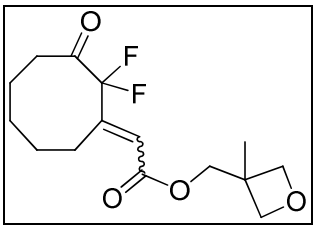

Cyclooctane-1,3-dione (433.0 mg, 3.1 mmol, 1 equiv) was dissolved in a flame-dried Schlenk flask with dry acetonitrile (22.5 mL) under an argon atmosphere. Cesium carbonate (2.06 g, 6.3 mmol, 2 equiv) was added and the system was stirred for 30 min at rt and then cooled to 0 °C. Selectfluor (2.63 g, 7.4 mmol, 2.4 equiv) was added. The reaction mixture was stirred for 15 min at 0 °C and 1.5 h at rt before it was diluted with dry dichloromethane (17.5 mL). The reaction mixture was added into a solution of phosphonium iodide (545.8 mg, 3.1 mmol, 1 equiv) and DBU (471.8 mg, 3.1 mmol, 1 equiv) in dry dichloromethane (23.5 mL), and stirred at rt for 6 h under an argon atmosphere. The reaction mixture was diluted in diethylether (250 mL). The organic layer was washed five times with a saturated solution of NH_4Cl (5 x 150 mL) and brine (200 mL). It was then dried over anhydrous $MgSO_4$, filtered and concentrated under reduced pressure. The crude product was purified by flash chromatography (9:1 to 4:1 hexanes/EtOAc), affording a white solid (412.10 mg, 1.4 mmol, 44 %). *Rf* 0.29 (4:1 hexanes/EtOAc).
The analytical data were in accordance with reported characterization.[2]

^{1}H NMR:

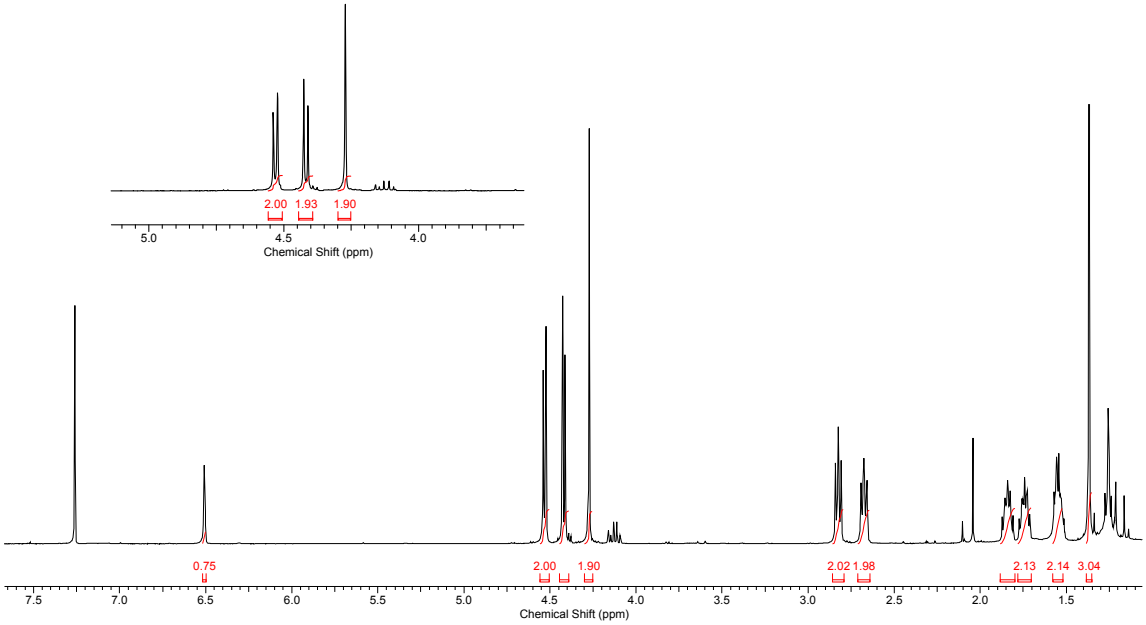

(3-methyloxetan-3-yl)methyl (2,2-difluoro-3-oxocyclooctyl)acetate

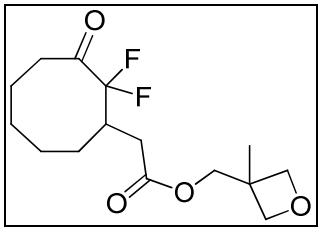

(3-methyloxetan-3-yl)methyl(2Z)-(2,2-difluoro-3-oxocyclooctylidene)ethanoate (500.90 mg, 1.7 mmol, 1 equiv) was dissolved with dry methanol (18 mL) in a flame-dried two-neck round-bottom flask. The system was flushed with argon and a catalytic amount of Pd/C was added. The system was flushed again with argon followed by dihydrogen, and stirred for 5 h. The system was then flushed with argon thoroughly and the mixture was filtered on syringe filters and concentrated under reduced pressure to yield a solid (435.40 mg, 1.4 mmol, 86 %). The analytical data were in accordance with reported characterization.[2]

2,2.difluoro-3-[(4-methyl-2,6,7-trioxabicyclo[2.2.2]oct-1-yl)methyl]cyclooctanone

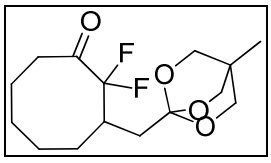

All pieces of glassware were carefully flame-dried and dry dichloromethane was put on activated 4 Å molecular sieves under stirring for 2 h. (3-methyloxetan-3-yl)methyl (2,2-difluoro-3-oxocyclooctyl)acetate (217.70 mg, 0.72 mmol, 1 equiv) was dissolved with dry dichloromethane (26.4 mL) in a flame-dried round-bottom flask containing activated 4 Å molecular sieves under argon atmosphere. The reaction mixture was cooled to 0 °C. In a

separate flame-dried round-bottom flask, a 0.02 M solution of BF_3OEt_2 (99 μL, 0.78 mmol in 39 mL of dry dichloromethane) was prepared and a portion of this solution (7.15 mL, 0.14 mmol, 0.2 equiv) was added to the reaction mixture. The reaction mixture was allowed to warm up at rt and it was stirred for 20 h. The reaction was then quenched with 1 mL of NEt_3. The reaction mixture was filtered to remove molecular sieves, concentrated under reduced pressure and purified by flash chromatography (20:1 Hexanes/EtOAc with 1% NEt_3 over deactivated silica gel) to yield a pale-yellow transparent oil (167.20 mg, 0.6 mmol, 85 %).
The analytical data were in accordance with reported characterization.[2]

(1E)-8,8-difluoro-7-[(4-methyl-2,6,7-trioxabicyclo[2.2.2]oct-1-yl)methyl]cyclooct-1-en-1-yl trifluoromethanesulfonate

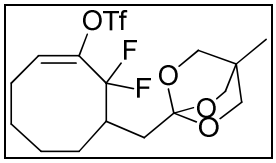

All pieces of glassware were carefully flame-dried and dry THF was put on activated 4 Å molecular sieves under stirring for 2 h. A portion of a 0.5 M solution of KHMDS (1.98 mL, 1.0 mmol, 1.5 equiv) was dissolved in dry THF (17 mL) in a flame-dried round-bottom flask under an argon atmosphere, and the solution was cooled to -78 °C. A solution of 2,2.difluoro-3-[(4-methyl-2,6,7-trioxabicyclo[2.2.2]oct-1-yl)methyl]cyclooctanone **9** (200 mg, 0.7 mmol, 1 equiv) in 8.5 mL of dry THF was added dropwise to the previous one over 15 min and stirred for 3 h. A solution of Tf_2NPh (353.67 mg, 1.0 mmol, 1.5 equiv) in 8.5 mL of THF was added. Then the reaction mixture was allowed to reach rt and was stirred for 19 h before that the reaction was quenched with deactivated silica gel. The mixture was concentrated under reduced pressure and purified by flash chromatography (20:1 to 15:1 Hexanes/EtOAc with 1% NEt_3 over deactivated silica gel) to yield the desired product (193 mg, 0.4 mmol, 67 %).
The analytical data were in accordance with reported characterization.[2]

1-[(2,2-difluorocyclooct-3-yn-1-yl)methyl]-4-methyl-2,6,7-trioxabicyclo[2.2.2]octane

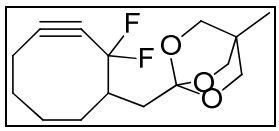

All pieces of glassware were carefully flame-dried and dry THF was put on activated 4 Å molecular sieves under stirring for 2 h. Vinyl triflate (146.0 mg, 0.3 mmol, 1 equiv) was dissolved in toluene and concentrated under reduced pressure. This operation was repeated three times to remove all traces of moisture. Vinyl triflate was then dissolved in dry THF (7.5 mL) and the reaction mixture was cooled to -20 °C. In a separate round-bottom flask a solution of LDA was prepared. Distilled diisopropylamine (212 μL, 1.5 mmol) was dissolved in dry THF (6.1 mL) and a portion of a titrated 2 M solution of n-butyllithium (0.70 mL, 1.4 mmol) was added dropwise after that the solution was cooled to -78 °C. A portion of the LDA solution (2.0 mL, 0.4 mmol, 1.23 equiv) was added dropwise to the reaction mixture over 1 h at -20 °C. The reaction mixture was brought to rt and stirred for 30 min. the reaction was then quenched by adding deactivated silica and concentrated under reduced pressure. The mixture was then purified by flash chromatography (20:1 to 15:1 Hexanes/EtOAc with 1% of NEt_3 over deactivated silica gel) to yield the desired product (87.40 mg, 0.3 mmol, 93 %). R_f = 0.45 (4:1 Hexanes/EtOAc).
The analytical data were in accordance with reported characterization.[2]

^{1}H NMR:

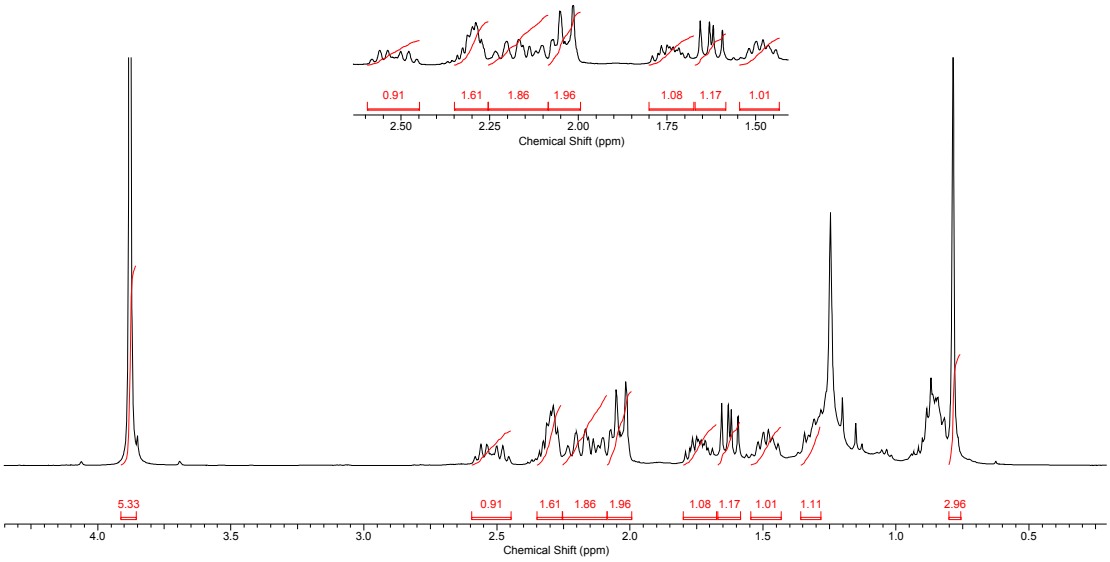

3-hydroxy-2-(hydroxymethyl)-2-methylpropyl (2,2-difluorocyclooct-3-yn-1-yl)acetate

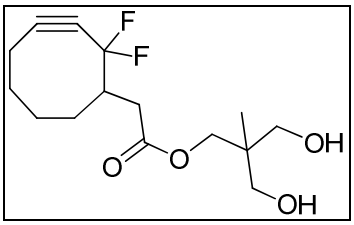

In a round-bottom flask, difluorinatedcyclooctyne orthoester (43.60 mg, 0.15 mmol, 1 equiv) and pyridinium p-toluenesulfonate (76.70 mg, 0.3 mmol, 2 equiv) were dissolved in methanol (2.2 mL) and water (217 μL). The system was stirred at rt for 24 h under an air atmosphere before that the reaction was quenched by adding a saturated aqueous solution of $NaHCO_3$ (970 μL). The crude product was concentrated under reduced pressure. It was then diluted with brine (3.9 mL) and extracted with EtOAc (3 x 5.2 mL). The organic layers were combined and washed with brine (5.2 mL) and with an HCl/brine solution (1:1 1M HCl/brine, 2 x 5.2 mL). The organic layer was then dried over anhydrous $MgSO_4$, filtered and concentrated under reduced pressure to afford the desired product (40.90 mg, 0.1 mmol, 90 %).
The analytical data were in accordance with reported characterization.[2]

(2,2-difluorocyclooct-3-yn-1-yl)acetic acid

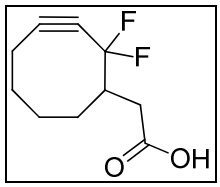

In a round-bottom flask, product 3-hydroxy-2-(hydroxymethyl)-2-methylpropyl (2,2-difluorocyclooct-3-yn-1-yl)acetate (61.20 mg, 0.2 mmol, 1 equiv) was dissolved in dioxane (1.1 mL) and water (212 μL) and lithium hydroxide (96.30 mg, 4.0 mmol, 20 equiv) was

added. The reaction mixture was stirred at rt overnight under an air atmosphere. The reaction was quenched by diluting the reaction mixture with a saturated aqueous solution of NaH_2PO_4 (10 mL) and was extracted with EtOAc (5 x 20 mL). The combined organic layers were dried over $MgSO_4$, filtered, concentrated under reduced pressure and purified by flash chromatography (98:2 to 96:4 CH_2Cl_2/MeOH) to afford a white solid (10.0 mg, 0.1 mmol, 25 %).
The analytical data were in accordance with reported characterization.[3]

^{1}H NMR:

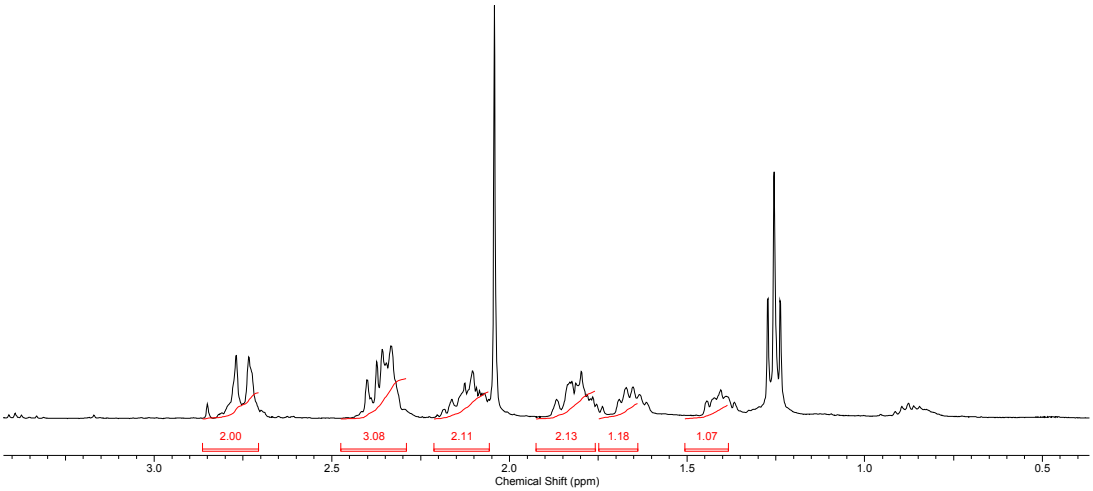

2-(2-(2-azidoethoxy)ethoxy)ethanemine HCl salt

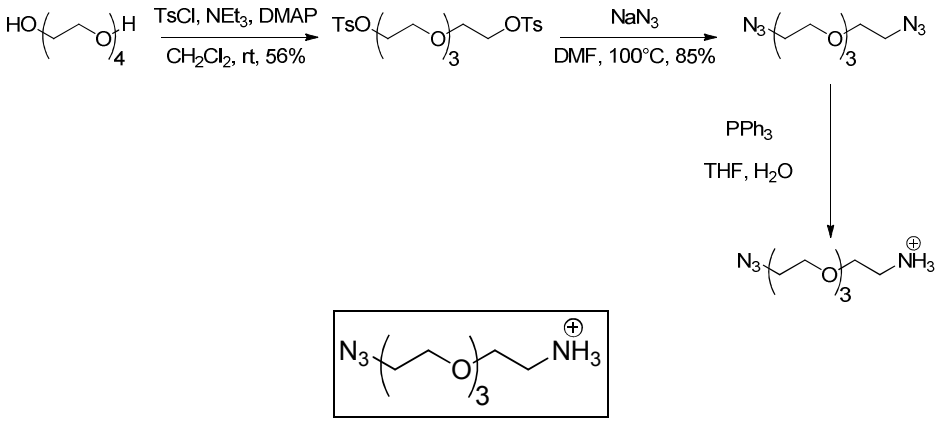

Tetraethylene glycol (50.0 g, 257.4 mmol, 1 equiv) was dissolved in dichloromethane (500 mL) and put under an argon atmosphere. Tosylchloride (147.2 g, 772.1 mmol, 3 equiv), triethylamine (107.0 mL, 772.1 mmol, 3 equiv) and DMAP (1.57 g, 12.9 mmol, 0.05 equiv) were added and the system was stirred for 16 h at rt. The reaction mixture was then washed with water. The organic layer was dried over $MgSO_4$, concentrated under reduced pressure and purified by flash chromatography (1:2 Hexanes/EtOAc) to afford the desired product (71.67 g, 142.7 mmol, 56 %).
The analytical data were in accordance with reported characterization.[4]

Oxybis(ethane-2,1-diyloxyethane-2,1-diyl) bis(4-methylbenzenesulfonate) (10.0 g, 19.9 mmol, 1 equiv) was dissolved in DMF (48 mL). NaN_3 (3.11 g, 47.8 mmol, 2.4 equiv) was

then added and the reaction mixture was stirred overnight at 100 °C. After that the system has reached rt, water was added and the mixture was extracted with ethyl acetate. The organic layer was then dried over anhydrous $MgSO_4$, filtered and concentrated under reduced pressure to yield the desired product (4.13 g, 16.9 mmol, 85 %).
The analytical data were in accordance with reported characterization.[4]

An 5 % aqueous HCl solution (32 mL) was added to a cooled solution of 1-azido-2-{2-[2-(2-azidoethoxy)ethoxy]ethoxy}ethane (7.88 g, 32.3 mmol, 1 equiv) in toluene (32 mL) at 0 °C. Triphenylphosphine (8.06 g, 30.6 mmol, 0.95 equiv) was then added and the reaction mixture was allowed to reach rt and was stirred for 16 h. The aqueous layer was removed and concentrated under reduced pressure. HCL was removed by coevaporation with toluene to afford the desired product (7.64 g, 30.1 mmol, 94 %).
The analytical data were in accordance with reported characterization.[4]

Biotin succinimidyl ester

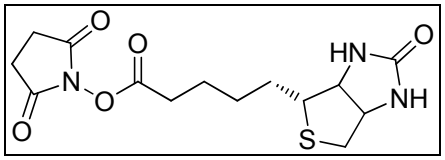

D-biotin (2.0 g, 8.2 mmol, 1 equiv) was dissolved in DMF under an argon atmosphere. N-hydroxysuccinimide (1.50 g, 13.1 mmol, 1.6 equiv) and N-ethyl-N'-(3-dimethylaminopropyl)-carboiimide hydrochloride (EDCI) (2.04 g, 10.6 mmol, 1.3 equiv) were added to the reaction mixture and the system was stirred at rt overnight.
The reaction mixture was then poured into ice (400 mL) and the precipitate was filtered over Büchner. The precipitate was recovered and dried under reduced pressure to yield a white powder (2.29 g, 6.7 mmol, 82 %).
The analytical data were in accordance with reported characterization.

***N*-(2-{2-[2-(2-azidoethoxy)ethoxy]ethoxy}ethyl)-5-[(4R)-2-oxohexahydro-1*H*-thieno[3,4-*d*]imidazol-4-yl]pentanamide**

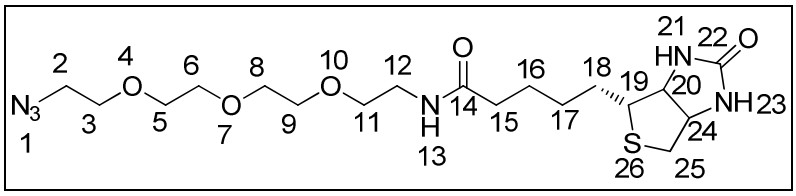

Triethylamine (1.57 g, 15.5 mmol, 2.5 equiv) was added to a solution of 2-(2-(2-azidoethoxy)ethoxy)ethanamine HCl salt (1.35 g, 6.2 mmol, 1 equiv) in DMF (37 mL). A solution of D-biotin N-succinimidyl ester (2.11 g, 6.7 mmol, 1 equiv) in 25 mL of DMF was added to the previous solution and stirred at rt overnight. The reaction mixture was diluted in a saturated solution of ammonium chloride (50 mL) and washed six times with ethyl acetate (6 x 40 mL). The organic layers were combined and concentrated under reduced pressure to afford a white solid (800.0 mg, 1.8 mmol, 30 %).

IR (film): 3250, 2925, 2860, 2105, 1695, 1650, 1550, 1465 1325, 1265 1105, 940, 870, 825, 695, 655, 595, 555, 520, 515 cm^{-1}.

^{1}H-NMR (400 MHz, $CDCl_3$): δ= 6.51 (s, 1H, amine), 5.92 (s, 1H, amine), 5.01 (s, 1H, amine), 4.50 (m, 1H, C(24)**H**), 4.33 (m, 1H, C(20)**H**), 3.69-3.61 (m, 8H, C(5)$\mathbf{H_2}$C(6)$\mathbf{H_2}$-O-C(8)$\mathbf{H_2}$C(9)$\mathbf{H_2}$), 3.56 (t, ^{3}J= 4.8 Hz, 2H, C(11)$\mathbf{H_2}$-O), 3.45 (t, 2H, ^{3}J= 5.3 Hz, C(3)$\mathbf{H_2}$-O), 3.40 (t, 2H,^{3}J= 3.4 Hz, C(12)$\mathbf{H_2}$-NH-(C=O)), 3.16 (dt, 1H, ^{2}J= 7.4, ^{3}J= 4.6 Hz, C(19)H), 2.92 (dd, 1H, ^{2}J= 12.8, ^{3}J= 5.0 Hz, C(25)$\mathbf{H_2}$-S), 2.73 (d, 1H,^{3}J= 12.8 Hz C(25)$\mathbf{H_2}$-S), 2.22 (m, 2H, C(15)$\mathbf{H_2}$), 1.78-1.64 (m, 6H, C(16)$\mathbf{H_2}$, C(18)$\mathbf{H_2}$, C(2)$\mathbf{H_2}$-N_3), 1.46 (m, 2H, C(17)$\mathbf{H_2}$) ppm.

^{13}C-NMR (100 MHz, $CDCl_3$) : δ= 173.6 (**C**(1)=O), 164.4 (**C**(2)=O), 70.6 to 70 (**C**(3)H_2, **C**(5)H_2, **C**(6)H_2, **C**(8)H_2, **C**(9) H_2, **C**(11) H_2), 61.8 (**C**(20)H_2), 60.2 (**C**(24)H_2), 55.8 (**C**(19)H_2), 50.7 (**C**(2)-N_3), 40.6 (**C**(12)-NH), 39.1 (**C**(25)-S), 36.0 (**C**(15)H_2), 28.1-28.3 (**C**(16)H_2, **C**(18)H_2), 25.7 (**C**(17)H_2) ppm.

MS (ESI-TOF): calculated: 445.2233; found: 445.2249
Optical rotation (CH_2Cl_2, 25 °C, c = 0.065 g / 100 mL): $[\alpha]_D^{25}$ = -15.3

^{1}H NMR:

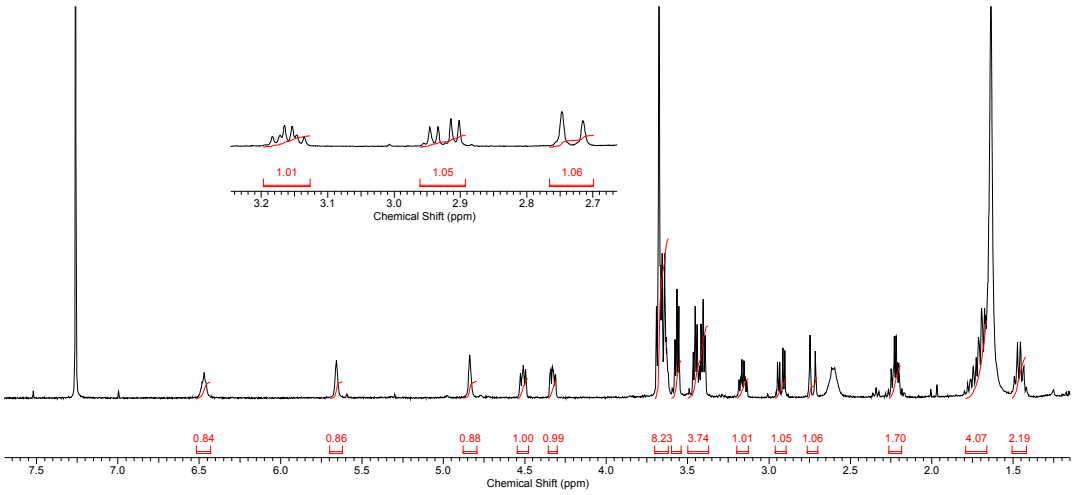

^{13}C NMR:

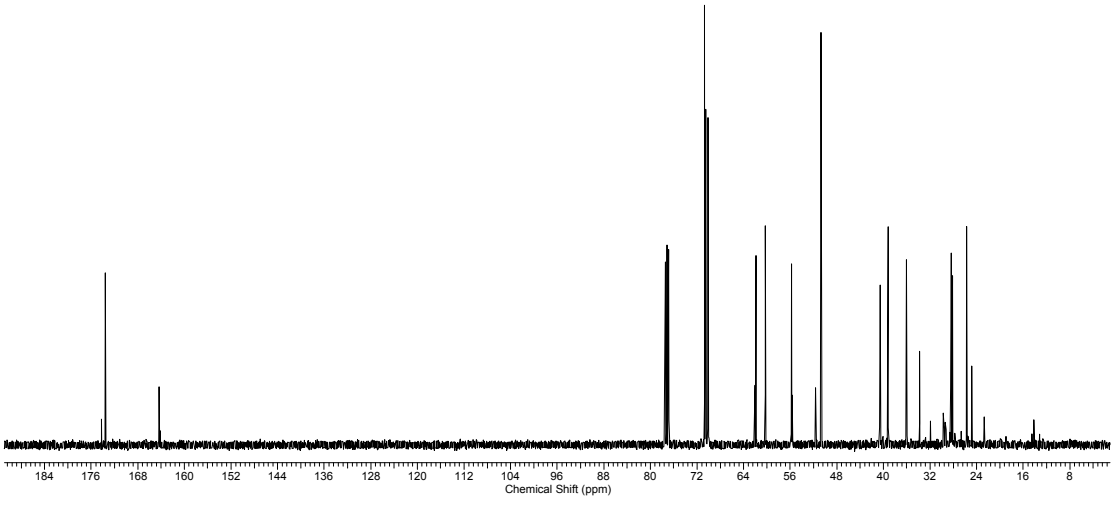

***N*-(2-{2-[2-(2-aminoethoxy)ethoxy]ethoxy}ethyl)-5-[(4R)-2-oxohexahydro-1*H*-thieno[3,4-*d*]imidazol-4-yl]pentanamide**

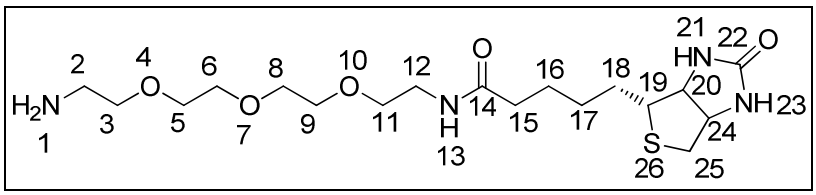

Triphenylphosphine (708.20 mg, 2.7 mmol, 1.5 equiv) was added to a stirred solution of N-(2-(2-(2-azidoethoxy)ethoxy)ethyl)biotinylamide (800.0 mg, 1.8 mmol, 1 equiv) in 17.5 mL of THF. The reaction mixture was stirred at rt under an argon atmosphere. After 30 min, 0.6 mL of water were added and the reaction mixture was stirred at rt for 20 h. The reaction mixture was then diluted in 70 mL of water and the aqueous phase was washed 5 times with toluene (5 x 55 mL). The aqueous phase was evaporated under reduced pressure to afford a viscous transparent yellow oil (540.0 mg, 1.3 mmol, 71 %).

IR (film): 3250 (br), 2925, 2860, 2360, 2335, 2110, 1700, 1645, 1550, 1460, 1350, 1325, 1265, 1245, 1205, 1100, 1035, 940, 870, 835, 720, 685, 645, 630, 610 cm^{-1}.

^{1}H NMR (400MHz, MeOD-d_4): δ= 4.49 (dd, 1H, ^{2}J= 7.9, ^{3}J= 4.3 Hz, C(24)**H**), 4.30 (dd, 1H, ^{2}J= 7.9, ^{3}J= 4.4 Hz C(20)**H**), 3.66-3.61 (m, 8H, C(5)**H**$_2$C(6)**H**$_2$-O-C(8)**H**$_2$C(9)**H**$_2$), 3.59 (t, 2H, ^{3}J= 5.2 Hz C(3)**H$_2$**-O), 3.54 (t, 2H, ^{3}J= 5.6 Hz, C(11)**H$_2$**-O), 3.36 (m, 2H, C(12)**H$_2$**-NH-(C=O)), 3.21 (m, 1H, C(19)**H**), 2.94 (d, 1H, ^{3}J= 5.0 Hz, C(25)**H**$_2$-S), 2.92 (t, 2H, ^{3}J= 5.5 Hz C(2)**H$_2$**-NH$_2$), 2.70 (d, 1H, ^{3}J= 12.7 Hz, C(25)**H**$_2$-S)), 2.22 (t, 2H, ^{3}J= 7.4 Hz C(15)**H$_2$**-(C=O)-NH)), 1.76-1.55 (m, 4H, C(16)**H$_2$**,C(18)**H$_2$**), 1.45 (m, 2H, C(17)**H$_2$**) ppm.

^{13}C NMR (100MHz, D_2O): δ= 176.9 (**C**(22)), 165.3 (**C**(14)), 69.6-68.8 (**C**(3)H$_2$, **C**(5)H$_2$, **C**(6)H$_2$, **C**(8)H$_2$, **C**(9)H$_2$, **C**(11)H$_2$), 62.0 (**C**(24)H), 60.2 (**C**(20)H), 55.3 (**C**(19)H), 39.6 (**C**(2)H$_2$), 39.5 (**C**(12)H$_2$), 38.8 (**C**(25)H$_2$), 35.4 (**C**(15)H$_2$), 27.8 (**C**(17)H$_2$), 27.6 (**C**(16)H$_2$), 25.1 (**C**(18)H$_2$) ppm.

MS (ESI-TOF): calculated: 419.2328; found: 419.2333
Optical rotation (CH_2Cl_2, 25 °C, c = 0.105 g / 100 mL): $[\alpha]_D^{25}$ = -14

^{1}H NMR:

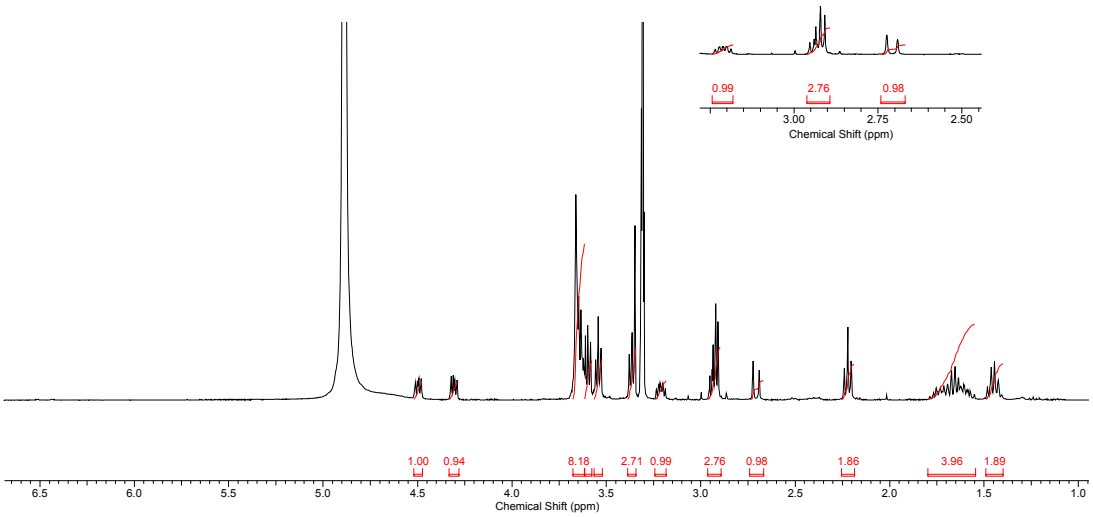

^{13}C NMR:

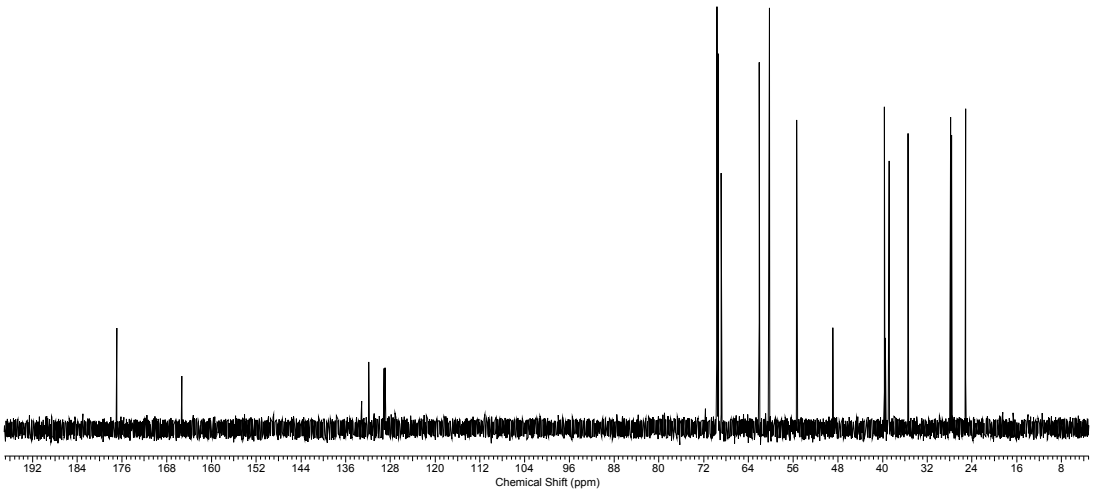

***N*-[14-(2,2-difluorocyclooct-3-yn-1-yl)-13-oxo-3,6,9-trioxa-12-azatetradec-1-yl]-5-(2-oxohexahydro-1*H*-thieno[3,4-*d*]imidazol-4-yl)pentanamide (16)**

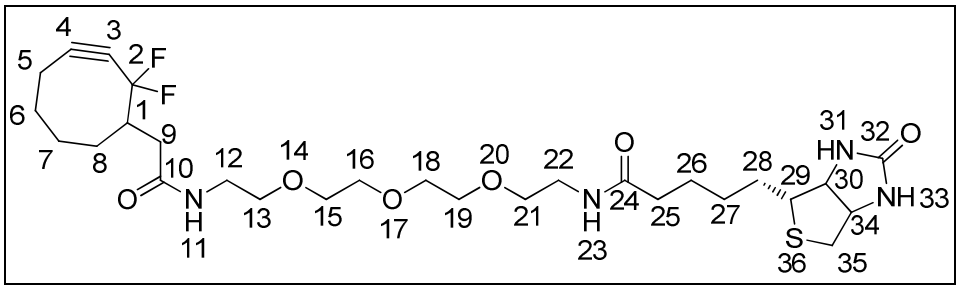

The (2,2-difluorocyclooct-3-yn-1-yl)acetic acid (10 mg, 0.05 mmol, 1 equiv) was dissolved with dry dichloromethane (0.38 mL) in a flame-dried round-bottom flask and put under an argon atmosphere. A solution of amino-PEG-biotin (20.70 mg, 0.05 mmol, 1 equiv) and N-ethyldiisopropylamine (12.69 mg, 0.07 mmol, 1.5 equiv) in dry dichloromethane (0.38 mL) was added to the reaction mixture. The system was stirred at rt for 5 h, and then purified by flash chromatography (9:1 to 8:2 EtOAc/MeOH) to afford a white solid (12.10 mg, 0.02 mmol, 41 %).

IR (film): 3265, 2930, 2870, 2220, 1705, 1645, 1555, 1460, 1385, 1280, 1240, 1130, 1030, 1010, 940, 750, 690, 665, 650, 605 cm^{-1}.

^{1}H NMR (400MHz, MeOD-d_4): δ= 4.50 (dd, 1H, ^{2}J= 7.7, ^{3}J= 5.0 Hz, C(34)**H**), 4.31(dd, 1H, ^{2}J= 7.7, ^{3}J= 4.5 Hz, C(30)**H**), 3.64 (app. d, 8H, ^{3}J= 5.6 Hz, C(15)**H$_2$**C(16)**H$_2$**-O-C(18)**H$_2$**C(19)**H$_2$**), 3.55 (t, 4H, ^{3}J= 5.4 Hz, C(13)**H$_2$**, C(21)**H$_2$**), 3.37 (m, 4H, C(12)**H$_2$**, C(22)**H$_2$**), 3.21 (m, 1H, C(29)**H**), 2.93 (dd, 1H, ^{2}J= 12.8, ^{3}J= 4.9 Hz, C(35a)**H$_2$**), 2.83-2.74 (m, 1H, C(1)**H**), 2.71 (d, 1H, ^{3}J= 12.7 Hz, C(35b)**H$_2$**), 2.51 (dd, 1H, ^{2}J= 12.7, ^{3}J= 3.8 Hz, C(9a)**H$_2$**), 2.47-2.31 (m, 2H, C(5)**H$_2$**), 2.22 (app. t, 3H, ^{3}J= 6.9 Hz, C(25)**H$_2$**, C(9b)**H$_2$**), 2.17-2.08 (m, 2H, C(6)**H**$_2$), 1.86-1.51 (m, 6H, C(26)**H$_2$**, C(28)**H$_2$**, C(7)**H$_2$**), 1.48-1.29 (m, 4H, C(27)**H$_2$**, C(8)**H$_2$**) ppm.

^{13}C NMR (100MHz, MeOD-d_4) : δ= 176.1 (**C**=O), 173.8 (**C**=O), 166.1 (**C**=O), 111.7 (**C**≡C), 111.5 (**C**≡C), 71.6, 71.27, 71.26, 70.6, 70.5, 63.3, 61.6, 57.0, 54.4 (t, **C**(2)F_2, J = 24.2 Hz), 41.0, 40.4, 40.3, 36.7, 35.9, 33.77, 33.75, 33.3, 33.2, 29.8, 29.5, 28.9, 26.8, 20.6 ppm.

MS (ESI-TOF): calculated: 603.3028; found: 603.3027
Optical rotation (CH_2Cl_2, 25 °C, c = 0.105 g / 100 mL): $[\alpha]_D^{25}$ = 130.0

^{1}H NMR:

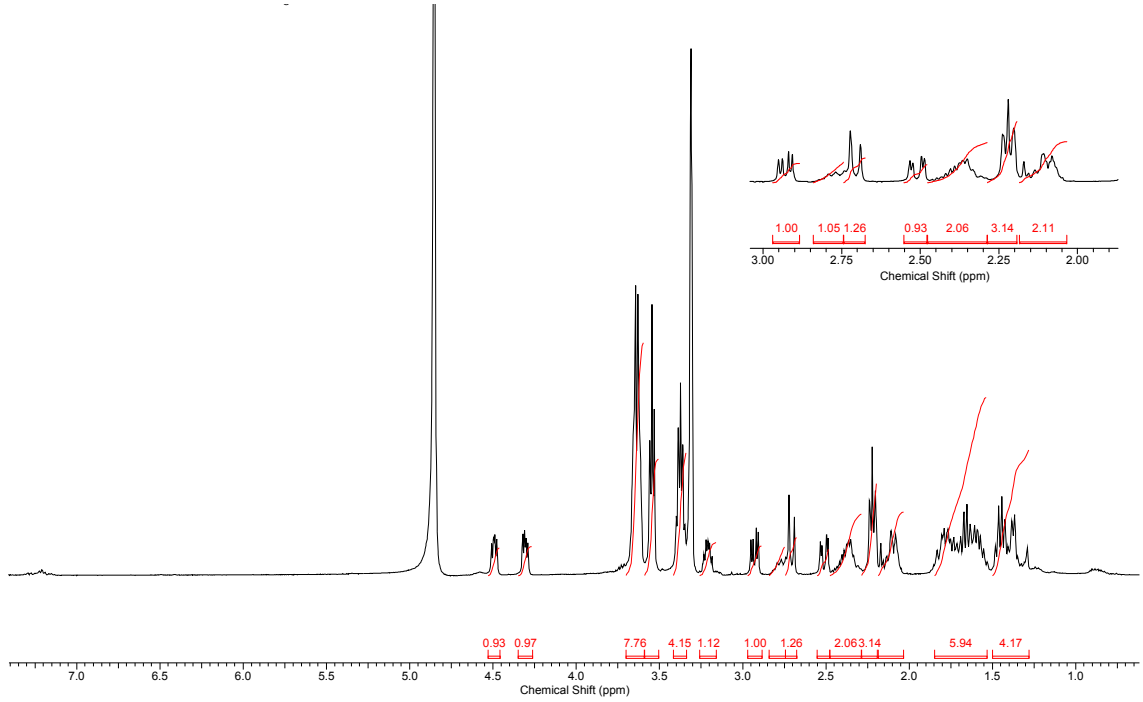

^{13}C NMR:

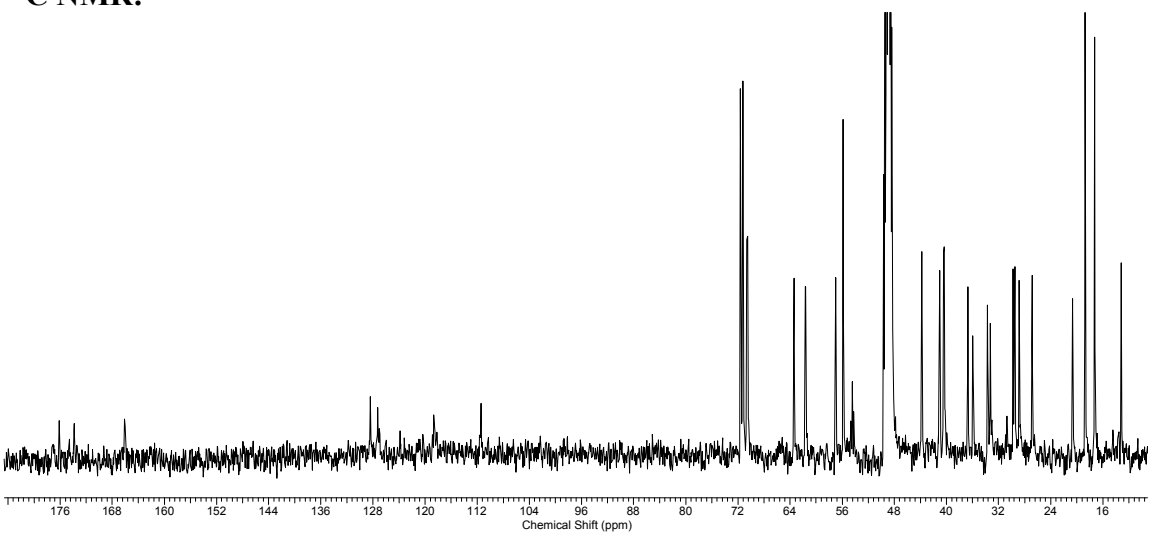

Tris-(hydroxypropyltriazolylmethyl)amine (THPTA)

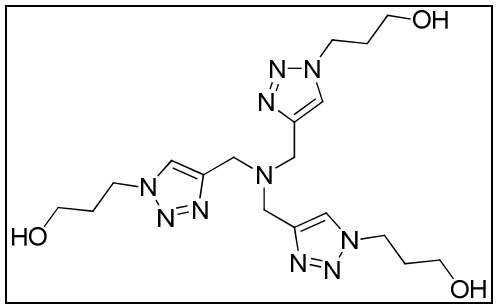

Sodium azide (3.58 g, 55.0 mmol) was added to a solution of 3-bromo-1-propanol (1.54 g, 11.1 mmol) in DMF (9 mL). After stirring at boiling under reflux for 36 h the mixture was filtered and coconcentrated with toluene. The residue was diluted with CH_2Cl_2 and washed twice with aqueous NaCl. The organic layer was dried, filtered and concentrated to give the desired 3-azido-1-propanol (723 mg, 65 %).

Tripropargylamine (0.13 g, 1 mmol) in acetonitrile/methanol solution (3 mL) was treated sequentially with 3-azido-1-propanol (0.35 g, 3.5 mmol), 2,3-lutidine (0.11 g, 1 mmol) and $Cu(MeCN)_4PF_6$ (2 mol % with respect to total alkyne units). Upon addition of the copper salt, the reaction was cooled in an ice bath. The mixture was stirred at room temperature for 3 days. The reaction mixture was evaporated and dissolved in methanol. The crude product was precipitated in acetonitrile (146 mg, 60 %).
The analytical data were in accordance with reported characterization.[5]

^{1}H NMR:

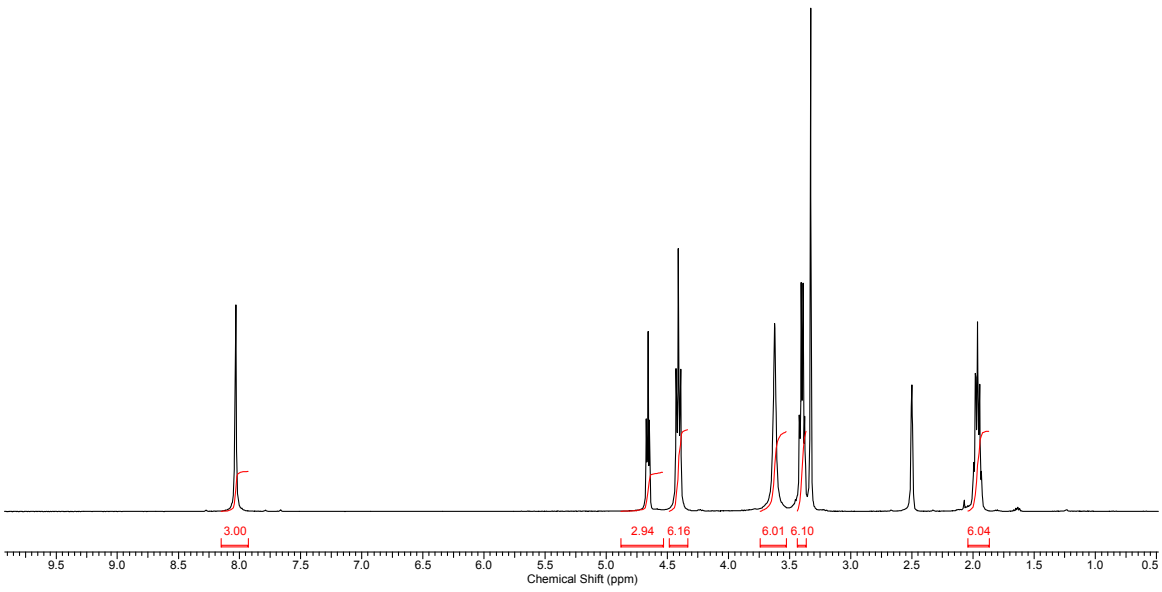

References

(1) Pirrung, M. C., Webste, N. J. G. (1987) Mechanism of intramolecular photocycloaddition of cycloctenones. *J. Org. Chem*. *52*, 3603-3613

(2) Baskin, J. M., Prescher, J.A., Laughlin, S. T., Agard, Chang, P. V., Miller, I. A., Lo, A., N. J., Codelli, J. A., Bertozzi, C. R. (2007) Copper-free click chemistry of dynamic *in vivo* imaging. *Proc. Natl. Acad. Sci. USA*, *104*, 16793-16797.

(3) Codelli, J. A., Baskin, J. M., Agard, N. J., Bertozzi, C. R. (2008) Second-generation difluorinated cyclooctynes for copper-free click chemistry. *J. Am. Chem. Soc. 130*, 11486-11493.

(4) Bonger, K. M., Van den Berg, R. J. B. H. N., Heitman, L. H., Ijzerman, A. P., Oosterom, J., Timmers, C. M., Overkleeft, H. S., Van der Marel, G. A. (2007) Synthesis and evaluation of homo-bivalent GnRHR ligands. *Bioorg. Med. Chem*. *15*, 4841-4856.

(5) Liu, X.-M., Thakur, A., Wang, D. (2007) Efficient synthesis of linear multifuntional poly(ethyleneglycol) by copper(I)-catalyzed Huisgen 1,3-dipolar cycloaddition. *Biomacromol. 8*, 2653-2658.

Bioconjugate Chemistry

ARTICLE

pubs.acs.org/bc

Long-Wavelength Absorbing and Fluorescent Chameleon Labels for Proteins, Peptides, and Amines

Hans H. Gorris,[*,†,§] Sayed M. Saleh,[†,§] Dominik B. M. Groegel,[†] Steffen Ernst,[‡] Knut Reiner,[‡] Heinz Mustroph,[‡] and Otto S. Wolfbeis[*,†]

[†]University of Regensburg, Institute of Analytical Chemistry, Chemo- and Biosensors, D-93040 Regensburg, Germany

[‡]FEW Chemicals, D-06766 Bitterfeld-Wolfen, Germany

Supporting Information

ABSTRACT: Long-wavelength absorbing labels that change their color and fluorescence upon conjugation to proteins and other biomolecules provide two critical advantages over the wealth of conventional amine-reactive labels. At first, the progress of the labeling reaction can be monitored continuously either visually or by spectrometry without prior purification. Then, the labeled biomolecule can be investigated with red or near-infrared light, which minimizes background interference in biological samples. These unique characteristics are met by a group of long-wavelength absorbing cyanine dyes carrying a reactive chloro substituent for nucleophilic substitution with primary amines, which is accompanied by a color change from green to blue. In addition to this so-called chameleon effect, the dyes display an increase in fluorescence during the labeling reaction. Despite their structural similarity, the reactivity of the dyes differs strongly. The fastest labeling kinetics is observed with dye S 0378 as its five-membered ring affords a stabilizing effect on the intermediate carbocation during an S_N1-type of nucleophilic substitution. The reaction mechanism of the amine-reactive cyanine dyes provides a blueprint for the design of future long-wavelength absorbing chameleon dyes.

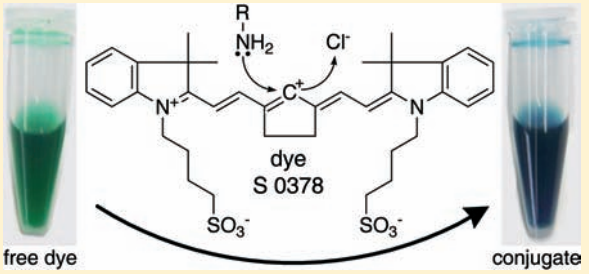

INTRODUCTION

Modification by amine-reactive probes constitutes the prevalent route for labeling proteins, peptides, and other amines. These labels undergo an addition reaction (e.g., the isothiocyanates) or a nucleophilic substitution reaction (e.g., the sulfochlorides) with deprotonated amino groups of lysine and the amino-terminus on the surface of proteins, or with amino groups of other biomolecules to form a stable covalent bond. The absorbance of most current labels is not affected by the labeling reaction, so any label that has not reacted cannot be distinguished spectrally from a label bound to a protein. Consequently, it is necessary to separate the free label from the labeled protein after the reaction has completed. To address this shortcoming of conventional labels, we have introduced pyrylium (Py) dyes as a group of so-called chameleon labels that undergo a visually detectable color shift to a shorter wavelength as well as a change in fluorescence upon conjugation to amino groups.[1,2] As a result of this chameleon effect, the labeled protein can be easily differentiated even if the free label is present in large excess. Py labels have found various applications in areas such as protein assay and labeling,[3] in studies on neuropeptides,[4] gel electrophoresis,[5] capillary electrophoresis,[6−8] fluorescence-based cytometric single cell analysis,[9] and in surface chemistry.[10] Py labels were also used in immobilized form.[11,12] Kostenko et al.[13] presented another class of chameleon labels which leads to long-wave-shifted rather than to shortwave-shifted conjugates.

Long-wavelength absorbing labels are of substantial interest because red and near-infrared (NIR) light penetrates more deeply into biological materials and generates much less background fluorescence than short-wavelength light.[14] Cyanine (Cy) dyes are a prominent class of fluorescent dyes that—depending on their molecular structure—cover the whole spectrum from the blue to the NIR.[15−17] Some red- and NIR-absorbing cyanine dyes are equipped with a chloro group in the center of their conjugated π-electron system (Figure 1) that undergoes facile nucleophilic substitution by amines and thiols in organic solution at elevated temperatures.[18−20] Patonay et al.[18] substituted the chloro group by thiophenols followed by several modification steps to obtain amino-reactive labels. This complex label design, however, omits a key feature of these cyanine dyes: If the electron withdrawing chloro group is substituted by an electron donating amine, the dye's absorbance strongly shifts to shorter wavelengths.[21] We perceived that this chameleon effect may be amenable to direct protein labeling in aqueous solutions and temperatures below 40 °C. To confer water solubility, we chose three exemplary cyanine dyes containing sulfo groups (Figure 1) and investigated them with respect to their reactivity toward proteins, peptides, and various amines.

Received: April 14, 2011
Revised: June 14, 2011
Published: June 15, 2011

ACS Publications © 2011 American Chemical Society

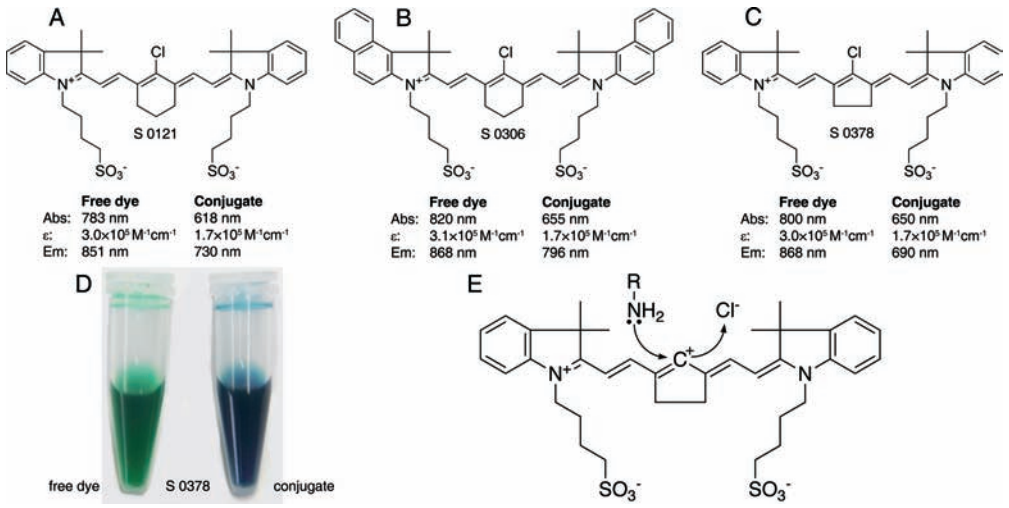

Figure 1. Chemical structures of the water-soluble cyanine dyes S 0121 (A), S 0306 (B), and S 0378 (C). Conjugation to amines leads to a color change from green to blue and a change in the emission spectrum. Absorbance maxima, molar absorbances, and emission maxima of each dye and its conjugate to HSA are shown. (D) Photograph of microtubes containing dye S 0378 (200 μg/mL) in the unconjugated form (left) and conjugated to HSA (5 mg/mL, right). The labeling reaction can be followed visually by the color change from green to blue. (E) Nucleophilic substitution of dye S 0378 by primary amines. The five-membered-ring structure in combination with the polymethine chain sustains the formation of a carbocation and directs the reaction toward an S_N1 mechanism.

EXPERIMENTAL PROCEDURES

Materials and Instruments. Goat antimouse IgG antibodies and human serum albumin (HSA) were purchased from Sigma-Aldrich (Munich, Germany; www.sigmaaldrich.com). The peptide angiotensin II with the sequence H_2N-Asp-Arg-Val-Tyr-Ile-His-Pro-Phe-COOH was purchased from Bachem (Weilam Rhein, Germany; www.bachem.com). The long-wavelength absorbing cyanine dyes S 0121, S 0306, and S 0378 were obtained from FEW Chemicals (Wolfen, Germany; www.few.de). Other reagents and solvents were of the highest grade available. Size exclusion chromatography was performed using Sephadex G-75 (GE Healthcare, Munich, Germany; www.gehealthcare.com). Fluorescence spectra were acquired on an FP-6300 fluorescence spectrometer from Jasco (Essex, UK; www.jasco.co.uk) and mass spectra on a MALDI-TOF mass spectrometer from GSG (Bruchsal, Germany; www.gsg-analytical.com).

Labeling of Proteins and Peptides. Stock solutions of 10 mg of the dyes S 0121, S 0306, and S 0378 in 1 mL of methanol, as well as 1 mg/mL of HSA, IgG, and peptide in 20 mM sodium carbonate buffer, pH 8.4, were prepared. Two microliters of the dye solution and 200 μL of the protein/peptide solution were added to 20 mM sodium carbonate buffer, pH 8.4, to give a total reaction volume of 1 mL. The solutions were shaken in a thermomixer (950 rpm) at 37 °C for various periods of time. For further characterization, labeled proteins (blue) were purified from the free dye (green) by size exclusion chromatography on Sephadex G-75.

MALDI-TOF Mass Spectrometry. A small quantity of unlabeled or labeled HSA was dissolved in 50 μL water and mixed in a 1:1 (v/v) ratio with an oversaturated solution of sinapic acid in methanol/acetonitrile (1:1, v/v). One drop of the mixture was deposited onto a metal plate and, after solvent evaporation, the spot was analyzed by MALDI-TOF mass spectrometry.

Labeling of Primary Amines with Dye S 0378. Solutions of 272 μM of dye S 0378, 408 μM of primary amine (β-alanine, dodecylamine, ethanolamine, histamine, propargylamine, or tyramine), and 408 μM of triethylamine in methanol were incubated either for 15 h at 25 °C or for 4 h at 70 °C.

RESULTS AND DISCUSSION

Selection of Long-Wavelength Absorbing Chameleon Dyes. Protein labeling is preferably performed in aqueous solutions and at ambient temperature in order to leave the protein structure intact. Furthermore, the labeling reaction is expected to be fast to save time and prevent microbial growth in a sample. On the other hand, the label has to be chemically stable with respect to storage and preventing spontaneous reactions in a sample.

The nucleophilic ε-amino-group of lysine presents a labeling site on proteins for which various amine-reactive reagents are available. In most cases, the labels feature two distinct subsites: one for coupling to amines and the other one for generating a signal—usually a conjugated π-electron system that serves as a chromophore or fluorophore. As the coupling site and the conjugated π-system are separated, the color or fluorescence of the label is not affected by the coupling reaction. Consequently, the labeling reaction is not detectable by a color change and the labeled protein needs to be purified from the free dye. In the chameleon dyes, by contrast, the π-system takes part in the coupling reaction and the coupled amino group exerts an electron shifting effect. Polyenes, however, undergo addition reactions with nucleophiles, which would ultimately destroy the conjugated π-system and prevents their use as a conjugation site. Aromatic rings that are part of the delocalized electron system may undergo substitution reactions by amines under conditions that are suitable for labeling proteins,[22] but in most cases, such aromatic residues tend to be rather inert. A highly reactive aromatic cation such as pyrylium as part of the delocalized electron system is an alternative.[1] The reaction of the blue pyrylium label with amines yields a red and fluorescent pyridinium analogue.

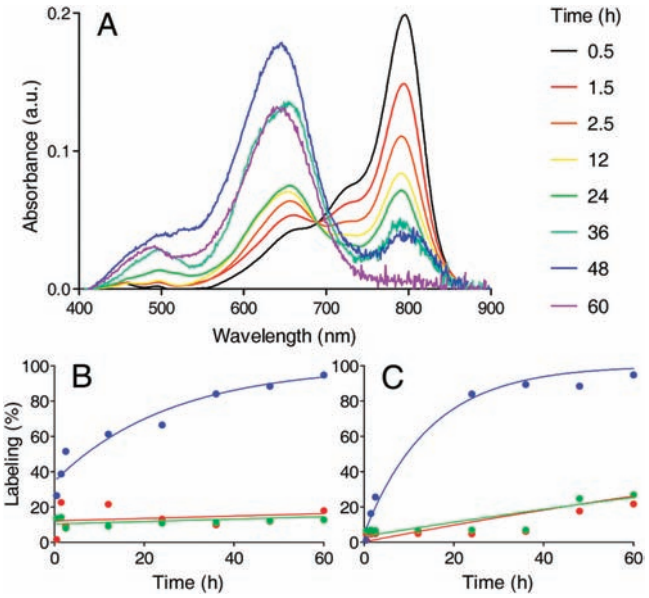

Figure 2. (A) Changing absorbance spectra of dye S 0378 upon binding to HSA at 37 °C. The degree of labeling (%) of HSA (B) and IgG (C) by the dyes S 0121 (red), S 0306 (green), and S 0378 (blue) was calculated according to eq 1. Half-times of the labeling kinetics were obtained by fitting the data points to $y = (100 - bg) \times (1 - e^{-kx}) + bg$, where bg denotes the background and k the reaction rate coefficient. Dye S 0378 displayed the fastest labeling kinetics (half-time for labeling HSA, 18 h; and for labeling IgG, 10 h). The reactions of labels S 0121 and S 0306 were too slow to determine accurate half-times.

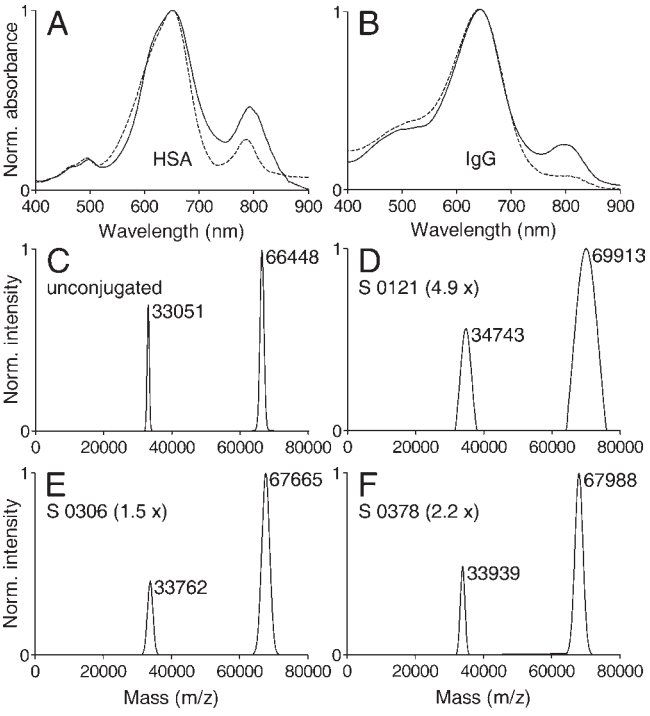

Figure 3. Characterization of labeled proteins. HSA (A) and IgG (B) were labeled with S 0378 and purified by size exclusion chromatography. An absorbance spectrum was recorded before (solid line) and after (hatched line) purification. Unlabeled and labeled HSA preparations were purified by size exclusion chromatography and analyzed by MALDI-TOF mass spectrometry. (C) In the MALDI spectra, the second peak indicates the mass of unconjugated HSA (66.45 kDa (mean) ± 0.57 kDa (standard deviation). (D) HSA labeled with S 0121 (69.91 ± 2.79 kDa). (D) HSA labeled with S 0306 (67.67 ± 1.14). (D) HSA labeled with S 0378 (67.99 ± 1.16). The average number of dye molecules per HSA molecule was calculated by [mass (HSA labeled with dye_x) − mass (unconjugated HSA)]/[mass (dye_x) − mass (Cl)].

Here, we extend this approach to another kind of cationic π-electron system. Cyanine dyes and rhodamines can be regarded as resonance-stabilized carbocations that are more electronically delocalized than neutral conjugated hydrocarbons.[23] In search of a long-wavelength absorbing dye for labeling amines, we found that the chloro atoms at the polymethine chain of cyanine dyes undergo nucleophilic substitution under mild conditions. This particular reactivity places polymethine dyes between polyenes with high chemical reactivity (in terms of addition reactions) and aromatic π-systems with their low chemical reactivity (in terms of substitution reactions).[24] Only a few long-wavelength absorbing cyanine dyes that contain both a chloro group for nucleophilic substitution by amines and sulfo groups to confer water-solubility are available. We chose three exemplary dyes S 0121, S 0306, and S 0378 (the absorbance and emission spectra are shown in the Supporting Information Figure 1) that display a large spectral shift in their absorbance as well as in their emission spectrum when conjugated to amines (Figure 1). Dye S 0306 is a derivative of indocyanine green, which is commonly administered intravenously for medical diagnostics and thus attests to the dye's excellent biocompatibility and nontoxicity.[25]

The chameleon dyes were conjugated to (a) an IgG antibody, (b) human serum albumin (HSA), and (c) the peptide angiotensin II. These compounds can be found in blood and thus represent valuable bioanalytical targets. While labeling of the two proteins is assumed to proceed mainly via their lysine side chains, which typically have a pK_a of 10, the amino terminus of the peptide with its distinctly lower pK_a value is the only conjugation site of the peptide. To account for the high pK_a of lysine side chains, reactions were carried out in bicarbonate buffer of pH 8.4.

Monitoring the Labeling Reaction of Chameleon Dyes. The labeling reaction of all three dyes is visible by eye due to a hypsochromic (shortwave) color shift from green to blue (Figure 1D) as the electron-withdrawing chloro group is replaced by an electron-donating amino group. The reaction can be monitored quantitatively if the changes in absorbance are recorded over time. The absorbance maxima of the free labels and their conjugates to amines are listed in Figure 1.

A single absorbance measurement, however, is sensitive to the dye concentration as well as the light source and the sensitivity of the sensor. Ratiometric measurements, by contrast, are resistant to such fluctuations but rely on a constant reference value.[26] Although the intensity at the isosbestic point between both maxima should provide a reference value, it is too weak and thus prone to fluctuations. We therefore devised a new ratiometric approach for chameleon dyes based on the absorbance at both maxima, which can be used to report the degree of labeling at any time over the course of the labeling reaction. The sum of the absorbance readings at the absorption maxima of the free dye and the conjugate provide a constant reference value after correcting for the different molar absorption coefficients (listed for each dye in Figure 1; in eq 1, the maxima of label S 0378 are shown). Then, the degree of labeling is defined by the ratio of the absorbance

dx.doi.org/10.1021/bc200192k |*Bioconjugate Chem.* 2011, 22, 1433–1437

Table 1. Absorbance at 650 and 800 nm of Dye S 0378 after Reaction with Various Primary Amines[a]

	S 0378 only	β-alanine	dodecylamine	ethanolamine	histamine	propargylamine	tyramine
650 nm	0.03	0.52	0.06	0.35	0.32	0.23	0.33
800 nm	0.59	0.20	0.56	0.00	0.29	0.05	0.02
labeling (%)		82	17	99	66	89	97

[a] The degree of labeling (%) was calculated according to eq 1.

maximum of the conjugate to the reference value.

$$Labeling\ (\%) = \frac{100 \times A_{650\mathrm{nm}}}{A_{650\mathrm{nm}} + A_{800\mathrm{nm}}\left[\varepsilon_{650\mathrm{nm}}(conj)/\varepsilon_{800\mathrm{nm}}(free)\right]} \quad (1)$$

It should be noted that the absorbance of the free dye at 650 nm amounts to about 10% of the absorbance at 800 nm, which changes the degree of labeling slightly. Equation 1 is amenable to any type of chameleon dye as long as there is only a small overlap in the absorbance spectra of the free dye and the conjugate.

Variation of Chameleon Dyes. The labeling of HSA, IgG, and the peptide angiotensin II by the dyes S 0121, S 0306, and S 0378 was monitored by measuring the changes in the absorbance spectra over time. Figure 2A shows the spectra of the reaction of label S 0378 with HSA after correction for stray light. The degree of labeling at each time point was then calculated by eq 1 as shown for HSA (Figure 2B) and IgG (Figure 2C). Similar results were obtained for the peptide. Although all dyes react to some degree with the proteins and the peptide after extended periods of time, only the reaction of dye S 0378 was fast enough to calculate accurate half-times for labeling HSA (18 h), IgG (10 h), and angiotensin II (36 h).

The remarkably better labeling kinetics of dye S 0378 can be attributed to the five-membered ring at the conjugation site, where the structurally very similar dyes S 0306 and S 0378 feature six-membered rings. Both the five-membered and the six-membered rings favor an S_N1 mechanism over an S_N2 mechanism because the concomitant carbocation is stabilized by the carbon double bonds and the ring structure increases steric hindrance. The five-membered ring of dye S 0378, however, shows higher reactivity because cyclopentenyl cations are more stable than cyclohexenyl cations.[27−29] The stabilizing effect of the ring structure thus may also reduce electronic rearrangement along the polymethine chain and retains the carbocation at the site of origin. Figure 1E outlines the inferred reaction mechanism of amines with dye S 0378.

Fluorescence Measurements. In addition to the changes in color, the dyes also exhibit a change in fluorescence upon binding to amines. While the free dyes are weakly fluorescent, the conjugates display deep-red fluorescence that can be detected with red-sensitive photomultipliers. The reaction of label S 0378 with amines can be monitored by excitation at 600 nm and recording the increase in the emission intensity at 690 nm (Supporting Information Figure 2). Monitoring the labeling reaction by absorbance spectrometry, however, is preferable, because it is ratiometric and thus more precise.

Characterization of Labeled Proteins. IgG and HSA were labeled with dye S 0378 and excess dye was removed by size exclusion chromatography. The fast eluting proteins can be readily distinguished from the unreacted green dye by their blue color. The absorbance at 800 nm shows that some unreacted S 0378 remained noncovalently bound to HSA after the purification step (Figure 3A), while the amount of free dye left on the antibody is negligible (Figure 3B).

Next, the average number of label molecules per protein molecule was determined by MALDI-TOF mass spectrometry. All samples were prepared under the same reaction conditions (37 °C; overnight) and purified by size exclusion chromatography. Figure 3C shows the exact molecular mass of HSA with a small standard deviation (66.4 kDa ± 0.6 kDa). The higher molecular masses indicated in Figure 3D−F confirm that the labeling reaction of all three dyes has occurred. HSA was labeled, on average, 4.9-fold by S 0121, 1.5-fold by S 0306, and 2.2-fold by S 0378. The labeled HSA preparations have a broader size distribution than the unconjugated protein because the 58 lysine residues in one HSA molecule can be labeled differentially and to various degrees. The widest distribution of labels on HSA was found with S 0121.

Labeling of Primary Amines. Biogenic and synthetic primary amines (β-alanine, dodecylamine, ethanolamine, histamine, propargylamine, and tyramine) were labeled with dye S 0378. These primary amines are less sensitive to solvents such that the labeling reaction can be carried out in methanol. As the primary amines and dyes react in a molar ratio of 1:1, a 2-fold excess of amines was adequate to allow for a complete turnover of the dye molecules. Labeling for 15 h at room temperature (25 °C), however, was only partially successful. Better results were obtained by labeling for 4 h at 70 °C and adding a tertiary amine (triethylamine) as a catalyst and base that cannot react with the dye. In all cases, the reaction can be monitored by the increase in absorbance at 650 nm and the decrease at 800 nm (Table 1). Different primary amines show a remarkably diverse reactivity with dye S 0378. While dodecylamine was only marginally labeled (17%), the reaction was almost complete with ethanolamine (99%) and tyramine (97%).

CONCLUSION

Long-wavelength absorbing and fluorescent cyanine dyes were established as a new class of amine-reactive chameleon labels for proteins, peptides, and amines. The reactivity of the cyanine dyes is conferred by a chloro substituent in the center of the methine chain that can undergo an S_N1-type nucleophilic substitution with primary amines. Replacement of the chloro substituent results in a visually detectable color change from green to blue as well as a change in fluorescence. A new ratiometric method was devised to study the labeling kinetics. Dye S 0378 showed the fastest kinetics because the reactive chloro group is located at a five-membered ring. Although the reaction of dye S 0378 was slower than the reaction of Py labels,[1] proteins and peptides can be easily labeled in aqueous solutions at 37 °C. Even better results can be obtained when the labeling procedure is performed in methanol at 70 °C, which is an additional option for many amines. The outlined reaction mechanism of the long-wavelength absorbing cyanine dyes

holds great potential for the design of future amine-reactive chameleon dyes.

■ ASSOCIATED CONTENT

Supporting Information. Absorption and emission spectra of the free dyes and the changes in the fluorescence spectra during the labeling reaction. This material is available free of charge via the Internet at http://pubs.acs.org.

■ AUTHOR INFORMATION

Corresponding Authors

*Hans H. Gorris & Otto S. Wolfbeis, Institute of Analytical Chemistry, Chemo- and Biosensors, University of Regensburg, Universitätsstr. 31 D-93040, Regensburg, Germany. H.H.G.: Tel. +49 941 943 4008, Fax +49 941 943 4064, Hans-Heiner.Gorris@chemie.uni-r.de. O.S.W.: Tel. +49 941 943 4065, Fax +49 941 943 4064, Otto.Wolfbeis@chemie.uni-r.de.

Author Contributions

§These authors contributed equally to the work.

■ ACKNOWLEDGMENT

We thank Daniela Meyer for additional fluorescence measurements. S. M. S. thanks the Egyptian Government for a fellowship for performing his PhD study in Regensburg.

■ REFERENCES

(1) Wetzl, B. K., Yarmoluk, S. M., Craig, D. B., and Wolfbeis, O. S. (2004) Chameleon labels for staining and quantifying proteins. *Angew. Chem., Int. Ed. 43*, 5400–5402.

(2) Craig, D. B., Wetzl, B. K., Duerkop, A., and Wolfbeis, O. S. (2005) Determination of picomolar concentrations of proteins using novel amino reactive chameleon labels and capillary electrophoresis laser-induced fluorescence detection. *Electrophoresis 26*, 2208–2213.

(3) Hoefelschweiger, B. K., Duerkop, A., and Wolfbeis, O. S. (2005) Novel type of general protein assay using a chromogenic and fluorogenic amine-reactive probe. *Anal. Biochem. 344*, 122–129.

(4) Schneider, E., Keller, M., Brennauer, A., Hoefelschweiger, B. K., Gross, D., Wolfbeis, O. S., Bernhardt, G., and Buschauer, A. (2007) Synthesis and characterization of the first fluorescent nonpeptide NPYY1 receptor antagonist. *ChemBioChem 8*, 1981–1988.

(5) Meier, R. J., Steiner, M. S., Duerkop, A., and Wolfbeis, O. S. (2008) SDS-PAGE of proteins using a chameleon-type of fluorescent prestain. *Anal. Chem. 80*, 6274–6279.

(6) Wojcik, R., Swearingen, K. E., Dickerson, J. A., Turner, E. H., Ramsay, L. M., and Dovichi, N. J. (2008) Reaction of fluorogenic reagents with proteins - I. Mass spectrometric characterization of the reaction with 3-(2-furoyl)quinoline-2-carboxaldehyde, Chromeo P465, and Chromeo P503. *J. Chromatogr., A 1194*, 243–248.

(7) Ramsay, L. M., Dickerson, J. A., Dada, O., and Dovichi, N. J. (2009) Femtomolar concentration detection limit and zeptomole mass detection limit for protein separation by capillary isoelectric focusing and laser-induced fluorescence detection. *Anal. Chem. 81*, 1741–1746.

(8) Steiner, M. S., Meier, R. J., Spangler, C., Duerkop, A., and Wolfbeis, O. S. (2009) Determination of biogenic amines by capillary electrophoresis using a chameleon type of fluorescent stain. *Microchim. Acta 167*, 259–266.

(9) Cohen, D., Dickerson, J. A., Whitmore, C. D., Turner, E. H., Palcic, M. M., Hindsgaul, O., and Dovichi, N. J. (2008) Chemical cytometry: Fluorescence-based single-cell analysis. *Annu. Rev. Anal. Chem. 1*, 165–190.

(10) Hoffmann, K., Mix, R., Resch-Genger, U., and Friedrich, J. F. (2007) Monitoring of amino functionalities on plasma-chemically modified polypropylene supports with a chromogenic and fluorogenic pyrylium reporter. *Langmuir 23*, 8411–8416.

(11) Steiner, M. S., Meier, R. J., Duerkop, A., and Wolfbeis, O. S. (2010) Chromogenic sensing of biogenic amines using a chameleon probe and the red-green-blue readout of digital camera images. *Anal. Chem. 82*, 8402–8405.

(12) Garcia-Acosta, B., Comes, M., Bricks, J. L., Kudinova, M. A., Kurdyukov, V. V., Tolmachev, A. I., Descalzo, A. B., Marcos, M. D., Martinez-Manez, R., Moreno, A., Sancenon, F., Soto, J., Villaescusa, L. A., Rurack, K., Barat, J. M., Escriche, I., and Amoros, P. (2006) Sensory hybrid host materials for the selective chromo-fluorogenic detection of biogenic amines. *Chem. Commun.* 2239–2241.

(13) Kostenko, O. M., Kovalska, V. B., Volkova, K. D., Shaytanov, P., Kocheshev, I. O., Slominskiy, Y. L., Pisareva, I. V., and Yarmoluk, S. M. (2006) New method for covalent fluorescent biomolecule labeling with hemicyanine dye. *J. Fluoresc. 16*, 589–593.

(14) Miller, J. N. (2008) *Long-wavelength and near-infrared fluorescence: State of the Art, Future applications, and Standards*, Springer, Berlin.

(15) Oswald, B., Patsenker, L., Duschl, J., Szmacinski, H., Wolfbeis, O. S., and Terpetschnig, E. (1999) Synthesis, spectral properties, and detection limits of reactive squaraine dyes, a new class of diode laser compatible fluorescent protein labels. *Bioconjugate Chem. 10*, 925–931.

(16) Oswald, B., Gruber, M., Bohmer, M., Lehman, F., Probst, M., and Wolfbeis, O. S. (2001) Novel diode laser-compatible fluorophores and their application to single molecule detection, protein labeling and fluorescence resonance energy transfer immunoassay. *Photochem. Photobiol. 74*, 237–245.

(17) Pham, W., Lai, W. F., Weissleder, R., and Tung, C. H. (2003) High efficiency synthesis of a bioconjugatable near-infrared fluorochrome. *Bioconjugate Chem. 14*, 1048–1051.

(18) Patonay, G., Salon, J., Sowell, J., and Strekowski, L. (2004) Noncovalent labeling of biomolecules with red and near-infrared dyes. *Molecules 9*, 40–49.

(19) Kele, P., Li, X. H., Link, M., Nagy, K., Herner, A., Lorincz, K., Beni, S., and Wolfbeis, O. S. (2009) Clickable fluorophores for biological labeling-with or without copper. *Org. Biomol. Chem. 7*, 3486–3490.

(20) Li, X. H., Shi, W., Chen, S. M., Jia, J., Ma, H. M., and Wolfbeis, O. S. (2010) A near-infrared fluorescent probe for monitoring tyrosinase activity. *Chem. Commun. 46*, 2560–2562.

(21) Zollinger, H. (2003) *Color chemistry, synthesis properties, and applications of organic dyes and pigments*, 3rd ed., Wiley-VCH, Weinheim, Germany.

(22) Ghosh, P. B., and Whitehou, Mw. (1968) 7-chloro-4-nitrobenzo-2-oxa-1,3-diazole - a new fluorigenic reagent for amino acids and other amines. *Biochem. J. 108*, 155–156.

(23) Thorley, K. J., Hales, J. M., Anderson, H. L., and Perry, J. W. (2008) Porphyrin dimer carbocations with strong near infrared absorption and third-order optical nonlinearity. *Angew. Chem., Int. Ed. 47*, 7095–7098.

(24) Reichardt, C. (1995) Chiral polymethine dyes: A remarkable but forgotten conjugated pi system. *J. Phys. Org. Chem. 8*, 761–773.

(25) Landsman, M. L. J., Kwant, G., Mook, G. A., and Zijlstra, W. G. (1976) Light-absorbing properties, stability, and spectral stabilization of indocyanine green. *J. Appl. Physiol. 40*, 575–583.

(26) Gorris, H. H., Ali, R., Saleh, S. M., and Wolfbeis, O. S. (2011) Tuning the dual emission of photon-upconverting nanoparticles for ratiometric multiplexed encoding. *Adv. Mater. 23*, 1652–1655.

(27) Brown, H. C., Rao, C. G., and Ravindranathan, M. (1978) Structural effects in solvolytic reactions 0.29. Solvolysis of tertiary allylic para-nitrobenzoates - Effect of allylic double-bond on rates of solvolysis of representative tertiary para-nitrobenzoates. *J. Org. Chem. 43*, 4939–4943.

(28) Schleyer, P. V., Bentley, T. W., Koch, W., Kos, A. J., and Schwarz, H. (1987) Structures and energies of isomeric cyclopentenyl cations. Resolution of the question of anchimeric assistance in cyclopenten-4-yl solvolysis. *J. Am. Chem. Soc. 109*, 6953–6957.

(29) Sorensen, T. S. (1969) The equilibria and kinetics of the cyclohexenyl-cyclopentenyl cation rearrangement. *J. Am. Chem. Soc. 91*, 6398–6403.

Supporting information:

Long-Wavelength Absorbing and Fluorescent Chameleon Labels for Proteins, Peptides, and Amines

Hans H. Gorris, Sayed M. Saleh, Dominik B. M. Groegel, Steffen Ernst, Knut Reiner, Heinz Mustroph, Otto S. Wolfbeis

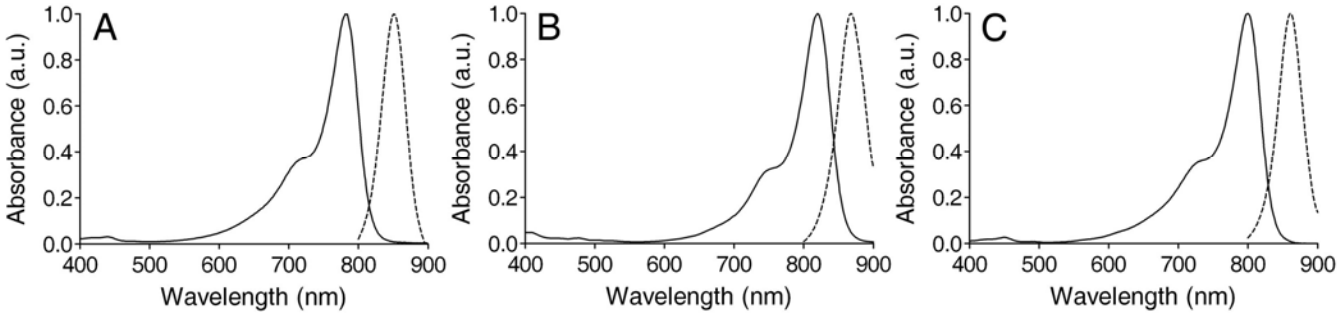

Supporting Figure 1. Absorbance (solid line) and emission spectra (hatched line) of the free dyes (A) S 0121, (B) S 0306 and (C) S 0378.

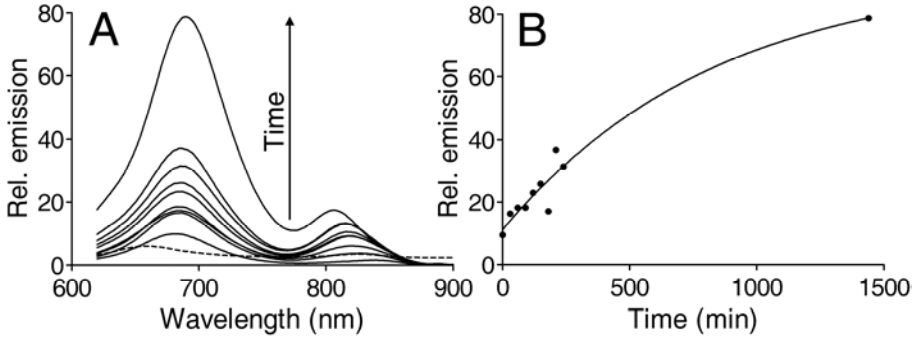

Supporting Figure 2. (A) Fluorescence changes of dye S 0378 upon binding to HSA at 37 °C. The reaction was monitored every 30 min for 4 hours and after 24 h. Upon excitation at 600 nm, the emission spectrum shows a main peak at 690 nm. The small side peak can be attributed to an inner filter effect: The emission at 690 nm is reabsorbed by the remaining free dye that displays its own emission at 800 nm. The hatched line shows the emission spectrum of dye S 0378 without HSA. (B) The increase of the emission intensity at 690 nm indicates the reaction kinetics.

Bioconjugate Chemistry

ARTICLE

pubs.acs.org/bc

Folate Receptor-Targeted Aggregation-Enhanced Near-IR Emitting Silica Nanoprobe for One-Photon *in Vivo* and Two-Photon *ex Vivo* Fluorescence Bioimaging

Xuhua Wang,[†] Alma R. Morales,[†] Takeo Urakami,[§] Lifu Zhang,[†,∥] Mykhailo V. Bondar,[⊥] Masanobu Komatsu,[§] and Kevin D. Belfield*[,†,‡]

[†]Department of Chemistry, University of Central Florida, Orlando, Florida 32816, United States

[‡]CREOL, The College of Optics and Photonics, University of Central Florida, Orlando, Florida 32816, United States

[§]Sanford-Burnham Medical Research Institute at Lake Nona, Orlando, Florida 32827, United States

[∥]School of Electrical Engineering, Anhui Polytechnic University, Wuhu, 241000, China

[⊥]Institute of Physics, Prospect Nauki, 46, Kiev-28, 03094 Ukraine

Supporting Information

ABSTRACT: A two-photon absorbing (2PA) and aggregation-enhanced near-infrared (NIR) emitting pyran derivative, encapsulated in and stabilized by silica nanoparticles (SiNPs), is reported as a nanoprobe for two-photon fluorescence microscopy (2PFM) bioimaging that overcomes the fluorescence quenching associated with high chromophore loading. The new SiNP probe exhibited aggregate-enhanced emission producing nearly twice as strong a signal as the unaggregated dye, a 3-fold increase in two-photon absorption relative to the DFP in solution, and approximately 4-fold increase in photostability. The surface of the nanoparticles was functionalized with a folic acid (FA) derivative for folate-mediated delivery of the nanoprobe for 2PFM bioimaging. Surface modification of SiNPs with the FA derivative was supported by zeta potential variation and ^{1}H NMR spectral characterization of the SiNPs as a function of surface modification. *In vitro* studies using HeLa cells expressing a folate receptor (FR) indicated specific cellular uptake of the functionalized nanoparticles. The nanoprobe was demonstrated for FR-targeted one-photon *in vivo* imaging of HeLa tumor xenograft in mice upon intravenous injection of the probe. The FR-targeting nanoprobe not only exhibited highly selective tumor targeting but also readily extravasated from tumor vessels, penetrated into the tumor parenchyma, and was internalized by the tumor cells. Two-photon fluorescence microscopy bioimaging provided three-dimensional (3D) cellular-level resolution imaging up to 350 μm deep in the HeLa tumor.

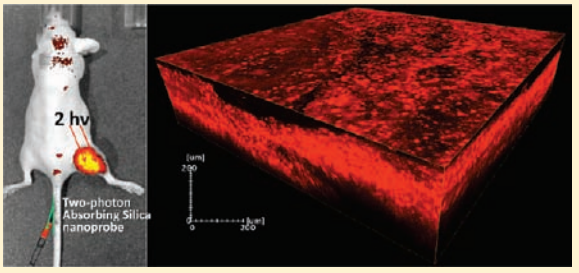

INTRODUCTION

In comparison with conventional bioimaging techniques, such as computed tomography (CT) or magnetic resonance imaging (MRI), fluorescence-based optical bioimaging affords much higher sensitivity and has been widely exploited to track biological processes.[1−4] Two-photon fluorescence microscopy (2PFM), one of the advanced fluorescence imaging techniques, has been investigated as a powerful tool for fundamental studies, cancer diagnosis, and oncologic drug development.[5−9] This technique has a number of advantages over traditional one-photon fluorescence microscopy (1PFM), including highly localized 3D spatial excitation, lower photo-induced damage, longer possible observation time, less interference by autofluorescence, and deeper penetration in tissue and thick samples.[10−13] A series of two-photon absorbing organic dyes[14] was reported for 2PFM imaging while a number of nanoparticles such as gold nanorods,[15] quantum dots,[16] and carbon nanoparticles[17] also show promise in 2PFM applications. However, one major challenge to the development and implementation of 2PFM for molecular bioimaging is a lack of biocompatible probes with sufficient two-photon absorption (2PA) cross-section, high fluorescence quantum yield, and high photostability in physiological environments.[10,18] For 2PFM applications, 2PA dyes are required to be hydrophilic or dispersible in aqueous media while maintaining high fluorescence efficiency.[19−21] Generally, organic materials with large 2PA cross-sections are synthetically more accessible in hydrophobic forms, and their fluorescence efficiencies are dramatically reduced in aqueous media due to self-aggregation-induced fluorescence quenching.[22,23]

Recently, ceramic-based nanoparticles encapsulating hydrophobic dyes have been reported as biocompatible fluorescent probes for bioimaging.[24−26] Although the strategy to disperse hydrophobic dyes in aqueous media has been relatively successful in improving photostability, the amount of dye remained at

Received: May 12, 2011
Revised: June 20, 2011
Published: June 21, 2011

ACS Publications © 2011 American Chemical Society

quite a low concentration, limiting the intensity of the fluorescence signal from individual nanoparticles due to aggregation-induced fluorescence quenching at high chromophore loading.[27] Typically, fluorescence quantum yields of organic dyes are decreased by self-quenching in the aggregated stage. However, a series of organic dyes with a self-distorted structure were reported to exhibit fluorescence enhancement via aggregation rather than the customary decrease.[28−32] This phenomenon was exploited to develop a high-signal output silica nanoprobe for 2FPM imaging.[33] Although enhanced two-photon fluorescence was achieved, surface modification of the nanoparticles for *in vivo* targeting bioimaging has rarely been reported, and the 2PA cross-section of the dyes employed were generally low. A series of compounds were reported to exhibit aggregation-enhanced emission,[34] but their two-photon based optical properties and application for 2PFM have not been reported. The development of silica nanoparticles (SiNPs) encapsulating an aggregation-enhanced emitting dye with a large 2PA cross-section and high photostability as a nanoprobe for 2PFM would be significant.

To increase the stability of SiNPs for *in vivo* imaging, polyethylene glycol (PEG) is often introduced to their surface. PEGylation of a drug or therapeutic protein often masks the agent from the host's immune system, reducing antigenicity and immunogenicity. PEGylation also increases the hydrodynamic size of the agent, prolonging its circulatory time by reducing renal clearance. It also can decrease the toxicity of the system and provide water solubility to hydrophobic drugs and proteins.[35] The PEG group has also been used to reduce normal tissue uptake of various materials, decrease toxicity, and increase tumor accumulation.[36] Beyond passive targeting through the enhanced permeability and retention (EPR) effect, delivery of particles to smaller solid tumors and metastatic cells can be achieved by modifying particle surfaces with moieties directed at cell surface markers unique to the tumor cells.[37] With developments in cell biology, a variety of disease-specific ligand−receptor pairs have been identified, e.g., ligands based on antibodies, antibody fragments, proteins, and peptides.[38] Because of their high selectivity to specific cell receptors, ligands based on antibodies, antibody fragments, proteins, and peptides were fervently investigated for drug and bioimaging agent delivery.[39] Among the receptors of interest, the folate receptor (FR) is overexpressed by a spectrum of malignant tumors, including cancers of the lung, ovary, breast, brain, kidney, colon, and endometrium.[40] Recently, folic acid conjugated nanoparticles were investigated as carriers for delivering magnetic agents for MRI bioimaging,[41] photosensitizers for photodynamic therapy,[42] anticancer drugs for cancer therapy,[43] and quantum dots for two-photon fluorescence microscopy.[44] Folic acid has been widely used for the selective delivery of attached imaging and therapeutic agents to tumors because of its high affinity to the folate receptor ($K_d = 10^{-10}$ M).[45] However, the cellular-level understanding of how nanoparticles distribute within a solid tumor has not been thoroughly investigated due to the lack of fluorophores suitable for high resolution 3-D analysis in deep tissues. Herein, a two-photon absorbing, aggregation-enhanced near-infrared (NIR) emitting and folate receptor-targeting silica nanoprobe is reported to probe the cellular distribution of the folate nanoprobe within a solid tumor. The FR-targeted, highly selective tumor accumulation of the new SiNP probe was demonstrated by *in vivo* one-photon fluorescence imaging of tumor-bearing mice and *ex vivo* two-photon fluorescence imaging of whole-mounted tumors. Our study presents a critical advancement in SiNP technology for disease diagnostics and therapeutics.

EXPERIMENTAL SECTION

Materials and Methods. Triethoxyvinylsilane (VTES, 97%), 1-butanol (99%), folic acid (FA), dicyclohexylcarbodiimide (DCC), *N*-hydroxysuccinimide (NHS), 2-aminoethanethiol, and the surfactant Tween-80, *N*′-[3-(trimethoxysilyl)propyl]diethylenetrimaine (DETA), were obtained from Sigma-Aldrich. *N*-Methyl-2-pyrrolidinone (NMP, 99%), triethylamine (TEA), and dimethyl sulfoxide (DMSO) were obtained from Acros. 2-(2,6-Bis((*E*)-2-(7-(diphenylamino)-9,9-diethyl-9*H*-fluoren-2-yl)vinyl)-4*H*-pyran-4-ylidene)malononitrile (DFP) was prepared as described in the Supporting Information. Maleimide-poly(ethylene glycol)-succinimidyl carboxymethyl, with an average MW of 3400 (MAL-PEG-SCM), was obtained from Laysan Bio Inc. Rat anti-mouse CD31 was obtained from BD Biosciences. Alexa Fluor 350 goat antimouse IgM was obtained from Invitrogen. The preceding chemicals or biological regents were used as received without further purification, except where otherwise noted. Thermo Slide-A-Lyzer 10K cut off dialysis cassettes and 0.22 μm cutoff membrane filters were obtained from Fisher Inc. HeLa and MG63 cells were obtained from ATCC (America Type Culture Collection, Manassas, VA, USA). All cells were incubated in RPMI-1640 medium (Invitrogen, Carlsbad, CA, USA), supplemented with 10% fetal bovine serum (FBS, Atlanta Biologicals, Lawrenceville, GA, USA), 100 units/mL penicillin−streptomycin (Atlanta Biologicals, Lawrenceville, GA, USA), and incubated at 37 °C in a 95% humidified atmosphere containing 5% CO_2. Details of pyran derivative DFP, including preparation and characterization, will be reported elsewhere. ^{1}H NMR spectra were recorded at 300 MHz.

Synthesis of Dye-Encapsulated Amine Terminated SiNPs. The amine and PEG-terminated nanoparticles, with or without encapsulation of the fluorenyl derivative DFP, were synthesized according to the method described by Prasad et al. with moderate modification.[28] Briefly, the nanoparticles were prepared by coprecipitating the dyes with polymeric organically modified silica sol in the nonpolar core of Tween-80/1-butanol micelles in deionized water. NMP was used as a hydrophilic solvent, which has unlimited water miscibility as well as suitable solubility for DFP. First, 1.0 g of VTES in 10 mL of NMP was hydrolyzed and condensed in the presence of 200 μL of ammonium hydroxide (28.0−30%) at room temperature for 16 h to obtain a clear solution of prepolymerized silica sol. Then, the prepolymerized silica sol was filtered with a membrane filter (0.22 μm pore size) for further SiNP preparation. Micelles were prepared with 0.2 g of Tween-80 and 0.4 mL of 1-butanol in 10 mL of deionized water. To obtain dye-encapsulation in SiNPs, 100 μL of the sol solution was homogeneously mixed with 0.38 mL of NMP solutions without or with DFP (0 mg, 0 wt %; 0.9 mg, 10 wt %; 1.8 mg, 20 wt %; 2.7 mg, 30 wt %), followed by the addition of 0.4 mL of the NMP solution by one-shot syringe injection into the prepared micelle dispersions to induce nanoprecipitation under vigorous magnetic stirring. After 30 min, 20 μL of EDTA was added to functionalize the surface of the nanoparticles with amine. To ensure completion of sol−gel condensation within the coprecipitated nanoparticles, the mixtures were further stirred at room temperature for 24 h. Nanoparticle purification was conducted by dialyzing the dispersion against deionized water in a 10 kDa cutoff cellulose membrane to remove Tween-80 and 1- butanol for 48 h. The dialyzed solution was then filtered through a 0.22 μm cutoff membrane filter. The resulting nanoparticles were stored at 4 °C for later experiments.

Conjugation of Amine-Terminated SiNPs with MAL-PEG-SCM. To 10 mL of DFP-doped silica nanoparticles dispersed in deionized water, 0.5 mL of PBS (20×, pH 7.4) and 10 mg MAL-PEG-SCM (M. W. 3400) in 300 μL water were added. The mixture was stirred for 30 min in the dark. The unreacted MAL-PEG-SCM polymer was removed by dialyzing the dispersion against deionized water in a 10 kDa cutoff cellulose membrane for 48 h. Finally, the dialyzed solution was filtered through a 0.22 μm cutoff membrane filter and stored at 4 °C for later experiments.

Surface Modification of Maleimide-Terminated SiNPs with FA. To 2 mL of the MAL terminated SiNPs dispersed in deionized water, 0.1 mL of PBS (20×, pH 7.4) and (*S*)-2-(2-(4-((2-amino-4-hydroxypteridin-6-yl)methylamino)-phenyl) acetamido)-5-(2-mercaptoethylamino)-5-oxopentanoic acid (FA-SH) (1 mg/mL in DMSO, 500 μL) was added, and the mixture was stirred for 1 h. The unreacted FA-SH and DMSO were removed by dialyzing the reaction mixture against deionized water in a 10 kDa cutoff cellulose membrane for 48 h. Finally, the dialyzed solution was filtered through a 0.22 μm cutoff membrane filter and stored at 4 °C for subsequent experiments.

Characterization of Dye-Encapsulating SiNPs. Transmission electron microscopy (TEM) images were obtained using a JEOL-JEM 1011 transmission electron microscope (JEOL, Ltd., Japan) operating at 100 kV in bright field for the nanoparticles. A drop of SiNPs dispersed in water was placed on a holey carbon film copper grid and left to evaporate. The zeta potential measurement and particle size analysis by a light scattering method were conducted using the Zetasizer Nano-ZS90 (Malvern Instruments). ^{1}H NMR spectra of SiNPs dispersed in D_2O were recorded at 300 MHz.

Uptake of SiNPs by Cancer Cells. HeLa or MG63 cells were placed onto poly-D-lysine coated glasses in 24-well plates (15,000 cells per well), and the cells were incubated for 48 h before incubating with dye-doped SiNPs. Stock solution of dye-doped SiNPs suspended in water was prepared as ∼50 μM solution. The solution was diluted to 0.1, 1, and 5 μM solutions by complete growth medium, RPMI-1640, and freshly placed over the cells for a 2 h period. After incubation, the cells were washed with PBS for 3 min at 37 °C (3−5×) and fixed using 3.7% formaldehyde solution for 15 min at 37 °C. To reduce autofluorescence, a fresh solution of $NaBH_4$ (1 mg/mL) in PBS (pH 8.0), which was prepared by adding few drops of 6 N NaOH solution into PBS (pH 7.2), was used for treating the fixed cells for 15 min (2×). The plates were then washed twice with PBS and once with water. After this, the glass coverslips were mounted by Prolong gold mounting medium for microscopy.

Animal Model, *in Vivo* and *ex Vivo* Imaging. Eight-week-old female athymic nude mice were obtained from Harlan Laboratories (Indianapolis, IN). HeLa cells (5×10^6 cells) were inoculated subcutaneously into the right thighs of mice. Imaging studies were performed 10 days after tumor inoculation; SiNPs dispersed in PBS (300 μM, ∼0.2 mL, 3 nmol/g body weight) or vehicle (PBS, ∼0.2 mL) were injected to the mice via the tail vein. At different times after the injection of SiNPs or the vehicle, the mice were imaged using an IVIS Spectrum imaging system (Caliper Life Sciences) while under anesthesia. Fluorescence images were recorded by two channels. One channel, excitation at 500 nm and emission at 720 nm, was used to record the fluorescence from the SiNPs, while the other channel, excitation at 605 nm and emission at 720 nm, was used to record background tissue autofluorescence. The resulting images were processed by subtracting the background tissue autofluorescence from the fluorescence from the SiNPs with software of the IVIS Spectrum imaging system. After *in vivo* imaging, the mice were euthanized with i.v. injections of xylazine, and the tissue samples were collected after 20 mL of PBS perfusion through the heart, fixed in 4% paraformaldehyde, and cryprotected in PBS solution for *ex vivo* one- and two-photon fluorescence microscopy imaging. Two mice were examined for each sample.

1PFM Cell, Tissue, and *ex Vivo* 2PFM Imaging. Conventional single-photon fluorescence cell images were obtained using an inverted microscope (Olympus IX70) equipped with a QImaging cooled CCD (Model Retiga EXi) and excitation with the filtered emission of a 100 W mercury lamp. In order to improve the fluorescence background-to-image ratios, one-photon confocal fluorescence images of the fixed cells were taken using a custom-made filter cube for dye-doped SiNPs. The specifications of the filter cube were tailored to match the excitation wavelength of probes and to capture most of its emission profile. 1PFM imaging of *ex vivo* tissue sections was performed on a Leica TCS SP5 II Tandem Scanner upright multiphoton laser scanning microscopy system. Frozen tumors were sectioned by a freeze microtome (Leica, CM1900) to ∼20 μm thick sections. For labeling the of endothelia of blood vessels, the MEC13.3 antibody (1:50 dilution in PBS) was used to react with CD31, and a labeled goat antimouse IgM antibody Alexa Fluor 350 (1 μg/mL in PBS) was used to label the primary antibody MEC13.3. The nuclei of the sectioned tissues were stained with Hoechst 33285 (0.2 μg/mL in PBS). The section tissues were imaged and examined by laser-scanning confocal microscopy (Leica, TCS SP5). 2PFM cell imaging was performed using a modified Olympus Fluoview FV300 microscope system coupled to a tunable Coherent Mira 900F Ti:sapphire laser (76 MHz, modelocked, 200 fs pulse width, tuned to 840 nm). A short-pass emission filter (cutoff 690 nm) was placed in the microscope scanhead to avoid background irradiance from the excitation source. Consecutive layers, separated by approximately 0.15 μm for cell imaging and 0.3 μm for tumor imaging, were recorded to create a 3D reconstruction from overlaid 2PFM images. Two-photon induced fluorescence was collected with a 60× microscope objective (UPLANSAPO 60×, NA = 1.35, Olympus). 2PFM thick tissue imaging was performed using a Leica TCS SP5 microscope system coupled to a tunable Coherent Chameleon Vision S (80 MHz, modelocked, 75 fs pulse width, tuned to 980 nm). A short-pass emission filter (cutoff 840 nm) was placed before the CCD camera to avoid background irradiance from the excitation source. Consecutive layers, separated by approximately 0.5 μm for thick tumor imaging, were recorded to create a 3D reconstruction from overlaid 2PFM images. Two-photon induced fluorescence was collected with a water immersion high NA/low magnification objective lens HC X APO L20× (NA = 1.0, Leica) with the magnification changer in the CCD camera mode (3× magnification was used).

■ RESULTS AND DISCUSSION

Aggregation Enhanced Emission of DFP. To study and exploit the potential utility of pyran derivatives, which were reported to exhibit aggregation-enhanced emission,[30] a pyran derivative 2-(2,6-bis((*E*)-2-(7-(diphenylamino)-9,9-diethyl-9*H*-fluoren-2-yl)vinyl)-4*H*-pyran-4-ylidene)malononitrile (DFP) (Figure 1, left) was prepared and its photophysical properties were investigated herein for 2PFM bioimaging. A simple precipitation method was employed to prepare the stable DFP

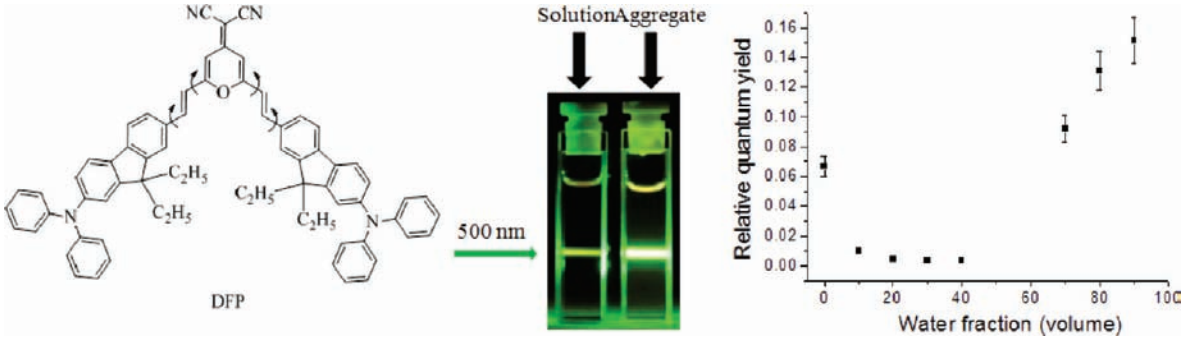

Figure 1. Molecular structure of DFP (left), the florescence emission of DFP (5×10^{-6} mol·L^{-1}) in THF and the THF/water mixture (90% volume fraction of water, ca. 20 nm nanoparticle suspension) under 500 nm laser excitation (middle), and the relative fluorescence quantum yields (Φ_f) of DFP (5×10^{-6} mol·L^{-1}) vs water fraction in THF (right).

nanoaggregates dispersed in water,[24,26] with THF as a water-miscible solvent for DFP. The roles of water in the organic nanoparticle preparation by precipitation included lowering the solubility of DFP and stabilizing a colloidal dispersion by promoting surface charge. Figure S1 (Supporting Information) shows a representative transmission electron microscopy (TEM) image of the nanoaggregates made from 90% v/v of water in THF, having a diameter of 20 ± 6 nm. The results pictured in Figure 1 (right) indicated that the relative fluorescence quantum yield (Φ_f) of DFP with the same concentration of 5×10^{-6} mol·L^{-1} decreased dramatically from 0.067 to 0.003 when the volume fraction of the water increased from 0 to 40%. Bulk precipitation occurred in the range of 50−60% water volume fraction, possibly because this amount of water decreased the solubility of DFP but did not stabilize the colloid enough by promoting surface charge.[24] The relative fluorescence quantum yield, Φ_f, of DFP at 50−60% was not measured due to bulk precipitation. After the volume fraction of the water was increased above 60%, stable nanoaggregates of DFP formed, and the relative Φ_f of DFP under the same conditions varied from 0.09 to 0.15 with the volume fraction of water increasing from 70 to 90%. It is apparent that the fluorescence of DFP was intensified by aggregation. Figure 1(middle) illustrates that the relative fluorescence intensity of DFP with the same concentration at the aggregate state was much stronger than it was in THF solution under 500 nm laser excitation. The absorption and emission spectra of DFP in different water fraction solutions are presented in Figure S2 (Supporting Information). The emission spectra showed that the fluorescence intensity was enhanced by aggregation with a minimal shift, whereas the absorption of DFP broadened, and the intensity decreased with increasing water.

This relatively abnormal phenomenon exhibited by DFP may be explained by rotation upon the axes of the olefinic double bonds adjacent to the fluorenyl rings and pyranyl ring in DFP (Figure 1, left) so that the conformational flexibility may result in the molecule being relatively nonemissive in dilute solution. However, when the molecule formed nanoaggregates in more hydrophilic solution, the intramolecular rotations were restricted, and the molecular conformation was stiffened, resulting in aggregation-enhanced emission (i.e., the favored conformations were radiative).[34,46] This presumption was supported by the blue-shifted monomer fluorescence in a dilute solid solution of DFP in a polymethylmethacrylate (PMMA) film, where isolated molecules are stiffened and distorted by the rigid matrix (Figure 4a). The DFP emission is red-shifted without quenching at concentrations that normally would be high enough to induce self-quenching because the intermolecular steric hindrance between DFP molecules not only extends the π-conjugation but also diminishes intermolecular quenching effects.[47]

Synthesis, Characterization, and Photophysical Properties of Amine-Terminated DFP Doped SiNPs. To apply the observed aggregation-enhanced emission property of the hydrophobic 2PA dye DFP for 2PFM bioimaging, dye-doped SiNPs encapsulating different amounts of DFP were prepared according to a moderately modified reported method.[33] Dye-doped SiNPs have been reported to be biocompatible,[48,49] stable without releasing encapsulated hydrophobic molecules,[50] and facile to be modified with biomolecules.[51] The synthesis and surface modification of the dye-doped SiNPs are schematically described in Scheme 1. To prepare the high loading dye-doped or nonlabeled SiNPs, a prepolymerized triethoxyvinylsilane (VTES) sol solution was first prepared. Then the sol solution and a solution with or without a certain amount of DFP were mixed and coprecipitated within the nonpolar interior of aqueous Tween-80 micelles through a solvent displacement process.[52] *N*′-[3-(Trimethoxysilyl)-propyl]diethylenetriamine (DETA) was the added to the reaction mixture to introduce free amine groups on the SiNP surface for subsequent bioconjugation.

The zeta potential was analyzed to determine the change in surface charge of the SiNPs. Results in Figure 2a indicated that the nonlabeled SiNPs presented an overall positive charge with a zeta potential value of +10.4 ± 0.5 mW, presumably because of the presence of amine moieties on the surface of the SiNPs.[52] With increasing dye loading, the overall surface charge of the SiNPs became more and more negative, and the 30 wt % (defined as DFP/[DFP+VTES] by weight) loading SiNPs exhibited a zeta potential of +2.14 ± 0.4 mV. The overall surface charge of SiNPs encapsulating different amounts of DFP varied possibly due to increasing surface hydrophobicity that promoted preferential adsorption of anions (OH^-) on the surface. The SiNP particle size was analyzed by transmission electron microscopic (TEM) and dynamic light scattering (DLS). The results from DLS (Figure 2b) indicated that the particle size of SiNPs increased with increased loading ratios of DFP in the particles. A representive TEM image of 20 wt % SiNPs (Figure 2c) was in good agreement with their number-averaged size distribution in water. The diameters were in the range of 20−30 nm with an average diameter of ca. 25 nm. This size is small enough to minimize the clearance of the host's immune system, prolong the circulation time of the SiNPs in live animals, and, hence, increase accumulation of the SiNPs in the targeted tumor.

Scheme 1. Synthesis and Surface Modification of DFP-Doped SiNPs with FA Surface Modification

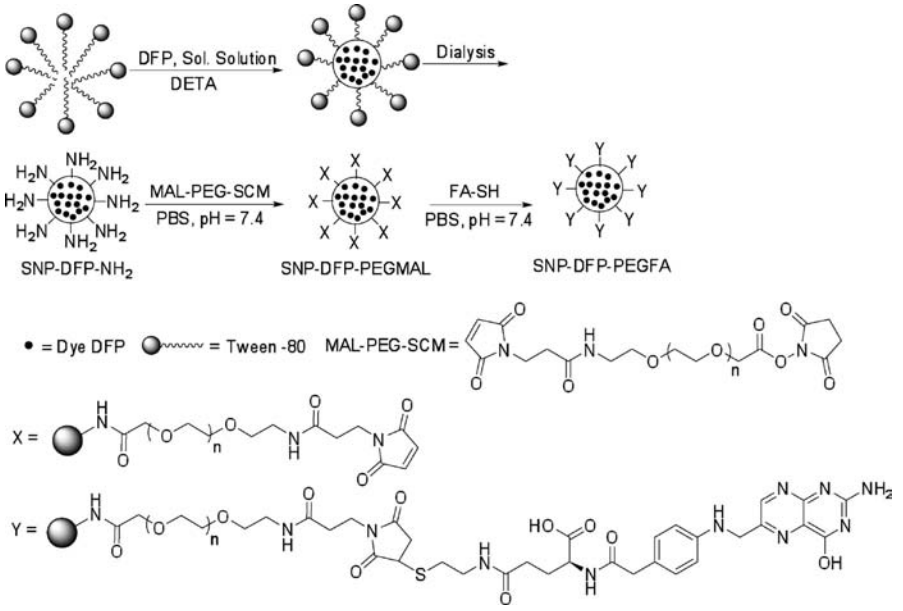

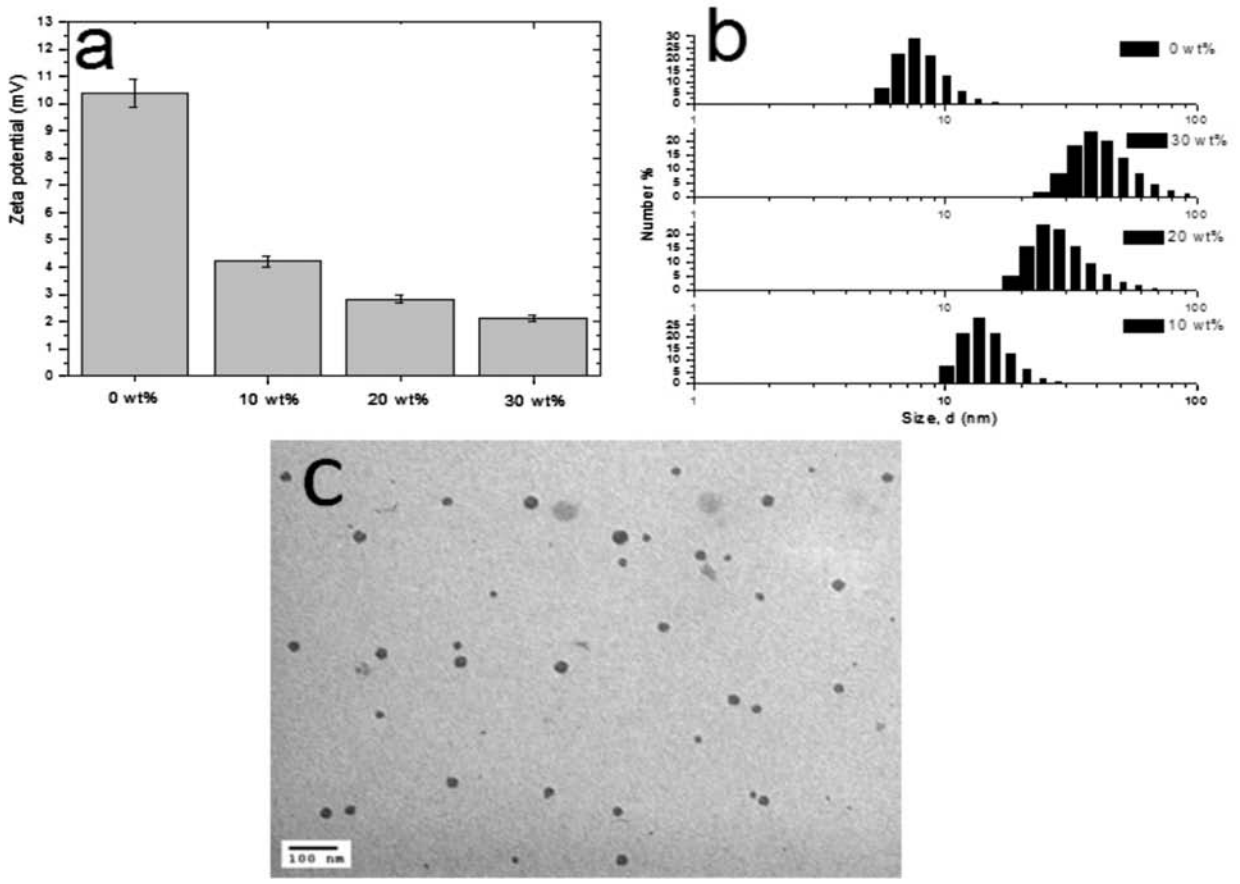

Figure 2. (a) Zeta potential, (b) number-averaged particle size distribution by light scattering, and (c) and representive TEM image (20 wt % SiNPs) of SiNPs encapsulating different amounts of DFP; the scale bar is 100 nm.

The fluorescence quantum yield, Φ_f, and luminescence lifetime, τ_f, of the dye-doped SiNPs encapsulating various amounts of DFP, dispersed in water, were analyzed to optimize conditions for their use in 2PFM bioimaging. The results shown in Figure 3a indicate that the fluorescence quantum yield, Φ_f, achieved a highest value of 0.18 ± 0.04 at a 20 wt % DFP concentration.

dx.doi.org/10.1021/bc2002506 |*Bioconjugate Chem.* 2011, 22, 1438–1450

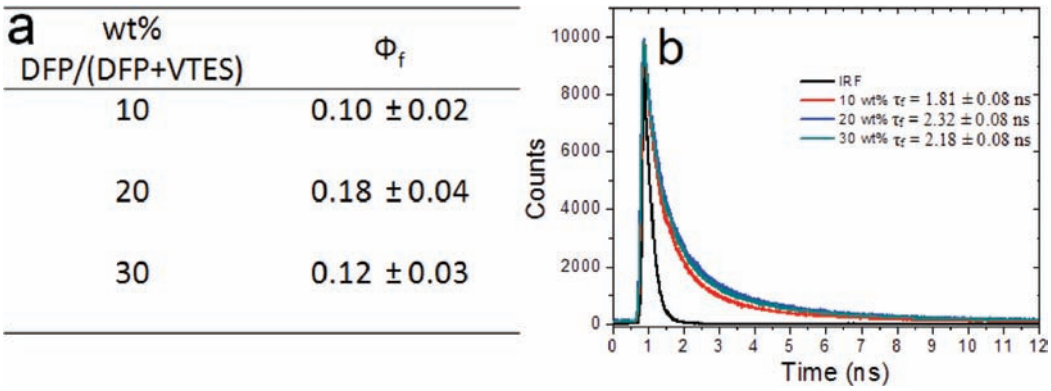

Figure 3. (a) Fluorescence quantum yield (Φ_f) and (b) fluorescence lifetime decay of SiNPs encapsulating differing quantities of DFP.

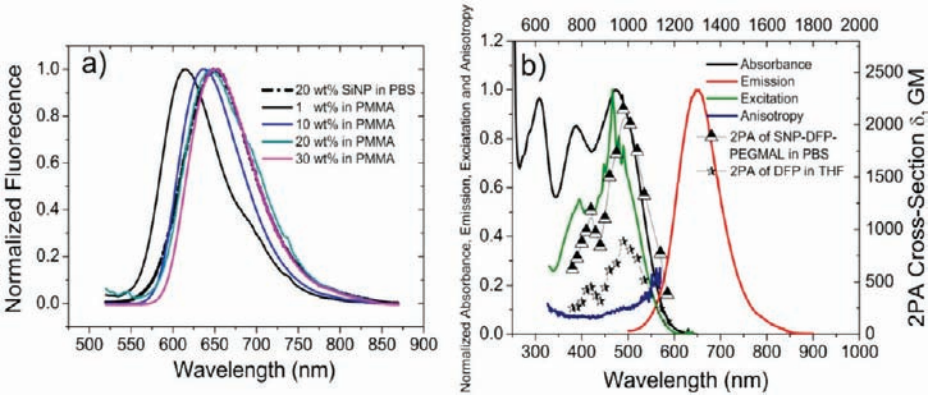

Figure 4. (a) Fluorescence emission spectra of DFP with different concentrations in PMMA and 20 wt % SiNPs dispersed in PBS (1×). (b) Absorption, emission, excitation, and 2PA spectra of 20 wt % SiNPs (SNP-DFP-PEGMAL) and an anisotropy spectrum in PBS (1×), as well as 2PA spectra of DFP in THF.

According to the fluorescence decay presented in Figure 3b, the fluorescence lifetime of the SiNPs reached the highest value (2.32 ± 0.08 ns) at 20 wt % DFP and the lowest value (1.81 ± 0.08 ns) at 10 wt % DFP, consistent with fluorescence quantum yield measurements.

The 20 wt % SiNPs were chosen for the 2PFM bioimaging not only because of their higher fluorescence quantum yield but also because of their suitable particle size for *in vivo* bioimaging. The linear and nonlinear photophysical properties of silica nanoprobe were investigated in phosphate buffered saline (PBS, 1×) to determine the potential utility of the silica nanoprobe for 2PFM bioimaging applications. The emission spectra of the 20 wt % SiNPs matrix was close to the emission spectra of 20 wt % DFP in PMMA (Figure 4a), indicating that DFP in 20 wt % SiNPs was in the same aggregate state as DFP in PMMA solid solution. The absorption, emission, excitation, 2PA cross-section, and the excitation anisotropy spectra of the silica nanoprobe in PBS (1×) are shown in Figure 4b. The linear absorption spectrum (dark) and excitation spectrum (green) were sufficiently close to each other, and the emission spectrum (red) showed a maximum emission in the red (~650 nm), extending into the near-IR. The values of excitation anisotropy (Figure 4b, blue) were not constant in the range of the main 1PA band (450−550 nm), indicating its relatively complex nature. Presumably, this band corresponds to at least two electronic transitions with different orientations of its transition dipoles.

By employing a standard z-scan method[53] with a femtosecond laser system, the silica nanoprobe afforded an impressive maximum 2PA cross-section (δ) of ~2100 GM (1 GM = 10^{-50} · cm^4 · s · $photon^{-1}$) at 980 nm (Figure 4b, triangle), which was ca. three times higher than free DFP in THF (Figure 4b, star). The aggregation enhanced two-photon absorption of DFP in SiNPs may be due to the considerably hindered internal rotation of the dye molecule in the solid silica matrix.[28] The 2PA efficiency of our nanoprobe is much higher than those previously reported, typically <300 GM, for two-photon fluorescence microscopy (2PFM) bioimaging.[54]

Surface Modification, Characterization, and Photophysical Properties of the FA Conjugated DFP Doped SiNPs. In order to mask the silica nanoprobe from the host's immune system and target FR overexpressing tumors, the surface of the SiNPs was further modified with maleimide-terminated PEG and then FA. The succinimidyl carboxyl group on maleimide-poly(ethylene glycol)-succinimidyl carboxymethyl (MAL-PEG-SCM, M.W. 3400) was first used to react with the amine group on the surface of the SiNPs, yielding a maleimide functional group on the surface to react with the thiol group on (*S*)-2-(2-(4-((2-amino-4-hydroxypteridin-6-yl)methylamino)-phenyl) acetamido)-5-(2-mercaptoethylamino)-5-oxopentanoic acid (FA-SH) in the next step (Scheme 1). Finally, the FA-conjugated SiNPs were purified by dialysis to remove unreacted molecules. The success of FA conjugation to the SiNPs was confirmed by

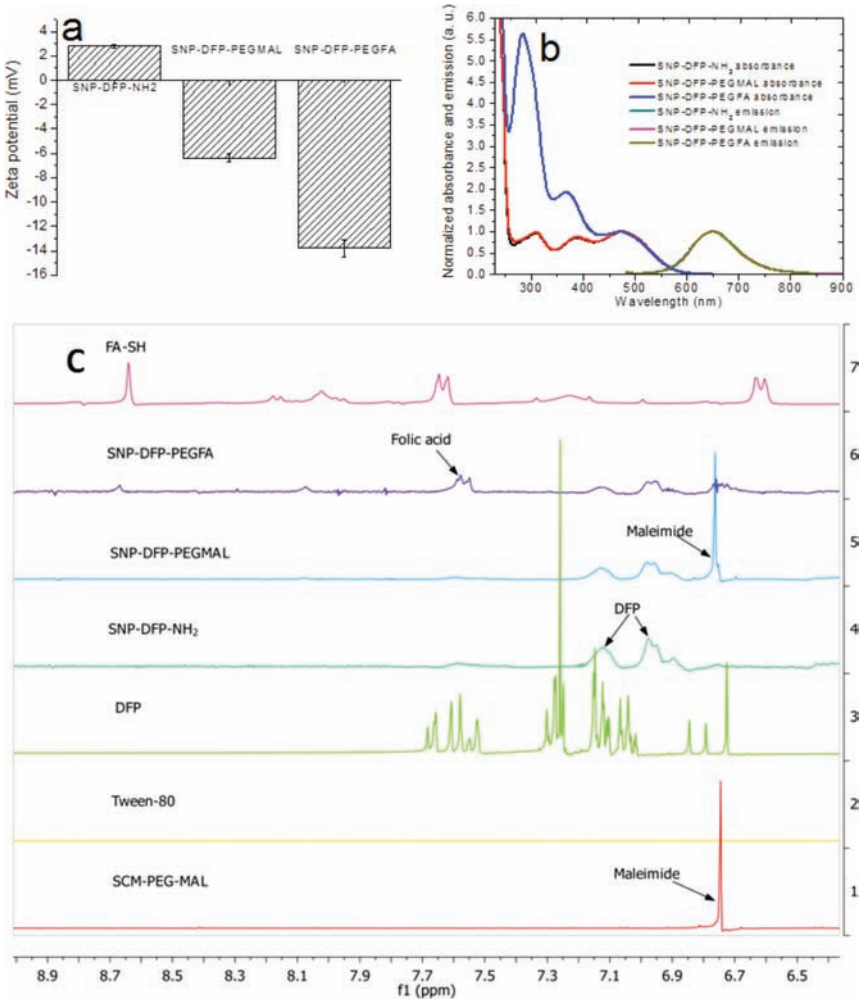

Figure 5. (a) Zeta potential values of surface modified DFP-doped SiNPs dispersed in water. (b) Absorption and fluorescence emission spectra of surface modified DFP-doped SiNPs dispersed in PBS. (c) ^{1}H NMR spectra of different surface modified DFP-doped SiNPs dispersed in D_2O, as well as SCM-PEG-MAL and Tween-80 in D_2O, FA-SH in DMSO-d_6, and DFP in $CDCl_3$.

zeta potential measurement (Figure 5a). The zeta potential value of amine-terminated SiNPs (SNP-DFP-NH_2) decreased from +2.8 mV to −6.4 mV after reaction of surface amino groups with MAL-PEG-SCM to form the MAL-terminated SiNPs (SNP-DFP-PEGMAL) since most of the positive charge from NH_3^+ was eliminated. After FA-SH conjugation with SNP-DFP-PEGMAL and formation of FA-terminated SiNPs (SNP-DFP-PEGFA), the zeta potential value decrease continuously to −13.8 mV, possibly because the positive charge on the surface was shielded by the FA derivative.

In addition, proton NMR spectra of the SiNPs in D_2O, as well as SCM-PEG-MAL and Tween-80 in D_2O, FA-SH in DMSO-d_6, DFP in CD_3Cl (Figure 5c and ^{1}H NMR spectra in Supporting Information), confirmed the surface modification of the DFP-doped SiNPs modified by FA. A signal at δ = 6.76 ppm from the maleimide was present after the amine-terminated SiNPs reacted with MAL-PEG-SCM, producing maleimide groups on the surface of the SiNPs. Then the signal from maleimide at δ = 6.76 ppm disappeared after the maleimide reacted with the thiol of FA-SH, and the signal at δ = 7.62 ppm from folic acid appeared in the proton NMR spectrum of FA-modified SiNPs. Because of the presence of PEG on the surface of the SiNPs, the FA-conjugated SiNPs dispersed well in phosphate buffered saline (PBS, 1×) solution and were quite stable. A representative TEM image and dynamic light scattering (DLS) size distribution of the FA conjugated nanoparticles dispersed in PBS is shown in Figure S5 (Supporting Information). The average particle size was ∼28 nm with a polydispersity index (PdI) value of 0.375, and no aggregation or decomposition was observed through all experiments.

The photostability of SNP-DFP-PEGFA in PBS was evaluated resulting in a photodecomposition quantum yield, Φ_d, of 3.7×10^{-7} that was ca. 25% of the value for DFP in Tween-80 micelles in PBS (1.3×10^{-6}). This result is significant in that the photostability of the DFP probe encased in the SiNP (SNP-DFP-PEGFA) was ca. four times higher than that of free DFP (in solution). It is possible that when the nanoprobe was irradiated, the silica matrix protected the dye molecules from the aqueous environment and reduced the oxidation of the dye molecules by slowing the diffusion of oxygen, an aspect of future investigations.

The linear and nonlinear photophysical and photochemical properties of the silica nanoprobe resulted in a highly desirable figure of merit ($F_M = \delta\Phi_f/\Phi_d$) value of $\sim 1.1 \times 10^9$ GM in PBS, a value that is about two times higher than a previously reported high-fidelity small molecule probe.[5] The absorption and emission spectra of SNP-DFP-NH_2, SNP-DFP-PEGMAL, and

dx.doi.org/10.1021/bc2002506 |*Bioconjugate Chem.* 2011, 22, 1438–1450

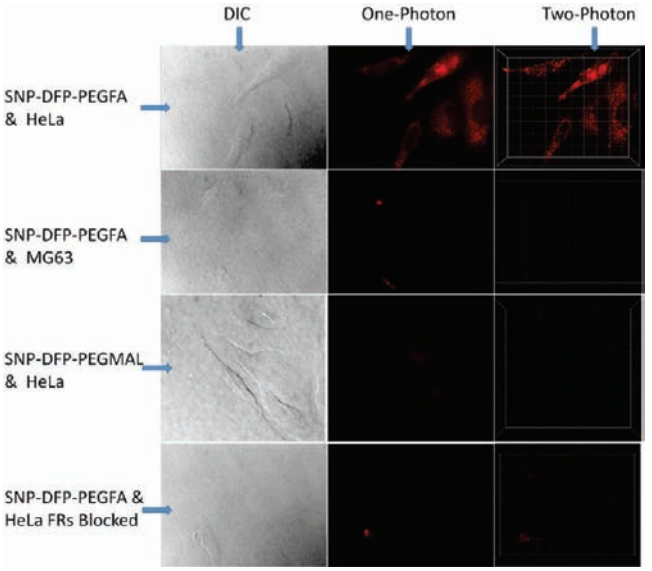

Figure 6. Images of HeLa cells incubated with SNP-DFP-PEGFA (5 μM, 2 h) (top row), MG63 cells incubated with SNP-DFP-PEGFA (5 μM, 2 h) (second row), HeLa cells incubated with SNP-DFP-PEGMAL (5 μM, 2 h) (third row), and HeLa cells incubated with 2 mg/mL FA for 1 h first followed by incubation with SNP-DFP-PEGFA (5 μM, 2 h) (bottom row). Left panel, differential interference contrast (DIC); middle panel, 1PFM image; right panel, 3D reconstruction from overlaid 2PFM images (Ex, 840 nm; power, 90 mW, ~14% on the focal plane; Em, short-pass filter 690 nm); 10 μm grid. All images were acquired and processed with the same conditions.

SNP-DFP-PEGFA are presented in Figure 5b, and after FA conjugation, the absorption of FA in the short wavelength was presented, and, as can be seen, the emission spectrum did not change.

Cytotoxicity, *in Vitro* 1PFM and 2PFM Folate Receptor-Targeted Cell Imaging of the DFP SiNP Nanoprobe. Before applying the FA-conjugated SiNPs for FR-targeted bioimaging, the probe's cytotoxicity with HeLa and MG63 cells was investigated using an MTS assay.[5] The results (Figure S4, Supporting Information) indicated that the FA-conjugated SiNPs are compatible with these cell lines (~85% cell viability) over a DFP concentration range from 0.01−5 μM, which was high enough for imaging. DFP concentrations were determined from the absorption of SNP-DFP-PEGFA at 472 nm (absorbance coefficient, $\varepsilon_{472\ nm}$ = 5.4 × 10^4 $M^{-1}\cdot cm^{-1}$ in PBS). The results suggested that the FA-conjugated SiNPs will be suitable for FR-targeted 2PFM *in vitro* cell imaging.

In preparation for *in vivo* imaging studies, *in vitro* cell imaging was conducted to test the selectivity of the FA-conjugated silica nanoprobe to FRs. HeLa cells, known to overexpress FRs, and low FR expressing MG63 cancer cells were incubated with the same concentration of the FA-conjugated SiNPs for the same time. 1PFM and 2PFM images are presented in Figure 6 demonstrating that HeLa cells (top row) incubated with FA-conjugated SiNPs (SNP-DFP-PEGFA) were much brighter than the MG 63 cells (a negative control, second row from the top) incubated with the same nanoprobe. In addition, two additional control experiments were performed. In one control, HeLa cells (third row from the top) incubated with non-FA-conjugated SiNPs (SNP-DFP-PEGMAL) under the same conditions showed no significant uptake of the probe. In the additional control experiment, HeLa cells (bottom low) whose FRs were first blocked with FA and, subsequently incubated with FA-conjugated SiNPs, also demonstrated no specific uptake of the SiNPs. These results indicated that the HeLa cancer cells, which are well-known to overexpress FRs, internalized the FA-conjugated SiNPs, presumably by FR mediation but that those cells which do not overexpress FRs or whose FRs were blocked did not take up the silica nanoprobe effectively.

Folate Receptor-Targeted *in Vivo* Tumor Imaging with Nanoprobes and Biodistribution Study. The *in vitro* studies demonstrated that the FA-conjugated SiNPs can target FRs, providing motivation to investigate the SiNPs for FR-targeting bioimaging in mice. Athymic nude mice bearing HeLa tumors (10 days post-inoculation of 5 × 10^6 HeLa cells on the right thigh), which overexpress FRs, were administered with the SNP-DFP-PEGFA or SNP-DFP-PEGMAL probe (3 nmol DFP per gram of animal body weight) via tail vein injection. The mice were imaged at different time points post-injection (p.i.), using an IVIS Spectrum imaging system; the fluorescence signals from the nanoprobes were collected in one channel with excitation at 500 nm and emission at 720 nm. The tissue background autofluorescence signals were recorded with a second channel with excitation at 605 nm and emission at 720 nm. The efficiency of the channels to separate the probe fluorescence signals from the background autofluorescence signals was checked by imaging standard samples with different concentrations of SNP-DFP-NH_2 in PBS (Figure S6, Supporting Information). In this experiment, two groups of mice were analyzed in the same way. The resulting images presented in Figure 7 were corrected by subtracting the animal autofluorescence background images from the silica probe fluorescence images using the vendor's software. Just after 30 min p.i., a fluorescence signal was detected in the tumor. A steady increase in the tumor fluorescence intensity in the mice injected with SNP-DFP-PEGFA was observed during the next few hours, and the tumor fluorescence intensity reached its maximum at 6 h p.i. No significant fluorescence signal was detected in the tumor for the SNP-DFP-PEGMAL injected mouse. These results indicate that the FA-conjugated SiNPs accumulated in the tumor and demonstrated that the FA-conjugated nanoprobes can be delivered to tumor sites effectively.

At 6 h p.i., the mice injected with SNP-DFP-PEGFA or SNP-DFP-PEFMAL were sacrificed, and their HeLa tumors and organs were harvested and imaged immediately with the IVIS Spectrum imaging system using the same collection channels described above. The fluorescence images of the organs and tumors are shown in Figure S7 (Supporting Information). The SiNPs' biodistribution was determined by their relative fluorescence intensity from these organs (Figure 8a). The biodistribution of the nanoprobes in normal organs, e.g., liver, kidney, spleen, heart, lung, intestine, muscle, and brain, were similar between the FA-conjugated and nonconjugated probes and consistent with the biodistribution of other SiNPs reported previously.[26] The most important difference in the biodistribution was the ca. three times higher HeLa tumor uptake observed for FA-conjugated SiNPs, supporting FR-mediated accumulation of the nanoparticles. For a better comparison and higher resolution, the excised tumors of the mice injected with SNP-DFP-PEGFA or SNP-DFP-PEGMAL were imaged and presented in Figure 8b. The fluorescence signal intensity of the tumor from the mouse injected with SNP-DFP-PEGFA was ca. three times higher than the one from the mouse injected with SNP-DFP-PEGMAL. The efficiency of tumor targeting of the FA-conjugated nanoprobe was impressive, particularly considering that the mice used in this study were fed

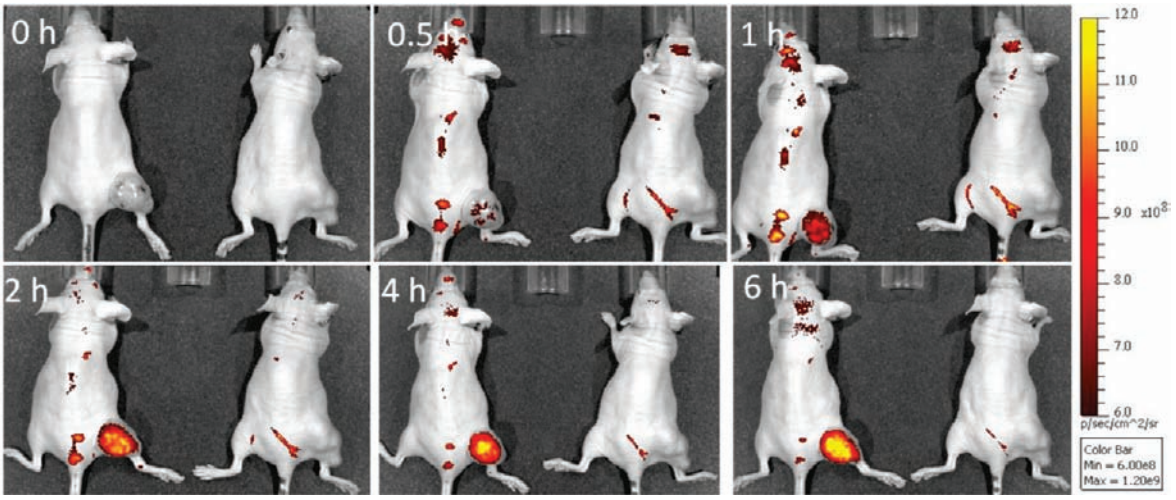

Figure 7. Representative whole-body *in vivo* fluorescence images of mice bearing HeLa tumors. The mice were intravenously administered with DFP-containing folate SiNP conjugate (left: SNP-DFP-PRGFA) or DFP-containing SiNP without folic acid derivatization (right: SNP-DFP-PEGMAL) at 3 nmol/g body weight, and the fluorescence signal was monitored at different time points post-probe administration.

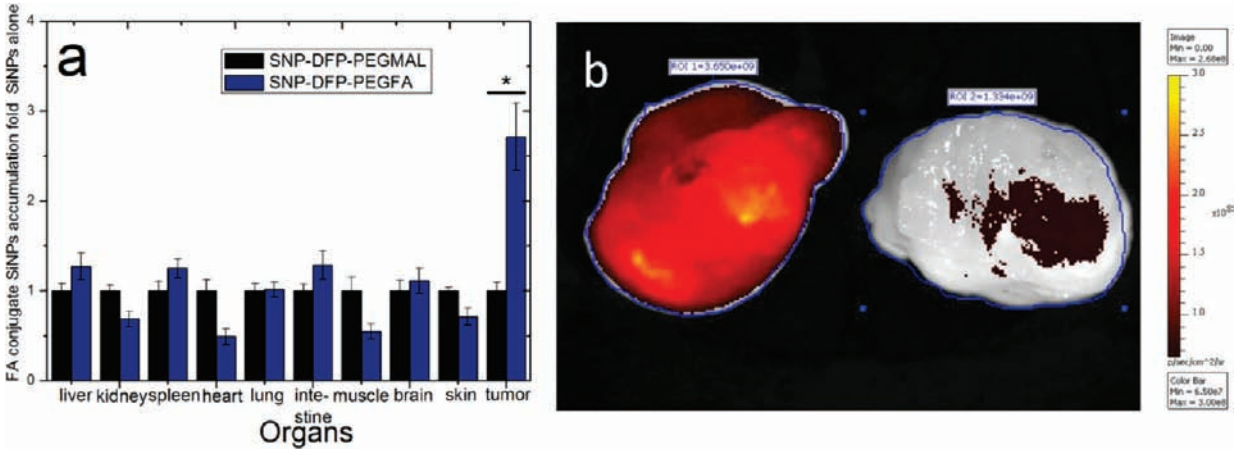

Figure 8. (a) Comparison of the SiNPs delivery efficiency (organ accumulation) of the FA-conjugated silica nanoprobe and non-FA containing silica nanoprobe (Student's *t* test, $n = 2$ mice per group, error bars denote mean ± SEM, $^*P < 0.05$) and (b) *ex vivo* image of the HeLa tumor of mice injected with SNP-DFP-PEGFA (left) and SNP-DFP-PEGMAL (right).

a regular diet rather than a folate-free diet, which is usually necessary to increase the detection sensitivity of the folate receptor-targeted probes.[55] In addition, because the *ex vivo* tumor fluorescence signal appeared to be fairly homogeneous and FRs are overexpressed by cancer cells, it is reasonable to predict that the fluorescence signal should emanate from cells distributed throughout the tumor rather than being localized in the vasculature, an aspect explored in the following section.

Histology Studies of HeLa Tumors from the Mice Administered with Nanoprobes. After *in vivo* and *ex vivo* imaging of the tumor by the IVIS spectrum imaging system, the collected tumors were sectioned to ~20 μm thick sections. In order to determine the location of the nanoprobe in the tumor, the nuclei of the tumor were stained with Hoechst 33285 before visualizing with a Leica 1P-FCS confocal microscope. The confocal fluorescence image of the FA-conjugated nanoprobe accumulated in the tumor together with the localized fluorescence spectrum is illustrated in Figure 9. The 1PFM image of the tissue indicated that the FA-conjugated nanoprobe accumulated in the tumor cells (Figure 9d and f). The HeLa cancer cells internalized the nanoprobe and accumulated in specific organelles within the cancer cells (likely endosomes), and the localized fluorescence spectrum (Figure 9e) confirmed that the localized fluorescence (pointed out by triangles in Figure 9f) was from the internalized nanoprobe ($\lambda_{em\ max}$ = 650 nm) rather than tissue autofluorescence ($\lambda_{em\ max}$ = 524 nm), and the fluorescence signals from the folate nanoprobe was about three times higher than the autofluorescence signals.

Significantly, no fluorescence for the nanoprobe channel was observed in the HeLa tumors from the mice injected with non-folic acid-conjugated nanoprobe SNP-DFP-PEGMAL (Figure S8, Supporting Information). In addition, blood vessels were stained to show how far the nanoprobe penetrates into the tumor; the result shown in Figure S9 (Supporting Information) indicated that the folate nanoprobe leaked out of the blood vessels (Figure S9 (Supporting Information), pointed out by triangles) and spread throughout the tumor.

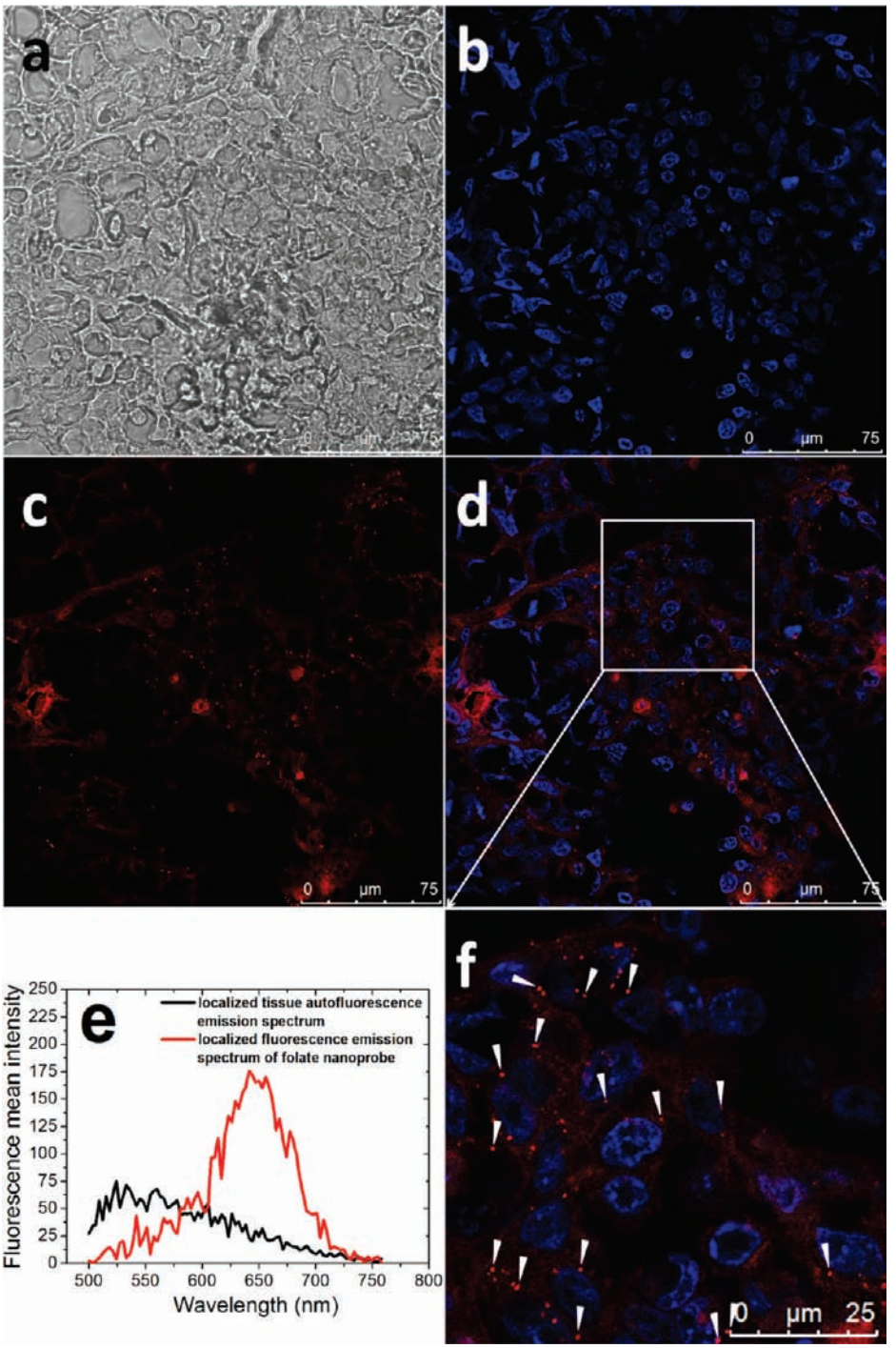

Figure 9. One-photon confocal fluorescence images of the HeLa tumor (~20 μm sections) from the tail vein of mice injected with SNP-DFP-PEGFA (3 nmol/g body weight, 6 h p.i.). (a) Bright field; (b) image of the nuclei of the tumor stained with Hoechst 33285 (0.2 μg/mL); Ex, 405 nm; Em, 520−560 nm; DM, RSP500 nm; (c) image of the tumor with the channel for SNP-DFP-PEGFA; Ex, 476 nm; Em, 620−680 nm; DM, RSP 500 nm; (d) merged image of Hoechst 33285 and SNP-DFP-PEGFA; (e) localized tissue autofluorescence emission spectrum and localized fluorescence emission spectrum of the folate nanoprobe; Ex, 476 nm; Em, 500−760 nm; DM, RSP 500 nm; (f) Higher magnification of panel d where the arrowheads indicate clusters of the nanoprobe taken up by the tumor cells; objective 63×, NA = 1.4; representative fields from multiple sections of two tumors are shown.

2PFM Folate Receptor-Targeted Imaging of HeLa Tumors. The tumors excised from the nanoprobe-administered mice were whole-mounted and imaged, optical layer-by-layer, using a 2PFM imaging system. The fs laser excitation was tuned to 980 nm in order to achieve cellular-level 2PFM images of the tumors. The thick 2PFM images of a tumor are presented in Figure 10. The 2PFM tumor images showed that the FA-conjugated nanoprobes appeared to be primarily distributed in the cytoplasm of cancer cells (a few cells are indicated by arrowheads in Figure 10c) though some may be associated with the cell membrane. Deep tissue 2PFM imaging (ca. 350 μm) was achieved (Figure 10e) with cellular-level visual information of a solid tumor. While the

dx.doi.org/10.1021/bc2002506 |*Bioconjugate Chem.* 2011, 22, 1438–1450

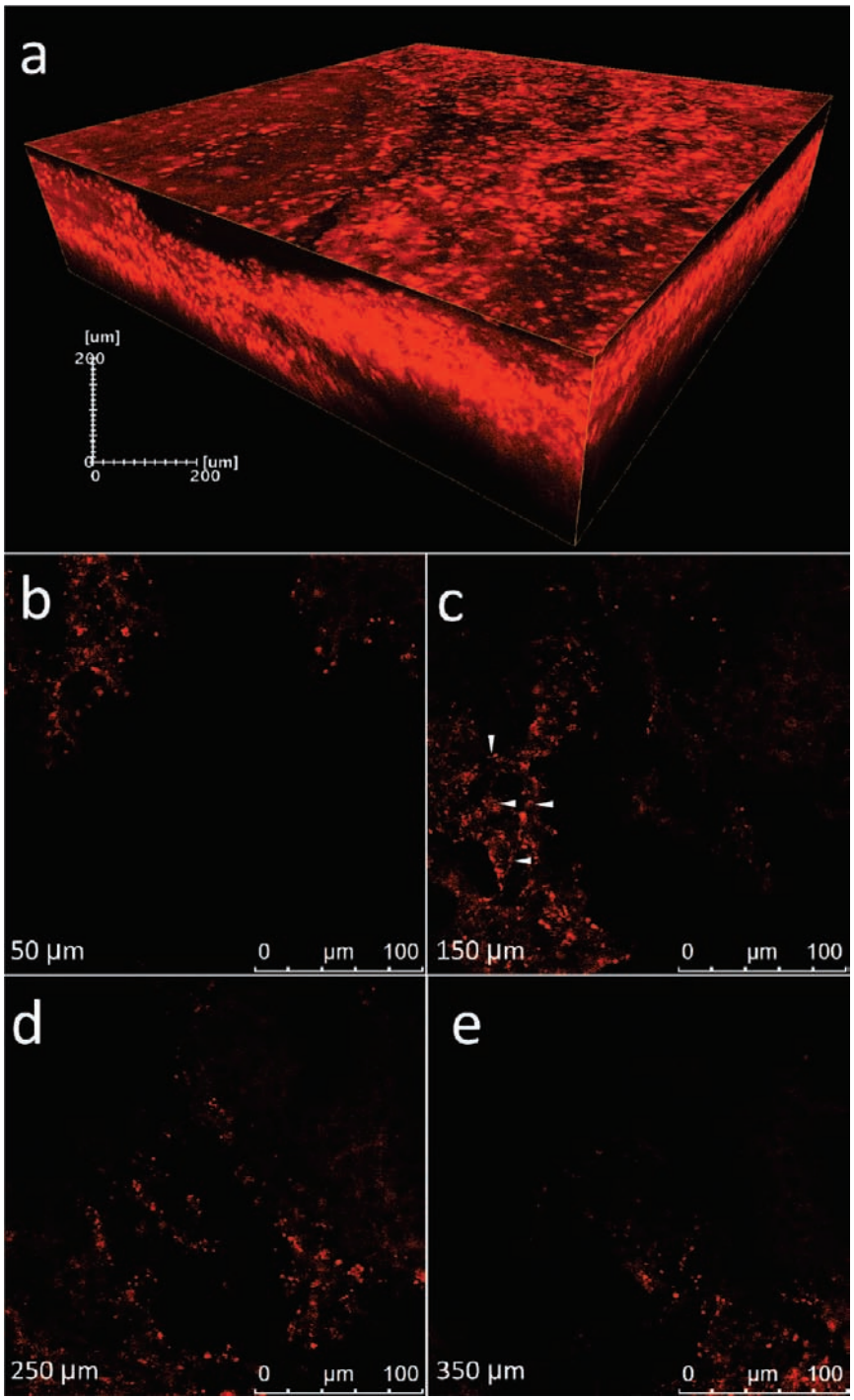

Figure 10. (a) Representative 3D two-photon fluorescence images of the HeLa tumor from a mouse that was injected with SNP-DFP-PEGFA (3 nmol/g) in the tail vein; (b) 50 μm deep image; (c) 150 μm deep image; (d) 250 μm deep image; (e) 350 μm deep image; Ex, 980 nm; power, 300 mW; ~20% on the focal plane; short-pass filter, 840 nm; 20× (NA = 1.0, Leica).

tumor from the mouse that was administered with FA-conjugated SiNPs clearly showed cells with SiNP accumulation (Figure 10a), no significant signal was observed for non-FA-conjugated SiNPs (Figure S10, Supporting Information). The results are consistent with FR-binding of the FA-conjugated SiNPs and accumulation in the tumor cells. Thus, imaging nanoprobes can be effectively and specifically delivered to tumors that overexpress FRs. These results suggest that the FA-mediated active targeting strategy is more effective than passive targeting strategies via enhanced permeability and retention (EPR).

CONCLUSIONS

In this study, we developed an aggregation-enhanced long wavelength emission, 2PA pyran derivative (DFP) that exhibits much stronger fluorescence upon aggregation than in THF

solution. In order to harness the potential of the hydrophobic DFP probe for biological imaging and stabilize its aggregation, DFP-encapsulating SiNPs that target folate receptors were synthesized and characterized. In order to specifically deliver the two-photon fluorescent SiNPs to a tumor, the surface of the nanoparticles was functionalized with PEG and then modified with a folic acid derivative at the outer terminus of the PEG group. Nanoparticle surface functionalization was characterized by measuring changes in the zeta potential and NMR spectra of the SiNPs. The DFP aggregate-encapsulating SiNPs exhibited enhanced fluorescence emission (twice the fluorescence quantum yield relative to that of unaggregated DFP). Importantly, these nanoparticles exhibited a 3-fold increase in two-photon absorption relative to that of the DFP in solution. In addition, the photostability of the fluorescent SiNPs was ca. four times higher than the free DFP dye, resulting in an impressively high figure of merit for the new nanoparticle probe. TEM and DLS provided information regarding nanoparticle size and size distribution, indicating an average particle size of ca. 25 nm.

The cytotoxicity of the new SiNPs was assessed in two cell lines and found to be suitable for *in vitro* cell imaging. The FA-modified DFP-containing SiNPs were selectively taken up by HeLa cells overexpressing folate receptors (FR) as determined by 1PFM and 2PFM imaging experiments. The target specificity of the SiNPs was further demonstrated by three independent control experiments (1) using a FR-negative cell line, (2) testing a non-FA labeled SiNP probe on HeLa cells, and (3) blocking FR-mediated HeLa cell binding of the SiNPs with free FA.

These FR-targeting DFP-encapsulating SiNPs were demonstrated as efficient probes for *in vivo* fluorescence bioimaging upon intravenous administration into mice bearing HeLa tumors. The real-time fluorescence image monitoring for the biodistribution of the SiNPs indicated that the SiNPs selectively accumulated in the tumor, most likely via FA-mediated active targeting. Furthermore, the nanoprobe not only targeted the tumor but also penetrated deep into the tumor parenchyma as demonstrated by cellular-level 2PFM *ex vivo* imaging of whole-tumor mounts. Thus, 2PFM of the tumor provided near cell culture-image quality up to 350 μm deep in the tumor tissue. This comprehensive study of an aggregate-enhanced emission probe sets the stage for its future use in *in vivo* biomarker 2PFM imaging, in which the probe can be deliberately modified with vectors to target various tumor biomarkers.

■ ASSOCIATED CONTENT

Ⓢ Supporting Information. Synthesis of DFP, preparation process, and TEM image of DFP nanoaggregates; cell viability results, photostability, and two-photon absorption cross-section measurement methods; and ^{1}H NMR spectra of the SiNPs and compounds, as well as fluorescence images of organs showing nanoprobe distribution of mice injected with different SiNPs. This material is available free of charge via the Internet at http://pubs.acs.org.

■ AUTHOR INFORMATION

Corresponding Author
*E-mail: Belfield@ucf.edu.

■ ACKNOWLEDGMENT

We wish to acknowledge the National Institutes of Health (1 R15 EB008858-01 to K.D.B. and 1 R01 CA125255 to M.K.), the U.S. Civilian Research and Development Foundation (UKB2-2923-KV-07), the Ministry of Education and Science of Ukraine (grant M/49-2008), the National Science Foundation (CHE-0840431 and CHE-0832622), and Florida Department of Health, Bankhead-Coley Cancer Research Program (10BD-11 to T.U). Dr. Zixi Cheng is acknowledged for the use of a freeze microtome.

■ REFERENCES

(1) Pawley, J. B. (2005) *Handbook of Biological Confocal Microscopy*, 3rd ed., Springer, New York.
(2) Prasad, P. N. (2003) *Introduction to Biophotonics*, John Wiley & Sons, Hoboken, NJ.
(3) Weissleder, R. (2002) Scaling down imaging: molecular mapping of cancer in mice. *Nature Rev. Cancer 2*, 11–18.
(4) Yang, M., Baranov, E., Jiang, P., Sun, F., Li, X., Li, L., Hasegawa, S., Bouvet, M., Tuwaijri, M., Chishima, T., Shimada, H., Moossa, A. R., Penman, S., and Hoffman, R. M. (2002) Whole-body optical imaging of green fluorescent protein-expressing tumors and metastases. *Proc. Natl. Acad. Sci. U.S.A. 97*, 1206–1211.
(5) Wang, X., Nguyen, D. M., Yanez, C. O., Rodriguez, L., Ahn, H., Bondar, M. V., and Belfield, K. D. (2010) High-fidelity hydrophilic probe for two-photon fluorescence lysosomal imaging. *J. Am. Chem. Soc. 132*, 12237–12239.
(6) Zoumi, A., Yeh, A., and Tromberg, B. J. (2002) Imaging cells and extracellular matrix in vivo by using second-harmonic generation and two-photon excited fluorescence. *Proc. Natl. Acad. Sci. U.S.A. 99*, 11014–11019.
(7) Svoboda, K., and Yasuda, R. N. (2006) Principles of two-photon excitation microscopy and its applications to neuroscience. *Neuron 50*, 823–839.
(8) Pavlova, I., Hume, K. R., Yazinski, S. A., Peters, R. M., Weiss, R. S., and Webb, W. W. (2010) Multiphoton microscopy as a diagnostic imaging modality for lung cancer. *Proc. Soc. Photo. Opt. Instrum. Eng. 7569*, 756918.
(9) Kelloff, G. F., Krohn, K. A., Larson, S. M., Weissleder, R., Mankoff, D. A., Hoffman, J. M., and Link, J. M. (2005) The progress and promise of molecular imaging probes in oncologic drug development. *Clin. Cancer Res. 11*, 7967–7985.
(10) Master, B. R., and So, P. T. C. (2008) *Handbook of Biomedical Nonlinear Optical Microscopy*, Oxford University Press: New York.
(11) Helmchen, F., and Denk, W. (2005) Deep tissue two-photon microscopy. *Nat. Methods 2*, 932–940.
(12) Wang, B. G., Känig, K., and Halbhuber, K. J. (2010) Two-photon microscopy of deep intravital tissues and its merits in clinical research. *J. Microsc. 238*, 1–20.
(13) Nguyen, D. M., Wang, X., Ahn, H., Rodriguez, L., Bondar, M. V., and Belfield, K. D. (2010) Novel hydrophilic bis(1,2,3-triazolyl)-fluorenyl probe for in vitro zinc ion sensing. *ACS Appl. Mater. Interfaces 2*, 2978–2981.
(14) He, G. S., Tan, L., Zheng, Q., and Prasad, P. N. (2008) Multiphoton absorbing materials: molecular designs, characterizations, and applications. *Chem. Rev. 108*, 1245–1330.
(15) Durr, N. J., Larson, T., Smith, D. K., Korgel, B. A., Sokolov, K., and Ben-Yakar, A. (2007) Two-photon luminescence imaging of cancer cells using molecularly targeted gold nanorods. *Nano lett. 7*, 941–945.
(16) Larson, D. R., Zipfei, W. R., William, R. W., Clark, S. W., Bruzhez, M. P., Wise, F. W., and Webb, W. W. (2003) Water-soluble quantum dots for multiphoton fluorescence imaging in vivo. *Science 300*, 1434–1436.
(17) Cao, L., Wang, X., Meziani, M. J., Lu, F., Wang, H., Luo, P. G., Lin, Y., Harruff, B. A., Veca, L. M., Murray, D., Xie, S., and Sun, Y. (2007) Carbon dots for multiphoton bioimaging. *J. Am. Chem. Soc. 129*, 11318–11319.
(18) Diaspro, A. (2002) *Confocal and Two-Photon Microscopy, Foundations, Applications, and Advances*, Wiley-Liss, New York.
(19) Morales, A. R., Schafer-Hales, K. J., Marcus, A. I., and Belfield, K. D. (2008) Amine-reactive fluorene probes: synthesis, optical characterization, bioconjugation, and two-photon fluorescence imaging. *Bioconjugate Chem. 19*, 2559–2567.

(20) Morales, A. R., Yanez, C. O., Schafer-Hales, K. J., Marcus, A. I., and Belfield, K. D. (2009) Biomolecule labeling and imaging with a new fluorenyl two-photon fluorescent probe. *Bioconjugate Chem. 20*, 1992–2000.

(21) Morales, A. R., Luchita, G., Yanez, C. O., Bondar, M. V., Przhonska, O. V., and Belfield, K. D. (2010) Linear and nonlinear photophysics and bioimaging of an integrin-targeting water-soluble fluorenyl probe. *Org. Biomol. Chem. 8*, 2600–2608.

(22) Yao, S., Ahn, H., Wang, X., Fu, J., Van Stryland, E. W., Hagan, D. J., and Belfield, K. D. (2010) Donor−acceptor−donor fluorene derivatives for two-photon fluorescence lysosomal imaging. *J. Org. Chem. 75*, 3965–3974.

(23) Andrade, C. D., Yanez, C. O., Rodriguez, L., and Belfield, K. D. (2010) A series of fluorene-based two-photon absorbing molecules: synthesis, linear and nonlinear characterization, and bioimaging. *J. Org. Chem. 75*, 3975–3982.

(24) Rosenholm, J. M., Meinander, A., Peuhu, E., Niemi, R., Eriksson, J. E., Sahlgren, C., and Lindén, M. (2009) Targeting of porous hybrid silica nanoparticles to cancer cells. *ACS Nano 3*, 197–206.

(25) Nakamura, M., Shono, M., and Ishimura, K. (2007) Synthesis, characterization, and biological applications of multifluorescent silica nanoparticles. *Anal. Chem. 79*, 6507–6514.

(26) Kumar, R., Roy, I., Ohulchanskky, T. Y., Vathy, L., Bergey, E. J., Sajjad, M., and Prasad, P. N. (2010) *In vivo* biodistribution and clearance studies using multimodal organically modified silica nanoparticles. *ACS Nano 4*, 699–708.

(27) Wang, X., Yao, S., Ahn, H., Zhang, Y., Bondar, M. V., Torres, J. A., and Belfield, K. D. (2010) Folate receptor targeting silica nanoparticle probe for two-photon fluorescence bioimaging. *Biomed Opt. Express 1*, 453–462.

(28) Kim, S., Zheng, Q., He, G. S., Bharali, D. J., Pudavar, H. E., Baev, A., and Prasad, P. N. (2006) Aggregation-enhanced fluorescence and two-photon absorption in nanoaggregates of a 9,10-bis[4′-(4″-aminostyryl)styryl]anthracene derivative. *Adv. Funct. Mater. 16*, 2317–2323.

(29) Luo, J., Xie, Z., Lam, J. W. Y., Cheng, L., Chen, H., Qiu, C., Kwok, H. S., Zhan, X., Liu, Y., Zhu, D., and Tang, B. Z. (2001) Aggregation-induced emission of 1-methyl-1,2,3,4,5-pentaphenylsilole. *Chem. Commun. 18*, 1740–1741.

(30) An, B., Kwon, S., Jung, S. D., and Park, S. Y. (2002) Enhanced emission and its switching in fluorescent organic nanoparticles. *J. Am. Chem. Soc. 124*, 14410–14415.

(31) An, B., Kwon, S., and Park, S. Y. (2007) Photopatterned arrays of fluorescent organic nanoparticles. *Angew. Chem., Int. Ed. 46*, 1978–1982.

(32) Lim, S., An, B., Jung, S. D., Chung, M., and Park, S. Y. (2004) Photoswitchable Organic Nanoparticles and a polymer film employing multifunctional molecules with enhanced fluorescence emission and bistable photochromism. *Angew. Chem., Int. Ed. 116*, 6506–6510.

(33) Kim, S., Pudavar, H. E., Boniu, A., and Prasad, P. N. (2007) Aggregation-enhanced fluorescence in organically modified silica nanoparticles: a novel approach toward high-signal-output nanoprobes for two-photon fluorescence bioimaging. *Adv. Mater. 19*, 3719–3795.

(34) Tong, H., Hong, Y., Dong, Y., Ren, Y., Häussler, M., Lam, J. W. Y., Wong, K. S., and Tang, B. Z. (2007) Color-tunable, aggregation-induced emission of a butterfly-shaped molecule comprising a pyran skeleton and two cholesteryl wings. *J. Phys. Chem. B 111*, 2000–2007.

(35) Pasult, G., and Veronese, F. M. (2009) PEG conjugates in clinical development or use as anticancer agents: An overview. *Adv. Drug Delivery Rev. 61*, 1177–1188.

(36) Harris, J. M., and Chess, R. B. (2003) Effect of pegylation on pharmaceuticals. *Nature Rev. Drug Discovery 2*, 214–221.

(37) Davis, M. E., Chen, Z., and Shin, D. M. (2008) Nanoparticle therapeutics: an emerging treatment modality for cancer. *Nature Rev. Drug Discovery 7*, 771–782.

(38) Xiong, J., Stehle, T., Zhang, R., Joachimiak, A., Frech, M., Goodman, S. L., and Arnaout, M. A. (2002) Crystal structure of the extracellular segment of integrin $\alpha_v\beta_3$ in complex with an Arg-Gly-Asp ligand. *Science 296*, 151–155.

(39) Brigger, I., Dubernet, C., and Couvreur, P. (2002) Nanoparticles in cancer therapy and diagnosis. *Adv. Drug Delivery Rev. 54*, 631–651.

(40) Low, P. S., and Antony, A. C. (2004) Folate receptor-targeted drugs for cancer and inflammatory diseases. *Adv. Drug Delivery Rev. 56*, 1055–1058.

(41) Sun, C., Veiseh, O., Gunn, J, Fang, C., Hansen, S., Lee, D., Sze, R., Ellenbogen, R. G., Olson, J., and Zhang, M. (2008) In vivo MRI detection of gliomas by chlorotoxin-conjugated superparamagnetic nanoprobes. *Small 4*, 372–379.

(42) Yang, S., Lin, F., Tsai, K., Wei, M., Tsai, H., Wong, J., and Shieh, M. (2010) Folic acid-conjugated chitosan nanoparticles enhanced protoporphyrin IX accumulation in colorectal cancer cells. *Bioconjugate Chem. 21*, 679–689.

(43) Liu, Y., Li, K., Pan, J., and Feng, S. (2010) Folic acid conjugated nanoparticles of mixed lipid monolayer shell and biodegradable polymer core for targeted delivery of Docetaxel. *Biomaterials 31*, 330–338.

(44) Bharali, D. J., Lucey, D. W., Jyakumar, H., Pudavar, H. E., and Prasad, P. N. (2005) Folate-receptor-mediated delivery of InP quantum dots for bioimaging using confocal and two-photon microscopy. *J. Am. Chem. Soc. 127*, 11364–11371.

(45) Low, P. S., Henne, W. A., and Doorneweerd, D. D. (2008) Discovery and development of folic-acid-based receptor targeting for imaging and therapy of cancer and inflammatory diseases. *Acc. Chem. Res. 41*, 120–129.

(46) Yu, G., Yin, S. W., Liu, Y. Q., Chen, J. S., Xu, X. J., Sun, X. B., Ma, D. G., Zhan, X. W., Peng, Q., Shuai, Z. G., Tang, B. Z., Zhu, D. B., Fang, W. H., and Luo, Y. (2005) Structures, electronic states, photoluminescence, and carrier transport properties of 1,1-disubstituted 2,3,4,5-tetraphenylsiloles. *J. Am. Chem. Soc. 127*, 6335–6346.

(47) Kim, S., Ohulchanskyy, T. Y., Pudavar, H. E., Pandey, R. K., and Prasad, P. N. (2007) Organically modified silica nanoparticles co-encapsulating photosensitizing drug and aggregation-enhanced two-photon absorbing fluorescent dye aggregates for two-photon photodynamic therapy. *J. Am. Chem. Soc. 129*, 2669–2675.

(48) Zhao, X., Bagwe, R. P., and Tan, W. (2004) Development of organic-dye-doped silica nanoparticles in a reverse microemulsion. *Adv. Mater. 16*, 173–176.

(49) Bharali, D. J., Klejbor, I., Stachowiak, E. K., Dutta, P., Roy, I., Kaur, N., Bergey, E. J., Prasad, P. N., and Stachowiak, M. K. (2005) Organically modified silica nanoparticles: a nonviral vector for *in vivo* gene delivery and expression in the brain. *Proc. Natl. Acad. Sci. U.S.A. 102*, 11539–11544.

(50) Roy, I., Ohulchanskyy, T. Y., Bharali, D. J., Pudavar, H. E., Mistretta, R. A., Kaur, N., and Prasad, P. N. (2005) Optical tracking of organically modified silica nanoparticles as DNA carriers: A nonviral, nanomedicine approach for gene delivery. *Proc. Natl. Acad. Sci. U.S.A. 102*, 279–284.

(51) Kumar, R., Roy, I., Ohulchanskyy, T. Y., Goswami, L. N., Bonoiu, A. C., Bergey, E. J., Tramposch, K. M., Maitra, A., and Prasad, P. N. (2008) Covalently dye-linked, surface-controlled, and bioconjugated organically modified silica nanoparticles as targeted probes for optical imaging. *ACS Nano 2*, 449–456.

(52) Horn, D., and Rieger, J. (2001) Organic nanoparticles in the aqueous phase—theory, experiment, and use. *Angew. Chem., Int. Ed. 40*, 4330–4361.

(53) Sheik-Bahae, M., Said, A. A., Wei, T. H., Hagan, D. J., and Van Stryland, E. W. (1990) Sensitive measurement of optical nonlinearities using a single beam. *IEEE J. Quantum Electron. 26*, 760–769.

(54) Kim, S., Huang, H., Pudavar, H. E., Cui, Y., and Prasad, P. N. (2007) Intraparticle energy transfer and fluorescence photoconversion in nanoparticles: an optical highlighter nanoprobe for two-photon bioimaging. *Chem. Mater. 19*, 5650–5656.

(55) Gravier, J., Schneider, R., Frochot, C., Bastogne, T., Schmitt, F., Didelon, J., Guillemin, F., and Barberi-Heyob, M. (2008) Improvement of meta-tetra(hydroxyphenyl)chlorin-like photosensitizer selectivity with folate-based targeted delivery. synthesis and in vivo delivery studies. *J. Med. Chem. 51*, 3867–3877.

Supporting Information

for

Folate Receptor-targeted Aggregation-enhanced Near-IR Emitting Silica Nanoprobe for One-photon *in vivo* and Two-photon *ex vivo* Fluorescence Bioimaging

Xuhua Wang,[†] Alma R. Morales,[†] Takeo Urakami,[§] Lifu Zhang,[†£] Mykhailo V. Bondar[⊥], Masanobu Komatsu,[§] and Kevin D. Belfield[†‡]*

[†] Department of Chemistry University of Central Florida, Orlando, FL 32816, USA

[‡] CREOL, The College of Optics and Photonics, University of Central Florida, Orlando, FL 32816, USA

[§] Sanford-Burnham Medical Research Institute at *Lake Nona* Orlando, FL 32827, USA

[£]School of Electrical Engineering, Anhui Polytechnic University, Wuhu, 241000, China

[⊥] Institute of Physics, Prospect Nauki, 46, Kiev-28, 03094 Ukraine

Table of Contents

Table of Contents 2

List of Figures 2

1. Synthesis of 2-(2,6-bis((E)-2-(7-(diphenylamino)-9,9-diethyl-9H-fluoren-2-yl)vinyl)-4H-pyran-4-ylidene)malononitrile (DFP) 4

2. Preparation of DFP organic nanoparticles. 4

3. Preparation of (S)-2-(2-(4-((2-amino-4-hydroxypteridin-6-yl)methylamino)phenyl) acetamido)-5-(2-mercaptoethylamino)-5-oxopentanoic acid (FA-SH) 6

4. Spectroscopic measurements and quantum yield determination. 7

5. Two-photon absorption cross section determination. 7

6. Photostability measurement 8

7. Cytotoxicity Assay. 9

References 23

List of Figures

Figure S1. TEM image of DFP nanoparticles obtained from nanoparticle suspension containing 80% volume fraction of water in THF, Scar bar: 100 nm. 5

Figure S2. a) UV-vis absorption spectral changes of DFP (5×10^{-6} mol·L^{-1}) as a function of the water fraction in THF; b) fluorescence emission spectral changes of DFP (5×10^{-6} mol·L^{-1}) as a function of the water fraction in THF. 5

Figure S3. Photobleaching of SNP-DPF-PEGFA and DFP encapsulated in Tween-80 micelles in PBS at 501 nm with a power of 10 mW. 9

Figure S4. Viability of HeLa and MG63 cells incubated with SNP-DFP-PEGFA. Error bars represent standard error of the mean of 3 replicates. 10

Figure S5. A representative TEM image (a) and DLS size distribution (b) of the FA conjugated nanoparticles in PBS. 10

Figure S6. Standard samples with different concentration of SNP-DFP-NH_2 in PBS (1, 0.5, 0.1, 0.01, and 0.001 μM). Filter sets for the images of standard samples in tubes are: left 500/720 and right 605/720. 11

Figure S7. *Ex vivo* images of the HeLa tumor and organs of the mice injected with (a) SNP-DFP-PEGFA and (b) SNP-DFP-PEGMAL. 11

Figure S8. One-photon confocal images of HeLa tumor tissue sections (~20 μm thick sections) from mice tail vein injected with SNP-DFP-PEGMAL (3 nmol/g body weight, 6 h p.i.); a) bright field, b) image of the nuclei of the tumor stained with Hoechst 33285 (0.2 μg/mL), Ex: 405 nm, Em: 520 – 560 nm, DM: RSP500 nm; c) image of tumor with the channel for SNP-DFP-PEGFA, Ex: 476 nm, Em: 620 - 680 nm, DM: RSP 500 nm; and d) merged image; objective 63×, NA: 1.4. Representive fields from multiple sections of two tumors are shown. 12
Figure S9. One-photon confocal images of HeLa tumor (~ 20 μm sections) from mice tail vein injected with SNP-DFP-PEGFA (3 nmol/g body weight, 6 h p.i.); a) image of the CD31, primary antibody MEC13.3 (1 : 50 dilution in PBS), secondary antibody Alexa Fluor 350 goat anti-mouse IgG antibody (1 μg/mL), Ex: 351nm, Em: 450 – 560 nm; b) image of tumor with the channel for SNP-DFP-PEGFA, Ex: 476 nm, Em: 620 - 680 nm, DM: RSP 500 nm; c) merged image; Objective 10×, NA: 0.4; Representive fields from multiple sections of two tumors are shown. 13
Figure S10. Representative thick 3D-two-photon fluorescence image of the HeLa tumor from a mouse that was injected with SNP-DFP-PEGMAL (3 nmol/g) into the tail vein. Ex: 980 nm; Power: 300 mW, ~20% on the focal plane; short-pass filter 840 nm, 20× (N.A. 1.0, Leica). 14
Figure S11. ^{1}H NMR spectra of FA-SH in DMSO-6d. 15
Figure S12. ^{1}H NMR spectra of SCM-PEG-MAL in D_2O. 16
Figure S13. ^{1}H NMR spectra of Tween-80 in D_2O..... 17
Figure S14. ^{1}H NMR spectra of DFP in $CDCl_3$. 18
Figure S15. ^{1}H NMR spectra of SNP-DFP-NH_2 in D_2O. 19
Figure S16. ^{1}H NMR spectra of SNP-DFP-PEGMAL in D_2O. 20
Figure S17. ^{1}H NMR spectra of SNP-DFP-PEGFA in D_2O. 21
Figure S18. Stacked plot of the ^{1}H NMR spectra of the materials. 22

1. Synthesis of 2-(2,6-bis((E)-2-(7-(diphenylamino)-9,9-diethyl-9H-fluoren-2-yl)vinyl)-4H-pyran-4-ylidene)malononitrile (DFP).

A mixture of 7-(diphenylamino)-9,9-diethyl-9H-fluorene-2-carbaldehyde (0.6 g, 1.43 mmol), and commercial 2,6-dimethyl-4-dicyanomethylene-4H-pyran (0.13 g, 0.71 mmol) were dissolved in EtOH (35 mL). After adding piperidine (0.4 mL) slowly via syringe while stirring, the reaction mixture was refluxed for 72 h. Reddish precipitate was obtained after cooling the reaction to room temperature. DFP was obtained after purifying the product through a silica gel column using hexanes/ethyl acetate (4:1) as eluent. A red solid was obtained (0.35 g, 25% yd); m.p. 229-230 °C. ^{1}H NMR (300 MHz, $CDCl_3$) δ: 7.68 (s, 1H), 7.66 (s, 2H), 7.60-7.52 (m, 8H), 7.30-7.24 (m, 10H), 7.15-7.10 (m, 10H), 7.06-7.01 (m, 5H) 6.84 (s, 1H), 6.79 (s, 1H), 6.72 (s, 2H), 2.01-1.94 (m, 8H), 0.39 (t, J = 14.7 Hz, 12H). ^{13}C NMR (75 MHz, $CDCl_3$) δ: 158.6, 155.8, 152.0, 150.8, 148.2, 147.7, 144.2, 138.6, 135.1, 132.5, 129.2, 127.8, 124.2, 1232.2, 122.9, 121.6, 121.0, 119.5, 118.6, 117.1, 115.4, 106.8, 59.0, 56.1, 32.6, 8.6. HRMS-ESI theoretical m/z $[M+H]^+$ = 971.47, found, 971.46, theoretical; m/z $[2M+H]^+$ = 1941.93, found, 1941.92, theoretical.

2. Preparation of DFP organic nanoparticles.

The DFP organic nanoaggregate dispersion was prepared by injecting a 0.125 mL stock solution of DFP in THF (2×10^{-4} M) into 4.825 mL of a THF/water mixture, with vigorous stirring. In all samples, the final concentration of DFD (5×10^{-6} M) was constant after stock solution injection. The relative fluorescence quantum yield values of those were measured at the same concentration of 5×10^{-6} M.

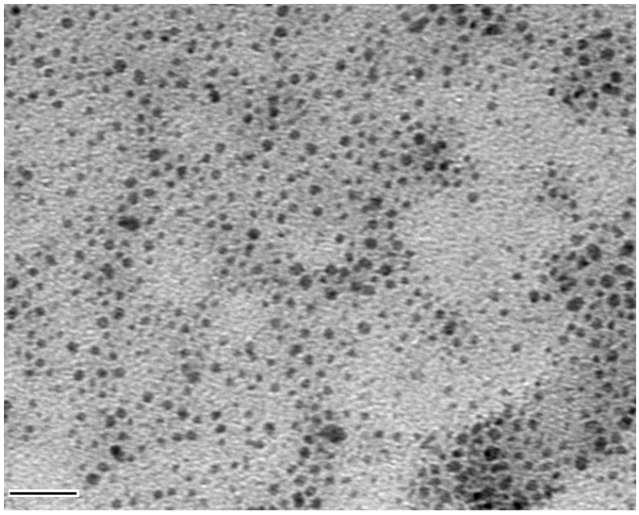

Figure S1. TEM image of DFP nanoparticles obtained from nanoparticle suspension containing 80% volume fraction of water in THF, Scar bar: 100 nm.

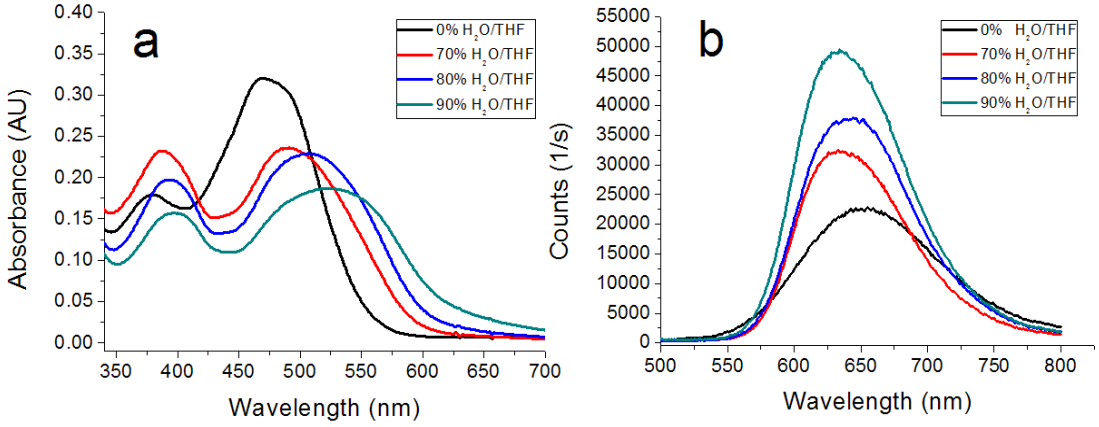

Figure S2. a) UV-vis absorption spectral changes of DFP (5×10^{-6} mol·L^{-1}) as a function of the water fraction in THF; b) fluorescence emission spectral changes of DFP (5×10^{-6} mol·L^{-1}) as a function of the water fraction in THF.

3. Preparation of (S)-2-(2-(4-((2-amino-4-hydroxypteridin-6-yl)methylamino)phenyl) acetamido)-5-(2-mercaptoethylamino)-5-oxopentanoic acid (FA-SH)

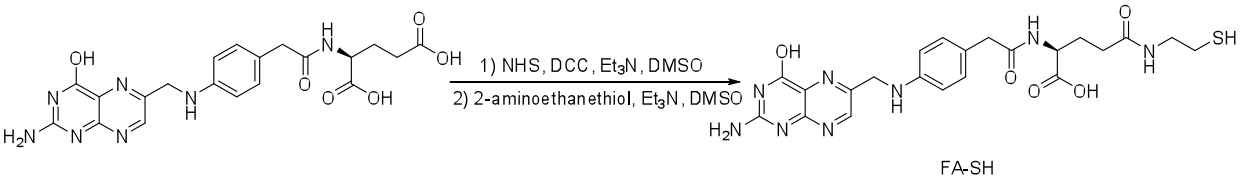

FA-SH

N-Hydroxysuccinimide ester of folic acid (NHS-FA (*γ*)) was prepared in accordance to a reported procedure.[1] Briefly, folic acid (1.0 g, 2.2 mmole) was added into a mixture of anhydrous dimethyl sulfoxide (DMSO, 30 mL) and triethylamine (TEA, 0.5 ml, 3.6 mmol). Folic acid dissolved while stirring the mixture under nitrogen and in the dark overnight. Folic acid was mixed with dicyclohexylcarbodiimide (DCC, 0.5 g, 2.4 mmole) and *N*-hydroxysuccinimide (NHS, 0.52 g, 4.5 mmole), and stirred in the dark for a further 18 h. The side product, dicyclohexylurea (DCU), precipitated and was removed by vacuum filtration. An equimolar amount of 2-aminoethanethiol (0.170 g, 2.2 mmole) and 10 mL TEA was added to the filtrate, and the reaction was conducted under nitrogen overnight. Subsequently, 30 mL CH_2Cl_2 and 30 mL hexanes were added to the reaction mixture to precipitate the crude product that was collected by filtration. The crude product was then dissolved in 30 mL water whose pH was adjusted to 10.0 by ammonium hydroxide. The solution was washed thrice with CH_2Cl_2. After neutralization with HCl, the yellow product was precipitated and collected by filtration; 66% yd; m.p. dec at 187 °C. ^{1}H NMR (d-DMSO, 300 MHz) δ (TMS ppm): 12.27 (b, COOH, 1H), 8.64 (s, pteridine moiety, 1H), 8.05- 8.23 (b, NH-CO, 2H), 7.66 (d, Ar ring, 2H), 7.20 (b, NH_2, 2H), 6.65 (d, Ar ring, 2H), 4.51 (d, CH_2-N, 2H), 4.27 (m, NCH-CO-,1H), 3.31 (t, N-CH_2, 2H), 2.74 (t, CH_2-S, 1H), 2.20 (m, CH_2, 2H), 1.90-2.16 (m, CH_2, 2H, SH, 1H).

4. Spectroscopic measurements and quantum yield determination.

Steady-state absorption spectra were obtained with an Agilent 8453 UV-vis spectrophotometer in 10 mm path length quartz cuvettes. Steady-state fluorescence emission spectra and fluorescence quantum yield measurements were carried out using a PTI QuantaMaster spectrofluorimeter. The fluorescence quantum yields were recorded by using cresyl violet in methanol (Φ_f = 0.54)[2] as standard since its emission was similar to DFP. The optical density of the standard was less than 0.1. The values of fluorescence quantum yields, $\Phi_{f(sample)}$, were calculated according to equation 1:

$$\Phi_{f(sample)} = \Phi_{f(ref)} \frac{OD_{(ref)} I_{(sample)} n_{(sample)}^2}{OD_{(sample)} I_{(ref)} n_{(ref)}^2} \quad (1)$$

where Φ_f is the quantum yield, I is integrated emission signal, OD is optical density at the excitation wavelength, and n is the refractive index; subscript 'ref' stands for standard (reference sample, 'sample' stands for samples (DFP).

5. Two-photon absorption cross section determination.

The 2PA spectra of DFP in THF and $CHCl_3$ and 20 wt% SiNPs (SNP-DFP-PEGMAL) in PBS, were determined over a broad spectral region by a typical z-scan method.[3] We used a femtosecond regenerative Ti:sapphire amplifier (Coherent Legend-HE), which is seeded by a Ti:sapphire femtosecond oscillator (Coherent Mira 900). An optical parametric amplifier (OPA) (Coherent OperA-Solo) pumped by the Coherent Legend-HE provided laser pulses of 100 fs duration with a broadly adjustable wavelength. The tuning range of 700–1200 nm was used in this experiment. The z-scan measurements were performed in 1 mm quartz cuvettes with DFP at

~ 10^{-2} M in THF and SNP-DFP-PEGMAL at ~ 3×10^{-4} M in PBS. In addition, the scattering affect of the nanoparticles was checked by non-dye labeled nanoparticles with the same concentration and no significant signal was observed from the blank particles at this concentration. The uncertainty in the measured cross sections was ca. 15%.

6. Photostability measurement.

The photostability of dye-doped SiNPs and free dye DFP encapsulated in Tween-80 micelles in PBS were determined by the absorption method previously described.[4] A solution of SNP-DFP-PEGFA in PBS or DFP encapsulated in Tween-80 micelles in PBS was irradiated in 1 cm path length quartz cuvettes with a 501 nm Argon laser at 10 mW. The values of photodecomposition quantum yields, Φ_d, were calculated according to equation 2, and the results are the average of ten pairs of adjacent absorbance maxima. The normalized absorbance maxima of two solutions according to the bleaching time are presented in Figure S3,

$$\Phi_d = \frac{(A_1 - A_0)N_A}{10^3 \times \varepsilon \times \mathrm{I} \times (1-10^{(A_1+A_0)/2})(t_1 - t_0)} \qquad (2)$$

where Φ_d is the photobleaching decomposition quantum yield, A_1 is absorbance maxim at t_1, A_0 is absorbance max at t_0, N_A is Avogadro's number, ε is molar absorbance, t_1-t_0 is time exposed (s), and I is the intensity of laser in photon·cm^{-2}·s^{-1}.

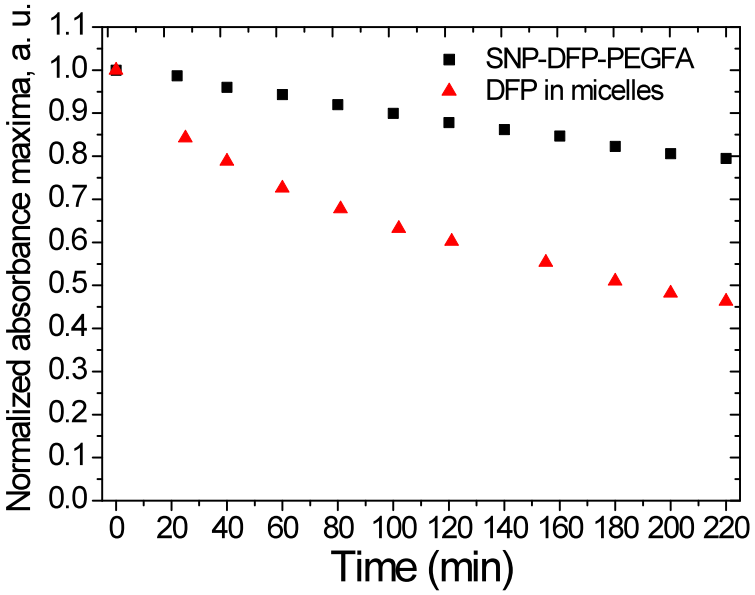

Figure S3. Photobleaching of SNP-DPF-PEGFA and DFP encapsulated in Tween-80 micelles in PBS at 501 nm with a power of 10 mW.

7. Cytotoxicity Assay.

To assess the cytotoxicity of silica nanoprobes, 1×10^3 per well of HeLa or MG63 cells in 96-well plates were incubated in 90 µL of RPMI-1640 medium without phenol red, supplemented with 10% FBS and 100 units/mL penicillin-streptomycin for 24 h. The cells were then incubated with various amounts of SiNPs containing a certain amount of DFP (0.01, 0.1, 0.5, 1, and 5 µM) for an additional 20 h. Subsequently, 20 µL of CellTiter 96® AQueous One Solution reagent was added to each well, followed by further incubation for 4 h at 37 °C. The relative viability of the cells incubated with the silica nanoprobes to untreated cells was determined by measuring the MTS-formazan absorbance on a microplate reader (Spectra Max M5, Molecular Devices, Sunnyvale, CA, USA) at 538 nm with subtraction of the absorbance of the cell-free nanoprobe at

538 nm. The results from three individual experiments were averaged. The cell viability data are presented in Figure S4.

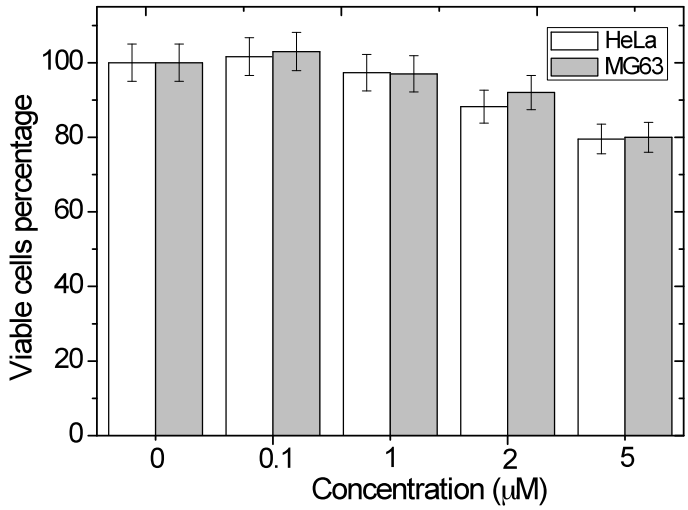

Figure S4. Viability of HeLa and MG63 cells incubated with SNP-DFP-PEGFA. Error bars represent standard error of the mean of 3 replicates.

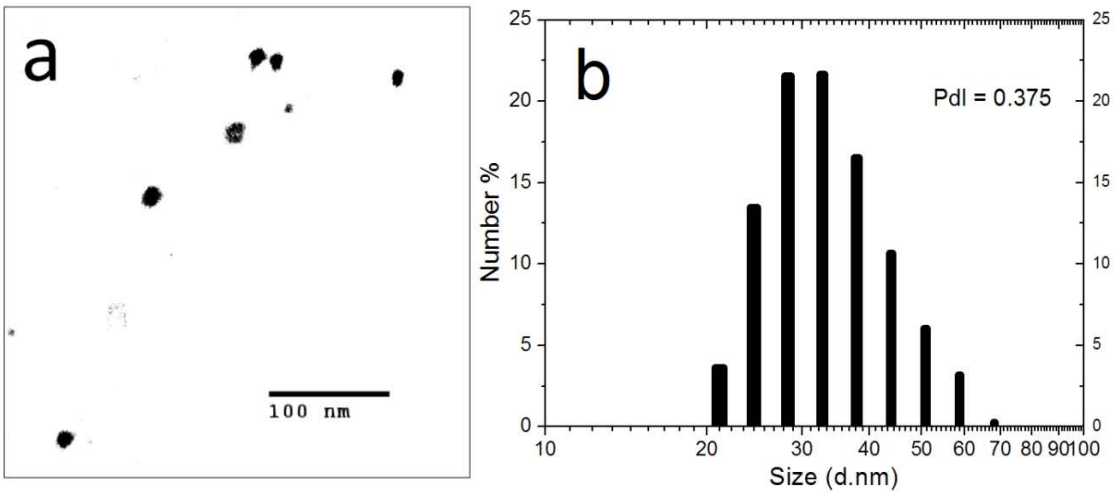

Figure S5. A representative TEM image (a) and DLS size distribution (b) of the FA conjugated nanoparticles in PBS.

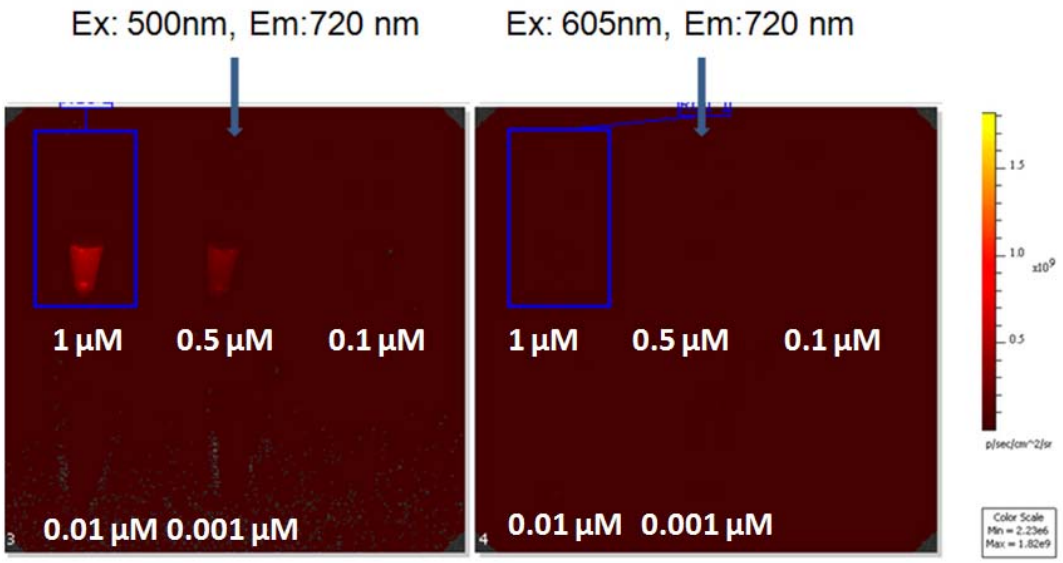

Figure S6. Standard samples with different concentration of SNP-DFP-NH_2 in PBS (1, 0.5, 0.1, 0.01, and 0.001 μM). Filter sets for the images of standard samples in tubes are: left 500/720 and right 605/720.

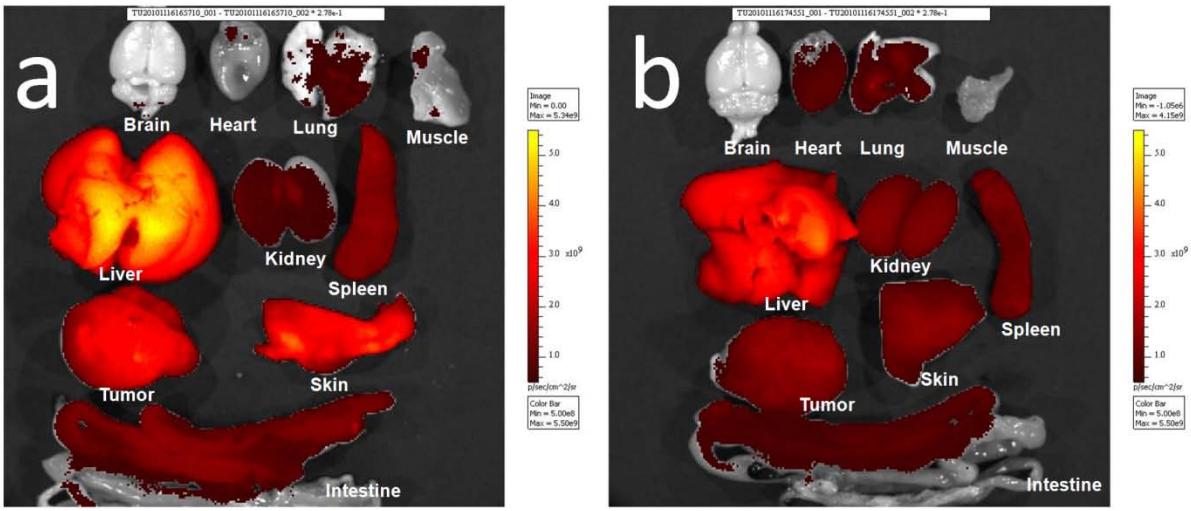

Figure S7. *Ex vivo* images of the HeLa tumor and organs of the mice injected with (a) SNP-DFP-PEGFA and (b) SNP-DFP-PEGMAL.

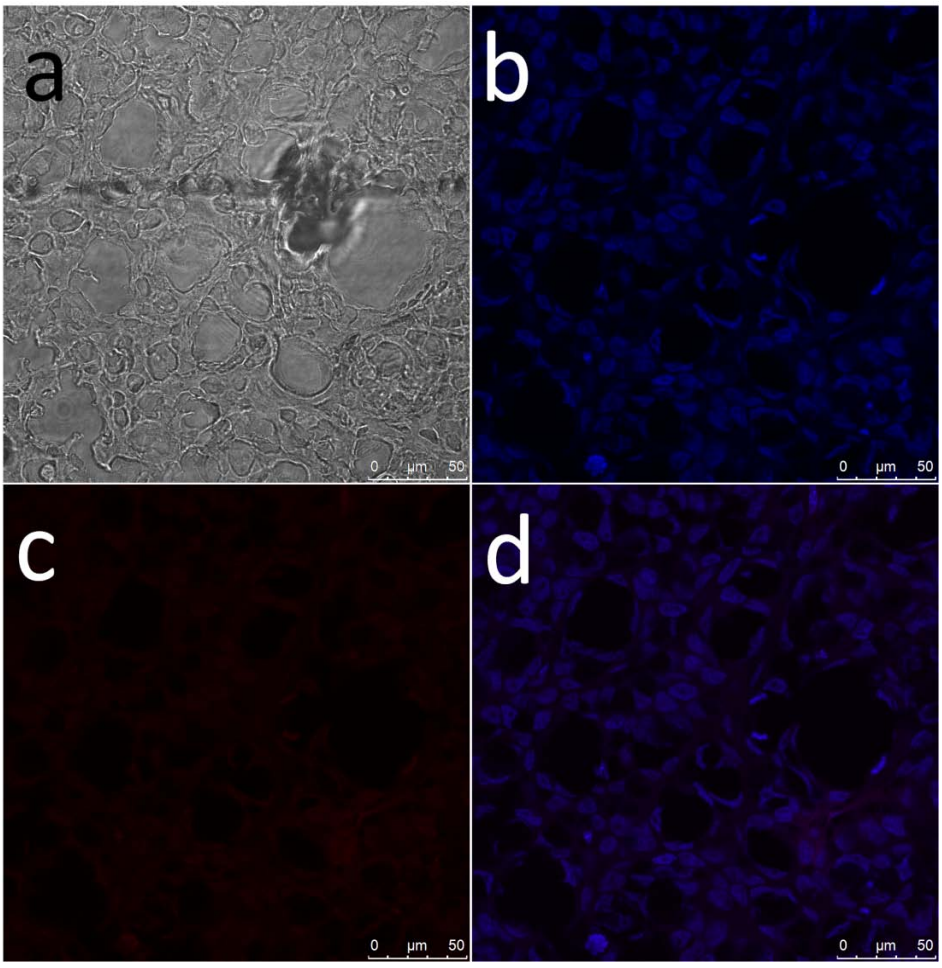

Figure S8. One-photon confocal images of HeLa tumor tissue sections (~20 µm thick sections) from mice tail vein injected with SNP-DFP-PEGMAL (3 nmol/g body weight, 6 h p.i.); a) bright field, b) image of the nuclei of the tumor stained with Hoechst 33285 (0.2 µg/mL), Ex: 405 nm, Em: 520 – 560 nm, DM: RSP500 nm; c) image of tumor with the channel for SNP-DFP-PEGFA, Ex: 476 nm, Em: 620 - 680 nm, DM: RSP 500 nm; and d) merged image; objective 63×, NA: 1.4. Representative fields from multiple sections of two tumors are shown.

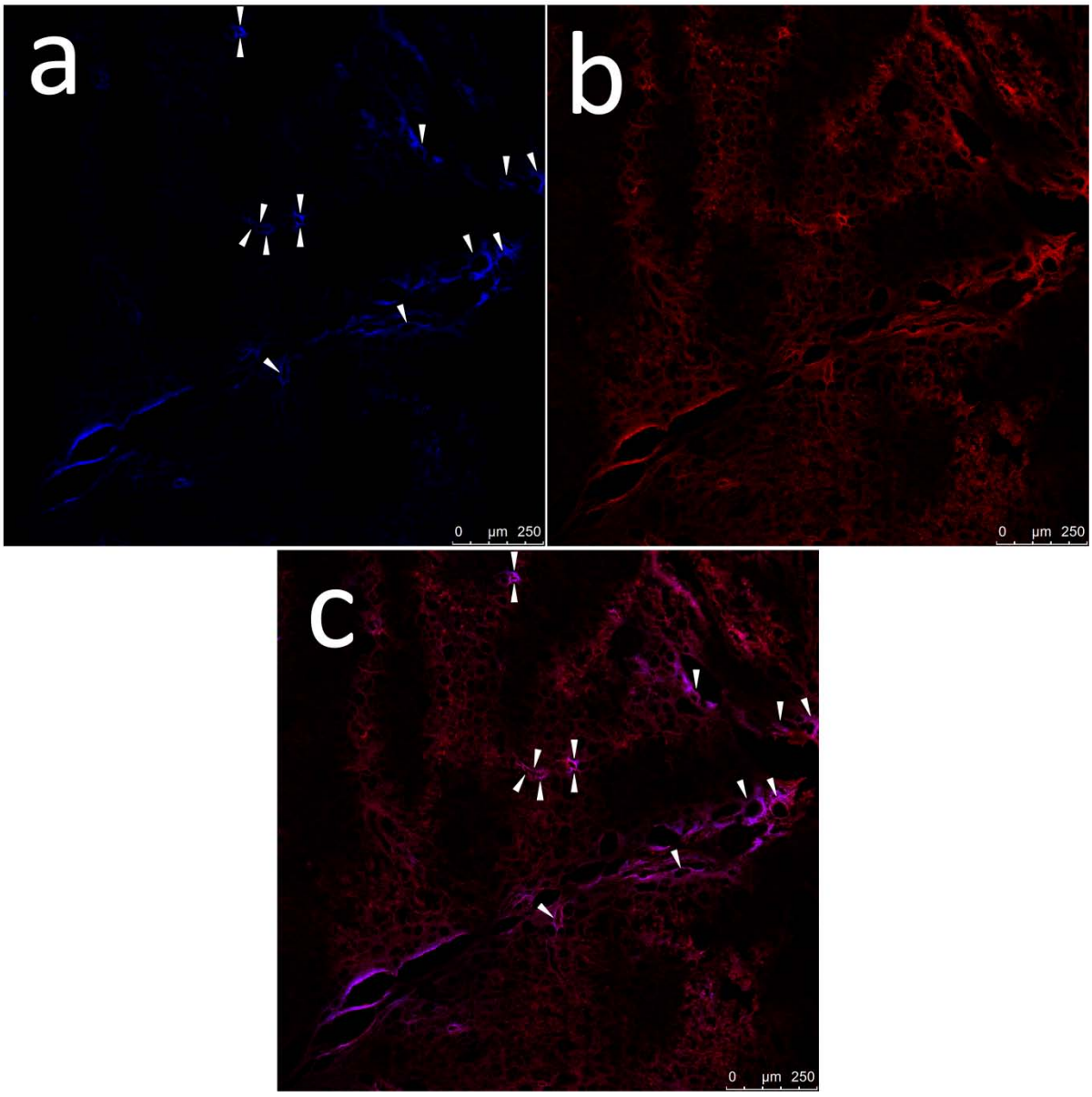

Figure S9. One-photon confocal images of HeLa tumor (~ 20 µm sections) from mice tail vein injected with SNP-DFP-PEGFA (3 nmol/g body weight, 6 h p.i.); a) image of tumor vessels stained for CD31, primary antibody MEC13.3 (1 : 50 dilution in PBS), secondary antibody Alexa Fluor 350 goat anti-mouse IgG antibody (1 µg/mL), Ex: 351nm, Em: 450 – 560 nm; b) image of tumor with the channel for SNP-DFP-PEGFA, Ex: 476 nm, Em: 620 - 680 nm, DM: RSP 500 nm; c) merged image; Objective 10×, NA: 0.4; Representive fields from multiple sections of two tumors are shown.

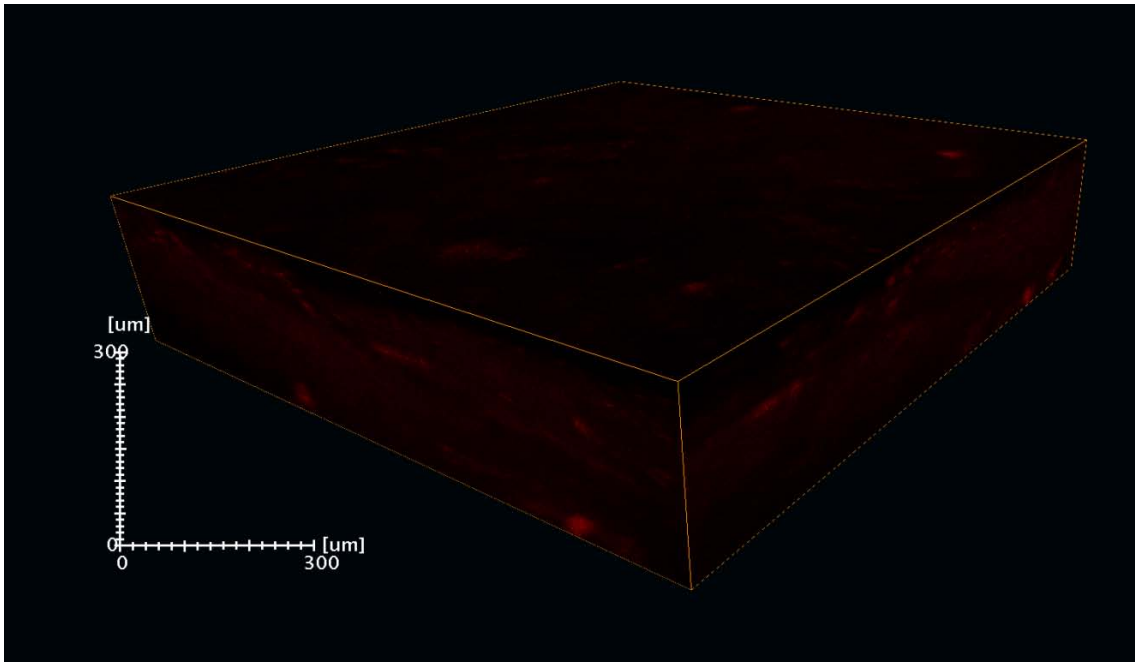

Figure S10. Representative thick 3D-two-photon fluorescence image of the HeLa tumor from a mouse that was injected with SNP-DFP-PEGMAL (3 nmol/g) into the tail vein. Ex: 980 nm; Power: 300 mW, ~20% on the focal plane; short-pass filter 840 nm, 20× (N.A. 1.0, Leica).

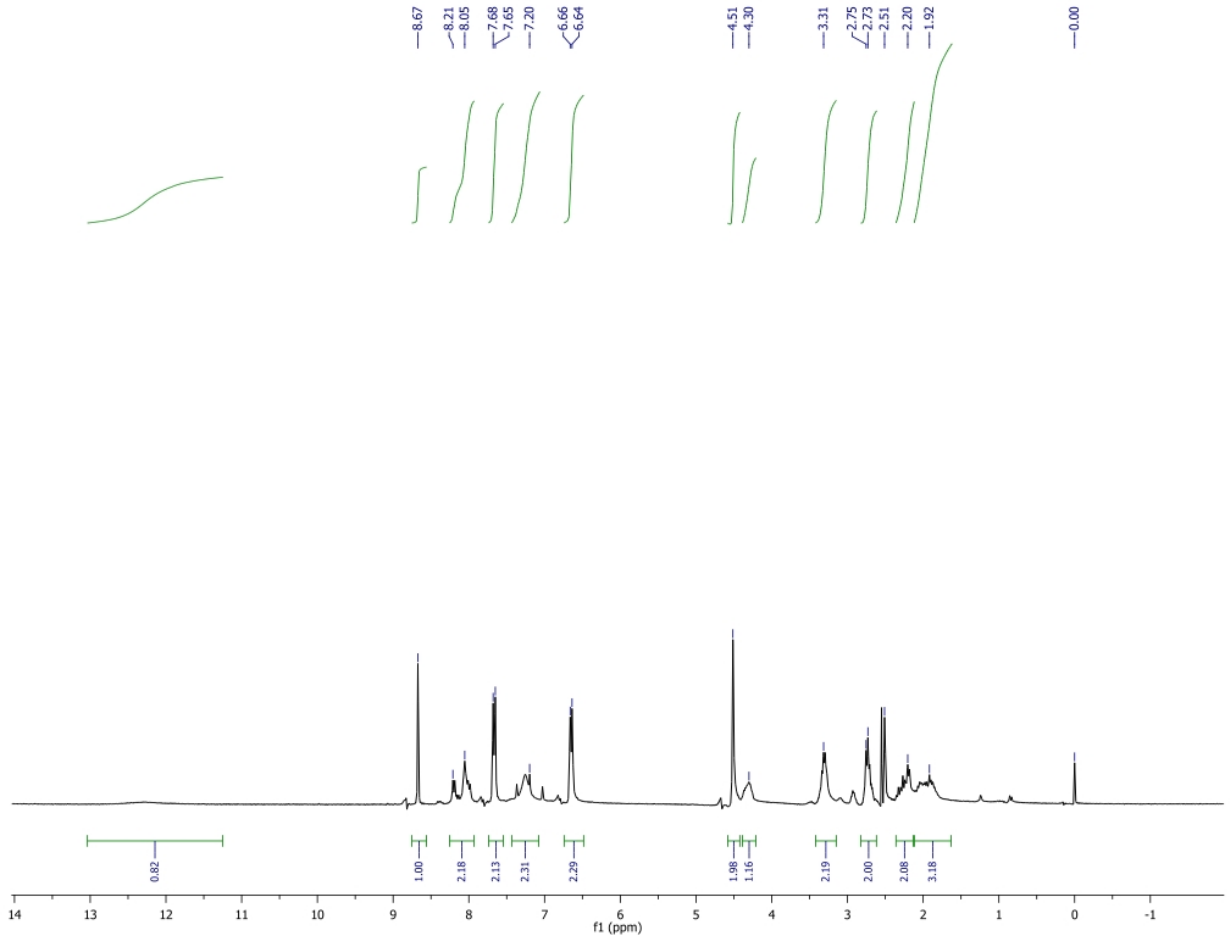

Figure S11. ^{1}H NMR spectra of FA-SH in DMSO-6d.

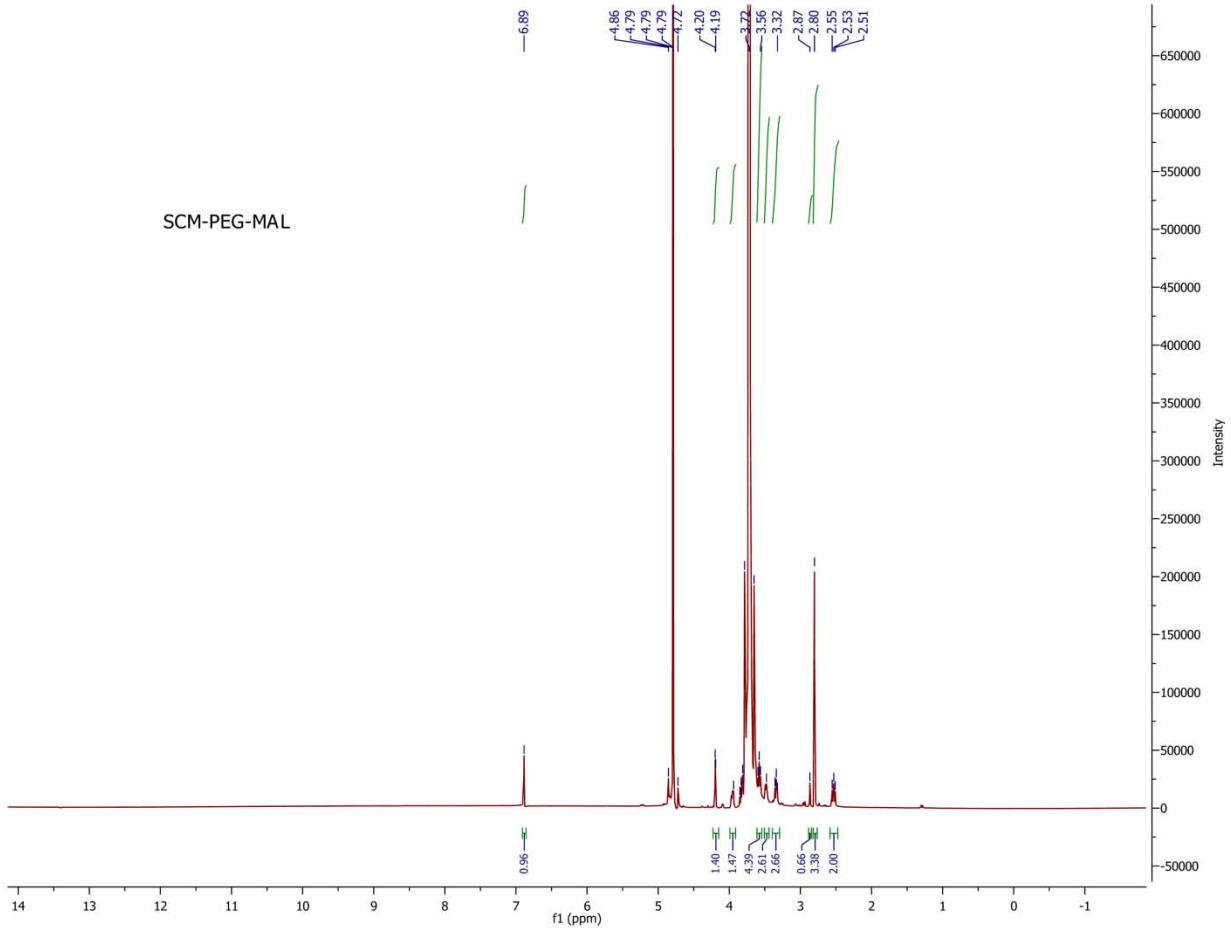

Figure S12. ^{1}H NMR spectra of SCM-PEG-MAL in D_2O.

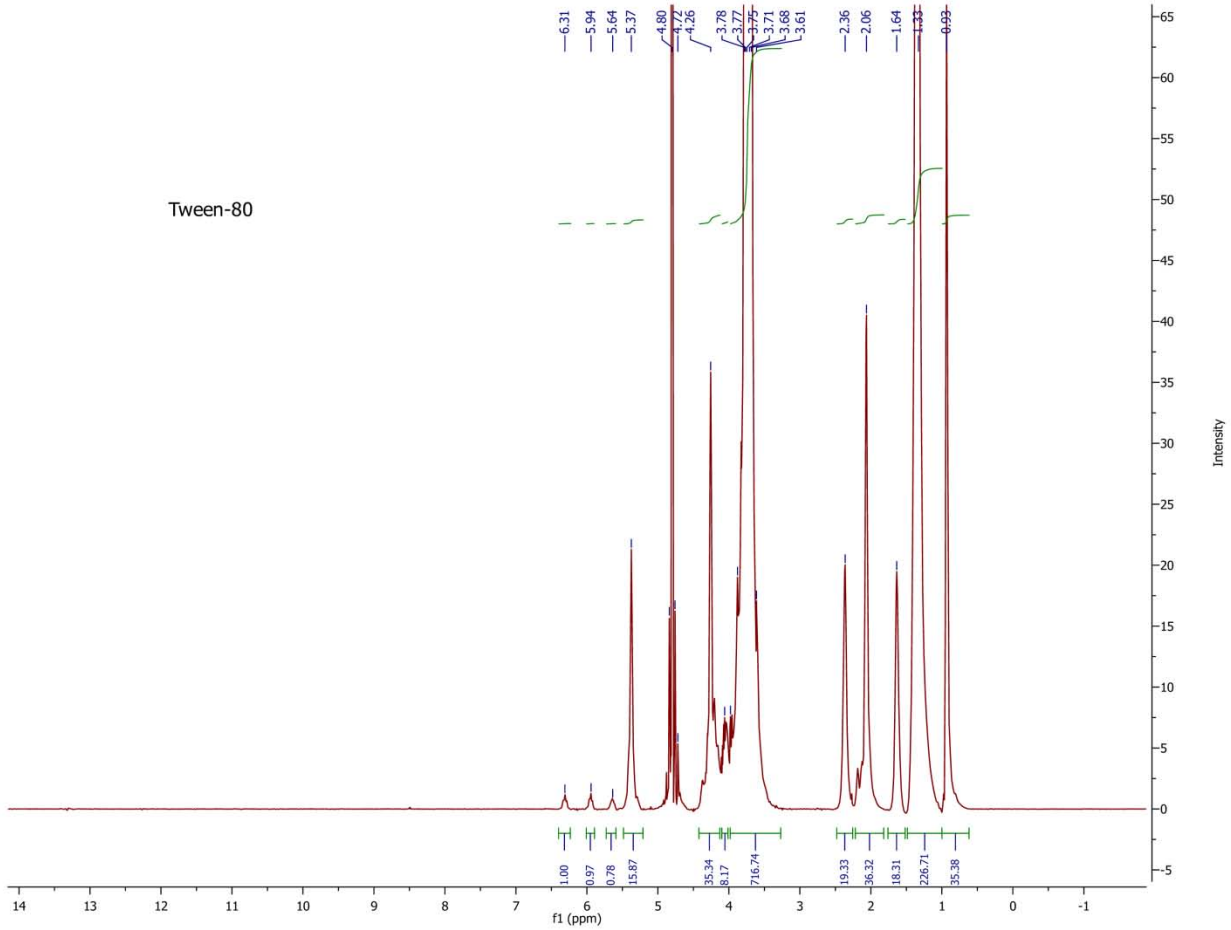

Figure S13. ^{1}H NMR spectra of Tween-80 in D_2O.

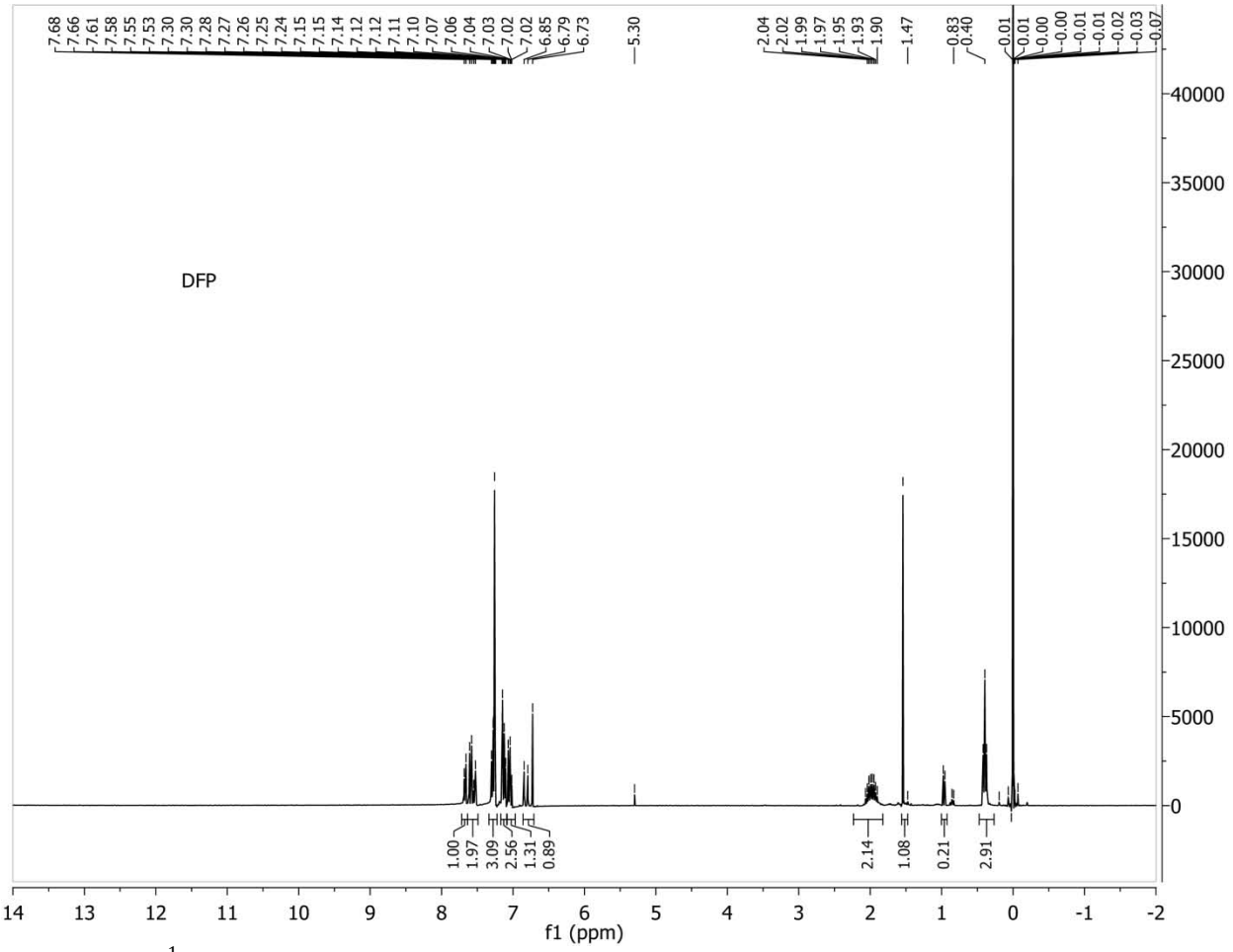

Figure S14. ^{1}H NMR spectra of DFP in $CDCl_3$.

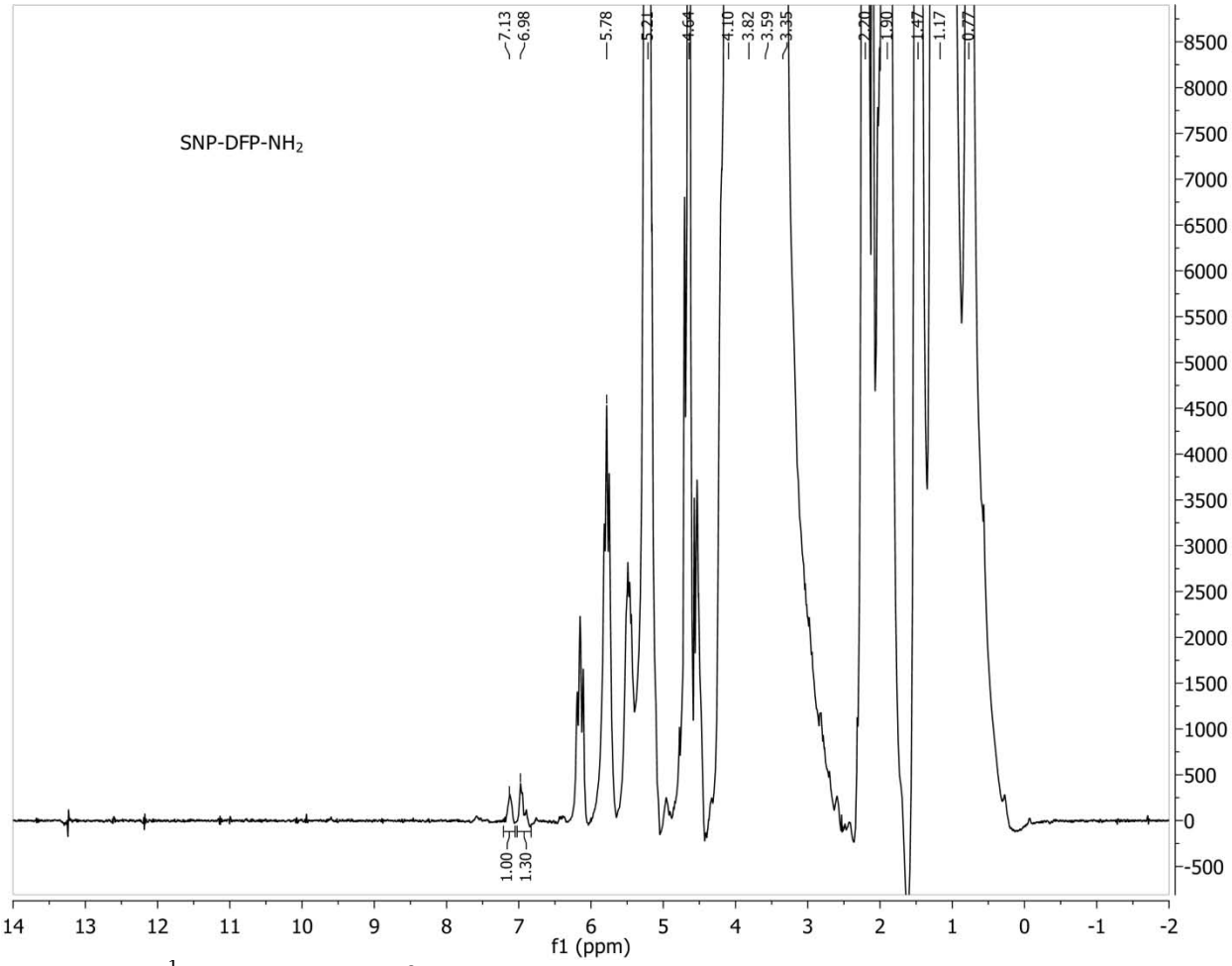

Figure S15. ^{1}H NMR spectra of SNP-DFP-NH_2 in D_2O.

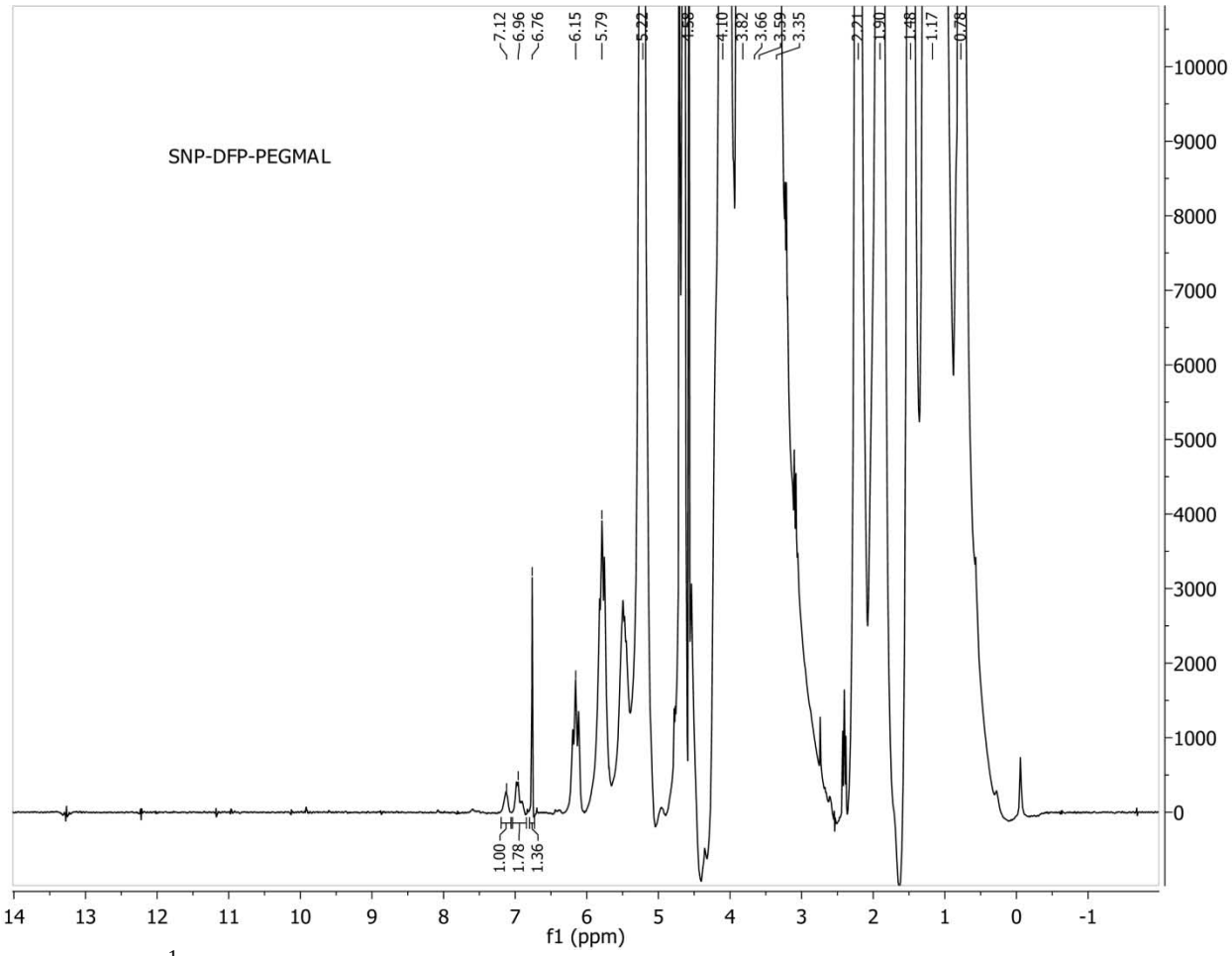

Figure S16. ^{1}H NMR spectra of SNP-DFP-PEGMAL in D_2O.

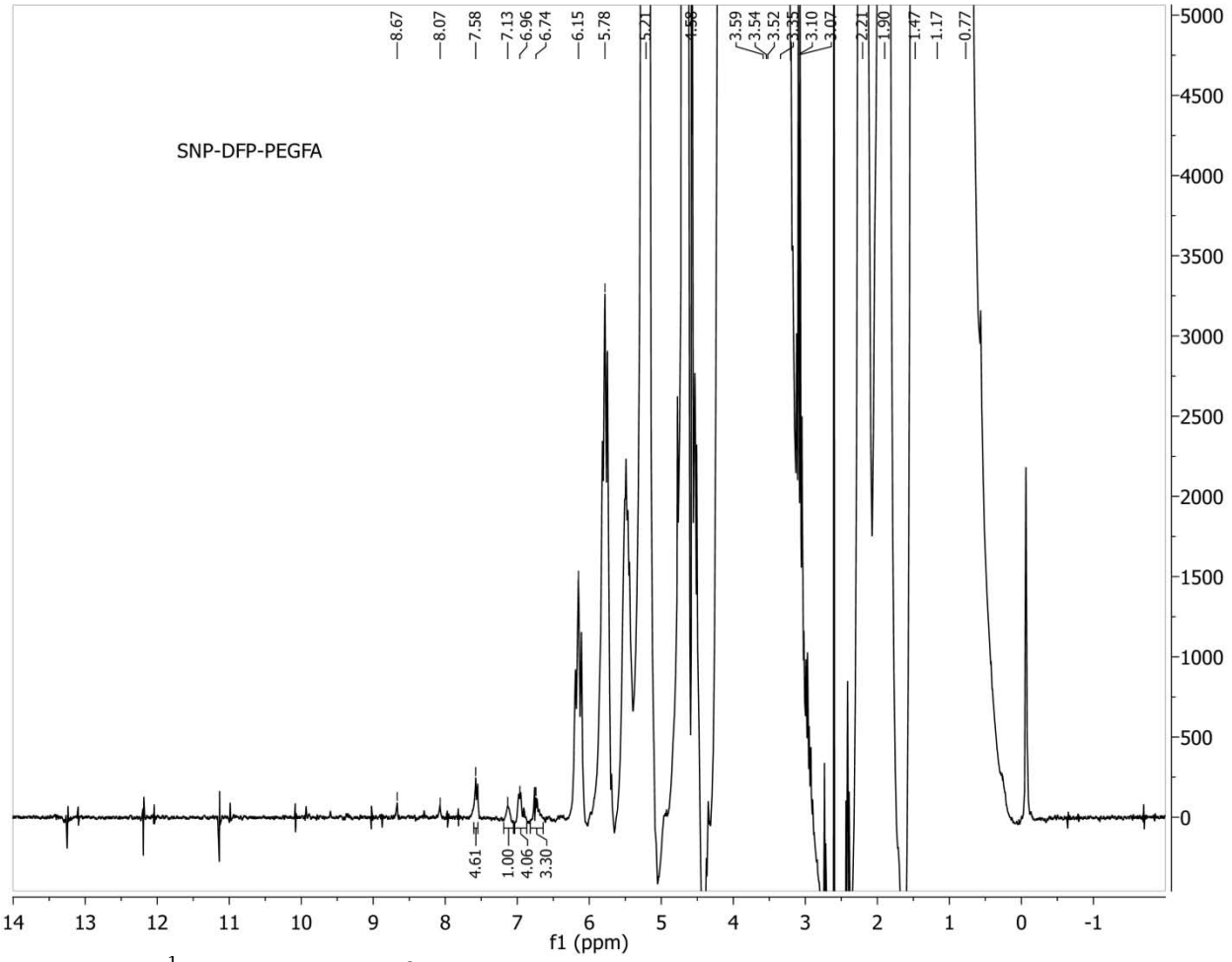

Figure S17. ^{1}H NMR spectra of SNP-DFP-PEGFA in D_2O.

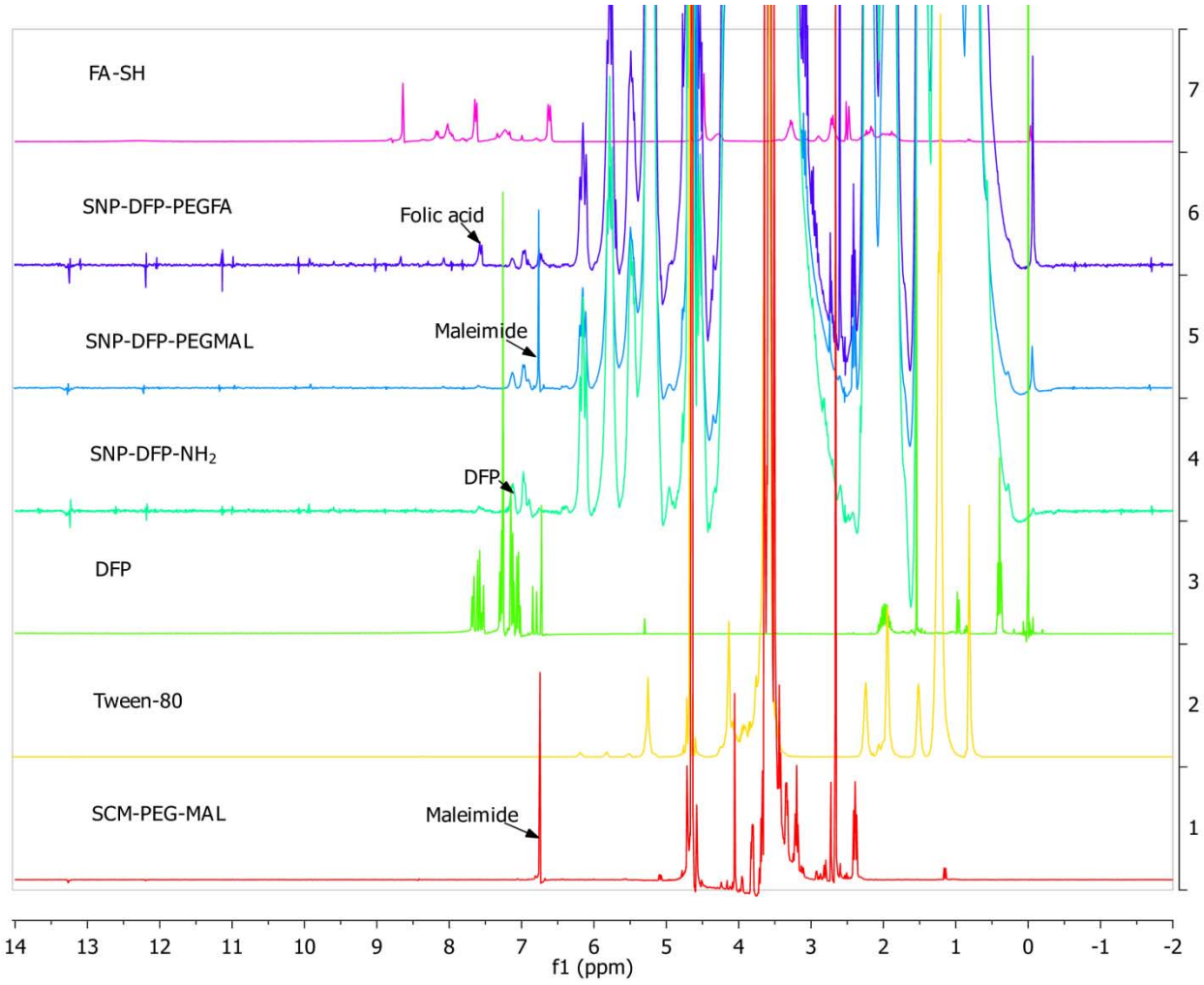

Figure S18. Stacked plot of the ^{1}H NMR spectra of the materials.

References

(1) a) Hu, X., Chen, X., Liu, S. Shi, Q., and Jing, X. (2008) Novel aliphatic poly(ester-carbonate) with pendant allyl ester groups and its folic acid functionalization. *J. Polym. Sci. A: Polym. Chem. 46*, 1852-1861. b) Chan, P., Kurisawa, M., Chung, J. E., and Yang, Y. (2007) Synthesis and characterization of chitosan-*g*-poly(ethylene glycol)-folate as a non-viral carrier for tumor-targeted gene delivery. *Biomaterials 28*, 540-549.

(2) Lakowicz, J. R. Principles of Fluorescence Spectroscopy, Plenum Press: New York, 1999, pp 53.

(3) Sheik-Bahae, M., Said, A. A., Wei, T. H., Hagan, D. J., and Van Stryland, E. W. (1900) Sensitive measurement of optical nonlinearities using a single beam. *IEEE J. Quantum Electron. QE-26*, 760–769.

(4) Corredor, C. C., Belfield, K. D., Bondar, M. V., Przhonska, O. V., and Yao, S. (2006) One- and two-photon photochemical stability of linear and branched fluorene derivatives. *J. Photochem. Photobiol. A: Chem. 184*, 105-112.

Bioconjugate Chemistry

TECHNICAL NOTE

pubs.acs.org/bc

Physicochemical Conjugation with Deoxycholic Acid and Dimethylsulfoxide for Heparin Oral Delivery

Sang Kyoon Kim,[†,‡] June Huh,[†,§] Sang Yoon Kim,[∥] Youngro Byun,[‡] Dong Yun Lee,[*,⊥,#] and Hyun Tae Moon[*,□]

[‡]WCU Department of Molecular Medicine and Biopharmaceutical Sciences, College of Pharmacy, Seoul National University, Seoul 151-742, Republic of Korea

[§]Department of Materials Science and Engineering, Yonsei University, Seoul 120-749, Republic of Korea

[∥]Department of Otolaryngology, Asan Medical Center, College of Medicine, University of Ulsan, Seoul 138-736, Republic of Korea

[⊥]Department of Bioengineering, College of Engineering, and Institute for Bioengineering and Biopharmaceutical Research, Hanyang University, Seoul 133-791, Republic of Korea

[#]Hanyang University Institute of Aging Society, Seoul 133-791, Republic of Korea

[□]Research and Development Center, Mediplex Corp., Seoul 151-742, Republic of Korea

Supporting Information

ABSTRACT: Heparin, as therapeutic medications, cannot be administered orally because of its hydrophilic and high molecular weight. Here, we present a new technology to enhance the absorption of heparin in the intestine through its chemical conjugation with deoxycholic acid (DOCA) that can interact with bile acid transporter in the intestine. For the ampiphilic property and complete dissolution, the modified heparin was physically complexed with dimethylsulfoxide (DMSO). The DOCA-conjugated heparin could form nanoparticles in aqueous solution, whereas it was completely dissolved when treated with above 10% DMSO solution. Molecular dynamics computation study and two-dimensional homonulcear ^{1}H nuclear overhauser effect spectroscopy (NOESY) NMR spectra demonstrated that one heparin molecule was chemically conjugated with two DOCA molecules that were physically interacted with six DMSO molecules within 4 Å via hydrophobic interactions and partly via hydrogen bonding. Its therapeutic efficacy was also pharmaceutically analyzed. When the DMSO-bound DOCA-conjugated heparin was orally administered into mice, its therapeutic efficacy was enhanced according to the amount of bound DMSO. Also, after oral administration of fluorescence-labeled DMSO-bound DOCA-conjugated heparin, it was circulated in the whole body for above 2 h. However, the DOCA-conjugated heparin without DMSO binding was fast eliminated after oral absorption. This study demonstrates that the interaction of structural constraints, DOCA and DMSO, with heparin can serve as a platform technology for potential macromolecule oral delivery.

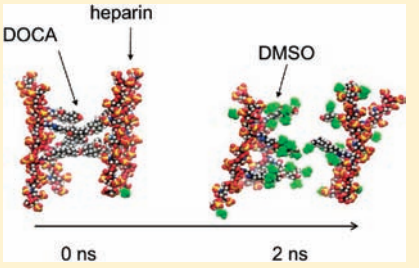

INTRODUCTION

Macromolecules such as proteins, polysaccharides, and DNA are rapidly being developed as specific and potent therapeutic materials. In drug delivery systems, by far the most convenient and preferred route is the oral route. For macromolecule oral delivery, formulation and delivery as much as the development of the medication itself are significant hurdles to clinical applications. Heparin, one of macromolecules, is the most potent anticoagulant for deep vein thrombosis (DVT) and pulmonary embolism (PE) prevention. Venous thromboembolisms, i.e., DVT and PE, are diagnosed in hospitalized patients annually. Currently, 5 days of parenteral heparin injections followed by 3 months of oral warfarin therapy prevents PE in 95% of patients with proximal DVT.[1] However, although heparin and warfarin are effective anticoagulants, oral warfarin therapy varies by individual patients because warfarin has a slow onset due to predominant protein binding and drug−drug interactions.[2] However, heparin does not have teratogenic effects and has rapid onset with a half-life of <4 h.[3] Therefore, chronic heparin administration is a highly attractive alternative therapy for the prevention of venous thromboembolism. Unfortunately, heparin can only be given parenterally due to its high charge density and large molecular weight. Thus, there is a need for an orally absorbable heparin because the long-term use of intravenous heparin is not a practical option.

Recently, we have designed a novel technology for oral delivery of macromolecules, e.g., heparin, insulin, and chemical drugs.[4,5] The main technology for oral absorption of macromolecules is that the amine group of macromolecules is chemically conjugated with the carboxylic group of deoxycholic acid (DOCA), which consequentially causes increased hydrophobicity and interactions with

Received: December 24, 2010
Revised: May 1, 2011
Published: May 31, 2011

ACS Publications © 2011 American Chemical Society

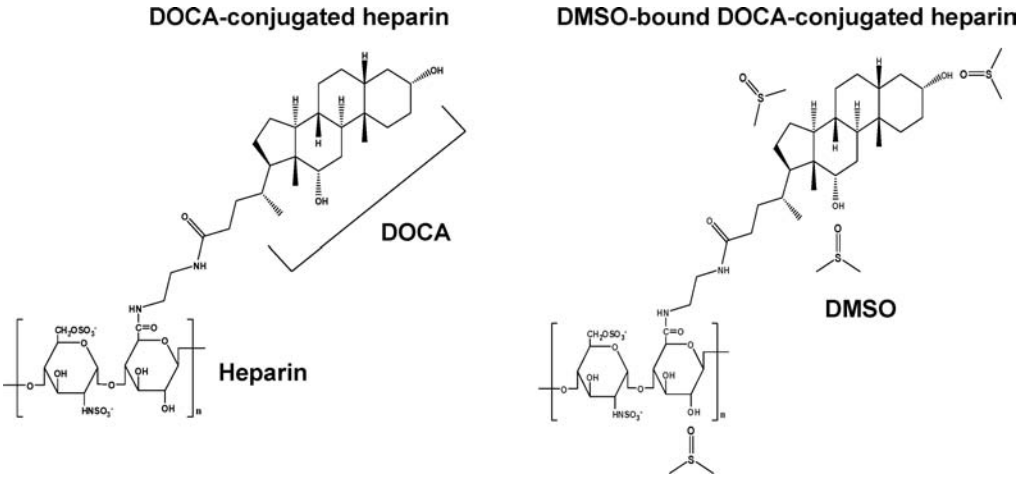

Figure 1. Chemical scheme of designed DMSO-bound DOCA-conjugated heparin without or with DMSO molecules.

bile acid transporters in the small intestine.[6] When orally administered in animals, the modified heparin molecules could cure the experimentally induced thrombotic diseases.[7] However, the oral bioavailability of DOCA-conjugated heparin was affected due to the formation of its self-assembled nanoparticles in the aqueous solution. Therefore, preventing DOCA-conjugated macromolecules from particularizing in water is of utmost importance in achieving high therapeutic efficacy.

In this study, we newly designed an oral absorption system of DOCA-conjugated heparin using physical interaction with dimethylsulfoxide (DMSO). DMSO as an organic solvent is widely used in biology as a cryoprotect agent and muscle relaxant agent, and for perfusion of organs before transplant. The advantage of DMSO over other organic solvents arises from its aprotic physical properties (such as its relatively small dielectric constant (ε^2 = 46.8[2]) and high dipole moment (4.0 D^2)), enabling it to solubilize hydrophobic molecules by secondary interaction.[8] Therefore, to achieve intramolecular mechanical information about the interaction among heparin, DOCA, and DMSO for clinical application, we carried out atomistic molecular dynamics simulation and the 2D-NOESY NMR spectra of DMSO-bound DOCA-conjugated heparin. Then, we evaluated the optimal oral absorption of DOCA-conjugated heparin in mice according to the different concentration of DMSO molecules.

EXPERIMENTAL PROCEDURES

Preparation of DMSO-Bound DOCA-Conjugated Heparin. The chemical conjugate of low-molecular-weight heparin and deoxycholic acid (DOCA) was synthesized by conjugating the carboxylic group of DOCA with carboxylic group of heparin as described in the previous study[4] (Supporting Information Figure S1). Briefly, DOCA (196 mg) was mixed with *N*,*N*′-dicyclohexylcarbodiimide (DCC) (165 mg) and *N*-hydroxy succinimide (HOSu) (92 mg) in 15 mL of dimethylformamide (DMF). The feed mole ratio of DOCA, DCC, and HOSu was 1:1.6:1.6. The concentrations of DCC and HOSu were higher than that of DOCA in order to activate DOCA completely. The mixture was reacted for 5 h at room temperature under vacuum and the precipitated dicyclohexylurea was filtered. The unreacted DCC was precipitated by adding 1 mL of distilled water and filtered. The filtrated solution was poured in 15 mL of distilled water. The remaining HOSu was dissolved in water and the activated DOCA was precipitated and filtered. The activated DOCA was mixed with ethylenediamine in DMF and reacted for 5 h at room temperature, thereby forming deoxycholylethylamine. To eliminate the byproducts, the product was purified by preparative adsorption chromatography on a column packed with silica gel (0.04−0.063). A mixture of chloroform, methanol, and NH4OH (8:2:0.25) was used as eluent. The feed mole ratio of activated DOCA to ethylenediamine was 3:1. The product deoxycholylethylamine was characterized using ^{1}H NMR, FT-IR (SPECTRUM 2000, Perkin-Elmer Co., UK), and LC/MS (Agilent 1100 series, Agilent technologies, Inc., CA).

On the other hand, heparin (100 mg), dissolved in 2 mL of formamide and 1-ethyl-3-(3-dimethylaminopropyl) carbodiimide (EDAC) solution (11.5 mg) was added in order to activate carboxylic groups of heparin. Deoxycholylethylamine was coupled with activated carboxylic groups of heparin. The reaction mixture was incubated at 25 °C for 12 h. The feed mole ratio of deoxycholylethylamine to heparin was 3:1. After the product was precipitated in acetone, followed by lyophilization, DOCA-conjugated heparin was obtained as white powder. The synthesized product was analyzed using proton nuclear magnetic resonance (^{1}H NMR) (Avance 500 FT-NMR, Bruker, MA), and its anticoagulant activity was determined using anti-FXa chromogenic assay (Chromogenix kit, Chromgenic, Milano, Italy), where S-2222 was used as the substrate.

In order to physically bind DMSO molecules to DOCA-conjugated heparin, 20 mg/mL of DOCA-conjugated heparin was dissolved in different concentrations of DMSO solution (0%, 2%, 5%, 10%, and 20%) and freeze−dried at −85 °C for 3 days. Finally, the DMSO-bound DOCA-conjugated heparin was obtained as a white powder (Figure 1). The amount of DMSO bound to DOCA-conjugated heparin was obtained by calculating the weight change of DOCA-conjugated heparin powder before and after it had been freeze−dried. To check the particles using an electrophoretic light scattering spectrophotometer (ELS-8000, Otsuka Electronics, Osaka, Japan), 2 mg/dL of DMSO-bound DOCA-conjugated heparin or DOCA-conjugated heparin itself was dissolved in water solution and the particle sizes were measured.

Evaluation of Correlation between DMSO and DOCA-Conjugated Heparin by Nuclear Magnetic Resonance Spectrometer. The direct interaction between DMSO and DOCA-conjugated heparin was evaluated by using ^{1}H NMR and two-dimensional (2D) homonuclear ^{1}H nuclear Overhauser

effect spectroscopy (NOESY) (Bruker Avance DRX500 MHz NMR; Bruker Biospin GmbH, Rheinstetten, Germany), equipped with a gradient unit. To eliminate the peak shift by DMSO in this experiment, DOCA-conjugated heparin was physically complexed with DMSO-d_6 (Sigma) instead of DMSO. The sample concentration in this experiment was 10 mg/mL in D_2O solution and 2D NOESY was carried out at DW 83.200 μs, AQ 0.17 s, NS 16, and with mixing time of 1000 ms.

All-Atom Molecular Dynamics by Computational Simulations. The DOCA-conjugated heparin with DMSO molecules was simulated in explicit aqueous solution by all-atom molecular dynamics with general AMBER force fields (GAFF).[9] The ANTECHAMBER was used to generate the force-field parameters for DOCA-conjugated heparin and DMSO.[10] The charges of DOCA-conjugated heparin and DMSO were assigned according to the AM1-BCC model.[11] For an initial configuration, four DOCA-conjugated heparin molecules, each of which is composed of two DOCA side chains grafted to a heparin backbone consisting of six iduronic acids and six hexosamines (I_6H_6) with alternating sequence, were generated with cosolvents of ~15 000 explicit TIP3P water molecules and ~500 DMSO molecules inside the simulation box.[12] The initial dimension of simulation box is 95 × 95 × 65 Å^3 and the periodic boundary condition is imposed on each direction. The weight fraction of DMSO molecules in cosolvent is about 13%, consistent with this experiment. The generated initial configuration was first energy-minimized by the conjugate gradient method, and the system was subsequently equilibrated using *NAMD* simulation program for 4 ns in the NPT ensemble at 300 K and 1 atm.[13] For calculating long-range electrostatic forces, the particle mesh Ewald (PME) method was employed.[14] The interaction behavior in the DOCA-conjugated heparin/water/DMSO systems was analyzed based on the run trajectories of a time span (typically 1 ns) after 3 ns equilibration and various properties (e.g., pair correlation function) were calculated by time-averaging over the time span. Supporting Information Figure S2 shows the theoretical equation for computation simulation.

Oral Absorption Profiles of DMSO-bound DOCA-Conjugated Heparin in Mice. To administer DMSO-bound DOCA-conjugated heparin to mice, different kinds of DMSO-bound DOCA-conjugated heparin were dissolved in small quantities of water and vortexed. The final volume administered (dosage administered: 10 mg/kg) was adjusted to 200 μL/mouse. Different kinds of DMSO-bound DOCA-conjugated heparin solutions were administered through an oral gavage into the stomach of ICR (imprinting control regions) mice (Samtako Bio Korea; Osan, Korea), which had been fasted for 4 h. Blood samples (450 μL) were collected from the retro-orbital plexus at 0, 10, 20, 30, 60, and 120 min using a capillary; collected samples were directly mixed with 50 μL of sodium citrate (3.8% solution), centrifuged at 2500 × *g*, and allowed to stand for 5 min at 4 °C. Then, to confirm the oral absorption of the heparin, the anticoagulant activity of orally absorbed heparin in the plasma was measured by anti-FXa chromogenic assay (COATESTHeparin, Milano, Italy).

All animal experimentation was reviewed and approved by our Institutional Animal Care and Use Committee, which is certified by the Institute of Laboratory Animal Resources at Seoul National University.

Optical Imaging to Visualize the Distribution of Orally Administered DMSO-Bound DOCA-Conjugated Heparin Orally. To visualize the distribution of DMSO-bound DOCA-conjugated heparin in the body, florescence-labeled DMSO-bound DOCA-conjugated heparin was chemically synthesized. Briefly, Alexa 488 of 5 mg was dissolved in 1 mL of 10% DMSO solution and it was reacted with DOCA-conjugated heparin by 1:1 mol ratio. After dialysis to remove the unreacted Alexa 488 (molecular cutoff: 2000) in dark condition for 3 days, the Alexa-labeled DMSO-bound DOCA-conjugated heparin was freeze−dried. For oral administration experiment, the Alexa-labeled DMSO-bound DOCA-conjugated heparin was dissolved in water and orally administered in mice (final concentration: 10 mg/kg). After that, fluorescence distribution in the body was measured by using a Kodak Image Station 4000 MM (Digital Imaging Systems, New Haven, CT), equipped with a special C-mount lens and a FITC emission filter.

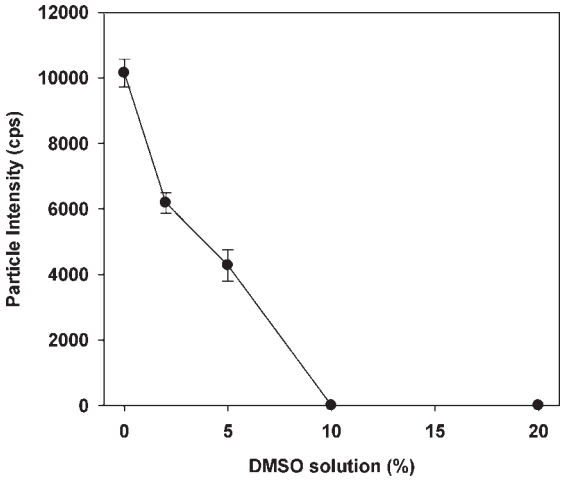

Figure 2. Measurement of solubilization of DMSO-bound DOCA-conjugated heparin after DOCA-conjugated heparin (20 mg/mL) was bound in different concentration of DMSO solution (0%, 2%, 5%, 10%, 20%). The data were plotted as the means ± SD, n = 3.

Statistical Analysis. The cumulative data from animal experiments were expressed as mean ± SD, and a paired t test was used for comparisons between groups. A value of $P \leq 0.05$ was considered as statistically significant.

RESULT AND DISCUSSION

Characteristics of DOCA-Conjugated Heparin. Heparin is known as the most potent anticoagulant and is widely used for the treatment and prevention of deep vein thrombosis and pulmonary embolism.[15−17] Currently, however, heparin is available to patients only by parenteral administration since it is both hydrophilic and highly negatively charged.[18] To enhance delivery of oral heparin, we eyed on the hydrophobic character of deoxycholic acid (DOCA), which is a bile acid and can be generally reabsorbed in the intestine via interaction with bile acid receptors. The chemical conjugation of heparin and DOCA was carried out, as reported in our previous study (Supporting Information Figure S1).[4,19] The peaks at 1720 and 1585 cm^{-1} in the FT-IR spectrum indicated the presence of amide bonds in DOCA-conjugated heparin (data not shown). Also, in the ^{1}H NMR and the ^{13}C NMR spectra, the amide peak was found at 7.58 and 178 ppm, respectively (data not shown). These results indicated the presence of amide bonds between the carboxylic groups of heparin and the amine groups of deoxychorylethylamine (Figure 1). The conjugation ratio of DOCA to heparin was 2.4:1, and the anticoagulant activity of DOCA-conjugated

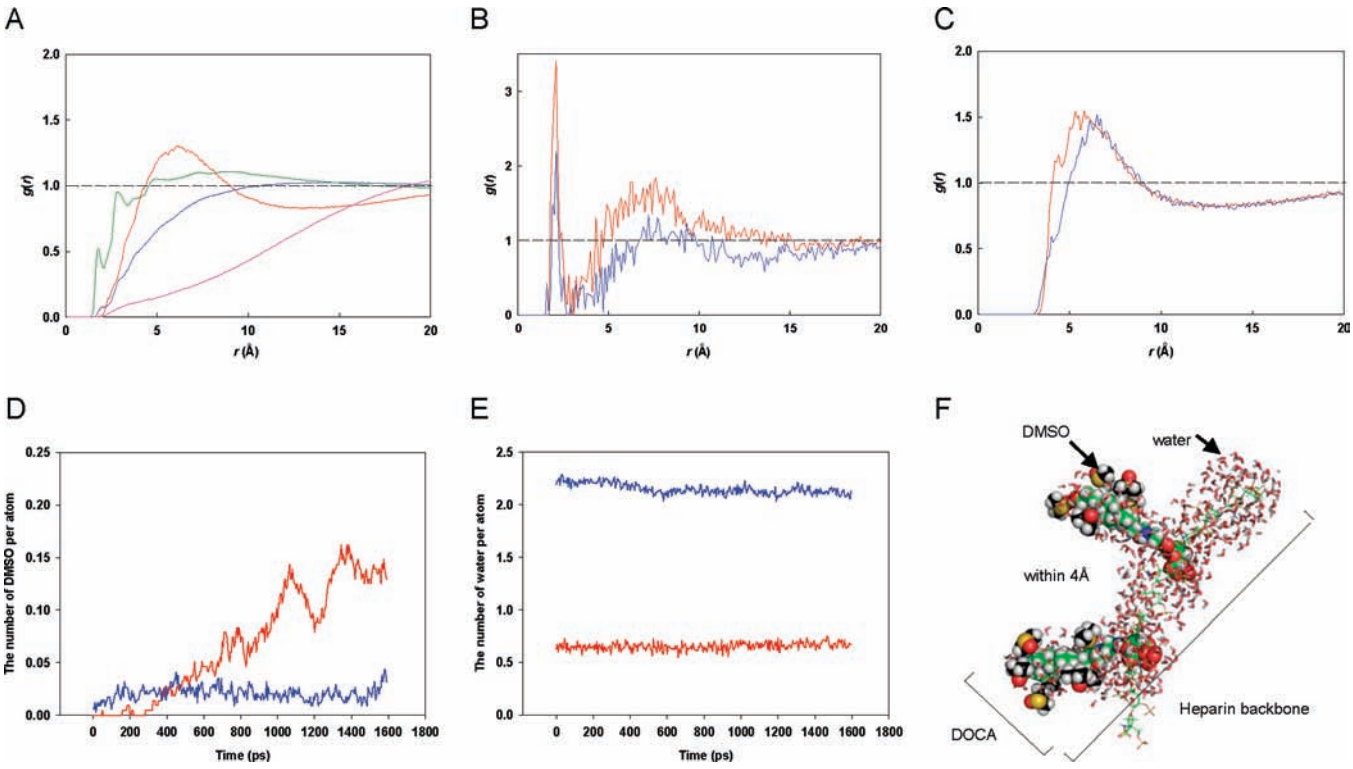

Figure 3. All-atom molecular dynamics by computational simulations. (A) Pair correlation functions $g_{\alpha\beta}(r)$ between DOCA and water molecules (blue), heparin and water molecules (cyan), DOCA and DMSO molecules (red), or heparin and DMSO molecules (purple). The dashed line indicates the bulk value: $g(r_{\infty}\rightarrow) = 1$. (B) Pair correlation functions between oxygen atom of DMSO molecules and hydroxyl group of end position (red) or middle position (blue) of the ring. (C) Pair correlation functions between hydrophobic ring and methyl groups (red) or oxygen (blue) of DMSO molecules. (D) Number of DMSO molecules in each interaction between DMSO and DOCA (red) or DMSO and heparin (blue). (E) Number of water molecules in each interaction between water and DOCA (red) or water and heparin (blue). (F) Simulated structure of DMSO-bound DOCA-conjugated heparin in water. For clear visualization of DMSO binding, only DMSO molecules are represented by CPK model while other components are represented by stick model. Only DMSO and water molecules within 4 Å distance from DOCA-conjugated heparin were displayed to visualize how favorably DMSO and water molecules interacted with DOCA-conjugated heparin.

heparin measured by anti-FXa chromogenic assay was 86 ± 0.4 IU/mg, while that of heparin itself was 97 ± 0.0 IU/mg (data not shown). The bioactivity in both cases was statistically different ($P < 0.05$).

DMSO-Bound DOCA-Conjugated Heparin. The DOCA-conjugated heparin formed self-assembled nanoparticles in water (~350 nm).[7] However, when DOCA-conjugated heparin physically interacted with DMSO molecule in 2%, 5%, 10%, 20% DMSO solution, 3.3, 11.9, 20.5, and 25.4 wt % DMSO molecules were physically bound with DOCA-conjugated heparin, respectively. As the content of the bound DMSO increased, the particle intensities, which reflect the tendency of self-aggregation, were dramatically attenuated (Figure 2). Eventually, when the bound amount of DMSO content was above 20 wt %, the powder form of DMSO-bound DOCA-conjugated heparin was completely dissolved in aqueous solution and did not form any particles.

Molecular Dynamic Simulation Study of DMSO-Bound DOCA-Conjugated Heparin. To develop this DMSO-bound DOCA-conjugated heparin as a therapeutic medicine, we should evaluate the interaction mechanism between them. To this end, the molecular dynamics simulation can provide a detailed atomistic description for the binding of DMSO molecules to DOCA-conjugated heparin. We analyzed how favorably the DOCA-conjugated heparin interacted with DMSO and water molecules by calculating the pair correlation function, $g_{\alpha\beta}(r)$, which is the probability of how far apart α-species are from β-species by distance r, relative to the probability expected for a completely random distribution (Supporting Information Figure S2). First, we analyzed the pair correlations of interaction between DOCA and water, heparin and water, DOCA and DMSO, or heparin and DMSO molecules (Figure 3A). The DOCA−water (blue line) correlation function did not show any peaks as it gradually reached unity (corresponding to a bulk concentration) at r = 11 Å, whereas the heparin−water (cyan line) correlation function reached a bulk value at a shorter distance of r = 4 Å, before which two small peaks also emerged at 2 Å and 3 Å. These results suggested that water molecules could interact more favorably with the heparin backbone than the hydrophobic DOCA. Two small peaks at 2 Å and 3 Å for the heparin−water correlation were attributed to the primary hydrogen bonding of water molecules with hydroxyl groups of disaccharides and the secondary hydrogen bonding of water with the primarily bonded water molecules, respectively. However, rather than hydrogen bonding between water oxygen and hydroxyl group, it is the hydrophilic nature of heparin, which has largely originated from the negatively charged sulfate and carboxylate groups found abundantly in the heparin backbone, that strongly attracts water hydrogens. On the other hand, the value of DOCA−DMSO (red line) correlation function was larger than unity at r = 4−8 Å, where a broad peak emerged, while

dx.doi.org/10.1021/bc100594v |*Bioconjugate Chem.* 2011, 22, 1451–1458

the value for heparin−DMSO (purple line) correlation function was far below unity until it reached the bulk value only at $r = 20$ Å. These results suggest that, unlike the case of water molecules, DMSO can attract DOCA much more than heparin.

We analyzed here how DMSO molecules were bound to DOCA. Since a DMSO molecule consists of two nonpolar methyl groups attached to a polar sulfoxide group, we could consider two major DMSO binding sites: (i) hydrogen bonding interaction between oxygen atom of DMSO and hydroxyl group at the end or in the middle position of DOCA (Supporting Information Figure S3A, site A and B respectively), and (ii) hydrophobic interaction between carbon 4-rings and oxygen atom or methyl groups of DMSO (Supporting Information Figure S3B, site C and D, respectively). Figure 3B represents the pair correlation functions for hydrogen bonding interaction at sites A (red line) and B (blue line). The site A correlation function was sharply peaked at $r = 2$ Å, consistent with the typical H−O hydrogen bonding distance (1.6−2 Å), indicating that the hydrogen bonding at site A was completed. A relatively broad peak also appeared in the range of $r = 4-10$ Å. At site B, a similar correlation curve was observed but the peak was less than at the site A. It should be pointed out that the DOCA−DMSO correlation function (red line) in Figure 3A was a result of averaging all the possible pair atoms of DOCA−DMSO. Since a DOCA molecule is composed of ∼50 atoms, the strong correlation of sites A and B at 2 Å gives almost negligible contributions to the overall DOCA−DMSO correlation, which is the reason the peak at 2 Å is absent in the DOCA−DMSO correlation curve in Figure 3A. Therefore, the main driving force responsible for DOCA−DMSO binding is not hydrogen bonding interaction but something else associated with the broad peak at 4−8 Å. This speculation is also rationalized in the sense that the site A and B can form hydrogen bonding not only with DMSO, but also with water molecules so that the hydrogen bonding alone cannot explain a favorable DOCA−DMSO interaction as compared to the DOCA−water interaction. In this respect, it is interesting to investigate the orientation of DMSO binding to DOCA with respect to the sites at C and D. At $r > 7$ Å, both curves collapsed similarly, since there was no preferred DMSO orientation when the DMSO−DOCA distance was large (Figure 3C). However, in the region of $r < 7$ Å, the two curves start to separate from each other: the peak in site D correlation curves (red line) emerged at $r = 5-6$ Å slightly shorter than at the peak position ($r = 7$ Å) in the site C correlation curve (blue line). Obviously, this result suggests that the methyl groups of DMSO preferably interacted with the nonpolar 4-ring of DOCA via hydrophobic interaction as the sulfoxide groups of DMSO interacted favorably with water molecules. The hydrophobic correlation curves at sites C and D were nearly similar to the DMSO−DOCA interaction in Figure 3A, meaning that the broad peak appearing at $r = 4-8$ Å in the DOCA−DMSO is largely attributed to the hydrophobic interaction between methyl group of DMSO and the hydrophobic 4-ring of DOCA. Therefore, the solubilization mechanism of DMSO-bound DOCA-conjugated heparin was due to the amphiphilicity of DMSO molecule that was bound to DOCA largely via hydrophobic interaction at the site D while the hydrophilic sulfoxide group shielded the DOCA from aggregation.

With increased time, the number of the DMSO molecules bound to DOCA (red line) increased, but the amount to heparin (blue line) was negligible (Figure 3D). On the other hand, the number of water molecules bound to heparin (blue line) was highly saturated, whereas that to DOCA (red line) did not change (Figure 3E). These tendencies of DMSO and water molecules interacting with DOCA-conjugated heparin were visualized in Figure 3F, where DMSO and water molecules positioned within 4 Å from the heparin backbone were displayed. The heparin backbone was surrounded by water molecules, whereas DMSO molecules were bound predominantly to DOCA. In addition, the hydrogens of water molecules tend to face toward the heparin backbone, which supports the aforementioned notion that the heparin−water interaction was driven mainly by sulfate or carboxylate groups rather than hydrogen bonding between water oxygen and hydroxyl group. Figure 4 shows the DMSO effect on the dissociation of the aggregated DOCA-conjugated heparin according to a different time scale. At zero time, two heparin backbones were aggregated via hydrophobic interaction of DOCA molecules. At 2 ns after the presence of DMSO molecules in aqueous solution, 5−6 DMSO molecules were strongly interacting with DOCA molecules, thereby inducing dissociation of the aggregated heparins. Finally, we simulated the mobility of one or two chains of DMSO-bound DOCA-conjugated heparin in solution (Supporting Information Movie S1).

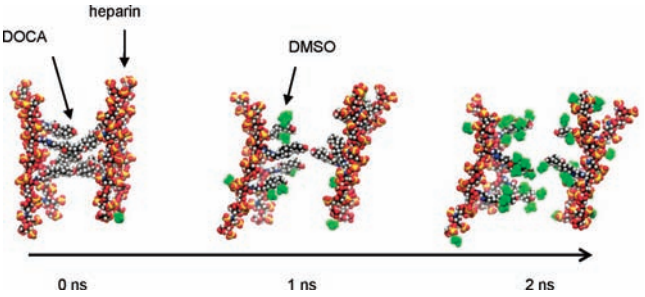

Figure 4. Molecular dynamics simulation of dispersing DOCA-conjugated heparin by DMSO binding. In aqueous solution, the bound DMSO could dissociate the aggregation of two chains of DOCA-conjugated heparin according to the different time scale. The simulation time is indicated in each snapshot.

NMR Spectrometry Study of DMSO-Bound DOCA-Conjugated Heparin. In our previous study, we indirectly showed that the physical binding of DMSO to DOCA-conjugated heparin could produce the shifted or stretched peaks in the FT-IR spectrum and thermal analysis such as differential scanning calorimetry and thermal gravimetry analysis, which was caused by the binding of DMSO to DOCA-conjugated heparin via secondary interactions.[20] For the precise evaluation of DMSO binding to DOCA-conjugated heparin, we used ^{1}H NMR and 2D-NOESY NMR spectrometry. In this experiment, to clearly detect the peak shift of ^{1}H of heparin and DOCA in DMSO-d_6 and D_2O solution, original peaks of heparin and DOCA were observed in the regions 3.0−5.0 ppm and 0.5−2.5 ppm, respectively (Figure 5A and B, purple color). After binding with DMSO-d_6, the peaks of heparin and DOCA were shifted (Figure 5A and B, green color). In the 2D-MOSEY NMR spectrum of heparin and DOCA, heparin had a lot of cross-peaks by inter- or intramolecular interactions, while the cross-peaks of DOCA were simple (Figure 5C and D, purple color). Chemical shifts of backbone and residues of heparin were altered by the binding of DMSO to heparin (Figure 5C, green). We also found that NMR peaks for DOCA were also shifted by DMSO binding (Figure 5D, green). These results indicated that both heparin and DOCA in DOCA-conjugated heparin were affected by the interaction with DMSO molecules.

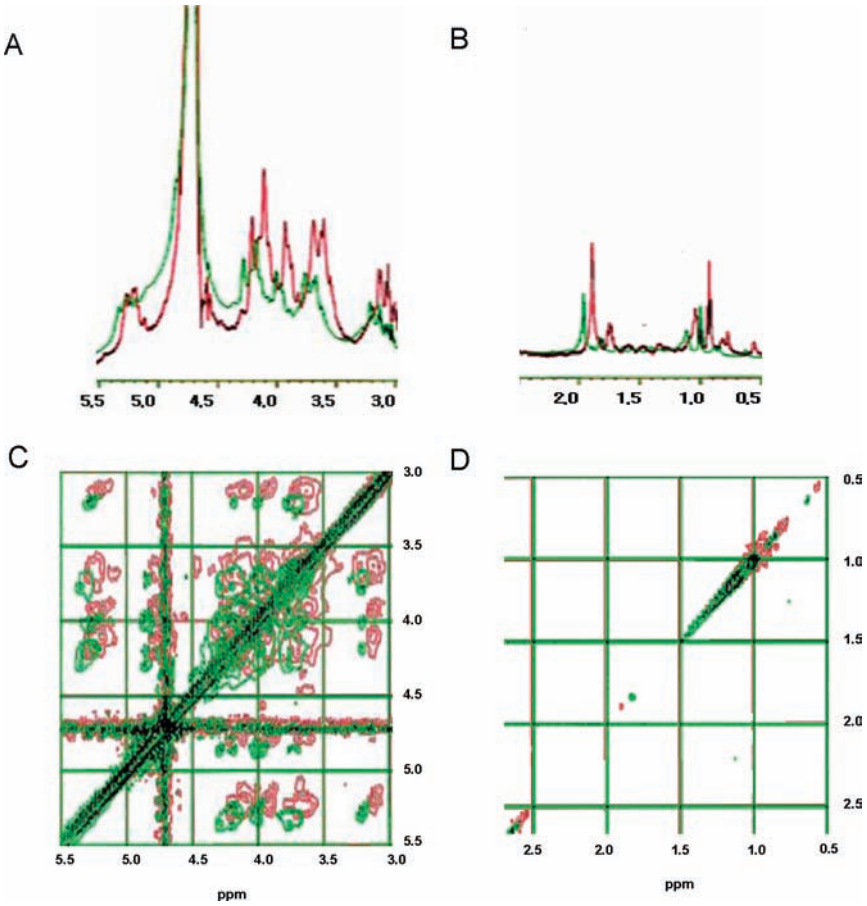

Figure 5. Correction between DMSO and DOCA-conjugated heparin molecules by NMR spectrometry. (A) ^{1}H NMR spectrum of heparin with (green color) or without (purple color) 10% DMSO-d_6 binding. (B) ^{1}H NMR spectrum of DOCA with (green color) or without (purple color) DMSO-d_6 binding. (C) 2D-NOESY spectrum of heparin with (green) or without (purple) 10% DMSO-d_6 binding. (D) 2D-NOESY spectrum of DOCA with (green) or without (purple) 10% DMSO-d_6 binding.

In Vivo Oral Administration of DMSO-Bound DOCA-Conjugated Heparin. After the physical binding of DOCA-conjugated heparin was completed in 2%, 5%, 10%, and 20% DMSO solution, 10 mg/kg DMSO-bound DOCA-conjugated heparin in water solution (200 μL/mouse) was orally administered to mice. Heparin activity in plasma increased according to the increased amount of bound DMSO contents, as indicated by the maximum concentration (C_{max}) values of heparin in plasma as well as the AUC (area under curve). For 0%, 3.3%, 11.9%, 20.5%, and 25.4% bound DMSO contents, the C_{max} values were 0.34 $\pm$ 0.04, 0.33 $\pm$ 0.04, 0.34 $\pm$ 0.03, 0.48 $\pm$ 0.03, and 0.54 $\pm$ 0.10 IU/mL, respectively (Figure 6A). The AUC were 12.5 $\pm$ 0.9, 21.8 $\pm$ 2.3, 21.2 $\pm$ 1.8, 30.9 $\pm$ 1.6, and 31.5 $\pm$ 1.9 IU/mL/min, respectively (Figure 6B). To visualize the distribution of DMSO-bound DOCA-conjugated heparin in the body, optical imaging was carried out after the oral administration of 10 mg/kg of DMSO-bound Alexa-488 and DOCA-conjugated heparin (physical binding in 20% DMSO solution) or Alexa-488 and DOCA-conjugated heparin itself (control group) in mice (Figure 6C). At 10 min after oral administration, strong fluorescence intensity was observed in both cases. However, at 40 and 120 min after oral administration, the fluorescence intensity of DMSO-bound DOCA-conjugated heparin in the whole body was still strongly observed for 2 h. The reason was that the physically bound DMSO could completely solubilize the nanoparticles of DOCA-conjugated heparin, and then, the conjugated DOCA molecules could be highly exposed to increase the binding opportunity onto bile acid transporters in the small intestine.[6] However, the fluorescence intensity of DOCA-conjugated heparin was gradually diminished in the body due to its low opportunity for binding bile acid transporter in the intestine. Therefore, physical binding of DMSO could improve the pharmacokinetics, i.e., bioavailability, of the orally administered heparin.

On the other hand, in this study we did not show the toxicity of the orally administered DMSO-bound DOCA-conjugated heparin. Also, we previously showed no cytotoxicity to the Caco-2 cell monolayer in vitro.[21] The reason was that the amount of bound DMSO was not too much to show cytotoxicity (DMSO content in 10 mg/kg of the modified heparin was about 20 wt %). It is known that the oral NOEL (no observable effects limit) of DMSO in rhesus monkey is 3 g/kg/day during an 18 month study. If extrapolated to humans, the oral monkey NOEL of 3 g/kg/day is comparable to an average human (70 kg) consuming approximately 210 g DMSO per day. In reality, the U.S. Food and Drug Administration (FDA) announced that DMSO was pharmaceutically placed in the safest category (class 3 solvents) with low toxicity potential. Therefore, we can conclude that the amount of bound DMSO in the heparin has no cytotoxicity.

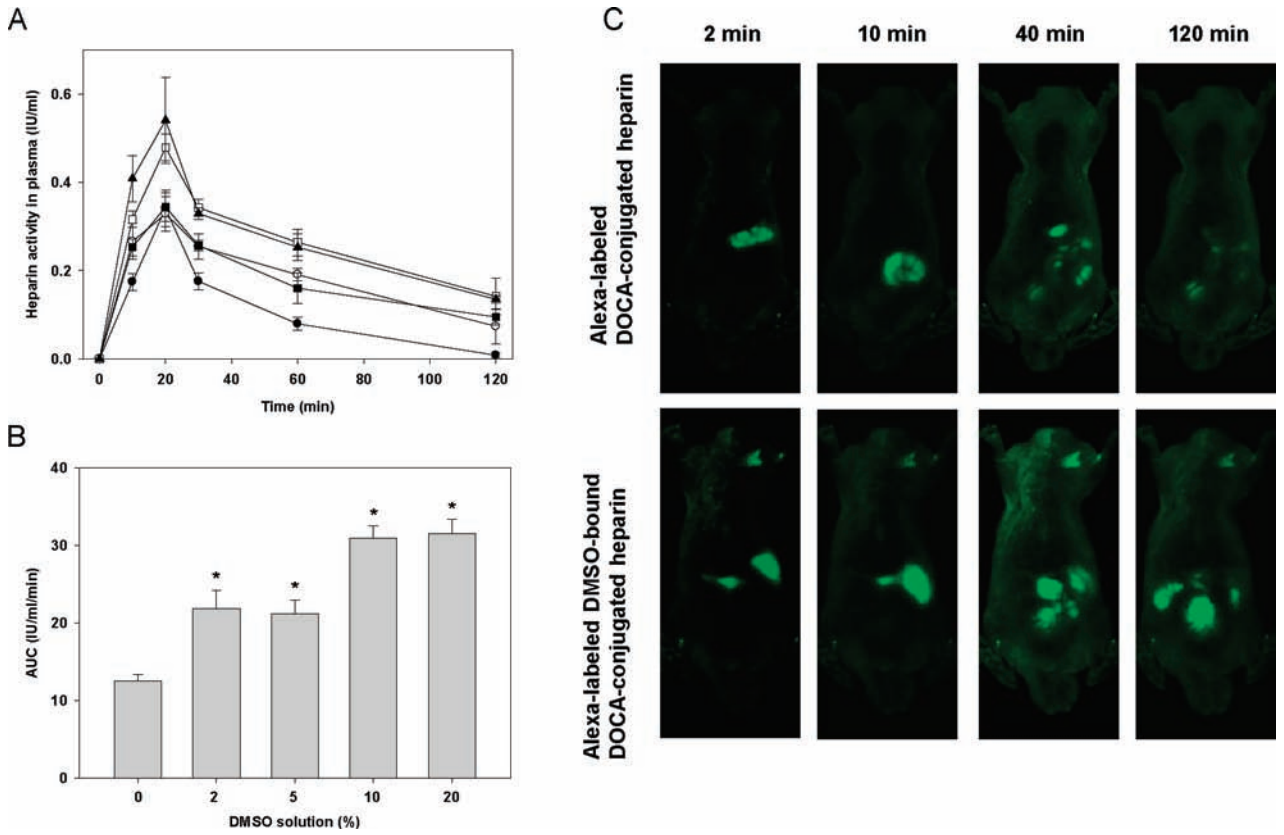

Figure 6. Oral absorption of DMSO-bound DOCA-conjugated heparin in mice. (A) Absorption profiles of DMSO-bound DOCA-conjugated heparin according to different amounts of bound DMSO contents after oral administration into mice: 0% (●; control), 2% (○), 5% (■), 10% (□), and 20% (▲). (B) Area under the curve (AUC; IU/mL/min) after its oral administration. (C) Optical imaging of the distribution of DMSO-bound Alexa-labeled DOCA-conjugated heparin in mice after oral administration according to different times. The data were expressed as the means ± SD ($n = 5$). *$P < 0.05$.

In conclusion, the mechanism study through the simulation revealed that DMSO molecules are rarely bound to the heparin backbone whereas water molecules are very crowded around the heparin backbone that is mainly driven by the electrostatic interaction between negatively charged sulfate (or carboxylate groups) and water hydrogen rather than hydrogen bonding between hydroxyl group and water oxygen. Also, the main driving force responsible for DMSO−DOCA binding is not hydrogen bonding but hydrophobic interaction between the methyl group of DMSO and the 4-ring of DOCA. The sulfoxides of DMSO facing outward with respect to DOCA shield DOCAs to prevent self-assembled particulation. Therefore, the solubilization mechanism of DMSO-bound DOCA-conjugated heparin is due to the amphiphilic action of DMSO molecules that is bound to DOCA largely via hydrophobic interaction, while the hydrophilic sulfoxide group shields the DOCA from their aggregation, which is reminiscent in many ways of colloidal particle stabilization in an amphiphilic system. Therefore, the observed main dissolution effect would be given via "hydrophobic hydration" by DMSO/water mixture. These results open new perspectives for improved oral formulation of macromolecules with DOCA and DMSO as structural constraints in nanoscale. Finally, the structural constraints-based oral formulation can open new opportunities to use DMSO and DOCA in a newly designed platform technology for oral delivery of macromolecules as drug additives.

■ ASSOCIATED CONTENT

Supporting Information. Additional graphics as described in the text. This material is available free of charge via the Internet at http://pubs.acs.org.

■ AUTHOR INFORMATION

Corresponding Author

*Dong Yun Lee, Ph.D., Department of Bioengineering, College of Engineering, Institute for Bioengineering and Biopharmaceutical Research, Hanyang University, and Hanyang University Institute of Aging Society, Seoul 133-791, Republic of Korea; Phone (82-2) 2220-2348; Fax (82-2) 2220-4741; E-mail dongyunlee@hanyang.ac.kr. Hyun Tae Moon, Ph.D., Research and Development Center, Mediplex Corp., #21-315, College of Pharmacy, Seoul National University, San 56-1, Shinlim-dong, Gwanak-gu, Seoul 151-742, Republic of Korea; Phone (82-2) 880-2537; Fax (82-2) 872-7864; E-mail htmoon@mediplex.co.kr.

Author Contributions

†These authors contributed equally to this work as first authors.

■ ACKNOWLEDGMENT

This study was supported by a grant from the Next Generation New Technology Development Program (grant no. 10011353) of the Korean Ministry of Commerce, Industry, and Energy (MOCIE), and supported by the World Class University

(WCU) program (grant no. R31-2008-000-10103), the Converging Research Center Program (2009-0081879) and the Basic Science Research Program (grant no. 2010-0002994) through the National Research Foundation of Korea (NRF) funded by the Ministry of Education, Science and Technology, Republic of Korea.

REFERENCES

(1) Hyers, T. M., Hull, R. D., and Weg, J. G. (1995) Antithrombotic therapy for venous thromboembolic disease. *Chest 108*, 335S–351S.

(2) Hull, R., Delmore, T., Carter, C., Hirsh, J., Genton, E., Gent, M., Turpie, G., and McLaughlin, D. (1982) Adjusted subcutaneous heparin versus warfarin sodium in the long-term treatment of venous thrombosis. *N. Engl. J. Med. 306*, 189–94.

(3) Hardman, J. G., Limbird, L. E., Molinoff, P. B., Ruddon, R. W., and Gilman, A. G. (1996) *The pharmacological basis of therapeutics*, Vol. 9, McGraw-Hill, New York.

(4) Lee, Y., Nam, J. H., Shin, H. C., and Byun, Y. (2001) Conjugation of low-molecular-weight heparin and deoxycholic acid for the development of a new oral anticoagulant agent. *Circulation 104*, 3116–20.

(5) Lee, S., Kim, K., Kumar, T. S., Lee, J., Kim, S. K., Lee, D. Y., Lee, Y. K., and Byun, Y. (2005) Synthesis and biological properties of insulin-deoxycholic acid chemical conjugates. *Bioconjugate Chem. 16*, 615–20.

(6) Kim, S. K., Kim, K., Lee, S., Park, K., Park, J. H., Kwon, I. C., Choi, K., Kim, C. Y., and Byun, Y. (2005) Evaluation of absorption of heparin-DOCA conjugates on the intestinal wall using a surface plasmon resonance. *J. Pharm. Biomed. Anal. 39*, 861–70.

(7) Kim, S. K., Vaishali, B., Lee, E., Lee, S., Lee, Y. K., Kumar, T. S., Moon, H. T., and Byun, Y. (2006) Oral delivery of chemical conjugates of heparin and deoxycholic acid in aqueous formulation. *Thromb. Res. 117*, 419–27.

(8) Haynes, W. M. (1999) (Haynes, W. M., Ed.) CRC Press/Taylor and Francis, Boca Raton, FL.

(9) Wang, J., Wolf, R. M., Caldwell, J. W., Kollman, P. A., and Case, D. A. (2004) Development and testing of a general amber force field. *J. Comput. Chem. 25*, 1157–74.

(10) Ponder, J. W., and Case, D. A. (2003) Force fields for protein simulations. *Adv. Protein Chem. 66*, 27–85.

(11) Jakalian, A., Bush, B. L., Jack, B. D., and Bayly, C. I. (2000) Fast, efficient generation of high-quality atomic charges. AM1-BCC model: I. *J. Comput. Chem. 21*, 132–46.

(12) Jorgensen, W. L., Chandrasekhar, J., Madura, J. D., Impey, R. W., and Klein, M. L. (1983) Comparison of simple potential functions for simulating liquid water. *J. Chem. Phys. 79*, 926–935.

(13) Kale, L., Skell, R., Bhandarkar, M., Brunner, R., Gursoy, A., Krawetz, N., Phillips, J., Shinozaki, A., Varadarajan, K., and Schulten, K. (1999) NAMD2: greater scalability for parallel molecular dynamics. *J. Comput. Phys. 151*, 283–312.

(14) Darden, T., York, D., and Pdersen, L. (1993) Particle mesh Ewald: An N⊕log(N) method for Ewald sums in large systems. *J. Chem. Phys. 98*, 10089–10092.

(15) Freiman, D. G., Suyemoto, J., and Wessler, S. (1965) Frequency of pulmonary thromboembolism in man. *N. Engl. J. Med. 272*, 1278–80.

(16) Casu, B. (1989) Structure of heparin and heparin fragments. *Ann. N.Y. Acad. Sci. 556*, 1–17.

(17) Breddin, H. K., Hach-Wunderle, V., Nakov, R., and Kakkar, V. V. (2001) Effects of a low-molecular-weight heparin on thrombus regression and recurrent thromboembolism in patients with deep-vein thrombosis. *N. Engl. J. Med. 344*, 626–31.

(18) Jaques, L. B. (1979) Heparins--anionic polyelectrolyte drugs. *Pharmacol. Rev. 31*, 99–166.

(19) Lee, Y., Kim, S. H., and Byun, Y. (2000) Oral delivery of new heparin derivatives in rats. *Pharm. Res. 17*, 1259–64.

(20) Kim, S. K., Lee, D. Y., Kim, C. Y., Nam, J. H., Moon, H. T., and Byun, Y. (2007) A newly developed oral heparin derivative for deep vein thrombosis: non-human primate study. *J. Controlled Release 123*, 155–63.

(21) Kim, S. K., Lee, D. Y., Lee, E., Lee, Y. K., Kim, C. Y., Moon, H. T., and Byun, Y. (2007) Absorption study of deoxycholic acid-heparin conjugate as a new form of oral anti-coagulant. *J. Controlled Release 120*, 4–10.

Supporting Information

Manuscript for ‘Bioconjugate Chemistry’

Nanoscale Rule of Deoxycholic Acid and Dimethylsulfoxide Structural Constraint for Macromolecule Oral Delivery

Sang Kyoon Kim[1,*], June Huh[2,*], Sang Yoon Kim[3], Youngro Byun[1], Dong Yun Lee[4,**] and Hyun Tae Moon[5,**]

1. Synthesis of DMSO-bound DOCA-conjugated heparin

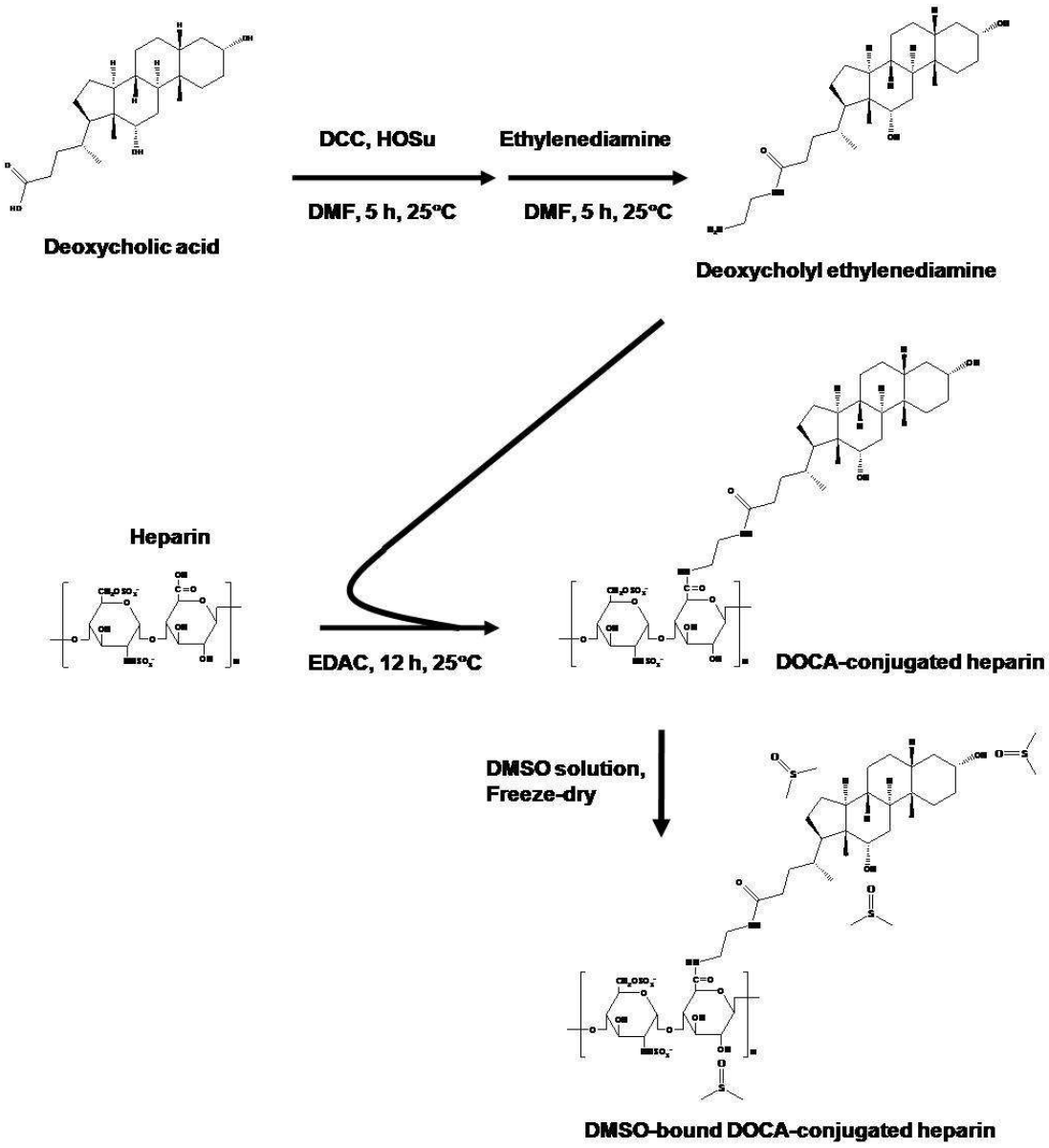

Supporting Information Figure S1. Synthesis of DMSO-bound DOCA-conjugated heparin

2. Theoretical equation for computation simulation

a

$$m_i \ddot{\mathbf{r}}_i = \mathbf{F}_i$$

$$\mathbf{r}_i(t+\Delta t) \cong 2\mathbf{r}_i(t) - \mathbf{r}_i(t-\Delta t) + \frac{\mathbf{F}_{tot,i}}{2!m_i}\Delta t^2$$

b

$$U(\mathbf{r}^n) \equiv U\left(b,\theta,\phi,r_{ij}\right)$$
$$\cong \sum_{bonds} k_b\left(b-b_o\right)^2 + \sum_{angle} k_\theta\left(\theta-\theta_o\right)^2 + \sum_{dihedrals} k_\phi\left[1+\cos\left(m\phi-\delta\right)\right] +$$
$$+ \sum_{nonbonded} 4\varepsilon_{ij}\left[\left(r_{ij}/\sigma_{ij}\right)^{-12} - \left(r_{ij}/\sigma_{ij}\right)^{-6}\right]$$
$$+ \sum_{H-bonds}\left[\left(r_{ij}/C_{ij}\right)^{-12} - \left(r_{ij}/D_{ij}\right)^{-10}\right] + \sum_{nonbonded}\frac{q_i q_j}{\varepsilon r_{ij}}$$

c

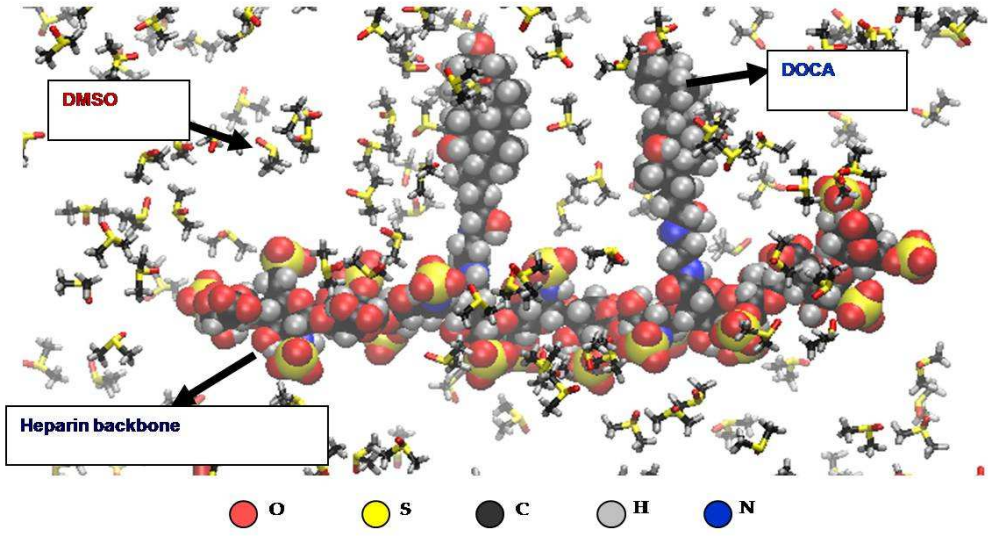

Supporting Information Figure S2. (A) Equation of motion (solved by verlet algorithm). F_i: inter-atomic force field of *i*-atom (nonbonded interaction: van der Waals, electrostatic, hydrogen bonding, etc bonded interaction: bond stretching, bond bending, etc) **(B) AMBER Potential**. Force Field Parameterization for DOCA-conjugated heparin in DMSO solution (by Quantum Calculation). The force field

parameters (k_b, k_θ, k_φ, σij, C_{ij}, D_{ij}, etc) for all the atoms in DOCA-conjugated heparin/DMSO/water were determined thorough quantum mechanical calculation. Force field parameters depend not only on atom type but also on other atoms bonded to it. So, it cannot be generalized by listing up the pairwise interatomic interaction. The determination of force field parameter for heparin alone is something new as well as DOCA-conjugated heparin. **c)** Heparin backbone: 12 heparin repeating group of iduronic acid and hexosamine by α1-4 linkage. DOCA: 2 DOCA bound chemically to carboxylic site of heparin backbone (evenly spaced). DMSO: the DOCA-conjugated heparin was disolved in 10 wt% of DMSO solution. Water: water molecule with a bulk density (background; water molecules are not shown).

3. The possible interaction site of DMSO and DOCA molecule

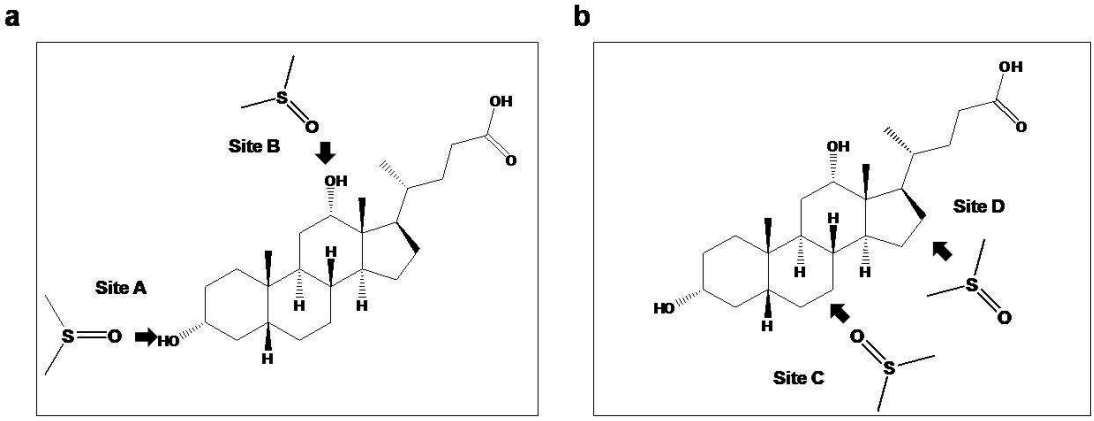

Supporting Information Figure S3. The possible interaction site of DMSO molecules and DOCA molecules. **(A)** Site A, hydrogen bonding between oxygen of DMSO and hydroxyl group in end position of DOCA; site B hydrogen bonding between oxygen DMSO and hydroxyl group in middle position of DOCA. **(B)** site C hydrophobic interaction between oxygen of DMSO and DOCA ring; site D methyl group of DMSO and DOCA ring.

Supporting information movie 1. Two Chain Simulation of DOCA-conjugated heparin in DMSO Solution (12 wt % relative to water content). Only DMSO (green) within 3Å from LHD were shown. DMSO become more populated near DOCA than near heparin backbones. Light blue color represented water molecules. DMSOs tend to screen out hydrophobic interaction between DOCAs dynamically by lasting the formation and breakage hydrogen bonds between hydroxy groups of DOCA and DMSO. Running time: 2ns.

Bioconjugate Chemistry

REVIEW

pubs.acs.org/bc

^{64}Cu-Labeled Phosphonium Cations as PET Radiotracers for Tumor Imaging

Yang Zhou and Shuang Liu*

School of Health Sciences, Purdue University, 550 Stadium Mall Drive, West Lafayette, Indiana 47907, United States

ABSTRACT: Alteration in mitochondrial transmembrane potential ($\Delta\Psi_m$) is an important characteristic of cancer. The observation that the enhanced negative mitochondrial potential is prevalent in tumor cell phenotype provides a conceptual basis for development of mitochondrion-targeting therapeutic drugs and molecular imaging probes. Since plasma and mitochondrial potentials are negative, many delocalized organic cations, such as rhodamine-123 and ^{3}H-tetraphenylphosphonium, are electrophoretically driven through these membranes, and able to localize in the energized mitochondria of tumor cells. Cationic radiotracers, such as ^{99m}Tc-Sestamibi and ^{99m}Tc-Tetrofosmin, have been clinically used for diagnosis of cancer by single photon emission computed tomography (SPECT) and non-invasive monitoring of the multidrug resistance (MDR) transport function in tumors of different origin. However, their diagnostic and prognostic values are often limited due to their insufficient tumor localization (low radiotracer tumor uptake) and high radioactivity accumulation in the chest and abdominal regions (low tumor selectivity). In contrast, the ^{64}Cu-labeled phosphonium cations represent a new class of PET (positron emission tomography) radiotracers with good tumor uptake and high tumor selectivity. This review article will focus on our recent experiences in evaluation of ^{64}Cu-labeled phosphonium cations as potential PET radiotracers. The main objective is to illustrate the impact of radiometal chelate on physical, chemical, and biological properties of ^{64}Cu radiotracers. It will also discuss some important issues related to their tumor selectivity and possible tumor localization mechanism.

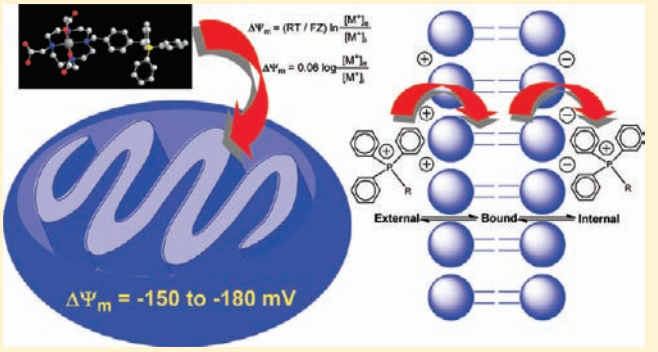

INTRODUCTION

Early Detection of Cancer. Cancer is the second leading cause of death worldwide. The most prevalent forms of this disease are solid tumors of the lung, breast, prostate, colon, and rectum.[1] Most cancer patients can survive for a long period of time after surgery, radiation, and chemotherapy or a combination thereof if it can be detected at the early stage. Therefore, accurate early detection is highly desirable so that various therapeutic regimens can be given before tumors become widely spread. Many imaging modalities are currently available for early cancer detection. Ultrasonography (US), computed tomography (CT), and magnetic resonance imaging (MRI) can provide details of structural changes, variations in density, and differences in proton content in tissues. However, it remains a significant challenge to use US, CT, and MRI methods for molecular imaging of cancer. Nuclear medicine procedures using radiolabeled receptor ligands can provide the *in vivo* characterization of cellular structure, and are able to monitor biological changes in tumor tissues at the cellular and molecular levels. A "fatal flaw" for most of the receptor-based target-specific radiotracers is that not all tumors overexpress that specific receptor. Thus, it is of great benefit to develop a molecular imaging probe that could detect cancers by targeting a biomarker found in the majority, if not all, of human cancer lesions.

Targeting Energized Mitochondria. Alteration in mitochondrial transmembrane potential ($\Delta\Psi_m$) is an important characteristic of cancer caused directly by mitochondrial dysfunction, such as DNA mutation and oxidative stress.[2−5] It has been reported that the mitochondrial transmembrane potential in carcinoma cells (regardless of the tumor origin) is significantly higher than that in normal epithelial cells.[6−11] For example, the difference in $\Delta\Psi_m$ between the colon carcinoma cell line CX-1 and the control green monkey kidney epithelial cell line CV-1 was approximately 60 mV (163 mV in tumor cells vs 104 mV in normal cells). The observation that the enhanced negative mitochondrial potential is prevalent in tumor cell phenotype provides the conceptual basis for development of mitochondrion-targeting therapeutic pharmaceuticals and molecular imaging probes.[2−5,12−25]

Measuring Mitochondrial Potential with Lipophilic Organic Cations. Mitochondrial potential measurement provides the most comprehensive reflection of mitochondrial bioenergetic function primarily because it directly depends on the proper integration of diverse metabolic pathways that converge at mitochondria. Since both plasma and mitochondrial potentials

Received: February 28, 2011
Revised: June 14, 2011
Published: June 22, 2011

ACS Publications © 2011 American Chemical Society

are negative, many delocalized cationic molecules with appropriate structural features are electrophoretically driven through these transmembranes, and tend to accumulate inside the energized mitochondria of tumor cells.[2−5,12−17] This is exemplified by the use of rhodamine-123 and ^{3}H-tetraphenylphosphonium (^{3}H-TPP) for measurement of mitochondrial potential in tumor cells on the basis of their intracellular and mitochondrial concentration.[6−10,13,15,16] In addition, rhodamine derivatives have also been used as fluorescent probes for optical imaging of tumors in animal models.[18−25]

Imaging Tumors with Cationic Radiotracers. Cationic radiotracers, such as ^{99m}Tc-Sestamibi and ^{99m}Tc-Tetrofosmin, were developed as radiotracers for myocardial perfusion imaging by single photon emission computed tomography (SPECT).[26−31] It was found that these cationic radiotracers are also able to localize in tumors due to the increased negative plasma and mitochondrial potential in tumor cells as compared to normal cells of surrounding tissues.[32−42] ^{99m}Tc-Sestamibi and ^{99m}Tc-Tetrofosmin have been clinically used for diagnosis of cancer and noninvasive monitoring of the tumor multidrug resistance (MDR) transport function.[33,36−42] However, their diagnostic and prognostic values are often limited due to their insufficient tumor localization and high radioactivity accumulation in the chest and abdominal regions.

Radiolabeled Phosphonium Cations as Radiotracers. More than 20 years ago, radiolabeled quaternary ammonium, phosphonium, and arsonium cations were studied as perfusion radiotracers for heart imaging.[43,44] Recently, several groups proposed to use radiolabeled triphenylphosphonium, such as 4-(^{18}F-benzyl)triphenylphosphonium (^{18}F-BzTPP), cations as PET radiotracers for myocardial perfusion and tumor imaging.[45−52] It has been reported that ^{3}H-tetraphenylphosphonium (^{3}H-TPP) has better tumor uptake than ^{99m}Tc-Sestamibi,[53] but its tumor selectivity is poor with tumor/heart ratios of $\ll$1.0. Since ^{3}H-TPP is not suitable for PET imaging, the ^{11}C-labeled TPP cation has been proposed as the alternative.[45,46] In addition, the high uptake of ^{18}F-BzTPP in the heart and liver may impose a significant challenge for its application in diagnosis of cancer in chest and abdominal regions. Even though biodistribution and imaging studies in small animals[45,52] and dogs[45,46,49] have clearly demonstrated the utility of ^{11}C and ^{18}F-labeled TPP cations for imaging heart and tumors by PET, the combination of short half-life of ^{11}C ($T_{1/2}$ = 20.4 min, 98% abundance) and ^{18}F ($T_{1/2}$ = 110 min, 97% abundance) with their poor availability and high cost of infrastructure makes it very difficult to use ^{11}C and ^{18}F-labeled TPP cations for PET studies of cancer patients in most of the clinic settings. Therefore, there is an urgent need for new and better PET radiotracers that can be readily prepared, have high tumor selectivity, and are able to provide the information of the tumor mitochondrial function in a noninvasive fashion.

About This Review. Many review articles have appeared covering the nuclear medicine applications of cationic radiotracers for tumor imaging and noninvasive monitoring of tumor MDR transport function by SPECT or PET.[36−42] This article is not intended to be an exhaustive review of current literature on cationic radiotracers and their nuclear medicine applications. Instead, it will focus on our recent experiences in evaluations of ^{64}Cu-labeled phosphonium cations as highly tumor selective PET radiotracers. This review will also discuss some important issues related to their tumor selectivity and localization mechanism. The main objective is to illustrate the impact of bifunctional chelators (BFCs) and radiometal chelate on physical, chemical, and biological properties of ^{64}Cu-labeled phosphonium cations. It is very important to note that the mitochondrion-targeted radiotracers described in this article are not intended to measure the exact mitochondrial potential in tumor cells as ^{3}H-TPP and the rhodamine derivatives are used for many *in vitro* assays.[6−10,13,15,16] Considering the heterogeneity of tumor cells in different regions of the same tumor tissue and among different types of tumors, these mitochondrion-targeted radiotracers are designed to noninvasively determine the contrast between the tumor and surrounding normal tissues.

RADIOTRACER DESIGN

Characteristics of Optimal Radiotracers. For a new tumor-specific radiotracer to be successful, it must show clinical indications for high-incidence tumors (breast, lung, and prostate cancers). The radiotracer should have high tumor uptake and target-to-background (T/B) ratios in a short period of time postinjection (p.i.). To achieve this goal, the radiotracer should have a rapid blood clearance to minimize background radioactivity. Since most high-incidence tumors occur in the chest and abdominal regions, renal excretion is needed to avoid excessive radioactivity accumulation in the gastrointestinal tract, which might interfere with interpretation of tumor radioactivity.

Radiotracer Design. Figure 1 shows selected phosphonium cations, bifunctional chelators (BFCs), and PKM (pharmacokinetic modifying) linkers. The phosphonium cation serves as a targeting moiety to carry ^{64}Cu into the energized mitochondria of tumor cells. The BFC is required for chelation of ^{64}Cu. PKM linkers are used to improve pharmacokinetics of ^{64}Cu radiotracers. In principle, the ^{64}Cu-labeled phosphonium cations should be useful for imaging most tumors, if not all, since the higher negative mitochondrial potential is prevalent in tumor cell phenotypes.[47−53] Their high tumor selectivity provides a unique opportunity to develop radiotracers that are sensitive to the early change in tumor mitochondrial potential. Successful development of such a radiotracer will be beneficial for the early detection of cancer. It must be noted that the ^{64}Cu-labeled phosphonium cations are significantly different from their ^{18}F-analogues with respect to their physical, chemical, and biological properties. Replacing ^{18}F with a ^{64}Cu-BFC chelate has a significant impact on the biological characteristics of phosphonium cations due to its large size, hydrophilicity, and the change in overall molecular charge.

Why ^{64}Cu or ^{62}Cu? ^{64}Cu has a half-life of 12.7 h and a β^{+} emission (18%, E_{max} = 0.655 meV). Despite its low β^{+} abundance, the long half-life makes it feasible to prepare, transport, and deliver the ^{64}Cu radiotracer for its clinical applications.[54,55] Recent breakthroughs in production of ^{64}Cu with high specific activity have made it more available to small institutions without the on-site cyclotron facilities.[54] Thus, ^{64}Cu is a viable alternative to ^{18}F for research programs that wish to incorporate high sensitivity and high spatial resolution of PET, but cannot afford to maintain the expensive radionuclide production infrastructure. ^{62}Cu is a generator-produced radionuclide. Its 9.7 min half-life allows the repeated dosing without imposing a significant radiation burden to the patient. Copper radionuclides, related radiochemistry, and nuclear medicine applications of ^{64}Cu-radiotracers have been reviewed extensively.[54−60] We have evaluated several metallic radionuclides (^{99m}Tc, ^{64}Cu, and ^{111}In) for radiolabeling of phosphonium cations. It was found that only the ^{64}Cu-labeled phosphonium cations are able to localize in U87MG glioma tumors with long tumor retention, while the corresponding ^{99m}Tc and

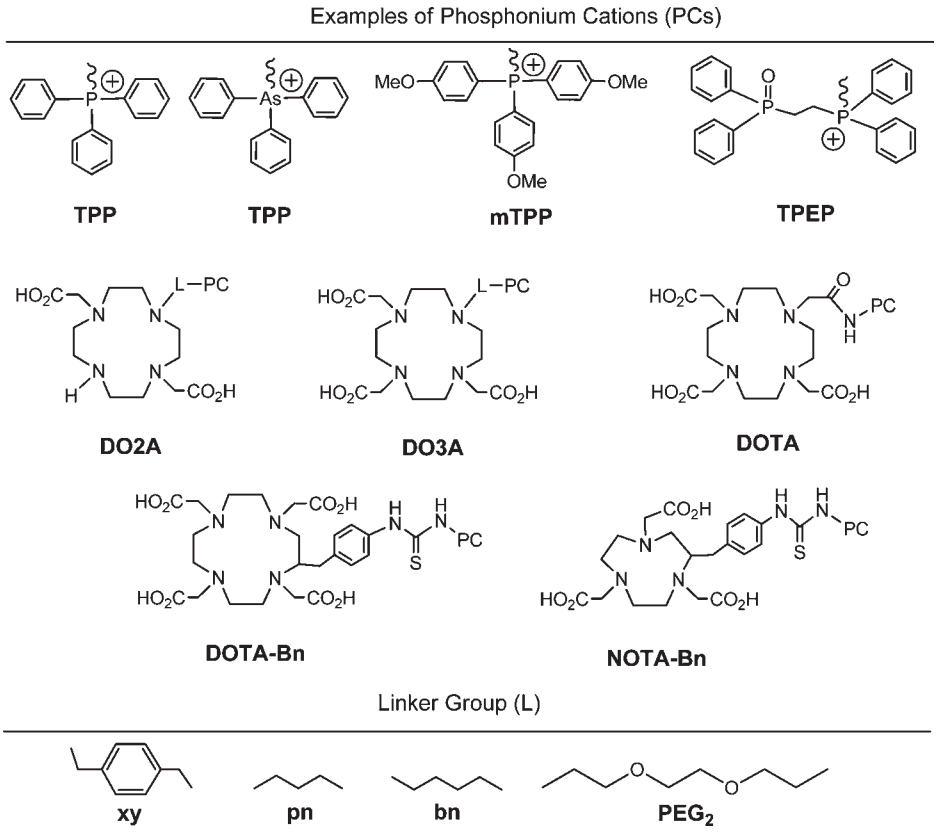

Figure 1. Phosphonium cation conjugates for preparation of ^{64}Cu radiotracers. The phosphonium cation (PC) is used as the mitochondrion-targeting biomolecule to carry ^{64}Cu into the tumor cells where the negative mitochondrial potential is elevated as compared to normal cells. DOTA, DO3A, DO2A, NOTA, and their derivatives are used as BFCs for ^{64}Cu chelation. Different linkers (L) are useful for modification of pharmacokinetics of ^{64}Cu radiotracers.

^{111}In radiotracers tend to have significant tumor washout. Since ^{64}Cu and ^{62}Cu share identical coordination chemistry, ^{62}Cu-labeled phosphonium cations are expected to have the same biodistribution characteristics as their ^{64}Cu analogues.

Bifunctional Chelators for ^{64}Cu Chelation. Due to the d^9 configuration, Cu(II) complexes are kinetically labile. BFCs for $^{62/64}$Cu-labeling are often macrocyclic and form Cu(II) complexes with high thermodynamic stability and kinetic inertness.[61−76] Since most phosphonium cations are relatively small, the optimal BFCs would be those which form low-molecular-weight ^{64}Cu chelates. That is why DO3A (1,4,7,10-tetraazacyclododecane-1,4,7-tetraacetic acid), DO2A (1,4,7,10-tetraazacyclododecane-1,4-diacetic acid), DOTA (1,4,7,10-tetraazacyclododecane-1,4,7,10-tetraacetic acid), and NOTA (1,4,7-tritazacyclononane-1,4,7-triacetic acid) are used as the BFCs for ^{64}Cu-labeling of phosphonium cations.[61−64] These BFCs are able to form anionic or neutral ^{64}Cu chelates so that the overall molecular charge of the ^{64}Cu radiotracers is either neutral or positive under physiological conditions.

SYNTHESIS OF CONJUGATED ORGANIC CATIONS

DO3A conjugates were readily prepared according to Chart 1 by reacting the DO3A(OBu-t)$_3$ with the respective bromide in DMF in the presence of sodium carbonate.[61,63,64] Hydrolysis of the *t*-butyl ester in hydrochloric acid gave the expected DO3A conjugates (**1**: DO3A-pn-TPP; **2**: DO3A-bn-TPP; **3**: DO3A-xy-TPP; **4**: DO3A-xy-TPA; **5**: DO3A-xy-mTPP; and **6**: DO3A-xy-TPEP). DO2A-xy-TPP (**7**) and DO2A-(xy-TPP)$_2$ (**8**) were prepared according to Chart 2 by N-alkylation of DO2A(OBu-t)$_2$ with 4-(bromomethylbenzyl)triphenylphosphonium.[63] DOTA-Bn-xy-TPP (**9**), DOTA-Bn-xy-TPEP (**10**), NOTA-Bn-xy-TPP (**11**), and NOTA-Bn-xy-TPEP (**12**) were prepared according to Chart 3.[56] The key intermediates were (4-(aminomethyl)benzyl)(2-(diphenylphosphoryl)ethyl)diphenylphosphonium and 4-(aminomethylbenzyl)triphenylphosphonium.[63,64] Conjugates **1**−**12** were synthesized to explore the impact of phosphonium moiety, linker, and BFCs on the biodistribution and excretion kinetics of their corresponding ^{64}Cu radiotracers.

COORDINATION CHEMISTRY OF DO3A-CONJUGATED TPP

Solid State Structures. To understand coordination chemistry of DO3A-conjugated phosphonium cations, we prepared complexes In(**3**)$^+$ and Ga(**3**)$^+$ as model compounds for ^{111}In-(**3**)$^+$ and ^{68}Ga(**3**)$^+$, respectively, and Cu(**3**) as the model for ^{64}Cu(**3**). Mn(**3**) was prepared because of its similarity to Cu(**3**) with respect to molecular charge.[62] Despite their difference in overall molecular charge, In(**3**)$^+$ and Mn(**3**) have almost identical solid-state structures with DO3A bonding to In(III) and Mn(II) in a monocapped octahedral coordination geometry (Figure 2).[62] Because of the smaller size of Ga(III), DO3A in Ga(**3**)$^+$ is only hexadentate with four amine-N and two carboxylate-O atoms bonding to Ga(III) in a distorted octahedral coordination geometry (Figure 2). One carboxylic acid group in DO3A is deprotonated in order to balance the positive charge of Ga(III).[62] Since the ionic radius of Cu(II) is close to that of Ga(III), it is reasonable to believe that the coordinated DO3A in

Chart 1. Synthesis of DO3A Conjugates

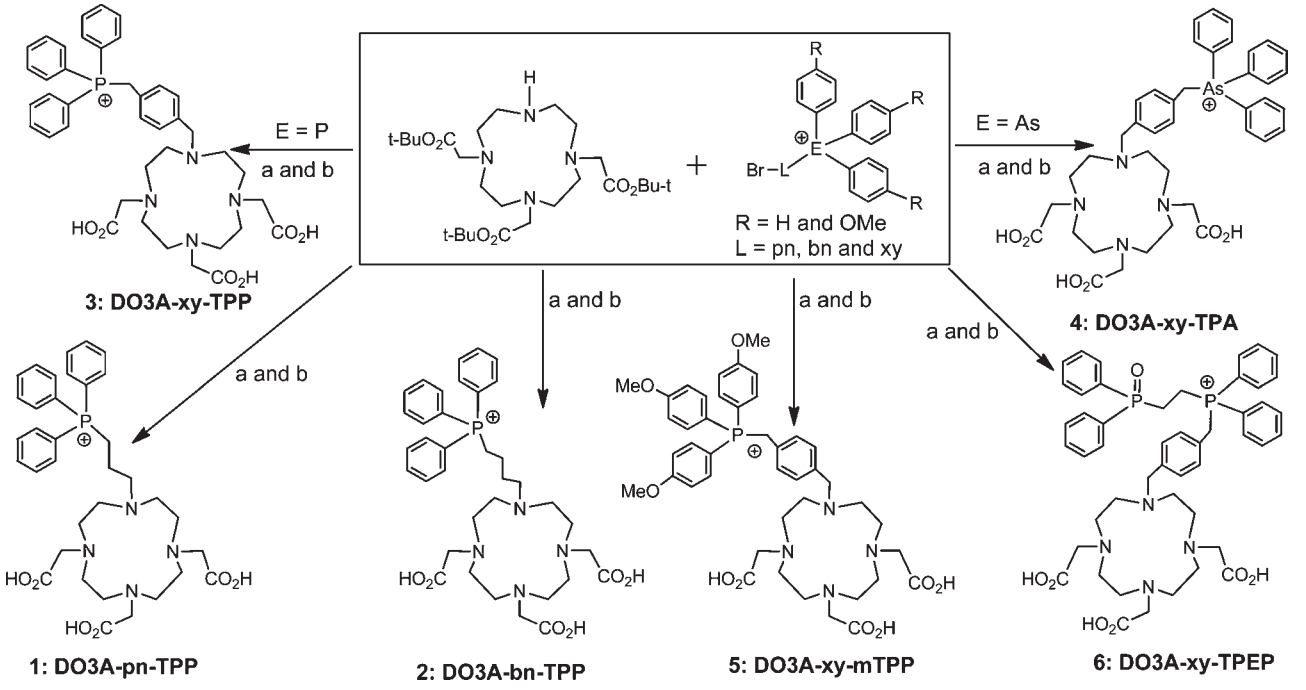

Chart 2. Synthesis of DO2A Conjugates

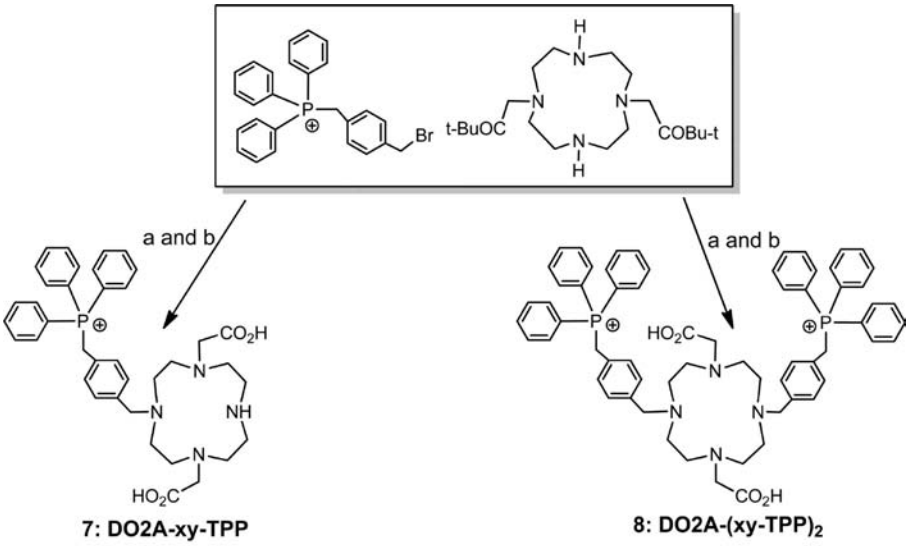

Cu(**3**) is most likely hexadentate, as observed in Cu(DO3A),[77] with one acetate group being deprotonated to balance the cationic charge from TPP.

Solution Structures. Since ^{64}Cu(**3**) and ^{111}In(**3**)$^+$ are used as radiotracers in biological systems, it is necessary to study their solution properties (structure, isomerism, and stability) in aqueous solution. On the basis of HPLC concordance experiments (Figure 3), it was concluded that ^{111}In(**3**)$^+$ and In(**3**)$^+$ have the same composition due to their identical HPLC retention times.[62] In(**3**)$^+$ remains symmetrical in aqueous solution with no dissociation of acetate chelating arms.[62] The presence of a single peak in the region of interest (Figure 3) suggests that they exist in solution as a single or "averaged" species. The HPLC retention times for In(**3**)$^+$ and Ga(**3**)$^+$ are almost identical (14.5 and 14.7 min, respectively), but they are significantly shorter than that of Mn(**3**) (16.8 min) and Cu(**3**) (17.2 min). Obviously, Ga(**3**)$^+$ and In(**3**)$^+$ with the +1 overall molecular charge are more hydrophilic than Mn(**3**) in its zwitterion form.[62] The HPLC

Chart 3. Synthesis of DOTA and NOTA Conjugates

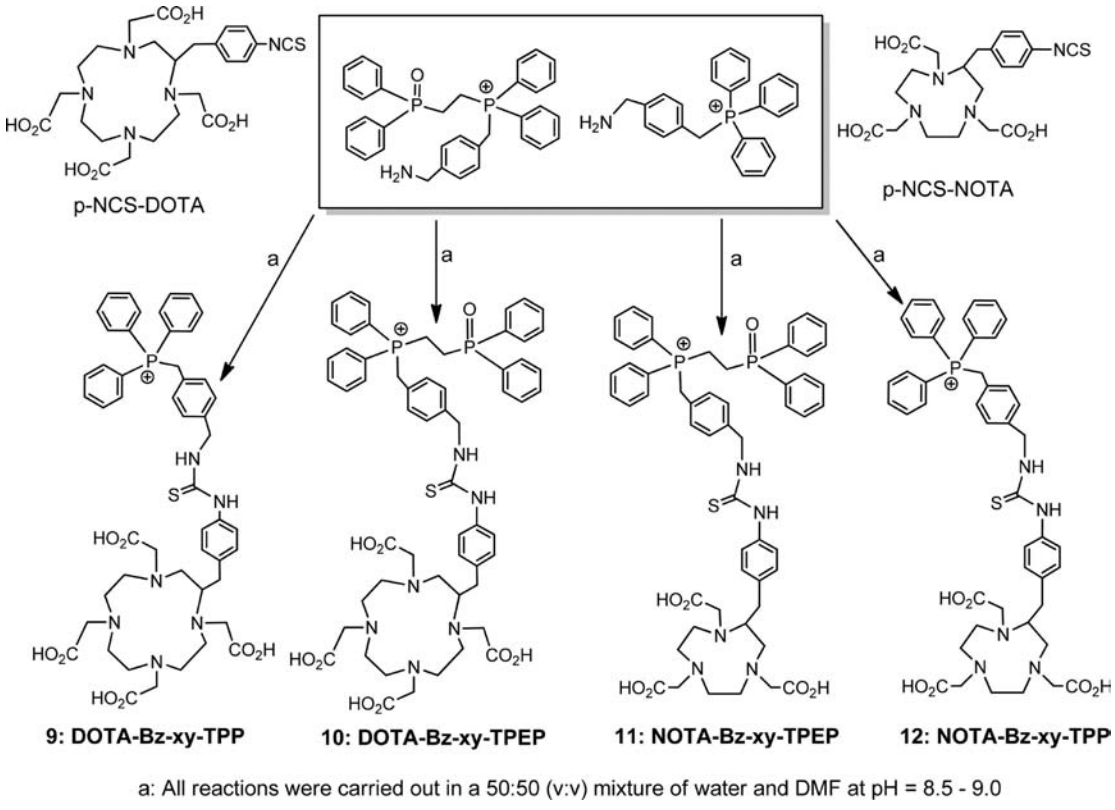

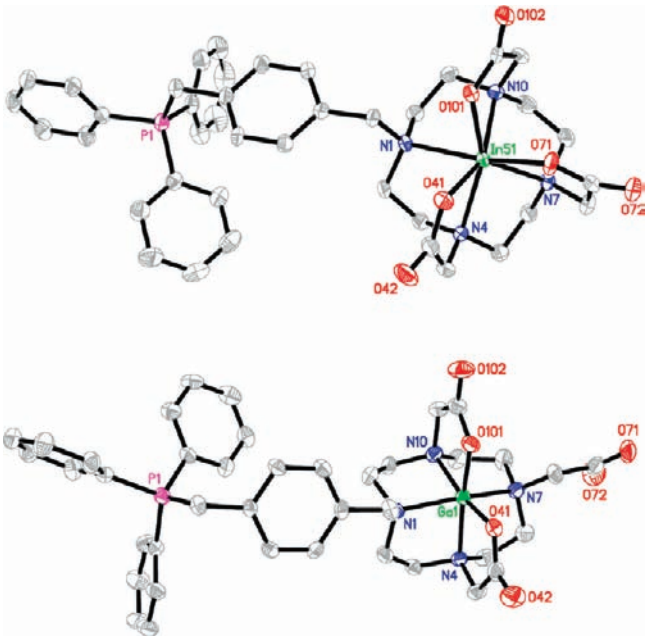

Figure 2. ORTEP drawings of $In(3)^+$ (top) and $Ga(3)^+$ (bottom). Crystallization water molecules and hydrogen atoms are omitted for the sake of clarity. The structure of Mn(3) is almost identical to that of $In(3)^+$ despite their difference in the overall molecular charge.

retention time of Mn(3) (16.8 min) is close to that of Cu(3) (17.2 min) under identical chromatographic conditions (Figure 3), suggesting that Cu(3) may also exist in solution as its zwitterion form.[62−64] However, it is unclear if the two acetate chelating arms in ^{64}Cu(3) remain coordinated in solution. Because of its low concentration in the blood circulation, it is quite possible that ^{64}Cu-DO3A in ^{64}Cu(3) might become 4-coordinated with a square planar coordination sphere. The lower pH value (pH = 4.5−5.0) inside tumor cells as compared to normal cells (pH = 6.5−7.4) also makes it easier for the two acetate chelating arms to become dissociated from ^{64}Cu. This conclusion is supported by the fact that ^{64}Cu(6) underwent extensive tranchelation in the liver,[64] and completely consistent with the instability of the ^{64}Cu-DOTA chelate.[78−82]

BIOLOGICAL EVALUATION

Biodistribution Characteristics. More than 25 ^{64}Cu-labeled phosphonium cations have been evaluated for their biodistribution characteristics and excretion kinetics in athymic nude mice bearing U87MG human glioma xenografts.[61,63,64] We were interested in this tumor-bearing animal model because the U87MG human glioma cell line has been used to evaluate the cellular uptake kinetics of ^{99m}Tc-Sestamibi and ^{99m}Tc-Tetrofosmin[83] due to its lack of MDR1 P-glycoprotein (MDR1 Pgp) expression.[84,85] Western blotting studies also showed that the xenografted U87MG glioma tissues have little expression of MRP1, MRP2, and MRP4.[65] Figure 4 compares ^{99m}Tc-Sestamibi and three ^{64}Cu-labeled phosphonium cations for their uptake in the tumor, heart, liver, and muscle, as well as tumor/heart and tumor/lung ratios. ^{99m}Tc-Sestamibi was used for comparison purposes since it has been clinically used for tumor imaging and monitoring of the tumor MDR transport function.[36−42] The most striking difference is that all ^{64}Cu radiotracers have heart uptake of <0.6% ID/g while the heart uptake of ^{99m}Tc-Sestamibi

dx.doi.org/10.1021/bc200106p |*Bioconjugate Chem.* 2011, 22, 1459–1472

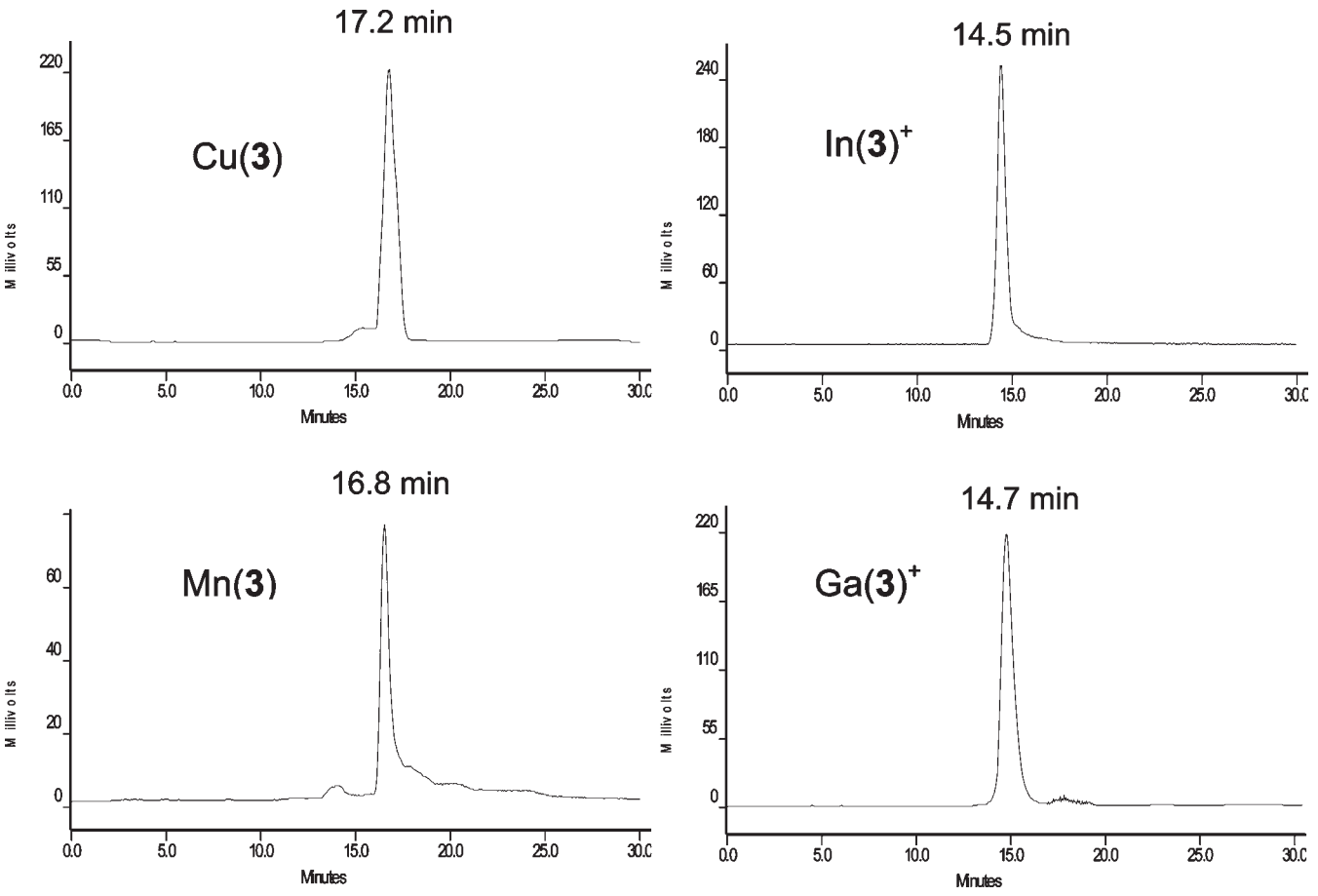

Figure 3. Typical HPLC chromatograms of Cu(**3**), Mn(**3**), In(**3**)$^+$, and Ga(**3**)$^+$. The presence of a single peak suggests that they exist in solution as a single or "averaged" species. Obviously, Ga(**3**)$^+$ (14.7 min) and In(**3**)$^+$ (14.5 min) with the +1 overall molecular charge are more hydrophilic than Mn(**3**) (16.8 min) and Cu(**3**) (17.2 min) in their zwitterion forms.

was >15% ID/g over the 2 h period. As a result, ^{64}Cu radiotracers have tumor/heart ratios much better than that of ^{99m}Tc-Sestamibi. The muscle uptake of ^{99m}Tc-Sestamibi was high (~5%ID/g), whereas the muscle uptake of ^{64}Cu radiotracers was almost undetectable at >30 min p.i. Thus, the ^{64}Cu-labeled phosphonium cations have significant advantages over ^{99m}Tc-Sestamibi. The biodistribution of ^{64}Cu(**3**) and ^{64}Cu(**4**) was almost identical, suggesting that the heteroatom (P vs As) had very little impact on biodistribution of radiotracers.[61] ^{64}Cu(**3**) has the tumor uptake comparable to that of ^{64}Cu(**5**); but ^{64}Cu(**5**) has the lower liver uptake, indicating that the presence of methoxy groups improves the radiotracer liver clearance.[63] ^{64}Cu(**6**) had higher tumor uptake (Figure 4) than ^{64}Cu(**3**), but its liver uptake was much lower than that of ^{64}Cu(**3**).[64] This indicates that the high liver uptake of ^{64}Cu(**3**) is caused by TPP cation, not the *in vivo* instability of ^{64}Cu-DO3A. On the basis of tumor uptake and T/B ratios (Figure 4), we believe that TPEP has better tumor-targeting capability than TPP.

Impact of BFC. The tumor uptake of ^{64}Cu(**10**) is comparable to that of ^{64}Cu(**6**) at 30−60 min p.i. (Figure 5A), but its tumor/heart ratios are lower than those of ^{64}Cu(**6**), probably due to the benzene ring in ^{64}Cu(**10**).[64] Among ^{64}Cu-labeled phosphonium cations evaluated in the glioma model, ^{64}Cu(**11**) (Figure 5A) and ^{64}Cu(**12**) (Figure 5B) had very low tumor uptake, probably due to NOTA,[63,64] which forms the Cu-NOTA chelate with better solution stability than that of Cu-DOTA.[75] The extra xy-TPP moiety in ^{64}Cu(**8**) also results in decreased tumor uptake (Figure 5B) and increased liver uptake, probably due to the +2 overall molecular charge and increased lipophilicity.[64] On the basis of biodistribution data, it becomes clear that (1) DO3A is the best BFC for ^{64}Cu-labeling of phosphonium cations; (2) NOTA-Bn has significant adverse effect on radiotracer tumor uptake; (3) DOTA derivatives might be useful BFCs if the aromatic benzene ring can be eliminated; and (4) the ^{64}Cu chelate should have the neutral or negative charge. The combination of relatively high tumor uptake and high T/B ratios makes ^{64}Cu(**6**) the most promising PET radiotracer for tumor imaging.[63,64]

Impact of Metal Chelate. Figure 5C compares tumor uptake of ^{111}In(**3**), ^{64}Cu(**3**), ^{111}In(**6**), and ^{64}Cu(**6**). It is surprising that ^{64}Cu and ^{111}In radiotracers have such a significant difference in their tumor uptake. For example, both ^{64}Cu(**3**) and ^{64}Cu(**6**) have a steady increase in tumor uptake at 30−120 min p.i.[63,64] while ^{111}In(**3**) and ^{111}In(**6**) had a significant tumor washout over the 2 h study period. At this moment, it is not clear what causes the difference between ^{111}In and ^{64}Cu-labeled phosphonium cations. It seems that the radiotracers with an octahedral solution structure and high *in vivo* stability (^{111}In-DO3A) tend to have much lower tumor uptake with shorter tumor retention time than those with a square-planar solution structure and relatively low *in vivo* stability (^{64}Cu-DO3A). More studies are still in progress to further define the role of radiometal chelates on the tumor uptake and tumor retention time of radiolabeled phosphonium cations.

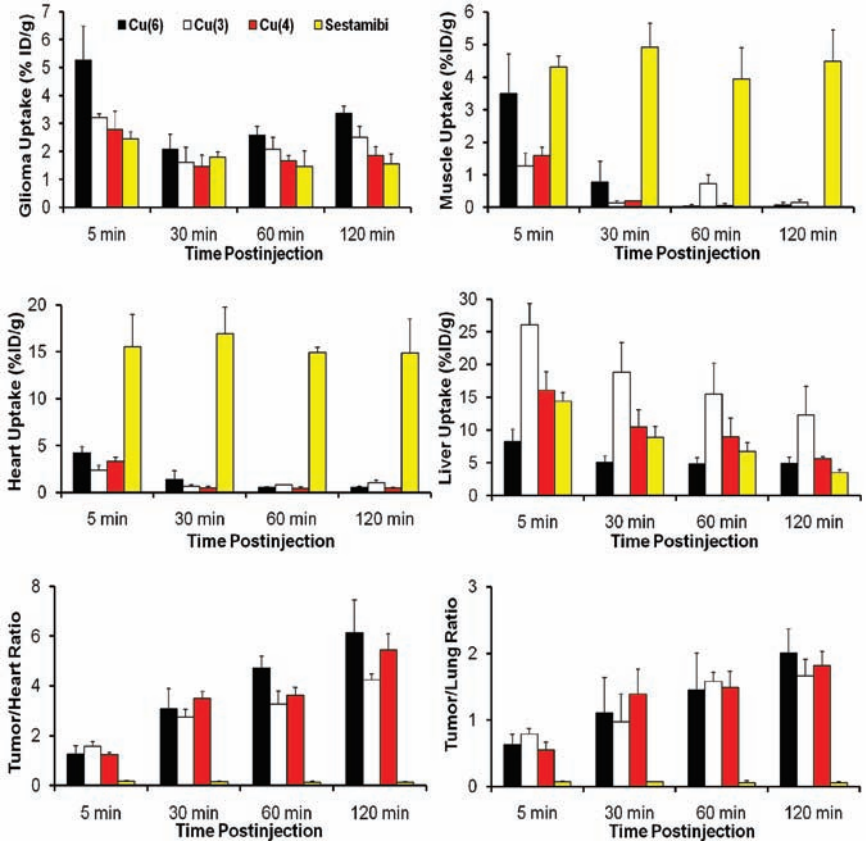

Figure 4. Comparison between the ^{64}Cu-labeled phosphonium cations and ^{99m}Tc-Sestamibi with respect to their uptake in the glioma tumor, heart, liver, and muscle, as well as their tumor/heart and tumor/lung ratios in the athymic nude mice bearing U87MG glioma xenografts.

MicroPET Imaging. Figure 6 illustrates microPET images for ^{64}Cu(**2**), ^{64}Cu(**3**), and ^{64}Cu(**6**) in athymic nude mice bearing U87MG glioma xenografts at 4 h p.i.[61,63,64] The tumors were clearly visualized with excellent T/B contrast. It is interesting to note that the tumor uptake of ^{64}Cu(**2**) was much lower than that of ^{64}Cu(**3**), but its background radioactivity was also much lower.[63] Therefore, all three ^{64}Cu radiotracers are useful for imaging MDR-negative tumors by PET.

Metabolism and ^{64}Cu-Transchelation in Liver. The metabolism studies showed that ^{64}Cu(**3**) and ^{64}Cu(**6**) are excreted via renal and hepatobiliary routes.[61,64] There was no significant metabolism detectable for ^{64}Cu(**6**) in the feces sample at 120 min p.i. In contrast, only ~15% of ^{64}Cu(**3**) remains intact in feces during the same study period. The radio-HPLC analysis of the liver homogenate suggest that ^{64}Cu(**6**) underwent extensive ^{64}Cu-tranchelation in the liver.[64] While the identity of detected metabolites remains unknown, the radio-HPLC profile of ^{64}Cu-(**6**) is very similar to that of ^{64}Cu-labeled TETA-Octreotide in rat liver homogenate.[81] Thus, it is reasonable to believe that these metabolites are likely caused by ^{64}Cu-transchelation from ^{64}Cu-DO3A chelate to the proteins, such as superoxide dismutase (SOD), which are abundant in the liver.[82]

Stability of ^{64}Cu-BFC Chelate and Radiotracer Liver Uptake. Cu(II) has a d^9 configuration with coordination number being 4, 5, or 6 depending on chelator. The 4-coordinated Cu(II) complexes are normally square-planar while the square-pyramid coordination geometry is often seen in 5-coordinated Cu(II) complexes. In 6-coordinated Cu(II) complexes, the two apical donor atoms are weakly bonded to Cu(II) in a distorted octahedral arrangement due to John-Teller distortion. As discussed previously, BFCs for copper radionuclides are often macrocyclic chelators that form Cu(II) complexes with high thermodynamic stability and kinetic inertness.[55,56] This was exemplified by early use of cyclam and cyclen derivatives for ^{67}Cu-labeling of monoclonal antibodies,[66] and further development of cross-bridged cyclam derivatives, such as CB-TE2A (2,2′-(1,4,8,11-tetraazabicyclo[6.6.2]hexadecane-4,11-diyl)diacetic acid).[76,78−80] It was reported that ^{64}Cu-CB-TE2A had higher *in vivo* stability than ^{64}Cu-DOTA and ^{64}Cu-TETA.[76,78−80] Since Cu(II) complexes are kinetically labile due to its d^9 configuration, the high liver uptake of ^{64}Cu radiotracers is often attributed to their *in vivo* instability, which leads to ^{64}Cu-transchelation from ^{64}Cu-BFC to copper-binding proteins, such as superoxide dismutase abundant in liver.[82] The metabolism of ^{64}Cu-labeled biomolecules and ^{64}Cu complexes of tetraazamacrocycles has been investigated extensively.[66,76,78−80] These studies clearly show that kinetic inertness of ^{64}Cu chelates is particularly important for *in vivo* stability of ^{64}Cu radiotracers. However, the results from our studies suggested that the high radiotracer liver uptake is mainly caused by phosphonium cations, not instability of ^{64}Cu-DO3A.[61,63,64] This conclusion is supported by the fact that ^{64}Cu(**7**) has significantly lower liver uptake than ^{64}Cu(**3**) even though ^{64}Cu-DO3A is expected to have better *in vivo* stability than ^{64}Cu-DO2A.[63] It is important to note that the tumor uptake of target-specific ^{64}Cu radiotracers is almost exclusively determined by receptor binding of targeting

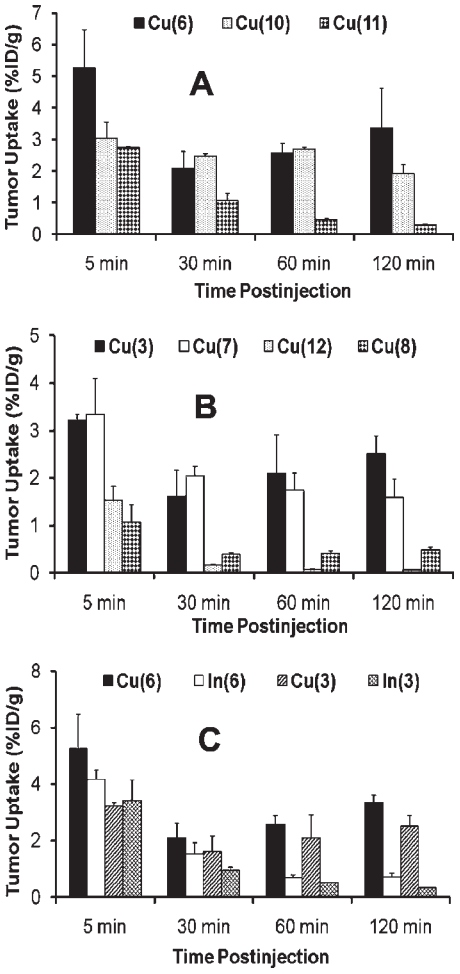

Figure 5. Histograms to illustrate impacts of BFCs, overall charge, and radiometal on the tumor uptake of ^{64}Cu and ^{111}In-labeled phosphonium cations in the athymic nude mice bearing U87MG human glioma xenografts.

biomolecules. The BFCs for ^{64}Cu chelation should be those which form ^{64}Cu-BFC chelates with high kinetic inertness to minimize liver radioactivity accumulation. In contrast, the optimal BFC should be those which result in the ^{64}Cu radiotracer with high tumor uptake and the best T/B ratios, since it has great impact on both tumor uptake and excretion kinetics of ^{64}Cu-labeled phosphonium cations. From this point of view, DO3A and DOTA are suitable BFCs for ^{64}Cu-labeling of phosphonium cations.

TUMOR LOCALIZATION MECHANISM

Mitochondrial Potential: Driving Force for Tumor Localization. It is believed that mitochondrial potential is a major factor contributing to the tumor uptake of cationic radiotracers.[3,13,46,47,52] Various tumor cell lines exhibit differences in the number, size, and shape of their mitochondria relative to normal control cells.[4] It has been reported that the mitochondria of rapidly growing tumors tend to be fewer in number and have fewer cristae than those from slowly growing tumors; the latter are larger and have characteristics closely resembling those of normal cells.[4] The main difference between tumor cells and normal cells is mitochondrial potential (163 mV in carcinoma tumor cells vs 104 mV in normal cells).[7−10] According to the Nernst equation, the ~60 mV increase in mitochondrial potential will result in approximately 10-fold more accumulation of cationic compounds in the energized mitochondria of tumor cells (Figure 7). It is this mitochondrial potential difference that provides the contrast (differential uptake of radiotracer) between tumor and surrounding normal tissues. In addition, the plasma potential (−30 to −60 mV) also preconcentrates cationic species relative to the external medium, thus affecting their cytoplasma concentration and availability for the mitochondrial uptake.[13,86−88]

Activation Energy: Barrier to Crossing Lipid Membranes. Lipophilic cations, such as TPPs, are lipid-soluble despite their positive charge. They can readily pass through the phospholipid bilayer into the mitochondria.[13] In contrast, hydrophilic cations, such as Na^+ and K^+, can cross the plasma and mitochondrial transmembranes only with the help of ionophores or carrier proteins. The impermeability of biological membranes to hydrophilic cations is largely due to the high activation energy required to move them from an aqueous environment into the lipid core (Figure 8) of the membrane.[86] The activation energy is composed of two components: the repulsive electrostatic interactions and the attractive hydrophobic forces.[87] The main repulsive electrostatic energy component, Born energy, is due to the enthalpy required to overcome charge repulsion and to remove salvation water molecules from the cation upon transfer from aqueous environment to the lipid core of the membrane.[13,88] The Born energy (W_B) is given by the following equation:

$$W_B = \frac{q^2}{8\pi\varepsilon_0 r}\left(\frac{1}{\varepsilon_1}+\frac{1}{\varepsilon_2}\right) \xrightarrow[\varepsilon_2 = 80(\text{water})]{\varepsilon_1 = 2(\text{lipid})} \frac{339Z^2}{r}$$

where ε_o is the vacuum permittivity, ε_1 is the dielectric constant within the lipid core of the membrane (~2), ε_2 is the dielectric of water (~80), q is the charge per mole of cation, r is the ionic radius, and Z is the charge per cation.[13,88] Born energy is decreased when cation becomes bigger (larger r value). The attractive component of activation energy is due to hydrophobicity of the cation (Figure 8). This energy is required to move an uncharged molecule with identical size and hydrophobicity from aqueous environment into lipid core of the phospholipid bilayer.[86,87] This component of activation energy is attractive for lipophilic organic cations due to increased entropy (loss of water structure when moving a molecule into the lipid core). The combination of decreased Born energy due to their much larger size and high attractive hydrophobic effect might contribute to 10^7-10^8-fold faster permeation kinetics through the phospholipid bilayer for triphenylphosphonium cations (Figure 9) as compared to that of Na^+ and K^+.[87,89]

Membrane Penetration Kinetics: Control of Tumor Selectivity. Another important factor influencing the radiotracer's tumor uptake and selectivity is mitochondrial density in different organs or tissues. Myocardium has the highest mitochondrial density and may occupy up to 40% of total volume of myocytes. Other mitochondrion-rich organs also include the salivary gland, liver, and kidneys. For lipophilic cationic radiotracers (log P = 0.5−1.5), such as ^{99m}Tc-Sestamibi (log P = 1.1), their membrane diffusion kinetics are so fast that they tend to localize in the mitochondrion-rich organs, such as heart, liver, kidneys, and salivary gland. For hydrophilic cations (log P = −1.0 to −3.0),

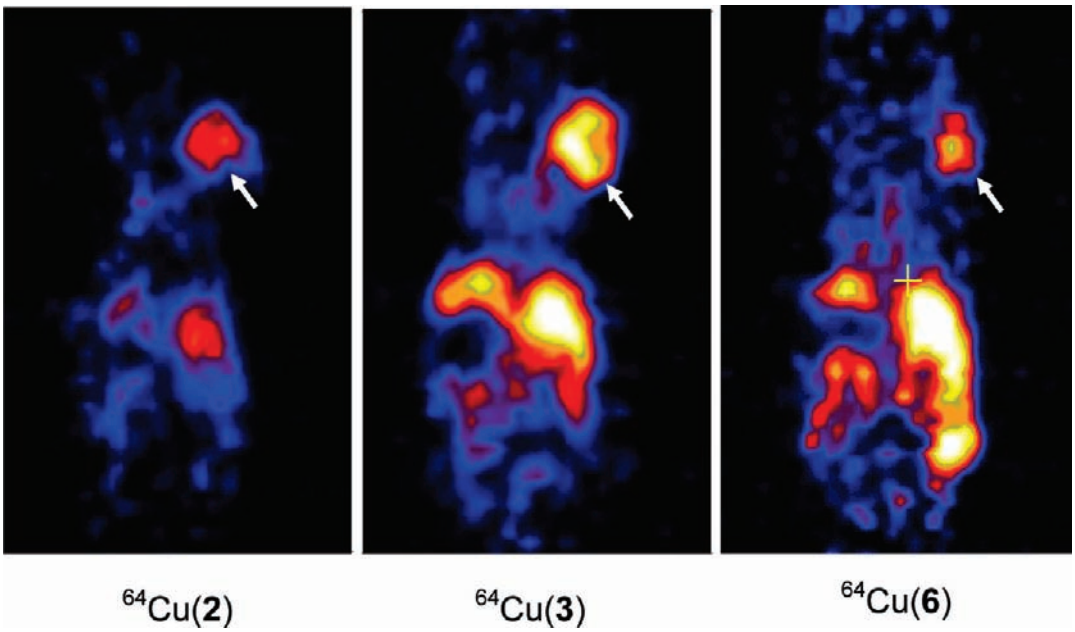

Figure 6. Representative microPET images of the glioma-bearing mice administered with ~250 μCi of ^{64}Cu(**2**), ^{64}Cu(**3**), and ^{64}Cu(**6**) at 4 h p.i. Arrows indicate the presence of tumors.

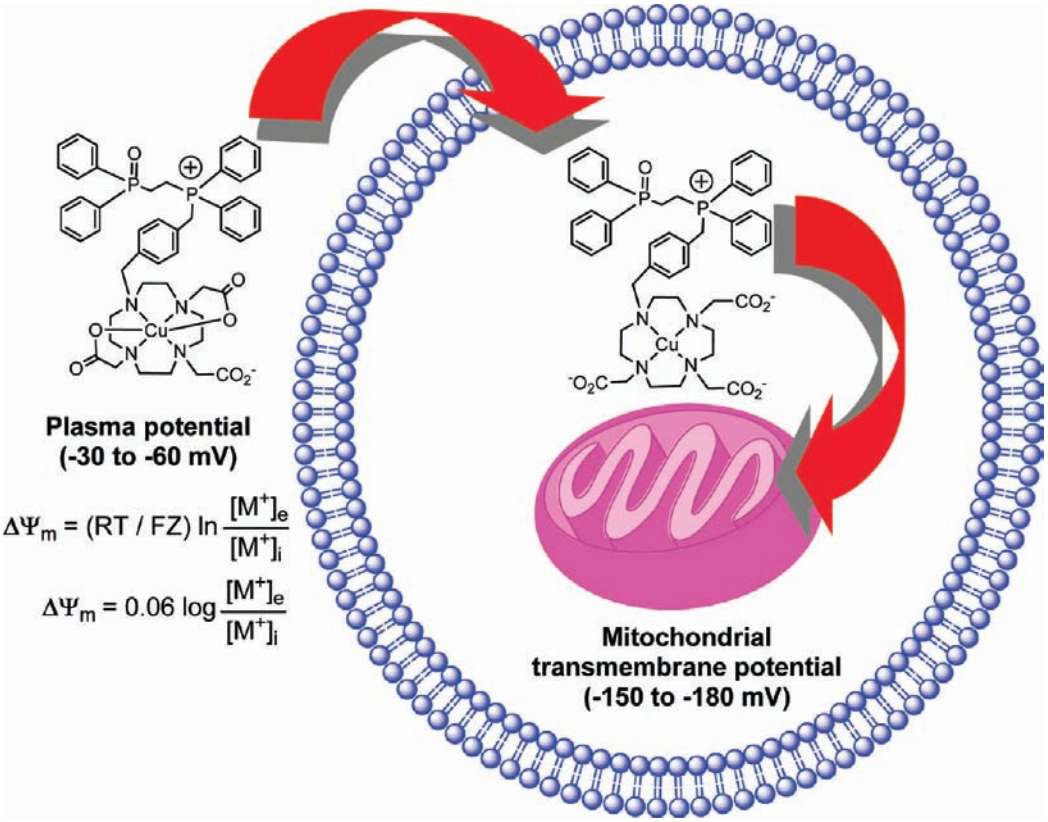

Figure 7. Schematic presentation of the process for ^{64}Cu(**6**) to across the plasma and mitochondrial membranes. The main difference between tumor cells and normal cells is the mitochondrial potential. The difference in mitochondrial potential ($\Delta\Psi_m$) between carcinoma cells and epithelial cells is ~60 mV, which contributes to ~10-fold more accumulation of ^{64}Cu(**6**) in mitochondria according to the Nernst equation. The plasma potential (−30 to −60 mV) also preconcentrates ^{64}Cu(**6**) in the plasma. The lower pH value (pH = 4.5−5.0) inside tumor cells makes it easier for the two acetate chelating arms to become dissociated from ^{64}Cu.

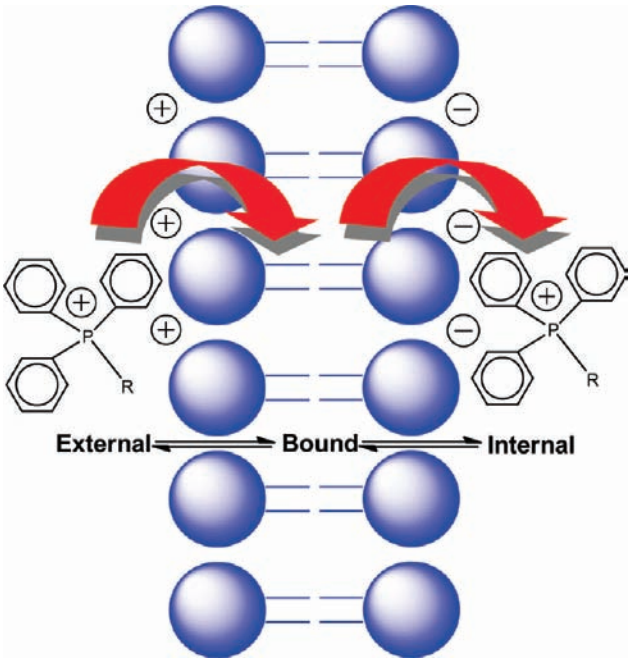

Figure 8. Schematic illustration to move a triphenylphosphonium cation across a lipophilic membrane. The electrostatic interaction between the triphenylphosphonium cation and positive charges outside the membrane is repulsive. This component of activation energy is due to the enthalpy input required to overcome charge repulsion and to remove salvation water molecules from the cation upon transfer into the membrane lipid core. In contrast, the hydrophobic interaction between the triphenylphosphonium cation and the lipid core is attractive due to hydrophobicity of the lipophilic phosphonium cation and increased entropy (loss of water structure when moving a molecule into the lipid core).

such as ^{64}Cu(**6**) (log P = −1.7), the low lipophilicity makes it more difficult for them to across mitochondrial membranes,[63,64] and often leads to a slow membrane diffusion kinetics, thereby forcing them to localize in tissues where the negative mitochondrial potential is elevated. Thus, it is not surprising that ^{64}Cu(**6**) (log P = −1.7) and ^{64}Cu(**3**) (log P = −2.7) have excellent tumor selectivity (Figure 9) with very low uptake in the heart and muscle. In this respect, cationic radiotracers with log P values in the range 0.5−1.3 are particularly useful for imaging organs (heart, liver, and salivary gland) with high mitochondrial density due to their fast membrane-penetration kinetics. In contrast, cationic radiotracers with log P values in the range of −1.0 to −3.0 are best fitted for imaging tumors with the elevated mitochondrial potential. This conclusion is completely consistent with the results from preclinical studies on cationic anticancer drugs and triarylmethane dyes for their phototoxicity toward tumor cells.[90−94]

Optimal Lipophilicity. There is little information available with regard to the optimal lipophilicity for a radiotracer to achieve high tumor selectivity. A predictive model has been reported for selective accumulation of generic chemicals in carcinoma tumor cells.[95] It was predicted that the optimal log P value for an organic cation to achieve high tumor selectivity is between 0.0 and −1.5. However, caution must be taken in using this predictive model because the molecular shape of ^{64}Cu-labeled cations is significantly different from that of their parent phosphonium cations. On the basis of the results from biodistribution studies in the glioma model, it seems that the optimal log P value for a ^{64}Cu-labeled phosphonium cation to achieve high tumor selectivity is between −1.0 and −3.0 (Figure 9). This conclusion should be further confirmed for other ^{64}Cu-labeled organic cations.

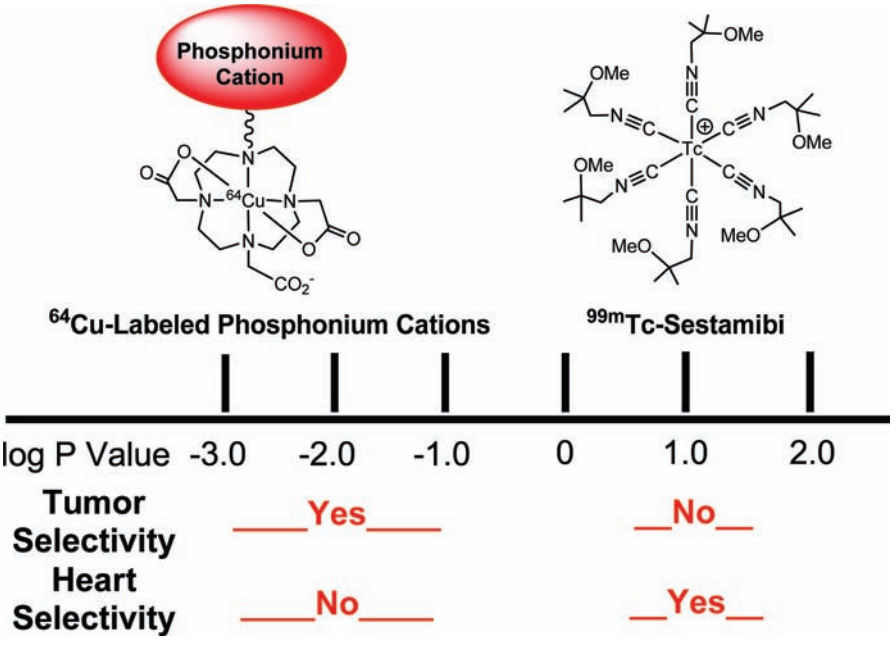

Figure 9. Schematic presentation to illustrate the selectivity of cationic radiotracers based on their lipophilicity. ^{99m}Tc-Sestamibi is lipophilic (log P = 1.1), and its membrane diffusion rate is so fast that it can readily localize in mitochondrion-rich areas, such as the heart, liver, and kidneys. The ^{64}Cu-labeled phosphonium cations, such as in ^{64}Cu(**3**), are very hydrophilic (log P = −1.5 to −2.7) due to the hydrophilic ^{64}Cu-DO3A chelate. The slow diffusion kinetics makes it difficult for the ^{64}Cu-labeled phosphonium cations to cross plasma and mitochondrial membranes, thereby forcing them to localize in the tumor where mitochondrial potential is elevated (∼60 mV). While the enhanced negative mitochondrial potential provides the thermodynamic driving force for the ^{64}Cu-labeled phosphonium cations to localize in energized mitochondria of tumor cells, the hydrophilicity offers control of their cell-penetrating kinetics and tumor selectivity.

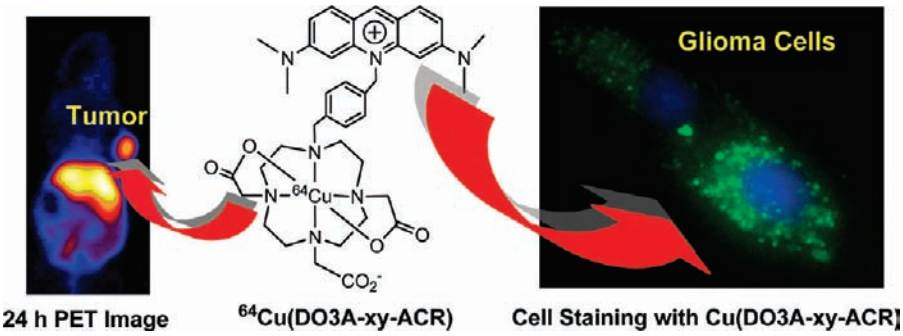

Figure 10. Schematic presentation to show the capability of ^{64}Cu(DO3A-xy-ACR) to localize in glioma. ^{64}Cu(DO3A-xy-ACR) is the PET radiotracer for tumor imaging, while Cu(DO3A-xy-ACR) is used as the fluorescent probe to demonstrate their mitochondrial localization. The results from this study provided strong indirect evidence to suggest that ^{64}Cu-labeled phosphonium cations are able to localize in the energized mitochondria of tumor cells.

Subcellular Distribution Characteristics. To understand the tumor localization mechanism of ^{64}Cu-labeled phosphonium cations, subcellular distribution studies were performed on ^{64}Cu(**3**) and ^{64}Cu(**6**) using a standard differential centrifugation method.[63,64] ^{99m}Tc-Sestamibi was used for comparison purposes since ^{99m}Tc-Sestamibi is widely used for imaging tumors in cancer patients. It was found that ^{64}Cu(**3**), ^{64}Cu(**6**), and ^{99m}Tc-Sestamibi share similar subcellular distribution patterns.[63,64] Since it is well-accepted that ^{99m}Tc-Sestamibi is a mitochondrion-targeting cationic radiotracer, we believe that ^{64}Cu(**3**) and ^{64}Cu(**6**) are able to target tumor mitochondria.

^{64}Cu(DO3A-xy-ACR): A Close "Relative" of ^{64}Cu-Labeled Phosphonium Cations. To further demonstrate the mitochondrion-targeting capability of ^{64}Cu-labeled phosphonium cations, we recently evaluated ^{64}Cu(DO3A-xy-ACR) (Figure 10: DO3A-xy-ACR = 2,6-bis(dimethylamino)-10-(4-((4,7,10-tris(carboxymethyl)-1,4,7,10-tetraazacyclo-dodecan-1-yl)methyl)benzyl)acridin-10-ium) in the glioma-bearing animal model.[96] We also prepared Cu(DO3A-xy-ACR) for cell-staining assays. We found that ^{64}Cu(DO3A-xy-ACR) remained in the glioma for >24 h while Cu(DO3A-xy-ACR) was able to localize in the mitochondria of glioma cells (Figure 10). Although ^{64}Cu(DO3A-xy-ACR) is not an ideal PET radiotracer for tumor imaging due to its high liver uptake,[96] the results from this study provided strong indirect evidence to suggest that ^{64}Cu-labeled phosphonium cations are able to localize in the energized mitochondria of tumor cells, where the negative transmembrane potential is elevated.

CONCLUSION

^{64}Cu-labeled phosphonium cations are a new class of PET radiotracers with high tumor selectivity. While their high tumor uptake can be attributed to the enhanced mitochondrial potential, the tumor selectivity of ^{64}Cu-labeled phosphonium cations is most likely attributed to their low lipophilicity and slow membrane-penetration kinetics. It is appreciated that ^{18}F-labeling of phosphonium cations usually results in minimal changes in their physical and biological properties. In contrast, the radiolabeling of phosphonium cations with metallic radionuclide (such as ^{64}Cu, ^{99m}Tc, and ^{111}In) requires the use of a BFC and results in significant changes in the molecular size, lipophilicity, and biodistribution properties. Even though the exact structural requirements for radiometal chelates remain unknown, one thing is certain: attachment of the ^{64}Cu-DO3A chelate onto phosphonium cations results in radiotracers with good tumor uptake and high tumor selectivity. Among the ^{64}Cu-labeled phosphonium cations evaluated in the glioma-bearing animal model, ^{64}Cu(**6**) has the best tumor uptake with very high tumor selectivity. Future studies will be directed toward understanding of solution structures of radiometal (^{64}Cu, ^{99m}Tc, and ^{111}In) chelates and their impact on cellular uptake kinetics of radiolabeled phosphonium cations.

AUTHOR INFORMATION

Corresponding Author

*Phone: 765-494-0236. E-mail: liu100@purdue.edu.

ACKNOWLEDGMENT

The author would like to thank Dr. Xiaoyuan Chen at the National Institute of Biomedical Imaging and Bioengineering (NIBIB) for PET imaging studies. This work is supported, in part, by Purdue University and research grants: R01 CA115883 from National Cancer Institute (NCI).

ABBREVIATIONS

DO3A-bu-TPP (**1**), triphenyl(4-((4,7,10-tris(carboxymethyl)-1,4,7,10-tetraazacyclododecan-1-yl)methyl)-3-propyl)phosphonium; DO3A-bu-TPP (**2**), triphenyl(4-((4,7,10-tris(carboxymethyl)-1,4,7,10-tetraazacyclododecan-1-yl)methyl)-4-butyl) phosphonium; DO3A-xy-TPP (**3**), triphenyl(4-((4,7,10-tris(carboxymethyl)-1,4,7,10-tetraazacyclododecan-1-yl)methyl)benzyl) phosphonium; DO3A-xy-TPA (**4**), triphenyl(4-((4,7,10-tris-(carboxymethyl)-1,4,7,10-tetraazacyclododecan-1-yl)methyl) benzyl)arsonium; DO3A-xy-mTPP (**5**), tris(4-methoxyphenyl)-(4-((4,7,10-tris(carboxymethyl)-1,4,7,10-tetraazacyclododecan-1-yl)methyl)benzyl)phosphonium; DO3A-xy-TPEP (6), (2-(diphenylphosphoryl)ethyl)diphenyl(4-((4,7,10-tris(carboxymethyl)-1,4,7,10-tetraazacyclododecan-1-yl)methyl)benzyl)phosphonium; DO2A-xy-TPP (7), (4-((4,10-bis(carboxymethyl)-1,4,7,10-tetraazacyclododecan-1-yl)methyl)benzyl)triphenylphosphonium; DO2A-(xy-TPP)$_2$ (8), (4,4′-(4,10-bis(carboxymethyl)-1,4,7,10-tetraazacyclododecane-1,7-diyl)bis(methylene)bis(4,1-phenylene))bis(methylene)bis(triphenylphosphonium); NOTA-Bn-xy-TPP (9), triphenyl(4-((3-(4-((1,4,7,10-tetrakis(carboxymethyl)-1,4,7,10-tetraazacyclododecan-2-yl)methyl)phenyl)thioureido)methyl)benzyl)phosphonium;

DOTA-Bn-xy-TPEP (10), (2-(diphenylphosphoryl)ethyl)diphenyl(4-((3-(4-((1,4,7,10-tetrakis(carboxymethyl)-1,4,7,10-tetraazacyclododecan-2-yl)methyl)phenyl)thioureido)methyl)benzyl)phosphonium; NOTA-Bn-xy-TPEP (11), (2-(diphenylphosphoryl)ethyl)diphenyl(4-((3-(4-((1,4,7-tris(carboxymethyl)-1,4,7-triazonan-2-yl)methyl)phenyl)thioureido)methyl)benzyl)phosphonium and; NOTA-Bn-xy-TPP (**12**), triphenyl(4-((3-(4-((1,4,7-tris(carboxymethyl)-1,4,7-triazonan-2-yl)methyl)phenyl)thioureido)methyl)benzyl)phosphonium

REFERENCES

(1) Jemal, A., Siegel, R., Xu, J., and Ward, E. (2010) Cancer statistics, 2010. *CA Cancer J. Clin. 60*, 277–300.

(2) Kroemer, G., Dallaporta, B., and Resche-Rigon, M. (1998) The mitochondrial death/life regulator in apoptosis and necrosis. *Annu. Rev. Physiol. 60*, 619–642.

(3) Modica-Napolitano, J. S., and Aprille, J. R. (2001) Delocalized lipophilic cations selectively target the mitochondria of carcinoma cells. *Adv. Drug Delivery Rev. 49*, 63–70.

(4) Duchen, M. R. (2004) Mitochondria in health and disease: perspectives on a new mitochondrial biology. *Mol. Aspects Med. 25*, 365–451.

(5) Modica-Napolitano, J. S., and Singh, K. K. (2002) Mitochondria as targets for detection and treatment of cancer. *Expert Rev. Mol. Med. 4*, 1–19.

(6) Johnson, L. V., Walsh, M. L., and Chen, L. B. (1980) Localization of mitochondria in living cells with rhodamine 123. *Proc. Natl. Acad. Sci. U. S. A. 77*, 990–994.

(7) Summerhayes, I. C., Lampidis, T. J., Bernal, S. D., Nadakavukaren, J. J., Nadakavukaren, K. K., Shepard, E. L., and Chen, L. B. (1982) Unusual retention of rhodamine 123 by mitochondria in muscle and carcinoma cells. *Proc. Natl. Acad. Sci. U. S. A. 79*, 5292–5296.

(8) Modica-Napolitano, J. S., and Aprille, J. R. (1987) Basis for the selective cytotoxicity of rhodamine 123. *Cancer Res. 47*, 4361–4365.

(9) Davis, S., Weiss, M. J., Wong, J. R., Lampidis, T. J., and Chen, L. B. (1985) Mitochondrial and plasma membrane potentials cause unusual accumulation and retention of rhodamine 123 by human breast adenocarcinoma-derived MCF-7 cells. *J. Biol. Chem. 260*, 13844–13850.

(10) Dairkee, S. H., and Hackett, A. J. (1991) Differential retention of rhodamine 123 by breast carcinoma and normal human mammary tissue. *Breast Cancer Res. Treat. 18*, 57–61.

(11) Mannella, C. A. (2006) The relevance of mitochondrial membrane topology to mitochondrial function. *Biochim. Biophys. Acta 1762*, 140–147.

(12) Gottlieb, E., and Thompson, C. B. (2003) Targeting the mitochondria to enhance tumor suppression. *Methods Mol. Biol. 223*, 543–554.

(13) Ross, M. F., Kelso, G. F., Blaikie, F. H., James, A. M., Cochemé, H. M., Filipovska, A., Da Ros, T., Hurd, T. R., Smith, R. A., and Murphy, M. P. (2005) Lipophilic triphenylphosphonium cations as tools in mitochondrial bioenergetics and free radical biology. *Biochemistry (Mosc.) 70*, 222–230.

(14) Jakobs, S. (2006) High resolution imaging of live mitochondria. *Biochim. Biophys. Acta 1763*, 561–575.

(15) Lichtshtein, D., Kaback, H. R., and Blume, A. J. (1979) Use of a lipophilic cation for determination of membrane potential in neuroblastoma-glioma hybrid cell suspensions. *Proc. Natl. Acad. Sci. U. S. A. 76*, 650–654.

(16) Hockings, P. D., and Rogers, P. J. (1996) The measurement of transmembrane electrical potential with lipophilic cations. *Biochim. Biophys. Acta 1282*, 101–106.

(17) Huang, S. G. (2002) Development of a high throughput screening assay for mitochondrial membrane potential in living cells. *J. Biomol. Screen. 7*, 383–389.

(18) Lefevre, C., Kang, H. C., Haugland, R. P., Malekzadeh, N., Arttamangkul, S., and Haugland, R. P. (1996) Texas Red-X and rhodamine Red-X, new derivatives of sulforhodamine 101 and lissamine rhodamine B with improved labeling and fluorescence properties. *Bioconjugate Chem. 7*, 482–489.

(19) Lavis, L. D., Chao, T. Y., and Raines, R. T. (2006) Fluorogenic label for biomolecular imaging. *ACS Chem. Biol. 1*, 252–260.

(20) Mao, C., and Kisaalita, W. S. (2004) Determination of resting membrane potential of individual neuroblastoma cells (IMR-32) using a potentiometric dye (TMRM) and confocal microscopy. *J. Fluoresc. 14*, 739–743.

(21) Scaduto, R. C., Jr, and Grotyohann, L. W. (1999) Measurement of mitochondrial membrane potential using fluorescent rhodamine derivatives. *Biophys. J. 76*, 469–477.

(22) Hama, Y., Urano, Y., Koyama, Y., Kamiya, M., Bernardo, M., Paik, R. S., Shin, I. S., Paik, C. H., Choyke, P. L., and Kobayashi, H. (2007) A target cell-specific activatable fluorescence probe for in vivo molecular imaging of cancer based on a self-quenched avidin-rhodamine conjugate. *Cancer Res. 67*, 2791–2799.

(23) Glunde, K., Foss, C. A., Takagi, T., Wildes, F., and Bhujwalla, Z. M. (2005) Synthesis of 6′-*O*-lissamine-rhodamine B-glucosamine as a novel probe for fluorescence imaging of lysosomes in breast tumors. *Bioconjugate Chem. 16*, 843–851.

(24) Longmire, M. R., Ogawa, M., Hama, Y., Kosaka, N., Regino, C. A., Choyke, P. L., and Kobayashi, H. (2008) Determination of optimal rhodamine fluorophore for in vivo optical imaging. *Bioconjugate Chem. 19*, 1735–1742.

(25) Yova, D., Atlamazoglou, V., Kavantzas, N., and Loukas, S. (2000) Development of a fluorescence-based imaging system for colon cancer diagnosis using two novel rhodamine derivatives. *Lasers Med. Sci. 15*, 140–147.

(26) Saha, G. B., Go, R. T., and Maclntyre, W. J. (1992) Radiopharmaceuticals for cardiovascular imaging. *Int. J. Rad. Appl. Instrum. B 19*, 1–20.

(27) Jain, D. (1999) Technetium-99m labeled myocardial perfusion imaging agents. *Semin. Nucl. Med. 29*, 221–236.

(28) Acampa, W., Di Benedetto, C., and Cuocolo, A. (2000) An overview of radiotracers in nuclear cardiology. *J. Nucl. Cardiol. 7*, 701–707.

(29) Dilsizian, V. (2000) The role of myocardial perfusion imaging in vascular endothelial dysfunction. *J. Nucl. Cardiol. 7*, 180–184.

(30) Beller, G. A., and Zaret, B. L. (2000) Contributions of nuclear cardiology to diagnosis and prognosis of patients with coronary artery disease. *Circulation 101*, 1465–1478.

(31) Parker, J. A. (2001) Cardiac nuclear medicine in monitoring patients with coronary heart disease. *Semin. Nucl. Med. 31*, 223–237.

(32) Herman, L. W., Sharma, V., Kronauge, J. F., Barbarics, E., Herman, L. A., and Piwnica-Worms, D. (1995) Novel hexakis-(arenisonitrile)technetium(I) complexes as radioligands targeted to the multidrug resistance P-glycoprotein. *J. Med. Chem. 38*, 2955–2963.

(33) Luker, G. D., Fracasso, P. M., Dobkin, J., and Piwnica-Worms, D. (1997) Modulation of the multidrug resistance P-glycoprotein: detection with technetium-99m-sestamibi in vivo. *J. Nucl. Med. 38*, 369–372.

(34) Liu, Z., Stevenson, G. D., Barrett, H. H., Kastis, G. A., Bettan, M., Furenlid, L. R., Wilson, D. W., and Woolfenden, J. M. (2004) Imaging recognition of multidrug resistance in human breast tumors using ^{99m}Tc-labeled monocationic agents and a high-resolution stationary SPECT system. *Nucl. Med. Biol. 31*, 53–65.

(35) Liu, Z., Stevenson, G. D., Barrett, H. H., Furenlid, L. R., Wilson, D. W., Kastis, G. A., Bettan, M., and Woolfenden, J. M. (2005) Imaging recognition of inhibition of multidrug resistance in human breast cancer xenografts using ^{99m}Tc-labeled sestamibi and tetrofosmin. *Nucl. Med. Biol. 32*, 573–583.

(36) Schomäcker, K., and Schicha, H. (2000) Use of myocardial imaging agents for tumor diagnosis: a success story? *Eur. J. Nucl. Med. 27*, 1845–1863.

(37) Del Vecchio, S., and Salvatore, M. (2004) ^{99}Tc-MIBI in the evaluation of breast cancer biology. *Eur. J. Nucl. Med. Mol. Imaging 31* (Suppl. 1), S88–S96.

(38) Sharma, V., and Piwnica-Worms, D. (1999) Metal complexes for therapy and diagnosis of drug resistance. *Chem. Rev. 99*, 2545–2560.

(39) Sharma, V. (2004) Radiopharmaceuticals for assessment of multidrug resistance P-glycoprotein-mediated drug transport activity. *Bioconjugate Chem. 15*, 1464–1474.

(40) Sharma, V., and Piwnica-Worms, D. (2005) Monitoring multidrug resistance P-glycoprotein drug transport activity with single-photon emission computed tomography and positron emission tomography radiopharmaceuticals. *Top. Curr. Chem. 252*, 155–178.

(41) Vaidyanathan, G., and Zalutsky, M. R. (2004) Imaging drug resistance with radiolabeled molecules. *Curr. Pharm. Des. 10*, 2965–2979.

(42) Filippi, L., Santoni, R., Manni, C., Danieli, R., Floris, R., and Schillaci, O. (2005) Imaging primary brain tumors by single-photon emission computerized tomography (SPECT) with technetium-99m Sestamibi (MIBI) and Tetrofosmin. *Curr. Med. Imaging Rev. 1*, 61–66.

(43) Srivastava, P. C., and Knapp, F. F., Jr. (1984) [(*E*)-1-[^{123}I]Iodopenten-5-yl]triphenylphosphonium iodide: convenient preparation of a potential useful myocardial perfusion agent. *J. Med. Chem. 27*, 978–981.

(44) Srivastava, P. C., Hay, H. G., and Knapp, F. F., Jr. (1985) Effects of alkyl and aryl substitution on the myocardial specificity of radioiodinated phosphonium, arsonium, and ammonium cations. *J. Med. Chem. 28*, 901–904.

(45) Krause, B. J., Szabo, Z., Becker, L. C., Dannals, R. F., Scheffel, U., Seki, C., Ravert, H. T., Dipaola, A. F., Jr., and Wagner, H. N., Jr. (1994) Myocardial perfusion with [^{11}C]methyl triphenyl phosphonium: measurements of the extraction fraction and myocardial uptake. *J. Nucl. Biol. Med. 38*, 521–526.

(46) Madar, I., Anderson, J. H., Szabo, Z., Scheffel, U., Kao, P. F., Ravert, H. T., and Dannals, R. F. (1999) Enhanced uptake of [^{11}C]TPMP in canine brain tumor: a PET study. *J. Nucl. Med. 40*, 1180–1185.

(47) Madar, I., Weiss, L., and Izbicki, G. (2002) Preferential accumulation of ^{3}H-tetraphenylphosphonium in non-small cell lung carcinoma in mice: comparison with ^{99m}Tc-MIBI. *J. Nucl. Med. 43*, 234–238.

(48) Ravert, H. T., Madar, I., and Dannals, R. F. (2004) Radiosynthesis of 3-[^{18}F]fluoropropyl and 4-[^{18}F]fluorobenzyl triarylphosphonium ions. *J. Label. Compd. Radiopharm. 47*, 469–476.

(49) Madar, I., Ravert, H. T., Du, Y., Hilton, J., Volokh, L., Dannals, R. F., Frost, J. J., and Hare, J. M. (2006) Characterization of uptake of the new PET imaging compound ^{18}F-fluorobenzyl triphenyl phosphonium in dog myocardium. *J. Nucl. Med. 47*, 1359–1366.

(50) Cheng, Z., Subbarayan, M., Chen, X., and Gambhir, S. S. (2005) Synthesis of (4-[^{18}F]fluorophenyl)triphenylphosphonium as a potential imaging agent for mitochondrial dysfunction. *J. Label. Compd. Radiopharm. 48*, 131–137.

(51) Cheng, Z., Winant, R. C., and Gambhir, S. S. (2005) A new strategy to screen molecular imaging probe uptake in cell culture without radiolabeling using matrix-assisted laser desorption/ionization time-of-flight mass spectrometry. *J. Nucl. Med. 46*, 878–886.

(52) Min, J. J., Biswal, S., Deroose, C., and Gambhir, S. S. (2004) Tetraphenylphosphonium as a novel molecular probe for imaging tumors. *J. Nucl. Med. 45*, 636–643.

(53) Steichen, J. D., Weiss, M. J., Elmaleh, D. R., and Martuza, R. L. (1991) Enhanced in vitro uptake and retention of ^{3}H-tetraphenylphosphonium by nervous system tumor cells. *J. Neurosurg. 74*, 116–122.

(54) Anderson, C. J., Green, M. A., and Fujibayashi, Y. (2003) Chemistry of copper radionuclides and radiopharmaceutical products, *Handbook of Radiopharmaceuticals: Radiochemistry and Applications* (Welch, M. J., and Redvanly, C., Eds.) pp 401−422, John Wiley & Sons, Ltd.

(55) Smith, S. V. (2004) Molecular imaging with copper-64. *J. Inorg. Biochem. 98*, 1874–1901.

(56) Blower, P. J., Lewis, J. S., and Zweit, J. (1996) Copper radionuclides and radiopharmaceuticals in nuclear medicine. *Nucl. Med. Biol. 23*, 957–980.

(57) Liu, S. (2004) The role of coordination chemistry in development of target-specific radiopharmaceuticals. *Chem. Soc. Rev. 33*, 1–18.

(58) Reichert, D. E., Lewis, J. S., and Anderson, C. J. (1999) Metal complexes as diagnostic tools. *Coord. Chem. Rev. 184*, 3–66.

(59) Anderson, C. J., and Welch, M. J. (1999) Radiometal-labeled agents (non-technetium) for diagnostic imaging. *Chem. Rev. 99*, 2219–2234.

(60) Liu, S. (2008) Bifunctional coupling agents for radiolabeling of biomolecules and target-specific delivery of metallic radionuclides. *Adv. Drug Delivery Rev. 60*, 1347–1370.

(61) Wang, J., Yang, C. T., Kim, Y. S., Sreerama, S. G., Cao, Q., Li, Z. B., He, Z., Chen, X., and Liu, S. (2007) ^{64}Cu-labeled triphenylphosphonium and triphenylarsonium cations as highly tumor-selective imaging agents. *J. Med. Chem. 50*, 5057–5069.

(62) Yang, C. T., Li, Y., and Liu, S. (2007) Synthesis and structural characterization of complexes of a DO3A-conjugated triphenylphosphonium cation with diagnostically important metal ions. *Inorg. Chem. 46*, 8988–8997.

(63) Kim, Y. S., Yang, C. T., Wang, J., Wang, L., Li, Z. B., Chen, X., and Liu, S. (2008) Effects of targeting moiety, linker, bifunctional chelator, and molecular charge on biological properties of ^{64}Cu-labeled triphenylphosphonium cations. *J. Med. Chem. 51*, 2971–2984.

(64) Yang, C. T., Kim, Y. S., Wang, J., Wang, L., Shi, J., Li, Z. B., Chen, X., Fan, M., Li, J. J., and Liu, S. (2008) ^{64}Cu-labeled 2-(Diphenylphosphoryl)ethyldiphenylphosphonium cations as highly selective tumor imaging agents: effects of linkers and chelates on radiotracer biodistribution characteristics. *Bioconjugate Chem. 19*, 2008–2022.

(65) Liu, S., Kim, Y. S., Zhai, S., Shi, J., and Hou, G. (2009) Evaluation of ^{64}Cu(DO3A-xy-TPEP) as a potential PET radiotracer for monitoring tumor multidrug resistance. *Bioconjugate Chem. 20*, 790–798.

(66) Deshpande, S. V., DeNardo, S. J., Meares, C. F., McCall, M. J., Adams, G. P., Moi, M. K., and DeNardo, G. L. (1988) Copper-67-labeled monoclonal antibody Lym-1, a potential radiopharmaceutical for cancer therapy: labeling and biodistribution in RAJI tumored mice. *J. Nucl. Med. 29*, 217–225.

(67) Anderson, C. J., Pajeau, T. S., Edwards, W. B., Sherman, E. L., Rogers, B. E., and Welch, M. J. (1995) In vitro and in vivo evaluation of copper-64-octreotide conjugates. *J. Nucl. Med. 36*, 2315–2325.

(68) Anderson, C. J., Jones, L. A., Bass, L. A., Sherman, E. L., McCarthy, D. W., Cutler, P. D., Lanahan, M. V., Cristel, M. E., Lewis, J. S., and Schwarz, S. W. (1998) Radiotherapy, toxicity and dosimetry of copper-64-TETA-octreotide in tumor-bearing rats. *J. Nucl. Med. 39*, 1944–1951.

(69) Lewis, J. S., Srinivasan, A., Schmidt, M. A., and Anderson, C. J. (1999) In vitro and in vivo evaluation of ^{64}Cu-TETA-Tyr^{3}-octreotate. A new somatostatin analog with improved target tissue uptake. *Nucl. Med. Biol. 26*, 267–273.

(70) Lewis, J. S., Lewis, M. R., Cutler, P. D., Srinivasan, A., Schmidt, M. A., Schwarz, S. W., Morris, M. M., Miller, J. P., and Anderson, C. J. (1999) Radiotherapy and dosimetry of ^{64}Cu-TETA-Tyr^{3}-octreotate in a somatostatin receptor-positive, tumor-bearing rat model. *Clin. Cancer Res. 5*, 3608–3616.

(71) Chen, X., Liu, S., Hou, Y., Tohme, M., Park, R., Bading, J. R., and Conti, P. S. (2004) MicroPET imaging of breast cancer α_v-integrin expression with ^{64}Cu-labeled dimeric RGD peptides. *Mol. Imaging Biol. 6*, 350–359.

(72) Wu, Y., Zhang, X., Xiong, Z., Cheng, Z., Fisher, D. R., Liu, S., Gambhir, S. S, and Chen, X. (2005) MicroPET imaging of glioma integrin $\alpha_v\beta_3$ expression using ^{64}Cu-labeled tetrameric RGD peptide. *J. Nucl. Med. 46*, 1707–1718.

(73) McQuade, P., Miao, Y., Yoo, J., Quinn, T. P., Welch, M. J., and Lewis, J. S. (2005) Imaging of melanoma using ^{64}Cu- and ^{86}Y-DOTA-ReCCMSH(Arg^{11}), a cyclized peptide analogue of α-MSH. *J. Med. Chem. 48*, 2985–2992.

(74) Shi, J., Kim, Y. S., Zhai, S., Liu, Z., Chen, X., and Liu, S. (2009) Improving tumor uptake and pharmacokinetics of ^{64}Cu-labeled cyclic RGD peptide dimers with Gly_3 and PEG_4 linkers. *Bioconjugate Chem. 20*, 750–759.

(75) Prasanphanich, A. F., Nanda, P. K., Rold, T. L., Ma, L., Lewis, M. R., Garrison, J. C., Hoffman, T. J., Sieckman, G. L., Figueroa, S. D.,

and Smith, C. J. (2007) [^{64}Cu-NOTA-8-Aoc-BBN(7−14)NH_2] targeting vector for positron-emission tomography imaging of gastrin- releasing peptide receptor-expressing tissues. *Proc. Natl. Acad. Sci. U. S. A. 104*, 12462–12467.

(76) Garrison, J. C., Rold, T. L., Sieckman, G. L., Figueroa, S. D., Volkert, W. A., Jurisson, S. S., and Hoffman, T. J. (2007) In vivo evaluation and small-animal PET/CT of a prostate cancer mouse model using ^{64}Cu bombesin analogs: side-by-side comparison of the CB-TE2A and DOTA chelation systems. *J. Nucl. Med. 48*, 1327–1337.

(77) Kumar, K., Tweedle, M. F., Malley, M. F., and Gougoutas, J. Z. (1995) Synthesis, stability, and crystal structure studies of some Ca^{2+}, Cu^{2+}, and Zn^{2+} complexes of macrocyclic polyamino carboxylates. *Inorg. Chem. 34*, 6472–6480.

(78) Boswell, C. A., Sun, X., Niu, W., Weisman, G. R., Wong, E. H., Rheingold, A. L., and Anderson, C. J. (2004) Comparative in vivo stability of copper-64-labeled cross-bridged and conventional tetraaza-macrocyclic complexes. *J. Med. Chem. 47*, 1465–1474.

(79) Boswell, C. A., McQuade, P., Weisman, G. R., Wong, E. H., and Anderson, C. J. (2005) Optimization of labeling and metabolite analysis of copper-64-labeled azamacrocyclic chelators by radio-LC-MS. *Nucl. Med. Biol. 32*, 29–38.

(80) Sprague, J. E., Peng, Y., Fiamengo, A. L., Woodin, K. S., Southwick, E. A., Weisman, G. R., Wong, E. H., Golden, J. A., Rheingold, A. L., and Anderson, C. J. (2007) Synthesis, characterization and in vivo studies of Cu(II)-64-labeled cross-bridged tetraazamacrocycle-amide complexes as models of peptide conjugate imaging agents. *J. Med. Chem. 50*, 2527–2535.

(81) Bass, L. A., Wang, M., Welch, M. J., and Anderson, C. J. (2000) In vivo transchelation of copper-64 from TETA-octreotide to superoxide dismutase in rat liver. *Bioconjugate Chem. 11*, 527–532.

(82) Anderson, C. J. (2001) Metabolism of radiometal-labeled proteins and peptides: what are the real radiopharmaceuticals in vivo? *Cancer Biother. Radiopharm. 16*, 451–455.

(83) Le Jeune, N., Perek, N., Denoyer, D., and Dubois, F. (2004) Influence of glutathione depletion on plasma membrane cholesterol esterification and on Tc-99m-sestamibi and Tc-99m-tetrofosmin uptakes: a comparative study in sensitive U-87-MG and multidrug-resistant MRP1 human glioma cells. *Cancer Biother. Radiopharm. 19*, 411–421.

(84) Bähr, O., Rieger, J., Duffner, F., Meyermann, R., Weller, M., and Wick, W. (2003) P-glycoprotein and multidrug resistance-associated protein mediate specific patterns of multidrug resistance in malignant glioma cell lines, but not in primary glioma cells. *Brain Pathol. 13*, 482–494.

(85) Nakatsu, S., Kondo, S., Kondo, Y., Yin, D., Peterson, J. W., Kaakaji, R., Morimura, T., Kikuchi, H., Takeuchi, J., and Barnett, G. H. (1997) Induction of apoptosis in multi-drug resistant (MDR) human glioblastoma cells by SN-38, a metabolite of the camptothecin derivative CPT-11. *Cancer Chemother. Pharmacol. 39*, 417–423.

(86) Ketterer, B., Neumcke, B., and Läuger, P. (1971) Transport mechanism of hydrophobic ions through lipid bilayer membranes. *J. Membr. Biol. 5*, 225–245.

(87) Flewelling, R. F., and Hubbel, W. L. (1986) Hydrophobic ion interactions with membranes. Thermodynamic analysis of tetraphenylphosphonium binding to vesicles. *Biophy. J. 49*, 531–540.

(88) Honig, B. H., Hubell, W. L., and Flewelling, R. F. (1986) Electrostatic interactions in membranes and proteins. *Annu. Rev. Biophys. Biophys. Chem. 15*, 163–193.

(89) Grunwald, E., Baughman, G., and Kohnstam, G. (1960) The solvation of electrolytes in dioxane-water mixtures, as deduced from the effect of solvent change on the standard partial molar free energy. *J. Am. Chem. Soc. 82*, 5801–5811.

(90) Kandela, I. K., Lee, W., and Indig, G. L. (2003) Effect of the lipophilic/hydrophilic character of cationic triarylmethane dyes on their selective phototoxicity toward tumor cells. *Biotech. Histochem. 78*, 157–169.

(91) Kandela, K., Bartlett, J. A., and Indig, G. L. (2002) Effect of molecular structure on the selective phototoxicity of triarylmethane dyes towards tumor cells. *Photochem. Photobiol. Sci. 1*, 309–314.

(92) Horobin, R. W. (2001) Uptake, distribution, and accumulation of dyes and fluorescent probes within living cells. A structure-activity modeling approach. *Adv. Colour Sci. Technol. 4*, 101–107.

(93) Fantin, V. R., Beradi, M. J., Scorrano, L., Korsmeyer, S. J., and Leder, P. (2002) A novel mitochondriotoxic small molecule that selectively inhibits tumor cell growth. *Cancer Cell 2*, 29–42.

(94) Britten, C. D., Rowinsky, E. K., Baker, S. D., Weiss, G. R., Smith, L., Stephenson, J., Rothenberg, M., Smetzer, L., Cramer, J., Collins, W., Von Hoff, D. D., and Eckhardt, S. G. (2000) A phase I and pharmacokinetic study of the mitochondrial-specific rhodacyanine dye analog MKT 077. *Clin. Cancer Res. 6*, 42–49.

(95) Trapp, S., and Horobin, R. W. (2005) A predictive model for the selective accumulation of chemicals in tumor cells. *Eur. Biophys. J. 34*, 959–966.

(96) Zhou, Y., Kim, Y. S., Shi, J., Jacobson, O., Chen, X., and Liu, S. (2011) Evaluation of ^{64}Cu-labeled acridinium cation: a PET radiotracer targeting tumor mitochondria. *Bioconjugate Chem. 22*, 700−708.

Bioconjugate Chemistry

COMMUNICATION

pubs.acs.org/bc

Engineering a Synthetic Ligand for Tumor Necrosis Factor−Alpha

Nidhi Gupta,[⊥] Paul E. Belcher,[⊥] Stephen Albert Johnston,* and Chris W. Diehnelt*

Center for Innovations in Medicine, The Biodesign Institute at Arizona State University, Tempe, Arizona 85287, United States

Supporting Information

ABSTRACT: One approach to prepare protein binding ligands is to join two low-affinity ligands that bind different sites on the target protein to create a high-affinity bivalent ligand. This typically requires some knowledge of the ligand binding site and requires exquisite orientation of the ligands in order to achieve maximum binding affinity. Here, we explored the limit of affinity improvement possible with no a priori knowledge of peptide binding site and with minimal effort spent in linking the lead peptides. We compared the affinity enhancement from linking two peptides with low affinity for tumor necrosis factor-α (TNFA) to the affinity enhancement from linking affinity improved versions of these peptides using several different scaffolds. We found that we achieved the highest affinity gain not by the precise positioning of the peptides, but rather by using affinity improved versions of the lead peptides to produce synbodies with apparent K_D's of 9 to 48 nM. Kinetic analysis showed that the binding kinetics of the synbody are strongly influenced by the kinetics of the starting peptide. This suggests that careful selection of peptides based on their kinetic profile prior to linking will influence the kinetics of the final binding agent.

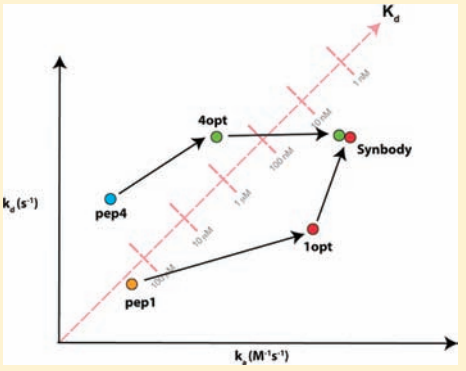

In the post-genomic era, a major challenge is to characterize the human proteome in order to understand individual cells, disease mechanisms, and therapeutic modes of action. A systematic and comprehensive collection of specific affinity reagents directed against all human proteins is essential for characterizing the human proteome, and numerous groups are working to discover protein binding ligands for this effort.[1] Ligands are typically discovered via directed evolutionary technologies (phage, mRNA display), consisting of multiple recursive cycles, each with library generation and subsequent screenings in functional assays.[2−5] Directed evolution approaches and combinatorial chemistry approaches have also been used to discover peptides and peptidomimetics with high affinity (K_D < 100 nM) for a protein target.[6−9] Another approach to create high-affinity ligands is to link together two low-affinity ligands that bind different sites on the target protein to produce a ligand with an affinity that approaches the product of the affinities of each ligand. The basis of this approach was developed by Jencks[10] and demonstrated by Fesik, who linked two small molecules together to produce a ligand whose affinity approached the product of the affinities of the individual ligands.[11] This method, referred to as SAR by NMR, required an in-depth knowledge of the target structure and position of the small molecule binding sites to allow the correct linker length to be elucidated. We are interested in simpler methods to creating ligands based on the same principle.

We recently applied this basic approach, in which two low affinity 12 amino acid (aa) peptides (K_D = 2 and 5 μM) that bound different sites on Gal80 were linked using a DNA scaffold to produce a high-affinity (K_D = 5 nM) protein ligand, called a synbody.[12] While this technique yielded high-affinity ligands, the linkage of peptide pairs was quite sensitive to distance and orientation in order to maximize the binding affinity of the ligand. This was likely a consequence of targeting specific binding sites on Gal80 using short peptides but might not hold true if longer peptides were used. The structural constraint of the DNA linker may also have been limiting. If longer peptides (20 aa in length) were used in a synbody, it could be possible that the linkage requirements are less strict than those for small molecules. Peptides of this length are not expected to adopt stable secondary structures and should be free to bind regions on the protein surface rather than small, well-defined binding sites,[13] thus making the requirements for linkage less strict. We have also shown that, due to the linear nature of many 20-aa peptides, it is possible to make single amino acid substitutions to identify substitutions that increase affinity and then add up positive substitutions to produce an optimized peptide whose affinity is the sum of the ΔG's of each substitution.[14] Additionally, rather than use a rigid DNA scaffold to link the peptides, the use of a flexible linker should allow each peptide to explore conformational space after binding, meaning the distance between each ligand becomes less important.[15] If these suppositions hold true, it should be possible to identify peptides with modest affinity for a target and then optimize the peptides binding affinity prior to linking with a flexible linker in order to create a high-affinity ligand. We propose a method (Figure 1A) in which a small library of random peptides is screened to identify lead peptides with micromolar affinity for a target protein. The lead peptides are then affinity improved using a thermodynamic additivity method

Received: February 18, 2011
Revised: June 23, 2011
Published: July 18, 2011

ACS Publications © 2011 American Chemical Society

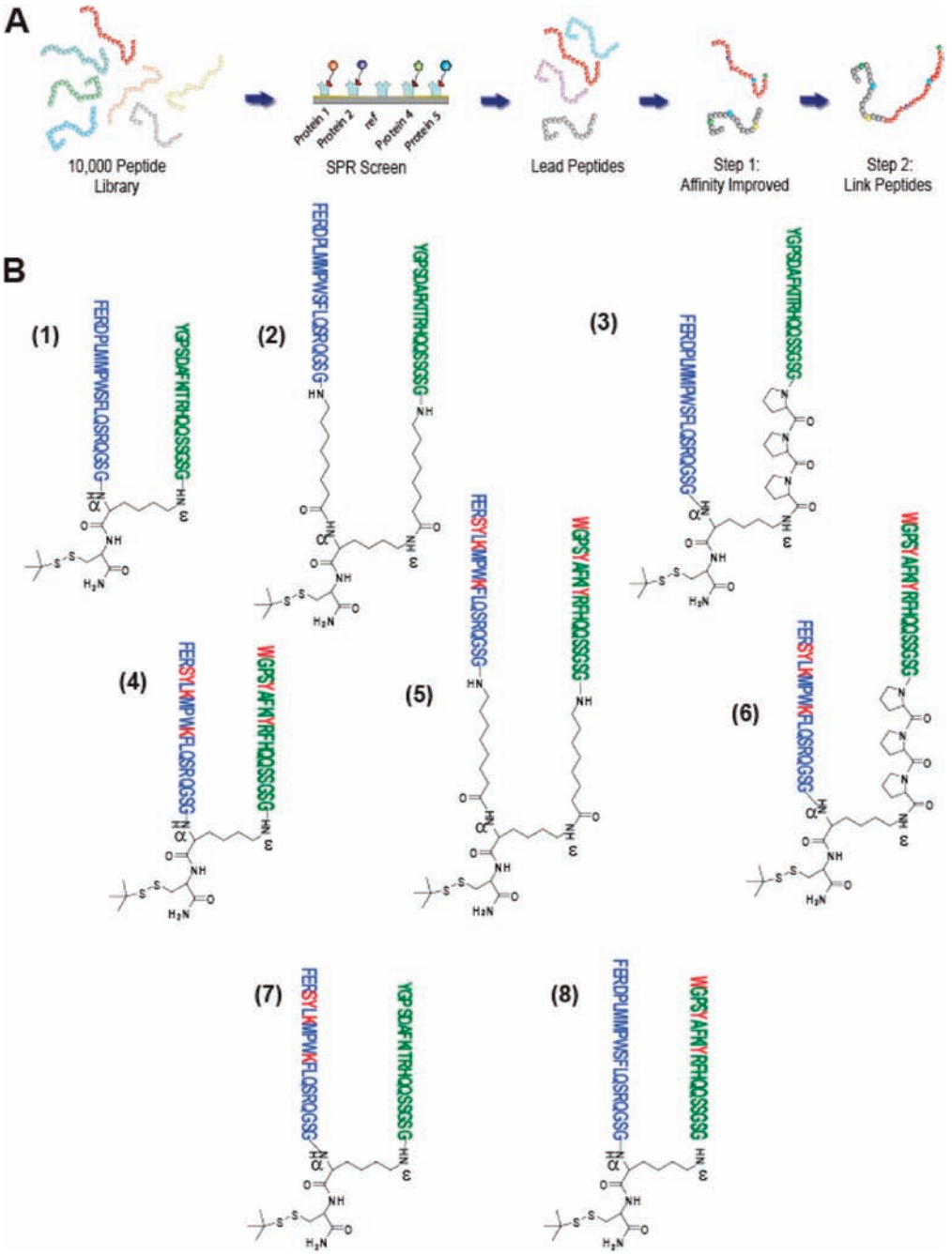

Figure 1. (A) Scheme to engineer protein affinity agents starting from a small library of peptides. (B) Chemical structures of synbodies tested for TNFA.

to increase the affinity from 50- to 200-fold over the starting peptide.[14] The affinity-improved peptides are then linked together using a variety of scaffolds to yield another 10- to 100-fold affinity improvement. Simple bivalent linking should produce a 10- to 500-fold improvement in binding affinity over the starting peptides, as similar affinity improvements have been reported in the literature.[9] In principle, this should convert two peptides with modest binding affinity into a high affinity ligand with a K_D that is 1000 to 10 000 times better than the starting peptide without having a priori knowledge of each peptide's binding site.

To test this concept, we used peptide ligands for TNFA that were previously identified and optimized in our group.[14] The peptides were identified from a SPR screen of a 10 000-peptide library of 20-mers against TNFA and were then affinity-improved using a thermodynamic additivity method we developed. The lead peptides are referred to as **pep1** (FERDPLMMPWSFLQSRQGSC) and **pep4** (YGPSDAFKITRHQQSSGSC) and have equilibrium dissociation constants (K_D) of 160 ± 16 μM and 23 ± 2 μM, respectively, while the affinity optimized peptides referred to as **1opt** (FERSYLKMPWKFLQSRQGSC) and **4opt** (WGPSYAFKYRFHQQSSGSC) have K_D's = 1.6 ± 0.3 μM for **1opt** and K_D = 90 ± 2 nM for **4opt**. The details of the peptide discovery and optimization are found in ref 14. We then joined **pep1** and **pep4** on three different scaffolds to create candidate synbodies and joined **1opt** and **4opt** on the same scaffolds to create optimized synbodies (Figure 1B). As we had no knowledge

Scheme 1. Synthesis Scheme for Synbody (2) and (5)

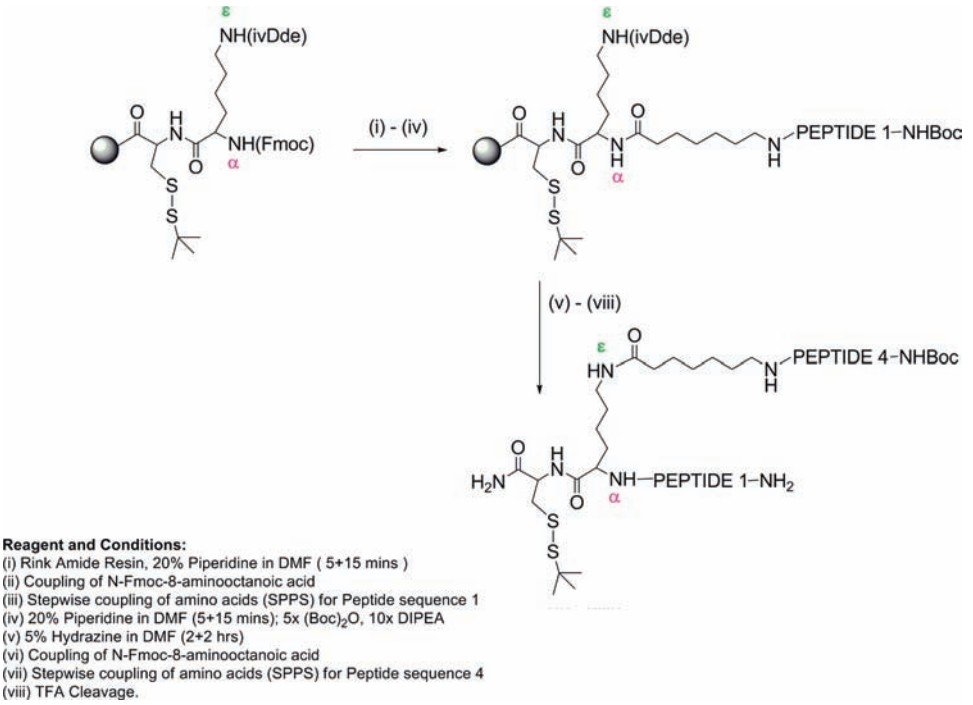

of the peptide binding sites, we chose scaffolds with varying degrees of flexibility and linker length, since soluble TNFA is a homotrimer with a diameter of ~7 nm,[16] and each peptide is approximately 7 nm in length if fully extended. Lysine was chosen as a core scaffold to link **pep1** and **pep4**, as this is a widely used linking strategy referred to as a MAP (multiple antigenic peptide),[17] and we have successfully used this scaffold to make a high affinity synbody to AKT1.[18] Utilizing both α- and ε-amino functional groups of lysine, **pep1** and **pep4** were synthesized respectively using modified divergent stepwise SPPS. Additional synbodies were constructed from the lysine core by the addition of 8-amino octanoic acid (Scheme 1) or Pro-Pro-Pro[19] in order to explore differences in peptide positioning, orientation, and rigidity. These were synthesized in a similar manner as synbody (**1**) to preserve the linkage chemistry. Each synbody was purified by HPLC and analyzed by MALDI to confirm identity (Supporting Information). Synbodies (**4**), (**5**), and (**6**) were synthesized in the same manner.

As an initial test of the binding affinity of each synbody, different amounts of TNFA were immobilized on four spots of one flow cell using a Biacore A-100 SPR and a 100 nM solution of each synbody was injected. TNFA was immobilized by amine coupling to yield surfaces with 1000 to 7000 response units (RU's) of TNFA. This high level of TNFA was used to ensure that each synbody produced an observable sensorgram. The chart in Figure 2A shows the response from each synbody on all four TNFA surfaces. It can be seen that there is little difference in the binding levels produced by synbodies (**1**) and (**2**), yet there is roughly half as much binding from synbody (**3**). This could be indicative of synbody (**3**) having lower affinity than (**1**) or (**2**) or that the binding site of (**3**) is partially blocked due to immobilization of TNFA. The responses for the synbodies composed of the optimized peptides are much higher than their wild-type analogues indicating that they have higher binding affinity. However, due to the high levels of TNFA immobilized, we could not accurately determine the binding affinity of each synbody, as the dissociation rate was artificially slowed due to rebinding of the synbody during the dissociation phase (data not shown).

To determine the binding affinity and kinetics of each synbody, we again used SPR but used two different TNFA immobilization strategies to prepare low-density TNFA surfaces to control for immobilization artifacts. In the first method, we used amine immobilization to prepare low-density TNFA surfaces that would produce R_{max} values less than 100 RU's. In the second approach, monobiotinylated TNFA was prepared according to the protocol outlined in ref 16 and captured on an SPR surface coated with Neutravidin. We captured different densities of biotin-TNFA per flow cell in order to produce R_{max} values less than 100 RU's. Increasing concentrations of synbody (**1**) were injected over the TNFA surfaces, and the resulting sensorgrams were globally fit using Biacore software to a 1:1 binding model to determine the association rate (k_a), dissociation rate (k_d), and dissociation constant $K_D = k_d/k_a$. The quality of the fitting was assessed by the χ^2 goodness-of-fit test and was less than 2.0 for each TNFA surface. Representative sensorgrams from synbody (**1**) on the biotin-TNFA surface are shown in Figure 2B (top). Comparison with sensorgrams from the amine-immobilized surface showed that there was no statistically significant difference (at the 0.05 level) between the K_D values determined on the two different surfaces. Therefore, replicate injections across multiple surfaces were averaged and the results are summarized in Table 1 which shows that that synbody (**1**) has an apparent $K_D = 766 \pm 405$ nM. Synbody (**2**) and (**3**) were analyzed in a similar manner and it can be seen that the choice of scaffold does have an effect on the binding affinity (representative sensorgrams are shown in Supporting Information). In fact, the rapid kinetics of (**3**) could not be accurately fit and the K_D was estimated to be >1 μM. This result is in concordance with other observations

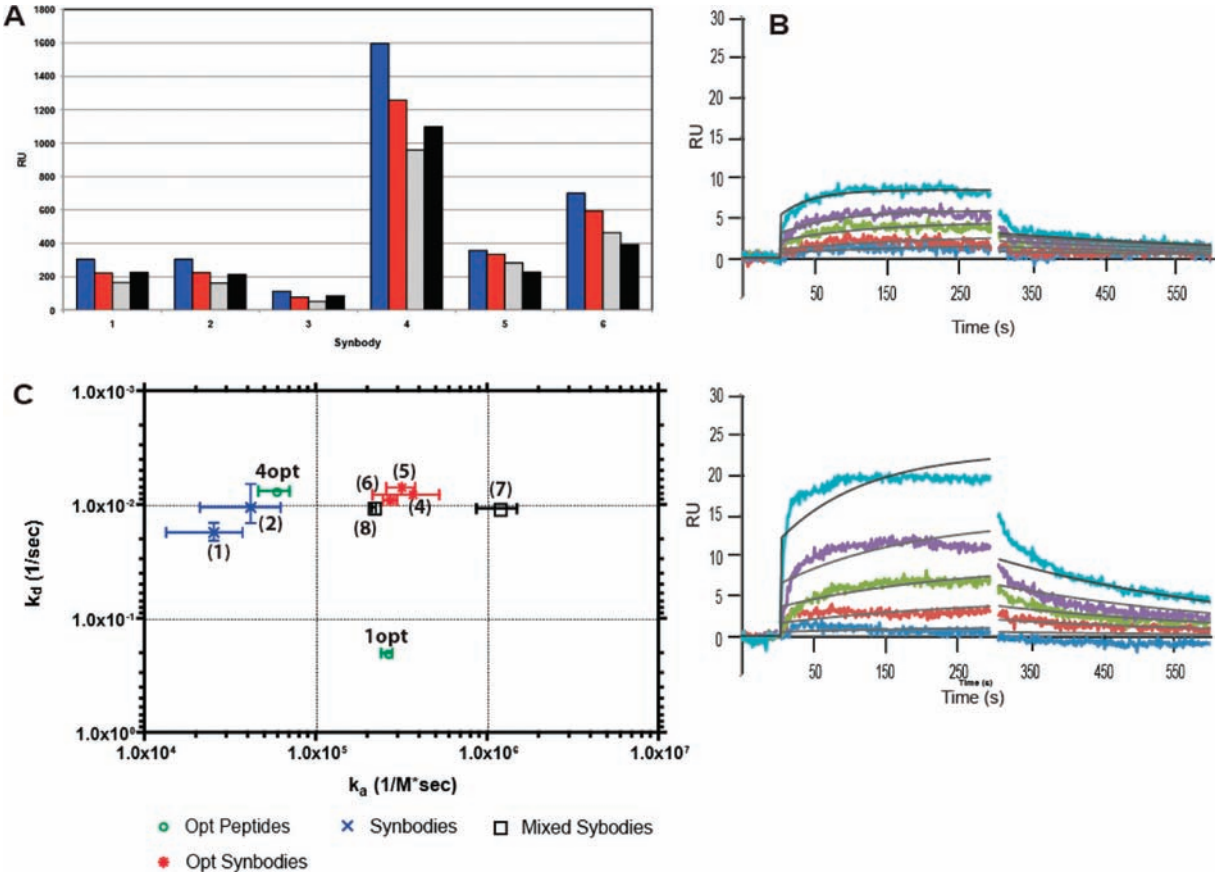

Figure 2. (A) Binding responses from a 100 nM injection of each synbody injected on a SPR flow cell with 4 different levels of immobilized TNFA. The blue bar corresponds to the surface with the highest level of immobilized TNFA, while the gray bar corresponds to binding on the surface with the lowest level of immobilized TNFA. (B) SPR sensorgrams of synbody (**1**) (top) and synbody (**4**) (bottom) binding to immobilized TNFA. The data set was globally fit using a 1:1 binding model as represented by the solid lines. (C) Plot of k_a vs k_d to illustrate the differences in binding kinetics of the different TNFA ligands.

Table 1. Equilibrium Dissociation Constants and Kinetic Rate Constants for TNFA Synbodies

synbody	k_a (M^{-1} s^{-1})	k_d (S^{-1})	K_D (M) bivalent ligand	K_D (M) ligand	β
[a]pep1	n.d.	n.d.	-	1.60×10^{-4} (±0.16)	-
[a]pep4	n.d.	n.d.	-	2.30 × 105 (± 0.20)	-
(**1**)	2.53×10^{4} (±1.20)	1.74×10^{-2} (±0.93)	7.66×10^{-7} (±4.05)	-	209
(**2**)	4.15×10^{4} (±2.05)	1.05×10^{-2} (±0.79)	2.31×10^{-7} (+0.92)	-	693
(**3**)	n.d.	n.d.	$>1 \times 10^{-6}$	-	<100
[a]1opt	2.6×10^{5} (±0.2)	2.0×10^{-1} (±0.2)	-	7.0×10^{-7} (±0.02)	-
[a]4opt	5.8×10^{4} (±1.2)	7.5×10^{-3} (±0.8)	-	1.3×10^{-7} (±0.30)	-
(**4**)	3.67×10^{5} (±1.54)	8.15×10^{-3} (±1.55)	2.57×10^{-8} (±1.18)	-	27
(**5**)	3.17×10^{5} (±0.61)	7.05×10^{-3} (±0.34)	2.28×10^{-8} (±0.54)	-	16
(**6**)	2.71×10^{5} (±0.25)	9.09×10^{-3} (±0.94)	3.39×10^{-8} (±0.66)	-	17
(**7**)	1.17×10^{6} (±0.31)	1.07×10^{-2} (±0.22)	9.14×10^{-9} (±2.71)	-	2516
(**8**)	2.17×10^{5} (±0.06)	1.05×10^{-2} (±0.21)	4.81×10^{-8} (±1.75)	-	3326

[a] Data from ref 14. Data were fit with a 1:1 Langmuir binding model and are the average of 2 or more runs over surfaces with ligand densities that will produce an R_{max} < 100 RU. Each sensorgram included had a χ^2 goodness-of-fit value of <10. n.d. = not determined.

of the importance of the orientation of the peptide pairs in order to achieve maximum binding affinity.[12] However, the optimized synbodies had apparent dissociation constants in a narrow range from 33.9 ± 7 nM for (**6**), to 25.7 ± 12 nM for (**4**) (Figure 2B), to a low of 22.8 ± 5 nM for (**5**). This somewhat surprising result suggests that the orientation or positioning of these peptides is not as critical as for the lower affinity **pep1** and **pep4**. This could be a consequence of the affinity improvement method altering the binding region on each peptide as the amino acid substitutions that increased the affinity for **1opt** and **4opt** were located in

the first 12 amino acids of each peptide. This implies that the N-terminal region of each peptide interacts with TNFA and as such is less sensitive to the scaffold type located on the C-terminal side of each peptide. To find out if it is necessary to optimize both peptides to maximize the apparent K_D, we prepared two additional synbodies composed of the lead peptide coupled to an optimized peptide on the lysine scaffold. Synbody (**7**) was prepared from a combination of **1opt** and **pep4** while (**8**) was prepared from a combination of **pep1** and **4opt**. The affinity and kinetics of these synbodies were measured in the same manner as before, and it was found that (**7**) had a $K_D = 9.14 \pm 2.7$ nM while (**8**) had a $K_D = 48.1 \pm 2.7$ nM. Thus, it is possible to get a large increase in apparent affinity by linking an affinity optimized peptide with an unoptimized one.

A rate map was prepared in order to compare the binding kinetics between different synbodies (Figure 2C). In this plot, k_a values were plotted on the *x*-axis and k_d values were plotted on the *y*-axis; data points to the right on the *x*-axis represents faster on-rates, while data points higher on the *y*-axis represent slower off-rates. Synbodies with highest affinity appear in the upper right-hand quadrant of the plot, whereas lowest affinity is in the lower left-hand corner. Synbodies composed of **pep1** and **pep4** had a larger spread in k_a and k_d than those composed of the optimized peptides. It is also evident that the increase in affinity of the optimized synbodies is driven mostly by an increase in k_a with only a small change in k_d versus the starting synbodies. The kinetic data for **1opt** and **4opt**[14] were also plotted and show that the kinetic profile of the optimized synbodies appears to incorporate the k_a of **1opt** and the k_d of **4opt** into the resulting synbodies. It is interesting to note that there does not appear to be an avidity effect observed for the optimized synbodies, as there was no decrease in k_d that is usually observed for avid binding.

As we began this work with the aim of improving the affinity of two modest affinity ligands in an engineered fashion, the enhancement factor, β,[20] was calculated for each synbody in order to quantify the affinity enhancement of the bivalent synbody versus the starting peptides. β was defined as $\beta = K_{D(peptide)}/K_{D(synbody)}$ where $K_{D(peptide)}$ of the weakest binding peptide was used. As can be seen in Table 1, linking **pep1** and **pep4** with three different scaffolds results in β values from <100 to 690. It seems that for this peptide pair the peptide orientation is important in order to achieve a large affinity improvement over the individual peptides. However, when the optimized peptides are linked, there is a small range of β values. Whether the smaller enhancements observed are a product of the difficulty in linking together two peptides with higher affinity or some other effect is unclear. This result though is consistent with other reports of modest enhancements when linking together two peptides with submicromolar affinity.[9] Large enhancements were observed when a single optimized peptide was linked to **pep1** or **pep4**, β values of 2516 and 3326, respectively. Nevertheless, whether a single optimized peptide or two optimized peptides are used, the net effect of this two-step process is *a* > 6400-fold improvement in affinity from the starting peptides to several ligands with K_D's that range from 9 to 34 nM without any knowledge of the peptide binding sites. Additionally, the lax linkage requirement implies that these peptides likely do not bind in a tightly defined binding pocket but rather make a few contacts with the surface of the protein. If each peptide had targeted a small binding pocket, then it would be expected that small changes in peptide orientation would have significant effects on affinity.

This work demonstrates that it is possible to discover two peptides with modest affinity for a target protein and gain a >5000-fold improvement in affinity when a thermodynamic optimization method is used in conjunction with different methods of bivalent linking. The in vitro system presented here enables the screening for kinetic properties of each ligand, and the data demonstrate the possibility that a "mix-and-match" strategy could be used to engineer a ligand with a desired kinetic profile. By combining one peptide with $k_a \approx 10^5\ M^{-1}\ s^{-1}$ with a second peptide with $k_d \approx 10^{-3}\ s^{-1}$ we were able to build a 23 nM ligand with $k_a \approx 10^5\ M^{-1}\ s^{-1}$ and $k_d \approx 10^{-3}\ s^{-1}$. With these lessons in mind, it could be possible to modify the thermodynamic additivity process to tailor the kinetic profile of each peptide, which should then translate into a kinetic profile optimized for the final ligand. This two-step process should enable the engineered construction of future synbodies.

■ ASSOCIATED CONTENT

Supporting Information. Materials and methods, characterization of synbodies by MALDI-TOF and binding analysis by SPR. This material is available free of charge via the Internet at http://pubs.acs.org.

■ AUTHOR INFORMATION

Corresponding Author

*E-mail addresses: stephen.johnston@asu.edu; chris.diehnelt@asu.edu.

Author Contributions

⊥These two authors contributed equally to this work.

■ ACKNOWLEDGMENT

We thank John Lainson for assistance with SPR experiments and Melanie Hadlock for her assistance in various parts of this work. We also thank Seongmin Hahn, Monica Kot, Mike Ewing, Donnie Shepard, Loren Howell, Zhan-Gong Zhao, and Zbigniew Cichacz for synbody synthesis and purification. We also wish to thank Phillip Stafford, Matthew Greving, and Neal Woodbury for their contribution to this work. The Arizona Translational Research Initiative Funds to SAJ and C.W.D supported this work.

■ REFERENCES

(1) Uhlen, M., Graslund, S., and Sundstrom, M. (2008) A pilot project to generate affinity reagents to human proteins. *Nat. Methods 5*, 854–855.

(2) Ellington, A. D., and Szostak, J. W. (1990) In vitro selection of RNA molecules that bind specific ligands. *Nature 346*, 818–822.

(3) Tuerk, C., and Gold, L. (1990) Systematic evolution of ligands by exponential enrichment: RNA ligands to bacteriophage T4 DNA polymerase. *Science 249*, 505–510.

(4) Smith, G. P., and Petrenko, V. A. (1997) Phage display. *Chem. Rev. 97*, 391–410.

(5) Roberts, R. W., and Szostak, J. W. (1997) RNA-peptide fusions for the in vitro selection of peptides and proteins. *Proc. Natl. Acad. Sci. U. S. A. 94*, 12297–302.

(6) Devlin, J. J., Panganiban, L. C., and Devlin, P. E. (1990) Random peptide libraries: a source of specific protein binding molecules. *Science 249*, 404–6.

(7) Alluri, P. G., Reddy, M. M., Bachhawat-Sikder, K., Olivos, H. J., and Kodadek, T. (2003) Isolation of protein ligands from large peptoid libraries. *J. Am. Chem. Soc. 125*, 13995–14004.

(8) Kodadek, T., Reddy, M. M., Olivos, H. J., Bachhawat-Sikder, K., and Alluri, P. G. (2004) Synthetic molecules as antibody replacements. *Acc. Chem. Res. 37*, 711–718.

(9) Shrivastava, A., Wronski, M. A. v., Sato, A. K., Dransfield, D. T., Sexton, D., Bogdan, N., Pillai, R., Nanjappan, P., Song, B., Marinelli, E., DeOliveira, D., Luneau, C., Devlin, M., Muruganandam, A., Abujoub, A., Connelly, G., Wu, Q. L., Conley, G., Chang, Q., Tweedle, M. F., Ladner, R. C., Swenson, R. E., and Nunn, A. D. (2005) A distinct strategy to generate high-affinity peptide binders to receptor tyrosine kinases. *Protein Eng. Des. Sel. 18*, 417–424.

(10) Jencks, W. P. (1981) On the attribution and additivity of binding energies. *Proc. Natl. Acad. Sci. U. S. A. 78*, 4046–4050.

(11) Shuker, S. B., Hajduk, P. J., Meadows, R. P., and Fesik, S. W. (1996) Discovering high-affinity ligands for proteins: SAR by NMR. *Science 274*, 1531–1534.

(12) Williams, B., Diehnelt, C. W., Belcher, P, Greving, M, Woodbury, N. W., Johnston, S. A., and Chaput, J. C. (2009) Creating protein affinity reagents by combining peptide ligands on synthetic DNA scaffolds. *J. Am. Chem. Soc. 131*, 17233–17241.

(13) Oyama, T., Sykes, K. F., Samli, K. N., Minna, J. D., Johnston, S. A., and Brown, K. C. (2003) Isolation of lung tumor specific peptides from a random peptide library: generation of diagnostic and cell-targeting reagents. *Cancer Lett. 202*, 219–230.

(14) Greving, M. P., Belcher, P. E., Diehnelt, C. W., Gonzalez-Moa, M. J., Emery, J., Fu, J., Johnston, S. A., and Woodbury, N. W. (2010) Thermodynamic additivity of sequence variations: an algorithm for creating high affinity peptides without large libraries or structural information. *PLoS One 5*, e15432.

(15) Krishnamurthy, V. M., Semetey, V., Bracher, P. J., Shen, N., and Whitesides, G. M. (2007) Dependence of effective molarity on linker length for an intramolecular protein−ligand system. *J. Am. Chem. Soc. 129*, 1312–1320.

(16) He, M. M., Smith, A. S., Oslob, J. D., Flanagan, W. M., Braisted, A. C., Whitty, A., Cancilla, M. T., Wang, J., Lugovskoy, A. A., Yoburn, J. C., Fung, A. D., Farrington, G., Eldredge, J. K., Day, E. S., Cruz, L. A., Cachero, T. G., Miller, S. K., Friedman, J. E., Choong, I. C., and Cunningham, B. C. (2005) Small-molecule inhibition of TNF-alpha. *Science 310*, 1022–5.

(17) Tam, J. P. (1988) Synthetic peptide vaccine design: synthesis and properties of a high-density multiple antigenic peptide system. *Proc. Natl. Acad. Sci. U. S. A. 85*, 5409–13.

(18) Diehnelt, C., Shah, M, Gupta, N, Belcher, P. E., Greving, M. P., Stafford, P, and Johnston, S. A. (2010) Discovery of high-affinity protein binding ligands - backwards. *PLoS One 5*, e10728.

(19) Arora, P. S. (2002) Design of artificial transcriptional activators with rigid poly-L-proline linkers. *J. Am. Chem. Soc. 124*, 13067–13071.

(20) Mammen, M., Choi, S.-K., and Whitesides, G. M. (1998) Polyvalent interactions in biological systems: implications for design and use of multivalent ligands and inhibitors. *Angew. Chem., Int. Ed. 37*, 2754–2794.

Supplementary Materials and Methods

Supporting Figures

Supporting Table 1. Percent purity, calculated m/z and measured m/z of each synbody used.

Synbody	Percent Purity (A_{280})	Calculated m/z	Measured m/z
(1)	100%	4841.3	4840.8
(2)	95%	5122.9	5123.1
(3)	90%	5131.9	5132.6
(4)	71%	5050.6	5050.6
(5)	75%	5332.2	5333.0
(6)	100%	5341.2	5342.9
(7)	87%	4917.4	4916.2
(8)	90%	4974.5	4973.5

Supporting Figure 1. MALDI spectrum from each synbody.

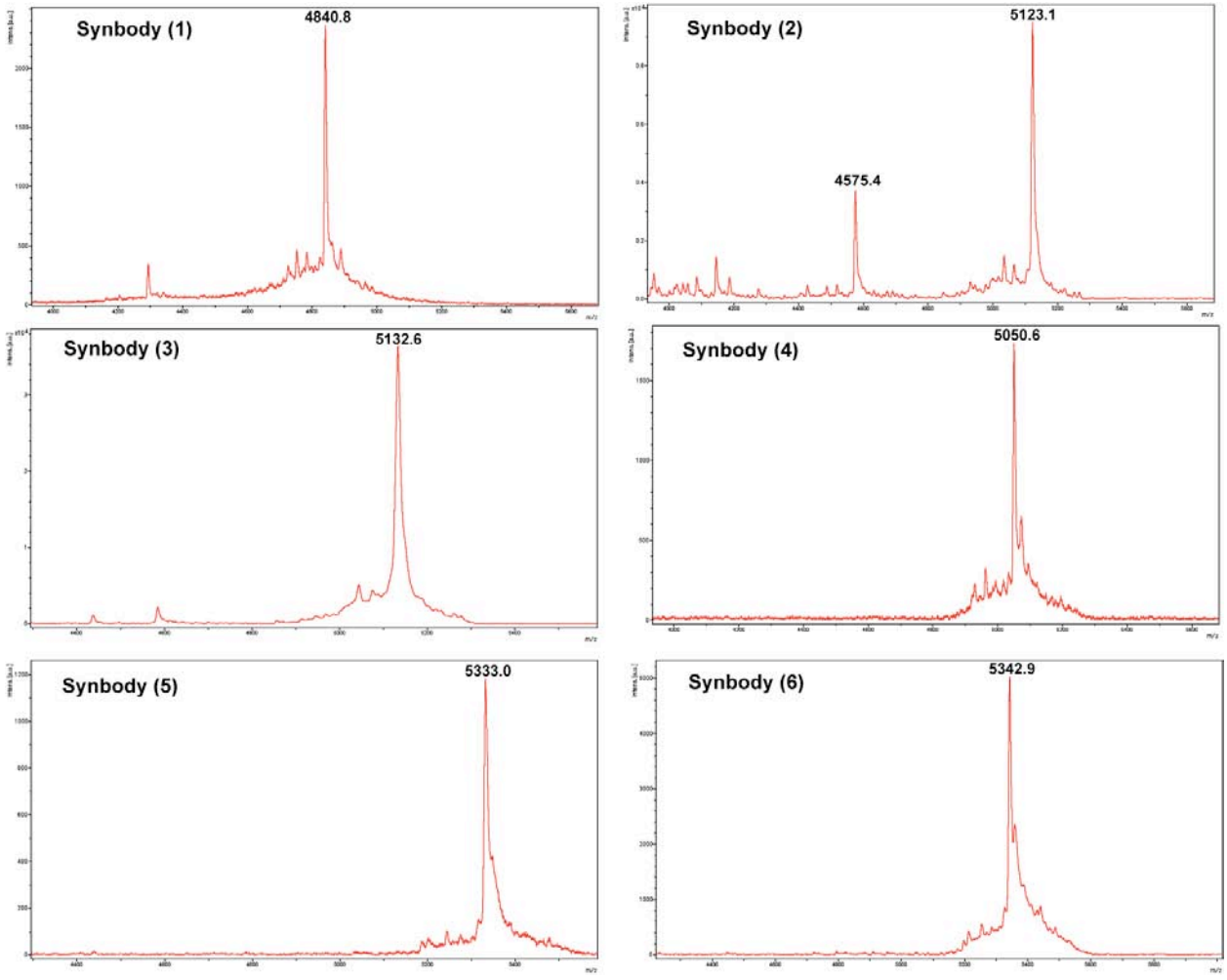

Supporting Figure 2. Representative sensorgrams from (A) synbodies composed of starting peptides and (B) synbodies composed of optimized peptides.

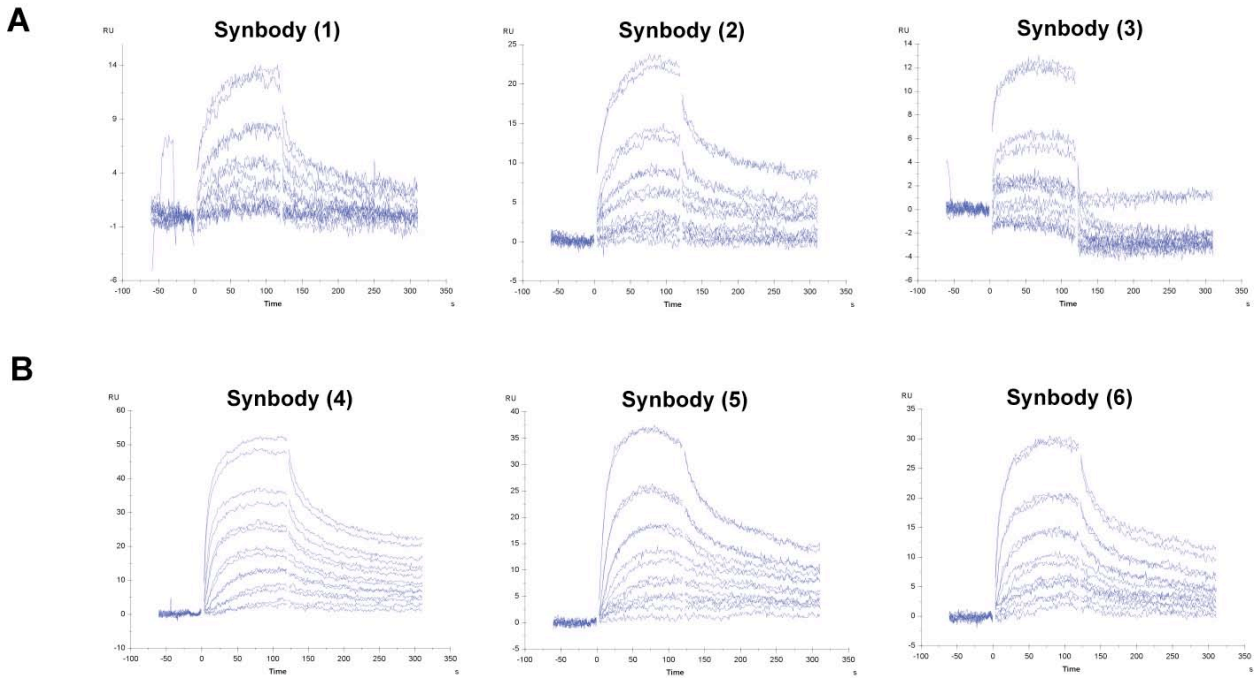

Synbody Synthesis

Reagents: All reagents and solvents were analytical, HPLC, or peptide synthesis grade. Commercial reagents and solvents were obtained from Aldrich and Fisher respectively and used without further purification unless otherwise noted. All amino acids and resins were purchased from Novabiochem, Chem Impex International Inc. as well as from Advanced Chem Tech and used without further purification. Linker, 8-(Fmoc-amino)octanoic acid was purchased from Sigma-Aldrich. All peptides were synthesized *via* standard Fmoc stepwise solid phase peptide synthesis (SPPS) on a Symphony Multiple Peptide Synthesizer at 25umole scale. Matrix-assisted laser desorption/ionization time-of-flight mass spectrometry (MALDI-TOF/MS) was carried out on Bruker Daltonics Microflex. UV measurements were carried out on a ND-1000 spectrophotometer instrument. All reversed-phase HPLC analysis and purifications were conducted on an Agilent 1200. Phenomenex Luna 5u analytical (4.6 x 250 mm) and semi-preparative (10 x 250 mm) C-18 columns were used for the analysis and purification.

Abbreviations: 9-Fluorenylmethyloxycarbonyl (Fmoc), Dimethylsulphoxide (DMSO), N,N-Dimethylformamide (DMF), Acetonitrile (AcCN), Methyl alcohol (MeOH), Dichloromethane (DCM), 1-Hydroxybenzotriazole (HOBt), 2-(1-*H*-benzotroazole-1-yl)-1,3,3-tetramethyluronium Hexafluorophosphate (HBTU), N-methylmorpholine (NMM), Trifluoroacetic acid (TFA), N,N-Diisopropylethylamine (DIPEA), Triisopropylsilane (TIPS), 1-(4,4-Dimethyl-2,6-dioxo-cyclohexylidene)-3-methyl-butyl (ivDde), Kaiser reagents [1.) Ninhydrine solution; 6% in ethanol, 2.) Potassium cynide in pyridine, 3.) Phenol in 80%ethanol]

Synbody Synthesis Protocol

All synbody candidates shown in Fig.1 (B) were synthesized *via* standard Fmoc stepwise solid phase peptide synthesis using orthogonal protecting groups on branched lysine. Two orthogonal groups were introduced using Fmoc-Lys(ivDde)-OH at the very C-terminus. The synthesis was carried out at 25umole scale on Rink amide resin (0.7mmole/g). The general strategy followed for the synthesis of synbody constructs was published (*18*). Linker was treated as protected amino acids and coupled in similar manner. Following the removal of Fmoc-protecting group by 20% piperidine in DMF for 5+15 mins, **pep1** was synthesized via stepwise addition of Fmoc amino acids on α-amino group of lysine. In the case of synbodies **(2)** and (**5**), 8-amino octanoic acid was added at the newly generated free α-amino group followed by assembly of **pep1**. The N-terminal Fmoc group was substituted with Boc group manually by treating with 5 fold excess of $(Boc)_2O$ (125umol, 0.027g) in presence of 10x DIPEA (250umol, 2.6nL). The resin was agitated at room temperature for 1 hr followed by standard washings with DMF (3x, 1min each), MeOH (2x, 1min each), DCM (2x, 1min each), DMF (3x, 1min each). An aliquot of resin was taken after MeOH wash for qualitative Kaiser Test. At this point, N^{ε}-(ivDde) protecting group was deprotected manually using 5% hydrazine monohydrate in DMF followed by standard washings. Removal of (ivDde) was monitored spectrophotometrically by absorption of the resulting 3,6,6-trimethyl-4-oxo-4,5,6,7-tetrahydra-1*H*-indazole at 300nm and was completed in 2 hrs. Deprotection was also determined by a standard qualitative Kaiser Test. The stepwise assembly of **pep4** was then accomplished at N^{ε}-lysine position using the peptide synthesizer. A five fold molar excess of Fmoc-amino acids, HOBt and NMM was used throughout the synthesis in a stepwise manner. The linker was coupled on ε -amino group followed by the stepwise addition amino acids to yield **pep4**. The final protected synbody construct was treated with cleavage cocktail (TFA: phenol: H_2O: TIPS :: 90:3: 5:2) for 2 hours at

room temperature and precipitated in cold diethyl ether. The precipitated construct was cooled for 15 mins in -80°C refrigerator to ensure complete precipitation. The solid was separated from the diethyl ether by centrifugation and the top phase was decanted off and pellet re-suspended with another addition of dry diethyl ether. The cooling and centrifugation process was done in triplicate. Upon completion, the constructs were dried and dissolved in water for HPLC purification. All the constructs were purified on reverse-phase HPLC on Phenomenex Luna 5u semi-preparative (10 x 250 mm) C-18 column using solvent system A: 0.1 % TFA in H_2O; solvent B: 90 % CH_3CN in 0.1 % TFA with a linear gradient method, 0 min, 10% B; 2 min, 10% B; 20 min, 45% B; 25 min, 95% B; 27 min, 95% B; 30 min, 100% B; 33 min, 10% B) with flow rate of 4 mL/min at a wavelength of 280 nm. The fractions were pooled and analyzed by MALDI-TOF mass spectrometry. The correct fraction was lyophilized and quantified using a ND-1000 spectrophotometer.

Surface Plasmon Resonance – Biotin-TNFA surface preparation

A Biacore A-100 SPR system was used for all affinity and kinetic determinations. The series S sensor chip CM5, amine coupling reagents and HBS-EP were obtained from GE Biacore. A standard amine immobilization protocol was performed at 25 °C using sodium acetate (10mM in 150mM sodium chloride, pH 4.5) as the immobilization buffer. Spots 1, 2 and 3 on each of the four flow cells of the CM-5 dextran chip were activated by a 10 minute injection of a freshly prepared 1:1 solution of 400mM 1-ethyl-3-(3-dimethylaminopropyl)-carbodimide (EDC): 100mM *N*-hydroxysuccimide (NHS) in water. The NHS-carboxy groups of spot 1 of the dextran surface were treated with a solution of neutravidin (50μg/ml) in sodium acetate (pH 5.0) for 8 mins at a flow rate of 10 μl/min. Any residual active sites were then quenched by a 5 min pulse of ethylene diamine (1M, pH 8.5). Similarly neutravidin was coupled to spots 2 and 3 via a 12 and 16 min injection cycle respectively, followed by quenching. An additionally 7 min injection of ethylene diamine was then pulsed over spots 1-3 to ensure no activated sites remained. This immobilization process was then repeated to couple neutravidin spots 4 and 5.

Prior to capture of the affinity tagged protein, the chip surface was conditioned with 8 - 30 second pulses of 10mM hydrochloride acid. Biotinylated TNFA was injected at 10uL/min until the desired level of capture was achieved. Two consecutive 30-second pulses of amino-

PEG_2-Biotin (1mM in HBS-N) were used to quench any excess biotin binding capacity of neutravidin.

For high-resolution kinetics, biotin-tagged TNFA was captured in multiple spot densities with Rmax's ranging from 20-100 RUs. Synbody samples in a range of concentrations were injected in a random order at a flow rate of 30µl/min over the flow cell surface. Buffer injections identical to the analyte were included throughout the analysis for the purpose of double referencing. Association and dissociation were monitored for 3 and 16 min, respectively. The surfaces were regenerated with 1 30-s injection of pH 2.5 glycine.

Amine Immobilization

A standard amine immobilization protocol was used as for neutravidin immobilization except TNFA (50µg/ml in sodium acetate pH 5.0) was injected on spot 1 for 5 minutes, spot 2 for 3 minutes, spot 4 for 2 minutes, and spot 5 for 4 minutes.

Data Analysis

To determine the kinetic parameters of the interaction, each data set was double referenced and fit globally using a 1:1 interaction model using Biacore A100 Evaluation or BiaEvaluation Software. Dissociation (k_d) and association (k_a) rate constants were obtained by nonlinear regression analysis of the primary sensorgram data according to a 1:1 binding model using the BIAevaluation version 3.2 software provided by the manufacturer. The dissociation constant K_D was calculated using the formula $K_D = k_d / k_a$.

Bioconjugate Chemistry

COMMUNICATION

pubs.acs.org/bc

New Covalent Capture Probes for Imaging and Therapy, Based on a Combination of Binding Affinity and Disulfide Bond Formation

Tolulope A. Aweda,[†] Vahid Eskandari,[†] David L. Kukis,[‡] David L. Boucher,[‡] Bernadette V. Marquez,[†] Heather E. Beck,[†] Gregory S. Mitchell,[‡] Simon R. Cherry,[‡] and Claude F. Meares*[,†]

[†]Chemistry Department and [‡]Center for Molecular and Genomic Imaging, University of California, Davis, California 95616, United States

Supporting Information

ABSTRACT: We describe the synthesis and development of new reactive DOTA-metal complexes for covalently targeting engineered receptors *in vivo*, which have superior tumor uptake and clearance properties for biomedical applications. These probes are found to clear efficiently through the kidneys and minimally through other routes, but bind persistently in the tumor target. We also explore the new technique of Cerenkov luminescence imaging to optically monitor radiolabeled probe distribution and kinetics *in vivo*. Cerenkov luminescence imaging uniquely enables sensitive noninvasive *in vivo* imaging of a β^- emitter such as ^{90}Y with an optical imager.

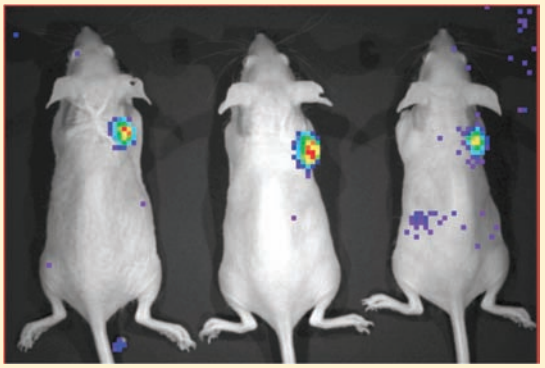

Developing synthetic molecules that specifically target cancer cells is a major goal of biomedical science. Among the most promising approaches are those based on affinity for a molecular target prominently displayed on the target cells, such as the RGD peptides for binding to cell surface integrins[1] or the somatostatin analogue octreotide for binding to type 2 somatostatin receptors.[2] This strategy may be complemented by the development of molecules with connector functions that link selectable sites of disease *in vivo* to validated probes, such as the widely used synthetic DOTA-metal complexes. Though there are variations, such connector molecules usually are engineered proteins derived from antibodies and are useful for "pretargeting", where the connector is administered before the probe.[3,4] An example is the streptavidin-scFv fusion proteins used as connectors for pretargeted imaging and therapy, along with biotin-tagged DOTA-metal probes possessing optimized biodistribution properties.[5] An alternative to the biotin−streptavidin system is infinite affinity probe capture using an engineered binding site that forms a stable covalent bond to the probe.[6] When formulated using a humanized antibody, the latter system presents fewer concerns about protein immunogenicity than streptavidin. Altering the cell-binding moiety of the connector protein while retaining the probe-binding receptor should make it practical to image a choice of biological targets with the same small probe molecule. Other approaches related to pretargeting include the dock-and-lock technique[7] and a tetrazine/trans-cyclooctene cycloaddition strategy.[8]

Previously, we engineered an antibody into a specific DOTA probe-binding receptor site, with a cysteine side chain placed for permanent probe capture.[9,10] Wei et al. have inserted this into reporter gene DAbR1 and demonstrated its favorable probe-capture properties in an animal model (Figure 1A).[11] Here, we consider changes in the structure and function of the synthetic DOTA probe, to further improve its biodistribution properties. Our prior work employed Michael addition of the cysteine thiol to an acrylamide side chain on the AABD(Y) probe, here denoted as **1**-Y (Figure 1C).[9,10] This reaction is clean and efficient *in vivo* and forms a stable thioether bond between probe and receptor, but clearance of the free probe occurs significantly through both the urinary and the slower intestinal route,[11] delaying removal of uncaptured probe from the organism. With the goal of identifying new probes that clear efficiently through the kidneys and minimally through other routes, we considered thiol−disulfide interchange, which has several features that allow manipulation of the probe's properties *in vivo*.

The DAbR1 tumor model system described by Wei et al.[11] provides an excellent starting point for testing the properties of candidate probe molecules *in vivo*. Because of the abundance of the free thiol form of the essential cysteine demonstrated for U-87 glioma expressing the DAbR1 reporter,[12] we chose to explore probes such as **5**-^{90}Y carrying the disulfide group as replacements for the electrophilic acryloyl group. This chemistry involves displacement of the leaving group RSH after the probe binds to the receptor, forming a new disulfide bond between the

Received: April 21, 2011
Revised: July 11, 2011
Published: July 14, 2011

ACS Publications © 2011 American Chemical Society

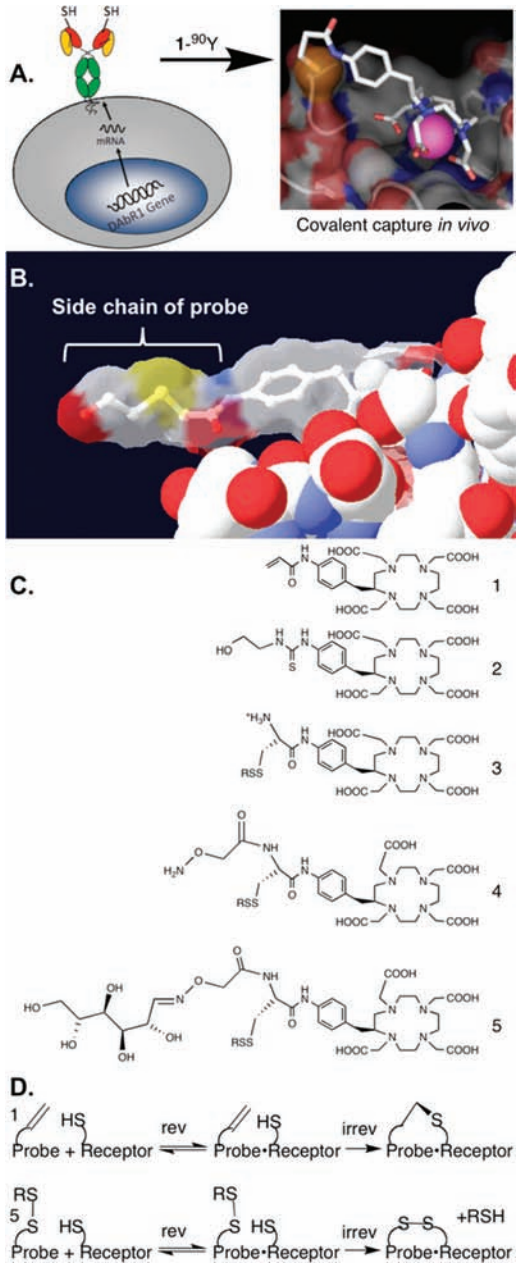

Figure 1. (A) Flow chart illustrating irreversible probe capture. First, the receptor is placed on the surface of a target cell, either by transfection of the receptor gene as shown,[11] or by pretargeting with a bispecific molecule;[5] then, the receptor captures the probe **1**-^{90}Y to form a reversible complex, which converts to a stable covalent complex (see D below). The pink sphere in the probe structure represents the chelated ^{90}Y (modified from ref 17 with permission). (B) From PDB file 1NC2,[13] the structure of compound **2**-Y bound to monoclonal antibody 2D12.5, from which the engineered receptor DAbR1 was derived; this shows the lack of interaction between the antibody (solid space fill) and the side chain of the probe (stick model inside transparent molecular surface), suggesting that the complex will accommodate probes with a variety of side chain shapes and sizes. For orientation, the benzene ring of **2**-Y can be compared to the benzene ring of **1**-^{90}Y in A. (C) Probe structures discussed here, before metal is added. See Scheme 1 for the structures of group R. (D) Comparison of Michael addition of probe **1**-^{90}Y with thiol−disulfide interchange of probe **5**-^{90}Y. Presumably, the latter reaction occurs *in vivo* as shown by the results in Figure 2.

probe and the engineered cysteine on the protein. A motivation for changing from Michael addition to thiol−disulfide interchange was that, if any probe−receptor conjugates are taken into endosomes inside cells, the disulfide bond between protein and probe is likely to be reduced and cleaved, releasing the probe and lessening concerns about triggering an immune response.

To implement the use of thiol−disulfide chemistry, it is necessary to address several points. The disulfide group on the new class of probes reacts only with thiols under physiological conditions, but this raises the question whether it would tag naturally occurring thiols in the body such as Cys-34 on albumin; what's more, it is possible that any such potential side reactions would be influenced by the nature of the side chain R in Figure 1C,D. A separate concern is that a disulfide linkage to receptor DAbR1 might prove less stable *in vivo* than the thioether linkage; if so, this could diminish the advantage of covalent bond formation.

Another consideration is that the side chain R might be varied to modify the clearance properties of the probe, for example, by increasing its hydrophilicity, in addition to adjusting the reactivity of the probe's disulfide group. The structure of the parent protein−probe complex from which DAbR1 was designed shows that the DOTA moiety of the probe interacts directly with the protein, while the probe's side chain protrudes into solution (Figure 1B).[13] This gives rise to the further possibility that a branched side chain can be introduced in order to add additional functions, such as a carbohydrate group to modify biodistribution.[14] Here, we report the first studies exploring these questions, using the new technique of Cerenkov luminescence imaging to optically monitor radiolabeled probe distribution and kinetics *in vivo*.[15] Cerenkov luminescence imaging uniquely enables sensitive noninvasive *in vivo* imaging of a β^- emitter such as ^{90}Y and offers informative qualitative images with relatively simple instrumentation.

MULTIMODAL DAbR1-2A-mCHERRY REPORTER GENE AND STABLE EXPRESSION IN U-87 GLIOMA CELLS

DNA sequences encoding the DAbR1 and mCherry reporter genes were subcloned to a lentiviral expression vector and linked by sequence encoding a 2A "self-cleaving" peptide to enable bicistronic expression of both reporter genes driven by a single CMV promoter. U-87 glioma cells were exposed to lentiviral particles delivering the basic reporter/selectable marker expression cassette to establish the U-87/DAbR1-2A-mCherry, or U-87/DC cell line. This cell line was then used for paired injections into the subscapular region of SCID Hairless Outbred (SHO) mice, with U-87/DC injected to the right shoulder and the parental U-87 line injected to the left shoulder. Details are provided in Supporting Information.

PROBE SYNTHESIS AND IMAGING

Prior to introduction of radiolabeled probe, mice were imaged on a Maestro 2 (Cambridge Research and Instrumentation) to verify fluorescent mCherry (and indirectly DAbR1) expression in U-87/DC derived tumors (Figure 2A). The new probes were synthesized as outlined in Scheme 1 and radiolabeled with ^{90}Y by the methods detailed in Supporting Information. Probes (8 μCi in 100 μL total volume) were administered via tail vein injection to mice sedated with 2% isoflurane. Following administration, Cerenkov luminescence images of the ^{90}Y distributions were

Scheme 1. Synthesis of New Probes[a]

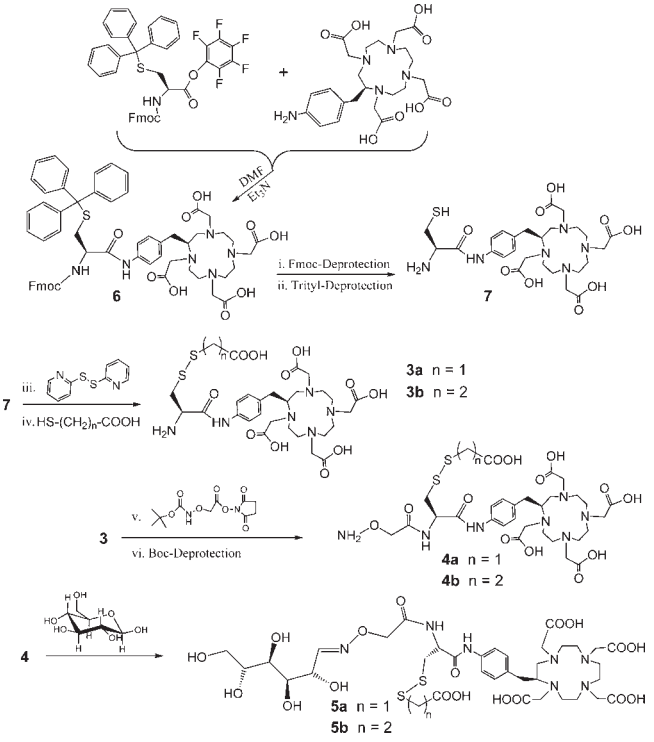

[a] The linear carbohydrate represented for **5** is one of several possible isomers. The leaving group may be selected to improve the biodistribution properties of the probe; e.g., **5a** and **5b** differ by $-CH_2-$ in the R group that is lost by displacement when the probe attaches to the DAbR1 receptor as shown in Figure 1D. Synthesis details are provided in Supporting Information.

acquired dynamically for a period of 45 min—Figure 2B shows the image acquired beginning at 9 min post injection on an IVIS 100 system (Caliper Life Sciences)—after which time the mice were awakened and returned to their cage. Cerenkov images were acquired again at 1.5 and 3.5 h post injection (Figure 2C,D).

IMAGES

As shown in Figure 2, tail-vein injection of **5b**-^{90}Y in 3 animals led to clear visualization of the U-87 tumor on the right shoulder, harboring the DAbR1 gene. A matching tumor on the left shoulder lacked this gene and was not visualized. Parallel results were observed *in vivo* with the homologous probe **5a**-^{90}Y. Uncaptured probes cleared almost exclusively through the kidney, leading to excellent tumor/background ratios one to two hours after injection.

BIODISTRIBUTIONS

To address whether the disulfide bond formed between the DAbR1 receptor and either of the **5**-^{90}Y probes persists *in vivo*, biodistributions were carried out 48 h after probe injection. Results are plotted in Figure 3. Even at 48 h, both **5**-^{90}Y probes show excellent concentration in tumor (6.3 ± 2.1%/g for **5b**-^{90}Y; 14.4 ± 4.5%/g for **5a**-^{90}Y; $p < 0.05$). The kidneys showed highest normal organ uptake (0.38 ± 0.03%/g for **5b**-^{90}Y; 1.71 ± 0.19%/g for **5a**-^{90}Y; $p < 0.05$); all other organs were <0.2%/g. Both **5**-^{90}Y probes persist in the tumor to a degree that compares favorably with **1**-^{90}Y (see below), implying that the attachment to DAbR1 is stable *in vivo*. This stability may be related to the noncovalent binding affinity of probe for receptor ($K_D = 2 \times 10^{-9}$ M),[12] which facilitates the specific disulfide bond formation. Note that without covalent attachment, the dissociation of similar probes from DAbR1 occurs with a half-life of ~100 s.[12]

It is notable that side reactions with the free cysteine side chain on the abundant (0.5 mM) albumin molecules in circulation evidently did not occur to a significant degree. Part of the reason for this may be that the disulfide bonds in **5a** or **5b** are not activated in the way that disulfide bonds are when they contain the familiar thiopyridine or thionitrobenzoate leaving groups, so there is little thermodynamic driving force to propel thiol−disulfide interchange between molecules diffusing freely in solution. On the other hand, after the reversible probe−receptor complex has been formed, release of the RSH leaving group (Figure 1D) may be entropically favorable due to the extra translational and rotational degrees of freedom created by this process.[16] Thiol−disulfide interchange between the probes and small thiols may be more difficult to detect, but the significant differences between the biodistributions of **5a**-^{90}Y and **5b**-^{90}Y suggest that interchange between these probes and small thiols is not important, since that would tend to make the probe distributions similar. For example, if both probes rapidly reacted with free cysteine in circulation and lost their original leaving groups, we would expect their biodistributions to be identical.

Previously, Wei et al. used a related model system, finding 24 h tumor uptake of **1**-^{90}Y was 4.9 ± 0.6%/g. Other organs showed some uptake of **1**-^{90}Y at 24 h, notably spleen (1.3 ± 0.5%/g), liver (0.8 ± 0.3%/g), and small intestine (0.3 ± 0.3%/g); bone uptake was a satisfactory 0.2 ± 0.1%/g.[11] In contrast to **1**-^{90}Y, the **5**-^{90}Y probes exhibit very little residue in spleen, liver, or intestine; instead, they show modestly higher kidney uptake. This is corroborated by the Cerenkov images, which imply clearance mainly through the kidney with very little through the liver and intestines. It is interesting to note that the **5b**-^{90}Y probe shows significantly lower concentration in both tumor and kidney than **5a**-^{90}Y (Figure 3). While the cause requires more investigation, it may be that compared to the acetate group of **5a**, the bulkier propionate group of **5b** reduces the accessibility of the disulfide bond. Further explorations of alternative leaving groups may refine the properties of this family of probes.

TIME SCALE FOR TARGET VISUALIZATION

As shown in Figure 2, substantial tumor uptake occurs within a few minutes, and background clears within a few hours. This is a highly favorable set of results that suggests, for example, that glucose might be replaced by 2-[^{18}F]fluorodeoxyglucose for PET imaging on this time scale. On the other hand, the very long persistence in the target indicates stable attachment of the probe to the receptor, which would be favorable for multiday procedures such as targeted radiotherapy with ^{90}Y.[5] While imaging requires good target/background ratios, preferably at short times, therapy benefits from long residence times of the radiopharmaceutical on the target, for the delivery of the maximum radiation dose. The therapeutic radionuclide ^{90}Y decays with a physical half-life of 64 h, making it advantageous to bind a probe such as **5**-^{90}Y on the target for at least that long; permanent binding is excellently suited for this application.

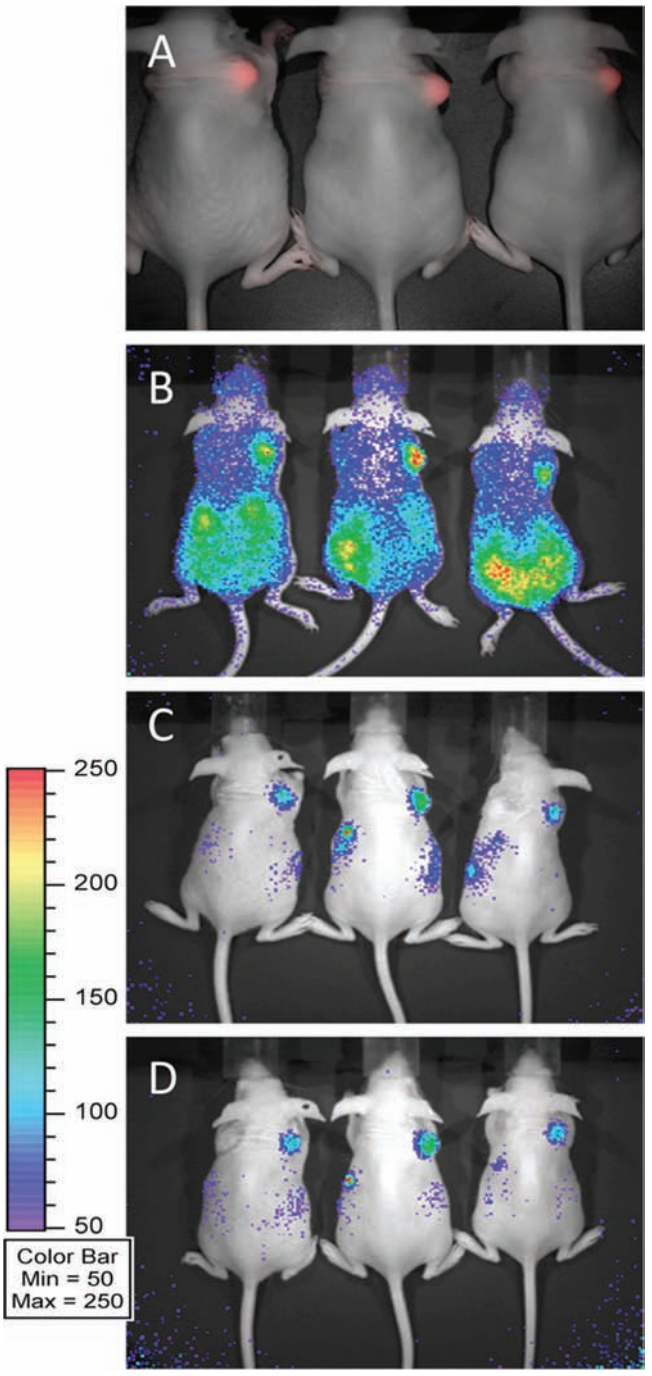

Figure 2. *In vivo* imaging of **5b**-^{90}Y. (A) Spectrally unmixed fluorescent image (overlaid with the corresponding monochrome image) acquired for three mice, each of which received bilateral injections of 3×10^6 U-87 glioma cells to the scapular region. Tumors on right shoulders are derived from U-87/DC cells engineered to express DAbR1 and the fluorescent protein mCherry. There are also tumors on the left shoulders, derived from parental U-87 cells without the reporter gene. (B,C,D) Cerenkov luminescence images acquired following tail vein injection of 8 μCi **5b**-^{90}Y. The color scale units (common to B,C,D) indicate counts per pixel. Images were acquired at (B) 9 min, (C) 1.5 h, and (D) 3.5 h postinjection. Similar images were obtained for **5a**-^{90}Y. The color scale units common to B, C, D indicate counts per pixel, and correspond to the radiance range 3.4×10^3 to 1.7×10^4 photons/s/cm^2/sr.

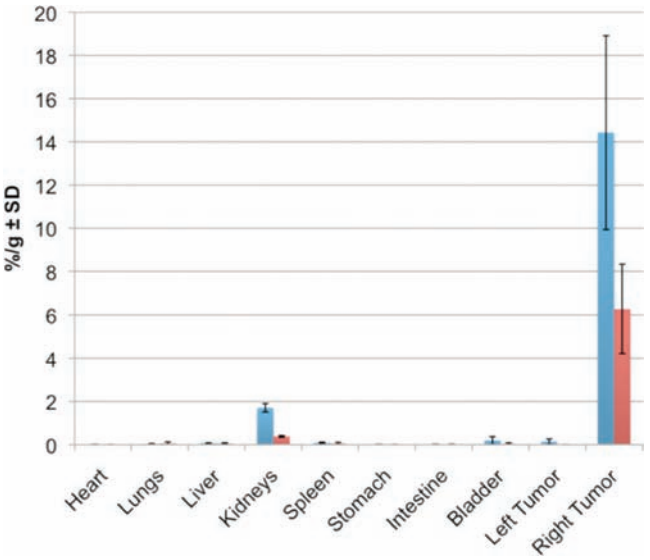

Figure 3. Mouse biodistributions 48 h after injection of **5a**-^{90}Y (blue) or **5b**-^{90}Y (red). Percent dose per gram tissue ± standard deviation ($n = 3$). See Scheme 1 for structures of **5a** and **5b**. Right tumor expresses the DAbR1 receptor gene.

■ ASSOCIATED CONTENT

Supporting Information. Experimental details for all syntheses and experimental methods. This material is available free of charge via the Internet at http://pubs.acs.org.

■ AUTHOR INFORMATION

Corresponding Author

*Claude F. Meares, Chemistry Department, University of California, Davis, CA 95616. E-mail cfmeares@ucdavis.edu; phone 530-752-0936; fax 530-752-8938.

■ ACKNOWLEDGMENT

Imaging and animal expenses were supported in part by NIH research grant CA143098 (SRC). Chemical synthesis was supported in part by NIH research grants CA016861 (CFM) and CA136639 (CFM). Jennifer Fung and Michelle Connell, Center for Molecular and Genomic Imaging, UC Davis, provided technical support for the imaging studies.

■ REFERENCES

(1) Liu, S. (2009) Radiolabeled cyclic RGD Peptides as integrin alphavbeta3-targeted radiotracers: maximizing binding affinity via bivalency. *Bioconjugate Chem. 20*, 2199–2213.

(2) Maresca, K. P., Marquis, J. C., Hillier, S. M., Lu, G., Femia, F. J., Zimmerman, C. N., Eckelman, W. C., Joyal, J. L., and Babich, J. W. (2010) Novel polar single amino acid chelates for technetium-99m tricarbonyl-based radiopharmaceuticals with enhanced renal clearance: application to octreotide. *Bioconjugate Chem. 21*, 1032–1042.

(3) Goodwin, D. A., Meares, C. F., Watanabe, N., McTigue, M., Chaovapong, W., Ransone, C. M., Renn, O., Greiner, D. P., Kukis, D. L., and Kronenberger, S. I. (1994) Pharmacokinetics of pretargeted monoclonal antibody 2D12.5 and Y-88-janus-2-(p-nitrobenzyl)-1,4,7,10-tetraazacyclododecanetetraacetic acid (DOTA) in Balb/c mice with KHJJ mouse adenocarcinoma - a model for Y-90 radioimmunotherapy. *Cancer Res. 54*, 5937–5946.

(4) Weiden, P., Breitz, H., Press, O., Appelbaum, J., Stone, D., Bryan, K., Su, F., Axworthy, D., Hylarides, M., Theodore, L., Beaumier, P., and Reno, J. (1998) Radioimmunotherapy (RIT) in the treatment of non-Hodgkins lymphoma (NHL): Advantage of pretargeted RIT (PRITR). *Blood 92*, 414A–414A.

(5) Lin, Y. K., Pagel, L. M., Axworthy, D., Pantelias, A., Hedin, N., and Press, O. W. (2006) A genetically engineered anti-CD45 single-chain antibody-streptavidin fusion protein for pretargeted radioimmunotherapy of hematologic malignancies. *Cancer Res. 66*, 3884–3892.

(6) Chmura, A. J., Orton, M. S., and Meares, C. F. (2001) Antibodies with infinite affinity. *Proc. Natl. Acad. Sci. U. S. A. 98*, 8480–8484.

(7) Goldenberg, D. M., Rossi, E. A., Sharkey, R. M., McBride, W. J., and Chang, C.-H. (2008) Multifunctional antibodies by the dock-and-lock method for improved cancer imaging and therapy by pretargeting. *J. Nucl. Med. 49*, 158–163.

(8) Devaraj, N., Upadhyay, R, Haun, J. B., Hilderbrand, S. A., and Weissleder, R. (2009) Fast and sensitive pretargeted labeling of cancer cells through a tetrazine/trans-cyclooctene cycloaddition. *Angew. Chem. Intl. Ed. 48*, 7013–7016.

(9) Corneillie, T. M., Lee, K. C., Whetstone, P. A., Wong, J. P., and Meares, C. F. (2004) Irreversible engineering of the multielement-binding antibody 2D12.5 and its complementary ligands. *Bioconjugate Chem. 15*, 1392–1402.

(10) Corneillie, T. M., Whetstone, P. A., Lee, K. C., Wong, J. P., and Meares, C. F. (2004) Converting weak binders into infinite binders. *Bioconjugate Chem. 15*, 1389–1391.

(11) Wei, L. H., Olafsen, T., Radu, C., Hildebrandt, I. J., McCoy, M. R., Phelps, M. E., Meares, C., Wu, A. M., Czernin, J., and Weber, W. A. (2008) Engineered antibody fragments with infinite affinity as reporter genes for PET imaging. *J. Nucl. Med. 49*, 1828–1835.

(12) Aweda, T. A., Beck, H. E., Wu, A. M., Wei, L. H., Weber, W. A., and Meares, C. F. (2010) Rates and equilibria for probe capture by an antibody with infinite affinity. *Bioconjugate Chem. 21*, 784–791.

(13) Corneillie, T. M., Fisher, A. J., and Meares, C. F. (2003) Crystal structures of two complexes of the rare-earth-DOTA-binding antibody 2D12.5: Ligand generality from a chiral system. *J. Am. Chem. Soc. 125*, 15039–15048.

(14) Schottelius, M., Rau, F., Reubi, J. C., Schwaiger, M., and Wester, H.-J. (2005) Modulation of pharmacokinetics of radioiodinated sugar-conjugated somatostatin analogues by variation of peptide net charge and carbohydration chemistry. *Bioconjugate Chem. 16*, 429–437.

(15) Robertson, R., Germanos, M. S., Li, C., Mitchell, G. S., Cherry, S. R., and Silva, M. D. (2009) Optical imaging of cerenkov light generation from positron-emitting radiotracers. *Phys. Med. Biol. 54*, N355–365.

(16) Page, M. I., and Jencks, W. P. (1971) Entropic contributions to rate accelerations in enzymic and intramolecular reactions and chelate effect. *Proc. Natl. Acad. Sci. U. S. A. 68*, 1678–1683.

(17) Day, J. J., Marquez, B. V., Beck, H. E., Aweda, T. A., Gawande, P. D., and Meares, C. F. (2010) Chemically modified antibodies as diagnostic imaging agents. *Curr. Opin. Chem. Biol. 14*, 803–809.

Supporting Information - New covalent capture probes

New covalent capture probes for imaging and therapy, based on a combination of binding affinity and disulfide bond formation.

Tolulope A. Aweda, Vahid Eskandari, David L. Kukis[†], David L. Boucher[†], Bernadette V. Marquez, Heather E. Beck, Gregory S. Mitchell[†], Simon R. Cherry[†], Claude F. Meares*

Chemistry Department, and Center for Molecular and Genomic Imaging,[†] University of California, Davis, CA 95616

Materials & Methods

Reagents: Aminobenzyl-DOTA (ABD) was purchased from Macrocyclics. Triethylamine (Et_3N), diisopropylethylamine (DIPEA), acetonitrile (CH_3CN) and plastic backed thin layer silica (TLC) plates were purchased from EMD Chemicals. Thioglycolic acid (mercaptoacetic acid, MAA), 3-mercaptopropionic acid (MPA), N-hydroxysuccinimide (NHS), tributylamine, yttrium chloride (YCl_3) and piperidine were purchased from Sigma Aldrich. Methylmethanethiosulfanate (MMTS) was purchased from Pierce. Biotechnical grade glucose, peptide grade tetrahydrofuran and methanol were purchased from Fisher Scientific. 2, 2'-Dithiodipyridine (DTP), trisopropylsilane (TIS), dimethylformamide (DMF), dichloromethane (CH_2Cl_2) and DTPA were purchased from Acros Organics. Boc-aminooxy acetic acid (Boc-AOA), *N,N'*-Dicyclohexylcarbodiimide **(**DCC) and Fmoc-Cys(trt)-Opfp were purchased from Novabiochem. 18 mΩ-cm water was used where HPLC or mass spec grade water was not required. $^{90}YCl_3$ and $^{111}InCl_3$ solutions in 0.05 M HCl were purchased from PerkinElmer Life Sciences, Boston, MA.

Syntheses:

(S)-2-(4-acrylamidobenzyl)-1,4,7,10-tetraazacyclododecane-N,N′,N″,N‴-tetraacetic acid (AABD) **1** (Figure 1). This was prepared by a modification of the previous method.(1-2) ABD (40 mg, 0.056 mmol) was dissolved in triethylammonium acetate (Et_3N•HOAc), pH 8.0 (0.1 M, 200 µL). The pH was adjusted to 9 with neat Et_3N . Acryloyl chloride (187 µL, 2.24 mmol) was dissolved in CH_2Cl_2 (213 µL). 200 µL of the acryloyl chloride/CH_2Cl_2 mixture (0.56 mmol) was added to 200 µL of the ABD and vortex mixed for 30 sec. The pH was adjusted to 8, while stirring with Et_3N until a stable pH 8 was achieved. The mixture was vortex mixed for another 15 min. A negative test to fluorescamine confirmed complete acylation of the amino group on ABD. The CH_2Cl_2 was removed and reaction mixture extracted 20× with Et_2O (1 mL each time). The pH

was maintained at ~2 with 6 M HCl during the Et_2O extraction. The last two extractions tested negative to 4-(p-nitrobenzyl)-pyridine confirming complete removal of the alkylating agent, acryloyl chloride (3). Residual Et_2O was removed by blowing Argon through the crude mixture. The crude mixture was purified by reverse phase chromatography and the fractions analyzed by TLC and mass spec. HPLC gradient: solvent A, water with 0.1% CF_3COOH; solvent B, CH_3CN, 0-5 min, 3-18% B, 5-45 min, 18-38%, 45-55 min, 38-100%, 55-60 min, 100% B, 60-62 min, 100-3% B, 62-65 min 3% B, 3 mL/min. Desired peak was collected between 21 and 23 min. (ESI-MS *m/z* calc'd (MH^+): 564.27. Observed: (MH^+): 564.4 and $(M-H)^-$: 562.4, Figure S1 and S2). TLC solvent: equal volumes of aqueous 0.1 M Et_3N•HOAc and methanol.

(S)-2-(4-N_α-Fmoc-S-trityl-L-cysteinylamidobenzyl)-1,4,7,10-tetraazacyclododecane-N,N′,N″,N‴-tetraacetic acid (fmoc-Cys(Trt)-ABD) **6** (Scheme 3). ABD (100 mg, 0.138 mmol, FW 705) was dissolved in 5 mL of H_2O, to which 20 mL of tributylamine was added. The solution was stirred for 4 h at room temperature. The aqueous layer was separated from the organic layer and taken to dryness under high vacuum. The dried product was completely dissolved in 3 mL of DMF. Fmoc-Cys(Trt)-OpFp (420 mg, 4 molar equiv, 0.55 mmol, FW 751.76) was added to the ABD-tributylamine and mixed until complete dissolution was achieved. The reaction mixture was stirred for 48 h at room temperature. Mass spec analysis shows approximately 90% conversion to product. The reaction was quenched with twelve 50 µL aliquots of water and stirred for an additional 30 min. The crude product was dried under high vacuum to an oily brownish-yellow paste. (ESI-MS m/z calc'd (MH^+): 1077.44, (MNa^+): 1099.42. Found: 1077.5, 1099.2 and 1100.3, Figure S3).

Removal of fmoc from **6.** The crude fmoc-Cys(Trt)-ABD was fmoc deprotected with 6 mL of 33% piperidine in DMF for 18-24 h at room temperature. The crude mixture was dried under vacuum, re-dissolved in 3 mL of DMF and concentrated again to give an oily paste. Purification of the crude Cys(Trt)-ABD was accomplished using preparative reverse phase chromatography, adding small portions of the paste to 0.8 mL of CH_3OH (0.15 mL of DMF was added to obtain complete dissolution). Yield: 58 mg, 68 µmol (49%). HPLC gradient: solvent A, water with 0.1% CF_3COOH; solvent B, CH_3CN with 0.075% CF_3COOH; 0-37 min, 3-45% B; 37-42 min, 45-100% B; 42-62 min, 100% B; 62-67 min, 100-3% B, 7mL/min. (ESI-MS m/z calc'd (MH+): 855.37, (MNa+): 877.36. Found: 855.5 and 877.2, Figure S4).

(S)-2-(4-L-cysteinylamidobenzyl)-1,4,7,10-tetraazacyclododecane-N,N′,N″,N‴-tetraacetic acid (Cys-ABD) **7**. HPLC-purified Cys(Trt)-ABD (58 mg, 68 µmol by UV, ε_{280}=17,800 $M^{-1}cm^{-1}$) was deprotected in 2 mL of CF_3COOH:CH_2Cl_2:TIS (50:50:2). The mixture was stirred at room temperature until positive to DTNB test (about 2.5 h). The resulting **7** was confirmed by mass spec analysis and taken to complete dryness under high vacuum. (ESI-MS m/z calc'd (MH^+): 613.27, (MNa^+): 635.68 Found: 613.5 and 635.4, Figure S5). Crude yield: 62 µmol by UV, (91%). A portion of the crude **7** to be used as a positive control was purified using preparative reverse phase chromatography. HPLC gradient: solvent A, water with 0.1% CF_3COOH; solvent B, CH_3CN with 0.075%

CF_3COOH, 0-37 min, 3-45% B; 37-42 min, 45-100% B; 42-62 min, 100% B; 62-67 min, 100-3% B, 7 mL/min.

(S)-2-(4-L-Cysteinyl(methyldisulfide)-amidobenzyl)-1,4,7,10-tetraazacyclododecane-N,N′,N″,N‴-tetraacetic acid (CH_3SSCys-ABD) **3** ($R^1=CH_3$). The dried, crude **7** (62 μmol) was dissolved in 1 mL of CH_3OH and the pH carefully adjusted with DIPEA with alternating additions of MMTS (40 μL total volume, 420 μmol) to a final pH between 5 and 6. The reaction mixture was stirred at room temperature for 1 h. The crude **3** ($R^1=CH_3$) was taken to dryness and left under high vacuum for another 2 h. (ESI-MS m/z calc'd (MH^+): 659.25, (MNa^+): 681.24 Found: 659.0 and 681.4, Figure S6).

(S)-2-(4-L-cysteinyl-(mercaptopropionic acid-disulfide)amidobenzyl)-1,4,7,10-tetraazacyclododecane-N,N′,N″,N‴-tetraacetic acid (MPASSCys-ABD) **3b** (Scheme 1). Vacuum-dried **7** (28 μmol) was dissolved in 400 μL of CH_3OH and 2 equiv of 2, 2′-Dithiodipyridine (DTP, 56 μmol, 120 μL of 0.5M DTP stock in CH_3OH, 220.31g/mol) was added. The pH of the mixture was approximately 4 due to residual CF_3COOH from the HPLC purification. The reaction mixture was stirred at room temperature for 5 h. Mass spec analysis after 5 h shows complete conversion of the free cysteine thiol group to the disulfide pyridine. (ESI-MS m/z calc'd (MH^+): 722.26, (MNa^+): 744.24 Found: 722.5 and 744.3, Figure S7). The crude **3** (R=2-pyridyl) was taken to dryness. A disulfide exchange was done with 3-mercaptopropionic acid (MPA). MPA (3 equiv relative to the initial **7**, 8 μL of 11.4 mM stock, FW: 106.14, d: 1.218) was added to the crude **3** (R^1=2-pyridyl) dissolved in 400 μL of CH_3OH. This solution was stirred at room temperature for 3 h. Mass spec analysis showed complete conversion to **3b**. (ESI-MS m/z calc'd (MH^+): 717.24, (MNa^+): 739.24 Found: 717.1 and 739.4, Figure S8). The crude product in CH_3OH was mixed with an equal volume of H_2O and the pH adjusted to 6 with Et_3N . About 75% of the free 2-thiopyridone was extracted from the mixture with an equal volume of chloroform. The crude **3b**, found both in the aqueous phase and interface layer, was purified by reverse-phase preparative HPLC to yield a yellowish solid. Yield: 6.1 mg, 8.5 μmol (30%). HPLC gradient: solvent A, water with 0.1% CF_3COOH; solvent B, CH_3CN with 0.075% CF_3COOH, 0-45 min, 3-40% B; 45-50 min, 40-100% B; 50-60 min, 100% B; 60-70 min, 100-3% B, 7mL/min. Peak containing the product as confirmed by mass spec was eluted between 25 and 28.3 min, 22.3 to 25% B.

(S)-2-(4-L-cysteinyl(mercaptoacetic acid-disulfide)-amidobenzyl)-1,4,7,10-tetraazacyclododecane-N,N′,N″,N‴-tetraacetic acid (MAASSCys-ABD) **3a** (Scheme 1). A similar disulfide exchange was carried out with mercaptoacetic acid (MAA) on the vacuum-dried, crude **3** (R=2-pyridyl). MAA (3 equiv relative to initial **7** (14 μmol), 3 μL of 14 mM stock, FW: 92.1g/mol, d: 1.32) was added to the crude **3** (R=2-pyridyl) dissolved in 200 μL of CH_3OH. This solution was stirred at room temperature for 3 h. Mass spec analysis showed complete conversion. The crude **3a** was HPLC purified. Yield: 2.5 mg, 3.5 μmol (25%). HPLC gradient: solvent A, water with 0.1% CF_3COOH; solvent B, CH_3CN with 0.075% CF_3COOH, 0-30 min, 3-45% B; 30-35 min, 45-100% B; 35-40 min, 100% B; 40-45 min, 100-3% B, 7mL/min. Peak containing the sample as

confirmed by mass spec was eluted between 19 and 20.8 min, 26.9% B. (ESI-MS m/z calc'd (MH+): 703.24, (MNa+): 725.22 Found: 703.5 and 725.4, Figure S9).

N'-Boc-aminooxyacetyl-N-hydroxysuccinimide Ester (BocAOA-NHS(4)). N-Boc-aminooxyacetic acid, Boc-AOA (100 mg, 520 μmol) was stirred in a mixture of ethyl acetate/dioxane (1:1, 2 mL) on an ice bath for 5 min. N-hydroxysuccinimide, NHS (62 mg, 540 μmol) was added to this mixture, then dicyclohexylcarbodiimide DCC (94 mg, 450 μmol, 0.8 equiv to NHS and BocAOA) was added. The reaction mixture was stirred at room temperature for 22 h under argon. Ethyl acetate (2mL) was added to the reaction mixture before filtering through a coarse-grade pyrex filter followed by a medium-grade filter. The resulting filtrate was dried under high vacuum and then re-crystallized in 1050 μL of 1:1:1 CH_2Cl_2/Et_2O/pentane to yield about 90 mg of pure Boc-AOA-NHS ester (yield was approximately 60%). IR analysis shows the presence of the ester group at 1739cm^{-1} and the complete disappearance of the carboxylic acid stretch at 1719cm^{-1}. A portion of the resulting Boc-AOA-NHS ester was dried and stored in -80 ºC under argon. ^{1}H NMR (300 MHz, CD_2Cl_2) δ 8.95 (s, 1H), 5.64 (s, 2H), 3.72 (s, 4H), 2.34 (d, *J*=3.4, 9H).

(S)-2-(4-(2-aminooxy-acetylamido)-L-cysteinyl(methyldisulfide)-amidobenzyl)-1,4,7,10-tetraazacyclododecane-N,N′,N″,N‴-tetraacetic acid (AOCD-SS-CH_3) **4** (R=CH_3). The vacuum-dried crude **3** (R^1=CH_3) (approximately 20 μmol) was dissolved and stirred in 300 μL of DMF, adjusted to pH 8 with 50 μL of DIPEA for about 5 min. Boc-AOA-NHS ester (60 μmol in 500 μL CH_2Cl_2) was added and pH adjusted to 8 again using an additional 20 μL of DIPEA. The mixture was maintained at pH 8 for another 3 h by adding DIPEA, and then stirred under argon at room temperature for 21 h. The Boc group of the crude product was removed in 2 mL CF_3COOH:CH_2Cl_2:TIS (50:50:2) solution for 4 h at room temperature. The crude **4** (R=CH_3) was HPLC purified. Peak containing the sample was eluted between 17.3 and 18 min, 26.8-27.6% B as confirmed by mass spec (ESI-MS m/z calc'd (MH^+): 732.26, (MNa^+): 754.25 Found: 732.1 and 754.3, Figure S10).

HPLC purification of all the aminooxy adducts was done using the same solvents and gradients: solvent A, water with 0.1% CF_3COOH; solvent B, CH_3CN with 0.075% CF_3COOH, 0-10 min, 3-25% B; 10-50 min, 25-40% B; 50-55 min, 40-100% B; 55-75 min, 100% B, 2 mL/min.

(S)-2-(4-(2-aminooxyacetylamido)-L-cysteinyl(mercaptopropionic acid-disulfide)-amidobenzyl)-1,4,7,10-tetraazacyclododecane-N,N′,N″,N‴-tetraacetic acid (AOCD-SS-MPA) **4b** (Scheme 1). The purified **3b**, approximately 3.4 μmol, was dissolved and stirred in 150 μL of DMF with pH adjusted to 8 using 10 μL of DIPEA for about 5 min (pH check was done on 1 μL aliquot of the mixture diluted with 3 μL of water). Boc-AOA-NHS ester (20 μmol in 20 μL of CH_2Cl_2) was added and the pH adjusted to 8 again, using DIPEA. The mixture was maintained at pH 8 for another 3 h by adding DIPEA as required, and then stirred under argon at room temperature for 21 h. The reaction was quenched with excess H_2O for 1 h and then dried under high vacuum. The

Boc group of the crude product was removed in 2 mL CF_3COOH:CH_2Cl_2:TIS (50:50:2) solution for 3 h at room temperature. The reaction was dried under high vacuum and the residue containing **4b** was stored at –80 ºC until needed. Yield: 1.7 mg, 2.2 μmol (64%). (ESI-MS m/z calc'd (MH^+): 790.27, (MNa^+): 812.26 Found: 790.3 and 812.1, Figure S11).

(S)-2-(4-(2-aminooxyacetylamido)-L-cysteinyl(mercaptoacetic acid-disulfide)-amidobenzyl)-1,4,7,10-tetraazacyclododecane-N,N′,N″,N‴-tetraacetic acid (AOCD-SS-MAA) **4a** (Scheme 1). The purified **3a**, approximately 1.65 μmol, was dissolved and stirred in 100 μL DMF with pH adjusted to 8 using 5 μL DIPEA. Boc-AOA-NHS ester (10 μmol in 10 μL CH_2Cl_2) was added and the pH adjusted to 8 again, using DIPEA. The mixture was maintained at pH 8 for another 3 h by adding DIPEA as required, and then stirred under argon at room temperature for 21 h. The reaction was quenched with H_2O for 1 h and then dried under high vacuum. The Boc group of the crude product was removed in 1.5 mL CF_3COOH:CH_2Cl_2:TIS (50:50:2) solution for 3 h at room temperature. The reaction was dried under high vacuum and stored at -80 ºC until needed. (ESI-MS m/z calc'd (MH^+): 776.25, (MNa^+): 798.24 Found: 776.8 and 798.5, Figure S12).
Analytical fractions of the crude **4a** and **4b** were separately HPLC purified using the same column conditions described above. The peak containing **4b** eluted between 17 and 17.4 min at 27.4-27.9% B while **4a** eluted between 16.2 and 16.5 min at 27.4% B, as confirmed by mass spec.

Glucose-AOCD-SS-MPA **5b** (Scheme 1). Glucose (26 mg, 144 μmol, 20 equiv to total **4b**) was dissolved and stirred in 70 μL normal saline with 1 μL CF_3COOH for 10 min. In another vial, crude **4b** was dissolved in 200 μL of 100% ethanol with 30 μL of normal saline added to achieve complete dissolution. The acidic glucose solution was added into the **4b** ethanolic solution and incubated while stirring at 100 ºC for 40 min. The solution was cooled and taken to dryness before HPLC purification using the gradient described above. Yield: 3.2 mg, 3.3 μmol (46%). (ESI-MS m/z calc'd (MH+): 952.32, Found: 952.4, Figure S13).

Glucose-AOCD-SS-MAA **5a** (Scheme 1) was dissolved and stirred in 35 μL normal saline with 0.6 μL CF_3COOH for 10 min. In another vial, **4a** was dissolved in 100 μL of 100% ethanol with 15 μL of normal saline added to achieve complete dissolution. The acidic glucose solution was added into the **4a** ethanolic solution and incubated while stirring at 100 ºC for 40 min. The solution was cooled and taken to dryness before HPLC purification using the gradient described above. Yield: 1.3 mg, 1.4 μmol (38%). (ESI-MS m/z calc'd (MH+): 938.30 Found: 938.4, Figure S14).

Radiochemistry. HPLC was performed on a Waters Breeze system with RA and UV (220 and 254 nm) detection, using a Luna C18 10 x 250 mm, 10 micron column (Phenomenex). Solvents 0.1% (v/v) TFA (aq) (A) and CH_3CN (B) were eluted at 3.0 mL/min using the linear gradient: 0 min, 97% A; 2 min, 97% A; 52 min, 0% A; 54 min, 0% A; 58 min, 97% A, 60 min, 97% A. The following elution times were observed: **1**,

16.96 min; **1**-^{90}Y, 16.43 min; **5b** (Scheme 1), 15.82 min; **5b**-^{90}Y (Figure 1), 15.06 and 15.39 min (two peaks); **5a**, 14.92 min; and **5a**-^{90}Y, 14.06 and 14.45 min (two peaks).

$^{90}YCl_3$ (0.5 to 2.6 mCi; Perkinelmer), supplied in dilute HCl, was buffered and added to DOTA constructs (80 to 270 nmol), such that the reaction solutions contained 0.7 to 2.6 mM DOTA construct in 0.1 to 0.6 M ammonium acetate, pH 6 to 7. The reactions were incubated for an hour or longer at 40 to 60 ^{o}C. DTPA was added to a final concentration of 10 mM to scavenge unchelated $^{90}Y^{3+}$, and the ^{90}Y-DOTA constructs were purified and evaluated for radiochemical yield (>95% of ^{90}Y chelated) by HPLC. The chelated ^{90}Y-DOTA products were well resolved from unchelated starting material, and 80 per cent or more of the latter was removed. The product HPLC peaks were dried at 110 ^{o}C under gentle helium, formulated for injection in PBS, and evaluated by HPLC for radiochemical purity (>95%) and mass content. Doses for injection contained 8 to 10 μCi of ^{90}Y-DOTA construct on 0.06 to 0.15 nmol total (chelated plus unchelated) DOTA construct.

Mass Spectra:

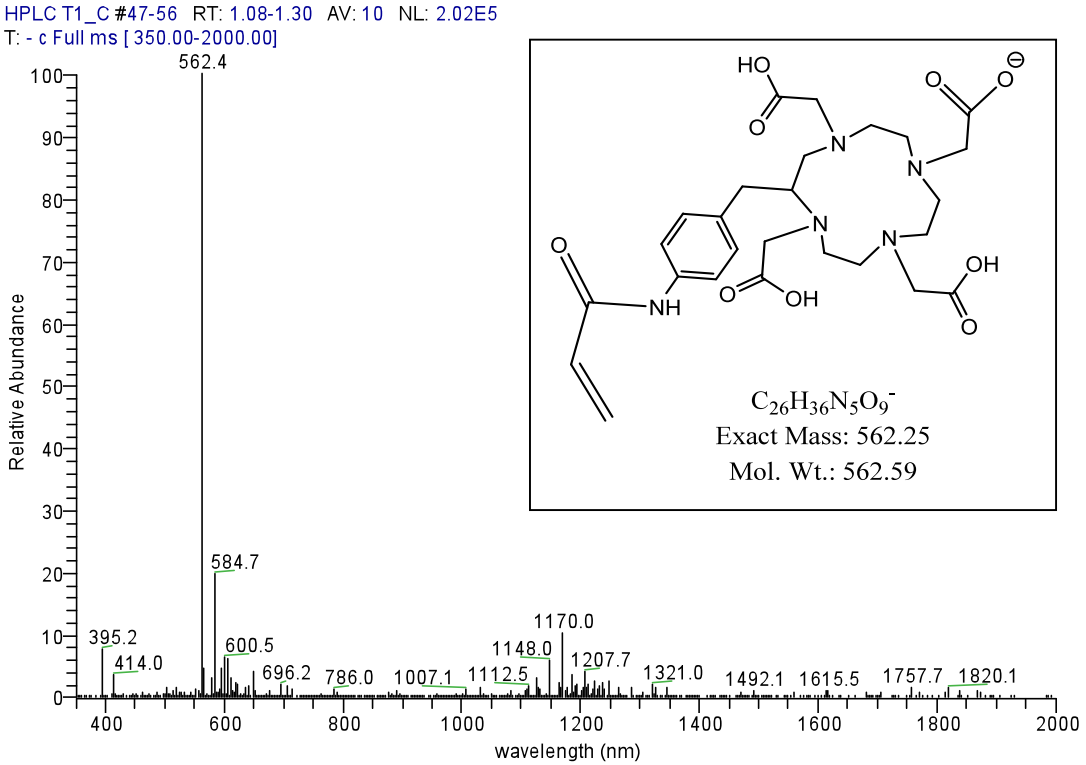

Figure s1. Mass spectrum for **1** after HPLC purification in the negative mode.

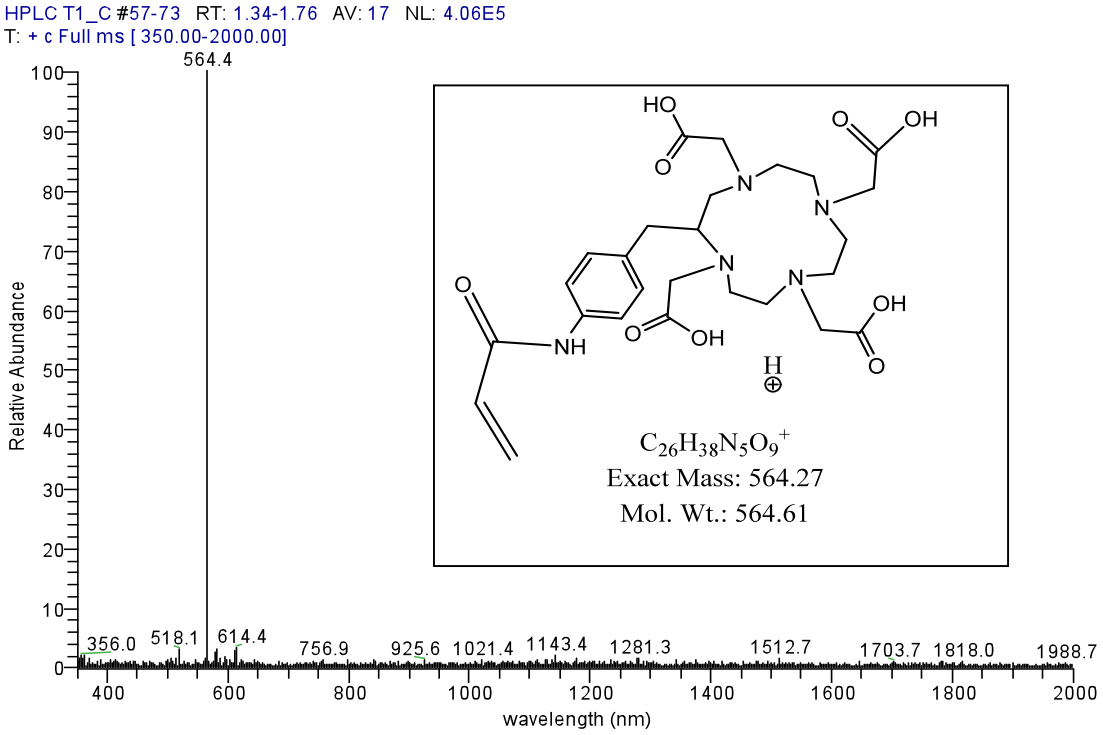

Figure s2. Mass spectrum for **1** after HPLC purification in the positive mode.

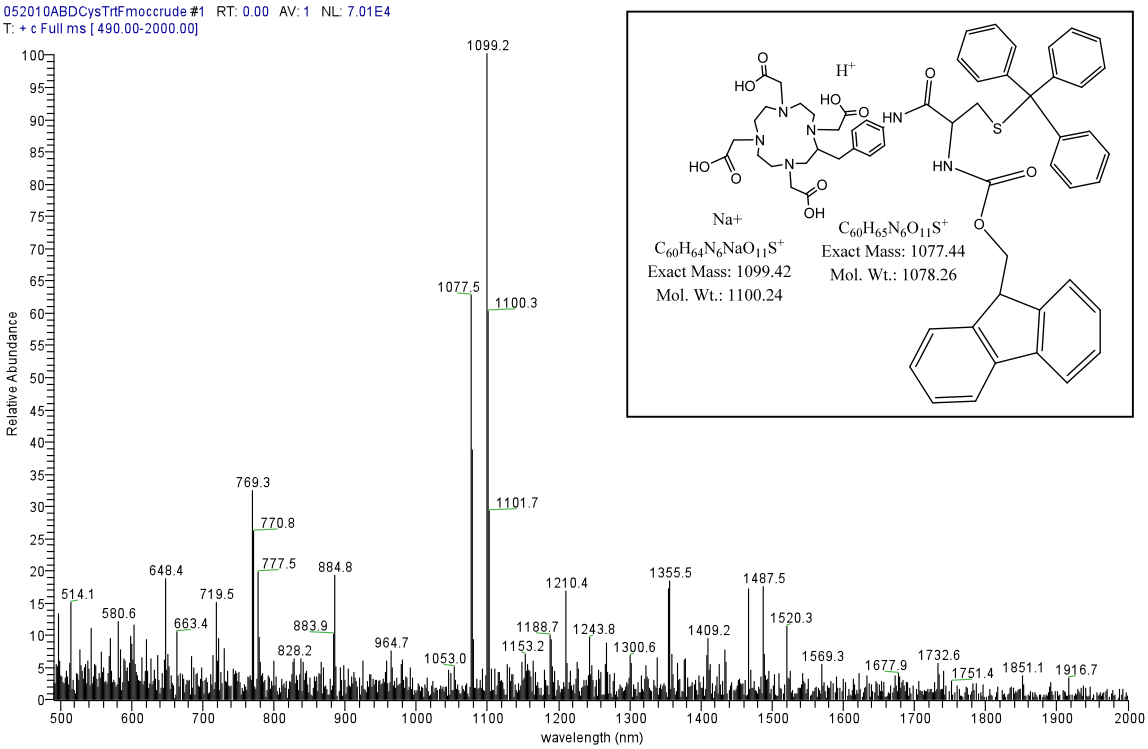

Figure s3. Mass Spec of ABD-Cys(Trt)-Fmoc after 48 h of incubation

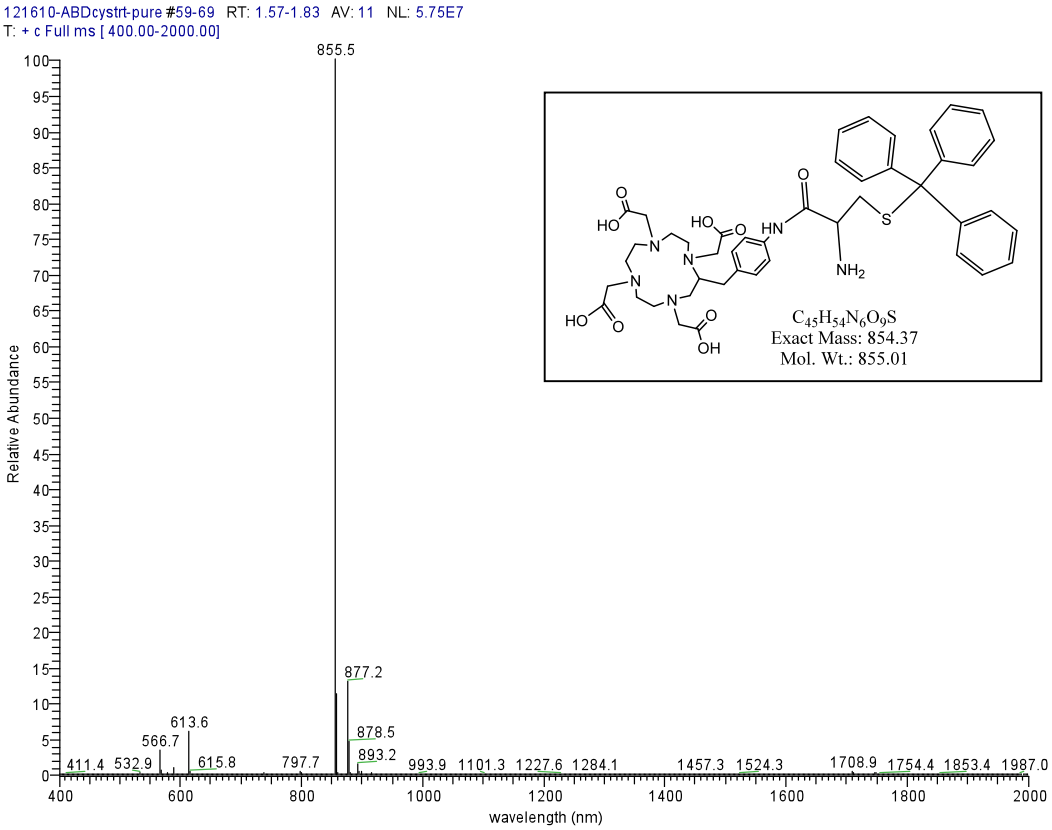

Figure s4. Mass spectrum for ABD-Cys(Trt) after HPLC purification in the positive mode.

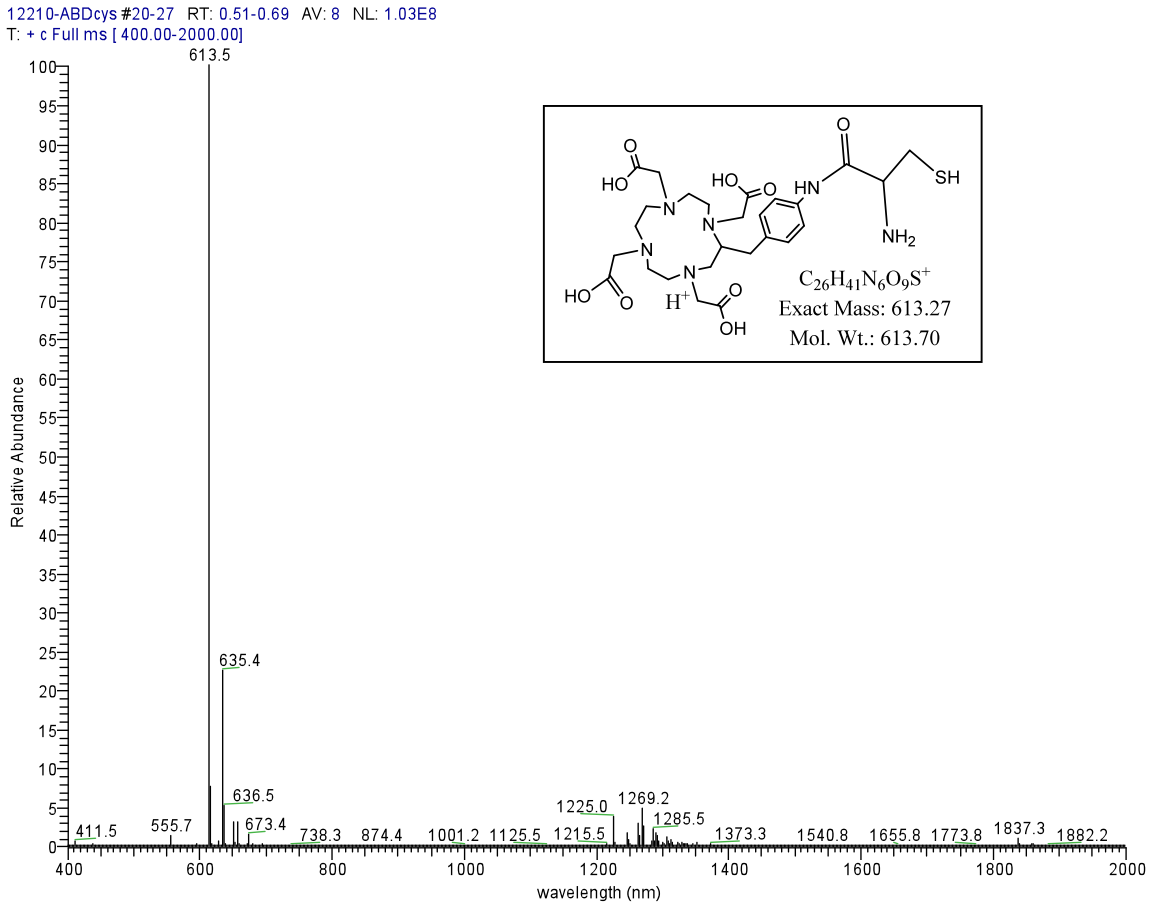

Figure s5. Mass spectrum for Cys-ABD after HPLC purification in the positive mode.

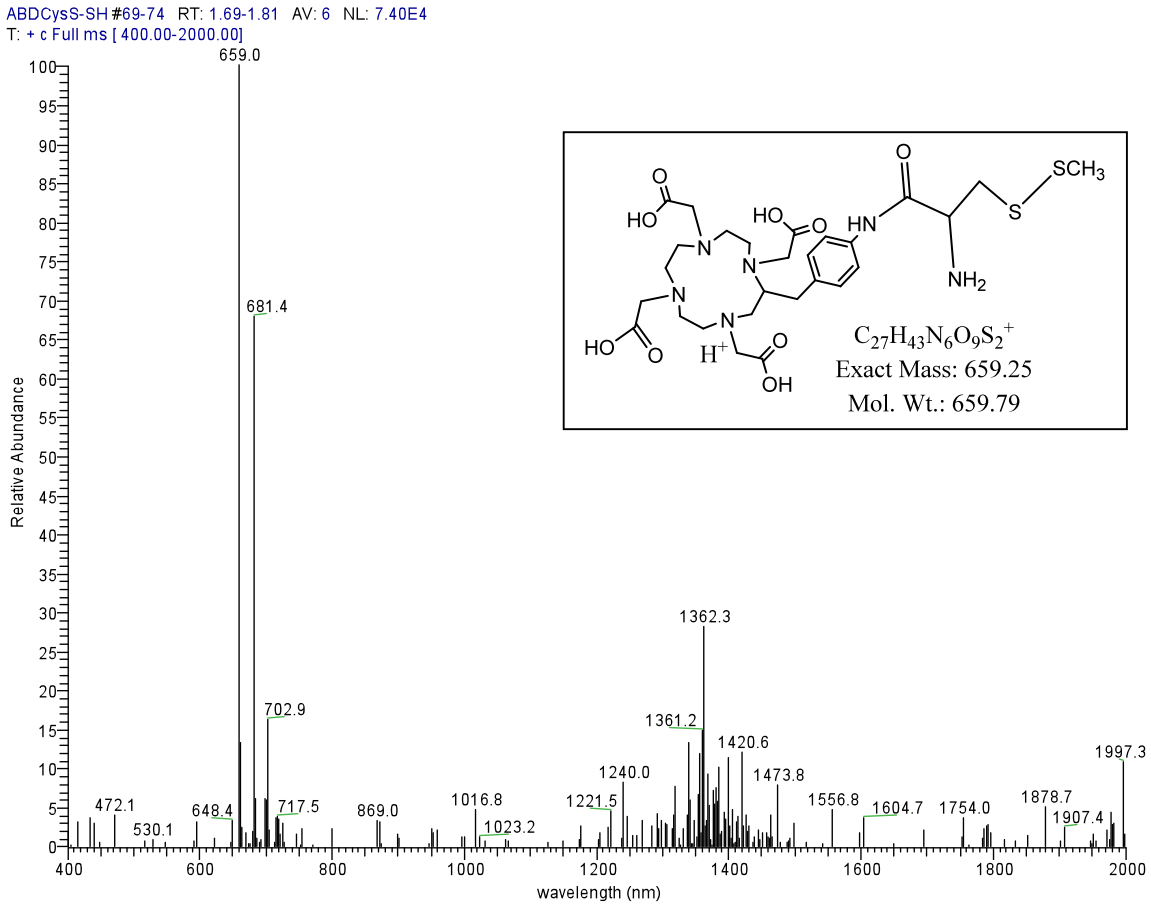

Figure s6. Mass spectrum for CH_3SSCys-ABD after HPLC purification in the positive mode.

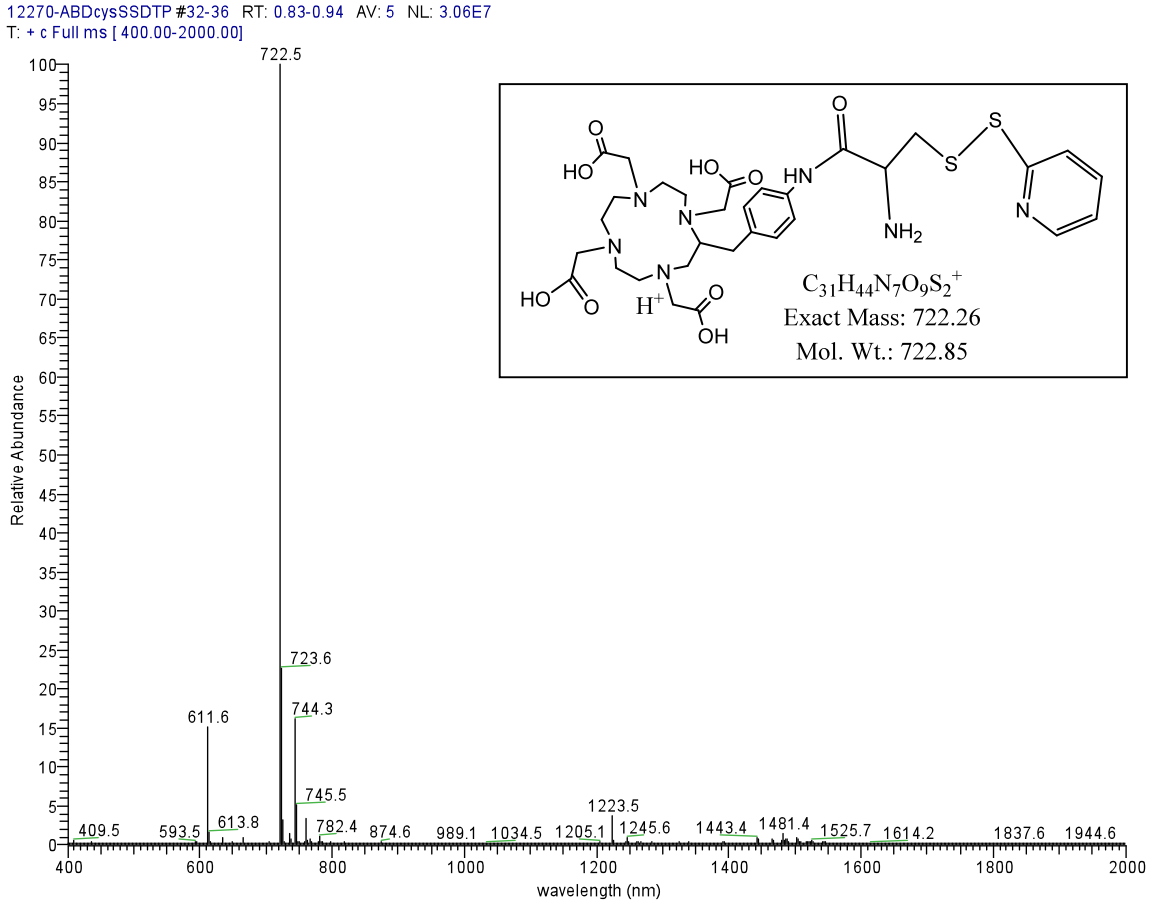

Figure s7. Mass spectrum for Pyr-SS-Cys-ABD in the positive mode.

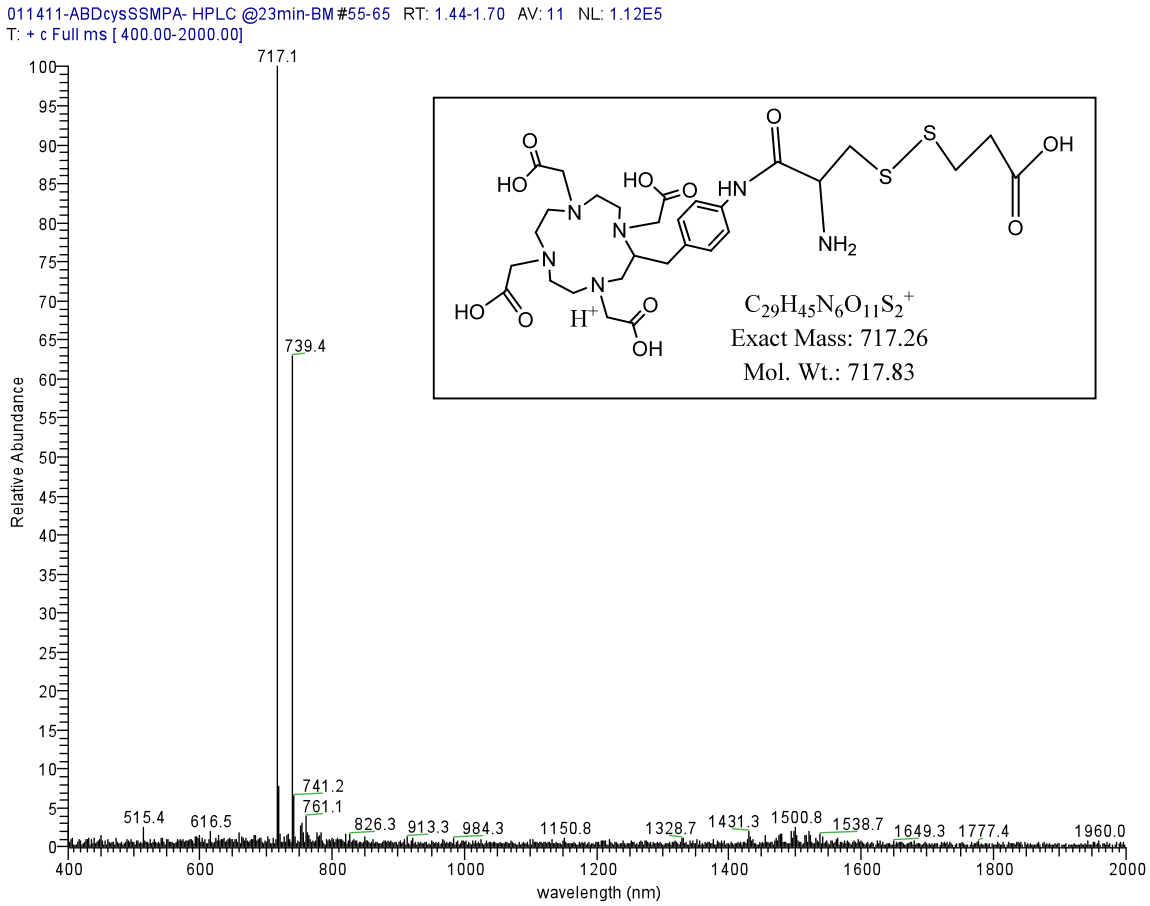

Figure s8. Mass spectrum for **3b** (Scheme 1) after HPLC purification in the positive mode.

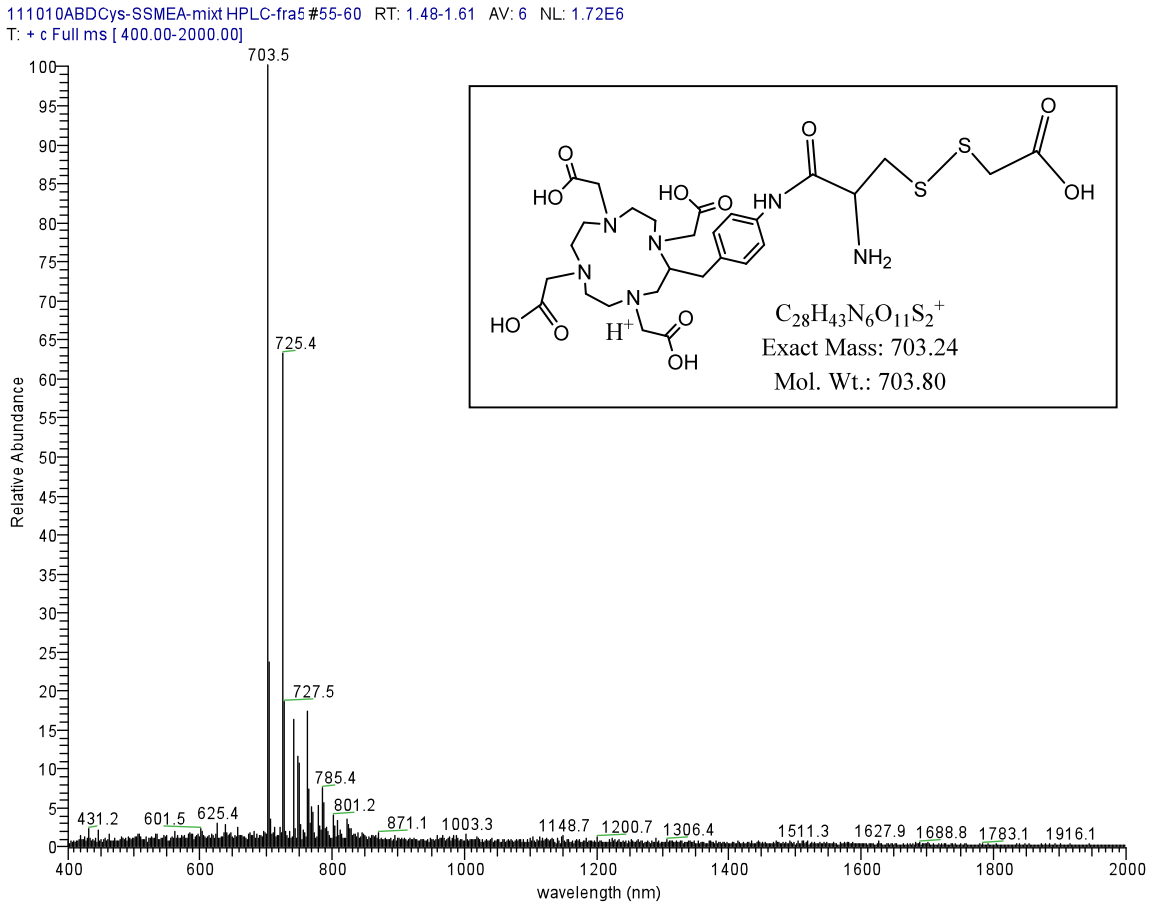

Figure s9. Mass spectrum for **3a** (Scheme 1) after HPLC purification in the positive mode.

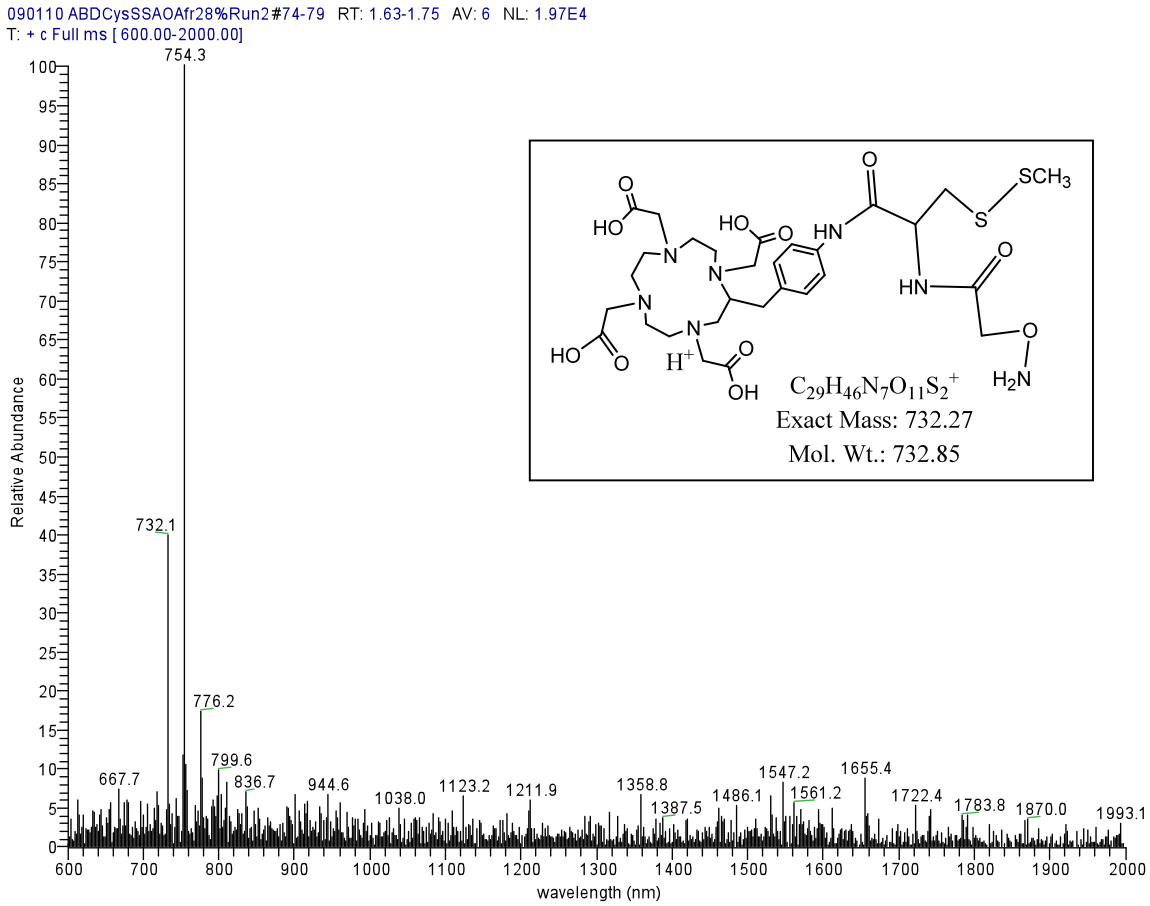

Figure s10. Mass spectrum for AOCD-SS-CH_3 after HPLC purification in the positive mode.

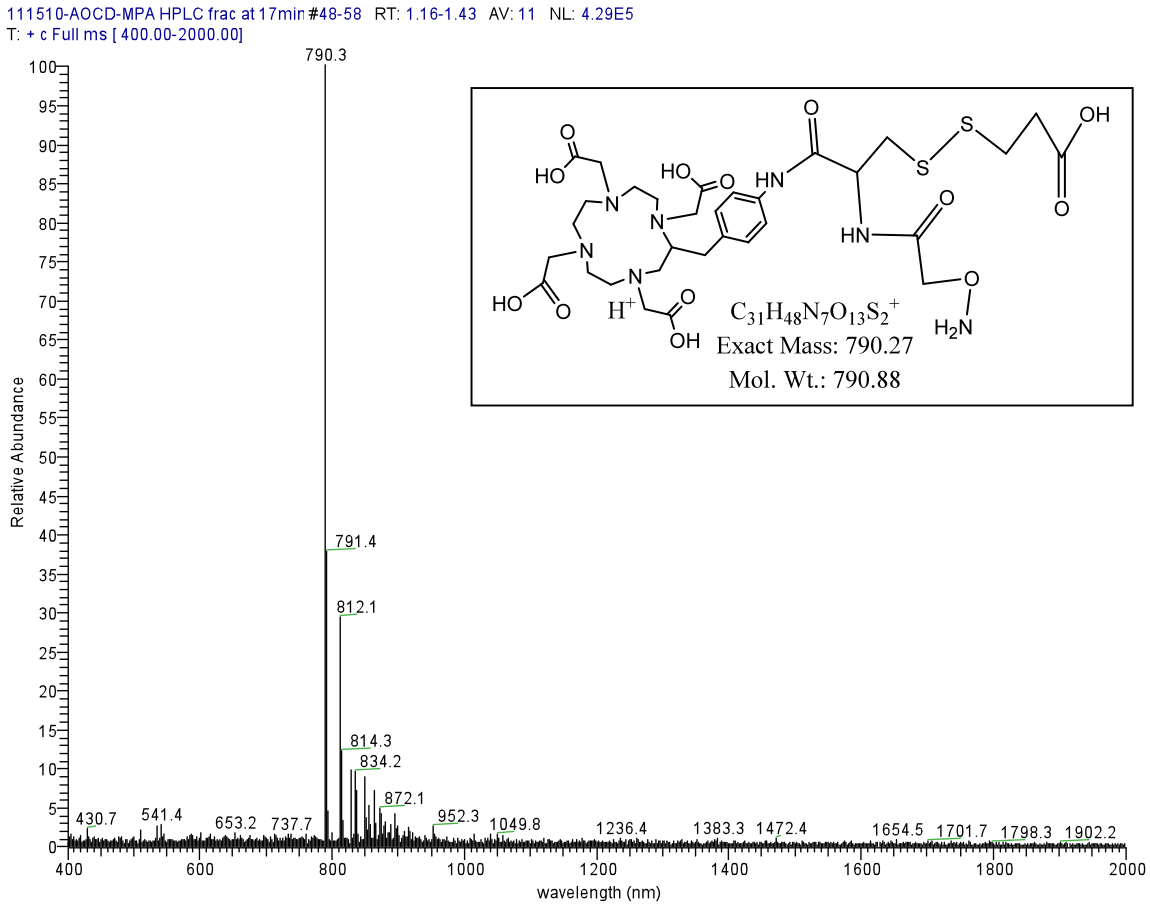

Figure s11. Mass spectrum for **4b** (Scheme 1) after HPLC purification in the positive mode.

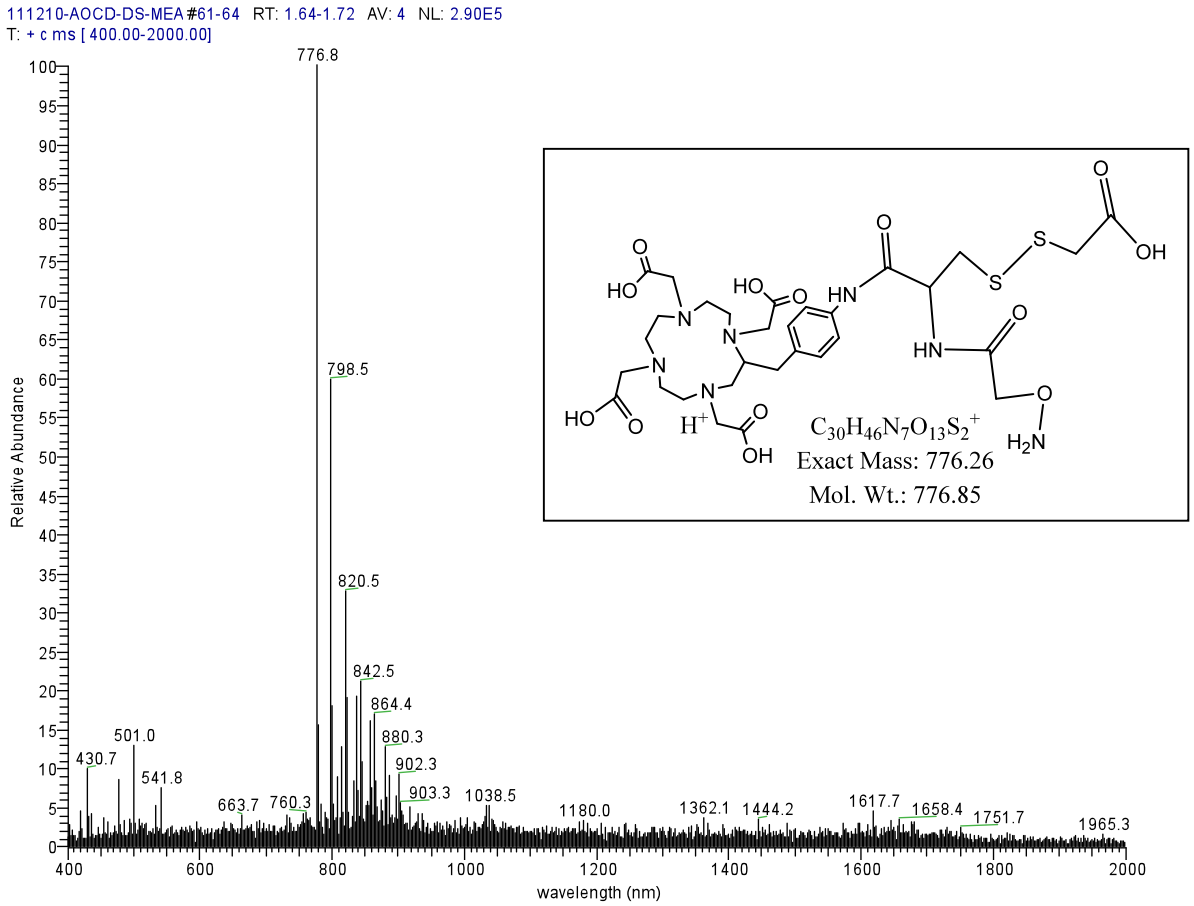

Figure s12. Mass spectrum for **4a** (Scheme 1) after HPLC purification in the positive mode.

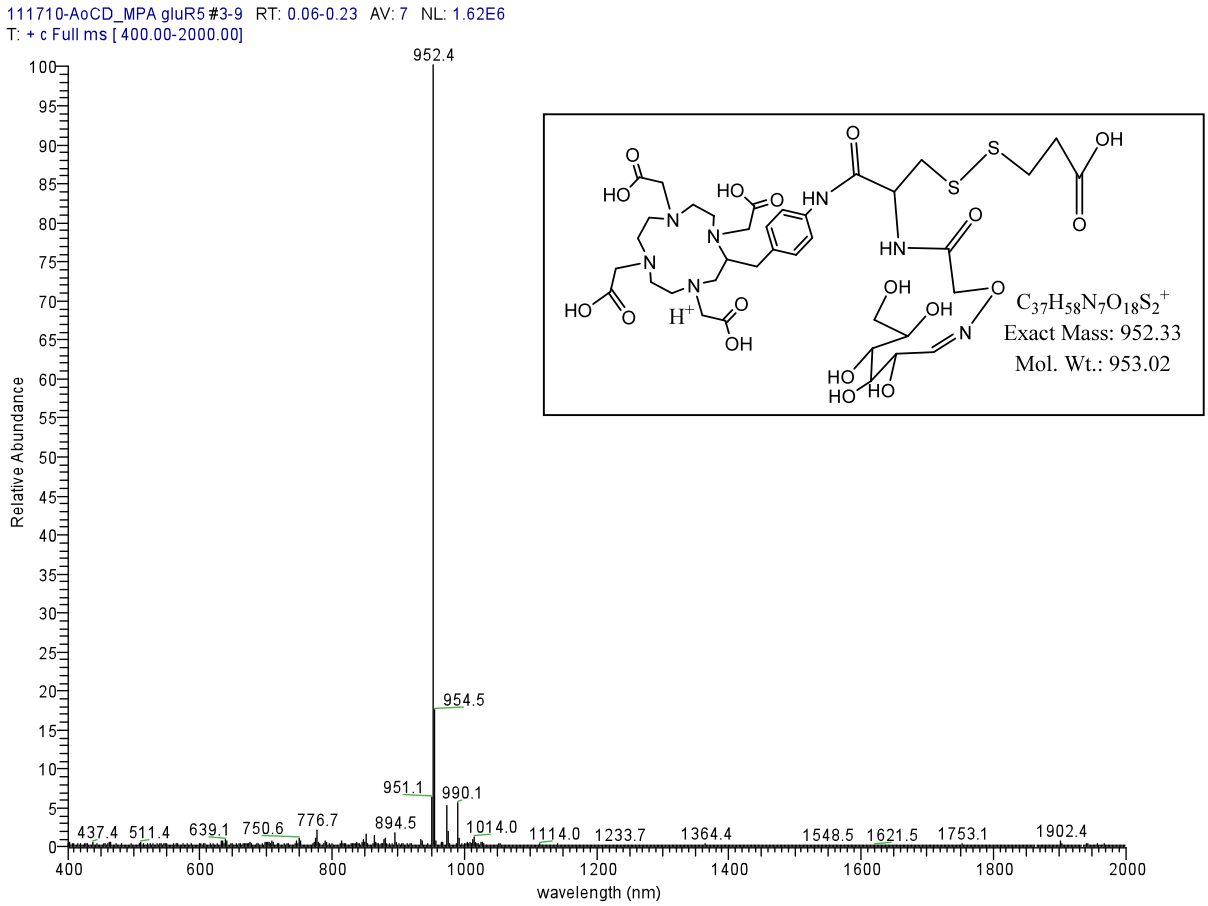

Figure s13. Mass spectrum for **5b** (Scheme 1) after HPLC purification, in the positive mode.

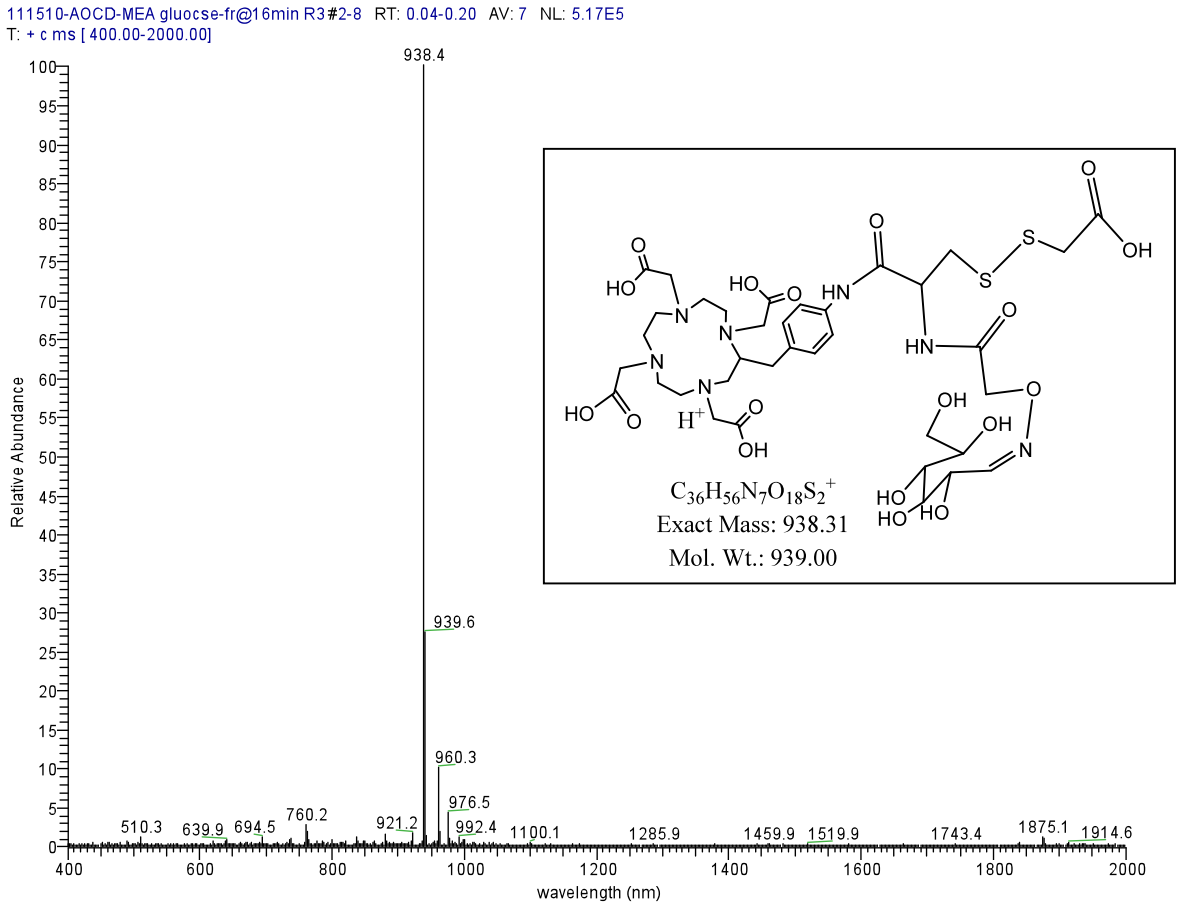

Figure s14. Mass spectrum for **5a** (Scheme 1) after HPLC purification, in the positive mode.

Supporting Information - New covalent capture probes

Construction of DAbR1-2A-mCherry multimodal reporter. The lentiviral plasmid backbone used for mammalian delivery in this study is a modified form of pLenti6/TR (Invitrogen). Briefly, the sequence containing the β-Globin Intron II and tetracycline receptor was excised and replaced with a customized multiple cloning sequence designed specifically for acceptance of a variety of similarly cloned reporter genes. Relevant to this manuscript, the MCS contains recognition sites for *CpoI*, *BamHI* and *XbaI*, in that order, immediately downstream from the cytomegalovirus (CMV) immediate early promoter.

Sequence encoding DAbR1 was PCR-amplified from pcDNA3.1/DAbR1 (a generous gift from Dr. Anna Wu, UCLA) using the following primer pair:

F: 5'-cggtccggccaccatggagacagacacactcc-3'
R: 5'-ggatccggcgtctgcgctcctgctgaac-3'

The PCR amplicon was TOPO cloned and verified for sequence accuracy. It was then digested with *CpoI* and *BamHI* (Fermentas) and ligated into the modified form of the pLenti6/CMV vector to create pLenti6/CMV/DAbR1. Sequence encoding the fluorescent protein mCherry was PCR-amplified from pmCherry-N1 (Clontech) using the following primers (with sequence encoding the 2A peptide shown in bold):

F: 5'-
ggatcc**gagggcagaggaagtcttctaacatgcggtgacgtggaggagaatcccggccct**atggtgagcaagggcgagg-3'
R: 5'-tctagacggaccgcttgtacagctcgtccatgcc-3'

The PCR amplicon was TOPO cloned and verified for sequence accuracy. It was then digested with *BamHI* and *XbaI* (Fermentas) and ligated into the similarly digested pLenti6/CMV/DAbR1 to create pLenti6/CMV/DAbR1-2A-mCherry.

Establishment of the U-87/DC cell line. 293T cells were obtained from ATCC and cultured in Dulbecco's Modified Eagle Medium (DMEM) supplemented with 10% fetal bovine serum and 1% penicillin/streptomycin/L-Glutamine (complete DMEM) and maintained at 37 C in the presence of 5% CO_2 in air. 293T cells were seeded to 10cm culture dishes and, at approximately 75% confluency, were co-transfected with pLenti6/CMV/DAbR1-2A-mCherry and the pLP1, pLP2 and pVSV-G series of viral packaging plasmids (Invitrogen) in a 1:1:1:1 ratio. Transfected cells were cultured 48-hours (with a single medium change at 24-hours post-transfection) and lentiviral particles were harvested and filtered through a 0.45 μM acrodisc (PALL Corporation) to remove cell debris and residual 293T cells. Filtered supernatant containing lentiviral particles was then applied to a culture of U-87 glioma cells (ATCC). Beginning 48 h post-transduction, stably transduced U-87 cells were selected for with 10 μg/mL blasticidin (Invitrogen) in complete DMEM for 30 days to generate the mixed U-87/DC cell line. Expression of mCherry (and indirectly DAbR1) was verified by fluorescent microscopy prior to *in vivo* studies.

Supporting Information - New covalent capture probes

Establishment of U-87 and U-87/DC tumors. Cultures of U-87 and U-87/DC were expanded in T150 flasks in complete DMEM. Expression of the DAbR1-2A-mCherry reporter was maintained in U-87/DC with 5 μg/mL blasticidin until five days prior to injection. At that time, selection was removed in order to prevent negative effects on tumor take rate. At approximately 80% confluency, cells were trypsinized, resuspended in complete DMEM and centrifuged (2000 rpm, 5 min, RT). The cell pellet was then washed with PBS, centrifuged and resuspended in fresh PBS at a concentration of $3x10^7$ cells/mL. One hundred microliters of the cell slurry ($3x10^6$ cells) was injected bilaterally into the subscapular region of six SCID Hairless Outbred (SHO) mice (Charles River) with U-87/DC cells delivered to the right shoulder and U-87 cells delivered to the left shoulder.

In vivo fluorescent imaging. Two hours prior to injection of radiolabeled probe, mice were imaged on a Maestro 2 (CRi) to verify mCherry expression. Images were acquired using the yellow filter set (excitation filter range – 576 to 621 nm; emission filter – 635 nm longpass; acquisition settings – 630 to 800 nm in 10 nm increments), 1x1 binning and an exposure time of 8 s. The spectrally unmixed composite images were overlaid with corresponding monochrome images using ImageJ software (http://rsweb.nih.gov).

In vivo Cerenkov Luminescence Imaging. At denoted intervals following administration of radiolabeled probe, Cerenkov luminescence imaging (CLI) was conducted for all mice. Images were acquired on an IVIS 100 (Caliper Life Sciences) using field of view "B" (15 cm), *f*/1, medium binning (binning factor 8), and an exposure time of 180 s. Luminescence images were overlaid with corresponding white light photograph images using Living Image software.

Ex vivo biodistribution. Animals (two cohorts, n=3 each) were euthanized by cervical dislocation following deep anesthesia 48 h after injection. Heart, lung, liver, kidney, spleen, stomach, intestine, bladder, and two (left and right) tumor tissues were removed, weighed, and counted for radioactivity with a calibrated gamma counter (1470 Wallac Wizard, Perkin Elmer) which measured the bremsstrahlung produced by the ^{90}Y radioactivity. Uptakes of radioisotope were calculated as the percentage of the injected dose per gram of tissue (%ID/g).

Literature Cited

(1) Corneillie, T. M., Lee, K. C., Whetstone, P. A., Wong, J. P., and Meares, C. F. (2004) Irreversible Engineering of the Multielement-Binding Antibody 2D12.5 and Its Complementary Ligands. *Bioconjugate Chemistry 15*, 1392-1402.

(2) Corneillie, T. M., Whetstone, P. A., Lee, K. C., Wong, J. P., and Meares, C. F. (2004) Converting Weak Binders into Infinite Binders. *Bioconjugate Chemistry 15*, 1389-1391.

(3) Thomas, J. J., Kim, J. H., and Mauro, D. M. (1992) 4-(4-nitrobenzyl)pyridine tests for alkylating agents following chemical oxidative activation. *Archives of Environmental Contamination and Toxicology 22*, 219-227.

(4) Foillard, S., Rasmussen, M. O., Razkin, J., Boturyn, D., and Dumy, P. (2008) 1-Ethoxyethylidene, a New Group for the Stepwise SPPS of Aminooxyacetic Acid Containing Peptides. *The Journal of Organic Chemistry 73*, 983-991.

Bioconjugate Chemistry

ARTICLE

pubs.acs.org/bc

Bimodal Quantitative Monitoring for Enzymatic Activity with Simultaneous Signal Increases in ^{19}F NMR and Fluorescence Using Silica Nanoparticle-Based Molecular Probes

Kazuo Tanaka, Narufumi Kitamura, and Yoshiki Chujo*

Department of Polymer Chemistry, Graduate School of Engineering, Kyoto University, Katsura, Nishikyo-ku, Kyoto 615-8510, Japan

ABSTRACT: We describe the bimodal quantitative assay for enzymatic activity in ^{19}F NMR spectroscopy and fluorescence spectroscopy using a nanoparticle-based molecular probe. Perfluorinated dendrimers were tethered on silica nanoparticles with a phosphate-caged fluorescein as a linker. Before enzymatic reaction, the molecular rotation of the perfluorinated dendrimers should be highly restricted, and the ^{19}F NMR signals from the perfluorinated dendrimers were too broad to be detected relative to the noise level. Fluorescence signals of fluorescein were suppressed by the presence of the diphosphate groups. Following the enzymatic reaction with an alkaline phosphatase, perfluorinated dendrimers and fluorescein were released, and the NMR signals of perfluorinated dendrimers and strong fluorescence from fluorescein were correspondingly observed. The enzymatic activity and reaction rates of the hydrolysis of alkaline phosphatase were detected from the increases of fluorescence and ^{19}F NMR signals. Finally, the feasibility of the probe in the presence of miscellaneous molecules under biomimetic conditions was demonstrated by determining of the enzymatic activity in cell lysate. Quantitative analysis using both ^{19}F NMR spectroscopy and fluorescence spectroscopy can be accomplished.

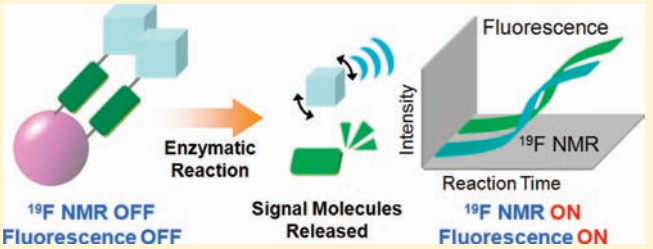

INTRODUCTION

Magnetic resonance imaging (MRI) contrast agents enable us to receive information from the spots deep inside vital bodies with site and time specificities. Next, interest has been directed to developing the advanced imaging protocols or contrast agents which realize the quantitative assay as executed in chemical exchange saturation transfer MRI.[1−3] A variety of fluorinated compounds have recently been used as a versatile platform to construct functional ^{19}F MR probes[4−7] for monitoring biological events such as gene expression,[8] protein distribution,[9,10] cell activity[11−13] or enzymatic reaction,[14] environmental alteration,[15−18] and biological reactions.[19] In addition, bimodal imaging probes which show corresponding[19,20] or complementary signal changes[21,22] between ^{19}F NMR spectroscopy and another modality have been developed. However, very few examples have been reported to apply ^{19}F MRI for quantitative assays.

A "turn-on" probe that can show the enhanced signal after the target detection throughout all conditions may have better measurement precision. The kinetic information can be readily calculated from signal increases per unit time. The noises caused by the intrinsic signals from unreacted probes or background can be excluded by adjusting the threshold level. These advantages may enhance the simplicity of the measurements. Moreover, bimodal turn-on probes which offer simultaneous increases of the magnitudes of the respective signals between different modalities during the detections have potential advantages such as data reliability and yet also have potential limitations such as protein aggregation that affects both signaling systems, so that bimodal probes deserve to be investigated in order to maximize advantages and minimize disadvantages.

Herein, we report bimodal probes with ^{19}F NMR spectroscopy and fluorescence spectroscopy for the quantitative assay of an enzymatic reaction. Perfluorinated dendrimers were anchored on silica nanoparticles (NPs) with the phosphate-caged fluorescein (Scheme 1). On silica NPs, the molecular rotation of the perfluorinated dendrimers should be highly restricted, and the NMR signals from the perfluorinated dendrimers can be suppressed.[23] During enzymatic reaction with an alkaline phosphatase (AP), the NMR signals from perfluorinated dendrimers would be enhanced due to recovery of the molecular rotation, increasing the fluorescence emission from the released fluorescein. Consequently, the enzymatic activity and reaction rates of the hydrolysis of AP can be evaluated from the increases of fluorescence and ^{19}F NMR signals. This is the first effort, to the best of our knowledge, to quantitatively evaluate a single enzymatic reaction with both ^{19}F NMR and fluorescence spectroscopies.

EXPERIMENTAL SECTION

General. ^{1}H NMR and ^{13}C NMR spectra were measured with a JEOL EX-400 spectrometer operating at 400 MHz for ^{1}H and 100 MHz for ^{13}C. ^{19}F and ^{29}Si NMR spectra were measured with

Received: August 27, 2010
Revised: June 23, 2011
Published: July 11, 2011

ACS Publications © 2011 American Chemical Society

Scheme 1. Detection Mechanism for Enzymatic Reaction Using the NP Probes

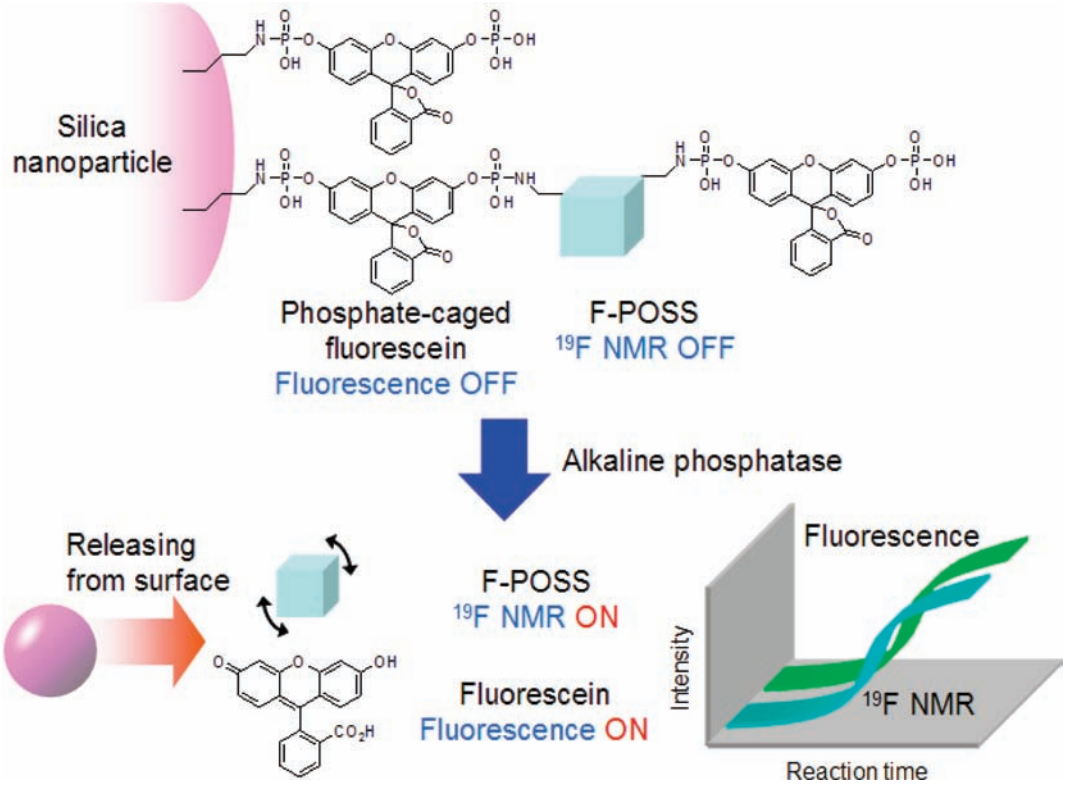

a JEOL JNM-A400 spectrometer operating at 370 MHz for ^{19}F and 80 MHz for ^{29}Si. Coupling constants (J value) are reported in Hertz. The chemical shifts in ^{19}F NMR are expressed in ppm downfield from trifluoroacetic acid as an external reference. Masses were determined with a MALDI-TOF mass spectroscopy (acceleration voltage 21 kV, negative mode) with 2,5-dihydroxybenzoic acid (DHB) as a matrix. Transmission electron microscopy (TEM) was performed using a JEOL JEM-100SX microscope operating at 100 kV. Emission spectra of the samples were monitored by a Perkin-Elmer LS50B fluorometer at 25 °C using a 1 cm path length cell. The excitation bandwidth was 0.1 nm. The emission bandwidth was 0.1 nm. Calf intenstine alkaline phosphatase (AP) was purchased from Invitrogen Corporation (USA). The dynamic light scattering (DLS) measurements were carried out at 90° scattering angle and 25 ± 0.2 °C using a FPAR-1000 particle analyzer with a He−Ne laser as a light source. The CONTIN program was used for data analysis to extract information on the average hydrodynamic radius (r_H).

F-POSS 2.[19,22,23]. To a suspension of octaammonium POSS[24−26] (**1**, 1 g, 0.852 mmol) and ethyl trifluoroacetate (406 μL, 3.41 mmol) in methanol (20 mL), triethylamine (2 mL, 14.4 mmol) was added, and the reaction mixture was stirred at room temperature for 3 h. The resulting mixture was evaporated, and the crude was directly used in the next step. A clear oil was obtained after dialysis (895 mg, 83%); ^1H NMR (D_2O, 400 MHz) δ 3.26 (t, 8H, J = 7.0 Hz), 2.94 (t, 8H, J = 7.0 Hz), 1.70 (brs, 8H), 1.61 (brs, 8H), 0.64 (m, 16H); ^{13}C NMR (D_2O, 100 MHz) δ 155.9, 117.4, 41.52, 40.92, 21.76, 20.05, 8.77, 8.72; ^{29}Si NMR (D_2O, 80 MHz) δ −68.7, −68.4; ^{19}F NMR (D_2O, 373 MHz) δ −75.4; MALDI-TOF [$(M+H)^+$], [POSS-TFA_2] calcd. 1074.52, found 1073.29, [POSS-TFA_3] calcd. 1170.53, found 1170.00, [POSS-TFA_4] calcd. 1266.53, found 1266.16, [POSS-TFA_5] calcd. 1362.54, found 1361.76.

Preparation of the Amino-Presenting Silica Nanoparticles.[23,27] A solution containing 2 mL of tetraethoxysilane, 1 mL of 3-aminopropyltriethoxysilane, 7 mL of water, and 2 mL of ammonium hydroxide in 50 mL of ethanol was stirred at ambient temperature for 16 h, and then the white precipitate was separated by centrifugation. After washing with ethanol three times, the particles (117 ± 15 nm diameter from TEM, 280 ± 44 nm diameter from DLS) were obtained as a white powder. In this step, 960 nmol of trifluoroacetyl groups were attached to the particles.

Preparation of the NP Probes. A solution containing 1.24 g of fluorescein (3.75 mmol) and $POCl_3$ (20 mL) was refluxed for 2 h. The reaction was monitored by ^1H NMR in $CDCl_3$, and after finishing the reaction, the excess $POCl_3$ was removed by evaporation. The brown residue containing **3** was used without purification for the next procedures. Identification was performed using the hydrolysis product of the compound **3** with 3,6-fluorescein diphosphate in ^1H NMR and MS measurements. F-POSS obtained above (0.852 mmol) and **3** were mixed in 20 mL of chloroform containing 2 mL of triethylamine (14.4 mmol). The phosphorylation of amino groups of F-POSS was monitored by the observation of the chemical shift at the 2-position of the hydrogen atoms which exhibited a downfield shift after the amide formation. After finishing the reaction, 100 mg of the amino-presenting silica nanoparticles was added to the mixture. The reaction was monitored by ninhydrin reagents for consumption of the amino groups on the NPs. After stirring 1 h at room temperature, nanoparticles were centrifuged and washed with chloroform, water, and methanol. The white powder was obtained after drying (119 ± 16 nm diameter from TEM, 288 ± 46 nm

dx.doi.org/10.1021/bc100381x |*Bioconjugate Chem.* 2011, 22, 1484–1490

diameter from DLS). To estimate the amount of F-POSS on the NP (81 nmol/mg), the ^{19}F NMR spectrum of the solution containing the NP probe was dissolved in 1 N aqueous sodium hydroxide and compared to spectra of the standard samples with various concentrations of trifluoroacetic acid. The amount of fluorescein (471 nmol/mg) was estimated from the fluorescence intensity and UV absorption of the dissolved solutions. At the surface of the particles, 49% of the amino groups were tethered with fluorescein, and 34% with F-POSS.

Enzymatic Reaction with the NP Probe. The NP probe (2.5 mg) was incubated in 500 μL of the reaction solution containing AP in 50 mM sodium phosphate, 100 mM Tris−HCl, and 0.05 mM EDTA (pH = 7.0) at 37 °C. The reaction was terminated by centrifuging the reaction mixture, and then the supernatants were analyzed by ^{19}F NMR. UV−vis absorption measurements were performed with the diluted supernatants (×10). Fluorescence measurements were executed with the diluted supernatants (×1000).

^{19}F NMR Measurements for Determining Reaction Yields in Enzymatic Reactions and Relaxation Times. Relaxation times of F-POSS and trifluoroacetic acid in ^{19}F NMR were taken with the following parameter sets: relaxation delay, 15 s; pulse width (90°), 51 μs; acquisition time, 88 ms; scan time, 4 times. ^{19}F longitudinal (T_1) relaxation data were collected with ten delay times (1, 5, 10, 20, 50, 100, 250, 500, 1000, and 3000 ms) using a standard 1D inverse recovery pulse sequence. ^{19}F transverse (T_2) relaxation data were collected with 9 delay times (400, 500, 600, 700, 800, 900, 1000, 2000, and 8000 ms) using a standard 1D Carr-Purcel-Meiboom-Gill pulse sequence. Resonance intensities in relaxation experiments were measured and fit to an exponential function. The reaction yields were determined according to our previous work.[23] ^{19}F NMR spectra for the analysis of synthetic compounds were taken at 25 °C with the following parameter sets: relaxation delay, 6 s; pulse width (45°), 12 μs; acquisition time, 88 ms; scan time, 8 times. In total, 1 min was required for 1D NMR acquisition. Standard solutions containing F-POSS with the concentration region 100 μM to 4 mM were prepared, and the linear relationship was determined between the concentration and the signal height of trifluoromethyl groups in F-POSS in the ^{19}F NMR spectra. The reaction yields were determined by fitting the signal height to the standard line.

Preparation for HeLa Cell Lysate. HeLa cells (1.0×10^6 cells) were cultured in a dish (90% confluent in ϕ100 mm dishes) and washed twice with ice-cold PBS(−). The cell lysate was then harvested with 2 mL of ice-cold CelLytic M Cell Lysis Reagent (Sigma-Aldrich, Inc., St. Louis, MO), kept at ambient temperature for 15 min, and centrifuged at 12 000 rpm for 5 min to remove the cell debris. The enzymatic volume activity (U/mL) of the supernatant was measured from the hydrolysis rate of *p*-nitrophenyl phosphate. The solutions (100 μL) containing 1 μL of the cell lysate, 6.7 mM *p*-nitrophenyl phosphate, and 2.0 mM magnesium chloride in 50 mM sodium phosphate buffer (pH = 6.0) were incubated at 37 °C, and the absorption changes at 405 nm were monitored. The volume activity was estimated from the fitting of the standard curve with CIAP.

RESULTS AND DISCUSSION

Scheme 1 illustrates the bimodal detection mechanism using the NP-based probe for enzymatic activity in this study. The probe consists of three significant components, the signal unit, the NP moiety, and the linker. As a ^{19}F NMR signal unit, we used water-soluble perfluorinated polyhedral oligomeric silsesquioxane (F-POSS) which can be a good scaffold to construct functional ^{19}F MR probes by modification with the signal regulation modulus because of high water-solubility and stability under biological conditions.[19,22,23] The silica NPs work as a quencher for ^{19}F NMR signals of the surface-tethered F-POSS molecules.[23] On the surface of the NP, the molecular rotation of F-POSS should be restricted like in the solid phase, which suppresses the NMR signals. Indeed, the T_1 and T_2 relaxation times of fluorine atoms were determined to be 2.90 and 1.94 s in trifluoroacetic acid and 1.067 and 0.992 s in F-POSS, respectively. On the other hand, those values in the NP probes were not determined because of shorter transverse relaxation times and the low signal intensity of the ^{19}F resonance. These results clearly indicate that the silica particles can accelerate the relaxation for ^{19}F NMR signals and work as a quencher for NMR signals. By the enzymatic digestion of the linker, F-POSS can be released, and the ^{19}F NMR signals of F-POSS would be enhanced. To evaluate the AP activity, the diphosphate-caged fluorescein was used as the biodegradable linker between F-POSS and the surface of NPs. The 3,6-diphospholyrated fluorescein shows less fluorescence emission, and the intrinsic strong emission can be recovered after

Scheme 2. Synthetic Sheme of the NP Pobes[a]

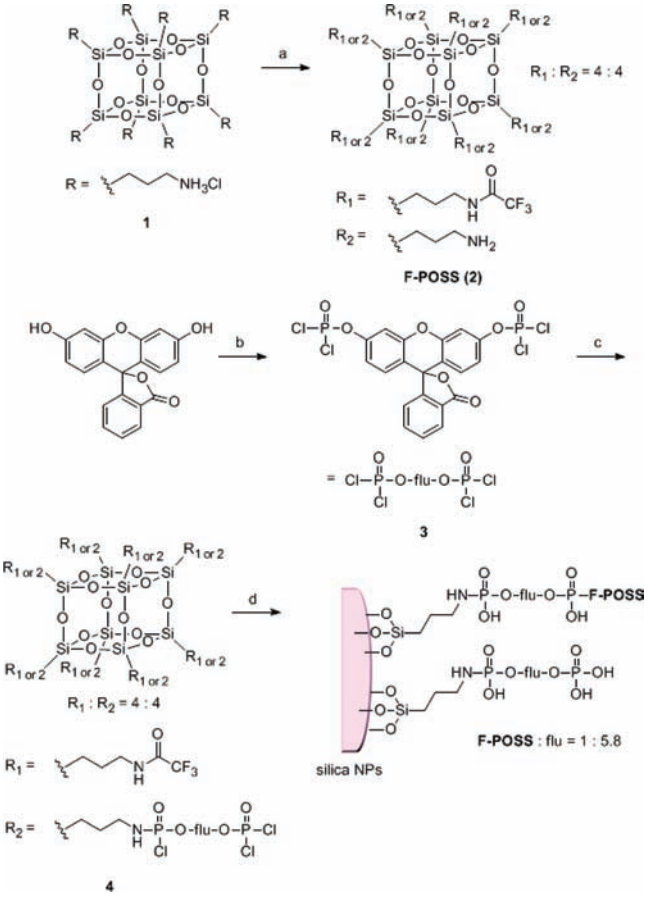

[a] Reagents: (a) ethyl trifluoroacetate, triethylamine, methanol, 83%; (b) fluorescein, phosphorus oxytrichloride, triethylamine, chloroform, quant.; (c) F-POSS, chloroform; (d) amino-modified silica nanoparticles, chloroform.

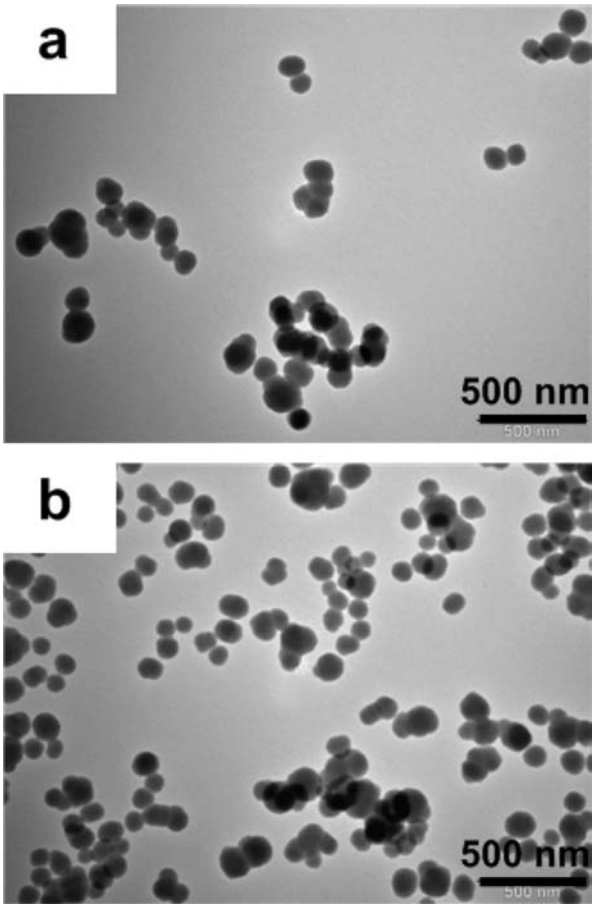

Figure 1. TEM images of (a) the amino-presenting silica NPs and (b) the F-POSS-coated silica NPs. The scale bar represents 500 nm length.

the elimination of both phosphate groups by AP.[28−36] Hence, the enzymatic reaction can be assessed by the increases of two signal molecules, F-POSS and fluorescein, in ^{19}F NMR and fluorescence measurements, respectively.

F-POSS were synthesized using octaamino-POSS as a starting material by introducing trifluoroacetyl groups according to a previous report.[23] We prepared amino-presenting silica NPs averaging 150 nm in diameter with the Stöber method.[27] The amino groups of F-POSS were modified with the precursor of the diphosphate-caged fluorescein **3** to yield the compound **4** (Scheme 2). Because compounds **3** and **4** can be readily degraded, we used these compounds without purification for the next steps. Subsequently, the phosphoryl chloride groups of compound **4** were reacted with the amino groups on the surface of NPs. After washing with water and methanol thoroughly, the monodispersed modified NPs were obtained (Figure 1). From the measurements of the particle radii with TEM and DLS, the slight increases were observed. These data indicate that the interparticle cross-linking should hardly occur in the product.

The amounts of F-POSS and fluorescein were determined by comparing the signal intensities with the standard samples as 81 nmol and 471 nmol on 1 mg of the NPs, respectively. The smaller existing ratio of F-POSS (1:5.8) than the theoretical value calculated from the reaction condition (1:4) indicates desorption of F-POSS from the particle surface during purification. This fact suggests that the phosphate-caged fluorescein not tethered to F-POSS should exist on the surface. The significant degradation

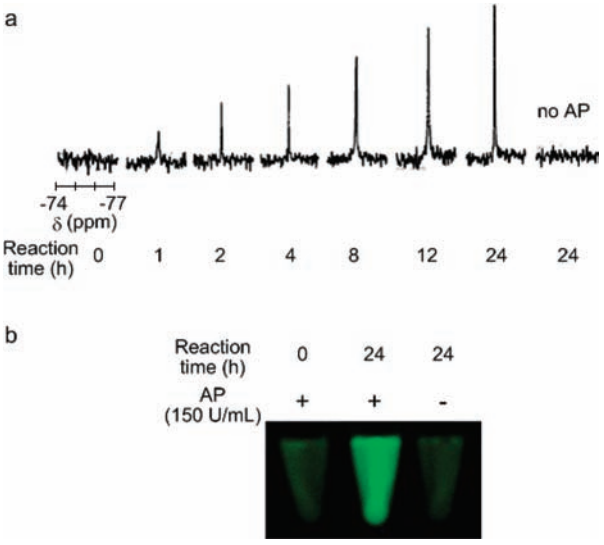

Figure 2. (a) ^{19}F NMR spectra of the supernatants after the incubation. The reactions were executed with the NP probes (F-POSS, 0.41 mM; F atom, 4.86 mM; fluorescein, 2.36 mM) in the presence or absence of AP (150 U/mL) in 50 mM sodium phosphate, 100 mM Tris−HCl, and 0.05 mM EDTA (pH = 7.0) at 37 °C. (b) The fluorescence image of the 10-fold diluted supernatants before (left) and after 24 h incubation in the presence (center) or absence (right) of AP. The samples were irradiated at 365 nm with the transilluminator.

following undesired signal output or aggregation was not observed by adding the agent to BSA (1 mg/mL) or serum, or by altering the pH between pH 5 and 9. In addition, the signals were not observed after 24 h incubation at 37 °C at pH 7.0 in the presence of proteinase K. These results suggest that our probe could provide clear signals without the loss of sensitivity caused by unexpected interactions in vivo.

A class of AP generally exists in the cell cytoplasm or surface in the whole body, and they can digest phosphodiester analogues without specificity.[37,38] The AP activity is particularly enhanced in tumor regions.[39,40] In addition, several tens to hundred nanometer-sized macromolecules can be specifically delivered to the tumor region by the enhanced permeability and retention (EPR) effect.[41−47] Therefore, we can set the scenarios so that the AP-responsive probes based on the nanoparticles can be expected to show enhanced signals after reaching tumor regions via the EPR effect or much vigorous AP activity. Hence, this system of assessing the AP activity could be a valid technique for early cancer diagnosis. ^{19}F MRI is an insensitive detection method, so accumulation of the probe with sufficient concentrations would be necessitated for in vivo usages. Nanoparticle-based probes are advantageous because the EPR effect could possibly solve the problems on the sensitivity and the delivery of the probe. The reactivity of the probe toward AP was investigated. The reaction mixtures (0.5 mL) containing 5 mg/mL of the modified NPs (F-POSS, 0.41 mM; F atom, 4.86 mM; fluorescein, 2.36 mM) and AP (150 U/mL) in 50 mM sodium phosphate and 100 mM Tris−HCl buffer (pH = 7.0) were incubated at 37 °C. ^{19}F NMR signals and fluorescence intensity at 512 nm from the mixture were monitored. Both signals increased after incubation in the presence of AP (Figure 2). From the fitting to the standard line, the reaction yields were calculated as approximately 10% after 1 h incubation. On the other hand, signal intensities were continuously under the detection limit (less than 5% of the reaction

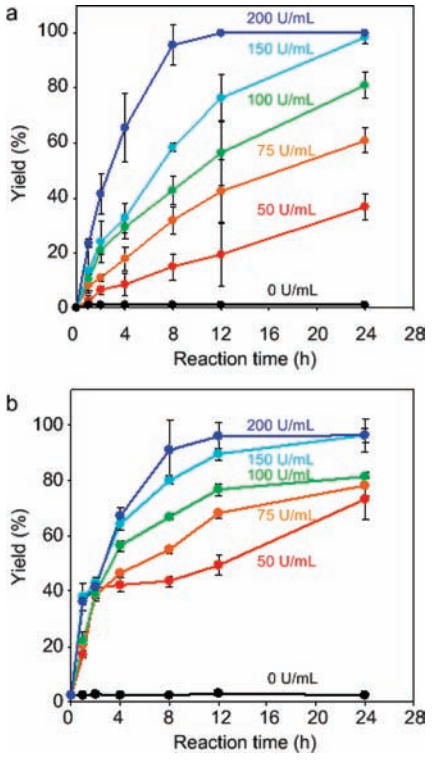

Figure 3. (a) Time-course of the intensity changes of ^{19}F NMR signals from the supernatants after enzymatic reactions. The NP probes (2.5 mg) were incubated in 500 μL of the reaction solutions (F-POSS, 0.41 mM; F atom, 4.86 mM; fluorescein, 2.36 mM) containing various concentration of AP in 50 mM sodium phosphate, 100 mM Tris−HCl, and 0.05 mM EDTA (pH = 7.0) at 37 °C. The reaction yields were monitored with ^{19}F NMR and calculated by fitting on the standards. The errors represent the standard deviation calculated from the three data sets. (b) Time-courses of the emission changes at 512 nm from the 10-fold diluted supernatants after reaction with various concentrations of AP. The errors represent the standard deviation calculated from the three data sets.

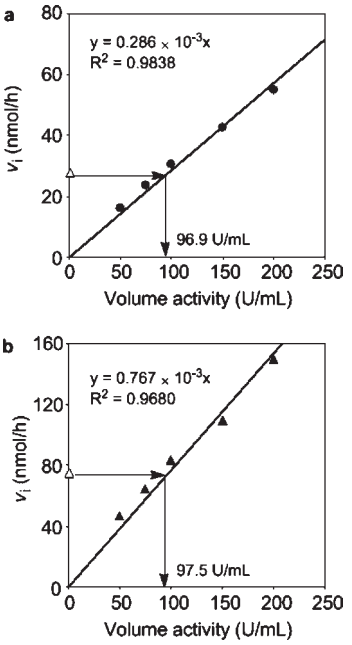

Figure 4. Determination of AP activity in the HeLa cell lysate. (a) Fitting of the obtained value (clear triangular dot) from the ^{19}F NMR measurements to the standard line according to the results of Figure 3a. (b) Fitting of the obtained value (clear triangular dot) from the fluorescence measurements to the standard line according to the results of Figure 3b. The plots represent the averages calculated from the three data sets.

yield) after 24 h incubation in the absence of AP. These results indicate that the AP activity can be detected using our probe as the corresponding increases of ^{19}F NMR and fluorescence signals as we designed.

We executed the reactions with various concentrations of AP, and the signal intensities from the reaction mixtures were monitored with ^{19}F NMR and fluorescence measurements (Figure 3). The increases of the signal intensities were compared with the standard line prepared with the concentration-definitive F-POSS solutions and converted as the reaction yields. The increases of the yields calculated from ^{19}F NMR and fluorescence signals showed good agreement. In the presence of 200 U/mL of AP, the reactions reached a plateau after the 8 h incubation. The detection limits were correspondingly 50 U/mL of AP. These data suggest that enzymatic reaction can be assessed by the synchronized increases of fluorescence and ^{19}F NMR signals. This fact proposes that the signal change of the probe in one modality could be corrected by the signal response in the other modality. The rapid increase of fluorescence intensity within 2 h could be caused from the fluorescein molecules tethered to the surface of the NPs directly and the amino-terminal of F-POSS.

To demonstrate feasibility of the quantitative analysis of the probe in the presence of the miscellaneous molecules under biomimetic conditions, the reactions were performed in the HeLa cell lysate. Initially, the AP activity was calculated from the hydrolysis rate of *p*-nitrophenyl phosphate in the lysate, and it was determined to be 95 ± 9 U/mL. The linear increases of the magnitude of both the ^{19}F NMR and fluorescence signal intensity were observed from our probes. Consequently, the enzymatic activities of the cell lysate were evaluated to be 97 (^{19}F NMR) and 98 (fluorescence) U/mL from the slope fitted to the standard line, respectively (Figure 4). These data suggest that the NP probe can be used for bimodal quantitative assay with biological samples.

CONCLUSION

In summary, we present here the bimodal detection in ^{19}F NMR and fluorescence for a single enzymatic reaction. The NP probes can gradually release perfluorinated dendrimers and fluorescein with the progress of enzymatic reactions. The enzymatic activity can be evaluated from the increasing rates of the signal magnitudes in ^{19}F NMR and fluorescence during the reaction. Finally, it was demonstrated that the enzymatic activity of the cell lysate evaluated with our probes showed good agreement with that with the conventional method. We conclude that this system could provide a feasible strategy for receiving quantitative information in MRI.

AUTHOR INFORMATION

Corresponding Author

*E-mail: chujo@chujo.synchem.kyoto-u.ac.jp. Fax: +81-75-383-2605. Phone: +81-75-383-2604.

■ ACKNOWLEDGMENT

This research was partly supported by Nakatani Foundation of Electronic Measuring Technology Advancement (for K.T.) and Grant-in-Aid for Young Scientists (B), no. 22750107, from the Ministry of Education, Culture, Sports, Science, and Technology, Japan.

■ REFERENCES

(1) Terreno, E., Castelli, D. D., Viale, A., and Aime, S. (2010) Challenges for molecular magnetic resonance imaging. *Chem. Rev. 110*, 3019–42.

(2) Ali, M. M., Liu, G., Shah, T., Flask, C. A., and Pagel, M. D. (2009) Using two chemical exchange saturation transfer magnetic resonance imaging contrast agents for molecular imaging studies. *Acc. Chem. Res. 42*, 915–24.

(3) Shapiro, M. G., Atanasijevic, T., Faas, H., Westmeyer, G. G., and Jasanoff, A. (2006) Dynamic imaging with MRI contrast agents: quantitative considerations. *Magn. Reson. Imaging 24*, 449–62.

(4) Srinivas, M., Heerschap, A., Ahrens, E. T., Figdor, C. G., and de Vries, I. J. M. (2010) ^{19}F MRI for quantitative *in vivo* cell tracking. *Trends Biotechnol. 28*, 363–70.

(5) Morawski, A. M., Winter, P. M., Yu, X., Fuhrhop, R. W., Scott, M. J., Hockett, F., Robertson, J. D., Gaffney, P. J., Lanza, G. M., and Wickline, S. A. (2004) Quantitative "magnetic resonance immunohistochemistry" with ligand-targeted ^{19}F nanoparticles. *Magn. Reson. Med. 52*, 1255–62.

(6) Yu, J., Kodibagkar, V. D., Cui, W., and Mason, R. P. (2005) ^{19}F: A versatile reporter for non-invasive physiology and pharmacology using magnetic resonance. *Curr. Med. Chem. 12*, 819–48.

(7) Senanayake, P. K., Kenwright, A. M., Parker, D., and van der Hoorn, S. K. (2007) Responsive fluorinated lanthanide probes for ^{19}F magnetic resonance spectroscopy. *Chem. Commun.* 2923–5.

(8) Cui, W., Otten, P., Li, Y., Koeneman, K. S., Yu, J., and Mason, R. P. (2004) Novel NMR approach to assessing gene transfection: 4-Fluoro-2-nitrophenyl-β-$_D$-galactopyranoside as a prototype reporter molecule for β-galactosidase. *Magn. Reson. Med. 51*, 616–20.

(9) Takaoka, Y., Sakamoto, T., Tsukiji, S., Narazaki, M., Matsuda, T., Tochio, H., Shirakawa, M., and Hamachi, I. (2009) Self-assembling nanoprobes that display off/on ^{19}F nuclear magnetic resonance signals for protein detection and imaging. *Nat. Chem. 1*, 557–61.

(10) Higuchi, M., Iwata, N., Matsuba, Y., Sato, K., Sasamoto, K., and Saido, T. C. (2005) ^{19}F and ^{1}H MRI detection of amyloid β plaques in vivo. *Nat. Neurosci. 8*, 527–33.

(11) Zimmermann, U., Nöth, U., Gröhn, P., Jork, A., Ulrichs, K., Lutz, J., and Haase, A. (2000) Non-invasive evaluation of the location, the functional integrity and the oxygen supply of implants: ^{19}F nuclear magnetic resonance imaging of perfluorocarbon-loaded Ba^{2+}-alginate beads. *Artif. Cells Blood Substit. Immobil. Biotechnol. 28*, 129–46.

(12) Ahrens, E. T., Flores, R., Xu, H. Y., and Morel, P. A. (2005) In vivo imaging platform for tracking immunotherapeutic cells. *Nat. Biotechnol. 23*, 983–87.

(13) Maki, J., Masuda, C., Morikawa, S., Morita, M., Inubushi, T., Matsusue, Y., Taguchi, H., and Tooyama, I. (2007) The MR tracking of transplanted ATDC5 cells using fluorinated poly-$_L$-lysine-CF_3. *Biomaterials 28*, 434–40.

(14) Mizukami, S., Takikawa, R., Sugihara, F., Hori, Y., Tochio, H., Wälchli, M., Shirakawa, M., and Kikuchi, K. (2008) Paramagnetic relaxation-based ^{19}F MRI probe to detect protease activity. *J. Am. Chem. Soc. 130*, 794–5.

(15) Okada, S., Mizukami, S., and Kikuchi, K. (2010) Application of a stimuli-responsive polymer to the development of novel MRI probes. *ChemBioChem 11*, 785–7.

(16) Tanabe, K., Harada, H., Narazaki, M., Tanaka, K., Inafuku, K., Komatsu, H., Ito, T., Yamada, H., Chujo, Y., Matsuda, T., Hiraoka, M., and Nishimoto, S. (2009) Monitoring biological one-electron reduction by ^{19}F-NMR: Hypoxia selective activation of ^{19}F-labeled indolequinone derivative. *J. Am. Chem. Soc. 131*, 15982–3.

(17) Oishi, M., Sumitani, S., and Nagasaki, Y. (2007) On-off regulation of ^{19}F magnetic resonance signals based on pH-sensitive PEGylated nanogels for potential tumor-specific smart ^{19}F MRI probes. *Bioconjugate Chem. 18*, 1379–82.

(18) Kenwright, A. M., Kuprov, I., Luca, E. D., Parker, D., Pandya, S. U., Senanayake, P. K., and Smith, D. G. (2008) ^{19}F NMR based pH probes: lanthanide(III) complexes with pH-sensitive chemical shifts. *Chem. Commun.* 2514–6.

(19) Tanaka, K., Kitamura, N., Takahashi, Y., and Chujo, Y. (2009) Reversible signal regulation system of ^{19}F NMR by redox reactions using a metal complex as a switching module. *Bioorg. Med. Chem. 17*, 3818–23.

(20) Mizukami, S., Takikawa, R., Sugihara, F., Shirakawa, M., and Kikuchi, K. (2009) Dual-function probe to detect protease activity for fluorescence measurement and ^{19}F MRI. *Angew. Chem., Int. Ed. 48*, 3641–3.

(21) Langereis, S., Keupp, J., van Velthoven, J. L. J., de Roos, I. H. C., Burdinski, D., Pikkemaat, J. A., and Grüll, H. (2009) A temperature-sensitive liposomal ^{1}H CEST and ^{19}F contrast agent for MR image-guided drug delivery. *J. Am. Chem. Soc. 131*, 1380–1.

(22) Tanaka, K., Inafuku, K., and Chujo, Y. (2008) Ratiometric multimodal chemosensors based on cubic silsesquioxanes for monitoring solvent polarity. *Bioorg. Med. Chem. 16*, 10029–33.

(23) Tanaka, K., Kitamura, N., Naka, K., and Chujo, Y. (2008) Multimodal ^{19}F NMR probe using perfluorinated cubic silsesquioxane-coated silica nanoparticles for nonitoring enzymatic activity. *Chem. Commun.* 6176–8.

(24) Feher, F. J., and Wyndham, K. D. (1998) Amine and ester-substituted silsesquioxanes: Synthesis, characterization and use as a core for starburst dendrimers. *Chem. Commun.* 323–4.

(25) Gravel, M.-C., Zhang, C., Dinderman, M., and Laine, R. M. (1999) Octa(3-chloroammoniumpropyl) octasilsesquioxane. *Appl. Organomet. Chem. 13*, 329–36.

(26) Tanaka, K., Kitamura, N., Naka, K., Morita, M., Inubushi, T., Chujo, M., Nagao, M., and Chujo, Y. (2009) Improving proton relaxivity of dendritic MRI contrast agents by rigid silsesquioxane core. *Polym. J. 41*, 287–92.

(27) Stöber, W., Fink, A., and Bohn, E. (1968) Controlled growth of monodisperse silica spheres in the micron size range. *J. Colloid Interface Sci. 26*, 62–9.

(28) Gee, K. R. (1999) Novel fluorogenic substrates for acid phosphatase. *Bioorg. Med. Chem. Lett. 9*, 1395–6.

(29) Fomine, S., Pineda, A., Ogawa, T., Perez, R., and Sotelo, M. (1995) Novel polymers containing fluorescein moieties. *Polym. J. 27*, 712–8.

(30) Tlenkopatchev, M., Fomine, S., Miranda, E., Fomina, L., and Ogawa, T. (1995) Synthesis of polynorbornene containing fluorescein moiety. *Polym. J. 27*, 1173–9.

(31) Subauste, M. C., List, B., Guan, X., Hahn, K. M., Lerner, R., and Gilula, N. B. (2001) A catalytic antibody produces fluorescent tracers of gap junction communication in living cells. *J. Biol. Chem. 276*, 49164–8.

(32) Mitchison, T. J. (1989) Polewards microtubule flux in the mitotic spindle: evidence from photoactivation of fluorescence. *J. Cell Biol. 109*, 637–52.

(33) Politz, J. C. (1999) Use of caged fluorochromes to track macromolecular movement in living cells. *Trends Cell Biol. 9*, 284–7.

(34) Mitchison, T. J., Sawin, J. A., Gee, T. K., and Mallavarapu, A. (1998) Caged fluorescent probes. *Methods Enzymol. 291*, 63–78.

(35) Funakoshi, T., and Hirokawa, N. (1998) Application of caged fluorescein-labeled tubulin to studies of microtubule dynamics and transport of tubulin molecules in axons. *Methods Enzymol. 291*, 348–56.

(36) Tanaka, K., Kitamura, N., and Chujo, Y. (2010) Biodegradable main-chain phosphate-caged fluorescein polymers for the evaluation of enzymatic activity. *Macromolecules 43*, 6180–4.

(37) Lange, P. H., Millan, J. L., Stigbrand, T., Vessella, R. L., Ruoslahti, E., and Fishman, W. H. (1982) Placental alkaline phosphatase as a tumor marker for seminoma. *Cancer Res. 42*, 3244–7.

(38) Keshaviah, A., Dellapasqua, S., Rotmensz, N., Lindtner, J., Crivellari, D., Collins, J., Colleoni, M., Thürlimann, B., Mendiola, C., Aebi, S., Price, K. N., Pagani, O., Simoncini, E., Castiglione Gertsch, M., Gelber, R. D., Coates, A. S., and Goldhirsch, A. (2007) CA15−3 and alkaline phosphatase as predictors for breast cancer recurrence: A combined analysis of seven International Breast Cancer Study Group trials. *Ann. Oncol. 18*, 701–8.

(39) Kojima, Y., and Sakurada, T. (1976) Increasing in alkaline phosphatase activity in the liver of mice bearing ehrlich ascites tumor. *Cancer Res. 36*, 23–7.

(40) Fishman, W. H. (1987) Clinical and biological significance of an isozyme tumor marker—PLAP. *Clin. Biochem. 20*, 387–92.

(41) Kong, G., Braun, R. D., and Dewhirst, M. W. (2000) Hyperthermia enables tumor-specific nanoparticle delivery: Effect of particle size. *Cancer Res. 60*, 4440–5.

(42) Ishida, O., Maruyama, K., Sasaki, K., and Iwatsuru, M. (1999) Size-dependent extravasation and interstitial localization of polyethyleneglycol liposomes in solid tumor-bearing mice. *Int. J. Pharm. 190*, 49–56.

(43) Litzinger, D. C., Buiting, A. M. J., Van Rooijen, N., and Huang, L. (1994) Effect of liposome size on the circulation time and intraorgan distribution of amphipathic poly(ethylene glycol)-containing liposomes. *Biochim. Biophys. Acta 1190*, 99–107.

(44) Yuan, F., Leunig, M., Huang, S. K., Berk, D. A., Papahadjopoulos, D., and Jain, R. K. (1994) Microvascular permeability and interstitial penetration of sterically stabilized (stealth) liposomes in a human tumor xenograft. *Cancer Res. 54*, 3352–6.

(45) Hobbs, S. K., Monsky, W. L., Yuan, F., Roberts, W. G., Griffith, L., Torchilin, V. P., and Jain, R. K. (1998) Regulation of transport pathways in tumor vessels: Role of tumor type and microenvironment. *Proc. Natl. Acad. Sci. U. S. A. 95*, 4607–12.

(46) Maeda, H. (2001) The enhanced permeability and retention (EPR) effect in tumor vasculature: The key role of tumor-selective macromolecular drug targeting. *Adv. Enzyme Regul. 41*, 189–207.

(47) Maeda, H., Fang, J., Inutsuka, T., and Kitamoto, Y. (2003) Vascular permeability enhancement in solid tumor: Various factors, mechanisms involved and its implications. *Int. Immunopharmacol. 3*, 319–28.

Bioconjugate Chemistry

ARTICLE

pubs.acs.org/bc

Fluorescent DNA Nanotags Featuring Covalently Attached Intercalating Dyes: Synthesis, Antibody Conjugation, and Intracellular Imaging

Andrea L. Stadler,[†,⊥] Junriz O. Delos Santos,[†,§] Elizabeth S. Stensrud,[‡] Anna Dembska,[†,§] Gloria L. Silva,[†,§] Shengpeng Liu,[†,§] Nathaniel I. Shank,[†,§] Ezgi Kunttas-Tatli,[‡] Courtney J. Sobers,[†] Philipp M. E. Gramlich,[∥] Thomas Carell,[∥] Linda A. Peteanu,[†,§] Brooke M. McCartney,[‡] and Bruce A. Armitage*[,†,§]

[†]Department of Chemistry, [‡]Department of Biological Sciences, and [§]Center for Nucleic Acids Science and Technology, Carnegie Mellon University, 4400 Fifth Avenue, Pittsburgh, Pennsylvania 15213, United States

[∥]Department of Chemistry and Biochemistry, Ludwig Maximilians University, Munich, 81377 Munich, Butenandtstrasse, 5-13, Haus F, Germany

Supporting Information

ABSTRACT: We have synthesized fluorescent DNA duplexes featuring multiple thiazole orange (TO) intercalating dyes covalently attached to the DNA via a triazole linkage. The intercalating dyes stabilize the duplex against thermal denaturation and show bright fluorescence in the green region of the spectrum. The emission color can be changed to orange or red by addition of energy-accepting Cy3 or Cy5 dyes attached covalently to the DNA duplex. The dye-modified DNA duplexes were then attached to a secondary antibody for intracellular fluorescence imaging of centrosomes in *Drosophila* embryos. Bright fluorescent foci were observed at the centrosomes in both the donor (TO) and acceptor (Cy5) channels, because the energy transfer efficiency is moderate. Monitoring the Cy5 emission channel significantly minimized the background signal because of the large shift in emission wavelength allowed by energy transfer.

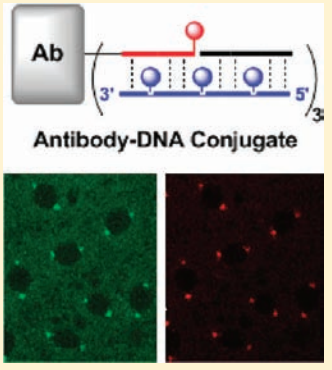

INTRODUCTION

A wide range of fluorescence technologies are available for biological imaging, allowing users to select virtually any color in the visible and near-IR region and a variety of orthogonal labeling strategies that permit imaging of multiple targets simultaneously.[1,2] Both chemical approaches to fluorescence labeling (e.g., dye-conjugated antibodies) and biological fusion constructs based on inherently fluorescent proteins such as green fluorescent protein or other tags that can recognize dyes have allowed cell biologists to develop an increasingly detailed understanding of the spatiotemporal patterns of molecular interactions occurring within cells and/or on cell surfaces.

While fluorescence technologies provide a palette of colors and labeling strategies, an area in which there is still room for improvement is the brightness of the labels. For stoichiometric labels such as fusion proteins, a single dye is attached to the protein of interest. If the protein is expressed in small amounts or is not strongly localized to a specific region, the resulting signal might not be sufficiently bright to detect, particularly in the complex environment of a cell.

The brightest fluorescent labels typically exhibit extraordinarily high molar extinction coefficients (ε). This includes semiconductor nanocrystals (i.e., quantum dots),[3] inorganic[4,5] and polymeric[6,7] nanoparticles, and phycobiliproteins.[8] These materials have found uses in certain labeling and detection applications. Nevertheless, one challenge that remains in adapting these high-ε materials more broadly is installing surface chemistry that allows single-point attachment to molecules of interest.

In prior work, we created a new class of fluorescent labeling reagents based on DNA nanostructures and fluorogenic intercalating dyes.[9,10] DNA can readily be designed to form one-, two-, or three-dimensional nanostructures, and intercalating dyes can insert into the helix at high densities, up to one fluorophore per two base pairs (Figure 1, top). Intercalating dyes of many fluorescence colors are commercially available, as is DNA bearing a variety of end group modifications that can be used to attach the DNA to various surfaces or other molecules. Thus, a noncovalent nanotag can be assembled from readily available materials and can be easily applied in labeling of biomolecules via standard conjugation chemistries.

While assembly of noncovalent nanotags is facile, the lack of a stable linkage between the dye and the DNA template allows the fluorophore to dissociate from the DNA, leading to weaker fluorescence from the labeled molecule and potentially unintended

Received: November 5, 2010
Revised: July 5, 2011
Published: July 14, 2011

ACS Publications © 2011 American Chemical Society

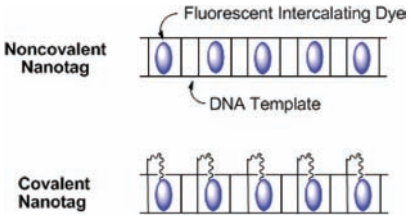

Figure 1. Schematic of noncovalent (top) and covalent (bottom) fluorescent DNA nanotags. A simple linear nanotag is shown, but multidimensional versions are readily assembled.

fluorescence from other molecules. For example, we observed that a noncovalent nanotag targeted to a cell-surface protein gave the intended peripheral fluorescence surrounding the cell, but also strong intracellular fluorescence from other cells.[9] This was due to dissociation of the dye from the nanotag, uptake into (presumably dead) cells, and staining of nucleic acids within those cells.

To enhance the utility of this class of fluorescent labels, we sought to develop covalent versions of our nanotags based on a robust "click" reaction.[11] In addition to providing stable conjugates between DNA and intercalating dyes, we have attached the resulting constructs to antibodies and used them to stain intracellular proteins. Efficient Förster resonance energy transfer in these tags allows wavelength shifting of the emission to minimize background fluorescence.

EXPERIMENTAL PROCEDURES

General Materials and Methods. Reagents for the synthesis of thiazole orange azides were purchased from Sigma-Aldrich and Alfa-Aesar. Solvents were high-performance liquid chromatography (HPLC) grade. DNA oligonucleotides were purchased from Integrated DNA Technologies, Inc., as lyophilized powders unless specified. Unmodified and 5′-biotinylated oligonucleotides were purified by gel-filtration chromatography, while Cy3- and Cy5-labeled oligonucleotides were purified by HPLC. Alkyne-modified DNA strands were synthesized in the Carell laboratory or by BaseClick GmbH. Streptavidin polystyrene beads (2 μm diameter) were purchased from Spherotech, Inc. (Libertyville, IL). Intermediate **4** (2-methylthiobenzothiazole) was provided by B. Schmidt. ^{1}H NMR spectra were recorded at 300 MHz on a Bruker Avance instrument in either MeOD-d_3 or $CDCl_3$ as the solvent, with TMS as the internal standard. Electrospray ionization mass spectrometry (ESI-MS) experiments were conducted on a Finnigan LCQ quadrupole ion trap mass spectrometer in positive ion mode using Xcalibur version 1.2.

*2-(2-Chloroethoxy)ethyl Trifluoromethanesulfonate (**1a**).* Poly(vinylpyridine) (PVPy, 1.10 g) was suspended in 60 mL of dry dichloromethane, and 1.85 mL (11 mmol) of trifluoromethanesulfonate anhydride was added followed by 1.90 mL (9 mmol) of 2-(2-chloroethoxy)ethanol. The mixture was stirred at room temperature for 2 h. The resin was gravity filtered, and the reaction mixture was washed with 1% sodium bicarbonate followed by brine and dried with anhydrous sodium sulfate and the solvent evaporated to dryness to give 1.28 g (5 mmol, 56% yield) of brown oil shown to be compound **1a**: ^{1}H NMR (300 MHz, $CDCl_3$) δ 4.67 (br t, 2H, J = 4.5 Hz), 3.88 (m, 2H), 3.82 (m, 2H), 3.68 (m, 2H).

*2-[2-(2-Chloroethoxy)ethoxy]ethyl Trifluoromethanesulfonate (**1b**).* PVPy (550 mg) was suspended in 30 mL of dry dichloromethane, and 925 μL (5.5 mmol) of trifluoromethanesulfonate anhydride was added followed by 645 μL (4.5 mmol) of 2-[2-(2-chloroethoxy)ethoxy]ethanol. The mixture was stirred at room temperature for 2 h. The resin was gravity filtered, and the solvent was washed with 1% sodium bicarbonate followed by brine and dried with sodium sulfate. Solvent evaporation yielded 1.13 g (3.8 mmol) of compound **1b** as an oil. Its identity was determined by ^{1}H NMR: 84% yield; ^{1}H NMR (300 MHz, $CDCl_3$) δ 4.66 (t, 2H, J = 4.5 Hz), 3.88 (m, 2H), 3.79 (m, 2H), 3.72 (m, 4H), 3.66 (m, 2H).

*1-[2-(2-Chloroethoxy)ethyl]-4-methylquinolinium Trifluoromethanesulfonate (**2a**).* Compound **1a** (640 mg, 2.5 mmol) was reacted with 298 μL (2.5 mmol) of 4-methylquinoline at 80 °C overnight. The reaction mixture was washed several times with ethyl ether giving 814 mg (2.2 mmol) of a gray powder shown to be the product (**2a**) by ^{1}H NMR: 88% yield; ^{1}H NMR (300 MHz, MeOD-d_3) δ 9.18 (d, 1H, J = 6.1 Hz), 8.60 (br d, 2H, $J \sim$ 8.8 Hz, two overlapped protons), 8.27 (ddd, 1H, J = 8.9, 7.0, 1.4 Hz), 8.08 (ddd, 1H, J = 8.9, 6.9, 1.0 Hz), 7.99 (dd, 1H, J = 6.1, 0.6 Hz), 5.27 (t, 2H, J = 4.8 Hz), 4.10 (t, 2H, J = 4.5 Hz), 3.69 (m, 2H), 2.54 (m, 2H), 3.10 (s, 3H).

*1-{2-[2-(2-Chloroethoxy)ethoxy]ethyl}-4-methylquinolinium Trifluoromethanesulfonate (**2b**).* Compound **1b** (1.08 g, 3.58 mmol) was reacted with 426 μL (3.22 mmol) of 4-methylquinoline at 90 °C for 48 h. The reaction mixture was washed several times with ethyl ether and the residue purified by column chromatograpy using reversed phase C-18 silica gel and mixtures of water and methanol as eluents giving 1.69 g (2.8 mmol) of intermediate **2b**. The product was shown to be pure by ^{1}H NMR: 78% yield; ^{1}H NMR (300 MHz, $CDCl_3$) δ 9.30 (d, 1H, J = 6.1 Hz), 8.53 (d, 1H, J = 9.0 Hz), 8.37 (dd, 1H, J = 8.5, 1.3 Hz), 8.21 (ddd, 1H, J = 9.0, 7.1, 1.3 Hz), 7.99 (ddd, 1H, J = 9.1, 7.1, 0.8 Hz), 7.90 (d, 1H, J = 6.1 Hz), 5.30 (t, 2H, J = 4.7 Hz), 4.14 (t, 2H, J = 4.7 Hz), 3.62−3.67 (m, 4H), 3.53−3.60 (m, 4H), 3.04 (s, 3H).

*3-{2-[2-(2-Chloroethoxy)ethoxy]ethyl}-2-(methylthio)-1,3-benzothiazol-3-ium Trifluoromethanesulfonate (**5**).* 2-Methylthiobenzothiazole (**4**, 362.6 mg, 2.0 mmol) was reacted with compound **1b** (600 mg, 2.0 mmol) at 80 °C. After a few minutes, it formed a hard solid that was allowed to stand for 3 h before ethanol was added and the mixture refluxed with stirring overnight. The solvent was evaporated and the solid washed several times with ethyl ether to give 474.8 mg (1.0 mmol) of a white solid identified as **5** by ^{1}H NMR and ESI-MS (50% yield): ^{1}H NMR (300 MHz, $CDCl_3$) δ 8.10 (d, 1H, J = 8.2 Hz), 8.06 (d, 1H, J = 8.5 Hz), 7.81 (ddd, 1H, J = 8.2, 7.2, 1.2 Hz), 7.69 (ddd, 1H, J = 8.5, 7.2, 0.9 Hz), 4.94 (t, 2H, J = 5.0 Hz), 4.11 (t, 2H, J = 5.0 Hz), 3.66−3.60 (m, 4H), 3.60−3.51 (m, 4H), 3.13 (s, 3H).

*1,4-Dimethylquinolinium Iodide (**6**).* 4-Methylquinoline (950 mg, 6.6 mmol) was reacted with iodomethane (1.14 g, 0.5 mL, 8.0 mmol) and potassium carbonate (46 mg, 0.3 mmol) under reflux overnight. The yellow solid formed was crushed into a fine powder, washed several times with ethyl ether, boiled in ethyl acetate, and hot filtered. After cooling to room temperature, the solid was filtered and dried under vacuum giving 1.85 g (6.5 mmol) of product **6**: 98% yield; ^{1}H NMR (300 MHz, $CDCl_3$) δ 10.26 (d, 1H, J = 6.0 Hz), 8.40 (dd, 1H, J = 8.5, 1.4 Hz), 8.31 (br d, 1H, J = 8.9 Hz), 8.24 (ddd, 1H, J = 8.9, 7.0, 1.4 Hz), 8.04 (d, 1H, J = 8.9, 7.0, 1.4 Hz), 7.99 (br d, 1H, J = 6.0 Hz), 4.89 (s, 3H), 3.06 (s, 3H).

*2-{1-[2-(2-Chloroethoxy)ethyl]-1H-quinolin-4-ylidenemethyl}-3-methylbenzothiazol-3-ium Trifluoromethanesulfonate (**TO-Cl-1**).* Intermediate **2a** (125 mg, 0.25 mmol) was reacted with 3-methyl-2-(methylthio)-1,3-benzothiazol-3-ium iodide (**3**, 81 mg,

0.25 mmol) in 1 mL of anhydrous ethanol added with triethylamine (34.8 μL). The reaction mixture turned orange almost immediately, and a solid appeared. After 90 min, the solvent was evaporated under vacuum and the solid washed exhaustively with ethyl ether. The crude dye was purified by vacuum liquid chromatography on a reversed phase C18 column using a gradient of water with methanol and methanol containing 0.05% TFA. Further purification was conducted on a silica gel column using 10% MeOH in dichloromethane yielding 54.7 mg of pure **TO-Cl-1** (0.11 mmol, 44% yield): ^{1}H NMR (300 MHz, $CDCl_3$) δ 8.72 (d, 1H, J = 7.1 Hz), 8.58 (dd, 1H, J = 8.5, 1.0 Hz), 7.93 (dd, 1H, J = 8.5, 1.0 Hz), 7.82 (td, 1H, J = 7.0, 1.4 Hz), 7.70 (m, 2H), 7.54 (ddd, 1H, J = 8.5, 7.5, 1.2 Hz), 7.37 (m, 2H), 6.74 (s, 1H), 4.85 (br t, 2H, J = 4.9 Hz), 4.08 (br t, 2H, J = 4.9 Hz), 3.99 (s, 3H), 3.78 (m, 2H), 3.59 (m, 2H); ESI-MS (positive mode) m/z 397.27 (M^+), calcd for $C_{22}H_{22}ClN_2OS$ m/z 397.21.

*2-{1-[2-(2-Iodoethoxy)ethyl]-1H-quinolin-4-ylidenemethyl}-3-methylbenzothiazol-3-ium Trifluoromethanesulfonate (**TO-I-1**).* **TO-Cl-1** (15.0 mg, 0.029 mmol) was reacted with 4 equiv of sodium iodide (60.0 mg) in dry acetone under reflux overnight. Approximately 97% of the dye was converted into **TO-I-1** according to the ^{1}H NMR integral of the triplet at δ 3.2 ($-CH_2I$). The dye was isolated by evaporation of the acetone and extraction with dichloromethane; after evaporation of the solvent, the dye was washed with water. The resulting oil was dissolved in a small volume of methanol and mixed with water to give a 10% methanol solution; it was put onto a RPC18 silica gel column and eluted with water and water/methanol mixtures of increasing strength: ^{1}H NMR (300 MHz, $CDCl_3$) δ 8.85 (d, 1H, J = 7.2 Hz), 8.64 (br d, 1H, J = 8.4 Hz), 7.98 (br t, 1H, J = 8.4 Hz), 7.84 (br t, 1H, J = 7.4 Hz), 7.73 (br d, 1H, J = 8.2 Hz), 7.54 (ddd, 1H, J = 8.4, 7.2, 1.3 Hz), 7.44−7.31 (m, 4H), 6.77 (s, 1H), 4.98 (br t, 2H, J = 4.8 Hz), 4.10 (br t, 2H, J = 4.8 Hz), 4.04 (s, 3H), 3.77 (m, 2H), 3.20 (m, 2H); ESI-MS (positive mode) m/z 489.13 (M^+), calcd for $C_{22}H_{22}IN_2OS$ m/z 489.05.

*2-{1-[2-(2-Azidoethoxy)ethyl]-1H-quinolin-4-ylidenemethyl}-3-methylbenzothiazol-3-ium Trifluoromethanesulfonate (**TO-N_3-1**).* **TO-I-1** (15.0 mg, 0.024 mmol) was reacted with sodium azide (15.0 mg, 0.23 mmol) in dimethylformamide (750 μL) overnight at room temperature. The *N*,*N*-dimethylformamide (DMF) was eliminated by adding excess of water to the reaction mixture and washing the dye on a reversed phase C18 column with 1 L of distilled water. The dye was finally eluted with pure methanol; **TO-N_3-1** (11.6 mg, 0.022 mmol) was obtained in 92.0% yield (overall yield of 39.2%): ^{1}H NMR (300 MHz, $CDCl_3$) δ 8.80 (d, 1H, J = 7.5 Hz), 8.48 (br d, 1H, J = 8.5, 1.2 Hz), 8.10 (br d, 1H, J = 8.5 Hz), 7.93 (td, 1H, J = 7.5, 1.2 Hz), 7.79 (br d, 1H, J = 7.5 Hz), 7.72 (td, 1H, J = 8.5, 1.2 Hz), 7.57 (br t, 1H, J = 7.5 Hz), 7.41 (m, 2H), 6.77 (s, 1H), 4.97 (br t, 2H, J = 4.9 Hz), 4.10 (br t, 2H, J = 4.9 Hz), 3.99 (s, 3H), 3.69 (m, 2H), 3.31 (br t, 2H, J = 4.6 Hz); ESI-MS (positive mode) m/z 404.20 (M^+), calcd for $C_{22}H_{22}N_5OS$ m/z 404.15.

*3-[2-(2-Chloroethoxyethoxy)ethyl]-2-(1-methyl-1H-quinolin-4-ylidenemethyl)-benzothiazol-3-ium Trifluoromethanesulfonate (**TO-Cl-3**).* Intermediate **5** (385.6 mg, 0.8 mmol) and 1,4-dimethylquinolinium iodide (**6**, 228.0 mg, 0.8 mmol) were dissolved in 3 mL of warm absolute ethanol, added with triethylamine (80 mg, 110 μL, 0.8 mmol). The reaction mixture turned red and was allowed to stand overnight at room temperature. The red crystals formed were filtered and purified by column chromatography on silica gel using dichloromethane with increasing concentrations of methanol (2−5% total) as the eluent. The fractions were analyzed by TLC and pooled together according to their composition; 125 mg (0.2 mmol) of intermediate dye **TO-Cl-3** was obtained: 26.4% yield; ^{1}H NMR (300 MHz, $CDCl_3$) δ 8.61 (d, 1H, J = 6.9 Hz), 8.59 (dd, 1H, J = 8.0, 1.5 Hz), 7.74 (m, 2H), 7.59 (br d, 1H, J = 8.0 Hz), 7.53 (dd, 1H, J = 8.2, 1.2 Hz), 7.42 (m, 2H), 7.24 (m, 2H), 6.87 (s, 1H), 4.70 (br t, 2H, J = 5.0 Hz), 4.08 (br t, 2H, J = 5.0 Hz), 4.05 (s, 3H), 3.60 (m, 2H), 3.50 (m, 4H), 3.39 (m, 2H); ESI-MS (positive mode) m/z 441.27 (M^+), calcd for $C_{24}H_{26}ClN_2O_2S$ m/z 441.14.

*3-[2-(2-Iodoethoxyethoxy)ethyl]-2-(1-methyl-1H-quinolin-4-ylidenemethyl)benzothiazol-3-ium Trifluoromethanesulfonate (**TO-I-3**).* Intermediate **TO-Cl-3** (125.0 mg, 0.2 mmol) and a large excess of sodium iodide (3 g) were refluxed in 3 mL of dry acetone for 32 h. Dichloromethane was then added to the round-bottom flask, and sodium chloride and excess sodium iodide precipitated. Dichloromethane washes continued until the precipitate was no longer pink. The isolated product **TO-I-3** was concentrated in vacuo giving a total of 120.0 mg (0.18 mmol): 90% yield; ^{1}H NMR (300 MHz, $CDCl_3$) δ 8.99 (d, 1H, J = 7.3 Hz), 8.58 (d, 1H, J = 8.2 Hz), 7.90 (br t, 1H, J = 7.7 Hz), 7.82−7.70 (m, 3H), 7.58−7.42 (m, 3H), 7.36 (br t, 1H, J = 7.5 Hz), 7.02 (s, 1H), 4.73 (br t, 2H, J = 4.9 Hz), 4.30 (s, 3H), 4.14 (br t, 2H, J = 4.8 Hz), 3.66−3.47 (m, 4H), 3.07 (t, 2H, J = 6.6 Hz); ESI-MS (positive mode) m/z 533.13 (M^+), calcd for $C_{24}H_{26}IN_2O_2S$ m/z 533.08.

*3-[2-(2-Azidoethoxyethoxy)ethyl]-2-(1-methyl-1H-quinolin-4-ylidenemethyl)benzothiazol-3-ium Trifluoromethanesulfonate (**TO-N_3-3**).* The final azide-substituted dye, **TO-N_3-3**, was prepared by reacting **TO-I-3** (120.0 mg, 0.18 mmol) with sodium azide (35.1 mg, 0.5 mmol) in DMF (2 mL) at room temperature with stirring overnight. The solution was diluted with 500 mL of distilled water, put onto a reversed phase C18 silica gel column, and washed with 1.5 L of water; after the column had dried, the dye was eluted with methanol containing 0.1% TFA. Additional purification was conducted by reversed phase C18 silica gel column chromatography to produce pure **TO-N_3-3** (97.0 mg, 0.17 mmol) in 93.6% yield: 22.2% overall yield; ^{1}H NMR (300 MHz, $CDCl_3$) δ 8.63 (d, 1H, J = 7.4 Hz), 8.44 (br d, 1H, J = 8.1 Hz), 7.92 (br t, 1H, J = 7.9 Hz), 7.83−7.70 (m, 3H), 7.58−7.50 (m, 2H), 7.46 (br d, 1H, J = 8.0 Hz), 7.38 (br t, 1H, J = 7.4 Hz), 7.00 (s, 1H), 4.65 (br t, 2H, J = 5.2 Hz), 4.25 (s, 3H), 4.11 (br t, 2H, J = 5.1 Hz), 3.71−3.56 (m, 4H), 3.52 (t, 2H, J = 4.9 Hz), 3.24 (t, 2H, J = 4.9 Hz); ESI-MS (positive mode) m/z 448.20 (M^+), calcd for $C_{24}H_{26}N_5O_2S$ m/z 448.18.

Conjugation of Azido Dyes to Alkyne-Modified DNA Oligonucleotides. To 25 μL of a 0.5 mM alkyne-functionalized DNA solution (12.5 nmol) in water were added 6.25 μL of a 100 mM dye/azide solution (625 nmol, 50 equiv) in DMSO and 5 μL of a freshly prepared solution containing a 1:1 ratio of CuBr (Sigma) and TBTA ligand (Sigma) in a degassed 3:1 DMSO/tBuOH mixture (0.05 M, 125 nmol, 20 equiv). The mixture was vortexed and shaken at 20 °C for 1 h. A second 5 μL portion of the CuBr/TBTA solution mixture was added, and the reaction mixture was again vortexed and shaken at 20 °C for an additional 1 h. The reaction mixture was evaporated to almost complete dryness and dissolved in 200 μL of 0.3 M NaOAc. The DNA was precipitated via addition of 1 mL of cold absolute ethanol and left overnight at −20 °C. The reaction mixture was centrifuged at 14000 rpm, and the supernatant was removed. The product pellet was washed three times with 70% ethanol and again centrifuged at 14000 rpm, and the supernatant was removed. The final product was suspended in 200 μL of water [or 10 mM

Tris (pH 7.5) for enhanced solubility] and desalted using a MicroSpin G-25 column (GE Healthcare) to remove any remaining unconjugated dye. MALDI-TOF mass spectrometry of ODN4, a 39mer bearing three thiazole orange (TO) dyes, gave a peak at m/z 13607.3 (calcd m/z 13596.8).

Characterization of Covalent Dye−DNA Single Strands and Duplexes. DNA solutions were prepared in 10 mM aqueous sodium phosphate (NaP_i) buffer (pH 7.0) and stored at −4 °C. Concentrations were determined by UV absorbance at 260 nm using a Varian Cary 3 Bio UV−vis spectrophotometer. The extinction coefficient of ODN4 at 260 nm was calculated to be 375500 M^{-1} cm^{-1} using an online calculator developed by Owczarzy and co-workers[12] and available at http://www.idtdna.com. We accounted for the contribution of the three TO dyes to the absorbance at this wavelength using an ε_{260}(TO) of 6600 M^{-1} cm^{-1}.[13] The molar extinction coefficient of the TO at 509 nm was then determined on the basis of the absorbance and DNA strand concentration. The value obtained was 161100 M^{-1} cm^{-1} (53700 M^{-1} cm^{-1} per TO).

Equal concentrations of each strand were used, and the DNA strands were annealed by being heated to 90 °C and then slowly cooled to 25 °C in 10 mM NaP_i. UV melting curves were measured by monitoring the absorbance at 260 nm while the temperature was increased at a rate of 1 °C/min. The molar extinction coefficient at the TO maximum (509 nm) was 178900 M^{-1} cm^{-1} (59600 M^{-1} cm^{-1} per TO).

Fluorescence Measurements. The fluorescence quantum yield of the ODN4 duplex was determined to be 0.16, relative to fluorescein as the standard (ϕ_f = 0.95 in 0.1 M NaOH). For FRET experiments, 0.1 μM solutions of duplexes were analyzed using either a Cary Eclipse or a Photon Technology International fluorimeter. All samples were excited at 485 nm, and the fluorescence intensity was measured from 500 to 750 nm. The bandpass for both the excitation and emission monochromators was 5 nm. The FRET efficiency (E) for Cy5-labeled duplexes was measured on the basis of the relative fluorescence intensity of the TO donor in the presence (F_{DA}) and absence (F_D) of the acceptor Cy5:

$$E = 1 - F_{DA}/F_D$$

Fluorescence lifetimes of the bulk nanotags in buffer were obtained using a home-built spectrometer consisting of a pulsed diode laser emitting at 437 nm (LDP-PC-440, Picoquant GmbH, ~100 ps fwhm), 10 nm band-pass filters to isolate specific emission frequencies, time-correlated single-photon counting electronics (Picoharp 300, Picoquant), and detection by an actively quenched photodiode (SPD-5-CTC, Micro Photon Devices). Sample concentrations were all ~100 nM.

Bead-Based Confocal Microscopy. For bead labeling experiments, DNA duplexes were biotinylated at the 3′-terminus of the DNA strand complementary to the TO-modified strand. (For FRET duplexes, Cy3 or Cy5 was attached to the 5′-terminus of this strand.) Cy3- and Cy5-labeled and unlabeled TO-modified duplexes were annealed by being heated to 90 °C and then cooled to 25 °C over a period of ~60 min. Nanotags were then added to aliquots of streptavidin beads in 0.02% Tween PBS free of calcium and magnesium. Samples were incubated in the dark for 20 min. Labeled beads were washed twice with PBS supplemented with 0.02% Tween 20 and placed onto a glass slide. Images of the nanotag-conjugated beads were collected following excitation at 488 nm with a Zeiss LSM 510 META confocal microscope. Fluorescence emission was collected with 500−550 nm bandpass (unlabeled duplex), 570−615 nm bandpass (duplex−Cy3), and 650 nm long-pass (duplex−Cy5) filters, respectively.

Synthesis and Characterization of Antibody−DNA Conjugates. AffiniPure goat anti-rabbit IgG (H+L) antibody (Ab) with minimal cross-reaction to human, mouse, and rat serum proteins was purchased from Jackson ImmunoResearch Laboratories. Prior to modification, Ab was desalted using a MicroSpin G-50 column (GE Healthcare) and buffer exchanged [150 mM NaCl and 100 mM sodium phosphate (pH 7.3)] using YM-50 centrifugal filters (50 kDa molecular mass cutoff; Millipore Corp.). Hydralink SANH reagent (EMD Chemicals/Merck) in DMF was added to the Ab in a 10:1 ratio (SANH:Ab). Separately, Hydralink SFB reagent (EMD Chemicals/Merck) in DMF was added to a 5′-aminated DNA oligonucleotide (Integrated DNA Technologies, Inc.) dissolved in modification buffer supplied by the manufacturer in a 10:1 ratio (SFB:DNA). Both Ab and DNA coupling reactions were conducted at room temperature for 2 h. Excess SANH and SFB were removed using MicroSpin G-50 and G-25 columns, respectively. Molar substitution ratio (MSR) assays using a standard protocol (SoluLink) were performed to determine the number of modifications per Ab and DNA molecule. A 2-fold excess of SFB-derivatized DNA was then combined with the SANH-derivatized Ab and allowed to react overnight at room temperature. Noncoupled DNA was removed using YM-50 centrifugal filters. Fractions from each filtration round were tested for the presence of unbound free DNA (A_{260} using the NanoDrop spectrophotometer). The conjugation of Ab to DNA was verified spectrophotometrically, confirming the presence of the hydrazone linkage (λ = 354 nm) formed between SANH and SFB.

Determination of the Ab:DNA Ratio. To quantitatively determine the number of DNA strands conjugated per Ab molecule, a calibration experiment was conducted for each of the Ab−DNA conjugates; 20 μL solutions with various ratios of Ab to DNA were mixed as follows: 1:0.25 (4 and 1 μM, respectively), 1:0.50 (4 and 2 μM, respectively), 1:1 (4 and 4 μM, respectively), 1:2 (4 and 8 μM, respectively), and 1:4 (4 and 16 μM, respectively). Using the NanoDrop spectrophotometer, the A_{260}/A_{280} absorbance ratios were determined and recorded for each solution. The obtained calibration curve was then used to determine the number of DNA molecules per Ab in the conjugate. This procedure accounts for the fact that the absorbance of the DNA nucleobases (260 nm) overlaps with the absorbance of the Ab protein (280 nm). For DNA−Ab conjugates reported here, three DNA strands (i.e., nine TO dyes) were attached to each antibody.

Immunofluorescence Microscopy. Wild-type fly stocks (w^{1118}) were maintained at room temperature. Embryos were collected after 0−2 h at 27 °C and fixed in a 1:1 37% formaldehyde/heptane mixture. Embryos were blocked in 1% goat serum and 0.1% Triton X-100 in phosphate-buffered saline (PBS) for 1 h. To label the centrosomes, embryos were incubated with anti-Centrosomin (1:4000) (gift from T. Megraw, Florida State University, Tallahassee, FL) in PBS supplemented with 1% goat serum and 0.1% Triton X-100 overnight at 4 °C. Secondary antibody staining was performed with either a goat anti-aabbit Alexa Fluor 488 antibody (2 mg/mL, 1:1000) (Invitrogen) incubated in PBS or a goat anti-rabbit nanotag conjugate (~0.5 mg/mL, 1:1000) supplemented with 1% goat serum and 0.1% Triton X-100 at 4 °C overnight. Images were collected on a Zeiss LSM 510 META confocal microscope with a 63× 1.40 NA Plan-Achromat objective using ZEN 2009 software.

Scheme 1

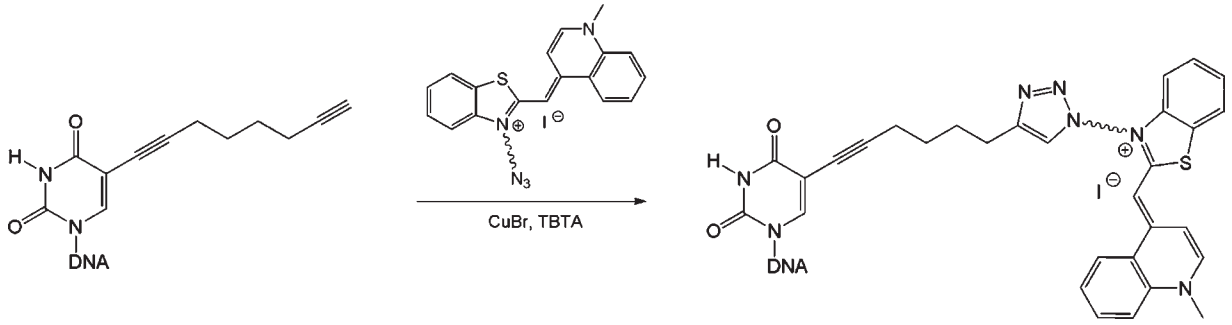

Fluorescence emission was collected for Alexa Fluor 488 and TO (505−550 nm) and FRET (λ > 650 nm) channels after excitation at 488 nm. Fluorescence emission profiles were collected at a spectral bandwidth of 10.7 nm. Images were analyzed with ImageJ (version 1.44). The emission profiles of the Ab−nanotag conjugate were obtained by utilizing the average pixel intensity within a 0.84 μm × 0.84 μm field encompassing each centrosome, and the average pixel intensity of three or four embryos is reported.

RESULTS AND DISCUSSION

Rationale. To expand the potential utility of fluorescent DNA nanotags, we pursued a strategy by which the intercalating dyes could be attached covalently to the DNA (Figure 1). In our approach, intercalation is a key element because this minimizes self-quenching when multiple dyes are held within the proximity of each other.[9] Intercalated dyes are also well-known to stabilize DNA duplexes and higher-order nanostructures against both thermal denaturation and enzymatic degradation.[10]

Conjugation of unsymmetrical cyanine dyes to nucleic acid strands has been motivated by the tendency of these dyes to exhibit enhanced fluorescence when constrained by end stacking or intercalation. These dyes have been useful noncovalent stains for nucleic acids[14,15] and have recently found additional applications as covalent conjugates with DNA or PNA oligonucleotides. For example, Ishiguro and co-workers first attached oxazole yellow to DNA termini as a hybridization reporter.[16] Kubista and Svanvik reported similar properties for PNA "light-up" probes in which TO was attached to the PNA terminus.[17] A variety of other TO conjugates with DNA and PNA have been reported in which the TO was attached to internal or terminal positions.[13,18−25]

We relied on a Cu(I)-mediated Huisgen cyclization ("click") reaction to covalently attach the dye molecules to the DNA.[26,27] As shown in Scheme 1, an alkyne group linked through a flexible spacer to C5 of a uracil residue can react with an azide-substituted intercalator dye (TO) to covalently attach the two via a newly formed triazole linkage. A variety of methods have been reported for conjugating TO to DNA,[13,18−22,24,28−30] but we chose this reaction because Carell and co-workers recently reported that it can be used to incorporate six consecutive fluorescein dyes onto a DNA single strand in high yield.[11,31] Seela and Pujari have reported successful conjugation of coumarin dyes to alkyne-functionalized DNA.[31,32]

In contrast to cases where the cyanine dye was attached to DNA terminus, we expect the TO in our systems to intercalate into the helix. This is distinct from earlier work where TO was used as a nucleobase replacement, as originally reported by Seitz and co-workers for PNA conjugates[33] and subsequently by Wagenknecht and co-workers for DNA conjugates.[25,30] In our approach, the TO residues should intercalate into fully base paired helices, leading to higher thermal stabilities for the dye-modified duplexes.

TO is readily functionalized at multiple positions, allowing optimization of the linkage to the DNA. Three TO azides were synthesized: **TO-N_3-1**, **TO-N_3-2**, and **TO-N_3-3** (Chart 1). These dyes feature two points of attachment and variable linker lengths. (We also synthesized a version with a shorter linker on the benzothiazole side but did not pursue DNA conjugation with it.)

Dye Synthesis and DNA Conjugation. The synthetic method for the azido-substituted thiazole orange dyes is outlined in Scheme 2. Quaternization of the 2-methyl heterocyclic ammonium salts is generally performed by heating the corresponding heteroaromatic base with a molar equivalent or an excess of an alkylating agent such as an alkyl iodide, bromide, sulfate, or tosylate.[34,35] This alkylation reaction requires high temperatures and long reaction times for the achievement of acceptable yields. We chose an alternative route in which the corresponding alcohols were first converted to trifluoromethanesulfonic acid esters via reaction with triflic anhydride in the presence of the polymer-bound non-nucleophilic base poly(vinylpyridine).[36] This reaction proceeds rapidly at room temperature, and the alkyl triflates (**1a** and **1b**) are obtained in high yield after filtration. Quaternization of the heterocycle to give **1a**, **1b**, and **5** then proceeded smoothly at room temperature as demonstrated by the formation of white powdery solids. To ensure complete alkylation, the reaction mixture was refluxed overnight in anhydrous ethanol. Previously reported methods were used to condense the two dye halves.[37] The purified chloro dyes (**TO-Cl-1**, **TO-Cl-2**, and **TO-Cl-3**) were refluxed in dry acetone and subjected to iodo exchange with a large excess of sodium iodide. The iodo dyes were isolated by multiple washes with dichloromethane and then underwent efficient azide exchange at room temperature in the presence of a 3-fold excess of sodium azide in DMF. The reaction mixture was diluted in water and loaded onto a C-18 reversed phase column to remove the DMF and isolate the final dyes **TO-N_3-1**, **TO-N_3-2**, and **TO-N_3-3**.

The TO azide dyes were conjugated to a 16mer DNA oligonucleotide bearing a single alkyne-modified uracil residue at position 8: **ODN1−ODN3**, 5′-GCG CTG T<u>X</u>C ATT CGC G-3′, where <u>X</u> is the TO−uracil conjugate

The DNA−TO conjugates were purified by HPLC and exhibited a single band on a polyacrylamide gel. The modified strands are labeled **ODN1−ODN3**, corresponding to attachment of **TO-N_3-1**, **TO-N_3-2**, and **TO-N_3-3**, respectively.

dx.doi.org/10.1021/bc100485f |*Bioconjugate Chem.* 2011, 22, 1491–1502

Chart 1

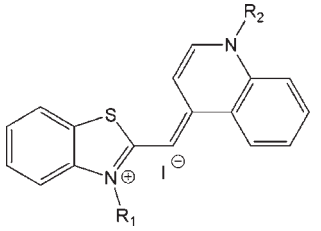

TO-N_3-1: $R_1 = CH_3$, $R_2 = CH_2CH_2OCH_2CH_2N_3$

TO-N_3-2: $R_1 = CH_3$, $R_2 = (CH_2CH_2O)_2CH_2CH_2N_3$

TO-N_3-3: $R_1 = (CH_2CH_2O)_2CH_2CH_2N_3$, $R_2 = CH_3$

Scheme 2

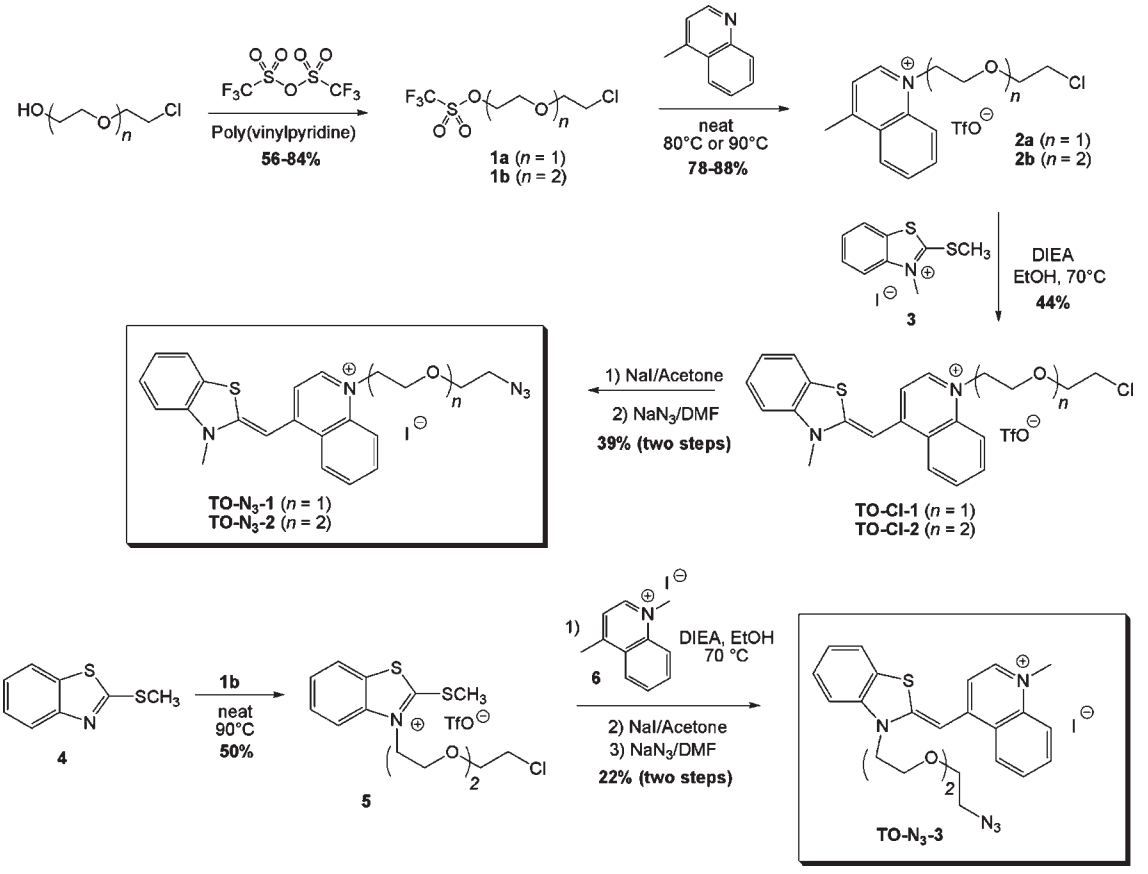

Characterization of Click DNA Duplexes. *UV Melting Curves.* DNA strands **ODN1**−**ODN3** were hybridized to their complementary strand to form 16 bp duplexes, which were then subjected to UV melting analysis. For comparison, we included a duplex formed from the alkyne−DNA precursor, i.e., without a clicked dye. As shown in Figure 2A, the **ODN1** and **ODN2** duplexes exhibited higher, but less cooperative, melting transitions than the unmodified duplex control (T_m = 51 °C vs 49 °C). This suggests that the linker between the TO intercalator and the DNA is too short because the higher T_m could result from partial intercalation of the dye into the base pair stack, but a distortion of the helix due to the linker length could weaken the cooperativity. In contrast, the duplex formed by **ODN3** exhibits an even higher melting transition (T_m = 56 °C), and the cooperativity is similar to that of the unmodified duplex.

Fluorescence Spectroscopy. We also compared the fluorescence intensities of the three TO−DNA conjugates in single- and double-stranded forms. In the absence of a complementary strand, the order of fluorescence intensity was as follows: **ODN2** > **ODN1** > **ODN3** (Figure S1 of the Supporting Information). The fluorescence in all three cases is much higher than for the individual unconjugated **TO-N_3** dyes in aqueous solution (data not shown). However, after hybridization to form duplexes, **ODN3** exhibits the strongest fluorescence (Figure 2B). The higher fluorescence and higher and more cooperative UV melting transition for the **ODN3** duplex perhaps reflect better intercalation of the dye into the helix, facilitated by the longer linker connecting the dye to the uracil and the attachment through the benzothiazole side of the dye. On the basis of these results, further experiments were performed using DNA functionalized with **TO-N_3-3**.

dx.doi.org/10.1021/bc100485f |*Bioconjugate Chem.* 2011, 22, 1491–1502

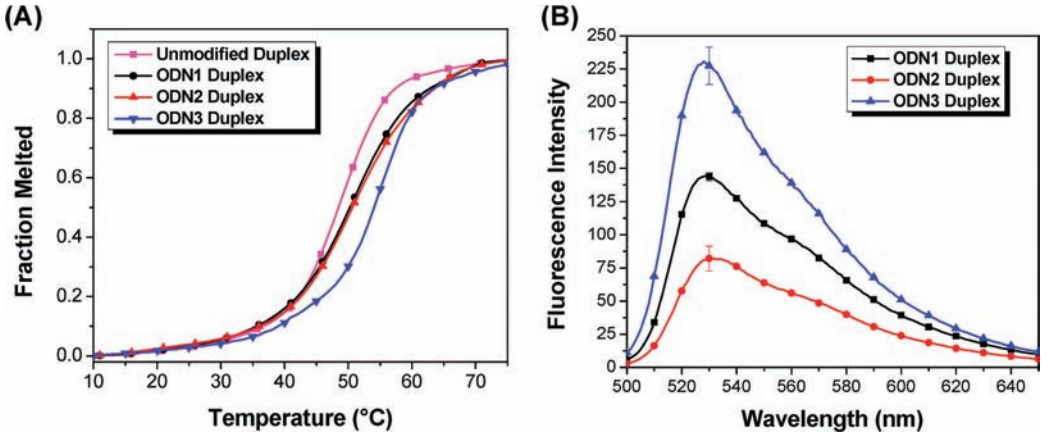

Figure 2. UV melting curves (A) and fluorescence spectra (B) for DNA duplexes based on **ODN1**−**ODN3**. Samples contained 1.0 (A) or 0.1 μM duplex (B) in 10 mM NaP_i, 100 mM NaCl, and 0.1 mM EDTA.

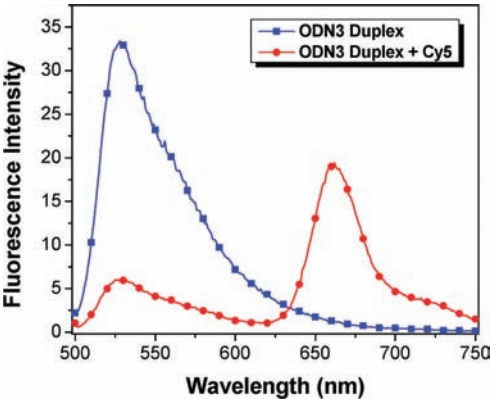

Figure 3. Fluorescence emission spectra recorded for the **ODN3** duplex in the absence or presence of the Cy5 energy acceptor dye on the complementary strand. Samples contained 0.1 μM duplex in 10 mM NaP_i, 100 mM NaCl, and 0.1 mM EDTA. Samples were excited at 488 nm.

Photophysics. The fluorescence lifetimes of TO-conjugated nanotags were measured using time-correlated single-photon counting to probe the binding properties of the dyes and the effects of dye−dye interactions in the multiply substituted nanotags. The **ODN3** duplex was found to exhibit a minimum of two resolvable lifetime components of 4.4 and 2.1 ns in a 1:1.4 ratio (Figure S2 of the Supporting Information). The multiexponential decay suggests multiple binding orientations for this tethered dye and is consistent with prior work by Netzel and coworkers on noncovalently bound intercalating TO dyes.[38] We also determined the fluorescence quantum yield for the **ODN3** duplex (ϕ_f) to be 0.2 (relative to fluorescein in 0.1 N NaOH), which is comparable to the value reported for a noncovalently intercalated TO derivative in calf thymus DNA (ϕ_f = 0.25[30]). Thus, covalent attachment to the DNA does not significantly alter the photophysics of the dye.

Energy Transfer in the Clicked Duplex. In our noncovalent nanotags, Förster resonance energy transfer (FRET) from the intercalated dyes to covalently attached acceptor dyes placed at one or more of the DNA strand termini was exceptionally efficient, allowing shifting of the emission wavelength by nearly 300 nm. We investigated FRET in the covalent construct by attaching a single Cy5 acceptor dye to the 5′-end of the complementary strand.[28] As shown in Figure 3, excitation of the TO intercalator in the presence of the Cy5 results in 82% FRET, as calculated from the apparent quenching of the TO fluorescence. This result is supported by lifetime measurements, showing that the TO lifetime components are reduced from 4.4 and 2.1 ns (1:1.4 ratio) to 4.0 and 1.1 ns (1:1.5 ratio), respectively, in the presence of Cy5 (Figure S2 of the Supporting Information).

Labeling of Polymer Beads. An important application of fluorescent labels is in bead-based assays, where the beads are tagged with a variety of different colors and intensities for both encoding and sensing strategies.[39−41] We synthesized duplexes in which **ODN3** was hybridized to a complementary strand having a biotin at the 3′-terminus and no dye, a Cy3, or a Cy5 at the 5′-terminus. These duplexes were then mixed with streptavidin-coated polystyrene beads and imaged in a fluorescence microscope. As shown in Figure 4, the three sets of beads can be excited at the same wavelength but fluoresce green, orange, or red depending on whether the duplexes were tagged with no acceptor, Cy3, or Cy5, respectively. The beads can be distinguished by emission wavelength and by variation of the amount of DNA used for labeling that would allow the beads to be distinguished by intensity, all while being excited at the same wavelength.

Synthesis and Characterization of a Trifunctionalized DNA Strand. Our ultimate goal is to label the DNA with many TO dyes to further increase the fluorescence intensity compared to a label bearing a single fluorophore. As a first step, we designed a DNA 39mer (**ODN4**) having three alkynes at positions 7, 20, and 33. The alkyne-modified DNA was then conjugated to **TO-N_3-3** as described above. After removal of the unincorporated dye, MALDI-TOF mass spectrometric analysis was consistent with three dyes per DNA strand. UV−vis spectra of ODN4 in single- and double-stranded contexts are provided as Supporting Information (Figure S3) (**ODN4**, 5′-TAC TAA XTA CAT TTG CTA GXC CAG ATC GGC AGX GCA GGC-3′).

The trifunctionalized DNA was hybridized to the complementary 39mer and gave a satisfactory UV melting curve and fluorescence spectrum (panels A and B of Figure 5, respectively). The molar extinction coefficient and fluorescence quantum yield of the trifunctionalized DNA duplex were as follows: ε_{509} = 184850 M^{-1} cm^{-1} (61600 M^{-1} cm^{-1} per dye), and ϕ_f = 0.16,

dx.doi.org/10.1021/bc100485f |*Bioconjugate Chem.* 2011, 22, 1491–1502

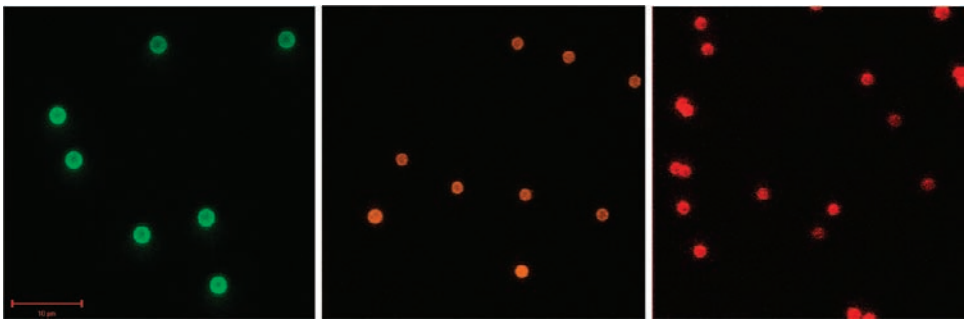

Figure 4. Confocal fluorescence imaging of streptavidin-coated polystyrene microspheres (2 μm diameter) conjugated with biotinylated **ODN3** duplex (left) or **ODN3** duplex labeled with Cy3 (center) or Cy5 (right) FRET acceptor dyes. The following bandpass (BP) or long-pass (LP) filters were used: for TO (left) 500−550 nm BP, for Cy3 (center) 570−615 nm (BP), and for Cy5 (right) 650 nm LP. The scale bar is 10 μm.

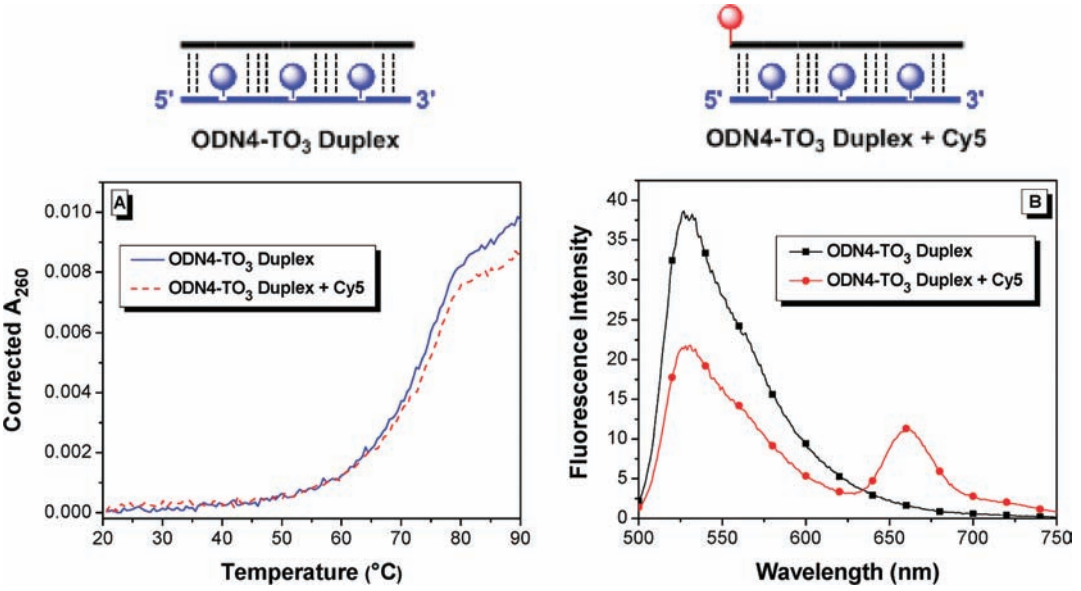

Figure 5. (A) UV melting curves of the trifunctionalized **ODN4-TO$_3$** duplex with and without the Cy5 label. The initial absorbance (T = 20 °C) was subtracted from the rest of the curve to set both curves to zero. (B) Fluorescence emission spectra of the **ODN4-TO$_3$** duplex with and without the Cy5 label. The duplex concentration was 50 nM in both cases.

respectively. The molar extinction coefficient and quantum yield values are comparable to values determined for PNA-conjugated TO after hybridization to cDNA.[23] Time-resolved experiments with the **ODN4** duplex yielded values of 3.6 and 1.8 ns (ca. 1:2 ratio), similar to those of the monofunctionalized **ODN3** duplex (data not shown).

Hybridization of the trifunctionalized **ODN4-TO$_3$** to a complementary strand having a 3′-Cy5 label gave a similar melting curve (Figure 5A). The corresponding duplexes exhibited 44% FRET efficiency, based on TO quenching (Figure 5B). Although this efficiency is considerably lower than that for **ODN3**, this is not a surprising result because the Cy5 is approximately 109, 65, and 24 Å from the three TO intercalators and the critical transfer distance at which FRET is 50% efficient (R_0) for TO−Cy5 is estimated to be 41 Å based on the ϕ_f of 0.2 determined for the **ODN3** duplex.

We were interested in determining whether an internal Cy5 might provide better FRET because of the greater proximity on average to all three TO intercalators. We separated the complementary strand into 19- and 20-nucleotide fragments that can be combined with the triclick DNA strand to form a ternary duplex (Figure 6). This design provides greater flexibility in the synthesis of antibody conjugates as described in the next section and is also considerably less expensive than purchasing a full-length DNA oligonucleotide with an internal Cy5 modification. UV melting curves verified assembly of the ternary duplexes (Figure S3 of the Supporting Information). Duplex A contains no Cy5 acceptor and provides the maximum TO fluorescence. Duplexes B and C place a single Cy5 at an internal position, closer on average to all three TO dyes than in the case of a terminal Cy5 (duplex D). Interestingly, duplex D exhibited the greatest TO quenching, but also the lowest Cy5 fluorescence, while duplex B exhibits the least TO quenching (~25%) but the brightest Cy5 fluorescence. Clearly, the different environment of the Cy5 in the internal versus terminal configurations has a significant effect on the quantum yields. This was verified by direct excitation of the Cy5, which resulted in similar relative fluorescence intensities as observed due to the transfer of energy from TO (data not shown).

Antibody Conjugation and Fluorescence Labeling in Cells. To test the utility of TO-functionalized DNA strands in cellular imaging, we designed an antibody construct depicted in

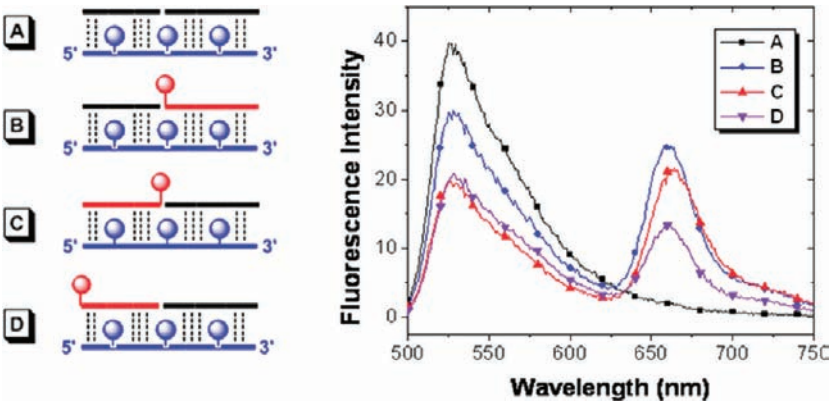

Figure 6. Fluorescence emission spectra of various ternary duplexes based on trifunctionalized **ODN4-TO$_3$** 39mer. The duplex concentration was 50 nM in both cases.

Scheme 3

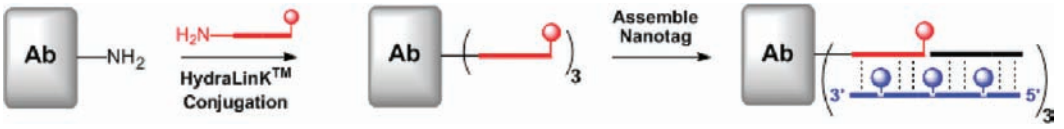

Scheme 3. Starting with an anti-rabbit antibody IgG, we conjugated a 19mer DNA strand bearing a 5′-amino group and a 3′-Cy5 dye using a commercially available HydraLinK kit. (This chemistry involves conjugating the amino groups from the DNA terminus and antibody side chains to succinimidyl ester reagents bearing aldehyde and hydrazine groups. The DNA and antibody can then be reacted with one another to produce a stable hydrazone linkage.) UV−vis analysis indicated that three or four DNA strands were conjugated per antibody. The trifunctionalized DNA 39mer was then hybridized to the antibody along with a 20mer to complete the duplex assembly. The tripartite design of this nanotag (design B in Figure 5) leaves open the option of adding a second acceptor dye to the 20mer component, leading to more efficient energy transfer, although we have not yet explored this.

The utility of the Ab−nanotag conjugate as a secondary antibody for intracellular labeling was demonstrated by immunofluorescence microscopy. Centrosomin, a protein that localizes to the centrosomes, was selected as a target protein. Centrosomes are the microtubule-organizing centers of cells and localize in well-characterized punctate foci, allowing easy visualization when stained with a conventional Alexa-tagged fluorescent secondary antibody (Figure 7A).[42] Thus, Centrosomin provides a convenient marker for testing the ability of the Ab−nanotag conjugate to recognize and report the localization of a specific primary Ab.

Syncytial (0−2 h) wild-type *Drosophila* embryos were fixed and stained for Centrosomin localization first using a Centrosomin-specific primary antibody followed by the Ab−nanotag conjugate as a secondary Ab (Scheme 3) and visualized with fluorescence microscopy (Figure 7B,C). Imaging the TO intercalator donor signal from the duplex reports Centrosomin localization (Figure 7B). This indicates that the secondary antibody is still functional after conjugation of multiple DNA duplexes to increase the magnitude of the fluorescence signal. The observation of donor TO fluorescence is consistent with the fact that the transfer of energy to the Cy5 acceptor is only ∼25% efficient in solution (Figure 6, design B); i.e., there are unquenched TO intercalators in the assemblies.

The centrosomes are clearly evident as bright foci; however, some background fluorescence is present in the TO channel even after utilizing a zwitterionic buffer (0.5 M PIPES and 0.5 M HEPES) to minimize nonspecific binding of the oligonucleotides.[43] The excess background fluorescence could be due to (i) autofluorescence from the embryo, (ii) excess TO-conjugated strand from the initial assembly, and/or (iii) partial dehybridization of the TO-conjugated strand from the antibody reagent during the washing step prior to imaging. Importantly, TO fluorescence is not observed in the nuclei, showing that the conjugated TO dyes do not stain the cellular DNA. (Compare panels B and D of Figure 7, where genomic DNA is stained with DAPI.) In our prior work with noncovalent nanotags, the dissociation of dyes from the DNA framework led to nonspecific staining of cellular DNA, compromising the quality of cellular images acquired with these reagents.[9] Covalent conjugation of the TO dyes to the DNA eliminates genomic DNA staining.

The background fluorescence is significantly reduced upon collection of the FRET signal [exciting the nanotag donor TO at 488 nm and collecting the emission of the Cy5 acceptor (Figure 7C)]. Thus, the emission wavelength of the nanotags can be red-shifted by >100 nm by FRET. In addition, the acquisition of the FRET signal indicates that the nanotag remains at least partially hybridized, because dissociation of the TO-conjugated strand would prevent sensitized emission from the Cy5, which is covalently attached to the antibody. Line profiles of both the TO and FRET signals show an improved signal-to-noise ratio (Figure 7E,F).

Spectral imaging with a confocal microscope was utilized to acquire the emission spectra of the Ab−nanotag conjugates in fixed syncytial embryos (Figure 8). The emission spectrum

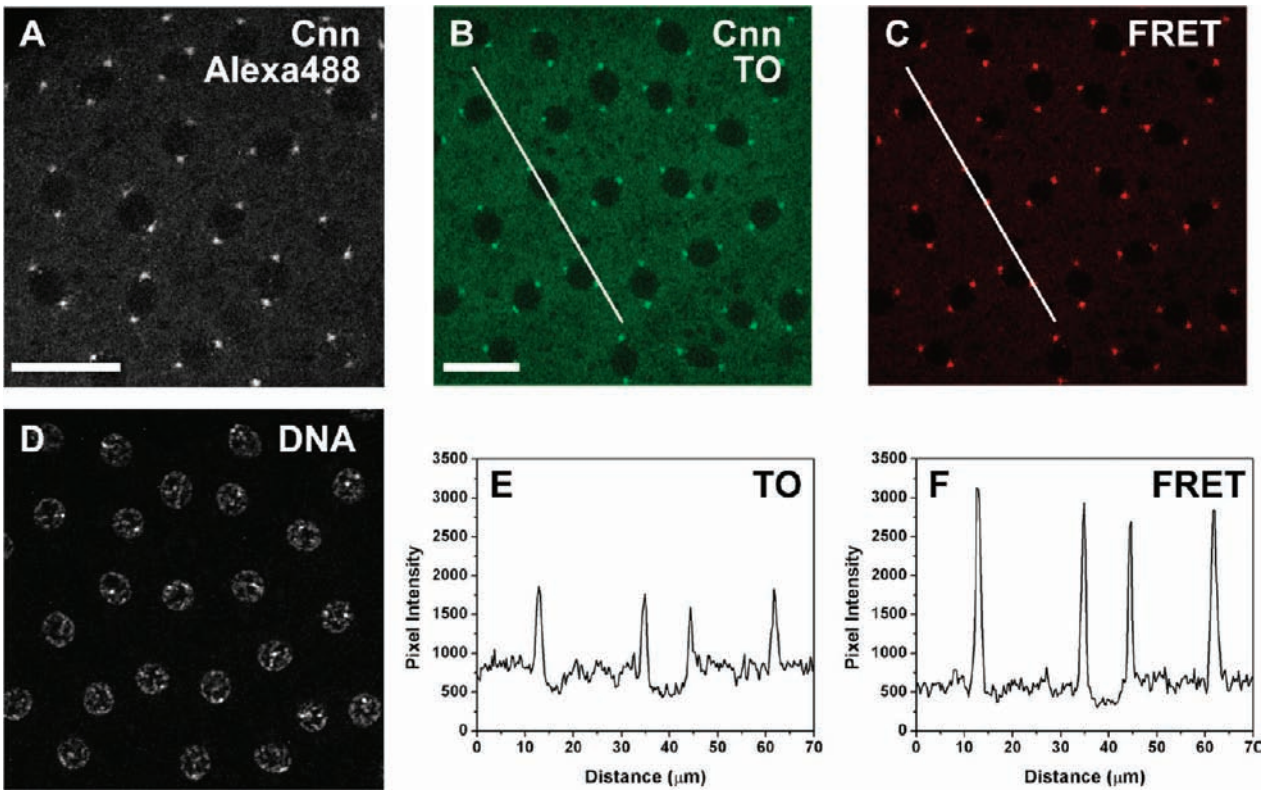

Figure 7. Localization of Centrosomin (Cnn) in fixed 0−2 h syncytical *Drosophila* embryos. (A) Centrosomin localization within the embryo probed with a conventional Alexa Fluor 488-labeled secondary antibody. Centrosomin stained with an Ab−nanotag conjugate containing TO and Cy5. Images were recorded following excitation at 488 nm and collection of either the TO (B) or FRET (C) emission. (D) Nuclei are shown by DNA staining (DAPI). The same embryo was imaged for micrographs B−D. (E and F) Intensity profiles collected along the lines shown in panels B and C for the TO (E) and FRET (F) emission show that the FRET emission has improved the brightness and signal-to-noise ratio compared to those of the TO emission. The scale bar is 20 μm.

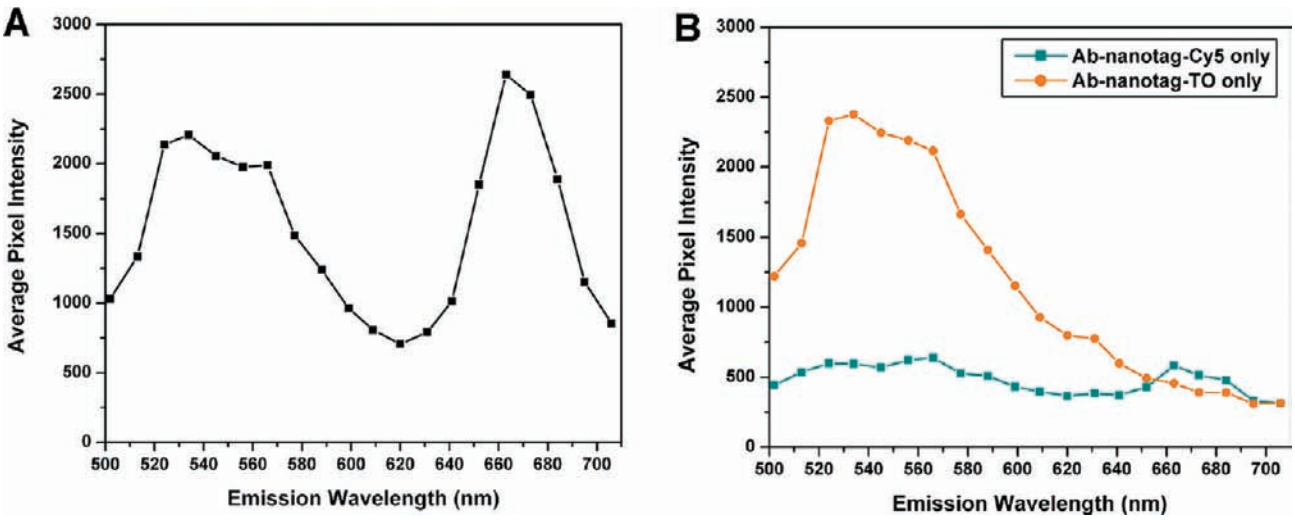

Figure 8. Average fluorescence emission spectra of the Ab−nanotag conjugates in fixed syncytical *Drosophila* embryos. The emission spectra were recorded after excitation at 488. (A) Average pixel intensity at the centrosome of an Ab−nanotag conjugate containing both TO and Cy5 at a given emission wavelength (n = 120−140 centrosomes in four embryos). (B) Average pixel intensity of Ab−nanotag conjugates containing only the TO donor (orange) or Cy5 acceptor (green).

shown is the average pixel intensity of Centrosomin−Ab−nanotag foci of four different embryos (n = 30−35 centrosomes per embryo) (Figure 8A). The emission spectrum of the Ab−nanotag conjugates containing both TO and Cy5 fluorophores is similar to the solution data of the duplex in Figure 6 (duplex B). Emission profiles recorded in the absence of the Cy5 acceptor molecule

dx.doi.org/10.1021/bc100485f |*Bioconjugate Chem.* 2011, 22, 1491–1502

within the Ab−nanotag conjugate do not show an emission peak at 663 nm (Figure 8B). In addition, the emission spectrum of the Ab−nanotag construct without the TO donor shows only a minimal amount of Cy5 fluorescence following excitation at 488 nm. It is difficult to compare the immunofluorescence results directly to the FRET efficiency results in solution (Figure 6), as the amount of protein at the centrosome can vary during the cell cycle, differences in immunolabeling between embryos can occur (Figure S4 of the Supporting Information), and differences in fluorescence emission filters can exist. However, a similar emission spectrum of the Ab−nanotag conjugate is observed in both the in vitro and the in vivo spectral imaging, illustrating efficient transfer of energy to the Cy5 acceptor.

CONCLUSION

The results described above illustrate the value of DNA as a scaffold on which to assemble multifluorophore arrays for fluorescence imaging. Alkyne-functionalized nucleotides based on uracil[11] or 8-aza-7-deazaadenine[31] allow click chemistry to be used to attach fluorescent or fluorogenic dyes to internal positions of a DNA strand without interfering with hybridization. Our results demonstrate that a trifunctionalized DNA strand labeled with TO intercalators provides sufficiently bright fluorescence, efficient energy transfer, and facile hybridization to antibodies conjugated to complementary strands for the creation of useful immunofluorescence reagents. While there have been numerous other examples of DNA−antibody conjugates, most prior work has relied on the DNA component to hybridize either to a target DNA or RNA strand in solution, as in proximity-based ligation assays,[44] or to a cDNA immobilized on a surface for the preparation of antibody microarrays.[45−47] A recent report demonstrated DNA-based labeling of antibodies, but the DNA was labeled noncovalently with a cationic fluorescent polymer and antibody conjugation was achieved using biotinylated DNA and Ab, with streptavidin cross-linking the two.[48]

Ongoing work is directed toward increasing the number of dyes attached to a given DNA strand to increase the brightness of a given DNA-functionalized antibody and/or reduce the number of DNA strands that need to be attached to an antibody to achieve a given level of brightness. (The brightness of our trifunctionalized ODN4 duplex label is lower than that of a single Cy5 dye, primarily because of the lower quantum yield of TO, although this would be offset by a much higher extinction coefficient in systems that incorporated more and/or brighter intercalator dyes.) We are also working on developing nanotags based on shorter wavelength dyes, such as the coumarin recently reported by Seela and Pujari, which emits at 420 nm.[31] On the basis of the efficient energy transfer in our nanotags, even in the absence of large spectral overlap, excitation with the increasingly common violet laser line (405 nm) will allow emission across the visible spectrum, allowing for simultaneous multicolor imaging of different targets, provided orthogonal recognition components (e.g., antibodies) are used.

ASSOCIATED CONTENT

Supporting Information. Synthetic details for compound **TO-N_3-2**, fluorescence spectra of TO-modified DNA oligonucleotides **ODN1**−**ODN3**, fluorescence lifetime measurements of TO-modified **ODN3** duplex with or without the Cy5 acceptor, details of R_0 calculation, MALDI-TOF mass spectrum of the **ODN4** single strand, UV−vis spectra of the **ODN4** single strand and duplex, UV melting curves of termolecular duplexes, and spectral imaging analysis of individual *Drosophila* embryos. This material is available free of charge via the Internet at http://pubs.acs.org.

AUTHOR INFORMATION

Corresponding Author

*Telephone: (412) 268-4196. Fax: (412) 268-1061. E-mail: army@cmu.edu.

Present Addresses

⊥Biology Department, Brookhaven National Laboratory, Upton, NY 11973.

ACKNOWLEDGMENT

We are grateful to the National Institutes of Health (Grant R01GM080994) and the donors of the American Chemical Society's Petroleum Research Fund (44470-AC4) for financial support of this research. NMR instrumentation at Carnegie Mellon University was partially supported by the National Science Foundation (Grant CHE-0130903). Mass spectrometers were funded by the National Science Foundation (DBI-9729351).

REFERENCES

(1) Waggoner, A. (2006) Fluorescent Labels for Proteomics and Genomics. *Curr. Opin. Chem. Biol. 10*, 62–66.

(2) Giepmans, B. N. G., Adams, S. R., Ellisman, M. H., and Tsien, R. Y. (2006) The Fluorescent Toolbox for Assessing Protein Location and Function. *Science 312*, 217–224.

(3) Bruchez, M. J., Moronne, M., Gin, P., Weiss, S., and Alivisatos, A. P. (1998) Semiconductor Nanocrystals as Fluorescent Biological Labels. *Science 281*, 2013–2016.

(4) Zhao, X., Bagwe, R. P., and Tan, W. (2004) Development of Organic-Dye-Doped Silica Nanoparticles in a Reverse Microemulsion. *Adv. Mater. 16*, 173–176.

(5) Burns, A., Ow, H., and Wiesner, U. (2006) Fluorescent Core-Shell Silica Nanoparticles: Towards "Lab on a Particle" Architectures for Nanobiotechnology. *Chem. Soc. Rev. 35*, 1028–1042.

(6) Wu, C., Zheng, Y., Szymanski, C., and McNeill, J. (2008) Energy Transfer in a Nanoscale Multichromophoric System: Fluorescent Dye-Doped Conjugated Polymer Nanoparticles. *J. Phys. Chem. C 112*, 1772–1781.

(7) Sun, G., Berezin, M. Y., Fan, J., Lee, H., Ma, J., Zhang, K., Wooley, K. L., and Achilefu, S. (2010) Bright Fluorescent Nanoparticles for Developing Potential Optical Imaging Contrast Agents. *Nanoscale 2*, 548–558.

(8) Glazer, A. N. (1994) Phycobiliproteins: A Family of Valuable, Widely Used Fluorophores. *J. Appl. Phycol. 6*, 105–112.

(9) Benvin, A. L., Creeger, Y., Fisher, G. W., Ballou, B., Waggoner, A. S., and Armitage, B. A. (2007) Fluorescent DNA Nanotags: Supramolecular Fluorescent Labels Based on Intercalating Dye Arrays Assembled on Nanostructured DNA Templates. *J. Am. Chem. Soc. 129*, 2025–2034.

(10) Özhalici-Ünal, H., and Armitage, B. A. (2009) Fluorescent DNA Nanotags Based on a Self-Assembled DNA Tetrahedron. *ACS Nano 3*, 425–433.

(11) Gierlich, J., Burley, G. A., Gramlich, P. M. E., Hammond, D. M., and Carell, T. (2006) Click Chemistry as a Reliable Method for the High-Density Postsynthetic Functionalization of Alkyne-Modified DNA. *Org. Lett. 8*, 3639–3642.

(12) Tataurov, A. V., You, Y., and Owczarzy, R. (2008) Predicting Ultraviolet Spectrum of Single Stranded and Double Stranded Deoxyribonucleic Acids. *Biophys. Chem. 33*, 66–70.

(13) Bethge, L., Singh, I., and Seitz, O. (2010) Designed Thiazole Orange Nucleotides for the Synthesis of Single Labelled Oligonucleotides that Fluoresce upon Matched Hybridization. *Org. Biomol. Chem. 8*, 2439–2448.

(14) Lee, L. G., Chen, C., and Liu, L. A. (1986) Thiazole Orange: A New Dye for Reticulocyte Analysis. *Cytometry 7*, 508–517.

(15) Rye, H. S., Yue, S., Wemmer, D. E., Quesada, M. A., Haugland, R. P., Mathies, R. A., and Glazer, A. N. (1992) Stable Fluorescent Complexes of Double-Stranded DNA with Bis-Intercalating Asymmetric Cyanine Dyes: Properties and Applications. *Nucleic Acids Res. 20*, 2803–2812.

(16) Ishiguro, T., Saitoh, J., Yawata, H., Otsuka, M., Inoue, T., and Sugiura, Y. (1996) Fluorescence Detection of Specific Sequence of Nucleic Acids by Oxazole Yellow-Linked Oligonucleotides. Homogeneous Quantitative Monitoring of *In Vivo* Transcription. *Nucleic Acids Res. 24*, 4992–4997.

(17) Svanvik, N., Westman, G., Wang, D., and Kubista, M. (2000) Light-Up Probes: Thiazole Orange-Conjugated Peptide Nucleic Acid for Detection of Target Nucleic Acid in Homogeneous Solution. *Anal. Biochem. 281*, 26–35.

(18) Privat, E., Melvin, T., Mérola, F., Schweizer, G., Prodhomme, S., Asseline, U., and Vigny, P. (2002) Fluorescent Properties of Oligonucleotide-Conjugated Thiazole Orange Probes. *Photochem. Photobiol. 75*, 201–210.

(19) Wang, X., and Krull, U. J. (2005) Synthesis and Fluorescence Studies of Thiazole Orange Tethered onto Oligonucleotide: Development of a Self-Contained DNA Biosensor on a Fiber Optic Surface. *Bioorg. Med. Chem. Lett. 15*, 1725–1729.

(20) Hara, Y., Fujii, T., Kashida, H., Sekiguchi, K., Liang, X., Niwa, K., Takase, T., Yoshida, Y., and Asanuma, H. (2010) Coherent Quenching of a Fluorophore for the Design of a Highly Sensitive In-Stem Molecular Beacon. *Angew. Chem., Int. Ed. 49*, 5502–5506.

(21) Ikeda, S., Kubota, T., Yuki, M., Yanagisawa, H., Tsuruma, S., and Okamoto, A. (2010) Hybridization-Sensitive Fluorescent DNA Probe with Self-Avoidance Ability. *Org. Biomol. Chem. 8*, 546–551.

(22) Ikeda, S., Yuki, M., Yanagisawa, H., and Okamoto, A. (2009) Doubly Thiazole Orange-Labeled Cytidine for Functional Expansion of a Hybridization-Sensitive Probe. *Tetrahedron Lett. 50*, 7191–7195.

(23) Jarikote, D. V., Krebs, N., Tannert, S., Röder, B., and Seitz, O. (2006) Exploring Base-Pair-Specific Optical Properties of the DNA Stain Thiazole Orange. *Chem.—Eur. J. 13*, 300–310.

(24) Lartia, R., and Asseline, U. (2006) New Cyanine-Oligonucleotide Conjugates: Relationships between Chemical Structures and Properties. *Chem.—Eur. J. 12*, 2270–2281.

(25) Menacher, F., Rubner, M., Berndl, S., and Wagenknecht, H.-A. (2008) Thiazole Orange and Cy3: Improvement of Fluorescent DNA Probes with Use of Short Range Electron Transfer. *J. Org. Chem. 73*, 4263–4266.

(26) Kolb, H. C., Finn, M. G., and Sharpless, K. B. (2001) Click Chemistry: Diverse Chemical Function from a Few Good Reactions. *Angew. Chem., Int. Ed. 40*, 2004–2021.

(27) Rostovtsev, V. V., Green, L. G., Fokin, V. V., and Sharpless, K. B. (2002) A Stepwise Huisgen Cycloaddition Process: Copper(I)-Catalyzed Regioselective "Ligation" of Azides and Terminal Alkynes. *Angew. Chem., Int. Ed. 41*, 2596–2599.

(28) Algar, W. R., Massey, M., and Krull, U. J. (2006) Fluorescence Resonance Energy Transfer and Complex Formation Between Thiazole Orange and Various Dye-DNA Conjugates: Implications in Signaling Nucleic Acid Hybridization. *J. Fluoresc. 16*, 555–567.

(29) Berndl, S., and Wagenknecht, H.-A. (2009) Fluorescent Color Readout of DNA Hybridization with Thiazole Orange as an Artificial DNA Base. *Angew. Chem., Int. Ed. 48*, 2418–2421.

(30) Holzhauser, C., Berndl, S., Menacher, F., Breunig, M., Göpferich, A., and Wagenknecht, H.-A. (2010) Synthesis and Optical Properties of Cyanine Dyes as Fluorescent DNA Base Substitutions for Live Cell Imaging. *Eur. J. Org. Chem.*, 1239–1248.

(31) Seela, F., and Pujari, S. S. (2010) Azide-Alkyne "Click" Conjugation of 8-Aza-7-deazaadenine-DNA: Synthesis, Duplex Stability, and Fluorogenic Dye Labeling. *Bioconjugate Chem. 21*, 1629–1641.

(32) Seela, F., Sirivolu, R., and Chittepu, P. (2008) Modification of DNA with Octadiynyl Side Chains: Synthesis, Base Pairing, and Formation of Fluorescent Coumarin Dye Conjugates of Four Nucleobases by the Alkyne-Azide "Click" Reaction. *Bioconjugate Chem. 19*, 211–224.

(33) Koehler, O., and Seitz, O. (2003) Thiazole Orange as Fluorescent Universal Base in Peptide Nucleic Acids. *Chem. Commun.*, 2938–2939.

(34) Pardal, A. C., Ramos, S. S., Santos, P. F., Reis, L. V., and Almeida, P. (2002) Synthesis and Spectroscopic Characterization of N-Alkyl Quaternary Ammonium Salts, Typical Precursors of Cyanines. *Molecules 7*, 320–330.

(35) Hamer, F. M. (1971) *The Cyanine Dyes and Related Compounds*, Vol. 18, Interscience Publishers, New York.

(36) Ross, S. A., Pitie, M., and Meunier, B. (2000) A Straightforward Preparation of Primary Alkyl Triflates and Their Utility in the Synthesis of Derivatives of Ethidium. *J. Chem. Soc., Perkin Trans. 1*, 571–574.

(37) Silva, G. L., Ediz, V., Armitage, B. A., and Yaron, D. (2007) Experimental and Computational Investigation of Unsymmetrical Cyanine Dyes: Understanding Torsionally Responsive Fluorogenic Dyes. *J. Am. Chem. Soc. 129*, 5710–5718.

(38) Netzel, T. L., Nafisi, K., Zhao, M., Lenhard, J. R., and Johnson, I. (1995) Base-Content Dependence of Emission Enhancements, Quantum Yields, and Lifetimes for Cyanine Dyes Bound to Double-Stranded DNA: Photophysical Properties of Monomeric and Bichromophoric DNA Stains. *J. Phys. Chem. 99*, 17936–17947.

(39) Krishhan, V. V., Khan, I. H., and Luciw, P. A. (2009) Multiplexed Microbead Immunoassays by Flow Cytometry for Molecular Profiling: Basic Concepts and Proteomics Applications. *Crit. Rev. Biotechnol. 29*, 29–43.

(40) Borisov, S. M., Mayr, T., Karasyov, A. A., Klimant, I., Chojnacki, P., Moser, C., Nagl, S., Schaeferling, M., Stich, M. I., Kocincova, A. S., and Wolfbeis, O. S. (2008) New Plastic Microparticles and Nanoparticles for Fluorescent Sensing and Encoding. *Springer Ser. Fluoresc. 4*, 431–463.

(41) Yang, J., Sena, M. P., and Gao, X. (2009) Quantum Dot-Encoded Fluorescent Beads for Biodetection and Imaging. *Rev. Fluoresc. 4*, 139–156.

(42) Megraw, T. L., Li, K., Kao, L., and Kaufman, T. C. (1999) The Centrosomin Protein is Required for Centrosome Assembly and Function during Cleavage in *Drosophila*. *Development 126*, 2829–2839.

(43) Stanlis, K. K., and McIntosh, J. R. (2003) Single-Strand DNA Aptamers as Probes for Protein Localization in Cells. *J. Histochem. Cytochem. 51*, 797–808.

(44) Soederberg, O., Gullberg, M., Jarvius, M., Ridderstrale, K., Leuchowius, K.-J., Jarvius, J., Wester, K., Hydbring, P., Bahram, F., Larsson, L.-G., and Landegren, U. (2006) Direct Observation of Individual Endogenous Protein Complexes in situ by Proximity Ligation. *Nat. Methods 3*, 995–1000.

(45) Wacker, R., Schroder, H., and Niemeyer, C. M. (2004) Performance of Antibody Microarrays Fabricated by either DNA-Directed Immobilization, Direct Spotting or Streptavidin-Biotin Attachment: A Comparative Study. *Anal. Biochem. 330*, 281–287.

(46) Ng, J. K., Ajikumar, P. K., Tang, Y. C., Lee, J. Y., Stephanopoulos, G., and Too, H.-P. (2007) Spatially Addressable Protein Array: ssDNA-Directed Assembly for Antibody Microarray. *Electrophoresis 28*, 4638–4644.

(47) Bailey, R. C., Kwong, G. A., Radu, C. G., Witte, O. N., and Heath, J. R. (2007) DNA-Encoded Antibody Libraries: A Unified Platform for Multiplexed Cell Sorting and Detection of Genes and Proteins. *J. Am. Chem. Soc. 129*, 1959–1967.

(48) Zheng, W., and He, L. (2010) Multiplexed Detection of Protein Cancer Biomarkers on Au/Ag-Barcoded Nanorods using Fluorescent-Conjugated Polymers. *Anal. Bioanal. Chem. 397*, 2261–2270.

Fluorescent DNA Nanotags Featuring Covalently Attached Intercalating Dyes: Synthesis, Antibody Conjugation and Intracellular Imaging

Andrea L. Stadler,[†ℓ] Junriz Delos Santos, [†,‡] Elizabeth S. Stensrud,[§] Anna Dembska,[†,‡] Gloria L. Silva,[†,‡] Shengpeng Liu,[†,‡] Nathaniel I. Shank,[†,‡] Ezgi Kunttas-Tatli,[§] Courtney J. Sobers,[†] Philipp M. E. Gramlich,[€] Thomas Carell,[€] Linda A. Peteanu,[†,‡] Brooke M. McCartney,[§] Bruce A. Armitage[†,‡*]

Departments of Chemistry[†] and Biological Sciences[§] and Center for Nucleic Acids Science and Technology[‡], Carnegie Mellon University, 4400 Fifth Avenue, Pittsburgh, PA 15213
Department of Chemistry and Biochemistry, Ludwig Maximilians University, Munich, 81377 Munich, Butenandtstr, 5-13, Haus F, Germany[€]

* Tel: 412-268-4196; Fax: 412-268-1061; e-mail: army@cmu.edu

Abstract: We have synthesized fluorescent DNA duplexes featuring multiple thiazole orange (TO) intercalating dyes covalently attached to the DNA via a triazole linkage. The intercalating dyes stabilize the duplex against thermal denaturation and show bright fluorescence in the green. The emission color can be changed to orange or red by addition of energy-accepting Cy3 or Cy5 dyes attached covalently to the DNA duplex. The dye-modified DNA duplexes were then attached to a secondary antibody for intracellular fluorescence imaging of centrosomes in ***Drosophila*** embryos. Bright fluorescent foci were observed at the centrosomes in both the donor (TO) and acceptor (Cy5) channels, due to the fact that the energy transfer efficiency is moderate. Monitoring the Cy5 emission channel significantly minimized the background signal due to the large shift in emission wavelength allowed by energy transfer.

ℓ Current address: Biology Department, Brookhaven National Lab, Upton, NY 11973

Synthesis of TO-N_3-2.

Synthesis of **TO-Cl-2**. Intermediate **2b** (331.0 mg, 1.00 mmol), was reacted with 3-methyl-2-(methylthio)-1,3-benzothiazol-3-ium iodide (443.0 mg, 1.00 mmol) in 2 mL of anhydrous ethanol and added with triethylamine (139 μL). It was heated briefly and left overnight at room temperature. The solvent was evaporated under vacuum and the residue washed exhaustively with ethyl ether. The crude dye was purified by column chromatography on silica gel using dichloromethane and 5% methanol in dichloromethane. Fractions were pooled together according to their TLC profile and purified further using the same elution solvent. A total of 77.1 mg (7.4%) of pure **TO-Cl-2** was obtained. ^{1}H NMR (300 MHz, $CDCl_3$) δ: 8.56 (d, 1H, ***J*** = 8.5 Hz); 8.4 (d, 1H, ***J*** = 7.2 Hz); 7.79-7.66 (m, 2H); 7.66-7.57 (m, 2H); 7.40 (ddd, 1H, ***J*** = 8.5; 7.2; 1.1 Hz); 7.30-7.11 (m, 3H); 6.60 (s, 1H); 4.66 (br t, 2H, ***J*** = 4.22 Hz); 3.96 (br t, 2H, ***J*** = 4.42 Hz); 3.90 (s, 3H); 3.67-3.52 (m, 8H). ESIMS (positive mode) ***m/z***: 441.40 (M+); calculated for $C_{24}H_{26}ClN_2O_2S$ ***m/z***: 441.14.

The iodo exchange to obtain **TO-I-2** was achieved by dissolving the dye (77.1 mg, 0.14 mmol) in acetone (10 mL), adding sodium iodide (2.0 g, 30 mmol) and refluxing overnight. Progress of the reaction was followed by ESI-MS. The acetone was evaporated and the excess sodium iodide was eliminated by dissolving the dye with dichloromethane and decanting the salt. The dichloromethane was evaporated and the dye was dissolved into a minimum amount of dimethylformamide and added with 91.0 mg (1.4 mmol) of sodium azide. It was stirred at room temperature overnight. The reaction mixture was added with 130 mL of distill water, loaded onto a reversed phase C-18 column and eluted with 1.5 L of distill water (to eliminate the residual solvent and salt) and the dye eluted with 100 mL of methanol containing 0.05% TFA. The counterion was exchanged by adding excess potassium iodide in dry acetone and stand at room temperature overnight. After the evaporation of acetone the dye was extracted with dichloromethane. **TO-N_3-2** was shown to be pure by ^{1}H NMR, 69.5 mg (0.12 mmol) were recovered (yield 86 %). ^{1}H NMR (300 MHz, $CDCl_3$) δ: 8.53 (d, 1H, ***J*** = 8.6 Hz); 8.50 (d, 1H, ***J*** = 7.4 Hz); 7.91-7.87 (m, 2H); 7.78 (dd, 1H, ***J*** = 8.0; 0.9 Hz); 7.72 (ddd, 1H, ***J*** = 8.6; 8.4; 2.5 Hz); 7.57 (ddd, 1H, ***J*** = 8.6; 7.1; 1.1 Hz); 7.47 (d, 1H, ***J*** = 7.1 Hz); 7.42 (br d, 1H, ***J*** = 8.6 Hz); 7.38 (br dd, 1H, ***J*** = 7.8; 0.9 Hz); 6.78 (s, 1H); 4.78 (t, 2H, ***J*** = 4.9 Hz); 4.04 (t, 2H, ***J*** = 4.9 Hz); 3.99 (s, 3H); 3.70-3.64 (m, 2H); 3.64-3.58 (m, 4H); 3.34 (t, 2H, ***J*** = 4.9 Hz). ESIMS (positive mode) ***m/z***: 448.13 (M+); calculated for $C_{24}H_{26}N_5O_2S$ ***m/z***: 448.18.

1. Fluorescence Spectra of TO-Modified DNA Oligonucleotides ODN1-ODN3

The fluorescence spectra for the single-stranded TO-modified DNA strands are shown below. In contrast to the order of fluorescence intensity observed for the ***duplexes*** (**ODN3** > **ODN1** > **ODN2**), the order of fluorescence for the single strands is **ODN2** > **ODN1** > **ODN3**.

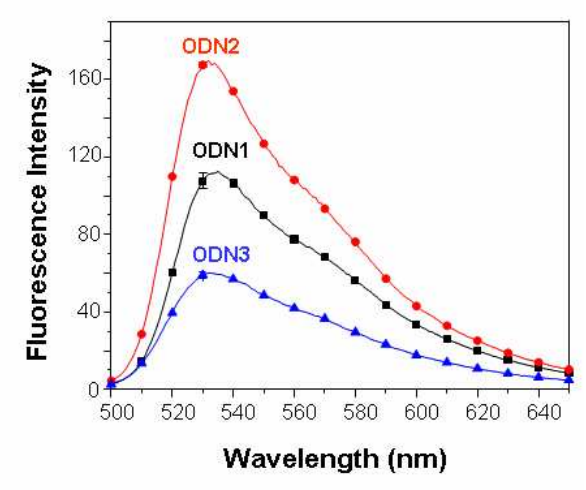

Figure S1. Fluorescence spectra recorded for TO-conjugated DNA strands **ODN1**, **ODN2** and **ODN3**. DNA concentration was 0.1 μM. 10 mM NaPi (pH 7), 100 mM NaCl and 0.1 mM EDTA. Samples were excited at 485 nm.

2. Fluorescence Lifetime Measurements of TO-Modified ODN3 Duplex ± Cy5 Acceptor

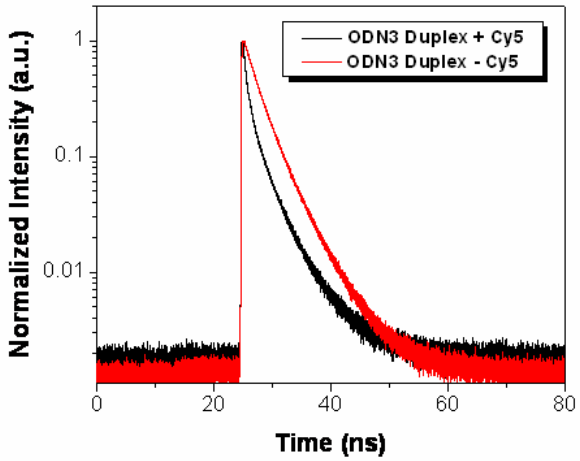

	ODN3 Duplex – Cy5	ODN3 Duplex + Cy5
A_1	11899.8	5224
t_1	4.4251	3.9774
A_2	16723	8006
t_2	2.0838	1.1222
X^2	1.05	1.44
Weighted Lifetime (ns)	3.057	2.250

Figure S2. Fluorescence lifetimes for **ODN3** duplex recorded in absence or presence of 5'-Cy5 on complementary strand. DNA concentration was 0.1 µM. Buffer contained 10 mM NaPi (pH 7), 100 mM NaCl and 0.1 mM EDTA. Samples were excited at 450 nm.

3. R_0 Calculation

Following Algar and coworkers, who determined the spectral overlap integral $\boldsymbol{J} = 1.6 \times 10^{-10}$ cm^6 and using refractive index $\boldsymbol{n}$ = 1.48, orientation factor κ^2 = 2/3, and ϕ_D = 0.2 (i.e. the fluorescence quantum yield of the donor, TO), we calculate the critical energy transfer distance (R_0) according to the formula:

$R_0 = [8.79 \times 10^{-28} \text{ mol} \times (\boldsymbol{n}^4\ \kappa^2\ \phi_D\ \boldsymbol{J}]^{1/6} = 40.6$ Å

This value is significantly greater than that calculated by Algar and coworkers (R_0 = 26 Å) due to the larger quantum yield of our covalently attached TO compared with the noncovalently bound TO monocation used in the previous work (ϕ_D = 0.01).

4. MALDI-TOF Mass Spectrum of ODN4 Single Strand

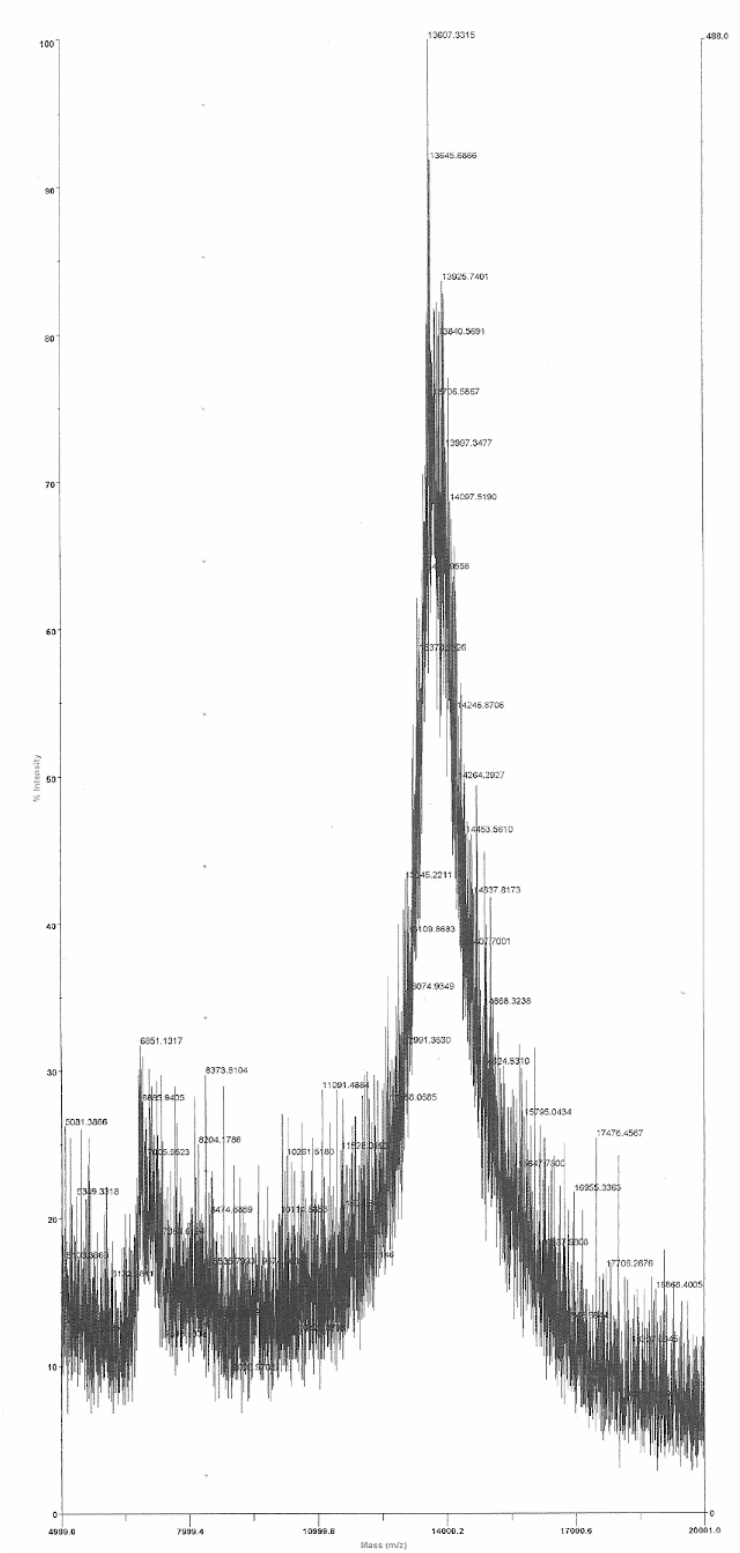

Figure S3. MALDI-TOF mass spectrum of ODN4 single strand. Molecular ion is observed at m/z = 13,607.3. (Calculated mass = 13,596.8.)

5. UV-Vis Spectra of ODN4 Single Strand and Duplex

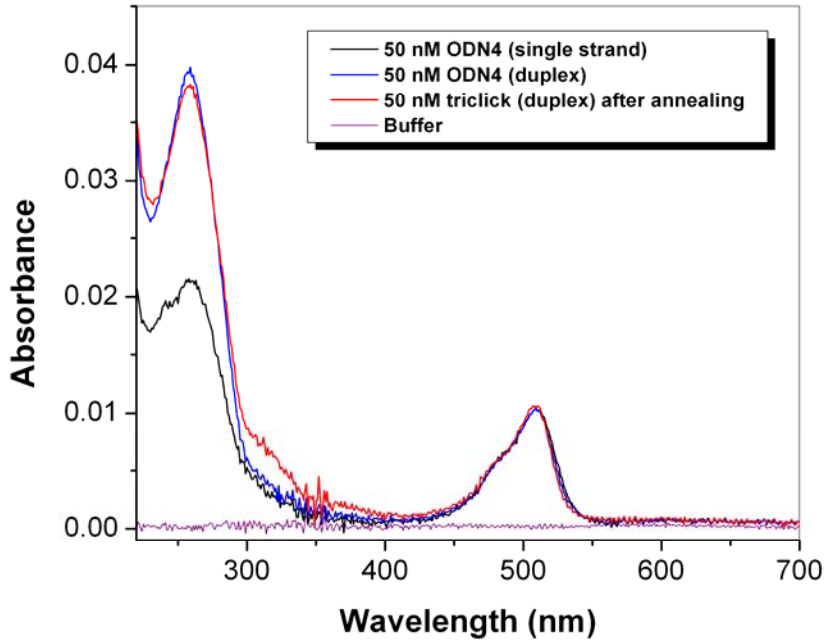

Figure S4. UV-vis spectra of ODN4 single strand and duplex. Samples included 1.0 μM DNA, 10 mM NaPi (pH 7), 100 mM NaCl and 0.1 mM EDTA.

6. UV Melting Curves of Termolecular Duplexes (X = Uracil-linked TO, Red and Black indicate different strands.)

A termolecular duplex consisting of the three strands shown below was prepared. The red strand was 5'-endlabeled with Cy5. Note that the red and black sequences correspond to different strands.

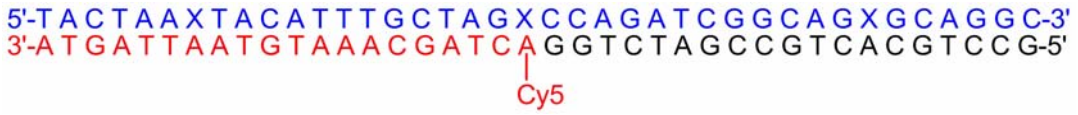

Two duplexes were prepared. In the first, no TO dyes were attached to the 39mer, meaning three alkynyl-uracil residues were present at the positions labeled "X" in the sequence above. In the second duplex, **TO-N_3-3** was attached to the DNA strand to give a final ratio of 2.4-2.7 dyes per strand. The UV melting curves reflect the stabilizing effect of the TO intercalators. Two transitions are evident in the TO-free duplex: the upper transition at 66.3 °C is assigned to melting of the 19mer strand, due to the significantly higher GC content, leaving the 20mer melting at 53.3 °C. Conjugation of TO dyes to the 39mer strand results in increases in T_m by 5.0 and 7.4 °C. (The corresponding values observed in the absence of the Cy5 label differed by less than 1 °C.)

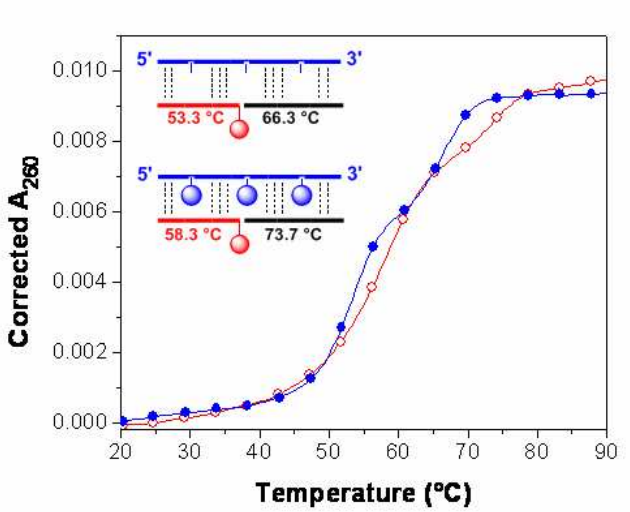

Figure S5. UV melting curves for ternary duplexes shown schematically above. Samples included 1.0 μM DNA, 10 mM NaPi (pH 7), 100 mM NaCl and 0.1 mM EDTA. Data were corrected by subtracting the initial absorbance at 20 °C from the curve. Intercalation of TO dyes stabilizes both transitions.

7. Spectral Imaging of Individual *Drosophila* Embryos

This figure provides spectral imaging results for individual embryos showing the range of brightness values that are obtained for different embryos. Thus, there is a fluctuation of approximately 10-15% around the mean value (for 31 different embryos), as shown in the lower figure. The similarity in the spectral profiles for the individual embryos indicates that the variation arises from differences in brightness, which is a function of antibody staining efficiency, not FRET efficiency, which would indicate variable hybridization of the triclicked DNA strand to the antibody.

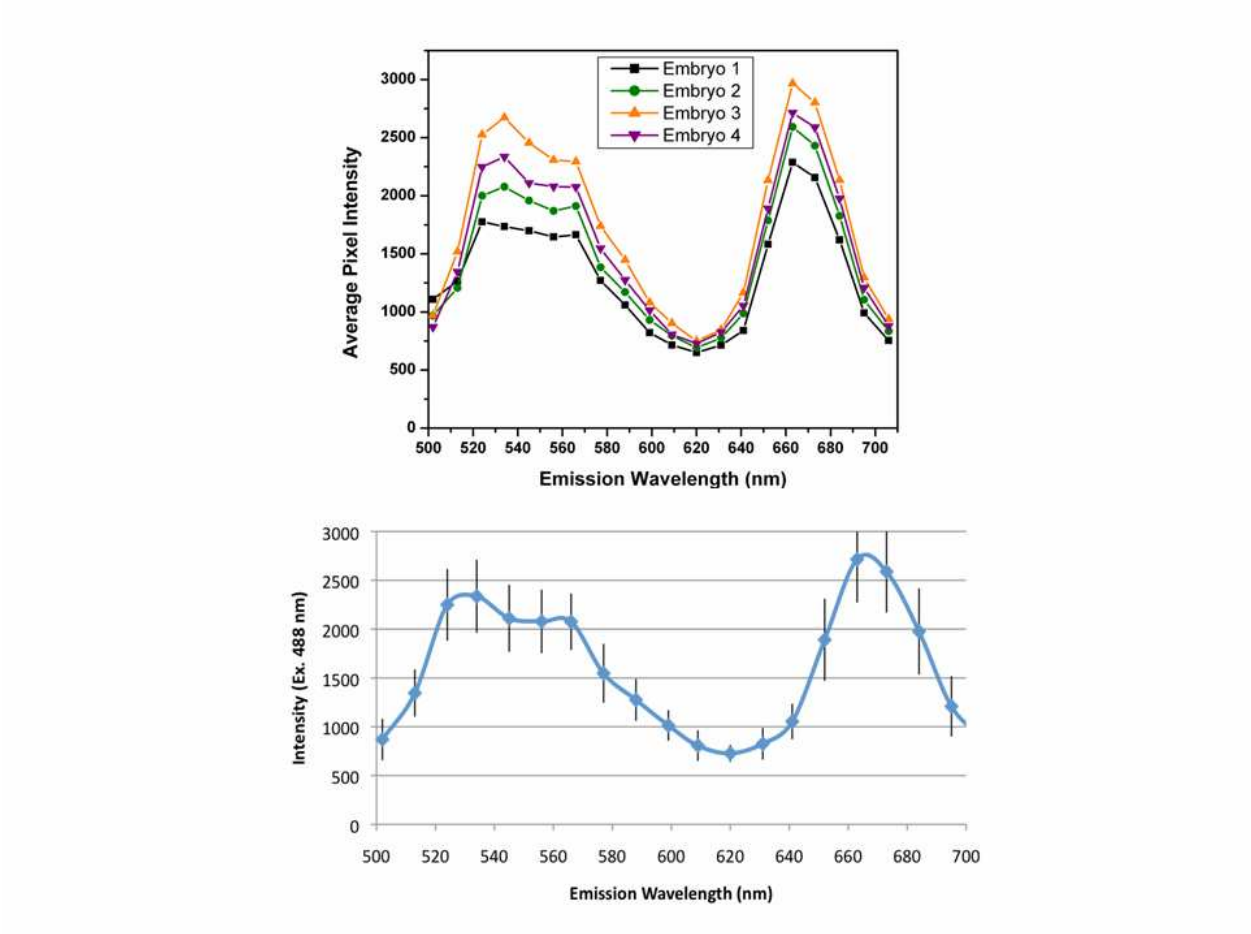

Figure S6. The average pixel intensity at the centrosome of the Ab-nanotag conjugate in 4 different fixed syncytial ***Drosophila*** embryos. Each point is represented as the average pixel intensity at the centrosome at a given emission wavelength (n = 30 – 35 centrosomes per embryo).

Bioconjugate Chemistry

ARTICLE

pubs.acs.org/bc

Galactosylated *N*-2-Hydroxypropyl Methacrylamide-*b*-*N*-3-Guanidinopropyl Methacrylamide Block Copolymers as Hepatocyte-Targeting Gene Carriers

Zhu Qin, Wei Liu, Ling Li, Liang Guo, Chen Yao, and Xinsong Li*

Biomaterials and Drug Delivery Laboratories, School of Chemistry and Chemical Engineering, Southeast University, Nanjing 211189, China

ABSTRACT: As alternatives of viral and cationic lipid gene carriers, cationic polymer-based vectors may provide flexible chemistry for the attachment of targeting moieties. In this report, galactosylated *N*-2-hydroxypropyl methacrylamide-*b*-*N*-3-guanidinopropyl methacrylamide block copolymers (galactosylated HPMA-*b*-GPMA block copolymers, or abbreviated as GHG) were prepared in order to develop hepatocyte targeting gene transfection carriers. The block copolymers were synthesized by aqueous reversible addition−fragmentation chain transfer (RAFT) polymerization of *N*-2-hydroxypropyl methacrylamide (HPMA) and *N*-3-aminopropyl methacrylamide (APMA), followed by galactosylation and guanidinylation. The molecular weight of GHG copolymers determined by static light scattering method was in the range from 48 600 to 76 240 g/mol. In addition, the galactose content in the GPMA block in the copolymers was determined to be 6.5−8.0 mol % according to the sulfuric acid method. The GHG copolymers complexed completely with plasmid DNA (pDNA) to show positive zeta-potential values with diameter 100−250 nm from charge ratio of 4, which demonstrated the excellent DNA condensing ability of guanidino groups. Furthermore, the MTT assay data of GHG/pDNA complexes on HepG2 cells and HeLa cells indicated that GHG copolymers had significantly lower cytotoxicity than PEI. In addition, the copolymers with GPMA component from 30.23% showed higher transfection efficiency than PEI at charge ratio of 12 in HepG2 cells. The result revealed that the conjugation of galactose groups in the copolymers brought asialoglycoprotein-receptor (ASGP-R) mediated transfection. The employing of HPMA component decreased the aggregation of protein in transfection presence of serum. The GHG copolymers combined the advantages of galactose moieties, guanidino groups, and HPMA component might show potential in safe hepatocyte targeting gene therapy.

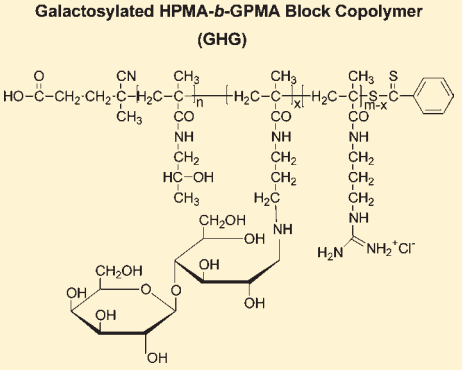

INTRODUCTION

Nonviral gene delivery carriers based on cationic polymers have attracted much attention facilitating the entry of plasmid DNA (pDNA) or siRNA into cells in the past decade. As alternatives of viral and cationic lipid gene carriers, cationic polymer-based vectors may have advantages such as safety and stability, avoidance of immunogenicity, and ease of structure modification and manufacturing practice.[1−3] *N*-(3-Aminopropyl)methacrylamide hydrochloride (APMA), a primary amine containing monomer with the backbone of methacrylate, was potentially useful in the development of gene delivery carriers of cationic polymers.[4] *N*-(2-Hydroxypropyl) methacrylamide (HPMA), a permanently hydrophilic monomer with the similar methacrylamide backbone, can be copolymerized with APMA to shield the surface charge of the latter and create a steric barrier against aggregation. It is shown that APMA-HPMA copolymers were efficient carriers for delivery of anticancer agents in the literature.[5−7]

Aqueous reversible addition−fragmentation chain transfer (RAFT) technology is a living radical polymerization process, which is a powerful method for the synthesis of well-defined polymers for biomedical applications. Compared with traditional radical polymerization, recent advances in controlled radical polymerization (CRP) especially RAFT polymerization have facilitated the synthesis of narrowly dispersed copolymers with controlled molecular weight, polymer architecture, and reactive structopendant or structoterminal functionality for bioconjugation.[8−12] Furthermore, Narain and McCormick have reported the aqueous RAFT polymerization method for the direct preparation of well-defined primary amine-based homopolymers, block and statistical copolymers, without protecting group chemistry.[13,14] It may be a significant step toward the tailored construction of well-defined copolymers for targeted gene delivery.[15]

Gene delivery to a very specific set of cells might be highly demanded in cancer therapies. Cationic polymers generally do not have the capacity for cell-specific targeting but provide flexible chemistry for the attachment of targeting moieties that allow both increased cell uptake and, often, cell specificity. A wide range of targeting moieties, such as folate,[16] epidermal growth factor,[17] transferrin,[18] or antibodies [19] have been conjugated to the residues of side chains or the backbone of cationic polymers. It is reported that

Received: November 24, 2010
Revised: May 18, 2011
Published: June 20, 2011

ACS Publications © 2011 American Chemical Society

Table 1. Composition for the Preparation of HPMA-*b*-APMA Block Copolymer (HA) by Aqueous RAFT Polymerization, and Galactosylated HPMA-*b*-GPMA Copolymer (GHG) by Galactosylation and Guanidinylation

HPMA-*b*-APMA block copolymer (HA)				galactosylated HPMA-*b*-GPMA block copolymer (GHG)			
	target DP[a]						
sample	HPMA	APMA	actual content of primary amino groups[b], mol %	sample	content of galactose[c] in feed, mol %	actual content of galactose[c,d], mol %	M_W[e], g/mol
HA1	60	30	16.75	GHG1	10	6.5	76 240
HA2	60	60	30.23	GHG2	10	7.2	68 000
HA3	60	120	41.20	GHG3	10	6.5	69 600
HA4	30	150	55.60	GHG4	10	8.0	48 600

[a] The $[M]_0/[CTA]_0$ ratio was equal to the target degree of polymerization (DP), while the $[CTA]_0/[ACVA]_0$ ratio was kept at 2/1. [b] As determined by the Ninhydrin assay. [c] Divided by the content of GPMA block in copolymers. [d] As determined by sulfuric acid micromethod. [e] As determined by a static light scattering instrument, dn/dc = 0.17 mL/g.

the asialoglycoprotein receptors (ASGP-R) of hepatocytes could recognize and internalize glycoproteins bearing terminal galactose or *N*-acetylglucosamine residues via clathrin-coated pits.[20] Therefore, the employments of lactose[21,22] and galactose[23−25] as conjugation partners with cationic polymers have been studied to deliver gene into liver parenchymal cells. Zanta et al. and Cook et al.'s reports revealed that 5% galactose conjugated to PEI could show high transfection efficiency in hepatocyte-derived cell lines.[26,27]

Cell-penetrating peptides (CPPs) such as Tat and other arginine-rich peptides has been reported that they can be taken up by cells via other receptor- or protein-independent transmembrane pathway than endocytosis and localize in the nucleus[28,29] in the past several years. A common feature of these peptides is that they consist of a large number of positively charged amino acids, especially arginine.[30−32] Compared with primary amino groups (pK_a = 10.8), the stronger basic guanidino group of arginine with pK_a of 12.5 may provide greater DNA condensing capability. The guanidino groups conjugated to linear poly(L-lysine) (PLL),[33] chitosan,[34] poly(propylene imine) (PEI),[35] and poly(amido amine) (PAMAM) dendrimer,[36] have showed greatly enhanced transfection efficiency than unmodified amino ones. Furthermore, Koo et al. reported that poly(L-arginine) (PArg) possessed both higher transfection efficiency and lower cytotoxicity than PLL, and PArg could be promising as an efficient gene delivery carrier.[37] Therefore, it is supposed that changing the primary amino groups of cationic polymer to guanidino groups should be beneficial for enhancing cellular uptake and transfection efficiency of gene delivery.

In this report, galactosylated *N*-2-hydroxypropyl methacrylamide-*b*-*N*-3-guanidinopropyl methacrylamide block copolymers (galactosylated HPMA-*b*-GPMA block copolymers, or abbreviated as GHG) was developed as a novel nonviral gene transfection vector. They were synthesized by aqueous RAFT polymerization of HPMA and APMA, followed by galactosylation for hepatocyte targeting and guanidinylation for cell penetrating. The complexes of galactosylated HPMA-*b*-GPMA block copolymers with plasmid DNA were investigated by agarose gel electrophoresis, particle size, and zeta potential measurements. In addition, the cytotoxicity, and transfection experiment of GHG/pDNA complexes were examined in HepG2 cells and HeLa cells.

EXPERIMENTAL PROCEDURE

Materials. *N*-3-Aminopropyl methacrylamide hydrochloride (APMA) and *N*-2-hydroxypropyl methacrylamide (HPMA) were purchased from PolySciences. 4,4′-Azobis(4-cyanovaleric acid) (ACVA), β-lactose, sodium cyanoborohydride, 1-*H*-pyrazole-1-carboxamidine hydrochloride, and branched PEI (MW 25 000) were purchased from Sigma-Aldrich. 1,4-Dioxane, acetone, boric acid, sodium borate, and Na_2CO_3 were purchased from Sinopharm (China). 4-Cyanopentanoic acid dithiobenzoate (CTP) was synthesized in our lab. The Endo-Free Plasmid Maxi Kit was purchased from Omega (China). Fetal bovine serum (FBS), Dulbecco's modified Eagle's medium (DMEM), antibiotics, trypsin, and 3-(4,5-dimethylthiazol-2-yl)-2,5-diphenyltetrazolium bromide (MTT) were purchased from Gibco. The plasmid pGL3-control luciferase reporter vector and Luciferase assay system were purchased from Promega. BCA protein assay kit was purchased from Biocolor (China).

Syntheses of HPMA-*b*-APMA Block Copolymers (HA) (13, 15). A series of *N*-2-hydroxypropyl methacrylamide-*b*-*N*-3-aminopropyl methacrylamide (HPMA-*b*-APMA) block copolymers was prepared by aqueous RAFT polymerization at 70 °C, employing 4,4′-azobis(4-cyanovaleric acid) (ACVA) as the radical initiator and 4-cyanopentanoic acid dithiobenzoate (CTP) as the RAFT chain transfer agent (CTA) with the feeds as cited in Table 1. $[M]_0$ was defined as the initial monomer concentration. The $[M]_0/[CTA]_0$ ratio was equal to the target degree of polymerization (DP), while the $[CTA]_0/[ACVA]_0$ ratio was kept at 2/1. The typical synthesis was as follows: HPMA (7.0 mmol) was dissolved in double distilled water (2 mL) before the addition of CTP (0.12 mmol, target DP = 60) and ACVA (0.06 mmol) in 1,4-dioxane stock solution. After degassing via three freeze−thaw cycles, the flask was placed in a preheated oil bath for 24 h at 70 °C. The reaction was then quenched by cooling the reaction vessel in an ice bath and exposure to air. The obtained HPMA homopolymer was purified by precipitation in acetone. Then, the HPMA homopolymer was subsequently used as macro-CTA. A typical protocol described for the copolymerization of HPMA to APMA was as follows: In a 5 mL flask, APMA (1.2 mmol), HPMA homopolymer (0.02 mmol, target DP = 60), and ACVA (0.01 mmol, dissolved in dioxane) were mixed with double distilled water (2 mL). The copolymerization protocol was the same as the homopolymerization of HPMA described previously.

The HPMA-*b*-APMA block copolymers were obtained as white powder. The content of primary amino group which

represented the ratio of APMA in the copolymer was determined by the Ninhydrin assay[38] as indicated in Table 1. The composition of the copolymers was determined by ^{1}H NMR and ^{13}C NMR as follows. ^{1}H NMR (300 MHz, D_2O): δ (ppm) 0.99−1.20 ($CH_2CH(OH)CH_3$, $CH_2C(CH_3)CO$), 1.80−1.92 ($CH_2C(CH_3)CO$, $CH_2CH_2CH_2NH_2$), 3.08 ($CH_2CH_2CH_2NH_2$), 3.24 ($CONHCH_2CH(OH)CH_3$, $CONHCH_2CH_2CH_2NH_2$), 3.94 ($CH_2CH(OH)CH_3$). ^{13}C NMR (125 MHz, D_2O): δ (ppm) 19.50 ($CH_2CH(CH_3)CH_2$), 22.80 ($CH_2CH(OH)CH_3$), 28.70 ($NHCH_2CH_2CH_2NH_2$), 39.63−40.04 ($CONHCH_2CH_2$, $CH_2CH_2CH_2NH_2$), 47.80 ($CONHCH_2CH(OH)CH_3$), 49.72 ($CH_2C(CH_3)CO$), 56.66 ($CH_2C(CH_3)CO$), 68.21 ($CH_2CH(OH)CH_3$), 181.81 (C═O).

Galactosylation of HPMA-*b*-APMA Block Copolymers. Galactosylated HPMA-*b*-APMA block copolymers (GHA) were synthesized by reductive amination reaction.[26,27] Briefly, HPMA-*b*-APMA block copolymers (127 μmol of primary amino groups) and β-lactose (12.7 μmol) were dissolved in 1 mL of sodium borate buffer (200 mM, pH 8.2), followed by the addition of sodium cyanoborohydride (5-fold molar excess of lactose). Then, the reaction mixture was stirred at room temperature for 24 h. The obtained galactosylated copolymers were purified by dialysis against distilled water (MWCO = 7000) and lyophilized. The content of galactose in the APMA block in galactosylated HPMA-*b*-APMA block copolymers was determined by sulfuric acid micromethod.[39]

Guanidinylation of Galactosylated HPMA-*b*-APMA Block Copolymers. The residue primary amino groups (13 mM) of galactosylated HPMA-*b*-APMA block copolymers were guanidinylated with 1*H*-pyrazole-1-carboxamidine hydrochloride (65 mM) in water which was adjusted to pH 9.0 with Na_2CO_3 at room temperature for 24 h.[35] Then, they were extensively dialyzed against distilled water (MWCO = 7000) and lyophilized. The obtained copolymers can be named as galactosylated *N*-2-hydroxypropyl methacrylamide-*b*-*N*-3-guanidinopropyl methacrylamide (galactosylated HPMA-*b*-GPMA block copolymers, or abbreviated as GHG). The absolute molecular weights of the GHG copolymers were determined by a static light scattering instrument (BI-200SM, Brookhaven, USA).The chemical compositions of GHG were estimated by ^{1}H, ^{13}C NMR as follows. ^{1}H NMR (300 MHz, D_2O): δ (ppm) 0.96−1.20 ($CH_2CH(OH)CH_3$, $CH_2C(CH_3)CO$), 1.79 ($CH_2C(CH_3)CO$, $CH_2CH_2CH_2NHC(NH)NH_2$), 2.64 ($CH_2CH_2CH_2NHCH_2CH_2(OH)$), 2.82 ($NHCH_2CH_2(OH)$), 3.21 ($CONHCH_2CH(OH)CH_3$, $CONHCH_2CH_2CH_2NH$, $CH_2CH_2CH_2NHC(NH)NH_2$), 3.58−3.78 ($CH_2(OH)$ and $CH(OH)$ in galactose), 3.94 ($CH_2CH(OH)CH_3$), 4.56 ($CH(OCH)(CH_2OH)OCH$ in galactose). ^{13}C NMR (125 MHz, D_2O): δ (ppm) 19.24 ($CH_2CH(CH_3)CH_2$), 22.23 ($CH_2CH(OH)CH_3$), 29.18 ($NHCH_2CH_2CH_2NH$), 40.08−41.65 ($CONHCH_2CH_2$, $CH_2CH_2NHC(NH)NH_2$), 47.77 ($CONHCH_2CH(OH)CH_3$), 52.02 ($CH_2C(CH_3)CO$), 55.51 ($CH_2C(CH_3)CO$), 63.69 ($CH_2(OH)$ in galactose), 68.20 ($CH_2CH(OH)CH_3$), 71.15−77.95 ($CH(OH)$ in galactose), 113.57 ($CH(OCH)(CH_2OH)OCH$ in galactose), 159.50 ($CH_2NHC(NH)NH_2$), 181.93 (C═O).

The guanidinylation of HPMA-*b*-APMA block copolymers without galactose groups were also prepared, which were named as HPMA-*b*-GPMA block copolymers, or abbreviated as HG. The guanidinylation was detected by ^{1}H, ^{13}C NMR as follows. ^{1}H NMR (300 MHz, D_2O): δ (ppm) 0.94−1.19 ($CH_2CH(OH)CH_3$, $CH_2C(CH_3)CO$), 1.79 ($CH_2C(CH_3)CO$, $CH_2CH_2CH_2NHC(NH)NH_2$), 3.21 ($CONHCH_2CH(OH)CH_3$, $CONHCH_2CH_2CH_2NHC(NH)NH_2$), 3.92($CH_2CH(OH)CH_3$). ^{13}C NMR (125 MHz, D_2O): δ (ppm) 18.80 ($CH_2CH(CH_3)CH_2$), 22.00 ($CH_2CH(OH)CH_3$), 29.37 ($NHCH_2CH_2CH_2NHC(NH)NH_2$), 39.70−41.3 ($CONHCH_2CH_2$, $CH_2CH_2NHC(NH)NH_2$), 47.74 ($CONHCH_2CH(OH)CH_3$), 49.70 ($CH_2C(CH_3)CO$), 56.29 ($CH_2C(CH_3)CO$), 67.99 ($CH_2CH(OH)CH_3$), 159.21 ($CH_2NHC(NH)NH_2$), 181.62 (C═O).

Agarose Gel Electrophoresis. DNA condensing ability of galactosylated HPMA-*b*-GPMA block copolymers (GHG) was examined by agarose gel electrophoresis, HPMA-*b*-GPMA block copolymers (HG) was employed as controls. In this assay, the charge ratios were presented as the molar ratio of the positively charged guanidino groups of GHG to negatively charged phosphate backbone of DNA. GHG/pDNA complexes were formed at a series of charge ratios.

In each case, an appropriate amount of GHG dissolved in PBS (pH = 7.2) was mixed with 0.2 μg of pDNA to a volume of 6 μL, and incubated at room temperature for 30 min. After adding 1 μL of loading buffer, each complex solution was loaded into a well for electrophoretic separation on 1.0% agarose gel with Tris-boric acid EDTA (TBE) running buffer and electrophoresced at 100 V for 10 min. The visualization of DNA was illuminated with ethidium bromide (0.2 μg/mL).

Particle Size and Zeta Potential Measurements. The average sizes and zeta potential values of GHG/pDNA and HG/pDNA complexes were examined by a dynamic light scattering instrument (90Plus/BI-MAS, Brookhaven, USA) equipped with a He−Ne laser (632.2 nm, fixed scattering angle of 90°) at 25 °C. For these experiments, GHG or HG/pDNA complexes were prepared in PBS (pH = 7.2) at charge ratios (+/−) of 1, 4, 8, 12, and 16. After 30 min incubation, complex solutions were diluted to a final volume of 1.5 mL containing a final pDNA concentration of 10 μg/mL. Measured sizes and zeta potential values were presented as the average values of triplicate.

Cell Culture. HepG2 (human hepatocellular liver carcinoma cells) and HeLa (human cervix epithelial carcinoma cells) were cultured in DMEM medium, supplemented with 10% heat inactivated FBS, and antibiotics (10 U/mL penicillin and 10 μg/mL streptomycin). Cells were incubated at 37 °C in a 5% CO_2 humidified atmosphere and split using trypsin when almost confluent.

Cytotoxicity. The cytotoxicity of galactosylated HPMA-*b*-GPMA block copolymers (GHG) was measured by MTT assay. HPMA-*b*-GPMA block copolymers (HG) were also evaluated in comparison with GHG, and PEI was used as a control. HepG2 cells and HeLa cells were seeded at a density of 10^4 cells/well in 96-well plates and grown in 100 μL DMEM medium containing 10% FBS for 24 h at 37 °C. After treating cells with GHG/pDNA complexes (0.1 μg pDNA) at different charge ratios for 6 h in 50 μL serum- and antibiotic-free DMEM medium, the medium was replaced with DMEM medium containing 10% FBS and the cells were incubated for 48 h. After this period, 20 μL of MTT solution (5 mg/mL in PBS) was added and the cells were further incubated for 4 h at 37 °C. Subsequently, medium were removed carefully and 150 μL of DMSO was added to each well to dissolve the formazan crystal formed by proliferating cells. UV absorbance was measured at 490 nm using a microplate reader (model 680, Bio-Rad, USA). The cell viability was calculated as a percentage of complex-treated cells to untreated negative control cells. All experiments were performed in sextuplicate.

Scheme 1. Synthesis of Galactosylated HPMA-*b*-GPMA Block Copolymer (GHG)

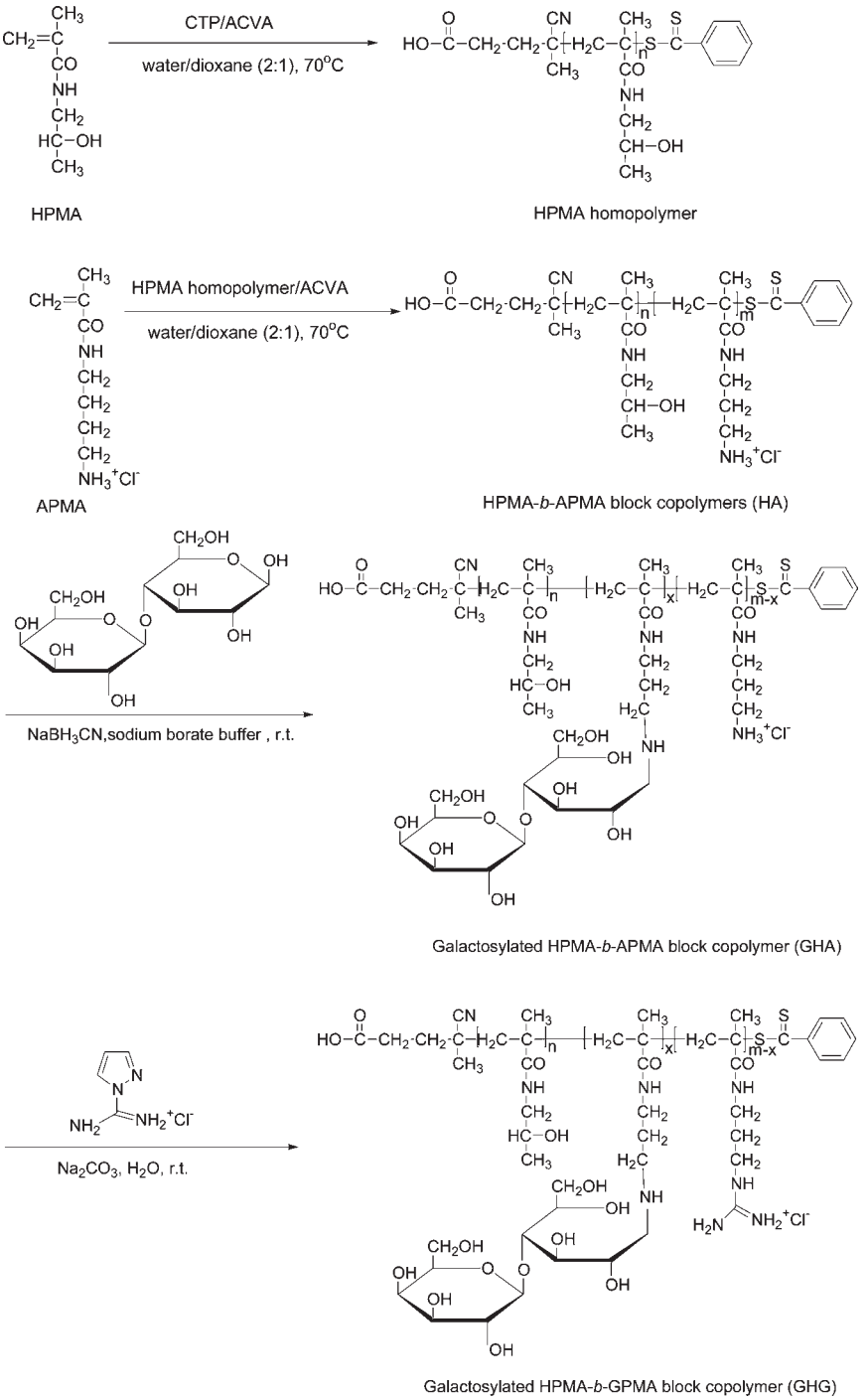

Transfection Experiments. The transfection efficiency of galactosylated HPMA-*b*-GPMA block copolymers (GHG) was measured by luciferase expression assay using plasmid PGL3 luciferase vector as a reporter gene. HPMA-*b*-GPMA block copolymers (HG) were also evaluated in comparison with GHG, and PEI was used as a control. HepG2 cells and HeLa cells were seeded at a density of 10^4 cells/well in 96-well plates and incubated in 100 μL DMEM medium containing 10% FBS for 24 h to 90−95% confluence. Before transfection, the growth medium was removed from each well, and the cells were washed twice with serum- and antibiotic-free medium. Then, cells were treated with GHG/pDNA complexes (0.1 μg pDNA) at different charge ratios for 6 h in 50 μL serum- and antibiotic-free DMEM medium. After exchange with DMEM medium containing 10% FBS, cells were further incubated for 48 h at 37 °C. Then, the medium was removed and the cells were washed twice with PBS before adding 20 μL Cell Culture Lysis reagent. The luciferase assay was carried out according to the manufacture's instruction (Promega, USA). The luciferase activity expressed as relative light units (RLUs) was

measured with a luminometer (Chameleon V L, Hidex, Finland). The protein concentration in the cell lysates was measured by BCA protein assay kit. The final results were reported in terms of RLU/mg cellular protein. All experiments were performed in triplicate.

Transfection experiments in the presence of serum were conducted in DMEM medium containing 10% FBS with the same procedure as above.

RESULTS AND DISCUSSION

Syntheses of Galactosylated HPMA-*b*-GPMA Block Copolymers. Galactosylated HPMA-*b*-GPMA block copolymers (GHG) were synthesized by aqueous RAFT copolymerization of HPMA and APMA, followed by galactosylation and guanidinylation as described in Scheme 1. A series of HPMA-*b*-APMA block copolymers HA1, HA2, HA3, and HA4 were synthesized with different target degree of polymerization (DP) as listed in Table 1. In order to control the molecular weight of HPMA-*b*-APMA block copolymers, 4-cyanopentanoic acid dithiobenzoate (CTP) was used as chain transfer agent. The content of primary amino groups which represented the ratio of APMA in the copolymer was determined by the Ninhydrin assay[38] as indicated in Table 1. The concentration of primary amine groups in the copolymers was less than that present in the feed indicating disparate monomer reactivities.

Partial primary amino groups of HPMA-b-APMA block copolymers were further modified by galactosylation for hepatocyte targeting through reductive amination reaction,[26,27] and subsequently, the residue primary amino groups of galactosylated HPMA-*b*-APMA block copolymers were totally guanidinylated with 1*H*-pyrazole-1-carboxamidine hydrochloride under very gentle condition. The chemical composition of the galactose groups in galactosylated HPMA-*b*-GPMA block copolymers (GHG) were determined by ^{1}H and ^{13}C NMR measurements. The peaks at 3.58−3.78 and 4.56 ppm in the ^{1}H NMR spectra of GHG were assigned to the protons from 2-carbon to 6-carbon and 1-carbon of galactose, respectively. The peaks at 63.69, 71.15−77.95, and 113.57 ppm in the ^{13}C NMR spectra of GHG were assigned to the carbon of 6-carbon, 2-carbon to 5-carbon, and 1-carbon in galactose, respectively. The quantitative composition of the galactose group to the content of GPMA block in galactosylated HPMA-*b*-GPMA block copolymers was determined to be 6.5−8.0 mol % as indicated in Table 1 by the sulfuric acid method.[39] As literature reported that more than 5% galactose conjugation could show high transfection efficiency in hepatocyte-derived cell lines,[26,27] the obtained galactosylated copolymers could be used as ASGP-R targeting gene carriers.

The guanidinylation of residue primary amino groups was also established by ^{1}H and ^{13}C NMR spectroscopy. Attention was given to the region 3.0−3.4 ppm in the ^{1}H NMR spectra of HA and GHG copolymers, where the proton peak of methylene next to the primary amino groups of HA copolymer was shifted from 3.08 ppm to 3.21 ppm as the guanidinylation completed.[35] The disappearance of the methylene peak at 3.08 ppm indicated that the residue primary amino groups were thoroughly replaced by the guanidino ones. Furthermore, in the ^{13}C NMR spectra of HA and GHG copolymers, the guanidinylation of primary amino group is demonstrated by the appearance of a new peak at 159.50 ppm corresponding to the C atoms of the guanidino groups. The results indicated that the residue primary amino groups of galactosylated HPMA-*b*-APMA block copolymers were converted to guanidino groups of galactosylated HPMA-*b*-GPMA block copolymers after a total guanidinylation.

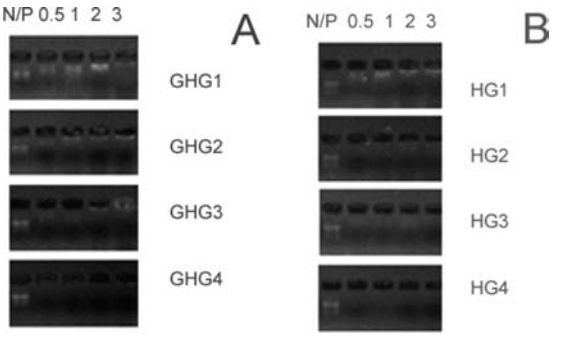

Figure 1. Agarose gel electrophoresis images of (A) GHG/pDNA and (B) HG/pDNA complexes at different charge ratios.

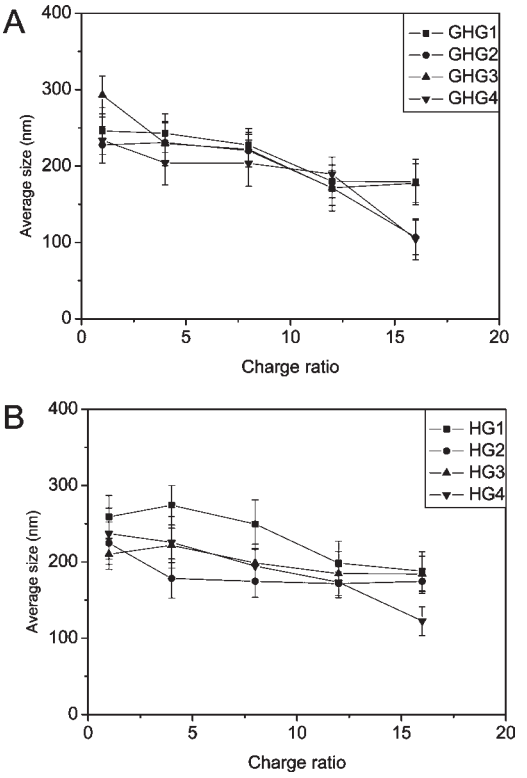

Figure 2. Average particle sizes of (A) GHG/pDNA and (B) HG/pDNA complexes at different charge ratios examined by the dynamic light scattering instrument.

The absolute molecular weights of galactosylated HPMA-*b*-GPMA block copolymers GHG1, GHG2, GHG3, and GHG4 were in the range 48 600−76 240 g/mol determined by static light scattering method as shown in Table 1.

Agarose Gel Electrophoresis. Agarose gel electrophoresis was performed in order to examine pDNA condensing ability of galactosylated HPMA-*b*-GPMA block copolymers (GHG), using HPMA-*b*-GPMA block copolymers (HG) as controls. The results revealed that the complete complex formation occurred at charge ratios 3, 3, 2, and 0.5 for GHG1, GHG2, GHG3, and GHG4 with 16.75%, 30.23%, 41.20%, and 55.60% GPMA component in the GHG copolymers, respectively, as shown in Figure1. Meanwhile, the complete complex formation

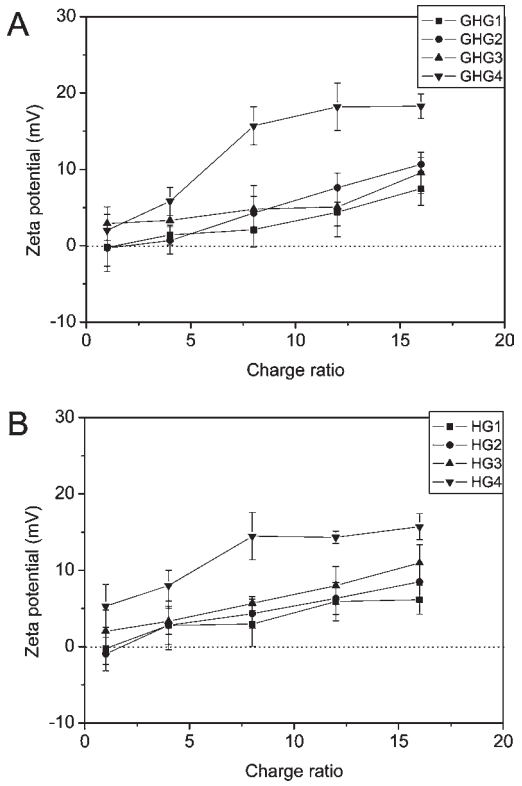

Figure 3. Zeta potential values of (A) GHG/pDNA and (B) HG/pDNA complexes at different charge ratios examined by the dynamic light scattering instrument.

occurred at charge ratios 3, 0.5, 0.5, and 0.5 for HG1, HG2, HG3, and HG4 copolymers, respectively.

Since the guanidino group (pK_a = 12.5) is fully protonated at physiological pH, all the GHG and HG copolymers can condense pDNA efficiently via electrostatic and hydrogen bond interactions between the strong positive charges of guanidino groups and negative charges of pDNA phosphates. As indicated in Figure 1, GHG1 and HG1 completely complexed with pDNA at charge ratio of 3. It is suggested that the presence of HPMA component in the GHG and HG copolymers provides the main shielding effect on the complex formation. Compared with HG2 and HG3, GHG2 and GHG3 condensed pDNA completely at relatively higher charge ratios. It is supposed that the abundant hydroxyl groups in the galactose group also enhanced the shielding effect. GHG4/pDNA and HG4/pDNA complexes both formed at charge ratio of 0.5; it might be that the component of guanidino groups took the dominant position in more than half the copolymers. Therefore, the HPMA and galactose components in galactosylated HPMA-*b*-GPMA block copolymers play an important role in the efficient formation of GHG/pDNA complex.

Average Sizes and Zeta Potential Measurements. The average particle size of GHG/pDNA and HG/pDNA complexes prepared in PBS (pH 7.2) with different charge ratios is measured by dynamic light scattering as shown in Figure 2. The results indicated that the copolymers can condense pDNA sufficiently to form particles with the diameter less than 300 nm at charge ratio from 1 to 16. In addition, the particle size of the complexes showed the tendency to decrease with the increase in charge ratio and GPMA component in the copolymers. While the charge ratio rose to 12, the particle sizes of GHG/pDNA and HG/pDNA

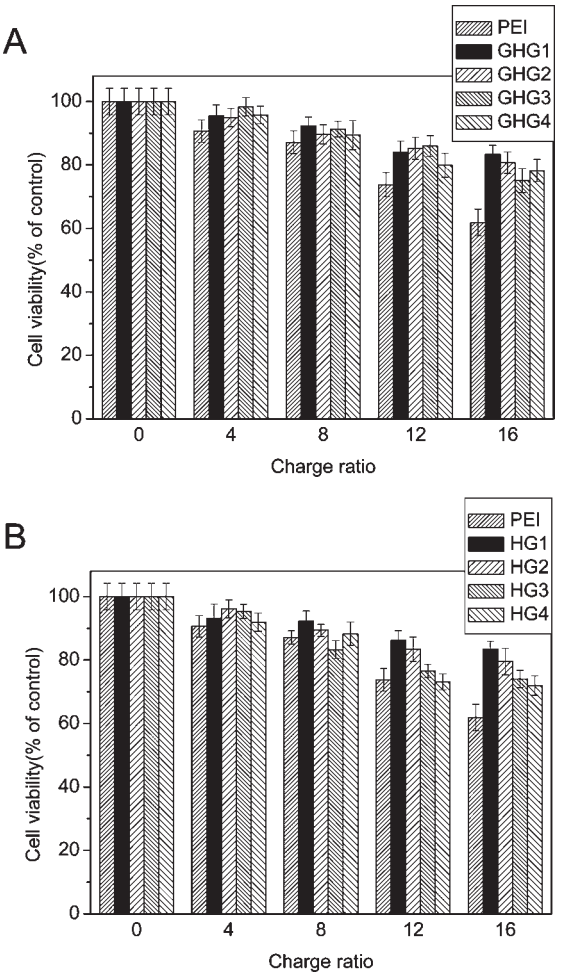

Figure 4. Cytotoxicity of (A) GHG/pDNA and (B) HG/pDNA complexes at different charge ratios in HepG2 cells by MTT assay (branched PEI 25K as a control).

complexes reduced to less than 200 nm. It is revealed that GHG4 and HG4 with 55.60% GPMA component in the copolymers had the best DNA condensing ability, which formed particles with the smallest diameter of nearly 100 nm at charge ratio of 16. The particle sizes of cationic polymer/gene complexes are very important for gene expression, and the GHG/pDNA complexes with diameters of 100−250 nm from the charge ratio of 4 may be to the satisfaction of this prerequisite. It is also found that the average particle sizes of GHG/pDNA complexes showed no significant difference by comparison with the corresponding HG/pDNA.

The zeta potential values of GHG/pDNA and HG/pDNA complexes were shown in Figure 3. It is revealed that GHG1/pDNA and GHG2/pDNA complexes with 16.75% and 30.23% GPMA component in the copolymers displayed positive values at the charge ratio more than 1, suggesting that the negatively charged pDNA was packed into the complex completely, while GHG3/pDNA and GHG4/pDNA complexes with 41.20% and 55.60% GPMA component in the copolymers showed positive surface values even at charge ratio of 1, demonstrating the strong pDNA condensing ability of the guanidino groups. Also, each GHG/pDNA complex had its highest zeta potential value at the charge ratio of 16, indicating complete shielding of DNA negative charges and condensed particulates with smallest size (Figure 2).

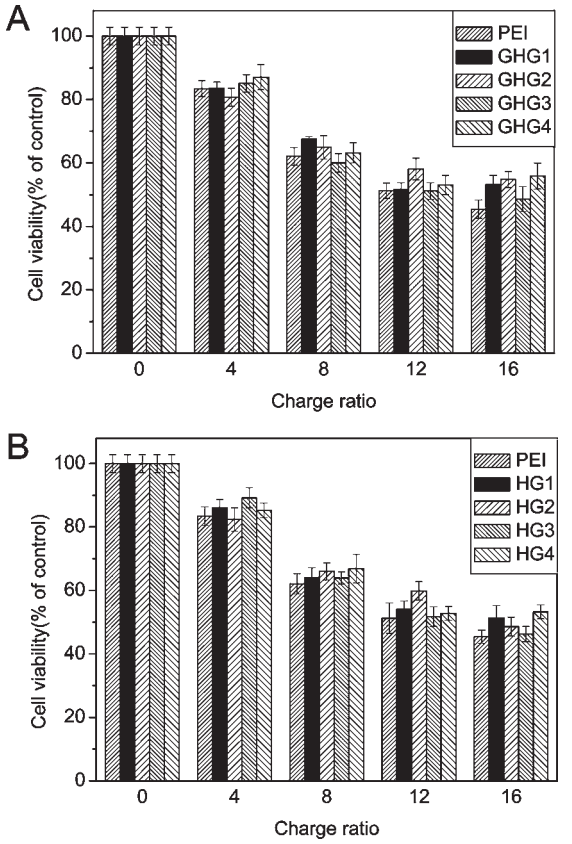

Figure 5. Cytotoxicity of (A) GHG/pDNA and (B) HG/pDNA complexes at different charge ratios in HeLa cells by MTT assay (branched PEI 25K as a control).

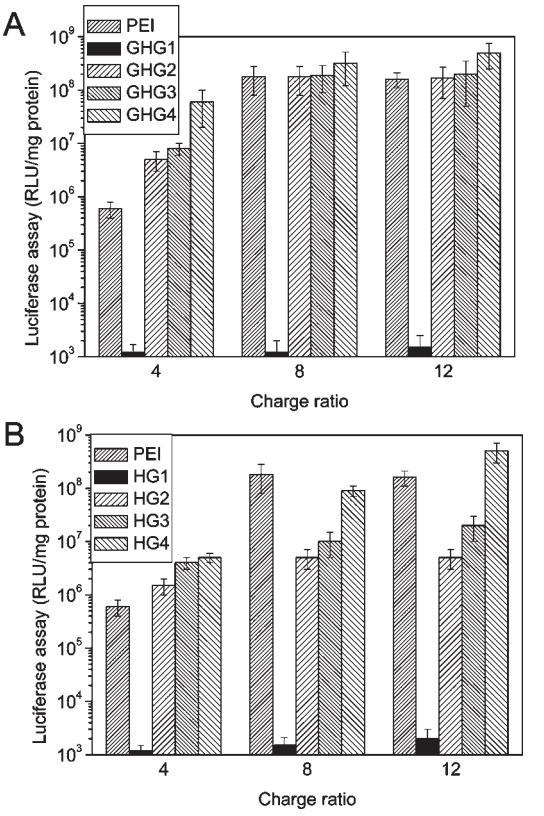

Figure 6. Transfection efficiencies of (A) GHG/pDNA and (B) HG/pDNA complexes at different charge ratios in the absence of serum measured by luciferase expression assay in HepG2 cells (branched PEI 25K as a control).

Furthermore, the GHG4/pDNA complex reached the positive peak value of 18.27 at charge ratio of 16, which was consistent with the corresponding smallest particle size of 104.2 nm as shown in Figure 2. Apparently, the positive surface charge of the complexes increases gradually with the increasing GPMA component and charge ratios. Compared with HG/pDNA complexes, the zeta potential values of GHG/pDNA complexes showed no obvious decrease, indicating that the hydroxyl groups of galactose groups did not make sense in the decreasing surface potential values. The positive charge of cationic polymer/pDNA complexes is thought to be helpful for its absorption to negatively charged cellular membrane, also leading to efficient intracellular trafficking and influencing transfection efficiency.[40] So, GHG/pDNA complexes with positive surface charge from the charge ratio of 4 may be advantageous for absorption onto cellular membrane.

Cytotoxicity. Cytotoxicity of GHG/pDNA and HG/pDNA complexes was examined using HepG2 and HeLa cells as shown in Figures 4 and 5. PEI, the most commonly used gene carrier, was involved for comparison. The results revealed that GHG and HG copolymers exhibited less cytotoxicity than PEI at charge ratios from 4 to 16 in both cell lines, which suggested better cell viability for the application of gene delivery. All the complexes had obviously less cytotoxic effect on HepG2 cells than HeLa cells at the same charge ratios, which is supposed to be the different dependency between cell lines. In each cell line, it is found that the cytotoxicity of complexes increases with increasing charge ratio. Compared with GHG/pDNA and HG/pDNA complexes at the same charge ratio, there seems to be no significant difference in HeLa cells. However, in HepG2 cells, GHG3/pDNA and GHG4/pDNA complexes with 41.20% and 55.60% GPMA component in the copolymers showed better cell viability than corresponding HG/pDNA complexes. It is considered to be the reduction of GHG concentration in medium by receptor-mediated endocytosis to HepG2 cells through ASGP-R,[26] whereas the HG copolymers without galactose groups remaining in medium bring more cytotoxic effects. Bulmus[41] reported that polyHPMA could be noncytotoxic or cytotoxic depending on the choice of RAFT agent as the interplay between polymer and RAFT end-group can be a significant factor in cytotoxicity. However, the toxic effect of dithiobenzoate-ended polyHPMA could be eliminated at low concentrations ($\leq$200 μM). Since the concentration of the galactosylated HPMA-*b*-GPMA copolymers with the end-group dithiobenzoate of the RAFT agent in DMEM medium was much less than 200 μM in the cytotoxicity experiments conducted in this paper, the interplay between the copolymer and the RAFT end-group could have no significant contribution to the cytotoxicity, and the positively charged GPMA component might be the key factor in the cytotoxicity of this experiment.

Transfection Experiments. The transfection of galactosylated HPMA-*b*-GPMA block (GHG) copolymers/pDNA complexes was performed on HepG2 expressing high levels of ASGP-R and HeLa cells lacking ASGP-R using plasmid PGL3 luciferase vector as a reporter gene. HPMA-*b*-GPMA block copolymers (HG) were also evaluated in comparison with GHG, and PEI was used as a control. Complexes of GHG

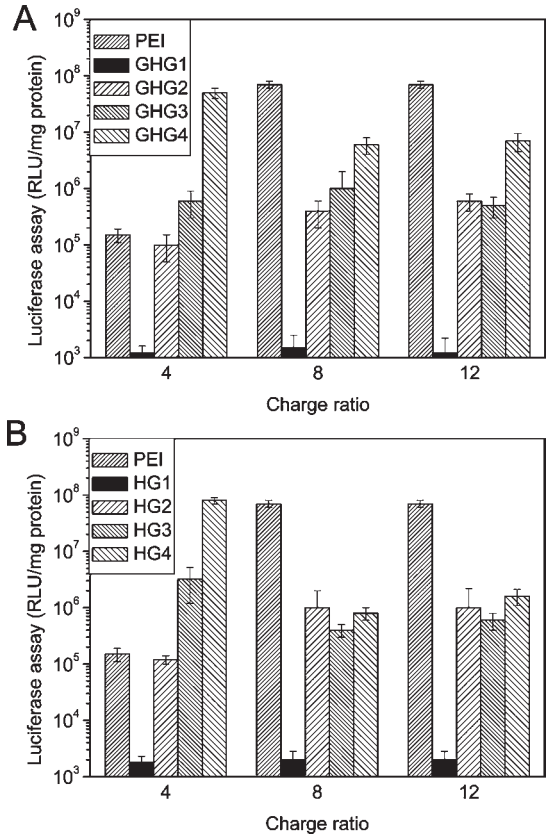

Figure 7. Transfection efficiencies of (A) GHG/pDNA and (B) HG/pDNA complexes at different charge ratios in the absence of serum measured by luciferase expression assay in HeLa cells (branched PEI 25K as a control).

and HG copolymers with pDNA were prepared at charge ratios of 4, 8, and 12, respectively. The charge ratios employed for the transfection efficiency experiments were within the range applied for the cytotoxicity evaluation as shown in the cytotoxicity section above.

The transfection efficiency of GHG and HG copolymers was increased with the increase of the content of guanidino groups in the copolymers as shown in Figure 6 and Figure 7. GHG4 and HG4 with 55.60% GPMA component showed the highest transfection in both cell lines, whereas GHG1 and HG1 with 16.75% GPMA component revealed much lower transfection efficiency. The results demonstrated that the guanidino groups of the GPMA block brought a significant increase of transfection efficiency analogous to CPP mediated internalization[28,30]

The data shown in Figure 6 and Figure 7 also revealed that the transfection efficiency of GHG and HG copolymers was intensively influenced by the targeting groups and charge ratios. At charge ratio of 4, the transfection efficiency of GHG and HG was much higher than that of PEI control in HepG2 cells and HeLa cell. However, as charge ratio increased, most GHG copolymers in HeLa cells and HG copolymers in both cells exhibited less transfection than PEI, except HG4 with 55.6% GPMA component at charge ratio of 12 in HepG2 cells. Notably, as GHG copolymers in HepG2 cells were taken into account, GHG copolymers with guanidino groups from 30.23% revealed similar or higher transfection than that of PEI at charge ratios of 8 and 12. Furthermore, GHG4 exhibited the highest efficiency of 5×10^8 RLU/mg

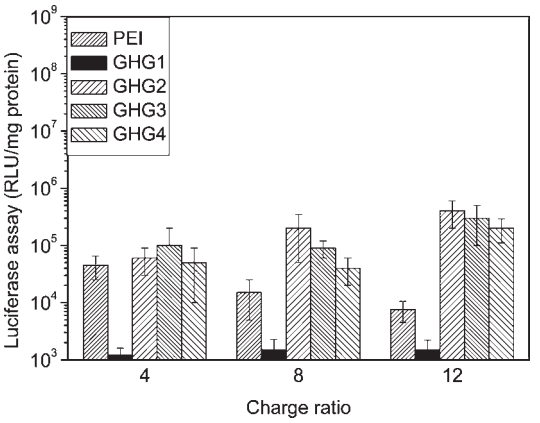

Figure 8. Transfection efficiencies of GHG/pDNA complexes at different charge ratios in the presence of serum (10% FBS) measured by luciferase expression assay in HepG2 cells (branched PEI 25K as a control).

protein at charge ratio of 12. The results can be attributed to the conjugation of galactose content in the copolymers which induced the ASGP-R mediated transfection in hepatocyte-derived cell lines. It confirmed that the galactose groups enhanced the transfection efficiency as targeting moieties.

The transfection efficiency was dependent on the cell lines and cytotoxicity as well. The best transfection of GHG and HG copolymers in HeLa cells occurred at a magnitude of 10^7 RLU/mg protein and charge ratio of 4 (Figure 7). As charge ratios increased, the transfection of CHG and GH copolymers was sharply reduced, which might be inhibited by the relative low cell viability of <70% as cited in Figure 5. On the contrary, in HepG2 cells, GHG/pDNA and GH/pDNA complexes with cell viability of >70% at charge ratio from 4 to 12 (Figure 4) showed increasing transfection efficiency with the increase of charge ratios. In addition, the highest transfection efficiency of GHG and GH copolymers with magnitude of 10^8 RLU/mg protein was revealed at charge ratios of 12 (Figure 6). The GHG/pDNA and HG/pDNA complexes in HeLa cells showed relatively higher cytotoxicity than in HepG2 cells at the same charge ratios. Therefore, the different tendency of transfection efficiency in HepG2 and HeLa cells balanced the cytotoxicity contributed to the dependence of cell lines.

Figure 8 showed the transfection efficiency of GHG/pDNA complexes in the presence of serum (10% FBS) in HepG2 cells at different charge ratios. The results indicated that the transfection efficiency of all the complexes decreased after addition of serum in the medium. In addition, the down regulation of transfection efficiency was reduced as the HPMA component in the copolymers increased. GHG2 and GHG3 with HPMA components of 58.80% and 69.77% had relatively high transfection efficiency. It is suggested that the hydrophilic HPMA component prevents aggregation of protein in the serum on the complexes before being taken up by cells. All the GHG/pDNA complexes showed higher transfection efficiency than PEI/pDNA complexes at charge ratios as indicated in the experiments. It is suggested that GHG copolymers have a potential for gene delivery in vivo as well as in vitro.

CONCLUSIONS

A series of galactosylated HPMA-*b*-GPMA block (GHG) copolymers were synthesized by aqueous RAFT polymerization of HPMA and APMA, followed by partial galactosylation for

hepatocyte targeting and total guanidinylation for cell penetration. The GHG copolymers combined completely with pDNA to form complexes at charge ratios no more than 3. The complexes revealed positive zeta potential values with diameter 100−250 nm from charge ratio of 4, which demonstrated excellent DNA condensing ability of guanidino groups in the copolymers. GHG copolymers had significantly lower cytotoxicity than PEI on HepG2 cells and HeLa cells. GHG copolymers with guanidino groups from 30.23% revealed higher transfection than PEI and GHG4 with 55.60% guanidino groups exhibited the highest efficiency at charge ratio of 12 in HepG2 cells, which confirmed that the conjugation of galactose content in the copolymers brought the ASGP-R mediated transfection. The employment of HPMA content decreases the aggregation of protein in the presence of serum transfection. Therefore, GHG copolymers combining the advantages of galactose content, guadino groups, and the HPMA component might show potential in safe hepatocyte targeting gene therapy.

AUTHOR INFORMATION

Corresponding Author

*Phone: (86-25) 8379-3456. Fax: (86-25) 8379-3456. E-mail: lixs@seu.edu.cn.

REFERENCES

(1) Liu, F., and Huang, L. (2002) Development of non-viral vectors for systemic gene delivery. *J. Controlled Release 78*, 259–266.

(2) Thomas, M., and Klibanov, A. M. (2003) Non-viral gene therapy: polycation-mediated DNA delivery. *Appl. Microbiol. Biotechnol. 62*, 27–34.

(3) Park, T. G., Jeong, J. H., and Kim, S. W. (2006) Current status of polymeric gene delivery systems. *Adv. Drug Delivery Rev. 58*, 467–486.

(4) Verbaan, F. J., Bos, G. W., Snel, C., Oussoren, C., Woodle, M. C., Hennink, W. E., and Storm, G. (2004) A comparative study of different cationic transfection agents for in vivo gene delivery after intravenous administration. *J. Drug Delivery Sci. Technol. 14*, 1–7.

(5) Gianasi, E., Wasil, M., Evagorou, E. G., Keddle, A., Wilson, G., and Duncan, R. (1999) HPMA copolymer platinates as novel antitumour agents: in vitro properties, pharmacokinetics and antitumour activity in vivo. *Eur. J. Cancer 35*, 994–1002.

(6) Nori, A., Jensen, K. D., Tijerina, M., Kova, P. K., and Kopecek, J. (2003) Tat-conjugated synthetic macromolecules facilitate cytoplasmic drug delivery to human ovarian carcinoma cells. *Bioconjugate Chem. 14*, 44–50.

(7) Yuan, F., Chen, F., Xiang, Q. Y., Qin, X., Zhang, Z. R., and Huang, Y. (2008) Synthesis and characterization of HPMA copolymer-5-FU conjugates. *Chin. Chem. Lett. 19*, 137–140.

(8) Kulkarni, S., Schilli, C., Grin, B., Muller, A. H. E., Hoffman, A. S., and Stayton, P. S. (2006) Controlling the aggregation of conjugates of streptavidin with smart block copolymers prepared via the RAFT copolymerization technique. *Biomacromolecules 7*, 2736–2741.

(9) Yanjarappa, M. J., Gujraty, K. V., Joshi, A., Saraph, A., and Kane, R. S. (2006) Synthesis of copolymers containing an active ester of methacrylic acid by RAFT: Controlled molecular weight scaffolds for biofunctionalization. *Biomacromolecules 7*, 1665–1670.

(10) Nicolas, J., Mantovani, G., and Haddleton, D. M. (2007) Living radical polymerization as a tool for the synthesis of polymer-protein/peptide bioconjugates. *Macromol. Rapid Commun. 28*, 1083–1111.

(11) Boyer, C., Bulmus, V., Liu, J., Davis, T. P., Stenzel, M. H., and Barner-Kowollik, C. (2007) Well-defined protein-polymer conjugates via in situ RAFT polymerization. *J. Am. Chem. Soc. 129*, 7145–7154.

(12) Boyer, C., Bulmus, V., Davis, T. P., Ladmiral, V., Liu, J., and Perrier, S. (2009) Bioapplications of RAFT polymerization. *Chem. Rev. 109*, 5402–5436.

(13) Deng, Z., Bouchekif, H., Babooram, K., Housni, A., Choytun, N., and Narain, R. (2008) Facile synthesis of controlled-structure primary amine-based methacrylamide polymers via the reversible addition-fragmentation chain transfer process. *J. Polym. Sci., Polym. Chem. 46*, 4984–4996.

(14) York, A. W., Zhang, Y., Holley, A. C., Guo, Y., Huang, F., and McCormick, C. L. (2009) Facile synthesis of multivalent folate-block copolymer conjugates via aqueous RAFT polymerization: targeted delivery of siRNA and subsequent gene suppression. *Biomacromolecules 10*, 936–943.

(15) Scales, C. W., Vasilieva, Y. A., Convertine, A. J., Lowe, A. B., and McCormick, C. L. (2005) Direct, controlled synthesis of the nonimmunogenic, hydrophilic polymer, poly (N-(2-hydroxypropyl) methacrylamide) via RAFT in aqueous media. *Biomacromolecules 6*, 1846–1850.

(16) Cho, K. C., Kim, S. H., Jeong, J. H., and Park, T. G. (2005) Folate receptor-mediated gene delivery using folate-poly(ethylene glycol)-poly(L-lysine) conjugate. *Macromol. Biosci. 5*, 512–519.

(17) Schaffer, D. V., Neve, R. L., and Lauffenburger, D. A. (1997) Use of the green fluorescent protein as a quantitative reporter of epidermal growth factor receptor-mediated gene delivery. *Tissue Eng. 3*, 53–63.

(18) Kircheis, R., Schuller, S., Brunner, S., Ogris, M., Heider, K. H., Zauner, W., and Wagner, E. (1999) Polycation-based DNA complexes for tumor-targeted gene delivery in vivo. *J. Gene Med. 1*, 111–120.

(19) Kircheis, R., Kichler, A., Wallner, G., Kursa, M., Ogris, M., Felzmann, T., Buchberger, M., and Wagner, E. (1997) Coupling of cell-binding ligands to polyethylenimine for targeted gene delivery. *Gene Ther. 4*, 409–418.

(20) Stockert, R. J. (1995) The asialoglycoprotein receptor: relationships between structure, function and expression. *Physiol. Rev. 75*, 591–609.

(21) Bandyopadhyay, P., Ma, X., Linehan-Stieers, C., Kren, B. T., and Steer, C. J. (1999) Nucleotide exchange in genomic DNA of rat hepatocytes using RNA/DNA oligonucleotides. Targeted delivery of liposomes and polyethylenimine to the asialoglycoprotein receptor. *J. Biol. Chem. 274*, 10163–10172.

(22) Choi, Y. H., Liu, F., Choi, J. S., Kim, S. W., and Park, J. S. (1999) Characterization of a targeted gene carrier, lactose-polyethylene glycol-grafted poly-l-lysine and its complex with plasmid DNA. *Hum. Gene Ther. 10*, 2657–2665.

(23) Bettinger, T., Remy, J. S., and Erbacher, P. (1999) Size reduction of galactosylated PEI/DNA complexes improves lectin-mediated gene transfer into hepatocytes. *Bioconjugate Chem. 10*, 558–561.

(24) Niidome, T., Urakawa, M., Sato, H., Takahara, Y., Anai, T., Hatakayama, T., Wada, A., Hirayama, T., and Aoyagi, H. (2000) Gene transfer into hepatoma cells mediated by galactose-modified a-helical peptides. *Biomaterials 21*, 1811–1819.

(25) Hashida, M., Takemura, S., Nishikawa, M., and Takakura, Y. (1998) Targeted delivery of plasmid DNA complexed with galactosylated poly (l-lysine). *J. Controlled Release 53*, 301–310.

(26) Cook, S. E., Park, I. K., Kim, E. M., Jeong, H. J., Park, T. G., Choi, Y. J., Akaike, T., and Cho, C. S. (2005) Galactosylated polyethylenimine-graft-poly(vinyl pyrrolidone) as a hepatocyte-targeting gene carrier. *J. Controlled Release 105*, 151–163.

(27) Zanta, M. A., Boussif, O., Adib, A., and Behr, J. P. (1997) In vitro gene delivery to hepatocytes with galactosylated polyethylenimine. *Bioconjugate Chem. 8*, 839–844.

(28) Funhoff, A. M., Nostrum, C. F., Lok, M. C., Fretz, M. M., Crommelin, D. J. A., and Hennink, W. E. (2004) Poly (3-guanidinepropyl methacrylate): a novel cationic polymer for gene delivery. *Bioconjugate Chem. 15*, 1212–1220.

(29) Kim, T., Ou, M., Lee, M., and Kim, S. W. (2009) Arginine-grafted bioreducible poly (disulfide amine) for gene delivery systems. *Biomaterials 30*, 658–664.

(30) Brooks, H., Lebleu, B., and Vive's, E. (2005) Tat peptide-mediated cellular delivery: back to basics. *Adv. Drug Delivery Rev. 57*, 559–577.

(31) Deshayes, S., Morris, M. C., Divita, G., and Heitz, F. (2006) Interactions of amphipathic carrier peptides with membrane components in relation with their ability to deliver therapeutics. *J. Pept. Sci. 12*, 758–765.

(32) Tung, C. H., and Weissleder, R. (2003) Arginine containing peptides as delivery vectors. *Adv. Drug Delivery Rev. 55*, 281–294.

(33) Choi, S. W., Sato, Y., Akaike, T., and Maruyama, A. (2004) Preparation of cationic comb-type copolymer having guanidino moieties and its interaction with DNAs. *J. Biomater. Sci. Polym. Ed. 15*, 1099–1110.

(34) Gao, Y., Xu, Z., Chen, S., Gu, W., Chen, L., and Li, Y. (2008) Arginine-chitosan /DNA self-assemble nanoparticles for gene delivery: In vitro characteristics and transfection efficiency. *Int. J. Pharm. 359*, 241–246.

(35) Tzivelekaa, L. A., Psarrab, A. M., Tsiourvasa, D., and Paleosa, C. M. (2007) Synthesis and characterization of guanidinylated poly-(propylene imine) dendrimers as gene transfection agents. *J. Controlled Release 117*, 137–146.

(36) Choi, J. S., Nam, K., Park, J. Y., Kim, J. B., Lee, J. K., and Park, J. S. (2004) Enhanced transfection efficiency of PAMAM dendrimer by surface modification with L-arginine. *J. Controlled Release 99*, 445–456.

(37) Koo, H., Kang, H., and Lee, Y. (2009) Analysis of the relationship between the molecular weight and transfection efficiency/cytotoxicity of Poly-L-arginine on a mammalian cell line. *Bull. Korean Chem. Soc. 30*, 927–930.

(38) Crrotto, E., and Aros, R. (1993) Quantitative determination of chitosan and the percentage of free amino groups. *Anal. Biochem. 211*, 240–241.

(39) Masuko, T., Minami, A., Iwasaki, N., Majima, T., Nishimura, S. I., and Lee, Y. C. (2005) Carbohydrate analysis by a phenol−sulfuric acid method in microplate format. *Anal. Biochem. 339*, 69–72.

(40) Pack, D. W., Hoffman, A. S., Pun, S., and Stayton, P. S. (2005) Design and development of polymers for gene delivery. *Nat. Rev. Drug Discovery 4*, 581–593.

(41) Pissuwan, D., Boyer, C., Gunasekaran, K., Davis, T. P., and Bulmus, V. (2010) In vitro cytotoxicity of RAFT-Polymers. *Biomacromolecules 11*, 412–420.

Bioconjugate Chemistry

ARTICLE

pubs.acs.org/bc

Solubilization of Native Integral Membrane Proteins in Aqueous Buffer by Noncovalent Chelation with Monomethoxy Poly(ethylene glycol) (mPEG) Polymers

Thamara K. Janaratne,[†] Linda Okach,[§,‡] Ansgar Brock,[‡] and Scott A. Lesley[*,†,§,‡]

[†]The Joint Center for Structural Genomics and The Scripps Research Institute, Department of Molecular Biology, La Jolla, California 92037, United States

[§]The Joint Center for Structural Genomics, San Diego, California 92121, United States

[‡]The Genomics Institute of the Novartis Research Foundation, San Diego, California 92121, United States

Supporting Information

ABSTRACT: Highly hydrophobic integral membrane proteins (IMPs)are typically purified in excess detergent media, often resulting in rapid inactivation and denaturation of the protein. One promising approach to solve this problem is to couple hydrophilic polymers, such as monomethoxypolyethylene glycol (mPEG) to IMPs under mild conditions in place of detergents. However, the broad application of this approach is hampered by poor reaction efficiencies, low tolerance of detergent stabilized membrane proteins to reaction conditions, and a lack of proper site-specific reversible approaches. Here, we have developed a straightforward, efficient, and mild approach to site-specific noncovalent binding of long-chain polymers to recombinant IMPs. This method uses the hexa-histidine tag (His-Tag) often used for purification of recombinant proteins as an attachment site for mPEGs. Solubility studies performed using five different IMPs confirmed that all tested mPEG-bound IMPs were completely soluble and stable in detergent free aqueous buffer compared to their precipitated native proteins under the identical circumstances. Activity assays and circular dichroism (CD) spectroscopy confirmed the structural integrity of modified IMPs.

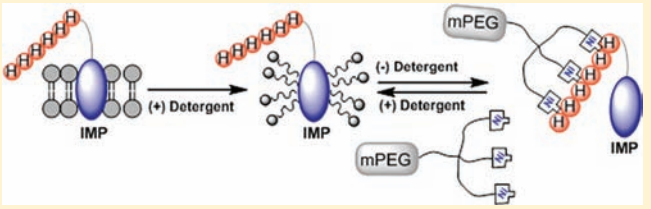

INTRODUCTION

Integral membrane proteins (IMPs) comprise about 25−30% of all encoded proteins in genomes.[1] However, *in vitro* structure−function studies of IMPs are technically challenging and require extracting the protein from the lipid membrane and solubilizing with detergents.[2−4] These detergents are dissociating amphiphiles and tend to disrupt the protein−protein, protein−lipid, and lipid−lipid interactions that stabilize the three-dimensional structure of IMPs leading to denaturation and precipitation of protein.[5−7] The poor stability and denaturing effects of detergent solubilized IMPs are the main technical barriers limiting their study.

Considerable efforts have been devoted to developing methods for membrane protein stabilization. One preferred approach is substituting detergents with amphiphilic polymers named amphipols.[8−10] Amphipols are polyacrylamide-based surfactants that bind noncovalently to the transmembrane surfaces of proteins in a quasi-irreversible manner. IMPs have been stabilized in aqueous buffers using zwitterionic, anionic, or neutral amphipols. Although, in some cases addition of such amphipols has been observed to destabilize the protein.[9,11]

Amphipathic α-helical peptides known as peptitergents were also being explored to solubilize IMPs in detergent free buffer. They are predicted to shield the hydrophobic regions of the protein in a rigid, well-ordered, parallel α-helical arrangement. Thus far, this method has had limited success. In previous studies, the method was limited to partially solubilizing only two of the three tested proteins.[12,13] Other studies have shown that covalent modification of IMPs with PEG or PEGylation can stabilize IMPs in an aqueous environment.[14−16] However, covalent PEGylation of IMPs requires significant optimization for each unique protein and can be difficult to localize to a unique site. For example, depending on the PEGylation method, type of protein, site of modification, PEGylated MscL[14] maintained the native structure in aqueous buffer, whereas bacteriorhodopsin[15] and porin[16] resulted in partially denatured water-soluble proteins. Performing covalent modifications to fragile IMPs embedded in detergent micelles requires harsh conditions including low pH, higher temperatures, longer reaction times, and requirement of organic reagents leading to protein denaturation.

Ni(II) doped tris-NTA chelation to His-Tag protein has been successfully applied for many different applications including fluorescence labeling,[17] biotinylation,[18] and protein immobilization on solid support.[19] These studies also have established that

Received: January 25, 2011
Revised: June 25, 2011
Published: July 10, 2011

ACS Publications © 2011 American Chemical Society

the stability of tris-NTA chelation to His-Tag protein is ~4-fold stronger than mono-NTA chelation and the resulting derivatized protein solution can be diluted to pM concentration without dissociating the chelation bond.[20]

Herein, we report the reversible attachment of mPEG polymers through nickel (Ni^{2+})-chelated NTA (nitrilotriacetic acid) to solubilize and stabilize recombinant IMPs in their native form either in low-detergent or aqueous buffer solutions. The generality of the noncovalent method was tested using five IMPs of different size, function, and structure. Reactive mPEG-$NTA_3(Ni^{2+})$ polymers of 5 kDa and 10 kDa (average molecular weight) bearing three NTA units (tris-NTA) were synthesized and noncovalently chelated to recombinant IMPs via their His-Tag. We compare our method with the PMAL-12 [Poly(maleic anhydride-alt-1-tetradecene) substituted with 3-(dimethylamino)propylamine] amphipol-stabilized approach.[8] Given the widespread use of His-Tags for Ni-NTA mediated protein purification and the fact that tags are typically located on termini of recombinant proteins where they minimally effect protein structure and function, our tris-NTA(Ni^{2+})-mediated noncovalent polymer chelation approach provides a straightforward means to chemically modify IMPs for the solubilization and stabilization of delicate IMPs in aqueous environment without the need for excessive detergents.

EXPERIMENTAL PROCEDURE

Proton (^1H) and carbon (^{13}C) NMR spectra were recorded on a Bruker 300 MHz NMR spectrometer. Unless otherwise stated, spectra were acquired at 25 °C in deuterated chloroform ($CDCl_3$).

Pyruvate kinase (PK), lactate dehydrogenase (LDH), phosphoenol pyruvate (PEP), nicotinamide adenine dinucleotide (NADH), 4-(*N*,*N*-dimethylamino)pyridine (DMAP), *N*-(3-dimethylaminopropyl)-*N*′-ethylcarbodiimide (EDAC·HCl), 2-(trimethylsilyl)ethanol (TMSE), sodium sulfate (Na_2SO_4), trifluoroacetic acid (TFA), magnesium acetate ($Mg(OAc)_2$), and 10% palladium on charcoal (10% Pd/C) were purchased from Sigma-Aldrich; 1-palmitoyl-2-oleoyl-*sn*-glycero-3-phospho-(1′-sn-glycerol) (sodium salt) [POPG] from Avanti Polar Lipids; *n*-decyl-β-D-maltoside (DM), 5-cyclohexyl-1-pentyl-β-D-maltoside (CY-5), 6-cyclohexyl-1-pentyl-β-D-maltoside (CY-6), and *n*-octyl-β-D-glucopyranoside (OG), PMAL-12 [poly(maleic anhydride-*alt*-1-tetradecene) substituted with 3-(dimethylamino)propylamine] were from Anatrace; dichloromethane (CH_2Cl_2), hexane, ethylacetate (EtOAc), diethyl ether, and chloroform were from Fisher and used without further purification.

Lys-NTA_3TMSE_9 (compound **1**),[21] mPEG-CH_2-COOH (compound **2**),[22] and dibutyrylglycerol (DBG)[23] were synthesized according to the literature procedure.

Cloning and Expression. *Escherichia coli* diacylglycerol kinase (DGK) was cloned to pSpeedET vector as described previously.[24,25] Expression clones for *Thermotoga maritima* IMPs, TM0561, TM0407, TM1122, and TM0307 were obtained from The Joint Center for Structural Genomic (JCSG) clone collection.[26] Each vector encodes a hexa-histidine (His-Tag) purification tag at the N-terminus of the full-length recombinant protein. Protein expression of all the selected clones was performed using *E. coli* HK100 cells in modified terrific broth media (24 g of yeast extract, 16 g of tryptone, 10 g of bacto-casamino acid, 100 mM Tris-Cl, pH 8, and 2% glycerol per liter culture containing 100 μg/mL ampicillin or 50 μg/mL kanamycin). After approximately three hours at 37 °C, protein expression was induced with 0.02% L-arabinose for an additional four hours. Cells were harvested by centrifugation at 3000*g* for 15 min.

Purification of Integral Membrane Proteins. Cells were resuspended in 50 mL of lysis buffer (50 mM Tris-Cl, pH 7.9, 150 mM NaCl containing one protease inhibitor cocktail [Roche] minitablet per liter of original culture) and then lysed at 4 °C by passage through a M110S Microfluidizer (Microfluidic Corporation, Newtown). The cell lysate was centrifuged at 20 000*g* for 30 min. The clarified supernatant was equilibrated with 0.5% (w/v) detergent (DDM) for 2−3 h at room temperature prior to passage through a Ni-NTA (Qiagen) column (10 mL). The column was washed with 50−100 mL of wash buffer (25 mM sodium phosphate, pH 7.9, 150 mM NaCl, 25 mM imidazole) containing 2× detergent (CY-6/CY-5) CMC. The protein was then eluted with the 10−15 mL elution buffer (25 mM sodium phosphate, pH 7.9, 100 mM NaCl, 400 mM imidazole) containing 1% (w/v) of selected detergents. The protein in elution buffer was concentrated by ultrafiltration using 30 kDa (Millipore) concentrator and the buffer was exchanged to Tris-Cl, pH 7.9, and 150 mM NaCl buffer using PD-10 (GE Healthcare) columns.

Synthesis of Compound 3: mPEG(10K)-NTA_3TMSE_9 (average molecular weight 10 kDa). Compound **2** (1.3 g; 0.13 mmoL; MW ≈ 10 000 Da)[22] and DMAP (28 mg; 0.18 mmol) were dissolved in 200 mL of dry CH_2Cl_2 under argon atmosphere at 0 °C. EDAC·HCl (70 mg; 0.37 mmol) was added under argon and the resulting mixture was maintained at 0 °C for 0.5 h. Then, the compound **1**[21] (0.34 g; 0.18 mmol) solubilized in 10 mL of dry CH_2Cl_2 was added and the ensuing mixture was continuously stirred at 0 °C for an additional 1 h prior to stirring at room temperature for 3 days. Following the reaction, the light yellow organic layer was washed twice with distilled water (400 mL), dried (Na_2SO_4), and concentrated to 20 mL under reduced pressure. The product was precipitated with excess diethyl ether (200 mL) and the precipitate was filtered and washed thoroughly with excess diethyl ether and dried under vacuum overnight to yield compound **3** (1.4 g, 90%). ^1H NMR and negative ninhydrin staining of thin layer chromatography (TLC) analysis of compound **3** confirmed the final product. ^1H NMR 4.10−4.23 (18H, m, −O−CH_2−), 3.10−3.30 (19H, m, -OCH_3 of mPEG, −NH−CH_2−, 4× -NCH−CO-, 2× -NCH_2−CO-NH-, and 3× −CO-NH−CH_2−), 1.21−1.89 (24H, m, 4× -NCH_2−$(CH_2)_3$-), 0.84−1.05 (18H, m, 9× −CH_2Si-), 0.02 (81H, m, 27× -$Si(CH_3)_3$).

Synthesis of Compound 4: mPE(10K)-NTA_3, Average Molecular Weight 10 kDa. Compound **3** (1.5 g, 0.11 mmol) was dissolved in 5 mL of dry CH_2Cl_2. Trifluoroacetic acid (TFA; 5 mL) was added dropwise to the reaction mixture at room temperature. After stirring the reaction at room temperature for 4 h, the solvent was removed under vacuum and the product was precipitated with excess diethyl ether. The precipitate was filtered, washed thoroughly with ether, and dried under vacuum to yield compound **4** (1.2 g, 90%) as a yellowish solid, which gave a negative staining with ninhydrin test. Structure of compound **4** was confirmed by ^1H NMR and MALDI MS. ^1H NMR (D_2O) 3.28 (3H, s, -OCH_3 of mPEG), 1.1−2.0 (24H, m, -$NHCH_2$−$(CH_2)_3$- of tris-NTA), 3.15−3.25 (12H, m, -NCH_2−CO-O−); MALDI: Found, 11225 Da; required 11118 Da (MALDI MS measured against the mPEG(10K)-CH_2COOH starting material: 10230 Da).

Synthesis of Compound 5 (Average Molecular Weight, 10 kDa): mPEG(10K)-$NTA_3(Ni^{2+})_3$. Compound **4** (0.2 g, 0.017 mmol) in 1 mL of 20 mM Tris-Cl, pH 7.5, 150 mM NaCl buffer

Scheme 1. Synthesis of mPEG-NTA$_3$(Ni^{2+})$_3$ (Average Molecular Weight = 5000 or 10 000) Polymers

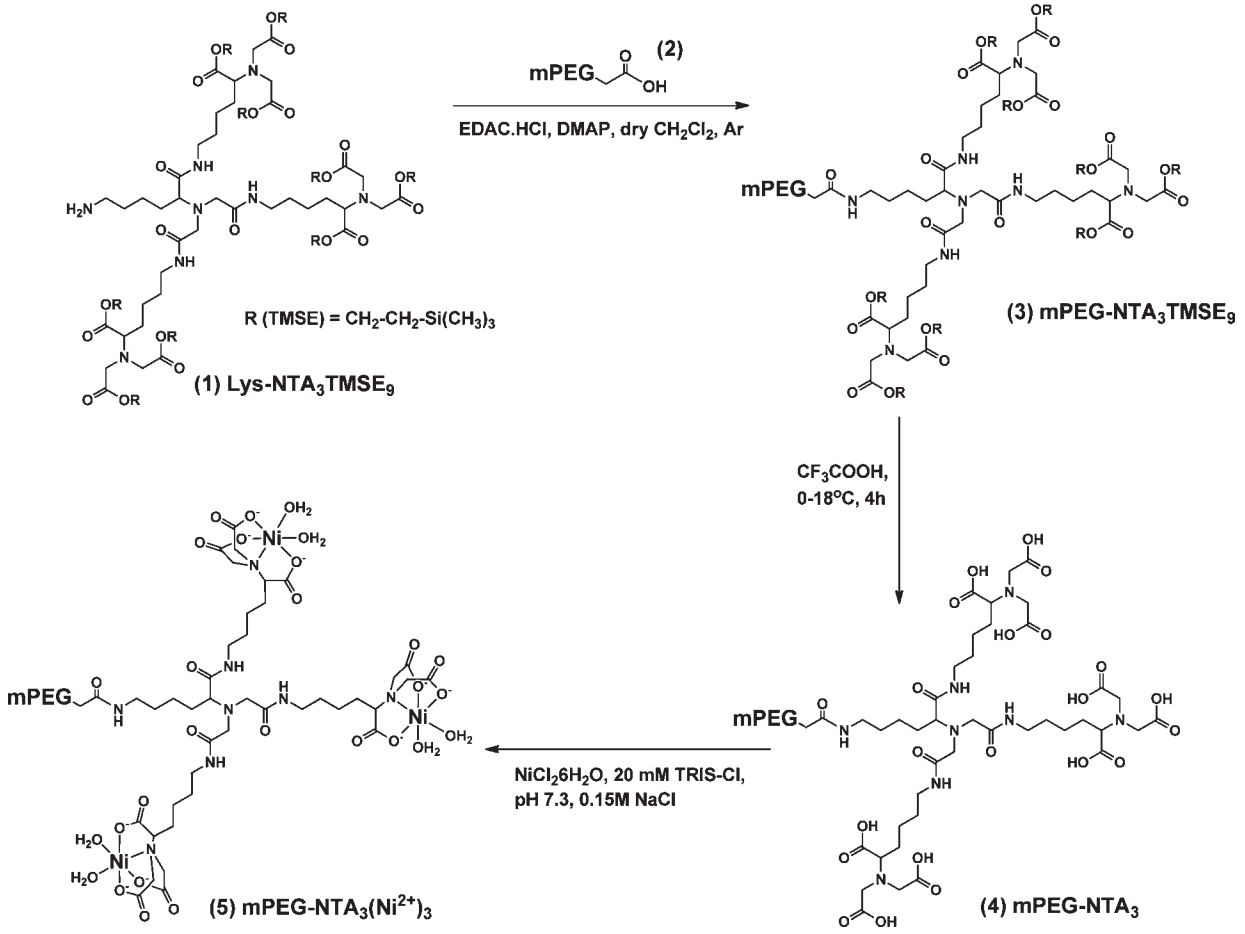

was stirred with 48 mg of $NiCl_2$ $6H_2O$ (0.1 mmol) at room temperature. After stirring for 30 min, the excess $NiCl_2$ was removed by dialysis to yield the compound **5**. The successive Ni(II) chelated compound **5** in Tris buffer was subsequently reacted with recombinant IMPs.

Synthesis of Compound 5 (Average Molecular Weight, 5 kDa): mPEG(5K)NTA$_3$(Ni^{2+})$_3$. mPEG(5K)NTA$_3$(Ni^{2+})$_3$ was synthesized from mPEG(5K)-CH_2-COOH[22] similar to compounds **3** to **5** (10 kDa) and confirmed by MALDI MS spectrometry. mPE(5K)-NTA$_3$: MALDI MS: Found, 5760; required: 5988 (MALDI MS measured against mPEG(5K)-CH_2COOH: 5100).

Noncovalent Coordination of mPEG Polymers to Recombinant IMPs. One equivalent of purified protein (between 10 and 100 μM concentration) in 20 mM Tris-Cl, pH 7.5, 150 mM NaCl was mixed with 1−1.1 equiv of mPEG-NTA$_3$(Ni^{2+})$_3$ [5 or 10 kDa][5] at 4 °C for 15 min. After mixing, detergent was completely removed from the protein solution by dialysis. The final detergent concentration in solution was measured colorimetrically by following the literature procedure.[27]

Enzyme Activity Assays. Activity of DGK (*E. coli* diacylglycerol kinase) was assayed following published procedures.[23,28] The assay mixture contained 3 mM Na_3ATP, 15 mM $Mg(OAc)_2$, 0.25 mM NADH, 1 mM PEP, 20 units/mL PK, 20 units/mL LDH, 10 mM DBG (substrate), and 0.42 mM POPG (lipid activator) in 0.8 mL of buffer (75 mM PIPES pH 6.9, 0.1 mM EGTA, 0.1 mM EDTA, 50 mM LiCl). The reaction was initiated by adding 0.04−0.1 μM DGK or derivatized DGK to the assay mixture at 30 °C. Activity of mPEG-bound or wild-type DGK was calculated in units/mg from the absorbance (340 nm) vs time plots as described.[23,28]

Circular Dichroism Spectroscopy. Circular dichroism spectra of DGK derivatives were recorded using a JASCO J-720 circular dichroism spectrophotometer in 1 mm optical path length quartz cuvettes between 260 and 190 at 0.1 nm intervals. Spectra were recorded in 20 μM protein concentration in 20 mM Tris-Cl, pH 7.9, and 100 mM NaCl buffer.

RESULTS

Noncovalent Coordination of IMPs with mPEG-NTA$_3$(Ni^{2+})$_3$. Tris-NTA(Ni^{2+})-activated mPEG polymers, mPEG(5K)-NTA$_3$(Ni^{2+})$_3$, and mPEG(10K)-NTA$_3$(Ni^{2+})$_3$ [5 or 10 kDa] employed in this study were synthesized from mPEG−OH as described in Methods (Scheme 1). The recombinant IMPs were purified in excess detergents and noncovalently bound to mPEG-NTA$_3$(Ni^{2+})$_3$ through N-terminal His-Tag chelation (4 °C, 10 min). All the IMPs tested in Table 1 were chelated with mPEG-(10K)NTA$_3$(Ni^{2+})$_3$ polymer. Protein concentration measurements at 280 nm showed that all the mPEG-bound IMPs in detergents have extended shelf lives as compared to the native proteins in detergents alone (Table 1). Polymer (mPEG)

Table 1. Comparison of mPEG-Bound IMPs Stability Vs Their Detergent Counterparts[a]

IMPs	detergent	TM[b]	MW (kDa)	stability[c]	stability[d]	stability[e]
TM0561	Cymal-6	2	43	-	++	++
DGK	Cymal-5	3	15	+	++	++
TM0407	Cymal-5	4	20	-	++	++
TM1122	OG	6	32	-	++	++
TM0317	Cymal-5	7	81	-	++	++

[a] − protein started precipitating in less than two weeks; + protein started precipitating after two weeks; ++ protein didn't precipitate after two months. [b] Number of transmembrane helices (TM) were determined using http://www.cbs.dtu.dk/services/TMHMM/ server. [c] Stability of IMPs in detergent. [d] Stability of mPEG(10K)$NTA_3(Ni^{2+})_3$ chelated IMPs in detergent. [e] Stability of mPEG(10K)$NTA_3(Ni^{2+})_3$ chelated IMPs in aqueous buffer; MW = Molecular weight.

chelated IMPs maintained solubility under detergent depleted conditions as well as in aqueous buffer (20 mM Tris-Cl, pH 7.5, 150 mM NaCl) (Table 1). During dialysis, the detergent distribution was followed by absorbance at 490 nm.[27] The amount of detergent present in the 10 kDa mPEG polymer bound IMPs in aqueous buffer was less than 10 molecules per IMP after dialysis. Derivatized IMPs with the smaller size mPEG-(5K)$NTA_3(Ni^{2+})_3$ with N-terminal His-Tag precipitated partially or fully in detergent free buffer. Depending on the protein, mPEG-(5K)$NTA_3(Ni^{2+})_3$-bound-IMPs required retaining 7−15% of the native protein detergent concentration to sustain solubility. As a negative control, derivatization of IMPs with non-Ni(II)-chelated mPEG(10K)NTA_3 was tested. In the absence of chelated Ni(II), all these tested proteins precipitated out upon detergent removal demonstrating the contribution of Ni(II)-mediated coordination of mPEG for the His-Tag protein stability.

Activity Assays. To investigate the influence of noncovalent tris-NTA(Ni^{2+})-mediated polymer binding toward maintaining 3D structural integrity, we performed activity assays using *E. coli* DGK as a model IMP.[29−32] DGK was purified in CY-5 (CMC = 2−5 mM) and the kinase activity of the protein was measured in the presence of phosphatidylglycerol (PG) lipid activator. PG is the major anionic lipid component of the *E. coli* lipid membrane constituting 15−20% by weight compared to 2−5% of cardiolipin.[33] Kinetic activity of DGK derivatives was studied by coupling their production of MgADP to NADH oxidation measured at 340 nm.[28]

Table 2 compares the kinase activity of different mPEG-chelated DGK derivatives during phase transitions from detergent to aqueous phase under identical conditions.[23,28] DGK-mPEG(5K)$NTA_3(Ni^{2+})_3$ sustains the original activity at its lowest soluble detergent concentration (15% of the original native DGK detergent concentration) confirming that protein activity, which is used as a symbol of structural integrity, is unaffected by the change from detergent media to hydrophilic polymer (Table 2, row 5). Enzyme activity of native DGK was not measured under identical conditions, as it remained predominantly in precipitated form.

Substitution of mPEG(5K)$NTA_3(Ni^{2+})_3$ with the longer chain length mPEG(10K)$NTA_3(Ni^{2+})_3$ allowed completed removal of detergents. Chelation efficiency did not change in comparison to mPEG(5K)$NTA_3(Ni^{2+})_3$. However, the increasing mPEG polymer chain length yielded reduced enzyme activity. DGK-mPEG(10K)$NTA_3(Ni^{2+})_3$ could be solubilized in detergent free buffer with 32% of residual activity of the DGK native protein (Table 2, row 7).

Table 2. Activity of DGK Derivatives in Different CY-5/DGK Ratio

DGK derivative	CY-5/DGK	% of CY-5	*A* (units/mg)	% *A*
[a]DGK-CY-5	220	100%	108 ± 1.5	100%
[b]DGK-PMAL	14	6.3%	86 ± 0.6	80%
[c]DGK-mPEG(5K)$NTA_3(Ni^{2+})_3$	220	100%	108 ± 0.6	100%
[c]DGK-mPEG(5K)$NTA_3(Ni^{2+})_3$	32	14.5%	96 ± 0.6	90%
[c]DGK-mPEG(10K)$NTA_3(Ni^{2+})_3$	220	100%	97 ± 1	90%
[c]DGK-mPEG(10K)$NTA_3(Ni^{2+})_3$	<7	<3.1%	35 ± 1	32%
[d]DGK-CY-5	225	102%	105 ± 2.5	97%

[a] Native DGK protein in the presence of minimum detergent needed to stabilize the protein in aqueous buffer. We normalize the native protein's detergent/protein ratio, 220, and the activity (A) as 100% for comparison. [b] Kinase activity of amphipol-stabilized DGK in trace detergent. [c] Kinase activity of mPEG-bound DGK proteins was shown during different detergent/protein ratio. [d] Kinase activity of DGK after reincorporating back to detergents from mPEG(10K)$NTA_3(Ni^{2+})_3$ media; *A* = Activity in units/mg.

Tris-NTA(Ni^{2+}) mediated chelation of DGK-mPEG-(10K)$NTA_3(Ni^{2+})_3$ was reversed using imidazole and EDTA and introduced the mPEG free protein back into the detergent phase (see Supporting Information). Activity measured in re-introduced DGK in detergents yielded the original activity (Table 2, row 8). ANSEC analysis of mPEG chelated DGK derivatives suggests that the reduced activity with increasing mPEG chain length can be attributed to the formation of large discrete structures in aqueous media which reverse back to the original protein size distribution upon removal of the mPEG (Figure S1 in Supporting Information). Expansion of the hydrodynamic volume is a general result of protein PEGylation and is widely employed to improve serum half-life of protein-based therapeutics.[34,35] Protein unfolding and aggregation as a cause of the observed increase in hydrodynamic volume can be excluded based on the enzyme activity data and the CD spectroscopy data discussed below.

CD Spectroscopy. The secondary structure of mPEG-bound and unbound DGK derivatives in low detergent concentration or aqueous buffer was analyzed by far-UV CD spectroscopy to provide further evidence of structural integrity of mPEG chelated proteins. As shown in Figure 1, mPEG-bound DGK derivatives have very similar CD spectral patterns to those of native DGK than DGK-PMAL as reflected by the characteristic CD bands around 195, 209, and 223 nm.

DISCUSSION

The noncovalent mPEG-chelating approach presented here provides a successful method to couple mPEGs site-specifically to IMPs in excess detergent media. It has been shown in previous work that the harsh reaction conditions employed in covalent derivatization of IMPs with mPEG polymers (5 kDa) resulted in partially denatured proteins.[15,16] Chelation is an extremely mild, reversible, and efficient coupling method for rapid recovery of active IMPs from detergent micelles. PEGylation of proteins is a well established technique which has many advantages including improved protein solubility, stability, and serum half-life.[36−38] We have demonstrated application of Tris-NTA(Ni^{2+}) mediated mPEG chelation to stabilize active recombinant IMPs in low-detergent or detergent-free environment.

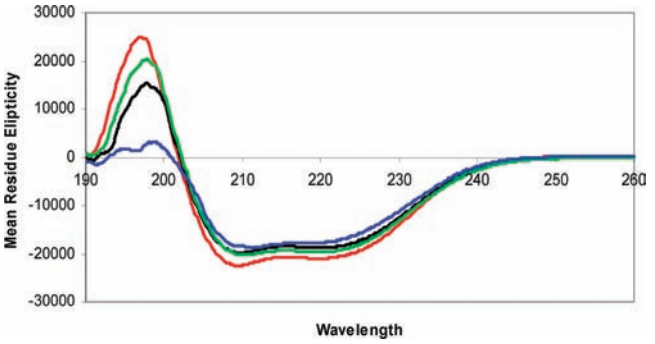

Figure 1. Far-UV CD spectra (selected DGK derivatives in Table 2) of DGK-WT (red; in 100% detergent; Table 2, row 2), DGK-PMAL (blue; in 6.3% residual detergent; Table 2, row 3), DGK-mPEG(5K)$NTA_3(Ni^{2+})_3$ (green; in 14.5% residual detergent; Table 2, row 5), and DGK-mPEG(10K)$NTA_3(Ni^{2+})_3$ (black; in <3.1% residual detergent; Table 2, row 7) in 20 mM Tris-Cl, pH 7.9 and 100 mM NaCl buffer.

Reactive mPEG-$NTA_3(Ni^{2+})_3$ derivatives of different chain lengths were synthesized and confirmed by NMR and MALDI MS. All IMPs tested were successfully chelated with both 5 kDa and 10 kDa mPEGs under mild conditions. It has been shown in this study that approximately 85−90% of the detergent required to stabilize the native proteins could be removed using mPEG(5K)$NTA_3(Ni^{2+})_3$ chelation and practically 100% using mPEG(10K)$NTA_3(Ni^{2+})_3$. Therefore, our current noncovalent coupling method has been able to produce stable mPEG-bound IMPs to significantly improve stability and solubility in aqueous buffer solutions over their detergent solubilized counterparts.

All mPEG-bound DGK derivatives tested were found to be enzymatically active. Observed activity of the protein varied with length of the chelated mPEG chain. Although the detergents could not be removed completely from the DGK-mPEG-(5K)$NTA_3(Ni^{2+})_3$, the derivatized DGK retained full activity while amphipol-stabilized DGK (DGK-PMAL) was less active. Chelation of the protein with a longer 10 kDa mPEG chain supported the solubility of protein in detergent free buffer, but the activity was reduced. DGK-mPEG(10K)$NTA_3(Ni^{2+})_3$ retained 32% (Table 2, row 7) of native DGK protein's activity and regained original enzyme activity upon introduction into detergent media (Table 2, row 8). Further, the similar CD spectra of all DGK derivatives suggest that the backbone configuration of the protein has not changed following the post-translational modification. The least enzymatically active DGK-mPEG-(10K)$NTA_3(Ni^{2+})_3$ yielded a much more similar CD spectrum to that of the native protein than DGK-PMAL (Figure 1, blue spectrum). This leads to the conclusion that the observed activity loss upon increasing mPEG chain length is not the result of structural changes within DGK. Activity loss as a result of PEGylation is well documented in the literature.[34,35] The ANSEC profile of DGK-mPEG(10K)$NTA_3(Ni^{2+})_3$ in aqueous phase and detergent inclusion supports that DGK-mPEG(10K)$NTA_3(Ni^{2+})_3$ formed larger discrete structures in aqueous media that reversed after reintroduction into detergent media (Supporting Information Figure S1). Therefore, the observed activity reduction is likely due to interference of the enlarged PEG chains with substrate access to the active site.

CONCLUSION

The present work establishes that highly hydrophobic recombinant IMPs can be successfully solubilized and stabilized in low detergent or in aqueous buffer by noncovalently coupling with tris-$NTA(Ni^{2+})$-mediated mPEGs. The reaction is straightforward, efficient, and utilizes a common protein purification tag. The solubility of IMPs can readily be adjusted by varying the size of the mPEG chain. CD spectroscopy and enzyme assay of derivatized DGK confirmed the retention of secondary structure upon chelation with mPEG. This method will be useful for structure−functional studies of IMPs where the use of detergent is deemed problematic. Multiple efforts that encompass crystallization of IMPs in detergent free medium, the attachment of different crystallizable polymers to the IMP backbone, and the introduction of native, detergent free protein into different matrixes (lipid cubic phase, lipid bilayer) for crystallization purposes are currently in progress.

ASSOCIATED CONTENT

Supporting Information. Analytical SEC behavior of DGK in detergent phase and polymer phase, and re-extraction of DGK from DGK-mPEG(10K)$NTA_3(Ni^{2+})_3$ to detergent medium. This material is available free of charge via the Internet at http://pubs.acs.org.

AUTHOR INFORMATION

Corresponding Author

*The Scripps Research Institute, Department of Molecular Biology, SP30-101, 10550 North Torrey Pines Rd, La Jolla, California 92037, USA. e-mail: slesley@scripps.edu. Tel: 858-784-7424. Fax: 858-784-7443.

ACKNOWLEDGMENT

We thank Kurt Wüthrich for access to the CD spectrophotometer, Linda Columbus and David Jones for helpful discussion, Heath Klock for providing us *T. maritima* membrane protein clones and Bernhard Geierstanger and Susan Cellitti for providing materials for covalent PEG coupling experiments. This work was supported by the NIH National Institute of General Medical Sciences, Protein Structure Initiative Grant U54 GM074898.

REFERENCES

(1) Wallin, E., and von Heijne, G. (1998) Genome-wide analysis of integral proteins from eubacterial, archaean, and eukaryotic organisms. *Protein Sci. 7*, 1029–1038.

(2) Hjelmeland, L. M., and Chrambach, A. (1984) Solubilization of functional membrane-bound receptors, in *Receptor Biochemistry and Methodology* (Venter, J. C., and Harrison, L. C., Eds.) pp 35−46, Alan R. Liss, New York.

(3) Seddon, A. M., Curnow, P., and Booth, P. J. (2004) Membrane proteins, lipids and detergents: Not just a soap opera. *Biochim. Biophys. Acta 1666*, 105–117.

(4) Thomas, C. T., and McNamee, M. G. (1990) Purification of membrane proteins. *Methods Enzymol. 182*, 499–520.

(5) Bowie, J. U. (2001) Stabilizing membrane proteins. *Curr. Opin. Struct. Biol. 11*, 397–402.

(6) Gohon, Y., and Popot, J.-L. (2003) Membrane protein-surfactant complexes. *Curr. Opin. Colloid Interface Sci. 8*, 15–22.

(7) Garavito, R. M., and Ferguson-Miller, S. (2001) Detergents as tools in membrane biochemistry. *J. Biol. Chem. 276*, 32403–32406.

(8) Gorzelle, B. M., Hoffman, A. K., Keyes, M. H., Gray, D. N., Ray, D. G., and Sanders, C. R. (2002) Amphipols can support the activity of a membrane enzyme. *J. Am. Chem. Soc. 124*, 11594–11595.

(9) Tribet, C., Audebert, R., and Popot, J.-L. (1996) Amphipols: Polymers that keep membrane proteins soluble in aqueous solutions. *Proc. Natl. Acad. Sci. U. S. A. 93*, 15047–15050.

(10) Popot, J.-L., Berry, E. A., Charvolin, D., Creuzenet, C., Ebel, C., Engelman, D. M., Flötenmeyer, M., Giusti, F., Gohon, Y., Hervé, P., Hong, J. H., Lakey, J. H., Leonard, K., Shuman, H. A., Timmins, P., Warschawski, D. E., Zito, F., Zoonens, M., Pucci, B., and Tribet, C. (2003) Amphipols: polymeric surfactants for membrane biology research. *Cell. Mol. Life Sci. 60*, 1559–1574.

(11) Champeil, P., Menguy, T., Tribet, C., Popot, J.-L., and Maire, M. l. (2000) Interaction of amphipols with sarcoplasmic reticulum Ca2+-ATPase. *J. Biol. Chem. 275*, 18623–18637.

(12) Schafmeister, C. E., Miercke, L. J. W., and Stroud, R. M. (1993) Structure at 2.5 A of a designed peptide that maintains solubility of membrane proteins. *Science 262*, 734–738.

(13) Soomets, U., Kairane, C., Zilmer, M., and Langel, U. (1997) Attempt to solubilize Na+/K+-exchanging ATPase with amphiphilic peptide PD1. *Acta Chem. Scand. 51*, 403–6.

(14) Becker, C. F. W., Strop, P., Bass, R. B., Hansen, K. C., Locher, K. P., Ren, G., Yeager, M., Rees, D. C., and Kochendoerfer, G. G. (2004) Conversion of a mechanosensitive channel protein from a membrane-embedded to a water-soluble form by covalent modification with amphiphiles. *J. Mol. Biol. 343*, 747–758.

(15) Sirokman, G., and Fasman, G. D. (1993) Refolding and proton pumping activity of a polyethylene glycol-bacteriorhodopsin water-soluble conjugate. *Protein Sci. 2*, 1161–1170.

(16) Wei, J., and Fasman, G. D. (1995) A poly(ethylene glycol) water-soluble conjugate of porin: refolding to the native state. *Biochemistry 34*, 6408–6415.

(17) Lata, S., Martynas, G., Tampe', R., and Piehler, J. (2006) Specific and stable fluorescence labeling of histidine-tagged proteins for dissecting multi-protein complex formation. *J. Am. Chem. Soc. 128*, 2365–2375.

(18) Reichel, A., Schaible, D., Furoukh, N. A., Cohen, M., Schreiber, G., and Piehler, J. (2007) Noncovalent, site-specific biotinylation of histidine-tagged proteins. *Anal. Chem. 79*, 8590–8600.

(19) Alonso, J. M., Reichel, A., Piehler, J., and Campo, A. d. (2008) Photopatterned surfaces for site-specific and functional immobilization of proteins. *Langmuir 24*, 448–457.

(20) Lata, S., Reichel, A., Brock, R., Tampe', R., and Piehler, J. (2005) High-affinity adaptors for switchable recognition of histidine-tagged proteins. *J. Am. Chem. Soc. 127*, 10205–10215.

(21) Altin, G. J., Banwell, M. G., Coghlan, P. A., Easton, C. J., Nairn, M. R., and Offermann, D. A. (2006) Synthesis of NTA3-DTDA- A chelator-lipid that promotes stable binding of his-tagged proteins to membranes. *Aust. J. Chem. 59*, 302–306.

(22) Fishman, A., Acton, A., and Lee-Ruff, E. (2004) A simple preparation of PEG-carboxylates by direct oxidation. *Synth. Commun. 34*, 2309–2312.

(23) Czerski, L., and Sanders, C. R. (2000) Functionality of a membrane protein in bicelles. *Anal. Biochem. 284*, 327–333.

(24) Klock, H. E., and Lesley, S. A. (2009) The polymerase incomplete primer extension (PIPE) method applied to high-throughput cloning and site-directed mutagenesis. *Methods Mol. Biol. 498*, 91–103.

(25) Klock, H. E., Koesema, E. J., Knuth, M. W., and Lesley, S. A. (2008) Combining the polymerase incomplete primer extension method for cloning and mutagenesis with microscreening to accelerate structural genomics efforts. *Proteins: Struct., Funct., Bioinformatics 71*, 982–994.

(26) Lesley, S. A., Kuhn, P., Godzik, A., Deacon, A. M., Mathews, I., Kreusch, A., Spraggon, G., Klock, H. E., McMullan, D., Shin, T., Vincent, J., Robb, A., Brinen, L. S., Miller, M. D., McPhillips, T. M., Miller, M. A., Scheibe, D., Canaves, J. M., Guba, C., Jaroszewski, L., Selby, T. L., Elsliger, M.-A., Wooley, J., Taylor, S. S., Hodgson, K. O., Wilson, I. A., Schultz, P. G., and Stevens, R. C. (2002) Structural genomics of the Thermotoga maritima proteome implemented in a high-throughput structure determination pipeline. *Proc. Natl. Acad. Sci. U. S. A. 99*, 11664–11669.

(27) Urbani, A., and Warne, T. (2005) A clorimetric determination for glycosidic and bile salt-based detergents: applications in membrane protein research. *Anal. Biochem. 336*, 117–124.

(28) Badola, P., and Sanders, C. R. (1997) Escherichia coli diacylglycerol kinase Is an evolutionarily optimized membrane enzyme and catalyzes direct phosphoryl transfer. *J. Biol. Chem. 272*, 24176–24182.

(29) Partridge, A. W., Melnyk, R. A., Yang, D., and Bowie, J. U. (2003) A Transmembrane segment mimic derived from Escherichia coli diacylglycerol kinase inhibits protein activity. *J. Biol. Chem. 278*, 22056–22060.

(30) Smith, R. L., O'Toole, J. F., Maguire, M. E., and Sanders, C. R. (1994) Membrane topology of Escherichia coli diacylglycerol kinase. *J. Bacteriol. 176*, 5459–5465.

(31) Vinogradova, O., Badola, P., Czerski, L., Sonnichsen, F. D., and Sanders, C. R. (1997) Escherichia coli diacylglycerol kinase: A case study in the application of solution NMR methods to an integral membrane protein. *Biophys. J. 72*, 2688–2701.

(32) Lau, F. W., Chen, X., and Bowie, J. U. (1999) Active sites of diacylglycerol kinase from Escherichia coli are shared between subunits. *Biochemistry 38*, 5521–5527.

(33) Morein, S., Andersson, A.-S., Rilfors, L., and Lindblom, G. (1996) Wild-type Escherichia coli cells regulate the membrane lipid composition in a window between gel and non-lamellar structures. *J. Biol. Chem. 271*, 6801–6809.

(34) Yang, K., Basu, A., Wang, M., Chintala, R., Hsieh, M., Liu, S., Hua, J., Zhang, Z., Zhou, J., Li, M., Phyu, H., Petti, G., Mendez, M., Janjua, H., Peng, P., Longley, M., Borowski, V., Mehlig, M., and Filpula, D. (2003) Tailoring structure-function and pharmacokinetic properties of single-chain Fv proteins by site-specific PEGylation. *Protein Eng. 16*, 761–770.

(35) Lee, L. S., Conover, C., Shi, C., Whitlow, M., and Filpula, D. (1999) Prolonged circulating lives of single-chain Fv proteins conjugated with polyethylene glycol: a comparison of conjugation chemistries and compounds. *Bioconjugate Chem. 10*, 973–981.

(36) Mehvar, R. (2000) Modulation of the pharmacokinetics and pharmacodynamics of proteins by polyethylene glycol conjugation. *J. Pharm. Pharm. Sci. 3*, 125–136.

(37) Delgado, C., Francis, G. E., and Fisher, D. (1992) The uses and properties of PEG-linked proteins. *Crit. Rev. Ther. Drug Carrier Syst. 9*, 249–304.

(38) Harris, J. M., and Chess, R. B. (2003) Effect of pegylation on pharmaceuticals. *Nat. Rev. Drug Discovery 2*, 214–221.

SUPPORTING INFORMATION

Analytical Size Exclusion Chromatography (AnSEC):

AnSEC (Agilent 1100) analysis of native-DGK and mPEG-bound DGK derivatives was performed in 20mM Tris-HCl, pH 7.5 and 150 mM NaCl running buffer at 0.35 mL/min flow rate using Shodex KW-803 column. Native and mPEG-bound DGK derivatives in excess detergent were analyzed in running buffer containing more than detergent CMC (5 mM CY-5). mPEG-bound DGK derivatives in aqueous buffer or in detergent concentrations below CMC were analyzed by maintaining the similar environment of the derivatized protein. Before analysis samples were centrifuged at 15,000 rpm for 20 min for particulate removal.

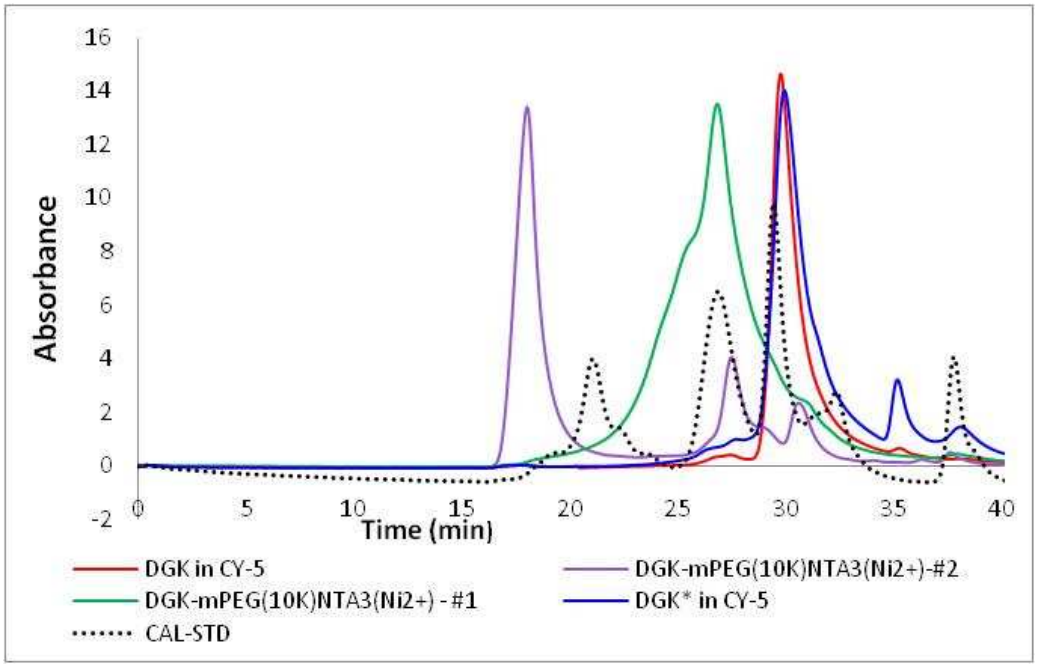

Figure S1: Analytical SEC profile of DGK in detergent phase and polymer phase: Native DGK protein in detergent CY-5, 100% detergent (red), DGK-mPEG(10K)$NTA_3(Ni^{2+})_3$-#1 in 100% detergent (green), DGK-mPEG(10K)$NTA_3(Ni^{2+})_3$-#2 in aqueous buffer (purple) and DGK

reincorporated to detergent media from DGK-mPEG(10K)$NTA_3(Ni^{2+})_3$-#2 (blue). Bio-Rad protein standard (Black dotted line).

Reextraction of DGK from DGK-mPEG(10K)$NTA_3(Ni^{2+})_3$ to Detergent Medium:

1mL of DGK-mPEG(10K)$NTA_3(Ni^{2+})_3$ (2mg/mL) was incubated with 2.5 mL of buffer (25mM Tris-Cl, pH 7.5, 150 mM NaCl, 300 mM Imidazole, 5 mM EDTA and 10 mM CY-5 buffer) for 6 hours at 4^oC. Following incubation, the solution was exchanged to 25 mM Tris-Cl, 150 mM NaCl and 5mM CY-5 buffer and was purified using Ni-affinity chromatography to isolate mPEG free DGK protein.

Bioconjugate Chemistry

ARTICLE

pubs.acs.org/bc

Intracellular Trafficking of Polyamidoamine−Poly(ethylene glycol) Block Copolymers in DNA Delivery

Daniel K. Bonner,[†,‡,§] Cheuk Leung,[†] Jane Chen-Liang,[†] Loice Chingozha,[†] Robert Langer,[†,‡,§] and Paula T. Hammond[*,†,‡]

[†]Department of Chemical Engineering, Massachusetts Institute of Technology, 77 Massachusetts Avenue, Cambridge, Massachusetts 02139, United States

[‡]David H. Koch Institute for Integrative Cancer Research at MIT

[§]Harvard-MIT Division of Health Science and Technology

Supporting Information

ABSTRACT: The delivery of nucleic acids has the potential to revolutionize medicine by allowing previously untreatable diseases to be clinically addressed. Viral delivery systems have shown immunogenicity and toxicity dangers, but synthetic vectors have lagged in transfection efficiency. Previously, we developed a modular, linear−dendritic block copolymer architecture with high gene transfection efficiency compared to commercial standards. This rationally designed system makes use of a cationic dendritic block to condense the anionic DNA and forms complexes with favorable endosomal escape properties. The linear block provides biocompatibility and protection from serum proteins, and can be functionalized with a targeting ligand. In this work, we quantitate performance of this system with respect to intracellular barriers to gene delivery using both high-throughput and traditional approaches. An image-based, high-throughput assay for endosomal escape is described and applied to the block copolymer system. Nuclear entry is demonstrated to be the most significant barrier to more efficient delivery and will be addressed in future versions of the system.

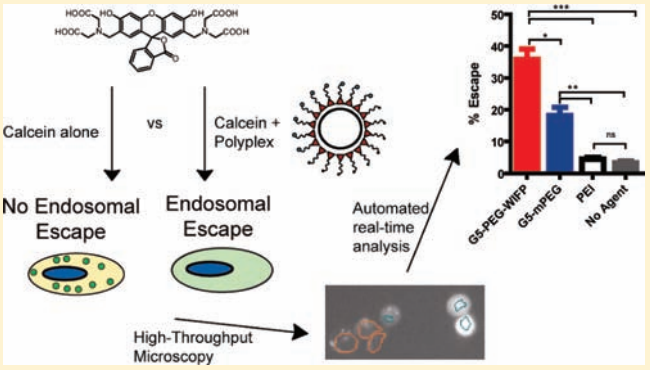

INTRODUCTION

Nucleic acid therapies have unique potential as a transformative element in clinical medicine over the coming decades. The primary barrier to clinical application of gene therapy has been the lack of safe, efficient materials to deliver genes to appropriate tissues.[1,2] A variety of viral vectors, including adenoviruses, adeno-associated viruses (AAVs), and retroviruses, have been studied as gene delivery agents.[3] While these materials can achieve high levels of protein expression, they have suffered from concerns of safety, immunogenicity, scale-up for manufacturing, and limited size of the delivered gene.[1] When viral vectors are used for transient gene expression, the increased immune response upon repeat injections becomes a limiting factor.[4,5]

Synthetic systems have been developed as a safer alternative to viral transfection, but have struggled to achieve efficiency (protein produced per plasmid) on the same order of magnitude as viral vectors. Synthetic delivery systems include cationic polymers,[6,7] liposomes,[8−10] and dendrimers,[11,12] among other material classes. Polymeric systems developed include linear and branched polyethyleneimine (PEI),[13] linear and dendritic polyamidoamine (PAMAM),[11] poly-β-amino esters (PBAE),[14−16] as well as many other linear and branched polyamines.[17] The molecular design of such polymeric systems must overcome several extracellular and intracellular barriers to achieve therapeutic levels of protein expression. In the bloodstream, DNA complexes must avoid hepatic and renal clearance, detection and removal by the immune system, binding to charged serum proteins, intercomplex aggregation, degradation by plasma nucleases, and uptake by nontargeted somatic cells.[18−21] Complexes then must be taken up efficiently by the cells of interest, and escape the endosomal compartment into which they are initially trafficked. Failure to do so results in degradation in the lysosome or recycling to the cell membrane, and lack of transfection. Once out of the endosome, the complex must translocate to the nucleus and cross the nuclear membrane . Unpackaging of the DNA from the complex is also necessary prior to expression of the delivered plasmid by the host cell. As synthetic vectors do not contain transcription factors as viruses do, the final expression of uncomplexed plasmids in the nucleus has been shown to be a bottleneck as well.[24]

In order to address these barriers to transfection, our lab has previously developed a linear−dendritic block copolymer

Received: January 28, 2011
Revised: May 23, 2011
Published: July 15, 2011

ACS Publications © 2011 American Chemical Society

system, in which a generation 5.0 PAMAM dendron is conjugated to a poly(ethylene glycol) (PEG) linear block, which itself is end-linked to a targeting moiety.[25,26] This PAMAM-G5-PEG system performed well *in vitro*, with transfection efficiencies nearly 10-fold greater than commercially available branched PEI, and it displayed targeted, receptor-mediated uptake with cytotoxicities significantly lower than unmodified PAMAM or PEI. The targeting moiety on the targeted PAMAM-G5-PEG conjugates is a short peptide, WIFPWIQL, identified from *in vivo* phage display techniques by the Arap/Pasqualini lab.[27] WIFPWIQL binds GRP78/BiP/HSP70—a glucose-response protein found intracellularly at the endoplasmic reticulum (ER) in benign cell types—but on the cell membrane of many solid tumor cell types.[28,29] In our previous publication, we reported on the synthesis, DNA complexation, and overall *in vitro* transfection efficiency of these conjugates. In this work, we characterize the intracellular trafficking of this system in order to identify the bottlenecks to more efficient delivery with these synthetic vectors, and further elucidate the mechanisms which enable any enhanced efficiency of this system over other common polyamines. We also introduce a new method for high-throughput screening of the endosomal escape properties of various polyplex formulations.

MATERIALS AND METHODS

Materials. Generation 5.0 cystamine core PAMAM dendrimers were obtained from Dendritic Nanotechnologies (Mount Pleasant, MI) and used without further purification. Heterobifunctional poly(ethylene glycol) (Maleimide-PEG5k-*N*-hydroxysuccinimide) was obtained from Laysan Bio (Arab, AL). WIFPWIQL peptide was synthesized and purified by the MIT Biopolymers lab in the Swanson Core facilities at the Koch Institute. Immobilized tris(2-carboxyethyl)phosphine (TCEP) reducing gel was obtained from Pierce (Thermo Fisher Scientific, Rockford, IL). Branched 25 000 g/mol (M_w) polyethyleneimine (PEI) and other chemical reagents were purchased from Sigma Aldrich (St. Louis, MO). DU145 cells and cell culture media were obtained from ATCC (Manassas, VA). pCMV-EGFP-N1 plasmid DNA was obtained from Aldevron Inc. (Fargo, ND). All other cell culture reagents were obtained from Invitrogen (Carlsbad, CA).

Block Copolymer Synthesis. PAMAM-G5-PEG block copolymers were prepared in a three-step synthesis. In the first step, generation 5.0 cystamine core PAMAM dendrimer (60.0 mg, 2.05 μmol) was reduced using immobilized TCEP gel (1.5 mL) for 90 min. Confirmation of the reduction was done using (5,5′-dithiobis-(2-nitrobenzoic acid) (DTNB, Ellman's reagent) to quantify free thiols and fluorescamine to quantify primary amines. Reduction was greater than 80%. In parallel, targeting peptide WIFPWIQL (7.1 mg, 6.5 μmol) was dissolved in DMSO at 5 mg/mL and added to a solution of Mal-PEG5k-NHS (30 mg, 5.4 μmol) in DMSO at 5 mg/mL. Twenty microliters of triethylamine (TEA) was added to facilitate the reaction. After 30 min, this reaction was twice precipitated in cold ether, dissolved in PBS, and reacted with the reduced PAMAM dendrimer for 24 h. Untargeted polymers were synthesized by substituting monofunctional MAL-mPEG5k for the WIFPWIQL-PEG-MAL. The synthesized polymers were dialyzed against 8000 MWCO SpectraPOR (Spectrum Laboratories, Rancho Dominguez, CA) and lyophilized. Structure was confirmed by ^{1}H NMR (400 MHz, D_2O) δ (ppm) = 3.69 (s, CH_2CH_2O), 3.48 (t, $CONHCH_2CH_2NH_2$), 3.30 (t, $CONHCH_2CH_2NR$), 3.11 (t, $CONHCH_2CH_2NH_2$), 2.85 (m, NCH_2CH_2CONH), 2.64 (t, $CONHCH_2CH_2NR$), 2.45 (m, NCH_2CH_2CONH).

Cell Culture. DU145 cells were cultured in Minimum Essential Media (MEM) supplemented with 10% heat-inactivated fetal bovine serum (FBS) and 1% penicillin−streptomycin in a humidified 37 °C atmosphere at 5% CO_2.

Transfection. Cells were trypsinized prior to transfection and seeded in 96-well plates at 5000 cells/well overnight in a humidified 37 °C atmosphere at 5% CO_2. PAMAM-PEG block copolymers were diluted in 25 mM sodium acetate buffer (NaAc) (pH 5.5) at 1.5 mg/mL initially and then further diluted into 25 μL of the same buffer in a separate 96-well plate at varying concentrations. Twenty-five microliters of pDNA at 0.06 mg/mL in NaAc was then added to each well and mixed by gentle pipetting. After 10 min for complex formation, 30 μL aliquots of the complexes were added to 200 μL of Opti-MEM supplemented with 10% FBS. After further mixing, 150 μL aliquots of the complexes in Opti-MEM were added to the cells (after growth media had been removed). After 4 h, the complexes in Opti-MEM were removed and growth media was added. Cells were assayed at 48 h for GFP production using flow cytometry. 4000−10 000 live cells per sample were analyzed. GFP production was normalized to that from transfection with an optimized formulation of 25 kDa branched PEI.[30] *p*-values were calculated using a two-way analysis of variation and Bonferroni post-tests were performed on all conditions shown.

Flow Cytometry. Flow cytometry was performed in U-bottom 96-well plates using an LSR II HTS Flow cytometer (Becton-Dickinson, Mountain View, CA). To prepare samples, media was removed from cells and replaced with 25 μL trypsin for 5 min. 50 μL of PBS supplemented with 2% FBS was then added to each well, mixed, and the entire 75 μL cell suspension transferred into a U-bottom 96-well plate. Representative 2D histograms are included in the Supporting Information.

Polyplex Uptake. Block copolymers and PEI were labeled with fluorescein isothiocyanate (FITC) at a molar ratio of 4:1 (dye/polymer). Using the labeled polymers, polyplexes were formed and cells treated as described in the above section. At the time indicated, cells were removed from the incubator and analyzed using flow cytometry. *p*-values were calculated using a two-way analysis of variation and Bonferroni post-tests were performed on all conditions shown.

High-Throughput Endosomal Escape. Complexes were assembled and transfection was conducted as described above, except that the Opti-MEM containing 25 μM calcein and cells were seeded in black-sided, clear-bottom 96-well plates. Four hours after transfection, 5 μL of a solution of Hoechst 33342 diluted to 1:30 in PBS was added. After 20 min of staining, complexes and free dye were removed, and the cells were washed 3 times with PBS. 150 μL of phenol-free Opti-MEM with 10% serum was added to each well before the plate was covered with an opaque sticker, foiled, and analyzed. Imaging was done using a Cellomics ArrayScan VTI HCS Reader (Thermo Fisher, Waltham, MA) and analysis was done using the included software (see Supporting Information for details). 300−3000 live cells per sample were analyzed. *p*-values were calculated using an unpaired *t* test.

Confocal Microscopy. 8-well Lab-Tek chamber slides (Thermo Fisher, Waltham, MA) were treated for 20 min with human fibronectin in PBS at 0.01 mg/mL. The fibronectin was

Scheme 1. Synthesis of PAMAM-G5-PEG-WIFP Conjugates[a]

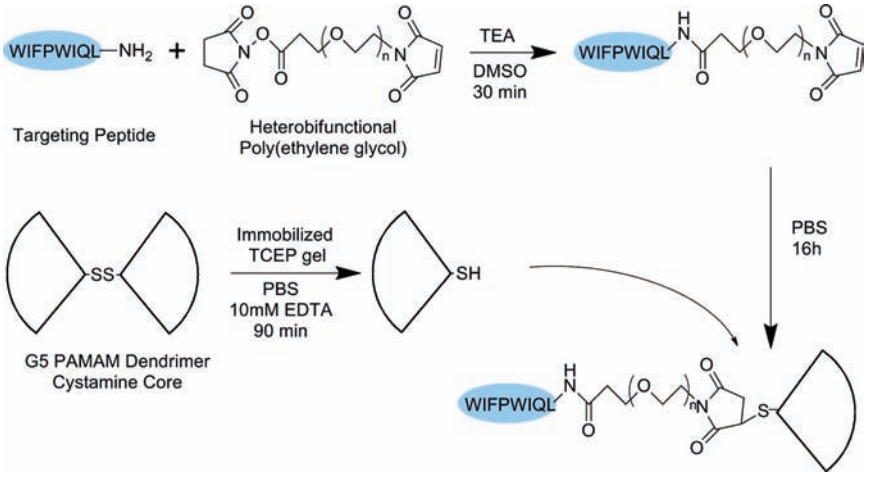

[a] The targeting peptide is first reacted with a bifunctional linker before being precipitated and added to reduced G5 PAMAM dendrimer.

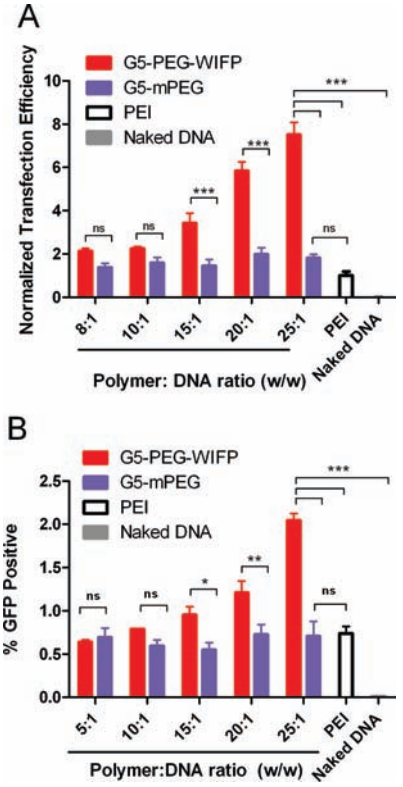

Figure 1. Normalized transfection efficiency (A) and percentage of cells transfected (B) of targeted and untargeted block copolymer formulations at various polymer/DNA ratios. Transfections of EGFP were performed in 10% serum and analyzed 48 h later using flow cytometry. An optimized formulation of PEI at a polymer/DNA ratio of 2:1 was used and data is reported as mean fluorescence intensity normalized to that of the PEI transfected cells. Error bars represent SEM of 5 replicate experiments (*** = $p < 0.001$, ** = $p < 0.01$, * = $p < 0.05$, ns = not significant). These results are in agreement with previously published reports of transfection efficiency of this block copolymer system.[26]

removed and DU145 cells were trypsinized and seeded in each well at a concentration of 1000 cells/well 24 h before transfection. Plasmid DNA was labeled with Rhodamine-CX using the Label-IT kit (Mirus Bio, Madison, WI). Polymers were FITC-labeled as described earlier. Polyplexes between labeled DNA and labeled polymers were formed in NaAc buffer as described earlier. 40 μL of complexes were added to 160 uL phenol-free Opti-MEM (supplemented with 10% serum) and added to each well. Complexes were removed after 4 h and replaced with growth media. At 24 h, cells were fixed with 3.7% formaldehyde in PBS, stained with Hoechst 33342, and washed 3 times with PBS. Imaging was done on a PerkinElmer Ultraview spinning disk confocal microscope (PerkinElmer, Waltham, MA).

RESULTS AND DISCUSSION

Synthesis. Synthesis of the PAMAM-G5-PEG linear—dendritic block copolymers was similar to that reported previously by our group[26] and is shown in Scheme 1. Briefly, generation 5.0, cystamine core dendrimers were first reduced to expose dendrons with a single thiol moiety (yielding two dendron-thiols per dendrimer). In parallel, the *N*-hydroxysuccinimide (NHS) group of a heterobifunctional PEG was first reacted with the terminal lysine on the WIFPWIQL peptide, leaving the maleimide group of the PEG block free for subsequent conjugation to the exposed thiol on the reduced PAMAM dendrimer. This synthetic approach is managed easily in aqueous solutions and can be generally applied to most targeting ligands.

Overall Transfection. While the overall transfection efficiency of a gene carrier is a critical parameter to characterize, it is ultimately necessary to determine the bottlenecks—quantitatively if possible—in order to better design future iterations of the system. As shown in Figure 1A, the targeted block copolymers transfected DU145 cells nearly 8-fold better than 25 kDa bPEI and nearly 4-fold better than an untargeted control block copolymer, which is consistent with our previously published studies using this system.[26] Figure 1B shows that the presence of serum in the system limited the absolute percentage of cells transfected to less than 3% and the increase of targeted block copolymer was 3-fold over both the untargeted control and PEI. While PEI is an efficient gene carrier in serum-free media, in more biologically relevant conditions (i.e., 10% or more serum),

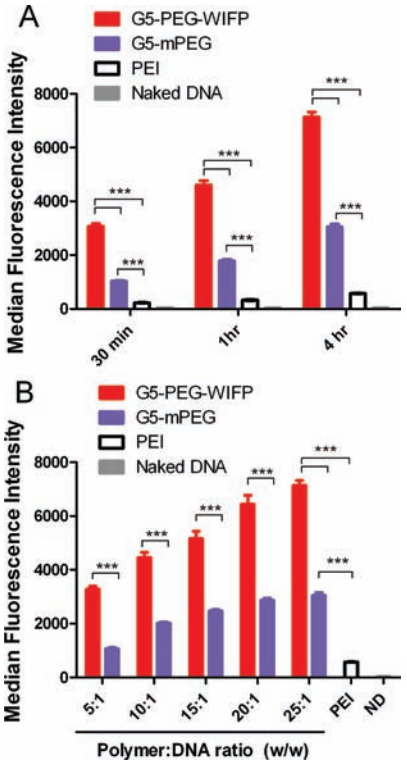

Figure 2. Uptake of polyplexes formed by targeted and untargeted block copolymers against PEI. FITC-labeled polymers were complexed with EGFP plasmids and added to DU145 cells in 10% serum. Median cell associated fluorescence was measured at 30 min, 1 h, and 4 h as indicated in panel A (w/w = 25:1 for block copolymers). Panel B shows the effect of varying the polymer/DNA ratio of the block copolymers. Fluorescence was measured at 4 h in panel B. PEI was used at an optimized w/w ratio of 2:1. Error bars represent SEM of 5 replicate experiments (*** = $p < 0.001$, ** = $p < 0.01$, * = $p < 0.05$, ns = not significant).

the advantage of the PEGylation in the block copolymer system becomes apparent.[31]

Uptake. Once in the immediate vicinity of the target cell, the polyplex must first undergo binding and internalization. While it is possible to characterize many aspects of the binding and internalization process,[32] at this time we chose to simply focus on the degree of polyplex association with the target cells. In this study, each polymer system was labeled with a fluorophore (FITC) and the labeled polyplexes were added to DU145 cells. Figure 2 shows the median cell associated fluorescence achieved by the various delivery vehicles after up to 4 h of incubation, as measured by flow cytometry. Intracellular uptake of the PAMAM-G5-PEG WIFP block copolymer complexes exhibits a 12-fold increased cellular uptake over PEI; the untargeted PAMAM-G5-PEG also yielded a 5-fold gain versus the PEI control. This is consistent with other reports that the PEG exterior shell generated in the block copolymer polyplexes gives a significant advantage in shielding them from adsorption of proteins.[33] The presence of serum proteins (particularly albumin) can abrogate the uptake of PEI by binding PEI complexes prior to cell uptake.[31] Of note is that the general relationship between the uptake efficiencies and overall transfection efficiencies of these polymers is similar, implying that at least one principal difference between their effectiveness is their differential uptake ability. However, the increases in the percentage of transfected cells of the block copolymers over PEI are much less than the increases in uptake, suggesting that PEI may be more effective at mediating downstream events. Another difference could lie in the endosomal trafficking of polyplexes internalized via GRP78 binding[34] versus those internalized via nonreceptor mediated endocytosis, as increased uptake resulted in increased transfection efficiency for the targeted polymer, but not for the untargeted control. This effect could also be due to potential downstream effects of the peptide in mediating endosomal escape or nuclear translocation. For each of the polymers, even though significant uptake is achieved, further evaluation is necessary to understand the subsequent barriers to transfection that result in relatively low transgene expression in comparison to viral vectors. A block copolymer with a scrambled peptide may have been a more ideal targeting control; however, the polyplex size, charge, and loading are unchanged by the presence of the peptide, indicating that the PEG control should be a good control of a nontargeted system (see Supporting Information). Additionally, our earlier communication[26] shows that the addition of competing ligand suppresses overall transfection efficiency, indicating that the uptake of these particles is receptor-mediated.

Endosomal Escape. Endosomal escape is a critical barrier to overcome in the delivery of nucleic acids. Measurement of endosomal escape is done frequently using fluorescence microscopy.[35] Commonly, a fluorescent marker for the endosomes (transferrin, fluorophore-modified dextrans, endosome/lysosome tracking dye) is employed, and escape is considered achieved if there is no colocalization between the polyplex and the endosomal marker.[36] However, this is difficult to measure and quantify in high throughput, thus screening a large library of materials or formulations for differences in endosomal escape performance is complex. Akinc et al.[37] describe a novel method for measuring the pH of the polyplex environment via high-throughput flow cytometry, but here we describe a direct method for quantifying the disruption of the endosome using an image-based high-throughput screening approach.

The high-throughput approach uses the fact that calcein is a membrane-impermeable fluorophore that can be taken up by cells and trafficked through endosomes to lysosomes, but cannot achieve endosomal/lysosomal escape.[38,39] In the presence of an escape agent, calcein will be released and is seen throughout the cell (Figure 3A). Using an automated fluorescent microscope, the two phenotypes can be differentiated in real time by algorithms using spatial fluorescence information. Figure 3B shows a representative image (20× magnification) in which the algorithm has identified cells which have undergone endosomal escape vs those that have not. Figure 3C is an example of an assay validation experiment in which increasing amounts of PEI were added and the escape measured at different time points. As expected, escape percentage increased with increasing concentrations of PEI and increasing incubation time. When applied to the block copolymer systems studied, a similar pattern to that of the uptake and overall transfection efficiency was observed (Figure 3D). The observed escape percentage relationship between targeted and untargeted PAMAM block copolymers was similar to that of the uptake, suggesting the endosomal escape properties were relatively unchanged between the two polymers. This is consistent with the fact that these two polymers differ only in the presence of a targeting ligand, and thus, the pH-responsive PAMAM structure remains the same. The low escape percentage of the PEI is likely due to its poorer uptake relative to the block copolymers as its escape percentage is greatly enhanced in the absence of serum (see Supporting Information).

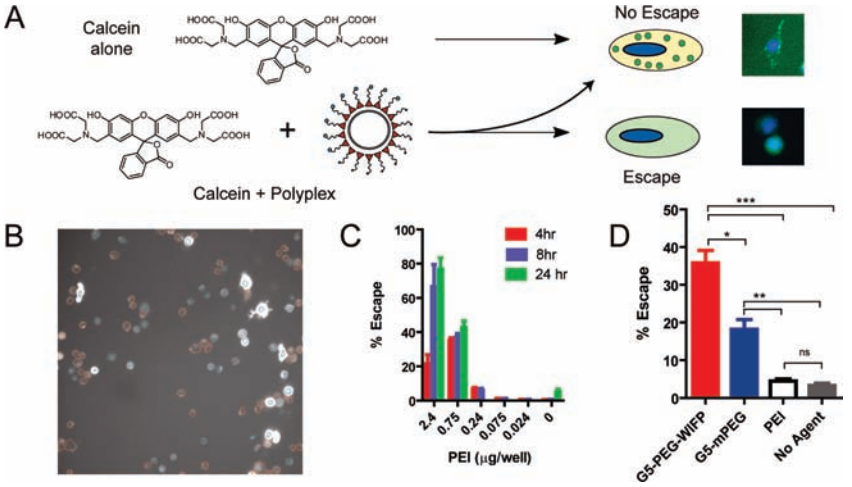

Figure 3. Panel A is a schematic of the high-throughput calcein assay used to quantify endosomal escape. When calcein alone is taken up by cells, it remains in the endosomal compartments and thus a punctuate pattern of fluorescence in the cytoplasm is visible. With the addition of an endosomal escape agent, e.g., a polymer or polyplex, the calcein is released into the cytosol yielding a uniform pattern of fluorescence. The images in panel A are representative of these morphologies and taken at 20×. The images have been intensity normalized for this figure in order to more easily visualize the punctuate vs diffuse pattern of fluorescence. Nuclei are shown in blue, calcein as green. Panel B is a grayscale image of the calcein channel of DU145 cells treated with G5-PEG-WIFP polyplexes. The Cellomics algorithm has differentiated cells with endosomal escape (blue circle overlay) vs those without (orange circle overlay). In panel C, the concentration of PEI is increased as is the time in which the cells were exposed to the calcein/escape agent. Panel D shows the percentage of escaped cells from treatments with various polyplex formulations in OPTI-MEM with 10% serum. PAMAM based polyplexes were used at a 25:1 w/w ratio. PEI was used at 2:1 w/w ratio. Error bars are SEM of 3 replicates (*** = $p < 0.001$, ** = $p < 0.01$, * = $p < 0.05$, ns = not significant).

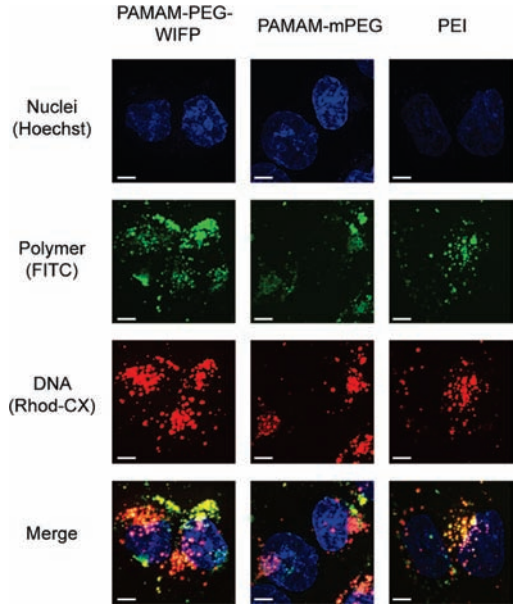

Figure 4. Confocal fluorescence micrographs of cells transfected with targeted/untargeted block copolymers as well as PEI. Transfection took place in 10% serum, and micrographs were taken on fixed cells 24 h after polyplexes were added. Scale bars are 5 μm. In the merged channel, yellow indicates colocalization of polymer (green) and DNA (red). PAMAM based polyplexes were used at a 25:1 w/w ratio. PEI was used at a 2:1 w/w ratio.

Nuclear Uptake and DNA Unpackaging. While endosomal escape could be visualized and quantitated using a high-throughput approach, dissociation of the polyplex and nuclear uptake were followed using traditional confocal microscopy techniques. In this case, both the plasmid DNA and polymers were labeled in order to track polyplex dissociation. Figure 4 shows representative images of a 24 h incubation of dual-labeled polyplexes. There is substantially more plasmid DNA delivered by the targeted block copolymer in comparison with the untargeted polymer or PEI. Again, this is due primarily to the differential uptake between the three systems. Additionally, it is apparent that the PAMAM-PEG micelles are not completely dissociated, as there is significant colocalization between the polymer and DNA channels. In the case of the targeted PAMAM-PEG, it is possible to visualize a yellow core at the center of areas of red fluorescence, indicating that there is still polymer associated with most polyplexes. Finally, it is evident that the polyplexes are localized to an area near the nucleus, but not inside, such as a microtubule organization center (MTOC).[40] Uptake into the nucleus should be readily seen 24 h after initial application, but the fact that it is not observed with these materials indicates nuclear localization to be a significant barrier to delivery. The observed gene expression can likely be attributed to either the small percentage of decomplexed DNA that is nonspecifically chaperoned into the nucleus or to cells in which the nuclear membrane was not intact (e.g., in the process of dividing).[41] In this case, some polyplexes accessing the nucleus may still be fully or partially condensed, but even partially complexed polyplexes could participate in gene transcription.[42] The lack of efficient nuclear uptake and polyplex decondensation represents a significant barrier to further transfection efficiency and an area in which these polymers can be improved, possibly by the incorporation of a nuclear localization sequence.

For the targeted block copolymers, nearly 100% of cells took up complexes (see Supporting Information), 36% achieved endosomal escape, but only 2% were ultimately transfected. Less than 6% of cells which experienced escape were transfected by either targeted or untargeted block copolymer, while over 15% of escaped cells were transfected by PEI. This underscores that,

while the escape of these block copolymers polymers is efficient, downstream events after endosomal escape represent the most important challenges going forward. Addressing these challenges will be important, because even as currently designed, these promising targeted block copolymers are capable of superior transfection relative to PEI in the presence of serum.

CONCLUSIONS

PAMAM-PEG block copolymers have shown promise as gene delivery agents. Here, we have shown this system to be nearly an order of magnitude more potent than PEI *in vitro* and have examined the bottlenecks the system faces. While targeted uptake remains efficient, even in the presence of serum, endosomal escape and unpackaging of DNA polyplexes afterward could be further improved. To that end, we have demonstrated a tool to screen libraries of compounds to rapidly determine the best structures and formulations for endosomal escape. Finally, we have shown that nuclear translocation appears to be the primary obstacle to more efficient transfection in this system—further engineering of the system to promote active delivery of polyplexes into the nucleus could greatly enhance transfection.

ASSOCIATED CONTENT

Supporting Information. Additional information as described in the text. This material is available free of charge via the Internet at http://pubs.acs.org.

AUTHOR INFORMATION

Corresponding Author

*E-mail: Hammond@mit.edu.

ACKNOWLEDGMENT

Funding for this research was provided by National Institutes of Health (NIH) NIBIB grant R01EB008082. This work was also supported by National Defense Science and Engineering Graduate Fellowship and the National Science Foundation Graduate Research Fellowship Program, as well as The MIT-Harvard Center of Cancer Nanotechnology Excellence Center, NCI grant 1U54CA151884. The authors acknowledge the Swanson Biotechnology Center in the Koch Institute at MIT, the Keck Imaging facility at the Whitehead Institute, and the Genome Technology Core at the Whitehead Institute. The authors also thank James Evans, Roberto Zoncu, and Nicki Watson for helpful imaging advice and assistance.

REFERENCES

(1) Somia, N., and Verma, I. M. (2000) Gene therapy: trials and tribulations. *Nat. Rev. Genet. 1*, 91–99.

(2) Schaffert, D., and Wagner, E. (2008) Gene therapy progress and prospects: synthetic polymer-based systems. *Gene Ther. 15*, 1131–8.

(3) Walther, W., and Stein, U. (2000) Viral vectors for gene transfer - A review of their use in the treatment of human diseases. *Drugs 60*, 249–271.

(4) Zaiss, A. K., and Muruve, D. A. (2008) Immunity to adeno-associated virus vectors in animals and humans: a continued challenge. *Gene Ther. 15*, 808–816.

(5) Nayak, S., and Herzog, R. W. (2010) Progress and prospects: immune responses to viral vectors. *Gene Ther. 17*, 295–304.

(6) Glover, D. J., Lipps, H. J., and Jans, D. A. (2005) Towards safe, nonviral therapeutic gene expression in humans. *Nat. Rev. Genet. 6*, 299–310.

(7) Kan, P. L., Schatzlein, A. G., and Uchegbu, I. F. (2006) Polymers used for the delivery of genes in gene therapy, in *Polymers in drug delivery* (Uchegbu, I. F., and Schatzlein, A. G., Eds.) CRC Press, Boca Raton.

(8) Felgner, P. L., Gadek, T. R., Holm, M., Roman, R., Chan, H. W., Wenz, M., Northrop, J. P., Ringold, G. M., and Danielsen, M. (1987) Lipofection - a highly efficient, lipid-mediated dna-transfection procedure. *Proc. Natl. Acad. Sci. U. S. A. 84*, 7413–7417.

(9) Kogure, K., Akita, H., Yamada, Y., and Harashima, H. (2008) Multifunctional envelope-type nano device (MEND) as a non-viral gene delivery system. *Adv. Drug Delivery Rev. 60*, 559–571.

(10) Legendre, J.-Y., and Szoka, F. C., Jr. (1992) Delivery of plasmid DNA into mammalian cell lines using pH-sensitive liposomes: comparison with cationic liposomes. *Pharm. Res. 9*, 1235–1242.

(11) Haensler, J., and Szoka, F. C. (1993) Polyamidoamine cascade polymers mediate efficient transfection of cells in culture. *Bioconjugate Chem. 4*, 372–379.

(12) Tang, M. X., Redemann, C. T., and Szoka, F. C. (1996) In vitro gene delivery by degraded polyamidoamine dendrimers. *Bioconjugate Chem. 7*, 703–714.

(13) Abdallah, B., Hassan, A., Benoist, C., Goula, D., Behr, J. P., and Demeneix, B. A. (1996) A powerful nonviral vector for in vivo gene transfer into the adult mammalian brain: Polyethylenimine. *Hum. Gene Ther. 7*, 1947–1954.

(14) Anderson, D. G., Akinc, A., Hossain, N., and Langer, R. (2005) Structure/property studies of polymeric gene delivery using a library of poly(beta-amino esters). *Mol. Ther. 11*, 426–34.

(15) Anderson, D. G., Lynn, D. M., and Langer, R. (2003) Semi-automated synthesis and screening of a large library of degradable cationic polymers for gene delivery. *Angew. Chem., Int. Ed. Engl. 42*, 3153–8.

(16) Lynn, D. M., Anderson, D. G., Putnam, D., and Langer, R. (2001) Accelerated discovery of synthetic transfection vectors: parallel synthesis and screening of a degradable polymer library. *J. Am. Chem. Soc. 123*, 8155–6.

(17) Fukushima, S., Miyata, K., Nishiyama, N., Kanayama, N., Yamasaki, Y., and Kataoka, K. (2005) PEGylated polyplex micelles from triblock catiomers with spatially ordered layering of condensed pDNA and buffering units for enhanced intracellular gene delivery. *J. Am. Chem. Soc. 127*, 2810–2811.

(18) Chiou, H. C., Tangco, M. V., Levine, S. M., Robertson, D., Kormis, K., Wu, C. H., and Wu, G. Y. (1994) Enhanced resistance to nuclease degradation of nucleic-acids complexed to asialoglycoprotein-polylysine carriers. *Nucleic Acids Res. 22*, 5439–5446.

(19) Dash, P. R., Read, M. L., Barrett, L. B., Wolfert, M., and Seymour, L. W. (1999) Factors affecting blood clearance and in vivo distribution of polyelectrolyte complexes for gene delivery. *Gene Ther. 6*, 643–650.

(20) Patel, H. M. (1992) Serum opsonins and liposomes: their interaction and opsonophagocytosis. *Crit. Rev. Ther. Drug Carrier Syst. 9*, 39–90.

(21) Mislick, K. A., and Baldeschwieler, J. D. (1996) Evidence for the role of proteoglycans in cation-mediated gene transfer. *Proc. Natl. Acad. Sci. U. S. A. 93*, 12349–12354.

(22) Lam, A. P., and Dean, D. A. (2010) Progress and prospects: nuclear import of nonviral vectors. *Gene Ther.* 1–9.

(23) Dean, D. A., Strong, D. D., and Zimmer, W. E. (2005) Nuclear entry of nonviral vectors. *Gene Ther. 12*, 881–90.

(24) Hama, S., Akita, H., Iida, S., Mizuguchi, H., and Harashima, H. (2007) Quantitative and mechanism-based investigation of post-nuclear delivery events between adenovirus and lipoplex. *Nucleic Acids Res. 35*, 1533–43.

(25) Wood, K. C., Little, S. R., Langer, R., and Hammond, P. T. (2005) A family of hierarchically self-assembling linear-dendritic hybrid polymers for highly efficient targeted gene delivery. *Angew. Chem., Int. Ed. 44*, 6704–8.

(26) Wood, K. C., Azarin, S. M., Arap, W., Pasqualini, R., Langer, R., and Hammond, P. T. (2008) Tumor-targeted gene delivery using molecularly engineered hybrid polymers functionalized with a tumor-homing peptide. *Bioconjugate Chem. 19*, 403–5.

(27) Arap, M. A., Lahdenranta, J., Mintz, P. J., Hajitou, A., Arap, W., and Pasqualini, R. (2004) Cell surface expression of the stress response chaperone GRP78 enables tumor targeting by circulating ligands. *Cancer Cell 6*, 275–284.

(28) Lee, A. S. (2007) GRP78 induction in cancer: therapeutic and prognostic implications. *Cancer Res. 67*, 3496–3499.

(29) Li, J., and Lee, A. S. (2006) Stress induction of GRP78/BiP and its role in cancer. *Current* 45–54.

(30) Gabrielson, N. P., and Pack, D. W. (2006) Acetylation of polyethylenimine enhances gene delivery via weakened polymer/DNA interactions. *Biomacromolecules 7*, 2427–2435.

(31) Forrest, M. L., Meister, G., Koerber, J., and Pack, D. (2004) Partial acetylation of polyethylenimine enhances in vitro gene delivery. *Pharm. Res. 21*, 365–371.

(32) Sahay, G., Alakhova, D. Y., Kabanov, A. V. Endocytosis of nanomedicines. *J. Controlled Release 145*, 182-195.

(33) Giri, J., Diallo, M. S., Simpson, A. J., Liu, Y., Goddard, W. A., Kumar, R., and Woods, G. C. Interactions of poly(amidoamine) dendrimers with human serum albumin: binding constants and mechanisms. *ACS Nano*[Online early Online].

(34) Ni, M., Zhang, Y., and Lee, A. S. (2011) Beyond the endoplasmic reticulum: atypical GRP78 in cell viability, signalling and therapeutic targeting. *Biochem. J. 434*, 181–8.

(35) Payne, C. K. (2007) Imaging gene delivery with fluorescence microscopy. *Nanomedicine 2*, 847–60.

(36) Akita, H., Ito, R., Khalil, I. A., Futaki, S., and Harashima, H. (2004) Quantitative three-dimensional analysis of the intracellular trafficking of plasmid DNA transfected by a nonviral gene delivery system using confocal laser scanning microscopy. *Mol. Ther. 9*, 443–451.

(37) Akinc, A., Thomas, M., Klibanov, A. M., and Langer, R. (2005) Exploring polyethylenimine-mediated DNA transfection and the proton sponge hypothesis. *J. Gene Med. 7*, 657–63.

(38) Hu, Y., Litwin, T., Nagaraja, A. R., Kwong, B., Katz, J., Watson, N., and Irvine, D. J. (2007) Cytosolic delivery of membrane-impermeable molecules in dendritic cells using pH-responsive core-shell nanoparticles. *Nano Lett. 7*, 3056–3064.

(39) Jones, R. A., Cheung, C. Y., Black, F. E., Zia, J. K., Stayton, P. S., Hoffman, A. S., and Wilson, M. R. (2003) Poly(2-alkylacrylic acid) polymers deliver molecules to the cytosol by pH-sensitive disruption of endosomal vesicles. *Biochem. J. 372*, 65–75.

(40) Barua, S., and Rege, K. The influence of mediators of intracellular trafficking on transgene expression efficacy of polymer-plasmid DNA complexes. *Biomaterials 31*, 5894-5902.

(41) Pouton, C. W., Wagstaff, K. M., Roth, D. M., Moseley, G. W., and Jans, D. A. (2007) Targeted delivery to the nucleus. *Adv. Drug Delivery Rev. 59*, 698–717.

(42) Bielinska, A. U., Kukowska-Latallo, J. F., and Baker, J. R. (1997) The interaction of plasmid DNA with polyamidoamine dendrimers: mechanism of complex formation and analysis of alterations induced in nuclease sensitivity and transcriptional activity of the complexed DNA. *Biochim. Biophys. Acta 1353*, 180–190.

Supporting information for "Intracellular Trafficking of Polyamidoamine – Polyethylene Glycol Block Copolymers in DNA Delivery" *by Daniel K. Bonner, Cheuk Leung, Jane Chen-Liang, Loice Chingozha, Robert Langer, and Paula T. Hammond.*

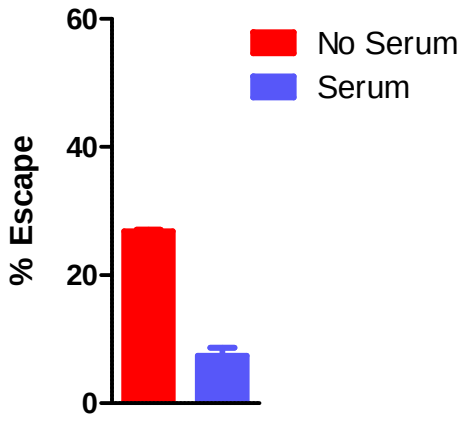

Supplementary Figure S1

This figure shows the percentage of escaped cells from treatments with 25k bPEI at a 2:1 w/w ratio in OPTI-MEM with either 10% serum or no serum at all.

As mentioned in the text, the addition of serum in the transfection media greatly decreases the percentage of escaped cells for branched polyethyleneimine. We hypothesize that this is due to the binding of polyplexes to serum proteins.

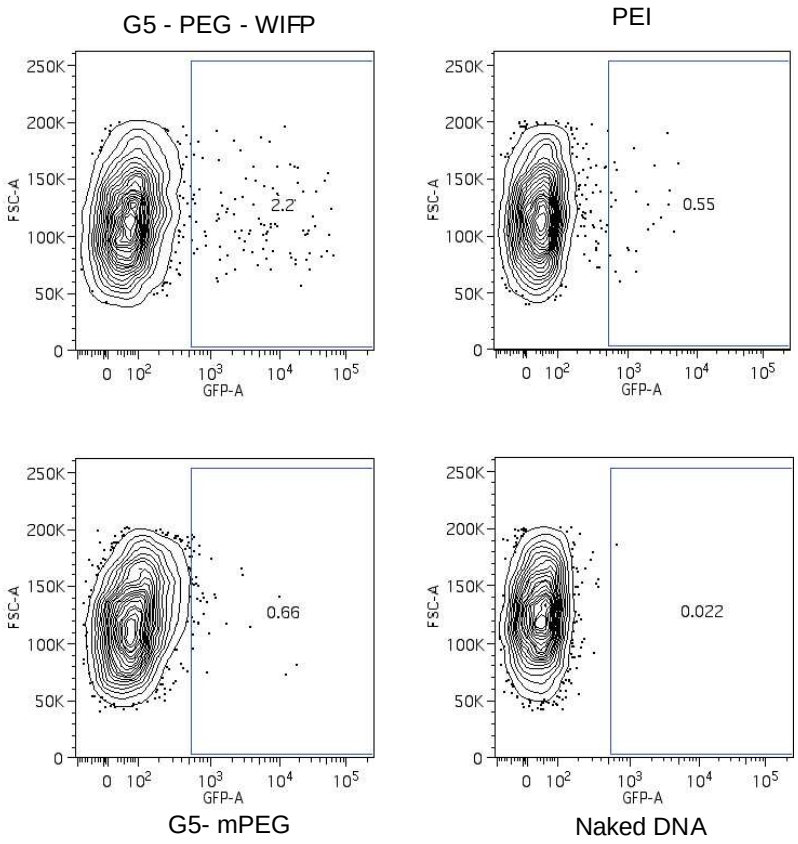

Supplementary Figure S2

Transfections of EGFP were performed in 10% serum and analyzed 48 hrs later using flow cytometry as described in the methods in the main text. Figure S2 shows the flow cytometry 2D histograms and gates used to calculate the GFP positive percentages in Figure 1B. An optimized formulation of PEI at a polymer:DNA ratio of 2:1 was used in this experiment. G5-PEG-WIFP and G5-mPEG are shown at the 25:1 w/w ratio.

As mentioned in the text, the absolute percentages of transfected cells are low due to the presence of serum, but are nonetheless meaningful because they are 3-fold higher than that of a standard polymer transfection agent, bPEI, in a more relevant physiological condition than serum-free.

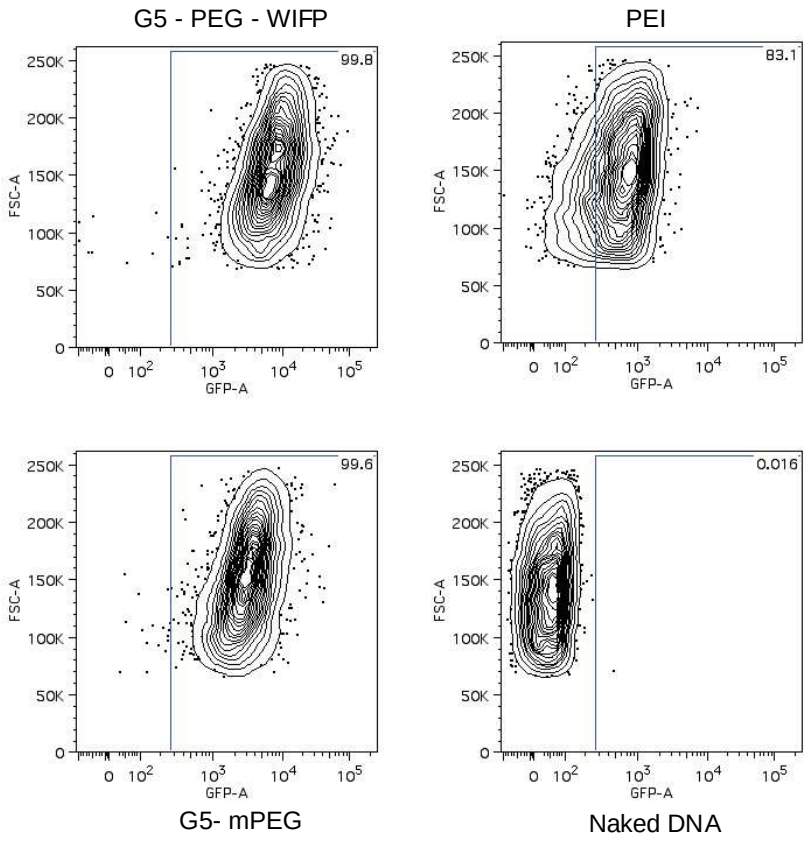

Supplementary Figure S3

Figure S3 shows the flow cytometry 2D histograms and gates used to characterize the uptake of polyplexes shown in Figure 2. FITC-labeled polymers were complexed with EGFP plasmids and added to DU145 cells in 10% serum. Cell associated fluorescence was measured at 30 min, 1h, and 4h. Plots shown are from polyplexes formed at 25:1 (w/w) and taken after 4 h of uptake.

Figure S3 shows 100% of cells treated with G5-PEG constructs take up polyplexes, whereas only 85% of those labeled with PEI do. Figure 2 quantifies the median fluorescence and demonstrates that G5-PEG-WIFP shows a 2-fold increase in uptake over the untargeted G5-mPEG.

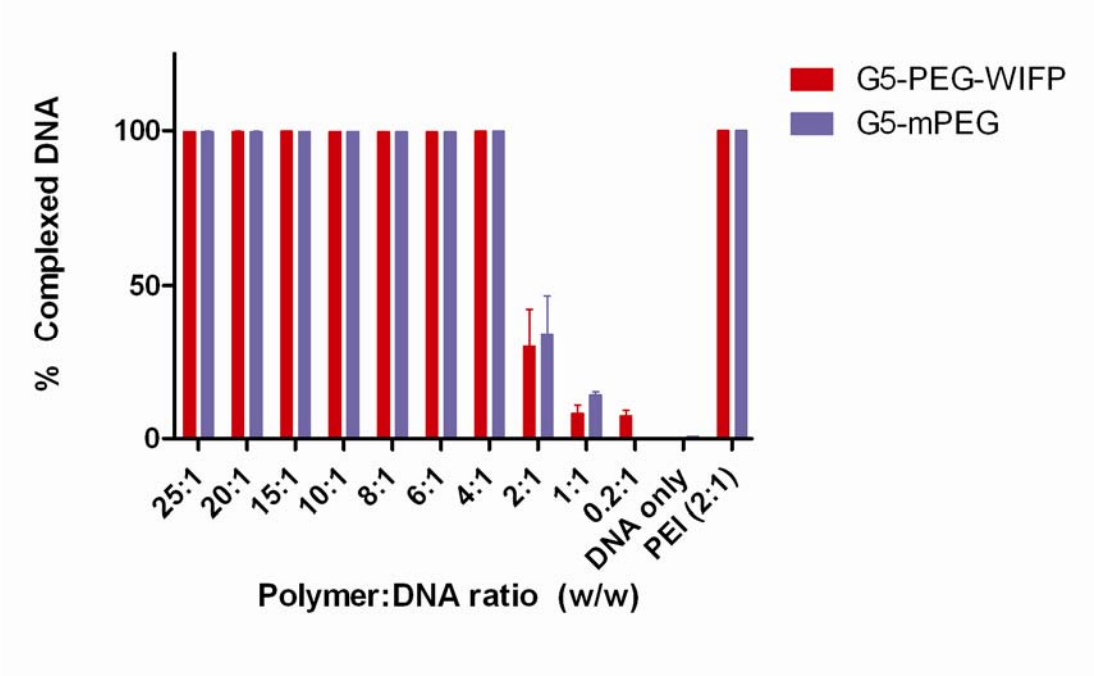

Supplementary Figure S4

DNA Complexation of targeted and untargeted block copolymers as measured by exclusion of Picogreen.

Polyplexes were prepared as described in the *Transfection* portion of the Materials and Methods in the main text. Following complexation, particles were added to a 1:200 solution of Picogreen (Invitrogen) and their fluorescence measured on a Perkin Elmer 1420 Multilabel Plate Reader. Background was subtracted from all measurements and 0% complexation defined by the amount of fluorescent from a DNA only control. PAMAM-PEG block copolymers are able to condense DNA completely at a w/w ratio of 4:1 and higher. The presence of the peptide does not alter the degree of complexation of the polyplexes.

Supplementary Methods

High Throughput Endosomal Escape Assay - Image Processing

Complexes were assembled and transfection was conducted as described in the manuscript, except that 25 μM calcein was added to the Opti-MEM and cells were seeded in black-sided, clear-bottom 96-well plates. 4 hours after transfection, 5 μL of a solution of Hoechst 33342 diluted to 1:30 in PBS was added. After 20 minutes of staining, complexes and free dye were removed, and the cells were washed 3 times with PBS. 150 μL of phenol-free Opti-MEM with 10% serum was added to each well before the plate was covered with an opaque sticker, foiled, and analyzed. Imaging was done using a Cellomics ArrayScan VTI HCS Reader (Thermo Fisher, Waltham, MA) and analysis was done using the included software.

20 fields per well were imaged with a 20x objective, yielding 300 – 3000 cells. Autofocus was used for each field, based on the nuclear (Hoechst) channel with no Z-Offset. Exposure time was fixed at 0.15 s. Objects (nuclei) were identified using the Isodata thresholding method and considered single cell nuclei if the object area was between 40 and 400 square pixels. After the nuclei were identified, the cytoplasmic area was defined as being a ring a fixed distance outside the nucleus. After defining “escaped” and “non-escaped” cells, the most accurate combination of parameters for separating the two was based on the average calcein channel intensity in the central nuclear region. Since the majority of the cytoplasmic volume appeared to be present outside this region, calcein-filled endosomes rarely existed in this region. However, in escaped cells, the cytoplasmic region above & below the nucleus, even with relatively low volume, would always have some calcein signal. A threshold in this value was empirically set and could

vary based on camera type, light source, and exposure time. Methods defining the number of cytoplasmic spots and their intensity relative to the rest of the cytoplasm were ultimately inferior to this method. Future iterations of this assay may determine degree of escape or identify cells with both diffuse and punctuate calcein staining. Finally, note the images shown in Figure 3 are intensity normalized in order to better visualize the punctate staining pattern – all calculations are done with unstreched images (and thus the apparently different level of background in Figure 3 is not a problem).

Bioconjugate Chemistry

ARTICLE

pubs.acs.org/bc

Fluorescent Nanoparticles Consisting of Lipopeptides and Fluorescein-Modified Polyanions for Monitoring of Protein Kinase Activity

Haruka Koga,[†,‡] Riki Toita,[†,‡,§] Takeshi Mori,[†,∥] Tetsuro Tomiyama,[†] Jeong-Hun Kang,[∥,⊥] Takuro Niidome,[†,∥,#] and Yoshiki Katayama[*,†,∥,#,▽]

[†]Graduate School of Systems Life Sciences, [∥]Department of Applied Chemistry, Faculty of Engineering, and [#]Center for Future Chemistry, Kyushu University, 744 Motooka, Nishi-ku, Fukuoka 819-0395, Japan

[▽]Center for Advanced Medical Innovation, Kyushu University, 3-1-1 Maidashi, Higashi-ku, Fukuoka, 812-8582, Japan

Supporting Information

ABSTRACT: Protein kinase (PK)-responsive nanoparticles (NPs) comprising a hydrophobically modified peptide substrate for PKs and a fluorescein-labeled polyanion (pA-F) were reported for monitoring PK activity via fluorescence intensity measurements. In this system, the formation of NPs by mixing lipopeptides and pA-Fs results in fluorescence quenching, while the quenched fluorescence recovered following dissociation of the NPs owing to the phosphorylation reaction of PKs. Eleven lipopeptides with different hydrophobic moieties (hydrocarbon and lithocholic acid) and four pA-Fs having main chains with differing flexibilities and fluorescein contents were synthesized and used to fabricate a series of twenty-four PK-responsive NP probes. The responses of the PK-responsive NP probes to PKs were evaluated to screen the most suitable NP probes. The assay system was then used to determine the IC_{50} values for five inhibitors, the results of which were very similar to those previously reported. Thus, PK-responsive NPs are useful tools for high-throughput screening (HTS) of PK inhibitors.

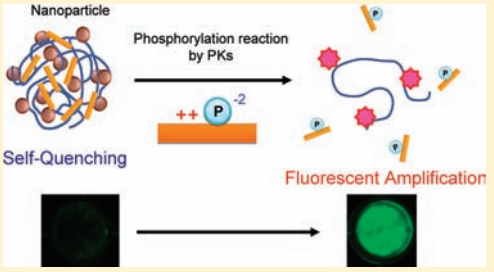

INTRODUCTION

Protein kinases (PKs) have important roles in regulating various cellular functions (e.g., growth, differentiation, motility, apoptosis, and survival) through the signal transduction system. It has been estimated that the human genome involves over 500 different genes encoding PKs, which corresponds to around 20,000 distinct phosphorylation reactions occurring in human cells.[1,2] Because the dysregulation of PK activities is associated with devastating diseases such as cancers, diabetes, autoimmune disorders, and neurological diseases, PK inhibitors have been regarded as potential drugs for their treatment.[3−5] In addition, PKs are also related to stem cell modulation (e.g., differentiation, self-renewal, reprogramming), and as such, they are of particular interest in stem-cell biology and regenerative medicine.[6] Thus, the development of chemical modulators for PK activity (e.g., inhibitors, activators) is of great significance. As such, powerful high-throughput screening (HTS) systems are necessary for the discovery of novel chemical compounds to regulate the activity of particular PKs.

Pharmaceutical companies have large libraries of chemical compounds that need to be evaluated for the discovery of PK inhibitors. As such, the development of homogeneous assays (mix-and-measure), which do not require substrates to be immobilized onto a solid phase or a washing step, are considered to be suitable for HTS formats as compared with heterogeneous assays (e.g., enzyme-linked immunosorbent assays).[7] Of the many homogeneous PK activity detection systems known, fluorescence-based assays have certain advantages as practical HTS formats due to their simple and sensitive readout and their high potential for miniaturization and automation.[7−27] Fluorescence PK assays can be classified into two large groups: antibody-based assays which employ antibodies of phospho-amino acid and non-antibody-based assays. In the case of antibody-based assays, direct detection with fluorophore-labeled antibodies,[8−11] fluorescence polarization[12,13] and fluorescence resonance energy transfer (FRET)[14,15] have been reported to date. However, most of the antibody-based assays have only been applied to end-point assays. In addition, unlike the well-known anti-phospho-tyrosine, antibodies against phospho-serine and phospho-threonine having satisfactory affinity and specificity have yet to be developed. This is the biggest obstacle to the wide application of antibody-based assays for many well-known PKs.[13]

In the case of non-antibody-based assays, a number of peptide-[16−23] and polymer-based probes[24−26] have been reported. Of these assays, some are available not only for HTS but also for PK imaging in living cells. Although polymer-based probes show good performance in cell-free and living-cell assays, their synthesis is difficult when compared with that of peptide-based probes, which are not only easy to synthesize but also have high reproducibility

Received: February 3, 2011
Revised: June 27, 2011
Published: July 11, 2011

ACS Publications © 2011 American Chemical Society

when used in automated systems. Imperiali and co-workers reported fluorophore-modified peptide probes that enhanced the original fluorescence intensity after the phosphorylation reaction via chelation of Mg^{2+} between the phosphate groups and the internal chelator of the probes.[19−22] Lee's group reported the synthesis of self-assembled micelle-like probes comprising fluorophores and long alkyl chain modified peptide substrates with a neutral net charge that elevate fluorescence intensity through a phosphorylation reaction owing to disassembly of the micelle.[23] However this probe should have cationic or anionic amino acids added to the peptide substrate to neutralize the net charges, although this modification may reduce the reactivity of the peptide toward target Ser/Thr and Tyr PKs.[28−33]

Thus, we aimed to develop a novel probe according to the following criteria: (1) homogeneous, (2) non-antibody use, (3) simple synthesis, (4) real time measurement, and (5) without any change of original peptide sequence. Especially, criterion (5) is important to avoid reducing both the reactivity and specificity of the peptide for target PKs.

In this report, we described the novel homogeneous fluorescent-PK assay using nanoparticles (NPs), each consisting of a hydrophobically modified peptide substrate (i.e., a lipopeptide) and a fluorescein-labeled polyanion (pA-F). The well-known Ser/The PKs, cAMP-dependent protein kinase (PKA)[34−36] and protein kinase C (PKC)α,[36−38] were selected as target PKs. The hyperactivations of these PKs have often been observed in many cancers, and thus, these PKs show high potential as drug targets. As specific and sensitive peptide substrates, Kemptide[28] and Alphatomega[39−42] were used for the NP probes of PKA and PKCα, respectively. When the NPs are formed between pA-Fs and lipopeptides via the electrostatic interaction, fluorescence is effectively self-quenched owing to the concentration of the fluorescein moieties. In contrast, after the phosphorylation reaction of the lipopeptides in the NPs, the fluorescence intensity is amplified owing to dissociation of the NPs because phosphorylation reaction with PKs reduces the net cationic charges of the lipopeptides. The system was available to evaluate the IC_{50} values of some well-known inhibitors of PKA and PKCα. Our system offers a simple, rapid, sensitive and accurate monitoring of PK activity which is suitable to the high-throughput screening (HTS) of PK inhibitors.

EXPERIMENTAL SECTION

Synthesis of Lipopeptides. Various lipopeptides modified with methacrylic acid or a fatty acid (hexanoic acid, decanoic acid, tetradecanoic acid, octadecanoic acid, and lithocholic acid; all from Sigma-Aldrich, Tokyo, Japan) at the *N*-terminus were synthesized according to standard Fmoc-chemistry procedures, as described previously.[39−42] The peptide sequences used for the PKA and PKCα substrates were X-LRRASLG-NH_2 and X-FKKQGSFAKKK-NH_2, respectively: X indicates a hydrophobic moiety. Crude lipopeptides were purified by reverse phase HPLC by using a linear A−B gradient at a flow rate of 3 mL/min, where eluent A was 0.1% TFA in water and eluent B was 0.1% TFA in acetonitrile, and analyzed by MALDI-ToF MS (Bruker, Kanagawa, Japan). Reverse phase HPLC and MALDI-ToF-MS analysis showed that the lipopeptides were of >95% purity.

Synthesis of Poly(L-aspartic acid) Modified with Fluorescein (pAsp-F-*X*). Poly aspartic acid in the sodium salt form (100 mg, 10 μmol) (M_w 10,500, −COOH 720 μmol; Sigma-Aldrich), 1-ethyl-3-(3-dimethylaminopropyl)carbodiimide hydrochloride (EDC) (138 mg, 720 μmol) (DOJINDO, Kumamoto, Japan), and HOBt monohydrate (110 mg, 720 μmol) (Watanabe Chem., Hiroshima, Japan) were dissolved in $NaHCO_3$ buffer (6.8 mL, 0.1 M, pH 8.5), followed by addition of various amounts of a DMF solution of Boc-ethylenediamine (Fluka, Tokyo, Japan) at 0 °C. The reaction mixture was stirred at room temperature for one day and dialyzed against distilled water by using a dialysis membrane (molecular weight cutoff, 3500) for four days, followed by lyophilization to obtain a white powder.

After deprotection of the Boc groups using TFA/DCM (1/1, v/v), the reactant was precipitated in an excess volume of diethyl ether. This suspension was centrifuged at 5000*g* for 5 min at 4 °C, and the precipitate was dried in vacuo to obtain a white powder. The primary amine contents in the polymers were determined by 2,4,6-trinitrobenezenesulfonic acid (TNBS) assay.

Fluorescein modification of pAsp-ethylenediamine was carried out briefly as follows: pAsp-ethylenediamine (100 mg) with different amine contents and a two-times excess equivalent of 5- (and 6-) carboxyfluorescein succinimidyl ester (Pierce, Tokyo, Japan) were dissolved in 350 μL of DMSO/pyridine (5/2 = v/v) containing a five-times equivalent of diisopropylethylamine, and the resulting mixture was stirred overnight. After adjusting the pH of the solution to11 with 2 M NaOH, the solution was dialyzed against water for five days by using a dialysis membrane with a molecular weight cutoff of 3,500, followed by lyophilization to obtain a yellow powder. The fluorescein content was determined by measuring the absorbance at 494 nm in PBS (pH 7.4) (ε = 68,000) using UV−vis spectroscopy (Shimadzu, Kyoto, Japan) and pAsp-F-*X*, where *X* means the content of fluorescein as mol %.

Synthesis of poly(acrylic acid)-Modified with Fluorescein (pAA-F). A mixture of poly(acrylic acid) in the free salt form (26.1 mg, Wako, Osaka, Japan) and EDC (138 mg, 720 μmol) were dissolved in $NaHCO_3$ buffer (6.0 mL, 0.1 M, pH 8.5), followed by the addition of 5-(aminoacetamido)fluorescein (4 mg, 10 μmol, Invitrogen, Tokyo, Japan) at 0 °C. The mixture was stirred overnight and then dialyzed against water for five days by using a dialysis membrane with a molecular weight cutoff of 3,500, followed by lyophilization to obtain a yellow powder. The fluorescein content was calculated using the method described above.

Quenching Assay for Optimization of NP Preparation. Lipopeptide/pAsp-F-*X* NPs at various cation/anion (C/A) ratios were prepared by simply mixing lipopeptide and pAsp-F-*X* in water. The C/A ratio is defined as the ratio of residual molar concentration of amino groups in lipopeptides to that of carboxyl groups in pAsp-F-*X*. The NPs were incubated on ice for 15 min, after which the final volume was adjusted to 100 μL with PKA reaction buffer [0.2 mM ATP, 1 mM $MgCl_2$, and 10 mM HEPES, pH 7.3; all as final concentrations] or PKCα reaction buffer [0.2 mM ATP, 1 mM $MgCl_2$, 0.5 mM $CaCl_2$, 2.0 μg/mL diacylglycerol (DAG), 2.5 μg/mL phosphatidylserine (PS), and 10 mM HEPES, pH 7.3; all as final concentrations]. The fluorescence intensity was measured at 37 °C using the multilabel counter ARVO Sx (Wallac Inc., Turku, Finland). Excitation and emission wavelengths were 485 and 535 nm, respectively. The relative fluorescence intensity (RFI) was determined using the following equation:

$$relative fluorescence intensity (RFI) = (F_{obs} - F_b)/(F_{pAsp\text{-}F\text{-}X} - F_b)$$

In this formula, F_{obs}, F_b, and $F_{pAsp\text{-}F}$ are the fluorescence intensities of the lipopeptide/pAsp-F-*X* NPs at each C/A ratio,

that of reaction buffer, and that of pAsp-F-*X* without lipopeptides, respectively.

Fluorescent Amplification Assay. Lipopeptide/pAsp-F-*X* NPs were prepared at optimal C/A ratios, as shown in Table 1. The NPs were incubated on ice for 15 min, after which the final volume was adjusted to 100 μL with PKA or PKCα reaction buffer containing 0.1 U/μL PKA (Promega, Tokyo, Japan) or 1.1 ng/μL PKCα (Sigma-Aldrich), respectively. Before the addition of PKs, the fluorescence intensity of the sample solution was measured and was plotted at t = 0 in all figures. Fluorescence measurements of the sample solutions were taken at each time interval using the multilabel counter ARVO Sx following the addition of PK or heat-inactivated PK. The inactivation of the PKs was performed by heating the sample solution at 97 °C for 5 min. The phosphorylation ratio at each time interval was also determined by MALDI-ToF-MS as described previously.[39−41]

Measurement of Light-Scattering Intensity (LSI). Dissociation of the lipopeptide/pAsp-F-*X* NPs by PKs was confirmed by monitoring the LSI using Zetasizer Nano Series particle analyzer (Malvern Instruments, U.K.), as described previously.[40] The final volume of the NP dispersion was adjusted to 100 μL with PKA or PKCα reaction buffer as described above. The reaction was initiated by adding PKs to each buffer at 37 °C.

Determination of IC_{50}. The time course of fluorescence amplification in the PK reaction in the presence of various concentrations of known PK inhibitors was measured as described above. IC_{50} factors were calculated by using Graph Prism sigmoidal dose response software. EC_{50} factors were also calculated according to the same procedures.

Table 1. Efficiency of Quenching and Fluorescence Amplification in Various Lipopeptides and pAsp-F-*X*s

lipopeptides	pAsp-F-*X*	C/A[a]	QE[b]/%	RFI changes[c]	time[d]/min
Ma-PKA[e]	all types	—[f]	—	—	—
6-PKA[e]	all types	—	—	—	—
10-PKA	pAsp-F-1.1	3.0	85	3.9	5
	pAsp-F-3.7	3.0	90	6.3	5
	pAsp-F-10.8	2.0	90	2.3	5
14-PKA	pAsp-F-1.1	3.0	62	—	—
	pAsp-F-3.7	1.5	87	4.1	5
	pAsp-F-10.8	3.0	90	—	—
18-PKA	pAsp-F-1.1	0.5	39	—	—
	pAsp-F-3.7	1.0	75	3.1	30
	pAsp-F-10.8	1.5	84	—	—
Lith-PKA	pAsp-F-1.1	3.0	21	—	—
	pAsp-F-3.7	3.0	64	2.7	20
	pAsp-F-10.8	4.0	75	—	—

[a] C/A ratio showing the highest quenching efficiency. [b] QE means quenching efficiency. QE is calculated from the following equation: $QE/\% = (1 - RFI_{NP}) \times 100$. RFI_{NP} is relative fluorescent intensity of nanoparticle. [c] Maximum RFI changes. [d] The time of maximum RFI changes. [e] Quenching assays and PKA amplification assays were not performed because NP formation was not observed in the DLS experiment. [f] "—" means "not determined".

RESULTS AND DISCUSSION

Design of PK-Responsive Fluorescent NPs. The concept of PK-responsive fluorescent NPs is shown in Figure 1. For this strategy, various cationic lipopeptides (the net charge for the PKA and PKCα peptide substrates is +2 and +5, respectively) modified with different lengths of fatty acids or lithocholic acid at the *N*-terminus of the peptide substrates were synthesized to increase their interaction (Chart 1). The electrostatic formation of NPs between these cationic lipopeptides and fluorescein-modified polyanions (pA-Fs) results in fluorescence quenching because the fluorescein moieties associated with the pA-Fs are in close proximity to each other so as to allow intermolecular energy transfer owing to the compaction of the pA-F chains (i.e., the Förster radius of fluorescein−fluorescein = 4.4 nm).[43] On the other hand, when the lipopeptide was phosphorylated by the target PKs, the NPs dissociated because the electrostatic interactions between the pA-Fs and the lipopeptides were weakened owing to a decrease of the net cationic charges of the lipopeptides as a result of the introduction of negatively charged phosphate groups into the lipopeptides (i.e., +2 to 0 in the PKA peptide substrate and +5 to +3 in the PKCα peptide substrate), leading to amplification of the fluorescence intensity.

Effect of Main Chain Structures of pA-F. Two types of polyanions, poly(aspartic acid) (pAsp) and poly(acrylic acid) (pAA) (Chart 1), were compared as pA-Fs: pAsp is more rigid than pAA. Each pA-F, which contains fluorescein from 1 to 11 mol %, was dissolved in HEPES buffer (10 mM, pH 7.3) or PK reaction buffer (10 mM HEPES buffer (pH 7.3) with 100 μM ATP and 1 mM $MgCl_2$), and then their fluorescence intensity was measured using a microplate reader (Figure S1 in the Supporting Information). No obvious difference in fluorescence intensity was detected between the two buffered pAsp-F-*X* solutions (*X* means the content of fluorescein as mol %). In contrast, the fluorescence intensity in the two buffered pAA-F-1.3 solutions was four times lower in the PK reaction buffer containing Mg^{2+} than in the HEPES buffer indicating

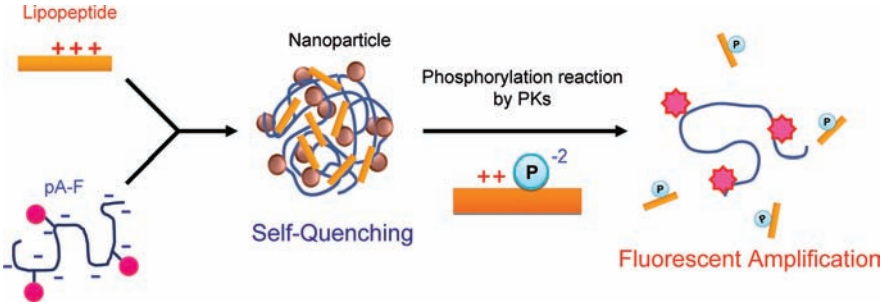

Figure 1. Schematic illustration of the PK-responsive system. Fluorescence is quenched via the formation of nanoparticles (NPs) between cationic lipopeptides and fluorescein-labeled polyanions (pA-Fs). Phosphorylation reactions by PKs decrease the net cationic charges of the lipopeptides, causing the NPs to dissociate, and then the fluorescence intensity is amplified.

Chart 1. Chemical Structures of Lipopeptide and pA-F

Lipopeptide

Lipopeptide	Peptide sequence
X-PKA	X-LRRASLG-NH_2
X-PKC	X-FKKQGSFAKKK-NH_2

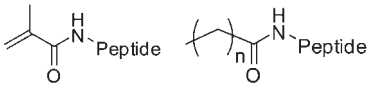

X = Ma

X = 6, 10, 14 and 18
(n = 4, 8, 12 and 16)

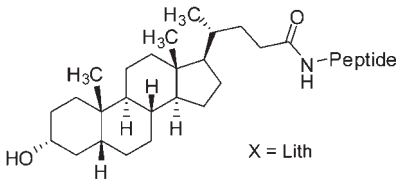

X = Lith

pA-F

pAA-F

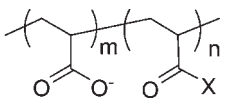

X = Aminofluorescein

pAsp-F-X

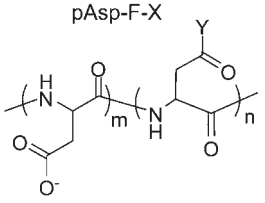

Y = Fluorescenyl ethylenediamine
or ethylenediamine

self-quenching of pAA-F-1.3 in the PK reaction buffer. This difference in quenching behavior between pAsp-F and pAA-F is considered to be due to the difference in the rigidity of the polymer chain. The pAA chain will be flexible enough to form a compaction state by hydrophobic interaction of the fluorescein moieties. Another possibility to explain the difference observed in the two polyanions is the hydrophobicity of the pA-F main chain. In the PK reaction buffer, Mg^{2+} ions will be chelated by the carboxylic acid moiety of the main chain, which will enhance the compaction of pA-F due to the decrease in the electrostatic repulsion. More hydrophilic nature of the main chain of pAsp-F-*X* may contribute to avoid the self-aggregation. These results suggest that a rigid and hydrophilic polymer main chain is more suitable to avoid self-quenching without lipopeptides. Thus, pAsp-F-*X* was selected as the optimal chemical structure for the polyanions for this strategy.

Fluorescence Quenching by NP Formation. We examined the optimum C/A ratio for mixing of lipopeptides and pAsp-F-*X* to find a suitable quenching condition in NP formation; the results of the study are summarized in Table 1. First, we investigated the effects of the *N*-terminus hydrophobic moiety of the lipopeptides on the formation of NPs using dynamic light scattering (DLS) measurement. The less hydrophobic Ma-PKA and 6-PKA did not form detectable NPs with the pAsp-F-*X* used in this study at any C/A ratio due to their low hydrophobicity. On the other hand, those longer fatty acid- or lithocholic acid-modified lipopeptides (10-PKA, 14-PKA, 18-PKA and Lith-PKA) were able to form NPs with pAsp-F-*X* with a diameter of 200–1000 nm depending on the content of fluorescein in pAsp-F-*X* and the C/A ratio. Previous reports demonstrated that NPs comprising polycations and polyanions modified with hydrophobic groups are generally more stable than NPs consisting of unmodified polycations and polyanions even in high salt concentration owing to hydrophobic interactions.[44−46] Thus we concluded that hydrophobic interactions among the *N*-terminus hydrophobic moieties of the lipopeptides play a critical role in increasing the interaction with polyanions. To our knowledge, this is the first report demonstrating the importance of hydrophobic groups on NP formation between polyanions and cationic peptides with low net cationic charges.

Next, we examined the quenching efficiency (QE) of pAsp-F-*X*/lipopeptide NPs in PKA reaction buffer without PKA, and the result is shown in Figure 2 and Table 1. The relative fluorescence intensity (RFI) of NPs with 10-PKA, 14-PKA and Lith-PKA decreased with increasing C/A ratio, and became saturated above particular C/A ratios depending on the combination of pAsp-F-*X* and lipopeptides. In contrast, NPs with 18-PKA showed a different behavior. For example, the RFI of the 18-PKA/pAsp-F-3.7 NPs decreased with increasing C/A ratio, and reached a minimum at a C/A ratio of 1.0, while a further increase of the C/A ratio led to an elevation of the RFI. Similar behaviors were also observed in the systems of pAsp-F-1.1 and pAsp-F-10.8. This observation is not fully understood as yet, but it is considered that, at higher C/A ratios, 18-PKA may assemble with itself to form micelles.

In comparison with the pAsp-F-*X*/Lith-PKA system, the RFI reached about 0.4 at a C/A ratio of 1.5 in pAsp-F-3.7 and pAsp-F-10.8 NPs (Figure 2B,C), while that in the pAsp-F-1.1 NPs was reduced only to 0.8 even at a C/A ratio of 3 (Figure 2A). In addition, weak quenching caused by the formation of NPs in pAsp-F-1.1 was also observed with 14-PKA and 18-PKA, as compared with those in pAsp-F-3.7 and pAsp-F-10.8 (Table 1). These results indicated a lower QE for the pAsp-F-1.1 NPs compared with others. This lower QE was due to the low content of fluorescein in pAsp-F-*X*. Thus, we concluded that pAsp-F-1.1 was not suitable as a pAsp-F-*X* to achieve effective quenching.

In the case of pAsp-F-3.7 NPs, 18-PKA (75%) and Lith-PKA (64%) showed insufficient fluorescent quenching at C/A ratios of 1 and 3, respectively. In contrast, both 10-PKA and 14-PKA showed more effective fluorescent quenching at about 90% at C/A ratios of 3 and 1.5, respectively (Figure 2B and Table 1). Similarly in the system of pAsp-F-10.8 NPs, slightly higher quenching efficiencies from both 10-PKA and 14-PKA (90%) were detected compared with 18-PKA (84%) and Lith-PKA (75%) (Figure 2C). Clearly, as the hydrophobicity of the *N*-terminus moiety in the lipopeptides increased, the quenching efficiency tended to reduce probably due to steric hindrance of the *N*-terminus moieties. Thus, the less hydrophobic

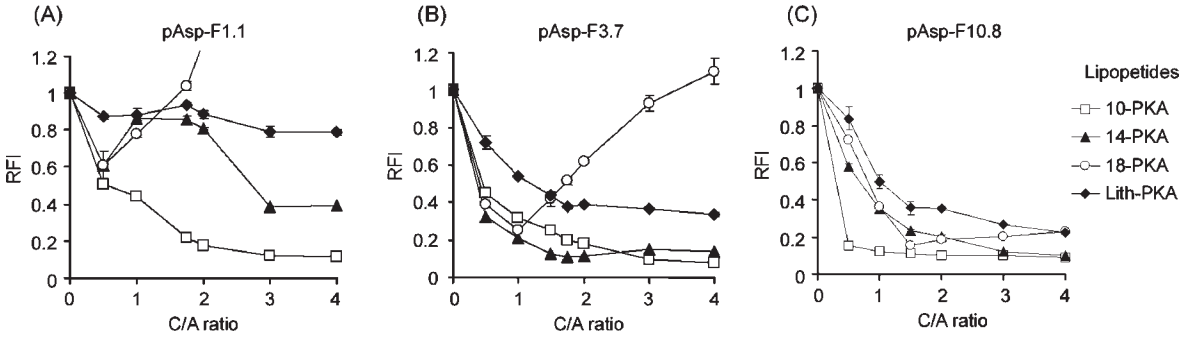

Figure 2. Evaluation of fluorescence intensity of NPs at each C/A ratio. After the formation of NPs between lipopeptides and (A) pAsp-F-1.1, (B) pAsp-F-3.7 and (C) pAsp-F-10.8 in PKA reaction buffer without PKA, the fluorescence intensity was measured using a microplate reader. Data are represented as relative fluorescence intensity (RFI), as described in the Experimental Section.

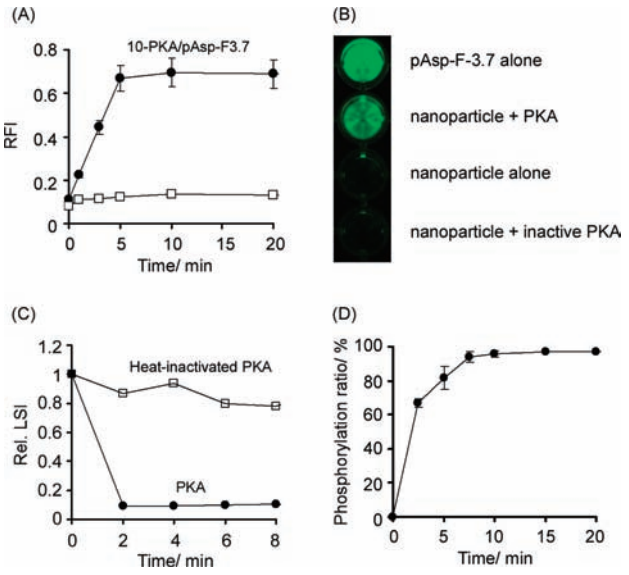

Figure 3. Fluorescence amplification of 10-PKA/pAsp-F-3.7 NPs (C/A ratio 3.0) by the phosphorylation reaction with PKA. (A) Change of fluorescence intensity after addition of 100 U/mL PKA (closed circles) and heat-inactive PKA (open squares) to a dispersion containing 10-PKA/pAsp-F-3.7 NPs. (B) Fluorescence images from microplate wells 20 min after PKA addition. (C) Change of light scattering intensity (LSI) of NP dispersion after addition of PKA (closed circles) and heat-inactivated PKA (open squares). Data are represented as relative LSI, where the initial LSI was defined as 1. (D) Time course of phosphorylation ratio. Phosphorylation ratios of NPs were determined by MALDI-ToF-MS analysis.

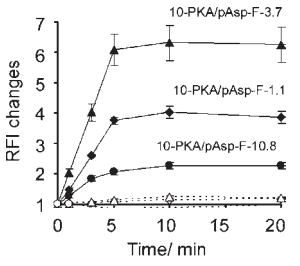

Figure 4. Change of fluorescence intensity of various 10-PKA NPs by PKA (closed marks) and heat-inactivated PKA (open marks). Diamonds, triangles and circles indicate 10-PKA/pAsp-F-1.1, 10-PKA/pAsp-F-3.7 and 10-PKA/pAsp-F-10.8 NPs, respectively. Data are represented as fold fluorescence changes after the phosphorylation reaction.

lipopeptides such as 10-PKA and 14-PKA were superior in quenching efficiency.

Fluorescent Amplification by Phosphorylation Reaction. Six NPs (summarized in Table 1) were investigated to see whether their fluorescence intensities were amplified by the phosphorylation reaction with PKA. After addition of active or heat-inactivated PKA (negative control) to the NP dispersions in 96-well-microplates, the time course of fluorescence intensity was monitored using a microplate reader. As shown in Figure 3A,B, the RFI of the 10-PKA/pAsp-F-3.7 NPs did not change for 20 min after addition of heat-inactivated PKA. On the other hand, a drastic increase of RFI was detected after addition of PKA, in which the RFI reached a maximum after 5 min (6.3-fold increase).

To clarify whether fluorescence amplification is caused by dissociation of the NPs during the phosphorylation reaction with PKA, the time course of both the light scattering intensity (LSI) and the phosphorylation ratio of 10-PKA/pAsp-F-3.7 was monitored with DLS and MALDI-ToF MS analysis, respectively. As shown in Figure 3C, when heat-inactivated PKA was added to the 10-PKA/pAsp-F-3.7 NP dispersion, no change in LSI was detected. In contrast, an immediate and drastic decrease of LSI was observed after addition of PKA. Moreover, the time course of the phosphorylation ratio of 10-PKA/pAsp-F-3.7 NPs was almost concerted with that of the RFI and LSI changes (Figure 3D). These results strongly suggest that the 10-PKA/pAsp-F-3.7 NPs dissociated as a result of the phosphorylation reaction with PKA, leading to amplification of the fluorescence intensity.

Effect of Fluorescein Content in pAsp-F-*X* and Hydrophobicity of Lipopeptide. A fluorescence amplification assay with PKA was conducted against NPs consisting of 10-PKA and three kinds of pAsp-F-*X* with different fluorescein contents (Figure 4). In all of the 10-PKA/pAsp-F-*X* systems, a gradual increase of the fluorescence intensity was observed by the addition of active PKA, but such amplification was not observed with inactivated PKA. However, there was a significant difference in fluorescence amplification; 3.9-, 6.3-, and 2.3-fold for 10-PKA/pAsp-F-1.1, 10-PKA/pAsp-F-3.7 and 10-PKA/pAsp-F-10.8, respectively, at 5 min after PKA addition in which the changes in RFI were saturated. From a comparison of the 10-PKA/pAsp-F-1.1 and 10-PKA/pAsp-F-3.7 NPs (Table 1), it was speculated that a higher quenching efficiency is better for larger RFI changes.

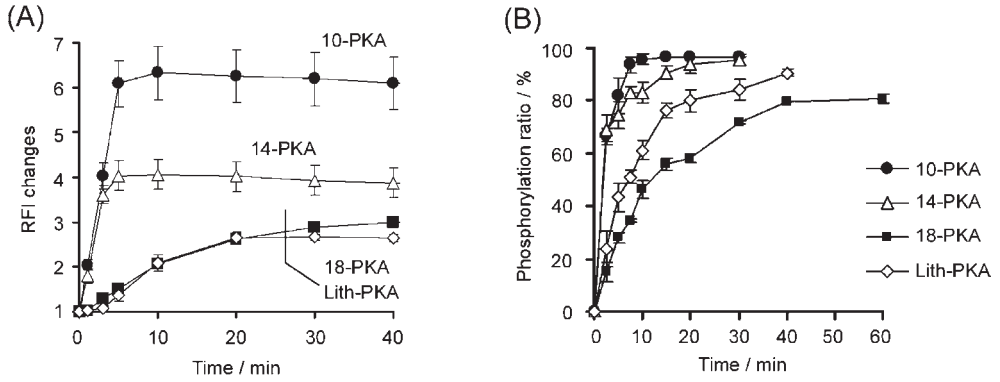

Figure 5. Effect of the hydrophobic moiety of the lipopeptide on fluorescence amplification by PKA. (A) Time course of fluorescence change of NPs involving various lipopeptides and pAsp-F3.7 by PKA. Data are represented as fold changes with initial RFI. (B) Change of phosphorylation ratio of various pAsp-F-3.7 NPs.

However, the RFI change in 10-PKA/pAsp-F-10.8 was the lowest in spite of the high quenching efficiency. This poor fluorescence recovery of the 10-PKA/pAsp-F-10.8 NPs is considered to be due to the incomplete dissociation of the NPs to recover their original fluorescence intensity. These results indicated that effective dissociation as well as effective quenching is important to achieve large fluorescent amplification. We found that pAsp-F-3.7 was the best polyanion in this study because it achieved not only effective quenching but effective dissociation.

Figure 5A shows a comparison of pAsp-F-3.7 NPs with each lipopeptide. The fluorescence intensities of the NPs increased with PKA addition in all cases. However, those NPs with more hydrophobic lipopeptides (18-PKA and Lith-PKA) showed less RFI changes than those with less hydrophobic lipopeptides (10-PKA and 14-PKA). This was due to less quenching of the more hydrophobic lipopeptides as discussed above (Table. 1). In addition, when the hydrophobicity of the lipopeptides was increased, longer reaction times were needed to reach the maximum RFI. Thus the phosphorylation time course of each NP system was determined by MALDI-ToF-MS (Figure 5B). The NPs of 10-PKA/pAsp-F-3.7 and 14-PKA/pAsp-F-3.7 were phosphorylated with a comparable time course, and they were almost concerted with that of the RFI changes. In contrast, the phosphorylation ratio of Lith-PKA/pAsp-F-3.7 and 18-PKA/pAsp-F-3.7 proceeded more slowly compared with that of 10-PKA/pAsp-F-3.7 and 14-PKA/pAsp-F-3.7. Thus, the slow RFI development in NPs involving highly hydrophobic lipopeptides reflected a slow phosphorylation reaction. We concluded that the 10-PKA/pAsp-F-3.7 and 14-PKA/pAsp-F-3.7 NPs were suitable to achieve drastic and rapid fluorescence amplification on reaction with PKA.

Optimal NPs for High-Throughput Assay of PK Inhibitors. To evaluate the sensitivities of this system, fluorescence amplification during phosphorylation reactions was monitored against 14-PKA/pAsp-F-3.7 and 10-PKA/pAsp-F-3.7 NPs in the presence of several concentrations of PKA (0.1−100 U/mL) (Figure S2A,B in the Supporting Information). The 10-PKA/pAsp-F-3.7 NPs showed fluorescence amplification with phosphorylation above 50 U/mL of PKA, whereas the 14-PKA/pAsp-F-3.7 NPs increased the RFI above 10 U/mL. One of the reasons for the higher sensitivity of the 14-PKA/pAsp-F-3.7 NPs is the much smaller size of the 14-PKA/pAsp-F-3.7 NPs (627 and 194 nm for 10-PKA/pAsp-F-3.7 and 14-PKA/pAsp-F-3.7 NPs, respectively), which corresponds to a larger specific surface area, enabling the efficient PKA reaction. The EC_{50} value, which is the concentration of enzyme required for 50% of maximum phosphorylation of the peptide, was determined to be 11 U/mL for 14-PKA/pAsp-F-3.7 NPs (Figure S2C in the Supporting Information). Thus, the 14-PKA/pAsp-F-3.7 NPs were used for determination of the IC_{50} of the PKA inhibitor described below.

Application to Another Kinase, PKCα. To demonstrate the generality of our assay, we applied the system to PKCα, another Ser/Thr kinase. Because PKCα plays key roles in abnormal proliferation of cancer cells, it is hyperactivated in many cancer cells or tissues (e.g., melanoma, hepatoma, glioma, and breast cancer).[36−41] Thus, monitoring of PKCα activity is considered to be useful for cancer diagnosis. A PKCα-specific peptide (H-FKKQGSFAKKK-NH_2)[38−40] was used as a motif of lipopeptides (Table 1). However, there were two issues for applying the peptide to our system. First, PKCα needs a lipid cofactor for enzyme activation. It was reported that cationic detergent-like molecules with longer alkyl chains (i.e., 1,12-diaminododecane and octadodecylamine) act as competitive inhibitors against phospholipid-sensitive PKC families including PKCα, whereas octylamine, which has a shorter alkyl chain, showed no inhibitory effect.[47,48] Because the chemical structures of lipopeptides resemble cationic detergents, they may have some effect on PKCα activity. Thus, we examined the phosphorylation ratios of lipopeptides involved in NPs with PKCα by MALDI-ToF-MS to select the optimal hydrophobic moieties of the PKC lipopeptides (Figure S3 in the Supporting Information). The phosphorylation ratio of NPs with 10-PKC or Lith-PKC was similar to that of the free peptide substrate (Ma-PKC), but NPs with 14-PKC or 18-PKC showed lower phosphorylation ratios, suggesting that lipopeptides with longer fatty acids are not suitable as lipopeptides for PKCα. Thus, we selected 10-PKC for the fluorescence amplification assay of PKCα.

Another issue is the high cationic charge (+5) of the peptide. The peptide still has +3 net charges after phosphorylation in contrast to the PKA substrate that changes its net charge to neutral. This may be unfavorable for fluorescence development with phosphorylation of the NPs, because the responsiveness of the system is based on the decrease of positive charge on the peptide. Thus, we investigated the fluorescence characteristics during NP formation and its phosphorylation. When 10-PKC formed NPs with pAsp-F-3.7 or pAsp-F-10.8, the fluorescence intensities were effectively quenched (70%) above a C/A ratio of 0.5 or 1.5, respectively (Figure 6A). After forming 10-PKC/pAsp-F-10.8 NPs at a C/A ratio of 2.0, the fluorescence intensity

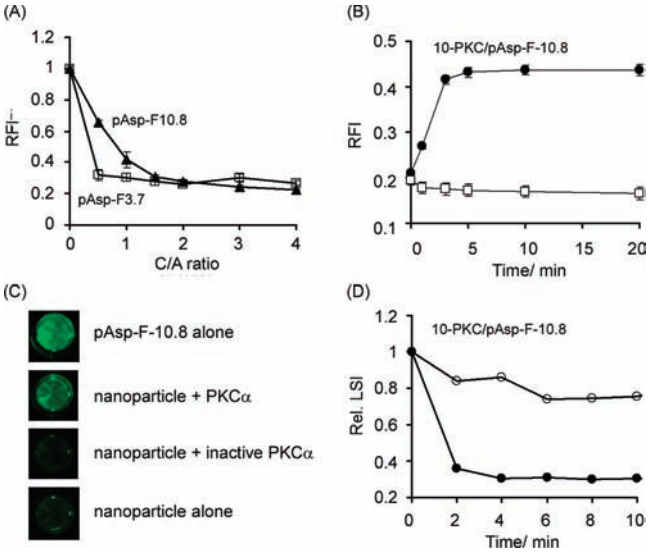

Figure 6. Fluorescence amplification of NPs by PKCα. (A) Fluorescence quenching of 10-PKC/pAsp-F-3.7 (open squares) or 10-PKC/pAsp-F-10.8 (closed triangles) NPs at each C/A ratio in PKCα reaction buffer without PKCα. (B) Change of RFI after addition of 1.1 pg/μL PKCα (closed circles) and heat-inactive PKCα (open squares) to dispersions containing 10-PKC/pAsp-F-10.8 NP (C/A ratio = 3.0). (C) Fluorescence images from microplate wells obtained 20 min after PKCα addition. (D) Change of LSI of 10-PKC/pAsp-F-10.8 (closed circles) and 10-PKC-A/pAsp-F-10.8 (open circles) NP dispersions by PKCα. 10-PKC-A was used as the negative control of 10-PKC, where a phosphorylation site serine was substituted with alanine, meaning no phosphorylation occurred with PKCα.

was monitored in the presence of active or inactivated PKCα. No change of RFI was detected after addition of heat-inactivated PKCα, whereas the RFI increased after adding PKCα (Figure 6B). These changes were also clearly detected visually under a UV illuminator (Figure 6C). In addition, dissociation of the 10-PKC/pAsp-F-10.8 NPs by phosphorylation was confirmed by a decrease in LSI after addition of PKCα (Figure 6D).

These results demonstrated the wide applicability of our system for PKs that prefer cationic substrate peptides having net charges ranging from +2 to +5. Such PKs include many kinds of Ser/Thr kinases such as Ca^{2+}/calmodulin-dependent PK II (CaMK-II), mitogen-activated PK-2 (MAPK-2), MAP-activated PK-2 (MAPKAPK-2), and PKB/Akt.[29−33,49] However, it may be difficult to apply our methodology to PKs that phosphorylates acidic peptides (e.g., casein kinase[50]).

Determination of IC_{50} Values of PK Inhibitors. Finally, we applied the PK-responsive fluorescent NPs for evaluation of the IC_{50} values of certain PK inhibitors. 14-PKA/pAsp-F-3.7 and 10-PKC/pAsp-F-10.8 NPs were used for the IC_{50} determination of inhibitors against PKA and PKCα, respectively. When the fluorescence intensity was monitored during the PKA reaction in the presence of various concentrations of staurosporine and H-89, a concentration-dependent suppression of the fluorescence amplification was observed (Figure 7A for staurosporine), which could also be observed visually (Figure 7B). By using the fluorescence intensity value obtained 20 min after the PKA reaction (Figure 7C), we determined the IC_{50} values of staurosporine and H-89 as 18 nM and 241 nM, respectively. These values were consistent with those previously reported (15 nM and 135 nM) (Table 2). The use of the 10-PKC/pAsp-F-10.8 NPs enabled us to calculate the IC_{50} values of certain PKCα inhibitors (Table 2). These results show that our NP systems are useful in high-throughput screening (HTS) to search for novel PK inhibitors.

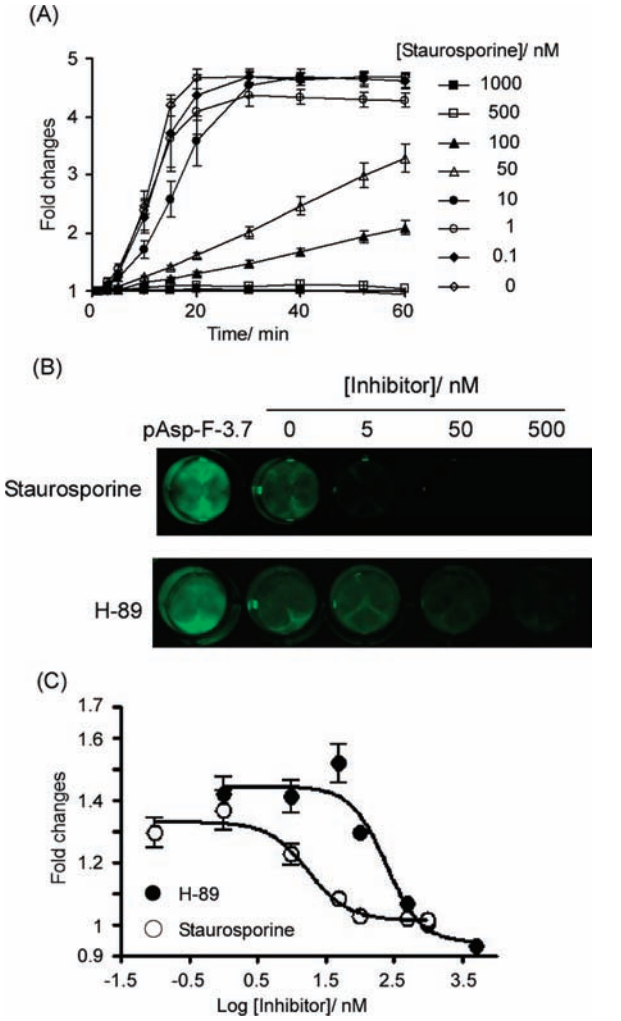

Figure 7. Determination of IC_{50} values of PKA inhibitors using 14-PKA/pAsp-F-3.7 NPs. (A) Change of fluorescence intensity by PKA in the presence of various concentrations of staurosporine (0.1−1000 nM). (B) Fluorescence optical images of microplate wells obtained 20 min after PKA addition. (C) IC_{50} data for H-89 (closed circles) and staurosporine (open circles).

Table 2. IC_{50} Values for Each Inhibitor Determined by Using Optimized NPs

		IC_{50} value/nM	
target PKs[a]	inhibitors	found	reported
PKA	staurosporine	18	15[51]
	H-89	241	135[52]
PKCα	Ro-31-7549	64	53[53]
	Ro-31-8425	17	8[53]
	rottlerin	>5,000	30,000[54]

[a] 14-PKA/pAsp-F-3.7 and 10-PKC/pAsp-F-10.8 NPs were used for PKA and PKCα assay, respectively.

■ ASSOCIATED CONTENT

Supporting Information. Characterizations of NPs. This material is available free of charge via the Internet at http://pubs.acs.org.

■ AUTHOR INFORMATION

Corresponding Author

*Phone: +81-92-802-2849. Fax: +81-92-802-2849. E-mail: ykatatcm@mail.cstm.kyushu-u.ac.jp.

Present Addresses

[§]Innovation Center for Medical Redox Navigation, Kyushu University, 3-1-1 Maidashi, Higashi-ku, Fukuoka 812-8582, Japan. [⊥]Laboratory for Advanced Diagnostic Devices and Department of Biomedical Engineering, Advanced Medical Engineering Center, National Cardiovascular Center Research Institute, 5-7-1 Fujishirodai, Suita, Osaka 565-8565, Japan.

Author Contributions

[‡]These authors contributed equally to this work.

■ ACKNOWLEDGMENT

This work was financially supported by a grant-in-aid for Scientific Research from the Ministry of Education, Culture, Sports, Science and Technology (MEXT) of Japan. R.T. is grateful to the Japan Society for the Promotion of Science (JSPS) for the doctor course scholarship.

■ REFERENCES

(1) Hunter, T. (2000) Signaling—2000 and beyond. *Cell 100*, 113–127.

(2) Cohen, P. (2001) The role of protein phosphorylation in human health and disease. *Eur. J. Biochem. 268*, 5001–5010.

(3) Zhang, J., Yang, P. L., and Gray, N. S. (2009) Targeting cancer with small molecule kinase inhibitors. *Nat. Rev. Cancer 9*, 28–39.

(4) Knight, Z. A., Lin, H., and Shokat, K. M. (2010) Targeting the cancer kinome through polypharmacology. *Nat. Rev. Cancer 10*, 130–137.

(5) Lapenna, S., and Giordano, A. (2009) Cell cycle kinases as therapeutic targets for cancer. *Nat. Rev. Drug Discovery 8*, 547–566.

(6) Xu, Y., Shi, Y., and Ding, S. (2008) A chemical approach to stem-cell biology and regenerative medicine. *Nature 453*, 338–344.

(7) Ahsen, O. V., and Bömer, U. (2005) High-throughput screening for kinase inhibitors. *ChemBioChem 6*, 481–490.

(8) Kupcho, K., Somberg, R., Bulleit, B., and Goueli, S. A. (2003) A homogeneous, nonradioactive high-throughput fluorogenic protein kinase assay. *Anal. Biochem. 317*, 210–217.

(9) Rodems, M., Hamman, B. D., Lin, C., Zhao, J., Shah, S., Heidary, D., Makings, L., Stack, J. H., and Pollok, B. A. (2002) A FRET-based assay platform for ultra-high density drug screening of protein kinases and phosphatases. *Assay Drug Dev. Technol. 1*, 9–19.

(10) Park, Y. W., Cummings, R. T., Wu, L., Zheng, S., Cameron, P. M., Woods, A., Zaller, D. M., Marcy, A. I., and Hermes, J. D. (1999) Homogeneous proximity tyrosine kinase assays: scintillation proximity assay versus homogeneous time-resolved fluorescence. *Anal. Biochem. 269*, 94–104.

(11) Turek-Etienne, T. C., Lei, M., Terracciano, J. S., Langsdorf, E. F., Bryant, R. W., Hart, R. F., and Horan, A. C. (2004) Use of red-shifted dyes in a fluorescence polarization AKT kinase assay for detection of biological activity in natural product extracts. *J. Biomol. Screening 9*, 52–61.

(12) Fowler, A., Swift, D., Longman, E., Acornley, A., Hemsley, P., Murray, D., Unitt, J., Dale, I., Sullivan, E., and Coldwell, M. (2002) An evaluation of fluorescence polarization and lifetime discriminated polarization for high throughput screening of serine/threonine kinases. *Anal. Biochem. 308*, 223–231.

(13) Turek, T. C., Small, E. C., Bryant, R. W., and Hill, W. A. G. (2001) Development and validation of a competitive AKT serine/threonine kinase fluorescence polarization assay using a product-specific anti-phospho-serine antibody. *Anal. Biochem. 299*, 45–53.

(14) Freeman, R., Finder, T., Gill, R., and Willner, I. (2010) Probing protein kinase (CK2) and alkaline phosphatase with CdSe/ZnS quantum dots. *Nano Lett. 10*, 2192–2196.

(15) Ghadiali, J. E., Cohen, B. E., and Stevens, M. M. (2010) Protein kinase-actuated resonance energy transfer in quantum dot−peptide conjugates. *ACS Nano 4*, 4915–4919.

(16) Sharma, V. R., Agnes, S., and Lawrence, D. S. (2007) Deep quench: an expanded dynamic range for protein kinase sensors. *J. Am. Chem. Soc. 129*, 2742–2743.

(17) Yeh, R. H., Yan, X., Commer, M., Bresnick, A. R., and Lawrence, D. S. (2002) Real time visualization of protein kinase activity in living cells. *J. Biol. Chem. 277*, 11527–11532.

(18) Kikuchi, K., Hashimoto, S., Mizukami, S., and Nagano, T. (2009) Anion sensor-based ratiometric peptide probe for protein kinase activity. *Org. Lett. 11*, 2732–2735.

(19) Shults, M. D., and Imperiali, B. (2003) Versatile fluorescence probes of protein kinase activity. *J. Am. Chem. Soc. 125*, 14248–14249.

(20) Shults, M. D., Janes, K. A., Lauffenburg, D. A., and Imperiali, B. (2005) A multiplexed homogeneous fluorescence-based assay for protein kinase activity in cell lysates. *Nat. Methods 2*, 277–284.

(21) Shults, M. D., Moniz, D. C., and Imperiali, B. (2006) Optimal Sox-based fluorescent chemosensor design for serine/threonine protein kinases. *Anal. Biochem. 352*, 198–207.

(22) Luković, E., González-Vera, J. A., and Imperiali, B. (2008) Recognition-domain focused chemosensors: versatile and efficient reporters of protein kinase activity. *J. Am. Chem. Soc. 130*, 12821–12827.

(23) Sun, H., Low, K. E., Woo, S., Noble, R. L., Graham, R. J., Connaughton, S. S., Gee, M. A., and Lee, L. G. (2005) Real-time protein kinase assay. *Anal. Chem. 77*, 2043–2049.

(24) Kim, J. H., Lee, S., Kim, K., Jeon, H., Park, R. W., Kim, I. S., Choi, K., and Kwon, I. C. (2007) Polymeric nanoparticles for protein kinase activity. *Chem. Commun 13*, 1346–1348.

(25) Kim, J. H., Lee, S., Park, K., Nam, H. Y., Jang, S. Y., Youn, I., Kim, K., Jeon, H., Park, R. W., Kim, I. S., Choi, K., and Kwon, I. C. (2007) Protein-phosphorylation-responsive polymeric nanoparticles for imaging protein kinase activities in single living cells. *Angew. Chem., Int. Ed. 46*, 5779–5782.

(26) Rininsland, F., Xia, W., Wittenburg, S., Shi, X., Stankewicz, C., Achyuthan, K., McBranch, D., and Whitten, D. (2004) Metal ion-mediated polymer superquenching for highly sensitive detection of kinase and phosphatase activities. *Proc. Natl. Acad. Sci. U.S.A. 101*, 15295–15300.

(27) Lee, S., Park, K., Kim, K., Choi, K., and Kwon, I. C. (2008) Activatable imaging probes with amplified fluorescent signals. *Chem. Commun. 36*, 4250–4260.

(28) Kemp, B. E., Graves, D. J., Benjamini, E., and Krebs, E. D. (1977) Role of multiple basic residues in determining the substrate specificity of cyclic AMP-dependent protein kinase. *J. Biol. Chem. 252*, 4888–4894.

(29) Stokoe, D., Caudwell, B., Cohen, P. T. W., and Cohen, P. (1993) The substrate specificity and structure of mitogen-activated protein (MAP) kinase-activated protein kinase-2. *Biochem. J. 296*, 843–849.

(30) Songtang, Z., Lu, K. P., Kwon, Y. T., Tsai, L. H., Filhol, O., Cochet, C., Brickey, D. A., Bartleson, T. R. C., Graves, D. J., and DeMaggio, A. (1996) A structural basis for substrate specificities of protein Ser/Thr kinases: primary sequence preference of casein kinases I and II, NIMA, phosphorylase kinase, calmodulin-dependent kinase II, CDK5, and Erk1. *Mol. Cell. Biol. 16*, 6486–6493.

(31) Hutti, J. E., Jarrell, E. T., Chang, J. D., Abbott, D. W., Storz, P., Toker, A., Cantley, L. C., and Turk, B. E. (2004) A rapid method for determining protein kinase phosphorylation specificity. *Nat. Methods 1*, 27–29.

(32) Songyang, Z., Carraway, K. L., III, Eck, M. J., Harrison, S. C., Feldman, R. A., Mohammadi, M., Schlessinger, J., Hubbard, S. R., Smith, D. P., Eng, C., Lorenzo, M. J., Ponder, B. A. J., Mayer, B. J., and Cantley, L. C. (1995) Catalytic specificity of protein-tyrosine kinases is critical for selective signaling. *Nature 373*, 536–539.

(33) Hofmann, J. (1997) The potential for isoenzyme-selective modulation of protein kinase C. *FASEB J. 11*, 649–667.

(34) Carlson, C. C., Smithers, S. L., Yeh, K. A., Burnham, L. L., and Dransfield, D. T. (1999) Protein kinase A regulatory subunits in colon cancer. *Neoplasia 4*, 373–378.

(35) Ludwig, K. W., Lowey, B., and Niles, R. M. (1980) Retinoic acid increases cyclic AMP-dependent protein kinase activity in murine melanoma cells. *J. Biol. Chem. 255*, 5999–6002.

(36) Hulme, P. C., Clegg, M. J., Miler, R. A., and Gordge, W. R. (1996) Elevation of protein kinase A and protein kinase C activities in malignant as compared with normal human breast tissue. *Eur. J. Cancer 32A*, 2120–2126.

(37) Hofmann, J. (2004) Protein kinase C isozymes as potential targets for anti cancer therapy. *Curr. Cancer Drug Targets 4*, 125–146.

(38) Mackay, H. J., and Twelves, C. J. (2007) Targeting the protein kinase C family: are we there yet? *Nat. Rev. Cancer 7*, 554–562.

(39) Kang, J. H., Asai, D., Yamada, S., Toita, R., Oishi, J., Mori, T., Niidome, T., and Katayama, Y. (2008) A short peptide is a protein kinase C (PKC) α-specific substrate. *Proteomics 8*, 2006–2011.

(40) Kang, J. H., Asai, D., Kim, J. H., Mori, T., Toita, R., Tomiyama, T., Asami, Y., Oishi, J., Sato, Y. T., Niidome, T., Jun, B., Nakashima, H., and Katayama, Y. (2008) Design of polymeric carriers for cancer-specific gene targeting: utilization of abnormal protein kinase Cα activation in cancer cells. *J. Am. Chem. Soc. 130*, 14906–14907.

(41) Kang, J. H., Asai, D., Toita, R., Kitazaki, H., and Katayama, Y. (2009) Plasma protein kinase C (PKC)α as a biomarker for the diagnosis of cancers. *Carcinogenesis 30*, 1927–1931.

(42) Oishi, J., Asami, Y., Mori, T., Kang, J. H., Tanabe, M., Niidome, T., and Katayama, Y. (2007) Measurement of homogeneous kinase activity for cell lysates based on the aggregation of gold nanoparticles. *ChemBioChem 8*, 875–879.

(43) Wu, P., and Brand, L. (1994) Resonance energy transfer: methods and applications. *Anal. Biochem. 218*, 1–13.

(44) Akagi, T., Watanabe, K., Kim, H., and Akashi, M. (2009) Stabilization of polyion complex nanoparticles composed of poly(amino acid) using hydrophobic interactions. *Langmuir 26*, 2406–2413.

(45) Müller, M., Kesseler, B., and Richter, S. (2005) Preparation of monomodal polyelectrolyte complex nanoparticles of PDADMAC/poly(maleic acid-alt-α-methylstyrene) by consecutive centrifugation. *Langmuir 21*, 7044–7051.

(46) Voets, I. K., de Keizer, A., Shuart, M. A. C., Justynska, J., and Schlaad, H. (2007) Irreversible structural transitions in mixed micelles of oppositely charged diblock copolymers in aqueous solution. *Macromolecules 40*, 2158–2164.

(47) Hannun, Y. A., Loomis, C. R., Merrill, A. H., Jr., and Bell., R. M. (1986) Sphingosine inhibition of protein kinase C activity and of phorbol dibutyrate binding in vitro and in human platelets. *J. Biol. Chem. 261*, 12604–12609.

(48) Qi, D. F., Schatzman, R. C., Mazzei, G. J., Turner, R. S., Raynor, R. L., Liao, S., and Kuo., J. F. (1983) Polyamines inhibit phospholipid-sensitive and calmodulin-sensitive Ca^{2+}-dependent protein kinases. *Biochem. J. 213*, 281–288.

(49) Oishi, J., Han, X., Kang, J. H., Asami, Y., Mori, T., Niidome, T., and Katayama., Y. (2008) High-throughput colorimetric detection of tyrosine kinase inhibitors based on the aggregation of gold nanoparticles. *Anal. Biochem. 373*, 161–163.

(50) Caravatti, G., Meyer, T., Fredenhagen, A., Trinks, U., Mett, H., and Fabbro, D. (1994) Inhibitory activity and selectivity of staurosporine derivatives towards protein kinase C. *Bioorg. Med. Chem. Lett. 4*, 399–404.

(51) Kuenzel, E. A., Mulligan, J. A., Sommercorn, J., and Krebs, E. G. (1987) Substrate specificity determinants for casein kinase II as deduced from studies with synthetic peptides. *J. Biol. Chem. 262*, 9136–9140.

(52) Davies, S. P., Reddy, H., Caivano, M., and Cohen, P. (2000) Specificity and mechanism of action of some commonly used protein kinase inhibitors. *Biochem. J. 351*, 95–105.

(53) Wilkinson, S. E., Parker, P. J., and Nixon, J. S. (1993) Isoenzyme specificity of bisindolylmaleimides, selective inhibitors of protein kinase C. *Biochem. J. 294*, 335–337.

(54) Gschwendt, M., Müller, H. J., Kielbassa, K., Zang, R., Kittstein, W., Rincke, G., and Marks, F. (1994) Rottlerin, a Novel Protein Kinase Inhibitor. *Biochem. Biophys. Res. Commun. 199*, 93–98.

Supporting Information

Fluorescent Nanoparticles Consisting of Lipopeptides and Fluorescein-Modified Polyanions for Monitoring of Protein Kinase Activity

Haruka Koga,[†,¶] Riki Toita,[†,¶] Takeshi Mori,[†,‡] Tetsuro Tomiyama,[†] Jeong-Hun Kang,[§] Takuro Niidome,[†,‡,‖] and Yoshiki Katayama*[,†,‡,‖,□]

[†] Graduate School of Systems Life Sciences, Kyushu University, 744 Motooka, Nishi-ku, Fukuoka 819-0395, Japan.

[‡] Department of Applied Chemistry, Faculty of Engineering, Kyushu University, 744 Motooka, Nishi-ku, Fukuoka 819-0395, Japan.

[§] Laboratory for Advanced Diagnostic Devices and Department of Biomedical Engineering, Advanced Medical Engineering Center, National Cardiovascular Center Research Institute, 5-7-1 Fujishirodai, Suita, Osaka 565-8565, Japan.

[‖] Center for Future Chemistry, Kyushu University, 744 Motooka, Nishi-ku, Fukuoka 819-0395, Japan.

[□] Center for Advanced Medical Innovation, Kyushu University, 3-1-1 Maidashi, Higashi-ku, Fukuoka, 812-8582, Japan.

[¶] These authors contributed equally to this work.

*To whom correspondence should be addressed. Phone: +81-92-802-2849. Fax: +81-92-802-2849. E-mail: ykatatcm@mail.cstm.kyushu-u.ac.jp

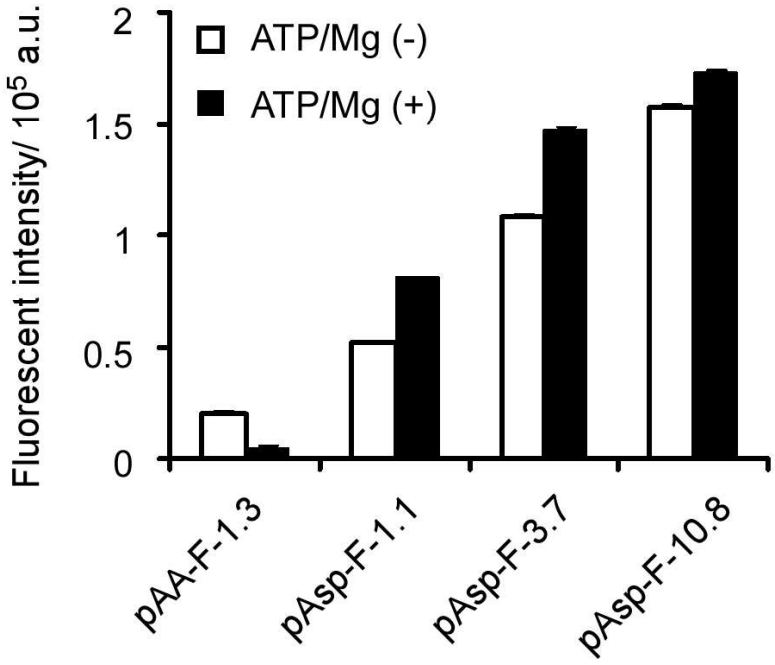

Figure S1. Effect of flexibility of polymer main chain of pA-Fs with or without ATP and $MgCl_2$.

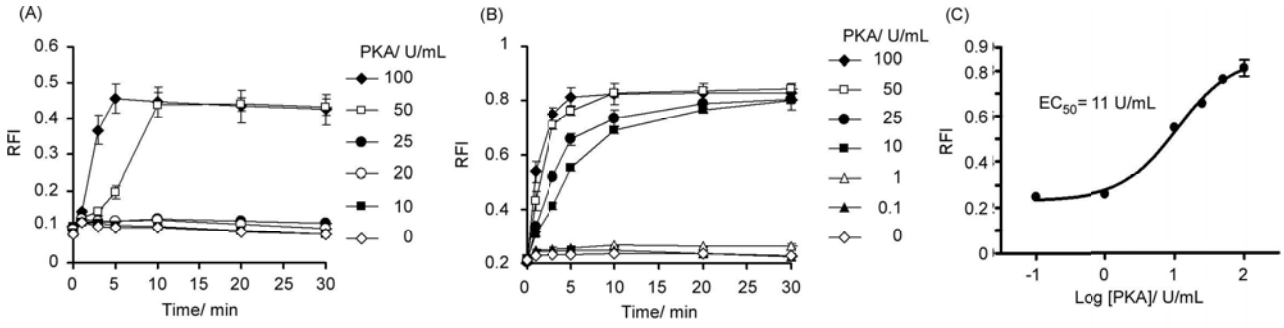

Figure S2. Changes of fluorescence intensity after addition of various concentrations of PKA (0.1–100 U/mL) to dispersions containing (A) **10-PKA/pAsp-F-3.7** (C/A ratio=3.0) and (B) **14-PKA/pAsp-F-3.7** (C/A ratio=1.5) NPs. (C) EC_{50} values of NPs.

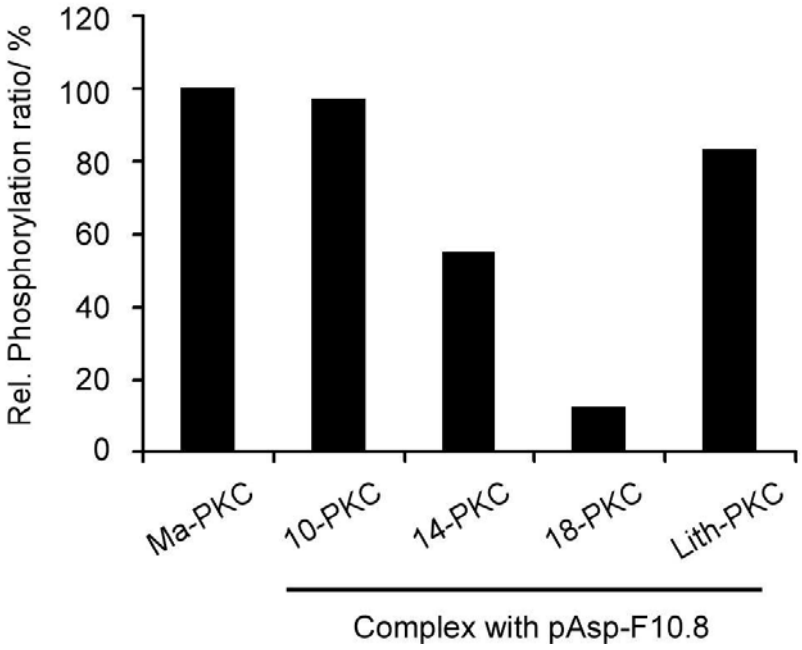

Figure S3. Comparison of phosphorylation ratios of NPs consisting of various lipopeptides and **pAsp-F10.8** at 60 min after PKCα phosphorylation.

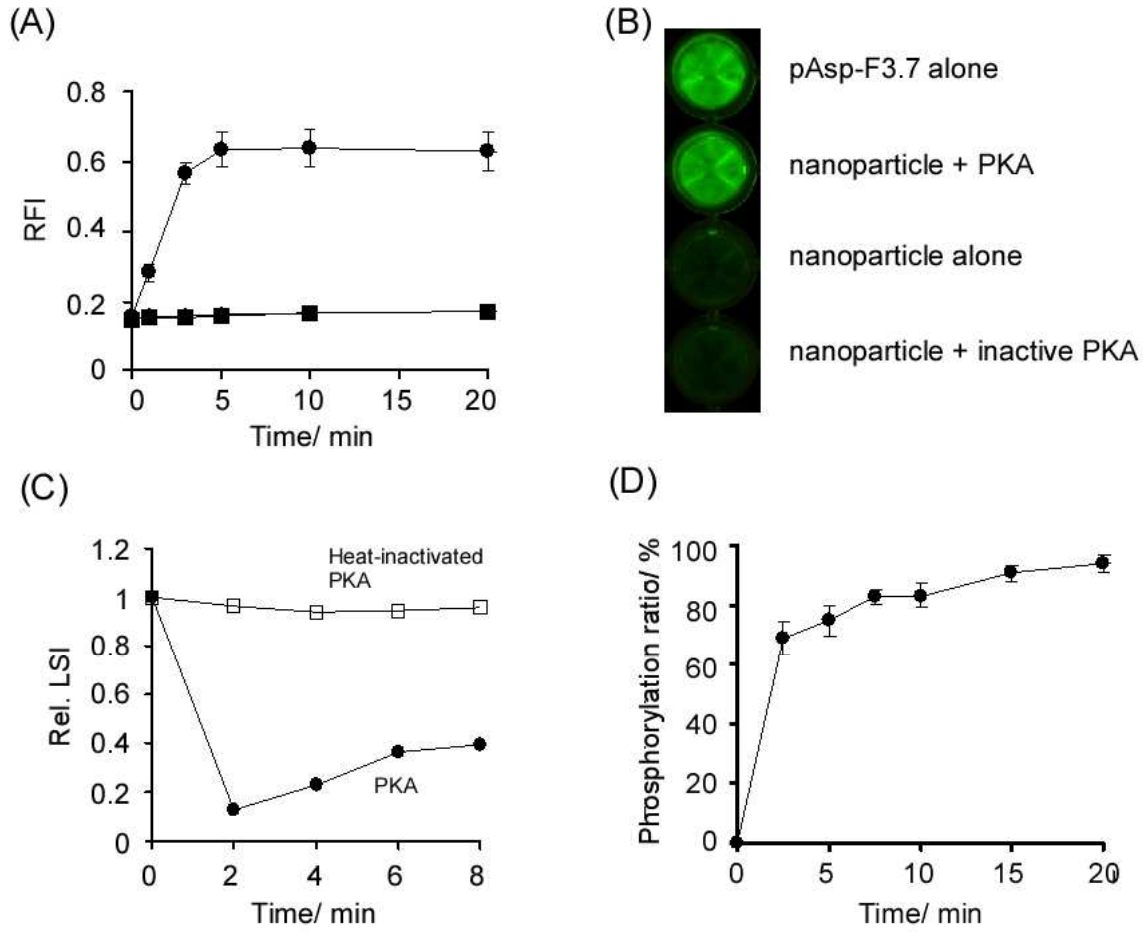

Figure S4. Fluorescence amplification of **14-PKA/pAsp-F-3.7** NPs (C/A ratio=1.5) by PKA. (A) Change of RFI after addition of PKA (closed circles), heat-inactive PKA (closed squares) to dispersion containing **14-PKA/pAsp-F-3.7** NPs. (B) Fluorescent images from wells 20 minutes after PKA addition. (C) Change of light scattering intensity (LSI) of NP dispersion after addition of PKA (closed circles) and heat-inactivated PKA (open squares). Data are represented as relative LSI, where initial LSI was defined as 1. (D) Change of phosphorylation ratio. Phosphorylation ratios of the NPs were determined by MALDI-ToF-MS analysis.

Bioconjugate Chemistry

ARTICLE

pubs.acs.org/bc

Chemically Programmed Antibodies Targeting Multiple Alpha(v) Integrins and Their Effects on Tumor-Related Functions in Vitro

Rajib K. Goswami,[†] Krishna M. Bajjuri,[†] Jane S. Forsyth,[‡] Sanjib Das,[†,§] Wolf Hassenpflug,[‡] Zheng-Zheng Huang,[†,#] Richard A. Lerner,[*,†] Brunhilde Felding-Habermann,[*,‡] and Subhash C. Sinha[*,†]

[†]The Departments of Molecular Biology and [‡]The Skaggs Institute for Chemical Biology, and The Department of Molecular and Experimental Medicine, The Scripps Research Institute, 10550 North Torrey Pines Road, La Jolla, California 92037, United States

Supporting Information

ABSTRACT: Integrins αvβ3 and αvβ6 are highly expressed on tumor cells and/or by the tumor vasculature of many human cancers, and represent promising targets for anticancer therapy. Novel chemically programmed antibodies (cpAbs) targeting these integrins were prepared using the catalytic aldolase Antibody (Ab) programming strategy. The effects of the cpAbs on cellular functions related to tumor progression were examined in vitro using tumor cell lines and their cognate integrin ligands, fibronectin and osteopontin. The inhibitory functions of the conjugates and their specificity were examined based on interference with cell−cell and cell−ligand interactions related to tumor progression. Cell binding analyses of the anti-integrin cpAbs revealed high affinity for tumor cells that overexpressed αvβ3 and αvβ6 integrins, and weak interactions with αvβ1 and αvβ8 integrins, *in vitro*. Functional analyses demonstrated that the cpAbs strongly inhibited cell−cell interactions through osteopontin binding, and they had little or no immediate effects on cell viability and proliferation. On the basis of these characteristics, the cpAbs are likely to have a broad range of activities *in vivo*, as they can target and antagonize one or multiple αv integrins expressed on tumors and tumor vasculatures. Presumably, these conjugates may inhibit the establishment of metastastatic tumors in distant organs through interfering with cell adhesion more effectively than antibodies or compounds targeting one integrin only. These anti-integrin cpAbs may also provide useful reagents to study combined effect of multiple αv integrins on cellular functions *in vitro*, on pathologies, including tumor angiogenesis, fibrosis, and epithelial cancers, *in vivo*.

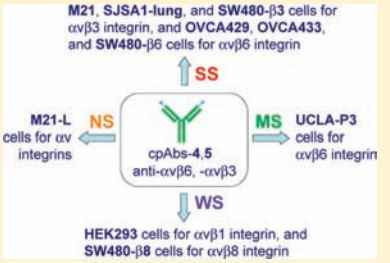

INTRODUCTION

Integrin adhesion receptors, expressed as heterodimers at the surface of all mammalian cells, regulate various cellular processes, including adhesion, migration, proliferation, differentiation, and cell death.[1−4] Integrins mediate cell−cell and cell−matrix attachment through interaction with their cognate ligands, and expression of these receptors in normal cells is well controlled. In contrast, under pathologic conditions such as cancer, expression levels of certain integrins are altered. Often, more than one heterodimeric integrin is overexpressed on cancer cells during disease progression, and inhibition of one specific integrin type does not necessarily affect the cellular function to be targeted as, in some cases, integrins can substitute for each other to influence a given cellular process.[5] In cancer patients, overexpression of key integrins, such as αvβ3 and αvβ5, has been observed on tumor cells, especially on highly metastatic cells.[6] In addition, certain host responses such as angiogenic endothelial cell sprouting rely on de novo expression of integrin αvβ3 in the tumor vasculature. Similarly, integrin αvβ6 is overexpressed especially on cells of many epithelial cancers, including squamous carcinoma of the breast, cervix, esophagus, head and neck, lung, ovaries, and skin.[7−14] Notably, these tumor cells were shown to express αvβ6 in 33−92% of the studied cases while the integrin is missing on the normal epithelial cells of these organs.[7] The effects of upregulation of these αv integrins in the above cancers are manifold, but mechanisms of their involvement in disease progression and consequences of their inhibition are not fully understood. An important clinical aspect that is certain, however, is that these integrins are associated with tumor angiogenesis, growth, and metastasis.[15] Therefore, these integrins are considered important targets for cancer therapy and diagnosis, and development of their inhibitors remains subject of intense research. Whereas selective inhibitors of various heterodimeric integrins are needed to examine their functions, broad-acting inhibition of multiple key integrins in the clinic could be necessary to achieve effective cancer therapy.

Previously, we have reported the Aldolase antibody (Ab) programming technology that involves covalent conjugation of a compound, usually a small molecule, peptidomimetic, or peptide, with an aldolase Ab, such as 38C2, and provides chemically programmed Ab (cpAb).[16−21] Conjugation takes place selectively in the Ab binding site, and is mediated by a designed linker usually possessing a β-diketone (DK),[16−18] an acetone adduct of vinyl ketone (pVK) as a latent VK,[19,20] or a lactam function.[21]

Received: February 16, 2011
Revised: July 20, 2011
Published: July 20, 2011

ACS Publications © 2011 American Chemical Society

dx.doi.org/10.1021/bc2000879 | *Bioconjugate Chem.* 2011, 22, 1535–1544

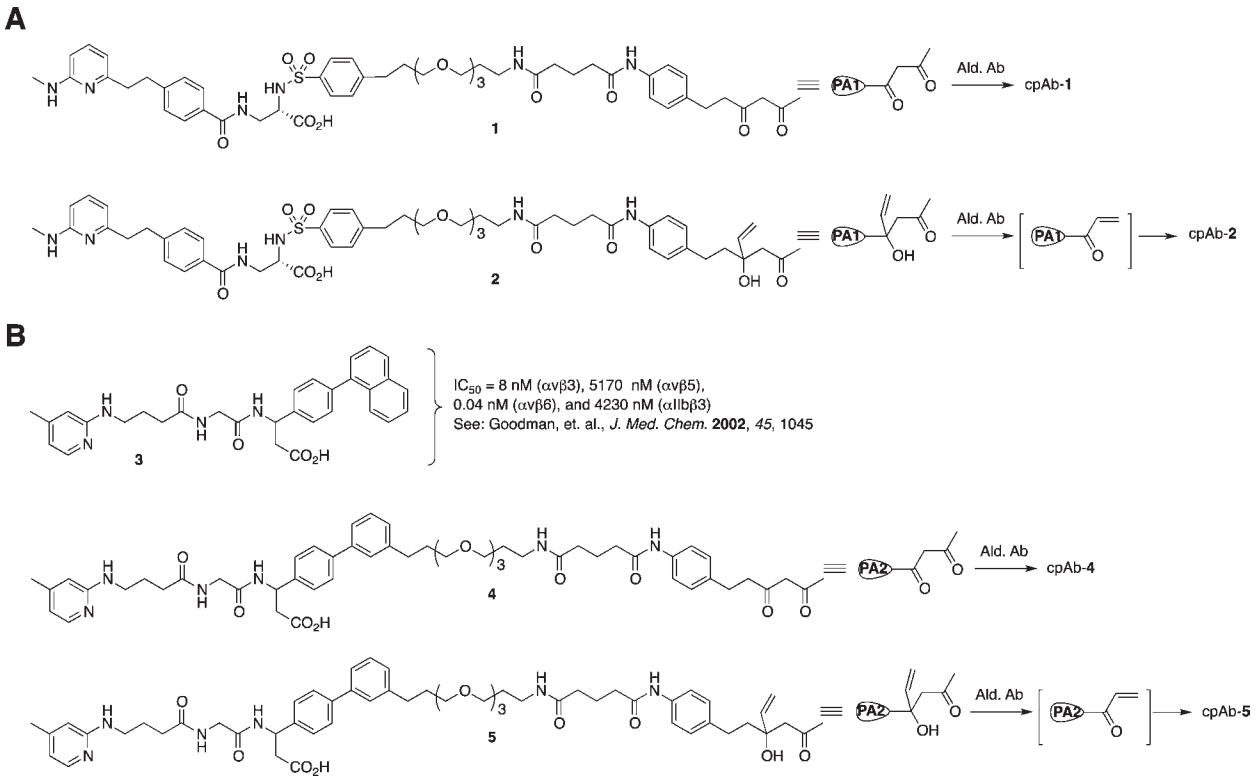

Figure 1. (A) Potent αvβ3 and (B) αvβ3/αvβ6 integrin inhibitors with and without DK and p-VK linkers, and their conjugation to an aldolase Ab showing the Ab-programming strategy. **PA1** and **PA2**, Programming Agents (compounds).

Importantly, the pVK compound undergoes retro aldol reaction to give a reactive VK linker, before the latter reacts with the Ab (Figure 1). We have also examined the programming of all available aldolase Abs, including 33F12, 38C2, 84G3, 84H9, 84G11, 85A2, 85C7, 85H6, 90G8, 92F9, and 93F3,[22,23] using multiple integrin inhibitors. The results revealed that most Abs could be programmed, yet the resultant cpAbs did not necessarily exhibit cell-targeting properties.[20] Nonetheless, using the aldolase Ab-programming strategy, we have prepared numerous integrin-targeting cpAbs, including those directed to integrins αvβ3 and αvβ5. We anticipate that a library of cpAbs that can target various integrins can be developed in this manner, particularly those for which low molecular weight inhibitors are known.[4] These cpAbs may find uses as chemical biology and drug discovery tools, whereas some may also possess therapeutic and diagnostic applications.[24−26] In this article, we summarize the details of aldolase Ab programming using a dual inhibitor of integrins αvβ3 and αvβ6, and *in vitro* evaluation of the cell binding characteristics and functional properties of the resulting cpAbs.

EXPERIMENTAL PROCEDURES

Materials. All chemicals were purchased from Sigma-Aldrich. Generation and purification of mouse mAbs 38C2, 84G3, 85H6, and 90G8 are described elsewhere.[22,23] Human cancer cell lines, M21 and M21-L melanoma,[27] BMS and BCM1 breast cancer,[28] UCLA-P3 lung carcinoma,[29] SJSA1-Lung, a lung metastasis derived osteosarcoma,[30] and OVCA 429 and OVCA 433 ovarian carcinoma,[31] are available or generated in this laboratory. SW480 puro, SW480-β3, SW480-β6, and SW480-β8 cells, and antiαvβ8 integrin 14E5 mouse Ab were kindly provided by Dr. Stephen Nishimura of UCSF Medical Center, San Francisco, California.[32,33] Antibody L230 (antiαv, ATCC Cat. No. HB8448) was a gift from the Pfizer, Inc. Antibodies M21−3 (anti-β3), and P1F6 (anti-αVβ5) and P5D2 (anti-β1) (hybridoma cells gifted by Elizabeth Wayner) were prepared in house in Felding-Habermann laboratory. Antibodies BHA2.1 (anti-α2β1, Cat. No. MAB1998) and 10D5 (anti-αVβ6, Cat. No. MAB2077Z) were purchased from Millipore, Billerica, MA. FITC conjugated antimouse Ab was purchased from Jackson Laboratories, and APC conjugated antimouse Ab was purchased from Invitrogen, California. Human fibronectin (Cat. No. 341635) was purchased from EMD Biosciences. Human osteopontin (OPN) was cloned from SJSA1 human osteosarcoma cells, expressed as a His-tagged protein in *E. coli*, and purified under nondenaturing conditions on Ni-NTA agarose.

Synthesis of Compounds. *Compound* ***7***. Malonic acid (446 mg, 4.28 mmol) and ammonium acetate (660 mg, 8.56) were added sequentially to a stirring solution of 3′-bromo-[1,1′-biphenyl]-4-carbaldehyde (**6**, 2 g, 4.28 mmol) in EtOH (30 mL).[34,35] After the mixture was refluxed for 24 h, it was cooled to room temperature and filtered using EtOH and ether to give the corresponding β amino acid as white solids. The latter product was taken to the next step without further purification.

The above-described β amino acid was suspended in 100 mL MeOH, and $SOCl_2$ (1.6 mL, 21.4 mmol) was added dropwise to the suspension at −5 °C. After all $SOCl_2$ was added, the mixture was refluxed for 4 h and solvents were removed. The residue was taken in EtOAc (50 mL) and aqueous $NaHCO_3$ (50 mL), and CbzCl (0.9 mL, 6.42 mmol) was added dropwise to the mixture at 0 °C. After the mixture was stirred overnight, it was worked up using EtOAc and water. The combined organic layer was washed

with brine, dried over Na_2SO_4, and purified by column chromatography to give pure Cbz-protected amino ester **7** (3.3 g, yield 92% from ***6***). ^{1}H NMR ($CDCl_3$, 500 MHz): δ 7.69 (s, 1H), 7.51−7.37 (m, 4H), 7.32−7.11 (m, 8H), 6.03 (d, 1H, J = 2.7 Hz), 5.21 (m, 1H), 5.16−5.05 (m, 2H), 3.62 (s, 3H), 2.96−2.73 (m, 2H). HRMS-ESI: Calc. for $C_{24}H_{22}BrNO_4$, 467.07, Found 467.072.

Compound ***9***. $PdCl_2(PPh_3)_2$ (495 mg, 0.7 mmol) and CuI (268 mg, 1.4 mmol) were added to a degassed solution of the β amino ester **7** (3.3 g, 7.1 mmol) and NEt_3 (2 mL) in CH_3CN (30 mL), and the reaction mixture was heated to the reflux temperature.[36] A solution of alkyne **8** (2.25 g, 10.6 mmol) in degassed CH_3CN (30 mL) was added dropwise to the reaction mixture over one hour, and heating was continued for 24 h. After the reaction was complete, as judged by TLC, the mixture was diluted with EtOAC, washed with NH_4Cl and brine, and dried over Na_2SO_4. Solvents were removed in vacuo and the residue was chromatographed over silica gel giving the pure coupled product (3.7 g, 87% yield). ^{1}H NMR (300 MHz, $CDCl_3$): δ 7.64 (s, 1H), 7.53−7.45 (m, 4H), 7.41−7.29 (m, 8H), 5.93 (d, 1H, J = 2.7 Hz), 5.22 (m, 1H), 5.17−5.01 (m, 3H), 4.42 (s, 2H), 3.62−3.57 (m, 2H), 3.42−3.39 (m, 2H), 3.37−3.24 (m, 2H), 3.63 (s, 3H), 3.62−3.59 (s, 2H), 3.57−3.49 (m, 2H), 3.49−3.31 (m, 2H), 2.95−2.87 (m, 2H), 1.79−1.68 (m, 2H), 1.48 (s, 9H), HRMS-ESI: Calc. for $C_{35}H_{40}N_2O_7$, 601.28 $(M+H)^+$, Found 601.276.

Pd−C (10% w/w, 500 mg) was added to a solution of the above-described coupled product (3.7 g, 6.2 mmol) in EtOH (20 mL) and the mixture was stirred under hydrogen atmosphere for 24 h. The mixture was filtered to remove insoluble materials, solvents removed under vacuum, and the resultant product **9** (2.89 g) was taken to next reaction without further purification.

Compound ***10***. EDC (3.79 g, 19.8 mmol) and DIPEA (9.5 mL, 54 mmol) were added successively to a mixture of Gly-OMe hydrochloride salt (2.47 g, 19.8 mmol), 4-(pyridine-2-ylamino)butanoic acid (3.5 g, 18 mmol), and HOBt (2.68 g, 19.8 mmol) in DMF (40 mL) at 0 °C, and the mixture was stirred at room temperature overnight. The mixture was concentrated and worked up using EtOAc−aq NH_4Cl, saturated $NaHCO_3$, and brine. The organic layer was dried over Na_2SO_4 and purified, giving the methyl ester of compound **10** (4.1 g, 87% yield). ^{1}H NMR (300 MHz, $CDCl_3$): δ 7.87 (d, 1H, J = 2.7 Hz), 7.61 (t, 1H, J = 3.1 Hz), 6.39 (d, 1H, J = 2.7 Hz), 6.21 (s, 2H), 4.99 (t, 1H, J = 2.9 Hz), 4.07 (d, 2H, J = 3.7 Hz), 3.71 (s, 3H), 3.41−3.31 (m, 2H), 2.36 (t, 2H, J = 7.1 Hz), 2.39 (s, 3H), 2.83 (q, 2H, J = 7.1 Hz).

A solution of 2 M aq NaOH (22.6 mL, 45.2 mmol) was added to a solution of the above-described ester (4 g, 15.1 mmol) in dioxane (50 mL), and the mixture was stirred at room temperature overnight. When the starting material had disappeared, the reaction mixture was acidified to pH 2 and the solvent was evaporated to give the corresponding free acid **10** (3.8 g) that was taken to next step without further purification.

Compound ***11***. EDC (1.3 g, 6.8 mmol), HOBt (915 mg, 6.78 mmol), and NMM (3.4 mL, 30.8 mmol) were added sequentially to a solution of the above-described free amine **9** (2.89 g, 6.2 mmol) and acid **10** (3.09 g, 12.3 mmol) in DMF (30 mL) at 0 °C, and the reaction mixture was stirred at room temperature overnight. Solvents were removed in vacuo, and the residue was dissolved in EtOAC, and washed with saturated $NaHCO_3$, NH_4Cl, followed by brine. The organic layer was dried over Na_2SO_4, solvents were removed, and the residue was purified by column chromatography to give compound **11** (3.76 g, 87% yield based on amine). ^{1}H NMR (300 MHz, $CDCl_3$): δ 8.01−7.97 (m, 2H), 7.62−7.47 (m, 6H), 7.44−7.29 (m, 5H), 7.12 (d, 1H, J = 5.1 Hz), 6.39 (m, 1H), 6.17 (bs, 1H), 5.47 (m, 1H), 5.07 (bs, 1H), 4.77 (t, 1H, J = 3.7 Hz), 4.01−3.98 (m, 2H), 3.72 (s, 1H), 3.68−3.61 (m, 5H), 3.62 (s, 3H), 3.61−3.54 (m, 4H), 3.53−3.47 (m, 4H), 3.42−3.31 (m, 3H), 3.23−3.18 (m, 2H), 2.97−2.86 (m, 2H), 2.77−2.73 (m, 2H), 2.37 (t, 3H, J = 7.1 Hz), 2.21−2.17 (m, 2H), 2.14 (s, 3H). HRMS-ESI: Calc. for $C_{39}H_{53}N_5O_7$, 704.39 $(M+H)^+$, Found 704.388.

Compounds ***4*** *and* ***5***. A solution of 2 M aq NaOH (1.06 mL, 2.12 mmol) was added to a solution of the above-described ester (500 mg, 0.70 mmol) in dioxane (2 mL), and the mixture was stirred at room temperature overnight. When the starting material had disappeared, the reaction mixture was acidified to pH 2.0 and the solvent was evaporated to give the corresponding free acid quantitatively which was taken to next step without further purification. See Scheme 1

The above-described crude acid was treated with 25% TFA/CH_2Cl_2 (v/v, 1 mL, 1 drop of anisole) at room temperature overnight, and then the solvent was removed under vacuum and used for the next reaction without further purification.

To a solution of the above-described amino acid (100 mg, 0.17 mmol) in CH_3CN (1 mL) was added NEt_3 (0.09 mL, 0.51 mmol) followed by the NHS ester **12**[17,37] (127 mg, 0.34 mmol), and the mixture was stirred at room temperature for 2 h. Solvents were removed in vacuo and the residue was purified by column chromatography to give the title product **4** (151 mg, 91% yield). ^{1}H NMR (300 MHz, $CDCl_3$ + CD_3OD): δ 7.92−7.77 (m, 1H), 7.57−7.26 (m, 10H, 7.20−7.07 (m, 3H), 6.61 (s, 1H), 6.47 (d, 1H, J = 2.3 Hz), 5.28 (t, 1H, J = 2.7 Hz), 4.10−4.03 (m, 1H), 3.83−3.75 (m, 1H), 3.68−3.55 (m, 8H), 3.52−3.43 (m, 5H), 3.35−3.28 (m, 2H), 3.27−3.13 (m, 4H), 2.94−2.79 (m, 4H), 2.77−2.65 (m, 3H), 2.64−2.46 (m, 3H), 2.44−2.33 (m, 2H), 2.27−2.16 (m, 4H), 2.16−2.13 (6H), 2.09−1.86 (m, 2H), 1.81−1.69 (m, 3H), 1.31 (t, 3H, J = 6.9 Hz). HRMS-ESI: Calc. for ($C_{54}H_{70}N_6O_{11}$), 979.5175 $(M+H)^+$, Found 979.5171.

Similarly, to the above-described amino acid (100 mg, 0.17 mmol) was reacted with NHS ester **13**[19,37] (127 mg, 0.34 mmol) giving **5** (155 mg, 91% yield). ^{1}H NMR (CD_3OD + $CDCl_3$, 600 MHz): δ 7.58 (bs, 1H), 7.53 (s, 1H), 7.49−7.41 (m, 4H), 7.38 (d, J = 7.8 Hz, 2H), 7.35−7.29 (m, 4H), 7.15 (bd, J = 6.0 Hz, 1H), 7.11 (d, J = 7.2 Hz, 2H), 6.53 (bs, 1H), 6.46 (bs, 1H), 5.91 (dd, J = 17.4, 10.8 Hz, 1H), 5.30 (d, J = 16.8 Hz, 1H), 5.26 (bs, 1H), 5.18 (d, J = 10.8 Hz, 1H), 4.11 (d, J = 17.4 Hz, 1H), 3.8 (d, J = 17.4 Hz, 1H), 3.70−3.63 (m, 6H), 3.63−3.57 (m, 4H), 3.55−3.49 (m, 4H), 3.36−3.30 (m, 3H), 3.28 (t, J = 6.6 Hz, 2H), 2.78 (s, 1H), 2.76−2.68 (m, 4H), 2.65−2.50 (m, 4H), 2.37 (t, J = 7.2 Hz, 2H), 2.29−2.24 (m, 4H), 2.19 (s, 3H), 2.12−2.02 (m, 2H), 2.00−1.90 (m, 4H), 1.88−1.82 (m, 1H), 1.80−1.74 (m, 2H), 1.30−1.25 (m, 6H). MS-ESI (m/z): 1007 (M^+), 1008 $(M+H)^+$, 1030 $(M+Na)^+$.

Formation of the Programmed Antibodies (cpAbs)—General Method.[37] Compounds **1** and **2** or **4** and **5** (100 μM in CH_3CN, 2.5−3 μL) were added separately to Aldolase Abs (1 μM, 100 μL) in Eppendorf tubes at pH 6.0, 7.4, and 8.5, and the mixtures were incubated at room temperature for 0.5 h (for the DK compounds **1** and **4**), or 37 °C for 1.5 h (for the pVK compounds **2** and **5**). Mixture of the antibodies (1 μM, 100 μL) and CH_3CN (3 μL) was incubated at 37 °C (1.5 h) and used as the control group. Subsequently, the mixtures were transferred to the 96 well fluorescence reader plate, and a solution of methodol (10 mM in EtOH, 2 μL) was added to each well containing the Ab or the resulting cpAbs, and progress of the retro aldol reaction

Table 1. Aldolase Ab Programming Using the DK and pVK Compounds 1 and 2[a]

	pH 6.0, 1.5 h					pH 7.4, 1.5 h					pH 8.5, 1.5 h				
	Catalytic activity (%)			Ab Prog. (%)		Catalytic activity (%)			Ab Prog. (%)		Catalytic activity			Ab Prog. (%)	
Ab	Ab	Ab-**1**	Ab-**2**	Ab-**1**	Ab-**2**	Ab	Ab-**1**	Ab-**2**	Ab-**1**	Ab-**2**	Ab	Ab-**1**	Ab-**2**	Ab-**1**	Ab-**2**
24H6	0	1	0	-	-	2	0	0	-	-	2	0	1	-	-
38C2	25	0	0	100	-	24	0	1	100	96	23	0	3	100	87
33F12	7	0	0	100	100	5	1	0	-	-	6	0	0	100	100
84G3	83	0	64	100	23	100	0	50	100	50	97	0	50	100	48
84G11	2	0	0	-	-	28	0	3	100	89	34	0	3	100	91
85A2	3	1	2	-	-	21	0	3	100	86	23	0	2	100	91
85C7	0	0	1	-	-	2	0	0	-	-	4	0	1	-	-
85H6	4	1	4	-	-	25	1	3	96	88	12	0	1	100	92
90G8	2	0	4	-	-	19	0	1	100	95	19	0	2	100	91
92F9	1	0	0	-	-	8	0	0	100	100	9	0	0	100	100
93F3	22	0	18	100	18	25	0	7	100	72	23	0	5	100	78

[a] Key: Three sets of reactions were performed by incubating the Abs with compounds **1** and **2** for 0.5 and 1.5 h, respectively, at pH 6.0, 7.4, and 8.5, and the methodol assay was used to determine the extent of the Ab programming. Catalytic rates of the untreated Abs and the cpAbs are compared to the highest activity that was observed with the untreated Ab 84G3 at pH 7.4.

of methodol giving fluorescent 6-methoxy-2-naphthaldehyde was measured using a fluorometer,[37,39] λ_{abs} 330 nm and λ_{em} 452 nm. Inhibition of the retro aldol reaction was used as the measurement of the Ab programming using compounds **1**, **2** and **4**, **5**. Similarly, the cpAbs 38C2-**4**,**5**, 84G3-**4**,**5**, 85H6-**4**,**5**, and 90G8-**4**,**5** were prepared by mixing a solution of compound **4** (125 μM in DMSO, 6.7 μL) or **5** (150 μM in DMSO, 6.7 μL) with Abs 38C2, 84G3, 85H6, or 90G8 (50 μM, 6.7 μL), as needed, in PBS buffer (pH 7.4, total volume 100 μL) and incubating the mixtures at room temperature for 0.5 h (for compound **4**) or at 37 °C for 1.5−36 h (for compound **5**).

Evaluation of the Binding of the cpAbs to αvβ3, αvβ5, and αvβ6 Integrin-Expressing Cells. *Flow Cytometry.* Cells were detached by brief trypsinization with 0.25% (w/v) trypsin, 1 mM EDTA, washed with PBS, and resuspended at 2×10^6 cells/mL in ice cold flow cytometry buffer (for anti integrin binding: 1% BSA in TBS pH 7.4; for chemically programmed Abs (cpAbs): 1% BSA, 100 μM $MnCl_2$, TBS pH 7.4). Aliquots of 50 μL containing 10^5 cells were distributed into tubes for indirect immunofluorescence staining in the presence of 20 μg/mL of cpAbs or 10 μg/mL of anti-integrin mAbs. After incubation for 45 min on ice and washing, cells were incubated with FITC or APC conjugated goat antimouse polyclonal antibodies (at a 1:100 dilution, i.e., 10 μg/mL in FACS buffer) for 45 min on ice. After a final wash, cells were analyzed using flow cytometry using a FACScalibur (Becton-Dickinson) as described earlier.[20] All binding experiments were repeated at least three times at different time points using independent cell batches to determine the consistency of the results. Representative analyses are shown.

Cell-Adhesion Assay. To measure the effects of cpAbs on integrin mediated tumor cell adhesion, nontissue culture treated 96-well plates were coated with human fibronectin or osteopontin (2 μg/mL in PBS) overnight at 4 °C. The plates were washed and blocked with 2% BSA in TBS for 1 h at RT. Tumor cells were harvested with Versene and washed in serum-free EMEM medium containing 0.5% BSA which was also used as adhesion buffer. Before plating onto the matrix proteins, the cells were preincubated with cpAbs at 2 μM final concentration with or without function blocking monoclonal anti-integrin antibodies at 100 μg/mL for 15 min at RT. The cells were then seeded at 2×10^4/well in the presence of the antibodies. Adhesion time was 20 min on fibronectin and 30 min on osteopontin. To harvest attached cells, the nonadhered cells were removed by adding floatation medium (0.9% NaCl, 80% Percoll) which sinks to the bottom and gently lifts unbound cells, followed by fixation of the adhered cells with 3.3% glutaraldehyde and 20% Percoll. The attached cells were stained with crystal violet, washed, lyzed with 0.5% Triton X 100 in water, and quantified by measuring optical absorbance at 595 nm. All cell adhesion experiments were carried out in triplicates.

Cell Survival Assay. To measure effects of cpAbs on tumor cell viability and proliferation, 5×10^4 cells were plated into 24 well plates and incubated with or without cpAbs at 0.4 and 2 μM concentration. On days 1, 2, 3, and 4, cells were harvested and counted. Live cells were identified and counted based on trypan blue exclusion. Cell-survival assay was carried out once, and there were no replicates.

RESULTS AND DISCUSSION

Programming of Ab 38C2 was previously achieved using numerous low molecular weight inhibitors of integrin αvβ3, including compounds **1** and **2**, which possessed a DK or a pVK (an aldol adduct of the VK) linker (Figure 1).[17,19] Both DK compounds and VK compounds reacted in the Ab binding sites, as evident from the fact that the conjugates were catalytically inactive. We further anticipated that the ε amine function of the reactive lysine residue (pK < 6.0) residing in the hydrophobic environment in Ab binding sites reacted with both the DK and VK compounds giving an enaminone and the β-aminoketone derivative, respectively. Indeed, formation of the enaminone function was confirmed using UV spectroscopy that shows a characteristic λ_{max} at 318 nm,[22] and subsequently using the X-ray crystallographic study of the Ab 33F12 Fab that was reacted with the diketone hapten.[38] On the other hand, the proposed mode of conjugation of the highly reactive VK compounds through the ε amine functionality of the reactive lysine residue of an aldolase Ab[19,20] remained to be confirmed. In any case, it was certain that the VK compound also reacted in the Ab binding sites. Thus,

Table 2. Aldolase Ab Programming Using the DK and pVK Compounds 4 and 5[a]

	pH 7.4, 0.5, or 1.5 h					pH 7.4, 36 h		
	Catalytic activity (%)			Ab Prog. (%)		Catalytic activity (%)		Ab Prog. (%)
Ab	Ab	Ab-**4**	Ab-**5**	Ab-**4**	Ab-**5**	Ab	Ab-**5**	Ab-**5**
38C2	22	0	0	100	100			
84G3	90	0	46	100	49	100	8	92
85H6	22	1	3	95	86	21	0	100
90G8	18	0	1	100	94	17	0	100

[a] Key: Reactions were performed by incubating the Abs with compounds **4** for 0.5 and compound **5** for 1.5 or 36 h at pH 7.4, and progress of the chemical programming was determined using the methodol assay, as described earlier (Table 1). Catalytic rates of the untreated Abs and the cpAbs are compared to the highest activity that was observed with the untreated Ab 84G3.

Scheme 1. Synthesis of Integrin αvβ3/αvβ6 Antagonists Coupled with a DK and p-VK Linker for Production of the cpAbs (PA2, Programming agent)[a]

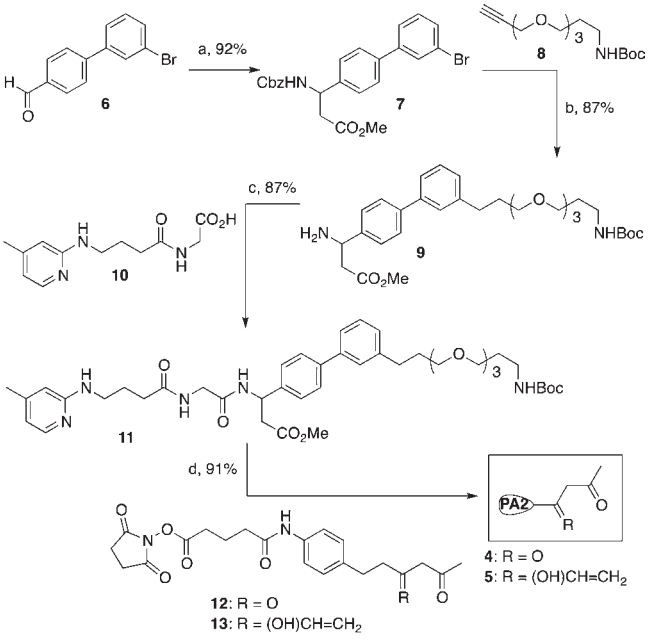

[a] Key: (a) (i) NH_4OH, malonic acid, EtOH, reflux, 24 h, (ii) MeOH, $SOCl_2$, reflux, 4 h, (iii) CbzCl, aq. Na_2CO_3, EtOAc, 0 °C - RT, 16 h; (b) (i) $Pd(PPh_3)_2Cl_2$, CuI, NEt_3, CH_3CN, 24 h, (ii) H_2, Pd−C, 0.1 M HCl, MeOH, 24 h; (c) EDC, HOBt, DIPEA, DMF, 0 °C - RT, 16 h; (d) (i) 2 M aq. NaOH, MeOH, RT, 16 h, (ii) TFA, anisole, CH_2Cl_2, RT, 16 h, (iii) **12**, or **13**, Et_3N, CH_3CN, RT, 2 h.

most Abs, including 38C2, 84G3, 85H6, and 90G8, which possessed appreciable activity and catalyzed the retro aldol reaction of the pVK linker were programmed efficiently with compound **2**.[20]

Chemical programming of the aldolase Abs is determined using the methodol assay, in that methodol is used as a substrate that undergoes a retro aldol reaction catalyzed by all of the above-described aldolase Abs to produce fluorescent 6-methoxy-2-naphthaldehyde.[37,39] In contrast, a programmed Ab is no longer active and does not catalyze the retro aldol reaction of methodol, and therefore, no fluorescence is detected. Thus, we found that the programming of all Abs was complete in less than 0.5 h (room temperature) using the DK compound **1**, and was over 95−98% complete upon 2−24 h incubation (37 °C) with the pVK compound **2**, at pH 7.4 (Table 1, also see Supporting Information (SI) Figure S-1). We further confirmed that the Ab-programming using compounds **1** and **2** is best achieved at pH 7.4, though most Abs, including Ab 38C2, can also be programmed at pH 6.0 and 8.5. On the other hand, all Abs, except 38C2, 84G3, and 93F3, possessed reduced catalytic activity at pH 6.0 as compared to that at pH 7.4, which we analyzed using the methodol assay. Apparently, the catalytic ω amine of the lysine residue in these Abs, but not in 38C2, 84G3, and 93F3, was already protonated at pH 6.0.

To prepare novel αvβ3 and αvβ6 integrin directed cpAbs, we used the aldolase Abs 38C2, 84G3, 85H6, and 90G8, and compounds **4** and **5**, which are analogues of the highly potent dual inhibitor of integrins αvβ3 and αvβ6, viz., compound **3**.[40] The latter binds strongly to integrins αvβ3 (IC_{50} = 8 nM) and αvβ6 (IC_{50} = 0.04 nM), and weakly to αvβ5 (IC_{50} = 5170 nM) and αIIbβ3 (IC_{50} = 4230 nM). The inhibitory activity of compound **3** has been determined using immobilized integrins as the target; biotinylated human serum vitronectin have been used as ligands for integrins αvβ3 and αvβ5, fibronectin for αvβ6, and fibrinogen for αIIbβ3.[40] The site of the linker arm in compounds **4** and **5** that connects the targeting agent **3** to Ab was determined on the basis of a series of compounds, including **1** and **2**, which were used earlier in Ab programming.[17,19,20] Upon the basis of the selectivity of compound **3**, described above, we anticipated that the new cpAbs prepared with compound **4** or **5** and the aldolase Abs should also bind efficiently to integrin αvβ6 and somewhat less efficiently to αvβ3, but not to integrins αvβ5 and αIIbβ3.[40]

Compounds **4** and **5** were prepared by modifying the synthesis of compound **3** using the readily available aldehyde **6**[41] and acid **10**, as shown in Scheme 1. Thus, aldehyde **6** was prepared by Suzuki reaction[36] of 4-formylphenylboronic acid with 3-bromo-1-iodobenzene and subsequently converted to β-amino acid ester **7** by using Rodionov-Johnson reaction[34,35] with malonic acid and ammonium hydroxide in refluxing ethanol, followed by protection of the free amine and carboxylic acid functions. Compound **7** was then reacted with alkyne **8** using $Pd(PPh_3)_2Cl_2$ as catalyst to give a coupled alkyne product that was hydrogenated over Pd−C giving **9**. The latter product underwent peptide coupling with acid **10** giving compound **11**. Methyl ester and Boc function in compound **11** were deprotected, and the resulting amino acid was reacted with the DK-NHS ester, **12**, and VK-NHS ester, **13**, yielding target compounds **4** and **5**, respectively.

dx.doi.org/10.1021/bc2000879 |*Bioconjugate Chem.* 2011, 22, 1535–1544

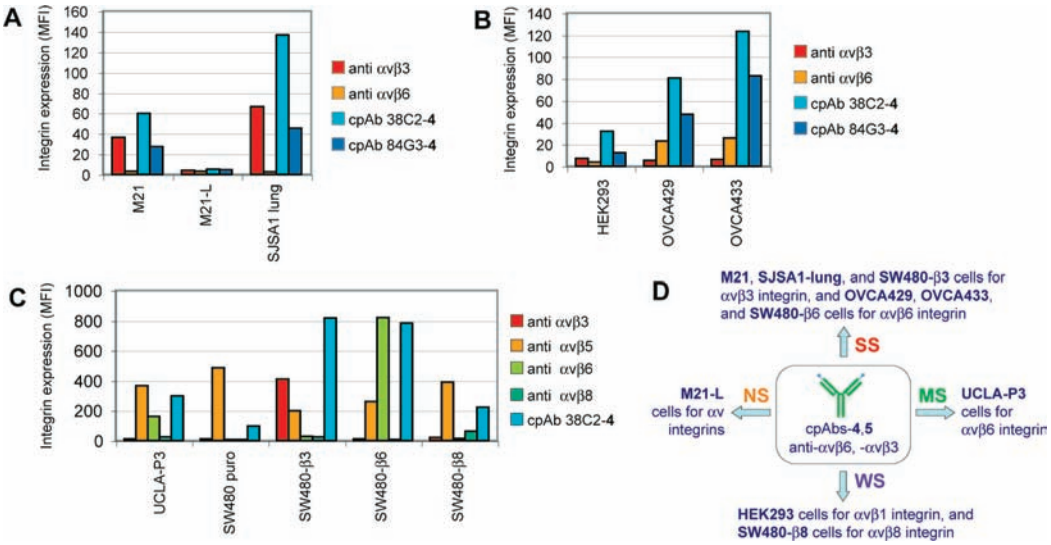

Figure 2. Binding specificity of cpAbs 38C2-**4** and 84G3-**4** to αv integrins expressed by human tumor cells. Flow cytometry analysis showing the level of cpAb binding to various tumor cells, including (A) M21, M21-L, and SJSA1-lung, (B) HEK293, OVCA429, and OVCA433, and (C) UCLA-P3, SW480 puro, SW480-*β*3, SW480-*β*6, and SW480-*β*8, expressing/deficient in various integrins. "Anti-integrin" denotes monoclonal anti-integrin complex specific antibodies used to report integrin expression. FITC labeled antimouse Abs were used to detect the binding of the Abs and cpAbs in A and B, and APC labeled antimouse Abs were used in C. (D) Schematic summary of the major integrin heterodimer recognized by the cpAbs (SS, strong staining; MS, moderate staining; WS, weak staining; and NS, no apparent staining observed or interpreted due to specific integrin heterodimers).

Subsequently, Abs 38C2, 84G3, 85H6, and 90G8 were programmed by incubating the individual Abs with compound **4** or **5**. As expected, complete programming of all Abs using compound **4** took place in 0.5 h at room temperature by using 2.2−2.5 mol equiv of the compound. Similarly, they were 95−98% programmed using 2.5−3.0 mol equiv of compound **5** in 2−16 h at 37 °C. Completion of the programming was determined using the methodol assay (Table 2, also see SI Figure S-2) and/or MALDI-TOF analysis.

To investigate whether compound **4** or **5** can redirect the Abs to integrins αv*β*3 and αv*β*6, we used the above-mentioned cpAbs prepared with Abs 38C2 or 84G3, i.e., 38C2-**4** or **5**, 84G3-**4** or **5**, and determined the cell binding properties and integrin specificity of these conjugates by using a series of human cancer cell lines, including M21 and M21-L melanoma,[27] OVCA 429 and OVCA 433 ovarian carcinoma cells,[31] BMS and BCM1 breast cancer,[28] SJSA1-lung osteosarcoma,[30] and HEK293 cells.[42] The expression levels of target and control integrins on these tumor cells were analyzed by flow cytometry with monoclonal antibodies against αv*β*3 (VNR1), αv*β*5 ((P1F6), αv*β*6 (10D5), α2*β*1 (BHA2.1), α5 (P1D6), *β*1 (P5D2), αv (L230), and *β*3 (M21.3.3). As shown in Figure 2A and SI Figure S-3A, M21 and SJSA1 lung cells have high expression levels of integrin αv*β*3 and low levels of integrins αv*β*5 and αv*β*6. Similar results were found for BMS and BCM1 breast carcinoma cells (not shown). In contrast, OVCA 429 and OVCA 433 cells overexpress αv*β*6, and do not or weakly express αv*β*3 and αv*β*5 (Figure 2B and SI Figure S-3A), and HEK293 cells lack both αv*β*3 and αv*β*6 (Figure 2B), but express αv*β*1 integrin.[42] M21-L cells lack αv integrin expression and were used as a control.[27] All of the used cells express high levels of *β*1 integrins. On the basis of this information, our cell model includes cancer cells that overexpress—or lack—our target integrins αv*β*3 and/or αv*β*6, and either carry or lack other relevant integrins such as αv*β*1 and αv*β*5 and other major integrins not recognized or weakly recognized by our targeting agents.

Using this cell model, we determined binding and specificity of cpAbs 38C2-**4**, 38C2-**5**, and 84G3-**4** by flow cytometry (Figure 2A,B and SI Figure S-3C). Evidently, cpAb 38C2-**4** and 84G3-**4** bind to M21, SJSA1 lung, HEK293, and OVCA429 and 433 cells that either express αv*β*3, αv*β*1, or αv*β*6. CpAbs 38C2-**4** and 84G3-**4** did not bind to M21-L cells (Figure 2A,B) confirming that these cpAbs do not recognize any non-αv integrin, and therefore are αv integrin specific. Similarly, cpAb 38C2-**5**, which possessed the targeting moiety identical to 38C2-**4**, but differed in the linker (DK for **4** and pVK for **5**), bound to M21, BMS, and BCM1 cells (see SI Figure S-3C). Interestingly, binding of 38C2-**4** to target tumor cells is superior to that of 84G3-**4**, but we anticipate that the latter's binding could also be improved through the linker length optimization. Nonetheless, these findings clearly show that the cpAbs prepared from Abs 38C2 or 84G3 and compound **4** or **5** were capable of binding strongly to tumor cells that express either integrin αv*β*3 and/or αv*β*6, but not to those that lack αv integrin.

To determine specificities and cross-reactivities of the cpAbs among all the av integrins, next we used cpAb 38C2-**4** and determined its binding to SW480 (wild type as well as those transfected with *β*3, *β*6, or *β*8 integrin) colon cancer[32] and UCLA-P3 lung carcinoma cells.[29] Whereas UCLA-P3 cells express αv*β*5 and αv*β*6, and lack αv*β*3 integrin, all SW480 cells express αv*β*5, and SW480-*β*3, SW480-*β*6, and SW480-*β*8 cells also express αv*β*3, αv*β*6 and αv*β*8 integrin, respectively, besides αv*β*5 and α5*β*1 integrins. Again, we confirmed the expression levels of various integrins in these cells by flow cytometry and using the appropriate Abs (see Figure 2C and SI Figure S-3). As expected, cpAb 38C2-**4** bound strongly to SW480-*β*3 and SW480-*β*6, but only weakly to SW480 (puro). Interestingly, however, 38C2-**4** also bound to SW480-*β*8 cells, which express αv*β*8 integrin. On the basis of all the findings, we conclude that all cpAbs, prepared with the aldolase Abs 38C2 or 84G3 and compounds **4** or **5**, have strong affinity for both αv*β*3 and αv*β*6

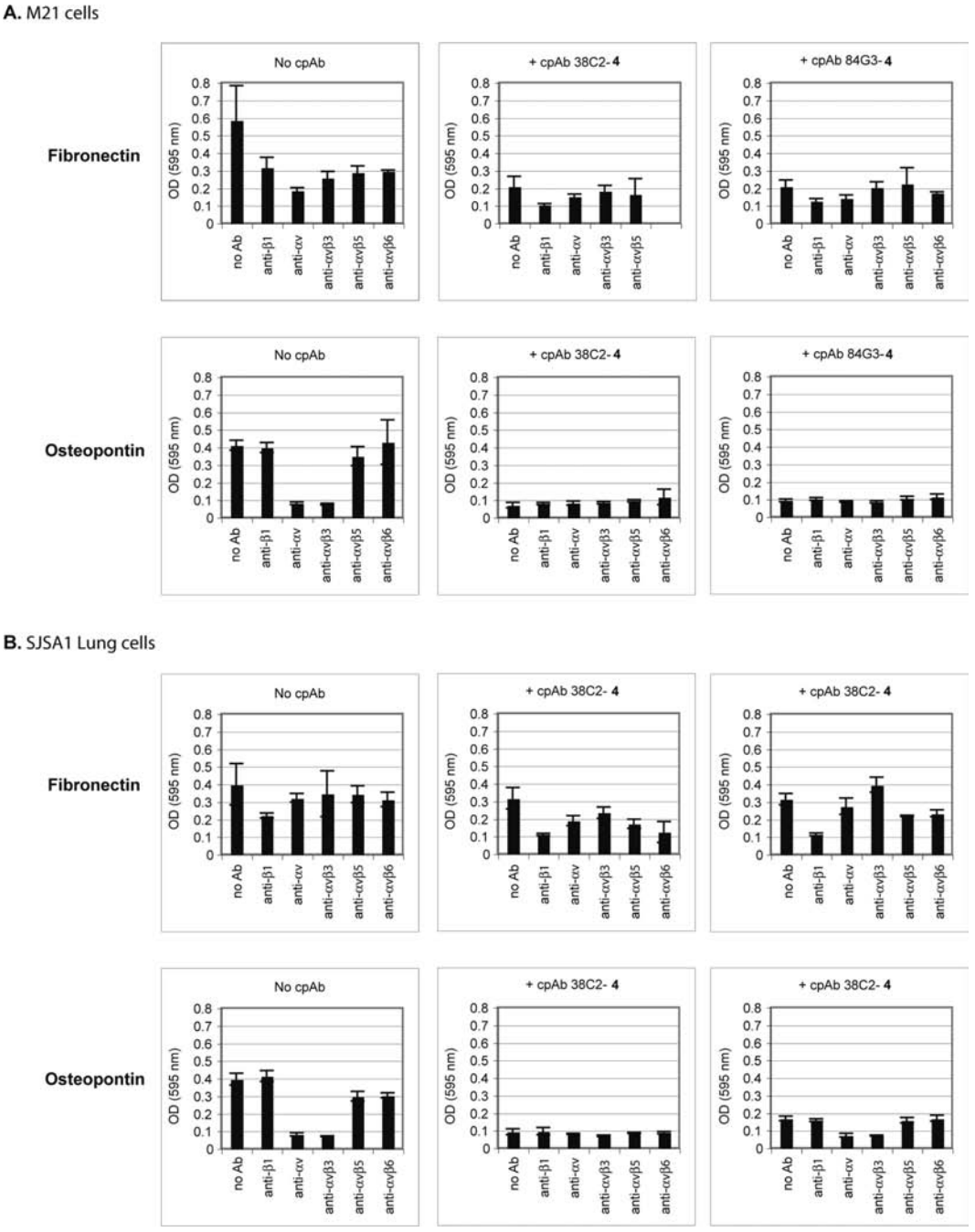

Figure 3. Effect of function-blocking control Abs and aldolase Ab-derived cpAbs on adhesion of (A) M21 cells and (B) SJSA1 lung cells to fibronectin (FN) or osteopontin (OPN). Use of function blocking monoclonal anti-β1, αv, β3, αvβ3, αvβ5, and αvβ6 antibodies indicates that adhesion of (A, Upper Left) M21 cells or (B, Upper Left) SJSA1 lung cells to FN is substantialy inhibited by most Abs used, but to OPN can be inhibited mainly by anti-av and anti-avb3 integrin Abs for both (A, Lower Left) M21 cells and (B, Lower Left) SJSA1 lung cells and to some extent using anti-αvβ5 Ab for M21 cells, anti-αvβ5, and anti-αvβ6 Abs for SJSA1 Lung cells. Use of cpAb 38C2-**4** or 84G3-**4** also moderately inhibits adhesion of (A, Upper Middle and Upper Right) M21 cells and (B, Upper Middle and Upper Right) SJSA1-lung cells to FN, which may be further enhanced with the addition of most Abs used. In contrast, a use of cpAb 38C2-**4** or 84G3-**4** causes a substantial inhibition of (A, Lower Middle and Lower Right) M21 cells and (B, Lower Middle and Lower Right) and SJSA1-lung cells to OPN, and remains unaffected when combined with all other Abs used.

integrins, and a weak affinity for the αvβ1 and αvβ8 integrins. These cpAbs are unlikely to have any appreciable affinity to αvβ5 integrin, because the binding affinity of the parent compound **3** to αvβ5 integrin is over 500 and 100 000 times weaker than to αvβ3 and αvβ6 integrins.[40] The observed weak binding of the cpAb 38C2-**4** to SW480 puro cells (Figure 2C) could be due to the αvβ1 integrin; it should be noted that all SW480 cells have a high level of αv and β1 integrins (SI Figure 3B) besides the αvβ5 integrin.

Therapeutic applicability of the above-described dual αvβ3 and αvβ6 integrin-targeting cpAbs, including 38C2-**4** and 84G3-**4**, as antitumor and anti-angiogenic agents would depend upon

their ability to interfere with the functions of these integrins on cancer and endothelial cells. A key function in tumor progression and angiogenesis is cell adhesion to natural integrin ligands within the extracellular matrix.[1−3] Most integrin binding matrix proteins are recognized by more than one integrin and the cognate receptors cooperate to mediate cell adhesion. To specifically address cpAbs effects on tumor cell adhesion mediated by integrins, we used fibronectin (FN) and osteopontin (OPN) as matrix ligands that are recognized by a number of integrins, including αvβ3 and αvβ6, overexpressed on tumor cells.[43] The cell−ligand adhesion studies were carried out, *in vitro*, using M21 human melanoma and SJSA1 osteosarcoma cells. Both of these cell types are aggressively metastatic and both ligands are highly relevant for tumor cell adhesion, migration, and invasion during tumor progression. Cell adhesion assays with the cpAbs 38C2-**4** and 84G3-**4** were conducted in both the presence and absence of known function blocking anti-integrin Abs, in order to assess the effects that the cpAbs would cause on individual integrins. In some experiments, we also examined cpAbs 85H6-**4** and 90G8-**4**, which were prepared using compound **4** and Abs 85H6 and 90G8, respectively (see SI Figure S-5).

Before interrogating the effects of the cpAbs on tumor cell-FN and OPN ligands interactions, we defined the tumor cell adhesion model and determined the time course of cell adhesion and the best interception time for function blocking antibodies. For this, effects of various function blocking anti-integrin Abs, including anti-β1, antiαv, antiαvβ3, and antiαvβ5 were examined on adhesion of M21 and SJSA1 lung cancer cells to FN and OPN as substrates. The results are shown in Figure 3A and B (upper and lower-left) (and SI Figures S-4, S-5, and S-6). Evidently, integrin αvβ3 was the main integrin that mediated the adhesion of these cells to OPN, whereas the cell adhesion to FN is mediated by multiple αv and β1 integrins. While the expression levels of αvβ5 and αvβ6 are low (Figure 2A and SI Figure 3D), it is possible that these integrins engage in binding cooperating with other fibronectin receptors. This may explain the partial inhibition by anti αvβ5 and αvβ6 directed Abs of M21 cell adhesion (Figure 3A-Upper and B-Upper).

Next, we evaluated the effects of the cpAbs on adhesion of M21 melanoma and SJSA1-lung carcinoma cells to FN and OPN. As shown in Figure 3A,B (Upper and Lower: Middle and Right), all cpAbs inhibited adhesion of both M21 and SJSA1-lung cells to FN and OPN. By combining anti-β1, anti-αv, anti-αvβ3, anti-αvβ5, or anti-αvβ6 Abs (100 μg/mL) with our aldolase Ab-based cpAbs in the adhesion experiments, and the results of our FACS assays described earlier in Figure 2, we can confidently state that our cpAbs inhibited adhesion of M21 and SJSA1 cells to both OPN and FN through specific interference with integrin αvβ3, and to some extent through αvβ1. The unconjugated aldolase Abs had no effect on the adhesion of any of our tumor cell models. Together, these data demonstrate a high efficacy of the cpAbs for interfering with multiple αv integrin mediated tumor cell adhesive functions.

Integrin αvβ3-targeting cpAbs were previously shown to discern their therapeutic efficacies by causing both antitumor and/or antiangiogenic effects *in vivo*.[16,19,24] To assess whether such effects could be mediated, at least in part, through direct cytotoxic or cytostatic impact of the antibody conjugates, we examined tumor cell viability in the presence of the cpAbs. In a pilot study, we found that these integrin targeting cpAbs cause no or only very low toxicity or cytostatic effects to the tumor cells. This was measured based on cell growth and viability *in vitro*. As

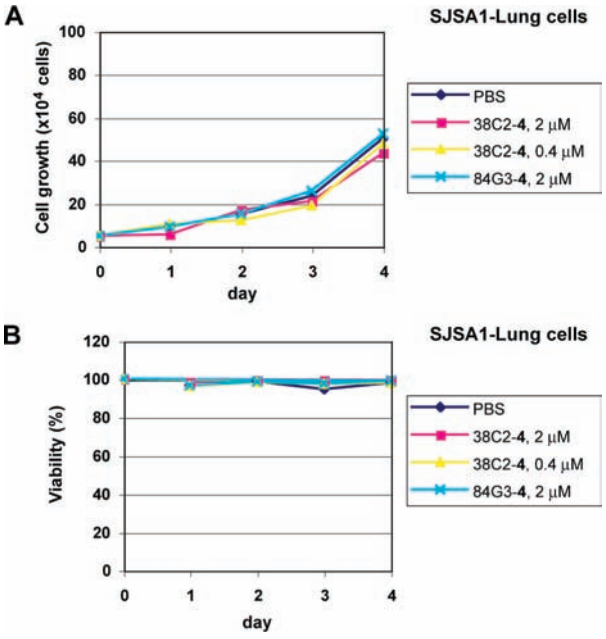

Figure 4. Viability and proliferation of SJSA1 cells in the absence and presence of 38C2-**4** (0.4 μM or 2 μM) and 84G3-**4** (2 μM).

shown in Figure 4, essentially no changes were observed in growth and viability of SJSA1 cells in the presence of the cpAbs. Generally, more than 90% cells were found viable in each study. This observation is in close agreement with our prior studies using an anti-αvβ3 integrin cpAb, which also had little toxicity at 2 μM concentration, except on MAEC mouse endothelial cell line ($IC_{50} \approx 1$ μM).[16] The results suggest that the anti-αvβ3 and dual αvβ3,αvβ6 integrin directed cpAbs may suppress tumor growth, presumably through interfering with the cell functions that control cell division and involve integrin mediated matrix contact survival signals. However, the cpAbs targeting multiple αv integrins per se do not mediate cell-killing at least at a low micromolar concentration.

Earlier, we found that an anti-αvβ3 cpAb, including that prepared with compounds **1** or **2** and Ab 38C2, inhibited the growth of both primary and metastatic tumors of several human cancers in mouse models.[19] On the basis of our results, we argue that an anti-αvβ3 compound or a cpAb can inhibit primary tumor growth and metastasis to distant organs presumably by invoking several pathways, including inhibiting angiogenesis and preventing initial adhesion of the cancer cells to their distant organ vasculature and tissues. Therefore, it seems to be less likely that an anti-integrin compound, Ab, or our cpAbs may cause actual regression of an established primary tumor or have major effects on established metastases. Moreover, if tumor cells overexpress more than one integrin type, it may be essential to inhibit all integrins that functionally contribute to primary tumor growth and/or metastasis of such cells, as the integrins compensate each other's function. Indeed, in a separate pilot study, we found that the anti-αvβ3,αvβ6 integrin cpAb 84G3-**4** had little effect on an established mouse metastasis model of human SJSA1-lung osteosarcoma, which also overexpresses multiple integrins, including α5β1 and α2β1, besides αvβ3, *in vivo* (not shown).

In summary, novel cell-targeting cpAbs were prepared based on the aldolase Ab-programming strategy using a series of Abs, including 38C2, 84G3, 85H6, and 90G8, and a dual inhibitor of integrins αvβ3 and αvβ6. The resulting cpAbs bound efficiently

and specifically to a variety of highly metastatic human cells expressing integrins αvβ3 and αvβ6. Importantly, the cpAbs specifically inhibited adhesion of target tumor cells from various metastatic human cancers to extracellular matrix proteins that are relevant during tumor growth and metastatic progression. *In vitro*, these cpAbs have little toxicity on cell growth and viability at low micromolar or nanomolar concentrations. We anticipate that the anti-αvβ3 and αvβ6 compounds and cpAbs can be best used for directing agents to specifically deliver therapeutic agents, and that they can be used in combination with cytotoxins or other therapeutic agents to tumors, the tumor vasculature and tumor microenvironments. A dual targeting strategy against integrins αvβ3 and αvβ6 by our specific cpAb is likely to have application in the diagnosis and therapy of a broader range of human cancers expressing either or both integrins. Moreover, an anti-αvβ3 and αvβ6 integrin cpAb can provide reagents to study combined effect of αvβ3 and αvβ6 *in vitro*, and αvβ3 and αvβ6-mediated pathologies *in vivo*, including tumor angiogenesis, fibrosis, and epithelial cancers.[31,44] Finally, this study highlights the versatility and specificity of our aldolase antibody programming approach to generate highly efficient tools for diagnostic and possibly therapeutic applications, and as an alternative to the classical antibody−integrin inhibitor conjugates.[45,46]

■ ASSOCIATED CONTENT

Supporting Information. Additional figures depicting the extent of the chemical antibody programming using the methodol assay. This material is available free of charge via the Internet at http://pubs.acs.org.

■ AUTHOR INFORMATION

Corresponding Author

*E-mail: subhash@scripps.edu.

Present Addresses

[§]Glenmark Pharmaceuticals Ltd., Plot No. A-607, TTC, Industrial Area, MIDC, Mahape, Navi Mumbai-400709.

[#]DuPont Central Research and Development, Experimental Station-E328/207B, Rt 141 and Henry Clay, Wilmington, DE 19880.

■ ACKNOWLEDGMENT

We express our thanks to Professor Carlos F. Barbas of this Institute for the helpful discussions and the aldolase antibodies, Dr. Ronny Drapkin and the Dana-Farber Cancer Institute, Boston, MA for OVCA-429 and OVCA-433 cell lines, and to Dr. Stephen Nishimura of UCSF Medical Center, San Francisco, California, for the SW480 cell lines and the anti-αvβ8 integrin 14E5 mouse Ab. This work was supported by NIH grants CA120289 to SCS and CA112287 to BFH, California Breast Cancer Research Program grants 12NB0176 and 13NB0180 to BFH, and Department of Defense grants W81XWH-07-1-0421 and W81XWH-09-1-0690 to SCS and W81XWH-08-1-0468 to BFH.

■ REFERENCES

(1) Caswell, P. T., Vadrevu, S., and Norman, J. C. (2009) Integrins: masters and slaves of endocytic transport. *Nat. Rev. Mol. Cell Biol. 10*, 843–853.

(2) Shattil, S. J., Kim, C., and Ginsberg, M. H. (2010) The final steps of integrin activation: the end game. *Nat. Rev. Mol. Cell Biol. 11*, 288–300.

(3) Desgrosellier, J. S., and Cheresh, D. A. (2010) Integrins in cancer: biological implications and therapeutic opportunities. *Nat. Rev. Cancer 10*, 9–22.

(4) Cox, D., Brennan, M., and Moran, N. (2010) Integrins as therapeutic targets: lessons and opportunities. *Nat. Rev. Drug Discovery 9*, 804–820.

(5) van der Flier, A., Badu-Nkansah, K., Whittaker, C. A., Crowley, D., Bronson, R. T., Lacy-Hulbert, A., and Hynes, R. O. (2010) Endothelial α5 and αv integrins cooperate in remodeling of the vasculature during development. *Development 137*, 2439–2449.

(6) Erdreich-Epstein, A., Shimada, H., Groshen, S., Liu, M., Metelitsa, L. S., Kim, K. S., Stins, M. F., Seeger, R. C., and Durden, D. L. (2000) Integrins alpha(v)beta3 and alpha(v)beta5 are expressed by endothelium of high-risk neuroblastoma and their inhibition is associated with increased endogenous ceramide. *Cancer Res. 60*, 712–721.

(7) Koopman Van Aarsen, L. A., Leone, D. R., Ho, S., Dolinski, B. M., McCoon, P. E., LePage, D. J., Kelly, R., Heaney, G., Rayhorn, P., Reid, C., Simon, K. J., Horan, G. S., Tao, N., Gardner, H. A., Skelly, M. M., Gown, A. M., Thomas, G. J., Weinreb, P. H., Fawell, S. E., and Violette, S. M. (2008) Antibody-mediated blockade of integrin αvβ6 inhibits tumor progression in vivo by a transforming growth factor-B−regulated mechanism. *Cancer Res. 68*, 561–570.

(8) Breuss, J. M., Gallo, J., DeLisser, H. M., Klimanskaya, I. V., Folkesson, H. G., Pittet, J. F., Nishimura, S. L., Aldape, K., Landers, D. V., and Carpenter, W. (1995) Expression of the β6 subunit in development, neoplasia and tissue repair suggests a role in epithelial remodeling. *J. Cell. Sci. 108*, 2241–2251.

(9) Jones, J., Watt, F. M., and Speight, P. M. (1997) Changes in the expression of alpha v integrins in oral squamous cell carcinomas. *J. Oral Pathol. Med. 26*, 63–68.

(10) Hakkinen, L., Hildebrand, H. C., Berndt, A., Kosmehl, H., and Larjava, H. (2000) Immunolocalization of tenascin-C, α9 integrin subunit, and αvβ6 integrin during wound healing in human oral mucosa. *J. Histochem. Cytochem. 48*, 985–998.

(11) Regezi, J. A., Ramos, D. M., Pytela, R., Dekker, N. P., and Jordan, R. C. K. (2002) Tenascin and β6 integrin are overexpressed in floor of mouth in situ carcinomas and invasive squamous cell carcinomas. *Oral Oncol. 38*, 332–336.

(12) Ahmed, N., Pansino, F., Baker, M., Rice, G., and Quinn, M. (2002) Association between αvβ6 integrin expression, elevated p42/44 kDa MAPK, and plasminogen-dependent matrix degradation on ovarian cancer. *J. Cell. Biochem. 84*, 675–686.

(13) Bates, R. C., Bellovin, D. I., Brown, C., Maynard, E., Wu, B., Kawakatsu, H., Sheppard, D., Oettgen, P., and Mercurio, A. M. (2005) Transcriptional activation of integrin β6 during the epithelialmesenchymal transition defines a novel prognostic indicator of aggressive colon carcinoma. *J. Clin. Invest. 115*, 339–347.

(14) Hazelbag, S., Kenter, G., Gorter, A., Dreef, E., Koopman, L., Violette, S., Weinreb, P., and Fleuren, G. (2007) Overexpression of the αvβ6 integrin in cervical squamous cell carcinoma is a prognostic factor for decreased survival. *J. Pathol. 212*, 316–324.

(15) Lafrenie, R. M., Buckner, C. A., and Bewick, M. A. (2007) Cell adhesion and cancer: is there a potential for therapeutic intervention? *Expert Opin Ther. Targeting 11*, 727–731.

(16) Rader, C., Sinha, S. C., Popkov, M., Lerner, R. A., and Barbas, C. F., III (2003) A chemically programmed monoclonal antibody for cancer therapy. *Proc. Natl. Acad. Sci. U.S.A. 100*, 5396–5400.

(17) Li, L.-S., Rader, C., Matsushita, M., Das, S., Barbas, C. F., III, Lerner, R. A., and Sinha, S. C. (2004) Chemical-adaptor immunotherapy: design, synthesis and evaluation of novel integrin-targeting devices. *J. Med. Chem. 47*, 5630–5640.

(18) Rader, C., Turner, J. M., Heine, A., Shabat, D., Sinha, S. C., Wilson, I. A., Lerner, R. A., and Barbas, C. F., III (2003) A humanized aldolase antibody for selective chemotherapy and adaptor immunotherapy. *J. Mol. Biol. 332*, 889–899.

(19) Guo, F., Das, S., Mueller, B. M., Barbas, C. F., III, Lerner, R. A., and Sinha, S. C. (2006) Breaking the one antibody-one target axiom. *Proc. Natl. Acad. Sci. U.S.A. 103*, 11009–11014.

(20) Goswami, R. K., Huang, Z.-Z., Forsyth, J. S., Felding-Habermann, B., and Sinha, S. C. (2009) Multiple catalytic aldolase antibodies suitable for chemical programming. *Bioorg. Med. Chem. Lett. 19*, 3821–3824.

(21) Gavrilyuk, J. I., Wuellner, U., Salahuddin, S., Goswami, R. K., Sinha, S. C., and Barbas, C. F., III (2009) An efficient chemical approach to bispecific antibodies and antibodies of high valency. *Bioorg. Med. Chem. Lett. 19*, 3716–3720.

(22) Wagner, J., Lerner, R. A., and Barbas, C. F., III (1995) Efficient aldolase catalytic antibodies that use the enamine mechanism of natural enzymes. *Science 270*, 1797–1800.

(23) Zhong, G., Lerner, R. A., and Barbas, C. F., III (1999) Broadening the aldolase catalytic antibody repertoire by combining reactive immunization and transition state theory: new enantio- and diastereoselectivities. *Angew. Chem., Int. Ed. 38*, 3738–3741.

(24) Popkov, M., Rader, C., Gonzalez, B., Sinha, S. C., and Barbas, C. F., III (2006) Small molecule drug activity in melanoma models may be dramatically enhanced with an antibody effector. *Int. J. Cancer 119*, 1194–1207.

(25) Doppalapudi, V. R., Tryder, N., Li, L., Aja, T., Griffith, D., Liao, F.-F., Roxas, G., Ramprasad, M. P., Bradshaw, C., and Barbas, C. F. (2007) Chemically programmed antibodies: endothelin receptor targeting CovX-bodies. *Bioorg. Med. Chem. Lett. 17*, 501–506.

(26) Doppalapudia, V. R., Huanga, J., Liua, D., Jina, P., Liua, B., Lia, L., Desharnaisa, J., Hagena, C., Levina, N. J., Shieldsa, M. J., Parisha, M., Murphya, R. E., Del Rosarioa, J., Oatesa, B. D., Laia, J.-Y., Matina, M. J., Ainekulua, Z., Bhata, A., Bradshawa, C. W., Woodnutta, G., Lerner, R. A., and Lappe, R. W. (2010) Chemical generation of bispecific antibodies. *Proc. Natl. Acad. Sci. U.S.A. 107*, 22611–22616.

(27) Felding-Habermann, B., Mueller, B. M., Romerdahl, C. A., and Cheresh, D. A. (1992) Involvement of integrin αv gene expression in human melanoma tumorigenicity. *J. Clin. Invest. 89*, 2018–2022.

(28) Rolli, M., Fransvea, E., Pilch, J., Saven, A., and Felding-Habermann, B. (2003) Activated integrin alphavbeta3 cooperates with metalloproteinase MMP-9 in regulating migration of metastatic breast cancer cells. *Proc. Natl. Acad. Sci. U.S.A. 100*, 9482–9487.

(29) Wayner, E. A., Orlando, R. A., and Cheresh, D. A. (1991) Integrins alpha v beta 3 and alpha v beta 5 contribute to cell attachment to vitronectin but differentially distribute on the cell surface. *J. Cell Biol. 113*, 919–929.

(30) Alkhalaf, M., and Jaffal, S. (2006) Potent antiproliferative effects of resveratrol on human osteosarcoma SJSA1 cells: novel cellular mechanism involving the ERKs/p53 cascade. *Free Radical Biol. Med. 41*, 318–325.

(31) Lidor, Y. J., Shpall, E. J., Peters, W. P., and Bast, R. C., Jr. (1991) Synergistic cytotoxicity of different alkylating agents for epithelial ovarian cancer. *Int. J. Cancer 49*, 704–710.

(32) Weinreb, P. H., Simon, K. J., Rayhorn, P., Yang, W. J., Leone, D. R., Dolinski, B. M., Pearse, B. R., Yokota, Y., Kawakatsu, H., Atakilit, A., Sheppard, D., and Violette, S. M. (2004) Function-blocking integrin αvβ6 monoclonal antibodies: distinct ligand-mimetic and nonligand-mimetic classes. *J. Biol. Chem. 279*, 17875–17887.

(33) Cambier, S., Mu, D.-Z., O'Connell, D., Boylen, K., Travis, W., Liu, W.-H., Broaddus, V. C., and Nishimura, S. L. (2000) A Role for the Integrin αvβ8 in the Negative Regulation of Epithelial Cell Growth. *Cancer Res. 60*, 7084–7093.

(34) Rodionov, V. M., and Postovskaja, E. A. (1929) Mechanism of formation of β-aryl-β-amino fatty acids by the condensation of aroatic aldehydes with malonic acid and its derivatives. *J. Am. Chem. Soc. 51*, 841–847.

(35) Johnson, T. B., and Livak, J. E. (1936) Pyrimidines. CXLIX. The synthesis of aryl-substituted dihydrouracils and their conversion into uracil derivatives. *J. Am. Chem. Soc. 58*, 299–303.

(36) Miyaura, N., and Suzuki, A. (1995) Palladium-catalyzed cross-coupling reactions of organoboron compounds. *Chem. Rev. 95*, 2457–2483.

(37) Sinha, S. C., Das, S., Li, L.-S., Lerner, R. A., and Barbas, C. F., III (2007) Preparation of integrin alpha(v)beta(3)-targeting Ab 38C2 constructs. *Nat. Prot. 2*, 449–456.

(38) Zhu, X., Tanaka, F., Lerner, R. A., Barbas, C. F., III, and Wilson, I. A. (2009) Direct observation of an enamine intermediate in amine catalysis. *J. Am. Chem. Soc. 131*, 18206–18207.

(39) List, B., Barbas, C. F., III, and Lerner, R. A. (1998) Aldol sensors for the rapid generation of tunable fluorescence by antibody catalysis. *Proc. Natl. Acad. Sci. U.S.A. 95*, 15351–15355.

(40) Goodman, S. L., Hölzemann, G., Sulyok, G. A. G., and Kessler, H. (2002) Nanomolar small molecule inhibitors for αvβ6, αvβ5 and αvβ3 integrins. *J. Med. Chem. 45*, 1045–1051.

(41) Simoni, D., Rondanin, R., Baruchello, R., Rizzi, M., Grisolia, G., Eleopra, M., Grimaudo, S., Di Cristina, A., Pipitone, M. R., Bongiorno, M. R., Arico, M., Invidiata, F. P., and Tolomeo, M. (2008) Novel terphenyls and 3,5-diaryl isoxazole derivatives endowed with growth supporting and antiapoptopic properties. *J. Med. Chem. 51*, 4796–4803.

(42) Li, E., Brown, S. L., Stupack, D. G., Puente, X. S., Cheresh, D. A., and Nemerow, G. R. (2001) Integrin αvβ1 Is an Adenovirus Coreceptor. *J. Virol. 75*, 5405–5409.

(43) Humphries, J. D., Byron, A., and Humphries, M. J. (2006) Integrin ligands at a glance. *J. Cell Sci. 119*, 3901–3903.

(44) Humphries, M. J. (2004) Monoclonal antibodies as probes of integrin priming and activation. *Biochem. Soc. Trans. 32*, 407–411.

(45) Kok, R. J., Schraa, A. J., Bos, E. J., Moorlag, H. E., Ásgeirsdóttir, S. A., Everts, M., Meijer, D. K. F., and Molema, G. (2002) Preparation and functional evaluation of RGD-modified proteins as αvβ3 integrin directed therapeutics. *Bioconjugate Chem. 13*, 128–135.

(46) Shin, I. S., Jang, B.-S., Danthi, S. N., Xie, J., Yu, S., Le, N., Maeng, J.-S., Hwang, I. S., Li, K. C. P., Carrasquillo, J. A., and Paik, C. H. (2007) Use of antibody as carrier of oligomers of peptidomimetic αvβ3 antagonist to target tumor-induced neovasculature. *Bioconjugate Chem. 18*, 821–828.

Chemically Programmed Antibodies Targeting Multiple Alpha(v) Integrins and Their Effects on Tumor-Related Functions in vitro

Rajib K. Goswami,[1] Krishna M. Bajjuri,[1] Jane S. Forsyth,[2] Sanjib Das,[1] Wolf Hassenpflug,[2] Zheng-Zheng Huang,[1] Richard A. Lerner,[1,*] Brunhilde Felding-Habermann,[2,*] Subhash C. Sinha,[1,*]

The Departments of Molecular Biology, and Molecular and Experimental Medicine, and The Skaggs Institute for Chemical Biology. The Scripps Research Institute, 10550 North Torrey Pines Road, La Jolla, CA 92037

E-mail: subhash@scripps.edu

Supporting Information

Fig. S-1. Determination of the Ab-programming using the methodol assay Page S-1

Fig. S-2. Determination of the Ab-programming with compounds **4** and **5** Page S-2

Fig. S-3. Flow cytometry analysis Page S-2

Fig. S-4. Effect of function-blocking control Abs on adhesion of M21, BCM2, and SJSA1 lung cells to fibronectin or osteopontin Page S-3

Fig. S-5. Effect of function-blocking control Abs and cpAbs alone or in combination on adhesion of M21 cells to fibronectin or osteopontin Page S-4

Table S-1. Binding of anti-integrin Abs and cpAb 38C2-**4** to multiple cell lines determined using FACS. Page S-5

[1] Molecular Biology and The Skaggs Institute
[2] Molecular and Experimental Medicine

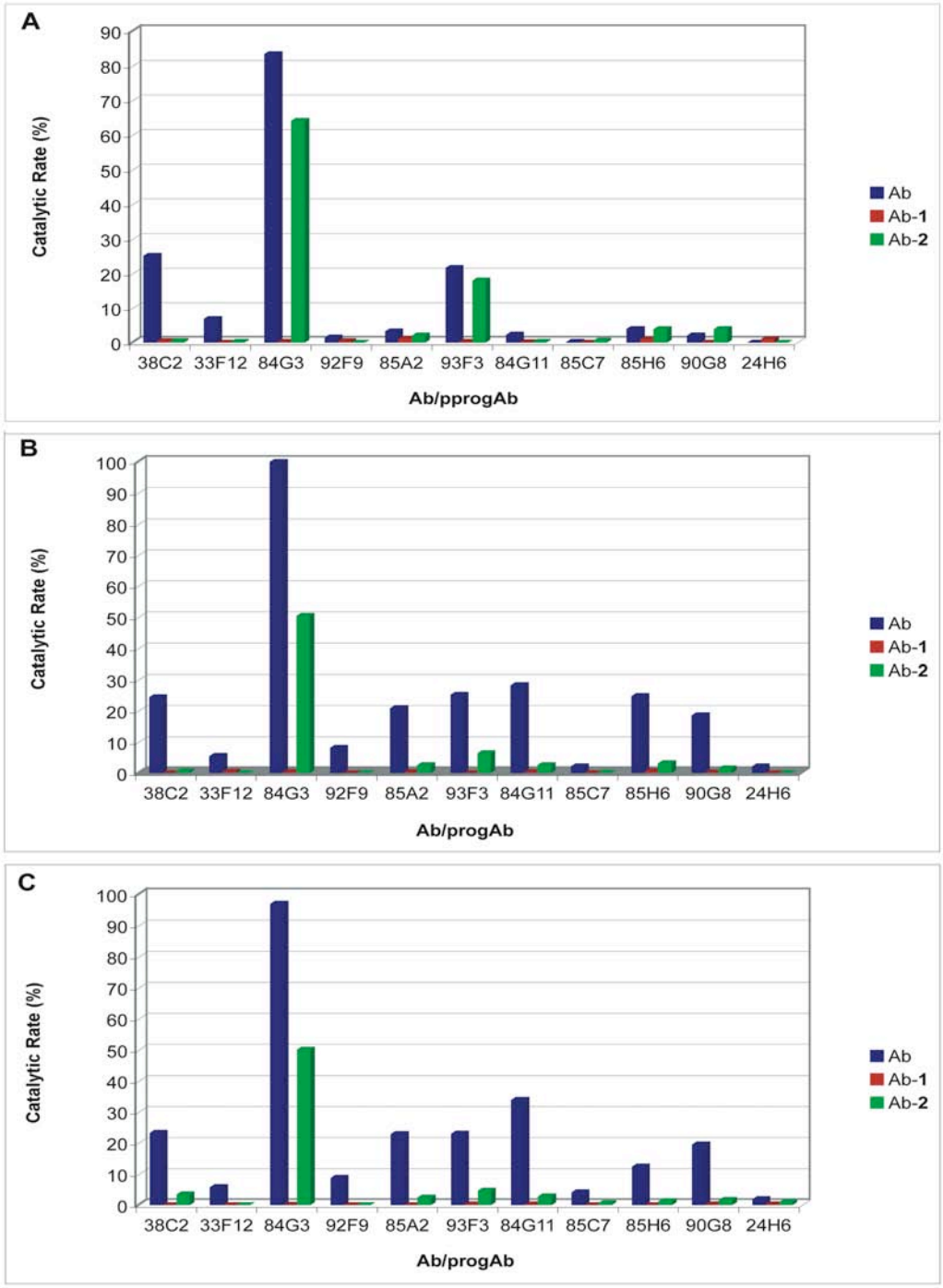

Fig. S-1. Determination of the Ab-programming using the methodol assay. Ab programming was carried out using the DK compound **1** for 30 mins (room temperature) or with the pVK compound **2** for 1.5 h (37 ˚C) at pH (A) 6.0, (B) 7.4, and (C) 8.5.

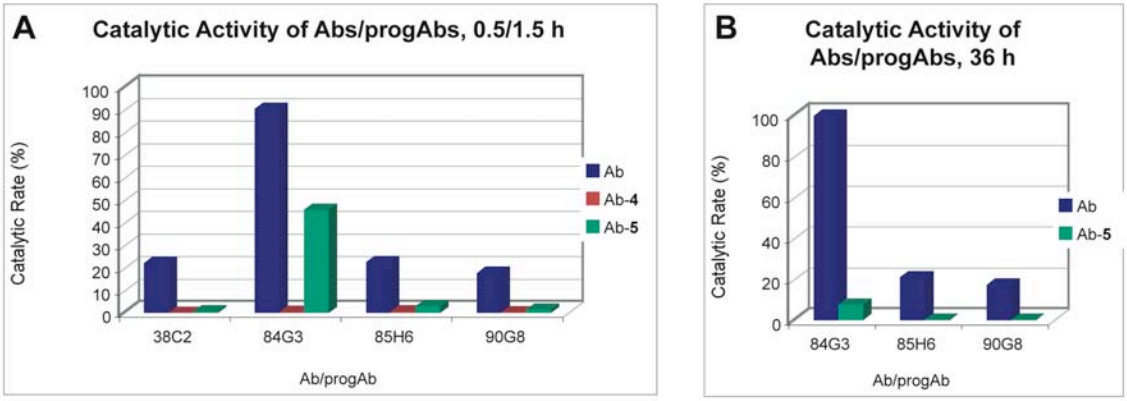

Fig. S-2. Determination of the Ab-programming with compounds **4** and **5** using the methodol assay. Ab programming was carried out using the DK compound **4** for 30 mins (room temperature) or with the pVK compound **5** for 1.5 h (37 ˚C) at pH 7.4. Programming of Ab 84G3 using the pVK compound **5** (3 equivalent) was 50% complete in 1.5 hrs, but only 92% in 36 hrs. To achieve nearly complete programming (>98%), the mixture was incubated another 36-48 hrs.

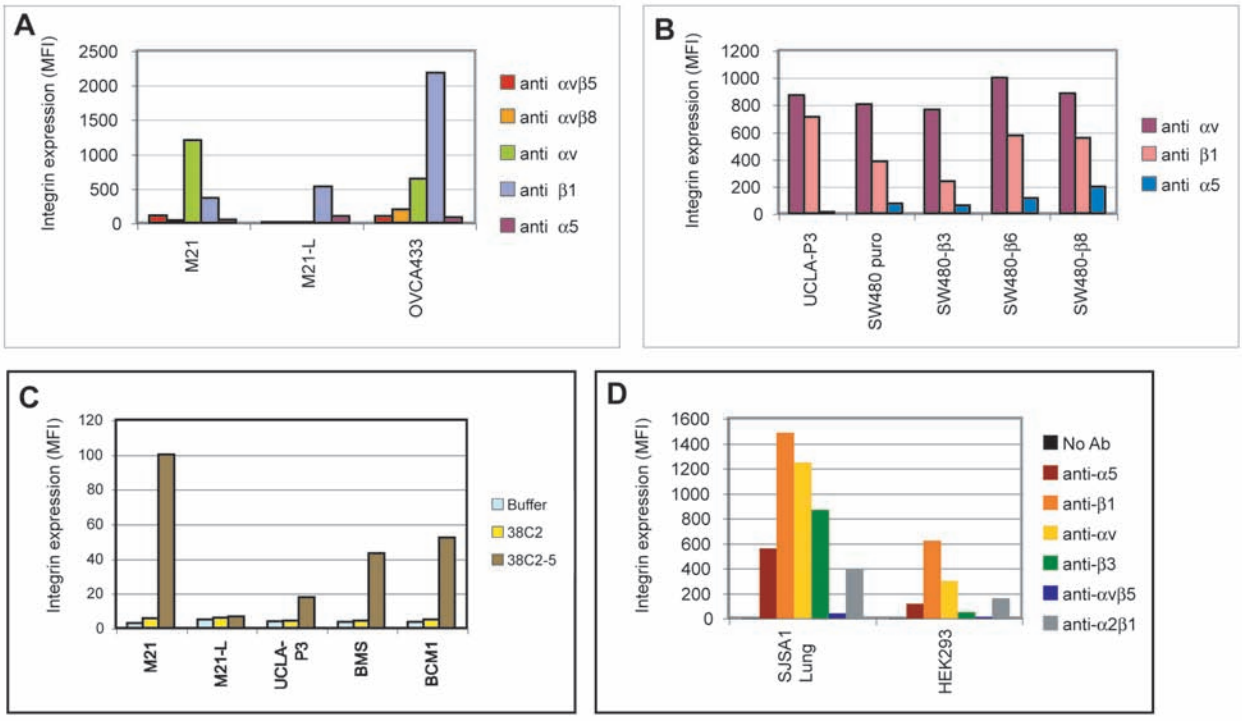

Fig. S-3. Flow cytometry analysis showing the integrin expression on various tumor cells, including (A) M21, M21-L, and OVCA433, (B) UCLA-P3, SW480 puro, SW480-β3, SW480-β6, and SW480-β8, and (D) SJSA1 lung and HEK293 cells. 'Anti-integrin' denotes monoclonal anti-integrin complex specific antibodies used to report integrin expression. Shown in (C) are the

binding specificity of cpAb 38C2-**5** to αv integrins expressed by human M21, M21-L, UCLA-P3, BMS, and BCM1 tumor cells. APC labeled anti-mouse Abs were used to detect the binding in A, B and D, and FITC labeled anti-mouse Abs were used in C.

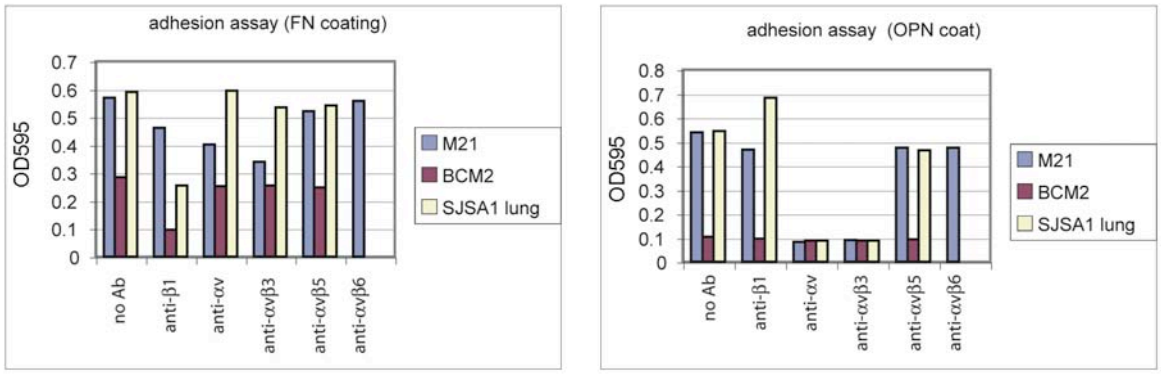

Fig. S-4. Effect of function-blocking control Abs on adhesion of M21, BCM2, and SJSA1 lung cells to (Upper) fibronectin (FN) or (Lower) osteopontin (OPN). Use of function blocking monoclonal anti-β1, -αv, -β3, αvβ3, αvβ5, and αvβ6 antibodies indicates that adhesion of BCM2 and SJSA1 lung cells to fibronectin (FN) can be substantially inhibited using anti-β1 antibody, whereas adhesion of M21 and SJSA1 lung cells to osteopontin (FN) can be substantially inhibited using anti-αvβ3 antibody.

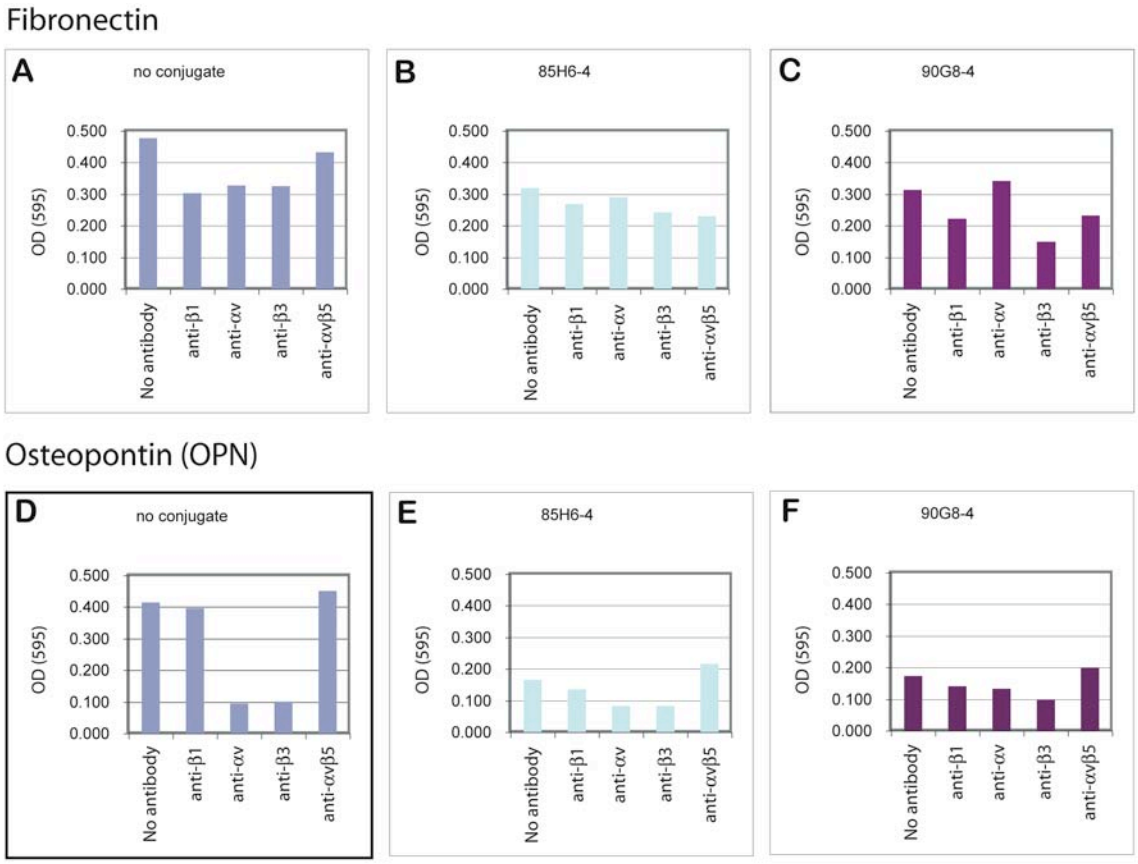

Fig. S-5. Effect of function-blocking control Abs and cpAbs alone or in combination on adhesion of M21 cells to (Upper) fibronectin (FN) or (Lower) osteopontin (OPN). Use of function blocking monoclonal anti-β1, -αv, -β3, and αvβ5 antibodies indicates that adhesion of M21 cells to OPN can be substantially inhibited using anti-αv, and anti-β3 antibodies, as well as the cpAbs 85H6-**4** and 90G8-**4**. All Abs and cpAbs have some effect on the adhesion of M21 cells to FN.

Table S-1. Binding of anti-integrin Abs and cpAb 38C2-**4** to multiple cell lines determined using FACS.

Cells	Antibodies							
	VNR1	P1F6	10D5	14E5	L230	P5D2	P1D6	cpAb 38C2-**4**
	Integrin targets							
	anti αvβ3	anti αvβ5	anti αvβ6	anti αvβ8	anti αv	anti β1	anti α5	anti αvβ3/ αvβ6
	Mean fluorescence Intensities							
M21	528.71	104.39	6.18	30.93	1195.53	357.92	47.68	1361.76
M21-L	5.79	6.02	5.41	6.1	8.24	522.76	91.87	10.22
OVCA 433	12.58	92.86	298.99	196	639.66	2175.39	80.87	1119.7
UCLA-P3	10.85	365.68	159.77	23.18	865.95	706.88	6.84	296.07
SW480 puro	11	485.04	7.47	7.63	803.08	381.56	69.87	94.79
SW480 β3	407.98	197.39	26.02	25.39	760.96	233.25	58.71	815.99
SW480 β6	8.7	258.81	819.97	6.34	997.6	569.27	112.14	781.14
SW480 β8	20.5	388.5	14.49	63.04	881.87	552.58	194.56	222.73

Key: Antibody binding was detected using APC-labeled secondary anti-mouse Ab.

Bioconjugate Chemistry

ARTICLE

pubs.acs.org/bc

Aldehyde PEGylation Kinetics: A Standard Protein versus a Pharmaceutically Relevant Single Chain Variable Fragment

Anna Moosmann,[*,#,†] Jessica Blath,[#,‡] Robert Lindner,[†] Egbert Müller,[§] and Heiner Böttinger[†]

[†]Institute of Cell Biology and Immunology, University of Stuttgart, Allmandring 31, 70569 Stuttgart, Germany

[‡]Institute of Interfacial Engineering, University of Stuttgart, Nobelstrasse 12, 70569 Stuttgart, Germany

[§]Tosoh Bioscience GmbH, Zettachring 6, 70567 Stuttgart, Germany

ABSTRACT:

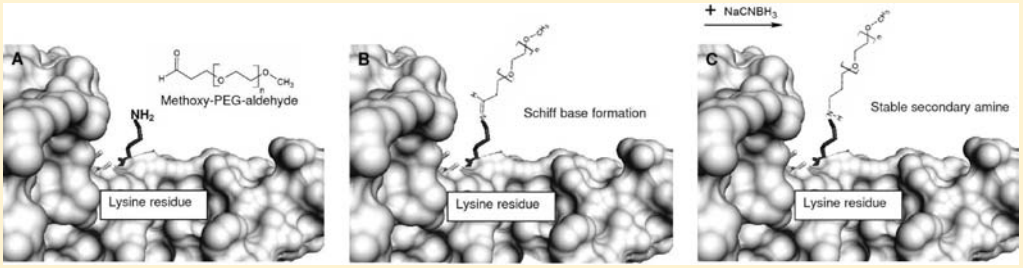

The mPEG-aldehyde PEGylation with two different PEG sizes and two proteins was experimentally determined with respect to yield, conversion, and selectivity. The kinetic behavior of these PEGylation reactions was simulated using a numerically solved set of differential equations. We show that the assumption of an inactivation of mPEG-aldehyde is crucial for the simulation of the overall PEGylation and that the inactivation is pH-dependent. We further demonstrate that ideal PEGylation parameters such as pH, temperature, reaction time, and protein concentration need to be chosen carefully depending on the protein and PEG size. In terms of selectivity and yield, we show that the reaction should be stopped before the highest mono-PEG concentration is reached. Moreover, room temperature and a slightly acidic pH of approximately 6 are good starting points. In conclusion, selectivity can be optimized choosing a shorter reaction time and a reduced reaction temperature.

INTRODUCTION

There are numerous drugs based on proteins of different classes, such as enzymes and antibodies, both having great potential in pharmaceutical use. However, the usage of proteins in general is restricted by their biocompatibility and in situ half-life. In particular, small molecules have very short half-lives, which restricts the use of small proteins in drug design.[1,2] For example, antibody fragments have many characteristics that would make them ideal drug candidates, such as easy and cheap production and high efficacy; however, due to their small size blood and renal clearance are very high.[1,2] An effective way of prolonging the in situ half-life of such proteins is polymer modification, which artificially enlarges the hydrodynamic radius and leads to a masking effect.[2−5] As the renal clearance depends highly on the hydrodynamic radius, renal filtration as a fast excretion step will be overcome. The masking effect by polymer modification will also decrease the target sites for proteases[1,2,6] and thereby prolong the half-life, too. One possible way of polymer modification is PEGylation, which denominates the chemical attachment of a poly(ethylene glycol) chain to molecules such as proteins or peptides. Since the first reports in PEGylation in the 1970s,[3,7] the method has now become a state-of-the-art technology. Eight PEGylated protein drugs are approved by the FDA by now,[8] such as PEGasys (Hoffman-La Roche) and PEG Intron (Schering-Plough/Enzon),[9,10] both α-Interferon products for hepatitis C treatment. PEG is the polymer of choice because it is a neutral, nonimmunogenic, and inert polymer.[6,11,12] PEG has to be functionalized with a reactive end group to enable attachment to another molecule. Each functionalization of PEG results in altered PEGylation kinetics, but additionally the protein itself affects the kinetic characteristics of the PEGylation reaction as well as the ambient conditions. One of the most frequently used functionalities is aldehyde-modified PEG, which reacts with free amino groups of the protein.[6,8] This reaction is random, as all available amino groups can react. The pK_a and the accessibility of each free amino group define the probability for PEGylation.[2,6,8,13,14] These characteristics can be influenced by the ambient conditions. The pH is a critical factor in PEGylation characteristics, as well as temperature and concentrations of protein and PEG.[6,8,15] PEGylation changes the physicochemical properties of a protein,[9,16] and the

Received: February 21, 2011
Revised: July 18, 2011
Published: July 24, 2011

ACS Publications © 2011 American Chemical Society

chromatographic behavior of proteins is modified by PEGylation, too. The altered behavior of PEGylated proteins in comparison with the non-PEGylated parental proteins could be shown by ion-exchange chromatography (IEX),[9,16,17] hydrophobic interaction chromatography,[9] as well as size exclusion chromatography (SEC).[9] In this study, we thus focus on IEX for the rapid separation of PEGylated and non-PEGylated proteins to follow the PEGylation reaction as fast as possible.

Furthermore, studies on the standard protein lysozyme have already been performed regarding its behavior in chromatography,[18,19] as well as accessible PEGylation sites for aldehyde chemistry,[20] but thus far, no detailed survey on the kinetics of the aldehyde PEGylation reaction itself has been published. We compare the PEGylation kinetics of two different proteins, a pharmaceutically relevant single-chain variable fragment produced in *E. coli* and the enzyme lysozyme. Both proteins were PEGylated and the reaction was closely observed to obtain the relevant data for kinetic analysis. Different factors influencing the environmental conditions such as pH and temperature have additionally been analyzed and two different PEG sizes were used. Finally, to gather deeper insight into the reaction kinetics, a model was developed to simulate the reaction behavior.

MATERIAL AND METHODS

Chemicals. Methoxy-PEG-aldehyde (mPEG-AL) with average molecular weights of 5 and 30 kDa were purchased from NOF Corp. (Grobbendonk, Belgium). Lysozyme (98% pure, chicken egg white) was provided by Sigma (St. Louis, USA). All other chemicals were provided by Merck (Darmstadt, Germany).

Production of scFv. The single-chain variable fragment used in this study was produced in *E. coli BL21 DE3 rha*$^-$ using the rhamnose induction system.[21,22] Following a modified osmotic shock procedure according to Rathore,[23] the pellet was solubilized in 100 mM phosphate buffer containing 50% glucose followed by adding pure water. After centrifugation, the protein solution was purified using protein L-chromatography (GenScript, Piscataway, USA). The purified scFv was further diafiltered and lyophilized for long-term storage.

PEGylation of scFv and Lysozyme. Protein and 5 or 30 kDa PEG of the desired concentration were dissolved in a 20 mM sodium phosphate buffer pH 6.0 or 7.0 or a 20 mM sodium acetate buffer pH 3.0, 4.0, or 5.0 containing 20 mM $NaCNBH_3$.[4,18,19] The PEGylation reaction was performed in a final volume of 1 mL at temperatures between 10 and 30 °C and a protein concentration in the range 1−10 g/L. The reaction time was up to 20 h; the monitoring was carried out continuously. All discussed factors were analyzed individually; each reaction was replicated at least two times. The following standard conditions were used as starting conditions for each factor analysis: for lysozyme, pH 6, 21 °C, 20 h reaction time, 2-fold PEG excess, 1 g/L; for scFv, 1 g/L, pH 4, 21 °C, 20 h reaction time, 5-fold PEG excess.

Lysozyme and scFv both possess a N-terminal amino group, and lysozyme possesses 6 lysine residues whereas the scFv has 9. Therefore, more than one mono-PEGylated isoform and also different di-PEGylated forms as well as higher PEGylated species can be formed in the random reaction.

Analytical Procedures. An analytical TSKgel SP-NPR column (ID 4.6 mm × L 35 mm, Tosoh Bioscience GmbH, Stuttgart, Germany) was used to track the PEGylation reaction. For lysozyme, the buffer consisted of 25 mM sodium phosphate buffer, pH 6.0. For elution, 1 M NaCl was added. For scFv, the buffer consisted of 20 mM sodium acetate buffer, pH 4.5. For elution, 1 M NaCl was added. The analytical IEX was carried out on a Thermo Separation HPLC SpectraSYSTEM (Thermo Fisher Scientific GmbH, Dreieich, Germany).

SDS-PAGE under reducing conditions was performed according to Laemmli.[24] Protein samples were solubilized in sample buffer and heated at 95 °C for 3 min. SDS-PAGE was performed with precast NuPAGE Novex 10% Bis-Tris Midigels (Invitrogen Corporation, Carlsbad, USA) in an XCell4 SureLock Midi-Cell (Invitrogen) according to the manufacturer's procedure. The gels were stained with PageBlue Protein Staining solution (Fermentas, St. Leon-Rot, Germany) according to the manufacturer's instruction. To stain specifically the PEGylated proteins, barium−iodine staining was carried out. The procedure was modified according to Kurfürst,[25] following the instructions of Bailon et al.[26]

SEC was carried out on an analytical TSKgel G3000SW_{XL} column (7.8 mm × 30 cm, Tosoh Bioscience GmbH). As mobile phase, a 100 mM sodium phosphate buffer, pH 6.7, containing 100 mM Na_2SO_4 and 0.05% NaN_3 was used. The SEC chromatography was performed on a Thermo Separation HPLC SpectraSYSTEM (Thermo Fisher Scientific GmbH).

Mathematic Modeling. For the PEGylated forms and the unmodified forms at all time points, the concentration was estimated via the peak area from IEX chromatography, under the assumption of PEG being undetectable for UV absorbance. As PEG is undetectable, no experimental data for the PEG concentration were utilizable; rather, the PEG concentration, needed for the modeling, was calculated from the protein concentration by the following equation:

$$c(\mathrm{PEG})^t = c(\mathrm{PEG})^0 - c(\text{mono-PEG-protein})^t - 2 \times c(\textit{di-PEG-protein})^t - 3 \times c(\textit{tri-PEG-protein})^t$$

The set of differential equations describing the reaction (see Kinetic Studies and Mathematic Modeling section) was solved numerically with the program *MatLab* (v R2010a, MathWorks, Ismaning, Germany).[14] The MatLab ode23s solver implemented in our case uses a modified Rosenbrock formula of order 2. Furthermore, an optimization was carried out using the *MatLab* toolbox fminsearch to fit the reaction kinetic parameters to the measured data.

Calculation of Conversion, Yield, and Selectivity. The calculation of conversion, yield, and selectivity followed the conventions.[27]

Conversion X:

$$X = \frac{{c_E}^0 - c_E}{{c_E}^0}$$

where c_E = reactant concentration and c_E^0 = reactant concentration at start of reaction.

Yield Y:

$$Y = \frac{c_P}{{c_E}^0}$$

where c_P = product concentration (Mono-PEGylated protein for the present study).

Selectivity S:

$$S = \frac{Y}{X}$$

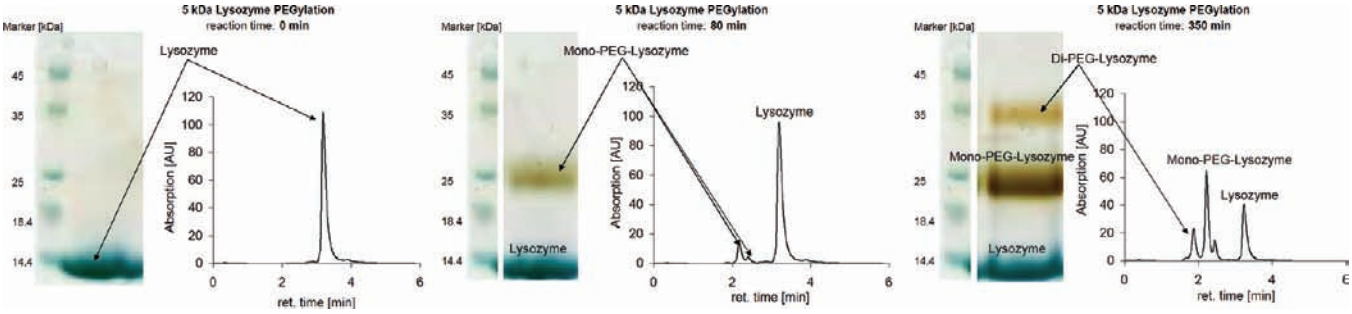

Figure 1. PEGylation reaction of lysozyme and 5 kDa PEG after 0, 80, and 350 min reaction time. Analyzed via cation-exchange and SDS-PAGE. Peaks and bands were labeled as results of MALDI-TOF and SDS-PAGE indicated. Left chromatogram, reaction time 0 min; center chromatogram, reaction time 80 min; right chromatogram, reaction time 350 min. Blue, Coomassie stained proteins; green, PEGylated proteins Coomassie and barium−iodine stained. For chromatographic conditions, see Analytical procedures.

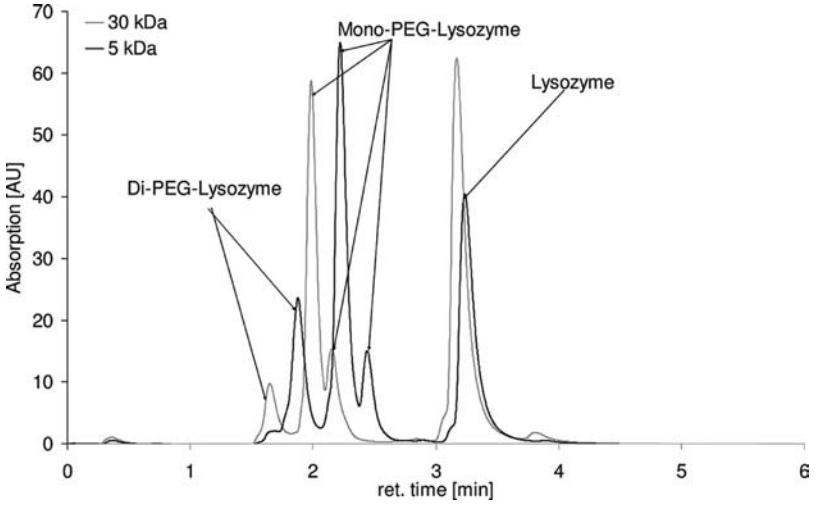

Figure 2. PEGylation reaction of lysozyme with 5 and 30 kDa PEG after 20 h reaction time. Analyzed via cation-exchanger. Peaks were labeled as results of MALDI-TOF and SDS-PAGE indicated. Black line, 5 kDa PEGylated lysozyme; gray line, 30 kDa PEGylated lysozyme. For chromatographic conditions, see Analytical procedures.

RESULTS AND DISCUSSION

PEGylation of Lysozyme. The PEGylation reaction was closely followed using an analytical SP-NPR column (Tosoh Bioscience GmbH) with a total analysis time of 6 min. Chromatograms were evaluated using the peak area as given by the program ChromQuest (Thermo Separations). Figure 1 shows typical chromatograms and the corresponding bands in SDS-PAGE of lysozyme and PEGylated lysozyme before the start of the reaction and after a reaction time of 80 and 350 min with a 5 kDa PEG. Lysozyme remained in the mixture, as PEG did, which is not visible in UV and thereby not shown. In SDS-PAGE, PEG of 5 kDa was not visible because it migrated out of the gel. During the reaction, two isoforms of Mono-PEGylated lysozyme were formed, as well as a Di- and a Tri-PEGylated form.[4,20] The Tri-PEGylated form did appear after more than 350 min and is not shown in Figure 1. The other PEGylation products are shown in Figure 1 to clarify the peak identification process. In a former study,[18] fractions of the elution peaks shown in Figure 1 were collected and sent to the Friedrich-Alexander University (Erlangen, Germany) to perform the MALDI-TOF analysis.[4] The peaks were identified as labeled in Figure 1 with the help of SDS-PAGE and MALDI-TOF. Analogue experiments were done for PEGylation with 30 kDa PEG and the results were comparable, but the retention times were slightly shorter. A resolution comparison between a 5 and 30 kDa PEGylated lysozyme is shown in Figure 2. The resolution was not affected by the different sizes used in this work. In prior work, it could already be shown that the retention times in IEX decreased with increasing PEG length and increasing number of added PEG chains.[16,18,29] Additionally, SDS-PAGE with the reaction mixtures was carried out after 20 h (Figure 3). The Coomassie staining revealed the protein fractions in blue, whereas a barium−iodine staining showed PEG in brown. For the PEGylated proteins, a mixture of both colors can be seen, resulting in green to brownish bands (Figures 1 and 3). It is well-known that PEG in SDS-PAGE migrates more slowly than proteins, so the protein standard used leads to higher molecular weights of PEG and PEGylated proteins.[8,15,26] PEG of 5 kDa size is not visible in Figure 3 because it migrated out of the gel during the washing and staining procedure, but it was visible after the very first barium−iodine staining (results not shown). The apparent size of 5 kDa PEG in SDS-PAGE was estimated to be 8 kDa; for 30 kDa PEG, the apparent size in SDS-PAGE was about 50 kDa. Wiyh these values

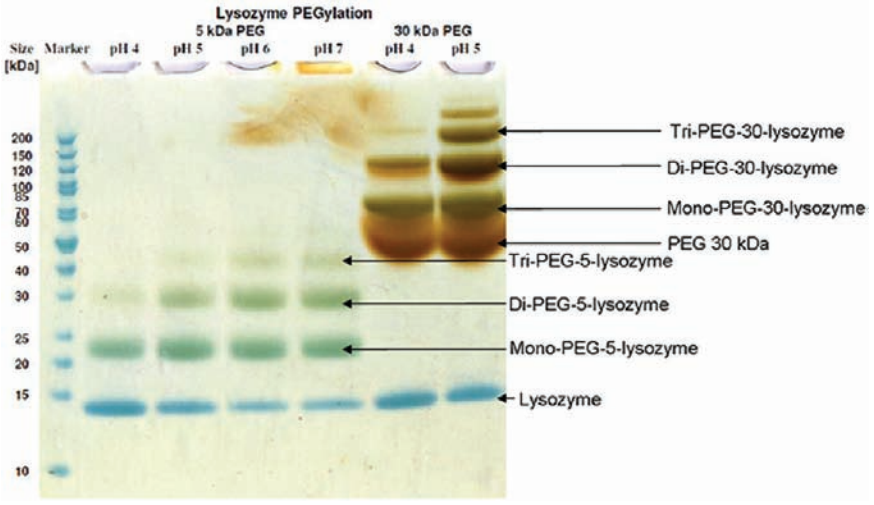

Figure 3. SDS-PAGE of a lysozyme PEGylation with 5 kDa PEG (left) and 30 kDa PEG (right) at different pH values after a reaction time of approximately 1200 min. Blue, Coomassie stained proteins; brown, barium−iodine stained PEG. Mixed colors represent PEGylated proteins. The marker proteins are on the left side.

Table 1. Relative Migration Length (Rf), Theoretical Size, and Calculated Size [a]for Analyzed Samples of PEGylated Lysozyme

Rf [cm]	sample	theoretical size [kDa]	calculated size [kDa]	theoretical apparent size of PEGylated protein in SDS-PAGE [kDa]
0.55	Poly-PEG-30-Lys	134.4	588.45	214.4
0.9	Tri-PEG-30-Lys	104.4	258.07	164.4
1.35	Di-PEG-30-Lys	74.4	130.92	114.4
2	Mono-PEG-30-Lys	44.4	67.81	64.4
2.4	PEG 30 kDa	30	49.98	50
2.8	Tri-PEG-5-Lys	29.4	38.61	38.4
3.3	Di-PEG-5-Lys	24.4	29.33	30.4
4	PEG-5-Lys	19.4	21.26	22.4
4.95	Lysozym	14.4	14.88	14.4

[a] Column 4 calculated with the protein marker only; column 5 calculated theoretical apparent size taking into account the calculated size of PEG (column 4) as it appeared in SDS-PAGE.

taken into account, a new theoretical size in SDS-PAGE could be estimated (Table 1). This estimated size correlated well with the measured size gained with the help of the protein standard. The bigger the size of the PEGylated proteins, the more imprecise the size estimation was; however, this could be a gel-specific problem and was therefore not further investigated. The MALDI-TOF analyses confirmed the results of the SDS-PAGE. Thus, SDS-PAGE can alternatively be used as a tool for size estimation of PEGylated proteins and peak identification in IEX.

PEGylation of scFv. The PEGylation reaction was followed as described for lysozyme. Again, SDS-PAGE at different time points correlated the peaks with the bands, both appearing after varying reaction times (Figure 5). The scFv monomer and dimer peak were identified using SEC because the dimerized scFv was not stable in the presence of SDS (data not shown).

In the course of the PEGylation reaction, the dimer of the scFv disappeared and several peaks of shorter retention times appeared (Figure 5). This matches the chromatographic behavior of PEGylated lysozyme. Retention times in IEX decreased the higher the PEGylation degree got.[16,18,29] Small peaks with a longer retention time than scFv also emerged during the PEGylation reaction. These peaks were not visible in a SDS-PAGE and thereby could be aggregated proteins, PEGylated dimer-scFv, or small amounts of PEGylated impurities. The SDS-PAGE revealed clear bands, matching the presumption, as Mono-, Di-, and Tri-PEGylated forms were clearly visible and the sizes could be estimated as defined for lysozyme (see Table 2). For the PEGylation with 30 kDa PEG, an unexpected band appeared above the Mono-PEGylated scFv, which was light brown (Figure 4). The absence of blue color is evidence for the absence of a protein fraction. In addition, the calculated size of about 116 kDa indicated that this band was a PEG 30 kDa dimer, which should migrate at about 100 kDa in SDS-PAGE. This assumption was further supported by the slightly visible band in Figure 3 below the Di-PEG-30-lysozyme band, and the appearance of this band in SDS-PAGE of both proteins confirmed that it was not a protein-specific phenomenon. To verify the assumption of having a dimer PEG 30 kDa, another SDS-PAGE was carried out with PEG of 5 and 30 kDa in PEGylation reaction buffer of pH 5 and $NaCNBH_3$ without the presence of protein (Figure 6). For 30 kDa PEG, a second band was clearly visible, for 5 kDa PEG the second band was barely visible and disappeared very fast. This is evidence for a dimerization of PEG under the present reaction conditions.

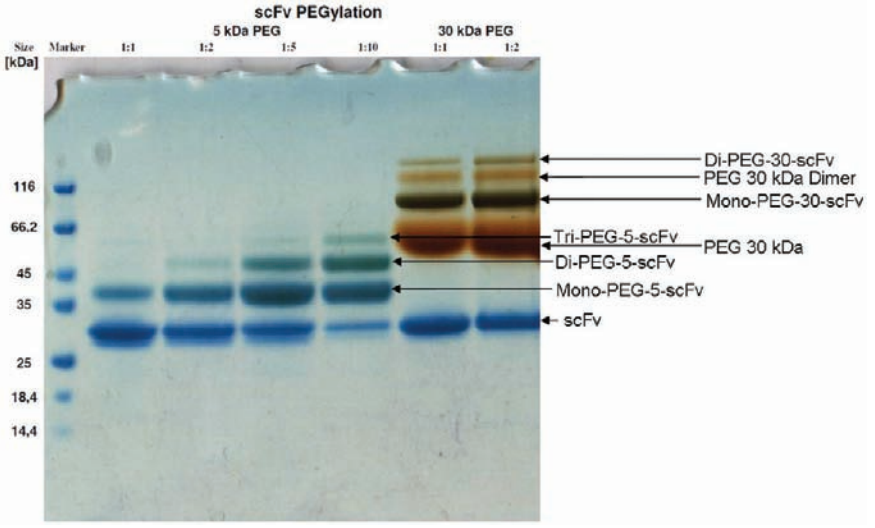

Figure 4. SDS-PAGE of a scFv PEGylation with 5 kDa PEG (left) and 30 kDa PEG (right) at different protein-to-PEG ratios after a reaction time of approximately 1200 min. Blue, Coomassie stained proteins; brown, barium−iodine stained PEG. Mixed colors represent PEGylated proteins. The marker proteins are on the left side.

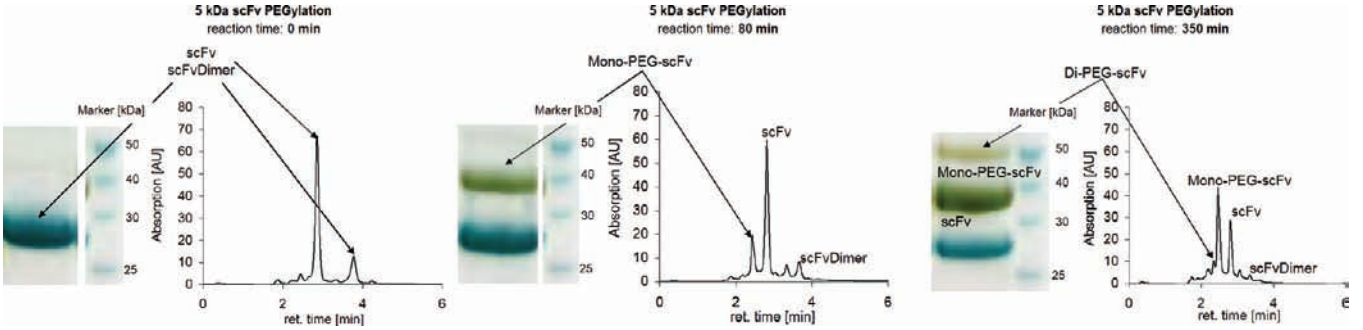

Figure 5. PEGylation reaction of scFv and 5 kDa PEG after 0, 80, and 350 min reaction time. Analyzed via cation-exchanger and SDS-PAGE. Peaks and bands were labeled as results of SDS-PAGE indicated. Left chromatogram, reaction time 0 min; center chromatogram, reaction time 80 min; right chromatogram, reaction time 350 min. Blue, Coomassie stained proteins; green, PEGylated proteins Coomassie and barium−iodine stained. For chromatographic conditions, see Analytical procedures.

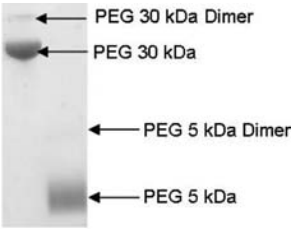

Figure 6. SDS-PAGE of 30 (left) and 5 kDa PEG (right) solubilized in reaction buffer at pH 5. Black: barium−iodine stained PEG.

According to this result, the peaks of the IEX chromatogram were labeled as shown in Figure 4. For the PEGylated scFv, only one peak containing Mono-PEGylated protein was visible. The PEGylation of the scFv with 30 kDA PEG showed an analogue performance to lysozyme.

Kinetic Studies and Mathematic Modeling. To monitor the PEGylation reaction all Mono-PEGylated isoforms were summed up to Mono-PEG-protein and the monomer and dimer peaks of scFv were also summed up to unmodified protein. Peak areas were used to determine the concentrations of the PEGylated forms. In the case of the unmodified proteins, the concentration in the beginning of the reaction was known.

In a first attempt, the following reaction model was stated:

$$\text{PEG} + \text{protein} \rightarrow \text{Mono-PEG-protein} \quad (1)$$

$$\text{Mono-PEG-protein} + \text{PEG} \rightarrow \text{Di-PEG-protein} \quad (2)$$

$$\text{Di-PEG-protein} + \text{PEG} \rightarrow \text{Tri-PEG-protein} \quad (3)$$

The reaction rates r were thereby defined:

$$r_1 = \text{PEG} \times \text{protein} \times k_1$$

$$r_2 = \text{PEG} \times \text{Mono-PEG-protein} \times k_2$$

$$r_3 = \text{PEG} \times \text{Di-PEG-protein} \times k_3$$

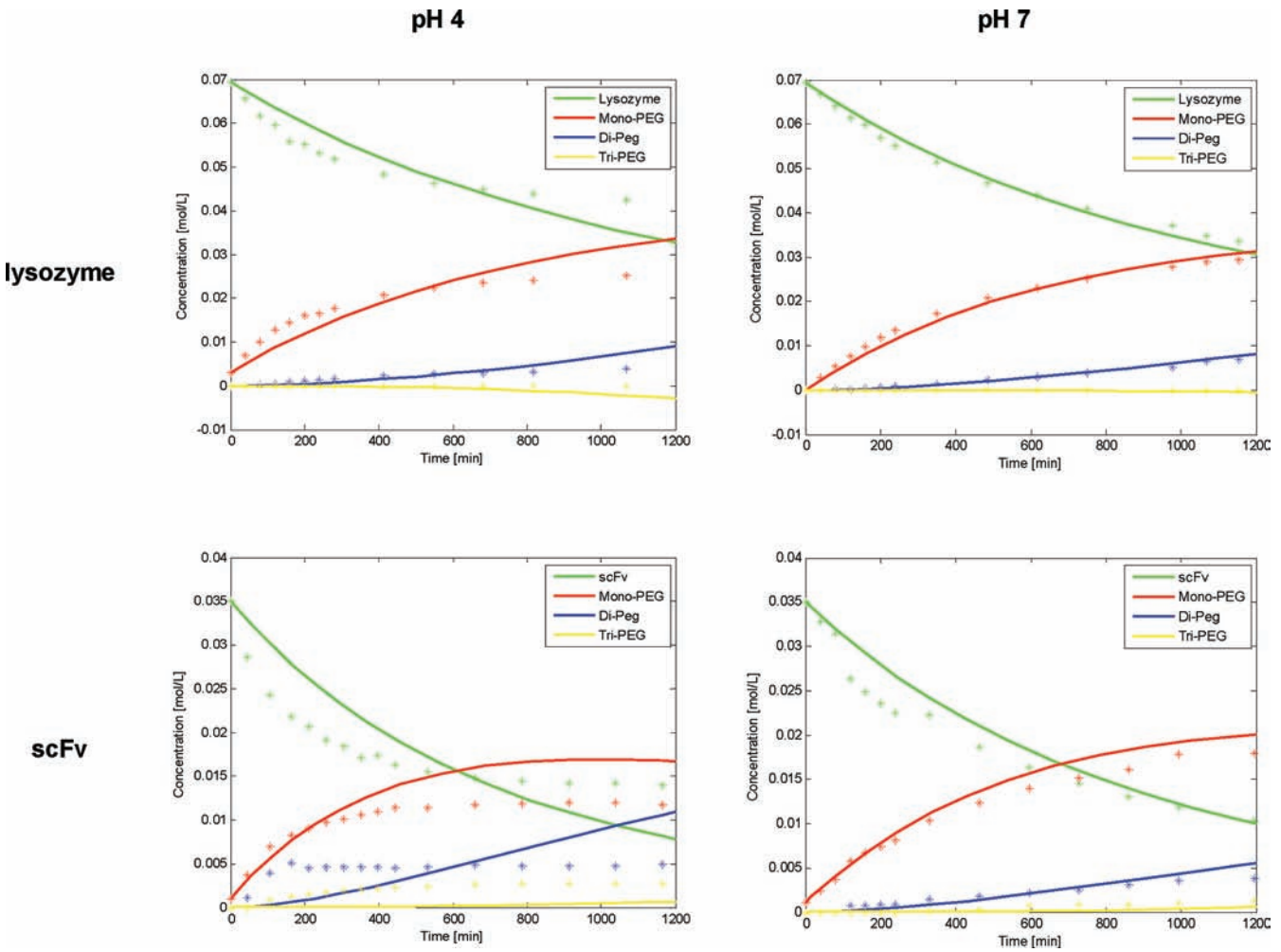

Figure 7. PEGylation reaction for lysozyme and 5 kDa PEG at a pH of 4 (top left), at a pH of 7 (top right), scFv, and 5 kDa PEG at pH 4 (bottom left) and 7 (bottom right). For lysozyme PEGylation, 21 °C, 20 h reaction time, 2-fold PEG excess, 1 g/L protein; and for scFv, 1 g/L protein, 21 °C, 20 h reaction time, 5-fold PEG excess. Experimental data shown as crosses; simulated data shown as straight lines. Green, unmodified protein; red, Mono-PEG-protein; blue, Di-PEG-protein; yellow, Tri-PEG-protein.

and the differential equations were specified:

$$\mathrm{d}x(\mathrm{PEG}) = -r_1 - r_2 - r_3$$

$$\mathrm{d}x(\mathrm{protein}) = -r_1$$

$$\mathrm{d}x(\text{Mono-PEG-protein}) = r_1 - r_2$$

$$\mathrm{d}x(\text{Di-PEG-protein}) = r_2 - r_3$$

$$\mathrm{d}x(\text{Tri-PEG-protein}) = r_3$$

With the program *MatLab*, the differential equations were numerically solved, the experimental data was compared to the calculated results, and an optimization was carried out as specified.[14] As a result, *MatLab* showed the experimental data as crosses and the calculated concentrations as lines (exemplarily shown in Figure 7 for four data sets).

The first attempt at reaction modeling seemed to work well at a pH of 7 (Figure 7, right side). However, the more acidic the pH got, the worse the simulated reaction fitted the data (Figure 7 left column). The real reaction worked faster on a short time scale and then reached a plateau.

With the knowledge that dimerized PEG could be detected in SDS-PAGE (Figure 6), the next step was to include another reaction that inactivates PEG with the ability to form a PEG molecule that can no longer react. For example, a reaction with $NaCNBH_3$ or an aldol reaction leading to PEG-multimers is a possibility for PEG inactivation. In SDS-PAGE, dimers were detected, but they appeared at different pH values (see Figure 6 for pH 5), whereas the kinetic simulation seems to favor a reaction that is pH dependent. Thus, an aldol reaction seems to be unlikely, but the nature of the inactivation reaction was not further observed. In a second attempt, an undefined inactivation step for PEG was included in the reaction set as done by Buckley and co-workers for mPEG-succinimidyl propionate:[14]

$$\text{PEG} + \text{protein} \rightarrow \text{Mono-PEG-protein} \quad (1)$$

$$\text{Mono-PEG-protein} + \text{PEG} \rightarrow \text{Di-PEG-protein} \quad (2)$$

$$\text{Di-PEG-protein} + \text{PEG} \rightarrow \text{Tri-PEG-protein} \quad (3)$$

$$\text{PEG}_{\text{reacting}} \rightarrow \text{PEG}_{\text{inactive}} \quad (4)$$

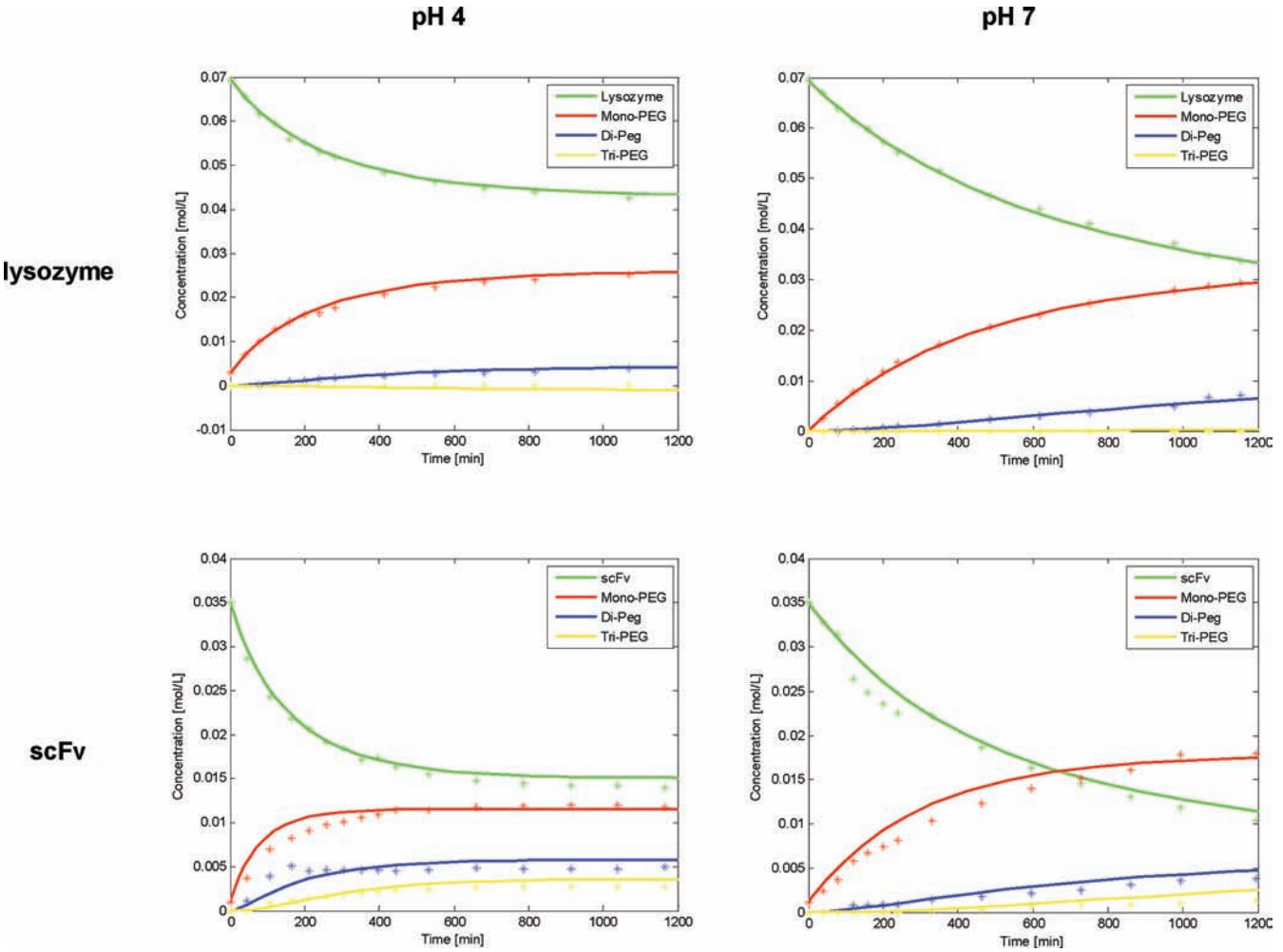

Figure 8. PEGylation reaction for lysozyme and 5 kDa PEG at a pH of 4 (top left) and at a pH of 7 (top right), scFv, and 5 kDa PEG at pH 4 (bottom left) and 7 (bottom right). For lysozyme PEGylation, 21 °C, 20 h reaction time, 2-fold PEG excess, 1 g/L protein; and for scFv, 1 g/L protein, 21 °C, 20 h reaction time, 5-fold PEG excess. Experimental data shown as crosses, simulated data shown as straight lines. Green, unmodified protein; red, Mono-PEG-protein; blue, Di-PEG-protein; yellow, Tri-PEG-protein.

The reaction rates r were thereby defined

$$r_1 = \mathrm{PEG}_{\mathrm{reacting}} \times \mathrm{protein} \times k_1$$

$$r_2 = \mathrm{PEG}_{\mathrm{reacting}} \times \mathrm{Mono\text{-}PEG\text{-}protein} \times k_2$$

$$r_3 = \mathrm{PEG}_{\mathrm{reacting}} \times \mathrm{Di\text{-}PEG\text{-}protein} \times k_3$$

$$r_4 = \mathrm{PEG}_{\mathrm{reacting}} \times k_4$$

and the differential equations were specified

$$\mathrm{d}x(\mathrm{PEG}_{\mathrm{all}}) = -r_1 - r_2 - r_3$$

$$\mathrm{d}x(\mathrm{protein}) = -r_1$$

$$\mathrm{d}x(\mathrm{Mono\text{-}PEG\text{-}protein}) = r_1 - r_2$$

$$\mathrm{d}x(\mathrm{Di\text{-}PEG\text{-}protein}) = r_2 - r_3$$

$$\mathrm{d}x(\mathrm{Tri\text{-}PEG\text{-}protein}) = r_3$$

$$\mathrm{d}x(\mathrm{PEG}_{\mathrm{reacting}}) = -r_1 - r_2 - r_3 - r_4$$

$$\mathrm{d}x(\mathrm{PEG}_{\mathrm{inactive}}) = r_4$$

The differential equations were solved as described above. The results of the kinetic simulation now fitted the experimental data very well. For lysozyme, an excellent match at all pH values could be achieved, and for scFv, the simulated data fitted the experimental data relatively good (Figure 8). All experimental data sets were simulated with the above demonstrated set of differential equations. The rate constants k_1 and k_2 were determined and are listed for different temperatures in Tables 3 and 4. The rate constant k_1 was always higher than k_2 in the case of lysozyme, indicating that the Mono-PEGylation was much faster than the addition of a second PEG. In contrast, the rate constant k_2 exceeded k_1 in an acidic pH and at very high protein concentrations in the case of the PEGylation of scFv with a 5 kDa PEG. However, using the 30 kDa PEG the rate constant k_1 exceeded k_2 in the case of both scFv and lysozyme (data not shown). The calculated rate constants k_1 for the reaction of protein to Mono-PEGylated protein were in the range 0.002−0.016 L/mol min for lysozyme and 0.009−0.3 L/mol min for scFv. The rate constants k_2 generally were about half of the calculated values for k_1.

The rate constants should behave constant at different protein concentrations; this could be observed for lysozyme PEGylation with both PEG sizes. However, when using different protein

dx.doi.org/10.1021/bc200090x |*Bioconjugate Chem.* 2011, 22, 1545–1558

Table 2. Relative Migration Length (Rf), Theoretical Sizes, and Calculated Sizes[a] for Analyzed Samples of PEGylated scFv

Rf [cm]	sample	theoretical size [kDa]	calculated size [kDa]	theoretical apparent size of PEGylated protein in SDS-PAGE [kDa]
1.75	Di-PEG-30-scFv	88.5	156.82	128.5
2.1	PEG 30 kDa Dimer	60	116.01	100
2.6	Mono PEG-30-scFv	58.5	81.50	78.5
3.5	PEG 30 kDa	30	49.86	50
3.25	Tri-PEG-5-scFv	43.5	56.36	52.5
3.7	Di-PEG-5-scFv	38.5	45.48	44.5
4.25	PEG-5-scFv	33.5	36.17	36.5
5	scFv	28.5	27.65	28.5

[a] Column 4: calculated with the protein marker only. Column 5: calculated theoretical apparent size, taking into account the calculated size of PEG as it appeared in SDS-PAGE.

Table 3. PEGylation of Lysozyme at Different Temperatures and the Resulting Rate Constants k_1, k_2, and Yield, Conversion, and Selectivity after 20 h Reaction Time

temp [°C]	PEG [kDa]	k_1 [L/mol min]	k_2 [L/mol min]	yield	conversion	selectivity
10	5	0.0037	0.0017	0.34	0.36	0.94
21	5	0.0125	0.0061	0.5	0.66	0.76
30	5	0.0165	0.0089	0.49	0.68	0.72
10	30	0.0028	0.0013	0.29	0.29	1.00
21	30	0.0075	0.003	0.43	0.45	0.96
30	30	0.0124	0.0022	0.51	0.59	0.86

Table 4. PEGylation of scFv at Different Temperatures and the Resulting Rate Constants k_1, k_2, and Yield, Conversion, and Selectivity after 20 h Reaction Time

temp [°C]	PEG [kDa]	k_1 [L/mol min]	k_2 [L/mol min]	yield	conversion	selectivity
10	5	0.0199	0.0101	0.56	0.73	0.77
20	5	0.0144	0.0086	0.48	0.61	0.79
30	5	0.0727	0.0424	0.43	0.87	0.50
10	30	0.0153	0.0071	0.52	0.67	0.78
20	30	0.0115	0.0011	0.45	0.50	0.91
30	30	0.0657	0.0312	0.53	0.86	0.61

concentrations of scFv a wide difference in the rate constants was obtained (data not shown). An explanation could be that the evaluation of the chromatograms obtained at very high scFv concentrations was difficult due to a poor separation. In addition, it could be possible that the chosen reaction mechanism did not describe the reaction perfectly. Especially at high protein concentrations, the formation of protein aggregates could be a problem for peak evaluation and the reaction model.

The influence of temperature on reaction velocities was very high. At 30 °C, the PEGylation reaction for lysozyme was fastest, and at a temperature of 10 °C, it was slowest. For scFv, this behavior changed; the reaction at 10 °C was faster than at 20 °C. In theory, a temperature rise should increase the reaction velocity.[30] For lysozyme, with 5 and 30 kDa PEG the reaction velocity doubled with a temperature increase of 10 °C. For example, a reaction with 30 kDa PEG and lysozyme at 10 °C had a k_1 of 0.0028 L/mol min; at 21 °C, k_1 was 0.0063 L/mol min, and at 30 °C, 0.0124 L/mol min. For scFv, the 20 °C value was lower than the 10 °C value, whereas the 30 °C value was nearly four times the 10 °C value. Thus, there seems to be a problem in the mid-temperature range. The reaction did not follow the usual standards in this temperature range (Tables 3 and 4). The modeling of the scFv PEGylation thereby showed two problems, one was the dependence of the reaction rate constant on the scFv concentration, which indicates that the reaction is influenced by a different mechanism and might not follow a reaction of first order as lysozyme did. The second problem was the temperature dependent behavior.

Production Parameters. To decide which reaction conditions should be chosen for a scale-up, the conversion, yield, and selectivity of each reaction were monitored after 5, 10, and 20 h and plotted against different ambient conditions such as the pH ranging from 4 to 7, the temperature from 10 to 30 °C as well as the protein concentration from 1 to 10 g/L and the PEG-to-protein ratio from 1- to 5-fold excess. All factors were analyzed individually, starting conditions are listed in the PEGylation of scFv section.

Reaction Time. For all reactions, the selectivity slightly decreased over the time, whereas the yield and conversion increased continuously (Figure 9).

pH. Yield increased with increasing pH for the 30 kDa version of scFv PEGylation, whereas the pH did not influence the lysozyme PEGylation significantly (data not shown). Likewise,

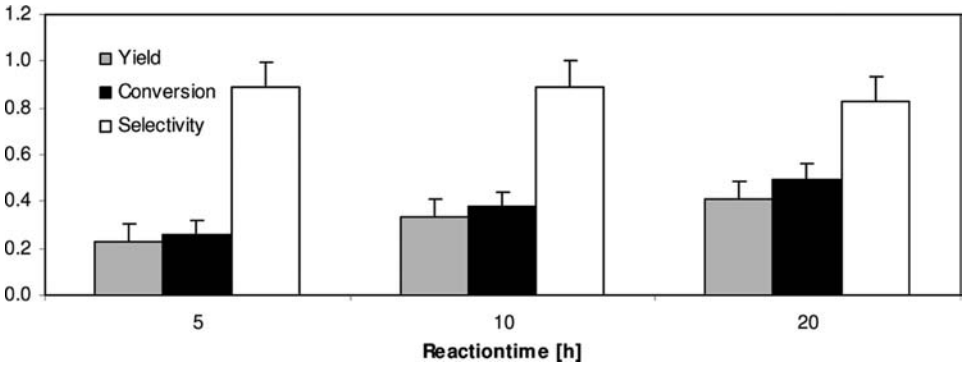

Figure 9. Conversion, yield, and selectivity over the reaction time. Shown exemplarily for lysozyme PEGylation with 5 kDa PEG at standard conditions. Gray bars, yield; black bars, conversion; white bars, selectivity.

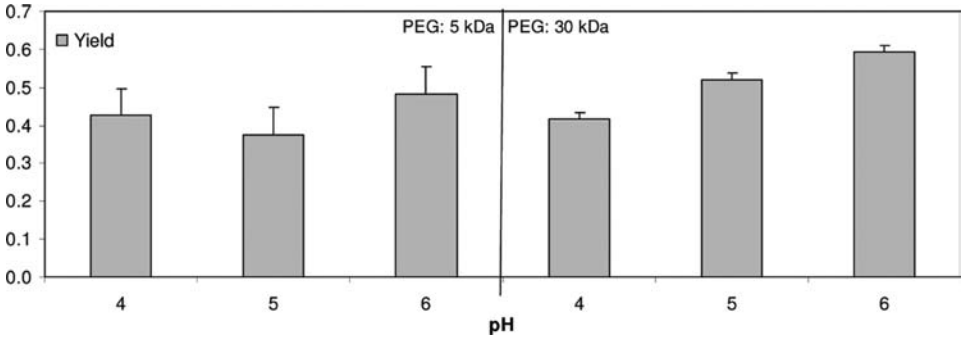

Figure 10. Yield over pH. Shown exemplarily for scFv PEGylation with 5 kDa PEG (left) and 30 kDa (right) at 21 °C after 20 h. Gray bars: yield.

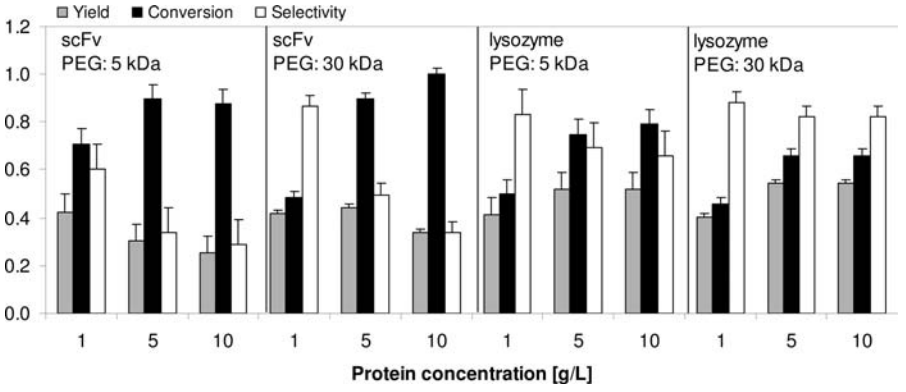

Figure 11. Conversion, yield, and selectivity over the total protein concentration for scFv and 5 kDa PEG (left), 30 kDa PEG (mid left), and lysozyme with 5 kDa PEG (mid right) and 30 kDa PEG (right). Gray bars, yield; black bars, conversion; white bars, selectivity. The reactions were done at 21 °C, for lysozyme at a pH of 6, and for scFv, at pH 4, both with 20 h reaction time.

the scFv PEGylation with 5 kDa PEG was not affected significantly by pH changes (Figure 10). The increase in yield with increasing pH was congruent with the observation made for mPEG-aldehyde, namely, that inactivating side reactions decreased the more neutral the pH was (see mPEG-Aldehyde Inactivation). Regarding selectivity, a pH dependent trend was not visible (data not shown).

Protein Concentration. An increase in total lysozyme concentration with unchanged PEG-to-protein ratio led to increased conversion and yield, whereas the selectivity decreased. A plateau was reached between 5 and 10 g/L protein (Figure 11). The increase in conversion at a constant PEG-to-protein ration was also visible for scFv PEGylation; however, a plateau was not reached when 30 kDa PEG was used. For scFv, the yield decreased with increasing protein concentration whereas the conversion rose slightly for 5 kDa PEG and heavily for 30 kDa PEG (Figure 11). Selectivity decreased rapidly with increasing protein concentration for all proteins and PEGs. An explanation for the decrease in yield with rising scFv concentration is the massive decrease in selectivity leading to a reduced yield despite the rising conversion.

PEG-to-Protein Ratio. The PEG-to-protein ratio was studied only for scFv PEGylation. With increasing PEG excess, the yield increased as did conversion. This could be observed using 30 kDa

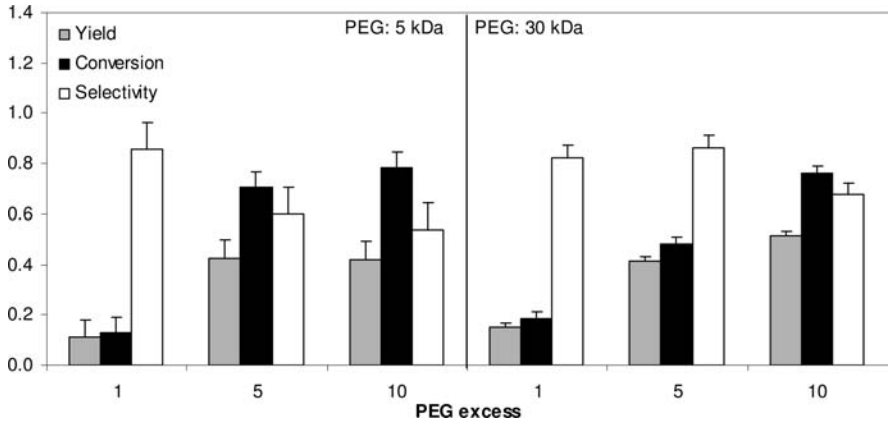

Figure 12. Conversion yield and selectivity over the PEG excess at constant 1 g/L scFv. For 5 kDa PEG (left), 30 kDa PEG (right). Gray bars, yield; black bars, conversion; white bars, selectivity. The reactions were done at 21 °C at a pH of 4 and 20 h reaction time.

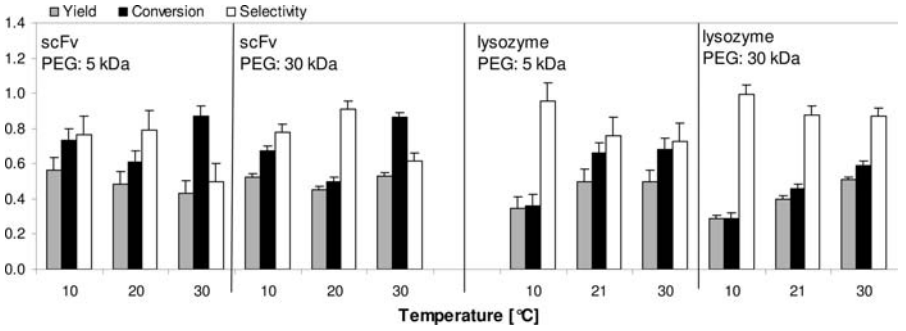

Figure 13. Conversion, yield, and selectivity over the temperature at constant 1 g/L protein. For scFv and 5 kDa PEG (left), 30 kDa PEG (mid left). For lysozyme and 5 kDa PEG (mid right) and 30 kDa PEG (right). Gray bars, yield; black bars, conversion; white bars, selectivity. The reaction pH was 4 for scFv and 6 for lysozyme. The reaction time was 20 h.

PEG, whereas the use of 5 kDa PEG resulted in a plateau in yield between 5- and 10-fold PEG excess. The selectivity decreased with increasing PEG-to-protein ratio except for PEG 30 kDa where no difference between 1- and 5-fold PEG excess could be found (Figure 12).

Temperature. The temperature rise for lysozyme PEGylation led to increased yield and conversion; a plateau was reached for PEG 5 kDa between 21 and 30 °C; however, the selectivity decreased with increasing temperature. Selectivity also decreased when the scFv was used, though a trend was not that clearly visible for all factors. The yield decreased for a PEGylation of scFv with 5 kDa PEG; using 30 kDa PEG, a trend was not visible (Figure 13). An irregularity in the temperature range of 20 °C could also be shown for the reaction rate constants of the scFv PEGylation (Table 4). A different mechanism could be responsible for the unexpected behavior of the reaction rate and yield, for example, an interaction between PEG and scFv. The temperature had no effect on the scFv PEGylation with 30 kDa PEG, whereas for 5 kDa PEG, the rising temperature led to a decrease of yield and selectivity. For lysozyme, an increase in yield and a decrease in selectivity was visible regardless of the PEG size.

Best Conditions. The best condition for a PEGylation reaction is the best possible combination of high yield and high selectivity. An increasing reaction time increased yield as well as conversion independent of the conditions used. Of note, the selectivity was slightly reduced between 10 and 20 h reaction time. Consequently, the reaction should be stopped before reaching a plateau. Indeed, a reaction time around 15 h guaranteed high yield and selectivity at the tested starting conditions. Regarding the pH, big differences were not visible; however, it could be shown (see mPEG-Aldehyde Inactivation) that mPEG-aldehyde gets inactivated at low pH values. Thereby, the best pH should be chosen with respect to the solubility of the protein. For example, solubility of lysozyme, which has a pI of 11, was not critical within the pH range used in this study. In contrast, the solubility of scFv, which has a pI in the neutral range, was strongly dependent on the pH value. It could be shown that scFv was more soluble in more acidic surroundings, which are therefore recommended for its PEGylation. However, studies exist, which discovered a pH dependency of the selectivity for certain PEGylation sites, especially at the N-terminus,[31,32] that was not further investigated here.

A rising protein concentration led to an increase in conversion though to a decrease in selectivity. The ideal protein concentration thus depends on the protein used. In the case of lysozyme, a concentration of 5 g/L was found to be a good compromise, whereas the ideal protein concentration of scFv was in the lower range and dependent on the PEG size. Long PEG chains require a higher protein concentration than short PEG chains. For example, 2 g/L was used for scFv PEGylation with 30 kDa PEG and only 1 g/L for PEGylation with 5 kDa PEG, because in the case of scFv PEGylation, with 5 kDa PEG an increase in protein concentration led to a decrease in yield. This can be

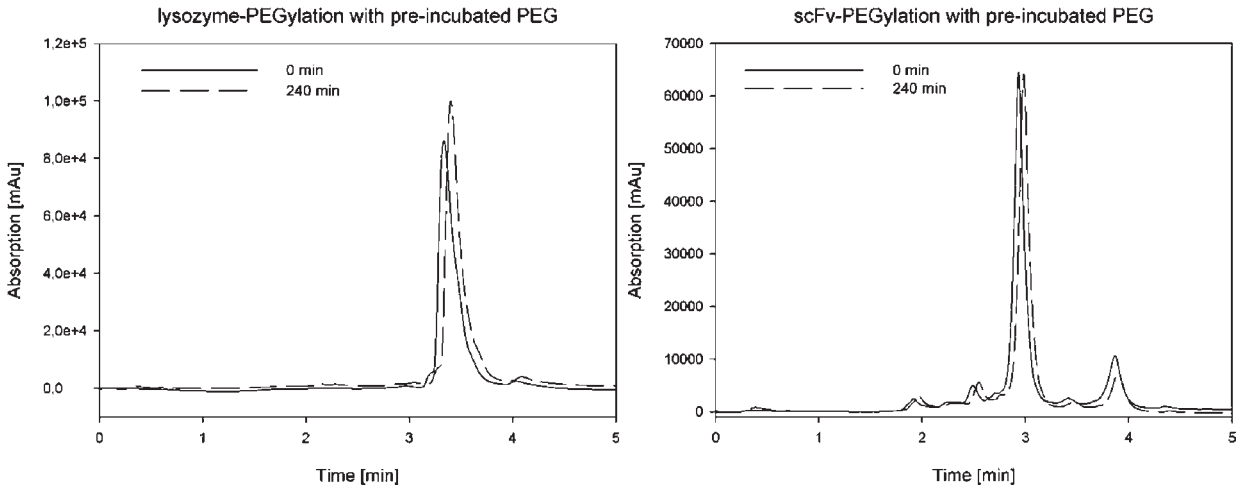

Figure 14. PEGylation reaction of lysozyme (left) and scFv (right), exemplarily shown with a 5 kDa PEG (right) and a 30 kDa PEG (left). PEG was preincubated in reaction buffer containing 20 mM $NaCNBH_3$ at a pH of 4 in the absence of protein. Continuous line, 0 min reaction time; dashed line, 4 h reaction time. No reaction occurred regardless the protein or PEG size.

explained by a lower solubility of scFv and possibly the formation of aggregates. Of note, upon PEGylation with a 30 kDa PEG the decrease in yield was not apparent. It is thus possible that long chain PEG increases the solubility of scFv. In addition, the concentration-dependent reaction rates of scFv point toward difficulties with the PEGylation reaction mechanism. For lysozyme, the reaction rates were concentration independent, as they should be with a working model, but for the scFv PEGylation, this was not the case. Here, an additional factor seems to disturb the expected reaction mechanism. The formation of aggregates of the hydrophobic scFv might have to be taken into account in future research.

In addition, the temperature dependence of scFv PEGylation also did not show the expected behavior. In the case of lysozyme, an increase of the reaction rate with increasing temperature was determined as predicted by Arrhenius.[27] The yield and reaction rate of scFv PEGylation at 30 °C were highest; however, at 10 °C these parameters were still higher than those obtained at 20 °C, which does not fit with the theory of van't Hoff and Arrhenius.[27] A different reaction mechanism could be responsible here, for example, an interaction between PEG and protein or an aggregation phenomenon could explain this protein concentration and temperature-dependent behavior, respectively. In addition, a hydrophobic force-driven interaction could easily be temperature dependent, leading to a higher interaction at lower temperature and a better reactivity at 10 °C because of a higher probability of PEG and protein to interact. The interaction could reach an end point at 30 °C prevented by the Brownian motion. A normal reaction progression is thus reached again. Apparently, this interaction would also influence the dependence of the reaction rate constant on the protein concentration, which showed an unusual behavior as already discussed above. Our suggestion would thus be using a reaction temperature of 15 °C for scFv PEGylation and 20 °C for lysozyme PEGylation.

In the case of scFv PEGylation, a lower PEG-to-protein ratio led to higher selectivity but lower yield and conversion. A compromise would be to use a relatively high PEG-to-protein ratio such as 5:1.

The optimized conditions were tested for lysozyme at a pH of 6 and a temperature of 20 °C with a 2-fold PEG excess and a lysozyme concentration of 5 g/L. These conditions were chosen for both PEG sizes; only the reaction time varied. For PEGylation with 5 kDa, 15 h reaction time was chosen, whereas the PEGylation with 30 kDa proceeded for 20 h. Yield, conversion, and selectivity were very good for both PEG sizes. Especially, the yield could be improved to 0.54 for 5 kDa and 0.59 for 30 kDa PEG. Both values were the best ever tested and accompanied by a conversion of 0.7 and 0.6, respectively. The combination of optimal values for all parameters was an important improvement, which could also be approved for scFv PEGylation. Here, the yield could be increased to 0.6 and 0.57 for 5 and 30 kDa PEG, respectively, both together with excellent conversion and selectivity.

mPEG-Aldehyde Inactivation. The inactivation reaction for mPEG-AL seems to be essential for mathematical modeling (see Kinetic Studies and Mathematic Modeling) even though mPEG-AL should not be susceptible to hydrolysis.[14] At a neutral pH, inactivation of PEG did not occur; however, at acidic pH values inactivation took place. To analyze the inactivation process in more detail, mPEG-AL was incubated overnight in different buffers without the presence of protein followed by a PEGylation reaction the next day. It could be shown that the reaction did not take place with PEG preincubated in a $NaCNBH_3$-containing buffer of pH 4 using neither lysozyme nor scFv as PEGylation protein. The size of the PEG molecule also did not affect the inactivation reaction (Figure 14).The hydrolysis of the imine can be ruled out or is only a part of the inactivation, as no protein and thereby no amino group was present during the inactivation overnight. It was not further investigated to determine what driving force or which chemical compound of the reaction mix play a role in the inactivation reaction.

In the following experiments, the inactivation reaction was observed, as it also took place in the PEGylation reactions without preincubation. All factors mentioned above were observed. Especially, temperature and pH had a significant influence. Increasing temperature led to increased inactivation reaction rates though the factor of temperature dependent changes also seemed to be dependent on the protein. In the case of lysozyme, a change was visible within the low temperature

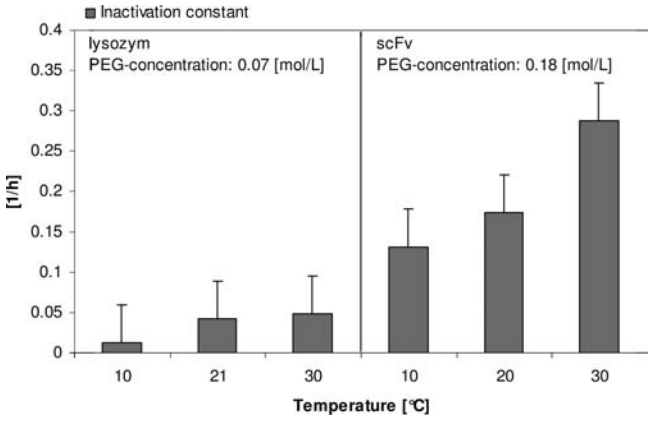

Figure 15. Inactivation reaction rate constant k_4 (gray bars) over the temperature, shown exemplarily for 5 kDa PEG with lysozyme and a PEG concentration of 0.07 mol/L at a pH of 6 (left) and scFv with a PEG concentration of 0.18 mol/L at a pH of 4 (right).

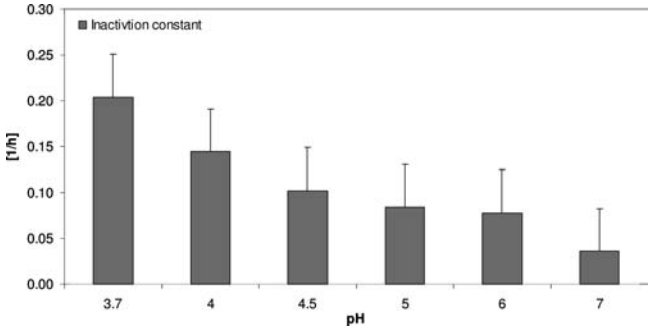

Figure 16. Inactivation reaction rate constant k4 (gray bars) over the pH, shown for scFv and 30 kDa PEG at 21 °C at a constant PEG concentration of 0.18 mol/L.

ranges. The reaction rate remained constant between 21 and 30 °C. In the case of the scFv PEGylation, only small changes were visible within the low temperature regions; however, between 20 and 30 °C a considerable difference could be found (Figure 15). The temperature dependence was independent of the PEG size (data not shown). Nevertheless, it cannot be excluded that the pH is the factor influencing the absolute values of this experiment most, as the PEGylation of lysozyme was carried out at a pH of 6 whereas scFv-PEGylation took place at a pH of 4. In line with this, the pH dependence was clearly visible; the inactivation increased in acidic pH and decreased the more basic the environment got (Figure 16). This was visible for all proteins and all PEG sizes (Figure 16, shown exemplarily for scFv and 30 kDa PEG). The PEG concentration influenced the PEG inactivation slightly, increasing PEG concentration led to inactivation rate constants that are changed significantly only for the highest and lowest PEG-to-protein ratio. For example, the inactivation rate constant varied in the range 0.18−0.29 L/h between 1- and 10-fold excess of PEG in the case of scFv PEGylation with 5 kDa PEG.

Buckley and co-workers calculated a rate constant of 1.31 L/h for mPEG-succinimidyl propionate inactivation.[14] Of note, this inactivation rate is approximately 3-fold higher than the inactivation rate for mPEG-AL found at a pH of 3.2 in the present study. Hu et al. already found the PEGylation rate to be dependent on the PEG functionalization even when the same PEGylation chemistry was used.[28] This could also account for the different PEG inactivation rates for differently functionalized PEGs.

This clearly shows the higher stability of mPEG-AL in comparison with mPEG-succinimidyl propionate.

CONCLUSIONS

Lysozyme and a scFv were PEGylated successfully via aldehyde chemistry. The PEGylation reaction was monitored and a mathematical model was established. An additional inactivation reaction for mPEG-AL was included and the reaction could be simulated closely. In the case of lysozyme, an excellent working reaction model could be obtained, whereas in the case of scFv, the model did not work perfectly.

By analyzing the reaction parameters such as reaction rates, conversion, yield, and selectivity, lysozyme PEGylation turned out to be a real model reaction. All factors behaved as expected; however, scFv PEGylation didn not display such an exemplary characteristic.

Unfortunately, conditions used to obtain the best selectivity did not result in highest conversion. For example, the highest conversion was obtained at 30 °C; however, the selectivity was not good at such a high temperature. Furthermore, the reaction time appeared to be an important feature: The longer the reaction time, the better the yield and conversion, although selectivity decreased.

Several studies describe that the pH is a crucial factor;[6,8,13,15] however, we could only partly confirm this hypothesis. In our hands, PEGylation of lysozyme was pH-independent. However, PEGylation of scFv was improved at a neutral pH, although the solubility of the scFv is restricted to acidic pH values. Of note, the inactivation of mPEG-AL was found to be pH dependent. At acidic pH values, PEG inactivation is accelerated, and the pH should be chosen in the neutral or slightly acidic range, depending on the protein's solubility behavior. Previous studies[13,15] have described the isoform formation to be pH dependent; however, this will be investigated in future studies. The PEG-to-protein ratio was also examined. The lower it got, the more selective the reaction was. To obtain a compromise between selectivity and yield, the PEG excess should be approximately 2- to 5-fold. An ideal protein concentration of about 5 g/L for lysozyme was determined, whereas the scFv PEGylation requires a lower protein concentration dependent on the used PEG size.

On the basis of the results obtained so far, optimal PEGylation conditions were obtained that resulted in a combination of high yield, conversion, and selectivity. The selected conditions used for lysozyme were 5 g/L protein concentration, 20 °C, 2-fold PEG excess, and a reaction time of 15 h for 5 kDa PEG and 20 h for 30 kDa PEG at a pH of 6. In the case of scFv PEGylation, the conditions used were a pH of 4, a reaction temperature of 15 °C, 15 h, and 5-fold PEG excess for both PEG sizes. Using 5 kDa PEG, a protein concentration of only 1 g/L was favorable, whereas in the case of 30 kDa PEG, 2 g/L was found to be the ideal concentration.

Small mPEG-AL inactivation rates can be obtained by avoiding acidic pH values and high temperatures. The inactivation rate for m-PEG-AL could be calculated between 0.01 L/h and 0.5 L/h depending on environmental conditions. This is about a third of 1.31 L/h, the inactivation rate reported previously for mPEG-succinimidyl propionate inactivation.[14] MPEG-AL was found to be more stable than mPEG-succinimidyl propionate in the

present study. The conducted experiments lead to the conclusion that the PEGylation reaction parameters need to be chosen and tested carefully for each protein and PEG size. Dependiong on the protein, the reaction mechanism seems to show slight differences. The presented model worked perfectly for the ideal lysozyme PEGylation, whereas the PEGylation of scFv was not simulated perfectly because of some unknown changes in reaction mechanism, which might be the formation of aggregates but were not further investigated here. Only minimal general predictions can be made, which are all defined by the mPEG-AL inactivation. Thus, high temperatures and acidic pH values should be avoided for aldehyde PEGylation.

AUTHOR INFORMATION

Corresponding Author

*Anna Moosmann, Dipl. Biol. t.o., phone: +49 711 685 60262, e-mail: anna.moosmann@izi.uni-stuttgart.de.

Author Contributions

#Equal contributions.

ACKNOWLEDGMENT

We thank the Bundesministerium fuer Bildung und Forschung (BMBF), Germany for supporting this work.

ABBREVIATIONS USED

IEX, ion-exchange chromatography; mPEG-AL, methoxy-PEG-aldehyde; PEG, poly(ethylene glycol); Rf, relative migration length; scFv, single chain variable fragment; SEC, size exclusion chromatography

REFERENCES

(1) Chowdhury, P. S., and Wu, H. (2005) Tailor-made antibody therapeutics. *Methods 36*, 11–24.

(2) Chapman, A. P. (2002) PEGylated antibodies and antibody fragments for improved therapy: a review. *Adv. Drug Delivery Rev. 54*, 532–545.

(3) Abuchowski, A., McCoy, J. R., Palczuk, N. C., van Es, T., and Davis, F. F. (1977) Effect of covalent attachment of polyethylene glycol on immunogenicity and circulating life of bovine liver catalase. *J. Biol. Chem. 252*, 3582–3586.

(4) Veronese, F. M. (2001) Peptide and protein PEGylation: a review of problems and solutions. *Biomaterials 22*, 405–417.

(5) Yang, K., Basu, A., Wang, M., Chintala, R., Hsieh, M., Liu, S., Hua, J., Zhang, Z., Zhou, J., Li, M., Phyu, H., Petti, G., Mendez, M., Janjua, H., Peng, P., Longley, C., Borowski, V., Mehlig, M., and Filpula, D. (2003) Tailoring structure-function and pharmacokinetic properties of single-chain Fv proteins by site-specific PEGylation. *Protein Eng. 16*, 761–770.

(6) Zalipsky, S. (1995) Functionalized poly(ethylene glycol) for preparation of biologically relevant conjugates. *Bioconjugate Chem. 6*, 150–165.

(7) Abuchowski, A., Van Es, T., Palczuk, N. C., and Davis, F. F. (1977) Alteration of immunological properties of bovine serum albumin by covalent attachment of polyethylene glycol. *J. Biol. Chem. 252*, 3578–3581.

(8) Veronese, F. M. (2009) *PEGylated protein drugs: Basic Science and Clinical Applications*, Birkhäuser Verlag, Switzerland.

(9) Fee, C. J., and Van Alstine, J. M. (2006) PEG-Proteins: Reaction engineering and separation issues. *Chem. Eng. Sci. 61*, 924–939.

(10) Wang, Y., Youngster, S., Grace, M., Bausch, J., Bordens, R., and Wyss, D. F. (2002) Structural and biological characterization of pegylated recombinant interferon alpha-2b and its therapeutic implications. *Adv. Drug Delivery Rev. 54*, 547–570.

(11) Monfardini, C., and Veronese, F. (1998) Stabilization of substances in circulation. *Bioconjugate Chem. 9*, 418–450.

(12) Webster, R., Elliott, V., Park, B. K., Walker, D., Hankin, M., and Taupin, P. (2009) PEG and PEGconjugates toxicity. In *PEGylated protein drugs: Basic Science and Clinical Applications*. (Veronese, F. M., Ed.) pp 127−147, Birkhäuser Verlag, Switzerland.

(13) Wang J., Hu T., Liu, Y., Zhang, G., Ma, G., Su, and Z. (2010) Kinetic and stoichiometric analysis of the modification process for N-terminal PEGylation of staphylokinase. *Anal. Biochem.* doi:10.1016/j.ab.2010.12.030

(14) Buckley, J. J., Finn, R. F., Mo, J., Bass, L. A., and Ho, S. V. (2008) PEGylation of biological macromolecules. In *Process chemistry in the pharmaceutical industry*, Vol. 2, *Challenges in an ever changing climate* (Gadamasetti, K., and Braish, T., Eds.) pp 383−402, CRC Press, Boca Raton.

(15) Nojima, Y., Iguchi, K., Suzuki, Y., and Sato, A. (2009) The pH-dependent formation of PEGylated bovine lactoferrin by branched polyethylene glycol (PEG)-N-hydroxysuccinimide (NHS) active esters. *Biol. Pharm. Bull. 32*, 523–526.

(16) Pabst, T. M., Buckley, J. J., Ramasubramanyan, N., and Hunter, A. K. (2007) Comparison of strong anion-exchangers for the purification of a PEGylated protein. *J. Chromatogr., A 1147*, 172–182.

(17) Caserman, S., Kusterle, M., Kunstelj, M., Milunovic, T., Schiefermeier, M., Jevševar, S., and Porekar, V. G. (2009) Correlations between in vitro potency of polyethylene glycol−protein conjugates and their chromatographic behavior. *Anal. Biochem. 389*, 27–31.

(18) Moosmann, A., Christel, J., Boettinger, H., and Mueller, E. (2010) Analytical and preparative separation of PEGylated lysozyme for the characterization of chromatography media. *J. Chromatogr., A 1217*, 209–215.

(19) Müller, E., Josic, D., Schröder, T., and Moosmann, A. (2010) Solubility and binding properties of PEGylated lysozyme derivatives with increasing molecular weight on hydrophobic-interaction chromatographic resins. *J. Chromatogr., A 1217*, 4696–4703.

(20) Lee, H., and Park, T. G. (2003) A novel method for identifying PEGylation sites of protein using biotinylated PEG derivatives. *J. Pharm. Sci. 92*, 97–103.

(21) Bornscheuer, U. T., Altenbuchner, J., and Meyer, H. H. (1999) Directed evolution of an esterase: screening of enzyme libraries based on pH-indicators and a growth assay. *Bioorg. Med. Chem. 7*, 2169–2173.

(22) Khalameyzer, V., Fischer, I., Bornscheuer, U. T., and Altenbuchner, J. (1999) Screening, nucleotide sequence, and biochemical characterization of an esterase from Pseudomonas fluorescens with high activity towards lactones. *Appl. Environ. Microbiol. 65*, 477–482.

(23) Rathore, A. S., Bilbrey, R. E., and Steinmeyer, D. E. (2003) Optimization of an osmotic shock procedure for isolation of a protein product expressed in E. coli. *Biotechnol. Prog. 19*, 1541–1546.

(24) Laemmli, U. K. (1970) Cleavage of structural protein during assembly of the head bacteriophage T4. *Nature 227*, 680–685.

(25) Bailon, P., Palleroni, A., Schaffer, C. A., Spence, C. L., Fung, W.-J., Porter, J. E., Ehrlich, G. K., Pan, W., Xu, Z.-X., Modi, M. W., Farid, A., and Berthold, W. (2001) Rational design of a potent, long-lasting form of interferon: A 40 kDa branched polyethylene glycol-conjugated interferon r-2a for the treatment of hepatitis C. *Bioconjugate Chem. 12*, 195–202.

(26) Kurfürst, M. M. (1992) Detection and molecular weight determination of polyethylene glycol-modified hirudin by staining after sodium dodecyl sulfate-polyacrylamide gel electrophoresis. *Anal. Biochem. 200*, 244–248.

(27) Hillebrand, U. (2009) Stöchiometrie: Eine Einführung in die Grundlagen mit Beispielen und Übungsaufgaben, Springer Verlag, Berlin Heidelberg.

(28) Hu, T., Prabhakaran, M., Acharya, S. A., and Manjula, B. N. (2005) Influence of the chemistry of conjugation of poly(ethylene glycol) to Hb on the oxygen-binding and solution properties of the PEG-Hb conjugate. *Biochem. J. 392*, 555–564.

(29) Seely, J. E., and Richey, C. W. (2001) Use of ion-exchange chromatography and hydrophobic interaction chromatography in the preparation and recovery of polyethylene glycol-linked proteins. *J. Chromatogr., A 908*, 235–241.

(30) Arnaut, L., Formosinho, S., and Burrows, H. (2007) Chemical kinetics: from molecular structure to chemical reactivity, Elsevier, Dordrecht.

(31) Kinstler, O., Molineux, G., Treuheit, M., Ladd, D., and Gegg, C. (2002) Mono-N-terminal poly(ethylene glycol)−protein conjugates. *Adv. Drug Delivery Rev. 54*, 477–485.

(32) Lee, H., Jang, I. H., Ryu, S. H., and Park, T. G. (2003) N-terminal site-specific mono-PEGylation of epidermal growth factor. *Pharm. Res. 5*, 818–825.

■ NOTE ADDED AFTER ASAP PUBLICATION

This paper was published on the Web on Aug 1, 2011, with errors in Table 2. The corrected version was reposted on Aug 17, 2011.

Bioconjugate Chemistry

ARTICLE

pubs.acs.org/bc

Synthesis of Aminoglycoside-3′-Conjugates of 2′-*O*-Methyl Oligoribonucleotides and Their Invasion to a ^{19}F labeled HIV-1 TAR Model

Anu Kiviniemi and Pasi Virta*

Department of Chemistry, University of Turku, FIN-20014 Turku, Finland

Supporting Information

ABSTRACT: The potential of aminoglycosides to induce RNA-invasion has been demonstrated. For this purpose, aminoglycoside-3′-conjugates of 2′-*O*-methyl oligoribonucleotides have been synthesized entirely on a solid phase. The synthesis includes an automated oligonucleotide chain elongation to solid-supported neomycin, ribostamycin, and methyl neobiosamine, and a two-step deprotection/release of the solid-supported conjugate, which allows exploitation of a simple protecting group scheme. Conjugates have been targeted to a ^{19}F labeled HIV-1 TAR RNA model (Trans Activation Response element of HIV), which allows monitoring of the invasion by ^{19}F NMR spectroscopy. A remarkably enhanced invasion, compared to that resulting from the corresponding unmodified 2′-*O*-methyl oligoribonucleotide (5′-CAGGCUCA-3′), has been obtained by the neomycin conjugate. The increased affinity results from a cooperative binding of the neomycin moiety and hybridization, though the invasion may also follow a mechanism, in which the first molar equivalent of the conjugate induces hybridization of the second.

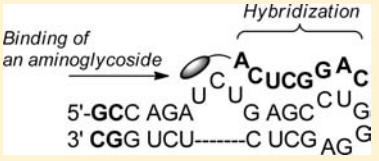

INTRODUCTION

Aminoglycosides are antibiotics, which interact with a variety of RNA targets. Binding to the ribosomal decoding site (A−site) is the basis of their bactericidal effect,[1−5] and comparable affinities to other RNA targets, e.g., to several ribozymes[6−16] and to important RNA motifs of HIV (TAR, RRE and DIS),[17−20] show their potential as more general RNA-targeting drugs. Aminoglycosides are also able to stabilize DNA- and RNA-triplexes, DNA-RNA hybrid triplexes, and hybrid duplexes.[21−23] The recognition of a certain RNA target is usually based on a bulge or an internal loop, in which the canonical base-pairing is disrupted by few mismatches.[24] As an example, the site-specific binding of neomycin to the HIV-1 TAR region occurs below the UCU bulge through the minor groove.[25] Although the nonionic interactions may play an important role in the recognition, aminoglycosides' affinity to RNA mainly originates from electrostatic interaction of their protonated amino groups with phosphodiester linkages. The binding, hence, is promiscuous, which is the main bottleneck of aminoglycoside-based RNA-targeting.[24] In principle, the promiscuity may be overcome by appropriate structural modifications, but conformational adaption of an RNA target upon complex formation makes development of specific ligands extremely complex.[26] One option to increase the specificity is the conjugation of aminoglycosides to other recognition moieties. By conjugation to oligonucleotides or PNA, the aminoglycoside's binding may be cooperatively directed by hybridization, and the specificity may be expectedly improved. In view of the antisense approach,[27,28] such conjugates are attractive, since the binding of the covalently attached aminoglycoside may enhance hybridization and direct the drug design to shorter oligonucleotide sequences. Improvements considering the cellular uptake may additionally be provided since neomycin has been shown to assist the lipid-mediated delivery of oligonucleotides.[29] Pioneering work for the aminoglycoside-induced antisense oligonucleotides has already been done. Neomycin has been covalently attached into an oligodeoxyribonucleotide, complementary to a seven-bases-long α-sarcin loop RNA sequence, and its ability to enhance duplex formation has been studied.[30] A 14-mer PNA-neamine conjugate targeted to HIV-1 TAR has displayed anti-HIV-1 activity and sequence-specific metal-ion-independent cleavage of the target RNA.[31,32] A set of neamine- and ribostamycin-2′-*O*-methyl oligoribonucleotide conjugates has been prepared in order to study their nuclease activity,[33] and DNA-duplex stabilization has been obtained by 4′-*C*-conjugated paromamine.[34,35] It is worth noting that conjugation of neamine with dinucleotides has been reported to remarkably decrease affinity to HIV-1 TAR RNA, due to electrostatic repulsion between the phosphates, whereas conjugates of the corresponding PNA show about 2-fold binding affinities compared to that of neamine.[36]

HIV-1 TAR RNA is a potential target for antisense oligonucleotides since it occurs at the 5′-end of all HIV-1 RNA transcripts and is regulated by the cognate protein Tat during transcriptional elongation.[37−40] The target region in HIV-1 TAR is a relatively short but chemically interesting RNA-construct, which consists of a trinucleotide UCU bulge and a

Received: February 24, 2011
Revised: June 14, 2011
Published: June 21, 2011

ACS Publications © 2011 American Chemical Society

Scheme 1. Synthesis of Conjugates 10−16[a]

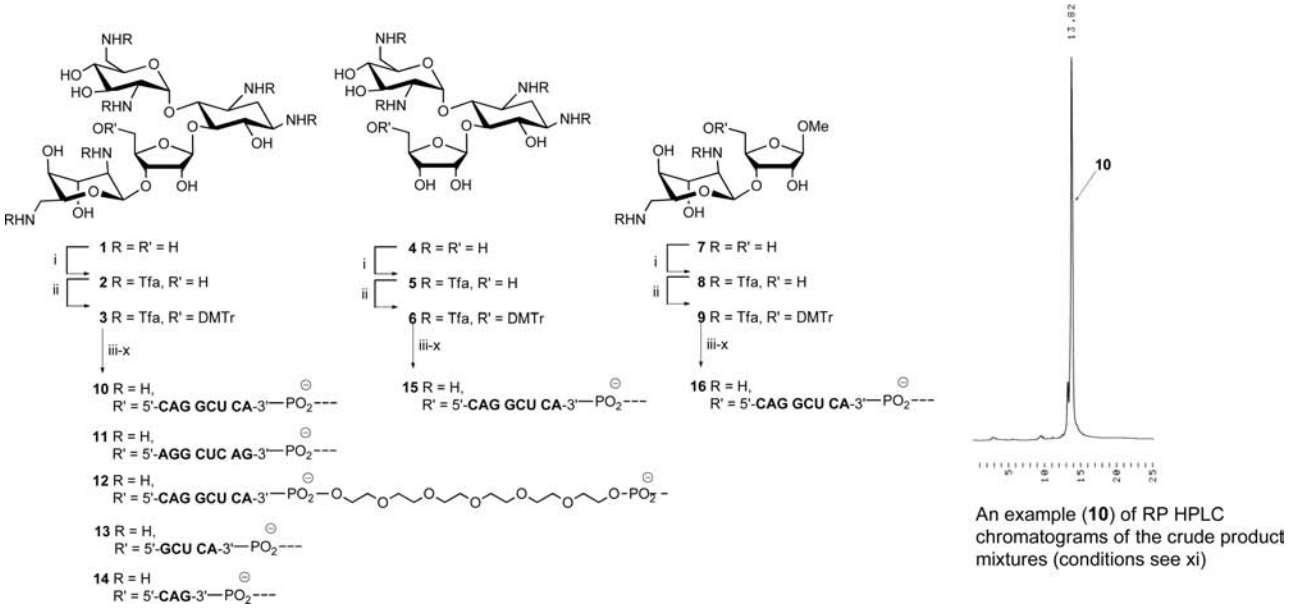

[a] Reagents and conditions: (i) TfaOMe, MeOH, Et_3N; (ii) DMTrCl, Py, overall yields (from **1**, **4** and **7**), **3**, 73%; **6**, 59%; and **9**, 51%; (iii) succinanhydride, DMAP, pyridine; (iv) LCAA-CPG, HATU, DIEA, DMF; (v) benzylamine, HATU, DIEA, DMF; (vi) acetic anhydride, lutidine, 1-methyl imidazole, THF; (vii) standard automated RNA synthesis; (ix) 0.1 mol L^{-1} NaOMe in MeOH; (x) ammonolysis; (xi) RP HPLC conditions, a gradient elution from 10% to 40% acetonitrile in 0.1 mol L^{-1} aq. $Et_3NH^+AcO^-$ over 25 min, Thermo ODS Hypersil column (250 × 4.6 mm, 5μm) at a flow rate of 1.0 mL min^{-1}.

Scheme 2. Invasions of 8-Mer 2′-*O*-Methyl Oligoribonucleotide (17) and Its Neomycin-3′-conjugate (10) to the ^{19}F Labeled HIV-1 TAR RNA Model (A)

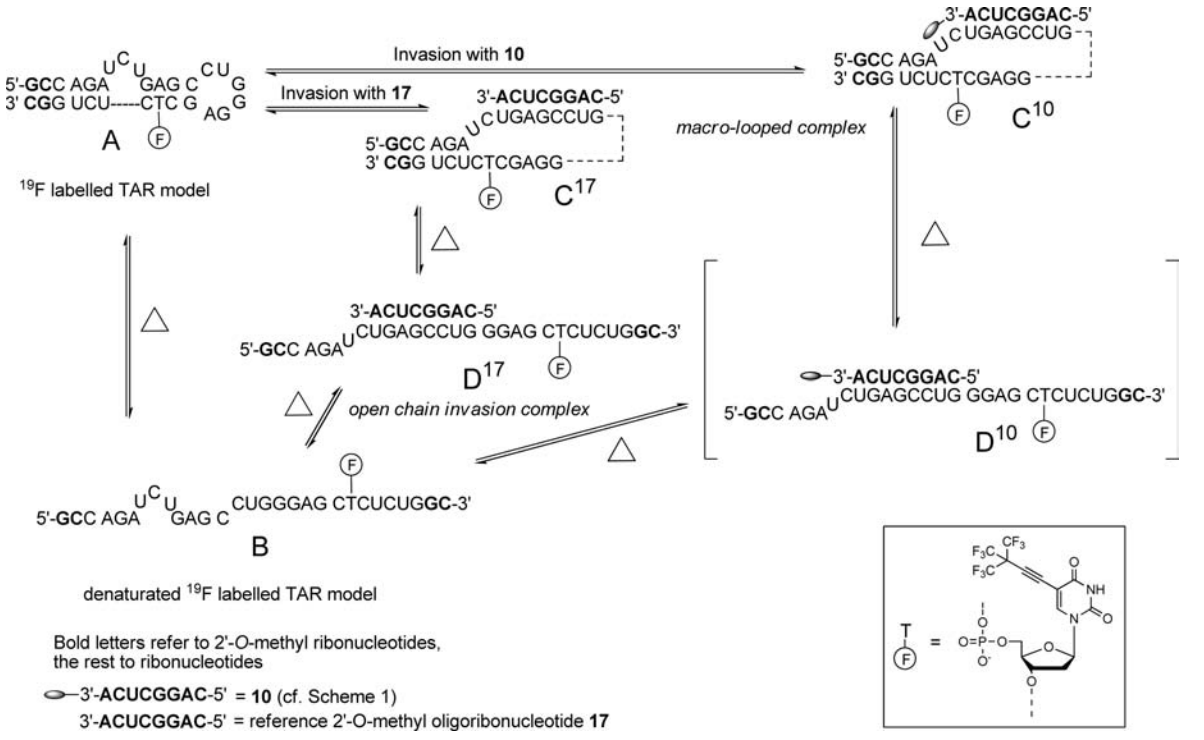

hairpin loop linked together by a tetranucleotide stem region. The essential elements for HIV-1 TAR targeting may, however, be applied more generally to oligonucleotide-based drug design since related RNA-constructs exist in many biologically relevant

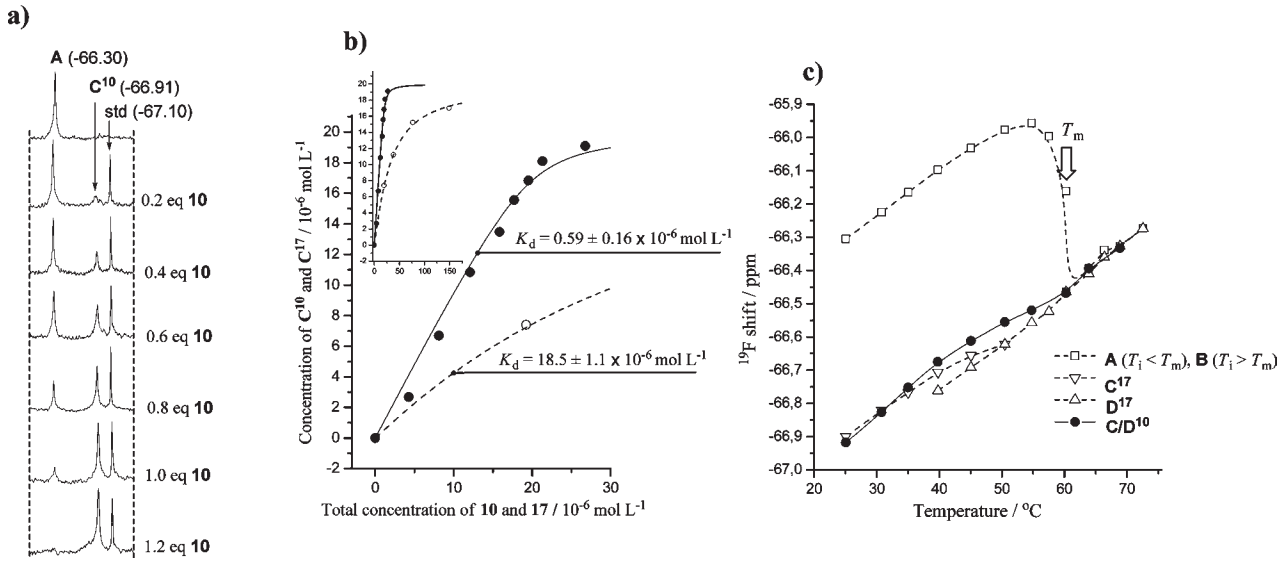

Figure 1. (a) ^{19}F NMR spectra of **A** (20 μmol L^{-1} in 25 mmol L^{-1} NaH_2PO_4 buffered H_2O-D_2O (9:1, v/v, pH 6.5) in the presence of increasing concentrations of **10**. 5-[4,4,4,-Trifluoro-3,3,-bis(trifluoromethyl)but-ynyl]-2′-deoxyuridine (10 μmol L^{-1}) was used as an internal standard (std). (b) Titration curves obtained by integrals of ^{19}F resonances in different concentrations of **10** (●) and **17** (○), {[$\mathbf{C}^n$] = [$\mathbf{A}_{tot}$] × a relative ^{19}F peak area $\mathbf{C}^n/(\mathbf{C}^n + \mathbf{A})$. (c) ^{19}F shift versus temperature profiles. **A**, **B**, $\mathbf{C}^{17}$, $\mathbf{D}^{17}$, and $\mathbf{C}/\mathbf{D}^{10}$; cf. Schemes 1 and 2.

RNAs. Among them are microRNAs, which recently have been reassessed as potential of antisense targets.[41] We have recently shown that neomycin induces invasion of a 2′-*O*-methyl oligoribonucleotide to a HIV-1 TAR model.[42] In the present study, neomycin, ribostamycin, and methyl neobiosamine have been covalently attached to the 3′-terminus of 2′-*O*-methyl oligoribonucleotides (**10**−**16**), and influence of the conjugated aminoglycosides on RNA invasion has been studied. As done previously, a ^{19}F labeled HIV-1 TAR RNA model **A** (Scheme 2) has been used as a target, which allows monitoring of the secondary structural arrangement upon invasion by ^{19}F NMR spectroscopy. For the preparation of the conjugates (**10**−**16**), a straightforward procedure was applied (Scheme 1). Partially protected aminoglycosides (**3**, **6**, and **9**), bearing the dimethoxitrityl protected primary hydroxyl group and trifluoroacetyl protected amino groups, were covalently attached to a LCAA CPG-support via succinyl linker. After capping of the remaining reactive functionalities, 2′-*O*-methyl oligoribonucleotide sequences were automatically elongated to these solid-supported aminoglycosides. A two-step procedure (1, NaOMe/MeOH; 2, ammonolysis) was used for the deprotection/release, to avoid *O*→*N*-acyl migration on the aminoglycoside moieties. A relatively simple protecting group scheme may, hence, be utilized. For K_d determinations, a mixture of the ^{19}F labeled HIV-1 TAR model was titrated by these conjugates. According to ^{19}F NMR spectroscopic monitoring (Figure 1a), the neomycin moiety remarkably induces invasion of 2′-*O*-methyl oligoribonucleotides (Figure 1b). The right side (rings I, II, and III, i.e., ribostamycin) of the neomycin moiety also resulted in a slight enhancement, but influence of the left side (rings III and IV, i.e., biosamine) remained marginal (Table 2). The enhanced invasion was attributed to a formation of a stabilized macro-looped complex, by concurrent hybridization and binding of the neomycin moiety (Scheme 2 and Figure 1c). Interestingly, if the neomycin moiety is not appropriately available, the invasion may also follow a mechanism, in which the first molar equivalent of the conjugate induces hybridization of the second.

EXPERIMENTAL PROCEDURES

General Remarks. The NMR spectra of **3**, **6**, and **9** were recorded at 500 MHz. The chemical shifts are given in ppm from internal TMS and coupling constants in hertz. Peak assignments were supported by COSY and HSQC. The mass spectra of **3**, **6**, and **9** and oligonucleotide conjugates **10**−**16** were recorded by ESI ionization. Oligonucleotides **10**−**16** were assembled on an Applied Biosystems 392 DNA synthesizer using commercially available 2′-*O*-methyl ribonucleoside phosphoramidites. Standard RNA coupling protocol was followed. The ^{19}F labeled TAR model (**A**) was prepared as previously described.[42] A Thermo Hypersil ODS column (250 × 4.6 mm, 5 μm) at a flow rate of 1 mL min^{-1} was used for the RP HPLC purification of the conjugates (**10**−**16**). A gradient elution from 10% to 40% acetonitrile in 0.1 mol L^{-1} $Et_3NH^+AcO^-$-buffer over 25 min was used.

^{19}F NMR Spectroscopy. Oligonucleotides (triethylammonium salts) were lyophilized to dryness and dissolved in 25 mmol L^{-1} NaH_2PO_4-buffer (pH 6.5) in D_2O-H_2O (1:9 v/v). For the titration experiments, conjugates were added as 1 mmol L^{-1} solutions to a 20 μmol L^{-1} solution of ^{19}F labeled HIV-1 TAR model (**A**). Prior to each spectroscopic detection, the mixtures were heated to 90 °C for 1 min and then allowed to cool down to room temperature. Spectra were recorded at a frequency of 376.1 MHz on a Bruker Avance 400 MHz spectrometer. Typical experimental parameters were chosen as follows: ^{19}F excitation pulse, 12.6 μs; acquisition time, 0.675 s; relaxation delay, 1.0 s; and usual number of scans, 2400 or 4800. ^{19}F resonances were referenced relative to external CCl_3F. Sample temperature for the ^{19}F shift versus temperature profiles (cf. Figure 1c) was calibrated by using known shifts of ethylene glycol at different temperatures. K_d values were calculated from relative peak areas of ^{19}F resonance signals of the free HIV-1 TAR model (**A**) and

dx.doi.org/10.1021/bc200101r |*Bioconjugate Chem.* 2011, 22, 1559–1566

of the complexes (**C**) according to the following equations: $K_d[\mathbf{C}] = [\mathbf{A}][\mathbf{ON}]$, $[\mathbf{A}] + [\mathbf{C}] = [\mathbf{A}_{tot}]$, $[\mathbf{ON}] = [\mathbf{ON}_{tot}]-[\mathbf{C}] \rightarrow [\mathbf{C}]^2 - ([\mathbf{A}_{tot}] + [\mathbf{ON}_{tot}] + K_d)[\mathbf{C}] + [\mathbf{ON}_{tot}][\mathbf{A}_{tot}] = 0$, where $[\mathbf{C}]$ = concentration of the invasion complex = $X[\mathbf{A}_{tot}]$, X = a relative ^{19}F signal peak area (cf. Figure 1a) of the invasion complex, $[\mathbf{A}_{tot}]$ = the total concentration of **A**, $[\mathbf{A}]$ = concentration of free **A**, $[\mathbf{ON}_{tot}]$ = total concentration of the conjugate, and $[\mathbf{ON}]$ = concentration of the free conjugate. Titrations were additionally performed in the presence of the 5-[4,4,4,-trifluoro-3,3-bis(trifluoromethyl)but-1-ynyl]-2′-deoxyuridine (10 μmol L^{-1}) standard,[43] to which the peak areas were referenced.

Thermal UV Denaturation Studies. Absorbance versus temperature profiles (Supporting Information) were recorded at 260 nm on a Perkin-Elmer Lambda 35 UV−vis spectrometer equipped with a multiple cell holder and a Peltier temperature-controller. The temperature was changed at a rate of 0.5 °C/min (from 20 to 90 °C). The measurements were performed in 25 mM NaH_2PO_4 buffer (pH 6.5). T_m values were determined as the maximum of the first derivate of the melting curve.

5′-*O*-(4,4′-Dimethoxytrityl)-1,3,2′,6′,2‴,6‴-hexa-*N*-trifluoroacetylneomycin (3). Triethylamine (3.6 mL, 26 mmol) and methyl trifluoroacetate (2.6 mL, 26 mmol) were added to neomycin trisulfate (**7**, 2.0 g, 2.2 mmol) in methanol (10 mL). The mixture was stirred overnight at room temperature and evaporated to dryness. Saturated $NaHCO_3$ was added to the residue, and the crude product (**2**) was extracted with ethyl acetate. The organic layers were combined, dried over Na_2SO_4, filtered, and evaporated to dryness. The residue was further dried by coevaporation with dry pyridine and dissolved in dry pyridine, and then 4,4′-dimetoxytrityl chloride (0.80 g, 2.4 mmol) was added to the mixture. After overnight reaction, saturated $NaHCO_3$ was added, and the product was extracted with ethyl acetate. The organic layers were combined, dried over anhydrous Na_2SO_4, filtered, and evaporated to dryness. The residue was purified by silica gel chromatography (10% MeOH, 1% Et_3N in CH_2Cl_2) to yield 2.35 g (73%) of the product (**3**) as white foam. ^1H NMR (CD_3OD, 500 MHz) δ: 7.46 (m, 2H), 7.36−7.30 (m, 6H), 7.21 (m, 1H), 6.90 (m, 4H), 5.78 (d, 1H, J = 3.3 Hz), 5.16 (d, 1H, J = 4.6 Hz), 5.09 (d, 1H, J = 1.5 Hz), 4.29 (dd, 1H, J = 4.8 Hz, both), 4.21−4.20 (m, 2H), 4.14 (m, 1H), 4.11 (dd, 1H, J = 6.7 Hz, both), 4.01 (m, 1H), 3.97 (m, 1H), 3.92 (m, 1H), 3.87 (dd, 1H, J = 9.9 and 8.8 Hz), 3.80 (s, 6H), 3.75−3.63 (m, 5H), 3.60 (dd, 1H, J = 13.5 and 7.4 Hz), 3.56−3.51 (m, 2H), 3.35−3.31 (m, 3H), 3.19 (dd, 1H, J = 10.5 and 3.1 Hz), 2.00 (ddd, 1H, J = 12.9 Hz, 4.2 and 4.2 Hz), 1.77 (ddd, 1H, J = 12.7 Hz, each). ^{13}C NMR (CD_3OD, 125 MHz) δ: 157.93, 157.85, 145.0, 136.0, 135.6, 130.2, 129.9, 128.0, 127.4, 126.3, 112.7, 109.0, 97.6, 96.3, 87.4, 86.3, 81.9, 76.9, 75.6, 74.8, 73.0, 72.1, 71.5, 70.3, 69.8, 69.2, 67.1, 62.5, 54.3, 53.5, 51.3, 49.6, 49.1, 40.4, 39.6, 31.5 (Tfa related peaks not listed). HRMS(ESI): found 1515.3239, $[M + Na]^+$ requires 1515.3265 (error 1.7 ppm).

5′-*O*-(4,4′-Dimethoxytrityl)-1,3,2′,6′-tetra-*N*-trifluoroacetylribostamycin (6). Compound **6** was synthesized from **4** (as a disulfate salt, 0.25 g, 0.38 mmol) as described for the neomycin derivative **3** from **1** above. After silica gel chromatography (5% MeOH and 0.2% Et_3N in CH_2Cl_2) 0.26 g (59%) of **6** was obtained as white foam. ^1H NMR (CD_3OD, 500 MHz) δ: 7.46 (m, 2H), 7.34 (m, 4H), 7.29 (m, 2H), 7.20 (m, 1H), 6.86 (m, 4H), 5.67 (d, 1H, J = 2.7 Hz), 5.22 (d, 1H, J = 4.0 Hz), 4.18−4.10 (m, 3H), 4.02−3,97 (m, 3H), 3.92 (m, 1H), 3.81 (m, 1H), 3.78 (s, 6H), 3.76−3.64 (m, 4H), 3.60 (m, 2H), 3.30−3.25 (m, 2H), 3.23 (dd, 1H, J = 10.2 and 3.8 Hz), 2.01 (ddd, 1H, J = 12.9 Hz, 4.2 and 4.2 Hz), 1.75 (ddd, 1H, J = 12.8 Hz each). ^{13}C NMR (CD_3OD, 125 MHz) δ: 158.7, 145.0, 136.0, 135.8, 130.02, 129.95, 128.0, 127.4, 126.3, 112.7, 109.2, 96.6, 86.7, 83.2, 76.4, 75.5, 72.9, 72.1, 70.9, 70.2, 70.1, 63.1, 54.3, 53.8, 49.7, 49.2, 40.5, 31.5 (Tfa related peaks not listed). HRMS(ESI): found 1163.2786, $[M + Na]^+$ requires 1163.2771 (error 1.3 ppm).

Methyl-2′,6′-Bis-*N*-trifluoroacetyl Neobiosamine B (9). Compound **9** was synthesized from **7** (as free amine, β:α = 0.77:0.23, 0.63 g, 1.9 mmol) as described for the neomycin derivative **3** from **1** above, but 2 mol equiv of DMTrCl was used. After silica gel chromatography (5% MeOH and 0.2% Et_3N in CH_2Cl_2), 0.63 g (51%) of **8** (pure β isomer) was obtained as white foam. ^1H NMR (CD_3OD, 500 MHz) δ: 7.60 (m, 2H), 7.47 (m, 4H), 7.28 (m, 2H), 7.20 (m, 1H), 6.87 (m, 4H), 5.36 (b, 1H), 4.36 (d, 1H, J = 7.3 Hz), 4.34 (b, 1H), 4.27 (b, 1H), 4.20 (dd, 1H, J = 6.8 and 6.7 Hz), 4.07 (b, 1H), 3.77 (s, 6H), 3.71 (dd, 1H, J = 12.8 and 8.8 Hz), 3.62 (b, 1H), 3.54 (b, 1H), 3.52 (dd, J = 12.8 and 4.9 Hz), 3.36 (s, 3H), 3.32 (b, 1H), 3.18 (m, 2H), 2.33 (b, 1H). ^{13}C NMR (CD_3OD, 125 MHz) δ: 157.4, 144.4, 135.3, 135.0, 128.7, 127.0, 125.9, 124.9, 111.3, 111.1, 100.2, 96.3, 85.4, 75.3, 69.9, 69.6, 67.8, 67.5, 65.6, 60.7, 54.1, 52.8, 50.1 (Tfa related peaks not listed). HRMS(ESI): found 842.2415, $[M + Na]^+$ requires 841.2383 (error 3.8 ppm).

Synthesis of the Conjugates 10−14. Succinanhydride (3.4 mg, 33 μmol) and a catalytic amount of DMAP were added to a mixture of **3**, **6**, or **9** (33 μmol, each) in dry pyridine (0.50 mL). The mixtures were stirred overnight at ambient temperature and evaporated to dryness. (According to MS(ESI), the crude product mixtures also contained multiply succinated side products in addition to monosuccinates.) The residues were dissolved in DMF (1.0 mL), and HATU (25 mg, 67 μmol), DIEA (23 μL, 130 μmol), and LCAA-CPG support (100 mg) were added to the mixtures. After overnight shaking, the suspensions were filtered, and the supports were washed with DMF and CH_2Cl_2 and dried under vacuum. The potential unreacted carboxylic acid groups on the supports were capped by amide bond formation. Accordingly, the supports were suspended in DMF (1.0 mL), and benzylamine, HATU, and DIEA were added to the suspensions. After overnight shaking, the supports were filtered, washed with DMF and CH_2Cl_2, and dried under vacuum. The unreacted hydroxyl groups of the solid supported aminoglycosides and the unreacted amino groups of the initial support were then acetylated by double syringe method using a mixture of acetic anhydride, lutidine, and *N*-methyl imidazol in THF (5:5:8:82, v/v/v/v, for 15 min at 25 °C). After acetylation, the resins were washed with THF and CH_2Cl_2 and dried under vacuum. A small aliquot of each resin was analyzed by the DMTr-cation assay. Loadings of 17 μmol g^{-1} (neomycin resin), 14 μmol g^{-1} (ribostamycin resin), and 19 μmol g^{-1} (methyl neobiosamine resin) were obtained. The appropriate oligonucleotide chains were then assembled (0.5 μmol scale) by standard automated RNA protocol. After chain assembly, supports were treated with 0.1 M NaOMe in MeOH (1.0 mL, for 2 h at 25 °C) and filtered. One molar aqueous ammonium chloride (100 μL) was added to the filtrates, and the mixtures were evaporated to dryness. Supports and the filtrates were combined and treated with saturated ammonia for 15 h at 55 °C. Finally, the mixtures were filtered, evaporated to dryness, dissolved in water, and purified by RP HPLC [a gradient elution from 10% to 40% acetonitrile in 0.1 mol L^{-1} aq. $Et_3NH^+AcO^-$ over 25 min, Thermo ODS Hypersil column (250 × 4.6 mm, 5 μm) at a flow rate of 1.0 mL min^{-1}; an example of the RP HPLC chromatogram is shown in Scheme 1].

Table 1

conjugate	observed mass	calculated mass
10	1646.9[a]	1646.4
11	909.0[b]	909.0
12	1666.9[c]	1666.4
13	1136.3[a]	1136.3
14	816.7[a]	816.7
15	1566.9[a]	1566.8
16	1501.8[a]	1501.8

[a] $[M - 2H]^{2-}$. [b] $[M - 4H]^{4-}$. [c] $[M + K - 3H]^{2}$.

The isolated products were desalted and lyophilized to dryness. Authenticity of the isolated products **10**−**16** was verified by MS (ESI) spectroscopy (Table 1).

RESULTS AND DISCUSSION

Synthesis of the Aminoglycoside 3′-Conjugates of 2′-*O*-Methyl Oligoribonucleotides (10−16). Synthesis of the conjugates (**10**−**16**) is described in Scheme 1. The protecting group scheme was simplified by using a one-pot anchoring/protection procedure of partially protected aminoglycosides (**3**, **6**, and **9**). Neomycin (**1**), ribostamycin (**4**), and methyl neobiosamine (**7**) were *N*-trifluoroacetylated (**2**, **5**, and **8**), and the primary hydroxyl group was selectively protected by the 4,4′-dimethoxytrityl group. Compounds (**3**, **6**, or **9**) were then treated with one molar equivalent of succinanhydride (iii), the crude products were attached to the LCAA-CPG support (iv), and the potential free carboxyl and hydroxyl groups on the supports were capped by amide bond formation (v) and acetylation (vi), respectively. An automated oligonucleotide chain elongation (vii) was successfully performed on the obtained aminoglycoside supports. In order to avoid potential *O*→*N*-acyl migration on the aminoglycoside moieties, a two-step deprotection-procedure was performed. The solid-supported conjugates were subjected to a mixture of NaOMe in methanol (ix, ester cleavage), and then the deprotection was continued by ammonolysis (x, amide cleavage). The sodium methoxide pretreatment favors transesterification, in which the trifluoroacetamides stay intact. According to RP HPLC chromatograms (an example is shown in Scheme 1) and MS (ESI) spectra (Table 1), products were successfully obtained without *O*→*N*-acyl migration.

Invasion of the Conjugates to the ^{19}F Labeled TAR Model (A). ^{19}F is biologically nonexistent and has an NMR-sensitive nucleus (83% compared to ^{1}H), which additionally offers wide chemical shift dispersion. These properties make the ^{19}F nucleus a useful probe for the monitoring of conformational transitions in RNA.[42−51] Closely related to this work, 2′-deoxy-2′-fluoronucleosides incorporated in RNA have been used for the monitoring RNA-aminoglycoside interactions,[47] and 2,4-difluorotoluene nucleosides have been used for the quantification of hairpin/hairpin and duplex/hairpin equilibria of self-complementary RNAs.[49] We have recently demonstrated the applicability of ^{19}F NMR spectroscopy to the monitoring of RNA invasion, by studying the binding of 2′-*O*-methyl oligoribonucleotides to the ^{19}F labeled HIV-1 TAR RNA model **A**.[42] The 5-[4,4,4-trifluoro-3,3-bis(trifluoromethyl)but-1-ynyl]-2′-deoxyuridine sensor[43] within the model decreases the stability of the four nucleotide stem between the loop and the UCU-bulge (ΔT_m = −2.7 °C), slightly facilitating the invasion. The model (**A**) is, hence, useful for comparative evaluation of the affinities of different invader oligonucleotides. A distinct ^{19}F resonance signal from that referring to the initial hairpin structure may be obtained, when a structural change, such as invasion (**C**/**D**) or thermal denaturation (**B**), takes place. Additionally, temperature-dependent behavior of the complexes may be followed by ^{19}F shift vs temperature profiles since the potential macro-looped (**C**) and the open-chain invasion complex (**D**) may, in a favorable case, result in ^{19}F signals with different resonance shifts (Figure 1c). Note that there is a linear temperature-dependent ^{19}F shift downfield with the slope 0.014 ppm K^{-1}. Deviations from this passive shift refer to structural changes in RNA. In the present study, model **A** was titrated with conjugates **10**−**13**, (**14** + **17**), **15**, and **16**, and their invasion efficiency was evaluated by ^{19}F NMR spectroscopy. We recently showed that invasion of 2′-*O*-methyl oligoribonucleotide **17** (Scheme 2) to **A** may be induced by the presence of neomycin (as a discrete molecule).[42] Therefore, neomycin, when covalently attached to the same 2′-*O*-methyl oligoribonucleotide (**10**), may be expected to result in a cooperative effect, in which the complex is stabilized by concurrent hybridization and binding of the neomycin moiety. The site-specific binding of neomycin occurs below the bulged nucleotides of the native HIV-1 TAR region through the minor groove.[25] Stabilization of the complex should, hence, be based on the formation of the macro-looped complex ($\mathbf{C}^{10}$) since the open-chain invasion complex ($\mathbf{D}^{10}$) contains only the canonical double strand with a modest affinity to aminoglycosides. ^{19}F NMR spectra during the titration of **A** with **10** is shown in Figure 1a, and the titration curve recording the relative ^{19}F peak areas is shown in Figure 1b. As seen from Figure 1b, conjugate **10** provides a significantly enhanced invasion compared to that obtained by unmodified 2′-*O*-methyl oligoribonucleotide **17**. Fitting the titration curve to the stoichiometric (1:1) complex formation, gave K_d = 0.59 ± 0.16 μmol L^{-1} with **10**, whereas K_d = 18.5 ± 1.1 μmol L^{-1} was obtained with **17**. An interesting observation was additionally done, when the mixture of the complex $\mathbf{C}/\mathbf{D}^{10}$ was heated. The ^{19}F shift vs temperature profile of the complex ($\mathbf{C}/\mathbf{D}^{10}$) followed the prolonged downfield curve of the complex ($\mathbf{C}/\mathbf{D}^{17}$) with unmodified 2′-*O*-methyl oligoribonucleotide **17** (Figure 1c). We have previously concluded that the downfield curve (∇ in Figure 1c) refers to the macrolooped complex ($\mathbf{C}^{17}$) and the upfield curve (Δ in Figure 1c) to the open-chain invasion complex ($\mathbf{D}^{17}$).[42] The prolonged downfield curve (●) refers to neomycin binding and is consistent with the expectation that the enhanced invasion is related to the stabilized macro-looped complex ($\mathbf{C}^{10}$).

Invasion by the other conjugates was similarly studied (see titration curves in the Supporting Information), and the K_d

Table 2.[a]

oligonucleotide	K_d (μmol L^{-1})
10	0.59 ± 0.16
11	4.9 ± 1.5
12	0.32 ± 0.22
13	37.0 ± 2.0
15	3.8 ± 0.7
16	25.0 ± 0.4
17	18.5 ± 1.1
17 + **14** (1:1, *n*/*n*)	3.6 ± 0.8

[a] Each K_d is simplified to stoichiometric (1:1) complexes.

values for each complex are listed in Table 2. Comparing K_d of $\mathbf{C^{11}}$ ($4.9 \pm 1.5\ \mu mol\ L^{-1}$) to that of $\mathbf{C^{10}}$ ($0.59 \pm 0.16\ \mu mol\ L^{-1}$) shows that shifting of the 2′-*O*-methyl oligoribonucleotide sequence by one nucleotide (C at 5′-end deleted and G at 3′-end added) significantly decreases the affinity. More interestingly, the titration curve obtained by $\mathbf{C^{11}}$ hardly follows 1:1-complex formation, but the saturation is deviated to a 2:1-stoichiometry. An explanation to this phenomenon is that the above-mentioned cooperative effect could not be gained with **11** but that the first molar equivalent of the conjugate may induce invasion of the second. In order to evaluate the efficiency of this ternary mechanism, titration was additionally performed with a 1:1-mixture of unmodified octamer **17** and neomycin conjugate **14**, which with the short CAG-strand cannot alone invade **A** (cf. **13** below). Conjugate **14**, however, does induce the invasion of **17** of **A**, for which $K_d = 3.6 \pm 0.8\ \mu mol\ L^{-1}$ (simplified to 1:1-complex formation) may be determined. This verifies that invasion with conjugate **11** may be induced in a ternary manner. The ternary induction may partly take place also with **10** (or with other conjugates as well), but the titration profile may be more overlapped by that of the stoichiometric (1:1) complex formation. In order to avoid potential structural constraints for the cooperative recognition, conjugate **12**, bearing a flexible polyethylene glycol spacer between the neomycin moiety and 2′-*O*-methyl oligoribonucleotide, was targeted to **A**. As expected, the more flexible spacer facilitates cooperativity, and a higher affinity ($K_d = 0.32 \pm 0.22\ \mu mol\ L^{-1}$) compared to that of **10** was obtained. Noteworthy, this strongly stoichiometric complex formation approach's limitations can be reliably detected by the adopted method (based on integrals of ^{19}F resonance signals). Importance of the left (biosamine) and right (ribostamycin) sides of the neomycin moiety may be seen in K_d values of $\mathbf{C^{16}}$ and $\mathbf{C^{17}}$. The affinities were expectedly weaker than that of **10** ($\mathbf{C^{10}}$: $K_d = 0.59 \pm 0.16\ \mu mol\ L^{-1}$), and the ribostamycin moiety still promotes invasion ($\mathbf{C^{13}}$: $K_d = 3.8 \pm 0.7\ \mu mol\ L^{-1}$), but influence of the biosamine moiety ($\mathbf{C^{14}}$: $K_d = 25 \pm 0.4\ \mu mol\ L^{-1}$) to that of **17** ($\mathbf{C^{17}}$: $K_d = 18.5 \pm 1.1\ \mu mol\ L^{-1}$) was marginal (slightly negative). Titration with neomycin conjugate **13**, bearing a short pentanucleotide sequence, resulted in a broad and fragmented signal into the ^{19}F NMR spectrum. This is a consequence of weak hybridization, in which unspecific binding of the neomycin moiety (conjugate in excess) already predominates. Only a weak invasion ($K_d = 36.9 \pm 2.0\ \mu mol\ L^{-1}$ simplified to stoichiometric 1:1-complex formation) was observed. Mixtures of the complexes were also heated to provide the ^{19}F shift vs temperature profiles (see Supporting Information). The stable complex $\mathbf{C^{12}}$ expectedly followed the prolonged downfield curve similar to $\mathbf{C^{10}}$ (cf. Figure 1c), and a slightly prolonged downfield curve was obtained also with $\mathbf{C^{11}}$. Similar downfield shifting was not obtained with complexes ($\mathbf{C^{15}}$ and $\mathbf{C^{16}}$) of ribostamycin and neobiosamine conjugates. Consistent with ^{19}F shift vs temperature profiles, complexes $\mathbf{C^{10-12}}$ were stable upon heating (at a temperature lower than T_m), but equilibrium between **A** and **15** or **16** was dynamic, and hence, the amount of complexes $\mathbf{C^{15}}$ or $\mathbf{C^{16}}$ decreased upon heating. UV-melting profiles of the complexes were also measured. Noteworthy, these are performed in a diluted 2 $\mu mol\ L^{-1}$ solution of **A** in the presence of the conjugates (**10**, **11**, **14** + **17**, **15**, and **16**, 2 equiv; **12**, 1 equiv; and **13**, 5 equiv), in which the weak complexes are mainly dissociated. The only conjugate which resulted in an increased T_m was **12** (1 equiv, $T_m = 62.7\ °C$; **A**, $T_m = 60.7\ °C$). No change or a slightly decreased $T_m = 59.2-60.6\ °C$ was observed with other conjugates.

CONCLUSIONS

Aminoglycoside (neomycin, ribostamycin, and methyl neobiosamine) 3′-conjugates of 2′-*O*-methyl oligoribonucleotides have been synthesized entirely on a solid phase, and their invasion efficiency to a ^{19}F labeled HIV-1 TAR model has been evaluated by ^{19}F NMR spectroscopy. In addition to the determined K_d-values, ^{19}F shift versus temperature profiles of the complexes have been measured. A significantly enhanced invasion in the presence of the neomycin moiety (conjugates **10** and **12**) has been obtained. Enhancement has been concluded to be involved in the stabilized macrolooped complex, which allows concurrent hybridization and binding of the neomycin moiety. Aminoglycoside-promoted RNA-invasion has hence been verified, which may give new ideas for the oligonucleotide-based RNA targeting.

ASSOCIATED CONTENT

Supporting Information. ^{1}H NMR and ^{13}C NMR spectra, RP HPLC chromatograms, titration curves, ^{19}F shift vs the temperature profile, and UV-melting curves. This material is available free of charge via the Internet at http://pubs.acs.org.

AUTHOR INFORMATION

Corresponding Author

*Fax: +35823336700. E-mail: pamavi@utu.fi.

ACKNOWLEDGMENT

The financial support from the Academy of Finland is gratefully acknowledged.

REFERENCES

(1) Davies, J., Gorini, L., and Davis, B. D. (1965) Misreading of RNA codewords induced by aminoglycoside antibiotics. *Mol. Pharmacol. 1*, 93–106.

(2) Moazed, D., and Noller, H. F. (1987) Interaction of antibiotics with functional sites in 16S ribosomal RNA. *Nature 327*, 389–394.

(3) Francois, B., Russell, R. J. M., Murray, J. B., Aboul-ela, F., Masquida, B., Vicens, Q., and Westhof, E. (2005) Crystal structures of complexes between aminoglycosides and decoding site oligonucleotides: role of the number of rings and positive charges in the specific binding leading to miscoding. *Nucleic Acid Res. 33*, 5677–5690.

(4) Recht, M. I., Fourmy, D., Blanchard, S. C., Dahlquist, K. D., and Puglisi, J. D. (1996) RNA sequence determinants for aminoglycoside binding to an A-site rRNA model oligonucleotide. *J. Mol. Biol. 261*, 421–436.

(5) Purohit, P., and Stern, S. (1994) Interaction of a small RNA with antibiotic and RNA ligands of the 30S subunit. *Nature 370*, 659–662.

(6) Von Ahsen, U., and Noller, H. F. (1993) Footprinting the sites of interaction of antibiotics with catalytic group I intron RNA. *Science 260*, 1500–1503.

(7) Von Ahsen, U., Davies, J., and Schroeder, R. (1991) Antibiotic inhibition of group I ribozyme function. *Nature 353*, 368–370.

(8) Herman, T. (2005) Drugs targeting the ribosome. *Current Opin. Struct. Biol. 15*, 355–366.

(9) Hoch, I., Berens, C., Westhof, E., and Schroeder, R. (1998) Antibiotic inhibition of RNA catalysis: Neomycin B binds to the catalytic core of the td group I intron displacing essential metal ions. *J. Mol. Biol. 282*, 557–569.

(10) Mikkelsen, N. E., Brannval, M., Virtanen, A., and Kirsebom, L. A. (1999) Inhibition of RNAse P RNA cleavage by aminoglycosides. *Proc. Natl. Acad. Sci. U.S.A. 96*, 6155–6160.

(11) Earnshaw, D. J., and Gait, M. J. (1998) Hairpin ribozyme cleavage catalyzed by aminoglycoside antibiotics and the polyamine spermine in the absence of metal ions. *Nucleic Acid Res. 26*, 5551–5561.

(12) Tor, Y., Hermann, T., and Westhof, E. (1998) Deciphering RNA recognition: aminoglycoside binding to the hammerhead ribozyme. *Chem. Biol. 5*, 277–283.

(13) Stage, T. K., Hertel, K. J., and Uhlenbeck, O. C. (1995) Inhibition of the hammerhead ribozyme by neomycin. *RNA 1*, 95–101.

(14) Cloudet-d'Orval, B., Stage, T. K., and Uhlenbeck, O. C. (1995) Neomycin inhibition of the hammerhead ribozyme involves ionic interactions. *Biochemistry 34*, 11186–11190.

(15) Chia, J. S., Wu, H. L., Wang, H. W., Chen, D. S., and Chen, P. J. (1997) Inhibition of hepatisis delta virus genomic ribozyme self-cleavage by aminoglycosides. *J. Biomed. Sci. 4*, 208–216.

(16) Tok, J. B. H., Cho, J., and Rando, R. R. (1999) Aminoglycoside antibiotics are able to specifically bind the 5′-untranslated region of thymidylate synthase messenger RNA. *Biochemistry 38*, 199–206.

(17) Mei, H.-Y., Galan, A. A., Halim, N. S., Mack, D. P., Morelan, D. W., Sanders, K. B., Truong, H. N., and Czarnik, A. W. (1995) Inhibition of an HIV-1 Tat-derived peptide binding to TAR RNA by aminoglycoside antibiotics. *Bioorg. Med. Chem. Lett.e> 5, 27552760.*

(18) Zapp, M. L., Stern, S., and Green, M. R. (1993) Small molecules that selectively block RNA binding of HIV-1 rev protein inhibit rev function and viral production. *Cell 74*, 969–978.

(19) Tam, V. K., Kwong, D., and Tor, Y. (2007) Fluorescent HIV-1 dimerization initiation site: design, properties, and use for ligand discovery. *J. Am. Chem. Soc. 129*, 3257–3266.

(20) Ennifar, E., Paillart, J.-C., Bodlenner, A., Walter, P., Weibel, J.-M., Aubertin, A.-M., Pale, P., Dumas, P., and Marquet, R. (2006) Targeting the dimerization initiation site of HIV-1 RNA with aminoglycosides: from crystal to cell. *Nucleic Acid Res. 34*, 2328–2339.

(21) Arya, D. P., and Coffee, R. L., Jr. (2000) DNA triple helix stabilization by aminoglycoside antibiotics. *Bioorg. Med. Chem. Lett. 10*, 1897–1899.

(22) Arya, D. P., Xue, L., and Tennant, P. (2003) Combining the best in triplex recognition: synthesis and nucleic acid binding of a BQQ-neomycin conjugate. *J. Am. Chem. Soc. 125*, 8070–8071.

(23) Arya, D. P., Coffee, R. L., Jr., and Charles, I. (2001) Neomycin induced hybrid triplex formation. *J. Am. Chem. Soc. 123*, 11093–11094.

(24) Thomas, J., and Hergenrother, P. J. (2008) Targeting RNA with small molecules. *Chem. Rev. 108*, 1171–1224.

(25) Wang, S., Huber, P. W., Cui, M., Czarnik, A. W., and Mei, H.-Y. (1998) Binding of neomycin to the TAR element of HIV-1 RNA induces dissociation of Tat protein by an allosteric mechanism. *Biochemistry 37*, 5549–5557.

(26) Blount, K. F., Zhao, F., Hermann, T., and Tor, Y. (2005) Conformational constraint as a means for understanding RNA-aminoglycoside specificity. *J. Am. Chem. Soc. 127*, 9818–9829.

(27) Zamecnik, P. C., and Stephenson, M. L. (1978) Inhibition of Rous sarcoma virus replication and cell transformation by a specific oligodeoxynucleotide. *Proc. Natl. Acad. Sci. U.S.A. 75*, 280–284.

(28) Stephenson, M. L., and Zamecnik, P. C. (1978) Inhibition of Rous sarcoma viral RNA translation by a specific oligodeoxyribonucleotide. *Proc. Natl. Acad. Sci. U.S.A. 75*, 285–288.

(29) Napoli, S., Carbone, G. M., Catapano, C., Shaw, N., and Arya, D. P. (2005) Neomycin improves cationic lipid-mediated transfection of DNA in human cells. *Bioorg. Med. Chem. Lett. 15*, 3467–3469.

(30) Irudayasamy, C., Xi, H., and Arya, D. P. (2007) Sequence-specific targeting of RNA with an oligonucleotide-neomycin conjugate. *Bioconjugate Chem. 18*, 160–169.

(31) Riguet, E., Tripathi, S., Désire, J., Pandey, V. N., and Décout, J.-L. (2004) A peptide nucleic acid-neamine conjugate that targets and cleaves HIV-1 TAR RNA inhibits viral replication. *J. Med. Chem. 47*, 4806–4809.

(32) Chaubey, B., Tripathi, S., Désire, J., Baussanne, I., Décout, J.-L., and Pandey, V. N. (2007) Mechanism of RNA cleavage catalyzed by sequence specific polyamide nucleic acid-neamine conjugate. *Oligonucleotides 17*, 302–313.

(33) Ketomäki, K., and Virta, P. (2008) Synthesis of aminoglycoside conjugates of 2′-O-methyl oligoribonucleotides. *Bioconjugate Chem. 19*, 766–777.

(34) Kiviniemi, A., Virta, P., and Lönnberg, H. (2010) Solid-supported synthesis and click conjugation of 4′-*C*-alkyne functionalized oligodeoxyribonucleotides. *Bioconjugate Chem. 21*, 1890–1901.

(35) Kiviniemi, A., Virta, P., and Lönnberg, H. (2008) Utilization of intrachain 4′-*C*-azidomethylthymidine for preparation of oligodeoxyribonucleotide conjugates by click chemistry in solution and on a solid support. *Bioconjugate Chem. 19*, 1726–1734.

(36) Mei, H., Xing, L., Cai, L., Hong-Wei, J., Zhao, P., Yang, Z.-J., Zhang, L.-R., and Zhang, L.-H. (2008) Studies on the synthesis of neamine-dinucleosides and neamine-PNA conjugates and their interaction with RNA. *Bioorg. Med. Chem. Lett. 18*, 5355–5358.

(37) Vickers, T., Baker, B. F., Cook, P. D., Zounes, M., Buckheit, R. W., Jr., Germany, J., and Ecker, D. J. (1991) Inhibition of HIV-LTR gene expression by oligonucleotides targeted to the TAR element. *Nucleic Acids Res. 19*, 3359–3368.

(38) Ecker, D. J., Vickers, T. A., Bruice, T. W., Freier, S. M., Jenison, R. D., Manoharan, M., and Zounes, M. (1992) Pseudo-half-knot formation with RNA. *Science 257*, 958–961.

(39) Mestre, B., Arzumanov, A., Singh, M., Boulme, F., Litvak, S., and Gait, M. J. (1999) Oligonucleotide inhibition of the interaction of HIV-1 Tat protein with the trans-activation responsive region (TAR) of HIV RNA. *Biochim. Biophys. Acta 1445*, 86–98.

(40) Arzumanov, A., Walsh, A. P., Rajwanshi, V. K., Kumar, R., Wengel, J., and Gait, M. J. (2001) Inhibition of HIV-1 Tat-dependent trans activation by steric block chimeric 2′-O-methyl/LNA oligoribonucleotides. *Biochemistry 40*, 14645–14654.

(41) Kota, S. K., and Balasubramanian, S. (2010) Cancer therapy via modulation of micro RNA levels: a promising future. *Drug Discovery Today 15*, 733–740.

(42) Kiviniemi, A., and Virta, P. (2010) Characterization of RNA invasion by ^{19}F NMR spectroscopy. *J. Am. Chem. Soc. 132*, 8560–8562.

(43) Barhate, N. B., Barhate, R. N., Cekan, P., Drobny, G., and Th. Sigurdsson, S. (2008) A nonafluoro nucleoside as a sensitive ^{19}F NMR probe of nucleic acid conformation. *Org. Lett. 10*, 2745–2747.

(44) Kreutz, C., Kählig, H., Konrat, R., and Micura, R. (2005) Ribose 2′-*F* labeling: A simple tool for the characterization of RNA secondary structure equilibria by ^{19}F NMR spectroscopy. *J. Am. Chem. Soc. 127*, 11558–11559.

(45) Olsen, G. L., Edwards, T. E., Deka, P., Varani, G., Sigurdsson, S. Th., and Drobny, G. P. (2005) Monitoring tat peptide binding to TAR RNA by solid-state ^{31}P-^{19}F REDOR NMR. *Nucleic Acid Res. 33*, 3447–3454.

(46) Hennig, M., Munzárova, M. L., Bermel, W., Scott, L. G., Sklenár, V., and Williamson, J. R. (2006) Measurement of long-range ^{1}H-^{19}F scalar coupling constants and their glycosidic torsion dependence in 5-fluoropyrimidine-substituted RNA. *J. Am. Chem. Soc. 128*, 5851–5858.

(47) Kreutz, C., Kählig, H., Konrat, R., and Micura, R. (2006) A General approach for the identification of site-specific RNA binders by ^{19}F NMR spectroscopy: Proof of concept. *Angew. Chem., Int. Ed. 45*, 3450–3453.

(48) Hennig, M., Scott, L. G., Sperling, E., Bermel, W., and Williamson, J. R. (2007) Synthesis of 5-fluoropyrimidine nucleotides as sensitive NMR probes of RNA structure. *J. Am. Chem. Soc. 129*, 14911–14921.

(49) Graber, D., Moroder, H., and Micura, R. (2008) ^{19}F NMR spectroscopy for the analysis of RNA secondary structure populations. *J. Am. Chem. Soc. 130*, 17230.

(50) Tanabe, K., Sugiura, M., and Nishimoto, S. (2010) Monitoring of duplex and triplex formation by ^{19}F NMR using oligonucleotides possessing 5-fluorodeoxyuridine unit as ^{19}F signal transmitter. *Bioorg. Med. Chem. 18*, 6690–6694.

(51) Moumné, R., Pasco, M., Prost, E., Lecourt, T., Micouin, L., and Tisné, C. (2010) Fluorinated diaminocyclopentanes as chiral sensitive NMR probes of RNA structure. *J. Am. Chem. Soc. 132*, 13111–13113.

Supporting Information to:

Synthesis of Aminoglycoside-3'-Conjugates of 2'-*O*-Methyl Oligoribonucleotides and Their Invasion to a ^{19}F labelled HIV-1 TAR Model

Anu Kiviniemi and Pasi Virta*

Department of Chemistry, University of Turku, FIN-20014 Turku, Finland

CONTENTS

Figure S1. ^{1}H NMR (CD_3OD, 500 MHz) of **3** S2
Figure S2. ^{13}C NMR (CD_3OD, 125 MHz) of **3** S2
Figure S3. ^{1}H NMR (CD_3OD, 500 MHz) of **6** S3
Figure S4. ^{13}C NMR (CD_3OD, 125 MHz) of **6** S3
Figure S5. ^{1}H NMR (CD3OD, 500 MHz) of **9** S4
Figure S6. ^{13}C NMR (CD_3OD, 125 MHz) of **9** S4
Figure S7. RP HPLC chromatogram and MS(ESI) spectra of **10.** S5
Figure S8. Titration curve of **A** + **10** S5
Figure S9. ^{19}F shift *vs.* temperature profile of **C**[10] S5
Figure S10. RP HPLC chromatogram and MS(ESI) spectra of **11.** S6
Figure S11. Titration curve of **A** + **11**. S6
Figure S12. ^{19}F shift *vs.* temperature profile of **C**[11] S6
Figure S13. RP HPLC chromatogram and MS(ESI) spectra of **12** S7
Figure S14. Titration curve of **A** + **12**. S7
Figure S15. ^{19}F shift *vs.* temperature profile of **C/D**[12] S7
Figure S16. RP HPLC chromatogram and MS(ESI) spectra of **13** S8
Figure S17. Titration curve of **A** + **13** S8
Figure S18. RP HPLC chromatogram and MS(ESI) spectra of **14** S9
Figure S19. Titration curve of **A** + **14** + **17**. S9
Figure S20. RP HPLC chromatogram and MS(ESI) spectra of **15** S10
Figure S21. Titration curve of **A** + **15** S10
Figure S22. ^{19}F shift *vs.* temperature profile of **C/D**[15] S10
Figure S23. RP HPLC chromatogram and MS(ESI) spectra of **16** S11
Figure S24. Titration curve of **A** + **16** S11
Figure S25. ^{19}F shift *vs.* temperature profile of **C/D**[16] S11
Figure S26. ^{19}F NMR spectra of the titrations of **A** with the conjugates S12
Figure S27. The UV-melting curves of ^{19}F labelled TAR RNA with the conjugates S13

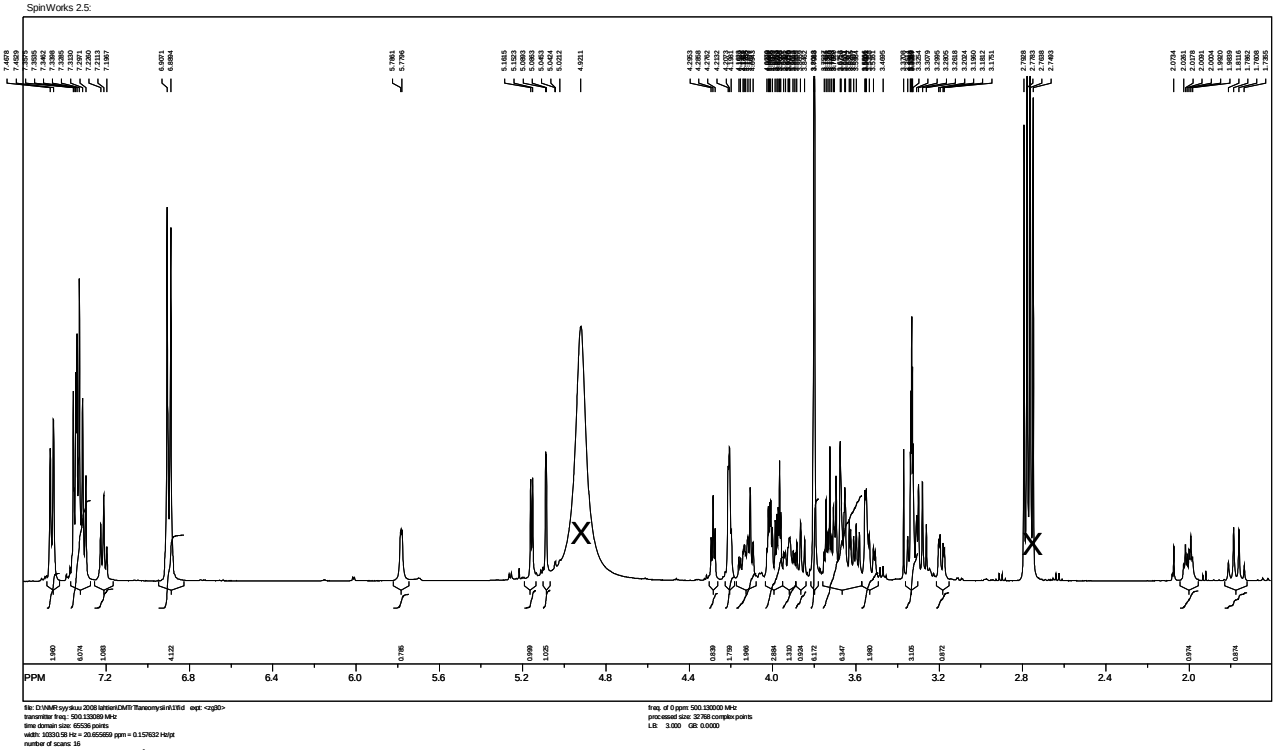

Figure S1. ^{1}H NMR (CD_3OD, 500 MHz) of **3**

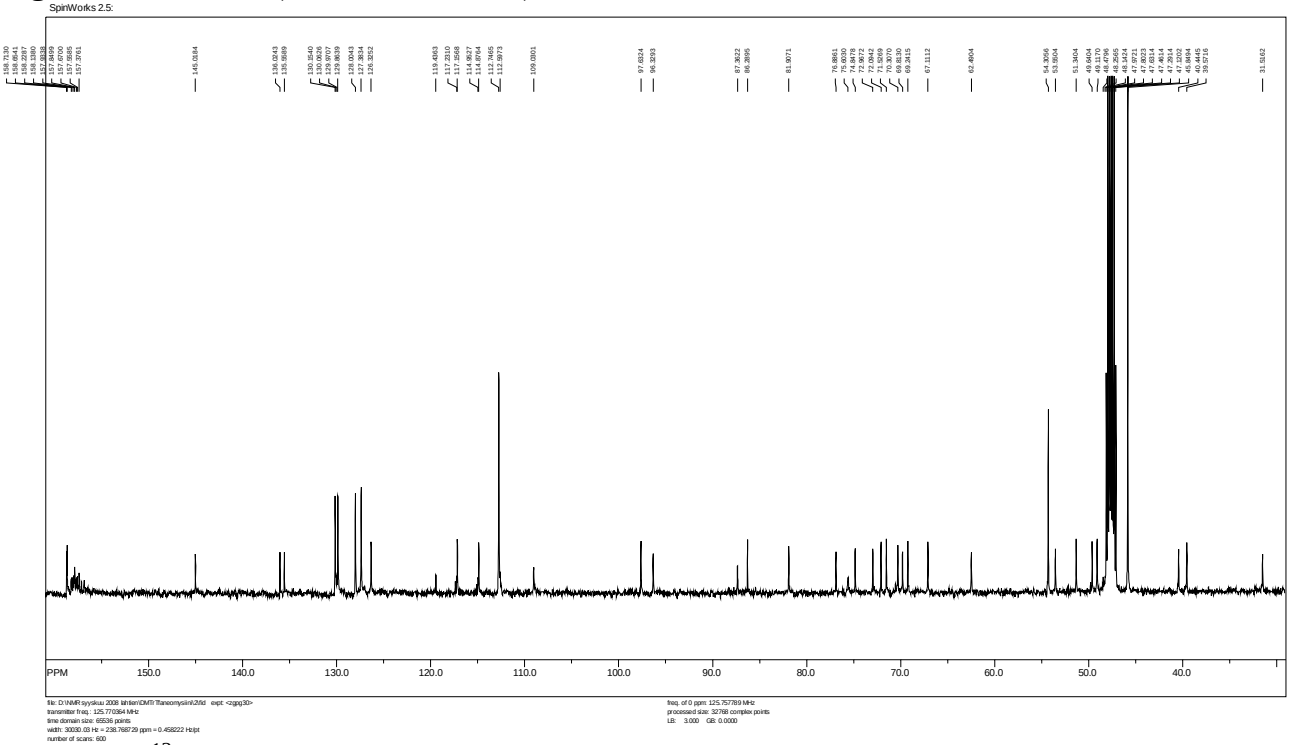

Figure S2. ^{13}C NMR (CD_3OD, 125 MHz) of **3**

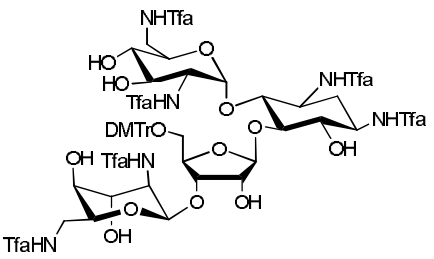

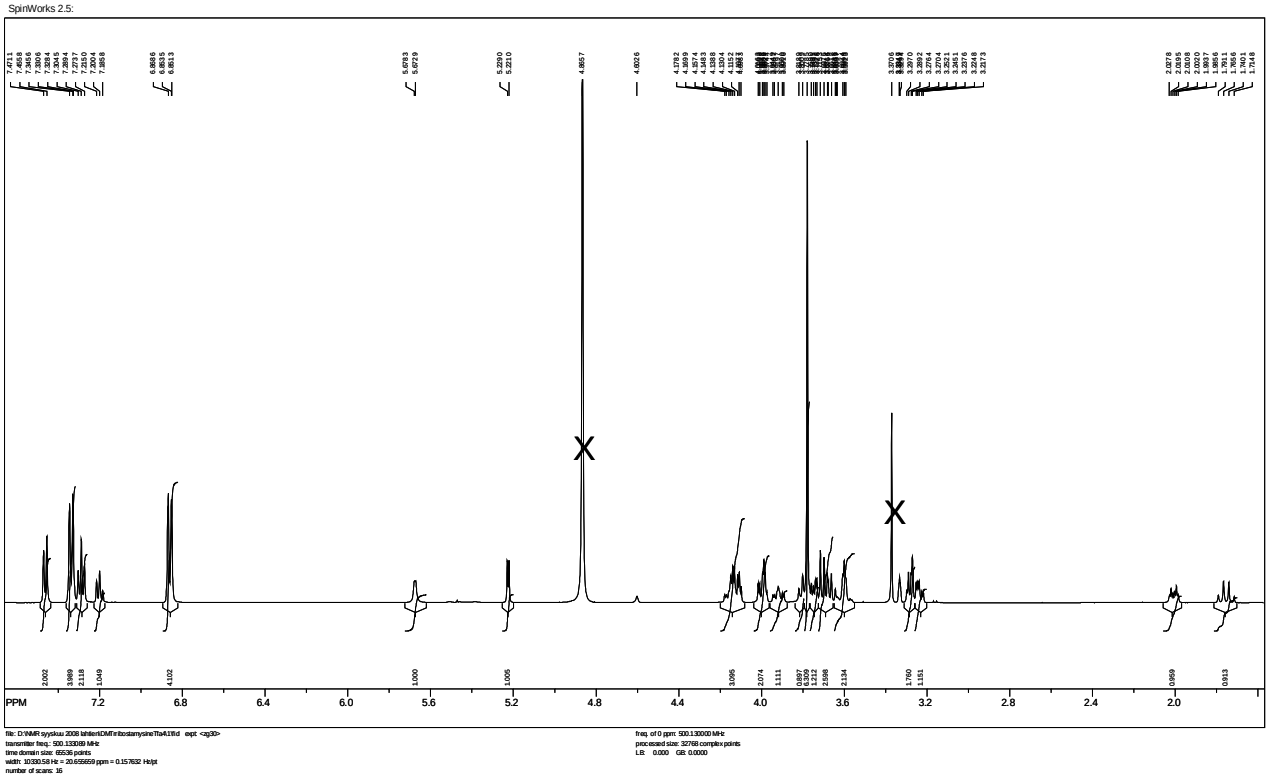

Figure S3. ^{1}H NMR (CD_3OD, 500 MHz) of **6**

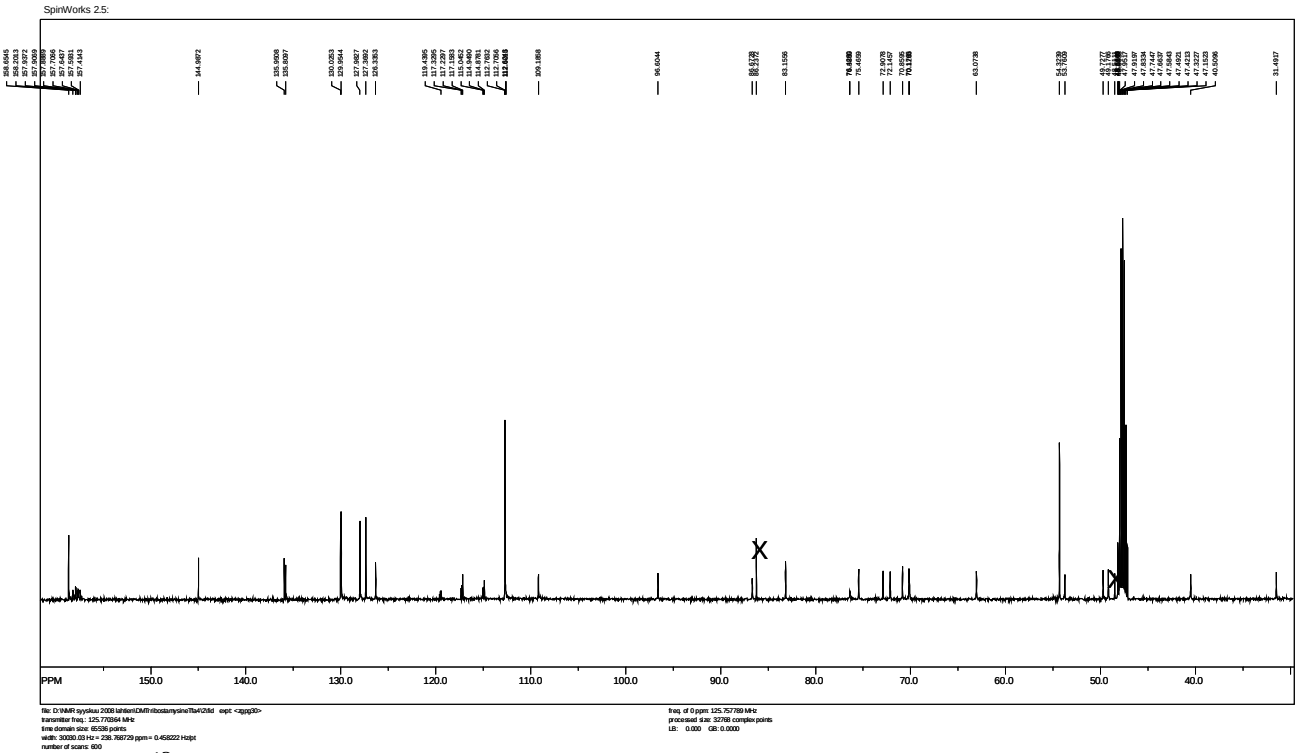

Figure S4. ^{13}C NMR (CD_3OD, 125 MHz) of **6**

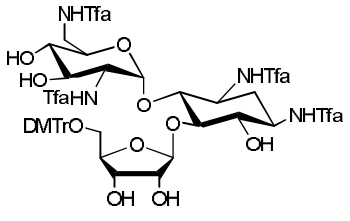

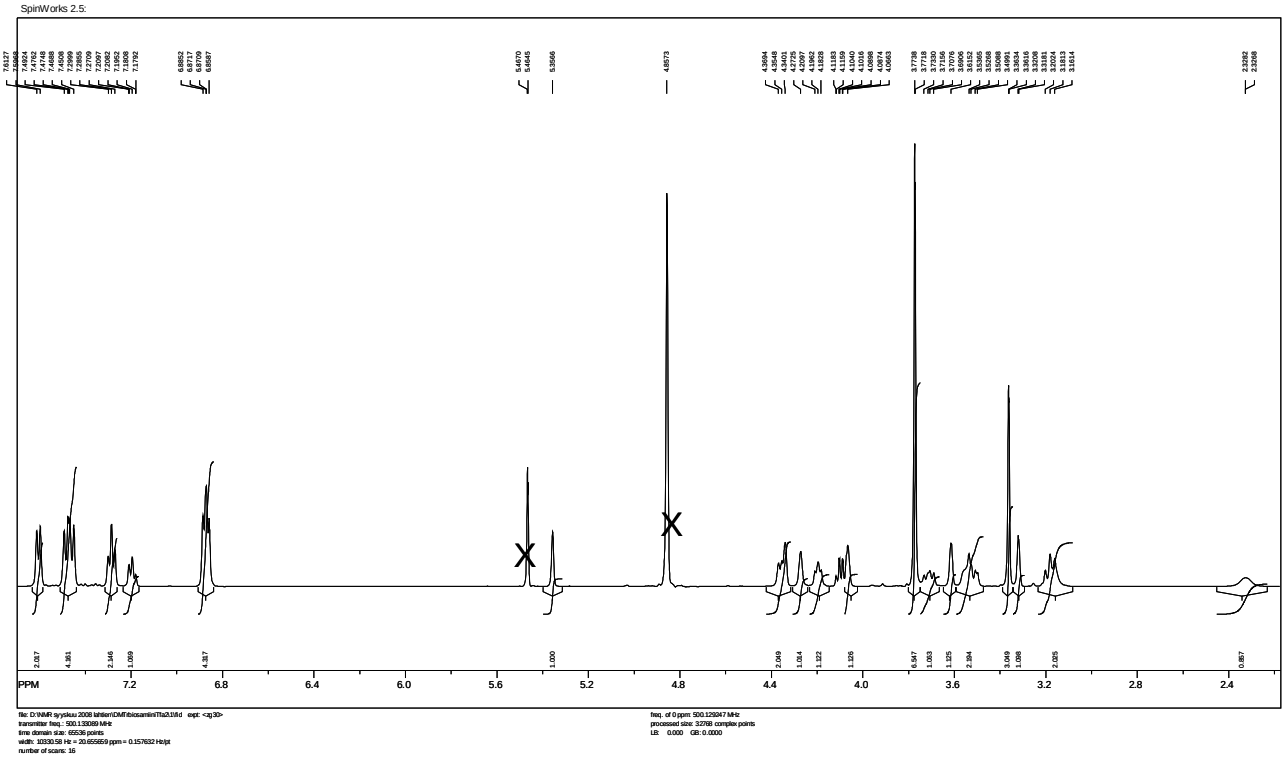

Figure S5. ^{1}H NMR (CD3OD, 500 MHz) of **9**

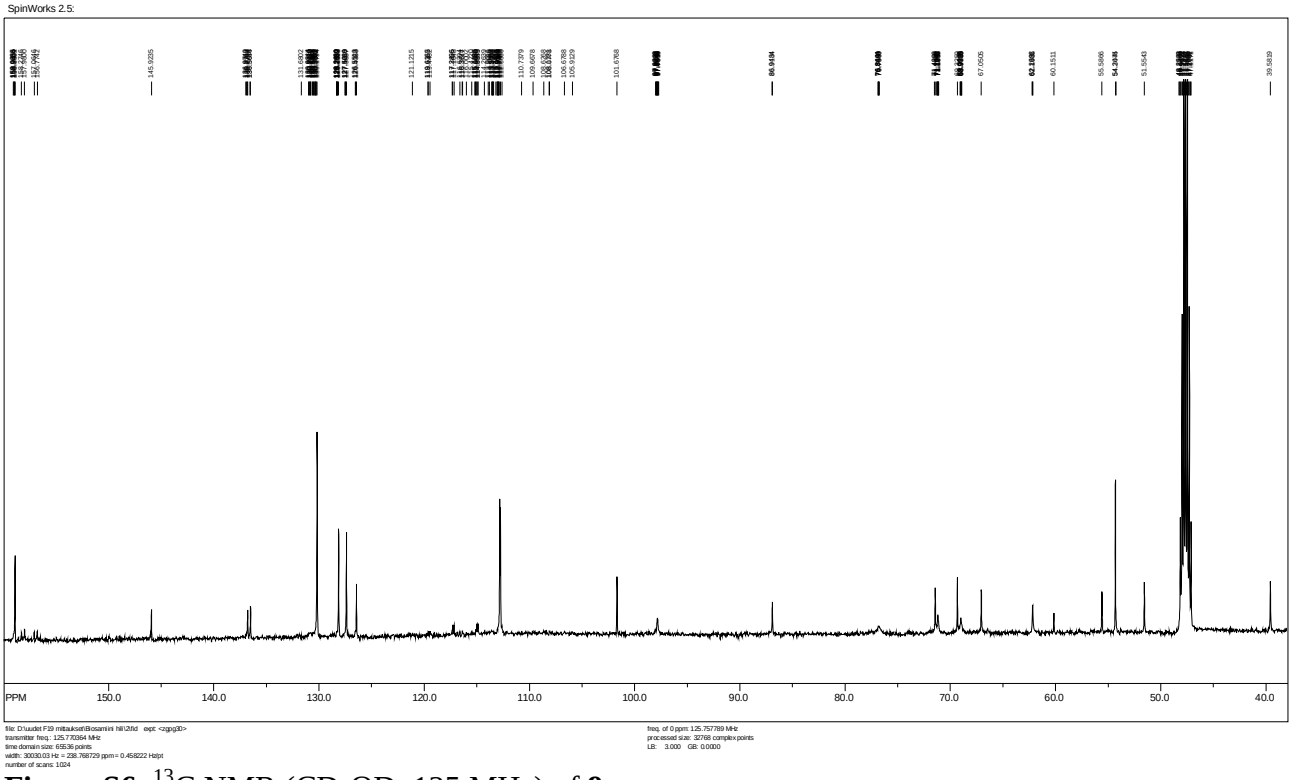

Figure S6. ^{13}C NMR (CD_3OD, 125 MHz) of **9**

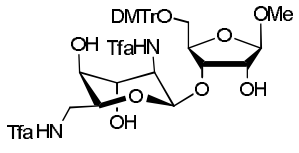

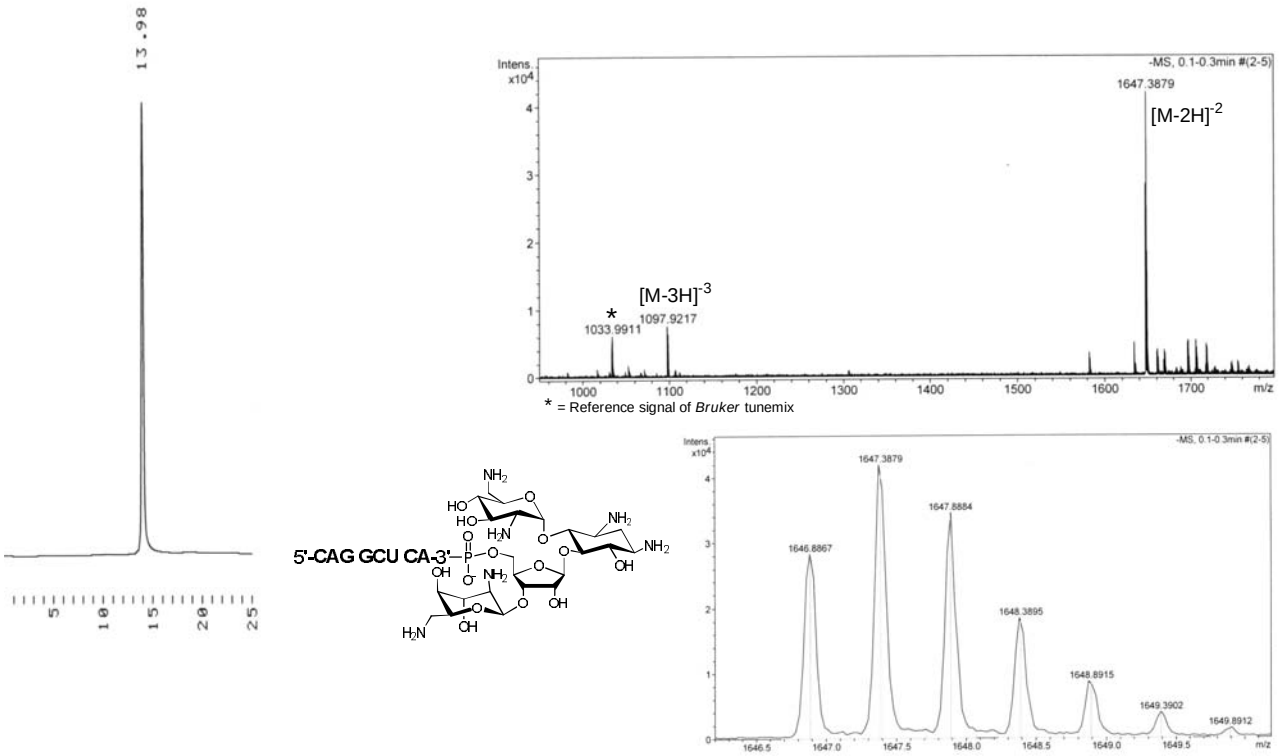

Figure S7. RP HPLC chromatogram and MS(ESI) spectra of **10.**

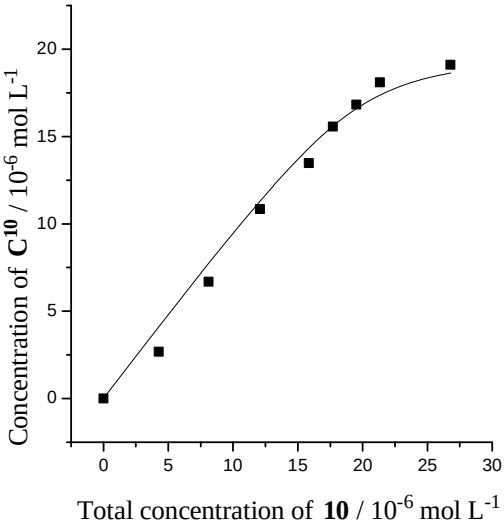

Figure S8. Titration curve of **A** + **10**.
K_d = 0.59 ± 0.16 μmol L^{-1}

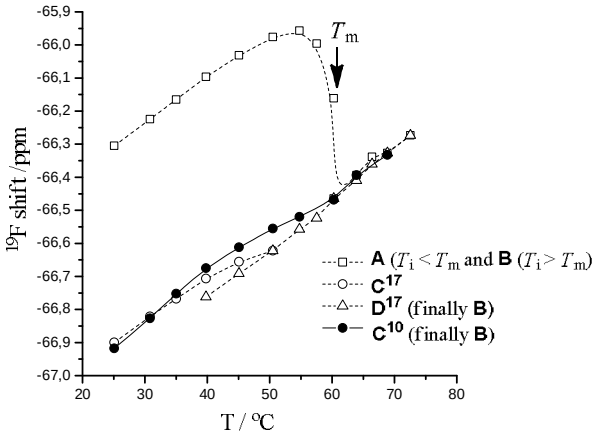

Figure S9. ●) ^{19}F shift *vs.* temperature profile of $\mathbf{C^{10}}$.

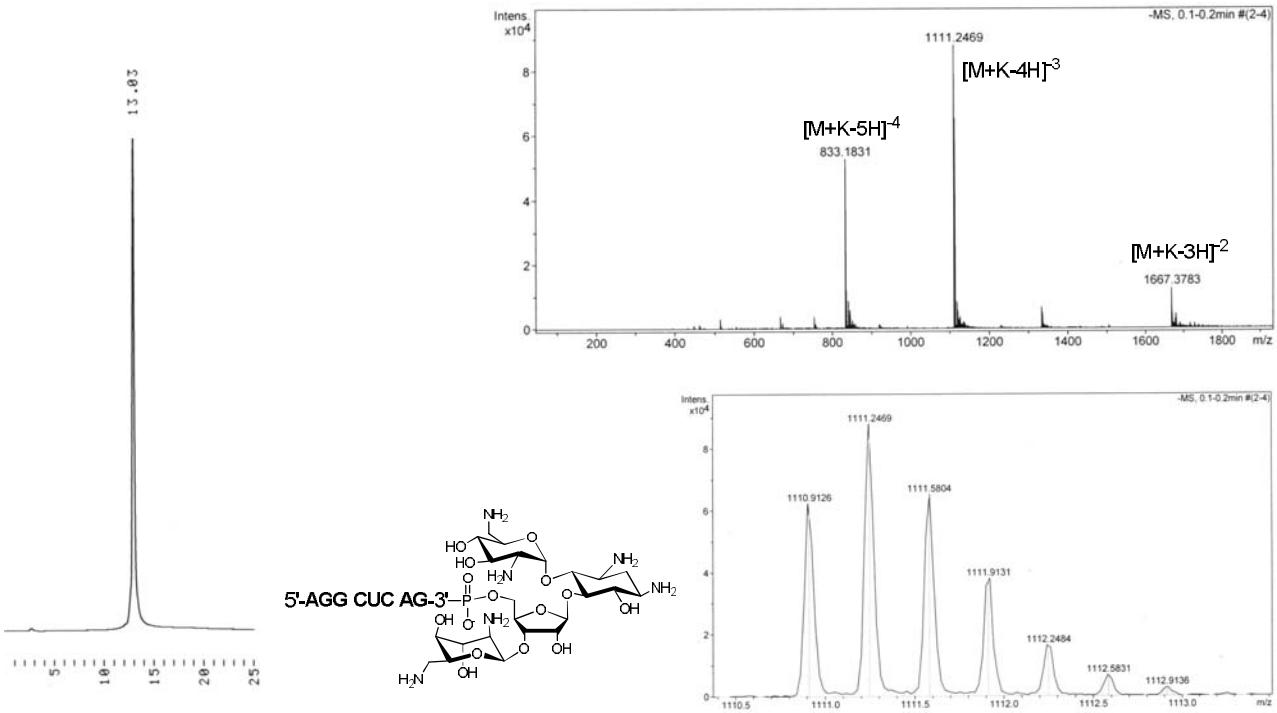

Figure S10. RP HPLC chromatogram and MS(ESI) spectra of **11**

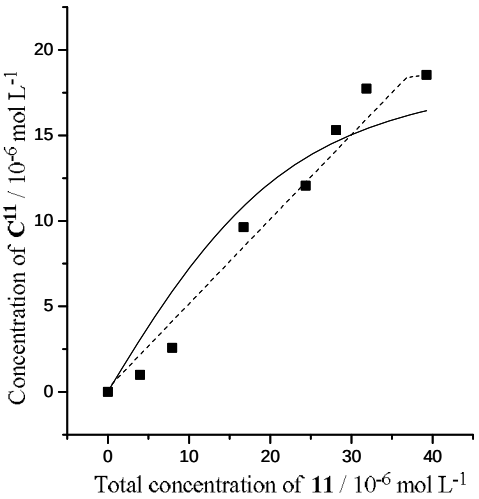

Figure S11. Titration curve of **A** + **11**. K_d = 4.9 ± 1.5 μmol L^{-1}

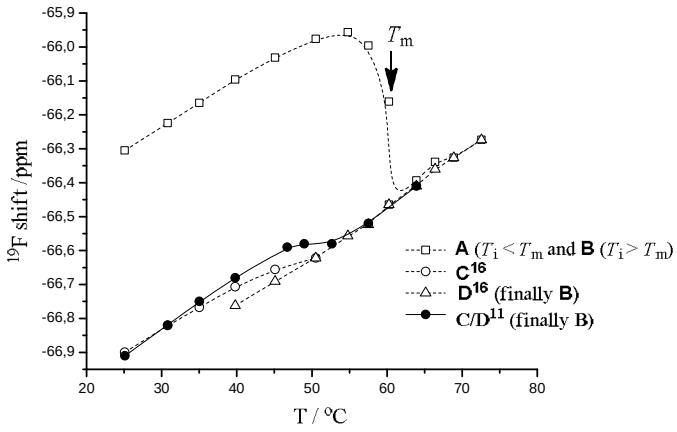

Figure S12. ●) ^{19}F shift *vs.* temperature profile of **C/D**^{12}.

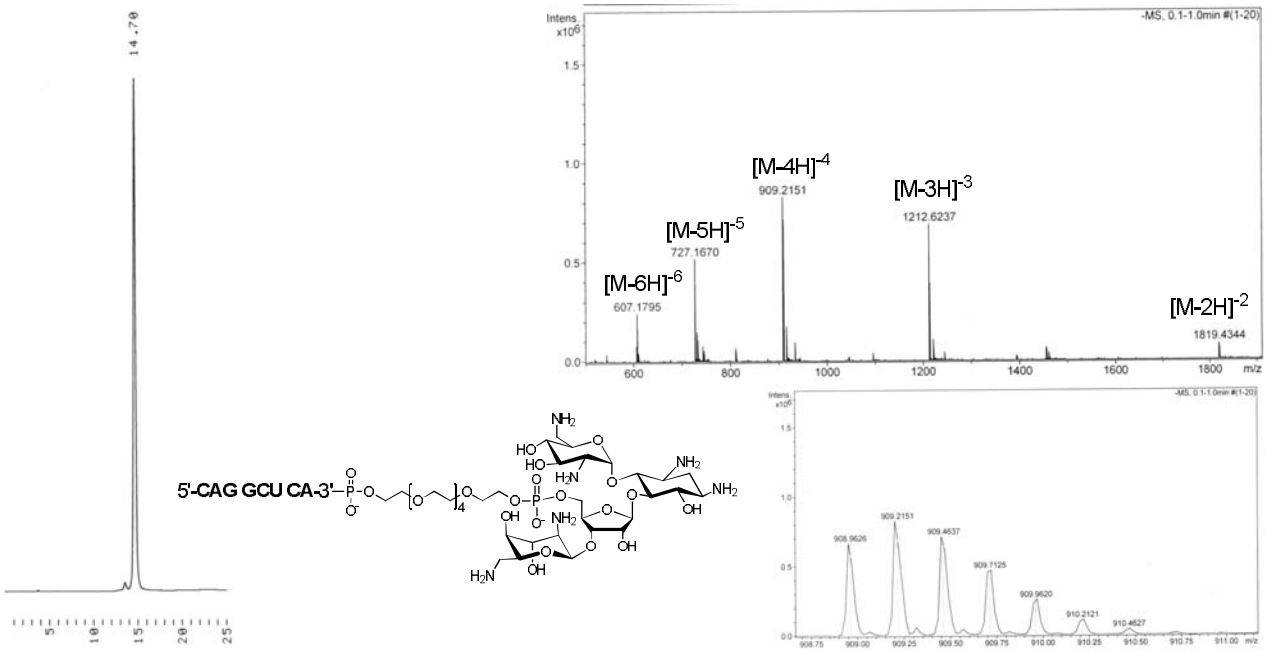

Figure S13. RP HPLC chromatogram and MS(ESI) spectra of **12.**

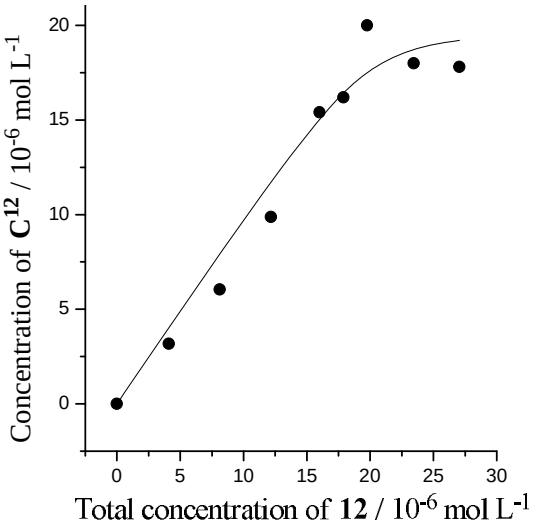

Figure S14. Titration curve of **A** + **12**.
K_d = 0.32 ± 0.22

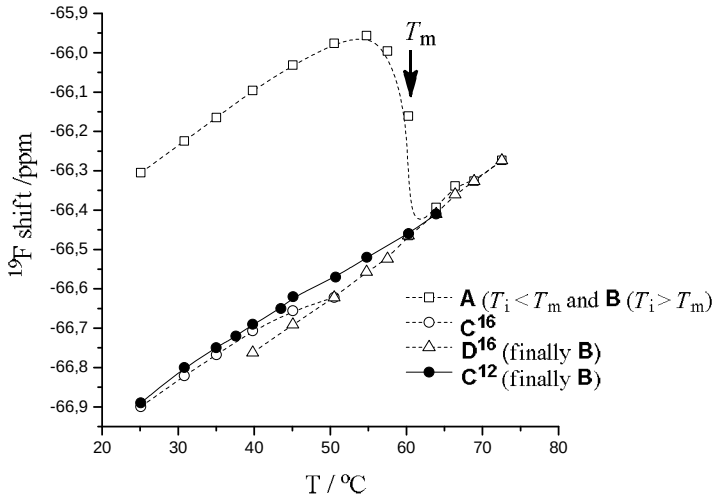

Figure S15. ●) ^{19}F shift *vs.* temperature profile of $\mathbf{C}^{12}$.

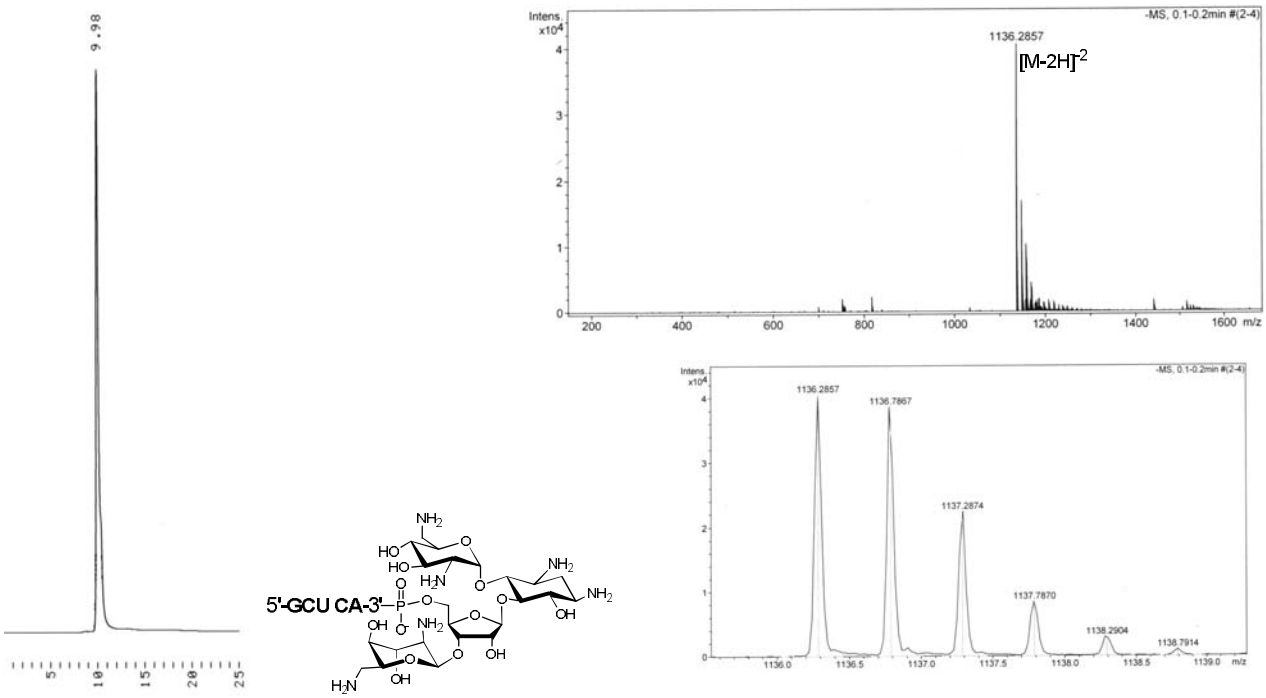

Figure S16. RP HPLC chromatogram and MS(ESI) spectra of **13**.

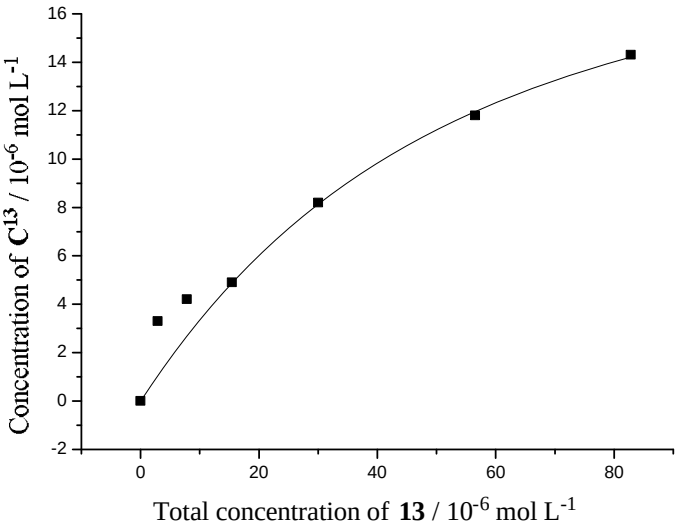

Figure S17. Titration curve of **A** + **13**. K_d = 36.9 ± 2.0 µmol L^{-1} (simplified to stoichiometric 1:1-complex). As seen in ^{19}F NMR spectrum (**S26e**) the resulted complex was undefined (a broad and fragmented ^{19}F signal).

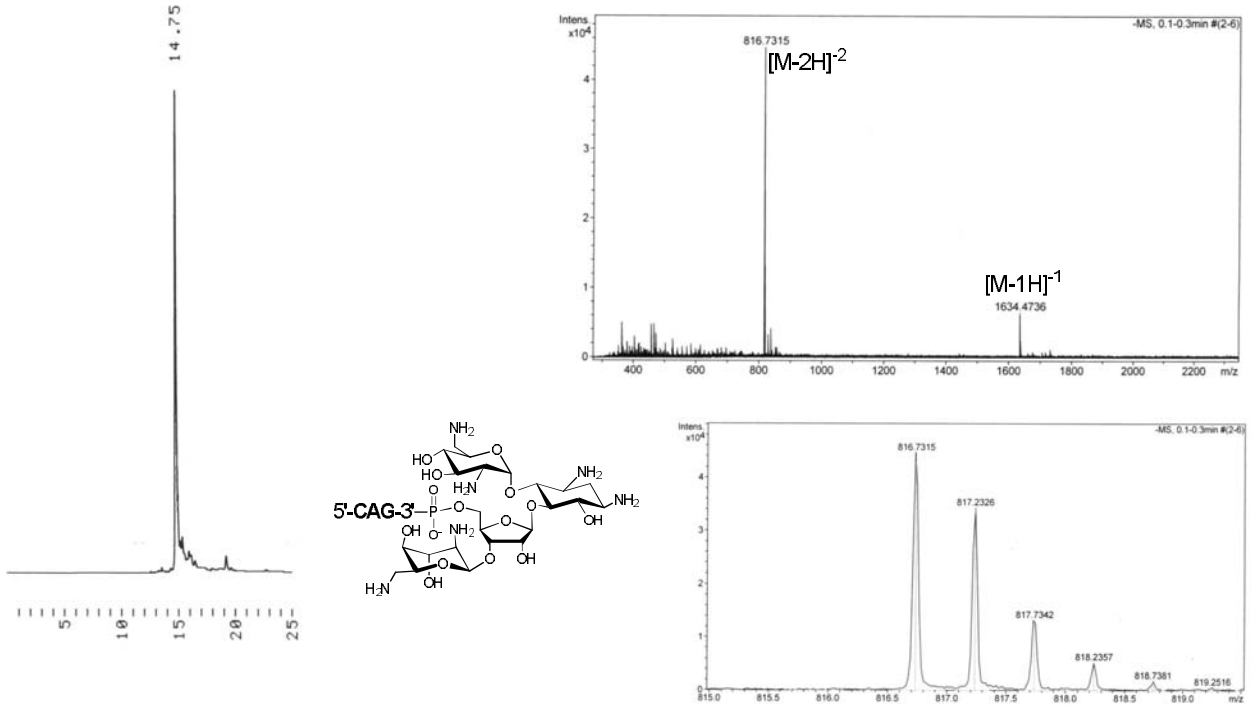

Figure S18. RP HPLC chromatogram and MS(ESI) spectra of **14**.

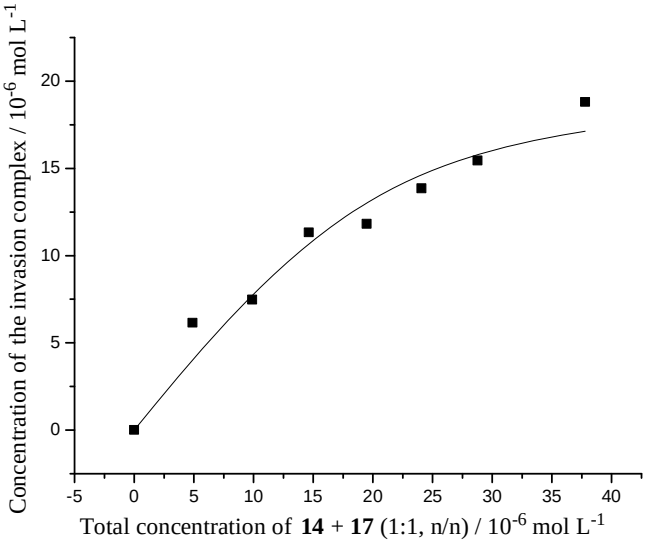

Figure S19. Titration curve of **A** + mixture of (**14** + **17,** 1:1, *n/n*)**.** K_d = 3.6 ± 0.8 µmol L^{-1} (simplified to stoichiometric 1:1-complex)

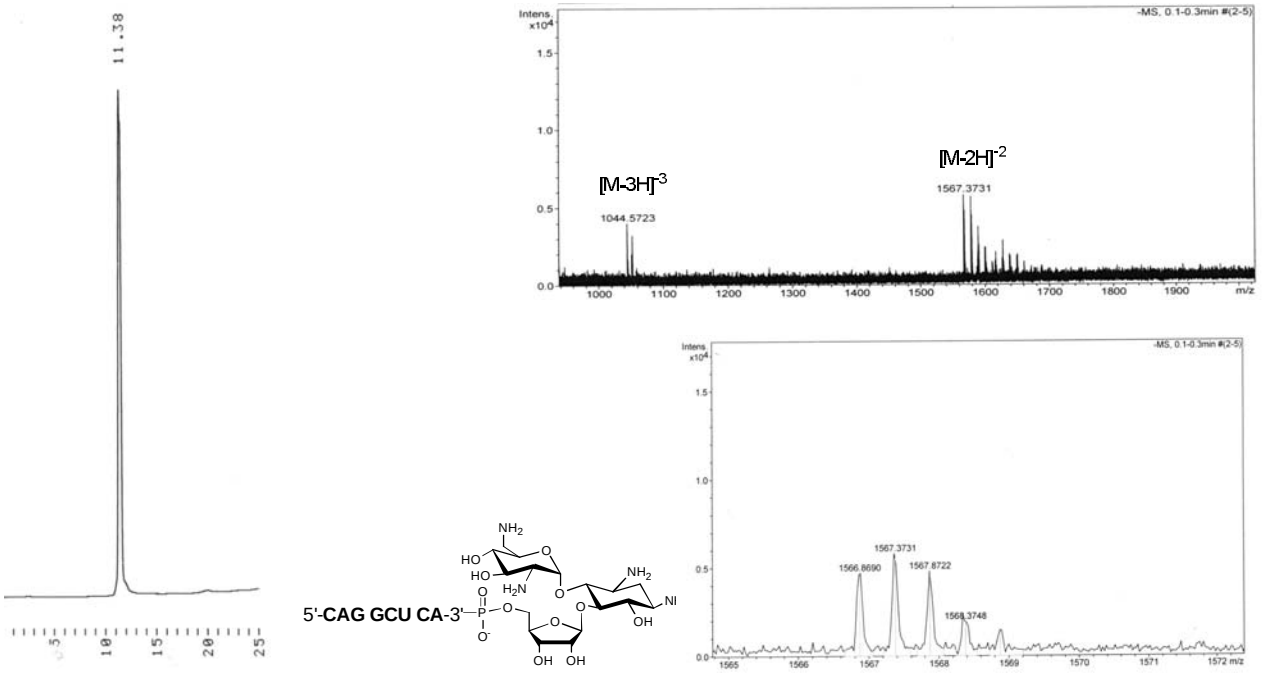

Figure S20. RP HPLC chromatogram and MS(ESI) spectra of **15**

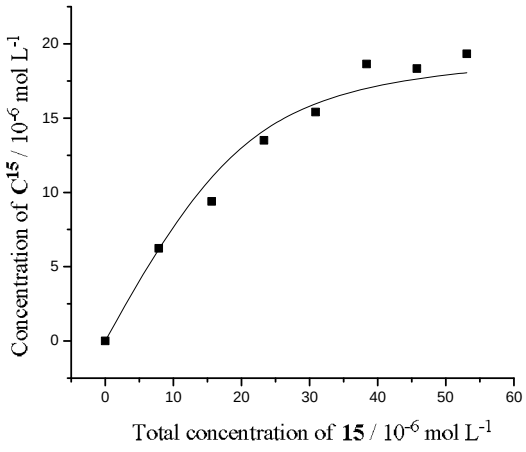

Figure S21. Titration curve of **A** + **15**.
K_d = 3.8 ± 0.7 μmol L^{-1}

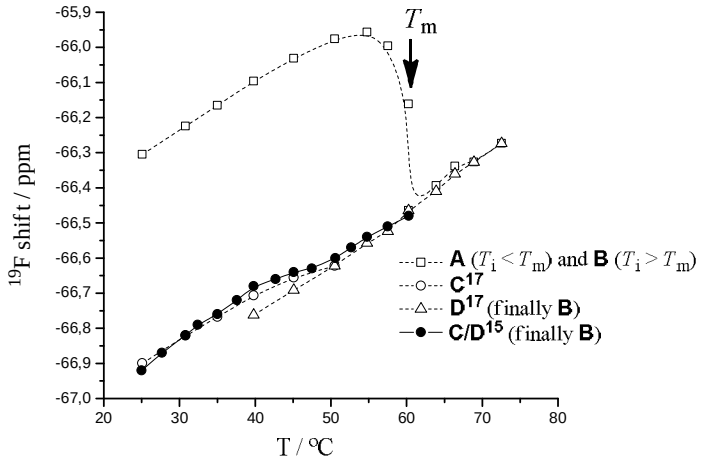

Figure S22. ●) ^{19}F shift *vs.* temperature profile of **C/D**^{15}.

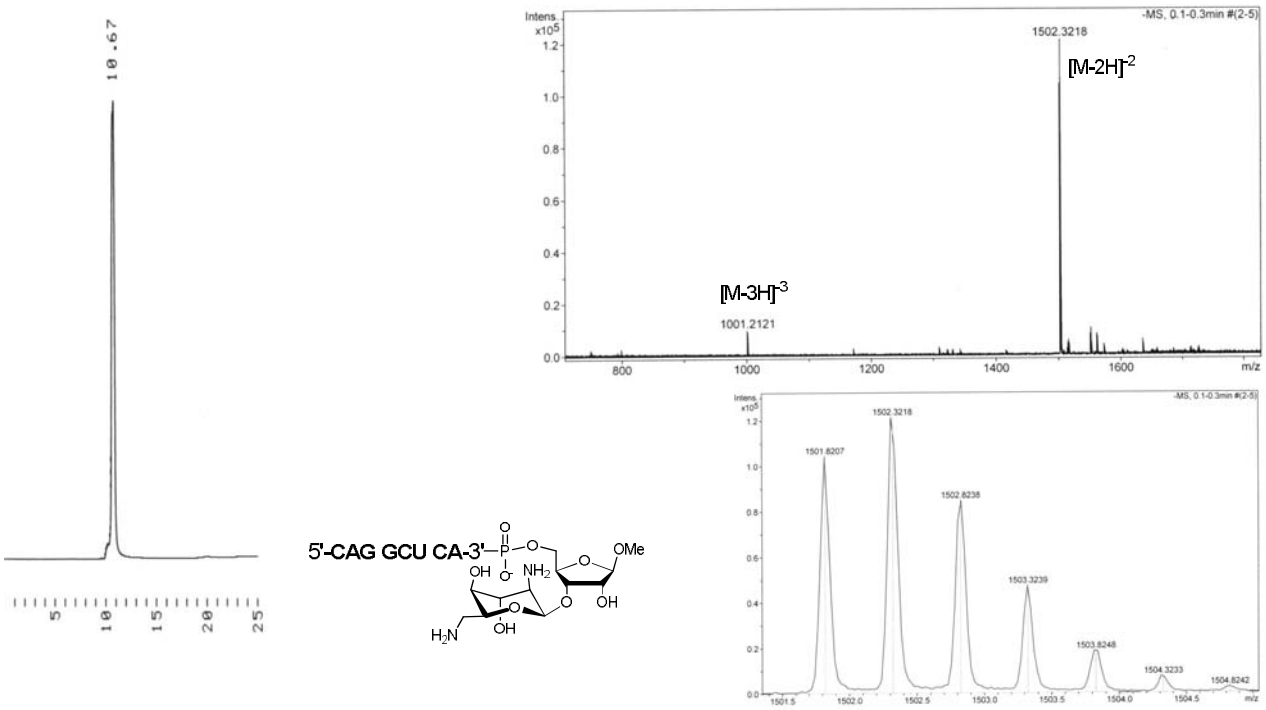

Figure S23. RP HPLC chromatogram and MS(ESI) spectra of **16**

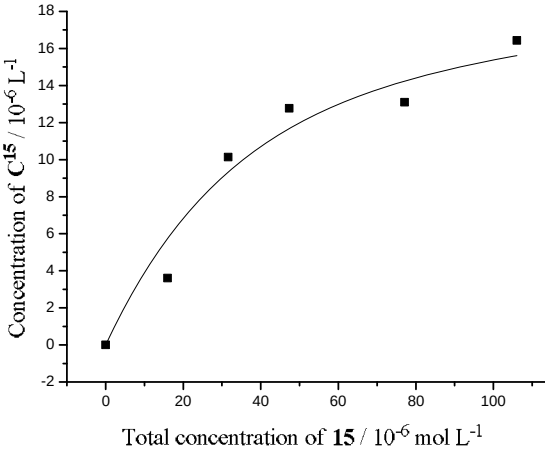

Figure S24. Titration curve of **A** + **16**. K_d = 25 ± 0.4 μmol L^{-1}

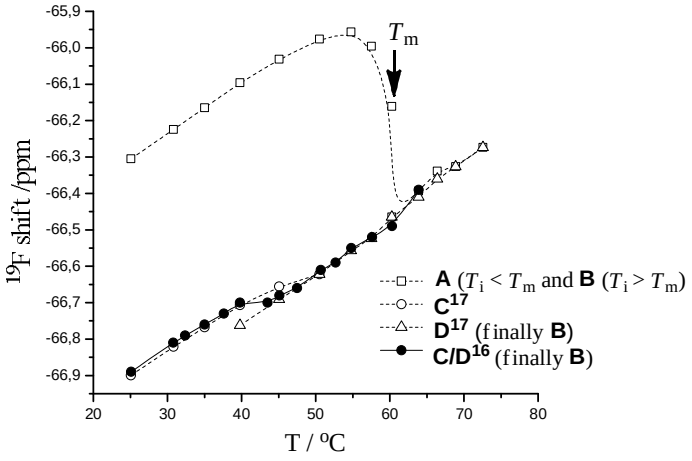

Figure S25. ●) ^{19}F shift *vs.* temperature profile of **C/D**^{16}.

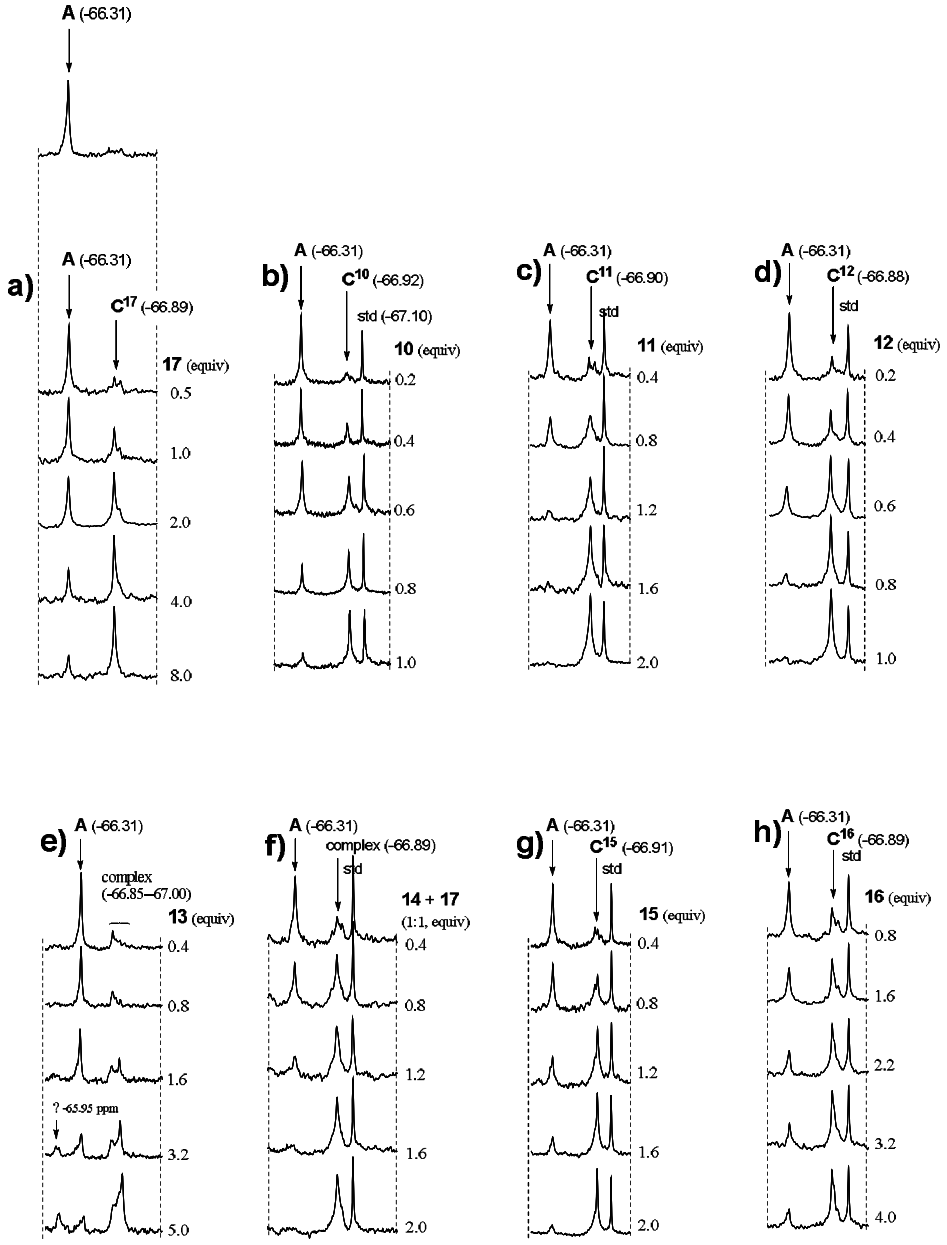

Figure S26. ^{19}F NMR spectra of the titrations of **A** with the conjugates (**a** measured in previous work: Kiviniemi, A. and Virta P. *J. Am. Chem. Soc.* **2010**, *132*, 8560-8562).

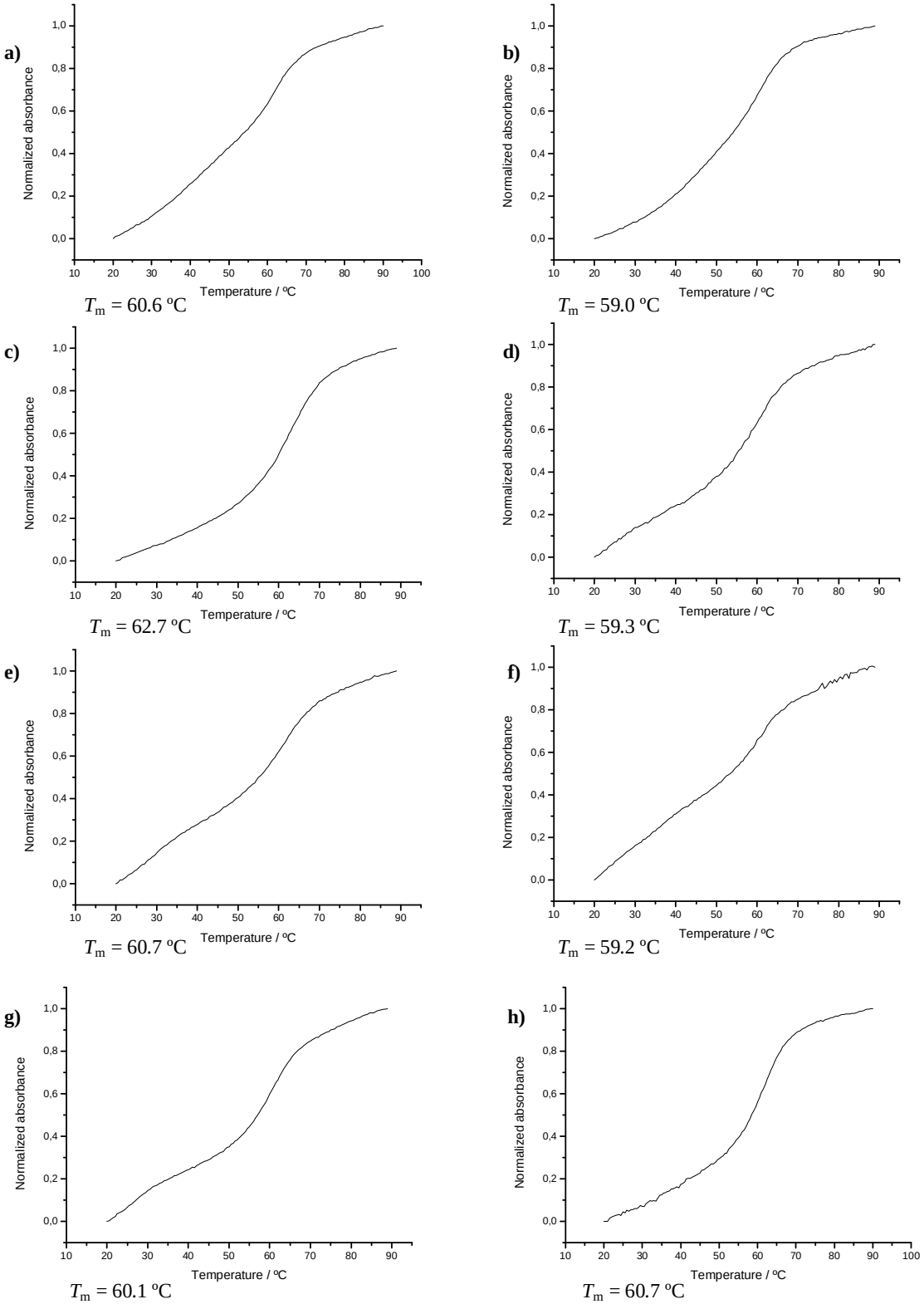

Figure S27. The UV-melting curves of ^{19}F labelled TAR RNA (2 μM in 25 mM NaH_2PO_4 buffer, pH 6.5) with **a)** 5´-CAGGCUCA-neomycin **10** (1 equiv), **b)** 5´-AGGCUCAG-neomycin **11** (2 equiv), **c)** 5´-CAGGCUCA-PEG-neomycin **12** (1 equiv), **d)** 5-GCUCA-neomycin **13** (5 equiv), **e)** 5'-CAG-neomycin **14** + 5´-CAGGCUCA-3´ **17** (2 equiv both), **f)** CAGGCUCA-ribostamycin **15** (2 equiv), **g)** 5´-CAGGCUCA-methyl biosamine **16** (2 equiv), **h)** ^{19}F labelled TAR RNA (measured in previous work: Kiviniemi, A. and Virta P. *J. Am. Chem. Soc.* **2010**, *132*, 8560-8562).

Bioconjugate Chemistry

ARTICLE

pubs.acs.org/bc

Targeted Delivery in Breast Cancer Cells via Iodine: Nuclear Localization Sequence Conjugate

Hui-Yuan Wang, Cao Li, Wen-Jie Yi, Yun-Xia Sun, Si-Xue Cheng, Ren-Xi Zhuo, and Xian-Zheng Zhang*

Key Laboratory of Biomedical Polymers of Ministry of Education & Department of Chemistry, Wuhan University, Wuhan 430072, P. R. China

ABSTRACT: The nonviral vector with iodine-nuclear localization sequence (namely, NLS-I) targeting breast cancer cells was fabricated. Ternary complexes were formed via charge interactions among NLS-I peptides, PEI 1800, and DNA, and we investigated their cellular internalization, nuclear accumulation as well as transfection efficiency. All the experiments were assessed by employing MCF-7 cells that express sodium/iodide symporter and HeLa cells that lack the expression of the symporter. In MCF-7 cells, cell internalization and nuclear accumulation of NLS-I was markedly increased compared to that in NLS. In addition, compared to that of the PEI1800/DNA complex, PEI1800/DNA/NLS-I complexes exhibited much enhanced luciferase reporter gene expression by up to 130-fold. By contrast, in HeLa cells, the evident improvements of cellular internalization, nuclear accumulation, and transfection efficiency by NLS-I were not observed. This study demonstrates an alternative method to construct a nonviral delivery system for targeted gene transfer into breast cancer cells.

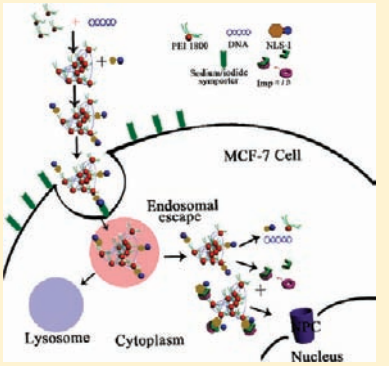

INTRODUCTION

Among women, the three leading sites of cancer are the breast, lung and bronchus, and colon and rectum and causes one-half of female cancer deaths. Breast cancer incidence rates are higher than any other cancers throughout the world both in developed and developing countries. Currently, breast cancer is a major source of morbidity throughout the world. Ten percent of all new cancer cases are cancer of the female breast, and more than 410,000 patients die of it each year.[1−3]

After the first human gene therapy trial succeeded in 1989, thousands of clinical trials have been completed for treating various forms of diseases, and its potential in cancer treatment is widely recognized. In addition to target genes, a gene delivery system which would be nontoxic and efficient is essential for gene therapy. Although viral vectors are efficient DNA delivery systems, there also exist some disadvantages, such as the risk of an immune response and the size limitations of the gene that can be used.[4] Hence, nonviral vectors have acquired more attention due to low immune response and simplicity of preparation.

Among thousands of nonviral vectors, cationic polyethylenimine (PEI), a synthetic polymer, is still considered as one of the most efficient candidates to effectively condense DNA, deliver genes in many cell lines with high efficiency, and often serve as a "golden standard".[5,6] However, its transfection efficiency was strongly associated with cytotoxicity, and both efficiency and cytotoxicity are depended on the molecular weight of the polycation.[7] Previous reports demonstrated that low-molecular-weight PEI (LMW PEI) exhibited negligible cytotoxicity but also showed poor transfection activity.

One possible avenue to design efficient LMW PEI-based vectors is to incorporate functional peptides to overcome low gene transfer capacity of LMW PEI.[8] It is known that the nuclear target is believed to be a key requirement for enhancing the transfection efficiency. One of the attempts to improve the transport of DNA to the nucleus is the use of nuclear localization signals (NLS). The best studied NLS sequence is the SV40 large-T antigen (especially in its shortest form Pro-Lys-Lys-Lys-Arg-Lys-Val), which mediates the interaction with carrier proteins.[9,10] Nevertheless, these attempts have achieved little success as NLS shows limited effect on cellular uptake.[11,12]

It is well known that in a variety of species, the iodide concentration in milk is 10- to 30-fold higher than that in maternal plasma, and researchers have identified and characterized a sodium/iodide symporter (Na^+/I^- symporter, called NIS), an essential glycoprotein, which is located in the membrane and actively transports iodide from the maternal plasma into the alveolar epithelial cells of the mammary gland.[13−15] This symporter has also been reported to be expressed in human MCF-7 mammary cancer cells,[16] and the expression of this symporter in the breast cancer specimens was significantly higher than that in the normal mammary gland.[15,17] Consequently, iodide uptake in these breast cancer cells is higher than that in the healthy mammary gland.

Here, to improve the transfection ability of an LMW PEI1800 based vector, an iodine-nuclear localization sequence, i.e., NLS-I was synthesized and introduced to improve cellular internalization and nuclear accumulation in breast cancer cells. The NLS-I was mixed with PEI1800/DNA by a physical method, and then the ternary complexes were obtained through charge interaction, which can be used as a human mammary cancer targeting gene

Received: March 6, 2011
Revised: May 13, 2011
Published: June 20, 2011

ACS Publications © 2011 American Chemical Society

Scheme 1. Targeting Mechanism of the PEI/DNA/NLS-I Complexes to Breast Cancer Cells[a]

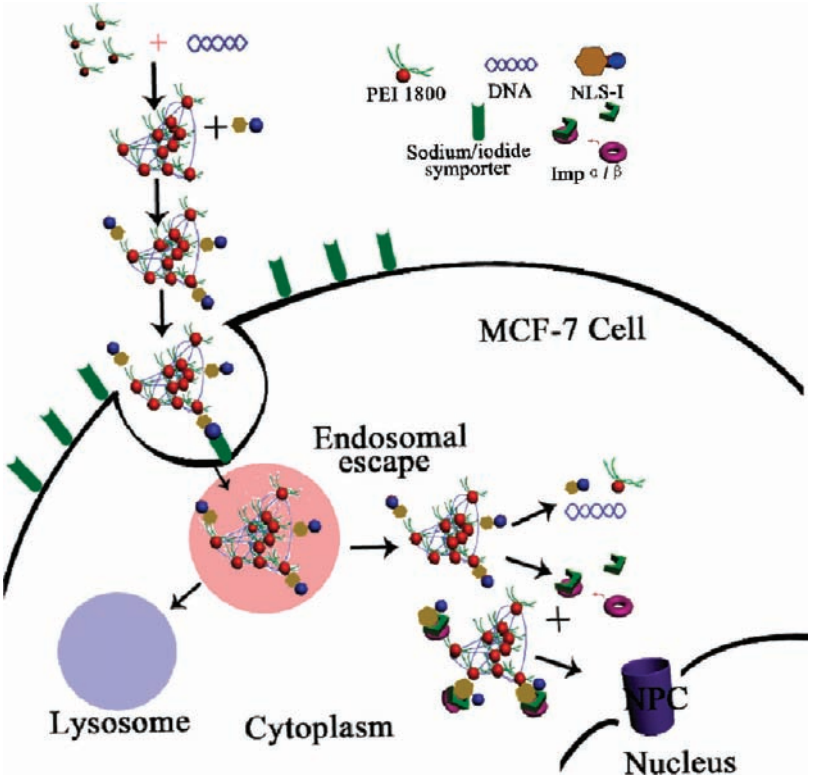

[a] Sodium/iodide symporter (Na^+/I^- symporter) is an essential glycoprotein, which is located in the membrane of MCF-7 cells and actively transports iodide from the media into the cells. The cellular uptake of complexes containing an iodine atom is strongly dependent on the symporter, and the complex with plasmid DNA is translocated into the nucleus through the nuclear pore complex (NPC) by successive docking of Imp β and nucleoporins.

delivery system. The targeting mechanism of the NLS-I peptide to breast cancer cells is represented in Scheme 1.

EXPERIMENTAL PROCEDURES

Materials. QIAfilterTM plasmid purification Giga Kit (5) was purchased from Qiagen (Hilden, Germany). GelRed was purchased from Biotium (CA, USA). Dulbecco's modified Eagle's medium (DMEM), RPMI medium 1640, fetal bovine serum (FBS), 3-[4, 5-dimethylthiazol-2-yl]-2,5-diphenyltetrazoliumbromide (MTT), penicillin−streptomycin, and phosphate buffered saline (PBS) were purchased from Invitrogen Corp. The Micro BCA protein assay kit was purchased from Pierce. Acetate and methanol were of analytical grade and used as received. Hydroxyurea was purchased from Alfa Aesar (USA). *N*-Fluorenyl-9-methoxycarbonyl (FMOC) protected L-amino acids (FMOC-Pro-OH, FMOC-Arg(Pbf)-OH, FMOC-Val-OH, FMOC-Lys(Trt)-OH, and 2-chlorotrityl chloride resin (100−200 mesh, loading: 1.32 mmol/g)) were purchased from GL Biochem Ltd. (Shanghai, China) and used as received. *N*-Hydroxybenzotriazole (HOBt), trifluoroacetic acid (TFA), *O*-benzotriazole-*N*,*N*,*N*,*N*-tetramethyl-uronium-hexafluorophosphate (HBTU), and piperidine were provided by Shanghai Reagent Chemical Co. (China) and used directly. Dimethylformamide (DMF) and diisopropylethylamine (DiEA) were obtained from Shanghai Reagent Chemical Co. (China) and distilled prior to use. Triisopropylsilane (TIS) was purchased from ACROS (USA) and used without further purification. PEI 1800 Da, PEI 25 kDa, 2-iodobenzoic acid, and FITC were purchased from Sigma-Aldrich (Taufkirchen, Germany). All other reagents and solvents were of analytical grade and used directly.

Peptide Synthesis. The peptide was synthesized manually using standard solid phase methodologies based on classical Fmoc (1-(9*H*-fluoren-9-yl)-methoxycarbonyl)/*tert*-butyl chemistry.[18,19] Briefly, the peptide sequence was assembled on a 2-chlorotrityl chloride resin (1.32 mmol/g), using DiEA/HBTU/HOBt in *N*, *N*-dimethylformamide to promote coupling of the Fmoc-protected amino acid-OH and 20% piperidine in *N*,*N*-dimethylformamide for Fmoc-removal cycles. The coupling efficacy was monitored via the ninhydrin assay. Iodobenzoic acid was coupled to the last amino acids. The peptide was fully deprotected and cleaved from resin by trifluoroacetic acid (28.5 mL), water (1.5 mL), and triisopropylsilane (1.5 mL) per gram of peptide resin, for 2 h at room temperature. The resin was removed by filtration, and the cleavage mixture and three subsequent TFA washings were collected. The combined solution was concentrated to a viscous solution by rotary evaporation. Cold ether was added to precipitate the product. After washing with cold ether (five times) to remove TFA residual, the precipitate was dissolved in distilled water and then freeze-dried under vacuum for 3 days and stored at −20 °C until used. The purity of the products was examined by high-pressure liquid chromatography (HPLC) with a C18 column and using a linear gradient of acetonitrile and DI water containing 0.1% TFA. The purity of the products was examined by high-pressure liquid chromatography (HPLC) with a C18 column and using a linear gradient of acetonitrile and DI water containing 0.1% TFA, and the molecular weights were

confirmed using by electrospray ionization mass spectrometry (ESI/MS).

For labeling of NLS-I, NLS-I-FITC was synthesized. FITC (7.79 mg; 20 μmol) was mixed with 11.13 mg of NLS-I (10 μmol) in EtOH, and the reaction mixture was stirred overnight at room temperature in a dark place. In order to separate labeled NLS-I from unreacted FITC, an ultrafiltration technique was performed using an ultrafiltration membrane. Simultaneously, to explore the effect of iodide on cellular uptake, NLS-FITC was also synthesized. Peptides were lyophilized and stored at −20 °C until use.

Cell Culture and Amplification of Plasmid DNA. Human breast cancer cell line (MCF-7) and human cervix carcinoma cell line (HeLa) were used for transfection and were incubated in 1640 medium and DMEM medium, respectively, with 10% FBS and 1% antibiotics (penicillin−streptomycin, 10000 U/mL) at 37 °C in a humidified atmosphere containing 5% CO_2.

PGL-3 plasmid was transformed in *Escherichia coli* JM109 and was amplified in terrific broth media at 37 °C overnight at 250 rpm. The plasmid was purified by EndoFree QiAfilter Plasmid Giga Kit (5) (QIAGEN, Germany). Then the purified plasmid was dissolved in TE buffer solution and stored at −20 °C.

Preparation of PEI1800/DNA Complexes with or without NLS-I. The PEI1800/DNA binary complexes at various N/P ratios ranging from 0.2 to 20 were prepared by adding appropriate volumes of PEI1800 solution (in 150 mM NaCl solution) to1 μg of pGL-3 DNA (100 ng/μL in 40 mM Tris−HCl buffer solution), and then the complexes were diluted to a total volume of 100 μL with 150 mM NaCl and vortexed for 5 s. The complexes were incubated at 37 °C for 30 min to allow the formation of complexes.

To form ternary complexes, the "PEI1800 first" method and the "NLS-I first" method were both used. In terms of the "PEI1800 first" method, the PEI 1800/DNA binary complexes were first incubated at 37 °C for 30 min, and then different volumes of NLS-I solution (0.5 mg/mL in 150 mM NaCl solution) were added to the PEI1800/DNA complexes for another 30 min incubation period, and the complexes with NLS-I were obtained. For the "NLS-I first" method, PEI1800/DNA/NLS-I complexes at indicated N/P ratios were prepared similarly with the contrary formation order between PEI1800 and peptides. The suitable N/P ratios of ternary complexes were used for preparing complexes with NLS-I addition. All complexes were used immediately after their preparation.

Agarose Gel Electrophoresis Assay. The vector/DNA binary complexes at varying N/P ratios were prepared as 2.4. The complexes were diluted to a total volume of 8 μL with 150 mM NaCl solution, and then the complexes were incubated at 37 °C for 30 min. After that, the complexes were loaded on the 0.7% (w/v) agarose gel containing GelRed and with Tris-acetate (TAE) running buffer at 80 V for 60 min. DNA was visualized with a UV lamp using a Vilber Lourmat imaging system (France).

Particle Size and ζ-Potential Measurement. The particle size and ζ-potential were measured by Nano-ZS ZEN3600 (Malvern Instruments) at 25 °C. The vector/DNA binary complexes were prepared as 2.4 and distilled water to 1 mL volume for the size and ζ-potential measurements, respectively.

Cytotoxicity Assay *in Vitro*. The cytotoxicity assay was performed with MCF-7 and HeLa cells by MTT assay. Briefly, the cells were seeded, respectively, in a 96-well plate at a density of 6000 cells/well, and then cells were incubated in 100 μL medium containing 10% FBS for 1 day prior to adding the vectors. After the PEI or NLS-I was added for 2 days, the medium was replaced with 200 μL of fresh medium. Then, 20 μL MTT (5 mg/mL) solutions were added to each well and further incubated for 4 h. After that, the medium was removed, and 200 μL of DMSO was added. The absorbance was measured at 570 nm using a microplate reader (Bio-Rad, Model 550, USA). The relative cell viability was calculated as follows: cell viability (%) = $(OD_{570(samples)}/OD_{570(control)}) \times 100$, where $OD_{570(control)}$ was obtained in the absence of peptides, and $OD_{570(samples)}$ was obtained in the presence of peptides.

Cellular Uptake Study. The cellular internalization and nuclear accumulation ability of NLS-I in MCF-7 and HeLa cells were evaluated using a confocal laser scanning microscope and FACS.[20]

The MCF-7 and HeLa cells were seeded at a density of 1×10^5 cells/well into biohousing chamber slide dishes loaded with a 25 mm diameter slide on cover-glass slides and cultured for 24 h, and then NLS-I-FITC and NLS-FITC were added. The terminal concentration was 100 μmol/L. They were further incubated for 4 h at 37 °C, and after that, the medium was removed, and the cells were washed with PBS three times. Then, the nucleus was stained with Hoechst 33258 (2 μg/mL) for 15 min at 37 °C, after which the cells were further washed with PBS three times and incubated with 200 μL of medium. The fluorescence was observed with a confocal laser scanning microscope (C1−Si, Nikon, Japan) equipped with a 405 nm diode for Hoechst 33258 and a 488 nm argon laser.

To analyze the internalization of the two peptides by FACS, MCF-7 and HeLa cells in fresh culture medium were plated at a density of 1×10^4 cells/well into 24-well microplates and cultured for 24 h in medium containing 10% FBS. After complete adhesion, the cells were incubated at 37 °C for 4 h with fresh medium containing peptides (the terminal concentration was 100 μmol/L) prior to washing with PBS. The cells were then treated with 0.25% trypsin at 37 °C for 3 min prior to the addition of 500 μL of PBS. The cells were centrifuged at 1000 rpm for 10 min, and after the supernatant was removed, they were washed with 500 μL of PBS and centrifuged at 1000 rpm for 10 min. After this washing cycle was repeated, the cells were suspended in PBS (200 μL) and subjected to fluorescence analysis on a Beckman Flow Cytometer (Epics XL) using 488-nm laser excitation and a 515- to 545-nm emission filter.

***In Vitro* Transfection.** The transfection efficiency of vector/DNA complexes were evaluated at various N/P ratios. The cells were seeded in the 24-well plate at a density of 6×10^4 cells/well and cultured with 1 mL of medium containing 10% FBS for 1 day at 37 °C to give 50% confluence at the time of transfection. Then the complexes formed by the "PEI1800 first" method and the "NLS-I first" method were added into the plate with serum-free medium for 4 h at 37 °C. After this period, the medium was replaced with fresh medium containing 10% FBS, and the cells were further incubated for 2 days to allow gene expression. For the luciferase assay, the medium was removed, and cells were washed with 0.25 mL of PBS, then the cells were lysed using 200 μL of reporter lysis buffer (Pierce).

The luciferase activity was measured with a chemiluminometer (Lumat LB9507, EG&G Berthold, Germany). Luciferase activity was normalized to the amount of total protein in the sample, which was determined using a BCA protein assay kit (Pierce).

Furthermore, transfections were conducted in the presence of 10% serum on MCF-7 and HeLa cells. In contrast to the NLS-I peptide, the NLS peptides were also used as vectors by the "PEI1800 first" and "NLS first" methods.

RESULTS AND DISCUSSION

Synthesis and Characterization of Peptides. In this study, 2-iodobenzoic acid was directly conjugated to the N-terminal of the NLS sequences during peptide synthesis. The conjugates were assayed for purity by analytical high performance liquid chromatography, and the purity of the product was at least 90%. The nomenclatures, sequences, and molecular weights, determined by electrospray ionization mass spectrometry (ESI/MS) are listed in Table 1.

Gel Retardation Assay. The binding capability of materials to condense DNA is a prerequisite for the gene vector. Figure 1 shows the results of agarose gel electrophoresis of vector/DNA complexes with increasing N/P ratios. As shown in Figure 1A, the PEI1800/DNA complexes were condensed compactly at N/P ratios higher than 1. In contrast, NLS-I in Figure 1B shows visible lower condensable ability; the peptide could not retard DNA migration even at the high N/P ratio (N/P ratio = 30) tested. As shown in Figure 1C, no significant differences were observed by the addition of different NLS-I peptide contents into PEI1800/DNA complexes, which indicated that the ability of PEI 1800 to condense DNA was not affected by peptides.

Particle Size and ζ-Potential Measurement. The ability of vectors to condense DNA was also evaluated in terms of particle size and ζ-potential measurements. Figures 2 and 3 show the mean particle diameter and surface charge of PEI1800/DNA with or without NLS-I.

The particle size and ζ-potential of PEI1800/DNA complexes were examined at N/P ratios ranging from 0.2 to 30. As shown in Figure 2A, the particle size decreased from 900 nm to 600 nm with increasing N/P ratios first, then the size increased from 600 nm up to 1200 nm when the N/P ratios were higher than 5, which is in agreement with the literature report.[22] Figure 3A shows that the ζ-potential of PEI1800/DNA complexes increased with increasing N/P ratios. Moreover, at an N/P ratio of 5, the surface charge of PEI1800/DNA complexes was 5 mV, close to neutrality. However, the surface charge of PEI1800/DNA complexes with N/P ratios higher than 5 ranged from 10 to 16 mV, which may be too high to form the noncovalent binding of peptides to the complexes via charge interactions. Hence, the N/P ratio of 5 between PEI1800 and plasmid DNA was chosen for further studies.

As shown in Figures 2B and 3B, the particle size and ζ-potential of complexes with NLS-I incorporated by the "PEI1800 first" method with different contents of peptide were examined. The PEI1800 solution was added to the DNA solution at the N/P ratio of 5, and after 30 min of incubation, various amounts of the peptide were added to the complexes at N/P ratios between the peptide and DNA from 0 to 25 to form ternary complexes. The complexes were incubated for another 30 min before being used for experiments. The final N/P ratios listed as PEI1800/DNA/NLS-I are indicated from 5/1/0 to 5/1/25. As shown in Figure 2B, the size of these complexes increased first, then decreased when the N/P ratio of PEI1800/DNA/NLS-I was higher than 5/1/2, whereas the size of the complex increased again when N/P ratios of PEI1800/DNA/NLS-I were higher than 5/1/10. This result indicates that the optimal N/P ratio of PEI1800/DNA/NLS-I may be 5/1/10. Figure 3B shows that the ζ-potential of complexes with NLS-I increased slightly with increasing content of NLS-I peptide due to the slight positive charge of peptide.

***In Vitro* Cytotoxicity.** The cytotoxicity of the vectors was monitored in MCF-7 and HeLa cells by the MTT assay, and 25 kDa PEI was used as the control. As shown in Figure 4, for PEI 1800 or NLS-I, no significant cytotoxicity was observed even at the highest incubation condition (200 mg/L) in both cell lines. Generally, the cytotoxicity of cationic materials depends on the molecular weight, cell binding ability, and membrane permeability.[21] Hence, the lower cytotoxicity of PEI 1800 or NLS-I perhaps is ascribed to their lower molecular weight.

Cellular Uptake Study of Peptides by Confocal Laser Scanning Microscopy and FACS. The effect of iodide on cellular internalization and nuclear localization was further investigated. To determine intracellular localization by confocal laser scanning microscopy, fluorescein isothiocyanate (FITC) as the fluorescent probe was coupled to the two peptides, and MCF-7 cells and HeLa cells were both treated with NLS-I and NLS. Then the cellular uptake and nuclear localization could be directly visualized under fluorescence microscopy (Figure 5). In this experiment, the amount of internalized peptide was also assessed by FACS (Figures 6 and 7).

In MCF-7 cells, a dramatic increased accumulation of fluorescence in the nucleus was observed after incubation with NLS-I-FITC (Figure 5A), whereas less accumulation of fluorescence was

Table 1. Sequences and Molecular Weights of Peptides

		molecular weight	
vector	sequence	expected	found
NLS	PKKKRKV	883.15	883.2
NLS-I	Iodinated-PKKKRKV	1113.17	1113.2

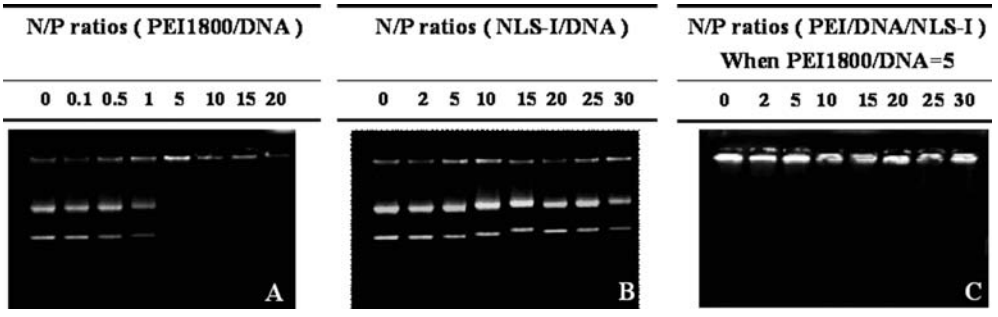

Figure 1. Agarose gel electrophoresis retardation assay of (A) PEI1800/DNA; (B) NLS-I/DNA; and (C) PEI1800/DNA/NLS-I with the "PEI1800 first" method. To prepare the ternary complexes, DNA was packed with PEI polymers first, following by the addition of peptides at the indicated N/P ratios from 0 to 25. The N/P ratio between PEI1800 and DNA was 5/1 for all groups, and the final N/P ratios listed as PEI1800/DNA/NLS-I are indicated from 5/1/0 to 5/1/25.

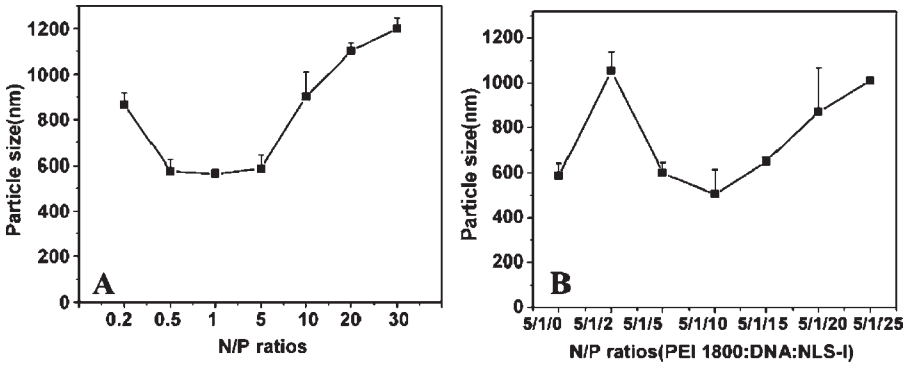

Figure 2. Particle size of complexes. (A) PEI1800/DNA at N/P ratios ranging from 0.2 to 20; (B) "PEI1800 first" method, PEI1800/DNA/NLS-I at N/P ratios ranging from 5/1/0 to 5/1/25. Data are shown as the mean ± SD (n = 3).

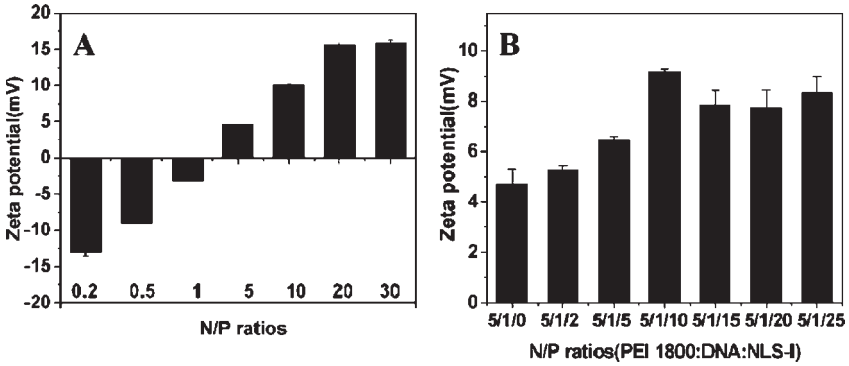

Figure 3. Zeta potential of complexes. (A) PEI1800/DNA at N/P ratios ranging from 0.2 to 30; (B) "PEI1800 first" method, PEI1800/DNA/NLS-I at N/P ratios ranging from 5/1/0 to 5/1/25. Data are shown as the mean ± SD (n = 3).

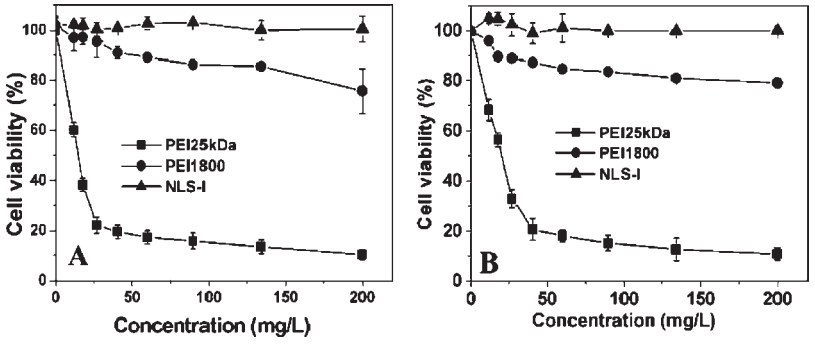

Figure 4. Cell viabilities of vectors and 25 kDa PEI in (A) MCF-7 cells and (B) HeLa cells. Data are shown as the mean ± SD (n = 3).

found in the nucleus of cells treated with NLS-FITC (Figure 5B). As judged by FACS analysis (Figure 6A_1 and A_2), the percentage of NLS-I-FITC labeled cells was increased by 80% (Figure 7A), and the mean fluorescence intensity (MIF) was markedly heightened by 380% (Figure 7B). Via quantification of FITC-labeled peptides in cells, they identified that the percentage of stained cells by NLS-I-FITC was almost one time greater than that of NLS-FITC peptide, but the MIF was nearly four times greater, indicating that the amount of NLS-I-FITC peptide in every stained cell was in fact significantly higher than that of the NLS-FITC peptide. We inferred that the addition of iodide to the conjugate (NLS-I-FITC) could very much increase the peptide's cellular internalization in MCF-7 cells.

By contrast, we further confirmed the contribution of iodide to the internalization of peptide in HeLa cells, and only few FITC-labeled NLS-I and NLS were taken up by the nuclei of cells (Figure 5C and D). Incubation with NLS-I-FITC gave no significant effect on the cellular uptake compared to that of NLS-FITC (Figures 6B_1,B_2 and 7). The cellular uptake was slightly higher under the incubation with NLS-I-FITC, and FACS analysis showed an average increase of 8.6% in NLS-I-FITC uptake compared with that of NLS-FITC. The observation indicated that

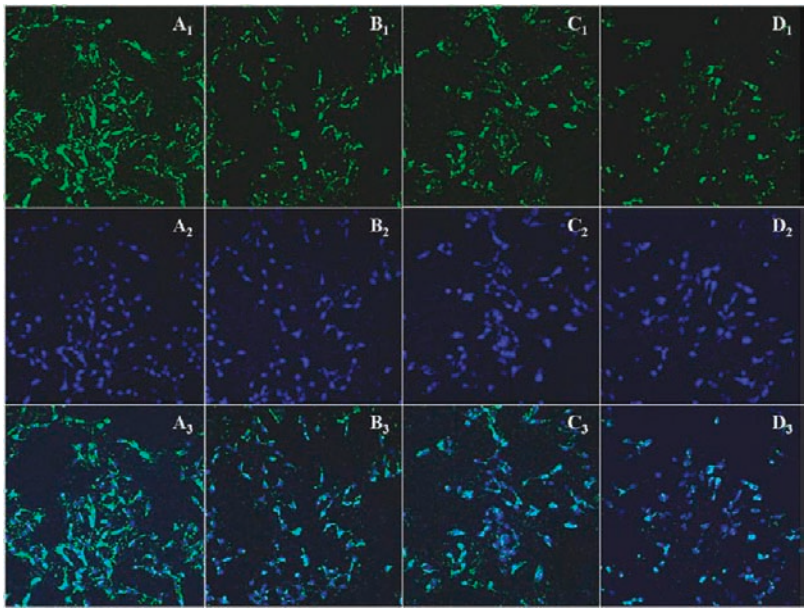

Figure 5. Confocal microscopy images of intracellular trafficking of peptides. The localization of peptides labeled with FITC was observed in A_1-D_1, the nuclei were stained with Hoechst 33258 in A_2 and B_2, and the merged photo is presented in A_3-D_3. (A) NLS-I-FITC in MCF-7 cells; (B) NLS-FITC in MCF-7 cells; (C) NLS-I-FITC in HeLa cells; (D) NLS-FITC in HeLa cells.

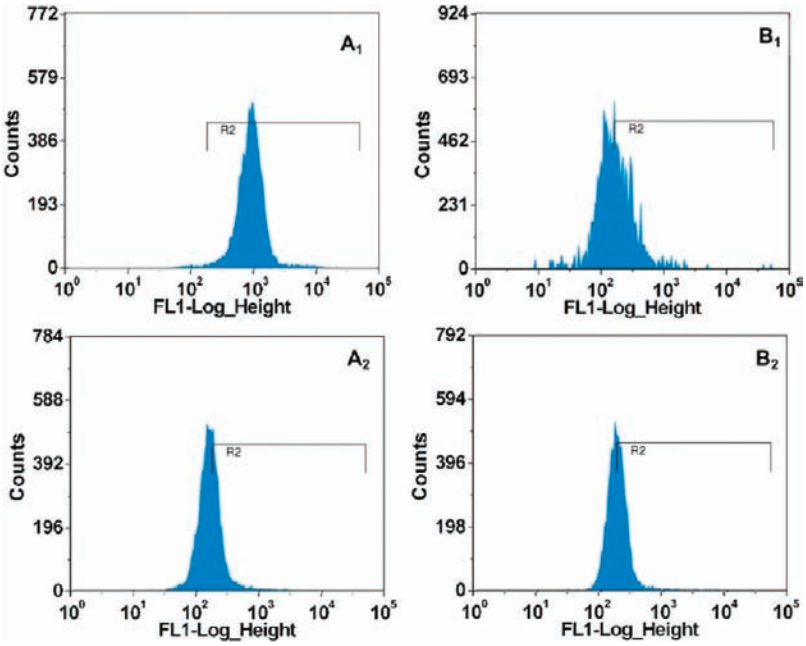

Figure 6. FACS analysis of cellular uptake of peptides. Cells were incubated with peptides (100 μmol/L) for 4 h at 37 °C prior to trypsinization and FACS analysis. A_1, NLS-I-FITC in MCF-7 cells; A_2, NLS-FITC in MCF-7 cells; B_1, NLS-I-FITC in HeLa cells; B_2, NLS-FITC in HeLa cells.

the iodide in the peptide sequence had only a minor influence on its internalization characteristic in HeLa cells.

Obviously, phase-contrast observation demonstrated that the coupling of the iodine atom to the NLS peptide seems to play a decisive role in the augmentation of cellular and nuclear uptake processes only in MCF-7 cells. As described above, iodide is transported actively across the membrane of breast cancer cells by the sodium/iodide symporter, which is also expressed on the surface of breast cancer cells as thyroid cells. In contrast to MCF-7 cells, the cellular uptake of NLS-I-FITC and NLS-FITC in HeLa cells was similar, possibly due to the absence of the sodium/iodide symporter in Hela cells. These results indicated that we could choose the NLS-I as a vehicle to transport DNA into breast cells selectively.

Enhancement of Plasmid DNA Transfection Efficiency by NLS-I in MCF-7 Cells. For human gene therapy, gene delivery vectors are usually modified by integrating targeting moieties that recognize particular types of cellular receptors to achieve cell-specific targeting. In this study, we chose the NLS-I as a targeting peptide to recognize breast cancer cells. Functional peptides

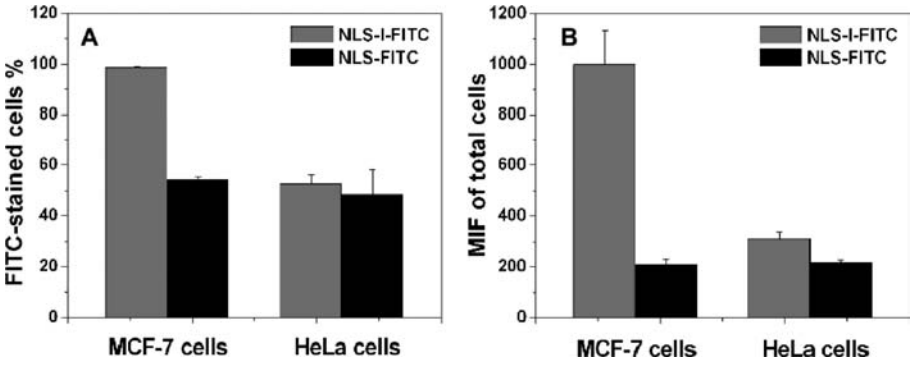

Figure 7. Quantification of cellular uptake of peptides by FACS analysis. (A) The number of positively labeled cells was represented as the percentage of total counting cells in each panel. (B) The mean fluorescence intensity (MIF) of total counting cells in each panel.

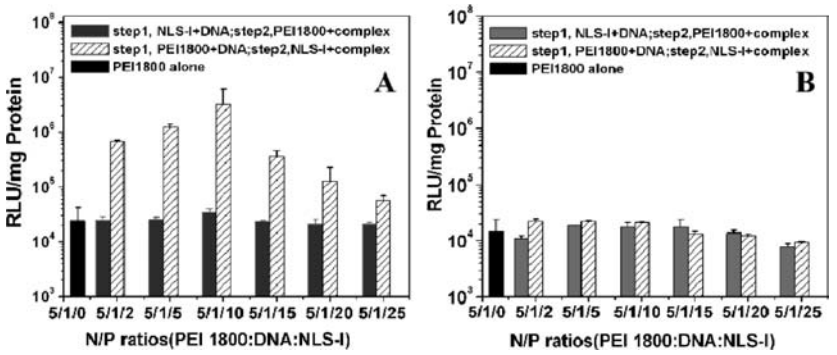

Figure 8. Luciferase expression mediated by PEI1800/DNA/NLS-I complexes at N/P ratios ranging from 5/1/0 to 5/1/25 with the "NLS-I first" method and the "PEI1800 first" method. (A) In MCF-7 cells; (B) in HeLa cells. Data are shown as the mean ± SD (n = 3).

were widely chemically conjugated to PEI/plasmid DNA complexes, resulting in nonviral gene delivery vectors with high efficiency. However, chemical conjugation may be detrimental to the biological activities of peptides. Thus, we fabricated a ternary complex via electrostatic interactions between targeting peptides and PEI1800/DNA complexes in the current study.

As indicated earlier, PEI1800 was found to be inefficient as a gene vector even though it is able to condense DNA; however, without PEI addition, naked DNA and the NLS-I/DNA complex did not accomplish significant transfection (data not show). For the transfection study, the polycationic transfection reagent PEI1800 was required for neutralization and condensation of the DNA first. We prepared PEI1800/DNA complexes at an N/P ratio of 5 that displayed a weak positive surface charge which facilitates the binding of cationic peptide to complexes.[23] On the one hand, PEI1800/DNA complexes with N/P ratios less than 5 failed to form stable vector/DNA complexes; on the other hand, complexes with ratios higher than 5 inhibit the interaction of the complexes with the targeting peptide because of the electrostatic repulsion.

In the current study, we prepared PEI1800/DNA/NLS-I complexes with the "NLS-I first" method and the "PEI1800 first" method. However, the formation order to make complexes had an outstanding effect on gene transfection. As shown in Figure 8A, the addition of peptide produced no effect on the transfection efficiency when ternary complexes were prepared with the "NLS-I first" method, while the complexes prepared by the "PEI1800 first" method increased gene expression conspicuously. We speculated that addition of NLS-I after PEI1800/DNA might result in a ternary structure with the targeting peptide on the surface of the complexes due to the interaction of the peptide with the sodium/iodide symporter. Therefore, the "PEI1800 first" method was used for the rest of study.

To establish the maximal DNA transfection efficiency by NLS-I with the "PEI1800 first" method, the N/P ratio between nitrogen residues of NLS-I and phosphate residues of DNA was optimized. PEI1800/DNA (N/P ratio of 5) complex was mixed with different concentrations of NLS-I (N/P ratios from 2 to 25) for transfection. Figure 8A shows that the inclusion of peptide with complexes at NLS-I/DNA ratios from 2 to 25 exhibited increasing transfection efficiency in MCF-7 cells, compared to that in complexes containing no peptides. This result suggests that with the increased peptide content to PEI800/DNA complexes, transgene expression levels in MCF-7 cells got increased. Also, as shown in Figure 8A, the increase in transgene expression level is dependent on the peptide content, and the complex with the N/P ratio of 10 between NLS-I and DNA can achieve the best transgene expression level. In detail, the PEI1800/DNA/NLS-I complex with the N/P ratio of 5/1/10 with a small size, a positive zeta-potential, and a relatively required amount of surface-displayed peptides can achieve the highest transfection efficiency by up to 130-fold compared to that of complexes with PEI1800 alone. It was also found that when the N/P ratios were higher than 10, the gene expression level got decreased, probably due to the increased aggregation of peptide on the surface of complexes, which resulted in large particles and weak internalization ability. However, excess NLS-I may compete with the ternary complexes for binding sodium/iodide symporter, leading to reduced

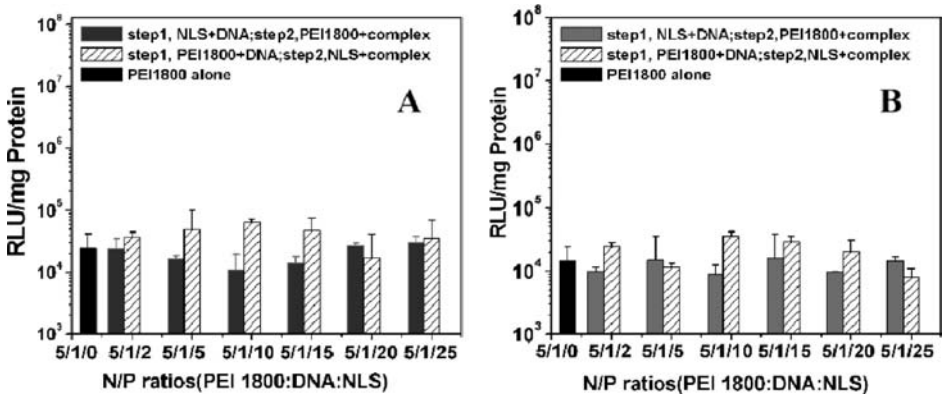

Figure 9. Luciferase expression mediated by PEI1800/DNA/NLS complexes at N/P ratios ranging from 5/1/0 to 5/1/25 with the "NLS first" method and the "PEI1800 first" method. (A) In MCF-7 cells; (B) in HeLa cells. Data are shown as the mean ± SD (n = 3).

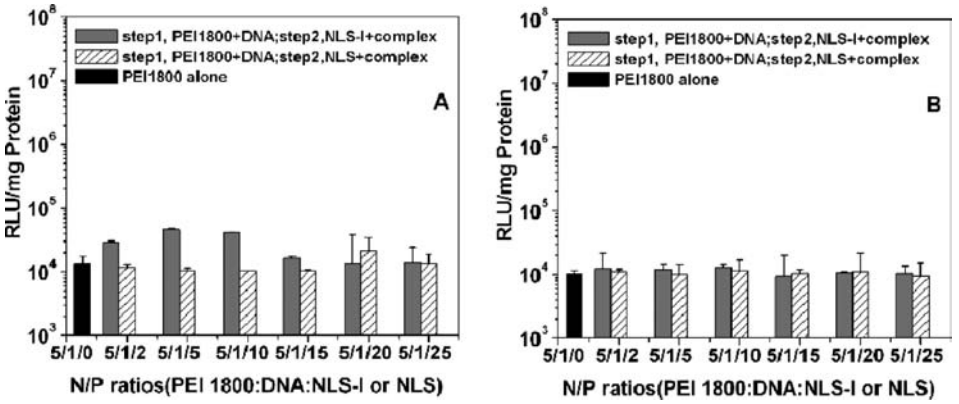

Figure 10. Luciferase expression mediated by PEI1800/DNA/NLS-I complexes and PEI1800/DNA/NLS complexes at N/P ratios ranging from 5/1/0 to 5/1/25 with the "PEI1800 first" method in the presence of 10% serum. (A) In MCF-7 cells; (B) in HeLa cells. Data are shown as the mean ± SD (n = 3).

cellular uptake of complexes and plasmid DNA. In fact, when the N/P ratio is higher than 25, the effect of NLS-I dis appeared (data not show).

To further examine targeted gene delivery by the NLS-I-containing ternary complexes, we compared the transfection efficiency of the ternary complexes both in MCF-7 cells with stable sodium/iodide symporter expression and HeLa cells without the symporter. In contrast to MCF-7 cells, in HeLa cells, as shown in Figure 8B, using PEI/DNA/NLS-I complexes did not significantly affect gene transfection efficiency compared to that of the PEI/DNA complexes. These results revealed that the NLS-I is much more potent in MCF-7 cells than that in HeLa cells and also clearly demonstrate that the improved gene transfection by NLS-I was related to the interaction of NLS-I with the sodium/iodide symporter.

We now know that PEI/DNA/NLS-I complexes can cause significant effects in transfection efficiency in MCF-7 cells; subsequently, to obtain further information on the effects of iodine on gene delivery, we next examined the effects of NLS as peptide vectors. The NLS peptide used in Figure 9 did not yield improvements as palpable as NLS-I, presumably due to the process of internalization (Figures 5−7). Consequently, all the visible effects on intracellular quantities and transfection efficiencies in MCF-7 cells by NLS-I demonstrated that iodine had a significant influence on breast cancer cell targeting.

As described above, the sodium/iodine symporter (NIS) is expressed on the surface of MCF-7 cells [14−16], which can actively transport iodide from the medium into the cells, the cellular uptake of complexes and plasmid DNA is strongly dependent on the iodine atom introduced into vectors. Then, the nuclear localization sequence may transport DNA into the nucleus through the nuclear pore complex (NPC) by the successive docking of Imp β and nucleoporins (Nups) (Scheme 1).

To evaluate the effect of serum on transfection activity, transfections of PEI1800/DNA/NLS-I complexes and PEI1800/DNA/NLS complexes at N/P ratios ranging from 5/1/0 to 5/1/25 in the presence of 10% serum were also assessed with the "PEI1800 first" method (Figure 10). The results shows that PEI/DNA/NLS-I complexes can also cause positive effects on transfection efficiency in MCF-7 cells compared to that of complexes containing no NLS-I. In detail, the PEI1800/DNA/NLS-I complex with the N/P ratio of 5/1/5 can achieve the highest transfection efficiency by up to 4-fold compared to that of complexes with PEI1800 alone in the presence of 10% serum. However, using PEI1800/DNA/NLS-I complexes in HeLa cells did not affect gene transfection efficiency compared to that of PEI1800/DNA complexes.

It was found that the transfection efficiency of the delivery systems is inhibited by the presence of serum. It was reported that the competitive binding of particles with serum proteins leads to subsequent blood clearance and inhibition of gene delivery

for cationic gene delivery vehicles such as low molecular weight PEI and polyethylenimine-grafted vectors.[24,25] Here, the reduction in transfection efficiency was attributed to serum inhibition of PEI1800.

CONCLUSIONS

In this article, we introduced an iodine atom to a nuclear localization signal (PKKKRKV) by chemically attaching 2-iodobenzoic acid to the peptide to obtain the NLS-I peptide for cell targeting and nuclear transport. During the preparation of the ternary complexes, DNA was first bound to PEI1800, and then NLS-I was added to prepare the PEI1800/DNA/NLS-I complex. It was found, in MCF-7 cells, that cell internalization and nuclear accumulation of NLS-I was markedly increased compared to those in NLS; in addition, the luciferase reporter gene expression by PEI1800/DNA/NLS-I complexes exhibited much enhanced efficiency. By contrast, in HeLa cells, the improvements were not observed. The studies demonstrate that the iodine atom of the NLS peptide does induce enhancement of gene transfer in MCF-7 cells selectively, which will find great potential in breast cancer therapy.

AUTHOR INFORMATION

Corresponding Author

*Tel: 86-27-68755993. Fax: 86-27-68754509. E-mail: xz-zhang@whu.edu.cn.

ACKNOWLEDGMENT

We acknowledge the financial support from the Ministry of Science and Technology of China (2009CB930300, 2011CB606202) and Open Project of State Key Laboratory for Supramolecular Structure and Materials (SKLSSM201001).

REFERENCES

(1) Howlader, N., Altekruse, S. F., and Edwards, B. K. (2010) Monitoring the Burden of Cancer in the United States, in *Bioactive Compounds and Cancer* (Milner, J. A., and Romagnolo, J. A., Eds.) pp 3−23, Humana Press, New York.

(2) Morris, G. J., and Mitchell, E. P. (2008) Higher incidence of aggressive breast cancers in African-American women: A review. *J. Natl. Med. Assoc. 100*, 698–702.

(3) Ferlay, J., Héry, C., Autier, P., and Sankaranarayanan, R. (2010) Global Burden of Breast Cancer, in *Breast Cancer Epidemiology* (Li, C. I., Ed.) pp 1−19, Springer Science + Business Media, New York.

(4) Edelstein, M. L., Abedi, M. R., and Wixon, J. (2007) Gene therapy clinical trials worldwide to 2007: an update. *J. Gene Med. 9*, 833–42.

(5) Lungwitz, U., Breunig, M., Blunk, T., and Gopferich, A. (2005) Polyethylenimine-based non-viral gene delivery systems. *Eur. J. Pharm. Biopharm. 60*, 247–66.

(6) Neu, M., Fischer, D., and Kissel, T. (2005) Recent advances in rational gene transfer vector design based on poly(ethylene imine) and its derivatives. *J. Gene Med. 7*, 992–1009.

(7) Kunath, K., Harpe, von A., Fischer, D., Petersen, H., Bickel, U., Voigt, K., and Kissel, T. (2003) Low-molecular-weight polyethyleneimine as a non-viral vector for DNA Delivery: comparison of physicochemical Properties, transfection efficiency and in vivo distribution with high-molecular- weight polyethyleneimine. *J. Controlled Release 89*, 113–25.

(8) Zeng, J., Wang, X., and Wang, S. (2007) Self-assembled ternary complexes of plasmid DNA, low molecular weight polyethylenimine and targeting peptide for nonviral gene delivery into neurons. *Biomaterials 28*, 1443–51.

(9) Pouton, C. W., Wagstaff, K. M., Roth, D. M., Moseley, G. W., and Jans, D. A. (2007) Targeted delivery to the nucleus. *Adv. Drug Delivery Rev. 59*, 698–717.

(10) Arenal, A., Pimentel, R., Garcia, C., Pimentel, E., and Alestrom, P. (2004) The SV40 T antigen nuclear localization sequence enhances Nuclear import of vector DNA in embryos of a crustacean (*Litopenaeus schmitti*). *Gene 337*, 71–7.

(11) Nagasaki, T., Myohoji, T., Tachibana, T., Futaki, S., and Tamagaki, S. (2003) Can nuclear localization signals enhance nuclear localization of plasmid DNA?. *Bioconjugate Chem. 14*, 282–6.

(12) van der Aa., M, Koning, G. A., d'Oliveira, C., Oosting, R. S., Wilschut, K. J., Hennink, W. E., and Crommelin, D. J. (2005) An NLS peptide covalently linked to linear DNA does not enhance transfection efficiency of cationic polymer based gene delivery systems. *J. Gene Med. 7*, 208–17.

(13) Spitzweg, C., Joba, W., Eisenmenger, W., and Heufelder, A. E. (1998) Analysis of human sodium iodide symporter gene expression in extra-thyroidal tissues and cloning of its complementary deoxyribonucleic acids from salivary gland, mammary gland, and gastric mucosa. *J. Clin. Endocr. Metab. 83*, 1746–51.

(14) Kilbane, M. T., Ajjan, R. A., Weetman, A. P., Dwyer, R., Mcdermott, E. W. M., O' Higgins, N. J., and Smith, P. P. A. (2000) Tissue iodine content and serum-mediated 125I uptake-blocking activity in breast cancer. *J. Clin. Endocr. Metab. 85*, 1245–50.

(15) Tazebay, U. H., Wapnir, I. L., Levy, O., Dohan, O., Zuckier, L. S., Zhao, Q. H., Deng, H. F., Amenta, P. S., Fineberg, S., Pestell, R. G., and Carrasco, N. (2000) The mammary gland iodide transporter is expressed during lactation and in breast cancer. *Nat. Med. 6*, 871–8.

(16) Kogai, T., Schultz, J. J., Johnson, L. S., Huang, M., and Brent, G. A. (2000) Retinoic acid induces sodium/iodide symporter gene expression and radioiodide uptake in the MCF-7 breast cancer cell line. *Proc. Natl. Acad. Sci. U.S.A. 97*, 8519–24.

(17) Perron, B., Rodriguez, A. M., Leblanc, G., and Pourcher, T. (2001) Cloning of the mouse sodium iodide symporter and its expression in the mammary gland and other tissues. *J. Endocrinol. 170*, 185–96.

(18) Fields, G. B., and Noble, R. L. (1990) Solid phase peptide synthesis utilizing 9-fluorenylmethoxycarbonyl amino acids. *Int. J. Pept. Protein Res. 35*, 161–214.

(19) Moore, N. M., Barbour, T. R., and Sakiyama-Elbert, S. E. (2008) Synthesis and characterization of four-arm poly(ethylene glycol)-based gene delivery vehicles coupled to integrin and DNA-binding peptides. *Mol. Pharmaceutics 5*, 140–50.

(20) Nakase, I., Niwa, M., Takeuchi, T., Sonomura, K., Kawabata, N., Koike, Y., Takehashi, M., Tanaka, S., Ueda, K., Simpson, J. C., Jones, A. T., Sugiura, Y., and Futaki, S. (2004) Cellular uptake of arginine-rich peptides: roles for macropinocytosis and actin rearrangement. *Mol. Ther. 10*, 1011–1022.

(21) Xiong, M. P., Forrest, M. L., Ton, G., Zhao, A., Davies, N. M., and Kwon, G. S. (2007) Poly(aspartate-g-PEI800), a polyethylenimine analogue of low toxicity and high transfection efficiency for gene delivery. *Biomaterials 28*, 4889–900.

(22) Godbey, W. T., Wu, K. K., and Mikos, A. G. (1999) Poly(ethylenimine) and its role in gene delivery. *J. Controlled Release 60*, 149–60.

(23) Rea, J. C., BarronC, A. E., and Shea, L. D. (2008) Peptide-mediated lipofection is governed by lipoplex physical properties and the density of surface-displayed amines. *J. Pharm. Sci. 97*, 4794–806.

(24) Fischer, D., Bieber, T., Lin, Y. X., Elsässer, H. P., and Kissel, T. (1999) A novel non-viral vector for DNA delivery based on low molecular weight, branched polyethylenimine: effect of molecular weight on transfection efficiency and cytotoxicity. *Pharm. Res. 16*, 1273–9.

(25) Ma, K., Hu, M. X., Xie, M., Shen, H. J., Qiu, L. Y., Fan, W. M., Sun, H. Y., Chen, S. Q., and Jin, Y. (2010) Investigation of polyethylenimine-grafted-triamcinolone acetonide as nucleus-targeting gene delivery systems. *J. Gene Med. 12*, 669–80.

Bioconjugate Chemistry

ARTICLE

pubs.acs.org/bc

Intracellular Protein Target Detection by Quantum Dots Optimized for Live Cell Imaging

Youngseon Choi,*,† Keumhyun Kim,† Sukmin Hong,† Hichul Kim,‡ Yong-Jun Kwon,‡ and Rita Song*,†

†Chemical Biology Laboratory

‡Discovery Biology Group

Institut Pasteur Korea (IP-K), 696 Sampyeong-dong, Bundang-gu, Seongnam-Si, Gyeonggi-Do, 463-400, South Korea

Supporting Information

ABSTRACT: Imaging of specific intracellular target proteins in living cells has been of great challenge and importance for understanding intracellular events and elucidating various biological phenomena. Highly photoluminescent and water-soluble semiconductor nanocrystal quantum dots (QDs) have been extensively applied to various cellular imaging applications due to the long-term photostability and the tunable narrow emission spectra with broad excitation. Despite the great success of various bioimaging and diagnostic applications, visualization of intracellular targets in live cells still has been of great challenge. Nonspecific binding, difficulty of intracellular delivery, or endosomal trapping of nanosized QDs are the main reasons to hamper specific target binding in live cells. In this context, we prepared the polymer-coated QDs (pcQD) of which the surface was optimized for specific intracellular targeting in live cells. Efficient intracellular delivery was achieved through PEGylation and subsequent cell penetrating peptide (i.e., TAT) conjugation to the pcQD in order to avoid significant endosomal sequestration and to facilitate internalization of the QDs, respectively. In this study, we employed HEK293 cell line overexpressing endothelin A receptor (ET_AR), a family of G-protein coupled receptor (GPCR), of which the cytosolic c-terminal site is genetically engineered to possess green fluorescent protein (GFP) as our intracellular protein target. The fluorescence signal of the target protein and the well-defined intracellular behavior of the GPCR help to evaluate the targeting specificity of QDs in living cells. To test the hypothesis that the TAT-QDs conjugated with antibody against intracellular target of interest can find the target, we conjugated anti-GFP antibody to TAT-PEG-pcQD using heterobifunctional linkers. Compared to the TAT-PEG-pcQD, which was distributed throughout the cytoplasm, the antiGFP-functionalized TAT-PEG-pcQD could penetrate the cell membrane and colocalize with the GFP. An agonist (endothelin-1, ET-1) treatment induced GFP-ET_AR translocation into pericentriolar region, where the GFP also significantly colocalized with antiGFP-TAT-PEG-pcQD. These results demonstrate that stepwise optimization of PEG-pcQD conjugation with both a cell penetrating peptide and an antibody against a target of interest allows specific binding to the intracellular target protein with minimized nonspecific binding.

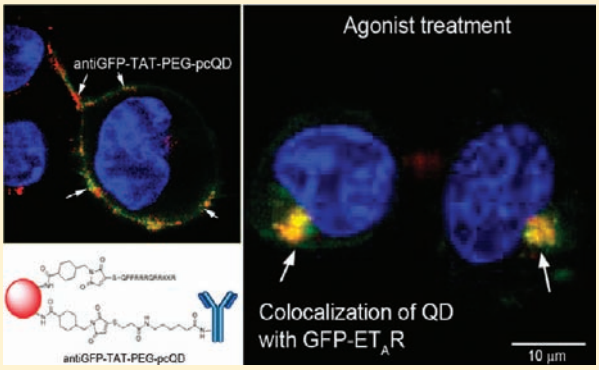

INTRODUCTION

Imaging of specific intracellular target proteins in living cells has been of great challenge and importance for understanding intracellular events and elucidating various biological phenomena in cell biology and drug discovery.[1] Highly photolumminescent and water-soluble semiconductor nanocrystal quantum dots (QDs) have been extensively exploited for the various bioimaging applications because of their narrow spectra, tunable fluorescence, and long-term photostability.[2−5] Despite the great success in biological applications, QDs without proper surface modification suffer from nonspecific binding as well as instability in the cells, resulting in incapability of subcellular targeting in complex intracellular environments.[6,7] Endosomal trapping and subsequent transport to the perinuclear region has been known to hamper the specific targeting of the functionalized nanoparticles.[8,9] This inherent endocytosis process of nanosized QDs and the active machinery of the endocytosis trafficking system remain problems for the application of QDs toward efficient intracellular labeling of specific targets in live cells.[5,10−14]

Recent advancements in conjugation chemistry and live cell imaging techniques, however, have allowed us to significantly address these issues. Nonspecific binding of QDs can be significantly reduced by appropriate PEGylation (750−6000 Da) because of the well-known stealth effect of the PEG molecules.[15,16] Bentzen et al. also reported the efficacy of PEGylated QDs in HEK and 3T3 cell lines, where they found that the nonspecific uptake of

Received: March 15, 2011
Revised: June 14, 2011
Published: June 30, 2011

ACS Publications © 2011 American Chemical Society

QDs depends on cell types.[17] Most recently, Tan et al. showed that the cellular interaction of oleyl-modified QDs (20−50 nm) depends on the balance between surface charge and hydrophobicity.[18] Numerous studies have corroborated the fact that the cellular interaction of nanoparticles depends on the size, charge, shape, and surface properties,[14,19,20] reflecting the importance of surface chemistry as well as complexity of nanoparticle−cell interactions.

With the reduced nonspecific binding and cytotoxicity of the PEGylated QD surface, various efforts have been made to image and track cell-surface membrane proteins such as integrins,[21] folate receptors,[22] neurotransmitter receptors,[23] epidermal growth factor receptor (EGFR),[24,25] and G-protein coupled receptors (GPCRs)[26] using the PEG-QDs conjugated with receptor-specific small molecules or antibodies. The QDs used in these studies are designed to bind the receptors on the cellular surface membrane, where the QDs conjugated with small ligands or antibodies are delivered into cells via receptor-mediated endocytosis. This approach, however, may not be employed for directly detecting targets of interest if the targets exist in the cytosol.

Therefore, another approach has been implemented to deliver various nanoparticles into cells using a cell-penetrating peptide (CPP).[27−31] In particular, a CPP derived from human immunodeficiency virus-1 transactivator (TAT) protein, or TAT peptide, has been widely used to facilitate delivery of various nanoparticles into cells, where TAT-conjugated QDs has been known to be uptaken via macropinocytosis, followed by accumulation in perinuclear region.[32−34] Though intracellular distribution, cytotoxicity as well as mechanistic studies of the QDs have been extensively performed, few studies have yet explored the specific detection of targets located inside living cells. This may be potentially due to the difficulty of avoiding nonspecific uptake which interferes the correct interpretation of target localization by live cellular imaging.

Herein, we report the study on the detection of the specific intracellular target protein in live cells based on TAT-conjugated QDs. First, to find optimum surface chemistry for polymer-coated QD (pcQD) which allows minimization of nonspecific uptake and cytotoxicity, we investigated several aspects of cellular interaction of pcQD in live cells. The surface functionality, concentration, incubation time, and cytotoxicity were considered important factors for affecting the intracellular behavior of QDs. We performed controlled PEGylation of pcQDs (PEG-pcQDs), followed by stepwise modification with TAT and an antibody against a specific target protein.

To demonstrate the specific binding capability of the QD conjugate, we employed the HEK293 cell line overexpressing green fluorescent protein (GFP) as our intracellular target of interest, which is genetically engineered to be tethered to the cytosplasmic c-terminal site of endothelin A receptor (ET_AR). ET_AR is one of two mammalian receptor subtypes (ET_AR and ET_BR) of 7-transmembrane GPCR family, widely present in most cells and tissues related with cardiovascular and renal diseases and cancer.[35,36] Given the biological complexity of living cells, we designed a simplified cellular model system, where the target is a fluorescent protein and the intracellular behavior of the target can be easily detected by fluorescence imaging. Thus, we constructed the fluorescent target protein which is fused with the cytoplasmic region of the GPCR. This cellular model may help us to identify the specific binding of QD probe to the target via colocalization of the GFP signal with the different-colored QD signals (red emission in this study). Also, the well-defined mechanisms of cell-surface expression, internalization, and agonist-induced translocation of the GPCR allows us to confirm the specific binding of the probe in a reliable manner.[37,38] Further, the emerging interest of GPCRs as a major therapeutic target in drug discovery may provide additional significance for this study using a cellular model overexpressing GPCR transmembrane protein.

Using confocal fluorescence microscopy, we could observe the PEG-pcQDs modified with TAT and anti-GFP antibody specifically bind the intracellular target GFP in live cells. The antiGFP-TAT-PEG-pcQD which initially colocalized with the GFP at the cellular membrane also translocated with the GFP after the ET-1 agonist treatment in agreement with the characteristic of the GPCR. These results suggest that the controlled functionalization of PEGylated pcQD with both TAT and an antibody against a specific target protein can afford efficient cellular entry of QDs as well as specific detection of an intracellular target without significant nonspecific uptake or binding.

EXPERIMENTAL SECTION

Materials. Cadmium nitrate (99.99%), sodium myristate (99%), hexamethyldisilathiane ($(TMS)_2S$), diethylzinc ($ZnEt_2$), trioctylphosphine (TOP, 90%), trioctylphosphine oxide (TOPO, 99%), 1-octadecene (ODE), selenium powder (99.9%), poly(acrylic acid) (PAA, M.W. = 1800 g/mol), and octylamine (99%) were purchased from Aldrich. All organic solvents were purchased from Junsei (Japan). 1-Ethyl-3-(3-dimethylaminopropyl) carbodiimide hydrochloride (EDC) and sodium tetraborate were purchased from Sigma. Monoamino methoxy PEGs (PEG molecular weights 750, 2000, 5000 Da) and diamino-PEG5000 were purchased from SunBio (Korea). Alexa Fluor 634-labeled human transferrin conjugate (AF634-transferrin), 2′-(4-ethoxyphenyl)-5-(4-methyl-1-piperazinyl)-2,5′-bi-1H-benzimidazole trihydrochloride trihydrate (Hoechst33342), and 3-(4,5-dimethylthiazol-2-yl)-2,5-diphenyltetrazolium bromide (MTT) were obtained from Invitrogen (USA). Sulfo-succinimidyl 4-[*N*-maleimidomethyl]-cyclohexane-1-carboxylate (sulfo-SMCC) and sulfosuccinimidyl 6-(3′-[2-pyridyldithio]-propionamido)hexanoate (sulfo-LC-SPDP) were purchased from Pierce (Thermo Scientific, USA). Monoclonoal anti-GFP antibody was obtained from Calbiochem (USA). The cystein-modified cell penetrating peptide TAT possessing the sequence Ac-RKKRRQRRRPPQC−$CONH_2$ (N-terminal acetyl, C-terminal amide capping; c-TAT) was obtained from Peptron Inc. (Daejon, Korea). All the chemicals were used without further purification. All the solutions were prepared using deionized water (18 MΩ) or autoclaved water.

General Characterization Methods. All absorption spectra were obtained in a quartz cuvette using Cary 5000 UV−vis spectrometer (Varian Inc., CA, USA) with a spectral range of 200−800 nm, a scan rate of 600 nm/min, and a slit width of 2 nm. Agarose gel electrophoresis was performed with 1% agarose in 0.5× Tris-borate EDTA buffer (pH 8.0) at 25 V cm^{-1} for 50 min. The resulting gel image was obtained using LAS 3000 gel imager (Fuji, Japan). Dynamic light scattering (DLS) measurements were performed using Nano-ZS (Malvern, UK) at room temperature.

NH_2-PEG Modification of Carboxylated Polymer-Coated QDs. Polymer-coated QDs possessing carboxyl terminal groups (pcQD) were prepared according to the procedure described in the literature.[36] The pcQDs (100 pmol) were reacted with

Scheme 1. Synthetic Scheme for Anti-GFP Antibody-Conjugated TAT-PEG-pcQD[a]

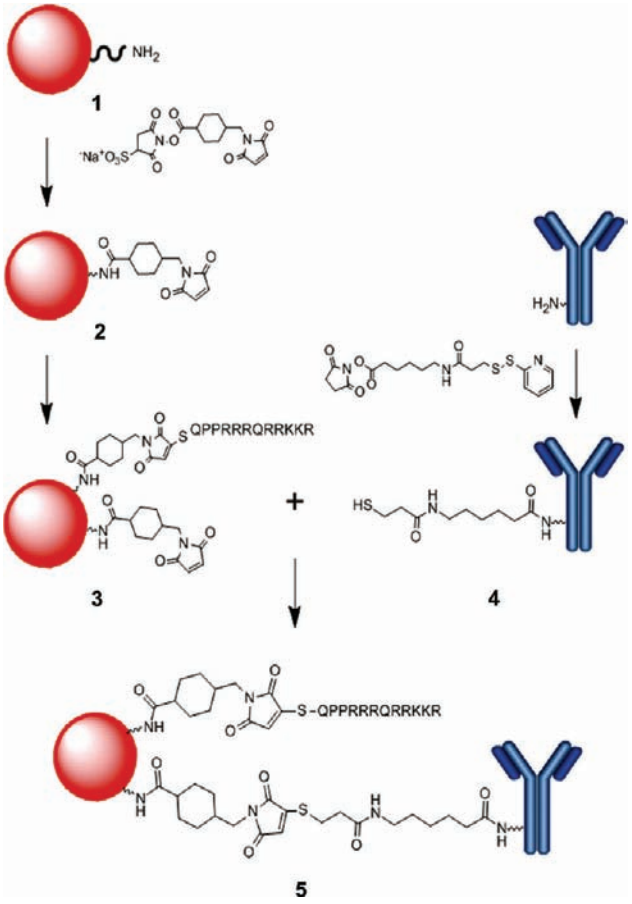

[a] Diamino-PEG5k modified pcQD (NH_2-PEG-pcQD, **1**) was reacted with sulfo-SMCC to give SMCC-PEG-pcQD **2**, followed by coupling reaction with cystein-modified TAT peptide. The partially modified TAT-PEG-pcQD **3** was further reacted with SPDP-modified antiGFP **4** to yield antiGFP-TAT-PEG-pcQD **5**. As a control, antiGFP-pcQD without TAT was synthesized by reacting **2** with **4** to yield antiGFP-PEG-pcQD.

20 000 equiv of diamino-PEG5k in 10 mM borate buffer (pH 8) in the presence of 5000 equiv of EDC for 16 h at room temperature. The reaction mixture was purified by membrane filtration using Microcon (MWCO, 100 kDa, Milipore) with 5× centrifugation in deionized water. The final conjugate (NH_2-PEG-pcQD, **1**) in Scheme 1 was characterized using agarose gel electrophoresis for the electrophoretic mobility and DLS for the hydrodynamic size. The QD concentration was determined by the absorption at the first exciton peak using the extinction coefficent according to the literature.[39,40]

TAT Peptide Conjugation of NH_2-PEG-pcQD. To conjugate TAT peptide to the amine-functionalized PEG-pcQD, 100 pmol of QD **1** was first reacted with 5000 equiv of sulfo-SMCC in 1 mL of 1×PBS (10 mM phosphate buffer, 150 mM NaCl, pH 7.4) for 1 h at room temperature before purification with membrane filter (MWCO 100 kDa, Milipore). Twenty picomoles of SMCC-modified PEG-pcQDs (SMCC-PEG-pcQD, **2**) was then added to the cystein-modified TAT peptide (c-TAT; QPPRRRQRRKKR; 1 nmol) in 200 μL of 1×PBS buffer and reacted for 1 h at room temperature. The partially modified TAT-PEG-pcQD **3** conjugate was purified five times with 1×PBS by using 100 kDa MWCO membrane filter. The filtrate was collected and concentrated for determination of the number of TAT molecules per QD using BCA assay.

Anti-GFP antibody Conjugation of TAT-PEG-pcQD. First, the anti-GFP antibody (molecular weight 150 kDa, 67 pmol) was activated with 1000 equiv of sulfo-LC-SPDP in 1×PBS for 30 min at room temperature. To avoid oxidation of the resulting thiol group of the SPDP-modified anti-GFP antibody (SPDP-antiGFP, **4**), 0.1 M DTT (10 μL) was added and reacted for an additional 10 min and the conjugate was purified three times with 1× PBS using 30 kDa MWCO membrane filter. Finally, 4 equiv of **4** was added to the partially modified TAT-PEG-pcQD **3** and incubated for 3 h at room temperature with gentle shaking. The reaction mixture was then purified using a size exclusion column filled with S-200 resin. The fluorescent fractions monitored by hand-held UV lamp for QD fluorescence were collected and concentrated using 100 kDa MWCO membrane filter in 1×PBS before agarose gel electrophoresis analysis and DLS measurement.

Cell Culture. The human epidermal carcinoma cell line HeLa was cultured at 37 °C in a humidified atmosphere and 5% CO_2 in Dulbecco's modified eagle's medium (DMEM) supplemented with 10% fetal bovine serum, 100 IU/mL penicillin, and 100 IU/mL streptomycin (all from Invitrogen). HEK293 cells were cultured in DMEM/F12 medium supplemented with 10% fetal calf serum, 1% penicillin streptomycin, and 1% Geneticin under humidified air containing 5% CO_2 at 37 °C.

Construction of a Stable HEK293 Cell Line Expressing GFP-Tagged ET_AR. A human endothelin A receptor (ET_AR) cDNA clone (www.cDNA.org) was fused to the eGFP coding sequence of the pEGFP-N1 vector (Clontech, USA) and ligated in the pCDNA3.1(-) vector. The resulting endothelin A-EGFP DNA was cloned, checked by sequencing, and used for transfection of HEK293 cells using standard protocols. A recombinant clone was obtained through several selections with 1% of v/v Geneticin (Invitrogen).

Cytotoxicity Test. MTT assay was performed to evaluate the cytotoxicity of the pcQDs at various concentrations (10 nM to 1 μM). HeLa cells were incubated with the QDs in a dose-dependent manner for 1 and 5 days and the percentage of viable cell was measured by MTT assay. At each time point, MTT (0.5 mg/mL) was added to each well, and the plates were incubated at 37 °C for 4 h. Spectrophotometric data were obtained by Victor3 microplate reader (Perkin-Elmer, USA) at 531 nm. The MTT assay was performed in duplicates for each condition.

Live Cell Imaging. Cellular uptake of the QDs in live cells was investigated by confocal laser scanning fluorescence microscope (LSM5 Live, Carl Zeiss) in HeLa cell line. HeLa cells (5000 cells/well) were seeded in glass-bottomed 8-well chamber slide (Lab-Tek) with 0.4 mL DMEM medium. For the study on nonspecific endocytosis of the QDs, the cells were treated with various concentrations of the QDs (10−500 nM) and incubated up to 24 h at 37 °C in the CO_2 incubator. For the targeting of the intracellular GFP tethered to the c-terminal region of the ET_AR, antiGFP-TAT-PEG-pcQD conjugate solution (2.5 μM) was added to the HEK293 cells expressing GFP-tagged ET_AR with the final concentration 10 nM for 30 min. For endosomal labeling, 1 μL of AF634-transferrin (1 mg/mL in 1×PBS) was

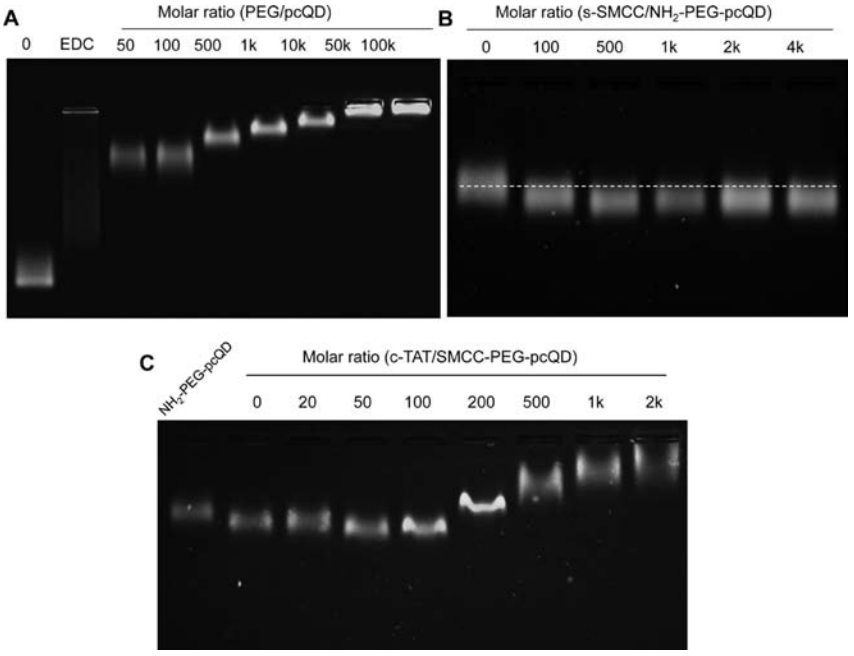

Figure 1. Gel electrphoresis analysis for various QD conjugation reactions: (A) conjugation of pcQD with diamno-PEG5k, (B) sulfo-SMCC conjugation to NH_2-PEG-pcQD **1**, (C) c-TAT conjugation to SMCC-PEG-pcQD **2**. 1% agarose gel was run for 50 min at 50 V in 0.5×TBE buffer (pH 8).

also added to the cell medium. After incubation for 20 min at 37 °C, the cells were washed three times with fresh DMEM medium.

Fluorescence Microscopy and Image Analysis. Fluorescence images of the cells were obtained with the confocal microscope at 37 °C in a live cell chamber using a 63×/1.4 NA oil immersion objective and scan speed of 1−5 frame/s. For the excitation of QD, 488 Ar-ion laser line was used with emission bandpass filter (550−615 nm), while the AF634-transferrin conjugate was excited with a 633 He−Ne laser and observed with a long pass filter (650 nm). The confocal fluorescence images were processed using *Zen 2008* software (Carl Zeiss).

■ RESULTS AND DISCUSSION

Synthesis and Characterization of AntiGFP-TAT-pcQD Conjugate 5. Conjugation of anti-GFP antibody to TAT-PEG-pcQD **3** was performed using two different heterobifunctional linkers, sulfo-SMCC and sulfo-LC-SPDP, as shown in Scheme 1.

Diamino-PEG Conjugation to pcQD. The carboxyl groups of the pcQD (50 pmol) were reacted with various amounts of diamino-PEG5k (50−100 k equiv) in the presence of EDC (25 nmol). The mobility of pcQD was highly reduced after conjugation of PEG molecules due to the decrease of negative charges and the increase of the size of the pcQD. The pcQD activated with EDC alone were destabilized and aggregated, while PEGylated pcQDs **1** showed high stability in various buffer conditions showing the decrease in mobility with the increase in molar ratios of the PEG to pcQD (Figure 1A). DLS analysis also showed the increase of hydrodynamic diameter from 12 ± 1 nm (pcQD) to 14 ± 1.5 nm. The electrophoretic mobility was maximized at the molar ratios of PEG over 10k, with the apparent mobility of 2.0×10^{-9} cm V^{-1} s^{-1}. Considering the potential cytotoxic effects, the decreased negative charges inducing colloidal instability, and the higher content of PEGs, we used NH_2-PEG-pcQD **2** prepared with 1:500 molar ratio of QD to PEG for further reaction. See Supporting Information Figure S1 for the agarose gel electrophoresis characterization of PEGylated pcQDs with different molecular weights of PEGs.

*Sulfo-SMCC Conjugation to QD **1**.* The *N*-hydroxyl succinimide group of the sulfo-SMCC reacts with the amino groups of QD **1**. The agarose gel electrophoresis exhibited the increasing mobility of sulfo-SMCC activated QD **2** with the increase of the molar ratio of sulfo-SMCC to QD **1** (100−4000) (Figure 1B). It may be due to the fact that the overall negative charges relatively increase as the SMCC reacts with amino groups of QD **1**. On the basis of this result, the molar ratio of 1000 (SMCC to QD **1**) was used for further conjugation.

*TAT Peptide Conjugation to Sulfo-SMCC-PEG-QD **2**.* QD **2** bearing an optimized number of SMCC moieties was used for both TAT and anti-GFP antibody conjugation. We first performed a titration experiment using c-TAT with the increasing molar ratios of the c-TAT to QD **2** (20−2000 equiv). The mobility of QD **2** gradually decreased as more c-TAT molecules reacted with QD **2** (Figure 1C) due to the positively charged arginine-rich TAT peptide. This result allowed us to determine the amount of c-TAT per QD **2** for partial TAT modification, while the remaining SMCC groups can be further conjugated to the anti-GFP antibody. In the molar ratio of 200, we found that approximately 50 TAT peptides were conjugated to QD **2**, which was determined by BCA protein assay.

*Anti-GFP Antibody Conjugation to TAT-PEG-pcQD **3**.* To minimize the steric hindrance of antibody, we introduced a long chain heterobifunctional linker, sulfo-LC-SPDP, to the anti-GFP antibody to afford antibody **4**. The 4-fold molar excess of SPDP-anti-GFP antibody **4** was then allowed to react with QD **3** for 3 h, followed by purification with S-200 size exclusion column equilibrated with 1×PBS (pH 7.4) to remove unreacted anti-GFP antibodies. The successful conjugation of antibody to QD **3** was confirmed through both agarose gel electrophoresis and

dx.doi.org/10.1021/bc200126k |*Bioconjugate Chem.* 2011, 22, 1576–1586

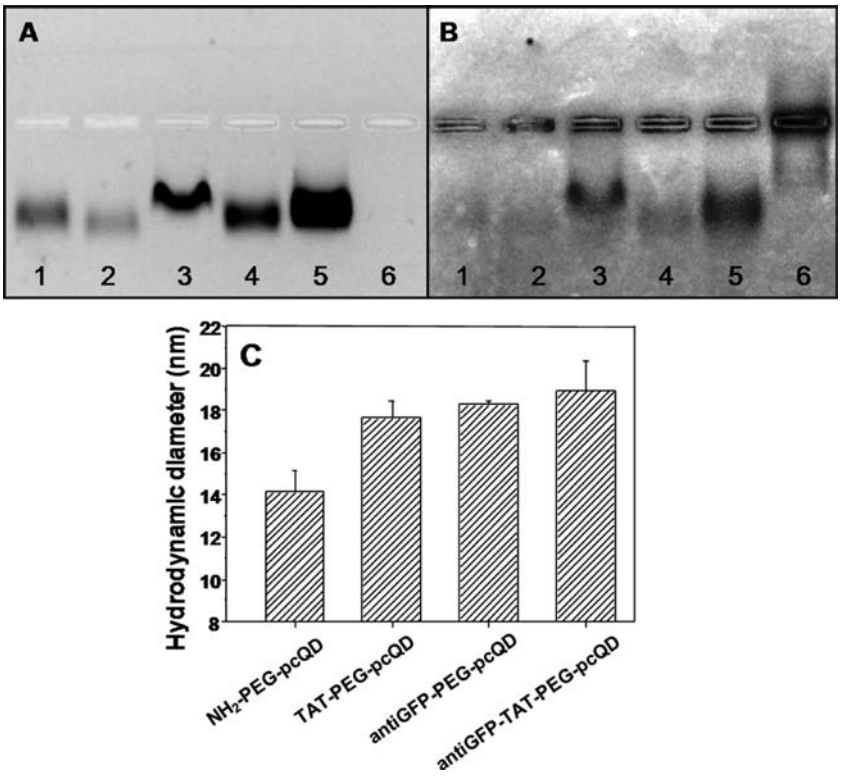

Figure 2. Characterization of anti-GFP antibody-conjugated TAT-PEG-pcQD using agrose gel electrophoresis (A,B) and dynamic light scattering analysis (C). (A) Fluorescence image of the gel with lane 1: NH_2-PEG-pcQD **1** (Em = 600 nm), lane 2: SMCC-pcQD **2**, lane 3: partially modified TAT-PEG-pcQD **3**, lane 4: antiGFP-PEG-pcQD, lane 5: antiGFP-TAT-pcQD **5**, lane 6: anti-GFP antibody (10 μg). 1% agarose gel was run at 50 V for 60 min in 0.5×TBE buffer (pH 8). The loading amount of QD was 1−3 pmol per well, and the same gel was consecutively stained with colloidal blue staining kit. (C) The conjugates showed the size range of 18−19 nm, compared with the starting NH_2-PEG-pcQD **1** (∼14 nm). The values were the average of five measurements in 1×PBS at room temperature.

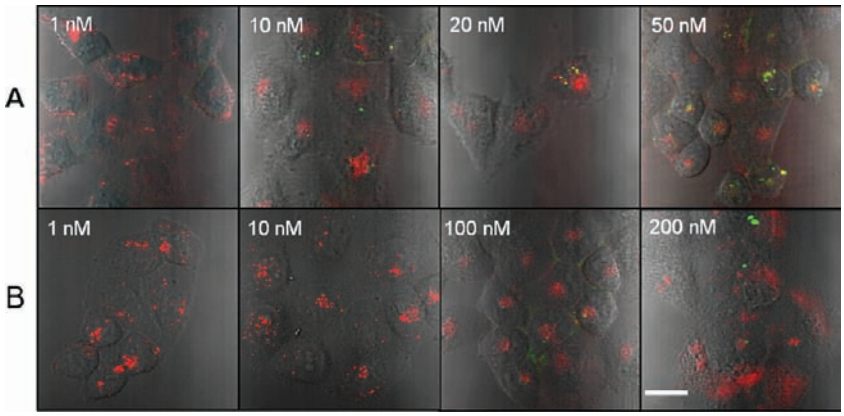

Figure 3. Comparison of nonspecific uptake of various concentrations of unmodified pcQD (A) with NH_2-PEG-pcQD (B). The green QDs (emission peak at 525 nm) were incubated with live HeLa cells for 3 h before confocal fluorescence imaging. The images are the overlay of differential interference contrast (DIC) image (for cell morphology), green channel (for QDs) and red channel (for endosomes labeled with AF634-transferrin). Scale bar = 20 μm.

dynamic light scattering analysis (Figure 2). The electrophoretic mobility of the antiGFP-TAT-PEG-pcQD (lane 5) slightly increased when compared to the TAT-PEG-pcQD (lane 3), and also showing increasing hydrodynamic size (19 ± 1.5 nm). Importantly, high purity of antiGFP-TAT-PEG-pcQD **4** was clearly shown after the column purification, which can be compared with the free antibody control (lane 6) stained with colloidal blue. The number of TAT peptides and anti-GFP antibodies per QD was determined to be 50 ± 5 and 2 ± 0.8, respectively, based on the calibration curve of antibody and TAT peptide according to BCA assay.

Nonspecific Uptake of NH_2-PEG-pcQD versus Unmodified pcQD. The nonspecific endocytosis of unmodified polymer-coated QDs with carboxyl groups are problematic in the case where the specific binding to a target of interest should be observed in cellular imaging. To avoid these undesirable

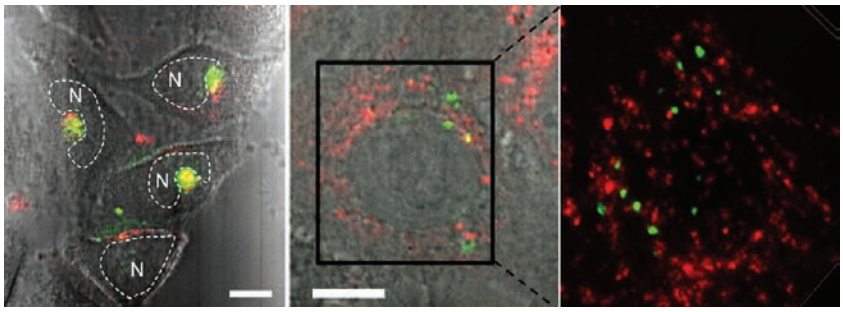

Figure 4. Twenty-four hour incubation of unmodified pcQD (left, 50 nM) and PEG-pcQD (middle and right, 100 nM). The green pcQDs (emission peak at 525 nm) were accumulated predominantly in the perinuclear region and colocalized with late endosomal vesicles. The endosomes were labeled with the red AF634-transferrin conjugate (1 μg/mL). N indicates nucleus region marked with dotted line. The 3D projection of the boxed area in the middle image is represented in the right with only green and red channels for clarity. The scale bar indicates 10 μm.

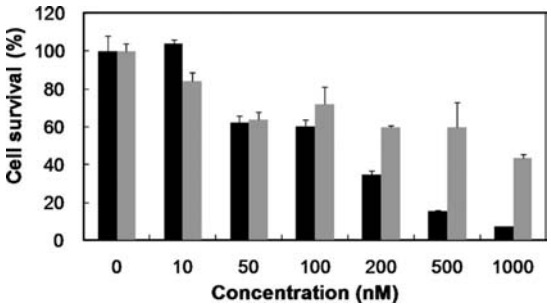

Figure 5. MTT assay of unmodified pcQD (black bar) and NH_2-PEG-pcQD (gray bar) for cytoxicity evaluation.

interactions of nanoparticles with cells, various PEG molecules have been used in biology, pharmaceutics, and polymer chemistry.[41]

Figure 3 shows the comparison of the nonspecific uptake of PEGylated pcQDs with the unmodified pcQD after 3 h incubation in live HeLa cells. The uptake of the pcQD with carboxyl surface (pcQD) was first observed at 10 nM, significantly accumulating in the cells at 50 nM. However, the PEGylated pcQD (NH_2-PEG-pcQD **1**) exhibited no significant cellular uptake in the concentration range 1−50 nM. However, at a higher concentration range (100−200 nM), the PEGylated pcQD showed a slight cellular uptake, though the number of cells showing the QD signal was less than 1% of total cell population (∼10 000 cells per well).

The uptake of PEG-pcQD **1** was hardly observed in the cell even after 24 h incubation at a concentration of 50 nM, which is in contrast with the abundant distribution of carboxylated pcQDs in the cytoplasm, mostly in the perinuclear region (Figure 4). A few PEG-pcQDs **1** found in the cytoplasm were not colocalized with endosomes labeled with AF634-transferrin. Three-dimensional cellular image analysis clearly showed the separate location of PEG-pcQDs from endosomes, indicating that the PEGylation helps to avoid not only nonspecific cellular uptake, but also endosomal sequestration. In addition, the effect of different molecular weights of PEG molecules (750, 2000, 5000) on the cellular uptake of pcQDs was negligible (see Supporting Information Figure S2).

Cytotoxicity of PEGylated pcQD. To quantitatively assess the cytotoxicity of NH_2-PEG-pcQD **1** compared with pcQD, MTT assay was performed according to the standard protocol. The unmodified pcQDs showed significant cytotoxicity with an effective concentration at 50% cell survival (EC_{50}) of ∼120 nM (Figure 5). The NH_2-PEG-pcQDs revealed less cytotoxic effect than pcQD overall, while exhibiting similar cytotoxicity with the unmodified pcQD in the range 10−50 nM. This result indicates that the amino-PEG can reduce the cytotoxicity of pcQD. It is worth noting that the survival ratio of the cell in the presence of PEG-QD was kept in a constant range (∼60%) at the entire concentration range tested (10−500 nM). However, the cytotoxicity of pcQD remarkably increased depending on the concentration. In a separate experiment, we also prepared methoxy PEG-modified pcQD which showed significantly reduced cytotoxicity (see the Supporting Information for the preparation of methoxy PEG-pcQD).

Efficient Intracellular Delivery of PEG-pcQDs via TAT Peptide. The significantly reduced nonspecific binding and the low cytotoxicity of the PEG-pcQDs enabled us to pursue an efficient intracellular delivery using a well-known cell penetrating peptide, human immunodeficiency virus-1 transactivator protein (TAT) peptide. The arginine-rich TAT peptide (RKKRRQRRRPPQ) has been successfully used to promote the internalization of a range of polymeric or inorganic nanoparticles into living cells.[5,28,42,43]

Figure 6 showed the cellular uptake of TAT-PEG-pcQD **3** which was remarkably facilitated, exhibiting characteristic punctate distribution of the QDs throughout the cytoplasm even at 1 nM after 30 min incubation. This facilitated delivery of the PEGylated pcQDs is attributed to the presence of the cationic TAT, which has been known to enhance the interactions with negatively charged cellular membranes.[31]

In the live cell experiment using HeLa cells, the QDs delivered via TAT peptide were not significantly colocalized with endosomes labeled with AF634-transferrin (red fluorescence). This observation potentially indicates that the TAT-PEG-pcQDs enter into cells via the pathway independent of clathrin-mediated endocytosis because transferrin has been well-documented for the clathrin-mediated internalization pathway.[43] Though still being elucidated for the mechanisms of nanoparticle uptake via cell penetrating peptides, recent reports have shown that TAT conjugation to streptavidin-QDs allows for the QDs to follow lipid-dependent macropinocytosis and active transport into cytosol.[29,32,33]

Specific Targeting of Cytoplasmic GFP. Despite the proven efficiency of TAT-mediated facilitated delivery of pcQDs, TAT-PEG-pcQDs alone cannot recognize any specific intracellular targets since they are easily taken up into cells and nonspecifically distributed in the cytoplasm in live cells. However, we hypothesized that the TAT-PEG-pcQD conjugated with an antibody against a specific target protein can find the intracellular target in

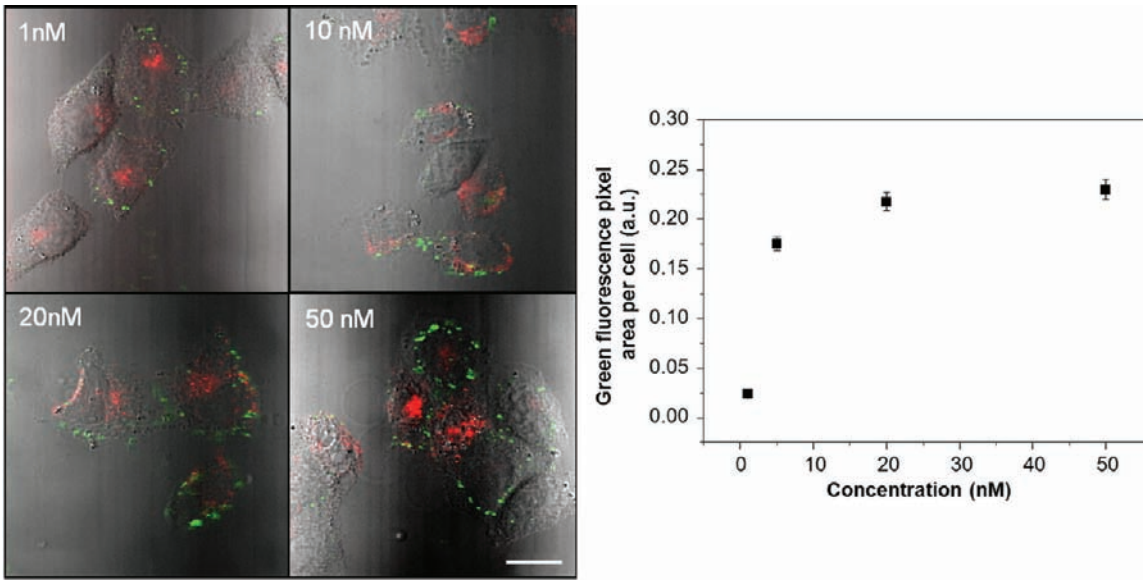

Figure 6. Facilitated intracellular delivery of PEGylated pcQDs mediated by TAT peptide. (Left) Live HeLa cells were incubated with varying concentration of the TAT-PEG-pcQD (1−50 nM) for 30 min at 37 °C before confocal imaging. The representative images at each concentration (1, 5, 20, 50 nM) were the overlays of DIC, green channel for QD, and red channel for endosomes labeled with transferrin-AF634 conjugates. (Right) To quantify the green channel fluorescence per cell, the average pixel areas per cell (n = 10−15) were obtained from the z-section images (10 μm depth with 1 μm interval) stacked in *Zen 2008* software using *ImageJ* plug-in (v 1.43).

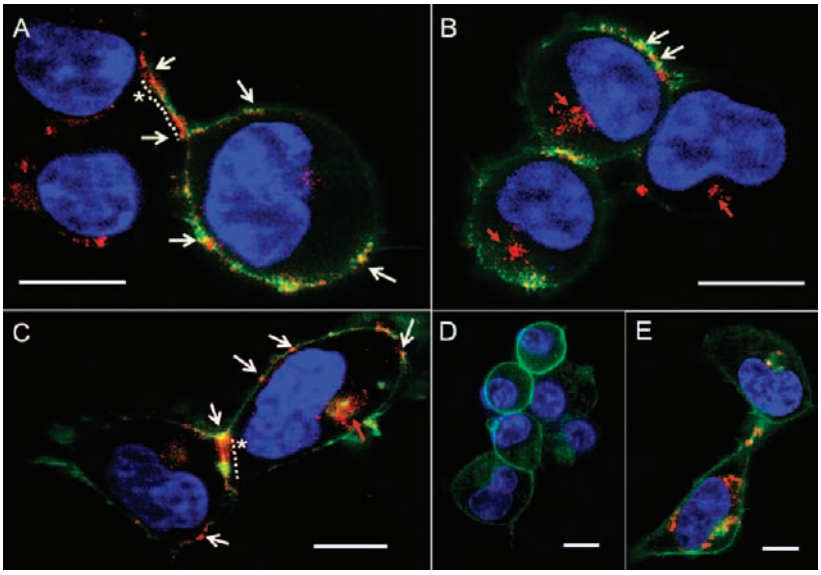

Figure 7. Targeting of the GFP tagged at the c-terminal cytoplamic site of the endothelin A receptor (ET_AR) of HEK293 cells using antiGFP-TAT-PEG-pcQD **5** conjugate (20 nM, emission peak at 605 nm). (A−C) After 30 min incubation, the red QD **5** were delivered to the plasma membrane (white arrows), preferentially localized with GFP signal as indicated by overlaid yellow color; QDs are often observed in the cytosol (red arrow); see Supporting Information Figures S3 and S4 for the separate channel images to identify QD colocalizing with GFP. QDs seemingly entrapped in the plasma membrane were moving rapidly along the membrane or traversing the filipodia of the cells (A; dotted line with asterisk) or along the cellular contacts (C; dotted line with asterisk); see the Supporting Information for the movies (Movie S1 for A and Movie S2 for C). (D,E) Control cell images at the same conditions with the antiGFP-PEG-pcQD (without TAT) showing nonsignificant endocytosis (D) and with the TAT-PEG-pcQD displaying punctuate and evenly distributed cellular uptake mostly in the cytoplasm (E). The images are overlays of blue channel (Hoechst33342 for nucleus), green channel (GFP), and red channel (pcQD). The scale bars correspond to 10 μm.

live cells. We tested this hypothesis by employing the GFP-ET_AR cell model, where the GFP as our target protein is designed to be tethered at the cytoplasmic c-terminal site of the transmembrane receptor ET_AR. To allow for the TAT-PEG-pcQD to target the GFP located in the intracellular region after membrane penetration, we conjugated anti-GFP antibody to the TAT-PEG-pcQD using heterobifunctional linker strategy as schematically shown in Scheme 1.

As shown in Figure 7A−C, antiGFP-TAT-PEG-pcQDs were initially bound to the plasma membrane (white arrows) and

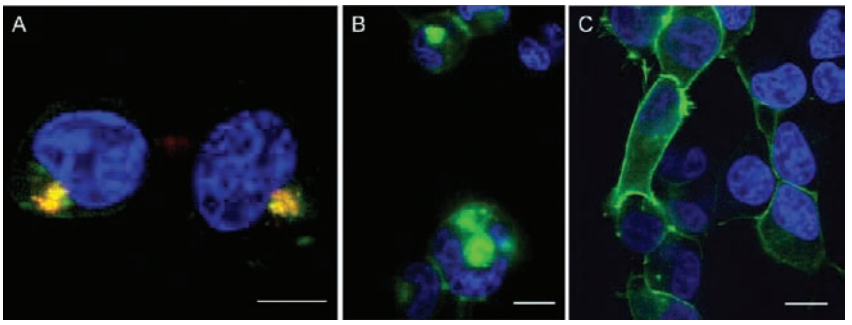

Figure 8. Confocal microscope images of live GFP-ET_AR expressing HEK293 cells incubated with 30 nM antiGFP-TAT-PEG-pcQD (red) for 1 h, followed by an agonist treatment (40 nM ET-1) for additional 1 h (A). The colocalization of the red QD mostly with the GFP cluster shown in yellow color was observed in the pericentriolar region. Notice the concomitant decrease of membrane GFP signal, as the GFP-ET_AR translocated. The characteristic perinuclear clustering of the translocated GFP-ET_AR was shown (B) along with the untreated HEK293 expressing GFP-ET_AR (C). The images are overlays of blue channel (Hoechst33342 nuclear stain), green channel (GFP), and red channel (QD). The scale bars correspond to 10 μm.

some QDs were also observed in the cytoplasm (red arrow) after 30 min incubation at 37 °C. To ensure that the QDs are specifically bound with the target GFP of our interest, the control cellular images were also obtained. The antiGFP-PEG-pcQD (without TAT) showed negligible cellular uptake due to the presence of PEG molecules (Figure 7D). As expected, the nontargeted TAT-PEG-pcQD (without antiGFP) showed punctate and even distribution mostly in the cytoplasm with no significant colocalization with GFP or membrane (Figure 7E). These results indicate that the localization of the antiGFP-TAT-PEG-pcQD in the membrane region can be the result of the facilitated internalization of the QDs owing to TAT conjugation and target binding due to the presence of anti-GFP antibody.

Since our target GFP is tethered to the membrane receptor ET_AR and the anti-GFP antibody is bound to QD, it may be difficult to bind efficiently to each other because of steric hindrance. Accordingly, we noticed that some of GFP signal seemed not to colocalize with the QD, which may be due to the decreased affinity of the conjugated GFP antibodies. In addition, the faster photobleaching of GFP compared to the stable QD signal during the confocal imaging, which is an inherent problem of most fluorescent proteins, could not make complete colocalization of the QD with the GFP signal. Despite this, as noticed from the separate fluorescence channel images of Figure 7A−C in the Supporting Information (Figure S3 and S4), it seemed more evident that the majority of the QD signal was colocalized with the GFP. In addition, the separate channel image of the TAT-PEG-pcQD control (Figure 7E) clearly exhibited cytoplasmic distribution mainly surrounding the nucleus with no significant QD signal at the membrane region (see the Supporting Information Figure S5).

It is noteworthy that a portion of the antiGFP-TAT-PEG-pcQD also appeared colocalized with the GFP in the cytoplasmic endosomal structures as indicated by the red arrows (Figure 7B, C), while some remained on the cellular membrane. This may be related with heterogeneous expression of GFP-ET_AR, which is also in agreement with data in the literature, where CFP- or YFP-tagged ET_AR distribution were found mainly on plasma membrane and slightly within endosomal structure.[44]

Time-Course Imaging. We also performed the time-course imaging to monitor the intracellular behavior of the antiGFP-TAT-PEG-pcQD which is associated with GFP. Tracking of QDs in live cells in real time may provide information on the mechanism of binding of the QD probe to the target given the possibilities of receptor-mediated endocytosis or nonspecific endocytosis (non-TAT mediated); for example, the receptor-mediated endocytosis leads to perinuclear accumulation of QD-receptor after 30 min to 1 h (data not shown), while the nonspecific endocytosis requires at least 3 h to show the similar phenomena as demonstrated in Figure 4.

During the 30 min to 1 h period of imaging time, we found that QD controls without anti-GFP antibody showed negligible binding (PEG-pcQD) or facilitated uptake (TAT-PEG-pcQD) into the cytoplasm. Unlike these control QDs, the colocalized antiGFP-TAT-QD and GFP were moving rapidly along the membrane with an average speed of 0.15 μm/s (n = 10) at the membrane region. Some are traversing between the two cells through the filipodia of the cells (Figure 7A; dotted line with asterisk) or along the cell periphery (Figure 7C; dotted line with asterisk); see the Supporting Information movie for lateral movement of QD along the membrane: Movie S1 for Figure 7A and Movie S2 for Figure 7C. These types of lateral movement on the membrane were not observed in the case of the TAT-PEG-pcQD or other cases of nonspecific endocytosis using, i.e., carboxylated QDs. This spatiotemporal information from the time-course imaging further indicated that the localization of the antiGFP-TAT-PEG-pcQD is associated with the intracellular target GFP.

Despite the limit of optical resolution of confocal fluorescence microscope for the plasma membrane with a thickness of approximately 10 nm, it is technically challenging to differentiate the location of QDs at the inner membrane region from the outer membrane region. However, the unique photochemical properties of QD such as great brightness and resistance to photobleaching allowed for imaging the lateral movement of the antiGFP-TAT-PEG-pcQD in the membrane region. Interestingly, these features of QD movements seem to reflect the dynamic nature of GPCR on the plasma membrane as described in the literature.[38,45−48] It has been reported that various GPCRs including β-adrenergic and GABA receptors, and TGF β-receptors have shown surface mobility with the lateral diffusion coefficients ($(1-12) \times 10^{-9}$ cm^2/s).[45,49−51] Though the measurement of the exact diffusion coefficient of the GFP-ET_AR is not within the scope of this study, our relevant data (0.15 μm/s of QD movement along the membrane) apparently yields 5.6×10^{-10} cm^2/s, when applied with a free diffusion equation; diffusion length = $4Dt$, where D is diffusion coefficient (cm^2/s) and t is the time (s). It is noteworthy that the present GPCR tracking method can be applied to GPCR-related drug screening if the condition for quantifying the endocytosis of GPCR is established.

Ligand-Induced Translocation of Target Protein. To further confirm that QD **5** is specifically bound with the GFP of the ET_AR, we treated the cells with a well-known agonist, endothelin-1 (ET-1), which stimulates the ET_AR to be internalized and translocated into pericentriolar recycling endosomes.[52−54] It was reported that endocytosis of ET_AR occurs in an agonist-dependent manner, and the ET_AR bound to ET-1 remains a stable complex for at least 2 h in the cell.[55]

As shown in Figure 8, ET-1 treatment on the cells preincubated with QD **5** (30 nM) for 1 h resulted in the decrease of membrane GFP signal and the increase of perinuclear GFP signal. The majority of the red QDs colocalized with the green ET_AR cluster as appeared in yellowish color in the pericentriolar region (Figure 8A). This is attributed to the ET-1 induced ET_AR translocation from cellular membrane to perinuclear region, which allows for the GFP tethered to ET_AR to translocate together. See the Supporting Information Figure S5 for separate channel images for identification of colocalization. Also, we found that a small portion of QDs are still present in the membrane region at the different focal plane. This may be due to a heterologous translocation pattern of the ET_AR, or potential oligomerization of the ET_AR, leading to the aggregation on the surface.[38] See the Supporting Information Figure S6 for the *z*-section images of Figure 8A. For comparison purposes, the characteristic perinuclear clustering of the translocated ET_AR after ET-1 treatment was shown in Figure 8B. Also, no activated translocation of GFP-ET_AR without agonist treatment during the 2 h was observed in the naïve cells (Figure 8C). These results suggest that the QD signal is associated with ET-1-dependent ET_AR receptor pathway, confirming the specific binding of the antiGFP-TAT-PEG-pcQD to the target GFP.

CONCLUSIONS

Specific intracellular target detection in live cells using QD was demonstrated by the antibody-functionalized TAT-PEG-pcQD prepared by stepwise optimization of the conjugation of pcQDs with PEG, TAT, and anti-GFP antibody. To demonstrate the intracellular targeting specificity of the QD conjugate, a model cell line overexpressing cytoplasmic GFP as an intracellular target at the c-terminal site of endothelin A receptor (ET_AR) was constructed. The GFP-ET_AR cellular model allowed for identification of specific binding of the red-emitting antiGFP-TAT-PEG-pcQD with the cytoplasmic GFP of the ET_AR via colocalization. To further confirm the specificity of the probe to the target GFP, the ET_AR agonist (ET-1)-induced translocation phenomenon of GPCR was utilized. When compared with the controls (PEG-pcQD, TAT-PEG-pcQD, and antiGFP-PEG-pcQD), the antiGFP-TAT-PEG-pcQD was significantly colocalized with the translocated GFP-ET_AR cluster in the pericentriolar region after the ET-1 treatment. High luminescence and photostability of the QDs also allowed us to obtain spatiotemporal information of the target protein in live cells, offering the potential of the QD for target visualization in living cells.

These results suggested successful specific binding of the antiGFP-TAT-PEG-pcQD with the intracellular target GFP in living cells. This study demonstrated that controlled functionalization of PEGylated pcQDs with both TAT and an antibody against a target of interest can afford efficient cellular entry of QDs as well as specific detection of an intracellular target without significant nonspecific uptake or binding. Further studies are underway to explore the potential of the TAT-PEG-pcQD-based probes for visualizing multiple targets in live cells. The detection of target proteins without any fluorescent tagging should be the ultimate goal of this study. We are currently applying this strategy to pursue drug-target identification in live cells.

ASSOCIATED CONTENT

Supporting Information. Details of synthesis and characterization of polymer-coated quantum dot and methoxy PEGylated pcQDs; cellular uptake of PEGylated pcQDs with different molecular weights of PEG molecules; separate confocal fluorescence channel images of Figure 7A,B,C, and Figure 8A; *z*-section image of Figure 8A; cellular entry of TAT-PEG-pcQD. This material is available free of charge via the Internet at http://pubs.acs.org.

AUTHOR INFORMATION

Corresponding Author

*Dr. Youngseon Choi, Chemical Biology Laboratory, Institut Pasteur Korea (IP-K), 696 Sampyeong-dong, Bundang-gu, Seongnam-Si, Gyeonggi-Do, 463-400, South Korea; (Tel) +82-31-8018-8234, (Fax) +82-31-8018-8014, E-mail: yschoi@ip-korea.org. Dr. Rita Song, Chemical Biology Laboratory, IP-K; (Tel) +82-31-8018-8230, (Fax) +82-31-8018-8014, E-mail: rsong@ip-korea.org.

ACKNOWLEDGMENT

This research was supported by the National Research Foundation of Korea funded by Ministry of Education and Science and Technology through National R&D Program (no. 2010-0019107) and Basic Science Research Program (no. 2010-0024880).

REFERENCES

(1) Lang, P., Yeow, K., Nichols, A., and Scheer, A. (2006) Cellular imaging in drug discovery. *Nat. Rev. Drug Discovery 5*, 343–356.

(2) Alivisatos, P. (2004) The use of nanocrystals in biological detection. *Nat. Biotechnol. 22*, 47–52.

(3) Michalet, X., Pinaud, F. F., Bentolila, L. A., Tsay, J. M., Doose, S., Li, J. J., Sundaresan, G., Wu, A. M., Gambhir, S. S., and Weiss, S. (2005) Quantum dots for live cells, in vivo imaging, and diagnostics. *Science 307*, 538–544.

(4) Medintz, I. L., Uyeda, H. T., Goldman, E. R., and Mattoussi, H. (2005) Quantum dot bioconjugates for imaging, labelling and sensing. *Nat. Mater. 4*, 435–446.

(5) Delehanty, J. B., Boeneman, K., Bradburne, C. E., Robertson, K., and Medintz, I. L. (2009) Quantum dots: a powerful tool for understanding the intricacies of nanoparticle-mediated drug delivery. *Expert Opin. Drug Delivery 6*, 1091–1112.

(6) Kirchner, C., Liedl, T., Kudera, S., Pellegrino, T., Javier, A. M., Gaub, H. E., Stolzle, S., Fertig, N., and Parak, W. J. (2005) Cytotoxicity of colloidal CdSe and CdSe/ZnS nanoparticles. *Nano Lett. 5*, 331–338.

(7) Gopalakrishnan, G., Danelon, C., Izewska, P., Prummer, M., Bolinger, P. Y., Geissbuhler, I., Demurtas, D., Dubochet, J., and Vogel, H. (2006) Multifunctional lipid/quantum dot hybrid nanocontainers for controlled targeting of live cells. *Angew. Chem., Int. Ed. 45*, 5478–5483.

(8) Howarth, M., Liu, W. H., Puthenveetil, S., Zheng, Y., Marshall, L. F., Schmidt, M. M., Wittrup, K. D., Bawendi, M. G., and Ting, A. Y. (2008) Monovalent, reduced-size quantum dots for imaging receptors on living cells. *Nat. Methods 5*, 397–399.

(9) Mok, H., Bae, K. H., Ahn, C. H., and Park, T. G. (2009) PEGylated and MMP-2 specifically dePEGylated quantum Dots: comparative evaluation of cellular uptake. *Langmuir 25*, 1645–1650.

(10) Parak, W. J., Boudreau, R., Le Gros, M., Gerion, D., Zanchet, D., Micheel, C. M., Williams, S. C., Alivisatos, A. P., and Larabell, C. (2002) Cell motility and metastatic potential studies based on quantum dot imaging of phagokinetic tracks. *Adv. Mater. 14*, 882–885.

(11) Jaiswal, J. K., Mattoussi, H., Mauro, J. M., and Simon, S. M. (2003) Long-term multiple color imaging of live cells using quantum dot bioconjugates. *Nat. Biotechnol. 21*, 47–51.

(12) Hoshino, A., Fujioka, K., Oku, T., Nakamura, S., Suga, M., Yamaguchi, Y., Suzuki, K., Yasuhara, M., and Yamamoto, K. (2004) Quantum dots targeted to the assigned organelle in living cells. *Microbiol. Immunol. 48*, 985–994.

(13) Lovric, J., Bazzi, H. S., Cuie, Y., Fortin, G. R. A., Winnik, F. M., and Maysinger, D. (2005) Differences in subcellular distribution and toxicity of green and red emitting CdTe quantum dots. *J. Mol. Med. 83*, 377–385.

(14) Maysinger, D., Lovric, J., Eisenberg, A., and Savic, R. (2007) Fate of micelles and quantum dots in cells. *Eur. J. Pharm. Biopharm. 65*, 270–281.

(15) Hild, W. A., Breunig, M., and Goepferich, A. (2008) Quantum dots - Nano-sized probes for the exploration of cellular and intracellular targeting. *Eur. J. Pharm. Biopharm. 68*, 153–168.

(16) Chang, E., Yu, W. W., Colvin, V. L., and Drezek, R. (2005) Quantifying the influence of surface coatings on quantum dot uptake in cells. *J. Biomed. Nanotechnol. 1*, 397–401.

(17) Bentzen, E. L., Tomlinson, I. D., Mason, J., Gresch, P., Warnement, M. R., Wright, D., Sanders-Bush, E., Blakely, R., and Rosenthal, S. J. (2005) Surface modification to reduce nonspecific binding of quantum dots in live cell assays. *Bioconjugate Chem. 16*, 1488–1494.

(18) Tan, S. J., Jana, N. R., Gao, S. J., Patra, P. K., and Ying, J. Y. (2010) Surface-ligand-dependent cellular Interaction, subcellular Localization, and cytotoxicity of polymer-coated quantum dots. *Chem. Mater. 22*, 2239–2247.

(19) Zhang, L. W., and Monteiro-Riviere, N. A. (2009) Mechanisms of quantum Dot nanoparticle cellular uptake. *Toxicol. Sci. 110*, 138–155.

(20) Verma, A., and Stellacci, F. (2010) Effect of surface properties on nanoparticle-cell interactions. *Small 6*, 12–21.

(21) Winter, J. O., Liu, T. Y., Korgel, B. A., and Schmidt, C. E. (2001) Recognition molecule directed interfacing between semiconductor quantum dots and nerve cells. *Adv. Mater. 13*, 1673–1677.

(22) Bharali, D. J., Lucey, D. W., Jayakumar, H., Pudavar, H. E., and Prasad, P. N. (2005) Folate-receptor-mediated delivery of InP quantum dots for bioimaging using confocal and two-photon microscopy. *J. Am. Chem. Soc. 127*, 11364–11371.

(23) Gussin, H. A., Tomlinson, I. D., Little, D. M., Warnement, M. R., Qian, H. H., Rosenthal, S. J., and Pepperberg, D. R. (2006) Binding of muscimol-conjugated quantum dots to GABA(c) receptors. *J. Am. Chem. Soc. 128*, 15701–15713.

(24) Lidke, D. S., Nagy, P., Heintzmann, R., Arndt-Jovin, D. J., Post, J. N., Grecco, H. E., Jares-Erijman, E. A., and Jovin, T. M. (2004) Quantum dot ligands provide new insights into erbB/HER receptor-mediated signal transduction. *Nat. Biotechnol. 22*, 198–203.

(25) Lee, J., Choi, Y., Kim, K., Hong, S., Park, H. Y., Lee, T., Cheon, G. J., and Song, R. (2010) Characterization and cancer cell specific binding properties of Anti-EGFR antibody conjugated quantum dots. *Bioconjugate Chem. 21*, 940–946.

(26) Zhou, M., Nakatani, E., Gronenberg, L. S., Tokimoto, T., Wirth, M. J., Hruby, V. J., Roberts, A., Lynch, R. M., and Ghosh, I. (2007) Peptide-labeled quantum dots for imaging GPCRs in whole cells and as single molecules. *Bioconjugate Chem. 18*, 323–332.

(27) Fischer, R., Fotin-Mleczek, M., Hufnagel, H., and Brock, R. (2005) Break on through to the other side - Biophysics and cell biology shed light on cell-penetrating peptides. *ChemBioChem 6*, 2126–2142.

(28) Patel, L. N., Zaro, J. L., and Shen, W. C. (2007) Cell penetrating peptides: Intracellular pathways and pharmaceutical perspectives. *Pharm. Res. 24*, 1977–1992.

(29) Richard, J. P., Melikov, K., Brooks, H., Prevot, P., Lebleu, B., and Chernomordik, L. V. (2005) Cellular uptake of unconjugated TAT peptide involves clathrin-dependent endocytosis and heparan sulfate receptors. *J. Biol. Chem. 280*, 15300–15306.

(30) Richard, J. P., Melikov, K., Vives, E., Ramos, C., Verbeure, B., Gait, M. J., Chernomordik, L. V., and Lebleu, B. (2003) Cell-penetrating peptides - A reevaluation of the mechanism of cellular uptake. *J. Biol. Chem. 278*, 585–590.

(31) Wadia, J. S., Stan, R. V., and Dowdy, S. F. (2004) Transducible TAT-HA fusogenic peptide enhances escape of TAT-fusion proteins after lipid raft macropinocytosis. *Nat. Med. 10*, 310–315.

(32) Ruan, G., Agrawal, A., Marcus, A. I., and Nie, S. (2007) Imaging and tracking of tat peptide-conjugated quantum dots in living cells: new insights into nanoparticle uptake, intracellular transport, and vesicle shedding. *J. Am. Chem. Soc. 129*, 14759–14766.

(33) Chen, B., Liu, Q. L., Zhang, Y. L., Xu, L., and Fang, X. H. (2008) Transmembrane delivery of the cell-penetrating peptide conjugated semiconductor quantum Dots. *Langmuir 24*, 11866–11871.

(34) Wei, Y., Jana, N. R., Tan, S. J., and Ying, J. Y. (2009) Surface coating directed cellular delivery of TAT-functionalized quantum dots. *Bioconjugate Chem. 20*, 1752–1758.

(35) Paasche, J. D., Attramadal, T., Kristiansen, K., Oksvold, M. P., Johansen, H. K., Huitfeldt, H. S., Dahl, S. G., and Attramadal, H. (2005) Subtype-specific sorting of the ETA endothelin receptor by a novel endocytic recycling signal for G protein-coupled receptors. *Mol. Pharmacol. 67*, 1581–1590.

(36) Bhowmick, N., Narayan, P., and Puett, D. (1998) The endothelin subtype A receptor undergoes agonist- and antagonist-mediated internalization in the absence of signaling. *Endocrinology 139*, 3185–3192.

(37) Drake, M. T., Shenoy, S. K., and Lefkowitz, R. J. (2006) Trafficking of G protein-coupled receptors. *Circ. Res. 99*, 570–582.

(38) Bohme, I., and Beck-Sickinger, A. G. (2009) Illuminating the life of GPCRs. *Cell Commun. Signal 7*, 16.

(39) Choi, Y., Kim, H. P., Hong, S. M., Ryu, J. Y., Han, S. J., and Song, R. (2009) In situ visualization of gene expression using polymer-coated quantum-dot-DNA conjugates. *Small 5*, 2085–2091.

(40) Yu, W. W., Qu, L. H., Guo, W. Z., and Peng, X. G. (2003) Experimental determination of the extinction coefficient of CdTe, CdSe, and CdS nanocrystals. *Chem. Mater. 15*, 2854–2860.

(41) Otsuka, H., Nagasaki, Y., and Kataoka, K. (2003) PEGylated nanoparticles for biological and pharmaceutical applications. *Adv. Drug Delivery Rev. 55*, 403–419.

(42) Kaplan, I. M., Wadia, J. S., and Dowdy, S. F. (2005) Cationic TAT peptide transduction domain enters cells by macropinocytosis. *J. Controlled Release 102*, 247–253.

(43) Traub, L. M. (2009) Tickets to ride: selecting cargo for clathrin-regulated internalization. *Nat. Rev. Mol. Cell Biol. 10*, 583–596.

(44) Gregan, B., Jurgensen, J., Papsdorf, G., Furkert, J., Schaefer, M., Beyermann, M., Rosenthal, W., and Oksche, A. (2004) Ligand-dependent differences in the internalization of endothelin A and endothelin B receptor heterodimers. *J. Biol. Chem. 279*, 27679–27687.

(45) Pooler, A. M., and McIlhinney, R. A. J. (2007) Lateral diffusion of the GABA(B) receptor is regulated by the GABA(B2) C terminus. *J. Biol. Chem. 282*, 25349–25356.

(46) Ostrom, R. S., and Insel, P. A. (2004) The evolving role of lipid rafts and caveolae in G protein-coupled receptor signaling: implications for molecular pharmacology. *Br. J. Pharmacol. 143*, 235–245.

(47) Hur, E. M., and Kim, K. T. (2002) G protein-coupled receptor signaling and cross-talk - Achieving rapidity and specificity. *Cell Signal 14*, 397–405.

(48) Nelson, S., Horvat, R. D., Malvey, J., Roess, D. A., Barisas, B. G., and Clay, C. M. (1999) Characterization of an intrinsically fluorescent gonadotropin-releasing hormone receptor and effects of ligand binding on receptor lateral diffusion. *Endocrinology 140*, 950–957.

(49) Barak, L. S., Ferguson, S. S. G., Zhang, J., Martenson, C., Meyer, T., and Caron, M. G. (1997) Internal trafficking and surface mobility of a functionally intact beta(2)-adrenergic receptor-green fluorescent protein conjugate. *Mol. Pharmacol. 51*, 177–184.

(50) Hebert, T. E., Gales, C., and Rebois, R. V. (2006) Detecting and imaging protein-protein interactions during g protein-mediated signal

transduction in vivo and in situ by using fluorescence-based techniques. *Cell Biochem. Biophys. 45*, 85–109.

(51) Ma, X. Y., Wang, Q., Jiang, Y. X., Xiao, Z. Y., Fang, X. H., and Chen, Y. G. (2007) Lateral diffusion of TGF-beta type I receptor studied by single-molecule imaging. *Biochem. Biophys. Res. Commun. 356*, 67–71.

(52) Chun, M. Y., Lin, H. Y., Henis, Y. I., and Lodish, H. F. (1995) Endothelin-induced endocytosis of cell-surface ET(a) receptors - endothelin remains intact and bound to the ET(a) receptor. *J. Biol. Chem. 270*, 10855–10860.

(53) Abe, Y., Nakayama, K., Yamanaka, A., Sakurai, T., and Goto, K. (2000) Subtype-specific trafficking of endothelin receptors. *J. Biol. Chem. 275*, 8664–8671.

(54) Bagnato, A., Spinella, F., and Rosano, L. (2008) The endothelin axis in cancer: the promise and the challenges of molecularly targeted therapy. *Can. J. Physiol. Pharmacol. 86*, 473–484.

(55) Chun, M. Y., Liyanage, U. K., Lisanti, M. P., and Lodish, H. F. (1994) Signal transduction of a G-protein-coupled receptor in caveolae - colocalization of endothelin and its receptor with caveolin. *Proc. Natl. Acad. Sci. U. S. A. 91*, 11728–11732.

Supporting Information

Intracellular Target Protein Detection by Quantum Dots Optimized for Live Cell Imaging

Youngseon Choi, Keumhyun Kim, Sukmin Hong, HiChul Kim,† Yong-Jun Kwon,† and Rita Song**

Nano/Bio Chemistry Laboratory, †Discovery Biology Group, Institut Pasteur Korea, Seongnam-Si, Gyeonggi-Do, 464-400, South Korea

*Email address: yschoi@ip-korea.org, rsong@ip-korea.org

(1) Synthesis and characterization of polymer-coated QDs (pcQD)

Polymer-coated QDs were prepared by the method reported in the literature with a slight modification.[1-3] Briefly, trioctylphosphine oxide (TOPO)-capped CdSe/ZnS QDs were encapsulated with amphiphilic polymer molecules via hydrophobic interactions.

Synthesis of TOPO-capped CdSe/ZnS QDs. Selenium powder and cadmium precursors was added into a 50 mL three-neck flask with ODE (20.0 g). The mixture was degassed for 10 min under vacuum at room temperature. Under Ar flow, the solution was stirred and heated to the reaction

temperature (300 °C). After the reaction had terminated, a solution of oleic acid in ODE (0.05 M, 2.5 mL) was added dropwise into the reaction solution to stabilize the growth of nanocrystals. The solution was cooled down to room temperature. To prepare ZnS shell-coated QDs, CdSe nanocrystals were mixed with 2 g of TOPO and 2 g of hexadecylamine (HDA), and chloroform was evaporated completely. The solution was heated to 170 °C in Ar atmosphere. A capping solution containing 2 mL of diethylzinc (2mL) and 400 μL of hexamethyldisilathiane ($(TMS)_2S$) and 10 mL of trioctylphosphine (TOP) were added slowly to the reaction flask for 3 h, after which the solution was cooled down to room temperature. Finally, the solution was filtered through a 0.2 μm pore size polypropylene syringe filter

Synthesis of octylamine-modified poly (acrylic acid). Poly (acrylic acid) (PAA, 3.6 g; M.W. 1800, Aldrich) and EDC (2.3 g) were transferred into a 100 mL round-bottom flask. 40mL of DMF was added to dissolve the mixture. About 1.2 mL of octylamine (99 %, Aldrich) was added dropwise into the reaction flask. When the reaction was complete, DMF was removed by evaporator, and the residue was mixed with 10mL of acetone and transferred into a centrifuge tube. 40 mL of water was added, and the gummy precipitated product was separated by centrifugation (3000 rpm for 10 min) and washed thoroughly with water. The amount of octylamine conjugation was ~ 15 % as determined by NMR analysis. The octylamine-modified PAA with this range of ratio showed the best water solubility and the highest quantum yield (QY) of 30 % ~ 60 %.

Polymer coating of TOPO-capped CdSe/ZnS. The octylamine-modified PAA was dissolved in 2 mL of chloroform. Tetramethyl-ammonium hydroxide was added to the polymer solution to raise the pH of the solution up to 10. The polymer solution was added to 5 mL of chloroform in a 20 mL round bottom flask and the solution was stirred for 1 min to ensure complete admixture of the polymer solution. With continued stirring, CdSe/ZnS QD solution was added dropwise to the polymer solution. The mixed solution was then stirred for two minutes to ensure the complete homogeneous solution and then the chloroform was removed in vacuo with a slight heating to yield a thin film of the particle-polymer complex on the wall of the flask. 5 mL of distilled water was added to the flask and swirled along the walls of the flask to disperse the particles in the aqueous medium. The dispersion was then allowed to stir overnight at room temperature. Finally, the solution was centrifuged (4,000 g, 15 min) to remove aggregates and filtered through a 0.2 μm pore size PVDF syringe filter. The resulting polymer-coated QDs in water, further used for DNA conjugation, was characterized by fluorescence spectrometer, transmission electron microscope (TEM), gel permeation chromatography (GPC), agarose gel electrophoresis, and dynamic light scattering (DLS) method.

(2) Characterization of PEGylated pcQDs

Amine-functionalized monomethoxy PEGs with different molecular weights (750, 2000, 5000) were conjugated to the pcQD using carbodiimide chemistry. Successful conjugation was confirmed

by agarose gel electrophoresis (**Figure S1**). Electrophoretic mobility of pcQD gradually decreased depending on the amount of mPEGs (750, 2000, 5000) at the fixed amount of EDC (5,000 equiv.). Considering that the electrophoretic mobility depends on mass, size and charge of the molecules, the decreased mobility upon PEGylation is mainly due to the increased hydrodynamic size and the decreased negative charges of pcQD. Also, the electrophoretic mobility profile of pcQDs with higher molecular weight PEGs (mPEG2k-pcQD and mPEG5k-pcQD) are similar to each other, reaching the maximum values at 2.0 $x10^{-5}$ $cmV^{-1}sec^{-1}$, while the pcQD with short PEG molecule (750) showed nearly 4 times higher maximum mobility. These results suggest that maximum conjugation efficiency can be reached when at least 10,000 equiv. of mPEGs regardless of lengths of PEG molecules. For the endocytosis study, the surface –COOH groups of pcQD were partially conjugated with methoxy amino PEG molecules with different molecular weights (750, 2000, 5000) using EDC chemistry. This partial PEGylation will allow for further conjugation with other biomacromolecules such as antibody or DNA.

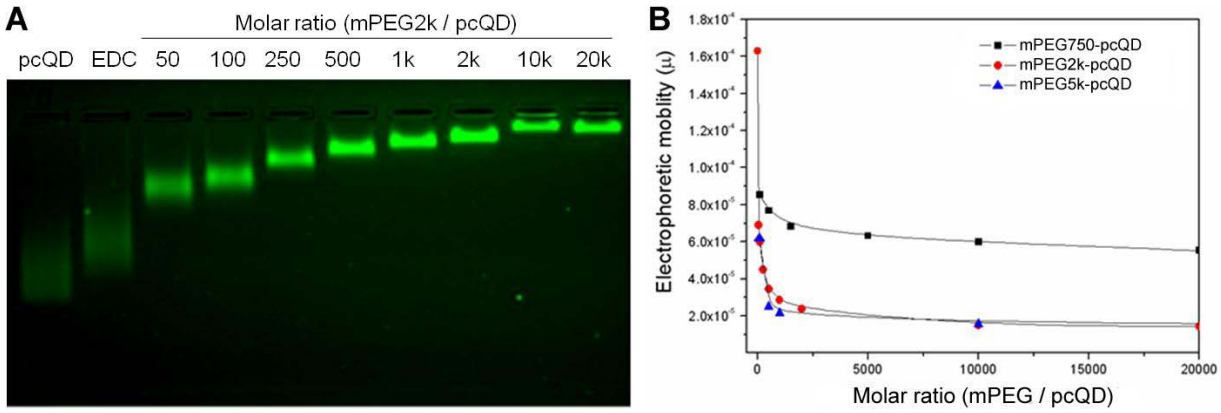

Figure S1. Agarose gel electrophoresis characterization of PEGylated pcQDs with different molecular weights of PEGs. (A) mPEG2k-pcQD (emission at 510 nm) conjugates, where the pcQD were reacted with amine-functionalized monomethoxy PEG2k at varying molar ratios (50 ~ 20,000) in a borate buffer (pH 8) for 16h. (B) Comparison of electrophoretic mobilities (μ; unit = $cmV^{-1}sec^{-1}$) of pcQDs modified with different molecular weights of PEGs (750, 2000, 5000). 1.5% agarose gel was run at 50V for 60 min in 0.5XTBE buffer.

(3) Cellular uptake of PEGylated pcQDs with different molecular weights of PEG molecules

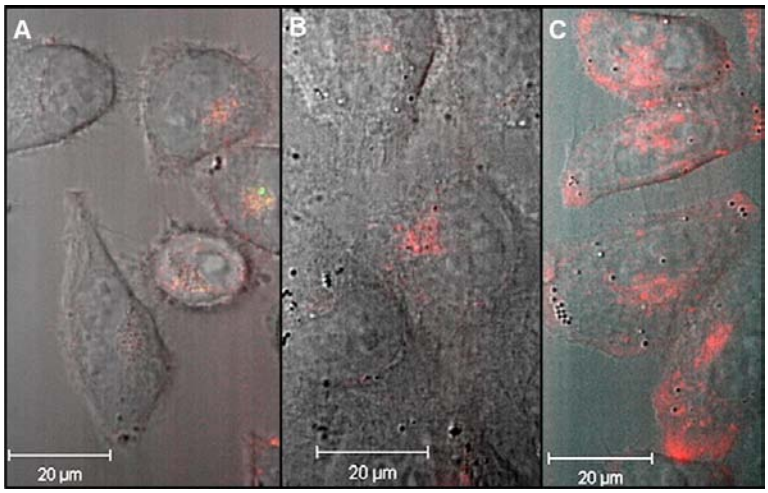

Figure S2. Effect of molecular weight of PEG molecules (750, 2000, 5000) on the non-specific uptake of pcQDs was negligible. Representative confocal microscope images of live HeLa cells were shown after 24 h incubation of mPEG750-pcQD (A), mPEG2k-pcQD (B), and mPEG5k-pcQD (C). The cells were post-labeled with transferrin-Alexafluor 634 conjugate for endosomes.

(4) Targeting of GFP tethered at the cytoplasmic c-terminal site of ET_AR using antiGFP-TAT-PEG-pcQD

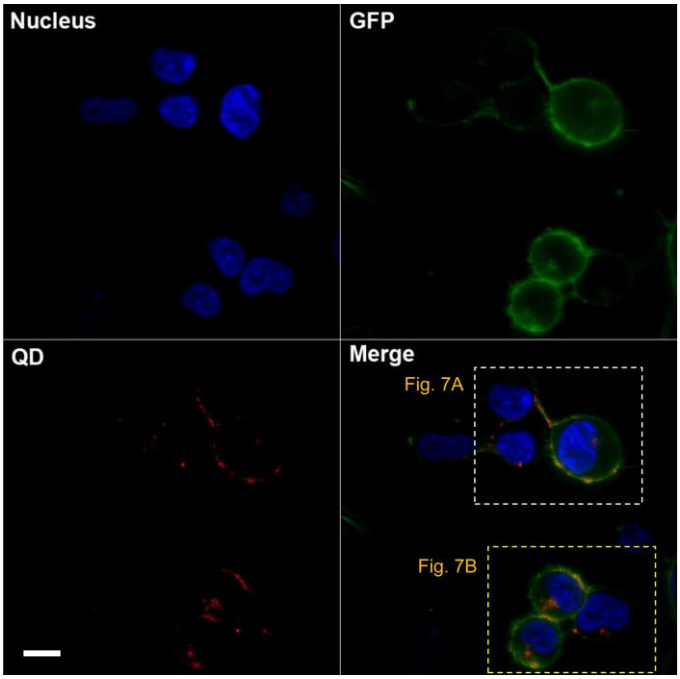

Figure S3. Separate fluorescent channel image of Figure 7A (white dotted box) and 7B (yellow dotted box), where the colocalization of antiGFP-TAT-PEG-pcQD with the target GFP was demonstrated in a magnified view. The scale bar = 10 μm.

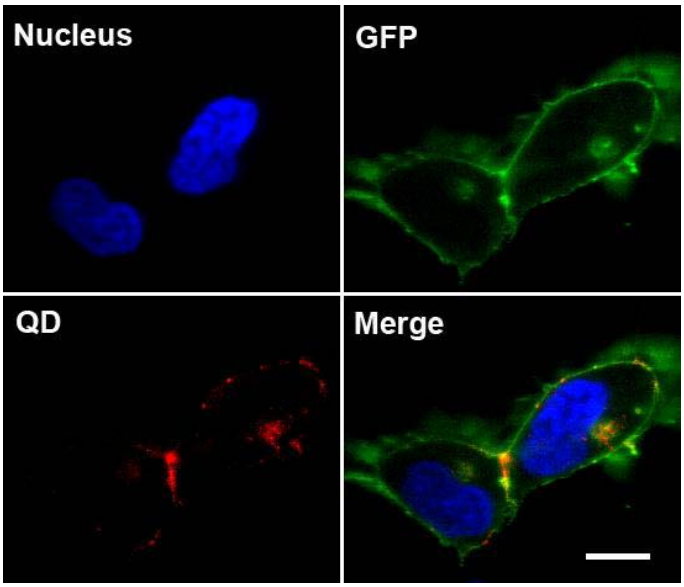

Figure S4. Separate fluorescent channel image of Figure 7C, where the colocalization of antiGFP-TAT-PEG-pcQD with the target GFP was demonstrated. The scale bar = 10 μm.

(5) Cellular entry of TAT-PEG-pcQD without anti-GFP antibody

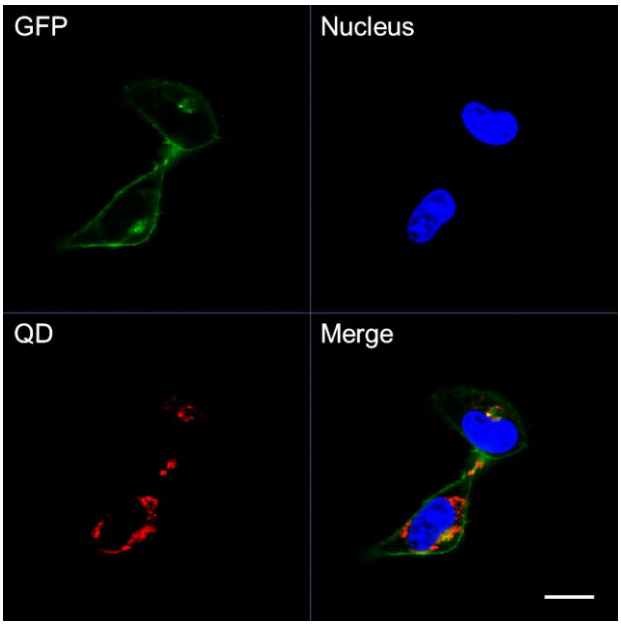

Figure S5. Intracellular delivery of PEG-pcQD via TAT. Incubation of TAT-PEG-pcQD without anti-GFP antibody conjugation exhibited punctated distribution in the cytoplasm surrounding the nucleus with no significant QD signal at the membrane region. The scale bar = 10 μm.

(6) Agonist-induced translocation of GFP-ET_AR

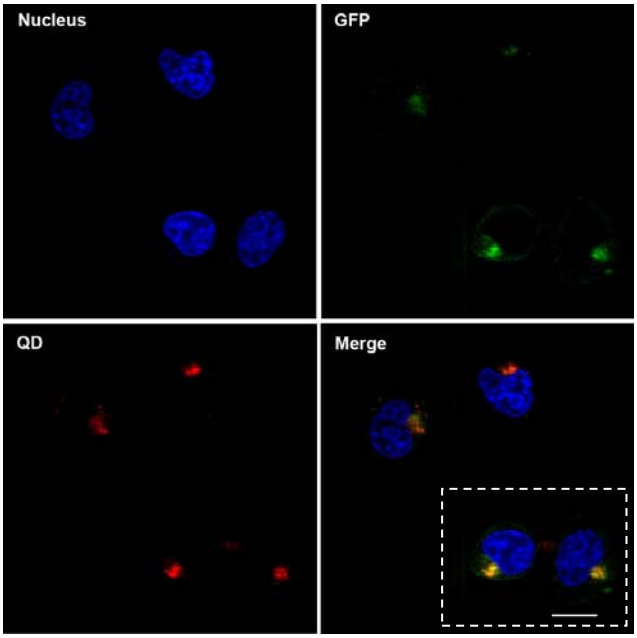

Figure S6. Separate fluorescent channel image of the Figure 8A (dotted box), where the colocalization of antiGFP-TAT-PEG-pcQD with the target GFP after agonist (ET-1) stimulation of ET_AR was demonstrated in a magnified view. The scale bar = 10 μm.

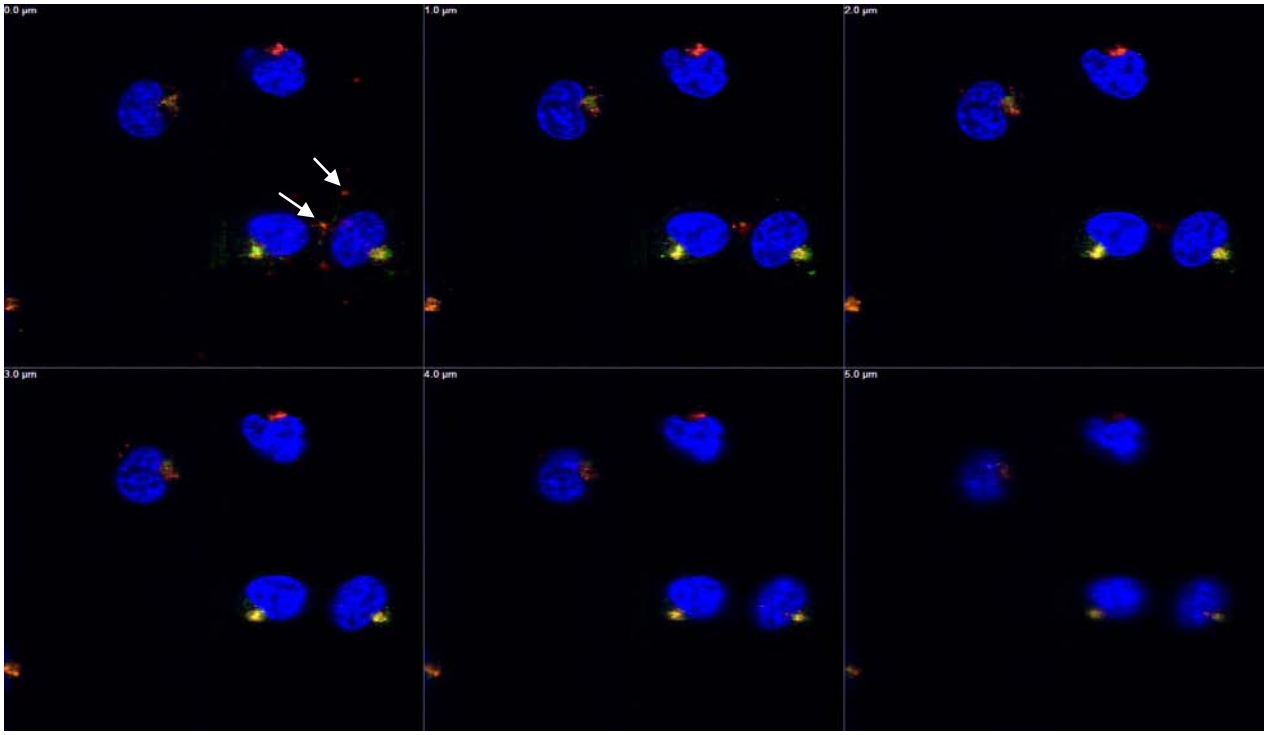

Figure S7. Z-section images (1 µm interval) of Figure 8A, where a small portion of antiGFP-TAT-PEG-pcQD are still found on the membrane at different focal planes (arrows) even 1h after ET-1 treatment. The scale bar = 10 µm.

References

(1) Peng, Z. A., and Peng, X. G. (2001) Formation of high-quality CdTe, CdSe, and CdS nanocrystals using CdO as precursor. *J. Am. Chem. Soc. 123*, 183-184.

(2) Wu, X. Y., Liu, H. J., Liu, J. Q., Haley, K. N., Treadway, J. A., Larson, J. P., Ge, N. F., Peale, F., and Bruchez, M. P. (2003) Immunofluorescent labeling of cancer marker Her2 and other cellular targets with semiconductor quantum dots. *Nat. Biotechnol. 21*, 41-46.

(3) Gao, X. H., Cui, Y. Y., Levenson, R. M., Chung, L. W. K., and Nie, S. M. (2004) In vivo cancer targeting and imaging with semiconductor quantum dots. *Nat. Biotechnol. 22*, 969-976.

Bioconjugate Chemistry

ARTICLE

pubs.acs.org/bc

In Vivo Imaging of Transplanted Islets with ^{64}Cu-DO3A-VS-Cys^{40}-Exendin-4 by Targeting GLP-1 Receptor

Zhanhong Wu,[†] Ivan Todorov,[†] Lin Li,[‡] James R. Bading,[§] Zibo Li,[∥] Indu Nair,[†] Kohei Ishiyama,[†] David Colcher,[§] Peter E. Conti,[∥] Scott E. Fraser,[⊥] John E. Shively,[‡] and Fouad Kandeel*[,†]

[†]Department of Diabetes, Endocrinology and Metabolism

[‡]Department of Immunology

[§]Department of Cancer Immunotherapy and Tumor Immunology

Beckman Research Institute of City of Hope, Duarte, California 91010, United States

[∥]Molecular Imaging Center, Department of Radiology, University of Southern California, Los Angeles, California 90033, United States

[⊥]Division of Biology, California Institute of Technology, Pasadena, California 91125, United States

Supporting Information

ABSTRACT: Glucagon-like peptide 1 receptor (GLP-1R) is highly expressed in pancreatic islets, especially on β-cells. Therefore, a properly labeled ligand that binds to GLP-1R could be used for in vivo pancreatic islet imaging. Because native GLP-1 is degraded rapidly by dipeptidyl peptidase-IV (DPP-IV), a more stable agonist of GLP-1 such as Exendin-4 is a preferred imaging agent. In this study, DO3A-VS-Cys^{40}-Exendin-4 was prepared through the conjugation of DO3A-VS with Cys^{40}-Exendin-4. The in vitro binding affinity of DO3A-VS-Cys^{40}-Exendin-4 was evaluated in INS-1 cells, which overexpress GLP-1R. After ^{64}Cu labeling, biodistribution studies and microPET imaging of ^{64}Cu-DO3A-VS-Cys^{40}-Exendin-4 were performed on both subcutaneous INS-1 tumors and islet transplantation models. The subcutaneous INS-1 tumor was clearly visualized with microPET imaging after the injection of ^{64}Cu-DO3A-VS-Cys^{40}-Exendin-4. GLP-1R positive organs, such as pancreas and lung, showed high uptake. Tumor uptake was saturable, reduced dramatically by a 20-fold excess of unlabeled Exendin-4. In the intraportal islet transplantation models, ^{64}Cu-DO3A-VS-Cys^{40}-Exendin-4 demonstrated almost two times higher uptake compared with normal mice. ^{64}Cu-DO3A-VS-Cys^{40}-Exendin-4 demonstrated persistent and specific uptake in the mouse pancreas, the subcutaneous insulinoma mouse model, and the intraportal human islet transplantation mouse model. This novel PET probe may be suitable for in vivo pancreatic islets imaging in the human.

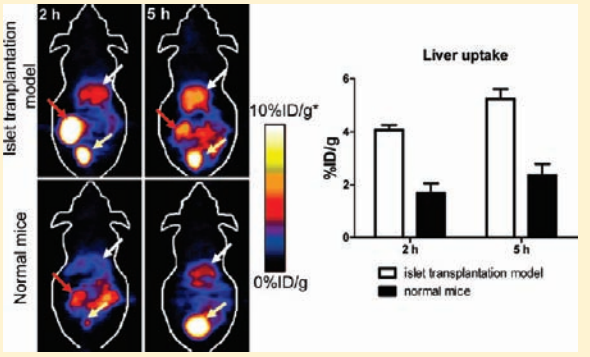

INTRODUCTION

In 2007, 23.6 million children and adults in the United States (7.8% of the population) had diabetes. The pathophysiology of diabetes is complex, but the main clinical features result from impairment of insulin secretion and/or function. In humans, the pancreas is a small, elongated organ that lies behind the stomach and adjacent to the liver, duodenum, and spleen. The insulin-producing β-cells that govern glucose homeostasis are located in the islets of Langerhans, which comprise only 2−3% of all pancreatic tissues. β-cells represent up to 80% of the islets, while other types of cells (mainly α, δ, and pancreatic polypeptide (PP) cells) contribute to the remaining islet cell mass.

Islet transplantation is a promising treatment option for Type 1 diabetes (T1D) patients; however, the fate of the graft over time remains difficult to follow, due to the lack of available tools capable of monitoring islet graft loss. Currently, the estimates of islet survival and function are limited to indirect assessments based on exogenous insulin requirements or metabolic studies. Therefore, the development of noninvasive imaging methods for the assessment of the pancreatic β-cell mass and status is becoming important for monitoring patients after islet transplantation.

A variety of currently available imaging techniques, including magnetic resonance imaging (MRI),[1−6] bioluminescence imaging (BLI),[7−9] and nuclear imaging (positron emission tomography (PET) and single photon emission computed tomography (SPECT)), have been tested for the study of β-cells. In particular, PET is a noninvasive functional imaging technique that provides adequate resolution, high sensitivity, and accurate quantification of physiological, biochemical, and pharmacological processes in living subjects.

Received: March 15, 2011
Revised: June 20, 2011
Published: June 21, 2011

ACS Publications © 2011 American Chemical Society

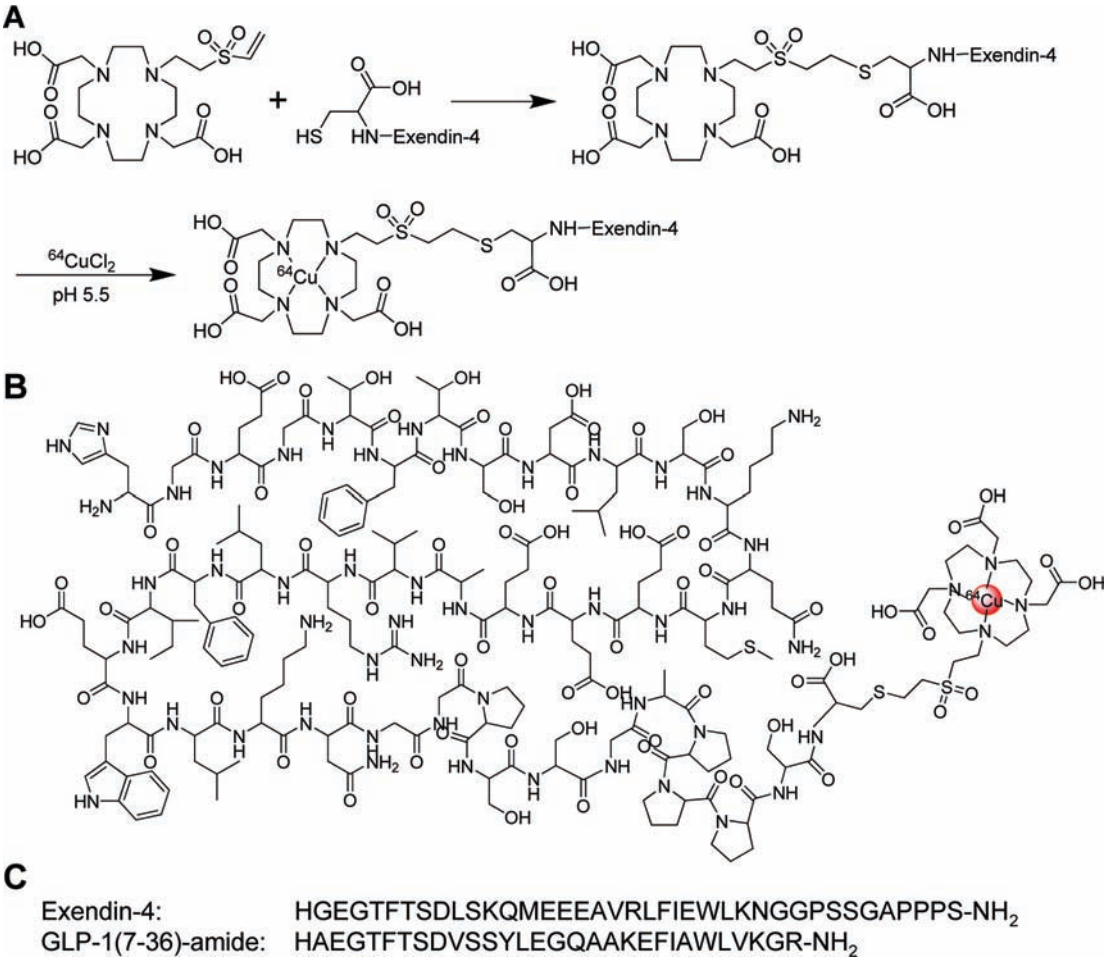

Figure 1. (A) Synthesis and Cu-64 labeling of ^{64}Cu-DO3A-VS-Cys^{40}-Exendin-4. (B) Chemical structure of ^{64}Cu-DO3A-VS-Cys^{40}-Exendin-4. (C) Sequences of Exendin-4 and GLP-1(7−36)-amide.

Glucagon-like peptide 1 (GLP-1) is an incretin peptide released from the intestine in response to nutrient ingestion; its binding to the GLP-1 receptor (GLP-1R) augments glucose-induced insulin secretion from pancreatic β-cells.[10,11] Since GLP-1R is highly expressed in islets, and especially highly expressed on β-cells, ligands of GLP-1R could be ideal probes for pancreatic β-cell imaging.[12,13] Exendin-4, a peptide hormone first isolated by Dr. John Eng from the saliva of the gila monster in 1992, is especially attractive as an affinity ligand.[14,15] Exendin-4 displays biological properties similar to human GLP-1, with which it shares 53% sequence identity;[12] however, it is metabolically much more stable than GLP-1. Previously, Exendin analogues have been labeled with ^{111}In,[16−20] ^{125}I,[21] ^{99m}Tc,[18] and ^{68}Ga.[18,22] However, most tracers were only evaluated in GLP-1 receptor positive insulinoma with experimental models and in humans.[19,20] To date, imaging of transplanted human β-cells in humans has been limited to one study of SPECT imaging with Lys^{40}(Ahx-DTPA-^{111}In)NH_2]Exendin-4 in one patient who received transplants in muscle.[23] Here, we report the development of ^{64}Cu-labeled Exendin-4 for in vivo imaging of GLP-1 receptor. Cu-64 ($t_{1/2}$ = 12.7 h) decays by β^+ (20%) and β^- emission (37%), as well as electron capture (43%), making it well-suited for radiolabeling proteins, antibodies, and peptides for PET imaging.[24] In addition to characterizing the performance of ^{64}Cu-labeled Exendin-4 in a rodent insulinoma model, we also explored its feasibility for imaging intraportal islet transplantation.

EXPERIMENTAL PROCEDURES

General. All commercially available chemical reagents were purchased from Aldrich (St. Louis, MO) and used without further purification. Cys^{40}-Exendin-4 was synthesized by standard FMOC chemistry by the Synthetic and Biopolymer Chemistry Core at City of Hope (Duarte, CA). 1,4,7,10-Tetraazacyclododecane-1,4,7-tris(*t*-butyl acetate) was purchased from Macrocyclics Inc. (Dallas, TX). $^{64}CuCl_2$ was obtained from Washington University (St. Louis, MO) by the ^{64}Ni(p,n)^{64} Cu nuclear reaction. ^{125}I-Exendin(9−39) was purchased from Perkin-Elmer (Wellesley, MA).

Preparation of DO3A-VS Conjugated Exendin-4 (DO3A-VS-Cys^{40}-Exendin-4). DO3A-VS (1,4,7-tris(acetic acid)-10-vinylsulfone-1,4,7,10-tetraazacyclododecane) was prepared as previously reported.[25] Cys^{40}-Exendin-4 (0.7 μmol) in 250 μL of water was added to 0.77 μmol of DO3A-VS in 100 μL of water (pH 8.0) (Figure1). The solution was stirred under argon overnight at 25 °C and the product was purified by HPLC (Phenomenex Gemini C18, Torrance, CA; flow = 1 mL/min). The product was characterized by LTQ FT mass spectrometer (Thermo, Waltham, MA) (m/z: 4752.30, calcd: 4752.93).

Radiolabeling of DO3A-VS-Cys^{40}-Exendin-4. DO3A-VS-Cys^{40}-Exendin-4 (10 μg) was labeled by adding of 74 MBq of $^{64}Cu^{2+}$ in 0.1 M sodium acetate buffer (pH 5.5) followed by 45 min of incubation at 43 °C. DTPA (10 mM, 5 μL) was added to chelate unlabeled ^{64}Cu. The radiochemical yield was determined by radio-ITLC and HPLC (flow = 1 mL/min; the mobile phase was changed from 95% solvent A [0.1% trifluoroacetic acid (TFA) in water] and 5% solvent B [0.1% TFA in acetonitrile (ACN)] (0−2 min) to 35% solvent A and 65% solvent B at 32 min). ^{64}Cu-DO3A-VS-Cys^{40}-Exendin-4 was purified by C-18 Sep-Pak cartridge, and the eluant was evaporated and reconstituted in saline for animal studies.

Cells. Rat insulinoma cell line INS-1 (GLP-1R positive, kindly donated by Dr. Ian Sweet, University of Washington, Seattle, WA) was maintained under standard conditions: the INS-1 insulinoma cells were grown in RPMI-1640 medium supplemented with 10% fetal bovine serum (Atlanta Laboratories, Atlanta, GA), 20 mM Hepes, 2 mM L-glutamine, 1 mM sodium pyruvate, 1% antibiotic−antimycotic solution (Mediatech, Manassas, VA), and 50 mM 2-mercaptoethanol at 37 °C in humidified atmosphere containing 5% CO_2. The INS-1 insulinoma cells were grown in culture until sufficient cells were available.

Human pancreatic islets were isolated by the Southern California Islet Cell Resources Center (SC-ICRC, Duarte, CA) from human pancreata from healthy adult donors with a proper consent for research use and approval by the Institutional Review Board of the City of Hope. Islet isolations were performed using the standard collagenase method for pancreas digestion and islet purification[26] following the operating procedures of the SC-ICRC. Islets cultured for 48−72 h in CMRL1066 based islet culture medium (Mediatech, Manassas, VA) were used in the experiments.

In Vitro Cell Binding Assay. The in vitro GLP-1R-binding affinity and specificity of DO3A-VS-Cys^{40}-Exendin-4 and Exendin-4 were assessed via competitive cell binding assays using ^{125}I-Exendin(9−39) (PerkinElmer, Waltham, MA) as the GLP-1R specific radioligand. In detail, INS-1 cells were harvested, washed three times with phosphate buffered saline (1×, Mediatech, Manassas, VA), and resuspended (2×10^6 cells/mL) in the binding buffer.[27] Filter multiscreen DV plates (96-well, pore size, 0.65 μm, Millipore, Billerica, MA) were seeded with 10^5 cells and incubated with ^{125}I-Exendin(9−39) (0.74 kBq/well) in the presence of increasing concentrations of different Exendin-4 analogues (0−1.0 μmol/L). The truncated Exendin(9−39) is an antagonist of GLP-1R and a competitive inhibitor of Exendin-4. The total incubation volume was adjusted to 200 μL. After the cells were incubated for 2 h at room temperature, the plates were filtered through a multiscreen vacuum manifold and washed three times with binding buffer. The hydrophilic polyvinylidenedifluoride (PVDF) filters were collected, and the radioactivity was determined using a gamma counter. The best-fit 50% inhibitory concentration (IC_{50}) values for INS-1 cells were calculated by fitting the data with nonlinear regression using *GraphPad Prism* (GraphPad Software, La Jolla, CA). Experiments were performed on triplicate samples.

Animals. Male, NOD/SCID mice (the City of Hope Animal Resource Center, Duarte, CA), 8−10 weeks old, served as recipients for insulinoma cells and human islet cells. All animal experiments were performed in compliance with the Guidelines for the Care and Use of Research Animals established by the City of Hope/Beckman Research Institute's Animal Use Committee.

Xenograft Tumor Model. NOD/SCID mice were injected with INS-1 rat insulinoma cells (5×10^6, suspended in 0.1 mL of 1× phosphate buffered saline) subcutaneously in the thigh. Tumors were established within 18−21 days postinjection. Blood glucose values were monitored daily and 6% glucose solution was fed ad libitum once the blood glucose level was lower than 3.3 mmol/L.

Islet Transplantation. Islets with a diameter of less than 250 μm were used for transplantation. Islets were transplanted into the livers of NOD/SCID mice via the portal vein. Immediately before intraportal infusion, 1000 islet equivalents were suspended in 200 μL of Hank's balanced salt solution (Mediatech, Manassas, VA), and loaded in a 1 mL syringe. Under general anesthesia, the portal vein was exposed by extra-abdominal repositioning of the bowel and the islets were infused into the portal vein via a 27-gauge needle.

Biodistribution and MicroPET Imaging. Biodistribution and microPET imaging of ^{64}Cu-DO3A-VS-Cys^{40}-Exendin-4 were performed in mice bearing INS-1 tumor or islet grafts to evaluate the in vivo specific binding to GLP-1R. For blocking studies, Exendin-4 (20 μg) was coinjected with the radiotracer. For biodistribution studies, NOD/SCID mice bearing INS-1 tumor (n = 3, for each time point) were injected intravenously with ^{64}Cu-DO3A-VS-Cys^{40}-Exendin-4 (0.05 μg, 0.37 MBq, 100 μL). Activity injected into each mouse was measured in a dose calibrator (Capintec, Ramsey, NJ). Animals were sacrificed under inhalation anesthesia at 1 h, 4 h, and 22 h postinjection (p.i.). Tissues and organs of interest were excised and weighed. Radioactivity in each excised specimen was measured using a gamma counter; radioactivity uptake was expressed as percent injected dose per gram (%ID/g). Mean uptake (%ID/g) and corresponding standard deviation was calculated for each group of animals.

For microPET imaging, mice were injected via the tail vein with 3.7−7.4 MBq of ^{64}Cu-DO3A-VS-Cys^{40}-Exendin-4 (0.5−1 μg). Serial imaging of INS-1 tumor (at 1, 4, and 22 h; scan duration 20, 20, and 45 min, respectively) and islet transplantation model (at 2 and 5 h; scan duration 10 and 20 min, respectively) was performed using a microPET R4 scanner (Concorde Microsystems, Knoxville, TN; 8 cm axial field of view, spatial resolution 2.0 mm). Images were reconstructed with a MAP iterative algorithm using the *microPET Manager* software (Concorde Microsystems, Knoxville, TN). Images were then analyzed using the Acquisition Sinogram Image Processing (ASIPro) software (Concorde Microsystems, Knoxville, TN). Average radioactivity accumulation within liver was obtained from a three-dimensional region of interest (ROI) drawn within the central portion of the PET liver image. Image intensities were converted to units of activity concentration (Bq/cm^3) using a calibration factor obtained by scanning a cylindrical phantom filled with a known activity concentration of ^{64}Cu. Assuming a tissue density of 1 g/mL, measured tissue activity concentrations were converted to units of Bq/g, then multiplied by 100 and divided by the injected dose to obtain an image-derived percent injected dose per gram of tissue (% ID/g).

Histology Study. Livers of mice transplanted with human islets and human pancreas were fixed with 10% formalin and processed for paraffin embedding. 5 μm parallel sections were stained with hematoxylin and eosin or immunostained for insulin and GLP-1R, as described previously.[28,29] Guinea pig antihuman insulin (DAKO, Carpinteria, CA) and rabbit antihuman GLP-1R (Novus Biologicals, Littleton, CO) were used as primary antibodies. The corresponding secondary antibodies were conjugated

with FITC or Texas Red (Jackson Immunoresearch, West Grove, PA). The slices were counter-stained for DNA with diamidinophenylindole (DAPI) (Sigma, St. Louis, MO) and visualized with an Olympus BX51 fluorescent microscope equipped with a Pixera 600 camera.

Statistical Analysis. Quantitative data were expressed as mean ± SD. Means were compared using one-way ANOVA and Student's *t* test. *P* values of <0.05 were considered statistically significant.

RESULTS

Chemistry and Radiolabeling. The identity of DO3A-VS-Cys^{40}-Exendin-4 (Figure 1) was confirmed by HPLC and mass spectrometry. The ^{64}Cu-labeling (n = 5) was achieved in ^{64}Cu-DO3A-VS-Cys^{40}-Exendin-4 with more than 95% decay-corrected yield and radiochemical purity of >99%. ^{64}Cu-DO3A-VS-Cys^{40}-Exendin-4 was analyzed by ITLC and HPLC. The HPLC retention time of ^{64}Cu-DO3A-VS-Cys^{40}-Exendin-4 was 23 min. For radio-TLC analysis, ^{64}Cu-DO3A-VS-Cys^{40}-Exendin-4 remained at the origin of the TLC plate, while the retention factor (Rf) value for free ^{64}Cu-DTPA was 0.9−1.0. The specific activity of ^{64}Cu-DO3A-VS-Cys^{40}-Exendin-4 was around 3.3×10^{15} Bq/mol.

In Vitro Cell Binding Affinity. We compared the receptor-binding affinity of DO3A-VS-Cys^{40}-Exendin-4 with that of Exendin-4 using a competitive cell-binding assay (Figure 2). Both peptides inhibited the binding of ^{125}I-Exendin(9−39) to GLP-1R positive INS-1 cells in a dose-dependent manner.

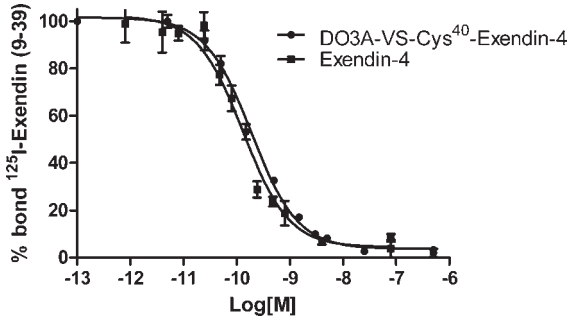

Figure 2. Competitive binding assays of ^{125}I-Exendin(9−39) and DO3A-VS-Cys^{40}-Exendin-4 or Exendin-4 in INS-1 cells . Data are mean ± SE (n = 3). X axis reflects concentration of nonradolabeled competitor. IC_{50} values for DO3A-VS-Cys^{40}-Exendin-4 and Exendin-4 were 190.6 ± 3.5 and 131.07 ± 8.3 pM, respectively.

The IC_{50} value for DO3A-VS-Cys^{40}-Exendin-4 (190.6 ± 3.5 pmol/L) was comparable to that of Exendin-4 (130.7 ± 8.3 pmol/L). The results showed that DO3A conjugation had a minimal effect on the receptor-binding affinity.

Biodistribution Studies and MicroPET Imaging. The GLP-1R targeting efficacy and biodistribution patterns of ^{64}Cu-DO3A-VS-Cys^{40}-Exendin-4 in NOD/SCID mice bearing INS-1 rat insulinoma xenografts (GLP-1R positive) were evaluated at multiple time points (1, 4, and 22 h) with static microPET scans. Representative sliced decay-corrected coronal images at different time points are shown in Figure 3A. The INS-1 tumors were clearly visualized with high tumor-to-background contrast for ^{64}Cu-DO3A-VS-Cys^{40}-Exendin-4.

To obtain quantitative biodistribution data, we performed dissection and direct assay of tissue activity concentration in groups of insulnoma-bearing mice sacrificed at 1, 4, and 22 h. The data are shown in Figure 3B. Uptake of ^{64}Cu-DO3A-VS-Cys^{40}-Exendin-4 in INS-1 insulinomas was 12.7 ± 2.9, 14.2 ± 2.6, and 9.2 ± 4.0% ID/g at 1, 4, and 22 h p.i., respectively (Figure 3B). This result is consistent with the excretion pattern from the microPET imaging results. Similar to the microPET imaging result, ^{64}Cu-DO3A-VS-Cys^{40}-Exendin-4 mainly accumulated in the kidneys, which remained at 46.8 ± 11.4%ID/g at 23 h p.i..

The GLP-1 receptor specificity of ^{64}Cu-DO3A-VS-Cys^{40}-Exendin-4 was confirmed by a blocking experiment where the radiotracer was coinjected with excess amount of cold Exendin-4 (20 μg). As can be seen from Figure 4A, in the presence of unlabeled Exendin-4, the INS-1 tumor uptake was significantly lower (2.7 ± 2.0% ID/g) than that without Exendin-4 blocking (14.2 ± 2.6% ID/g, P < 0.01) at 4 h p.i. In the blocking experiment, the uptake of ^{64}Cu-DO3A-VS-Cys^{40}-Exendin-4 in other GLP-1 positive organs (pancreas, lungs, and duodenum) was significantly decreased (Figure 4B).

To test the tracer in an islet transplant model, we implanted 1000 IEQ human islets into mouse liver via portal vein. Nine days after implantation, mice were imaged with ^{64}Cu-DO3A-VS-Cys^{40}-Exendin-4 (Figure 5A). Liver uptake of the radiotracer was significantly higher (P < 0.01) in transplanted mice (4.0 ± 0.2 and 5.3 ± 0.7%ID/g at 2 and 5 h p.i., respectively) than in control mice (1.7 ± 0.6 and 2.4 ± 0.8%ID/g at 2 and 5 h p.i., respectively) (Figure 5B). Histology studies (Figure 6) clearly demonstrated that human islet grafts were present in mouse liver and that most insulin-positive cells are also GLP-1R-positive, which are similar to those for native human islets in the pancreas. This study confirmed that the higher liver uptake of

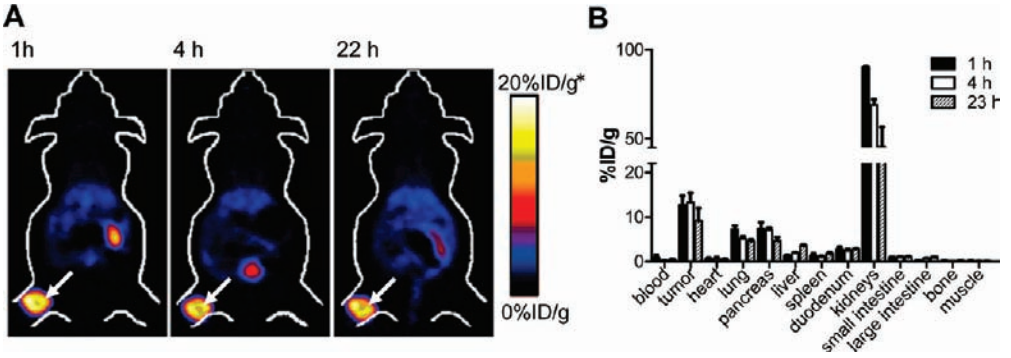

Figure 3. (A) Representative coronal microPET images of a NOD/SCID mouse bearing an INS-1 xenograft and injected with ^{64}Cu-DO3A-VS-Cys^{40}-Exendin-4 (arrows point to the tumor; image is saturated if uptake ≥20%ID/g). (B) Biodistribution of ^{64}Cu-DO3A-VS-Cys^{40}-Exendin-4 in NOD/SCID mice bearing INS-1 xenograft at 1 h, 4 h, and 23 h p.i.. The data are mean ± SD (n = 3).

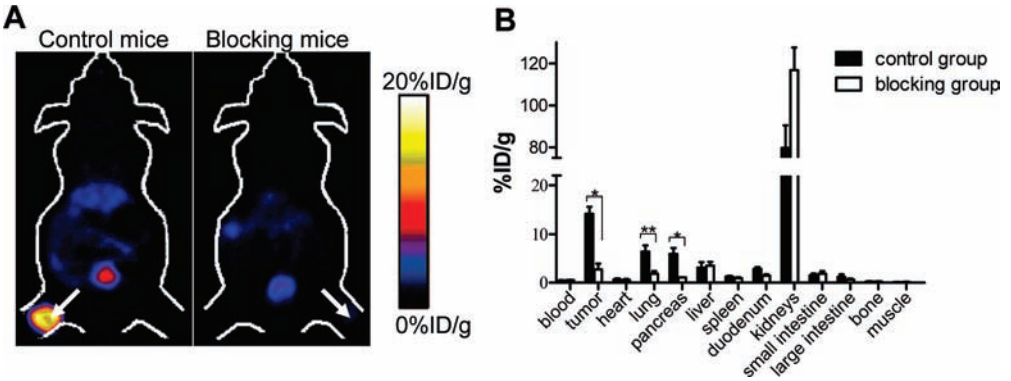

Figure 4. (A) Representative coronal microPET images of NOD/SCID mice bearing INS-1 xenograft 4 h after injection of ^{64}Cu-DO3A-VS-Cys^{40}-Exendin-4 in the absence/presence of excess Exendin-4 (arrows point to the tumors, image is saturated if uptake ≥20%ID/g). (B) Biodistribution of ^{64}Cu-DO3A-VS-Cys^{40}-Exendin-4 in NOD/SCID mice bearing INS-1 xenograft in the absence/presence of excess Exendin-4 at 4 h p.i. The data are mean ± SD (n = 3; *P < 0.01, **P < 0.015).

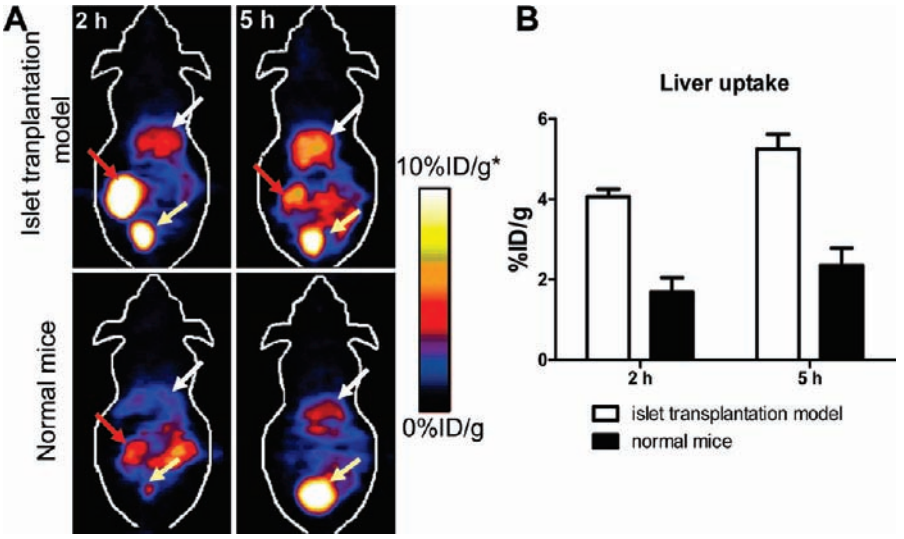

Figure 5. (A) Coronal microPET images of ^{64}Cu-DO3A-VS-Cys^{40}-Exendin-4 in NOD/SCID mice transplanted with human islets into liver or native NOD/SCID mice (white arrows point to the livers, red arrows point to kidneys, and yellow arrows point to bladders). Images are normalized to reflect radiodecay-corrected relative image intensity per unit injected activity (image is saturated if uptake ≥10%ID/g). (B) Image-derived liver uptake compared between the islet transplant model and normal mice. The data are the mean ± SD (n = 3). Uptake was higher in transplanted mice at both time points (P < 0.01).

the islet transplantation model was due to a GLP-1R targeting effect.

DISCUSSION

A major challenge for both experimental diabetes research and clinical diabetes care is to obtain spatial and quantitative information about islet or β-cell mass (BCM). Imaging technology has advanced rapidly in recent years, making it possible to noninvasively image small and/or deep structures within the body. It would be of great benefit to the diabetes community to be able to image the pancreatic BCM noninvasively. Such a method would not only facilitate early clinical diagnosis of beta-cell loss during development of T1D, but also provide an approach with which to evaluate antidiabetic drugs with the potential to stimulate β-cell regeneration. Noninvasive imaging could also be very important for monitoring the fate of transplanted islets.

It is difficult to quantify β-cell mass noninvasively due to the small size (50−500 μm in diameter) of islets and their scattered distribution pattern throughout the pancreas. Therefore, a ligand with high affinity and specificity for pancreatic β-cells is required. Several receptors and their ligands have been reported for β-cell imaging, including sulfonylurea receptor 1 (SUR1),[30−32] the vesicular acetylcholine transporter (VAChT),[33] and monoamine transporter 2 (VMAT2);[34−38] however, most of the imaging results are suboptimal, and an ideal probe for accurate and noninvasive imaging of pancreatic β-cells has not yet been developed.

GLP-1R is highly expressed in islets, especially on β-cells in the pancreas. Therefore, the ligands of GLP-1R could be ideal probes for pancreatic β-cell imaging. In this study, ^{64}Cu-DO3A-VS-Cys^{40}-Exendin-4 was prepared and shown to have high binding affinity to GLP-1R in vitro. The high and specific expression of GLP-1R on INS-1 cells makes the rodent insulinoma model an

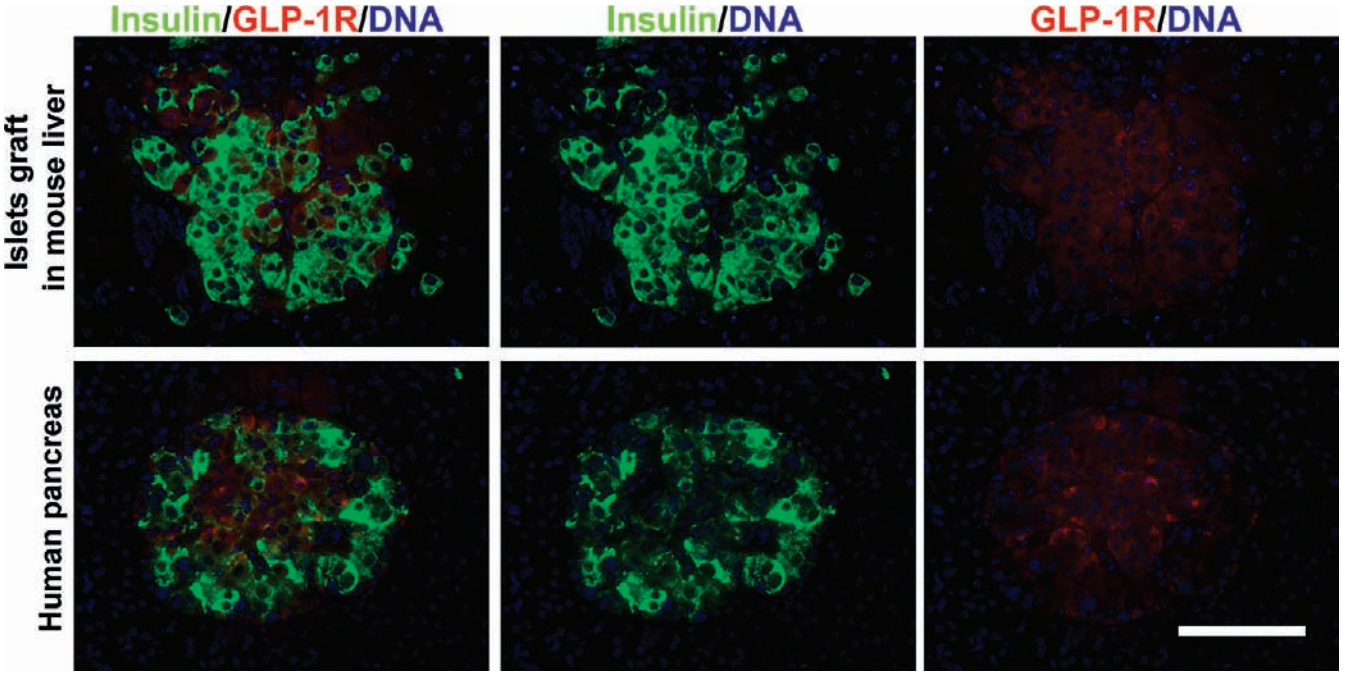

Figure 6. Human islet grafts in the liver of NOD/SCID mice and native human pancres. Parallel mice liver and human pancreas sections were stained with hematoxylin/eosin and immunostained for insulin (green), GLP-1R (red), and DNA (blue). Scale bar, 100 μm.

ideal platform to test the GLP-1R targeting efficacy and specificity. As expected, the GLP-1R positive INS-1 tumor demonstrated high and persistent uptake of ^{64}Cu-DO3A-VS-Cys^{40}-Exendin-4. Receptor specificity was confirmed by a blocking experiment. The pancreas and lung, which have high GLP-1R expression, showed relatively high specific uptake. The uptake of pancreas was reduced by unlabeled Exendin-4 from 5.9 $\pm$ 0.8% ID/g to 1.1 $\pm$ 0.1%ID/g at 4 h p.i. ($P < 0.01$), and the lung uptake was reduced from 6.4 $\pm$ 2.2%ID/g to 1.8 $\pm$ 0.9%ID/g ($P < 0.015$). It needs to be pointed out that the human lung expressed significantly smaller amounts of GLP-1 receptor compared with rodent lung.[39]

High kidney uptake of ^{64}Cu-DO3A-VS-Cys^{40}-Exendin-4 was observed in both the microPET imaging and biodistribution studies, which was similar with other radiometal-labeled Exendin analogues.[16−18,22] Previously, other researchers have demonstrated that GLP-1R has low expression in kidney.[39−41] It has been shown that the kidneys are of great importance for the removal of ^{64}Cu-DO3A-VS-Cys^{40}-Exendin-4 and/or its metabolites from the circulation.[42,43] In our research, we have found ^{64}Cu-labeled Exendin-4 was cleared rapidly from blood (Supporting Information Figure S1) and the high kidney uptake could not be reduced by the blocking study (coinjection with nonradiolabeled Exendin-4). L-Polyglutamic acid (PGA), Gelofusine, or the combination of PGA and Gelofusine pretreatment could significant reduce kidney uptake of Ga-68 labeled Exendin-4, while the tumor uptake was not affected.[18,44] Although ^{64}Cu-DO3A-VS-Cys^{40}-Exendin-4 is stable in vitro (Supporting Information Figure S2-A), metabolites was observed in kidney homogenate (Supporting Information Figure S2-C). Therefore, the most likely reason for the high kidney uptake is that the peptide is filtered through glomerulus and subsequently degraded by enzymes in the tubuli brush border membrane.[42]

Human islets were transplanted into NOD/SCID mice livers through the portal vein, and a subsequent histological study clearly showed the presence of functional human islets at the time of imaging. Higher liver uptake was observed with microPET imaging on day 10 after transplantation compared with that of normal mice. As shown in Figure 5B, liver uptake in the islet transplantation model was almost twice that in controls. Thus, ^{64}Cu-DO3A-VS-Cys^{40}-Exendin-4 PET can noninvasively detect transplanted islets in the liver. It is noted that liver uptake increased between 2 and 5 h, which may be caused by metabolism and transchelation of Cu^{2+} to superoxide dismutase.[45−48]

This is a principle proof study and only a single number of human islets were transplanted into mice liver and a single time point microPET scan was performed post islet transplantation. Further studies are needed to test the feasibility of long-term monitoring of transplanted islets with ^{64}Cu-DO3A-VS-Cys^{40}-Exendin-4. In future studies, we will transplant different numbers of islets into mice liver and perform microPET scan at different time points post-transplantation to correlate the β-cell mass and uptake of mice livers.

CONCLUSION

In summary, GLP-1R targeted ^{64}Cu-DO3A-VS-Cys^{40}-Exendin-4 showed high and specific uptake in INS-1 tumors. Moreover, we also demonstrated the feasibility of ^{64}Cu-DO3A-VS-Cys^{40}-Exendin-4 for in vivo imaging intraportally transplanted islets in mice. These results suggest that ^{64}Cu-DO3A-VS-Cys^{40}-Exendin-4 is a very promising PET probe for transplanted islets imaging and may be useful for clinical translation.

ASSOCIATED CONTENT

Supporting Information. Additional figures as described in text. This material is available free of charge via the Internet at http://pubs.acs.org.

AUTHOR INFORMATION

Corresponding Author

*Fouad Kandeel, M.D., Ph.D. Address: Department of Diabetes, Endocrinology and Metabolism City of Hope, 1500 East Duarte Road, Duarte, CA 91010. Phone: (626)301-8282. Fax: (626)301-8489. E-mail: fkandeel@coh.org.

ACKNOWLEDGMENT

This work was supported by the grant from the Juvenile Diabetes Research Foundation International (JDRF-37-2009-20). The authors thank Dr. Ismail Al-Abdullah and the islet isolation team of the Southern California Islet Cell Resource Center at City of Hope for providing the human islets.

REFERENCES

(1) Leoni, L., and Roman, B. B. (2010) MR imaging of pancreatic islets: tracking isolation, transplantation and function. *Curr. Pharm. Des. 16*, 1582–94.

(2) Medarova, Z., and Moore, A. (2009) MRI as a tool to monitor islet transplantation. *Nat. Rev. Endocrinol. 5*, 444–52.

(3) Medarova, Z., and Moore, A. (2009) MRI in diabetes: first results. *Am. J. Roentgenol. 193*, 295–303.

(4) Marzola, P., Longoni, B., Szilagyi, E., Merigo, F., Nicolato, E., Fiorini, S., Paoli, G. T., Benati, D., Mosca, F., and Sbarbati, A. (2009) In vivo visualization of transplanted pancreatic islets by MRI: comparison between in vivo, histological and electron microscopy findings. *Contr. Media Mol. Imaging 4*, 135–42.

(5) Tai, J. H., Foster, P., Rosales, A., Feng, B., Hasilo, C., Martinez, V., Ramadan, S., Snir, J., Melling, C. W., Dhanvantari, S., Rutt, B., and White, D. J. (2006) Imaging islets labeled with magnetic nanoparticles at 1.5 T. *Diabetes 55*, 2931–8.

(6) Evgenov, N. V., Medarova, Z., Dai, G., Bonner-Weir, S., and Moore, A. (2006) In vivo imaging of islet transplantation. *Nat. Med. 12*, 144–8.

(7) Virostko, J., Radhika, A., Poffenberger, G., Chen, Z., Brissova, M., Gilchrist, J., Coleman, B., Gannon, M., Jansen, E. D., and Powers, A. C. (2010) Bioluminescence imaging in mouse models quantifies beta cell mass in the pancreas and after islet transplantation. *Mol. Imaging Biol. 12*, 42–53.

(8) Roth, D. J., Jansen, E. D., Powers, A. C., and Wang, T. G. (2006) A novel method of monitoring response to islet transplantation: bioluminescent imaging of an NF-kB transgenic mouse model. *Transplantation 81*, 1185–90.

(9) Villalobos, C., Nadal, A., Nunez, L., Quesada, I., Chamero, P., Alonso, M. T., and Garcia-Sancho, J. (2005) Bioluminescence imaging of nuclear calcium oscillations in intact pancreatic islets of Langerhans from the mouse. *Cell Calcium 38*, 131–9.

(10) Holst, J. J. (2007) The physiology of glucagon-like peptide 1. *Physiol. Rev. 87*, 1409–39.

(11) Baggio, L. L., and Drucker, D. J. (2007) Biology of incretins: GLP-1 and GIP. *Gastroenterology 132*, 2131–57.

(12) Goke, R., Fehmann, H. C., Linn, T., Schmidt, H., Krause, M., Eng, J., and Goke, B. (1993) Exendin-4 is a high potency agonist and truncated exendin-(9−39)-amide an antagonist at the glucagon-like peptide 1-(7−36)-amide receptor of insulin-secreting beta-cells. *J. Biol. Chem. 268*, 19650–5.

(13) Malhotra, R., Singh, L., Eng, J., and Raufman, J. P. (1992) Exendin-4, a new peptide from Heloderma suspectum venom, potentiates cholecystokinin-induced amylase release from rat pancreatic acini. *Regul. Pept. 41*, 149–56.

(14) Eng, J., Kleinman, W. A., Singh, L., Singh, G., and Raufman, J. P. (1992) Isolation and characterization of exendin-4, an exendin-3 analogue, from Heloderma suspectum venom. Further evidence for an exendin receptor on dispersed acini from guinea pig pancreas. *J. Biol. Chem. 267*, 7402–5.

(15) Edwards, C. M., Stanley, S. A., Davis, R., Brynes, A. E., Frost, G. S., Seal, L. J., Ghatei, M. A., and Bloom, S. R. (2001) Exendin-4 reduces fasting and postprandial glucose and decreases energy intake in healthy volunteers. *Am. J. Physiol. Endocrinol. Metab. 281*, E155–61.

(16) Gotthardt, M., Lalyko, G., van Eerd-Vismale, J., Keil, B., Schurrat, T., Hower, M., Laverman, P., Behr, T. M., Boerman, O. C., Goke, B., and Behe, M. (2006) A new technique for in vivo imaging of specific GLP-1 binding sites: first results in small rodents. *Regul. Pept. 137*, 162–7.

(17) Wild, D., Behe, M., Wicki, A., Storch, D., Waser, B., Gotthardt, M., Keil, B., Christofori, G., Reubi, J. C., and Macke, H. R. (2006) [Lys^{40}(Ahx-DTPA-^{111}In)NH$_2$]exendin-4, a very promising ligand for glucagon-like peptide-1 (GLP-1) receptor targeting. *J. Nucl. Med. 47*, 2025–33.

(18) Wild, D., Wicki, A., Mansi, R., Behe, M., Keil, B., Bernhardt, P., Christofori, G., Ell, P. J., and Macke, H. R. (2010) Exendin-4-based radiopharmaceuticals for glucagonlike peptide-1 receptor PET/CT and SPECT/CT. *J. Nucl. Med. 51*, 1059–67.

(19) Christ, E., Wild, D., Forrer, F., Brandle, M., Sahli, R., Clerici, T., Gloor, B., Martius, F., Maecke, H., and Reubi, J. C. (2009) Glucagon-like peptide-1 receptor imaging for localization of insulinomas. *J. Clin. Endocrinol. Metab. 94*, 4398–405.

(20) Wild, D., Macke, H., Christ, E., Gloor, B., and Reubi, J. C. (2008) Glucagon-like peptide 1-receptor scans to localize occult insulinomas. *N. Engl. J. Med. 359*, 766–8.

(21) Mukai, E., Toyoda, K., Kimura, H., Kawashima, H., Fujimoto, H., Ueda, M., Temma, T., Hirao, K., Nagakawa, K., Saji, H., and Inagaki, N. (2009) GLP-1 receptor antagonist as a potential probe for pancreatic beta-cell imaging. *Biochem. Biophys. Res. Commun. 389*, 523–6.

(22) Brom, M., Oyen, W. J., Joosten, L., Gotthardt, M., and Boerman, O. C. (2010) ^{68}Ga-labelled exendin-3, a new agent for the detection of insulinomas with PET. *Eur. J. Nucl. Med. Mol. Imaging 37*, 1345–55.

(23) Pattou, F., Kerr-Conte, J., and Wild, D. (2010) GLP-1-receptor scanning for imaging of human beta cells transplanted in muscle. *N. Engl. J. Med. 363*, 1289–90.

(24) Kumar, R., Dhanpathi, H., Basu, S., Rubello, D., Fanti, S., and Alavi, A. (2008) Oncologic PET tracers beyond [^{18}F]FDG and the novel quantitative approaches in PET imaging. *Q. J. Nucl. Med. Mol. Imaging 52*, 50–65.

(25) Li, L., Tsai, S. W., Anderson, A. L., Keire, D. A., Raubitschek, A. A., and Shively, J. E. (2002) Vinyl sulfone bifunctional derivatives of DOTA allow sulfhydryl- or amino-directed coupling to antibodies. Conjugates retain immunoreactivity and have similar biodistributions. *Bioconjugate Chem. 13*, 110–5.

(26) Ricordi, C., Lacy, P. E., and Scharp, D. W. (1989) Automated islet isolation from human pancreas. *Diabetes 38* (Suppl 1), 140–2.

(27) Gallwitz, B., Witt, M., Folsch, U. R., Creutzfeldt, W., and Schmidt, W. E. (1993) Binding specificity and signal transduction of receptors for glucagon-like peptide-1(7−36)amide and gastric inhibitory polypeptide on RINm5F insulinoma cells. *J. Mol. Endocrinol. 10*, 259–68.

(28) Todorov, I., Nair, I., Avakian-Mansoorian, A., Rawson, J., Omori, K., Ito, T., Valiente, L., Iglesias-Meza, I., Orr, C., Shiang, K. D., Ferreri, K., Al-Abdullah, I. H., Mullen, Y., and Kandeel, F. (2010) Quantitative assessment of beta-cell apoptosis and cell composition of isolated, undisrupted human islets by laser scanning cytometry. *Transplantation 90*, 836–42.

(29) Tornehave, D., Kristensen, P., Romer, J., Knudsen, L. B., and Heller, R. S. (2008) Expression of the GLP-1 receptor in mouse, rat, and human pancreas. *J. Histochem. Cytochem. 56*, 841–51.

(30) Amartey, J. K., Esguerra, C., Al-Jammaz, I., Parhar, R. S., and Al-Otaibi, B. (2006) Synthesis and evaluation of radioiodinated substituted beta-naphthylalanine as a potential probe for pancreatic beta-cells imaging. *Appl. Radiat. Isot. 64*, 769–77.

(31) Wangler, B., Schneider, S., Thews, O., Schirrmacher, E., Comagic, S., Feilen, P., Schwanstecher, C., Schwanstecher, M., Shiue,

C. Y., Alavi, A., Hohnemann, S., Piel, M., Rosch, F., and Schirrmacher, R. (2004) Synthesis and evaluation of (S)-2-(2-[^{18}F]fluoroethoxy)-4-([3-methyl-1-(2-piperidin-1-yl-phenyl)-butyl -carbamoyl]-methyl)-benzoic acid ([^{18}F]repaglinide): a promising radioligand for quantification of pancreatic beta-cell mass with positron emission tomography (PET). *Nucl. Med. Biol. 31*, 639–47.

(32) Wangler, B., Beck, C., Shiue, C. Y., Schneider, S., Schwanstecher, C., Schwanstecher, M., Feilen, P. J., Alavi, A., Rosch, F., and Schirrmacher, R. (2004) Synthesis and in vitro evaluation of (S)-2-([^{11}C]methoxy)-4-[3-methyl-1-(2-piperidine-1-yl-phenyl)-butyl-carbam oyl]-benzoic acid ([^{11}C]methoxy-repaglinide): a potential beta-cell imaging agent. *Bioorg. Med. Chem. Lett. 14*, 5205–9.

(33) Clark, P. B., Gage, H. D., Brown-Proctor, C., Buchheimer, N., Calles-Escandon, J., Mach, R. H., and Morton, K. A. (2004) Neurofunctional imaging of the pancreas utilizing the cholinergic PET radioligand [^{18}F]4-fluorobenzyltrozamicol. *Eur. J. Nucl. Med. Mol. Imaging 31*, 258–260.

(34) Inabnet, W. B., Milone, L., Harris, P., Durak, E., Freeby, M. J., Ahmed, L., Sebastian, M., Lifante, J. C., Bessler, M., and Korner, J. (2010) The utility of [^{11}C] dihydrotetrabenazine positron emission tomography scanning in assessing beta-cell performance after sleeve gastrectomy and duodenal-jejunal bypass. *Surgery 147*, 303–9.

(35) Eriksson, O., Jahan, M., Johnström, P., Korsgren, O., Sundin, A., Halldin, C., and Johansson, L. (2010) In vivo and in vitro characterization of [^{18}F]-FE-(+)-DTBZ as a tracer for beta-cell mass. *Nucl. Med. Biol. 37*, 357–363.

(36) Kung, M. P., Hou, C., Lieberman, B. P., Oya, S., Ponde, D. E., Blankemeyer, E., Skovronsky, D., Kilbourn, M. R., and Kung, H. F. (2008) In vivo imaging of beta-cell mass in rats using ^{18}F-FP-(+)-DTBZ: a potential PET ligand for studying diabetes mellitus. *J. Nucl. Med. 49*, 1171–6.

(37) Freeby, M., Goland, R., Ichise, M., Maffei, A., Leibel, R., and Harris, P. (2008) VMAT2 quantitation by PET as a biomarker for beta-cell mass in health and disease. *Diabetes Obes. Metab. 10* (Suppl 4), 98–108.

(38) Simpson, N. R., Souza, F., Witkowski, P., Maffei, A., Raffo, A., Herron, A., Kilbourn, M., Jurewicz, A., Herold, K., Liu, E., Hardy, M. A., Van Heertum, R., and Harris, P. E. (2006) Visualizing pancreatic beta-cell mass with [^{11}C]DTBZ. *Nucl. Med. Biol. 33*, 855–64.

(39) Korner, M., Stockli, M., Waser, B., and Reubi, J. C. (2007) GLP-1 receptor expression in human tumors and human normal tissues: potential for in vivo targeting. *J. Nucl. Med. 48*, 736–43.

(40) Bullock, B. P., Heller, R. S., and Habener, J. F. (1996) Tissue distribution of messenger ribonucleic acid encoding the rat glucagon-like peptide-1 receptor. *Endocrinology 137*, 2968–78.

(41) Orskov, C., and Poulsen, S. S. (1991) Glucagonlike peptide-I-(7−36)-amide receptors only in islets of Langerhans. Autoradiographic survey of extracerebral tissues in rats. *Diabetes 40*, 1292–6.

(42) Ruiz-Grande, C., Alarcon, C., Alcantara, A., Castilla, C., Lopez Novoa, J. M., Villanueva-Penacarrillo, M. L., and Valverde, I. (1993) Renal catabolism of truncated glucagon-like peptide 1. *Horm. Metab. Res. 25*, 612–6.

(43) Hassan, M., Eskilsson, A., Nilsson, C., Jonsson, C., Jacobsson, H., Refai, E., Larsson, S., and Efendic, S. (1999) In vivo dynamic distribution of ^{131}I-glucagon-like peptide-1 (7−36) amide in the rat studied by gamma camera. *Nucl. Med. Biol. 26*, 413–20.

(44) Gotthardt, M., van Eerd-Vismale, J., Oyen, W. J., de Jong, M., Zhang, H., Rolleman, E., Maecke, H. R., Behe, M., and Boerman, O. (2007) Indication for different mechanisms of kidney uptake of radiolabeled peptides. *J. Nucl. Med. 48*, 596–601.

(45) Boswell, C. A., Sun, X., Niu, W., Weisman, G. R., Wong, E. H., Rheingold, A. L., and Anderson, C. J. (2004) Comparative in vivo stability of copper-64-labeled cross-bridged and conventional tetraazamacrocyclic complexes. *J. Med. Chem. 47*, 1465–74.

(46) Bass, L. A., Wang, M., Welch, M. J., and Anderson, C. J. (2000) In vivo transchelation of copper-64 from TETA-octreotide to superoxide dismutase in rat liver. *Bioconjugate Chem. 11*, 527–32.

(47) Rogers, B. E., Anderson, C. J., Connett, J. M., Guo, L. W., Edwards, W. B., Sherman, E. L., Zinn, K. R., and Welch, M. J. (1996) Comparison of four bifunctional chelates for radiolabeling monoclonal antibodies with copper radioisotopes: biodistribution and metabolism. *Bioconjugate Chem. 7*, 511–22.

(48) Anderson, C. J., and Ferdani, R. (2009) Copper-64 radiopharmaceuticals for PET imaging of cancer: advances in preclinical and clinical research. *Cancer Biother. Radiopharm. 24*, 379–93.

Supporting Information:

Dynamic microPET scan. NOD/SCID mouse was intravenously injected with 7.4 MBq of ^{64}Cu-DO3A-VS-Cys^{40}-Exendin-4 and then subjected to a 30-min dynamic scan (2 × 1 min, 3 ×3 min, 2 × 5 min, 1 × 9 min; total of 8 frames) starting right after injection. Five-minute static PET images were also acquired at 1h after injection. The images were reconstructed by 2-dimensional ordered-subsets expectation maximization (OSEM) algorithm.

Solution Stability. The solution stability of ^{64}Cu-DO3A-VS-Cys^{40}-Exendin-4 was studied by measuring the radiochemical purity with HPLC after incubation in serum solution at 37 ^{o}C. The purified product was reconstituted in serum solution to 1 mCi/mL. Sample of the resulting solution were analyzed by radio-HPLC at 7 h post incubation.

Metabolic Stability. The metabolic stability of ^{64}Cu-DO3A-VS-Cys^{40}-Exendin-4 was evaluated in a NOD/SCID mouse. Sixty minutes after the intravenous injection of 7.4 MBq of ^{64}Cu-DO3A-VS-Cys^{40}-Exendin-4, the mouse was sacrificed and liver and kidneys were harvested. The liver and kidneys were homogenized using a homogenizer, suspended in 1 mL of PBS buffer, and then centrifuged for 5 min at 14,000 rpm. For each sample, after the removal of the supernatant, 50% TFA in 100 μL PBS was added to the solution, followed by mixing and centrifugation for 5 min. The upper solution was then taken and injected for HPLC analysis. The eluent was collected with a fraction collector (1.0 min/fraction), and the radioactivity of each fraction was measured with a gamma counter.

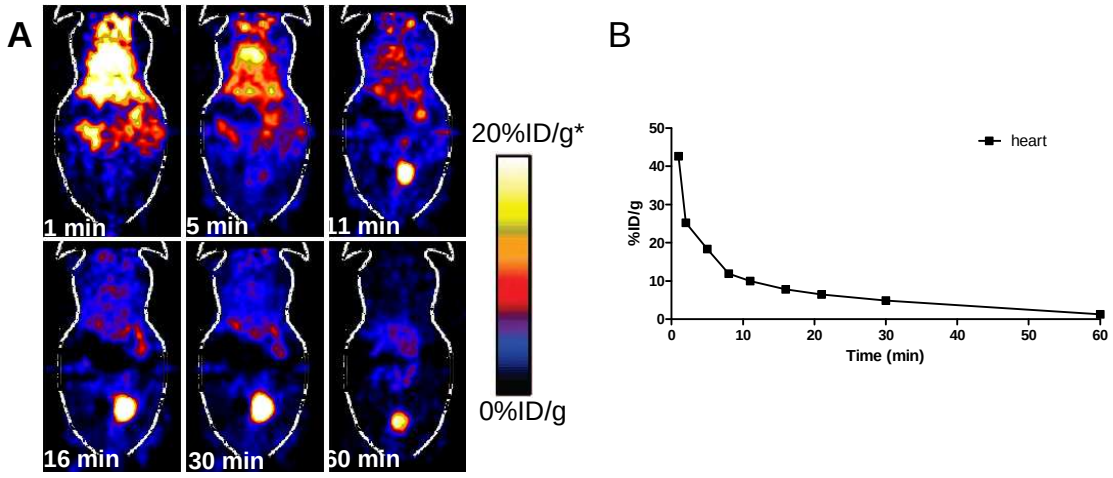

Figure S1. (A) Representative coronal microPET images of a NOD/SCID mouse at 1, 5, 11, 16, 30, and 60 min after injection of ^{64}Cu-DO3A-VS-Cys^{40}-Exendin-4. (B) Time–activity curves of heart after intravenous injection of ^{64}Cu-DO3A-VS-Cys^{40}-Exendin-4. Data were derived from a multiple time-point microPET study.

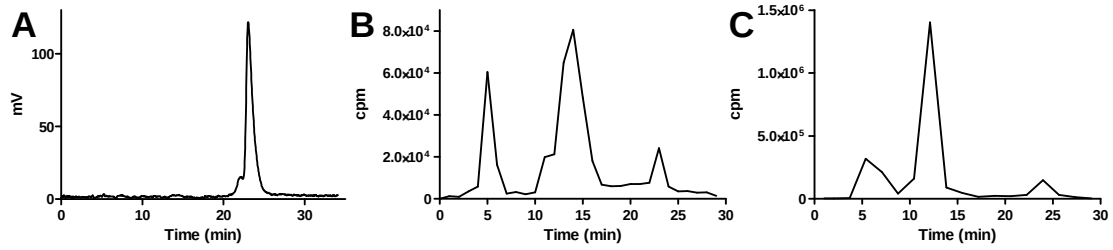

Figure S2. (A) The HPLC profile of ^{64}Cu-DO3A-VS-Cys^{40}-Exendin-4 at 7 h post purification. Metabolic stability of ^{64}Cu-DO3A-VS-Cys^{40}-Exendin-4 in the liver (B) and kidneys (C) at 1 h post-injection.

Bioconjugate Chemistry

ARTICLE

pubs.acs.org/bc

Characterization of Morphine−Glucose-6-phosphate Dehydrogenase Conjugates by Mass Spectrometry

May L. Chiu,[†] A. Jimmy Ytterberg,[⊥,‡] Rachel R. Ogorzalek Loo,[§] Joseph A. Loo,[‡,§] and Harold G. Monbouquette*[,†]

[†]Department of Chemical and Biomolecular Engineering, [‡]Department of Chemistry and Biochemistry, [§]Molecular Biology Institute, David Geffen School of Medicine at UCLA, and UCLA-DOE Institute of Genomics and Proteomics, University of California, Los Angeles, California 90095-1592, United States

ABSTRACT: A key characteristic of the analyte−reporter enzyme conjugate used in the enzyme-multiplied immunoassay technique (EMIT) is the inhibition of the conjugate enzyme upon anti-analyte antibody binding. To improve our understanding of the antibody-induced inhibition mechanism, we characterized morphine−glucose-6-phosphate dehydrogenase (G6PDH) conjugates as model EMIT analyte−reporter enzyme conjugates. Morphine−G6PDH conjugates were prepared by acylating predominantly the primary amines on G6PDH with morphine 3-glucuronide NHS ester molecules. In this study, morphine−G6PDH conjugates were characterized using a combination of methods, including tryptic digestion, immunoprecipitation, matrix-assisted laser desorption ionization mass spectrometry, and electrospray ionization tandem mass spectrometry. Twenty-six conjugation sites were identified. The identified sites all were found to be primary amines. The degree of conjugation was determined to be less than the number of conjugation sites, suggesting heterogeneity within the morphine−G6PDH conjugate population. Two catalytically important residues in the active site (K22 and K183) were among the identified conjugation sites, explaining at least partially the cause of loss of activity due to the coupling reaction.

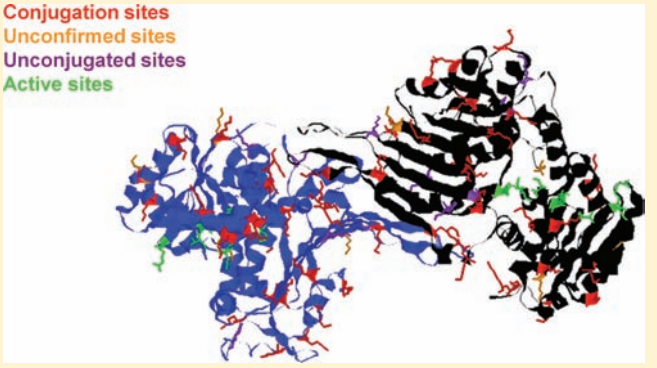

INTRODUCTION

The enzyme-multiplied immunoassay technique (EMIT) is a homogeneous assay technique widely used for small-molecule drug testing.[1,2] Similar to other enzyme immunoassays (EIA), EMIT relies on a reporter enzyme for signal generation. However, the reliance of EMIT on antibody-induced inhibition of the reporter enzyme distinguishes it from other EIA. Conceptually, EMIT is based on the reversible repression of reporter enzyme activity caused by an anti-analyte antibody binding to an analyte−reporter enzyme conjugate.[3] When an antibody binds to an analyte or analyte analogue covalently coupled to the reporter enzyme, a physical blockage and/or conformational change of the enzyme active site occurs, thereby reducing its catalytic activity. When introduced, free analyte competes for antibody binding and at least partially prevents repression. Because the concentration of antibody binding sites available to inhibit the enzyme depends on the concentration of free analyte, the measurable reporter enzyme activity is related to the free analyte concentration.

Some advantages of EMIT include simple assay protocols, a rapid assay time, and a low detection limit. Perhaps most importantly, EMIT-based assays are conducted conveniently in a homogeneous solution without the need for washing and separation steps [in contrast to the enzyme-linked immunosorbent assay (ELISA), for instance]. The assay time for commercial EMIT, at less than 1 min,[4] is much shorter than that for ELISA, yet a low detection limit (<1 nM) still can be achieved with EMIT.[5] These qualities have made EMIT attractive for lower-molecular weight analytes in which suitable reporter enzyme conjugates can be synthesized.

Glucose-6-phosphate dehydrogenase (G6PDH, EC 1.1.1.49) from *Leuconostoc mesenteroides* is certainly the most commonly used reporter enzyme for EMIT.[4] The bacterial G6PDH is a 109 kDa homodimer[6] that catalyzes oxidization of glucose 6-phospate (G6P) to 6-phosphogluconate with a high specific activity using NAD^+ as the electron acceptor.[7] The rate of NADH production can be monitored either spectrophotometrically or fluorometrically. Analyte−G6PDH conjugates usually are prepared by acylating the primary amine (NH_2) groups of lysines and the N-terminus with activated carboxyl (COOH) groups of the analyte or analyte derivative. In a common coupling reaction, the hydroxyl (OH) groups of tyrosines also can be acylated, but to a much lesser extent.[8] It has been established that analyte−G6PDH conjugates prepared in this fashion give significant repression of conjugate enzyme activity upon antibody binding,[9,10] a key requirement for EMIT.

Received: March 16, 2011
Revised: June 14, 2011
Published: June 16, 2011

ACS Publications © 2011 American Chemical Society

Figure 1. Amino acid sequence of *L. mesenteroides* G6PDH used in this study as available from the Swiss-Prot protein sequence database (accession number P11411) with the 36 lysines (black) and 21 tyrosines (gray) highlighted. This sequence differs from that in the RCSB Protein Data Bank (PDB entry 1DPG) by the addition of a methionine at the N-terminus and the substitution of a serine for cysteine at position 62 (both in italics).

Although many EMIT assays have been constructed successfully with analyte−G6PDH conjugates made using the approach described herein, little is understood about the inhibition mechanism and conjugation sites. One of a few previously published reports showed that antibody-induced inhibition was caused by conformational change and noncooperative antibody binding because anti-analyte Fab fragments can inhibit the analyte−G6PDH conjugate as effectively as the bivalent IgG.[8] In this report, the data regarding O^3-carboxymethylmorphine−G6PDH conjugate inhibition versus anti-morphine concentration were analyzed using a probability model. The modeling results suggested that most morphine was conjugated to G6PDH via a random subset of 12 readily available NH_2 groups and three or four tyrosine residues. Less frequent conjugation to other NH_2 groups was implied. The model also suggested that only one or two NH_2 groups (on the homodimer) were associated with antibody-induced inhibition. However, among the 37 NH_2 groups (lysines and the N-terminus) on each G6PDH monomer subunit, it still was not established which residues conjugated with morphine and/or were involved in the antibody-induced inhibition (Figure 1). Further, the conclusions drawn from the probability model were not substantiated with experimental data. Aside from this work, an unsuccessful attempt to identify antibody-induced inhibition sites by proteolytic hydrolysis methods was mentioned in a meeting abstract; however, no experimental details or data were published.[11] Finally, a claim was made in a patent regarding genetically modified G6PDH that suggested that some of the lysine residues (after conjugation with the analyte) did not contribute to the antibody-induced inhibition.[12] However, the patent did not identify the lysine residues that are important to antibody-induced inhibition. Further, only eight of the lysine residues were discussed in the patent.

A more thorough understanding of the analyte−G6PDH conjugate population created by following a typical coupling reaction protocol can help improve EMIT assays. For example, via identification of sites that are important for antibody-induced inhibition, genetically modified G6PDH mutants can be created to allow more site-specific conjugations, thereby lowering the level of deactivation caused by general conjugations and allowing for more efficient coupling. In fact, Dade Behring Inc. created a category of inhibitable, genetically modified G6PDH mutants that have a single conjugation per monomer subunit, thereby preventing deactivation caused by unnecessary conjugation.[11] The conjugation site is located within the region of residues 45−60; it is created by an opportunistic cysteine substitution, because *L. mesenteroides* G6PDH includes no natural cysteine residues. However, the inhibition exhibited by the G6PDH conjugates based on the mutants follows a cooperative antibody binding mechanism, which differs from that with the native reporter enzyme. Further, little information about the G6PDH mutants and the EMIT systems employing the mutants has been disclosed; therefore, it is difficult to build upon this development.

To improve our understanding of the antibody-induced inhibition mechanism involving noncooperative antibody binding, we prepared a model morphine conjugate based on native G6PDH and characterized the model in this study. A specific aim of this work was to identify the conjugation sites on the G6PDH reporter enzyme. Because the sites that are responsible for antibody-induced inhibition (AII sites) must be a subset of all conjugation sites, it was hoped that this study could narrow the field of candidate AII sites. A combination of methods, including tryptic digestion, immunoprecipitation (IP), matrix-assisted laser desorption ionization mass spectrometry (MALDI MS),[13,14] and electrospray ionization tandem mass spectrometry (ESI-MS/MS),[15] was used to identify sites of attachment of morphine to G6PDH. The conjugation site identity data also can be useful for developing strategies to improve EMIT assays. Further, the methods developed in this work could be applicable for characterizing and improving other analyte−reporter enzyme systems designed for EMIT.

MATERIALS AND METHODS

Materials. Morphine 3-β-D-glucuronide (M3G), glucose-6-phosphate dehydrogenase (G6PDH) from *L. mesenteroides* (lyophilized powder), *N*,*N*-dimethylformamide (anhydrous, 99.8%) (DMF), D-glucose 6-phosphate sodium salt (G6P), β-nicotinamide adenine dinucleotide hydrate (NAD^+), magnesium chloride hexahydrate ($MgCl_2 \cdot 6H_2O$), gelatin from porcine skin (type A), sodium phosphate monobasic salt, sodium phosphate dibasic salt, Trizma Preset crystals (pH 8.0), sinapinic acid (SA), 2,5-dihydroxybenzoic acid (DHB), α-cyano-4-hydroxycinnamic acid (recrystallized prior use), and bovine serum albumin (BSA) were purchased from Sigma Aldrich (St. Louis, MO). Sheep anti-morphine antibody (whole serum) was obtained from AbD Serotec (Raleigh, NC). 1-Ethyl-3-[3-(dimethylamino)propyl]-carbodiimide hydrochloride (EDC), *N*-hydroxysuccinimide (NHS), Protein-G Spin Columns, and Luminol Enhancer Solutions were purchased from Thermo Fisher Scientific (Rockford, IL). Amersham Biosciences PD-10 desalting columns and nitrocellulose membranes were obtained from GE Healthcare (Waukesha, WI). Microcon YM-30 centrifugal filters were obtained from Millipore (Billerica, MA). Methanol, acetonitrile (ACN), trifluoroacetic acid (TFA), lanolin, phosphoric acid, and Tween 20 were obtained from Fisher Scientific (Pittsburgh, PA). NuPAGE Novex 4 to 12% Bis-Tris gel, MOPS SDS running buffer (20×), NuPAGE LDS sample buffer (4×), and NuPAGE transfer buffer (20×) were purchased from Invitrogen (Carlsbad, CA). Rabbit anti-sheep antibody bound to horseradish peroxidase (HRP) was obtained from Bio-Rad (Hercules, CA). Modified trypsin was obtained from Promega (Madison, WI). GELoader tips were purchased from Eppendorf (Westbury, NY). PolySULFOETHYL aspartamide strong cation exchange material (4 μm) was obtained from PolyLC, Inc. (Columbia, SC). Jupiter Proteo reversed phase medium (4 μm, C12) was purchased

from Phenomenex (Torrance, CA). POROS R1 and POROS R2 reversed phase material were purchased from Applied Biosystems (Framingham, MA). Finally, Empore C8 extraction disks were obtained from 3M Bioanalytical Technologies (St. Paul, MN).

Morphine−G6PDH Conjugation. The COOH groups of M3G in a 10 mM solution were first activated in 20 mM EDC and 40 mM NHS in DMF for 1−2 h. The activated M3G (M3G-NHS-ester) solution was added to G6PDH in 100 mM sodium phosphate buffer (SPB) (pH 7.3) to give final concentrations of 5.4 μM (500 units/mL) G6PDH and 20% DMF. G6PDH concentrations ranging from 10 to 500 units/mL, in combination with different M3G concentrations (0.1−1.6 mM), were used to prepare different conjugate samples. The mixtures were allowed to react for 4 h to form the morphine−G6PDH conjugate. At the end of the 4 h period, the excess cross-linkers and M3G were removed by gel filtration with PD-10 columns and three rounds of centrifugal filtration with Microcon YM-30 centrifuge filters. The conjugation reaction and purification steps were conducted under ambient conditions.

Western Blot. Western blots were performed according to standard procedures.[16] Briefly, protein samples were denatured in NuPAGE LDS sample buffer at 70 °C for 10 min. The denatured samples were loaded onto a Bis-Tris gel. Electrophoresis was conducted at 200 V for 55 min in MOPS SDS running buffer. The proteins then were transferred to a nitrocellulose membrane in NuPAGE transfer buffer via application of 30 V for 90 min. Subsequently, the membrane was incubated in blocking solution consisting of 50% Qiagen blocking reagent and 2.5% milk in Tris-buffered saline (200 mM Tris buffer and 150 mM NaCl) with 0.5% Tween (TBST) overnight at 4 °C, then in a sheep anti-morphine Ab solution (diluted 500-fold in TBST) for 2 h at room temperature, and finally in a rabbit anti-sheep IgG−HRP solution (diluted 2000-fold in TBST) for 1 h at room temperature. Between each incubation step, the membrane was washed three times in TBST. The HRP signal was amplified using Luminol Enhancer Solutions.

Repression of Morphine−G6PDH Conjugate Activity upon Antibody Binding. In a 1 cm path length cuvette, 3 μL of calibrator solution was added to 136 μL of Syva Reagent 1, which consisted of 4.2 μg/mL sheep polyclonal antibodies to morphine, 10 mM G6P, and 6 mM NAD^+. Purified water and 1 mM M3G were used as the calibrator solutions for the repressed and unrepressed state measurements, respectively. The mixture was allowed to equilibrate at 37 °C for 6 min. Ten microliters of the 2.5 nM morphine−G6PDH solution [in 50 mM Tris-HCl (pH 8.0), 0.1 M NaCl, and 0.1% gelatin] was added to the mixture and mixed by repeated micropipetting. The optical density at 340 nm (OD_{340}) was recorded at 37 °C, and the initial change in OD_{340} per minute (ΔOD_{340}/min) was determined. From ΔOD_{340}, the enzyme activity in units per milliliter was calculated using Beer's law, where 6.22 mM^{-1} cm^{-1} was used as the NADH extinction coefficient.

MALDI MS of Intact Morphine−G6PDH Conjugates. The MALDI MS spectra were recorded using an Applied Biosystems Voyager DE-STR MALDI-TOF mass spectrometer. The protein sample was desalted using a Microcon YM-30 centrifugal filter to obtain a final salt concentration of <1 mM, and a final protein concentration of ~5 μM. Sinapinic acid dissolved in a 70:30 (v/v) ACN/water mixture and 0.1% TFA at a concentration of 20 mg/mL was used as the MALDI matrix. The sample (1.0 μL) and the matrix (1.2 μL) were spotted on the MALDI stainless steel target using the sandwich spotting method.[17] Spectra were recorded in linear mode at 25 kV. The resulting data were processed and analyzed using Voyager Data Explorer (Applied Biosystems, Foster City, CA). The average molecular weight of a conjugate was calculated from the average centroid mass of three to eight mass spectra.

Trypsin Digestion. In-solution trypsin digestion was performed according to the protocol described by Ytterberg et al.[18] Briefly, proteins were precipitated with >90% acetone at −20 °C overnight. The precipitates were collected by centrifugation, resuspended, and subsequently incubated in 80% acetone, 10% methanol, and 0.2% acetic acid at −20 °C for 30 min. The resuspended precipitates then were centrifuged; the supernatant was removed, and residual acetone was evaporated. Next, the pellets were dissolved in 20 μL of DMSO and subsequently diluted to 50 mM NH_4HCO_3 and 30% DMSO. Trypsin was added to a final protease:protein ratio of 1:20, and proteins were digested overnight at 37 °C. The peptide mixtures were dried completely and then resuspended in 5% formic acid (FA). For in-gel digestion, proteins were separated by sodium dodecyl sulfate−polyacrylamide gel electrophoresis and stained with Coomassie blue. Stained protein spots were manually excised, washed, and digested with trypsin as described by Rosenfeld et al.[19]

Immunoprecipitation of Tryptic Digest. Ten microliters of the tryptic digest sample was dried under vacuum and subsequently resuspended in 20 μL of binding buffer [100 mM SPB (pH 7.3)]. To the resuspended tryptic digest was added 20 μL of sheep anti-morphine antibody (whole serum). The resulting mixture was incubated at 4 °C overnight to allow for binding of antibody to M3G tryptic peptides. After this incubation, the mixture was added to 40 μL of protein-G resin (binding capacity of 11−15 mg of human IgG/mL), which had been equilibrated with binding buffer. The sample was incubated at room temperature with mixing for 30−60 min. Subsequently, the sample was centrifuged at 5000*g* for 2 min, and the supernatant was collected for analysis. The pellet was washed three times with 400 μL of water and resuspended in 60 μL of 5% FA to elute the antibody and antibody-bound tryptic peptide from the protein-G resins. The preparation then was centrifuged, and the resulting eluate (supernatant) was collected and desalted using a POROS R2-packed microcolumn.[20]

MALDI MS of Tryptic Digest. The tryptic digest was dried and resuspended in 5% FA. One-half microliter of the sample was spotted on the target; subsequently, 0.5 μL of the matrix was mixed into the sample spot. The sample and matrix were allowed to dry and cocrystallize. DHB in 25% ACN, 15% 2-propanol, and 0.5% phosphoric acid at a concentration of 10 mg/mL or CHCA in a 70:30 ACN/water with 0.1% TFA at a concentration of 7 mg/mL was used as the matrix. MALDI mass spectra were recorded in reflector mode (Voyager DE-STR MALDI-TOF) at 20 kV.

Fractionation of Modified Peptides and ESI-MS/MS Analysis. In-gel-digested G6PDH and the morphine−G6PDH conjugate were analyzed by liquid chromatography−tandem mass spectrometry (LC−MS/MS) (Synapt HDMS, Waters Corp., Manchester, U.K.) using a 40 min HPLC gradient between 10 and 95% ACN with 0.1% FA (v/v). The data were processed by searching against an in-house version of the Swiss-Prot sequence databases using Mascot (Matrix Science, London, U.K.). The mass tolerances for precursor and fragment ions were set to 0.3 Da. A maximum of two missed cleavages in the tryptic digestion was allowed. Variable modifications used in the search

included oxidation of methionine; addition of morphine 3-glucuronide (443.1580 Da, neutral loss of 285.1365 Da) to tyrosine, lysines, and the N-terminus; and formation of pyroglutamate from the N-terminal glutamine and glutamate. All MS/MS spectra were verified manually.

To improve the sequence coverage of modified peptides, the in-solution-digested morphine−G6PDH conjugate was fractionated manually using strong cation exchange (SCX) chromatography. In brief, a plug of 3M Empore C8 extraction disks was put into a P10 pipet tip, and polysulfethyl aspartamide stationary phase was added to a height of 4 mm. After equilibration, the sample was loaded onto the column in 20% ACN and 1% FA. The peptides were eluted with elution steps at increasing concentrations of ammonium formate, followed by evaporation. The peptides were then resuspended in 5% FA, loaded onto a microcolumn packed with POROS R2 resins, and eluted directly into the glass capillaries (Proxeon Biosystems, Odense, Denmark) to be analyzed manually via ESI-MS/MS (Synapt HDMS). One of the SCX fractions contained several of the potentially modified peptides and was therefore fractionated further. Similar to the fractionation using SCX chromatography, C12 reversed phase material was packed into P10 tips to a height of 4 mm. Fractions were eluted stepwise using increasing ACN concentrations in 1% FA. After evaporation and resuspension in 5% FA, the peptides were loaded onto microcolumns and eluted directly into glass capillaries to be analyzed by ESI-MS/MS.

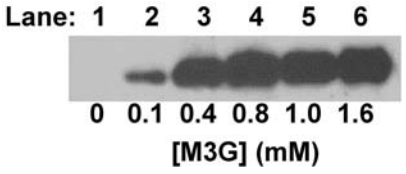

Figure 2. Western blot (using the anti-morphine antibody) of morphine−G6PDH conjugates prepared with the NHS-enhanced carbodiimide-mediated coupling method. Morphine−G6PDH conjugates were prepared with 0.1 μM G6PDH and varying M3G concentrations: 0.1, 0.4, 0.8, 1.0, and 1.6 mM (lanes 2−6, respectively). The absence of signals corresponding to unmodified G6PDH (lane 1) indicated that the binding of the anti-morphine antibody was specific to the M3G molecules.

Hydroxylamine Treatment. An equal volume of a 2 M hydroxylamine solution (pH 8.5) (prepared fresh daily) was added to the intact morphine−G6PDH conjugate and G6PDH (27 μM) samples. The mixture was incubated for 1−5 h at room temperature. After the incubation, the hydroxylamine was removed using a POROS R1 microcolumn. For tryptic digest samples, 10 μL of tryptic digest was dried and subsequently resuspended in 10 μL of purified water with vortex treatment. Next, 10 μL of 2 M hydroxylamine (pH 8.5) (prepared fresh daily) was added to the tryptic digest and incubated for 1−5 h. After the incubation, hydroxylamine was removed using a POROS R2 microcolumn.

RESULTS AND DISCUSSION

Morphine−G6PDH Conjugation. Morphine was conjugated to G6PDH using an NHS-enhanced carbodiimide-mediated coupling method.[21] The COOH group of M3G, a morphine derivative, was first activated by EDC and NHS, forming an NHS-ester. The NHS-ester was then reacted with an NH_2 group from lysines or the N-terminus of G6PDH to form an amide bond. Although coupling could also occur between the NHS-ester and the OH group from tyrosine, the majority of the labeling is expected to occur at the NH_2 groups because the NH_2 group is substantially more nucleophilic than the OH group at pH 7.3 at which conjugation took place.

To confirm morphine−G6PDH conjugation using this approach, Western blot analysis was employed. The anti-morphine antibody exhibited affinity for the morphine−G6PDH conjugate samples as indicated by the band that appeared above the molecular mass of a single 54 kDa G6PDH monomer

Sample	Representative MALDI Spectra (Degree of conjugation 0 1 2 3 4 5 6)	[M3G] in conjugation (mM)	*m/z*	FWHM (Da)	Degree of conjugation (M3G/ monomer)	Repression
G6PDH		0	54,420 ± 30	660 ± 30	0	3 ± 2 %
MG1		0.4	54,860 ± 60	1380 ± 50	1.0 ± 0.1	13 ± 2 %
MG2		0.8	55,200 ± 40	1780 ± 90	1.8 ± 0.1	27 ± 2 %
MG3		1.2	55,600 ± 100	2050 ± 60	2.6 ± 0.2	38 ± 2 %
MG4		1.6	55,950 ± 60	2180 ± 60	3.4 ± 0.2	45 ± 1 %
	53000 56000 *m/z*					

Figure 3. MALDI mass spectra and data (*m/z* and fwhm), degrees of conjugation, and levels of repression of intact G6PDH and morphine−G6PDH conjugates (MG1−MG4). The $[M + H]^+$ (centroid mass at 50% of peak height) and fwhm values are average values of three to six independent samples; the ± values represent standard errors. The degree of conjugation was calculated on the basis of the difference in $[M + H]^+$ between the conjugate sample and unmodified G6PDH divided by the mass increase of each M3G modification (443 Da). The ± values on % repression data represent standard errors ($n = 3$).

(Figure 2). The absence of signals corresponding to the G6PDH bands also indicated that the binding of the anti-morphine antibody was specific to the M3G molecules. This result verified that the G6PDH monomers were linked covalently to M3G molecules.

Characterization of the Intact Morphine−G6PDH Conjugate. The degree of conjugation and the repression level upon antibody binding are important characteristics of an analyte−G6PDH conjugate used in EMIT assays, and they often are related. To determine these characteristics and to study their relationship, we performed MALDI MS and activity assay analyses on morphine−G6PDH conjugate samples prepared using coupling reaction mixtures containing M3G and G6PDH at molar ratios of approximately 75:1 (MG1), 150:1 (MG2), 225:1 (MG3), and 300:1 (MG4). MALDI MS was employed to determine the average mass increase of the modified protein from the covalent attachment of M3G to G6PDH, thereby providing an estimate of the degree of conjugation. Figure 3 shows representative MALDI MS spectra of unmodified G6PDH, as well as the MG1−MG4 preparations. The G6PDH sample gave a peak at m/z 54420 ± 30, which corresponds to the expected molecular mass of a G6PDH monomer. For the conjugate samples, the attachment of each M3G molecule is expected to give a mass increase of 443 Da. The M3G molecular mass is 461 Da, but the coupling reaction results in the release of one water molecule (18 Da). The average molecular masses of the MG1−MG4 preparations were found to be m/z 54860 ± 60, 55200 ± 40, 55600 ± 100, and 55950 ± 60, respectively, which indicated that there were averages of 1.0 ± 0.1, 1.8 ± 0.1, 2.6 ± 0.2, and 3.4 ± 0.2 M3G molecules attached to each G6PDH monomer, respectively. With an increased degree of conjugation, an increase in the level of deactivation of the conjugate also was observed. The full width at half-maximum (fwhm) of the peaks from all four morphine−G6PDH conjugate populations was larger than that of the unmodified G6PDH peak, suggesting there was a distribution in the number of M3G attachments. The fwhm also increased with the degree of conjugation, implying a broader distribution as expected.

A high level of antibody-induced reporter enzyme repression is an important EMIT assay characteristic because it contributes directly to higher assay sensitivity through a lower background signal. To determine the achievable repression level, the enzyme activities measured in the presence and absence of excess anti-morphine antibody were compared. The repression levels were found to be 13 ± 2, 27 ± 2, 38 ± 2, and 45 ± 1% for MG1−MG4, respectively, as summarized in Figure 3. The unmodified G6PDH exhibited a negligible level of repression (3 ± 2%), indicating that the specific binding of antibody to the conjugated M3G caused the observed repression of reporter enzyme activity. The increase in reporter enzyme repression activity with an increased degree of conjugation is expected, because the probability of attachment of M3G on enzyme sites that cause repression upon antibody binding increases with the degree of conjugation.

Studies of morphine−G6PDH conjugates prepared at varying G6PDH concentrations in the coupling reaction mixture revealed that the G6PDH concentration did not affect the degree of conjugation. Using 1.6 mM M3G, morphine−G6PDH conjugates were prepared with G6PDH concentrations ranging from 0.1 to 5.4 μM. The resulting conjugates displayed the same levels of repression, implying the same degree of conjugation. Further, the MALDI MS analysis showed that the degree of conjugation

(a)

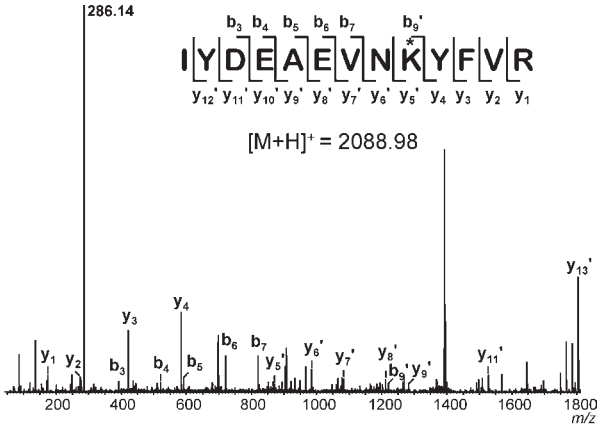

(b)

[M+H]+ (calc.)	Fragmentation pattern	Conjugation site(s)	Mascot score
1561.79	AAKNAAFNALK	K266	22
1576.72	KNTPEPYER	K410	8
1814.93	KLYPSVFNLYK	K22	10
1907.90	LNAKSVEDAFNTR	K387	27
2004.02	GYLQKHFAIVGTAR	K38	38
2018.97	QALNDDEFKQLVR	K56	14
2026.02	TLVTFFGGTGDLAKR	K20	23
2049.95	TIDLGWTVSDEDKK	K409	18
2088.98	IYDEAEVNKYFVR	K283	37
2143.02	YLKSEGLLADTGYNR	K132	58
2235.99	EAIEEAADKFDIDGNR	K106	17
2430.16	IDHYLGKEMVQNIAALR	K183	57
2573.28	MVSEIKTLVTFFGGTGDLAK	N-term. or K6	34
2645.29	FVDATSAVYTADKAPLETYK	K455	32
3066.45	AAKNAAFNALKIYDEAEVNK	K266 & K274	

Figure 4. (a) ESI-MS/MS spectrum (deconvoluted with MaxENT3) of the IYDEAEVNKYFVR tryptic peptide with a single M3G attachment ($[M + H]^+$ = 2088.98). The $[M + H]^+$ = 286.14 signal corresponds to the mass of the morphine moiety from M3G, indicating the loss of morphine from the backbone fragment. A series of expected b- and y-ions accounted for the morphine loss (b′ and y′ denote ions with the morphine loss), confirmed the peptide identity, and allowed the assignment of the M3G conjugation site, which is the ninth residue of the tryptic peptide or K283 of the G6PDH monomer. (b) Fragmentation patterns of the M3G tryptic peptides obtained from ESI-MS/MS spectra (asterisks denote the conjugation sites, and degree signs denote oxidized residues). Spectra were deconvoluted with either MaxENT3 or Mascot Distiller. While most spectra identified the modified peptide with the highest score when searching the Mascot database, others had to be interpreted manually. The fragmentation pattern of the $[M + H]^+$ = 2573.28 peptide suggested either the N-terminus or K6 to be a conjugation site.

of the morphine−G6PDH conjugate prepared at a concentration of 1.1 μM was also ~3.4. These observations, indicating that the degree of conjugation depended on the M3G concentration but not the G6PDH concentration, suggest that spontaneous M3G-NHS-ester hydrolysis limited the progress of the conjugation reaction.

ESI-MS/MS Analysis of MG4 Tryptic Digests. Proteolytic digestion in combination with MALDI MS and MS/MS methods is widely used in protein characterization.[22] In this work,

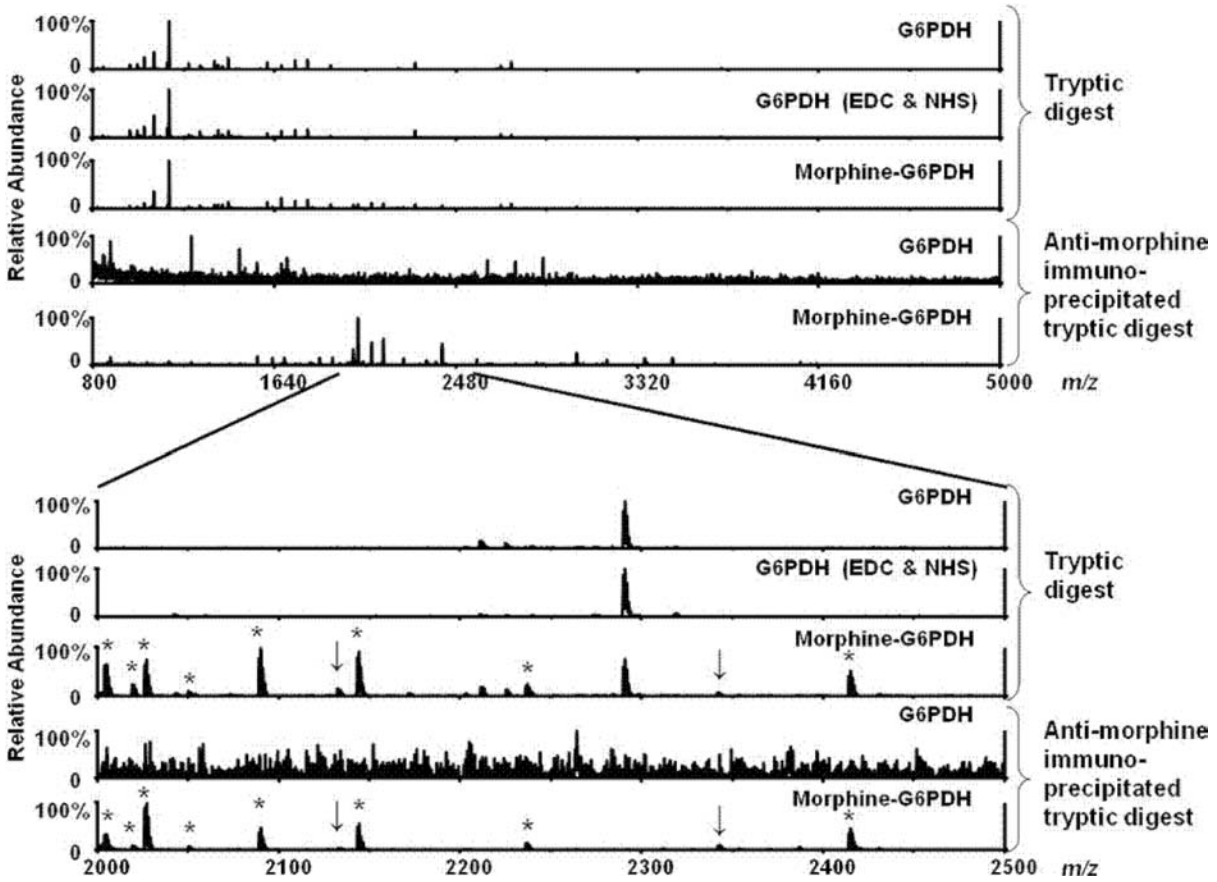

Figure 5. MALDI MS spectra (top, m/z 800−5000; bottom, m/z 2000−2500) of G6PDH tryptic digest, G6PDH-EN tryptic digest, MG4 tryptic digest, G6PDH IP-digest, and MG4 IP-digest. The y-axes were scaled relative to the peak with the highest intensity in the selected range. Asterisks and arrows denote peaks that represent M3G tryptic peptides; asterisks denote M3G tryptic peptides that also were identified by the MS/MS method.

morphine−G6PDH conjugates and unmodified G6PDH were digested by trypsin, which cleaves specifically at the carboxyl side of lysine and arginine with the exception of the cases where there is a succeeding proline[23,24] or a M3G-modified lysine. Subsequently, the tryptic digest was analyzed by ESI MS/MS and MALDI MS methods to locate conjugation sites.

MS/MS spectra were obtained for peptides in the MG4 tryptic digest samples. Fifteen M3G tryptic peptides (peptides with bound M3G) were identified. Figure 4a shows a typical deconvoluted ESI-MS/MS spectrum of a M3G tryptic peptide. The deconvoluted ESI-MS/MS spectrum was transformed from the triply charged ion at m/z 697.01, which corresponds closely to the m/z of the expected IYDEAEVNKYFVR tryptic peptide with a single M3G attachment (m/z 696.99 or 2087.98 Da). An abundant product ion at m/z 286.14 also was observed in the spectrum that is consistent with the loss of morphine from M3G. Further, a series of expected b- and y-product ions resulting from cleavage of the peptide backbone amide bonds confirmed the peptide identity and led to the assignment of the M3G conjugation site, which was determined to be the lysine residue of the tryptic peptide, or K283 of the G6PDH monomer.

The morphine fragment ion (m/z 286.14) also was used as a reporter ion, which aided the screening of other M3G tryptic peptides. Figure 4b shows the fragmentation pattern of the 15 M3G tryptic peptides identified using ESI-MS/MS. Left-facing bars indicate b-ions, and right-facing bars indicate y-ions. In 10 of 15 peptides, the modification sites could be assigned unambiguously, while in four cases, the sites were assigned assuming only lysine and tyrosine residues could be modified. In addition, another conjugation site was determined to be at either the N-terminus or K6 based on the fragmentation pattern of the N-terminal peptide (2572.3 Da). As expected, missed trypsin cleavage was observed at all the M3G-modified lysine residues.[24]

MALDI MS Analysis of Tryptic Digests. MALDI MS analyses of tryptic digests and anti-morphine immunoprecipitated tryptic digests (IP-digest) also were utilized to identify M3G tryptic peptides. Although the MALDI MS method does not provide amino acid content information, the amino acid sequence of the measured masses can be inferred from the G6PDH sequence. Because the mass and corresponding amino acid sequence of each G6PDH tryptic peptide can be predicted, it is straightforward to deduce the amino acid sequence of the measured masses.

Figure 5 shows representative MALDI MS spectra of the G6PDH tryptic digest (G6PDH-TD), the MG4 tryptic digest (MG4-TD), the G6PDH IP-digest (G6PDH-IPTD), and the MG4 IP-digest (MG4-IPTD) samples. In addition to G6PDH, another control sample, G6PDH that reacted with EDC and NHS (G6PDH-EN), was prepared and subsequently subjected to tryptic digestion. As shown in Figure 5, the MALDI MS spectrum of G6PDH-EN showed no detectable difference from that of G6PDH. Therefore, only the G6PDH control was considered in further analyses.

The overall patterns of MALDI MS spectra (m/z 800−5000) for G6PDH-TD and MG4-TD were similar, but the m/z 2000−2500 region revealed some minor peaks present only in the MG4-TD spectrum. This observation was anticipated, because peaks representing M3G tryptic peptides were expected to appear only in the MG4-TD spectrum. By identifying peaks that were present in the morphine-conjugated G6PDH mass spectra and absent from the G6PDH mass spectra, we determined masses of M3G tryptic peptides. These measured masses were further matched against the masses of expected M3G tryptic peptides, thereby yielding the corresponding amino acid sequences. On the basis of this MALDI−tryptic digest (MALDI−TD) analysis, 45 M3G tryptic peptides were identified.

Anti-morphine immunoprecipitation (IP) also was employed to search for additional M3G tryptic peptides and to further substantiate the previously identified peptides. Because the IP eluate should contain only peptides with affinity for the anti-morphine antibody, the peaks on the MG4-IPTD mass spectra were expected to represent the masses of M3G tryptic peptides. Although background signals were present from nonspecific binding, significantly weaker signals were measured for G6PDH-IPTD, suggesting nonspecific binding was minimal. From the MALDI−IPTD analysis, 46 M3G tryptic peptides were found, 32 of which were identified in the MALDI−TD study.

Although the MALDI MS method did not provide direct sequence information about M3G conjugation, the results obtained from the MALDI−TD and MALDI−IPTD analyses nonetheless are convincing for several reasons. M3G tryptic peptides were present in the MG4-TD and/or MG4-IPTD samples but absent from the control samples. Moreover, the MALDI MS results were consistent with the ESI-MS/MS data. More than 90% (14 of 15) of the peptides identified by MS/MS also were identified by the MALDI−TD and/or MALDI−IPTD analysis. Finally, the results from these two analyses corroborated one another to a large extent as illustrated by Figure 5 (m/z 2000−2500). MG4-TD and MG4-IPTD spectra displayed similar peaks that were absent in the control spectra. In fact, more than 70% (32 of 45) of the M3G tryptic peptides identified by the MALDI−TD analysis showed affinity for the anti-morphine antibody. It was expected that some of the M3G tryptic peptides (14 in this case) could only be identified by the MALDI−IPTD analysis and not the MALDI−TD analysis because IP generally amplifies signals allowing the identification of modified peptides present at lower concentrations. There were 13 peptides that appeared only in the MG4-TD spectra but not the MG4-IPTD spectra, and this observation could be caused by material loss during the wash of the IP experiment. The MALDI−TD and MALDI−IPTD results both confirm and complement one another.

The exact conjugation sites of many M3G tryptic peptides identified by MALDI MS were unknown, because many of the peptides have more than a single lysine or tyrosine residue. To narrow down the possible conjugation sites, several MG4 samples were subjected to hydroxylamine treatment to remove any conjugation that occurred via the OH groups of tyrosine. This process was useful in determining whether the M3G molecule was conjugated through an NH_2 or OH group for a given tryptic peptide. Three MG4 samples from different batches were treated with hydroxylamine prior to tryptic digestion. The intact mass and repression level of the hydroxylamine-treated MG4 preparation were statistically the same as those of the untreated MG4, suggesting that conjugation occurring through OH groups was absent or insignificant. However, MALDI−TD and MALDI−IPTD analyses of the hydroxylamine-treated MG4 samples revealed the loss of four tryptic peptide peaks, suggesting that M3G was conjugated to OH groups on these peptides. However, different results were obtained when the same analyses were performed on two MG4 samples that underwent hydroxylamine treatment after tryptic digestion. Three of four peptides that were lost after hydroxylamine pretreatment reappeared; moreover, two different M3G tryptic peptide peaks disappeared. Because MG4 samples treated with hydroxylamine before and after tryptic digestion produced different results, no peptide was confirmed to have M3G conjugation through an OH group. Nevertheless, the M3G tryptic peptides that remained after hydroxylamine treatment (whether before or after digestion) helped in the identification of NH_2 conjugation sites on M3G peptides identified by MALDI.

Identification of Conjugation Sites of M3G Peptides Identified by MALDI MS. A given peptide sequence could have more than one possible conjugation site (e.g., it could contain more than a single lysine or tyrosine), and thus, the exact amino acid residues engaged in coupling to M3G may not be determined unambiguously without additional information. The task was simplified in several cases by making the following commonly accepted assumptions. (1) Lysine, the N-terminus, and tyrosine are the only possible conjugation sites. (2) Modification of lysines causes missed cleavage. (3) Hydroxylamine removes all M3G groups coupled to tyrosine. These assumptions are well-established in the literature,[8,25,26] and they also are consistent with the MS/MS results obtained with this particular system. The MS/MS data directly support the first two assumptions, as shown by the fact that all the conjugation sites identified by MS/MS are amines and missed cleavages are observed on all the M3G-modified lysines. The MS/MS results also indirectly support the third assumption. Because all conjugation sites found by the MS/MS method were NH_2 groups, it is consistent with hydroxylamine results, which also suggest that most, if not all, conjugation sites were NH_2 groups. On the basis of these assumptions, 12 additional lysine residues were identified as conjugation sites, yet the exact conjugation sites for a number of remaining peptides still could not be determined.

Conjugation Site Categorization. Conjugation sites were categorized into three tiers based on the certainty of their identities. The M3G tryptic peptides identified by ESI-MS/MS based on their masses and sequences were highly certain, and they were categorized into tier 1. Peptides that were identified by both MALDI−TD and MALDI−IPTD analyses showed that the peptides had affinity for the anti-morphine antibody; these peptides were assigned to tier 2. Tier 3 M3G peptides were identified by only MALDI−TD or MALDI−IPTD analysis. After M3G peptides had been assigned to different tiers, conjugation sites were then categorized accordingly. The conjugation sites were placed into the same tier as the peptide(s) from which they were deduced. If a conjugation site was identified by multiple peptides, the conjugation site was placed in the highest tier. A total of 26 conjugation sites were confirmed by the data, 14 of which were placed in tier 1, six in tier 2, and six in tier 3 (Table 1a).

All 26 identified sites were found to be lysine residues, and an additional conjugation site was identified (by MS/MS) as either the N-terminus or K6. Three other lysine residues, K97, K149, and K209, were potential conjugation sites as suggested by peptides observed at m/z 4119.87, 4147.90, and 2633.32, respectively (Table 1b). However, these sites could not be further pinpointed because of the existence of other possible

Table 1. M3G Conjugation Sites (a) and Potential M3G Conjugation Sites (b) Categorized into Three Tiers[a]

	(a) M3G Conjugation Sites		
	M3G conjugation site	peptide *m/z*	peptide sequence[b]
tier 1	K20	2025.02	TLVTFFGGTGDLA**K**R
	K22	1813.93	**K**LYPSVFNLYK
	K38	2003.02	GYLQ**K**HFAIVGTAR
	K56	2017.97	QALNDDEF**K**QLVR
	K106	2234.99	EAIEEAAD**K**FDIDGNR
	K132	2142.02	YL**K**SEGLLADTGYNR
	K183	2413.21	IDHYLG**K**EMVQNIAALR
	K266	1560.79	AA**K**NAAFNALK
	K274	3065.45	AAKNAAFNAL**K**IYDEAEVNK
	K283	2087.98	IYDEAEVN**K**YFVR
	K387	1906.90	LNA**K**SVEDAFNTR
	K409	2048.95	TIDLGWTVSDED**K**K
	K410	1575.72	**K**NTPEPYER
	K455	2644.29	FVDAISAVYTAD**K**APLETYK
tier 2	K64	3175.40	DSI**K**DFTDDQAQAEAFIEHFSYR
	K129	1629.84	FFGTIA**K**YLK
	K205	2341.10	FGNPIFDAAWN**K**DYIK
	K299	3128.41	AQYGAGDSADF**K**PYLEELDVPADSK
	K462	2310.03	APLETY**K**SGSMGPEASDK
	K485	1803.88	LLAANGDAWF**K**G
tier 3	K32	2846.41	LYPSVFNLY**K**K**G**YLQ**K**
	K33	2846.41	LYPSVFNLY**K**K**G**YLQ**K**
	K339	889.43	SG**K**R
	K344	1229.64	LAA**K**QTR
	K383	1498.80	GAIEL**K**LNAK
	K473	2793.29	SGSMGPEASD**K**LLAANGDAWFK

	(b) Potential M3G Conjugation Sites		
	potential M3G conjugation site	peptide *m/z*	peptide sequence[b,c]
tier 1	N-terminus	2572.28	**NH_2**-MVSEI**K**TLVTFFGGTGDLAK
	K6	2572.28	NH_2-MVSEI**K**TLVTFFGGTGDLAK
tier 2	K209	2633.32	DYI**K**NVQVTLSEVLGVEER
tier 3	K97	4119.87	AHDVTDAASYAVL**K**EAIEEAADKFDIDGNR
	K149	4147.90	LMIE**K**PFGTSYDTAAELQNDLENAFDDNQLFR

[a] Tier 1, conjugation sites derived from MS/MS data; tier 2, conjugation sites derived from M3G tryptic peptides identified by both MALDI−TD and MALDI−IPTD analyses; tier 3, conjugation sites derived from M3G tryptic peptides identified by either MALDI−TD or MALDI−IPTD analysis. [b] Residues in bold denote conjugation sites and potential conjugation sites indicated in the second column. [c] The underlined residues indicate other possible conjugation sites suggested by the M3G tryptic peptide.

M3G attachment sites on the peptides. This study demonstrated the primary conjugation sites to be NH_2 groups. It also demonstrated that, among the 37 NH_2 groups on each G6PDH monomer, at least 27 of the groups can be acylated by activated COOH compounds (in this case M3G-NHS-ester), with perhaps a small amount of modified tyrosines. It also may be worth noting that four of the six remaining NH_2 sites (K253, K260, K312, and K442), if modified, would generate M3G tryptic peptides with masses of >4400 Da, which could be difficult to detect with the MALDI MS method. On the basis of the results, all NH_2 groups except for K353 and K377 were found to be at least potential conjugation sites. Therefore, K353 and K377 can be excluded as AII (antibody-induced inhibition) sites.

Although the number of conjugation sites was determined to be at least 27 for MG4, a degree of conjugation of 3.4 suggests that there is a heterogeneous population of morphine−G6PDH conjugates; i.e., different G6PDH monomers have different M3G conjugation sites. Solely on the basis of the MALDI−TD data, 17 conjugation sites were found in the MG1 samples. Because the repression level for MG4 (46%) was higher than that for MG1 (11%), the conjugation sites present only in MG4 may be particularly important for AII. However, the magnitude of the MALDI MS signal of many of the modified peptides also decreases with a decreasing degree of conjugation, which could cause a decrease in the level of repression. No information about identifying AII sites could be obtained from this result.

The results of this study are mostly consistent with a previous study conducted by Ullman et al.,[8] which focused on the characterization of a similar conjugate, O^3-carboxymethylmorphine (O^3-CMM)−G6PDH, fitting inhibition versus anti-

morphine concentration data to a probability model. Both studies showed that the level of inhibition increased with the degree of conjugation, and lysines were the primary conjugation sites for activated COOH analyte. A heterogeneous population of analyte−G6PDH conjugate was suggested by both studies. There were, however, a few different conclusions between the studies. First, the O^3-CMM−G6PDH study assigned a higher fraction of conjugation sites to tyrosine residues. This inconsistency perhaps could be explained by the different conjugation reaction pH used in the two studies. The O^3-CMM−G6PDH conjugate was prepared at pH 8, while the morphine−G6PDH conjugate in this work was prepared at pH 7.3. A higher pH could increase the nucleophilicity of the OH group, thereby making the OH groups more likely to be acylated. Some more minute details, such as the number of conjugation sites and the repression level, also were different between the two systems. Despite a few minor differences, the majority of the conclusions between the two studies were generally consistent.

Implications for EMIT. An analyte−G6PDH conjugate is a major component in an EMIT system. Therefore, the characterization of analyte−G6PDH conjugates is important for understanding and improving EMIT systems. Although a previous study focused on characterization of O^3-CMM−G6PDH conjugates, this work describes a different approach for characterizing the morphine−G6PDH conjugate using a combination of several methods, including an enzyme activity assay, proteolytic digestion, immunoprecipitation, and mass spectrometry. Unlike the previous study, the current approach uses MALDI MS to determine the degree of conjugation, obviating the need to handle radioisotopes. More importantly, this study identified conjugation sites via tryptic digestion and MS analysis, information not provided in the previous study.

A useful finding of this study was that two catalytically important residues in the active sites, K22 and K183,[12,27,28] were conjugated with M3G molecules. This explains at least a partial cause of enzyme activity loss due to the conjugation reaction. Within the heterogeneous morphine−G6PDH population, the deactivated morphine−G6PDH molecules are useless for the EMIT assay, because antibody binding to a deactivated enzyme would not generate any change in activity. Further, the M3G molecules on the deactivated enzyme also compete for antibody binding, and as a result, the detection limit would increase. The ability to prevent conjugation on the catalytically important residues could improve the performance of the EMIT assay, yet it would be even more useful to be able to perform site-specific conjugation. An existing patent described two mutation schemes for creating genetically modified G6PDH toward site-specific conjugation, but scarce results on the first scheme and no results on the second scheme were reported.[12] The first scheme involved mutation of specific lysine residues to arginine. Because arginine is not reactive to activated COOH compounds, conjugation on undesired amino acid positions could be prevented. The second proposed scheme involved genetically modifying residues that are important for antibody-induced inhibition to cysteines, and subsequently conjugating the analyte to the cysteine residues. Because our study reveals that K22 and K183 are conjugation sites for M3G, the lysine to arginine mutation approach would be inadequate. Although it is still unknown which conjugation sites are important for antibody-induced inhibition, the second scheme is a better approach, because it could prevent alteration of catalytically important residues through either genetic modification or covalent conjugation. Perhaps creating a series of G6PDH mutants such that each mutant has a different lysine substituted with cysteine could be a part of the development strategy.

To estimate the number of important sites for AII, the inhibition and degree of conjugation data obtained in this study were utilized. On the basis of probability, the total number of combinations (T) of N conjugation sites at a degree of conjugation of x is

$$T = \frac{N!}{x!(N-x)!} \tag{1}$$

If there are d deactivation sites, which cause complete deactivation if modified with M3G, the number of combinations that are still active (not deactivated) is T_{nd}

$$T_{nd} = \frac{N-d!}{x!(N-d-x)!} \tag{2}$$

Now, if in addition to d deactivation sites, there are also r sites that if bound by the anti-morphine antibody will cause complete inhibition, then the number of combinations that are still active is $T_{nd,nr}$

$$T_{nd,nr} = \frac{N-d-r!}{x!(N-d-r-x)!} \tag{3}$$

and the % repression measured will be

$$\%\ \text{repression} = 1 - \frac{T_{nd,nr}}{T_{nd}} \times 100\% \tag{4}$$

To estimate r, the values for $N-d$, x, and % repression are required. The degree of conjugation (x) and the corresponding % repression have been measured in this study. The value of $N-d$ is not clear, because N and d are unknown. However, $N-d$ has an upper bound of 68. This is because K22, K149, and K183 have been shown to be catalytically important,[27−29] meaning that there are at least six catalytically important lysine residues per G6PDH homodimer ($d \geq 6$). Because N cannot exceed 74 (the total number of NH_2 groups), $N - d \leq 68$. By fitting the % repression versus x to eqs 2−4 with the constraint that $N - d \leq 68$, the result shows that r cannot exceed 6. Because r represents the number of repression sites on each G6PDH homodimer, this suggests at most 3 unique amino acid residues that are important for AII. This is consistent with Ullman's study, which estimated 1 important unique amino acid residue.

CONCLUSIONS

In this work, morphine−G6PDH conjugates have been characterized using a combination of methods, including an enzyme activity assay, tryptic digestion, immunoprecipitation, and mass spectrometry. This study utilized MALDI MS to determine the degree of conjugation, obviating the need to handle radioisotopes while providing results consistent with a previous O^3-carboxymethylmorphine−G6PDH conjugate characterization study. Further, tryptic digestion and MS analyses allowed for conjugation site identification, information not provided in the previous studies. The 26 unambiguously identified conjugation sites all were found to be lysine residues, demonstrating that lysines are the primary conjugation sites and that a large portion of the 36 lysines on the G6PDH are accessible to and can be modified by activated COOH compounds. Further, the catalytically important lysine residues were

among the 26 identified conjugation sites. The insights gained in this study partially explain the cause of enzyme deactivation resulting from the conjugation reaction and are useful in devising strategies for creating new G6PDH mutants to improve EMIT.

AUTHOR INFORMATION

Corresponding Author

*Telephone: (310) 825-8946. Fax: (310) 206-4107. E-mail: hmonbouq@ucla.edu.

Present Addresses

[⊥]Department of Medical Biochemistry and Biophysics, Karolinska Institute, Stockholm, Sweden.

ACKNOWLEDGMENT

The UCLA Mass Spectrometry and Proteomics Technology Center was established with a grant from the W. M. Keck Foundation. J.A.L. acknowledges support from the National Institutes of Health (R01 RR 20004).

REFERENCES

(1) Ullman, E. F. (1999) Homogeneous immunoassays: Historical perspective and future promise. *J. Chem. Educ. 76*, 781–788.

(2) Scharpé, S., Cooreman, W. M., Blomme, W. J., and Laekeman, G. M. (1976) Quantitative enzyme immunoassay: Current status. *Clin. Chem. 22*, 733–738.

(3) Rubenstein, K. E., Schneider, R. S., and Ullman, E. F. (1972) Homogeneous enzyme immunoassay. A new immunochemical technique. *Biochem. Biophys. Res. Commun. 47*, 846–851.

(4) Deshpande, S. S. (1996) *Enzyme Immunoassays. From Concept to Product Development*, pp 244, 258, 259, Chapman & Hall, New York.

(5) Rosenthal, A. F., Vargas, M. G., and Klass, C. S. (1976) Evaluation of enzyme-multiplied immunoassay technique (EMIT?) for determination of serum digoxin. *Clin. Chem. 22*, 1899–1902.

(6) Lee, W. T., Flynn, T. G., Lyons, C., and Levy, H. R. (1991) Cloning of the gene and amino acid sequence for glucose 6-phosphate dehydrogenase from *Leuconostoc mesenteroides*. *J. Biol. Chem. 266*, 13028–13034.

(7) Olive, C., Geroch, M. E., and Levy, H. R. (1971) Glucose 6-phosphate dehydrogenase from *Leuconostoc mesenteroides*. Kinetic Studies. *J. Biol. Chem. 246*, 2047–2057.

(8) Ullman, E. F. (1980) Principles of homogeneous enzyme-immunoassay. In *Enzyme Immunoassay* (Maggio, E. T., Ed.) pp 105–134, CRC Press, Boca Raton, FL.

(9) Rubenstein, K. E., and Ullman, E. F. (1975) Enzyme immunoassays with glucose-6-phosphate dehydrogenase. U.S. Patent 3,875,011.

(10) Chang, J., Gotcher, S., and Gushaw, J. B. (1982) Homogeneous enzyme immunoassay for theophylline in serum and plasma. *Clin. Chem. 28*, 361–367.

(11) Ullman, E. F. (1999) Homogeneous immunoassays: EMIT® and beyond. *J. Clin. Ligand Assay 22*, 221–227.

(12) Jakobovits, E. B., Silen, J. L., Levy, M. J., Goodman, T. C., Becker, M., Ullman, E. F., Caldwell, R. M., Bott, R. R., and Barnett, C. C. (2000) Homogeneous immunoassays using mutant glucose-6-phosphate dehydrogenases. U.S. Patent 6,033,890.

(13) Karas, M., and Hillenkamp, F. (1988) Laser desorption ionization of proteins with molecular masses exceeding 10,000 Da. *Anal. Chem. 60*, 2299–2301.

(14) Tanaka, K., Waki, H., Ido, Y., Akita, S., Yoshida, Y., and Yoshida, T. (1988) Protein and polymer analyses up to m/z 100 000 by laser ionization time of flight mass spectrometry. *Rapid Commun. Mass Spectrom. 2*, 151–153.

(15) Fenn, J. B., Mann, M., Meng, C. K., Wong, S. F., and Whitehouse, C. M. (1990) Electrospray ionization: Principles and practice. *Mass Spectrom. Rev. 9*, 37–70.

(16) *NuPAGE Technical Guide*, version E (2003) Invitrogen Corp., Carlsbad, CA.

(17) Kussmann, M., Nordhoff, E., Rahbek-Nielsen, H., Haebel, S., Rossel-Larsen, M., Jakobsen, L., Gobom, J., Mirgorodskaya, E., Kroll-Kristensen, A., Palm, L., and Roepstorff, P. (1997) Matrix-assisted laser/desorption ionization mass spectrometry sample preparation techniques designed for various peptide and protein analytes. *J. Mass Spectrom. 32*, 593–601.

(18) Ytterberg, A. J., Peltier, J.-B., and van Wijk, K. J. (2006) Protein profiling of plastoglobules in chloroplasts and chromoplasts. A surprising site for differential accumulation of metabolic enzymes. *Plant Physiol. 140*, 984–997.

(19) Rosenfeld, J., Capdevielle, J., Guillemot, J. C., and Ferrara, P. (1992) In-gel digestion of proteins for internal sequence analysis after one or two-dimensional gel electrophoresis. *Anal. Biochem. 203*, 173–179.

(20) Gobom, J., Nordhoff, E., Mirgorodskaya, E., Ekman, R., and Roepstorff, P. (1999) Sample purification and preparation technique based on nano-scale reversed-phase columns for the sensitive analysis of complex peptide mixtures by matrix-assisted laser desorption/ionization mass spectrometry. *J. Mass Spectrom. 34*, 105–116.

(21) Staros, J. V., Wright, R. W., and Swingle, D. M. (1986) Enhancement by *N*-hydroxysulfosuccinimide of water-soluble carbodiimide-mediated coupling reactions. *Anal. Biochem. 156*, 220–222.

(22) Chapman, J. R. (2000) *Mass Spectrometry of Proteins and Peptides*. Humana Press, Totowa, NJ.

(23) Barret, A. J., Rawlings, N. D., and Woessner, J. F. (2004) Trypsin. In *Handbook of Proteolytic Enzymes*, pp 1483−1488, Elsevier Academic Press, San Diego.

(24) Allen, G. (1989) Sequencing of proteins and peptides. In *Laboratory Technique in Biochemistry and Molecular Biology* (Burdon, R. H., and van Knippenberg, P. H., Eds.) Vol. 9, pp 85−89, Elsevier/North-Holland, Amsterdam.

(25) Rice, R. H., Means, G. E., and Brown, W. D. (1977) Stabilization of bovine trypsin by reductive methylation. *Biochim. Biophys. Acta 492*, 316–321.

(26) Rowley, G. L., Rubenstein, K. E., Rubenstein, J. H., and Ullman, E. F. (1975) Mechanism by which antibodies inhibit hapten-malate dehydrogenase conjugates. *J. Biol. Chem. 250*, 3759–3766.

(27) Lee, W. T., and Levy, H. R. (1992) Lysine-21 of *Leuconostoc mesenteroides* glucose 6-phosphate dehydrogenase participates in substrate binding through charge-charge interaction. *Protein Sci. 1*, 329–334.

(28) Rowland, P., Basak, A. K., Gover, S., Levy, H. R., and Adams, M. J. (1994) The three-dimensional structure of glucose 6-phosphate dehydrogenase from *Leuconostoc mesenteroides* refined at 2.0 Å resolution. *Structure 2*, 1073–1087.

(29) Naylor, C. E., Gover, S., Basak, A. K., Cosgrove, M. S., Levy, H. R., and Adams, M. J. (2001) $NADP^+$ and NAD^+ binding to the dual coenzyme specific enzyme *Leuconostoc mesenteroides* glucose 6-phosphate dehydrogenase: Different interdomain hinge angles are seen in different binary and ternary complexes. *Acta Crystallogr. D57*, 635–648.

Bioconjugate Chemistry

ARTICLE

pubs.acs.org/bc

Spider Silk-Based Gene Carriers for Tumor Cell-Specific Delivery

Keiji Numata,[†,§] Michaela R Reagan,[†] Robert H Goldstein,[‡] Michael Rosenblatt,[‡] and David L Kaplan[*,†]

[†]Department of Biomedical Engineering, Tufts University, 4 Colby Street, Medford, Massachusetts 02155, United States

[‡]Department of Physiology, Tufts University School of Medicine, 136 Harrison Avenue, Boston, Massachusetts 02111-1800, United States

ABSTRACT: The present study demonstrates pDNA complexes of recombinant silk proteins containing poly(L-lysine) and tumor-homing peptides (THPs), which are globular and approximately 150−250 nm in diameter, show significant enhancement of target specificity to tumor cells by additions of F3 and CGKRK THPs. We report herein the preparation and study of novel nanoscale silk-based ionic complexes containing pDNA able to home specifically to tumor cells. Particular focus was on how the THP, F3 (KDEPQRRSARLSAKPAPPKPEPKPKKAPAKK), and CGKRK, enhanced transfection specificity to tumor cells. Genetically engineered silk proteins containing both poly(L-lysine) domains to interact with pDNA and the THP to bind to specific tumor cells for target-specific pDNA delivery were prepared using *Escherichia coli*, followed by *in vitro* and *in vivo* transfection experiments into MDA-MB-435 melanoma cells and highly metastatic human breast tumor MDA-MB-231 cells. Non-tumorigenic MCF-10A breast epithelial cells were used as a control cell line for in vitro tumor-specific delivery studies. These results demonstrate that combination of the bioengineered silk delivery systems and THP can serve as a versatile and useful new platform for nonviral gene delivery.

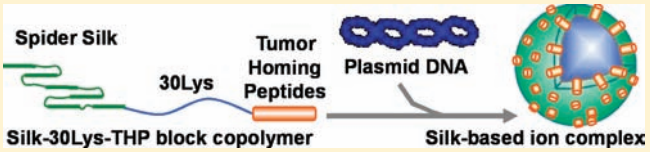

INTRODUCTION

Gene delivery is an important technique to treat various diseases including cancers and inherited diseases. Recently, nonviral vectors, i.e., cationic polymer-based vectors, have attracted attention as safer gene vectors compared to viral vectors.[1−3] Nonviral plasmid DNA (pDNA) delivery systems using cationic liposomes or chemically derived synthetic polymers such as polyethyleneimine have improved over the past decade in terms of transfection efficiency, cell-binding, and endosomal release.[4,5] Nevertheless, cytotoxicity and target specificity remain key challenges with lipid- and synthetic polymer-based gene delivery systems. A suitable nonviral gene vector would be biocompatible, biodegradable, nontoxic, efficient, and able to be designed to target specific cell types. These are challenging design goals to meet with liposomes or chemically synthesized polymers, mainly due to the limits inherent with chemically synthesis.

Silk proteins have been used successfully in the biomedical field as sutures for decades, and also explored as biomaterials for cell culture and tissue engineering, achieving Food and Drug Administration approval for such expanded utility because of their excellent mechanical properties, versatility in processing, and biocompatibility.[6−8] Virgin silk with the associated contaminant sericin proteins was reported as a potential allergen causing a Type I allergic, due to upregulated IgEs in response to the sericins; however, once the sericins are properly removed, there is minimal response from the core fibroin structural proteins.[9,10] Further, α-chymotrypsin degradation products of silk proteins are nontoxic.[9−11] Silk-based gene delivery systems have recently been reported to provide biodegradability, biocompatibility, high transfection efficiency, and DNase resistance.[12−14] The secondary structure of the silk sequences in these pDNA complexes can be used to regulate enzymatic degradation rates of the complexes, and hence control the release profile of carried genes from these complexes.[13] Therefore, if target specificity can be added into these silk-based gene delivery systems via recombinant techniques, then a more efficient and useful nonviral gene delivery system can be realized, in which the chemistry can be precisely tailored for cell targeting. To our knowledge, there is no such nonviral tailored gene delivery system currently available.

In the present study, we report the preparation and study of novel nanoscale silk-based ionic complexes containing pDNA able to home specifically to tumor cells. Silk-based block copolymers were bioengineered with both poly(L-lysine) domains to interact with pDNA and the tumor-homing peptide (THP) to bind to specific tumor cells for target-specific pDNA delivery. Particular focus was on how the THP, F3 (KDEPQRRSARLSAKPAPPKPEPKPKKAPAKK) and CGKRK, enhanced transfection specificity to tumor cells. F3 peptides have been reported to home to nucleolin, which is expressed at the surface of tumor angiogenic endothelial cells, and bind specifically to MDA-MB-435 cells.[15,16] CGKRK peptides were reported to bind specifically to heparan sulfate in tumor vessels.[17,18] Genetically engineered silk proteins containing poly(L-lysine) and the THPs were prepared using *Escherichia coli*, followed by *in vitro* and *in vivo* transfection experiments into MDA-MB-435 melanoma cells and highly metastatic human breast tumor MDA-MB-231 cells. Non-tumorigenic MCF-10A breast epithelial cells were used as a control cell line for *in vitro* tumor-specific delivery studies.

Received: April 4, 2011
Revised: June 30, 2011
Published: July 08, 2011

ACS Publications © 2011 American Chemical Society

Silk6mer-30lys-monomeric F3 (SL-mF3) Theoretical pI/Mw: 10.72 / 28737.77 Da
MHHHHHHSSGLVPRGSGMKETAAAKFERQHMDSPDLGTDDDDKAMAA
SGRGGLGGQGAGAAAAAGGAGQGGYGGLGSQGT
SGRGGLGGQGAGAAAAAGGAGQGGYGGLGSQGT
SGRGGLGGQGAGAAAAAGGAGQGGYGGLGSQGT
SGRGGLGGQGAGAAAAAGGAGQGGYGGLGSQGT
SGRGGLGGQGAGAAAAAGGAGQGGYGGLGSQGT
SGRGGLGGQGAGAAAAAGGAGQGGYGGLGSQGT
SKKKKKKKKKKKKKKKTSKKKKKKKKKKKKKKT
SKDEPQRRSARLSAKPAPPKPEPKPKKAPAKKTS

Silk6mer-30lys-monomeric CGKRK (SL-mCGKRK) Theoretical pI/Mw: 10.66 / 25897.10 Da
MHHHHHHSSGLVPRGSGMKETAAAKFERQHMDSPDLGTDDDDKAMAA
SGRGGLGGQGAGAAAAAGGAGQGGYGGLGSQGT
SGRGGLGGQGAGAAAAAGGAGQGGYGGLGSQGT
SGRGGLGGQGAGAAAAAGGAGQGGYGGLGSQGT
SGRGGLGGQGAGAAAAAGGAGQGGYGGLGSQGT
SGRGGLGGQGAGAAAAAGGAGQGGYGGLGSQGT
SGRGGLGGQGAGAAAAAGGAGQGGYGGLGSQGT
SKKKKKKKKKKKKKKKTSKKKKKKKKKKKKKKT
S**CGKRK**TS

Silk6mer-30lys-dimeric CGKRK (SL-dCGKRK) Theoretical pI/Mw: 10.68 / 26657.50 Da
MHHHHHHSSGLVPRGSGMKETAAAKFERQHMDSPDLGTDDDDKAMAA
SGRGGLGGQGAGAAAAAGGAGQGGYGGLGSQGT
SGRGGLGGQGAGAAAAAGGAGQGGYGGLGSQGT
SGRGGLGGQGAGAAAAAGGAGQGGYGGLGSQGT
SGRGGLGGQGAGAAAAAGGAGQGGYGGLGSQGT
SGRGGLGGQGAGAAAAAGGAGQGGYGGLGSQGT
SGRGGLGGQGAGAAAAAGGAGQGGYGGLGSQGT
SKKKKKKKKKKKKKKKTSKKKKKKKKKKKKKKT
S**CGKRK**TS**CGKRK**TS

Figure 1. Amino acid sequences of the recombinant proteins with 30 lysines and tumor-homing peptides (THP). Bold: THP sequences. Underline: representative 6mer of spider silk sequence.

EXPERIMENTAL PROCEDURES

Design and Cloning of Recombinant Silk Sequence. The spider silk repeat unit was selected based on the consensus repeat (SGRGGLGGQGAGAAAAAGGAGQGGYGGLGSQGT) derived from the native sequence of the dragline protein MaSp1 sequence from the spider *Nephila clavipes* (Accession P19837). The Silk6mer-30lys containing six contiguous copies of this repeat and 30 lysines was developed through the transfer of cloned inserts to pET-30a, according to our previously published procedures.[12,15−18] The sequences of the synthetic oligonucleotides encoding F3 and CGKRK residues were as follows: F3-a: 5′-*CTAGC*AAAGATGAACCGCAGCGCCGCAGCGCGCGCCTGAGCGCGAAACCGGCGCCGCCGAAACCGGAACCGAAACCGAAAAAAGCGCCGGCGAAAAAAA-3′, F3-b: 5′-*CTAGT*TTTTTTCGCCGGCGCTTTTTTCGGTTTCGGTTCCGGTTTCGGCGGCGCCGGTTTCGCGCTCAGGCGCGCGCTGCGGCGCTGCGGTTCATCTTTG-3′, CGKRK-a: 5′-*CTAGC*TGCGGCAAACGCAAAA-3′, CGKRK-b: 5′-*CTAGT*TTTGCGTTTGCCGCAG-3′. The restriction sites for *Spe*I are italicized. F3-a and F3-b as well as CGKRK-a and CGKRK-b are complementary oligonucleotides which were annealed to form double-stranded DNA. The double-stranded DNAs of the sequences were ligated into pET30-Silk6mer-30lys to generate pET30-Silk6mer-30lys-monomeric F3 (mF3), pET30-Silk6mer-30lys-monomeric CGKRK (mCGKRK), and pET30-Silk6mer-30lys-dimeric CGKRK (dCGKRK), as shown in Figure 1, by DNA ligase (New England Biolabs Inc., Ipswich, MA).

Protein Expression and Purification. The constructs pET30-Silk6mer-30lys-mF3, pET30-Silk6mer-30lys-mCGKRK, and pET30-Silk6mer-30lys-dCGKRK were used to transform *E. coli* strain RY-3041, and the expression and purification of these proteins were carried out by methods reported previously.[14,19−21] SDS-polyacrylamide gel electrophoresis (PAGE) was performed using 4−12% precast NuPage Bis-Tris gels (Invitrogen, Carlsbad, CA). The gel was stained with colloidal blue (Invitrogen, Carlsbad, CA). Purified samples were extensively dialyzed against acetic buffer and then Milli-Q water. For dialysis, Spectra/Por Biotech Cellulose Ester Dialysis Membranes with MWCO of 100−500 Da (Spectrum Laboratories Inc., Rancho Dominguez, CA) were used.

Preparation and Characterization of pDNA Complexes. pDNA encoding Firefly Luciferase (Luc, 7041 bp) was amplified in competent DH5α *E. coli* (Invitrogen) and purified using EndoFree Plasmid Maxi Kits (Qiagen, Hilden, Germany). The DNA concentration was determined by absorbance at 260 nm. To prepare the complexes of the recombinant silk proteins with pDNA, a solution containing silk protein (0.1 mg/mL) was mixed with the pDNA solution (370 μg/mL) at various N/P ratios. Here, N/P ratio refers to the ratio of number of amines/phosphates from pDNA. The mixture of recombinant silk and pDNA was incubated at room temperature (∼20 °C) overnight prior to characterization. The pDNA complexes were characterized by zeta potential meter (Zetasizer Nano-ZS, Malvern Instruments Ltd., Worcestershire, UK) and atomic force microscopy (AFM, Dimension V, Veeco Instruments Inc., Plainview, NY). The pDNA complex solution (around 70 μL) was added to ultrapure water (450 μL, Invitrogen) and then used as a sample for zeta potential and size measurement. Zeta potential and zeta deviation of samples were measured three times by a zeta potential meter, and the average data were obtained using *Dispersion Technology* software v 5.03 (Malvern Instruments Ltd.). The pDNA complex solution was cast on cleaved mica, and observed in air at room temperature using a 200−250 μm long silicon cantilever with a spring constant of 2.8 N/m in tapping mode AFM. Calibration of the cantilever tip convolution effect was carried out to obtain the true dimensions of objects by previously reported methods.[19,20]

Cell Culture, *in Vitro* Transfection, and Cell Viability. The MDA-MB-435 melanoma cell line, MDA-MB-231 human breast tumor cell line, and MCF10A non-tumorigenic mammary breast epithelial cells were also used to investigate target specificity of the pDNA complexes. Cultures were grown to confluence using media consisting of Dulbecco's Modified Eagle Medium (DMEM) and 10% FBS for MDA-MB-435 and MDA-MB-231 cells. The medium for MCF10A was composed of DMEM/F12, 5% horse serum, 20 ng/mL EGF, 0.5 μg/mL hydrocortisone, 0.1 μg/mL cholera toxin, and 10 μg/mL insulin. The cultures were detached from their substrates using 0.25% trypsin (Invitrogen), and then replated in the 24-multiwell plate at a density of 8000 cells/well. Before transfection experiments, the cells were washed with PBS to remove antibiotic and insulin. Media for the *in vitro* transfection experiments consisted of DMEM and 10% FBS. pDNA (1.2 μg) and recombinant silk (appropriate amount) complexes were added into each well. After incubation of the cells for 6 h at 37 °C, the media was exchanged with media without pDNA complexes. To evaluate luciferase gene expression quantitatively, a Luciferase assay (Promega, Madison, WI) was performed (n = 4). The amount of protein in each well was determined using a BCA protein assay (Pierce Biotechnology, Rockford, IL), and then the relative light units (output)/weight of protein (RLU/mg) was obtained. Lipofectamine 2000 (Invitrogen) was used as a positive control vector. For cell viability, MCF10A cells (8000 cells/well) were seeded into the 96-well plates containing the pDNA complexes and cultured for 48 h in the media (100 μL) used in the transfection experiment. Cytotoxicity to the cells of the pDNA complexes was characterized by standard 3-(4,5-dimethylthiazol-2-yl)-5-(3-carboxymethoxyphenyl)-2-(4-sulfophenyl)-2*H*-tetrazolium (MTS) assay (Promega, Madison, WI) according to the manufacturer's instructions (n = 8).

***In Vivo* Transfection.** All experimental procedures involving animals were performed under an animal protocol approved by Tufts Institutional Animal Care and Use Committee. The MDA-MB-231 breast tumor was established by injecting a mixture of 5 $\times$ 10^5 MDA-MB-231 cells suspended in 13.3 μL of phosphate buffer solution (PBS, Invitrogen) and 6.7 μL of matrigel (BD Bioscience, San Jose, CA) into both the left and right mammary fat pads. Tumors were allowed to grow for 2 weeks to reach an average diameter of 5 mm. The pDNA complexes (pDNA: 1.2 μg, N/P: 2) in PBS were delivered via multiple tail vain injections to the tumor-bearing mice (n = 4) twice a week. As a control experiment, the pDNA complexes were also injected to mice without tumor (n = 2) twice a week. Three days, one week, and four weeks later, the mice were subjected to optical imaging on Xenogen IVIS200 (Xenogen Corp., Alameda, CA). Mice were anesthetized with 3% isoflurane and injected with D-luciferin (10 mg/kg intraperitoneal injection) approximately 10 min before imaging. Light emitted from the tumors was quantified using *Living Image* software (Xenogen). Photons produced by luciferase were normalized as photons per second per centimeter squared per steradian.

Statistical Analysis. The particle sizes on mica substrates were measured by AFM using a *Research Nanoscope* software version 7.30 (Veeco Instruments Inc.). The average value of 20 measurements was used. Statistical differences in particle sizes by AFM, cell transfection efficiency, and cell viability were determined by unpaired t-test with a two-tailed distribution and differences were considered statistically significant at $p < 0.05$. The data in the AFM, cell transfection efficiency, and cell viability experiments are expressed as means $\pm$ standard deviation.

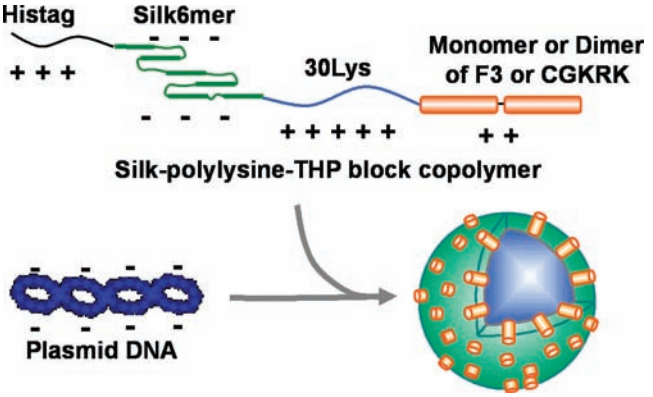

Figure 2. Schematic of formation of the pDNA complexes of the recombinant silk proteins, namely, the silk-poly(L-lysine)-THP block copolymers.

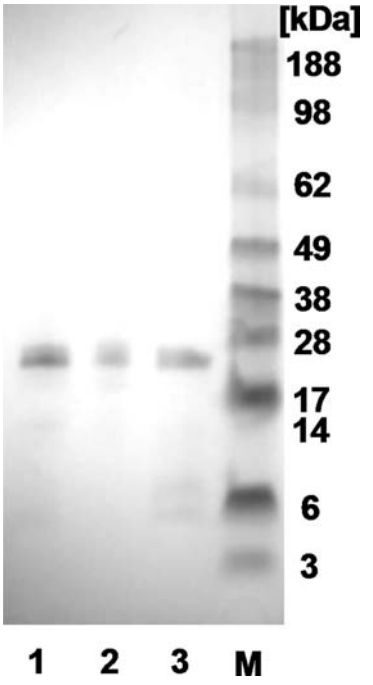

Figure 3. SDS-PAGE of the silk-poly(L-lysine)-THP block copolymers after the purification with Ni-NTA chromatography and dialysis. Lane 1: SL-mCGKRK, lane 2: SL-dCGKRK, lane 3: SL-mF3, and M: molecular weight marker.

RESULTS AND DISCUSSION

Biosynthesis of Recombinant Silk Proteins. The recombinant silk proteins containing poly(L-lysine) (30 aa) and THP, monomeric F3 (SL-mF3), monomeric CGKRK (SL-mCGKRK), or dimeric CGKRK (SL-dCGKRK), were expressed in *E. coli* and purified with Ni-NTA chromatography. The domain structure and amino acid sequences of the spider silk variants generated with poly(L-lysine) and THPs are shown in Figures 1 and 2. Yields of the recombinant silk proteins were approximately 0.8 mg/L after purification and dialysis. The proteins after purification by Ni-NTA

Table 1. Sizes and Zeta Potentials of the pDNA Complexes Prepared in This Study

	sizes and PDI [nm][a]			zeta potential and deviation [mV]		
	SL-mF3	SL-mCGKRK	SL-dCGKRK	SL-mF3	SL-mCGKRK	SL-dCGKRK
N/P 0.1	631 (0.384)	826 (0.608)	218 (0.778)	8.17 (4.5)	−32.5 (5.9)	−21.2 (11)
N/P 1	331 (0.645)	323 (0.558)	239 (0.842)	11.0 (5.5)	−20.5 (5.9)	−12.5 (7.6)
N/P 2	143 (0.176)	261 (0.157)	274 (0.687)	13.8 (3.6)	−11.1 (6.6)	−14.5 (6.5)
N/P 5	167 (0.460)	244 (0.139)	258 (0.622)	14.6 (4.6)	−10.6 (4.4)	−10.5 (5.9)
Silk polymer only without pDNA	170 (0.790)	363 (0.813)	204 (0.882)	10.9 (4.3)	−7.17 (4.4)	−9.76 (4.9)

[a] Determined by zeta-nanosizer.

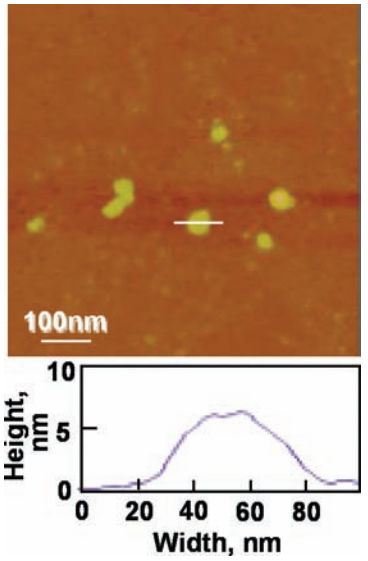

Figure 4. AFM height images of the pDNA complexes with silk-poly(L-lysine)-monomeric F3 (SL-mF3) casted on a mica substrate in air.

chromatography and dialysis were analyzed by SDS-PAGE and stained with Colloidal blue to evaluate purity (Figure 3). SL-mF3, SL-mCGKRK, and SL-dCGKRK showed a major band corresponding to a molecular weight of approximately 24 kDa, respectively, almost identical to the theoretical molecular weights (monoisotopic mass) of 28737.77, 25897.10, and 26657.50 Da, respectively, by consideration of silk-based polymers generally do not run true to size on SDS-PAGE gels, due to the hydrophobic nature of the protein,[14,17] confirming that the bioengineered proteins were the expected recombinant proteins.

Characterization of pDNA Complexes. Ionic complex formation with pDNA encoding a reporter gene and the recombinant silk proteins (SL-mF3, SL-mCGKRK, and SL-dCGKRK) were characterized with different N/P ratios (the ratio of number of amines/phosphates from pDNA) by zeta-nanosizer and AFM. The hydrodynamic diameter and zeta potential of the pDNA complexes of the recombinant silks are listed in Table 1. The average diameters of the SL-mF3, SL-mCGKRK, and SL-dCGKRK at the concentration of 0.1 mg/mL without pDNA were 170, 363, and 204 nm, respectively, indicating that the recombinant silk proteins formed monodispersed micelles without pDNA via hydrophobic interaction of the silk sequences. The recombinant silk proteins with pDNA formed ionic complexes via ionic polylysine−pDNA interactions and played a role in core of the ionic complexes, in consideration of the previous reports on ionic complexes of silk-like polymer and pDNA,[14] which means THPs and silk sequences could exist at the surface of the complexes and also neutralized their electrical charges as shown in Figure 2. This micelle structure will help the complex to interact with the tumor cells via THPs. The average diameters of the complexes with pDNA decreased from over 500 nm to approximately 200 nm with an increase in N/P ratio, and the pDNA complexes prepared at N/P of 5 demonstrated almost the same values as the complexes at N/P of 2. The zeta potential of pDNA complexes increased slightly with an increase in N/P ratio. Also, the SL-mF3 showed positive zeta potentials. On the basis of these sizes and zeta potentials as well as previous studies,[12,14] the most suitable pDNA complexes for *in vitro* transfection were determined to be those prepared at an N/P of 2, because of their smaller and less negative charge features of the complexes. The complexes (N/P 2) of SL-mF3, SL-mCGKRK, and SL-dCGKRK were 143, 261, and 274 nm in diameter and 13.8 ± 3.6, 11.1 ± 6.6, and −14.5 ± 6.5 mV in zeta potential, respectively (Table 1).

The pDNA complexes of SL-mF3 prepared at N/P of 2 were cast on mica and imaged by AFM (Figure 4). On the basis of these AFM observations, all of the complexes prepared at N/P of 2 formed homogeneous globular complexes, and the pDNA complexes of SL-mF3 at N/P of 2 demonstrated an average diameter and height of 95 ± 46 nm and 6.5 ± 2.3 nm, respectively (n = 20). The calibration of the cantilever tip convolution effect was performed to obtain the true dimensions of the pDNA complexes using the methods reported previously.[19,20] On the basis of the volume of the pDNA complexes, the dimensions determined by zeta nanosizer (dynamic light scattering) were slightly larger than those by AFM, since the pDNA complexes on mica were shrunk due to drying in air.[20]

The cytotoxicity of the pDNA complexes with an N/P ratio of 2 for SL-mF3, SL-mCGKRK, and SL-dCGKRK was determined using the standard MTS assay with MCF10A mammary breast epithelial cells, which represent healthy cells in the present study. The pDNA complexes of SL-mF3, SL-mCGKRK, and SL-dCGKRK showed 106 ± 17%, 111 ± 3%, and 105 ± 8% of cell viability, respectively, indicating that the present silk-based systems have reasonably low cytotoxicity against non-tumorigenic cells; suitable to be used in drug and gene deliveries.

***In Vitro* Transfection.** *In vitro* transfection experiments were performed with MDA-MB-435, MDA-MB-231, and MCF10A cells in order to evaluate the effects of the THPs, F3 and CGKRK, on target specificity of the silk-based gene delivery. MDA-MB-435 cells had been considered to be breast cancer cells but were recently reported to show melanoma-like properties.[21] Nevertheless, F3 peptides are reported to bind MDA-MB-435 and MDA-MB-231 via nucleolin or nucleolin-related proteins, whereas CGKRK peptides may bind to MDA-MB-435 by

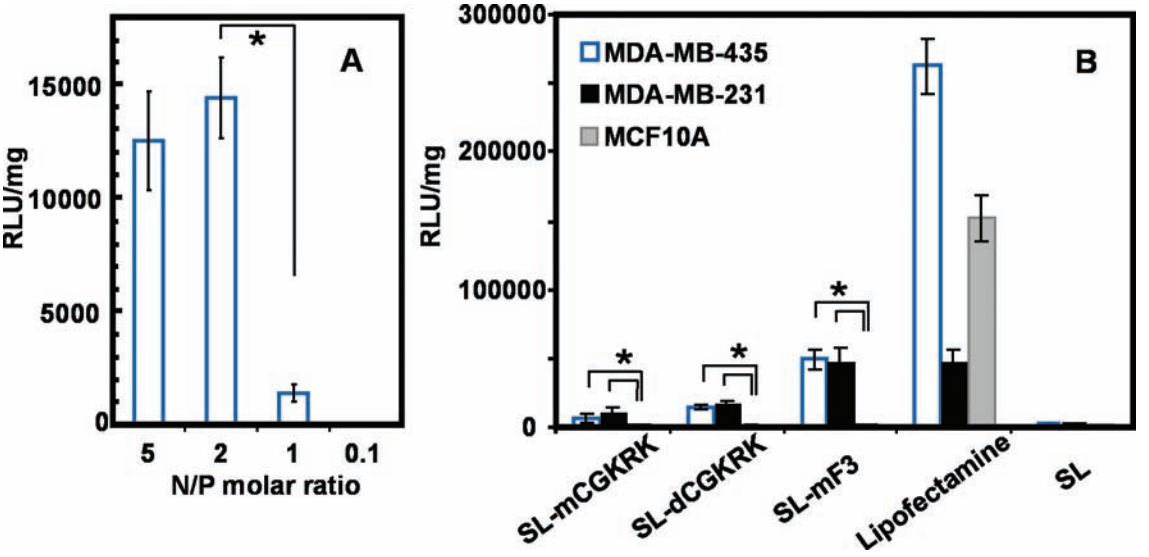

Figure 5. *In vitro* transfection results in loading pDNA complexes of the recombinant silk proteins. (A) *In vitro* transfection results of silk-poly(L-lysine)-dimeric CGKRK (SL-dCGKRK) with different N/P ratios in MDA-MB-435 cells. (B) Transfection results of silk-poly(L-lysine)-monomeric CGKRK (SL-mCGKRK), silk-poly(L-lysine)-dimeric CGKRK (SL-dCGKRK), silk-poly(L-lysine)-monomeric F3 (SL-mF3), and silk-poly(L-lysine) (SL: negative control) prepared at N/P 2 in MDA-MB-435, MDA-MB-231, and MCF10A cells. Lipofectamine 2000 was used as a positive control sample. Data are shown as means ± standard deviation ($n = 4$). *Significant difference between two groups at $p < 0.05$. The transfection results of SL-mCGKRK, SL-dCGKRK, and SL-mF3 in MCF10A are significantly different from in MDA-MB-435 and MDA-MB-231 cells.

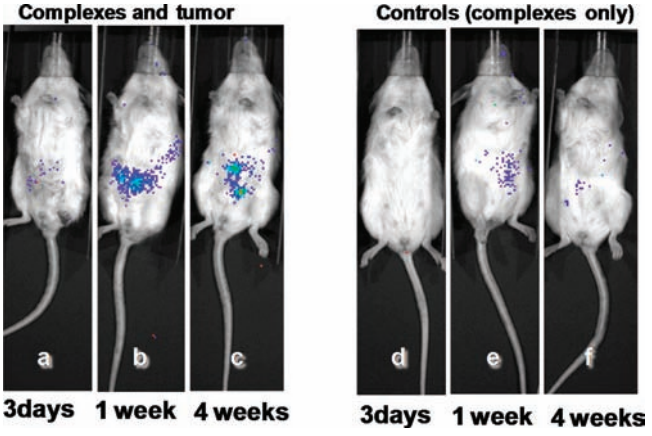

Figure 6. *In vivo* transfection results in loading pDNA complexes of SL-mF3 prepared at N/P 2 in MDA-MB-231 tumor cells in mice (a,b,c) and their control experiments without tumor cells (d,e,f). Typical bioluminescent images of 3 days (a,d), 1 week (b,e), and 4 weeks (c,f) luciferase expression in mice.

recognizing heparan sulfates in tumor vessels.[22−26] MDA-MB-231 human breast tumor cells were used as a representative model for breast cancer cells. On the other hand, MCF10A non-tumorigenic mammary breast epithelial cells were used as a negative control to evaluate target specificity. To determine the most efficient N/P ratio of the pDNA complexes, MDA-MB-435 cells were transfected via the SL-dCGKRK with luciferase pDNA as a reporter gene. Figure 5A show the transfection efficiencies to MDA-MB-435 cells for pDNA complexes of SL-dCGKRK with N/P ratios ranging from 0.1 to 5 based on the luciferase assay ($n = 4$). pDNA complexes prepared at N/P of 2 demonstrated the highest transfection efficiency among the different N/P ratios, followed by a steep decrease in efficacy, presumably due to excess recombinant silk interacting with the cells and pDNA. The transfection efficiency of the pDNA complexes prepared at N/P of 5 was nearly identical to that at N/P of 2. Therefore, the complexes at N/P of 2, which contained fewer recombinant silk proteins, were used for the transfection experiments. Figure 5B shows the transfection efficiencies to MDA-MB-435, MDA-MB-231, and MCF10A cells for pDNA complexes of the recombinant silk proteins (N/P 2), as well as for the transfection regent Lipofectamine 2000 (Invitrogen), as a positive control. The silk block copolymers containing only silk6mer and poly(L-lysine) (30aa) sequences did not show useful transfection to these cell lines (Figure 5B). The pDNA complexes of SL-dCGKRK showed higher transfection efficiency in comparison with SL-mCGKRK. This may be because of fewer negative surface charges on the dimeric CGKRK sequences of SL-dCGKRK. The pDNA complexes of all three types of silk polymers exhibited transfection to only MDA-MB-435 and MDA-MB-231 cells, whereas they did not demonstrate useful transfection efficiency to MCF10A nontumorigenic mammary breast epithelial cells, indicating that the target specificity of the present silk-based gene delivery systems was significantly improved by the additions of THP into the silk and poly(L-lysine) sequences. This also suggests that parts of THPs were present at the surface of the complexes with pDNA to specifically interact with the tumorigenic cells. The pDNA complexes were digested by enzymes in lysosomes inside cells, resulting in pDNA release, as in our prior study.[12] DNase I showed no significant degradation of the pDNA complexed with the silk block copolymers.[13]

***In Vivo* Transfection.** *In vivo* transfection experiments were also carried out using SL-mF3 (N/P 2), which showed the highest transfection efficiency to MDA-MB-231 tumor cells (Figure 5B). Bioluminescent images of live tumor-bearing mice at 3 days, 1 week, and 4 weeks after injections of the pDNA complexes were captured to evaluate the luciferase expression (Figure 6). Three days were insufficient for expression of the

pDNA in tumor cells in the mice (Figure 6a,d). Each tumor-bearing mouse significantly expressed luciferase in the tumor at day 7, one week after the first injection, whereas the mice without tumor cells did not show significant luciferase expression (Figure 6b,e). The expression level slightly increased for 4 weeks, while the control mice did not show significant expression (Figure 6c,f). More importantly, no significant toxicity was observed with the mice. On the basis of these limited *in vivo* results, the pDNA complexes containing F3 THP have potential to treat tumors specifically, but more importantly, without side effects associated with toxicity. A more comprehensive study will be required to clarify the longevity of transfection, as well as to fully evaluate the potential of these new systems.

In conclusion, the present study demonstrated that pDNA complexes of recombinant silk proteins containing poly(L-lysine) and THP, which are globular and approximately 150−250 nm in diameter, show significant enhancement of target specificity to tumor cells by additions of F3 and CGKRK THPs. The low cytotoxicity of the silk-based pDNA complexes is significant based on MTS assays, *in vitro* and *in vivo* transfection experiments, which is an important advantage for biomedical applications. The present study also suggests that the silk-based delivery systems containing functional peptides, such as THP, can be tailormade delivery systems by virtue of those peptides as well as have shown potentials as a versatile and useful new platform polymer for nonviral gene delivery.

AUTHOR INFORMATION

Corresponding Author

*David. L. Kaplan, Department of Biomedical Engineering, Tufts University, 4 Colby Street, Medford, Massachusetts, 02155 USA. Phone: (+1)-617-627-3251. Fax: (+1)-617-627-3231. E-mail: david.kaplan@tufts.edu.

Present Addresses

§Enzyme Research Team, Biomass Engineering Program, RIKEN Institute, 2−1 Hirosawa, Wako-shi, Saitama, 351−0198, Japan.

ACKNOWLEDGMENT

This work has been supported by grants from the NIH (P41 Tissue Engineering Resource Center, EB002520) and the NSF (D.K.). K.N. was supported by a JSPS Postdoctoral Fellowship for Research Abroad.

REFERENCES

(1) Edelstein, M. L., Abedi, M. R., and Wixon, J. (2007) Gene therapy clinical trials worldwide to 2007--an update. *J. Gene Med. 9*, 833–842.

(2) Edelstein, M. L., Abedi, M. R., Wixon, J., and Edelstein, R. M. (2004) Gene therapy clinical trials worldwide 1989−2004-an overview. *J. Gene Med. 6*, 597–602.

(3) Lundstrom, K. (2003) Latest development in viral vectors for gene therapy. *Trends Biotechnol. 21*, 117–122.

(4) Fischer, D., Bieber, T., Li, Y. X., Elsasser, H. P., and Kissel, T. (1999) A novel non-viral vector for DNA delivery based on low molecular weight, branched polyethylenimine: Effect of molecular weight on transfection efficiency and cytotoxicity. *Pharm. Res. 16*, 1273–1279.

(5) Ross, P. C., and Hui, S. W. (1999) Lipoplex size is a major determinant of in vitro lipofection efficiency. *Gene Ther. 6*, 651–659.

(6) Altman, G. H., Diaz, F., Jakuba, C., Calabro, T., Horan, R. L., Chen, J., Lu, H., Richmond, J., and Kaplan, D. L. (2003) Silk-based biomaterials. *Biomaterials 24*, 401–416.

(7) Numata, K., and Kaplan, D. L. (2010) Silk-based delivery systems of bioactive molecules. *Adv. Drug Delivery Rev. 62*, 1497–1508.

(8) Wang, Y., Kim, H. J., Vunjak-Novakovic, G., and Kaplan, D. L. (2006) Stem cell-based tissue engineering with silk biomaterials. *Biomaterials 27*, 6064–6082.

(9) Dewair, M., Baur, X., and Ziegler, K. (1985) Use of immunoblot technique for detection of human ige and igg antibodies to individual silk proteins. *J. Allergy Clin. Immunol. 76*, 537–542.

(10) Zaoming, W., Codina, R., FernandezCaldas, E., Lockey, F., and Bukanz, S. C. (1996) Partial characterization of the silk allergens in mulberry silk extract. *J. Allergy Clin. Immunol. 97*, 109–109.

(11) Numata, K., Cebe, P., and Kaplan, D. L. (2010) Mechanism of enzymatic degradation of beta-sheet crystals. *Biomaterials 31*, 2926–2933.

(12) Numata, K., Hamasaki, J., Subramanian, B., and Kaplan, D. L. (2010) Gene delivery mediated by recombinant silk proteins containing cationic and cell binding motifs. *J. Controlled Release 146*, 136–143.

(13) Numata, K., and Kaplan, D. L. (2010) Silk-based gene carriers with cell membrane destabilizing peptides. *Biomacromolecules 11*, 3189–3195.

(14) Numata, K., Subramanian, B., Currie, H. A., and Kaplan, D. L. (2009) Bioengineered silk protein-based gene delivery systems. *Biomaterials 30*, 5775–5784.

(15) Bini, E., Foo, C. W., Huang, J., Karageorgiou, V., Kitchel, B., and Kaplan, D. L. (2006) RGD-functionalized bioengineered spider dragline silk biomaterial. *Biomacromolecules 7*, 3139–3145.

(16) Huang, J., Valluzzi, R., Bini, E., Vernaglia, B., and Kaplan, D. L. (2003) Cloning, expression, and assembly of sericin-like protein. *J. Biol. Chem. 278*, 46117–46123.

(17) Prince, J. T., McGrath, K. P., DiGirolamo, C. M., and Kaplan, D. L. (1995) Construction, cloning, and expression of synthetic genes encoding spider dragline silk. *Biochemistry 34*, 10879–10885.

(18) Yan, S. Z., Beeler, J. A., Chen, Y. B., Shelton, R. K., and Tang, W. J. (2001) The regulation of type 7 adenylyl cyclase by its C1b region and Escherichia coli peptidylprolyl isomerase, SlyD. *J. Biol. Chem. 276*, 8500–8506.

(19) Numata, K., Hirota, T., Kikkawa, Y., Tsuge, T., Iwata, T., Abe, H., and Doi, Y. (2004) Enzymatic degradation processes of lamellar crystals in thin films for poly[(R)-3-hydroxybutyric acid] and its copolymers revealed by real-time atomic force microscopy. *Biomacromolecules 5*, 2186–2194.

(20) Numata, K., Kikkawa, Y., Tsuge, T., Iwata, T., Doi, Y., and Abe, H. (2006) Adsorption of biopolyester depolymerase on silicon wafer and poly[(R)-3-hydroxybutyric acid] single crystal revealed by real-time AFM. *Macromol. Biosci. 6*, 41–50.

(21) Rae, J. M., Creighton, C. J., Meck, J. M., Haddad, B. R., and Johnson, M. D. (2007) MDA-MB-435 cells are derived from M14 melanoma cells--a loss for breast cancer, but a boon for melanoma research. *Breast Cancer Res. Treat. 104*, 13–19.

(22) Porkka, K., Laakkonen, P., Hoffman, J. A., Bernasconi, M., and Ruoslahti, E. (2002) A fragment of the HMGN2 protein homes to the nuclei of tumor cells and tumor endothelial cells in vivo. *Proc. Natl. Acad. Sci. U. S. A. 99*, 7444–7449.

(23) Christian, S., Pilch, J., Akerman, M. E., Porkka, K., Laakkonen, P., and Ruoslahti, E. (2003) Nucleolin expressed at the cell surface is a marker of endothelial cells in angiogenic blood vessels. *J. Cell Biol. 163*, 871–878.

(24) Hoffman, J. A., Giraudo, E., Singh, M., Zhang, L., Inoue, M., Porkka, K., Hanahan, D., and Ruoslahti, E. (2003) Progressive vascular changes in a transgenic mouse model of squamous cell carcinoma. *Cancer Cell 4*, 383–391.

(25) Makela, A. R., Matilainen, H., White, D. J., Ruoslahti, E., and Oker-Blom, C. (2006) Enhanced baculovirus-mediated transduction of human cancer cells by tumor-homing peptides. *J. Virol. 80*, 6603–6611.

(26) Soundararajan, S., Chen, W. W., Spicer, E. K., Courtenay-Luck, N., and Fernandes, D. J. (2008) The nucleolin targeting aptamer AS1411 destabilizes bcl-2 messenger RNA in human breast cancer cells. *Cancer Res. 68*, 2358–2365.

Bioconjugate Chemistry

ARTICLE

pubs.acs.org/bc

Delivery of a Peptide Radiopharmaceutical to Brain with an IgG-Avidin Fusion Protein

Qing-Hui Zhou,[†] Jeff Zhiqiang Lu,[‡] Eric Ka-Wai Hui,[‡] Ruben J. Boado,[†,‡] and William M. Pardridge*[,†]

[†]Department of Medicine, University of California at Los Angeles, California 90024, United States

[‡]ArmaGen Technologies, Inc., Santa Monica, California 90401, United States

ABSTRACT: The genetic engineering, host cell expression, purity, identity, and in vivo brain drug targeting properties are described for a new IgG-fusion protein, designated the cTfRMAb-AV fusion protein. Avidin (AV) is fused to the carboxyl terminus of the heavy chain of the genetically engineered chimeric monoclonal antibody (mAb) against the mouse transferrin receptor (TfR). The TfRMAb binds the endogenous TfR on the blood-brain barrier (BBB), which triggers transport into brain from blood. The cTfRMAb-AV fusion protein is produced in stably transfected Chinese hamster ovary cells, which are grown in serum free medium under conditions of biotin starvation. Following affinity purification, the purity and identity of the cTfRMAb-AV fusion protein were verified by electrophoresis and Western blotting. The affinity of the cTfRMAb for the murine TfR is high, $K_I = 4.6 \pm 0.5$ nM, despite fusion of avidin to the antibody heavy chain. The model peptide radiopharmaceutical used in this study is the Aβ^{1-40} amyloid peptide of Alzheimer's disease (AD), which in a brain-penetrating form could be used to image the amyloid plaque in brain in AD. The BBB transport and brain uptake of the [^{125}I]-Aβ^{1-40} peptide was measured in mice injected intravenously (IV) with the peptide either free or conjugated to the cTfRMAb-AV fusion protein. The brain uptake of the free Aβ^{1-40} peptide was very low, 0.1% of injected dose (ID)/gram brain following IV injection, and is comparable to the brain uptake of a brain blood volume marker. However, the brain uptake of the Aβ^{1-40} peptide was high, 2.1 ± 0.2% ID/gram brain, following attachment of the biotinylated peptide to the cTfRMAb-AV fusion protein. Capillary depletion analysis showed the peptide penetrated the brain parenchyma from blood. The cTfRMAb-AV fusion protein is a new drug delivery system that can target to mouse brain monobiotinylated peptide or antisense radiopharmaceuticals.

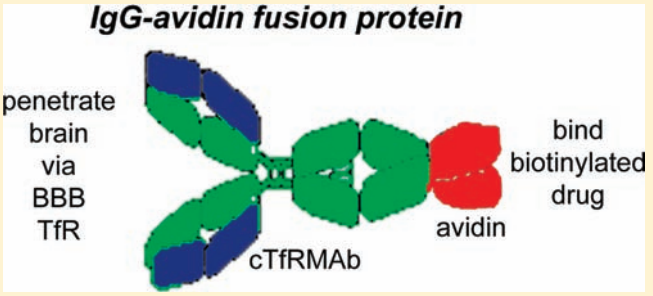

INTRODUCTION

Peptides and antisense agents are potential radiopharmaceuticals for imaging brain disorders. However, peptides and antisense agents do not cross the blood-brain barrier (BBB). Peptides and antisense agents can be reformulated for brain penetration with BBB transport technology using molecular Trojan horses (MTH). A BBB MTH is an endogenous peptide or peptidomimetic monoclonal antibody (mAb) that binds an endogenous BBB receptor transporter, such as the insulin receptor or transferrin receptor (TfR), which triggers receptor-mediated transport into brain.[1] A peptide or protein drug, which is not normally transportable across the BBB, is genetically fused to the MTH, and the fusion protein is transported into brain via endogenous BBB transporters. However, it is often not feasible to engineer a fusion protein of the MTH and a peptide radiopharmaceutical. In addition, it is not possible to engineer a fusion protein of a MTH and an antisense radiopharmaceutical. An alternative strategy for linking the peptide or antisense imaging agent to the MTH is avidin−biotin technology. With this approach, a fusion protein is engineered that is composed of avidin (AV) and the MTH. Prior work has described the genetic engineering of a fusion protein of avidin and a mAb to the human insulin receptor (HIR), and this fusion protein is designated HIRMAb-AV.[2] However, the HIRMAb-AV fusion protein cannot be validated in rodent models, because the HIRMAb only cross reacts with the insulin receptor of Old World primates.[3] There is no known mAb against the rat or mouse insulin receptor that can be used as a BBB MTH in rodents. Therefore, a surrogate MTH has been engineered for brain drug delivery in the mouse, which is a chimeric mAb against the mouse TfR, and designated as the cTfRMAb.[4]

The present work describes the genetic engineering and eukaryotic host cell expression of a fusion protein of avidin and the cTfRMAb, designated as the cTfRMAb-AV fusion protein. This IgG-avidin fusion protein is formed by fusion of the amino terminus of avidin to the carboxyl terminus of the heavy chain of the cTfRMAb (Figure 1). The model peptide radiopharmaceutical used in these studies is the Aβ^{1-40} amyloid peptide of Alzheimer's disease (AD). The monobiotinylated Aβ^{1-40} peptide is captured by the avidin moiety of the fusion protein (Figure 1). AD is caused by the formation of amyloid plaque in brain, and this plaque is composed of the A$\beta^{1-42/43}$ amyloid peptide.[5,6] Radiolabeled forms of the Aβ^{1-40} amyloid peptide are used to detect plaque in tissue sections in vitro in the AD brain.[7]

Received: April 5, 2011
Revised: May 17, 2011
Published: June 27, 2011

ACS Publications © 2011 American Chemical Society

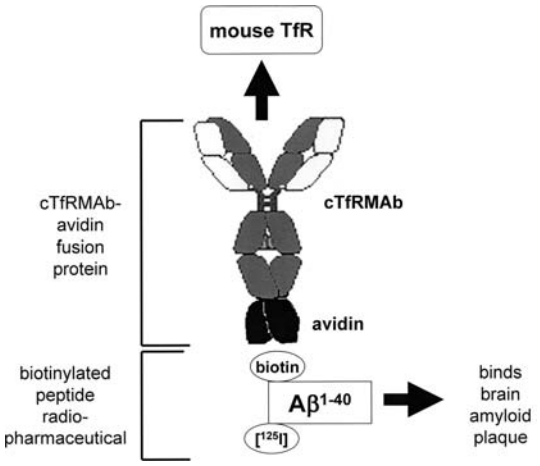

Figure 1. cTfRMAb-AV fusion protein is formed by fusion of avidin to the carboxyl terminus of the heavy chain of the chimeric monoclonal antibody against the mouse transferrin receptor (cTfRMAb). The $A\beta^{1-40}$ peptide radiopharmaceutical is biotinylated on the amino terminus of the peptide, to enable attachment to the cTfRMAb-AV fusion protein, and is radio-iodinated on internal lysine residues with the [^{125}I]-Bolton-Hunter reagent. The cTfRMAb-AV fusion protein is formulated in one vial, and the [^{125}I, N-biotinyl]-$A\beta^{1-40}$ peptide is formulated in a second vial, and the two vials are mixed prior to intravenous administration in mice. The cTfRMAb part of the fusion protein delivers the $A\beta^{1-40}$ peptide across the BBB, where the peptide then attaches to $A\beta$ amyloid plaque, which forms in AD brain behind the BBB.

Owing to the self-assembly of amyloid plaque, the $A\beta^{1-40}$ peptide radiopharmaceutical selectively associates with amyloid plaque in brain. This property makes the $A\beta^{1-40}$ peptide a potential radiopharmaceutical for imaging the brain amyloid plaque burden in AD brain in vivo. However, the $A\beta^{1-40}$ does not cross the BBB.[8] The present work describes the formulation of a brain penetrating peptide radiopharmaceutical, wherein the cTfRMAb-AV fusion protein is formulated in one vial, and the [^{125}I, N-biotinyl]-$A\beta^{1-40}$ peptide is formulated in a second vial. The vials are mixed just prior to intravenous administration in the mouse. The cTfRMAb-AV fusion protein is produced by stably transfected Chinese hamster ovary (CHO) cells under conditions of biotin depletion, and the N-biotinyl-$A\beta^{1-40}$ is radiolabeled with the [^{125}I]-Bolton-Hunter reagent.

EXPERIMENTAL PROCEDURES

Production of CHO Line. A tandem vector (TV) containing within a single plasmid DNA the expression cassettes encoding the cTfRMAb heavy chain-AV fusion protein, the cTfRMAb light chain (LC), and the murine dihydrofolate reductase (DHFR) was engineered similarly to a TV described previously.[9] The cDNA encoding the 128 amino acid (AA) avidin protein was amplified by PCR as described previously,[2] and subcloned at the 3′-end of the cTfRMAb HC to form the pcTfRMAb-AV tandem vector. The structure of the TV has been described previously.[9] The sequence of the TV was confirmed by bidirectional DNA sequencing performed at Eurofins MWG Operon (Huntsville, AL) using custom sequencing oligodeoxynucleotides synthesized at Midland Certified Reagent Co. (Midland, TX). The TV was linearized and CHO cells were electroporated, followed by selection in hypoxanthine-thymine deficient medium and amplification with graded increases in methotrexate (MTX) up to 80 nM in serum free medium (SFM). The CHO line was dilutionally cloned at 1 cell/well, and high producing clones were selected by measurement of medium mouse IgG concentrations by enzyme-linked immunosorbent assay (ELISA). The CHO line was stable through multiple generations, and produced medium IgG levels of 5−10 mg/L in shake flasks at a cell density of 1−2 million cells/mL in serum free medium (Hyclone, Logan, UT, HYQ SFM4CHO-Utility, catalogue number SH30516.02), which contains 800 nM biotin.

The IgG-avidin fusion protein must be expressed in biotin-free medium. Otherwise, the expressed fusion protein would be fully saturated with biotin. Owing to the very slow dissociation of biotin from avidin,[10] it is very difficult to strip biotin from avidin. Therefore, IgG-avidin fusion proteins are expressed in CHO cells cultured in biotin-depleted medium.[2] Following propagation in biotin-containing medium, the CHO cells were centrifuged and resuspended in custom, biotin-free medium from Hyclone (HYQ SFM4CHO-Utility without biotin, catalogue number RR10659−01), which was supplemented with 20 nM biotin. The cells were expanded to a volume of 0.8 L in shake flasks in medium containing 20 nM biotin, followed by expansion to 2.4 L with biotin-free medium. Over the course of 4 weeks, a total of 7.7 L of conditioned medium was harvested and replaced by biotin-free medium. The medium pool was concentrated to 2 L with tangential flow filtration, clarified by depth filtration, and applied to a protein G column.

Protein G Affinity Purification. The medium was ultrafiltered with a 0.2 um Sartopore-2 sterile-filter unit (Sartorius Stedim Biotech, Goettingen, Germany), and applied to a 25 mL protein G Sepharose 4 Fast Flow (GE Life Sciences, Chicago, IL) column equilibrated in 25 mM Tris/25 mM NaCl/5 mM EDTA/pH = 7.1. The column was washed with 25 mM Tris/1 M NaCl/5 mM EDTA/pH = 7.1, and the fusion protein was eluted with 0.1 M glycine/pH = 2.8. The acid eluate was pooled and neutralized to pH = 6.0 with 1 M Tris base, aliquoted, and stored at −70 °C. Protein content was determined with the bicinchoninic acid (BCA) assay from Pierce-Thermo (Rockford, IL).

SDS-PAGE and Western Blotting. The homogeneity of the cTfRMAb-AV fusion protein was evaluated with sodium dodecyl sulfate polyacrylamide gel electrophoresis (SDS-PAGE) under reducing and nonreducing conditions using 4−15% and 7.5% Tris-HCl gels (Biorad Life Science, Hercules, CA), respectively. Western blot analysis was performed with a goat antimouse IgG (H+L) antibody (Bethyl Laboratories, Montgomery, TX) for the mouse IgG Western, and with a rabbit antiavidin antibody (Abcam, Cambridge, MA) for the avidin Western. The immunoreactivity of the cTfRMAb-AV fusion protein was compared with the cTfRMAb described previously[4] and with avidin (Pierce-Thermo).

TfR Radio-Receptor Assay. Binding of the cTfRMAb-AV fusion protein to the mouse TfR was measured with a radioreceptor assay (RRA) using the [^{125}I]-labeled 8D3 rat mAb to the mouse TfR as the binding ligand, as described previously.[4] The 8D3 TfRMAb was purified from ascites with a protein G affinity column, and the antibody was radiolabeled with [^{125}I]-iodine and chloramine T to a specific activity of 4.5 uCi/ug and a trichloroacetic acid (TCA) precipitability of 99%. Mouse 3T3 fibroblasts were plated on collagen-coated BD Biocoat 24-well dishes (Becton-Dickinson, Franklin Lakes, NJ), and the binding assay was performed at 4 °C for 3 h.[4] The [^{125}I]-8D3 TfRMAb was added at a tracer concentration of 0.4 nM, and increasing

concentrations of either unlabeled 8D3 TfRMAb, to measure the K_D of binding, or the cTfRMAb-AV fusion protein, to measure the K_I of binding, were co-mixed with the labeled 8D3 TfRMAb. The 8D3 self-inhibition study allowed for computation of the dissociation constant, K_D, and the maximal binding, B_{max}, and the cTfRMAb-AV fusion protein cross-inhibition study allowed for determination of the K_I of binding to the mouse TfR.[9] Binding curves were fit by nonlinear regression analysis using the BMDP2007e software (Statistical Solutions, Dublin, Ireland).

Biotin Binding. The quantitative binding of biotin to the cTfRMAb-AV fusion protein was determined with an ultrafiltration assay, as described previously.[2] The assay used [^{3}H]-biotin (Perkin-Elmer, Boston, MA), which had a specific activity of 50 uCi/nmol, and an Ultrafree-MC filter unit (Millipore, Billerica, MA), which has a low protein binding regenerated cellulose filter with a 10 kDa molecular weight cutoff. A 100 uL volume of PBS (0.01 M Na_2HPO_4/0.15 M NaCl/pH = 7.4) was added to a microfuge tube (MFT), which contained 0.1 uCi/mL of ^{3}H-biotin (2 nM), various concentrations of unlabeled biotin (25−1000 nM), and a fixed concentration of either avidin (5 ug/mL, 80 nM) or the cTfRMAb-AV fusion protein (15 ug/mL, 80 nM). After a 30 min incubation at room temperature, the solution was transferred to the Ultrafree-MC ultrafiltration unit, which was placed in a 1.5 mL MFT, and the unit was centrifuged at 10 000 *g* for 5 min at room temperature. The total biotin binding was determined from the total biotin concentration and the percent binding of the [^{3}H]-biotin, which was determined by sampling the ultrafiltrate for ^{3}H radioactivity using a Perkin-Elmer liquid scintillation counter. The number of biotin binding sites per protein was determined from the ratio of the bound biotin concentration relative to the concentration of the avidin or the cTfRMAb-AV fusion protein.

Cell Biotin Uptake Assay. Mouse 3T3 fibroblasts (400 000 cells/well) were plated in 24 well dishes as described above, and cultured in DMEM medium with 10% fetal bovine serum. The incubation was initiated by aspiration of medium, washing with Tris-buffered saline (TBS), and addition of 400 uL/well of TBS (pH = 7.4) containing 0.5 uCi/mL of [^{3}H]-biotin, 0 or 1.0 ug/mL recombinant streptavidin (Sigma Chemical Co, St. Louis, MO), or 0 or 5.0 ug/mL cTfRMAb-AV fusion protein. The incubation at 37 °C was terminated at 2, 10, 30, 60, or 120 min by aspiration followed by washing of the monolayer 3 times with cold TBS. The monolayer was solubilized with 0.5 mL/well of 1 N NaOH, followed by heating at 60 °C for 30 min. The [^{3}H] radioactivity was determined with a Perkin-Elmer liquid scintillation counter using Ultima-Gold (Downers Grove, IL), and the monolayer protein was determined with the BCA assay. The cell uptake was expressed as a volume of distribution (VD), which is equal to the (DPM/mg protein)/(DPM/uL medium).

Radio-Iodination of N-Biotinyl-Aβ^{1-40}. The N-biotinyl-LC-Aβ^{1-40} amyloid peptide was purchased from AnaSpec, Fremont, CA (catalogue no. 24645−01), where LC = 6-carbon long chain linker between the biotin and the peptide amino terminus. The N-biotinyl-Aβ^{1-40} peptide was radiolabeled with [^{125}I]-Bolton-Hunter reagent from American Radiolabeled Chemicals (St. Louis, MO). The peptide was solubilized in 60% dimethylsulfoxide in water, and 50 ug of peptide was reacted with 2.0 mCi of [^{125}I]-Bolton-Hunter reagent. The labeled peptide was purified with a 1 × 28 cm Sephadex G-25 gel filtration column, with an elution buffer of 0.01 M Na_2HPO_4/0.15 M NaCl/pH = 7.4/0.1% Tween-20. The N-biotinyl-Aβ^{1-40} peptide was labeled to a specific activity of 31 uCi/ug and a trichloroacetic acid (TCA) precipitability of >99%.

Pharmacokinetics and Brain Uptake in the Mouse. Adult male C57BL/6J mice, weighing 24 g, were obtained from Jackson Laboratories (Bar Harbor, ME). All procedures were carried out in accordance with the Guide for the Care and Use of Laboratory Animals as adopted and promulgated by the U.S. National Institutes of Health. Mice in groups of 3 were anesthetized with intraperitoneal (IP) ketamine (100 mg/kg) and xylazine (10 mg/kg), and injected intravenously (IV) in the tail vein with 60 uL (0.11 nmol/mouse, 15 uCi/mouse) of [^{125}I, N-biotinyl]-Aβ^{1-40} either alone or co-mixed with the cTfRMAb-AV fusion protein. The injection dose (ID) of the cTfRMAb-Av fusion protein was 0.14 nmol/mouse, which is equivalent to 1 mg/kg of fusion protein. An aliquot (50 uL) of venous blood was collected at 0.25, 2, 5, 15, 30, and 60 min after injection by sampling the orbital vein. The blood was centrifuged for collection of plasma, which was analyzed for radioactivity. At 60 min after injection, the mice were euthanized, and major organs (liver, spleen, kidney, heart, lung) and the cerebral hemispheres were removed and weighed for each mouse. One hemisphere was homogenized for capillary depletion analysis, as described below. The radioactivity of plasma and tissue samples was determined with a Wizard gamma counter (Perkin-Elmer, Downers Grove, IL). Organ uptake at 60 min after injection was expressed as % of injected dose (ID)/gram tissue. The plasma radioactivity that was precipitable with cold 10% TCA was determined at each time point.

The TCA-precipitable plasma radioactivity, DPM/mL, was converted to % injected dose (ID)/mL, and the %ID/mL was fit to a biexponential equation

$$\%\mathrm{ID/mL} = A_1 e^{-k_1 t} + A_2 e^{-k_2 t}$$

The intercepts (A_1, A_2) and the slopes (k_1, k_2) were used to compute the pharmacokinetic (PK) parameters, including the median residence time (MRT), the central volume of distribution (V_c), the steady-state volume of distribution (V_{ss}), the area under the plasma concentration curve (AUC) at 60 min, the steady-state AUC (AUC_{ss}), and the systemic clearance (CL). Nonlinear regression analysis used the AR subroutine of the BMDP Statistical Software. Data were weighted by $1/(\%\mathrm{ID/mL})^2$.

The BBB permeability-surface area (PS) product is computed from the terminal brain uptake (%ID/g) and the 60 min plasma AUC (%IDmin/mL) as follows:

$$\text{PS product} = [(\%\mathrm{ID/g})/\mathrm{AUC}] \times 1000$$

Capillary Depletion Method. One cerebral hemisphere from each mouse was processed for the capillary depletion method as described previously,[11] which separates the brain homogenate into the capillary pellet and the postvascular supernatant. The volume of distribution (VD) was determined for each of the 3 fractions from the ratio of total ^{125}I radioactivity in the fraction, DPM/gram brain, divided by the ^{125}I radioactivity in the 60 min terminal plasma, DPM/uL. A high VD in the postvascular supernatant, as compared to the VD in the capillary pellet, is evidence for transport of the protein through the BBB into brain parenchyma.

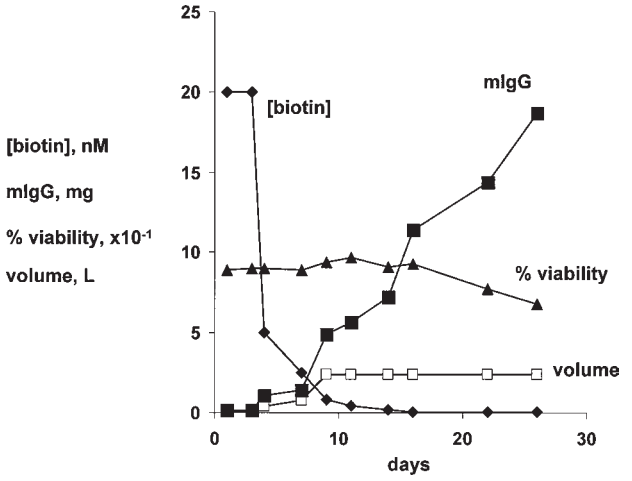

Figure 2. Medium biotin concentration, nM (♦); medium mouse IgG (mIgG) by ELISA, mg produced (■); medium volume, liters (□); and CHO cell viability, % (▲); over the course of 28 days in culture in serum free, biotin-depleted medium.

RESULTS

DNA sequencing of the cTfRMAb-AV expression plasmid encompassed 6475 nucleotides (nt), which spanned 3 separate and tandem expression cassettes encoding the fusion protein of the cTfRMAb heavy chain (HC) and avidin, the cTfRMAb light chain (LC), and the murine DHFR selection gene. The LC was formed by 234 AA, including a 20 AA signal peptide, and had a predicted molecular weight of 23 554 Da and an isoelectric point (pI) of 5.73. The HC fusion protein was formed by 592 AA, including a 19 AA signal peptide, a 118 AA cTfRMAb HC variable region, a 324 AA mouse IgG1 constant (C) region, a 3 AA linker (Ser-Ser-Ser), and the 128 AA avidin, and had a predicted molecular weight of 63 375 Da and a pI of 7.64. The fusion HC contained 2 predicted N-linked glycosylation sites, with one site in the mouse IgG1 C-region and one site within the AV domain. The predicted molecular weight of the cTfRMAb-AV heterotetramer, without glycosylation, is 173 858 Da.

The CHO cells, stably transfected with the cTfRMAb-AV tandem vector, were propagated in serum free medium in 1 L flasks on an orbital shaker with a medium biotin concentration of 20 nM. Over the next 7 days, the medium was replaced with biotin-free medium until the medium biotin was <0.05 nM (Figure 2). The CHO cells were propagated for an additional 3 weeks in medium with <0.05 nM biotin, and during this time, the production of the cTfRMAb-AV fusion protein increased linearly (Figure 2). The cell viability was >90% for 3 weeks and then the viability decreased to 70% during the fourth week of biotin starvation (Figure 2). The cTfRMAb-AV fusion protein was affinity purified from the terminal, serum free conditioned medium by protein G affinity chromatography to homogeneity on reducing (Figure 3A) and nonreducing (Figure 3B) SDS-PAGE. The molecular weight (MW) of the cTfRMAb and the cTfRMAb-AV heavy and light chains was estimated by linear regression analysis based on the migration of the MW standards in Figure 3. The light chain of both proteins migrated at 28 kDa, while the heavy chain of the cTfRMAb and the cTfRMAb-AV fusion protein migrated at 59 kDa and 75 kDa, respectively, on the reducing SDS-PAGE (Figure 3A). The cTfRMAb and the cTfRMAb-AV fusion protein migrated at a MW of 181 kDa and

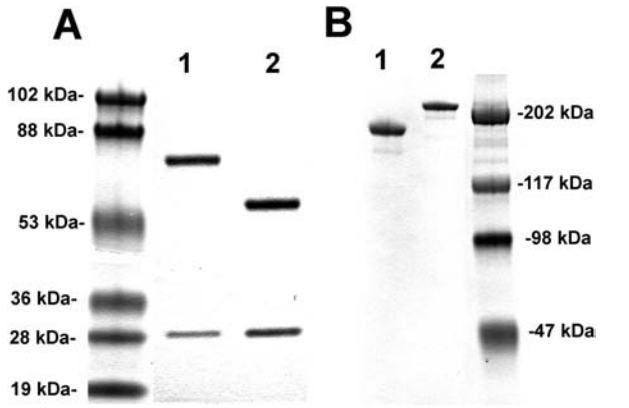

Figure 3. (A) Reducing SDS-PAGE of the cTfRMAb-AV fusion protein (lane 1) and the cTfRMAb (lane 2). (B) Nonreducing SDS-PAGE of the cTfRMAb (lane 1) and the cTfRMAb-AV fusion protein (lane 2).

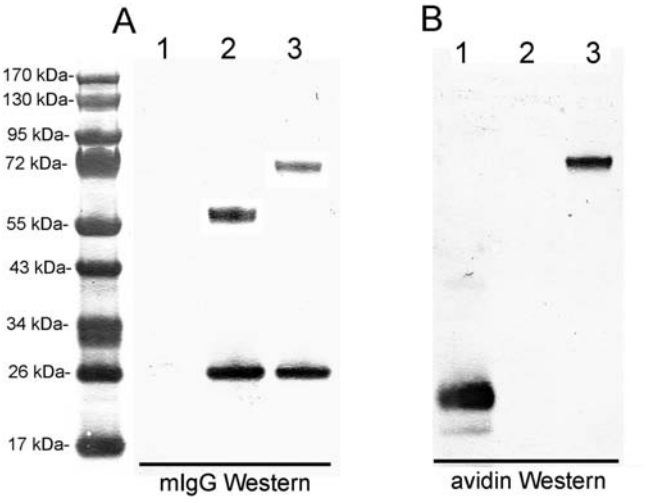

Figure 4. Western blot with primary antibody against mouse IgG (mIgG) (A) or avidin (B) of avidin (lane 1), cTfRMAb (lane 2), or cTfRMAb-AV fusion protein (lane 3).

214 kDa, respectively, on the nonreducing SDS-PAGE gel (Figure 3B). The identity of the cTfRMAb-AV fusion protein was verified by mouse IgG and avidin Western blotting (Figure 4). An antimouse IgG primary antibody reacted equally well with the light chain of either the cTfRMAb or the cTfRMAb-AV fusion protein, but did not react with avidin (Figure 4A). An antiavidin primary antibody reacted equally well with avidin or the heavy chain of the cTfRMAb-AV fusion protein, but did not react with the heavy chain of the cTfRMAb (Figure 4B).

The cTfRMAb-AV fusion protein retained high-affinity binding to the mouse TfR, as the K_I of fusion protein binding to the mouse TfR, 4.6 ± 0.5 nM, was no different from the K_D of binding of the 8D3 rat mAb to the mouse TfR, 5.0 ± 0.6 nM (Figure 5). The biotin binding assay demonstrated that there were 1 and 4 free biotin binding sites per cTfRMAb-AV fusion protein and avidin molecule, respectively. The cellular uptake of [^{3}H]-biotin by mouse 3T3 fibroblasts was low in the presence of either buffer or recombinant streptavidin (SA), but was increased following co-mixing with the cTfRMAb-AV fusion protein (Figure 6).

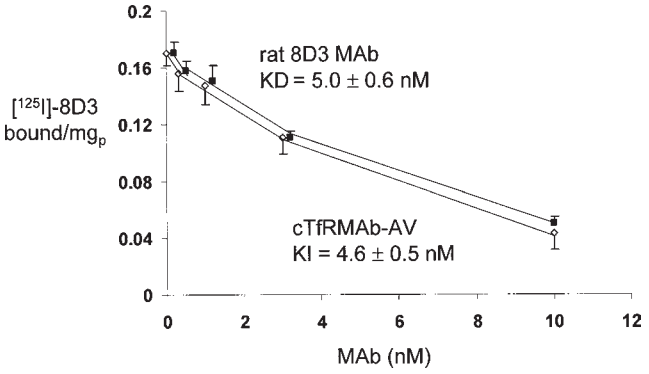

Figure 5. Binding of [^{125}I]-labeled rat 8D3 mAb against the mouse TfR is either self-competed by unlabeled 8D3 mAb (■) or cross-competed by unlabeled cTfRMAb-AV fusion protein (◊). Data are mean ± SE (n = 4 per point).

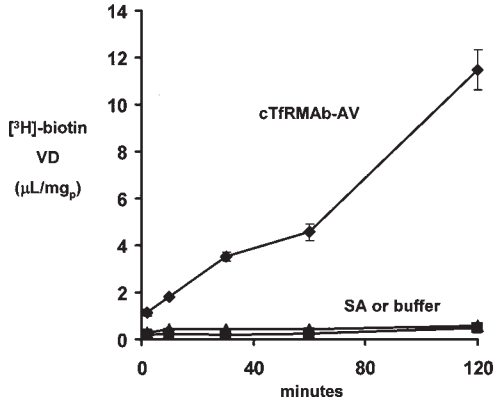

Figure 6. The cell/medium ratio, or volume of distribution (VD), of [3H]-biotin during a 120 min incubation in the presence of buffer, streptavidin (SA), or the cTfRMAb-AV fusion protein. Data are mean ± SE (n = 4 per point).

The rate of clearance of [^{125}I, N-biotinyl]-Aβ^{1-40} from plasma in the mouse was comparable following IV injection of the peptide either with or without premixing with the cTfRMAb-AV fusion protein (Figure 7). The PK analysis showed there was no difference in the systemic clearance (CL) of the labeled peptide with or without attachment to the cTfRMAb-AV fusion protein (Table 1). However, the organ uptake of the [^{125}I, N-biotinyl]-Aβ^{1-40} was altered following coinjection with the fusion protein. Organ uptake by the kidney was suppressed, while organ uptake by brain, liver, spleen, and lung was increased following conjugation of the [^{125}I, N-biotinyl]-Aβ^{1-40} to the cTfRMAb-AV fusion protein (Table 2). The brain uptake of the free [^{125}I, N-biotinyl]-Aβ^{1-40} was nil, while there was a >20-fold increase in the brain uptake of the peptide following coinjection with the cTfRMAb-AV fusion protein (Figure 8C). The 60 min plasma AUC was comparable in mice injected with either the free [^{125}I, N-biotinyl]-Aβ^{1-40} or the conjugate of [^{125}I, N-biotinyl]-Aβ^{1-40} bound to the cTfRMAb-AV fusion protein (Figure 8A). The marked increase in brain uptake of the peptide following attachment to the cTfRMAb-AV fusion protein was caused by an increase in the BBB permeability coefficient (Figure 8B).

The increase in brain uptake of the biotinyl-Aβ^{1-40} peptide following conjugation to the cTfRMAb-AV fusion protein

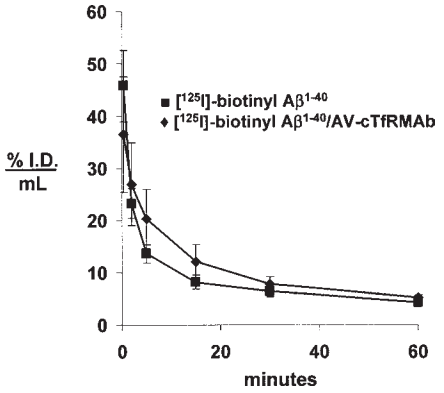

Figure 7. Plasma concentration, expressed as % ID/mL, of [^{125}I]-biotinyl Aβ^{1-40} following injection of labeled peptide either alone (■) or coinjected with 1:1 molar ratio of the cTfRMAb-AV fusion protein (♦). Data are mean ± SE (n = 3 mice per point).

represented distribution into brain parenchyma, as demonstrated by the capillary depletion method (Table 3). The VD in whole brain homogenate of the free biotinyl-Aβ^{1-40} peptide, 12 ± 2 uL/g, is no different from the brain plasma volume. Conversely, the VD in whole brain homogenate of the biotinyl-Aβ^{1-40} peptide conjugated to the cTfRMAb-AV fusion protein, 308 ± 2 uL/g, is 26-fold greater than the homogenate VD for the free biotinyl-Aβ^{1-40} peptide (Table 3). The VD of the conjugate in the postvascular supernatant is 12-fold greater than the VD in the vascular pellet (Table 3), indicating >90% of the conjugate taken up by brain has distributed into brain parenchyma beyond the BBB. The TCA precipitability of the radioactivity in the post-vascular supernatant is 19 ± 2% and 93 ± 1% for the unconjugated biotinyl-Aβ^{1-40} peptide and for the biotinyl-Aβ^{1-40} peptide conjugated to the cTfRMAb-AV fusion protein, respectively (Table 3).

The brain uptake of the conjugate of biotinyl-Aβ^{1-40} bound to the cTfRMAb-AV fusion protein declined with time after IV administration. The brain uptake at 6 h after IV injection was 0.63 ± 0.08% ID/gram (mean ± SE, n = 4 mice), which is reduced 70% compared to the brain uptake of the targeted peptide at 1 h after IV injection, 2.1 ± 0.2% ID/gram (Figure 8C).

■ DISCUSSION

The results of this study are consistent with the following conclusions. First, the cTfRMAb-AV fusion protein is expressed well by stably transfected CHO cells cultured in serum free medium, and the cells can be maintained with high viability under conditions of biotin starvation for at least 4 weeks (Figure 2). Second, the affinity purified cTfRMAb-AV fusion protein is structurally intact with no degradation products or aggregation (Figures 3−4) and is a bifunctional protein, which binds both biotin (Figure 6) and the murine TfR with high affinity (Figure 5). Third, the cTfRMAb-AV fusion protein mediates the brain uptake of a model peptide radiopharmaceutical, biotinyl-Aβ^{1-40}, and the brain uptake of the conjugate is on the order of 2% ID/gram brain (Figure 8).

Avidin, and avidin fusion proteins, have been produced in bacterial and baculovirus expression systems,[12,13] as well as mammalian host cells, such as myeloma cells.[14] However, cell culture medium contains very high concentrations of biotin (Methods), and any avidin fusion protein expressed in mammalian host cells

Table 1. Pharmacokinetic Parameters in the Mouse[a]

parameter	units	[^{125}I]-biotinyl Aβ^{1-40}	[^{125}I]-biotinyl Aβ^{1-40}/ cTfRMAb-AV
A_1	%ID/mL	38.6 ± 3.5	23.2 ± 2.7
A_2	%ID/mL	10.1 ± 0.8	12.8 ± 1.9
k_1	min^{-1}	0.477 ± 0.059	0.195 ± 0.050
k_2	min^{-1}	0.014 ± 0.002	0.015 ± 0.003
MRT	min	64 ± 9	58 ± 11
V_c	mL/kg	81 ± 4	120 ± 8
V_{ss}	mL/kg	308 ± 23	263 ± 29
AUC_{ss}	%IDmin/mL	797 ± 62	958 ± 91
CL	mL/min/kg	4.8 ± 0.4	4.5 ± 0.4

[a] Parameters estimated from the plasma clearance data in Figure 7. The parameters are defined in Methods.

Table 2. Organ Uptake in the Mouse of Biotinyl-Aβ^{1-40} with and without Conjugation to the cTfRMAb-AV Fusion Protein[a]

organ	[^{125}I]-biotinyl Aβ^{1-40}	[^{125}I]-biotinyl Aβ^{1-40}/ AV-cTfRMAb
brain	0.10 ± 0.06	2.1 ± 0.2
heart	1.6 ± 0.2	1.8 ± 0.3
lung	3.3 ± 0.5	9.9 ± 2.5
kidney	32.3 ± 3.8	15.8 ± 4.8
spleen	2.3 ± 0.5	29.7 ± 2.4
liver	18.1 ± 4.1	26.1 ± 4.3

[a] Data are % ID/gram; mean ± SE (n = 3 mice/group).

cultured in high biotin medium will be secreted already complexed with biotin. Owing to the extremely high affinity of avidin binding of biotin, which is characterized by a K_D of 10^{-15} M, and a dissociation half-time of 89 days,[15] it is difficult to separate biotin from avidin. Therefore, prior work on the expression of an IgG-AV fusion protein in CHO cells developed a 1-month biotin starvation protocol for production of biotin-depleted IgG-AV fusion protein by CHO cells,[2] and this method was used in the present work to produce the cTfRMAb-AV fusion protein. The biotin concentration was reduced from the maintenance level of 800 nM (Methods) to <0.05 nM (Figure 2). The failure to produce the IgG-AV fusion protein under conditions of biotin starvation will generate a biotin-loaded fusion protein with minimal capacity for binding biotinylated therapeutics.

The cTfRMAb-AV fusion protein is a heterotetrameric protein comprising 2 heavy and 2 light chains (Figure 1). The fusion of avidin to the carboxyl terminus of each heavy chain of the cTfRMAb has no effect on the affinity of the cTfRMAb part of the fusion protein for the murine TfR, as shown by the cell-based radio-receptor assay in vitro (Figure 5). The retention of the high affinity of the cTfRMAb part of the fusion protein for the TfR predicts high brain uptake of the cTfRMAb-AV fusion protein, and this is observed (Figure 8C). The brain uptake (%ID/gram) of the conjugate of the [^{125}I, N-biotinyl]-Aβ^{1-40} and the cTfRMAb-AV fusion protein, 2.1 ± 0.2% ID/gram (Figure 8C), is equal to the brain uptake of the cTfRMAb.[4] The enhanced uptake in liver and spleen (Table 2) is due to the highly fenestrated capillary wall in these organs, which enables rapid distribution of the conjugate to the TfR on the parenchymal cells in liver and spleen. The suppression of uptake by kidney (Table 2) is due to the greater molecular size of the [^{125}I, N-biotinyl]-Aβ^{1-40} following conjugation to the cTfRMAb-AV fusion protein.

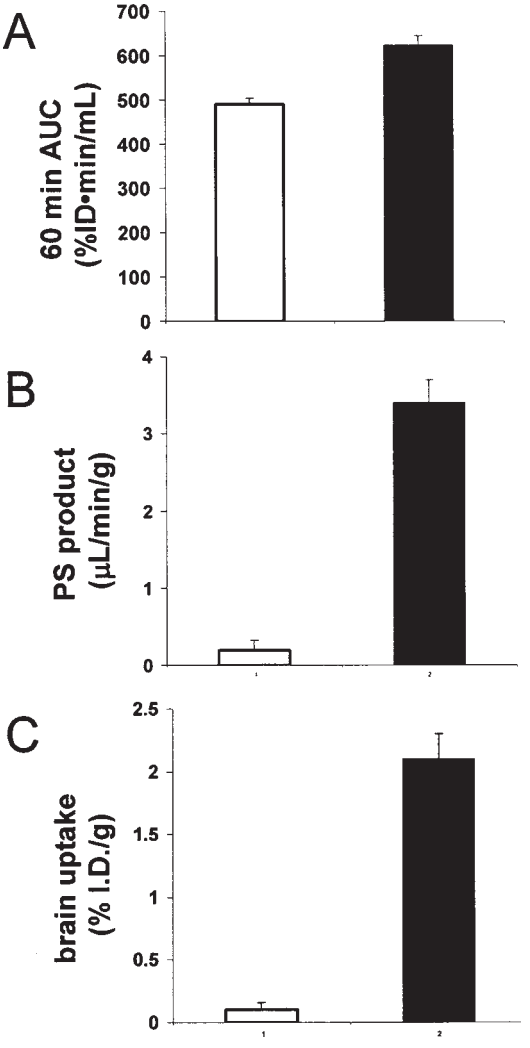

Figure 8. Plasma AUC at 60 min after injection (A), BBB PS product (B), or brain uptake (C) of [^{125}I]-biotinyl Aβ^{1-40} following injection of labeled peptide either alone (open bars) or coinjected with 1:1 molar ratio of the cTfRMAb-AV fusion protein (closed bars). Data are mean ± SE (n = 3 mice per point).

The use of the cTfRMAb-AV fusion protein as a BBB drug delivery system has the potential to deliver to brain virtually any monobiotinylated therapeutic, and this is demonstrated in the present study for the biotinylated Aβ^{1-40} amyloid peptide of AD.

Table 3. Capillary Depletion Analysis of Biotinyl-Aβ^{1-40} Distribution in Brain with and without Conjugation to the cTfRMAb-AV Fusion Protein[a]

parameter	[^{125}I]-biotinyl Aβ^{1-40}	[^{125}I]-biotinyl Aβ^{1-40}/ AV-cTfRMAb
homogenate VD	12 ± 2	308 ± 9
postvascular supernatant VD	12 ± 2	141 ± 12
brain capillary pellet VD	2.5 ± 0.5	12 ± 1
TCA precipitation (%), 60 min postvascular supernatant	19 ± 2	93 ± 1
TCA precipitation (%), 60 min plasma	65 ± 3	76 ± 1

[a] VD = volume of distribution (uL/g); TCA = trichloroacetic acid. Mean ± SE (n = 3 mice/group).

The cTfRMAb-AV fusion protein is formulated in one vial, and the [^{125}I, N-biotinyl]-Aβ^{1-40} peptide radiopharmaceutical is formulated in a second vial. The two vials are mixed just prior to intravenous administration to form the conjugate shown in Figure 1. In the absence of the drug delivery system, the N-biotinyl-Aβ^{1-40} peptide does not penetrate the brain, owing to the lack of transport of the peptide across the BBB (Figure 8). The brain volume of distribution (VD) of the N-biotinyl-Aβ^{1-40}, 12 ± 2 uL/gram (Table 3), or the brain uptake of the N-biotinyl-Aβ^{1-40}, 0.10 ± 0.06%ID/gram (Figure 8C), is no different than the brain VD, or brain %ID/gram, of a brain blood volume marker. The OX26 murine mAb against the rat TfR does not recognize the mouse TfR, and is a blood volume marker in the mouse brain.[16] The brain VD of the OX26 mAb in the mouse is 11 ± 1 uL/gram, and the brain uptake of the OX26 mAb in the mouse is 0.1% ID/gram, and these parameters are equal to the brain uptake parameters of the N-biotinyl-Aβ^{1-40} amyloid peptide, which shows that the biotinylated peptide alone does not cross the BBB. However, following conjugation to the cTfRMAb-AV fusion protein, the brain uptake of the N-biotinyl-Aβ^{1-40} amyloid peptide increases to 2.1 ± 0.2% ID/gram (Figure 8C). This level of brain uptake in the mouse is comparable to the brain uptake of lipid soluble small molecules. For example, the brain uptake in the mouse of lipid-soluble, small molecule brain amyloid imaging agents is 2−3% ID/gram at 60 min after IV injection,[17] which is comparable to the brain uptake of the Aβ peptide radiopharmaceutical conjugated to the cTfRMAb-AV fusion protein (Figure 8C). The transport of the cTfRMAb-AV fusion protein across the BBB in the mouse in vivo results in distribution into brain parenchyma, as demonstrated by the capillary depletion method. The brain VD of the cTfRMAb-AV fusion protein in the postvascular supernatant is 12-fold greater than the VD in the brain vasculature (Table 3), which indicates that 90% of the fusion protein bound by the vasculature in brain has transcytosed into brain parenchyma. The measurement of activity of brain capillary specific enzymes in the fractions produced with the capillary depletion method shows that this technique results in a 95% removal of the microvasculature from the postvascular supernatant.[18] The distribution of the conjugate radioactivity into the postvascular supernatant was not an artifact caused by the brain uptake of TCA soluble metabolites, as the TCA precipitability of the radioactivity in the postvascular supernatant of mice injected with the conjugate, 93 ± 1% (Table 3), was high compared to the TCA precipitability in the postvascular supernatant of mice injected with the unconjugated [^{125}I, N-biotinyl]-Aβ^{1-40} peptide, 19 ± 2% (Table 3).

The N-biotinyl-Aβ^{1-40} peptide used in these studies is monobiotinylated. The biotin is incorporated at the amino terminus of the 40 amino acid amyloid peptide. It is important that the targeted therapeutic contain no more than 1 biotin moiety per molecule. Higher degrees of biotinylation could lead to aggregation of the complex, owing to the multivalency of avidin binding of biotin. In the case of peptide or antisense radiopharmaceuticals, such as peptide nucleic acids,[19] a single biotin moiety can be incorporated at the level of solid-phase synthesis.

The cTfRMAb-AV fusion protein is specific for the mouse, and is the homologue of the HIRMAb-AV fusion protein described previously for use in humans.[2] With regard to potential immune reactions in humans, the primary immunogenic component of the IgG-avidin delivery system is avidin. However, there are several factors that may reduce the potential immunogenicity of avidin in humans. The delivery agent is an IgG-avidin fusion protein, and the constant region of IgG contains amino acid sequences called Tregitopes, which induce T-cell immune tolerance.[20] Humans may be immune tolerant to avidin. Avidin is abundant in Western diets, as avidin is a major protein of egg whites, and oral antigen feeding induces immune tolerance.[21] Avidin has been administered to humans intravenously at high doses without immune reactions.[22,23] Finally, diagnostic agents are not intended for chronic use.

In summary, the present study describes the genetic engineering, CHO cell expression, purification, and validation of a novel IgG-avidin fusion protein that selectively targets the TfR in the mouse. The cTfRMAb-AV fusion protein can potentially deliver a wide variety of peptide radiopharmaceuticals to the brain of the mouse for in vivo imaging applications. Following reformulation of peptide radiopharmaceuticals with the IgG-avidin fusion protein, the brain uptake of the large molecule brain imaging agents is comparable to the brain uptake of small molecule, lipid soluble brain imaging agents.

AUTHOR INFORMATION

Corresponding Author

*Dr. William M. Pardridge, UCLA, Warren Hall, 13-164 900 Veteran Ave., Los Angeles, CA 90024. Ph: +1 310 825 8858. Fax: +1 310 206 5163. E-mail address: wpardridge@mednet.ucla.edu.

ACKNOWLEDGMENT

Winnie Tai and Phuong Tram provided expert technical assistance. This work was supported by NIH grant R43-NS-062458.

REFERENCES

(1) Pardridge, W. M. (2008) Re-engineering biopharmaceuticals for delivery to brain with molecular Trojan horses. *Bioconjugate Chem. 19*, 1327–1338.

(2) Boado, R. J., Zhang, Y., Xia, C. F., Wang, Y., and Pardridge, W. M. (2008) Genetic engineering, expression, and activity of a chimeric

monoclonal antibody-avidin fusion protein for receptor-mediated delivery of biotinylated drugs in humans. *Bioconjugate Chem. 19*, 731–739.

(3) Pardridge, W. M., Kang, Y. S., Buciak, J. L., and Yang, J. (1995) Human insulin receptor monoclonal antibody undergoes high affinity binding to human brain capillaries in vitro and rapid transcytosis through the blood-brain barrier in vivo in the primate. *Pharm. Res. 12*, 807–816.

(4) Boado, R. J., Zhang, Y., Wang, Y., and Pardridge, W. M. (2009) Engineering and expression of a chimeric transferrin receptor monoclonal antibody for blood-brain barrier delivery in the mouse. *Biotechnol. Bioeng. 102*, 1251–1258.

(5) Glenner, G. G., and Wong, C. W. (1984) Alzheimer's disease: initial report of the purification and characterization of a novel cerebrovascular amyloid protein. *Biochem. Biophys. Res. Commun. 120*, 885–890.

(6) Masters, C. L., Simms, G., Weinman, N. A., Multhaup, G., McDonald, B. L., and Beyreuther, K. (1985) Amyloid plaque core protein in Alzheimer disease and Down syndrome. *Proc. Natl. Acad. Sci. U. S. A. 82*, 4245–4249.

(7) Maggio, J. E., Stimson, E. R., Ghilardi, J. R., Allen, C. J., Dahl, C. E., Whitcomb, D. C., Vigna, S. R., Vinters, H. V., Labenski, M. E., and Mantyh, P. W. (1992) Reversible in vitro growth of Alzheimer disease beta-amyloid plaques by deposition of labeled amyloid peptide. *Proc. Natl. Acad. Sci. U. S. A. 89*, 5462–5466.

(8) Saito, Y., Buciak, J., Yang, J., and Pardridge, W. M. (1995) Vector-mediated delivery of 125I-labeled beta-amyloid peptide A beta 1−40 through the blood-brain barrier and binding to Alzheimer disease amyloid of the A beta 1−40/vector complex. *Proc. Natl. Acad. Sci. U. S. A. 92*, 10227–10231.

(9) Boado, R. J., Zhou, Q. H., Lu, J. Z., Hui, E. K., and Pardridge, W. M. (2010) Pharmacokinetics and brain uptake of a genetically engineered bifunctional fusion antibody targeting the mouse transferrin receptor. *Mol. Pharmaceutics 7*, 237–244.

(10) Wilchek, M., and Bayer, E. A. (1990) Applications of avidin-biotin technology: literature survey. *Methods Enzymol. 184*, 14–45.

(11) Zhou, Q. H., Boado, R. J., Lu, J. Z., Hui, E. K., and Pardridge, W. M. (2010) Monoclonal antibody-glial-derived neurotrophic factor fusion protein penetrates the blood-brain barrier in the mouse. *Drug Metab. Dispos. 38*, 566–572.

(12) Hytonen, V. P., Laitinen, O. H., Airenne, T. T., Kidron, H., Meltola, N. J., Porkka, E. J., Horha, J., Paldanius, T., Maatta, J. A., Nordlund, H. R., Johnson, M. S., Salminen, T. A., Airenne, K. J., Yla-Herttuala, S., and Kulomaa, M. S. (2004) Efficient production of active chicken avidin using a bacterial signal peptide in Escherichia coli. *Biochem. J. 384*, 385–390.

(13) Airenne, K. J., Oker-Blom, C., Marjomaki, V. S., Bayer, E. A., Wilchek, M., and Kulomaa, M. S. (1997) Production of biologically active recombinant avidin in baculovirus-infected insect cells. *Protein Expr. Purif. 9*, 100–108.

(14) Penichet, M. L., Kang, Y. S., Pardridge, W. M., Morrison, S. L., and Shin, S. U. (1999) An antibody-avidin fusion protein specific for the transferrin receptor serves as a delivery vehicle for effective brain targeting: initial applications in anti-HIV antisense drug delivery to the brain. *J. Immunol. 163*, 4421–4426.

(15) Green, N. M. (1975) Avidin. *Adv. Protein Chem. 29*, 85–133.

(16) Lee, H. J., Engelhardt, B., Lesley, J., Bickel, U., and Pardridge, W. M. (2000) Targeting rat anti-mouse transferrin receptor monoclonal antibodies through blood-brain barrier in mouse. *J. Pharmacol. Exp. Ther. 292*, 1048–1052.

(17) Ono, S., Cheng, Y., Kimura, H., Cui, M., Kagawa, S., Nishii, R., and Saji, H. (2011) Novel ^{18}F-labeled benzofuran derivatives with improved properties for positron emission tomography (PET) imaging of β-amyloid plaques in Alzheimer's brains. *J. Med. Chem. 54*, 2971–2979.

(18) Triguero, D., Buciak, J., and Pardridge, W. M. (1990) Capillary depletion method for quantification of blood-brain barrier transport of circulating peptides and plasma proteins. *J. Neurochem. 54*, 1882–1888.

(19) Suzuki, T., Wu, D., Schlachetzki, F., Li, J. Y., Boado, R. J., and Pardridge, W. M. (2004) Imaging endogenous gene expression in brain cancer in vivo with 111In-peptide nucleic acid antisense radiopharmaceuticals and brain drug-targeting technology. *J. Nucl. Med. 45*, 1766–1775.

(20) De Groot, A. S., Moise, L., McMurry, J. A., Wambre, E., Van Overtvelt, L., Moingeon, P., Scott, D. W., and Martin, W. (2008) Activation of natural regulatory T cells by IgG Fc-derived peptide "Tregitopes. *Blood 112*, 3303–11.

(21) Weiner, H. L. (1994) Oral tolerance. *Proc. Natl. Acad. Sci. U. S. A. 91*, 10762–10765.

(22) Paganelli, G., Magnani, P., Zito, F., Lucignani, G., Sudati, F., Truci, G., Motti, E., Terreni, M., Pollo, B., Giovanelli, M., Canal, N., Scotti, G., Comi, G., Koch, P., Maecke, H. R., and Fazio, F. (1994) Pre-targeted immunodetection in glioma patients: tumour localization and single-photon emission tomography imaging of [99mTc]PnAO-biotin. *Eur. J. Nucl. Med. 21*, 314–321.

(23) Samuel, A., Paganelli, G., Chiesa, R., Sudati, F., Calvitto, M., Melissano, G., Grossi, A., and Fazio, F. (1996) Detection of prosthetic vascular graft infection using avidin/indium-111-biotin scintigraphy. *J. Nucl. Med. 37*, 55–61.

Bioconjugate Chemistry

ARTICLE

pubs.acs.org/bc

Pushing Antibody-Based Labeling Systems to Higher Sensitivity by Linker-Assisted Affinity Enhancement

Hans H. Gorris,[†,‡] Steffen Bade,[†] Niels Röckendorf,[†] Milan Fránek,[§] and Andreas Frey*[,†]

[†]Division of Mucosal Immunology and Diagnostics, Research Center Borstel, Parkallee 22, 23845 Borstel, Germany

[‡]Institute of Analytical Chemistry, Chemo- and Biosensors, University of Regensburg, 93040 Regensburg, Germany

[§]Department of Analytical Biotechnology, Veterinary Research Institute, Hudcova 70, 621 32 Brno, Czech Republic

Supporting Information

ABSTRACT: The sensitivity of antibody/hapten-based labeling systems is limited by the natural affinity ceiling of immunoglobulins. Breaking this limit by antibody engineering is difficult. We thus attempted a different approach and investigated if the so-called bridge effect, a corecognition of the linker present between hapten and carrier protein during antibody generation, can be utilized to improve the affinity of such labeling systems. The well-known haptens 2,4-dinitrophenol (2,4-DNP) and 2,4-dichlorophenoxyacetic acid (2,4-D) were equipped with various linkers, and the resulting affinity change of their cognate antibodies was analyzed by ELISA. Anti-2,4-DNP antibodies exhibited the best affinity to their hapten when it was combined with aminobutanoic acid or aminohexanoic acid. The affinity of anti-2,4-D antibodies could be enhanced even further with longer aliphatic spacers connected to the hapten. The affinity toward aminoundecanoic acid-2,4-D derivatives, for instance, was improved about 100-fold compared to 2,4-D alone and yielded detection limits as low as 100 amoles of analyte. As the effect occurred for all antibodies and haptens tested, it may be sensible to implement the bridge effect in future antibody/hapten-labeling systems in order to achieve the highest sensitivity possible.

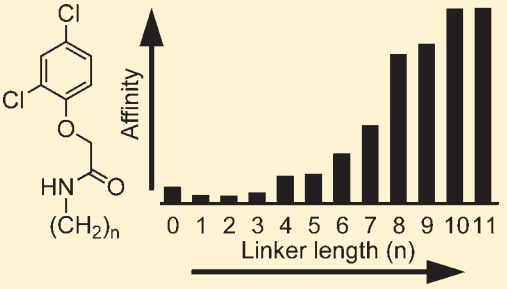

INTRODUCTION

As most biomolecules lack an intrinsic reporter unit for sensitive detection, bioanalytical set-ups usually require analyte labeling, either with direct labels, such as fluorophores,[1] or with indirect labels for binding secondary detection reagents.[2] Although direct labels are read out faster, indirect labels can be more sensitive when used in combination with signal amplification reagents. For indirect labeling, a small molecule is attached covalently to a biomolecule, e.g. by using click chemistry.[3] This ligand is subsequently detected by a specific receptor/probe molecule. One of the most widely used indirect labeling strategies exploits the exceptionally high affinity of (strept)avidin to biotin,[4] which lies in the pico- to femtomolar range. Here, biotin usually serves as a ligand and (strept)avidin, equipped with a reporter molecule (enzyme, dye, radio nuclide), acts as the probe. A drawback of labeling with biotin, however, is its endogenous occurrence in biological samples which may interfere with analyte detection.[5] Most other indirect labels, such as the digoxigenin (DIG) system,[6] are based on the binding of antibodies to ligands of low molecular weight, so-called haptens. Albeit similar in design, such antibody-based labeling systems are inferior to (strep)avidin−biotin as they have a natural upper affinity ceiling[7] of approximately 10^{-10} M^{-1}. In practice, their affinity may even be lower, as it cannot be ruled out that the antibody requires the context of the carrier protein onto which the hapten was coupled for immunization in order to optimally recognize the hapten structure, a phenomenon known as the bridge effect.[8] The affinity reconstitution or improvement caused by a hapten-carrier bridge has usually been considered an adverse effect in particular for competitive ELISAs that rely on similar antibody affinities to the analyte, i.e. the free hapten, and the labeled hapten used for detection, the so-called tracer.[9−13] For example, the herbicide 2,4-dichlorophenoxyacetic acid (2,4-D) can only be detected accurately in environmental samples if the bridge effect is avoided.[14,15] As most studies are focused on avoiding the bridge effect of 2,4-D and other haptens, its potential benefits for high affinity labeling have not been investigated in detail before.

We have recently introduced 2,4-D as a nonbiogenic label that avoids cross-reactivity with biological materials. This labeling strategy was applied to the detection of large (ovalbumin) and small (insulin) proteins, glycoproteins (mucin), DNA, and peptides.[16] Moreover, the efficient immobilization and detection of 2,4-D labeled peptides on microtiter plates allowed the design of a robust proteolysis assay[17] that operates even with crude intestinal juice preparations.[18] In the course of these studies, we observed that the affinity between the 2,4-D label and its cognate antibody was strongly enhanced when an aliphatic linker was attached to

Received: April 7, 2011
Revised: July 11, 2011
Published: July 12, 2011

ACS Publications © 2011 American Chemical Society

dx.doi.org/10.1021/bc2001787 | *Bioconjugate Chem.* 2011, 22, 1619–1624

the carboxyl group of 2,4-D. Here, we explore this phenomenon in depth by investigating the binding of 2,4-D equipped with various linkers to three anti-2,4-D antibody clones and comparing this setup to the classical and extensively described 2,4-dinitrophenyl (2,4-DNP) hapten−antibody pair.[19,20]

EXPERIMENTAL SECTION

Reagents and Buffers. Synthesis reagents were purchased from Sigma-Aldrich (Taufkirchen, Germany), Merck (Darmstadt, Germany), Merck Biosciences (Schwalbach, Germany), Advanced Chemtech (Louisville, KY, USA), Peptech (Burlington, MA, USA), MP Biomedicals (Eschwege, Germany), Molecular Biosciences (Boulder, CO, USA), and Polypure (Oslo, Norway). Monoclonal anti-2,4-D IgG antibodies (clone E2/G2, E4/C2, and F6/C10) were generated in mice against the 2,4-D hapten coupled to thyroglobulin according to standard procedures.[21] Monoclonal rat anti-DNP IgG antibodies (clone LO−DNP-1 and LO−DNP-61, affinity purified) were purchased from Interchim (Montlucon Cedex, France), casein (Hammarsten grade) from BDH (Poole, England), and horseradish-peroxidase-labeled streptavidin (SA-HRP) from Vector (Burlingame, CA, USA). L(ite)-PBS: 10 mM sodium phosphate, pH 7.0, 10 mM NaCl. D(ulbecco's)-PBS: 2.7 mM KCl, 1.5 mM KH_2PO_4, 136 mM NaCl, 8.1 mM Na_2HPO_4, pH 7.3. P(hysiological)-PBS:[22] 8 mM phosphate, pH 7.2, 4.6 mM K^+, 111.3 mM Na^+, 101.5 mM Cl^-). ELISA substrate solution: 3 mM H_2O_2, 1 mM 3,3′,5,5′-tetramethylbenzidine in 200 mM potassium citrate buffer, pH 4.0.[23]

Conjugate Synthesis. Conjugate libraries were SPOT-synthesized on a cellulose membrane[24] using standard fluorenylmethoxycarbonyl (Fmoc) amino acid protection chemistry as described earlier.[17] To allow the release of the synthesis products from the cellulose support, each individual peptide was anchored C-terminally on the cellulose via a proline-ε-lysine sequence, which can be cleaved off the support under diketopiperazine formation.[25] The cellulose sheets used as synthesis support were first uniformly derivatized with proline. In the next step, synthesis areas (SPOTs) of the individual conjugates were defined by applying an ε-Fmoc-protected lysine. Onto this anchor, the conjugate chain was assembled by stepwise reactions with active esters of Fmoc-protected "amino acid" building blocks: Biocytin was coupled first on the SPOTs, introducing the biocytin label. Next followed *O*-(3-aminopropyl)-*O*′-(*N*-diglycolyl-3-aminopropyl)-nonaethyleneglycol, establishing a poly(ethylene glycol) (PEG) spacer, then a single alanine (or a series of amino acids to form a short peptide sequence) was added. Then, one of various linker moieties was added, either an aminoalkanoic acid (H_2N-$(CH_2)_n$-COOH, $n = 1-11$) or a PEG (*O*-(3-aminopropyl)-*O*′-(*N*-diglycolyl-3-aminopropyl)-diethyleneglycol). As the last building block, 2,4-DNP or 2,4-D was coupled. After the last coupling round, all protection groups were removed, the conjugates were cleaved off the individual membrane SPOTs, dried in vacuo, dissolved in 1.5 mL of L-PBS × 0.005% (w/v) Tween 20, and stored at −80 °C. Conjugates were used without further purification as the antibody capture step on the microtiter plate (see below) already constitutes a purification step (for a detailed protocol on conjugate synthesis see Supporting Information).

Conjugate and Antibody Concentrations. SPOT synthesis yields of conjugates were quantitated with a competitive ELISA by determining the half maximal effective concentration (EC_{50}), where the signal intensity is reduced to 50% of the maximal signal, indicating that equal amounts of competitor and conjugate are present.[17] 2,4-DNP-antibody concentrations were provided by the manufacturer. Purity of 2,4-D-antibodies was confirmed by gel electrophoresis, and their concentrations were determined by Lowry- and BCA-assay.

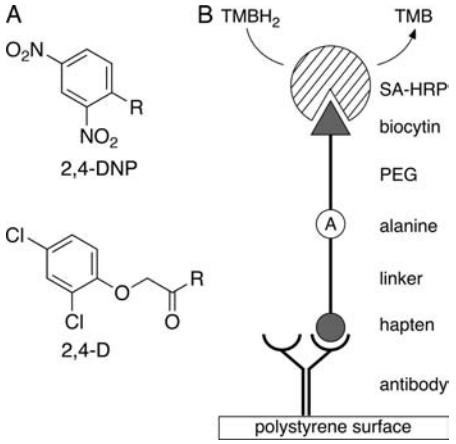

Figure 1. Analyte detection setup. (A) 2,4-Dinitrophenyl (2,4-DNP) and 2,4-dichlorophenoxyacetyl (2,4-D) residues. (B) Analyte constructs consist of alanine flanked C-terminally by a short PEG stretch and a biocytin handle and N-terminally by a linker moiety and 2,4-DNP- or 2,4-D-hapten. Adherence of the analyte onto an antibody-coated microtiter plate occurs via the 2,4-D- or 2,4-DNP-label. For analyte detection, a streptavidin−horseradish peroxidase (SA-HRP) conjugate binds to the biocytin handle and oxidizes chromogenic $TMBH_2$ to the chromophore TMB.

ELISA. High-bind polystyrene 96-well microtiter plates (Corning, Wiesbaden, Germany) were coated overnight at 4 °C with 75 μL/well of 50 ng/mL antibody in L-PBS. The microtiter plates were then washed three times with 300 μL/well of D-PBS × 0.05% (w/v) Tween 20 (D-PBST), blocked with 250 μL/well of 1% (w/v) casein/D-PBS for 3−4 h at RT, and washed again four times with D-PBST. Conjugates were serially diluted in 75 μL/well of P-PBS × 0.005% (w/v) Tween 20 (P-PBST) on the antibody-coated microtiter plate. After 2 h 30 min, microtiter plates were washed four times with 300 μL/well of D-PBST and incubated for 60 min at RT using 75 μL/well of 1 μg/mL SA-HRP in 1% (w/v) casein in D-PBS. After six washes with 300 μL/well of D-PBST, microtiter plates were developed by adding 75 μL/well of ELISA substrate solution. The enzyme reaction was terminated after 30 min by adding 125 μL/well of 1 M H_2SO_4. Signal intensities in wells were measured at $\lambda = 450$ nm with a microtiter plate reader and fitted to a four-parameter logistic function (eq 1):[26]

$$OD_c = \frac{OD_{max} - OD_{bg}}{1 + \left(\frac{c}{EC_{50}}\right)^s} + OD_{bg} \quad (1)$$

where c is the conjugate concentration, OD_c the optical density as a function of c. The curve fit yields the maximum signal intensity (OD_{max}), the background intensity (OD_{bg}), the half maximal effective conjugate concentration (EC_{50}), and the slope at the inflection point (s).

RESULTS AND DISCUSSION

Detection System. The effects of different linkers on hapten−antibody interaction were analyzed using a specially designed

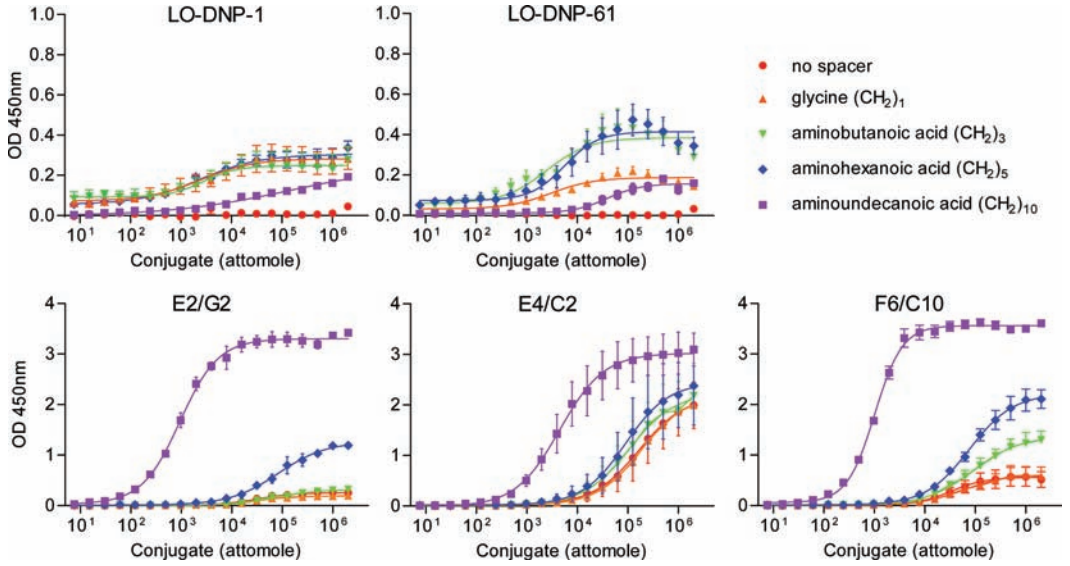

Figure 2. Influence of different linkers on hapten−antibody binding. Microtiter plates were coated with 50 ng/mL of either anti-2,4-DNP- (LO−DNP-1, LO−DNP-61) or anti-2,4-D-antibodies (E2/G2, E4/C2, F6/C10). Analytes carrying the corresponding haptens in combination with various aliphatic linkers were added in serial dilutions and detected via their biocytin label (mean ± SEM of three experiments).

ELISA where an immobilized antibody captures an analyte molecule that is equipped with a tag via which the binding is recorded. The analyte was designed as a peptidic conjugate with the hapten label on one side and a detection handle on the other and was synthesized from C-terminus to N-terminus using SPOT-synthesis on a cellulose membrane.[24] As 2,4-D and 2,4-DNP (Figure 1A) do not carry an amino function that is necessary for chain elongation, they were positioned on the N-terminus. On the C-terminus, we introduced biocytin (biotin attached to the side chain of lysine) as a detection handle because of its exceptionally high binding constant with streptavidin (10^{15} M^{-1}).[4] In addition to the terminal labels, the conjugates contained an aliphatic linker adjacent to 2,4-D or 2,4-DNP for analyzing the bridge effect and a hydrophilic PEG-spacer next to the biocytin handle to improve water solubility. The two halves of the construct were connected by a single amino acid (alanine). After the synthesis was completed, the conjugates were released into solution for ELISA analysis. Anti-2,4-D- or anti 2,4-DNP-antibodies where coated on a microtiter plate to immobilize the conjugates via the hapten constructs of interest. Bound conjugate was detected and quantified by a streptavidin−horseradish peroxidase conjugate mediating a colorogenic reaction (Figure 1B).

ELISA signals are fitted with a logistic function (eq 1) that provides OD_{max} and EC_{50}. It has been discussed whether and how the affinity is reflected in OD_{max} and EC_{50}.[27] Although logistic functions appear to represent the law of mass action,[28] care has to be taken as hapten binding to surface immobilized antibodies can be diffusion limited rather than reaction limited.[29] Consequently, comparing the affinities of various hapten−antibody combinations requires similar surface conditions and analyte sizes in all experiments. The analytes used in our experiments were structurally identical except for the hapten/linker combination, and homogeneity was conferred by the defined synthetic nature of the analyte molecules. Moreover, we coated the microtiter plate surface with the same antibody concentration (50 ng/mL) in all experiments, which we had found to result in an optimal absorbance span between OD_{bg} and OD_{max}. Finally, it should be noted that the antibody−analyte binding is not affected by bivalent interactions[30] as each conjugate carries a single hapten label only.

Label and Antibody Specificity. Franek et al.[21] demonstrated that the anti-2,4-D antibodies used in our experiments are highly specific for 2,4-D and display very limited cross reactivities to structural analogues. Accordingly, replacement of the oxy acetic acid moiety of 2,4-D by acetic acid or oxybutanoic acid lead to a complete loss of binding, whereas extensions at the carboxyl group of the 2,4-D yielded similar results as native 2,4-D. Thus, only derivatizations that result from coupling of amino-functionalized linkers to the carboxyl group of 2,4-D and that leave the original hapten structure intact may increase sensitivity. This is consistent with the bridge effect.

Nevertheless, two possible scenarios independent of the hapten−antibody interaction but also causative for a signal increase with hapten/linker constructs are conceivable. First, the high sensitivity could be a mere spacer effect that facilitates the accessibility of the captured analyte for the detection reagent on the microtiter plate surface. When we substituted the linker aminoundecanoic acid adjacent to 2,4-D by a hydrophilic polyethylene glycol (PEG) of comparable length, however, no increase in the detection sensitivity was observable, ruling out control of the signal intensity by mere sterical constraints. Second, the aliphatic linker could mediate nonspecific binding of the conjugate to the solid support by interactions with the hydrophobic polystyrene body of the microtiter plate. In fact, aminohexanoic acid-conjugation has already been used to immobilize peptides directly on microtiter plates.[31] However, when we applied peptide conjugates carrying an aminoundecanoic acid linker and the structural analogue phenoxyacetic acid instead of 2,4-D onto a microtiter plate coated with anti-2,4-D-antibodies, no signals were detectable. Consequently, the high sensitivity observed with our hapten/linker conjugates cannot result from hydrophobic binding of long aliphatic linkers to the plate material.

Influence of Antibody Clones and Different Linkers. The bridge effect has been attributed to a corecognition of the chemical linkage between the hapten and the carrier protein

Table 1. OD_{max} and EC_{50} (amole) for Anti-DNP- and Anti-2,4-D Antibodies Obtained with Different Hapten/Linker Combinations[a]

hapten	moAb		no linker	$(CH_2)_1$	$(CH_2)_3$	$(CH_2)_5$	$(CH_2)_{10}$
DNP	LO−DNP-1	OD_{max}	nd	0.28	0.25	0.30	nd
		EC_{50}	nd	2434	2820	2367	nd
	LO−DNP-61	OD_{max}	nd	0.19	0.39	0.41	0.16
		EC_{50}	nd	2997	2448	5532	38983
2,4-D	E2/G2	OD_{max}	0.26	0.19	0.33	1.26	3.30
		EC_{50}	32172	33989	69230	82714	943
	E4/C2	OD_{max}	2.19	2.20	2.24	2.44	3.02
		EC_{50}	167535	182901	105113	89140	4462
	F6/C10	OD_{max}	0.56	0.62	1.37	2.22	3.56
		EC_{50}	32988	59016	89924	76128	1019

[a] nd; not determinable.

used for antibody generation.[13] Usually, a hapten is coupled to the carrier protein via an amino function, either on a lysine side chain or on the N-terminus. In the latter case, antibodies should recognize the hapten in context with the N-terminal amino acid sequence of the carrier protein. We tested this for three anti-2,4-D-antibody clones which had been generated with thyroglobulin as a carrier.[21] When we investigated 2,4-D-Asn-Ile-Phe-Glu-Tyr-Gln-labeled conjugates, however, OD_{max} and EC_{50} were similar to those obtained with a 2,4-D-label not bearing this amino acid stretch, which shows that the N-terminal amino acid sequence of the carrier protein did not contribute to the bridge effect for any of our 2,4-D-antibodies.

We hence concentrated on the effect of aliphatic linkers which may mimic the configuration of a lysine side chain. Dose−response curves with serially diluted analytes reflect the influence of such bridges on assay performance (Figure 2). None of the bridges had a marked adverse effect on assay performance, but not all linkers improved the ELISA curves. Whether or not a gain in slope and OD_{max} and a reduction of EC_{50} occurred was dependent on the specific hapten−linker−antibody combination. The OD_{max} and EC_{50} values of each combination are summarized in Table 1.

For the 2,4-DNP-system, the results were in good agreement with the bridge theory: both anti-2,4-DNP-antibody clones recognize 2,4-DNP most efficiently when an aliphatic linker similar in length (aminobutanoic acid or aminohexanoic acid) to a lysine side chain was used. All anti-2,4-D-antibody clones, by contrast, show a remarkably different relationship between affinity and linker length. While shorter linkers such as glycine lead to a similar OD_{max} as obtained with the respective construct in the 2,4-DNP label system, the 2,4-D system meets no maximum with aminobutanoic acid or aminohexanoic acid. Instead, OD_{max} is further increasing up to aminoundecanoic acid. This tendency is followed by all anti-2,4-D antibody clones, albeit with individual variations in the strength of the bridge effect, e.g. with clone E2/G2, we observe a 13-fold increase in OD_{max} with the aminoundecanoic acid linker compared to the hapten alone, with clone E4/C2 only a 1.4-fold increase was detected. An increased OD_{max} can be attributed in part to lower release rates (k_{off}) of the analyte with long aliphatic linkers, effectuating an equilibrium shift toward more bound analyte and hence a higher OD_{max}: the stronger the capture antibody binds the analyte the less the analyte will be released from the complex during subsequent washing and incubation steps.[16] Additionally, conformational

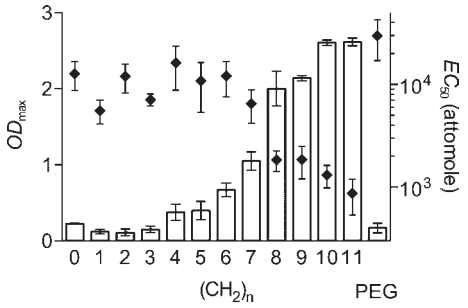

Figure 3. Influence of increasing linker length and composition on hapten−antibody affinity. Analytes carried linear aliphatic linkers ($(CH_2)_n$), varying from glycine ($n = 1$) to aminododecanoic acid ($n = 11$), coupled to the carboxyl group of 2,4-D. Microtiter plates were coated with 50 ng/mL of anti-2,4-D antibody clone E2/G2 to capture different analyte constructs, and analyte binding was quantitated via the biotin label. OD_{max} (□) increases and EC_{50} (◆) decreases with the length of the aliphatic linker. By contrast, a hydrophilic PEG linker of similar length as aminododecanoic acid does not improve analyte binding compared to 2,4-D alone ($(CH_2)_0$) (mean ± SEM of three experiments).

effects may play a role. It was shown that haptens can induce conformational changes at the antibody binding sites during the binding process,[32,33] and structural evidence was provided for conformational diversity in monoclonal antibodies.[34] Thus, a population of monoclonal antibodies can be composed of different preexisting isomers that may be converted to a "high-affinity conformation" by an induced-fit isomerization. If hapten binding is not strong enough, it may not be able to induce a conformational shift in some antibody isomers necessary for accommodating the hapten. Consequently, only a fraction of capture antibodies will be occupied, even if the antibody seems to be "saturated", eventually resulting in a lower OD_{max}.

When looking at the EC_{50} values, the 2,4-DNP conjugates performed best when short aliphatic linkers were used. By contrast, 2,4-D binding by all antibody clones improved considerably with linkers above aminobutanoic acid, displaying a 30- to 40-fold decrease in EC_{50} with the aminoundecanoic acid linker compared to 2,4-D alone. Here, the lowest EC_{50} of 1 fmole conjugate was obtained with the anti-2,4-D-antibody clones E2/G2 and F6/C10, and an analyte detection limit (the so-called end point titer) of approximately 100 amoles was achieved. Thus, labeling with 2,4-D-aminoundecanoic acid leads to "superoptimal" analyte detection, which seems to be largely independent of the anti-2,4-D-antibody clone.

The superoptimal bridge effect prompted us to investigate the conjugate detection with 2,4-D in detail. Aliphatic linkers were elongated successively by $(CH_2)_n$ from glycine ($n = 1$) to aminododecanoic acid ($n = 11$) (Figure 3). An increasing aliphatic linker length resulted in a sigmoid-like response profile of OD_{max} and $1/\log_{10}(EC_{50})$, with an inflection point between $(CH_2)_7$ and $(CH_2)_8$. The inflection point indicates where increments in the length of the aliphatic linker enhance the affinity most efficiently. While longer linkers still yield higher affinities, the gain in affinity is less pronounced and levels down to a point where further increases are insignificant.

CONCLUSION

We could show that aliphatic spacers next to the hapten exert distinct bridge effects, considerably improving the binding of

2,4-D or 2,4-DNP to their cognate antibodies. In contrast to 2,4-DNP conjugates, 2,4-D does not tap the full potential of antibody binding when adjacent to aliphatic linkers which have the length of a lysine side chain, but it clearly outperforms the 2,4-DNP system when combined with long aliphatic linkers. Our findings demonstrate the potential of the bridge effect when using haptens in combination with aliphatic linkers for high affinity labeling and provide a guideline for optimizing other antibody−hapten pairs as sensitive labeling/detection systems for biomolecules.

■ ASSOCIATED CONTENT

Supporting Information. Details on conjugate synthesis and analysis. This material is available free of charge via the Internet at http://pubs.acs.org.

■ AUTHOR INFORMATION

Corresponding Author

*Phone: + 49-4537-188 5620. Fax: + 49-4537-188 6930. E-mail: afrey@fz-borstel.de.

■ ACKNOWLEDGMENT

This work was funded in part by grants from the German Ministry for Education and Research (BMBF, grants 01KO0113 and 13N8473) and from the German Research Council (DFG, grant Fr 958/4-1).

■ REFERENCES

(1) Kele, P., Mezo, G., Achatz, D., and Wolfbeis, O. S. (2009) Dual labeling of biomolecules by using click chemistry: a sequential approach. *Angew. Chem. Int. Ed. 48*, 344–347.

(2) Zhang, Q., and Guo, L. H. (2007) Multiple labeling of antibodies with dye/DNA conjugate for sensitivity improvement in fluorescence immunoassay. *Bioconjugate Chem. 18*, 1668–1672.

(3) Rostovtsev, V. V., Green, L. G., Fokin, V. V., and Sharpless, K. B. (2002) A stepwise Huisgen cycloaddition process: Copper(I)-catalyzed regioselective "ligation" of azides and terminal alkynes. *Angew. Chem. Int. Ed. 41*, 2596–2599.

(4) Green, N. M. (1990) Avidin and streptavidin. *Methods Enzymol. 184*, 51–67.

(5) Hamblett, K. J., Kegley, B. B., Hamlin, D. K., Chyan, M. K., Hyre, D. E., Press, O. W., Wilbur, D. S., and Stayton, P. S. (2002) A streptavidin-biotin binding system that minimizes blocking by endogenous biotin. *Bioconjugate Chem. 13*, 588–598.

(6) McCreery, T. (1997) Digoxigenin labeling. *Mol. Biotechnol. 7*, 121–124.

(7) Foote, J., and Eisen, H. N. (1995) Kinetic and affinity limits on antibodies produced during immune-responses. *Proc. Natl. Acad. Sci. U.S.A. 92*, 1254–1256.

(8) Franek, M. (1987) Structural aspects of steroid-antibody specificity. *J. Steroid Biochem. 28*, 95–108.

(9) Luttrell, B. M., and Henniker, A. J. (1991) Reaction coupling of chelation and antigen-binding in the calcium ion-dependent antibody-binding of cyclic-AMP. *J. Biol. Chem. 266*, 21626–21630.

(10) Abuknesha, R. A., and Luk, C. (2005) Paraquat enzyme-immunoassays in biological samples: assessment of the effects of hapten−protein bridge structures on assay sensitivity. *Analyst 130*, 956–963.

(11) Nara, S., Tripathi, V., Chaube, S. K., Rangari, K., Singh, H., Kariya, K. P., and Shrivastav, T. G. (2008) Influence of hydrophobic and hydrophilic spacer-containing enzyme conjugates on functional parameters of steroid immunoassay. *Anal. Biochem. 373*, 18–25.

(12) Nordblom, G. D., Counsell, R. E., and England, B. G. (1984) A specific radioimmunoassay for androstenedione with reduced bridge-binding. *Steroids 44*, 275–282.

(13) Tiefenauer, L. X., Bodmer, D. M., Frei, W., and Andres, R. Y. (1989) Prevention of bridge binding in immunoassays: A general estradiol tracer structure. *J. Steroid Biochem. 32*, 251–257.

(14) Matuszczyk, G., Knopp, D., and Niessner, R. (1996) Development of an ELISA for 2,4-D: Characterization of two polyclonal antisera. *Fresenius' J. Anal. Chem. 354*, 41–47.

(15) Hatzidakis, G. I., Tsatsakis, A. M., Krambovitis, E. K., Spyros, A., and Eremin, S. A. (2002) Use of L-lysine fluorescence derivatives as tracers to enhance the performance of polarization fluoroimmunoassays. A study using two herbicides as model antigens. *Anal. Chem. 74*, 2513–2521.

(16) Bade, S., Röckendorf, N., Franek, M., Gorris, H. H., Lindner, B., Olivier, V., Schaper, K. J., and Frey, A. (2009) Biolabeling with 2,4-dichlorophenoxyacetic acid derivatives: The 2,4-D tag. *Anal. Chem. 81*, 9695–9702.

(17) Gorris, H. H., Bade, S., Röckendorf, N., Albers, E., Schmidt, M. A., Franek, M., and Frey, A. (2009) Rapid profiling of peptide stability in proteolytic environments. *Anal. Chem. 81*, 1580–1586.

(18) Bade, S., Gorris, H. H., Koelling, S., Olivier, V., Reuter, F., Zabel, P., and Frey, A. (2010) Quantitation of major protein constituents of murine intestinal fluid. *Anal. Biochem. 406*, 157–165.

(19) Landsteiner, K., and Chase, M. W. (1937) Studies on the sensitization of animals with simple chemical compounds: IV. Anaphylaxis induced by picryl chloride and 2:4 dinitrochlorobenzene. *J. Exp. Med. 66*, 337–351.

(20) Eisen, H. N. (2001) Specificity and degeneracy in antigen recognition: Yin and Yang in the immune system. *Annu. Rev. Immunol. 19*, 1–21.

(21) Franek, M., Kolar, V., Granatova, M., and Nevorankova, Z. (1994) Monoclonal ELISA for 2,4-dichlorophenoxyacetic acid: characterization of antibodies and assay optimization. *J. Agric. Food Chem. 42*, 1369–1374.

(22) Lockwood, J. S., and Randall, H. T. (1949) The place of electrolyte studies in surgical patients. *Bull. New York Acad. Med. 25*, 228–243.

(23) Frey, A., Meckelein, B., Externest, D., and Schmidt, M. A. (2000) A stable and highly sensitive 3,3′,5,5′-tetramethylbenzidine-based substrate reagent for enzyme-linked immunosorbent assays. *J. Immunol. Methods 233*, 47–56.

(24) Frank, R. (1992) Spot-synthesis: an easy technique for the positionally addressable, parallel chemical synthesis on a membrane support. *Tetrahedron 48*, 9217–9232.

(25) Bray, M. B., Maeji, N. J., and Geysen, H. M. (1990) The simultaneous multiple production of solution phase peptides; assessment of the Geysen method of simultaneous peptide synthesis. *Tetrahedron Lett. 31*, 5811–5814.

(26) Rodbard, D., and Hutt, D. M. (1974) In *Proceedings of the Symposium on Radioimmunoassay and Related Procedures in Medicine, International. Atomic Energy Agency*, pp 165−192, Unipub, New York, Vienna.

(27) Steward, M. W., and Lew, A. M. (1985) The importance of antibody affinity in the performance of immunoassays for antibody. *J. Immunol. Methods 78*, 173–190.

(28) Finney, D. J. (1983) Response curves for radioimmunoassay. *Clin. Chem. 29*, 1762–1766.

(29) Stenberg, M., and Nygren, H. (1988) Kinetics of antigen-antibody reactions at solid-liquid interfaces. *J. Immunol. Methods 113*, 3–15.

(30) Nygren, H., Czerkinsky, C., and Stenberg, M. (1985) Dissociation of antibodies bound to surface-immobilized antigen. *J. Immunol. Methods 85*, 87–95.

(31) Pyun, J. C., Cheong, M. Y., Park, S. H., Kim, H. Y., and Park, J. S. (1997) Modification of short peptides using epsilon-aminocaproic acid for improved coating efficiency in indirect enzyme-linked immunosorbent assays (ELISA). *J. Immunol. Methods 208*, 141–149.

(32) Lancet, D., and Pecht, I. (1976) Kinetic evidence for hapten-induced conformational transition in immunoglobulin Mopc 460. *Proc. Natl. Acad. Sci. U.S.A. 73*, 3549–3553.

(33) Foote, J., and Milstein, C. (1994) Conformational isomerism and the diversity of antibodies. *Proc. Natl. Acad. Sci. U.S.A. 91*, 10370–10374.

(34) James, L. C., Roversi, P., and Tawfik, D. S. (2003) Antibody multispecificity mediated by conformational diversity. *Science 299*, 1362–1367.

Supporting information:

Pushing antibody-based labeling systems to higher sensitivity by linker-assisted affinity enhancement

Hans H. Gorris, Steffen Bade, Niels Röckendorf, Milan Fránek & Andreas Frey

Conjugate synthesis and characterization

Synthesis scheme. All hapten conjugates were prepared by solid-phase synthesis on cellulose membranes ("SPOT-synthesis") using standard fluorenylmethoxycarbonyl (Fmoc) amino acid protection chemistry[1] (Fig. S-1). To allow the release of the synthesis products from the cellulose support, each conjugate was anchored C-terminally on the cellulose via a proline-lysine sequence which can be cleaved off the support under diketopiperazine formation[2]. To achieve this, the cellulose sheets used as synthesis support were first uniformly derivatized with proline (Fig. S-1, step A). In the next step, synthesis-SPOTs of the individual conjugates were defined by applying an ε-Fmoc-protected lysine (step B). Onto this anchor, the conjugate chain was assembled by stepwise reactions with active esters of Fmoc-protected "amino acid" building blocks: Biocytin was coupled first on the SPOTs (step C), introducing the biocytin label. Next followed O-(3-aminopropyl)-O'-(N-diglycolyl-3-aminopropyl)-nonaethyleneglycol (step D), establishing a poly(ethylene glycol) (PEG) spacer, then a single alanine (or a series of amino acids to form a short peptide sequence) was added (step E). Next, one of various linker moieties was added, either an aminoalkanoic acid (H_2N-$(CH_2)_n$-COOH, n = 1 – 11) (step F) or a PEG (O-(3-aminopropyl)-O'-(N-diglycolyl-3-aminopropyl)-diethyleneglycol). As the last building block, 2,4-DNP or 2,4-D was coupled (step G). After the last coupling round, all protection groups were removed, and the conjugates were cleaved off the individual SPOTs.

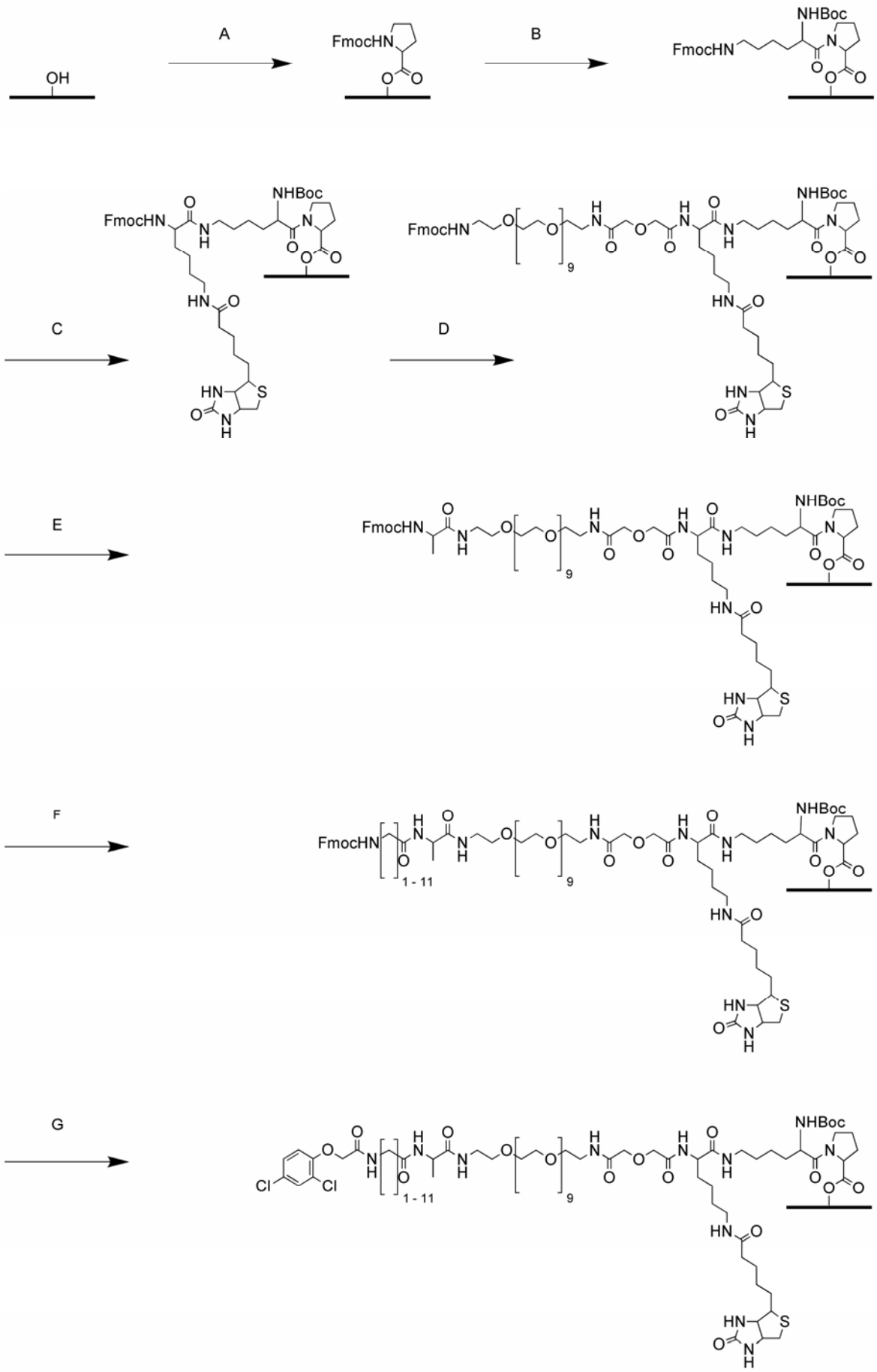

Supporting Figure S-1: Conjugation scheme

Materials. Cellulose membranes (Whatman 540) were from GE Healthcare (Whatman GmbH, Dassel, Germany). Synthesis reagents were purchased from Sigma-Aldrich (Taufkirchen, Germany), Merck (Darmstadt, Germany), Merck Biosciences (Schwalbach, Germany), Advanced Chemtech (Louisville, KY, USA), Peptech (Burlington, MA, USA), MP Biomedicals (Eschwege, Germany), Molecular Biosciences (Boulder, CO, USA), and Polypure (Oslo, Norway). Anhydrous hydroxybenzotriazole (HOBt) was from Dojindo Laboratories (Kumamoto, Japan) and dimethylformamide (DMF) from Promochem (Wesel, Germany). DMF and N-methyl-2-pyrrolidone (NMP; Fluka, Taufkirchen, Germany) were deionised by treatment with dried ion exchange mixed bed resin AG501-X8 (Bio Rad Laboratories, München, Germany) and desiccated with molecular sieve 4 Å (Fluka). All other chemicals and solvents were used without further purification.

Experimental details. All reactions were performed at room temperature if not stated otherwise. A stack of four vacuum dried Whatman 540 cellulose membranes cut to a size of 9 × 13 cm was esterified in a closed container for 24 h with 10 ml of Fmoc-protected proline (0.2 M Fmoc-proline, 0.25 M diisopropylcarbodiimide (DICD) and 0.46 M NMP in DMF). The proline-derivatized sheets were then separated and in all following steps incubated under agitation. Unreacted hydroxyl functions on the cellulose sheets were acetylated ("blocking step") by treatment with 2 % (v/v) acetic anhydride in DMF for 24 h (the solution was changed repeatedly), the sheets were washed with DMF (1 × 30 s, 2 × 2 min) and the Fmoc group was cleaved off the proline residues ("deprotection step") by treatment with 20 % (v/v) piperidine in DMF for 5 min. The sheets were washed with DMF (1 × 30 s, 4 × 2 min) and ethanol (1 × 30 s, 2 × 2 min) before drying in the cold air flow of a fan. A solution of 0.2 M Boc-Lys(Fmoc)-OH, 0.35 M HOBt and 0.4 mM 5(6)-carboxytetramethylrhodamine (for visualization of the SPOTs) in NMP was prepared and activated for 30 min with DICD (final concentration: 0.25 M). Using the pipetting device ASP 222 (Intavis AG, Cologne, Germany), 0.1 µl of this solution were applied to define an array of 25 × 17 SPOTs on each sheet. Each amino acid application step was performed three times followed by an incubation time of at least 40 min. Unreacted amino functions were blocked by acetylation with 2 % (v/v) acetic anhydride in DMF for 24 h, and the sheets were washed with DMF, deprotected and washed

with DMF as before. To confirm the presence of free amino groups, the SPOTs were stained by repeated treatments with a solution of 0.01 % (w/v) bromophenol blue in DMF for 10 min. The sheets were washed with DMF and ethanol and dried as before. For each of the following synthesis cycles 0.2 µl of the respective Fmoc-protected amino acid solutions were activated for 30 min with HOBt and DICD in the same concentrations as given above and applied to the SPOTs. The washing, blocking, deprotection, staining and drying procedure was performed as before, though with an acetylation time of 20 min.

For side chain deprotection and anchor cleavage, the dried sheets were incubated under agitation with a freshly prepared solution of 3 % triisobutylsilane, 2 % water and 50 % trifluoroacetic acid in dichloromethane (v/v) for 2 × 1 h. After washing with dichloromethane (1 × 1 min, 3 × 10 min), 0.1 % HCl / 50 % methanol in water (1 × 1 min, 3 × 20 min) and 1 M acetic acid (1 × 1 min, 3 × 20 min) the sheets were dried *in vacuo*. The individual SPOTs were punched out of the cellulose sheets and transferred to microtubes. The conjugates were released from the cellulose support by shaking in 0.5 ml of 0.1 M triethylammonium acetate / 20 % ethanol in water (v/v) overnight at 30 °C. Supernatants were transferred to a second tube and another 0.5 ml triethylammonium acetate buffer was applied to the SPOTs for 2 h. Supernatants were pooled and lyophilized. The conjugates were dissolved in 1.5 ml L-PBS (10 mM sodium phosphate, pH 7.0, 10 mM NaCl) containing 0.005 % (w/v) Tween 20 , snap-frozen in liquid N_2 and stored at -80 °C.

Conjugate characterization. The synthesis products were characterized by high resolution electrospray ionization mass spectrometry. As an example, the ESI-MS spectrum of the conjugate carrying the aminoundecanoic acid spacer and 2,4-D is shown (Fig S-2).

Fig. S-2 A depicts the molecular structure of the SPOT-synthesized conjugate as it is obtained after side chain deprotection and cleavage of the lysyl-proline anchor. The lyophilized conjugate was dissolved in a solution of 74 % (v/v) water, 25 % (v/v) acetonitrile and 1 % (v/v) acetic acid (adjusted to pH 2.8) and analyzed on a Bruker Daltonics Apex II ESI-FT-MS (Bruker Daltonics, Bremen, Germany) with a 7-tesla activity shielded magnet und an Apollo electrospray ion source. The ESI-MS spectrum (Fig. S-2 B) shows a main peak at 1649.801 m/z. The difference of 16 compared to the calculated mass of 1633.81 m/z can be attributed to

the oxidation of biocytin to biocytin sulfoxide. The occurrence of that oxidation reaction under our synthesis conditions was confirmed by incubating just biocytin in the deprotection solution and recording a mass spectrum. As biotin sulfoxide is bound by streptavidin nearly as well as biotin[3] we did not surmise any detrimental effect of this modification for the ensuing affinity measurements by ELISA. The peak at 1570.760 m/z results from an incomplete diketopiperazine rearrangement of the lysyl-proline anchor where the conjugate carries a terminal lysine residue only. As this modification is confined to the anchor residue no influence on the affinity measurements is to be expected. Since all minor peaks do not display the typical isotope pattern of a chlorinated species they do not carry the 2,4-D moiety and hence cannot be bound by the capture antibody on the microtiter plate in the ELISA.

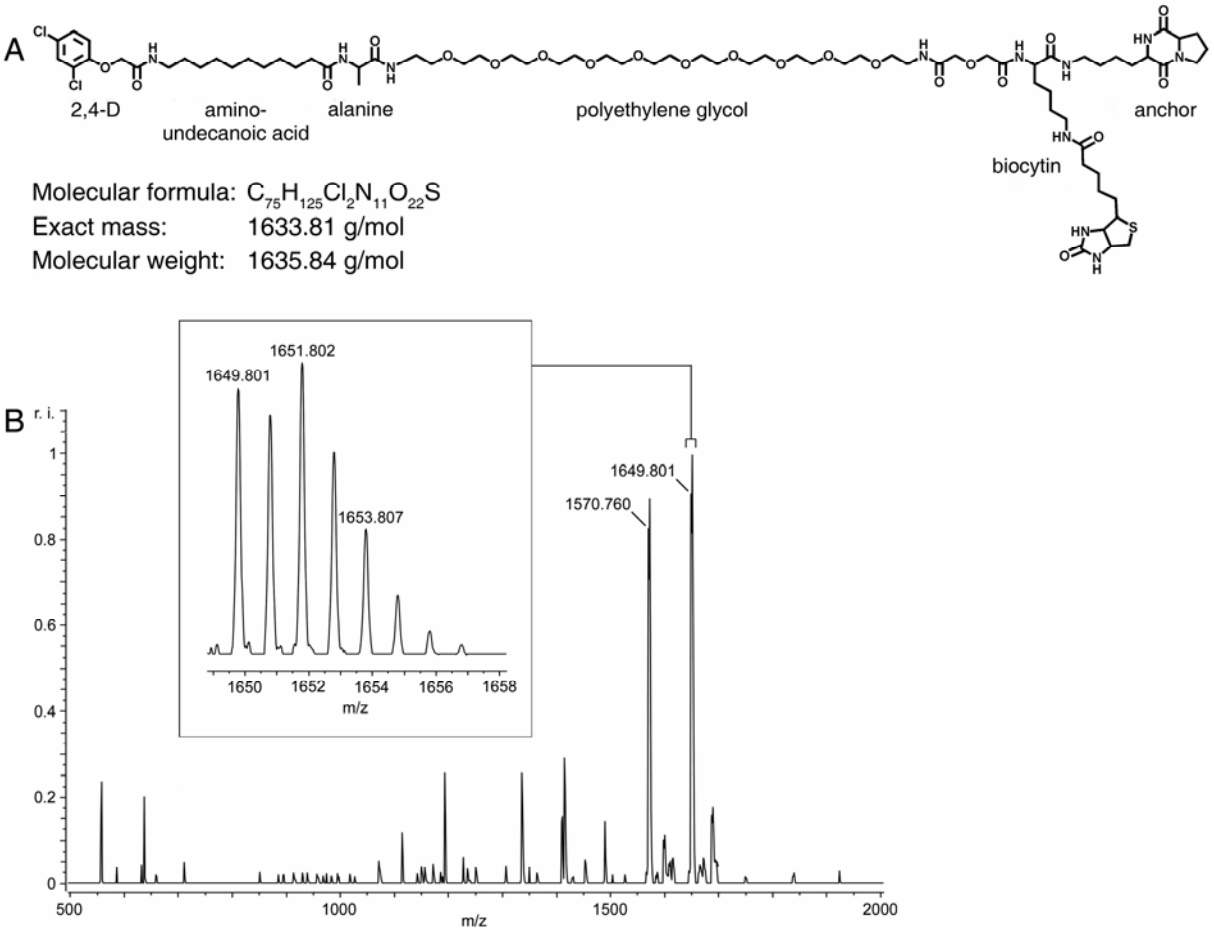

Supporting Figure S-2: Molecular structure (A) and deconvoluted ESI-MS (B) of a SPOT-synthesized conjugate carrying the aminoundecanoic acid spacer and 2,4-D. The enlarged inset shows the typical isotope pattern consistent with the two chloro groups in 2,4-D.

References

(1) Frank, R. (1992) Spot-synthesis: an easy technique for the positionally addressable, parallel chemical synthesis on a membrane support. *Tetrahedron 48*, 9217-9232.

(2) Bray, M. B., Maeji, N. J., and Geysen, H. M. (1990) The simultaneous multiple production of solution phase peptides; assessment of the Geysen method of simultaneous peptide synthesis. *Tetrahedron Lett 31*, 5811-5814.

(3) Lichstein, H. C., and Birnbaum, J. (1965) Combinability of avidin and streptavidin with analogs of biotin. *Biochem Biophys Res Commun 20*, 41-45.

Bioconjugate Chemistry

ARTICLE

pubs.acs.org/bc

Cy5-Conjugated Hybridization-Sensitive Fluorescent Oligonucleotides for Ratiometric Analysis of Nuclear Poly(A)$^+$ RNA

Takeshi Kubota,[†] Shuji Ikeda,[†] Hiroyuki Yanagisawa,[†] Mizue Yuki,[†] and Akimitsu Okamoto*[,†,‡]

[†]RIKEN Advanced Science Institute, 2-1 Hirosawa, Wako, Saitama 351-0198, Japan

[‡]PRESTO, Japan Science and Technology Agency, 4-1-8 Honcho, Kawaguchi, Saitama 332-0012, Japan

ABSTRACT: Subnuclear poly(A)$^+$ RNA localization in living mammalian cells was visualized by ratiometric analysis using hybridization-sensitive fluorescent oligonucleotide probes. Probes were oligonucleotides, which contained a Cy5 fluorescent dye at the strand end and a thiazole orange double-labeled nucleotide inside strand. A ratiometric analysis using poly(A)-targeting probes revealed a distribution of the probe itself as red fluorescence and localization of the target RNA sequence in cell nuclei as green fluorescence. The fluorescence of the subnuclear poly(A)$^+$ RNA hybridized with the poly(A)-targeting probes was observed as puncta in interchromatin areas.

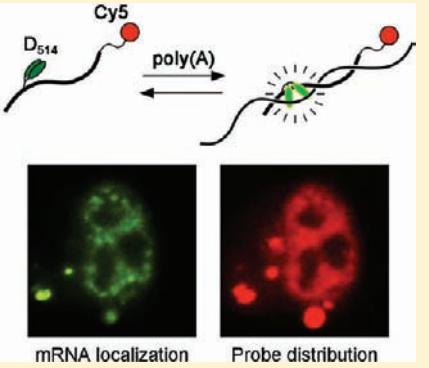

INTRODUCTION

mRNAs are transcribed from active chromosomal loci and spliced or edited at distinct domains known as speckles,[1,2] and then transported to nuclear membranes by specific proteins to pass through a nuclear pore.[3,4] Effective monitoring of the expression and behavior of mRNA in a cell nucleus is significant for cell biologists. To detect subnuclear mRNA localization using a fluorescence signal, development of fluorescent probes binding with the poly(A) sequence of mRNA may be one of the most effective approaches. Much information regarding transcription and translocation in cells has already been provided by poly(A)$^+$ RNA imaging.[5,6]

However, conventional probes, which are simply labeled with fluorescent dyes, may not be suitable for live cell imaging, because they inherently emit fluorescence even in the absence of their target. The distribution and intensity of probe fluorescence corresponds to the distribution and concentration of the probe itself, not always reflecting the distribution and concentration of its target RNA. For greater precision in RNA monitoring, observation of both the distribution of probes and the localization of their target RNA is important; thus, development of probes with properties allowing this simultaneous observation is required. The latest hybridization-sensitive fluorescent probes, which possess an ability for fluorescence to be emitted only when they are hybridized with the target RNA, have been reported.[7−9] However, they often require the formation of higher-order structures or covalent bonds, which is disadvantageous in living cells.

In this article, we report the design of a hybridization-sensitive fluorescent probe with a reference fluorophore for more effective detection of poly(A)$^+$ RNA localization. Addition of a red fluorescent dye, Cy5, as a reference signal for monitoring probe distribution to probes with a hybridization-sensitive fluorescence emission function served visualization of not only the distribution of the probe itself, but also its target RNA localization in living cells.

EXPERIMENTAL PROCEDURES

Synthesis of a Cy5-Conjugated ECHO Probe. Probes were synthesized using a conventional phosphoramidite method. A diamino-modified nucleoside phosphoramidite (a precursor of D_{514}) was synthesized as described in our previous paper.[10] Cy5 of the 5′ end was incorporated using Cy5 phosphoramidite (Glen Research), of which one hydroxy group was protected with a 4-monomethoxytrityl group. The synthesized probes were cleaved from the support and deprotected (except for the Cy5 monomethoxytrityl group) in 28% aqueous ammonia at 25 °C for 8 h. After removal of ammonia under reduced pressure, the unlabeled probes were purified by reversed-phase HPLC on a 5-ODS-H column (10 mm × 150 mm, eluted with a solvent mixture of 0.1 M triethylammonium acetate (TEAA), pH 7.0, in a linear gradient of from 5% to 60% acetonitrile over 30 min at a flow rate of 3.0 mL/min). A solution of a succinimidyl ester of the thiazole orange dye (50 equiv per active amino group of the synthesized oligomer) in DMF was added to a solution of the unlabeled probe in 100 mM sodium carbonate buffer (pH 9.0) and incubated at 25 °C for 30 min.[10] The reaction mixture was

Received: April 12, 2011
Revised: July 11, 2011
Published: July 14, 2011

ACS Publications © 2011 American Chemical Society

dx.doi.org/10.1021/bc200184a | *Bioconjugate Chem.* 2011, 22, 1625–1630

treated with ethanol (−80 °C, 30 min) to precipitate the reaction products. After centrifugation at 4 °C for 30 min, the supernatant was removed. The pellet was incubated in 500 μL of 20% acetic acid at 25 °C for 20 min to deprotect the Cy5 monomethoxytrityl group. After extraction three times with ethyl acetate, the aqueous phase was passed through a 0.45 μm filter. The product was purified by reversed-phase HPLC on a 5-ODS-H column (10 mm × 150 mm, elution with a solvent mixture of 0.1 M TEAA, pH 7.0, in a linear gradient of from 5% to 37.5% acetonitrile over 30 min at a flow rate of 3.0 mL/min). The synthesized probes were identified by MALDI-TOF mass spectrometry. (Here, the molecular weight of the counteranions of one Cy5 and two D_{514} dyes was not included in the value of M.): ProbeU, calcd. for $C_{329}H_{431}N_{54}O_{198}P_{24}S_2$, 9117.7 $[M - 2H]^+$, found 9118.5; ProbeA, calcd. for $C_{350}H_{452}N_{117}O_{156}P_{24}S_2$, 9601.5 $[M - 2H]^+$, found 9599.7. The probe concentration was determined by absorption at 260 nm with a UV-2550 spectrophotometer (Shimadzu).

Fluorescence Spectra. Fluorescence spectra of the probes (0.5 μM) were measured in a HEPES-buffered solution (120 mM potassium chloride, 5 mM sodium chloride, 25 mM HEPES, pH 7.2), using a quartz cuvette with a 1 cm path length at 25 °C. The excitation and emission bandwidths were 1.5 nm. D_{514} and Cy5 of probes were excited at 514 and 633 nm, respectively. Spectra were recorded using a RF-5300PC spectrofluorophotometer (Shimadzu).

Cell Culture. Culture reagents were purchased from Invitrogen. HeLa cells and COS7 cells were cultured in Dulbecco's modified Eagle's medium (DMEM) containing 10% heat-inactivated fetal bovine serum (FBS), 50 U/mL penicillin, and 50 mg/mL streptomycin. Madin−Darby canine kidney (MDCK) cells were cultured in MEM containing 10% heat-inactivated FBS, 0.1 mM nonessential amino acids, 50 U/mL penicillin, and 50 mg/mL streptomycin. NIH3T3 cells were cultured in DMEM containing 10% heat-inactivated calf serum, 50 U/mL penicillin, and 50 mg/mL streptomycin. All cells were cultured at 37 °C under a humidified atmosphere of 5% CO_2 in air. HeLa cells were a gift from Dr. Shinichi Nakagawa (RIKEN Advanced Science Institute). Other cell lines were provided by the RIKEN BioResource Center through the National Bio-Resource Project of the Ministry of Education, Culture, Sports, Science, and Technology of Japan (MEXT), Japan. For experimental use, cells (passage numbers 5−9) were cultured in glass-based dishes. Prior to microscope observation, the culture medium was washed and exchanged to phenol red free DMEM.

Transfection and Fluorescence Imaging. The Cy5-conjugated hybridization-sensitive fluorescent probe (50 pmol) in water were introduced using 2 μL Lipofectamine 2000 (Invitrogen) following the manufacturer's protocol. After 1 h incubation at 37 °C with the Lipofectamine 2000 and a probe, the cells were washed three times with PBS and observed in phenol red free serum-supplemented DMEM. The cells were maintained under culture conditions using an incubation system during fluorescence imaging. For DAPI staining, the probe-transfected cells were fixed with 4% paraformaldehyde for 15 min at room temperature, and subsequently, after washing three times with PBS, the cells were stained with 0.5 μg/mL DAPI in PBS for 10 min at room temperature. Fluorescence images were acquired with a motorized inverted microscope (Axio Observer Z1; Zeiss) equipped with an EM-CCD (Evolve, Roper) and a 63× (oil immersion NA 1.4) objective and filter sets (ex 500/24−25, dm 520, em 542/25−27 for D_{514}, ex 575−625, dm 645, em 660−710 for Cy5, ex 365, dm 396, em 445/50 for DAPI). Acquired images were analyzed and processed with *AxioVision* software (version 4.8). The fluorescence and differential interference contrast (DIC) images were acquired sequentially within 2 s with a motorized microscope.

RESULTS AND DISCUSSION

Design and Synthesis. A fluorescent double-labeled nucleotide probe has recently been developed to achieve high fluorescence intensity for a hybrid with its target nucleic acid, and effective quenching of the unhybridized probe.[10,11] The main mechanism for the effective fluorescence suppression is based on exciton coupling theory,[i−14] thus, the probe is known as an exciton-controlled hybridization-sensitive fluorescent oligonucleotide (ECHO) probe. Fluorescence switching depending on hybridization with their target RNA would be useful for cellular RNA detection.[15,16] However, ECHO probes have the disadvantage that the detection of the distribution of the probe itself within a cell is difficult because they usually show very weak fluorescence in the absence of a target RNA, although this is also an advantage because the background fluorescence arising from an excess of probes in the cell is inconspicuous. Therefore, installation of a fluorescence indicator into the probe to show its distribution is required for RNA localization analysis with a fair degree of precision.

We designed a new ECHO probe to monitor both the distribution of the probe and localization of the target RNA using ratiometric analysis. A green fluorescent nucleotide, D_{514}, in ECHO probes was adopted for hybridization-sensitive fluorescence emission and 2′-*O*-methylribose nucleotides were used for ECHO probes (except D_{514}) to increase resistance to intracellular nucleases.[17−19] In addition, a red fluorescent dye, Cy5, was attached as a reference signal to the 5′ end of the ECHO probes. The two dyes were spatially separated in the probe using two hexaethylene glycol spacers and fifteen nucleotides. One of the Cy5-conjugated ECHO probes, ProbeU, has a sequence Cy5-s-s-$U_{15}D_{514}U_6$, where 's' denotes a hexaethylene glycol and 'U' is 2′-*O*-methyluridine. This probe is expected to recognize a repeated-adenine sequence, e.g., a poly(A) tail of mRNA (Figure 1). We also synthesized ProbeA, Cy5-s-s-$A_{15}D_{514}A_6$ (where A is 2′-*O*-methyladenosine), as a control probe.

Fluorescence of Probes. Cy5-conjugated ECHO probes exhibited on−off switching of fluorescence at the D_{514} emission wavelength depending on addition of the complementary RNA strand. The emission spectrum of single-stranded ProbeU (500 nM) excited at 514 nm showed a negligible fluorescence in HEPES buffer, whereas ProbeU hybridized with poly(A) RNA displayed much stronger D_{514} fluorescence (29-fold increase at 532 nm) (Figure 2a). On the other hand, the fluorescence spectra of the ProbeU excited at 633 nm almost overlapped, regardless of hybridization with poly(A) RNA (within 1.01 fold at 660 nm). The fluorescence spectra of ProbeA also showed similar emission properties (Figure 2b). Fluorescence intensity of D_{514} and Cy5 in ProbeU was also measured in various probe concentrations from 500 nM to 50 nM in 50 nM steps. The fluorescence decreased proportionally and the ratio of the fluorescence intensities of D_{514} and Cy5 was almost constant through the experiment (Figure 2c and d).

The Cy5 fluorescence intensity of ProbeU exhibited a linear relationship with the amount of ProbeU at a constant concentration of A_{22} RNA even in the presence of excess probe (Figure 3).

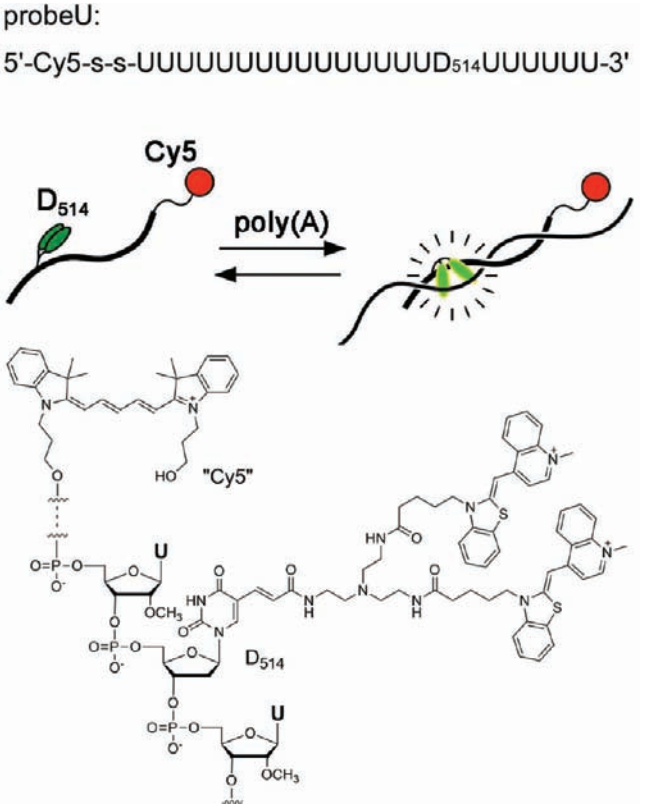

Figure 1. Sequence and structure of Cy5-conjugated ECHO probe (probeU). 's' denotes a hexaethylene glycol linker.

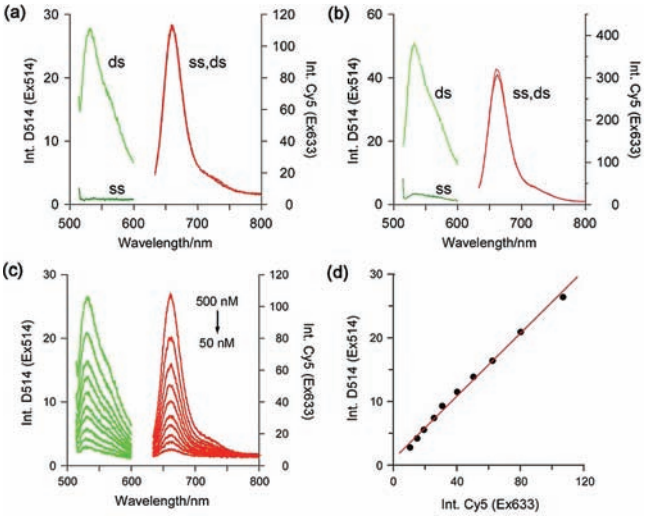

Figure 2. Fluorescence of Cy5-conjugated ECHO probes. (a) Fluorescent spectra of ProbeU (500 nM). The spectra of the single-stranded probe (ss) and hybrid with 2 equiv of poly(A) RNA (ds) were measured in 5 mM sodium chloride, 120 mM potassium chloride, and 25 mM HEPES (pH 7.2)−KOH at 25 °C. Green, fluorescence spectra of ProbeU D_{514} excited at 514 nm; red, spectra of ProbeU Cy5 excited at 633 nm. (b) Fluorescent spectra of ProbeA (500 nM). (c) Change in the fluorescence intensities of D_{514} and Cy5 in the hybrid of ProbeU and poly(A) RNA depending on ProbeU concentration. The concentration of ProbeU was changed from 500 nM to 50 nM in 50 nM steps. (d) Relationship between ProbeU D_{514} and Cy5 fluorescence intensities. The fluorescence intensities of D_{514} at 530 nm and Cy5 at 660 nm in the spectra in (c) were plotted. There was a linear relationship among different probe concentrations (R^2 = 0.995).

In contrast, the D_{514} fluorescence intensity of a ProbeU-containing solution increased in proportion to the amount of added ProbeU until the ProbeU/A_{22} RNA ratio became 1:1, but it almost reached a plateau when the concentration of ProbeU exceeded that of A_{22} RNA. The fluorescence behavior of the probe, where both a hybridization-sensitive fluorescent dye (D_{514}) and a hybridization-insensitive fluorescent dye (Cy5) were installed into a single nucleic acid strand, suggested its strong potential as a probe for ratiometric fluorescence analysis simultaneously visualizing both the distribution of the probe and the location of the target poly(A)$^+$ RNA in a cell. In addition, the fluorescence of Cy5 regardless of hybridization and the proportional change in the probe fluorescence intensities depending on probe concentration suggested that the Cy5 fluorescence of the probe would be effective as a standard for the normalization of fluorescence intensity in the inter- and intracellular D_{514} fluorescence comparison experiments.

RNA Localization and Probe Distribution in HeLa Cells. Having established the fluorescence behavior of Cy5-conjugated ECHO probes in vitro, we examined the fluorescence imaging of human cancer cells, HeLa cells, where a Cy5-conjugated ECHO probe was transfected. ProbeU (50 pmol) was transfected into HeLa cells by 1 h incubation with Lipofectamine 2000, and then the fluorescence emission from cells was examined using a green filter set (ex 500/24−25, dm 520, em 542/25−27) and a red filter set (ex 575−625, dm 645, em 660−710).

The fluorescence images from D_{514} and Cy5 of ProbeU in the cells appeared different. Cy5 fluorescence, which indicates distribution of the probe, was strong and uniform in nuclei except for nucleoli, whereas relatively weaker fluorescence was observed

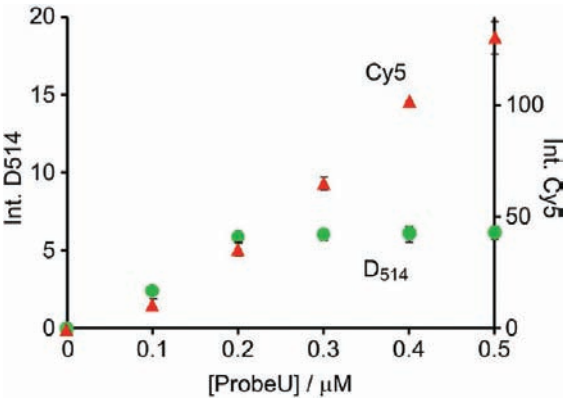

Figure 3. Change in the fluorescence intensities of D_{514} and Cy5 in the hybrid of ProbeU and A_{22} RNA depending on ProbeU concentration. The fluorescence intensity of ProbeU in the presence of A_{22} RNA (0.2 μM) was measured in 50 mM sodium phosphate (pH = 7.0) and 100 mM sodium chloride. The concentration of ProbeU was changed from 0 μM to 0.5 μM in 0.1 μM steps. Green circles, fluorescence intensities of ProbeU D_{514} at 532 nm, excited at 514 nm; red triangles, fluorescence intensities of ProbeU Cy5 at 660 nm, excited at 633 nm.

in the cytoplasmic area (Figure 4a). The fluorescence from the nucleoli, whose shape can be confirmed in DIC images, showed weak fluorescence, suggesting that almost all of the probe was excluded from nucleoli. The nucleolus is a subnuclear organelle in which rRNA is transcribed and assembled, and thus, it may be difficult for the probe to penetrate the highly rRNA-accumulated

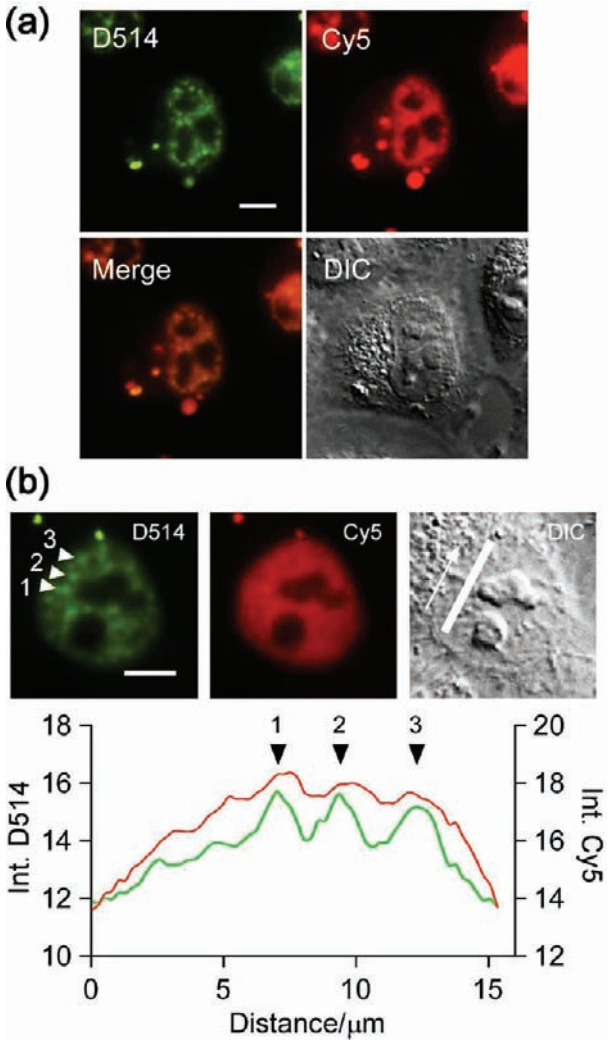

Figure 4. Fluorescence images of probeU-transfected HeLa cells. (a) Cell images. The fluorescence from D_{514} and Cy5 of ProbeU was acquired with green and red filter sets, respectively. Bar: 10 μm. (b) Puncta emerging in the nucleus. Fluorescent intensities along the white line drawn in the DIC image (right) were plotted. Green, ProbeU D_{514}; red, Cy5. Bar: 10 μm.

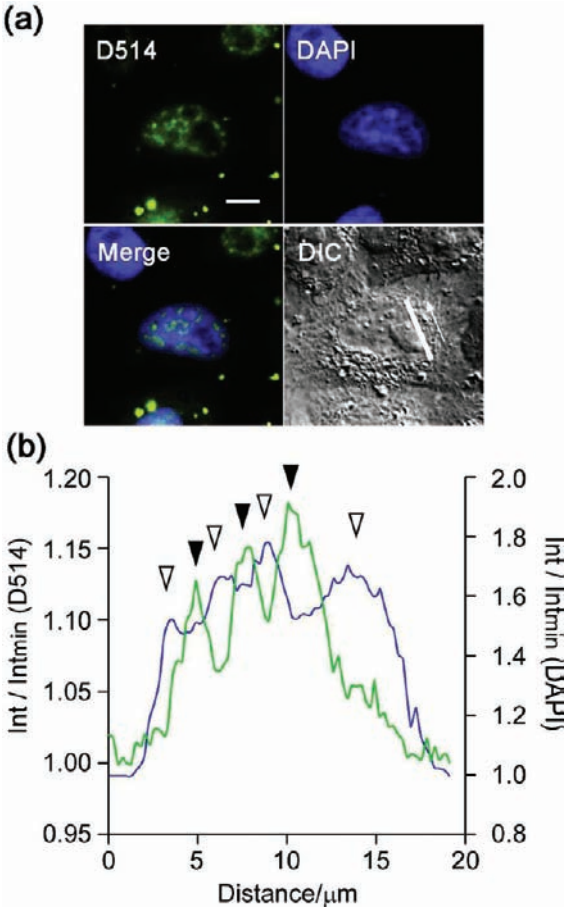

Figure 5. DAPI staining of ProbeU-transfected HeLa cells. (a) Cell images. ProbeU-transfected cells were stained with DAPI after being fixed with 4% paraformaldehyde. Green, fluorescence from D_{514}; blue, fluorescence from DAPI. Bar: 10 μm. (b) Distinct patterns of the ProbeU D_{514} and DAPI fluorescence images. Fluorescence intensities along the white line drawn in the DIC image of (a) were plotted. Green, ProbeU D_{514}; blue, DAPI. Filled arrowheads, ProbeU D_{514}-predominant region; open arrowheads, DAPI-predominant region.

nucleolus area. On the other hand, D_{514} fluorescence, which indicates localization of poly(A)$^+$ RNA through probe hybridization, was mainly observed in nuclei as clear puncta. A line profile showing the fluorescence intensities of D_{514} and Cy5 of ProbeU in a HeLa cell showed the striking difference of fluorescence distribution seen in Figure 4b. The fluorescence arising from D_{514} exhibited three sharp signal peaks (arrowheads 1, 2, and 3) along the line indicated in the DIC image, whereas the fluorescence intensity of Cy5 was stronger, but gave a profile with blunted responses. The fluorescence profile of ProbeU Cy5 in a HeLa cell suggests that the cell nucleus was filled with the probe and the probe D_{514} fluorescence showed the localization of the poly(A)$^+$ RNA hybridized with the probe.

The fluorescence image of the D_{514} of ProbeU was also quite different from the image of the chromatin structure stained with DAPI. When the chromatin structures of HeLa cells were stained with DAPI (0.5 μg/mL) after the probe transfection process into the cells was fixed with paraformaldehyde, the fluorescence signals arising from the D_{514} of ProbeU and DAPI appeared alternately in the cell nucleus (Figure 5a). The region stained by DAPI is a DNA condensed region, and it is also a region with a relatively low transcription activity.[20,21] On the other hand, the region stained by ProbeU D_{514} probably has a relatively high transcription activity because D_{514} emits strong fluorescence when the probe is hybridized with poly(A)$^+$ RNA. The line profile of the fluorescence intensities in the cell clearly indicates the different distributions of DNA and poly(A)$^+$ RNA represented by mRNA (Figure 5b). Open arrowheads in the figure show the regions where the signal from DNA (i.e., fluorescence of DAPI) is predominant and filled arrowheads indicate the regions where the signal from poly(A)$^+$ RNA (i.e., fluorescence of hybridized ProbeU) is predominant. The distribution of fluorescence suggests that poly(A)$^+$ RNA was detected in interchromatin spaces, as reported by Politz et al.[5]

The fluorescence image obtained from the ProbeA-transfected HeLa cells also explained the fluorescence property of Cy5-conjugated ECHO probes. ProbeA, which can be hybridized with RNA containing a U_6AU_{15} sequence, seems to have only a small

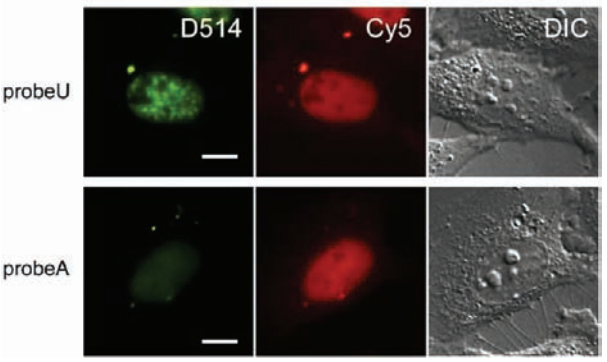

Figure 6. Fluorescence images of ProbeU- or ProbeA-transfected HeLa cells.

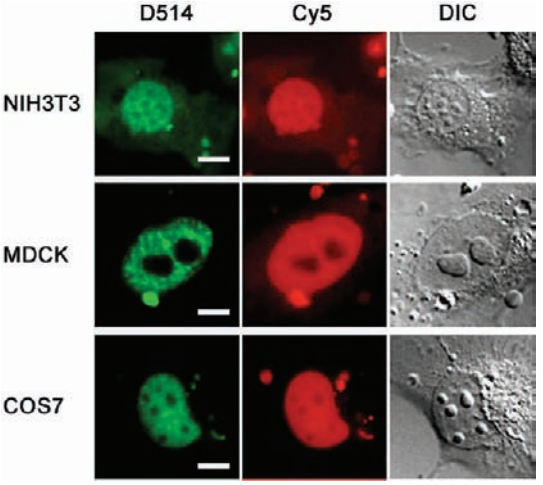

Figure 7. Fluorescence images of ProbeU in various mammalian cell types. ProbeU was transfected into NIH3T3, MDCK, and COS7 cells according to the protocol for transfection into HeLa cells. Bar: 10 μm.

chance of binding with RNA in cells. When ProbeA was transfected into HeLa cells, cell uptake of the probe was confirmed by the fluorescence of Cy5. The fluorescence of ProbeA Cy5 distributed mainly in the nuclei, which was strong and uniform (Figure 6). Cy5 fluorescence indicates the distribution of all ProbeA in the cell, which contains excess probes, and it is regardless of hybridization with RNA. The fluorescence distribution pattern observed for ProbeA Cy5 was similar to that of ProbeU Cy5. In contrast, the distribution of the fluorescence of ProbeA D_{514} was different from that of ProbeU D_{514}. D_{514} fluorescence arises from hybridization with the complementary RNA; i.e., the distribution of the fluorescence of D_{514} in cell indicates the localization of the complementary RNA. The fluorescence arising from D_{514} of ProbeA was much weaker than that from ProbeU, and no punctum was observed in the nucleus. Although the reason for the weak nonspecific fluorescence emission of ProbeA remains unknown, the fluorescence was suppressed in the cell, compared with that of ProbeU. In contrast, the puncta with D_{514} fluorescence observed for ProbeU indicates that they are not a result of accumulation of the fluorescent probe, but an accumulation of the poly(A)$^+$ RNA hybridized with ProbeU. The fluorescence images of Cy5-conjugated ECHO probes in the cells showed both the distribution of the probe and the RNA localization in nuclei.

Poly(A)$^+$ RNA Localization in Other Cell Types. The ratiometric RNA analysis using Cy5-conjugated ECHO probes also facilitated the observation of a similar poly(A)$^+$ RNA localization pattern in other mammalian cell types. We tested the fluorescence imaging for NIH3T3 (mouse), MDCK (dog), and COS7 (monkey) cells, which were transfected according to the ProbeU lipofection protocol (efficiency of lipofection was 30−60%). The fluorescence of ProbeU Cy5 was observed to be strongly uniform in the nuclei of these cells except for in their nucleoli, whereas several puncta appeared in the fluorescence of the ProbeU D_{514} (Figure 7).

CONCLUSION

An oligonucleotide, which contained a Cy5 fluorescent dye at the strand end and a thiazole orange double-labeled nucleotide at the strand inside was designed for fluorescence imaging of poly(A)$^+$ RNA in a cell. Subnuclear poly(A)$^+$ RNA localization in living mammalian cells was visualized by a ratiometric analysis using the Cy5-conjugated ECHO probe. Ratiometric analysis using the poly(A)-targeting probe revealed the distribution of the probe itself as a red fluorescence and localization of target RNA sequence in cell nuclei as a green fluorescence. The fluorescence of the subnuclear poly(A)$^+$ RNA hybridized with the poly(A)-targeting probe was observed as puncta in interchromatin areas.

AUTHOR INFORMATION

Corresponding Author

*Phone: (+81) 48-467-9238. Fax: (+81) 48-467-9205. E-mail: aki-okamoto@riken.jp.

ACKNOWLEDGMENT

This work was supported by a Grant-in-Aid for Young Scientists (B) (#21,750,182) (TK) and a Grant-in-Aid for Scientific Research (B) (#20,350,083) (AO) from the Japan Society for the Promotion of Science, and a Grant-in-Aid for Scientific Research on Priority Areas (Cancer) (#20,014,030) (AO) from the Ministry of Education, Culture, Sports, Science and Technology of Japan (MEXT).

REFERENCES

(1) Misteli, T., Cáceres, J. F., and Spector, D. L. (1997) The dynamics of a pre-mRNA splicing factor in living cells. *Nature 387*, 523–527.

(2) Lamond, A. I., and Spector, D. L. (2003) Nuclear speckles: a model for nuclear organelles. *Nat. Rev. Mol. Cell Biol. 4*, 605–612.

(3) Tokunaga, K., Shibuya, T., Ishihama, Y., Tadakuma, H., Ide, M., Yoshida, M., Funatsu, T., Ohshima, Y., and Tani, T. (2006) Nucleocytoplasmic transport of fluorescent mRNA in living mammalian cells: nuclear mRNA export is coupled to ongoing gene transcription. *Genes Cells 11*, 305–317.

(4) Enninga, J., Levy, D. E., Blobel, G., and Fontoura, B. M. (2002) Role of nucleoporin induction in releasing an mRNA nuclear export block. *Science 295*, 1523–1525.

(5) Politz, J. C., Tuft, R. A., Pederson, T., and Singer, R. H. (1999) Movement of nuclear poly(A) RNA throughout the interchromatin space in living cells. *Curr. Biol. 9*, 285–291.

(6) Taneja, K. L., Lifshitz, L. M., Fay, F. S., and Singer, R. H. (1992) Poly(A) RNA codistribution with microfilaments: evaluation by in situ hybridization and quantitative digital imaging microscopy. *J. Cell Biol. 119*, 1245–1260.

(7) Tyagi, S., and Kramer, F. R. (1996) Molecular beacons: Probes that fluoresce upon hybridization. *Nat. Biotechnol. 14*, 303–308.
(8) Sando, S., and Kool, E. T. (2002) Imaging of RNA in bacteria with self-ligating quenched probes. *J. Am. Chem. Soc. 124*, 9686–9687.
(9) Mahara, A., Iwase, R., Sakamoto, T., Yamana, K., Yamaoka, T., and Murakami, A. (2002) Bispyrene-conjugated 2′-O-methyloligonucleotide as a highly specific RNA-recognition probe. *Angew. Chem., Int. Ed. 41*, 3648–3650.
(10) Ikeda, S., and Okamoto, A. (2008) Hybridization-sensitive on-off DNA probe: Application of the exciton coupling effect to effective fluorescence quenching. *Chem. —Asian J. 3*, 958–968.
(11) Ikeda, S., Kubota, T., Kino, K., and Okamoto, A. (2008) Sequence dependence of fluorescence emission and quenching of doubly thiazole orange-labeled DNA: Effective design of a hybridization-sensitive probe. *Bioconjugate Chem. 19*, 1719–1725.
(12) Sagawa, T., Tobata, H., and Ihara, H. (2004) Exciton interactions in cyanine dye—hyaluronic acid (HA) complex: reversible and biphasic molecular switching of chromophores induced by random coil-to-double-helix phase transition of HA. *Chem. Commun.* 2090–2091.
(13) West, W., and Sandra, P. (1965) The dimeric state of cyanine dyes. *J. Phys. Chem. 69*, 1894–1903.
(14) Khairutdinov, R. F., and Serpone, N. (1997) Photophysics of cyanine dyes: Subnanosecond relaxation dynamics in monomers, dimers, and H- and J-aggregates in solution. *J. Phys. Chem. B 101*, 2602–2610.
(15) Kubota, T., Ikeda, S., and Okamoto, A. (2009) Doubly thiazole orange-labeled DNA for live cell RNA imaging. *Bull. Chem. Soc. Jpn. 82*, 110–117.
(16) Kubota, T., Ikeda, S., Yanagisawa, H., Yuki, M., and Okamoto, A. (2010) Sets of RNA repeated tags and hybridization-sensitive fluorescent probes for distinct images of RNA in a living cell. *PLoS ONE 5*, e13003.
(17) Inoue, H., Hayase, Y., Imura, A., Iwai, S., Miura, K., and Ohtsuka, E. (1987) Synthesis and hybridization studies on two complementary nona(2′-O-methyl)ribonucleotides. *Nucleic Acids Res. 15*, 6131–6148.
(18) Majlessi, M., Nelon, N. C., and Becker, M. M. (1998) Advantages of 2′-O-methyl oligoribonucleotide probes for detecting RNA targets. *Nucleic Acids Res. 26*, 2224–2229.
(19) Kubota, T., Ikeda, S., Yanagisawa, H., Yuki, M., and Okamoto, A. (2009) Hybridization-sensitive fluorescent probe for long-term monitoring of intracellular RNA. *Bioconjugate Chem. 20*, 1256–1261.
(20) Cabral, J. S., Felix, L. P., and Guerra, M. (2006) Heterochromatin diversity and its co-localization with 5S and 45S rRNA sites in chromosomes of four Maxillaria species (Orchidaceae). *Genet. Mol. Biol. 29*, 659–664.
(21) Black, J. C., and Whetstine, J. R. (2011) Chromatine landscape. *Epigenetics 6*, 9–15.

Bioconjugate Chemistry

ARTICLE

pubs.acs.org/bc

PEGylated TNF-Related Apoptosis-Inducing Ligand (TRAIL) Analogues: Pharmacokinetics and Antitumor Effects

Tae Hyung Kim,[†] Yu Seok Youn,[†] Hai Hua Jiang,[†] Seulki Lee,[§] Xiaoyuan Chen,[§] and Kang Choon Lee*[,†]

[†]College of Pharmacy, SungKyunKwan University, 300 Chonchon-dong, Jangan-ku, Suwon City 440-746, Korea

[§]Laboratory of Molecular Imaging and Nanomedicine, National Institute of Biomedical Imaging and Bioengineering (NIBIB), National Institutes of Health (NIH), Bethesda, Maryland 20892, United States

ABSTRACT: The low stability and fast clearance of tumor necrosis factor (TNF)-related apoptosis-inducing ligand (TRAIL) are the main obstacles to its implementation as an antitumor agent. Here, we attempted to improve its pharmacokinetic and pharmacodynamic profiles by using PEGylation. N-terminal PEGylated TRAIL (PEG−TRAIL) was synthesized using 2, 5, 10, 20, and 30 kDa PEG. Antitumor effect assessments in HCT116 tumor bearing nude mice showed that all PEG−TRAIL analogues efficiently suppressed mean tumor growth, with mean tumor growth inhibition (TGI) values (5K-, 20K-, 30K-PEG−TRAIL) of 43.5, 61.7, and 72.3%, respectively. In particular, 30K-PEG−TRAIL was found to have antitumor efficacy for five days after a single administration (1 mg/mouse, ip). The different antitumor effects of these PEG−TRAIL analogues were attributed to augmented pharmacokinetics and metabolic resistance. All analogues were found to have higher metabolic stabilities in rat plasma, extended pharmacokinetic profiles, and greater circulating half-lives (3.9, 5.3, 6.2, 12.3, and 17.7 h for 2, 5, 10, 20, and 30K-PEG−TRAIL, respectively, versus 1.1 h for TRAIL, ip) in ICR mice. Our findings suggest that TRAIL derivatized with PEG of an appropriate M_w might be useful antitumor agent with protracted activity.

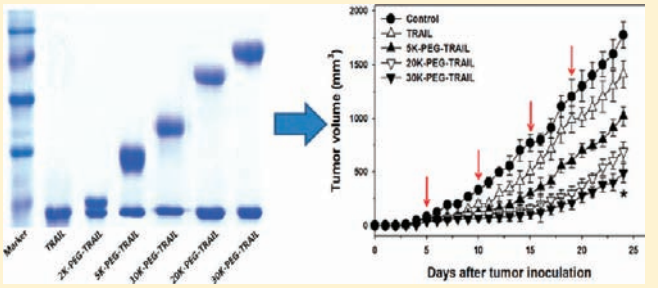

INTRODUCTION

Tumor necrosis factor (TNF)-related apoptosis-inducing ligand (TRAIL) is a member of the TNF superfamily, members of which selectively induce apoptosis in tumor cells but not in most normal cells. This novel selectivity and cytotoxicity are due to the ability of trimeric TRAIL to bind to the death receptors DR4 and DR5, which are overexpressed on tumor cells. Furthermore, only the complex formed between DR4, DR5, and trimeric TRAIL has apoptotic activity. During apoptosis, the activation of caspases leads to the cleavage of vital cellular substrates and subsequent cell death.[1−5] However, although TRAIL has a potent apoptotic effect on tumor cells, its rapid inactivation, poor stability and solubility, rapid renal clearance, and severe hepatotoxicity[6−8] after systemic delivery represent critical obstacles to its clinical application.

PEGylation, a type of covalent modification with polyethylene glycol (PEG), is viewed as a practical way of improving the therapeutic values of peptide and protein drugs,[3,9,10] and it has been well documented that this technique increases metabolic resistance and reduces renal clearance and tissue affinity.[11,12] Furthermore, the pharmacokinetic profiles of PEGylated peptides and proteins can be controlled by simply changing the M_w of the PEG and thus increasing PEG M_w enhances the above properties.[11,12] Nevertheless, increases in PEG M_w can reduce the biological activities of PEGylated proteins due to the steric effect of the pendant PEG.

PEGASYS (a 40 kDa branched PEG-conjugated interferon (IFN) α-2a, Roche), has only 5−10% of the in vitro bioactivity of wild type IFN-α-2a, and yet it was significantly more effective in vivo activity in human than the standard interferon so its pharmacokinetic potency is superior.[13,14] Accordingly, it is important that PEG size be optimized to achieve an appropriate balance between in vitro biological activity and in vivo pharmacokinetics.

We previously reported on an N-terminal specific PEGylated (PEG M_w: 5 kDa) TRAIL.[3] This 5K-PEG−TRAIL displayed preserved biological activity and profoundly improved physicochemical stability. Moreover, 5K-PEG−TRAIL showed a much longer pharmacokinetic profile and enhanced antitumor activity than native TRAIL, with fewer side effects (hepatotoxicity). However, despite these encouraging results, the antitumor activity of 5K-PEG−TRAIL was achieved by daily administration. To reduce the administration frequency and thus increase convenience to patients, we decided to develop longer lasting PEG−TRAIL analogues. Accordingly, in the present study, we investigated the antitumor activities of PEG−TRAIL analogues substituted with different M_w PEG (2, 5, 10, 20, 30 kDa). In addition, we performed experiments to determine the

Received: April 13, 2011
Revised: July 6, 2011
Published: July 14, 2011

ACS Publications © 2011 American Chemical Society

physicochemical stabilities, biological activities, and pharmacokinetic behaviors of these analogues.

EXPERIMENTAL PROCEDURES

Materials. PEG−TRAIL analogues were prepared as previously described.[3] Briefly, trimeric TRAIL was constructed by incorporating trimer-forming zipper sequences and then PEGylated in an N-terminal specific manner. Monomethoxy PEG−aldehyde (mPEG−ALD, M_w 2, 5, 10, 20, 30 kDa) was purchased from Nippon Oil and Fats (NOF, Tokyo). All other chemicals were of analytical grade and were used as obtained. Cell lines were obtained from the Korean Cell Line Bank (Seoul).

Experimental Animals. BALB/c athymic nude mice (male, 4−5 weeks old) and ICR mice (male, 4−5 weeks old, weighing 16−18 g) were purchased from the Hanlim Experimental Animal Laboratory (Seoul). Animals were cared for in accordance with the guidelines issued by the National Institutes of Health (NIH) for the care and use of laboratory animals (NIH publication 80−23, revised in 1996). Animals were housed in groups of 6−8 under a 12 h light/dark cycle (lights on 6 a.m.), allowed food and water ad libitum, and acclimatized for 2 weeks. This study was approved by the Ethical Committee on Animal Experimentation of SungKyunKwan University.

Preparation and Characterization of PEG−TRAIL Analogues. PEG−TRAIL analogues were prepared using 2, 5, 10, 20, and 30 kDa mPEG−ALD in the presence of 20 mM sodium cyanoborohydride ($NaCNBH_3$) in 50 mM sodium acetate buffer at pH 5, as described previously.[3] In brief, PEG/TRAIL molar ratios and reaction times were optimized by size exclusion chromatography monitoring. PEG−TRAIL analogues were recovered by gel-filtration chromatography, concentrated by ultrafiltration, and stored at −20 °C until required. Analogues were identified by SDS-PAGE. Coomassie blue was used to visualize the PEG−TRAIL analogues.

In Vitro Biological Activities of PEG−TRAIL Analogues. The in vitro cytotoxicities of PEG−TRAIL analogues were determined using MTT assays, as previously described.[3] In brief, in vitro cytotoxicities were investigated using human colon tumor cells (HCT116). The cells were maintained in DMEM supplemented with 10% FBS containing 1% penicillin/streptomycin. For dose-dependent cytotoxicity assays, cells were seeded in 96-well plates at 1×10^4 cells/well and preincubated for 24 h. Media were then replaced with fresh serum-free DMEM, and predetermined amounts of TRAIL or PEG−TRAIL analogues were added to final concentrations of 0−1000 ng/mL. The in vitro cytotoxicities of TRAIL and of the PEG−TRAIL analogues were determined by performing MTT assays after incubation for 24 h.

To determine apoptotic activities, apoptosis and necrosis were determined using Annexin-V-FLUOS staining kits (Roche, Applied Science, Mannheim, Germany). The apoptotic activities of free TRAIL and PEG−TRAIL analogues (each IC_{50} concentration treated) were compared using a FACS Calibur unit (BD Bioscience Mountain View, CA).

In Vitro Stabilities of PEG−TRAIL Analogues. In vitro stabilities in PBS were investigated by measuring solubility changes in isotonic buffer solution, as previously described.[3] In brief, solutions of TRAIL or of the PEG−TRAIL analogues (400 μg/mL in PBS pH 7.4) were incubated at 37 °C for 0, 10, or 30 min and 1, 2, 3, 6, 12, 24, 48, or 72 h. Aliquots (100 μL) were then centrifuged at 10000 rpm for 20 min to remove denatured protein aggregates. Protein concentrations in supernatants were determined using BCA protein assays using BSA as a standard. The biological stabilities of TRAIL and of the analogues were also investigated by measuring their cytotoxic effects on HCT116 colon tumor cells. Briefly, after preparing TRAIL or PEG−TRAIL analogue solutions (10 μg/mL) in 50% rat plasma, samples were incubated at 37 °C for 0, 15, and 30 min, and for 1, 3, 6, 12, and 24 h. Aliquots (100 μL) were the centrifuged at 10000 rpm for 20 min to remove debris, and HCT116 cells in 96-well cell culture plates were treated with supernatants for 24 h. Cell viabilities were determined using MTT assays.

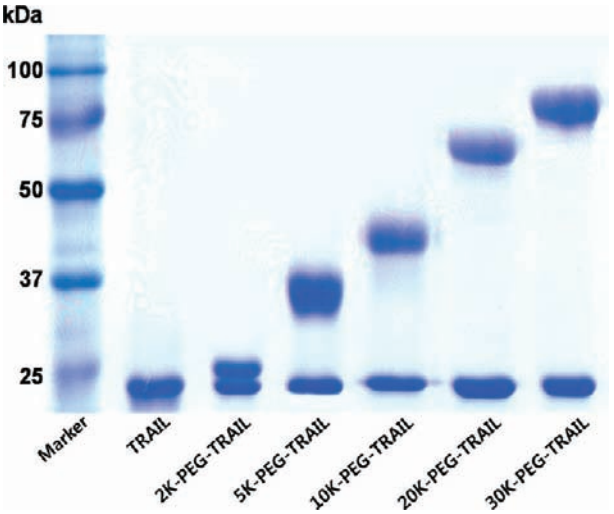

Figure 1. Characterization of PEG−TRAIL analogues. SDS-PAGE patterns of PEG−TRAIL analogues obtained by N-terminal specific PEGylation.

Radioiodine (^{125}I) Labeling of PEG−TRAIL Analogues. Radioiodinated TRAIL and PEG−TRAIL analogues were prepared using a modification of the IODO-GEN method previously described.[4,15,16] Briefly, 100 μL of an IODO-GEN (Pierce, Rockford, IL) solution in methylene chloride (1.0 mg/mL) was dispensed into a fresh tube, and evaporated under a nitrogen stream. Aliquots (100 μL) of TRAIL or PEG−TRAIL analogues (0.5 mg/mL) and 50 μCi of $Na^{125}I$ (Perkin-Elmer, Boston, MA) diluted to 100 mM with PBS (pH 7.4) were then added. The reaction was allowed to proceed for 2 min, and supernatants were then loaded into a Superose 12 HR 10/30 column connected to a flow-through radioisotope detector (Ramona 200, Raytest, Straubenhardt, Germany). ^{125}I-labeled protein fractions were collected and stored at 4 °C until required.

In Vivo Pharmacokinetic Disposition Study. Pharmacokinetic dispositions were examined using a modification of a previously described method.[4,15,16] Radioiodinated TRAIL or PEG−TRAIL analogues were administered to ICR mice ($n = 4$) by ip injection (approximately 10 μg, 13000 cpm), and mice were then sacrificed at predetermined times. Blood samples were obtained by heart puncture, and livers and kidneys were quickly excised and rinsed three times with saline solution. Radioactivities of blood (100 μL) and whole tissue organs were measured by γ-counting (Cobra, Packard Instruments Co., Groningen, The Netherlands), and the results obtained were used to calculate percentage radioactivities in blood and organs versus total dose administered. In the case of blood, total blood volume

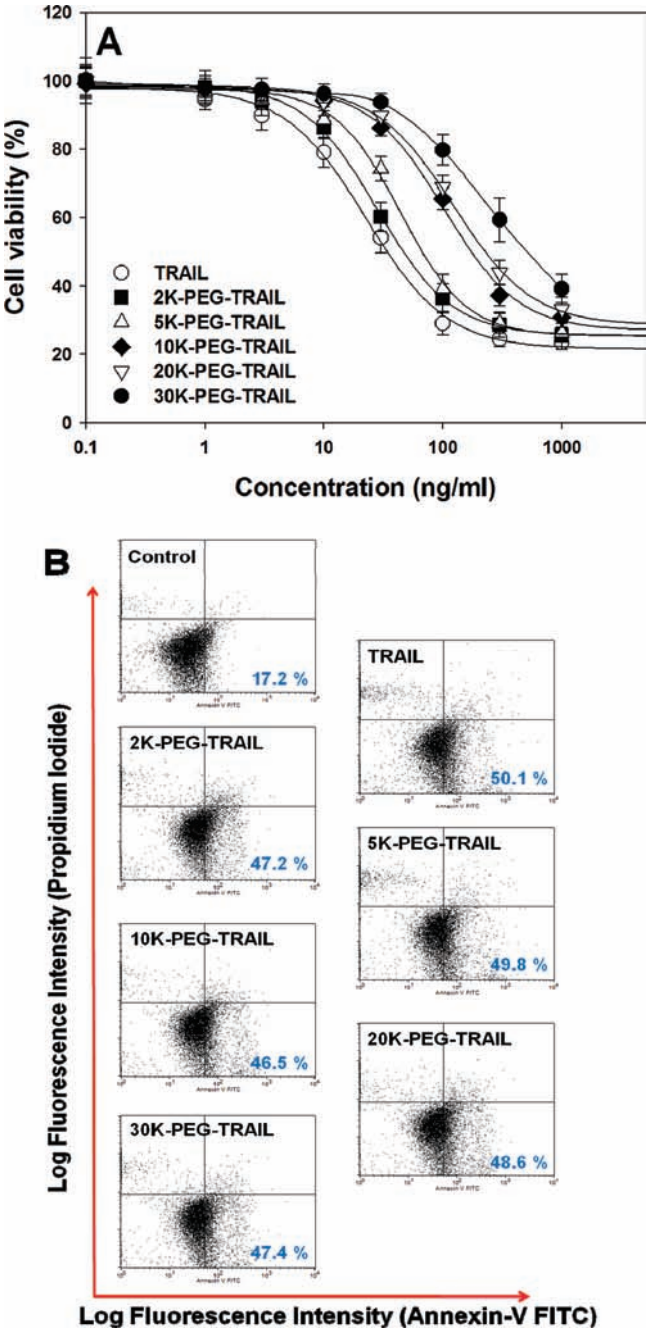

Figure 2. In vitro biological activity of PEG−TRAIL analogues. (A) Cytotoxicity of TRAIL and PEG−TRAIL analogues on HCT116. (B) Apoptotic activities of TRAIL and PEG−TRAIL analogues (each IC_{50} concentration treated) were compared using a FACS Calibur unit.

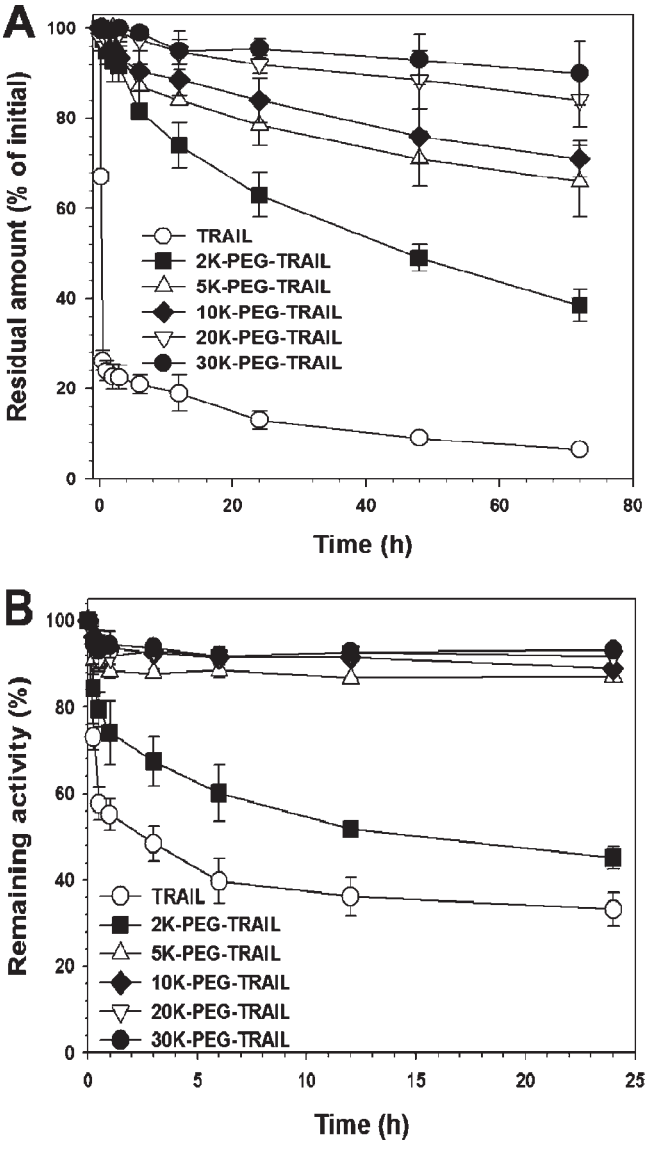

Figure 3. In vitro physicochemical characterizations of PEG−TRAIL analogues. (A) Time-dependent solubility changes of TRAIL and PEG−TRAIL analogues (n = 3) in PBS (pH 7.4) at 37 °C. (B) time-dependent activity changes of TRAIL and PEG−TRAIL analogues (n = 3) in 50% rat plasma (1:1 mixture of plasma and PBS, 37 °C for 24 h, activity test was conducted using HCT116 cells using MTT).

to body weight for ICR mice was presumed to be 70 mL/kg, and this figure was used to calculate percentages of radioiodinated TRAIL and radioiodinated PEG−TRAIL analogues in whole blood. All pharmacokinetic parameters were calculated by two-compartmental analysis using WinNolin version 1.1 (Scientific Consulting, Inc., Cary, NC). In particular, the AUC_{inf} value was obtained by the computational calculation of the area under the curve from zero to infinite time based on the trapezoidal rule, and the circulating half-life ($t_{1/2}$) was obtained by the same method about the elimination phase after ip injections.

In Vivo Antitumor Activity Study. The antitumor effects of PEG−TRAIL analogues were investigated in HCT116 tumor bearing mice (n = 6). Briefly, freshly harvested HCT116 cells (3×10^6 cells/mouse) were inoculated sc into BALB/c athymic mice, and 5 days later, mice were treated with TRAIL (1 mg/mouse, ip) or the PEG−TRAIL analogues (1 mg/mouse, ip) every 5 days. Tumor volumes were monitored for 24 days after tumor cell administration. Tumor volumes were calculated using longitudinal (L) and transverse (W) diameters using $V = (L \cdot W^2)/2$, and tumor growth inhibition (TGI) percent values were calculated using the formula TGI % = $(1 - TV_{sample}/TV_{control}) \times 100$, where TV is tumor volume.

In vivo tumor cell apoptosis were also investigated in HCT116 tumor-bearing BALB/c athymic mice. Briefly, at 24 days after HCT116 administration, tumor tissues were recovered from

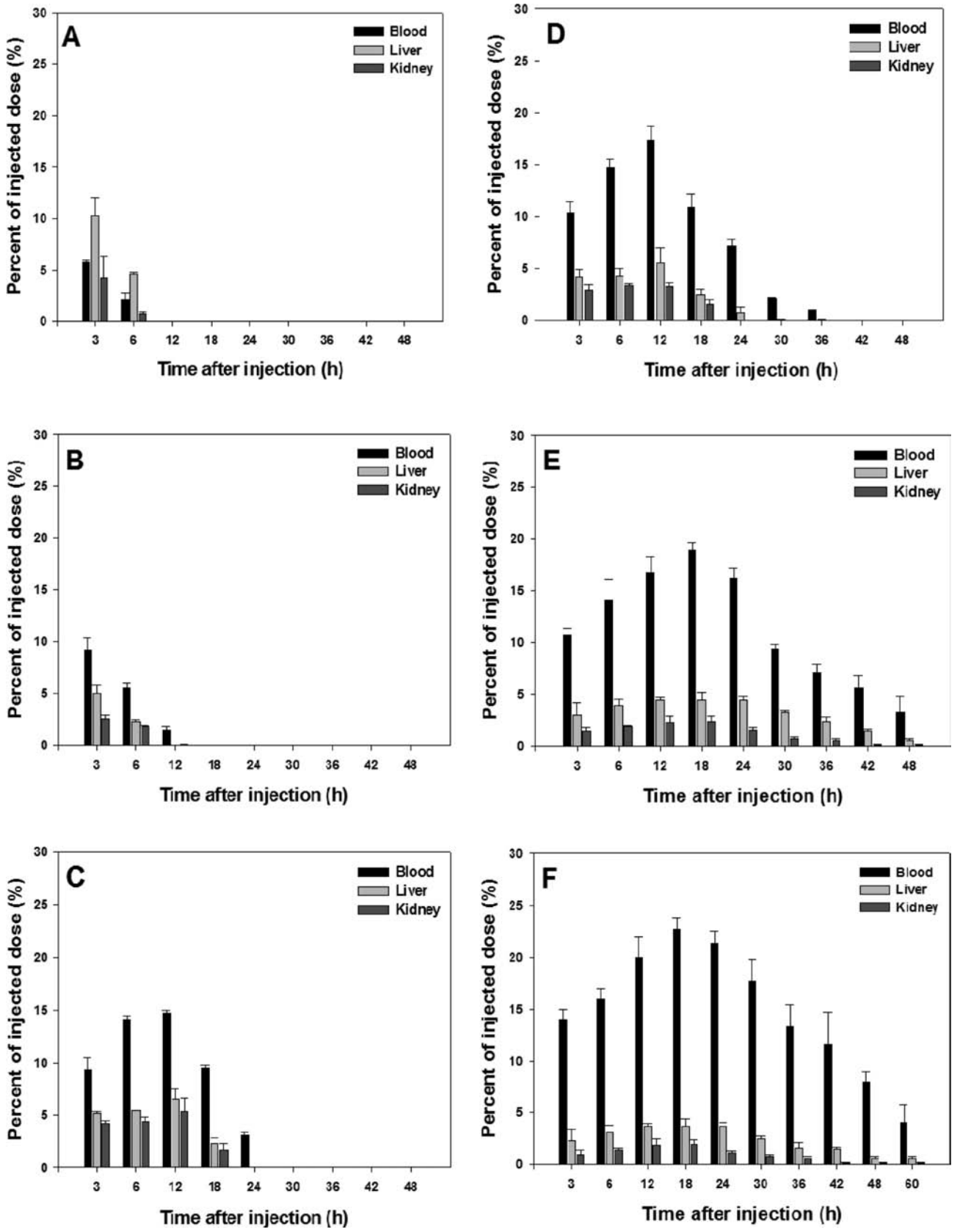

Figure 4. Pharmacokinetic profiles of TRAIL (A) and PEG−TRAIL analogues ((B) PEG 2 kDa, (C) 5 kDa, (D) 10 kDa, (E) 20 kDa, and (F) 30 kDa) in blood and tissue organs (liver and kidney) of ICR mice (n = 4). Results were then used to calculate percentages versus injected doses in blood and tissue organs (liver and kidney).

Table 1. Pharmacokinetic Parameters of TRAIL and PEG−TRAIL Analogues in ICR Mice[a]

PK parameters	TRAIL	2K-PEG−TRAIL	5K-PEG−TRAIL	10K-PEG−TRAIL	20K-PEG−TRAIL	30K-PEG−TRAIL
AUC_{inf} (%·h)	28.4 ± 2.8	66.3 ± 1.7	273.7 ± 5.4	338.5 ± 23.0	612.7 ± 49.2	957.2 ± 67.8
C_{max} (%)	5.8 ± 0.1	9.2 ± 1.2	14.7 ± 0.2	17.3 ± 1.4	18.8 ± 0.8	22.7 ± 1.2
$t_{1/2}$ (h)	1.1 ± 0.0	3.9 ± 0.7	5.3 ± 0.3	6.2 ± 0.2	12.3 ± 2.2	17.7 ± 2.6

[a] Data are means ± SDs. AUC_{inf} = area under the curve from zero to infinity; C_{max} = maximum concentration expressed as a percentage of injected dose (%); $t_{1/2}$: half-life during the elimination phase.

euthanized animals. Sections (5 μm) were then cut from 10% neutral buffered, formalin-fixed, paraffin-embedded tissue blocks. Apoptotic cell death in tumor tissues was visualized by performing TdT-mediated dUTP nick end labeling (TUNEL) assays using a commercial kit (In Situ Cell Death Detection Kit, Roche, Applied Science, Mannheim, Germany).

Data Analysis. Data are presented as mean ± SDs. Statistical significances were determined using One-Way ANOVA, and P values of <0.05 were considered statistically significant. Pharmacokinetic parameters were calculated by two-compartmental analysis (WinNolin, Scientific Consulting, Inc., Cary, NC).

RESULTS

Characterization of PEG−TRAIL Analogues. N-terminal specific TRAIL PEGylation was performed under acidic conditions (pH 5). PEG−TRAIL analogues were obtained by selective fractionation using gel filtration chromatography, and the analogues were examined by SDS-PAGE (Figure 1). Because of denaturation during sample preparation, TRAIL produced only one band at 22 kDa (monomer) by Coomassie blue/SDS-PAGE. However, the PEGylated TRAIL analogues produced two distinct bands corresponding to TRAIL monomer and N-terminal-PEGylated TRAIL monomer.

In Vitro Biological Activity of PEG−TRAIL Analogues. The in vitro cytotoxicities of PEG−TRAIL analogues were examined using MTT assays and HCT116 cells. TRAIL has a marked apoptotic effect on HCT116 cells (IC_{50} 35.2 ng/mL; Figure 2A). However, the cytotoxicities of the PEG−TRAIL analogues reduced with increasing PEG size (M_w: 2, 5, 10, 20, 30 kDa) and had IC_{50} values of 46.1, 69.6, 170.3, 229.2, 494.7 ng/mL, respectively. In addition, apoptosis induced by TRAIL and by the PEG−TRAIL analogues at a concentration of IC_{50} was investigated using Annexin-V-FLUOS apoptosis detection kits. TRAIL and the five analogues were all found to induce apoptosis (Figure 2B).

In Vitro Stabilities of PEG−TRAIL Analogues. Solution stabilities were investigated in physiological PBS. As shown in Figure 3A, TRAIL precipitated and aggregated rapidly under these conditions, whereas the five analogues showed much greater stability, which increased with PEG M_w. In particular, 20K- and 30K-PEG−TRAIL were found to have half-lives more than 100 times greater than TRAIL. Furthermore, although TRAIL did not aggregate at a concentration of 10 μg/mL, which is below its solubility limit (Figure 3A), its biological activity continuously diminished, presumably because of proteolytic degradation and/or denaturation. In addition, 5K-, 10K-, 20K-, and 30K-PEG−TRAIL maintained 80% of their apoptotic activities on HCT116 tumor cells after 24 h of incubation in rat plasma (Figure 3B), whereas 2K-PEG−TRAIL only maintained 40% of its apoptotic activity.

In Vivo Pharmacokinetic Disposition Study. The pharmacokinetic dispositions of PEG−TRAIL analogues were assessed in the blood and various organs of ICR mice. TRAIL was found to be rapidly removed from the circulation, with a circulating $t_{1/2}$ of 1.1 ± 0.0 h (Figure 4A and Table 1), whereas 2K-, 5K-, 10K-, 20K-, and 30K-PEG−TRAIL had $t_{1/2}$ values of 3.9 ± 0.7, 5.3 ± 0.3, 6.2 ± 0.2, 12.3 ± 2.2, and 17.7 ± 2.6 h, respectively (Figure 4B−F and Table 1). In addition, the AUC_{inf} values (%·h) of the analogues in blood also increased with increasing PEG M_w, and in particular, 30K-PEG−TRAIL was found to have an AUC_{inf} 33.7 times greater than that of TRAIL. In contrast to blood profiles, TRAIL distributions were significantly reduced by PEGylation in livers and kidneys, and importantly, increased PEG M_w reduced and delayed distributions to livers and kidneys, which are the principal sites of TRAIL metabolism (Table 1).

In Vivo Antitumor Activity Study. The antitumor effect of free TRAIL and PEG−TRAIL analogues were investigated in HCT116 tumor bearing mice. Five days after inoculation, mice were treated with TRAIL (1 mg/mouse, ip) or PEG−TRAIL analogues (1 mg/mouse, ip) every 5 days; tumor volumes were continuously monitored. 5K-, 20K-, and 30K-PEG−TRAIL were found to efficiently suppress mean tumor growth, with mean TGI values (24 day) of 43.5, 61.7, and 72.3%, respectively (Figure 5A). In particular, 30K-PEG−TRAIL retained antitumor activity at five days after a single administration. Furthermore, whereas TUNEL assays of tumor tissues from TRAIL treated mice showed some signs of cell death, TUNEL assays of tumor tissues from 30K-PEG−TRAIL treated mice showed obvious tumor cell apoptosis (Figure 5C).

DISCUSSION

TRAIL is of considerable clinical interest for cancer therapy due to its unique tumor-directed apoptotic activities.[17,18] Despite its clinical advantages, several pharmaceutical issues such as the instability of TRAIL under physiological conditions, its inability to form an active trimer, and its weak pharmacokinetic characteristics hinder its use as a cancer treatment.[6,8] To address these obstacles, researchers have focused on the development of TRAIL derivatives with improved tumor specificities and enhanced trimer-forming abilities.[19−22] As occurs in natural systems, in which post-translational modifications play important roles during the production of new biologic entities, numerous strategies have been adopted to overcome the physicochemical and pharmaceutical shortcomings of therapeutic proteins.

PEGylation is a well-established means of prolonging the lifespan of short living, potent proteins. However, the clinical efficacies of randomly PEGylated proteins are low because they contain a substantial nonbiologic entity. Previously, we synthesized an N-terminal specific PEGylated TRAIL (5K-PEG−TRAIL; PEG M_w: 5000) with enhanced physicochemical, pharmacokinetic, and antitumor characteristics.[3] 5K-PEG−TRAIL showed improved physiological stability and had a better pharmacokinetic profile than TRAIL, and the activity loss was minimal. Nevertheless, although our 5K-PEG−TRAIL showed better

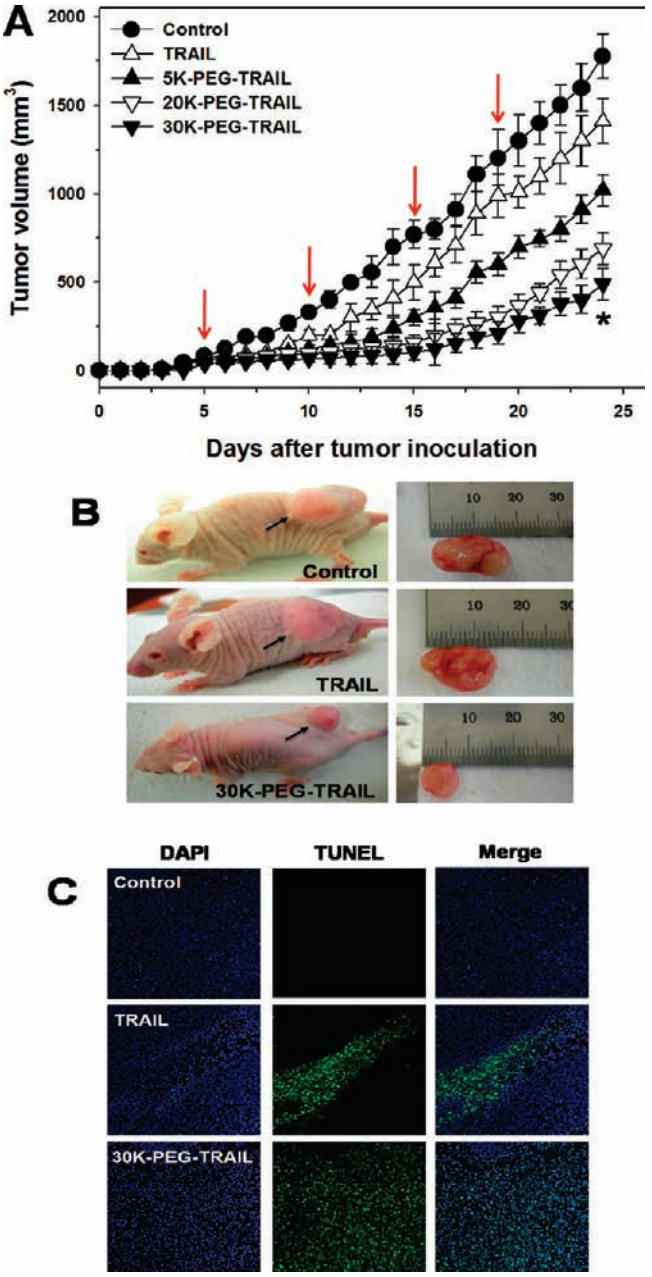

Figure 5. In vivo antitumor activity of PEG−TRAIL analogues. (A) Tumor growth suppressions by TRAIL and PEG−TRAIL analogues (5K-, 20K-, 30K-PEG−TRAIL) (drugs were injected every five days at 1 mg/mouse, protein base, ip). (n = 6; *p < 0.05 versus control). (B) Representative mouse at end point (24 day) for control, TRAIL and 30K-PEG−TRAIL were shown (left) alongside images of excised tumors (right). (C) Histological observations of control, TRAIL and 30K-PEG−TRAIL after TUNEL staining of apoptotic cell death in tumor (nuclei are stained blue and apoptotic cells green) (×400).

antitumor activity that TRAIL, a greater in vivo half-life was required for the promising efficacy in frequency of administration.

The pharmacokinetic properties of PEGylated peptides and proteins can be modulated by changing the M_w of the PEG component. In general, PEGylated molecules have much larger (~9 times) "effective" molecular sizes than theoretical because of their linear natures and the water affinity of PEG.[23−25] Accordingly, changes of PEG M_w can result in substantial pharmacokinetic changes. For this reason, we hypothesized that increasing PEG M_w in PEG−TRAIL analogues could be used to design pharmacokinetic profiles and pharmacologic effects by altering renal clearance, metabolism, and body distribution.

In the present study, we initially investigated the impact of PEG M_w on the biological activities and stability of TRAIL in vitro. Increasing the M_w of TRAIL was found to have contrary effects on the biological activities and stabilities of the PEGylated adducts. Increasing PEG size deprives TRAIL of its inherent biological activity in vitro, and the cytotoxicities of PEG−TRAIL analogues were reduced by increasing PEG M_w due to the disruption of TRAIL binding to death receptors by PEG. Despite reduced cytotoxicities due to PEGylation, these cytotoxicities were retained (7.1% of the efficacy of native TRAIL for 30K-PEG−TRAIL). Conversely, the PEG−TRAIL analogues were found to have greatly enhanced metabolic resistance in rat plasma due to the disturbance of proteolysis by the PEG stand attached (Figure 3B). Specifically, such improvements appeared to be substantial impetuses to extend the functional lifespan of TRAIL when exposed to those in vivo milieus. However, unlike the biological activity loss observed in vitro, PEGylation greatly improved the pharmacokinetic profile of TRAIL by prolonging its survival time (Figure 4 and Table 1). The improved in vitro physicochemical characteristics of PEG−TRAIL analogues also improved in vivo pharmacokinetic characteristics. Several researches have reported that TRAIL is rapidly eliminated and has a short half-life (~30 min), mainly due to renal clearance.[6] However, the increased molecular weight and the molecular shielding afforded by PEG dramatically enhance the pharmacokinetic profiles of PEG−TRAIL analogues. In particular, the PEG−TRAIL analogues were found to exhibit the discriminated pharmacokinetic profiles with the escalated elimination half-lives depending on PEG size and increasing PEG M_w reduced liver and kidney distributions. Importantly, the delayed and reduced kidney accumulation of 30K-PEG−TRAIL explains in part its extended presence in plasma because TRAIL itself is susceptible to glomerular filtration.[6]

To determine whether the PEG−TRAIL analogues are potentially useful cancer treatments, we examined their antitumor activity using HCT116 colon tumor-bearing BALB/c athymic mice. The results obtained showed that increasing PEG M_w from 5K produced the desired biological effects. Furthermore, the pharmacologic effectivenesses of the PEG−-TRAIL analogues matched their observed pharmacokinetic durations. In particular, 30K-PEG−TRAIL displayed the most effective antitumor potential in terms of its effect duration, despite its reduced biological activity in vitro, which we attributed to its persistence and altered pharmacokinetic distribution. In the present study, 30K-PEG−TRAIL was found to be the strongest antitumor agent candidate.

To summarize, this study demonstrates that N-terminal-specific PEGylated TRAIL analogues offer improved enzyme resistance and increased half-lives in the circulation. In addition, their improved antitumor potencies suggest that these analogues potentially offer the opportunity of a practical, convenient, and safe long-acting cancer therapy.

AUTHOR INFORMATION

Corresponding Author

*Phone: +82-31-290-7704. Fax: +82-31-290-7724. E-mail: kclee@skku.edu.

■ ACKNOWLEDGMENT

This work was supported by a grant from the Korean Ministry of Education, Science, and Technology (grant no. 2010K001256).

■ REFERENCES

(1) Ashkenazi, A., Pai, R. C., Fong, S., Leung, S., Lawrence, D. A., Marsters, S. A., Blackie, C., Chang, L., McMurtrey, A. E., Hebert, A., DeForge, L., Koumenis, I. L., Lewis, D., Harris, L., Bussiere, J., Koeppen, H., Shahrokh, Z., and Schwall, R. H. (1999) Safety and antitumor activity of recombinant soluble Apo2 ligand. *J. Clin. Invest. 104*, 155–162.

(2) French, L. E., and Tschopp, J. (1999) The TRAIL to selective tumor death. *Nature Med. 5*, 146–147.

(3) Chae, S. Y., Kim, T. H., Park, K., Jin, C. H., Son, S., Lee, S., Youn, Y. S., Kim, K., Jo, D. G., Kwon, I. C., Chen, X., and Lee, K. C. (2010) Improved antitumor activity and tumor targeting of NH(2)-terminal-specific PEGylated tumor necrosis factor-related apoptosis-inducing ligand. *Mol. Cancer Ther. 9* (6), 1719–1729.

(4) Kim, T. H., Jiang, H. H., Youn, Y. S., Park, C. W., Lim, S. M., Jin, C. H., Tak, K. K., Lee., H. S., and Lee, K. C. (2011) Preparation and characterization of Apo2L/TNF-related apoptosis-inducing ligand-loaded human serum albumin nanoparticles with improved stability and tumor distribution. *J. Pharm. Sci. 100* (2), 482–491.

(5) Kim, T. H., Jiang, H. H., Park, C. W., Youn, Y. S., Lee, S, Chen, X, and Lee, K. C. (2011) PEGylated TNF-related apoptosis-inducing ligand (TRAIL)-loaded sustained release PLGA microspheres for enhanced stability and antitumor activity. *J. Controlled Release 150* (1), 63–69.

(6) Xiang, H., Nguyen, C. B., Kelley, S. K., Dybdal, N., and Escandón, E. (2004) Tissue distribution, stability, and pharmacokinetics of Apo2 ligand/tumor necrosis factor-related apoptosis-inducing ligand in human colon carcinoma COLO205 tumor-bearing nude mice. *Drug Metab. Dispos. 32*, 1230–1238.

(7) Jo, M., Kim, T. H., Seol, D. W., Esplen, J. E., Dorko, K., Billiar, T. R., and Strom, S. C. (2000) Apoptosis induced in normal human hepatocytes by tumor necrosis factor-related apoptosis-inducing ligand. *Nature Med. 6*, 564–567.

(8) Kelley, S. K., Harris, L. A., Xie, D., Deforge, L., Totpal, K., Bussiere, J., and Fox, J. A. (2001) Preclinical studies to predict the disposition of Apo2L/tumor necrosis factor-related apoptosis-inducing ligand in humans: characterization of in vivo efficacy, pharmacokinetics, and safety. *J. Pharmacol. Exp. Ther. 299*, 31–38.

(9) Lee, S., Youn, Y. S., Lee, S. H., Byun, Y., and Lee, K. C. (2006) PEGylated glucagon-like peptide-1 displays preserved effects on insulin release in isolated pancreatic islets and improved biological activity in db/db mice. *Diabetologia 49*, 1608–1611.

(10) Youn, Y. S., Kwon, M. J., Na, D. H., Chae, S. Y., Lee, S., and Lee, K. C. (2008) Improved intrapulmonary delivery of site-specific PEGylated salmon calcitonin: optimization by PEG size selection. *J. Controlled Release 125* (1), 68–75.

(11) Kang, J. S., DeLuca, P. P., and Lee, K. C. (2009) Emerging PEGylated drugs. *Expert Opin. Emerging Drugs 14* (2), 363–380.

(12) Caliceti, P., and Veronese, F. M. (2003) Pharmacokinetic and biodistribution properties of poly(ethylene glycol)−protein conjugates. *Adv. Drug Delivery Rev. 55* (10), 1261–1277.

(13) Bailon, P., Palleroni, A., Schaffer, C. A., Spence, C. L., Fung, W. J., Porter, J. E., Ehrlich, G. K., Pan, W., Xu, Z. X., Modi, M. W., Farid, A., Berthold, W., and Graves, M. (2001) Rational design of a potent, long-lasting form of interferon: a 40 kDa branched polyethylene glycol-conjugated interferon alpha-2a for the treatment of hepatitis C. *Bioconjugate Chem. 12* (2), 195–202.

(14) Grace, M. J., Lee, S., Bradshaw, S., Chapman, J., Spond, J., Cox, S., Delorenzo, M., Brassard, D., Wylie, D., Cannon-Carlson., S., Cullen, C., Indelicato, S., Voloch, M., and Bordens, R. (2005) Site of pegylation and polyethylene glycol molecule size attenuate interferon-alpha antiviral and antiproliferative activities through the JAK/STAT signaling pathway. *J. Biol. Chem. 280* (8), 6327–6336.

(15) Kim, I., Kim, T. H., Ma, K., Lee, E. S., Kim, D., Oh, K. T., Lee, D. H., Lee, K. C., and Youn, Y. S. (2010) Synthesis and evaluation of human serum albumin-modified exendin-4 conjugate via heterobifunctional polyethylene glycol linkage with protracted hypoglycemic efficacy. *Bioconjugate Chem. 21* (8), 1513–1519.

(16) Lee, K. C., Chae, S. Y., Kim, T. H., Lee, S., Lee, E. S., and Youn, Y. S. (2009) Intrapulmonary potential of polyethylene glycol-modified glucagon-like peptide-1s as a type 2 anti-diabetic agent. *Regul. Pept. 152* (1−3), 101–107.

(17) Griffith, T. S., and Lynch, D. H. (1998) TRAIL: a molecule with multiple receptors and control mechanisms. *Curr. Opin. Immunol. 10*, 559–563.

(18) LeBlanc, H. N., and Ashkenazi, A. (2003) Apo2L/TRAIL and its death and decoy receptors. *Cell Death Differ. 10*, 66–75.

(19) Walczak, H., Miller, R. E., Ariail, K., Gliniak, B., Griffith, T. S., Kubin, M., Chin, W., Jones, J., Woodward, A., Le, T., Smith, C., Smolak, P., Goodwin, R. G., Rauch, C. T., Schuh, J. C., and Lynch, D. H. (1999) Tumoricidal activity of tumor necrosis factor-related apoptosis-inducing ligand in vivo. *Nature Med. 5*, 157–163.

(20) Kim, M. H., Billiar, T. R., and Seol, D. W. (2004) The secretable form of trimeric TRAIL, a potent inducer of apoptosis. *Biochem. Biophys. Res. Commun. 321*, 930–935.

(21) Seol, D. W., and Billiar, T. R. (2000) Cysteine 230 modulates tumor necrosis factor related apoptosis-inducing ligand activity. *Cancer Res. 60*, 3152–3154.

(22) Cao, L., Du, P., Jiang, S. H., Jin, G. H., Huang, Q. L., and Hua, Z. C. (2008) Enhancement of antitumor properties of TRAIL by targeted delivery to the tumor neovasculature. *Mol. Cancer Ther. 7*, 851–861.

(23) Uchio, T., Baudys, M., Liu, F., Song, S. C., and Kim, S. W. (1999) Site-specific insulin conjugates with enhanced stability and extended action profile. *Adv. Drug Delivery Rev. 35* (2−3), 289–306.

(24) Harris, J. M., Martin, N. E., and Modi, M. (2001) Pegylation: a novel process for modifying pharmacokinetics. *Clin. Pharmacokinet. 40* (7), 539–551.

(25) Harris, J. M. (1991) *Poly(ethylene glycol) Chemistry, Biotechnical and Biomedical Applications*, Plenum Press, New York.

Bioconjugate Chemistry

ARTICLE

pubs.acs.org/bc

Assembly and Targeting of Liposomal Nanoparticles Encapsulating Quantum Dots

Rajesh Mukthavaram,[†] Wolf Wrasidlo,[†,‡] David Hall,[§] Santosh Kesari,[*,†,‡] and Milan Makale[*,†,‡]

[†]Neuro-oncology Program, Moores Cancer Center

[‡]Department of Neurosciences

[§]Department of Radiology

University of California, San Diego

Supporting Information

ABSTRACT: Quantum dots (QDs) are attracting intense interest as fluorescence labeling agents for biomedical imaging because biocompatible coatings and relatively nontoxic rare earth metal QDs have emerged as possible options. QD photoemissions are bright, of narrow wavelength range, and very stable. We sought to encapsulate QDs within targeted PEGylated liposomes to reduce their propensity for liver uptake and to amplify the already strong QD emission signal. A novel lipid−QD conjugate initialized a process by which lipids in solution coalesced around the QDs. The liposomal structure was confirmed with size measurements, SEM, and IR spectroscopy. PEGylated QD liposomes injected into a xenograft tumor model largely cleared from the body within 24 h. Residual liver labeling was low. Targeted QD liposomes exhibited robust tumor labeling compared with controls. This study highlights the potential of these near IR emitting QD liposomes for preclinical/clinical applications.

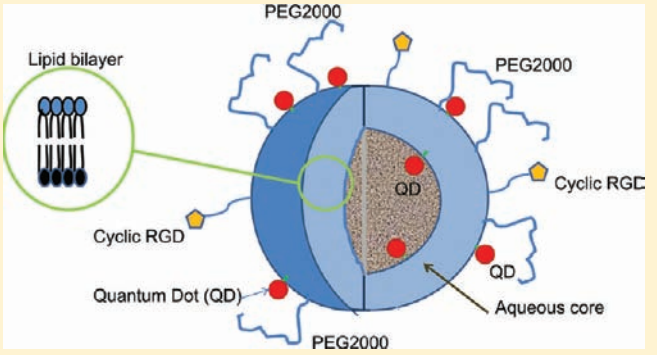

INTRODUCTION

Nanoparticles are increasingly being explored as labeling agents in fluorescence-based biomedical imaging. Fluorescence label-based laparoscopic/endoscopic imaging of the blood vessels, bronchi, esophagus, stomach, intestines, skin, and oral cavity, along with intraoperative fluorescence imaging, have the potential to facilitate the detection and assessment of pathological structures such as tumors, inflamed and/or infected tissue, ulcers and fibrotic lesions.[1−5] Quantum dot (QD) nanoparticles in particular are attracting considerable interest as imaging labels, as they produce a very intense, narrow wavelength band photoemission, and they are two orders of magnitude more photostable than conventional fluorophores.[6]

Newer QD variants such as the rare earth metal compositions are relatively nontoxic, while the toxic cadmium-based QDs can be coated with poly(ethylene glycol) (PEG) to possibly render them sufficiently inert for uneventful clearance from the body, if they are less than 15 nm in size and not too densely PEGylated.[7−11] In the absence of UV irradiation, QDs with a stable coating have been found to be essentially nontoxic, so IR fluorescence may be preferable for cadmium-based QDs.[12] However, when they are intravenously injected, nontargeted, targeted, and micelle-encapsulated QDs concentrate in the liver, spleen, and bone marrow and may clear slowly if at all, and this accumulation is undesirable from the standpoint of toxicological and pharmacokinetic considerations.[7−12]

Liposomes offer an attractive potential solution to coating QDs to prevent liver accumulation. Liposomal nanoparticles are stable and long circulating when PEGylated.[13] They are comparatively large (∼100 nm) and have favorable charge characteristics even with a payload. They can be made multifunctional by at the same time accommodating any combination of QDs, a drug payload, an MRI or PET labeling agent, and a targeting ligand.[14−16] Gel core liposomes have favorable loading of all drug chemotypes.[17] Liposomes are already FDA approved for human use and there are currently two liposome-based products, Doxil and Depocyte, that are used clinically, making liposomes an appealing and readily translatable potential platform for QD delivery in patients.

The goal of the present study was to address two key issues to support further investigations of QD liposomes as labeling agents for preclinical and clinical fluorescence imaging. First, various strategies of loading QDs into liposomes can be problematic for various reasons: (1) the approach of simply entrapping particles such as QDs and iron oxide within the liposomal bilayer may lead to leaching of these hydrophobic molecules *in vivo*,[18] (2) conjugation of QDs to the external liposome surface only via PEG

Received: April 26, 2011
Revised: July 11, 2011
Published: July 25, 2011

ACS Publications © 2011 American Chemical Society

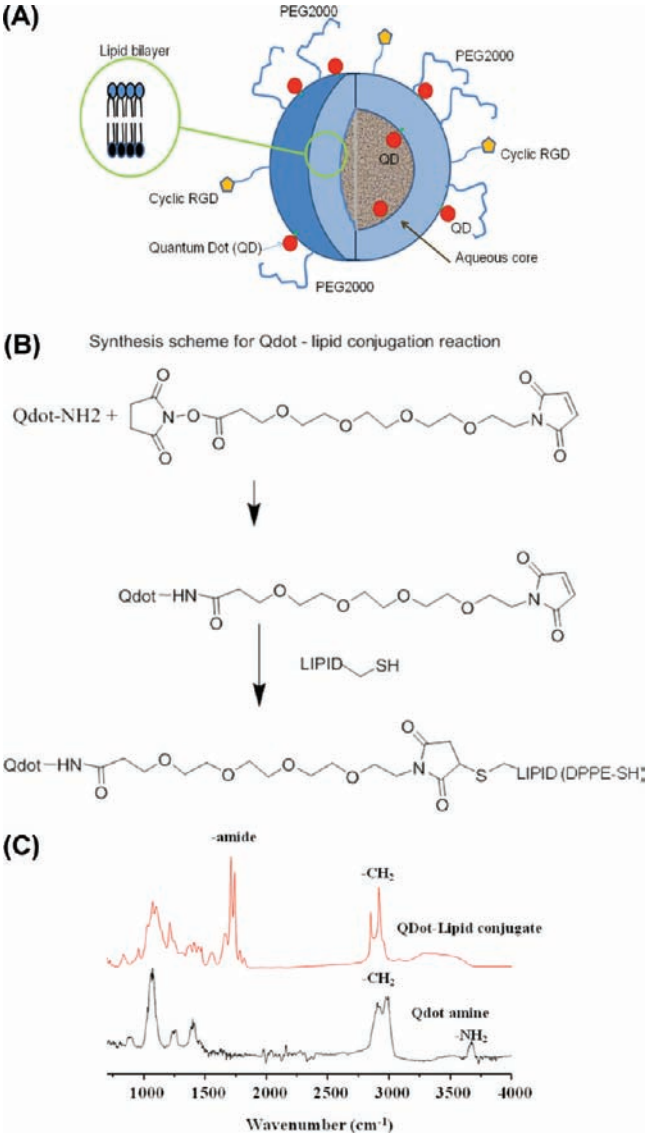

Figure 1. (A) Cutaway drawing showing liposomal nanoparticle lipid bilayer (inset) and cyclic RGD peptides bound to the exterior liposomal surface. The QDs denoted by filled red circles are conjugated to a lipid moiety and reside inside and external to the bilayer. The liposome is in effect initiated at these QD—lipid conjugates and forms around them. The interior volume of this liposome is aqueous, but can be filled with a hydrogel to facilitate the loading of a broad range of drug chemotypes. (B) Schematic diagram depicting the conjugation of the QD and the DPPE-SH lipid prior to liposomal nanoparticle assembly. The first step is to couple the QD to the linker. The maleamide group of the linker reacts with the lipid-thiol to create a stable thioether bond. (C) IR spectroscopy, the lower tracing shows the spectrum for QDs alone. The top tracing shows the spectrum of the putative lipid-QD conjugate. The doublet resulting from stretch of the amide bond is clearly indicated and is not present within the QD alone tracing. This data provides strong evidence that QD-lipid conjugation was successful. Fluorescence intensity of the QD800 nanocrystals was not diminished by encapsulation (data not shown).

would not be expected to result in the most extensive QD loading, (3) the use of long PEG chains (PEG2000) to bind the QDs to the external liposomal surface may expose the QDs and result in heavy liver concentrations even >24 h after intravenous injection, and (4) additional moieties used to encapsulate the QDs can affect their emission spectrum.[19,20] The second major issue is that poor signal-to-noise *in vivo* is a limitation of virtually all labeling fluorophores.[21] The strong emission generated by QDs helps overcome this signal degradation by tissue autofluorescence, but further enhancement of signal by concentrating the QDs at the target is clearly an important objective.

Liposomal QD encapsulation was achieved using a novel and efficient linking of the QDs to a lipid anchor by covalent binding, so that initiation of the liposomal outer shell began at the lipid—QD conjugate and extended in all directions to effect complete QD encapsulation (Figure 1). This allows a higher density of QDs to be loaded, and this specific approach has been attempted previously but for micelles which have drug loading limitations and stability issues.[22,23] The signal-to-background issue was addressed by preparing QD liposomes targeted to the $\alpha v\beta 3$ integrin expressed exclusively on angiogenic microvessels.[24−26] Our hypothesis was that unbound QD liposomes would wash out after several hours while targeted liposomes would remain bound to the target to generate a readily discriminated signal.[27]

We present physical measurements confirming the predicted structure of the QD liposomes with our assembly approach. Furthermore, in a xenograft tumor model targeted QD liposomes (near IR 800 nm; non-UV emission) 24 h after intravenous injection robustly labeled the tumor but not the liver, as they showed significant clearance. These results highlight the potential of QD liposomes as biomedical labeling agents and support subsequent, more comprehensive investigations of QD-based multifunctional particles for clinical diagnostic—therapeutic applications.

EXPERIMENTAL PROCEDURES

Preparation of QD—Lipid Conjugates. *Synthesis of QD—Lipid Conjugate and Assembly of Lipsomes.* The final structure of the liposomal nanoparticle is shown in Figure 1A. Note the QD—lipid conjugates adorning the exterior and interior. To accomplish this, initially the amino-QD800 (1 μM; Invitrogen) in 300 μL water was conjugated to a short linker, succinimidyl ester-$(PEO)_4$-maleimide (2.5 μM) in DMSO, as shown in the reaction scheme in Figure 1B. The reaction mixture was stirred at room temperature for one hour. Then, DOPE-SH (2.5 μM; Avanti Polar Lipids, Inc., Alabaster, Alabama) containing the free thiol group in 200 μL chloroform was reacted with the QD-$(PEO)_4$-maleimide for one hour at room temperature in a biphasic solution to produce the QD—lipid conjugate. We performed thin layer chromatography of the QD—lipid conjugate, and then acquired the IR spectroscopic profile in order to prove the presence of the QD to lipid amide bond thus confirming conjugation.

The liposomal formulation comprised cholesterol/DOPE/DSPC/DOPE-$(PEO)_4$-QD/DSPE-mPEG2000 (3:3:3:0.5:0.5 molar ratio) dissolved in chloroform and was evaporated under argon gas. The dried lipid film was hydrated in sterile water to create large multilamellar vesicles (LMVs). Liposomes were vortexed for 2—3 min to remove any adhering lipid film and sonicated in a bath sonicator (Ultrasonik 28X) for 2—3 min at room temperature. MLVs were then sonicated with a Ti-probe (Branson 450 sonicator) for 1—2 min to produce small unilamellar vesicles (SUVs) as indicated by the formation of a translucent solution. To reduce the size of the SUVs, stepwise extrusion was performed with the final step being extrusion through a polycarbonate filter with 100 nm

pore size (Whatman). Unencapsulated QDs were separated from the QD liposomes by size exclusion chromatography using Sepharose CL-4B column, with PBS as an eluent.

Physical Characterization of Bioconjugates. *Particle Size and Net Charge (Zeta Potential).* The liposome suspension was diluted in 1/10 in Milli-Q water, and 100 μL of the dilution was sized using light backscattering (Malvern Zetasizer, ZEN 3600). The same instrument was used to measure the particle net charge which was expressed in mV. The QD liposome size and surface ζ-potential were obtained from three repeat measurements with a backscattering angle of 173°. Liposome morphology and size were further characterized using scanning electron microscopy (SEM). Samples were prepared by dropping 5 μL of QD liposome suspension onto a polished silicon wafer. After drying the droplet at room temperature overnight, the sample was coated with chromium and then imaged by SEM.

Electron Microscopy (SEM) for Structure Confirmation. Further confirmation of liposome size and structure was obtained with SEM. The particle samples were diluted 1/10 in Milli-Q water, drying 5 μL onto polished silicon wafers overnight, coating with chromium, and then imaged on a Philips XL-30 electron microscope to 30 000×. Particular emphasis was placed on confirming that the liposomes were spherical.

Fluorescent Emission Peak and IR Spectrum. For the emission peak, QDs alone and QD800-lipsomes were prepared using known volumes and concentrations, followed by purification with size exclusion chromatography. A Tecan fluorescence spectrophotometer was used to measure the peak emission of the intact nanoparticles at an excitation wavelength of 405 nm, and to confirm that the emission peak (780 nm) was that expected for the QD800 nanocrystals. For the IR spectrum, the QD−lipid conjugate and the QDs alone were prepared in solution and the emitted IR was measured using a Thermo Scientific Nicolet 6700 FT-IR spectrometer.

Particle Stability. Liposomal nanoparticles encapsulating QDs were prepared and were characterized in terms of size and charge using a Malvern Zetasizer. The particles were stored at room temperature for 7 days and then were rescanned, and changes quantified in terms of percent change from the prestorage data.

Biological Characterization. *Cell Viability Study.* U87 cells were maintained in Dulbecco's modified Eagle's medium (DMEM) supplemented with 10% fetal bovine serum (FBS); cells were cultured at 37 °C in a humidified atmosphere containing 5% CO_2. For cell viability study, 3-(4,5-dimethylthiazol-2-yl)-2,5-diphenyltetrazolium bromide (MTT) reduction assay was performed. For MTT assay, 2000 cells (U87) per well were seeded into a 96 well plate and cultured overnight, then incubated with 10 different concentrations of the QD liposomes starting from 0.2 uM to 0.39 nM. Ten microliters of MTT was added 72 h after addition of the QD particles to the cells. Results were expressed as percent viability = $\{[A_{540}(\text{treated cells}) - \text{background}]/[A_{540}(\text{untreated cells}) - \text{background}]\} \times 100$.

In Vitro Imaging of Targeted QD−Liposomes. U87 cells were seeded onto a 6 well culture plate at a density of 200K cell per well and incubated in DMEM with 10% FBS for 24 h, QD encapsulated particles or native QDs were added to the wells at a final concentration of 0.5 nM. Cells were incubated for 4 h, washed with PBS twice, and observed with a laser scanning confocal microscope. QD conjugates in the cytoplasm excited with 450 nm and fluorescence emission was observed at 780 nm.

In Vivo Imaging of Native QDs, and Targeted vs Nontargeted QD−Lipsomes. Athymic nude mice were anesthetized with ketamine/medetomidine and subcutaneously inoculated in the left flank with 4×10^6 cells/100 μL PBS of the U87 glioblastoma cell line. When the flank tumors grew to a volume of 60 mm^3, the animals were anesthetized with isofluorane administered via a nose cone, and imaged in an Advanced Research Technologies (ART) Optix-MX2 imaging system. This apparatus includes four pulsed lasers (picosecond pulse, 80 MHz duty cycle) of different wavelengths to excite a variety of fluorophores with corresponding emission filters and a time-correlated single photon counting (TCSPC) photomultiplier tube for fluorescence time domain detection, which can provide both fluorescence intensity and fluorescence lifetime imaging. Here, 470 nm/780 nm excitation/emission wavelengths were employed to image the nanoparticles. The nanoparticles were intravenously injected via the tail vein and the mice were imaged before injection, and at 2 and 24 h after injection. A brightfield image was acquired first, followed by fluorescence intensity images based on single photon counting. The image data were saved directly on a PC for later processing. Images were acquired both before and after nanoparticle injection.

Data Processing. The data was processed using *ART Optix* analysis software and the counts represented as heat maps superimposed on the brightfield grayscale image. Identity of the fluorophore (QD800) was confirmed by fluorescence lifetime determination.

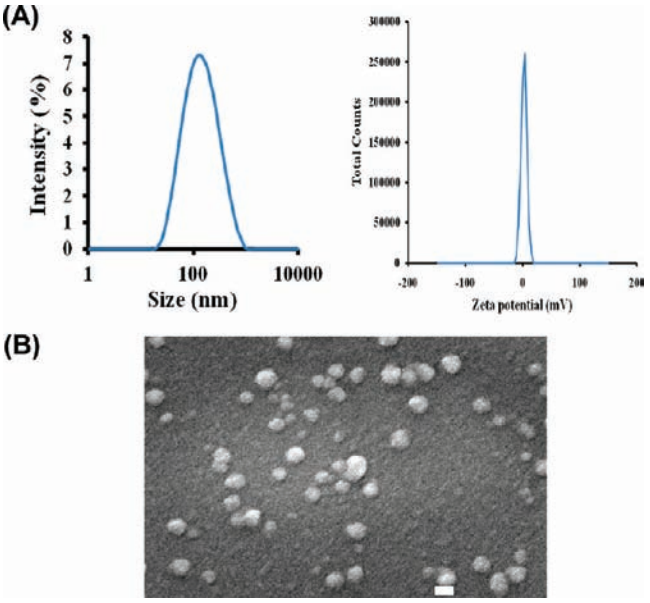

Figure 2. (A) Left panel is the Zetasizer plot of a QD liposome suspension and reveals an average QD liposome size of 109 nm and a symmetrical size distribution. This data confirm that the nanoparticles containing QDs are of the desired size, which indicates that the encapsulation of the relatively large QDs did occur. The right panel is the plot of charge distribution indicating that the liposomal nanoparticles containing QDs were neutral, indicating that encapsulation of the QDs was complete. The lack of charge allows for a much longer in vivo circulation time. (B) Electron microscope image of liposomal nanoparticles containing QDs. The spherical shape of the nanoparticles is clearly visible and they are the correct size, approximately 100 nm, as indicated by the white bar which denotes 100 nm.

RESULTS

Physical Characterization of QD−Lipid Conjugates. *Confirmation of Conjugation.* Thin layer chromatography revealed

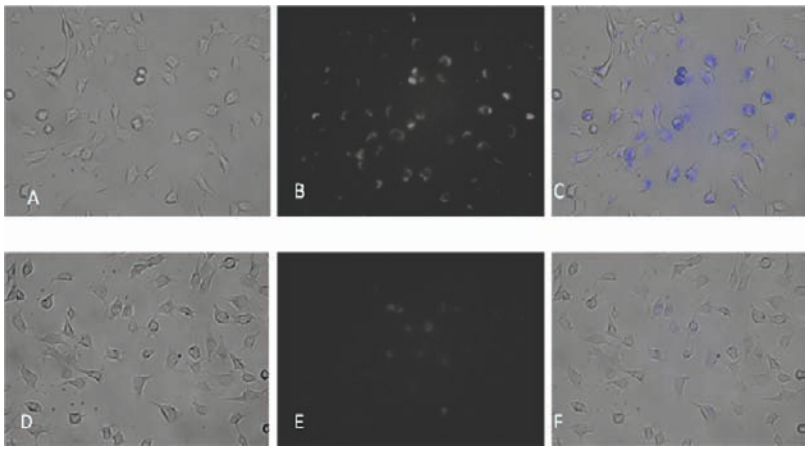

Figure 3. Panels A−C depict the uptake of particles in cultured U87 glioblastoma cells. Panel A is the phase contrast image, while B is the fluorescence acquisition. Panel C shows the merge and it can be seen that a significant proportion of the cells have internalized the targeted QD liposomes. In comparison, panels D−F show the uptake of nontargeted QD liposomes by U87 cells. The merge of D and E, denoted by panel F, reveals that endocytosis of the nontargeted QDs resulted in considerably less internalization than was the case with targeted particles.

the presence both a QD and QD conjugate in the mobile phase (shown in Supporting Information). IR spectroscopy clearly indicated the amide bond linking the QD with the lipid (DPPE-SH) and therefore confirmed the existence of the QD−lipid conjugate (Figure 1C). The QD emission peak wavelength was unchanged by the lipid conjugation (shown in Supporting Information).

Particle Size and Net Charge (Zeta Potential). Figure 2A, left panel, shows that the average particle size was 100 nm indicating that fully formed liposomes were present in the suspension mixture, since this was the final extrusion pore size. The right panel of Figure 2A indicates the zeta potential, or net charge, which was close to the desired neutrality, consistent with complete QD encapsulation. We found that the zeta potential and average particle size were not significantly changed after storage in PBS at 4 °C for 7 days (not shown).

Electron Microscopy (SEM) for Structure Confirmation. Figure 2B is the SEM of the QD liposomes. The white bar indicates 100 nm, and the SEM confirmed that the particles were 100 or greater in size, that they had a spherical shape, and were intact.

Biological Characterization. *Cell Viability Study.* We found that the QD liposomes and the QDs were nontoxic in the concentrations tested (0.01 to 0.20 μM) when applied to U87 cells in culture (shown in Supporting Information). These data show that encapsulating the QDs within liposomes did not make them toxic at physiologically relevant doses.

In Vitro Imaging. The QD targeted QD liposomes were taken up more avidly by U87 cells than nontargeted QD liposomes. In Figure 3, panels A−C depict the uptake of particles in cultured U87 glioblastoma cells. Panel A is the phase contrast image, while B is the fluorescence acquisition. Panel C shows the merge and it can be seen that a significant proportion of the cells have internalized the targeted QD liposomes. In comparison, panels D−F, which are arranged according to the same format, reveal the lower uptake of nontargeted QD liposomes into U87 cells. The merge of D and E, denoted by panel F, reveals that endocytosis alone of the nontargeted QDs resulted in considerably less internalization than was the case with targeted particles. These data suggest that that targeting $\alpha v\beta 3$ integrins, which are expressed by U87 cells, confers a delivery advantage with tumor cells. The targeted QD liposomes are most probably being taken up via the $\alpha v\beta 3$ receptor and internalized, while the nontargeted liposomes are mostly being taken up via endocytosis.

In Vivo Imaging of Native QDs, and Targeted vs Nontargeted QD-Liposomes. Targeted and nontargeted QD liposomes were widely distributed at two hours after injection of the mice as shown in Figure 4A−D. The photon counts were high in images taken with the animal in both the prone and supine positions. Peak counts for both targeted and nontargeted QD liposomes were measured in the liver, kidney, and bone marrow. After 24 h, the unbound QD liposomes had washed out of most body areas and the liver labeling has substantially declined (Figure 4E,F). However, these PEGylated QD liposomes had evidently cleared the liver. In view of the extensive clearance and the finding that QD liposomes were not toxic in cell culture, there exists the possibility that even cadmium-based QD liposomes may be practicable in terms of some cancer-related clinical applications.

The targeted particles remained bound to the tumor and produced strong labeling that could be cleanly discriminated from background. The identity of the QD800 liposomes was unambiguously confirmed by measuring the species specific fluorescence lifetime, which as expected was much longer than the surrounding tissue autofluorescence (inset in Figure 4G).[28−30] The mouse which received nontargeted QD liposomes had a low degree of liver labeling and no tumor labeling. None of the acquired images were filtered or modified from the original.

DISCUSSION

QDs have attracted attention owing to their photoemission qualities which include the generation of an intense narrow wavelength band of fluorescent light and resistance to photobleaching. Cadmium-based QDs unfortunately are toxic to cultured human cells and little is known about their clearance from the human body. Several reports have indicated that coating cadmium-based QDs with inert materials renders them essentially nontoxic as long as exposure to UV light is avoided.[11,12] Newer rare earth metal and organic QDs are much less toxic, but encapsulation is still desirable for purposes of targeting, stealth, and drug loading.[12] Micelles tend to be unstable and drug uptake into a micelle already containing a QD would be challenging.[23]

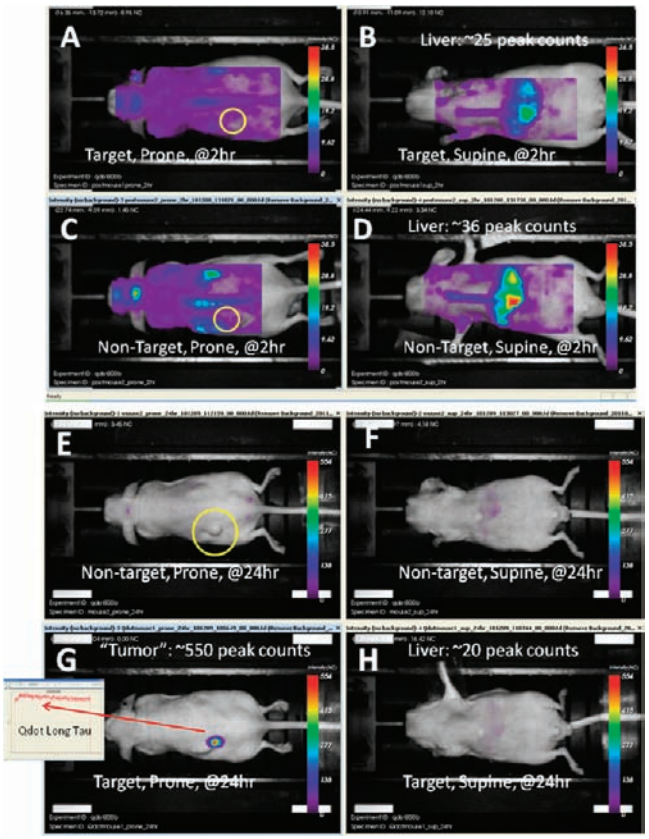

Figure 4. Panels A−D above and E−H below. Series of brightfield grayscale images fused with fluorescence intensity images. Panels A through D were obtained at 2 h after the intravenous injection of either targeted or nontargeted QD liposomes. The tumor site is indicated by a yellow circle on the prone images. Note that there is considerable liver uptake of both targeted and nontargeted QD liposomes resulting in strong liver labeling. At 24 h after injection, denoted by panels E though H, the QD liposomes, or at least the QDs have cleared the body either from renal clearance or via the feces. However, in panel G the targeted QD liposomes have bound to the tumor and/or its blood vessels to generate robust, clearly defined labeling. The identity of this fluorescence is confirmed to be the nanoparticle by the characteristic long fluorescence lifetime . The tumor site in the mouse that received nontargeted liposomes is shown by the yellow circle in panel E. In panels F and H, the decline in liver labeling is quite substantial. The images were not processed and are original.

Liposomes are ideal QD coating candidates, but liposomal encapsulation is technically complex.

The present study was designed to develop a practicable and reliable liposomal QD encapsulation protocol to create a fluorescence labeling platform that could be targeted and also used as a drug delivery vehicle. We sought to determine whether lipid encapsulation reduced toxicity in vitro, and facilitated targeting for amplification of the QD signal using an in vivo system. A novel chemistry was implemented to allow conjugation of the QD to a lipid anchor which acted as an initiation site for lipid encapsulation. Conjugation rather than simple encapsulation alone is required, as otherwise the hydrophobic QDs will prematurely leach out from between the liposomal bilayer.

PEG2000 represents an optimized PEG variant in terms of toxicity and increasing circulation stability. PEG2000 has been chosen as it is nontoxic[17,25,31] and because it is used in many clinical liposomal formulations, such as Doxil. It prevents opsonization and removal from the circulation, thereby enhancing liposomal circulation half-life.

A near-IR emitting QD (QD800) was tested to demonstrate that near IR fluorescence imaging of QDs in vivo was feasible, since avoidance of UV light prevents coated QDs from becoming toxic.[12] The targeted QD liposomes largely cleared the test mice within 24 h, suggesting that coated QDs may be cleared rapidly and thus represent a lower toxicity hazard. Since the QD liposomes were too large (100 nm plus) for kidney clearance, it is possible that the route of excretion was through the liver and the intestines and then finally via the feces.[7,8] Importantly, the targeting results suggest that targeting allowed for washout to reduce unbound, background QDs.[27] This may have facilitated an amplification of the target labeling with enhanced signal to noise.

The focus of future studies will be to more comprehensively characterize QD liposomal clearance and toxicity, and to combine target fluorescence labeling with drug delivery.[16,32−35] This "theranostic" combination within a single nanoplatform would potentially allow the tumor to be located and drug delivery to be chronicled and related to the response of the tumor. Some reports describe the loading of doxorubicin into lipsomes, but this is an older compound and relatively straightforward to load into liposomes. Newer agents such as taxol are more challenging owing to their hydrophobicity.[36] Gel core liposomes allow drug compounds of virtually all chemotypes to be loaded effectively.[16,36−39]

In summary, the present study has shown that QD encapsulation within a large (100 nm plus) liposome can be accomplished and that such a QD liposome may be targeted. Moreover, the lipid coating and PEGylation renders the QD essentially nontoxic and coupled with rapid clearance may allow both cadmium-based and less toxic rare earth metal and organic QDs to be feasible for patient use. The data provide a basis for pursuing subsequent, comprehensive studies involving the targeted delivery of a therapeutic agent using a QD bearing liposomal platform, the chronicling of the therapeutic effect of such a nanoparticle on an in vivo implanted tumor, and the detailed characterization of particle biodistribution and clearance.

■ ASSOCIATED CONTENT

Supporting Information. We characterized the effects of conjugation in terms of emission wavelength and liposomal toxicity. We found that the QD emission peak wavelength was unchanged by the lipid conjugation. Moreover, encapsulating the QDs within liposomes did not make them more toxic at the doses typically used in vitro. This material is available free of charge via the Internet at http://pubs.acs.org.

■ AUTHOR INFORMATION

Corresponding Author

*Milan Makale,UCSD Moores Cancer Center, 3855 Health Sciences Drive, La Jolla, CA 92093-0803. E-mail: mmakale@ucsd.edu. Tel: 858-822-6922. Santosh Kesari, UCSD Moores Cancer Center, 3855 Health Sciences Drive, La Jolla, CA 92093-0803. Email: skesari@ucsd.edu. Tel: 858-822-7524.

■ ACKNOWLEDGMENT

This work was supported in part by grants from NIH (NIH 3P30CA023100-25S8). The authors wish to thank Dr. Santosh

Aryal for the SEM image, Dr. Kersi Pestonjamasp and Mr. Joseph Aguilera for the in vitro fluorescence images, and Mr. Ying Chao for the in vivo tumor implantations. The authors gratefully acknowledge ICMIC NCI-P50-CA128346 and the UCSD In Vivo Small Animal Imaging Resource for the in vivo imaging.

REFERENCES

(1) Roberts, D. W., Valdés, P. A, Harris, B. T., Fontaine, K. M., Hartov, A., Fan, X., Ji, S., Lollis, S. S., Pogue, B. W., Leblond, F., Tosteson, T. D., Wilson, B. C., and Paulsen, K. D. (2011) Coregistered fluorescence-enhanced tumor resection of malignant glioma: relationships between delta-aminolevulinic acid-induced protoporphyrin IX fluorescence, magnetic resonance imaging enhancement, and neuropathological parameters. *J. Neurosurg. 114* (3), 595–603.

(2) Zou, P., Xu, S., Povoski, S. P., Wang, A., Johnson, M. A., Martin, E. W., Jr., Subramaniam, V., Xu, R., and Sun, D. (2009) Near-infrared fluorescence labeled anti-TAG-72 monoclonal antibodies for tumor imaging in colorectal cancer xenograft mice. *Mol. Pharmaceutics 6*, 428–440.

(3) Liu, R. C., and Traverso, L. W. (2005) Diagnostic laparoscopy improves staging of pancreatic cancer deemed locally unresectable by computed tomography. *Surg. Endosc. 19*, 638–642.

(4) Loning, M., Diddens, H., Kupker, W., Diedrich, K., and Huttmann, G. (2004) Laparoscopic fluorescence detection of ovarian carcinoma metastases using 5-aminolevulinic acid-induced protoporphyrin IX. *Cancer 100*, 1650–1656.

(5) He, Y., Xu H., Chen C., Peng J., Tang H., Zhang Z., and Li Z, P. (2011) *In situ* spectral imaging of marker proteins in gastric cancer with near-infrared and visible quantum dots probes. *Talanta* EPub ahead of print.

(6) Smith, A. M., Dave, S., Nie, S., True, L., and Gao, X. (2006) Multicolor quantum dots for molecular diagnostics of cancer. *Expert Rev. Mol. Diagn. 6* (2), 231–244.

(7) Schipper, M. L., Iyer, G., Koh, A. L., Cheng, Z., Ebenstein, Y., Aharoni, A., Keren, S., Bentolila, L. A., Li, J., Rao, J., Chen, X., Banin, U., Wu, A. M., Sinclair, R., Weiss, S., and Gambhir, S. S. (2009) Particle size, surface coating, and PEGylation influence the biodistribution of quantum dots in living mice. *Small 5* (1), 126–34.

(8) Choi, H. S., Liu, W., Misra, P., Tanaka, E., Zimmer, J. P., Itty Ipe, B., Bawendi, M. G., and Frangioni, J. V. (2007) Renal clearance of quantum dots. *Nat. Biotechnol. 25* (10), 1165–70.

(9) Pozzi-Mucelli, S., Boschi, F., Calderan, L., Sbarbati, A., and Osculati, F. (2009) Quantum Dots: proteomics characterization of the impact on biological systems. *J. Phys.: Conf. Ser. 170*, 1–5.

(10) Lewinski, N., Zhu, H., and Drezek, R. (2009) Evaluating strategies for risk assessment of nanomaterials. In *Nanotoxicity: from in vivo and in vitro models to health risks* (Sahu, S. C., and Casciano, D., Eds.) p 476, Wiley, New Delhi.

(11) Das, G. K., Chan, P. P., Teo, A., Loo, J. S., Anderson, J. M., and Tan, T. T. (2010) In vitro cytotoxicity evaluation of biomedical nanoparticles and their extracts. *J. Biomed. Mater. Res. A 93* (1), 337–46.

(12) Lee, J., Ji, K., Kim, J., Park, C., Lim, K. H., Yoon, T. H., and Choi, K. (2010) Acute toxicity of two CdSe/ZnSe quantum dots with different surface coating in Daphnia magna under various light conditions. *Environ. Toxicol. 25* (6), 593–600.

(13) Remaut, K., Lucas, B., Braeckmans, K., Demeester, J., and De Smedt, S. C. (2007) Pegylation of liposomes favours the endosomal degradation of the delivered phosphodiester oligonucleotides. *J. Controlled Release 117* (2), 256–66.

(14) Hu, R., Yong, K.-T., Roy, I., Ding, H., Law, W.-C., Cai, H., Zhang, X., Vathy, L. A., Bergey, E. J., and Prasad, P. N. (2010) Functionalized near-infrared quantumdots for *in vivo* tumor vasculature imaging. *Nanotechnology 21*, 1–9.

(15) Garg, A., Tisdale, A. W., Haidari, E., and Kokkoli, E. (2009) Targeting colon cancer cells using PEGylated liposomes modified with a fibronectin-mimetic peptide. *Int. J. Pharm. 366*, 201–210.

(16) Zhang, L., and Granick, S. (2006) How to stabilize phospholipid liposomes (using nanoparticles). *Nano Lett. 6* (4), 694–698.

(17) Erten, A., Wrasidlo, W., Scadeng, M., Esener, S., Hoffman, R., Bouvet, M., and Makale, M. (2010) MR and fluorescence imaging of doxorubicin loaded nanoparticles using a novel *in vivo* model. *Nanomedicine 6* (6), 797–807.

(18) Bulte, J. W. M., and Modo, H. M. J. (2008) Introduction: The Emergence of Nanoparticles as an Imaging Platform in Biomedicine. In *Nanoparticles in Biomedical Imaging - Fundamental Biomedical Technologies*, pp 2−3, Vol 102, Springer, New York.

(19) Weng, K. C., Noble, C. O., Papahadjopoulos-Sternberg, B., Chen, F. F., Drummond, D. C., Kirpotin, D. B., Wang, D., Hom, Y. K., Hann, B., and Park, J. W. (2008) Targeted tumor cell internalization and imaging of multifunctional quantum dot-conjugated immunoliposomes *in vitro* and *in vivo*. *Nano Lett. 8* (9), 2851–7.

(20) Chen, C. S., Yao, J., and Durst, R. A. (2006) Liposome encapsulation of fluorescent nanoparticles: quantum dots and silica nanoparticles. *J. Nanopart. Res. 8*, 1033–1038.

(21) Hinterdorfer, P., and van Oijen, A., Eds. (2009) *Handbook of Single Molecule Biophysics*, pp 2−5 and 143, Springer, New York.

(22) Kim, Y. H., Subramanyam, E., Im, J. H., Huh, K. M., Choi, H., Choi, J. S., Lee, Y. K., and Park, S. W. (2010) A new PEG-lipid conjugate micelle for encapsulation of CdSe/ZnS quantum dots. *J. Nanosci. Nanotechnol. 10* (5), 3275–9.

(23) Kim, K. S., Hur, W., Park, S. J., Hong, S. W., Choi, J. E., Eun Goh, E. J., Yoon, S. K., and Hahn, S. K. (2010) Bioimaging for targeted delivery of hyaluronic acid derivatives to the livers in cirrhotic mice using quantum dots. *ACS Nano 4* (6), 3005–3014.

(24) Cai, W., Zhang, X., Wu, Y., and Chen, X. (2005) RGD peptide-labeled quantum dots for integrin $\alpha v\beta 3$ targeting. In *Understanding Biology Using Peptides* (Blondelle, S. E., Ed.) pp463−464, American Peptide Society.

(25) Murphy, E. A., Majeti, B. K., Barnes, L. A., Makale, M., Weis, S. M., Lutu-Fuga, K., Wrasidlo, W., and Cheresh, D. A. (2008) Nanoparticle-mediated drug delivery to tumor vasculature suppresses metastasis. *Proc. Natl. Acad. Sci. U.S.A. 105* (27), 9343–8.

(26) Arap, W., Pasqualini, R., and Ruoslahti, E. (1998) Cancer treatment by targeted drug delivery to tumor vasculature in a mouse model. *Science 279* (5349), 377–80.

(27) Papagiannaros, A., Upponi, J., Hartner, W., Mongayt, D., Levchenko, T., and Torchilin, V. (2010) Quantum dot loaded immunomicelles for tumor imaging. *BMC Med. Imaging 10*, 22.

(28) Tadrous, P. J. (2000) Methods for imaging the structure and function of living tissues and cells: 2. Fluorescence lifetime imaging. *J. Pathol. 191*, 229–234.

(29) Elson, D. et al. (2004) et al. Time-domain fluorescence lifetime imaging applied to biological tissue. *Photochem. Photobiol. Sci. 3*, 795–801.

(30) Hall, D. J., Sunar, U., Farshchi-Heydari, S., and Han, S. H. (2009) *In vivo* simultaneous monitoring of two fluorophores with lifetime contrast using a full-field time domain system. *Appl. Opt. 48*, D74–D78.

(31) Liao, D., Liu, Z., Wrasidlo, W., Chen, T., Luo, Y., Xiang, R., and Reisfeld, R. A. (2011)Synthetic enzyme inhibitor: a novel targeting ligand for nanotherapeutic drug delivery inhibiting tumor growth without systemic toxicity. *Nanomedicine* [Epub ahead of print]

(32) Kim, S. H., Tan, J. P., Nederberg, F., Fukushima, K., Colson, J., Yang, C., Nelson, A., Yang, Y. Y., and Hedrick, J. L. (2010) Hydrogen bonding-enhanced micelle assemblies for drug delivery. *Biomaterials 31* (31), 8063–71.

(33) May, A., Bhaumik, S., Gambhir, S. S., Zhan, C., and Yazdanfar, S. (2009) Whole-body, real-time preclinical imaging of quantum dot fluorescence with time-gated detection. *J. Biomed. Opt. 14*, 060504.

(34) Botchway, S. W., Charnley, M., Haycock, J. W., Parker, A. W., Rochester, D. L., Weinstein, J. A., and Williams, J. A. (2008) Time-resolved and two-photon emission imaging microscopy of live cells with inert platinum complexes. *Proc. Natl. Acad. Sci. U. S. A 105*, 16071–16076.

(35) Akers, W. J., Berezin, M. Y., Lee, H., and Achilefu, S. (2008) Predicting in vivo fluorescence lifetime behavior of near-infrared fluorescent contrast agents using in vitro measurements. *J. Biomed. Opt. 13*, 054042.

(36) Kan, P., Tsao, C.-W., Wang, A.-J., Su, W.-C., and Liang, H.-F. (2011) A liposomal formulation able to incorporate a high content of paclitaxel and exert promising anticancer effect. *J. Drug Delivery 2011*, 1–9.

(37) Casadei, M. A., Cerreto, F., Cesa, S., Giannuzzo, M., Feeney, M., Marianecci, C., and Paolicelli, P. (2006) Solid lipid nanoparticles incorporated dextran hydrogels. A new drug delivery system for oral formulations. *Int. J. Pharm. 325*, 140–146.

(38) Kim, I., Jeong, Y., and Kim, S-ZH. (2000) Self-assembled hydrogel nanoparticles compoused of dextran and polyethyleneglycol macromer. *Int. J. Pharm. 205*, 109–116.

(39) De Geest, B. G., Stubbe, B. G., Jonas, A. M., Van Thienen, T., Hinrichs, W. L., Demeester, J, and De Smedt, S. C. (2006) Self-exploding lipid coated microgels. *Biomacromolecules 7*, 373–379.

SUPPORTING INFORMATION

The bar graph in SI Figure 1 shows the same peak wavelength emission intensity for the QDs before and after lipid conjugation. SI Figure 2 indicates that the QD liposomes and the QDs were non-toxic in the concentrations tested (0.01 to 0.20 μM) when applied to U87 cells in culture.

SI Figure 1

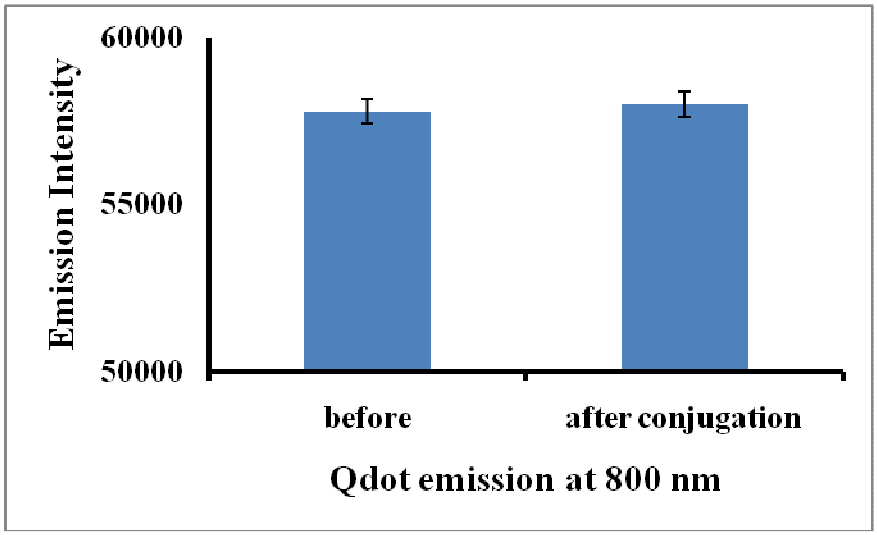

SI Figure 2

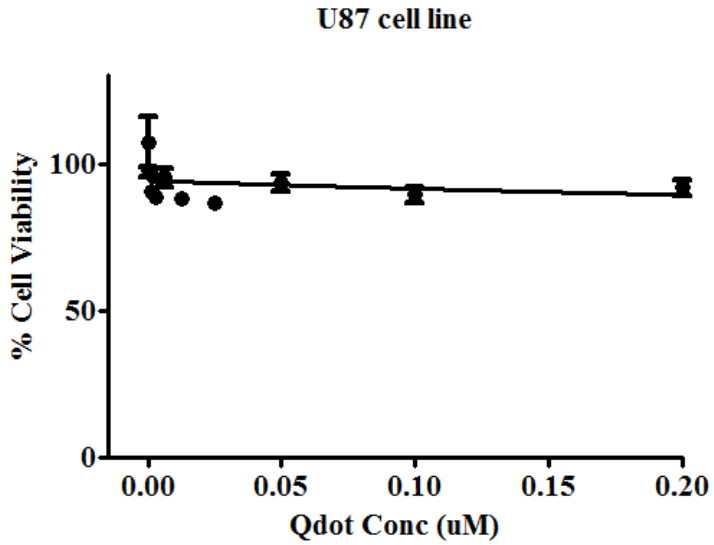

Bioconjugate Chemistry

ARTICLE

pubs.acs.org/bc

Use of Model Peptide Reactions for the Characterization of Kinetically Controlled Ligation

Joongoo Lee,[†] Yoonjin Kwon,[†] Brad L. Pentelute,[‡] and Duhee Bang*[,†]

[†]Department of Chemistry, Yonsei University, Shinchon 134 Seoul 120-749 Korea

[‡]Department of Microbiology and Molecular Genetics, Harvard Medical School, Boston, Massachusetts

Supporting Information

ABSTRACT:

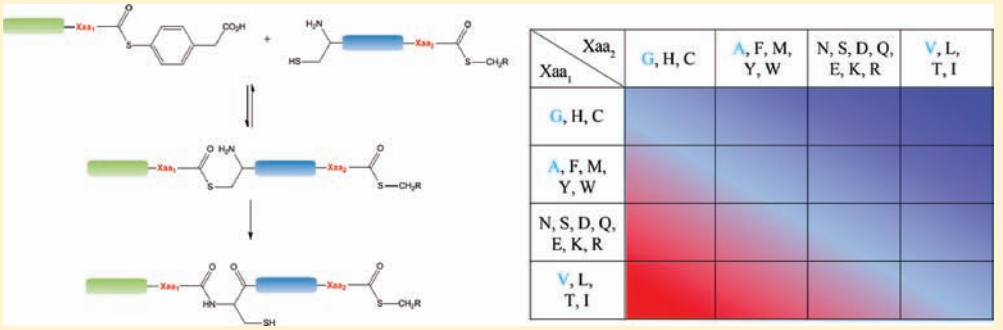

Since the introduction of kinetically controlled ligation (KCL), a chemoselective reaction between a peptide-$^{\alpha}$thioarylester and a Cys-peptide-$^{\alpha}$thioalkylester, KCL has been utilized for the total chemical synthesis of large proteins (i.e., lysozyme and HIV-protease) by providing fully convergent synthetic routes. Although KCL has the potential to become an important chemistry for protein synthesis, the principle of KCL is not fully characterized. In particular, prior work on KCL has focused on the reactivity difference of the two different -$^{\alpha}$thioester forms—alkyl vs aryl. Another equally important feature of KCL, Xaa−Cys ligation sites, has not been investigated. The work reported here describes combinatorial KCL reactions using model peptides to dissect the interplay of the Xaa_1, Xaa_2, -$^{\alpha}$thioarylester, and -$^{\alpha}$thioalkylester. Results from these studies provide fundamental insights into the KCL reaction, and will lead to the optimal synthetic route for the routine chemical synthesis of large target protein molecules.

INTRODUCTION

The chemical synthesis of proteins may allow for the creation of artificial proteins with novel function.[1,2] However, due to solid-phase peptide synthesis size limitations (ca. 50 amino acids (aa)), the preparation of large synthetic proteins requires the ligation of multiple peptides. Native chemical ligation (NCL) has provided the most practical solution for the ligation of polypeptides, whereby native peptide bonds are formed from a chemoselective reaction of unprotected peptide segments (i.e., a peptide-$^{\alpha}$thioester and a Cys-peptide).[3,4] NCL has allowed for the total synthesis of a number of proteins with full biological activity.[2,5,6]

Although NCL can provide a facile route for the synthesis of proteins, this amide-bond forming chemistry has been limited to the sequential ligation of peptides in the C-to-N direction, and most synthetic proteins have been prepared by sequential NCL of two to four peptide segments.[6−8] Sequential ligation is possible because of the facile transformation of Thz- to Cys-, where Thz is the cryptic form of Cys.[7,9] However, N-to-C directional ligation has been a challenging task because of the dual reactivity of the Cys-peptide-$^{\alpha}$thioalkylester which undergoes side-reactions.

Recently, the KCL method was introduced to enable the convergent ligation of multiple unprotected peptide segments.[10] A key feature of KCL chemistry is to exploit the reactivity differences between the -$^{\alpha}$thioarylester and the -$^{\alpha}$thioalkylester. A KCL between a peptide1-$^{\alpha}$thioarylester and a Cys-peptide2-$^{\alpha}$thioalkylester leads to the desired ligation product (i.e., peptide1-Cys-peptide2-$^{\alpha}$thioalkylester) because the -$^{\alpha}$thioalkylester acts as a synthon compared to the highly reactive -$^{\alpha}$thioarylester group. Other chemistries have been developed for the introduction of chemical groups that can be transformed to -$^{\alpha}$thioesters.[11−16] Notably, a strategy utilizing N-alkylated Cys at the C-terminal peptide is promising for the use in convergent chemical protein synthesis because the peptide can generate peptide-$^{\alpha}$thioester upon treatment with 3-mercaptopropionic acid.[5,11,12] However, the conversion may be limited to the generation of peptide-$^{\alpha}$thioester containing only C-terminal Gly due to the incomplete conversion with other C-terminal amino acids.

Received: May 2, 2011
Revised: June 27, 2011
Published: July 10, 2011

ACS Publications © 2011 American Chemical Society

dx.doi.org/10.1021/bc2002242 | *Bioconjugate Chem.* 2011, 22, 1645–1649

KCL is the only method that can be used for both N-to-C[17] and C-to-N ligations because of the reaction modularity of the dual functional groups including the -$^{\alpha}$thioalkylester and -$^{\alpha}$thioarylester as well as conversion between the Thz- and Cys-. Due to the reactivity control of the Cys-peptide-$^{\alpha}$thioester, KCL has the potential to be used for the routine preparation of large proteins in a fully convergent manner.[18] In fact, kinetically controlled convergent ligation of multiple peptides has enabled the preparation of lysozyme[19] and one of the largest synthetic protein molecules, the 203aa HIV protease.[20]

Although KCL has the potential to become an important chemistry for convergent peptide ligation, its reaction kinetics is not fully understood. We assumed that the KCL reaction, originally developed by utilizing reactivity differences between the different -$^{\alpha}$thioesters forms, would also be highly dependent on the Xaa reactivity at the two reactants; the peptide-$\underline{Xaa_1}$-$^{\alpha}$thioarylester and Cys-peptide-$\underline{Xaa_2}$-$^{\alpha}$thioalkylester. This assumption was based on previous NCL research; Dawson et al. performed combinatorial ligations of LYRA-Xaa-$^{\alpha}$thioester peptides to a Cys-RANK peptide to illustrate that NCL reaction kinetics are highly dependent on the Xaa-Cys ligation site.[21] Because two reactive "Xaa-Cys" ligation sites (at the two C-terminal -$^{\alpha}$thioesters) were present during the KCL reaction, the synthetic design of KCL for chemical protein synthesis is more complex. To gain insight into the KCL reaction, we set out to perform a characterization of KCL by combinatorial reactions of model peptides, including the peptide-Xaa_1-$^{\alpha}$thioarylester and the Cys-peptide-Xaa_2-$^{\alpha}$thioalkylester. Results from these studies provide fundamental insight into the KCL reaction, and lead to the optimal synthetic route for the routine chemical synthesis of large target protein molecules.

EXPERIMENTAL SECTION

Materials. *p*-Methyl-benzhydrylamine resin·HCl, Boc-amino acids, *S*-trityl-β-mercaptopropionic acid, and 2-(1*H*-benzotriazol-1-yl)-1,1,3,3-tetramethyluronium hexafluorophosphate (HBTU) were obtained from Peptide International (Louisville, KY). *N*,*N*-Diisopropylethylamine (DIEA) was obtained from Applied Biosystems (Foster City, CA). *N*,*N*-Dimethylformamide (DMF) was purchased from Burdick & Jackson (Muskegon, MI). Dichloromethane (DCM) was purchased from Duksan (Ahnsan, Korea). Trifluoroacetic acid (TFA) was from Daejung (Siheong, Korea).

Peptide Synthesis. Peptide-$^{\alpha}$thioesters were prepared by manual in situ neutralization Boc chemistry[22] peptide synthesis on a *p*-methyl-benzhydrylamine resin. Amino acid side-chain protection was as follows: Arg(Tos), Cys(4-CH_3Bzl), Lys(Cl-Z), Tyr(Br-Z). Peptides were prepared on a 0.2 mmol scale. In brief, each synthetic cycle consisted of N$^{\alpha}$-Boc removal by two TFA treatments, two DMF washes, a 10 min coupling time with 1.0 mmol preactivated Boc-amino acid, and a DMF flow wash. Exceptions to this protocol were for the coupling of C-terminal amino acid (Gly, Ala, Val) and S-trityl-β-mercaptopropionic acid, which had a 30 min coupling time. N$^{\alpha}$-Boc-amino acids (1.0 mmol, 5-fold excess) were preactivated for 1 min with 0.95 mmol HBTU (0.4 M in DMF) in the presence of excess DIEA (2.85 mmol). After chain assembly was completed, the peptides were deprotected and cleaved from the resin by treatment with anhydrous hydrogen fluoride (HF) containing *p*-cresol (5%, v/v) for 1 h at 0 °C. Peptide composition was verified by LC-MS as follows: LYRA-Gly-$^{\alpha}$thioester, observed mass (ob.) 728.7 Da, calculated average mass (ca.) 728.8 Da; LYRA-Ala-$^{\alpha}$thioester, ob. 742.7 Da, ca. 742.9 Da; LYRA-Val-$^{\alpha}$thioester, ob. 770.8 Da, ca. 770.9 Da; CLAFK-Gly-$^{\alpha}$thioester, ob. 724.5 Da, ca. 724.9 Da; CLAFK-Ala-$^{\alpha}$thioester, ob. 738.7 Da, ca. 738.9 Da; and CLAFK-Val-$^{\alpha}$thioester peptides, ob. 766.7 Da, ca. 767.0 Da.

Scheme 1[a]

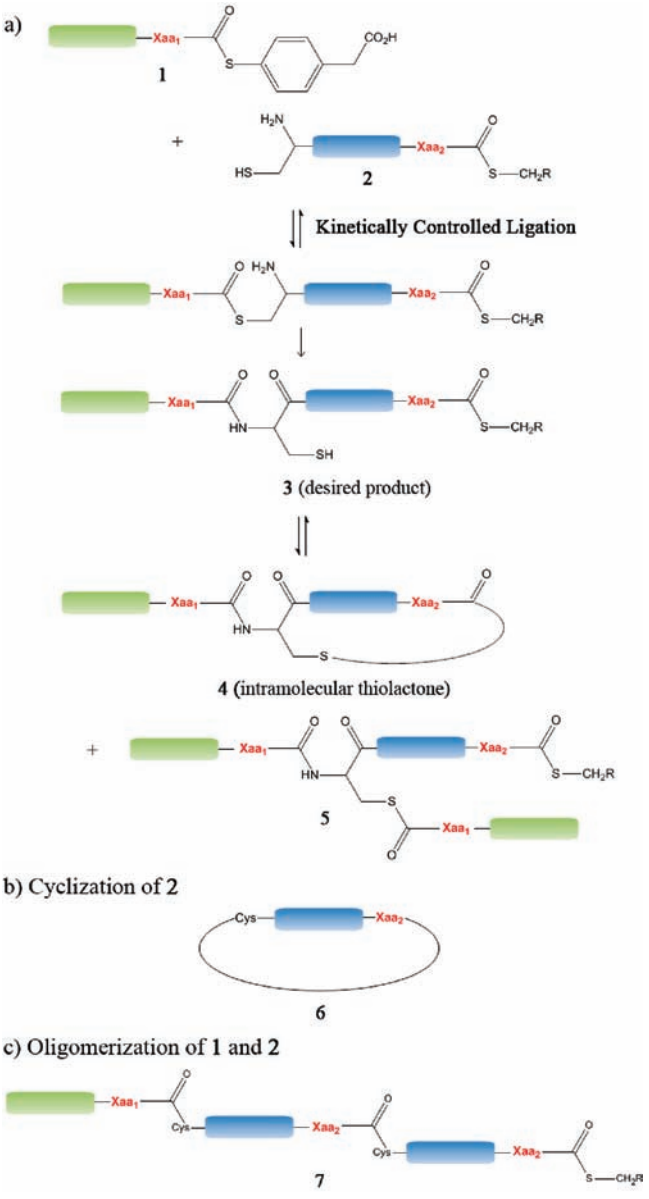

[a] (a) Kinetically controlled ligation (KCL) reaction with peptide-Xaa_1-$^{\alpha}$thioarylester (**1**) and Cys-peptide-Xaa_2-$^{\alpha}$thioalkylester (**2**). The Xaa_1 and Xaa_2 represent Gly, Ala, or Val residues resulting in nine possible combinatorial reactions. Peptide (**3**) was transformed to the by-products (**4** and **5**) through intramolecular transthioesterification and self-ligation. KCL side-reactions: (b) cyclization and (c) oligomerization.

LC-MS Analysis. Reaction aliquots for each time point were characterized by LC-MS, using a Vydac C4 column (5 μm, 0.46 × 5 cm). The analysis of species present in the resulting solution was performed by integrating the peak area from the UV−vis spectra measured at 214 nm in analytical HPLC profiles at each time point.

Conversion of LYRA-Xaa$_1$-$^{\alpha}$thioalkylester Peptides to LYRA-Xaa$_1$-$^{\alpha}$thioarylester Peptides. Conversion of peptide-$^{\alpha}$thioalkylester to peptide-$^{\alpha}$thioarylester was performed by dissolving crude peptide-$^{\alpha}$thioalkylester (ca. 1 mM) in a pH 6.8 aqueous buffer containing 6 M guanidine hydrochloride and 4-mercaptophenylacetic acid (200 mM).[10,23] The conversion reaction was monitored by LC-MS. The desired peptide-$^{\alpha}$thioarylester was isolated by preparative HPLC, and fractions were confirmed by mass spectrometry and subsequently lyophilized.

KCL. Nine model reactions for the ligation of two peptides (ca. 0.5 mM each, **1** and **2** in Scheme 1) were conducted in 200 mM phosphate buffer, pH 6.8, containing 6 M guanidine hydrochloride, and 30 mM tris(2-carboxyethyl)phosphine hydrochloride (TCEP).[10] No thiol additive was added during the ligation reaction. At each time point (7.5, 15, 30, 60, 120, and 240 min), an aliquot (20 μL) was extracted from the reaction and quenched with 2.5% TFA (16 μL) in water. Peptides in each aliquot were characterized by LC-MS.

RESULTS AND DISCUSSION

For the analysis of all possible KCL reactions, a large number of combinatorial KCL reactions (400 reactions from 20 different peptide-Xaa$_1$-$^{\alpha}$thioarylester peptides, and 20 different Cys-peptide-Xaa$_2$-$^{\alpha}$thioalkylester peptides) are needed. KCL (unlike NCL) reactions produce multiple products, which further complicates the process for tracking the reaction pathways in detail.[20]

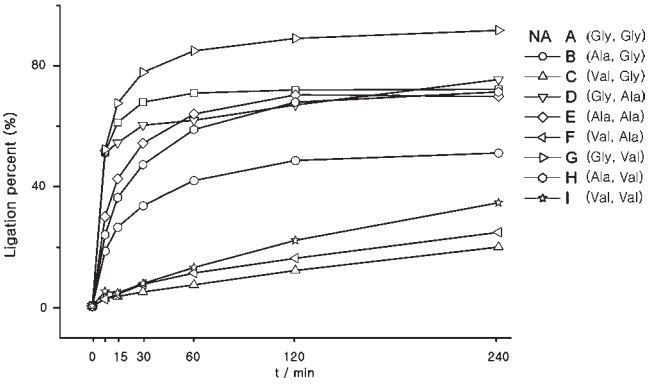

Figure 1. Yield of the nine KCL model reactions as a function of time.

Thus, we focused on the preparation of the most representative model peptides to gain insights for the KCL reaction process (Scheme 1). Three LYRA-Xaa$_1$-$^{\alpha}$thioarylester peptides (Xaa$_1$ = Gly, Ala, or Val) and three CLAFK-Xaa$_2$-$^{\alpha}$thioalkylester peptides (Xaa$_2$ = Gly, Ala, or Val) were chosen based on the Xaa-Cys ligation sites;[21] Gly-Cys shows one of the fastest ligation sites, Val-Cys as one of the slowest, and Ala-Cys with an intermediate rate. A total of nine (3^2) model KCL reactions were conducted.

Yields for the nine KCL model reactions are reported in Figure 1. In addition to the desired KCL product (**3**), we included thiolactone (**4**) and trimer (**5**) as desired product peaks because these molecules can be converted to the product peak by the addition of excess thiol additives.[20] To evaluate the percentage of ligated peptide molecules, reaction aliquots for each time point were characterized by integrating the HPLC peak area at each time point (up to four hours).

Figure 1 and Table 1 show that Xaa$_1$ of the peptide-Xaa$_1$-$^{\alpha}$thioarylester greatly affected ligation yield over the Xaa$_2$ of the Cys-peptide-Xaa$_2$-$^{\alpha}$thioalkylester. For example, the top three KCL yields were obtained for Gly as Xaa$_1$. The next highest yields were obtained when KCL was performed with Ala as Xaa$_1$. We also observed that Xaa$_2$ with bulkier side chains affected KCL yields with a general trend of increased ligation yield. However, magnitude of the Xaa$_2$ effect was smaller than the Xaa$_1$. For example, ligation yield increased when Xaa$_2$ was Val rather than Ala or Gly (Figure 1). Dependence of the higher ligation yield on Xaa$_1$ rather than Xaa$_2$ is most likely due to the fact that the Xaa$_1$ is an -$^{\alpha}$thioarylester peptide.

To dissect the KCL reaction in detail, we determined the rate constants for each of the nine KCL model reactions (Supporting Information Figure S2). The peptide-Xaa$_1$-$^{\alpha}$thioarylester concentration (C_t) change over time was used for evaluation of the rate constant. The observed rate constant (k_{obs}) for each reaction (Table 2) was estimated directly from slopes of the straight lines shown in Figure S2. A linear relationship of $1/C_t$ versus time was observed for these model reactions, indicating that most of the KCL reactions follow second-order kinetics. Exceptions to the linear relationships are discussed below.

The observed ligation yields for each KCL reaction indicate that Xaa$_1$ is the important factor for reaction kinetics (Figure 1, Table 1). Change of Xaa$_1$ from Gly to Ala to Val led to a two- to

Table 1. Cyclized and Ligated Peptides Resulting from KCL Reactions[a]

		Cys-peptide-Xaa$_2$-$^{\alpha}$thioalkylester		
cyclized peptide/ligated peptides (%)		Gly	Ala	Val
Peptide-Xaa$_1$ -$^{\alpha}$thioarylester	Gly	22/71 (reaction **A**)	22/74 (reaction **D**)	0/90 (reaction **G**)
	Ala	11/50 (reaction **B**)	13/68 (reaction **E**)	0/70 (reaction **H**)
	Val	33/19 (reaction **C**)	25/24 (reaction **F**)	0/34 (reaction **I**)

[a] Percent cyclization was determined by calculating the fraction of UV−vis peak area (%) of **6**. Percent ligation was determined by integration of the peak areas of **3**, **4**, and **5**.

Table 2. KCL Rate Constants (k_{obs}) between Peptide-Xaa$_1$-$^{\alpha}$thioarylester and Cys-peptide-Xaa$_2$-$^{\alpha}$thioalkylester

		Cys-peptide-Xaa$_2$-$^{\alpha}$thioalkylester		
k_{obs} (M^{-1} s^{-1})		Gly	Ala	Val
Peptide-Xaa$_1$-$^{\alpha}$thioarylester	Gly	2.00×10^{-7} (reaction **A**)	4.17×10^{-6} (reaction **D**)	2.33×10^{-6} (reaction **G**)
	Ala	1.37×10^{-8} (reaction **B**)	6.50×10^{-8} (reaction **E**)	1.67×10^{-8} (reaction **H**)
	Val	6.83×10^{-9} (reaction **C**)	9.67×10^{-9} (reaction **F**)	1.30×10^{-8} (reaction **I**)

Table 3. R^2 Values for the KCL Reaction Straight Lines

R^{2a}		Cys-peptide-Xaa$_2$-$^{\alpha}$thioalkylester		
		Gly	Ala	Val
Peptide-Xaa$_1$-$^{\alpha}$thioarylester	Gly	0.624 (reaction **A**)	0.921 (reaction **D**)	0.984 (reaction **G**)
	Ala	0.894 (reaction **B**)	0.954 (reaction **E**)	0.984 (reaction **H**)
	Val	0.809 (reaction **C**)	0.944 (reaction **F**)	0.985 (reaction **I**)

[a] R^2 was evaluated from the method of least-squares and indicates the proportion of variation. Values were close to unity, as the data were close to the straight trend line. Although rate constants were evaluated from the slope of the straight line, they were calculated on the assumption that the concentration of cyclized peptide remained constant over the reaction and satisfied the pseudo-second-order reaction. However, R^2 values obtained from KCL reactions with Cys-peptide-Gly-$^{\alpha}$thioalkylester (reactions **A**, **B**, and **C**) deviated from the straight line as shown in Figure S2. In contrast, reactions of Cys-peptide-Ala-$^{\alpha}$thioalkylester and Cys-peptide-Val-$^{\alpha}$thioalkylester (reactions **D**-**F** and **G**-**I**) were in almost perfect accord with the pseudo=second-order reaction kinetics.

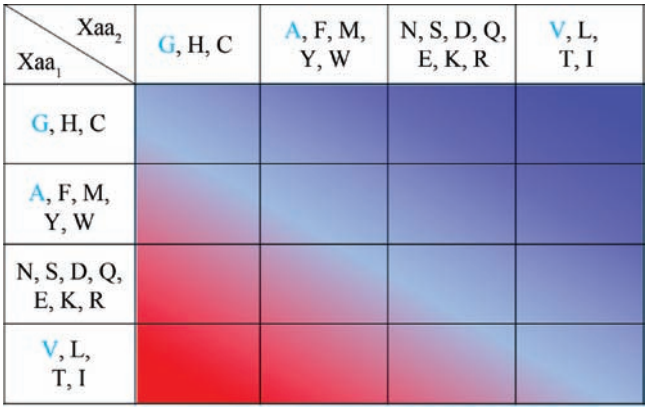

Figure 2. Optimal KCL reactions based on the combination of a Xaa$_1$ and Xaa$_2$. The blue area represents the combination of Xaa$_1$ and Xaa$_2$ exhibiting efficient KCL reactions while the combinations highlighted in red show inefficient KCL reactions. Gly, Ala, and Val in blue indicate the Xaa amino acids investigated in this study. Reactions with the other 19 amino acids except Pro are inferred from previous NCL kinetics studies.[21] Pro/Pro as Xaa$_1$/Xaa$_2$ is not presented here because Pro/Pro is in a largely blue square and is misleading given a recent report to the contrary.[24]

three-order decrease in the rate constant. In contrast, the reaction rate increased as the C-terminal amino acid residue in the Cys-peptide-Xaa$_2$-$^{\alpha}$thioalkylester varied from Gly to Ala to Val. In addition, kinetics from Xaa$_2$ were affected less (on the order of ~50-fold) compared to Xaa$_1$. The KCL with Cys-peptide-Gly-$^{\alpha}$thioalkylester (reactions **A**, **B**, and **C**) had smaller rate constants compared to the Cys-peptide-Ala-$^{\alpha}$thioalkylester (reaction **D**, **E**, and **F**) or Cys-peptide-Val-$^{\alpha}$thioalkylester (reaction **G**, **H**, and **I**) reactions.

Possible reactions with Cys-peptide-Xaa$_2$-$^{\alpha}$thioalkylesters in KCL reactions include ligation with peptide-Xaa$_1$-$^{\alpha}$thioarylester, intramolecular cyclization, and oligomerization between Cys-peptide-Xaa$_2$-$^{\alpha}$thioalkylesters.[20] However, a negligible amount of oligomerization product was detected in the nine KCL reactions conducted here (Supporting Information Figure S1). This implies that reaction priority is as follows: first, the desired KCL reaction is faster than intramolecular cyclization, and second, intramolecular cyclization is faster than oligomerization between Cys-peptide-Xaa$_2$-$^{\alpha}$thioalkylesters.

Because the major competing reaction for KCL is Cys-peptide-$^{\alpha}$thioalkylester reactant cyclization, less cyclization during the reaction leads to a large percent of ligated product (Table 1). All KCL reactions with Cys-peptide-Val-$^{\alpha}$thioalkylester resulted in the highest ligation yield compared to the other reactions involving Xaa$_2$ with less bulkier side chains. For example, increased blocking of intramolecular cyclization by the Cys-peptide-Val-$^{\alpha}$thioalkylester made the reaction follow second-order kinetics (Table 3). In contrast, the Cys-peptide-Gly-$^{\alpha}$thioalkylester readily underwent rapid intramolecular cyclization prior to the ligation reaction with the peptide-$^{\alpha}$thioarylester. This cyclization reduced the effective concentration of Cys-peptide-Gly-$^{\alpha}$thioalkylester during the KCL reaction resulting lower KCL yields.

CONCLUSIONS

In this work, combinatorial KCL reactions were performed to dissect how Xaa and -$^{\alpha}$thioester combinations contribute to overall reaction yields and kinetics. On the basis of the KCL results presented here and previous NCL studies,[21] we conclude that optimal KCL reactions can be achieved by the combination of a reactive Xaa$_1$ and a less reactive Xaa$_2$ (blue colors, Figure 2). For example, the use of Ala for the Xaa$_1$ would preclude the use of more reactive Gly, His, or Cys as the Xaa$_2$. Our study further illustrates the following aspects of the KCL. First, ligation yields and kinetics were highly dependent on the nature of Xaa$_1$. For example, the KCL with a peptide-Gly-$^{\alpha}$thioarylester resulted in the fastest ligation, while the peptide-Val-$^{\alpha}$thioarylester showed the slowest ligation rate due to the hindered β-branched side chain of Val. Second, Xaa$_2$ affected ligation kinetics, with the Xaa$_2$ contribution largely being due to the concentration decrease of the Cys-peptide-Xaa$_2$-$^{\alpha}$thioalkylester reactant from the intramolecular cyclization reaction. The reaction rate increased as the Xaa$_2$ contained a bulkier side chain by preventing cyclization of the reacting peptide. However, the effect of Xaa$_2$ was not as profound as the effect of Xaa$_1$. In conclusion, the KCL reaction coordinates are highly dependent on the interplay between Xaa$_1$, Xaa$_2$, -$^{\alpha}$thioarylester, and -$^{\alpha}$thioalkylester of the reacting peptides. It is anticipated that understanding the influence of Xaa and different -$^{\alpha}$thioester forms will play an important role in the development of efficient KCL reactions. We also expect that the kinetic studies described here can be generalized to amino acids (Xaa$_1$ and Xaa$_2$) not investigated here (Figure 2).

ASSOCIATED CONTENT

Supporting Information. Two figures as described in the text. This material is available free of charge via the Internet at http://pubs.acs.org.

AUTHOR INFORMATION

Corresponding Author
*Email: duheebang@yonsei.ac.kr.

ACKNOWLEDGMENT

Grants from the National Research Foundation of Korea, Basic Science Research Program (2009-0072688) and the BK21 program of the Ministry of Education, Science and Technology funded this work. D.B. is a TJ Park junior faculty fellow supported by the Posco TJ Park Foundation.

REFERENCES

(1) Dawson, P. E., and Kent, S. B. (2000) Synthesis of native proteins by chemical ligation. *Annu. Rev. Biochem. 69*, 923–960.

(2) Kent, S. B. H. (2009) Total chemical synthesis of proteins. *Chem. Soc. Rev. 38*, 338–351.

(3) Dawson, P. E., Muir, T. W., Clark-Lewis, I., and Kent, S. B. (1994) Synthesis of proteins by native chemical ligation. *Science 266*, 776–779.

(4) Macmillan, D. (2006) Evolving strategies for protein synthesis converge on native chemical ligation. *Angew. Chem., Int. Ed. 45*, 7668–7672.

(5) Byun, E., Kim, J., Kang, S. M., Lee, H., Bang, D., and Lee, H. (2011) Surface PEGylation via native chemical ligation. *Bioconjugate Chem. 22*, 4–8.

(6) Hackenberger, C. P. R., and Schwarzer, D. (2008) Chemoselective ligation and modification strategies for peptides and proteins. *Angew. Chem., Int. Ed. 47*, 10030–10074.

(7) Bang, D., and Kent, S. B. H. (2004) A one-pot total synthesis of crambin. *Angew. Chem., Int. Ed. 43*, 2534–2538.

(8) Kochendoerfer, G. G., Chen, S. Y., Mao, F., Cressman, S., Traviglia, S., Shao, H. Y., Hunter, C. L., Low, D. W., Cagle, E. N., Carnevali, M., Gueriguian, V., Keogh, P. J., Porter, H., Stratton, S. M., Wiedeke, M. C., Wilken, J., Tang, J., Levy, J. J., Miranda, L. P., Crnogorac, M. M., Kalbag, S., Botti, P., Schindler-Horvat, J., Savatski, L., Adamson, J. W., Kung, A., Kent, S. B. H., and Bradburne, J. A. (2003) Design and chemical synthesis of a homogeneous polymer-modified erythropoiesis protein. *Science 299*, 884–887.

(9) Villain, M., Vizzavona, J., and Rose, K. (2001) Covalent capture: a new tool for the purification of synthetic and recombinant polypeptides. *Chem. Biol. 8*, 673–679.

(10) Bang, D., Pentelute, B. L., and Kent, S. B. H. (2006) Kinetically controlled ligation for the convergent chemical synthesis of proteins. *Angew. Chem., Int. Ed. 45*, 3985–3988.

(11) Erlich, L. A., Kumar, K. S. A., Haj-Yahya, M., Dawson, P. E., and Brik, A. (2010) N-Methylcysteine-mediated total chemical synthesis of ubiquitin thioester. *Org. Biomol. Chem. 8*, 2392–2396.

(12) Kumar, K. S. A., Spasser, L., Erlich, L. A., Bavikar, S. N., and Brik, A. (2010) Total chemical synthesis of di-ubiquitin chains. *Angew. Chem., Int. Ed. 49*, 9126–9131.

(13) Ackrill, T., Anderson, D. W., and Macmillan, D. (2010) Towards biomolecular assembly employing extended native chemical ligation in combination with thioester synthesis using an N -> S acyl shift. *Biopolymers 94*, 495–503.

(14) Zheng, J. S., Cui, H. K., Fang, G. M., Xi, W. X., and Liu, L. (2010) Chemical protein synthesis by kinetically controlled ligation of peptide O-esters. *ChemBioChem 11*, 511–515.

(15) Yuan, Y., Chen, J., Wan, Q., Tan, Z. P., Chen, G., Kan, C., and Danishefsky, S. J. (2009) Toward homogeneous erythropoietin: fine tuning of the C-terminal acyl donor in the chemical synthesis of the Cys(29)-Gly(77) glycopeptide domain. *J. Am. Chem. Soc. 131*, 5432–5437.

(16) Kawakami, T., and Aimoto, S. (2007) Sequential peptide ligation by using a controlled cysteinyl prolyl ester (CPE) autoactivating unit. *Tetrahedron Lett. 48*, 1903–1905.

(17) Rajagopal, S., and Kent, S. B. H. (2007) Total chemical synthesis and biophysical characterization of the minimal isoform of the KChIP2 potassium channel regulatory subunit. *Protein Sci. 16*, 2056–2064.

(18) Lee, J. Y., and Bang, D. (2010) Challenges in the chemical synthesis of average sized proteins: sequential vs. convergent ligation of multiple peptide fragments. *Biopolymers 94*, 441–447.

(19) Durek, T., Torbeev, V. Y., and Kent, S. B. H. (2007) Convergent chemical synthesis and high-resolution x-ray structure of human lysozyme. *Proc. Natl. Acad. Sci. U. S. A. 104*, 4846–4851.

(20) Torbeev, V. Y., and Kent, S. B. H. (2007) Convergent chemical synthesis and crystal structure of a 203 amino acid "covalent dimer" HIV-1 protease enzyme molecule. *Angew. Chem., Int. Ed. 46*, 1667–1670.

(21) Hackeng, T. M., Griffin, J. H., and Dawson, P. E. (1999) Protein synthesis by native chemical ligation: Expanded scope by using straightforward methodology. *Proc. Natl. Acad. Sci. U. S. A. 96*, 10068–10073.

(22) Schnolzer, M., Alewood, P., Jones, A., Alewood, D., and Kent, S. B. H. (1992) In situ neutralization in boc-chemistry solid phase peptide synthesis - Rapid, high yield assembly of difficult sequences. *Int. J. Pept. Res. Ther. 40*, 180–193.

(23) Johnson, E. C. B., and Kent, S. B. H. (2006) Insights into the mechanism and catalysis of the native chemical ligation reaction. *J. Am. Chem. Soc. 128*, 6640–6646.

(24) Pollock, S. B., and Kent, S. B. (2011) An investigation into the origin of the dramatically reduced reactivity of peptide-prolyl-thioesters in native chemical ligation. *Chem. Commun. (Camb.) 47*, 2342–2344.

Supporting Information for

Use of Model Peptide Reactions for the Characterization of a Kinetically Controlled Ligation

*Joongoo Lee, Yoonjin Kwon, Brad L. Pentelute, and Duhee Bang**

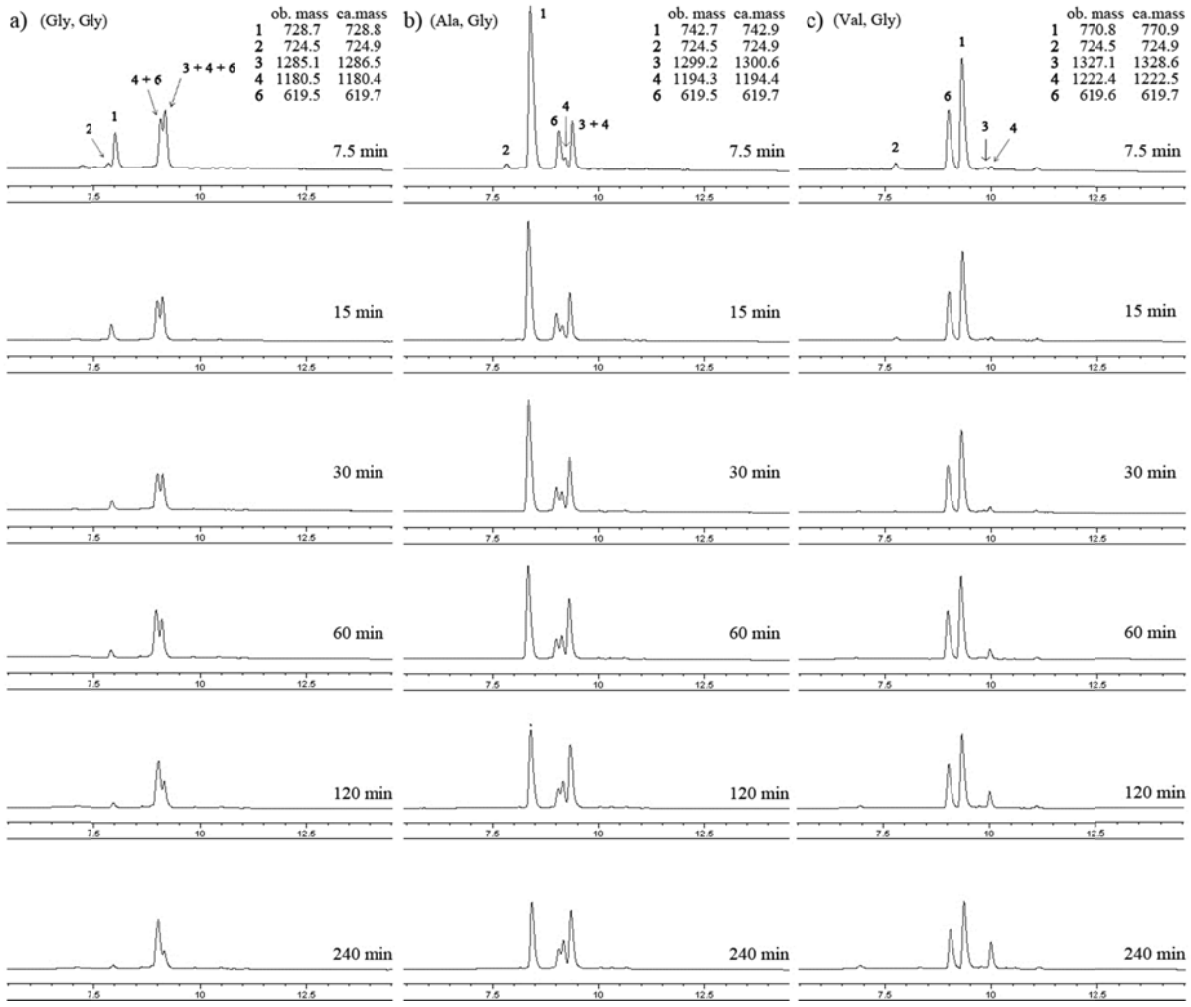

Figure S1. UV-Vis spectral changes for the nine KCL reactions. Change was monitored by LC-MS and measured at λ=214 nm. The UV-Vis spectra for the **A**, **B**, **C**, **D**, **E**, **F**, **G**, **H**, and **I** reactions are shown in a), b), c), d), e), f), g), h), and i), respectively.

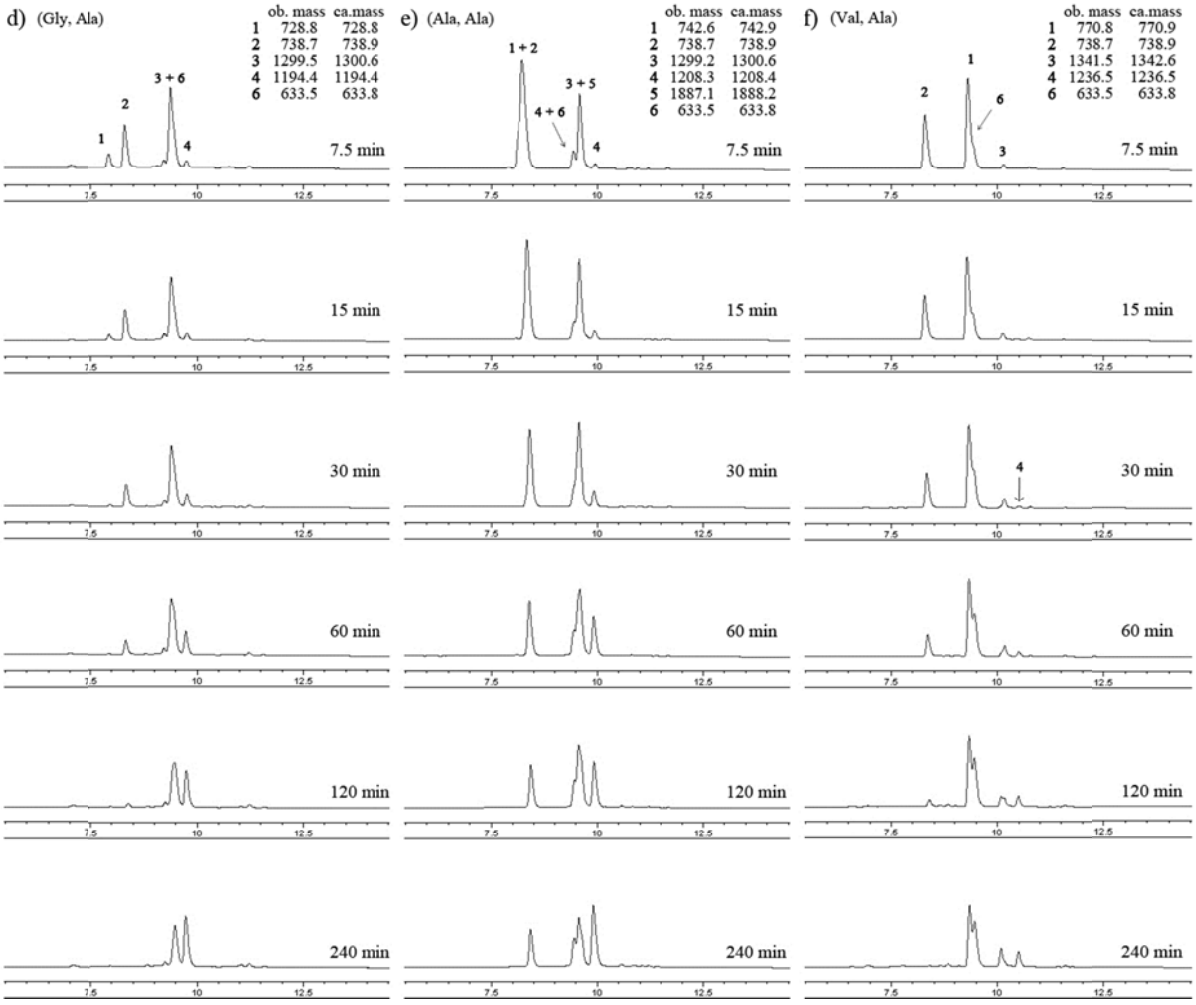
d) (Gly, Ala)
ob. mass ca.mass
1 728.8 728.8
2 738.7 738.9
3 1299.5 1300.6
4 1194.4 1194.4
6 633.5 633.8
1
2
3 + 6
4
7.5 min
15 min
30 min
60 min
120 min
240 min
e) (Ala, Ala)
ob. mass ca.mass
1 742.6 742.9
2 738.7 738.9
3 1299.2 1300.6
4 1208.3 1208.4
5 1887.1 1888.2
6 633.5 633.8
1 + 2
3 + 5
4 + 6
4
7.5 min
15 min
30 min
60 min
120 min
240 min
f) (Val, Ala)
ob. mass ca.mass
1 770.8 770.9
2 738.7 738.9
3 1341.5 1342.6
4 1236.5 1236.5
6 633.5 633.8
2
1
6
3
4
7.5 min
15 min
30 min
60 min
120 min
240 min
7.5
10
12.5

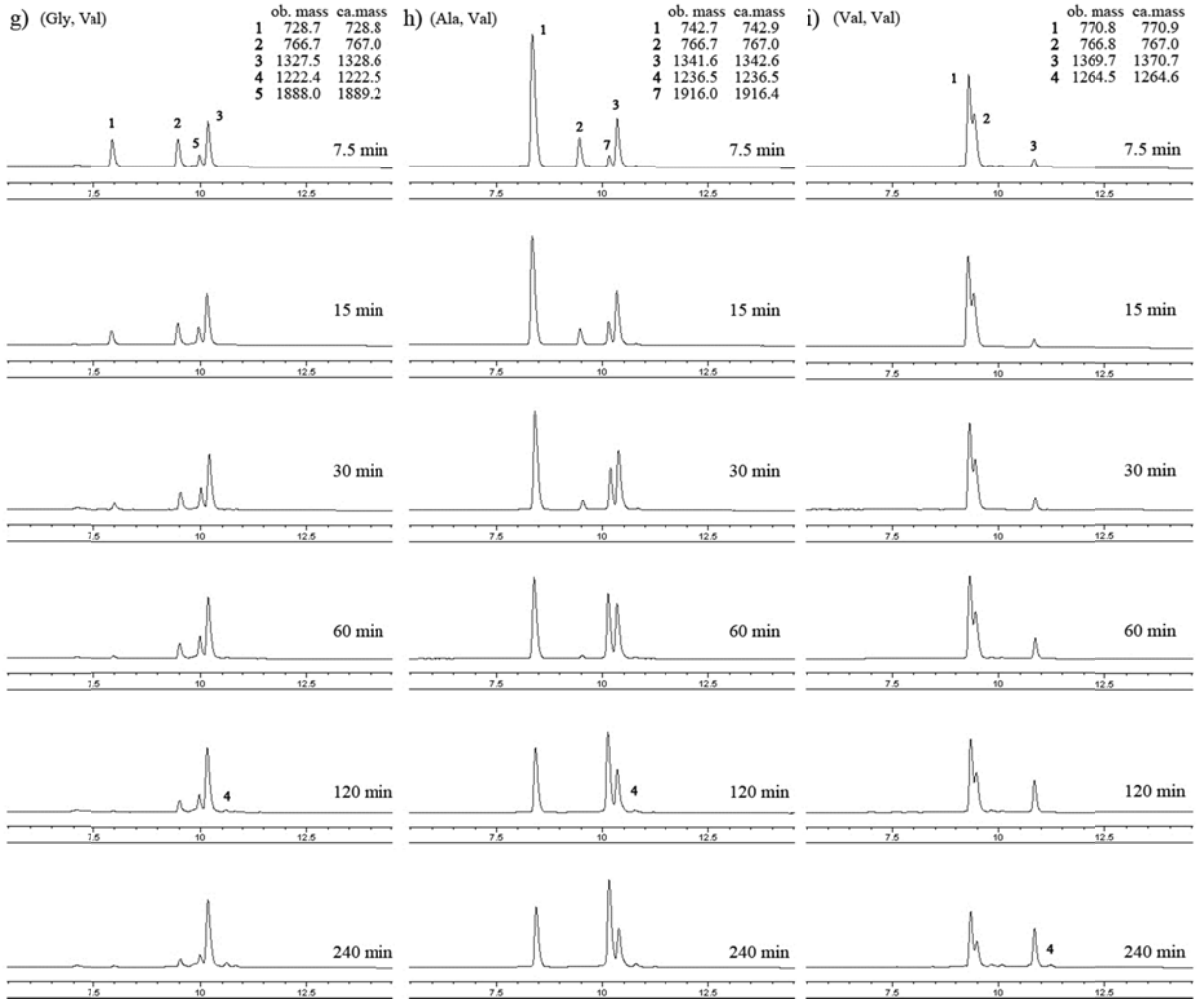
g) (Gly, Val)
ob. mass ca.mass
1 728.7 728.8
2 766.7 767.0
3 1327.5 1328.6
4 1222.4 1222.5
5 1888.0 1889.2
h) (Ala, Val)
ob. mass ca.mass
1 742.7 742.9
2 766.7 767.0
3 1341.6 1342.6
4 1236.5 1236.5
7 1916.0 1916.4
i) (Val, Val)
ob. mass ca.mass
1 770.8 770.9
2 766.8 767.0
3 1369.7 1370.7
4 1264.5 1264.6
7.5 min
15 min
30 min
60 min
120 min
240 min
7.5
10
12.5

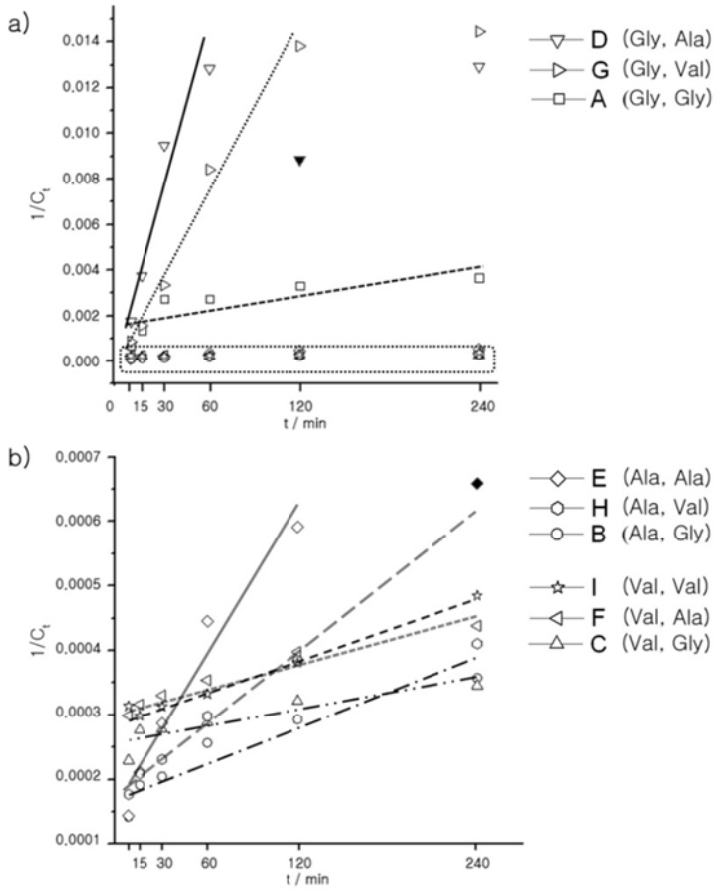

Figure S2. Plot of $1/C_t$ versus time and the rate constants (k_{obs}) for each KCL. The dotted box in a) is expanded in b) for clarification of data linearity. The rate constant was evaluated from the slope of each straight line. For **A**, **D**, and **G**, the concentration change for the first 30 min, 60 min, and 120 min were used to draw the straight line, respectively. The black reverse-triangle in reaction **C** and the black diamond in reaction **E** represent data not used for analysis due to aberrance. The parentheses represent the combination of (Xaa_1, Xaa_2) in the reacting peptides.

Bioconjugate Chemistry

ARTICLE

pubs.acs.org/bc

Multivalent Bifunctional Chelator Scaffolds for Gallium-68 Based Positron Emission Tomography Imaging Probe Design: Signal Amplification via Multivalency

Ajay N. Singh,[†,□] Wei Liu,[†,∥,□] Guiyang Hao,[†] Amit Kumar,[†] Anjali Gupta,[†] Orhan K. Öz,[†] Jer-Tsong Hsieh,[‡] and Xiankai Sun*[,†,§]

[†]Departments of Radiology and [‡]Urology, [§]Advanced Imaging Research Center, University of Texas Southwestern Medical Center, Dallas, Texas, United States

[∥]State Key Lab of Crystal Materials, Shandong University, Jinan, Shandong, P. R. China

Supporting Information

ABSTRACT: The role of the multivalent effect has been well recognized in the design of molecular imaging probes toward the desired imaging signal amplification. Recently, we reported a bifunctional chelator (BFC) scaffold design, which provides a simple and versatile approach to impart multivalency to radiometal based nuclear imaging probes. In this work, we report a series of BFC scaffolds ($^{t}Bu_3$-**1**-COOH, $^{t}Bu_3$-**2**-$(COOH)_2$, and $^{t}Bu_3$-**3**-$(COOH)_3$) constructed on the framework of 1,4,7-triazacyclononane-1,4,7-triacetic acid (NOTA) for ^{68}Ga-based PET probe design and signal amplification via the multivalent effect. For proof of principle, a known integrin $\alpha_v\beta_3$ specific ligand (c(RGDyK)) was used to build the corresponding NOTA conjugates (H_3**1**, H_3**2**, and H_3**3**), which present 1−3 copies of c(RGDyK) peptide, respectively, in a systematic manner. Using the integrin $\alpha_v\beta_3$ binding affinities (IC_{50} values), enhanced specific binding was observed for multivalent conjugates (H_3**2**: 43.9 ± 16.1 nM; H_3**3**: 14.7 ± 5.0 nM) as compared to their monovalent counterpart (H_3**1**: 171 ± 60 nM) and the intact c(RGDyK) peptide (204 ± 76 nM). The obtained conjugates were efficiently labeled with $^{68}Ga^{3+}$ within 30 min at room temperature in high radiochemical yields (>95%). The in vivo evaluation of the labeled conjugates, ^{68}Ga-**1**, ^{68}Ga-**2**, and ^{68}Ga-**3**, was performed using male severe combined immunodeficiency (SCID) mice bearing integrin $\alpha_v\beta_3$ positive PC-3 tumor xenografts (n = 3). All ^{68}Ga-labeled conjugates showed high in vivo stability with no detectable metabolites found by radio-HPLC within 2 h postinjection (p.i.). The PET signal amplification in PC-3 tumor by the multivalent effect was clearly displayed by the tumor uptake of the ^{68}Ga-labeled conjugates (^{68}Ga-**3**: 2.55 ± 0.50%ID/g; ^{68}Ga-**2**: 1.90 ± 0.10%ID/g; ^{68}Ga-**1**: 1.66 ± 0.15%ID/g) at 2 h p.i. In summary, we have designed and synthesized a series of NOTA-based BFC scaffolds with signal amplification properties, which may find potential applications as diagnostic gallium radiopharmaceuticals.

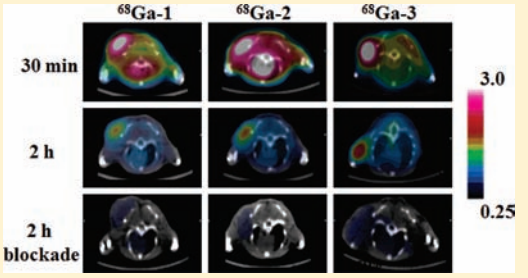

INTRODUCTION

Positron emission tomography (PET), a nuclear imaging technique, has become a standard-of-care tool for diagnosis, staging treatment planning, and therapeutic efficacy monitoring of patients with cancer or other diseases.[1−5] In addition to clinical applications, PET is also widely used in laboratory research to study the underlying mechanisms of diseases and to facilitate the discovery of new treatments.[6] Development and application of PET imaging probes from the standard PET radionuclides (^{15}O: $t_{1/2}$ = 2.04 min; ^{13}N: $t_{1/2}$ = 9.96 min; ^{11}C: $t_{1/2}$ = 20.4 min; and ^{18}F: $t_{1/2}$ = 110 min) suffers from the short half-lives of the radionuclides, which mandates the presence of a radiochemistry laboratory in close proximity to a cyclotron facility.[7] To date, PET probe development using nonstandard PET radionuclides (e.g., ^{64}Cu, ^{68}Ga, ^{89}Zr, ^{124}I) has drawn considerable interest given its independence from a cyclotron facility.[8,9] Among the nonstandard PET radionuclides, ^{68}Ga ($t_{1/2}$ = 68 min, 89% β^+, $E_{\beta+max}$ = 1.92 MeV, 11% EC) has the most clinical significance as it can be obtained on as-needed basis from a benchtop ^{68}Ge/^{68}Ga generator system thereby negating the onsite cyclotron requirement.[10−14] Compared to ^{18}F, the shorter half-life of ^{68}Ga is not necessarily a hindrance in preclinical or clinical applications because its well-established coordination chemistry enables rapid radiolabeling with high radiochemical yields,[15,16] which provides an opportunity to develop commercial kits to prepare PET probes onsite for diagnostic and prognostic imaging of diseases.

A macrocyclic chelator, 1,4,7-triazacyclononane-1,4,7-triacetic acid (NOTA), and its derivatives are particularly suitable for ^{68}Ga incorporation due to their fast and efficient radiolabeling and in vivo stability (Figure 1).[10,11,16] The stability of the Ga(III)-NOTA complex results from the perfect hole-size match between the NOTA cavity and the Ga(III) metal ion, which is

Received: May 2, 2011
Revised: June 9, 2011
Published: July 10, 2011

ACS Publications © 2011 American Chemical Society

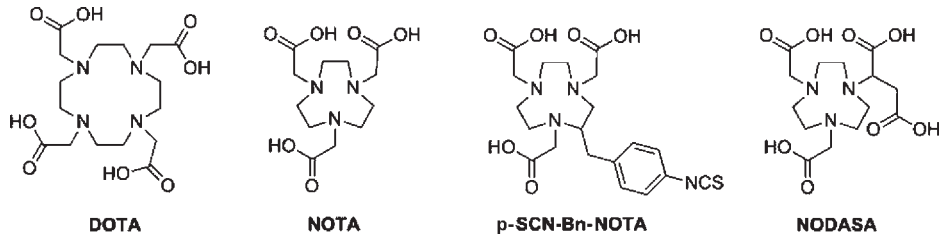

Figure 1. Structures of commonly used BFCs for gallium radiopharmaceuticals.

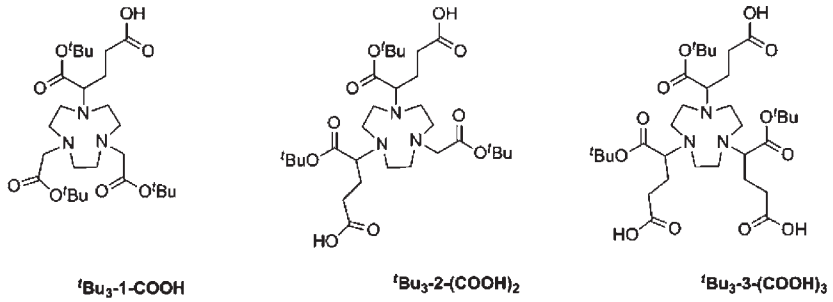

Figure 2. Structures of ^{t}Bu-protected BFC scaffolds: ^{t}Bu$_3$-**1**-COOH, ^{t}Bu$_3$-**2**-(COOH)$_2$, and ^{t}Bu$_3$-**3**-(COOH)$_3$.

accentuated by the tight embrace of the three coordinating carboxylate groups (Figure 1).[17−23] However, application of NOTA for a targeted PET probe design is restricted because of its limited bifunctionality. Once the pendent carboxylic acid of the NOTA is conjugated with a targeting vector, the coordinating ability of the NOTA with ^{68}Ga is compromised due to the loss of a coordinating pendant carboxylate group. Several NOTA derivatives such as *S*-2-(4-isothiocyanatobenzyl)-1,4,7-triazacyclononane-1,4,7-triaceticacid (p-SCN-Bn-NOTA), 1,4,7-triazacyclononane-1-succinic acid-4,7-diacetic acid (NODASA), and 2-(4,7-bis-(carboxymethyl)-1,4,7-triazonan-1-yl)pentanedioic acid (NODAGA) have been designed to circumvent this problem.[15,18,19,23,24] The general concept of these modifications is the presence of an additional functionality on the macrocylic core for vector conjugation, while preserving NOTA's capability of stable Ga(III) chelation (Figure 1).

A PET probe design is aimed towards facilitating the accurate detection and quantitative analysis of a disease state, which requires high imaging sensitivity and specificity of the designed probe toward the target. To date, the multivalent effect has become a well-accepted concept in the design of molecular imaging probes for specific signal amplification by enhancing the binding affinity of a probe to the specific cell surface receptor.[25] The most common way to incorporate the multivalent effect into a PET probe design is through the conjugation of a multimeric targeting vector on a bifunctional chelator (BFC). For instance, dimeric, tetrameric, and octameric forms of a cyclic-RGD (Arginine-Glycine-Aspartic Acid) peptide have been used to enhance the in vivo imaging properties of PET probes by the resulting multivalent effect.[26,27]

Recently, we reported a BFC scaffold design, which provides a simple and effective way to impart multivalency to PET imaging probes labeled with ^{64}Cu.[28] This unique design of BFC scaffolds provides multiple peripheral functional points for multipresentation of targeting vectors in a BFC without compromising the metal chelate stability of the chelating core. In this work, we have extended this approach to NOTA-based radiopharmaceuticals by synthesizing a series of NOTA BFC scaffolds, ^{t}Bu$_3$-**1**-COOH, ^{t}Bu$_3$-**2**-(COOH)$_2$, and ^{t}Bu$_3$-**3**-(COOH)$_3$ (Figure 2). The NOTA BFC scaffold design maintains the intact Ga(III) chelating NOTA core (after ^{t}Bu deprotection) and varies the number of peripheral carboxylate groups from 1 to 3 to anchor the corresponding number of targeting molecules. This allows us to investigate the multivalent effect on ^{68}Ga-labeled PET probe design in a systematic way. In this study, a well-validated integrin $\alpha_v\beta_3$ ligand (c(RGDyK)) was used as a model targeting molecule to generate monovalent H$_3$**1**, divalent H$_3$**2**, and trivalent H$_3$**3** (Figure 3). For comparison, a monovalent analogue (H$_3$**1a**) made from the commercially available p-SCN-Bn-NOTA was used as a positive control (Figure 3).[26]

EXPERIMENTAL SECTION

General Methods and Materials. All reactions were carried out under N_2 atmosphere in degassed dried solvents. Commercially available starting materials were purchased from commercial vendors and used directly without further purification unless otherwise stated. Milli-Q water (18 MΩ-cm) was obtained from a Millipore Gradient Milli-Q water system (Billerica, MA). All aqueous solutions were prepared with Milli-Q water. Silica gel 60 (70−230 mesh, Merck) was used for column chromatography. Analytical thin-layer chromatography (TLC) was performed using Merck 60 F254 silica gel (precoated sheets, 0.2 mm thick) (Lawrence, KS). The ^{1}H and ^{13}C NMR spectra were recorded on a Varian 400 or 500 MHz spectrometer; chemical shifts are expressed in ppm relative to TMS as reference peak (0.0 ppm). Matrix-assisted laser desorption/ionization (MALDI) mass spectra were acquired on an Applied Biosystems Voyager-6115 mass spectrometer. Radiolabeled conjugates were purified by Light C-18 Sep-Pak cartridges (Waters, Milford, MA). Radioactivity of tissue samples and radioactive standards was counted by an automatic γ-counter, Wizard$_2$ 3″ (PerkinElmer).

Bulk solvents were removed by rotary evaporator under reduced pressure, and trace solvents were removed by vacuum

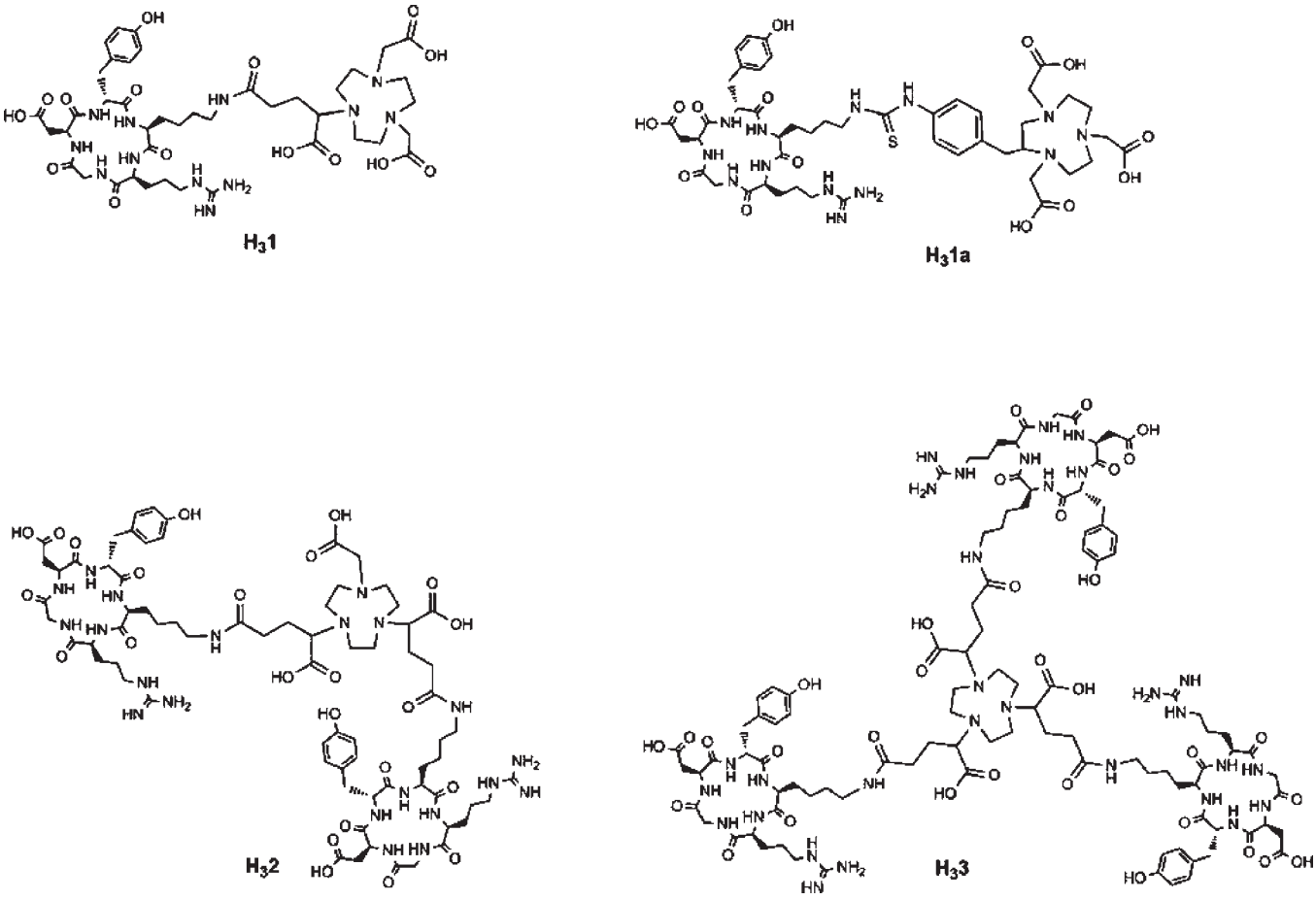

Figure 3. Structures of peptide conjugates: H_3**1**, H_3**1a**, H_3**2**, and H_3**3**.

pump. The α-bromoglutaric acid-1-*tert*-butyl ester-4-benzyl ester (**4**) was synthesized according to the published procedure.[29] The 1,4,7-triazacyclononane (TACN) and p-SCN-Bn-NOTA were purchase from Macrocyclics (Dallas, TX); and L-glutamic acid-5-benzyl ester was purchased from Sigma-Aldrich. The ^{68}Ge/^{68}Ga generator system was purchased from iThemba Laboratories (Somerset west, South Africa).

High Performance Liquid Chromatography (HPLC) Methods. HPLC separation was performed on a Waters 600 Multisolvent Delivery System equipped with a Waters 2996 Photodiode Array detector. The mobile phase consisted of H_2O with 0.1% TFA (solvent A) and acetonitrile with 0.1% TFA (solvent B). The analytical HPLC was performed on an XTerra RP18 column (150 × 4.6 mm) with a gradient of 0% B to 100% B in 50 min at a flow rate of 1.0 mL/min. The HPLC separation was performed on a semipreparative XTerra RP18 Column (250 × 10 mm) with a gradient of 0% B to 100% B in 50 min at a flow rate of 4.0 mL/min.

Integrin $\alpha_v\beta_3$ Receptor-Binding Assay. The $\alpha_v\beta_3$ integrin-binding affinities of c(RGDyK), H_3**1**, H_3**1a**, H_3**2**, and H_3**3** were determined by a competitive cell-binding assay using ^{125}I-echistatin (PerkinElmer) as the $\alpha_v\beta_3$-specific radioligand. The experiments were performed on U87MG human glioblastoma cells following a previously reported method.[28] Briefly, U87MG cells were grown in RPMI 1640 medium supplemented with penicillin, streptomycin, and 10% (v/v) fetal bovine serum (FBS) at 37 °C under 5% CO_2. Suspended U87MG cells in binding buffer (20 mM Tris, pH 7.4, 150 mM NaCl, 2 mM $CaCl_2$, 1 mM $MgCl_2$, 1 mM $MnCl_2$, 0.1% bovine serum albumin) were seeded on multiwell DV plates (Millipore) with 5 × 10^4 cells per well and then incubated with ^{125}I-echistatin (10 000 cpm/well) in the presence of increasing concentrations (0−5000 nM) of c(RGDyK) peptide conjugates for 2 h. The final volume in each well was maintained at 200 μL. At the end of incubation, unbound ^{125}I-echistatin was removed by filtration followed by three rinses with cold binding buffer. The retentate was collected and the radioactivity was measured using a γ-counter. The best-fit IC_{50} values (inhibitory concentration where 50% of the ^{125}I-echistatin bound on U87MG cells are displaced) of c(RGDyK), H_3**1**, H_3**2**, and H_3**3** were calculated by fitting the data with nonlinear regression using GraphPad Prism (GraphPadSoftware, Inc.). Experiments were repeated with quintuplicate samples.

Tissue Culture and Animal Model. All animal studies were performed in compliance with guidelines set by the UT Southwestern Institutional Animal Care and Use Committee (IACUC). The PC-3 cell line was obtained from the American Type Culture Collection (ATCC, Manassas, VA), and was cultured in T-media (Invitrogen, Carlsbad, CA) at 37 °C in an atmosphere of 5% CO_2 and were passaged at 75% confluence in P150 plates. T-media was supplemented with 5% fetal bovine serum (FBS) and 1× penicillin/streptomycin. PC-3 cells were harvested from monolayer using PBS and trypsin/EDTA, and suspended in T-media with 5% FBS. The cell suspension was then injected subcutaneously (5 × 10^6 cells in 100 μL media)

into the front left flanks of male SCID mice. After injection, general health of the animals was monitored three times a week. The tumor was allowed to grow three weeks to reach a palpable size (50−150 mm^3) for biodistribution and microPET-CT imaging studies.

Biodistribution. Male SCID mice bearing PC-3 prostate tumor xenograft were injected with 0.56−0.74 MBq of a ^{68}Ga-labeled conjugate to evaluate the tissue distribution of the tracer in mice. All mice were sacrificed at 30 min and 2 h p.i. The organs of interest (tumor, blood, heart, lung, liver, spleen, kidneys, fat, bone, muscle, brain, small intestine, large intestine, and stomach) were harvested, weighed, and radioactivity was quantified using a γ-counter. Standards were prepared and counted along with the tissue samples to calculate the percent injected dose per gram (%ID/g) and percent injected dose per organ (%ID/organ). To determine the pharmacokinetic parameters, mice injected with the tracer were blood sampled from the retro-orbital sinus at 2, 5, 10, 30, 60, and 120 min. The pharmacokinetic parameters were calculated based on a two-compartment open model.[30] For in vivo stability evaluation, three SCID mice were used for each conjugate; each mouse was injected with 5.5−7.4 MBq of a ^{68}Ga labeled conjugate in 150 μL of saline via the tail vein. The mouse urine was collected within 2 h post injection (p.i.) and the lower part of the abdomen was pressed as necessary. The collected urine was filtered and analyzed by radio-HPLC.

Mouse PET/CT Imaging. The imaging studies were performed on a Siemens Inveon Multimodality PET/CT system (Siemens Medical Solutions Inc., Knoxville, TN, USA). Ten minutes prior to imaging, the animals were anesthetized using 3% isofluorane at room temperature until stable vitals were established. Once the animal was sedated, the animal was placed onto the imaging bed under 2% Isofluorane anesthesia for the duration of the imaging. The CT imaging was acquired at 80 kV and 500 μA with a focal spot of 58 μm. The total rotation of the gantry was 360° with 360 rotation steps obtained at an exposure time of approximately 180 ms/frame. The images were attained using CCD readout of 4096 × 3098 with a binning factor of 4 and an average frame of 1. Under low magnification, the effective pixel size was 103.03 μm. Total microCT scan time was approximately 6 min. The CT images were reconstructed with a down sample factor of 2 using Cobra Reconstruction Software. The PET imaging was acquired directly following the acquisition of CT data. Each PC-3 tumor bearing mouse was injected with 3.7−4.2 MBq of a ^{68}Ga-labeled conjugate in 100 μL of saline via tail vein. Immediately after the injection, a dynamic PET scan was performed from 0 to 30 min. The 0−30 min dynamic imaging data were reconstructed into six frames (5 min each frame), where each frame represented the average value of the respective 5 min interval. At 2 h p.i., a 15 min static scan was performed. PET images were reconstructed using Fourier Rebinning and Ordered Subsets Expectation Maximization 3D (OSEM3D) algorithm. Reconstructed CT and PET images were fused and analyzed using Inveon Research Workplace (IRW) software. For quantification, regions of interest were placed in the areas expressing the highest ^{68}Ga-labeled conjugate activity as determined by PET and guided by visual inspection of CT images. The tissues examined include the tumor, heart, liver, lung, kidney, and muscle. The resulting quantitative data were expressed in %ID/g.

Synthesis (Scheme 1). *Compounds **5** and **6**.*[23] A solution of α-bromoglutaric acid 1-*tert*-butyl ester 5-benzyl ester[29] (**4**, 0.40 g, 1.12 mmol) in 30 mL of chloroform was added over a period of 3 h to a solution of 1,4,7-triazacyclononane (**TACN**, 0.29 g, 2.24 mmol) in 40 mL of chloroform. The mixture was stirred over 3 d at room temperature and concentrated to give yellow oil. The crude product was purified by column chromatography (silica gel, $CHCl_3$/EtOH/NH_4OH 7:3:0.5) to give **5** (0.15 g, 50%) and **6** (40 mg, 15%) as colorless oil.

*Compound **5**.* ^{1}H NMR ($CDCl_3$, 500 MHz) δ 1.5 (s, 9H, $C(CH_3)_3$); 2.2−1.85 (m, 2H, $CHNCH_2$); 2.9−2.5 (m, 14H, NCH_2, $CH_2COOBzl$); 3.25 (dd, 1H, CHBr); 5.1 (s, 2H, CH_2Ph); 7.35 (m, 5H, Ph); MALDI-TOF/MS calcd for $C_{22}H_{35}N_3O_4$ $[M+H]^+$: 406.23. Found: 406.40.

*Compound **6**.* ^{1}H NMR ($CDCl_3$, 500 MHz) δ 1.4 (s, 18H, $C(CH_3)_3$); 1.9 (m, 2H); 2.05 (m, 2H); 2.45 (m, 2H); 2.55 (m, 2H); 2.8 (d, 2H); 3.0 (bs, 4H); 3.25 (m, 6H); 5.17 (s, 4H, CH_2Ph); 7.28 (m, 10H, Ph); MALDI-TOF/MS calcd for $C_{38}H_{55}N_3O_8$ $[M+H]^+$: 682.40. Found: 682.28.

*Compound $^tBu_3$-**1**-Bn.*[23] The mixture of **5** (0.300 g, 0.740 mmol) and K_2CO_3 (0.20 g, 1.45 mmol) in 50 mL of anhydrous MeCN was cooled to 0 °C. To the above solution, *t*-butyl-2-bromoacetate (0.26 g, 1.35 mmol) in 20 mL of anhydrous MeCN was added dropwise for 4 h. The reaction mixture was stirred at 0 °C for 6 h and at room temperature for 24 h. The mixture was filtered over Celite and the filtrate was evaporated to dryness. The crude product was purified by column chromatography (silica gel, CH_3Cl/EtOH 95:5) to provide $^tBu_3$-**1**-Bn as yellow oil (0.27 g, 57%). ^{1}H NMR ($CDCl_3$, 500 MHz) δ 1.5 (s, 27H, $C(CH_3)_3$); 1.85−3.6 (m, 21H, $CHNCH_2$, NCH_2, CH_2−COOBn, CH_2COO^tBu); 5.1 (s, 2H, CH_2Ph); 7.35 (m, 5H, Ph); MALDI-TOF/MS calcd for $C_{34}H_{55}N_3O_8$ *m/z*: 635.40. Found: 635.75.

*Compound $^tBu_3$-**1**-COOH*[23]. Compound $^tBu_3$-**1**-Bn (150 mg, 0.237 mmol) was dissolved in 20 mL of 2-propanol and the solution was degassed (N_2) for 5 min. To the above solution was added 10% Pd/C (50 mg) suspended in 0.5 mL of H_2O. The suspension was shaken in a hydrogenator (Parr, Moline, Illionis) at room temperature for 16 h under a H_2 atmosphere (60 psi). The suspension was filtered through Celite and the solvent was evaporated under vacuum. The obtained crude oil was purified by column chromatography (silica gel, 2-propanol/ammonia 95:5) to provide $^tBu_3$-**1**-COOH (85 mg, 66%) as yellow oil. ^{1}H NMR ($CDCl_3$, 500 MHz) δ 1.5 (s, 27H, $C(CH_3)_3$); 2.0 (m, 2H); 2.5 (m, 2H); 2.8−3.2 (m, 12H); 3.45−3.75 (m, 5H); MALDI-TOF/MS calcd for $C_{27}H_{49}N_3O_8$ $[M+H]^+$: 544.35. Found: 544.68.

*Compound H_3**1***. To a mixture of compound $^tBu_3$-**1**-COOH (5.0 mg, 9.0 μmol), *N*-hydroxysuccinimide (NHS, 10.0 mg, 88.7 μmol) and EDC·HCl (1-ethyl-3-(3-dimethylaminopropyl) carbodiimide)(15.0 mg, 90.0 μmol) in 800 μL of anhydrous MeCN was added 20 μL of *N*,*N*-diisopropylethylamine (DIPEA). The mixture was then stirred under N_2 for 24 h. After removal of the solvent under reduced pressure, the resulting residue was redissolved in $CHCl_3$ (1.0 mL) and then promptly washed with water (3 × 2 mL). The organic layer was evaporated, and the residue was dried by a lyophilizer to yield the NHS-activated ester as pale yellow solid (MALDI-TOF/MS calcd for $C_{31}H_{52}N_4O_{10}$ $[M+H]^+$: 641.37. Found: 641.42), The NHS-activated ester was used directly for the next step without further purification. Cyclic RGD peptide [c(RGDyK)] (7.0 mg, 11 μmol) was mixed with the NHS-activated ester in 500 μL of anhydrous DMF, to which 50 μL of DIPEA was added. The mixture was then stirred at room temperature for two days under N_2. After removal of the solvent, the crude product was purified by semipreparative reverse-phase HPLC. The collected fractions of multiple runs were combined and lyophilized to afford 2.0 mg of *t*-butyl protected H_3**1** as white powder. MALDI-TOF/MS

Scheme 1. Synthetic Routes to $H_3$1, $H_3$1a, $H_3$2, and $H_3$3[a]

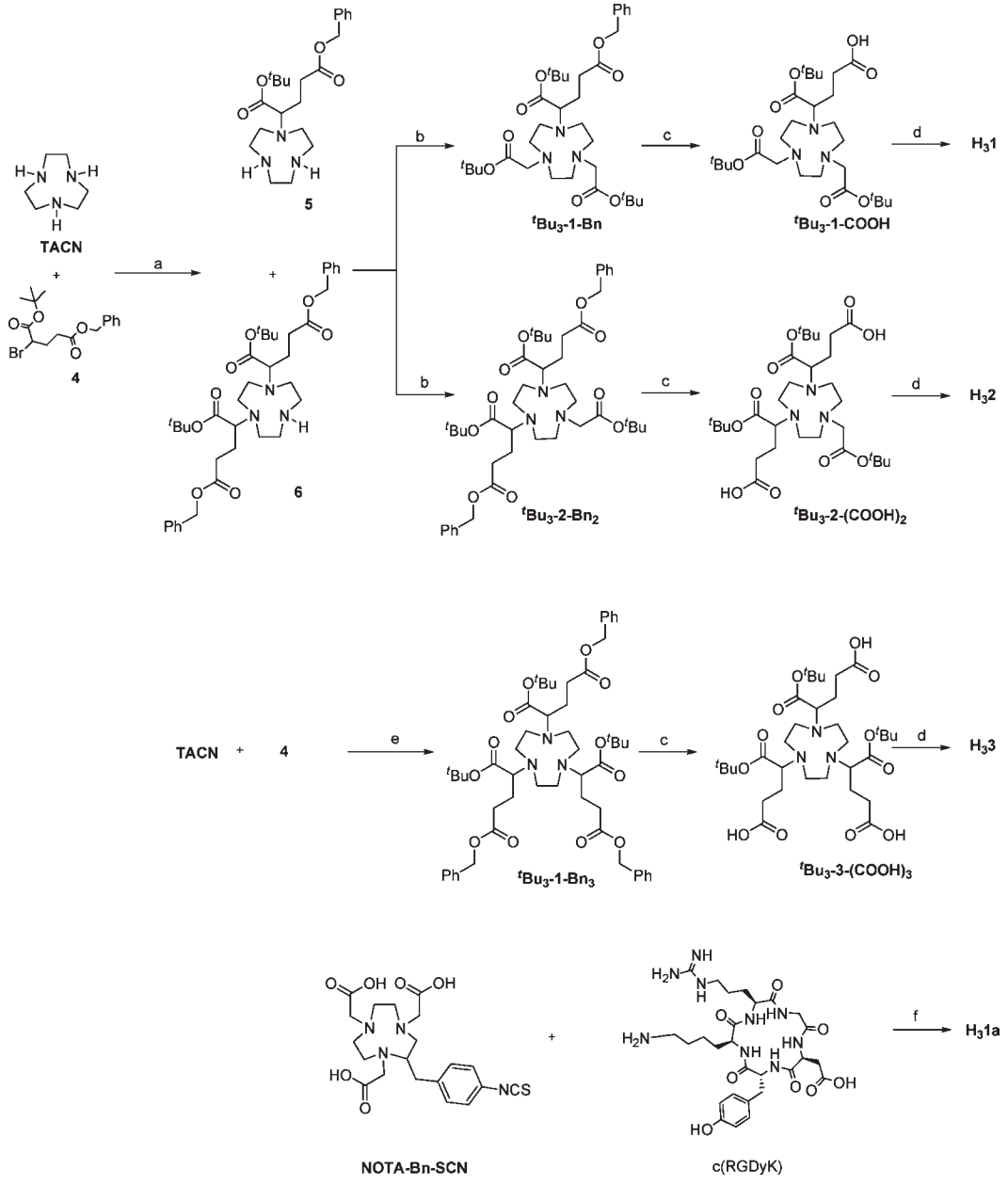

[a] (a) $CHCl_3$; (b) MeCN, K_2CO_3, *t*-butyl-2-bromoacetate; (c) 2-propanol, 10% Pd/C, H_2; (d) (i) NHS, EDC·HCl; (ii) c(RGDyK), DIPEA, DMF; (iii) TFA; (e) MeCN, K_2CO_3; (f) DIPEA, DMF.

calcd for $C_{54}H_{88}N_{12}O_{15}$ $[M+H]^+$: 1144.65. Found: 1144.37. The *t*-butyl protected H_3**1** (2.0 mg, 1.74 μmol) was dissolved in 95% of TFA and stirred at room temperature for 12 h. After evaporation of the solvent, the residue was purified by semipreparative reverse-phase HPLC. The collected fractions of multiple runs were pooled and lyophilized to afford H_3**1** as white solid in quantitative yield. MALDI-TOF/MS calcd for $C_{42}H_{64}N_{12}O_{15}$ *m/z*: 976.46. Found: 976.43.

*Compound ^{t}Bu$_3$-**2**-Bn$_2$.* The mixture of **6** (85 mg, 0.12 mmol) and K_2CO_3 (86 mg, 0.62 mmol) in 40 mL of anhydrous MeCN was cooled to 0 °C. To the above solution *t*-butyl-2-bromoacetate (24 mg, 0.125 mmol) in 10 mL of anhydrous MeCN was added dropwise for 3 h. The reaction was stirred at 0 °C for 6 h and room temperature for 24 h. The mixture was filtered over Celite and the filtrate was evaporated to dryness. The crude product was purified by column chromatography (silica gel, $CHCl_3$/EtOH, 95: 5) to give ^{t}Bu$_3$-**2**-Bn$_2$ (80 mg, 80%) as yellow oil. ^{1}H NMR ($CDCl_3$, 500 MHz) δ 1.5−1.7 (s, 27H, C$(CH_3)_3$); 1.91−2.10 (m, 4H); 2.42−2.61 (m, 4H); 2.83 (bs, 3H); 3.1 (bs, 5H); 3.3 (bs, 3H); 3.5 (bs, 2H); 3.80−4.14 (m, 3H); 5.1 (s, 4H, CH_2Ph); 7.25 (m, 10H, Ph); ^{13}C NMR ($CDCl_3$,100 MHz) δ 25.20, 28.16, 31.05, 53.38, 55.28, 58.59, 64.46, 77.00, 80.90, 81.97, 85.21, 126.79, 128.08, 135.92, 171.99, 172.87. MALDI-TOF/MS calcd for $C_{44}H_{65}N_3O_{10}$ $[M+H]^+$: 796.47. Found: 796.67.

*Compound ^{t}Bu$_3$-**2**-(COOH)$_2$.* Compound ^{t}Bu$_3$-**2**-Bn$_2$ (50 mg, 0.15 mmol) was dissolved in 20 mL of 2-propanol and the solution was degassed (N_2) for 5 min. To the above solution was

dx.doi.org/10.1021/bc200227d |*Bioconjugate Chem.* 2011, 22, 1650–1662

added 10% Pd/C (30 mg) suspended in 0.5 mL of H_2O. The suspension was shaken in a hydrogenator at room temperature for 16 h under a H_2 atmosphere (60 psi). The suspension was filtered through Celite and the solvent was evaporated under vacuum. The obtained crude oil was purified by column chromatography (silica gel, 2-propanol/ammonia 95:5) to provide ^{t}Bu$_3$-**2**-(COOH)$_2$ (30 mg, 66%) as yellow oil. ^{1}H NMR ($CDCl_3$, 500 MHz) δ 1.6 (s, 27H, C$(CH_3)_3$); 2.4−2.8 (m, 7H); 3.0−3.3 (m, 12H); 3.45−3.75 (m, 5H); MALDI-TOF/MS calcd for $C_{30}H_{53}N_3O_{10}$ *m/z*: 615.37. Found: 615.56.

*Compound H$_3$**2***. To a mixture of compound ^{t}Bu$_3$-**2**-(COOH)$_2$ (5.0 mg, 8.5 μmol), NHS (10.0 mg, 80.0 μmol) and EDC·HCl (10.5 mg, 55.0 μmol) in 500 μL of dry MeCN was added 20 μL of DIPEA, which was then stirred under N_2 for 24 h. Solvent was removed under reduced pressure, the residue was redissolved in $CHCl_3$ (1 mL) and then promptly washed with water (3 × 2 mL). The $CHCl_3$ was evaporated, the residue was dried by a lyophilizer to yield NHS-activated ester as pale yellow solid (MALDI-TOF/MS calcd for $C_{38}H_{59}N_5O_{14}$ $[M+H]^+$: 808.41. Found: 808.18), NHS-activated ester was used directly for the next step without further purification. Cyclic RGD peptide [c(RGDyK)] (10.5 mg, 17 μmol) was mixed with the above yellow solid in 500 μL of anhydrous DMF, to which 50 μL of DIPEA was added. The mixture was then stirred at room temperature for two days under N_2. After evaporation of the solvent under vacuum, the crude product was purified by a semipreparative reverse-phase HPLC. The collected fractions of multiple runs were combined and lyophilized to afford *t*-butyl protected H$_3$**2** as white powder. MALDI-TOF/MS calcd for $C_{84}H_{131}N_{21}O_{24}$ $[M+H]^+$: 1818.97. Found: 1818.74. The *t*-butyl protected H$_3$**2** (3.5 mg, 1.9 μmol) was dissolved in 95% of TFA and stirred at room temperature for 12 h. After evaporation of the solvent, the residue was purified by semipreparative reverse-phase HPLC. The collected fractions of multiple runs were pooled and lyophilized to afford a white solid H$_3$**2** in quantitative yield. MALDI-TOF/MS calcd for $C_{72}H_{107}N_{21}O_{24}$ *m/z*: 1649.78. Found: 1649.38.

*Compound ^{t}Bu$_3$-**3**-Bn$_3$*. To a suspension of **TACN** (68 mg, 0.525 mmol) and K_2CO_3 (1.2 g, 8.68 mmol) in 3 mL of anhydrous MeCN at room temperature, compound **4** (620 mg, 1.74 mmol) in 3 mL of anhydrous MeCN was added dropwise. After the addition, the reaction was allowed to proceed at room temperature for 24 h and then at 55 °C for 24 h. The solids were removed by filtration and washed with chloroform (2 × 20 mL). The combined filtrate was concentrated under vacuum and purified by column chromatography (silica gel, 60−230 mesh) using $CHCl_3$ to EtOAc for elution. Compound ^{t}Bu$_3$-**3**-Bn$_3$ was obtained as a sticky oil (350 mg; yield, 70%): ^{1}H NMR ($CDCl_3$, 400 MHz) δ 1.42 (s, 27H), 1.76−1.88 (m, 3H), 1.90−2.04 (m, 3H), 2.38−2.58 (m, 8H), 2.64−2.84 (m, 8H), 2.86−2.96 (m, 2H), 3.04−3.14 (m, 3H), 5.08 (s, 6H), 7.32 (s, 15H); ^{13}C NMR ($CDCl_3$,100 MHz) δ 25.63, 28.55, 31.31, 52.61−54.42 (br), 66.42, 67.22, 81.08, 128.41, 128.47, 128.77, 136.28, 172.74, 173.47. MALDI-TOF/MS calcd for $C_{54}H_{75}N_3O_{12}$ $[M+H]^+$: 958.54. Found: 958.77. Anal. Calcd for $C_{54}H_{75}N_3O_{12}\cdot H_2O$: C, 66.44; H, 7.95; N, 4.30. Found: C, 66.41; H, 7.65; N, 4.30.

*Compound ^{t}Bu$_3$-**3**-(COOH)$_3$*. To a solution of ^{t}Bu$_3$-**3**-Bn$_3$ (100 mg, 0.128 mmol) in 5 mL of 2-propanol was added portionwise 10 mg of 10% Pd/C. The suspension was shaken in a hydrogenator at room temperature for 16 h under a H_2 atmosphere (60 psi). After removal of the solids, evaporation of solvent under vacuum gave the target compound ^{t}Bu$_3$-**3**-(COOH)$_3$ as white solid in nearly quantitative yield. ^{1}H NMR ($CDCl_3$, 400 MHz) δ 1.48 (s, 27H), 2.07 (br, 6H), 2.50 (br, 8H), 3.15 (br, 10H), 3.62 (br, 3H), 8.35 (br. 3H); ^{13}C NMR (CD_3OD, 100 MHz) δ 25.16, 27.34, 31.27, 45.55, 63.39, 82.89, 171.41, 175.24; MALDI-TOF/MS calcd for $C_{33}H_{57}N_3O_{12}$ *m/z*: 687.39. Found: 688.89. Anal. Calcd for $C_{33}H_{54}N_3Na_3O_{12}$: C, 52.58; H, 7.22; N, 5.57. Found: C, 52.58; H, 7.22; N, 5.59.

*Compound H$_3$**3***. To a mixture of compound ^{t}Bu$_3$-**3**-(COOH)$_3$ (3.8 mg, 5.5 μmol), NHS (6.2 mg, 55.0 μmol) and EDC HCl (10.5 mg, 55.0 μmol) in 500 μL of dry MeCN was added 20 μL of DIPEA, which was then stirred under N_2 for 24 h. After the solvent was removed under reduced pressure, the residue was redissolved in $CHCl_3$ (1 mL) and then washed 3 times (3 × 2 mL) with water promptly. The organic layer was evaporated to remove $CHCl_3$, and the resulting residue was then dried by a lyophilizer to NHS-activated ester as pale yellow solid (MALDI-TOF/MS calcd for $C_{45}H_{60}N_6O_{18}$ $[M+H]^+$: 979.44. Found: 979.40), NHS-activated ester was used directly for the next reaction without further purification. Cyclic RGD peptide [c(RGDyK)] (10.5 mg, 17 μmol) was mixed with the above yellow solid in 500 μL of anhydrous DMF, to which 50 μL of DIPEA was added. The mixture was then stirred at room temperature for two days under N_2. After evaporation of the solvent under vacuum, the crude product was purified by a semipreparative reverse-phase HPLC. The collected fractions of multiple runs were combined and lyophilized to afford 4.5 mg of *t*-butyl protected H$_3$**3** as white powder (33%). MALDI-TOF/MS calcd for $C_{114}H_{174}N_{30}O_{33}$ $[M+H]^+$: 2490.29. Found: 2490.21. The *t*-butyl protected H$_3$**3** (2.0 mg, 0.80 μmol) was dissolved in 95% of TFA and stirred at room temperature for 12 h. After evaporation of the solvent, the residue was purified by semipreparative reverse-phase HPLC. The collected fractions of multiple runs were pooled and lyophilized to afford a white solid H$_3$**3** in quantitative yield. MALDI-TOF/MS calcd for $C_{102}H_{150}N_{30}O_{33}$ $[M+H]^+$: 2321.10. Found: 2321.43.

*Compound H$_3$**1a***. To a solution of *p*-SCN-Bn-NOTA (10 mg, 22 μmol) in 200 μL of anhydrous DMF was added a mixture of [c(RGDyK)] (3.3 mg, 5 μmol) and DIPEA (20 μL) in 200 μL of anhydrous DMF. The mixture was then stirred at room temperature for 24 h. After evaporation of the solvent, the residue was purified by semipreparative reverse-phase HPLC. The collected fractions from multiple runs were pooled and lyophilized to afford 5.0 mg of H$_3$**1a** as white solid (88%). MALDI-TOF/MS calcd for $C_{47}H_{67}N_{13}O_{14}$ $[M+H]^+$: 1070.47. Found: 1070.48.

Radiolabeling of H$_3$1, H$_3$1a, H$_3$2, and H$_3$3 with ^{68}Ga. To a 2.0 mL vial containing 5−10 μg of respective conjugate in 1400 μL of 1 M 4-(2-hydroxyethyl)-1-piperazineethanesulfonic acid (HEPES, pH = 6.5) solution, 74−111 MBq of $^{68}GaCl_3$ in 0.6 N HCl was added. The reaction mixture was shaken and incubated at 75 °C for 0.5 h. Then, 2 μL of 5 mM ethylendiaminetetraacetic acid (EDTA) was added to the reaction mixture, which was allowed to incubate for another 5 min (EDTA was used to remove nonspecifically bound or free ^{68}Ga from the ^{68}Ga-labeled conjugate). The purification of ^{68}Ga-labeled conjugate was carried out by passing the mixture through a preconditioned Sep-Pak C-18 light cartridge. After thorough rinsing (3 × 3 mL, water) of the cartridge, the ^{68}Ga-labeled conjugate was eluted by an ethanol−water mixture (70:30). The product was first analyzed by a Rita Star Radioisotope TLC Analyzer (Straubenhardt, Germany) on instant thin-layer chromatography (ITLC-SG) plates (Pall Life Sciences, East Hills, NY) and then by radio-HPLC to determine the radiochemical purity of the product.

Statistical Analysis. Quantitative data were expressed as the mean ± SD. Unpaired *t* test (two-tailed, confidence intervals: 95%) was performed using GraphPad Prism. *P* values of <0.05 were considered statistically significant.

RESULTS

Synthesis. The synthesis of H_3**1**, H_3**2**, and H_3**3** can be divided into two parts (Scheme 1): first, synthesis of $^tBu_3$-**1**-COOH, $^tBu_3$-**2**-$(COOH)_2$, and $^tBu_3$-**3**-$(COOH)_3$; second, conjugation of c(RGDyK) with $^tBu_3$-**1**-COOH, $^tBu_3$-**2**-$(COOH)_2$, and $^tBu_3$-**3**-$(COOH)_3$, followed by the deprotection of the *t*-butyl protected carboxylate groups. The side arm, α-bromoglutaric acid-1-*tert*-butyl ester-4-benzyl ester **4** was synthesized by two steps from commercially available L-glutamic acid-5-benzyl ester.[29] Alkylation of the commercially available **TACN** with **4** in $CHCl_3$ at room temperature gave both mono (**5**, 50%) and dialkylated (**6**, 15%) products. Compounds **5** and **6** were separated using column chromatography, where compound **6** was eluted first. Further alkylation of **5** and **6** with bromo-*t*-butyl ester afforded $^tBu_3$-**1**-Bn (57%) and $^tBu_3$-**2**-Bn_2 (80%), respectively. Overalkylation was observed during the reaction between **5** or **6** with bromo-*t*-butyl ester, which led to the respective quaternary ammonium salt. However, the salt formation was avoided by slow addition of bromo-*t*-butyl ester to the diluted solution of **5** or **6**. Alkylation of **TACN** with **4** (3.3 equiv) afforded $^tBu_3$-**3**-Bn_3 in a yield of over 70% without formation of mono- or disubstituted analogues under the given reaction conditions.

The protected BFC scaffolds, $^tBu_3$-**1**-Bn, $^tBu_3$-**2**-Bn_2, and $^tBu_3$-**3**-Bn_3, contain two protected carboxylate groups at α and γ positions of the side arm. The benzyl protected γ-carboxylate groups in $^tBu_3$-**1**-Bn, $^tBu_3$-**2**-Bn_2, and $^tBu_3$-**3**-Bn_3 were selectively deprotected and reserved for peptide (c(RGDyK)) conjugation. Catalytic debenzylation of $^tBu_3$-**1**-Bn, $^tBu_3$-**2**-Bn_2, and $^tBu_3$-**3**-Bn_3 was achieved using 10% Pd/C in 2-propanol under hydrogen atmosphere to afford $^tBu_3$-**1**-COOH, $^tBu_3$-**2**-$(COOH)_2$, and $^tBu_3$-**3**-$(COOH)_3$ in quantitative yield. The obtained γ-carboxylic acids were then activated by NHS for acid−amine conjugation chemistry and used as received for further conjugation. The conjugation of NHS-activated $^tBu_3$-**1**-COOH, $^tBu_3$-**2**-$(COOH)_2$, and $^tBu_3$-**3**-$(COOH)_3$ with 1−3 equiv of c(RGDyK) in the presence of DIPEA provided the *t*-butyl protected conjugates in 30−45% yields. Finally, the α-carboxylate group was deprotected using 95% trifluoroacetic acid to provide H_3**1**, H_3**2**, and H_3**3**, each containing three internal carboxylic acids for ^{68}Ga labeling. The H_3**1a** conjugate was prepared by directly reacting *p*-SCN-Bn-NOTA with c(RGDyK) peptide at room temperature in DMF using a reported procedure.[15,26]

All the intermediates and final products were characterized by ^{1}H NMR, mass spectroscopy, and HPLC. Analysis of ^{1}H NMR spectra was facilitated by addition or removal of characteristic *t*-butyl and/or benzyl groups. Also, these compounds were characterized by their molecular ion peak by MALDI-mass spectrometry, and the purity of these conjugates was assured by observing a single peak in the reverse-phase HPLC.

Radiochemistry. The ^{68}Ga labeling efficiencies were evaluated under an acidic condition (pH = 3.0−3.5)[31] for all the conjugates by varying the reaction temperature and time. At room temperature, conjugates H_3**1** and H_3**1a** showed a high ^{68}Ga incorporation rate (>90%) within 10 min of the radiochemical reaction, while H_3**2** and H_3**3** only had 71% and 84%, respectively. When the reaction proceeded to 30 min, all the conjugates were radiolabeled with >95% of ^{68}Ga. At 70 °C, all conjugates showed nearly instant labeling with ^{68}Ga. The ^{68}Ga labeled conjugates were purified in one step using a preactivated C-18 Sep-Pak light cartridge with a > 90% recovery rate. The radiochemical purity of the ^{68}Ga-labeled conjugates after cartridge purification was >99% as determined by radio-HPLC. The overall radiochemical procedure including the purification and HPLC steps took less than 45 min and gave a decay-corrected radiochemical yield of >90%. The specific activity of the purified ^{68}Ga-labeled conjugates was in the range 33−44 MBq/nmol. The ^{68}Ga-labeled conjugates were eluted from HPLC less than 1 min earlier than their respective conjugate.

Cell-Binding Assay. The in vitro $\alpha_v\beta_3$ binding affinities of c(RGDyK), H_3**1**, H_3**2**, and H_3**3** were determined by a competitive cell-binding assay using ^{125}I-echistatin as the integrin-specific radioligand.[32] The receptor binding experiments were performed using $\alpha_v\beta_3$ integrin-positive U87MG human glioma cells containing a high $\alpha_v\beta_3$ integrin density on its cell surface.[33] All the conjugates inhibited the binding of ^{125}I-echistatin to the $\alpha_v\beta_3$ integrin-positive U87MG cells in a dose-dependent manner (Supporting Information Figure S1). Calculated IC_{50} values expressed by the 50% inhibitory concentration of the ^{125}I-echistatin binding were 204 ± 76 nM (c(RGDyK)), 218 nM (H_3**1a**),[26] 171 ± 60 nM (H_3**1**), 43.9 ± 16.1 nM (H_3**2**), and 14.7 ± 5.0 nM (H_3**3**). The in vitro $\alpha_v\beta_3$ binding affinity of c(RGDyK) was used as a reference. The binding affinity of H_3**1** is similar to that of c(RGDyK), indicating that the conjugation of a NOTA scaffold to c(RGDyK) had minimal effect on the receptor binding affinity of c(RGDyK). The multivalent enhancement ratio (MVE) calculated by dividing the IC_{50} value of H_3**1** by that of H_3**2** or H_3**3** and the respective number of c(RGDyK) molecules was 3.9 for H_3**2** and 11.6 for H_3**3**, indicative of the anticipated multivalent effect.[28,34]

In Vivo Stability. The metabolic stability of ^{68}Ga-**1**, ^{68}Ga-**1a**, ^{68}Ga-**2**, and ^{68}Ga-**3** in SCID mice was evaluated by examining their metabolites in urine at 2 h p.i. Impressively, no metabolites were detected for any of the conjugates by radio-HPLC analysis (Supporting Information Figure S2), indicating high in vivo stability of ^{68}Ga-labeled conjugates.

Biodistribution. The pharmacokinetics (PK) parameters for ^{68}Ga-**1**, ^{68}Ga-**1a**, ^{68}Ga-**2**, and ^{68}Ga-**3** were evaluated in SCID mice using a two-compartment open model. The time-activity curves of the ^{68}Ga-labeled conjugates in blood showed a biphasic clearance (Figure 4). As shown in Table 1, all the ^{68}Ga-labeled conjugates displayed a rapid distribution half-life ($t_{1/2(\alpha)}$ < 5 min) and a short terminal half-life ($t_{1/2(\beta)}$ < 50 min).

The tissue distribution profiles of ^{68}Ga-**1**, ^{68}Ga-**1a**, ^{68}Ga-**2**, and ^{68}Ga-**3** in SCID mice bearing the $\alpha_v\beta_3$ integrin-positive PC-3 tumor are summarized in Figure 5 and Supporting Information Table S3. Among the organs evaluated, kidney showed the highest uptake (^{68}Ga-**1a**: 6.25 ± 0.61%ID/g; ^{68}Ga-**1**: 5.40 ± 0.61%ID/g; ^{68}Ga-**2**: 3.18 ± 2.76%ID/g; ^{68}Ga-**3**: 8.41 ± 0.99%ID/g) at 30 min p.i., indicating that all the conjugates were primarily excreted through the renal route. At 2 h p.i., less than 60% of the kidney uptake was retained for monovalent conjugates (^{68}Ga-**1a**: 2.95 ± 0.76%ID/g; ^{68}Ga-**1**: 3.14 ± 0.13%ID/g), while the divalent and trivalent ones showed *a* > 90% retention (^{68}Ga-**2**: 3.86 ± 1.80% ID/g; ^{68}Ga-**3**: 7.50 ± 0.95%ID/g). At 30 min p.i., no significant difference was observed for the liver uptake of the conjugates (^{68}Ga-**1a**: 1.98 ± 0.29%ID/g; ^{68}Ga-**1**: 1.91 ± 0.30% ID/g; ^{68}Ga-**2**: 2.07 ± 0.05%ID/g; ^{68}Ga-**3**: 3.10 ± 0.77%ID/g). Interestingly, the liver uptake retention was independent of the valency of the conjugates at 2 h p.i. However, the tumor uptake of

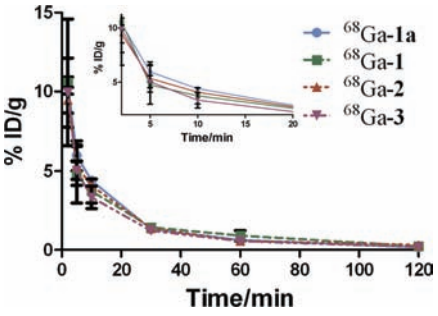

Figure 4. Time activity curves of ^{68}Ga-**1**, ^{68}Ga-**1a**, ^{68}Ga-**2**, and ^{68}Ga-**3**. Data obtained from blood sampling are presented as %ID/g ± s.d. (n = 3).

Table 1. In Vivo Pharmacokinetic Parameters of ^{68}Ga-1, ^{68}Ga-1a, ^{68}Ga-2, and ^{68}Ga-3

conjugates	$t_{1/2(\alpha)}$, min	$t_{1/2(\beta)}$, min
^{68}Ga-**1a**	4.0 ± 1.1	29.8 ± 7.1
^{68}Ga -**1**	2.7 ± 0.0	32.9 ± 8.0
^{68}Ga -**2**	3.8 ± 1.4	48.2 ± 9.0
^{68}Ga -**3**	3.4 ± 0.9	36.8 ± 1.1

the conjugates showed a positive correlation with the valency (^{68}Ga-**1a**: 1.63 ± 0.19%ID/g; ^{68}Ga-**1**: 1.67 ± 0.16%ID/g; ^{68}Ga-**2**: 1.94 ± 0.32%ID/g; ^{68}Ga-**3**: 4.41 ± 1.00%ID/g) at 2 h p.i., which clearly reflects the multivalent effect and is consistent with the cell binding affinities of the conjugates. Impressively, the tumor retention rate of the uptake shown at 2 h p.i. was on the order of trivalent ^{68}Ga-**3** (79%) > divalent ^{68}Ga-**2** (61%) > monovalent ^{68}Ga-**1** (55%) ≈ monovalent ^{68}Ga-**1a** (57%) at 2 h p.i.

Mouse PET-CT Imaging. The PET-CT imaging was performed on SCID mice bearing integrin $\alpha_v\beta_3$-positive PC-3 prostate cancer xenograft. Representative decay-corrected coronal images at 30 min (dynamic frame of 25−30 min) and 2 h p.i. are shown in Figure 6a. The PC-3 tumors were clearly visualized by all four probes at 30 min p.i. but without significant tumor uptake difference observed among the conjugates (^{68}Ga-**1a:** 3.24 ± 0.41%ID/g; ^{68}Ga-**1**: 3.26 ± 0.70%ID/g; ^{68}Ga-**2**; 3.06 ± 0.21% ID/g; and ^{68}Ga-**3**: 3.55 ± 0.85%ID/g) (Supporting Information Table S1). Uptake of ^{68}Ga-**1**, ^{68}Ga-**1a**, ^{68}Ga-**2**, and ^{68}Ga-**3** at 30 min p.i. in other organs, especially muscle and blood, was also high, which resulted in the low tumor-to-background contrast. At 2 h p.i., the tumor-to-background contrast clearly increased as the ^{68}Ga-labeled conjugate was cleared from the nontarget organs (Figure 6d). Of the ^{68}Ga-labeled conjugates, ^{68}Ga-**3** showed the highest tumor uptake at 2 h p.i. (2.55 ± 0.50%ID/g), which is significantly (p < 0.05) higher than all other ^{68}Ga-labeled conjugates (^{68}Ga-**2**: 1.90 ± 0.10%ID/g; ^{68}Ga-**1**: 1.66 ± 0.15% ID/g; and ^{68}Ga-**1a**: 1.40 ± 0.36%ID/g) (Figure 6c). This observation can be explained by the enhanced binding affinity of the trivalent ^{68}Ga-**3** conjugate, which led to its prolonged retention in the target, integrin $\alpha_v\beta_3$-positive tumor. Compared to the corresponding 30 min uptake value, the tumor uptake retention at 2 h p.i. follows the same order as observed in the biodistribution result: trivalent ^{68}Ga-**3** (72%) > divalent ^{68}Ga-**2** (62%) > monovalent ^{68}Ga-**1** (51%) ≈ monovalent ^{68}Ga-**1a** (43%). A blockade experiment was performed by coinjecting the ^{68}Ga-labeled conjugate with the blocking dose of c(RGDyK) (10 mg/kg). The drastic reduction of tumor uptake for all

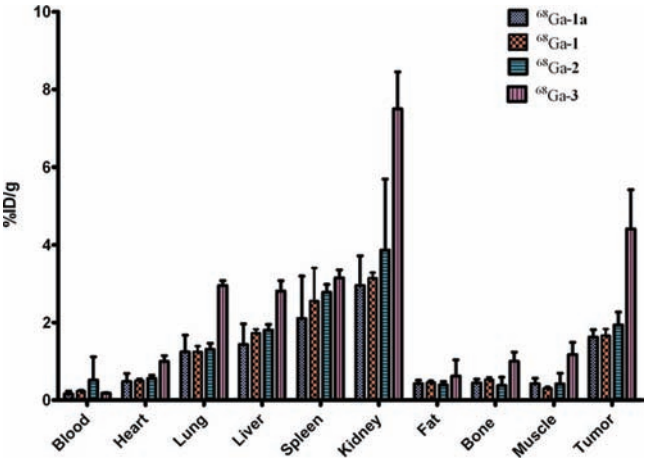

Figure 5. Tissue distribution of ^{68}Ga-**1**, ^{68}Ga-**1a**, ^{68}Ga-**2**, and ^{68}Ga-**3** in PC-3 tumor bearing SCID mice at 2 h p.i. Data are presented as %ID/g ± s.d. (n = 3).

^{68}Ga-labeled conjugates unequivocally indicated their imaging specificity of integrin $\alpha_v\beta_3$ (Supporting Information Table S1).

Consistent with the biodistribution data, all ^{68}Ga-labeled conjugates showed efficient clearance from the kidney (Supporting Information Table S1). Possibly due to the multivalent effect, ^{68}Ga-**3** showed the highest kidney uptake (4.03 ± 1.75%ID/g) at 2 h p.i., which is significantly higher than other ^{68}Ga-labeled conjugates (p < 0.01) (Figure 6b, Supporting Information Table S1). In the liver, no significant uptake and retention difference was observed for the ^{68}Ga-labeled conjugates at either 30 min or 2 h p.i. Low to negligible level (<1.14% ID/g) of uptake was observed in other major organs (e.g., heart, lungs, muscle) at 2 h p.i.

DISCUSSION

The design of a BFC for metal-based radiopharmaceuticals is largely influenced by the ability of the BFC to form a kinetically inert chelate with a metal radionuclide and the ease to covalently anchor a targeting vector. To date, both cyclic and acyclic BFCs containing coordinating atoms (e.g., nitrogen, oxygen, and sulfur) have been reported for Ga(III) chelation.[35−38] For a BFC to be considered for nuclear imaging probe design, its complex with the metal ion of interest must have desirable thermodynamic and in vivo kinetic stability, specifically resistance to trans-metalation with serum proteins. The most commonly used macrocyclic chelator, 1,4,7,10-tetraazacyclododecanetetraacetic acid (DOTA), is a choice of convenience for ^{68}Ga PET imaging design due to its commercial availability and the fact that it is in the composition of several FDA-approved agents. However, the DOTA complex with Ga(III) has a thermodynamic stability constant (log K = 21.33)[39] comparable to that of the transferrin complex with Fe(III) (log K = 20.3),[40] which may lead to in vivo transmetalation.[40] Also, the complexation kinetics of DOTA with Ga(III) often require an elevated temperature and a long reaction time, which could be detrimental to the activity of the biomolecule and not advantageous to ^{68}Ga, a radionuclide with a decay half-life barely longer than one hour. Given the small ionic radius of Ga(III) (76 pm),[18] NOTA, a nine-membered triazamacrocyclic chelator, would provide a perfect cavity size match for Ga(III) coordination. Indeed, the thermodynamic stability constant of Ga(III)-NOTA complex (log K = 30.98)[22,24] is approximately 10 orders of

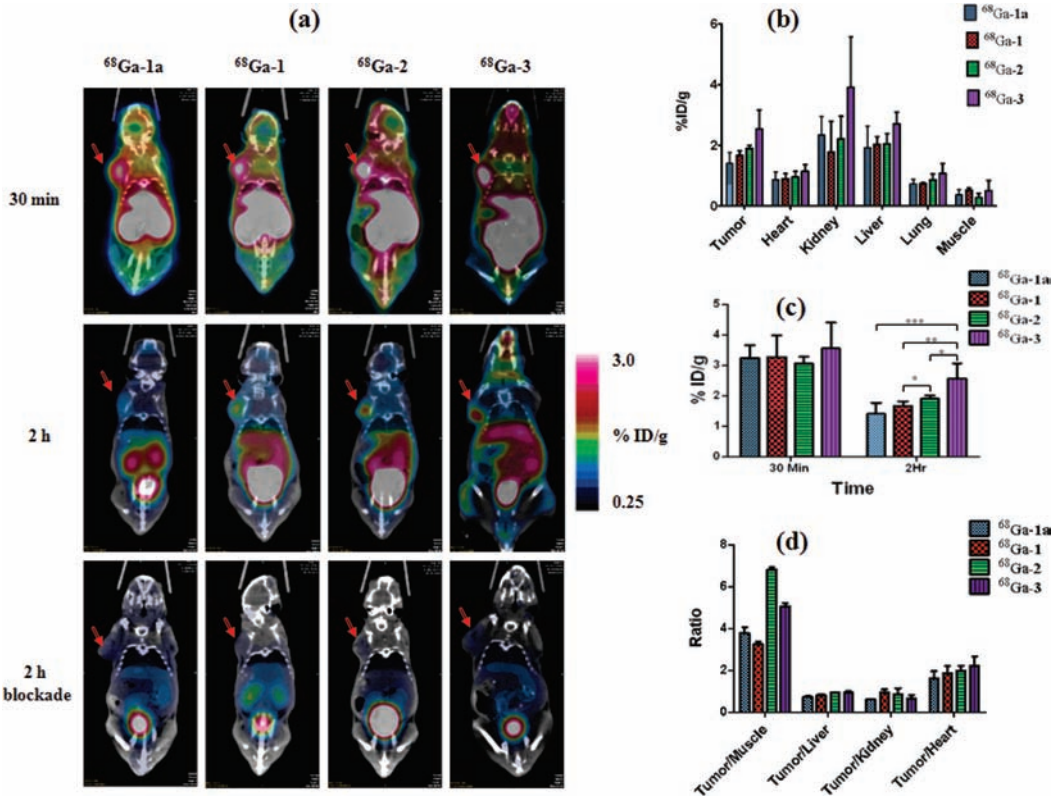

Figure 6. (a) Decay-corrected whole-body coronal microPET images of SCID mice bearing PC-3 tumor xenografts following injection of ^{68}Ga-**1**, ^{68}Ga-**1a**, ^{68}Ga-**2**, and ^{68}Ga-**3**: 30 min (dynamic frame of 25−30 min); 2 h (static scan); and 2 h blockade (coinjection with 10 mg/kg of c(RGDyK)). Tumors are indicated by red arrows. For comparison, the images are shown at the same signal intensity scale. (b) Uptake of the ^{68}Ga labeled conjugates at 2 h p.i. in tumor and major organs obtained from quantitative imaging analysis. Data are presented as %ID/g ± s.d. (n = 3). (c) Comparative tumor uptake of the ^{68}Ga labeled conjugates at 30 min and 2 h p.i. Data are presented as %ID/g ± s.d. (n = 3). (d) Ratios of tumor to major organs for the ^{68}Ga labeled conjugates.

magnitude higher than that of its DOTA counterpart. More impressively, the neutral Ga(III)-NOTA complex was reported to stay inert against the acid-catalyzed dissociation in 6N HNO_3 for 6 days.[20] When NOTA is used without modification as a BFC, however, one of its three pendent coordinating carboxylic acids would be consumed to form an amide linkage with the targeting vector. Although the coordinating atoms (N_3O_3) stay the same before and after the conjugation, the stability of the metal complex moiety is compromised due to the formation of an amide linkage.[41,42] In order for NOTA to keep its three coordinating acetate arms intact for Ga(III) chelation, an additional functional group is necessary. Indeed, various C- or N-functionalized NOTA derivatives have been reported as modified NOTA for gallium radiopharmaceuticals.[23,43−46] Of the reported methods, the N-functionalization of TACN provides a simple and versatile way of introducing additional functionalities to the triazamacrocyclic ring, which makes the NOTA derivatives bifunctional.[23,24]

The multivalent effect is widely used to enhance the desired biological potency of a bioactive molecule.[47−50] For instance, the tumor targeting efficacy of a targeting vector can be enhanced by orders of magnitude through the strengthened specific ligand−receptor binding.[28,34,51−54] In principle, multimeric presentation of a ligand increases its local concentration on the cell surface thus increasing the probability of the specific ligand−receptor interaction, which results in enhanced target accumulation. Furthermore, the juxtaposition of the conjoined ligands can facilitate the desired ligand−receptor interaction. In the field of molecular imaging, the multivalent effect can certainly be exploited to amplify the imaging signal in target organs or tissues in the same manner. Indeed, several groups have reported that imaging contrast can be significantly improved by taking advantage of multivalent effect in the imaging probe design.[27,28,32,55−58] For instance, multivalent PET imaging probes featuring multimeric peptides have demonstrated better imaging properties than their monomeric counterpart.[32,55,59−64]

Recently, we reported a BFC scaffold design for ^{64}Cu-based PET imaging probes, which provides multiple peripheral functional points for multipresentation of targeting vectors in a BFC without compromising the metal chelate stability of the chelating core.[28] An important role of such a BFC scaffold is to provide PET signal enhancement through the resulted multivalent effect. Similarly, we designed a series of NOTA-based scaffolds for ^{68}Ga PET imaging probes, $^{t}Bu_3$-**1**-Bn,[23] $^{t}Bu_3$-**2**-Bn_2, and $^{t}Bu_3$-**3**-Bn_3, which contain two orthogonally protected carboxylic acid groups on each side arm. All three BFC scaffolds have three *t*-butyl protected α-carboxylic acid groups intended for Ga(III) coordination, while the number of the terminal benzyl protected γ-carboxylic acid differs to systematically vary the valency of a targeting vector from 1 to 3. The orthogonality of the protecting groups on the side arm enables the selective deprotection of the γ-carboxylate and α-carboxylate groups by different procedures at the corresponding step. Further, the four-carbon alkyl chain is incorporated as a spacer between the NOTA core and the peripheral carboxylate groups so as to minimize the interference of the NOTA motif with the properties of the targeting vector. Indeed, it was reported that replacing one of the acetic acid side

arms of NOTA with succinic acid, a 4-carbon spacer, has a negligible effect on the geometry or the thermodynamic stability of the resulting Ga(III) complex (Ga-NODASA: log K = 30.9; Ga-NOTA: log K = 30.98).[24] Impressively, the exchange kinetics of ^{67}Ga-NODASA with transferrin at the physiological pH and temperature showed no metal transchelation over the period of 5 days.[24] Therefore, we believe the replacement of the acetate side arm with α-bromoglutaric acid 1-*tert*-butyl ester 5-benzyl ester (**4**) would not adversely influence the structural integrity and thermodynamic stability of the resulting Ga-complexes.

The NOTA BFC scaffolds, ^{t}Bu$_3$-**1**-COOH, ^{t}Bu$_3$-**2**-(COOH)$_2$, and ^{t}Bu$_3$-**3**-(COOH)$_3$, were synthesized by alkylation of TACN using appropriate equivalents of **4.** Synthesis of ^{t}Bu$_3$-**1**-COOH and ^{t}Bu$_3$-**2**-(COOH)$_2$ was performed in a three-step route with the first step determining the overall yield. The alkylation of TACN with **4** afforded both **5** and **6**. The two subsequent steps were quantitative. Synthesis of ^{t}Bu$_3$-**3**-(COOH)$_3$ was straightforward, and can be scaled to produce grams of the product. The NOTA scaffolds (^{t}Bu$_3$-**1**-COOH, ^{t}Bu$_3$-**2**-(COOH)$_2$, and ^{t}Bu$_3$-**3**-(COOH)$_3$) possess one, two, and three peripheral carboxylate groups, respectively, for the covalent attachment of a targeting vector in a systematic fashion. For proof of concept, a well-validated integrin $\alpha_v\beta_3$ ligand, c(RGDyK), was conjugated to ^{t}Bu$_3$-**1**-COOH, ^{t}Bu$_3$-**2**-(COOH)$_2$, and ^{t}Bu$_3$-**3**-(COOH)$_3$ to yield ^{t}Bu-protected monvalent, divalent, and trivalent peptide conjugates. The ^{t}Bu-protected α-carboxylate was later deprotected in 95% TFA to give H$_3$**1**, H$_3$**2**, and H$_3$**3** in quantitative yield as peptide conjugates ready for labeling with ^{68}Ga.

Radiolabeling of the conjugates of H$_3$**1**, H$_3$**2**, and H$_3$**3** with ^{68}Ga was tested by varying reaction conditions, such as pH, temperature, and time, in order to reach the highest achievable specific activity of the labeled tracers within a short time, given the 68-min half-life of ^{68}Ga. Because radiolabeling of NOTA with ^{68}Ga is pH-sensitive, HEPES was used as the reaction buffer to provide the optimal labeling pH (3.0−3.5).[16] At room temperature, we were able to label the conjugates in high radiochemical yields (RCY > 95%) within 30 min. Comparatively speaking, the ^{68}Ga labeling of multivalent conjugates (H$_3$**2** and H$_3$**3**) was slower than that of the monvalent ones (H$_3$**1** and H$_3$**1a**) in part due to the steric hindrance by the additional copies of c(RGDyK) peptide. However, the difference virtually disappeared when the radiolabeling was conducted at 70 °C. One of the desired features of a PET imaging agent for clinical application is the ease of postlabeling purification. By a simple separation procedure through a C-18 cartridge, all the radiolabeled conjugates reached >99% radiochemical purity as determined by radio-HPLC.

Both H$_3$**1** and H$_3$**1a** have one copy of c(RGDyK) peptide, while H$_3$**2** and H$_3$**3** have two and three copies of c(RGDyK), respectively. The multipresentation of the c(RGDyK) peptide in H$_3$**2** and H$_3$**3** is expected to enhance the affinity of the receptor−ligand interaction through the phenomenon of multivalent effect. By a competitive cell-binding assay using ^{125}I-echistatin as the integrin-specific radioligand,[32] the multivalent effect, as measured by the enhanced specific ligand−receptor binding affinity, was evaluated. The determined IC$_{50}$ values of monvalent H$_3$**1** (171 ± 60 nM), divalent H$_3$**2** (43.9 ± 16.1 nM), and trivalent H$_3$**3** (14.7 ± 5.0 nM) were found to be similar to the measurements reported for the monovalent (H$_3$**1a**, 218 nM), divalent (60 nM), and tetravalent (16 nM) conjugates constructed from peptide multimerization of c(RGDyK).[26] The cell-binding assay clearly demonstrated the anticipated multivalent effect of H$_3$**2** and H$_3$**3** as compared to their monovalent counterpart (H$_3$**1**). Of note, the multivalent effect resulting from the BFC scaffold-based multivalency (H$_3$**3**, 13 nM) is similar to that resulting from the tetramerization of c(RGDyK) (p-SCN-Bn-NOTA-tetramer, 16 nM).[26]

The in vivo behavior of ^{68}Ga-**1**, ^{68}Ga-**1a**, ^{68}Ga-**2**, and ^{68}Ga-**3**, was evaluated in SCID mice bearing integrin $\alpha_v\beta_3$-positive PC-3 prostate cancer xenograft. Like other c(RGDyK) based agents, all the ^{68}Ga-labeled conjugates were efficiently cleared from the kidneys, while the excretion through feces was negligible within 2 h p.i. The radio-HPLC analysis of collected urine demonstrated that the ^{68}Ga-labeled conjugates stayed intact (>99%) within 2 h p.i, which is roughly twice the physical half-life of ^{68}Ga. This high metabolic stability of the ^{68}Ga-labeled conjugates likely resulted from the kinetic inertness of the Ga-NOTA complex.

The integrin $\alpha_v\beta_3$ positive PC-3 tumor was visualized with ^{68}Ga-**1**, ^{68}Ga-**1a**, ^{68}Ga-**2,** and ^{68}Ga-**3** at 30 min and 2 h p.i. (Figure 6a). Irrespective of the valency, all the ^{68}Ga-labeled conjugates showed similar tumor uptake with poor contrast at 30 min p.i. due to their relatively high level in the nontarget organs (e.g., blood and muscle; Supporting Information Table S3). At 2 h p.i., the enhanced tumor uptake and retention of ^{68}Ga-**2** and ^{68}Ga-**3** can be partially attributed to their increased binding affinities resulting from multivalent effect. Interestingly, the tumor PET signal amplification level by the multivalent effect (^{68}Ga-**3**: 2.55 ± 0.50%ID/g; ^{68}Ga-**2**: 1.90 ± 0.10%ID/g; ^{68}Ga-**1**: 1.66 ± 0.15% ID/g) is similar to that in a published work using peptide multimerization of c(RGDyK) as an approach to realize multivalent effect for PET probe design (tetramer: 2.1%ID/g; dimer: 1.9%ID/g; monomer: 1.1%ID/g).[26] In addition to the increased binding affinity, the prolonged in vivo half-life of multivalent conjugates, resulting from the molecule size increase, may also contribute to the enhanced tumor uptake over the time course. The prolonged in vivo half-life of multivalent conjugate is believed to be able to sustain the desired tumor accumulation and retention.[26,65] However, similar distribution and elimination half-lives were observed for all radiolabeled conjugates. Therefore, we think that the observed tumor uptake increase and PET signal amplification were predominately caused by the multivalency of ^{68}Ga-**2** and ^{68}Ga-**3**. It is important to note that the imaging specificity is not compromised because of the added multivalency as was shown by the complete signal loss in the blockade experiment (Figure 6a and Supporting Information Table S2). The liver signal intensity difference between 2 and 2 h blockade was likely caused by the diluting effect of the excess cold ligand. However, we acknowledge that the kidney uptake was also increased by the multivalent effect, which might affect how the peptide conjugates are handled in the proximal tubule and their binding to megalin. While the same phenomenon is common in peptide-based radiopharmaceuticals, the exact mechanism for such an increase is unknown.

Statistical analyses proved a strong correlation between the biodistribution and quantitative imaging data as indicated by the calculated Pearson correlation coefficients for the four conjugates (r: ^{68}Ga-**1a** > 0.77; ^{68}Ga-**1** > 0.85; ^{68}Ga-**2** > 0.90; ^{68}Ga-**3** > 0.87).

■ CONCLUSIONS

A series of NOTA-based BFC scaffolds were synthesized to take advantage of multivalent effect for ^{68}Ga PET imaging probe design. Using a well-validated integrin $\alpha_v\beta_3$ ligand, c(RGDyK), peptide conjugates varying multivalency from 1 to 3 were prepared. The in vitro and in vivo evaluations of the peptide

conjugates demonstrated that the preservation of the intact NOTA core in the BFC scaffold design guaranteed rapid and efficient ^{68}Ga incorporation and high in vivo stability, while the multivalency rendered by the BFC scaffold design was able to significantly enhance the specific imaging of the targeted $\alpha_v\beta_3$ receptor in a prostate cancer xenograft mouse model. Together with our previously reported BFC scaffold design for ^{64}Cu PET imaging probes, we have validated the design concept that multivalent effect can be realized on a simple BFC scaffold to amplify the desired imaging signal. It is noteworthy that the peptide multimerization method reported by others can be combined with our BFC scaffold design to achieve multilayered multivalency if necessary. Further, our design allows enhanced specific targeting to heteromeric receptors by incorporating mutually independent targeting molecules on the BFC scaffold.

■ ASSOCIATED CONTENT

Supporting Information. Figure S1−2 and Table S1−3, as described in the text. This material is available free of charge via the Internet at http://pubs.acs.org.

■ AUTHOR INFORMATION

Corresponding Author

*Correspondence to Xiankai Sun, Ph.D., Department of Radiology and Advanced Imaging Research Center, University of Texas Southwestern Medical Center at Dallas, 2201 Inwood Road, Texas 75390-8542, USA; E-mail: Xiankai.Sun@UTSouthwestern.edu.

Author Contributions

□A. Singh and W. Liu contributed equally to this work.

■ ACKNOWLEDGMENT

This work was partially supported by a USAMRMC grant (W81XWH-08-1-0305) and two NIH grants (P01 DK058398; U24 CA126608). The authors acknowledge the generous support of a private donor that allowed the purchase of the Inveon PET-CT system.

■ REFERENCES

(1) Kelloff, G., Hoffman, J. M., Johnson, B., Scher, H. I., Siegel, B. A., Cheng, E. Y., Cheson, B. D., O'Shaughnessy, J., Guyton, K. Z., Mankoff, D. A., Shankar, L., Larson, S. M., Sigman, C. C., Schilsky, R. L., and Sullivan, D. C. (2005) Progress and promise of FDG-PET imaging for cancer patient management and oncologic drug development. *Clin. Cancer Res. 11*, 2785–2808.

(2) von Schulthess, G. K., Steinert, H. C., and Hany, T. F. (2006) Integrated PET/CT-3: Current applications and future directions. *Radiology 238*, 405–422.

(3) Harry, V. N., Semple, S. I., Parkin, D. E., and Gilbert, F. J. (2010) Use of new imaging techniques to predict tumour response to therapy. *Lancet Oncol. 11*, 92–102.

(4) de Rosales, R. T. M., Arstad, E., and Blower, P. J. (2009) Nuclear imaging of molecular processes in cancer. *Target Oncol. 4*, 183–197.

(5) Gambhir, S. S. (2002) Molecular imaging of cancer with positron emission tomography. *Nat. Rev. Cancer 2*, 683–693.

(6) Phelps, M. E. (2000) Positron emission tomography provides molecular imaging of biological processes. *Proc. Natl. Acad. Sci. U. S. A. 97*, 9226–9233.

(7) Miller, P. W., Long, N. J., Vilar, R., and Gee, A. D. (2008) Synthesis of ^{11}C, ^{18}F, ^{15}O, and ^{13}N radiolabels for positron emission tomography. *Angew. Chem., Int. Ed. 47*, 8998–9033.

(8) Pagani, M., Stone-Elander, S., and Larsson, S. A. (1997) Alternative positron emission tomography with non-conventional positron emitters: effects of their physical properties on image quality and potential clinical applications. *Eur. J. Nucl. Med. Mol. Imaging 24*, 1301–1327.

(9) Hao, G., Singh, A. N., Liu, W., and Sun, X. (2010) PET with non-standard nuclides. *Curr. Topics Med. Chem. 10*, 1096–1112.

(10) Al-Nahhas, A., Win, Z., Szyszko, T., Singh, A., Khan, S., and Rubello, D. (2007) What can gallium-68 PET add to receptor and molecular imaging? *Eur. J. Nucl. Med. Mol. Imaging 34*, 1897–901.

(11) Al-Nahhas, A., Win, Z., Szyszko, T., Singh, A., Nanni, C., Fanti, S., and Rubello, D. (2007) Gallium-68 PET: a new frontier in receptor cancer imaging. *Anticancer Res. 27*, 4087–94.

(12) Khan, M. U., Khan, S., El-Refaie, S., Win, Z., Rubello, D., and Al-Nahhas, A. (2009) Clinical indications for Gallium-68 positron emission tomography imaging. *Eur. J. Surg. Oncol. 35*, 561–7.

(13) Schottelius, M., Berger, S., Poethko, T., Schwaiger, M., and Wester, H. J. (2008) Development of novel Ga-68- and F-18-labeled GnRH-I analogues with high GnRHR-targeting efficiency. *Bioconjugate Chem. 19*, 1256–1268.

(14) Ehrhardt, G. J., and Welch, M. J. (1978) A new germanium-63/gallium-68 generator. *J. Nucl. Med. 19*, 925–9.

(15) Jeong, J. M., Hong, M. K., Chang, Y. S., Lee, Y.-S., Kim, Y. J., Cheon, G. J., Lee, D. S., Chung, J.-K., and Lee, M. C. (2008) Preparation of a promising angiogenesis PET imaging agent: ^{68}Ga-labeled c-(RGDyK)-isothiocyanatobenzyl-1,4,7-triazacyclononane-1,4,7-triacetic acid and feasibility studies in mice. *J. Nucl. Med. 49*, 830–836.

(16) Velikyan, I., Maecke, H., and Langstrom, B. (2008) Convenient preparation of ^{68}Ga-based PET-radiopharmaceuticals at room temperature. *Bioconjugate Chem. 19*, 569–573.

(17) Lee, J., Garmestani, K., Wu, C., Brechbiel, M. W., Chang, H. K., Choi, C. W., Gansow, O. A., Carrasquillo, J. A., and Paik, C. H. (1997) In vitro and in vivo evaluation of structure-stability relationship of ^{111}In- and ^{67}Ga-labeled antibody via 1B4M or C-NOTA chelates. *Nucl. Med. Biol. 24*, 225–230.

(18) Prata, M. I. M., Santos, A. C., Geraldes, C. F. G. C., and de Lima, J. J. P. (2000) Structural and in vivo studies of metal chelates of Ga(III) relevant to biomedical imaging. *J. Inorg. Biochem. 79*, 359–363.

(19) Prata, M. I., Santos, A. C., Geraldes, C. F., and de Lima, J. J. (1999) Characterisation of $^{67}Ga^{3+}$ complexes of triaza macrocyclic ligands: biodistribution and clearance studies. *Nucl. Med. Biol. 26*, 707–10.

(20) Broan, C. J., Cox, J. P. L., Craig, A. S., Kataky, R., Parker, D., Harrison, A., Randall, A. M., and Ferguson, G. (1991) Structure and solution stability of indium and gallium complexes of 1,4,7-triazacyclononanetriacetate and of yttrium complexes of 1,4,7,10-tetraazacyclododecanetetraacetate and related ligands - kinetically stable complexes for use in imaging and radioimmunotherapy - X-ray molecular-structure of the indium and gallium complexes of 1,4,7-triazacyclononane-1,4,7-triacetic acid. *J. Chem. Soc., Perkin Trans. 2*, 87–99.

(21) Craig, A. S., Parker, D., Adams, H., and Bailey, N. A. (1989) Stability, Ga-71 NMR, and crystal-structure of a neutral gallium(III) complex of 1,4,7-triazacyclononanetriacetate - a potential radiopharmaceutical. *J. Chem. Soc., Chem. Commun.* 1793–1794.

(22) Clarke, E. T., and Martell, A. E. (1991) Stabilities of the Fe(III), Ga(III), and In(III) chelates of N,N′,N″-triazacyclononanetriacetic acid. *Inorg. Chim. Acta 181*, 273–280.

(23) Eisenwiener, K.-P., Prata, M. I. M., Buschmann, I., Zhang, H.-W., Santos, A. C., Wenger, S., Reubi, J. C., and Maecke, H. R. (2002) NODAGATOC, a new chelator-coupled somatostatin analogue labeled with [$^{67/68}$Ga] and [^{111}In] for SPECT, PET, and targeted therapeutic applications of somatostatin receptor (hsst2) expressing tumors. *Bioconjugate Chem. 13*, 530–541.

(24) Andre, J. P., Maecke, H. R., Zehnder, M., Macko, L., and Akyel, K. G. (1998) 1,4,7-triazacyclononane-1-succinic acid-4,7-diacetic acid

(NODASA): a new bifunctional chelator for radio gallium-labelling of biomolecules. *Chem. Commun.* 1301–1302.

(25) Deyev, S. M., and Lebedenko, E. N. (2008) Multivalency: the hallmark of antibodies used for optimization of tumor targeting by design. *Bioessays 30*, 904–18.

(26) Li, Z. B., Chen, K., and Chen, X. (2008) ^{68}Ga-labeled multimeric RGD peptides for microPET imaging of integrin $\alpha_v\beta_3$ expression. *Eur. J. Nucl. Med. Mol. Imaging 35*, 1100–8.

(27) Liu, Z., Niu, G., Shi, J., Liu, S., Wang, F., Liu, S., and Chen, X. (2009) ^{68}Ga-labeled cyclic RGD dimers with Gly3 and PEG4 linkers: promising agents for tumor integrin $\alpha_v\beta_3$ PET imaging. *Eur. J. Nucl. Med. Mol. Imaging 36*, 947–957.

(28) Liu, W., Hao, G., Long, Michael, A., Anthony, T., Hsieh, J.-T., and Sun, X. (2009) Imparting multivalency to a bifunctional chelator: a scaffold design for targeted PET imaging probes. *Angew. Chem., Int. Ed. 48*, 7346–7349.

(29) Eisenwiener, K. P., Powell, P., and Macke, H. R. (2000) A convenient synthesis of novel bifunctional prochelators for coupling to bioactive peptides for radiometal labelling. *Bioorg. Med. Chem. Lett. 10*, 2133–5.

(30) Welling, P. G. (1997) *Pharmacokinetics: Processes, mathematics, and applications*, American Chemical Society, Washington, DC.

(31) Velikyan, I., Maecke, H., and Langstrom, B. (2008) Convenient preparation of ^{68}Ga-based PET-radiopharmaceuticals at room temperature. *Bioconjugate Chem. 19*, 569–73.

(32) Li, Z. B., Cai, W., Cao, Q., Chen, K., Wu, Z., He, L., and Chen, X. (2007) ^{64}Cu-labeled tetrameric and octameric RGD peptides for small-animal PET of tumor $\alpha_v\beta_3$ integrin expression. *J. Nucl. Med. 48*, 1162–71.

(33) Zhang, X., Xiong, Z., Wu, Y., Cai, W., Tseng, J. R., Gambhir, S. S., and Chen, X. (2006) Quantitative PET imaging of tumor integrin $\alpha_v\beta_3$ expression with ^{18}F-FRGD2. *J. Nucl. Med. 47*, 113–121.

(34) Montet, X., Funovics, M., Montet-Abou, K., Weissleder, R., and Josephson, L. (2006) Multivalent effects of RGD peptides obtained by nanoparticle display. *J. Med. Chem. 49*, 6087–93.

(35) Wadas, T. J., Wong, E. H., Weisman, G. R., and Anderson, C. J. (2010) Coordinating radiometals of copper, gallium, indium, yttrium, and zirconium for PET and SPECT imaging of disease. *Chem. Rev. 110*, 2858–2902.

(36) Fani, M., Andre, J. P., and Maecke, H. R. (2008) ^{68}Ga-PET: a powerful generator-based alternative to cyclotron-based PET radiopharmaceuticals. *Contr. Media Mol. Imaging 3*, 67–77.

(37) Maecke, H. R., and Andre, J. P. (2007) ^{68}Ga-PET radiopharmacy: A generator-based alternative to ^{18}F-radiopharmacy. *Ernst Schering Res. Found. Workshop* 215–42.

(38) Bandoli, G., Dolmella, A., Tisato, F., Porchia, M., and Refosco, F. (2009) Mononuclear six-coordinated Ga(III) complexes: A comprehensive survey. *Coord. Chem. Rev. 253*, 56–77.

(39) Clarke, E. T., and Martell, A. E. (1991) Stabilities of trivalent metal ion complexes of the tetraacetate derivatives of 12-, 13- and 14-membered tetraazamacrocycles. *Inorg. Chim. Acta 190*, 37–46.

(40) Decristoforo, C., Hernandez Gonzalez, I., Carlsen, J., Rupprich, M., Huisman, M., Virgolini, I., Wester, H.-J., and Haubner, R. (2008) ^{68}Ga- and ^{111}In-labelled DOTA-RGD peptides for imaging of $\alpha_v\beta_3$ integrin expression. *Eur. J. Nucl. Med. Mol. Imaging 35*, 1507–1515.

(41) Hoigebazar, L., Jeong, J. M., Choi, S. Y., Choi, J. Y., Shetty, D., Lee, Y.-S., Lee, D. S., Chung, J.-K., Lee, M. C., and Chung, Y. K. (2010) Synthesis and characterization of nitroimidazole derivatives for ^{68}Ga-labeling and testing in tumor xenografted mice. *J. Med. Chem. 53*, 6378–6385.

(42) Woods, M., Caravan, P., Geraldes, C. F., Greenfield, M. T., Kiefer, G. E., Lin, M., McMillan, K., Prata, M. I., Santos, A. C., Sun, X., Wang, J., Zhang, S., Zhao, P., and Sherry, A. D. (2008) The effect of the amide substituent on the biodistribution and tolerance of lanthanide(III) DOTA-tetraamide derivatives. *Invest. Radiol. 43*, 861–70.

(43) Brechbiel, M. W., McMurry, T. J., and Gansow, O. A. (1993) A direct synthesis of a bifunctional chelating agent for radiolabeling proteins. *Tetrahedron Lett. 34*, 3691–3694.

(44) Cox, J. P. L., Craig, A. S., Helps, I. M., Jankowski, K. J., Parker, D., Eaton, M. A. W., Millican, A. T., Millar, K., Beeley, N. R. A., and Boyce, B. A. (1990) Synthesis of C- and N-functionalised derivatives of 1,4,7-triazacyclononane-1,4,7-triyltriacetic acid (NOTA), 1,4,7,10-tetraazacyclododecane-1,4,7,10-tetrayltetra-acetic acid (DOTA), and diethylenenetriaminepenta-acetic acid (DTPA): bifunctional complexing agents for the derivatisation of antibodies. *J. Chem. Soc., Perkin Trans. 1*, 2567–2576.

(45) McMurry, T. J., Brechbiel, M., Wu, C., and Gansow, O. A. (1993) Synthesis of 2-(p-thiocyanatobenzyl)-1,4,7-triazacyclononane-1,4,7-triacetic acid: Application of the 4-methoxy-2,3,6-trimethylbenzenesulfonamide protecting group in the synthesis of macrocyclic polyamines. *Bioconjugate Chem. 4*, 236–245.

(46) Studer, M., and Meares, C. F. (1992) Synthesis of novel 1,4,7-triazacyclononane-N,N′,N″-triacetic acid derivatives suitable for protein labeling. *Bioconjugate Chem. 3*, 337–41.

(47) Gestwicki, J. E., Cairo, C. W., Strong, L. E., Oetjen, K. A., and Kiessling, L. L. (2002) Influencing receptor-ligand binding mechanisms with multivalent ligand architecture. *J. Am. Chem. Soc. 124*, 14922–33.

(48) Hotez, P. J., Bethony, J. M., Oliveira, S. C., Brindley, P. J., and Loukas, A. (2008) Multivalent anthelminthic vaccine to prevent hookworm and schistosomiasis. *Expert Rev. Vaccines 7*, 745–52.

(49) Hudson, P. J., and Kortt, A. A. (1999) High avidity scFv multimers; diabodies and triabodies. *J. Immunol. Methods 231*, 177–89.

(50) Reulen, S. W. A., Dankers, P. Y. W., Bomans, P. H. H., Meijer, E. W., and Merkx, M. (2009) Collagen targeting using protein-functionalized micelles: the strength of multiple weak interactions. *J. Am. Chem. Soc. 131*, 7304–7312.

(51) Almutairi, A., Rossin, R., Shokeen, M., Hagooly, A., Ananth, A., Capoccia, B., Guillaudeu, S., Abendschein, D., Anderson, C. J., Welch, M. J., and Fréchet, J. M. J. (2009) Biodegradable dendritic positron-emitting nanoprobes for the noninvasive imaging of angiogenesis. *Proc. Natl. Acad. Sci. U. S. A. 106*, 685–690.

(52) Hong, S., Leroueil, P. R., Majoros, I. J., Orr, B. G., Baker, J. R., Jr., and Banaszak Holl, M. M. (2007) The binding avidity of a nanoparticle-based multivalent targeted drug delivery platform. *Chem. Biol. 14*, 107–15.

(53) Todorovska, A., Roovers, R. C., Dolezal, O., Kortt, A. A., Hoogenboom, H. R., and Hudson, P. J. (2001) Design and application of diabodies, triabodies and tetrabodies for cancer targeting. *J. Immunol. Methods 248*, 47–66.

(54) Ye, Y., Bloch, S., Xu, B., and Achilefu, S. (2006) Design, synthesis, and evaluation of near infrared fluorescent multimeric RGD peptides for targeting tumors. *J. Med. Chem. 49*, 2268–2275.

(55) Chen, X., Liu, S., Hou, Y., Tohme, M., Park, R., Bading, J. R., and Conti, P. S. (2004) MicroPET imaging of breast cancer α_v-integrin expression with ^{64}Cu-labeled dimeric RGD peptides. *Mol. Imaging Biol. 6*, 350–9.

(56) Dijkgraaf, I., Rijnders, A. Y., Soede, A., Dechesne, A. C., Esse, G. W. v., Brouwer, A. J., Corstens, F. H. M., Boerman, O. C., Rijkers, D. T. S., and Liskamp, R. M. J. (2007) Synthesis of DOTA-conjugated multivalent cyclic-RGD peptide dendrimers via 1,3-dipolar cycloaddition and their biological evaluation: implications for tumor targeting and tumor imaging purposes. *Org. Biomol. Chem. 5*, 935–944.

(57) Jia, B., Liu, Z., Shi, J., Yu, Z., Yang, Z., Zhao, H., He, Z., Liu, S., and Wang, F. (2008) Linker effects on biological properties of ^{111}In-labeled DTPA conjugates of a cyclic RGDfK dimer. *Bioconjugate Chem. 19*, 201–10.

(58) Thumshirn, G., Hersel, U., Goodman, S. L., and Kessler, H. (2003) Multimeric cyclic RGD peptides as potential tools for tumor targeting: solid-phase peptide synthesis and chemoselective oxime ligation. *Chemistry 9*, 2717–25.

(59) Liu, S. (2006) Radiolabeled multimeric cyclic RGD peptides as integrin $\alpha_v\beta_3$ targeted radiotracers for tumor imaging. *Mol. Pharm. 3*, 472–87.

(60) Liu, S. (2009) Radiolabeled cyclic RGD peptides as integrin $\alpha_v\beta_3$-targeted radiotracers: maximizing binding affinity *via* bivalency. *Bioconjugate Chem. 20*, 2199–213.

(61) Dijkgraaf, I., Kruijtzer, J. A., Liu, S., Soede, A. C., Oyen, W. J., Corstens, F. H., Liskamp, R. M., and Boerman, O. C. (2007) Improved targeting of the $\alpha_v\beta_3$ integrin by multimerisation of RGD peptides. *Eur. J. Nucl. Med. Mol. Imaging 34*, 267–73.

(62) Janssen, M., Oyen, W. J., Massuger, L. F., Frielink, C., Dijkgraaf, I., Edwards, D. S., Radjopadhye, M., Corstens, F. H., and Boerman, O. C. (2002) Comparison of a monomeric and dimeric radiolabeled RGD-peptide for tumor targeting. *Cancer Biother. Radiopharm. 17*, 641–6.

(63) Wang, J., Kim, Y. S., and Liu, S. (2008) 99mTc-labeling of HYNIC-conjugated cyclic RGDfK dimer and tetramer using EDDA as coligand. *Bioconjugate Chem. 19*, 634–42.

(64) Zhang, X., Liu, H., Miao, Z., Kimura, R., Fan, F., and Cheng, Z. (2011) Macrocyclic chelator assembled RGD multimers for tumor targeting. *Bioorg. Med. Chem. Lett. 21*, 3423–3426.

(65) Nasongkla, N., Chen, B., Macaraeg, N., Fox, M. E., Frechet, J. M. J., and Szoka, F. C. (2009) Dependence of pharmacokinetics and biodistribution on polymer architecture: effect of cyclic versus linear polymers. *J. Am. Chem. Soc. 131*, 3842–3843.

Multivalent Bifunctional Chelator Scaffolds for Gallium-68 Based Positron Emission Tomography Imaging Probe Design: Signal Amplification *via* Multivalency

Ajay N. Singh[1†], Wei Liu[1,2†], Guiyang Hao[1], Amit Kumar[1], Anjali Gupta[1], Orhan K. Öz[1], Jer-Tsong Hsieh[3], Xiankai Sun*[1,4].

Departments of [1]Radiology and [3]Urology, [4]Advanced Imaging Research Center, University of Texas Southwestern Medical Center, Dallas, Texas, USA

[2]State Key Lab of Crystal Materials, Shandong University, Jinan, Shandong, P. R. China

[†] A. Singh and W. Liu contributed equally to this work.

*Correspondence to Xiankai Sun, Ph.D., Department of Radiology and Advanced Imaging Research Center, University of Texas Southwestern Medical Center at Dallas, 2201 Inwood Road, Texas 75390-8542, USA; E-mail: Xiankai.Sun@UTSouthwestern.edu

Supporting Information

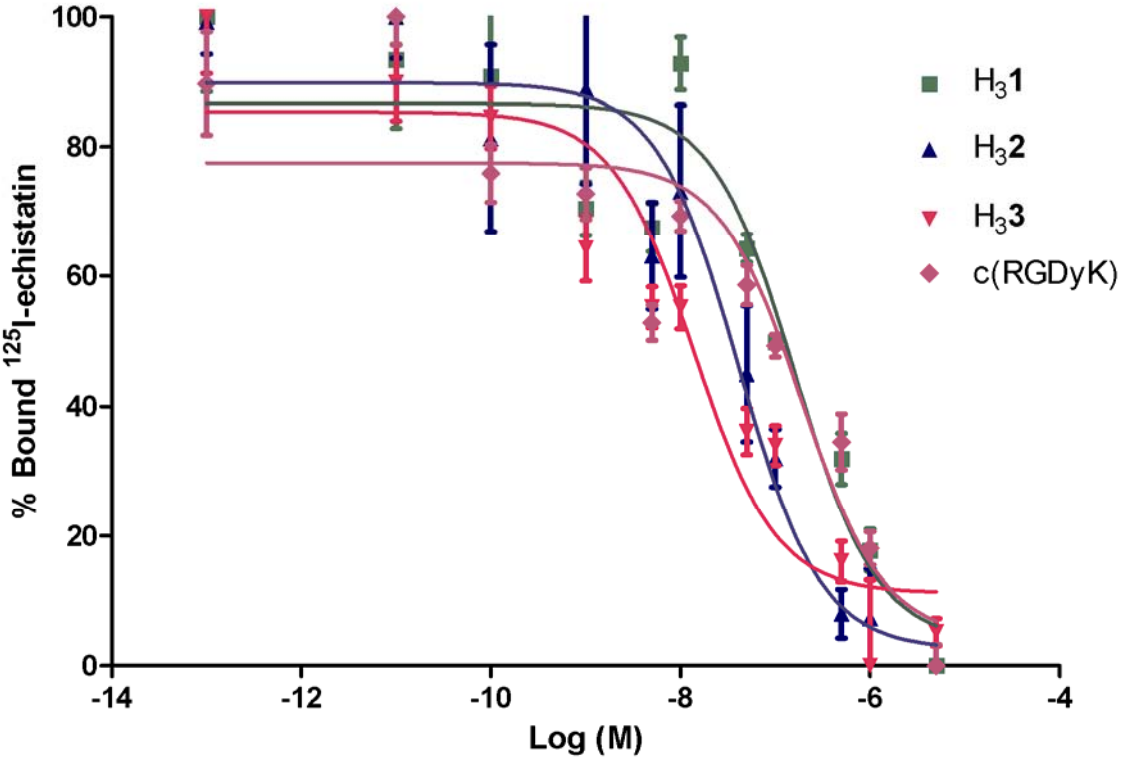

Figure S1. The integrin $\alpha_v\beta_3$ binding affinities of c(RGDyK), H_3**1,** H_3**2,** and H_3**3** measured by a competitive cell-binding assay using ^{125}I-echistatin as the integrin-specific radioligand. The IC_{50} values were calculated to be 204 ± 76 nM, 171 ± 60 nM, 43.9 ± 16.1 nM, and 14.7 ± 5.0 nM for c(RGDyK), H_3**1**, H_3**2**, and H_3**3**, respectively (two-tailed t-test: $p < 0.01$). Goodness of fit (R^2): 0.80 – 0.82.

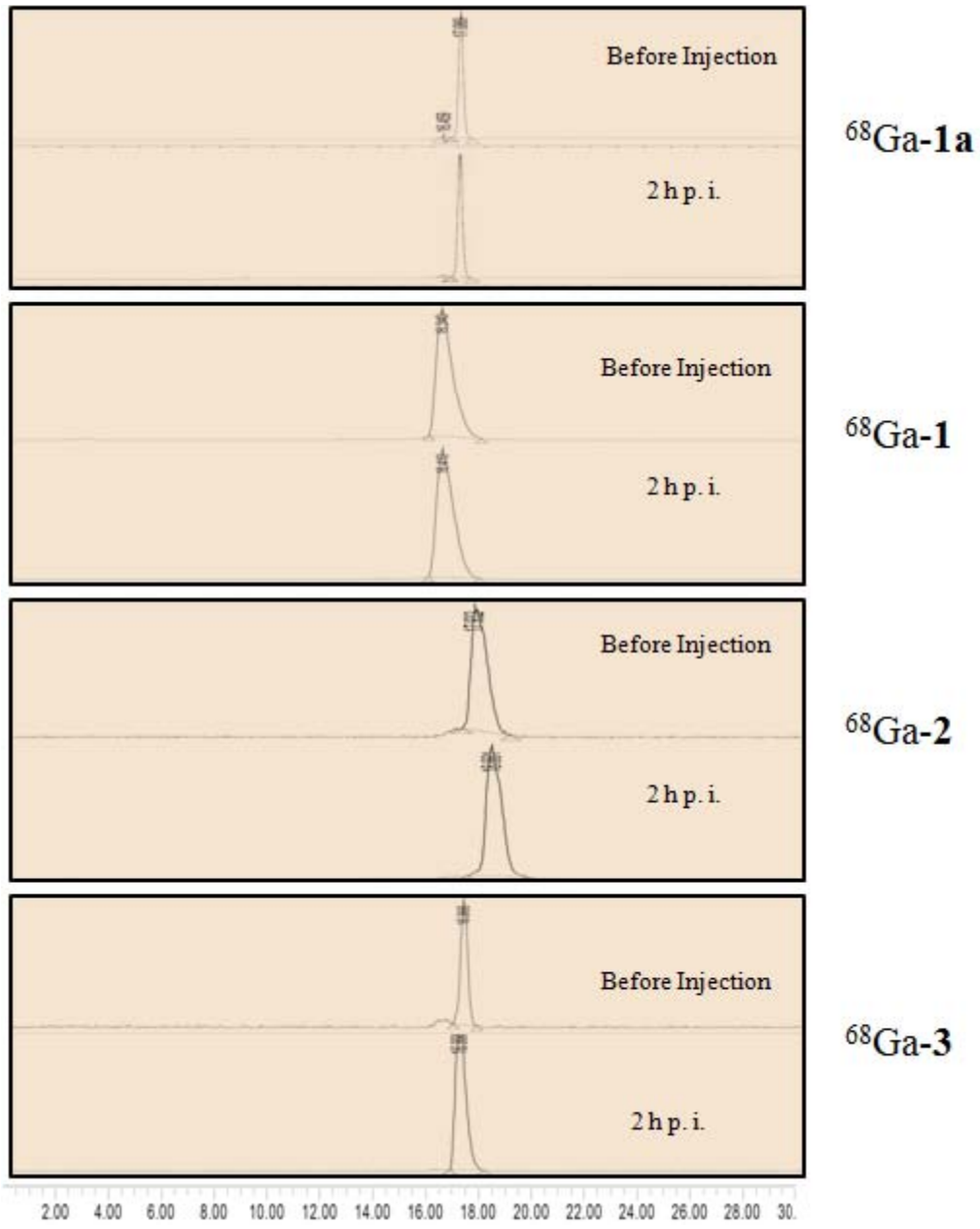

Figure S2. Radio-HPLC analysis of the metabolites of ^{68}Ga-**1a**, ^{68}Ga-**1**, ^{68}Ga-**2** and ^{68}Ga-**3** in mouse urine at 2 h p.i. (n = 4)

Table S1. Uptake of ^{68}Ga-**1**, ^{68}Ga-**1a**, ^{68}Ga-**2** and ^{68}Ga-**3** at 30 min and 2 h p.i. in major organs and tumor determined by quantitative PET imaging analysis. Data are presented as %ID/g ± s.d. (n = 3).

Organ	^{68}Ga-**1a**		^{68}Ga-**1**		^{68}Ga-**2**		^{68}Ga-**3**	
	(30 min)	(2 h)	(30 min)	(2 h)	(30 min)	(2 h)	(30 min)	(2 h)
Tumor	3.24±0.41	1.40±0.36	3.26±0.70	1.66±0.15	3.06±0.21	1.90±0.10	3.55±0.85	2.55±0.50
Heart	4.48±0.74	0.86±0.25	3.16±0.50	0.89±0.17	3.44±0.51	0.95±0.18	3.26±0.81	1.14±0.21
Lung	2.76±0.35	0.73±0.15	2.13±0.30	0.73±0.03	2.22±0.10	0.85±0.19	2.6±0.72	1.07±0.31
Liver	3.92±0.70	1.92±0.71	3.16±0.32	2.03±0.25	3.5±0.55	2.04±0.35	3.88±0.92	2.70±0.39
Kidney	12.52±4.0	2.34±0.60	9.73±5.0	1.77±1.01	11.22±3.8	2.22±0.73	9.23±3.78	3.90±1.60
Muscle	1.03±0.32	0.37±0.17	0.77±0.63	0.51±0.07	0.85±0.33	0.27±0.13	1.34±0.55	0.50±0.34

Table S2. Uptake of ^{68}Ga-**1**, ^{68}Ga-**1a**, ^{68}Ga-**2** and ^{68}Ga-**3** co-injected with c(RGDyK) (10mg/kg) at 30 min and 2 h p.i. in major organs and tumor determined by quantitative PET imaging analysis. Data are presented as %ID/g ± s.d. (n = 3).

Organ	^{68}Ga-**1a**		^{68}Ga-**1**		^{68}Ga-**2**		^{68}Ga-**3**	
	(30 min)	(2 h)	(30 min)	(2 h)	(30 min)	(2 h)	(30 min)	(2 h)
Tumor	2.40 ±0.12	0.64±0.21	2.55±0.32	0.3 1±0.02	2.98±1.5	0.44±0.19	1.69±0.42	0.51±0.15
Heart	3.81±1.00	0.55±0.21	4.09±1.00	0.45±0.02	4.33±3.2	0.60±0.08	3.18±0.04	0.77±0.46
Lung	2.14±0.46	0.37±0.04	1.93±0.37	0.30±0.05	2.32±1.7	0.45±0.43	1.70±0.02	0.48±0.21
Liver	2.81±0.66	0.81±0.10	2.89±0.47	0.92±0.10	2.81±1.9	0.93±0.75	2.23±0.00	0.91±0.26
Kidney	6.92±3.17	1.95± 0.33	9.97±5.61	1.55±0.77	8.26±7.2	1.54±0.40	7.09±2.53	3.40±1.52
Muscle	1.49±0.11	0.22±0.05	1.51±0.20	0.15±0.04	1.77±0.97	0.17±0.04	1.31±0.02	0.35±0.18

Table S3. Biodistribution data of ^{68}Ga-**1**, ^{68}Ga-**1a**, ^{68}Ga-**2** and ^{68}Ga-**3** at 30 min and 2 h p.i. in major organs and tumor. Data are presented as %ID/g ± s.d. (n = 3) (S. Int.: Small intestines; L. Int = Large intestines).

Organ	^{68}Ga-**1a**		^{68}Ga-**1**		^{68}Ga-**2**		^{68}Ga-**3**	
	(30min)	(2 h)	(30min)	(2 h)	(30min)	(2 h)	(30min)	(2 h)
Tumor	2.84±0.24	1.63±0.19	3.04±0.24	1.67±0.16	3.16±0.22	1.94±0.32	5.58±0.45	4.41±1.00
Blood	1.31±0.11	0.16±0.06	1.43±0.25	0.23±0.03	1.24±0.09	0.51±0.60	1.21±0.28	0.18±0.00
Heart	1.00±0.07	0.47±0.21	0.96±0.25	0.50±0.05	1.08±0.02	0.55±0.08	1.78±0.23	1.00±0.14
Lung	2.74±0.11	1.24±0.42	2.62±0.24	1.25±0.13	2.93±0.10	1.31±0.15	5.29±1.25	2.94±0.12
Liver	1.98±0.29	1.43±0.53	1.91±0.30	1.72±0.09	2.07±0.05	1.80±0.14	3.10±0.77	2.81±0.26
Spleen	2.66±0.94	2.10±1.08	3.17±0.70	2.55±0.84	2.44±0.54	2.78±0.19	3.42±0.91	3.14±0.20
Kidney	6.25±0.61	2.95±0.76	5.40±0.61	3.14±0.13	3.18±2.76	3.86±1.80	8.41±0.99	7.50±0.95
Fat	0.40±0.21	0.42±0.09	1.34±0.74	0.45±0.04	0.66±0.28	0.39±0.08	1.08±0.51	0.61±0.42
Bone	0.97±0.17	0.44±0.09	0.94±0.05	0.52±0.06	0.91±0.81	0.37±0.21	1.23±0.10	1.00±0.24
Muscle	0.70±0.10	0.42±0.14	0.62±0.02	0.30±0.03	0.91±0.73	0.41±0.27	1.57±0.24	1.17±0.31
Brain	0.08±0.01	0.05±0.00	0.07±0.01	0.06±0.01	0.06±0.02	0.06±0.02	0.13±0.01	0.10±0.03
S.Int	2.01±0.18	2.39±0.88	2.01±0.22	2.20±0.28	2.01±0.19	1.59±0.15	3.97±0.30	3.14±0.69
L.Int	0.84±0.03	0.92±0.08	1.04±0.10	0.98±0.24	1.07±0.68	1.40±0.19	1.96±0.17	1.60±0.65
Stomach	0.82±0.33	1.83±0.18	0.75±0.07	0.99±0.11	0.59±0.02	1.20±0.34	3.36±0.43	1.86±0.61

Bioconjugate Chemistry

ARTICLE

pubs.acs.org/bc

Use of 5′-γ-Ferrocenyl Adenosine Triphosphate (Fc-ATP) Bioconjugates Having Poly(ethylene glycol) Spacers in Kinase-Catalyzed Phosphorylations

Sanela Martić, Meghan K. Rains, Daniel Freeman, and Heinz-Bernhard Kraatz*

Chemistry Department, The University of Western Ontario, London, Ontario, Canada

Supporting Information

ABSTRACT:

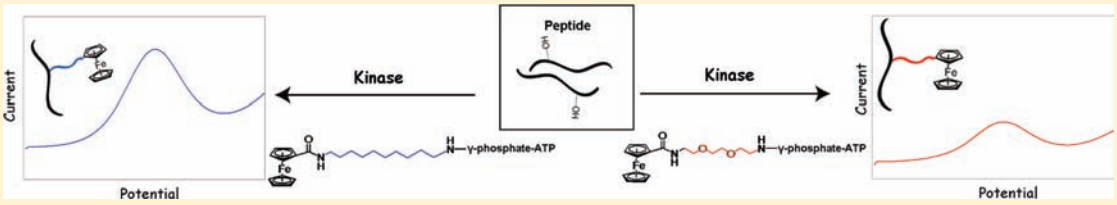

The 5′-γ-ferrocenyl adenosine triphosphate (Fc-ATP) bioconjugates (**3** and **4**), containing the poly(ethylene glycol) spacers, were synthesized and compared to a hydrophobic analogue as co-substrates for the following protein kinases: sarcoma related kinase (Src), cyclin-dependent kinase (CDK), casein kinase II (CK2α), and protein kinase A (PKA). Electrochemical kinase assays indicate that the hydrophobic Fc-ATP analogue was an optimal co-substrate for which K_M values were determined to be in the 30−200 μM range, depending on the particular protein kinase. The luminescence kinase assay demonstrated the kinase utility for all Fc-ATP conjugates, which is in line with the electrochemical data. Moreover, Fc-ATP bioconjugates exhibit competitive behavior with respect to ATP. Relatively poor performance of the polar Fc-ATP bioconjugates as co-substrates for protein kinases was presumably due to the additional H-bonding and electrostatic interactions of the poly(ethylene glycol) linkers of Fc-ATP with the kinase catalytic site and the target peptides. Phosphorylation of the full-length protein, His-tagged pro-caspase-3, was demonstrated through Fc-phosphoamide transfer to the Ser residues of the surface-bound protein by electrochemical means. These results suggest that electrochemical detection of the peptide and protein Fc-phosphorylation via tailored Fc-ATP co-substrates may be useful for probing protein−protein interactions.

INTRODUCTION

Protein phosphorylation, catalyzed by protein kinase, is a critical biological event that regulates cellular life and death and has been linked to diseases such as cancer.[1,2] A number of analytical methods have been developed to detect and monitor protein kinase activity and to screen for inhibitors of kinases as drug targets in cancer research.[3−13] Monitoring phosphorylation reactions of peptides and proteins is generally achieved by two approaches based on the modified peptide substrates or modified adenosine triphosphate (ATP) analogues. A modification of ATP at the γ-phosphate position by a reporter group, such as a redox or fluorescence label, positions the probe in close proximity to the kinase active site, catalytic pocket, and peptide (protein) substrate to be phosphorylated.[14−17] By using γ-modified ATP, the phosphorylation-dependent kinase−substrate cross-linking was recently used to identify phosphorylation sites and active kinases.[18] Other γ-substitutions of ATP include biotinylation,[19,20] dansylation,[21] and thiophosphate[22,23] labeling and were used for quantitative determination of kinase activity, identification of peptide (protein) substrates, and screening of kinase inhibitors. An electrochemical strategy was recently developed based on 5′-γ-ferrocenyl phosphate ATP co-substrate (Fc-ATP) to monitor phosphorylation of surface-bound peptides.[13] As depicted in Scheme 1A, the protein kinase-driven Fc-phosphoamide transfer to the Ser, Thr, or Tyr residues of the immobilized peptides resulted in the current response that was subsequently measured. Herein, we explore the utility of new Fc-ATP analogues containing poly(ethylene glycol) linkers between the ferrocene group and the ATP fragment in order to compare the protein kinase promiscuity and co-substrate variability with highly polar co-substrates. By comparing the alkyl and poly(ethylene glycol) spacers of comparable length in Fc-ATP bioconjugates, we electrochemically explored the structural and electronic factors surrounding the kinase-catalyzed reactions, which are less accessible by using unmodified ATP.

We decided to synthesize two new polar Fc-poly(ethylene glycol)-ATP conjugates with poly(ethylene glycol) (PEG) spacer -$(CH_2)_2$−O−$(CH_2)_2$−O−$(CH_2)_2$− (**3**) and -$(CH_2)_3$−O−$(CH_2)_2$−O−$(CH_2)_2$−O−$(CH_2)_3$ (**4**) and compare their efficiency as kinase cosubstrates with Fc-alkyl-ATP analogue (**5**) of

Received: May 2, 2011
Revised: June 21, 2011
Published: June 22, 2011

ACS Publications © 2011 American Chemical Society

Scheme 1. Schematic Representation of the Electrochemical Kinase Assays Based on the Fc-ATP Co-Substrate 5 for (A) Phosphorylation of the Surface-Bound Peptide[a] and (B) Phosphorylation of the Surface-Bound Protein in the Presence of Kinase[a]; (C) Competitive Solution Fluorescence Assay for Peptide Phosphorylation in the Presence of ATP, Fc-ATP Co-Substrate 5, and Protein Kinase[b]

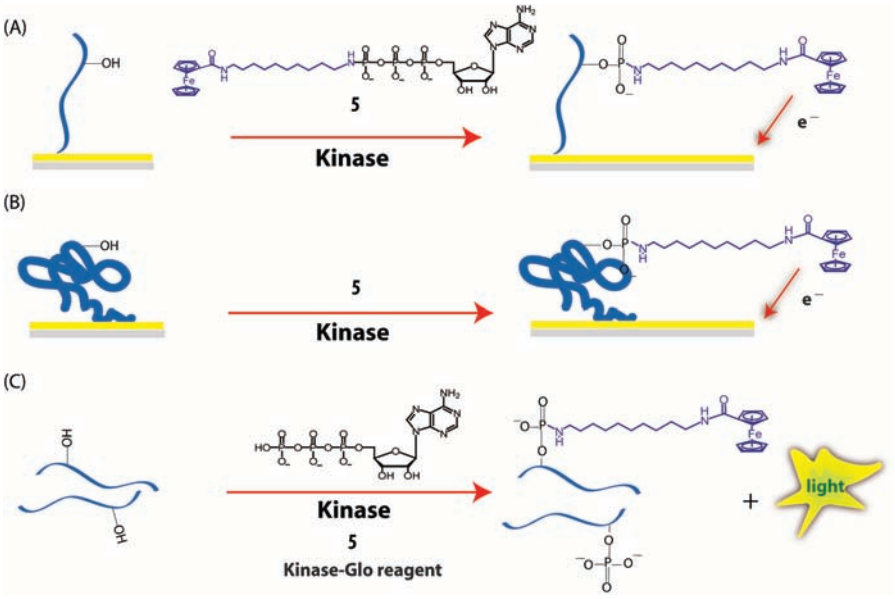

[a] Fc-phosphoamide transfer to the surface results in the redox response. [b] Following the kinase reaction, the subsequent addition of kinase-glo reagent produces light proportional to the leftover ATP amount.

similar spacer length.[14] Here, we explore the kinase promiscuity, only with respect to Fc-ATP, and investigate the usefulness of hydrophobic and hydrophilic Fc-ATP co-substrates for peptide phosphorylations by multiple protein kinases. We probe the effects of the polar versus nonpolar Fc-ATP conjugates on four protein kinases and their ability to drive peptide phosphorylation. By electrochemical means, we demonstrate the usefulness of the analytical method for detection of protein phosphorylation as well, as presented in Scheme 1B. The kinase reaction parameters were estimated electrochemically, and the electrochemical trends were compared to the fluorescence kinase assay for the first time (Scheme 1C).

EXPERIMETNAL PROCEDURES

General Methods. All organic solvents were freshly distilled unless otherwise specified. All reagents were used without further purification. Ferrocene, triethylamine, *O*-benzotriazole-*N*,*N*,*N*′,*N*′-tetramethyl-uronium-hexafluoro-phosphate (HBTU), hydroxybenzotriazole (HOBt), *N*,*N*′-dicyclohexylcarbodiimide (DCC), and adenosine triphosphate (ATP) were purchased from Sigma Aldrich, while diaminopoly(ethylene glycol) starting material was obtained from TCI America. The peptide substrates Arg-Arg-Arg-Asp-Asp-Asp-**Ser**-Asp-Asp-Asp and Arg-Arg-Leu-**Ser**-**Ser**-Leu-Arg-Ala, and proteins CK2α, and PKA protein kinases were donated by D. W. Litchfield's laboratories (The University of Western Ontario, Canada). Src protein kinase and Glu-Gly-Ile-**Tyr**-Asp-Val-Pro peptide substrate were obtained from Cell Signaling (New England Biolabs Ltd., Pickering, Ontario). CDK2/Cyclin A kinase and peptide substrate His-His-Ala-**Ser**-Pro-Arg-Lys were purchased from Enzo Life Sciences. All NMR experiments (^{1}H, ^{13}C, and ^{31}P) were performed on INOVA 400 spectrometer at room temperature. An external reference 85% H_3PO_4 was used for all ^{31}P NMR experiments. MALDI-TOF MS spectra were collected on Applied Biosystems 4700 Proteomics Analyzer (Applied Biosystems, USA). All organic solvents were freshly distilled, and the experiments in aqueous conditions were prepared using ultrapure water (18.3 MΩ cm) from Millipore Milli Q system.

General Procedure for the Synthesis of the Fc-Poly-(ethylene glycol)-Boc 1−2. To a solution of HBTU (1.36 g, 3.59 mmol), HOBt (0.55 g 3.59 mmol), and triethylamine (0.50 mL, 3.57 mmol) in CH_2Cl_2 (50 mL) was added a solution of ferrocene monocarboxylic acid (0.69 g 3.01 mmol) in CH_2Cl_2 (10 mL). The resulting mixture was stirred for 2 h at room temperature and washed with saturated aqueous $NaHCO_3$ (3 × 50 mL), then 10% citric acid (3 × 50 mL) and water (3 × 50 mL). The organic layer was dried over Na_2SO_4 and evaporated prior to purification. Fc-active ester was purified using flash silica chromatography CH_2Cl_2/ethyl acetate (90:10% v/v) and isolated in 75% yield. To a solution of Fc-active ester (0.30 g, 0.83 mmol) in CH_2Cl_2 (30 mL) was added NH_2-poly(ethylene glycol)-Boc ligand (0.19 g, 0.79 mmol) in CH_2Cl_2 (10 mL). The solution was stirred at room temperature for 2 h and then washed with saturated aqueous $NaHCO_3$ anhydrous (3 × 50 mL), then 10% citric acid (3 × 50 mL) followed by water (3 × 50 mL). The organic layer was dried over Na_2SO_4 and evaporated. The organics were purified using silica chromatography and a $CHCl_3$/MeOH (95:5% v/v) solvent system to afford compounds **1** and **2** as viscous liquids in 86% (0.32 g) and 85% (0.31 g) yield, respectively.

Compound 1. ^{1}H NMR ($CDCl_3$, 400 MHz): δ 6.26 (s, 1H, Fc-CO-NH), 5.04 (s, 1H, NH-Boc), 4.69 (s, 2H, Fc), 4.34 (s, 2H, Fc), 4.21 (s, 5H, Fc), 3.66 (s, 4H, O−CH_2−CH_2−O), 3.62 (m, 2H, CH_2), 3.59 (m, 4H, NH−CH_2, CH_2), 3.36 (q, 2H, NH−CH_2, J = 5.1, 9.9 Hz), 1.46 (s, 9H, Boc). ^{13}C NMR ($CDCl_3$, 400 MHz): δ 156.0 (2C), 79.1, 72.9 (2C), 70.2 (4C), 70.1 (5C), 52.0, 45.9,

41.4, 40.3, 31.2, 28.4 (3C). IR (KBr pellet): ν (cm^{-1}) 3400, 2942, 2924, 1653, 1541, 1457. MS-EI$^+$: m/z (%) 460.1 (100) [M^+]. HRMS EI$^+$ m/z (%) calcd 460.1661 for $C_{22}H_{32}FeN_2O_5^+$, found 460.1666.

Compound 2. ^{1}H NMR ($CDCl_3$, 400 MHz): δ 6.55 (s, 1H, Fc-CO-NH), 4.95 (s, 1H, NH-Boc), 4.71 (t, 2H, Fc, J = 1.7 Hz), 4.31 (t, 2H, Fc, J = 1.8 Hz), 4.20 (s, 5H, Fc), 3.75−3.45 (m, 14H, CH_2), 3.23 (q, 2H, NH−CH_2, J = 5.5, 11.5 Hz), 1.88 (m, 2H), 1.75 (m, 2H), 1.44 (s, 9H, Boc). ^{13}C NMR ($CDCl_3$, 400 MHz): δ 169.9, 156.0, 70.7, 70.5, 70.4, 70.3 (2C), 70.2 (2C), 70.1 (4C), 69.7 (5C), 68.1 (2C), 38.5, 38.3, 29.3, 28.5 (3C). IR (KBr pellet): ν (cm^{-1}) 3443, 2954, 2924, 2362, 2079, 1636, 1539, 1173. MS-EI$^+$: m/z (%) 532.2 (100) [M^+]; HRMS EI$^+$: m/z (%) calcd 532.2236 for $C_{26}H_{40}FeN_2O_6^+$, found 532.2252.

General Procedure for Deprotection of Fc-Poly(ethylene glycol)-Boc 1−2. To a solution of compound **1**−**2** (1.21 mmol) in CH_2Cl_2 (20 mL) was added a solution of trifluoroacetic acid (TFA) (50.1 mmol) in CH_2Cl_2 (20 mL). The reaction mixture was stirred for 1 h at room temperature. The progress of the reaction was monitored with TLC analysis, and additional TFA was added as a 50% v/v solution in CH_2Cl_2 as necessary to complete deprotection. The resulting solution was slowly treated with triethylamine (4.21 mL) until a pH of 9 was reached. This solution was washed with water (3 × 10 mL), and organic layers were dried over Na_2SO_4, and evaporated to dryness prior to their use.

General Procedure for the Synthesis of the Fc-ATP Conjugates 3−4. The disodium salt of ATP (0.12 g, 0.19 mmol) was equilibrated in 0.1 M triethylammonium bicarbonate (TEAB) buffer (pH 7.4), and passed through a DOWEX ion exchange column. After ion exchange, the volume was reduced with rotary evaporation, and then coevaporated with dry methanol (3 × 5 mL). The triethylammonium ATP salt was dissolved in dry DMF (5 mL) and stirred at room temperature under an Ar atmosphere. DCC (0.15 g, 0.72 mmol) was added and the reaction mixture was allowed to stir under Ar for 3 h at room temperature to form adenosine metaphosphate (AMP). In the final coupling step, this solution was added to a solution of Fc-poly(ethylene glycol)-NH_2 in dry methanol (10 mL) and stirred under Ar for 30 min at room temperature. The resulting mixture was then poured into water (20 mL) and a fine precipitate was filtered. The mother liquor was loaded onto a diethylaminoethyl (DEAE)-cellulose column that was pre-equilibrated with 0.1 M TEAB buffer, and flushed with water to remove excess starting ferrocene material. DEAE column was further treated with a gradient 0.1−0.5 M TEAB buffer to isolate ATP-containing fractions. These fractions were further purified by HPLC as described below. The overall yields after HPLC separation were 8% and 14% for compounds **3** and **4**, respectively.

Compound 3. ^{1}H NMR (D_2O, 400 MHz): δ 8.50 (s, 1H, H_8), 8.19 (s, 1H, H_2), 6.07 (d, 1H, $H_{1'}$, J = 6.0 Hz), 4.78 (m, 3H, $H_{2'}$, Fc), 4.57 (dd, 1H, $H_{3'}$, J = 3.3, 3.5 Hz), 4.48 (t, 2H, Fc, J = 1.8 Hz), 4.39 (q, 1H, $H_{4'}$, J = 3.0, 5.7 Hz), 4.25−4.24 (m, 2H, $H_{5'}$, $H_{5''}$), 4.24 (s, 5H, Fc), 3.66 (t, 4H, J = 5.1 Hz), 3.56 (t, 2H, NH−CH_2, J = 5.8 Hz), 3.49 (t, 2H, NH−CH_2, J = 5.3 Hz), 3.09 (m, 4H). ^{31}P NMR (D_2O, 400 MHz): δ −0.45 (d, J = 20.4 Hz), −10.56 (d J = 19.3 Hz), −21.88 (t, J = 19.4 Hz). IR (KBr): ν (cm^{-1}) 3300−3600 (b, O−H), 3444 (b, N−H free), 2913 (C−H aliphatic), 2740, 2678, 1653 cm^{-1} (s, C═O, amide); MALDI-TOF MS m/z (%): 904.0463 (44) [M+K]$^+$ (exp), 904.0933 (100) [M+K]$^+$ (calcd) for $C_{28}H_{42}N_7O_{15}P_3FeK$.

Compound 4. ^{1}H NMR (D_2O, 400 MHz): δ 8.51 (s, 1H, H_8), 8.21 (s, 1H, H_2), 6.08 (d, 1H, $H_{1'}$, J = 6.0 Hz), 4.73 (m, 3H, $H_{2'}$, Fc), 4.53 (t, 1H, $H_{3'}$, J = 3.4 Hz), 4.45 (t, 2H, Fc, J = 1.9 Hz), 4.36 (q, 1H, $H_{4'}$, J = 2.6 Hz), 4.25−4.20 (m, 2H, $H_{5'}$, $H_{5''}$), 4.21 (s, 5H, Fc), 3.60−3.50 (m, 4H), 3.49 (t, 2H, NH−CH_2, J = 6.8 Hz), 3.33 (t, 2H, NH−CH_2, J = 5.3 Hz), 3.27 (m, 4H), 2.86 (q, 2H, CH_2, J = 7.3, 16.2 Hz), 1.83 (q, 2H, CH_2, J = 6.5, 12.9 Hz), 1.66 (q, 2H, CH_2, J = 6.9, 13.3 Hz). ^{31}P NMR (D_2O, 400 MHz): δ −0.18 (d, J = 22.7 Hz), −10.51 (d J = 18.2 Hz), −21.85 (t, J = 19.4 Hz). IR (KBr): ν (cm^{-1}) 3300−3600 (b, O−H), 3406 (b, N−H free), 2933 (C−H aliphatic), 2739, 2492, 1648 cm^{-1} (s, C═O, amide); MALDI-TOF MS m/z (%): 976.1231 (36) [M+K]$^+$ (exp), 976.1508 (100) [M+K]$^+$ (calcd) for $C_{32}H_{50}N_7O_{16}P_3FeK$.

HPLC Separation. The resulting mixture was evaporated to dryness and purified using HPLC chromatography (Varian Modular reverse-phase Dynamax Macro-HPLC System C_{18} (21.4 mm × 25 cm)). The flow rate was 15 mL/min, UV detector was set at 254 nm, and a 30 min linear gradient composed of A TEAB (pH 7.4) and B CH_3CN as solvent system was used. The mobile phase was composed of 100% A to 97% A over 2 min, from 97% A to 92% A over 2 min, from 92% A to 90% A over 2 min, from 90% A to 85% A over 4 min, at 85% A for 2 min, from 85% A to 88% A over 3 min, from 88% A to 90% A over 3 min, from 90% A to 92% A over 2 min, from 92% A to 96% A over 4 min, and from 96% A to 100% A over 4 min.

Electrochemical Studies. All electrochemical studies were performed on a CH instrument potentiostat 660B (Austin, TX). For solution experiments, glassy carbon electrode (surface area = 0.02 cm^2) was the working electrode, Ag/AgCl in 3 M KCl was a reference electrode, and Pt wire was an auxiliary electrode. Compounds **1** and **2** were tested in dry acetonitrile solutions at 0.1 mM in the presence of 0.1 M tetrabutylammonium perchlorate (TBAP). Compounds **3** and **4** were tested at 0.1 mM in Milli-Q water containing 0.1 M $NaClO_4$. Surface characterization of biosensor interface was performed using a protein-modified gold electrode (0.02 cm^2) as a working electrode, Ag/AgCl 3 M KCl as reference electrode, and Pt wire as an auxiliary electrode. CV electrochemical measurements for surface characterization were carried out in the presence of 1 mM solution of $K_4[Fe(CN)_6]\cdot 3H_2O$ and $K_3[Fe(CN)_6]\cdot 3H_2O$ in 10 mM sodium phosphate buffer (pH 7.5) in the presence of 50 mM KNO_3. All EIS spectra were collected under the same conditions and at the formal potential of $Fe^{-4/-3}$ redox couple (0.25 V vs Ag/AgCl) at 5 mV amplitude and in the 0.1 Hz to 100 kHz range. All impedance spectra are represented as Nyquist plots with real impedance (Z_{re}) vs imaginary impedance (Z_{im}) values. The experimental data were fitted to an appropriate equivalent circuit by using the *ZSimWin* 2.0 (EChem software).

Preparation of Peptide (Protein)-Modified Gold Electrode. Gold electrodes (surface area 0.02 cm^2) were cleaned by etching in piranha solution (3:1% v/v H_2SO_4/30% H_2O_2) for 5 min, then rinsed with a copious amount of water, and subsequently polished over alumina slurry (0.3 μm then at 0.05 μm). Next, the electrochemical cleaning by cycling was done in H_2SO_4 (0.5 M) within the potential range 0−1.5 V until a stable gold oxidation peak was obtained. Finally, gold electrodes were sonicated in freshly distilled ethanol for 10 min and dried under N_2. For film formation, gold electrodes were immersed in lipoic acid *N*-hydrosuccinimide ester (Lip-NHS) solution (2 mM) in ethanol for 3 days at 5 °C. Electrodes were subsequently rinsed with ethanol and incubated in the selected peptide substrate solution

(100 μM) or protein solution (100 ng/mL) in dH_2O for 1 day at 5 °C. The peptide substrates used were Glu-Gly-Ile-**Tyr**-Asp-Val-Pro, His-His-Ala-**Ser**-Pro-Arg-Lys, Arg-Arg-Arg-Asp-Asp-Asp-**Ser**-Asp-Asp-Asp, and Arg-Arg-Leu-**Ser-Ser**-Leu-Arg-Ala and the protein target was His-tagged pro-caspase-3. Electrodes were further rinsed with water and incubated in ethanolamine solution (100 mM) in ethanol for 1 h. Surface blocking of the electrodes was omitted when protein immobilization was performed. After rinsing with freshly distilled ethanol and drying under N_2, the peptide-modified gold electrodes or protein-modified gold electrodes were ready for use.

Electrochemical Kinase Assay. For kinase reactions, electrodes were immersed in the kinase reaction buffer and kept at 37 °C in a moist incubation chamber for 2 h. The kinase reaction buffer consisted of the kinase assay buffer specific to the kinase, 400 μM Fc-ATP (compound **3**−**5**), 1 μg/mL kinase protein (Src, CDK2, and PKA), and 10 ng/mL of CK2α due to limited availability of the given kinase. The kinase buffer recipes used were similar to those suggested by the protein providers, except with the omission of dithiothrietol (DTT). Electrodes were rinsed with 10 mM sodium phosphate buffer (pH 7.5) prior to electrochemical measurements.

A typical electrochemical experiment was performed in 10 mM sodium phosphate buffer (pH 7.5) in the presence of modified gold electrode as the working electrode, Ag/AgCl 3 M KCl as reference, and Pt wire as auxiliary electrode.

Control experiments were performed by incubating gold electrodes, previously modified with Lip-NHS, into the solution of bovine serum albumin (60 mg/mL) in dH_2O. The phosphorylation reactions were performed as described above.

The second type of control experiment was carried out on the His-tagged pro-caspase-3 protein modified gold electrodes in the presence of CDK2 protein kinase and in the absence of CK2α.

CK2α concentration-dependent kinase assays were carried out at 400 μM compound **5** at following kinase concentrations: 0, 0.1, 0.5, 0.6, 2.5, 5, and 10 ng/mL. Concentration-dependent studies with respect to compound **5** were performed for all four kinases and their respective target peptides at following Fc-ATP concentrations: 5, 10, 25, 50, 75, 100, 200, and 400 μM. These studies were used to determine the K_M values for compound **5** with respect to all 4 kinases.

Luciferase Kinase Assays. Screening protocol was based on the Kinase-Glo Max luminescent kinase assay.[25] Kinase-Glo Max reagent was purchased from SignalChem (USA) and the fluorescence assays were performed as suggested by the provider. A typical reaction mixture consisted of kinase assay buffer specific for a given kinase protein under study, 100 ng/mL of specific protein kinase (CK2α was at 0.5 ng/mL), and 100 μM peptide substrate, at variable ATP concentrations (0, 0.5, 1, 2.5, 5, 10, 25, 35, 50 μM) in the presence or absence of compound **3**−**5** (10 μM). The kinase reaction was carried out in a 20 μL reaction volume in a 96-half-well white microtiter plate at 37 °C for 4 h. The microtiter plate was cooled down to RT before adding 20 μL of Kinase-Glo Max reagent. After 15 min of further reacting with Kinase-Glo Max reagent at room temperature, the luminescence signal was recorded with the PerkinElmer Wallac 1420 Multichannel Counter.

RESULTS AND DISCUSSION

Synthesis of Hydrophilic Ferrocene Conjugates. *N-tert*-Butoxycarbonyl (Boc) protected amino poly(ethylene glycol)

Scheme 2. Synthesis of the Ferrocene Conjugates 1−4 and the Structure of Fc-Bioconjugate 5

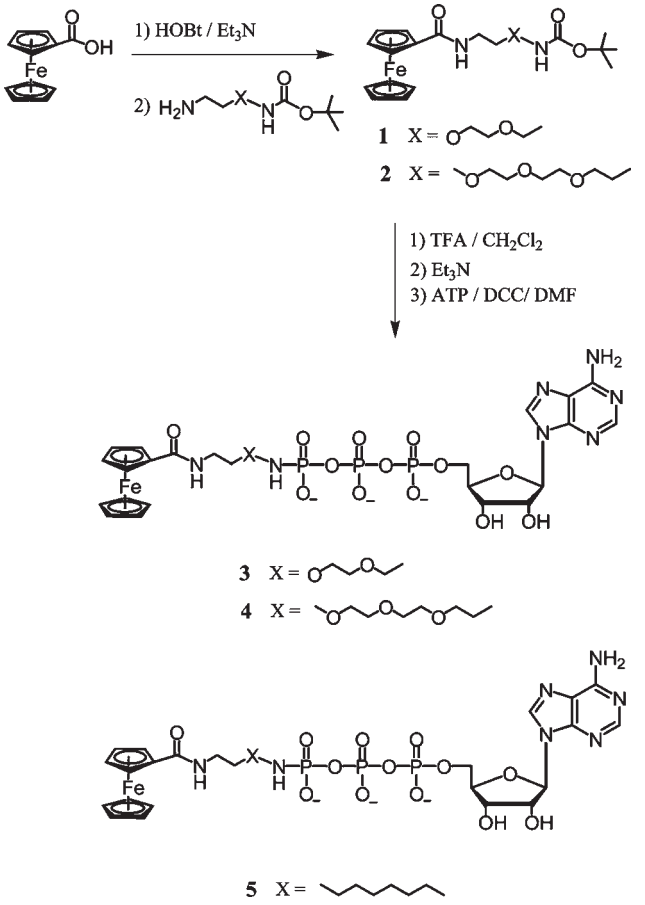

intermediates were synthesized according to the literature procedure.[26] The synthesis of the ferrocene-polyethylene glycol-(*N-tert*-butoxycarbonyl) (Fc-CO-NH-(polyethylene glycol)$_n$-NHBoc) (n = 2 (**1**), 3 (**2**)) conjugates was performed in two steps as shown in Scheme 2. First, activated ferrocene-benzotriazole ester was prepared in the presence of HBTU, HOBt, and triethylamine and isolated.[27] Subsequently, Boc-protected poly(ethylene glycol) amines were coupled to the Fc-active ester to yield target compounds **1** and **2** in 80−90% yield. The compounds were characterized by NMR and mass spectrometry. For the coupling protocol to ATP, the Boc-protected Fc-conjugates were deprotected under acidic conditions, in the presence of an excess trifluoroacetic acid in CH_2Cl_2. The coupling procedure to ATP was performed as reported in the literature, wherein in situ formed adenosine metaphosphate was reacted with the Fc-poly(ethylene glycol)-NH_2 under basic conditions.[28,29] The crude reaction mixture was first purified on diethylaminoethyl (DEAE) cellulose column equilibrated with 0.1 M triethylammonium bicarbonate (TEAB) (pH 7.5), in order to remove excess Fc-linker starting material. Additional treatment with 0.1−0.5 M TEAB afforded the Fc-ATP-containing fractions which were subjected to the reverse-phase HPLC purification. HPLC conditions employed were based on the TEAB/CH_3CN solvent system with gradient 100%/0% to 85%/15% to isolate Fc-ATP conjugates **3** and **4** in 8% and 14% yield, respectively. HPLC traces of Fc-ATP bioconjugates **3** and **4** are shown in Figure 1A. Fc-ATP

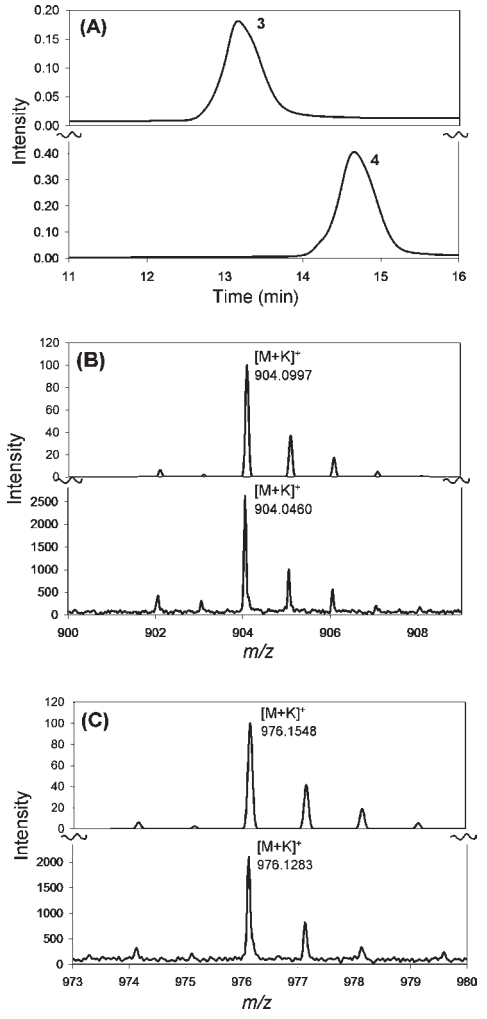

Figure 1. (A) HPLC traces of Fc-ATP conjugates **3** and **4**. The purification was performed on C18 reverse-phase column, at 10 mL/min flow rate and in TEAB/CH_3CN gradient (100% to 85% TEAB). Fc-ATP conjugates are characterized with the retention times of 13.2 (**3**) and 14.6 min (**4**) which are higher than that of unmodified ATP (~6 min). Partial mass spectra of purified compound **3** (B) and **4** (C) showing $[M + K]^+$ molecular ion splitting pattern for experimental (bottom) and theoretical isotope peaks (top).

derivatives were characterized by 1D and 2D NMR and MALDI-TOF mass spectrometry.

Solution Characterization of Ferrocene Conjugates. A distinguishing feature of the $^{31}P\{^1H\}$-NMR spectra of the Fc-ATP conjugates **3** and **4** is the characteristic doublet for the γ-P, observed at −0.45 ppm for compound **3** and −0.15 ppm for compound **4** (vs H_3PO_4 85%), indicative of the resulting Fc-γ-phosphoamide formation. By contrast, an unmodified ATP exhibits a ^{31}P NMR γ-doublet at approximately −8 ppm. Further characterization of Fc-ATP bioconjugates was performed by MALDI-TOF MS in Figure 1B,C, which shows the molecular ion peak $[M+K]^+$ and isotope pattern for **3** and **4** with the matching theoretical predictions.

Solution electrochemical behavior of Fc-linker compounds **1** and **2**, presented in Figure 2A, was investigated by means of cyclic voltammetry in CH_3CN solution containing TBAP electrolyte. Notably, both compounds exhibit the potential difference, ΔE, in the 57−62 mV range, half-wave potential, $E_{1/2}$, at ~600 mV and peak current ratios, i_{pa}/i_{pc}, at ~1.1, characteristic of ferrocene compounds. Unlike ATP-free compounds, Fc-bioconjugates **3** and **4** are characterized by a cathodic shift in redox potential to lower values that fall in the 410−425 mV range; however, they exhibit i_{pa}/i_{pc} values close to unity and ΔE values in the 40−65 mV range (Figure 2B). Comparison of the diffusion coefficients for all four compounds clearly demonstrates the effect of molecule size on its mobility and redox activity in solution, and as expected, Fc-ATP conjugates have smaller D values (~5×10^{-5} cm^2/s) than their parent compounds **1** and **2** (~11×10^{-5} cm^2/s). Diffusion coefficient values were calculated using the Randles-Sevcic equation.[30] Electrochemical and solution data for Fc-conjugates **1**−**4** are presented in Table 1.

Utility of Fc-ATP Co-Substrates in Peptide Phosphorylation Reactions. This study is aimed at addressing the generality of the Fc-ATP co-substrates and elucidates the effects of the linker polarity in Fc-ATP on four protein kinases under study. Previous studies showed that Fc-ATP conjugates of optimal alkyl linker length are readily consumed in kinase-catalyzed phosphorylation of surface-bound peptide.[13,24] However, the effects of the linker variation in Fc-ATP, which includes a more polar poly(ethylene glycol) spacer, on the kinase phosphorylation reaction were unknown. With this goal in mind, we developed and initially investigated compounds **3** and **4** as phosphorylation co-substrates using the general electrochemical kinase assay shown in Scheme 1A. To compare the abilities of polar Fc-ATP compounds **3** and **4** to serve as co-substrates, the aliphatic Fc-ATP analogue **5** was investigated as well, under identical experimental conditions. This allowed for a direct comparison of hydrophobic versus hydrophilic Fc-ATP conjugates while keeping the spacer length relatively constant. The comparative study may reveal more information about the kinase active site and kinase interactions with the peptide substrates. It is also expected that comparative Fc-ATP study will hint toward tolerance of kinases in terms of the structural and electronic effects as they pertain to the co-substrate. Four different kinases were chosen as representative protein kinases that act on Tyr, Ser, or Thr residues. Sarcoma-related (Src) kinase is a protein Tyr kinase that is overexpressed in certain solid cancer tumors.[31] Cyclin-dependent kinase (CDK2), in combination with cyclin A, is primarily involved in the cell cycle and division and it phosphorylates Ser residues on the target peptides or proteins.[32] While CDK2 is a Pro-directing protein kinase, casein kinase II (CK2α) is an acidophilic kinase and relies on acidic residues as the dominant specificity determinants of peptide and protein substrates.[33] CK2α is directly involved in the cellular metabolism and differentiation and phosphorylates Ser/Thr residues in key regulatory proteins.[34] Last, protein kinase A (PKA) was chosen as another Ser/Thr kinase that is largely dependent on the presence of cyclic adenosine monophosphate whose binding activates kinase and allows for binding of ATP and subsequent phosphorylation reaction.[35]

Cyclic voltammetry (CV) and square-wave voltammetry (SWV) were used for electrochemical studies on peptides bound to gold surfaces. These films were prepared by immobilization of the Lip-NHS on gold, followed by conjugation with the target peptide sequences: Glu-Gly-Ile-**Tyr**-Asp-Val-Pro (Src), His-His-Ala-**Ser**-Pro-Arg-Lys (CDK2), Arg-Arg-Arg-Asp-Asp-Asp-**Ser**-Asp-Asp-Asp (CK2α), and Arg-Arg-Leu-**Ser**-**Ser**-Leu-Arg-Ala (PKA) and finally blocking with ethanolamine, which reacted with any remaining NHS groups.

Next, phosphorylation reactions were performed by incubating peptide-modified gold electrodes in the kinase assay buffer

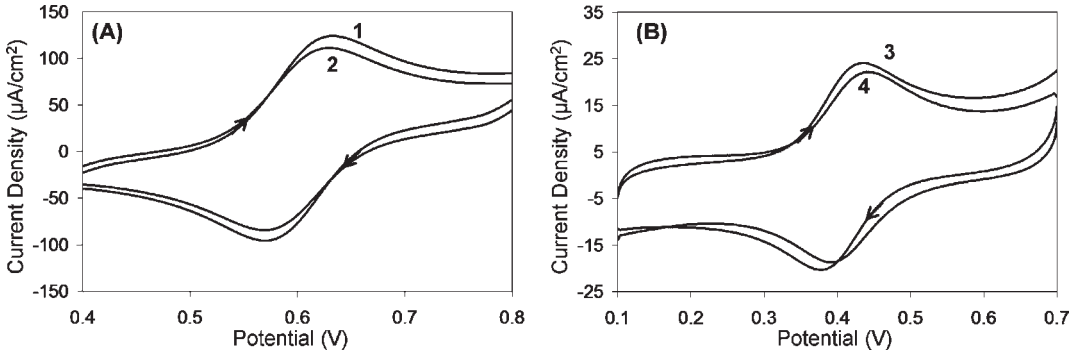

Figure 2. Cyclic voltammograms of (A) compounds **1** and **2** (0.1 mM in 0.1 M TBAP in CH_3CN) and (B) compounds **3** and **4** (0.1 mM in 0.1 M $NaClO_4$ in water).

Table 1. Solution Characterization Data of Fc-conjugates 1−5[a]

Fc-compound	R_t (min)[b]	^{31}P NMR (ppm)[c]	$E_{1/2}$ (mV)	ΔE (mV)	i_{pa}/i_{pc}	D[d]
1	—	—	600 ± 5	61 ± 5	1.1	12.1 ± 0.13
2	—	—	601 ± 5	57 ± 5	1.1	11.4 ± 0.18
3	13.2	−0.45	411 ± 5	61 ± 4	0.9	5.25 ± 0.09
		−10.54				
		−21.88				
4	14.6	−0.15	422 ± 3	55 ± 10	1.1	5.77 ± 0.19
		−10.51				
		−21.82				
5[e]	10.1	−0.71	424 ± 3	55 ± 10	0.9	4.82 ± 0.32
		−11.40				
		−22.80				

[a] Electrochemical data for compounds **1** and **2** were obtained at 0.1 mM ligand in CH_3CN in the presence of 0.1 M TBAP and the compounds **3** and **4** were measured at 0.1 mM in the presence of 0.1 M $NaClO_4$ as supporting electrolyte. Ag/AgCl as reference electrode, Pt as auxiliary electrode, glassy carbon as working electrode, scan rate = 100 mV/s. Electrochemical data measured by cyclic voltammetry. The reported error was obtained from the triplicate measurements. $E_{1/2}$ = half-wave potential; ΔE = peak separation; i_{pa}/i_{pc} = peak current ratio. [b] HPLC conditions: reverse-phase C18 column, solvent gradient: 100% triethylammonium bicarbonate (TEAB), 85% TEAB and 15% CH_3CN, 100% TEAB over 30 min. [c] D_2O, 298 K, H_3PO_4 85% as an external NMR reference. [d] Diffusion coefficient is given in $\times 10^{-5}$ cm^2/s and was determined electrochemically. [e] Solution data for Fc-conjugate **5** was added as reference.[24]

containing the appropriate protein kinase (1 μg/mL for all kinases, except for CK2α which was at 10 ng/mL for all peptide assays) and Fc-ATP conjugates **3**−**5** (400 μM). Following the kinase-catalyzed phosphorylation reactions and extensive washing with buffer, CVs and SWVs were collected with all the compounds studied (see Supporting Information, Figure SI-19−21). Figure 3A,B shows representative CVs and SWVs for Src-catalyzed reactions in the presence of all Fc-ATP conjugates. The largest current densities were observed for the phosphorylation reactions performed with compound **5**. The formal redox potential, $E°$, located at ∼420 V in the case of compound **5** and ∼505 mV in the case of compound **3** suggested the presence of redox active groups on the surface. The current response was directly related to the transfer of ferrocenyl-phosphate group from Fc-ATP co-substrate to the hydroxyl residues of the surface-bound peptide. Similarly, the electrochemical assays were performed in the presence of other kinases and the compilation of all the electrochemical data is shown in Figure 3C. From Figure 3C, it is evident that the greatest electrochemical signal was observed for CDK2 kinase reactions performed in the presence of hydrophobic compound **5**, followed by compounds **4** and **3**. In all cases, hydrophobic Fc-ATP conjugate **5** outperformed the polar Fc-ATP compounds and led to the greatest current density. Relative to each other, compounds **3** and **4** exhibited some difference in their performance depending on the type of kinase protein studied. In the case of Src and CK2α, compound **3** was a better co-substrate, while compound **4** gave the greater signal in the case of CDK2. Given that different kinases exhibit slightly different kinase activities with specific peptide substrates, it is not surprising that the electrochemical signal varies from kinase to kinase protein even with the best Fc-ATP co-substrate, such as **5**. However, differences observed between the conjugates for a specific protein kinase can be attributed to the abilities of these compounds to function as co-substrates. Because of the low sensitivity toward polar Fc-ATP compounds, we have investigated kinetic parameters for compound **5** with all four kinases. From the plot of the steady-state current density versus compound **5** concentrations, the Lineweaver−Burk plot was derived and the K_M values were estimated, with respect to the co-substrate, and found to be 30, 150, 90, and 180 μM for Src, CDK2, PKA, and CK2α kinases, respectively. The electrochemical data indicated that the bioconjugate **5** displayed K_M values similar to those of ATP, which are typically in the 10−100 μM range, depending on the kinase type and the target peptide.

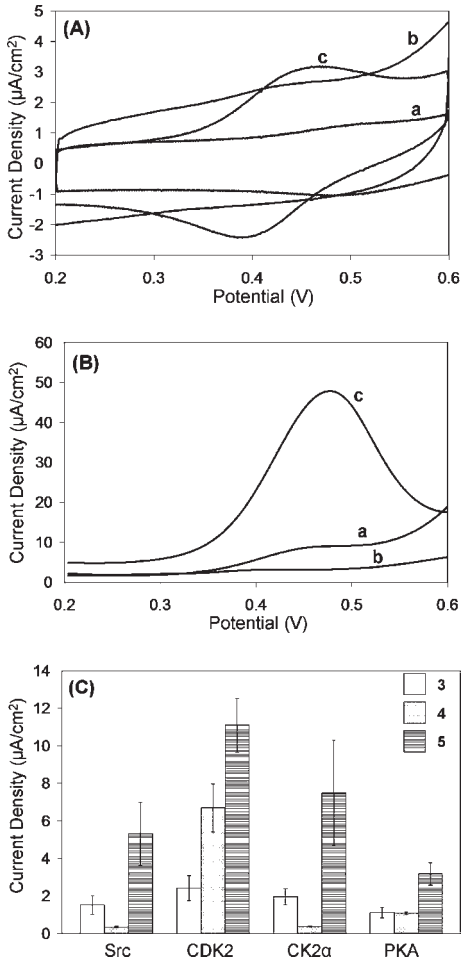

Figure 3. (A) Cyclic voltammograms and (B) square-wave voltammograms showing current densities of surface-bound peptides following the Src kinase-catalyzed phosphorylation reaction in the presence of compounds **3** (a), **4** (b), and **5** (c). (C) Plot of current densities of surface-bound peptides following the phosphorylation reactions with different kinases (Src, CDK2, CK2α, and PKA) in the presence of compounds **3**−**5**. Data points are the average of triplicate measurements taken from normalized SWVs.

Finally, we used the solution biochemical luminescent kinase-glo assay, an ATP depletion assay, to investigate the ability of Fc-ATP to act as co-substrates in the presence of unmodified ATP. The fluorescence intensity is directly proportional to the ATP concentration and inversely proportional to the extent of the phosphorylation reaction.[25] As presented in Scheme 1C, following the kinase reaction, the greater amount of leftover ATP produces greater fluorescence signal. Initially, the variable ATP concentration experiments were performed with all four kinase proteins and their respective peptide substrates. Next, in a competitive fluorescence assay, all three Fc-ATP conjugates were added at 10 μM in the presence of protein kinases and at variable ATP concentrations (Scheme 1C). The addition of Fc-ATP to ATP assay resulted in the fluorescence increase, as shown in Figure 4A. This observation was not simply due to the addition of Fc-ATP bioconjugates **3**−**5**, since no fluorescence increase was observed in the kinase assays in the absence of kinase and substrate under identical experimental conditions. Moreover, the leftover ATP in the kinase reaction was directly related to the overall fluorescence. Luminescence increase due to the addition of Fc-conjugates **3**−**5** was in the 26−60% range, depending on the protein kinase as depicted in Figure 4B. The increase in the fluorescence might be due to the ability of compounds **3**−**5** to compete with ATP for kinase and subsequent phosphorylation. Hence, an increase in fluorescence is due to the increased leftover ATP concentration. Overall, Fc-ATP conjugates produced a significant increase in the fluorescence intensities for all four kinases, which was similar to the electrochemical data. Discrepancies between the fluorescence and electrochemical assays were potentially due to the state of the peptide substrate, which is free in the solution studies and surface-bound in the electrochemical analysis. However, the electrochemical and fluorescence data indicate that Fc-ATP conjugates are viable substrates for Tyr and a variety of Ser/Thr protein kinases. Moreover, the fluorescence data show that all three Fc-ATP bioconjugates are competitive with respect to ATP and, hence, support the notion that Fc-ATP co-substrates are being utilized by protein kinases.

Polar Fc-ATP Co-Substrates in Protein Phosphorylation Reactions. In order to test the compatibility of Fc-ATP co-substrates with whole protein targets, a kinase-catalyzed phosphorylation of a full-length protein was investigated. As a representative example, His-tagged pro-caspase-3 (dead) (Caspase-3, for short) protein was chosen as the substrate for CK2α protein. Caspases play a major role in the regulation of cell survival,[36] and a number of phosphorylated proteins are less susceptible to caspase cleavage.[37] Hyperphosphorylation by protein kinases promotes cancerous cell activity through direct interactions with caspase-mediated signaling pathways.[38,39] For example, the phosphorylation of pro-caspase-2 by CK2 prevents dimerization and activation.[40] In the electrochemical assay, depicted in Scheme 1B, protein Caspase-3 was immobilized on the gold surface in a similar manner to the peptide immobilization. Surface characterization of the biosensor interface was performed by CV and electrochemical impedance spectroscopy (EIS) and in the presence of $Fe^{-4/-3}$ redox couple in order to demonstrate the surface coverage and blocking. CVs revealed a reversible redox behavior characteristic for $Fe^{-4/-3}$ on bare gold, but a significant reduction in overall current following the protein immobilization. EIS spectra for bare electrodes are characterized by a small resistance component. By contrast, incubation in Lip-NHS solution produces a film resistance in the shape of a semicircle that is magnified when protein was attached. The diameter of the semicircle corresponds to the interfacial resistance at the electrode surface and is quite small in the case of bare Au electrode. The low-frequency loop observed for bare Au surface is due to the diffusion-limited electrochemical process and is lessened upon formation of self-assembled monolayer by Lip-NHS. The large semicircle is evident following the protein binding and suggests the film's resistance to the ion diffusion. Electrochemical data were fitted to a suitable equivalent circuit that reflects the real electrochemical process. The chosen circuit includes the ohmic resistance, R_s, of the electrolyte solution, the electronic charge transfer resistance, R_{CT}, in parallel with a constant phase element, CPE, which is associated with the double layer and reflects the interface between the assembled film and the electrolyte solution. In addition, the electronic charge transfer resistance is in series with another capacitive component, CPE, that is in parallel with resistance, R_X. The R_{CT} value increased from 36 to 1309 Ω cm^2 upon formation of Lip-NHS self-assembled monolayer on the gold surface, followed by immobilization of Caspase-3.

The phosphorylation reactions were performed for all three Fc-ATP conjugates in the presence of 0.5 ng/mL CK2α protein

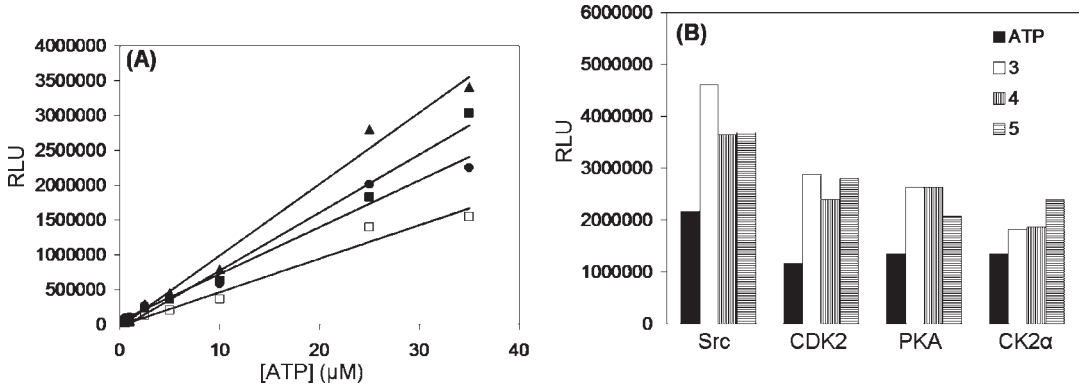

Figure 4. (A) Luminescence intensity versus ATP concentration in the absence (□) and presence of 10 μM compounds **3** (▲), **4** (●), and **5** (■) for Src kinase-catalyzed phosphorylation reaction. (B) Plot of the fluorescence intensities for variety of protein kinase phosphorylation reactions in the presence of 50 μM ATP and following the addition of 10 μM Fc-conjugates **3**−**5**.

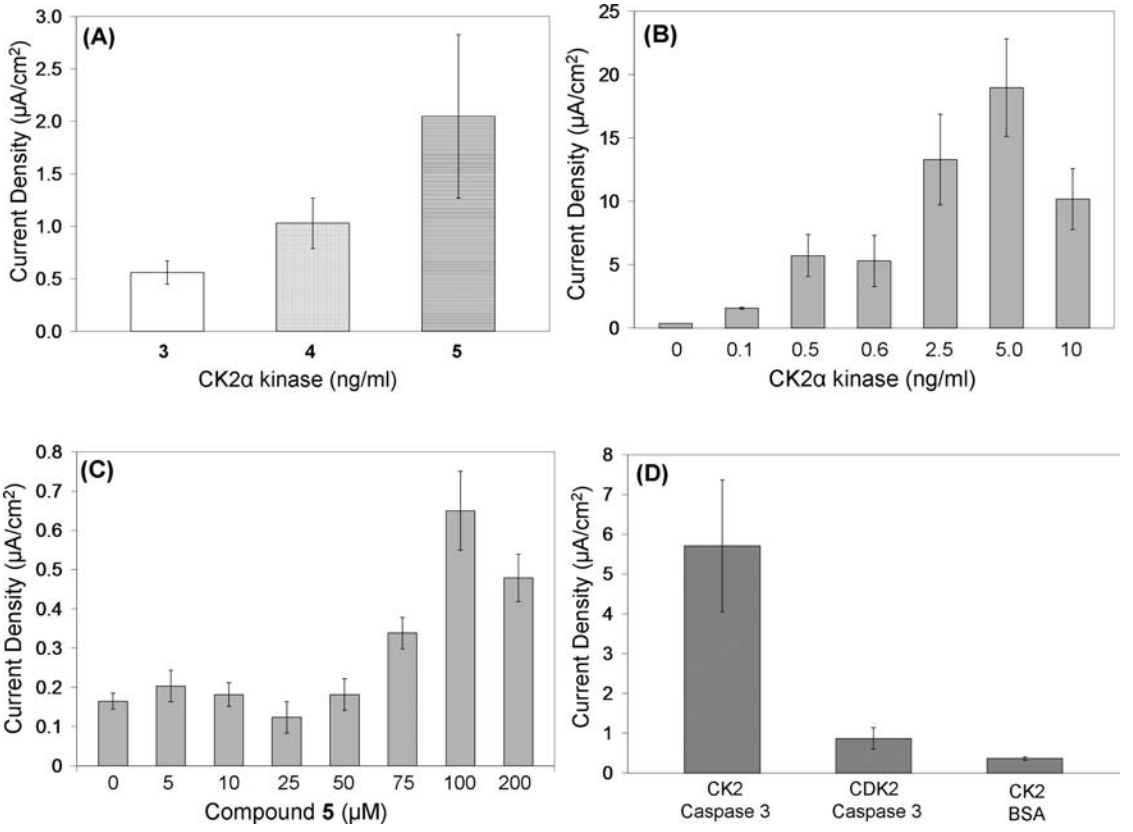

Figure 5. Plot of current densities for CK2α-catalyzed phosphorylation of Caspase-3 protein in the presence of (A) Fc-ATP compounds **3**−**5** at 0.5 ng/mL kinase, (B) Fc-conjugate **5** at varying CK2α kinase concentrations, and (C) compound **5** at various concentrations. (D) Current densities for the phosphorylations of Caspase-3 and BSA in the presence of 0.5 ng/mL CK2α and phosphorylation of Caspase-3 in the presence of CDK2 kinase. Error bars obtained from triplicate measurements.

kinase. The highest current density, in Figure 5A, was observed after phosphorylation reaction with aliphatic congener Fc-ATP conjugate **5**. CVs and SWVs indicated that the efficiency of the ferrocenyl-phosphate group transfer followed the order: compound **5** > **4** > **3** (Figure 5A). The relative order of the hydrophilic compounds was reversed when compared to the phosphorylation of the surface-bound peptide. These differences could be ascribed to many factors including the nature of the substrate to be phosphorylated which are beyond the scope of this paper and have not been further investigated. We have, however, focused on the most promising compound **5** and investigated the effect of CK2α protein concentration on the extent of phosphorylation reaction and the electrochemical signal. From the plot of current density versus CK2α concentration in Figure 5B, the saturation point at ~2.5 ng/mL is evident. Fc-ATP concentration studies shown in Figure 5C clearly indicate that the optimal concentration of Fc-conjugate **5** is ~100 μM.

We next investigated the selectivity and specificity of protein phosphorylation by using bovine serum albumin (BSA), which is not a kinase substrate, and CK2α protein kinase. Figure 5D indicates a relatively low current density when BSA was used compared to the phosphorylation of the Caspase-3 result. In order to further probe the phosphorylation of Caspase-3 protein, alternative Ser protein kinase, CDK2 was used. While the extent of protein phosphorylation is quite low, judging from the lower current density, the probability of the CDK2-driven phosphorylation can be explained. Caspase-3 is a poor substrate of CDK2, but two Ser residues can potentially be phosphorylated to a lesser extent. As a Pro-directing protein kinase, CDK2 phosphorylation may also overlap with caspase recognition site, which might explain the positive electrochemical response.[41]

Electrochemical studies suggested that the dramatic differences between the Fc-ATP conjugates might be due to the steric and electronic factors, which surround the phosphorylation event. We have previously established that the optimal linker length in Fc-ATP was necessary to observe Fc-phosphorylation in the electrochemical assay. Since all Fc-ATP conjugates presented here contain relatively long spacers, the steric considerations in the kinase active site are minimal. Despite the fact that the catalytic site of protein kinase, at the γ-phosphate, is shallow and solvent-exposed, the inherently polar amino acid residues are critical for catalysis. The residues that line the ATP-binding site are hydrophobic by large, but the catalytic site of protein kinase is typically populated with charged amino acid residues such as Lys33 and Asp145, as in case of CDK2/Cyclin A complex.[42] The γ-phosphate group of ATP is held together in position by ionic and H-bonding interactions which are critical. Similarly, the catalytic unit in CK2α is lined with Lys68, Asp175, and Glu81 from C-helix.[43] Notably, the side chain of Lys168 in the catalytic loop of PKA kinase, in combination with the backbone Ser53 residue, is involved in H-bonding with γ-phosphate, which orients it for a transfer to the substrate.[44] In the case of Src kinase, a conserved Lys295 and Asp404 in the activation loop are required for the catalytic action of the kinase, and any changes in the position of the loop regulates the access of the substrate to the active-site cleft and also modulates the phosphorylation.[45]

In our system, polar poly(ethylene glycol) linkers in Fc-ATP **3**−**4** were not optimal for kinase-catalyzed reactions, as indicated by the relatively low current densities. Presumably, the H-bonding interactions of the poly(ethylene glycol) chains in Fc-ATP with the catalytic pocket of the kinase, and most likely with the incoming peptide (protein) substrate, might negatively affect the outcome of the phosphorylation reaction. Since the aliphatic Fc-conjugate **5** is highly nonpolar, we propose that the extent of the electrostatic and H-bonding interactions is lessened and hence does not greatly interfere with the phosphorylation process. To identify the exact nature of the interactions between the Fc-ATP conjugates with the protein kinase, we are currently attempting the co-crystallization of protein kinase with Fc-ATP co-substrate.

CONCLUSIONS

Comparative electrochemical study between polar and nonpolar Fc-ATP conjugates was utilized in peptide (protein) phosphorylation reactions catalyzed by a variety of protein kinases. Electrochemical data reveal that a long hydrophobic Fc-ATP conjugate outperforms the polar Fc-ATP analogues as an efficient kinase co-substrate. Despite the use of a long spacer, which alleviates any steric constraints during the phosphorylation reaction, the additional H-bonding and electrostatic interactions make polar Fc-ATP a poor co-substrate. The electronic factors are the major reasons for large differences observed between the Fc-ATP conjugates. We are currently working on crystallizing out protein kinases with Fc-ATP co-substrates in order to fully understand the exact nature of the interactions.

ASSOCIATED CONTENT

Supporting Information. Full characterization of all Fc-conjugates, solution CVs and SWVs for compounds **1**−**4**, CVs and SWVs for kinase reactions with compounds **3** and **4**, enzyme kinetic studies and EIS table. This material is available free of charge via the Internet at http://pubs.acs.org.

AUTHOR INFORMATION

Corresponding Author

*E-mail: hkraatz@uwo.ca. Fax: +1-519-661-3022. Tel: +1-519-661-2111 ext. 81561.

ACKNOWLEDGMENT

S.M. thanks the Ontario Ministry of Research and Innovation for a postdoctoral fellowship. This work was funded by the NSERC strategic grants program and the University of Western Ontario. We are grateful to Prof. D. W. Litchfield for CK2α and PKA protein kinases and RRRDDDSDDD and RRLSSLRA peptides.

REFERENCES

(1) Maning, G., Whyte, D. B., Martinez, R., Hunter, T., and Sudarsanam, S. (2002) The protein kinase complement of the human genome. *Science 298*, 1912–1934.

(2) Blume-Jensen, P., and Hunter, T. (2001) Oncogenin kinase signalling. *Nature 411*, 355–365.

(3) Braunwalder, A. F., Yarvood, D. R., Hall, T., Missbach, M., Lipson, K. E., and Sills, M. A. (1996) A solid-phase assay for the determination of protein tyrosine kinase activity of c-src using scintillating microtitration plates. *Anal. Biochem. 234*, 23–26.

(4) Houseman, B. T., Huh, J. H., Kron, S. J., and Mrkisch, M. (2002) Peptide chips for the quantitative evaluation of protein kinase activity. *Nat. Biotechnol. 20*, 270–274.

(5) Shults, M. D., and Imperiali, B. (2003) Versatile fluorescence probes of protein kinase activity. *J. Am. Chem. Soc. 125*, 14248–14249.

(6) Wang, Z., Lee, J., Cossins, A. R., and Brust, M. (2005) Microarray-based detection of protein binding and functionality by gold nanoparticle probes. *Anal. Chem. 77*, 5770–5774.

(7) Wilner, O. I., Guidotti, C., Wieckowska, A., Gill, R., and Willner, I. (2008) Probing kinase activities by electrochemistry, contact-angle measurements and moelcular-force interactions. *Chem.—Eur. J. 14*, 7774–7781.

(8) Green, K. D., and Pflum, M. K. H. (2007) Kinase-catalyzed biotinylation for phosphoprotein detection. *J. Am. Chem. Soc. 129*, 10–11.

(9) Sato, M., Ozawa, T., Yoshida, T., and Umezawa, Y. (1999) A fluorescent indicator for tyrosine phosphorylation-based insulin signalling pathways. *Anal. Chem. 71*, 3948–3954.

(10) Yoshida, T., Sato, M., Ozawa, T., and Umezawa, Y. (2000) An SPR-based screening method for agonist selectivity for insulin signalling pathways based on the binding of phosphotyrosine to its specific binding protein. *Anal. Chem. 72*, 6–11.

(11) Matsuno, H., Furusawa, H., and Okahata, Y. (2004) Kinetic study of phosphorylation-dependent complex formation between the kinase-inducible domain (KID) of CREB and the KIX domain of CBP on a quartz crystal microbalance. *Chem.—Eur. J. 10*, 6172–6178.

(12) Kerman, K., Vestergaard, N., and Tamiya, E. (2007) Label-free electrical sensing of small molecule inhibition on tyrosine phosphorylation. *Anal. Chem. 79*, 6881–6885.

(13) Song, H., Kerman, K., and Kraatz, H. B. (2008) Electrochemical detection of kinase-catalyzed phosphorylation using ferrocene-conjugates ATP. *Chem. Commun.* 502–504.

(14) Parang, K., Kohn, J. A., Saldanha, A., and Cole, P. A. (2002) Development of photo-crosslinking reagents for protein kinase-substrate interactions. *FEBS Lett. 520*, 156–160.

(15) Lee, S. E., Elphick, L. M., Anderson, A., Bonnac, L., Child, E. S., Mann, D. J., and Gouverneur, V. (2009) Synthesis and reactivity of novel γ-phosphate modified ATP analogues. *Bioorg. Med. Chem. Lett. 19*, 3804–3807.

(16) Elphick, L. M., Lee, S. E., Gouverneur, V., and Mann, D. J. (2007) Using chemical genetics and ATP analogues to dissect protein kinase function. *Chem. Biol. 2*, 299–314.

(17) Freeman, R., Finder, T., Gill, R., and Willner, I. (2010) Probing protein kinase (CK2) and alkaline phosphatase with CdSe/ZnS quantum dots. *Nano Lett. 10*, 2192–2196.

(18) Suwal, S., and Pflum, M. K. H. (2010) Phosphorylation-dependent kinase-susbtrate cross-linking. *Angew. Che. Int. Ed. 49*, 1627–1630.

(19) Green, K. D., and Pflum, M. K. (2007) Kinase catalyzed biotinylation for phosphoprotein detection. *J. Am. Chem. Soc. 129*, 10–11.

(20) Wang, Z., Levy, R., Fernig, D. G., and Brust, M. (2006) Kinase-catalyzed modification of gold nanoparticles: a new approach to colorimetric kinase activity screening. *J. Am. Chem. Soc. 128*, 2214–2215.

(21) Green, K. D., and Pflum, K. H. (2009) Exploring kinase cosubstrate promiscuity: monitoring kinase activity through dansylation. *ChemBioChem 10*, 234–237.

(22) Eckstein, F. (1985) Nucleoside phosphorothioates. *Annu. Rev. Biochem. 54*, 367–402.

(23) Allen, J. J., Lazerwith, S. E., and Shokat, K. M. (2005) Bioorthogonal affinity purification of direct kinase substrates. *J. Am. Chem. Soc. 127*, 5288–5289.

(24) Martic, S., Labib, M., Freeman, D., and Kraatz, H. B. Probing the role of the linker in Fc-ATP conjugates: monitoring protein kinase-catalyzed phosphorylations electrochemically. *Chem.—Eur. J.* **2011**, *17*, 6744−6752.

(25) Koresawa, M., and Okabe, T. (2004) High-throughput screening with quantitation of ATP consumption: A universal non-radioisotope, homogenenous assay for protein kinase. *Assay Drug Dev. Technol. 2*, 153–160.

(26) N'Da, D. D, and Neuse, E. W. (2006) Polyamidoamines as drug carriers: synthesis of polymers featuring extrachain-type primary amino groups as drug-anchoring sites. *S. Afr. J. Chem. 59*, 65–70.

(27) Carpino, L. A. (1993) 1-Hydroxy-7azabenzotriazole. An efficient peptide coupling additive. *J. Am. Chem. Soc. 115*, 4397–4398.

(28) Knorre, D. G., Kurbatov, V. A., and Samukov, V. V. (1976) General method for the synthesis fo ATP gamma-derivatives. *FEBS Lett. 70*, 105–108.

(29) Suto, R. K., Whalen, M. A., Bender, B. R., and Finke, R. G. (1998) Synthesis of γ-phosphate-linked nucleoside affinity chromatography resins for protein purification, including ribonucleoside triphosphate reductase. *Nucleosides, Nuleotides Nucleic Acids 17*, 1453–1471.

(30) Laviron, E. (1979) General expression of the linear potential sweep voltammogram in the case of diffusionless electrochemical systems *J. Electroanal. Chem. Interfacial Electrochem. 101*, 19–28.

(31) Slack-Davis, J., Da Silva, J. O., and Parson, S. J. (2010) LKB1 and Src: antagonistic regulators of tumor growth and metastasis. *Cancer Cell 17*, 527–529.

(32) Malumbres, N., and Barbacid, M. (2009) Cell cycle, CDKs and cancer: a changing paradigm. *Nat. Rev. 9*, 153–166.

(33) Duncan, J. S., Turowec, J. P., Vilk, G., Li, S. S. C., Gloor, G. B., and Litchfield, D. W. (2010) Regulation of cell proliferation and survival: Convergence of protein kinases and caspases. *Biochim. Biophys. Acta 1804*, 505–510.

(34) Litchfield, D. (2003) Protein kinase CK2: structure, regulation and role in cellular decisions of life and death. *Biochem. J. 369*, 1–15.

(35) Wu, K. J., Mattioli, M., Morse, H. C., and Dalla-Favera, R. (2002) c-MYC activates protein kinase A (PKA) by direct transcriptional activation fo the PKA catalytic subunit beta (PKA-Cβ) gene. *Oncogene 21*, 7872–7882.

(36) McStay, G. P., Salvensen, G. S., and Green, D. R. (2008) Overlapping cleavage motif selectivity of caspases: implications for analysis of apoptotic pathways. *Cell Death Differ. 15*, 322–331.

(37) Desagher, S., Osen-Sand, A., Montessuit, S., Magnenat, E., Vilbois, F., Hochmann, A., Journot, L., Antonsson, B., and Martinou, J. C. (2001) Phosphorylation of bid by casein kinase I and II regulates its cleavage by caspase 8. *Mol. Cell 8*, 601–611.

(38) Okun, I., Balakin, K. V., Tkachenko, S. E., and Ivachtchenko, A. V. (2008) Caspase activity modulators as anticancer agenets. *Anticancer Agents Med. Chem. 8*, 322–341.

(39) Torres, J., Rodriguez, M. P., Myers, M., Valiente, M., Graves, J. D., Tonks, N. K., and Pulido, R. (2003) Phosphorylation-regulated cleavage of the tumour suppressor PTEN by caspase-3: implications for the control of protein stability and PETN-protein interactions. *J. Biol. Chem. 278*, 30652–30660.

(40) Li, P. F., Li, J., Muller, E. C., Otto, A., Dietz, R., and Harsdorf, R. (2002) Phosphorylation by protien kinaseCK2: a singling switch for the caspase-inhibiting protien ARC. *Mol. Cell 10*, 247–258.

(41) Schweigreiter, R., Stasyk, T., Contarini, S., Frauscher, S., Oertle, T., Klimaschewski, L. A., Huber, C. E., and Bandtlow, C. E. (2007) Phosphorylation-regulated cleavage of the reticulon protein Nogo-B by caspase-7 at a noncanonical recognition site. *Proteomics 7*, 4457–5567.

(42) De Bondt, H. L., Rosenblatt, J., Jancarik, J., Jones, H. D., Morgan, D. O., and Kim, S. H. (1993) Crystal structure of cyclin-dependent kinase 2. *Nature 363*, 595–602.

(43) Mazzorana, M., Pinna, L. A., and Battistutta, R. (2008) A structural insight into CK2 inhibition. *Mol. Cell. Biochem. 316*, 57–62.

(44) Taylor, S. S., Yang, J., Wu, J., Haste, N. M., Radzio-Andzelm, E., and Anand, G. (2004) PKA: a portrait of protein kinase dynamics. *Biochim. Biophys. Acta 1697*, 259–269.

(45) Williams, J. C., Weijland, A., Gonfloni, S., Thompson, A., Courtneidge, S. A., Superti-Furga, G., and Wierenga, R. K. (1997) The 2.35 Å crystal structure of the inactivated form of chicken Src: a dynamic molecule with multiple regulatory interactions. *J. Mol. Biol. 274*, 757–775.

Supporting Information Available

Tuning Peptide/Protein Phosphorylations *via* Ferrocene-Modified ATP Hydrophilicity

*Sanela Martic, Meghan K. Rains, Daniel Freeman and Heinz-Bernhard Kraatz**

Chemistry Department, The University of Western Ontario, London, Ontario, Canada

hkraatz@uwo.ca

Figure S1. ^{1}H NMR of compound **1**……...S3

Figure S2. ^{1}H-^{1}H COSY NMR of compound **1**……...……...S4

Figure S3. ^{13}C NMR of compound **1**……..S5

Figure S4. ^{1}H NMR of compound **2**……...S6

Figure S5. ^{1}H-^{1}H COSY NMR of compound **2**……...……...S7

Figure S6. ^{13}C NMR of compound **2**……..S8

Figure S7. ^{1}H NMR of compound **3**……...S9

Figure S8. ^{1}H-^{1}H COSY NMR of compound **3**……...……...S10

Figure S9. ^{32}P NMR of compound **3**……..S11

Figure S10. HPLC spectrum of compound **3**…….....S12

Figure S11. MALDI-TOF spectrum of compound **3**……...……..S13

Figure S12. ^{1}H NMR of compound **4**……S14

Figure S13. ^{1}H-^{1}H COSY NMR of compound **4**……...……S15

Figure S14. ^{32}P NMR of compound **4**……S16

Figure S15. HPLC spectrum of compound **4**…….....S17

Figure S16. MALDI-TOF spectrum of compound **4**……...……..S18

Figure S17. Cyclic voltammograms and the plots of current versus scan rate of compound **1**…….S19

Figure S18. Cyclic voltammograms and the plots of current versus scan rate of compound **3**…….S20

Figure S19. Cyclic voltammograms and square-wave voltammograms of peptide-modified electrode after CDK2/cyclin phosphorylation in the presence of compounds **3 - 5**……..…….S21

Figure S20. Cyclic voltammograms and square-wave voltammograms of peptide-modified electrode after CK2α phosphorylation in the presence of compounds **3 - 5**……..…….S22

Figure S21. Cyclic voltammograms and square-wave voltammograms of peptide-modified electrode after PKA phosphorylation in the presence of compounds **3 - 5**……..…….S23

Figure S22. (A) Plot of current density versus compound **5** concentration and (B) plot of reciprocal current density versus reciprocal of compound **5** concentration for Src phosphorylation……..…….S24

Figure S23. (A) Plot of current density versus compound **5** concentration and (B) plot of reciprocal current density versus reciprocal of compound **5** concentration for CDK2/cyclin A phosphorylation……..……..…….S25

Figure S24. (A) Plot of current density versus compound **5** concentration and (B) plot of reciprocal current density versus reciprocal of compound **5** concentration for PKA phosphorylation……..…….S26

Figure S25. (A) Plot of current density versus compound **5** concentration and (B) plot of reciprocal current density versus reciprocal of compound **5** concentration for CK2α phosphorylation……..…….S27

Figure S26. (A) CVs and (B) Nyquist plots for a) bare gold, b) lipoic-NHS and c) His-tagged pro-caspase-3……..…….S28

Figure S27. Luminescence signal as a function of ATP concentration for (A) Src, (B) CDK2, (C) PKA and (D) CK2 α protein kinase in the absence and presence of compounds **3 – 5**……...……..…….S29

Table S1. Electrochemical impedance values.……..…….…….S30

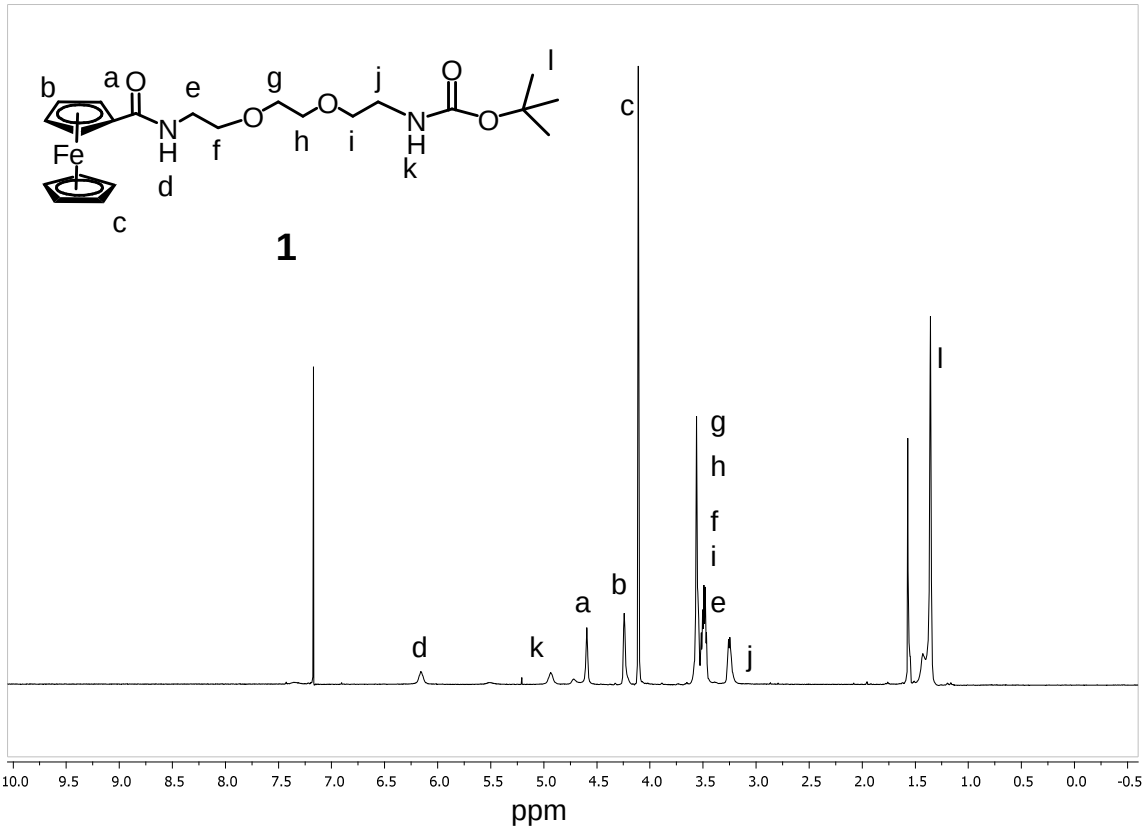

Figure S-1. ^{1}H NMR of compound **1** in $CDCl_3$ at 295 K.

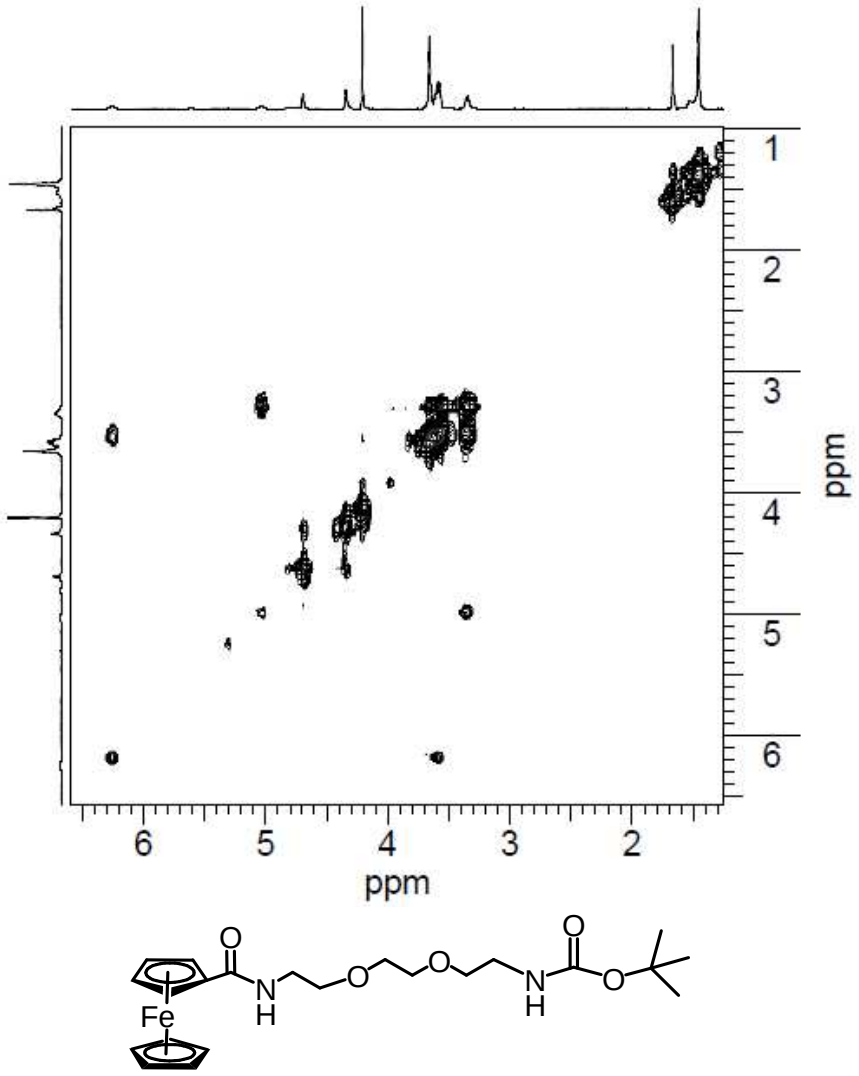

1

Figure S-2. ^{1}H-^{1}H COSY NMR of compound **1** in $CDCl_3$ at 295 K.

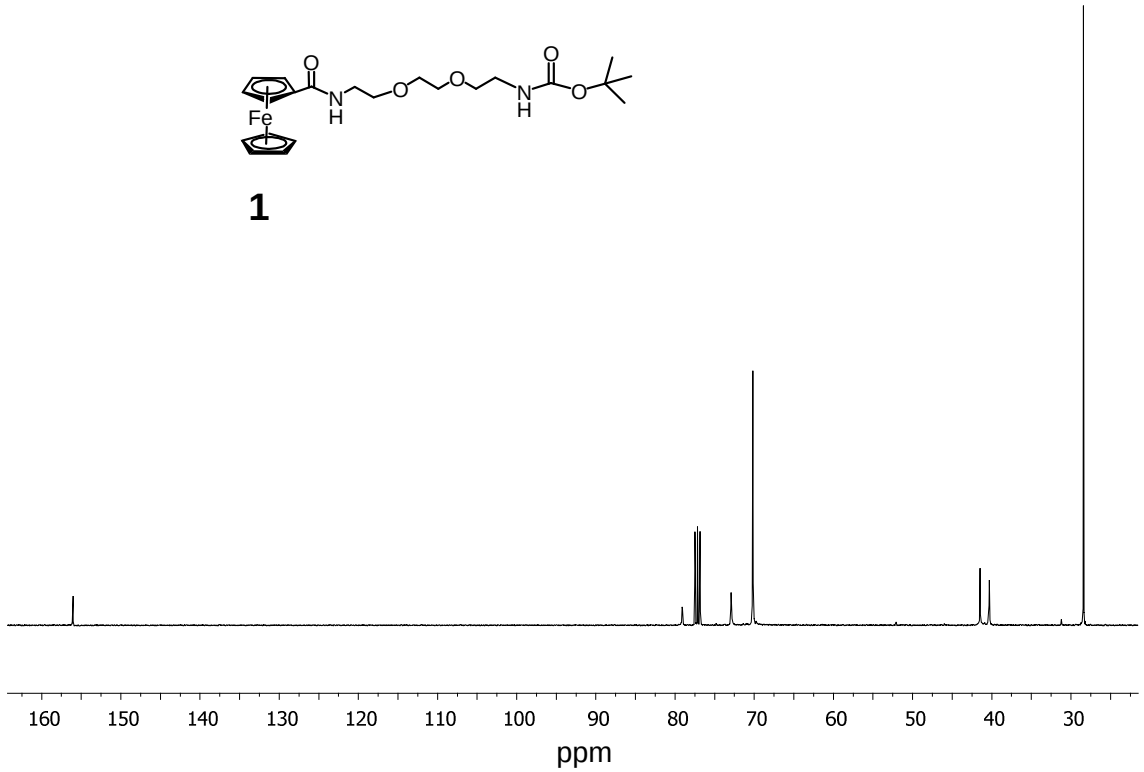

Figure S-3. ^{13}C NMR of compound **1** in $CDCl_3$ at 295 K.

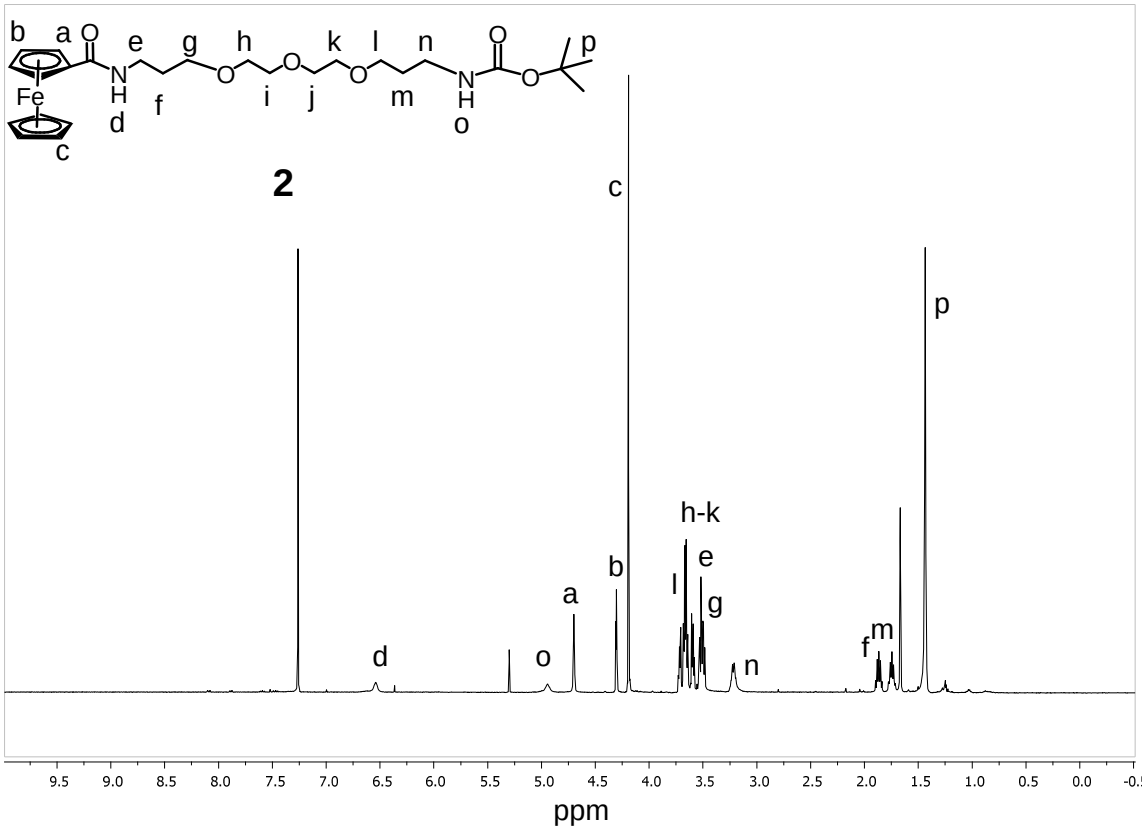

Figure S-4. ^{1}H NMR of compound **2** in $CDCl_3$ at 295 K.

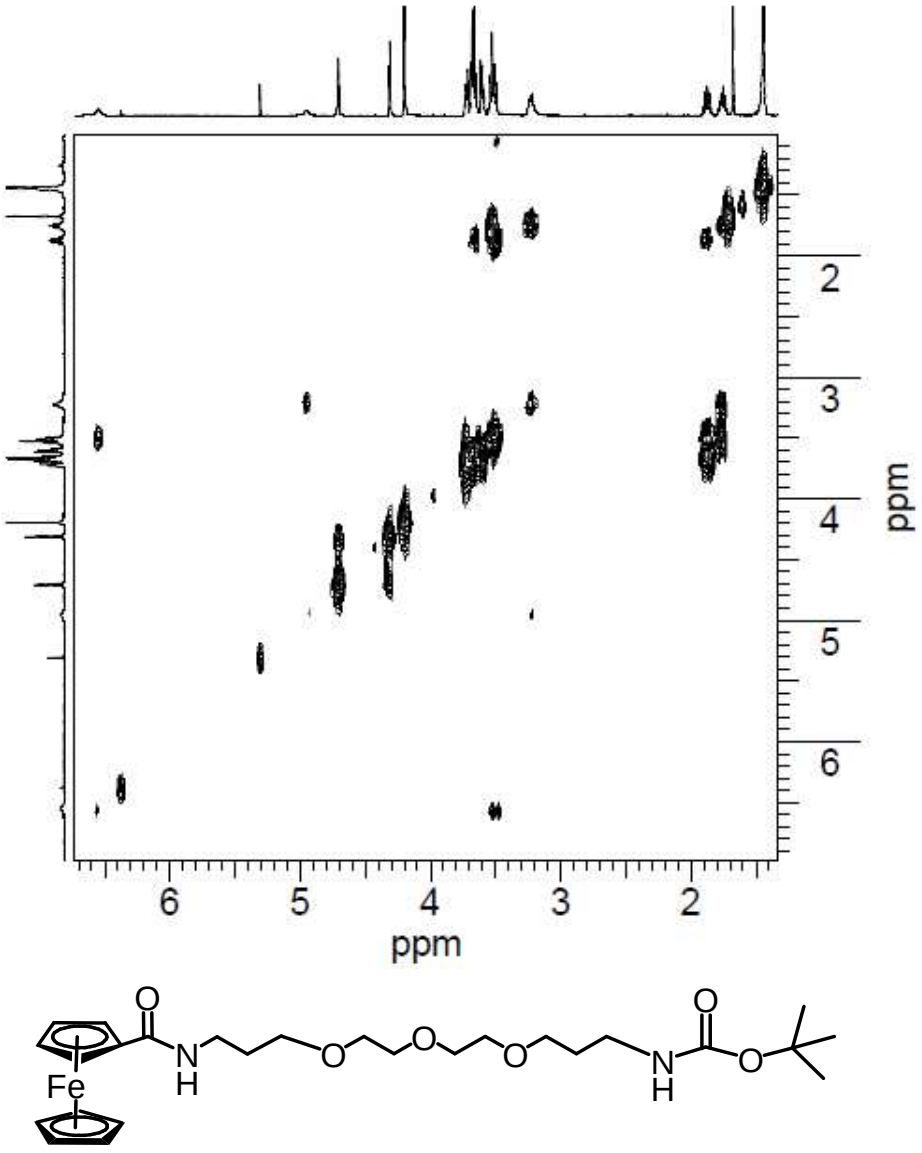

2

Figure S-5. ^{1}H-^{1}H COSY NMR of compound **2** in $CDCl_3$ at 295 K.

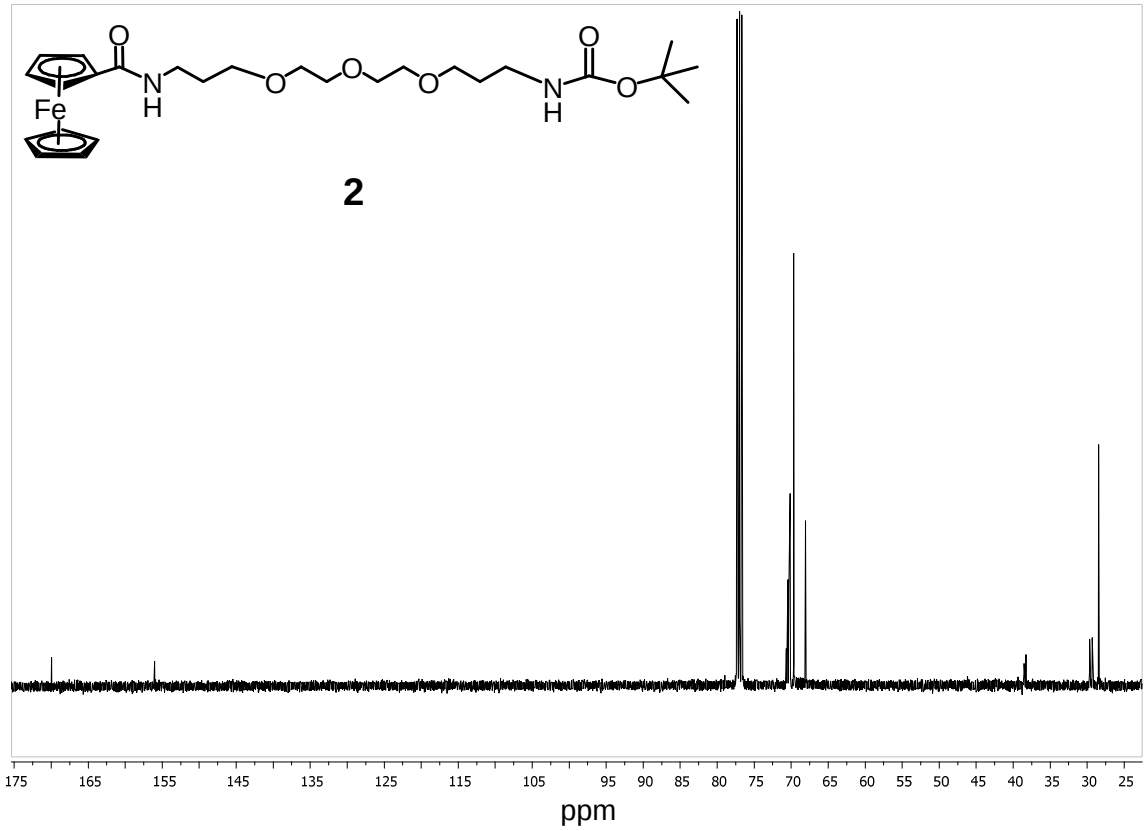

Figure S-6. ^{13}C NMR of compound **2** in $CDCl_3$ at 295 K.

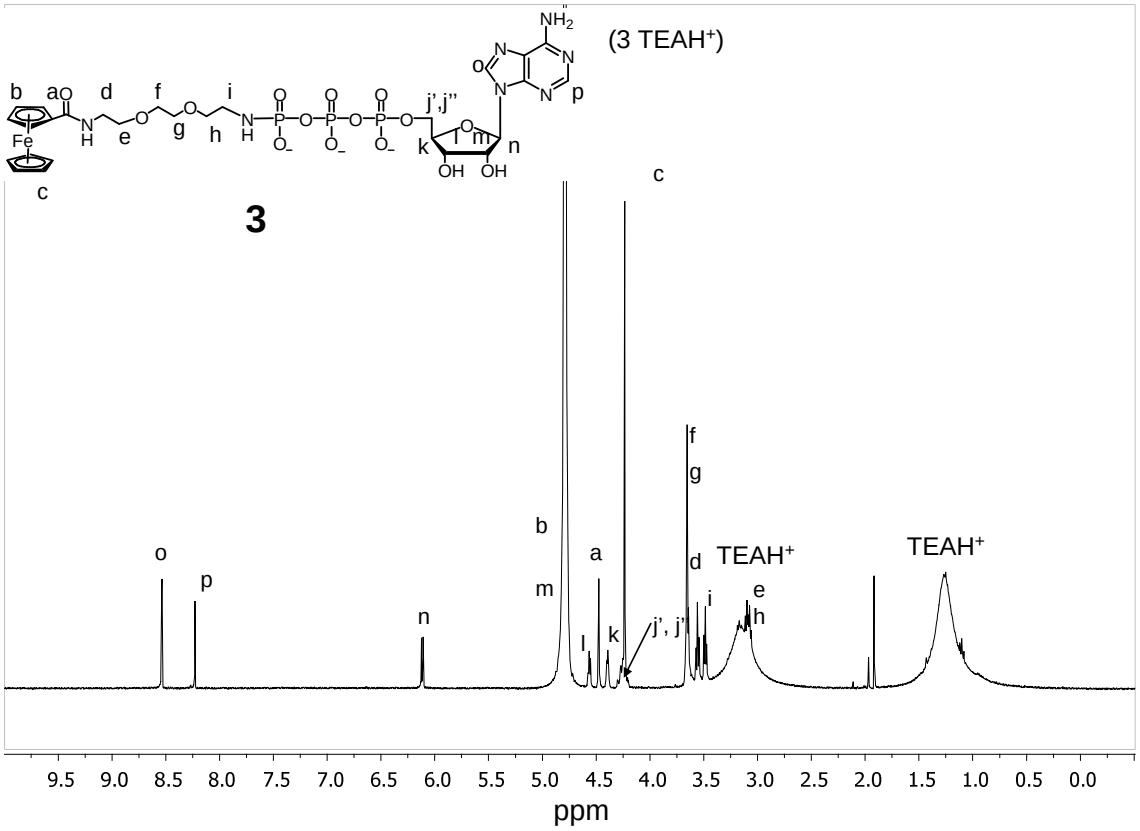

Figure S-7. ^{1}H NMR of compound **3** in D_2O at 295 K.

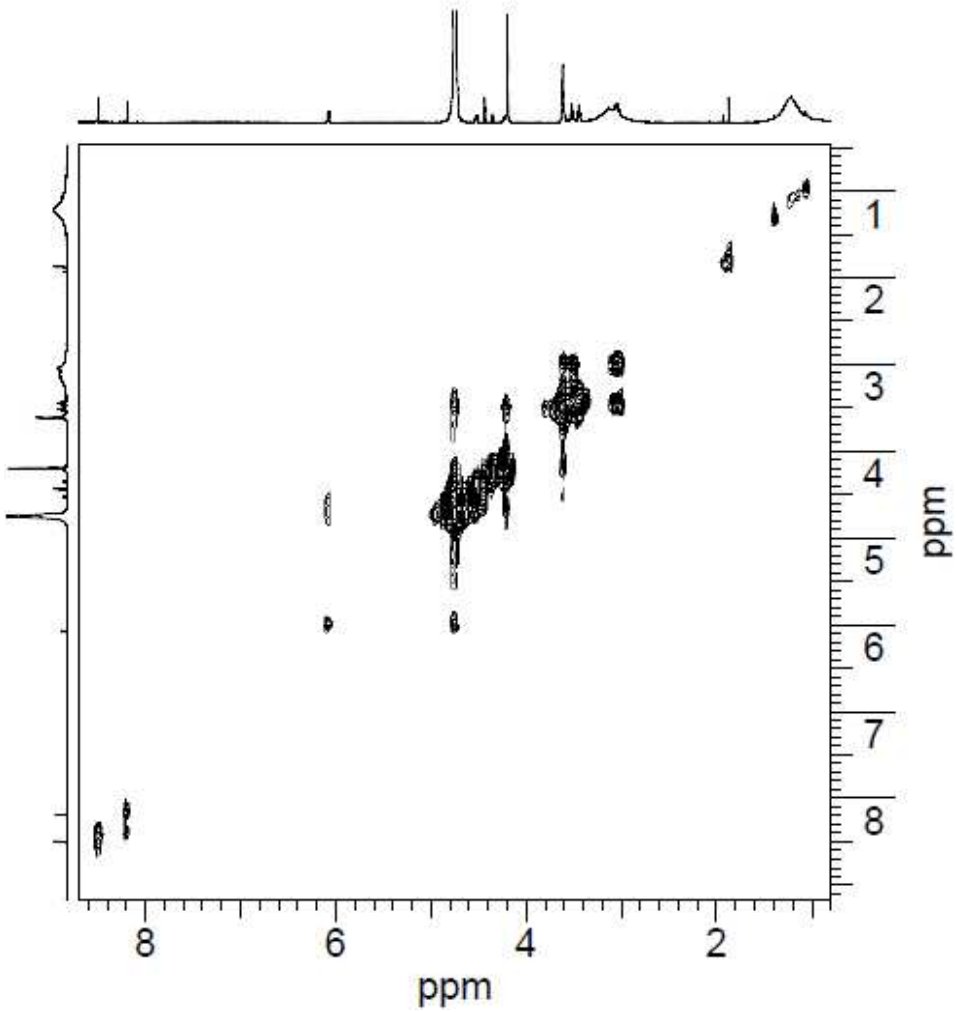

3

Figure S-8. ^{1}H-^{1}H COSY NMR of compound **3** in D_2O at 295 K.

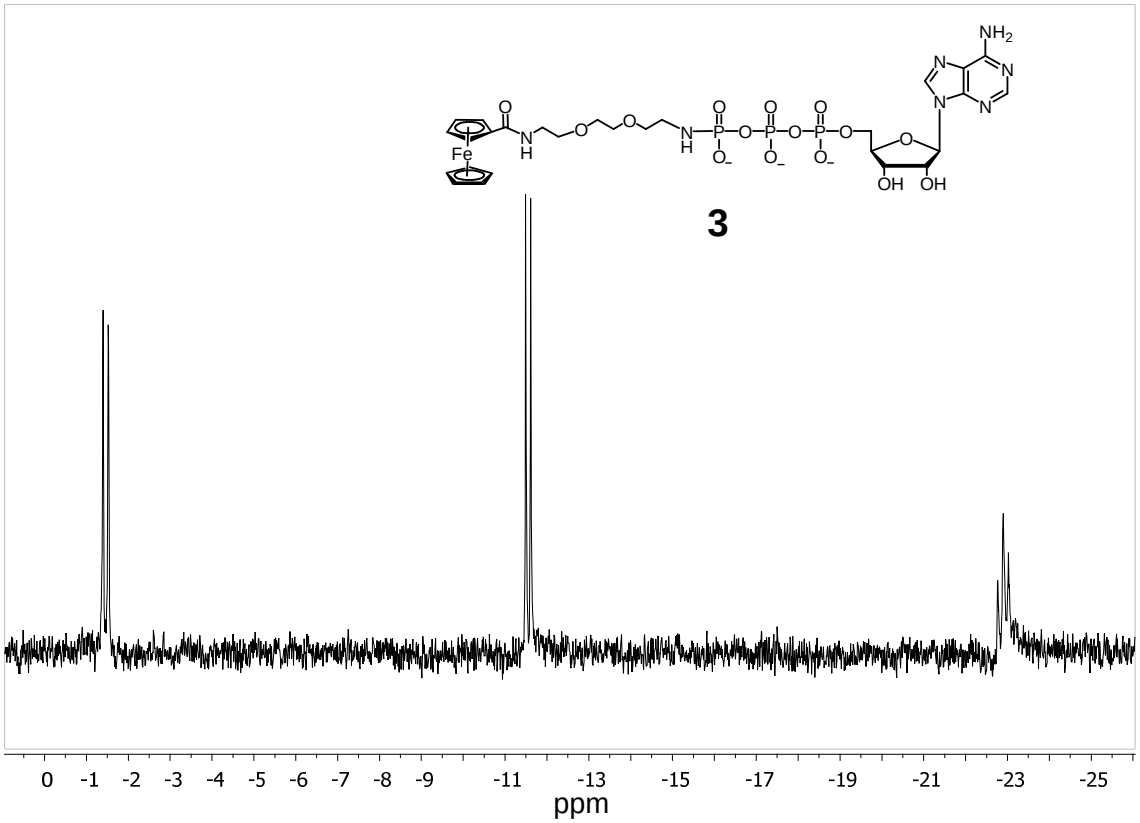

Figure S-9. ^{31}P NMR of compound **3** in D_2O at 295 K.

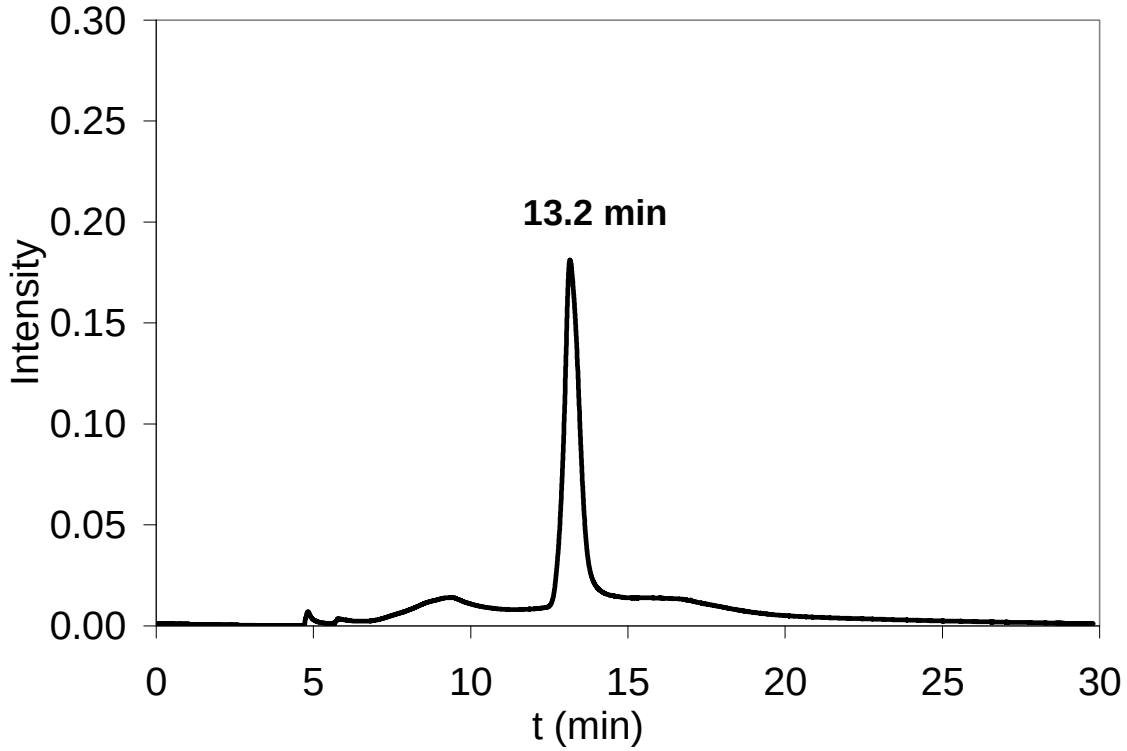

Figure S-10. HPLC trace of compound **3**.

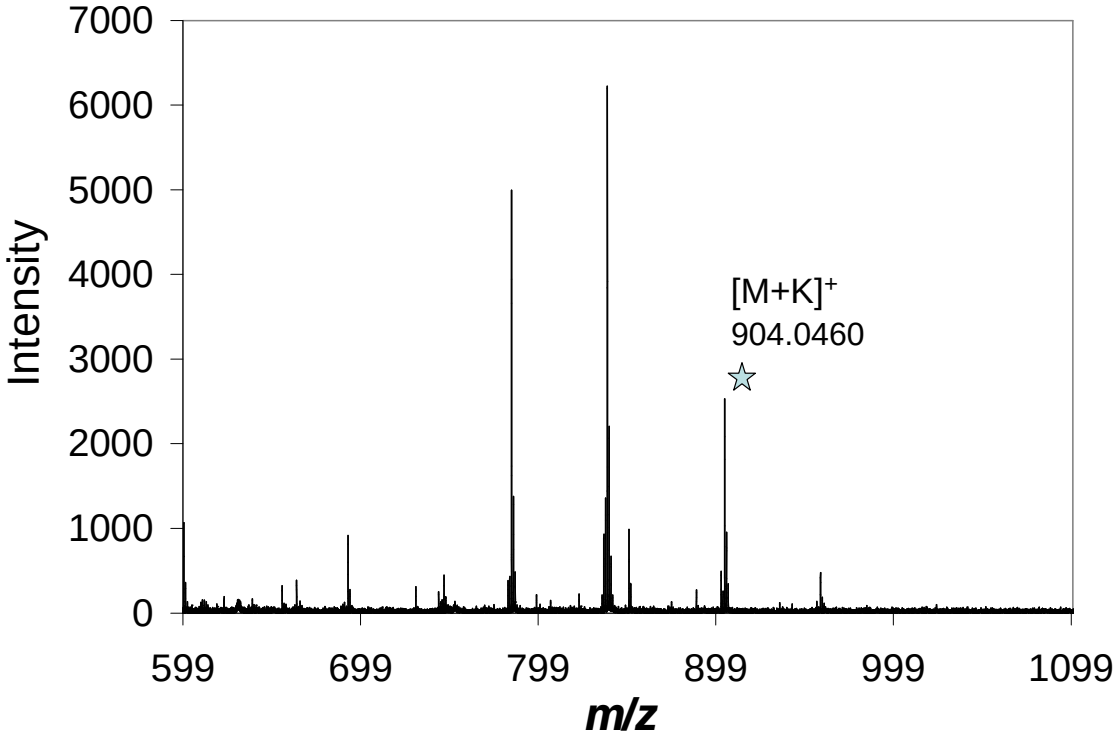

Figure S-11. MALDI-TOF MS spectra of compound **3**.

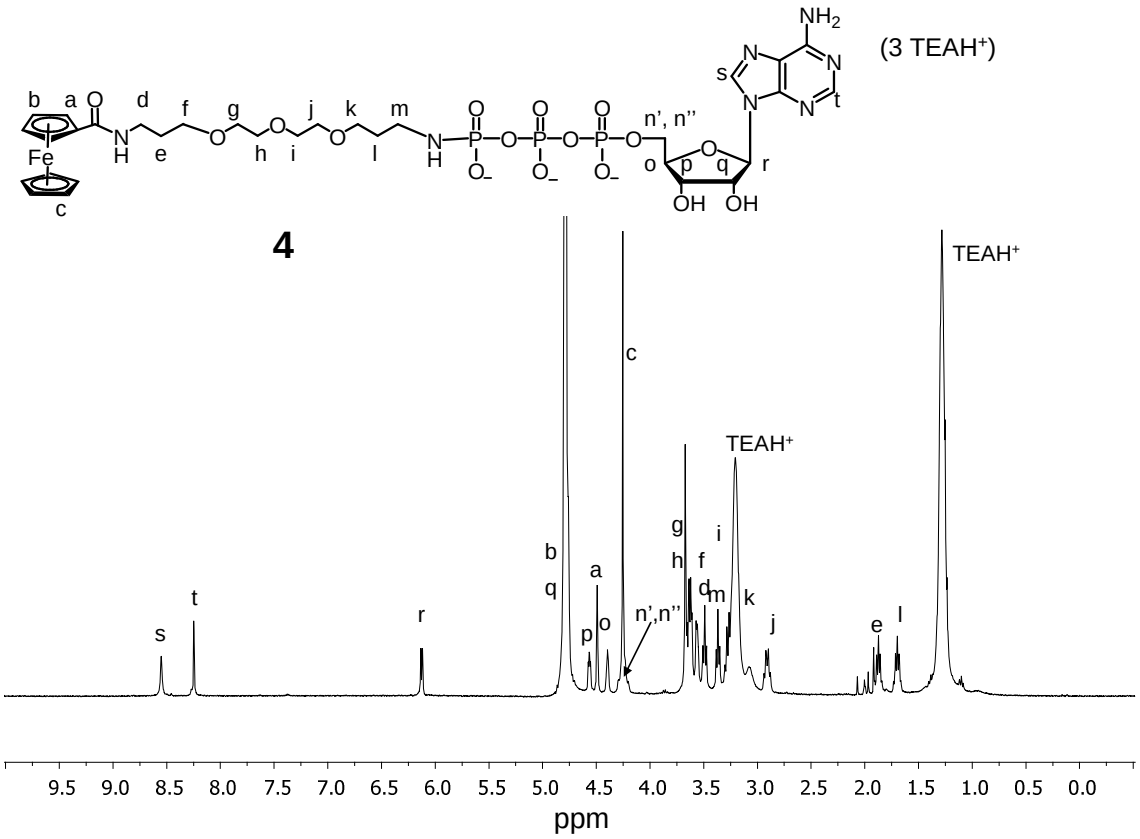

Figure S-12. ^{1}H NMR spectra of compound **4** in D_2O at 295K.

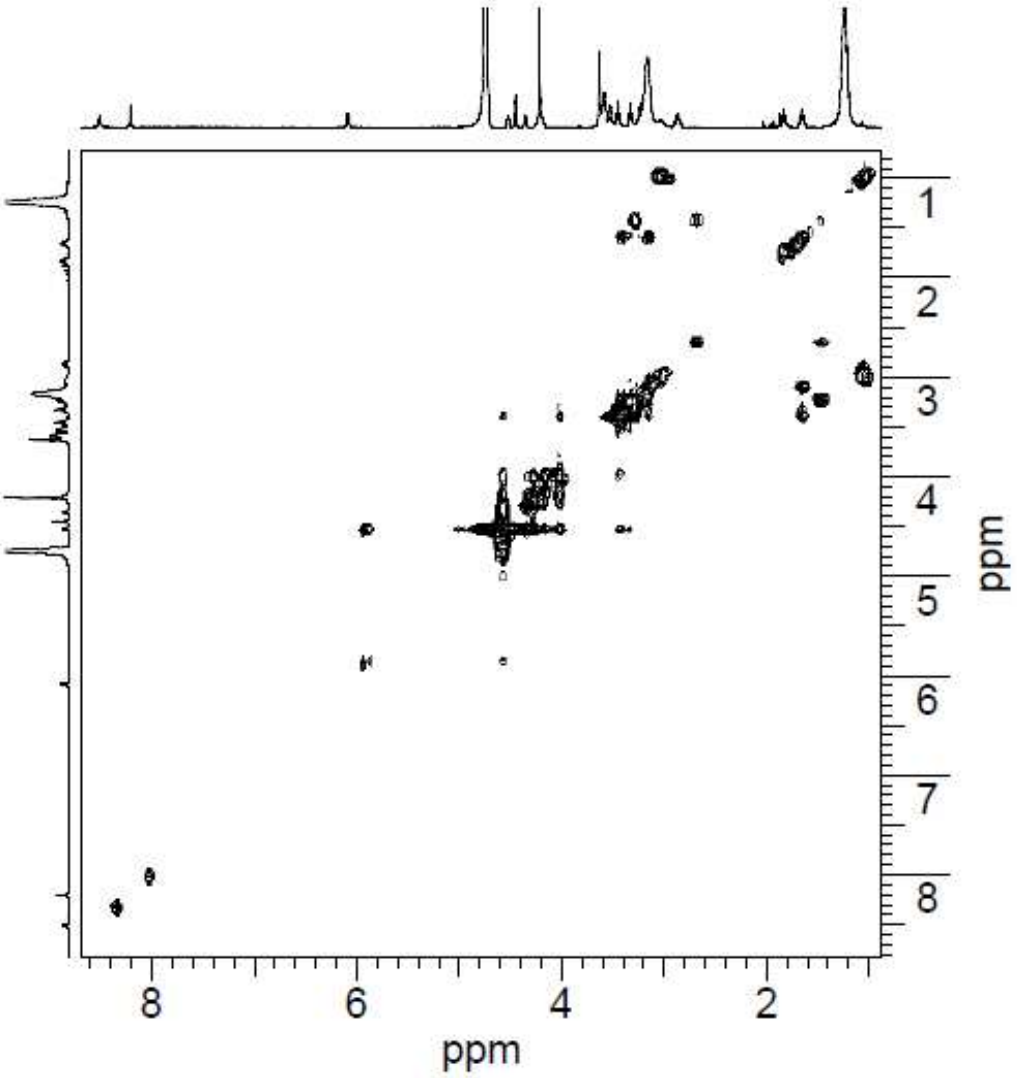

4

Figure S-13. ^{1}H-^{1}H COSY NMR spectra of compound **4** in D_2O at 295K.

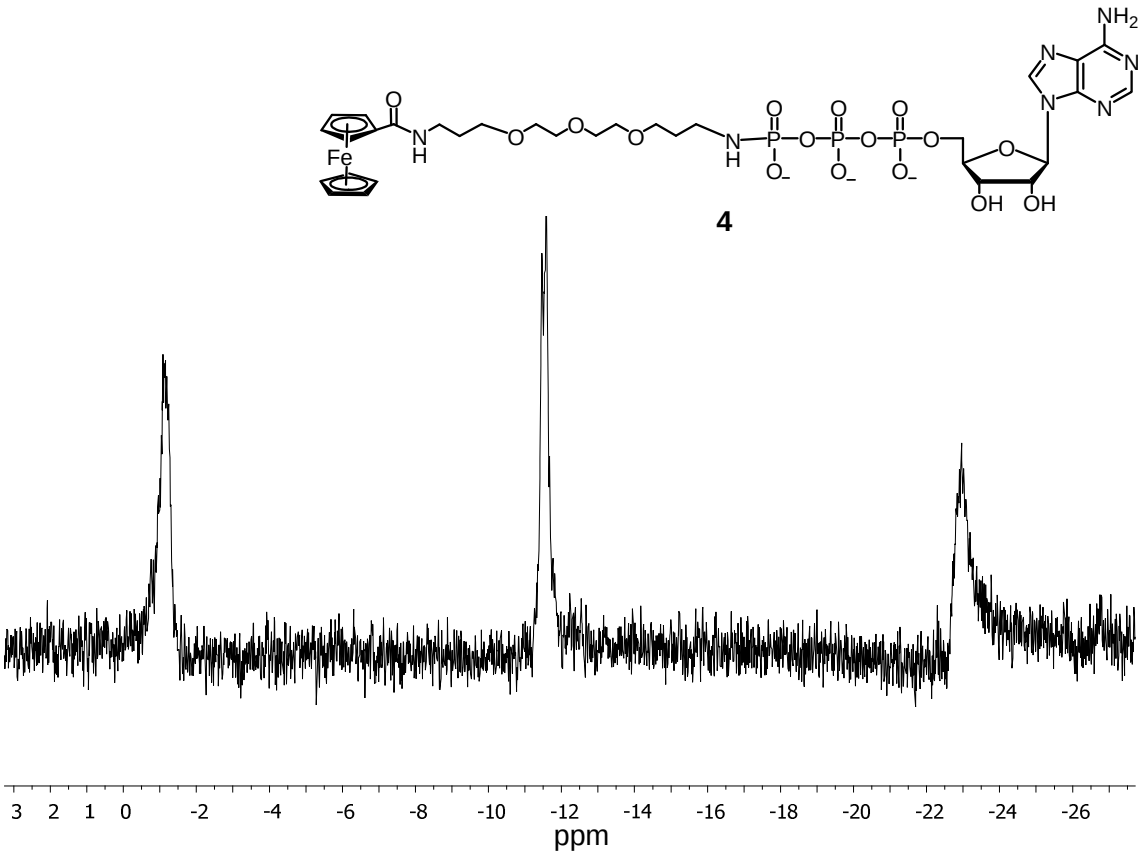

Figure S-14. ^{1}P NMR spectra of compound **4** in D_2O at 295K.

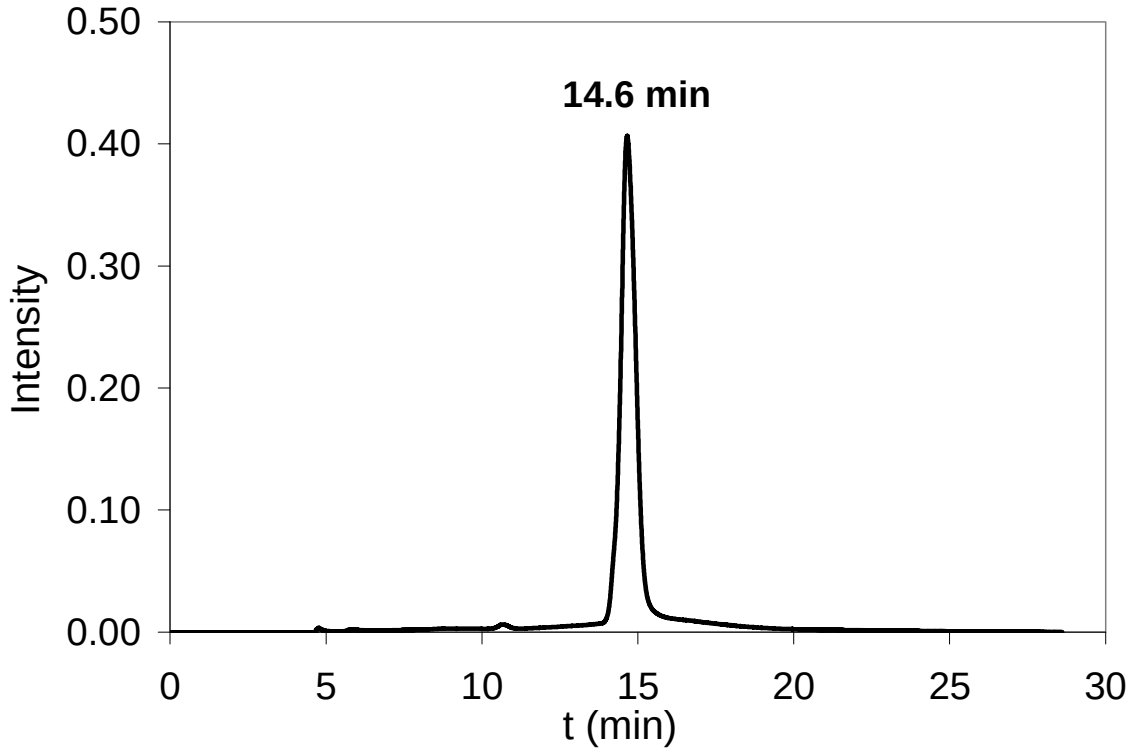

Figure S-15. HPLC trace of compound **4**.

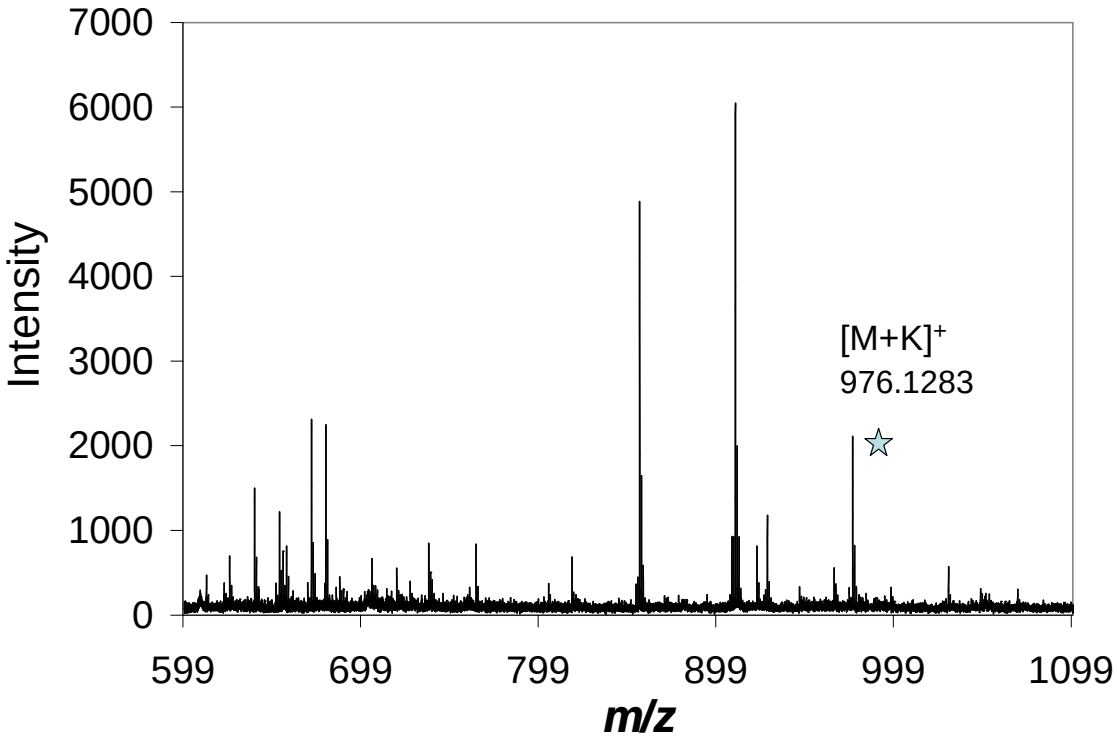

Figure S-16. MALDI-TOF MS of compound **4**.

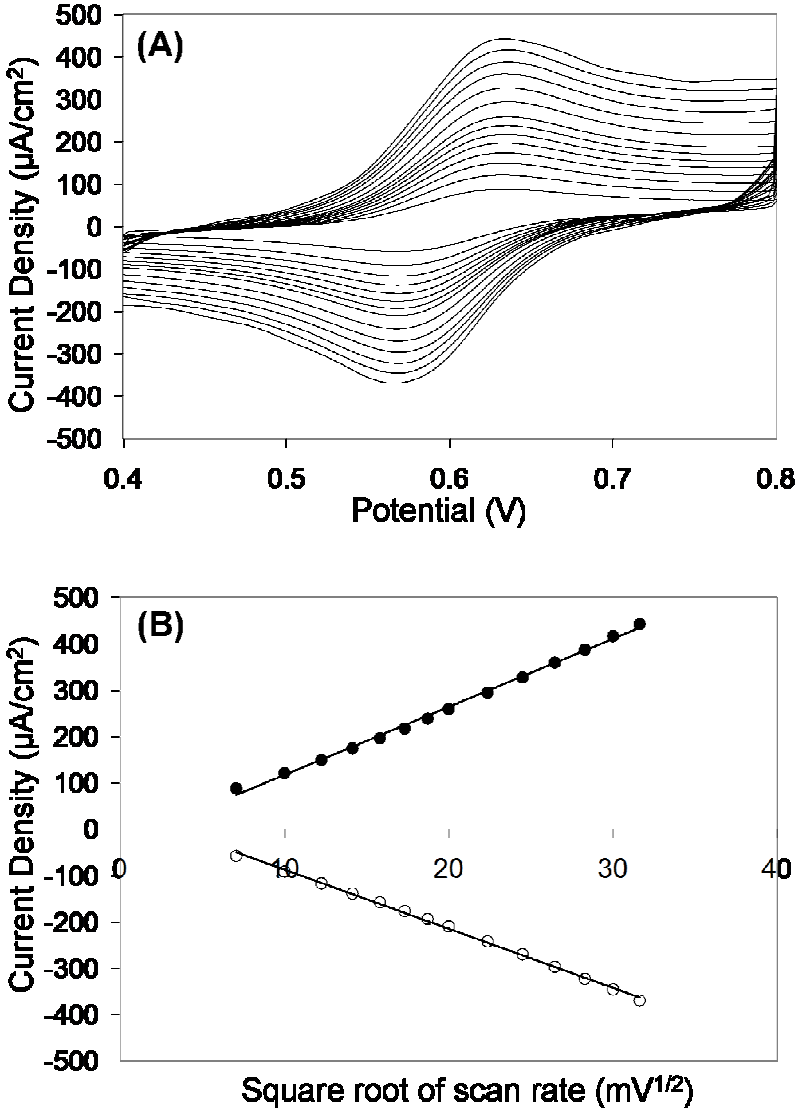

Figure S-17. (A) Cyclic voltmamograms of compound **1** as a function of the scan rate. (C) Plot of anodic and cathodic current densities as a function of square root of scan rate.

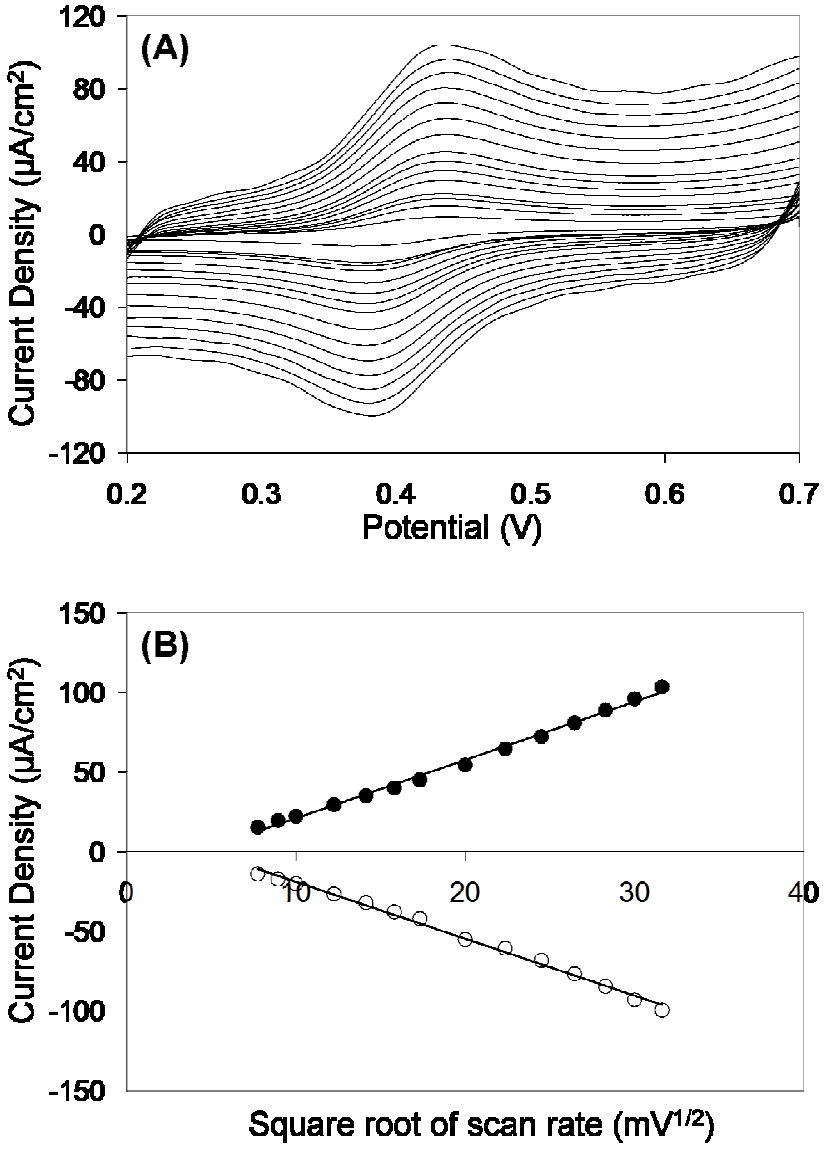

Figure S-18. (A) Cyclic voltmamograms of compound **3** as a function of scan rate. (C) Plot of anodic and cathodic current densities as a function of square root of scan rate.

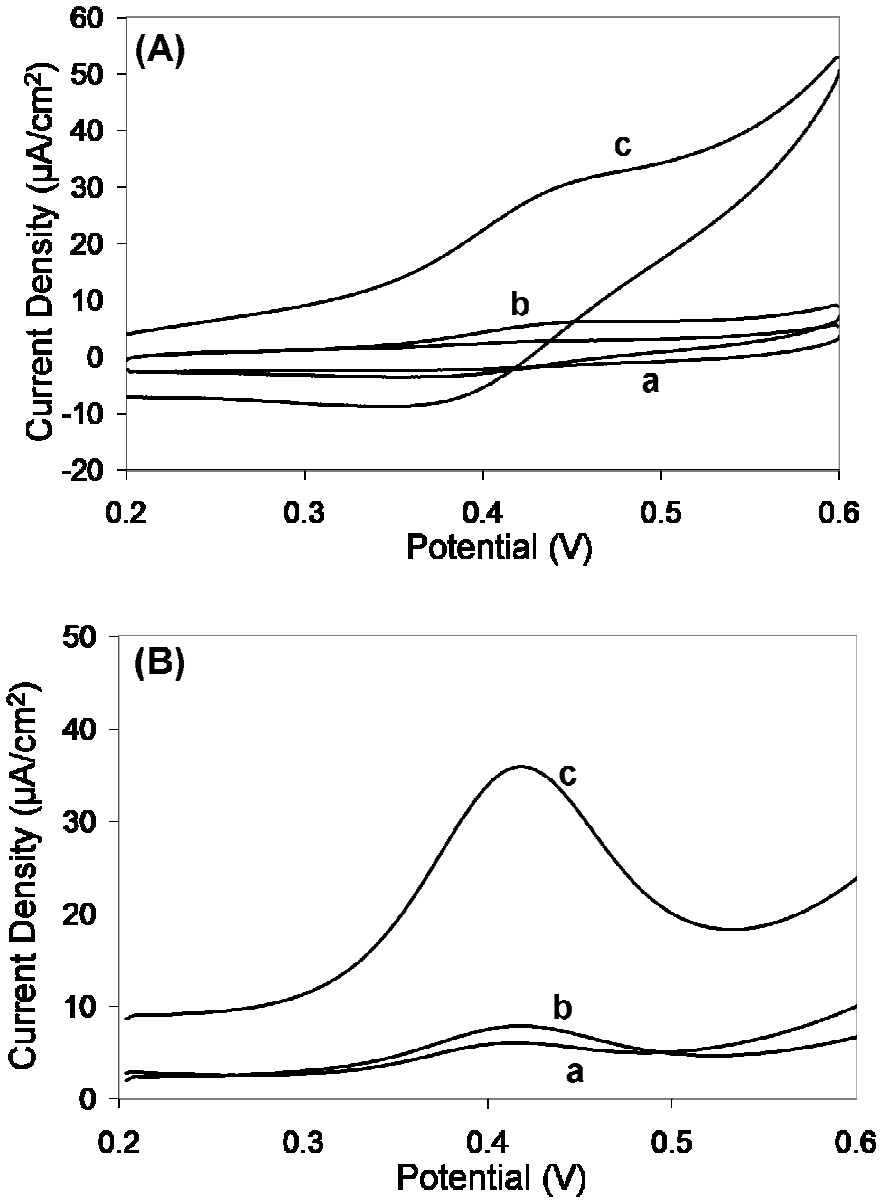

Figure S-19. (A) Cyclic voltmamograms and (B) square-wave voltammograms of surface-immobilized HHASPRK peptide following the phosphorylation with CDK2/cyclin A (1 μg/mL) and compounds **3** (a), **4** (b) and **5** (c).

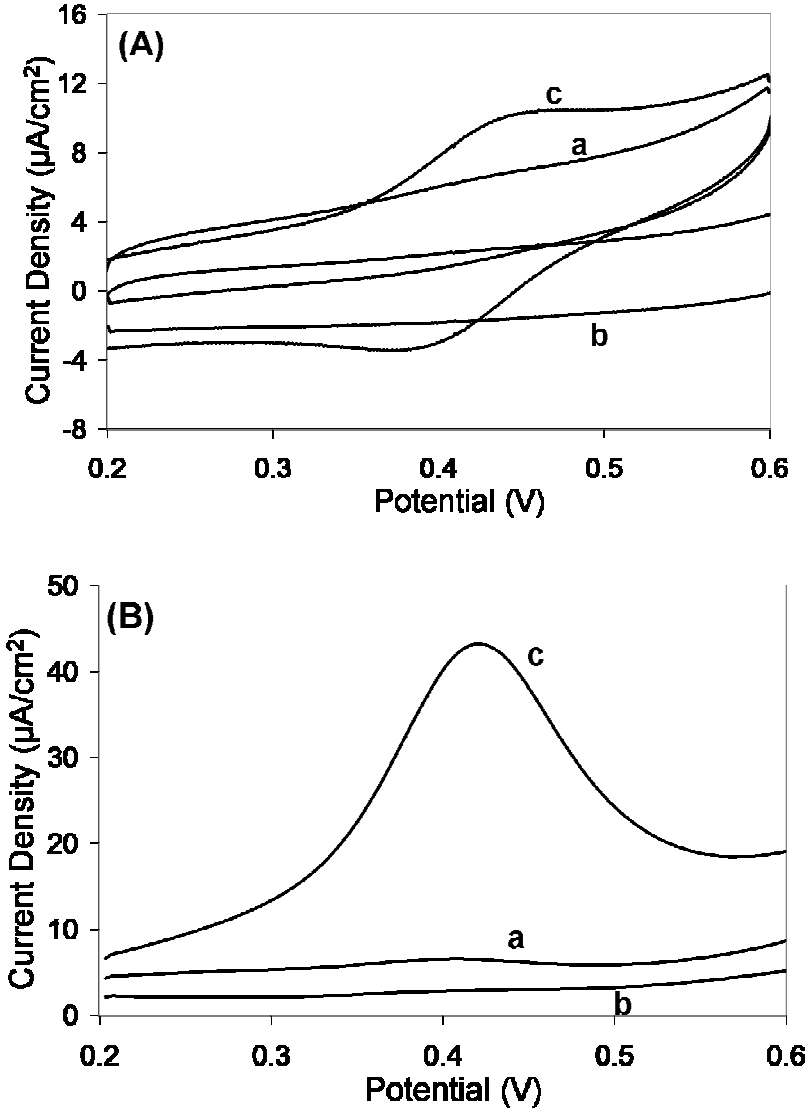

Figure S-20. (A) Cyclic voltmamograms and (B) square-wave voltammograms of surface-immobilized RRRDDD**S**DDD peptide following the phosphorylation with CK2α (0.2 ng/mL) and compounds **3** (a), **4** (b) and **5** (c).

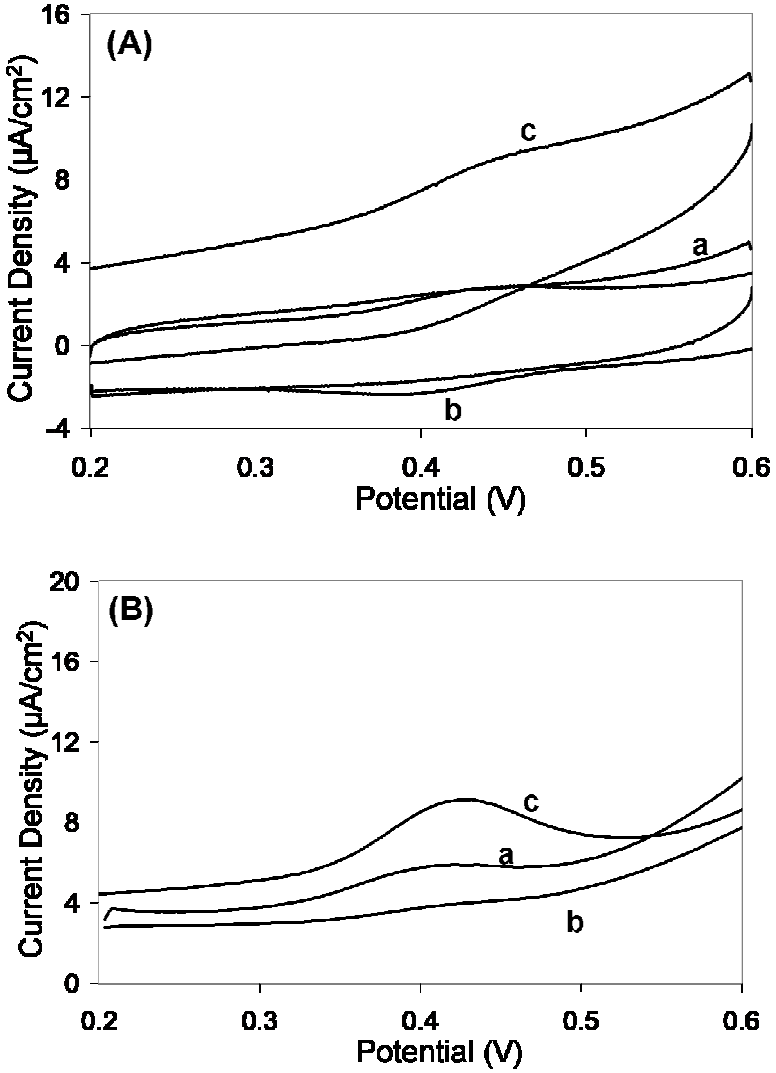

Figure S-21. (A) Cyclic voltmamograms and (B) square-wave voltammograms of surface-immobilized RRLSSLRA peptide following the phosphorylation with PKA (1 μg/mL) and compounds **3** (a), **4** (b) and **5** (c).

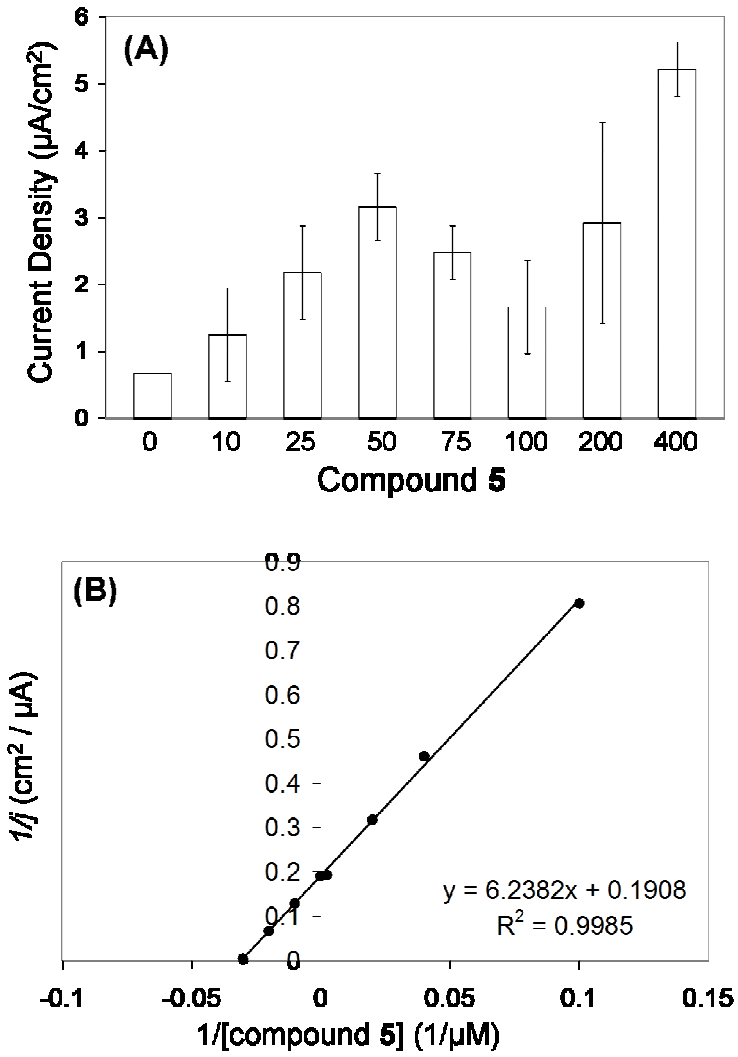

Figure S22. (A) Plot of current density versus compound **5** concentration and (B) Lineweaver-Burke plot of compound **5** showing reciprocal current density versus reciprocal of compound **5** concentration for Src phosphorylation reaction of the peptide-modified electrode.

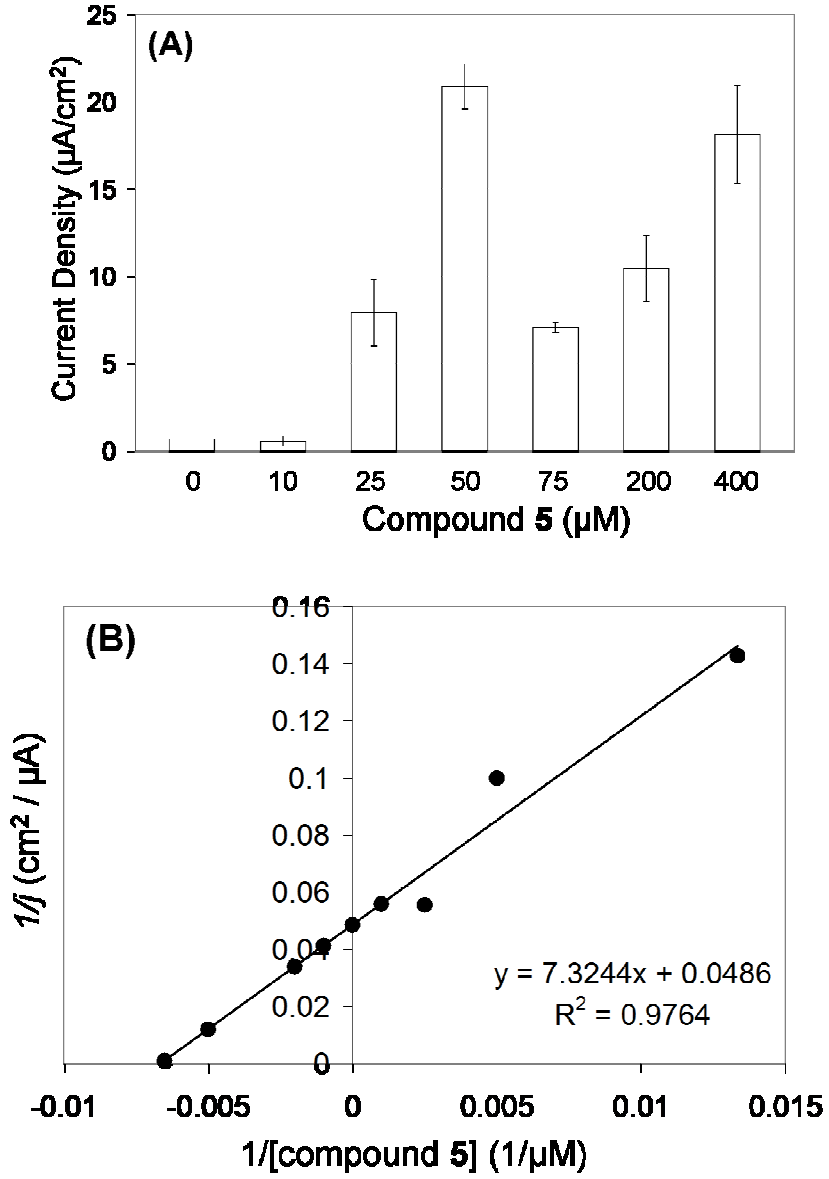

Figure S23. (A) Plot of current density versus compound **5** concentration and (B) Lineweaver-Burke plot of compound **5** showing reciprocal current density versus reciprocal of compound **5** concentration for CDK2/cyclin A phosphorylation reaction of the peptide-modified electrode.

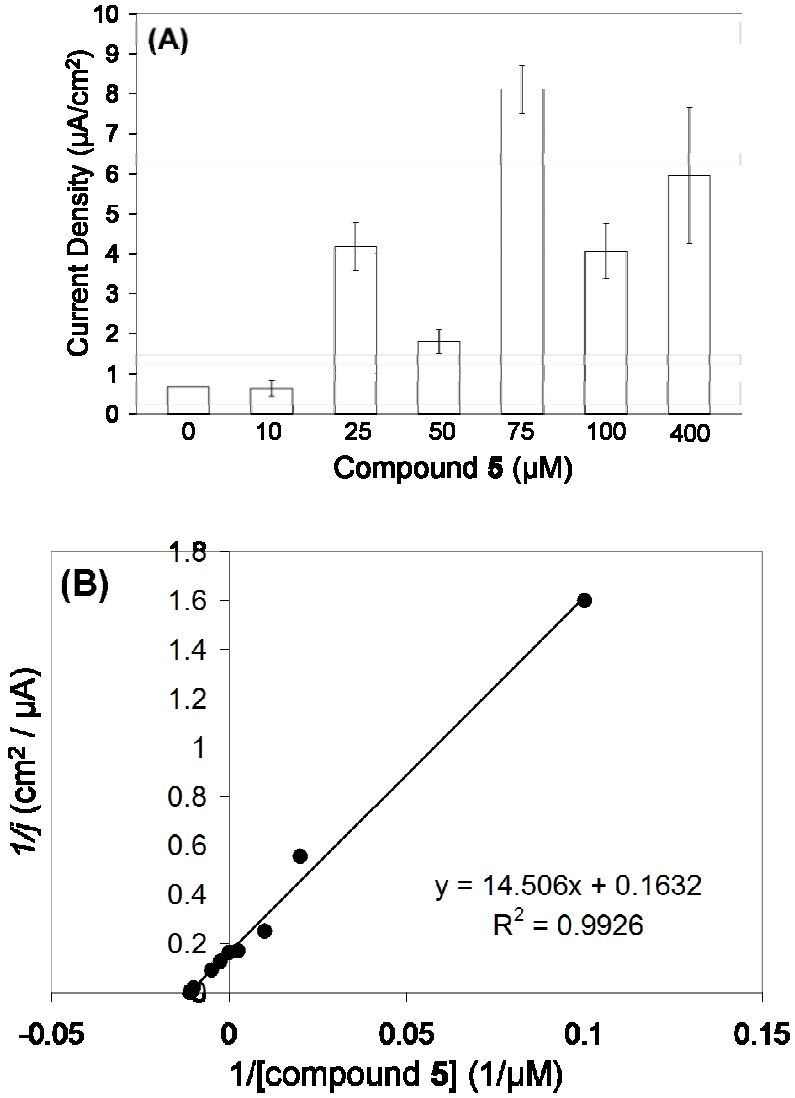

Figure S24. (A) Plot of current density versus compound **5** concentration and (B) Lineweaver-Burke plot of compound **5** showing reciprocal current density versus reciprocal of compound **5** concentration for PKA phosphorylation reaction of the peptide-modified electrode.

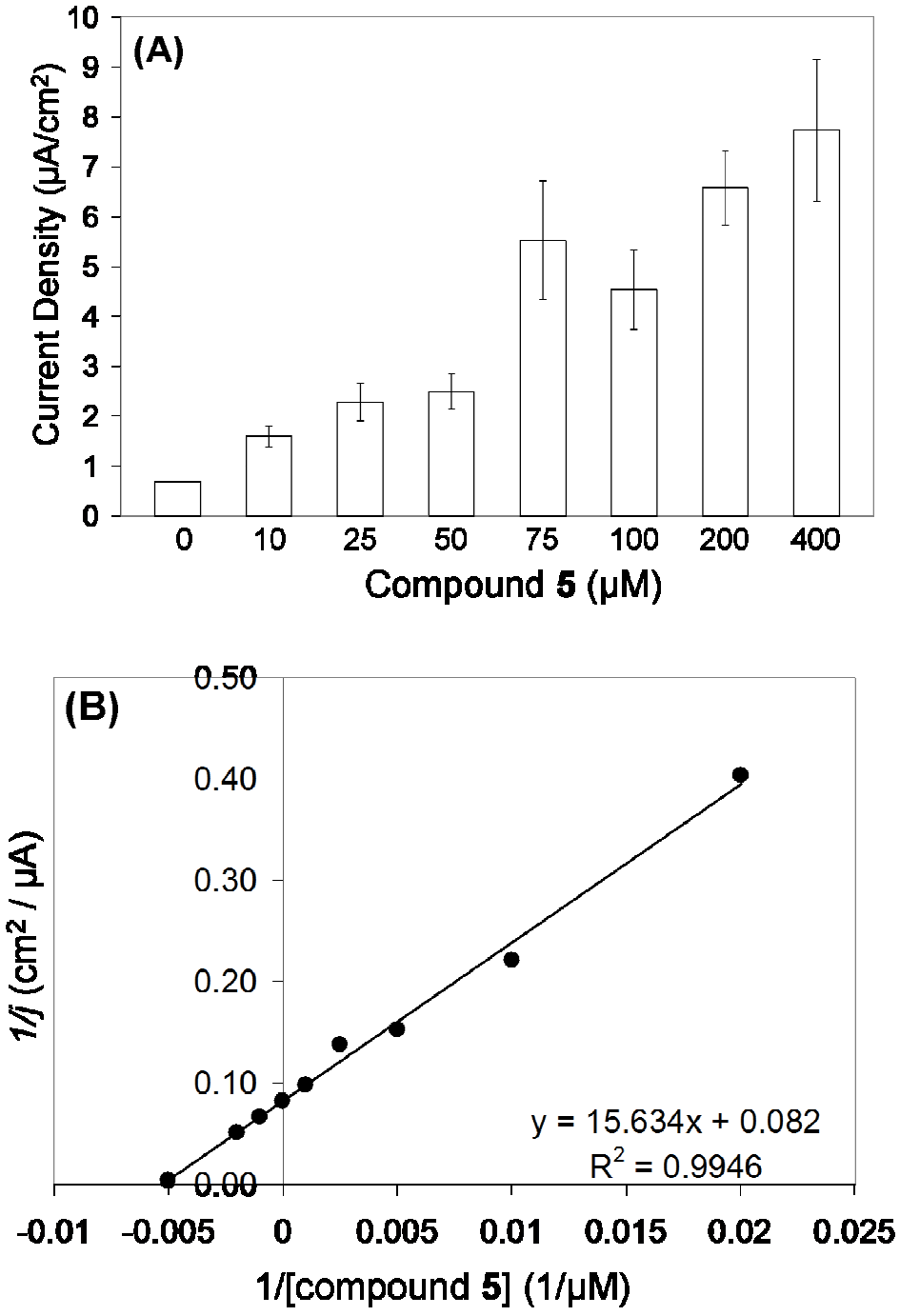

Figure S25. (A) Plot of current density versus compound **5** concentration and (B) Lineweaver-Burke plot of compound **5** showing reciprocal current density versus reciprocal of compound **5** concentration for CK2α phosphorylation reaction of the peptide-modified electrode.

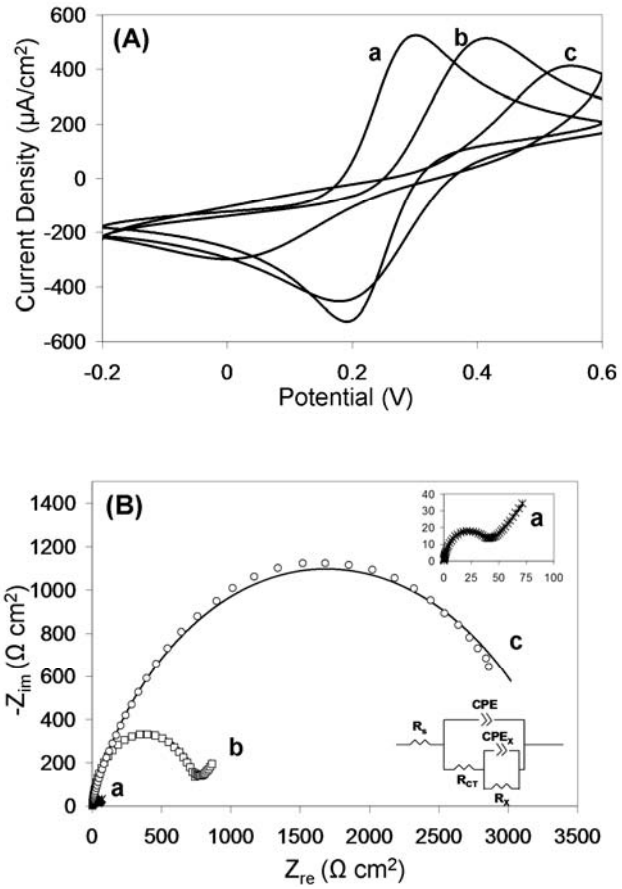

Figure S26. Characterization of the biosensor surface by (A) cyclic voltammetry and (B) Nyquist plot ($-Z_{im}$ *vs* Z_{re}) of electrochemical impedance spectra obtained for bare gold surface (a), following the immobilization of lipoic-*N*-hydroxysuccinimide (b) and immobilization of His-tagged pro-caspase-3 (dead) (c). Upper inset shows Nyquist plot for bare electrode. Measured data are shown as symbols with the fitting to the given equivalent circuit (lower inset) as solid lines. The equivalent circuit applied to fit the measured impedance data as R_s solution resistance, *CPE* and CPE_X constant phase elements, R_{CT} charge transfer resistance, R_X is the film resistance. Electrochemical measurements were done in 1 mM ferri/ferro redox couple in the presence of 50 mM KNO_3.

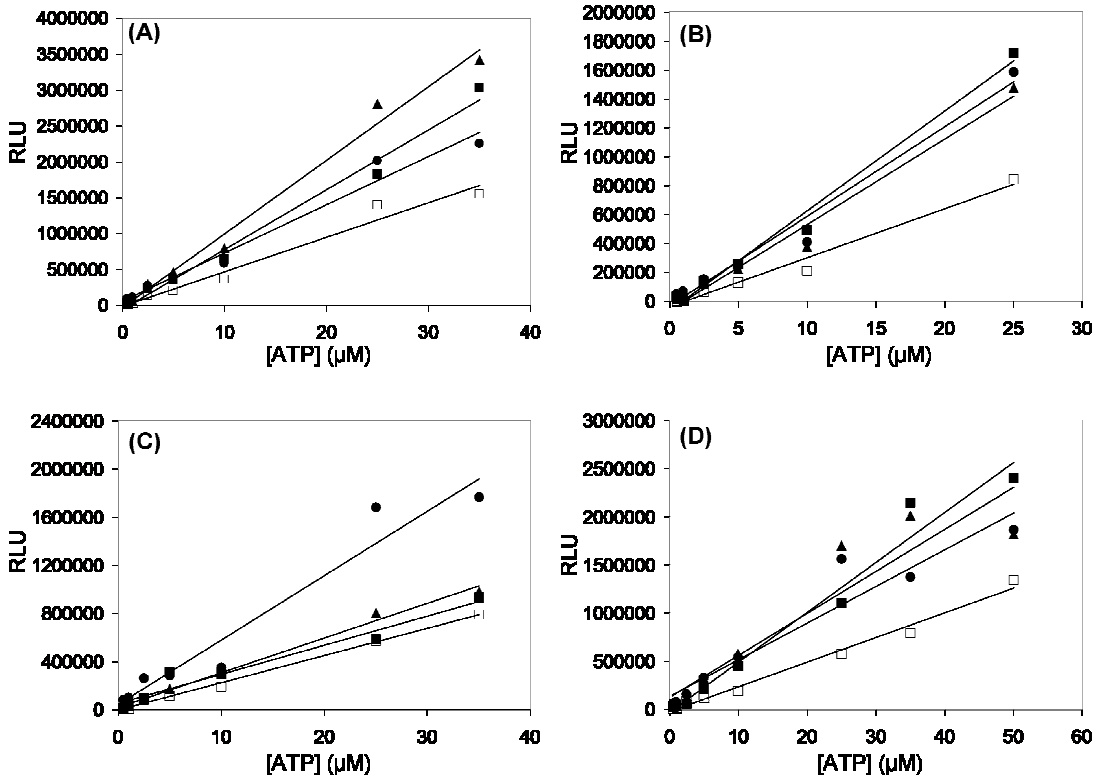

Figure S27. Luminescence signal as a function of ATP concentration for (A) Src, (B) CDK2, (C) PKA and (D) CK2α protein kinase in the absence (□) and presence of 10 μM compounds **3** (▲), **4** (●) and **5** (■).

Table S-1. Equivalent circuit element values for the bare gold electrode and following the modification with lipoic acid-NHS ester and His-tagged pro-caspase-3 protein. Standard error is provided as percentage in brackets.

Surface	R_S (Ω cm^2)	*CPE* (S sec^n cm^{-2})	*n*	R_{CT} (Ω cm^2)	*CPE* (S sec^n cm^{-2})	*n*	R_X (Ω cm^2)
Au	0.02 (17)	3.5×10^{-5} (5.5)	0.915 (0.5)	36.42 (5.6)	7.9×10^{-4} (28)	0.467 (16)	377×10^{8} (7.3)
Lipoic-acid NHS	0.792 (5.1)	3.79×10^{-5} (8.3)	0.899 (1.1)	784.6 (7.0)	5.98×10^{-4} (52.3)	0.7557 (93)	152×10^{17} (1.2)
His-tagged pro-caspase-3	0.91 (5.1)	4.91×10^{-5} (11)	0.680 (1.2)	1309 (56)	1.31×10^{-3} (76)	0.998 (1.3)	1338 (68)

Bioconjugate Chemistry

ARTICLE

pubs.acs.org/bc

Multivalent Cyclic RGD Conjugates for Targeted Delivery of Small Interfering RNA

Md. Rowshon Alam,[‡] Xin Ming,[†] Michael Fisher,[†] Jeremy G. Lackey,[‡] Kallanthottathil G. Rajeev,[‡] Muthiah Manoharan,[‡] and Rudy L. Juliano*[,†]

[†]Division of Molecular Pharmaceutics, UNC Eshelman School of Pharmacy, University of North Carolina, Chapel Hill, North Carolina 27599, United States

[‡]Alnylam Pharmaceuticals, 300 Third Street, Cambridge, Massachusetts 02142, United States

Supporting Information

ABSTRACT: We have designed, synthesized, and tested conjugates of chemically modified luciferase siRNA (Luc-siRNA) with bi-, tri-, and tetravalent cyclic-(arginine-glycine-aspartic) (cRGD) peptides that selectively bind to the $\alpha v\beta 3$ integrin. The cellular uptake, subcellular distribution, and pharmacological effects of the cRGD-conjugated Luc-siRNAs compared to those of unconjugated controls were examined using a luciferase reporter cassette stably transfected into $\alpha v\beta 3$ positive $M21^+$ human melanoma cells. The $M21^+$ cells exhibited receptor-mediated uptake of cRGD−siRNA conjugates but not of unconjugated control siRNA. The fluorophore-tagged cRGD−siRNA conjugates were taken up by a caveolar endocytotic route and primarily accumulated in cytosolic vesicles. The bi-, tri-, and tetravalent cRGD conjugates were taken up by $M21^+$ cells to approximately the same degree. However, there were notable differences in their pharmacological effectiveness. The tri- and tetravalent versions produced progressive, dose-dependent reductions in the level of luciferase expression, while the bivalent version had little effect. The basis for this divergence of uptake and effect is currently unclear. Nonetheless, the high selectivity and substantial "knock down" effects of the multivalent cRGD−siRNA conjugates suggest that this targeting and delivery strategy deserves further exploration.

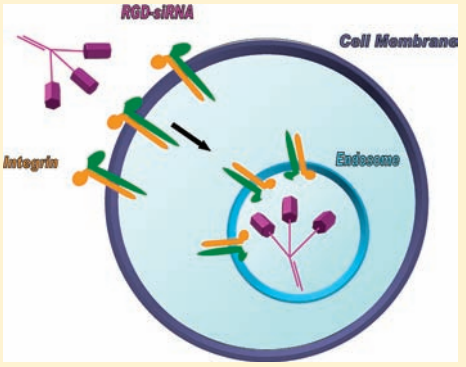

INTRODUCTION

Antisense and small interfering RNA (siRNA) oligonucleotides have displayed considerable promise for treatment of a variety of diseases. Advancement of new chemistries and design features have led to oligonucleotides that provide improved stability against nucleases, enhanced potency, weakened immune responses, and reduced toxicity profiles compared to those of early generations of oligonucleotides.[1−3] Excellent results for both antisense and siRNA have been attained in cell culture and animal models, and this has driven the initiation of multiple clinical trials.[1,4] However, despite important progress, a key impediment to the wider success of this approach is poor delivery of oligonucleotides to their sites of action within cells, because of the need to cross several biological barriers subsequent to administration.[5,6]

The endogenous regulatory mechanisms involved in RNA interference (RNAi) can be activated by the delivery of siRNAs to the cell interior.[7] The mechanism of targeted mRNA degradation by siRNA is highly complex and not completely understood. It includes the formation of an RNA-induced silencing complex (RISC) that contains the Argonaute 2 protein, while the Dicer RNase and other accessory proteins are also important in loading of siRNA onto the RISC.[8] The potency and specificity of siRNAs can be improved, and their impact on the innate immune system can be reduced via chemical modification guided by design algorithms.[3] Nonetheless, effective delivery of siRNA to its intracellular sites of action remains a challenge.

One important modality for delivery of both antisense and siRNA molecules has been the use of polymeric or lipid nanocarriers.[9] Lipid-based carriers have proven to be particularly efficacious in the delivery of siRNA to the liver.[10] A variety of polymeric[11] or other types of nanoparticles[12] have also been employed for siRNA delivery. Effective deployment of siRNA to tumors has been challenging, but recently, targeted lipid-based nanoparticles have exhibited substantial activity.[13]

An alternative approach for delivery of antisense and siRNA moieties involves covalent conjugation of high-affinity and receptor specific ligands that bind to cell surface receptors.[14−17] This strategy can be used to provide cell-type selective targeting and delivery and thereby to enhance tissue specific intracellular accumulation of oligonucleotides. For example, we have utilized peptide ligands with high affinity for integrins,[18,19] for a G protein-coupled receptor,[20] or for the sigma receptor[21] to enhance delivery of antisense oligonucleotides into tumor cells that overexpress these receptors.

Received: May 4, 2011
Revised: July 8, 2011
Published: July 14, 2011

ACS Publications © 2011 American Chemical Society

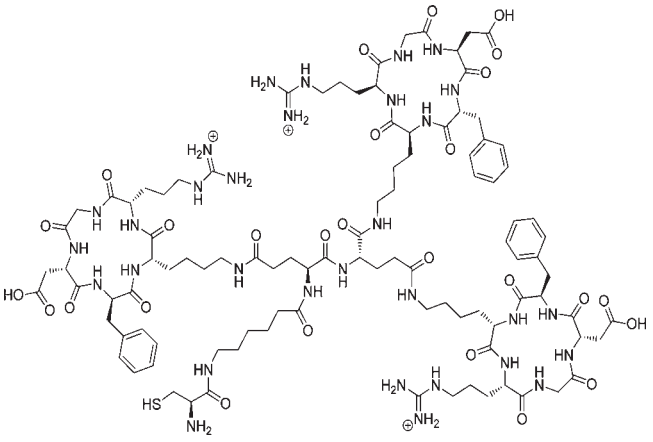

Figure 1. Trivalent cRGD **2**. The cysteine is connected to a 6-amino-hexanoic acid linker that joins two, three, and four cRGD moieties for the bi-, tri-, and tetravalent versions, respectively. Only the trivalent peptide is shown here.

In this work, we extend the strategy for tissue specific delivery of siRNAs by conjugating high-affinity cyclic(arginine-glycine-aspartic) (cRGD) ligands that are known to bind to $\alpha v\beta 3$ integrin to luciferase siRNA. The high-affinity bi-, tri-, and tetravalent cRGD ligands were conjugated to the 3′-end of the sense strand of the siRNA. We demonstrate enhanced receptor specific cellular uptake of cRGD−siRNA conjugates and dose dependent inhibition of a luciferase reporter gene in the absence of transfection agents. We also demonstrate uptake inhibition of cRGD−siRNA conjugates by preincubation of the $\alpha v\beta 3$ integrin positive cells[22] with excess RGD peptide, and association of the biological effect with the valency or cRGD content of the siRNA conjugate studied.

MATERIALS AND METHODS

Reagents. Bi-, tri-, and tetravalent cRGD peptides were obtained from Peptides International (Louisville, KY). The amino acid sequences of the bi-, tri-, and tetravalent cRGD peptides are H-Cys-Aca-Glu-[cyclo(Arg-Gly-Asp-D-Phe-Lys)]$_2$, H-Cys-Aca-Glu-[cyclo(Arg-Gly-Asp-D-Phe-Lys)]-Glu-[cyclo(Arg-Gly-Asp-D-Phe-Lys)]$_2$, and H-Cys-Aca-Glu-{Glu-[cyclo(Arg-Gly-Asp-D-Phe-Lys)]$_2$}$_2$, respectively. A thiol group was introduced into the cRGDs by attaching a cysteine residue via the spacer 6-aminocaproic acid to the α-amino group of glutamic acid to allow conjugation of the peptide to a maleimide-containing oligonucleotide under Michael addition conditions (Figure 1).

Solid-Phase Synthesis of Modified siRNA Targeting the Firefly Luciferase Gene. All oligonucleotides used in this study were synthesized on an ABI 394 DNA synthesizer using standard phosphoramidite chemistry with commercially available phosphoramidite monomers. The oligonucleotides were deprotected with a methylamine solution at 65 °C for 10 min (40 wt % in water) followed by DMSO wash and cooled on dry ice for 10 min and then treated with TEA·3HF at 65 °C for 12 min. All oligonucleotides were purified by anion-exchange high-performance liquid chromatography (HPLC) and characterized by liquid chromatography−mass spectroscopy (LC−MS) analysis. For peptide conjugation, an amino linker was introduced at the 3′-end of the sense strand by initiating the oligonucleotide synthesis on a *trans*-4-hydroxyproline-based support **4** under standard oligonucleotide synthesis conditions (Scheme 1).

Postsynthetic Conjugation of cRGD Peptides to Oligonucleotides. The HPLC-purified amino-linked sense strand **5** (23.6 mg, 3.35 μmol) was reacted with 6-maleimidohexanoic acid *N*-hydroxysuccinimide ester (EMCS) (21 mg, 68 μmol) in 1× PBS buffer (pH 7.2) for 20 min at room temperature to yield maleimido-modified sense strand **6** (Scheme 1). The reaction mixture was then diluted with HPLC grade water (15 mL) and directly loaded onto a Waters XTerra RP-18 column on an AKTA purifier (GE Healthcare) and purified using a gradient of buffers A and B. Buffer A was 0.1 M TEAA (pH 7.0), and buffer B was CH_3CN (gradient of 0% B for 1 column volume, from 10 to 50% B for 5 column volumes, and from 50 to 100% B for 2 column volumes; flow rate of 15 mL/min, UV at 260 nm). The HPLC fractions with the right mass were collected (22.6 mg, 3.11 μmol, 93%), aliquoted into the desired quantity, and treated immediately with peptides **1**−**3** individually to yield the desired cRGD-conjugated sense strands **7**−**9** (Scheme 1). The products formed were analyzed by analytical HPLC and LC−MS to confirm integrity.

Bivalent cRGD peptide **1** (1.6 mg, 1.02 μmol) was dissolved in water (1 mL) and added to the solution of maleimido oligonucleotide **6** (3 mg, 0.41 μmol) in 0.4 M KCl with 40% CH_3CN, and the mixture was incubated overnight at room temperature. The reaction mixture was dialyzed in water and loaded onto a Waters XTerra RP-18 column on the AKTA purifier and purified using buffers A and B under the same conditions that were used for the purification of maleimido oligonucleotide **6**. Fractions containing the bivalent conjugate **7** were pooled and lyophilized (3.4 mg, 0.39 μmol, 95%). The tri- and tetravalent cRGDs (**2** and **3**) were conjugated to maleimido oligonucleotide **6** under similar conditions to yield the corresponding oligonucleotide conjugates **8** and **9**, respectively (Scheme 1). Postsynthetic conjugation of trivalent cRGD peptide **3** (2.3 mg, 1.02 μmol) to maleimido oligonucleotide **6** (3 mg, 0.41 μmol) yielded the conjugate **8** (3.3 mg, 0.348 μmol, 84%). Conjugation of the peptide **3** (2.0 mg, 0.68 μmol) to oligonucleotide **6** (2 mg, 0.27 μmol) gave the desired conjugate **9** (1.8 mg, 0.18 μmol, 67%). The trivalent cRGD-conjugated sense strand **10** (Table 1) of a more potent luciferase siRNA was also synthesized under similar conditions. All conjugated oligonucleotides were analyzed by HPLC and LC−MS to confirm the integrity of the products formed (Table 1).

Similarly, antisense strand **15** with the fluorophore Alexa 488 at the 3′-end was obtained from the corresponding amino-linked antisense strand synthesized from the solid support **4** (Scheme 1). The amino-linked oligonucleotide obtained from **4** was postsynthetically reacted with commercially available Alexa 488 NHS ester to yield the fluorophore-tagged antisense strand **15** under conditions similar to those described for the synthesis of maleimido oligonucleotide **6**.

Preparation of Luciferase cRGD−siRNA Conjugates. cRGD−siRNA conjugates with and without the fluorophore Alexa 488 were prepared for this study. Annealing of cRGD-conjugated oligonucleotides **7**−**9** individually with equimolar amounts of antisense strand at 95 °C for 3 min in sterile water followed by slow cooling afforded the siRNAs **11**−**13**, respectively (Scheme 1 and Table 2). While our studies were in progress, we identified a more potent luciferase siRNA sequence, and a trivalent cRGD−siRNA conjugate **14** of the potent siRNA was also prepared for studying conjugate-mediated RNAi activity

Scheme 1. Conjugation of cRGD Peptides to siRNA[a]

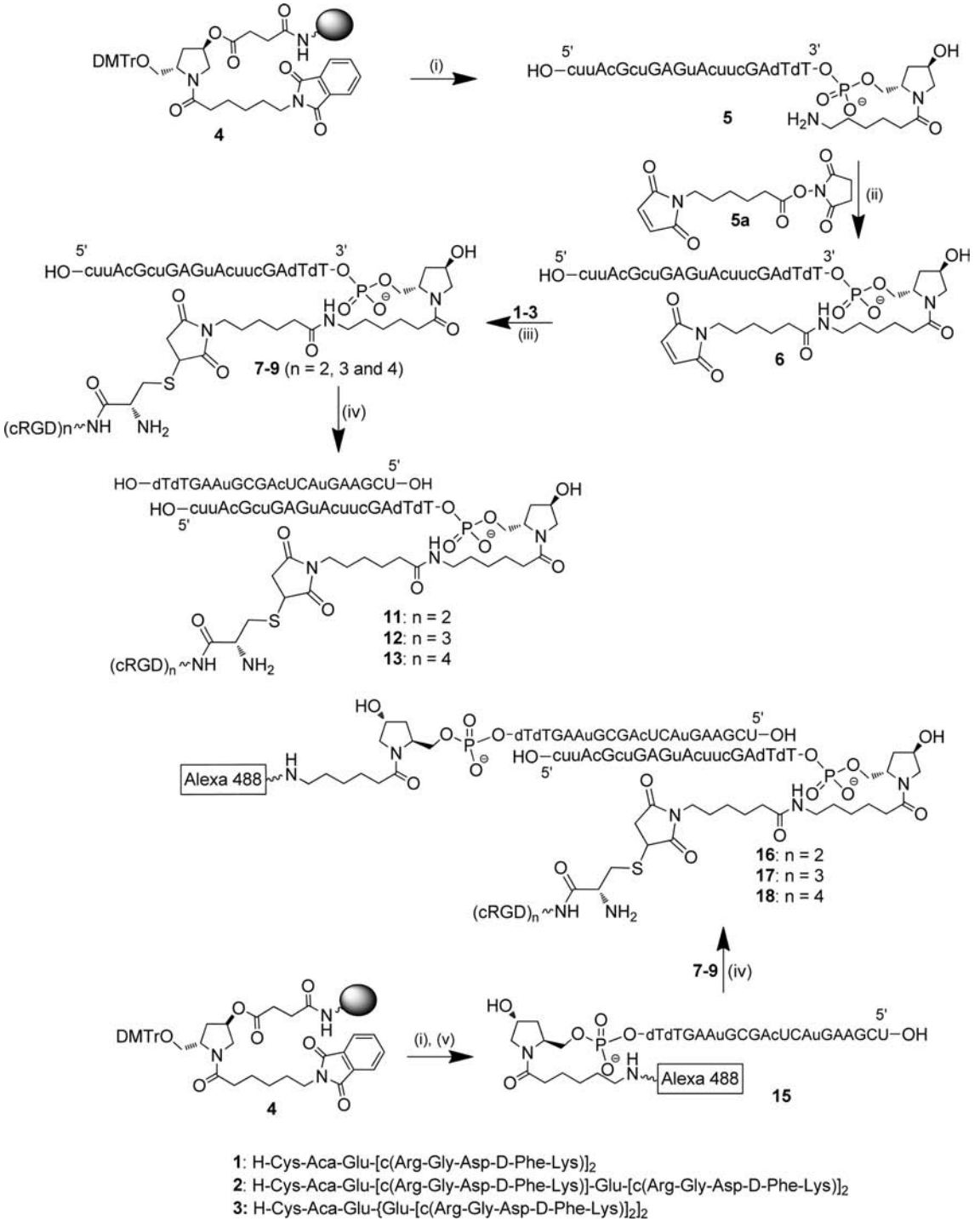

[a] (i) Solid-phase oligonucleotide synthesis and deprotection; (ii) PBS buffer, pH 7.2, room temperature, 20 min; (iii) 0.4 M KCl, 40% MeCN in H_2O, room temperature, overnight; (iv) antisense strand, annealing at 95 °C in H_2O; (v) Alexa 488 NHS ester, PBS buffer, pH 7.2, 20 min.

in vitro. Similarly, annealing of conjugates **7**−**9** with Alexa 488-tagged antisense strand **15** afforded the fluorophore-labeled siRNAs **16**−**18**, respectively (Scheme 1 and Table 2). Each set contains the control siRNAs **19** and **20** with no cRGD moiety. Duplex formation was confirmed by capillary gel electrophoresis and LC−MS analysis.

Cell Lines. $M21^+$ melanoma cells with a high level of expression of $\alpha v\beta 3$ integrin,[22] as well as $M21^-$ cells that lack this integrin, were obtained from D. Cheresh (University of California, San Diego, La Jolla, CA) and were cultured in DMEM medium (Gibco/Invitrogen) supplemented with 10% FBS (Sigma). $M21^+$ cells were transfected with a luciferase expression

Table 1. cRGD-Conjugated Sense Strands of Luciferase siRNA

				mass	
conjugate	valency of cRGD	sequence (5′−3′)[a]	yield[b] (%)	calcd	found
7	2	cuuuAcGcuGAGuAcuucGAdTdTX1	95	8779	8779
8	3	cuuuAcGcuGAGuAcuucGAdTdTX2	84	9494	9494
9	4	cuuuAcGcuGAGuAcuucGAdTdTX3	67	10208	10209
10	3	AccGAAAGGucuuAccGGAdTsdTX2	88	9579	9579

[a] X1−X3 represent bi-, tri-, and tetravalent cRGDs, respectively (see Table 2 for details); lowercase letters indicate 2′-*O*-methyl ribo sugar modification, and dT stands for 2′-deoxythymidine. [b] Postsynthetic conjugation yield from the amino-linked oligonucleotide (Scheme 1).

Table 2. Luciferase siRNAs Conjugated to Multivalent cRGD Peptides

siRNA	S/AS[a]	Sequence (5′-3′)[b]	cRGD content
19	S	cuuuAcGcuGAGuAcuucGAdTdT	0
	AS	UCGAAGuACUcAGCGuAAGdTdT	
11	S	cuuuAcGcuGAGuAcuucGAdTdTX1	2
	AS	UCGAAGuACUcAGCGuAAGdTdT	
12	S	cuuuAcGcuGAGuAcuucGAdTdTX2	3
	AS	UCGAAGuACUcAGCGuAAGdTdT	
13	S	cuuuAcGcuGAGuAcuucGAdTdT X3	4
	AS	UCGAAGuACUcAGCGuAAGdTdT	
14	S	AccGAAAGGucuuAccGGAdTsdTX2	3
	AS	UCCGGuAAGACCUUUCGGUdTsdT	
20	S	cuuuAcGcuGAGuAcuucGAdTdT	0
	AS	UCGAAGuACUcAGCGuAAGdTdTY	
16	S	cuuuAcGcuGAGuAcuucGAdTdT X1	2
	AS	UCGAAGuACUcAGCGuAAGdTdTY	
17	S	cuuuAcGcuGAGuAcuucGAdTdT X2	3
	AS	UCGAAGuACUcAGCGuAAGdTdTY	
18	S	cuuuAcGcuGAGuAcuucGAdTdTX3	4
	AS	UCGAAGuACUcAGCGuAAGdTdTY	

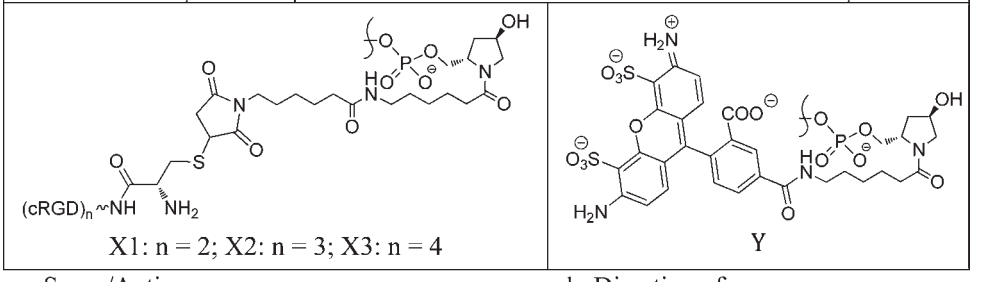

a. Sense/Antisense b. Direction of sequence

plasmid pGL3 promoter (Promega) and pcDNA3.1/hygro (Invitrogen) at a 10:1 ratio using an Amaxa Nucleoporation system following the manufacturer's instructions. Selection was conducted in DMEM containing 500 μg/mL hygromycin B

(Roche) and 10% FBS for 2 weeks. Individual clones were picked and screened for luciferase activity using a luciferase assay kit (Promega). The single cell clone with the highest activity was termed $M21^+GL_3$ and used in further studies.

Cell Uptake Studies. Uptake studies of the fluorescently labeled siRNA conjugates were performed similar to our previous studies of uptake of antisense oligonucleotides.[20] Briefly, the total cellular uptake of the Alexa 488-labeled siRNA was measured by flow cytometry using a LSR II cell analyzer (Becton-Dickenson, San Jose, CA). After treatment with oligonucleotides for various periods of time, the cells were trypsinized and analyzed by flow cytometry, with a 490 nm laser and 520 nm emission filters for Alexa 488 fluorescence. In all cases, oligonucleotide concentrations used were normalized with respect to Alexa 488 fluorescence.

Luciferase Knockdown Studies. $M21^+GL_3$ cells were treated with various concentrations of cRGD-conjugated or control siRNAs for 4 h in serum free medium. At that point, serum was added to a final concentration of 2% and the incubation continued for 96 h. Cells were lysed and luciferase activity and the amount of cell protein determined as previously described.[20]

Confocal Fluorescence Microscopy. The intracellular distribution of the Alexa 488-labeled siRNA conjugates in living cells was examined using an Olympus Confocal FV300 fluorescence microscope with 63×-oil immersion objectives. $M21^+GL_3$ cells were plated in 35 mm glass bottom microwell dishes (MatTek, Ashland, MA). The intracellular uptake of the siRNA conjugates (50 nM) was visualized by confocal microscopy after treatment for 4 or 24 h. Colocalization of the RGD−siRNA−Alexa 488 conjugates with Alexa 594-labeled transferrin (Tfn) or cholera toxin B (CTB) (Invitrogen), as markers for clathrin-coated vesicles or lipid rafts, respectively, was also accomplished via confocal microscopy. Transferrin (20 μg/mL) and cholera toxin B (4 μg/mL) were used for 15 and 30 min, respectively, prior to live cell imaging.

RESULTS

Synthesis and Characterization. The chemical structure of the trivalent cRGD peptide is illustrated in Figure 1; the bi- and tetravalent versions have analogous structures. Each peptide contains a cysteine residue attached to the 6-aminohexanoic acid that joins the cRGD moieties through the glutamic acid residue. The thiol (-SH) reactive group of the cysteine residue of each peptide undergoes chemical conjugation to the maleimide functionality of the sense strand of firefly luciferase siRNA via a Michael addition reaction. The amino-linked sense strand **5** of luciferase RNA obtained from the solid support **4** as shown in Scheme 1 was reacted with 6-maleimidohexanoic acid *N*-hydroxysuccinimide ester to yield maleimido-functionalized sense strand **6**. The reaction was performed under controlled conditions for only 20 min in 1× PBS buffer (pH 7.2) to prevent maleimide degradation. The product was immediately purified by RP-HPLC, and the purified material was directly used for the conjugation reaction. The peptide conjugation reaction occurred between the maleimido-functionalized sense strand **6** of luciferase siRNA and the reactive thiol group (-SH) of the multivalent cRGD peptides **1**−**3** (Scheme 1). Using 2.5 equiv of peptide in each conjugation reaction, almost all starting maleimido oligonucleotide **6** was consumed and converted to the corresponding cRGD-conjugated sense strand with an excellent yield (Table 1). The conjugates were purified by reverse-phase HPLC (RP-HPLC) using an AKTA purifier. The HPLC profiles for the purification of bi-, tri-, and tetravalent cRGD conjugates are shown in panels a−c of Figure 2, respectively. The arrows in each RP-HPLC chart indicate the position of maleimido oligonucleotide **6** and the corresponding cRGD conjugate. Each HPLC profile showed that the conjugate peak was clearly resolved from its precursor **6**. After purification, bivalent cRGD conjugate **7** was obtained at a relatively higher yield (95%) than trivalent cRGD conjugate **8** (84%), which in turn was higher than the yield of tetravalent conjugate **9** (67%). After lyophilization, the conjugates were redissolved in sterile water without any difficulty. We have not seen aggregation of these conjugates in water. For all cases, the structure of the final product was confirmed by LC−MS analysis.

Annealing of siRNA−cRGD Conjugates. After conjugation of cRGD peptides to the 3′-end of the sense strand of luciferase

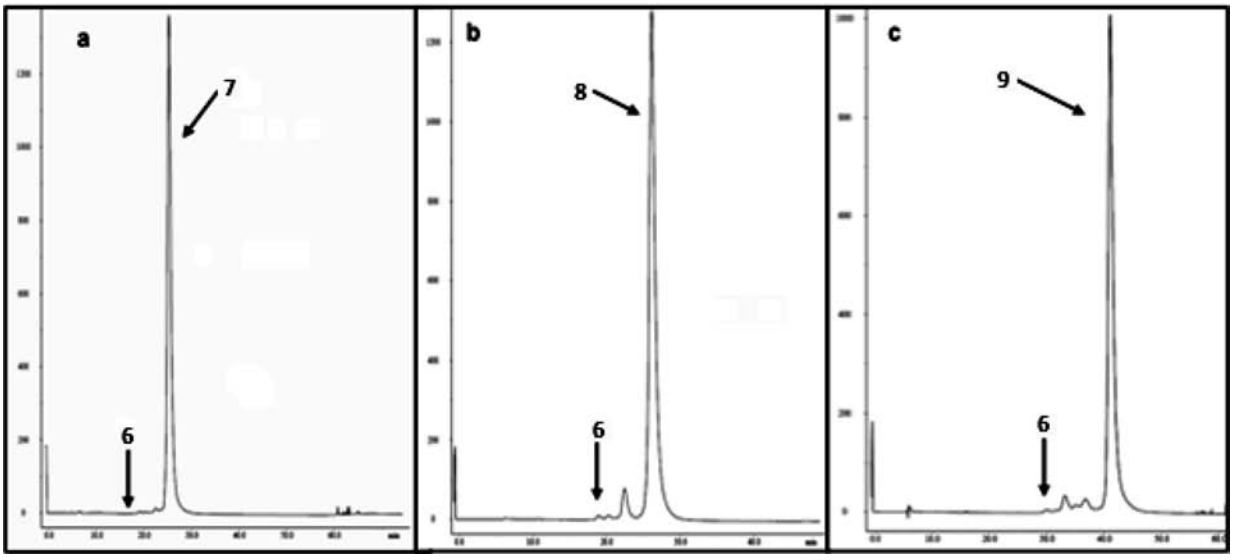

Figure 2. AKTA RP-HPLC purification profiles for the crude reaction mixture of (a) bivalent **7**, (b) trivalent **8**, and (c) tetravalent **9** cRGD−sense oligonucleotide conjugates. Arrows indicate the relative change of retention time of the conjugates (**7**−**9**) from the maleimide−RNA sense strand (**6**). HPLC analysis was performed as described in Materials and Methods.

Scheme 2[a]

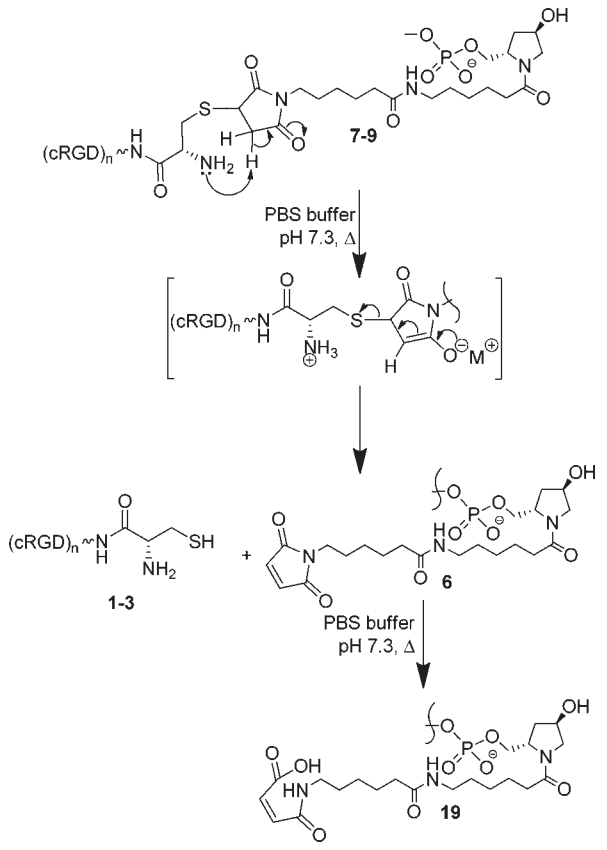

[a] Intramolecular amine-assisted retro-Michael addition of the cRGD−oligonucleotide conjugate at elevated temperatures (>90 °C) in PBS buffer (pH 7.4).

siRNA, we initially attempted to anneal the cRGD-conjugated sense strands **7**−**9** with the complementary antisense strand in 1× PBS buffer (pH 7.4) according to a standard annealing procedure.[23] However, we observed a degradation of the cRGD-conjugated sense strand during the annealing process, with the extent of degradation depending on annealing temperature. The degraded products were identified as the corresponding cRGD peptide and the carboxylic acid **19** by LC−MS analysis. The plausible mechanism of degradation of the cRGD−siRNA conjugate at elevated temperature in PBS buffer (pH 7.4) is the intramolecular amine-assisted retro-Michael addition reaction shown in Scheme 2. Interestingly, the degradation was not observed in metal free sterile water at elevated temperatures. Therefore, the annealing was performed in sterile water to yield the desired cRGD−siRNA conjugates **11**−**14** and **16**−**18** (Scheme 1). We prepared two sets of cRGD−siRNA conjugates in sterile water with fluorescently labeled antisense strand **15** or one without the fluorescent label (Table 2). The appendage of the reporter group to the antisense strand of cRGD−siRNA conjugates **16**−**18** allowed evaluation of cRGD-assisted cellular uptake and intracellular trafficking of the conjugates. The conjugates **11**−**14** with no fluorescent tag were used for the determination of the efficacy of the conjugates by the knockdown assay. After they had been annealed, the integrity of double-stranded cRGD−siRNA conjugates was analyzed and confirmed by capillary gel electrophoresis and LC−MS analysis.

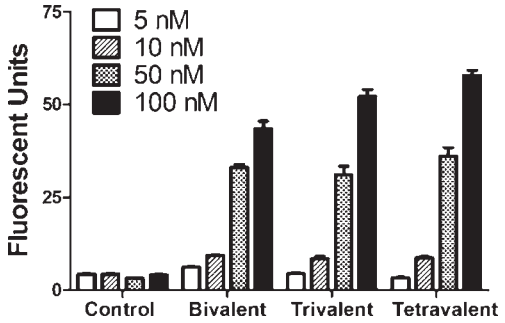

Figure 3. Uptake of cRGD−siRNA conjugates. Total cell uptake of Alexa 488-labeled bi-, tri-, and tetravalent cRGD−siRNA conjugates (**16**−**18**, respectively) as well as control siRNA (**20**) during a 4 h incubation was examined by flow cytometry as described in Materials and Methods.

Cellular Uptake. The conjugation of cRGD moieties dramatically enhanced the uptake of siRNA by $M21^{+}GL_3$ melanoma cells. As seen in Figure 3, the control nonconjugated siRNA **20** displayed little uptake at all concentrations tested. In contrast, the bi-, tri-, and tetravalent cRGD conjugates **16**−**18**, respectively, each displayed enhanced uptake that increased progressively with concentrations ranging from 5 to 100 nM. No evidence of saturation of uptake was noted in the concentration range tested. Previous studies have indicated that the affinities of multivalent RGD conjugates for $\alpha v\beta 3$ are in the range of 30−100 nM.[24] However, we did not seek to measure affinity in this study. There were no major differences in the uptake of the siRNA with bi-, tri-, or tetravalent conjugation. The uptake of the cRGD−siRNA conjugates clearly involved specific interactions of the RGD group with its receptor, because $\alpha v\beta 3$ positive $M21^{+}$ cells accumulated far more of the RGD-conjugated siRNA than the control nonconjugated siRNA while $\alpha v\beta 3$ negative $M21^{-}$ cells did not (Figure 4A). Further, excess RGD peptide competitively blocked the cRGD−siRNA conjugate uptake process (Figure 4B). In contrast, uptake was only slightly affected by the presence of serum proteins even though some potential competitors such as vitronectin and fibronectin are present in small amounts in serum (Figure 4C). Uptake and RGD inhibition experiments were also conducted with compound **14**, a trivalent conjugate with a more potent siRNA sequence. The results were similar to those of the other RGD conjugates and are shown in Figure S1 of the Supporting Information.

Inhibition of Luciferase Expression. cRGD conjugates **11**−**13**, as well as the control nonconjugated siRNA **19**, were designed to inhibit luciferase expression. The control siRNA **19** had no activity unless it was in a complex with a transfection agent. For example, when complexed with Lipofectamine 2000, the nonconjugated control at 100 nM caused an approximately 80% reduction in luciferase activity. The cRGD-conjugated siRNAs were tested in the absence of any transfection agent. Interestingly, the tri- and tetravalent cRGD conjugates **12** and **13**, respectively, produced progressive dose-dependent reductions in luciferase activity, while the bivalent version **11** had little effect (Figure 5). Using the original siRNA sequence, the trivalent cRGD conjugate **12** produced a 40% reduction in luciferase activity at 50 nM. During the course of our studies, we identified a more potent luciferase siRNA for cRGD conjugation, and it was conjugated to the trivalent cRGD ligand to yield conjugate **14** (Table 2). The newly designed conjugate **14**

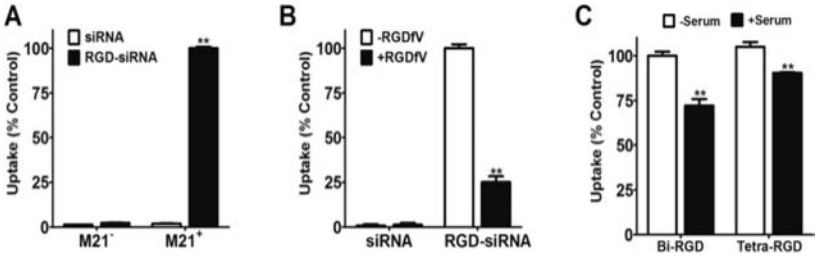

Figure 4. Effects on uptake. The effect of several factors on cell uptake of the cRGD−siRNA conjugates was examined. (A) Uptake of the tetravalent cRGD−siRNA conjugate (**18**) was compared in $\alpha v\beta 3$ positive $M21^+$ cells versus $M21^-$ cells that do not express this integrin. (B) Effect of an excess (1 μM) of free cRGD peptide on uptake of the tetravalent cRGD conjugate. (C) Effect of 10% serum on uptake of the bi- and tetravalent cRGD conjugates (**16** and **18**, respectively). In each case, the highest value was arbitrarily set as a 100% control and data were expressed as a percentage of the control.

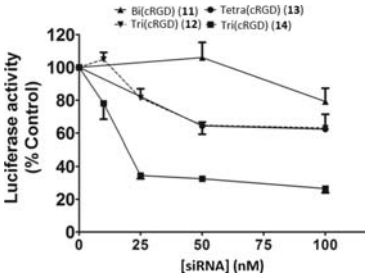

Figure 5. Inhibition of luciferase expression. Various concentrations of the bi-, tri-, and tetravalent cRGD−siRNA conjugates (**11**−**14**) were tested for their ability to reduce the level of expression of luciferase in $M21^+GL_3$ cells using the procedures described in Materials and Methods. Both the original trivalent cRGD conjugate (**12**) and the trivalent cRGD conjugate (**14**) using the more potent luciferase siRNA sequence were examined.

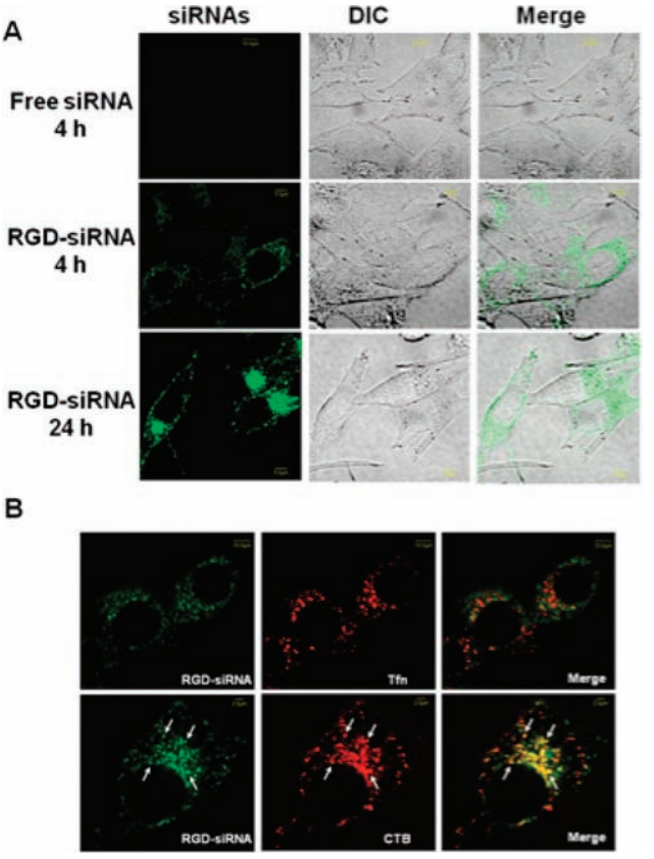

Figure 6. Subcellular localization of the conjugates. (A) Subcellular distribution of an Alexa 488-labeled tetravalent cRGD−siRNA conjugate (**18**) examined in live cells by confocal microscopy after treatment for 4 or 24 h. (B) Subcellular distribution of the Alexa 488-labeled tetravalent conjugate compared to that of Alexa 594-labeled transferrin or cholera toxin. (Figure S1 of the Supporting Information. Uptake of the trivalent cRGD−siRNA conjugate (**14**) compared in $\alpha v\beta 3$ positive $M21^+$ cells vs $M21^-$ cells that do not express this integrin. The effect of an excess (1 μM) of free cRGD peptide on uptake of the trivalent conjugate was also tested.)

produced a 70% reduction in luciferase activity at 25 nM (Figure 5). Interestingly, the biological effect of luciferase knockdown was not well-correlated with the total cell uptake. As shown in Figure 3, all three fluorophore-labeled cRGD conjugates **16**−**18** exhibited enhanced cell uptake, but as seen in Figure 5, only the tri- and tetravalent versions produced significant knockdown.

Subcellular Localization. We examined the subcellular localization of the Alexa 488-labeled siRNA at 4 and 24 h time points, comparing the unconjugated **20** and tetravalent cRGD conjugate **18**. As seen in Figure 6A, the unconjugated labeled siRNA **20** was not detectable while the cRGD conjugate **18** displayed substantial uptake into vesicular structures in the cytosol, these presumably being various types of endosomes. At 24 h, the accumulated fluorescence was more intense and was now concentrated in perinuclear locations. Most of the material continued to be vesicular, although some slight cytosolic fluorescence was discernible. To more precisely identify the endomembrane compartments involved in the uptake and trafficking of the RGD−siRNA conjugate, we co-incubated the Alexa 488-labeled oligonucleotide (green) with Alexa 594 (red)-labeled markers for well-known endocytotic pathways. Thus transferrin is known to be internalized via the clathrin-coated pit pathway, while cholera toxin is substantially internalized via the caveolar pathway or other lipid raft-dependent pathways.[25] As seen in Figure 6B, at 4 h there was virtually no overlap of the labels for transferrin and siRNA; in contrast, there was substantial overlap of the cholera toxin and the cRGD−siRNA conjugate **18**. This suggests that the initial uptake pathway for the cRGD−siRNA conjugate involves calveolae; this observation is consistent with literature about the mechanism of internalization of the $\alpha v\beta 3$ integrin.[26] We further investigated the uptake pathways by using a series of well-known pharmacological inhibitors of various endocytotic processes. The trivalent cRGD−siRNA conjugate **14** was incubated with $M21^+$ cells in the presence of nontoxic concentrations of selected inhibitors, and the results are summarized in Table 3. Methyl-β-cyclodextrin, an agent that affects lipid raft stability, had the

Table 3. Effects of Inhibitors on cRGD−siRNA Conjugate Uptake[a]

siRNA (50 nM)	drug or inhibitor	concn	endocytosis pathway putatively affected	cRGD−siRNA conjugate uptake (%)
14	none			100 ± 1.4
	chlorpromazine	2.5 μM	clathrin-mediated endocytosis	93.3 ± 1.9
	methyl-β-cyclodextrin	1 mM	lipid raft-mediated endocytosis	42.8 ± 1.0
	amiloride	100 μM	macropinocytosis	98.5 ± 2.3
	cytochalasin D	2 μM	actin inhibitor	37.9 ± 0.9

[a] $M21^+$ cells were treated with the indicated nontoxic concentration of drugs and trivalent cRGD−siRNA conjugate **14**. Uptake was measured after 3 h by flow cytometry. Results were normalized to the uptake of the siRNA conjugate **14** in the absence of inhibitors.

greatest inhibitory effect. This observation supports the notion that lipid raft/caveolar pathways are important in the internalization of the RGD conjugates.

Cytotoxicity. There was little toxicity associated with the use of the cRGD−siRNA conjugates at the concentrations examined. Thus, in the knockdown experiments whose results are depicted in Figure 5, the cell protein recovered in each of the treated samples was essentially the same as for the untreated control. The only exceptions were the cases in which Lipofectamine 2000 was used where some protein loss was observed (data not shown). Additionally, the cells treated with the cRGD−siRNA conjugates maintained normal morphology as illustrated in the DIC images of Figure 6.

DISCUSSION

It would be of substantial value to be able to effectively target antisense or siRNA oligonucleotides to specific cell types by making use of differential expression of cell surface receptors. In this study, we have focused on the αvβ3 integrin, a cell surface glycoprotein that is preferentially expressed in angiogenic endothelia and in certain tumor types, including melanomas.[27,28] The process of targeted oligonucleotide delivery using conjugates with high-affinity ligands involves several steps. First, there is selective association with the receptor followed by some form of endocytosis of the receptor−ligand complex. This is followed by trafficking through various endomembrane compartments such as early and late endosomes, the trans-Golgi apparatus, and lysosomes. Finally, there is release from membrane-bound compartments into the cytosolic or nuclear sites of action of siRNA and antisense oligonucleotides.[5] It has become clear that there are important relationships between the intracellular trafficking of receptors and their functional activity.[29] Likewise, we have developed initial evidence that intracellular trafficking pathways can influence the pharmacological activity of oligonucleotides.[19]

This report demonstrates that high-affinity cRGD ligands can strongly and specifically enhance uptake of siRNA by cells that express the αvβ3 integrin. Uptake was blocked by excess unconjugated RGD peptide, and receptor positive $M21^+$ cells accumulated the cRGD−siRNA conjugates to a much greater degree than receptor negative $M21^-$ cells. Interestingly, increasing the valency from bi- to tetravalent had little effect on the magnitude of the overall uptake process. Confocal microscopy and inhibitor studies indicated that initial uptake of the cRGD−siRNA conjugates occurred primarily via caveolar endocytosis.

A surprising result was the difference in the pharmacological effectiveness of conjugates with differing valencies. While the bivalent cRGD−siRNA conjugate exhibited an only slight effect, the tri- and tetravalent versions produced substantial dose-dependent reductions in the levels of luciferase expression. This was especially true of the trivalent conjugate **14** made with the more potent luciferase siRNA sequence. Because all of the conjugates were taken up approximately equally well, this suggests that events downstream of the initial uptake are responsible for the different observed effects. One possibility is that several conjugates follow different intracellular trafficking pathways or traverse those pathways at different rates. However, our current observations indicate that, at least at early time points, the tetravalent cRGD−siRNA conjugate follows the caveolar internalization pathway that we have previously described for bivalent cRGD−oligonucleotide conjugates.[18] It is possible that the higher-valency conjugates are retained more effectively within the cells at later time points, but this issue is difficult to study because of the inevitable degradation of the siRNA at longer times. Another possibility is that the presence of multiple cRGD peptides may cause a destabilization of the endosome membrane leading to more effective release of the oligonucleotide to the cytosol. However, at this point, we do not have a clear-cut mechanistic explanation of the differing efficacy of the bi- and multivalent conjugates. Nonetheless, these results are encouraging in that they clearly demonstrate receptor specific targeting and significant pharmacological effects of multivalent ligand−siRNA conjugates. This could emerge as an interesting alternative to the delivery of siRNA using various forms of lipid or polymer nanoparticles. However, further evolution of the chemical conjugation approach will require both a better understanding of mechanism and validation in an in vivo setting.

ASSOCIATED CONTENT

Supporting Information. A supplementary figure. This material is available free of charge via the Internet at http://pubs.acs.org.

ACKNOWLEDGMENT

We gratefully acknowledge Dr. D. Cheresh (University of California, San Diego) for providing $M21^+$ and $M21^-$ melanoma cells and Drs. Meena and C. Sherrill (Alnylam Pharmaceuticals) for providing amino-functionalized oligonucleotides for conjugation. This work was supported by National Institutes of Health Grant P01GM059299 to R.J. and by Alnylam Pharmaceuticals.

REFERENCES

(1) Bennett, C. F., and Swayze, E. E. (2010) RNA targeting therapeutics: Molecular mechanisms of antisense oligonucleotides as a therapeutic platform. *Annu. Rev. Pharmacol. Toxicol. 50*, 259–293.

(2) Prakash, T. P., and Bhat, B. (2007) 2′-Modified oligonucleotides for antisense therapeutics. *Curr. Top. Med. Chem. 7*, 641–649.

(3) Walton, S. P., Wu, M., Gredell, J. A., and Chan, C. (2010) Designing highly active siRNAs for therapeutic applications. *FEBS J. 277*, 4806–4813.

(4) Vaishnaw, A. K., Gollob, J., Gamba-Vitalo, C., Hutabarat, R., Sah, D., Meyers, R., de Fougerolles, T., and Maraganore, J. (2010) A status report on RNAi therapeutics. *Silence 1*, 14.

(5) Juliano, R., Bauman, J., Kang, H., and Ming, X. (2009) Biological barriers to therapy with antisense and siRNA oligonucleotides. *Mol. Pharmaceutics 6*, 686–695.

(6) Whitehead, K. A., Langer, R., and Anderson, D. G. (2009) Knocking down barriers: Advances in siRNA delivery. *Nat. Rev. Drug Discovery 8*, 129–138.

(7) Lares, M. R., Rossi, J. J., and Ouellet, D. L. (2010) RNAi and small interfering RNAs in human disease therapeutic applications. *Trends Biotechnol. 28*, 570–579.

(8) Czech, B., and Hannon, G. J. (2011) Small RNA sorting: Matchmaking for Argonautes. *Nat. Rev. Genet. 12*, 19–31.

(9) Akhtar, S., and Benter, I. F. (2007) Nonviral delivery of synthetic siRNAs in vivo. *J. Clin. Invest. 117*, 3623–3632.

(10) Love, K. T., Mahon, K. P., Levins, C. G., Whitehead, K. A., Querbes, W., Dorkin, J. R., Qin, J., Cantley, W., Qin, L. L., Racie, T., Frank-Kamenetsky, M., Yip, K. N., Alvarez, R., Sah, D. W., de Fougerolles, A., Fitzgerald, K., Koteliansky, V., Akinc, A., Langer, R., and Anderson, D. G. (2010) Lipid-like materials for low-dose, in vivo gene silencing. *Proc. Natl. Acad. Sci. U.S.A. 107*, 1864–1869.

(11) Kabanov, A. V., and Vinogradov, S. V. (2009) Nanogels as pharmaceutical carriers: Finite networks of infinite capabilities. *Angew. Chem., Int. Ed. 48*, 5418–5429.

(12) Tamura, A., and Nagasaki, Y. (2010) Smart siRNA delivery systems based on polymeric nanoassemblies and nanoparticles. *Nanomedicine (London, U.K.) 5*, 1089–1102.

(13) Tseng, Y. C., Mozumdar, S., and Huang, L. (2009) Lipid-based systemic delivery of siRNA. *Adv. Drug Delivery Rev. 61*, 721–731.

(14) Juliano, R., Alam, M. R., Dixit, V., and Kang, H. (2008) Mechanisms and strategies for effective delivery of antisense and siRNA oligonucleotides. *Nucleic Acids Res. 36*, 4158–4171.

(15) Zhu, L., and Mahato, R. I. (2010) Targeted delivery of siRNA to hepatocytes and hepatic stellate cells by bioconjugation. *Bioconjugate Chem. 21*, 2119–2127.

(16) Cesarone, G., Edupuganti, O. P., Chen, C. P., and Wickstrom, E. (2007) Insulin receptor substrate 1 knockdown in human MCF7 ER+ breast cancer cells by nuclease-resistant IRS1 siRNA conjugated to a disulfide-bridged D-peptide analogue of insulin-like growth factor 1. *Bioconjugate Chem. 18*, 1831–1840.

(17) Ming, X. (2011) Cellular delivery of siRNA and antisense oligonucleotides via receptor-mediated endocytosis. *Expert Opin. Drug Delivery 8*, 435–449.

(18) Alam, M. R., Dixit, V., Kang, H., Li, Z. B., Chen, X., Trejo, J., Fisher, M., and Juliano, R. L. (2008) Intracellular delivery of an anionic antisense oligonucleotide via receptor-mediated endocytosis. *Nucleic Acids Res. 36*, 2764–2776.

(19) Alam, M. R., Ming, X., Dixit, V., Fisher, M., Chen, X., and Juliano, R. L. (2010) The biological effect of an antisense oligonucleotide depends on its route of endocytosis and trafficking. *Oligonucleotides 20*, 103–109.

(20) Ming, X., Alam, M. R., Fisher, M., Yan, Y., Chen, X., and Juliano, R. L. (2010) Intracellular delivery of an antisense oligonucleotide via endocytosis of a G protein-coupled receptor. *Nucleic Acids Res. 38*, 6567–6576.

(21) Nakagawa, O., Ming, X., Huang, L., and Juliano, R. L. (2010) Targeted intracellular delivery of antisense oligonucleotides via conjugation with small-molecule ligands. *J. Am. Chem. Soc. 132*, 8848–8849.

(22) Felding-Habermann, B., Mueller, B. M., Romerdahl, C. A., and Cheresh, D. A. (1992) Involvement of integrin alpha V gene expression in human melanoma tumorigenicity. *J. Clin. Invest. 89*, 2018–2022.

(23) Wolfrum, C., Shi, S., Jayaprakash, K. N., Jayaraman, M., Wang, G., Pandey, R. K., Rajeev, K. G., Nakayama, T., Charrise, K., Ndungo, E. M., Zimmermann, T., Koteliansky, V., Manoharan, M., and Stoffel, M. (2007) Mechanisms and optimization of in vivo delivery of lipophilic siRNAs. *Nat. Biotechnol. 25*, 1149–1157.

(24) Li, Z. B., Cai, W., Cao, Q., Chen, K., Wu, Z., He, L., and Chen, X. (2007) ^{64}Cu-labeled tetrameric and octameric RGD peptides for small-animal PET of tumor $\alpha(v)\beta(3)$ integrin expression. *J. Nucl. Med. 48*, 1162–1171.

(25) Khalil, I. A., Kogure, K., Akita, H., and Harashima, H. (2006) Uptake pathways and subsequent intracellular trafficking in nonviral gene delivery. *Pharmacol. Rev. 58*, 32–45.

(26) Caswell, P. T., and Norman, J. C. (2006) Integrin trafficking and the control of cell migration. *Traffic 7*, 14–21.

(27) Desgrosellier, J. S., and Cheresh, D. A. (2010) Integrins in cancer: Biological implications and therapeutic opportunities. *Nat. Rev. Cancer 10*, 9–22.

(28) Eliceiri, B. P., and Cheresh, D. A. (2000) Role of alpha v integrins during angiogenesis. *Cancer J. 6* (Suppl. 3), S245–S249.

(29) Sadowski, L., Pilecka, I., and Miaczynska, M. (2009) Signaling from endosomes: Location makes a difference. *Exp. Cell Res. 315*, 1601–1609.

Alam et al. Multivalent Cyclic RGD Conjugates for Targeted Delivery of siRNA

Supplementary Figure 1. Uptake of the trivalent RGD-siRNA (**14**) was compared in avb3 positive M21+ cells versus M21- cells that do not express this integrin. The effect of an excess (1 μM) free cyclic RGD peptide on uptake of the trivalent conjugate was also tested.

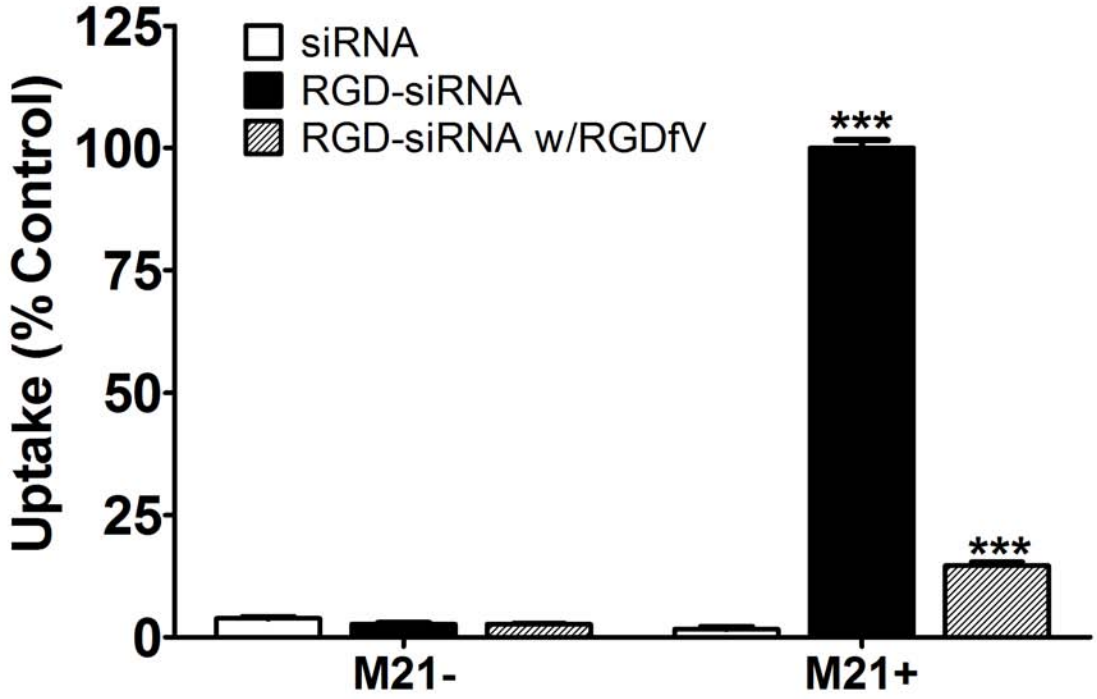

Bioconjugate Chemistry

ARTICLE

pubs.acs.org/bc

Synthesis and Evaluation of Novel Gonadotropin-Releasing Hormone Receptor-Targeting Peptides

Haixun Guo,[†] Jie Lu,[†] Helen Hathaway,[‡,§] Melanie E. Royce,[§,∥] Eric R. Prossnitz,[‡,§] and Yubin Miao*[,†,§,#]

[†]College of Pharmacy, [‡]Department of Cell Biology and Physiology, [∥]Department of Internal Medicine, [§]Cancer Research and Treatment Center, and [#]Department of Dermatology, University of New Mexico, Albuquerque, New Mexico 87131, United States

ABSTRACT: The purpose of this study was to develop novel radiolabeled gonadotropin-releasing hormone (GnRH) receptor-targeting peptides for breast cancer imaging. Three novel 1,4,7,10-tetraazacyclododecane-1,4,7,10-tetraacetic acid (DOTA)-conjugated GnRH peptides were designed and synthesized. The radiometal chelator DOTA was conjugated to the epsilon or alpha amino group of D-lysine, or the epsilon amino group of L-lysine via an Ahx {aminohexanoic acid} linker to generate DOTA−Ahx−(D-Lys^6-GnRH1), DOTA−Ahx−(D-Lys^6-GnRH2) and DOTA−Ahx−(L-Lys^6-GnRH3), respectively. The conjugation of the DOTA to the epsilon amino group of D-lysine (rather than alpha amino group of D-lysine nor epsilon amino group of L-lysine) maintained the nanomolar GnRH receptor binding affinity. The IC_{50} values of DOTA−Ahx−(D-Lys^6-GnRH1), DOTA−Ahx−(D-Lys^6-GnRH2) and DOTA−Ahx−(L-Lys^6-GnRH3) were 36.1 nM, 10.6 mM and 4.3 mM, respectively. Since only DOTA−Ahx−(D-Lys^6-GnRH1) displayed nanomolar receptor binding affinity, the specific GnRH receptor binding of ^{111}In-DOTA−Ahx−(D-Lys^6-GnRH1) was determined in human GnRH receptor membrane preparations. Furthermore, the biodistribution and tumor imaging properties of ^{111}In-DOTA−Ahx−(D-Lys^6-GnRH1) were examined in MDA-MB-231 human breast cancer-xenografted nude mice. ^{111}In-DOTA−Ahx−(D-Lys^6-GnRH1) exhibited specific GnRH receptor binding and rapid tumor uptake (1.76 ± 0.58% ID/g at 0.5 h postinjection) coupled with fast whole-body clearance through the urinary system. The MDA-MB-231 human breast cancer-xenografted tumor lesions were clearly visualized by single photon emission computed tomography (SPECT)/CT at 1 h postinjection of ^{111}In-DOTA−Ahx−(D-Lys^6-GnRH1). The profound impact of DOTA position on the binding affinity of the GnRH peptide provided a new insight into the design of novel radiolabeled GnRH peptides. The successful imaging of MDA-MB-231 human breast cancer-xenografted tumor lesions using ^{111}In-DOTA−Ahx−(D-Lys^6-GnRH1) suggested its potential as a novel imaging probe for human breast cancer imaging.

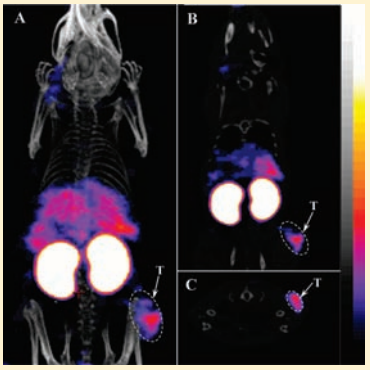

INTRODUCTION

Breast cancer is the most commonly diagnosed cancer and the second leading cause of cancer death in women in the United States. It was predicted that approximately 209,060 new cases would be diagnosed and 40,230 fatalities would occur in the US in 2010.[1] Unfortunately, no curative treatment exists for metastatic breast cancer. Early diagnosis of breast cancer followed by a prompt surgical removal provides patients the best opportunities for cures or prolonged survivals. Mammography is an effective diagnostic tool for primary breast cancer. However, it is less effective for women with breast implants, for women with postsurgical recurrence, and for women under age fifty as the breast tissue tends to be more dense.[2] Meanwhile, mammography cannot detect distant breast cancer metastases. Single photon emission computed tomography (SPECT) and positron emission tomography (PET) techniques[3,4] are more attractive noninvasive imaging modalities for metastatic breast cancer detection due to their high sensitivities and spatial resolutions. At present, 2-[^{18}F]fluoro-2-deoxy-D-glucose ([^{18}F]FDG) is the most commonly used PET imaging agent for the detection of various tumors including breast cancer.[5−15] However, the clinical application of [^{18}F]FDG is limited[10] by its unsatisfactory sensitivity for small tumors <1 cm (57%) and for tumors in situ (25%), and high false-positive results in the circumstance of inflammation. Hence, novel breast cancer-specific imaging probes are urgently needed to improve the detection accuracy for breast cancer.

Overexpression of gonadotropin-releasing hormone (GnRH) receptors on the breast cancer cells[16−20] highlights the potential of GnRH receptor as a molecular target for developing breast cancer-specific imaging probes. Clinical studies showed that 52% of breast cancer specimens removed by surgical resection overexpressed GnRH receptors.[19,20] Native GnRH peptide is a hypothalamic decapeptide (pGlu^1-His^2-Trp^3-Ser^4-Tyr^5-Gly^6-Leu^7-Arg^8-Pro^9-Gly^{10}-NH_2). Both motifs of pGlu^1-His^2-Trp^3 and Arg^8-Pro^9-Gly^{10}-NH_2 are critical for GnRH receptor binding.[21] The replacement of Gly^6 with a D-amino acid increases the binding affinity and decreases the metabolic clearance of the peptide.[22] The D-Lys^6-GnRH peptide has been used as a delivery vehicle to target

Received: May 12, 2011
Revised: July 10, 2011
Published: July 11, 2011

ACS Publications © 2011 American Chemical Society

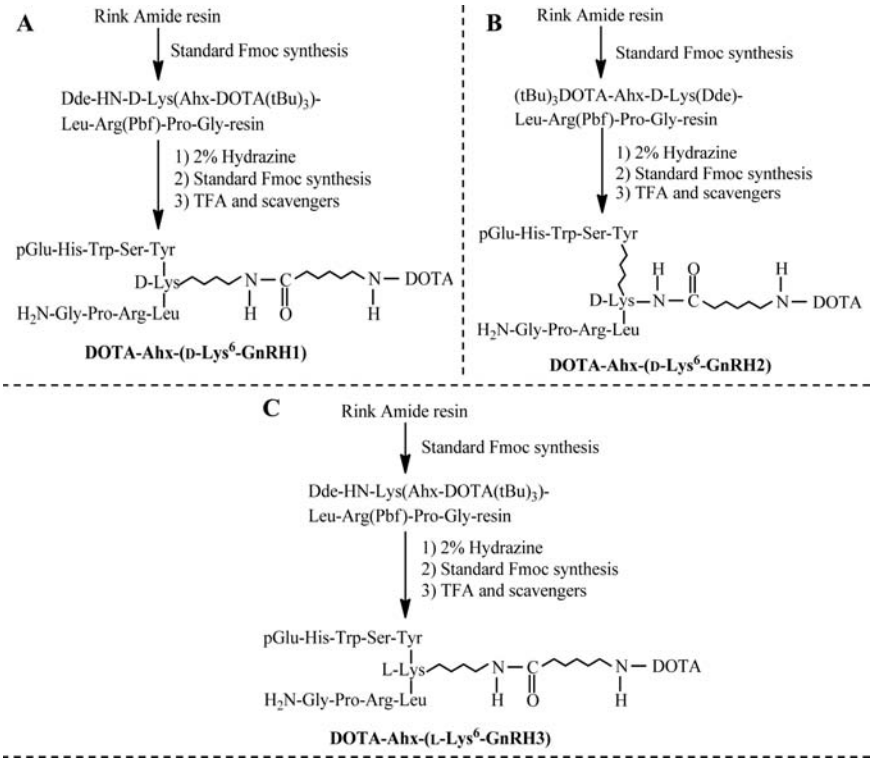

Figure 1. Synthetic schemes of three novel GnRH peptides.

the chemotherapy agent (2-pyrrolinodoxorubicin, AN201) to the GnRH receptors for breast cancer treatment.[23−31] The AN201 was coupled to the epsilon amino group of D-Lys^6 in D-Lys^6-GnRH to generate a cytotoxic compound named AN207.[23] The receptor-targeting AN207 exhibited enhanced remarkable therapeutic efficacy and decreased toxicity compared to the parent chemotherapy agent AN201. A single treatment of AN207 (250 nmol/kg) resulted in 100% cure for mice bearing MX-1 human mammary carcinomas (GnRH receptor-positive) without apparent toxicity.[28] These results on AN207 indicated that D-Lys^6-GnRH could selectively bind the GnRH receptor to target the chemotherapy agent to breast cancer cells.

We hypothesized that the radiolabeled GnRH peptide can specifically bind the GnRH receptors for human breast cancer imaging in this study. We designed and evaluated three novel DOTA-conjugated GnRH peptides to examine our hypothesis, as well as to determine the effect of DOTA position on the binding affinity of the GnRH peptide. Specifically, the metal chelator DOTA was coupled to the epsilon and alpha amino groups of D-Lys^6 in D-Lys^6-GnRH via an aminohexanoic acid (Ahx) hydrocarbon linker to yield DOTA−Ahx−(D-Lys^6-GnRH1) and DOTA−Ahx−(D-Lys^6-GnRH2), respectively. In a parallel study, the DOTA was coupled to the epsilon amino group of L-Lys^6 to generate DOTA−Ahx−(L-Lys^6-GnRH3). The GnRH receptor binding affinities of these three peptides were determined using Millipore ChemiScreen human GnRH receptor membrane preparations. Only DOTA−Ahx−(D-Lys^6-GnRH1) displayed low nanomolar GnRH receptor binding affinity. Hence, we further evaluated the tumor targeting and imaging properties of ^{111}In-DOTA−Ahx−(D-Lys^6-GnRH1) in MDA-MB-231 human breast cancer-xenografted nude mice.

EXPERIMENTAL PROCEDURES

Chemicals and Reagents. Amino acids and resin were purchased from Advanced ChemTech Inc. (Louisville, KY) and Novabiochem (San Diego, CA). DOTA-tri-*tert*-butyl ester was purchased from Macrocyclics Inc. (Richardson, TX). $^{111}InCl_3$ was purchased from MDS Nordion, Inc. (Vancouver, Canada) for radiolabeling. ^{125}I-[D-Trp^6]-LH-RH {pGlu-His-Trp-Ser-[^{125}I]Tyr-D-Trp-Leu-Arg-Pro-Gly-NH_2} was obtained from PerkinElmer Inc. (Boston, MA), and ChemiScreen human GnRH receptor membrane preparations were purchased from Millipore, Inc. (Billerica, MA), for receptor binding studies. GnRHR antibody (N-20, sc-8682) and the ABC Staining Systems were purchased from Santa Cruz Biotechnology, Inc. (Santa Cruz, CA) for immunohistochemistry (IHC) staining. All other chemicals used in this study were purchased from Thermo Fischer Scientific (Waltham, MA) and used without further purification. MDA-MB-231 human breast cancer cells were obtained from American Type Culture Collection (Manassas, VA).

Peptide Synthesis. Three GnRH peptides were synthesized using 9-fluorenylmethyloxycarbonyl (Fmoc) chemistry. Briefly, the intermediate scaffolds of Dde-HN-D-Lys(Ahx-DOTA-(tBu)$_3$)-Leu-Arg(Pbf)-Pro-Gly, (tBu)$_3$DOTA−Ahx−D-Lys(Dde)-Leu-Arg(Pbf)-Pro-Gly, and Dde-HN-Lys(Ahx-DOTA(tBu)$_3$)-Leu-Arg(Pbf)-Pro-Gly were synthesized on Rink amide resin by an Advanced ChemTech multiple-peptide synthesizer (Louisville, KY). Seventy micromoles of resin, 210 μmol of each Fmoc-protected amino acid and 210 μmol of (tBu)$_3$DOTA were used for the synthesis. The protecting group of Dde in each scaffold was removed by 2% hydrazine. The moiety of pGlu-His(Trt)-Trp(Boc)-Ser(tBu)-Tyr(tBu) was conjugated to the epsilon amino group of either L-Lys or D-Lys, or the alpha amino group

of D-Lys in the intermediate scaffolds. The protecting groups were totally removed by treating with a mixture of trifluoroacetic acid (TFA), thioanisole, phenol, water, ethanedithiol and triisopropylsilane (87.5:2.5:2.5:2.5:2.5:2.5) for 4 h at 25 °C. Each peptide was precipitated and washed with ice-cold ether four times, purified by reverse phase high performance liquid chromatography (RP-HPLC) and characterized by LC−MS.

***In Vitro* Receptor Binding Assay.** The GnRH receptor binding affinities (IC_{50} values) of DOTA−Ahx−(D-Lys^6-GnRH1), DOTA−Ahx−(D-Lys^6-GnRH2) and DOTA−Ahx−(L-Lys^6-GnRH3) were determined by *in vitro* competitive binding assay according to a published procedure[32] with modifications. Briefly, 5 μL of Millipore ChemiScreen human GnRH membrane preparations was incubated at 25 °C for 3 h with approximately 30,000 counts per minute (cpm) of ^{125}I-[D-Trp^6]-LH-RH in the presence of 10^{-11} to 10^{-5} M of each peptide in 95 μL of binding medium {50 mM *N*-(2-hydroxyethyl)-piperazine-*N*′-(2-ethanesulfonic acid), 5 mM $MgCl_2$, 1 mM $CaCl_2$, pH 7.4, 0.2% bovine serum albumin (BSA)}. After the incubation, 800 μL of ice-cold washing buffer (50 mM *N*-(2-hydroxyethyl)-piperazine-*N*′-(2-ethanesulfonic acid), 500 mM NaCl, pH 7.4, 0.1% BSA) was added to each mixture. Each resulting mixture was filtered through a GF/C filter (Whatman, Clifton, NJ) presoaked in 1% polyethylenimine. Each filter was rinsed with 1 mL of ice-cold washing buffer three times. The activities on the filters were measured in a Wallac 1480 automated gamma counter (PerkinElmer, Waltham, MA). The IC_{50} value of each peptide was calculated using Prism software (GraphPad Software, La Jolla, CA).

Peptide Radiolabeling with ^{111}In. Among these three synthetic GnRH peptides, only DOTA−Ahx−(D-Lys^6-GnRH1) displayed low nanomolar GnRH receptor binding affinity. Hence, we further evaluated DOTA−Ahx−(D-Lys^6-GnRH1). ^{111}In-DOTA−Ahx−(D-Lys^6-GnRH1) was prepared in a 0.5 M NH_4OAc buffer at pH 4.5 according to our published procedure.[33] Briefly, 50 μL of $^{111}InCl_3$ (37−74 MBq in 0.05 M HCl aqueous solution), 10 μL of 1 mg/mL DOTA−Ahx−(D-Lys^6-GnRH1) aqueous solution and 400 μL of 0.5 M NH_4OAc (pH 4.5) were added into a reaction vial and incubated at 75 °C for 45 min. After the incubation, 10 μL of 0.5% EDTA aqueous solution was added into the reaction vial to scavenge potential unbound $^{111}In^{3+}$ ions. The radiolabeled DOTA−Ahx−(D-Lys^6-GnRH1) was purified to single species by Waters RP-HPLC (Milford, MA) on a Grace Vydac C-18 reverse phase analytical column (Deerfield, IL) using the following gradient at a 1 mL/min flow rate. The mobile phase consisted of solvent A (20 mM HCl aqueous solution) and solvent B (100% CH_3CN). The gradient was initiated and kept at 85:15 A/B for 3 min followed by a linear gradient of 85:15 A/B to 75:25 A/B over 20 min. Then, the gradient was changed from 75:25 A/B to 10:90 A/B over 3 min followed by an additional 5 min at 10:90 A/B. Thereafter, the gradient was changed from 10:90 A/B to 85:15 A/B over 3 min. The purified peptide sample was purged with N_2 gas for 20 min to remove the acetonitrile. The pH of final peptide solution was adjusted to 7.4 with 0.1 N NaOH and sterile normal saline for specific binding and animal studies.

In vitro serum stability of ^{111}In-DOTA−Ahx−(D-Lys^6-GnRH1) was determined by incubation in mouse serum at 37 °C for 2 h and monitored for degradation by RP-HPLC. Briefly, 100 μL of HPLC-purified ^{111}In-DOTA−Ahx−(D-Lys^6-GnRH1) solution (~3.7 MBq) was added into 100 μL of mouse serum (Sigma-Aldrich Corp, St. Louis, MO) and incubated at 37 °C for 2 h. After the incubation, 200 μL of a mixture of ethanol and acetonitrile (v:v = 1:1) was added to precipitate the serum. The resulting mixture was centrifuged at 10000*g* for 5 min to collect the supernatant. The supernatant was purged with N_2 gas for 30 min to remove the ethanol and acetonitrile. The resulting sample was mixed with 500 μL of water and injected into RP-HPLC for analysis using the gradient described above.

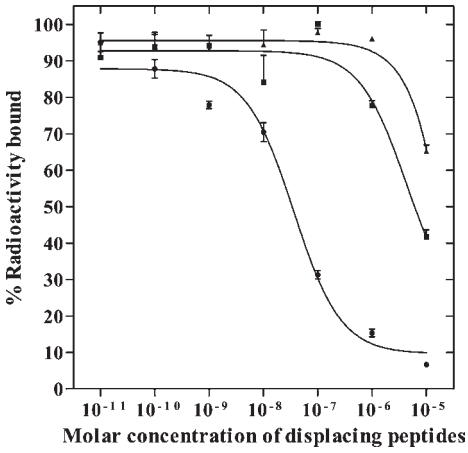

Figure 2. The competitive binding curves of the GnRH peptides. The IC_{50} values of DOTA−Ahx−(D-Lys^6-GnRH1), DOTA−Ahx−(D-Lys^6-GnRH2) and DOTA−Ahx−(L-Lys^6-GnRH3) were 36.1 nM, 10.6 mM and 4.3 mM, respectively.

Specific Human GnRH Receptor Binding of ^{111}In-DOTA−Ahx−(D-Lys^6-GnRH1). The specific human GnRH receptor binding of ^{111}In-DOTA−Ahx−(D-Lys^6-GnRH1) was determined using human GnRH receptor membrane preparations obtained from Millipore, Inc. (Billerica, MA). Briefly, 50 μL of Millipore ChemiScreen human GnRH receptor membrane preparations were incubated at 25 °C for 3 h with approximately 60,000 cpm of HPLC-purified ^{111}In-DOTA−Ahx−(D-Lys^6-GnRH1) in 50 μL of binding medium with or without 1 μM of DOTA−Ahx−(D-Lys^6-GnRH1) peptide blockade. After the incubation, each membrane preparation was mixed with 800 μL of ice-cold washing buffer first, and then filtered through a GF/C filter (Waterman, Clifton, NJ) presoaked in 1% polyethylenimine. Each filter was rinsed with 1 mL of ice-cold washing buffer three times and counted in a gamma counter.

Immunohistochemistry Staining of MDA-MB-231 Human Breast Cancer-Xenografted Tumor. The immunohistochemistry staining was performed on MDA-MB-231 human breast cancer-xenografted tumors to demonstrate the GnRH receptor expression. The MDA-MB-231 human breast cancer-xenografted tumors were generated through flank subcutaneous inoculations of MDA-MB-231 cells (1×10^7 cells/mouse) in female athymic nude mice. The tumor weights reached approximately 0.3 g at 18 days post cell inoculation. The immunoperoxidase staining of the xenografted MDA-MB-231 tumor slices (4 μm thickness) were performed according to the protocol of goat ABC staining system (sc-2023) purchased from Santa Cruz Biotechnology (Santa Cruz, CA). Briefly, the tumor slices were treated with 3% H_2O_2 for 15 min followed by a 20 min treatment with the blocking serum at 25 °C. Then, the tumor slices were incubated with primary goat anti-human GnRH antibody (1:40; Santa Cruz Biotechnology, Santa Cruz, CA) for 1.75 h at 25 °C. Thereafter, the tumor slices were incubated with biotinylated secondary antibody for 30 min and followed by a 30 min

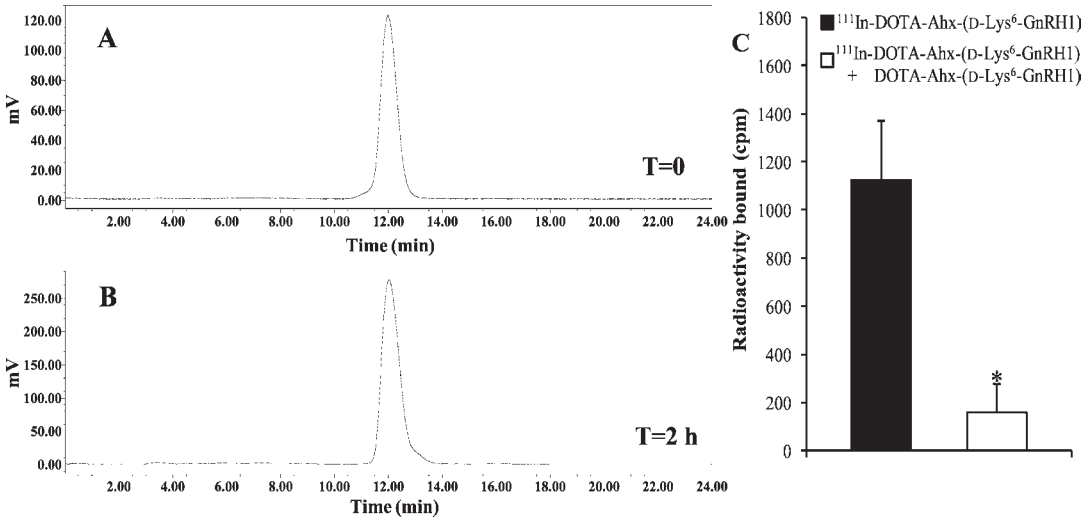

Figure 3. (A, B) Radioactive HPLC profiles of ^{111}In-DOTA−Ahx−(D-Lys^6-GnRH1) (A, T = 0) and its mouse serum stability (B, T = 2 h) after 2 h incubation at 37 °C. The retention time of ^{111}In-DOTA−Ahx−(D-Lys^6-GnRH1) was 12.0 min. (C) Binding of ^{111}In-DOTA−Ahx−(D-Lys^6-GnRH1) on human GnRH receptor membrane preparations with (□) or without (■) the presence of 1 μM of DOTA−Ahx−(D-Lys^6-GnRH1). *P < 0.05.

incubation with AB enzyme reagent. The tumor slices were incubated with the peroxidase substrate for 5 min followed by a dehydration process using ethanol and xylene. After the immunoperoxidase staining, the tumor slices were washed with deionized water and counterstained with Gill's formulation #2 hematoxylin. One to two drops of DPX permanent mounting medium were immediately added to the tumor slices after the counterstaining. Then, the tumor slices were covered with glass coverslips and observed by the light microscopy. As controls, the xenografted MDA-MB-231 tumor slices (4 μm thickness) were incubated (without primary goat anti-human GnRH antibody) with secondary biotinylated antibody, AB enzyme reagent and peroxidase substrate, respectively.

Biodistribution and Tumor Imaging. All the animal studies were conducted in compliance with Institutional Animal Care and Use Committee approval. The pharmacokinetics of ^{111}In-DOTA−Ahx−(D-Lys^6-GnRH1) was determined in MDA-MB-231 human breast cancer-xenografted female athymic nude mice (Harlan, Indianapolis, IN). The nude mice were subcutaneously inoculated with 1×10^7 MDA-MB-231 cells on the right flank of each mouse to generate MDA-MB-231 xenografted tumors. The tumor weights reached approximately 0.3 g at 18 days post cell inoculation. Each tumor-bearing mouse was injected with 0.037 MBq of ^{111}In-DOTA−Ahx−(D-Lys^6-GnRH1) via the tail vein. Groups of 5 mice were sacrificed at 0.5, 2, 4, and 24 h postinjection, and tumors and organs of interest were harvested, weighed and counted. Blood values were taken as 6.5% of the whole-body weight.

To determine the tumor imaging properties of ^{111}In-DOTA−Ahx−(D-Lys^6-GnRH1), approximately 5.6 MBq of ^{111}In-DOTA−Ahx−(D-Lys^6-GnRH1) was injected into a MDA-MB-231 human breast cancer-xenografted nude mouse (18 days post cell inoculation) via the tail vein. The mouse was sacrificed for small animal SPECT/CT (Nano-SPECT/CT, Bioscan) imaging at 1 h postinjection. The CT imaging was immediately followed by whole-body SPECT imaging. The SPECT scans of 24 projections were acquired. Reconstructed SPECT and CT data were visualized and coregistered using InVivoScope (Bioscan, Washington, DC).

Statistical Methods. Statistical analysis was performed using Student's t test for unpaired data to determine the significance of differences between the GnRH receptor binding of ^{111}In-DOTA−Ahx−(D-Lys^6-GnRH1) with or without 1 μM of DOTA−Ahx−(D-Lys^6-GnRH1) peptide blockade. Difference at the 95% confidence level (p < 0.05) was considered significant.

RESULTS

DOTA−Ahx−(D-Lys^6-GnRH1), DOTA−Ahx−(D-Lys^6-GnRH2) and DOTA−Ahx−(L-Lys^6-GnRH3) were successfully synthesized and purified by RP-HPLC. Figure 1 illustrates the synthetic schemes of the GnRH peptides. All three GnRH peptides displayed greater than 90% purity after the HPLC purification. The peptide identities were confirmed by electrospray ionization mass spectrometry. The calculated molecular weights of DOTA−Ahx−(D-Lys^6-GnRH1), DOTA−Ahx−(D-Lys^6-GnRH2) and DOTA−Ahx−(L-Lys^6-GnRH3) were 1752.9, 1752.9 and 1752.9, whereas the found molecular weights of DOTA−Ahx−(D-Lys^6-GnRH1), DOTA−Ahx−(D-Lys^6-GnRH2) and DOTA−Ahx−(L-Lys^6-GnRH3) were 1752.2, 1752.2 and 1752.4, respectively. The GnRH receptor binding affinities of the peptides are presented in Figure 2. The IC_{50} values of DOTA−Ahx−(D-Lys^6-GnRH1), DOTA−Ahx−(D-Lys^6-GnRH2) and DOTA−Ahx−(L-Lys^6-GnRH3) were 36.1 nM, 10.6 mM and 4.3 mM, respectively.

We further evaluated DOTA−Ahx−(D-Lys^6-GnRH1) since only DOTA−Ahx−(D-Lys^6-GnRH1) exhibited low nanomolar GnRH receptor binding affinity. DOTA−Ahx−(D-Lys^6-GnRH1) was readily labeled with ^{111}In in 0.5 M ammonium acetate solution at pH 4.5 with greater than 95% radiolabeling yield. ^{111}In-DOTA−Ahx−(D-Lys^6-GnRH1) was completely separated from its excess nonlabeled peptide by RP-HPLC. The retention times of ^{111}In-DOTA−Ahx−(D-Lys^6-GnRH1) and DOTA−Ahx−(D-Lys^6-GnRH1) were 12.0 and 8.3 min, respectively. ^{111}In-DOTA−Ahx−(D-Lys^6-GnRH1) was stable in mouse serum at 37 °C for 2 h. Only intact ^{111}In-DOTA−Ahx−(D-Lys^6-GnRH1) was detected by RP-HPLC after 2 h of incubation in mouse serum (Figure 3). The GnRH receptor binding of ^{111}In-DOTA−Ahx−(D-Lys^6-GnRH1) is shown in

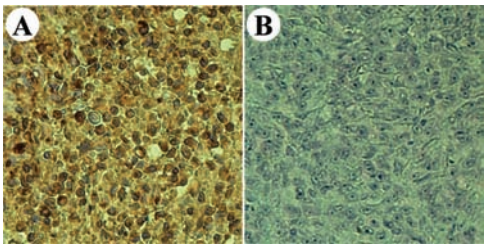

Figure 4. Immunohistochemistry staining of GnRH receptor expressions in MDA-MB-231 human breast cancer-xenografted tumor (A, ×400). The MDA-MB-231 xenografted tumor exhibited strong brown cytoplasmic staining. As a comparison, the MDA-MB-231 xenografted tumor were stained without primary goat anti-human GnRH antibody (B, ×400).

Table 1. Biodistribution of ^{111}In-DOTA−Ahx−(D-Lys^6-GnRH1) in MDA-MB-231 Human Breast Cancer-Xenografted Nude Mice[a]

tissue	0.5 h	2 h	4 h	24 h
	Percent Injected Dose/Gram (% ID/g)			
tumor	1.76 ± 0.58	0.29 ± 0.10	0.15 ± 0.05	0.18 ± 0.07
brain	0.34 ± 0.28	0.03 ± 0.02	0.02 ± 0.01	0.03 ± 0.01
blood	2.87 ± 0.71	0.20 ± 0.03	0.11 ± 0.02	0.04 ± 0.02
heart	1.11 ± 0.19	0.13 ± 0.04	0.09 ± 0.06	0.10 ± 0.06
lung	3.17 ± 0.69	0.28 ± 0.12	0.18 ± 0.10	0.11 ± 0.03
liver	1.60 ± 0.29	0.77 ± 0.06	0.97 ± 0.13	0.59 ± 0.16
spleen	0.80 ± 0.10	0.23 ± 0.04	0.39 ± 0.01	0.31 ± 0.11
stomach	0.66 ± 0.37	0.31 ± 0.31	0.50 ± 0.56	0.04 ± 0.01
kidneys	15.39 ± 4.59	8.88 ± 1.26	9.28 ± 1.18	4.43 ± 1.67
muscle	0.51 ± 0.34	0.03 ± 0.03	0.12 ± 0.03	0.16 ± 0.02
pancreas	0.55 ± 0.04	0.15 ± 0.02	0.13 ± 0.08	0.11 ± 0.08
bone	0.72 ± 0.19	0.35 ± 0.26	0.70 ± 0.50	0.37 ± 0.26
skin	3.07 ± 0.91	0.26 ± 0.04	0.24 ± 0.03	0.22 ± 0.05
	Uptake Ratio of Tumor/Normal Tissue			
tumor/blood	0.61	1.45	1.36	4.50
tumor/muscle	3.45	9.67	1.25	1.13
	Percent Injected Dose (% ID)			
intestines	1.43 ± 0.10	0.42 ± 0.10	0.63 ± 0.21	0.16 ± 0.02
urine	73.12 ± 5.36	94.61 ± 0.60	94.59 ± 0.27	96.81 ± 0.72

[a] The data are presented as percent injected dose/gram or as percent injected dose (mean ± SD, n = 5).

Figure 3. Incubation of 1 μM of DOTA−Ahx−(D-Lys^6-GnRH1) peptide blocked 86% of the binding of ^{111}In-DOTA−Ahx−(D-Lys^6-GnRH1), indicating that the binding of ^{111}In-DOTA−Ahx−(D-Lys^6-GnRH1) was GnRH receptor-specific.

The GnRH receptor expressions in MDA-MB-231 human breast cancer-xenografted tumors slices were confirmed by immunohistochemistry staining. The immunohistochemistry staining results are presented in Figure 4. The GnRH receptor expressions were positively stained in MDA-MB-231 human breast cancer-xenografted tumors. Hence, we used the MDA-MB-231 human breast cancer-xenografted nude mice to determine the tumor targeting and pharmacokinetic properties of ^{111}In-DOTA−Ahx−(D-Lys^6-GnRH1). The biodistribution results of ^{111}In-DOTA−Ahx−(D-Lys^6-GnRH1) are shown in

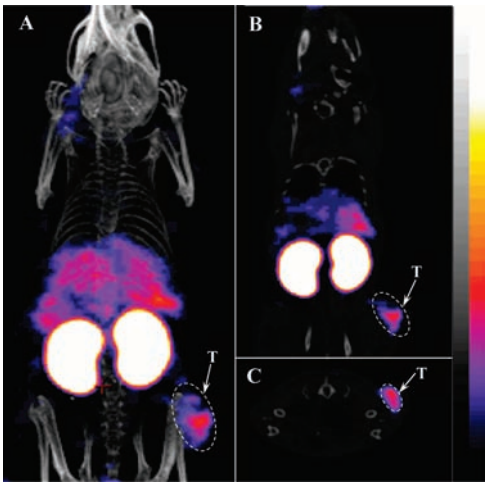

Figure 5. Three-dimensional (A), coronal (B) and transversal (C) SPECT/CT images of MDA-MB-231 human breast cancer-xenografted tumor at 1 h postinjection of 5.6 MBq of ^{111}In-DOTA−Ahx−(D-Lys^6-GnRH1). Flank breast cancer lesions (T) were highlighted with arrows on the images.

Table 1. ^{111}In-DOTA−Ahx−(D-Lys^6-GnRH1) exhibited rapid tumor uptake. The tumor uptake values were 1.76 ± 0.58 and 0.29 ± 0.10% ID/g at 0.5 and 2 h postinjection. The tumor uptake values decreased to 0.15 ± 0.05 and 0.18 ± 0.07% ID/g at 4 and 24 h postinjection. Blood clearance of ^{111}In-DOTA−Ahx−(D-Lys^6-GnRH1) was fast. The blood uptake was 0.20 ± 0.03% ID/g at 2 h postinjection. Meanwhile, whole-body clearance of ^{111}In-DOTA−Ahx−(D-Lys^6-GnRH1) was rapid, with approximately 95% of the injected radioactivity cleared through the urinary system by 2 h postinjection. The renal uptake values were 15.39 ± 4.59, 8.88 ± 1.26, 9.28 ± 1.18 and 4.43 ± 1.67% ID/g at 0.5, 2, 4, and 24 h postinjection. Besides the kidneys, the liver was the normal organ with second high uptake after 2 h postinjection. The liver uptake values were 0.77 ± 0.06, 0.97 ± 0.13 and 0.59 ± 0.16% ID/g at 2, 4, and 24 h postinjection. The tumor imaging properties of ^{111}In-DOTA−Ahx−(D-Lys^6-GnRH1) were examined in MDA-MB-231 human breast cancer-xenografted nude mice. The three-dimensional, coronal and transversal SPECT/CT images are presented in Figure 5. Flank MDA-MB-231 xenografted tumors were clearly visualized by SPECT/CT using ^{111}In-DOTA−Ahx−(D-Lys^6-GnRH1) as an imaging probe in all three images. The whole-body image (Figure 5A) showed high tumor to normal organ uptake ratios except for the kidneys and liver.

DISCUSSION

There is considerable interest to develop receptor-targeting peptide radiopharmaceuticals for cancer imaging including breast cancer. For instance, radiolabeled bombesin (BBN) peptides[34−37] have been utilized to target the gastrin-releasing peptide (GRP) receptors for breast cancer imaging. Both ^{99m}Tc-Cyc-Aca-BBN-(2−14)NH$_2$[34] and ^{99m}Tc-RP527[35] have been successfully used to visualize breast cancer in human, confirming the feasibility of using receptor-targeting radiolabeled peptides for breast cancer detection. In this study, the GnRH receptor is an attractive molecular target due to its overexpression on human breast cancer cells as well as tissue samples.[16−20] Wild-type

GnRH peptide (pGlu[1]-His[2]-Trp[3]-Ser[4]-Tyr[5]-Gly[6]-Leu[7]-Arg[8]-Pro[9]-Gly[10]-NH_2) can bend around the flexible Gly[6] for GnRH receptor binding. The substitution of Gly[6] with a D-amino acid enhances the binding affinity and reduces the metabolic clearance of the peptide.[22] It is known that both motifs of pGlu[1]-His[2]-Trp[3] and Arg[8]-Pro[9]-Gly[10]-NH_2 play crucial roles in GnRH receptor binding.[21] Several radiolabeled GnRH peptides have been reported over the past decade.[38−40] Initially, a bifunctional chelating agent (BFCA) of P_2S_2−COOH {6,8-bis-[3-(bis-(hydroxymethyl)phosphanyl)propylsulfanyl]octanoic acid} was conjugated to the epsilon amino group of D-Lys[6] in D-Lys[6]-GnRH peptide for ^{99m}Tc/^{188}Re radiolabeling.[38] The P_2S_2-D-Lys[6]-GnRH peptide was readily labeled with ^{99m}Tc/^{188}Re with greater than 88% radiolabeling yields, demonstrating the feasibility of using the P_2S_2−COOH as a BFCA for GnRH peptide radiolabeling with ^{99m}Tc/^{188}Re. However, neither receptor binding affinities nor biodistribution properties were reported for ^{99m}Tc/^{188}Re−P_2S_2-D-Lys[6]-GnRH.[38] Thereafter, a backbone metal cyclization strategy was employed to cyclize the N-terminus and C-terminus of the GnRH peptides to develop ^{99m}Tc-labeled GnRH peptides.[39] Unfortunately, the backbone metal cyclization dramatically decreased the GnRH receptor binding affinities of the peptides, confirming that both N-terminus and C-terminus need to be reserved for strong GnRH receptor binding.

In 2008, ^{18}F- and ^{68}Ga-labeled GnRH peptides were reported for GnRH receptor-targeting.[40] The motif of *p*-fluorobenzyloxime acetyl (FBOA) was conjugated to the epsilon amino group of D-Lys[6] in D-Lys[6]-GnRH via the β-alanine (β-Ala) or Ahx linker for ^{18}F radiolabeling, whereas the DOTA was directly coupled to the epsilon amino group of D-Lys[6] in D-Lys[6]-GnRH for ^{68}Ga radiolabeling. The results on receptor binding affinity and internalization property indicated that the lipophilicity of the moiety attached to the D-Lys[6] showed a significant impact on both receptor binding affinity and internalization property. The Ahx linker was more lipophilic and better than the β-Ala linker in terms of maintaining high receptor binding affinity and high internalization percentage of the GnRH peptide. Direct coupling of the hydrophilic ^{68}Ga-DOTA moiety to D-Lys[6]-GnRH dramatically reduced the receptor binding affinity and internalization percentage of the peptide.[36] No biodistribution result was reported for ^{18}F- and ^{68}Ga-labeled GnRH peptides.

In this study, instead of direct coupling the DOTA to the D-Lys[6], we conjugated the DOTA to the D-Lys[6] via the Ahx linker to enhance the lipophilicity of the moiety attached to D-Lys[6]-GnRH while retaining nanomolar GnRH receptor binding affinity of the peptide. Since both alpha and epsilon amino groups of D-Lys[6] can be used for DOTA conjugation, we separately conjugated the DOTA to each amino group of D-Lys[6] to determine which amino group was better for DOTA conjugation in terms of GnRH receptor binding affinity. The IC_{50} values of DOTA−Ahx−(D-Lys[6]-GnRH1) and DOTA−Ahx−(D-Lys[6]-GnRH2) revealed that the epsilon amino group of D-Lys[6] was better than the alpha amino group in maintaining nanomolar GnRH receptor binding affinity. The conjugation of the DOTA to the alpha amino group of D-Lys[6] dramatically decreased the GnRH receptor binding affinity by 293-fold. Furthermore, we conjugated the DOTA to the epsilon amino group of L-Lys[6] via the Ahx linker to examine the potential impact of D- and L-configuration of the Lys[6] on the GnRH receptor binding affinity. The IC_{50} values of DOTA−Ahx−(D-Lys[6]-GnRH1) and DOTA−Ahx−(L-Lys[6]-GnRH3) suggested that the D-configuration of the Lys[6] played a key role in maintaining the GnRH receptor binding affinity as well. The replacement of D-Lys[6] with L-Lys[6] sacrificed the GnRH receptor binding affinity by 119-fold. The dramatic differences in GnRH receptor binding affinities among these three novel GnRH peptides demonstrated the profound impact of the DOTA position on the binding affinity of the GnRH peptide.

DOTA−Ahx−(D-Lys[6]-GnRH1) displayed 36.1 nM GnRH receptor binding affinity, warranting its further evaluation. We chose to radiolabel DOTA−Ahx−(D-Lys[6]-GnRH1) with ^{111}In, which is an attractive diagnostic radionuclide and is commercially available. Importantly, the switch from the ^{68}Ga-DOTA moiety to the ^{111}In-DOTA moiety could further reduce one more negative charge of the radiometal-DOTA moiety since ^{111}In required one more −COOH group from the DOTA for coordination compared to ^{68}Ga. The radiolabeling of DOTA−Ahx−(D-Lys[6]-GnRH1) with ^{111}In was rapid and efficient (>95% radiolabeling yield). The metal chelator DOTA formed a stable complex with ^{111}In. ^{111}In-DOTA−Ahx−(D-Lys[6]-GnRH1) was stable in serum at 37 °C for 2 h (Figure 3). ^{111}In-DOTA−Ahx−(D-Lys[6]-GnRH1) exhibited GnRH receptor-specific binding, with 86% of the binding being blocked by 1 μM nonradiolabeled DOTA−Ahx−(D-Lys[6]-GnRH1) peptide blockade. The expressions of the GnRH receptors on MDA-MB-231 human breast cancer-xenografted tumor lesions were confirmed by immunohistochemistry staining (Figure 4). ^{111}In-DOTA−Ahx−(D-Lys[6]-GnRH1) exhibited rapid tumor uptake (1.76 ± 0.58% ID/g at 0.5 h postinjection) coupled with fast whole-body clearance in MDA-MB-231 human breast cancer-xenografted nude mice. As presented in Figure 5, the MDA-MB-231 human breast cancer-xenografted tumors were clearly visualized by SPECT/CT using ^{111}In-DOTA−Ahx−(D-Lys[6]-GnRH1) as an imaging probe at 1 h postinjection, highlighting the potential use of ^{111}In-DOTA−Ahx−(D-Lys[6]-GnRH1) for human breast cancer imaging. The radioactivity accumulation in kidneys and liver was observed in the SPECT/CT images as well. The kidneys were the normal organs with the highest radioactivity uptakes, which was consistent with the biodistribution results (Table 1). It is worthwhile to note that a positively charged side chain of Arg[8] is available in ^{111}In-DOTA−Ahx−(D-Lys[6]-GnRH1). Therefore, the renal uptake was likely attributed to the electrostatic interaction between the positively charged ^{111}In-DOTA−Ahx−(D-Lys[6]-GnRH1) and negatively charged renal tubular cells. A possible way to reduce the renal uptake of ^{111}In-DOTA−Ahx−(D-Lys[6]-GnRH1) would be the coinjection of positively charged lysine, which was successful in decreasing the renal uptakes of ^{111}In-labeled alpha-melanocyte stimulating hormone (α-MSH) peptides by 70%.[41]

Hydrocarbon linkers with various lengths were successfully coupled between the DOTA and bombesin peptide to optimize the receptor binding affinities of bombesin peptides.[42] The DOTA-conjugated bombesin peptides with the linkers ranging from 5-carbon to 8-carbon exhibited 0.6−1.7 nM receptor binding affinities. Either shorter or longer hydrocarbon linkers dramatically reduced the receptor binding affinity by 100-fold.[34] Despite the fact that the Ahx linker was utilized to improve the lipophilicity of the metal−DOTA moiety attached to D-Lys[6]-GnRH in this study, more studies would be needed to determine whether the Ahx linker is ideal or not for low nanomolar GnRH receptor binding of the peptide. Hence, it would be interesting to examine the impact of the hydrocarbon linker on GnRH receptor binding affinity of the peptide in the future.

In conclusion, the DOTA position displayed a profound impact on the binding affinity of the GnRH peptide. The coupling

of DOTA to the epsilon amino group of D-Lys^6 maintained nanomolar GnRH receptor binding affinity of the peptide, providing a new insight into the design of novel radiolabeled GnRH peptides. The successful imaging of MDA-MB-231 human breast cancer-xenografted tumor lesions using ^{111}In-DOTA−Ahx−(D-Lys^6-GnRH1) highlighted its potential as a novel imaging probe for human breast cancer imaging.

AUTHOR INFORMATION

Corresponding Author

*2502 Marble NE, MSC09 5360, College of Pharmacy, University of New Mexico, Albuquerque, NM 87131, USA. Phone: (505) 925-4437. Fax: (505) 272-6749. E-mail: ymiao@salud.unm.edu.

ACKNOWLEDGMENT

We appreciate Drs. Fabio Gallazzi and Jianquan Yang for their technical assistance. This work was supported in part by DOD Grant W81XWH-09-1-0105, NIH Grant NM-INBRE P20RR016480, the Oxnard Foundation Award and New Mexico Cancer Nanotech Training Center Postdoctoral Fellowship. The image in this article was generated by the Keck-UNM Small Animal Imaging Resource established with funding from the W.M. Keck Foundation and the University of New Mexico Cancer Research and Treatment Center (NIH P30 CA118100).

REFERENCES

(1) Jemal, A., Siegel, R., Xu, J., and Ward, E. (2010) Cancer statistics. *CA Cancer J. Clin. 60*, 277–300.

(2) Buist, D. S., Porter, P. L., Lehman, C., Taplin, S. H., and White, E. (2004) Factors contributing to mammography failure in women aged 40−49 years. *J. Natl. Cancer Inst. 96*, 1432–1440.

(3) Gambhir, S. S. (2002) Molecular imaging of cancer with positron emission tomography. *Nat. Rev. Cancer 2*, 683–693.

(4) Sharma, V., Luker, G. D., and Piwnica-Worms, D. (2002) Molecular imaging of gene expression and protein function in vivo with PET and SPECT. *J. Magn. Reson. Imaging 16*, 336–351.

(5) Bos, R., van Der Hoeven, J. J., van Der Wall, E., van Der Groep, P., van Diest, P. J., Comans, E. F., Joshi, U., Semenza, G. L., Hoekstra, O. S., Lammertsma, A. A., and Molthoff, C. F. (2002) Biologic correlates of ^{18}fluorodeoxyglucose uptake in human breast cancer measured by positron emission tomography. *J. Clin. Oncol. 20*, 379–387.

(6) Avril, N., Menzel, M., Dose, J., Schelling, M., Weber, W., Janicke, F., Nathrath, W., and Schwaiger, M. (2001) Glucose metabolism of breast cancer assessed by ^{18}F-FDG PET: histologic and immunohistochemical tissue analysis. *J. Nucl. Med. 42*, 9–16.

(7) Mankoff, D. A., Dunnwald, L. K., Gralow, J. R., Ellis, G. K., Charlop, A., Lawton, T. J., Schubert, E. K., Tseng, J., and Livingston, R. B. (2002) Blood flow and metabolism in locally advanced breast cancer: relationship to response to therapy. *J. Nucl. Med. 43*, 500–509.

(8) Oshida, M., Uno, K., Suzuki, M., Nagashima, T., Hashimoto, H., Yagata, H., Shishikura, T., Imazeki, K., and Nakajima, N. (1998) Predicting the prognoses of breast carcinoma patients with positron emission tomography using 2-deoxy-2-fluoro[^{18}F]-D-glucose. *Cancer 90*, 2227–2234.

(9) Inoue, T., Yutani, K., Taguchi, T., Tamaki, Y., Shiba, E., and Noguchi, S. (2004) Preoperative evaluation of prognosis in breast cancer patients by [(18)F]2-Deoxy-2-fluoro-D-glucose-positron emission tomography. *J. Cancer Res. Clin. Oncol. 130*, 273–278.

(10) Avril, N., Rose, C. A., Schelling, M., Dose, J., Kuhn, W., Bense, S., Weber, W., Ziegler, S., Graeff, H., and Schwaiger, M. (2000) Breast imaging with positron emission tomography and fluorine-18 fluorodeoxyglucose: use and limitations. *J. Clin. Oncol. 18*, 3495–3502.

(11) Eubank, W. B., Mankoff, D. A., Takasugi, J., Vesselle, H., Eary, J. F., Shanley, T. J., Gralow, J. R., Charlop, A., Ellis, G. K., Lindsley, K. L., Austin-Seymour, M. M., Funkhouser, C. P., and Livingston, R. B. (2001) ^{18}Fluorodeoxyglucose positron emission tomography to detect mediastinal or internal mammary metastases in breast cancer. *J. Clin. Oncol. 19*, 3516–3523.

(12) Isasi, C. R., Moadel, R. M., and Blaufox, M. D. (2005) A meta-analysis of FDG PET for the evaluation of breast cancer recurrence and metastases. *Breast Cancer Res. Treat. 90*, 105–112.

(13) Lonneux, M., Borbath, I. I., Berliere, M., Kirkove, C., and Pauwels, S. (2000) The place of whole-body PET FDG for the diagnosis of distant recurrence of breast cancer. *Clin. Positron Imaging 3*, 45–49.

(14) Vranjesevic, D., Filmont, J. E., Meta, J., Silverman, D. H., Phelps, M. E., Rao, J., Valk, P. E., and Czernin, J. (2002) Whole-body (18)F-FDG PET and conventional imaging for predicting outcome in previously treated breast cancer patients. *J. Nucl. Med. 43*, 325–329.

(15) Cook, G. J., Houston, S., Rubens, R., Maisey, M. N., and Fogelman, I. (1998) Detection of bone metastases in breast cancer by ^{18}FDG PET: differing metabolic activity in osteoblastic and osteolytic lesions. *J. Clin. Oncol. 16*, 3375–3379.

(16) Miller, W. R., Scott, W. N., Morris, R., Fraser, H. M., and Sharpe, R. M. (1985) Growth of human breast cancer cells inhibited by a luteinizing hormone-releasing hormone agonist. *Nature 313*, 231–233.

(17) Eidne, K. A., Flanagan, C. A., and Millar, R. P. (1985) Gonadotropin-releasing hormone binding sites in human breast carcinoma. *Science 229*, 989–991.

(18) Sharoni, Y., Bosin, E., Miinster, A., Levy, J., and Schally, A. V. (1989) Inhibition of growth of human mammary tumor cells by potent antagonists of luteinizing hormone-releasing hormone. *Proc. Natl. Acad. Sci. U.S.A. 86*, 1648–1651.

(19) Fekete, M., Wittliff, J. L., and Schally, A. V. (1989) Characteristics and distribution of receptors for [d-Trp6]-luteinizing hormone-releasing hormone, somatostatin, epidermal growth factor and sex steroids in 500 biopsy samples of human breast cancer. *J. Clin. Lab. Anal. 3*, 137–147.

(20) Baumann, K. H., Kiesel, L., Kaufmann, M., Bastert, G., and Runnebaum, B. (1993) Characterization of binding sites for a GnRH-agonist (buserelin) in human breast cancer biopsies and their distribution in relation to tumor parameters. *Breast Cancer Res. Treat. 25*, 37–46.

(21) Millar, R. P. (2005) GnRH and GnRH receptors. *Anim. Reprod. Sci. 88*, 5–28.

(22) Beckers, T., Bernd, M., Kutscher, B., Kuhne, R., Hoffman, S., and Reissmann, T. (2001) Structure-function studies of linear and cyclized peptide antagonists of the GnRH receptor. *Biochem. Biophys. Res. Commun. 289*, 653–663.

(23) Nagy, A., Schally, A. V., Armatis, P., Szepeshazi, K., Halmos, G., Kovacs, M., Zarandi, M., Groot, K., Miyazaki, M., Jungwirth, A., and Horvath, J. (1996) Cytotoxic analogs of luteinizing hormone-releasing hormone containing doxorubicin or 2-pyrrolinodoxorubicin, a derivative 500−1000 times more potent. *Proc. Natl. Acad. Sci. U.S.A. 93*, 7269–7273.

(24) Halmos, G., Nagy, A., Lamharzi, N., and Schally, A. V. (1999) Cytotoxic analogs of luteinizing hormone-releasing hormone bind with high affinity to human breast cancers. *Cancer Lett. 136*, 129–136.

(25) Wang, X., Krebs, L. J., Al-Nuri, M., Pudavar, H. E., Ghosal, S., Liebow, C., Nagy, A. A., Schally, A. V., and Prasad, P. N. (1999) A chemically labeled cytotoxic agent: two-photon fluorophore for optical tracking of cellular pathway in chemotherapy. *Proc. Natl. Acad. Sci. U.S.A. 96*, 11081–11084.

(26) Szepeshazi, K., Schally, A. V., Nagy, A., Halmos, G., and Groot, K. (1997) Targeted cytotoxic luteinizing hormone releasing hormone (LH-RH) analogs inhibit growth of estrogen-independent MXT mouse mammary cancer in vivo by decreasing cell proliferation and inducing apoptosis. *Anticancer Drugs 8*, 974–987.

(27) Szepeshazi, K., Schally, A. V., and Nagy, A. (1999) Effective treatment of advanced estrogen-independent MXT mouse mammary cancers with targeted cytotoxic LH-RH analogs. *Breast Cancer Res. Treat. 56*, 267–276.

(28) Kahan, Z., Nagy, A., Schally, A. V., Halmos, G., Arencibia, J. M., and Groot, K. (1999) Complete regression of MX-1 human breast cancer xenografts after targeted chemotherapy with a cytotoxic analog of luteinizing hormone-releasing hormone, AN-207. *Cancer 85*, 2608–2615.

(29) Bajo, A. M., Schally, A. V., Halmos, G., and Nagy, A. (2003) Targeted doxorubicincontaining luteinizing hormone-releasing hormone analogue AN-152 inhibits the growth of doxorubicin-resistant MX-1 human breast cancers. *Clin. Cancer Res. 9*, 3742–3748.

(30) Kahan, Z., Nagy, A., Schally, A. V., Halmos, G., Arencibia, J. M., and Groot, K. (2000) Administration of a targeted cytotoxic analog of luteinizing hormone releasing hormone inhibits growth of estrogen independent MDA-MB-231 human breast cancers in nude mice. *Breast Cancer Res. Treat. 59*, 255–262.

(31) Chatzistamou, I., Schally, A. V., Nagy, A., Armatis, P., Szepeshazi, K., and Halmos, G. (2000) Effective treatment of metastatic MDA-MD-435 human estrogen independent breast carcinomas with a targeted cytotoxic analog of luteinizing hormone-releasing hormone, AN-207. *Clin. Cancer Res. 6*, 4158–4165.

(32) Flanagan, C. A., Fromme, B. J., Davidson, J. S., and Millar, R. P. (1998) A high affinity gonadotropin-releasing hormone (GnRH) tracer, radioiodinated at position 6, facilitates analysis of mutant GnRH receptors. *Endocrinology 139*, 4115–4119.

(33) Guo, H., Yang, J., Gallazzi, F., and Miao, Y. (2010) Reduction of the ring size of radiolabeled lactam bridige-cyclized α-MSH peptide, resulting in enhanced melanoma uptake. *J. Nucl. Med. 51*, 418–426.

(34) Scopinaro, F., Varvarigou, A. D., Ussof, W., De Vincentis, G., Sourlingas, T. G., Evangelatos, G. P., Datsteris, J., and Archimandritis, S. C. (2002) Technetium-labeled bombesin-like peptide: preliminary report on breast cancer uptake in patients. *Cancer Biother. Radiopharm. 17*, 327–335.

(35) Van de Wiele, C., Dumont, F., Broecke, R. V., Oosterlinck, W., Cocquyt, V., Serreyn, R., Peers, S., Thornback, J., Slegers, G., and Dierck, R. A. (2000) Technetium-99m RP527, a GRP analogue for visualization of GRP receptor-expressing malignancies: a feasibility study. *Eur. J. Nucl. Med. 27*, 1694–1699.

(36) Prasanphanich, A. F., Retzloff, L., Lane, S. R., Nanda, P. K., Sieckman, G. L., Rold, T. L., Ma, L., Figueroa, S. D., Sublett, S. V., Hoffman, T. J., and Smith, C. J. (2009) In vitro and in vivo analysis of [^{64}Cu-NO_2A-8-Aoc-BBN(7−14)NH_2]: a site-directed radiopharmaceutical for positron-emission tomography imaging of T-47D human breast cancer tumors. *Nucl. Med. Biol. 36*, 171–181.

(37) Retzloff, L., Heinzke, L., Figueroa, S. D., Sublett, S. V., Ma, L., Sieckman, G. L., Rold, T. L., Santos, I., Hoffman, T. J., and Smith, C. J. (2010) Evaluation of [^{99m}Tc-$(CO)_3$-X-Y-Bombesin(7−14)NH_2] conjugates for targeting gastrin-releasing peptide receptors overexpressed on breast carcinoma. *Anticancer Res. 30*, 19–30.

(38) Gali, H., Hoffman, T. J., Sieckman, G. L., Owen, N. K., Katti, K. V., and Volkert, W. A. (2001) Synthesis, characterization, and labeling with ^{99m} Tc/^{188}Re of peptide, conjugates containing a dithia-bisphosphine chelating agent. *Bioconjugate Chem. 12*, 354–63.

(39) Barda, Y., Cohen, N., Lev, V., Ben-Aroya, N., Koch, Y., Mishani, E., Fridkin, M., and Gilon, C. (2004) Backbone metal cyclization: novel ^{99m}Tc labeled GnRH analog as potential SPECT molecular imaging agent in cancer. *Nucl. Med. Biol. 31*, 921–933.

(40) Schottelius, M., Berger, S., Poethko, T., Schwaiger, M., and Wester, H. J. (2008) Development of novel ^{68}Ga- and ^{18}F-labeled GnRH-I analogues with high GnRHR-targeting efficiency. *Bioconjugate Chem. 19*, 1256–1268.

(41) Guo, H., Yang, J., Gallazzi, F., Prossnitz, E. R., Sklar, L. A., and Miao, Y. (2009) Effect of DOTA position on melanoma targeting and pharmacokinetic properties of ^{111}In-labeled lactam bridge-cyclized alpha-melanocyte stimulating hormone peptide. *Bioconjugate Chem. 20*, 2162–2168.

(42) Hoffman, T. J., Gali, H., Smith, C. J., Sieckman, G. L., Hayes, D. L., Owen, N. K., and Volkert, W. A. (2003) Novel series of ^{111}In-labeled bombesin analogs as potential radiopharmaceuticals for specific targeting of gastrin-releasing peptide receptors expressed on human prostate cancer cells. *J. Nucl. Med. 44*, 823–831.

Bioconjugate Chemistry

ARTICLE

pubs.acs.org/bc

Quantification of Primary Amine Groups Available for Subsequent Biofunctionalization of Polymer Surfaces

Samantha Noel,[§,†] Benoit Liberelle,[§,†] Lucie Robitaille,[‡] and Gregory De Crescenzo*[,†]

[†]Department of Chemical Engineering, Groupe de Recherche en Sciences et Technologies Biomédicales, Bio-P^2 Research Unit, École Polytechnique de Montréal, P.O. Box 6079, succ. Centre-Ville, Montréal, Québec, Canada H3C 3A7

[‡]Functional Polymer Systems Group, Industrial Materials Institute, National Research Council Canada, Boucherville, Québec, Canada J4B 6Y4

ABSTRACT: Biocompatible polymers are commonly functionalized with specific moieties such as amino groups to modify their surface properties and/or to attach bioactive compounds. A reliable method is usually required to characterize amino group surface densities. In this study, aminated polyethylene terephthalate (PET) films were generated via an aminolysis reaction involving either ethylenediamine molecules (EtDA), in order to vary easily the amino group density on PET surfaces, or 25 kDa polyvinylamine (PVAm) as an alternative reagent preventing bulk damages resulting from the aminolysis reaction. Among commonly used dyes for amino group quantification, Orange II and Coomassie Brillant Blue (CBB) were selected to quantify the extent of amine grafting resulting from these derivatization procedures. Rapid and convenient colorimetric assays were compared to surface atomic compositions obtained from X-ray photoelectron spectroscopy (XPS) measurements. Orange II was found to be the most appropriate dye for quantifying primary amine groups in a reliable and specific way. Due to its unique negative charge and low steric hindrance compared to CBB, the Orange II dye was very sensitive and provided reliable quantification over a wide range of amino group surface densities (ca. 5 to at least 200 pmol/mm^2). In order to further validate the use of the Orange II dye for amino group quantification, a heterobifunctional linker reacting with amino groups was then grafted on modified PET surfaces. Interestingly, the good correlation between the densities of adsorbed Orange II and covalently grafted linkers suggests that the Orange II method is a relevant, reliable, easy, and inexpensive method to predict the amount of amino groups available for subsequent functionalization of polymer surfaces.

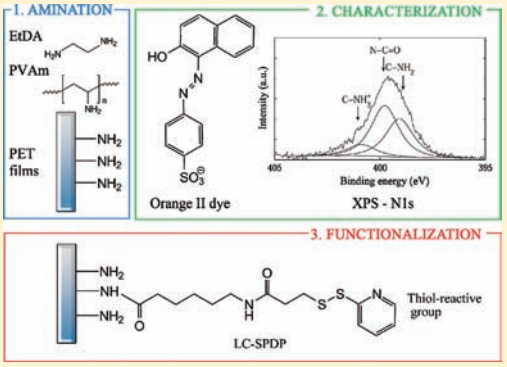

INTRODUCTION

With respect to the development of synthetic biomedical implants, biocompatible materials are needed for the devices to perform a specific function and to prevent any adverse effect inside the host. As biological responses take place on the material surface exposed to outer environment, conventional materials usually need to be enhanced to get new specific surface properties.[1,2] With the bulk materials of interest being mostly organic polymers,[3,4] the introduction of amino groups is often the first step of surface modification.[5] Amine moieties per se can indeed modify the macroscopic surface properties, i.e., modulate cell adhesion and tissue compatibility[6] or hydrophilicity[2,7] or promote specific differentiation of stem cells.[8] For more specific and controlled surface properties, amino groups can also be used to chemically attach bioactive molecules[1,9] such as oligosaccharides,[10] enzymes,[11,12] peptides,[13−15] or other polymers, e.g., PEG[16] or dextran[17] providing the surface with antifouling properties. The surface properties after amine derivatization, as well as subsequent grafting, are nevertheless dependent on the amino group density that has to be quantified in order to control the biomaterial functionalization.[8,10,11]

Primary amine content can be determined by several methods,[18] among which fluorometry,[19,20] colorimetry,[21−26] and spectroscopy[27−29] have already been reported. However, most of those methods are either expensive (e.g., fluorometry with *o*-phthaldehyde (OPA)[20]), time-consuming (e.g., colorimetry with 2,4,6-trinitrobenzenesulfonic acid (TNBS)[20]), or semiquantitative (e.g., X-ray photoelectron spectroscopy (XPS)[29]). In contrast, colorimetric assays that take advantage of anionic dyes are quantitative, economical, and convenient to perform on various material geometries.[6,25,30−32] The reliability of colorimetric techniques may however be questioned because of possible nonspecific adsorption of the dye to the substrate surface.[33,34] To the best of our knowledge, primary amine contents that are determined with anionic dyes are either used without any validation or only qualitatively supported by Fourier transformed infrared spectroscopy (FTIR) or XPS analyses.[7,10,14,21,24,33,35−37] Furthermore, correlations between the amine densities and the

Received: May 20, 2011
Revised: June 15, 2011
Published: July 07, 2011

ACS Publications © 2011 American Chemical Society

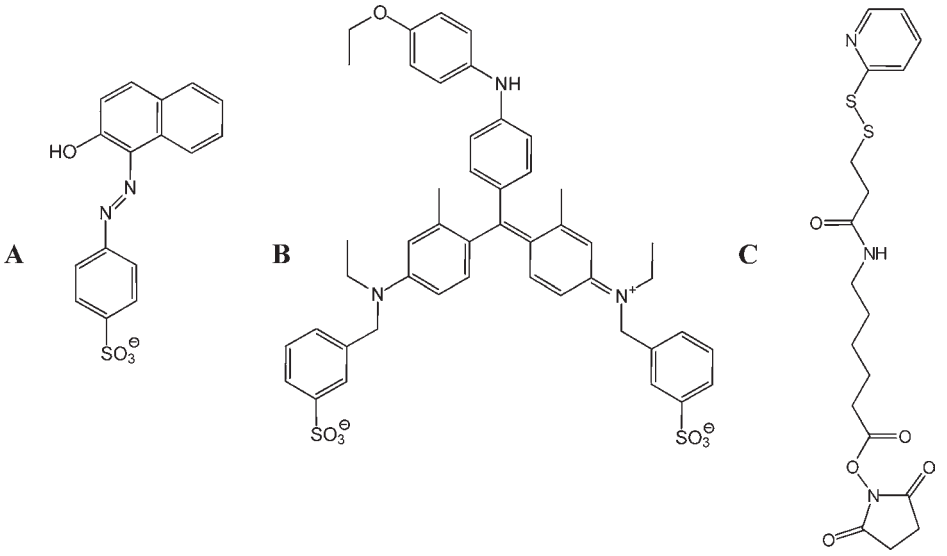

Figure 1. Molecules used for primary amine group quantification: Anionic dyes ((A) Orange II and (B) Coomassie Brillant Blue (CBB)) and (C) LC-SPDP heterobifunctional linker.

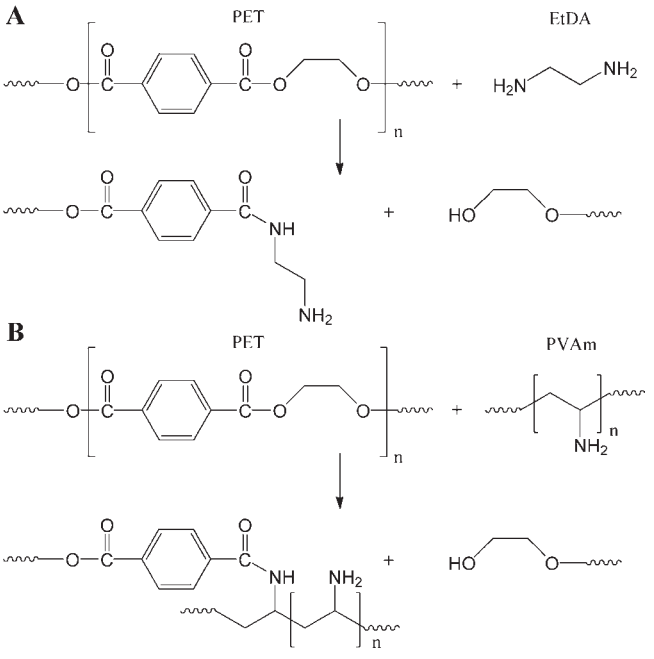

Figure 2. Aminolysis reaction scheme between PET and (A) EtDA or (B) PVAm.

amount of subsequently grafted molecules have never been clearly established.[10,11]

In this work, quantitative values of amino group density were determined via colorimetric methods based on two commonly used dyes, i.e., Orange II (Figure 1A)[7,10,14,23,33,35−37] and Coomassie Brilliant Blue (Figure 1B),[24,25,38,39] and were compared to atomic percent measurements made by XPS, as a reference. Those assays were performed on surfaces made of polyethylene terephthalate (PET), as this synthetic polymer is widely employed for its unique physical, chemical, and mechanical properties.[4] Due to its hydrophobic character and low adhesion properties, PET shows good stability in biological environments but moderate biocompatibility.[40] Therefore, this linear polyester is a relevant example of materials requiring surface functionalization, including bioactive molecules tethering,[13] for biomedical applications of PET-based devices. In this article, PET films were functionalized with primary amines via two different chemical treatments, involving a widely used small diamine molecule, namely, ethylenediamine (EtDA, Figure 2A),[10,11] or through the grafting of an aminated polymer (Figure 2B).[16] The various aminated films were then functionalized with an amino-reactive molecule (LC-SPDP linker, Figure 1C), which is of particular interest in the route of oriented immobilization of cysteine-tagged proteins.[13,41] The density of the grafted linker was further used to validate amine densities derived from Orange II assays.

MATERIALS AND METHODS

Chemicals and Reagents. Milli-Q quality water (18.2 MΩ. cm; total organic compounds (TOC) = 4 ppb) was generated with a Millipore Gradient A 10 purification system. Sodium hydroxide (NaOH, 99.3% purity), cysteine (99+% purity), acetic acid glacial (99.7% purity), ethanol (EtOH, 99.9% purity), methanol (MeOH, 99.9% purity), dioxane (99+% purity), and hydrochloric acid (HCl, 37.7% v/v) were obtained from VWR International, Ltd. (Mont-Royal, QC). Orange II sodium salt (92% purity), Coomassie Brillant Blue (100% purity), dimethylsulfoxide (DMSO, 99.7+% purity), 2-pyridinethiol (99% purity), phosphate buffered saline (10 mM PBS, NaCl − 0.138 M, KCl − 0.027 M, pH 7.4), potassium carbonate (K_2CO_3, 99% purity), and potassium chloride (KCl, 99+% purity) were purchased from Sigma-Aldrich Canada, Ltd. (Oakville, ON). Succinimidyl 6-[3-(2-pyridyldithio)-propionamido]hexanoate (LC-SPDP, 95+% purity) was obtained from Pierce Biotechnology, Inc. (Rockford, IL). Ethylenediamine (EtDA, 99+% purity) was purchased from Fisher Scientific, Ltd. (Nepean, ON). The linear aminated polymer polyvinylamine (PVAm) was obtained from Polysciences, Inc. (Warrington, PA). PET (Traytuf 9506 from M&G Group, Italy) films, 100 μm in thickness, were obtained by melt-extrusion using a Randcastle extrusion line.

PET Films Aminolysis. *Surface Preparation.* All glassware was carefully cleaned by overnight immersion in a bath of

KOH-saturated isopropyl alcohol, followed by intensive rinsing with Milli-Q water. The polyethylene terephthalate (PET) films (12 mm × 5 mm) were cleaned in an ultrasonic bath for 15 min in ethanol and then dried in a laminar flow cabinet at room temperature.

Ethylenediamine (EtDA) Functionalization. The protocol was adapted from those previously described in the literature.[10,11] Briefly, PET films were immersed in a reactive EtDA/methanol solution for 30 min at 50 °C. Six concentrations of EtDA (ranging from 30% to 40% v/v, by 2% steps) were tested to generate a wide range of amino group densities. At the end of the reaction, the films were intensively washed with Milli-Q water (at least 3 times) and dried in air. Untreated and EtDA-treated PET films were then observed under a scanning electron microscope (SEM; JSM-6100 Scanning Microscope, JEOL, Japan) at an accelerating voltage of 5.0 kV, to qualitatively assess the roughness of the films.

Polyvinylamine (PVAm) Functionalization. PVAm was grafted on PET films as previously described.[16] Briefly, PET films were immersed in a 4 g/L solution of PVAm dissolved in Milli-Q water and dioxane (73:27 v/v, pH 4). NaOH and KCl (1:1, 67 mM) was added to adjust pH and ionic strength (pH 10). The reaction was carried out for 24 h at 70 °C. At the end of the reaction, the films were rinsed with Milli-Q water and ethanol, washed again with Milli-Q water, and finally dried in air.

X-ray Photoelectron Spectroscopy. Functionalized PET surfaces were characterized with respect to their elemental chemical compositions (in at. %) and chemical bond types by X-ray photoelectron spectroscopy (XPS) analyses (surveys, as well as C, N, and O high-resolution spectra, respectively). XPS spectra were obtained using a VG ESCALAB 3MkII instrument using non-monochromatic Mg Kα radiation (12 kV, 18 mA). All samples were extensively washed and immersed for 20 min in an ultrasonic bath prior to analysis in order to remove any possible traces of unreacted chemicals that could affect XPS measurements. None of the samples exhibited any evidence of X-ray-induced damage during room-temperature XPS measurements. XPS spectra were acquired at 0° emission angle, normal to the sample surface, and possible charging was corrected by referencing all peaks to the carbon (C 1s) peak at binding energy BE = 284.7 eV in accordance with the literature.[42] Quantification of the constituent elements was performed using broad-scan spectra and *Avantage v4.12* software (Thermo Electron Corp., Waltham, MA) by integrating the areas under relevant peaks after a Shirley-type background subtraction, and using sensitivity factors from Wagner table. Deconvoluted C 1s peak areas of relevant chemical bonds (C═C, C═O, and C−O) in pristine PET were kept proportional for each subsequent analysis, in order to identify any new functional groups added after surface modification. Peak fitting to experimental data was carried out using a minimum number of peaks, consistent with a reasonable fit to the raw data and the molecular structure of modified polymer. Binding energies from XPS analysis are reported as mean ± standard deviation.

Colorimetric Assays on Surfaces. The areas of EtDA- and PVAm-coated films were determined prior to colorimetric assays. Two colorimetric methods were used to quantify the amount of exposed primary amine groups on the PET surfaces, i.e., the Orange II method and the Coomassie Brillant Blue method, based on the work of Uchida et al.[23] and Coussot et al.,[24,38] respectively.

Orange II Method. The amino-covered films were immersed in 1.5 mL of dye solution (14 mg/mL) in acidic solution (Milli-Q water adjusted to pH 3 with 1 M HCl) for 30 min at 40 °C. The samples were then intensively rinsed 3 times using the acidic solution (pH 3) to remove unbound dye. Once air-dried, the colored films were immersed in 1 mL of alkaline solution (Milli-Q water mixture adjusted to pH 12 with a 1 M NaOH solution). The pH of the solution containing the desorbed dye was adjusted to pH 3 by adding 1% v/v of 12.3 M HCl. The absorbance of the solution was then measured at 484 nm.

Coomassie Brillant Blue (CBB) Method. The modified PET films were immersed in 1.5 mL of dye solution (0.5 mg/mL) in acidic solution (pH 2.2, 85:10:5 v/v Milli-Q water/methanol/acetic acid) for 5 min at room temperature. The samples were then intensively rinsed with the acidic solution, to remove unbound dye. Once air-dried, the films were immersed in alkaline solution (pH 11.25, 0.125 M K_2CO_3 in 50:50 v/v Milli-Q water/methanol). The pH of the solution containing the desorbed dye was adjusted to pH 3 by adding 7.5% v/v of 3 M HCl. The absorbance of the solutions containing the desorbed dye was finally measured at 620 nm.

Linear correlation between Orange II densities and XPS atomic contents, as well as between Orange II and CBB densities, are described by the square of Pearson coefficient (R^2) and the associated *p*-value. Values for dye densities are reported as mean ± standard deviation.

Functionalization of Aminated Surfaces using LC-SPDP. EtDA- and PVAm-modified PET films were reacted with LC-SPDP molecules, as previously described.[43] Briefly, amino-modified films were placed in test tubes containing 1.0 mL of 1 mM LC-SPDP in 10 mM phosphate buffer (10% v/v DMSO) for 150 min at 40 °C, unless mentioned otherwise. The films were rinsed by soaking them in DMSO, in 10 mM phosphate buffer (pH 7.4), and in Milli-Q water. In a second step, the dried films were incubated in a 25 mM cysteine solution (1 M NaCl in 0.1 M sodium acetate, pH 4.0) for 1 h at room temperature in order to release 2-pyridinethiol groups. The absorbance of the solution was finally measured at 343 nm.

Stability of LC-SPDP Thiol-Reactive Groups. Absorbance measurements at 343 nm were performed using a stopped-flow apparatus (Bio-Logic SFM-4, Claix, France) for the release of 2-pyridinethiol groups from LC-SPDP to be evaluated all along the 300 min experiments. The sample temperature (20 to 50 °C) was kept constant using a Peltier cell device. The measurements were initiated by mixing a 1 mM LC-SPDP solution in DMSO with PBS to yield a final solution of 0.1 mM LC-SPDP.

The absorbance measurements were normalized to the plateau value (reached after 10 min) corresponding to the addition of 10% v/v of the previous cysteine solution. From that final absorbance value, it is possible to calculate the 2-pyridinethiol concentration using the reported extinction coefficient (ε = 8.08 $mM^{-1}.cm^{-1}$).[44] Of interest, we found that this concentration was equal to the initial LC-SPDP concentration, hence further validating that all 2-pyridinethiol groups had been released in the mixture due to cysteine addition.

RESULTS AND DISCUSSION

Primary amine groups were introduced on PET films via an aminolysis reaction occurring in the presence of a short molecule, i.e., ethylenediamine (EtDA), or a 25 kDa aminated polymer, i.e., polyvinylamine (PVAm) as presented in Figure 2. The aminolysis process involves an acyl group substitution in which the PET carbonyl group is used as an electrophile and is attacked by a

Table 1. Atomic Percentages Derived from XPS Analysis of EtDA-Treated PET Films

% v/v EtDA in MeOH (%)[a]	0	30	32	34	36	38	40
			C1s Peak Proportion (at. %)				
C═C	60.97	60.40	60.17	59.70	57.86	54.48	51.91
C−O	21.43	20.97	20.87	20.71	19.49	18.91	18.02
C═O, O═C−N	16.43	15.88	15.24	14.94	13.96	15.63	16.58
"Shake-up"[b]	1.16	2.33	2.24	1.11	1.37	1.58	1.81
C−N	0.00	0.42	1.48	3.55	7.32	9.40	11.69
			N1s Peak Proportion (at. %)				
NH_2	-	40.66	43.04	40.74	29.87	42.28	38.22
NH_3^+	-	3.30	8.23	6.17	19.48	6.50	11.46
O═C−N	-	56.04	48.73	53.09	50.64	51.22	50.32

[a] EtDA grafting was carried out as described in the Material and Methods section. ($n = 1$). [b] The "shake-up" peak, separated by 6.7 eV from C═C peak, is related to the excitations taking place in the π orbitals on the benzene rings.

Table 2. Atomic Percentages Derived from XPS Analysis of PVAm-Treated PET Films

	experimental conditions[a]		
	untreated	PVAm-treated	
	-	pH 4	pH 10
	C 1s Peak Proportion (% at)		
C═C	60.29	53.82	43.00
C−O	21.74	14.54	14.63
C═O, O═C—N	15.83	14.56	14.95
"Shake-up"[b]	1.61	1.85	1.31
C−C	-	7.61	13.05
C−N	-	7.61	13.07
	N 1s peak proportion (% at.)		
NH_2	-	37.50	33.86
NH_3^+	-	23.71	23.62
O═C—N	-	38.79	42.52

[a] PVAm grafting was carried out as described in the Material and Methods section ($n = 1$). [b] The "shake-up" peak, separated by 6.7 eV from C═C peak, is related to the excitations taking place in the π orbitals on the benzene rings.

nucleophilic amine group. As a result of the aminolysis reaction, an ester link (O═C—O) of the PET backbone is cleaved and a covalent amide bond (O═C—N) between the amino-based (macro)molecule and the PET surface is created.

XPS Characterization of Aminated PET Surfaces. XPS analysis was carried out to characterize EtDA and PVAm grafting on PET films as well as to quantify primary amine atomic percentage.

XPS spectrum of pristine PET (Tables 1 and 2, Figure 3A1) showed three main peaks in the C 1s region corresponding to C═C (284.7 eV), C−O (1.40 ± 0.12 eV shift), and C═O (3.68 ± 0.02 eV shift) environments, for which the positions and areas are in good agreement with values reported in the literature.[42] The satellite peak, corresponding to a shift of 6.7 eV, was most likely due to "shake-up" excitations taking place in the π orbitals on the benzene rings.[42]

For all EtDA-treated PET films (Table 1), the best envelope fit of C 1s spectra was obtained by adding one peak compared to untreated films (Figure 3B1); this additional peak was attributed to a C−N bond (0.61 ± 0.12 eV shift). The C−N peak indicated the presence of amino groups on PET surfaces but could not, on its own, confirm the covalent grafting of the EtDA molecule as O═C—N were not distinguishable from O═C—O (3.68 ± 0.02 eV shift). However, the high-resolution N 1s region revealed three components (Figure 3B2) that were attributed to C−NH_2 (398.76 ± 0.11 eV), O═C—N (399.74 ± 0.11 eV), and C−NH_3^+ (400.57 ± 0.11 eV), confirming the presence of both primary amines and covalent grafting. Altogether, as expected, the atomic percentages of C−N increased with EtDA concentration while the atomic percentages of C−O decreased (Table 1), due to EtDA grafting and chain scissions, respectively (Figure 2A). Interestingly, with the exception of the 30% EtDA concentration (for which some cross-linking is expected to be favored), about the same O═C—N/N content was obtained for all EtDA-modified films (ca. 50%). This suggests that, for each EtDA molecule, one of the two primary amine groups was involved in a covalent link to the PET matrix, while the other amino group was exposed to the surface, as already observed.[45]

For C 1s spectra of PVAm-treated PET films (Table 2), in addition to the three peaks assigned to the underlying PET layer, two new peaks were observed (Figure 3C1), i.e., C−N (0.93 ± 0 eV shift) and C−C (0 ± 0 eV shift), indicating the presence of PVAm on the surface. For all PVAm-treated films, the high-resolution N 1s spectra were deconvoluted into three peaks (Figure 3C2) that were attributed to C−NH_2 (398.76 ± 0.12 eV), O═C—N (399.74 ± 0.12 eV), and C−NH_3^+ (400.57 ± 0.12 eV). Once again, the presence of amide bonds suggested that PVAm chains were covalently grafted to the PET matrix.

For both series of functionalized films (Tables 1 and 2), it was observed that the higher the amount of C−N (at. %), the lower the amount of C═C (at. %). Given that the depth probed by XPS (ca. 50 Å) and the number of C═C bonds were constant, such a trend confirmed that the thicker the grafted layer (C−N) was, the thinner the probed underlying PET layer (C═C) was. Interestingly, the amount of C═C (at. %) for PVAm-treated films was found to be slightly lower than for EtDA-treated films, suggesting that the layer of grafted PVAm was thicker than the one obtained with EtDA, in good agreement with the size of the involved molecules.

Amino Group Quantification by Orange II Method. A wide range of amino group density was first generated on PET films by varying the concentration of EtDA in methanol (from 30% to

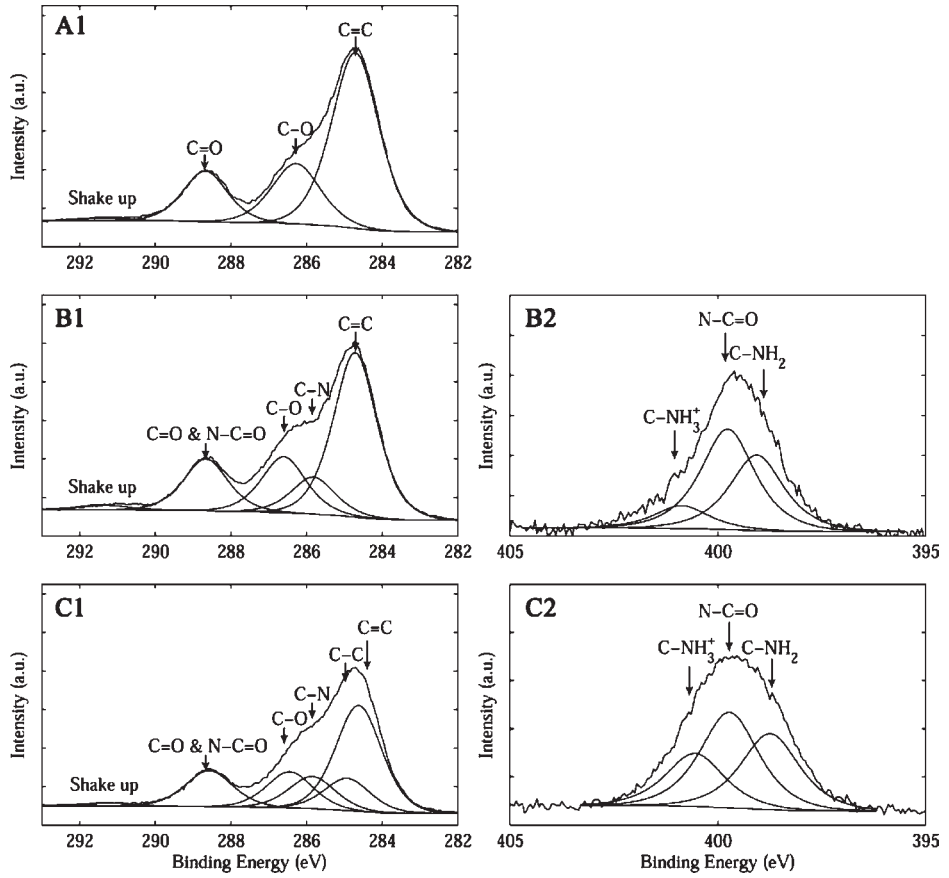

Figure 3. Characterization of EtDA and PVAm grafting by XPS. High-resolution XPS (1) C 1s and (2) N 1s spectra of (A) pristine, (B) EtDA-treated, and (C) PVAm-treated PET films. EtDA concentration was 40% v/v and PVAm grafting was carried out at pH 10.

40% v/v), according to previously described reaction parameters.[10,11] The amount of exposed primary amine groups was then quantified using the Orange II method, the latter being based on the reversible electrostatic interactions between the negatively charged sulfonated dye (Figure 1A) and the positive charge of protonated amino groups in acidic solution. Under alkaline conditions (pH 12), the neutral amino groups induced Orange II release into the solution, which absorbance was measured to evaluate the desorbed dye quantity.[37] The Orange II binding reaction onto protonated amino groups was complete after 30 min at 40 °C at pH 3 (data not shown), as previously observed.[23] Besides, the adsorbed dye content reached a plateau for pH values below 4.5 (data not shown), suggesting that all available amino groups were protonated under such conditions.

For pristine PET surfaces, a nonsignificant Orange II concentration (0.51 ± 0.04 pmol/mm^2) was obtained, suggesting that nonspecific interactions between the PET substrate and the dye were negligible. For EtDA-modified films, the concentration of desorbed dye in the solution, and therefore the density of EtDA grafted on the PET films, increased with the amount of EtDA used for derivatization (Figure 4A), validating a correlation between the amino group density and the Orange II concentration. The range of dye density was found to be between 6.0 ± 1.9 to 159.2 ± 24.8 pmol/mm^2 for EtDA concentration varying from 30% to 40% v/v in methanol, respectively. As previously reported for reaction time,[10] the Orange II density was observed to rise exponentially with EtDA concentration (Figure 4A). Such an exponential behavior is most likely attributable to an increase of surface roughness, as highlighted from SEM images (Figure 4B). That is, the specific polymer area accessible to the dye does increase due to a nonhomogeneous chain scission within the PET layer during the aminolysis reaction.

As an alternative to EtDA-based surface derivatization, we recently proposed the use of PVAm for PET surface modification,[16] as this method may preserve PET mechanical properties while introducing amino functionalities (unpublished results). Two experimental conditions, adapted from previous work,[16] were also explored in order to modulate the amino group density. More specifically, the chemical reactions were performed at pH 10 and 4 (see Materials and Methods section), giving rise to Orange II densities of 82.6 ± 2.4 and 5.1 ± 0.6 pmol/mm^2, respectively (data not shown). This difference was expected, since pH drastically influences the ratio of protonated versus unprotonated amino groups of PVAm ($pK_a \approx 9.25$)[46] and since the aminolysis reaction requires nucleophilic unprotonated amines (Figure 2B).

Comparison between Orange II Densities and XPS Measurements. Quantitative densities of Orange II adsorbed on aminated PET films were compared with the atomic content of C-NH_2 derived from XPS analysis (Figure 5). The C-NH_2 data corresponded to the product of %C−N by (%NH_2 + %NH_3^+), resulting from deconvolution of C 1s peak and N 1s peak, respectively (Tables 1 and 2). For EtDA-treated films, a linear correlation was obtained for EtDA concentration ranging from 0% to 38% v/v ($R^2 = 0.987$, $p < 0.001$), validating the Orange II method for primary amine quantification. The extreme experimental

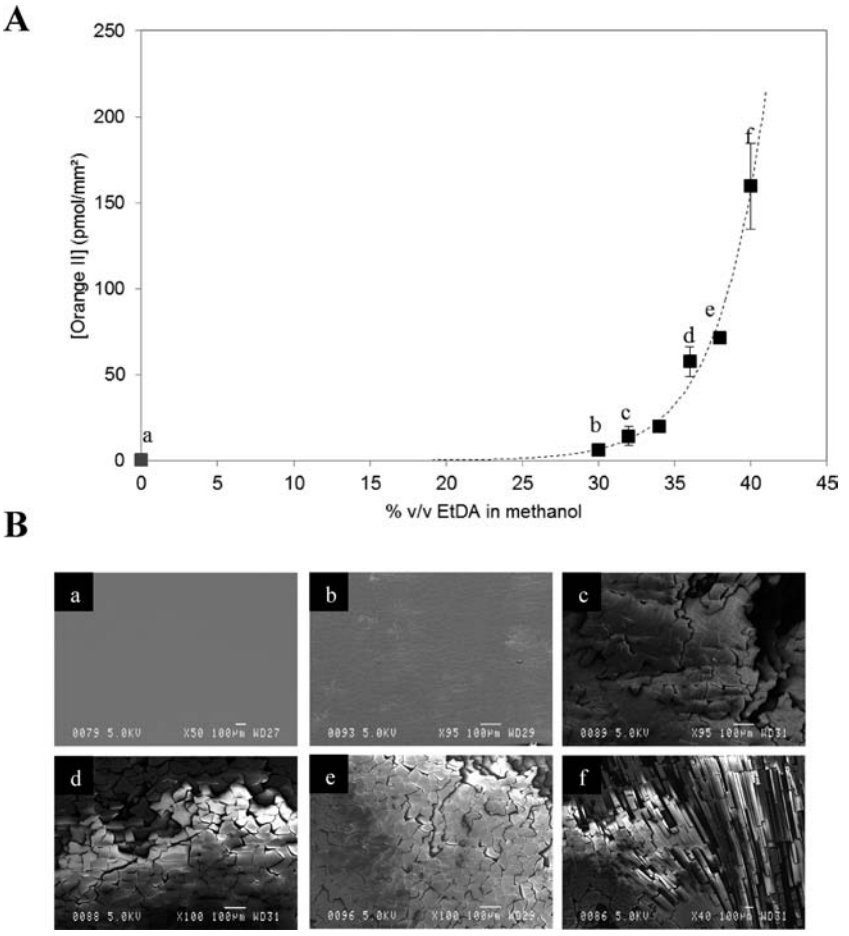

Figure 4. Characterization of EtDA-modified PET films by (A) the Orange II assay (n = 3) and by (B) SEM imaging for EtDA concentrations in methanol ranging from 30% to 40% v/v (a, 0%; b, 30%; c, 32%; d, 36%; e, 38%; f, 40%). The dashed line is only a guide for the eyes.

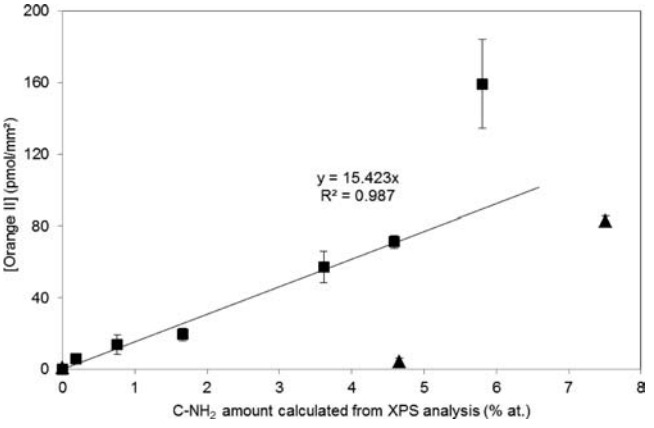

Figure 5. Correlation between amino group quantification from XPS analysis and adsorbed Orange II concentration for (■) EtDA-treated and (▲) PVAm-treated PET films (n = 3).

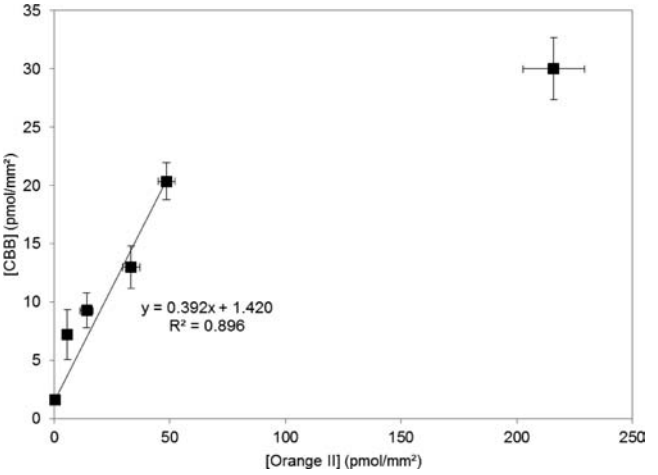

Figure 6. Correlation between Coomassie Brilliant Blue (CBB) and Orange II colorimetric methods for EtDA-treated PET films (n = 3). The highest point was excluded from the linear regression.

condition (i.e., 40% EtDA v/v) was characterized by relatively low C−NH_2 content, as determined from XPS measurements, and high Orange II value; this experimental condition was not properly described by the linear correlation. This outlier could be explained by the extreme roughness of the corresponding surfaces (Figure 4B, image f). That is, an excessive surface roughness could have indeed induced an overestimation of Orange II concentrations (due to a non-negligible increase of specific area) as well as undervalued C−NH_2 content from XPS measurements (since the analysis depth of XPS samples was kept constant, ca. 50 Å).[34]

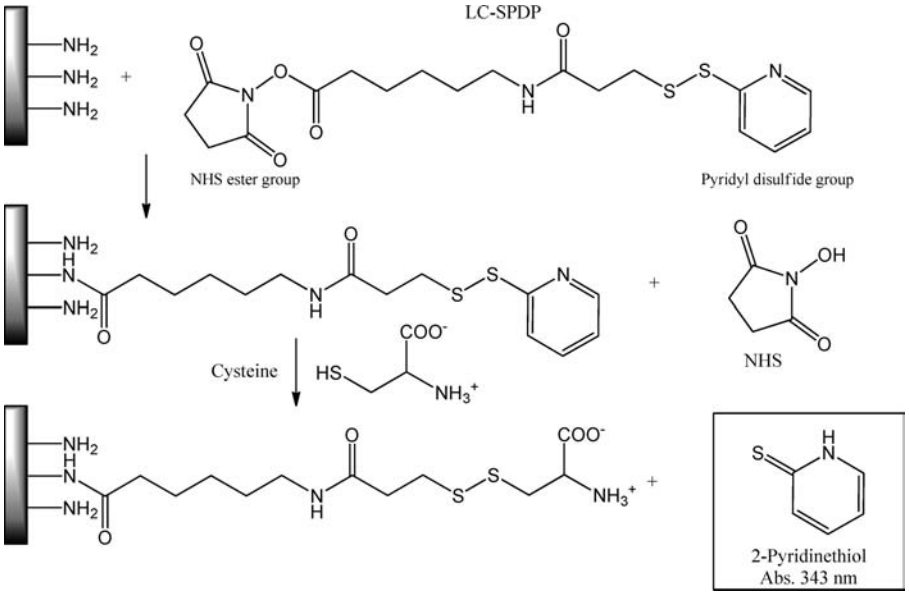

Figure 7. Schematic illustration of functionalization of amino-modified PET surfaces with heterobifunctional LC-SPDP molecules, followed by subsequent reaction with cysteine. The amount of released 2-pyridinethiol was measured at 343 nm.

The Orange II densities of PVAm-grafted films (i.e., 5.1 ± 0.6 and 82.6 ± 2.4 pmol/mm^2) were found to be in the same range as those obtained for EtDA-coated films (i.e., from 0.51 ± 0.04 to 159.2 ± 24.8 pmol/mm^2). However, the densities appeared to be underestimated when compared with the linear trend we previously determined for EtDA grafting (Figure 5), suggesting that all the PVAm amino groups detected by the XPS analysis were not able to interact with the dye. Such a difference between the two quantification techniques is most probably related to the polymer conformation at the PET surface, making some amino groups of the inner PVAm layer inaccessible to the dye. If our hypothesis is true, the Orange II method should provide a better quantitative prediction of the amount of primary amine groups that are readily accessible for subsequent chemical functionalization.

Comparison between Orange II and Coomassie Brilliant Blue Method. Many other dyes are commonly used to quantify primary amine groups onto solid surfaces.[23,38,39] Among these, the ability of Coomassie Brilliant Blue (a large divalent dye, Figure 1B) to quantify surface amino groups was compared to that of the small monovalent Orange II (Figure 1A) in terms of adsorbed densities onto aminated surfaces.

For both EtDA- and PVAm-treated PET films, dye densities obtained by the Coomassie Brilliant Blue (CBB) method were plotted as a function of those determined by the Orange II method (Figure 6). Interestingly, the CBB density measured on pristine PET (1.62 ± 0.19 pmol/mm^2) was found to be higher than that of Orange II (0.51 ± 0.04 pmol/mm^2), the former thus exhibiting higher nonspecific adsorption onto PET surfaces. As the experimental conditions (pH, time, temperature, solvent) were already optimized in the literature for the two colorimetric methods,[23,24] both dyes were supposed to detect accessible amino groups. However, for all the aminated PET films, densities determined by the CBB method were lower than those determined by the Orange II method (Figure 6). Such a result strongly suggests that steric hindrance between CBB molecules prevented them from binding to some amine moieties, inducing lower surface binding when compared to that of small Orange II molecules. Of interest, for Orange II densities below 50 pmol/mm^2, a linear correlation was found between the two dye densities (R^2 = 0.896, p < 0.01), showing a slope of 0.39 (Figure 6). This result suggests that, in this range, the CBB dye is indeed likely to bind to amino groups with a stoichiometry of 2:1 on account of its two charges per molecule, as previously proposed by Uchida et al.[23] As a consequence, Orange II dye appeared appropriate for amino group detection in a wide range of densities, in a quantitative and specific manner.

Functionalization of Aminated Surfaces with LC-SPDP. In order to confirm the ability of the Orange II dye to detect only available amino groups, a commonly used heterobifunctional linker (LC-SPDP, Figure 1C) was chemically grafted on both EtDA- and PVAm-modified PET films. The amine reactive N-hydroxysuccinimide (NHS) ester group of LC-SPDP reacted with the free primary amines on the modified PET surfaces at pH 7.4, to form a stable amide bond (Figure 7). The pyridyl disulfide group, located by the other end of the LC-SPDP linker, reacts specifically with thiol groups. Of interest, such a linker enables an oriented immobilization of cysteine-tagged protein. Proteins or other biomolecules grafted on LC-SPDP-covered surfaces can be quantified by UV readout thanks to the 2-pyridinethiol release induced by the reaction (Figure 7).[47] In order to eliminate any potential bias related to the size of the protein to be grafted, cysteine (i.e., the smallest thiol-containing proteinaceous unit) was reacted with the LC-SPDP-modified PET films. Under our conditions (i.e., large excess of cysteine and 60 min reaction), the reaction was observed to be complete in solution (1:1 stoichiometry between LC-SPDP and released groups) and thus allowed for the direct quantification of linker density.

The concentration of added LC-SPDP was optimized for a 15 min reaction at 20 °C (Figure 8A). The grafted linker density, assessed by released 2-pyridinethiol concentration upon cysteine addition, reached a plateau for LC-SPDP concentrations higher than 1 mM. Accordingly, 1 mM LC-SPDP solutions were used for subsequent grafting experiments.

LC-SPDP grafting kinetics were then studied by varying reaction time and temperature (Figure 8B) in order to get the

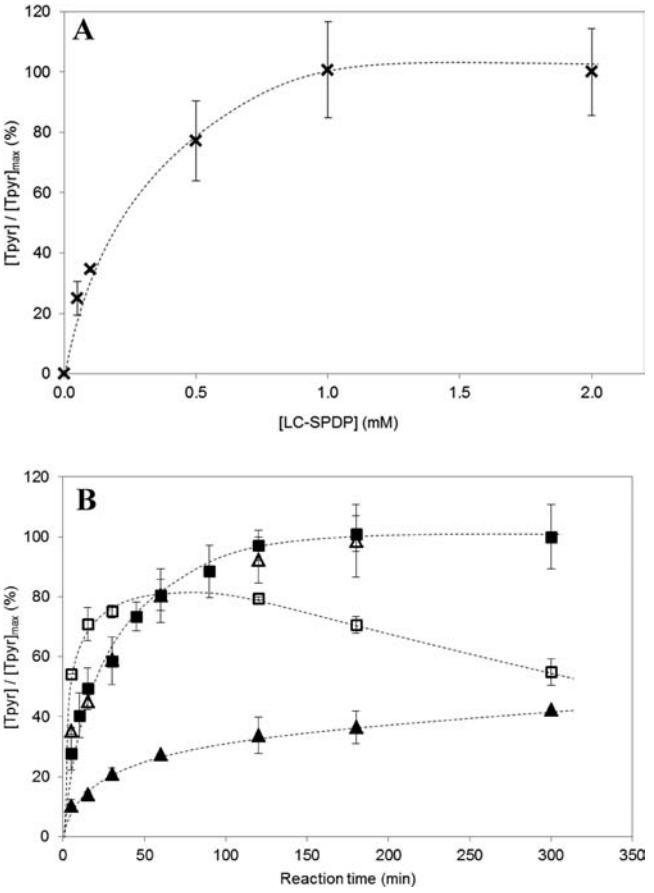

Figure 8. LC-SPDP grafting optimization on 38% EtDA-treated PET films (n = 3). (A) Influence of the LC-SPDP concentration in the reaction mixture for a reaction performed for 15 min at 20 °C. (B) Time course of the LC-SPDP grafting performed at (▲) 20 °C, (Δ) 30 °C, (■) 40 °C, and (□) 50 °C in a 1 mM linker solution. Grafted LC-SPDP densities were quantified thanks to 2-pyridinethiol release ([Tpyr]) determined by UV-readout, as described in the Materials and Methods section. The [Tpyr] values were normalized by the asymptotic value ($[Tpyr]_{max}$) obtained using a 2 mM solution and at 40 °C for (A) and (B), respectively. Dashed lines are guides for the eyes.

best surface coverage. As expected, the initial rate of the grafting reaction increased with temperature. After few hours (ca. 150 min), the same plateau value was reached at 30 and 40 °C (247 ± 15 pmol/mm^2), strongly suggesting that this maximum value could be accounted for a complete surface coverage. Quite different behaviors were observed for reactions carried out at both 20 and 50 °C. For the latter, the amount of released 2-pyridinethiol was found to decrease after a 60 min reaction, due to the instability of the thiol-reactive (pyridyl disulfide) groups at 50 °C (Figure 9). At 20 °C, the reaction was slower after 120 min of reaction, most likely due to the limited half-life of the NHS ester group of LC-SPDP at pH 7.4.[44] Accordingly, the grafted LC-SPDP density was found to be the best for a 150 min reaction at 40 °C in a 1 mM linker solution. Note that, for these experimental conditions, a loss of 7% of pyridyl disulfide groups was observed prior to cysteine grafting (Figure 9).

Comparison between Orange II Densities and Grafted LC-SPDP Densities. EtDA- and PVAm-covered PET films were reacted with LC-SPDP under our optimized conditions, i.e., at 40 °C for 150 min in a 1 mM solution. Linker densities on PET

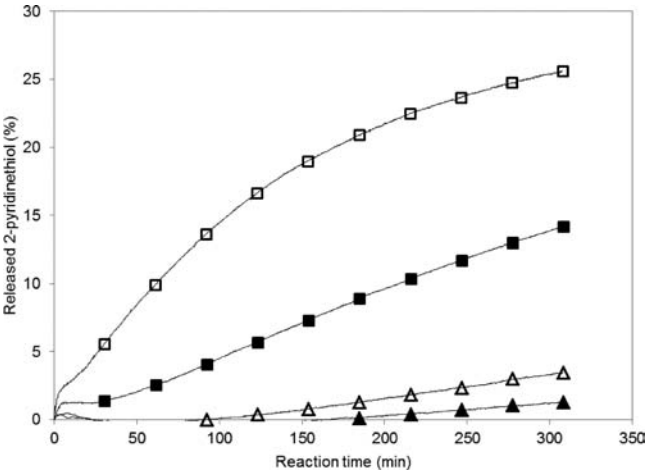

Figure 9. Stability of thiol-reactive groups of LC-SPDP. The release of 2-pyridinethiol was measured by stopped-flow absorbance at 343 nm in a LC-SPDP solution (0.1 mM, 90:10 v/v PBS/DMSO) at (—▲—) 20 °C, (—Δ—) 30 °C, (—■—) 40 °C, and (—□—) 50 °C. Absorbance values were normalized by the one measured after cysteine addition, as described in the Materials and Methods section.

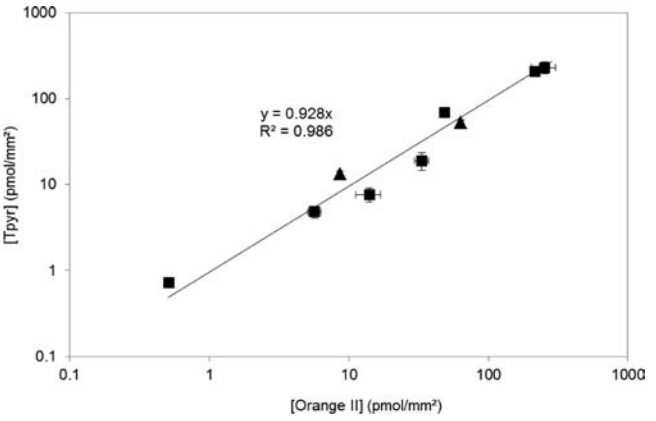

Figure 10. Correlation between released 2-pyridinethiol density and Orange II density assayed for (■) EtDA-treated and (▲) PVAm-treated PET films (n = 3). Treated PET films were reacted with a 1 mM LC-SPDP solution for 150 min at 40 °C. The 2-pyridinethiol concentration ([Tpyr]) corresponds to the grafted LC-SPDP density, as described in the Results and Discussion section.

films, thereby reaching maximized LC-SPDP surface coverage, were then determined thanks to the 2-pyridinethiol release induced by cysteine grafting, as described earlier (Figure 7). Quantification of LC-SPDP-modified amino groups was compared with Orange II densities (Figure 10), showing a linear correlation for all EtDA- and PVAm-covered films (R^2 = 0.986, p < 0.001), with a slope close to 1 (0.928). Such an excellent correlation thus demonstrates that all amino groups that were available for Orange II binding were also available for LC-SPDP grafting on EtDA- and PVAm-modified films. Primary amine density as determined by the Orange II colorimetric method being so closely correlated to the amount of grafted LC-SPDP unambiguously confirmed Orange II as an appropriate method for the quantification of amino groups available for subsequent biofunctionalization with a 1:1 stoichiometry.

CONCLUSION

In this article, a rapid and convenient method using the Orange II dye was validated to quantify the amount of primary amine groups grafted on PET surfaces and available for subsequent functionalization.

Aminated surfaces were first generated via the PET chain scission-based aminolysis reaction involving diamine molecules (EtDA). Results given by the Orange II assays were found to be reliable, quantitative, and specific for a wide range of amino group surface densities (ca. 5 to at least 200 pmol/mm^2). SEM images revealed that the PET chemical etching was significant for high EtDA concentrations (ca. 40% v/v). Induced PET surface roughness was found to strongly interfere with conclusions drawn from XPS measurements but not from those derived from Orange II measurements.

As an alternative to surface-damaging EtDA functionalization, PET films were aminolyzed with polyamine chains (PVAm). For PVAm-treated films, the correlation between Orange II densities and XPS measurements was significantly different from the linear behavior observed with EtDA-treated films, most likely due to the fact that amino groups of the inner PVAm layer were not available for Orange II binding. Interestingly, subsequent LC-SPDP grafting revealed that those unavailable amino groups were not accessible to the linker either. Therefore, as opposed to Coomassie Brilliant Blue assays or XPS measurements, the Orange II-based quantification of amino groups was shown to be appropriate to quantitatively predict subsequent functionalization of both EtDA- and PVAm-treated PET surfaces by LC-SPDP, and potentially other types of molecules.

AUTHOR INFORMATION

Corresponding Author

*E-mail: gregory.decrescenzo@polymtl.ca; Tel: (514) 340-4711 (#7428); Fax: (514) 340-2990.

Author Contributions

§Both authors contributed equally to this manuscript.

ACKNOWLEDGMENT

This work was supported by the Natural Sciences and Engineering Council of Canada (NSERC) and the Canada Research Chair Protein-enhanced Biomaterials (G.D.C.). The authors would also like to thank Suzie Poulin and Nathalie Raymond for their help or advice during the conduction of this experimental work.

REFERENCES

(1) Goddard, J. M., and Hotchkiss, J. H. (2007) Polymer surface modification for the attachment of bioactive compounds. *Prog. Polym. Sci. 32*, 698–725.

(2) Ma, Z. W., Mao, Z. W., and Gao, C. Y. (2007) Surface modification and property analysis of biomedical polymers used for tissue engineering. *Colloids Surf., B 60*, 137–157.

(3) Muthuvijayan, V., Gu, J., and Lewis, R. S. (2009) Analysis of functionalized polyethylene terephthalate with immobilized NTPDase and cysteine. *Acta Biomater. 5*, 3382–3393.

(4) Bide, M., Phaneuf, M., Brown, P., McGonigle, G., and LoGerfo, F. (2006) Modification of polyester for medical uses. *Modified fibers with medical and specialty applications* (Edwards, J. V., Buschle-Diller, G., and Goheen, S. C., Eds.) pp 91−124, Springer, Netherlands.

(5) Zhu, Y., Gao, C., He, T., and Shen, J. (2004) Endothelium regeneration on luminal surface of polyurethane vascular scaffold modified with diamine and covalently grafted with gelatin. *Biomaterials 25*, 423–430.

(6) Hamerli, P., Weigel, T., Groth, T., and Paul, D. (2003) Enhanced tissue-compatibility of polyethylenterephtalate membranes by plasma aminofunctionalisation. *Surf. Coating Technol. 174−175*, 574–578.

(7) Albrecht, W., Seifert, B., Weigel, T., Schossig, M., Hollander, A., Groth, T., and Hilke, R. (2003) Amination of poly(ether imide) membranes using di- and multivalent amines. *Macromol. Chem. Phys. 204*, 510–521.

(8) Mwale, F., Girard-Lauriault, P. L., Wang, H. T., Lerouge, S., Antoniou, J., and Wertheimer, M. R. (2006) Suppression of genes related to hypertrophy and osteogenesis in committed human mesenchymal stem cells cultured on novel nitrogen-rich plasma polymer coatings. *Tissue Eng. 12*, 2639–2647.

(9) Yan-Peng, J., and Fu-Zhai, C. (2007) Surface modification of polyester biomaterials for tissue engineering. *Biomed. Mater. 2*, R24–R37.

(10) Bech, L., Meylheuc, T., Lepoittevin, B., and Roger, P. (2007) Chemical surface modification of poly(ethylene terephthalate) fibers by aminolysis and grafting of carbohydrates. *J. Polym. Sci., Part A: Polym. Chem. 45*, 2172–2183.

(11) Irena, G., Jolanta, B., and Karolina, Z. (2009) Chemical modification of poly(ethylene terephthalate) and immobilization of the selected enzymes on the modified film. *Appl. Surf. Sci. 255*, 8293–8298.

(12) Dominick, W. D., Berhane, B. T., Mecomber, J. S., and Limbach, P. A. (2003) Covalent immobilization of proteases and nucleases to poly(methylmethacrylate). *Anal. Bioanal. Chem. 376*, 349–354.

(13) Boucher, C., Ruiz, J.-C., Thibault, M., Buschmann, M. D., Wertheimer, M. R., Jolicoeur, M., Durocher, Y., and De Crescenzo, G. (2010) Human corneal epithelial cell response to epidermal growth factor tethered via coiled-coil interactions. *Biomaterials 31*, 7021–7031.

(14) Papra, A., Hicke, H., and Paul, D. (1999) Synthesis of peptides onto the surface of poly (ethylene terephthalate) particle track membranes. *J. Appl. Polym. Sci. 74*, 1669–1674.

(15) Jiang, X.-S., Chai, C., Zhang, Y., Zhuo, R.-X., Mao, H.-Q., and Leong, K. W. (2006) Surface-immobilization of adhesion peptides on substrate for ex vivo expansion of cryopreserved umbilical cord blood CD34+ cells. *Biomaterials 27*, 2723–2732.

(16) Dimitrievska, S., Maire, M., Diaz-Quijada, G. A., Robitaille, L., Ajji, A., Yahia, L. H., Moreno, M., Merhi, Y., and Bureau, M. N. (2011) Low thrombogenicity coating of nonwoven PET fiber structures for vascular grafts. *Macromol. Biosci. 11*, 493–502.

(17) Liberelle, B., Boucher, C., Chen, J., Jolicoeur, M., Durocher, Y., and De Crescenzo, G. (2010) Impact of epidermal growth factor tethering strategy on cellular response. *Bioconjugate Chem. 21*, 2257–2266.

(18) Hinterwirth, H., Strobl, M., and Al-Dubai, H. (2010) Analytical methods for detection of small amounts of amino groups on solid surfaces: a survey. *Monatsh. Chem. 141*, 291–299.

(19) Ivanov, V. B., Behnisch, J., Holländer, A., Mehdorn, F., and Zimmermann, H. (1996) Determination of functional groups on polymer surfaces using fluorescence labelling. *Surf. Interface Anal. 24*, 257–262.

(20) Janolino, V., and Swaisgood, H. (1992) A spectrophotometric assay for solid phase primary amino groups. *Appl. Biochem. Biotechnol. 36*, 81–85.

(21) Cook, A. D., Pajvani, U. B., Hrkach, J. S., Cannizzaro, S. M., and Langer, R. (1997) Colorimetric analysis of surface reactive amino groups on poly(lactic acid-co-lysine):poly(lactic acid) blends. *Biomaterials 18*, 1417–1424.

(22) Kakabakos, S. E., Tyllianakis, P. E., Evangelatos, G. P., and Ithakissios, D. S. (1994) Colorimetric determination of reactive solid-supported primary and secondary amino groups. *Biomaterials 15*, 289–297.

(23) Uchida, E., Uyama, Y., and Ikada, Y. (1993) Sorption of low-molecular-weight anions into thin polycation layers grafted onto a film. *Langmuir 9*, 1121–1124.

(24) Coussot, G., Perrin, C., Moreau, T., Dobrijevic, M., Le Postollec, A., and Vandenabeele-Trambouze, O. (2011) A rapid and reversible colorimetric assay for the characterization of aminated solid surfaces. *Anal. Bioanal. Chem. 399*, 1061–1069.

(25) Coussot, G., Faye, C., Ibrahim, A., Ramonda, M., Dobrijevic, M., Le Postollec, A., Granier, F., and Vandenabeele-Trambouze, O. (2011) Aminated dendritic surfaces characterization: a rapid and versatile colorimetric assay for estimating the amine density and coating stability. *Anal. Bioanal. Chem. 399*, 2295–2302.

(26) Gaur, R. K., and Gupta, K. C. (1989) A spectrophotometric method for the estimation of amino groups on polymer supports. *Anal. Biochem. 180*, 253–258.

(27) Aflori, M., Drobota, M., Timpu, D., and Barboiu, V. (2008) Studies of amine treatments influence on poly(ethyleneterepthalate) films. *Optoelectron. Adv. Mater., Rapid Commun. 2*, 291–295.

(28) Nissen, K. E., Stuart, B. H., Stevens, M. G., and Baker, A. T. (2008) Characterization of aminated poly(ethylene terephthalate) surfaces for biomedical applications. *J. Appl. Polym. Sci. 107*, 2394–2403.

(29) Dauginet, L., Duwez, A. S., Legras, R., and Demoustier-Champagne, S. (2001) Surface modification of polycarbonate and poly(ethylene terephthalate) films and membranes by polyelectrolyte deposition. *Langmuir 17*, 3952–3957.

(30) Ohe, T., Yoshimura, Y., Abe, I., Ikeda, M., and Shibutani, Y. (2007) Chemical introduction of sugars onto PET fabrics using diamine and cyanuric chloride. *Text. Res. J. 77*, 131.

(31) Mangovska, B., Bogoeva-Gaceva, G., and Pohlers, A. (1996) Structure and basic properties of aminated PET. *J. Appl. Polym. Sci. 62*, 605–612.

(32) Hartwig, A., Mulder, M., and Smolders, C. A. (1994) Surface amination of poly(acrylonitrile). *Adv. Colloid Interface Sci. 52*, 65–78.

(33) Zemljic, F. (2009) Characterization of amino groups for cotton fibers coated with chitosan. *Text. Res. J. 79*, 219.

(34) Siow, K. S., Britcher, L., Kumar, S., and Griesser, H. J. (2006) Plasma methods for the generation of chemically reactive surfaces for biomolecule immobilization and cell colonization - A review. *Plasma Processes Polym. 3*, 392–418.

(35) Yu, D.-G., Lin, W.-C., and Yang, M.-C. (2007) Surface modification of poly(l-lactic acid) membrane via layer-by-layer assembly of silver nanoparticle-embedded polyelectrolyte multilayer. *Bioconjugate Chem. 18*, 1521–1529.

(36) Nakajima, N., and Ikada, Y. (1995) Mechanism of amide formation by carbodiimide for bioconjugation in aqueous media. *Bioconjugate Chem. 6*, 123–130.

(37) Goddard, J. M., and Hotchkiss, J. H. (2008) Tailored functionalization of low-density polyethylene surfaces. *J. Appl. Polym. Sci. 108*, 2940–2949.

(38) Chazalnoel, P., Coussot, G., Desvignes, I., Dobrijevic, M., Le Postollec, A., Vandenabeele, T. O., Vandenabeele-Trambouze, O. (2009) Method for detecting and quantifying a molecule including at least one proton group on a solid substrate. Eur. Patent 2928457 A1.

(39) Coussot, G., Nicol, E., Commeyras, A., Desvignes, I., Pascal, R., and Vandenabeele-Trambouze, O. (2009) Colorimetric quantification of amino groups in linear and dendritic structures. *Polym. Int. 58*, 511–518.

(40) Topala, I., Dumitrascu, N., and Pohoata, V. (2007) Influence of plasma treatments on the hemocompatibility of PET and PET + TiO_2 films. *Plasma Chem. Plasma Process 27*, 95–112.

(41) Ichinose, J., Morimatsu, M., Yanagida, T., and Sako, Y. (2006) Covalent immobilization of epidermal growth factor molecules for single-molecule imaging analysis of intracellular signaling. *Biomaterials 27*, 3343–3350.

(42) Beamson, G., and Briggs, D. (1992) *High resolution XPS of organic polymers: the Scienta ESCA300 database*, Wiley, Chichester.

(43) Boucher, C., Liberelle, B., Jolicoeur, M., Durocher, Y., and De Crescenzo, G. (2009) Epidermal growth factor tethered through coiled-coil interactions induces cell surface receptor phosphorylation. *Bioconjugate Chem. 20*, 1569–1577.

(44) Carlsson, J., Drevin, H., and Axen, R. (1978) Protein thiolation and reversible protein-protein conjugation. N-Succinimidyl 3-(2-pyridyldithio)propionate, a new heterobifunctional reagent. *Biochem. J. 173*, 723–37.

(45) Keen, I., Broota, P., Rintoul, L., Fredericks, P., Trau, M., and Grøndahl, L. (2006) Introducing amine functionalities on a poly(3-hydroxybutyrate-co-3-hydroxyvalerate) surface: comparing the use of ammonia plasma treatment and ethylenediamine aminolysis. *Biomacromolecules 7*, 427–434.

(46) Renken, A., and Hunkeler, D. (2007) Polyvinylamine-based capsules: A mechanistic study of the formation using alginate and cellulose sulphate. *J. Microencapsulation 24*, 323–336.

(47) Ghasemi, M., Minier, M., Tatoulian, M., and Arefi-Khonsari, F. (2007) Determination of amine and aldehyde surface densities: application to the study of aged plasma treated polyethylene films. *Langmuir 23*, 11554–61.

Bioconjugate Chemistry

ARTICLE

pubs.acs.org/bc

Targeted, Activatable, In Vivo Fluorescence Imaging of Prostate-Specific Membrane Antigen (PSMA) Positive Tumors Using the Quenched Humanized J591 Antibody−Indocyanine Green (ICG) Conjugate

Takahito Nakajima,[†] Makoto Mitsunaga,[†] Neil H. Bander,[‡] Warren D. Heston,[§] Peter L. Choyke,[†] and Hisataka Kobayashi*[,†]

[†]Molecular Imaging Program, Center for Cancer Research, National Cancer Institute, National Institutes of Health, Bethesda Maryland 20892, United States

[‡]Department of Urology, Weill Medical College of Cornell University, New York, New York 10065, United States

[§]Department of Cancer Biology and Urological Institute, Cleveland Clinic, Cleveland, Ohio 44195, United States

ABSTRACT: In patients with prostate cancer, a positive surgical margin is associated with an increased risk of cancer recurrence and poorer outcome, yet margin status cannot be determined during the surgery. An *in vivo* optical imaging probe that could identify the tumor margins during surgery could result in improved outcomes. The design of such a probe focuses on a highly specific targeting moiety and a near-infrared (NIR) fluorophore that is activated only when bound to the tumor. In this study, we successfully synthesized an activatable monoclonal antibody−fluorophore conjugate consisting of a humanized anti-Prostate-Specific Membrane Antigen (PSMA) antibody (J591) linked to an indocyanine green (ICG) derivative. Prior to binding to PSMA and cellular internalization, the conjugate yielded little light; however, after binding an 18-fold activation was observed permitting the specific detection of PSMA+ tumors up to 10 days after injection of a low dose (0.25 mg/kg) of the reagent. This agent demonstrates promise as a method to image the extent of prostate cancer in vivo and could assist with real-time resection of extracapsular extension of tumor and positive lymph nodes.

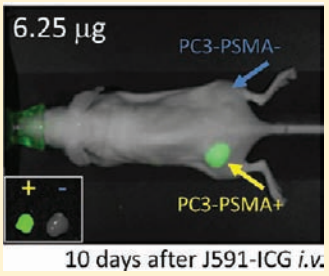

INTRODUCTION

Prostate cancer is the second leading cause of cancer mortality in men. Surgical resection is associated with a high cure rate in men with low risk tumors; however, the risk of recurrent disease rises with the Gleason score and clinical stage of the tumor. Nevertheless, especially in patients with locally invasive prostate cancer, long-term cancer control can be achieved if adequate margins are obtained at surgery. Unfortunately, despite improving clinical imaging modalities,[1−3] the process of achieving negative margins is retrospective and is determined post hoc by histopathology. A method to aid the surgeon in obtaining negative margins during the procedure would be welcomed and could be anticipated to result in better patient outcomes. In order to achieve this goal, a highly specific optical imaging probe must be developed that fulfills at least two criteria. The agent must be highly targeted to prostate cancer with few false positives, and the fluorescent probe to which the targeting ligand is attached must be activatable only at sites of tumor in order to achieve adequate target to background ratios (TBR) to display the tumor in real time to the surgeon. Additionally, the fluorescent probe should emit light in the near-infrared (NIR) to permit deeper tissue penetration than is possible with visible light.

Prostate specific membrane antigen (PSMA) is a type 2 integral membrane glycoprotein, also known as glutamate carboxypeptidase II (GCPII)[4] and folate hydrolase 1, found initially in prostate cancer cell lines (LNCaP)[5] and a few other tissues including kidney, intestine, and central nervous system.[6] It is considered the most well-established cell membrane marker of prostate cancer and therefore a plausible target for an optical probe. PSMA is expressed on tumor cells as a noncovalent homodimer.[7] PSMA has been used in imaging as a single photon emission computed tomography (SPECT) scan in which a PSMA antibody (capromab pentitide, ProstaScint) is labeled with radioactive indium-111.[8] Experimentally, small PSMA receptor binding ligands have also been tested[9] for imaging prostate cancer. These methods have met with variable success, in part owing to the specificity of the capromab antibody used: it recognizes an intracellular epitope that is only accessible to circulating antibody when the cell membrane is disrupted. Furthermore, while SPECT scans are potentially useful in the preoperative or postoperative setting, they are of little value for surgical guidance or on-site tissue diagnosis because they offer low spatial and temporal resolution. Optical probes, however, could provide higher resolution and near real time imaging without the risks to the patient and surgeon, associated with exposure to ionizing radiation.

Received: May 28, 2011
Revised: June 27, 2011
Published: July 10, 2011

ACS Publications © 2011 American Chemical Society

dx.doi.org/10.1021/bc2002715 | *Bioconjugate Chem.* 2011, 22, 1700–1705

Herein, we describe our initial experience with an optical antibody−flourophore conjugate consisting of an anti-PSMA humanized antibody (J591) coupled to an activatable NIR fluorophore indocyanine green (ICG).[10] We tested this agent in PSMA-expressing and non-expressing prostate cancer xenografts in mice and compared it to a comparable conjugate, trastuzumab−ICG (Tra−ICG) which targets HER2 expressing tumors.

EXPERIMENTAL PROCEDURES

Reagents. Two humanized monoclonal antibodies were used in this study: J591, a humanized PSMA-specific monoclonal antibody, was developed at Weill Cornell Medical College (New York, NY) by one of the authors (NHB); trastuzumab (Tra), a humanized anti-HER-2 antibody, was purchased from Genentech Inc. (South San Francisco, CA). For activatable labeling of antibodies, ICG-sulfo-OSu was purchased from Dojindo Molecular Technologies (Gaithersburg, MD) and IR700DX NHS ester (IR700) was purchased from LI-COR Biosciences (Lincoln, NE). All other chemicals used were of reagent grade.

Synthesis of Fluorophore Conjugated Antibodies. Both humanized monoclonal antibodies J591 and Tra (1 mg, 6.2 nmol) were incubated with ICG-sulfo-OSu (50 nmol, 1:8) or IR700 (31 nmol, 1:5) in 0.1 M Na_2HPO_4 (pH 8.5) at room temperature for 30 min. Then the mixture was purified with a Sephadex G50 column (PD-10; GE Healthcare, Piscataway, NJ). The elution fraction of 1.8 mL obtained from 2.6 to 4.4 mL of the elutant was collected. The concentration of ICG or IR700 was measured by absorption with a UV−vis system (model 8453 UV−visible value system; Agilent Technologies, Santa Clara, CA) to confirm the number of fluorophore molecules conjugated to each antibody molecule. The number of ICG per each antibody measured was ∼1 for ICG at the quenching state or ∼3 for IR700.

As a quality control of the J591−ICG conjugate, we performed SDS−PAGE and a binding assay with modified Lindmo's method [11] and Scatchard plot using ^{125}I-labeled J591 and J591−ICG, and PC3-PSMA+ cells, as previously described.[12]

Validation of Quenching Ability in Vitro. For validation of the quenching and dequenching ability of bound ICG, both J591−ICG and Tra−ICG conjugates were treated with 1% SDS to diminish hydrophobic k−k interactions and separate IgG chains. The change in fluorescence intensity for each conjugate was measured with an *in vivo* imaging system (Pearl Imager, LI-COR Biosciences) using 785 nm laser excitation and 820 nm emission.

Cell Culture. A PSMA transfected PC3 cell line PC3-PSMA+ (PC3pip) and a control blank-vector transfected PC3 cell line PC3-PSMA− (PC3flu) [13] were used for PSMA targeting studies with activatable J591−ICG conjugates. Both cells were established at the Cleveland Clinic Foundation. For HER2 targeting studies by trastuzumab conjugates, the HER2 transfected NIH3T3 (3T3/HER2) cell line and a control Balb/3T3 cell line were used.[14]

All cell lines were grown in RPMI 1640 medium (Life Technologies, Gaithersburg, MD) containing 10% fetal bovine serum (FBS) (Life Technologies) and 1% Pen-Strep (Biofluids, Camarillo, CA). All cell cultures were maintained in 5% carbon dioxide (CO_2) at 37.0 °C in a humidified incubator.

Flow Cytometry. Fluorescence signal from PC3 cells after incubation with ICG- or IR700-conjugated J591 agents was measured using a FACSCalibur flow cytometer (BD Biosciences, San Jose, CA) and CellQuest software (BD Biosciences). Briefly, for the binding experiment, 1×10^5 PC3-PSMA+ or PC3-PSMA− cells were incubated with J591−ICG or J591−IR700 at 37.0 °C for 8 h. To validate the specific binding of the antibody, excess J591 antibody (50 μg) was used to block 0.5 μg of J591−IR700 conjugates.

Fluorescence Microscopy Studies. PC3-PSMA+ cells (1×10^4) were plated on a covered glass-bottomed culture well and incubated for 16 h. Then J591−ICG was added to the medium (5 μg/mL) and the cells were incubated for either 1 or 8 h. Cells were washed once with PBS, and fluorescence microscopy was performed using an Olympus BX61 microscope (Olympus America, Inc.) equipped with the following filters: excitation wavelength 672.5−747.5 nm, emission wavelength 765−855 nm. Transmitted light differential interference contrast (DIC) images were also acquired. As a control, the conjugates were also incubated with PC3-flu (PSMA negative) cells.

Animal Tumor Model. All procedures were carried out in compliance with the Guide for the Care and Use of Laboratory Animal Resources (1996), National Research Council, and approved by the local Animal Care and Use Committee. The 7- to 8-week old, athymic nu/nu mice were used for all experiments. Both receptor positive and negative tumor cell lines were implanted in the same mice.

For PSMA targeting studies, 2×10^6 PC3-PSMA+ cells suspended in PBS were injected subcutaneously in the left dorsum of the mice, and the same number of PC3-PSMA− cells were injected subcutaneously into the right dorsum in each mouse.

For HER2 targeting studies, 1×10^6 3T3/HER2 cells suspended in PBS were injected subcutaneously in the left dorsum of the mice, 2 days prior to injecting with 1×10^6 Balb/3T3 cells in PBS into the right dorsum. The imaging experiments were performed at 5−7 days after cell injection, when tumor size is approximately 0.5 cm in diameter.

***In Vivo* PSMA Targeted Imaging Studies.** J591−ICG was diluted in 200 μL of PBS, and a dose of 50, 25, 12.5, or 6.25 μg was then injected via the tail vein into mice bearing both PC3-PSMA+ and PC3-PSMA− tumors. All mice were anesthetized with 2% isoflurane throughout all procedures. Then fluorescence images were obtained using the Pearl Imager (LI-COR Biosciences) at 800 nm at the following time points: 6 h and 1, 2, 3, 4, 6, and 10 days after injection.

Regions of interest were placed on ICG spectrum images with reference to white light to measure fluorescence intensities of PC3-PSMA+ and PC3-PSMA− tumors and body (background) at every time point up to day 6. The software Pearl Cam (LI-COR Biosciences) was used for calculating ROI signal data of each point. After acquisition of images at day 10, mice were sacrificed with carbon dioxide. *Ex vivo* images of resected tumors were obtained.

Comparison of Images between PSMA± and HER2± Tumors. To compare the signal obtained with J591−ICG from PC3-PSMA+ tumor with HER2 targeting images injected with Tra−ICG, both PSMA targeted and HER2 targeted images were serially acquired in side by side views 6 h and 1, 2, 3, and 4 days after injection of J591−ICG or Tra−ICG antibodies (12.5 μg in 200 μL of PBS) into PC3-PSMA± or 3T3-HER2± tumor bearing mice, respectively. The fluorescence intensities of tumors and body (background) were processed with the same method as above.

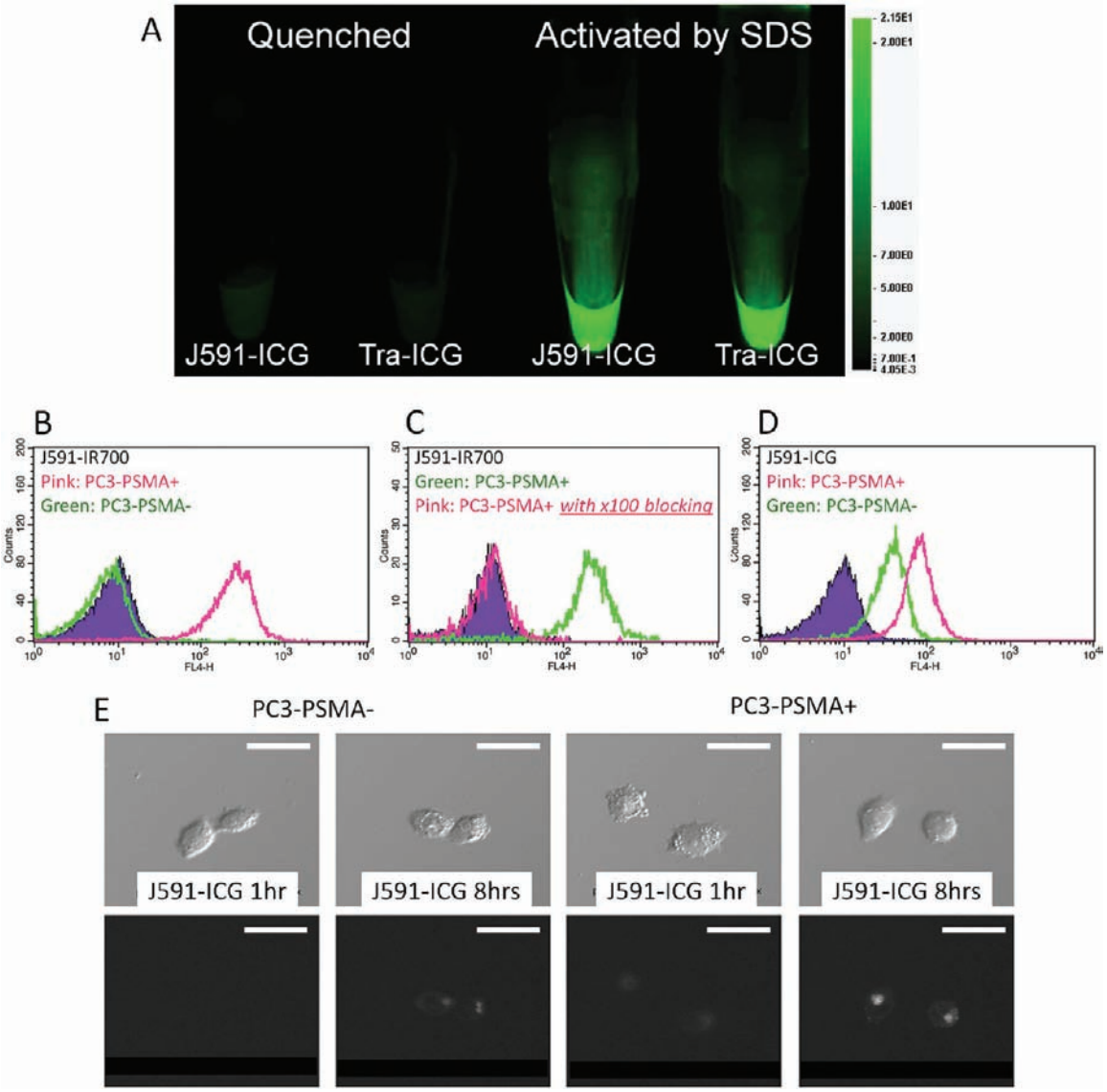

Figure 1. (A) Quenched (left) and chemically dequenched (right) J591−ICG and Tra−ICG. Dequenched conjugates show increased fluorescence signal shown in green. *In vitro* cell experiment with flow cytometry (B−D) and microscopy (E) showing specific binding of J591 to PSMA and activation of fluorescence signal after binding. Scale bar indicates 20 μm.

RESULTS

Antibody−Fluorophore Conjugates Showed High Quenching Capacity. Fluorescence intensity was low for both J591−ICG and Tra−ICG in their native states. After exposure to 1% SDS, a 18-fold and 15-fold increase in fluorescence signals was detected for J591−ICG and Tra−ICG, respectively (Figure 1A).

As defined by SDS−PAGE, 70% of ICG on the J591−ICG conjugate was covalently conjugated to the antibody. The specific immunoreactivity fraction of ^{125}I-labeled J591−ICG (69%) was only 7% less than the ^{125}I-labeled J591 without ICG (76%). The dissociation constant of ^{125}I-labeled J591 or J591−ICG as measured by Scatchard plot analysis was 2.8 nM, similar to published values.[15,16] In addition, the copy number of PSMA antigen on a single PC3-PSMA+ cell was calculated to be 2.0 million.

***In Vitro* Cell Analysis.** J591−IR700, a nonactivatable control conjugate, demonstrated intense signal arising from PC3-PSMA + cells and minimal signal from PC3-PSMA− cells (Figure 1B). Blocking experiments using 100-fold levels of unlabeled J591 showed almost complete competitive blocking of J591−IR700 uptake, indicating highly specific binding of J591−IR700 to PSMA (Figure 1C). Flow cytometry analysis using J591−ICG showed strong fluorescence from PC3- PSMA+ cells and weak signal from PC3-PSMA− cells (Figure 1D). Since this weak binding could not be blocked with a 100-fold excess of unlabeled J591 antibody, this signal represents low level, nonspecific activation of quenched ICG, which was seen only *in vitro*.

In vitro microscopy demonstrated results similar to flow cytometry experiments, namely, specific uptake by PSMA expressing cells that could be blocked with unlabeled J591 (Figure 1E).

***In Vivo* Imaging Studies Showed Specific Target Visualization with J591−ICG Even at Low Doses.** The time course of fluorescence intensity changes in PC3-PSMA+ and PC3-PSMA− tumors and of background signal after injection of various doses of J591−ICG are summarized in Figure 2A. PC3-PSMA+ tumors yielded significantly higher fluorescent signal at

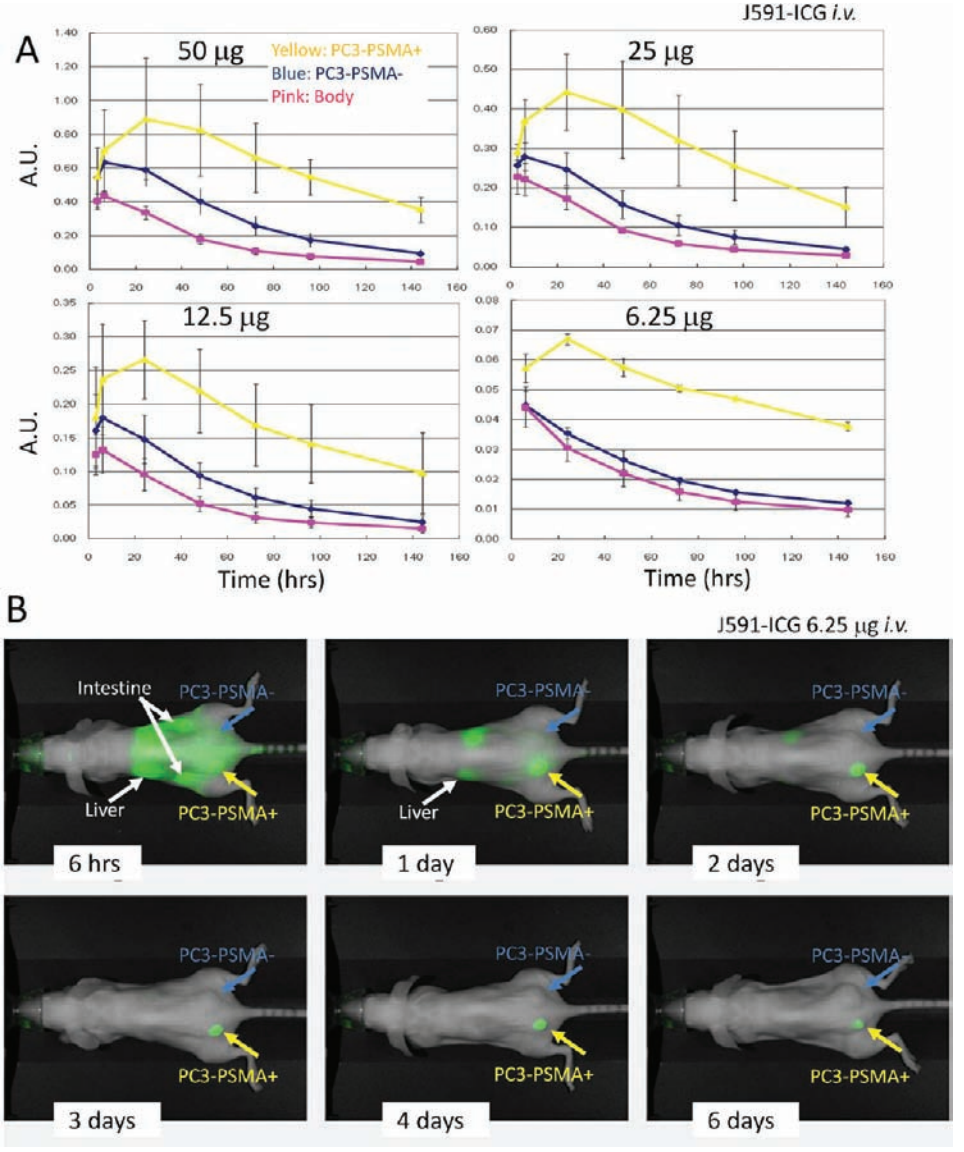

Figure 2. (A) *In vivo* serial fluorescence signals of PC3-PSMA+ and PC3-PSMA− tumor as well as background in the body of mice injected with 50, 25, 12.5, and 6.25 μg of J591−ICG. (B) *In vivo* serial fluorescence images of a PC3-PSMA+ and PC3-PSMA− tumor bearing mouse injected with 6.25 μg of J591−ICG. Only PC3-PSMA+ yields ICG fluorescence signal 3 days after injection or later.

all injected doses ≥1 day after injection. PC3-PSMA+ tumors were clearly depicted at all dose levels (50, 25, 12.5, and 6.25 μg) (Figure 2B) up to 10 days after injection (Figure 3A), although fluorescence signal from PC3-PSMA+ tumors increased with dose. While all PC3-PSMA+ tumor specimen, obtained 10 days after injection of 6.25 μg of J591−ICG, were clearly identified with ICG-specific fluorescence signal, no PC3-PSMA− tumor specimen did produce a detectable signal (Figure 3B). Signal intensity ratios between PC3-PSMA+ and PC3-PSMA− tumors increased with time, reaching 14 at 96 h after injection (Figure 3C). Since fluorescence from PC3-PSMA− tumors was practically equivalent to the background, ICG signals from scattered PC3-PSMA− tumors were often measured as negative numbers and thus were eliminated from the calculation. Therefore, the ratio of PC3-PSMA+ tumor to PC3-PSMA− tumor as shown in Figure 3C is an underestimate.

J591−ICG Yielded Brighter Fluorescence Signal from PC3-PSMA+ Tumor than Tra−ICG Yielded from 3T3/HER2+ Tumor. At the same dose injection (12.5 μg), the fluorescence signal arising from PSMA+ tumors after J591−ICG was higher than that from HER2+ tumors using the same dose of Tra−ICG (Figure 4), while these two cancer cells express similar numbers of respective receptors (~2 million copies) on the cell membrane.

DISCUSSION

This agent demonstrated several desirable features of a prostate cancer imaging optical probe. It appeared to be highly specific for PSMA expressing tumors, producing very bright targets within 24 h of administration. It appeared to have a favorable efficiency in comparison to a similar HER2 targeted Tra−ICG compound.[10] Its ability to be activated only at the PSMA+ cells led to very high target-to-background ratios

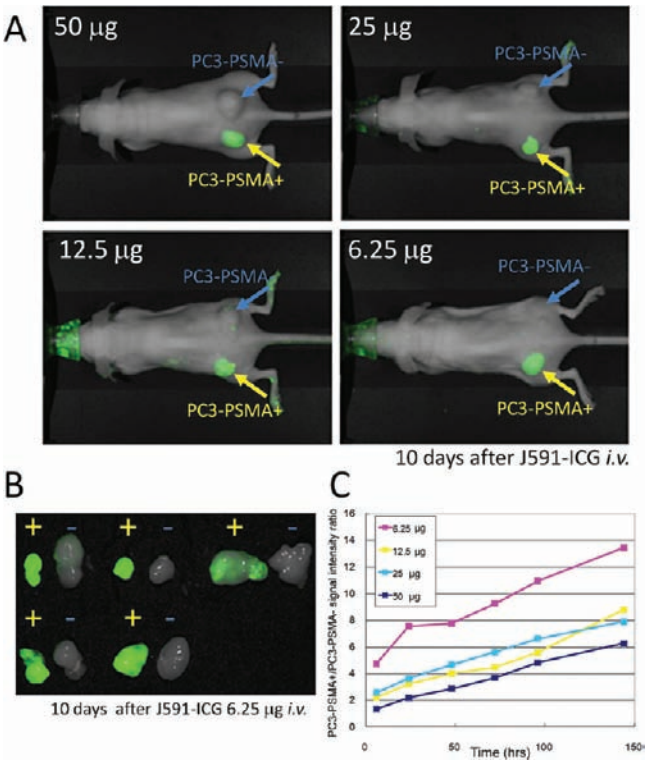

Figure 3. (A) *In vivo* fluorescence images of a PC3-PSMA+ and PC3-PSMA− tumor bearing mice 10 days after injection of 50, 25, 12.5, or 6.25 μg of J591−ICG are shown. Although ICG signal from PC3-PSMA + tumors is stronger in mice injected with a larger dose, all PC3-PSMA+ tumors show ICG fluorescence signal. (B) *Ex vivo* fluorescence images of five PC3-PSMA+ and PC3-PSMA− tumors obtained 10 days after injection of 6.25 μg of J591−ICG are shown. PC3-PSMA+ tumors clearly show specific fluorescence signal of ICG. (C) PC3-PSMA+ tumor to PC3-PSMA− tumor signal intensity ratio is plotted. All doses show a similar trend of changes on PC3-PSMA+ tumor to PC3-PSMA− tumor signal intensity ratio. Scattered PC3-PSMA− tumors, which showed signal below background, are eliminated from the calculation.

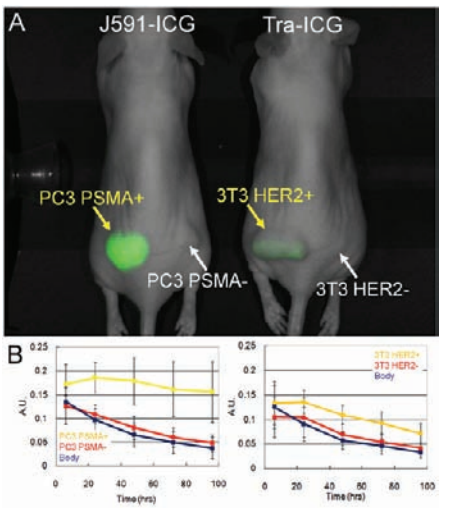

Figure 4. Side-by-side comparison of images (A) and serial fluorescence intensity curves (B) for PC3-PSMA+ and PC3-PSMA− tumor bearing mouse injected with 12.5 μg of J591−ICG versus 3T3HER2+ and 3T3HER2− tumor bearing mouse injected with 12.5 μg of Tra−ICG. Images (A) are obtained 3 days after injection of antibodies. The anti-PSMA conjugate yields higher signal than the anti-HER2 conjugate, suggesting better delivery and/or more efficient internalization.

(TBRs). This is related to a unique property of ICG, whereby it loses fluorescence when bound to the antibody but regains it once it has been chemically separated from the antibody as occurs after internalization and degradation of the conjugate in the lysosome. One drawback of this agent is that it requires 2 days to be sufficiently taken up by the tumor, internalized, and activated. However, once this has occurred the activation appears to last for at least 10 days. This suggests that there is a wide "window of opportunity" wherein the agent could be administered prior to a surgical procedure and still retain the desired benefits. Potential applications include detecting extracapsular extension, identifying lymph node metastasis, detecting residual tumor after resection, and validating at the point of care that tissue obtained via optical biopsy or surgery contains cancer.

Optical imaging is one of the few types of imaging that can be "activated".[17,18] Ideally, in the unbound state a targeted compound would yield no signal but after specific binding would become fluorescent. In its injected state the probe is quenched, emitting no light. After binding and internalization the ICG is separated from the antibody, allowing it to dequench and leading to high TBR. In this study, quenched J591−ICG was efficiently activated in PC3-PSMA+ tumors. This phenomenon occurred at all doses of PSMA and suggests that the injected dose for clinical applications could be minimized to 0.25 mg/kg that is comparable to the antibody doses used in radioimmunoscintigraphy. The flow cytometry results suggest that although the numbers of PSMA and HER2 antigens on respective PC3-PSMA+ cells and 3T3/HER2 cells were similar at 2.0 and 2.2 million copies per cell, respectively, the anti-PSMA conjugate was considerably more effective as an imaging agent than the anti-HER2 conjugate. The difference in fluorescence signal could derive from differences in the delivery of the antibody and/or the internalization/activation ratio.[17] In any case, the low dose of antibody required for effectiveness is encouraging for clinical translation.

Although safety was not specifically studied, there is reason for optimism regarding toxicity. Both major components of J591−ICG have been safely administered to patients. In the case of J591 this testing has been limited to several hundred patients in clinical trials at considerably higher doses,[19,20] but in the case of ICG there is more than 50 years of clinical experience, primarily in ophthalmology.[21] Of course, formal safety studies will be required prior to approval for human use, but the low dose needed for both components bodes well for a favorable toxicity profile.

In order to utilize a conjugate such as J591−ICG it will be necessary to have NIR cameras in the operating room.[22] Such cameras could be incorporated easily into existing endoscopic cameras, providing both white light and NIR imaging during the procedure. Such endoscopic cameras have already been developed experimentally.[23]

In conclusion, we successfully synthesized an activatable anti-PSMA humanized monoclonal antibody J591 conjugated with a linkable ICG derivative. The activatable antibody was able to depict PSMA+ tumors with high contrast compared to PSMA− tumors up to 10 days after injection of low dose of reagent (0.25 mg/kg). Activatable J591−ICG is a promising molecular imaging agent for detecting both primary and metastatic PSMA-positive prostate cancer based on the expression of PSMA and

dx.doi.org/10.1021/bc2002715 |*Bioconjugate Chem.* 2011, 22, 1700–1705

could be especially important in assisting surgeons performing biopsies and prostatectomies for cancer.

AUTHOR INFORMATION

Corresponding Author

*Phone: 301-451-4220. Fax: 301-402-3191. E-mail: Kobayash@mail.nih.gov.

ACKNOWLEDGMENT

This research was supported by the Intramural Research Program of the National Institutes of Health, National Cancer Institute, Center for Cancer Research. N.H.B. is a paid consultant to and owns stock in BZL Biologics, inc., the company to which the patents were licensed by Cornell Research Foundation for further research and development for the J591 antibody utilized in this article.

REFERENCES

(1) Hricak, H., Choyke, P. L., Eberhardt, S. C., Leibel, S. A., and Scardino, P. T. (2007) Imaging prostate cancer: a multidisciplinary perspective. *Radiology 243*, 28–53.

(2) Mease, R. C. (2010) Radionuclide based imaging of prostate cancer. *Curr. Top. Med. Chem. 10*, 1600–1616.

(3) Turkbey, B., Pinto, P. A., and Choyke, P. L. (2009) Imaging techniques for prostate cancer: implications for focal therapy. *Nat. Rev. Urol. 6*, 191–203.

(4) O'Keefe, D. S., Su, S. L., Bacich, D. J., Horiguchi, Y., Luo, Y., Powell, C. T., Zandvliet, D., Russell, P. J., Molloy, P. L., Nowak, N. J., Shows, T. B., Mullins, C., Vonder Haar, R. A., Fair, W. R., and Heston, W. D. (1998) Mapping, genomic organization and promoter analysis of the human prostate-specific membrane antigen gene. *Biochim. Biophys. Acta 1443*, 113–127.

(5) Israeli, R. S., Powell, C. T., Fair, W. R., and Heston, W. D. (1993) Molecular cloning of a complementary DNA encoding a prostate-specific membrane antigen. *Cancer Res. 53*, 227–230.

(6) Barinka, C., Sacha, P., Sklenar, J., Man, P., Bezouska, K., Slusher, B. S., and Konvalinka, J. (2004) Identification of the N-glycosylation sites on glutamate carboxypeptidase II necessary for proteolytic activity. *Protein Sci. 13*, 1627–1635.

(7) Schulke, N., Varlamova, O. A., Donovan, G. P., Ma, D., Gardner, J. P., Morrissey, D. M., Arrigale, R. R., Zhan, C., Chodera, A. J., Surowitz, K. G., Maddon, P. J., Heston, W. D., and Olson, W. C. (2003) The homodimer of prostate-specific membrane antigen is a functional target for cancer therapy. *Proc. Natl. Acad. Sci. U.S.A. 100*, 12590–12595.

(8) Gregorakis, A. K., Holmes, E. H., and Murphy, G. P. (1998) Prostate-specific membrane antigen: current and future utility. *Semin. Urol. Oncol. 16*, 2–12.

(9) Foss, C. A., Mease, R. C., Fan, H., Wang, Y., Ravert, H. T., Dannals, R. F., Olszewski, R. T., Heston, W. D., Kozikowski, A. P., and Pomper, M. G. (2005) Radiolabeled small-molecule ligands for prostate-specific membrane antigen: in vivo imaging in experimental models of prostate cancer. *Clin. Cancer Res. 11*, 4022–4028.

(10) Ogawa, M., Kosaka, N., Choyke, P. L., and Kobayashi, H. (2009) In vivo molecular imaging of cancer with a quenching near-infrared fluorescent probe using conjugates of monoclonal antibodies and indocyanine green. *Cancer Res. 69*, 1268–1272.

(11) Lindmo, T., Boven, E., Cuttitta, F., Fedorko, J., and Bunn, P. A., Jr. (1984) Determination of the immunoreactive fraction of radiolabeled monoclonal antibodies by linear extrapolation to binding at infinite antigen excess. *J. Immunol. Methods 72*, 77–89.

(12) Barrett, T., Koyama, Y., Hama, Y., Ravizzini, G., Shin, I. S., Jang, B. S., Paik, C. H., Urano, Y., Choyke, P. L., and Kobayashi, H. (2007) In vivo diagnosis of epidermal growth factor receptor expression using molecular imaging with a cocktail of optically labeled monoclonal antibodies. *Clin. Cancer Res. 13*, 6639–6648.

(13) Chang, S. S., Reuter, V. E., Heston, W. D., Bander, N. H., Grauer, L. S., and Gaudin, P. B. (1999) Five different anti-prostate-specific membrane antigen (PSMA) antibodies confirm PSMA expression in tumor-associated neovasculature. *Cancer Res. 59*, 3192–3198.

(14) Koyama, Y., Hama, Y., Urano, Y., Nguyen, D. M., Choyke, P. L., and Kobayashi, H. (2007) Spectral fluorescence molecular imaging of lung metastases targeting HER2/neu. *Clin. Cancer Res. 13*, 2936–2945.

(15) McDevitt, M. R., Barendswaard, E., Ma, D., Lai, L., Curcio, M. J., Sgouros, G., Ballangrud, A. M., Yang, W. H., Finn, R. D., Pellegrini, V., Geerlings, M. W., Jr., Lee, M., Brechbiel, M. W., Bander, N. H., Cordon-Cardo, C., and Scheinberg, D. A. (2000) An alpha-particle emitting antibody ([213Bi]J591) for radioimmunotherapy of prostate cancer. *Cancer Res. 60*, 6095–6100.

(16) Smith-Jones, P. M., Vallabahajosula, S., Goldsmith, S. J., Navarro, V., Hunter, C. J., Bastidas, D., and Bander, N. H. (2000) In vitro characterization of radiolabeled monoclonal antibodies specific for the extracellular domain of prostate-specific membrane antigen. *Cancer Res. 60*, 5237–5243.

(17) Kobayashi, H., and Choyke, P. L. (2011) Target-cancer-cell-specific activatable fluorescence imaging probes: rational design and in vivo applications. *Acc. Chem. Res. 44*, 83–90.

(18) Kobayashi, H., Ogawa, M., Alford, R., Choyke, P. L., and Urano, Y. (2010) New strategies for fluorescent probe design in medical diagnostic imaging. *Chem. Rev. 110*, 2620–2640.

(19) Bander, N. H., Milowsky, M. I., Nanus, D. M., Kostakoglu, L., Vallabhajosula, S., and Goldsmith, S. J. (2005) Phase I trial of 177lutetium-labeled J591, a monoclonal antibody to prostate-specific membrane antigen, in patients with androgen-independent prostate cancer. *J. Clin. Oncol. 23*, 4591–601.

(20) Bander, N. H., Trabulsi, E. J., Kostakoglu, L., Yao, D., Vallabhajosula, S., Smith-Jones, P., Joyce, M. A., Milowsky, M., Nanus, D. M., and Goldsmith, S. J. (2003) Targeting metastatic prostate cancer with radiolabeled monoclonal antibody J591 to the extracellular domain of prostate specific membrane antigen. *J. Urol. 170*, 1717–1721.

(21) Alford, R., Simpson, H. M., Duberman, J., Hill, G. C., Ogawa, M., Regino, C., Kobayashi, H., and Choyke, P. L. (2009) Toxicity of organic fluorophores used in molecular imaging: literature review. *Mol. Imaging 8*, 341–354.

(22) Gioux, S., Choi, H. S., and Frangioni, J. V. (2010) Image-guided surgery using invisible near-infrared light: fundamentals of clinical translation. *Mol. Imaging 9*, 237–255.

(23) Mitsunaga, M., Kosaka, N., Kines, R. C., Roberts, J. N., Lowy, D. R., Schiller, J. T., Ishihara, Y., Hasegawa, A., Choyke, P. L., and Kobayashi, H. (2011) In vivo longitudinal imaging of experimental human papillomavirus infection in mice with a multicolor fluorescence mini-endoscopy system. *Cancer Prev. Res. 4*, 767–773.

Bioconjugate Chemistry

ARTICLE

pubs.acs.org/bc

Synthesis and Evaluation of an Anti-MLC1 × Anti-CD90 Bispecific Antibody for Targeting and Retaining Bone-Marrow-Derived Multipotent Stromal Cells in Infarcted Myocardium

C. William Gundlach IV,[†] Amy Caivano,[†] Maria da Graca Cabreira-Hansen,[†] Amir Gahremanpour,[†] Wells S. Brown,[‡] Yi Zheng,[†] Bradley W. McIntyre,[‡] James T. Willerson,[†] Richard A. F. Dixon,[†] Emerson C. Perin,[†] and Darren G. Woodside*[,†]

[†]The Texas Heart Institute at St. Luke's Episcopal Hospital, Houston, Texas 77225, United States

[‡]The University of Texas MD Anderson Cancer Center, 1515 Holcombe Boulevard, Houston, Texas 77030, United States

ABSTRACT: A key issue regarding the use of stem cells in cardiovascular regenerative medicine is their retention in target tissues. Here, we have generated and assessed a bispecific antibody heterodimer designed to improve the retention of bone-marrow-derived multipotent stromal cells (BMMSC) in cardiac tissue damaged by myocardial infarction. The heterodimer comprises an anti-human CD90 monoclonal antibody (mAb) (clone 5E10) and an anti-myosin light chain 1 (MLC1) mAb (clone MLM508) covalently cross-linked by a bis-arylhydrazone. We modified the anti-CD90 antibody with a pegylated-4-formylbenzamide moiety to a molar substitution ratio (MSR) of 2.6 and the anti-MLC1 antibody with a 6-hydrazinonicotinamide moiety to a MSR of 0.9. The covalent modifications had no significant deleterious effect on mAb epitope binding. Furthermore, the binding of anti-CD90 antibody to BMMSCs did not prevent their differentiation into adipo-, chondro-, or osteogenic lineages. Modified antibodies were combined under mild conditions (room temperature, pH 6, 1 h) in the presence of a catalyst (aniline) to allow for rapid generation of the covalent bis-arylhydrazone, which was monitored at A_{354}. We evaluated epitope immunoreactivity for each mAb in the construct. Flow cytometry demonstrated binding of the bispecific construct to BMMSCs that was competed by free anti-CD90 mAb, verifying that modification and cross-linking were not detrimental to the anti-CD90 complementarity-determining region. Similarly, ELISA-based assays demonstrated bispecific antibody binding to plastic-immobilized recombinant MLC1. Excess anti-MLC1 mAb competed for bispecific antibody binding. Finally, the anti-CD90 × anti-MLC1 bispecific antibody construct induced BMMSC adhesion to plastic-immobilized MLC1 that was resistant to shear stress, as measured in parallel-plate flow chamber assays. We used mAbs that bind both human antigens and the respective pig homologues. Thus, the anti-CD90 × anti-MLC1 bispecific antibody may be used in large animal studies of acute myocardial infarction and may provide a starting point for clinical studies.

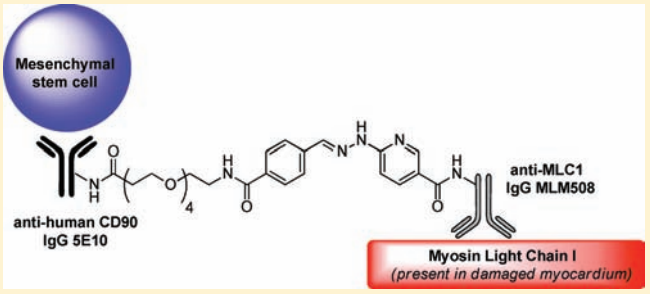

INTRODUCTION

Stem cell therapy is a promising therapeutic modality for restoring cardiac function in cardiovascular disease.[1,2] The preclinical findings that bone-marrow-derived multipotent stromal cells (BMMSCs) effect tissue repair[3] and have immunomodulatory activity[4] have led to the clinical testing of these cells in the treatment of a variety of diseases.[5] Furthermore, in a pig model of myocardial infarction, BMMSC engraftment and differentiation have been correlated with improved heart function.[6] However, the effectiveness of this therapy may be limited by low rates of cellular retention and engraftment in areas of cell delivery, even when cells are applied directly to the myocardium.[7,8]

One approach to address this issue is to target stem cells to ischemic tissue by creating a bispecific antibody that can bind to antigens specific for the stem cell and to the target tissue. This approach has been used in cancer therapy to target immune effector cells to tumor cells,[9] and catumaxomab, a first-generation bispecific antibody, has been approved recently in Europe for treating malignant ascites.[10] Lee and colleagues[11] have applied this methodology to cardiac stem cell therapy by generating a bispecific antibody construct to direct hematopoietic stem cells to infarcted myocardium in rodents.[11,12] In this construct, the tissue-targeting arm uses a monoclonal antibody (mAb) specific for myosin light chain 1 (MLC1) (mAb MLM508), which is found within the interstitial tissue of damaged hearts[13] and serves as an antigen marker for injured myocardium.[14−16] The other arm of the construct for binding hematopoietic stem cells is composed of a mAb to CD45,[11,12] which is a common leukocyte antigen[17] found on CD34$^+$ hematopoietic stem cells.[18]

In the present study, we have created a novel bispecific antibody for targeting BMMSCs to injured myocardium. The tissue-targeting arm of our reagent comprises the mAb MLM508 described

Received: June 13, 2011
Revised: July 11, 2011
Published: July 13, 2011

ACS Publications © 2011 American Chemical Society

above, which reacts with both pig and human MLC1.[19] Because BMMSCs do not express CD45[20] [the antigen used in the construct made by Lee and colleagues],[11,12] the stem-cell binding arm of our antibody was composed of mAb5E10, which recognizes the phenotypic cell surface marker CD90 (Thy-1)[21] found on BMMSCs. mAb 5E10 recognizes both pig and human BMMSCs.[22]

To generate an anti-CD90 × anti-MLC1 bispecific antibody construct, we used methods that labeled one mAb with a 6-hydrazinonicotinamide moiety via a conventional NHS ester. The second mAb in the bispecific construct was modified with a pegylated 4-formylbenzamide moiety, via a pentafluorophenyl ester. Formation of the bis-arylhydrazone, which is readily monitored by UV−vis spectroscopy, was rapid and precluded formation of homodimeric antibody products, which can occur with the use of other protein cross-linking chemistries. Herein, we describe the methodology involved in creating our bispecific antibody and the evaluation of its potential use as a BMMSC-targeting agent.

EXPERIMENTAL PROCEDURES

S-HyNic Modification of Anti-MLC1 Antibody. Anti-MLC1 (mouse anti-myosin light chain 1 antibody [MLM508, IgG2a]; Abcam, Cambridge, MA) was concentrated to 3.5 mg/mL and exchanged into modification buffer (100 mM sodium phosphate, 150 mM sodium chloride, pH 7.4) by using a spin column (Zeba, Thermo Fisher Scientific, Rockford, IL) according to the manufacturer's instructions. A portion of the resulting solution (30 μL, 2.7 mg/mL) was mixed with S-HyNic (0.8 μL, 35.5 mM; Solulink, San Diego, CA) in anhydrous dimethylformamide (DMF; Sigma-Aldrich, St. Louis, MO). After incubation at room temperature for 2 h, the reaction mixture was applied to a spin column equilibrated with coupling buffer (100 mM sodium phosphate, 150 mM sodium chloride, pH 6.0). HyNic-MLM508 (**1**, 35 μL, 2.0 mg/mL) was stored at 4 °C.

4FB(PEG)$_4$-PFP Modification of Anti-CD90 Antibody. Anti-CD90 (mouse anti-human CD90 antibody [5E10, IgG1]); BD Pharmingen, San Diego, CA) was concentrated to 3.5 mg/mL and subjected to buffer exchange as above. An aliquot of the resulting solution (25 μL, 3.5 mg/mL) was mixed with (4FB-(PEG)$_4$-PFP (Solulink) (0.5 μL, 6.9 mM) in anhydrous DMF. After incubation at room temperature for 2 h, the reaction mixture was applied to a spin column equilibrated with coupling buffer. 4FB(PEG)$_4$-5E10 (**2**, 30 μL, 2.2 mg/mL) was stored at 4 °C.

Measurement of Molar Substitution Ratio. An aliquot of modified antibody (3.3 μL) was mixed with either 2-hydrazinopyridine dihydrochloride (2-HP) or 4-nitrobenzaldehyde (4-NB) (both from Sigma-Aldrich) (6.7 μL, 0.5 mM in 100 mM MES, pH 6.0). The mixture was incubated at 37 °C for 0.5 h, and the absorbance at either 390 nm (4-NB) or 354 nm (2-HP) was recorded. UV−vis and absorbance spectra were measured with a Nanodrop 1000 (Nanodrop Products, Wilmington, DE). The MSR was calculated by using Beer's law and an extinction coefficient of 24 000 (4-NB) or 18 000 (2-HP).

ELISA Procedure. ELISA assays were performed to determine the functional activity of HyNic-MLM508 either alone or as part of the bispecific antibody construct. Briefly, recombinant human MLC1 (Abcam, 20 μg/mL) in TBS was immobilized onto wells of a 96-well plate (BD Falcon 353228) overnight at 4 °C. BSA (1% w/v) was added for 1 h at room temperature as a blocker. The wells were washed 3 times with PBS-T (0.1 mL, 10 mM sodium phosphate, 150 mM NaCl, 0.1% Tween-20 (v/v), pH 7.2) containing 1% FBS (v/v), and control antibodies or bispecific reagent were incubated in the wells for 1 h at room temperature in PBS-T containing 1% FBS (v/v). In competition experiments, wells were incubated with the excess MLM508 for 0.5 h, followed by 0.5 h with the bispecific reagent. The wells were washed with PBS-T containing 1% FBS (v/v), and the secondary antibody−HRP conjugate (Biosource International, Camarillo, CA; 1:500 dilution from commercial stock in PBS-T containing 1% FBS (v/v)) was incubated at room temperature for 1 h. For measurements of HyNic-MLM508 bound to MLC1, GAM-HRP was utilized. For measurements of the bispecific antibody binding to MLC1, anti-IgG1 (the isotype of mAb 5E10) was used. Wells were washed 4 times with PBS-T containing 1% FBS (v/v). Then the 1-Step Turbo TMB ELISA reagent (Thermo Fisher Scientific) was added to the wells. The colorimetric reaction was stopped with 1.5 M H_2SO_4, and the absorbance at 450 nm was recorded on a Safire2 (Tecan, Durham, NC) plate reader.

Pig-Bone-Marrow-Derived Multipotent Stromal Cells. BMMSCs were isolated on the basis of their ability to adhere to plastic surfaces. Bone marrow aspirates from male pigs were collected into 50 mL conical tubes through a cell strainer (70 μm mesh). Cells were counted and diluted in PBS to a final concentration of 10^7/mL. The mononuclear fraction was isolated by density-dependent cell separation (Ficoll, 1.077 g/mL, GE Healthcare, Uppsala, Sweden). After two washes with PBS, the mononuclear cells were plated in 175 cm^2 flasks at (0.5−1) × 10^6 cells per cm^2 in α minimal essential medium (αMEM, Invitrogen, Carlsbad, CA) containing ribonucleosides supplemented with 10% FBS (v/v) (Atlanta Biologicals, Lawrenceville, GA). One day later, fresh medium was added, and nonadherent cells were removed. At 70% confluence, cells were harvested with 0.25% trypsin (Invitrogen)/1 mM EDTA and further seeded at 10^3 cells per cm^2. The medium was changed every 3−4 days, and BMMSCs were further passaged at 70% confluency. BMMSCs between passages 3−6 were used in this study.

Bone-Marrow-Derived Multipotent Stromal Cell Differentiation Assays. Chondro-, osteo-, and adipogenesis differentiation assays were performed as previously described.[20,23] Briefly, monolayer cultures for osteogenesis and adipogenesis assays were initiated by seeding 2 × 10^3 cells in six-well tissue culture plates in αMEM. At 70% confluence, adipogenesis was induced by incubation with αMEM containing 10 mg/mL insulin, 10% FBS (v/v), 1 mM dexamethasone, 0.5 mM methylisobutylxanthine, and 100 mM indomethacine for 3 d, followed by 3 d in adipogenic maintenance medium (αMEM containing 10 mg/mL insulin and 10% (v/v) FBS). This alternating treatment was repeated until full adipogenic differentiation was obtained (approximately 2 weeks). Oil Red staining of neutral lipids was used to denote adipocytes.

Osteogenesis was induced in 70% confluent monolayers by incubation of BMMSCs with medium containing 50 mg/mL ascorbate 2-phosphate, 0.1 mM dexamethasone, and 10 mM β-glycerol phosphate and 10% FBS (v/v) for 21 days. The presence of osteoblasts was evaluated by the accumulation of intracellular alkaline phosphatase (Vector Red alkaline phosphatase substrate kit, Sigma-Aldrich).

For chondrogenic differentiation, 2 × 10^5 cells were centrifuged at 450 *g* for 5 min in 15 mL conical centrifuge tubes. The cell pellets were incubated for 21 days in differentiation medium (40 mg/mL proline, 100 mg/mL sodium pyruvate, 10 ng/mL TGF-β3, 0.1 mM dexamethasone, 50 mg/mL ascorbate 2-phosphate). To demarcate glycosaminoglycans, Alcian blue staining was applied to cell pellets fixed in 4% (w/v) paraformaldehyde.

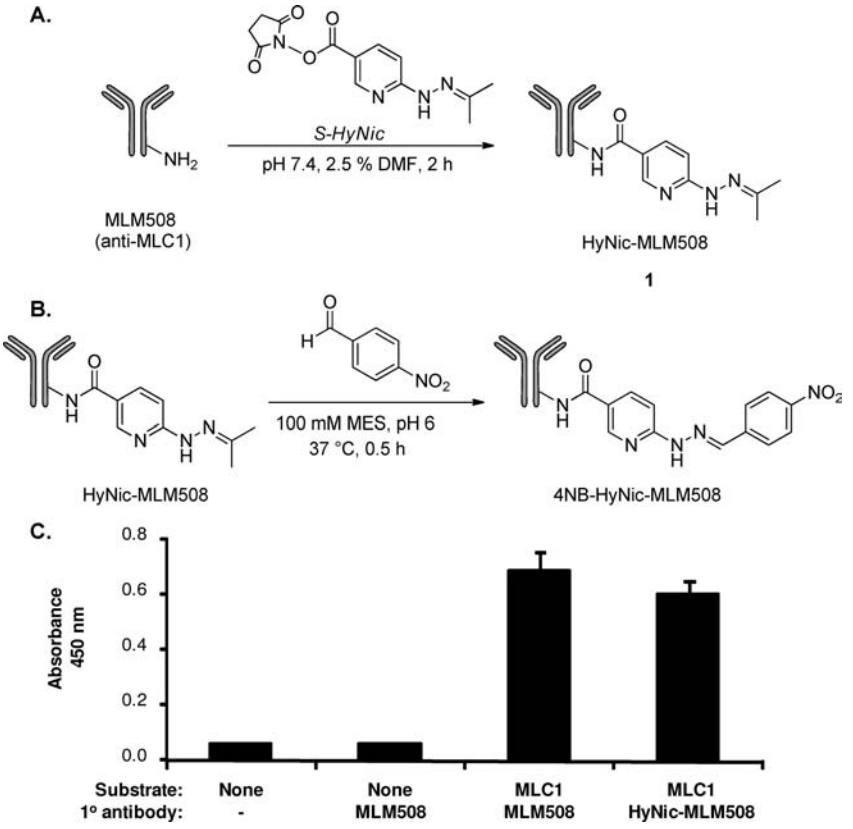

Figure 1. S-HyNic modification of anti-MLC1 antibody and retention of epitope specificity. (A) Reaction of anti-MLC1 antibody (mAb MLM508) with S-HyNic. The reaction products not shown include excess S-HyNic, *N*-hydroxysuccinimide (NHS), and unreacted mAb. S-HyNic and NHS were removed by buffer exchange before further testing and generation of the bispecific reagent. Modified antibodies are represented with one modification per molecule for simplicity. DMF is dimethylformamide; MES is 2-(*N*-morpholino)ethanesulfonic acid. (B) Reaction scheme followed to measure the molar substitution ratio (MSR). A portion of HyNic-MLM508 was incubated with 4-nitrobenzaldehyde (4-NB) to generate 4NB-HyNic-MLM508, which absorbs at 390 nm. During incubation at pH 6, the alkylhydrazone hydrolyzes *in situ* to produce the free hydrazine. The calculated MSR was 0.9. (C) ELISA analysis of HyNic-MLM508 binding to immobilized substrate recombinant human MLC1. Modified MLM508 binding was detected with GAM-HRP. All antibodies were used at 10 μg/mL. Results are presented as average A_{450} ± SD from triplicate wells. One of three experiments performed is shown.

Flow Cytometry. For analysis of 4FB(PEG)$_4$-5E10 binding to BMMSCs, cells (2×10^5) were incubated with 4FB(PEG)$_4$-5E10 for 0.5 h at 4 °C in PBS. After two washes in PBS containing 1% FBS (v/v), cells were incubated with GAM-IgG-FITC conjugate and analyzed on a LSRII (BD Biosciences, San Jose, CA). For analysis of bispecific antibody binding to BMMSCs, cells were treated as above except that secondary antibody treatment was GAM-IgG2a-FITC (BD Biosciences) to detect the MLM508 antibody.

Formation of Anti-MLC1 × Anti-CD90 Bispecific Antibody. HyNic-MLM508 (**1**, 27.5 μL) and 4FB(PEG)$_4$-5E10 (**2**, 25 μL) were combined with aniline (200 mM, 2.6 μL) in conjugation buffer to give a final aniline concentration of 10 mM. Reaction progress was monitored by measuring the UV−vis spectrum of 2 μL aliquots of the reaction mixture. After room-temperature incubation for 2.5 h, the reaction mixture was applied to a spin column equilibrated with 100 mM sodium phosphate, 150 mM sodium chloride, pH 7.2. The anti-MLC1 × anti-CD90 bispecific antibody mixture (**3**, 60 μL, 1.3 mg/mL) was stored at 4 °C.

Parallel-Plate Flow Experiments. Recombinant human MLC1 (20 μg/mL in 0.1 M $NaHCO_3$, pH 9.5) was immobilized overnight at 4 °C onto 24 mm × 50 mm slides cut from 15 mm × 100 mm polystyrene Petri dishes. The slides were washed with PBS, blocked with 2% (w/v) BSA for 2 h at room temperature, and assembled into a parallel-plate flow chamber. Control wells were coated with BSA (2%, w/v) only. Pig BMMSCs were either untreated or treated with bispecific antibody (5 μg/mL) for 0.5 h at 4 °C before washing and resuspension in running buffer (10 nM Tris, 103 mM NaCl, 24 mM $NaHCO_3$, 5.5 mM glucose, 5.4 mM KCl, 2 mg/mL BSA, pH 7.4). Then the BMMSCs (2.0×10^6 cells) were injected into the flow chamber and allowed to settle on the slides for 10 min. An increasing linear gradient of shear flow was pulled over the adherent cells for 300 s with the use of a computer-controlled syringe pump (Harvard Apparatus, Holliston, MA), and the number of adherent cells remaining was recorded by digital microscopy. Shear stress calculations were determined every 20 s. The shear stress in dyn/cm^2 is defined as $(6\mu Q)/(wh^2)$: μ is the viscosity of the medium (0.007); Q is the flow rate in cm^3/s; w is the width of the chamber (0.3175 cm); h is the height of the chamber (0.015 24 cm). The number of cells attached was recorded by digital microscopy (VI-470 charge-coupled device video camera, Optronics Engineering, Goleta, CA) at 20× on an inverted Nikon DIAPHOT-TMD microscope every 20 s and was plotted against time, as previously described.[24]

RESULTS

S-HyNic Modification of Anti-MLC1 mAb MLM508. mAb MLM508 (anti-MLC1) was modified by treatment with S-HyNic, yielding HyNic-MLM508 (**1**, Figure 1A). To determine the

molar substitution ratio (MSR), 4-NB was added to a portion of buffer-exchanged HyNic-MLM508 to generate 4NB-HyNic-MLM508 (Figure 1B) with an absorbance at 390 nm. The calculated MSR was 0.9, with a mass recovery of 86%. To determine whether the HyNic modification of MLM508 (**1**) altered epitope recognition of MLC1, we performed an ELISA assay utilizing purified recombinant human MLC1 as a substrate. The binding of HyNic-MLM508 (10 μg/mL) to immobilized MLC1 protein was measured relative to the binding of unmodified MLM508 (10 μg/mL) by ELISA, and the optical density values were within 1 standard deviation (Figure 1C). Thus, modifying MLM508 with S-HyNic had only a minimal effect on MLM508 interactions with MLC1.

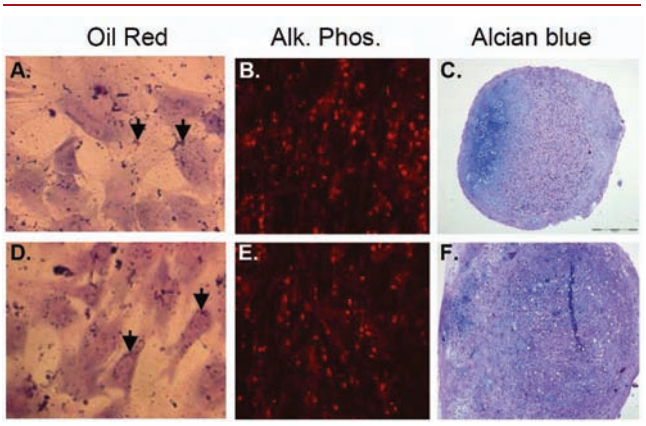

Figure 2. Differentiation capacity of BMMSCs treated with anti-CD90 antibody (mAb 5E10). BMMSCs were treated with anti-CD90 mAb 5E10 (A−C) or isotype control mAb (D−F). Differentiation of cells into adipogenic (A, D; arrows indicate neutral lipid accumulation), osteogenic (B, E), and chondrogenic (C, F) lineages was examined.

Effects of CD90 mAb on Bone-Marrow-Derived Multipotent Stromal Cell Differentiation. The anti-CD90 component of the bispecific antibody construct binds BMMSCs. To ensure that the binding of the CD90 antigen on BMMSCs did not affect the differentiation ability of BMMSCs, we performed osteo-, adipo-, and chrondogenic differentiation assays in the presence of the anti-CD90 mAb or an isotype control mAb (Figure 2). Anti-CD90 was used at 10 μg/mL, which was the saturating concentration as shown by flow cytometric analysis (data not shown). Under culture conditions for differentiation, BMMSCs showed the ability to differentiate along osteo-, adipo-, and chrondogenic lineages in the presence of the anti-CD90 antibody, indicating that binding of the CD90 surface antigen did not adversely affect cell differentiation (Figure 2).

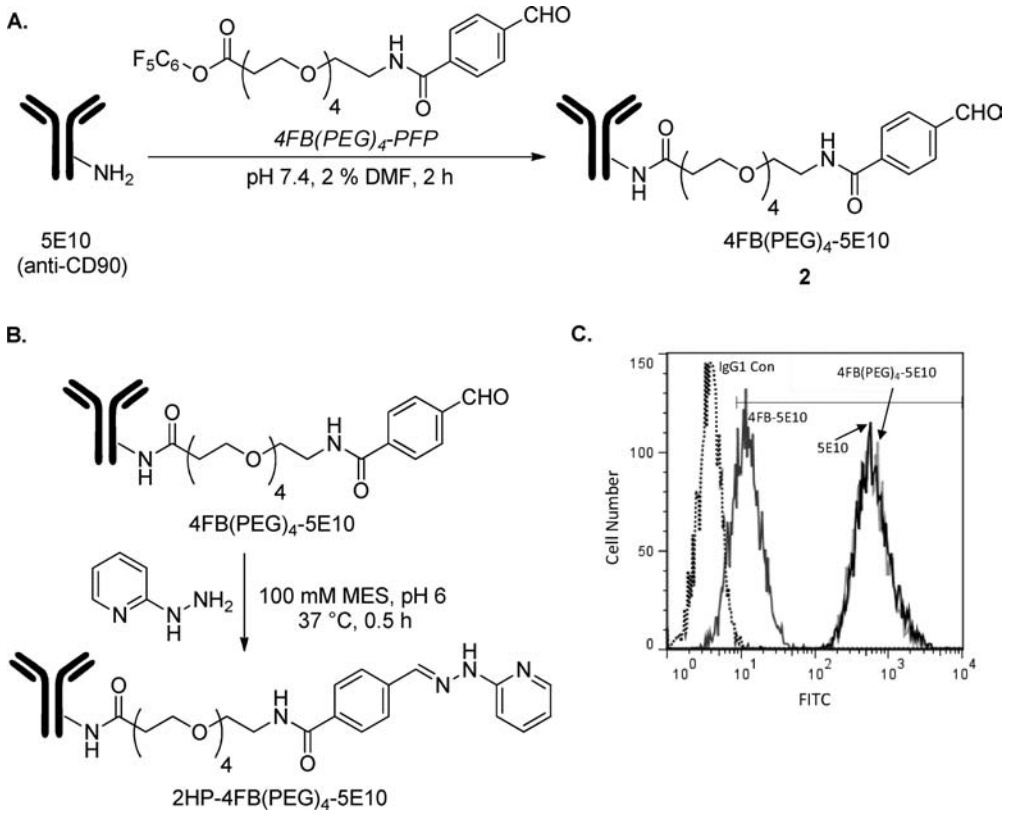

Figure 3. Modification of anti-CD90 antibody (mAb 5E10) with 4FB(PEG)$_4$-PFP and retention of antibody-binding specificity. (A) Reaction of mAb 5E10 with 4FB(PEG)$_4$-PFP. Reaction products not shown include excess 4FB(PEG)$_4$-PFP, pentafluorophenol, and unreacted antibody. Modified antibodies are represented with one modification per molecule for simplicity. 4FB(PEG)$_4$-PFP and pentafluorophenol were removed by buffer exchange before generation of the bispecific reagent and further use. DMF is dimethylformamide. (B) Reaction scheme to determine the molar substitution ratio (MSR). A portion of 4FB(PEG)$_4$-5E10 was incubated with 2-hydrazinopyridine dihydrochloride (2-HP) to form 2HP-4FB(PEG)$_4$-5E10, which absorbs at 354 nm. The calculated MSR was 2.6. (C) Flow cytometric analysis of 4FB-5E10 and 4FB(PEG)$_4$-5E10 binding to pig BMMSCs. Unmodified 5E10 (solid, black), 4FB(PEG)$_4$-5E10 (solid, light gray), 4FB-5E10 (solid, dark gray), and IgG1 control antibody (dotted, black) binding to BMMSCs was detected with GAM-FITC (10 μg/mL). 4FB-5E10 was synthesized in the same fashion as **2** (MSR = 3.0) using S-4FB. The histograms are representative of three experiments.

dx.doi.org/10.1021/bc200309h |*Bioconjugate Chem.* 2011, 22, 1706–1714

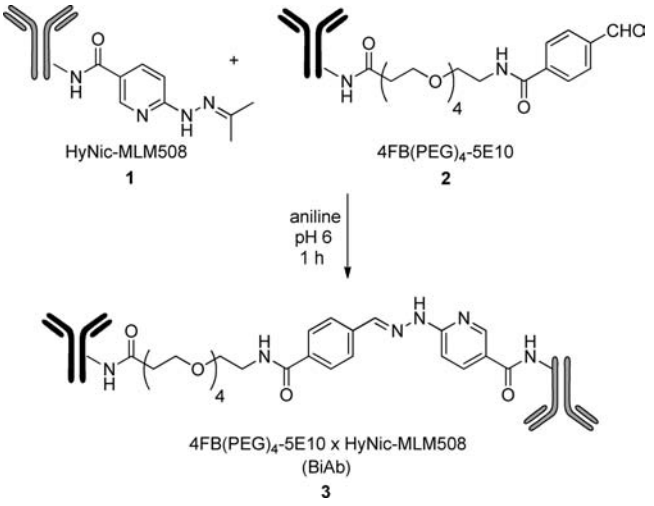

Figure 4. Reaction of two independently modified antibodies (HyNic-MLM508 and 4FB$(PEG)_4$-5E10) to form a bispecific construct mixture. The reactant-modified antibody mixtures are represented with one modification per molecule and without unmodified antibody for simplicity. Reaction products not shown include unmodified antibodies, **1**, **2**, heterodimers bearing multiple cross-links, and multimers.

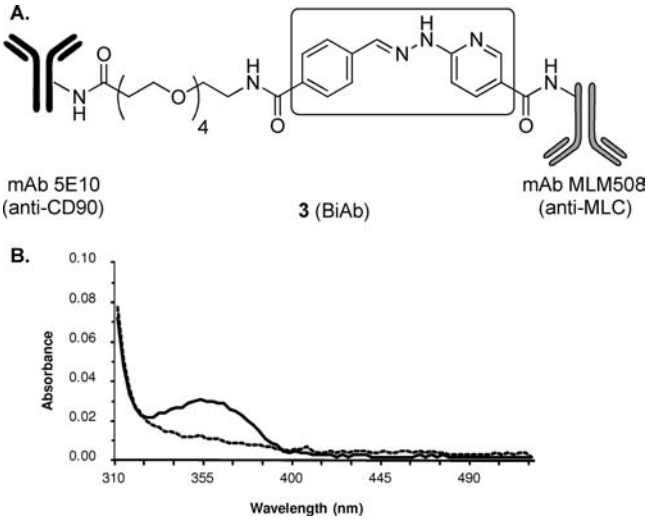

Figure 5. Generation of the bispecific antibody as monitored by UV—vis spectroscopy. (A) Bis-arylhydrazone (rectangle) generated in the reaction of 4FB$(PEG)_4$-5E10 with HyNic-MLM508 (see Figure 4). (B) The progress of the cross-linking reaction shown in Figure 4 was monitored by the absorbance of the bis-arylhydrazone at 354 nm (dashed, t = 0; solid, t = 1 h). A_{354} plateaued 1 h after initiation.

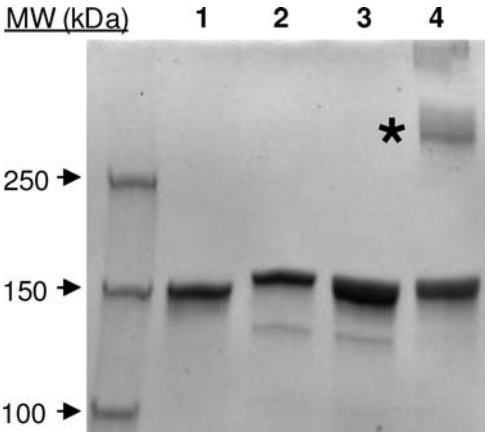

Figure 6. Analysis of reaction products by nonreducing SDS—PAGE: lane 1, unmodified MLM508 (2 μg); lane 2, unmodified mAb 5E10 (2 μg); lane 3, unmodified MLM508 and 5E10 combined (2 μg each, 4 μg total); lane 4, bispecific antibody reactant products (4 μg). Asterisk indicates bispecific antibody.

4FB$(PEG)_4$-PFP Modification of Anti-CD90 mAb 5E10. Anti-CD90 mAb 5E10 was modified by treatment with 4FB-$(PEG)_4$-PFP, yielding 4FB$(PEG)_4$-5E10 (**2**, Figure 3A). To determine the MSR, 2-HP was incubated with a portion of 4FB-$(PEG)_4$-5E10 to form 2HP-4FB$(PEG)_4$-5E10 (Figure 3B). On the basis of absorbance at 354 nm, we calculated an MSR of 2.6, and mass recovery was 75%. To determine whether 4FB$(PEG)_4$ modification of 5E10 affected its ability to bind to CD90 on the surface of pig BMMSCs, we compared the binding of 4FB-$(PEG)_4$-5E10 to BMMSCs with that of unmodified 5E10 by flow cytometric analysis (Figure 3C). The mean fluorescent intensity of 4FB$(PEG)_4$-5E10 (10 μg/mL) binding to BMMSCs in vitro was similar to that of unmodified 5E10 (10 μg/mL) (19 722 vs 22 029, respectively). This finding is in contrast to previous attempts to label mAb 5E10 with 4FB lacking the $(PEG)_4$ spacer, which inhibited 5E10 interactions with CD90 (Figure 3C).

Generation of Bispecific Antibody. To generate the bispecific antibody, HyNic-MLM508 (**1**) was combined with 4FB-(PEG_4)-5E10 (**2**) in a 1:1 molar ratio in the presence of 10 mM aniline[25] as a catalyst (Figure 4). The progress of the reaction was monitored over time by UV—vis spectroscopy, measuring A_{354} from the bis-arylhydrazone (Figure 5A, rectangle). The reaction reached a maximum A_{354} within 1 h, indicating that the reaction was complete (Figure 5B). Aniline was removed from the reaction mixture by buffer exchange of the bispecific antibody into PBS (pH 7.2) for storage. We analyzed a sample of the product (**3**) by nonreducing SDS—PAGE (Figure 6). As shown by densitometry, the reaction product comprised 61% mAb monomers, 25% dimers, and 14% multimers.

Antigen Specificity of the Bispecific Antibody. Individual modification of MLM508 and 5E10 did not result in the loss of antigen-binding activity (Figures 1C and 3C). However, to target BMMSCs to ischemic tissue, each arm of the bispecific antibody must remain functional after heterodimer formation. Thus, we tested the bispecific antibody reagent (**3**, Figure 7) to verify that the immunoreactivity of each half of the heterodimer was not reduced in the cross-linked species. First, we used an ELISA to verify that the bispecific antibody mixture could bind purified recombinant MLC1. We coated the wells with BSA (0.1% w/v) as a control or with MLC1 (10 μg/mL); unbound sites were blocked with BSA (0.1% w/v). HRP-conjugated goat anti-mouse IgG1 (the isotype of anti-CD90 mAb 5E10) was used as the detection antibody. Several control assays were performed to rule out nonspecific binding of the bispecific antibody to immobilized MLC1. No binding was observed when the bispecific antibody was incubated in wells coated with BSA only (Figure 7B). In addition, IgG2a (the isotype of MLM508) did not bind to immobilized MLC1, serving as a control for the MLM508 arm of the bispecific antibody. Furthermore, nonspecific binding of mAb 5E10 to immobilized MLC1 was not observed. Importantly, we saw significant binding of the bispecific antibody

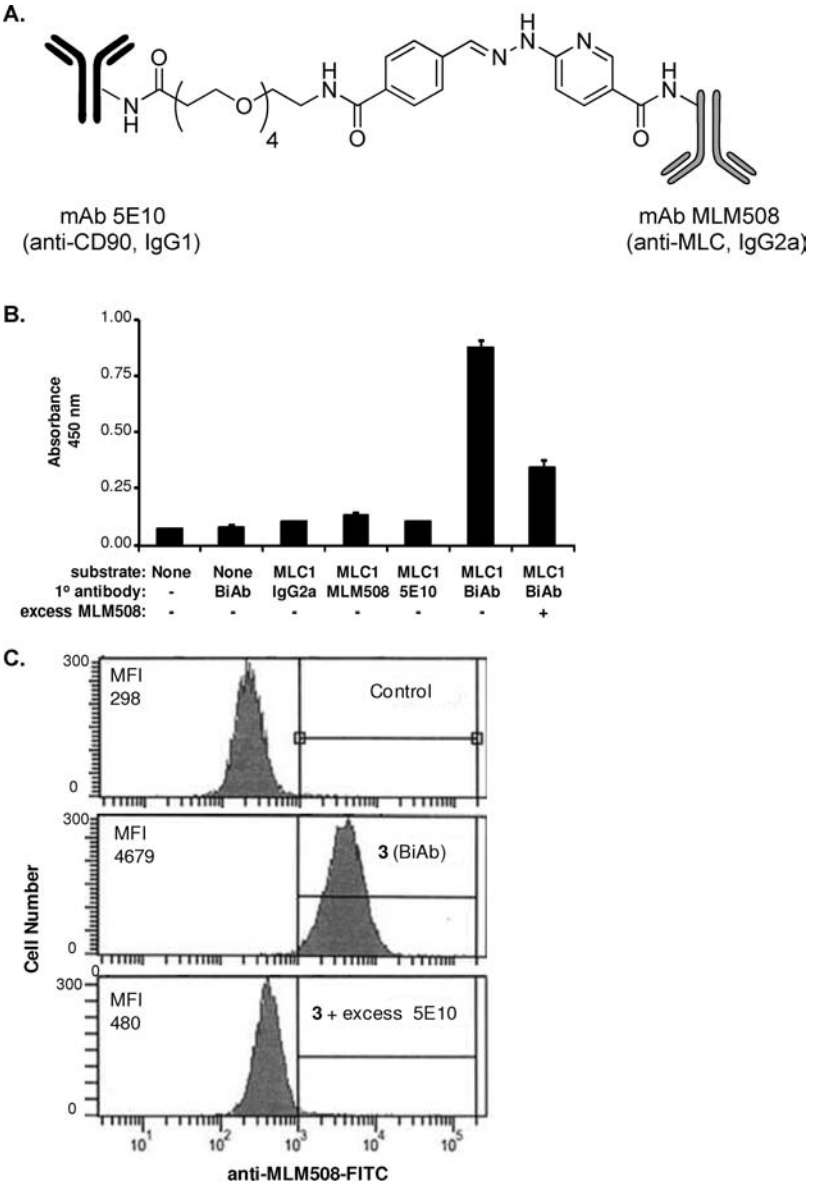

Figure 7. Antigen specificity of the bispecific antibody product (**3**). (A) Bispecific antibody (BiAb) highlighting the isotypes of the mAb of each respective arm. (B) ELISA analysis of BiAb binding to plastic immobilized recombinant human MLC1. MLC1 was immobilized at 10 μg/mL. After blocking with BSA, primary antibody was added at 10 μg/mL. In the case of "excess MLM508", unmodified MLM508 was added to the ELISA wells (20 μg/mL) 0.5 h before adding primary antibody. HRP-conjugated secondary antibody specific for IgG1 (the isotype of 5E10) was used for detection. Data are presented as average $A_{450} \pm$ SD from triplicate wells. One of three representative experiments is shown. (C) BiAb binding to pig BMMSCs as detected with anti IgG2a-FITC. To demonstrate specific BiAb binding, BMMSCs were pretreated with saturating levels of unlabeled mAb 5E10 (10 μg/mL) for 1 h before adding BiAb. Histograms are representative of three experiments.

to immobilized MLC1, and this binding was inhibited by preincubation of the ELISA wells with free, unmodified MLM508 (Figure 7B).

We used flow cytometry to test the anti-CD90 portion of the bispecific construct. Pig BMMSCs expressing CD90 were treated with individual unmodified antibodies, the bispecific antibody mixture, and excess unmodified anti-CD90 followed by the bispecific antibody mixture. No nonspecific binding of MLM508 to BMMSCs was observed (data not shown). Bispecific antibody binding to BMMSC was detected with goat-anti-mouse IgG2a-FITC (Figure 7C). Excess unmodified anti-CD90 inhibited the bispecific antibody from binding to BMMSCs by more than 90% (Figure 7C).

Functional Activity of the Bispecific Antibody. Parallel-plate flow chambers were used to test whether the bispecific agent we generated could increase the binding of pig BMMSCs to immobilized MLC1. MLC1 was immobilized in the chamber, and BMMSCs pretreated with bispecific antibody or left untreated (as controls) were perfused into the flow chamber. At 2.5 dyn/cm^2, 40% of the bispecific antibody-treated BMMSCs remained adherent to immobilized MLC1 substrate, whereas the percent of cells adhered in the control chambers was negligible (Figure 8). Even at high shear levels (15 dyn/cm^2), 10% of the bispecific antibody-treated BMMSCs were still attached (data not shown).

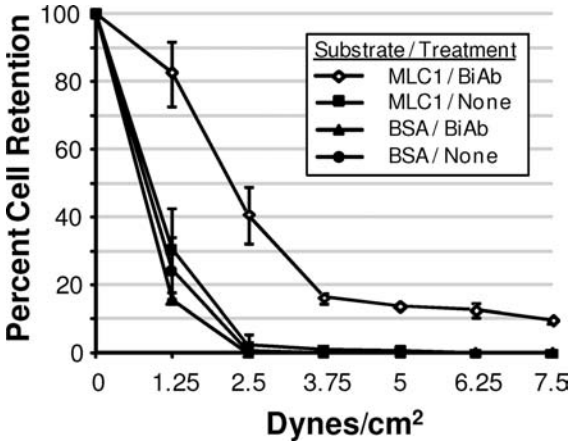

Figure 8. Bispecific antibody-induced retention of BMMSCs on MLC1 under conditions of shear stress. Parallel-plate flow chambers were coated with MLC1 or BSA as a control. Cells were either treated with the bispecific antibody (BiAb, 5 μg/mL) or untreated (controls) and then loaded onto the substrate and incubated for 0.5 h at room temperature. Cell detachment was measured as shear stress increased. Data represent the average percent of cell adhesion. Error bars indicate the data range (n = 2).

DISCUSSION

Developing an effective method for increasing the retention of transplanted stem cells in the injured myocardium would improve the benefits of cell therapy after myocardial infarction. Here, we describe the generation of a novel bispecific antibody designed to target BMMSCs to infarct tissue. The arms of the bispecific antibody are composed of the anti-CD90 mAb 5E10 and the anti-MLC1 mAb MLM508. The bis-arylhydrazone cross-linking chemistry we used in generating the construct allows for rapid quantification of antibody modifications, real-time nondestructive monitoring of bispecific antibody generation, and the assurance of heterodimer formation. Finally, our bispecific antibody product retained immunoreactivity of both arms of the construct (anti-CD90 and anti-MLC1) and mediated the retention of BMMSCs to MLC1 under stringent adhesion conditions.

The bispecific antibody approach has been used successfully to target human $CD34^+$ hematopoietic stem cells to ischemic myocardial tissue.[11,12] In these studies, the bispecific reagent comprised an anti-CD45 x anti-MLC1 antibody. This approach is not suitable for use in targeting BMMSCs because CD45 is not expressed on this cell population.[20] We used the anti-CD90 (Thy-1) mAb 5E10 in the heteroconjugate, as CD90 is a glycophosphatidylinositol-linked cell surface glycoprotein expressed on the surface of BMMSCs.[20] Although primarily used in the past as a phenotypic cell marker, CD90 has now been shown to regulate several cell surface signaling receptors.[21] Before using the anti-CD90 mAb 5E10 as one arm of the bispecific antibody, we showed that the binding of mAb 5E10 did not adversely affect BMMSC differentiation into adipogenic, chondrogenic, or osteogenic lineages (Figure 2). Furthermore, modification of mAb 5E10 with the extended linker 4FB$(PEG)_4$-PFP, at an MSR of 2.6, did not affect the binding of the mAB to CD90 expressed on the cell surface, thus maintaining antibody functionality (Figure 3). Previously, we had modified mAb 5E10 with S-4FB (the same moiety without the PEG extension, introduced via a NHS-ester), to an MSR of 3.0, but this modification inhibited mAb 5E10 from binding CD90 as indicated by flow cytometry experiments (Figure 3C). This indicates that the extended linker (4FB$(PEG)_4$) was superior in maintaining functionality after modification. Notably, in addition to human CD90, mAb 5E10 binds pig CD90 and thus is suitable for use in large animal studies.

In the present study, an antibody to MLC1 was used as the arm that binds antigens exposed within ischemic tissue. Because ischemia damages the myocyte cell membrane[26] and exposes intracellular contents to the extracellular environment,[27] MLC1 can be found within the interstitial tissue of damaged hearts.[13] Futhermore, MLC1 is not cleaved by caspases[28] that are active after myocardial apoptosis,[29] and circulating MLC1 can be detected as early as 6 h after an infarction.[14−16] We used S-HyNic to modify MLM508 (anti-MLC1). This modification allowed for the rapid determination of the MSR of MLM508 by its incubation with 4-nitrobenzaldehyde, as the resulting bis-arylhydrazone adsorbs at 390 nm. Modifying MLM508 with S-HyNic at an MSR of 0.9 did not affect the binding of MLM508 to MLC1 (Figure 1).

Many methods are available for generating bispecific antibodies, including the method of chemical cross-linking of purified mAbs to generate a heteroconjugate.[30] In the method used in our study, a covalent cross-link was formed between partners when a 6-hydrazinonicotinamide moiety reacted with a 4-formylbenzamide moiety, yielding a bis-arylhydrazone. These groups are readily introduced into proteins by using conventional NHS-ester or pentafluorophenyl ester reaction with free amines, presumably lysine side chains. We chose this approach because of its advantages in cross-linking specificity and the ability to readily quantify both mAb modifications and the extent of cross-link formation.

One common protein−protein cross-linking approach is to modify one partner with a thiol-reactive group, such as a malemide or pyridyl disulfide, and introduce free thiols into the other partner. When the two modified proteins are mixed, covalent intermolecular bonds are formed. A significant disadvantage of this method is the formation of homodimers. The thiol modified protein can form disulfide dimers and because of this, thiol-modified protein typically must be used immediately after production. Our approach of using two functional groups that do not naturally occur in proteins and are not self-reactive allows for storage of modified proteins before use and avoids homodimer formation. Additionally, the distinct chromophore of the bis-arylhydrazone cross-link allows for rapid monitoring of reactions by UV−vis spectroscopy. When a low-volume UV−vis spectrometer is used, small cross-linking reactions (10 μL) may be conducted and monitored in a nondestructive and nondilutive manner, making this approach suitable for using difficult-to-obtain proteins.

Several elegant strategies are now available to generate bispecific antibodies for clinical development, involving both whole IgG and Ig fragments such as Fab's and scFv's.[31] However, the majority of these strategies are recombinant protein based, which requires mAb sequence information and long lead times for development. An approach to generating bispecific antibodies that can be utilized even for antibodies that are only available commercially is advantageous because several different mAb can be tested before a candidate for clinical development can be developed and further evaluated. For *in vivo* studies, the bispecific antibody reaction product will be purified on an anti-IgG2a affinity column. This will result in the removal of free monomeric IgG1 (the anti-CD90 arm). Then the reagent will be incubated with BMMSCs, which will bind only the antibodies in the mixture that contain anti-CD90. Free antibody (e.g., monomeric anti-MLC1) will be washed away from the cells, leaving only bispecific reagent bound to cells before transplantation.

We have shown that each arm of the bispecific construct is functional and that the reagent can tether BMMSCs to immobilized MLC1 under conditions of shear stress. BMMSCs treated with the bispecific antibody resisted shear of up to 7.5 dyn/cm^2 (Figure 8) and continued to resist shear at levels of 15 dyn/cm^2 (data not shown). During inflammation, cell migration usually occurs at postcapillary venules, where vessel wall shear stress ranges from 1 to 10 dyn/cm^2.[32] These findings indicate that the bispecific antibody can bind BMMSCs to MLC1 during periods of physiologic shear stress. Thus, in addition to use in the direct administration of BMMSC by transendocardial injection, this feature would facilitate the administration of bispecific mAb-armed BMMSCs by intravenous injection.

In the present study, we describe the generation of a functional bispecific antibody comprising anti-CD90 and anti-MLC1 arms. Future studies will quantitatively assess whether this antibody can target human BMMSCs to injured myocardium in an NOD/SCID murine model. Moreover, because of its species cross-reactivity, this bispecific antibody can also be used in pig models of myocardial infarction.

AUTHOR INFORMATION

Corresponding Author

*Phone: 832-355-9084. Fax: 832-355-9692. Email:dwoodside@heart.thi.tmc.edu.

ACKNOWLEDGMENT

The authors thank Stephen N. Palmer, Ph.D., E.L.S., and Rebecca Bartow, Ph.D., of The Texas Heart Institute at St. Luke's Episcopal Hospital for their editorial assistance in the preparation of the manuscript. W. S. Brown was supported by Grant 2 T32-CA-09598-21 from the NIH.

REFERENCES

(1) Abdel-Latif, A., Bolli, R., Tleyjeh, I. M., Montori, V. M., Perin, E. C., Hornung, C. A., Zuba-Surma, E. K., Al-Mallah, M., and Dawn, B. (2007) Adult bone marrow-derived cells for cardiac repair: a systematic review and meta-analysis. *Arch. Intern. Med. 167*, 989–997.

(2) Lipinski, M. J., Biondi-Zoccai, G. G., Abbate, A., Khianey, R., Sheiban, I., Bartunek, J., Vanderheyden, M., Kim, H. S., Kang, H. J., Strauer, B. E., and Vetrovec, G. W. (2007) Impact of intracoronary cell therapy on left ventricular function in the setting of acute myocardial infarction: a collaborative systematic review and meta-analysis of controlled clinical trials. *J. Am. Coll. Cardiol. 50*, 1761–1767.

(3) Phinney, D. G., and Prockop, D. J. (2007) Concise review: mesenchymal stem/multipotent stromal cells: the state of transdifferentiation and modes of tissue repair—current views. *Stem Cells 25*, 2896–2902.

(4) Uccelli, A., Moretta, L., and Pistoia, V. (2008) Mesenchymal stem cells in health and disease. *Nat. Rev. Immunol. 8*, 726–736.

(5) Parekkadan, B., and Milwid, J. M. (2010) Mesenchymal stem cells as therapeutics. *Annu. Rev. Biomed. Eng. 12*, 87–117.

(6) Quevedo, H. C., Hatzistergos, K. E., Oskouei, B. N., Feigenbaum, G. S., Rodriguez, J. E., Valdes, D., Pattany, P. M., Zambrano, J. P., Hu, Q., McNiece, I., Heldman, A. W., and Hare, J. M. (2009) Allogeneic mesenchymal stem cells restore cardiac function in chronic ischemic cardiomyopathy via trilineage differentiating capacity. *Proc. Natl. Acad. Sci. U.S.A. 106*, 14022–14027.

(7) Chavakis, E., Urbich, C., and Dimmeler, S. (2008) Homing and engraftment of progenitor cells: a prerequisite for cell therapy. *J. Mol. Cell. Cardiol. 45*, 514–522.

(8) Fox, J. M., Chamberlain, G., Ashton, B. A., and Middleton, J. (2007) Recent advances into the understanding of mesenchymal stem cell trafficking. *Br. J. Haematol. 137*, 491–502.

(9) Baeuerle, P. A., and Reinhardt, C. (2009) Bispecific T-cell engaging antibodies for cancer therapy. *Cancer Res. 69*, 4941–4844.

(10) Sebastian, M., Kuemmel, A., Schmidt, M., and Schmittel, A. (2009) Catumaxomab: a bispecific trifunctional antibody. *Drugs Today 45*, 589–597.

(11) Lee, R. J., Fang, Q., Davol, P. A., Gu, Y., Sievers, R. E., Grabert, R. C., Gall, J. M., Tsang, E., Yee, M. S., Fok, H., Huang, N. F., Padbury, J. F., Larrick, J. W., and Lum, L. G. (2007) Antibody targeting of stem cells to infarcted myocardium. *Stem Cells 25*, 712–717.

(12) Zhao, T. C., Tseng, A., Yano, N., Tseng, Y., Davol, P. A., Lee, R. J., Lum, L. G., and Padbury, J. F. (2008) Targeting human CD34+ hematopoietic stem cells with anti-CD45 × anti-myosin light-chain bispecific antibody preserves cardiac function in myocardial infarction. *J. Appl. Physiol. 104*, 1793–1800.

(13) Mair, J., Wagner, I., Fridrich, L., Lechleitner, P., Dienstl, F., Puschendorf, B., and Michel, G. (1994) Cardiac myosin light chain-1 release in acute myocardial infarction is associated with scintigraphic estimates of myocardial scar. *Clin. Chim. Acta 229*, 153–159.

(14) Khaw, B. A., Beller, G. A., and Haber, E. (1978) Experimental myocardial infarct imaging following intravenous administration of iodine-131 labeled antibody (Fab′)2 fragments specific for cardiac myosin. *Circulation 57*, 743–750.

(15) Khaw, B. A., Gold, H. K., Fallon, J. T., and Haber, E. (1978) Detection of serum cardiac myosin light chains in acute experimental myocardial infarction: radioimmunoassay of cardiac myosin light chains. *Circulation 58*, 1130–1136.

(16) Khaw, B. A., Gold, H. K., Leinbach, R. C., Fallon, J. T., Strauss, W., Pohost, G. M., and Haber, E. (1978) Early imaging of experimental myocardial infarction by intracoronary administration of ^{131}I-labelled anticardiac myosin (Fab′)2 fragments. *Circulation 58*, 1137–1142.

(17) Fabre, J. W., and Williams, A. F. (1977) Quantitative serological analysis of a rabbit anti-rat lymphocyte serum and preliminary biochemical characterisation of the major antigen recognised. *Transplantation 23*, 349–359.

(18) Lansdorp, P. M., Sutherland, H. J., and Eaves, C. J. (1990) Selective expression of CD45 isoforms on functional subpopulations of CD34+ hemopoietic cells from human bone marrow. *J. Exp. Med. 172*, 363–366.

(19) Katoh, H., Sugi, M., Chino, S., Ishige, M., Kuroda, M., Fujimoto, M., Nagai, R., and Yazaki, Y. (1992) Development of an immunoradiometric assay kit for ventricular myosin light chain I with monoclonal antibodies. *Clin. Chem. 38*, 170–171.

(20) Pittenger, M. F., Mackay, A. M., Beck, S. C., Jaiswal, R. K., Douglas, R., Mosca, J. D., Moorman, M. A., Simonetti, D. W., Craig, S., and Marshak, D. R. (1999) Multilineage potential of adult human mesenchymal stem cells. *Science 284*, 143–147.

(21) Barker, T. H., and Hagood, J. S. (2008) Getting a grip on Thy-1 signaling. *Biochim. Biophys. Acta 1793*, 921–923.

(22) Wilschut, K. J., Jaksani, S., Van Den Dolder, J., Haagsman, H. P., and Roelen, B. A. (2008) Isolation and characterization of porcine adult muscle-derived progenitor cells. *J. Cell. Biochem. 105*, 1228–1239.

(23) Bosch, P., Fouletier-Dilling, C., Olmsted-Davis, E. A., Davis, A. R., and Stice, S. L. (2006) Efficient adenoviral-mediated gene delivery into porcine mesenchymal stem cells. *Mol. Reprod. Dev. 73*, 1393–1403.

(24) Woodside, D. G., Kram, R. M., Mitchell, J. S., Belsom, T., Billard, M. J., McIntyre, B. W., and Vanderslice, P. (2006) Contrasting roles for domain 4 of VCAM-1 in the regulation of cell adhesion and soluble VCAM-1 binding to integrin alpha4beta1. *J. Immunol. 176*, 5041–5049.

(25) Dirksen, A., Dirksen, S., Hackeng, T. M., and Dawson, P. E. (2006) Nucleophilic catalysis of hydrazone formation and transimination: implications for dynamic covalent chemistry. *J. Am. Chem. Soc. 128*, 15602–15603.

(26) Joggerst, S. J., and Hatzopoulos, A. K. (2009) Stem cell therapy for cardiac repair: benefits and barriers. *Expert Rev. Mol. Med. 11*, No. e20.

(27) Katus, H. A., Diederich, K. W., Hoberg, E., and Kubler, W. (1988) Circulating cardiac myosin light chains in patients with angina at rest: identification of a high risk subgroup. *J. Am. Coll. Cardiol. 11*, 487–493.

(28) Bott-Flügel, L., Weig, H. J., Uhlein, H., Nabauer, M., Laugwitz, K. L., and Seyfarth, M. (2008) Quantitative analysis of apoptotic markers in human end-stage heart failure. *Eur. J. Heart Failure 10*, 129–132.

(29) Prech, M., Marszalek, A., Schröder, J., Filas, V., Lesiak, M., Jemielity, M., Araszkiewicz, A., and Grajek, S. (2010) Apoptosis as a mechanism for the elimination of cardiomyocytes after acute myocardial infarction. *Am. J. Cardiol. 105*, 1240–1245.

(30) Fischer, N., and Léger, O. (2007) Bispecific antibodies: molecules that enable novel therapeutic strategies. *Pathobiology 74*, 3–14.

(31) Chan, A. C., and Carter, P. J. (2010) Therapeutic antibodies for autoimmunity and inflammation. *Nat. Rev. Immunol. 10*, 301–316.

(32) Lawrence, M. B., and Springer, T. A. (1993) Neutrophils roll on E-selectin. *J. Immunol. 151*, 6338–6346.

Bioconjugate Chemistry

ARTICLE

pubs.acs.org/bc

Evaluation of ^{99m}Tc-Labeled Cyclic RGD Peptide with a PEG_4 Linker for Thrombosis Imaging: Comparison with DMP444

Wei Fang,[†] Jia He,[†] Young-Seung Kim,[‡] Yang Zhou,[‡] and Shuang Liu*[,‡]

[†]Department of Nuclear Medicine, Cardiovascular Institute & Fu Wai Hospital, Chinese Academy of Medical Science & Peking Union Medical College, Beijing, China

[‡]School of Health Sciences, Purdue University, West Lafayette, Indiana, United States

Supporting Information

ABSTRACT: DMP444 is a ^{99m}Tc-labeled cyclic RGD peptide, which has been evaluated in preclinical canine deep vein thrombosis (DVT) and pulmonary embolism (PE) models, and in patients with DVT and PE by SPECT (single photon emission computed tomography). Clinical data indicated that DMP444 is useful for imaging DVT, but it had limited utility for imaging PE in patients. To understand its clinical findings, we prepared a new radiotracer P4-DMP444 by replacing the lipophilic 6-aminocaproic acid (CA) in DMP444 with a highly water-soluble PEG_4 (15-amino-4,7,10,13-tetraoxapentadecanoic acid) linker. The objective of this study was to explore the impact of PEG_4 on biological properties (biodistribution, excretion kinetics, and capability to image thrombi) of ^{99m}Tc radiotracer. We also used canine DVT and PE models to perform imaging studies with/without the heparin pretreatment. These studies were specifically designed to explore the impact of heparin treatment on thrombosis uptake of P4-DMP444. It was found that replacing the CA linker with PEG_4 could enhance the radiotracer clearance kinetics from blood and normal organs in both rats and dogs. The fact that P4-DMP444 and DMP444 share very similar thrombosis uptake in both DVT and PE models suggests that the PEG_4 linker has little effect on GPIIb/IIIa binding affinity of cyclic RGD peptide. Even though P4-DMP444 had less accumulation than DMP444 in the blood, heart, lungs, and muscle over the 2 h study period in both rats and dogs, the difference in PE/lung and DVT/muscle ratios is marginal, suggesting that one PEG_4 linker is not sufficient to dramatically change the contrast between thrombus and background. It is very important to note that the heparin treatment of dogs with DVT and PE resulted in dramatic decrease in accumulation of P4-DMP444 in fresh thrombi. On the basis of these results, we believe that DMP444 and P4-DMP444 are excellent radiotracers for imaging both DVT and PE, and should be used in patients without antithrombosis treatment at the time of imaging.

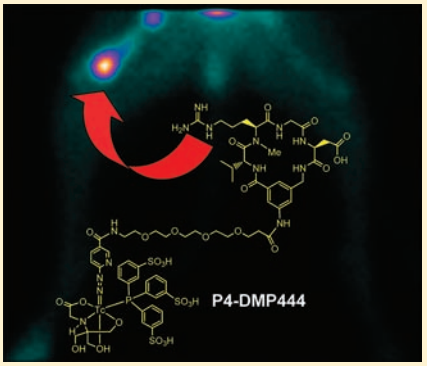

INTRODUCTION

Deep vein thrombosis (DVT) is the formation of blood clots in veins and is also known as venous thromboembolism.[1−3] DVT occurs when a thrombus forms in one of large veins in the lower extremities, leading to partially or completely blocked blood circulation. The condition may result in complications, such as a pulmonary embolism (PE) or death if not diagnosed and treated effectively. A majority of DVT patients will experience PE (~30% are symptomatic, and 40% are asymptomatic and at high risk) because the blood clot is unstable and can travel to and lodge in the lungs. More than one million people in the United States suffer from DVT every year. Complications from DVT kill almost 300 000 people a year—more than AIDS and breast cancer combined.[1,3] Thus, accurate early detection of DVT and PE is highly desirable so that various therapeutic regimens can be given.

Contrast-enhanced venography remains the gold standard for diagnosis of DVT, but compression ultrasonography is the most common technique used to detect DVT in the lower extremities. The main limitation of these procedures is that neither technique can distinguish between chronic and unstable thrombi.[1,4,5] Contrast venography and ultrasonography are imaging procedures that detect changes in venous anatomy. However, these procedures may overestimate the presence of active clots.[3] Nuclear imaging by single-photon emission computed tomography (SPECT) and positron emission tomography (PET) has the potential to furnish functional information on cell biologic events which determine the risk of plaque rupture and thrombosis formation.[6−8] Radiolabeled antibodies have been used to target the fibrin and activated platelets on acute thrombi in humans,[9−15] but they have limited clinical usage due to their long blood circulation time and radioactivity accumulation in the lungs. These limitations can be alleviated by using small peptides that are cleared quickly from the blood circulation.[16−33] Examples of small peptide radiotracers include ^{99m}Tc-apcitide[16−22] and DMP444,[23−32] both of which target GPIIb/IIIa receptors on the activated platelets. ^{99m}Tc-TP850 is a ^{99m}Tc-labeled small peptide targeting the fibrin component of thrombi.[33] The ^{99m}Tc-labeled peptide radiotracers have been reviewed extensively.[34−39]

Received: July 13, 2011
Published: July 24, 2011

ACS Publications © 2011 American Chemical Society

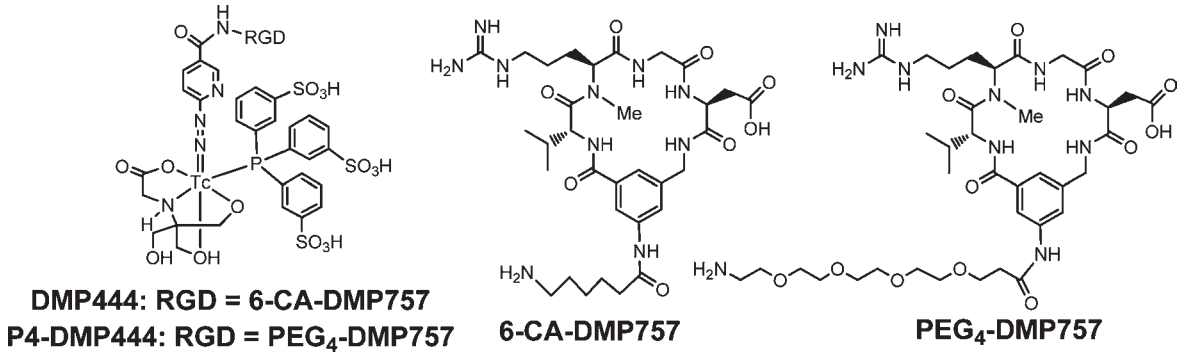

Figure 1. Structure of cyclic RGD peptides targeting GPIIb/IIIa receptors on activated platelets, and their corresponding ternary ligand ^{99m}Tc complexes [^{99m}Tc(HYNIC-RGD)(tricine)(TPPTS)] (DMP444: RGD = 6-CA-DMP757, and CA = 6-aminocaproic acid; P4-DMP444: RGD = PEG_4-DMP757, and PEG_4 = 15-amino-4,7,10,13-tetraoxapentadecanoic acid).

Activated platelets express GPIIb/IIIa receptors which recognize proteins and small peptides bearing RGD (arginine-glycine-glutamic acid) tripeptide sequences while nonactivated platelets express no GPIIb/IIIa receptors in their active conformation.[25] DMP444 (Figure 1) is a ^{99m}Tc-labeled cyclic RGD peptide,[23] and has been evaluated extensively in preclinical animal models,[24−30] and in the patients with DVT and PE.[31,32] Among the ^{99m}Tc radiotracers evaluated in canine DVT models, DMP444 had the best thrombus uptake and thrombus/blood and thrombus/muscle ratios.[24] It was reported that DMP444 has higher thrombus uptake and better thrombus-to-background ratios than ^{99m}Tc-apcitide.[25] It was also found that microthromboemboli could be detected after primary percutaneous transluminal coronary angioplasty, and the infarct size was proportional to the magnitude and extent of microthromboemboli.[30] At 10−40 min postinjection (p.i.), eight of ten patients with suspected DVT demonstrated an area of the increased radioactivity that was clearly related to the abnormality as noted by ultrasound methods.[31] On the basis of clinical data, it was concluded that DMP444 is useful for imaging DVT; but it had very limited utility for imaging PE in patients.[31,36,37] Its lack of sensitivity and specificity might be caused either by antithrombosis treatment (heparin alone or combination with Coumadin) in the patients suspected with thrombosis at the time of imaging[31] or by its slow blood clearance (45% of the injected dose at 2 h p.i. in the canine model) and lung radioactivity accumulation.[24,25]

To understand these clinical findings, we have prepared a new radiotracer P4-DMP444 (Figure 1) by replacing the lipophilic 6-aminocaproic acid (CA) linker in DMP444 with a highly water-soluble PEG_4 (15-amino-4,7,10,13-tetraoxapentadecanoic acid). The main purpose of using PEG_4 linker was to reduce radioactivity accumulation in the blood pool and lungs while maintaining high thrombosis uptake of ^{99m}Tc radiotracer. PEG_4 has been successfully used to improve excretion kinetics of many radiolabeled small peptides.[38−44] In addition, we also used the canine DVT and PE models to perform imaging studies in the dogs with/without heparin pretreatment. These studies were specifically designed to explore the impact of heparin treatment on thrombosis uptake of P4-DMP444. In this report, we present biological evaluations of P4-DMP444 in the rat and dog models.

EXPERIMENTAL SECTION

Materials and Instruments. Chemicals were purchased from Sigma/Aldrich (St. Louis, MO), and were used without further purification. Cyclic RGD peptide c[R(Me)GDV(Mamb(PEG_4))] (P4-DMP757) was custom-made by Peptides International, Inc. (Louisville, KY). Succinimidyl 6-(2-(2-sulfonatobenzaldehyde)-hydrazono)nicotinate (HYNIC-NHS), HYNIC-c[R(Me)GDV-(Mamb(CA)] (HYNIC-CA-DMP757) and [^{99m}Tc(HYNIC-CA-DMP757)(tricine)(TPPTS)] (DMP444) were prepared according to the procedures described in our previous report.[23] Na$^{99m}TcO_4$ was obtained from a commercial Lantheus ^{99}Mo/^{99m}Tc Technelite generator (North Billerica, MA). The ESI (electrospray ionization) mass spectral data were collected on a Finnigan LCQ classic mass spectrometer, School of Pharmacy, Purdue University.

HPLC Methods. The semiprep HPLC method (Method 1) used a LabAlliance HPLC system equipped with a UV/vis detector (λ = 254 nm) and Zorbax C_{18} semiprep column (9.4 nm × 250 mm, 100 Å pore size; Agilent Technologies, Santa Clara, CA). The flow rate was 2.5 mL/min and the mobile phase was isocratic with 70% A (0.1% TFA in water) and 30% B (0.1% TFA in methanol) at 0−5 min, followed by a gradient mobile phase going from 30% B at 5 min to 70% B at 20 min. The radio-HPLC method (Method 2) used the LabAlliance HPLC system equipped with a β-ram IN/US detector (Tampa, FL) and Zorbax C_{18} column (4.6 mm × 250 mm, 300 Å pore size; Agilent Technologies, Santa Clara, CA). The flow rate was 1 mL/min with a gradient mobile phase started with 90% A (25 mM NH_4OAc, pH = 6.8) and 10% B (acetonitrile) to 85% A and 15% B at 5 min, followed by another gradient mobile phase going from 15% B at 5 min to 20% B at 20 min and to 60% B at 25 min.

HYNIC-P4-DMP757. HYNIC-NHS (5.8 mg, 13 μmol) and PEG_4-DMP757 (2.2 mg, 2.6 μmol) were dissolved in anhydrous DMF (2 mL). To the mixture above was added diisopropylethylamine (DIEA: 3 drops). The reaction mixture was then stirred at room temperature for 20 h. After addition of 2 mL water and 2 drops of acetic acid, the solution was subjected to HPLC purification (Method 1). Fractions at 14.26 min were collected. Lyophilization of the combined collections afforded the expected product HYNIC-P4-DMP757 as a white powder 1.7 mg (yield 57.4%). ESI-MS: m/z = 1162 for $[M + Na]^+$ (1139.5 calcd. for $[C_{50}H_{69}N_{13}O_{16}S]$).

^{99m}Tc-Labeling and Dose Preparation. To a clean 5 cc vial filled with 1.0 mL solution (pH = 4.8) containing 5 mg TPPTS, 6.5 mg tricine, 40 mg mannitol, 38.5 mg disodium succinate hexahydrate, and 12.7 mg succinic acid were added 0.2 mL of the HYNIC-peptide conjugate solution (100 μg/mL in water) and 0.3 mL of Na$^{99m}TcO_4$ (10−30 mCi/mL) in saline. The vial was heated at 100 °C for 20 min in a lead-shielded water bath. After radiolabeling, the vial was placed back into the lead pig, and

allowed to stand at room temperature for 5−10 min. A sample of the resulting solution was analyzed by radio-HPLC (Method 2). The Log P values were determined using the literature procedure.[46,47] For biodistribution studies, all new radiotracers were prepared and purified by radio-HPLC. Volatiles in the HPLC mobile phase were removed under vacuum. Doses were prepared by dissolving the HPLC-purified radiotracer in saline to a concentration of ∼30 μCi/mL. For imaging studies, doses were prepared by dissolving the radiotracer in saline to 1−5 mCi/mL depending upon the animals (rats versus dogs). The resulting solution was filtered with a 0.20 μm Millex-LG filter to remove any foreign particles before being injected into animals.

Biodistribution Protocol. Biodistribution studies were performed using Sprague−Dawley (SD) rats in compliance with the NIH animal experiment guidelines (*Principles of Laboratory Animal Care*, NIH Publication No. 86−23, revised 1985). The animal protocol was approved by the Purdue University Animal Care and Use Committee. In short, 16 SD rats (200−250 g) were anesthetized with intramuscular injection of a mixture of ketamine (80 mg/kg) and xylazine (19 mg/kg). Each animal was administered with ∼3 μCi of ^{99m}Tc radiotracer by tail vein injection. Four animals were sacrificed by sodium pentobarbital overdose (∼200 mg/kg) at 5, 30, 60, and 120 min postinjection (p.i.). Blood samples were withdrawn from the heart of rats. The brain, eyes, heart, spleen, lungs, liver, kidneys, muscle, and intestine were harvested, washed with saline, dried with absorbent tissue, weighed, and counted on a Perkin-Elmer Wizard −1480 γ-counter (Shelton, CT). The organ uptake was calculated as the percentage of injected dose per gram of organ mass (%ID/g). Biodistribution data (%ID/g) are reported as an average plus the standard variation based on the results from four animals. Comparison between two radiotracers was made using the two-way ANOVA test (GraphPad *Prism 5.0*, San Diego, CA). The level of significance was set at $p < 0.05$.

Animal Preparation for Studies in Dogs. All experiments were performed in accordance with the NIH animal experiment guidelines (*Principles of Laboratory Animal Care*, NIH Publication No. 86−23, revised 1985). The protocols for animal studies in dogs have been approved by the Fu Wai Hospital Animal Care and Use Committee (Beijing, China). Five adult mongrel dogs (20.6 ± 1.8 kg, range 18−25 kg, fasted overnight) were anesthetized with intravenous (i.v.) injection of a mixture of ketamine (25 mg/kg) and diazepam (1.1 mg/kg), incubated with a cuffed endotracheal tube, and ventilated on a respirator with positive end-expiratory pressure of 4 cm H_2O. Additional sodium pentobarbital were used via i.v. injection to maintain anesthesia, when needed.

Blood Clearance Kinetics in Normal Dogs. Once under anesthesia, each animal was administered with 370 MBq of ^{99m}Tc radiotracer via the femoral vein. Venous blood samples (2 mL) were collected via a femoral vein catheter at 0.5, 2, 3, 4, 5, 10, 15, 30, 60, 90, and 120 min postinjection. The collected blood samples were weighed and counted for radioactivity in a gamma-counter (FT-646, Beijing Nuclear Instrument Factory, China). The radioactivity counts were corrected for radiation decay.

Planar Imaging in Normal Dogs. Once the animal was under anesthesia, it was placed supine on a dual-head γ-camera (E-cam, Siemens Medical Systems, Hoffman Estates, IL) equipped with a parallel-hole, low-energy, high-resolution collimator and 20% window centered on the 140 keV ^{99m}Tc photopeak. After administration of P4-DMP444 (∼370 MBq) via the contralateral femoral vein, anterior planar images were acquired at 5, 15, 30, 60, 90, and 120 min p.i., and were stored digitally in a 128 × 128 matrix. The acquisition count limits were set at 500 K. After completion of imaging, animals were allowed to recover at the Center for Experimental Animals (Fu Wai Hospital). To quantify images, regions of interest (ROIs) were drawn around heart, lung, and liver on each image acquired at each time-point. The raw radioactivity data in each ROI was expressed as counts/pixel per min. For comparison purposes, DMP444 was also evaluated for blood clearance and planar imaging in normal dogs using the same injection dose and same protocol. The time interval between two imaging studies for P4-DMP444 and DMP444 in the same dogs was at least 24 h.

Deep Venous Thrombosis (DVT) Model. ^{99m}Tc radiotracers were evaluated in vivo in canine model which has been reported previously for the evaluation of thrombus imaging radiotracers.[17,45] Five adult mongrel dogs were anesthetized with intravenous injection of a mixture of ketamine (25 mg/kg) and diazepam (1.1 mg/kg). In each animal, an 18-gauge angiocatheter was inserted into the distal half of right femoral vein and a 10 mm two-stranded spiral stainless steel coil was placed in the femoral vein at approximately the midfemur. The catheter was then removed, the wound was sutured, and the placement of the coils was documented by radiograph.

Pulmonary Embolism (PE) Model. Five adult mongrel dogs were anesthetized with pentobarbital (30 mg/kg) administered by intravenous injection. A 10 mm two-stranded spiral stainless steel embolization coil was inserted into left lower pulmonary artery through catheter in each dog. At 30 min after coil placement, X-ray angiography was performed to document the pulmonary embolism and the locations of the coils. After catheter was removed, the wound was sutured. During the operation for generating pulmonary embolism, the dogs were anesthetized, and electrocardiogram (ECG) and SaO_2 were recorded. ECG was changed during the insertion of catheter and was recovered quickly after removal. All animals were allowed to recover for 24 h before imaging with ^{99m}Tc radiotracer. There was no animal death before the completion of imaging.

Thrombus Imaging. The animal was placed supine under a SPECT camera (SIEMENS, Germany) which was equipped with a low-energy, all-purpose collimator and set to acquire the 140 keV photopeak of ^{99m}Tc with a 20% window. ^{99m}Tc radiotracer (∼370 MBq) were injected intravenously into a foreleg line and flushed in with saline. The 30° left anterior oblique images over the chest region (for PE) or the anterior images over leg (for DVT) were acquired at 15, 30, 60, 90, and 120 min p.i. The total counts over the chest region (for PE model) or the leg (for DVT model) were set up to 500 000. From the computer-stored images, thrombus-to-background ratios were determined. Average counts per pixel were computed from ROIs drawn manually around the areas of known thrombus (corresponding to the locations of coils in radiographs). ROIs were drawn over the thrombus-containing lung to evaluate adjacent lung background for PE models. The PE/Lung ratios were determined by dividing mean counts per pixel for PE by mean counts per pixel for lung background. Similarly, ROIs were drawn over both medial and lateral thigh in the thrombus-containing leg to calculate the muscle background for DVT models. The DVT/muscle ratios were determined by dividing mean counts per pixel for DVT by mean counts per pixel for muscle (average of medial and lateral ROIs).

Heparin Treatment on Radiotracer Thrombus Uptake. Two mongrel dogs with the PE were used to explore the impact of heparin treatment on the pulmonary thrombus uptake of

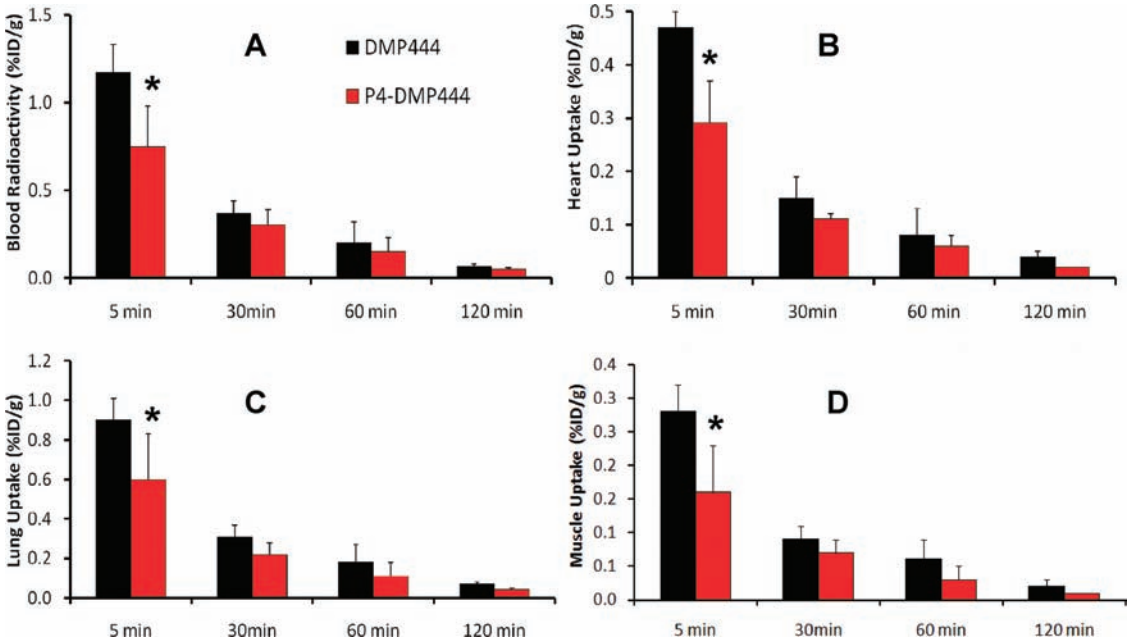

Figure 2. Comparison of organ uptake (%ID/g) of DMP444 and P4-DMP444 in the blood (A), heart (B), lung (C), and muscle (D) of Sprague−Dawley rats ($n = 4$) at 5, 30, 60, and 120 min p.i. At 5 min p.i., P4-DMP444 had significantly lower ($p < 0.05$) uptake than DMP444; but this difference disappeared at later times (>15 min p.i.).

P4-DMP444. A dose of 200 units/kg heparin (Changzhou Qianhong Bio-Pharma Co. Ltd., China) was intravenously injected at 10 min after the embolization coil was placed into left lower pulmonary artery. The chest region imaging protocol was performed as aforementioned.

Statistical Analysis. Statistical computations and analysis were made with *SPSS 13.0* software (SPSS Inc., Chicago, IL). The results are expressed as mean ± SD. Changes between the means within a group at different time points were assessed with one-way repeated-measures ANOVA test. Comparison between two radiotracers was made with two-way ANOVA test. The level of significance was set at $p < 0.05$.

RESULTS

HYNIC Conjugate Synthesis. Synthesis of HYNIC-P4-DMP757 was straightforward by reacting P4-DMP757 with excess HYNIC-OSu in anhydrous DMF in the presence of base, such as DIEA. It was purified from the reaction mixture by HPLC. Its composition has been confirmed by ESI-MS, and is completely consistent with the proposed structure (Figure 1). Its HPLC purity was >95% before being used for ^{99m}Tc-labeling.

Radiochemistry. P4-DMP444 was prepared according to the same method for DMP444.[23] No significant ^{99m}Tc-colloid (<0.5%) was detected using the non-$SnCl_2$ formulation, in which TPPTS acts as a reducing agent for $^{99m}TcO_4^-$ and a coligand at the same time to stabilize the ^{99m}Tc-HYNIC core. The partition coefficients of P4-DMP444 and DMP444 were determined in an equal volume mixture of 1-octanol and 25 mM phosphate buffer (pH = 7.4). The calculated Log P values for P4-DMP444 and DMP444 were −3.96 ± 0.20 and −4.02 ± 0.16, respectively. Apparently, there was no significant difference in their lipophilicity.

Biodistribution Properties. SD rats were used to compare biodistribution patterns of DMP444 and P4-DMP444. This animal model was used to evaluate peptide radiotracers, such as ^{99m}Tc-apcitide.[16,17] The selected biodistribution data are listed in Supporting Information Tables SI1 and SI2, respectively. Figure 2 compares organ uptake of P4-DMP444 and DMP444 in blood, heart, lungs, and muscle of SD rats. We are particularly interested in these organs because the radioactivity accumulation in the blood and heart will have significant impact on detection of arterial thrombi, in the lungs for PE, and in the muscle for DVT. The uptake of P4-DMP444 and DMP444 was low in the blood, heart, lung, and muscle. At 5 min p.i., P4-DMP444 had significantly lower ($p < 0.05$) uptake than DMP444. However, this difference disappeared at later times (>15 min p.i.). It was clear that replacing the CA linker with PEG_4 resulted in lower radioactivity accumulation in normal organs. These promising data led us to explore the blood clearance kinetics and normal organi biodistribution patterns of P4-DMP444 and DMP444 in dogs.

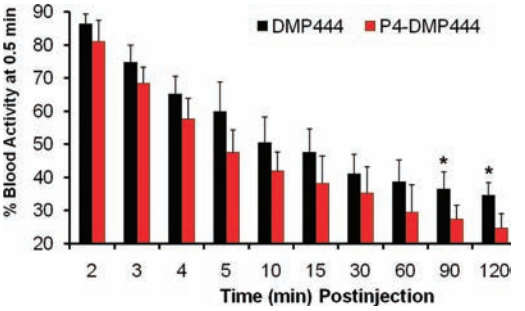

Figure 3. Comparison of blood clearance kinetics as determined by γ-counting between DMP444 and P4-DMP444 over 2 h study period. The blood radioactivity for P4-DMP444 was significantly lower ($P < 0.05$) than that for DMP444 at >90 min p.i.

Blood Clearance Kinetics. Figure 3 shows blood clearance curves of P4-DMP444 and DMP444 in normal dogs. The

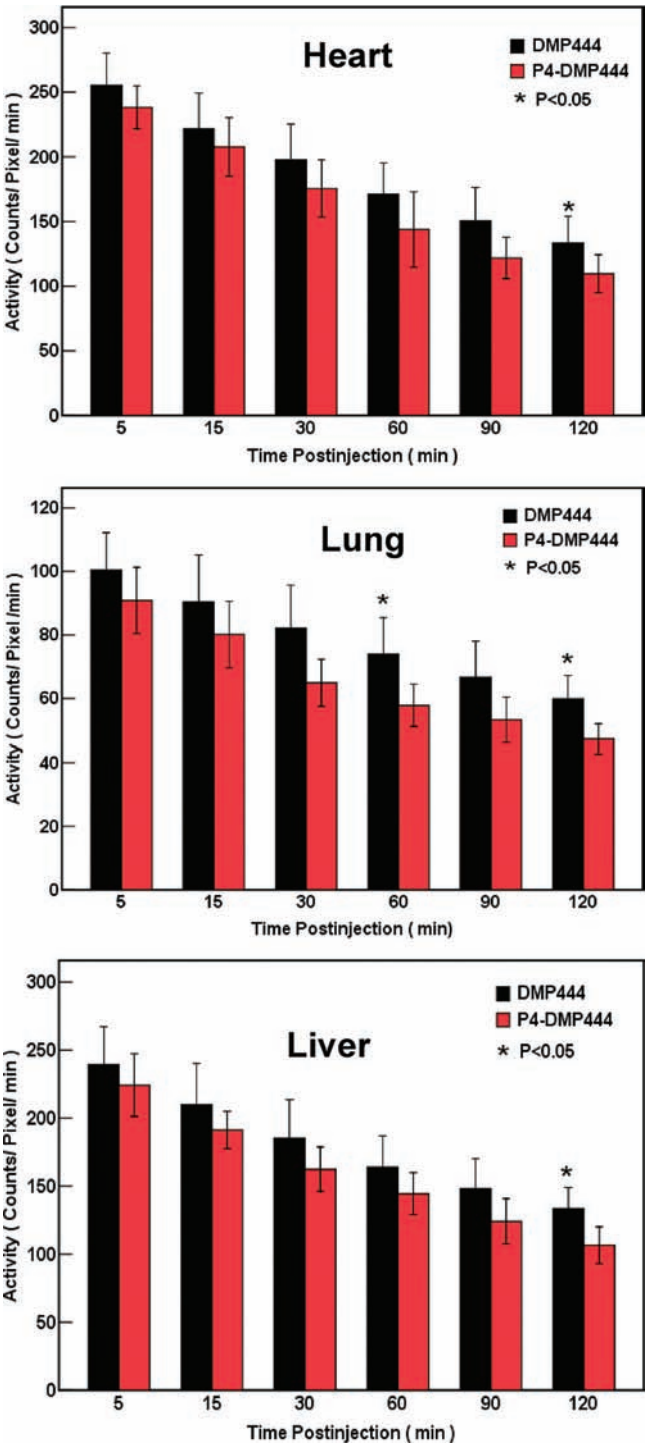

Figure 4. Organ distribution kinetics from imaging quantification in dogs administered with DMP444 and P4-DMP444 in the heart, lungs, and liver. There was a significant difference ($p < 0.05$) between DMP444 and P4-DMP444 for their heart, lung, and liver radioactivity at 120 min p.i.

radioactivity is expressed as a percentage of initial radioactivity level at 30 s p.i. Clearly, P4-DMP444 had faster blood clearance with >50% of initial radioactivity remaining at 5 min p.i. and 24.6% of initial radioactivity remaining at 120 min p.i. In contrast, DMP444 had nearly 50% of initial radioactivity remaining at 10 min p.i. and 34.6% of initial radioactivity

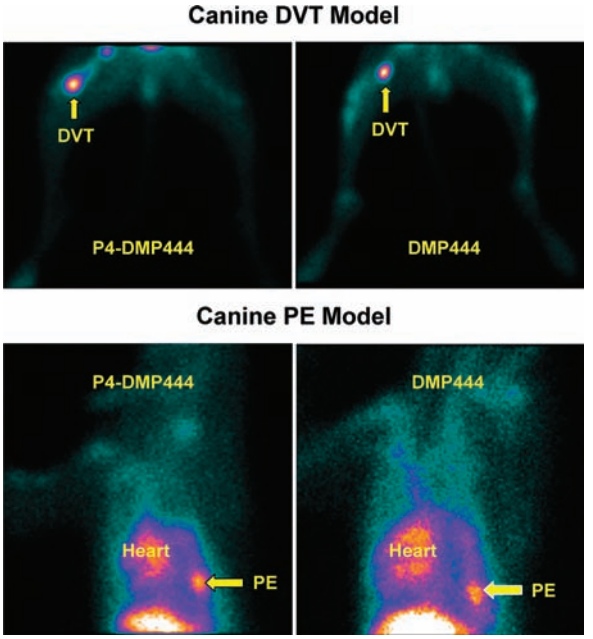

Figure 5. Top: planar images of lower body parts of the dogs with DVT in their right thigh at 120 min after injection of DMP444 (right) and P4-DMP444 (left). Bottom: planar images of chest region of the dog with PE in the right lung at 120 min after injection of DMP444 (right) and P4-DMP444 (left). The blood pool radioactivity in the heart was higher for DMP444 than that for P4-DMP444.

remaining at 120 min p.i. ($p < 0.05$ for P4-DMP444 vs DMP444 at 120 min p.i.)

Planar Imaging in Normal Dogs. Figure 4 illustrates the clearance kinetics of P4-DMP444 and DMP444 from normal organs in dogs. The radioactivity in the heart, lung and liver decreased markedly for both P4-DMP444 and DMP444 over the 2 h study period. P4-DMP444 had faster clearance than DMP444 from the heart, lung, and liver. There was a significant uptake difference ($p < 0.05$) between P4-DMP444 and DMP444 in the heart, lung, and liver at 120 min p.i.

Thrombus Imaging in Canine DVT and PE Models. Figure 5 compares the DVT (top: in right femoral vein) and PE (bottom: in the left lung) images obtained in dogs administered with P4-DMP444 and DMP444. Figure 6 shows the comparison of their PE/lung and DVT/muscle ratios at 15, 30, 60, 90, and 120 min p.i. in canine PE and DVT models. The lower uptake in the heart and lungs were observed for P4-DMP444. The PE/lung and DVT/muscle ratios were improved steadily from 15 min to 120 min p.i. P4-DMP444 had a significantly higher PE/lung ratio than DMP444 at 120 min p.i. (4.04 ± 0.13 vs 3.72 ± 0.14, $p < 0.05$). The difference between P4-DMP444 and DMP444 was not statistically significant for their DVT/muscle ratios (4.56 ± 0.41 vs 4.38 ± 0.28, $p > 0.05$) at 120 min p.i.

Impact of Heparin on Thrombus Uptake. Figure 7 shows planar images of the chest region in the dogs with PE (top: in the right lung) and DVT (bottom: in the right thigh) at 120 min after injection of P4-DMP444 with (right) and without (left) the antithrombosis treatment. It was quite clear that pretreatment of the dog with heparin at a dose of 200 units/kg significantly reduced the DVT and PE uptake of P4-DMP444.

dx.doi.org/10.1021/bc2003742 |*Bioconjugate Chem.* 2011, 22, 1715–1722

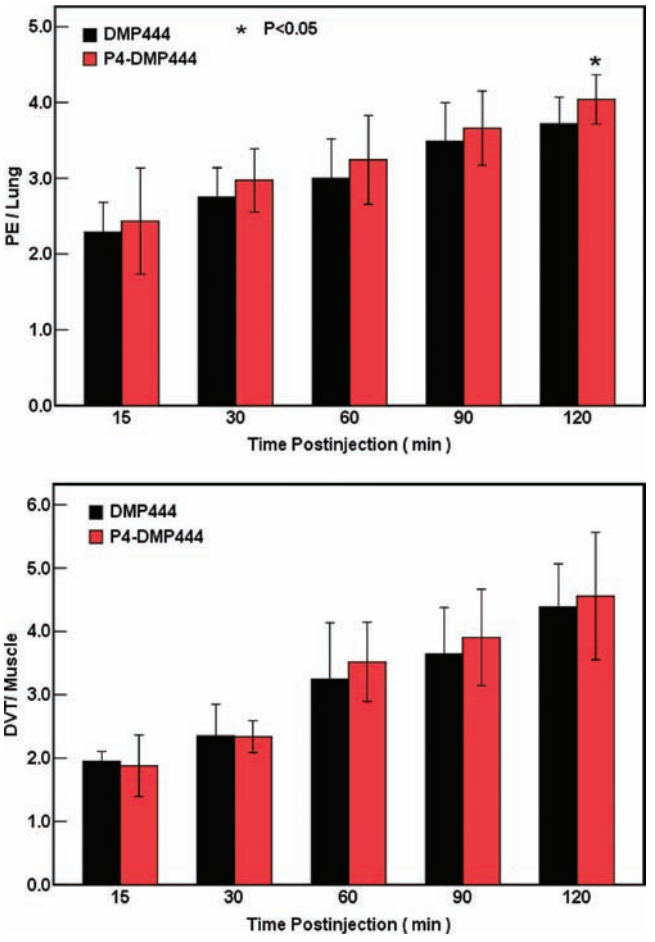

Figure 6. Comparison of PE/lung and DVT/muscle ratios for DMP444 (n = 5) and P4-DMP444 (n = 5) in dogs. The PE/lung ratio of ^{99m}Tc−P4-DMP444 was significantly better than that of DMP444 at 120 min p.i. There was no significant difference between DMP444 and P4-DMP444 for their DVT/muscle ratios.

DISCUSSION

In this study, we compared the biodistribution properties of DMP444 and P4-DMP444 (Figure 1) and their excretion kinetics from normal organs of the rats (Figure 2) and dogs (Figure 3). We are surprised to find out that replacing the lipophilic CA linker with PEG_4 had little effect on lipophilicity of ^{99m}Tc radiotracers (Log P = −3.96 ± 0.20 for P4-DMP444 and −4.02 ± 0.16 for DMP444). However, using the PEG_4 linker resulted in lower radioactivity accumulation in normal organs (e.g., blood, heart, liver, and lungs) of rats and dogs. These results are consistent with those obtained with radiolabeled PEG_4 containing small peptides in our previous studies.[38−44]

We also compared their capability to image thrombi in canine DVT and PE models. The fact that P4-DMP444 and DMP444 share similar thrombosis uptake (Figure 5) strongly suggests that replacing the CA linker with PEG_4 has little impact on GPIIb/IIIa binding affinity of cyclic RGD peptide. On the basis of their clearance kinetics from the blood, heart, liver, and lungs (Figures 3 and 4), one might expect better DVT/muscle and PE/lung ratios for P4-DMP444 as compared to DMP444. However, we found that P4-DMP444 and DMP444 shared very similar DVT/muscle ratios (Figure 6), probably because they both had low muscle uptake (Supporting Information Tables SI1 and SI2). Even though P4-DMP444 seems to have better PE/lung ratios (Figure 6) than DMP444 over the 2 h study period, their difference is marginal, suggesting that the addition of only one PEG_4 linker is not sufficient to dramatically change the contrast between thrombus and background, particularly muscle and lungs. Due to their very low lung uptake (Supporting Information Tables SI1 and SI2), it is reasonable to believe that the radioactivity accumulation in lungs is not the key factor contributing to the limited utility of DMP444 for imaging PE in patients.

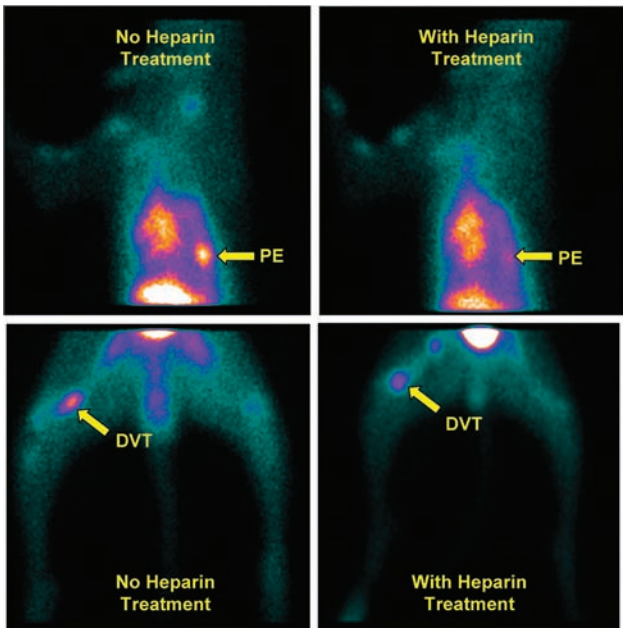

Figure 7. Planar images of the dogs with PE in the right lung (top) and DVT in their right thighs (bottom) at 120 min after injection of P4-DMP444 with (right) and without (left) the antithrombosis treatment with heparin (200 units/kg). Arrows indicate the presence of thrombus.

Heparin is a naturally occurring anticoagulant that prevents the formation of blood clots and extension of existing clots within the blood. Heparin and its low molecular weight derivatives (e.g., enoxaparin, dalteparin, tinzaparin) are used as antithrombosis agents to prevent DVT and PE in patients at risk.[48] In fact, most of the patients suspected with thrombosis take heparin alone or in combination with Warfarin (Coumadin) at the time of imaging.[31,36] Thus, we explored the impact of heparin treatment on imaging quality in the dogs administered with P4-DMP444. In this study, we found that the heparin treatment in dogs with DVT and PE before administration of P4-DMP444 resulted in dramatic decrease in radioactivity accumulation in the fresh thrombi (Figure 7). While heparin does not break down clots that have already formed, it allows the body's natural clot lysis mechanisms to work normally to break down blood clots that have formed. It is well-established that heparin binds to the enzyme inhibitor antithrombin III (AT) causing a conformational change, resulting in its activation through an increase in the flexibility of its reactive site loop.[49,50] The activated AT then inactivates thrombin and other proteases involved in blood clotting, most notable factor Xa,[49,50] which often leads to the deactivation of platelets and related receptors, such as GPIIb/IIIa. The rate of inactivation of these proteases by AT can increase by up to 1000-fold due to the binding of heparin.[57]

Thus, it is not surprising that DMP444 has very limited utility for imaging PE in the patients who were on antithrombosis medication at the time of imaging.[35,36] We believe that DMP444 and P4-DMP444 will have better sensitivity and specificity in the DVT and PE patients without antithrombosis treatment (heparin alone or in combination with Warfarin).

CONCLUSION

In this study, we found that replacing the CA linker with PEG_4 can improve the excretion kinetics from normal organs (blood, heart, liver, and lungs). Even though P4-DMP444 seems to have better PE/lung ratios than DMP444 over the 2 h study period, the addition of one PEG_4 linker in P4-DMP444 is not sufficient to dramatically change the contrast between thrombus and background. It is very important to note that the heparin pretreatment of dogs with DVT and PE can result in dramatic decrease in radioactivity accumulation in fresh thrombi. On the basis of the results from this study, we believe that P4-DMP444 is an excellent radiotracer for imaging both DVT and PE, and should be used in the patients without antithrombosis treatment at the time of imaging.

ASSOCIATED CONTENT

Supporting Information. Data tables as described in the text. This material is available free of charge via the Internet at http://pubs.acs.org.

AUTHOR INFORMATION

Corresponding Author

*Dr. Shuang Liu, School of Health Sciences, Purdue University, West Lafayette, IN 47907-2051. Phone: 765-494-0236; Fax 765-496-3367; E-mail: liu100@purdue.edu.

ACKNOWLEDGMENT

This work is supported, in part, by Purdue University and the research grant R01 CA115883 from the National Cancer Institute (NCI).

REFERENCES

(1) Blum, J. E., and Handmaker, H. (2002) Small peptide radiopharmaceuticals in the imaging of acute thrombus. *Curr. Pharm. Des. 8*, 1815–1826.

(2) Quinn, M. J., Byzova, T. V., Qin, J., Topol, E. J., and Plow, E. F. (2003) Integrin $\alpha_{IIb}\beta_3$ and its antagonism. *Arterioscler. Thromb. Vasc. Biol. 23*, 945–952.

(3) Chan, W. S., and Ginsberg, J. S. (2002) Diagnosis of deep vein thrombosis and pulmonary embolism in pregnancy. *Thromb. Res. 107*, 85–91.

(4) Nissen, S. E., and Yock, P. (2001) Intravascular ultrasound: novel pathophysiological insights and current clinical applications. *Circulation 103*, 604–616.

(5) Caussin, C., Ohanessian, A., Ghostine, S., Jacq, L., Lancelin, B., Dambrin, G., Sigal-Cinqualbre, A., Angel, C. Y., and Paul, J. F. (2004) Characterization of vulnerable nonstenotic plaque with 16-slice computed tomography compared with intravascular ultrasound. *Am. J. Cardiol. 94*, 99–104.

(6) de Feyter, P. J., and Nieman, K. (2002) New coronary imaging techniques: what to expect? *Heart 87*, 195–197.

(7) Jaffer, F. A., Libby, P., and Weissleder, R. (2006) Molecular and cellular imaging of atherosclerosis: emerging applications. *J. Am. Coll. Cardiol. 47*, 1328–1338.

(8) Choudhury, R. P., Fuster, V., and Fayad, Z. A. (2004) Molecular, cellular and functional imaging of atherothrombosis. *Nat. Rev. Drug Discovery 3*, 913–925.

(9) Moriwaki, H., Matsumoto, M., Handa, N., Isaka, Y., Hashikawa, K., Oku, N., Nakamura, M., Kamada, T., and Nishimura, T. (1995) Functional and anatomic evaluation of carotid atherothrombosis. A combined study of indium 111 platelet scintigraphy and B-mode ultrasonography. *Arterioscler. Thromb. Vasc. Biol. 15*, 2234–2240.

(10) Tsimikas, S., Palinski, W., Halpern, S. E., Yeung, D. W., Curtiss, L. K., and Witztum, J. L. (1999) Radiolabeled MDA2, an oxidation-specific, monoclonal antibody, identifies native atherosclerotic lesions in vivo. *J. Nucl. Cardiol. 6*, 41–53.

(11) Cerqueira, M. D., Stratton, J. R., Vracko, R., Schaible, T. F., and Ritchie, J. L. (1992) Noninvasive arterial thrombus imaging with ^{99m}Tc monoclonal antifibrin antibody. *Circulation 85*, 298–304.

(12) Matter, C. M., Schuler, P. K., Alessi, P., Meier, P., Ricci, R., Zhang, D., Halin, C., Castellani, P., Zardi, L., Hofer, C. K., Montani, M., Neri, D., and Lüscher, T. F. (2004) Molecular imaging of atherosclerotic plaques using a human antibody against the extradomain B of fibronectin. *Circ. Res. 95*, 1225–1233.

(13) Tsimikas, S., Shortal, B. P., Witztum, J. L., and Palinski, W. (2000) In vivo uptake of radiolabeled MDA2, an oxidation-specific monoclonal antibody, provides an accurate measure of atherosclerotic lesions rich in oxidized LDL and is highly sensitive to their regression. *Arterioscler. Thromb. Vasc. Biol. 20*, 689–697.

(14) Shaw, P. X., Hörkkö, S., Tsimikas, S., Chang, M. K., Palinski, W., Silverman, G. J., Chen, P. P., and Witztum, J. L. (2001) Human-derived anti-oxidized LDL autoantibody blocks uptake of oxidized LDL by macrophages and localizes to atherosclerotic lesions in vivo. *Arterioscler. Thromb. Vasc. Biol. 21*, 1333–1339.

(15) Ginsberg, H. N., Goldsmith, S. J., and Vallabhajosula, S. (1990) Noninvasive imaging of ^{99m}technetium-labeled low density lipoprotein uptake by tendon xanthomas in hypercholesterolemic patients. *Arteriosclerosis 10*, 256–262.

(16) Muto, P., Lastoria, S., Varrella, P., Vergara, E., Salvatore, M., Morgano, G., Lister-James, J., Bernardy, J. D., Dean, R. T., and Wencker, D. (1995) Detecting deep venous thrombosis with technetium-99m-labeled synthetic peptide P280. *J. Nucl. Med. 36*, 1384–1391.

(17) Lister-James, J., Knight, L. C., Maurer, A. H., Bush, L. R., Moyer, B. R., and Dean, R. T. (1996) Thrombus imaging with a technetium-99m-labeled activated platelet receptor-binding peptide. *J. Nucl. Med. 37*, 775–781.

(18) Bates, S. M., Lister-James, J., Julian, J. A., Taillefer, R., Moyer, B. R., and Ginsberg, J. S. (2003) Imaging characteristics of a novel technetium Tc-99m-labeled platelet glycoprotein IIb/IIIa receptor antagonist in patients with acute deep vein thrombosis or a history of deep vein thrombosis. *Arch. Intern. Med. 163*, 452–456.

(19) Taillefer, R., Therasse, E., Turpin, S., Lambert, R., Robillard, P., and Soulez, G. (1999) Comparison of early and delayed scintigraphy with ^{99m}Tc-apcitide and correlation with contrast-enhanced venography in detection of acute deep vein thrombosis. *J. Nucl. Med. 40*, 2029–2035.

(20) Carretta, R. F., Streek, P. V., and Weiland, F. L. (1999) Optimizing images of acute deep-vein thrombosis using technetium-99m-apcitide. *J. Nucl. Med. Technol. 27*, 271–275.

(21) Taillefer, R., Edell, S., Innes, G., and Lister-James, J. (2000) Acute thromboscintigraphy with ^{99m}Tc-apcitide: results of the phase 3 multicenter clinical trial comparing ^{99m}Tc-apcitide scintigraphy with contrast venography for imaging acute DVT. Multicenter trial investigators. *J. Nucl. Med. 41*, 1214–1223.

(22) Dunzinger, A., Hafner, F., Schaffler, G., Piswanger-Soelkner, J. C., Brodmann, M., and Lipp, R. W. (2008) ^{99m}Tc-apcitide scintigraphy in patients with clinically suspected deep venous thrombosis and pulmonary embolism. *Eur. J. Nucl. Med. Mol. Imaging 35*, 2082–2087.

(23) Edwards, D. S., Liu, S., Barrett, J. A., Harris, A. R., Looby, R. J., Ziegler, M. C., Heminway, S. J., and Carroll, T. R. (1997) New and versatile ternary ligand system for technetium radiopharmaceuticals: water soluble phosphines and tricine as coligands in labeling a hydrazinonicotinamide-modified cyclic glycoprotein IIb/IIIa receptor antagonist with ^{99m}Tc. *Bioconjugate Chem. 8*, 146–154.

(24) Barrett, J. A., Crocker, A. C., Damphousse, D. J., Heminway, S. J., Liu, S., Edwards, D. S., Lazewatsky, J. L., Kagan, M., Mazaika, T. J., and Carroll, T. R. (1997) Biological evaluation of thrombus imaging agents utilizing water soluble phosphines and tricine as coligands to label a hydrazinonicotinamide-modified cyclic glycoprotein IIb/IIIa receptor antagonist with ^{99m}Tc. *Bioconjugate Chem. 8*, 155–160.

(25) Mousa, S. A., Bozarth, J. M., Edwards, S., Carroll, T., and Barrett, J. A. (1998) Novel technetium-99m-labeled platelet GPIIb/IIIa receptor antagonists as potential imaging agents for venous and arterial thrombi. *Coron. Artery Dis. 9*, 131–141.

(26) Oyen, W. J., Boerman, O. C., Brouwers, F. M., Barrett, J. A., Verheugt, F. W., Ruiter, D. J., Corstens, F. H., and van der Meer, J. W. (2000) Scintigraphic detection of acute experimental endocarditis with the technetium-99m labelled glycoprotein IIb/IIIa receptor antagonist DMP444. *Eur. J. Nucl. Med. 27*, 392–399.

(27) Mitchel, J., Waters, D., Lai, T., White, M., Alberghini, T., Salloum, A., Knibbs, D., Li, D., and Heller, G. V. (2000) Identification of coronary thrombus with a IIb/IIIa platelet inhibitor radiopharmaceutical, technetium-99m DMP-444: a canine model. *Circulation 101*, 1643–1646.

(28) Scharn, D. M., Oyen, W. J., Klemm, P. L., Wijnen, M. H., and vanderVliet, J. A (2002) Assessment of prosthetic vascular graft thrombogenicity using the technetium-99m labeled glycoprotein IIb/IIIa receptor antagonist DMP444 in a dog model. *Cardiovasc. Surg. 10*, 566–569.

(29) Sakuma, T., Sari, I., Goodman, C. N., Lindner, J. R., Klibanov, A. L., and Kaul, S. (2005) Simultaneous integrin $\alpha_v\beta_3$ and glycoprotein IIb/IIIa inhibition causes reduction in infarct size in a model of acute coronary thrombosis and primary angioplasty. *Cardiovasc. Res. 66*, 552–561.

(30) Sakuma, T., Sklenar, J., Leong-Poi, H., Goodman, N. C., Glover, D. K., and Kaul, S. (2004) Molecular imaging identifies regions with microthromboemboli during primary angioplasty in acute coronary thrombosis. *J. Nucl. Med. 45*, 1194–1200.

(31) Klem, J. A., Schaffer, J. V., Crane, P. D., Barrett, J. A., Henry, G. A., Canestri, L., and Ezekowitz, M. D. (2000) Detection of deep venous thrombosis by DMP 444, a platelet IIb/IIIa antagonist: a preliminary report. *J. Nucl. Cardiol. 7*, 359–364.

(32) Brouwers, F. M., Oyen, W. J., Boerman, O. C., Barrett, J. A., Verheugt, F. W., Corstens, F. H., and Van der Meer, J. W. (2003) Evaluation of Tc-99m-labeled glycoprotein IIb/IIIa receptor antagonist DMP444 SPECT in patients with infective endocarditis. *Clin. Nucl. Med. 28*, 480–484.

(33) Aruva, M. R., Daviau, J., Sharma, S. S., and Thakur, M. L. (2006) Imaging thromboembolism with fibrin-avid ^{99m}Tc-peptide: evaluation in swine. *J. Nucl. Med. 47*, 155–162.

(34) Cerqueira, M. D. (1999) Current status of radionuclide tracer imaging of thrombi and atheroma. *Semin. Nucl. Med. 29*, 339–351.

(35) Taillefer, R. (2001) Radiolabeled peptides in the detection of deep venous thrombosis. *Semin. Nucl. Med. 31*, 102–123.

(36) Bernarducci, M. P. (2004) Radiolabeled peptides: overcoming the challenges of post-surgical patient management of venous thromboembolism. *Surg. Technol. Int. 12*, 50–67.

(37) Dobrucki, L. W., and Sinusas, A. J. (2010) PET and SPECT in cardiovascular molecular imaging. *Nat. Rev. Cardiol. 7*, 38–47.

(38) Wang, L., Shi, J., Kim, Y. S., Zhai, S., Jia, B., Zhao, H., Liu, Z., Wang, F., Chen, X., and Liu, S. (2009) Improving tumor-targeting capability and pharmacokinetics of ^{99m}Tc-labeled cyclic RGD dimers with PEG_4 linkers. *Mol. Pharmaceutics 6*, 231–245.

(39) Shi, J., Kim, Y. S., Zhai, S., Liu, Z., Chen, X., and Liu, S. (2009) Improving tumor uptake and pharmacokinetics of ^{64}Cu-labeled cyclic RGD dimers with triglycine and PEG_4 Linkers. *Bioconjugate Chem. 20*, 750–759.

(40) Liu, S., He, Z., Hsieh, W. Y., Kim, Y. S., and Jiang, Y. (2006) Impact of PKM linkers on biodistribution characteristics of the ^{99m}Tc-labeled cyclic RGDfK dimer. *Bioconjugate Chem. 17*, 1499–1507.

(41) Jia, B., Liu, Z., Shi, J., Yu, Z., Yang, Z., Zhao, H., He, Z., Liu, S., and Wang, F. (2008) Linker effects on biological properties of ^{111}In-labeled DTPA conjugates of a cyclic RGDfK dimer. *Bioconjugate Chem. 19*, 201–210.

(42) Liu, Z., Niu, G., Shi, J., Liu, S., Wang, F., Liu, S., and Chen, X. (2009) ^{68}Ga-labeled cyclic RGD dimers with Gly_3 and PEG_4 linkers: promising agents for tumor integrin $\alpha_v\beta_3$ PET imaging. *Eur. J. Nucl. Med. Mol. Imaging 36*, 947–957.

(43) Liu, Z., Liu, S., Wang, F., Liu, S., and Chen, X. (2009) Noninvasive imaging of tumor integrin expression using ^{18}F-labeled RGD dimer peptide with PEG_4 linkers. *Eur. J. Nucl. Med. Mol. Imaging 36*, 1296–1307.

(44) Liu, S. (2009) Radiolabeled cyclic RGD peptides as integrin $\alpha_v\beta_3$-targeted radiotracers: maximizing binding affinity via bivalency. *Bioconjugate Chem. 20*, 2199–2213.

(45) Meoli, D. F., Sadeghi, M. M., Krassilnikova, S., Bourke, B. N., Giordano, F. J., Dione, D. P., Su, H., Edwards, D. S., Liu, S., Harris, T. D., Madri, J. A., Zaret, B. L., and Sinusas, A. J. (2004) Noninvasive imaging of myocardial angiogenesis following experimental myocardial infarction. *J. Clin. Invest. 113*, 1684–1691.

(46) Agnelli, G., Piovella, F., Buoncristiani, P., Severi, P., Pini, M., D'Angelo, A., Beltrametti, C., Damiani, M., Andrioli, G. C., Pugliese, R., Iorio, A., and Brambilla, G. (1998) Enoxaparin plus compression stockings compared with compression stockings alone in the prevention of venous thromboembolism after elective neurosurgery. *N. Engl. J. Med. 339*, 80–5.

(47) Bergqvist, D., Agnelli, G., Cohen, A. T., Eldor, A., Nilsson, P. E., Le Moigne-Amrani, A., and Dietrich-Neto, F. (2002) Duration of prophylaxis against venous thromboembolism with enoxaparin after surgery for cancer. *N. Engl. J. Med. 346*, 975–980.

(48) Handoll, H. H., Farrar, M. J., McBirnie, J., Tytherleigh-Strong, G., Milne, A. A., and Gillespie, W. J. (2002) Heparin, low molecular weight heparin and physical methods for preventing deep vein thrombosis and pulmonary embolism following surgery for hip fractures. *Cochrane Database Syst. Rev. 4*, CD000305.

(49) Chuang, Y. J., Swanson, R., Raja, S. M., and Olson, S. T. (2001) Heparin enhances the specificity of antithrombin for thrombin and factor Xa independent of the reactive center loop sequence. Evidence for an exosite determinant of factor Xa specificity in heparin-activated antithrombin. *J. Biol. Chem. 276*, 14961–14971.

(50) Björk, I., and Lindahl, U. (1982) Mechanism of the anticoagulant action of heparin. *Mol. Cell. Biochem. 48*, 161–182.

Supplementary Materials for the Manuscript Entitled

"Evaluation of ^{99m}Tc-Labeled Cyclic RGD Peptide with a PEG_4 Linker for Thrombosis Imaging: Comparison with DMP444"

by

Wei Fang[1], Jia He[1], Young-Seung Kim[2], Yang Zhou[2], and Shuang Liu[2]*

[1]Department of Nuclear Medicine, Cardiovascular Institute & Fu Wai Hospital, Chinese Academy of Medical Science & Peking Union Medical College, Beijing, China

[2]School of Health Sciences, Purdue University, West Lafayette, USA

---

*To whom correspondence should be addressed.

Dr. Shuang Liu, School of Health Sciences, Purdue University, West Lafayette, IN 47907-2051. Phone: 765-494-0236; Fax 765-496-3367; Email: liu100@purdue.edu

Table SI1. Selected biodistribution data for DMP444 (Log P = -4.02 ± 0.16) in the SD rats (n = 5).

%ID/gram	5 min	30min	60 min	120 min
Blood	1.17 ± 0.16	0.37 ± 0.07	0.20 ± 0.12	0.07 ± 0.01
Brain	0.06 ± 0.01	0.02 ± 0.01	0.01 ± 0.01	0.01 ± 0.01
Eyes	0.17 ± 0.05	0.14 ± 0.11	0.06 ± 0.03	0.02 ± 0.02
Heart	0.47 ± 0.04	0.15 ± 0.04	0.08 ± 0.05	0.04 ± 0.01
Intestine	0.58 ± 0.14	0.26 ± 0.02	0.11 ± 0.04	0.07 ± 0.03
Kidney	3.96 ± 1.22	2.07 ± 0.32	0.86 ± 0.21	0.57 ± 0.12
Liver	0.33 ± 0.05	0.12 ± 0.01	0.09 ± 0.04	0.04 ± 0.01
Lungs	0.90 ± 0.11	0.31 ± 0.06	0.18 ± 0.09	0.07 ± 0.01
Muscle	0.28 ± 0.04	0.09 ± 0.02	0.06 ± 0.03	0.02 ± 0.01
Salivary	0.50 ± 0.06	0.16 ± 0.04	0.11 ± 0.06	0.04 ± 0.01
Spleen	0.31 ± 0.04	0.10 ± 0.03	0.06 ± 0.02	0.03 ± 0.01

Table SI2. Selected biodistribution data for P4-DMP444 (Log P = -3.96 ± 0.20) in the SD rats (n = 5).

%ID/gram	5 min	30min	60 min	120 min
Blood	0.75 ± 0.23	0.30 ± 0.09	0.15 ± 0.08	0.05 ± 0.01
Brain	0.08 ± 0.05	0.01 ± 0.00	0.01 ± 0.00	0.00 ± 0.00
Eyes	0.08 ± 0.05	0.05 ± 0.02	0.05 ± 0.02	0.01 ± 0.00
Heart	0.29 ± 0.08	0.11 ± 0.01	0.06 ± 0.02	0.02 ± 0.00
Intestine	0.38 ± 0.11	0.14 ± 0.02	0.07 ± 0.02	0.04 ± 0.01
Kidney	4.21 ± 1.97	1.64 ± 0.37	0.71 ± 0.12	0.55 ± 0.36
Liver	0.17 ± 0.06	0.09 ± 0.03	0.06 ± 0.03	0.03 ± 0.00
Lungs	0.60 ± 0.23	0.22 ± 0.06	0.11 ± 0.07	0.04 ± 0.01
Muscle	0.16 ± 0.07	0.07 ± 0.02	0.03 ± 0.02	0.01 ± 0.00
Salivary	0.27 ± 0.09	0.11 ± 0.01	0.07 ± 0.03	0.02 ± 0.01
Spleen	0.19 ± 0.08	0.06 ± 0.01	0.04 ± 0.02	0.02 ± 0.00

Bioconjugate Chemistry

TECHNICAL NOTE

pubs.acs.org/bc

Rapid HATU-Mediated Solution Phase siRNA Conjugation

Jeffrey G. Aaronson,*,† Lee J. Klein,‡ Aaron A. Momose,† Ann M. O'Brien,‡ Anthony W. Shaw,† Thomas J. Tucker,† Yu Yuan,† and David M. Tellers†

†Department of Medicinal Chemistry and ‡Department of Pharmaceutical Analytical Chemistry, Merck Research Laboratories, Merck & Co., Inc., West Point, Pennsylvania 19486, United States

ABSTRACT: Conditions for facile solution-phase amide conjugation of amine-modified siRNA with a diverse set of carboxylic acid partners using the coupling reagent HATU are described. These conditions eliminate the need for isolated activated esters and allow for rapid access to conjugates with a wide range of lipophilicity and functionality in good yield.

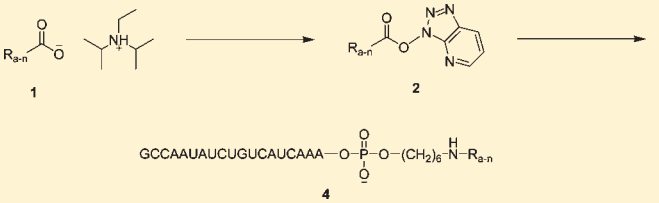

INTRODUCTION

The development of synthetic oligonucleotide therapeutics, particularly antisense and siRNA platforms, has highlighted the importance of robust methodologies for their modification with functional moieties.[1] Common conjugates include fluorescent tags,[2] targeting ligands,[3−5] and delivery-enhancing agents.[3,6−8] These moieties can be introduced at the 3′ or 5′ terminus during solid-phase synthesis employing the same phosphoramidite reactivity used to construct the oligonucleotide sequence or through the use of a compatible linker. The solid-phase approach benefits from streamlined chemistry and purification; however, relatively harsh cleavage and deprotection conditions limit its substrate scope.[9] Furthermore, 3′ terminal modifications are typically introduced by initiating oligonucleotide synthesis from a solid support modified with the desired conjugate.[10−12] This limits throughput and versatility in the discovery process by requiring a separate synthesis, deprotection, and purification for each unique conjugate (Scheme 1A). Even with parallel oligonucleotide synthesis capabilities, this approach to diverse 3′ modification is inefficient. Many of these issues can be circumvented via solution-phase synthetic modification after cleavage from the resin. The primary advantage of solution-phase synthesis is versatility: a single batch of linker-modified oligonucleotide can be derivatized to gain access to multiple diverse conjugates without a differentiated postsynthetic strategy for the 3′ and 5′ termini (Scheme 1B). Unfortunately, the scope of solution-phase siRNA modification is primarily limited by solvent compatibility. Deprotected oligonucleotides are insoluble in many of the organic solvents required for compatibility with hydrophobic coupling partners. Binary and tertiary mixed solvent systems[13,14] and lipophilic oligonucleotide counterions[15−17] have been reported in the literature to address this problem. Though these approaches are sufficient for many applications, the desire to better leverage the diversity-oriented attributes of solution-phase synthesis prompted development of the amidation conditions described herein.

MATERIALS AND METHODS

Amine modified passenger strand with the sequence 5′ GCCAAUAUCUGUCAUCAAA-$(CH_2)_6$-NH_2 (bold letters = ribonucleotides, underlined letters = 2′-O-methyl modified nucleotides) was synthesized using standard solid-support phosphoramide chemistry and isolation methods. The corresponding guide sequence was prepared in an analogous manner. Quantification of RNA solutions was carried out with a Thermo Scientific Nanodrop 2000c Spectrophotometer; the siRNA extinction coefficient was calculated using the nearest neighbor model.[18] A Milli-Q system (Millipore, Bedford, MA) was used to prepare deionized water (≥18 MΩ cm) for sample and buffer preparation. Organic solvents and reagents were obtained from various suppliers and were used without further purification.

Amidation Procedure. Stock solutions of siRNA (18.0 mM in DI water), carboxylic acid (200 mM in DMSO), and HATU (400 mM in DMSO) were prepared prior to conjugation. A stoichiometric amount of *N*,*N*-diisopropylethyamine (DIEA) was added to the carboxylic acid stock solution to form the carboxylate. siRNA (44.0 μL, 18.0 mM stock solution) was diluted with 396 μL DMSO and treated with DIEA (1.00 μL, 7.91 umol). Carboxylate (8.00 μL, 200 mM stock solution) and HATU (4.00 μL, 400 mM stock solution) were combined in a separate microcentrifuge tube and allowed to activate for 15 min with shaking. The siRNA solution was added to the activated carboxylic acid, and the resulting solution was shaken for an additional 15 min. The crude reaction mixture was diluted with 2 mL water and was purified via reverse-phase HPLC (linear gradient, 5−95% mobile phase B, where mobile phase A = aqueous 200 mM TEAA and mobile phase B = 200 mM TEAA in ACN, gradient over 20 min, Waters Xbridge phenyl OBD 5 μm 19 × 250 mm column). Centrifugal dialysis against DI water (Amicon Ultra 15, 3000 MW cutoff) was performed on

Received: March 7, 2011
Revised: May 9, 2011
Published: July 11, 2011

ACS Publications © 2011 American Chemical Society

Scheme 1. General Oligonucleotide Conjugation Strategies. (A) Solid-Phase Synthesis of 3′ Conjugates. Solid Sphere = Solid Support Resin. (B) Post-Synthetic 3′ Conjugation Utilizing an Amine Linker to Achieve Diversity

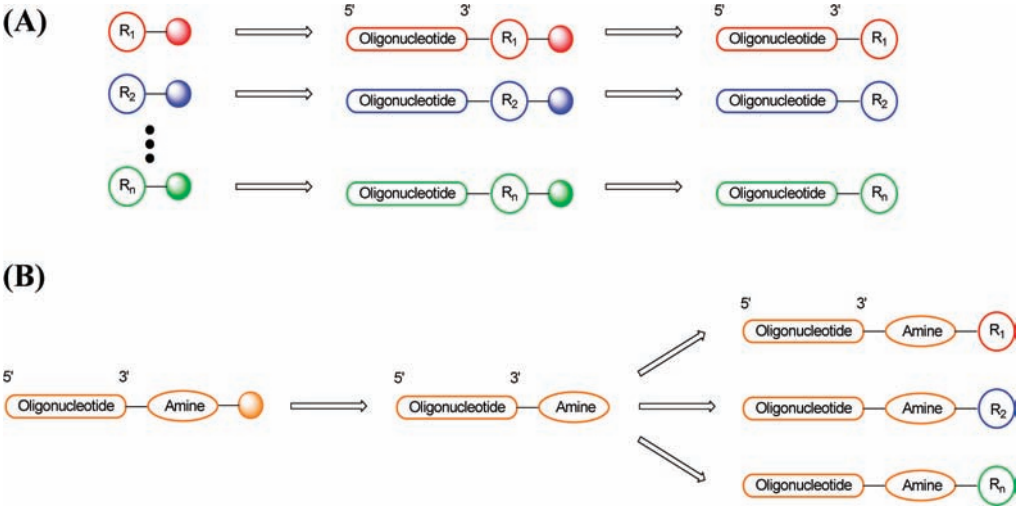

conjugate-containing fractions. Quantification by UV absorbance was followed by lyophilization to provide the isolated conjugate as an amorphous solid.

Hybridization. Isolated passenger strand conjugates **4h** and **4j** were reconstituted with DI water to concentrations of 0.38 mM and 0.44 mM, respectively, and were treated with an equimolar volume of 0.25 mM guide strand solution. The resulting solutions were heated at 90 °C for one minute and were allowed to slowly cool to room temperature. The final duplexes in solution were analyzed by capillary electrophoresis to assess duplex integrity and proper component strand stoichiometry.

HPLC of Crude Reactions. Crude reactions were assessed for conversion of starting siRNA using ion-pairing reverse-phase HPLC. An Agilent 1100 HPLC equipped with a Waters Xbridge phenyl 3.5 μm 4.6 × 150 mm column heated to 60 °C was used. The mobile phases consisted of aqueous 200 mM TEAA (mobile phase A) and 200 mM TEAA in ACN (mobile phase B). The method used for this analysis employed a gradient of 5−25% mobile phase B over 8 min, followed by 25−100% mobile phase B over 3 min and a two minute hold at 100% mobile phase B. A diode array was used to detect analyte at 260 nm.

UPLC-MS of Linker Conjugated Oligonucleotides. The linker-conjugated single-stranded oligonucleotides were analyzed for purity and mass identification via ion-pairing reversed-phase liquid chromatography mass spectrometry. An Acquity UPLC system using a Waters Acquity UPLC BEH 300 Å C4 1.7 μm, 2.1 × 100 mm column was employed for separation. The LC mobile phases were composed of 100 mM HFIP and 1.7 mM TEA in water (mobile phase A) and 20% THF in methanol (mobile phase B). The method was 10 min in duration with a linear gradient of 5−95% mobile phase B over 8 min followed by a 2 min equilibration. The flow rate was 200 μL/min. Samples were prepared to ∼0.1 mg/mL in water and 10 μL of sample solution was injected, giving an on-column sample mass of ∼1 μg. A TUV detector was used for analyte detection at 260 nm. The UPLC was interfaced to a Waters Synapt HDMS for mass analysis of the oligonucleotides. The MS instrument was used in electrospray ionization (ESI) negative ion mode, with the capillary voltage set to 2.8 kV, the source and desolvation temperatures at 150 °C, the cone gas flow at 30 L/h, and desolvation gas flow at 400 L/h. MS data were acquired in the range 500−3000 Da and deconvoluted using the maximum entropy algorithm software *MaxEnt 1*. Experimental mass data were compared to the theoretical mass of the linker-conjugated oligonucleotide for identification of the conjugate and any possible reaction impurities.

Capillary Electrophoresis (MEKC) Duplex Analysis. MEKC run buffer (BGE) consisted of 20 mM borate containing 50 mM Tween 20 and 50 mM SDS (pH 9.3, 1:1 Tween/SDS molar ratio). All CE experiments were carried out with the aid of the Agilent G1600 HPCE using bare silica capillaries having an internally flared "bubble cell" (50 μm × 56 cm eff.). Each capillary was preconditioned by flushing with 0.1 N NaOH solution, water, and BGE for 5 min each. Samples were prepared at ∼1 mg/mL in a total volume of 10 μL of either water or BGE (requiring ∼10 μg of total sample mass). Hydrodynamic injections were made by applying 50 mbar to the sample vial for 10 s. Finally, the capillary was operated in the normal mode at 25 °C with a field of +450 V/cm. For long, high-resolution runs, the injection was made at the inlet, resulting in a run time of approximately 35 min. For faster, lower resolution runs, injections were made at the outlet and the potentials were reversed, giving a run time of approximately 8 min. A photodiode array (PDA) detector was used to collect electropherograms and spectral data from 190 to 600 nm. Background-subtracted PDA spectra and migration times were compared against authentic samples of unconjugated oligonucleotides to aid identification while peak areas collected at 260 nm were used for quantitations.

■ RESULTS AND DISCUSSION

Reactions amenable to postsynthetic conjugation include activated disulfide exchange and maleimide addition,[10,19] cycloadditions,[20,21] and aldehyde condensations.[22] Our efforts for this communication have focused on the improvement and expansion of amidation reaction conditions. The amidation strategy was selected primarily because of the commercial and synthetic availability of carboxylated substrates, allowing for the preparation of a wide variety of desirable conjugates. Current

Scheme 2. HATU Coupling[a]

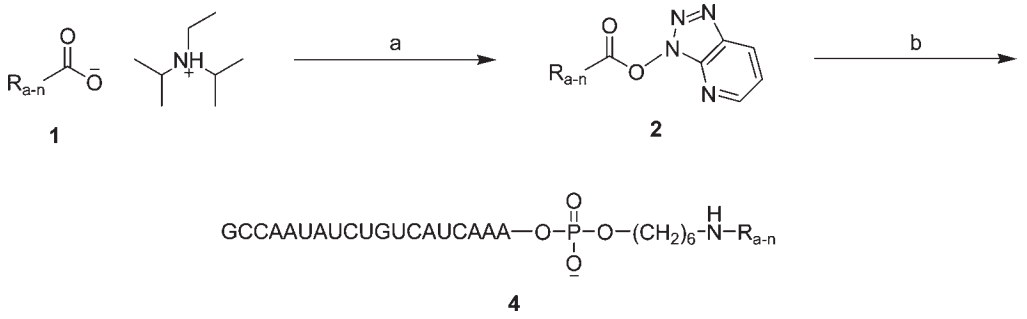

[a] Conditions: (a) HATU, DMSO, RT; (b) GCCAAUAUCUGUCAUCAAA-$(CH_2)_6$-NH_2, DIEA, 9:1 DMSO:water, RT.

amidation protocols require an oligonucleotide modified with a primary amine at one or both termini as well as an activated carboxylic acid coupling partner, often in large excess to compensate for competitive hydrolysis. Activation of the carboxylic acid is typically performed as a separate step that requires the additional effort of isolating the ester before proceeding with conjugation. (Note: Preactivation will also be used hereafter to denote carboxylic acid activation performed as a separate step before coupling. Unless otherwise noted, this operation is carried out without isolation of the activated ester or solvent switching before conjugation.)

To improve the overall efficiency of the process, a protocol was sought that would not require an isolated activated ester, would be expeditious, and would tolerate substrate diversity. These requirements were the impetus for exploring nontraditional coupling reagents for solution-phase siRNA conjugation. Uronium salts of hydroxybenzotriazoles are convenient "all in one" reagents that have been reported as efficient in peptide synthesis and small molecule applications;[23] HATU has distinguished itself from similar analogues as especially effective.[24,25]

Oligonucleotide conjugation using reagents in this class has been limited to on-resin reactions under anhydrous conditions.[26,27] This may be a result of the known hydrolytic liabilities of the parent reagent and the subsequent activated ester, particularly under basic conditions.[28,29] Condition development was therefore focused on minimizing water content in the solvent mixture. To this end, a brief screen of polar aprotic solvents was conducted to assess their ability to dilute siRNA passenger strand dissolved in a minimum volume of water. (Note: Initial efforts focused on strictly anhydrous conditions. Triethylammonium siRNA salts, as reported in the literature, successfully dissolved in 100% DMSO.[13] Treatment with DIEA and HATU-preactivated carboxylic acids produced efficient conversion to the desired conjugates [unpublished results from our laboratory]. While this result was encouraging, we sought to develop HATU-compatible conditions that did not require the additional step of counterion exchange.) This screen yielded DMSO in a ratio of 9:1 (v/v) with respect to water as a practical solvent system, completely dissolving the passenger strand at a concentration of 1.8 mM.

Activation of the carboxylic acid substrates with HATU was performed in a separate step using anhydrous DMSO as a solvent to further minimize contact of the coupling reagent with water (Scheme 2). (Note: One-pot coupling—in which HATU, carboxylic acid, and siRNA are introduced into the same reaction vessel without preactivation—was also investigated. Though the one pot method was successful for the example that was evaluated, the two-step preactivation/conjugation method is preferred because it allows for better reaction diagnosis with difficult substrates.) DMSO was chosen as the solvent for this step in the interest of simplicity and consistency. The feasibility of this approach was evaluated with **4c** as a test substrate; we were pleased to find that these conditions permitted successful coupling with 2 equiv of activated ester. With this result in hand, we began to explore the generality of the reaction with a diverse array of substrates.

The solubility of the carboxylic acid coupling partners in their DMSO stock solution was observed to be variable. Some examples, such as **1i**, were soluble at all stages of the coupling reaction. **1c** and **1h** were not consistently soluble throughout the procedure. Both were initially insoluble in DMSO; however, the carboxylates formed upon addition of a stoichiometric amount of DIEA enhanced their solubility. Precipitation was observed when these carboxylates were activated with HATU, though **1c** provided a homogeneous solution and **1h** only displayed slight heterogeneity when treated with siRNA. Both **1c** and **1h** demonstrated good conversion to their respective conjugates despite insolubility at the activation step. Substrate **1f**, a 20 carbon fatty acid, represents the approximate limit for saturated lipid chain length tolerated under these conditions. This example formed a viscous gel in DMSO when deprotonated with DIEA and precipitated when treated with siRNA. The restriction imposed by its physical properties is reflected in the observed conversion and recovery (Table 1).

Conversions for most coupling partners were good to excellent, and a range of lipophilicity and functionality were tolerated under these conditions (Table 1). The successful conjugation of lipophilic moieties (**4a**—**h**), an affinity ligand (**4i**), a fluorescent label (**4j**), a linear PEG (**4k**), and a protected amino acid (**4l**) illustrates the versatility and utility of this method. Notable exceptions were **4m** and **4n**, which were both soluble throughout the protocol and did not show appreciable conversion. Steric encumbrance presented by the fully substituted α carbon likely explains the low conversion observed for **4m**, but a similar rationale is not as satisfactory for **4n** and will require further investigation to assess.

The isolated yields of conjugates **4a**—**d** were conspicuously lower than the theoretical values derived from their conversions; this

Table 1. GCCAAUAUCUGUCAUCAAA-$(CH_2)_6$-NH-R

Compound	Substrate	Conversion[a]	Isolated Yield	Calculated Mass	Found Mass[b]
a	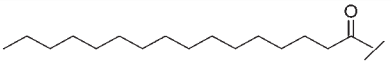	>99%	61%	6561.5	6560.6
b	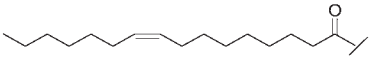	> 99%	62%	6559.5	6559.0
c	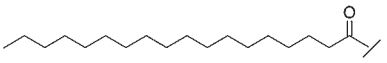	98%	65%	6589.5	6587.8
d	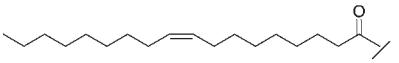	96%	65%	6587.5	6586.0
e	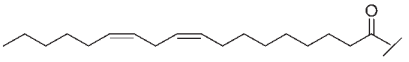	96%	84%	6585.6	6585.0
f	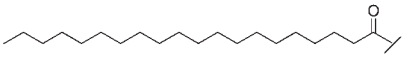	37%	31%	6617.7	6617.8
g	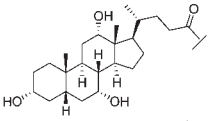	>99%	97%	6713.7	6712.4
h	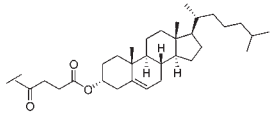	94%	82%	6791.8	6791.2
i	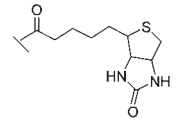	89%	74%	6549.4	6549.2
j	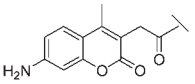	81%	75%	6538.3	6536.6
k	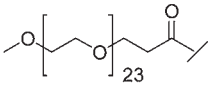	73%	67%	7422.4	7422.4
l	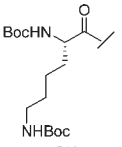	79%	71%	6651.5	6650.6
m	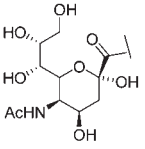	NR	-	-	-
n	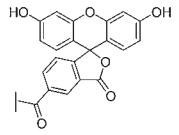	NR	-	-	-

[a] Conversions were assessed by analytical ion-pairing HPLC UV peak area percent. NR = no reaction. [b] Mass analysis of conjugates was conducted by UPLC-MS.

difference may be attributed to chromatographic purification recovery. The challenges of isolating lipophilic conjugates have been reported in the literature[9,30,31] and generally require additional purification optimization to improve recovery. The ion-pairing reverse-phase chromatography method described in the experimental section was not optimized for each substrate or substrate class and was intended as a general procedure to accommodate diverse conjugates with a wide range of physical properties.

The isolated passenger strands **4a**−**n** require hybridization with a complementary guide strand to engage the RNAi pathway.

dx.doi.org/10.1021/bc2001227 |*Bioconjugate Chem.* 2011, 22, 1723–1728

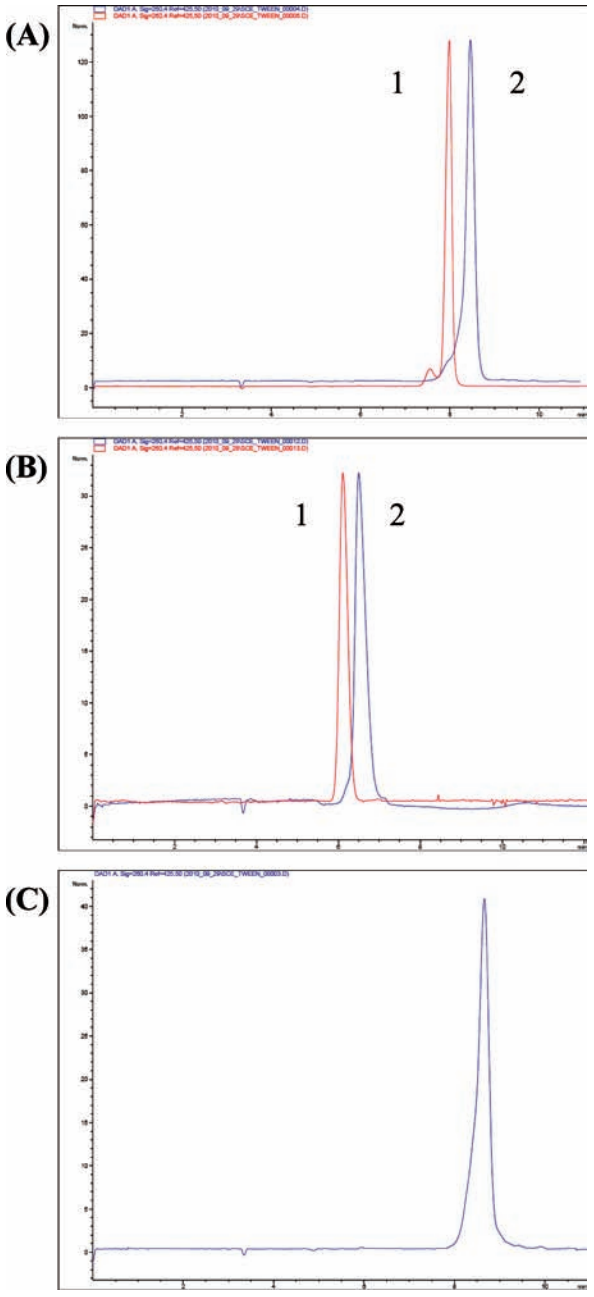

Figure 1. Duplex electropherograms. Hybridization analysis was conducted using MEKC. (A) Peak 1 = **4h**, Peak 2 = duplex. (B) Peak 1 = **4j**, Peak 2 = duplex. (C) Guide strand.

Conjugates **4h** and **4j** were annealed and duplex integrity confirmed by capillary electrophoresis (Figure 1). This technique accommodates a broad spectrum of conjugates and provides a quantitative analysis of duplex integrity and composition. (Note: While the literature is replete with examples of electrophoresis used to confirm oligonucleotide duplex formation, the capillary MEKC approach employed here offers rapid, quantitative results free from the concerns of dye-binding associated with slab gel techniques and appears to be nearly universally applicable to lipid-oligonucleotide constructs conferring a wide range of lipophilicities to the final duplexes. From that perspective, the MEKC method described here may be unique.) These examples, along with a number of similar siRNA conjugates, are currently being evaluated for biological activity and will be the subject of a future report from our laboratories.

CONCLUSION

The principal advantage of the protocol described in this technical note is the ability to rapidly access diverse conjugates without isolating a preactivated ester. This is particularly useful when carboxylic acid partners are synthetically precious or their activated ester is not commercially available. The relatively small excess of carboxylic acid required reduces waste, conserving expensive or difficult to synthesize coupling partners. In addition to eliminating the need to isolate a preactivated ester, this protocol is rapid, with a total reaction time of 30 min. Finally, these conditions are generally applicable to a diverse set of conjugates and do not require significant alterations to solvent composition or RNA counterions for different classes of substrates.

AUTHOR INFORMATION

Corresponding Author

*Jeffrey G. Aaronson, WP14-2147, 770 Sumneytown Pike P.O. Box 4, West Point, PA 19486. Phone: 215-652-7326. Fax: 215-652-3971. E-mail: jeffrey_aaronson@merck.com.

ACKNOWLEDGMENT

The authors thank Dr. Steven L. Colletti and Dr. Vasant Jadhav of Merck Research Laboratories for helpful discussions. The authors would also like to thank Enrique Vazquez, Amran Gowani, Rebecca Arvary, Dr. Francis Gosselin, Robert Fatula, and Lynn O'Neill-Davis for synthesis and characterization of the RNA sequences used in this work.

ABBREVIATIONS

ACN, acetonitrile; BGE, background electrolyte; DIEA, *N*,*N*-diisopropylethylamine; DMSO, dimethyl sulfoxide; HATU, *O*-(7-azabenzotriazol-1-yl)-*N*,*N*,*N*′,*N*′-tetramethyluronium hexafluorophosphate; HFIP, 1,1,1,3,3,3-hexafluoro-2-propanol; HOAT, 1-hydroxy-7-azabenzotriazole; HPLC, high performance liquid chromatography; MEKC, micellar electrokinetic capillary chromatography; SDS, sodium dodecyl sulfate; TEA, triethylamine; TEAA, triethylammonium acetate; THF, tetrahydrofuran; UPLC, ultraperformance liquid chromatography

REFERENCES

(1) Stanton, M. G., and Colletti, S. L. (2010) Medicinal chemistry of siRNA delivery. *J. Med. Chem. 53*, 7887–7901.

(2) Wojczewski, C., Stolze, K., and Engels, J. W. (1999) Fluorescent oligonucleotides — versatile tools as probes and primers for DNA and RNA analysis. *Synlett* 1667–1678.

(3) Marlin, F., Simon, P., Saison-Behmoaras, T., and Giovannangeli, C. (2010) Delivery of oligonucleotides and analogues: the oligonucleotide conjugate-based approach. *ChemBioChem 11*, 1493–1500.

(4) Zhu, L., and Mahato, R. I. (2010) Targeted delivery of siRNA to hepatocytes and hepatic stellate cells by bioconjugation. *Bioconjugate Chem. 21*, 2119–2127.

(5) Alam, M. R., Dixit, V., Kang, H., Li, Z., Chen, X., Trejo, J., Fisher, M., and Juliano, R. L. (2008) Intracellular delivery of an anionic antisense oligonucleotide via receptor-mediated endocytosis. *Nucleic Acids Res. 36*, 2764–2776.

(6) Wolfrum, C., Shi, S., Jayaprakash, K. N., Jayaraman, M., Wang, G., Pandey, R. K., Rajeev, K. G., Nakayama, T., Charrise, K., Ndungo,

E. M., Zimmermann, T., Koteliansky, V., Manoharan, M., and Stoffel, M. (2007) Mechanisms and optimization of in vivo delivery of lipophilic siRNAs. *Nat. Biotechnol. 25*, 1149–1157.

(7) Turner, J. J., Jones, S., Fabani, M. M., Ivanova, G., Arzumanov, A. A., and Gait, M. J. (2007) RNA targeting with peptide conjugates of oligonucleotides, siRNA and PNA. *Blood Cells, Molecules, and Diseases 38*, 1–7.

(8) Lorenz, C., Hadwiger, P., John, M., Vornlocher, H., and Unverzagt, C. (2004) Steroid and lipid conjugates of siRNAs to enhance cellular uptake and gene silencing in liver cells. *Bioorg. Med. Chem. Lett. 14*, 4975–4977.

(9) Rump, E. T., de Vrueh, R. L., Sliedregt, L. A., Biessen, E. A., van Berkel, T. J., and Bijsterbosch, M. K. (1998) Preparation of conjugates of oligodeoxynucleotides and lipid structures and their interaction with low-density lipoprotein. *Bioconjugate Chem. 9*, 341–349.

(10) Goodchild, J. (1990) Conjugates of oligonucleotides and modified oligonucleotides: a review of their synthesis and properties. *Bioconjugate Chem. 1*, 165–187.

(11) Lönnberg, H. (2009) Solid-phase synthesis of oligonucleotide conjugates useful for delivery and targeting of potential nucleic acid therapeutics. *Bioconjugate Chem. 20*, 1065–1094.

(12) Marshal, W. S., Vagle, K. (2010) Lipophilic Polynucleotide Conjugates. PCT Int. Appl. WO 2010/129672 A1.

(13) Agrawal, S., Christodoulou, C., and Gait, M. J. (1986) Efficient methods for attaching non-radioactive labels to the 5′-end of synthetic ligodeoxyribonucleotides. *Nucleic Acids Res. 14*, 6227–6245.

(14) Bannwarth, W., Schmidt, D., Stallard, R. L., Hornung, C., Knorr, R., and Müller, F. (1988) Bathophenanthroline-ruthenium(II) complexes as non-radioactive labels for oligonucleotides which can be measured by time-resolved fluorescence techniques. *Helv. Chim. Acta 71*, 2085–2099.

(15) Milesi, D, Kutyavin, I., Lukhtanov, E. A., Gorn, V. V., Reed, M. W. (2000) Synthesis of oligonucleotide conjugates in anhydrous dimethyl sulfoxide. *Methods in Enzymology. Vol. 313: Antisense Technology, Part A* (Phillips, M. I., Ed.) pp 164−173, Chapter 9, Academic Press, San Diego.

(16) Boutorine, A. S., Le Doan, T., Battioni, J. P., Mansuy, D., Dupré, D., and Hélène, C. (1990) Rapid route of synthesis of chemically reactive and highly radioactive labeled α- and β-oligonucleotide derivatives for in vivo studies. *Bioconjugate Chem. 1*, 350–356.

(17) Oberhauser, B., and Wagner, E. (1992) Effective incorporation of 2′-O-methyl-oligoribonucleotides into liposomes and enhanced cell association through modification with thiocholesterol. *Nucleic Acids Res. 20*, 533–538.

(18) Cantor, C. R., Warshaw, M. M., and Shapiro, H. (1970) Oligonucleotide interactions. III. circular dichroism studies of the conformation of deoxyoligonucleotides. *Biopolymers 9*, 1059–1077.

(19) Singh, Y., Murat, P., and Defrancq, E. (2010) Recent developments in oligonucleotide conjugation. *Chem. Soc. Rev. 39*, 2054–2070.

(20) Graham, D., and Enright, A. (2006) Cycloadditions as a method for oligonucleotide conjugation. *Curr. Org. Synth. 3*, 9–17.

(21) Jayaprakash, K. N., Peng, C., Butler, D., Varghese, J. P., Maier, M. A., Rajeev, K. G., and Manoharan, M (2010) Non-nucleoside building blocks for copper-assisted and copper-free click chemistry for the efficient synthesis of RNA conjugates. *Org. Lett. 12*, 5410–5413.

(22) Zatsepin, T. S., Stetsenko, D. A., Gait, M. J., and Oretskaya, T. S. (2005) Use of carbonyl group addition-elimination reactions for synthesis of nucleic acid conjugates. *Bioconjugate Chem. 16*, 471–489.

(23) Han, S., and Kim, Y. (2004) Recent development of peptide coupling reagents in organic synthesis. *Tetrahedron 60*, 2447–2467.

(24) Carpino, L. A. (1993) 1-Hydroxy-7-azabenzotriazole. An efficient peptide coupling additive. *J. Am. Chem. Soc. 115*, 4397–4398.

(25) Carpino, L. A., El-Faham, A., Minor, C. A., and Albericio, F. (1994) Advantageous applications of azabenzotriazole (triazolopyridine)-based coupling reagents to solid-phase peptide synthesis. *J. Chem. Soc., Chem. Commun.* 201–203.

(26) Vinayak, R. (1999) A convenient, solid-phase coupling of rhodamine dye acids to 5′amino-oligonucleotides. *Tetrahedron Lett. 40*, 7611–7613.

(27) Bleczinski, C. F., and Richert, C. (1999) Steroid-DNA interactions increasing stability, sequence-selectivity, DNA/RNA discrimination, and hypochromicity of oligonucleotide duplexes. *J. Am. Chem. Soc. 121*, 10889–10894.

(28) Albericio, F., Bofill, J. M., El-Faham, A., and Kates, S. A. (1998) Use of onium salt-based coupling reagents in peptide synthesis. *J. Org. Chem. 63*, 9678–9683.

(29) McCarthy, D. G., Hegarty, A. F., and Hathaway, B. J. (1977) N-Hydroxy-compounds as acyl transfer agents. Part 1. Kinetics and mechanism of nucleophilic displacements on 1-hydroxybenzotriazole esters and crystal and molecular structure of 1-benzoyloxybenzotriazole. *J. Chem. Soc., Perkin Trans. 2* (1972−1999), 224–231.

(30) Farooqui, F., Sarin, P. S., Sun, D., and Letsinger, R. L. (1991) Effect of structural bariations in cholesteryl-conjugated oligonucleotides in inhibitory activity toward HIV-1. *Bioconjugate Chem. 2*, 422–426.

(31) Boutorine, A. S., Tokuyama, H., Takasugi, M., Isobe, H., Nakamura, E., and Hélène, C. (1994) Fullerene-oligonucleotide conjugates: photoinduced sequence-specific DNA cleavage. *Angew. Chem., Int. Ed. Engl. 33*, 2462–2465.

Bioconjugate Chemistry

TECHNICAL NOTE

pubs.acs.org/bc

Evaluation of ^{64}Cu-Labeled Bifunctional Chelate−Bombesin Conjugates

Samia Ait-Mohand,[†] Patrick Fournier,[†] Véronique Dumulon-Perreault,[†] Garry E. Kiefer,[‡] Paul Jurek,[‡] Cara L. Ferreira,[§] François Bénard,[⊥] and Brigitte Guérin*[,†]

[†]Centre d'imagerie moléculaire de Sherbrooke (CIMS), Department of Nuclear Medicine and Radiobiology, Université de Sherbrooke, 3001, 12th North Avenue Sherbrooke, Qubec, Canada, J1H 5N4

[‡]Macrocyclics, Dallas, Texas, United States

[§]Nordion, Vancouver, British Columbia, Canada

[⊥]BC Cancer Agency Research Centre, Vancouver, British Columbia, Canada

ABSTRACT: Several bifunctional chelates (BFCs) were investigated as carriers of ^{64}Cu for PET imaging. The most widely used chelator for ^{64}Cu labeling of BFCs is DOTA (1,4,7,10-tetraazacyclododecane-*N*,*N*′,*N*″,*N*‴-tretraacetic acid), even though this complex exhibits only moderate *in vivo* stability. In this study, we prepared a series of alternative chelator−peptide conjugates labeled with ^{64}Cu, measured *in vitro* receptor binding affinities in human breast cancer T47D cells expressing the gastrin-releasing peptide receptor (GRPR) and compared their *in vivo* stability in mice. DOTA-, NOTA-(1,4,7-triazacyclononane-1,4,7-triacetic acid), PCTA-(3,6,9,15-tetraazabicyclo[9.3.1]pentadeca-1(15),11,13-triene-3,6,9-triacetic acid), and Oxo-DO3A-(1-oxa-4,7,10-triazacyclododecane-4,7,10-triacetic acid) peptide conjugates were prepared using H_2N-Aoc-[D-Tyr^6,βAla^{11},Thi^{13},Nle^{14}]bombesin(6−14) (BBN) as a peptide template. The BBN moiety was selected since it binds with high affinity to the GRPR, which is overexpressed on human breast cancer cells. A convenient synthetic approach for the attachment of aniline-BFC to peptides on solid support is also presented. To facilitate the attachment of the aniline-PCTA and aniline-Oxo-DO3A to the peptide via an amide bond, a succinyl spacer was introduced at the *N*-terminus of BBN. The partially protected aniline-BFC (*p*-H_2N-Bn-PCTA(O*t*-Bu)$_3$ or *p*-H_2N-Bn-DO3A(O*t*-Bu)$_3$) was then coupled to the resulting *N*-terminal carboxylic acid preactivated with DEPBT/ClHOBt on resin. After cleavage and purification, the peptide-conjugates were labeled with ^{64}Cu using [^{64}Cu]Cu(OAc)$_2$ in 0.1 M ammonium acetate buffer at 100 °C for 15 min. Labeling efficacy was >90% for all peptides; Oxo-DO3A-BBN was incubated an additional 150 min at 100 °C to achieve this high yield. Specific activities varied from 76 to 101 TBq/mmol. Competition assays on T47D cells showed that all BFC-BBN complexes retained high affinity for the GRPR. All BFC-BBN ^{64}Cu-conjugates were stable for over 20 h when incubated at 37 °C in mouse plasma samples. However, *in vivo*, only 37% of the ^{64}Cu/Oxo-DO3A complex remained intact after 20 h while the ^{64}Cu/DOTA-BBN complex was completely demetalated. In contrast, both ^{64}Cu/NOTA- and ^{64}Cu/PCTA-BBN conjugates remained stable during the 20 h time period. Our results indicate that it is possible to successfully conjugate aniline-BFC with peptide on solid support. Our data also show that ^{64}Cu-labeled NOTA- and PCTA-BBN peptide conjugates are promising radiotracers for PET imaging of many human cancers overexpressing the GRP receptor.

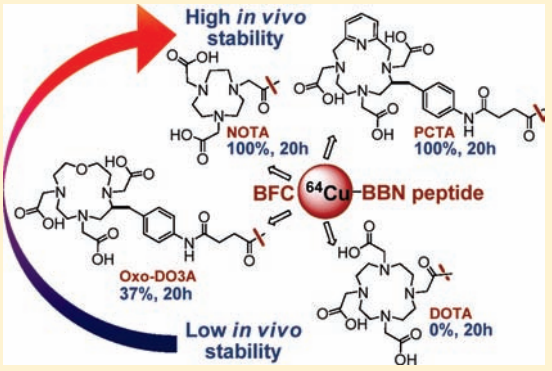

INTRODUCTION

Positron-emitting ^{64}Cu ($T_{1/2}$ = 12.7 h, β^+ 17.4%, E_{max} = 0.656 MeV, β^- 39%, E_{max} = 0.573 MeV) is a suitable isotope for PET imaging,[1] although the availability of appropriate Cu-chelating agents limits its wider application. Several bifunctional chelates (BFCs) have been investigated as carriers of radiometals for positron emission tomography (PET) imaging. Among them, DOTA is the most widely used for metal radioisotopes.[2] However, DOTA complexes with some radiometals such as ^{64}Cu show only moderate *in vivo* stability, resulting in demetalation and subsequent accumulation of the radiometal in nontarget tissues. Previous studies have described the potential of NOTA,[3] PCTA,[4,5] and Oxo-DO3A[4,5] as BFCs for divalent and trivalent metal ions. These chelators have been radiolabeled efficiently with ^{64}Cu and present higher resistance to transmetalation reactions *in vivo* as compared to DOTA.[3,4,6] We recently reported a practical synthetic approach for the preparation of NOTA-peptides directly on solid support.[7] However, no data on coupling of aromatic amine derivatives, such as PCTA and Oxo-DO3A, to peptides have been reported. The coupling of aromatic amine derivatives of BFC to antibodies or peptides require either large excesses of BFC or long reaction times.[8,9] In this

Received: May 25, 2011
Revised: July 15, 2011
Published: July 18, 2011

ACS Publications © 2011 American Chemical Society

dx.doi.org/10.1021/bc2002665 | *Bioconjugate Chem.* 2011, 22, 1729–1735

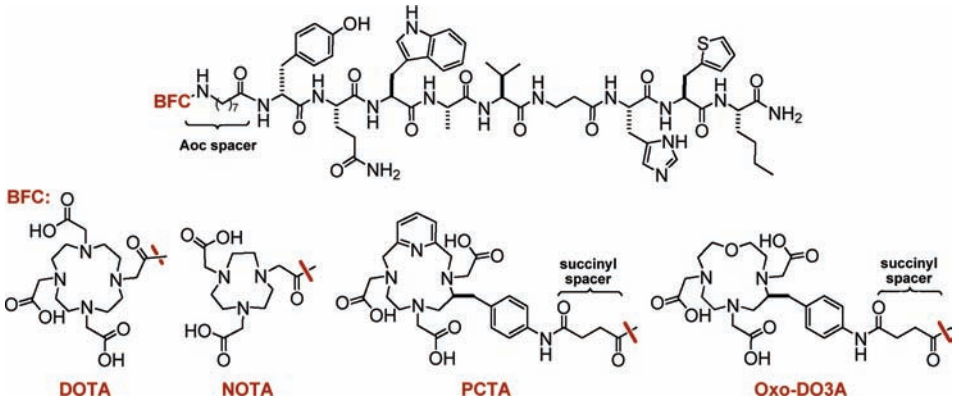

Figure 1. Structures of the BFC-BBN conjugate and bifunctional chelates DOTA, NOTA, PCTA, and Oxo-DO3A.

study, we report a convenient synthetic approach for the preparation of PCTA and Oxo-DO3A-peptide conjugates directly on solid support using H_2N-Aoc-[D-Tyr^6,βAla^{11}, Thi^{13},Nle^{14}]bombesin(6−14)^{10} (BBN) as peptide template. The two novel BFCs contain a 12-membered macrocyclic chelate, PCTA-(3,6,9,15-tetraazabicyclo[9.3.1]pentadeca-1(15),-11,13-triene-3,6,9-triacetic acid) or Oxo-DO3A-(1-oxa-4,7,10-triazacyclododecane-4,7,10-triacetic acid) and an aniline substituent, which can be attached to the BBN peptide via a succinyl spacer. The BBN derivative acts as an agonist and binds with high affinity to GRPR overexpressed on human prostate,[11,12] breast,[13−15] and other cancers.[16,17] GRPR belongs to a large family of G-protein-coupled receptors that are characterized by high or low affinity for agonist depending on the coupling of a guanine nucleotide (GDP or GTP) on the G-protein.[18] Furthermore, the level of GRPR has been shown to correlate positively to the presence of estrogen receptors.[14] For PET imaging, Schuhmacher et al. labeled a DOTA-PEG$_2$-[D-Tyr^6,β-Ala^{11},Thi^{13},Nle^{14}]BBN-(6−14) with ^{68}Ga,[19] while Chen et al. used DOTA-Lys^3-bombesin with ^{64}Cu.[20] Smith et al. successfully labeled modified BBN(7−14) analogues with ^{64}Cu for potential use in diagnostic imaging using NOTA or NO2A as chelating agents and obtained stable compounds.[3,21]

Our laboratory has reported the synthesis and the characterization of DOTA- and NOTA-BBN and showed that the NOTA peptide had an inhibition constant (K_i) value slightly lower than that of the analogous DOTA-peptide.[7] To determine whether PCTA-BBN and Oxo-DO3A-BBN offered an advantage over the currently used BFCs for Cu-based radiopharmaceuticals, we compared our novel BFCs to the analogous BFC-BBN conjugates containing the DOTA and NOTA moieties. The BFC-BBN conjugates (Figure 1) were examined with respect to ^{64}Cu-labeling efficacy, GRPR affinity, and stability. The availability of various copper chelators with high *in vivo* stability would allow fine-tuning of the various biological properties of ^{64}Cu-labeled BFC-BBN conjugates.

EXPERIMENTAL PROCEDURES

Materials. All chemicals and solvents (reagent grade) were used as supplied by the vendors without further purification, unless otherwise stated. NovaSyn TGR resin was obtained from NovaBiochem. Fmoc-protected amino acids were obtained from EMD NovaBiochem (Gibbstown, NJ, USA) or Chem-Impex International Inc. (Wood Dale, IL, USA). 1,4,7,10-Tetraazacyclododecane-1,4,7-tris-*tert*-butyl acetate-10-acetic acid (DOTA(O*t*-Bu)$_3$OH), 3,6,9,15-tetraazabicyclo[9.3.1]pentadeca-1(15),11,13-triene-3,6,9-tris-*tert*-butyl acetate (*p*-H_2N-Bn-PCTA-(O*t*-Bu)$_3$), and 1-oxa-4,7,10-triazacyclododecane-4,7,10-tris-*tert*-butyl acetate (*p*-H_2N-Bn-Oxo-DO3A-(O*t*-Bu)$_3$) were obtained from Macrocyclics (Dallas, TX, USA). 1.4.7-Triazacyclononane was obtained from TCI America (Portland, OR, USA). 2-(1*H*-7-Azabenzotriazol-1-yl)-1,1,3,3-tetramethyluronium hexafluorophosphate (HATU) was purchased from Chem-Impex International Inc. 3-(Diethoxy-phosphoryloxy)-3*H*-benzo[*d*]-[1,2,3] triazin-4-one (DEPBT) and 6-chloro-1-hydroxy-1*H*-benzotriazole (ClHOBt) were purchased from ChemPep (Wellington, FL, USA) and Matrix Innovation (Quebec, QC, CA), respectively. HEPES (4-(2-hydroxyethyl)-1-piperazineethanesulfonic acid), amphothericin B, RPMI-1640, PBS (phosphate-buffered saline), trypsin, penicillin, streptomycin, and fetal bovine serum (FBS) were purchased from Wisent (St-Bruno, QC, CA). *N,N*-Diisopropylethylamine (DIEA), thioanisole, and triisopropylsilane (TIPS) were obtained from Aldrich Chemical Co. Bovine serum albumin (BSA) and bombesin were purchased from Sigma-Aldrich (Saint-Louis, MO, USA). Acetonitrile, dichloromethane (DCM), *N,N*-dimetylformamide (DMF), and isopropyl alcohol (*i*-Pr-OH) were obtained from Fisher Scientific (Ottawa, ON, CA). ^{125}I-Bombesin was purchased from Perkin-Elmer Life Science Products (Boston, MA, USA). Finally, T47D human breast cancer cell line was obtained from ATCC (Manassas, VA, USA). DMF was dried over 4 Å molecular sieves for at least one week to remove trace amounts of amines and filtered before its use.

Peptide Synthesis. *DOTA-BBN (**1**) and NOTA-BBN (**2**).* We recently reported the synthesis, characterization, and biological activity of these peptides.[7]

General Procedure for the Coupling of Aniline-BFC to Peptide on Solid Support. The BBN derivative was synthesized by a continuous flow method on a Pioneer Peptide Synthesis System (PerSeptive Biosystems) using the Fmoc strategy. A 2-fold excess of Fmoc-protected amino acid over available resin substitution sites was used for coupling in amine free DMF. Fmoc-protected amino acids were activated for coupling with an equimolar amount of HATU and 2 equiv of DIEA. Fmoc deprotection was performed in 20% piperidine in DMF and monitored through absorbance at 364 nm. The resin was washed with trice with DMF, MeOH, DMF, MeOH, and DCM, respectively. After completion of the synthesis on the automated system, Fmoc-Aoc-OH and the succinyl spacer, as well as the aniline-BFC,

were coupled manually to the peptide. The Fmoc-Aoc-OH (2.5 equiv) was dissolved in 2 mL of DMF at 0 °C, DIEA (2.5 equiv) and PyBOP (2.5 equiv) were added to the cold solution. After 15 min of stirring, the mixture was added to the partially protected peptide on resin preswelled with DCM and mixed with ClHOBt (2.5 equiv) and DIEA (2.5 equiv). For this coupling, a mechanical agitation was maintained for 2 h at room temperature. The resin was washed thrice with DMF, MeOH, DMF, MeOH, and DCM, respectively. Fmoc deprotection was performed in 20% piperidine in DMF during 15 min, and the resin was washed as described above. The coupling and the Fmoc deprotection steps were followed by a Kaiser's test on resin; the reaction between resin and ninhydrin was followed colorimetrically whereby free primary amines after Fmoc deprotection were detected as blue beads and their absence as yellow beads. Reaction conditions were optimized by monitoring each step by analytical reversed-phase HPLC after cleavage of a small amount (10 mg) of the resin-bound peptide with 95% aqueous TFA. The partially protected peptide on resin was swelled in a minimal volume of DMF (2 mL), succinic anhydride (10 equiv), and DIEA (10 equiv) dissolved in DMF (3 mL) were added. This coupling procedure was performed twice (30 min and 1 h). The resin was washed as described above. The resulting *N*-terminal carboxylic acid group was activated with ClHOBt (1 equiv) and DIEA (2 equiv) in DMF. The preactivation mixture was stirred for 30 min, then DEPBT (1 equiv) and the aniline-BFC (*p*-H_2N-Bn-PCTA-(O*t*Bu)$_3$ or *p*-H_2N-Bn-Oxo-DO3A-(O*t*Bu)$_3$, 2 equiv) were added and the reaction was allowed to proceed overnight at room temperature, under mechanical agitation. The coupling was performed twice with 2 equiv of the amine. The resin was washed thrice as described above, and the desired peptide was deprotected and cleaved from the support by treatment with a cocktail of TFA/H_2O/thioanisole (92:2:6, v/v) for 4 h at room temperature under mechanical agitation. The resin was removed by filtration and washed with TFA. Combined filtrates were added dropwise to ethyl ether (1 mL of TFA/10 mL of ether). The precipitated peptides were centrifuged at 1200 rpm for 15 min. The ether solution was decanted and the white solid was dissolved in water, frozen, and lyophilized. The crude peptide was purified by flash chromatography on a Biotage SP4 system equipped with a C_{18} column. Purity of the peptides was verified by HPLC, and their identity was confirmed by API 3000 LC/MS/MS. Analytical high performance liquid chromatography (HPLC) was performed on an Agilent 1200 system equipped with a Zorbax Eclipse XDB C18 reversed-phase column (4.6 × 250 mm, 5 μ) and Agilent 1200 series diode array UV−vis detector, using a linear gradient of 0% to 100% acetonitrile in water with 0.1% TFA over 30 min at a flow rate of 1 mL/min.

*PCTA-BBN (**3**).* After purification, fractions containing the desired product were combined and lyophilized to yield peptide **3** as a white solid (10 mg, 23% yield based on resin substitution rate). Product purity was confirmed to be 95% by analytical reversed-phase HPLC: average retention time 16.2 min. MS Calc: 1846.9; Found: 924.6 (M/2 + 1), 1848.3 (M+1).

*Oxo-DO3A-BBN (**4**).* After purification on Biotage, fractions containing the desired product were combined and lyophilized to provide peptide **4** (8.3 mg, 20% yield based on resin substitution rate). Product purity was confirmed to be 99% by analytical reversed-phase HPLC: average retention time 16.2 min. MS Calc: 1813.9; Found: 908.5 (M/2 + 1), 1815.4 (M+1).

Cell Culture. The human breast cancer T47D cells were used in their 25th to 35th passages after receipt and cultured in RPMI 1640 medium containing phenol red supplemented with 2.5 mM glutamine, 100 U/mL penicillin, 100 μg/mL streptomycin, 100 ng/mL amphothericin B, and 10% FBS. Cells were grown in 5% CO_2 in air at 37 °C; the medium was changed 3 times per week.

***In Vitro* Receptor Binding.** Competition assays were performed on T47D human breast cancer cells expressing GRPR. In 24-well plates, the cells were cultured until near confluence and the medium was replaced by 400 μL of reaction medium (RPMI complemented with 2 mg/mL BSA, 4.8 mg/mL HEPES, 1 U/mL penicillin G, and 1 μg/mL streptomycin). For the assay, equal volumes of radioactive and nonradioactive ligands were added. The concentration of the radioactive ligand [^{125}I]I-Tyr^4-Bombesin (74 TBq/mmol) was 10^{-12} M. Increased concentrations (10^{-6} to 10^{-14} M) of the GRP ligand of interest were added to consecutive wells. The plates were incubated for 40 min at 37 °C with agitation. After the incubation, the reaction medium was removed and the cells were washed three times with PBS at room temperature. The cells were harvested and the bound [^{125}I]I-Tyr^4-Bombesin was counted in a gamma counter (Cobra II autogamma counter, Packard, MN). Finally, data were analyzed with *GraphPad Prism 5* software to determine the IC_{50} value. The K_i was calculated from the IC_{50} using the equation of Cheng and Prusoff.[22] The K_d = 1.5 × 10^{-10} M value for the [^{125}I]I-Tyr^4-Bombesin was determined by experiments done under similar conditions.[23]

Radiolabeling of BFC-Peptide Conjugate with ^{64}Cu. Our cyclotron facility provides ^{64}Cu isotope on a routine basis for research purposes, using a target system developed in collaboration with ACSI (Richmond, BC, CA). ^{64}Cu was prepared on a TR-19 cyclotron (ACSI) by the reaction ^{64}Ni(p,n)^{64}Cu using an enriched ^{64}Ni target electroplated on a rhodium disk.[24] $^{64}CuCl_2$ was recovered from the target following the procedure of McCarthy et al.[25] and converted to ^{64}Cu-acetate by dissolving the $^{64}CuCl_2$ in ammonium acetate (0.1 M; pH 5.5), followed by evaporation to dryness. BFC-peptide conjugates were labeled with ^{64}Cu following conditions optimized in our laboratory. Briefly, BFC-peptide (5 μg) was dissolved in a 0.1 M ammonium acetate buffer pH 5.5 with [^{64}Cu]Cu(OAc)$_2$ (296−370 MBq or 8−10 mCi) in a total volume of 250−300 μL, and then the resulting solution was incubated at 100 °C for 15 min, except for the Oxo-DO3A derivative which was incubated for 2.5 h at the same temperature. The labeled product was purified by HPLC equipped with a radiodetector. The peptide fraction was collected, evaporated, and ^{64}Cu counted in a Capintec Radioisotope Calibrator to calculate the specific activity of the product.

Plasma Stability Studies. ^{64}Cu-labeled DOTA-, NOTA-, PCTA-, and Oxo-DO3A-peptides were poorly soluble in a physiological solution; 10% DMF in PBS was used to solubilize the peptides. ^{64}Cu-labeled peptides (111 MBq (3 mCi); 30−50 μL) were incubated at 37 °C in 500 μL of fresh mouse plasma (n = 3) for different time periods, ice-cold acetonitrile was added, and the samples were vortexed and centrifuged. The supernatant was analyzed by reversed-phase HPLC to detect ^{64}Cu metabolites. For radioTLC analysis, plasma stability studies were achieved by incubating 1.85 MBq (50 μCi, 5−10 μL) of ^{64}Cu-labeled peptides at 37 °C in 100 μL of fresh mouse plasma (n = 3) for different time points. Free ^{64}Cu and ^{64}Cu/BFC-BBN conjugate were co-spotted with plasma samples (without treatment) and used as references. TLC was performed either on silica gel coated plastic sheets with methanol/0.1 M ammonium acetate pH 5.5 (1:1) as eluent or on C-18 bonded reversed-phase TLC

Table 1. Analytical Data for BFC-BBN Conjugates

		$[M]^+$					
entry	peptide	calcd	found[a]	yield (%)	purity[b] (%)	K_i[c] (nM)	labeling yield[d] (%)
1	Bombesin					0.76 ± 0.54	
2	DOTA-Aoc-BBN(6−14)	1667	1668	11	93	10.61 ± 4.55	>90
3	NOTA-Aoc-BBN(6−14)	1566	1567	16	98	6.13 ± 2.72	>95
4	^{64}Cu/NOTA-Aoc-BBN(6−14)					3.08 ± 0.74	
5	Oxo-DO3A-Suc-Aoc-BBN(6−14)	1814	1815	20	99	2.51 ± 1.50	>90[e]
6	PCTA-Suc-Aoc-BBN(6−14)	1847	1848	23	95	0.36 ± 0.05	>95

[a] Mass values were obtained by MALDI TOF mass spectroscopy or LC/MS/MS. [b] Purity was determined by HPLC analysis. [c] Affinities for GRPR were determined with [^{125}I-Tyr^4]bombesin in T47D human breast cancer cell line. [d] Labeling yield was determined by radio-HPLC analysis based on ^{64}Cu starting activity. [e] This peptide was incubated an extra 150 min at 100 °C.

Table 2. Peptide Coupling Optimization of *p*-H_2N-Bn-DO3A(O*t*Bu)$_3$ in Solution and Solid Phase

entry	carboxylic acid segment	coupling conditions	reaction time (h)	conversion[a] (%)
1	HO-Suc-Aoc-BBN(6−14)-resin	HATU (2.5 equiv), DMF	72	0
2	HO-Suc-Aoc-BBN(6−14)-resin	PyBOP and ClHOBt (2 equiv), DIEA (4 equiv), *N*-methylpyrrolidone:DMF (1:1)	72	trace
3	BOC-Gly-OH (2 equiv)	PyBOP and ClHOBt (2 equiv), DIEA (4 equiv), *N*-methylpyrrolidone:DMF (1:1)	72	>99
4	HO-Suc-Aoc-BBN(6−14)-resin	ClHOBt (1 equiv), DIEA (2 equiv), DMF, then DEPBT (1 equiv), (2×)	24	>99

[a] Conversion refers to fraction of the carboxylic acid fragment consumed in the reaction and was determined by TLC for coupling in solution or by HPLC and LC/MS/MS analysis after peptide cleavage.

plates with 0.1 M sodium citrate at pH 5, and ^{64}Cu was detected an Instant Imager system.

***In Vivo* Stability Studies.** ^{64}Cu-labeled peptides (15−25 MBq) were intravenously injected in female balb/c mice (n = 3). For the PCTA-BBN conjugate, this corresponded to about (6.47 ± 0.08) × 10^{-10} mol and in the case of the Oxo-DO3A-BBN derivative to about (1.06 ± 0.2) × 10^{-9} mol. Blood was taken from the mice's back paw at different times and directly analyzed by TLC either on silica gel with methanol/0.1 M ammonium acetate at pH 5.5 (1:1) or on C-18 coated plates with 0.1 M sodium citrate at pH 5.

RESULTS

Preparation and Characterization of BFC-BBN Conjugates. We previously reported the synthesis and characterization of DOTA- and NOTA-BBN peptides (Table 1).[7] These peptides were prepared with overall yields of 11−16% based on the substitution rate of the resin, determined photometrically from the amount of Fmoc chromophore released upon treatment of the resin with piperidine/DMF. According to analytical HPLC, the purity was 93% for DOTA-BBN and 98% for NOTA-BBN. For the preparation of the Oxo-DO3A-BBN, different coupling reagents were tested to activate the succinylated peptide on resin (Table 2). Our first attempt using HATU in DMF followed by the addition of *p*-H_2N-Bn-DO3A(O*t*-Bu)$_3$ failed to afford BFC-BBN conjugate, even after 72 h of mechanical agitation (Table 2, entry 1). A similar product pattern along with a trace amount of the desired Oxo-DO3A-BBN conjugate (LC/MS/MS analysis after peptide cleavage) was observed when the succinylated-BBN on resin was treated with PyBOP and ClHOBt in the presence of DIEA and a 1:1 ratio of *N*-methylpyrrolidone/DMF (Table 2, entry 2). Under similar conditions, coupling of *p*-H_2N-Bn-DO3A(O*t*-Bu)$_3$ to BOC-Gly-OH, a model compound, led to the desired BFC-BBN product when the reaction was performed in solution (Table 2, entry 3). We then found an effective coupling reagent, DEPBT, that was used for the activation of the carboxylic acid on resin and the subsequent coupling of the aniline-Oxo-DO3A chelate. As presented in Table 2, DEPBT was highly effective for the coupling of aniline-BFC to peptide on resin with complete conversion of the starting material (Table 2, entry 4). Using these conditions, the Oxo-DO3A-Suc-Aoc-BBN(6−14) and PCTA-Suc-Aoc-BBN(6−14) were prepared with overall yields of 20% and 26%, respectively, in >95% purity (Table 1).

BFC-BBN conjugates were also tested for their receptor binding affinity on T47D cells. DOTA-BBN peptide displayed good binding affinities to GRPR, while NOTA- and Oxo-DO3A-BBN peptides gave inhibition constant (K_i) values slightly lower than that of DOTA-peptide (Table 1). The lowest K_i value (0.36 ± 0.05 nM) was obtained with the PCTA-BBN derivative. The K_i value of the Cu/NOTA-BBN derivative is in the low nanomolar range and similar to that of the nonlabeled-peptide (Table 1, entries 3 and 4).

Preparation and Characterization (Radiolabeling, Purification, Stability) of ^{64}Cu-BFC-BBN Conjugates. We produce ^{64}$CuCl_2$ with a yield of 70 mCi/μA hr/μg using 99% enriched Ni-64, with typical production batches on the order of 3.70−9.25 GBq (100−250 mCi) with specific activity of 296−444 TBq/mmol (8000−12 000 Ci/mmol) of Cu determined by TETA titrations.[25] The BFC-BBN conjugate ^{64}Cu-labeling results are summarized in Table 1. An incubation time of 15 min at 100 °C was found to produce the highest labeling yields. Using this condition, labeling yields were greater than 90% for DOTA-,

NOTA-, PCTA-BBN, and the Oxo-DO3A-peptide; the latter was incubated for an additional 150 min to reach this yield (Table 1). The purification by HPLC using a C-18 column to remove unreacted ^{64}Cu yielded the radiolabeled BFC-BBN conjugate with >99% radiochemical purity and specific activity between 76 and 101 TBq/mmol (2050−2740 Ci/mmol) for all labeled peptides.

The stability of the ^{64}Cu-radiolabeled BFC-BBN, in terms of percentage of intact conjugate was determined in mouse plasma and female balb/c mice (Table 3). We monitored ^{64}Cu by both HPLC and radio-TLC on silica gel or C18 to determine any ^{64}Cu metabolites and free ^{64}Cu. Similar results were obtained using these two different approaches. Since radio-TLC can be performed directly on plasma and blood samples without precipitating plasma proteins, this approach was used to determine the stability of the other ^{64}Cu/BFC-BBN conjugates. As illustrated in Table 3, ^{64}Cu/DOTA-BBN was stable for 1 h in plasma, but for only 30 min after injection in mice. The radio-TLC analysis showed no degradation of the ^{64}Cu-labeled NOTA-and PCTA-BBN peptides after 20 h incubation in mouse plasma or in mice. The ^{64}Cu-labeled Oxo-DO3A derivative was stable *in vitro*, but only 37% intact conjugate remained 20 h post-injection in mice.

Table 3. ^{64}Cu/chelator Complex Stability of BBN(6-14) Derivatives

		^{64}Cu/BFC stability[a] (%)			
stability	time (min)	DOTA	NOTA	PCTA	Oxo-DO3A
plasma	60	>99	>99	>99	>99
	1200	n.d.	>99	>99	>99
in vivo (blood)	30	>99			
	60	67			
	90	41	>99	>99	>99
	1200	0	>99	>99	37−40

[a] Stability is presented as % intact ^{64}Cu-labeled BFC-peptide as determined by HPLC analysis or using TLC on silica gel with methanol/0.1 M ammonium acetate at pH 5.5 (1:1).

DISCUSSION

Previously, we reported the synthesis and characterization of two BFC-conjugated peptides: DOTA-BBN and NOTA-BBN.[7] It was found that NOTA-chelates are readily synthesized in a two-step process starting with bromo-acetylated peptides and that all NOTA peptides had inhibition constant (K_i) values slightly lower than the analogous DOTA-peptides. The synthesis of PCTA- and Oxo-DO3A-BBN conjugates on solid phase is summarized in Scheme 1. Although both isothiocyanate and aniline derivatives of PCTA and Oxo-DO3A are commercially available, we selected aniline derivatives for conjugation to our BBN peptide since they generally display greater long-term stability than their isothiocyanate analogues. To facilitate the coupling of the aniline-PCTA and the aniline-Oxo-DO3A to the peptide, a succinyl spacer was introduced at the *N*-terminus of BBN linked to the resin. Even if the activation of carboxylic moieties on resin is known to present challenges, a complete conversion of the succinylated-BBN was observed using DEPBT/ClHOBt as coupling reagents (Table 2, entry 4). Indeed, DEPBT has already been employed with success in difficult couplings, such as primary and secondary anilines.[26,27] Using their respective partially protected aniline chelates, milligram amounts of PCTA and Oxo-DO3A conjugates are rapidly and efficiently made and purified. An attractive aspect of this procedure is that a very stable amide bond between the BFC and the succinylated peptide is obtained. Also, increasing the distance between the chelate and the peptide backbone by using a succinyl spacer enhanced the BBN binding affinity. Indeed, the K_i values of Oxo-DO3A-BBN and PCTA-BBN conjugates were more than 5-fold and 30-fold lower, respectively, as compared to that found for DOTA-BBN when tested in T47D human breast cancer cells (Table 1). PCTA-Suc-Aoc-BBN(6−14) displayed the highest binding affinity of all BFC-BBN conjugates tested. The higher affinity of the NOTA conjugate for GRPR as compared to DOTA-BBN suggests that the introduction of a smaller chelating unit at the *N*-terminus of the peptide allowed the BBN peptide to interact more efficiently with its receptor. No significant

Scheme 1. Synthesis of PCTA- and Oxo-DO3A-BBN Conjugates on Solid Phase

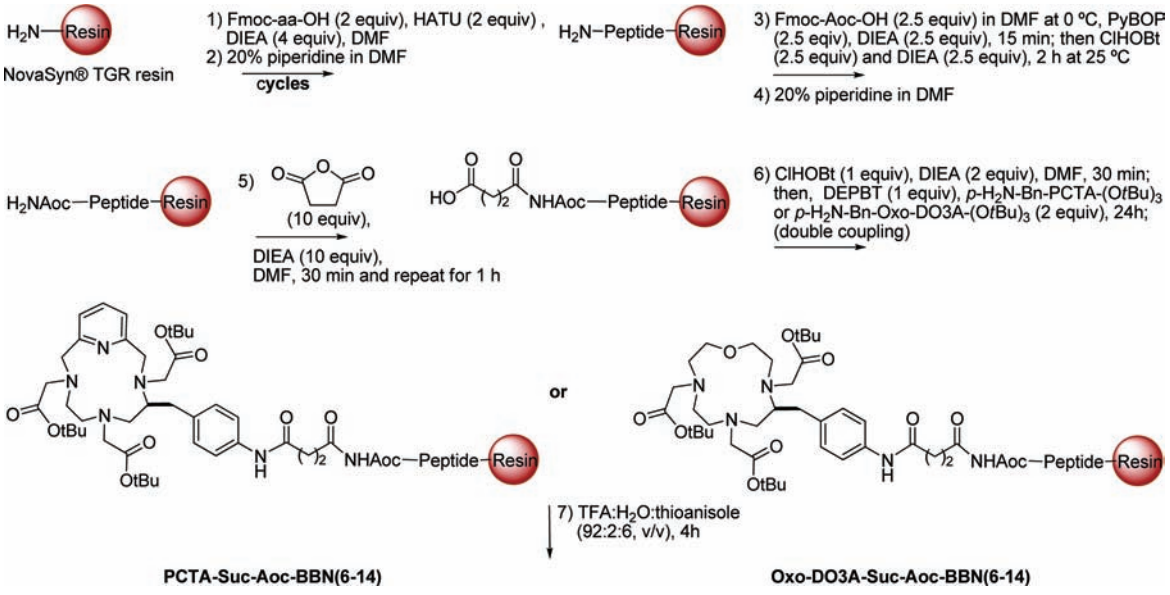

difference in affinity is observed between Cu-labeled and non-labeled peptides (Table 1).

After ^{64}Cu-labeling, the radiochemistry of the PCTA-BBN and Oxo-DO3A-BBN was compared to that of DOTA- and NOTA-BBN conjugates. All four ^{64}Cu complexing systems can be used to prepare peptide radioligands with high radiochemical purity and high specific activity. The radiolabeling yields for ^{64}Cu were found to depend on the temperature of the reaction mixture and the time with optimal results being obtained at 100 °C in 15 min. Even though previous publications reported that NOTA and DOTA are able to incorporate Cu-64 at much lower temperatures,[28] we used identical labeling conditions for all BFC-BBN conjugates in order to facilitate a proper comparison of the different peptides. Higher labeling efficacies are obtained when DOTA-, NOTA-, and PCTA-BBN conjugates are labeled using 0.1 M ammonium acetate buffer pH 5.5 and ^{64}Cu(OAc)$_2$ than with Oxo-DO3A-BBN. No radiation damage to the BBN peptide was observed even after heating at 100 °C for 150 min.

In vitro and *in vivo* stability assays confirm that ^{64}Cu-labeled NOTA- and PCTA-BBN conjugates remain stable over the 20 h time period. In contrast, both ^{64}Cu/DOTA- and ^{64}Cu/Oxo-DO3A-BBN have poor *in vivo* stability. Because the liver is one of the primary transchelation sites for Cu-64 complexes,[29] we also studied the stability of the ^{64}Cu/PCTA-BBN peptide in the liver 2 h post injection and detected 25% of free ^{64}Cu and 75% of the intact radiolabeled peptide. It appears that the free Cu-64 remains sequestered in liver (gallbladder) and does not go back in circulation, since only the ^{64}Cu/PCTA-BBN peptide is detected in blood after 20 h.

In conclusion, our data show that ^{64}Cu-labeled NOTA- and PCTA-BBN peptides are promising radiotracers for PET imaging. Their high binding affinity for GRP receptors and good stability in mice render them suitable as model compounds for the fine-tuning of biological properties of ^{64}Cu-labeled BFC-BBN conjugates. Further *in vitro*/*in vivo* evaluation of these tracers as potential cancer PET imaging agents is warranted.

AUTHOR INFORMATION

Corresponding Author

*Prof. Brigitte Guérin, Centre d'imagerie moléculaire de Sherbrooke (CIMS), Department of Nuclear Medicine and Radiobiology, Université de Sherbrooke, 3001, 12th North Avenue Sherbrooke, Qc, Canada, J1H 5N4. Phone: (819) 820-6868 ext. 15285; fax: (819) 829-3238. E-mail: brigitte.guerin2@usherbrooke.ca.

ACKNOWLEDGMENT

B.G. is a member of the FRSQ-funded Centre de recherche clinique Étienne-Le Bel. The work was financially supported by the Natural Sciences and Engineering Research Council of Canada (NSERC), the Canadian Institute of Health Research (CIHR grant MOP-89875), and the BC Leadership Chair in Functional Cancer Imaging. Conflicts of interest: Cara L. Ferreira is employed by Nordion. Paul Jurek and Garry Kiefer are employed by Macrocyclics Inc. The other authors declare that they have no conflicts of interest.

REFERENCES

(1) Williams, H. A., Robinson, S., Julyan, P., Zweit, J., and Hastings, D. (2005) A comparison of PET imaging characteristics of various copper radioisotopes. *Eur. J. Nucl. Med. Biol. 32*, 1473–1480.

(2) De Leon-Rodriguez, L. M., and Kovacs, Z. (2008) The synthesis and chelation chemistry of DOTA-peptide conjugates. *Bioconjugate Chem. 19*, 391–402.

(3) Prasanphanich, A. F., Nanda, P. K., Rold, T. L., Ma, L., Lewis, M. R., Garrison, J. C., Hoffman, T. J., Sieckman, G. L., Figueroa, S. D., and Smith, C. J. (2007) [^{64}Cu-NOTA-8-Aoc-BBN(7−14)NH$_2$] targeting vector for positron-emission tomography imaging of gastrin-releasing peptide receptor-expressing tissues. *Proc. Natl. Acad. Sci. U. S. A. 104*, 12462–12467.

(4) Ferreira, C. L., Yapp, D. T. T., Crisp, S., Sutherland, B. W., Ng, S. S. W., Gleave, M., Bensimon, C., Jurek, P., and Kiefer, G. E. (2010) Comparison of bifunctional chelates for ^{64}Cu antibody imaging. *Eur. J. Nucl. Med. Mol. Imaging 37*, 2117–2126.

(5) Ferreira, C. L., Lamsa, E., Woods, M., Duan, Y., Fernando, P., Bensimon, C., Kordos, M., Guenther, K., Jurek, P., and Kiefer, G. E. (2010) Evaluation of bifunctional chelates for the development of gallium-based radiopharmaceuticals. *Bioconjugate Chem. 21*, 531–536.

(6) Ferreira, C. L., Yapp, D. T., Lamsa, E., Gleave, M., Bensimon, C., Jurek, P., and Kiefer, G. E. (2008) Evaluation of novel bifunctional chelates for the development of Cu-64-based radiopharmaceuticals. *Nucl. Med. Biol. 35*, 875–882.

(7) Guérin, B., Ait-Mohand, S., Tremblay, M.-C., Dumulon-Perreault, V., Fournier, P., and Bénard, F. (2010) Total solid-phase synthesis of NOTA-functionalized peptides for PET or SPECT imaging. *Org. Lett. 12*, 280–283.

(8) Voss, S. D., Smith, S. V., DiBartolo, N., McIntosh, L. J., Cyr, E. M., Bonab, A. A., Dearling, J. L. J., Carter, E. A., Fischman, A. J. S., Treves, T., Gillies, S. D., Sargeson, A. M., Huston, J. S., and Packard, A. B. (2007) Positron emission tomography (PET) imaging of neuroblastoma and melanoma with ^{64}Cu-SarAr immunoconjugates. *Proc. Natl. Acad. Sci. U.S.A. 104*, 17489–17493.

(9) Luyt, L. G., and Katzenellenbogen, J. A. (2002) A trithiolate tripodal bifunctional ligand for the radiolabeling of peptides with gallium(III). *Bioconjugate Chem. 13*, 1140–1145.

(10) Mantey, S. A., Weber, H. ., Sainz, E., Akeson, M., Ryan, R. R., Pradhan, T. K., Searles, R. P., Spindel, E. R., Battey, J. F., Coy, D. H., and Jensen, R. T. (1997) Discovery of a high affinity radioligand for the human orphan receptor, bombesin receptor subtype 3, which demonstrates that it has a unique pharmacology compared with other mammalian bombesin receptors. *J. Biol. Chem. 272*, 26062–26071.

(11) Reile, H., Armatis, P. E., and Schally, A. V. (1994) Characterization of high-affinity receptors for bombesin/gastrin releasing peptide on the human prostate cancer cell lines PC-3 and DU-145: internalization of receptor bound ^{125}I-(Tyr^4) bombesin by tumor cells. *Prostate 25*, 29–38.

(12) Markwalder, R., and Reubi, J. C. (1999) Gastrin-releasing peptide receptors in the human prostate: relation to neoplastic transformation. *Cancer Res. 59*, 1152–1159.

(13) Pagani, A., Papotti, M., Sanfilippo, B., and Bussolati, G. (1991) Expression of the gastrin-releasing peptide gene in carcinomas of the breast. *Int. J. Cancer 47*, 371–375.

(14) Halmos, G., Wittliff, J. L., and Schally, A. V. (1995) Characterization of bombesin/gastrin-releasing peptide receptors in human breast cancer and their relationship to steroid receptor expression. *Canc. Res. 55*, 280–287.

(15) Gugger, M., and Reubi, J. C. (1983) Gastrin-releasing peptide receptors in non-neoplastic and neoplastic human breast. *Am. J. Pathol. 155*, 2067–2076.

(16) Moody, T. W., Bertness, V., and Carney, D. N. (1983) Bombesin-like peptides and receptors in human tumor cell lines. *Peptides 4*, 683–686.

(17) Reubi, J. C., Wenger, S., Schmuckli-Maurer, J., Schaer, J. C., and Gugger, M. (2002) Bombesin receptor subtypes in human cancers: detection with the universal radioligand ^{125}I-[D-Tyr^6, β-Ala^{11}, Phe^{13}, Nle^{14}] bombesin(6−14). *Clin. Cancer Res. 8*, 1139–1146.

(18) Conklin, B. R., and Bourne, H. R. (1993) Structural elements of Gα subunits that interact with G$\beta\gamma$, receptors and effectors. *Cell 73*, 631–641.

(19) Schuhmacher, J., Zhang, H., Doll, J., Mäcke, H. R., Matys, R., Hauser, H., Henze, M., Haberkorn, U., and Eisenhut, M. (2005) GRP receptor-targeted PET of a Rat pancreas carcinoma xenograft in nude mice with a ^{68}Ga-labeled bombesin(6−14) analog. *J. Nucl. Med. 46*, 691–699.

(20) Chen, X., Park, R., Hou, Y., Tohme, M., Shahinian, A. H., Bading, J. R., and Conti, P. S. (2004) MicroPET and autoradiographic imaging of GRP receptor expression with ^{64}Cu-DOTA-[Lys^3]bombesin in human prostate adenocarcinoma xenografts. *J. Nucl. Med. 45*, 1390–1397.

(21) Lane, S. R., Nanda, P., Rold, T. L., Sieckman, G. L., Figueroa, S. D., Hoffman, T. J., Jurisson, S. S., and Smith, C. J. (2010) Optimization, biological evaluation and microPET imaging of copper-64-labeled bombesin agonists, [^{64}Cu-NO_2A-(X)-BBN(7−14)NH_2], in a prostate tumor xenografted mouse model. *Nucl. Med. Biol. 37*, 751–761.

(22) Cheng, Y., and Prusoff, W. H. (1973) Relationship between the inhibition constant ([K_i]) and the concentration of inhibitor which causes 50% inhibition ([I_{50}]) of an enzymatic reaction. *Biochem. Pharmacol. 22*, 3099–3108.

(23) Aprikian, A. G., Han, K., Chevalier, S., Bazinet, M., and Viallet, J. (1996) Bombesin specifically induces intracellular calcium mobilization via gastrin-releasing peptide receptors in human prostate cancer cells. *J. Mol. Endocrinol. 16*, 297–306.

(24) Zeisler, S. K., Pavan, R. A., Orzechowski, J., Langlois, R., Rodrigue, S., and van Lier, J. E. (2003) Production of ^{64}Cu on the Sherbrooke TR-PET cyclotron. *J. Radioanal. Nucl. Chem. 257*, 175–177.

(25) McCarthy, D. W., Shefer, R. E., Klinkowstein, R. E., Bass, L. A., Margeneau, W. H., Cutler, C. S., Anderson, C. J., and Welch, M. J. (1997) Efficient production of high specific activity ^{64}Cu using a biomedical cyclotron. *Nucl. Med. Biol. 24*, 35–43.

(26) Auzzas, L., Larsson, A., Matera, R., Baraldi, A., Deschênes-Simard, B., Giannini, G., Cabri, W., Battistuzzi, G., Gallo, G., Ciacci, A., Vesci, L., Pisano, C., and Hanessian, S. (2010) Non-natural macrocyclic inhibitors of histone deacetylases: design, synthesis, and activity. *J. Med. Chem. 53*, 8387–8399.

(27) Woo, G. H. C., Beeler, A. B., and Snyder, J. K. (2007) 1,2,3, 4-Tetrahydro-1,5-naphthyridines and related heterocyclic scaffolds: exploration of suitable chemistry for library development. *Tetrahedron 63*, 5649–5655.

(28) Liu, Z., Yan, Y., Liu, S., Wang, F., and Chen X. (2009) ^{18}F, ^{64}Cu, and ^{68}Ga labeled RGD-bombesin heterodimeric peptides for PET imaging of breast cancer. *Bioconjugate Chem. 20*, 1016−1025, and refs cited therein.

(29) Boswell, C. A., Sun, X., Niu, W., Weisman, G. R., Wong, E. H., Rheingold, A. L., and Anderson, C. J. (2004) Comparative in vivo stability of copper-64-labeled cross-bridged and conventional tetraazamacrocyclic complexes. *J. Med. Chem. 47*, 1465–1474.

Bioconjugate Chemistry

REVIEW

pubs.acs.org/bc

Nucleic Acid Carriers Based on Precise Polymer Conjugates

Christina Troiber and Ernst Wagner*

Pharmaceutical Biotechnology, Center for System-based Drug Research and Center for NanoScience (CeNS), Ludwig-Maximilians-Universität, Butenandtstrasse 5-13, 81377 Munich, Germany

ABSTRACT: Polymer polydispersity, random conjugation of functional groups, and poorly understood structure−activity relationships have constantly hampered progress in the development of nucleic acid carriers. This review focuses on the synthetic concepts for the generation of precise polymers, site-specific conjugation strategies, and multifunctional conjugates for nucleic acid transport. Dendrimers, defined peptide carriers, sequence-defined polyamidoamines assembled by solid-phase supported synthesis, and precise lipopeptides or lipopolymers have been characterized for pDNA and siRNA delivery. Conjugation techniques such as click chemistries and peptide ligation are available for conjugating polymers with functional transport elements such as targeting or shielding domains and for direct covalent modification of therapeutic nucleic acids in a site-specific mode.

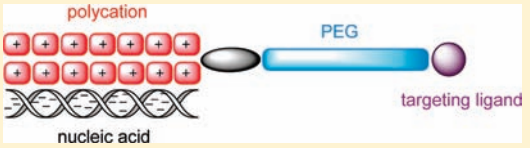

INTRODUCTION

A prerequisite for the successful delivery of genetic information into target cells of patients is the existence of appropriate carriers. Efficient viral and synthetic vectors already exist for the ex vivo nucleic acid delivery, whereas efficient and successful in vivo transport of DNA, RNA, or small interfering RNA (siRNA) to target cells is still limited. In terms of efficiency, viral vectors are still the most potent systems. Nonetheless, synthetic vectors possess distinct advantages, such as a lower immunogenic potential, a reduced mutagenic risk, and easier handling and manufacturing.[1−4] A combination of both worlds, the design of "synthetic viruses", might be most advantageous.[5−8]

Anionic charge, large size, and degradability of nucleic acids by nucleases make administration of naked nucleic acids rather inefficient in reaching the target location.[9,10] For these reasons, special carriers have been developed to aid the delivery of genetic material. They are designed to protect nucleic acids in the extracellular environment and to mediate their transport into the cytoplasm.[11] Several barriers, including stickiness to nontarget cells, extracellular fluids, and matrix, have to be overcome.[12] Cell entry, endolysosomal escape, cytoplasmic trafficking, and vector unpacking are further bottlenecks for successful delivery.[13−15] In the case of gene delivery the functional plasmid DNA (pDNA) encoding the protein has to be delivered into the nucleus.[16]

The most common synthetic vectors are cationic lipids and polymers, which form electrostatic complexes with the negatively charged nucleic acid. The payload is packaged into nanosized structures enabling uptake into cells.[14,17] In the case of polymers, the polyplex stability and transfection efficiency depend on the chemical type, molecular weight, and topology of the cationic polymer, as well as the ratio of polymer to nucleic acid.[18−20] Polyamine structures, including poly-L-lysine, linear and branched polyethylenimines (PEIs),or polyamidoamine (PAMAM) dendrimers, are an often used class of artificial vector system. In some polymers such as PEI or PAMAM, only a fraction of amine groups are protonated at physiological pH. The remaining basic groups may exhibit a buffering effect, the so-called proton-sponge effect, upon entry into the endosome. The pH-mediated creation of new cationic polymer charges triggers an influx of chloride counterions followed by water. The resulting osmotic pressure, together with interactions of the cationic polymer with the membrane, is assumed to rupture the lysosome/endosome, releasing the carrier and its cargo into the cytosol.[21−23]

PEI has been one of the gold standards for polymeric pDNA transfer in vitro and in vivo.[24] Frequently, various forms of branched PEI (bPEI) with molecular weights between 2 and 800 kDa have been used. bPEI contains primary, secondary, and tertiary amino groups. These amines have pK_a values spanning a broad pH range, resulting in high buffering capacity. The degree of protonation of the amines increases from roughly 20 to 45% as the pH decreases from 7 to 5.[23] bPEI is synthesized by polymerization of aziridine and hence has a very heterogeneous and polydisperse structure.

Branched PEI and many other related polymers and their derivatives show a heterogeneous distribution of molecular weight and isomers, which significantly influences physicochemical properties, biological efficiency, and cytotoxicity.[25−28] Moreover, random attachment of one or even several different functional domains results in heterogeneous conjugates that might be useful in experimental approaches, but are rather unsuitable for clinical developments.[29]

A possible solution to the inherent drawbacks of macromolecules derived by random polymerization is the synthesis of defined polymeric systems as nucleic acid carriers. Recently, different strategies were introduced for this purpose. Linear polymers can be generated by improved polymerization technologies, resulting in defined structures with low molecular weight polydispersity.[30−34] In this way, well-defined linear PEI

Received: May 12, 2011
Revised: July 6, 2011
Published: July 13, 2011

ACS Publications © 2011 American Chemical Society

(LPEI) was produced in GMP quality with very acceptable biological efficiency.[24,35] Early clinical studies with pDNA polyplexes highlight the potency of this polymer.[36] Other defined nucleic acid carriers result from dendrimers combining an extremely low polydispersity index with the high molecular mass of classical polymers.[37] Solid phase assisted synthetic strategies will be discussed for the preparation of defined polymeric structures with control over every monomer position in a sequence.

Novel efficient and orthogonal coupling techniques, as reviewed here and in other papers,[30] present a recent opportunity toward perfectly defined polymers. Furthermore, precise conjugation of polymers with functional groups, such as polyethylene glycol (PEG) shielding domains, targeting ligands, or chemically synthesized oligonucleotides, allow the synthesis of homogeneous nucleic acid carrier systems with exact composition.

DENDRIMERS

Dendritic structures are built from a series of branches extending outward from an inner core. Each iteration leads to a higher generation material and therefore to dendrimers with higher molecular weight. They consist of three distinct parts: a core, branching units, and branches, which can be chemically altered independently. As a result, an enormous variety of possible dendrimers exist.[38]

Dendritic Polylysines. Denkewalter[39] reported the synthesis of L-lysine based dendrimers (DPLs) in the early 1980s, which are usually synthesized via solid phase peptide synthesis (SPPS) introduced by Merrifield in 1963.[40] Boc-protected lysines were coupled to the core repeatedly after TFA deprotection, resulting in dendritic structures of different generations (G). Multiple antigen peptide (MAP) systems are a distinct type of dendritic structures containing an inner oligolysine core, multiple copies of synthetic peptide antigens, and a simple amino acid, such as alanine or glycine, as internal standard for monitoring the synthesis process.[41] These systems are used in vaccines to induce immunoreactions.

Hexaethylenediamine as initiator core led to symmetrical poly-L-lysine dendrimers, whereas the ε-peptide template, consisting of lysine residues, led to asymmetrical dendrimers. Those SPPS-derived structures were well-defined and monodisperse and displayed a precise number of surface amines.

DPLs of various generations were examined for their potential as antisense oligonucleotide (ODN) and plasmid DNA carriers.[42] They formed complexes with nucleic acids through ionic interactions with limited cell toxicity. The ODN and pDNA binding depended on the N/P (nitrogen to phosphate) ratios and the DPL generation. High N/P ratios and high-generation DPLs, with hyperbranched architecture, improved nucleic acid binding.

High-generation asymmetric DPLs complexed with ODN were less toxic than the free DPL. Only the highest generations of asymmetric DPLs showed moderate luciferase activity.[42]

The symmetric dendritic poly(L-lysine)s of generation 3 (G 3) or higher, built up on a hexamethylenediamine core,[43] formed complexes of 200−250 nm with pDNA, whereas size did not reflect compaction strength. Especially G 5 and G 6 dendrimers showed high transfection efficiencies in Caco-2, HepG2, and MKN45 cells. The efficiency of the G 6 pDNA complex was not significantly reduced when 50% serum was added. Eighty percent and higher cell viabilities were observed for the G 6 dendrimer alone and its polyplex. With regard to in vivo distribution, DPL pDNA polyplexes were found to possess favorable characteristics, such as delivery into tumors and prolonged circulation in the blood, but these polyplexes showed a low gene transfer efficiency.[44]

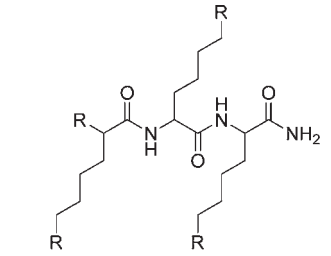

Figure 1. Dendritic copolymer of lysine and histidine.

To investigate the effect of the terminal cationic lysine group, arginine (R) and histidine (H) were coupled to the surface amines of DPL G 5 resulting in DPL GR6 and DPL GH6, respectively.[45] The arginine-modified DPL bound pDNA as effectively as the G 6 DPL, whereas histidine modification decreased the binding ability. Moreover, the transfection efficiency of DPL GR6 was significantly higher than that of DPL G 6, whereas DPL GH6 showed only a high efficiency when complexes were formed under acidic conditions (pH 5.0) due to the protonable imidazole groups of the histidine.[44]

Linear copolymers of lysine and histidine were not effective in the delivery of nucleic acids. To increase the polymer size and charge density, histidine−lysine (HK) branches were attached to one, two, or three lysines, resulting in 2-, 3-, and 4- branched structures, respectively (Figure 1).[46,47] The solid phase derived, branched HK dendrimers were additionally modified with branches of different histidine/lysine ratios, resulting in HK and HHK copolymers.

The pDNA binding and transfection efficiency positively correlates with the degree of branching and number of histidines in malignant cells with an endocytic pH >6.0. A negative correlation was found in primary cell lines with strong acidic endosomal pH.

For siRNA delivery the histidine/lysine ratio and branching were increased, resulting in HHHK copolymers with eight branches.[48,49] The repeating pattern of HHHK on the terminal branch augmented siRNA uptake in vitro more effectively than the HHK or HK pattern. Moreover, it had a reduced binding due to the lower content of lysines, but a higher buffering capacity due to the higher number of histidines. The addition of single lysines to the eight terminal branches of the HHHK copolymer led to increased siRNA binding, but reduced silencing.

For in vivo administration, 1,2-dioleoyl-3-trimethylammonium propane (DOTAP) liposomes were used as positive control. Surprisingly, the two four-branched polymers with lower lysine content (HHHK and HHK) were more effective as carriers for intratumoral delivery of rapidly growing fibrosarcoma 1 (Raf-1) siRNA than the eight-branched polymers. The four-branched HHHK copolymer was also superior in pDNA delivery after intratumoral injection.

The amphipathic, asymmetric lysine-based dendrimers $(\alpha/\varepsilon Lys)_7$-$(\alpha AMA)_3$amide and $(\alpha/\varepsilon Lys)_{15}$-$(\alpha AMA)_3$amide were synthesized by solid phase synthesis with 8 or 16 terminal amines, respectively.[50] Both primary amines of the lysine were used to generate higher generation dendrimers ($\alpha/\varepsilon Lys$), and the terminal amines were modified with the α-amino group of

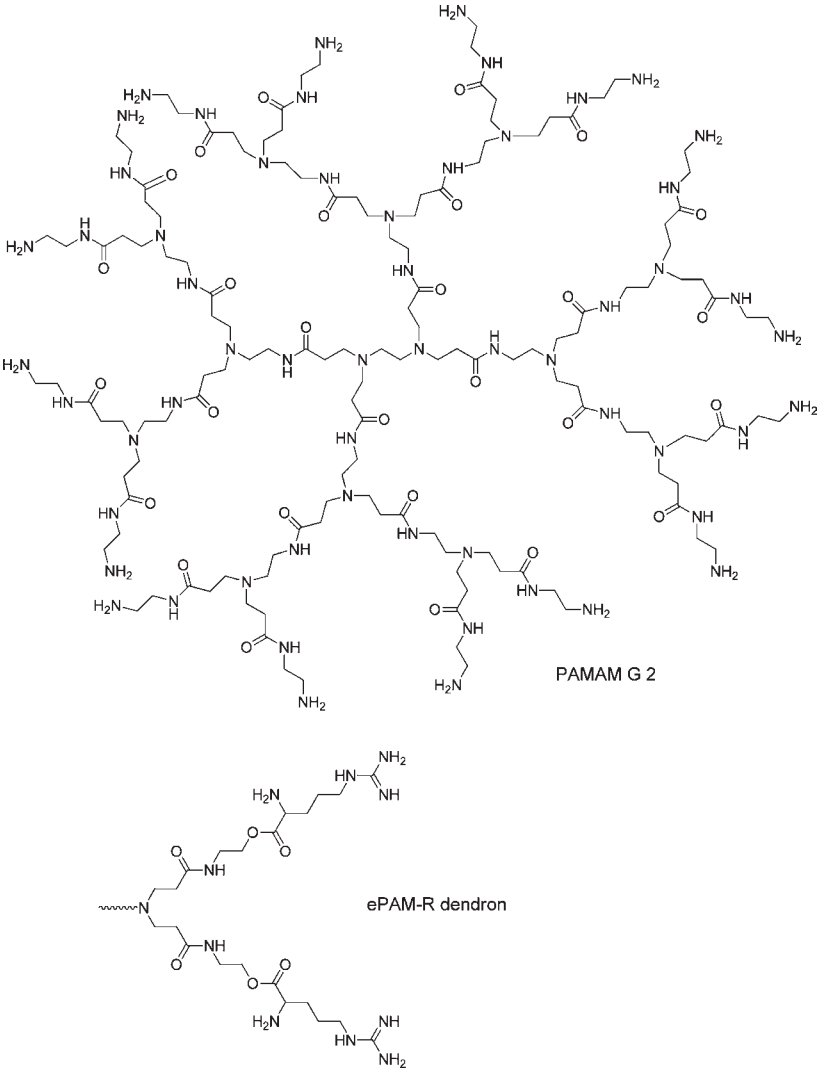

Figure 2. Starburst and arginine-grafted PAMAM dendrimer.

the amino-myristic acid (AMA). DNA dendrimer complexes formed high molecular weight aggregates with lower toxicity than the dendrimer alone. The complexes of $(\alpha/\varepsilon Lys)_{15}-(\alpha AMA)_3$-amide were able to transfect BHK cells as well as COS cells.[51]

PAMAM Dendrimers. Starburst polyamidoamine (PAMAM) dendrimers (Figure 2) are spherical, highly ordered, dendritic polymers with positively charged primary amino groups on their surface at physiological pH. The manufacturing process is a series of repetitive steps starting with a central initiator core. This core may consist of either an ammonium as trivalent initiator or an alkylenediamine as tetravalent initiator. Methyl acrylates are added to the core by exhaustive Michael addition followed by amidation of the resulting ester with an excess of alkylenediamine. Each complete growth step represents a new generation of polymer with a larger molecular diameter, twice the number of reactive surface sites, and approximately twice the molecular weight of the preceding generation.[52]

PAMAM dendrimers form stable complexes with plasmid DNA or oligonucleotides.[53−55] To investigate the potential use of PAMAM dendrimers for antisense ODN delivery, antisense-mediated correct splicing of a luciferase reporter was used as readout system.[56] G ≥ 5 dendrimers were moderately efficient in ODN delivery in serum-free medium while maintaining some activity even in the presence of high serum concentrations. The luciferase expression increased progressively with increasing oligonucleotide concentration for G 5 dendrimers. Moreover, G 5 dendrimers were less toxic in the presence of serum.

The carboxy group of Fmoc−L-arginine(pbf)−OH (R) or Fmoc−L-lysine(boc)−OH (K) was grafted to the primary amines of a PAMAM G 4 dendrimer, which resulted in PAMAM-R (Figure 2) or PAMAM-K dendrimers after deprotection.[57] The polymers formed pDNA polyplexes with a size around 200 nm. Compared to native PAMAM G 4 or PAMAM-K, PAMAM-R showed enhanced gene delivery expression in HepG2 and Neuro 2A cell lines, as well as in primary rat vascular smooth muscle cells. The modified PAMAM dendrimers displayed an increased toxicity in comparison to native PAMAM in 293 and HepG2 cells.

To reduce the toxicity of the arginine-grafted PAMAM dendrimer, the amide bonds were replaced by more rapidly biodegradable ester bonds. Therefore, hydroxyl-terminated PAMAM-OH G 2, 3, and 4 were modified with arginine by ester bond formation, resulting in e-PAM-R G 2, 3, and 4 dendrimers.[58] The core PAMAM-OH displayed low cell toxicity, transfection efficiency,

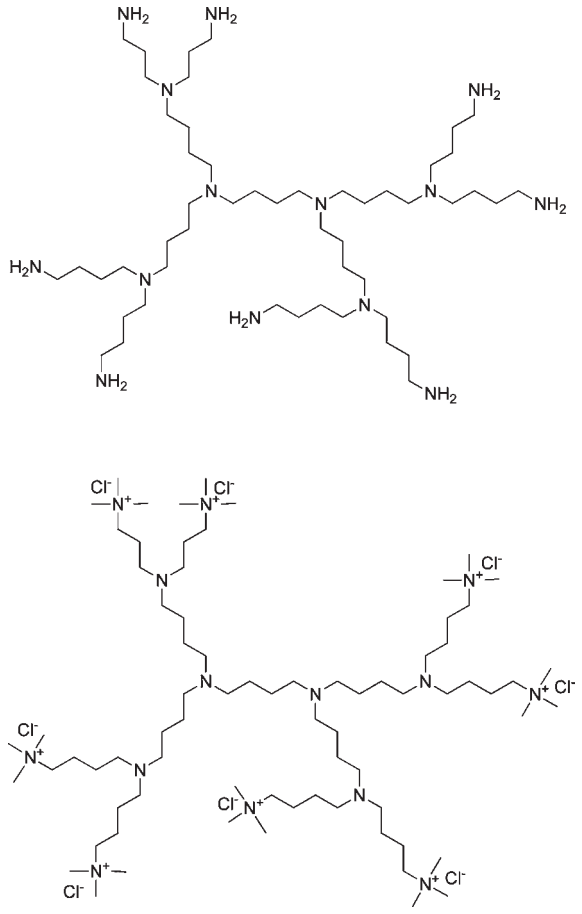

Figure 3. PPI DAB 8 and its quaternary ammonium derivative Q 8.

and DNA binding capacity due to the neutral hydroxyl groups on its surface. The polyplex size was 200−300 nm, and no significant difference in DNA binding between the e-PAM-R generations was observed. The e-PAM-R G 4 showed the highest transfection efficiency, similar to PAMAM-R with favorable cell viability due to the ester bond.

The proton buffering capacity of PAMAM-K was enhanced through the introduction of one to three Fmoc−His(trt)−OH into the L-arginine-grafted PAMAM G 4 dendrimer. The resulting PAMAM G4-$H_{(1-3)}$-K effectively condensed pDNA at low charge ratios, and pDNA was effectively delivered into the cells, especially into the nucleus. The transfection efficiency correlated positively with the number of histidine residues in different cell lines. Cytotoxicity was relatively low in all cell lines.[59]

Polypropylenimine Dendrimers. Native polypropylenimine (PPI) dendrimers derived from a 1,4-diaminobutane (DAB) core of different generations (DAB 4, 8, 16, 32, and 64) and their methyl quaternary ammonium derivatives (Q 4, 8, 16, and 32) were tested for their potential as nonviral gene delivery vectors (Figure 3).[60]

Quaternization of the lower generation DAB 4 and 8 improved DNA binding drastically and increased vector biocompatibility.[61] The toxicity of the native PPI dendrimers increased with molecular weight. DNA binding decreased the toxicity of the low-generation dendrimers, whereas the toxicity of the higher generations (DAB 16 and 32) was not modulated. DAB 16 was superior in in vitro gene transfer activity to DAB 8, especially at low DNA doses. The DAB 8/pDNA formulations were lethally toxic, whereas Q 8/pDNA complexes were tolerated on intravenous injection. Quaternization improved cell biocompatibility of higher DAB/DNA dendrimer complexes, but reduced transfection efficiency of higher generation native dendrimers. DAB 16 and Q 8/DNA formulations resulted predominantly in liver-targeted gene expression, presumably in Kupffer cells, and avoided lung delivery in contrast to LPEI.

PPI G 2 or G 3 was grafted with branched oligoethylenimine 800 Da (OEI) or PPI dendrimer via hexanediol diacrylate, providing bioreversible ester linkages.[62] Transfection levels of OEI-grafted dendrimer pDNA polyplexes were the best, similar to or even higher than those of standard PEI polyplexes. Intravenous injection of OEI-grafted PPI polyplexes into tumor-bearing mice mediated transgene expression predominantly in the subcutaneous tumors. Gene expression levels significantly increased with the higher dendrimer core generation.

DEFINED PEPTIDE CARRIERS

Key advantages of peptide polycations are monodispersity and exact composition defined by peptide sequence. This precise structure definition allows the evaluation of structure−activity relationships. Natural amino acids with cationic or protonated side chains are able to bind nucleic acids through electrostatic interactions and build positively charged polyplexes, which are then taken up through endocytosis.

Branched oligocationic peptides, which differ in number and type of cationic amino acids (lysines, arginine, ornithine) were coupled to the receptor ligand protein transferrin (Tf) via a spacer to ensure the flexibility of the peptide backbone of the pDNA binding moiety.[63] The pDNA binding ability increased with the number of cationic groups, whereas variations in the cationic side chain slightly effected pDNA compaction (arginyl > lysyl ≈ ornithyl). Incorporating tryptophan (Trp) into the DNA binding moiety did not affect binding affinity, but did affect DNA compaction. In the presence of chloroquine, DNA complexes of peptides with six to eight cationic amino acids were able to transfect K562 cells by transferrin receptor-mediated gene delivery.[64] Chloroquine acted as endosomolytic agent.[65]

A cationic amphipathic peptide suitable for oligonucleotide delivery contained repeating units of lysine−alanine−leucine−alanine (KALA).[66] The KALA peptide bound pDNA, and the complexes destabilized membranes. The efficiency of oligonucleotide delivery depended on the charge ratio. Moreover, positively charged polyplexes were necessary for nuclear accumulation and transfection.

Polyplex stabilization through interpeptide disulfide bonds was achieved by oxidation of peptides with low molecular weight after pDNA binding. Therefore, multiple cysteine residues were inserted into small synthetic oligolysines. One to four lysine residues were substituted with cysteines in Cys−Trp−Lys_{18}.[67,68] Peptides with three or more cysteines displayed increased polyplex stability and particle size and, therefore, led to a decrease in gene transfer. The cross-linked peptide with two terminal cysteines (Cys−Trp−Lys_{17}−Cys) mediated maximal gene expression without increasing DNA uptake. The Cys−Lys_4−Cys peptide exhibited equivalent particle size, DNA binding, and transfection efficiency. Addition of histidine resulted in the optimal peptide of Cys−His−Lys_6−His−Cys, with enhanced in vitro gene expression even in the absence of chloroquine due to its additional buffering capacity.

Another linear reducible polycation (RPC) with high molecular weight was prepared by oxidative polycondensation of

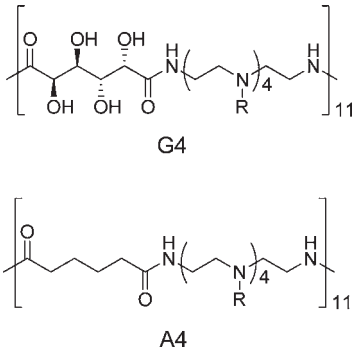

Figure 4. Poly(glycoamidoamine) G4 and analogue A4.

Cys−Lys_{10}−Cys prior to DNA condensation.[69] The cationic lipid DOTAP or chloroquine was used as endo/lysosomolytic agent for the RPC-based polyplexes. High levels of gene expression were observed in cancer cells in the presence of serum using RPC/DOTAP polyplexes with low toxicity due to the intracellular degradation of the polycation.

A short oligoarginine synthetic peptide (R_{15}) showed complete condensation of siRNA (N/P ≥ 3) with particle sizes between 220 and 270 nm and a positive zeta potential.[70] A charge-, time-, and dose-dependent luciferase gene silencing effect was achieved with heterogeneous polyplex distribution in the perinuclear region of COS-7 cells. A significant reduction of tumor growth was observed in subcutaneous SKOV-3 tumors when treated with R_{15}/Her-2-specific siRNA. In contrast, a treatment with R_{15}/Her-2-mismatch siRNA, naked siRNA, or 5% glucose solution showed no growth inhibition. Those results were confirmed with Western blot. In addition, mouse body weight did not change significantly during the oligoarginine/siRNA treatment.

LINEAR POLYAMIDOAMINES

Poly(glycoamidoamine)s (PGAAs) were synthesized as efficient and degradable carriers by solution reaction. Hexose-derived dicarboxylic acids were reacted with the terminal primary amines of defined protected oligoethylenimines under amide formation, followed by deprotection of the transient protected secondary amines of the polyamines.[71,72]

The PGAAs with four secondary amines with (D4, G4, M4, and T4) and analogues without (O4, S4, and A4) hydroxyl groups (Figure 4) within the dicarboxylic acid displayed differences in polymer degradation, pDNA complexation, toxicity, and transfection efficiency. Polymer degradation was facilitated through secondary amines and hydroxyls, which act as electron-withdrawing groups that formed hydrogen bonds. Degradation did not affect buffering capacity and was faster at pH 7.4 than at pH 5. Polymer degradation showed no effect on cell survival, but did on polyplex stability. Nearly 100% of cells were positive for Cy5 when exposed to PGAA/Cy5−pDNA polyplexes, whereas G4/DNA polyplexes showed the highest fluorescence intensity. All secondary amine containing PGAA polyplexes, formed with pDNA, showed luciferase gene expression. In contrast, GO2, in which the secondary amines were substituted with ethylene oxide units, did not show pDNA binding or gene transfer. In the nonhydroxylated analogues, pDNA binding affinity was slightly influenced by the length of the dicarboxylic acid (A4 > S4 > O4). DNA affinity increased slightly with the length of the methylene spacer in the repeat unit of the polymer due to electrostatic, van der Waals, and hydrogen bonding forces. These forces could be strengthened by the increasing distance between the amide monomer linkers. A substantial contribution of hydrophobic interactions to the binding mechanism was not observed. Carbohydrate hydroxyl groups were not necessary for binding and compaction of pDNA, but they enhanced binding strength. The latter correlated with transfection efficiency. Gene expression also appeared to be driven by degradation of the polymeric vehicle.[72] PGAAs were taken up via a complex, multifaceted internalization pathway.[73]

SEQUENCE-DEFINED POLYAMIDOAMINES

Solid phase peptide synthesis (SPPS) provided important technology such as orthogonal protective groups, which can be very useful also for synthesizing monodisperse sequence-defined polymers.[30] Instead of applying only protected natural amino acids in SPPS, artificial monomer building blocks are introduced to precisely position various functionalities. Natural and non-natural amino acids, but also monomers of completely different chemistries, chemical targeting ligands, PEG molecules, or lipophilic domains can be used as functionalities. Hartmann and Börner applied SPPS for the generation of sequence-defined multifunctional polyamidoamines.[74−79] Alternate coupling steps of diacids (succinic anhydride, Suc) and diamines, such as diamino-*N*-methyldipropylamine (Damp) or (*tBoc*)-spermine (*tBoc*-Spe), led to stepwise assembly of polyamidoamines (Figure 5).[78] Within the single-component PAA-block segment, functionalities were positioned precisely along the polymer, allowing local control of the chain properties. Addition of PEG to two different PAA block conjugates results in PEG-*block*-$(Suc\text{-}Spe)_{10}$ or PEG-*block*-$(Suc\text{-}Damp)_{10}$-Suc polymer.[77]

For further determination of the correlation between chemical structures and biological properties, PEG−PAAs containing only tertiary amines (PEG−*t*PAA), tertiary and secondary amines (PEG−*tp*PAA), or secondary and primary amines (PEG−*sp*PAA) were compared.[76] Interestingly, various structures were observed when polyplexes were formed with double-stranded DNA: PEG−*t*PAA formed ring-like structures, and PEG−*tp*PAA formed multimeric bundles and rod-like structures, whereas for PEG−*sp*-PAA uniform single-plasmid toroids and supercoiled pDNA were observed. The pDNA complexation and condensation properties of the PAAs were strongly dependent on concentration, volume, and mixing rates. PEG stabilized the polyplex and simultaneously produced "stealth" aggregates, which led not only to stable single-plasmid complexes but stabilized the pDNA itself. Moreover, the PEG−*t*PAA/DNA polyplexes were more stable to DNase digestion than PEG−*sp*PAA polyplexes due to the increased steric shielding. PEG−*sp*PAA stimulated cell activity to a small degree and showed no decrease of cell viability.

A bioreducible system with disulfide bonds stable in the oxidative surrounding of extracellular fluids was generated. This polyamidoamine-*block*-PEG with a single disulfide moiety was synthesized by the selective positioning of a cysteamine (Cya) into the polyamine backbone (PEG_{60}−Lys(Suc−Cya−Lys_2)−$(Suc-Damp-Lys_2)_4$).[75] The disulfide bonds of this linear polymer can be degraded in the intracellular reductive environment of cells. Gel electrophoresis revealed the formation of stable pDNA−polyplexes with polyplex size around 160 nm and a zeta potential of 0 due to the steric shielding effects of PEG.

Boc-L-alanine was used as starting material for the synthesis of a chiral diamine building block ADN (Figure 5).[79] The carboxylic

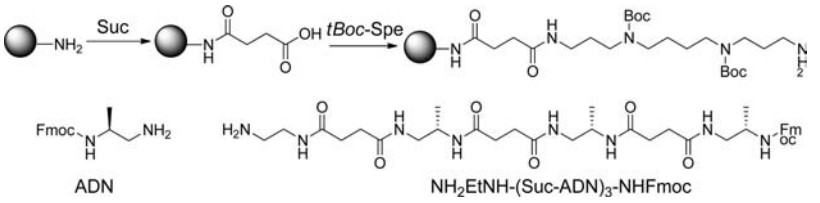

Figure 5. Alternate coupling steps of Suc and *tBoc*-Spe on solid phase and chrial building block ADN.

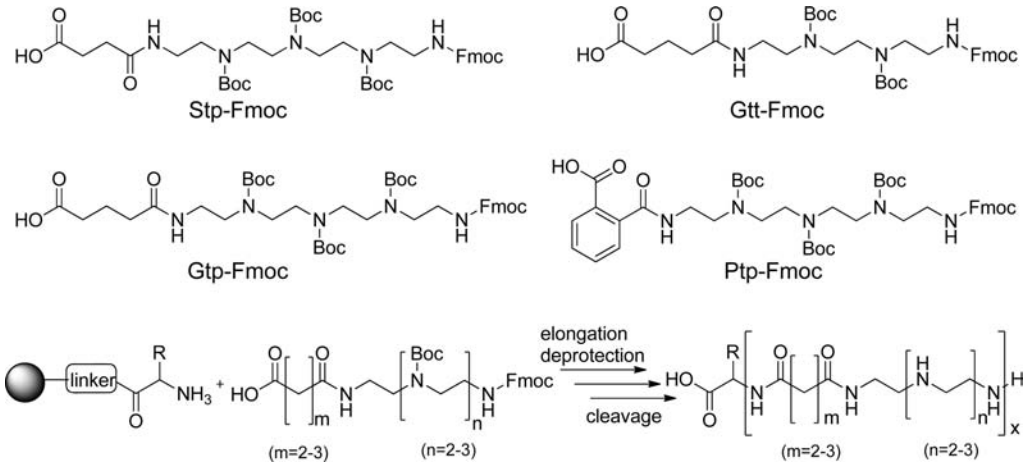

Figure 6. SPPS compatible building blocks and SPPS-based polymer assembly.

function of the α-amino acid was reduced, and afterward the hydroxyl group was transformed into a methanesulfonate. After nucleophilic addition of an azide, the Boc protection group was removed, and the obtained hydrochloride salt of the amino solid phase peptide synthesis group was protected with Fmoc. The azide was reduced to an amine, resulting in the chiral building block ADN. The iterative coupling of succinic anhydride and this chiral diamine building block on the solid phase led to chiral Suc−ADN−*block* polymers (Figure 5), which are under further investigation.

As a variation of the concept, Schaffert et al. introduced novel Fmoc/Boc-protected polyamino acids (Stp, Gtp, Gtt, Ptp; Figure 6) fully compatible with standard Fmoc-peptide synthesis.[80] The Fmoc-polyamino acids contain diacids as well as diamines in one building block. The secondary amines of tetraethylenepentamine (tp) or triethylenetetramine (tt) were protected with di-*tert*-butyl dicarbonate. The symmetrical Boc-protected diamines were monoacetylated in the first step with various cyclic anhydrides, succinic (S), phthalic (P), or glutaric (G) anhydride, followed by subsequent Fmoc protection. The novel building blocks were assembled by standard Fmoc/Boc SPPS, optionally in combination with natural amino acids (Figure 6), to provide defined polycations.[80] The presented strategy has recently been applied for the synthesis of a library of >300 defined polycationic carriers for nucleic acid delivery, including efficient pDNA and siRNA carriers.[81] The artificial amino acids Stp, Gtp, and Gtt were applied together with lysines as branching units, cysteines as bioreversible disulfide forming units, and various fatty acids as domains providing hydrophobic stabilization but also endosomal membrane destabilization. As topology can influence biophysical and biological properties, branched polymers or linear polymers optionally with modification in the center (T-shapes) or the end of chains (i-shapes, U-shapes) were designed and tested.

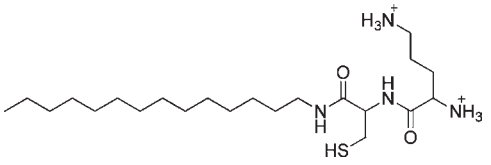

Figure 7. Cationic detergent $C_{14}CO$.

■ DEFINED LIPOPEPTIDES AND LIPOPOLYMERS (LIPOIDS)

pDNA lipoplexes formed by complexation of pDNA with liposomes usually present rather large nanoparticles containing several pDNA molecules. For monomolecular condensation of pDNA into small particles of around 20−30 nm, the group of J.-P. Behr designed cysteine-containing, amphiphilic, cationic detergents such as guanidinocysteine *N*-decylamide[82] or other thiol detergents with dodecane (C_{12}), tetradecane (C_{14}), or hexadecane (C_{16}) chains and spermine (S) or ornithine (O) headgroups[83] (see Figure 7).

The detergents were selected to possess a rather high critical micelle concentration (CMC), well above the concentration applied in pDNA complexation, and form small reversible unimolecular pDNA complexes. Upon oxidization of cysteines, which is accelerated in the presence of template pDNA, the detergent dimers behave like lipids with low CMC, making the pDNA complex stable. The monodisperse particles in early investigations had a negative surface potential and could not transfect cells.

Addition of cyclic pentapeptide RGD (cRGDfK) to $(C_{14}CO)_2$ for targeting endothelial cells in $\alpha_v\beta_3$ integrin-expressing primary endothelial cells resulted in the cRGDfK lipid.[84] The helper lipid dioleoylphosphatidylethanolamine (DOPE)

dx.doi.org/10.1021/bc200251r |*Bioconjugate Chem.* 2011, 22, 1737–1752

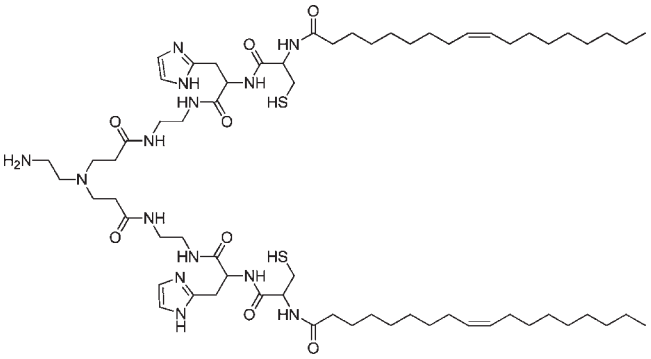

Figure 8. Amphiphilic siRNA vector EHCO.

was included to enhance the endosomolytic release. pDNA complexes containing the cRGDfK−lipid conjugate transfected more effectively than analogous nanoparticles containing a cRADfK−lipid control conjugate. Transfection was further increased by the addition of endosomal active chloroquine.

A further cationic detergent, built up of dodecanoic acid, cysteinyl-cysteine, and diaminopropane, formed 32 nm large, neutral DNA complexes, which were stable toward the exchange with extracellular polyanions.[85] Pharmacokinetics and biodistribution in mice showed 25% of the complexes still circulating after 30 min due to small particle size and the stabilizing effect of the surface cross-linking.

Lu introduced ethylenediamine (E) and spermine-based elivery systems derived by SPPS, combining the artificial monomers with selected natural amino acids.[86,87] Branching lysines, cross-linking cysteines, and oleic acid moieties were included in the polymers to form polyplexes with pDNA based on electrostatic and hydrophobic interactions, further stabilized by disulfide bond formation.

An ethylenediamine-containing, pH-sensitive, amphiphilic multifunctional siRNA carrier EHCO (Figure 8) displayed high cellular siRNA delivery in vitro, as well as in vivo.[88] EHCO forms stable nanoparticles with siRNA. However, at doses required for in vivo administration, both EHCO and DOTAP control siRNA complexes were turbid, which made intraperitoneal (ip) injection necessary. Nevertheless, luciferase activity of subcutaneous U87-Luc tumors could be silenced by ip EHCO (but not DOTAP) siRNA complexes by >50%. To possibly enhance bioavailability and render complexes suitable for intravenous administration, the EHCO polyplexes were modified with PEG. PEGylated EHCO/siRNA nanoparticles showed significantly lower luciferase gene silencing as compared to unmodified EHCO/siRNA nanoparticles.[89] For targeted delivery into tumor cells a RGD or bombesin (BN) peptide was attached to a PEG spacer with a maleimido (MAL) group, resulting in RGD−PEG−MAL or BN−PEG−MAL. The PEGylation of the surface thiol groups of EHCO−siRNA nanoparticles led to receptor-mediated uptake and high gene silencing efficiency. The systemic administration of targeted EHCO/siRNA PEG conjugates resulted in a significantly slower tumor growth rate. The RGD-targeted delivery system was more effective than the bombesin-targeted system in tumor inhibition after the last injection.

From a new small screen, EKHCO and EHHKCO were selected as polymerizable, pH-sensitive surfactants with nucleic acid binding capacity.[87] Complete pDNA condensation took place already at low N/P ratios, resulting in biologically inactive particles of 500−700 nm. Doubling of the polymer amount reduced the size to 150−200 nm. For complete siRNA condensation

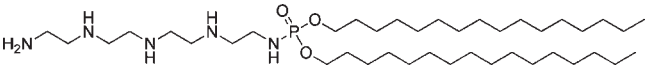

Figure 9. Dicetyl phosphate−tetraethylenepentamine.

a higher N/P ratio was necessary. Both the DNA and siRNA complexes of EHHKCO showed pH- and concentration-dependent hemolytic activity, whereas EKHCO had higher pH sensitivity. DNA and siRNA polyplexes exhibited a high intercellular uptake in U87, in additional to low cytotoxicity. GFP expression was observed in fewer than 10% of the cells, whereas luciferase knockdown resulted in 71.4 and 57.4% silencing effects with siRNA for EHHKCO and EKHCO, respectively.

The spermine (S)-based pH-sensitive carriers had a protonable headgroup, followed by natural amino acids (alanine, histidine, lysine, serine, and cysteine) and a lipophilic oleic acid tail.[86] Permutation of the natural amino acids resulted in several different gene delivery vectors, such as SKCO, SKHCO, SHKCO, SHHKCO, SKACO, SKAHCO, SHKACO, or SHHKACO. Polyplex sizes were around 100 nm (N/P 12). The pDNA condensation ability and uptake were comparable to those of the ethylenediamine-based polymers. However, GFP expression was found in an increased number of the transfected cells, whereas SKACO was identified as a promising lead carrier with the highest activity.

Several papers demonstrate encouraging siRNA delivery by lipophilic modified oligoethylenimines. Philipp et al. modified low molecular weight OEI by Michael addition with different lipophilic acrylate esters.[90] OEI-HA10, modified with 10 equiv of hexyl acrylate (HA), alone or in combination with the helper lipid DOPE, displayed high potency in siRNA-mediated gene silencing. Another related development for siRNA delivery, TEPA−polycationic liposomes (PCL), consists of dicetyl phosphate−tetraethylenepentamine (DCP−TEPA, Figure 9) and DOPE, dipalmitoylphosphatidylcholine, and cholesterol (Chol).[91]

The zeta potential of the TEPA−PCL was higher at low pH values than in the neutral pH, due to the increased protonation of the polycation. No cytotoxicity and highest GFP knockdown were observed at N/P ratios of 18 or 24. TEPA−PCL modified with PEG 2000 altered biodistribution and avoided reticuloendothelial system (RES) uptake. Moreover, the long-term circulation was increased. Unfortunately, free siRNA was detected after gel electrophoresis of the PEGylated TEPA−PCL/siRNA polyplexes. Thus, the siRNA was covalently attached to cholesterol at the 3′-position of the sense strand (PEG−TEPA−PCL/siRNA−Chol). Additionally, the Ala−Pro−Arg−Pro−Gly peptide was used as ligand for angiogenic vessels.[92] In vivo imaging resulted in an APRPG−TEPA−PCL/siRNA−Chol fluorescent signal in the whole body and accumulations in the bladder, liver, and tumor.

For gemini-like peptides, so-called geminoids, the amino acids serine (S), proline (P), lysine (K), and arginine (R) were assembled on solid phase and further modified with oleyl or oleoyl alkyl chains.[93] Proline and at least one cationic residue, either arginine or lysine, were necessary for the biological activity. The synthesized alanine derivatives were mutants in this setup, to investigate the importance of the single amino acids. 1-SPKR, a geminoid with two unsaturated C_{18}-alkyl chains, formed particles with diameters around 100 nm and bound pDNA completely. The transfection efficiency depended on the geminoid and DNA amount. 2-SPKR, a construct in which 1-octadecylamine was used instead of oleylamine and stearic acid instead of oleic acid,

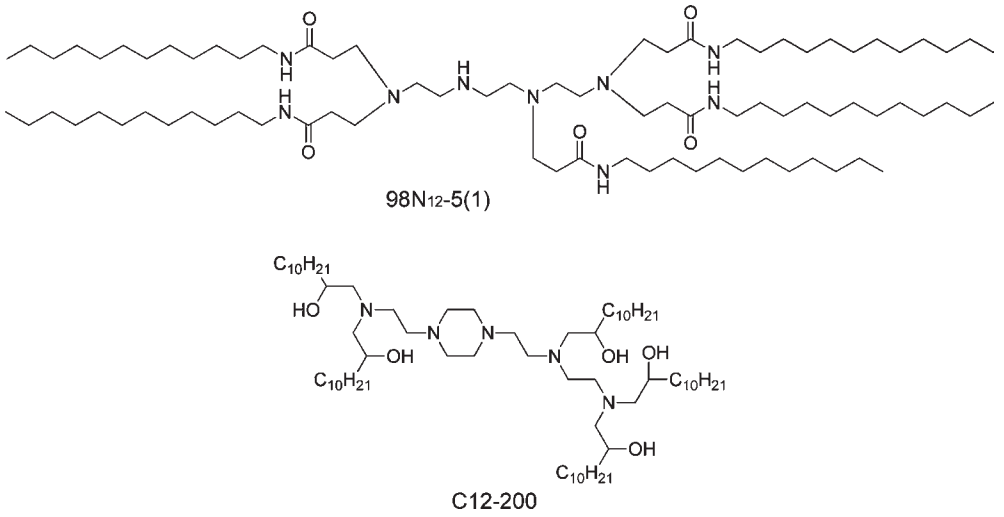

Figure 10. Lipidoids for nucleic acid transport.

was inefficient in HeLa cell transfection. Complexes of 1-SPKR and 1-APKR with anti-GFP-specific siRNA showed a knockdown, whereas no toxicity was observed when transfected with control siRNA.

A number of parameters were varied in a combinatorial library of lipidoids, which was synthesized through the addition of alkyl acrylates or alkyl acrylamides to primary or secondary amines.[94] Some structural prerequisites for efficient siRNA or micro RNA delivery were necessary: 8−12 carbons in the tail, >2 alkyl chain, amide linkages, and at least one secondary amine. All lipidoids, inducing gene silencing, displayed low cytotoxicity in different cell lines. One of the best performers, $98N_{12}$-5(1) (Figure 10), consisted of a tetraethylenepentamine core with five dodecylates. Based on a three-component delivery system containing this lipoid $98N_{12}$-5(1), cholesterol, and the PEG lipid $mPEG_{2000}$-C14 glyceride, a combinatorial approach was used to incorporate further diversities into this promising siRNA delivery candidate.[95] The new library of carriers was based on lipid-like tails with hydroxyl, carbamate, ether, or amine functional groups, attached to two different cores, 98 and 100.[96] The amine cores were modified by the addition of different arcylamides and acrylates. The luciferase expression was tested in HeLa cells at different weight to weight ratios. The knockdown at a w/w ratio of 15 (lipidoid: siRNA) was highest, whereas the efficiency decreased with decreasing ratios of lipidoids to siRNA. The efficacy of both amine cores was affected by tail modifications: core 100 was more efficient in silencing and more tolerant to the addition of the functional groups. Tails functionalized with ether, carbamate, or amine groups were most active. Only 4 of 17 lipidoids containing core 98 were effective, compared to 14 of 17 for core 100. PEG or long alkyl chains containing lipidoids were inactive, no matter to which core they were attached. The addition of a tertiary amine reduced the effectiveness specifically for core 98. All compounds had at least one w/w ratio for which the cell viability was >80%. Nevertheless, three active formulations of core 98 and one of core 100 had a viability of <60%. For improved serum stability the siRNA-containing lipidoids were mixed with cholesterol and PEG−ceramide. The in vivo efficacy was tested by a factor VII knockdown, and all tested derivates showed a decrease in factor VII serum levels, whereas all core 98 formulations were more effective than core 100 formulations.

Love et al. used a related combinatorial approach for the synthesis and screening of a library of oligonucleotide delivery systems.[97] This library consisted of nondegradable amino alcohols based on a polar amine-containing headgroup and a nonpolar hydrocarbon tail. Synthesis was achieved through the ring-opening of epoxides by amine substrates. The reaction was carried out without solvents, protection and deprotection steps, or further purification and was therefore well suited for the parallel synthesis approach and high-throughput screening. As a prerequisite for a knockdown at least 12 carbons in length was needed in the lipidoid tail.

To monitor the lipidoid-facilitated siRNA delivery, the mouse factor VII gene silencing model was used. To improve serum stability lipidoids were formulated with distearoylphosphatidylcholine, cholesterol, and PEG. After a single bolus administration, C12-200, the most promising candidate (Figure 10), resulted in reduced factor VII serum levels without observable toxicity. A simultaneous silencing of up to five genes was possible with C12-200. Additionally, C12-200-mediated silencing was investigated in nonhuman primates and siRNA specific to transthyretin (TTR). Dosing nonhuman primates with C12-200−TTR siRNA resulted in high levels of specific knockdown.[97]

■ FUNCTIONAL POLYMER CONJUGATES

A plain polymer, even when optimized and modified with lipid domains, may not be the perfect carrier for overcoming all delivery steps. Conjugation of additional natural or artificial biomimetic transport functions such as cell targeting ligands may further improve a carrier. A high percentage of human carcinomas overexpress the epidermal growth factor receptor (EGFR). LPEI, PEG−LPEI, and EGF−PEG−bPEI pDNA polyplexes were evaluated as synthetic gene vectors.[98] EGFR targeting led to a faster and more efficient internalization as compared to the untargeted LPEI and PEG−PEI pDNA nanoparticles. To facilitate the release of the polyplexes from the endosome into the cytosol, melittin (Mel), a bee venom peptide, was incorporated.[29] Moreover, polyinosine−cytosine (polyIC) was used as an antiproliferative double-stranded RNA. Melittin was either complexed with the nucleic acid as PEI−Mel conjugate together with EGF−PEG−bPEI or covalently attached,

Scheme 1. Cu(I)-Catalyzed 1,3-Dipolar Cycloaddition Reaction

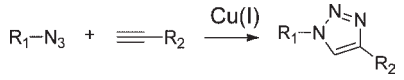

resulting in EGF−PEG−bPEI−Mel. Both melittin dsRNA conjugates released their payload polyIC into the cytosol, whereas polyIC/EGF−PEG−bPEI complexes were entrapped within vesicles. The EGF−PEG−bPEI−Mel conjugate demonstrated enhanced transfection efficiency in vitro and in vivo, as compared to all other polyplexes. The applied tetraconjugate, however, was very complex and chemically not well-defined. To make it more practical, branched PEI was substituted with linear PEI, and the chain length of PEG was optimized to 2 kDa, resulting in a EGF−PEG−LPEI conjugate that was most effective in polyIC-triggered killing of tumor cells, even in the absence of melittin.[99] Repeated intravenous injection of the more defined EGF−PEG−LPEI polyIC polyplex retarded tumor growth at least as effectively as the more heterogeneous EGF−PEG−bPEI−Mel polyplex.

More defined LPEI conjugates were obtained through site-specific coupling.[100] Linear PEI was terminated at one end by a highly nucleophilic hydrazine residue. The ω-regioselective conjugation to other molecules was possible through stable linkages. Transferrin was oxidized to obtain an aldehyde function and conjugated to hydrazino PEI. The resulting PEI−Tf vector had the targeting sequence precisely attached at one end. This precise conjugation technique and the resulting conjugates make structure−activity relationships possible.

■ PRECISE CONJUGATION TECHNIQUES

A series of "click chemistry" conjugation techniques have become available,[101−104] which can be very useful for precise conjugation at selected sites of macromolecules (Scheme 1). As a variation of the Huisgen 1,3-dipolar cycloaddition, the Cu(I)-catalyzed cycloaddition of terminal alkynes and azides (CuAAC)[105−107] proceeds efficiently and selectively under aqueous reaction conditions and in the presence of various other functionalities or biomolecules.[108,109]

Click chemistry is also fully compatible with the reaction conditions used for solid phase synthesis, in the synthesis of peptides and for modification of oligonucleotides. Copper-free click chemistries were even performed in living organisms.[110] Several applications for polymer polymerizations and conjugations for nucleic acid delivery have been reported.[111−116]

Lee et al. modified different cores with PAMAM dendrimers via click chemistry using a stitching method for the synthesis of dendrimers and di-*block* dendrimers.[117] The cycloaddition reaction took place between alkyne-functionalized PAMAM dendrons (1-*Dm*) and a multi(azides) building block as core unit.[118] The resulting emissive PAMAM dendrimers had 2,7-diazido-9*H*-fluorene as core chromophore.

Yu et al. applied click chemistry to introduce an EGF−PEG targeting group in a site-specific manner into PAMAM−pentaethylenehexamine (PEHA) dendrons.[119] As the copper-catalyzed chemistry is not compatible with copper-chelating oligoethylenimines, the click reaction with a bifunctional PEG derivative had to be performed using the PAMAM ester precursor, before introduction of the PEHA groups and EGF. Alternative novel PAMAM polymer conjugation concepts are based on copper-free click chemistries.[120]

Copper-assisted or copper-free click chemistry can also be used for the synthesis of siRNA conjugates.[121] Three possible synthesis routes were followed in CuAAC-mediated oligoribonucleotide−ligand conjugate synthesis: (i) The reaction took place at the monomer level prior to oligonucleotide synthesis, (ii) the solution phase postsynthetic "click conjugation" or (iii) the "click conjugation" on an immobilized and completely protected alkyne−oligonucleotide scaffold.[122] The last approach was the most efficient one. The ligand was introduced to a desired site within the oligonucleotide sequence, at selected positions on the sugar moiety (2′-, 3′-, or 5′-position) or at selected sites of the nucleobase. Azido-functionalized ligands bearing oligoamines, long lipophilic alkyl chains, and cholesterol were used to study the effect of physicochemical characteristics of the incoming azide on click conjugation to the alkyne−oligonucleotide scaffold in solution and on an immobilized solid support. The hydrophobic and cationic azides reacted with oligonucleotide−alkynes, which were attached to the solid support. Those siRNA conjugates effectively silenced luciferase gene expression with addition of lipofectamine 2000 in a stably transformed HeLa cell line. Interestingly, the siRNA activity was not hampered by the insertion of an extra modified nucleotide to the 5′-end of the sense strand, in contrast to the addition of a bulky nucleotide at the 3′-end of the sense strand, which was not well tolerated.

Another conjugation technique is native chemical ligation (NCL, Scheme 2). Native chemical ligation was originally developed to connect two unprotected peptides for the total synthesis of proteins.[123] An amide bond is formed by transthioesterification followed by intramolecular nucleophilic rearrangement between thioester and cysteine.

The chemoselective reaction occurs in mild aqueous solution, is simple, and gives almost quantitative yields. Byun attached cysteine−PEG to a titanium surface with thioester-containing phosphonic acid conjugates.[124] This approach indicates the usefulness of NCL as a toolkit for surface bioconjugation and functionalization. The potential of NCL in the synthesis of precise polymers or conjugates for nucleic acid delivery has to be investigated further.

■ DYNAMIC CONJUGATES

PEG shielding was found to improve polyplex stability and reduce nonspecific interactions, but stable, irreversible PEGylation drastically reduced transfection efficiency. To overcome this obstacle, the PEG functionality was incorporated into conjugates in a dynamic fashion, to be cleaved in the acidic environment of endosomes but remaining stable at extracellular physiological pH. Dynamic PEGylation of polymers was evaluated using various bioresponsive linkers.[125−128] For example, various pH-sensitive PEG hydrazones (HZN) were conjugated to poly-L-lysine.[125] The resulting PLL−HZN−PEG was then complexed with pDNA and Tf−PEI or EGF−PEI, conjugates containing a targeting receptor with endosomal uptake capacity. The in vitro transfection efficiency of those targeted, bioreversibly shielded polyplexes was up to >100-fold higher than those of the stably shielded polyplexes, similar to controls without shielding, and showed improved transfection to target tumor cells after intravenous application in vivo.

Amine-reactive PEG reagents, monofunctional PEG−HZN *N*-hydroxysuccinimide ester (NHS) and bifunctional

Scheme 2. Native Chemical Ligation

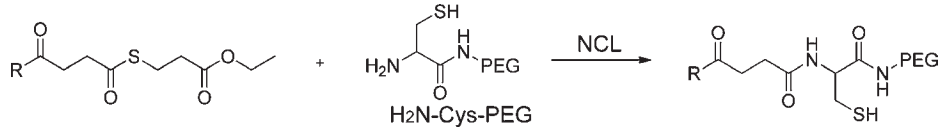

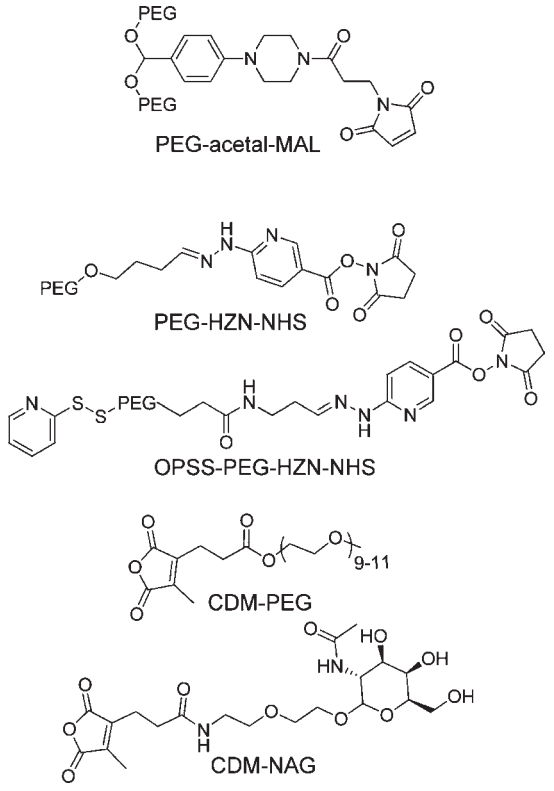

Figure 11. Monofunctional and bifunctional pH-sensitive bioreversible PEGylation reagents.

OPSS−PEG−HZN−NHS (Figure 11), were synthesized for post-PEGylation of bPEI and LPEI.[127] The heterobifunctional OPSS conjugate made a simultaneous PEGylation and incorporation of a targeting ligand possible. The targeting ligand EGF−PEG−bPEI was added to the PEG−HZN−NHS PEI−DNA polyplex. The EGF-containing, bioreducible polyplexes had improved transfection activity compared to polyplexes with stable PEGylation using PEG−NHS instead of PEG−HZN−NHS. Additionally, the labile PEG−HZN−NHS enhanced the efficiency of transgene delivery to distant tumor tissues with high specificity, even higher than pre-PEGylated polyplexes as described by Walker et al.[125]

The bifunctional, endosomal pH-cleavable reagent OPSS−PEG−HZN was further modified with cholesterol.[129] Both OPSS−PEG−HZN−Chol and its corresponding stable analogue OPSS−PEG−Chol spontaneously formed stable and shielded micelles at physiological pH. Lipopolyplexes composed of DNA complexed with LPEI, phospholipids including DOPE, and OPSS−PEG−HZN−Chol displayed an enhancement of gene expression compared to lipopolyplexes with stable PEG conjugates, without visible toxicity. After incorporation of B6, a peptidic ligand for the transferrin receptor, further improvement in transfection efficiency was observed for the acid-labile lipopolyplexes.

Dialkylated maleic acid anhydrides react with amines under ring-opening to form monoamides. These maleamates, however, are cleaved again at slightly acidic conditions, such as the endosomal pH due to steric strain. To exploit this for pH-reversible bioconjugation, Rozema and colleagues developed carboxylated forms of dimethylmaleic anhydride (CDM) and used them in CDM−PEG and related reagents.[128]

COVALENT NUCLEIC ACID CONJUGATES

The first polymer−oligonucleotide conjugates were prepared already more than 20 years ago.[130] The first paper, developing the concept of bioreversible covalent conjugates of bioresponsive polymers with antisense oligonucleotides, was published by the Hoffman and Stayton laboratory.[131,132] Asialoglycoprotein (ASGP) receptor targeted lactosylated and PEGylated antisense ODNs were developed for hepatocyte targeting.[133] For sigma-receptor targeting of cancer cells, splice switching antisense ODNs were covalently attached with mono- or multivalent anisamide ligands.[134] The trivalent anisamide−ODN conjugate displayed enhanced cellular uptake and higher efficacy than the monovalent conjugate in a luciferase reporter assay in tumor cell culture. An excellent overview of solid phase derived oligonucleotide conjugates is given by Lönnberg.[135]

siRNA Conjugates. For the synthesis of covalent siRNA conjugates (reviewed by Jeong et al.[136]) the four terminal ends are potential conjugation sites: the 3′- and 5′-ends of sense and antisense strand. The integrity of the 5′-terminus of the antisense strand plays an important role in the maintenance of the biological activity. Therefore, conjugation via cleavable linkers including acid-labile and reducible bonds is an elegant way to preserve the functionality of the siRNA. The chemical modifications, such as phosphorothioate, boranophosphate linkage, or modification of 2′-hydroxyl group of pentone sugar, enhance the stability of siRNA in biological fluids.[136]

Folate was evaluated as a ligand for siRNA delivery, with siRNA covalently bound via a linker resulting in enhanced intracellular uptake.[137] Conjugation of cholesterol to an apolipoprotein B siRNA (apoB siRNA) led to a lipophilic siRNA conjugate.[138] Cholesterol was attached to the 3′-terminus of the sense strand of siRNA by a pyrrolidone linker. The resulting Chol−apoB siRNA conjugate was biologically active, in contrast to unconjugated apoB siRNA. After systemic administration of Chol−apoB siRNA in vivo, an inhibition of apolipoprotein B was achieved by an RNAi mechanism of action. Nishina synthesized an α-tocopherol (vitamin E)−siRNA for systemic siRNA delivery to the liver.[139] Vitamin E was covalently attached to the 5′-terminus of the antisense strand of a 27/29mer siRNA, partially modified with 2′-O-methylated ribose and phosphorothioate linkages. After intracellular delivery, the lipophilic siRNA conjugate was processed in the dicer and the vitamin E moiety was released. This conjugate led to a significant reduction of the target gene apolipoprotein B after intravenous injection without inducing inflammatory interferons.

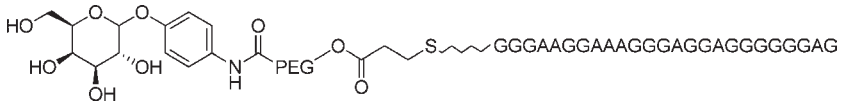

Figure 12. Covalent PEG−ODN conjugate with targeting ligand (Gal−PEG−ODN).

PEG Nucleic Acid Conjugates. Several publications report the covalent conjugation of siRNAs with PEG to improve pharmacological properties.[128,133,140−143] For example, PEG was attached via the cleavable disulfide linkage SPDP to the 3′-terminus of the sense strand of a vascular endothelial growth factor (VEGF) siRNA.[140] The resulting PEG−siRNA conjugate formed polyelectrolyte complex (PEC) micelles by interaction with the cationic PEI, as core forming agent. PEG−VEGF siRNA/PEI PEC micelles displayed high levels of serum stability over 48 h, whereas PEG−VEGF siRNA or naked siRNA was less stable. Prolonged circulation, prevention of aggregation, and blood compatibility were results of the PEG modification. The intact VEGF−siRNA was released from the conjugate under reductive conditions. Consequently, an effective silencing of VEGF gene expression in prostate carcinoma cells was observed for PEG−VEGF siRNA/PEI PEC micelles under optimized formulation conditions. Moreover, PEC micelles led to a far superior silencing than VEGF siRNA/PEI complexes in the presence of serum, demonstrating the crucial role of PEG for the application.

A sugar-modified PEG−siRNA conjugate containing the disaccharide lactose (Lac), which is derived from the condensation of galactose and glucose, was introduced by Oishi.[142] The siRNA was conjugated with lactosylated PEG through acid-labile linkage of thiopropionate, resulting in Lac−PEG−siRNA. Michael addition of the 5′-thiol-modified sense RNA with Lac−PEG gave a Lac−PEG conjugate with single-stranded RNA, which was then annealed with antisense RNA to undergo hybridization. Afterward, the Lac−PEG−siRNA was complexed with poly-L-lysine (PLL) with a polymerization degree of 40, leading to a quantitative complexation at the charge ratio of 1. Those PEG-based *block* ionomers self-assembled to lactosylated-polyion complex (PIC) micelles, which showed pH-sensitive dissolution properties. PEG-*block*-polycation/oligonucleotides, as well as PEG-*block*-oligonucleotide/polycation conjugates or PEG−oligonucleotide conjugate/polycation conjugates, were feasible for PIC micelle formulation. The PIC core was surrounded by PEG layers to increase biocompatibility and enzymatic tolerability. PIC micelles formed with Lac−PEG−siRNA/PLL were more effective, regarding silencing of the target gene in HUH-7 cells, compared to Lac−PEG−siRNA conjugates. Both conjugates exhibit RNA interference (RNAi) activities in a dose-dependent manner, even in the presence of serum.

For enhanced site-specific ASGP-receptor-mediated hepatocyte targeting with a covalently bound polycation, Zhu et al. conjugated galactosylated (Gal) PEG to ODN with an acid-labile β-thiopropionate ester linkage.[143]

After tail vein injection into rats, the Gal−PEG−ODN (Figure 12) was rapidly cleared from the circulation and accumulated in the liver.

Additionally, Zhu et al. evaluated two different targeting ligands in liver-targeted PEG−siRNA conjugates: galactose for ASGPR-mediated hepatocyte targeting and mannose-6-phosphate (M6P) for hepatic stellate cells.[133] The sugars attached to PEG, containing the acid labile ester linker OPSS, were coupled to the sense strand of luciferase and transforming growth factor β 1 (TGF-β1) siRNA. The functionality of the cleavable disulfide linker was investigated for both conjugates: When treated with dithiotreitol, the siRNA dissociated from the Gal/M6P−PEG−siRNA conjugates. The conjugates containing siRNA targeting firefly luciferase showed gene silencing. Even higher gene silencing was observed for the same siRNA amount when the conjugates formed complexes with pyridinium cationic liposomes. TGF-β1−siRNA with Gal−PEG and M6P−PEG silenced endogenous TGF-β1 gene expression comparably to the firefly luciferase conjugates without the cationic liposomes.

PEG−Polymer−siRNA Conjugates. A pH-sensitive reversible PEG reagent (CDM−PEG, Figure 11) was used in the formation of a hepatocyte-targeted polymer siRNA conjugate.[128] CDM−PEG was attached to the endosomolytic carrier polymer PBAVE, an amphipathic poly(vinyl ether) composed of butyl and amino vinyl ethers. The bifunctional maleamate linkage between PBAVE and the shielding agent PEG is reversible at endosomal pH. A CDM linker was also used for conjugating the polymer with *N*-acetylgalactosamine (NAG), an amino sugar derivative of galactose recognized by the asialoglycoprotein receptor of hepatocytes. The siRNA cargo was coupled to the PEG−PBAVE−NAG via a reversible disulfide linker, resulting in siRNA dynamic polyconjugates. Key features of these polyconjugates were a membrane active polymer, the ability to reversibly mask the activity of the polymer until it reached the acidic environment of endosomes, and the ability to target this polymer and its siRNA cargo specifically to hepatocytes in vivo. An effective knockdown of two endogenous genes in the mouse liver, with phenotype changes in vivo, was observable for 7−10 days. Therefore, two different siRNAs were used in the polyconjugates, one silencing apolipoprotein B and the other one silencing peroxisome proliferator-activated receptor α (pparα). Both conjugates targeted hepatocytes and avoided Kupffer cell uptake, resulting in no observable liver toxicity. Moreover, they were well tolerated. The apoB−siRNA dynamic polyconjugates led to a knockdown of 80−90% of apoB in vivo and, additionally, to lowered serum cholesterol and apoB protein levels, as well as a fatty liver. Readministration reduced serum cholesterol levels a second time. Mice treated with siRNA polyconjugates targeting pparα also displayed the gene-appropriate phenotype, characterized by a significant increase in serum triglycerides. Substitution of NAG with mannose resulted in redirection of the polyconjugate to nonparenchymal liver cells, away from hepatocytes.

DMMAn-Mel is an endosomolytic agent in which the lytic peptide melittin is masked by reaction with dimethyl maleic anhydride (DMMAn), a noncarboxylated analogue of CDM. The DMMAn group is removed at acidic pH and functional melittin is displayed, liberating the payload from the endosome.[144,145] A PLL-based dual responsive, that is, pH- and redox-responsive, polymer conjugate was developed.[141] PEG contributes to the conjugate solubility and shields the polymer. The siRNA was attached to the PEG−PLL−DMMAn-Mel at the 5′-terminus via a bioreducible disulfide bond. The conjugate was stable in the

presence of the polyanion heparin at conditions under which analogous electrostatic siRNA complexes disassembled. The pH-triggered, lytic activity of the conjugate was verified in an erythrocyte leakage assay; thus, it showed high in vitro biocompatibility due to the absence of cytotoxicity or hemolytic activity at neutral pH. Reduction, by low physiological concentrations of glutathione, resulted in the release of siRNA from the carrier conjugate. Moreover, an efficient and sequence-specific luciferase gene silencing was found for the PEG−PLL−DMMAn-Mel−siRNA conjugate comparable to the corresponding electrostatic polyplexes in Neuro2A-eGFPLuc cells. Unfortunately, the particular conjugate, based on a rather high molecular weight PLL (DP 153), displayed an unexpected high in vivo toxicity, requiring further optimization.[141]

CONCLUSION

In recent years, considerable progress has been made in discovering conditions and structural features that are required for nucleic acid transfer into mammalian cells. Precise polymers or conjugates are expected to play an important role in further refining structure−activity relationships. The ability of precise synthesis allows analysis of the influence of the conjugation site, single amino acids, or lipophilic domains in the polymer sequence. Up to now, PAMAM dendrimers have been the most promising precise polymers efficient in nucleic acid delivery. Solid phase supported peptide synthesis is an elegant tool for obtaining precise polymer conjugates. The concept has been extended to the synthesis of sequence-defined polyamidoamines, which, when properly modified, present very promising nucleic acid carriers. For example, lipophilic modifications play an important role in the carrier activity of lipopolymers. Several lipidoids, coformulated with cholesterol and PEG lipids, were already successfully applied for in vivo application of siRNA. Techniques such as click chemistry or native chemical ligation have great potential for the synthesis of precise conjugates of polymers with functional domains and nucleic acids. The application of these methods with precise polymers will provide exciting insights in structure−activity relationships of delivery systems and will be instrumental for the preparation of optimized clinically applicable delivery systems.

AUTHOR INFORMATION

Corresponding Author

*Phone: +49 89 2180 77841. Fax: +49 89 2180 77798; E-mail: ernst.wagner@cup.uni-muenchen.de.

ACKNOWLEDGMENT

Funding of the authors' work in the reviewed research area by the Cluster of Excellence "Nanosystems Initiative Munich" of the German Research Foundation and the BMBF Biotech cluster m4 project T12 is gratefully acknowledged.

ABBREVIATIONS

B6 peptide, Ac-CGHKAKGPRK-NH_2; Boc, *tert*-butoxycarbonyl; CDM, carboxy dimethyl maleic anhydride; DPL, dendritic polylysine; Fmoc, 9-fluorenyl methoxycarbonyl; GFP, green fluorescent protein; OEI, oligoethylenimine; OPSS, ω-2-pyridyldithio; pbf, 2,2,4,6,7-pentamethyldihydrobenzofuran-5-sulfonyl; PEG, polyethylene glycol; SPDP, *N*-succinimidyl 3-[2-pyridyldithio]-propionate; TFA, trifluoroacetic acetate; trt, trityl.

REFERENCES

(1) Gao, K., and Huang, L. (2008) Nonviral methods for siRNA delivery. *Mol. Pharmaceutics 6*, 651–658.

(2) Lin, C., Blaauboer, C.-J., Timoneda, M. M., Lok, M. C., van Steenbergen, M., Hennink, W. E., Zhong, Z., Feijen, J., and Engbersen, J. F. J. (2008) Bioreducible poly(amido amine)s with oligoamine side chains: synthesis, characterization, and structural effects on gene delivery. *J. Controlled Release 126*, 166–174.

(3) Schaffert, D., and Wagner, E. (2008) Gene therapy progress and prospects: synthetic polymer-based systems. *Gene Ther. 15*, 1131–1138.

(4) Wolff, J. A., and Rozema, D. B. (2008) Breaking the bonds: non-viral vectors become chemically dynamic. *Mol. Ther. 16*, 8–15.

(5) Wagner, E. (2004) Strategies to improve DNA polyplexes for in vivo gene transfer: will "artificial viruses" be the answer? *Pharm. Res. 21*, 8–14.

(6) Wagner, E. (2008) Converging paths of viral and non-viral vector engineering. *Mol. Ther. 16*, 1–2.

(7) Wagner, E., Plank, C., Zatloukal, K., Cotten, M., and Birnstiel, M. L. (1992) Influenza virus hemagglutinin HA-2 N-terminal fusogenic peptides augment gene transfer by transferrin−polylysine−DNA complexes: toward a synthetic virus-like gene-transfer vehicle. *Proc. Natl. Acad. Sci. U.S.A. 89*, 7934–7938.

(8) Zuber, G., Dauty, E., Nothisen, M., Belguise, P., and Behr, J. P. (2001) Towards synthetic viruses. *Adv. Drug Deliv. Rev. 52*, 245–253.

(9) Krebs, M. D., and Alsberg, E. (2011) Localized, targeted, and sustained siRNA delivery. *Chemistry 17*, 3054–3062.

(10) Mintzer, M. A., and Simanek, E. E. (2009) Nonviral vectors for gene delivery. *Chem. Rev. 109*, 259–302.

(11) Dekie, L., Toncheva, V., Dubruel, P., Schacht, E. H., Barrett, L., and Seymour, L. W. (2000) Poly-L-glutamic acid derivatives as vectors for gene therapy. *J. Controlled Release 65*, 187–202.

(12) Burke, R. S., and Pun, S. H. (2008) Extracellular barriers to in vivo PEI and PEGylated PEI polyplex-mediated gene delivery to the liver. *Bioconjugate Chem. 19*, 693–704.

(13) Chen, H. H., Ho, Y.-P., Jiang, X., Mao, H.-Q., Wang, T.-H., and Leong, K. W. (2008) Quantitative comparison of intracellular unpacking kinetics of polyplexes by a model constructed from quantum Dot-FRET. *Mol. Ther. 16*, 324–332.

(14) Midoux, P., Breuzard, G., Gomez, J. P., and Pichon, C. (2008) Polymer-based gene delivery: a current review on the uptake and intracellular trafficking of polyplexes. *Curr. Gene Ther. 8*, 335–352.

(15) Nishiyama, N., Arnida, Jang, W.-D., Date, K., Miyata, K., and Kataoka, K. (2006) Photochemical enhancement of transgene expression by polymeric micelles incorporating plasmid DNA and dendrimer-based photosensitizer. *J. Drug Targeting 14*, 413–424.

(16) Grosse, S., Thévenot, G., Monsigny, M., and Fajac, I. (2006) Which mechanism for nuclear import of plasmid DNA complexed with polyethylenimine derivatives? *J. Gene Med. 8*, 845–851.

(17) Parker, A. L., Newman, C., Briggs, S., Seymour, L., and Sheridan, P. J. (2003) Nonviral gene delivery: techniques and implications for molecular medicine. *Expert Rev. Mol. Med. 5*, 1–15.

(18) Christie, R. J., Nishiyama, N., and Kataoka, K. (2010) Minireview: Delivering the code: polyplex carriers for deoxyribonucleic acid and ribonucleic acid interference therapies. *Endocrinology 151*, 466–473.

(19) Kunath, K., von Harpe, A., Fischer, D., Petersen, H., Bickel, U., Voigt, K., and Kissel, T. (2003) Low-molecular-weight polyethylenimine as a non-viral vector for DNA delivery: comparison of physicochemical properties, transfection efficiency and in vivo distribution with high-molecular-weight polyethylenimine. *J. Controled Release 89*, 113–125.

(20) Itaka, K., Harada, A., Yamasaki, Y., Nakamura, K., Kawaguchi, H., and Kataoka, K. (2004) In situ single cell observation by fluorescence resonance energy transfer reveals fast intra-cytoplasmic delivery and easy

release of plasmid DNA complexed with linear polyethylenimine. *J. Gene Med. 6*, 76–84.
(21) Kichler, A., Leborgne, C., Coeytaux, E., and Danos, O. (2001) Polyethylenimine-mediated gene delivery: a mechanistic study. *J. Gene Med. 3*, 135–144.
(22) Sonawane, N. D., Szoka, F. C., Jr., and Verkman, A. S. (2003) Chloride accumulation and swelling in endosomes enhances DNA transfer by polyamine-DNA polyplexes. *J. Biol. Chem. 278*, 44826–44831.
(23) Akinc, A., Thomas, M., Klibanov, A. M., and Langer, R. (2005) Exploring polyethylenimine-mediated DNA transfection and the proton sponge hypothesis. *J. Gene Med. 7*, 657–663.
(24) Zou, S. M., Erbacher, P., Remy, J. S., and Behr, J. P. (2000) Systemic linear polyethylenimine (L-PEI)-mediated gene delivery in the mouse. *J. Gene Med. 2*, 128–134.
(25) Wightman, L., Kircheis, R., Rossler, V., Carotta, S., Ruzicka, R., Kursa, M., and Wagner, E. (2001) Different behavior of branched and linear polyethylenimine for gene delivery in vitro and in vivo. *J. Gene Med. 3*, 362–372.
(26) Jeong, G. J., Byun, H. M., Kim, J. M., Yoon, H., Choi, H. G., Kim, W. K., Kim, S. J., and Oh, Y. K. (2007) Biodistribution and tissue expression kinetics of plasmid DNA complexed with polyethylenimines of different molecular weight and structure. *J. Controlled Release 118*, 118–125.
(27) Werth, S., Urban-Klein, B., Dai, L., Hobel, S., Grzelinski, M., Bakowsky, U., Czubayko, F., and Aigner, A. (2006) A low molecular weight fraction of polyethylenimine (PEI) displays increased transfection efficiency of DNA and siRNA in fresh or lyophilized complexes. *J. Controlled Release 112*, 257–270.
(28) Russ, V., Elfberg, H., Thoma, C., Kloeckner, J., Ogris, M., and Wagner, E. (2008) Novel degradable oligoethylenimine acrylate ester-based pseudodendrimers for in vitro and in vivo gene transfer. *Gene Ther. 15*, 18–29.
(29) Shir, A., Ogris, M., Wagner, E., and Levitzki, A. (2006) EGF receptor-targeted synthetic double-stranded RNA eliminates glioblastoma, breast cancer, and adenocarcinoma tumors in mice. *PLoS Med. 3*, e6.
(30) Binauld, S., Damiron, D., Connal, L. A., Hawker, C. J., and Drockenmuller, E. (2011) Precise synthesis of molecularly defined oligomers and polymers by orthogonal iterative divergent/convergent approaches. *Macromol. Rapid Commun. 32*, 147–168.
(31) Lutz, J.-F. (2010) Sequence-controlled polymerizations: the next Holy Grail in polymer science?. *Polym. Chem. 1*, 55–62.
(32) Matyjaszewski, K., and Tsarevsky, N. V. (2009) Nanostructured functional materials prepared by atom transfer radical polymerization. *Nat. Chem. 1*, 276–288.
(33) Aoshima, S., and Kanaoka, S. (2009) A renaissance in living cationic polymerization. *Chem. Rev. 109*, 5245–5287.
(34) Adams, N., and Schubert, U. S. (2007) Poly(2-oxazolines) in biological and biomedical application contexts. *Adv. Drug Delivery Rev. 59*, 1504–1520.
(35) Bonnet, M. E., Erbacher, P., and Bolcato-Bellemin, A. L. (2008) Systemic delivery of DNA or siRNA mediated by linear polyethylenimine (L-PEI) does not induce an inflammatory response. *Pharm. Res. 25*, 2972–2982.
(36) Sidi, A. A., Ohana, P., Benjamin, S., Shalev, M., Ransom, J. H., Lamm, D., Hochberg, A., and Leibovitch, I. (2008) Phase I/II marker lesion study of intravesical BC-819 DNA plasmid in H19 over expressing superficial bladder cancer refractory to bacillus Calmette-Guerin. *J. Urol. 180*, 2379–2383.
(37) Kukowska-Latallo, J. F., Bielinska, A. U., Johnson, J., Spindler, R., Tomalia, D. A., and Baker, J. R., Jr. (1996) Efficient transfer of genetic material into mammalian cells using Starburst polyamidoamine dendrimers. *Proc. Natl. Acad. Sci. U.S.A. 93*, 4897–4902.
(38) Crespo, L., Sanclimens, G., Pons, M., Giralt, E., Royo, M., and Albericio, F. (2005) Peptide and amide bond-containing dendrimers. *Chem. Rev. 105*, 1663–1681.
(39) Denkewalter, R. G., Kolc, J., and Lukasavage, W. J. (1981) U.S. Patent 4 289 872.
(40) Merrifield, R. B. (1963) Solid phase peptide synthesis. I. The synthesis of a tetrapeptide. *J. Am. Chem. Soc. 85*, 2149–2154.
(41) Tam, J. P. (1988) Synthetic peptide vaccine design: synthesis and properties of a high-density multiple antigenic peptide system. *Proc. Nat. Acad. Sci. U.S.A. 85*, 5409–5413.
(42) Eom, K. D., Park, S. M., Tran, H. D., Kim, M. S., Yu, R. N., and Yoo, H. (2007) Dendritic α,ε-poly(L-lysine)s as delivery agents for antisense oligonucleotides. *Pharm. Res. 24*, 1581–1589.
(43) Ohsaki, M., Okuda, T., Wada, A., Hirayama, T., Niidome, T., and Aoyagi, H. (2002) In vitro gene transfection using dendritic poly(L-lysine). *Bioconjugate Chem. 13*, 510–517.
(44) Kawano, T., Okuda, T., Aoyagi, H., and Niidome, T. (2004) Long circulation of intravenously administered plasmid DNA delivered with dendritic poly(L-lysine) in the blood flow. *J. Controlled Release 99*, 329–337.
(45) Okuda, T., Sugiyama, A., Niidome, T., and Aoyagi, H. (2004) Characters of dendritic poly(L-lysine) analogues with the terminal lysines replaced with arginines and histidines as gene carriers in vitro. *Biomaterials 25*, 537–544.
(46) Chen, Q. R., Zhang, L., Stass, S. A., and Mixson, A. J. (2001) Branched co-polymers of histidine and lysine are efficient carriers of plasmids. *Nucleic Acids Res. 29*, 1334–1340.
(47) Chen, Q. R., Zhang, L., Luther, P. W., and Mixson, A. J. (2002) Optimal transfection with the HK polymer depends on its degree of branching and the pH of endocytic vesicles. *Nucleic Acids Res. 30*, 1338–1345.
(48) Leng, Q., Scaria, P., Zhu, J., Ambulos, N., Campbell, P., and Mixson, A. J. (2005) Highly branched HK peptides are effective carriers of siRNA. *J. Gene Med. 7*, 977–986.
(49) Leng, Q., and Mixson, A. J. (2005) Small interfering RNA targeting Raf-1 inhibits tumor growth in vitro and in vivo. *Cancer Gene Ther. 12*, 682–690.
(50) Sakthivel, T., Toth, I., and Florence, A. T. (1998) Synthesis and physicochemical properties of lipophilic polyamide dendrimers. *Pharm. Res. 15*, 776–782.
(51) Shah, D. S., Sakthivel, T., Toth, I., Florence, A. T., and Wilderspin, A. F. (2000) DNA transfection and transfected cell viability using amphipathic asymmetric dendrimers. *Int. J. Pharm. 208*, 41–48.
(52) Ravina, M., Paolicelli, P., Seijo, B., and Sanchez, A. (2010) Knocking down gene expression with dendritic vectors. *Mini Rev. Med. Chem. 10*, 73–86.
(53) Haensler, J., and Szoka, F. C., Jr. (1993) Polyamidoamine cascade polymers mediate efficient transfection of cells in culture. *Bioconjugate Chem. 4*, 372–379.
(54) Bielinska, A., Kukowska-Latallo, J. F., Johnson, J., Tomalia, D. A., and Baker, J. R. (1996) Regulation of in vitro gene expression using antisense oligonucleotides or antisense expression plasmids transfected using starburst PAMAM dendrimers. *Nucleic Acids Res. 24*, 2176–2182.
(55) Tang, M. X., Redemann, C. T., and Szoka, F. C., Jr. (1996) In vitro gene delivery by degraded polyamidoamine dendrimers. *Bioconjugate Chem. 7*, 703–714.
(56) Yoo, H., Sazani, P., and Juliano, R. L. (1999) PAMAM dendrimers as delivery agents for antisense oligonucleotides. *Pharm. Res. 16*, 1799–1804.
(57) Choi, J. S., Nam, K., Park, J.-y., Kim, J.-B., Lee, J.-K., and Park, J.-s. (2004) Enhanced transfection efficiency of PAMAM dendrimer by surface modification with L-arginine. *J. Controlled Release 99*, 445–456.
(58) Nam, H. Y., Hahn, H. J., Nam, K., Choi, W.-H., Jeong, Y., Kim, D.-E., and Park, J.-S. (2008) Evaluation of generations 2, 3 and 4 arginine modified PAMAM dendrimers for gene delivery. *Int. J. Pharm. 363*, 199–205.
(59) Yu, G. S., Bae, Y. M., Choi, H., Kong, B., Choi, I. S., and Choi, J. S. (2011) Synthesis of PAMAM dendrimer derivatives with enhanced buffering capacity and remarkable gene transfection efficiency. *Bioconjugate Chem. 22*, 1046–1055.
(60) Zinselmeyer, B. H., Mackay, S. P., Schatzlein, A. G., and Uchegbu, I. F. (2002) The lower-generation polypropylenimine

dendrimers are effective gene-transfer agents. *Pharm. Res. 19*, 960–967.

(61) Schatzlein, A. G., Zinselmeyer, B. H., Elouzi, A., Dufes, C., Chim, Y. T. A., Roberts, C. J., Davies, M. C., Munro, A., Gray, A. I., and Uchegbu, I. F. (2005) Preferential liver gene expression with polypropylenimine dendrimers. *J. Controlled Release 101*, 247–258.

(62) Russ, V., Gunther, M., Halama, A., Ogris, M., and Wagner, E. (2008) Oligoethylenimine-grafted polypropylenimine dendrimers as degradable and biocompatible synthetic vectors for gene delivery. *J. Controlled Release 132*, 131–140.

(63) Plank, C., Tang, M. X., Wolfe, A. R., and Szoka, F. C., Jr. (1999) Branched cationic peptides for gene delivery: role of type and number of cationic residues in formation and in vitro activity of DNA polyplexes. *Hum. Gene Ther. 10*, 319–332.

(64) Wagner, E., Zenke, M., Cotten, M., Beug, H., and Birnstiel, M. L. (1990) Transferrin-polycation conjugates as carriers for DNA uptake into cells. *Proc. Natl. Acad. Sci. U.S.A. 87*, 3410–3414.

(65) Cotten, M., Langle-Rouault, F., Kirlappos, H., Wagner, E., Mechtler, K., Zenke, M., Beug, H., and Birnstiel, M. L. (1990) Transferrin-polycation-mediated introduction of DNA into human leukemic cells: stimulation by agents that affect the survival of transfected DNA or modulate transferrin receptor levels. *Proc. Natl. Acad. Sci. U.S.A. 87*, 4033–4037.

(66) Wyman, T. B., Nicol, F., Zelphati, O., Scaria, P. V., Plank, C., and Szoka, F. C., Jr. (1997) Design, synthesis, and characterization of a cationic peptide that binds to nucleic acids and permeabilizes bilayers. *Biochemistry 36*, 3008–3017.

(67) McKenzie, D. L., Kwok, K. Y., and Rice, K. G. (2000) A potent new class of reductively activated peptide gene delivery agents. *J. Biol. Chem. 275*, 9970–9977.

(68) McKenzie, D. L., Smiley, E., Kwok, K. Y., and Rice, K. G. (2000) Low molecular weight disulfide cross-linking peptides as nonviral gene delivery carriers. *Bioconjugate Chem. 11*, 901–909.

(69) Read, M. L., Bremner, K. H., Oupicky, D., Green, N. K., Searle, P. F., and Seymour, L. W. (2003) Vectors based on reducible polycations facilitate intracellular release of nucleic acids. *J. Gene Med. 5*, 232–245.

(70) Kim, S. W., Kim, N. Y., Choi, Y. B., Park, S. H., Yang, J. M., and Shin, S. (2010) RNA interference in vitro and in vivo using an arginine peptide/siRNA complex system. *J. Controlled Release 143*, 335–343.

(71) Liu, Y., and Reineke, T. M. (2010) Degradation of poly(glycoamidoamine) DNA delivery vehicles: polyamide hydrolysis at physiological conditions promotes DNA release. *Biomacromolecules 11*, 316–325.

(72) Prevette, L. E., Lynch, M. L., and Reineke, T. M. (2010) Amide spacing influences pDNA binding of poly(amidoamine)s. *Biomacromolecules 11*, 326–332.

(73) McLendon, P. M., Fichter, K. M., and Reineke, T. M. (2010) Poly(glycoamidoamine) vehicles promote pDNA uptake through multiple routes and efficient gene expression via caveolae-mediated endocytosis. *Mol. Pharmaceutics 7*, 738–750.

(74) Hartmann, L. (2011) Polymers for control freaks: sequence-defined poly(amidoamine)s and their biomedical applications. *Macromol. Chem. Phys. 212*, 8–13.

(75) Hartmann, L., and Börner, H. G. (2009) Precision polymers: monodisperse, monomer-sequence-defined segments to target future demands of polymers in medicine. *Adv. Mater. 21*, 3425–3431.

(76) Hartmann, L., Hafele, S., Peschka-Suss, R., Antonietti, M., and Borner, H. G. (2008) Tailor-made poly(amidoamine)s for controlled complexation and condensation of DNA. *Chemistry 14*, 2025–2033.

(77) Hartmann, L., Häfele, S., Peschka-Süss, R., Antonietti, M., and Börner, H. G. (2007) Sequence positioning of disulfide linkages to program the degradation of monodisperse poly(amidoamines). *Macromolecules 40*, 7771–7776.

(78) Hartmann, L., Krause, E., Antonietti, M., and Borner, H. G. (2006) Solid-phase supported polymer synthesis of sequence-defined, multifunctional poly(amidoamines). *Biomacromolecules 7*, 1239–1244.

(79) Mosca, S., Wojcik, F., and Hartmann, L. (2011) Precise positioning of chiral building blocks in monodisperse, sequence-defined polyamides. *Macromol. Rapid Commun. 32*, 197–202.

(80) Schaffert, D., Badgujar, N., and Wagner, E. (2011) Novel Fmoc-polyamino acids for solid-phase synthesis of defined polyamidoamines. *Org. Lett. 13*, 1586–1589.

(81) Schaffert, D., Troiber, C., Salcher, E. E., Fröhlich, T., Martin, I., Badgujar, N., Dohmen, C., Edinger, D., Kläger, R., Maiwald, G., Farkasova, K., Seeber, S., Jahn-Hofmann, K., Hadwiger, P., and Wagner, E. (2011) Solid-phase synthesized sequence-defined T-shape, i-shape and U-shape polymers for pDNA and siRNA delivery. *Angew. Chem. Int. Ed. 50*, in press, DOI: 10.1002/anie.201102165.

(82) Blessing, T., Remy, J. S., and Behr, J. P. (1998) Monomolecular collapse of plasmid DNA into stable virus-like particles. *Proc. Natl. Acad. Sci. U.S.A. 95*, 1427–1431.

(83) Dauty, E., Remy, J.-S., Blessing, T., and Behr, J.-P. (2001) Dimerizable cationic detergents with a low cmc condense plasmid DNA into nanometric particles and transfect cells in culture. *J. Am. Chem. Soc. 123*, 9227–9234.

(84) Zuber, G., Dontenwill, M., and Behr, J.-P. (2009) Synthetic viruslike particles for targeted gene delivery to $\alpha v\beta 3$ integrin-presenting endothelial cells. *Mol. Pharmaceutics 6*, 1544–1552.

(85) Chittimalla, C., Zammut-Italiano, L., Zuber, G., and Behr, J.-P. (2005) Monomolecular DNA nanoparticles for intravenous delivery of genes. *J. Am. Chem. Soc. 127*, 11436–11441.

(86) Xu, R., and Lu, Z.-R. (2011) Design, synthesis and evaluation of spermine-based pH-sensitive amphiphilic gene delivery systems: multifunctional non-viral gene carriers. *Sci. China Chem. 54*, 359–368.

(87) Xu, R., Wang, X.-L., and Lu, Z.-R. (2010) New amphiphilic carriers forming pH-sensitive nanoparticles for nucleic acid delivery. *Langmuir 26*, 13874–13882.

(88) Wang, X.-L., Xu, R., and Lu, Z.-R. (2009) A peptide-targeted delivery system with pH-sensitive amphiphilic cell membrane disruption for efficient receptor-mediated siRNA delivery. *J. Controlled Release 134*, 207–213.

(89) Wang, X.-L., Xu, R., Wu, X., Gillespie, D., Jensen, R., and Lu, Z.-R. (2009) Targeted systemic delivery of a therapeutic siRNA with a multifunctional carrier controls tumor proliferation in mice. *Mol. Pharmaceutics 6*, 738–746.

(90) Philipp, A., Zhao, X., Tarcha, P., Wagner, E., and Zintchenko, A. (2009) Hydrophobically modified oligoethylenimines as highly efficient transfection agents for siRNA delivery. *Bioconjugate Chem. 20*, 2055–2061.

(91) Asai, T., Matsushita, S., Kenjo, E., Tsuzuku, T., Yonenaga, N., Koide, H., Hatanaka, K., Dewa, T., Nango, M., Maeda, N., Kikuchi, H., and Oku, N. (2011) Dicetyl phosphate−tetraethylenepentamine-based liposomes for systemic siRNA delivery. *Bioconjugate Chem. 22*, 429–435.

(92) Asai, T., and Oku, N. (2010) Angiogenic vessel-targeting DDS by liposomalized oligopeptides. *Methods Mol. Biol. 605*, 335–347.

(93) Damen, M., Aarbiou, J., van Dongen, S. F., Buijs-Offerman, R. M., Spijkers, P. P., van den Heuvel, M., Kvashnina, K., Nolte, R. J., Scholte, B. J., and Feiters, M. C. (2010) Delivery of DNA and siRNA by novel gemini-like amphiphilic peptides. *J. Controlled Release 145*, 33–39.

(94) Akinc, A., Zumbuehl, A., Goldberg, M., Leshchiner, E. S., Busini, V., Hossain, N., Bacallado, S. A., Nguyen, D. N., Fuller, J., Alvarez, R., Borodovsky, A., Borland, T., Constien, R., de Fougerolles, A., Dorkin, J. R., Narayanannair, J. K., Jayaraman, M., John, M., Koteliansky, V., Manoharan, M., Nechev, L., Qin, J., Racie, T., Raitcheva, D., Rajeev, K. G., Sah, D. W., Soutschek, J., Toudjarska, I., Vornlocher, H. P., Zimmermann, T. S., Langer, R., and Anderson, D. G. (2008) A combinatorial library of lipid-like materials for delivery of RNAi therapeutics. *Nat. Biotechnol. 26*, 561–569.

(95) Akinc, A., Goldberg, M., Qin, J., Dorkin, J. R., Gamba-Vitalo, C., Maier, M., Jayaprakash, K. N., Jayaraman, M., Rajeev, K. G., Manoharan, M., Koteliansky, V., Rohl, I., Leshchiner, E. S., Langer, R., and Anderson, D. G. (2009) Development of lipidoid-siRNA formulations for systemic delivery to the liver. *Mol. Ther. 17*, 872–879.

(96) Mahon, K. P., Love, K. T., Whitehead, K. A., Qin, J., Akinc, A., Leshchiner, E., Leshchiner, I., Langer, R., and Anderson, D. G. (2010)

Combinatorial approach to determine functional group effects on lipidoid-mediated siRNA delivery. *Bioconjugate Chem. 21*, 1448–1454.

(97) Love, K. T., Mahon, K. P., Levins, C. G., Whitehead, K. A., Querbes, W., Dorkin, J. R., Qin, J., Cantley, W., Qin, L. L., Racie, T., Frank-Kamenetsky, M., Yip, K. N., Alvarez, R., Sah, D. W., de Fougerolles, A., Fitzgerald, K., Koteliansky, V., Akinc, A., Langer, R., and Anderson, D. G. (2010) Lipid-like materials for low-dose, in vivo gene silencing. *Proc. Natl. Acad. Sci. U.S.A. 107*, 1864–1869.

(98) de Bruin, K., Ruthardt, N., von Gersdorff, K., Bausinger, R., Wagner, E., Ogris, M., and Brauchle, C. (2007) Cellular dynamics of EGF receptor-targeted synthetic viruses. *Mol. Ther. 15*, 1297–1305.

(99) Schaffert, D., Kiss, M., Rodl, W., Shir, A., Levitzki, A., Ogris, M., and Wagner, E. (2011) Poly(I:C)-mediated tumor growth suppression in EGF-receptor overexpressing tumors using EGF-polyethylene glycol-linear polyethylenimine as carrier. *Pharm. Res. 28*, 731–741.

(100) Pons, B., Mouhoubi, L., Adib, A., Godzina, P., Behr, J. P., and Zuber, G. (2006) ω-Hydrazino linear polyethylenimine: a monoconjugation building block for nucleic acid delivery. *Chembiochem 7*, 303–309.

(101) Hein, C., Liu, X.-M., and Wang, D. (2008) Click chemistry, a powerful tool for pharmaceutical sciences. *Pharm. Res. 25*, 2216–2230.

(102) Lutz, J.-F., and Zarafshani, Z. (2008) Efficient construction of therapeutics, bioconjugates, biomaterials and bioactive surfaces using azide-alkyne "click" chemistry. *Adv. Drug Delivery Rev. 60*, 958–970.

(103) Moses, J. E., and Moorhouse, A. D. (2007) The growing applications of click chemistry. *Chem. Soc. Rev. 36*, 1249–1262.

(104) Orski, S. V., Poloukhtine, A. A., Arumugam, S., Mao, L., Popik, V. V., and Locklin, J. (2010) High density orthogonal surface immobilization via photoactivated copper-free click chemistry. *J. Am. Chem. Soc. 132*, 11024–11026.

(105) Kolb, H. C., Finn, M. G., and Sharpless, K. B. (2001) Click chemistry: diverse chemical function from a few good reactions. *Angew. Chem. Int. Ed. 40*, 2004–2021.

(106) Rostovtsev, V. V., Green, L. G., Fokin, V. V., and Sharpless, K. B. (2002) A stepwise huisgen cycloaddition process: copper(I)-catalyzed regioselective "ligation" of azides and terminal alkynes. *Angew. Chem. Int. Ed. 41*, 2596–2599.

(107) Tornøe, C. W., Christensen, C., and Meldal, M. (2002) Peptidotriazoles on solid phase: [1,2,3]-triazoles by regiospecific copper(I)-catalyzed 1,3-dipolar cycloadditions of terminal alkynes to azides. *J. Org. Chem. 67*, 3057–3064.

(108) Mindt, T. L., Muller, C., Stuker, F., Salazar, J.-F., Hohn, A., Mueggler, T., Rudin, M., and Schibli, R. (2009) A "click chemistry" approach to the efficient synthesis of multiple imaging probes derived from a single precursor. *Bioconjugate Chem. 20*, 1940–1949.

(109) Schlossbauer, A., Schaffert, D., Kecht, J., Wagner, E., and Bein, T. (2008) Click chemistry for high-density biofunctionalization of mesoporous silica. *J. Am. Chem. Soc. 130*, 12558–12559.

(110) Chang, P. V., Prescher, J. A., Sletten, E. M., Baskin, J. M., Miller, I. A., Agard, N. J., Lo, A., and Bertozzi, C. R. (2010) Copper-free click chemistry in living animals. *Proc. Natl. Acad. Sci. U.S.A. 107*, 1821–1826.

(111) Jiang, X., Lok, M. C., and Hennink, W. E. (2007) Degradable-brushed pHEMA−pDMAEMA synthesized via ATRP and click chemistry for gene delivery. *Bioconjugate Chem. 18*, 2077–2084.

(112) Lee, C.-C., Grandinetti, G., McLendon, P. M., and Reineke, T. M. (2010) A polycation scaffold presenting tunable "click" sites: conjugation to carbohydrate ligands and examination of hepatocyte-targeted pDNA delivery. *Macromol. Biosci. 10*, 585–598.

(113) Liu, J., Jiang, X., Xu, L., Wang, X., Hennink, W. E., and Zhuo, R. (2010) Novel reduction-responsive cross-linked polyethylenimine derivatives by click chemistry for nonviral gene delivery. *Bioconjugate Chem. 21*, 1827–1835.

(114) Srinivasachari, S., Liu, Y., Zhang, G., Prevette, L., and Reineke, T. M. (2006) Trehalose click polymers inhibit nanoparticle aggregation and promote pDNA delivery in serum. *J. Am. Chem. Soc. 128*, 8176–8184.

(115) Srinivasachari, S., and Reineke, T. M. (2009) Versatile supramolecular pDNA vehicles via "click polymerization" of β-cyclodextrin with oligoethyleneamines. *Biomaterials 30*, 928–938.

(116) van Dijk, M., Rijkers, D. T. S., Liskamp, R. M. J., van Nostrum, C. F., and Hennink, W. E. (2009) Synthesis and applications of biomedical and pharmaceutical polymers via click chemistry methodologies. *Bioconjugate Chem. 20*, 2001–2016.

(117) Lee, J. W., Kim, H. J., Han, S. C., Kim, J. H., and Jin, S.-H. (2008) Synthesis and characterization of poly(amido amine) dendrimer containing fluorene as a core chromophore. *J. Nanosci. Nanotechnol. 8*, 4635–4639.

(118) Lee, J. W., Kim, H. J., Han, S. C., Kim, J. H., and Jin, S.-H. (2008) Designing poly(amido amine) dendrimers containing core diversities by click chemistry of the propargyl focal point poly(amido amine) dendrons. *J. Polym. Sci. Part A: Polym. Chem. 46*, 1083–1097.

(119) Yu, H., Nie, Y., Dohmen, C., Li, Y., and Wagner, E. (2011) Epidermal growth factor−PEG functionalized PAMAM-pentaethylene-hexamine dendron for targeted gene delivery produced by click chemistry. *Biomacromolecules 12*, 2039–2047.

(120) Huang, B., Desai, A., Zong, H., Tang, S., Leroueil, P., and Baker, J. R., Jr. (2011) Copper-free click conjugation of methotrexate to a PAMAM dendrimer platform. *Tetrahedron Lett. 52*, 1411–1414.

(121) Jayaprakash, K. N., Peng, C. G., Butler, D., Varghese, J. P., Maier, M. A., Rajeev, K. G., and Manoharan, M. (2010) Non-nucleoside building blocks for copper-assisted and copper-free click chemistry for the efficient synthesis of RNA conjugates. *Org. Lett. 12*, 5410–5413.

(122) Yamada, T., Peng, C. G., Matsuda, S., Addepalli, H., Jayaprakash, K. N., Alam, M. R., Mills, K., Maier, M. A., Charisse, K., Sekine, M., Manoharan, M., and Rajeev, K. G. (2011) Versatile site-specific conjugation of small molecules to siRNA using click chemistry. *J. Org. Chem. 76*, 1198–1211.

(123) Dawson, P., Muir, T., Clark-Lewis, I., and Kent, S. (1994) Synthesis of proteins by native chemical ligation. *Science 266*, 776–779.

(124) Byun, E., Kim, J., Kang, S. M., Lee, H., Bang, D., and Lee, H. (2010) Surface PEGylation via native chemical ligation. *Bioconjugate Chem. 22*, 4–8.

(125) Walker, G. F., Fella, C., Pelisek, J., Fahrmeir, J., Boeckle, S., Ogris, M., and Wagner, E. (2005) Toward synthetic viruses: endosomal pH-triggered deshielding of targeted polyplexes greatly enhances gene transfer in vitro and in vivo. *Mol. Ther. 11*, 418–425.

(126) Knorr, V., Allmendinger, L., Walker, G. F., Paintner, F. F., and Wagner, E. (2007) An acetal-based PEGylation reagent for pH-sensitive shielding of DNA polyplexes. *Bioconjugate Chem. 18*, 1218–1225.

(127) Fella, C., Walker, G. F., Ogris, M., and Wagner, E. (2008) Amine-reactive pyridylhydrazone-based PEG reagents for pH-reversible PEI polyplex shielding. *Eur. J. Pharm. Sci 34*, 309–320.

(128) Rozema, D. B., Lewis, D. L., Wakefield, D. H., Wong, S. C., Klein, J. J., Roesch, P. L., Bertin, S. L., Reppen, T. W., Chu, Q., Blokhin, A. V., Hagstrom, J. E., and Wolff, J. A. (2007) Dynamic PolyConjugates for targeted in vivo delivery of siRNA to hepatocytes. *Proc. Natl. Acad. Sci U.S.A. 104*, 12982–12987.

(129) Nie, Y., Günther, M., Gu, Z., and Wagner, E. (2011) Pyridylhydrazone-based PEGylation for pH-reversible lipopolyplex shielding. *Biomaterials 32*, 858–869.

(130) Leonetti, J. P., Degols, G., and Lebleu, B. (1990) Biological activity of oligonucleotide-poly(L-lysine) conjugates: mechanism of cell uptake 381. *Bioconjugate Chem. 1*, 149–153.

(131) Bulmus, V., Woodward, M., Lin, L., Murthy, N., Stayton, P., and Hoffman, A. (2003) A new pH-responsive and glutathione-reactive, endosomal membrane-disruptive polymeric carrier for intracellular delivery of biomolecular drugs. *J. Controlled Release 93*, 105–120.

(132) Hoffman, A. S., Stayton, P. S., Press, O., Murthy, N., Lackey, C. A., Cheung, C., Black, F., Campbell, J., Fausto, N., Kyriakides, T. R., and Bornstein, P. (2002) Design of "smart" polymers that can direct intracellular drug delivery. *Polym. Adv. Technnol. 13*, 992–999.

(133) Zhu, L., and Mahato, R. I. (2010) Targeted delivery of siRNA to hepatocytes and hepatic stellate cells by bioconjugation. *Bioconjugate Chem. 21*, 2119–2127.

(134) Nakagawa, T., Zhu, H., Morishima, N., Li, E., Xu, J., Yankner, B. A., and Yuan, J. (2000) Caspase-12 mediates endoplasmic-reticulum-specific apoptosis and cytotoxicity by amyloid-β. *Nature 403*, 98–103.

(135) Lönnberg, H. (2009) Solid-phase synthesis of oligonucleotide conjugates useful for delivery and targeting of potential nucleic acid therapeutics. *Bioconjugate Chem. 20*, 1065–1094.

(136) Jeong, J. H., Mok, H., Oh, Y.-K., and Park, T. G. (2008) siRNA conjugate delivery systems. *Bioconjugate Chem. 20*, 5–14.

(137) Thomas, M., Kularatne, S. A., Qi, L., Kleindl, P., Leamon, C. P., Hansen, M. J., and Low, P. S. (2009) Ligand-targeted delivery of small interfering RNAs to malignant cells and tissues. *Ann. N.Y. Acad. Sci. 1175*, 32–39.

(138) Soutschek, J., Akinc, A., Bramlage, B., Charisse, K., Constien, R., Donoghue, M., Elbashir, S., Geick, A., Hadwiger, P., Harborth, J., John, M., Kesavan, V., Lavine, G., Pandey, R. K., Racie, T., Rajeev, K. G., Rohl, I., Toudjarska, I., Wang, G., Wuschko, S., Bumcrot, D., Koteliansky, V., Limmer, S., Manoharan, M., and Vornlocher, H.-P. (2004) Therapeutic silencing of an endogenous gene by systemic administration of modified siRNAs. *Nature 432*, 173–178.

(139) Nishina, K., Unno, T., Uno, Y., Kubodera, T., Kanouchi, T., Mizusawa, H., and Yokota, T. (2008) Efficient in vivo delivery of siRNA to the liver by conjugation of α-tocopherol. *Mol. Ther. 16*, 734–740.

(140) Kim, S. H., Jeong, J. H., Lee, S. H., Kim, S. W., and Park, T. G. (2006) PEG conjugated VEGF siRNA for anti-angiogenic gene therapy. *J. Controlled Release 116*, 123–129.

(141) Meyer, M., Dohmen, C., Philipp, A., Kiener, D., Maiwald, G., Scheu, C., Ogris, M., and Wagner, E. (2009) Synthesis and biological evaluation of a bioresponsive and endosomolytic siRNA—polymer conjugate. *Mol. Pharmaceutics 6*, 752–762.

(142) Oishi, M., Nagasaki, Y., Itaka, K., Nishiyama, N., and Kataoka, K. (2005) Lactosylated poly(ethylene glycol)-siRNA conjugate through acid-labile β-thiopropionate linkage to construct pH-sensitive polyion complex micelles achieving enhanced gene silencing in hepatoma cells. *J. Am. Chem. Soc. 127*, 1624–1625.

(143) Zhu, L., Ye, Z., Cheng, K., Miller, D. D., and Mahato, R. I. (2007) Site-specific delivery of oligonucleotides to hepatocytes after systemic administration. *Bioconjugate Chem. 19*, 290–298.

(144) Meyer, M., Philipp, A., Oskuee, R., Schmidt, C., and Wagner, E. (2008) Breathing life into polycations: functionalization with pH-responsive endosomolytic peptides and polyethylene glycol enables siRNA delivery. *J. Am. Chem. Soc. 130*, 3272–3273.

(145) Philipp, A., Meyer, M., Zintchenko, A., and Wagner, E. (2011) Functional modification of amide-crosslinked oligoethylenimine for improved siRNA delivery. *Reactive Funct. Polymers 71*, 288–293.

Bioconjugate Chemistry

COMMUNICATION

pubs.acs.org/bc

Chemoselective Surface Immobilization of Proteins through a Cleavable Peptide

Monica Dettin,*[,§] Natali Muncan,[§] Antonella Bugatti,[‡] Francesca Grezzo,[§] Roberta Danesin,[§] and Marco Rusnati[‡]

[§]Department of Chemical Process Engineering, University of Padova, Padova, Italy

[‡]Department of Biomedical Sciences and Biotechnology, University of Brescia, Brescia, Italy

Supporting Information

ABSTRACT: Surface immobilization of biomolecules is a fundamental step in several experimental techniques such as surface plasmon resonance analysis and microarrays. Oxime ligation allows reaching chemoselective protein immobilization with the retention of native-like conformation by proteins. Beside the need for chemoselective ligation of molecules to surface/particle, equally important is the controlled release of the immobilized molecules, even after a specific binding event. For this purpose, we have designed and assessed in an SPR experiment a peptide linker able to (i) anchor a given protein (enzymes, receptors, or antibodies) to a surface in a precise orientation and (ii) release the immobilized protein after selective enzymatic cleavage. These results open up the possibility to anchor to a surface a protein probe leaving bioactive sites free for interaction with substrates, ligands, antigens, or drugs and successively remove the probe−ligand complex by enzymatic cleavage. This peptide linker can be considered both an improvement of SPR analysis for macromolecular interaction and a novel strategy for drug delivery and biomaterial developments.

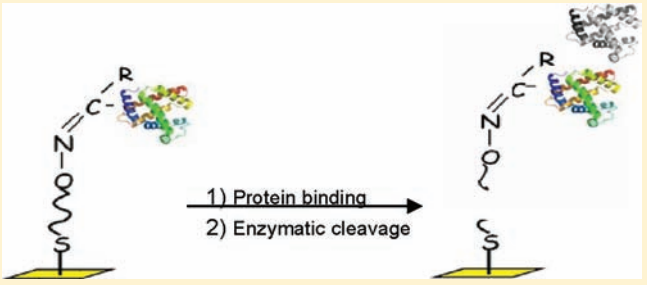

Surface immobilization of biomolecules is a key step in important experimental techniques including surface plasmon resonance (SPR) analysis[1] and microarrays[2] that are by now fundamental in research areas spanning from basic sciences to drug development. Surface functionalization with proteins is far more complex than with DNA, mainly due to the high number of different functional groups and to the structural complexity of folded proteins. Also, the need for an appropriate orientation of the immobilized protein on the surface is crucial for receptors, antibodies, and enzymes.[3] For these immobilizations, leaving the binding site or the catalytic pocket free can be satisfied only by chemoselective methods. An ideal chemoselective protein immobilization might exploit a selected functional group of the protein and may use experimental conditions that retain protein folding and its biological functions. Relevant to this point, classical protein immobilization via amine or thiol groups usually results in random conjugation without a defined protein orientation. On the other hand, among the various site-specific immobilization methods available, the bioorthogonal ligation reactions, like Staudinger ligation or Diels−Alder reaction, need the introduction of a peptide tag or a non-natural amino acid that may greatly affect protein folding and activity. Lempens et al. recently proposed oxime ligation as efficient protein immobilization strategy.[4] This method requests the site-specific introduction of a ketone in the N-terminal site of the protein by oxidation with pyridoxal-5′-phosphate (PLP);[5,6] the ketone is then used to link, through an oxime bond, an oxy-amine group on the surface. The conversion of the N-terminal group in ketone or aldehyde can be applied to many proteins without recombinant modification with the exclusion of those containing Q, W, H, P, or K as N-terminal residue or proteins whose N-terminus is blocked by post-translational modifications. Oxime ligation provides a fast and selective method for peptide and protein immobilization and its application has been demonstrated to increase the sensitivity of SPR analysis.[7]

Beside the need for chemoselective immobilization of molecules to surface/particle, equally important is the controlled release of the immobilized molecules (i.e., drugs) to target tissues/cells. This latter field of research has direct implications in the treatment of several important human diseases including cancer.[8,9]

On the basis of the above-mentioned considerations, we have attempted the design of a bifunctional peptide linker containing the matrix metallo proteinase (MMP)-2-cleavage site of CCL12[7] that could be selectively bound to a protein−ketone through its oxy-amine N-terminal group and anchored to a surface (i.e., a gold chip) through the thiol of its C-terminal Cys (Figure 1). The goal of this kind of strategy is twofold, probing both the possibility to chemoseletively immobilize a protein on a surface in a defined orientation and the possibility to collect the probe−ligand complex for further analyses and studies. Closely related to this

Received: May 13, 2011
Revised: July 25, 2011
Published: August 08, 2011

ACS Publications © 2011 American Chemical Society

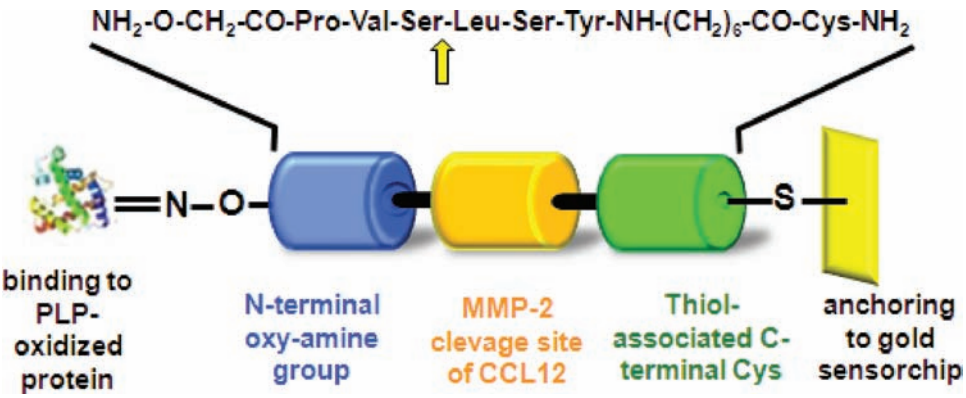

Figure 1. Schematic representation of the bifunctional peptide linker containing the MMP-2-cleavage site of CCL12.

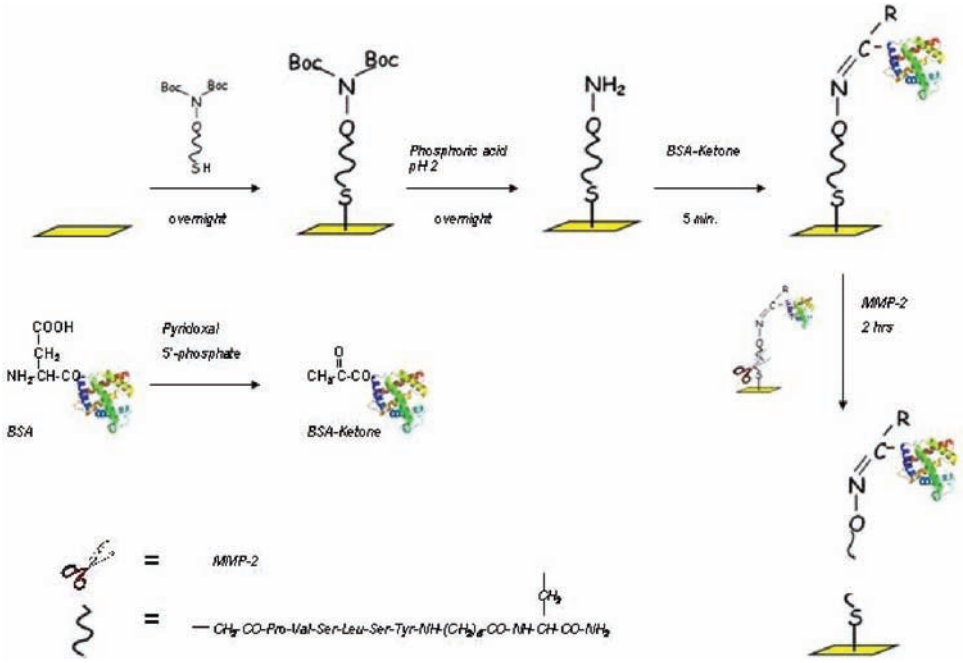

Figure 2. Schematic representation of the strategy for site-specific immobilization of proteins via a cleavable peptide linker here adopted. Boc = *tert*-butyloxycarbonyl.

latter point, the study performed here opens new possibilities in the field of controlled release of drugs from artificial surfaces for biomedical uses.

Figure 2 reports a schematic representation of the strategy adopted here. In detail, a premature and uncontrolled reaction of the highly reactive oxy-amino group of the peptide linker was avoided by protecting it with bis-*tert*-butyloxycarbonyl (Bis-Boc). The solid-phase synthesis of Bis-Boc-protected peptide linker was possible using super acid labile Mmt for Cys, 2-Cl-Trt for Tyr, and Trt for Ser instead of acid labile side chain protections and a super acid labile support (Sieber Amide resin). As this group is highly reactive with aldehyde, ketones, and nitriles, acetonitrile was avoided as eluent during HPLC purification.The Bis-Boc-protected peptide linker was then immobilized to a gold-coated sensorchip for SPR analysis via thiol group of its C-terminal Cys residue. Bovine serum albumin (BSA, here used as model protein) was PLP oxidized, obtaining the BSA-Ketone, and the sensorchip-immobilized peptide linker deprotected. Then, the chemoselective fusion to the oxy-amine N-terminal group of the immobilized peptide linker to BSA-Ketone was performed directly in the fluidic cell of the BIAcore apparatus (for technical details, see Experimental Section in the Supporting Information). The resulting sensorchip was then used to evaluate the possibility to remove BSA from the sensorchip by injecting MMP-2.

The sensorgram of a representative experiment (out of four other that gave similar results) is reported in Figure 3. The immobilization of the Bis-Boc-protected peptide linker produces a RU increase of 1513 units (approximately equal to 129 pmol/cm^2). The further functionalization of the surface with BSA-Ketone through oxime formation shows a further RU increase equal to 1165 units, that approximately corresponds to 1.75 pmol/cm^2 (thus with a reaction yield equal to 1% with respect to the anchored peptide surface density).

Addition of MMP-2 to the functionalized chip surface produces a transient, slight increase of RU that is possibly due to the association of the enzyme to the substrate. Relevant to this point,

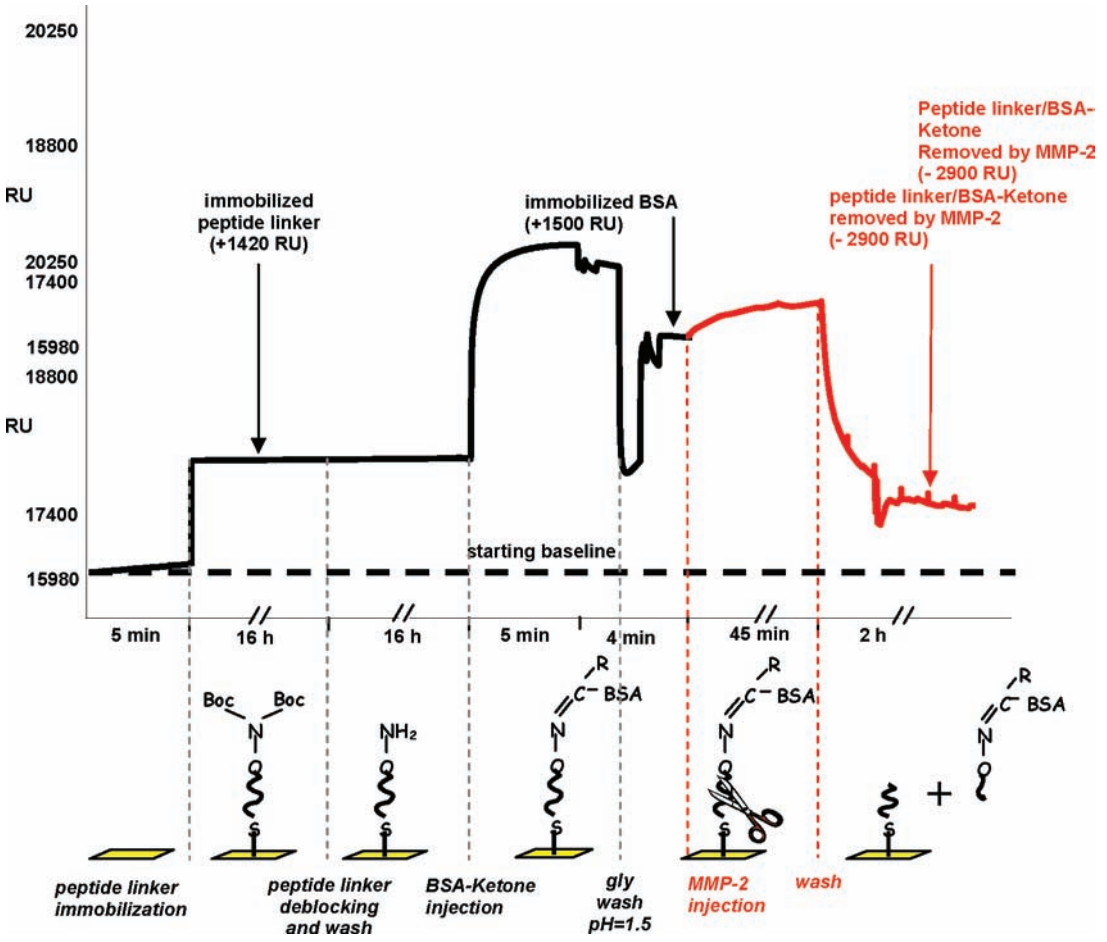

Figure 3. BIAcore responses during the procedure of chemoselective immobilization of BSA to a gold sensorchip followed by the enzymatic cleavage of the peptide linker. Boc = *tert*-butyloxycarbonyl.

the interaction of MMP-2 to CCL12 has been demonstrated to be very strong.[10] The slight increase of RU is, however, followed by a rapid decrement that reaches the level of RUs present on the sensorchip before BSA-Ketone injection.

To demonstrate the specificity of the protein association/cleavage observed, we injected BSA-Ketone on a gold sensorchip devoid of the peptide linker. In these experimental conditions, we observed an increase of RU equal to about 800 RU (due to unspecific adsorption of the protein to the gold surface[11]), but the subsequent treatment with MMP-2 did not produce any modification, in agreement with the lack of cleavable linker (data not shown). Relevant to this point, the observation that MMP2 completely removes peptide linker-associated BSA-Ketone suggests that, in our experimental conditions, no unspecific absorption of BSA-Ketone to the gold surface occurs, possibly due to the fact that the previous immobilization of the peptide linker has saturated the unspecific binding sites available on the gold surface. Finally, the reliability of the strategy proposed here is proven by the reproducibility of the results obtained in four repeated independent experiments (Figure 4).

In this paper, we have successfully designed and produced a bifunctional cleavable peptide that is able to efficiently link a protein to a gold surface through chemoselective immobilization and that effectively allows the controlled release of the protein by administering the appropriate enzyme. These results open up the possibility to immobilize to a surface enzymes, receptors, or antibodies with a precise orientation, leaving bioactive sites free for interaction with substrates, ligands, antigens, or drugs. This may impact the field of SPR analysis that, in the past years, has emerged as a powerful asset in the study of biomolecular interactions and drug development.[12] Actually, the strategy adopted here requires the exploitation of the N-terminus of the protein, hampering the immobilization of receptors in the proper orientation that would allow their interaction with extracellular ligands. Relevant to this point, alternative strategies have been individuated to overcome this limit: Carrico et al. have developed methods for site-specific introduction of aldehyde groups into recombinant proteins using the 6-amino-acid consensus sequence recognized by the formylglycine generating enzyme.[13] On the other hand, the N-terminal immobilization of the cytoplasmic tail of a receptors may be functional to the study of receptor interaction with intracellular second messengers or intracellular binders/inhibitors. Relevant to this point, tyrosine-kinase (TK) receptors play pivotal roles in important human diseases such as tumors[14] and the development of small, cell-permeable drugs that bind the intracellular portion of TK receptors (hampering their activation and/or the docking of second messengers) represents a promising therapeutical strategy.[15] In this field, the availability of a fast, reliable method for N-terminal chemoselective immobilization of TK receptors in SPR or other solid-phase assays would represent a formidable opportunity, especially for high-throughput screening of putative receptor binders/inhibitors.

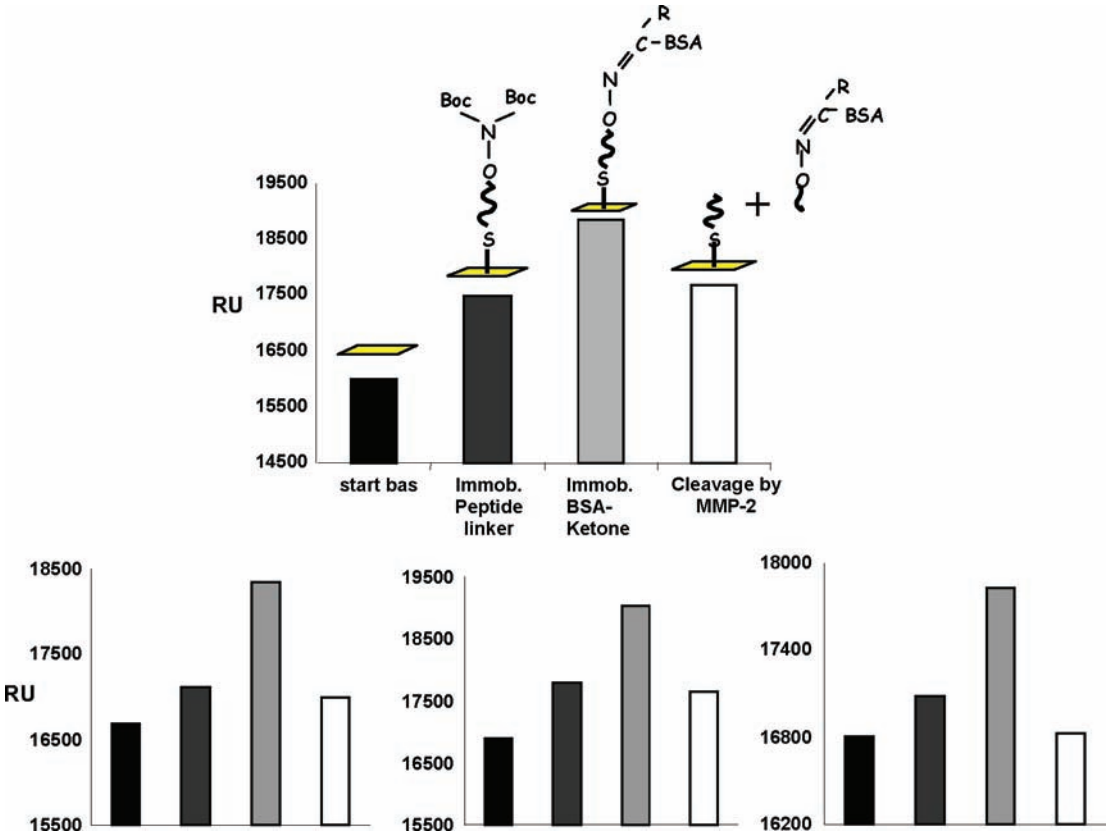

Figure 4. Immobilization levels for each of the four experiments performed. Boc = *tert*-butyloxycarbonyl.

Another promising evolution path that originates from the results presented here is the specific cleavage of a peptide linker with the consequent controlled release of the associated compound. Relevant to this point, the delivery and controlled release of drugs from artificial particles is an expanding field of research with implications in the treatment of several important human diseases including cancer.[8,9] Interestingly, our peptide linker is sensitive to MMP2. MMP2 is a zinc-dependent endopeptidase overexpressed in advanced stages of cancer where it plays a crucial role in tumor progression, angiogenesis, and metastasis.[16] It is thus possible to hypothesize that an anticancer drug immobilized to a particle via our peptide linker may be spontaneously and specifically released in MMP2-containing lesions. Also, our MMP2-labile peptide linker may behave in a "bioresponsive way", tuning drug release on the concentration of the metalloprotease that, in turn, is proportional to the extension/severity of the cancer lesion.[16]

Besides the approach reported here, a large number of advanced synthetic techniques have recently become available to achieve protein immobilization and modification with positional control. For example, the direct incorporation of noncanonical amino acids into proteins can be carried out via the subversion of the biosynthetic machinery:[17] the subsequent coupling of synthetic molecules to artificial amino acid side chains can yield novel bioconjugates. In an alternative approach, that mimics post-translational modifications, synthetic transformations can convert specific amino acid residues on expressed natural protein into other native or modified native groups.[18] When there is the necessity of protein labeling in a highly complex environment, new enzymatic strategies, able to append chemical functional groups to specific sequences, can be used.[19] In addition, antibodies represent another important class of bioconjugation targets: novel methods for the selective modification of antibodies are presented in the review of Meares et al.[20]

In conclusion, in this paper we have designed and produced a peptide linker able to (i) anchor a given protein to a surface in a precise orientation and (ii) release the immobilized protein after selective enzymatic cleavage. As it is, our peptide linker can be considered both an improvement of SPR analysis for macromolecular interaction and a novel strategy for drug delivery and biomaterial developments.

■ ASSOCIATED CONTENT

Supporting Information. Entire experimental section, including peptide synthesis, surface functionalization and BIAcore experiments. This material is available free of charge via the Internet at http://pubs.acs.org.

■ AUTHOR INFORMATION

Corresponding Author

*Prof. Monica Dettin, Department of Chemical Process Engineering, University of Padova, Via Marzolo, 9 35131 Padova, Italy. Tel. +39-049-8275553. Fax +39-049-8275555. E-mail: monica.dettin@unipd.it.

■ ACKNOWLEDGMENT

This work was supported by grants from MIUR, ISS (AIDS Project), and CARIPLO (grant 2008-2198) to M.R. The authors gratefully acknowledge support from the University of Padova

through the PLATFORMS strategic project "PLAsmonic nano-Textured materials and architectures FOR enhanced Molecular Sensing" -prot.STPD089KSC.

REFERENCES

(1) Jason-Moller, L., Murphy, M., and Bruno, J. (2006) Overview of Biacore systems and their applications. In *Current Protocols in Protein Science*, Chapter 19, Unit 19 13.

(2) Spisak, S., and Guttman, A. (2009) Biomedical applications of protein microarrays. *Curr. Med. Chem. 16*, 2806–2815.

(3) Kausaite-Minkstimiene, A., Ramanaviciene, A., Kirlyte, J., and Ramanavicius, A. (2010) Comparative study of random and oriented antibody immobilization techniques on the binding capacity of immunosensor. *Anal. Chem. 82*, 6401–6408.

(4) Lempens, E. H. M., Helms, B. A., Merkx, M., and Meijer, E. W. (2009) Efficient and chemoselective surface immobilization of proteins by using aniline-catalyzed oxime chemistry. *ChemBioChem 10*, 658–662.

(5) Gilmore, J. M., Scheck, R. A., Esser-Kahn, A. P., Joshi, N. S., and Francis, M. B. (2006) N- terminal protein modification through a biomimetic transamination reaction. *Angew. Chem. Int. 45*, 5307–5311.

(6) Scheck, R. A., Dedeo, M. D., Iavarone, A. T., and Francis, M. B. (2008) Optimization of a biomimetic transamination reaction. *J. Am. Chem. Soc. 130*, 11762–11770.

(7) Segers, V. F. M., Tokunou, T., Higgins, L. J., MacGillivray, C., Gannon, J., and Lee, R. T. (2007) Local delivery of protease-resistant stromal cell derived factor-1 for stem cell recruitment after myocardial infarction. *Circulation 116*, 1683–1692.

(8) Ogi, H., Fukunishi, Y., Nagai, H., Okamoto, K., Hirao, M., and Nishiyama, M. (2009) Nonspecific-adsorption behavior of polyethylenglycol and bovine serum albumin studied by 55-MHz wireless-electrodeless quartz crystal microbalance. *Biosens. Bioelectron. 24*, 3148–3152.

(9) Rich, R. L., and Myszka, D. G. (2009) Grading the commercial optical biosensor literature-Class of 2008: 'The Mighty Binders'. *J. Mol. Recognit. 23*, 1–64.

(10) McQuibban, G. A., Butler, G. S., Gong, J. H., Bendall, L., Power, C., Clark-Lewis, I., and Overall, C. M. (2001) Matrix metalloproteinase activity inactivates the CXC chemokine stromal cell-derived factor-1. *J. Biol. Chem. 276*, 43503–43508.

(11) Lemmon, M. A., and Schlessinger, J. (2010) Cell signaling by receptor tyrosine kinases. *Cell 141*, 1117–1134.

(12) Sharma, P. S., Sharma, S., and Tyagi, T. (2009) Receptor tyrosine kinase inhibitors as potent weapons in war against cancers. *Curr. Pharm. Des. 15*, 758–776.

(13) Carrico, I. S., Carlson, B. L., and Bertozzi, C. R. (2007) Introducing genetically encoded aldehydes into proteins. *Nat. Chem. Biol. 3*, 321–322.

(14) Wang, M., and Thanou, M. (2010) Targeting nanoparticles to cancer. *Pharmacol. Res. 62*, 90–99.

(15) Gullotti, E., and Yeo, Y. (2009) Extracellularly activated nanocarriers: a new paradigm of tumor targeted drug delivery. *Mol. Pharm. 6*, 1041–1051.

(16) Kessenbrock, K., Plaks, V., and Werb, Z. (2010) Matrix metalloproteinases: regulators of the tumor microenvironment. *Cell 141*, 52–67.

(17) Johnson, J. A., Lu, Y. Y., Van Deventer, J. A., and Tirrell, A. (2010) Residue-specific incorporation of non-canonical amino acids into proteins: recent developments and applications. *Curr. Opin. Chem. Biol. 14*, 774–780.

(18) Chalker, J. M., and Davis, B. G. (2010) Chemical mutagenesis: selective post-expression interconversion of protein amino acid residues. *Curr. Opin. Chem. Biol. 14*, 781–789.

(19) Rabuka, D. (2010) Chemoenzymatic methods for site-specific protein modification. *Curr. Opin. Chem. Biol. 14*, 790–796.

(20) Day, J. J., Marquez, B. V., Beck, H. E., Aweda, T. A., Gawande, P. D., and Meares, C. F. (2010) Chemically modified antibodies as diagnostic imaging agents. *Curr. Opin. Chem. Biol. 14*, 803–809.

Supporting Information

Chemoselective surface immobilization of proteins through a cleavable peptide

Monica Dettin, Natali Muncan, Antonella Bugatti, Francesca Ghezzo, Roberta Danesin and Marco Rusnati

Experimental section

Peptide linker synthesis

The peptide, whose sequence is reported in Fig.1, was synthesized by solid phase method using Fmoc chemistry. Sieber Amide resin (213 mg, 0.72 mmol/g) was used as solid support. The following side chain protecting groups were used: Mmt, Cys; 2Cl-Trt, Tyr; Trt, Ser. Each amino acid was condensed by double coupling using HBTU/HOBt condensing agent. The last insertion was carried out with $(Boc)_2N\text{-}O\text{-}CH_2\text{-}COOH$. The deprotection of the side chains and the cleavage of the peptide from the resin were carried out by treatment with 1% 2,2,2-trifluoroacetic acid, 5% triethylsilane in DCM for 10 minutes.

PLP Oxidation

BSA (60 nmoles) was dissolved together with pyridoxal-5'-phosphate (12 μmoles) in 1.2 mL phosphate buffer (25 mM, pH 6.5) and incubated for 24 hrs at 37°C.

SPR analysis

All experiments were performed on a BIAcore X instrument (GE-Healthcare, Milwaukee, WI). Bis-Boc-protected peptide linker was immobilized onto a gold-coated sensorchip for SPR analysis (Xantech Bioanalytics, Dusseldorf, Germany) as follows: after measuring the RU response of the naked gold surface (starting baseline), the sensorchip was removed from the BIAcore apparatus, a drop (30 μL) of methanol containing the Bis-Boc-protected peptide linker (1 mM) was deposited

onto the gold surface and incubated for 16 hrs at 25 °C in a methanol-satured chamber. The excess of peptide not immobilized was removed by washing the gold surface with three alternate washing with deionized water and ethanol. Then, the sensorchip was re-inserted in the BIAcore apparatus and the new RU response was measured to evaluate the amount of peptide linker effectively immobilized onto the gold surface. The sensorchip was removed again and deprotection of Bis-Boc groups was achieved by a 16-hrs incubation at 25 °C in 1 M phosphoric acid pH 2 followed by extensively washing with deionized water. The sensorchip was finally re-positioned in the BIAcore apparatus and regenerated with 2 injection of 100 mM HCl followed by one injection of 50 mM NaOH and of 0.5% SDS in HBS-EP buffer (flow rate equal to 100 μL/min for 30 s). The fusion of PLP-BSA to the immobilized peptide linker was obtained by injecting the protein (50 μM in 100 mM anilinium acetate pH 4.5) at a flow rate of 10 μL/min for 5 minutes followed by the regeneration the sensorchip with an injection of 10 mM glycine pH 1.5 in HBS-EP buffer at the same flow rate for 4 minutes. The enzymatic cleavage was performed by injecting MMP-2 (0.02 μg/mL in HBS-EP buffer) at a flow rate equal to 2 μL/min for 50 minutes. Then, HBS-EP buffer alone was fluxed at the same flow rate for 2 hrs.

Bioconjugate Chemistry

COMMUNICATION

pubs.acs.org/bc

Developing Visible Fluorogenic 'Click-On' Dyes for Cellular Imaging

Jianjun Qi, Myung-Shin Han, Yu-Cheng Chang, and Ching-Hsuan Tung*

Department of Radiology, Methodist Hospital Research Institute, Weill Cornell Medical College, Houston, Texas, United States

Supporting Information

ABSTRACT: New fluorogenic dyes were designed and synthesized based on Cu(I)-catalyzed 'click' reaction. Conjugating weakly fluorescent benzothiazole derivatives with an electron-deficient alkyne group at the 2-position with azide-containing molecules in aqueous solution form 'click-on' fluorescent adducts. Model reactions and cell culture experiment indicated that the developed 'click-on' dye could be applied to labeling various biomolecules, such as nucleic acids, proteins, and other molecules, in cells.

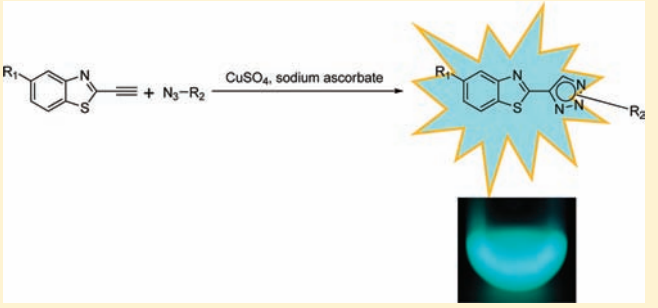

INTRODUCTION

Fluorescent dyes are a family of optical reporters widely used in studying biomolecules in cells[1] and animals.[2] With an appropriate fluorescent tag, the location and quantity of the target biomolecules or bioprocess can be conveniently tracked. Most dyes fluoresce continuously and show no difference in fluorescence property before and after labels; therefore, any leftover unreacted free dye could interfere with the dye attached to the molecules of interest, significantly lowering the signal to background contrast. An alternate way to label target molecules without worrying about the background issue is to use fluorogenic fluorochromes, whose emission wavelength or intensity shift or change after the labeling reaction.[3] Taking advantage of these unique fluorescent properties could minimize the high background issue. Although the benefit of using the fluorogenic fluorochromes is obvious, the approach has not been applied widely for at least two reasons: limited available fluorogenic fluorochromes and the nonselective reactivity of these dyes. Without specific chemical reactivity, labeling particular molecule remains challenging.

The 'click' reaction between an azide and alkyne group has recently been used to label various biomolecules in cells[4−7] and even animals.[8,9] The small size of the azide and alkyne groups enables them to 'trick' some natural synthases, and thus modified amino acids,[10] nucleosides,[11−13] and monosaccharide[14] with an azide or alkyne reactive group have been reported as the tagging residues for proteins,[15] nucleic acids,[13] and carbohydrates.[16] Since azide and alkyne reactive groups are not normally expressed in biological systems, the 'click' reaction is specific. Many existing dyes have been engineered with a reactive azide or alkyne functional group for labeling;[7,17] however, this modification only solves half of the problem, i.e., specific reactivity. The background signal remains an issue.

A new kind of 'click-on' fluorogenic dyes has lately been reported to overcome the aforementioned problems.[18] The 'click-on' fluorogenic dyes were designed to have low or no baseline fluorescence by masking the core fluorophore with an electron-donating azide group or electron-withdrawing alkyne group. After the 'click' reaction, the newly formed triazole conjugating structure delocalizes the local electrons and restores fluorescence. To date, only a handful of successful examples, derived from coumarin (**1**, **2**),[18−21] anthracene (**3**),[22] and naphthalimide (**4**, **5**),[23] have been reported (Figure 1). More 'click-on' dyes that fluoresce at different wavelengths are needed for various biomolecule labeling and applications.

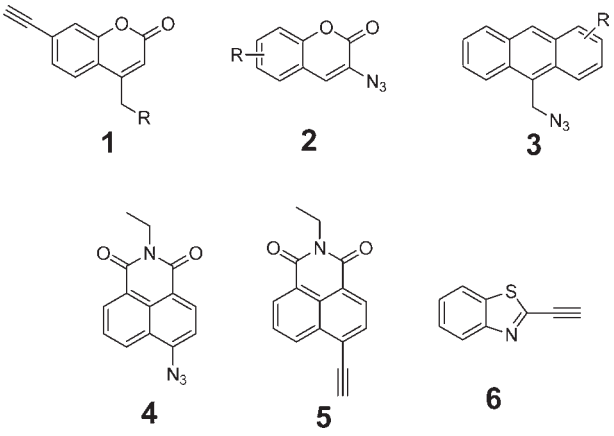

Figure 1. Examples of existing fluorogenic dyes.

Recently, we also reported an alkyne-containing benzothiazole 'click-on' dye (**6**), which has extremely low initial fluorescence, and its 'click-on' product shows 158-fold increase in fluorescence.[24] However, its low excitation and emission maxima which

Received: June 1, 2011
Revised: August 8, 2011
Published: August 09, 2011

ACS Publications © 2011 American Chemical Society

are approximately 290 and 360 nm, respectively, have restricted its biological application. In order to improve this shortcoming, we hypothesized that an electron-donating group such as dimethylamino or methoxyl group could enhance the effect of conjugating the parental aromatic benzothiazole ring, shifting the excitation and emission spectra into the visible range.

RESULT AND DISCUSSION

To add a methoxyl group at the 6-position of benzothiazole, 6-methoxybenzothiazole-2-alkyne **10** was synthesized using **7** as starting material (Scheme 1). Following a previously developed protocol,[24] **7** was initially transformed with 86% yield into iodobenzothiazole **8** via diazotization−Sandmeyer iodination in the presence of *p*-toluenesulfonic acid in acetonitrile.[25] The protected acetylenic benzothiazole **9** was obtained with 68.3% yield after a cross-coupling reaction of iodobenzothiazole **8** and a terminal alkyne with catalytic quantities of $Pd(PPh_3)_2Cl_2$ under basic condition.[26,27] The prepared **9** was deprotected with KF in MeOH at room temperature for 3 h, and then purified by a silica gel column to obtain **10** with 99% yield.

To prepare benzothiazole with dimethylamino at the 6-position, 6-dimethylbenzothiazole alkyne **16** was prepared from **11** (Scheme 2). Nitration of **11** was done with a mixture of concentrated sulfuric acid and fuming nitric acid to give **12**. The nitro group at the 6-position was then reduced with iron powder in MeOH under catalytic quantities of acetic acid to afford 6-amino-compound **13**.[28] Reductive amination of **13** with formaldehyde and triacetoxyborohydride in DCM formed 6-dimethyl compound **14**. Compound **16** was prepared, using a similar procedure for **10**, from **14** via cross-coupling and deprotection reaction with 44.5% and 84.6% yield, respectively.

The reactivity and 'click-on' fluorogenic properties of the prepared compounds **10** and **16** were tested by performing a [3 + 2] cycloaddition, also known as 'click' reaction, with model analogues **17**(**a**−**c**), representative analogues of nucleoside, amino acids, and linker (Scheme 3). Cu^{2+}/TBTA (Tris-[(1-benzyl-1*H*-1,2,3-triazol-4-yl)methyl] amine) was used as the catalyst in DMF/H_2O for 1 h at room temperature. Near-quantitative conversion was obtained for all reactions (Supporting Information).

Scheme 1[a]

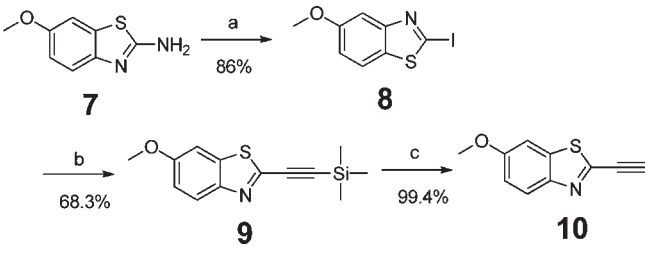

[a] Reagents and conditions: (a) 1. p-$MeC_6H_4SO_3H$, MeCN, RT-10 °C. 2. $NaNO_2$, H_2O, 10 min, 10-15 °C. 3. KI, RT, overnight. (b) 1. Ethynyltrimethylsilane, CuI, $PdCl_2(PPh_3)_2$, NEt_3, DCM. 2. $NaHCO_3$, H_2O. (c) KF, MeOH, RT, 3 h.

Scheme 2[a]

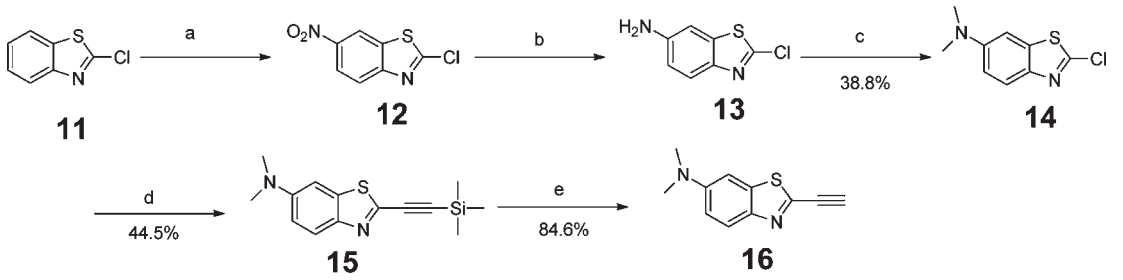

[a] Reagents and conditions: (a) HNO_3, H_2SO_4. (b) Fe, EtOH, AcOH, 55 °C, 3 h. (c) 36% formaldehyde, DCM, $NaBHAc_3$, HOAc, RT, 2 h. (d) 1. Ethynyltrimethylsilane, CuI, $PdCl_2(PPh_3)_2$, NEt_3, DCM. 2. $NaHCO_3$, H_2O. (e) KF, MeOH, RT, 3 h.

Scheme 3. Model 'Click' Reactions[a]

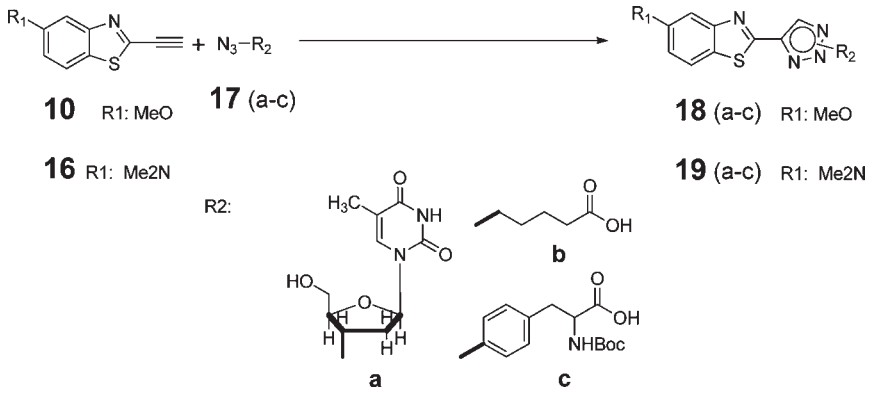

[a] Reagents and conditions: $CuSO_4$, sodium ascorbate, TBTA, DMF/H_2O(3/1), RT, 30 min.

dx.doi.org/10.1021/bc200282t |*Bioconjugate Chem.* 2011, 22, 1758–1762

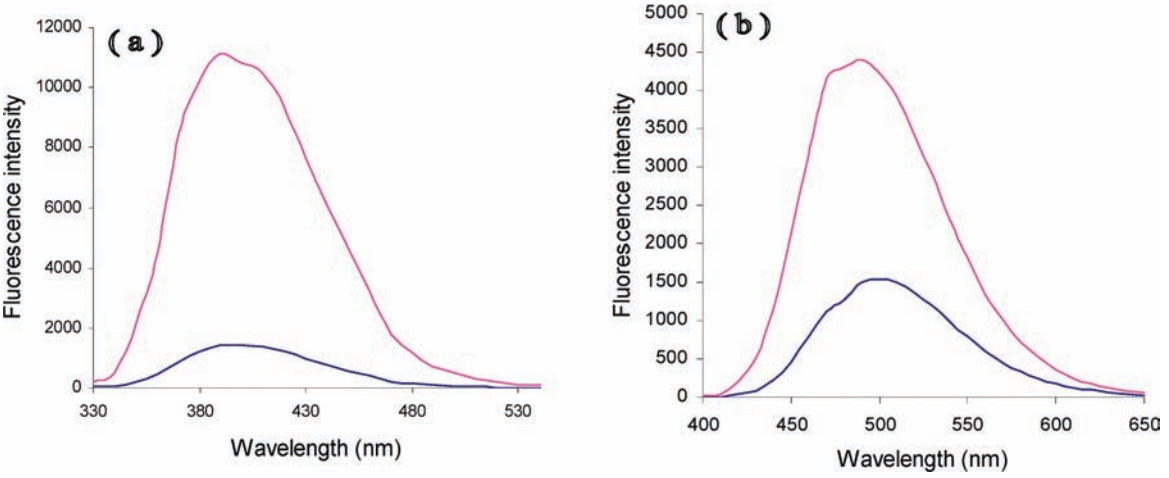

Figure 2. Emission spectra of benzothiazole derivatives (10 μM) in 3 mL pH = 7 buffer solution containing: (a) Compound **10** (blue) and **18b** (red) (λ_{ex} = 316 nm); (b) Compound **16** (blue) and **19b** (red) (λ_{ex} = 375 nm).

As expected, a red-shift was observed as an electron-donating group was added to the 6-position of benzothiazol. In aqueous buffer, the emission maxima of 6-methoxyl dye **10** and 6-dimethylamino dye **16** were approximately 390 and 500 nm, respectively. More red-shift was achieved with dimethylamino dye **16**. The emission maximum of the parent benzothiazole **6** is approximately 360 nm. Importantly, both dyes **10** and **16** were 'clickable' fluorogenic dyes whose 'clicked' products had a significant increase in fluorescence intensity (Figure 2). The quantum yield of **18b** was 0.36, but that of its parent compound **10** is only 0.05 in EtOH. The fluorescence intensity of **18b** (10 μM) in pH = 7.0 PBS buffer was 7.9-fold stronger than that of the parent dye **10** under the same condition. The quantum yield of **19b** and its parent compound **16** in EtOH were 0.65 and 0.49, respectively. The fluorescence intensity of **19b** (10 μM) in pH = 7.0 BPS buffer was 3.5-fold stronger than that of the parent dye **16**. Interestingly, the click reaction had little effect on wavelength.

Dimethylamino series, compounds **16** and **19**, had a long Stokes shift, 140−150 nm, in PBS buffer, while the Stokes shift of methoxyl series, compounds **10** and **18**, was approximately 70 nm. Solvent effect was also more significant for the dimethylamino series (Table 1). The Stokes shift for compounds **19** in methanol was shortened to 100−110 nm. In contrast, the 6-methoxy series only showed approximately 10 nm difference between the two solvents.

The fluorescent property of compounds **10** and **16**, and their corresponding 'clicked' products **18b** and **19b**, was further investigated in different pH conditions. As seen in Figure 3, compounds **10** and **18b** were relatively pH stable, while compounds **16** and **19b** showed clear pH dependency. From Figure 3b, the fluorescence intensities of compounds **16** and **19b** were down to zero at pH lower than 2. The fluorescence intensity of compounds **16** and **19b** increased with increasing pH, reaching the maxima at pH 6−8. The fluorescence intensity of **19b** dropped considerably on pH increase to 10, but the fluorescence intensity of **16** decreased only slightly. This clear pH dependence could be due to protonation of the dimethylamino group. In contrast, the methoxyl group cannot be protonated as easily as the amino group; thus, dyes **10** and **18b** are more pH stable.

The potential application of the developed 'click' fluorogenic dye was then validated in cell culture. For a better fluorescent contrast in biological application, dye **16** which has a long emission maximum and Stokes shift was selected for the study. The azide group was introduced into HeLa cells by incubating with AZT **17a** (2 μM) for 16 h. AZT is a nucleoside analogue which is known to be incorporated into DNA. After a thorough washing, cells were incubated with dye **16** and $CuSO_4$ for 3 h, followed by washes, and then, reducing agent NaAsc was added to initiate the 'click' reaction. Thirty minutes later, the cells were washed and monitored under a microscope. After 'click' reaction, an approximately 2-fold higher fluorescent signal was observed in the AZT treated cells using the common filter set for DAPI (4′,6-diamidino-2-phenylindole) stain (Figure 4). The fluorescent signal clearly highlight the nucleus, indicating that incorporated AZT reacted with dye **16**

Table 1. UV Absorption and Emission Spectra of Compounds 10, 16, 18(a-c), and 19(a-c)

	$\lambda_{max(abs)}$ (nm)	$\lambda_{max(em)}$ (nm)	Φ	Stokes shift (nm)
10	316 (MeOH)	379 (MeOH)	0.05[a]	63
	316 (H_2O)	393 (H_2O)		77
18a	316 (MeOH)	381 (MeOH)		65
	316 (H_2O)	392 (H_2O)		76
18b	315 (MeOH)	379 (MeOH)	0.36[a]	64
	315 (H_2O)	391 (H_2O)		76
18c	314 (MeOH)	381 (MeOH)		67
	314 (H_2O)	390 (H_2O)		76
16	364 (MeOH)	460 (MeOH)	0.49[b]	96
	343 (H_2O)	500 (H_2O)		157
19a	356 (MeOH)	466 (MeOH)		110
	350 (H_2O)	492 (H_2O)		142
19b	355 (MeOH)	459 (MeOH)	0.65[b]	104
	335 (H_2O)	493 (H_2O)		158
19c	352 (MeOH)	459 (MeOH)	0.63[b]	107
	332 (H_2O)	491 (H_2O)		159

[a] Quantum yield conditions: Solvent: EtOH, λ_{ex}: 330 nm; slit: 4 nm, λ_{em}: 345−550 nm; slit: 4 nm, Inc.: 1 nm; reference compound: 9, 10- diphenylanthracence, Φ = 0.90. [b] Quantum yield conditions: Solvent: EtOH, λ_{ex}: 360 nm, slit: 2 nm, λ_{em}: 375−650 nm; slit: 2 nm, Inc.: 1 nm; reference compound: 7-diethylamino-4-methylcoumarin, Φ = 0.73.

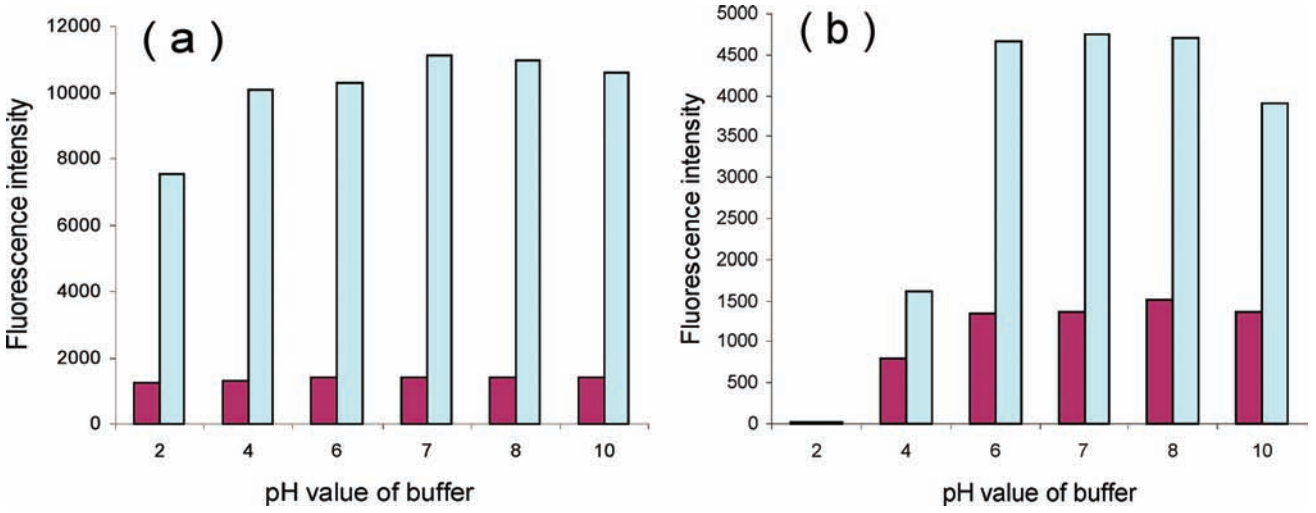

Figure 3. Effect of pH on fluorescence intensity ratio of benzothiazole derivatives in different pH PBS buffer. Conditions: (a) Compound **10** (Brown) and **18b** (Cyan), λ_{ex}: 316 nm, 10 μM. (b) Compound **16** (Brown) and **19b** (Cyan), λ_{ex}: 375 nm, 10 μM.

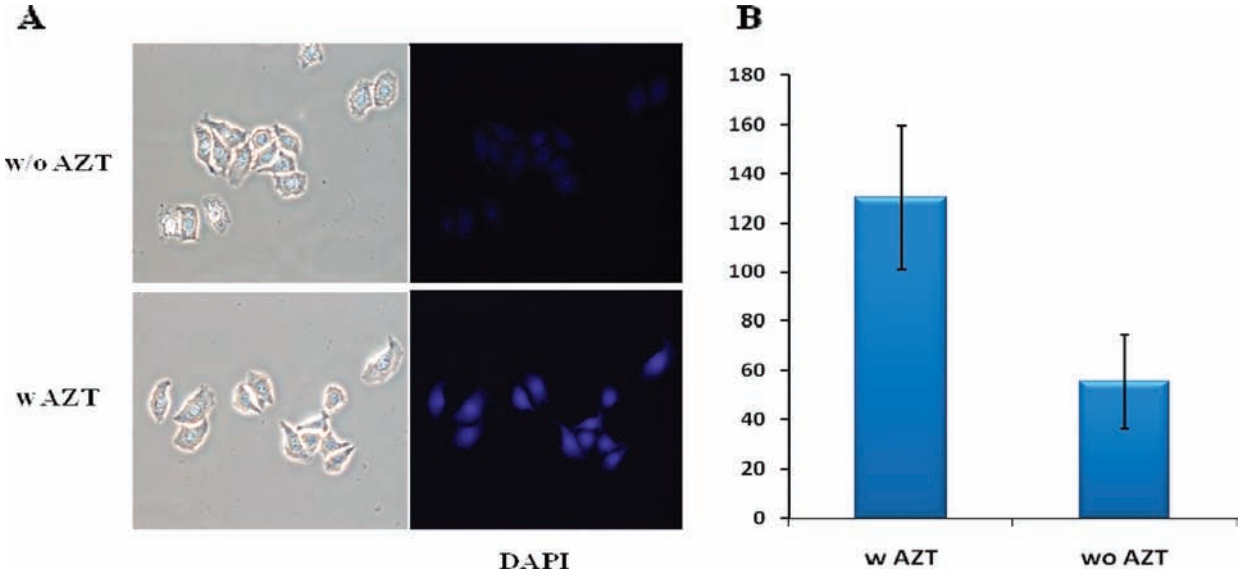

Figure 4. 'Click-on' fluorescence images of cells (A) and quantitation of fluorescent signal (B) after reacting with compound **16** (10 μM) in HeLa cells (20×). The fluorescent signal was imaged using the convention DAPI filter set.

and the 'click' reaction is able to brighten the fluorescent signal in cells. In a separate experiment, the cells were treated with AZT **17a** and dye **16**, but $CuSO_4$. The fluorescent signal level of these cells is compatible to that of the cells without AZT **17a**.

CONCLUSION

We describe the preparation of two 2-ethynyl-benzothiazole derivatized 'click-on' fluorogenic dyes. The two derivatives with an electron-donating dimethylamino or methoxyl group at the 6-position showed a 30 to 130 nm red-shift in fluorescence wavelength, compared to the parent benzothiazole fluorogenic dye. The model reactions with functionalized nucleoside and amino acid indicated that the developed 'click-on' dye could label various biomolecules, such as nucleic acids, proteins, and other molecules.

ASSOCIATED CONTENT

Supporting Information. Details of synthesis, characterization and cell culture validation. This material is available free of charge via the Internet at http://pubs.acs.org.

AUTHOR INFORMATION

Corresponding Author

Ching-Hsuan Tung, Department of Radiology, Methodist Hospital Research Institute, 6565 Fannin St. B5-009, Houston, TX 77030. Tel: +1 713-441-8682. Fax: +1 713-441-8689. E-mail: ctung@tmhs.org.

ACKNOWLEDGMENT

We thank the NMR facility at M. D. Anderson Cancer Center for acquiring all NMR data. This research was supported in part by NIH CA135312, and GM094880.

REFERENCES

(1) Hilderbrand, S. A. (2010) Labels and probes for live cell imaging: overview and selection guide. *Methods Mol. Biol. 591*, 17–45.

(2) Escobedo, J. O., Rusin, O., Lim, S., and Strongin, R. M. (2010) NIR dyes for bioimaging applications. *Curr. Opin. Chem. Biol. 14*, 64–70.

(3) Kucherak, O. A., Oncul, S., Darwich, Z., Yushchenko, D. A., Arntz, Y., Didier, P., Mely, Y., and Klymchenko, A. S. (2010) Switchable nile red-based probe for cholesterol and lipid order at the outer leaflet of biomembranes. *J. Am. Chem. Soc. 132*, 4907–4916.

(4) Kolb, H. C., and Sharpless, K. B. (2003) The growing impact of click chemistry on drug discovery. *Drug Discovery Today 8*, 1128–1137.

(5) Link, A. J., and Tirrell, D. A. (2003) Cell surface labeling of Escherichia coli via copper(I)-catalyzed [3 + 2] cycloaddition. *J. Am. Chem. Soc. 125*, 11164–11165.

(6) Jao, C. Y., and Salic, A. (2008) Exploring RNA transcription and turnover in vivo by using click chemistry. *Proc. Natl. Acad. Sci. U. S. A. 105*, 15779–15784.

(7) Kele, P., Li, X., Link, M., Nagy, K., Herner, A., Lorincz, K., Beni, S., and Wolfbeis, O. S. (2009) Clickable fluorophores for biological labeling--with or without copper. *Org. Biomol. Chem. 7*, 3486–3490.

(8) Prescher, J. A., and Bertozzi, C. R. (2005) Chemistry in living systems. *Nat. Chem. Biol. 1*, 13–21.

(9) Chang, P. V., Prescher, J. A., Sletten, E. M., Baskin, J. M., Miller, I. A., Agard, N. J., Lo, A., and Bertozzi, C. R. (2010) Copper-free click chemistry in living animals. *Proc. Natl. Acad. Sci. U. S. A. 107*, 1821–1826.

(10) Giepmans, B. N., Adams, S. R., Ellisman, M. H., and Tsien, R. Y. (2006) The fluorescent toolbox for assessing protein location and function. *Science 312*, 217–224.

(11) Diermeier-Daucher, S., Clarke, S. T., Hill, D., Vollmann-Zwerenz, A., Bradford, J. A., and Brockhoff, G. (2009) Cell type specific applicability of 5-ethynyl-2′-deoxyuridine (EdU) for dynamic proliferation assessment in flow cytometry. *Cytometry A 75*, 535–546.

(12) Chehrehasa, F., Meedeniya, A. C., Dwyer, P., Abrahamsen, G., and Mackay-Sim, A. (2009) EdU, a new thymidine analogue for labelling proliferating cells in the nervous system. *J. Neurosci. Methods 177*, 122–130.

(13) Salic, A., and Mitchison, T. J. (2008) A chemical method for fast and sensitive detection of DNA synthesis in vivo. *Proc. Natl. Acad. Sci. U. S. A. 105*, 2415–2420.

(14) Baskin, J. M., Prescher, J. A., Laughlin, S. T., Agard, N. J., Chang, P. V., Miller, I. A., Lo, A., Codelli, J. A., and Bertozzi, C. R. (2007) Copper-free click chemistry for dynamic in vivo imaging. *Proc. Natl. Acad. Sci. U. S. A. 104*, 16793–16797.

(15) Link, A. J., Vink, M. K., and Tirrell, D. A. (2004) Presentation and detection of azide functionality in bacterial cell surface proteins. *J. Am. Chem. Soc. 126*, 10598–10602.

(16) Chang, P. V., Dube, D. H., Sletten, E. M., and Bertozzi, C. R. (2010) A strategy for the selective imaging of glycans using caged metabolic precursors. *J. Am. Chem. Soc. 132*, 9516–9518.

(17) Nagy, K., Orban, E., Bosze, S., and Kele, P. (2010) Clickable long-wave "mega-stokes" fluorophores for orthogonal chemoselective labeling of cells. *Chem. Asian J. 5*, 773–777.

(18) Sivakumar, K., Xie, F., Cash, B. M., Long, S., Barnhill, H. N., and Wang, Q. (2004) A fluorogenic 1,3-dipolar cycloaddition reaction of 3-azidocoumarins and acetylenes. *Org. Lett. 6*, 4603–4606.

(19) Zhou, Z., and Fahrni, C. J. (2004) A fluorogenic probe for the copper(I)-catalyzed azide-alkyne ligation reaction: Modulation of the fluorescence emission via $^3(n,\pi^*)$-$^1(\pi,\pi^*)$ inversion. *J. Am. Chem. Soc. 126*, 8862–8863.

(20) Beatty, K. E., Liu, J. C., Xie, F., Dieterich, D. C., Schuman, E. M., Wang, Q., and Tirrell, D. A. (2006) Fluorescence visualization of newly synthesized proteins in mammalian cells. *Angew. Chem., Int. Ed. Engl. 45*, 7364–7367.

(21) Li, K., Lee, L. A., Lu, X., and Wang, Q. (2010) Fluorogenic "click" reaction for labeling and detection of DNA in proliferating cells. *Biotechniques 49*, 525–527.

(22) Xie, F., Sivakumar, K., Zeng, Q. B., Bruckman, M. A., Hodges, B., and Wang, Q. (2008) A fluorogenic 'click' reaction of azidoanthracene derivatives. *Tetrahedron 64*, 2906–2914.

(23) Sawa, M., Hsu, T. L., Itoh, T., Sugiyama, M., Hanson, S. R., Vogt, P. K., and Wong, C. H. (2006) Glycoproteomic probes for fluorescent imaging of fucosylated glycans in vivo. *Proc. Natl. Acad. Sci. U. S. A. 103*, 12371–12376.

(24) Qi, J., and Tung, C. H. (2011) Development of benzothiazole 'click-on' fluorogenic dyes. *Bioorg. Med. Chem. Lett. 21*, 320–323.

(25) Krasnokutskaya, E. A., Semenischeva, N. I., Filimonov, V. D., and Knochel, P. (2007) A new, one-step, effective protocol for the iodination of aromatic and heterocyclic compounds via aprotic diazotization of amines. *Synthesis* 81–84.

(26) Van den Hoven, B. G., and Alper, H. (2001) Remarkable synthesis of 2-(Z)-6-(E)-4H-[1,4]-thiazepin-5-ones by zwitterionic rhodium-catalyzed chemo- and regioselective cyclohydrocarbonylative ring expansion of acetylenic thiazoles. *J. Am. Chem. Soc. 123*, 1017–1022.

(27) Schlegel, J., and Maas, G. (1999) Propyne iminium salts by N-alkylation of alkynyl imines. *Synthesis* 100–106.

(28) Delmas, F., Avellaneda, A., Di Giorgio, C., Robin, M., De Clercq, E., Timon-David, P., and Galy, J. P. (2004) Synthesis and antileishmanial activity of (1,3-benzothiazol-2-yl) amino-9-(10H)-acridinone derivatives. *Eur. J. Med. Chem. 39*, 685–690.

Supporting Information

Developing visible fluorogenic ‘click-on’ dyes for cellular imaging

Jianjun Qi, Myung-Shin Han, Yu-Cheng Chang, Ching-Hsuan Tung*

List of contents

1. Chemical synthesis experiment procedure
    a. 2-iodo-5-methoxybenzo[d]thiazole
    b. 6-methoxy-2-((trimethylsilyl)ethynyl)benzo[d]thiazole
    c. 2-ethynyl-6-methoxybenzo[d]thiazole
    d. 2-chloro-6-nitrobenzo[d]thiazole
    e. 2-chlorobenzo[d]thiazol-6-amine
    f. 2-chloro-N,N-dimethylbenzo[d]thiazol-6-amine
    g. N,N-dimethyl-2-((trimethylsilyl)ethynyl)benzo[d]thiazol-6-amine
    h. 2-ethynyl-N,N-dimethylbenzo[d]thiazol-6-amine
    i. General ‘click’ reaction procedure
2. pH effect of fluorescent intensity experiment procedure
3. Cell culture experiment procedure
4. References

Materials and Reagents. Chemicals used in the syntheses were purchased from Aldrich or TCI without further purification. NMR spectra were recorded with a Bruker Avance Dpx 300 spectrometer and the δ values are in ppm vs $SiMe_4$ (0 ppm, 300MHz). Mass spectra were recorded using LCQ-Fleet mass spectrometer. UV spectra were recorded with a Varian 50 Bio UV-visible spectrometer; Fluorescence emission and excitation spectra were recorded using a FluoroMax-4 Spectrofluorometer and Spectra Max-M2 plate reader. HPLC was done by Varian 920-LC liquid chromatograph. Thin-layer chromatography (TLC) was performed on precoated silica gel 60F-254 glass plates.

2-iodo-5-methoxybenzo[d]thiazole (8)[1, 2]

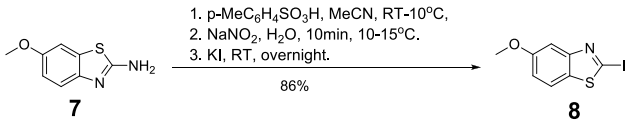

7 8

A solution of $NaNO_2$ (3.5 g, 50 mmol) and KI (10.5 g, 65 mmol) in H_2O was added dropwise to a mixture of 6-methoxybenzo[d]thiazol-2-amine (7) (4.5 g, 25 mmol), p-TsOH (15 g) in acetonitrile (100 ml) at 0°C around 30 min. The reaction was run overnight at RT, and then was quenched by 350 ml of water. The pH was adjusted to 8-9 with $NaHCO_3$. The precipitate was collected by filtration, and washed with water. The filter cake was dissolved in DCM, dried over Na_2SO_4, filtered through a silica gel column. The filtrate DCM solution was concentrated, and the crystallized pale brown solid (4.39 g) was collected by filtration. The remaining filtrate was further dried to give brown solid (1.87 g). The combined solid gave 6.25 g of compound **8** with 86% yield. TLC: Rf: 0.386 (hexane/ethyl acetate=6/1). MS (ESI) m/z 292 (M^+ +H); ^{1}HNMR ($CDCl_3$, 300MHz) δ 7.92 (1H, d, J=9Hz), 7.31 (1H, d, J=2.4Hz), 7.06 (1H, dd, J_1=9Hz, J_2=2.7Hz), 3.89 (3H, s).

6-methoxy-2-((trimethylsilyl)ethynyl)benzo[d]thiazole (9)[3, 4]

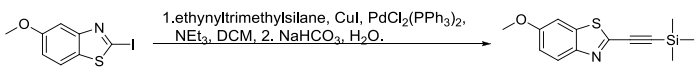

8 9

To a solution of 2-iodo-5-methoxybenzo[d]thiazole (8) (1.86 g, 6.39 mmol) and triethylamine (4 ml) in DCM (8 ml) was added ethynyltrimethylsilane (1.25 g, 12.78 mmol), CuI (26 mg), and $PdCl_2(PPh_3)_2$ (90

mg), and refluxed at 65 ^{o}C for 1h. The reaction solution was filtered through a short silica gel column, eluted with hexane/ethyl acetate=1/1. Solvent was removed by reduced pressure and the residue was purified by silica gel column using hexane/ethyl acetate=6/1 as eluent to give 1.14g yellow oil, 68.3% yield. TLC: Rf: 0.63 (hexane/ethyl acetate=6/1). MS (ESI) m/z 262 (M^+ + H); ^{1}HNMR ($CDCl_3$, 300MHz) δ 7.93 (1H, d, J=9Hz), 7.30 (1H, d, J=2.4Hz), 7.13 (1H, dd, J_1=9Hz, J_2=2.4Hz), 3.90 (3H, s), 0.32 (9H, s).

2-ethynyl-6-methoxybenzo[d]thiazole (10)

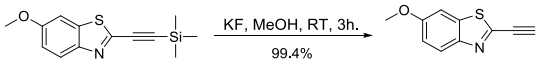

9 **10**

6-methoxy-2-((trimethylsilyl)ethynyl)benzo[d]thiazole (9) (1 g) in MeOH (30 ml) was reacted with KF (1 g) for 45 min at RT. Solvent was removed under reduced pressure, and the residue was purified by silica gel column using hexane/ethyl acetate=12/1 as eluent to give 0.72 g of pale yellow solid, yield 99.4%. TLC: Rf: 0.25 (hexane/ethyl acetate=6/1). MS (ESI) m/z 190 (M^+ +H); ^{1}HNMR ($CDCl_3$, 300MHz) δ 7.97 (1H, d, J=9Hz), 7.31 (1H, d, 2.4Hz), 7.15 (1H, dd, J_1=9Hz, J_2=2.4Hz), 3.91 (3H, s), 3.57 (1H, s).

2-chloro-6-nitrobenzo[d]thiazole (12)[(5)]

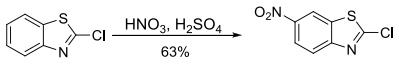

11 **12**

2-Chlorobenzothiazole (11) (25.1 g, 147 mmol) and potassium nitrate (16.4 g, 162 mmol) were added into conc. H_2SO_4 (135 mL) on ice. The mixture was stirred at 0 ^{o}C for 30 min and then room temperature for 1 h. The resulting mixture was poured onto ice and the precipitate was collected by filtration. The residue was washed with water and ethanol to give off-white solid (20.0 g, 63%). The crude product was used for next step without further purification.

2-chlorobenzo[d]thiazol-6-amine (13)

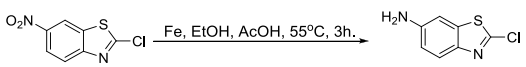

12 **13**

A suspension of Fe (10.00 g, 178.6 mmol) in ethanol (100 mL) and water (40 mL) was mixed with HCl (5 mL) at room temperature. The crude product from the previous step (5.00 g, 23.37 mmol) in ethanol (50

mL) was added to the suspension and refluxed at 90 ^{o}C for 3 hrs. The resulting mixture was extracted with chloroform (200 mL) and washed with water and brine. The solvent was removed under reduced pressure and the crude product was purified by flash column chromatography using ethyl acetate/hexane (5 to 30%) as eluent, giving yellow crystal solid 3.24 g (48% for two steps). ^{1}H NMR (300 MHz, $CDCl_3$) δ 7.72 (d, J = 8.7 Hz, 1 H), 7.01 (d, J = 2.4 Hz, 1 H), 6.83 (dd, J = 6.0, 2.4 Hz, 1 H); ESI-MS (ES^+) m/z calcd for $C_7H_5ClN_2S$ 184.0, found 185.0 ($M + H^+$).

2-chloro-N,N-dimethylbenzo[d]thiazol-6-amine (14)

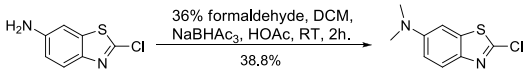

13 **14**

To a solution of 2-chlorobenzo[d]thiazol-6-amine (13) (920 mg, 5 mmol) in DCM (50 ml) was added 36% formaldehyde (5 ml) and $NaBHAc_3$ (3.25 g), and followed by HOAc (0.6 ml). The reaction solution was stirred overnight at RT. Extracted with DCM, washed with brine, and dried over Na_2SO_4. The solvent was removed, and the residue was purified by silica gel column using hexane/ethyl acetate=10/1 as eluent to give 411 mg white crystal **14** with 38.8% yield. TLC: Rf: 0.43 (hexane/ethyl acetate=5/1). MS (ESI) m/z 213 (M^+ +H); ^{1}HNMR ($CDCl_3$, 300MHz) δ 7.77 (1H, d, J=9Hz), 6.98 (1H, d, J=2.7Hz), 6.93 (1H, dd, J_1=9Hz, J_2=2.7Hz), 3.04 (6H, s).

N,N-dimethyl-2-((trimethylsilyl)ethynyl)benzo[d]thiazol-6-amine (15)

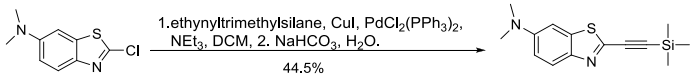

14 **15**

To a solution of 2-chloro-N,N-dimethylbenzo[d]thiazol-6-amine (14) (212 mg, 1.0 mmol) in DCM (2.2 ml) and NEt_3 (1.1 ml) was added ethynyltrimethylsilane (217 mg, 2 mmol), CuI (20 mg), and $PdCl_2(PPh_3)_2$ (20 mg) and refluxing at 65 ^{o}C for 3 h. The reaction solution was filtered through a short silica gel column, washed with hexane/ethyl acetate=1/1. The solvent was removed by reduced pressure, and the residue was purified by silica gel column using hexane/ethyl acetate=10/1 as eluent to give 122 mg yellow solid, 44.5% yield. TLC: Rf: 0.5 (hexane/ethyl acetate=5/1). MS (ESI) m/z 275 (M^+ +H); ^{1}HNMR ($CDCl_3$, 300 MHz) δ 7.87 (1H, d, J=9Hz), 7.02 (1H, d, J=2.7Hz), 6.98 (1H, dd, J_1=9Hz, J_2=2.7Hz), 3.06 (6H, s), 0.31 (9H, s).

2-ethynyl-N,N-dimethylbenzo[d]thiazol-6-amine (16)

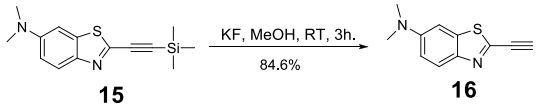

To a solution of N,N-dimethyl-2-((trimethylsilyl)ethynyl)benzo[d]thiazol-6-amine (15) (40 mg) in MeOH (10 ml) was added KF (250 mg) and stirred 3 h at RT. Solvent was removed under reduced pressure, the residue was purified by silica gel column, eluted by hexane/ethyl acetate=5/1 to give 25 mg of yellow solid, yield 84.7%. TLC: Rf: 0.3 (hexane/ethyl acetate=5/1). MS (ESI) m/z 203 (M^+ +H); ^{1}HNMR ($CDCl_3$, 300 MHz) δ 7.88 (1H, d, J=8.7Hz), 7.02 (1H, dd, J_1=4.2Hz, J_2=2.7Hz), 6.98 (1H, d, J=2.4Hz), 3.53 (1H, s), 3.07 (6H, s).

General 'click' reaction procedure (18, 19)

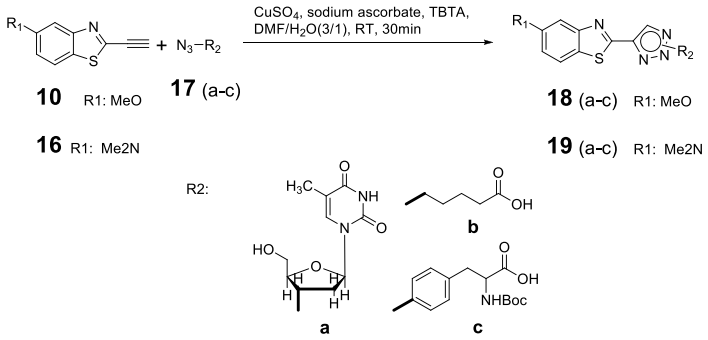

To a solution of AZT (**17a**) (14 mg, 0.052 mmol) in DMF (3 ml) and H_2O (1 ml) was added benzothiazole alkyne (**10**) (8 mg, 0.042 mmol), $CuSO_4$ (10 mg), sodium ascorbate (25 mg), and TBTA (2 mg), and stirred for 1 h at RT, followed by TLC and HPLC. No starting material **10** was detected after reaction (100% conversion), only the desired product **18a** was observed in HPLC. The reaction solution was extracted with EtOAc, washed with brine, and dried over Na_2SO_4. After removing solvent under reduced pressure, the residue was purified by silica gel column, eluted with 5% MeOH in EtOAc to give 11 mg white solid **18a** with 57% yield.

Compounds 18 (b, c) and **19 (a-c)** were prepared using the same procedure, the mole ratio of **10** or **16** and **7** were 1.1 to 1.5.

Table S-1 the Mass spectra and ^{1}HNMR data of the 'click on' products.

'Click' products	Mass	^{1}HNMR
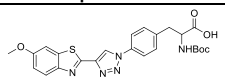	496 (M^{+}+H)	(CD_3OD) 9.09 (1H, s), 7.92 (1H, d, J=9.0Hz), 7.91 (2H, d, J=8.1Hz), 7.63 (1H, d, J=2.7Hz), 7.53 (2H, d, J=8.4Hz), 7.18 (1H, dd, J_1=9.0Hz, J_2=2.7Hz), 4.43 (1H, m), 3.93 (3H, s), 3.06 (1H,m), 1.4 (9H, s)
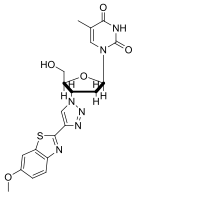	457 (M^{+}+H)	(CD_3OD) 8.72 (1H, s), 7.96 (1H, d, J=1.2Hz), 7.90 (1H, d, J=9.0Hz), 7.60 (1H, d, J=2.4Hz), 7.16 (1H, dd, J_1=9.0Hz, J_2=2.7Hz), 6.57 (1H, t, J=6.6Hz), 5.58 (1H,m), 4.48 (1H, m), 3.97 (1H, dd, J1= 12.3Hz, J_2= 3.3Hz), 3.92 (3H, s), 3.04 (1H, m), 2.84, (1H, m), 2.03 (1H, s), 1.94 (3H, s)
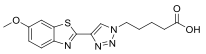	333 (M^{+}+H)	(CD_3OD) 8.59 (1H, s), 7.90 (1H, d, J=9.0Hz), 7.59 (1H, d, J=2.4Hz), 7.16 (1H, dd, J_1=9.0Hz, J_2=2.4Hz), 4.56 (2H, t, J=6.9Hz), 3.92 (3H, s), 2.03 (2H, m), 1.67 (2H, m)
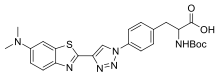	509 (M^{+}+H)	(CD_3OD) 9.08 (1H, s), 7.95 (1H, d, J=9.0Hz), 7.92 (2H, d, J=8.4Hz), 7.61 (1H, d, J=2.4Hz), 7.53 (2H, d, J=8.4Hz), 7.38 (1H, s), 7.30 (1H, dd, J_1=9.0Hz, J_2=2.4Hz), 4.46 (1H, m), 3.17 (6H, s), 3.08 (2H,m), 1.41 (9H, s)
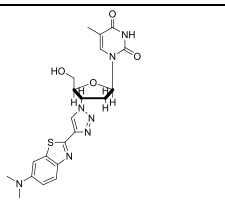	470 (M^{+}+H)	(CD_3OD) 8.68 (1H, s), 7.96 (1H, d, J=1.2Hz), 7.86 (1H, d, J=9.0Hz), 7.41 (1H, d, J=2.4Hz), 7.16 (1H, dd, J_1=9.0Hz, J_2=2.4Hz), 6.57 (1H, t, J=6.6Hz), 5.58 (1H,m), 4.48 (1H, m), 3.97 (1H, dd, J_1= 12.3Hz, J_2= 3.0Hz), 3.85(1H, dd, J_1= 12.3Hz, J_2= 3.0Hz), 3.10 (6H, s), 3.01 (1H, m), 2.83, (1H, m), 1.94 (3H, d, J=1.2Hz)
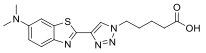	346 (M^{+}+H)	(D_2O+NaOD) 8.35 (1H, s) (very easy to be exchanged by D), 7.53 (1H, d, J=9.3Hz), 7.15 (1H, d, J=2.1Hz), 6.90 (1H, dd, J_1=9.3Hz, J_2=2.4Hz), 4.29 (2H, t, J=7.2Hz), 2.74 (6H, s), 2.08 (2H, t, J=7.5Hz), 1.79 (2H, m), 1.42 (2H, m).

pH effect of fluorescent intensity

The buffers of pH 3~10 were prepared by adding 0.1M citric acid or 0.1M NaOH solution to PBS Buffer. The pH 2 solution was prepared by adding 0.1M HCl solution. Compounds **10**, **18b, 16**, and **19b** (10μM) were dissolved in each pH and their fluorescence was measured by 316 nm or 375 nm excitation.

Cell culture

HeLa cells, human cervix adenocarcinoma epithelial cells, were cultured in Dulbecco's modified eagle medium (DMEM) supplemented with 10% fetal bovine serum (FBS),100 U/ml penicillin and 100 μg/ml streptomycin (Invitrogen). HeLa cells (2.5×10^4) were seeded with or without 2 μM AZT **17a** in a plastic petri dish with a bottom glass optical window (35 mm, MatTek) for 16 hrs at 37 ^{o}C. The cells were washed 3 times with medium before incubated with dye **16** (10 μM) and $CuSO_4$ (1 mM) for 3 hrs at 37 ^{o}C. After three washes with medium, reducing agent NaAsc (10 mM) in fresh medium was added to the cells and incubated for 30mins at 37 ^{o}C. The cell was fully washed by PBS and imaged by a fluorescence microscope using a conventional DAPI filter set. Exposure time was 125 ms. Fluorescence intensity of cells was quantified by manually outlined ROI (Region-of-interest) on 50 individual cells using an open source ImageJ program (v1.44, NIH). High resolution fluorescent images, 20X, were used for all quantitation.

References:

(1) Krasnokutskaya, E. A., Semenischeva, N. I., Filimonov, V. D., and Knochel, P. (2007) A new, one-step, effective protocol for the iodination of aromatic and heterocyclic compounds via aprotic diazotization of amines. *Synthesis*, 81-84.

(2) Qi, J., and Tung, C. H. (2011) Development of benzothiazole 'click-on' fluorogenic dyes. *Bioorg Med Chem Lett 21*, 320-323.

(3) Van den Hoven, B. G., and Alper, H. (2001) Remarkable synthesis of 2-(Z)-6-(E)-4H-[1,4]-thiazepin-5-ones by zwitterionic rhodium-catalyzed chemo- and regioselective cyclohydrocarbonylative ring expansion of acetylenic thiazoles. *J. Am. Chem. Soc. 123*, 1017-1022.

(4) Schlegel, J., and Maas, G. (1999) Propyne iminium salts by N-alkylation of alkynyl imines. *Synthesis*, 100-106.

(5) Delmas, F., Avellaneda, A., Di Giorgio, C., Robin, M., De Clercq, E., Timon-David, P., and Galy, J. P. (2004) Synthesis and antileishmanial activity of (1,3-benzothiazol-2-yl) amino-9-(10H)-acridinone derivatives. *Eur J Med Chem* 39, 685-690.

Bioconjugate Chemistry

COMMUNICATION

pubs.acs.org/bc

Chemical Synthesis of Cell-Permeable Apoptotic Peptides from *in Vivo* Produced Proteins

Thomas Fricke,[†] Robert J. Mart,[†] Catherine L. Watkins,[‡,§] Marie Wiltshire,[§] Rachel J. Errington,[§] Paul J. Smith,[§] Arwyn T. Jones,[‡] and Rudolf K. Allemann*[,†]

[†]School of Chemistry, Cardiff University, Park Place, Cardiff CF10 3AT, United Kingdom

[§]School of Medicine, Cardiff University, Heath Park, Cardiff, CF14 4XN, United Kingdom

[‡]Welsh School of Pharmacy, Cardiff University, King Edward VII Avenue, Cardiff, CF10 3XF, United Kingdom

Supporting Information

ABSTRACT: *In vivo* synthesis of peptides by bacterial expression has developed into a reliable alternative to solid-phase peptide synthesis. A significant drawback of *in vivo* methods is the difficulty with which gene products can be modified post-translationally. Here, we present a method for the facile modification of peptides generated in bacterial hosts after cyanogen bromide cleavage at C-terminal methionines. Reaction of the resulting homoserine lactones with propargylamine allows efficient and selective modification with a wide variety of chemicals such as fluorescent dyes, biotin derivatives, polyprenyls, lipids, polysaccharides, or peptides. Attachment of the cell penetrating peptide octa-arginine (R_8) to peptides derived from the proapoptotic tumor suppressor Bak BH3 led to efficient cellular uptake and subsequent cytochrome *c* release from mitochondria, culminating in induction of apoptosis similar to that observed with peptides linked to R_8 via the peptide backbone. These results highlight the significant potential for use of such tools in live cells.

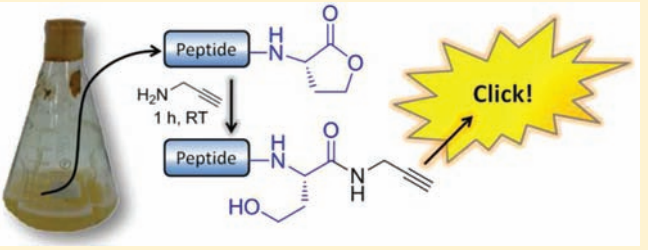

Protein−protein interactions are central to cellular processes and therefore provide opportunities for innovative research tools and medicines.[1−5] However, the interacting surfaces are generally hydrophobic, large, and shallow, and only a few examples exist of small molecules that target protein interfaces.[6−8] Mimicking Nature's strategy for protein recognition by using peptides is an elegant alternative and interest in therapeutic peptides is increasing;[2,9−12] the number of peptides in clinical studies has nearly doubled over the last 10 years.[13] The principal advantage of such peptides is the relative ease by which molecules with highly specific binding affinities can be synthesized through a series of simple amide bond formations. Concerns about short peptide lifetimes in the cellular environment and the difficulty with which most peptides pass across cell membranes have hitherto limited the use of peptides as therapeutics and as tools for biomedical research. However, the metabolic stability of peptides can be increased through additional chemical modification, while the use of cell penetrating peptides facilitates transport across cellular membranes. Examples of such transporter sequences include the HIV Tat peptide derived from the human immunodeficiency virus 1 trans-activating transcriptional activator,[14,15] penetratin from the *Drosophila* antennapedia homeodomain[16] and synthetic variants such as octa-arginine.[17] These peptides possess well-known abilities to enhance uptake of cargos such as peptides, proteins, DNA, and RNA into mammalian cells.[18−22] The additional length of such transporter sequences and any intervening spacer regions can, however make the chemical synthesis difficult and costly.

In recent years, new methods for high yielding syntheses of peptides in bacterial cells have been developed[23−25] and the production of peptides as fusions with larger carrier proteins has established a reliable alternative to standard solid-phase peptide synthesis. A significant drawback of the expression approach is the difficulty to efficiently and selectively modify the resulting peptides. Opportunities to attach molecules such as biotin, lipids, fluorescent dyes, glycans, or peptides in a selective way are limited by the availability of reactions that are selective for particular amino acid side chains. Here, we present a method to modify *in vivo* generated peptides to create a C-terminal alkyne group that can be transformed with a wide variety of azide reagents. Cleavage of methionine containing peptides with cyanogen bromide results in the formation of a C-terminal homoserine lactone,[26] which is amenable to nucleophilic attack. Previous reports have found homoserine lactones to be poor electrophiles that require the use of large excesses of expensive nucleophiles.[23,27] Here, the lactones were reacted with an excess of the relatively inexpensive propargylamine, resulting in the formation of a stable amide linkage between the peptide and an

Received: June 28, 2011
Revised: August 1, 2011
Published: August 08, 2011

ACS Publications © 2011 American Chemical Society

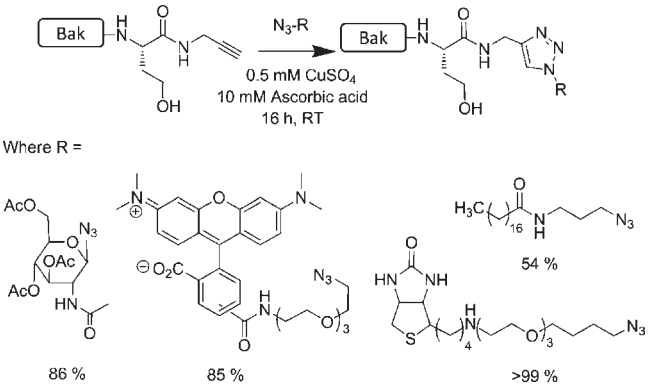

Figure 1. Structures of azides conjugated to alkyne modified peptides used in this study.

Scheme 1. Outline of the Facile Synthesis of Bioconjugates from Ketosteroid Isomerase Fusion Proteins[a]

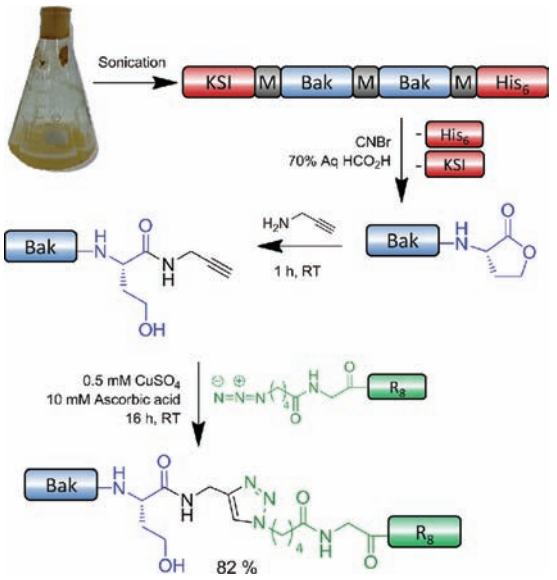

[a] Copper catalyzed [3 + 2] cycloaddition for the production of C-terminally modified Bak peptides from *in vivo* generated fusions with ketosteroid isomerase (KSI) that were cleaved with CNBr at methionines (M).

alkyne group. The alkyne could then be reacted with a variety of different azide containing molecules and commercially available dyes *via* high-yielding copper accelerated [3 + 2] cycloadditions (Figure 1).[28,29]

In addition to the conjugation of peptides with small molecules, this method was applied to the generation of peptides derived from the protein Bak, a member of the B-cell leukemia-2 (Bcl-2) family of proteins, which play key roles in the regulation of programmed cell death.[30] Bcl-2 family proteins are characterized by the presence of up to four conserved Bcl-2 homology domains that contain α-helical segments. The pro-apoptotic tumor suppressors Bax and Bak are antagonized by antiapoptotic Bcl-2 members (eg Bcl-2 and Bcl-x_L) via protein−protein interactions. Bak is often down regulated in cancer cells[31] with evidence that diverse apoptotic stimuli can preferentially engage the Bak pathway.[32] Peptides derived from the BH3 helix of Bak

Table 1. Amino Acid Sequences of Peptides Used in This Study and Binding Affinities to Bcl-x_L

name	sequence	K_D/nM [b]
Bak wt	CGGQVGRQLAIIGDDINR-Hsl[a]	90.9 ± 9.0
Bak GR_8-click	CGGQVGRQLAIIGDDINR-triazole-GR_8	28.3 ± 4.8
Bak-$SGGR_8$	CGGQVGRQLAIIGDDINRSGGR$_8$-Hsl[a]	25.9 ± 3.7
Bak L78A	CGGQVGRQAAIIGDDINR-Hsl[a]	No Binding
Bak L78A-GR_8-click	CGGQVGRQAAIIGDDINR-triazole-GR_8	No Binding
CGR_8	CGR_8	No Binding

[a] Homoserine lactone. [b] Measured by fluorescence anisotropy using Alexa 488 labeled peptides and Bcl-x_L.

have been shown to disrupt the interaction between native Bak and its partner Bcl-x_L.[33,34] Subsequent homo-oligomerization of activated Bak leads to the formation of channels that allow the release of cytochrome *c* from mitochondria, an early commitment step of apoptosis.[35]

The synthesis of a peptide modeled on the BH3 region of Bak with an additional N-terminal cysteine residue for selective functionalization was accomplished by introducing multiple repeats of a synthetic DNA sequence of the desired peptide into the expression vector pET-31b.[23] The peptides were produced in BL21(DE3) *E. coli* cells in high yields as protein fusions with ketosteroid isomerase (KSI). KSI is known to form poorly soluble inclusion bodies in *E. coli*, thereby protecting proteins from cellular proteases and allowing facile purification. The expressed fusion proteins were treated with cyanogen bromide in formic acid and the resulting peptides purified by standard reverse-phase HPL-chromatography (Scheme 1). The product peptides were isolated as a mixture of C-terminal homoserine lactone and homoserine forms; the latter could be converted quantitatively to the lactone with trifluoroacetic acid. Typical yields were 5 to 10 mg of purified lactone peptide per liter of bacterial cell culture (for details, see Supporting Information).

Treatment of the purified homoserine lactone peptides with propargylamine furnished peptidylpropargylamides in 75−85% yields. The peptide alkynes were treated with azides derived from Fluor 546, biotin, N-acetyl glucosamine, palmitic acid, and GR_8 (82% yield) to produce the corresponding triazoles in good yields (Figure 1, SI Figures S1−S7); these were readily purified by reversed-phase HPLC and identified from their mass spectra. The presence of an N-terminal cysteine allowed the synthesis of doubly labeled peptides through reaction of Alexa Fluor 488 maleimide with the sulfydryl of the *N*-terminal cysteine of the Fluor 546-triazole peptide (Supporting Information).

While the method described here allowed the efficient extension of the sequence of *in vivo* produced peptides, the presence of the triazole linkage could be envisaged to affect the physiological properties of the peptides. Literature reports indicate that Bak-R_8 peptides can induce cytochrome *c* release from mitochondria.[36] To demonstrate how our conjugation method can alter the properties of a peptide and assess the effect of the presence of the nonpeptidic linkage, we conjugated the Bak peptide and a mutant known to remove Bcl-x_L binding and apoptotic function (Bak L78A)[34] to an azido-GR_8 peptide. For comparison, an extended peptide, Bak-$SGGR_8$, was synthesized in *E. coli* and purified (Table 1). The N-terminal cysteine residue present in both peptides allowed for the conjugation of the Alexa Fluor 488 maleimide to monitor and measure the heterogeneity of cellular uptake and delivery.

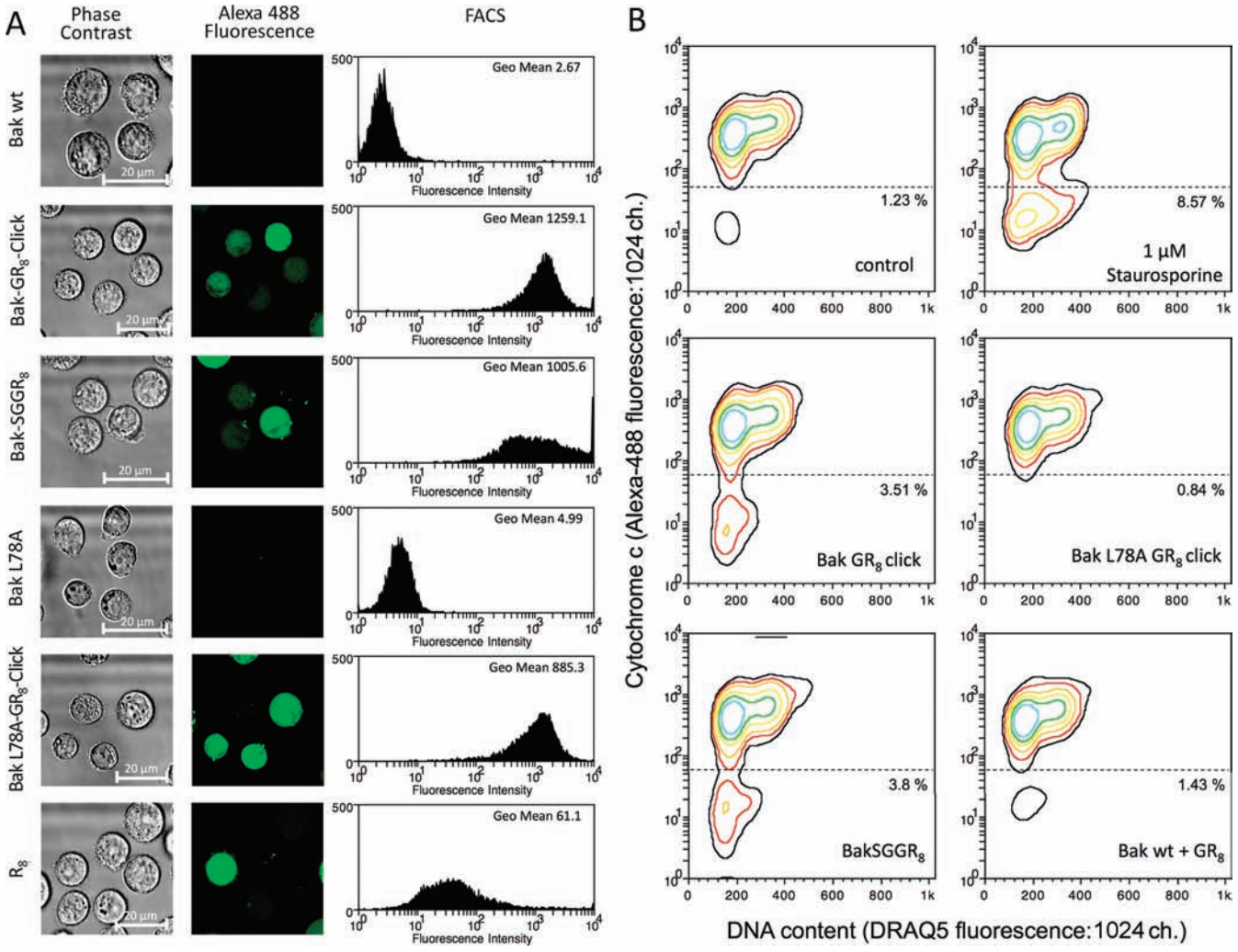

Figure 2. (a) Relative uptake of 5 μM Alexa Fluor 488 labeled peptides (Table 1) by KG1a cells for 1 h incubations at 37 °C analyzed by fluorescence microscopy and FACS (note the logarithmic scale; within the same cell population there was some degree of heterogeneity with respects to amount of internalized peptide and its subcellular distribution). (b) Contour plots from FACS (logarithmic contour spacing) showing cytochrome *c* release from mitochondria of KG1a cells after incubation with 20 μM peptides at 37 °C for 4 h.

Alexa Fluor 488 labeled $CGR_8{-}NH_2$ was synthesized by solid-phase chemistry to serve as a transporting, nonapoptotic control peptide. Fluorescence anisotropy measurements were used to determine the binding affinities of the labeled peptides to Bcl-x_L *in vitro* (Table 1).[33] As expected, no binding could be observed under the experimental conditions with Bak L78A, Bak L78A-GR_8-click, or CGR_8. Bak-$SGGR_8$ and Bak GR_8-click bound approximately 3 times more tightly to Bcl-x_L than Bak wt (Table 1 and Supporting Information). The K_D of 90.9 ± 9.0 nM for Bak wt was approximately 3 times lower than the value previously reported,[33] which is most likely attributable to the presence of Alexa Fluor 488.

Human leukemia myeloid KG1a cells were used to examine cellular uptake of the peptides. A cell population was incubated with peptide at 0.5 and 5 μM concentrations of peptides for 1 h at 37 °C and then analyzed by confocal microscopy and flow cytometry. As expected from literature precedents,[37,38] no Bak wt ingress was detectable at either concentration, whereas cells exposed to Bak GR_8-click, Bak-$SGGR_8$, and Bak L78A-GR_8-click showed fluorescent signals well above background, indicating peptide uptake. Furthermore, at 0.5 μM the fluorescence pattern was punctate indicating a possible endosomal mechanism for localization (Supporting Information). At the higher peptide concentration of 5 μM, the fluorescence signal per cell was higher and the cytoplasmic labeling diffuse, implying direct uptake (Figure 2a). Flow cytometry analysis of cells (FACS) indicated a ~350-fold increase of the mean fluorescence signal present in cells incubated with 5 μM Bak-$SGGR_8$, Bak GR_8-click, and Bak L78A-GR_8-click over control cells or those incubated with Bak wt and Bak L78A. A significant increase in fluorescence was even observed for cells incubated with 0.5 μM Bak-$SGGR_8$, Bak GR_8-click, and Bak L78A-GR8-click peptides (Supporting Information).

A further FACS experiment allowed the determination of apoptotic commitment as determined by the fraction (%) of cells showing release of cytochrome *c*. After incubation with peptides, cells are permeabilized and treated with an anti-cytochrome *c* antibody;[39] loss of signal (<60% compared to a control sample) indicated the cells had released cytochrome *c* from mitochondria into the cytoplasm and then into the buffer. As a consequence of high levels of the antiapoptotic Bcl-2 protein,[41] KG1a cells are known to be relatively resistant to the induction of apoptosis.[40] However, since effective delivery of R_8 peptide cargo into cells

dx.doi.org/10.1021/bc200338u |*Bioconjugate Chem.* 2011, 22, 1763–1767

was observed here, a medium term duration incubation (4 h) of KG1a cells was chosen as sufficient for determining the activity of the peptides in the cells in terms of cytochrome *c* release. As a positive control for cytochrome *c* release, cells were exposed to 1 μM staurosporine, an alkaloid known for its pro-apoptotic effect.[39,42] This treatment showed a 6-fold increase in cells undergoing cytochrome *c* release compared to no treatment. The DNA binding fluorochrome DRAQ5 was used to co-define cells with normal range DNA content and to assess any cell cycle specific apoptotic triggering and cytochrome *c* release was found to be cell cycle independent.[43] When exposed to our peptides, low levels of cytochrome *c* release were observed after coincubations with Bak wt (no uptake) and GR_8 peptide (no bioactive peptide) (Figure 2b). However, exposure to Bak GR_8-click and Bak $SGGR_8$ led to significant increases in cytochrome *c* release, three times higher relative to Bak L78A-GR_8-click, Bak wt, GR8, and the control sample. To validate the data, a Student's one-tailed *t* test was performed, showing $P > 0.05$ for samples with 1 μM staurosporine, Bak GR_8-click, and Bak $SGGR_8$ and for the coincubations with Bak wt and GR_8 peptide (Supporting Information).

In conclusion, a reliable method for the derivation of expressed peptides with a C-terminal propargyl amide through [3 + 2] cycloaddition with various azides has been developed. The resulting triazole linkage does not appear to affect the *in vitro* and *in vivo* properties of the resulting peptides, with Bak GR_8-click and Bak $SGGR_8$ showing very similar uptake and apoptosis induction. The octa-arginine sequence enhanced the cellular uptake of Bak peptides to a level sufficient to elicit an early apoptosis response in the acute myeloid leukemia cell line KG1a. The corresponding mutant Bak peptide Bak L78A-GR_8-click showed equivalent uptake (cargo delivery remained intact) but no apoptotic induction (bioactivity compromised), confirming the expected mechanism of apoptosis induction. Our methodology provides a unique combination of high-level *in vivo* synthesis of encoded peptides with the versatile options for derivatization, normally only associated with chemical peptide synthesis. The ability to tailor peptides in a flexible and robust manner offers many possibilities for the development of next-generation biomedical research tools. The results highlight the potential for the *in vivo* use of such tools to explore and manipulate biological process in live cells, for instance, to determine the hierarchical restrictions on the induction of apoptosis in cancer cell populations.

■ ASSOCIATED CONTENT

Supporting Information. Synthetic methods, spectroscopic data, micrographs, FACS histograms, binding data, mass spectra, HPLC traces. This material is available free of charge via the Internet at http://pubs.acs.org.

■ AUTHOR INFORMATION

Corresponding Author
*E-mail: allemannrk@cf.ac.uk.

■ ACKNOWLEDGMENT

We gratefully acknowledge financial support from the UK's Engineering and Physical Sciences Research Council through Basic Technology grant EP/F040954 and from Cardiff University. The authors wish to thank Piotr Wysoczanski for providing a sample of Bcl-x_L for affinity measurements and Dr. Robert Jenkins for expert assistance with mass spectrometry.

■ REFERENCES

(1) Fletcher, S., and Hamilton, A. D. (2006) Targeting protein-protein interactions by rational design: mimicry of protein surfaces. *J. R. Soc. Interface 3*, 215.

(2) Vlieghe, P., Lisowski, V., Martinez, J., and Khrestchatisky, M. (2010) Synthetic therapeutic peptides: science and market. *Drug Discovery Today 15*, 40.

(3) Che, Y., Brooks, B. R., and Marshall, G. R. (2007) Protein recognition motifs: design of peptidomimetics of helix surfaces. *Biopolymers 86*, 288.

(4) Robinson, J. A. (2008) β-hairpin peptidomimetics: design, structures and biological activities. *Acc. Chem. Res. 41*, 1278.

(5) Williamson, M. P., and Sutcliffe, M. J. (2010) Protein-protein interactions. *Biochem. Soc. Trans. 38*, 875.

(6) Vassilev, L. T., Vu, B. T., Graves, B., Carvajal, D., Podlaski, F., Filipovic, Z., Kong, N., Kammlott, U., Lukacs, C., Klein, C., Fotouhi, N., and Liu, E. A. (2004) In vivo activation of the p53 pathway by small-molecule antagonists of MDM2. *Science 303*, 844.

(7) Shangary, S., Qin, D. G., McEachern, D., Liu, M. L., Miller, R. S., Qiu, S., Nikolovska-Coleska, Z., Ding, K., Wang, G. P., Chen, J. Y., Bernard, D., Zhang, J., Lu, Y. P., Gu, Q. Y., Shah, R. B., Pienta, K. J., Ling, X. L., Kang, S. M., Guo, M., Sun, Y., Yang, D. J., and Wang, S. M. (2008) Temporal activation of p53 by a specific MDM2 inhibitor is selectively toxic to tumors and leads to complete tumor growth inhibition. *Proc. Natl. Acad. Sci. U.S.A. 105*, 3933.

(8) Tse, C., Shoemaker, A. R., Adickes, J., Anderson, M. G., Chen, J., Jin, S., Johnson, E. F., Marsh, K. C., Mitten, M. J., Nimmer, P., Roberts, L., Tahir, S. K., Mao, Y., Yang, X. F., Zhang, H. C., Fesik, S., Rosenberg, S. H., and Elmore, S. W. (2008) A potent and orally bioavailable Bcl-2 family inhibitor. *Cancer Res. 68*, 3421.

(9) Stewart, M. L., Fire, E., Keating, A. E., and Walensky, L. D. (2010) The MCL-1 BH3 helix is an exclusive MCL-1 inhibitor and apoptosis sensitizer. *Nat. Chem. Biol. 6*, 595.

(10) Bird, G. H., Madani, N., Perry, A. F., Princiotto, A. M., Supko, J. G., He, X., Gavathiotis, E., Sodroski, J. G., and Walensky, L. D. (2010) Hydrocarbon double-stapling remedies the proteolytic instability of a lengthy peptide therapeutic. *Proc. Natl. Acad. Sci. U.S.A. 107*, 14093.

(11) He, Y., Cheng, J., Lu, H., Li, J., Hu, J., Qi, Z., Liu, Z., Jiang, S., and Dai, Q. (2008) Potent HIV fusion inhibitors against Enfuvirtide-resistant HIV-1 strains. *Proc. Natl. Acad. Sci. U.S.A. 105*, 16332.

(12) Moellering, R. E., Cornejo, M., Davis, T. N., Del Bianco, C., Aster, J. C., Blacklow, S. C., Kung, A. L., Gilliland, D. G., Verdine, G. L., and Bradner, J. E. (2009) Direct inhibition of the NOTCH transcription factor complex. *Nature 462*, 182.

(13) Therapeutic peptides in clinical study in 2000−07 nearly doubled 1990s rate (2009) *Tufts CSDD Impact Report*, Tufts Center for the Study of Drug Development, Tuft University, Vol *11*.

(14) Frankel, A. D., and Pabo, C. O. (1988) Cellular uptake of the tat protein from human immunodeficiency virus. *Cell 55*, 1189.

(15) Green, M., and Loewenstein, P. M. (1988) Autonomous functional domains of chemically synthesized human immunodeficiency virus tat trans-activator protein. *Cell 55*, 1179.

(16) Joliot, A., Pernelle, C., Deagostini-Bazin, H., and Prochiantz, A. (1991) Antennapedia homeobox peptide regulates neural morphogenesis. *Proc. Natl. Acad. Sci. U.S.A. 88*, 1864.

(17) Wender, P. A., Mitchell, D. J., Pattabiraman, K., Pelkey, E. T., Steinman, L., and Rothbard, J. B. (2000) The design, synthesis, and evaluation of molecules that enable or enhance cellular uptake: peptoid molecular transporters. *Proc. Natl. Acad. Sci. U.S.A. 97*, 13003.

(18) Stewart, K. M., Horton, K. L., and Kelley, S. O. (2008) Cell-penetrating peptides as delivery vehicles for biology and medicine. *Org. Biomol. Chem. 6*, 2242.

(19) Nakase, I., Takeuchi, T., Tanaka, G., and Futaki, S. (2008) Methodological and cellular aspects that govern the internalization mechanisms of arginine-rich cell-penetrating peptides. *Adv. Drug Delivery Rev. 60*, 598.

(20) Futaki, S., Nakase, I., Tadokoro, A., Takeuchi, T., and Jones, A. T. (2007) Arginine-rich peptides and their internalization mechanisms. *Biochem. Soc. Trans. 35*, 784.

(21) Chugh, A., Eudes, F., and Shim, Y. S. (2010) Cell-penetrating peptides: nanocarrier for macromolecule delivery in living cells. *Iubmb. Life 62*, 183.

(22) Sawant, R., and Torchilin, V. (2010) Intracellular transduction using cell-penetrating peptides. *Mol. Biosyst. 6*, 628.

(23) Kuliopulos, A., and Walsh, C. T. (1994) Production, purification, and cleavage of tandem repeats of recombinant peptides. *J. Am. Chem. Soc. 116*, 4599.

(24) Fairlie, W. D., Uboldi, A. D., De Souza, D. P., Hemmings, G. J., Nicola, N. A., and Baca, M. (2002) A fusion protein system for the recombinant production of short disulfide-containing peptides. *Protein Expr. Purif. 26*, 171.

(25) Yonemoto, I. T., Wood, M. R., Balch, W. E., and Kelly, J. W. (2009) A general strategy for the bacterial expression of amyloidogenic peptides using BCL-XL-1/2 fusions. *Protein Sci. 18*, 1978.

(26) Gross, E., and Witkop, B. (1961) Selective cleavage of methionyl peptide bonds in ribonuclease with cyanogen bromide. *J. Am. Chem. Soc. 83*, 1510.

(27) Shi, T., Weerasekera, R., Yan, C., Reginold, W., Ball, H., Kislinger, T., and Schmitt-Ulms, G. (2009) Method for the affinity purification of covalently linked peptides following cyanogen bromide cleavage of proteins. *Anal. Chem. 81*, 9885.

(28) Kolb, H. C., Finn, M. G., and Sharpless, K. B. (2001) Click chemistry: Diverse chemical function from a few good reactions. *Angew. Chem., Int. Ed. 40*, 2004.

(29) Bock, V. D., Hiemstra, H., and van Maarseveen, J. H. (2005) Cu-I-catalyzed alkyne-azide "click" cycloadditions from a mechanistic and synthetic perspective. *Eur. J. Org. Chem.* 51.

(30) Chittenden, T., Harrington, E. A., O'Connor, R., Flemington, C., Lutz, R. J., Evan, G. I., and Guild, B. C. (1995) Induction of apoptosis by the Bcl-2 homologue Bak. *Nature 374*, 733.

(31) Rosen, K., Rak, J., Jin, J., Kerbel, R. S., Newman, M. J., and Filmus, J. (1998) Downregulation of the pro-apoptotic protein Bak is required for the ras-induced transformation of intestinal epithelial cells. *Curr. Biol. 8*, 1331.

(32) Neise, D., Graupner, V., Gillissen, B. F., Daniel, P. T., Schulze-Osthoff, K., Janicke, R. U., and Essmann, F. (2008) Activation of the mitochondrial death pathway is commonly mediated by a preferential engagement of Bak. *Oncogene 27*, 1387.

(33) Kneissl, S., Loveridge, E. J., Williams, C., Crump, M. P., and Allemann, R. K. (2008) Photocontrollable peptide-based switches target the anti-apoptotic protein Bcl-xL. *ChemBioChem 9*, 3046.

(34) Sattler, M., Liang, H., Nettesheim, D., Meadows, R. P., Harlan, J. E., Eberstadt, M., Yoon, H. S., Shuker, S. B., Chang, B. S., Minn, A. J., Thompson, C. B., and Fesik, S. W. (1997) Structure of Bcl-xL-Bak peptide complex: recognition between regulators of apoptosis. *Science 275*, 983.

(35) Adams, J. M., and Cory, S. (2007) The Bcl-2 apoptotic switch in cancer development and therapy. Structure of Bcl-xL-Bak peptide complex: recognition between regulators of apoptosis. *Oncogene 26*, 1324.

(36) Li, R., Boehm, A. L., Miranda, M. B., Shangary, S., Grandis, J. R., and Johnson, D. E. (2007) Targeting antiapoptotic Bcl-2 family members with cell-permeable BH3 peptides induces apoptosis signaling and death in head and neck squamous cell carcinoma cells. *Neoplasia 9*, 801.

(37) Holinger, E. P., Chittenden, T., and Lutz, R. J. (1999) Bak BH3 peptides antagonize Bcl-xL function and induce apoptosis through cytochrome c-independent activation of caspases. *J. Biol. Chem. 274* 13298.

(38) Albarran, B., Hoffman, A. S., and Stayton, P. S. (2011) Efficient intracellular delivery of a pro-apoptotic peptide with a pH-responsive carrier. *React. Funct. Polym. 71*, 261.

(39) King, M. A., Eddaoudi, A., and Davies, D. C. (2007) A comparison of three flow cytometry methods for evaluating mitochondrial damage during staurosporine-induced apoptosis in Jurkat cells. *Cytom. Part A 71A*, 668.

(40) Haag, P., Viktorsson, K., Lindberg, M. L., Kanter, L., Lewensohn, R., and Stenke, L. (2009) Deficient activation of Bak and Bax confers resistance to gemtuzumab ozogamicin-induced apoptotic cell death in AML. *Exp. Hematol. 37*, 755.

(41) Campos, L., Sabido, O., Rouault, J. P., and Guyotat, D. (1994) Effects of BCL-2 antisense oligodeoxynucleotides on in vitro proliferation and survival of normal marrow progenitors and leukemic cells. *Blood 84*, 595.

(42) King, M. A., Eddaoudi, A., and Davies, D. C. (2007) A comparison of three flow cytometry methods for evaluating mitochondrial damage during staurosporine-induced apoptosis in Jurkat cells. *Cytometry A 71*, 668.

(43) Smith, P. J., Blunt, N., Wiltshire, M., Hoy, T., Teesdale-Spittle, P., Craven, M. R., Watson, J. V., Amos, W. B., Errington, R. J., and Patterson, L. H. (2000) Characteristics of a novel deep red/infrared fluorescent cell-permeant DNA probe, DRAQ5, in intact human cells analyzed by flow cytometry, confocal and multiphoton microscopy. *Cytometry 40*, 280.

Supporting Information
for

Click chemistry for synthesis of cell permeable apoptotic peptides from expressed fusion proteins

Thomas Fricke, Robert J. Mart, Catherine L. Watkins, Marie Wiltshire, Rachel J. Errington, Paul J. Smith, Arwyn T. Jones, Rudolf K. Allemann*

Methods

Cloning, in vivo peptide synthesis, purification and cyanogen bromide cleavage. Oligonucleotides with the DNA sequence were purchased from Eurofin MWG Operon. They were phosphorylated at the 5'-end with polynucleotide kinase (NEB) and ligated into pET-31b (Novagen) that had been digested with the restriction enzyme AlwNI and dephosphorylated with calf intestinal phosphatase (NEB). For protein production, *E. coli* BL21(DE3) cells were transformed with the resulting plasmid. The cells were plated on LB agar containing 150 μg/mL ampicillin and grown overnight. 50 mL overnight cultures were used to inoculate 4 L of TB medium with addition of 0.2% (w/w) lactose and 0.05% (w/w) glucose. The cultures were grown at 37 °C for 16-20 h with rotary shaking at 250 rpm and harvested by centrifugation (3 000 g, 4 °C, 20 min). The cell pellet was resuspended in 50 mM possium phosphate buffer (pH 7), 300 mM NaCl, 1 mM PMSF and 0.1 mg/ml lysozyme, treated by sonication and centrifuged (12 000g, 4 °C, 20 min). The resulting pellet was washed with 50 mM potassium phosphate buffer (pH 7), 300 mM NaCl, 0.01% Tween 80 and centrifuged (12 000 g, 4 °C, 20 min). The resulting pellet was washed with 50 mM potassium phosphate buffer pH 7, 1 M NaCl, centrifuged (12 000 g, 4 °C, 20 min) and then redissolved in 6M guanidinium chloride. After centrifugation (30 000 g, 4 °C, 30 min) the supernatant was dialyzed twice against 4L H_2O. The precipitate was collected by centrifugation (10 000 g, 4 °C, 10 min) solubilized with 50 ml 70% formic acid and transferred to a 250 mL round bottom flask. The flask was wrapped in aluminum foil, 2 g of cyanogen bromide were added and the reaction was stirred for 16-24 h at room temperature under nitrogen atmosphere. The solvent was evaporated at 40 °C and the residue resuspended in 40% CH_3CN / 60% H_2O / 0.1% trifluoroacetic acid (TFA). The mixture was centrifuged at 10 000 g and 4 °C for 10 min. The supernatant was filtered through 0.22 μM filter and purified by reverse phase HPLC using a C18 column (Gemini, Phenomenex, 10 μm, 110 Å, 10 x 250 mm) using a linear acetonitrile gradient over 40 min from H_2O, 0.05 % TFA to 50% of CH_3CN, 0.05 % TFA with a flow rate of 5 ml min^{-1}.

For fluorescence labeling, the peptides were incubated with Alexa Fluor® 488-C5 maleimide sodium salt (Invitrogen) in 50 mM Tris-HCl (pH 8.3), 2 mM triscarboxyethyl phosphine (TCEP) at 4 °C over night, filtered through a 0.22 μM filter and purified by reverse phase HPLC as described above.

Purified peptides were analyzed for purity by analytical HPLC using a C18 column (Acclaim, Dionex, 3 μm, 120 Å, 4.6 x 150 mm) using a linear gradient over 40 minutes

from H_2O, 0.05 % TFA to 100% of CH_3CN, 0.05 % TFA with a flow rate of 5 ml min^{-1}**.** MALDI TOF MS (α-cyano-hydroxy-cinnamic acid in 50% CH_3CN / H_2O) confirmed the identity.

Synthesis of azides. The Azide-Fluor 545 and the Azide-PEG4-biotin conjugate were purchased from Click Chemistry Tools. 2-Acetamido-2-deoxy-β-D-glucopyranosyl azide 3,4,6-triacetate was purchased from Sigma.

Ethyl-5-azidovalerate

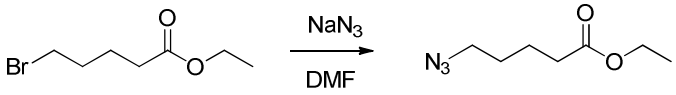

Ethyl-5-bromovalerate (5 g, 23.9 mmol, 1 eq) and sodium azide (2.5 g, 38.5 mmol, 1.6 eq) were dissolved in dimethylformamide (15 mL,) as stirred overnight at 85 °C. The suspension was then diluted with distilled water (200 mL) and extracted with ether (3 x 200 mL). The ether was then cautiously removed under reduced pressure. The compound was deliberately not evaporated to dryness, but the yield was calculated from the product/solvent ratio apparent in the ^{1}H NMR to be 3.73 g (91%). ^{1}H-NMR ($CDCl_3$, 400 MHz) δ 4.07 (2H, q, *J* = 7.0 Hz), 3.24 (2H, t, *J* = 6.4 Hz), 2.28 (2H, t, *J* = 7.3 Hz), 1.52-1.69 (4H, m), 1.14 (3H, t, *J* = 7.0 Hz). ^{13}C-NMR ($CDCl_3$, 100 MHz) δ 173.5, 60.7, 51.4, 34.0, 28.6, 22.4, 14.5. LRMS (APCI +ve) 172 $[M+H]^+$ (100%), 144 $[M-C_2H_5+2H]^+$ or $[M+H-N_2]^+$ (36%), 115 $[M-C_2H_5-N_2+H]^+$ (43%). HRMS (APCI +ve) found 172.1079 (calculated 172.1086 for $C_7H_{14}N_3O_2$).

5-Azidovaleric acid

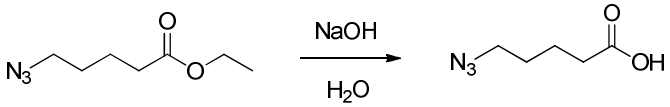

5-Azidovaleric acid was synthesized according to a literature procedure.[1] Ethyl-5-azidovalerate (588 mg, 3.4 mmol, 1 eq) was suspended in sodium hydroxide solution (41 mL, 1 M) and the minimum quantity of methanol required to achieve homogeneity was added. The solution was stirred for 4 h at room temperature then the methanol was evaporated under reduced pressure. The aqueous solution was washed with diethyl ether (2 x 20 mL), acidified with hydrochloric acid (conc) and the product extracted with diethyl ether (3 x 20 mL). These fractions were combined, dried over magnesium sulfate, filtered and evaporated to a yellow oil (464 mg, 94%). ^{1}H-NMR ($CDCl_3$, 400 MHz) δ 3.26-3.33 (2H, m), 2.36-2.42 (2H, m), 1.60-1.75 (4H, m). ^{13}C-NMR ($CDCl_3$, 125 MHz) δ 179.8, 51.4, 33.8, 28.6, 22.2. LRMS (APCI +ve) 144 $[M+H]^+$ (48%), (36%), 115 $[M-N_2]^+$ (100%). HRMS (APCI -ve) found 142.0620 (calculated 142.0617 for $C_5H_8N_3O_2$).

5-Azidovalerylpeptide

The peptide GR_8 was synthesised by standard solid phase synthesis techniques on Rink

amide resin (100-200 mesh, Merck Biosciences) using a CEM Liberty microwave-assisted peptide synthesiser. Azidovaleric acid (155 mg, 1.08 mmol 11 eq) was coupled to the sidechain-protected peptide on the resin (0.1 mmol) using diisopropylcarbodiimide (13 uL, 0.13 mmol 1.3 eq) and hydroxybenzotriazole (30 mg, 0.22 mmol, 2.2 eq) in dimethylformamide.

COMMENT [RM1]: The new figures are here.

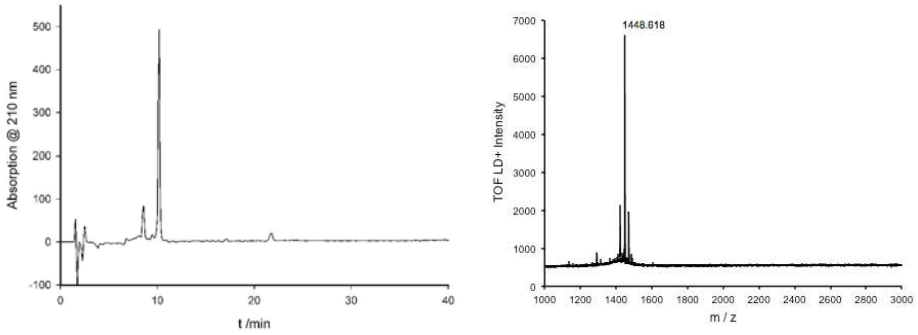

3-Azidopropylamine

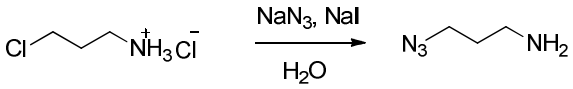

3-Azidopropylamine was synthesized by stirring 3-chloropropylamine hydrochloride (2.2 g, 17 mmol, 1 eq), sodium azide (3 g, 46 mmol, 2.7 eq) and potassium iodide (cat) at 80 °C for 5 h in water. The mixture was then cooled to room temperature and stirred overnight. The solution was cooled in ice and sodium hydroxide (2 g, 50 mmol) cautiously added portionwise. The aqueous was repeatedly extracted with diethyl ether (6 x 20 mL). The organic fractions were combined, dried over magnesium sulfate and cautiously evaporated under reduced pressure to yield an oil (1.07 g, 55%). ^{1}H-NMR ($CDCl_3$, 400 MHz) δ 3.31 (2H, t, *J* = 6.7 Hz), 2.74 (2H, t, *J* = 6.7 Hz), 1.67 (2H, p, *J* = 6.7 Hz), 1.12 (2H, br s). ^{13}C-NMR ($CDCl_3$, 125 MHz) δ 49.2, 39.3, 32.5. LRMS (APCI +ve) 101 $[M+H]^+$ (5%), 142 $[M+MeCN+H]^+$ (15%). HRMS (APCI +ve) found 101.0823 (calculated 101.0827 for $C_3H_9N_4$).

Palmityl-(3-azido)propylamide

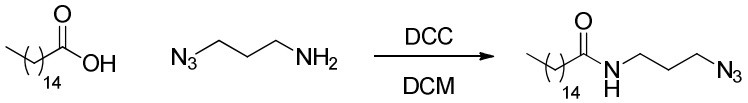

Palmitic acid (400 mg, 1.56 mmol, 1 eq.) was dissolved in thionyl chloride (3 mL) and dichloromethane (5 mL) and stirred at room temperature for 5 hours. The solvents were evaporated under reduced pressure and the residue dissolved in diethyl ether (10 mL). 3-azidopropylamine (400 mg, 4 mmol, 2.56 eq) was dissolved in dichloromethane (15 mL)

and slowly added to the palmitoyl chloride. The mixture was stirred overnight at room temperature then the solvents evaporated and the residue suspended in diethyl ether. The precipitate was washed thoroughly with further diethyl ether, then the resulting solid was dissolved in chloroform and evaporated to a yellow wax (91 mg, 17%). ^{1}H-NMR ($CDCl_3$, 400 MHz) δ 5.54 (1H, br s), 3.30 (2H, t, *J* = 6.6 Hz), 3.28 (2H, q, *J* = 6.6 Hz), 2.09 (2H, t, *J* = 7.6 Hz), 1.73 (2H, p, *J* = 6.6 Hz), 1.52-1.58 (2H, m), 1.16-1.25 (24H, m), 0.81 (3H, t, *J* = 6.9 Hz). ^{13}C-NMR ($CDCl_3$, 125 MHz) δ 173.4, 49.4, 37.1, 36.8, 31.9, 29.7, 29.7, 29.7, 29.6, 29.6, 29.5, 29.3, 29.3, 29.3, 28.9, 26.8, 25.7, 22.7, 14.1. LRMS (ESI +ve) 339 $[M+H]^+$ (100%), 266 (25%), 225(56%). HRMS (APCI +ve) 339.3122 (calculated 339.3124 for $C_{19}H_{39}N_4O$).

Purification of Bcl-x_L. pET 19b vector containing a truncated Bcl-x_L gene (1-212 Δ45-84) with a C-terminal His-tag was transformed into ***E.coli*** BL21(DE3), grown in LB medium at 37 °C until the OD at 600 reached 0.5. Gene expression was induced by addition of 0.5 mM IPTG, and the cells were allowed to grow for 5 h prior to harvesting by centrifugation (3 000g, 4 °C, for 20 min). The cells were resuspended in 100 mM sodium phosphate buffer pH 7.5, 500 mM NaCl, 5 mM Imidazol, 10 mM 2-mercaptoethanol and 1 mM PMSF. The cells were lysed by freeze-thawing and sonication. The lysate was centrifuged (30 000 g, 4 °C, 45 min) and filtered through an 0.22 μM filter and applied to a 5 ml Ni-Sepharose^{Tm} 6 Fast Flow (GE Heathcare Life Science) column equilibrated in the buffer above. The protein was eluted by a stepwise addition of imidazol in the lysis buffer to 500 mM. The elution fractions containing Bcl-x_L were pooled and dialyzed against 10 mM sodium phosphate buffer, pH 7.3, containing 5 mM 2-mercaptoethanol.

Lactone opening/Click reaction. The Bak peptides were dissolved in 30 μL of 100% TFA; the solvent was then removed in a speed vac (VR1, Heto) and the residue incubated with 50 μl 98 % propargylamine (Sigma) for 1 h. 200 μL acetylacetate was added to precipitate the product which after centrifugation was dissolved in 50% CH_3CN/50% H_2O containing 0.1% TFA, filtered through 0.22 μM filter and purified by reverse Phase HPLC using a C18 column (Gemini, Phenomenex, 10 μm, 110 Å, 10 x 250 mm) with a linear acetonitrile gradient over 40 minutes from H_2O, 0.05% TFA to 50% of CH_3CN, 0.05% TFA with a flow rate of 5 ml min^{-1}.

The propargylated peptides were mixed with the azides in 100 mM sodium phosphate buffer, pH 8.0, 500 mM NaCl, 5 mM ascorbic acid, 0.5 mM $CuSO_4$ and 10% DMSO. The reaction was then incubated for 20-24 h at room temperature with rotary shaking at 400 rpm, filtered through 0.22 μM filter and analyzed by reverse Phase HPLC using a C18 column (Gemini, Phenomenex, 10 μm, 110 Å, 10 x 250 mm). The reaction with the palmityl azide was performed in the buffer above with 50% DMSO and incubated at 60 °C for 20 h.

The peptides were analyzed by analytical HPLC using a C18 column (Acclaim, Dionex, 3 μm, 120 Å, 4.6 x 150 mm) with a linear acetonitrile gradient from H_2O, 0.05% TFA to 100% of CH_3CN, 0.05% TFA over 40 minutes with a flow rate of 5 ml min^{-1} and by MALDI TOF MS (MALDI micro MX, Waters**).**

Peptide	Observed m/z / calculated m/z	HPLC retention times min	% HPLC purity

A488-Bak wt F546	**3352.2 / 3354.2**	**18.47**	**96**
Bak wt N-acetyl-glucosamine	**2393.4 / 2394.2**	**14.07**	**95**
Bak wt palmityl	**2352.4 / 2353.8**	**27.25**	**98**
Bak wt biotin	**2450.4 / 2449.6**	**13.83**	**99**
A488-Bak-GR_8-click	**4170.1 / 4170.7**	**12.97**	**94**
A488-Bak L78A-GR_8 click	**4127.4 / 4126.9**	**12.76**	**96**

Table S1. Molecualar masses, retention times and purity of triazole peptides synthesized in this study (for conditions see text).

In vitro binding assay. The binding of Alexa488 labelled peptide to Bcl-x_L was monitored using a fluorescence anisotropy assay essentially as described previously[2] In short, measurements were made on a Perkin-Elmer Luminescence Spectrometer LS50B configured in the L-format. Excitation and emission (band-pass/wavelength) were (5 nm/494 nm) and (5 nm/519 nm), respectively. All measurements were performed in a 3 ml fluorescence quartz cuvette. The assay buffer was 100 mM sodium phosphate buffer pH 7.5 with 10 mM NaCl. Defined volumes of a 4-40 μM stock solution of Bcl-x_L were added successively to 10 nM fluorescently labelled peptide. The change of anisotropy was measured.
The *G* factor (ratio of sensitivities of the monochromator for horizontally and vertically polarized light) was calculated for each measurement using the equation where $I_\perp$ and $I_\parallel$ are intesities for fluorescent emission in parallel and perpendicular planes:

$G = I_\perp / I_\parallel$

Values for fluorescence anisotropy were determined from equation:

$A = (I_\parallel - G \tilde{I}_\perp I_\parallel + 2 G I_\perp$

COMMENT [RJM2]: This formula fails on a PC

The fraction of bound peptide (Φ) was derived by normalizing the anisotropy data. The resultant Φ values were fitted to the Langmuir equation using the program Sigmaplot to obtain K_D.

$\Phi = \{1 + (K_D/[\text{Bcl-}x_L])^n\}^{-1}$

The IC_{50} of unlabeled Bak wt peptide was measured by a fluorescence anisotropy competition assay. The unlabled peptide was titrated against 10 nM Alexa488 labeled Bak wt peptide and 300 mM Bcl-x_L in the assay buffer described above. The decrease in fluorescence intensity upon addition of the unlabled Bak wt peptide was monitored. The data was normalised and fit to the following equation to obtain values for IC_{50}:

$\Phi = 1 / 1 + ([\text{Bcl-}x_L] / IC_{50})$

The IC_{50} values can be related to the inhibitory constant K_i by applying the Cheng-Prusoff equation:

$K_i = IC_{50} / 1 + ([\text{Alexa 488 Bak wt}] / K_D)$

All binding curves were measured independently three times and resulting K_D or IC_{50} are reported as the mean with standard errors.

Cell Culture. All tissue culture reagents were purchased from Invitrogen or alternatively Sigma Aldrich (penicillin, streptomycin and glutamine) or Autogenbioclear (foetal bovine serum). Human KG1a cells were cultured and maintained at a density of (0.5–2) × 10^6 cells ml^{-1} in RPMI 1640 medium supplemented with 10% (v/v) foetal bovine serum (FBS), 100 I.U. ml^{-1} penicillin, 100 μg ml^{-1} streptomycin and 2 mM L-glutamine. The cells were maintained in a humidified 5% CO_2 incubator at 37 °C.

Microscopy to detect localization of Alexa488 labelled peptide. **Experiments were essentially as previously described [3] Briefly** KG1a cells (5×10^5 cells) were washed in complete medium and incubated with fresh complete medium containing 0.5 or 5 μM Alexa488 labelled peptide for 1 h. Cells were then washed twice in SFM (serum-free RPMI 1640 medium), once in imaging medium (SFM without Phenol Red) and resuspended in 500 μl of imaging medium. 100 μl aliquots of the cell suspension were transferred to the centre of glass-bottomed 35 mm culture dishes (MatTek), and the cells were allowed to settle for 30 s. They were then analysed on a Leica SP5 confocal laser-scanning microscope equipped with an Argon laser and a 63 × oil-immersion objective.

Flow Cytometry for Uptake study. KG1a cells (2.5×10^5/ml were incubated for 1 h with 0.5 or 5 μM Alexa488 labelled peptide at 37 °C. Cells were then washed three times with ice-cold PBS and resuspended in 200 μl of PBS. Cellular fluorescence was detected and analysed using a Becton Dickinson FACSCalibur. Live cells were obtained by gating (forward- versus side-scatter) to remove the low scattering debris (Figure S10), and 10000 events were acquired.

Cytochrome C assays. KG1a cells (2.5×10^5 in 100 μl complete medium) were incubated for 4 h with 20 μM peptide at 37 °C. 1 μM staurosporine was used as a positive control. The cells spun down and resuspended in 400 μl 30 μg ml^{-1} digitonin in respiration buffer (20 mM HEPES pH 7.1, 0.5 mM EGTA, 3 mM $MgCl_2$, 20 mM Taurine, 10 mM KH_2PO_4, 0.1% (w/w) BSA, 60 mM potassium-lactobionate, 110 mM mannitol, 0.3 mM DTT) for 5 min on ice to remove all cytoplasmic cytochrome c. The cells were then fixed (20 min at room temperature) by adding 400 μl 8% formaldehyde in respiration buffer. The cells were washed twice with PBS, resuspended in 1 ml blocking buffer (3% BSA, 0.05% saponin in PBS) and incubated for 1 h at room temperature. The cells were then incubated over night at 4 °C with anti-cytochrome C antibody (556432 BD Pharmingen) in blocking buffer. Two samples of KG1a cells without peptide were incubated without the antibody in blocking buffer as no primary controls. The samples were washed in blocking buffer, incubated for 1

h at room temperature with Alexa488 goat anti-mouse secondary antibody (Invitrogen A11001) at room temperature, washed in blocking buffer, resuspended in 0.5 ml PBS with 20 μM DRAQ5™ (Biostatus Ltd, Shepshed, UK) and then analysed using a Becton Dickinson FACSVantage flow cytometer (FL1-H [Alexa 488] 530/30 [Bandpass]; FL3-H [DRAQ5] LP695 [Longpass]) 10,000 events were collected per sample. For the analysis the cells were gated, according to the DRAQ5 fluorescence intensity (Figure S12). The experiments were performed 3 times in duplicates, averaged and normalized against the Bak wt response (Figure S14).

Supporting Figures

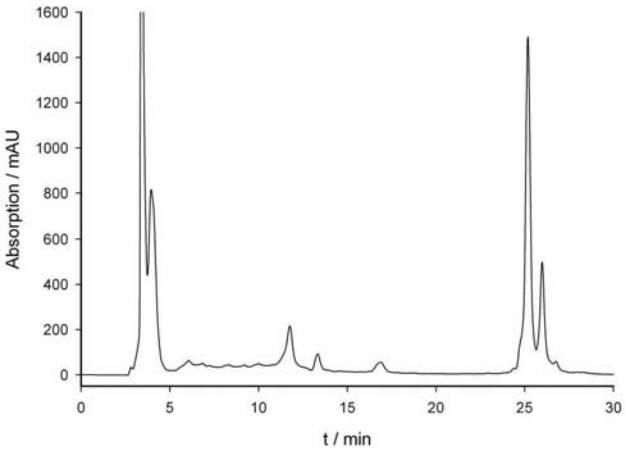

Figure S1. HPLC analysis of the reaction of Bak wt homoserine lactone with propargylamine (RT: alkyne peptide, 25 min; Bak wt 26 min).

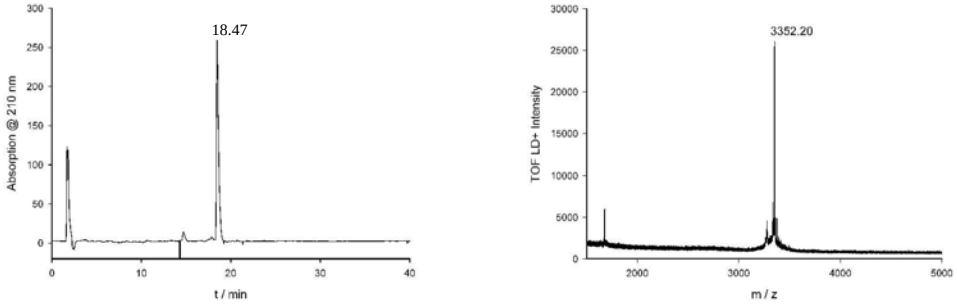

Figure S2. Left: Analytical HPLC trace of A488-Bak wt F546 peptide. Right: MALDI TOF mass spectrum of A488-Bak wt F546 peptide (calculated m/z: 3354.2).

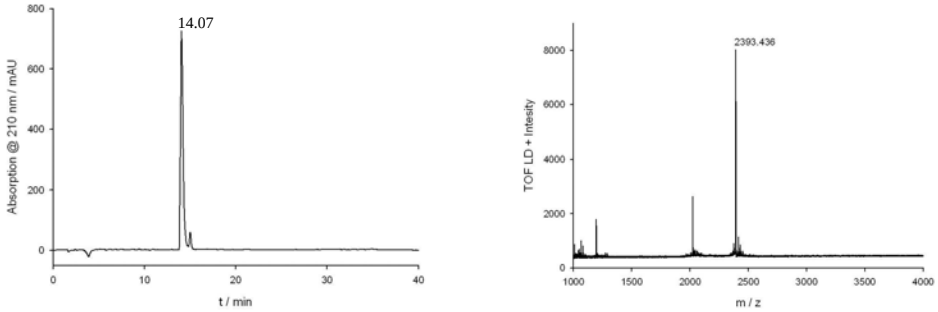

Figure S3. Left: Analytical HPLC trace of Bak wt N-acetyl-glucosamine peptide. Right: MALDI TOF mass spectra of Bak wt N-acetyl-glucosamine peptide (calculated m/z: 2394.22).

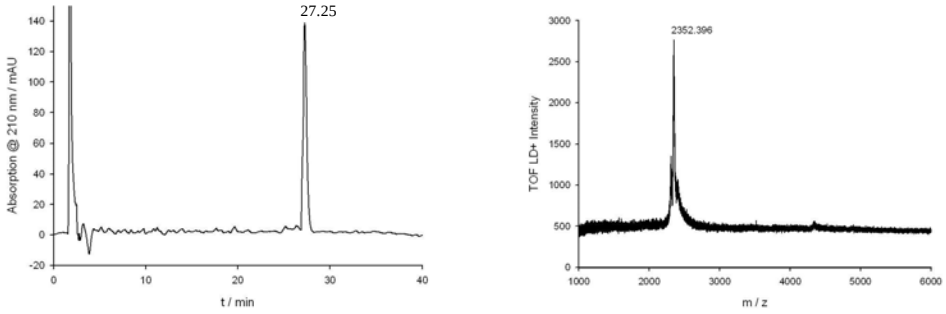

Figure S4. Left: Analytical HPLC trace of Bak wt palmityl peptide peptide. Right: MALDI TOF mass spectra of Bak wt palmityl peptide peptide (calculated m/z: 2353.82).

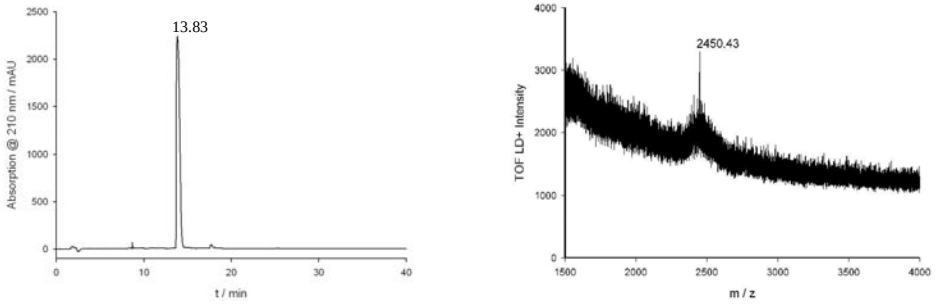

Figure S5. Left: Analytical HPLC trace of A488-Bak wt biotin peptide. Right: MALDI TOF mass spectrum of A488-Bak wt biotin peptide (calculated m/z: 2449.6).

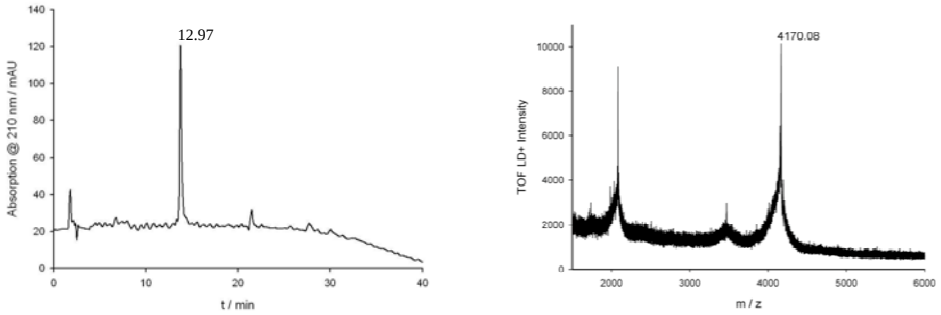

Figure S6. Left: Analytical HPLC trace of A488-Bak-GR_8-click peptide. Right: MALDI TOF mass spectrum of A488-Bak-GR_8-click peptide (calculated m/z: 4170.66)

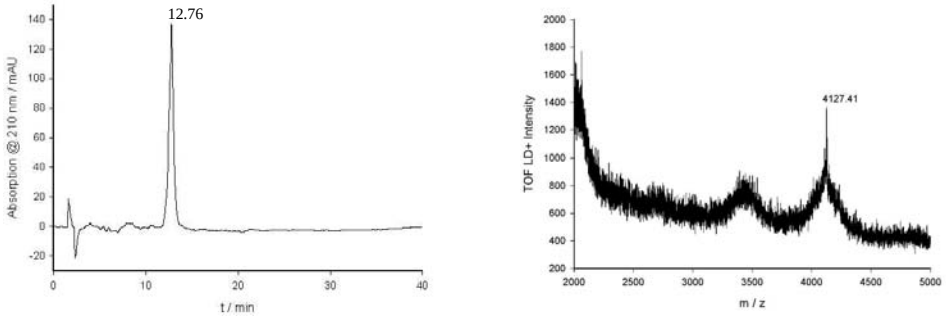

Figure S7. Left: Analytical HPLC trace of A488-Bak L78A-GR_8 click peptide. Right: MALDI TOF mass spectrum of A488-Bak L78A-GR_8-click peptide (calculated m/z: 4126.94)

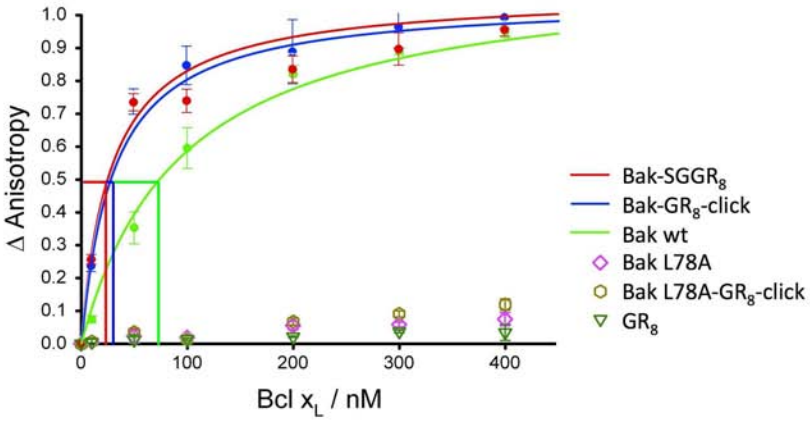

Figure S8. Typical binding curves for Bak-SGGR$_8$, Bak GR$_8$-click, Bak wt, Bak L78A, Bak L78A-GR8-click and GR8 binding to Bcl-x$_L$.

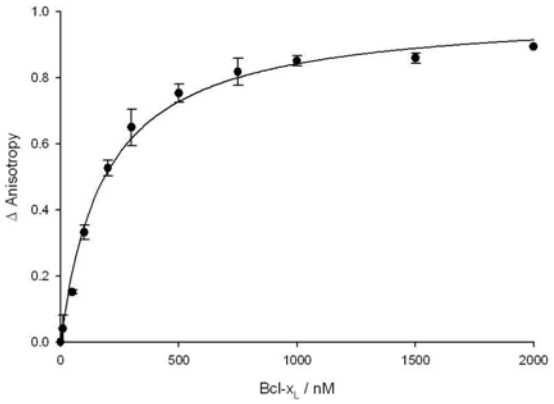

Figure S9. Competition assay. Unlabelled Bak wt peptide was titrated against 10 nM Alexa488 labeled Bak wt peptide and 300 mM Bcl-x$_L$. The resultant Φ values were fitted to the Langmuir equation using the program Sigmaplot to obtain IC$_{50}$. The IC$_{50}$ values can be related to the inhibitory constant K$_i$ by applying the Cheng-Prusoff equation. A K$_i$ of 167.7 nM ± 15.6 was calculated.

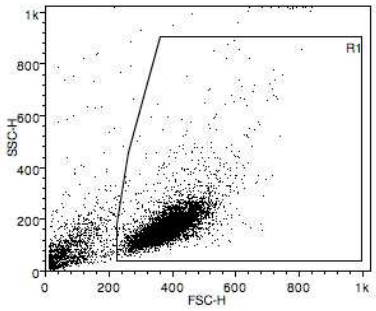

Figure S10. Side scatter / forward scatter dot plot in the cellular uptake assays as acquired by flow cytometry. Region R1, was used as the gate to remove debris and leave viable cells for analysis.

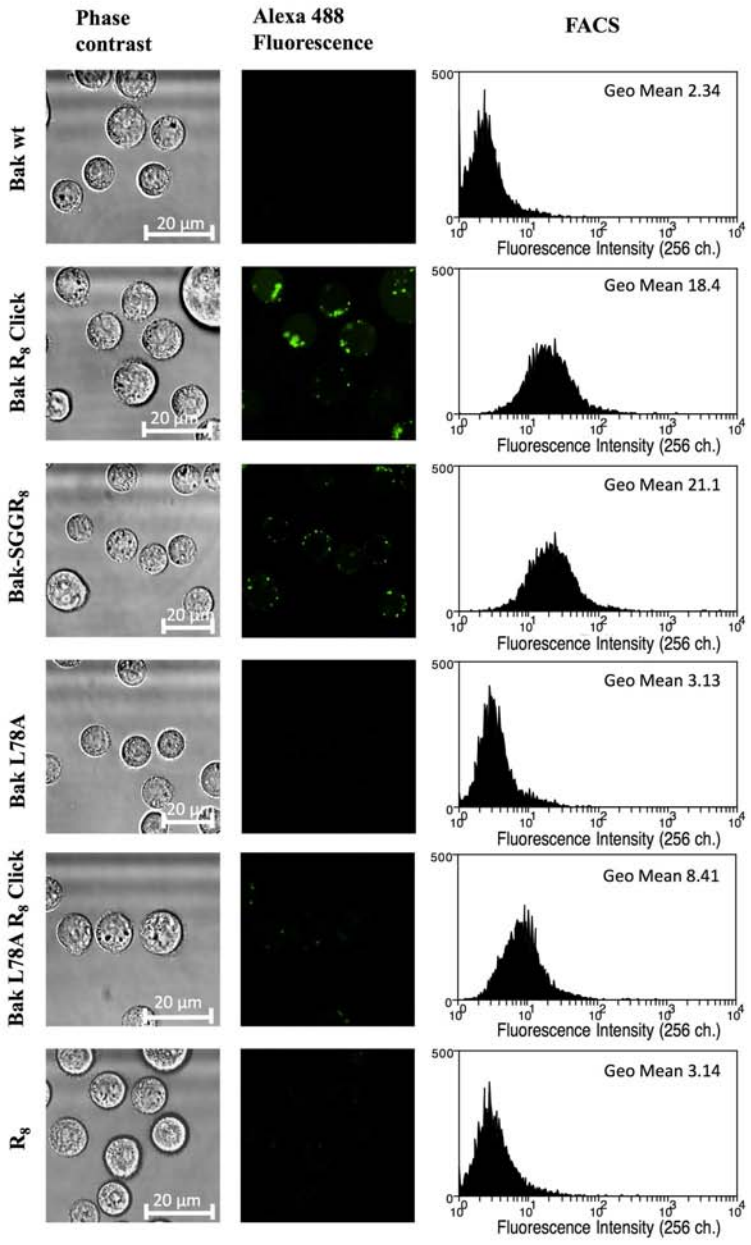

Figure S11. Relative uptake of 0.5 µM Alexa488 labelled peptides (Table 1) by KG1a cells for 1h incubations at 37°C analyzed by fluorescence microscopy and FACS (note the logarithmic scale).

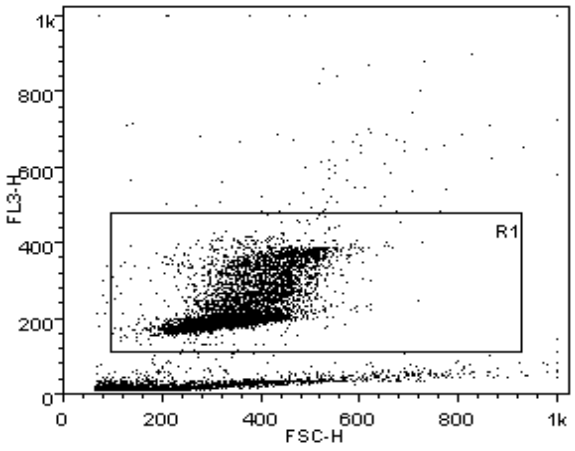

Figure S12. DRAQ5 / forward scatter dot plot. The region R1, which was used as a gate in the cytochrome c release assay, is indicated.

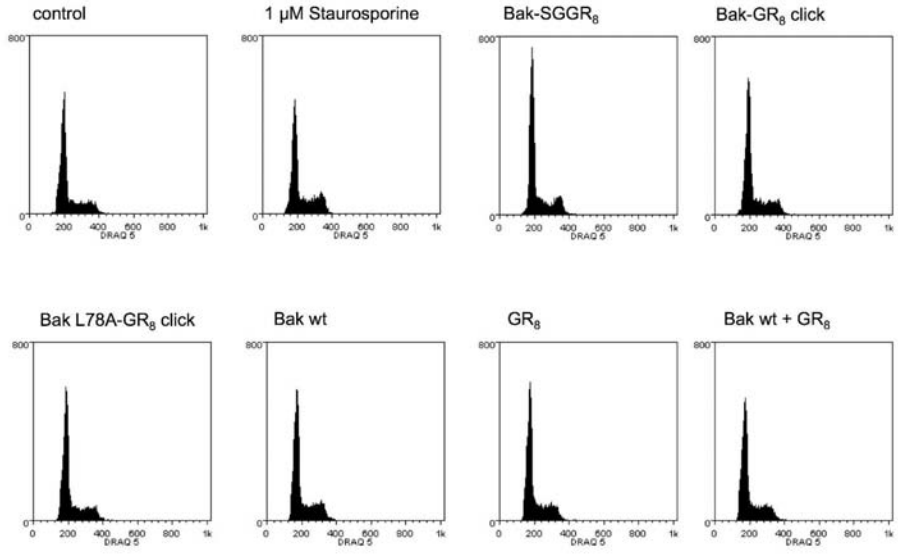

Figure S13. FACS histogram of DRAQ5 stained KG1a to define the cell cycle profile. This was used to show that there is no alteration in the cell cycle due to exposure to peptide (20µM) during the cytochrome c release assay over the 4 h incubation time.

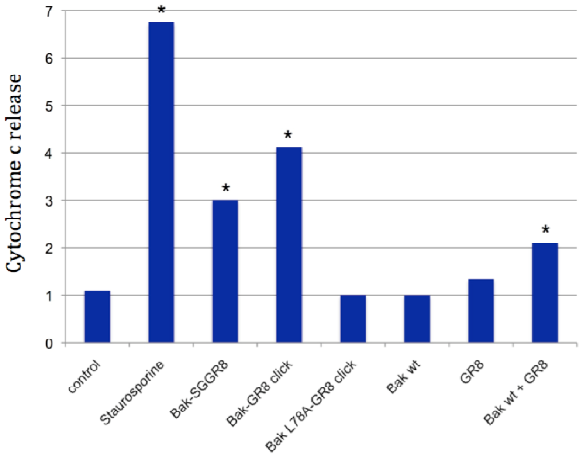

Figure S14. Relative cytochrome c release in KG1a cells after a 4h incubation with the corresponding peptides. The experiments were normalized to the Bak wt response and then averaged (x1 fold change). A Student's t-test was performed to validate the data (* $P > 0.05$).

References

(1) Khoukhi, N.; Vaultier, M.; and Carrie, R. (1987) Synthesis and Reactivity of Methyl Gamma-Azido Butyrates and Ethyl Delta-Azido Valerates and of the Corresponding Acid-Chlorides as Useful Reagents for the Aminoalkylation. *Tetrahedron*, *43* (8), 1811.

(2) Kneissl, S.; Loveridge, E. J.; Williams, C.; Crump, M. P.; and Allemann, R. K., (2008) Photocontrollable peptide-based switches target the anti-apoptotic protein Bcl-xL. *ChemBioChem.*, *9* (18), 3046-54.

(3) Watkins, C. L.; Schmaljohann, D.; Futaki, S.; and Jones, A. T. (2009) Low concentration thresholds of plasma membranes for rapid energy-independent translocation of a cell-penetrating peptide. *Biochem. J.*, *420*, 179-189.

Bioconjugate Chemistry

ARTICLE

pubs.acs.org/bc

Pharmacological Characterization of a Recombinant, Fluorescent Somatostatin Receptor Agonist

Varun K. A. Sreenivasan,[†] Oleg A. Stremovskiy,[§] Timothy A. Kelf,[†] Marika Heblinski,[‡] Ann K. Goodchild,[‡] Mark Connor,[‡] Sergey M. Deyev,[§] and Andrei V. Zvyagin*[,†]

[†]MQ Biofocus Research Centre

[‡]Australian School of Advanced Medicine

Macquarie University, Australia 2109

[§]Shemyakin & Ovchinnikov Institute of Bioorganic Chemistry, Russian Academy of Sciences, 117997 Russia

Supporting Information

ABSTRACT: Somatostatin (SST) is a peptide neurotransmitter/hormone found in several mammalian tissue types. Apart from its natural importance, labeled SST/analogues are utilized in clinical applications such as targeting/diagnosis of neuroendocrine tumors. We report on the development and characterization of a novel, recombinant, fluorescent somatostatin analogue that has potential to elucidate somatostatin-activated cell signaling. SST was genetically fused with a monomeric-red fluorescent protein (mRFP) as the fluorescent label. The attachment of SST to mRFP had no detectable effect on its fluorescent properties. This analogue's potency to activate the endogenous and transfected somatostatin receptors was characterized using assays of membrane potential and Ca^{2+} mobilization and immunocytochemistry. SST-mRFP was found to be an effective somatostatin receptor agonist, able to trigger the membrane hyperpolarization, mobilization of the intracellular Ca^{2+} and receptor−ligand internalization in cells expressing somatostatin receptors. This complex represents a novel optical reporter due to its red emission spectral band suitable for *in vivo* imaging and tracking of the somatostatin receptor signaling pathways, affording higher resolution and sensitivity than those of the state-of-the-art radiolabeling bioassays.

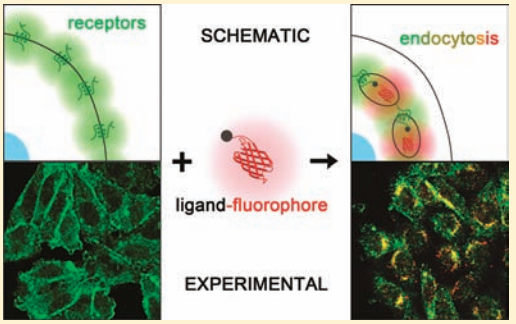

INTRODUCTION

Somatostatin-14 (SST) is a tetradecapeptide widely distributed in mammalian tissues participating in several crucial functions from regulating insulin release to modifying the central neural control of blood pressure and breathing.[1−3] SST, when bilaterally microinjected into discrete regions of the ventral medulla oblongata, evokes profound sympathoinhibition, leading to a precipitous fall in blood pressure. However, SST administered to the neighboring sites evokes a cessation of breathing, or apnea, but does not affect blood pressure.[4] SST functions via G-protein coupled receptors of 6 subtypes: sst_1, sst_{2A}, sst_{2B}, sst_3, sst_4, and sst_5 (in general, sst) which are found differentially distributed throughout the body and brain.[5] Of all these subtypes, the most abundant in human tissues and neuroendocrine tumors, hence the most studied, is sst_{2A}.[6] The physiological effects evoked following sst activation are mediated through several intracellular signaling pathways including adenylyl cyclase inhibition, K^+ channel opening, inhibition of voltage gated Ca^{2+} channels, and in some cases activation of phospholipase C or phospholipase A_2 leading to opening of intracellular Ca^{2+} stores.[3,7−9] Although the former three mechanisms are found to be pertussis toxin (PTX) sensitive, the latter is mostly found to occur following activation of sst in cells heterologously expressing the receptor and is only partially PTX sensitive and has been suggested to be mediated via $G_{i/o}$ and G_q/G_{11} proteins.[1,7,10] SST also acts via other PTX insensitive pathways which could result in stimulation of Na^+-H^+ exchange and inhibition of cell growth.[11,12] As sst(s) are overexpressed in neuroendocrine tumors, this inhibitory effect on cell-growth upon SST treatment is utilized for treatment of endocrine tumors and acromegaly[13] and also for imaging and diagnosis of neuroendocrine cancers using radiolabeled SST analogues.[14,15]

In most studies addressing tissue localization and trafficking of the somatostatin receptors, radioactively labeled SST peptide complexes were employed.[16−18] The intrinsic resolution limit of the radiolabeling approaches preclude capturing these processes with sufficient level of morphological and biomolecular detail. Moreover, radioactive techniques are potentially hazardous and demand setting up cumbersome laboratory safety procedures. In comparison, fluorescence labeling and optical imaging offers submicrometer resolution and noninvasiveness under nonhazardous conditions and provides high optical contrast in near-native

Received: February 27, 2011
Revised: August 7, 2011
Published: August 08, 2011

ACS Publications © 2011 American Chemical Society

cellular physiological environments. In addition, a specific spectroscopic signature of the fluorescent label allows efficient suppression of the cells morphological and autofluorescence background, pushing the sensitivity toward visualizing single ligand−receptor events. Multiplexed labeling of several proteins involved in a concerted molecular event is another attractive capability of fluorescent labels. This approach has thus far been restricted to labeling the sst (receptors) rather than SST (ligands), predominantly by immunofluorescence techniques.[16,19,20] As a result, important receptor functionality questions, for example, related to the postendocytosis fate of SST in certain cell types, whether the ligand is dissociated from the receptor, remains unresolved. A fluorescent label that renders SST observable will provide a comprehensive insight into the interaction of the ligand and the receptor, in combination with the existing methods of visualizing sst.

Development and applications of a few types of fluorescent somatostatin analogues have been reported in the literature. Nouel et al., Sarret et al., and Stroh et al. have reported employment of a Bodipy-conjugated [D-Trp^8]SST analogue to investigate the ligand internalization in COS-7,[21] AtT-20 cells,[22] and neurons,[23] respectively. The former investigated the differential internalization of the ligand by heterologously expressed sst_1 and sst_{2A} subtypes, and the latter two proposed sst_{2A} to be the subtype that contributed most to the ligand internalization in AtT-20 cells and neurons. Licha et al. and Becker et al. developed a new, cyanine dye-conjugated, octreotate analogue (a stabilized analogue of SST) and demonstrated labeling of the transfected somatostatin receptors *in vitro*[24] and in tumors expressing somatostatin receptors *in vivo*.[25] Kostenich et al. have also reported on labeling tumors using several types of fluorescent analogues of somatostatin pharmacore (a small peptide chain that facilitates the receptor binding).[26] Fluorescein-conjugated SST was employed to investigate the expression of somatostatin receptors in the immune system,[27] whereas fluorescein isothiocyanate (FITC)-conjugated octreotide was used for observation of its reuptake by the proximal tubular cells to be mediated by the scavenger receptors rather than sst.[28] Another fluorescent version of the octreotide aided elucidation of the mechanisms that dictated low permeation of the somatostatin-analogues and other drugs through the blood brain barrier.[29] However, the chemical attachment of a fluorescent organic dye to an SST molecule is prone to disruption of the optical or the biological activity, demanding a careful design of the conjugation procedure, with reproducibility of the chemical reaction yield being an inherent problem.[21,24,26]

In this paper, we report on the design and production of a robust, reproducible, genetically engineered fluorescent somatostatin analogue, somatostatin-monomeric red fluorescent protein (SST-mRFP), and evaluation of its fluorescent and pharmacological properties. The functionality of SST-mRFP in both endogenous and transfected cells expressing sst_{2A} is characterized. We also report, for the first time to the best of our knowledge, on an undissociated postendocytotic fate of the SST-sst_{2A} (ligand−receptor) complex in transfected Chinese Hamster Ovary (CHO-K1) cells.

EXPERIMENTAL PROCEDURES

Data analysis and curve fittings were performed either in *Matlab* R2009B or *Microcal Origin* academic version 8.1. Images were processed using *Image J*.

Genetic Engineering of Fluorescent Somatostatin (SST-mRFP). The genetic engineering procedure, microbial culturing, and cell lysis were carried out as per the standard protocols. In order to produce the chimeric protein, His-tagged SST-mRFP, the DNA fragment encoding SST (AGCKNFFWKTFTSC) was reconstituted using a pair of primers 5′-TCATGGGTACCG-GAGGTGGAGGTTCCGGAGGTGGAGGATCTGCTGGA-TGCAAGAACTTC-3′ and 5′-ATGACAAGCTTATCAGCAG-GATGTAAAGGTCTTCCAGAAGAAGTTCTTGCATCCA-GCAG-3′ followed by fusing to mRFP[30] using a flexible peptide $(Gly_4Ser)_2$ linker. This construct was subsequently cloned into pQE-30 vector (QIAGEN) using *Bam*HI and Hind III sites. This pQE-His-mRFP-SST plasmid was transfected to *E. coli* BL21 strain and incubated in LB (lysogeny broth) at 30 °C to express this recombinant protein. On reaching an optical density of 0.8 at 550 nm, the bacterial suspension was induced with 1 mM IPTG (isopropyl β-D-1-thiogalactopyranoside), and incubated for another 12 h.

Purification of the recombinant protein was carried out, as described earlier.[31] SDS/PAGE gel electrophoresis was performed in 12% polyacrylamide gel according to the standard protocol, and the resultant solution stored at 4 °C. The concentration of the recombinant protein in terms of mg/mL was estimated using absorption measurements at a wavelength of 280 nm. Prior to the cell experiments, the SST-mRFP solution was desalted with PD SpinTrap G-25 columns (GE Healthcare), pre-equilibrated with PBS (10× stock purchased from Invitrogen), and used within two months. The molar concentrations of SST and SST-mRFP were calculated based on the individual molecular masses of SST (1.63 kDa) and SST-mRFP (29.73 kDa).

Mass Spectroscopy. Mass spectroscopy analysis of the recombinant protein was carried out using Australian Proteome Analysis Facility (APAF), Sydney, Australia. In brief, two batches of the SST-mRFP solution were prepared in ammonium bicarbonate. One of the batches was reduced using dithiothreitol followed by alkylation using iodoacetamide. Later, both the batches were digested using trypsin, concentrated and desalted using zip-tip extraction, and analyzed by means of matrix assisted laser desorption/ionization (4800 Plus MALDI TOF/TOF). As a result, a number of peptides of known amino acid sequences (inferred from the DNA sequence template used for the SST-mRFP production) were produced. An Nd:YAG laser (355 nm) was used to irradiate the sample. Mass spectra were acquired for the mass range of 500−3500 Da. The near point calibration provided a mass accuracy greater than 500 ppm. The data was exported to a database search program, Mascot (Matrix Science Ltd., London, UK). The peaklists of the two analyzed batches were benchmarked against the fragments and their corresponding molecular masses determined *a priori*.

Spectral Measurements. The optical absorption spectrum of 1 μM SST-mRFP solution prepared in PBS was acquired using a spectrophotometer (Cary 5000 UV−vis-NIR, Varian Inc.). The spectrum was baseline corrected and presented here.

The fluorescence spectra of SST-mRFP and mRFP prepared in PBS were acquired using a fluorimeter (Fluorolog Tau3 system, JY Horiba). The mRFP fluorescence immunity to the cell preparation chemical procedures was evaluated by adding paraformaldehyde (final concentration of 3.7%) to the SST-mRFP solution and spectral acquisition after 20 min, followed by the spectral data analysis. The change in SST-mRFP concentration during this procedure was accounted for using a negative control experiment.

Cell Culture. The mouse AtT-20 neuroblastoma cell line was obtained from ATCC (VA, USA) and were grown in culture media composed of 90% DMEM (Dulbecco's modified Eagles Medium), 10% FBS (fetal bovine serum), and penicillin/streptomycin, 50/5 μg/mL, respectively (all reagents purchased from Invitrogen), in tissue culture treated flasks, inside an incubator maintained at 37 °C and 5% CO_2. AtT-20 cells are known to endogenously express sst_{2A} at a density of 1.2 pmol/mg.[32] For the membrane potential assay, they were grown on a 96-well glass bottomed, black-sided culture plate (Costar) until reaching confluency. For imaging, cells were seeded into an 4-well slide (BD Falcon) one day before the experiment.

The CHO-K1 cell line stably expressing the human somatostatin receptor type 2A (sst_{2A}) at a density of 10 pmol/mg was obtained from PerkinElmer Life and Analytical Sciences. The cells were grown in culture media composed of 90% F-12 Ham's, 10% FBS, and 400 μg/mL G-418 (all reagents purchased from Invitrogen), in tissue culture treated flasks (BD Falcon) inside an incubator maintained at 37 °C and 5% CO_2. For imaging, cells were seeded into an 8-well slide (BD Falcon) one day before the experiment. Cells used for the intracellular Ca^{2+} measurements were grown on 96-well plates until reaching confluency.

Membrane Potential Assay. A membrane potential change in the AtT-20 cells upon SST-induced activation was monitored using a fluorescence-based membrane potential assay (FLIPR bulk assay kit, Molecular Devices). AtT-20 cells grown in a 96-well plate were incubated overnight in Lebovitz L-15 media with 1% FBS (100 μL/well) inside a 37 °C incubator. The proprietary blue dye supplied with the FLIPR membrane potential assay kit was dissolved in a potassium-free modification of the recommended HEPES (*N*-[2-hydroxyethyl]piperazine-*N*′-[2-ethanesulphonic acid]) buffered Hank's balanced salt solution (in terms of mM: HEPES 18.5; Na_2HPO_4 0.34; $NaHCO_3$ 4.17; KH_2PO_4 0.44; $MgSO_4$ 0.83; $MgCl_2$ 1.05; NaCl 143.7; $CaCl_2$ 1.26; Glucose 5.5). 100 μL dye solution was added to each well in the 96-well plate and placed at 37 °C, 30 min prior to the experiment. The sst agonists or drugs (SST and SST-mRFP) of 5× final concentration were prepared in the above-described buffer and distributed in a 96-well plate (clear, v-bottom). The 96-well cell and drug plates were placed inside the flexstation (FlexStation 3, Molecular Devices). The membrane potential changes corresponding to the various drug concentrations were obtained by analyzing the recorded fluorescence signals (excitation/emission wavelengths, 530 nm/565 nm, respectively). Data fitting was performed by the following inbuilt logistic equation:

$$y = \frac{y_{min} - y_{max}}{1 + (x/EC50)^n} + y_{max}$$

where y_{min} and y_{max} are the minimum and saturation response, x is the concentration of the drug, EC50 is the drug concentration required to stimulate half-maximal response, and n is the fitting parameter that determines a slope for the fit.

Ca^{2+} Mobilization Assay. The CHO-K1 cells heterologously expressing sst_{2A} were used to characterize SST-mRFP activity in comparison with that of SST, using the Ca^{2+} mobilization assay. Fluorescence dye (Fura2-AM, Invitrogen) loaded into the cells reported the concentration of cytoplasmic Ca^{2+} ($[Ca^{2+}]$). The buffer used in $[Ca^{2+}]$ measurements contained, in terms of mM, the following: NaCl 140, KCl 2, $CaCl_2$ 2.5, $MgCl_2$ 1, HEPES 10, D-Glucose 10, and 0.05% BSA (pH and osomolality adjusted to 7.4 ± 0.1 and 330 ± 40 mosmol/kg, respectively), hereafter referred to as HBS. HBS-Ca was same as the above except that 2.5 mM $CaCl_2$ was replaced with 10 mM EGTA (ethylene glycol-bis[b-aminoethyl ether]-*N*,*N*,*N*′,*N*′-tetraacetic acid). HBS+Ca was similar to HBS, except for 20 mM of $CaCl_2$. Cells were washed once with HBS prior to loading with 2 μM Fura2-AM prepared in HBS. After 1 h of Fura2-AM incubation at 37 °C, the cells were washed 4 times with HBS and incubated again for 30 min at 37 °C. The cells were washed once immediately before the flexstation measurements. Drugs (SST and SST-mRFP), at 5× the final concentration, were prepared in HBS and loaded into the built-in drug chamber in a 96-well plate (clear, v-bottom). The instrument was programmed to record fluorescence emission at 510 nm under two consecutive excitations at wavelength bands centered at 340 and 380 nm, repeatedly every 4 s. The fluorescence was recorded before and after the addition of the drug. The autofluorescence background, acquired from cells lacking dye, was subtracted from the fluorescence assay signals. Minimum and maximum fluorescence measurements, acquired from the cells treated with HBS-Ca and HBS+Ca, respectively, in the presence of 50-μM digitonin, were used to calculate the exact intracellular $[Ca^{2+}]$ using the equation derived by Grynkiewicz et al.[33] The data were exported and fit to the logistic equation.

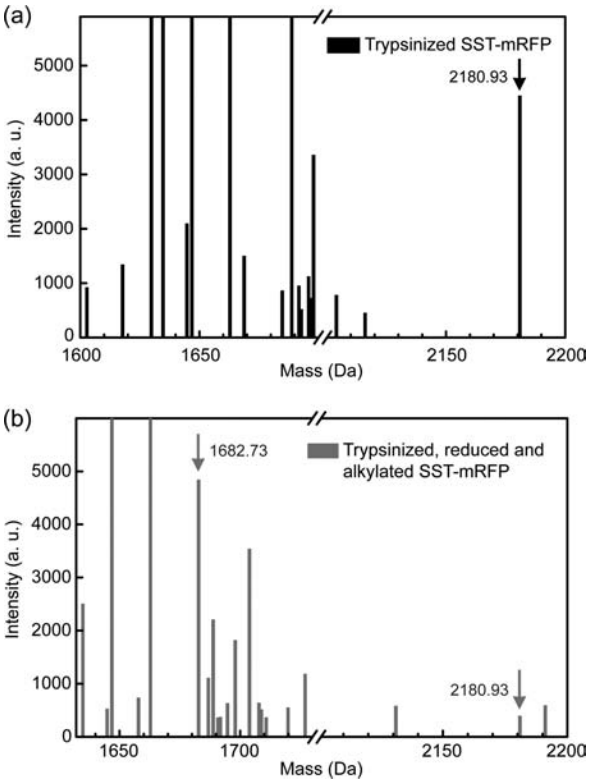

Figure 1. Mass spectrum of the trypsin-digested SST-mRFP (a) before and (b) after further reduction and alkylation. (a) A peak at 2180.93 Da and the peak absence at 1625.73 Da confirm the presence of disulfide bond in the SST module of the SST-mRFP complex. (b) Reduction of the disulfide bond diminished the peak at 2180.93 Da; instead, a new peak at 1682.73 Da appears.

Cell Imaging. The CHO-K1 cells were serum-starved overnight, with 1% FBS in the growth media. For the experiment, the cells were incubated with 100 nM SST, 100 nM mRFP, or 100 nM SST-mRFP prepared in PBS, supplemented with 0.1% bovine serum albumin (BSA), 20-mM D-glucose, 0.9-mM $CaCl_2$, and 0.5-mM $MgCl_2$ (hereafter referred to as PBS+CM), for

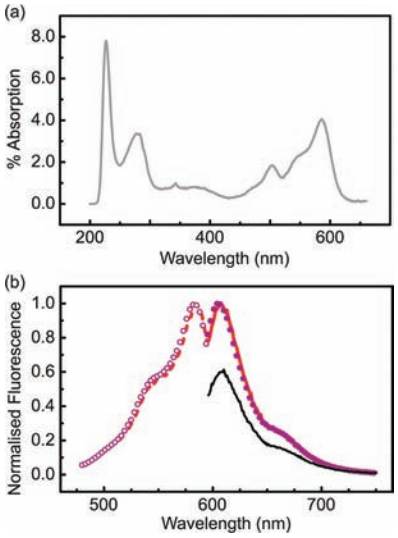

Figure 2. (a) Optical absorption spectrum of 1 μM SST-mRFP with a cuvette path length of 4.5 mm (baseline subtracted). (b) Normalized fluorescence spectra of mRFP and SST-mRFP. Excitation spectra of mRFP (open circles, purple) and SST-mRFP (thick dashed line, red). Emission spectra of mRFP (solid circles, purple) and SST-mRFP (thick solid line, red). Emission spectra of SST-mRFP in paraformaldehyde, thin solid line, black.

30 min at 37 °C to stimulate the cells. This step was avoided to evaluate the sst_{2A} distribution in the unstimulated cells. For the antagonist competition experiment, 10 μM BIM23627 was coincubated together with 100 nM SST-mRFP under the same conditions.

Immunocytochemistry (ICC) analysis of the cells under investigation was carried out as follows. The cells were fixed with 3.7% paraformaldehyde solution, prepared in PBSCM (same as PBS+CM, without glucose and BSA), for 20 min at room temperature. After washing once with PBSCM, the cells were permeabilized for 15 min with 0.2% Triton X-100, prepared in PBSCM, at room temperature. Subsequently, the cells were washed with PBSCM and blocked with 1% BSA solution prepared in PBSCM for 1 h at room temperature in order to reduce nonspecific binding of the antibodies to the substrates. As the next step, the rabbit-serum-derived primary antibody, against the carboxyl-terminal of sst_{2A} (diluted 1:125 times from the stock solution) (Biotrend Chemikalien GmBH), prepared 2 h prior to this step in PBSCM containing 1% BSA, was added to the cells and incubated for 1 h at room temperature while shaking. The cells were then thoroughly washed with PBS containing 1% BSA and incubated with antirabbit antibody conjugated with fluorescence dye FITC (Jackson Immunoresearch), prepared in PBS containing 1% BSA, for 1 h at room temperature while shaking. Finally, the cells were washed once with PBS containing 1% BSA, and sealed with a coverslip for imaging under either Leica TCS SP2 or Leica SP5 fluorescence confocal microscopes.

The AtT-20 cells were incubated with either 1 μM SST-mRFP or 1 μM mRFP (control) prepared in PBS+CM for 1 h at 37 °C. The cells were fixed with 3.7% paraformaldehyde solution, prepared in PBS, for 20 min at room temperature. Subsequently, 10 μM Hoechst solution, prepared in PBS, was added to the cells and incubated for 12 min, at room temperature, for nuclear labeling. The cells were washed two times with PBS and were prepared for imaging under the fluorescence confocal microscope.

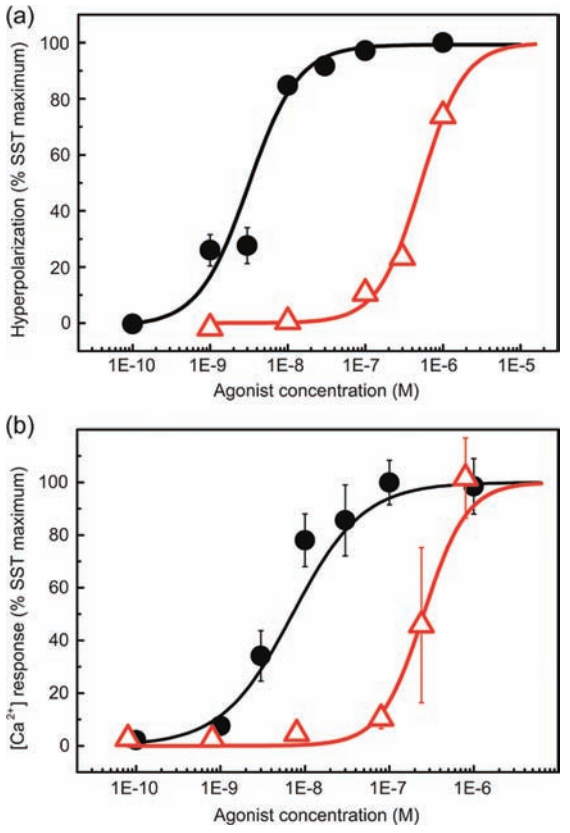

Figure 3. (a) Membrane potential response of the wild-type AtT-20 cells, containing endogenous sst and (b) intracellular [Ca^{2+}] response of the sst_{2A}-expressing CHO-K1 cell under stimulation by SST [solid black circles (mean ± SEM), solid black-sigmoid, logistic equation fit], and SST-mRFP [open red triangles (mean ± SEM), solid red-sigmoid, logistic equation fit]. The data shown here are representative of the four independent experiments, each performed in quadruplicate. The error bars, if not displayed, are smaller than the symbol size.

RESULTS AND DISCUSSION

The recombinant protein, SST-mRFP, molecular composition was characterized using the mass spectroscopy based analytical instrumentation. The activity of the mRFP module of the SST-mRFP was characterized by means of optical spectroscopy, while the biological activity of the SST group was characterized using several cell model experiments. In particular, the membrane hyperpolarization and fluorescence imaging reported on the endogenous receptor activity in the AtT-20 cells activated by SST-mRFP, whereas the intracellular Ca^{2+} mobilization and fluorescence imaging with auxiliary ICC reported on the transfected receptor activity of the SST-mRFP activated CHO-K1 cells.

Biochemical Characterization. The hairpin bend in a native SST molecule is stabilized by the disulfide bond between the amino acids Cys-3 and Cys-14 (amino acid numbers as per the native SST numbering). This disulfide bond has been shown to facilitate high biological activity; consequently, its absence results in reduced potency.[24] The correct disulfide bond was formed in the genetically engineered chimeric protein, SST-mRFP, as confirmed by the mass spectroscopy analysis. Prior to the analysis, a trypsin digestion procedure resulted in a controlled disintegration of the SST-mRFP recombinant protein. Among a number of resultant peptide fragments with amino acid sequence known *a*

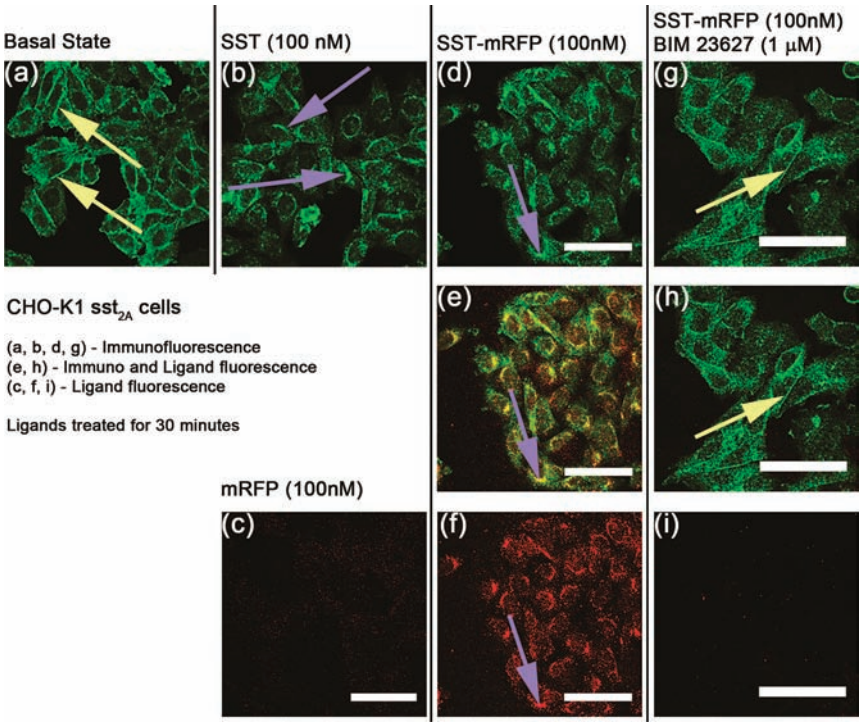

Figure 4. Fluorescence confocal images of CHO-K1 cells transfected with sst_{2A} receptors. mRFP and immunolabeled sst_{2A} fluorescence signals are color-coded red and green, respectively. ICC images of cells in (a) basal state or (b) treated with SST. (c) Cells treated with mRFP under 584 nm excitation that highlights mRFP. (d−f) Cells treated with SST-mRFP under (d) 488 nm excitation that highlights FITC, (f) 584 nm excitation that highlights mRFP, and (e) overlaid. (g−i) Cells treated with SST-mRFP along with BIM23627 under (g) 488 nm excitation, (i) 584 nm excitation, and (h) overlaid. Yellow arrows point to the sst_{2A} localized on the membrane; purple arrows point to the internalized sst_{2A} or sst_{2A}-ligand complex, localized in the perinuclear region. Scale bar, 50 μm.

priori, the following two peptides would report on the presence [HSTGAPSTPPGGGGSAG$_{TFTSC=}$CK (FW = 2180.95 Da)] or absence [HSTGAPSTPPGGGGSAGCK (FW = 1625.73 Da)] of the disulfide bond. As shown in Figure 1a, a peak at 2180.93 Da on the mass spectrum revealed the presence of the characteristic disulfide-bound peptides proving the hairpin bend in the recombinant SST-mRFP. The identity of this fragment was further confirmed by the disulfide reduction and alkylation of the trypsin-digested SST-mRFP. The resultant mass spectrum is shown in Figure 1b. The peak at 2180.93 Da is diminished and a new peak at 1682.73 Da, corresponding to the alkylated form of HSTGAPSTPPGGGGSAGCK, is clearly observable.

Optical Spectral Characterization. The absorption and excitation/emission spectra of SST-mRFP and pristine mRFP in PBS are shown in Figure 2a,b, respectively. The similarities in both absorption coefficient and the fluorescence spectra overlap suggest that the fluorescence property of the mRFP moiety in SST-mRFP was unaffected by the fused oligopeptide. The effect of the fixative, i.e., paraformaldehyde, was also evaluated to assess its potential influence on the mRFP spectral properties in the cell internalization experiments. The fluorescence emission of SST-mRFP was found to be reduced only by 40% under the presence of 3.7% paraformaldehyde in comparison with that in buffer (c.f., Figure 2), without any noticeable changes in the spectral profile, which was deemed acceptable for this investigation.

Membrane Potential Assay. The activity of SST-mRFP toward the endogenous sst in the wild-type AtT-20 was compared to that of the native SST by monitoring the $G_{i/o}$-protein induced membrane hyperpolarization, presumably, by means of activating the GIRK channels (G-protein coupled inwardly rectifying K^+ channels).[34] Figure 3a shows a representative SST and SST-mRFP dose−response curve activating the membrane potential response. The data from the 4 independent experiments, each performed in quadruplicate, for each ligand were analyzed. pEC50 values, defined as the negative log of drug concentration expressed in M that is required to reach half the maximum of the SST-induced saturation response, were found to be 8.4 ± 0.3 and 6.1 ± 0.2 for SST and SST-mRFP, respectively. It is likely that the lower pEC50 value of SST-mRFP compared to SST was due to the natural propensity for oligomerization of the coelenterate fluorescent proteins, despite the recent progress toward their monomerization.[25] Size-exclusion gel chromatography analysis of the SST-mRFP solution revealed the presence of dimers in the solution (detailed in the Supporting Information). Optimization of the purification and storage conditions of this recombinant protein is likely to diminish the SST-mRFP dimerization.

Ca^{2+} Mobilization Assay. Quantitative characterization of the activity of SST-mRFP toward activating the heterologously expressed sst_{2A} in CHO-K1 cells was carried out using the Ca^{2+} mobilization assay. Representative [Ca^{2+}] dose−response curves for SST and SST-mRFP are shown in Figure 3b. The calculated pEC50 values (from the data obtained from the four independent experiments, each in quadruplicate) for SST and SST-mRFP were found to be 7.8 ± 0.5 and 6.3 ± 0.3, respectively. The data point at the highest dose of SST-mRFP closely approaches the saturated SST dose−response. Sampling of the saturation region of the SST-mRFP dose−response curve was precluded by the SST-mRFP availability.

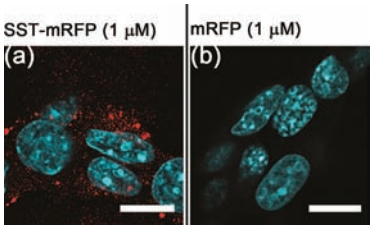

Figure 5. Fluorescence confocal images of wild-type AtT-20 cells expressing sst (receptors) treated with (a) SST-mRFP or (b) mRFP. The cell nuclei were stained with Hoechst fluorescent dye, for visual aid. mRFP and Hoechst fluorescence signals are color-coded red and cyan, respectively. Scale bar, 15 μm.

Further, the signaling pathway of SST-mRFP leading to the Ca^{2+} mobilization was found to be PTX sensitive (data not shown), in agreement with the literature.

Cell Imaging. It was previously demonstrated that heterologous sst_{2A} expressed in CHO-K1 cells were endocytosed upon the SST treatment within 15 min after stimulation.[9] This was confirmed by our immunocytochemical experiments, where the transfected CHO-K1 cells were subjected to SST treatment (results shown in Figure 4). The sst_{2A} receptors (color-coded green) were localized in the perinuclear region (Figure 4b, violet arrows) following the SST treatment, whereas they were found to be membrane-bound without the SST stimulation (Figure 4a, yellow arrows).

Despite the usefulness of ICC in receptor localization assessment, it provides little insight into the ligand pathway and fate. In order to demonstrate the potential of our recombinant fluorescent SST analogue for molecular trafficking studies, we performed the following experiment. The CHO-K1 cells were incubated with the recombinant SST-mRFP for 30 min under the conditions described above, which induced SST-mRFP internalization, with subsequent translocation to the perinuclear regions, as observed under SST activation. Due to the fluorescent nature of the SST analogue, it was clearly visible in the cells (Figure 4f, bright red color), relaxing the need to perform a cumbersome, time-consuming ICC procedure. At the same time, mRFP showed little internalization demonstrating the specificity of SST-mRFP toward sst_{2A} (Figure 4c). The possibility of dissociation of SST-mRFP from sst_{2A} postinternalization was investigated by ICC. The images displayed clear spatial overlap of the fluorescence from SST-mRFP (red) and sst_{2A} (green, immunolabeled) confirming the common intracellular fate of sst_{2A} and SST-mRFP, in the range of time scales investigated (Figure 4e, violet arrows). Importantly, this proves the specificity of the interaction between our novel, recombinant SST-mRFP complex and the sst_{2A} receptors. It is worthwhile to note that SST-mRFP at the concentration of 100 nM resulted in maximum internalization, with relatively low background overhead, and is useful for designing SST-mRFP imaging experiments. Co-incubation of the antagonist BIM23627 along with SST-mRFP inhibited the agonist internalization (as seen in Figure 4g–i), in accordance with previous studies,[35,36] again confirming the interaction specificity between SST-mRFP and sst_{2A}.

The sensitivity/specificity of SST-mRFP for labeling somatostatin receptors in wild type cells is demonstrated in Figure 5. The AtT-20 cells, known to express several receptor subtypes, sst_1, sst_2, sst_4, and sst_5,[22] when treated with SST-mRFP showed bright spots, mostly discretized in the cytoplasm, with no signs of nuclear penetration, as shown in the Figure 5a. The specificity of this labeling can be seen from Figure 5b, where mRFP showed no internalization.

CONCLUSION

We report on the design, production, and biochemical, optical, and pharmacological characterization of a genetically engineered somatostatin molecule fused with a monomeric red fluorescent protein (SST-mRFP). SST-mRFP was found to maintain its mRFP-derived fluorescent properties in the presence of chemical fixatives. The SST moiety in the SST-mRFP complex was demonstrated to be active and potent for triggering signaling in both wild-type and transfected cells expressing somatostatin receptors, although its potency was lower than that of SST, as confirmed by several bioassaying methods. Pinpointing possible reasons for the lower potency, we confirmed the complex integrity associated with SST's disulfide bond, but found the profound oligomerization of SST-mRFP, which lends itself straightforward improvement of the analogue performance. This analogue was demonstrated to be a useful fluorescent biomarker with potential to elucidate the intracellular fate of the somatostatin ligand–receptor complexes in transfected and wild-type cells. In perspective, fluorescent SST/analogues can serve as a model of a drug/gene delivery vehicle, since this small molecular weight peptide is highly mobile, with good prospects of surviving the blood enzymatic degradation.[37]

ASSOCIATED CONTENT

Supporting Information. Experimental methods and results from the characterization of SST-mRFP oligomerization. This material is available free of charge via the Internet at http://pubs.acs.org.

AUTHOR INFORMATION

Corresponding Author

*Department of Physics and Astronomy, Macquarie University, Herring Road, Sydney, NSW, Australia 2109. E-mail: andrei.zvyagin@mq.edu.au. Phone: 0061 2 9850 7760. Fax: 0061 2 9850 8115.

ACKNOWLEDGMENT

This research was primarily supported by a grant from the Macquarie University Research Innovation Fund. S.D. and O.S acknowledge the Russian Foundation of Basic Research and RAS Program Molecular & Cellular Biology for support of the recombinant protein synthesis. The authors express gratitude to Ms. Alisa Knapman for assistance with Flexstation 3 measurements. The mass spectroscopy analysis was undertaken at APAF, the infrastructure provided by the Australian Government through the National Collaborative Research Infrastructure Strategy (NCRIS).

ABBREVIATIONS

BSA, bovine serum albumin; CHO-K1, Chinese hamster ovary; FITC, fluorescein isothiocyanate; GIRK, G-protein coupled inwardly rectifying K^+; ICC, immunocytochemistry; LB, lysogeny broth; PBS, phosphate buffered saline; PBS+CM, PBS containing $CaCl_2$, $MgCl_2$, BSA, and D-Glucose; PBSCM, PBS containing

$CaCl_2$ and $MgCl_2$; SST, Somatostatin-14; SST-mRFP, somatostatin-monomeric-red fluorescent protein; sst_x, somatostatin receptor of subtype x; PTX, pertussis toxin

REFERENCES

(1) Cervia, D., and Bagnoli, P. (2007) An update on somatostatin receptor signaling in native systems and new insights on their pathophysiology. *Pharmacol. Ther. 116*, 322–341.

(2) Burke, P. G. R., Li, Q., Costin, M. L., McMullan, S., Pilowsky, P. M., and Goodchild, A. K. (2008) Somatostatin 2A receptor-expressing presympathetic neurons in the rostral ventrolateral medulla maintain blood pressure. *Hypertension 52*, 1127–U86.

(3) Strowski, M. Z., and Blake, A. D. (2008) Function and expression of somatostatin receptors of the endocrine pancreas. *Mol. Cell. Endocrinol. 286*, 169–179.

(4) Burke, P. G. R., Abbott, S. B. G., McMullan, S., Goodchild, A. K., and Pilowsky, P. M. (2010) Somatostatin selectively ablates post-inspiratory activity after injection into the Bötzinger complex. *Neuroscience (Amsterdam, Neth.) 167*, 528–539.

(5) Olias, G., Viollet, C., Kusserow, H., Epelbaum, J., and Meyerhof, W. (2004) Regulation and function of somatostatin receptors. *J. Neurochem. 89*, 1057–1091.

(6) Reubi, J. C., Kappeler, A., Waser, B., Schonbrunn, A., and Laissue, J. (1998) Immunohistochemical localization of somatostatin receptor sst2A in human pancreatic islets. *J. Clin. Endocrinol. Metab. 83*, 3746–3749.

(7) Tomura, H., Okajima, F., Akbar, M., Majid, M. A., Sho, K. M., and Kondo, Y. (1994) Transfected human somatostatin receptor-type-2, sstr2, not only inhibits adenylate-cyclase but also stimulates phospholipase-C and Ca^{2+} mobilization. *Biochem. Biophys. Res. Commun. 200*, 986–992.

(8) Taylor, J. E. (1995) Somatostatin (SSTR2) receptors mediate phospholipase C-independent Ca2+ mobilization in rat AR42J pancreas cells. *Biochem. Biophys. Res. Commun. 214*, 81–85.

(9) Liu, Q., Dewi, D. A., Liu, W., Bee, M. S., and Schonbrunn, A. (2008) Distinct phosphorylation sites in the SST2A somatostatin receptor control internalization, desensitization, and arrestin binding. *Mol. Pharmacol. 73*, 292–304.

(10) Nunn, C., Cervia, D., Langenegger, D., Tenaillon, L., Bouhelal, R., and Hoyer, D. (2004) Comparison of functional profiles at human recombinant somatostatin sst(2) receptor: simultaneous determination of intracellular Ca2+ and luciferase expression in CHO-K1 cells. *Br. J. Pharmacol. 142*, 150–160.

(11) Ren, J., Bell, G., Coy, D. H., and Brunicardi, F. C. (1997) Activation of human somatostatin receptor type 2 causes inhibition of cell growth in transfected HEK293 but not in transfected CHO cells. *J. Surg. Res. 71*, 13–18.

(12) Jacobs, S., and Schulz, S. (2008) Intracellular trafficking of somatostatin receptors. *Mol. Cell. Endocrinol. 286*, 58–62.

(13) Weckbecker, G., Lewis, I., Albert, R., Schmid, H. A., Hoyer, D., and Bruns, C. (2003) Opportunities in somatostatin research: biological, chemical and therapeutic aspects. *Nat. Rev. Drug Discovery 2*, 999–1017.

(14) Breeman, W. A. P., de Jong, M., Kwekkeboom, D. J., Valkema, R., Bakker, W. H., Kooij, P. P. M., Visser, T. J., and Krenning, E. P. (2001) Somatostatin receptor-mediated imaging and therapy: basic science, current knowledge, limitations and future perspectives. *Eur. J. Nucl. Med. 28*, 1421–1429.

(15) Slooter, G. D., Mearadji, A., Breeman, W. A. P., Marquet, R. L., De Jong, M., Krenning, E. P., and van Eijck, C. H. J. (2001) Somatostatin receptor imaging, therapy and new strategies in patients with neuroendocrine tumours. *Br. J. Surg. 88*, 31–40.

(16) Grant, M., Collier, B., and Kumar, U. (2004) Agonist-dependent dissociation of human somatostatin receptor 2 dimers - A role in receptor trafficking. *J. Biol. Chem. 279*, 36179–36183.

(17) Koenig, J. A., Kaur, R., Dodgeon, I., Edwardson, J. M., and Humphrey, P. P. A. (1998) Fates of endocytosed somatostatin sst(2) receptors and associated agonists. *Biochem. J. 336*, 291–298.

(18) Tulipano, G., Soldi, D., Bagnasco, M., Culler, M. D., Taylor, J. E., Cocchi, D., and Giustina, A. (2002) Characterization of new selective somatostatin receptor subtype-2 (sst2) antagonists, BIM-23627 and BIM-23454. Effects of BIM-23627 on GH release in anesthetized male rats after short-term high-dose dexamethasone treatment. *Endocrinology 143*, 1218–1224.

(19) Tulipano, G., Stumm, R., Pfeiffer, M., Kreienkamp, H. J., Hollt, V., and Schulz, S. (2004) Differential beta-arrestin trafficking and endosomal sorting of somatostatin receptor subtypes. *J. Biol. Chem. 279*, 21374–21382.

(20) Cescato, R., Schulz, S., Waser, B., Eltschinger, V., Rivier, J. E., Wester, H. J., Culler, M., Ginj, M., Liu, Q. S., Schonbrunn, A., and Reubi, J. C. (2006) Internalization of sst(2), sst(3), and sst(5) receptors: Effects of somatostatin agonists and antagonists. *J. Nucl. Med. 47*, 502–511.

(21) Nouel, D., Gaudriault, G., Houle, M., Reisine, T., Vincent, J. P., Mazella, J., and Beaudet, A. (1997) Differential internalization of somatostatin in COS-7 cells transfected with SST1 and SST2 receptor subtypes: A confocal microscopic study using novel fluorescent somatostatin derivatives. *Endocrinology 138*, 296–306.

(22) Sarret, P., Nouel, D., Dal Farra, C., Vincent, J. P., Beaudet, A., and Mazella, J. (1999) Receptor-mediated internalization is critical for the inhibition of the expression of growth hormone by somatostatin in the pituitary cell line AtT-20. *J. Biol. Chem. 274*, 19294–19300.

(23) Stroh, T., Jackson, A. C., Farra, C. D., Schonbrunn, A., Vincent, J. P., and Beaudet, A. (2000) Receptor-mediated internalization of somatostatin in rat cortical and hippocampal neurons. *Synapse (Hoboken, NJ, U. S.) 38*, 177–186.

(24) Licha, K., Hessenius, C., Becker, A., Henklein, P., Bauer, M., Wisniewski, S., Wiedenmann, B., and Semmler, W. (2001) Synthesis, characterization, and biological properties of cyanine-labeled somatostatin analogues as receptor-targeted fluorescent probes. *Bioconjugate Chem. 12*, 44–50.

(25) Becker, A., Hessenius, C., Licha, K., Ebert, B., Sukowski, U., Semmler, W., Wiedenmann, B., and Grotzinger, C. (2001) Receptor-targeted optical imaging of tumors with near-infrared fluorescent ligands. *Nat. Biotechnol. 19*, 327–331.

(26) Kostenich, G., Livnah, N., Bonasera, T. A., Yechezkel, T., Salitra, Y., Litman, P., Kimel, S., and Orenstein, A. (2005) Targeting small-cell lung cancer with novel fluorescent analogs of somatostatin. *Lung Cancer 50*, 319–328.

(27) Lichtenauer-Kaligis, E. G. R., Dalm, V. A. S., Oomen, S., Mooij, D. M., van Hagen, P. M., Lamberts, S. W. J., and Hofland, L. J. (2004) Differential expression of somatostatin receptor subtypes in human peripheral blood mononuclear cell subsets. *Eur. J. Endocrinol. 150*, 565–577.

(28) Barone, R., Van Der Smissen, P., Devuyst, O., Beaujean, V., Pauwels, S., Courtoy, P. J., and Jamar, F. (2005) Endocytosis of the somatostatin analogue, octreotide, by the proximal tubule-derived opossum kidney (OK) cell line. *Kidney Int. 67*, 969–976.

(29) Fricker, G., Nobmann, S., and Miller, D. S. (2002) Permeability of porcine blood brain barrier to somatostatin analogues. *Br. J. Pharmacol. 135*, 1308–1314.

(30) Campbell, R. E., Tour, O., Palmer, A. E., Steinbach, P. A., Baird, G. S., Zacharias, D. A., and Tsien, R. Y. (2002) A monomeric red fluorescent protein. *Proc. Natl. Acad. Sci. U. S. A. 99*, 7877–7882.

(31) Deyev, S. M., Waibel, R., Lebedenko, E. N., Schubiger, A. P., and Pluckthun, A. (2003) Design of multivalent complexes using the barnase-barstar module. *Nat. Biotechnol. 21*, 1486–1492.

(32) Heisler, S., and Srikant, C. B. (1985) Somatostatin-14 and somatostatin-28 pretreatment down-regulate somatostatin-14 receptors and have biphasic effects on forskolin-stimulated cyclic adenosine, 3′,5′-monophosphate synthesis and adrenocorticotropin secretion in mouse anterior pituitary tumor cells. *Endocrinology 117*, 217–225.

(33) Grynkiewicz, G., Poenie, M., and Tsien, R. Y. (1985) A new generation of Ca2+ indicators with greatly improved fluorescence properties. *J. Biol. Chem. 260*, 3440–3450.

(34) Pennefather, P. S., Heisler, S., and MacDonald, J. F. (1988) A potassium conductance contributes to the action of somatostatin-14 to suppress ACTH secretion. *Brain Res. 444*, 346–350.

(35) Stumm, R. K., Zhou, C., Schulz, S., Endres, M., Kronenberg, G., Allen, J. P., Tulipano, G., and Hollt, V. (2004) Somatostatin receptor 2 is activated in cortical neurons and contributes to neurodegeneration after focal ischemia. *J. Neurosci. 24*, 11404–11415.

(36) Lelouvier, B., Tamagno, G., Kaindl, A. M., Roland, A., Lelievre, V., Le Verche, V., Loudes, C., Gressens, P., Faivre-Baumann, A., Lenkei, Z., and Dournaud, P. (2008) Dynamics of somatostatin type 2A receptor cargoes in living hippocampal neurons. *J. Neurosci. 28*, 4336–4349.

(37) Xu, Z. P., Zeng, Q. H., Lu, G. Q., and Yu, A. B. (2006) Inorganic nanoparticles as carriers for efficient cellular delivery. *Chem. Eng. Sci. 61*, 1027–1040.

SUPPORTING INFORMATION

Pharmacological Characterization of a Recombinant, Fluorescent Somatostatin Receptor Agonist

Varun K. A. Sreenivasan[†], Oleg A. Stremovskiy[§], Timothy A. Kelf[†], Marika Heblinski[‡], Ann K. Goodchild[‡], Mark Connor[‡], Sergey M. Deyev[§], Andrei V. Zvyagin*[†]

[†] *MQ Biofocus Research Centre, Macquarie University, Australia 2109;* [‡] *Australian School of Advanced Medicine, Macquarie University, Australia 2109;* [§] *Shemyakin & Ovchinnikov Institute of Bioorganic Chemistry, Russian Academy of Sciences, 117997 Russia;*

**Department of Physics and Astronomy, Macquarie University, Herring Road, Sydney, NSW, Australia 2109*

Email: andrei.zvyagin@mq.edu.au

Phone: 0061 2 9850 7760

Fax: 0061 2 9850 8115

Gel Filtration analysis of SST-mRFP

The oligomerization effect of SST-mRFP was semi-quantified by gel filtration analysis (Superdex 200 10/300 GL Column; GE Healthcare). The observed peaks were benchmarked against to the peaks of the Tricorn Superdex 200 standard proteins.

Figure S1 shows the protein concentration in the eluate fractions obtained after the filtration. The peak labeled 'SST-mRFP (dimeric)' occurred at the protein mobility value that was calibrated to molecular mass of 60 kDa, corresponding to the dimeric form of SST-mRFP, whereas a second peak labeled 'SST-mRFP (monomeric)' was found to coincide with 30 kDa in the calibration chart that corresponds to the SST-mRFP monomer. The existence of this dimer is likely to be the reason for reduced potency of the recombinant protein. Optimization of purification and storage conditions can diminish this observed oligomerization.

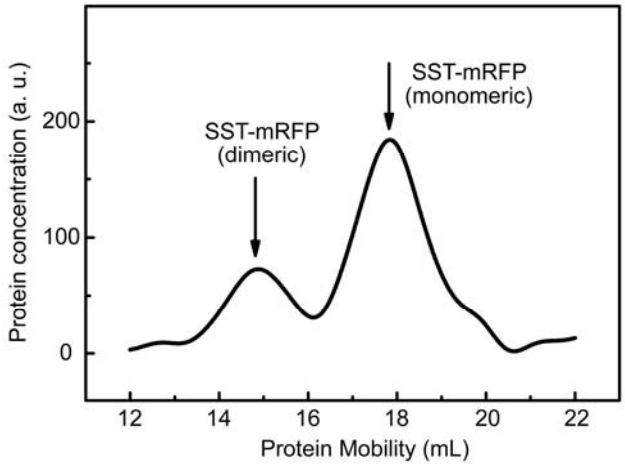

Figure S1. Plot of the SST-mRFP protein concentration versus the eluate mobility fractions using the size exclusion chromatography (baseline corrected). Two fractions, monomeric and dimeric, are demarcated by arrows.

Bioconjugate Chemistry

ARTICLE

pubs.acs.org/bc

Cancer-Stroma Targeting Therapy by Cytotoxic Immunoconjugate Bound to the Collagen 4 Network in the Tumor Tissue

Masahiro Yasunaga,[†] Shino Manabe,[‡] David Tarin,[§] and Yasuhiro Matsumura*[,†]

[†]Investigative Treatment Division, Research Center for Innovative Oncology, National Cancer Center Hospital East, 6-5-1 Kashiwanoha, Kashiwa, Chiba, 277-8577, Japan

[‡]Synthetic Cellular Chemistry Laboratory, RIKEN Advanced Science Institute, 2-1 Hirosawa, Wako, Saitama 351-0198, Japan

[§]Department of Pathology and Moores/UCSD Comprehensive Cancer Center, University of California, San Diego, 3855 Health Sciences Drive MC 0803, La Jolla, California, 92093-0803, United States

ABSTRACT: Some cytotoxic immunoconjugates have been approved for malignant lymphoma, a representative of hypervascular and stroma-poor tumors. However, many human solid tumors possess abundant intercellular stromata that prevent diffusion of cancer cell-specific monoclonal antibodies (mAb) and become a barrier preventing immunoconjugates from directly attacking cancer cells. Here we show the successful development of a new strategy that overcomes this drawback and achieves a highly localized concentration of a topoisomerase I inhibitor, SN 38, by conjugating it via an ester bond to a mAb targeted against collagen 4, a plentiful component of the tumor stroma. Poly(ethylene glycol) (PEG) was utilized as a spacer, close to each bond, to maintain stability in the blood. Immunoconjugates selectively extravasated from leaky tumor vessels and minimally from normal vessels because the immunoconjugates are too large to pass through normal vessel walls. Stroma-targeting immunconjugates bound to the stroma to create a scaffold, from which sustained release of cytotoxic agent occurred and the agent subsequently diffused throughout the tumor tissue to damage both tumor cells and vessels. Cancer-stroma-targeting immunoconjugate therapy was thus validated as a new modality of oncological therapy, especially for refractory, stromal-rich cancers.

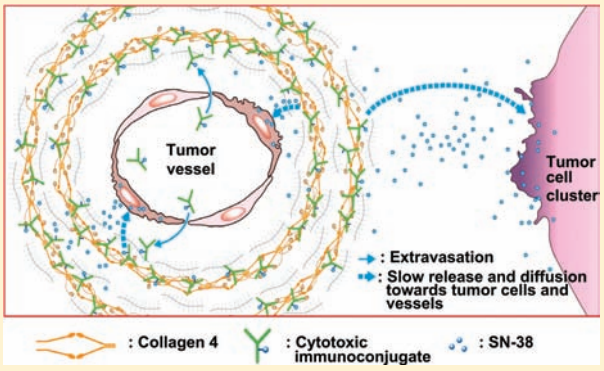

INTRODUCTION

In contrast to low molecular weight (LMW) agents, high molecular weight (HMW) agents such as monoclonal antibodies (mAbs) and nanoparticles have a long plasma half-life because they are too large to pass through the normal vessel walls, unless they are trapped by the reticuloendothelial system (RES) in various organs., However, HMW agents can reach tumor tissue sufficiently and extravasate efficiently from leaky tumor vessels to achieve tumor-selective accumulation of HMW agents by utilizing the enhanced permeability and retention (EPR) effect.[1−6] Even so, the use of HMW agents presents a dilemma for cancer therapy because the very properties that favor their high accumulation in the lesion also cause low diffusion of these macromolecules within a tumor.[7] Most human solid tumors possess abundant stromata that prevent mAb diffusion and, consequently, become a barrier preventing mAb from directly attacking cancer cells.[7−10] In fact, immunoconjugate therapies for common solid tumors (e.g., colorectal, lung, and pancreatic cancers) have not yet proven successful in clinical practice because of the heterogeneity of target antigens and the low uptake and retention of chemotherapeutic drugs in these types of cancer. This contrasts with the results seen in treatment of human hematologic malignancies and of tumor xenografts in mice, which usually have less inert interstitial tissue within the neoplasm.[11] The kinetics of drug distribution within tumors are considered to be functions of interstitial conductivity, which is determined by the quantity and density of the extracellular matrix (ECM e.g., proteoglycan, fibronectin), and fibrosis (e.g., collagen fibers) in the stroma.[7−10] Such compact assemblies of various tissue constituents in solid tumors cause reduced drug penetration and also act as a stromal barrier to prevent the diffusion of mAbs (HMW proteins).[7−9,11−13] Although there are a few papers describing tumor stromal targeting using immunoconjugates, the target molecule was still a surface antigen on cells in tumor stroma, or the ECM was used for targeting the tumor vascular endothelial cell.[14,15] The principle of our strategy is that our newly developed immunoconjugates selectively extravasated from leaky tumor vessels, bound to the collagen network in the stroma, and created a scaffold from which effective sustained release of the time-dependent ACA SN-38 occurred. This free SN-38 can easily reach the cancer cells by diffusion through the stromal barrier. Another important finding is that SN-38 released from immunoconjugates can attack and destroy the vascular endothelial cells (Figure1).

Received: March 29, 2011
Revised: June 30, 2011
Published: July 13, 2011

ACS Publications © 2011 American Chemical Society

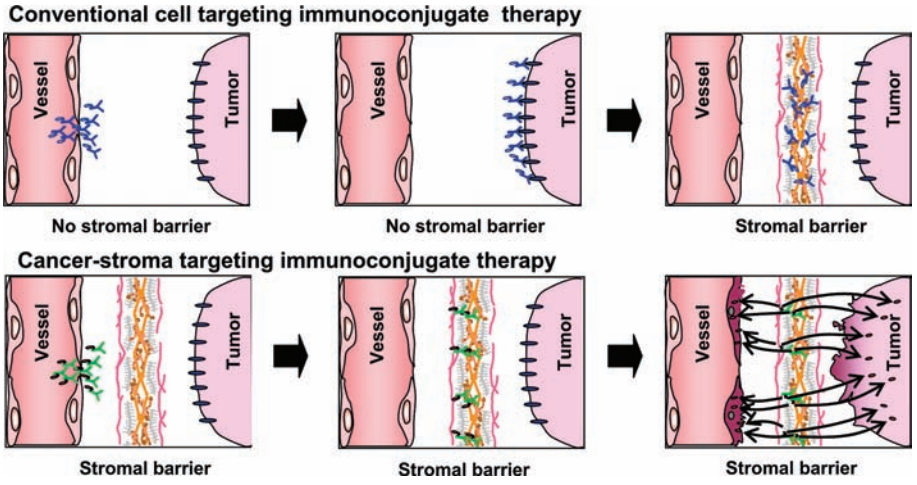

Figure 1. Therapeutic strategy of cancer-stroma targeting immunoconjugate. Conventional immunoconjugates can target cancer cells in the treatment of stroma-poor cancer such as malignant lymphoma. However, Many human solid tumors possess abundant stromata hindering the distribution of the immunoconjugates against cancer cells themselves (stromal barrier), whereas newly developed cancer-stroma-targeting immunoconjugates bound to the collagen 4 network of the cancer stroma, from which effective sustained release of the time-dependent anticancer agent SN-38 occurred. The SN-38 subsequently diffused throughout the tumor tissue to damage both cancer cells and vessels. Arrows show the distribution of SN-38 beyond the stromal barrier.

EXPERIMENTAL PROCEDURES

Antibody/Drug, Reagents, and Cells. Anti-EpCAM antibody-producing hybridoma (B8-4) was established from a mouse with immunizing recombinant protein (R&D Systems, Minneapolis, MN, USA). Anti-collagen 4 antibody-producing hybridoma (35-4) was obtained from a rat by immunization with purified mouse collagen 4 protein. A carrier protein was not used in either case.[16,17] Spleen cells from each immunized animal were fused with myeloma cells (P3X63Ag8.653). The specific hybridoma clones were selected using ELISA. Our anticollagen 4 antibody (35-4) was specific for mouse protein but not for human (data not shown). Antihuman CD20 antibody (rituximab) was purchased from Daiichi-Sankyo (Tokyo, Japan). For immunohistochemistry, polyclonal anti-collagen 4 antibody (LSL-LB-1403), monoclonal anti-CD31 antibody (MEC 13.3) and polyclonal anti-CD31 antibody (AF3628) were purchased from Cosmo. Bio. Inc. (Tokyo, Japan), Becton, Dickinson and Company (Franklin Lakes, NJ, USA), and R&D Systems, Inc. (Minneapolis, MN USA), respectively. SN-38 and CPT-11 (irinotecan) were purchased from Tokyo Chemical Industry Co. (Tokyo, Japan) and Yakult (Tokyo, Japan), respectively. Human pancreatic cancer cell line, PSN1 was purchased from the American Type Culture Collection (Rockville, MD, USA). Human pancreatic cancer cell line SUIT2 was purchased from the Health Science Research Resources Bank (Osaka, Japan). PSN1 and SUIT2 were maintained in DMEM (Sigma) supplemented with 10% fetal bovine serum (Tissue Culture Biologicals, CA, USA), penicillin, streptomycin, and amphotericin B (Sigma) in an atmosphere of 5% CO_2 at 37 °C. RL was maintained in RPMI1690 (Sigma) instead of DMEM.

Antibody Conjugate. A linker containing an ester bond between PEG and SN-38 was produced as follows. To a solution of SN-38 (102.1 mg, 0.260 mmol), BocHN-PEG_{27}-COOH (407.1 mg, 0.286 mmol) and 4-dimethylamino pyridine (15.9 mg, 0.130 mmol) in DMF (1 mL), 1-ethyl-3-(3-dimethyl aminopropyl)-carbodiimide·HCl (54.8 mg, 0.286 mmol) was added at 0 °C. The mixture was stirred at room temperature for 19 h, and the reaction mixture was purified by gel filtration column chromatography (LH20 $CHCl_3$/MeOH 1:1) and then silica gel column chromatography ($CHCl_3$/MeOH 15:1−9:1) to give the ester (420.1 mg, 90%) as a colorless oil.

^{1}H NMR (CD_3OD) δ 8.20 (d, J = 9.2 Hz, 1H), 7.99 (s, 1H), 7.66 (m, 2H), 5.60 (d, J = 16.5 Hz, 1H), 5.40 (d, J = 16.5 Hz, 1H), 5.32 (m, 2H), 3.93 (t, J = 6.4 Hz, 2H), 2.96 (t, J = 6.4 Hz, 2H), 1.97 (m, 2H), 1.43 (s, 9H), 1.40 (t, J = 7.6 Hz, 3H), 1,02 (t, J = 7.8 Hz, 3H); ^{13}C NMR (DMSO-d_6) δ 164.8, 161.9, 149.2, 148.5, 143.1, 142.7, 141.3, 138.2, 137.7, 137.5, 122.4, 119.5, 118.9, 117.2, 110.7, 106.5, 89.7, 70.4, 64.6, 62.3, 62.0, 62.0, 62.0, 61.9, 61.8, 61.8, 61.7, 61.5, 58.1, 58.0, 57.1, 41.2, 40.1, 31.8, 28.1, 26.3, 19.4, 14.4, 4.9, −1.1.

To a solution of BocHN-PEG_{27}-SN-38 (221.5 mg, 0.123 mmol) in CH_2Cl_2 (10 mL), trifluoroacetic acid (1 mL) was added at room temperature. After the mixture was stirred for 1.5 h, the solvent was removed in vacuo, and toluene was added. After evaporation, the residue was dried under high vacuum. The residue was dissolved in CH_2Cl_2 (5 mL) and MAL-PEG_{12}-NHS (128.2 mg, 0.148 mmol) and iPr_2NEt (48 μL, 0.246 mmol) were added at 0 °C. After 30 min, the mixture was purified by gel filtration column chromatography (LH-20, $CHCl_3/CH_3OH$ = 1:1) and silica gel column chromatography to give (276.0 mg, 91%) of the target product as a colorless oil.

^{1}H NMR (CD_3OD) δ 8.20 (d, J = 9.2 Hz, 1H), 8.00 (s, 1H), 7.66−7.64 (m, 2H), 6.83 (s, 2H), 5.60 (d, J = 16.0 Hz, 1H), 5.41 (d, J = 16.0 Hz, 1H), 5.34 (s, 1H), 3.93 (t, J = 6.0 Hz, 2H), 2.97 (t, J = 6.0 Hz, 2H), 2.49−2.45 (m, 4H), 2.00−1.98 (m, 2H), 1.41 (t, J = 7.6 Hz, 3H), 1.02 (t, J = 7.6 Hz, 3H); ^{13}C NMR (DMSO-d_6) δ 172.1, 170.4, 169.8, 169.7, 169.1, 156.5, 151.7, 149.7, 148.9, 146.2, 145.6, 145.0, 134.3, 131.1, 128.4, 126.8, 125.3, 118.8, 115.0, 96.5, 72.3, 69.9, 69.6, 69.5, 69.4, 69.0, 68.9, 66.7, 65.8, 65.1, 49.5, 36.0, 34.8, 34.1, 33.9, 31.6, 30.3, 25.4, 22.3, 13.9, 7.8.

Interchain disulfides of the antibodies were first reduced with 10 mM DTT (Sigma).[18] The numbers of free thiols were quantified with dinitrothiocyanobenzene (DNTB, Wako). After the purification by gel filtration (Amicon Ultra Centrifugal Filter Devices, Millipore, Billerica, MA, USA), reduced antibodies

dx.doi.org/10.1021/bc200158j |*Bioconjugate Chem.* 2011, 22, 1776–1783

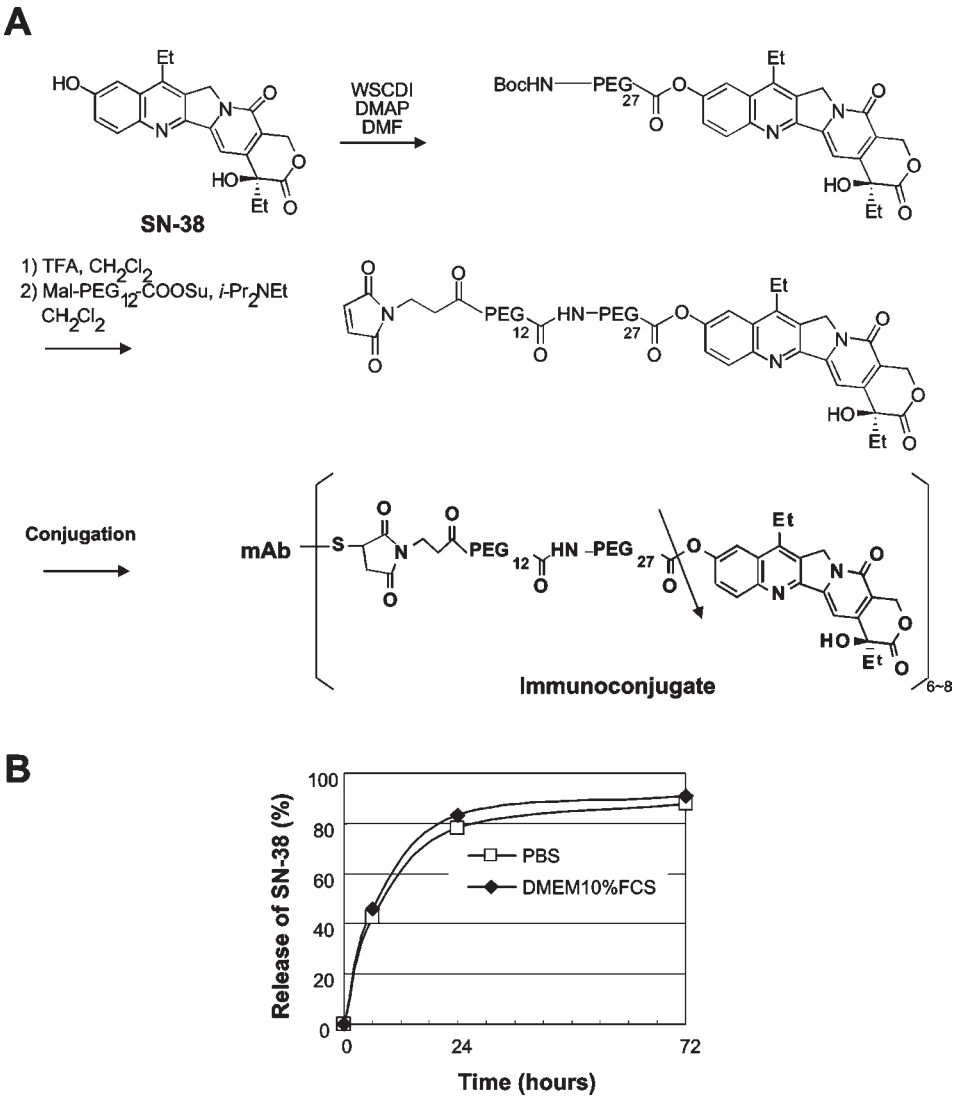

Figure 2. Structure and drug-release of the immunoconjugate. (A) Synthetic scheme of the immunoconjugate. The arrow indicates the cleavage site for releasing free active SN-38. PEG = poly(ethylene glycol). (B) The release behavior (nonenzymatic hydrolysis) of SN-38 from of the immunoconjugates.

(3.3 μM) were reacted with the SN-38 prodrugs (13.2 × [number of free thiols] μM) in PBS containing 5 mM EDTA (pH 6) at room temperature for 1 h, then at 4 °C overnight. SN-38-conjugated antibodies were purified by gel filtration (Amicon Ultra Centrifugal Filter Devices, Millipore). The concentration of antibody−prodrug conjugates was determined using the Bradford method (Bio-Rad Protein Assay, 500-0006JA, Bio-Rad). The numbers of residual thiols were quantified with DNTP. Each drug (SN-38)/antibody ratio was determined by comparison between the numbers of free and residual thiols (range from 6.7 to 8.4, Figure 2). For the evaluation of the antibody−drug coupling, the amount of forcibly detached SN-38 from the immunoconjugate was evaluated using HPLC (see next section).

High-Performance Liquid Chromatography (HPLC). The release behavior (nonenzymatic hydrolysis) of SN-38 from the immunoconjugates was investigated in vitro at 37 °C in DMEM with 10% FCS or PBS (pH 7.4). In addition to these reaction solutions at 6, 24, and 72 h in vitro, plasma and tumors on days 1, 3, and 7 after immunoconjugate injection in animal models were obtained. Reaction solutions and plasma were mixed with 0.1 M HCl at 50% (w/w). Tumors were rinsed with physiological saline, mixed with 0.1 M glycine-HCl buffer (pH 3.0) in methanol at 5% (w/w), and homogenized. To detect free SN-38 in the plasma, samples (50 μL) were mixed with 20 μL of 1 mM phosphoric acid in methanol (1:1) and 100 μL of camptothecin as internal standard solution. To detect free SN-38 in the tumor, samples (100 μL) were mixed with 20 μL of 1 mM phosphoric acid in methanol (1:1), 40 μL of ultrapure water, and 60 μL of internal standard solution. The samples were vortexed vigorously for 10 s and filtered through Ultrafree-MC centrifugal filter devices (Millipore, Bedford, MA, USA). To detect bound SN-38 in the immunoconjugate product itself, plasma or tumor samples (20 μL of plasma, 100 μL of tumor) were diluted with 20 μL of methanol (50% [w/w]) and 20 μL of NaOH (0.7 M). The samples were incubated for 15 min at room temperature. After incubation, 20 μL of HCl (0.7 M) and 60 μL of internal standard solution were added to the samples, and then the hydrolysate was filtered. Reverse-phase high-performance liquid chromatography (HPLC) was conducted at 35 °C on a Mightysil RP-18 GP column (150 mm × 4.6 mm; Kanto

dx.doi.org/10.1021/bc200158j |*Bioconjugate Chem.* 2011, 22, 1776–1783

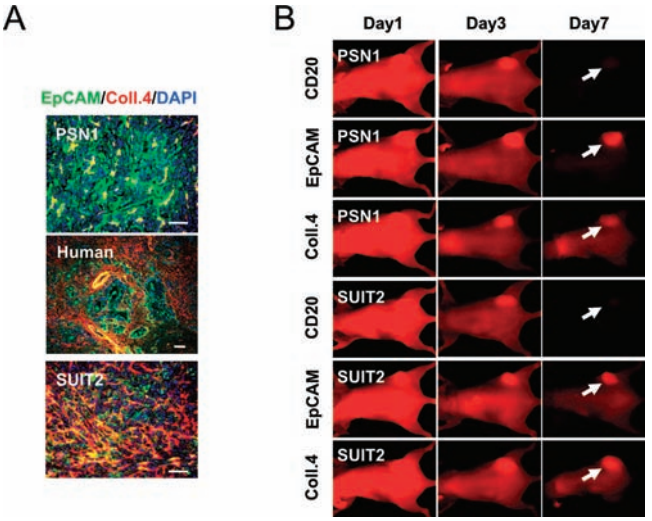

Figure 3. Intratumor accumulation of anti-EpCAM mAb and anti-collagen 4 mAb. (A) PSN1 and SUIT2 tumor and human pancreatic cancer were stained with anti-EpCAM (green), anticollagen 4 (red) mAb, and DAPI (blue). Scale bar = 100 μm. (B) In vivo imaging analysis of PSN1 and SUIT2 tumor was conducted using near-infrared labeled anti-CD20 (control), EpCAM, and collagen (coll.) 4 mAbs on days 1, 3, and 7 after injection. Arrows indicate each tumor position.

Chemical, Tokyo, Japan). The samples were injected into an Alliance Water 2795 HPLC system (Waters, Milford, MA, USA) equipped with a Waters 2475 multi-λ fluorescence detector. The detector was set at 365 and 540 nm (excitation and emission wavelengths, respectively) for SN-38.

In Vivo Imaging and Immunohistochemistry. Antibodies were conjugated with IRDye 800 (Li-Cor Biosciences, Lincoln, NE, USA) according to the manufacturer's protocol and injected to the tail vein at 100 μg. In vivo fluorescence imaging was performed by illuminating the animal using the OV110 small animal imaging system (Olympus Corp., Tokyo, Japan). Human specimens were purchased from US Biomax, Inc. (Rockville, MD, USA) and BioChain Institute, Inc. (Hayward, CA, USA). The tissues were incubated with anti-CD31 antibody (MEC 13.3 or AF3628), anti-collagen 4 antibody (35-4 or LSL-LB-1403), and anti-CD20 (rituximab) or anti-EpCAM antibody (B8-4) as first antibodies and Alexa 488- or 555-labeled anti-human, -mouse, -rat, or -goat IgG (Invitrogen) as second antibodies, respectively.

Animal Model and Antitumor Effects. Female BALB/c nude mice (5 weeks old) were purchased from SLC Japan (Shizuoka, Japan). Mice were inoculated subcutaneously in the flank with 2 $\times$ 10^6 cells of PSM1 and SUIT2. The length (L) and width (W) of tumor masses were measured every 4 days, and tumor volume was calculated using $(L \times W^2)/2$. All animal procedures were performed in compliance with the Guidelines for the Care and Use of Experimental Animals established by the Committee for Animal Experimental of the National Cancer Center. These guidelines meet the ethical standards required by law and also comply with the guidelines for the use of experimental animals in Japan. When the mean tumor volume reached approximately 90 mm^3 for PSM1 or approximately 70 mm^3 for SUIT2, mice were randomly divided into groups consisting of 5 mice each. Immunoconjugates were administered on day 0 by tail vein injection. The injection doses of antibody−SN-38 prodrug equal to an SN-38 dose of 3 mg/kg were determined by the calculation based on each drug (SN-38)/antibody ratio.

Statistical Analysis. Data were analyzed using ANOVA (Figure 4A,C) and Student's t test (Figure 4B). $P < 0.05$ was considered as significant.

RESULTS

Preparation of Cytotoxic Immunoconjugates. We developed two mAbs for tumor targeting, one against mouse collagen 4 abundantly found in the stroma of solid tumors, and another against human EpCAM which is strongly expressed in human cancer cells (Figure 3A). The third one was the mAb against CD20, which was used as a nonspecific control mAb for the human epithelial cancer cell lines. We used these three mAbs as vehicles to selectively exit the vascular system through the leaky tumor vessels and distribute within each tumor according to the nature of tumor stroma. Another special feature of our design was to conjugate highly cytotoxic SN-38 with each mAb using a specially selected linker, which provided both high serum stability and efficient, sustained drug release within the tumor lesion. SN-38 is a topoisomerase 1 inhibitor and an active component of CPT-11, which is used clinically for colorectal, lung, and other cancers. For the mAb conjugation to phenol−OH in SN-38, an ester bond was selected. In our design, poly(ethylene glycol) (PEG) was combined close to the bond mentioned above (Figure 2A). PEG is known to evade nonspecific capture by RES. The steric structure around the bond protects against immunoconjugate degradation in the blood. PEG has already been used for this purpose. [1−3,5,6] The drug (SN-38)/mAb ratio (the number of drugs attached to a mAb) of each immunoconjugate ranged from 6.7 to 8.4, which was calculated using DNTP method and validated by the evaluation of bound SN-38 in the conjugate using HPLC. Moreover, antigen recognition activity was estimated. In physiological conditions (nonenzymatic hydrolysis), the immunoconjugate can release SN-38 gradually and effectively (Figure 2B).

Intratumor Distribution of Anti-EpCAM mAb and Anti-collagen 4 mAb in Stroma-Poor or -Rich Tumors. We next clarified which types of xenograft tumors generated from human cell lines were stroma-rich or -poor. Immunohistochemistry using our 2 mAbs showed that tumors generated by the PSN1 cell line contained EpCAM-positive cells with interspersed collagen 4-positive stroma, different from that of freshly resected human pancreatic cancer (Figure 3A). On the other hand, SUIT2 tumor, reported as having histopathology relatively resembling the original human pancreatic cancer,[19,20] showed EpCAM-positive cells surrounded by a relatively high amount of collagen 4-positive stroma (Figure 3A). We then investigated the kinetics of entry of mAbs into the tumors using an in vivo imaging system with near-infrared fluorescence, which can provide deep tissue imaging with high fidelity.[21,22] Anti-CD20 mAb (rituximab), which is specific to human B cell lymphoma but not to carcinoma, was used as a nonspecific control because of its high specificity with less background.[11,23] Until day 3, all mAbs labeled with a near-infrared fluorescence dye including the control mAb were delivered to and retained in both PSN1 tumors, and SUIT2 tumors, indicating passive targeting by the EPR effect (Figure 3B). On day 7, anti-CD20 mAb was almost eliminated, but anti-EpCAM and anti-collagen 4 mAb were still retained in both types of tumors, indicating active targeting and retention, that is, binding to their respective ligands within the lesion.

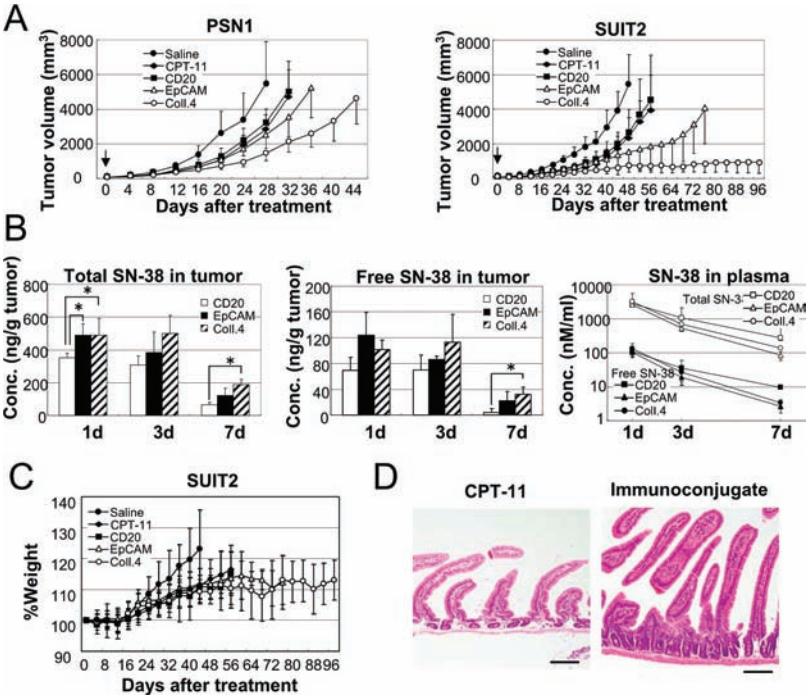

Figure 4. Antitumor effects, pharmacokinetics, and drug toxicities of anti-CD20, EpCAM, and collagen 4 immunoconjugates. (A) Antitumor activities in vivo were examined. In animal models of PSN1 and SUIT2, the three immunoconjugates or saline as control was administered to separate groups of mice by intravenous bolus injection on day 0. Arrows indicate day of administration, and the curves illustrate the effects of the treatments on tumor size. $P < 0.05$ (saline or CD20 vs EpCAM in PSN1), $P < 0.01$ (saline vs CPT11 or EpCAM in PSN1, CPT11 or CD20 vs EpCAM in SUIT2), $P < 0.001$ (saline vs CPT11 or CD20 or EpCAM in SUIT2, saline or CPT11 or CD20 or EpCAM vs collagen 4 in PSN1 or SUIT2). Bar = SD. (B) Tumor concentrations of total (bound and unbound) SN-38 (left) and free (unbound) SN-38 (center), and plasma concentrations (right) were determined using HPLC analysis. The concentrations on days 1, 3, and 7 are shown. ∗ indicates $P < 0.05$; bar = SD. (C) Changes in the % body weight of saline, CPT-11, CD20, EpCAM, and collagen 4 in the same treated SUIT2 group (panel A). Bar = SD. (D) Pathologic mucosal change of jejunum from mouse treated with CPT11 (upper) or anti-collagen 4 immunoconjugate (lower). Scale bar = 1 mm. Coll.4, Collagen 4; Conc., concentration.

In addition there was a signal of near-infrared fluorescence at the area of lung after the treatment with anti-collagen 4 mAb (Figure 3B). We recognized same signals with some other commercially available antibodies such as anti-EGFR mAb. Although we have never observed lung toxicity in mice following administration of our immunoconjugate, we certainly need further investigation of this issue.

Antitumor Activity and Pharmacokinetic Studies in Stroma-Poor or -Rich Pancreatic Tumor Xenografts. Antitumor activities of immunoconjugates with ester bond SN-38 were evaluated in vivo. CPT-11 (clinically approved prodrug of SN-38, 66.7 mg/kg at maximum tolerance dose of this mouse, human clinical application is 100−750 mg/m^2)[24] and three immunoconjugates (administered once, at an equivalent SN-38 dose of 3 mg/kg; cytotoxic effect of SN-38 is 20 times more potent than CPT-11)[25,26] showed significant antitumor activities compared with results in mice treated with saline, in mice bearing either PSN1 (EpCAM-positive and stroma-poor) or SUIT2 (EpCAM-positive and stroma-rich) tumors. In SUIT2 tumors, while the tumor continued to increase in mice treated with CPT-11, anti-CD20 immunoconjugate, and anti-EpCAM immunoconjugate, the tumor treated in mice with anti-collagen 4 immunoconjugate stopped growing by about 1 month and never resumed up to 3 months (Figure 4A). In mice bearing PSN1 tumors (stroma poor), differences were present but less marked. Thus, anti-collagen 4−SN-38 immunoconjugate exerted the most potent antitumor activity compared with anti-CD20 or anti-EpCAM immunoconjugates and CPT-11, but the PSN1 tumor volume continued to increase slowly (Figure 4A). In both tumor models, anti-EpCAM immunoconjugate exerted superior antitumor effect compared with CPT-11 and anti-CD20 immunoconjugate, but inferior antitumor effect compared with anti-collagen 4 SN38-immunoconjugate.

A pharmacokinetic analysis in SUIT2-tumor bearing mice showed that the same high tumor concentrations of either free or total SN-38 (free and conjugated SN-38) were observed for all three immunoconjugates by day 3. On day 7, the tumor concentration of free and total SN-38 was scarcely detected in the tumor treated with anti-CD20 immunoconjugate (Figure 4B). On the other hand, significantly higher concentrations of free and total SN-38 were detected in tumor tissues of mice treated with the anti-collagen 4 immunoconjugate compared with the anti-CD20 immunoconjugate (Figure 4B). The tumor concentration of free and total SN-38 treated with anti-EpCAM immunoconjugate was intermediate among them, but not significant (Figure 4B). Regarding normal tissue distribution and elimination of antibodies and SN-38, there was no difference among immunoconjugates on day 7 after the administration. There was no significant difference in body weight changes among saline, CPT-11, and immunoconjugate groups (Figure 4C). In addition, there was no hepatotoxicity, nephrotoxicity, or bone marrow toxicity in mice treated with all three immunoconjugates compared with controls (data not shown). In the small intestinal mucosa of mice, widespread villous atrophy and decreased crypt density were observed during the treatment with free unbound CPT-11, which is well-known to have severe intestinal toxicity in

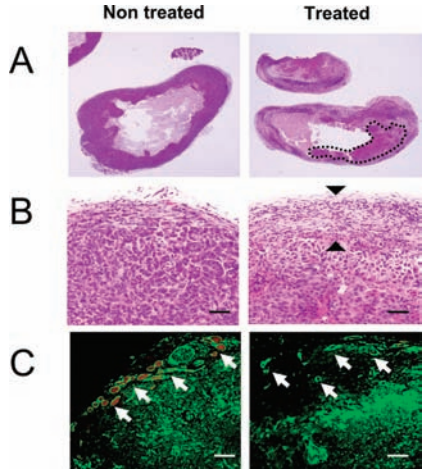

Figure 5. Histopathological features of SUIT2 tumors after anti-collagen 4 immunoconjugate treatment. (A) Hematoxylin and eosin staining of nontreated (left) and immunoconjugate-treated (right) SUIT2-tumors. A non-necrotic viable lesion in the treated tumor is enclosed by a dotted line. (B) The fibrotic capsule width in the treated tumor is indicated between black arrowheads. (C) Tumor vessels were examined by the CD31 (red)−collagen 4 (green) double-staining techniques. White arrows indicate tumor vessels or their traces in the boundary area. Scale bar = 100 μm.

clinics. On the other hand, the small intestinal mucosa of mice in groups treated with all immunoconjugates did not show any pathological change (Figure 4D).

Histopathological Features of SUIT2 Tumors after Anti-collagen 4 Immunoconjugate Treatment. The most important observation from a therapeutic standpoint was that only SUIT2 tumors treated with anti-collagen 4 immunoconjugate stopped growing about 1 month after treatment and remained dormant for more than 3 months. It is concluded that the strategy of orchestrating slow sustained release from a scaffold erected on the stable inert structural components of the tumor stroma is most effective. We compared histologically this nongrowing tumor with a size-matched, growing control tumor and found that both tumors showed central necrosis due to decreased blood flow, which is often observed in a murine xenotransplant model.[27,28] The striking difference was that large confluent necrotic zones and dense fibrotic capsule formation were observed only in the treated tumor (Figure 5A,B). In addition, CD31-positive endothelial cells, which may be tumor-feeding vessels in the peripheral part of the tumor, were never observed in the treated tumor compared with untreated control (Figure 5C). Instead, many collagen 4-positive round profiles corresponding to traces of destroyed vessels were observed in the peripheral area of the treated tumor (Figure 5C).

■ DISCUSSION

Cancer cells can acquire drug resistance via cellular and noncellular mechanisms.[7−9] The latter mechanisms involve various physiological barriers including excess interstitial stromal tissue, which prevents drug diffusion especially in human cancer.[7−10] Therefore, there is a rationale in overcoming this problem. In this study, we established two types of mAbs: anti-collagen 4 mAb for stroma targeting and anti-EpCAM mAb for tumor cell targeting. We then conjugated these mAbs with SN-38 using a newly designed linker assembly. Linker technology is an important part of immunoconjugate chemotherapy, and various linkers have been exploited to date. Among them, acid labile hydrazone linkage, thiol reduction of disulfide linkers, and enzymatic proteolysis of peptide linkers were favorably applied to ensure stability in plasma.[29,30] For these types of linkers, cell-mediated endocytosis and intracellular processing of the immunoconjugates were indispensable to make the active agent work. In our newly deployed linker construct, an ester bond was used for gradual cleavage in the extracellular space of the tumor. The interspaced PEG enables long survival of our immunoconjugates in the circulating plasma through a "stealth effect" permitting them to evade the RES. In addition, the immunoconjugates are too large to pass through the normal vessel wall, but they easily extravasate from leaky tumor vessels. Thus, our newly developed immunoconjugates can accumulate selectively in the tumor tissue and then exert sustained-release of SN-38. Our basic strategy for overcoming the stromal barrier as a protective shield for cancer cells is to make use of the stroma as a scaffold assembly of immunoconjugates, followed by the release of payload (anticancer agent) to the cancer cells. This free SN-38 can easily reach the cancer cells by diffusion, although the carrier mAb can hardly penetrate the stroma. Moreover, it was reported that collagen 4 in the outer layer of tumor vessels showed conspicuous structural abnormality and loose connection with both endothelial cells and pericytes, whereas that in normal tissue was well organized and tightly associated with the cells.[31] Therefore, SN-38-conjugated anti-collagen 4 mAb, which leaked out from tumor vasculature, can easily bind selectively to the collagen 4 matrix and accumulates within tumor tissues. It has been reported that tumor growth is angiogenesis-dependent and that tumors cannot grow if endothelial cell growth is limited. Moreover, there is evidence that accelerated tumor progression is only observed during the transition from the nonangiogenic stage to the angiogenic stage, a process termed "angiogenic switch".[32] Therefore, if this switch is turned off, tumors will stop growing and remain dormant indefinitely. Here, in our studies, only tumors treated with anti-collagen 4 mAb showed growth suppression and conversion to a dormant status, in keeping with reversal of the "switch". Our anti-collagen 4 immunoconjugate (mAb-bearing SN-38) can induce both tumor regression and the dormant state after a single, low-dose (SN-38, 3 mg/kg) injection. Interestingly, a dense fibrotic capsule was observed in the dormant tumor, which may be formed as a result of damage to the tumor vessels by released SN-38 and reaction of host defense in this lesion.

In our study, the antitumor activity of anti-EpCAM immunoconjugate was inferior to that of anti-collagen 4. We suggest that anti-EpCAM immunoconjugate may distribute unevenly within tumor cell areas and may possess less antivascular endothelial cell activity compared with anti-collagen 4 immunoconjugate.

The concentration of our immunoconjugate was much higher than that of trastuzumab−DM1 or other immunoconjugates used in previous studies.[33−35] The strategy of previous work was to reduce the dose of the mAb by selecting a very toxic agent and binding it to a mAb that can internalize into the tumor cells. Conversely, the principle of our strategy is that our immunoconjugate targets collagen 4 outside the tumor cells and allows the effective sustained release of SN-38 to attack tumor cells and vascular endothelial cells. The internalization ability of the antibody is irrelevant to our strategy. Therefore, in future we will have to exploit the linker to attach many drugs in combination with using a much more toxic agent like DM1 rather than SN-38

in order to reduce the administration dose of the antibody for clinical application.

There were a few papers describing tumor stromal targeting immunoconjugates, a mAb against a cell surface antigen FAP as fibroblast targeting therapy utilizing the internalization, or a mAb against fibronectin for the targeting of tumor vascular endothelial cells in photodynamic therapy.[14,15] In the latter, the drug directly damaged the stromal endothelial cells by the short and strong photochemical reaction. However, unlike those, our strategic concept is quite unique as follows:

(1) Newly developed SN-38-conjugated anti-collagen 4 Abs can extravasate from the leaky tumor vessels selectively and form a scaffold as it is captured by the collagen 4 network.

(2) The immunoconjugate allows the effective sustained release of SN-38 (a time-dependent anticancer agent) from the scaffold, and this released anticancer agent is distributed throughout the tumor.

(3) Consequently, the strategy described above was highly effective in causing arrest of tumor growth due to induced damage to tumor cells and tumor vessels without exerting adverse drug effects.The present method can be applied to other anticancer agents including molecular targeting agents by minor modification of chemical bonding between PEG and the drugs.

AUTHOR INFORMATION

Corresponding Author

*E-mail: yhmatsum@east.ncc.go.jp. Telephone and fax number: +81-4-7134-6857.

Notes

The authors declare that they have no conflict of interest.

ACKNOWLEDGMENT

This work was supported by Funding Program for World-Leading Innovative R&D on Science and Technology (FIRST Program) (Y.M.), Third Term Comprehensive Control Research for Cancer from the Ministry of Health, Labour and Welfare of Japan (Y.M.), a Grant-in-Aid for Scientific Research on Priority Areas from the Ministry of Education, Culture, Sports, Science and Technology, the Princess Takamatsu Cancer Research Fund (Y.M.), Japanese Foundation for Multidisciplinary Treatment of Cancer (Y.M.), Japanese Foundation for promotion of cancer research (M.Y.), and the Grant-in-Aid for Scientific Research from Japan Society for the Promotion of Science (M.Y.). We thank Dr. T. Sugino for his helpful discussion. We also thank Mrs. H. Koike and Miss M. Araake for their technical assistance and Mrs. K. Shiina for her secretarial support.

REFERENCES

(1) Peer, D., Karp, J. M., Hong, S., Farokhzad, O. C., Margalit, R., and Langer, R. (2007) Nanocarriers as an emerging platform for cancer therapy. *Nat. Nanotechnol. 2*, 751–760.

(2) Davis, M. E., Chen, Z. G., and Shin, D. M. (2008) Nanoparticle therapeutics: An emerging treatment modality for cancer. *Nat. Rev. Drug Discovery 7*, 771–782.

(3) Duncan, R. (2003) The dawning era of polymer therapeutics. *Nat. Rev. Drug Discovery 2*, 347–360.

(4) Matsumura, Y., and Maeda, H. (1986) A new concept for macromolecular therapeutics in cancer chemotherapy: mechanism of tumoritropic accumulation of proteins and the antitumor agent smancs. *Cancer Res. 46*, 6387–6392.

(5) Matsumura, Y. (2008) Poly(amino acid) micelle nanocarriers in preclinical and clinical studies. *Adv. Drug Delivery Rev. 22*, 899–914.

(6) Matsumura, Y., and Kataoka, K. (2009) Preclinical and clinical studies of anticancer agent-incorporating polymer micelles. *Cancer Sci. 100*, 572–579.

(7) Trédan, O., Galmarini, C. M., Patel, K., and Tannock, I. F. (2007) Drug resistance and the solid tumor microenvironment. *J. Natl. Cancer Inst. 99*, 1441–1454.

(8) Ghajar, C. M., and Bissell, M. J. (2008) Extracellular matrix control of mammary gland morphogenesis and tumorigenesis: insights from imaging. *Histochem. Cell Biol. 130*, 1105–1118.

(9) Minchinton, A. I., and Tannock, I. F. (2006) Drug penetration in solid tumors. *Nat. Rev. Cancer 6*, 583–592.

(10) Dvorak, H. F. (1986) Tumors: Wounds that do not heal. Similarities between tumor stroma generation and wound healing. *N. Engl. J. Med. 315*, 1650–1659.

(11) Ricart, A. D., and Tolcher, A. W. (2007) Technology insight: Cytotoxic drug immunoconjugates for cancer therapy. *Nat. Clin. Pract. Oncol. 4*, 245–255.

(12) Saito, Y., Yasunaga, M., Kuroda, J., Koga, Y., and Matsumura, Y. (2008) Enhanced distribution of NK012, a polymeric micelle-encapsulated SN-38, and sustained release of SN-38 within tumors can beat a hypovascular tumor. *Cancer Sci. 99*, 1258–1264.

(13) Mahadevan, D., and Von Hoff, D. D. (2007) Tumor-stroma interactions in pancreatic ductal adenocarcinoma. *Mol. Cancer Ther. 6*, 1186–1197.

(14) Ostermann, E., Garin-Chesa, P., Heider, K. H., Kalat, M., Lamche, H., Puri, C., Kerjaschki, D., Rettig, W. J., and Adolf, G. R. (2008) Effective immunoconjugate therapy in cancer models targeting a serine protease of tumor fibroblasts. *Clin. Cancer Res. 14*, 4584–4592.

(15) Palumbo, A., Hauler, F., Dziunycz, P., Schwager, K., Soltermann, A., Pretto, F., Alonso, C., Hofbauer, G. F., Boyle, R. W., and Neri, D. (2011) A chemically modified antibody mediates complete eradication of tumours by selective disruption of tumour blood vessels. *Br. J. Cancer 104*, 1106–1115.

(16) Herbert, W. J. (1978) Mineral-oil adjuvants and the immunisation of laboratory animals. *Handbook of Experimental Immunology*, 3rd ed (Weir, D. M., Ed.), pp A3.1−3.15, Blackwell, Oxford, U.K.

(17) Oi, V. T. Herzenberg, L. A. (1980) Immunoglobilin-producing hybrid cell lines.*Selected Methods in Cellular Immunology* (Misbell, B. B. Shiigi, S. M., Eds.). pp 351−372, WH Freeman & Co., New York.

(18) Sun, M. M., Beam, K. S., Cerveny, C. G., Hamblett, K. J., Blackmore, R. S., Torgov, M. Y., Handley, F. G., Ihle, N. C., Senter, P. D., and Alley, S. C. (2005) Reduction-alkylation strategies for the modification of specific monoclonal antibody disulfides. *Bioconjug Chem. 16*, 1282–1290.

(19) Iwamura, T., Katsuki, T., and Ide, K. (1987) Establishment and characterization of a human pancreatic cancer cell line (SUIT-2) producing carcinoembryonic antigen and carbohydrate antigen 19-9. *Jpn. J. Cancer Res. 78*, 54–62.

(20) Mauri, P., Scarpa, A., Nascimbeni, A. C., Benazzi, L., Parmagnani, E., Mafficini, A., Della Peruta, M., Bassi, C., Miyazaki, K., and Sorio, C. (2005) Identification of proteins released by pancreatic cancer cells by multidimensional protein identification technology: A strategy for identification of novel cancer markers. *FASEB J. 19*, 1125–1127.

(21) Folli, S., Westermann, P., Braichotte, D., Pèlegrin, A., Wagnières, G, van den Bergh, H, and Mach, J. P. (1994) Antibody-indocyanin conjugates for immunophotodetection of human squamous cell carcinoma in nude mice. *Cancer Res. 54*, 2643–2649.

(22) Mariani, G., Lasku, A., Balza, E., Gaggero, B., Motta, C., Di Luca, L., Dorcaratto, A., Viale, G. A., Neri, D., and Zardi, L. (1997) Tumor targeting potential of the monoclonal antibody BC-1 against oncofetal fibronectin in nude mice bearing human tumor implants. *Cancer 80*, 2378–2384.

(23) Armstrong, A., and Eck, S. L. (2003) EpCAM: A new therapeutic target for an old cancer antigen. *Cancer Biol. Ther. 2*, 320–326.

(24) Mathijssen, R. H., van Alphen, R. J., Verweij, J., Loos, W. J., Nooter, K., Stoter, G., and Sparreboom, A. (2001) Clinical pharmacokinetics and metabolism of irinotecan (CPT-11). *Clin. Cancer Res. 7*, 2182–2194.

(25) Senter, P. D., Beam, K. S., Mixan, B., and Wahl, A. F. (2001) Identification and activities of human carboxylesterases for the activation of CPT-11, a clinically approved anticancer drug. *Bioconjugate Chem. 12*, 1074–1080.

(26) Zhao, H., Rubio, B., Sapra, P., Wu, D., Reddy, P., Sai, P., Martinez, A., Gao, Y., Lozanguiez, Y., Longley, C., Greenberger, L. M., and Horak, I. D. (2008) Novel prodrugs of SN38 using multiarm poly(ethylene glycol) linkers. *Bioconjugate Chem. 19*, 849–859.

(27) Naito, S., von Eschenbach, A. C., and Fidler, I. J. (1987) Different growth pattern and biologic behavior of human renal cell carcinoma implanted into different organs of nude mice. *J. Natl. Cancer Inst. 78*, 377–385.

(28) Fallowfield, M. E. (1989) Blood flow distribution within transplantable tumors in the mouse. *Eur. J. Cancer Clin. Oncol. 25*, 1683–1688.

(29) Doronina, S. O., Torgov, M. Y., Mendelsohn, B. A., Cerveny, C. G., Chace, D. F., DeBlanc, R. L., Gearing, R. P., Bovee, T. D., Siegall, C. B., Francisco, J. A., Wahl, A. F., Meyer, D. L., and Senter, P. D. (2003) Development of potent monoclonal antibody auristatin conjugates for cancer therapy. *Nat. Biotechnol. 21*, 778–784.

(30) Wu, A. M., and Senter, P. D. (2005) Arming antibodies: Prospects and challenges for immunoconjugates. *Nat. Biotechnol. 23*, 1137–1146.

(31) Baluk, P., Morikawa, S., Haskell, A., Mancuso, M., and McDonald, D. M. (2003) Abnormalities of basement membrane on blood vessels and endothelial sprouts in tumors. *Am. J. Pathol. 163*, 1801–1815.

(32) Folkman, J. (2007) Angiogenesis: An organizing principle for drug discovery?. *Nat. Rev. Drug Discovery 6*, 273–286.

(33) Wahl, A. F., Donaldson, K. L., Mixan, B. J., Trail, P. A., and Siegall, C. B. (2001) Selective tumor sensitization to taxanes with the mAb-drug conjugate cBR96-doxorubicin. *Int. J. Cancer 93*, 590–600.

(34) Doronina, S. O., Bovee, T. D., Meyer, D. W., Miyamoto, J. B., Anderson, M. E., Morris-Tilden, C. A., and Senter, P. D. (2008) Novel peptide linkers for highly potent antibody-auristatin conjugate. *Bioconjugate Chem. 19*, 1960–1963.

(35) Burris, H. A., 3rd., Rugo, H. S., Vukelja, S. J., Vogel, C. L., Borson, R. A., Limentani, S., Tan-Chiu, E., Krop, I. E., Michaelson, R. A., Girish, S., Amler, L., Zheng, M., Chu, Y. W., Klencke, B., and O'Shaughnessy, J. A. (2011) Phase II Study of the antibody drug conjugate trastuzumab-DM1 for the treatment of human epidermal growth factor receptor 2 (HER2)-positive breast cancer after prior HER2-directed therapy. *J. Clin. Oncol. 29*, 398–405.

Bioconjugate Chemistry

ARTICLE

pubs.acs.org/bc

Development and Application of a Multimodal Contrast Agent for SPECT/CT Hybrid Imaging

Jason M. Criscione,[†] Lawrence W. Dobrucki,[§,⊥] Zhen W. Zhuang,[§] Xenophon Papademetris,[†,∥] Michael Simons,[§] Albert J. Sinusas,[§,∥] and Tarek M. Fahmy*[,†,‡]

[†]Department of Biomedical Engineering, [‡]Department of Chemical Engineering, Yale University, New Haven, Connecticut, United States

[§]Section of Cardiovascular Medicine, Department of Internal Medicine, [∥]Department of Diagnostic Radiology, Yale University School for Medicine, New Haven, Connecticut, United States

[⊥]Beckman Institute for Advanced Science and Technology, University of Illinois at Urbana−Champaign, Urbana, Illinois, United States

Supporting Information

ABSTRACT: Hybrid or multimodality imaging is often applied in order to take advantage of the unique and complementary strengths of individual imaging modalities. This hybrid non-invasive imaging approach can provide critical information about anatomical structure in combination with physiological function or targeted molecular signals. While recent advances in software image fusion techniques and hybrid imaging systems have enabled efficient multimodal imaging, accessing the full potential of this technique requires development of a new toolbox of multimodal contrast agents that enhance the imaging process. Toward that goal, we report the development of a hybrid probe for both single photon emission computed tomography (SPECT) and X-ray computed tomography (CT) imaging that facilitates high-sensitivity SPECT and high spatial resolution CT imaging. In this work, we report the synthesis and evaluation of a novel intravascular, multimodal dendrimer-based contrast agent for use in preclinical SPECT/CT hybrid imaging systems. This multimodal agent offers a long intravascular residence time ($t_{1/2}$ = 43 min) and sufficient contrast-to-noise for effective serial intravascular and blood pool imaging with both SPECT and CT. The colocalization of the dendritic nuclear and X-ray contrasts offers the potential to facilitate image analysis and quantification by enabling correction for SPECT attenuation and partial volume errors at specified times with the higher resolution anatomic information provided by the circulating CT contrast. This may allow absolute quantification of intramyocardial blood volume and blood flow and may enable the ability to visualize active molecular targeting following clearance from the blood.

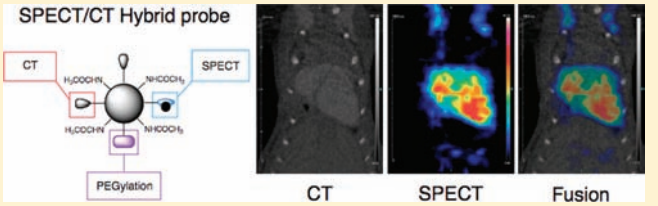

INTRODUCTION

Hybrid or multimodality imaging is often applied in the evaluation and management of cardiovascular disease, in order to take advantage of the unique and complementary strengths of individual imaging modalities.[1−5] This has become particularly critical when combining targeted molecular or physiological imaging with anatomic imaging. Toward this goal, efforts have been directed at combining modalities like magnetic resonance imaging (MRI) or X-ray computed tomography (CT) possessing high spatial resolution for evaluation of anatomical structure with those that possess high sensitivity like single photon emission tomography (SPECT) and positron emission tomography (PET) for detection of molecular or physiological signals. This has been accomplished by both design and implementation of hybrid imaging systems[6−11] and/or use of software fusion of images collected with multiple independent imaging systems.[12−14] Multimodal imaging with hybrid imaging systems combine multiple, independent probes to achieve high-sensitivity and high-resolution anatomic visualization with multiple modalities (e.g., SPECT/CT). On the other hand, software image fusion methodologies use a single probe incorporating multiple forms of contrast media along with multiple imaging modalities to adequately obtain desired information (e.g., MRI/optical). With recent advances in both hardware and software, hybrid imaging systems, specifically, PET/CT, PET/MRI, and SPECT/CT, have seen widespread implementation in preclinical and clinical applications.

Despite these technological advances, the development of multimodal contrast agents has lagged behind, necessitating the use of multiple independent imaging agents and application of software image fusion techniques.[12,13,15,16] The limiting factors in the design of multimodal contrast agents for hybrid imaging systems are twofold: (1) sensitivity differences inherent to the imaging modalities and (2) temporal restrictions related

Received: March 31, 2011
Revised: August 5, 2011
Published: August 18, 2011

ACS Publications © 2011 American Chemical Society

to image acquisition. The main challenge in developing these agents manifests itself within the sensitivities of the modalities.[17] Because the modalities providing high spatial resolution often exhibit poor sensitivity, and vice versa, it is essential to achieve the appropriate balance required for the selected application. The other significant challenge arises with the selection of the appropriate radionuclide for incorporation in a radiotracer-based imaging approach. The decay half-life governs not only the chemistry, but also the imaging protocols.

For targeted molecular imaging, one needs to design a single cardiovascular contrast agent that possesses long enough intravascular residence time to allow sufficient binding to the molecular target, with appropriate blood clearance to enable imaging of both the blood pool and the specific molecular target. This might require the use of radioisotopes with relatively long decay half-life. Radiotracer-based dynamic imaging approaches have remained the mainstay for evaluation of a physiological parameter like absolute regional myocardial blood flow or receptor binding. However, the lower resolution of SPECT and PET approaches require knowledge of anatomical structure in order to correct for attenuation and partial volume errors associated with limited resolution of these radiotracer approaches. To date, assessment of cardiovascular structure and function requires either software image fusion of multiple modalities with single multimodal probes[16,18−20] or hybrid system imaging with multiple probes, for example, Omnipaque and ^{99m}Tc-NC100692 for CT and SPECT, respectively.[21] An integrated imaging approach that employs a hybrid probe, incorporating contrast moieties to achieve both high spatial resolution (e.g., MRI or CT active) and high sensitivity (e.g., PET or SPECT active) with hybrid imaging systems, has the potential to efficiently and noninvasively generate the essential complementary sets of information required for diagnosis with a single dose and one imaging session.

Incorporation of the different contrast enhancing moieties within a single agent is greatly facilitated by core molecules manifesting multifunctional architectures. Because they satisfy this criterion, dendrimers, a class of hyperbranched polymers,[22] possess a high degree of surface functionality and have been routinely utilized as macromolecular contrast agents for many preclinical imaging modalities, including MRI,[15,23−28] CT,[12,29−31] PET,[32] and SPECT.[33−36] Though multimodal dendrimer-based contrast agents have been developed, their utility has been limited to software image fusion techniques (e.g., MRI/optical).

In this work, we report the synthesis and evaluation of a novel, multimodal blood pool dendrimer-based contrast agent designed for use in preclinical hybrid microSPECT/CT imaging systems with direct applicability to hybrid clinical imaging systems. This long-circulating dendrimer, comprising both triiodinated moieties and chelated ^{99m}Tc, provides effective, simultaneous contrast enhancement in both CT and SPECT, respectively.

MATERIALS AND METHODS

Synthesis of G4-[Ac]. Five hundred milligrams of ethylenediamine-core PAMAM generation 4 dendrimers (PAMAM(G4)) [Sigma Aldrich] were desiccated in a 100 mL round-bottom flask and subsequently dissolved in 100 mM sodium bicarbonate buffer (pH 9.0) to a final concentration of 10 mg/mL with magnetic stirring. To this dendrimer solution, 36 mol equiv of sulfosuccinimidyl acetate [Thermo Scientific] were added as a solid and allowed to dissolve. The pH of the reaction mixture was immediately adjusted to 8.5 with 1 N NaOH and the reaction was allowed to proceed for 2 h at 25 °C. The partially acetylated PAMAM(G4) product was purified by ultrafiltration with deionized water using 10K MWCO Amicon Ultra-15 filters [Millipore] and lyophilized to obtain a white crystalline solid (yield: 97%). The product was characterized by proton nuclear magnetic resonance (^{1}H NMR) spectroscopy (D_2O, 400 MHz); δ = 1.91 (105H, COCH_3), 2.28−2.42 (248H, C-CH_2-CONH), 2.50−2.61 (124H, N-CH_2CH_2NH), 2.68−2.80 (248H, N-CH_2CH_2CO), 3.14−3.36 (318H, CONH-CH_2). Extent of surface acetylation was determined according to the method of Majoros et al.[37]

Synthesis of G4-[[Ac]-TIBA]. *Activation of 2,3,5-Triiodobenzoic acid (TIBA).* Two hundred eighty-seven milligrams of 2,3,5-triiodobenzoic acid (18 mol equiv) were added to a 20 mL glass scintillation vial and dissolved in anhydrous dimethyl sulfoxide (DMSO) [Sigma Aldrich] to a final concentration of 50 mg/mL with magnetic stirring. To the solution of TIBA, 2 mol equiv of both *N*-hydroxysuccinimide [Thermo Scientific] and *N,N*-dicyclohexylcarbodiimide [Thermo Scientific] were added and allowed to dissolve. The reaction was allowed to proceed for 1 h at 25 °C in the absence of light. The reaction mixture was then filtered with a 0.22 μm PTFE syringe filter to remove the dicyclohexylurea (DCU) reaction byproduct and the filtrate was retained.

Coupling of G4-[Ac] to TIBA. A three-necked round-bottom flask was charged with 500 mg of G4-[Ac] and purged with argon. The G4-[Ac] was then dissolved in 60 mL anhydrous DMSO with magnetic stirring under an argon atmosphere. To this solution, the entire contents of the filtered activated TIBA solution were added via syringe without further purification. The reaction proceeded for 24 h at 25 °C under an argon atmosphere in the absence of light. The reaction mixture was then diluted with 10 volumes of deionized water and subsequently filtered with a 0.22 μm PES vacuum filtration system. The filtrate was purified into deionized water by ultrafiltration using 10K MWCO Amicon Ultra-15 filtrators and lyophilized to obtain a light brown solid (yield: 82%). The product was characterized by ^{1}H NMR spectroscopy (D_2O, 400 MHz); δ = 1.91 (105H, COCH_3), 2.28−2.42 (248H, C-CH_2CONH), 2.50−2.61 (124H, N-CH_2CH_2NH), 2.68−2.80 (248H, N-CH_2CH_2CO), 3.14−3.36 (348H, CONH-CH_2), 7.49 (15H, aromatic), 8.21 (15H, aromatic).

Synthesis of G4-[[[Ac]-TIBA]-DTPA]. Six hundred milligrams of G4-[[Ac]-TIBA] were added to a 100 mL round-bottom flask and subsequently dissolved in 100 mM sodium bicarbonate buffer (pH 9.0) to a final concentration of 10 mg/mL with magnetic stirring. To this dendrimer solution, 4 mol equiv of 2-(4-isothiocyanatobenzyl)-diethylenetriaminepentaacetic acid [Macrocyclics] dissolved in anhydrous DMSO were added. The pH of the reaction mixture was immediately adjusted to 8.5 with 1 N NaOH, and the reaction proceeded for 18 h at 25 °C in the absence of light. The product was purified by ultrafiltration with deionized water using 10K MWCO Amicon Ultra-15 filtrators and lyophilized to obtain a pale yellow solid (yield: 89%). The product was characterized by ^{1}H NMR spectroscopy (D_2O, 400 MHz); δ = 1.91 (105H, COCH_3), 2.28−2.42 (248H, C-CH_2CONH), 2.50−2.61 (124H, N-CH_2CH_2NH), 2.68−2.80 (248H, N-CH_2CH_2CO), 3.14−3.36 (348H, CONH-CH_2), 7.18 (8H, aromatic), 7.27 (8H, aromatic), 7.49 (15H, TIBA aromatic), 8.21 (15H, TIBA aromatic).

Synthesis of G4-[[[[Ac]-TIBA]-DTPA]-mPEG$_{12}$]. Four hundred ninety milligrams of G4-[[[Ac]-TIBA]-DTPA] were added to a 100 mL round-bottom flask and subsequently dissolved in 100 mM sodium bicarbonate buffer (pH 9.0) to a final concentration of

10 mg/mL with magnetic stirring. To this dendrimer solution, 8 mol equiv of succinimidyl-(*N*-methyl-dodecaethylene glycol) ester [Thermo Scientific] dissolved in anhydrous DMSO were added. The pH of the reaction mixture was immediately adjusted to 8.5 with 1 N NaOH and the reaction proceeded for 12 h at 25 °C in the absence of light. The product was purified by ultrafiltration with deionized water using 10K MWCO Amicon Ultra-15 filtrators, filtered with a 0.22 μm MCE syringe filtered, and lyophilized to obtain a pale yellow solid (yield: 83%). The product was characterized by ^{1}H NMR spectroscopy (D_2O, 400 MHz); δ = 1.91 (105H, $COCH_3$), 2.28−2.42 (248H, C-CH_2-CONH), 2.50−2.61 (124H, N-CH_2CH_2NH), 2.68−2.80 (248H, N-CH_2CH_2CO), 3.14−3.36 (360H, CONH-CH_2), 3.5−3.76 (336H, -OCH_2CH_2), 7.18 (8H, aromatic), 7.27 (8H, aromatic), 7.49 (15H, aromatic), 8.21 (15H, aromatic).

^{1}H NMR Spectroscopy. All samples were dissolved in D_2O (20 mg/mL) for characterization by proton nuclear magnetic resonance (^{1}H NMR) spectroscopy on a 400 MHz Bruker spectrometer with the solvent as a reference. Extent of surface conjugation was determined by analysis of peak integrations.

Dynamic Light Scattering (DLS). PAMAM(G4) and G4-[[[[Ac]-TIBA]-DTPA]-mPEG] were dissolved in sterile 1× PBS (pH 7.4) at a final concentration of 5 mg/mL and filtered with a 0.22 μm MCE syringe filter. Following filtration, the hydrodynamic diameter of the solutions was assessed with a Zetasizer Nano ZS-90 (Malvern Instruments) in triplicate sequential runs. The hydrodynamic diameter was obtained from volume distribution fitting averaged over the triplicate runs.

X-ray Attenuation Measurements. To evaluate the X-ray attenuation properties of G4-[[[[Ac]-TIBA]-DTPA]-$mPEG_{12}$], 50 mg of G4-[[[[Ac]-TIBA]-DTPA]-$mPEG_{12}$] dissolved in 0.3 mL of deionized water was serially diluted. Nine hundred projections of the serially diluted phantoms were acquired at 90 kVp and 40 mA on a preclinical microCT scanner [Explore CT120, GE Healthcare] with 16 ms exposure time in the presence of an external reference containing bone, air, and water for subsequent calibration. Three-dimensional (3D) CT images were reconstructed through a filtered back-projection algorithm and transferred to an image processing workstation [Advantage Windows 4.4, GE Healthcare] for analysis. X-ray attenuation values were obtained in Hounsfield units (HU) averaged over the 3D-based region of interest (ROI).

Animal Protocol. All animal experiments were performed in accordance with the regulations set by the Yale University Institutional Animal Care and Use Committee (IACUC). Healthy, wild-type C57BL/6 mice fed on a normal diet (n = 29, female, 6−8 weeks of age, 19−20 g, Jackson River Laboratories) were used in these studies. All surgical catheterizations with PE-10 polyethylene tubing and injections were performed under anesthesia (1−2% isoflurane/100% oxygen). All serial in vivo imaging studies were performed under anesthesia (1−2% isoflurane/100% oxygen) with electrocardiographical (ECG) monitoring [AccuSync 71, AccuSync Medical Research Corporation].

Preparation of Small-Volume Reduction Ampules. Small-volume reduction ampules were prepared according to a previously established method[38] with slight modifications. A 20 mL screw-cap glass scintillation vial was charged with 10 mL deionized water and purged with nitrogen for 30 min. To the purged deionized water, sodium bicarbonate (450 mg, 5.36×10^{-3} mol) [Sigma Aldrich], sodium carbonate (60 mg, 5.65×10^{-4} mol) [Sigma Aldrich], and sodium *p*-aminobenzoate (20 mg, 1.26×10^{-4} mol) were added as solids and mixed with magnetic stirring in a closed system. Tin(II) chloride (1.6 mg, 7×10^{-6} mol) [Sigma Aldrich] and methylene diphosphonic acid (2.5 mg, 1.42×10^{-5} mol) [Sigma Aldrich] were weighed together and added to the buffer salt solution as solids with magnetic stirring. The buffered solution was stirred until a clear solution was obtained. From this solution, 10, 20, 30, or 40 μL volumes were aliquotted to 1.7 mL Eppendorf ampules labeled A, B, C, or D, respectively, flash-frozen, and subsequently lyophilized. Reduction efficiency was assessed by thin layer chromatography (Supporting Information). The assembled reduction ampules were stored at −20 °C.

Radiolabeling for Biodistribution and Pharmacokinetics. Sodium pertechnetate (Na[$^{99m}TcO_4$]) was eluted from a ^{99m}Tc/^{99}Mo generator using 0.9% saline and diluted in deionized water. For each group (n = 4 per time point), 500 μCi of [$^{99m}TcO_4^-$] in 100 μL deionized water was added to a 40 μL assembled reduction ampule, vortexed, and allowed to equilibrate for 2 min at 25 °C. The entire contents of the ampule were then combined with a solution of G4-[[[[Ac]-TIBA]-DTPA]-$mPEG_{12}$] (20 mg dissolved in 600 μL sterile 1× PBS), vortexed, and allowed to equilibrate and chelate for 10 min at 25 °C. One hundred seventy-five microliters of the final radiolabeled construct (radiopurity >79.7%, Supporting Information) were loaded into 1 mL syringes without further purification.

Radiolabeling for MicroSPECT/CT Imaging. Sodium pertechnetate (Na[$^{99m}TcO_4$]) was eluted from a ^{99m}Tc/^{99}Mo generator using 0.9% saline and diluted in deionized water. 500 μCi of [$^{99m}TcO_4^-$] in 50 μL deionized water was added to a 20 μL assembled reduction ampule, vortexed, and allowed to equilibrate for 2 min at 25 °C. The entire contents of the ampule were then combined with a solution of G4-[[[[Ac]-TIBA]-DTPA]-$mPEG_{12}$] (50 mg dissolved in 250 μL sterile 1× PBS), vortexed, and allowed to equilibrate and chelate for 10 min at 25 °C. Three hundred microliters of the final radiolabeled construct (radiopurity >80%, Supporting Information) were loaded into 1 mL syringes without further purification.

Biodistribution and Pharmacokinetics. The biodistribution and pharmacokinetics of ^{99m}Tc-labeled G4-[[[[Ac]-TIBA]-DTPA]-$mPEG_{12}$] were evaluated in healthy, wild-type C57BL/6 mice (female, 6−8 weeks). Each mouse received a 115 ± 3 μCi dose of the radiolabeled dendrimer construct (^{99m}Tc chelated to 5 mg G4-[[[[Ac]-TIBA]-DTPA]-$mPEG_{12}$] dissolved in 0.175 mL chelation solution) injected intravenously via the left jugular vein (n = 4 per time point). Following suturing of the injection site, anesthesia was removed and the mice were euthanized at specific time points (0.5, 1, 2, 4, and 6 h). Blood samples were collected by cardiac puncture and organs (heart, lungs, liver, spleen, and kidneys) were harvested. The blood samples and organs were weighed and counted [Gamma Counter, Cobra Packard] with an appropriate energy window for ^{99m}Tc (full width at half-maximum of 140 keV photopeak) to determine their respective radioactivity counts per minute per gram (cpm/g). The obtained radioactivity counts (cpm/g) were decay-corrected to the time of injection and normalized to the injected dose.

MicroCT Imaging. Serial in vivo imaging of healthy, wild-type C57BL/6 mice (female, 6−8 weeks) was performed on a preclinical microCT scanner [Explore CT120, GE Healthcare] using the CT Fast Scan protocol (220 projections, 70 kVp, 32 mA, and a 16 ms exposure time). Following acquisition of a baseline, precontrast scan, either 0.15 mL (n = 2) or 0.30 mL (n = 2) of 166.7 mg/mL solutions of G4-[[[[Ac]-TIBA]-DTPA]-$mPEG_{12}$] dissolved in sterile 1× PBS were injected via

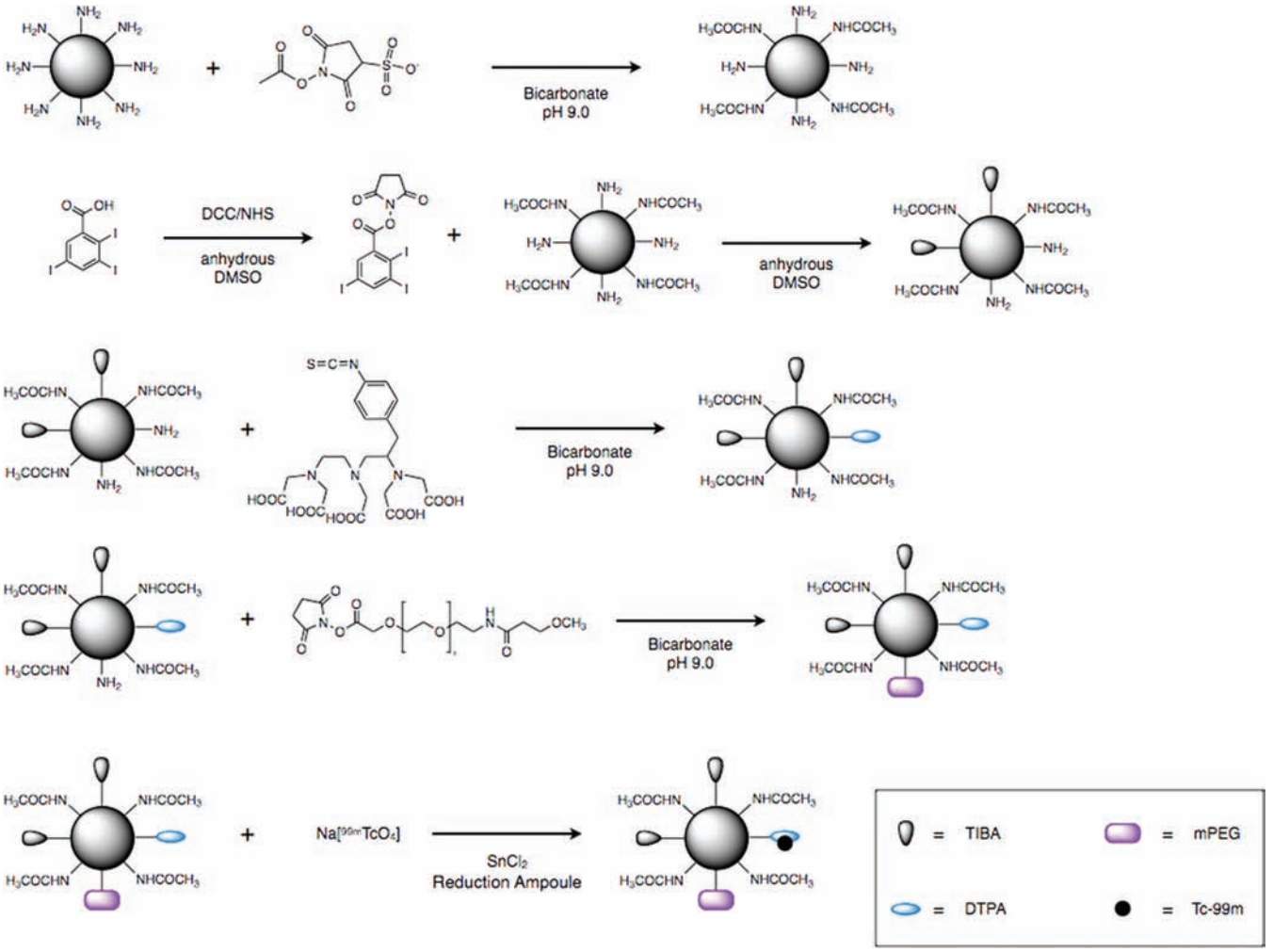

Figure 1. Schematic of the synthesis of ^{99m}Tc-labeled G4-[[[[Ac]-TIBA]-DTPA]-mPEG$_{12}$].

left jugular vein catheter over a 10 min duration to assess optimal dosage to achieve sufficient contrast-to-noise. Following injection of the contrast, mice were imaged serially from 0 to 90 min. Three-dimensional CT images were reconstructed through a filtered back-projection algorithm and further processed with *MicroView* software [GE Healthcare] and *BioImage Suite*.[39]

MicroSPECT/CT Imaging. The multimodal properties of ^{99m}Tc-labeled G4-[[[[Ac]-TIBA]-DTPA]-mPEG$_{12}$] were evaluated in five healthy, wild-type C57BL/6 mice (female, 6−8 weeks) using a preclinical microSPECT/CT hybrid system equipped with a gamma-camera having a 2 mm pinhole collimator [X-SPECT, Gamma Medica-Ideas]. Each mouse received a 440 ± 26 μCi dose of the radiolabeled dendrimer construct (^{99m}Tc chelated to 50 mg G4-[[[[Ac]-TIBA]-DTPA]-mPEG$_{12}$] dissolved in 0.3 mL chelation solution) intravenously via a left jugular vein catheter over a duration of 10 min. Following the injection and subsequent 5 min of circulation time, the mice were euthanized to eliminate motion artifacts from the chest cavity and imaged in the presence of two porous silica point sources to assist in image fusion. CT scans were acquired with 1024 projections at 75 kVp, 305 μA, 50 μm spot size, and magnification factor of 3. Nuclear scans were acquired with 360° counter-clockwise (CCW) rotation, 64 projections, 40 s per projection, ROR of 2.7 cm, FOV of 3.6 cm, and a 20% energy window centered around 140 keV. CT images were reconstructed with FLEX X-O CT software [Gamma Medica-Ideas] using a filtered back-projection algorithm. Nuclear images were reconstructed using FLEX SPECT software (8 iterations, 4 subsets) [Gamma Medica-Ideas], filtered with a Butterworth filter (Nyquist frequency = 0.5, order = 6) and subsequently fused with the CT images and visualized using Inveon Research Workstation [Siemens, USA].

RESULTS

Chemistry. Ethylenediamine-core, generation 4 poly(amidoamine) dendrimers (64 terminal amines) exhibit a highly cationic surface with limited water solubility. To increase the water solubility and decrease the overall surface charge arising from residual primary amines, we chose to partially acetylate the surface of PAMAM(G4) dendrimers[35,37,40] with sulfosuccinimidyl acetate (Figure 1). Partial acetylation was necessary to ensure the aqueous solubility of the subsequent intermediate and final products. ^{1}H NMR characterization of the isolated product G4-[Ac] shows the appearance of a peak at 1.91 ppm corresponding to the methyl protons of the acetyl surface groups (Figure 2a). The degree of acetylation was determined with ^{1}H NMR according to the method of Majoros et al.,[37] by calculating the ratio of the integrals obtained from the methyl protons of the acetyl groups and the sum

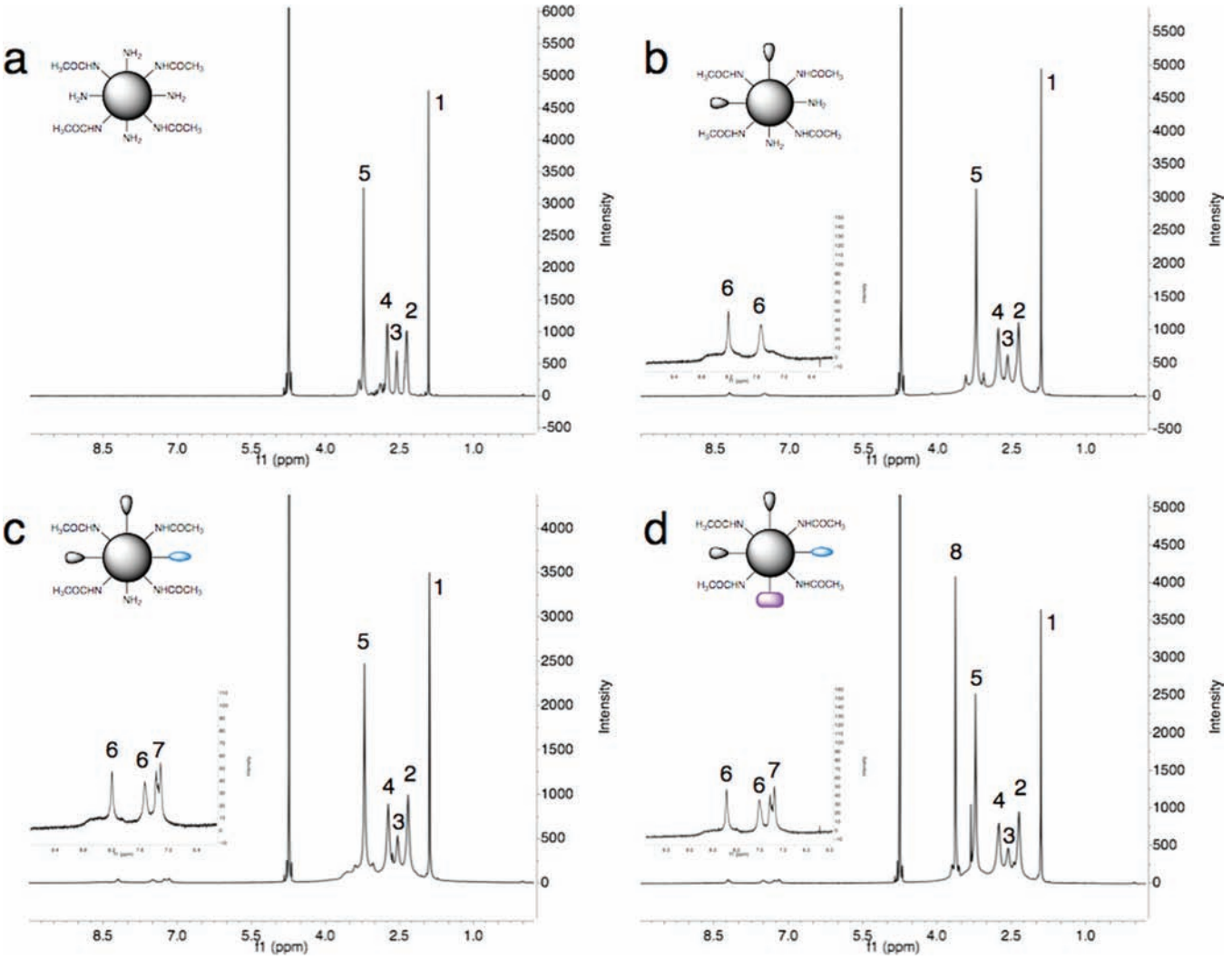

Figure 2. ^{1}H NMR characterization of the synthetic route to G4-[[[[Ac]-TIBA]-DTPA]-mPEG$_{12}$]. ^{1}H NMR spectra were acquired at 400 MHz for 20 mg/mL solutions of (a) G4-[Ac], (b) G4-[[Ac]-TIBA], (c) G4-[[[Ac]-TIBA]-DTPA], and (d) G4-[[[[Ac]-TIBA]-DTPA]-mPEG$_{12}$] in D_2O. Peaks are labeled according to the following: (1) 1.91 (COCH_3), (2) 2.28−2.42 (C-CH_2CONH), (3) 2.50−2.61 (N-CH_2CH_2NH), (4) 2.68−2.80 (N-CH_2CH_2CO), (5) 3.14−3.36 (CONH-CH_2), (6) 7.49 and 8.21 (TIBA aromatic), (7) 7.18 and 7.27 (DTPA aromatic), and (8) 3.5−3.76 (-OCH_2CH_2).

Table 1. Physicochemical Properties of G4-[[[[Ac]-TIBA]-DTPA]-mPEG$_{12}$]

compound	NH_2	$NHCOCH_3$	TIBA	DTPA	mPEG	molecular weight	d_{hyd} (nm)
G4	64	n/a	n/a	n/a	n/a	14 214[a]	4.47 ± 1.45
G4-[[[[Ac]-TIBA]-DTPA]-mPEG$_{12}$	3	35	15	4	7	29 762[b]	12.37 ± 6.09

[a] Obtained from Sigma Aldrich. [b] Obtained from ^{1}H NMR.

of all the methylene protons of the dendrimer (−CH_3/−CH_2 ratio). The number of acetyl groups coupled to the dendrimer surface was determined to be 35 (Table 1).

To transform the partially acetylated dendrimer into a radiopaque construct, we chose to couple 2,3,5-triiodobenzoic acid to 64% of the remaining dendrimer primary surface amines (Figure 1). To achieve the desired extent of conjugation, a slight molar excess of TIBA was converted to an amine-reactive NHS ester with DCC and NHS. The active NHS ester was retained after filtration to remove insoluble DCU and coupled immediately to the dendrimer surface without further purification. The product G4-[[Ac]-TIBA] showed the appearance of two broad peaks at 7.49 and 8.21 ppm corresponding to the two aromatic protons of TIBA in the ^{1}H NMR spectrum (Figure 2b). Further, the product showed an increase in the CONH-$\underline{CH_2}$ integral (3.14−3.36 ppm) corresponding to the coupling of ∼15 TIBA moieties (Table 1). The degree of acylation was further corroborated by comparing the integral values obtained for the aromatic protons of the TIBA moieties and the core methylene protons of the dendrimer (N-$\underline{CH_2}CH_2$-NH, 2.50−2.61 ppm). The changes in the dendrimer peak integrations and inherent line-broadening of the aromatic protons indicated covalent

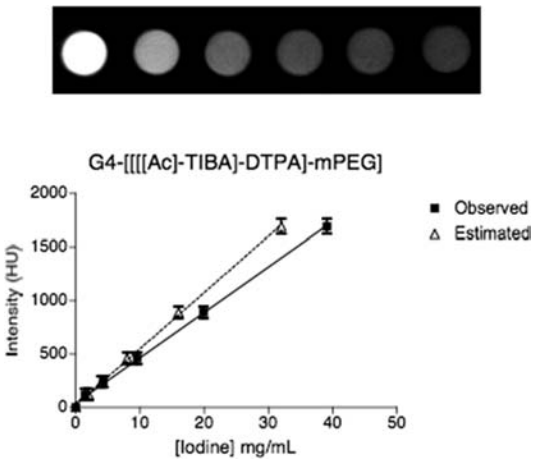

Figure 3. X-ray attenuation measurements. Phantom images of a serial dilution of G4-[[[[Ac]-TIBA]-DTPA]-mPEG$_{12}$] in deionized H_2O acquired at 90 kVp. The intensity values obtained in Hounsfield units averaged over 3D-based ROIs were plotted against iodine concentration. Iodine concentrations for G4-[[[[Ac]-TIBA]-DTPA]-mPEG$_{12}$] were extrapolated from the linear attenuation calibration curve for Omnipaque 350 (Supporting Information) and compared to those estimated from ^{1}H NMR.

attachment of TIBA, rather than complexation. Further, no reaction was observed in the absence of DCC and NHS.

Similar to the work of Zhang et al.,[35,36] we chose to couple p-SCN-Bn-DTPA, an acyclic chelator, to roughly 28% of the remaining dendrimer primary surface amines for subsequent chelation of the nuclear probe, ^{99m}Tc (Figure 1). The product G4-[[[Ac]-TIBA]-DTPA] showed the appearance of two overlapping broad peaks at 7.18 and 7.27 ppm in the ^{1}H NMR spectrum (Figure 2c) corresponding to the aromatic protons of the benzyl linker of p-SCN-Bn-DTPA. By comparing the integral values for the aromatic protons of the benzyl linker and the core methylene protons of the dendrimer (N-C$\underline{H_2}$C$\underline{H_2}$-NH, 2.50−2.61 ppm), the extent of conjugation via isothiocyanate linkage was determined to be ∼4 (Table 1). Again, the inherent line-broadening of the aromatic protons indicated covalent attachment of the DTPA via isothiocyanate linkage.

To further enhance the water solubility and intravascular residence time, we chose to PEGylate the remaining primary surface amines with mPEG$_{12}$-NHS (Figure 1). The product G4-[[[[Ac]-TIBA]-DTPA]-mPEG$_{12}$] showed the presence of a peak 3.5−3.76 ppm in the ^{1}H NMR spectrum (Figure 2d) corresponding to the methylene protons (-OC$\underline{H_2}$C$\underline{H_2}$) of the 12 ethylene oxide repeat units. By comparing the integral values for these methylene protons and the core methylene protons of the dendrimer (N-C$\underline{H_2}$CH$_2$-NH, 2.50−2.61 ppm), the extent of conjugation was determined to be ∼7 (Table 1). The final product, G4-[[[[Ac]-TIBA]-DTPA]-mPEG$_{12}$], was reproducibly attained in terms of both extent of surface conjugation and yield.

***In Vitro* Evaluation of G4-[[[[Ac]-TIBA]-DTPA]-mPEG$_{12}$].** To evaluate the X-ray attenuation properties of the dendrimer construct, we acquired images of serially diluted G4-[[[[Ac]-TIBA]-DTPA]-mPEG$_{12}$] in deionized water (Figure 3) and subsequently converted them to Hounsfield maps for quantitative analysis. Iodine concentrations of the serially diluted dendrimer construct were extrapolated from the linear attenuation versus iodine concentration calibration curve generated from the

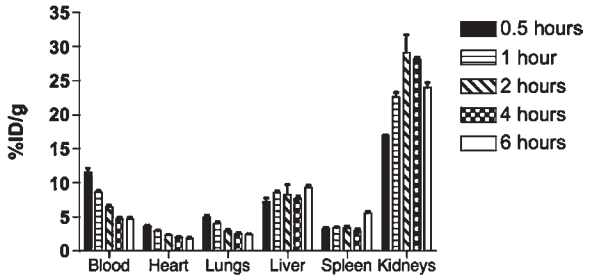

Figure 4. Biodistribution of ^{99m}Tc-labeled G4-[[[[Ac]-TIBA]-DTPA]-mPEG$_{12}$]. Biodistribution of ^{99m}Tc-labeled G4-[[[[Ac]-TIBA]-DTPA]-mPEG$_{12}$] revealed relatively long blood residence with predominant renal clearance and excretion.

serially diluted 20% Omnipaque 350 solution (Supporting Information Figure SI.2) for comparison to theoretical iodine concentrations estimated from ^{1}H NMR. A linear attenuation versus iodine concentration curve, an essential criterion for X-ray contrast agents, was obtained for G4-[[[[Ac]-TIBA]-DTPA]-mPEG$_{12}$]. The extrapolated iodine concentrations for G4-[[[-[Ac]-TIBA]-DTPA]-mPEG$_{12}$] were observed to be consistent with the estimated iodine weight percent (∼19% wt) determined with ^{1}H NMR.

Blood Clearance and Biodistribution. To assess the potential of the multimodal probe for blood pool imaging, we examined both the blood clearance pharmacokinetics and biodistribution of ^{99m}Tc-labeled G4-[[[[Ac]-TIBA]-DTPA]-mPEG$_{12}$]. Following intravenous injection of the radiolabeled dendrimer construct, the blood and organs were collected from healthy, female C57BL/6 mice (6−8 weeks, n = 4 per time point) and subsequently analyzed by gamma counting. To determine the circulation half-life of the construct, a blood clearance curve (Supporting Information Figure SI.5) was generated and fit to the monoexponential decay equation

$$A = A_0\, e^{-kt} + C \quad (1)$$

where k is the rate constant. From the curve-fitting analysis, the circulation half-life was calculated to be 0.72 h (43 min). Analysis of the biodistribution showed that the construct was cleared from the blood pool predominantly by the kidneys (Figure 4), as expected given the small hydrodynamic diameter (12.37 ± 6.09 nm) of the final dendrimer construct (Table 1).

Serial Blood Pool Imaging with MicroCT. The efficacy of G4-[[[[Ac]-TIBA]-DTPA]-mPEG$_{12}$] as a blood pool contrast agent was assessed in healthy, female C57BL/6 mice (6−8 weeks) with serial cardiac microCT following intravenous injection. We observed intravascular and intraventricular enhancement with an excellent contrast-to-noise ratio in the right and left ventricles of the heart across both doses. This enhancement persisted longer than 90 min postinjection (Figure 5a).

Multimodal Blood Pool Imaging with MicroSPECT/CT. To assess the multimodal capabilities of the dendrimer construct, ^{99m}Tc-labeled G4-[[[[Ac]-TIBA]-DTPA]-mPEG$_{12}$] was prepared and injected intravenously into healthy, female C57BL/6 mice (6−8 weeks, n = 5). Post-mortem microSPECT/CT imaging revealed substantial colocalization of the radioactivity and the dendritic iodinated contrast within the intravascular and intraventricular cavity in the absence of motion artifacts (Figure 5b−d). The intravascular retention, minimal liver accumulation, and colocalization of the different contrast media

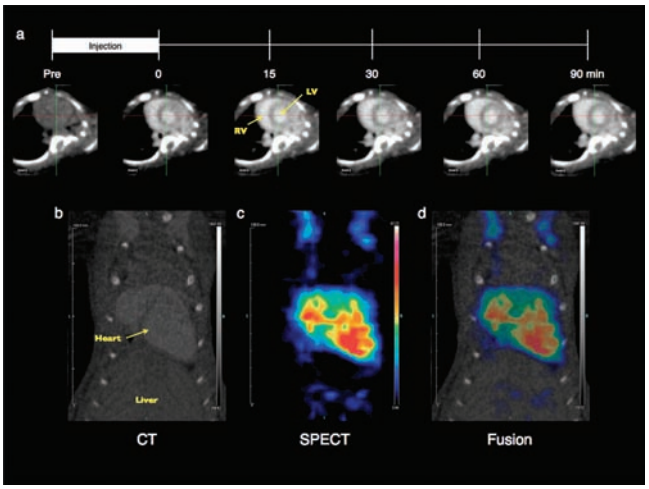

Figure 5. Serial microCT and multimodal microSPECT/CT blood pool imaging. (a) Following acquisition of a precontrast image and subsequent intravenous jugular vein injection of 50 mg of G4-[[[[Ac]-TIBA]-DTPA]-mPEG$_{12}$] dissolved in 0.3 mL sterile 1× PBS (10 min duration), serial short axis images of the RV/LV blood pool showing significant contrast enhancement were acquired from 0 to 90 min postinjection. Following intravenous jugular vein injection (10 min duration) of a 440 ± 26 μCi dose of the radiolabeled dendrimer construct (50 mg of ^{99m}Tc-labeled G4-[[[[Ac]-TIBA]-DTPA]-mPEG$_{12}$] dissolved in 0.3 mL chelation solution), post-mortem microSPECT/CT images of the heart were acquired. The fusion of the (b) microCT and (c) microSPECT coronal images presented in (d) shows significant colocalization of the nuclear and X-ray contrast components.

provides evidence for the formation of a sufficiently pure and stable chelate, as either colloidal or free hydrolyzed/reduced ^{99m}Tc would be cleared predominantly by the liver.[41,42]

DISCUSSION

With increasing desire to extract both structural and functional information with a single probe, the necessity for development of multimodal probes is evident. Along these lines, multimodal probes have been designed for software image fusion techniques, such as PET-MRI,[13] CT-MRI,[12,43,44] and optical-MRI;[15,16] however, the design of multimodal probes for hybrid imaging systems is relatively unexplored.[45] Thus, the primary objective of this work was to synthesize a single, multimodal blood pool agent designed to simultaneously offer complementary forms of contrast enhancement for small animal hybrid imaging systems, specifically, SPECT/CT.

We chose generation 4 PAMAM dendrimers as the core structure of the contrast agent for the following reasons: (1) the well-defined, multifunctional surface (64 primary amines) offers the ability to conjugate several different moieties with negligible steric hindrance, and (2) dendrimer-based contrast agents have been successfully designed and examined in single, noninvasive imaging modalities, including MRI,[15,23−28] CT,[12,29−31] and SPECT.[33−36] Partial acetylation of the PAMAM(G4) surface was performed to enhance the aqueous solubility[35,37,40] and abrogate the potential of cytotoxicity and hemolysis derived from the inherent positive surface charge.[40,46] We chose to couple TIBA to ∼25% of the initial surface amines to obtain sufficient iodine weight percent necessary for effective X-ray attenuation without sacrificing aqueous solubility. Further, TIBA was selected because it imparts similar X-ray attenuation properties to the FDA-approved, small-molecule triiodobenzoic acid derivative (Omnipaque 350, GE Healthcare) routinely used in clinical applications. To generate the multimodal character of the agent, the acyclic chelator, DTPA, was chosen to chelate tin(II)-reduced ^{99m}Tc because of its established chemistry and stability.[35,36,47] Design of effective macromolecular, polymeric contrast agents for blood pool imaging requires long intravascular residence times. To further enhance the circulation half-life and limit clearance by the reticulo-endothelial system (RES),[48] we chose to PEGylate the remainder of the surface with methoxy-terminated PEG.

The final dendrimer construct, G4-[[[[Ac]-TIBA]-DTPA]-mPEG$_{12}$], offers both sufficient X-ray contrast enhancement and sufficiently long circulation half-life for blood pool imaging with microCT. Following chelation of ^{99m}Tc, demonstration of the multimodal character of ^{99m}Tc-labeled G4-[[[[Ac]-TIBA]-DTPA]-mPEG$_{12}$] was successfully achieved with sequential cardiac microSPECT/CT image acquisition. This showed significant colocalization of nuclear and X-ray contrast in the heart. While others have reported long-circulating iodine-based contrast agents (e.g., Fenestra and liposomal formulations) and nuclear probes (e.g., ^{99m}Tc-Sestimibi), as well as, dendrimers, for CT and SPECT imaging, combining these forms of contrast into a single probe for hybrid imaging is virtually unexplored. Thus, this work represents the first report of a multimodal dendrimer-based contrast agent designed specifically for use with hybrid imaging systems to acquire blood pool images that exhibit both high spatial resolution and high sensitivity derived from a single probe. Further, the inherent long intravascular residence time offers the potential to enable assessment of cardiac function with both ECG and respiratory-gated microSPECT and microCT, which often imparts long image acquisition times.

Aside from integrating both the high spatial resolution of CT and the high sensitivity of nuclear imaging, the ability to combine the CT contrast and radionuclide in a single construct offers a great advantage for image processing and quantification. The fusion of sequentially obtained SPECT and CT images to gain information regarding anatomical structure and physiological function, such as absolute myocardial blood flow, relies heavily upon the ability to accurately correct the SPECT images for attenuation and partial volume effects. Specifically, this hybrid intravascular SPECT and CT probe would facilitate determination of intramyocardial blood volume and absolute myocardial blood flow using sequential, hybrid SPECT/CT imaging. Further, the probe would allow correction of SPECT partial volume errors by defining the endocardial and epicardial surfaces with CT imaging, while not compromising the ability to correct nonuniform attenuation within the chest. The multimodal properties of the contrast agent therefore offer the ability to perform these corrections directly with the circulating contrast agent at the precise time of image acquisition.

While the blood residence time is sufficiently long for blood pool imaging applications, simple synthetic modifications to the dendrimer and incorporation of targeting moieties would extend the utility of this construct to targeted imaging applications. For example, changing the acyclic chelator, DTPA, to the cyclic chelator, DOTA, would enable chelation of longer-lived radionuclides like ^{111}In for SPECT and ^{64}Cu for PET. Incorporation of these longer-lived radionuclides would provide sufficiently long nuclear half-lives for detection of the probe at active target sites following clearance from the blood. This would be essential for demonstrating site-specific targeting in vascular models such as angiogenesis and atherosclerosis.

CONCLUSIONS

We have successfully demonstrated the synthesis, characterization, and application of a radiolabeled, multimodal dendrimer-based contrast agent for preclinical microSPECT/CT imaging. The long intravascular residence time and predominant renal clearance of the agent provide optimal characteristics for intravascular and blood pool imaging with microSPECT/CT. The colocalization of the dendritic nuclear and X-ray contrast offers the potential to facilitate image analysis and quantification by enabling correction for SPECT attenuation and partial volume errors at specified times with the higher-resolution anatomic information provided by the circulating CT contrast. This may allow absolute quantification of intramyocardial blood volume and blood flow. Finally, the chelation of longer-lived SPECT (e.g., ^{111}In) or PET (e.g., ^{64}Cu) radionuclides might enable the ability to visualize active molecular targeting following sufficient clearance from the blood.

ASSOCIATED CONTENT

Supporting Information. Experimental details regarding the efficiency of ^{99m}Tc reduction and assessment of radiopurity of ^{99m}Tc-G4-[[[[Ac]-TIBA]-DTPA]-mPEG$_{12}$] are presented. This material is available free of charge via the Internet at http://pubs.acs.org.

AUTHOR INFORMATION

Corresponding Author

*Tel: 203-432-1043; Fax: 203-432-0030; E-mail: tarek.fahmy@yale.edu.

ACKNOWLEDGMENT

The authors would like to thank Xiangning Wang and Donald Dione for assistance with data collection and analysis. This work was partially supported by an NIH Autoimmunity Center of Excellence Pilot Award to Award (T.M.F.) and NIH grant HL65662 (A.J.S.).

REFERENCES

(1) Townsend, D. (2008) Dual-modality imaging: combining anatomy and function. *J. Nucl. Med. 49* (6), 938–955.

(2) Townsend, D. (2008) Multimodality imaging of structure and function. *Phys. Med. Biol. 53* (4), R1–R39.

(3) Townsend, D., and Cherry, S. (2001) Combining anatomy and function: the path to true image fusion. *Eur. Radiol. 11* (10), 1968–1974.

(4) Judenhofer, M., Wehrl, H., Newport, D., Catana, C., Siegel, S., Becker, M., Thielscher, A., Kneilling, M., Lichy, M., Eichner, M., Klingel, K., Reischl, G., Widmaier, S., Röcken, M., Nutt, R., Machulla, H., Uludag, K., Cherry, S., Claussen, C., and Pichler, B. (2008) Simultaneous PET-MRI: a new approach for functional and morphological imaging. *Nat. Med. 14* (4), 459–465.

(5) Schäfers, K., and Stegger, L. (2008) Combined imaging of molecular function and morphology with PET/CT and SPECT/CT: Image fusion and motion correction. *Basic Res. Cardiol. 103* (2), 191–199.

(6) Oconnor, M., and Kemp, B. (2006) Single-photon emission computed tomography/computed tomography: basic instrumentation and innovations. *Sem. Nucl. Med. 36* (4), 258–266.

(7) Pichler, B., Judenhofer, M., and Pfannenberg, C. (2008) Multimodal imaging approaches: PET/CT and PET/MRI. *Handb. Exp. Pharmacol.185* Pt 1, 109−132.

(8) Pichler, B., Judenhofer, M., and Wehrl, H. (2008) PET/MRI hybrid imaging: devices and initial results. *Eur. Radiol. 18* (6), 1077–1086.

(9) Pichler, B., Kolb, A., Nagele, T., and Schlemmer, H. (2010) PET/MRI: Paving the way for the next generation of clinical multimodality imaging applications. *J. Nucl. Med. 51* (3), 333–336.

(10) Pichler, B., Wehrl, H., Kolb, A., and Judenhofer, M. (2008) Positron emission tomography/magnetic resonance imaging: the next generation of multimodality imaging? *Sem. Nuc. Med. 38* (3), 199–208.

(11) Maurer, A. H. (2008) Combined imaging modalities: PET/CT and SPECT/CT. *Health Phys. 95*, 571–576.

(12) Regino, C. A., Walbridge, S., Bernardo, M., Wong, K. J., Johnson, D., Lonser, R., Oldfield, E. H., Choyke, P. L., and Brechbiel, M. (2008) A dual CT-MR dendrimer contrast agent as a surrogate marker for convection-enhanced delivery of intracerebral macromolecular therapeutic agents. *Contrast Med. Mol. Imaging 3* (1), 2–8.

(13) Choi, J., Park, J., Nah, H., Woo, S., Oh, J., Kim, K., Cheon, G., Chang, Y., Yoo, J., and Cheon, J. (2008) A hybrid nanoparticle probe for dual-modality positron emission tomography and magnetic resonance imaging. *Angew. Chem., Int. Ed. 47* (33), 6259–6262.

(14) Zaidi, H., Montandon, M., and Alavi, A. (2010) The clinical role of fusion imaging using PET, CT, and MR imaging. *Magnetic Resonance Imaging Clinics of North America 18* (1), 133–149.

(15) Talanov, V. S., Regino, C. A., Kobayashi, H., Bernardo, M., Choyke, P. L., and Brechbiel, M. (2006) Dendrimer-based nanoprobe for dual modality magnetic resonance and fluorescence imaging. *Nano Lett. 6* (7), 1459–1463.

(16) Strijkers, G., Kluza, E., Tilborg, G., Schaft, D., Griffioen, A., Mulder, W., and Nicolay, K. (2010) Paramagnetic and fluorescent liposomes for target-specific imaging and therapy of tumor angiogenesis. *Angiogenesis 13* (2), 161–173.

(17) Louie, A. (2010) Multimodality imaging probes: design and challenges. *Chem. Rev. 110*, 3146–3195.

(18) Skajaa, T., Cormode, D., Jarzyna, P., Delshad, A., Blachford, C., Barazza, A., Fisher, E., Gordon, R., Fayad, Z., and Mulder, W. (2011) The biological properties of iron oxide core high-density lipoprotein in experimental atherosclerosis. *Biomaterials 32* (1), 206–213.

(19) Kelly, K. (2005) Detection of vascular adhesion molecule-1 expression using a novel multimodal nanoparticle. *Circ. Res. 96* (3), 327–336.

(20) McCarthy, J. R., Patel, P., Botnaru, I., Haghayeghi, P., Weissleder, R., and Jaffer, F. A. (2009) Multimodal nanoagents for the detection of intravascular thrombi. *Bioconjugate Chem. 20*, 1251–1255.

(21) Dobrucki, L. W., Tsutsumi, Y., Kalinowski, L., Dean, J., Gavin, M., Sen, S., Mendizabal, M., Sinusas, A. J., and Aikawa, R. (2010) Analysis of angiogenesis induced by local IGF-1 expression after myocardial infarction using microSPECT-CT imaging. *J. Mol. Cell. Cardiol. 48* (6), 1071–1079.

(22) Tomalia, D. A., Naylor, A. M., and Goddard, W. A., III (1990) Starburst Dendrimers: Molecular-level control of size, shape, surface chemistry, topology, and flexibility from atoms to macroscopic matter. *Angew. Chem., Int. Ed. 29*, 138–175.

(23) Jászberényi, Z., Moriggi, L., Schmidt, P., Weidensteiner, C., Kneuer, R., Merbach, A., Helm, L., and Tóth, É. (2007) Physicochemical and MRI characterization of Gd3+-loaded polyamidoamine and hyperbranched dendrimers. *J. Biol. Inorg. Chem. 12* (3), 406–420.

(24) Kobayashi, H., and Brechbiel, M. (2005) Nano-sized MRI contrast agents with dendrimer cores. *Adv. Drug Delivery Rev. 57* (15), 2271–2286.

(25) Kobayashi, H., and Brechbiel, M. W. (2004) Dendrimer-based nanosized MRI contrast agents. *Curr. Pharm. Biotechnol. 5*, 539–549.

(26) Mounzer, R., Shkarin, P., Papademetris, X., Constable, T., Ruddle, N., and Fahmy, T. (2007) Dynamic imaging of lymphatic vessels and lymph nodes using a bimodal nanoparticulate contrast agent. *Lymph. Res. Biol. 5* (3), 151–158.

(27) Venditto, V. J., Regino, C. A., and Brechbiel, M. (2005) PAMAM dendrimer based macromolecules as improved contrast agents. *Mol. Pharmaceutics 2* (4), 302–311.

(28) Wiener, E. C., Brechbiel, M. W., Brothers, H., Magin, R. L., Gansow, O. A., Tomalia, D. A., and Lauterbur, P. C. (1994) Dendrimer-based metal-chelates - a new class of magnetic resonance imaging contrast agents. *Magn. Reson. Med. 31*, 1–8.

(29) Fu, Y., Nitecki, D. E., Maltby, D., Simon, G. H., Berejnoi, K., Raatschen, H. J., Yeh, B. M., Shames, D. M., and Brasch, R. C. (2006) Dendritic iodinated contrast agents with PEG-cores for CT imaging: Synthesis and preliminary characterization. *Bioconjugate Chem. 17*, 1043–1056.

(30) Yordanov, A. T., Lodder, A. L., Woller, E. K., Cloninger, M. J., Patronas, N., Milenic, D., and Brechbiel, M. W. (2002) Novel iodinated dendritic nanoparticles for computed tomography (CT) imaging. *Nano Lett. 2*, 595–599.

(31) Yordanov, A. T., Mollov, N., Lodder, A. L., Woller, E., Cloninger, M., Walbridge, S., Milenic, D., and Brechbiel, M. W. (2005) A water-soluble triiodo amino acid and its dendrimer conjugate for computerized tomography (CT) imaging. *J. Serb. Chem. Soc. 70*, 163–170.

(32) Almutairi, A., Rossin, R., Shokeen, M., Hagooly, A., Ananth, A., Capoccia, B., Guillaudeu, S., Abendschein, D., Anderson, C. J., Welch, M. J., and Fréchet, J. M. (2009) Biodegradable dendritic positron-emitting nanoprobes for the noninvasive imaging of angiogenesis. *Proc. Natl. Acad. Sci. U.S.A. 106* (3), 685–690.

(33) Agashe, H. B., Babbar, A. K., Jain, S., Sharma, R. K., Mishra, A. K., Asthana, A., Garg, M., Dutta, T., and Jain, N. K. (2007) Investigations on biodistribution of technetium-99m-labeled carbohydrate-coated poly(propylene imine) dendrimers. *Nanomed. Nanotechnol. 3*, 120–127.

(34) Parrott, M. C., Benhabbour, S. R., Saab, C., Lemon, J. A., Parker, S., Valliant, J. F., and Adronov, A. (2009) Synthesis, radiolabeling, and bio-imaging of high-generation polyester dendrimers. *J. Am. Chem. Soc. 131*, 2906–2916.

(35) Zhang, Y., Sun, Y., Xu, X., Zhang, X., Zhu, H., Huang, L., Qi, Y., and Shen, Y. (2010) Synthesis, biodistribution, and microsingle photon emission computed tomography (SPECT) imaging study of technetium-99m labeled PEGylated dendrimer poly(amidoamine) (PAMAM)-folic acid conjugates. *J. Med. Chem. 53*, 3262–3272.

(36) Zhang, Y., Sun, Y., Xu, X., Zhu, H., Huang, L., Zhang, X., Qi, Y., and Shen, Y. M. (2010) Radiosynthesis and micro-SPECT imaging of (99m)Tc-dendrimer poly(amido)-amine folic acid conjugate. *Bioorg. Med. Chem. Lett. 20* (3), 927–931.

(37) Majoros, I. J., Keszler, B., Woehler, S., Bull, T., and Baker, J. R. (2003) Acetylation of poly(amidoamine) dendrimers. *Macromolecules 36*, 5526–5529.

(38) Marino, M. E. C. P., Syud, F. A., Schaffer, P., Lee, B. D., Zhang, R., Lindborg, M., Gunneriusson, E., and Lendel, C. (2009) PDGF-RBeta binders. U.S. Patent Appl. 20090191124.

(39) Papademetris, X., Jackowski, M., Rajeevan, N., Constable, R. T., Staib, L. H. (2007) BioImage Suite: An integrated medical image analysis suite. Section of Bioimaging Sciences, Dept. of Diagnostic Radiology, Yale School of Medicine. Available from URL: http://www.bioimagesuite.org.

(40) Kolhatkar, R., Kitchens, K., Swaan, P., and Ghandehari, H. (2007) Surface acetylation of polyamidoamine (PAMAM) dendrimers decreases cytotoxicity while maintaining membrane permeability. *Bioconjugate Chem. 18* (6), 2054–2060.

(41) Banerjee, S., Samuel, G., Kothari, K., Unni, P. R., Sarma, H. D., and Pillai, M. R. (2001) Tc-99m and Re-186 complexes of tetraphosphonate ligands and their biodistribution pattern in animal models. *Nucl. Med. Biol. 28* (2), 205–213.

(42) Banerjee, T., Singh, A., Sharma, R., and Maitra, A. (2005) Labeling efficiency and biodistribution of Technetium-99m labeled nanoparticles: interference by colloidal tin oxide particles. *Int. J. Pharm. 289* (1−2), 189–195.

(43) Zheng, J., Liu, J., Dunne, M., Jaffray, D. A., and Allen, C. (2007) In vivo performance of a liposomal vascular contrast agent for CT and MR-based image guidance applications. *Pharm. Res. 24* (6), 1193–1201.

(44) Zheng, J., Perkins, G., Kirilova, A., Allen, C., and Jaffray, D. A. (2006) Multimodal contrast agent for combined computed tomography and magnetic resonance imaging applications. *Invest. Radiol. 41* (3), 339–348.

(45) Seevinck, P. R., Seppenwoolde, J. H., de Wit, T. C., Nijsen, J. F., Beekman, F. J., van Het Schip, A. D., and Bakker, C. J. (2007) Factors affecting the sensitivity and detection limits of MRI, CT, and SPECT for multimodal diagnostic and therapeutic agents. *Anticancer Agents Med. Chem. 7* (3), 317–334.

(46) Fischer, D., Li, Y., Ahlemeyer, B., Krieglstein, J., and Kissel, T. (2003) In vitro cytotoxicity testing of polycations: influence of polymer structure on cell viability and hemolysis. *Biomaterials 24* (7), 1121–1131.

(47) Narasimhan, D. V. S., Vanaja, P., Banodkar, S. M., and Mani, R. S. (1984) Studies on the chemistry of technetium-99m radiopharmaceuticals. *J. Radioanal. Nucl. Chem. 84*, 129–136.

(48) Chow, T., Lin, Y., Hwang, J., Wang, H., Tseng, Y., Pang, V., Liu, R., Lin, W., Yang, C., and Ting, G. (2009) Therapeutic efficacy evaluation of ^{111}In-labeled PEGylated liposomal vinorelbine in murine colon carcinoma with multimodalities of molecular imaging. *J. Nucl. Med. 50* (12), 2073–2081.

Development and application of a multimodal contrast agent for SPECT/CT hybrid imaging

Jason M. Criscione[1], Lawrence W. Dobrucki[2,3], Zhen W. Zhuang[2], Xenophon Papademetris[1,4], Michael Simons[2], Albert J. Sinusas[2,4] and Tarek M. Fahmy[1,5*]*

[1]*Department of Biomedical Engineering, Yale University, New Haven, CT*

[2]*Section of Cardiovascular Medicine, Department of Internal Medicine, Yale University School of Medicine, New Haven, CT*

[3]*Beckman Institute for Advanced Science and Technology, University of Illinois at Urbana-Champaign, Urbana, IL*

[4]*Department of Diagnostic Radiology, Yale University School of Medicine, New Haven, CT*

[5]*Department of Chemical Engineering, Yale University, New Haven, CT*

[*] Corresponding author: Tel: 203-432-1043; Fax: 203-432-0030; E-mail: tarek.fahmy@yale.edu

Supporting information.

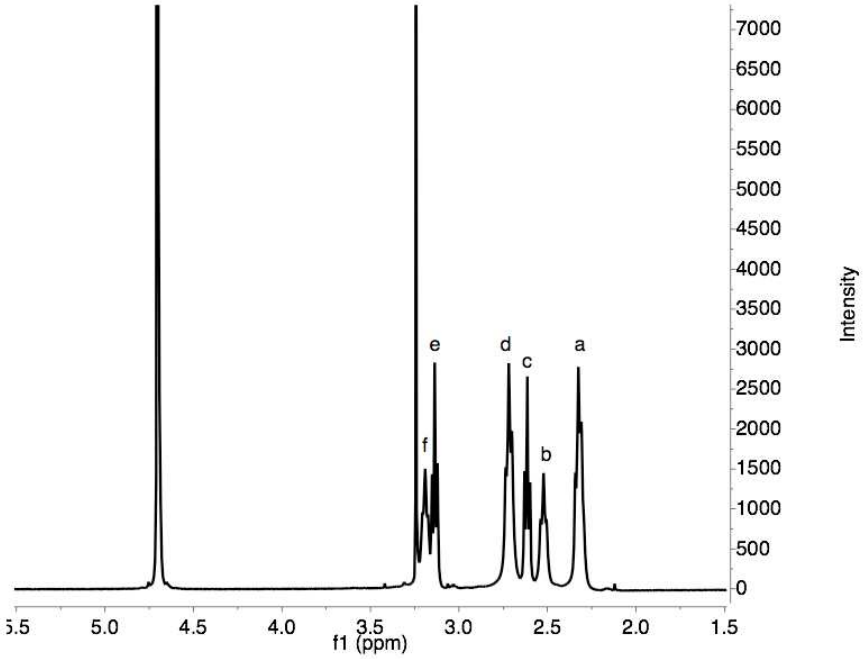

Figure SI.1. ^{1}H NMR spectrum of PAMAM(G4) (20 mg/mL in D_2O, 400 MHz). PAMAM(G4) was dissolved in D_2O (20 mg/mL) and characterized by ^{1}H NMR spectroscopy (D_2O, 400 MHz). Peaks are labeled according to the following: (a) -N-CH_2-C$\underline{H_2}$CONH, (b) -NH-CH_2C$\underline{H_2}$NR_2, (c) -NH-CH_2C$\underline{H_2}$NH_2 (d) -N-C$\underline{H_2}$$CH_2$CONH, (e) -NH-C$\underline{H_2}$$CH_2NH_2$ (f) -NH-C$\underline{H_2}$$CH_2NR_2$.

X-ray attenuation calibration curve. To evaluate the X-ray attenuation properties of G4-[[[[Ac]-TIBA]-DTPA]-mPEG_{12}], a standard curve was generated from a serial dilution of a 20% (v/v) Omnipaque 350 [GE Healthcare] solution in deionized water (70 mgI/mL). Nine hundred projections of the serially diluted phantoms were acquired at 90

kVp and 40 mA on a pre-clinical microCT scanner [Explore CT120, GE Healthcare] with 16 msec exposure time in the presence of an external reference containing bone, air and water for subsequent calibration. Three-dimensional (3D) CT images were reconstructed through a filtered back-projection algorithm and transferred to an image processing workstation [Advantage Windows 4.4, GE Healthcare] for analysis. X-ray attenuation values were obtained in Hounsfield units (HU) averaged over the 3D-based region of interest (ROI).

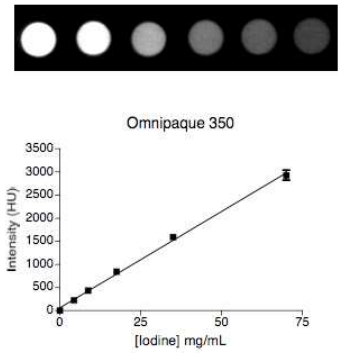

Figure SI.2. X-ray attenuation measurements. Phantom images of a serial dilution of a 20% (v/v) solution of Omnipaque 350 in deionized H_2O acquired at 90 kVp. The intensity values obtained in Hounsfield units averaged over 3D-based ROIs were plotted against iodine concentration to obtain a calibration curve.

Tc-99m reduction. Sodium pertechnetate ($Na[^{99m}TcO_4]$) was eluted from a $^{99m}Tc/^{99}Mo$ generator using 0.9% saline. To assess the efficiency of the assembled reduction ampoules, specific quantities of $Na[^{99m}TcO_4]$ diluted in deionized water were delivered to either 10 μL or 30 μL aliquotted reduction ampoules labeled "A" or "B", respectively. Specifically, 900 μCi in 75 μL deionized water was added to an ampoule labeled "B" and both 300 and 150 μCi in 25 μL deionized water were added to separated ampoules labeled "A". The combined kits were vortexed and equilibrated for 10 minutes at 25°C. $Na[^{99m}TcO_4]$ and the contents of the reduction ampoules were analyzed by thin layer chromatography (TLC). TLC was performed on a Silica Gel 60 stationary phase with acetone as the mobile phase. A static image of the TLC plate (**Figure SI.3**) was acquired over 10 minutes with a 20% energy window centered around 140 keV using a pre-clinical microSPECT/CT hybrid system equipped with a gamma-camera having a 1 mm pinhole collimator [X-SPECT, Gamma Medica-Ideas].

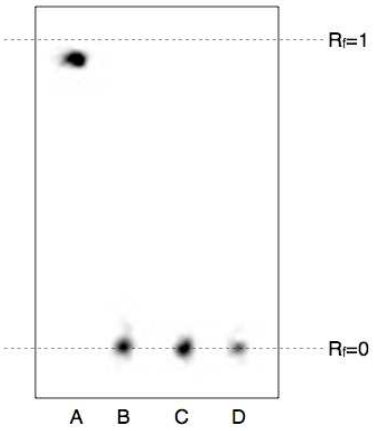

Figure SI.3. TLC analysis of the efficiency of ^{99m}Tc reduction by different aliquots of Sn(II)-containing reduction ampoules. (a) Na[^{99m}TcO$_4$] was observed to travel with the acetone solvent front, while reduced/hydrolyzed ^{99m}Tc remains at the origin. (b) shows the efficiency of a 30 μL reduction ampoule to reduce 900 μCi. (c) and (d) show the efficiency of a 10 μL reduction ampoule to reduce 300 and 150 μCi, respectively.

Radiopurity of ^{99m}Tc-G4-[[[[Ac]-TIBA]-DTPA]-mPEG$_{12}$]. The radiochemical purity of ^{99m}Tc to G4-[[[[Ac]-TIBA]-DTPA]-mPEG$_{12}$] utilized for the biodistribution studies was assessed with a size exclusion, spin-column method. Sodium pertechnetate (Na[^{99m}TcO$_4$]) was eluted from a ^{99m}Tc/^{99}Mo generator using 0.9% saline and diluted in deionized water. For consistency with the radiolabeling protocol for biodistribution, Na[^{99m}TcO$_4$] (500 μCi in 100 μL deionized water) was added to a 40 μL assembled

reduction ampoule, vortexed and allowed to equilibrate for 2 minutes at 25°C. The entire contents of the ampoule were then combined with a solution of G4-[[[[Ac]-TIBA]-DTPA]-mPEG$_{12}$] (20 mg dissolved in 600 μL sterile 1x PBS), vortexed and allowed to equilibrate and chelate for 10 minutes at 25°C. For consistency with the radiolabeling protocol for SPECT/CT, Na[^{99m}TcO$_4$] (500 μCi in 50 μL deionized water) was added to a 20 μL assembled reduction ampoule, vortexed and allowed to equilibrate for 2 minutes at 25°C. The entire contents of the ampoule were then combined with a solution of G4-[[[[Ac]-TIBA]-DTPA]-mPEG$_{12}$] (50 mg dissolved in 250 μL sterile 1x PBS), vortexed and allowed to equilibrate and chelate for 10 minutes at 25°C. In this particular preparation, the resulting chelation solution was diluted 1:2 in sterile 1x PBS to a final volume of 100 μL to avoid column saturation. As a control for column retention, 500 μCi Na[^{99m}TcO$_4$] in 100 μL deionized water was combined with 600 μL of sterile 1x PBS. Following chelation, 100 μL of the Na[^{99m}TcO$_4$] solution and the chelation solutions of ^{99m}Tc to G4-[[[[Ac]-TIBA]-DTPA]-mPEG$_{12}$] were aliquotted to a 0.5 mL Zeba desalting spin-column (equilibrated with sterile 1x PBS) and centrifuged at 4000 rpm for 1 minute. Following centrifugation, an additional 200 μL was delivered to the column and centrifuged again at 4000 rpm for 1 minute to minimize column losses. The inherent radioactivity of the filtrate and the column retenate were measured for the doses of Na[^{99m}TcO$_4$] and ^{99m}Tc to G4-[[[[Ac]-TIBA]-DTPA]-mPEG$_{12}$] in PBS using a ^{99m}Tc dose calibrator (Table SI.1). To validate the sensitivity of this method, Na[^{99m}TcO$_4$] was serially diluted and the linear range of the dose calibrator was assessed (Figure SI.4).

Dose	$Na[TcO_4]$	^{99m}Tc-G4 construct (Biodistribution)	^{99m}Tc-G4 construct (SPECT/CT)
Dose applied to Zeba Spin column (μCi)	80	72	77
Dose in column retenate (μCi)	78	14	15
Dose in column filtrate (μCi)	0	55	60
Radiopurity	n/a	79.7%	80.0%

Table SI.1. Assessment of radiopurity.

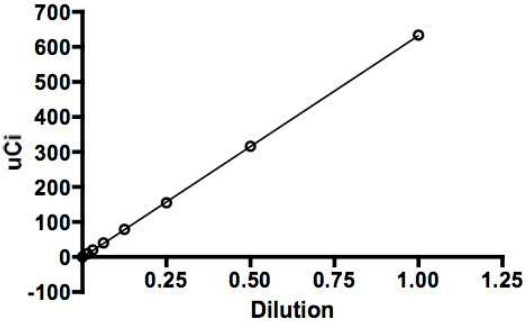

Figure SI.4. Dose calibrator response calibration. $Na[^{99m}TcO_4]$ was serially diluted into 1x PBS and the radioactivity for the ^{99m}Tc energy window was measured and plotted against the dilution factor to determine the limits of detection.

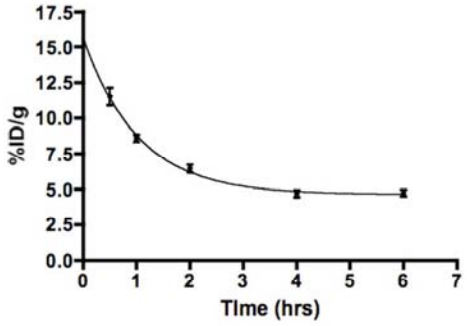

Figure SI.5. Evaluation of the pharmacokinetics of ^{99m}Tc-labeled G4-[[[[Ac]-TIBA]-DTPA]-mPEG$_{12}$]. Mono-exponential curve fitting of the blood clearance curve (r^2=0.9409), revealed a circulation half-life of 0.72 hours.

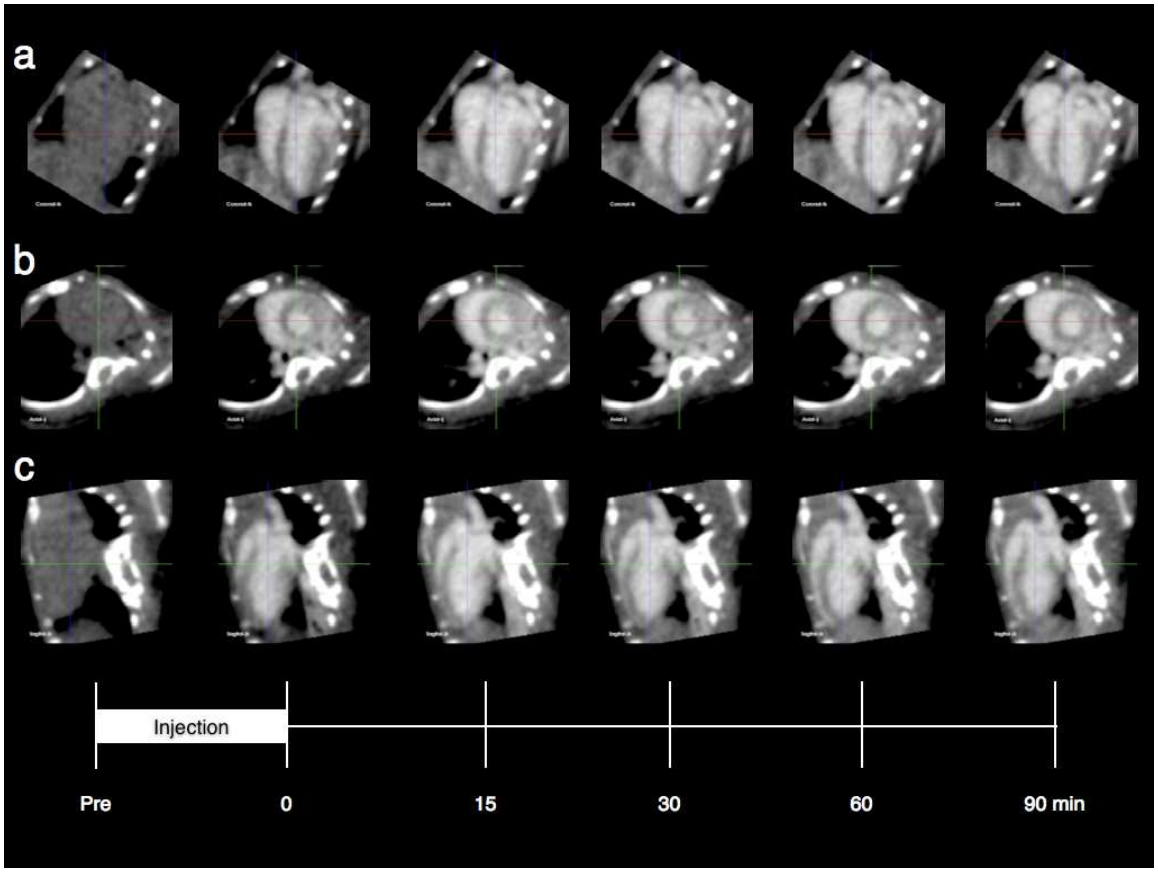

Figure SI.6. Serial cardiac microCT imaging. Following acquisition of a pre-contrast image and subsequent intravenous jugular vein injection of 50 mg of G4-[[[[Ac]-TIBA]-DTPA]-$mPEG_{12}$] dissolved in 0.3 mL sterile 1x PBS (10 minute duration), serial (a) horizontal long axis, (b) short axis and (c) vertical long axis images of the RV/LV blood pool showing significant contrast enhancement were acquired from 0-90 minutes post-injection.

Bioconjugate Chemistry

ARTICLE

pubs.acs.org/bc

High-Yielding Aqueous ^{18}F-Labeling of Peptides via Al^{18}F Chelation

Christopher A. D'Souza,*[,†] William J. McBride,[†] Robert M. Sharkey,[‡] Louis J. Todaro,[§] and David M. Goldenberg*[,‡]

[†]Immunomedics, Inc., 300 American Road, Morris Plains, New Jersey 07950, United States

[‡]Garden State Cancer Center, Center for Molecular Medicine and Immunology, Morris Plains, New Jersey 07950, United States

[§]Hunter College of the City University of New York, New York, New York 10065, United States

Supporting Information

ABSTRACT: The coordination chemistry of a new pentadentate bifunctional chelator (BFC), NODA-MPAA **1**, containing the 1,4,7-triazacyclononane-1,4-diacetate (NODA) motif with a methylphenylacetic acid (MPAA) backbone, and its ability to form stable Al^{18}F chelates were investigated. The organofluoroaluminates were easily accessible from the reaction of **1** and AlF_3. X-ray diffraction studies revealed aluminum at the center of a slightly distorted octahedron, with fluorine occupying one of the axial positions. The *tert*-butyl protected prochelator **7**, which can be synthesized in one step, is useful for coupling to biomolecules on solid phase or in solution. High yield (55−89%) aqueous ^{18}F-labeling was achieved in 10−15 min with a tumor-targeting peptide **4** covalently linked to **1**. Defluorination was not observed for at least 4 h in human serum at 37 °C. These results demonstrate the facile application of Al^{18}F chelation using BFC **1** as a versatile labeling method for radiofluorinating other heat-stable peptides for positron emission imaging.

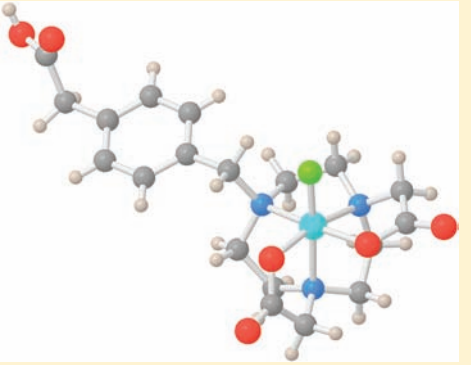

INTRODUCTION

Molecular imaging is the noninvasive visualization of cellular or molecular processes that promises to improve the diagnosis and monitoring of various diseases or conditions.[1,2] The most commonly used molecular imaging modalities include fluorescence, bioluminescence, positron-emission tomography (PET), and single-photon emission computed tomography (SPECT).[3] PET has emerged as a modality of choice because it yields images with good spatial resolution and excellent sensitivity.[4,5] Among the positron-emitting isotopes (^{11}C, ^{13}N, ^{15}O, ^{18}F, ^{68}Ga, ^{89}Zr, ^{124}I), ^{18}F has the advantages of suitable decay properties ($t_{1/2}$ = 109.7 min, ~97% β^+-emission, 635 keV), low β^+-trajectory (<2 mm), and small atomic size and is readily produced from a stable heavy atom (^{18}O) precursor.[6,7] Currently, one of the most widespread applications of PET/CT is the measurement of glucose metabolism using ^{18}F-fluorodeoxyglucose (^{18}F-FDG).[8] Radiofluorination traditionally has involved C−^{18}F bond formation that is performed in anhydrous polar aprotic solvents at 80−160 °C via S_N2 or S_NAr mechanism.[9−11] Although the aryl C−^{18}F bonds are generally stable in vivo, the aliphatic C−^{18}F is often prone to enzymatic cleavage. C−^{18}F bonds have also been introduced by the direct electrophilic addition of molecular fluorine ($^{18}F_2$) across double bonds.[12] New radiolabeling chemistries utilizing the fluorides of phosphorus, silicon, and boron have been explored.[13−15]

We previously reported a technique that exploits the fluorophilic nature of aluminum to afford direct aqueous ^{18}F-labeling by the formation of stable aluminum fluoride chelates.[16] Initial studies involved two chelation systems, the acyclic BFC diethylenetriaminepentaacetic acid (DTPA) and the macrocyclic BFC 1,4,7-triazacyclononane-1,4,7-triacetic acid (NOTA). While the former had excellent binding kinetics, its complexes were not stable, being prone to hydrolysis and demetalation in serum, whereas the NOTA derivative formed highly stable Al^{18}F complexes.[16]

The hexadentate *p*-SCN-Bn-NOTA was used to synthesize IMP449 (Figure 1), a hapten-peptide for in vivo targeting of cancer with a bispecific antibody (bsMAb) pretargeting system, a

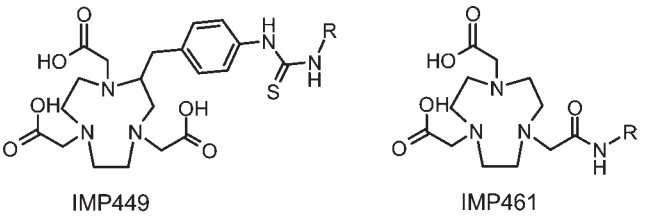

Figure 1. Structures of IMP449 and IMP461.

Received: April 5, 2011
Revised: July 26, 2011
Published: July 30, 2011

 © 2011 American Chemical Society

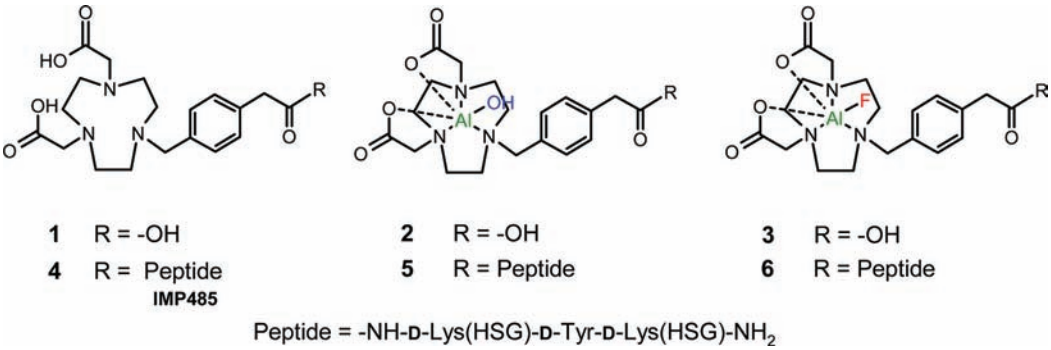

Figure 2. Structures of NODA-MPAA, IMP485, and their aluminum complexes.

highly sensitive and specific technique for localizing cancer.[17−19] Although the $Al^{18}F$(IMP449) was stable in vivo and displayed excellent tumor to blood (T/B) ratios, radiochemical yields (RCYs) were low (5−20%).[16] This could be due to the participation of all three *N*-acetate arms of the N_3O_3 donor set in the complexation, resulting in a restricted coordination site for binding ^{18}F. To address this issue, we synthesized IMP461 (Figure 1), a similar hapten-peptide with NOTA attached via one of its *N*-acetates, and obtained stable complexes, indicating that it was possible to diminish denticity without significant loss of ligand effectiveness.[20,21] This prompted us to focus on pentadentate derivatives of 1,4,7-triazacyclononane (TACN) that could form mononuclear octahedral complexes with aluminum and possess a single coordination site for binding fluorine. Herein, we report the coordination chemistry of a new pentadentate ligand **1**, containing the 1,4,7-triazacyclononane-1,4-diacetate motif, and its ability to form physiologically stable $Al^{18}F$-labeled chelates when covalently linked to a hapten-peptide (IMP485) **4** via an amide bond (Figure 2). These results establish the broad applicability of this chemical strategy in the development of ^{18}F-labeled biomolecules useful for PET imaging.

RESULTS

The reaction of **1** (Figure 2) with Al^{3+} was studied in the presence of $^{19}F^-$. Reacting equimolar amounts of $AlCl_3$ and **1** at 104 °C for 10 min yields a polar chelate **2** with retention time (t_R) of 8.98 min (Figure 3A). With equimolar amounts of NaF, $AlCl_3$, and **1**, the $Al^{19}F$ complex **3** (13.8%) was obtained, with t_R = 12.29 min (Figure 3B), along with **2** and unreacted **1**. Since $AlCl_3$ and NaF readily react[22] to produce $AlF_n^{(3-n)+}$, we investigated the reaction between AlF_3 and **1**. Although the AlF_3 remained as a fine suspension in the 2 mM AlF_3 solution, we reacted it with **1** at 105 °C for 10 min and obtained a low yield (4.3%) of **3** (Figure 3C). Suspecting that a hydrophilic organic solvent might better solubilize AlF_3, we carried out the reaction in the presence of 50 μL of methanol, which increased the yield of **3** to 27.7% (Figure 3D). Subsequent experiments revealed that the presence (50% or more v/v) of other hydrophilic organic solvents (e.g., acetonitrile, ethanol, *n*-propanol, isopropanol, *tert*-butyl alcohol, acetone, dioxane, tetrahydrofuran, dimethylsulfoxide, or dimethyl formamide) also improved the yield of **3**.

The next study determined if fluoride, which is bioisosteric with both the hydrogen atom and the hydroxyl group, could displace the hydroxide from **2**. When equimolar amounts of **2** and NaF were reacted at 100 °C for 10 min, a mixture containing **3** (32.3%) along with **1** and **2** (Figure 3E) was obtained, indicating a possible substitution mechanism, accompanied by demetalation. When the above reaction was performed in the presence of ethanol, we obtained a 2-fold increase in the yield of **3** (Figure 3F).

To determine their stability and structural features, **2** and **3** were synthesized by reacting **1** with $AlCl_3$ or AlF_3, respectively (Scheme 1). When the $Al^{19}F$ chelate **3** was incubated in PBS, pH 7.4, at 37 °C, no detectable loss of aluminum was observed by RP-HPLC after 24 h. However, the corresponding Al−OH chelate **2** was not as stable under the same conditions, undergoing progressive demetalation (e.g., 23% in 3 h, 61% in 12 h; see Supporting Information, Table S1).

The HRMS of **1** $(M + H)^+$ 394.20 and that of **3** with $(M + H)^+$ 438.16 confirm the presence of an aluminum fluoride complex (see Supporting Information, Figure S1). The mass spectrum of **2** has molecular ion peak $(M + H)^+$ 436.17 of low abundance, the parent peak being 418.16, molecular ion minus hydroxide, indicating that the sixth coordination site is occupied by hydroxide instead of chloride.

In the uncomplexed BFC **1**, the N−CH_2−Ph and Ph−CH_2−COOH protons appear as singlets at δ 4.32 and δ 3.61 (Figure 4A). Upon coordination with aluminum fluoride, the N−CH_2−Ph protons are split into a pair of doublets at δ 4.24 and δ 3.74 ppm. The region from δ 2.24 to 3.51 ppm is crowded, with several overlapping multiplets arising because of the splitting of the 12 N−CH_2−CH_2−N ring and 4 N−CH_2−COO^- protons, along with dissolved water (δ 3.3 ppm) molecules in DMSO-d_6 (Figure 4B). These multiplet patterns arise from ring conformational interconversions, which are not so rapid to hinder isomer detection by NMR spectroscopy.[23]

Monohydrated single crystals of **3** suitable for X-ray crystallography were grown from a concentrated solution of acetonitrile containing traces of water. The intensity data for **3** were measured on a Bruker-Nonius KappaCCD diffractometer (graphite-monochromated Mo Kα radiation, λ = 0.710 73 Å, $\phi-\omega$ scans) at 100 (1) K. The data were corrected for absorption. The single-crystal X-ray crystallography (Figure 5) reveals that **3** crystallizes with approximate dimensions of 0.060 mm × 0.080 mm × 0.52 mm and were monoclinic with space group $P2_1/c$. The final unit-cell constants of **3** were a = 20.463(4) Å, b = 8.495(2) Å, c = 12.692(3) Å, β = 107.52(3)°, V = 2103.9(7) Å^3, Z = 4, ρ = 1.438 g cm^{-1}, μ = 0.15 mm^{-1}, formula weight of 1821.66. The structure of **3** was solved with SHELXS-97 and refined by full-matrix least-squares on F^2 with SHELXL-97. The hydrogen atoms were calculated with the riding model in the structure-factor calculations, but their parameters were not refined. The final discrepancy indices, 2.93° < θ < 27.48°, were R = 0.0601 (calculated on F for 3241 reflections) and R_w = 0.1374

dx.doi.org/10.1021/bc200175c |*Bioconjugate Chem.* 2011, 22, 1793–1803

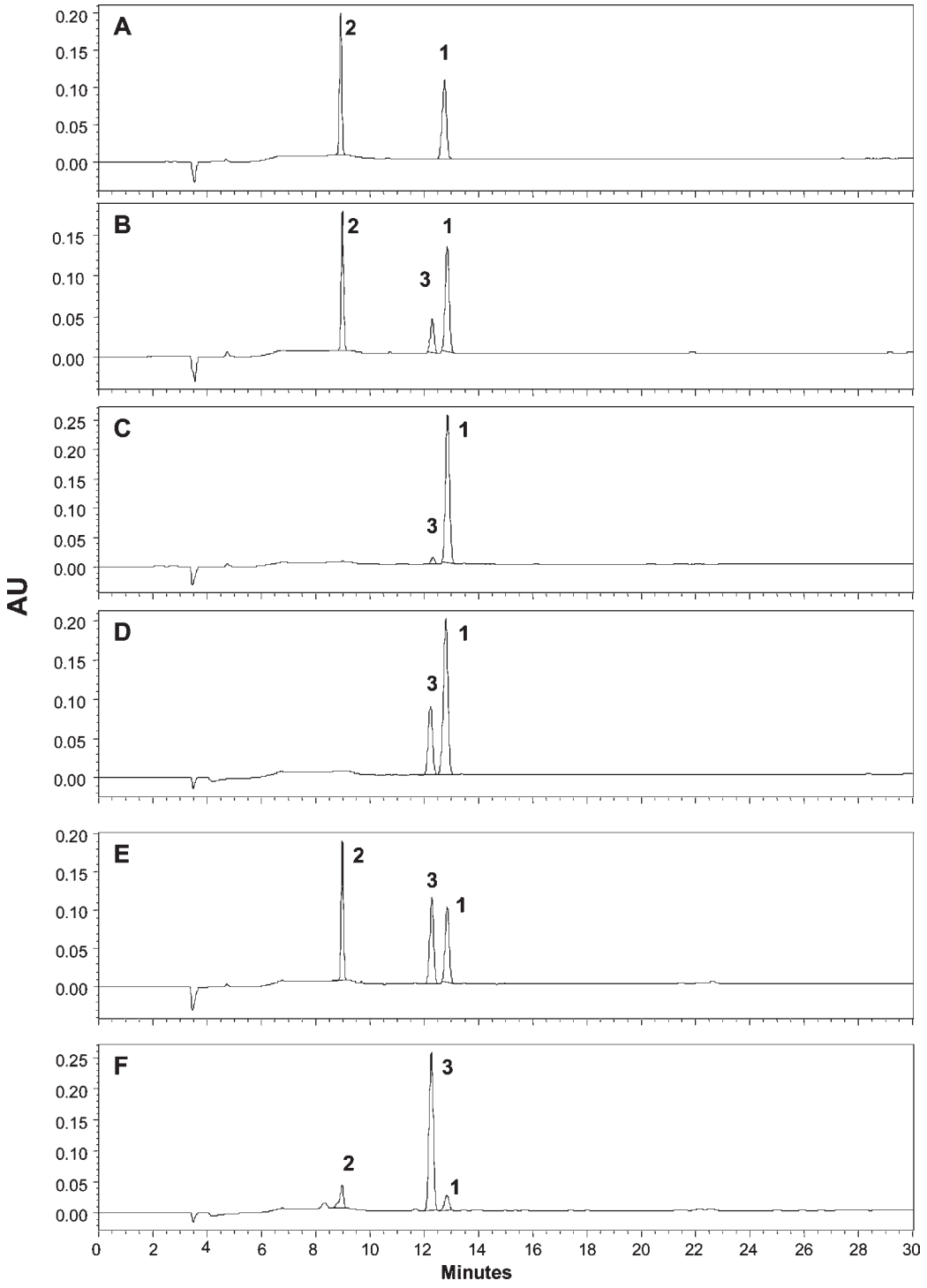

Figure 3. HPLC chromatograms using method **1**: (A) $AlCl_3$ with **1**; (B) $AlCl_3$ + NaF with **1**; (C) AlF_3 with **1**; (D) AlF_3 with **1** in the presence of MeOH; (E) NaF with **2**; (F) NaF with **2** in the presence of EtOH.

(calculated on F^2 for all 4812 reflections) with 281 parameters varied. The major peaks of the final difference map, −0.39 and +0.32 e Å^3, are near the aluminum atom. For crystallographic data (Table S2) and CIF file, see Supporting Information.

We next turned to examining radiolabeling yields using $^{18}F^-$ in saline. When a mixture of NODA-MPAA **1** (10 μL, 20 nmol), $AlCl_3$ (5 μL, 10 nmol), and 40 μL of $^{18}F^-$ (1.326 mCi) in 0.9% saline were reacted at 101 °C for 15 min, decay corrected RCY postpurification by solid-phase extraction (SPE) based on $^{18}F^-$ was 6.9%. With 50 μL of ethanol as cosolvent, RCY increased to 52.8%, validating our results with $^{19}F^-$. When the Al−OH chelate **2** (10 μL, 20 nmol) was reacted with 45 μL of $^{18}F^-$ in 0.9% saline at 101 °C for 15 min, in the absence and presence of ethanol, decay corrected RCYs were 29.6% and 63.9%, respectively.

Having established the suitability of NODA-MPAA for radiofluorination, the next studies focused on the radiolabeling of the

Scheme 1. Reaction of 1 with $AlCl_3$ and AlF_3

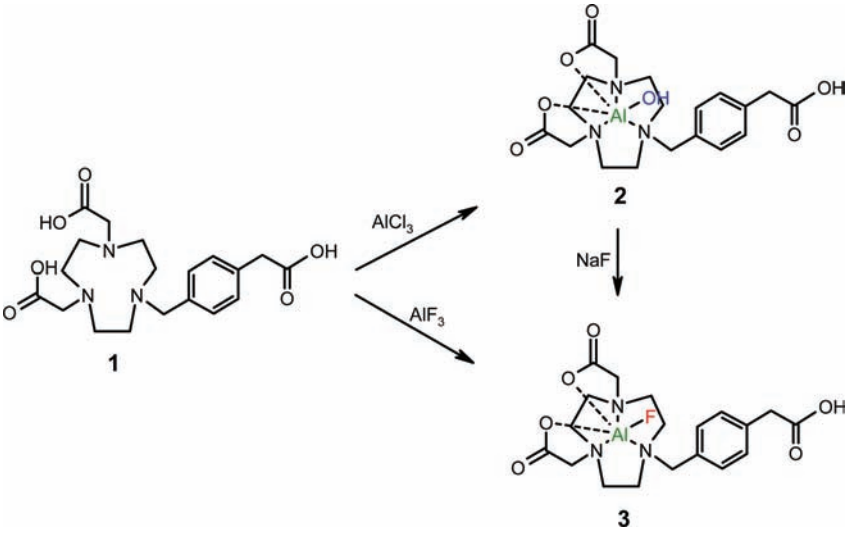

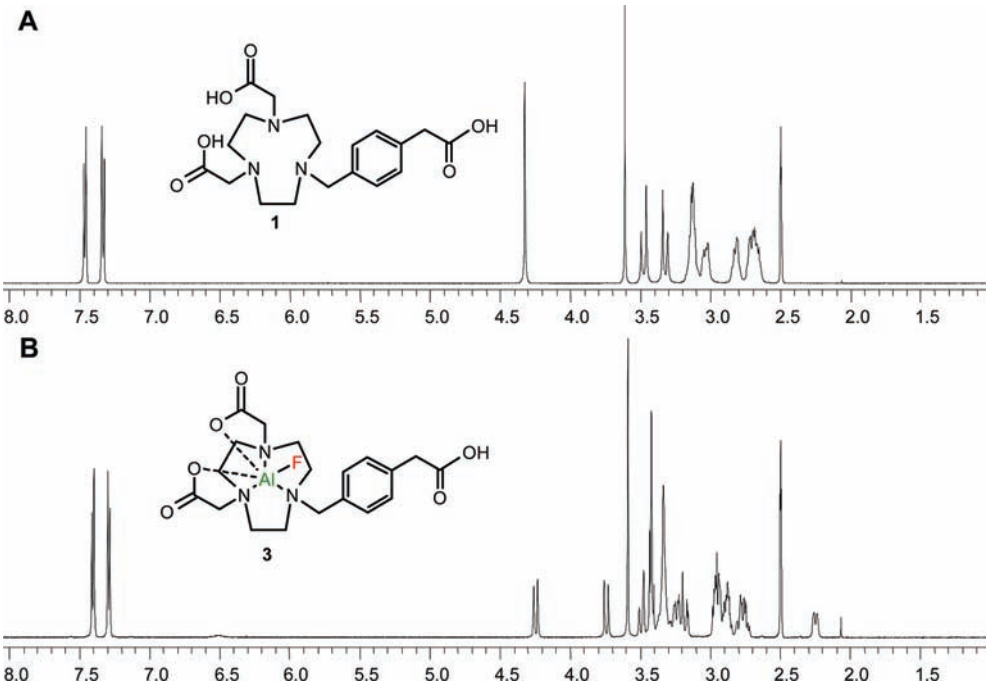

Figure 4. ^{1}H NMR of **1** and **3** in DMSO-d_6 at room temperature (500 MHz).

NODA-MPAA pretargeting hapten-peptide IMP485 **4**. Under the conditions shown in Table 1, RCYs increased from ~24% in aqueous conditions to 75−90% in the presence of ethanol and increasing amounts of $Na^{18}F$. A 2-fold increase in RCYs was also observed in the presence of other hydrophilic organic solvents (Table 2). The radio-HPLC chromatogram (method 2) of the SPE-purified peptide $Al^{18}F$(IMP485) shows a single peak with t_R = 15.789 min (Figure 6A), while the cold standard $Al^{19}F$-(IMP485) appears at 15.620 min (Figure 6B). There was no evidence of defluorination when $Al^{18}F$(IMP485) was incubated in human serum at 37 °C for 4 h (see Supporting Information, Figure S3). Efficient radiofluorination (decay corrected RCY of 72.3%, 1.28 Ci/μmol) was observed when a solution of AlOH(IMP485) **5** (10 μL, 20 nmol), 110 μL of ethanol, and 100 μL of $^{18}F^-$ (43.3 mCi) in 0.9% saline were reacted at 105 °C for 15 min (Table 3). Under identical conditions, labeling efficiency of IMP485 **4** was consistently higher than that observed with the NOTA-derived hapten-peptides IMP449 and IMP461 (see Supporting Information, Table S3−S5).

DISCUSSION

With the availability of compact cyclotrons, automated chemical modules, and microreactors, PET imaging using ^{18}F has become the modality of choice for molecular imaging of many small molecules.[24] Almost 90% of all clinical PET imaging is

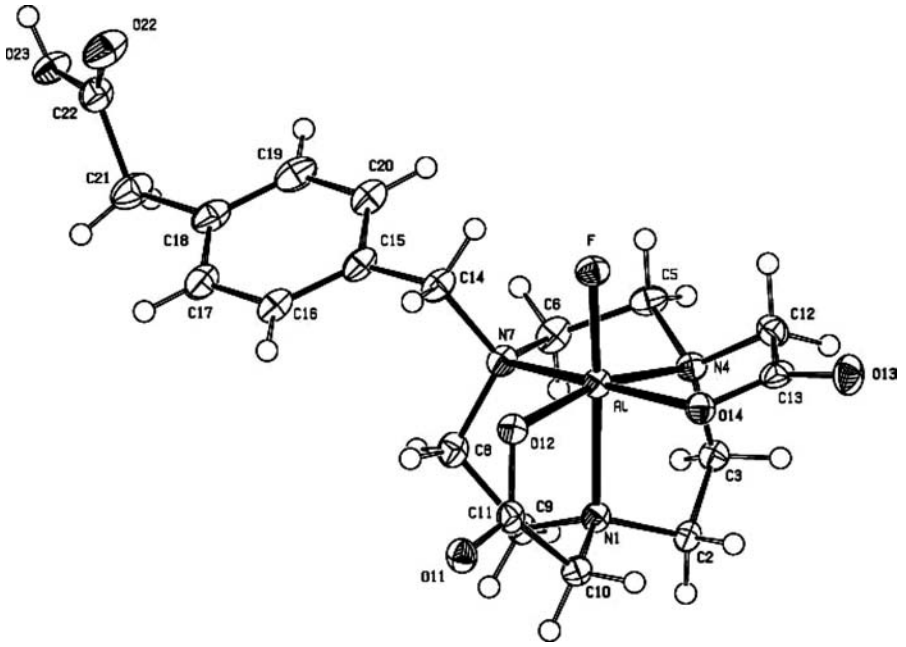

Figure 5. X-ray crystal structure of $Al^{19}F$(NODA-MPAA) **3**.

Table 1. ^{18}F-Labeling of 20 nmol of IMP485 + 10 nmol of Al^{3+} with Varying Amounts of $Na^{18}F$

activity[a] $Na^{18}F$ (mCi)	aqueous (μL)	ethanol (μL)	isolated activity[b] (mCi)	RCY[c] (%)
1.02	50	0	0.21	23.9
0.92	50	50	0.60	79.9
3.20	50	50	2.35	89.3
6.20	50	50	4.42	86.7
12.34	100	100	8.35	84.4
34.60	115	110	20.3	74.1[d]

[a] 10 μL of IMP485, 5 μL of Al^{3+}, 105−110 °C, 15 min. [b] Isolated activity in (1:1) EtOH/H_2O after HLB column purification (SPE). [c] Decay corrected RCY, based on synthesis time of 31−37 min. [d] Specific activity: 1.01 Ci/μmol.

Table 2. Effect of Solvent on the ^{18}F-Labeling of IMP485

activity[a] $Na^{18}F$ (mCi)	solvent (50 μL)	isolated activity[b] (mCi)	RCY[c] (%)
1.416		0.516	43.5
1.326	EtOH	1.006	89.4
1.206	DMF	0.886	86.5
1.608	DMSO	1.152	86.0
1.246	CH_3CN	0.966	91.3

[a] 35−50 μL of $Na^{18}F$, 10 μL of IMP485, 5 μL of Al^{3+}, 105 °C, 15 min. [b] Isolated activity in (1:1) EtOH/H_2O after HLB column purification (SPE). [c] Decay corrected RCY, based on synthesis time of 26−29 min.

performed using ^{18}F-FDG. The other 10% includes agents like ^{18}F-NaF used for bone imaging; ^{18}F-FLT, ^{18}F-choline, and ^{18}F-FET in oncology; and ^{18}F-fallypride, ^{18}F-DOPA, and ^{18}F-altanserin in neurosciences.[25] Despite its popularity, FDG cannot be used for many neurological, oncological, and cardiological conditions, making it imperative to seek other compounds.[26] There are numerous receptor-avid biomolecules, like folate, biotin, bombesin (BBN), gastrin-releasing peptide (GRP), RGD, somatostatin, antibodies, peptides, and proteins, which possess high specificity and affinity.[27,28] Development of a facile method of tagging these molecules with ^{18}F would enhance their utility in the detection of pathologically distinct cellular targets. Most ^{18}F-labeling methods are tedious to perform and require the efforts of specialized chemists. Multiple purifications of intermediates are commonly required, resulting in low RCYs. Additionally, ^{18}F-labeling involving C−^{18}F bond formation, which is employed in all clinically approved ^{18}F-labeled products, requires anhydrous conditions.[29] The newer labeling strategies, involving B−^{18}F and Si−^{18}F bond formation, have shown promise but suffer from the disadvantage of rather high lipophilicity of the building block,[30,31] a property that can enhance hepatobiliary clearance in vivo. An ideal method is one in which a peptide could be labeled rapidly in the final step with high specific activity in an aqueous medium.

With experience gained in rapid and quantitative binding of various radiometals with chelates and with the knowledge that $^{18}F^-$ avidly binds to Al^{3+}, we initiated a project to determine whether a stable $Al^{18}F$ complex could be formed with peptides coupled with an appropriate BFC. Our initial studies were performed with peptides covalently linked to the hexadentate *p*-SCN-Bn-NOTA and NOTA (Figure 1) via one of its *N*-acetates.[16,21] These peptides yield highly stable $Al^{18}F$-chelates (in vitro and in vivo) but with low RCYs. We rationalized that with a hexadentate ligand, one of the pendent carboxylates might not participate in the complexation, and the presence of uncoordinated donor atoms potentially could impose steric constraints on the coordinated ligand framework, resulting in isomerism and/or instability. We then set out to synthesize a BFC that could form mononuclear octahedral complexes with aluminum, leaving a vacant site for binding fluorine. Since TACN-derived BFCs are suitable for Al^{3+} (0.53 Å), we decided

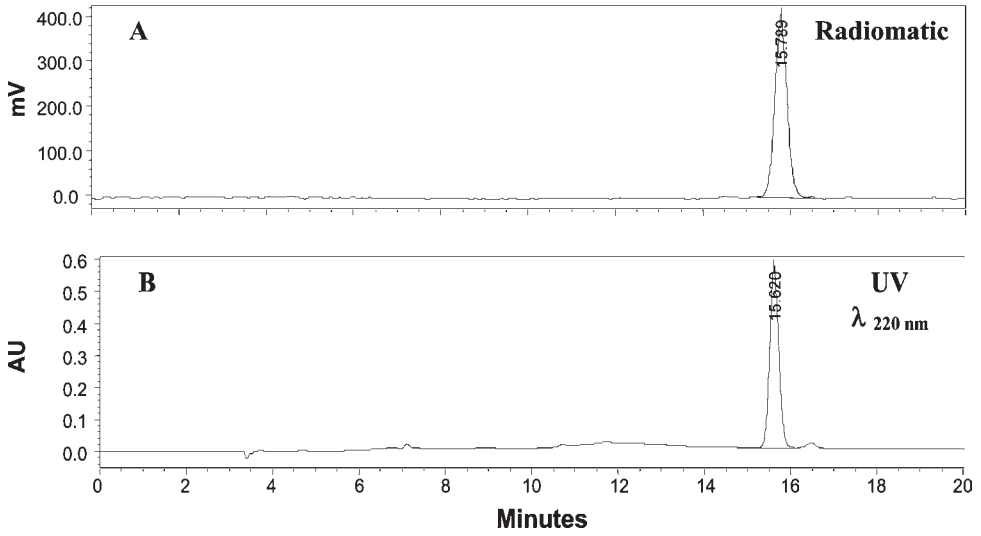

Figure 6. HPLC chromatograms: (A) SPE-purified $Al^{18}F$(IMP485); (B) $Al^{19}F$(IMP485).

Table 3. ^{18}F-Labeling of 20 nmol of AlOH(IMP485) with Varying Amounts of $Na^{18}F$

activity[a] $Na^{18}F$ (mCi)	aqueous (μL)	ethanol (μL)	isolated activity[b] (mCi)	RCY[c] (%)
3.51	70		1.019	36.4
3.34	70	100	2.21	83.6
4.07	60	75	2.44	73.8
43.3	110	110	25.6	72.3[d]

[a] 10 μL of AlOH(IMP485), 105 °C, 15 min. [b] Isolated activity in (1:1) EtOH/H_2O after HLB column purification (SPE). [c] Decay corrected RCY, based on synthesis time of 32−37 min. [d] Specific activity: 1.28 Ci/μmol.

to use NO2A*t*Bu with two pendent *N*-acetate arms as our building block. BFCs with pendent *N*-acetates are common, since they do not affect the molecular weight significantly and their high hydrophilicity favors rapid renal clearance. The pentadentate NODA-MPAA **1**, with its N_3O_2 donor set, was chosen because the *tert*-butyl protected prochelator **7** can be synthesized by one simple alkylation (Scheme 2). The methylphenylacetic acid (MPAA) backbone acts as a spacer and makes for easy linkage to biomolecules on solid phase or in solution.

The X-ray structure (Figure 5) confirms the ability of **1** to form an $Al^{19}F$ monohydrated complex, with the MPAA backbone distanced from the coordination sphere. The complex is neutral with aluminum located at the center of a slightly distorted octahedron, as evidenced by the deviation of the 12 quasi-orthogonal and 3 linear bond angles, from the ideal angles of 90° and 180° in a regular octahedron. The average of these 12 quasi-orthogonal angles and that of the three linear bond angles are 89.89° and 169.60°, respectively (Table 4). The two TACN ring nitrogens and two oxygens, one from each pendent carboxylate, lie in the equatorial plane. One axial plane is occupied by the third nitrogen of TACN, while the fluorine lies in the opposite axial position, completing the octahedral coordination sphere. The diversity of the bond distances between the aluminum and the heteroatoms N1, N4, N7, O12, O14, and F also contributes to the asymmetry of the aluminum coordination sphere. The Al−N4 bond is significantly shorter (2.036 Å) compared to the Al−N1 (2.074 Å) and Al−N7 (2.080 Å) bonds, while the Al−O14 (1.875 Å) and Al−O12 (1.854 Å) bond lengths are also slightly different. The longer Al−N1 (2.074 Å) bond could be a reflection of the high affinity of the *trans* fluoro ligand for aluminum. In comparison with the crystallized Al(NOTA), with Al−N and Al−O bond lengths of 2.06 and 1.84 Å, respectively,[32] the small difference in the average Al−N (2.063 Å) and Al−O (1.865 Å) bond lengths in **3** indicates that aluminum is strongly coordinated by the N_3O_2 donor set.

When incubated in PBS, pH 7.4, at 37 °C, $Al^{19}F$(NODA-MPAA) **3** was stable for over 24 h, while the corresponding Al−OH chelate **2** underwent demetalation to the extent of 23% in 3 h (see Supporting Information, Table S1). The fact that **3** did not undergo demetalation was gratifying, since a stable $Al^{18/19}F$ chelate is our most important prerequisite. It was interesting to note that fluoride, which is bioisosteric with both the hydrogen atom and the hydroxyl group, could displace the hydroxide from **2** (Figure 3E). The driving force for this reaction may be the formation of the strong Al−F bond (580−670 kJ/mol) in the product.

We believe that the improved labeling efficiency with peptides covalently linked to NODA-MPAA is due to the presence of a N_3O_2 donor set that can form stable mononuclear octahedral complexes with aluminum and possess a single coordination site for binding fluorine. The N_3O_3 donor set (hexadentate) of TACN derivatives like NOTA provides a suitable environment for the formation of highly stable aluminum chelates.[23] Low RCYs with IMP449 (N_3O_3 donor set) may result from the coordination sphere of aluminum being saturated, with limited access for fluorine. A similar situation, although with less restriction, could occur with IMP461, because of the participation of the amido oxygen in the complexation. Under identical conditions, RCYs were higher with IMP485 when compared to IMP449 and IMP461 (see Supporting Information, Tables S3−S5). These results suggest that pentadentate ligands with a free site for binding fluorine are ideal for stable $Al^{18}F$ chelation.

The $^{18}F^-$ produced in the cyclotron comes out as a dilute solution in $H_2{}^{18}O$ and is generally contaminated with metals from the target cell. Since our ^{18}F-labeling method involves the use of a BFC, the presence of competing metal ions would hamper

Scheme 2. Synthesis of NODA-MPAA 1 and (tBu)$_2$NODA-MPAA 7

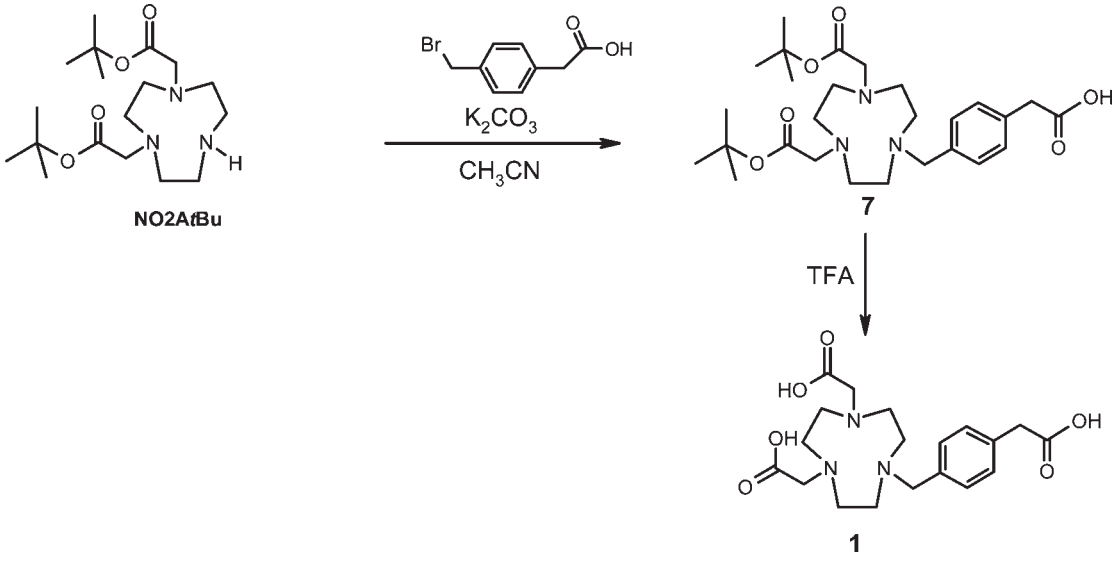

Table 4. Bond Lengths (Å) and Bond Angles (deg) for Complex 3

bond length (Å)		bond angle (deg)	
Al−F	1.714 (1)	F−Al−N1	176.2 (1)
Al−O12	1.854 (2)	F−Al−N4	96.8 (1)
Al−O14	1.875 (2)	F−Al−N7	91.8 (1)
Al−N1	2.074 (2)	F−Al−O12	97.7 (1)
Al−N4	2.036 (2)	F−Al−O14	93.3 (1)
Al−N7	2.080 (2)	O12−Al−O14	95.6 (1)
N1−C2	1.487 (3)	O12−Al−N1	82.6 (1)
N1−C9	1.506 (3)	O12−Al−N4	165.4 (1)
N1−C10	1.482 (3)	O12−Al−N7	95.3 (1)
N4−C3	1.505 (3)	O14−Al−N1	90.4 (1)
N4−C5	1.492 (3)	O14−Al−N4	83.3 (1)
N4−C12	1.483 (3)	O14−Al−N7	167.2 (1)
N7−C6	1.504 (3)	N1−Al−N4	82.9 (1)
N7−C8	1.496 (3)	N1−Al−N7	84.5 (1)
N7−C14	1.594 (2)	N4−Al−N7	84.4 (1)

effective labeling.[33] Initial labeling studies were performed with $^{18}F^-$ that was bound onto a (anion exchange resin) QMA cartridge, eluted with 0.4 M $KHCO_3$, followed by neutralization of the $KHCO_3$ with acetic acid. With pH being an important parameter for radiofluorination, inconsistencies in the neutralization resulted in varying RCYs. Recently, we found that QMA-bound $^{18}F^-$ could be eluted with 0.9% saline and used without making any pH adjustments.[20] Subsequently, we obtained high RCYs with the commercially available USP grade $Na^{18}F$, an approved bone-imaging agent.[34] This was convenient, since it eliminated the concentration, purification, and dry-down steps associated with other ^{18}F-labeling methods.

We also demonstrate herein two routes to synthesize the ^{18}F-labeled peptide: either heat the hapten-peptide (IMP485) **4** and Al^{3+} with commercially available $^{18}F^-$ in saline or synthesize the peptide−aluminum complex **5** and react it with $Na^{18}F$ (see Supporting Information, Scheme S1). The latter approach is attractive, since it is based on the reaction of a single reactant with $Na^{18}F$, eliminating any speculation regarding peptide to Al^{3+} ratios or inadvertently not adding any Al^{3+}. One of the key findings during the development of this methodology was that the presence of an added hydrophilic organic cosolvent (generally 50% or more v/v) doubled the RCYs (Table 2). However, ethanol was the cosolvent of choice for most of our subsequent radiofluorinations, since it is biocompatible and has the added advantage of preventing radiolysis.[35] On the basis of these findings, we explored the possibility of developing a single-vial kit, requiring only the addition of $^{18}F^-$ in saline.[36] These studies included an examination of the effects of temperature, reaction time, pH, amount of peptide, peptide to Al^{3+} ratio, and reaction volume on the radiolabeling efficiency. The development of the lyophilized kit formulation of IMP485, as well as kits for NODA-MPAA derived somatostatin receptor and bombesin binding peptides, will be reported elsewhere.

The theoretical specific activity (SA) of carrier-free $^{18}F^-$ is 1702 Ci/μmol but varies from 8.5 to 1162 Ci/μmol because of isotopic dilution from water, reagents, and reaction vessels.[37] In most clinical applications, 5−10 mCi ^{18}F-labeled product with specific activities of >1 Ci/μmol is required for imaging cellular targets.[38] We recently reported the development of a lyophilized kit formulation containing 20 nmol of IMP485 that has been radiolabeled to a specific activity of ~4 Ci/μmol.[36] This would allow for 4 h from start of radiolabeling to the injection of the patient to retain a SA of 1 Ci/μmol. When the reaction mixture is purified by SPE, one has to bear in mind that the product is a mixture consisting of unlabeled material (IMP485) **4** plus AlOH(IMP485) **5**, with $Al^{18/19}F$-labeled product. As seen in the Supporting Information Figures S4 and S5, excellent separation of $Al^{19}F$(IMP485) **6** from (IMP485) **4** and AlOH(IMP485) **5** using a C_{18} column is possible. Therefore, the SA could be increased if the postlabeling purification was by RP-HPLC instead of SPE. However, as mentioned earlier, the precise SA of the ^{18}F-labeled product will also depend on the SA of the $^{18}F^-$.[37] Because of the short half-life of ^{18}F, labeling is frequently performed with high levels of radioactivity, and this in turn imposes a requirement that the radiochemistry be performed in an apparatus that is shielded from the operator and is fully

automated.[39] Electrochemical methods, currently being explored for the concentration of no-carrier-added $^{18}F^-$, will help in reducing the reaction volume.[40] We are confident that ^{18}F-labeling via $Al^{18}F$ chelation, particularly using single-vial kits, can be adapted for use in these automated systems and would also benefit from microfluidic technology.[41]

Advancement of an ^{18}F-labeled peptide into the clinic requires that it possesses good in vivo stability, excellent targeting, and favorable excretion profile. Animal studies performed using kit formulated IMP485 have shown rapid clearance from the body via the kidneys with negligible presence in the bone, supporting in vivo stability.[42] To evaluate the true potential of this novel BFC **1**, we have synthesized and ^{18}F-labeled somatostatin receptor-binding and bombesin peptides and are currently investigating their tumor targeting capabilities.

Finally, while we appreciate that ^{18}F-labeling via $Al^{18}F$ chelation is facile, it has only been described for peptides that are stable at high temperatures. Recently, we reported a maleimide derivative of NODA-MPAA that can be ^{18}F-labeled and then coupled with high efficiency to thiol-containing peptides and proteins.[43] This two-step approach opens the possibility for adapting the $Al^{18}F$ chelation to heat-sensitive biomolecules.

CONCLUSIONS

A new pentadentate BFC **1** was synthesized and reacted with AlF_3 to yield an organofluoroaluminate **3**, which was characterized by RP-HPLC, ^1H and ^{13}C NMR, HRMS, and X-ray crystallography. The solid-state X-ray crystal structure of **3** reveals aluminum coordinated by an N_3O_2 donor set, in slightly distorted octahedron geometry, with fluorine occupying one of the axial positions. The stability of **3** was confirmed when it showed no signs of demetalation over 24 h when incubated in PBS, pH 7.4, at 37 °C. The partial solubility of AlF_3 led us to the realization that the addition of a hydrophilic organic cosolvent improves the yield of the organofluoroaluminate. It is interesting to note that the reaction of **1** with $AlCl_3$ and AlF_3 yields two distinct chelates, (Al−OH) **2** and (AlF) **3**, respectively. High yield aqueous radiofluorination was accomplished in a single step by heating a mixture of hapten-peptide **4** and Al^{3+} or the peptide−aluminum complex **5**, with commercially available $^{18}F^-$ in saline. The postlabeling purification method (SPE or RP-HPLC) employed was dictated by specific activity requirements. We hope that this robust, user-friendly ^{18}F-labeling methodology will stimulate the rapid development of new PET tracers for the imaging of disease states.

MATERIALS AND METHODS

General Information. All commercially obtained chemicals were analytical grade and used without further purification. $AlCl_3 \cdot 6H_2O$, NaF, $AlF_3 \cdot 3H_2O$, and 4-(bromomethyl)phenylacetic acid were purchased from Sigma-Aldrich (Milwaukee, WI) and sodium acetate and acetic acid from J. T. Baker (Phillipsburg, NJ). NO2A*t*Bu was purchased from CheMatech (Dijon, France).

Fmoc protected amino acids, Seiber amide resin, and trifluoroacetic acid were obtained from Creosalus (Louisville, KY). The peptides were synthesized using Protein Technologies, Inc. (Tucson, AZ) peptide synthesizer. The analytical and preparative reverse-phase HPLC (RP-HPLC) columns were purchased from Phenomenex (Torrance, CA) and Waters Corp. (Milford, MA). Two millimolar solutions of $AlCl_3$, NaF, AlF_3, and **1** were prepared in 2 mM NaOAc, the pH being maintained in the range 3.8−4.4. Since **1** and **4** displayed a high propensity for complexation with other metals (e.g., copper, gallium, and indium) at room temperature, care was taken to ensure that reactants were prepared in metal free containers. Reactions were performed in sealed 2 mL microcentrifuge tubes with cap and O-ring obtained from Fisher Scientific (Agawan, MA). Radiolabeled peptides were purified using Waters Oasis 1 or 3 cm^3 flangeless cartridges. $^{18}F^-$ in saline was purchased from PETNET (Hackensack, NJ). Solid-phase extraction (SPE) cartridges (Sep-Pak light QMA, Sep-Pak Accell plus CM, and Oasis HLB) were obtained from Waters (Milford, MA). ^1H and ^{13}C NMR spectra were recorded using a Varian Inova NMR spectrometer (Varian, Inc., Palo Alto, CA) at 500 MHz for ^1H and 125.7 MHz for ^{13}C at Rutgers University (Newark, NJ). ^1H NMR spectra are referenced to the tetramethylsilane peak ($\delta = 0$). Product identification was verified by high-resolution mass spectrometry (HRMS) using positive mode electrospray ionization with an Agilent time-of-flight LC−MS instrument at Immunomedics, Inc. (Morris Plains, NJ). X-ray crystallography data were collected on Bruker-Nonius KappaCCD (Mo Kα radiation) diffractometer at Hunter College of the City University of New York (New York, NY). All calculations were performed using Bruker SHELXS-97 software package, while SHELXL-97 was used for refinement.[44]

HPLC Methods. Analytical HPLC was performed using a Waters 2695 system equipped with a Phenomenex Gemini C_{18} reverse-phase column (250 mm × 4.6 mm, 5 μm, 110 Å).

Method 1. Parameters were as follows: gradient of 1 min with 100% A (0.1% TFA), then to 90:10 A/B over 5 min, followed by 85:15 A/B (90% acetonitrile, 10% water, 0.1% TFA) over 30 min at a flow rate of 1 mL/min. Absorbance was detected at 220 and 254 nm using a Waters 2996 photodiode array detector.

Method 2. Parameters were as follows: gradient of 1 min with 100% A (0.1% TFA), then to 90:10 A/B over 5 min, followed by 87:13 A/B (90% acetonitrile, 10% water, 0.1% TFA) over 20 min at a flow rate of 1 mL/min. Absorbance was detected at 220 and 254 nm using a Waters 2996 photodiode array detector. The column effluent was monitored using a Perkin-Elmer 610TR radiomatic flow scintillation analyzer.

Method 3. Parameters were as follows: linear gradient of 100% C (H_2O) to 30% D (50% ethanol) over 20 min at a flow rate of 1 mL/min. Absorbance was detected at 220 and 254 nm using a Waters 2996 photodiode array detector.

Method 4. Products were purified using a Waters PrepLC 4000 system with Sunfire Prep C_{18} OBD reverse-phase column (150 mm × 30 mm, 5 μm), using a linear gradient of 100% A (0.1% TFA) to 15% B (90% acetonitrile, 10% water, 0.1% TFA) over 80 min at a flow rate of 45 mL/min. Absorbance was detected at 220 nm using a Waters 486 tunable absorbance detector.

Method 5. Product was purified using a Waters PrepLC 4000 system with Sunfire Prep C_{18} OBD reverse-phase column (150 mm × 30 mm, 5 μm), using a linear gradient of 100% A (0.006 N HCl) to 100% B (acetonitrile) over 60 min at a flow rate of 45 mL/min. Absorbance was detected at 220 nm using a Waters 486 tunable absorbance detector.

Synthesis of the BFCs. *2-(4-(Carboxymethyl)-7-{[4-(carboxymethyl)phenyl]methyl}-1,4,7-triazacyclononan-1-yl) acetic Acid [H_2L] (**1**) (NODA-MPAA).* To a solution of 4-(bromomethyl)phenylacetic acid (15.7 mg, 0.68 mmol) in anhydrous CH_3CN at 0 °C was added dropwise over 20 min a solution of NO2A*t*Bu (26 mg, 0.73 mmol) in CH_3CN (5 mL). After 2 h, anhydrous K_2CO_3 (5 mg) was added to the reaction mixture, and the mixture was allowed to stir at

room temperature overnight. Solvent was evaporated, and the concentrate was acidified with 2 mL of TFA. After 3 h, the reaction mixture was diluted with water and purified by preparative RP-HPLC (method 4) to yield a white solid (11.8 mg, 43.7%). ^{1}H NMR (500 MHz, DMSO-d_6, 25 °C) δ 2.65−3.13 (m, 12 H), 3.32 (d, 2H), 3.47 (d, 2H), 3.61 (s, 2 H), 4.32 (s, 2 H), 7.33 (d, 2H), 7.46 (d, 2H); ^{13}C (125.7 MHz, DMSO-d_6) 40.8, 47.2, 49.6, 50.7, 55.2, 58.1, 130.4, 130.5, 130.9, 136.6, 158.4, 158.7, 172.8, 172.9. HRMS (ESI) calculated for $C_{19}H_{27}N_3O_6$ $(M + H)^+$ 394.1973; found 394.1979.

*2-{4-[(4,7-Bis-tert-butoxycarbonylmethyl)[1,4,7]-triazacyclononan-1-yl)methyl]phenyl}acetic Acid (**7**).* To a solution of 4-(bromomethyl)phenylacetic acid (593 mg, 2.59 mmol) in anhydrous CH_3CN (50 mL) at 0 °C was added dropwise over 1 h a solution of NO2A*t*Bu (1008 mg, 2.82 mmol) in CH_3CN (50 mL). After 4 h, anhydrous K_2CO_3 (100.8 mg, 0.729 mmol) was added to the reaction mixture, and the mixture was allowed to stir at room temperature overnight. Solvent was evaporated and the crude was purified by preparative RP-HPLC (method 5) to yield a white solid (713 mg, 54.5%). ^{1}H NMR (500 MHz, $CDCl_3$, 25 °C, TMS) δ 1.45 (s, 18 H), 2.64−3.13 (m, 16 H), 3.67 (s, 2 H), 4.38 (s, 2 H), 7.31 (d, 2H), 7.46 (d, 2H); ^{13}C (125.7 MHz, $CDCl_3$) δ 28.1, 41.0, 48.4, 50.9, 51.5, 57.0, 59.6, 82.3, 129.0, 130.4, 130.9, 136.8, 170.1, 173.3. HRMS (ESI) calculated for $C_{27}H_{43}N_3O_6$ $(M + H)^+$ 506.3225, found 506.3210.

Synthesis of Aluminum Chelates. *AlOH(NODA-MPAA) (**2**).* H_2L **1** (19.8 mg, 0.05 mmol) was dissolved in 1 mL of 2 mM NaOAc, pH 4.4, and treated with (12 mg, 0.05 mmol) $AlCl_3 \cdot 6H_2O$. The pH was adjusted to 4.5−5.0, and the reaction mixture was refluxed for 15 min. The crude was purified by preparative RP-HPLC (method 4) to yield a white solid (10.9 mg, 49.8%). HRMS (ESI) calculated for $C_{19}H_{26}AlN_3O_7$ $(M + H)^+$ 436.1659; found 436.1664.

*AlF(NODA-MPAA) (**3**).* H_2L **1** (40.6 mg, 0.103 mmol) was dissolved in 1 mL of 2 mM NaOAc, pH 4.4, and 0.5 mL of ethanol and treated with (19.5 mg, 0.141 mmol) $AlF_3 \cdot 3H_2O$. The pH was adjusted to 4.5−5.0, and the reaction mixture was refluxed for 15 min. When the mixture was cooled, the pH was once again raised to 4.5−5.0 and the reaction mixture refluxed for 15 min. The crude was purified by preparative RP-HPLC (method 4) to yield a white solid (22.4 mg, 49.6%). ^{1}H NMR (500 MHz, DMSO-d_6, 25 °C) δ 2.24−3.51 (m, 16 H), 3.59 (s, 2 H), 3.74 (d, 1H), 4.24 (d, 1H), 7.29 (d, 2H), 7.40 (d, 2H); ^{13}C (125.7 MHz, DMSO-d_6) 40.7, 46.0, 51.9, 52.7, 53.0, 54.5, 59.6, 64.0, 129.9, 131.3, 132.5, 135.8, 172.0, 172.2, 172.9. HRMS (ESI) calculated for $C_{19}H_{25}AlFN_3O_6$ $(M + H)^+$ 438.1616; found 438.1627.

Synthesis of the Peptide and Its Aluminum Chelates. *IMP485 (**4**).* NODA-MPAA-D-Lys(HSG)-D-Tyr-D-Lys(HSG)-NH_2 peptide was synthesized on Sieber amide resin with the amino acids added in the following order: Aloc-D-Lys(Fmoc)-OH, Trt-HSG-OH, Aloc removal, Fmoc-D-Tyr(But)-OH, Aloc-D Lys(Fmoc)-OH, Trt-HSG-OH, Aloc removal, and (tBu)$_2$NODA-MPAA. The peptide was then cleaved and purified by preparative RP-HPLC (method 4). HRMS (ESI) calculated for $C_{62}H_{89}N_{17}O_{15}$ $(M + H)^+$ 1312.6797; found 1312.6815.

*AlOH(IMP485) (**5**).* IMP485 (**3**) (21.5 mg, 0.016 mmol) was dissolved in 1 mL of 2 mM NaOAc, pH 4.4, and treated with (13.2 mg, 0.055 mmol) $AlCl_3 \cdot 6H_2O$. The pH was adjusted to 4.5−5.0, and the reaction mixture was refluxed for 15 min. The crude was purified by preparative RP-HPLC (method 4) to yield a white solid (11.8 mg). HRMS (ESI) calculated for $C_{62}H_{88}AlN_{17}O_{16}$ $(M + H)^+$ 1354.6483 ; found 1354.6431.

*Al^{19}F(IMP485) (**6**).* IMP485 (**3**) (16.5 mg, 0.013 mmol) was dissolved in 1 mL of 2 mM NaOAc, pH 4.43, and 0.5 mL of ethanol and treated with (2.5 mg, 0.018 mmol) $AlF_3 \cdot 3H_2O$. The pH was adjusted to 4.5−5.0, and the reaction mixture was refluxed for 15 min. When the mixture was cooled, the pH was once again raised to 4.5−5.0 and the reaction mixture refluxed for another 15 min. The crude was purified by preparative RP-HPLC (method 4) to yield a white solid (10.3 mg). HRMS (ESI) calculated for $C_{62}H_{87}AlFN_{17}O_{15}$ $(M + H)^+$ 1356.6440; found 1356.6458.

^{18}F-Labeling of IMP485. Amounts of 10 μL (20 nmol) of IMP485, 5 μL of $AlCl_3$ (10 nmol), 100 μL of Na^{18}F in 0.9% saline (34.6 mCi), and 110 μL of ethanol were reacted in a 2 mL microcentrifuge tube (sealed) at 105 °C for 15 min. The reaction mixture was cooled, diluted with 2−3 mL of deionized water, and then transferred into a HLB 3 cm^3 cartridge. The solution was eluted under vacuum into an empty 10 mL crimp-sealed vial. The reaction vessel and column were rinsed with 3 × 1 mL portions of water. The HLB cartridge was then transferred to another empty 3 mL vial and the product eluted with 4 × 150 μL of 1:1 ethanol/water to yield 20.3 mCi of Al^{18}F(IMP485) (decay corrected RCY of 74.1%; SA of 1.01 Ci/μmol).

^{18}F-Labeling of AlOH(IMP485). Amounts of 10 μL (20 nmol) of AlOH(IMP485), 100 μL of Na^{18}F in 0.9% saline (43.3 mCi), and 110 μL of ethanol were reacted in a 2 mL microcentrifuge tube (sealed) at 105 °C for 15 min. The reaction mixture was cooled, diluted with 2−3 mL of deionized water, and then transferred into a HLB 3 cm^3 cartridge. The solution was eluted under vacuum into an empty 10 mL crimp-sealed vial. The reaction vessel and column were rinsed with 3 × 1 mL portions of water. The HLB cartridge was then transferred to another empty 3 mL vial and the product eluted with 4 × 150 μL of 1:1 ethanol/water to yield 25.6 mCi of Al^{18}F(IMP485) (decay corrected RCY of 72.3%; SA of 1.28 Ci/μmol).

Radio-HPLC. The crude reaction mixture containing unbound ^{18}F$^-$ and the product obtained after purification by SPE were analyzed by RP-HPLC (method 2) using a Perkin-Elmer 610TR radiomatic flow scintillation analyzer (see Supporting Information, Figure S2), with recoveries of 79.7% and 100.6%, respectively.

Serum Stability. The SPE purified Al^{18}F(IMP485) in 20 μL of 1:1 EtOH/H_2O (66.3 μCi) was mixed with 200 μL of human serum and placed in the HPLC autosampler heated to 37 °C, injected 1, 2, and 4 μL at times 0, 2, and 4 h, respectively, to account for physical decay (see Supporting Information, Figure S3). No detectable ^{18}F$^-$ above background at the void volume was observed up to 4 h. In addition, percent recovery for each run was determined by counting the activity in six fractions over the entire 20 min run against a standard prepared from the original mixture. Total recoveries ranged from ∼76% to 91%.

■ ASSOCIATED CONTENT

Supporting Information. HPLC chromatograms, crystallographic data, and CIF file. This material is available free of charge via the Internet at http://pubs.acs.org.

■ AUTHOR INFORMATION

Corresponding Author

*For C.A.D.: e-mail, cdsouza@immunomedics.com.; phone, 973-605-8200, extension 299; fax, 973-605-1340. For D.M.G.: e-mail, dmg.gscancer@att.net.

Notes

C.A.D., W.J.M., and D.M.G. are employed or have financial interests in Immunomedics, Inc. R.M.S. and L.J.T. have disclosed no financial conflicts.

■ ACKNOWLEDGMENT

This work was funded in part by NIH Grant 5R44RR028018. The facility at which the X-ray crystallography was performed is supported by "Research Centers in Minority Institutions" Award RR-03037 from the National Center for Research Resources, NIH.

■ REFERENCES

(1) Signore, A., Mather, S. J., Piaggio, G., Malviya, G., and Dierckx, R. A. (2010) Molecular imaging of inflammation/infection: nuclear medicine and optical imaging agents and methods. *Chem. Rev. 110*, 3112–3145.

(2) Pysz, M. A., Gambhir, S. S., and Willmann, J. K. (2010) Molecular imaging: current status and emerging strategies. *Clin. Radiol. 65*, 500–516.

(3) Wong, F. C., and Kim, E. E. (2009) A review of molecular imaging studies reaching the clinical stage. *Eur. J. Radiol. 70*, 205–211.

(4) Ametamey, S. M., Honer, M., and Schubiger, P. A. (2008) Molecular imaging with PET. *Chem. Rev. 108*, 1501–1516.

(5) Chen, K., and Conti, P. S. (2010) Target-specific delivery of peptide-based probes for PET imaging. *Adv. Drug Delivery Rev. 62*, 1005–1022.

(6) Miller, P. W., Long, N. J., Vilar, R., and Gee, A. D. (2008) Synthesis of ^{11}C, ^{18}F, ^{15}O, and ^{13}N radiolabels for positron emission tomography. *Angew. Chem., Int. Ed. 47*, 8998–9033.

(7) Cai, L., Lu, S., and Pike, V. W. (2008) Chemistry with [^{18}F]fluoride ion. *Eur. J. Org. Chem.* 2853–2873.

(8) Wadsak, W., and Mitterhauser, M. (2010) Basic principles of radiopharmaceuticals for PET/CT. *Eur. J. Radiol. 73*, 461–469.

(9) Schirrmacher, R., Wängler, C., and Schirrmacher, E. (2007) Recent developments and trends in ^{18}F-radiochemistry: syntheses and applications. *Mini-Rev. Org. Chem. 4*, 317–329.

(10) Kim, D. W., Ahn, D.-K., Oh, Y.-H., Lee, S., Kil, H. S., Oh, S. J., Lee, S. J., Kim, J. S., Ryu, J. S., Moon, D. H., and Chi, D. Y. (2006) A new class of S_N2 reactions catalyzed by protic solvents: facile fluorination for isotopic labeling of diagnostic molecules. *J. Am. Chem. Soc. 128*, 16394–16397.

(11) Becaud, J., Mu, L., Karramkam, M., Schubiger, P. A., Ametamey, S. M., Graham, K., Stellfeld, T., Lehman, L., Borkowski, S., Berndorff, D., Dinkelborg, L., Srinivasan, A., Smits, K., and Koksch, B. (2009) Direct one-step ^{18}F-labeling of peptides via nucleophilic aromatic substitution. *Bioconjugate Chem. 20*, 2254–2261.

(12) Kachur, A. V., Dolbier, W. R., Xu, W., and Kock, C. J. (2010) Catalysis of fluorine addition to double bond: an improvement of method for synthesis of ^{18}F PET Agents. *Appl. Radiat. Isot. 68*, 293–296.

(13) Studenov, A. R., Adam., M. J., Wilson, J. S., and Ruth, T. J. (2005) New radiolabelling chemistry: synthesis of phosphorus-[^{18}F]-fluorine compounds. *J. Labelled Compd. Radiopharm. 48*, 497–500.

(14) Ting, R., Adam., M. J., Ruth, T. J., and Perrin, D. M. (2005) Arylfluoroborates and alkylfluorosilicates as potential PET imaging agents: high-yielding aqueous biomolecular ^{18}F-labeling. *J. Am. Chem. Soc. 127*, 13094–13095.

(15) Ting, R., Lo., J., Adam., M. J., Ruth, T. J., and Perrin, D. M. (2008) Capturing aqueous [^{18}F]-fluoride with an arylboronic ester for PET: synthesis and aqueous stability of a fluorescent [^{18}F]-labeled aryltrifluoroborate. *J. Fluorine Chem. 129*, 349–358.

(16) McBride, W. J., Sharkey, R. M., Karacay, H., D'Souza, C. A., Rossi, E. A., Laverman, P., Chang, C.-H., Boerman, O. C., and Goldenberg, D. M. (2009) A novel method of ^{18}F radiolabeling for PET imaging. *J. Nucl. Med. 50*, 991–998.

(17) Schoffelen, R., Sharkey, R. M., Goldenberg, D. M., Franssen, G., McBride, W. J., Rossi, E. A., Chang, C.-H., Laverman, P., Disselhorst, J. A., Eek, A., van der Graaf, W. T. A., Oyen, W. J. G., and Boerman, O. C. (2010) Pretargeted immunoPET imaging of CEA-expressing tumors with a bispecific antibody and a ^{68}Ga and ^{18}F-labeled hapten peptide in mice with human tumor xenografts. *Mol. Cancer Ther. 9*, 1019–1027.

(18) Sharkey, R. M., Karacay, H., Cardillo, T. M., Chang, C.-H., McBride, W. J., Rossi, E. A., Horak, I. D., and Goldenberg, D. M. (2005) Improving the delivery of radionuclides for imaging and therapy of cancer using pretargeting methods. *Clin. Cancer Res. 11*, 7109s–7121s.

(19) Rossi, E. A., Goldenberg, D. M., Cardillo, T. M., McBride, W. J., Sharkey, R. M., and Chang, C.-H. (2006) Stably tethered multifunctional structures of defined composition made by dock and lock method for use in cancer targeting. *Proc. Natl. Acad. Sci. U.S.A. 103*, 6841–6846.

(20) McBride, W. J., D'Souza, C. A., Sharkey, R. M., Karacay, H., Rossi, E. A., Chang, C.-H., and Goldenberg, D. M. (2010) Improved ^{18}F labeling of peptides with a fluoride-aluminum-chelate complex. *Bioconjugate Chem. 21*, 1331–1340.

(21) Laverman, P., McBride, W. J., Sharkey, R. M., Eek, A., Joosten, L., Oyen, W. J. G., Goldenberg, D. M., and Boerman, O. C. (2010) A novel facile method of labeling octreotide with ^{18}F-fluorine. *J. Nucl. Med. 51*, 454–461.

(22) Bodor, A., Tóth, I., Bányai, I., Szabó, Z., and Hefter, G. T. (2000) ^{19}F NMR study of the equilibria and dynamics of the Al^{3+}/F^- system. *Inorg. Chem. 39*, 2530–2537.

(23) de Sa, A., Prata, M. I. M., Geraldes, C. F. G. C., and André, J. P. (2010) Triaza-based amphiphilic chelators: synthetic route, in vitro characterization and in vivo studies of their Ga(III) and Al(III) chelates. *J. Inorg. Biochem. 104*, 1051–1062.

(24) Elizarov, A. M. (2009) Microreactors for radiopharmaceutical synthesis. *Lab Chip 9*, 1326–1333.

(25) Coenen, H. H., Elsinga, P. H., Iwata, R., Kilbourn, M. R., Pillai, M. R. A., Rajan, M. G. R., Wagner, H. N., and Zaknum, J. J. (2010) Fluorine-18 radiopharmaceuticals beyond [^{18}F]FDG in oncology and neurosciences. *Nucl. Med. Biol. 37*, 727–740.

(26) Nanni, C., Fantini, L., Nicolini, S., and Fanti, S. (2010) Non FDG PET. *Clin. Radiol. 65*, 536–548.

(27) Lee, S., Xie, J., and Chen, X. (2010) Peptide-based probes for targeted molecular imaging. *Biochemistry 49*, 1364–1376.

(28) Schottelius, M., and Wester, H.-J. (2009) Molecular imaging targeting peptide receptors. *Methods 48*, 161–177.

(29) Flavell, R. R., Kothari, P., Bar-Dagan, M., Synam, M., Vallabhajosula, S., Friedman, J. M., Muir, T. W., and Ceccarini, G. (2008) Site-specific ^{18}F-labeling of the protein hormone leptin using a general two-step ligation procedure. *J. Am. Chem. Soc. 130*, 9106–9112.

(30) Ting, R., Aguilera, T. A., Crisp, J. L., Hall, D. J., Eckelman, W. C., Vera, D. R., and Tsein, R. Y. (2010) Fast ^{18}F labeling of a near-infrared fluorophore enables positron emission tomography and optical imaging of sentinal lymph nodes. *Bioconjugate Chem. 21*, 1811–1819.

(31) Wängler, C., Waser, B., Alke, A., Iovkova, L., Buchholz, H.-G., Niedermoser, S., Jurkschat, K., Fottner, C., Schirrmacher, R., Reubi, J.-C., Wester, H.-J., and Wängler, B. (2010) One-step ^{18}F labeling of carbohydrate-conjugated octreotate-derivatives containing a silicon-fluoride-acceptor (SiFA): in vitro and in vivo evaluation as tumor imaging agents for positron emission tomography (PET). *Bioconjugate Chem. 21*, 2289–2296.

(32) Jyo, A., Kohno, T., Terazono, Y., and Kawano, S. (1990) Crystal structure of the aluminum(III) complex of 1,4,7-triazacyclononane-*N*,*N*′,*N*″-triacetate. *Anal. Sci. 6*, 629–630.

(33) Svadberg, A., Clarke, A., Dyrstad, K., Martinsen, I., and Hjelstuen, O. K. (2011) A critical study on borosilicate glassware and silica-based QMA's in nucleophilic substitution with [^{18}F]fluoride: influence of aluminum, boron and silicon on the reactivity of [^{18}F]-fluoride. *Appl. Radiat. Isot. 69*, 289–294.

(34) Hockley, B. G., and Scott, P. J. H. (2010) An automated method for preparation of [^{18}F]sodium fluoride for injection, USP to address the technetium-99m isotope shortage. *Appl. Radiat. Isot. 68*, 117–119.

(35) Jacobson, M. S., Dankwart, H. R., and Mahoney, D. W. (2009) Radiolysis of 2-[^{18}F]fluoro-2-deoxy-D-glucose and the role of ethanol and radioactive concentration. *Appl. Radiat. Isot. 67*, 990–995.

(36) McBride, W. J., D'Souza, C. A., Cardillo, T. M., and Goldenberg, D. M. (2011) A facile kit for rapid radiofluorination of peptides for PET. *J. Nucl. Med. 52* (Suppl. 1), 313.

(37) Füchtner, F., Preusche, S., Mäding, P., Zessin, J., and Steinbach, J. (2008) Factors affecting the specific activity of [^{18}F]fluoride from a [^{18}O]water target. *Nuklearmedizin 47*, 116–119.

(38) Lasne, M. C., Perrio, C., Rouden, J., Barre, L., Roeda, D., Dolle, F., and Crouzel, C. (2002) Chemistry of β^+-emitting compounds based on fluorine-18. *Top. Curr. Chem. 222*, 201–258.

(39) Yao, C.-H., Lin, K.-J., Weng, C.-C., Hsiao, I.-T., Ting, Y.-S., Yen, T.-C., Jan, T.-R., Skovronsky, D., Kung, M.-P., and Wey, S.-P. (2010) GMP-compliant automated synthesis of [^{18}F]AV-45 (Florbetapir F-18) for imaging β-amyloid plaques in human brain. *Appl. Radiat. Isot. 68*, 2293–2297.

(40) Saiki, H., Iwata, R., Nakanishi, H., Wong, R., Ishikawa, Y., Furumoto, S., Yamahara, R., Sakamoto, K., and Ozeki, E. (2010) Electrochemical concentration of no-carrier-added [^{18}F]fluoride from [^{18}O]water in a disposable microfluidic cell for radiosynthesis of ^{18}F-labeled radiopharmaceuticals. *Appl. Radiat. Isot. 68*, 1703–1708.

(41) Pascali, G., Mazzone, G., Saccomanni, G., Manera, C., and Salvadori, P. A. (2010) Microfluidic approach for fast labeling optimization and dose-on-demand implementation. *Nucl. Med. Biol. 37*, 547–555.

(42) D'Souza, C. A., McBride, W. J., Todaro, L. J., Sharkey, R. M., Karacay, H., Rossi, E. A., Chang, C.-H., and Goldenberg, D. M. (2011) Evaluation of 1,4,7-triazacyclononane-1,4-diacetate (NODA) ligand for development of PET imaging agents. *J. Nucl. Med. 52* (Suppl. 1), 171.

(43) McBride, W. J., D'Souza, C. A., Sharkey, R. M., and Goldenberg, D. M. (2011) A rapid method for F-18 labeling of proteins for PET. *J. Nucl. Med. 52* (Suppl. 1), 170.

(44) Sheldrick, G. M. (1997) *SHELXS-97* and *SHELXL-97*; University of Göttingen, Göttingen, Germany.

SUPPORTING INFORMATION

High-Yielding Aqueous ^{18}F-Labeling of Peptides via Al^{18}F Chelation

Christopher A. D'Souza,[*,†] William J. McBride,[†] Robert M. Sharkey,[‡] Louis J. Todaro,[¤] and David M. Goldenberg[*,‡]

[†]Immunomedics, Inc., Morris Plains, New Jersey 07950; [‡]Garden State Cancer Center, Center for Molecular Medicine and Immunology, Morris Plains, New Jersey 07950; [¤]Hunter College of the City University of New York, New York 10065.

* Corresponding author, Christopher A. D'Souza, Email cdsouza@immunomedics.com or David M. Goldenberg, Email: dmg.gscancer@att.net

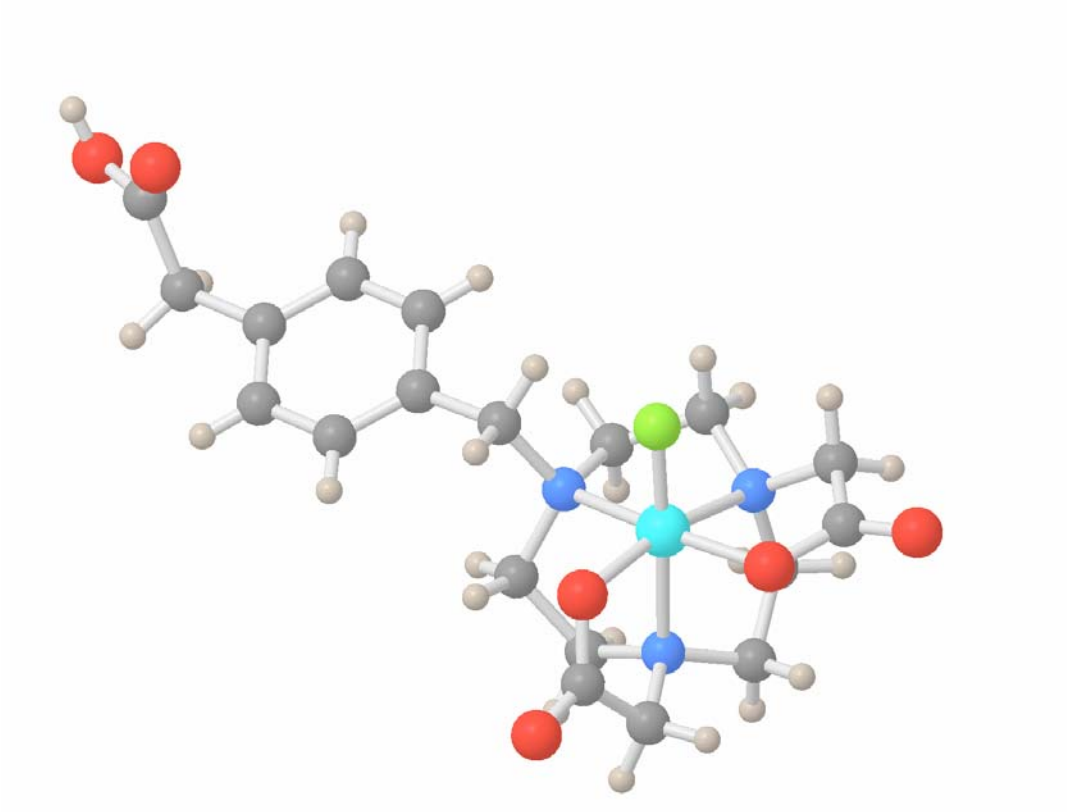

Table S1. Stability of AlOH(NODA-MPAA) **2** in PBS, pH 7.4, at 37 ^{o}C

Time (h)	AlOH(NODA-MPAA) 8.778 min[a]	NODA-MPAA 12.492 min[a]
0	100	0
1	92.95	7.05
2	84.32	15.68
3	76.94	23.06
4	70.56	29.44
6	59.37	40.63
9	45.51	54.49
12	38.62	61.38
22	25.41	74.59

[a]RP-HPLC: Method 1

Table S2. Crystallographic data for Al^{19}F(NODA-MPAA) **3**.

Empirical formula	$C_{19}H_{27}AlFN_3O_7$
Formula	$C_{19}H_{25}AlFN_3O_6.H_2O$
M (g/mol)	455.42
Crystal system	monoclinic
Space group	$P2_1/c$
a (Å)	20.463(4)
b (Å)	8.4950 (17)
c (Å)	12.692 (3)
α (^{o})	90.00
β (^{o})	107.52 (3)
γ (^{o})	90.00
V (Å^3)	2103.9 (7)
Z	4
F(000)	960
$D_{calc.}$ (g m^{-3})	1.438
μ (mm^{-1})	0.153
θ Range (^{o})	2.93 – 27.48
Reflections collected	13148
Reflections used	4812
No. of parameters/restraints	281/0
Goodness-of-fit on F^2	1.023

Table S3. ^{18}F-Labeling of 20 nmol IMP449 + 10 nmol Al^{3+} with $Na^{18}F$

Activity[a] $Na^{18}F$ (mCi)	Aqueous (μL)	Ethanol (μL)	Isolated activity[b] (mCi)	RCY[c] (%)
1.486	50	0	0.221	18.0
1.507	50	50	0.764	59.4
2.48	200	200	0.473	22.7

[a] 10 μL IMP449, 5 μL Al^{3+}, 105°C, 15 min.
[b] Isolated activity in (1:1) EtOH/H_2O after HLB column purification (SPE).
[c] decay corrected RCY – based on synthesis time of 25 – 34 minutes.

Table S4. ^{18}F-Labeling of 20 nmol IMP461 + 10 nmol Al^{3+} with $Na^{18}F$

Activity[a] $Na^{18}F$ (mCi)	Aqueous (μL)	Ethanol (μL)	Isolated activity[b] (mCi)	RCY[c] (%)
1.576	50	0	0.464	35.1
1.350	50	50	0.909	79.3
2.60	200	200	1.167	55.6

[a] 10 μL IMP461, 5 μL Al^{3+}, 105°C, 15 min.
[b] Isolated activity in (1:1) EtOH/H_2O after HLB column purification (SPE).
[c] decay corrected RCY – based on synthesis time of 26 – 34 minutes.

Table S5. ^{18}F-Labeling of 20 nmol IMP485 + 10 nmol Al^{3+} with $Na^{18}F$

Activity[a] $Na^{18}F$ (mCi)	Aqueous (μL)	Ethanol (μL)	Isolated activity[b] (mCi)	RCY[c] (%)
1.416	50	0	0.516	43.5
1.326	50	50	1.006	89.4
2.38	200	200	1.491	78.1

[a] 10 μL IMP485, 5 μL Al^{3+}, 105°C, 15 min.
[b] Isolated activity in (1:1) EtOH/H_2O after HLB column purification (SPE).
[c] decay corrected RCY – based on synthesis time of 26 – 35 minutes.

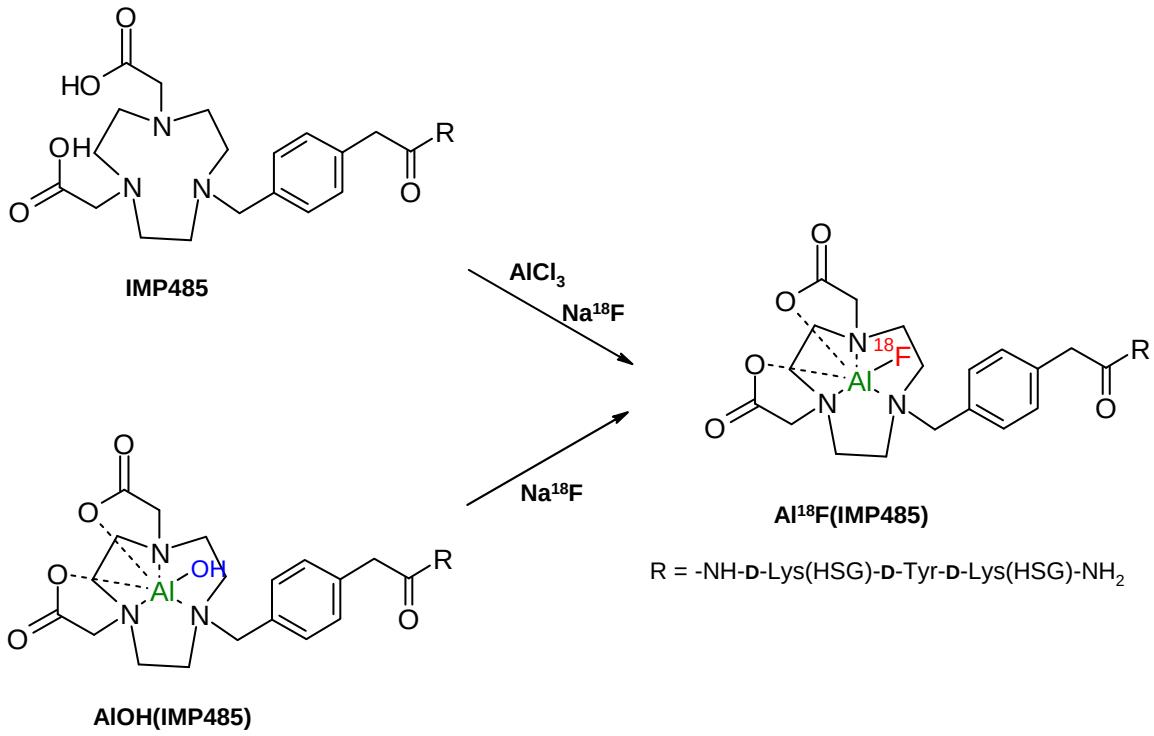

Scheme S1. ^{18}F-labeling of IMP485 and AlOH(IMP485).

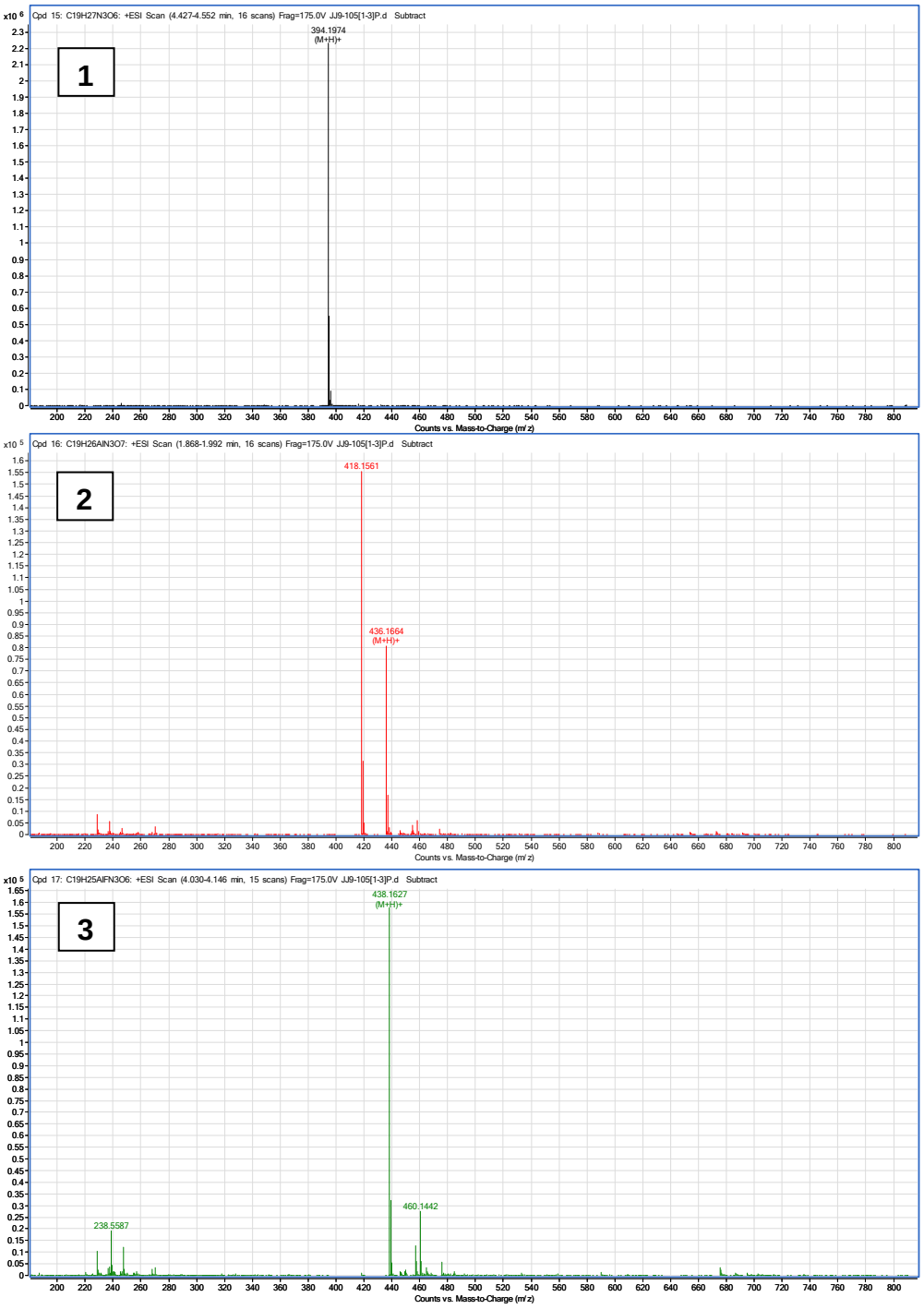

Figure S1. HRMS of **1**, **2** and **3**.

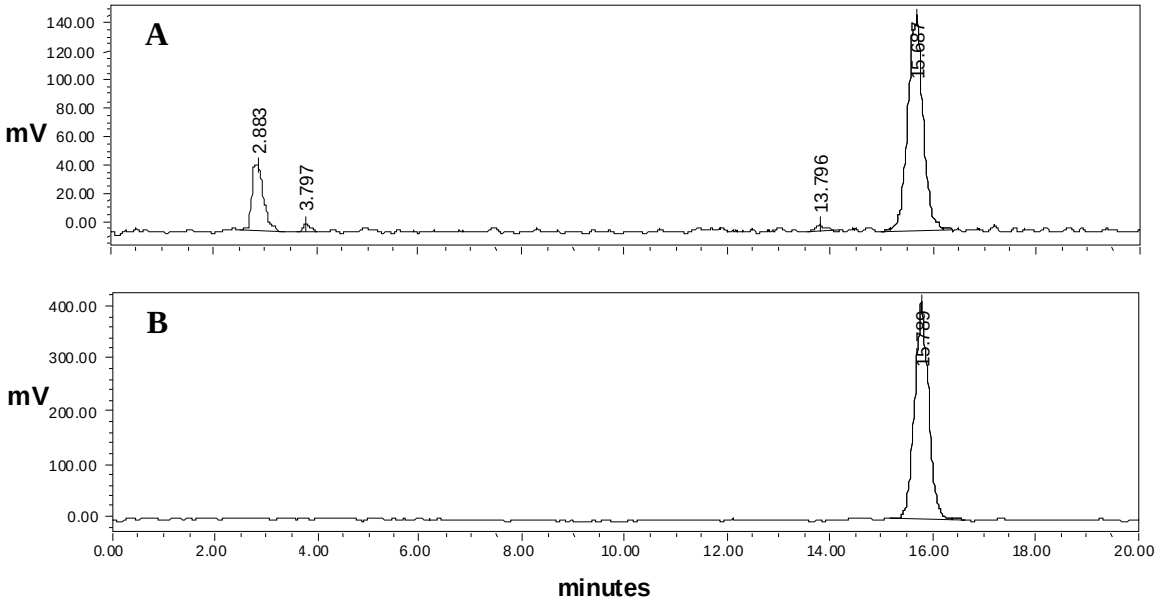

Figure S2. ^{18}F-labeling of IMP485 radio-HPLC chromatograms. (A) crude reaction mixture (B) SPE-purified Al^{18}F(IMP485).

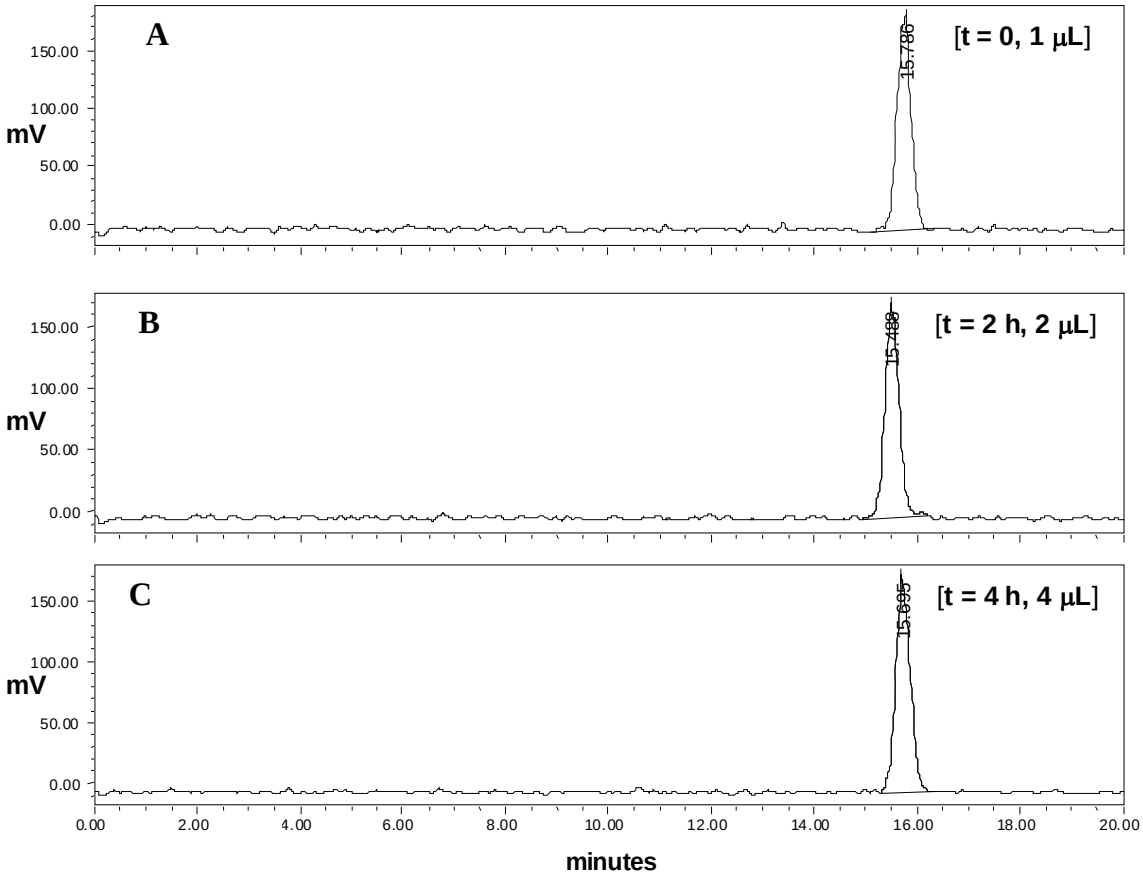

Figure S3. Stability of $Al^{18}F$(IMP485) in human serum at 37 ^{o}C. (A) time zero. (B) after 2 h. (C) after 4 h.

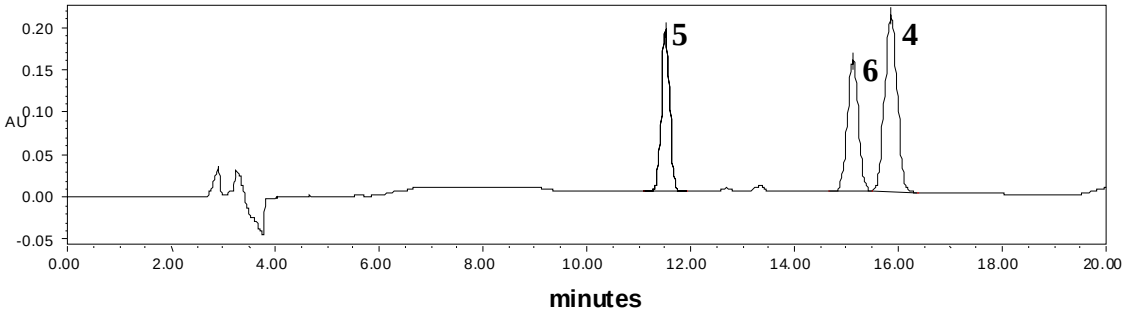

Figure S4. HPLC profile of a mixture containing AlOH(IMP485) **5**, $Al^{19}F$(IMP485) **6**, and IMP485 **4** using 0.1% TFA/acetonitrile as eluent (Method 2).

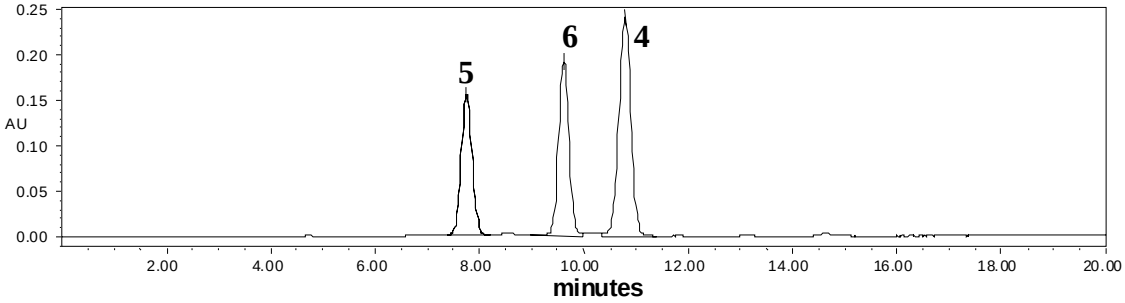

Figure S5. HPLC profile of a mixture containing AlOH(IMP485) **5**, $Al^{19}F$(IMP485) **6**, and IMP485 **4** using H_2O/Ethanol as eluent (Method 3).

Bioconjugate Chemistry

ARTICLE

pubs.acs.org/bc

C-Linked Antifreeze Glycoprotein (C-AFGP) Analogues as Novel Cryoprotectants

Mathieu Leclère,[†] Bonnie K. Kwok,[†] Luke K. Wu,[‡] David S. Allan,[‡] and Robert N. Ben*[,†]

[†]Department of Chemistry

[‡]Department of Medicine, Regenerative Medicine Program

University of Ottawa, Ontario, Canada, K1N 6N5

Supporting Information

ABSTRACT: Significant cell damage occurs during cryopreservation resulting in a decreased number of viable and functional cells post-thawing. Recent studies have correlated the unsuccessful outcome of regenerative therapies with poor cell viability after cryopreservation. Cell damage from ice recrystallization during freeze−thawing is one cause of decreased viability after cryopreservation. We have assessed the ability of two C-AFGPs that are potent inhibitors of ice recrystallization to increase cell viability after cryopreservation. Our results indicate that a 1−1.5 mg/mL (0.5−0.8 mM) solution of C-AFGP **1** is an excellent alternative to a 2.5% DMSO solution for the cryopreservation of human embryonic liver cells.

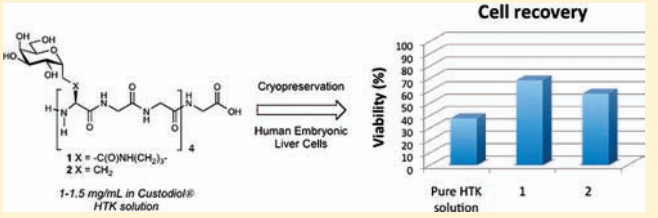

INTRODUCTION

Cryopreservation is a simple and economic option for the long-term storage of biological materials. However, one of the main drawbacks of this method is that large percentages of cells do not survive the freeze−thawing cycle. There are many reasons for this decreased viability which include cell necrosis due to intracellular freezing, mechanical damage to the external cell membrane by either ice or osmotic flux, and cold-induced apoptosis.[1−3] Cord blood banking has become routine in the past decade and this can be attributed to two reasons. The first is that stem cells from cord blood are now regarded as a practical alternative to autologous bone marrow stem cells,[4] and second, the documented successes of new stem cell-based regenerative therapies has increased dramatically in the last ten years. However, decreased cell viability after thawing is still a significant problem, particularly since recent studies have linked the successful outcome of regenerative therapies with the proportion of viable cells prior to transplant.[5,6] Consequently, improved cryopreservation protocols that increase cell viability are urgently required. Dimethyl sulfoxide (DMSO) is currently regarded as the "gold standard" for cryopreservation. While all cryoprotectants are potentially cytotoxic *in vitro*, DMSO has exhibited significant cytotoxic effects in the clinical setting.[7,8] While various biopolymers[9] have been explored as cryoprotectants, these fail to provide the high cell viabilities observed with DMSO or glycerol. Simple mono- and disaccharides have also been investigated as cryoprotectants; however, the structure of the carbohydrate, the freezing protocol, cell type, and reported cell viabilities vary dramatically between studies making it difficult to ascertain the true ability of these compounds to protect cells against cryoinjury. Native antifreeze glycoproteins (AFGPs) found in Teleost fish are naturally occurring antifreezes that have the ability to inhibit the growth of ice crystals *in vivo* (Figure 1).[10,11] Unfortunately, the thermal hysteresis (TH) properties of these proteins (the ability to selectively depress the freezing point of a solution relative to its melting point) actually exacerbates cell damage at temperatures outside of the TH gap during cryopreservation.[12] Despite this undesirable effect, biological antifreezes have been explored as cryoprotectants. The majority of this work has been carried out using antifreeze proteins (AFPs) and reports of AFGPs as cryoprotectants have been limited to preservation of cells via vitrification.[13] While AFGPs and AFPs also inhibit ice recrystallization in frozen samples, a property speculated to be beneficial in a cryoprotectant,[14] they have not proven to be effective cryoprotectants due to the TH activity that damages cells at cryopreservation temperatures. This has been demonstrated using AFP type I for the cryopreservation of red blood cells (RBCs) where it was observed that micromolar concentrations of AFP I appeared to confer some protection against cell damage, but millimolar concentrations fostered increased damage to cells during freeze−thawing.[14,15] It should be pointed out that these studies were performed using thawing rates that were nonoptimal, and thawing was performed slowly in order to increase the potential for ice recrystallization and subsequent cell damage. In typical cryopreservation protocols, thawing is done very quickly to mitigate cellular damage due to ice recrystallization. Given that an atypical thawing protocol was utilized, it is not clear whether inhibitors of ice recrystallization

Received: April 11, 2011
Revised: July 15, 2011
Published: August 04, 2011

ACS Publications © 2011 American Chemical Society

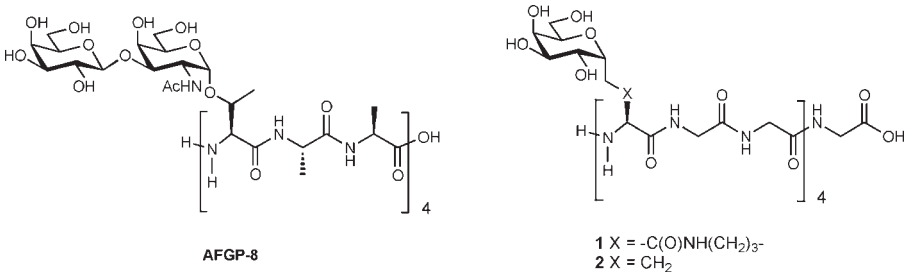

Figure 1. Structure of native AFGP 8 and *C*-linked analogues **1** and **2**.

would actually increase cell viabilities under conditions in which thawing was performed quickly.

EXPERIMENTAL PROCEDURES

The synthesis and characterization of precursors **8** and **9** as well as the general synthetic procedures details are described in the Supporting Information.

(*S*)-*N*-benzyloxycarbonyl-2,2-dimethyl-4-((*E*)-1′-deoxy-2′,3′;4′,6′-di-*O*-isopropylidene-α-D-galactopyranosyl)vinyl)-oxazolidine (7). Sulfone **9** (4.50 g, 10.0 mmol, 1.5 equiv) was dissolved in 20 mL of THF. The solution was cooled to −78 °C, and 10.0 mL of 1 M NaHMDS in THF (10 mmol, 1.5 equiv) was added. After 5 min of stirring, a solution of the crude aldehyde **8** (6.7 mmol) in 10 mL of THF was added via cannula. The stirring was continued for 1 h at −78 °C and the temperature slowly warmed to room temperature over 2 h. After an additional hour of stirring, the mixture was quenched with few drops of water and diluted with 100 mL of Et_2O. The organic layer was washed with water and brine, dried over Na_2SO_4, concentrated, and the crude purified by flash chromatography (Pet. Ether/AcOEt 5/2) to give 2.2 g of the alkene **7** (65% from **14**). ^{1}H NMR (DMSO-d_6, 500 MHz, 343 K) δ 7.36 (m, 5H), 5.82 (ddd, J = 16.2, 6.3, 1.9 Hz, 1H), 5.68 (dd, J = 16.2, 3.8 Hz, 2H), 5.06 (s, 2H), 4.78 (brt, J = 4.4 Hz, 1H), 4.49 (t, J = 6.2 Hz, 1H), 4.27−4.11 (br, 1H), 4.07 (dd, J = 9.0, 6.2 Hz, 1H), 4.04 (dd, J = 10.2, 5.81 Hz, 1H), 3.94 (d, J = 13.2 Hz, 1H), 3.75 (dd, J = 9.0, 2.0 Hz, 1H), 3.64 (d, J = 13.2 Hz, 1H), 3.41 (brs, 1H), 3.13 (brs, 1H), 1.54 (s, 3H), 1.47 (s, 6H), 1.38 (s, 6H), 1.33 (s, 6H) 1.29 (s, 3H), 1.27 (s, 3H). ^{13}C NMR (DMSO-d_6, 125 MHz, 343 K) δ 152.2, 137.1, 133.1, 128.8, 128.2, 127.9, 124.9, 109.5, 97.9, 94.0, 74.3, 73.6, 70.9, 68.4, 67.3, 66.5, 63.9, 63.0, 58.5, 29.5, 27.0, 26.8, 23.4, 18.5. HRMS (EI) m/z calcd. for $C_{27}H_{37}N_1O_8$ $[M]^+$ 503.2519 found 503.2521. IR (neat, cm^{-1}) 2985, 2935, 1701.

(*S*)-3-amino-4-(1′deoxy-2′,3′;4′,6′-di-*O*-isopropylidene-α-D-galactopyranosyl)-butanol (17). H_2 was bubbled for 5 min through a solution of the alkene **7** (2.10 g, 4.2 mmol) and $Pd(OH)_2/C$ (600 mg, 0.42 mmol, 0.1 equiv) in 20 mL of EtOH. Bubbling was stopped and stirring was continued for 1 h under H_2 atmosphere. The flask was then purged with N_2 and the mixture was filtered through Celite and the solvent removed *in vacuo*. After drying under high vacuum for several hours, 1.32 g of amino alcohol **17** was obtained (95%). ^{1}H NMR ($CDCl_3$, 400 MHz) δ 4.41 (brs, 1H), 4.32 (m, 1H), 4.25 (dd, J = 9.7, 5.4 Hz, 1H), 4.06 (dd, J = 12.9, 2.0 Hz, 1H), 3.85 (d, J = 12.9 Hz, 1H), 3.67 (dd, J = 9.9, 2.9 Hz, 1H), 3.59 (dd, J = 10.7, 3.3 Hz, 1H), 3.23 (brs, 1H), 3.20−3.00 (brs, 3H), 2.92 (brs, 1H), 1.61 (m, 3H), 1.44 (s, 3H), 1.43 (s, 3H), 1.42 (s, 3H), 1.38 (s, 3H), 1.36 (m, 1H). ^{13}C ($CDCl_3$, 100 MHz) δ 110.0, 98.6, 73.9, 70.8, 67.4, 65.6, 63.1, 52.8, 30.1, 29.2, 26.7, 26.5, 21.0, 18.4. MS(ESI) m/z calcd. for $C_{16}H_{30}N_1O_6$ $[M+H]^+$ 332.207 found 332.273. IR (neat, cm^{-1}) 3400, 2991, 2935.

((*S*)-3-(*N*-(9-fluorenylmethyloxycarbonyl)amino)-4-(1′-deoxy-2′,3′;4′,6′-di-*O*-isopropylidene-α-D-galactopyranosyl)-butanol (18). To a solution of **17** (1.30 g, 3.9 mmol) and $NaHCO_3$ (0.65 g, 7.8 mmol, 2 equiv.) in a mixture of 20 mL of 1,4-dioxane and 20 mL of water was added Fmoc-OSu (1.4 g, 4.2 mmol, 1.1 equiv) at 0 °C. The solution was stirred overnight at room temperature, then diluted with CH_2Cl_2, and the organic layer was washed with water, separated, dried over Na_2SO_4, and concentrated in vacuo. The crude was purified by flash chromatography (CH_2Cl_2/MeOH 98/2) to yield 1.60 g (75%) of the title compound **18**. ^{1}H NMR (C_6D_6, 500 MHz) δ 7.58 (dd, J = 6.5, 1.6 Hz, 2H), 7.51 (m, 2H), 7.22 (m, 4H), 4.87 (brs, 1H), 4.50 (dd, J = 10.0, 5.6 Hz, 1H), 4.45 (m, 2H), 4.27 (ddd, J = 9.2, 5.8, 2.8 Hz, 1H), 4.07 (m, 2H), 3.84 (dd, J = 12.8, 1.4 Hz, 1H), 3.65 (dd, J = 12.8, 2.4 Hz, 1H), 3.51 (dd, J = 10.0, 3.3 Hz, 1H), 3.44 (m, 1H), 3.37 (dd, J = 11.0, 5.1 Hz, 1H), 2.78 (s, 1H), 1.64 (m, 2H), 1.51 (m, 1H), 1.46 (s, 3H), 1.42 (s, 3H), 1.37 (s, 3H), 1.28 (m, 1H), 1.20 (s, 3H). ^{13}C NMR (C_6D_6, 125 MHz): δ 157.0, 144.7, 144.6, 141.9, 127.4, 125.4, 125.3, 120.3, 109.8, 98.4, 76.8, 74.4, 71.4, 67.9, 66.6, 65.4, 63.8, 63.5, 53.7, 48.0, 29.4, 29.0, 27.1, 26.9, 21.5, 18.8. MS (ESI) m/z calcd. for $C_{31}H_{40}NNaO_8$ $[M+Na]^+$ 576.257 found 576.288. IR (neat, cm^{-1}) 2989, 2937, 1703.

((*S*)-3-(*N*-(9-fluorenylmethyloxycarbonyl)amino)-4-(1′-deoxy-2′,3′;4′,6′-di-*O*-isopropylidene-α-D-galactopyranosyl)-butanoic acid (3b). Alcohol **18** (1.50 g, 2.7 mmol) was dissolved in 20 mL of acetonitrile. $NaHCO_3$ (0.68 g, 8.1 mmol, 3 equiv), TEMPO (42 mg, 0.27 mmol, 0.1 equiv), and $PhI(OAc)_2$ (1.3 g, 4.0 mmol, 1.5 equiv) were added and the mixture was stirred vigorously. The reaction was monitored by TLC (CH_2Cl_2/MeOH 98/2). Upon completion of the reaction (ca. 6 h), the mixture was diluted with CH_2Cl_2 and washed with water. The organic layer was separated, dried over Na_2SO_4, and the solvent evaporated. The crude aldehyde was redissolved in 20 mL of *t*-BuOH and 6 mL of 2-methyl-2-butene. The solution was then cooled to 0 °C and 14 mL of 1 M solution of aqueous KH_2PO_4 (14.0 mmol, 5.2 equiv) followed by 14 mL of 1 M solution of $NaClO_2$ (14.0 mmol, 5.2 equiv). After stirring at 0 °C for 2 h, the mixture was partitioned with AcOEt (100 mL) and water (50 mL). The organic layer was separated; the aqueous phase was extracted with 100 mL of AcOEt. The combined organic layers were dried over Na_2SO_4 and the solvents evaporated. Purification of the crude by flash chromatography (CH_2Cl_2/MeOH 96/4) yielded 1.22 g of the building block **3b** (80%). ^{1}H NMR (DMSO-d_6, 500 MHz, 343 K) δ 7.85 (d, J = 7.6 Hz, 2H), 7.70 (dd, J = 7.8, 7.4 Hz, 2H), 7.41 (dd, J = 7.5, 7.5 Hz, 2H), 7.32 (ddd, J = 7.8, 7.5, 1.6 Hz, 2H), 4.39 (d, J = 3.0 Hz, 1H), 4.30 (dd, J = 10.0, 7.0 Hz, 1H), 4.27 (d, J = 6.8 Hz, 1H), 4.25−4.28 (m, 2H), 4.07 (m, 2H), 3.72 (dd, J = 10.0, 2.8 Hz, 1H), 3.66 (dd,

J = 12.8, 1.0 Hz, 1H), 3.28 (brs, 1H), 1.89 (m, 1H), 1.74 (m, 2H), 1.58 (m, 1H), 1.39 (s, 3H), 1.33 (s, 6H), 1.30 (s, 3H). ^{13}C NMR (DMSO-d_6, 125 MHz, 293 K) δ 174.1 (br), 156.3 (br), 149.1, 149.0, 145.9, 132.9, 132.3, 130.4, 125.4, 114.0, 102.6, 80.5, 78.4, 75.5, 72.0, 70.9, 67.8, 67.7, 51.8, 34.5, 31.9, 23.9. MS (ESI) m/z calcd. for $C_{31}H_{37}N_1O_9Na$ $[M+Na]^+$ 590.237 found 590.286. IR (neat, cm^{-1}) 2987, 2933, 1712, 1704.

Glycoconjugate 2. A typical SPPS cycle consisted in the following steps: 300 mg (0.18 mmol) of Wang Fmoc-Gly-OH resin were swollen in DMF for 1 h. Fmoc deprotection was achieved by adding a mixture of piperidine/DBU/DMF 2/2/96 for 30 min. The resin was washed with DMF and treated with a premixed solution of Fmoc-Gly-Gly-OH and HCTU (6 equiv each) in DMF. DIPEA (12 equiv) was added and the resin was shaken gently for 3 h. After washing the resin with DMF, the Fmoc carbamate was cleaved as describe above. The resin was washed and treated with the premixed building block **3b** and HCTU (1.5 equiv each) and DIPEA (3 equiv) for 24 h. The resin was then washed with DMF (3 × 10 mL) and the Fmoc carbamate cleaved as described above. This cycle was repeated 3 more times in order to achieve the desired peptide length. The resin was washed with DMF, CH_2Cl_2, and MeOH and dried under high vacuum for 6 h. Final cleavage using a mixture of TFA/i-Pr_3SiH/H_2O 92.5/5/2.5 for 3 h furnished the crude glycoconjugate. The resin was filtered and washed with TFA and the combined filtrates were concentrated in vacuo at 35 °C. Acetone was added to precipitate the crude glycopeptide which was further purified by SPE on a Discovery C18 cartridge, followed by preparative HPLC (C18) to give 55 mg of the glycoconjugate **2** (20%). ^{1}H NMR (D_2O, 500 MHz, presaturated on HOD frequency) δ 4.21 (brs, 1H), 4.00−3.68 (brm, 8H), 3.65−3.47 (brm, 4H), 1.95−1.41 (brm, 4H). ^{13}C NMR (D_2O, 125 MHz) δ 174.5, 171.8, 171.6, 170.4, 75.2, 74.7, 71.8, 71.6, 69.5, 69.0, 68.0, 67.9, 61.1, 54.0, 52.9, 46.6, 42.5, 42.2, 41.5, 40.4, 27.3, 27.2, 20.2, 19.3. HRMS (MALDI-TOF) m/z calcd. for $C_{58}H_{97}N_{13}NaO_{34}$ $(M+Na)^+$ 1542.6159; found 1542.6965.

Cryopreservation Assay. WRL 68 cells were cultured and trypsinized as described above. Cells were diluted with culture media and counted using a hematocytometer. Aliquots containing 1 × 10^6 cells were added to 2 mL Eppendorf vial and cells were pelleted by centrifugation for 10 min at 2000 rpm. The supernatant was removed and the cells were resuspended in 0.1 mL HTK supplemented with glycoconjugate **1** or **2** to a concentration of 1, 1.5, 2, and 5 mg/mL. HTK supplemented with DMSO to a concentration 2.5% or 5% served as the positive controls. Cell suspensions were transferred to 2 mL cryogenic vials (Corning) and placed in a "Mr. Frosty" freezing container (Nalgene). The container was placed in an ultracold freezer (−80 °C) for 24 allowing a cooling rate of approximately 1 °C/min. Samples were then stored in a cryogenic tank in the vapor phase of liquid nitrogen (−150 °C) for 6 days. Following storage, samples were rapidly thawed in a 37 °C water bath with gentle agitation. Thawed samples were transferred to 2 mL centrifuge tubes and slowly diluted to 1 mL by dropwise addition of cell culture medium. Cells were pelleted by centrifugation for 10 min at 2000 rpm. The supernatant was decanted and the pellets resuspended in 0.5 mL of Annexin V binding buffer (BD Pharmingen).

Flow Cytometry. 100 μL of the suspension of cells in binding buffer was transferred to a flow cytometry tube. Subsequently, 5 μL of 7-Actinomycin D (7AAD) (BD Pharmingen) and 4 μL of Annexin V-PE (BD Pharmingen) were added and samples were incubated for 20 min in the dark. Following incubation, samples were diluted to 500 μL with 1× Annexin-V binding buffer. Flow cytometry analysis on 10 000 cells was carried out on a BD LSR flow cytometer using CellQuest (BD). Annexin V-PE was measured on FL-2 while 7-AAD was measured on FL-3. Complete viability was denoted as Annexin V-/7AAD- cells, early apoptotic as Annexin V+ /7AAD- cells, late apoptotic as Annexin V+ /7AAD+ cells, and Annexin V- /7AAD+ as necrotic cells. Compensation was set from single stain experiments with 7-AAD and Annexin-V. Aliquots from noncryopreserved samples labeled with equivalent fluorochromes were used to set the control gate excluding 99% 7AAD+ cells. Time between thawing and analysis by flow cytometry was 2 h. All trials were performed in duplicate.

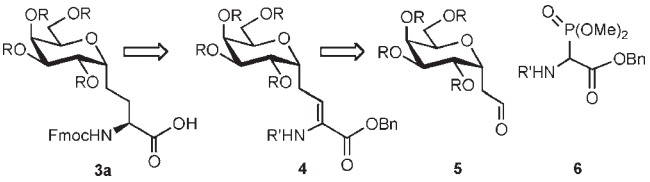

Figure 2. Retrosynthetic strategy to prepare building block **3a**.

RESULTS AND DISCUSSION

Our laboratory has successfully designed and synthesized a number of *C*-linked analogues of antifreeze glycoproteins (**1** and **2**, Figure 1) that are potent inhibitors of ice recrystallization but do not exhibit thermal hysteresis.[16−21] These compounds also possess increased chemical and biological stability relative to native AFGP. The two major structural differences between these *C*-linked AFGPs and native AFGP are that the disaccharide has been replaced with a *C*-linked galactosyl moiety and the alanine residues have been replaced with glycine residues. These structural changes were initially incorporated for ease of synthesis and to avoid C-terminal racemization during solid-phase synthesis. More recently, truncated versions of these structures bearing fluorine atoms have been prepared but these compounds failed to demonstrate the ability to inhibit ice recrystallization.[22] The "custom-tailored" antifreeze activity observed in **1** and **2** makes these compounds ideally suited for cryopreservative applications. In addition, **1** and **2** exhibit lower in vitro cytotoxicity and offer increased chemical stability relative to native AFGPs.[23] Unfortunately, the previously reported synthesis[20] of **2** was not amenable to the scale-up required for in vitro studies. The key step in our original synthesis of building block **3a** required for the solid-phase synthesis of **2** employed a catalytic asymmetric hydrogenation of the galactosyl enamide **4** as shown in Figure 2. This reaction proceeded with only moderate diastereoselectivity (69% de) yielding a complex mixture that was difficult to purify by HPLC making this approach unattractive for the preparation of **2**. A relatively small number of syntheses of *C*-galactosyl serines have been reported. In these examples, the key step has employed a Wittig olefination,[24] condensation of silyl enol-ether[25] or enolate[26] or a catalytic asymmetric hydrogenation[27] to incorporate the stereocenter at the α-carbon. In order to assess the ability of **2** as a cryoprotectant, a more efficient highly stereoselective synthesis affording a single diastereoisomer was desirable. Recently, Chen et al. reported the synthesis of *C*-galactosyl ceramides using the Julia-Kocienski-Lythgoe (JKL) olefination reaction.[28] We envisioned a similar approach in which a one-pot

JKL olefination[29,30] using carbohydrate derivative **8** and sulfone **9** as outlined in Figure 3 would furnish **7**.

Reduction of the carbon−carbon double bond in **7** with concomitant cleavage of the Cbz group was expected to furnish the amino alcohol, which could be converted to amino acid derivative **3b** necessary for the synthesis of **2**. In this approach, we chose to employ 5-phenyl-tetrazolyl (PT) sulfone **9** (prepared following a modified procedure reported by Albrecht et al.[31]), as it has been reported to be less prone to self-condensation than the benzothiazolyl sulfone.[32] The synthesis of **3b** is described in Scheme 1. Aldehyde **8** was prepared from α-*C*-allyl galactose derivative **11** which in turn was prepared by radical-mediated allylation of galactosyl bromide **10** using allyltributylstannane and Et_3B/air.[33] This afforded the α-*C*-allyl derivative **11** in 70% yield with a trace amount of **12** (6%) resulting from in situ acyl migration.[34] The terminal alkene was isomerized to 2-propenyl derivative **13** using $(Ph_2MeP)_2Ir(cod)PF_6$ catalyst.[35] Initial attempts to isomerize olefin **13** followed by ozonolysis failed to produce the desired aldehyde. Hence, isopropylidenes were installed in 75% yield and ozonolysis of **14** followed by reduction with PPh_3 yielded aldehyde **8** in 84% yield. Due to the propensity of this compound to epimerize and undergo elimination, it was not purified but used directly in the JKL olefination. Sulfone **9** was prepared from orthogonally protected L-serine methyl ester **15** via Mitsunobu reaction with 5-phenyl-tetrazolyl thiol to furnish **16** in 82% yield. Subsequent reduction with $LiBH_4$ followed by *N,O*-isopropylidene formation and oxidation using Sharpless conditions furnished the sulfone **9** in 65% yield. Sulfone **9** was then metalated at −78 °C with NaHMDS and followed by dropwise addition of aldehyde **8**. The reaction was then warmed to room temperature over 2 h. After workup, olefin **7** was obtained in 65% isolated yield. The geometry of the double bond was found to be exclusively *trans* by ^1H NMR spectroscopy. Reduction of the carbon−carbon double bond and removal of the Cbz carbamate using wet $Pd(OH)_2/C$ in ethanol was accompanied by concomitant cleavage of the *N,O*-isopropylidene moiety. The resulting amino-alcohol **17** was protected as the Fmoc carbamate (**18**) and oxidized furnishing carboxylic acid **3b** in 80% yield. Synthesis of glycoconjugate **2** using building block **3b** was carried out using standard Fmoc-based solid-phase synthesis with Wang resin. Cleavage of the glycoconjugate from the resin and simultaneous deprotection by treatment with TFA furnished the crude glycopeptide which was purified by solid-phase extraction on a C-18 SPE cartridge followed by reversed-phase HPLC to afford glycoconjugate **2** in 21% overall yield.

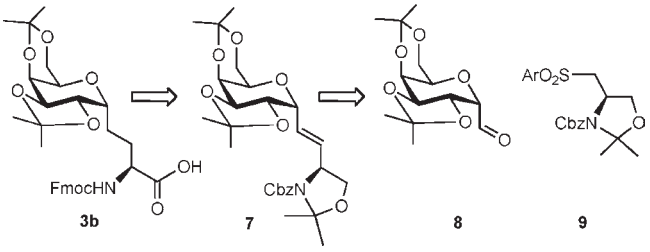

Figure 3. New retrosynthetic strategy to prepare building block **3b**.

C-AFGP analogues **1** and **2** were then assessed for cryoprotective abilities using human embryonic liver cells (WRL-68) as a model. This specific cell model was chosen because liver cells have been identified as a potential source of stem cells for various regenerative therapies.[36] Stem cells have changed the course of treatment for many malignant and nonmalignant conditions in adults and pediatric patients.[37,38] For instance, mesenchymal stem cells (MSCs) have been featured prominently as they have the ability to differentiate into many different cell types and have been successfully utilized to treat cartilage lesions,[39] spinal cord injury,[40] bone defects,[41] and cardiac disease.[42] Unfortunately, recent studies have correlated poor in vivo differentiation of these

Scheme 1. Synthesis of Building Block 3b

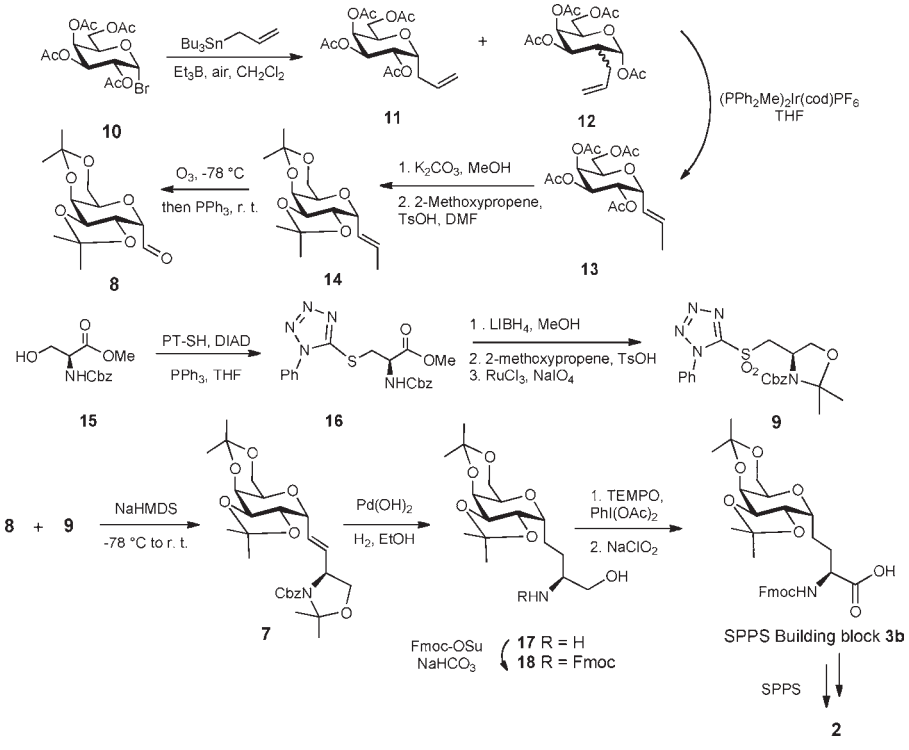

dx.doi.org/10.1021/bc2001837 |*Bioconjugate Chem.* 2011, 22, 1804–1810

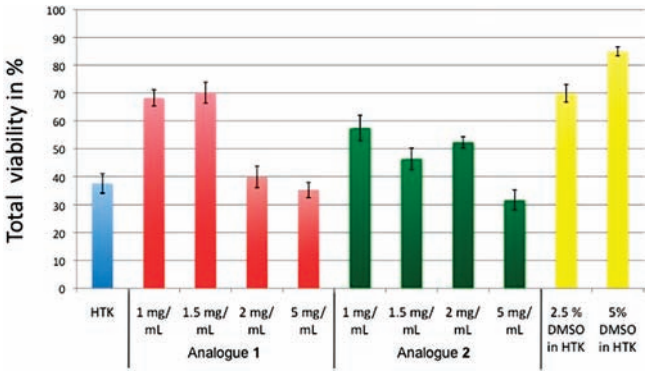

Figure 4. WRL-68 cell viability 2 h post thaw. Error bars indicate SEM.

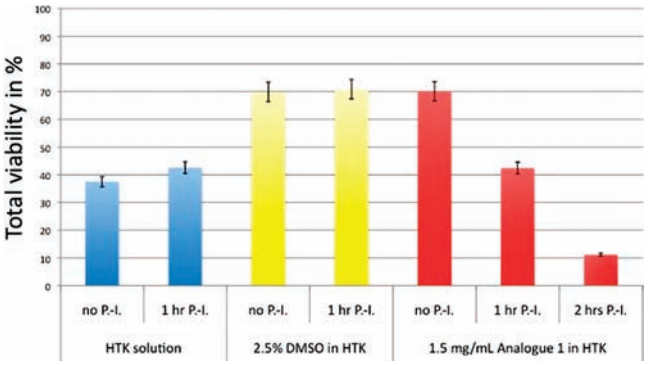

Figure 5. Viability of WRL-68 cells after 6 days cryopreservation using 1.5 mg/mL of analogue **1** with 1 and 2 h preincubation (P.-I.) at 37 °C. Error bars indicate SEM.

cells with low survival rates after cryopreservation, thus underscoring the need for improved cryopreservation protocols.[43]

It was hypothesized that, since these *C*-AFGPs were potent inhibitors of ice recrystallization and that this phenomenon has been implicated as a significant source of cell injury during cryopreservation,[15,44] addition of **1** and **2** to cell medium during freezing would enhance cell viabilities after thawing. In order to assess the cryoprotective potential of *C*-AFGP analogues **1** and **2**, a cryopreservation assay was developed, based on currently utilized cryopreservation protocols. Standard preservation conditions designed to minimize cell damage due to ice recrystallization were used. In this assay, *C*-AFGP analogue **1** or **2** was added to a suspension of 1×10^6 human embryonic liver cells (WRL-68) in a 100 μL histidine-tryptophane-ketoglutarate (HTK) custodiol solution. Custodiol HTK solution was a logical choice as it is routinely used in organ transplantation. The cryoprotection ability of **1** and **2** was directly compared to 2.5% and 5% DMSO solutions. This is a reasonable control, as cells are routinely frozen with DMSO in the medium.[45] Cell suspensions were transferred into 2 mL cryovials and placed into a Mister Frosty inside a −78 °C freezer to achieve rate controlled freezing of −1 °C/min. At a temperature of −80 °C, the cryovials were transferred into a liquid N_2 storage container. After 6 days, the samples were thawed quickly (to minimize ice recrystallization and subsequent cell damage) and resuspended in fresh medium. An aliquot was withdrawn and total cell viability was determined 2 h after thawing. A combination of 7-amino-actinomycin (7-AAD, an indicator of cell membrane integrity) and Annexin-V PE (a marker of apoptosis) was used to distinguish the viable cells from the apoptotic and necrotic ones.

Cell viabilities after freezing WRL 68 cells in the presence of *C*-AFGP analogues **1** and **2** using appropriate controls (DMSO and HTK solution) is presented in Figure 4. Experiments were performed using 1, 1.5, 2, and 5 mg/mL concentrations of **1** and **2**. WRL 68 cells cryopreserved using a 1 mg/mL solution of **1** resulted in total cell viability comparable to a 2.5% DMSO solution. This 1 mg/mL solution of **1** is 30% more effective than HTK solution alone but is approximately 10% less effective then the 5% DMSO solution. Similar results were obtained when a 1.5 mg/mL solution was utilized; however, 2 and 5 mg/mL concentrations of **1** proved detrimental, resulting in a marked decrease in total cell viability. While intercellular concentrations of 2 and 5 mg/mL are in the millimolar range, similar concentrations of AFP type I have been reported to result in significant cell damage during freezing and poor viabilities after thawing.[13] Analogue **2** gave similar results with maximum cryoprotective ability at 1 mg/mL. However, total viability was slightly lower than with analogue **1**. Cellular concentrations **1** and **2** greater than 2 mg/mL failed to increase post-thaw viabilities.

It has recently been reported that various cryoprotectants require preincubation with cells prior to freezing in order to ensure internalization[46] to confer cellular protection against intracellular ice formation.[1] This is an important property associated with cell penetrating cryoprotectants. Our laboratory has previously demonstrated that *C*-AFGP analogues **1** and **2** are readily internalized into liver cells within 10 min[23] and that this internalization is a receptor-mediated process likely involving the asialoglycoprotein receptor (ASGPr).[47,48] Encouraged by the fact that **1** and **2** where readily internalized, we investigated whether preincubation of cells with *C*-AFPGs would increase cell viabilities post-thaw. For this experiment, only *C*-AFGP analogue **1** was examined as it resulted in slightly better viabilities post-thaw than *C*-AFGP analogue **2** (Figure 4) at 1 and 1.5 mg/mL.

To ensure adequate time for internalization and thus maximize any cryoprotective effect, *C*-AFGP analogue **1** was preincubated with WRL 68 cells at 37 °C for 1 and 2 h prior to cryopreservation (Figure 5). No significant improvements in total cell viability were observed. This result suggests that adequate internalization occurs in a short amount of time and is consistent with our earlier studies.[22] Cell viability dramatically decreased when preincubation times were increased to 2 h. The cytotoxic nature of the 2 h preincubation is currently under investigation in our laboratory.

CONCLUSIONS

We have developed a new and highly selective synthesis of *C*-AFGP analogue **2**. Both *C*-AFGP analogues **1** and **2** are potent inhibitors of ice recrystallization but do not exhibit thermal hysteresis activity and can protect embryonic liver cells from cryo-injury at millimolar concentrations. *C*-AFGP analogue **1** at 1−1.5 mg/mL (0.5−0.8 mM) in cell culture is an effective cryoprotectant which appears to be as good as a 2.5% DMSO. It is particularly noteworthy that such a large increase in cell viability is observed under "ideal" thawing conditions that are designed to mitigate but cannot abrogate cell damage from ice recrystallization. This result further validates the hypothesis that inhibiting ice recrystallization during cryopreservation is important for improving cell viability. To the best of our knowledge, this is the first example where an analogue of a biological antifreeze possessing custom-tailored antifreeze activity has been

shown to be an effective cryoprotectant. While the mechanisms by which cryoprotectants protect cells against cryoinjury are complex, the results presented in this paper indicate that *C*-AFGP analogues **1** and **2** are effective cryoprotectants for human embryonic liver cells and that inhibition of ice recrystallization during cryopreservation is an important function for a cryoprotectant. Novel cryoprotectants such as these that are specifically designed to inhibit ice recrystallization may be instrumental in overcoming the current limitations associated with existing cryoprotectants, thus facilitating the efficient preservation of not just cells but tissues and even organs. *C*-AFGP glycoconjuages **1** and **2** are currently being investigated as cryoprotectants with other cell types, and the results of these studies will be reported in due course.

■ ASSOCIATED CONTENT

Supporting Information. Experimental procedures and spectroscopic data for all new compounds. This material is available free of charge via the Internet at http://pubs.acs.org.

■ AUTHOR INFORMATION

Corresponding Author
*rben@uottawa.ca.

■ ACKNOWLEDGMENT

This work was supported with grants from the Natural Sciences and Engineering Research Council (NSERC) of Canada and Canadian Blood Services (CBS).

■ REFERENCES

(1) Mazur, P. (1984) Freezing of living cells: mechanism and implications. *Am. J. Physiol.: Cell Physiol. 247*, C125–C142.

(2) Karlsson, J. O. M., and Toner, M. (1996) Long-term storage of tissues by cryopreservation: critical issues. *Biomaterials 17*, 243–256.

(3) Farrant, J., Walter, C. A., Lee, H., and McGann, L. E. (1977) Use of two-step cooling procedures to examine factors influencing cell survival following freezing and thawing. *Cryobiology 14*, 273–286.

(4) Broxmeyer, H. E. (2010) Will iPS cells enhance therapeutic applicability of cord blood cells and banking? *Cell Stem Cell 6*, 21–24.

(5) Allan, D. S., Keeney, M., Howson-Jan, K., Popma, J., K Weir, K., Bhatia, M., Sutherland, D. R., and Chin-Yee, I. H. (2002) Number of viable CD34 cells reinfused predicts engraftment in autologous hematopoietic stem cell transplantation. *Bone Marrow Transplant. 29*, 967–972.

(6) Abrahamsen, J. F., Wentzel-Larsen, T., and Bruserud, Ø. (2004) Autologous transplantation: the viable transplanted $CD34^+$ cell dose measured post-thaw does not predict engraftment kinetics better than the total $CD34^+$ cell dose measured pre-freeze in patients that receive more than 2×10^6 $CD34^+$ cells/kg. *Cytotherapy 6*, 356–362.

(7) Liseth, K., Abrahamsen, J. F., Bjørsvik, S., Grøttebø, K., and Bruserud, Ø. (2005) The viability of cryopreserved PBPC depends on the DMSO concentration and the concentration of nucleated cells in the graft. *Cytotherapy 7*, 328–333.

(8) Konuma, T., Ooi, J., Takahashi, S., Tomonori, A., Tsukada, T., Kobayashi, T., Sato, S., Kato, S., S., K., Ebihara, Y., Nagamura-Inoue, T., Tsuji, K., Tojo, A., and Asano, S. (2008) Cardiovascular toxicity of cryopreserved cord blood cell infusion. *Bone Marrow Transplant. 41*, 861–845.

(9) Matsumura, K., and Hyon, S.-H. (2009) Polyampholytes as low toxic efficient cryoprotective agents with antifreeze protein properties. *Biomaterials 30*, 4842–4849.

(10) Harding, M. M., Anderberg, P. I., and Haymet, A. D. J. (2003) 'Antifreeze' glycoproteins from polar fish. *Eur. J. Biochem. 270*, 1381–1392.

(11) Feeney, R. E., Burcham, T. S., and Yeh, Y. (1986) Antifreeze glycoproteins from polar fish blood. *Annu. Rev. Biophys. Biophys. Chem. 15*, 59–78.

(12) Wang, T., Zhu, Q., Yang, X., Layne, J. R., and Devries, A. L. (1994) Antifreeze glycoproteins from antarctic notothenioid fishes fail to protect the rat cardiac explant during hypothermic and freezing preservation. *Cryobiology 31*, 185–192.

(13) Rubinsky, B., Arav, A., and Devries, A. L. (1992) The cryoprotective effect of antifreeze glycopeptides from antarctic fishes. *Cryobiology 29*, 69–79.

(14) Carpenter, J. F., and Hansen, T. N. (1992) Antifreeze protein modulates cell survival during cryopreservation: mediation through influence on ice crystal growth. *Proc. Natl. Acad. Sci. U.S.A. 89*, 8953–8957.

(15) Chao, H., Davies, P. L., and Carpenter, J. F. (1996) Effects of antifreeze proteins on red blood cell survival during cryopreservation. *J. Exp. Biol. 199*, 2071–2076.

(16) Tam, R. Y., Rowley, C. N., Petrov, I., Zhang, T., Afagh, N. A., Woo, T. K., and Ben, R. N. (2009) Solution conformation of *C*-linked antifreeze glycoprotein analogues and modulation of ice recrystallization. *J. Am. Chem. Soc. 131*, 15745–15753.

(17) Eniade, A., Purushotham, M., Ben, R., N., Wang, J. B., and Horwath, K. (2003) A Serendipitous discovery of antifreeze protein-specific activity in c-linked antifreeze glycoprotein analogs. *Cell Biochem. Biophys. 38*, 115–124.

(18) Ben, R. N., Eniade, A., and Hauer, L. (1999) Synthesis of a *C*-linked antifreeze glycoprotein (AFGP) mimic: probes for investigating the mechanism of action. *Org. Lett. 1*, 1759–1762.

(19) Eniade, A., and Ben, R. N. (2001) Fully convergent solid phase synthesis of antifreeze glycoprotein analogues. *Biomacromolecules 2*, 557–561.

(20) Liu, S., and Ben, R. N. (2005) *C*-linked galactosyl serine AFGP analogues as potent recrystallization inhibitors. *Org. Lett. 7*, 2385–2388.

(21) Czechura, P., Tam, R. Y., Dimitrijevic, E., Murphy, A. V., and Ben, R. N. (2008) The importance of hydration for inhibiting ice recrystallization with *C*-linked antifreeze glycoproteins. *J. Am. Chem. Soc. 130*, 2928–2929.

(22) Chaytor, J. L., and Ben, R. N. (2010) Assessing the ability of a short fluorinated antifreeze glycopeptide and a fluorinated carbohydrate derivative to inhibit ice recrystallization. *Bioorg. Med. Chem. Lett. 20*, 5251–5254.

(23) Liu, S., Wang, W., Von Moos, E., Jackman, J., Mealing, G., Monette, R., and Ben, R. N. (2007) *In vitro* studies of antifreeze glycoprotein (AFGP) and a *C*-linked AFGP analogue. *Biomacromolecules 8*, 1456–1462.

(24) Bertozzi, C. R., Hoeprich, P. D. J., and Bednarski, M. D. (1992) Synthesis of carbon-linked glycopeptides as stable glycopeptide models. *J. Org. Chem. 57*, 6092–6094.

(25) Dondoni, A., Marra, A., and Massi, A. (1999) Design and use of an oxazolidine silyl enol ether as a new homoalanine carbanion equivalent for the synthesis of carbon-linked isosteres of *O*-glycosyl serine and *N*-glycosyl asparagine. *J. Org. Chem. 64*, 933–944.

(26) Nolen, E. G., Watts, M. M., and Fowler, D. J. (2002) Synthesis of *C*-linked glycopyranosyl serines via a chiral glycine enolate equivalent. *Org. Lett. 4*, 3963–3965.

(27) Debenham, S. D., Debenham, J. S., Burk, M. J., and Toone, E. J. (1997) Synthesis of carbon-linked glycopeptides through catalytic asymmetric hydrogenation. *J. Am. Chem. Soc. 119*, 9897–9898.

(28) Chen, G., Chien, M., Tsuji, M., and Franck, R. W. (2006) *E* and *Z* α-*C*-galactosylceramides by Julia−Lythgoe−Kocienski chemistry: a test of the receptor-binding model for glycolipid immunostimulant. *ChemBioChem 7*, 1017–1022.

(29) Baudin, J. B., Hareau, G., Julia, S. A., and Ruel, O. (1993) A direct synthesis of olefins by reaction of carbonyl compounds with lithio derivatives of 2-[alkyl or (2′-alkenyl)- or benzyl-sulfonyl]-benzothiazoles. *Tetrahedron Lett. 32*, 1175–1178.

(30) Bellingham, R., Jarowicki, K., Kocienski, P. J., and Martin, V. (1996) Synthetic approaches to Rapamycin: synthesis of a C10-C26 fragment via a one-pot Julia olefination reaction. *Synthesis* 285–296.

(31) Albrecht, B. K., and Williams, R. M. (2004) A concise, total synthesis of the TMC-95A/B proteasome inhibitors. *Proc. Natl. Acad. Sci. U.S.A. 101*, 11949–11954.

(32) Kocienski, P. J., Bell, A., and Blakemore, P. R. (2000) 1-*tert*-Butyl-1H-tetrazol-5-yl sulfones in the modified Julia olefination. *Synlett* 365–366.

(33) Guindon, Y., Lavallée, J.-F., Boisvert, L., Chabot, C., Delorme, D., Yoakim, C., Hall, D., Lemieux, R., and Simoneau, B. (1991) Stereoselective radical-mediated reduction and alkylation of α-halo esters. *Tetrahedron Lett. 32*, 27–30.

(34) Giese, B., Gröninger, K. S., Witzel, T., Korth, H.-G., and Sustmann, R. (1987) Synthese von 2-desoxyzuckern. *Angew. Chem. 99*, 246–247.

(35) Patman, R., Juárez-Ruiz, J. M., and Roy, R. (2006) Subtle stereochemical and electronic effects in iridium-catalyzed isomerization of *C*-allyl glycosides. *Org. Lett. 8*, 2961–2964.

(36) Petrenko, Y. A., Jones, D. R. E., and Petrenko, A. Y. (2008) Cryopreservation of human fetal liver hematopoietic stem/progenitor cells using sucrose as an additive to the cryoprotective medium. *Cryobiology 57*, 195–200.

(37) Barker, J. N., and Wagner, J. E. (2002) Umbilical cord blood transplantation: current state of the art. *Curr. Opin. Oncol. 14*, 160–164.

(38) Wagner, J. E., Broxmeyer, H. E., Byrd, R. L., Zehnbauer, B., Schmeckpeper, B., Shah, N., Griffin, C., Emanuel, P. E., Zuckerman, K. S., Cooper, S., Carow, C., Bias, W., and Santos, G. W. (1992) Transplantation of umbilical cord blood after myeloablative therapy: analysis of engraftment. *Blood 79*, 1874–1881.

(39) Can, A., and Karahuseyinoglu, S. (2007) Human umbilical cord stroma with regard to the source of fetus-derived stem cells. *Stem Cells 25*, 2886–2895.

(40) Syková, E., Jendelová, P., Urdzíková, L., Lesný, P., and Hejčl, A. (2006) Bone marrow stem cells and polymer hydrogels—two strategies for spinal cord injury repair. *Cell. Mol. Neurobiol. 26*, 1113–1129.

(41) Kraus, K. H., and Kirker-Head, C. (2006) Mesenchymal stem cells and bone regeneration. *Veterinary Surgery 35*, 232–242.

(42) Stamm, C., Kleine, H.-D., Westphal, B., Petzsch, M., Kittner, C., Nienaber, C. A., Freund, M., and Steinhoff, G. (2004) CABG and bone marrow stem cell transplantation after myocardial infarction. *Thorac. Cardiovasc. Surgeon* 152–158.

(43) Quevedo, H. C., Hatzistergos, K. E., Oskouei, B. N., Feigenbaum, G. S., Rodriguez, J. E., Valdes, D., Pattany, P. M., Zambrano, J. P., Hu, Q., McNiece, I., Heldman, A. W., and Hare, J. M. (2009) Allogeneic mesenchymal stem cells restore cardiac function in chronic ischemic cardiomyopathy via trilineage differentiating capacity. *Proc. Natl. Acad. Sci. U.S.A. 106*, 14022–14027.

(44) Fowler, A., and Toner, M. (2006) Cryo-injury and biopreservation. *Ann. N.Y. Acad. Sci. 1066*, 119–135.

(45) Morris, C. B. (2007) Cryopreservation of Animal and Human Cell Lines, in *Cryopreservation and Freeze-Drying Protocols*, 2nd ed. (Day, J. G., and Stacey, G. N., Eds.) pp 227−236, Humana Press, Totowa, NJ, USA.

(46) Mase, J., Mizuno, H., Okada, K., Sakai, K., Mizuno, D., Usami, K., Kagami, H., and Ueda, M. (2006) Cryopreservation of cultured periosteum: Effect of different cryoprotectants and pre-incubation protocols on cell viability and osteogenic potential. *Cryobiology 52*, 182–192.

(47) Stockert, R. J. (1995) The asialoglycoprotein receptor: relationships between structure, function, and expression. *Physiol. Rev. 75*, 591–609.

(48) Meier, M., Bider, M. D., Malashkevich, V. N., Spiess, M., and Burkhard, P. (2000) Crystal structure of the carbohydrate recognition domain of the h1 subunit of the asialoglycoprotein receptor. *J. Mol. Biol. 300*, 857–865.

SUPPLEMENTARY INFORMATION.

C-Linked Antifreeze Glycoprotein (*C*-AFGP) Analogues as Novel Cryoprotectants.

Mathieu Leclère[1], Bonnie K. Kwok[1], Luke K. Wu[2], David S. Allan[2] and Robert N. Ben[1,*]

[1]Department of Chemistry, D'Iorio Hall, 10 Marie Curie, University of Ottawa, Ottawa, ON, Canada, K1N 6N5.
[2]Department of Medicine, Regenerative Medicine Program, University of Ottawa, ON, Canada, K1N 6N5
rben@uottawa.ca

Table of contents.

General methods..……S2

Experimental procedures..…….….S3-S12

Cryopreservation assay.……S15

^{1}H and ^{13}C NMR spectra..……...……..S17-S38

Experimental Procedures

General Methods. All non-aqueous reactions were performed under argon in flame-dried glassware using dry solvents. Tetrahydrofuran and diethyl ether were distilled from sodium/benzophenone. Dichloromethane, triethylamine and diisopropylethylamine were distilled from calcium hydride. *N*,*N*-Dimethylformamide (HPLC grade) was dried over 4Å molecular sieves. Chemicals were purchased from Aldrich Chemical Company and used without further purification unless otherwise stated. Allyltributylstannane was obtained from Gelest Inc., lithium borohydride was purchased from Strem Chemicals and $Pd(OH)_2/C$ (20% Pd, 50% water) was obtained from TCI America. Low temperature baths were ice/water (0 °C) and solid CO_2/acetone (-78 °C). Reaction temperatures are those of the bath. Reactions were monitored by thin layer chromatography (TLC) using commercial aluminum-backed silica gel sheets coated with silica gel 60 F_{254} (E. Merck). TLC spots were developed by heating the plate after treatment with a cerium ammonium molybdate, phosphomolybdic acid or orcinol solutions. Room temperature corresponds to 22 ^{o}C. Supelco Discovery C-18 cartridges were used for solid phase extraction (SPE) and semi-preparative HPLC was performed on a Varian Polaris C-18 (21.2 x 250 mm).

^{1}H NMR (500 or 400 Mhz) and ^{13}C NMR (125 or 100 MHz) spectra were recorded on Bruker AVANCE 500 / 400 spectrometers. Chemical shifts are reported downfield from tetramethylsilane (δ scale) in ppm and calibrated on the residual proton signal of the solvent. ^{1}H NMR data are reported as follows: Chemical shift (multiplicity, coupling constants (Hz), and integration). Multiplicity is indicated by one or more of the following: s (singlet), d (doublet), t (triplet), q (quartet), m (multiplet), br (broad). High

resolution mass spectroscopy (HRMS) was performed on a Kratos Concept-11A mass spectrometer with an electron beam energy of 70 eV. Electrospray mass spectroscopy was performed on a Micromass Quatro-LC Electrospray spectrometer with a pump rate of 20 µL/min. MALDI-TOF spectra were recorded on an AB Voyager Elite mass spectrometer using DHB as the matrix. IR spectra were recorded on a SHIMADZU FTIR-8400S spectrometer.

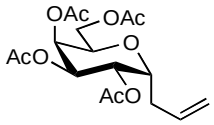

1-(2',3',4',6'-tetra-*O*-acetyl-1'-deoxy-α-D-galactopyranosyl)-prop-2-ene. (11).

To solution of Acetobromogalactose **10** (8.20 g, 20.0 mmol) in 20 mL of distilled CH_2Cl_2, was added 7.7 mL of allyltributyltin (50 mmol, 2.5 equiv.) and 2 mL of a 1 M solution of Et_3B in hexanes. Air was bubbled through the solution by means of a long 22-gauge needle connected to a 60-mL syringe at a flow rate of 5 mL/hr using a syringe pump. After 18 h (total of 90 mL of air), the reaction was concentrated *in vacuo*. The residue was dissolved in CH_3CN (100 mL) and washed with pentane (3 x 100 mL) to remove most of the organostannane. The CH_3CN layer was evaporated and the crude mixture was purified by flash chromatography (Toluene/Pet. Ether/AcOEt 5/4/1) of the *C*-allylated compound **11** as a waxy solid (5.41g, 70%, 94% purity). ^{1}H NMR (400 MHz, $CDCl_3$) δ 5.71 (m, 1H), 5.38 (dd, *J* = 3.1, 2.4 Hz, 1H), 5.24 (dd, *J* = 9.3, 5.1 Hz, 1H), 5.18 (dd, *J* = 9.3, 3.3 Hz, 1H), 5.08 (m, 2H), 4.26 (ddd, *J* = 9.9, 5.1, 4.7 Hz, 1H), 4.17 (dd, *J* = 12.2, 8.7 Hz, 1H), 4.05 (m, 2H), 2.44 (m, 1H), 2.24 (m, 1H), 2.08 (s, 3H), 2.03 (s, 3H), 2.00 (s, 3H), 1.99 (s, 3H). ^{13}C NMR (100 MHz, $CDCl_3$) δ 170.6, 170.1, 169.9,

169.8, 133.3, 117.7, 71.4, 68.3, 67.9, 67.6, 61.5, 30.9, 20.8, 20.7, 20.7. MS (ESI) *m/z* calcd. for $C_{17}H_{24}NaO_9$ $(M+Na)^+$ 395.132 found 395.208. IR (neat, cm^{-1}) 1743, 1396, 1224, 1047.

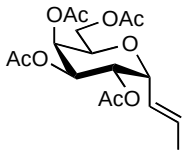

(*E*)-1-(2',3',4',6'-Tetra-*O*-acetyl-1'-deoxy-α-D-galactopyranose)-prop-1-ene (13).

Hydrogen was bubbled trough a suspension of $(Ph_2MeP)_2Ir(cod)PF_6$ (350 mg, 0.41 mmol, 0.03 equiv) in 5 mL of THF. The red suspension turned quickly into a yellow solution and bubbling was continued for 2 min. Excess of hydrogen was removed by bubbling argon for 10 min and the resulting activated catalyst was transferred to a degassed solution of **11** (5.1 g, 13.7 mmol) in 30 mL of THF. After stirring for 4 hrs under Ar, THF was evaporated and the crude product was purified by flash chromatography (Toluene/Pet. Ether/AcOEt 5/4/1) to give the alkene **13** as viscous oil (4.85 g, 95% yield, 94% purity). ^{1}H NMR (400 MHz, $CDCl_3$) δ 5.86 (dqd, *J* = 15.3, 6.6, 1.6 Hz, 1H), 5.61 (ddq, *J* = 15.5, 6.2, 1.6 Hz, 1H), 5.38 (dt, *J* = 3.2, 1.7 Hz, 1H), 5.26 (dd, *J* = 10.4, 5.6 Hz, 1H), 5.14 (dd, *J* = 10.4, 3.2 Hz, 1H), 4.72 (dd, *J* = 6.1, 5.9 Hz, 1H), 4.13 (m, 1H), 4.11-4.02 (m, 2H), 4.02 (s), 2.02-1.99 (m, 7H), 1.75 (dt, *J* = 6.5, 1.5 Hz, 3H), 4.06 (dd, *J* = 6.4, 4.0 Hz, 2H), 1.12 (s, 3H), 2.10 (s, 3H), 2.05 (s, 3H), 1.99 (s, 3H), 1.76 (dt, *J* = 6.7, 1.4 Hz, 3H). ^{13}C NMR (100 MHz, $CDCl_3$): δ 170.5, 170.2, 170.1, 169.9, 133.2, 122.6, 73.2, 68.3, 68.1, 68.0, 61.8, 20.8, 20.7, 20.7, 18.3. MS (ESI) *m/z* calcd. for $C_{17}H_{24}NaO_9$ $(M+Na)^+$ 395.132 found 395.184. IR (neat, cm^{-1}) ν 1739, 1369, 1213, 1041.

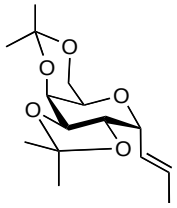

(*E*)-1-(1'-deoxy-2',3';4',6'-di-*O*-isopropylidene-α-D-galactopyranosyl)-prop-1-ene (14).

To a solution of **13** (4.70 g, 12.6 mmol) in 20 mL of MeOH was added 174 mg of K_2CO_3 (1.26 mmol, 0.1 equiv). After stirring for 6 hrs, the base was neutralized by addition of acidic resin (Dowex® 50WX8, H^+ form) until neutral pH. The resin was filtered off and the filtrate was concentrated *in vacuo*. After drying under high vacuum for several hours, the solid was re-dissolved in DMF (75 mL) under Ar. 190 mg of $TsOH.H_2O$ (1 mmol, 0.08 equiv) was added followed by dropwise addidion of 2-methoxypropene (5.4 mL, 56.7 mmol, 4.5 equiv.). After stirring for 1 hr at room temperature, the acid was neutralized with Et_3N (0.5 mL). The DMF was evaporated under high vaccum and the crude product was purified by flash chromatography (Pet. Ether/AcOEt 4.5/1 + 0.5% Et_3N) to give 2.69 g of the title compound **14** (75 %) as a colorless oil. ^1H NMR (400 MHz; $CDCl_3$): δ 5.87 (ddd, *J* = 15.6, 6.5, 1.7 Hz, 1H), 5.62-5.57 (m, 1H), 4.88-4.85 (m, 1H), 4.44 (dt, *J* = 1.5, 0.7 Hz, 1H), 4.27 (dd, *J* = 9.9, 5.7 Hz, 1H), 4.08 (dd, *J* = 12.9, 2.1 Hz, 1H), 3.89 (dd, *J* = 12.9, 1.5 Hz, 1H), 3.67 (dd, *J* = 9.9, 2.9 Hz, 1H), 3.37 (t, *J* = 1.5 Hz, 1H), 1.73 (dt, *J* = 6.5, 1.6 Hz, 3H), 1.46 (s, 3H), 1.46, (s, 3H), 1.44 (s, 3H), 1.40 (s, 3H). ^{13}C NMR (101 MHz; CDCl3): δ 131.3, 123.2, 110.0, 98.5, 75.2, 74.4, 70.9, 67.7, 63.5, 63.5, 29.3, 26.7, 26.5, 18.5, 18.3. MS (ESI) *m/z* calcd. for $C_{17}H_{28}NO_9$ $(M+NH_4)^+$ 390.2 found 390.2. IR (neat, cm^{-1}) ν 2988, 2916, 1668, 1379, 1371.

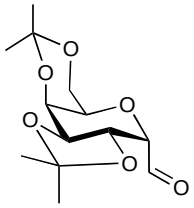

1-deoxy-1-formyl-2,3;4,6-di-*O*-isopropylidene-α-D-galactopyranose (8).

Alkene **14** (1.90 g, 6.7 mmol) in 20 mL of dry CH_2Cl_2 was treated with ozone at -78 °C until the solution turned blue. Excess of ozone was removed by bubbling nitrogen and PPh_3 (2.6 g, 10.0 mmol, 1.5 equiv.) was added at -78 °C. The mixture was slowly warmed to room temperature and stirred overnight. The reaction was monitored by ^{1}H NMR of the crude mixture. Solvent was then evaporated and the aldehyde **8** dried under high vacuum. Due to its instability it was not purified and used directly in the next step. However, it was found to be stable (^{1}H NMR) for several days when stored under Ar in a -20 °C freezer. ^{1}H NMR ($CDCl_3$, 400 MHz, aldehyde signals): δ 9.83 (s, 1H), 4.31 (d, *J* = 6.8 Hz, 1H), 4.46 (br, 1H), 4.40 (dd, *J* = 10.0, 6.7 Hz, 1H), 4.05 (dd, *J* = 13.2, 2.0 Hz, 1H), 3.97 (dd, *J* = 13.2, 1.4 Hz, 1H), 3.81 (m, 1H), 3.47 (dd, *J* = 10.0, 2.6 Hz, 1H), 1.47 (s, 3H), 1.44 (s, 3H), 1.42 (s, 3H), 1.37 (s, 3H). ^{13}C NMR ($CDCl_3$, 100 MHz, aldehyde signals) δ 200.8, 111.1, 98.6, 79,2, 76.1, 69.7, 67.4, 66.6, 63.1, 29.2, 26.4, 26.4, 18.4. HRMS (EI) *m/z* calcd. for $C_{12}H_{19}O_5$ $(M\text{-}CHO)^+$ 243.1232 found 243.1234. IR (neat, cm^{-1}) ν 2929, 1731.

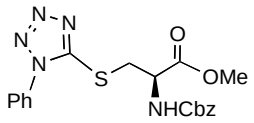

(*R*)-methyl 2-((benzyloxycarbonyl)amino)-3-((1-phenyl-1*H*-tetrazol-5-yl)thio) propanoate (16).

N-Cbz-L-serine methyl ester **15** (5.00 g, 19.8 mmol), 5-phenyl-tetrazole-1-thiol (7.0 g, 39.3 mmol, 2.0 equiv.) and PPh_3 (8.8 g, 33.7 mmol, 1.7 equiv) were dissolved in 50 mL of THF under Ar. The solution was cooled to 0 °C and 6.7 mL of diisopropyl azodicarboxylate (33.8 mmol, 1.7 equiv.) was added dropwise. The mixture was warmed to room temperature and stirred for 1 hr. The reaction was then quenched by addition of saturated solution of $NaHCO_3$ (5 mL) and the mixture was diluted with Et_2O. The organic layer was washed with sat. $NaHCO_3$, water, brine and dried over Na_2SO_4. Evaporation of the solvents followed by flash chromatography of the crude (Et_2O/Pet. Ether 2/1 then pure Et_2O) yielded 6.70 g of the sulfide **16** (82%) as a white solid. ^{1}H NMR (400 MHz, $CDCl_3$) δ 7.53 (m, 5H), 7.30 (m, 5H), 5.86 (d, *J* = 7.6 Hz, 1H), 5.07 (s, 2H), 4.79 (ddd, *J* = 7.6, 6.6, 4.5 Hz, 1H), 3.93 (dd, *J* = 14.0, 4.5 Hz, 1H), 3.81 (dd, *J* = 14.0, 6.6 Hz, 1H), 3.73 (s, 3H).^{13}C NMR (100 MHz, $CDCl_3$) δ 170.2, 133.4, 130.4, 129.9, 128.6, 128.3, 128.1, 124.0, 67.3, 53.5, 53.1, 35.4.HRMS (EI) *m/z* cald. for $C_{19}H_{19}N_5O_4S_1$ $(M)^+$ 413.1158 found 413.1133. IR (neat, cm^{-1}) ν 3260, 2875, 1716, 1498.

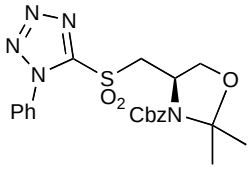

(*R*)-*N*-(benzyloxycarbonyl) 2,2-dimethyl-4-(((1-phenyl-1*H*-tetrazol-5-yl)sulfonyl)methyl) oxazolidine (9).

Methyl ester **16** (6.60 g, 16.0 mmol) was dissolved in a mixture of THF (20 mL) and Et_2O (80 mL). One millilitre of MeOH (24 mmol, 1.5 equiv.) and 0.52 g of $LiBH_4$ (24 mmol, 1.5 equiv.) were successfully added and the mixture was heated to reflux for 30 min. The reaction was then cooled with an ice bath and carefully quenched by dropwise

addition of water. The organic layer was washed with 1% HCl, water, sat. $NaHCO_3$, brine and dried over Na_2SO_4. After evaporation of the solvents and drying under high vacuum, the crude alcohol was re-dissolved in 50 mL dry CH_2Cl_2. 0.30 g of $TsOH.H_2O$ (1.6 mmol, 0.1 equiv.) were added and the solution was cooled to 0 °C. 3.9 mL of 2-Methoxypropene (40.0 mmol, 2.5 equiv.) were added and the mixture warmed to room temperature. After stirring for 1 hr, Et_3N (1 mL) was added and the DCM layer was washed twice with sat. $NaHCO_3$ and dried over Na_2SO_4. The solvent was evaporated and the crude dry compound was dissolved in 70 mL of a 2/2/3 mixture of $CH_2Cl_2/CH_3CN/H_2O$. Sodium periodate (15.4 g, 72.0 mmol, 4.5 equiv.) and $RuCl_3$ hydrate (66 mg, *ca.* 0.32 mmol, 2 mol%) was successively added and the mixture was stirred vigorously at room temperature for 2 h. One hundred milliliters of CH_2Cl_2 and 100 mL of water were added and the organic layer was separated, washed twice with water and once with brine. After drying over Na_2SO_4 and evaporation of the solvents, the crude was purified by flash chromatography (Pet. Ether/AcOEt 4/1) to give 4.71 g of the sulfone **9** (65% over 3 steps) as a waxy solid. ^{1}H NMR (DMSO-d_6, 500 MHz, 383 K) δ 7.63 (m, 5H), 7.31 (m, 5H), 5.08 (d, J = 12.5 Hz, 1H), 5.01 (d, J = 12.5 Hz, 1H), 4.47 (br s, 1H), 4.00 (m, 4H), 1.46 (s, 3H), 1.46 (s, 3H). ^{13}C NMR (DMSO-d_6, 125 MHz, 383 K) δ 154.2, 152.0, 136.8, 133.5, 131.9, 128.8, 128.3, 128.1, 126.6, 94.3, 67.1, 58.4, 31.0, 27.1, 24.2. HRMS (EI) *m/z* calcd. for $C_{20}H_{20}N_5O_5S_1$ $(M\text{-}CH3)^+$ 442.1185 found 442.1187. IR (neat, cm^{-1}) 1693, 1348.

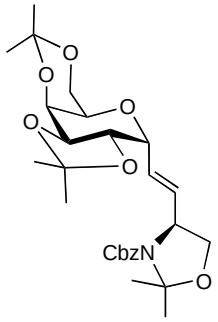

(*S*)-*N*-benzyloxycarbonyl-2,2-dimethyl-4-((*E*)-1'-deoxy-2',3';4',6'-di-*O*-isopropylidene-α-D-galactopyranosyl)vinyl)oxazolidine (7)

Sulfone **9** (4.50 g, 10.0 mmol, 1.5 equiv.) was dissolved in 20 mL of THF. The solution was cooled to -78 °C and 10.0 mL of 1M NaHMDS in THF (10 mmol, 1.5 equiv.) were added. After 5 min of stirring, a solution of the crude aldehyde **8** in 10 mL of THF was added *via cannula*. The stirring was continued for 1 hr at -78 °C and the temperature slowly warmed to room temperature over 2 hrs. After an additional hour of stirring, the mixture was quenched with few drops of water and diluted with 100 mL of Et_2O. The organic layer was washed with water and brine, dried over Na_2SO_4, concentrated and the crude purified by flash chromatography (Pet. Ether/AcOEt 2.5/1) to give 2.2 g of the alkene **7** (65% from **14**). ^{1}H NMR (DMSO-d_6, 500 MHz, 343 K) δ 7.36 (m, 5H), 5.82 (ddd, *J* = 16.2, 6.3, 1.9 Hz, 1H), 5.68 (dd, *J* = 16.2, 3.8 Hz, 2H), 5.06 (s, 2H), 4.78 (brt, *J* = 4.4 Hz, 1H), 4.49 (t, *J* = 6.2 Hz, 1H), 4.27-4.11 (br, 1H), 4.07 (dd, *J* = 9.0, 6.2 Hz, 1H), 4.04 (dd, *J* = 10.2, 5.81 Hz, 1H), 3.94 (d, *J* = 13.2 Hz, 1H), 3.75 (dd, *J* = 9.0, 2.0 Hz, 1H), 3.64 (d, *J* = 13.2 Hz, 1H), 3.41 (brs, 1H), 3.13 (brs, 1H), 1.54 (s, 3H), 1.47 (s, 6H), 1.38 (s, 6H), 1.33 (s, 6H) 1.29 (s, 3H), 1.27 (s, 3H). ^{13}C NMR (DMSO-d_6, 125 MHz, 343K) δ 152.2, 137.1, 133.1, 128.8, 128.2, 127.9, 124.9, 109.5, 97.9, 94.0, 74.3, 73.6, 70.9, 68.4, 67.3, 66.5, 63.9, 63.0, 58.5, 29.5, 27.0, 26.8, 23.4, 18.5. HRMS (EI) *m/z* calcd. for $C_{27}H_{37}N_1O_8$ $(M)^+$ 503.2519 found 503.2521.

IR (neat, cm^{-1}) ν 2985, 2935, 1701.

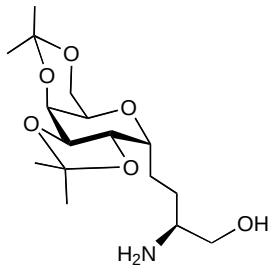

(*S*)-3-amino-4-(1'deoxy-2',3';4',6'-di-*O*-isopropylidene-α-D-galactopyranosyl)-butanol (17).

H_2 was bubbled for 5 min through a solution of the alkene **7** (2.10 g, 4.2 mmol) and $Pd(OH)_2/C$ (600 mg, 0.42 mmol, 0.1 equiv.) in 20 mL of EtOH for 5 min. Bubbling was stopped and stirring was continued for 1h under H_2 atmosphere. The flask was then purged with N_2 and the mixture was filtered through Celite® and the solvent removed *in vacuo*. After drying under high vacuum for several hours, 1.32 g of amino alcohol **17** were obtained (95%). ^{1}H NMR ($CDCl_3$, 400 MHz) d 4.41 (brs, 1H), 4.32 (m, 1H), 4.25 (dd, *J* = 9.7, 5.4 Hz, 1H), 4.06 (dd, *J* = 12.9, 2.0 Hz, 1H), 3.85 (d, *J* = 12.9 Hz, 1H), 3.67 (dd, *J* = 9.9, 2.9 Hz, 1H), 3.59 (dd, *J* = 10.7, 3.3 Hz, 1H), 3.23 (brs, 1H), 3.20-3.00 (brs, 3H), 2.92 (brs, 1H), 1.61 (m, 3H), 1.44 (s, 3H), 1.43 (s, 3H), 1.42 (s, 3H), 1.38 (s, 3H), 1.36 (m, 1H). ^{13}C ($CDCl_3$, 100 MHz) d 110.0, 98.6, 73.9, 70.8, 67.4, 65.6, 63.1, 52.8, 30.1, 29.2, 26.7, 26.5, 21.0, 18.4. MS(ESI) *m/z* calcd. for $C_{16}H_{30}N_1O_6$ $(M+H)^+$ 332.207 found 332.273. IR (neat, cm^{-1}) ν 3400, 2991, 2935.

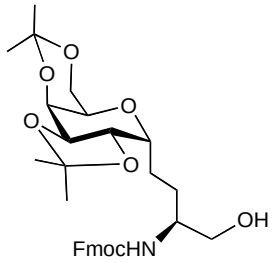

((*S*)-3-(*N*-(9-fluorenylmethyloxycarbonyl)amino)-4-(1'-deoxy-2',3';4',6'-di-*O*-isopropylidene-α-D-galactopyranosyl)-butanol (18).

To a solution of **17** (1.30 g, 3.9 mmol) and $NaHCO_3$ (0.65 g, 7.8 mmol, 2 equiv.) in a mixture of 20 mL of 1,4-dioxane and 20 mL of water was added Fmoc-OSu (1.4 g, 4.2 mmol, 1.1 equiv.) at 0 °C. The solution was stirred overnight at room temperature, then diluted with CH_2Cl_2 and the organic layer was washed with water, separated, dried over Na_2SO_4 and concentrated *in vacuo*. The crude was purified by flash chromatography (CH_2Cl_2/MeOH 98/2) to yield 1.60 g (75%) of the title compound **18**. ^{1}H NMR (C_6D_6, 500 MHz) δ 7.58 (dd, *J* = 6.5, 1.6 Hz, 2H), 7.51 (m, 2H), 7.22 (m, 4H), 4.87 (brs, 1H), 4.50 (dd, *J* = 10.0, 5.6 Hz, 1H), 4.45 (m, 2H), 4.27 (ddd, *J* = 9.2, 5.8, 2.8 Hz, 1H), 4.07 (m, 2H), 3.84 (dd, *J* = 12.8, 1.4 Hz, 1H), 3.65 (dd, *J* = 12.8, 2.4 Hz, 1H), 3.51 (dd, *J* = 10.0, 3.3 Hz, 1H), 3.44 (m, 1H), 3.37 (dd, *J* = 11.0, 5.1 Hz, 1H), 2.78 (s, 1H), 1.64 (m, 2H), 1.51 (m, 1H), 1.46 (s, 3H), 1.42 (s, 3H), 1.37 (s, 3H), 1.28 (m, 1H), 1.20 (s, 3H). ^{13}C NMR (C_6D_6, 125 MHz): δ 157.0, 144.7, 144.6, 141.9, 127.4, 125.4, 125.3, 120.3, 109.8, 98.4, 76.8, 74.4, 71.4, 67.9, 66.6, 65.4, 63.8, 63.5, 53.7, 48.0, 29.4, 29.0, 27.1, 26.9, 21.5, 18.8. MS(ESI) *m/z* calcd. for $C_{31}H_{40}N_1O_8$ $(M+Na)^+$ 576.257 found 576.288. IR (neat, cm^{-1}) ν 2989, 2937, 1703.

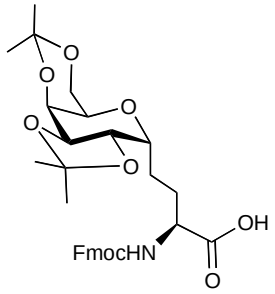

((*S*)-3-(*N*-(9-fluorenylmethyloxycarbonyl)amino)-4-(1'-deoxy-2',3';4',6'-di-*O*-isopropylidene-α-D-galactopyranosyl)-butanoic acid (3b).

Alcohol **18** (1.50 g, 2.7 mmol) was dissolved in 20 mL of acetonitrile. $NaHCO_3$ (0.68 g, 8.1 mmol, 3 equiv.), TEMPO (42 mg, 0.27 mmol, 0.1 equiv.) and $PhI(OAc)_2$ (1.3 g, 4.0 mmol, 1.5 equiv.) were added and the mixture was stirred vigorously. The reaction was monitored by TLC (CH_2Cl_2/MeOH 98/2). Upon completion of the reaction (*ca*. 6 hrs) the mixture was diluted with CH_2Cl_2 and washed with water. The organic layer was separated, dried over Na_2SO_4 and the solvent evaporated. The crude aldehyde was re-dissolved in 20 mL of *t*-BuOH and 6 mL of 2-methyl-2-butene. The solution was then cooled to 0°C and 14 mL of 1 M solution of aqueous KH_2PO_4 (14.0 mmol, 5.2 equiv.) followed by 14 mL of 1M solution of $NaClO_2$ (14.0 mmol, 5.2 equiv.). After stirring at 0 °C for 2 hrs, the mixture was partitioned with AcOEt (100 mL) and water (50 mL). The organic layer was separated; the aqueous phase was extracted with 100 mL of AcOEt. The combined organic layers were dried over Na_2SO_4 and the solvents evaporated. Purification of the crude by flash chromatography (CH_2Cl_2/MeOH 96/4) yielded 1.22 g of the building block **3b** (80%). ^{1}H NMR (DMSO-d_6/$CDCl_3$ 10/1, 500 Mhz, 343 K) δ 7.85 (d, *J* = 7.6 Hz, 2H), 7.70 (dd, *J* = 7.8, 7.4Hz, 2H), 7.41 (dd, *J* = 7.5, 7.5 Hz, 2H), 7.32 (ddd, *J* = 7.8, 7.5, 1.6 Hz, 2H), 4.39 (d, *J* = 3.0 Hz, 1H), 4.30 (dd, *J* = 10.0, 7.0 Hz, 1H), 4.27 (d, *J* =6.8 Hz, 1H), 4.25-4.28 (m, 2H), 4.07 (m, 2H), 3.72 (dd, *J* = 10.0, 2.8 Hz, 1H),

3.66 (dd, J = 12.8, 1.0 Hz, 1H), 3.28 (brs, 1H), 1.89 (m, 1H), 1.74 (m, 2H), 1.58 (m, 1H), 1.39 (s, 3H), 1.33 (s, 6H), 1.30 (s, 3H). ^{13}C NMR (DMSO-d_6/$CDCl_3$ 10/1, 125 MHz, 293 K) δ 174.1 (br), 156.3 (br), 149.1, 149.0, 145.9, 132.9, 132.3, 130.4, 125.4, 114.0, 102.6, 80.5, 78.4, 75.5, 72.0, 70.9, 67.8, 67.7, 51.8, 34.5, 31.9, 23.9. Note: the signals at 174.1 and 156.3 ppm are broadened due to the presence of rotamers. The resolution could be improved by heating the sample (343 K) but in these conditions, concomitant Fmoc cleavage occurred. MS (ESI) *m/z* calcd. for $C_{31}H_{37}N_1O_9Na$ $(M+Na)^+$ 590.237 found 590.286. IR (neat cm^{-1}) ν 2987, 2933, 1712, 1704.

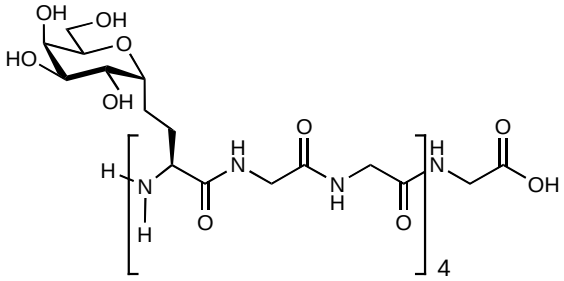

Glycoconjugate 2.

A typical SPPS cycle consisted in the following steps: 300 mg (0.18 mmol) of Wang Fmoc-Gly-OH resin were swollen in DMF for 1hr. Fmoc deprotection was achieved by adding a mixture of piperidine/DBU/DMF 2/2/96 for 30 min. The resin was washed with DMF and treated with a pre-mixed solution of Fmoc-Gly-Gly-OH and HCTU (6 equiv. each) in DMF. DIPEA (12 equiv.) was added and the resin was shaken gently for 3hrs. After washing the resin with DMF, the Fmoc carbamate was cleaved as describe above. The resin was washed and treated with the pre-mixed building block **3b** and HCTU (1.5 equiv. each) and DIPEA (3 equiv.) for 24 hrs. The resin was then washed with DMF (3x10 mL) and the Fmoc carbamate cleaved as described above. This cycle was repeated

3 more times in order to achieve the desired peptide length. The resin was washed with DMF, CH_2Cl_2, MeOH and dried under high vacuum for 6hrs. Final cleavage using a mixture of TFA/*i*-Pr_3SiH/H_2O 92.5/5/2.5 for 3 hrs furnished the crude glycoconjugate. The resin was filtered and washed with TFA and the combined filtrates were concentrated *in vacuo* at 35 °C. Acetone was added to precipitate the crude glycopeptide which was further purified by SPE on a Discovery® C18 cartridge followed by preparative HPLC (C18) to give 55 mg of the glycoconjugate **2** (20%). ^{1}H NMR (D_2O, 500 Mhz, pre-saturated on HOD frequency) δ 4.21 (brs, 1H), 4.00-3.68 (brm, 8H), 3.65-3.47 (brm, 4H), 1.95-1.41 (brm, 4H). ^{13}C NMR (D_2O, 125 MHz) δ 174.5, 171.8, 171.6, 170.4, 75.2, 74.7, 71.8, 71.6, 69.5, 69.0, 68.0, 67.9, 61.1, 54.0, 52.9, 46.6, 42.5, 42.2, 41.5, 40.4, 27.3, 27.2, 20.2, 19.3. HRMS (MALDI-TOF) *m/z* calcd. for $C_{58}H_{97}N_{13}NaO_{34}$ $(M+Na)^+$ 1542.6159 found 1542.6965.

Cryopreservation assays.

- *Cell culture.*

WRL 68 human embryonic liver cells (ATCC, CL-48) were cultured in Eagle's minimum essential media (MEM) supplemented with 10% fetal bovine serum (FBS) (Fisher) and 1% penicillin-streptomycin (Sigma) in 75 cm^2 flasks (Corning). Cells were incubated in a 37 °C incubator supplied with 5% CO_2. Cells from passage 90 to 100 of WRL 68 were used in this study. No evidence of overgrowth or morphological changes consistent with apoptosis was observed. All cells were detached using a trypsin-EDTA solution (0.25% trypsin, 1 mM EDTA-4Na). The suspension were diluted to 10 mL using growth medium and centrifuged at 2,000 rpm for 10 min. The supernatant was discarded and the cell re-suspended in 10 mL of medium. Final concentration of was determined using a hematocytometer.

- *Cryopreservation assay.*

WRL 68 cells were cultured and trypsinized as described above. Cells were diluted with culture media and counted using a hematocytometer. Aliquots containing $1x10^6$ cells were added to 2 mL Eppendorf vial and cells were pelleted by centrifugation for 10 min at 2,000 rpm. The supernatant was removed and the cells were re-suspended in 0.1 mL HTK supplemented with glycoconjugate **1** or **2** to a concentration of 1, 1.5, 2 and 5 mg/mL. HTK supplemented with DMSO to a concentration 2.5 or 5 % served as the positive controls. Cell suspensions were transferred to 2 mL cryogenic vials (Corning) and placed in a "Mr. Frosty" freezing container (Nalgene). The container was placed in an ultra-cold freezer (-80 °C) for 24 hrs allowing a cooling rate of approximately 1 °C

/min. Samples were then stored in a cryogenic tank in the vapour phase of liquid nitrogen (-150 °C) for 6 days. Following storage, samples were rapidly thawed in a 37 °C water bath with gentle agitation. Thawed samples were transferred to 2 mL centrifuge tubes and slowly diluted to 1 mL by dropwise addition of cell culture medium. Cells were pelleted by centrifugation for 10 min at 2,000 rpm. The supernatant was decanted and the pellets re-suspended in 0.5 mL of Annexin V binding buffer (BD Pharmingen).

- *Flow Cytometry*.

100 μL of the suspension of cells in binding buffer was transferred to a flow cytometry tube. Subsequently, 5 μL of 7-Actinomycin D (7AAD) (BD Pharmingen) and 4 μL of Annexin V-PE (BD Pharmingen) were added and samples were incubated for 20 min in the dark. Following incubation, samples were diluted to 500 μL with 1x Annexin-V binding buffer. Flow cytometry analysis on 10,000 cells was carried out on a BD LSR flow cytometer using CellQuest (BD). Annexin V-PE was measured on FL-2 while 7-AAD was measured on FL-3. Complete Viability was denoted as Annexin V-/7AAD- cells, early apoptotic as Annexin V+ /7AAD- cells, late apoptotic as Annexin V+ /7AAD+ cells and Annexin V- /7AAD+ as necrotic cells. Compensation was set from single stain experiments with 7-AAD and Annexin-V. Aliquots from non-cryopreserved samples labelled with equivalent fluorochromes were used to set the control gate excluding 99%7AAD+ cells. Time between thawing and analysis by flow cytometry was 2 hrs. All trials were performed in duplicate.

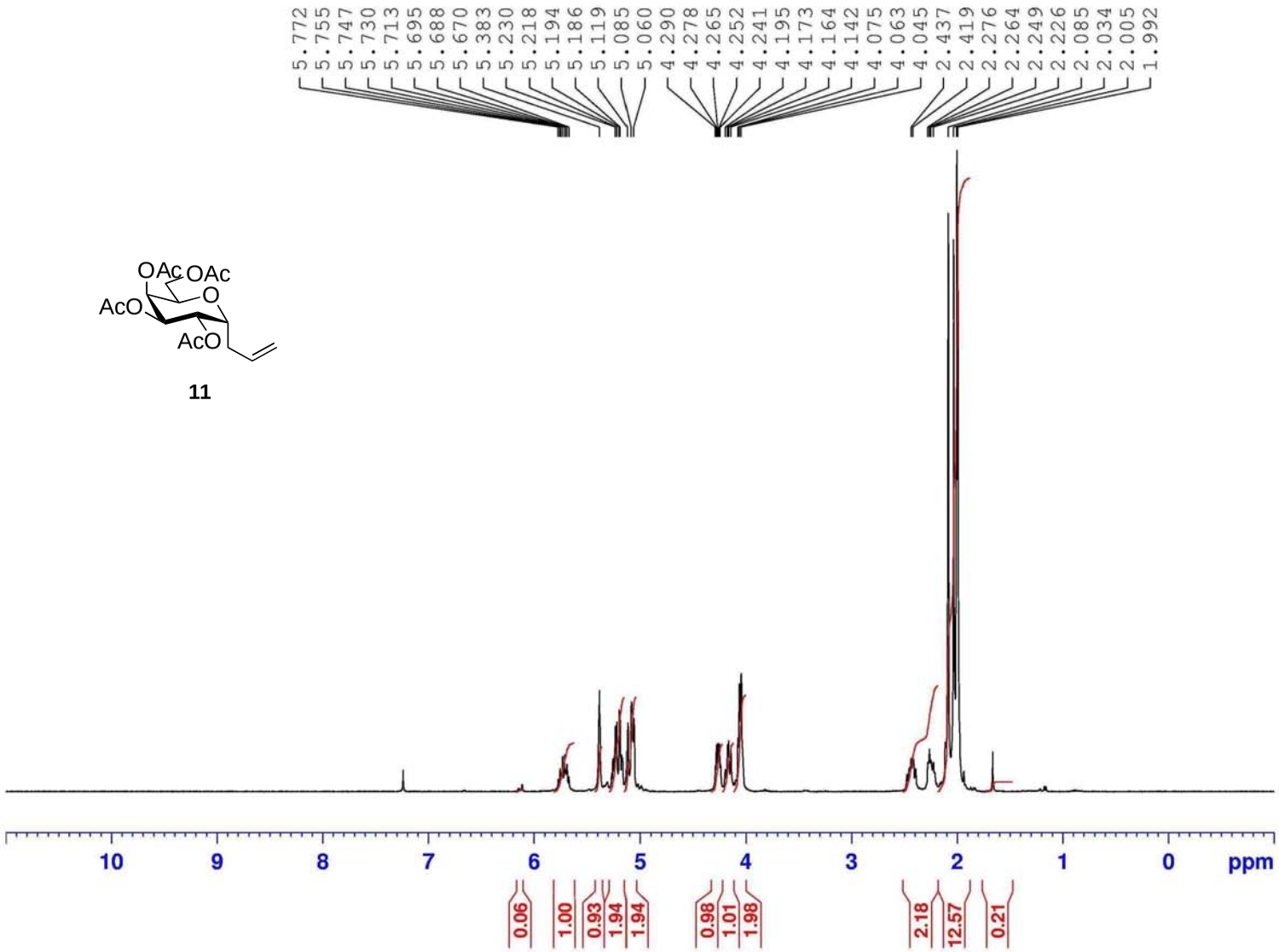
5.772
5.755
5.747
5.730
5.713
5.695
5.688
5.670
5.383
5.230
5.218
5.194
5.186
5.119
5.085
5.060
4.290
4.278
4.265
4.252
4.241
4.195
4.173
4.164
4.142
4.075
4.063
4.045
2.437
2.419
2.276
2.264
2.249
2.226
2.085
2.034
2.005
1.992
OAc
OAc
O
AcO
AcO
10
9
8
7
6
5
4
3
2
1
0
ppm
0.06
1.00
0.93
1.94
1.94
0.98
1.01
1.98
2.18
12.57
0.21

11

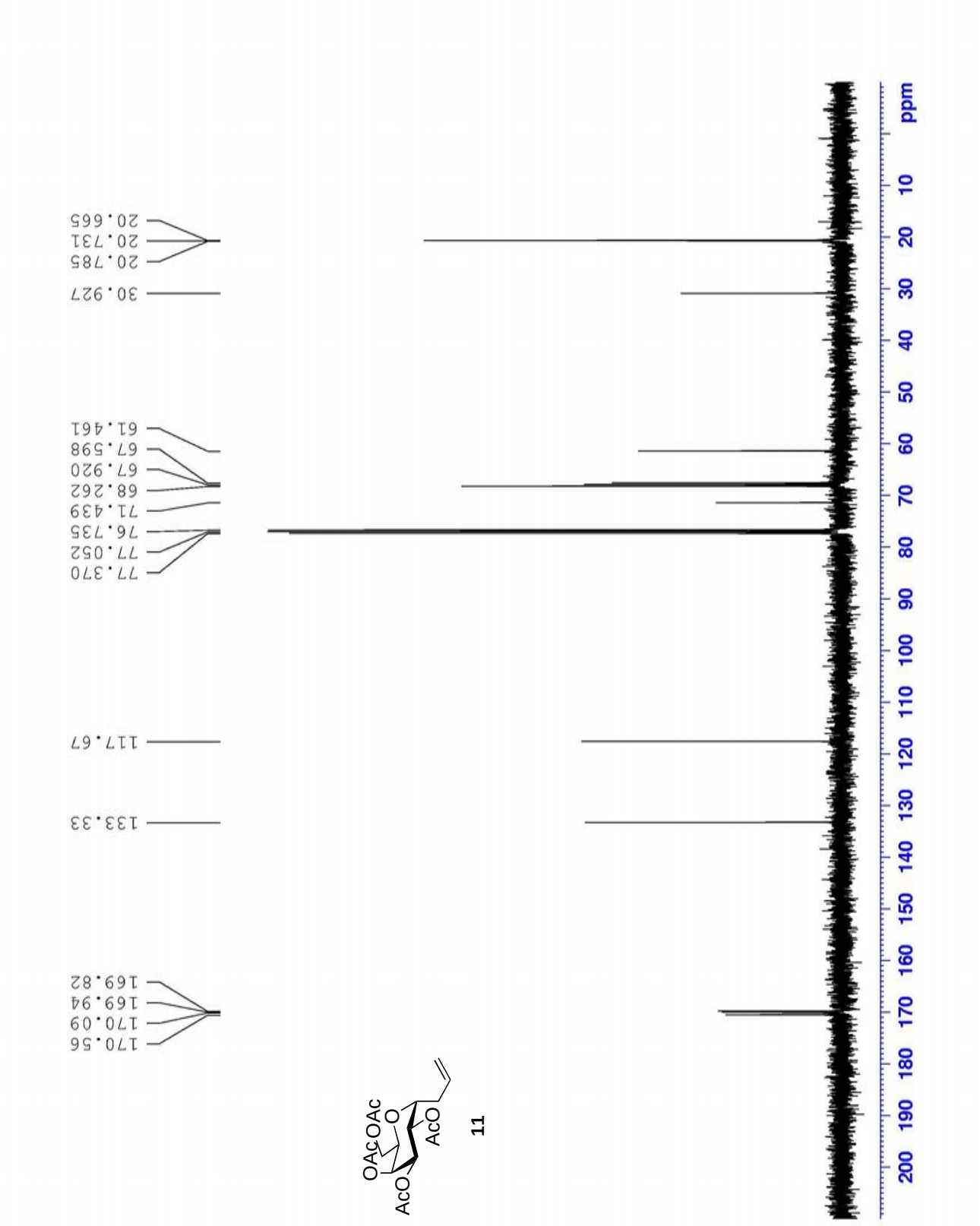
170.56
170.09
169.94
169.82
133.33
117.67
77.370
77.052
76.735
71.439
68.262
67.920
67.598
61.461
30.927
20.785
20.731
20.665
ppm
11

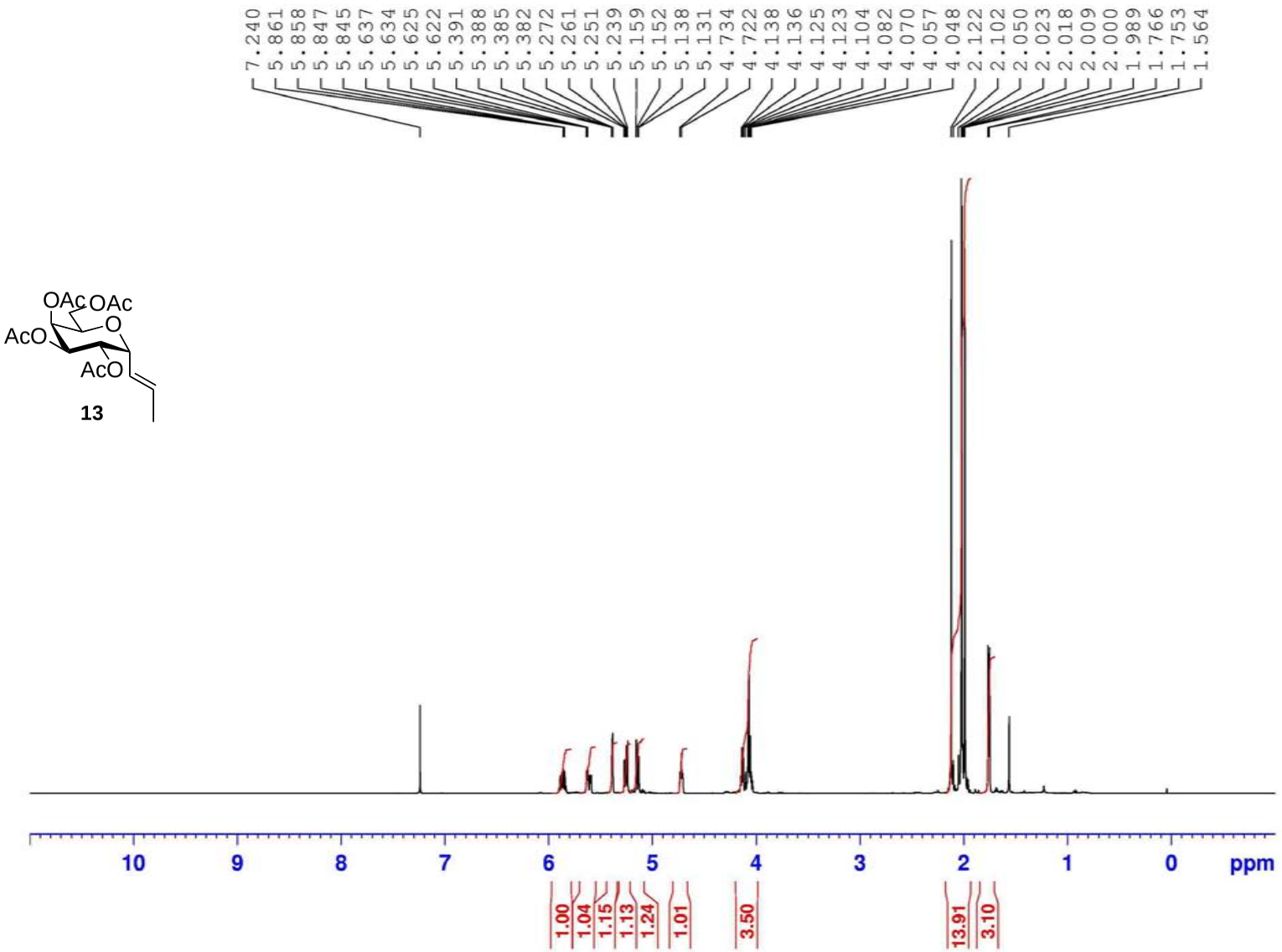
7.240
5.861
5.858
5.847
5.845
5.637
5.634
5.625
5.622
5.391
5.388
5.385
5.382
5.272
5.261
5.251
5.239
5.159
5.152
5.138
5.131
4.734
4.722
4.138
4.136
4.125
4.123
4.104
4.082
4.070
4.057
4.048
2.122
2.102
2.050
2.023
2.018
2.009
2.000
1.989
1.766
1.753
1.564
OAc
OAc
O
AcO
AcO
13
10
9
8
7
6
5
4
3
2
1
0
ppm
1.00
1.04
1.15
1.13
1.24
1.01
3.50
13.91
3.10

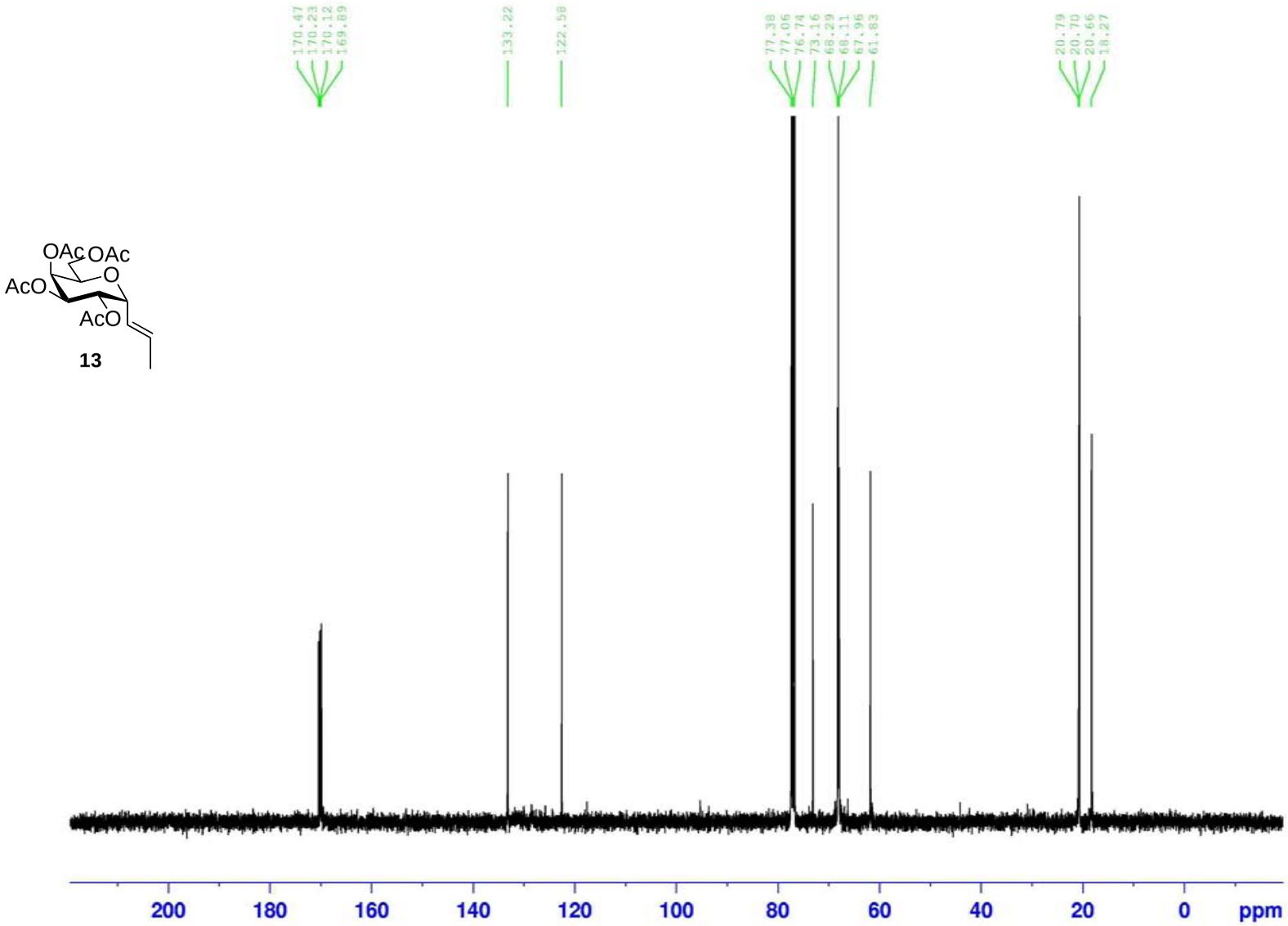
170.47
170.23
170.12
169.89
133.22
122.58
77.38
77.06
76.74
73.16
68.29
68.11
67.96
61.83
20.79
20.70
20.66
18.27
OAc
OAc
O
AcO
AcO
13
200
180
160
140
120
100
80
60
40
20
0
ppm

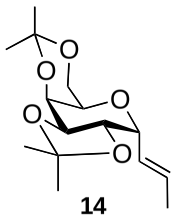
O
O
O
O
O

14

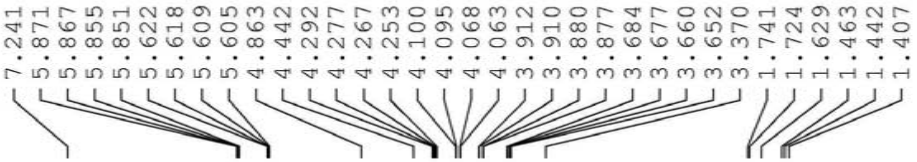
7.241
5.871
5.867
5.855
5.851
5.622
5.618
5.609
5.605
4.863
4.442
4.292
4.277
4.267
4.253
4.100
4.095
4.068
4.063
3.912
3.910
3.880
3.877
3.684
3.677
3.660
3.652
3.370
1.741
1.724
1.629
1.463
1.442
1.407

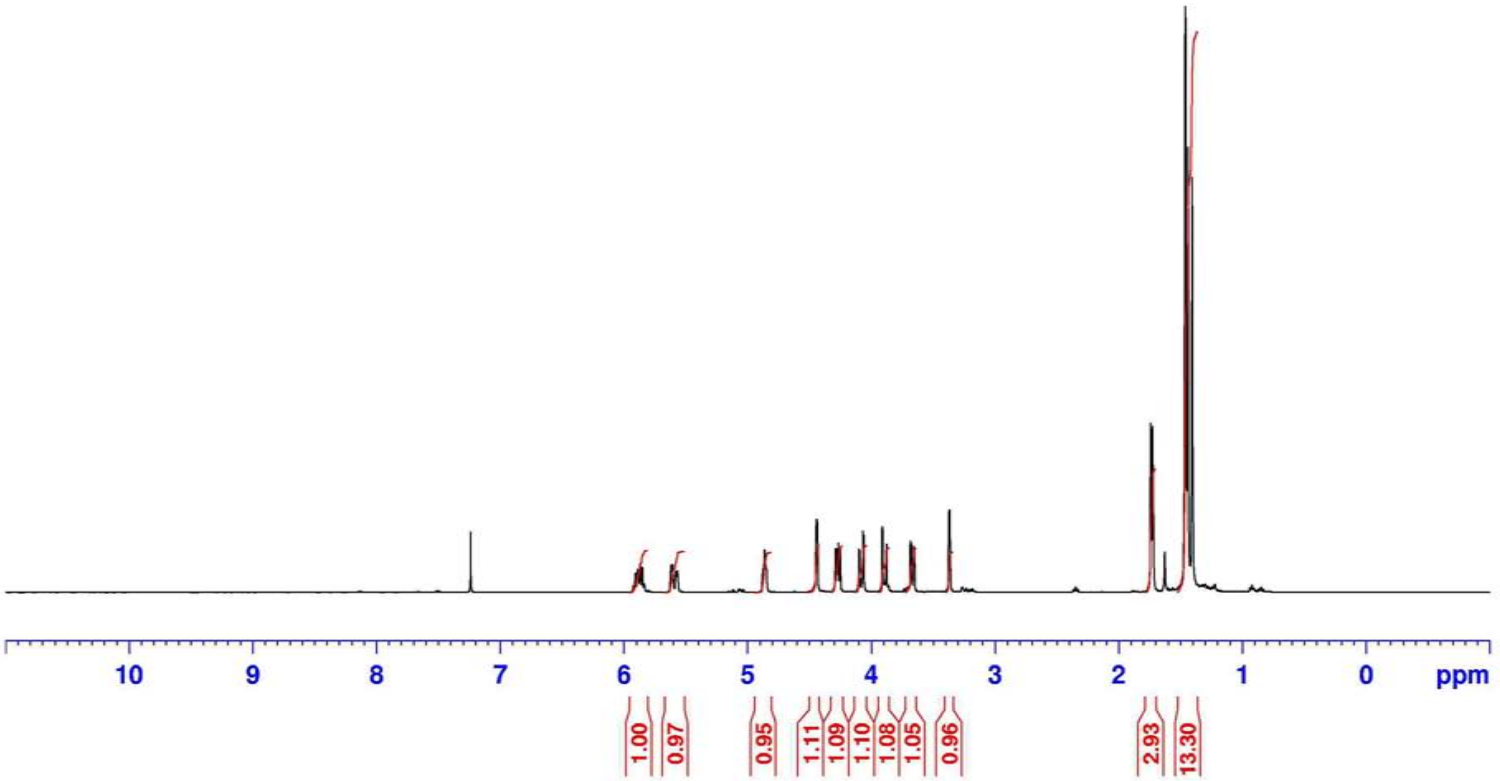
10
9
8
7
6
5
4
3
2
1
0
ppm
1.00
0.97
0.95
1.11
1.09
1.10
1.08
1.05
0.96
2.93
13.30

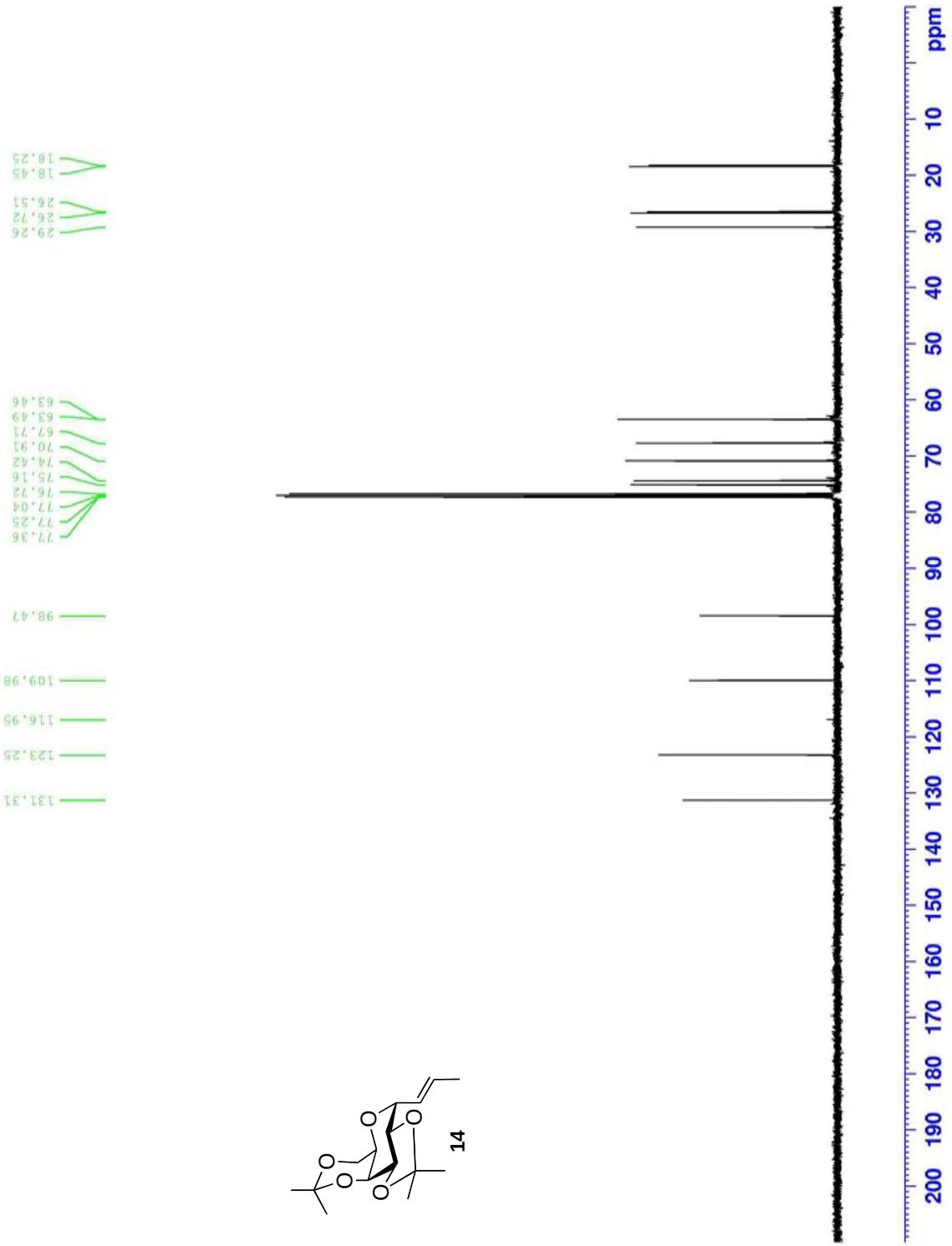
18.25
18.45
26.51
26.72
29.26
63.46
63.49
67.71
70.91
74.42
75.16
76.72
77.04
77.25
77.36
98.47
109.98
116.95
123.25
131.31
14
ppm
10
20
30
40
50
60
70
80
90
100
110
120
130
140
150
160
170
180
190
200

ppm
0
1
2
3
4
5
6
7
8
9
10
14.19
1.00
1.11
1.11
1.15
2.16
1.00
2.77
15.75
10.69
0.91
1.372
1.393
1.418
1.440
1.474
3.454
3.461
3.479
3.486
3.809
3.812
3.949
3.952
3.982
3.985
4.034
4.039
4.067
4.072
4.382
4.399
4.407
4.423
4.465
4.906
4.923
9.833
8

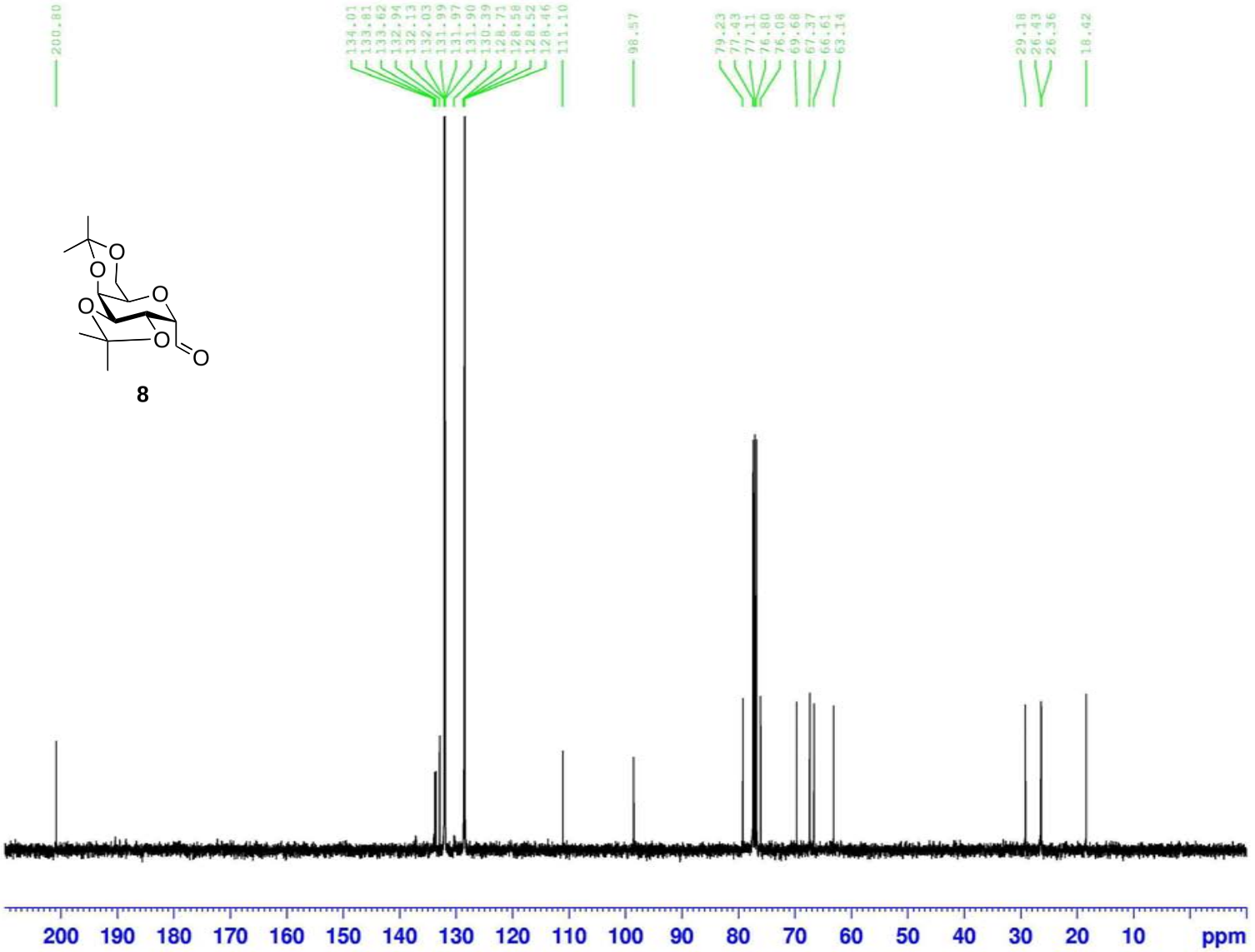
200.80
134.01
133.81
133.62
132.94
132.13
132.03
131.99
131.97
131.90
130.39
128.71
128.58
128.52
128.46
111.10
98.57
79.23
77.43
77.11
76.80
76.08
69.68
67.37
66.61
63.14
29.18
26.43
26.36
18.42
8
200 190 180 170 160 150 140 130 120 110 100 90 80 70 60 50 40 30 20 10 ppm

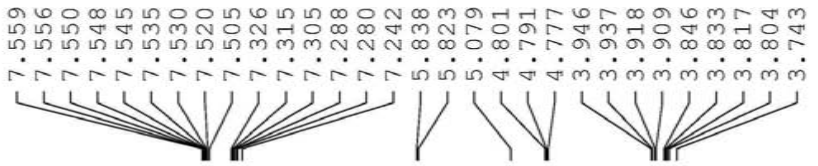
7.559
7.556
7.550
7.548
7.545
7.535
7.530
7.520
7.505
7.326
7.315
7.305
7.288
7.280
7.242
5.838
5.823
5.079
4.801
4.791
4.777
3.946
3.937
3.918
3.909
3.846
3.833
3.817
3.804
3.743
1.542

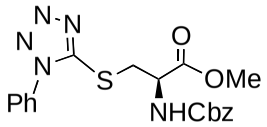
N
N
N
N
Ph
S
O
OMe
NHCbz

16

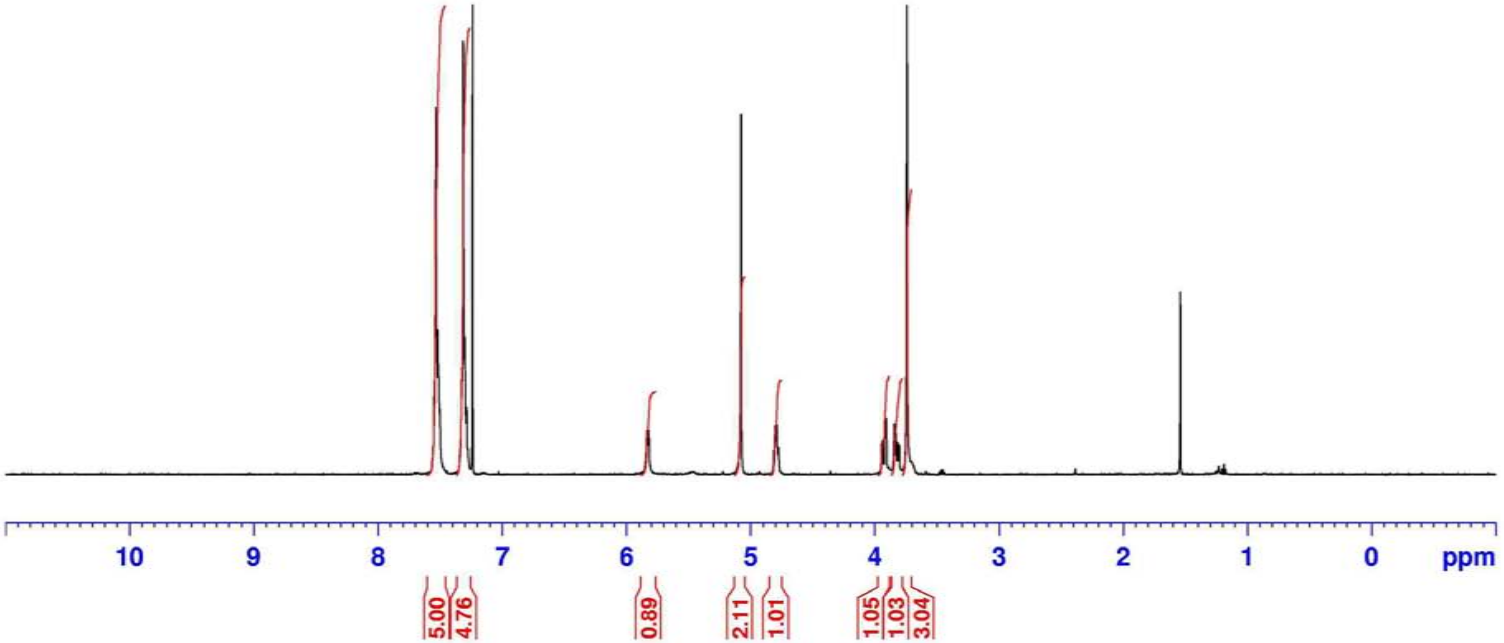
10
9
8
7
6
5
4
3
2
1
0
ppm
5.00
4.76
0.89
2.11
1.01
1.05
1.03
3.04

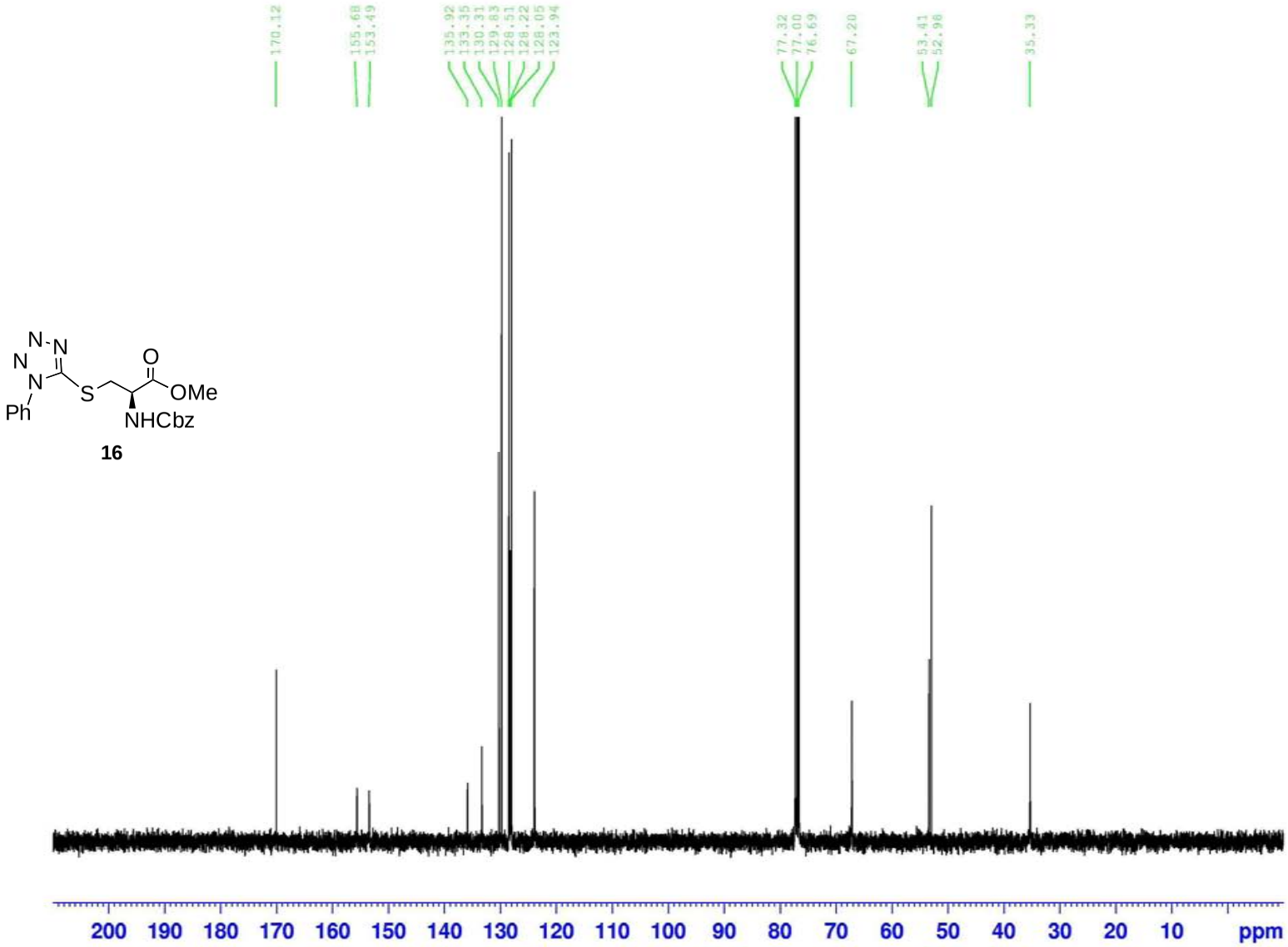
170.12
155.68
153.49
135.92
133.35
130.31
129.83
128.51
128.22
128.05
123.94
77.32
77.00
76.69
67.20
53.41
52.98
35.33
N
N
N
N
Ph
S
O
OMe
NHCbz
16
200
190
180
170
160
150
140
130
120
110
100
90
80
70
60
50
40
30
20
10
ppm

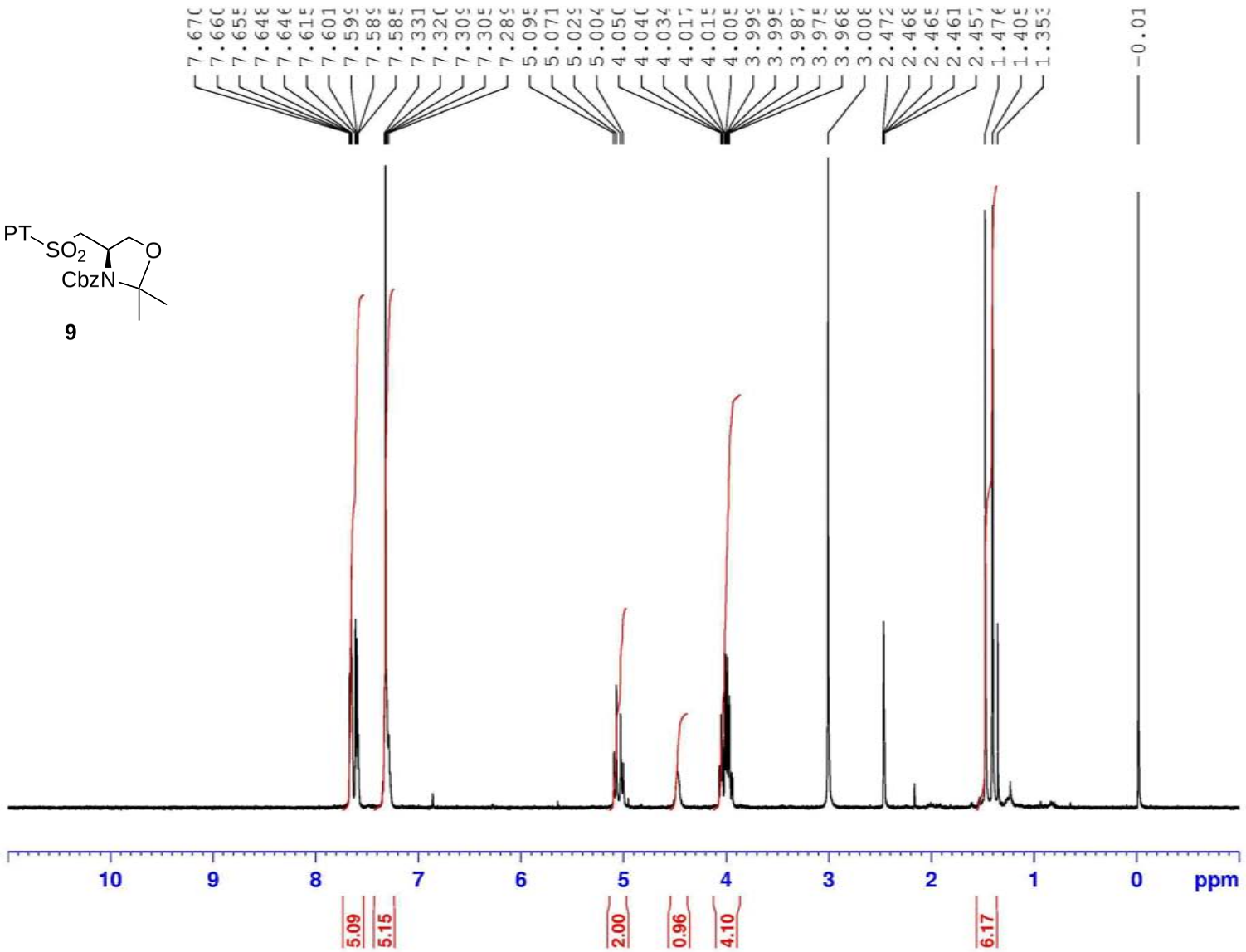
PT
SO2
CbzN
O
9
7.670
7.660
7.655
7.648
7.646
7.615
7.601
7.595
7.585
7.583
7.331
7.320
7.309
7.303
7.285
5.095
5.071
5.029
5.004
4.050
4.040
4.034
4.017
4.015
4.008
3.999
3.995
3.987
3.975
3.968
3.008
2.472
2.468
2.465
2.461
2.457
1.476
1.405
1.353
-0.01
10
9
8
7
6
5
4
3
2
1
0
ppm
5.09
5.15
2.00
0.96
4.10
6.17

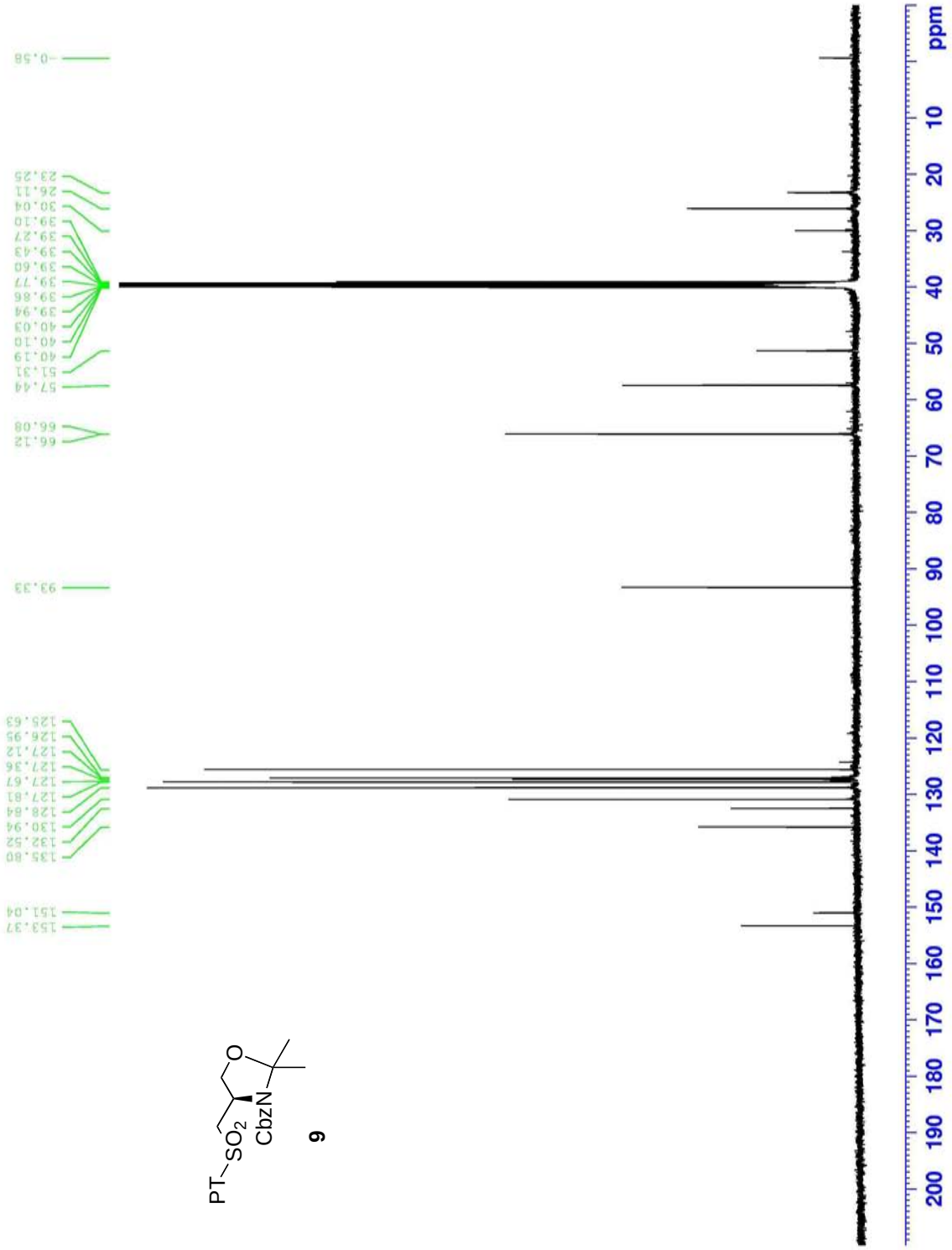
PT
SO2
CbzN
O
9
ppm
10
20
30
40
50
60
70
80
90
100
110
120
130
140
150
160
170
180
190
200
-0.58
23.25
26.11
30.04
39.10
39.27
39.43
39.60
39.77
39.86
39.94
40.03
40.10
40.19
51.31
57.44
66.08
66.12
93.33
125.63
126.95
127.12
127.36
127.67
127.81
128.64
130.94
132.52
135.80
151.04
153.37

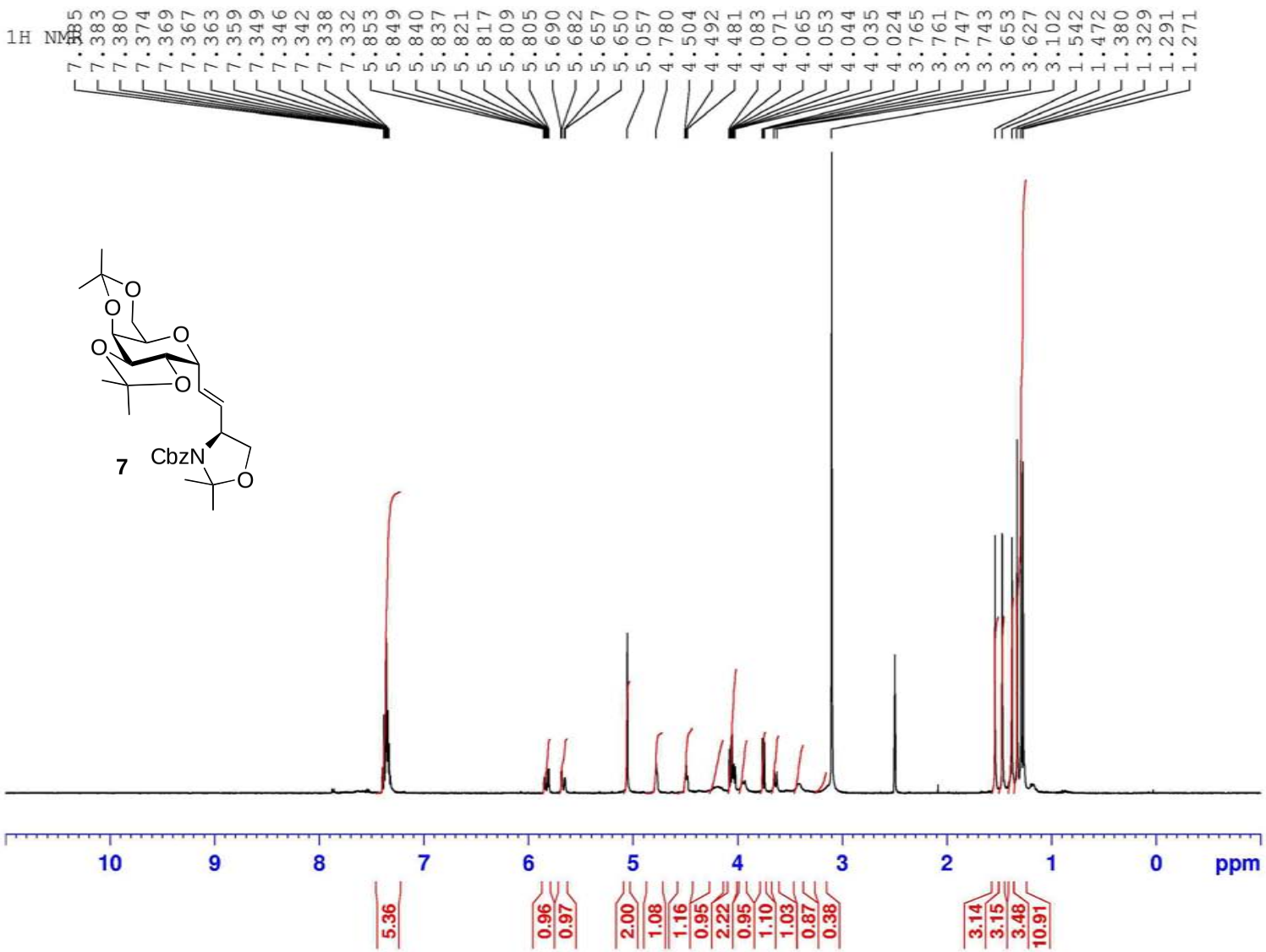
1H NMR
7.385
7.383
7.380
7.374
7.369
7.367
7.363
7.359
7.349
7.346
7.342
7.338
7.332
5.853
5.849
5.840
5.837
5.821
5.817
5.809
5.805
5.690
5.682
5.657
5.650
5.057
4.780
4.504
4.492
4.481
4.083
4.071
4.065
4.053
4.044
4.035
4.024
3.765
3.761
3.747
3.743
3.653
3.627
3.102
1.542
1.472
1.380
1.329
1.291
1.271
7
CbzN
10
9
8
7
6
5
4
3
2
1
0
ppm
5.36
0.96
0.97
2.00
1.08
1.16
0.95
2.22
0.95
1.10
1.03
0.87
0.38
3.14
3.15
3.48
10.91

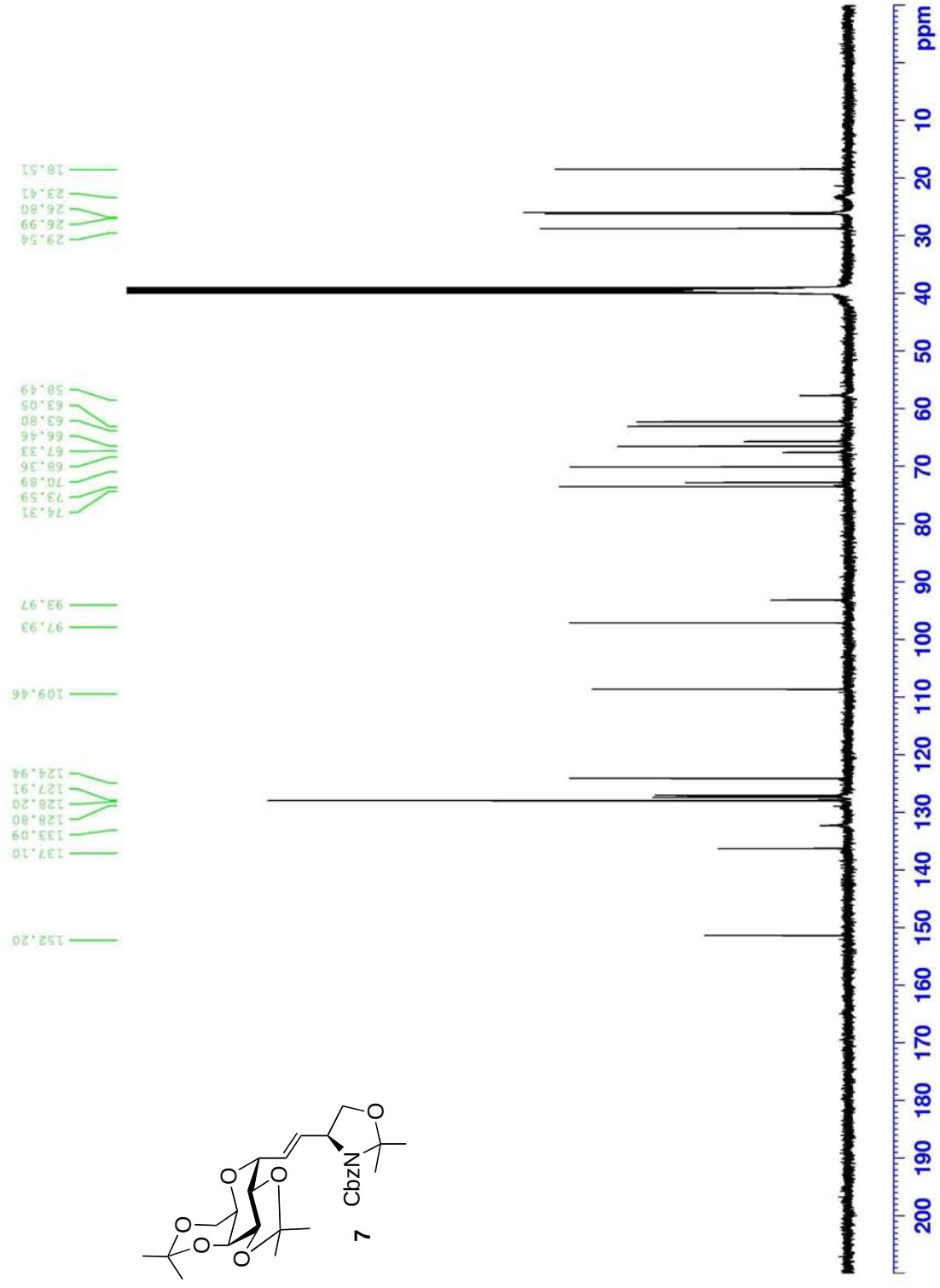
18.51
23.41
26.80
26.99
29.54
58.49
63.05
63.80
66.46
67.33
68.36
70.89
73.59
74.31
93.97
97.93
109.46
124.94
127.91
128.20
128.80
133.09
137.10
152.20
CbzN
7
ppm

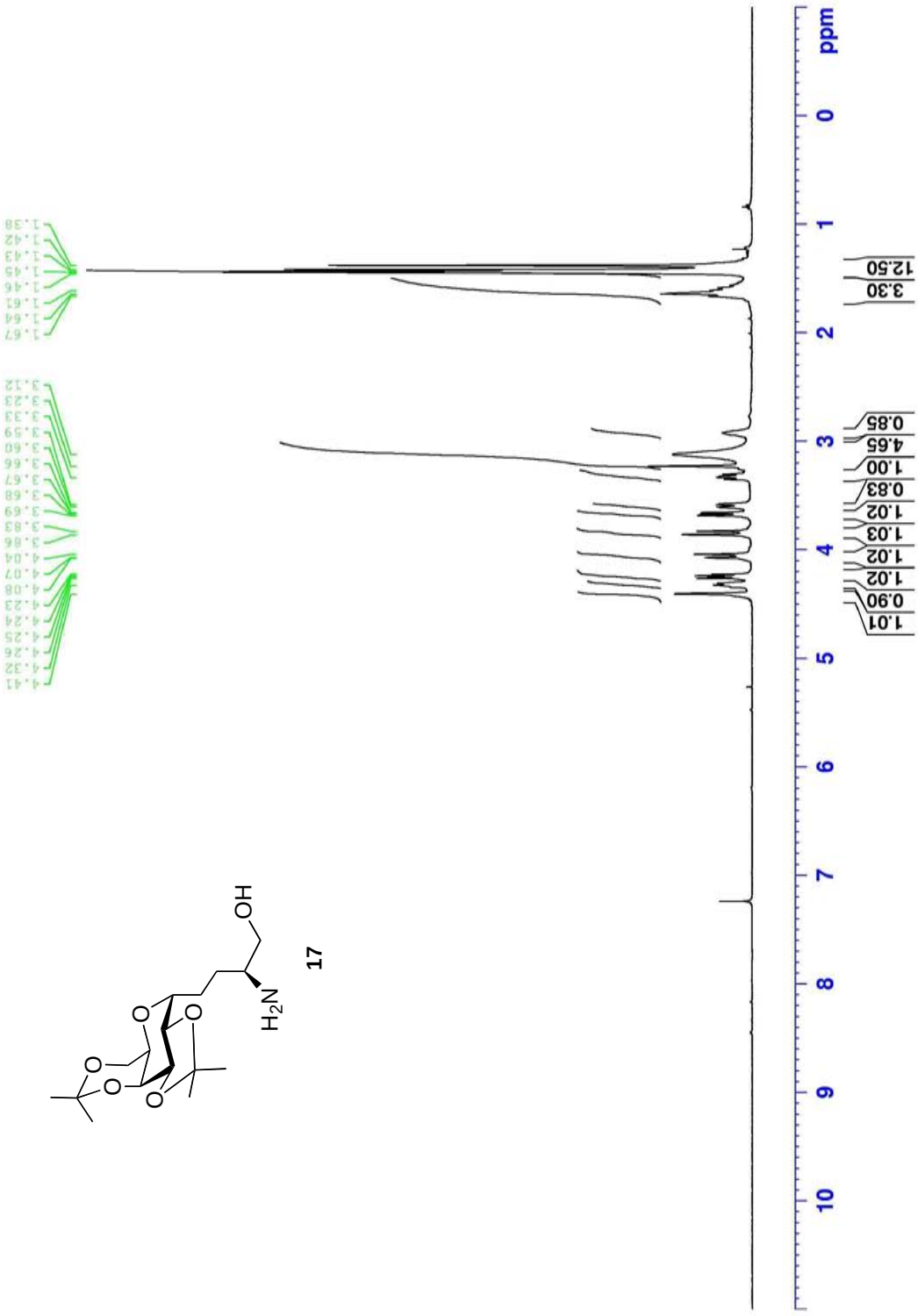
ppm
0 1 2 3 4 5 6 7 8 9 10
12.50
3.30
0.85
4.65
1.00
0.83
1.02
1.03
1.02
1.02
0.90
1.01
1.38 1.42 1.43 1.45 1.46 1.61 1.64 1.67
3.12 3.23 3.33 3.59 3.60 3.66 3.67 3.68 3.69 3.83 3.86 4.04 4.07 4.08 4.23 4.24 4.25 4.26 4.32 4.41
OH
H2N
O
O
O
O
O

17

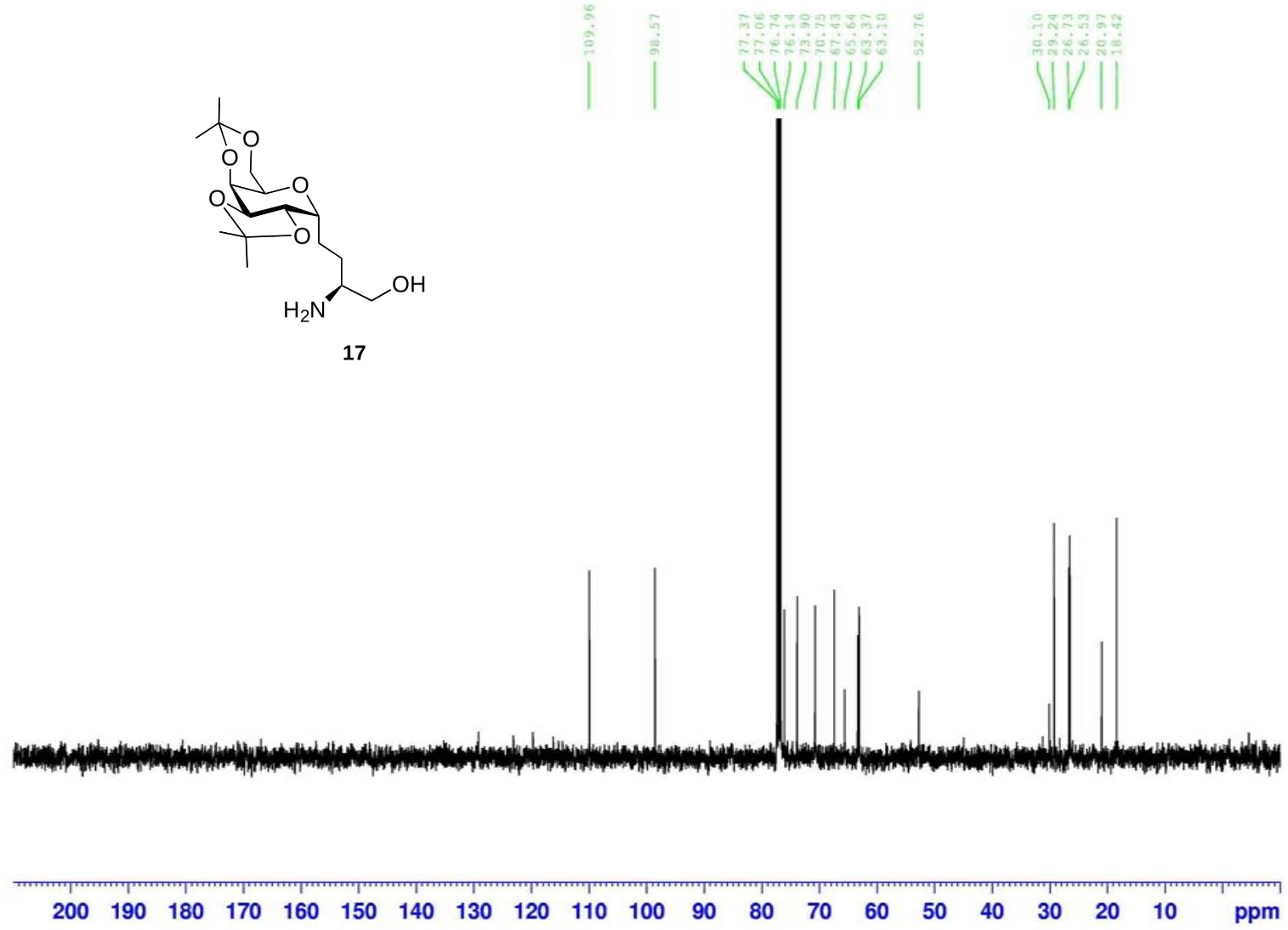
109.96
98.57
77.37
77.06
76.74
76.14
73.90
70.75
67.43
65.64
63.37
63.10
52.76
30.10
29.24
26.73
26.53
20.97
18.42
O
O
O
O
O
OH
H2N
200 190 180 170 160 150 140 130 120 110 100 90 80 70 60 50 40 30 20 10 ppm

17

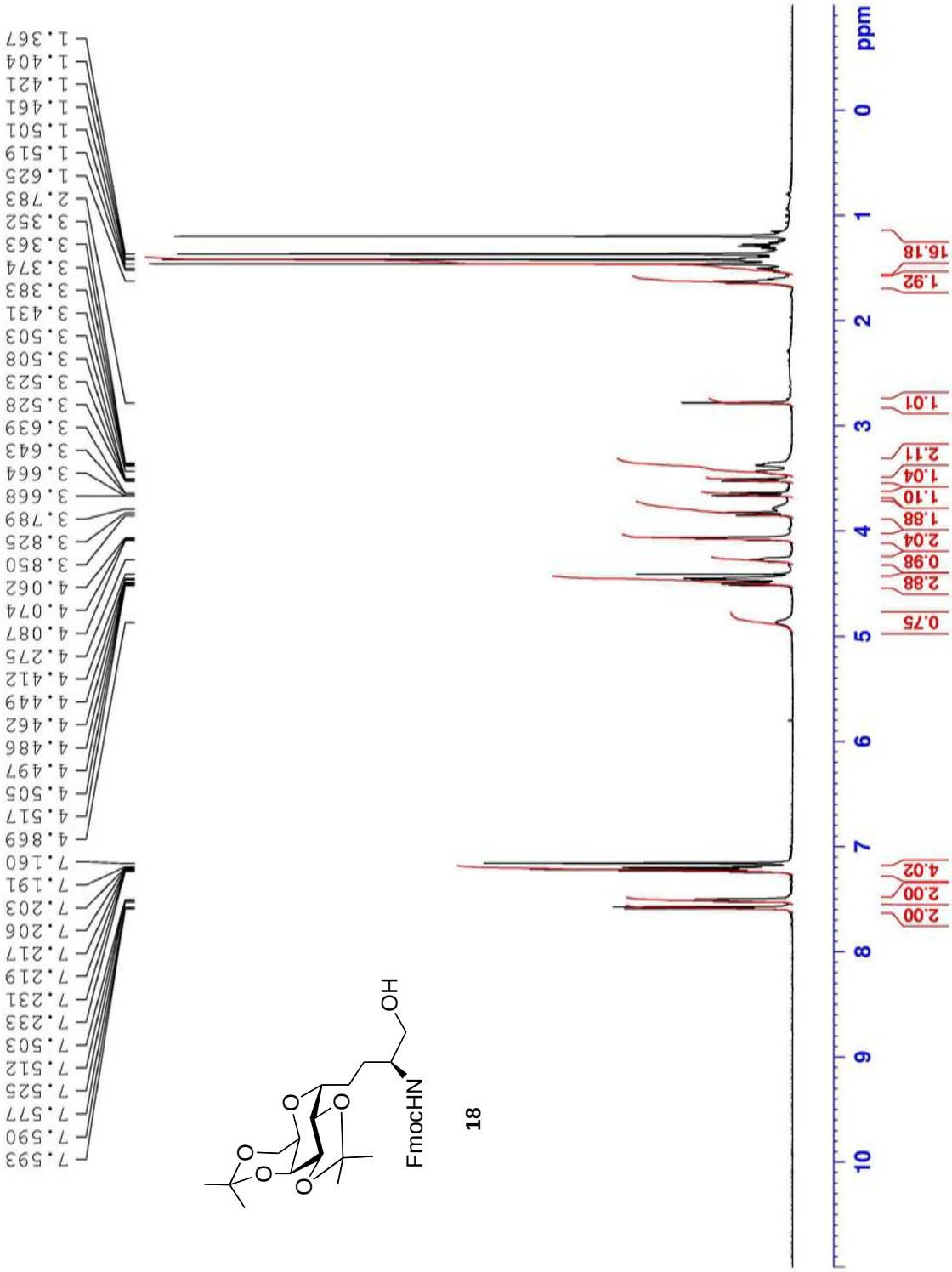
ppm
0
1
2
3
4
5
6
7
8
9
10
16.18
1.92
1.01
2.11
1.04
1.10
1.88
2.04
0.98
2.88
0.75
2.00
2.00
4.02
OH
FmocHN
O
O
O
O
O
7.593
7.590
7.577
7.525
7.512
7.503
7.233
7.231
7.219
7.217
7.206
7.203
7.191
7.160
4.869
4.517
4.505
4.497
4.486
4.462
4.449
4.412
4.275
4.087
4.074
4.062
3.850
3.825
3.789
3.668
3.664
3.643
3.639
3.528
3.523
3.508
3.503
3.431
3.383
3.374
3.363
3.352
2.783
1.625
1.519
1.501
1.461
1.421
1.404
1.367

18

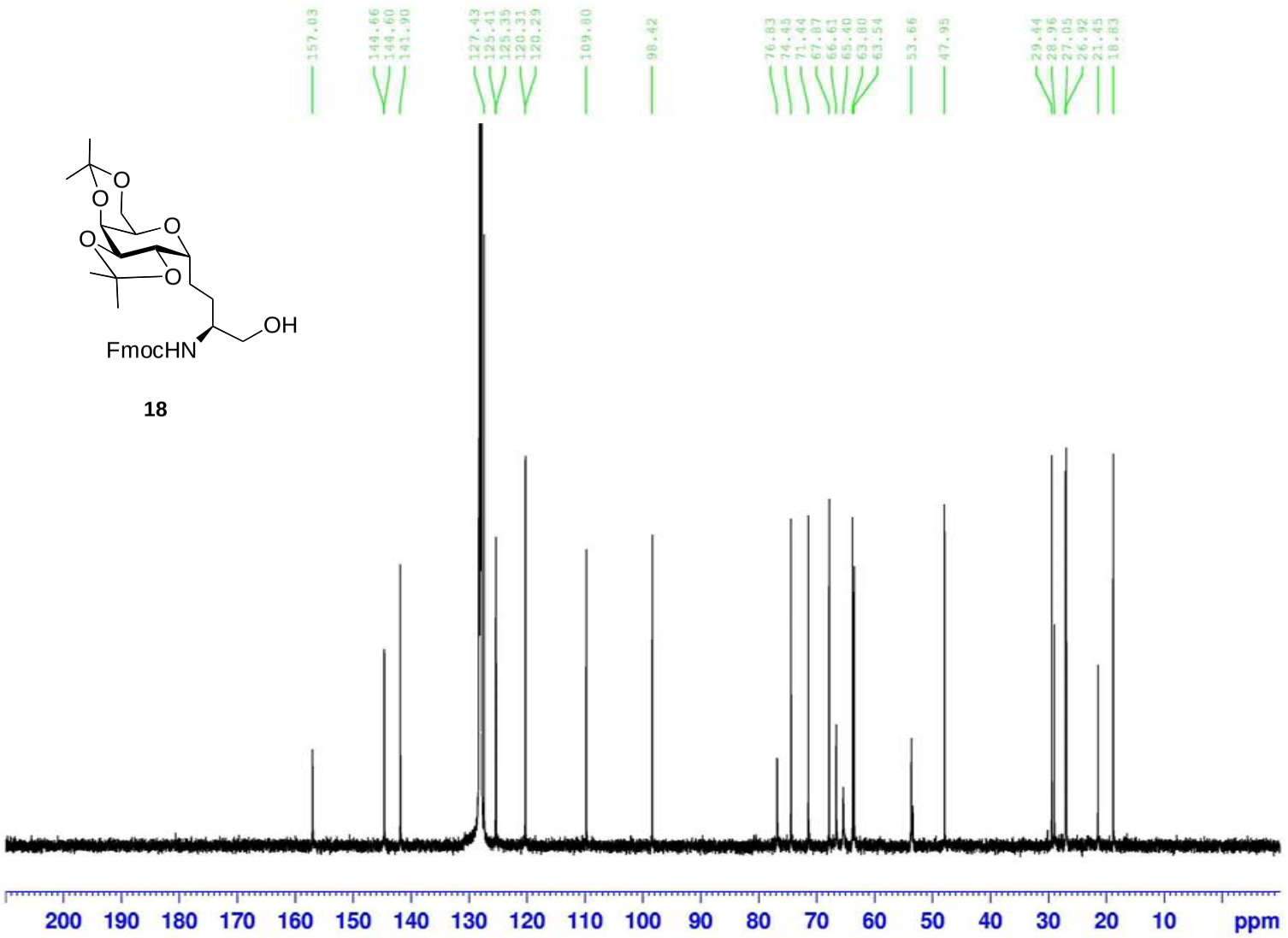
157.03
144.66
144.60
141.90
127.43
125.41
125.35
120.31
120.29
109.80
98.42
76.83
74.45
71.44
67.87
66.61
65.40
63.80
63.54
53.66
47.95
29.44
28.96
27.05
26.92
21.45
18.83
O
O
O
O
O
OH
FmocHN
200 190 180 170 160 150 140 130 120 110 100 90 80 70 60 50 40 30 20 10 ppm

18

7.829
7.814
7.679
7.664
7.649
7.389
7.374
7.359
7.302
7.301
7.288
7.273
4.358
4.271
4.266
4.251
4.248
4.234
4.213
4.202
4.187
4.173
4.165
4.157
4.147
4.046
4.035
4.027
4.015
3.939
3.914
3.701
3.696
3.681
3.676
3.635
3.610
3.244
1.868
1.857
1.850
1.841
1.726
1.709
1.691
1.566
1.559
1.539
1.528
1.370
1.365
1.350
1.300
1.266
1.221
FmocHN
OH
3b
ppm
10
9
8
7
6
5
4
3
2
1
0
2.00
1.95
4.58
1.00
4.20
2.13
0.98
1.14
1.13
1.02
1.00
2.03
1.07
12.91

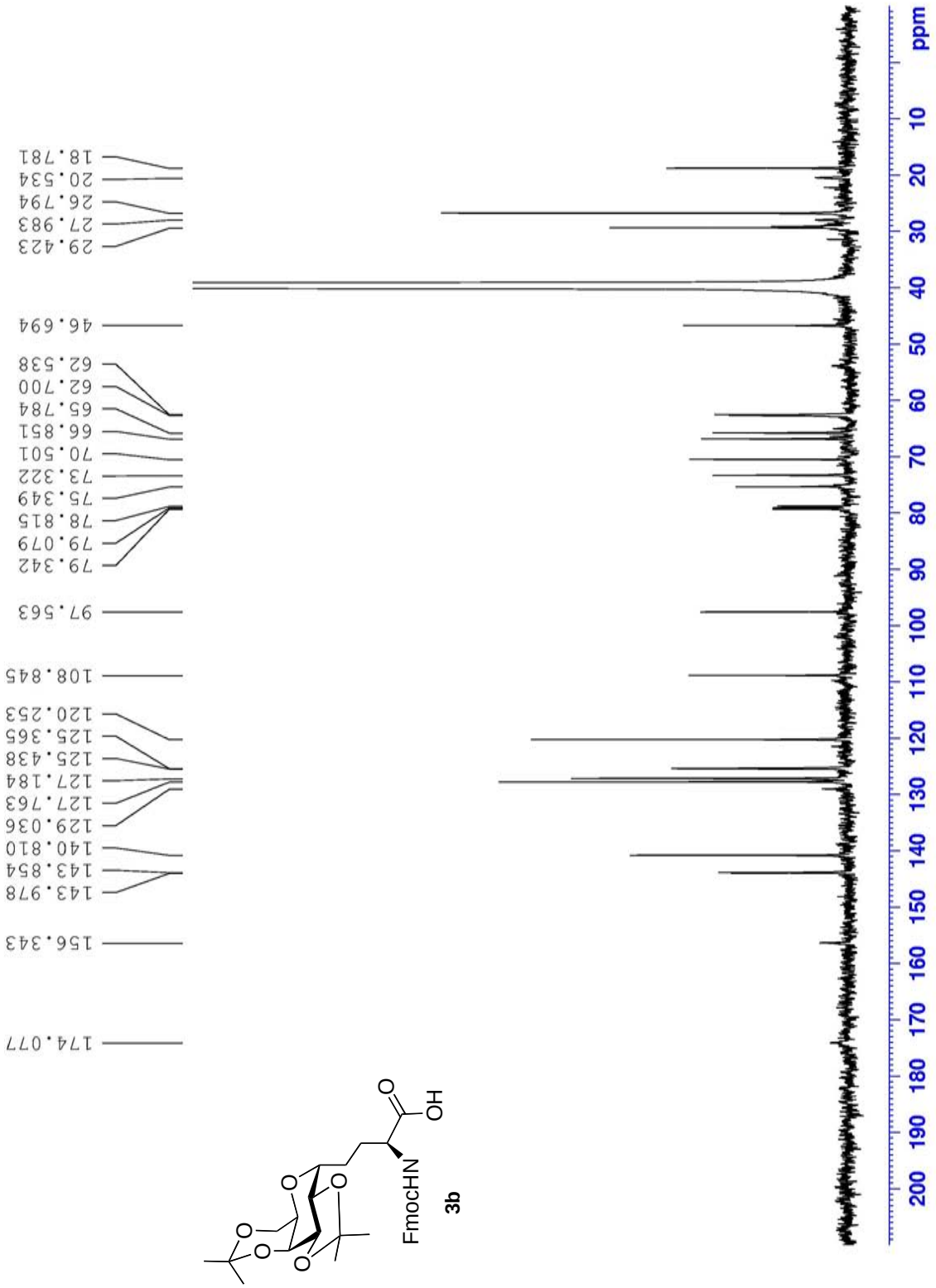
18.781
20.534
26.794
27.983
29.423
46.694
62.538
62.700
65.784
66.851
70.501
73.322
75.349
78.815
79.079
79.342
97.563
108.845
120.253
125.365
125.438
127.184
127.763
129.036
140.810
143.854
143.978
156.343
174.077
ppm
10
20
30
40
50
60
70
80
90
100
110
120
130
140
150
160
170
180
190
200
O
OH
FmocHN
O
O
O
O
O
O
3b

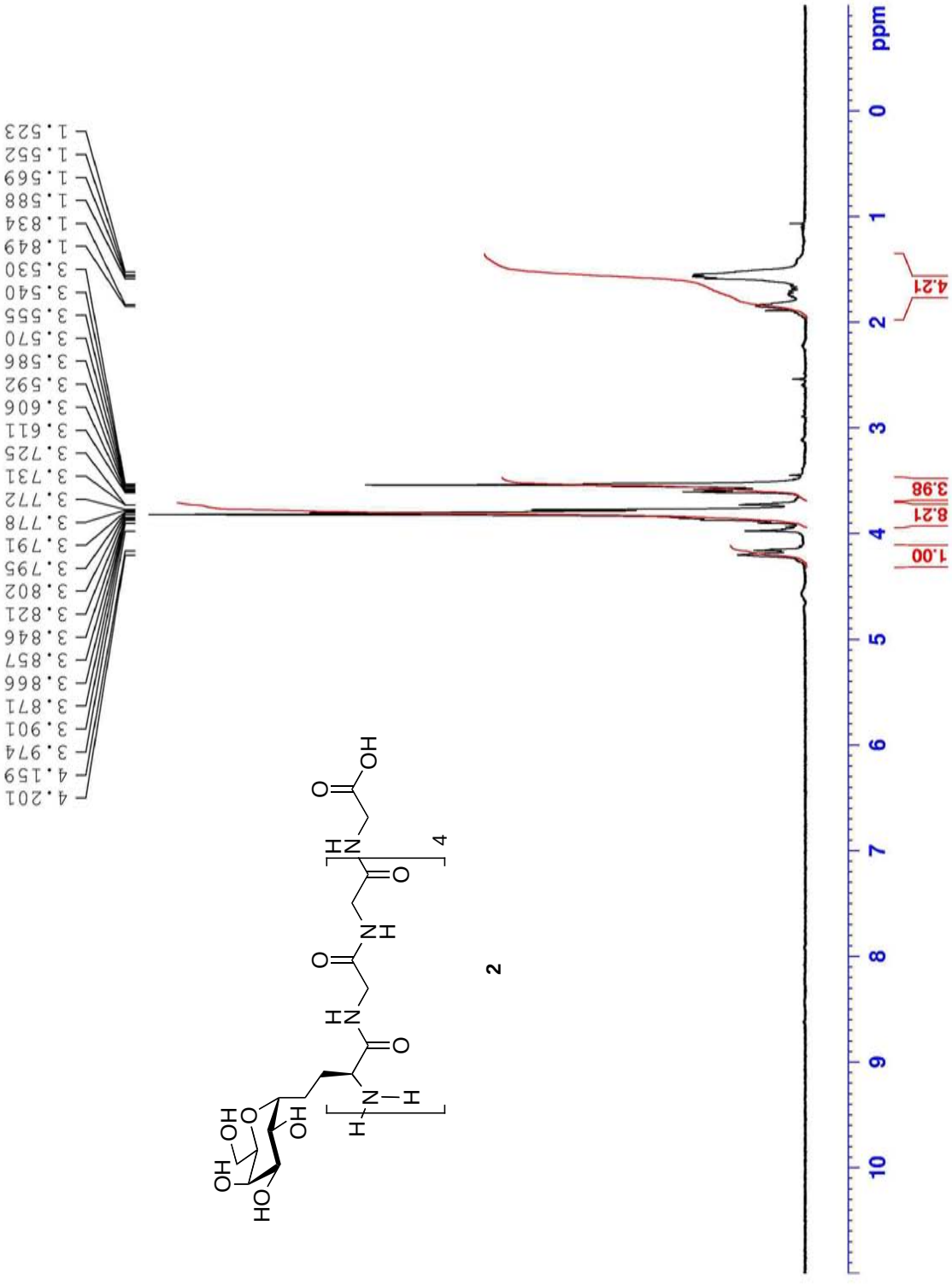
4.201
4.159
3.974
3.901
3.871
3.866
3.857
3.846
3.821
3.802
3.795
3.791
3.778
3.772
3.731
3.725
3.611
3.606
3.592
3.586
3.570
3.555
3.540
3.530
1.849
1.834
1.588
1.569
1.552
1.523
4.21
1.00
8.21
3.98
ppm
2

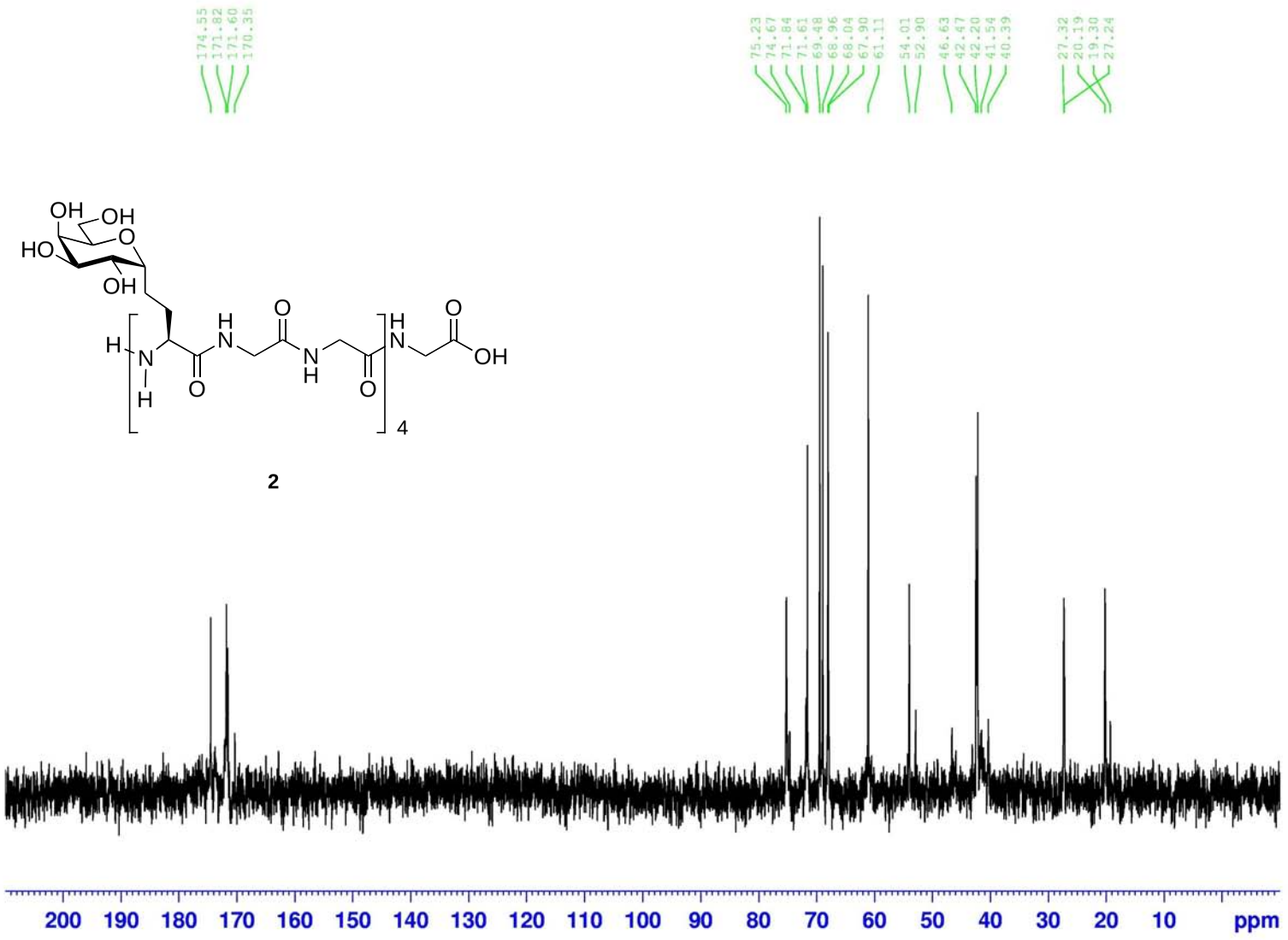
174.55
171.82
171.60
170.35
75.23
74.67
71.84
71.61
69.48
68.96
68.04
67.90
61.11
54.01
52.90
46.63
42.47
42.20
41.54
40.39
27.32
20.19
19.30
27.24
OH
OH
HO
O
OH
H
N
H
H
N
O
O
H
N
N
H
O
O
H
N
O
OH
4
2
200
190
180
170
160
150
140
130
120
110
100
90
80
70
60
50
40
30
20
10
ppm

Bioconjugate Chemistry

ARTICLE

pubs.acs.org/bc

Metabolism of Diazirine-Modified *N*-Acetylmannosamine Analogues to Photo-Cross-Linking Sialosides

Michelle R. Bond,[†,‡] Haochi Zhang,[‡] Jaekuk Kim,[‡] Seok-Ho Yu,[‡] Fan Yang,[‡] Steven M. Patrie,[‡] and Jennifer J. Kohler*[,‡]

[†]Department of Chemistry, Stanford University, Stanford, California 94305, United States

[‡]Division of Translational Research, Department of Internal Medicine, 5323 Harry Hines Boulevard, University of Texas Southwestern Medical Center, Dallas, Texas 75390, United States

Supporting Information

ABSTRACT: Terminal sialic acid residues often mediate the interactions of cell surface glycoconjugates. Sialic acid-dependent interactions typically exhibit rapid dissociation rates, precluding the use of traditional biological techniques for complex isolation. To stabilize these transient interactions, we employ a targeted photo-cross-linking approach in which a diazirine photo-cross-linker is incorporated into cell surface sialylated glycoconjugates through the use of metabolic oligosaccharide engineering. We describe three diazirine-modified *N*-acetylmannosamine (ManNAc) analogues in which the length of the linker between the pyranose ring and the diazirine was varied. These analogues were each metabolized to their respective sialic acid counterparts, which were added to both glycoproteins and glycolipids. Diazirine-modified sialic acid analogues could be incorporated into both α2−3 and α2−6 linkages. Upon exposure to UV irradiation, diazirine-modified glycoconjugates were covalently cross-linked to their interaction partners. We demonstrate that all three diazirine-modified analogues were capable of competing with endogeneous sialic acid, albeit to varying degrees. We found that larger analogues were less efficiently metabolized, yet could still function as effective cross-linkers. Notably, the addition of the diazirine substituent interferes with metabolism of ManNAc analogues to glycans other than sialosides, providing fidelity to selectively incorporate the cross-linker into sialylated molecules. These compounds are nontoxic and display only minimal growth inhibition at the concentrations required for cross-linking studies. This report provides essential information for the deployment of photo-cross-linking analogues to capture and study ephemeral, yet essential, sialic acid-mediated interactions.

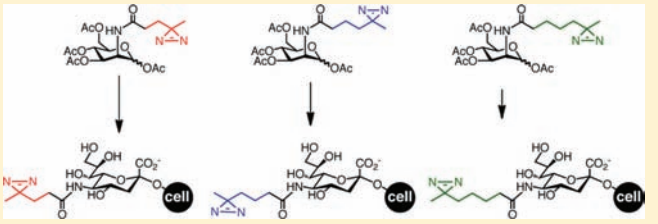

INTRODUCTION

Glycans are essential components of the mammalian cell surface, conferring an additional level of complexity to the heterogeneous compilation of proteins and lipids present on the plasma membrane. Glycoconjugates, including both glycoproteins and glycolipids, influence a diverse array of biological processes in eukaryotes, including mediating interactions among cells and between cells and the extracellular matrix. Alpha-keto acidic sugars known as sialic acids are key features of many cell surface glycoconjugates. The presence or absence of these nine-carbon sugars can significantly change the immunogenicity and bioactivity of glycoproteins and glycolipids.[1] Due to their privileged positions at the periphery of glycan structures, sialic acids are also crucial components of recognition elements.[2,3] For example, sialic acid-containing glycoconjugates are responsible for leukocyte homing to the sites of inflammation[4] and are critical for mediating cellular susceptibility to toxins[5] and viruses.[6]

Although burgeoning evidence points to essential roles for sialylation,[7] studying sialylated glycoconjugates, also called sialosides, remains challenging. Glycan-mediated interactions are often transient and characterized by low affinities with equilibrium dissociation constants typically in the micromolar to millimolar range.[4] The diversity and abundance of sialic acid-mediated interactions have yet to be explored fully due to the limited tools available for analyzing these labile complexes. Our strategy for studying a sialoside-mediated interaction is to covalently conjugate the complex via covalent photo-cross-linking, thereby capturing the interaction between the binding partners and enabling further analysis. By using metabolic oligosaccharide engineering,[8] a photoreactive moiety is selectively incorporated into sialylated glycoconjugates in their native cellular context. The photo-cross-linkers are then poised to capture biologically relevant complexes.

Metabolically incorporated photo-cross-linking sialic acids have been reported by our lab[9] and others,[10,11] and their utility has been demonstrated by the covalent capture of both glycoprotein−glycoprotein[9,10,12] and protein−glycolipid[13] interactions. Although several photo-cross-linking groups have demonstrated utility in biological settings,[14] we have focused

Received: April 27, 2011
Revised: August 2, 2011
Published: August 15, 2011

ACS Publications © 2011 American Chemical Society

dx.doi.org/10.1021/bc2002117 | *Bioconjugate Chem.* 2011, 22, 1811–1823

exclusively on the use of the alkyl diazirine. The diazirine is activated by exposure to 365 nm light, whereupon it is converted into a highly reactive carbene intermediate[15] that will insert into any nearby C−H or heteroatom−H bond. The diazirine's small size, high reactivity, and low selectivity offer advantages over other cross-linking moieties.[14]

Previously, we reported the synthesis of a diazirine-modified *N*-acetylmannosamine (ManNAc) analogue and showed that this compound could be metabolized to sialosides and used to cross-link a sialylated protein and a sialylated lipid to their binding partners.[9,13] While we successfully observed cross-linking, we were unsure whether the distance between the pyranose ring and the photo-cross-linker was optimal for efficient capture of sialoside binding partners. To address this concern, we prepared a panel of ManNAc analogues in which we varied the distance between the pyranose ring and the photo-cross-linker.

Here, we report the synthesis of variable-length photo-cross-linking ManNAc analogues and the results of their introduction in BJA-B, Daudi, and Jurkat cells. We examined the effects of these compounds on cell viability and growth. We show that these analogues are metabolized to photo-cross-linking sialosides, but not to other glycoconjugates. In addition, we compare the ability of the different photo-cross-linking sialic acids to covalently capture complexes containing either a sialylated glycoprotein or a sialylated glycolipid. Overall, we found that the compound with the shortest linker displayed the most efficient incorporation, also resulting in effective cross-linking. Compounds with a longer linker between the pyranose ring and the photo-cross-linker suffer from poor incorporation, yet are still capable of cross-linking. In studying the metabolism of these analogues, we discovered that the addition of the diazirine modification interferes with interconversion of ManNAc and *N*-acetylglucosamine (GlcNAc) analogues, thereby enabling selective incorporation of the diazirine into sialosides. Finally, we demonstrate that cross-linked complexes can be characterized by self-assembled monolayer (SAM) with matrix-assisted laser desorption/ionization (MALDI) time-of-flight mass spectrometry, providing a potential route to discovery and characterization of sialoside binding partners.

EXPERIMENTAL PROCEDURES

Chemical Synthesis of Photo-Cross-Linking Sugars. Syntheses of **1**−**4** have been reported previously.[9,16,17] Compounds **5** and **6** were prepared by a route analogous to **4** and described in detail in the Supporting Information. Acetylated sugars were purified by silica gel chromatography and reverse-phase HPLC. Synthetic details, NMR spectra, and HPLC traces demonstrating compound purity are found in the Supporting Information (Schemes S1−S3 and Figures S10−S24).

Cell Culture, Flow Cytometry, and Immunoblotting. BJA-B K88, BJA-B K20, and Daudi cells were cultivated in RPMI 1640 media containing 2 mM glutamine and supplemented with 10% fetal calf serum, 100 U/mL penicillin, and 100 μg/mL streptomycin. Unless otherwise noted, cells were maintained in a water-saturated atmosphere at 37 °C and 5% CO_2. Typically, cell densities were maintained between 2.5×10^5 and 2.0×10^6. To generate BJA-B cells in serum-free conditions, the cells were grown in RPMI 1640 with 2 mM L-glutamine containing 1× Nutridoma SP, 50 U/mL penicillin, and 50 μg/mL streptomycin. Cells were cultured for two passages at 2.5×10^5 cells/mL in serum-free media for 72 h prior to supplementation with monosaccharides.

Prior to the addition of cells to a 12 well plate, ethanol (EtOH), Ac_4ManNAc, Ac_4ManNDAz(2me), Ac_4ManNDAz-(3me), Ac_4ManNDAz(4me), Ac_4GlcNDAz(2me), or Ac_4ManNAz in EtOH was added to achieve a final concentration of 100 μM once media was added. EtOH was evaporated at ambient temperature and pressure prior to the addition of cells. Cells were seeded at a density of 3.0×10^5 cells/mL and cultured for 72 h with the compounds. After growth in the presence of the appropriate monosaccharides, cells were harvested by pelleting at 400*g* for 4 min and aspirating the supernatant. Cell viability was assessed using Trypan blue dye staining with the Countess Automated Cell Counter instrument (Invitrogen, Carlsbad, CA). When possible, cells were kept in the dark and on ice for subsequent procedures.

Jurkat cells were cultivated in RPMI 1640 media containing 2 mM L-glutamine and supplemented with 10% heat-inactivated FBS. Unless otherwise noted, cells were maintained in a water-saturated atmosphere at 37 °C and 5% CO_2. Typically, cell densities were maintained between 2.5×10^5 and 2.0×10^6. Cell viability was assessed using Trypan blue dye staining with the Countess Automated Cell Counter.

Flow cytometry and immunoblotting were performed according to reported procedures.[9,13,16] Details are provided in the Supporting Information.

Analysis of Ganglioside Content for Jurkat Cells Cultured with Compounds 1−6. All reagents, chemicals, and general supplies were purchased and used as received from Fisher Scientific (Waltham, MA) or Sigma-Aldrich (St. Louis, MO) unless otherwise noted. Dulbecco's phosphate buffered saline (DPBS) and cholera toxin subunit B-Alexa Fluor 488 (CTxB-488) were purchased from Invitrogen (Carlsbad, CA). Bovine serum albumin (BSA) Fraction V was purchased from Roche Applied Science (Indianapolis, IN). SepPak tC18 columns (0.3 g) were purchased from Fisher Scientific. HPTLC plates (20 × 20 cm, glass-backed, 200 μm thickness) were purchased from EMD Chemicals (Gibbstown, NJ). Matreya ganglioside standards 1408, 1510, and 1511 were purchased from Matreya LLC (Pleasant Gap, MD).

Jurkat cells were cultivated as described above. Prior to the addition of cells to a 25 cm plate, EtOH, Ac_4ManNAc, Ac_4ManNDAz(2me), Ac_4ManNDAz(3me), Ac_4ManNDAz-(4me), Ac_4GlcNDAz(2me), or Ac_4ManNAz in EtOH was added to achieve a final concentration of 100 μM once the media was added. The EtOH was pre-evaporated at ambient temperature and pressure. Jurkat cells were then seeded at a density of 2.5×10^5 cells/mL and incubated in the presence of the monosaccharides at 37 °C and 5% CO_2. After growth with the appropriate compounds for 72 h, cells were harvested, counted, and centrifuged at 650*g* for 5 min in 50 mL conical tubes and the supernatant aspirated. To ensure that all ganglioside concentrations were normalized, equal numbers of cells (2.7×10^7 cells) were collected for all samples. Cell pellets were stored at −80 °C overnight.

Cell pellets were thawed to RT and resuspended in 300 μL of ice-cold ddH_2O. They were then dounced 50 times with a Kontes tissue grinder, tube size 20. Following homogenization, cell suspension was added to a vial of stirring MeOH (800 μL). For the previous step and those following, glass Pasteur pipettes and glass vials were used; no plastic came in contact with samples. Samples were also shielded from light at every point possible during this procedure. To the stirring solution, 400 μL of chloroform was added and the

mixture stirred for 2.5 h at RT. The mixture was then transferred into a 13 × 100 mm glass culture tube and centrifuged at 2800*g* for 10 min at 30 °C. The resulting supernatant (total lipid extract - TLE) was transferred to a glass vial and the sample evaporated under a stream of nitrogen to dryness. The resulting yellow film was stored at RT in the dark.

For ganglioside isolation, the TLE was resuspended in 1200 μL of diisopropyl ether and 800 μL 1-butanol. This mixture was sonicated in a bath sonicator for 10 min. The resulting cloudy solution was transferred to a 13 × 100 mm glass culture tube. To the solution, 1 mL of 50 mM sodium chloride was added. Following mixing with a Pasteur pipet, the suspension was centrifuged at 2800*g* for 10 min at 30 °C to separate the two phases. The upper (organic) layer was then removed. To the aqueous layer, 1200 μL of diisopropyl ether and 800 μL of 1-butanol were added and mixed. Following centrifugation at 2800*g* for 10 min at 30 °C and removal of the organic layer; these last two steps were repeated once more.

For final purification, the remaining lipid mixture was loaded on a SepPak tC18 column (0.3 g size), washed, and eluted. First, the column was prepared by several washing steps: three washes with 2 mL of chloroform/MeOH/ddH_2O (C/M/W, 2:43:55) were followed by two washes with 2 mL of C/M (1:1) and last three additional washes with 2 mL of C/M/W (2:43:55). The sample was loaded onto the column and washed thrice with 2 mL of C/M/W (2:43:55) followed by three washes with 2 mL of M/W (1:1). Finally, the gangliosides were eluted in 2 mL of 100% MeOH. Ganglioside extracts were then transferred to a new 4 mL glass vial and evaporated to dryness under a stream of nitrogen. The clear, white film was stored at RT for further analysis.

A TLC chamber was pre-equilibrated with 140 mL of chloroform/MeOH/0.2% $CaCl_{2(aq)}$ (85:45:10). The HPTLC plate (EMD Chemicals #115534, 20 × 20 cm, glass-backed plates, silica gel 60 F_{254}, 200 μm thickness) was prerun and dried prior to sample loading to improve resolution. The syringe used for loading samples was cleaned with C/M/W, 4:8:3. Extracted ganglioside samples were redissolved in 50 μL C/M/W (2:1:0.1) and loaded onto the HPTLC plate along with ganglioside standards and dried. The HPTLC plate was then run in the chamber followed by drying under vacuum for 45 min.

To assess the presence of GM1a, the HPTLC plate was immersed in 0.5% polyisobutylmethacrylate in hexanes (diluted from a stock solution of 2% in chloroform) for 2 min to fix the gangliosides to the TLC plate. The plate was then fully dried followed by immersion in 1.0% BSA in DPBS for 30 min at RT. The plate was incubated with CTxB-Alexa Fluor 488 conjugate (1:20 000 dilution of a 1 mg/mL solution) in DBPS for 50 min at RT in the dark. The plate was washed briefly with DPBS, dried fully, and imaged by Typhoon with a 488 nm excitation laser and 520 nm emission filter. Global adjustments to image contrast and brightness were performed using Adobe Photoshop.

To visualize all gangliosides, the above plate was resorcinol-stained. The plate was sprayed with a resorcinol solution (0.1% resorcinol, 0.04% $CuSO_4$ in hydrochloric acid/water (4:1)). Following staining, the plate was thoroughly dried and sandwiched between two glass plates, then incubated at ∼100 °C for 15−20 min until bands were clearly visible. The plate was imaged with white light using an Alpha Innotech FluorChem HD2 imager and global adjustments to image contrast and brightness were made with Adobe Photoshop.

Cytosolic and Membrane-Bound Sialic Acid Analysis by DMB Derivatization. All reagents, chemicals, and general supplies were purchased and used as received from Fisher Scientific (Waltham, MA) or Sigma-Aldrich (St. Louis, MO) unless otherwise noted. PVDF membranes were purchased from Millipore, Immobilon (Billerica, CA). For chemiluminescent visualization, SuperSignal WestPico Chemiluminescent Substrate (ECL reagent) was purchased from Pierce (Rockford, IL). Polycarbonate centrifuge tubes (11 × 34 mm) were purchased from Beckman (Brea, CA). The bicinchoninic acid (BCA) Protein Assay Kit from Pierce was used to assess protein concentration. 1,2-diamino-4,5-methylenedioxybenzene (DMB) was purchased from Sigma Aldrich (we found other vendors' products to be inferior). Amicon Ultra Centrifugal Filters (0.5 mL; 10 kDa molecular weight cutoff (MWCO)) were purchased from Millipore. Complete Protease Inhibitor Cocktail Tablets, EDTA-free, were purchased from Santa Cruz Biotechnology. Tris-buffered saline Tween-20 was used in blocking solutions (TBST: 10 mM Tris·HCl pH 8.0, 150 mM NaCl, 0.1% v/v Tween 20). The hypotonic lysis buffer was composed of 10 mM Tris·HCl, pH 7.3, 10 mM $MgCl_2$, 1 mM EDTA, and 1 mM EGTA.

Jurkat cells were grown in the presence of sugars **1**−**6** as described above. Cells were harvested after 72 h and the number of cells normalized to 5 million. Cells were washed twice in 500 μL DPBS. Next, cells were swollen in hypotonic lysis buffer containing protease inhibitors for 15 min on ice. Cells were lysed by extrusion through a 25 gauge needle 30 times. Nuclei and unbroken cells were removed from the postnuclear supernatant by two rounds of centrifugation at 1000*g* for 15 min at 4 °C. Next, the postnuclear supernatant was transferred to heavy-walled polycarbonate tubes and centrifuged at 100 000*g* for 1 h in a Beckman TLA 120.2 rotor. The supernatant was designated the cytosolic fraction. The pellet was washed twice with cold 400 μL hypotonic lysis buffer and centrifuged at 100 000*g* for 1 h. The remaining pellet was designated the membrane fraction. Samples were either flash-frozen and the solvent removed by vacuum overnight or saved to assess fraction purity. To confirm that the membrane fraction was not contaminated by the nuclear fraction, protein concentration was normalized and proteins were resolved by SDS-PAGE. Proteins were then transferred to PVDF and probed for either lamin B (to identify the nuclear fraction) or calnexin (to identify the membrane fraction). DMB-derivatization (as described below) confirmed that no sialic acids were present in the membrane washes; this ensured that that no soluble sialic acid (free sialic acid or CMP-sialic acid) remained in the membrane fraction.

To release sialic acids, 50 or 100 μL of 2.0 M acetic acid was added for the membrane-bound and dried cytosolic samples, respectively. Solutions were incubated at 80 °C for 2 h. Samples were then cooled to room temperature. To the membrane-bound and cytosolic samples, 40 or 80 μL of 7 mM DMB, 0.75 M 2-mercaptoethanol, 18 mM $Na_2S_2O_4$, 1.4 M acetic acid were added, respectively. The samples were then incubated at 50 °C for 2 h. After this incubation period, 5 or 10 μL of 0.2 M NaOH was added to each membrane-bound or cytosolic sample, respectively. Samples were then filtered in 10 kDa MWCO filters by centrifugation and the resulting flowthrough was stored at −20 °C, in the dark until use. The derivatives were analyzed by online fluorescence detection using reverse-phase HPLC. Details are provided in the Supporting Information.

Mass Spectrometry Analysis of Cross-Linked CTxB-GM1a-SiaDAz(2me). Photo-cross-linking of CTxB-GM1a complexes

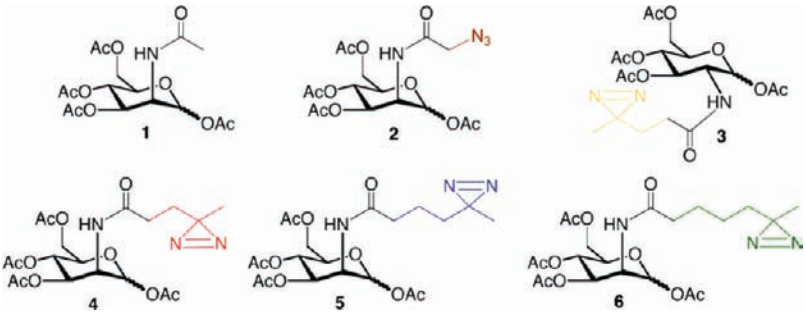

Figure 1. Per-*O*-acetylated *N*-acyl hexosamines. The *N*-acyl side chains of ManNAc and *N*-acetylglucosamine (GlcNAc) analogues were modified by the addition of a diazirine or an azide. Ac_4ManNAc (**1**) is a protected form of naturally occurring ManNAc. Ac_4ManNAz (**2**) is an azide-containing analogue that is metabolized to sialosides with high efficiency.[24] The names of the diazirine-modified sugars (**3**−**6**) are derived from the number of methylene groups separating the carbonyl and diazirine on the *N*-acyl side chain: Ac_4GlcNDAz(2me) (**3**), Ac_4ManNDAz(2me) (**4**), Ac_4ManNDAz-(3me) (**5**), and Ac_4ManNDAz(4me) (**6**).

was performed essentially as described previously.[13] The SAMDI mass spectrometry process was based on a literature procedure.[18] Details are provided in the Supporting Information.

RESULTS

Preparation of Photo-Cross-Linking Compounds and Control Molecules. Previously, we reported the synthesis of Ac_4ManNDAz(2me) (**4**), a precursor to photo-cross-linking sialosides.[9] Using a similar synthetic scheme (Scheme S1 and details in Supporting Information), we prepared two additional analogues, **5** and **6**, in which the distance between the pyranose ring and the photo-cross-linker was extended (Figure 1). In all cases, we prepared per-*O*-acetylated forms of the compounds. Acetylation of hydrophilic sugars improves passive diffusion through the plasma membrane[19] after which the acetyl groups are presumably removed by nonspecific esterases within the cytosol.[20]

Further metabolism of the photo-cross-linking compounds relies on the cells' endogenous machinery for biosynthesis of sialosides and the expression levels of each of the required enzymes (Figure 2). ManNAc, the first committed intermediate in sialic acid biosynthesis, is produced from UDP-GlcNAc by the action of the UDP-GlcNAc 2-epimerase. In addition, human cells also encode a GlcNAc 2-epimerase that is capable of interconverting GlcNAc and ManNAc, although the equilibrium favors the more stable GlcNAc.[21] Theoretically, the GlcNAc 2-epimerase could be capable of converting our photo-cross-linking ManNAc analogues to their GlcNAc counterparts, which might lead to photo-cross-linker incorporation into nonsialylated molecules such as *O*-GlcNAc-modified proteins or glycosaminoglycans. To confirm that any cross-linking we observe is due to diazirine-modified sialosides, as opposed to other possible diazirine-modified molecules, we use Ac_4GlcNDAz(2me) (**3**), the diazirine-modified analogue of GlcNAc, as a control molecule. If cross-linking is observed with **4**, but not with **3**, we conclude that the cross-linking is through a diazirine-modified sialoside, not another metabolite.

Maximizing Sialoside Production while Minimizing Growth Inhibition. We sought to define conditions under which these new photo-cross-linking ManNAc analogues are efficiently metabolized to cell surface sialosides. In these initial experiments, we used a cell line that is deficient in sialic acid production. BJA-B K20 cells are a subclone of the BJA-B B-cell lymphoma cell line and are distinguished by their deficiency in UDP-GlcNAc 2-epimerase activity.[22,23] Because BJA-B K20 cells lack the enzymatic activity required to convert UDP-GlcNAc to ManNAc, they cannot biosynthesize ManNAc or its metabolite sialic acid (Figure 2) from the UDP-GlcNAc precursor. Like many other cells, BJA-B K20 cells are capable of scavenging sialic acids from the culture medium. However, due to their inability to synthesize ManNAc, BJA-B K20 cells cultured in serum-free conditions fail to produce sialosides. If a ManNAc analogue is added to this deficient cell line, its metabolic conversion to sialic acid can be assessed by quantifying the total amount of sialic acids present in the cell. In addition to measuring sialoside formation in response to addition of diazirine-modified compounds, we cultured BJA-B K20 cells with the per-*O*-acetylated form of ManNAc (**1**), which we expect to be converted to sialosides effectively, and quantified cell surface sialylation. We also measured sialoside production due to Ac_4ManNAz (**2**),[17] an azide-modified analogue that is metabolized to sialosides with high efficiency.[24] Finally, we examined sialoside production in another BJA-B subclone, K88, which maintains UDP-GlcNAc 2-epimerase activity and has a high sialylation phenotype.[22]

First, we assessed the effects of protected ManNAc analogues on cell growth. BJA-B K20 cells were cultured in serum-free medium with **1**, **2**, **3**, **4**, **5**, or **6** at a range of concentrations, from 10 μM to 300 μM, for 72 h, after which Trypan blue staining was used to assess cell growth and viability. For all three photo-cross-linking ManNAc analogues, increases in analogue concentration correlated with decreased cell numbers (Supporting Information, Figure S1). The most dramatic example is the case of Ac_4ManNDAz(4me), where 45% fewer cells were observed when 300 μM compound was added to the culture, versus 10 μM compound. In contrast, when cells were supplemented with Ac_4ManNAz and Ac_4GlcNDAz(2me), the number of cells remained similar regardless of sugar concentration. Despite these different trends, relatively little growth inhibition was observed for any compound added at 100 μM. We also assessed cell viability using Trypan blue staining. We did not observe any significant viability trends and the fraction of live cells was high (86−94%) for all samples (Supporting Information, Figure S1). These data suggest that higher concentrations of the unnatural sugar analogues are detrimental to cell growth but do not significantly affect cell viability.

After assessing cell viability, we monitored the level of cell surface α2−6-linked sialic acids resulting from supplementation with compounds **1**−**6**. We used a fluorescently labeled *Sambucus*

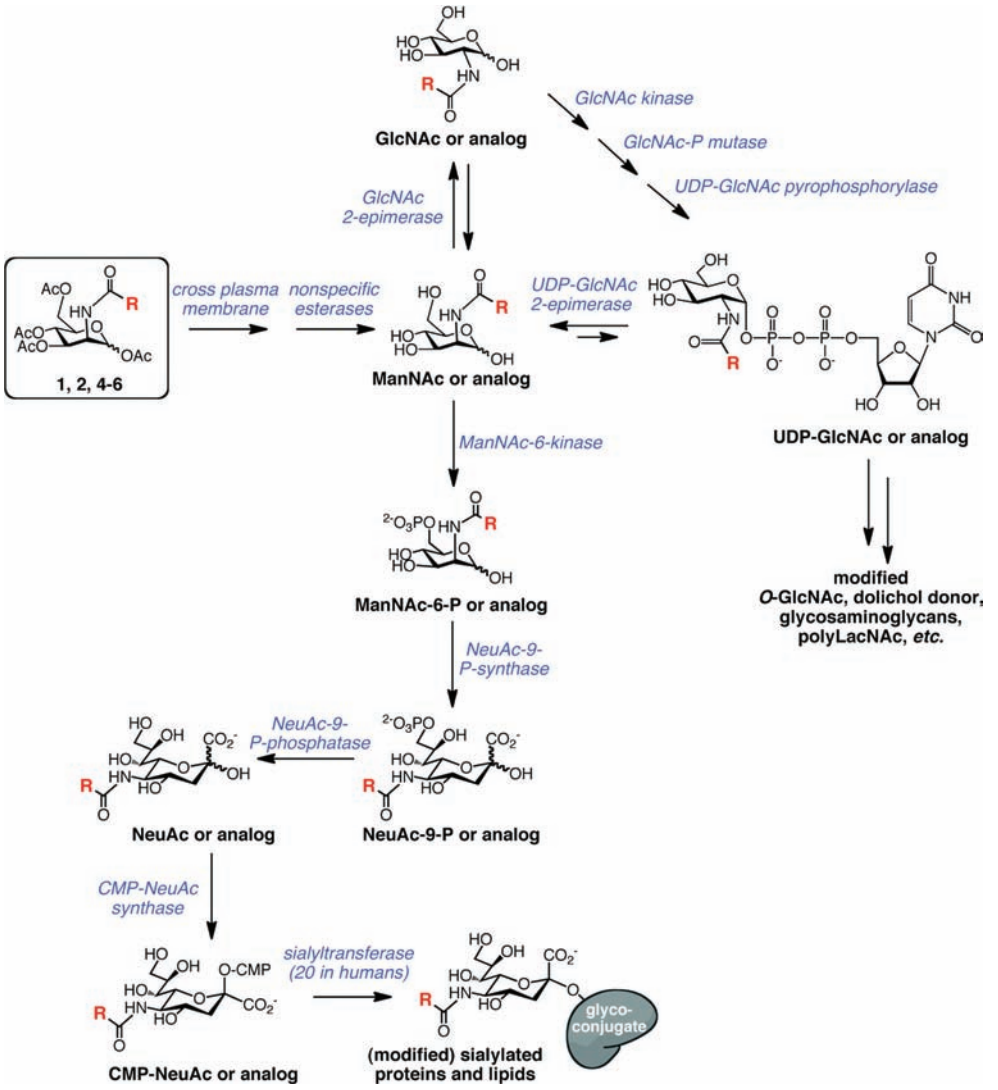

Figure 2. Metabolism of ManNAc and ManNAc analogues. Per-*O*-acetylated ManNAc analogues (boxed) diffuse across the plasma membrane after which acetyl groups are cleaved by nonspecific esterases. R is $-CH_3$ for naturally occurring ManNAc. ManNAc and analogues can be converted to the corresponding sialosides by a series of enzymatic transformations. Alternative possible fates for ManNAc analogues include conversion to GlcNAc analogues and UDP-GlcNAc analogues that are precursors for other glycoconjugates.

nigra agglutinin (SNA) conjugate (SNA-FITC) to measure production of cell surface α2−6-linked sialic acids. In the sialic acid-deficient BJA-B K20 cell line, essentially all of the sialic acids are derived from the exogenous addition of ManNAc analogues. Importantly, the SNA lectin tolerates deviations in the *N*-acyl side chain, so the diazirine modification is not expected to affect SNA binding.[25,26] For cells treated with Ac_4ManNAc, cell surface α2−6-linked sialic acid increased robustly, even at 10 μM (Figure 3). Cells treated with Ac_4ManNDAz(2me) and Ac_4ManNAz also displayed relatively high levels of cell surface α2−6-linked sialic acids. Conversely, to rise above the BJA-B K20 baseline level, cell cultures with Ac_4ManNDAz(3me) or Ac_4ManNDAz(4me) required sugar concentrations of 50 or 100 μM. BJA-B K20 cells treated with Ac_4GlcNDAz(2me) showed no increase in cell surface sialic acid, indicating that conversion of GlcNDAz(2me) to ManNDAz(2me) is negligible. These data, along with the growth data (Supporting Information Figure S1), led us to choose 100 μM as an optimal concentration of photo-cross-linking sugar to maximize incorporation while minimizing growth inhibition.

N-Acyl Side Chain Length Is Negatively Correlated with Incorporation Efficiency. To measure the total amount of cell surface photo-cross-linking sialic acid, we used the periodate oxidation and aniline-catalyzed oxime ligation (PAL) with flow cytometry detection essentially as reported by the Paulson lab.[27] In brief, photo-cross-linking sugar-supplemented cells were treated with sodium periodate to oxidize the polyol chain of cell surface sialic acids to an aldehyde, a functional group that is otherwise absent from the cell surface. We used an *in vitro* reaction to confirm that this oxidation reaction had no effect on the diazirine functionality (Supporting Information Figure S2). Oxidized cells were incubated with an aminooxy-biotin reagent in the presence of aniline catalyst, yielding cell surface sialic acids covalently conjugated to biotin through an oxime linkage. Finally, streptavidin-DTAF was added, yielding fluorescence labeling proportional to cell surface sialic acid. Fluorescence was quantified by flow cytometry (Figure 4A).

After PAL labeling, those cells with an intact sialic acid pathway (BJA-B K88) showed a much higher level of fluorescence than the

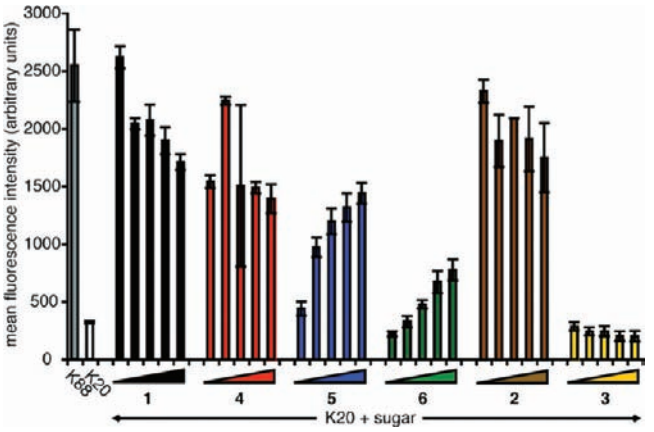

Figure 3. Metabolism of compounds to cell surface α2−6-linked sialic acids. BJA-B K20 cells were treated with increasing concentrations (10, 50, 100, 200, and 300 μM) of Ac_4ManNAc, Ac_4ManNAc analogues, or Ac_4GlcNDAz(2me). Cell surface α2−6-linked sialic acid levels of BJA-B K88 and K20 cells were assessed by SNA-FITC binding, as measured by flow cytometry. The standard deviation represents technical duplicate samples. Two biological replicates of the experiment were performed, yielding similar data (not shown).

BJA-B K20 cells that lack UDP-GlcNAc 2-epimerase activity (Figure 4A). Similarly, in comparison to unsupplemented BJA-B K20 cells, there was a marked increase in fluorescence for those BJA-B K20 cells incubated with certain ManNAc analogues. Our results demonstrate a robust conversion of Ac_4ManNDAz(2me) to cell surface sialic acid, similar to the levels seen for Ac_4ManNAc and Ac_4ManNAz. Conversion of Ac_4ManNDAz(3me) to the corresponding sialosides was demonstrated by the increase of fluorescence to slightly above baseline levels. Treatment with Ac_4ManNDAz(4me) did not yield a detectable increase in cell surface sialic acid. As expected, cells treated with the Ac_4GlcNDAz-(2me) control molecule displayed little difference from unsupplemented BJA-B cells, reflecting their inability to produce ManNDAz(2me) from Ac_4GlcNDAz(2me). These data are supported by results of a resorcinol assay (described in the Supporting Information) used to determine levels of total and glycoconjugate-bound sialic acids (Supporting Information Figure S3).

Photo-Cross-Linking Sialic Acids Are Incorporated in a Variety of Glycans. After confirming that photo-cross-linking ManNAc analogues are metabolized to cell surface sialic acids, we next examined whether our analogues were incorporated as both α2−3-linked and α2−6-linked sialic acids. We assessed the cell surface binding of lectins, proteins that recognize specific sugar epitopes, by flow cytometry. We used labeled SNA[28] and *Maackia amurenis* lectin (MAL-II)[29,30] which recognize Siaα2−6Gal and Siaα2−3Gal, respectively. For these experiments, BJA-B K20 cells were unsupplemented or cultured with 100 μM **1**−**6**, as described in the Supporting Information. Cells were washed and labeled with the appropriate lectins and their fluorescence assessed by flow cytometry.

Unsupplemented BJA-B K20 cells bound SNA and MAL-II at low levels (Figure 4B,C), unlike the BJA-B K88 cells, which bound both lectins at high levels. Culturing BJA-B K20 cells with Ac_4ManNAc yielded a dramatic increase in SNA and MAL-II binding, whereas culturing the cells with Ac_4GlcNDAz(2me) yielded no increase in lectin binding. When BJA-B K20 cells were supplemented with the unnatural photo-cross-linking ManNAc analogues, only those cultured with Ac_4ManNDAz(2me)

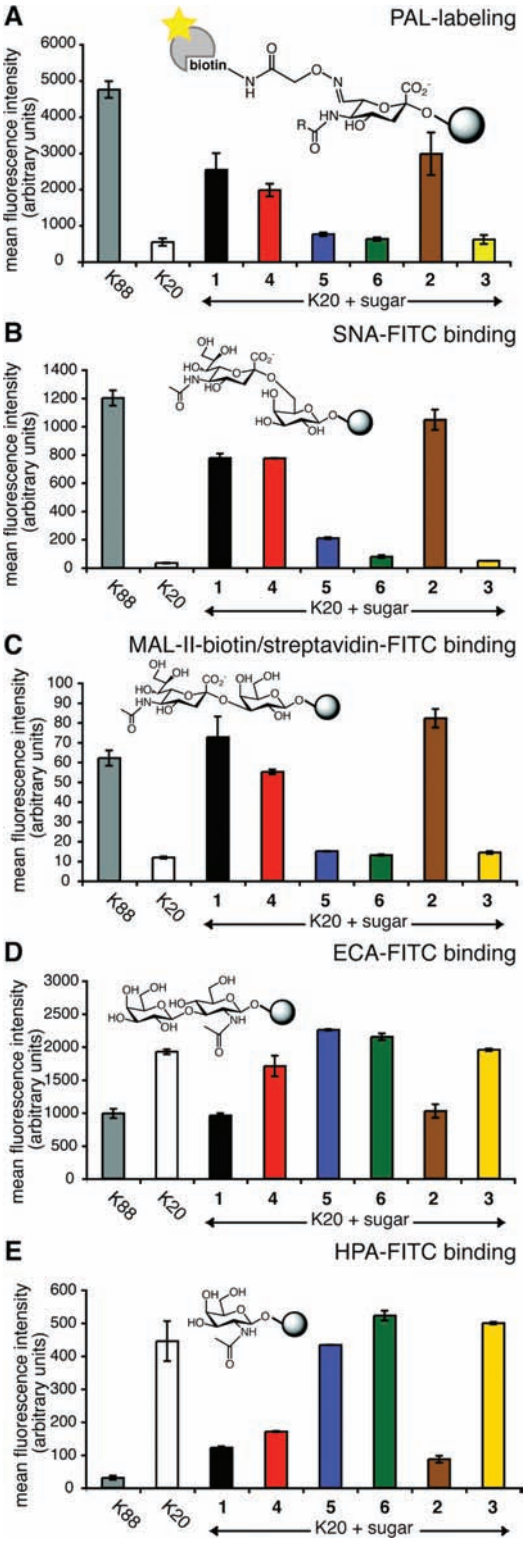

Figure 4. Cell surface sialic acid measured by flow cytometry. BJA-B K20 cells were grown in serum-free media supplemented with 100 μM **1**−**6**. (A) Total sialic acid detected by PAL; (B) Siaα2−6 galactose (Siaα2−6Gal) epitope detected by SNA lectin; (C) Siaα2−3Gal epitope detected by MAL-II lectin; (D) unsialylated terminal *N*-acetyllactosamine (LacNAc) detected by ECA lectin; (E) unsialylated terminal *N*-acetylgalactosamine (GalNAc) detected by HPA lectin. Error bars represent the standard deviation for three technical replicates.

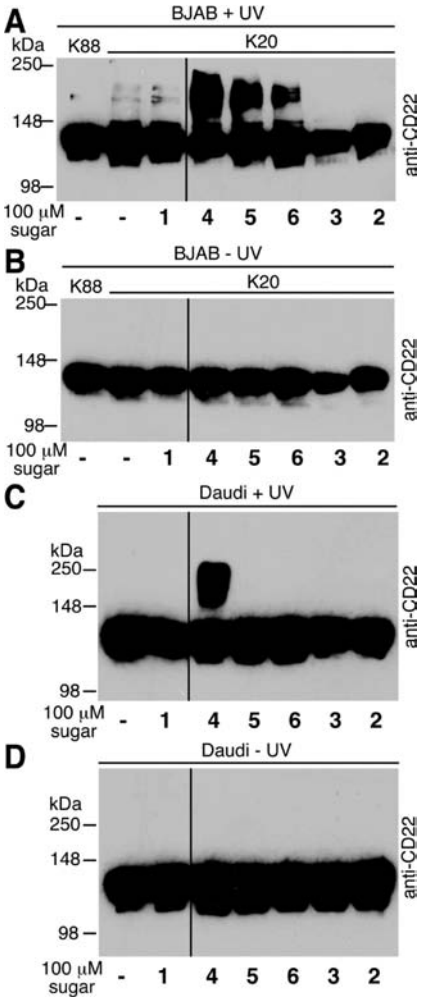

Figure 5. Photo-cross-linking of Siglec CD22 in BJA-B K20 and Daudi cells. BJA-B K20 or Daudi cells were cultured with photo-cross-linking sugars, photoirradiated, and lysed. Lysates from BJA-B K20 cells cultured with diazirine-containing sugars and exposed to UV light (A) or no UV light (B). Lysates from Daudi cells cultured with diazirine-containing sugars and exposed to UV light (C) or no UV light (D). For all blots, β-actin was used as a control to demonstrate similar levels of protein loading in every lane (data not shown).

showed significant levels of binding to MAL-II, while cells cultured with either Ac_4ManNDAz(2me) or Ac_4ManNDAz-(3me) bound to SNA. No detectable increases in lectin binding were observed for cells cultured with Ac_4ManNDAz(4me).

Although published data suggest that *N*-acyl substituents to sialic acid do not affect SNA or MAL-II binding,[26] we remained concerned that the lack of sialoside production we observed for the larger analogues could reflect lower affinity of the lectins to the modified sialic acids. To provide complementary information on the degree of sialylation, we also tested the binding of fluorescently conjugated lectins recognizing core glycan structures. The lectins used were *Erythrina cristagalli* agglutinin (ECA, specific for terminal LacNAc)[31] and *Helix pomatia* lectin (HPA, specific for terminal GalNAc).[32] Addition of sialic acid would be predicted to mask these core glycans, resulting in decreased lectin binding. Unsupplemented BJA-B K20 cells were bound by ECA and HPA at high levels (Figure 4D,E); BJA-B K88 cells bound the same lectins at lower levels. Culturing BJA-B K20 cells with Ac_4ManNAc yielded sharp decreases in ECA and HPA lectin binding. Cells cultured with Ac_4ManNDAz(2me) also displayed decreases in ECA and HPA binding, but cells cultured with Ac_4ManNDAz(3me) or Ac_4ManNDAz(4me) did not show dramatic changes. Culturing BJA-B K20 cells with Ac_4GlcNDAz(2me) had no effect on ECA or HPA binding. Taken together, our cell surface binding data provide strong evidence for the metabolism of Ac_4ManNDAz(2me) to both α2−6-linked and α2−3-linked sialic acids, and for the metabolism of Ac_4ManNDAz(3me) to at least α2−6-linked sialic acids. None of the flow cytometry data provide definitive evidence for metabolism of 100 μM Ac_4ManNDAz(4me) to cell surface sialic acid.

Photo-Cross-Linking Sialic Acids Cross-Link a Sialylated Glycoprotein. To confirm the utility of our photo-cross-linking sugar analogues, we captured a known sialic acid-mediated protein interaction and visualized the complex by immunoblot. The sialic acid binding IgG-like lectin (Siglec) CD22 is a protein that is not only modified by α2−6-linked sialic acid but it also binds sialic acid attached to other molecules, including other copies of CD22.[10,12] Several studies have demonstrated cross-linking of CD22 mediated by unnatural sialic acids.[9,10,12,14] Here, we monitored CD22 cross-linking in two different B cell lines: BJA-B K20 and Daudi. Using BJA-B K20 cells in serum-free media, we expected to observe high levels of cross-linking, since the photo-cross-linking sialic acid analogues do not need to compete with endogenous sialic acid for incorporation into sialosides. We cultured cells in the presence of the unnatural sugar analogues, photoirradiated the cells, and harvested the cell lysates. Lysates were resolved by denaturing sodium dodecyl sulfate polyacrylamide gel electrophoresis (SDS-PAGE), transferred to a polyvinylidine fluoride membrane (PVDF), and probed for the presence of CD22.

Monomeric CD22 displays an apparent molecular weight of ~120 kDa; a shift to higher molecular weight is indicative of production of a photo-cross-linked product (Figure 5A). As shown previously,[9] we observed photo-cross-linking of CD22 when cells were cultured with Ac_4ManNDAz(2me). Cells cultured with Ac_4ManNDAz(3me) or Ac_4ManNDAz(4me) also produced cross-linked species, although the amount of photo-cross-linked product was less. Cells cultured with Ac_4GlcNDAz-(2me) produced no photo-cross-linked product, consistent with our hypothesis that photo-cross-linking occurs through sialic acid, not other metabolites of the diazirine-modified sugars. Importantly, appearance of the putative cross-linked species was both UV- and diazirine-dependent. Lysates from cells that were not photoirradiated produced no bands other than monomeric CD22 (Figure 5B). All blots were stripped and reprobed for β-actin to demonstrate similar protein loading in every lane (data not shown).

The utility of photo-cross-linking sialic acid analogues will be limited if they can only be used in cell lines that are deficient in sialic acid synthesis. Therefore, we next tested whether the larger photo-cross-linking ManNAc analogues could engender sialoside cross-linking in cells that contain endogenous sialic acid. For these experiments, we analyzed CD22 cross-linking in the Daudi B cell line. When photoirradiated, only cells supplemented with Ac_4ManNDAz(2me) showed an anti-CD22 reactive band of increased molecular weight, corresponding to cross-linked CD22 (Figure 5C). Lysates from Daudi cells cultured with Ac_4Man NDAz(3me) or Ac_4ManNDAz(4me) did not display cross-linked CD22 even upon long exposures, suggesting inadequate

Table 1. DMB-Derivatization of Sialic Acids Reveals that SiaDAz(2me) and SiaDAz(3me) Effectively Compete with Endogenous Sialic Acid for Incorporation into Glycoconjugates[a]

		% of total sialic acid	
compound added	fraction analyzed	Neu5Ac	SiaDAz (2me, 3me, or 4me)
no added sugar	cytosol	100	0
	membrane	100	0
Ac_4ManNAc	cytosol	100	0
	membrane	100	0
Ac_4ManNDAz(2me)	cytosol	15	85
	membrane	26	74
Ac_4ManNDAz(3me)	cytosol	63, 70	37, 30
	membrane	92, 96	8, 4
Ac_4ManNDAz(4me)	cytosol	100	N.D.
	membrane	100	N.D.

[a] Jurkat cells were cultured with the indicated compounds, harvested, and fractionated. Sialic acids were derivatized by DMB and separated by reverse phase HPLC with fluorescence detection (see Figures S4−S6). Peaks were integrated to derive the percentages of Neu5Ac and other sialic acids. Multiple values indicate results from independent experiments. N.D. indicates that a peak corresponding to SiaDAz(4me) could not be identified.

competition with endogenous sialic acid. Lysates from Daudi cells not exposed to UV light did not reveal any cross-linked product (Figure 5D). Notably, Ac_4GlcNDAz(2me)-treated cells produced no photo-cross-linked product after UV exposure. These data suggest that Ac_4GlcNDAz(2me) is not metabolized to a photo-cross-linking sialic acid analogue even though Daudi cells have UDP-GlcNAc 2-epimerase activity and are therefore capable of converting UDP-GlcNAc to ManNAc.

Photo-Cross-Linking Sialic Acids Compete with Neu5Ac for Incorporation into Glycoconjugates. Having obtained indirect evidence that at least one photo-cross-linking sialic acid can compete with endogenous sialic acids, we wished to quantify the efficiency of photo-cross-linking sialic acid metabolism. We conducted this assessment in the Jurkat T cell line, because previous work indicated that sialic acid analogues can compete efficiently with Neu5Ac in this cell line.[24] We cultured Jurkat cells for 72 h with **1**, **3**, **4**, **5**, or **6**, then harvested the cells and fractionated them into cytosolic and membrane components. Cytosolic fractions should contain primarily free sialic acids and CMP-sialic acids, while the membrane fractions contain sialic acids that have been incorporated into glycoconjugates. Each sample was subjected to mild acid hydrolysis to release ketosidically linked sialic acids and then treated with 1,2-diamino-4,5-methylenedioxybenzene (DMB) to fluorescently derivatize the sialic acids. Separation by reverse-phase HPLC and fluorescence detection[24,33,34] enabled us to quantify the ratios of sialic acids present in each sample (raw data shown in Supporting Information Figures S4−S6).

Jurkat cells cultured in the absence of exogenous ManNAc analogues or in the presence of compounds **1** and **3** contained a single form of naturally occurring sialic acid, Neu5Ac (Table 1). Cells cultured with 100 μM Ac_4ManNDAz(2me) also contained significant quantities of a novel sialic acid species. Comparison of the retention time and mass to standard molecules revealed that this species is the sialic acid metabolite of Ac_4ManNDAz(2me), which we name SiaDAz(2me). SiaDAz(2me) comprised a greater portion of the total sialic acid in the cytosolic fraction (85%) than in the membrane fraction (74%). As expected from the cross-linking data, larger sialic acid analogues were less competitive with Neu5Ac. Supplementation with Ac_4ManNDAz(3me) yielded another novel peak, whose retention time and mass matched that of DMB-SiaDAz(3me) (**19**, Supporting Information Scheme S2), but it comprised only about a third of the cytosolic sialic acid and less than 10% of the membrane-associated sialic acid. We were unable to detect a sialic acid corresponding to SiaDAz(4me) in the lysates from cells supplemented with Ac_4ManNDAz(4me).

Taken together, the DMB derivatization data indicate that SiaDAz(2me) is efficiently incorporated into sialic acid-containing glycoconjugates, effectively replacing up to 74% of the cell surface Neu5Ac in Jurkat cells. Further, these results confirm that larger photo-cross-linking ManNAc analogues are less efficiently metabolized to sialic acid and to cell surface sialosides. Finally, our data indicate that the photo-cross-linking sialic acids are better represented among cytosolic sialic acids than among membrane sialic acids.

N-Acyl Diazirine Restricts ManNAc-GlcNAc Crosstalk. Next, we wished to examine whether diazirine-modified ManNAc could be metabolized to glycans other than sialosides. In cells, ManNAc is synthesized from UDP-GlcNAc by the UDP-GlcNAc 2-epimerase. While the reverse reaction is disfavored, a second enzyme, GlcNAc 2-epimerase, is capable of interconverting ManNAc and GlcNAc.[21] Therefore, the activity of GlcNAc 2-epimerase could potentially lead to incorporation of diazirine cross-linkers into GlcNAc-containing glycans, rather than sialic acid-containing glycans. To investigate this possibility, we cultured Jurkat cells with 100 μM Ac_4ManNDAz(2me), 100 μM Ac_4GlcNDAz(2me), or no exogenous sugar. After 72 h, the cells were harvested and lysed. Cell lysates were examined by high-performance anion exchange chromatography (HPAEC) to identify diazirine-containing nucleotide-sugar donors. As shown previously,[35] Jurkat cells cultured with Ac_4ManNDAz(2me) produce a new species, whose retention time is slightly longer than that of CMP-Neu5Ac (Supporting Information Figure S7). This new species is UV-sensitive and is therefore assigned as CMP-SiaDAz(2me). Notably, the CMP-SiaDAz(2me) peak was not observed in lysates from untreated Jurkat cells or from cells cultured with Ac_4GlcNDAz(2me). Next, we looked for evidence of UDP-GlcNDAz(2me) in the Jurkat lysates. None of the lysates displayed a peak with a retention time matching that of synthetic UDP-GlcNDAz(2me) (Supporting Information Scheme S3 and Figure S8). These results imply that the diazirine cross-linker in Ac_4ManNDAz(2me) is specifically directed toward incorporation into sialosides and not into other glycans.

Photo-Cross-Linking Sialic Acids Are Incorporated into Gangliosides. Our CD22 photo-cross-linking experiments in BJA-B K20 cells indicated that the larger photo-cross-linking ManNAc analogues were metabolized to sialic acids and incorporated into sialic acid-containing glycoproteins. We next tested if the new photo-cross-linking sialic acids could also be incorporated into sialic acid-containing glycolipids, as has been shown for other sialic acid analogues.[13,36−41] Briefly, Jurkat cells were cultured in the presence of sugars **1**−**6** for 72 h. After harvesting the cells, a series of extractions were employed to remove insoluble membrane components, proteins, phospholipids, and uncharged lipids.[42,43] Next, the resulting ganglioside fraction was

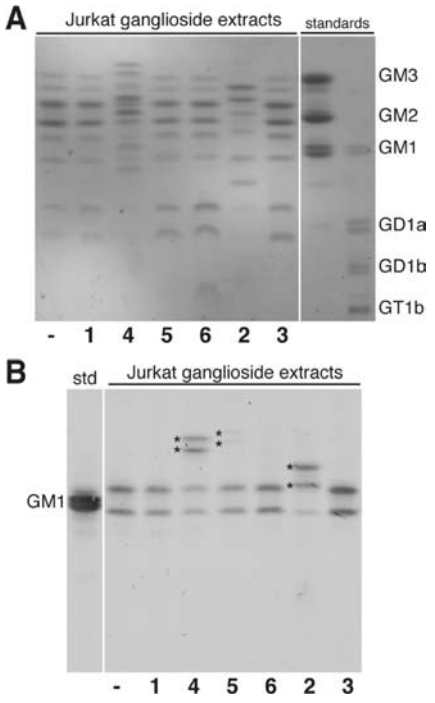

Figure 6. HPTLC analysis of gangliosides extracted from cultured Jurkat cells. Jurkat cells were cultured alone or with **1**−**6**. (A) The HPTLC plate was stained for sialic acid using resorcinol. Jurkat cells produce a variety of gangliosides: GM3, GM2, GM1a, and GD1a. The pattern of gangliosides changed upon introduction of unnatural sialic acid precursors Ac_4ManNDAz(2me) and Ac_4ManNAz, but not other compounds. (B) The HPTLC plate was probed with CTxB-488, which recognizes ganglioside GM1a. Naturally occurring GM1a molecules are present in all ganglioside extracts. Additional species with CTxB-488 reactivity (★) appeared when cells were cultured with Ac_4ManNDAz-(2me), Ac_4ManNDAz(3me), or Ac_4ManNAz.

separated by high-performance thin layer chromatography (HPTLC). The resolved sialylated lipids were detected using resorcinol staining. Resorcinol selectively reacts with sialic acid to yield gray−blue bands; asialo species appear brown. As we have observed previously,[13] Jurkat cells produce multiple gangliosides, identified as GD1a, GM1a, GM2, and GM3 based on their mobilities in comparison to standards (Figure 6A). Due to two different fatty acid chain lengths, the Jurkat gangliosides run in pairs. Resorcinol staining revealed a change in banding pattern for only two samples, corresponding to cells supplemented with Ac_4ManNDAz(2me) or Ac_4ManNAz (Figure 6A). Novel bands appearing in these lanes displayed R_f values higher than those in the control lanes; we interpret the addition of these to correspond to the production of diazirine- and azido-modified gangliosides, respectively. We previously confirmed the identity of the SiaDAz(2me)-modified gangliosides by matrix-assisted laser desorption ionization time-of-flight (MALDI-TOF) MS analysis.[13] Resorcinol staining did not provide evidence for SiaDAz(3me) or SiaDAz(4me) incorporation into gangliosides.

CTxB-488 Recognizes GM1a Analogues Modified by Photo-Cross-Linking Sialic Acids. We next investigated the ganglioside composition of these lysates using Alexa Fluor 488-labeled cholera toxin subunit B (CTxB-488) to probe the HPTLC plates. This analysis is about 1000 times more sensitive than resorcinol staining (Figure S9). We found that CTxB-488 efficiently bound natural GM1a in all Jurkat cell extracts (Figure 6B). Importantly, CTxB-488 also recognized additional species in extracts from cells supplemented with Ac_4ManNDAz(2me), Ac_4ManNDAz(3me), and Ac_4ManNAz, suggesting that SiaDAz-(2me), SiaDAz(3me), and SiaNAz are each incorporated into GM1a gangliosides. We did not observe CTxB-488 binding to any additional species in the lane corresponding to Ac_4ManNDAz-(4me)-treated cells, indicating that GM1a-SiaDAz(4me) was not produced at detectable levels or that the larger modification interferes with CTxB binding. In addition to confirming unnatural ganglioside production, these results provide evidence that CTxB can recognize and bind diazirine-modified ganglioside species.

Photo-Cross-Linking Sialic Acid Covalently Traps the GM1a-CTxB Complex. Previously, we showed that SiaDAz-(2me)-modified GM1a could be cross-linked to CTxB.[13] To determine if other diazirine-modified GM1a molecules could be used to covalently capture a ganglioside−protein complex, we cultured Jurkat cells with per-*O*-acetylated ManNAc analogues, incubated the cells with CTxB, and then irradiated the cells with 365 nm light for 45 min. Cells were lysed using a Triton X-100-based lysis buffer and the proteins separated by SDS-PAGE under reducing conditions. Separated proteins were transferred to a PVDF membrane and probed for the presence of CTxB by standard protein immunoblotting techniques. When Jurkat cells were cultured with Ac_4ManNDAz(2me) and Ac_4ManNDAz-(3me), we observed a new species whose mobility was slightly slower than CTxB (∼11.6 kDa), consistent with the covalent addition of a GM1a molecule (∼1.5 kDa) forming a ∼13 kDa complex (Figure 7A). Surprisingly, a modest amount of this lower mobility species was also observed in lysates from cells cultured with Ac_4ManNDAz(4me) or Ac_4ManNAz, suggesting that both the poorly incorporated SiaDAz(4me) and the inefficient cross-linker SiaNAz are each capable of mediating GM1a-CTxB cross-linking. In contrast, lysates from cells cultured with no compound, Ac_4ManNAc, or Ac_4GlcNDAz(2me) displayed a single band corresponding to unmodified CTxB. In complementary experiments, we probed membranes for the presence of GM1a with horseradish peroxidase-conjugated CTxB (CTxB-HRP). We observed GM1a present in all samples. For cells cultured with Ac_4ManNDAz(2me), we also observed an additional species that had a mobility consistent with cross-linked CTxB-GM1a-SiaDAz(2me) (Figure 7C). The intensity of the cross-linked band detected by CTxB-HRP is much less than that observed in the anti-CTxB blot; the source of the difference is not clear, but may reflect the fact that only a small fraction of GM1a is engaging in CTxB cross-linking, or that cross-linked GM1a is not strongly recognized by CTxB-HRP. Given the low intensity of the cross-linked CTxB-GM1a-SiaDAz(2me) detected by CTxB-HRP, it was not surprising that we did not observe cross-linked bands in any other lanes. Importantly, cells that were not exposed to 365 nm light revealed no formation of the CTxB-GM1a complex, demonstrating that complex formation was UV-dependent (Figure 7B and D). Furthermore, samples from Ac_4ManNAc-treated cells do not reveal any species with increased molecular weight, indicating that complex formation is dependent on the presence of a photoreactive moiety.

To solidify our assignment of the CTxB-GM1a-SiaDAz(2me) complex, we used self-assembled monolayer (SAM) with matrix-assisted laser desorption/ionization (MALDI) time-of-flight mass spectrometry (denoted SAMDI-TOF-MS) analysis of cell lysates. A detailed description of the analysis is provided in the Supporting Information. This procedure directly immunoprecipitates the CTxB and CTxB-GM1a-SiaDAz(2me) species onto

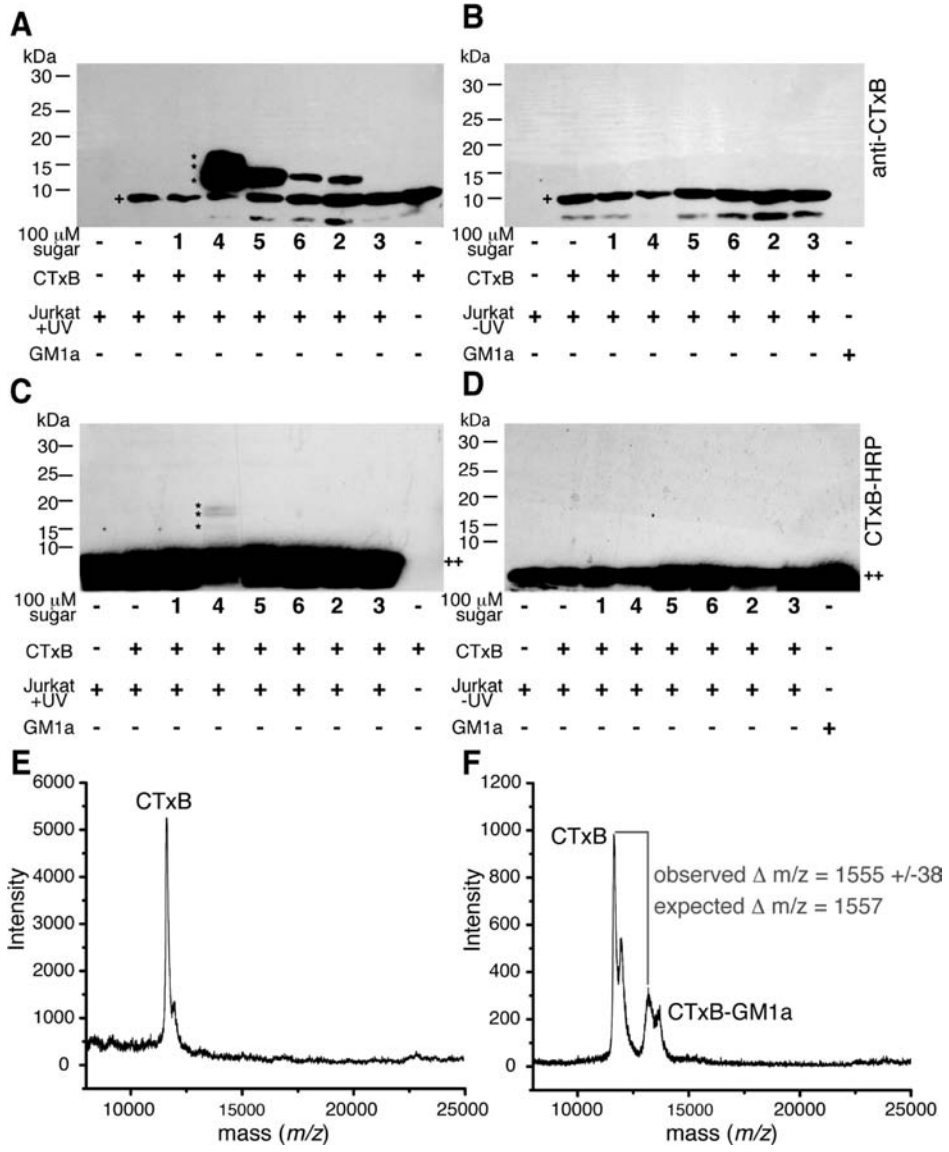

Figure 7. Photo-cross-linking sugar analogues covalently capture CTxB-GM1a interaction. Jurkat cells were cultured with or without sugar analogues **1**−**6** for 72 h and then incubated with CTxB for 45 min at 4 °C. Cells were photoirradiated, lysed, and the lysates separated by reducing SDS-PAGE followed by protein transfer to PVDF membranes. UV-irradiated (A) and non-UV-irradiated samples (B) were probed for the presence of CTxB (+) using an anti-CTxB antibody. A slower mobility band has an apparent molecular weight consistent with formation of a CTxB-GM1a complex (∼13 kDa, *). The identity of the very low molecular weight band (<10 kDa) is not known, but it appears to be related to a contaminant in the CTxB preparation. UV-irradiated (C) and non-UV-irradiated samples (D) were probed for the presence of GM1a (++) using CTxB-HRP. A slower mobility band has an apparent molecular weight consistent with formation of a CTxB-GM1a complex (∼13 kDa, *). Membranes were stripped and probed for β-actin to demonstrate equal protein loading in each lane (not shown). (E) SAMDI-TOF MS spectrum of SAM-bound monomeric CTxB species derived from cells cultured with Ac_4ManNAc, incubated with CTxB, and photoirradiated. (F) SAMDI-TOF MS spectrum of SAM-bound monomeric CTxB and cross-linked CTxB-GM1a-SiaDAz(2me) derived from cells cultured with Ac_4ManNDAz(2me), incubated with CTxB, and photoirradiated.

the gold chip followed by molecular weight determination of the bound analytes. Briefly, gold chips bearing NTA-based SAMs were first treated with $NiSO_4$ to generate the NTA/Ni^{2+} complex and then functionalized with His_6-tagged protein G followed by a rabbit anti-CTxB antibody.[18] These antibody-treated chips were then incubated with cell lysates, which were generated as described for the immunoblotting experiments. After washing the SAM chips, α-cyano-4-hydroxycinnamic acid (CHCA) matrix was deposited on top of the chips followed by MALDI-TOF MS analysis.

SAMDI experiments on lysates from cells cultured in the presence of Ac_4ManNAc revealed a molecular ion that corresponded to the singly charged monomeric CTxB (Figure 7E).[44,45] For the sample derived from cells cultured with Ac_4ManNDAz(2me), a second molecular ion at 1555 Da higher molecular weight was observed. This mass difference correlates (within experimental error) to the addition of the GM1a-SiaDAz(2me) (1557 Da) to CTxB (Figure 7F) and thus confirms the assignment of the covalently captured CTxB-GM1a-SiaDAz(2me) species in the immunoblot (Figure 7A and C).

DISCUSSION

Factors Affecting Conversion of Photo-Cross-Linking Sugars to Sialosides. Here, we investigated the metabolism of three photo-cross-linking ManNAc analogues of varying sizes. We discovered that each of these compounds could be metabolized to their sialic acid counterparts, incorporated into cellular sialosides, and employed to cross-link sialoside complexes. Consistent with previous reports,[11,46,47] we found that the size of the *N*-acyl chain modification was inversely correlated with the metabolism efficiency. Indeed, for the largest diazirine-modified sugar, detection of SiaDAz(4me)-containing glycoconjugates was difficult: we were only able to infer their presence from the CD22 cross-linking that we observed in BJA-B K20 cells and the CTxB-GM1a cross-linking that we observed in Jurkat cells. DMB derivatization of sialic acids present in the soluble, cytoplasmic fraction revealed that *N*-acyl chain length discrimination is a feature of one or more of the cytosolic or nuclear enzymes involved in converting the ManNAc analogues to sialic acid and CMP-sialic acid analogues. This finding is consistent with previous reports that ManNAc 6-kinase functions as a bottleneck for unnatural sialoside production.[46] Indeed, others have found that the use of sialic acid analogues, rather than ManNAc analogues, can offer a strategy to bypass restrictions on the types of sialosides that can be produced.[11,48] In addition, we observed that the fractional representation of the unnatural photo-cross-linking sialic acids is lower in the membrane fraction, as compared to the cytosolic fraction. While some of this difference might arise from a system that has not achieved equilibrium, we hypothesize that it could also reflect additional discrimination against the unnatural sialic acids, either at the level of transport of the CMP-sialic acids into the Golgi or tolerance for the CMP-sialic acids by various sialyltransferases.

Metabolic production of unnatural sialosides typically relies on the exogenous addition of ManNAc analogues, since the enzymes involved in the conversion of ManNAc to sialosides (Figure 2) have a well-documented tolerance in their substrate specificity.[8] Human cells can synthesize ManNAc from UDP-GlcNAc, by the action of UDP-GlcNAc 2-epimerase, but are also capable of directly interconverting ManNAc and GlcNAc, through the action of GlcNAc 2-epimerase, provided that this enzyme is expressed.[21] Therefore, GlcNAc analogues could theoretically be converted to ManNAc analogues and, further, to sialosides. However, none of our data indicated that Ac_4GlcNDAz(2me) could be metabolized to SiaDAz(2me), even in Daudi and Jurkat cells, which have UDP-GlcNAc 2-epimerase activity. Using Ac_4GlcNDAz(2me), we saw no evidence of photo-cross-linked species (Figures 5 and 7), no additional bands corresponding to a modified GM1a species (Figure 6), and no evidence of SiaDAz(2me) by DMB derivatization. Moreover, our HPAEC data indicated that not only is Ac_4GlcNDAz(2me) not converted to CMP-SiaDAz(2me), but also that Ac_4ManNDAz(2me) is not converted to UDP-GlcNDAz(2me) (Supporting Information Figures S7 and S8). In contrast, when Bertozzi and colleagues studied the metabolism of the smaller, azide-containing molecule Ac_4GlcNAz, they observed metabolism of GlcNAz to SiaNAz.[49] Our results suggest that the large substituent found on Ac_4GlcNDAz(2me) restricts entry into the sialic acid biosynthetic pathway and may provide a way to minimize crosstalk between strategies aimed at metabolic labeling of different classes of glycoconjugates. It is important to note that the metabolic fate of ManNAc analogues may vary in different cell lines, depending on the expression of different metabolic enzymes (Figure 2); we did not investigate those expression levels here.

Relationship between Incorporation and Photo-Cross-Linking Efficiencies. Our initial hypothesis was that introducing a longer, flexible linker between the pyranose ring and the diazirine might enhance cross-linking by allowing the cross-linker to sample a larger space. We were unable to test this hypothesis directly, because we found that analogues with longer linkers suffered from relatively poor metabolism to sialosides. Our data indicate that all three photo-cross-linking sugars—Ac_4ManNDAz(2me), Ac_4ManNDAz(3me), and Ac_4ManNDAz(4me)—are metabolized to effective photo-cross-linking sialosides, but the efficiency of metabolism limits the utility of the two larger compounds. We observed that the largest photo-cross-linking analogue, Ac_4ManNDAz(4me), yielded CD22 cross-linking in BJA-B K20 cells, but not Daudi cells (Figure 5). Given the poor efficiency of SiaDAz(4me) incorporation, we were surprised to observe CTxB-GM1a cross-linking in Jurkat cells that had been cultured with Ac_4ManNDAz(4me). This result indicates that the small amount of SiaDAz(4me) that is incorporated into GM1a is effective at cross-linking to CTxB and suggests that the diazirine cross-linker in SiaDAz(4me) is well-positioned for capturing this particular sialic acid-mediated interaction. Also surprising was the modest CTxB-GM1a cross-linking that we observed for Jurkat cells cultured with Ac_4ManNAz. Although Ac_4ManNAz is metabolized readily and incorporated into glycoconjugates with high efficiency,[24] we did not expect to observe cross-linking, since alkyl azides are poor photo-cross-linking moieties.[50]

Targeting Unnatural Sialic Acids to Sectors of the Sialome May Prove Challenging. Sialosides are a diverse set of molecules. Addition of sialic acid to glycoconjugates is catalyzed by one of the twenty sialyltransferases encoded in the human genome.[51,52] Although some functional redundancy exists within this family of enzymes, individual members exhibit divergent substrate specificities. Sialyltransferases can add sialic acid to both glycoproteins and glycolipids. Furthermore, sialic acids can be attached in α2−3, α2−6, or α2−8-linkages to a wide variety of underlying glycan structures. Although there are many examples of unnatural sugar incorporation into cellular sialosides,[8] there has been no systematic study to examine the unnatural substrate tolerance of individual sialyltransferases. We wondered whether differences in sialyltransferase specificity would enable selective incorporation of unnatural sialic acids into a particular subset of sialosides. When we examined the incorporation of our three photo-cross-linking sialic acid analogues, we found that the overall incorporation levels mirrored the efficiency of incorporation into glycolipids. Similarly, overall incorporation and incorporation into specific linkages and onto specific glycans displayed the same trends. While Golgi-resident sialyltransferases may collectively discriminate against diazirine-modified sialic acid analogues, none of the data presented here suggest that individual sialyltransferases differ in their discrimination patterns.

Achieving sialoside-specific incorporation may require other strategies. Turnover rates for both glycoproteins and glycolipids can vary dramatically,[53,54] suggesting that the optimal time for analysis of specific species may differ. Perhaps time-dependent metabolic labeling experiments could offer a way to selectively introduce unnatural sialic acids into a particular sector of the sialome. Alternatively, production of an orthogonal mutant sialyltransferase and nucleotide-sugar donor could also provide a directed incorporation strategy.

CONCLUSION

In summary, we described two new diazirine-modified sialic acid precursors, and compared them to a previously reported molecule with respect their efficiency of incorporation into sialosides and their ability to photo-cross-link two glycan-mediated interactions. All three diazirine-modified sialic acid precursors were incorporated into both glycoproteins and glycolipids. We found that the smallest diazirine-modified sialic acid precursor was most efficiently metabolized and completed well with endogenous sialic acid, resulting in up to 74% of cell surface sialic acid being diazirine-modified. We observed that even poorly incorporated analogues could function as cross-linkers. Metabolism of the largest diazirine-modified sialic acid precursor was so poor that we could not quantify its incorporation level, yet we could readily detect cross-linking of both sialylated glycoproteins and sialylated glycolipids. Notably, our data suggested that the photo-cross-linking substituent interferes with metabolic crosstalk between GlcNAc and ManNAc pathways, resulting in faithful incorporation of the diazirine into only sialylated glycoconjugates. In addition to these findings, we note that our ability to detect a cross-linked CTxB-GM1a complex by mass spectrometry provides a blueprint for future efforts to use photo-cross-linking for binding partner discovery.

ASSOCIATED CONTENT

Supporting Information. Additional figures and experimental data. This material is available free of charge via the Internet at http://pubs.acs.org.

AUTHOR INFORMATION

Corresponding Author

*Phone: 214-648-1214; fax: 214-648-4156; e-mail: jennifer.kohler@utsouthwestern.edu.

ACKNOWLEDGMENT

We thank Kim Orth (UT Southwestern Medical Center) for sharing Jurkat cells, Michael Pawlita (German Cancer Research Center), and James Paulson (The Scripps Research Institute) for sharing BJA-B K20, BJA-B K88 cells, and Ellen Vitetta (UT Southwestern Medical Center) for sharing Daudi cells. We thank Peter Vu (UT Southwestern Medical Center) for sharing reagents. We thank Yan Li (UT Southwestern Medical Center Protein Chemistry Technology Center) for mass spectrometry analysis of sugars, Angela Mobley (UT Southwestern Medical Center Flow Cytometry Core Facility) for help with flow cytometry, Luke Rice (UT Southwestern Medical Center) for access to the ultracentrifuge, and Wen-hong Li (UT Southwestern Medical Center) for access to the HPLC with a fluorescence detector. We also thank Yoshihito Tanaka and Chad M. Whitman for helpful discussions and suggestions. We acknowledge the following funding sources: the National Institutes of Health (GM090271), the March of Dimes (5-FY06-913), the Welch Foundation (I-1686), and the University of Texas Southwestern Medical Center. This content is solely the responsibility of the authors and does not necessarily represent the official views of the National Institute of General Medical Sciences or the National Institutes of Health. M. R. B. acknowledges the support of an NSF Graduate Research Fellowship and of Stanford University. J. J. K. is an Alfred P. Sloan Research Fellow.

REFERENCES

(1) Sinclair, A. M., and Elliott, S. (2005) Glycoengineering: The effect of glycosylation on the properties of therapeutic proteins. *J. Pharm. Sci. 94*, 1626–1635.

(2) Schauer, R. (2009) Sialic acids as regulators of molecular and cellular interactions. *Curr. Opin. Struct. Biol. 19*, 507–514.

(3) Varki, A. (2007) Glycan-based interactions involving vertebrate sialic-acid-recognizing proteins. *Nature 446*, 1023–1029.

(4) McEver, R. P., Moore, K. L., and Cummings, R. D. (1995) Leukocyte trafficking mediated by selectin-carbohydrate interactions *J. Biol. Chem. 270*, 11025–11028.

(5) Holmgren, J., Lönnroth, I., Månsson, J., and Svennerholm, L. (1975) Interaction of cholera toxin and membrane GM1 ganglioside of small intestine. *Proc. Natl. Acad. Sci. U. S. A. 72*, 2520–2524.

(6) Connor, R. J., Kawaoka, Y., Webster, R. G., and Paulson, J. C. (1994) Receptor specificity in human, avian, and equine H2 and H3 influenza virus isolates. *Virology 205*, 17–23.

(7) Varki, N. M., and Varki, A. (2007) Diversity in cell surface sialic acid presentations: implications for biology and disease. *Lab. Invest. 87*, 851–857.

(8) Du, J., Meledeo, M. A., Wang, Z., Khanna, H. S., Paruchuri, V. D. P., and Yarema, K. J. (2009) Metabolic glycoengineering: Sialic acid and beyond. *Glycobiology 19*, 1382–1401.

(9) Tanaka, Y., and Kohler, J. J. (2008) Photoactivatable crosslinking sugars for capturing glycoprotein interactions. *J. Am. Chem. Soc. 130*, 3278–3279.

(10) Han, S., Collins, B. E., Bengtson, P., and Paulson, J. C. (2005) Homomultimeric complexes of CD22 in B cells revealed by protein-glycan cross-linking. *Nat. Chem. Biol. 1*, 93–97.

(11) Luchansky, S. J., Goon, S., and Bertozzi, C. R. (2004) Expanding the diversity of unnatural cell-surface sialic acids. *ChemBioChem 5*, 371–374.

(12) Ramya, T. N. C., Weerapana, E., Liao, L., Zeng, Y., Tateno, H., Liao, L., Yates, J. R., Cravatt, B. F., and Paulson, J. C. (2010) *In situ trans* ligands of CD22 identified by glycan-protein photocross-linking-enabled proteomics. *Mol. Cell. Prot. 9*, 1339–1351.

(13) Bond, M. R., Whitman, C. M., and Kohler, J. J. (2010) Metabolically incorporated photocrosslinking sialic acid covalently captures a ganglioside-protein complex. *Mol. Biosyst. 6*, 1796–1799.

(14) Tanaka, Y., Bond, M. R., and Kohler, J. J. (2008) Photocrosslinkers illuminate interactions in living cells. *Mol. Biosyst. 4*, 473–480.

(15) Bayley, H. (1983) *Photogenerated Reagents in Biochemistry and Molecular Biology*, Elsevier.

(16) Bond, M. R., Zhang, H., Vu, P. D., and Kohler, J. J. (2009) Photocrosslinking of glycoconjugates using metabolically incorporated diazirine-containing sugars. *Nat. Protoc. 4*, 1044–1063.

(17) Saxon, E., and Bertozzi, C. R. (2000) Cell surface engineering by a modified Staudinger reaction. *Science 287*, 2007–2010.

(18) Patrie, S. M., and Mrksich, M. (2007) Self-assembled monolayers for MALDI-TOF mass spectrometry for immunoassays of human protein antigens. *Anal. Chem. 79*, 5878–5887.

(19) Jones, M. B., Teng, H., Rhee, J. K., Lahar, N., Baskaran, G., and Yarema, K. J. (2004) Characterization of the cellular uptake and metabolic conversion of acetylated N-acetylmannosamine (ManNAc) analogues to sialic acids. *Biotechnol. Bioeng. 85*, 394–405.

(20) Sarkar, A. K., Rostand, K. S., Jain, R. K., Matta, K. L., and Esko, J. D. (1997) Fucosylation of disaccharide precursors of sialyl Lewis(X) inhibit selectin-mediated cell adhesion. *J. Biol. Chem. 272*, 25608–25616.

(21) Luchansky, S. J., Yarema, K. J., Takahashi, S., and Bertozzi, C. R. (2003) GlcNAc 2-epimerase can serve a catabolic role in sialic acid metabolism. *J. Biol. Chem. 278*, 8035–8042.

(22) Keppler, O. T., Hinderlich, S., Langner, J., Schwartz-Albiez, R., Reutter, W., and Pawlita, M. (1999) UDP-GlcNAc 2-epimerase: A regulator of cell surface sialylation. *Science 284*, 1372–1376.

(23) Keppler, O. T., Peter, M. E., Hinderlich, S., Moldenhauer, G., Stehling, P., Schmitz, I., Schwartz-Albiez, R., Reutter, W., and Pawlita, M. (1999) Differential sialylation of cell surface glycoconjugates in a human B lymphoma cell line regulates susceptibility for CD95 (APO-1/Fas)-mediated apoptosis and for infection by a lymphotropic virus. *Glycobiology 9*, 557–569.

(24) Luchansky, S. J., Argade, S., Hayes, B. K., and Bertozzi, C. R. (2004) Metabolic functionalization of recombinant glycoproteins. *Biochemistry 43*, 12358–12366.

(25) Chokhawala, H. A., Huang, S. S., Lau, K., Yu, H., Cheng, J. S., Thon, V., Hurtado-Ziola, N., Guerrero, J. A., Varki, A., and Chen, X. (2008) Combinatorial chemoenzymatic synthesis and high-throughput screening of sialosides. *ACS Chem. Biol. 3*, 567–576.

(26) Brinkman-Van der Linden, E. C. M., Sonnenburg, J. L., and Varki, A. (2002) Effects of sialic acid substitutions on recognition by *Sambucus nigra* agglutinin and *Maackia amurensis* hemagglutinin. *Anal. Biochem. 303*, 98–104.

(27) Zeng, Y., Ramya, T. N. C., Dirksen, A., Dawson, P. E., and Paulson, J. C. (2009) High-efficiency labeling of sialylated glycoproteins on living cells. *Nat. Methods 6*, 207–209.

(28) Shibuya, N., Goldstein, I. J., Broekaert, W. F., Nsimba-Lubaki, M., Peeters, B., and Peumans, W. J. (1987) The elderberry (*Sambucus nigra* L.) bark lectin recognizes the Neu5Ac(α2−6)Gal/GalNAc sequence. *J. Biol. Chem. 262*, 1596–1601.

(29) Wang, W. C., and Cummings, R. D. (1988) The immobilized leukoagglutinin from the seeds of *Maackia amurensis* binds with high affinity to complex-type Asn-linked oligosaccharides containing terminal sialic acid-linked alpha-2,3 to penultimate galactose residues. *J. Biol. Chem. 263*, 4576–4585.

(30) Geisler, C., and Jarvis, D. L. (2011) Letter to the Glyco-Forum: Effective glycoanalysis with *Maackia amurensis* lectins requires a clear understanding of their binding specificities. *Glycobiology 21*, 988–993.

(31) Iglesias, J. L., Lis, H., and Sharon, N. (1982) Purification and properties of a D-galactose/N-acetyl-D-galactosamine-specific lectin from *Erythrina cristagalli*. *Eur. J. Biochem. 123*, 247–252.

(32) Brooks, S. A. (2000) The involvement of *Helix pomatia* lectin (HPA) binding N-acetylgalactosamine glycans in cancer progression. *Histol. Histopathol. 15*, 143–158.

(33) Hara, S., Yamaguchi, M., Takemori, Y., Furuhata, K., Ogura, H., and Nakamura, M. (1989) Determination of mono-O-acetylated N-acetylneuraminic acids in human and rat sera by fluorometric high-performance liquid chromatography. *Anal. Biochem. 179*, 162–166.

(34) Nakamura, S. M. H., Yamaguchi, M., Takemori, Y., and Ohkura, Y. (1987) 1,2-diamino-4,5-methylenedioxybenzene as a highly sensitive fluorogenic reagent for α-keto acids. *Chem. Pharm. Bull. 35*, 687–692.

(35) Yu, S.-H., Bond, M. R., Whitman, C. M., and Kohler, J. J. (2010) Metabolic labeling of glycoconjugates with photocrosslinking sugars. *Methods Enzymol. 478*, 541–562.

(36) Bussink, A. P., van Swieten, P. F., Ghauharali, K., Scheij, S., van Eijk, M., Wennekes, T., van der Marel, G. A., Boot, R. G., Aerts, J. M. F. G., and Overkleeft, H. S. (2007) N-azidoacetylmannosamine-mediated chemical tagging of gangliosides. *J. Lipid Res. 48*, 1417–1421.

(37) Chefalo, P., Pan, Y., Nagy, N., Guo, Z., and Harding, C. V. (2006) Efficient metabolic engineering of GM3 on tumor cells by N-phenylacetyl-D-mannosamine. *Biochemistry 45*, 3733–3739.

(38) Wang, Q., Zhang, J., and Guo, Z. (2007) Efficient glycoengineering of GM3 on melanoma cell and monoclonal antibody-mediated selective killing of the glycoengineered cancer cell. *Bioorg. Med. Chem. 15*, 7561–7567.

(39) Zou, W., Borrelli, S., Gilbert, M., Liu, T., Pon, R. A., and Jennings, H. J. (2004) Bioengineering of surface GD3 ganglioside for immunotargeting human melanoma cells. *J. Biol. Chem. 279*, 25390–25399.

(40) Pan, Y., Chefalo, P., Nagy, N., Harding, C., and Guo, Z. (2005) Synthesis and immunological properties of N-modified GM3 antigens as therapeutic cancer vaccines. *J. Med. Chem. 48*, 875–883.

(41) Whitman, C. M., Yang, F., and Kohler, J. J. (2011) Modified GM3 gangliosides produced by metabolic oligosaccharide engineering. *Bioorg. Med. Chem. Lett. 21*, 5006–5010.

(42) Ladisch, S., and Gillard, B. (1985) A solvent partition method for microscale ganglioside purification. *Anal. Biochem. 146*, 220–231.

(43) Schnaar, R. L. (1994) Isolation of glycosphingolipids. *Methods Enzymol. 230*, 348–370.

(44) Lai, C. Y. (1977) Determination of the primary structure of cholera toxin B subunit. *J. Biol. Chem. 252*, 7249–7256.

(45) Williams, J. P., Smith, D. C., Green, B. N., Marsden, B. D., Jennings, K. R., Roberts, L. M., and Scrivens, J. H. (2006) Gas phase characterization of the noncovalent quaternary structure of cholera toxin and the cholera toxin B subunit pentamer. *Biophys. J. 90*, 3246–3254.

(46) Jacobs, C. L., Goon, S., Yarema, K. J., Hinderlich, S., Hang, H. C., Chai, D. H., and Bertozzi, C. R. (2001) Substrate specificity of the sialic acid biosynthetic pathway. *Biochemistry 40*, 12864–12874.

(47) Keppler, O. T., Herrmann, M., von der Lieth, C. W., Stehling, P., Reutter, W., and Pawlita, M. (1998) Elongation of the N-acyl side chain of sialic acids in MDCK II cells inhibits influenza A virus infection. *Biochem. Biophys. Res. Commun. 253*, 437–442.

(48) Oetke, C., Brossmer, R., Mantey, L. R., Hinderlich, S., Isecke, R., Reutter, W., Keppler, O. T., and Pawlita, M. (2002) Versatile biosynthetic engineering of sialic acid in living cells using synthetic sialic acid analogues. *J. Biol. Chem. 277*, 6688–6695.

(49) Saxon, E., Luchansky, S. J., Hang, H. C., Yu, C., Lee, S. C., and Bertozzi, C. R. (2002) Investigating cellular metabolism of synthetic azidosugars with the Staudinger ligation. *J. Am. Chem. Soc. 124*, 14893–14902.

(50) Middaugh, C. R., Vanin, E. F., and Ji, T. H. (1983) Chemical crosslinking of cell membranes. *Mol. Cell. Biochem. 50*, 115–141.

(51) Harduin-Lepers, A., Vallejo-Ruiz, V., Krzewinski-Recchi, M. A., Samyn-Petit, B., Julien, S., and Delannoy, P. (2001) The human sialyltransferase family. *Biochimie 83*, 727–737.

(52) Datta, A. K. (2009) Comparative sequence analysis in the sialyltransferase protein family: Analysis of motifs. *Curr. Drug Targets 10*, 483–498.

(53) Baumann, H., and Doyle, D. (1978) Turnover of plasma membrane glycoproteins and glycolipids of hepatoma tissue culture cells. *J. Biol. Chem. 253*, 4408–4418.

(54) Tettamanti, G. (2004) Ganglioside/glycosphingolipid turnover: new concepts. *Glycoconj. J. 20*, 301–317.

Supporting information for:

Metabolism of diazirine-modified *N*-acetylmannosamine analogs to photocrosslinking sialosides

Michelle R. Bond,[1,2] Haochi Zhang,[2] Jaekuk Kim,[2] Seok-Ho Yu,[2] Fan Yang,[2] Steven M. Patrie,[2] and Jennifer J. Kohler[2,*]

[1]Department of Chemistry, Stanford University, Stanford, CA 94305
[2]Division of Translational Research, Department of Internal Medicine, University of Texas Southwestern Medical Center, Dallas, TX 75390
* To whom correspondence should be directed. phone: 214-648-1214; fax: 214-648-4156; email: jennifer.kohler@utsouthwestern.edu

Contents:

pp. 2-9	Syntheses of photocrosslinking sugars
p. 10	Effects of photocrosslinking sugars on cell growth and viability
pp. 11-14	Cell culture, flow cytometry, and immunoblotting
p. 15	Diazirine-containing sugars are stable to periodate oxidation conditions
p. 16	Sialic acid concentration determination using resorcinol/periodate assay
pp. 17-18	HPLC analysis of DMB derivatization
pp. 19-21	Analysis of CMP-SiaDAz(2me) and UDP-GlcNDAz(2me) in Jurkat cells by HPAEC
p. 22	HPTLC staining with CTxB-488 is more sensitive than resorcinol staining
pp. 23-24	Mass spectrometry analysis of CTxB-GM1a-SiaDAz(2me)
pp. 25-30	NMR spectra of purified compounds
pp. 31-32	HPLC evaluation of compound purity
p. 33	References

Syntheses of photocrosslinking sugars

Unless otherwise noted, chemicals were purchased from commercial suppliers and used as received without further purification. *N*-hydroxybenzyltriazole (HOBt) was purchased from AnaSpec (Fremont, CA). All other chemicals were purchased from Sigma-Aldrich (St. Louis, MO) or Fisher Scientific (Waltham, MA) unless otherwise noted. To monitor reactions, analytical thin layer chromatography (TLC) on silica gel 60 F254 glass plates (EM Science; Gibbstown, NJ) was used, followed by staining with ceric ammonium molybdate (CAM). CAM stain was composed of 0.4% wt/v $Ce(SO_4)_2$, 10% wt/v ammonium molybdate tetrahydrate, and 10% sulfuric acid. Products were purified by flash column chromatography on silica gel 60 (particle size 40-63 or 60-200 mm, EM Science). ^{1}H-NMR, ^{13}C-NMR, and ^{31}P-NMR were recorded with Varian 300, 400, or 500 MHz spectrometers and reported in δ ppm scale. ^{1}H-NMR were referenced to $CDCl_3$ (7.260 ppm). ^{13}C-NMR spectra were referenced to the center of the $CDCl_3$ triplet (77.0 ppm). ^{31}P-NMR spectra were referenced to 85% phosphoric acid (0 ppm). Electrospray ionization mass spectrometry (ESI-MS) data were collected at the Protein Chemistry and Technology Center at UT Southwestern Medical Center by Dr. Yan Li. Mass spectrometry methods: samples were dissolved or diluted into either a solution that contained 50% acetonitrile and 5% NH_4OH or an acetonitrile:H_2O 1:1 solution that contained 0.1% formic acid. Proxeon nano-tips were used to infuse the samples into a QStar XL mass spectrometer (Applied Biosystems, Framingham, MA). Spectra were acquired with mass range m/z 50-1000 or 300-1000. Molecular weights were calculated using the Baysesian Protein Reconstruct tool of the Analyst QS1.1 software. To confirm the purity of the unnatural analogs, samples were assessed using reverse phase HPLC.

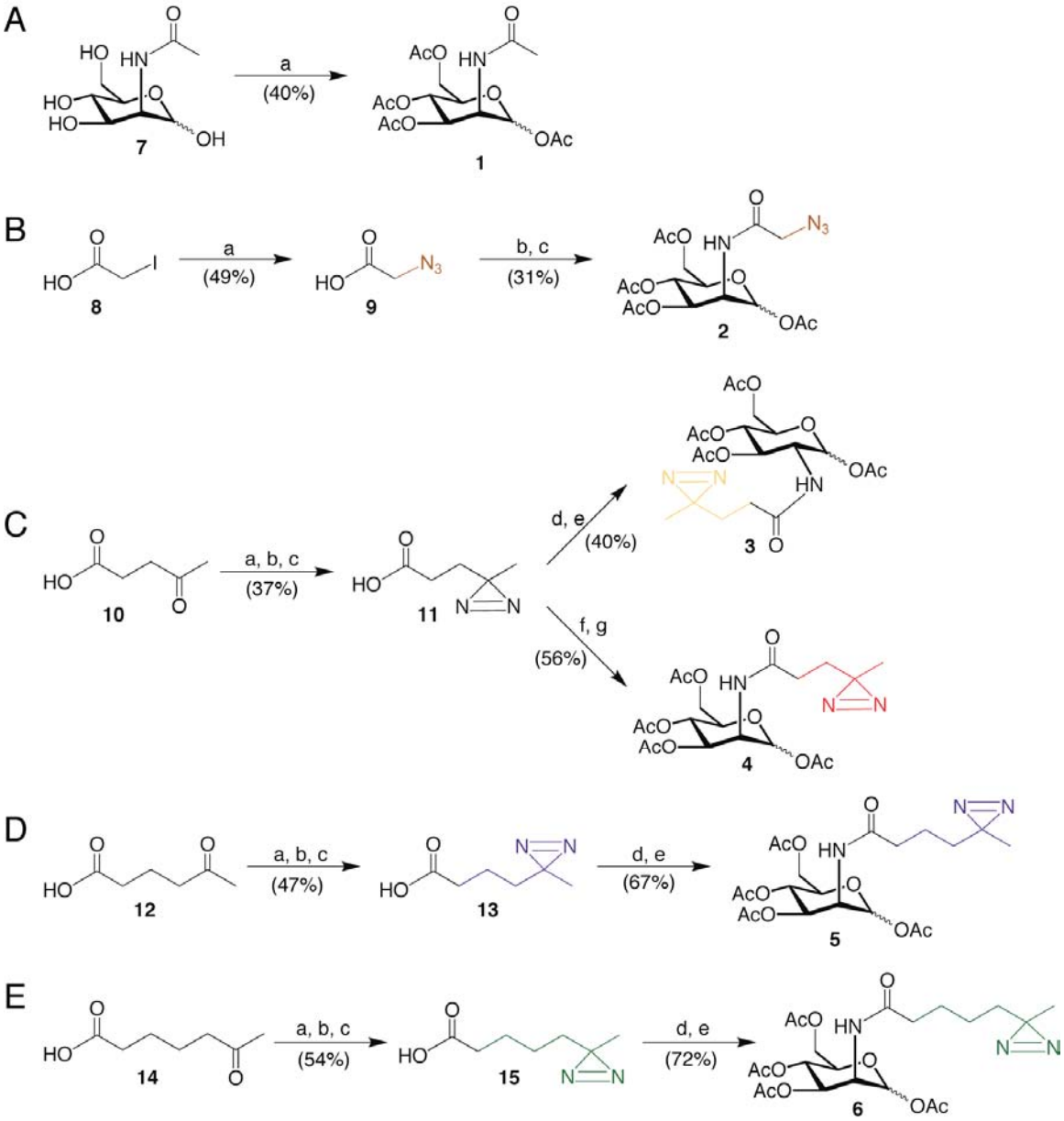

Scheme S1. **Synthesis of per-*O*-acetylated ManNAc and GlcNAc analogs.** (A) a) Ac_2O, pyridine. (B) a) NaN_3, ddH_2O, b) *D*-(+)-mannosamine hydrochloride, HOBt, 1-ethyl-3-(3-dimethylaminopropyl)carbodiimide hydrochloride (EDC), triethylamine (TEA), MeOH, c) Ac_2O, pyridine. (C) a) 7 M NH_3/MeOH, b) NH_2OSO_3H, MeOH, c) MeOH, TEA, I_2, d) *D*-(+)-glucosamine hydrochloride, HOBt, EDC, TEA, MeOH, e) Ac_2O, pyridine, f) *D*-(+)-mannosamine hydrochloride, HOBt, EDC, TEA, MeOH, g) Ac_2O, pyridine. (D) a) 7 M NH_3/MeOH, b) NH_2OSO_3H, MeOH, c) MeOH, TEA, I_2, d) *D*-(+)-mannosamine hydrochloride, HOBt, EDC, TEA, MeOH, e) Ac_2O, pyridine. (E) a) 7 M NH_3/MeOH, b) NH_2OSO_3H, MeOH, c) MeOH, TEA, I_2, d) *D* -(+)-mannosamine hydrochloride, HOBt, EDC, TEA, MeOH, e) Ac_2O, pyridine.

*Synthesis of Ac_4ManNAc (**1**)*

Ac_4ManNAc was synthesized as previously reported (Scheme S1A).[1] To a solution of *N*-acetylmannosamine (ManNAc, **7**) (124 mg, 0.56 mmol) in 5.5 mL of pyridine, 1.57 mL of acetic anhydride (Ac_2O) was added at 4 ºC. The reaction was allowed to warm to room temperature (RT) as it stirred for 20 h. The reaction mixture was diluted with CH_2Cl_2 and washed

successively by 1.0 M HCl, saturated sodium bicarbonate, and brine. The organic layer was dried over sodium sulfate and the solvent evaporated *in vacuo*. The resulting residue was purified by column chromatography (hexanes / ethyl acetate (EtOAc) gradient = 5/1, 3/1, 1/1) to afford **1** in 90 mg yield as a colorless gum in 40% yield as a mixture of anomers. ^{1}H-NMR (500 MHz, $CDCl_3$): δ 1.65 (3H, s), 2.02 (3H, s), 2.07 (3H, s), 2.11 (3H, s), 2.18 (3H, s), 4.10 (1H, dd, *J* = 2.3, 12.5 Hz), 4.28 (1H, t, *J* = 3.7 Hz), 4.78 (1H, ddd, *J* = 1.6, 3.9, 9.1 Hz), 5.06 (1H, d, 4.0 Hz), 5.13 (1H, t, *J* = 9.8 Hz), 5.33 (1H, d, *J* = 4.5 Hz), 5.79 (1H, d, *J* = 9.0 Hz), 5.86 (1H, d, *J* = 1.6 Hz). ^{13}C-NMR (125 MHz, $CDCl_3$): δ 20.88, 20.90, 20.92, 20.96, 20.97, 21.01, 21.08, 23.56, 23.65, 49.52, 49.74, 62.20, 65.41, 65.62, 68.99, 70.29, 71.56, 73.68, 90.86, 91.90, 168.34, 168.55, 169.92, 169.93, 170.23, 170.32, 170.73, 170.74, 170.82. ESI-MS for $C_{16}H_{23}NO_{10}$ [M], calcd. for 389.13, found 389.12. Representative ^{1}H-NMR spectrum, ^{13}C-NMR spectrum, and HPLC trace are shown in Supplemental Figures S13, S17, and S21, respectively.

Synthesis of 2-azido-acetic acid (9)

Synthesis of 2-azido-acetic acid was based on literature procedure.[2] To 50 mL of water, sodium azide (5.6 g, 86 mmol) and iodoacetic acid (8.0 g, 43 mmol) were added. The reaction was stirred overnight at RT. The solution was diluted with 1 M HCl, followed by extraction of the product into EtOAc. The organic layer was then washed with saturated sodium bicarbonate and brine. The organic layer was the dried with sodium sulfate and solvent was evaporated *in vacuo*, yielding the 1.5 g of the **9** as a yellow oil in 49% yield.

Synthesis of 4,4-azo-pentanoic acid (11)

As described previously,[1, 3] to levulinic acid (**10**, 8.19 g, 70.5 mol) at 4 ºC, 70 mL of 7 M NH_3/MeOH was added via syringe. Solution was stirred on ice for 3 h. NH_2OSO_3H (9.16 g, 81.1 mol) in 60 mL of MeOH was then added dropwise at 4 ºC. Solution stirred and reached RT overnight, yielding a white slurry. Precipitate was removed by vacuum filtration and filtrate was reduced to oil of the diaziridine *in vacuo*. Residue was dissolved in MeOH (50 mL) and solution was stirred on ice. 15 mL of TEA was then added. Under foil, iodine was added portionwise until the solution sustained a red-brown color for several min. Solvent was removed *in vacuo*. Residue was dissolved in EtOAc and washed successively with 1M HCl, 10% sodium thiosulfate, and brine. The organic layer was dried with anhydrous sodium sulfate and concentrated *in vacuo* to afford **11** in 37% yield as an orange liquid. ^{1}H-NMR (300 MHz, $CDCl_3$): δ 1.41 (3H, s), 1.72 (2H, t, *J* = 7.2 Hz), 2.24 (2H, t, *J* = 7.5 Hz). ESI-MS for $C_5O_2N_2H_8$ $[M-H]^-$, calcd. for 127.05, found 127.05. Representative ^{1}H-NMR spectrum is shown in Supplemental Figure S10.

Synthesis of 5,5-azo-hexanoic acid (13)

To 5-oxohexanoic acid (**12**, 2.56 g, 19.67 mol) and 20 mL of 7 M NH_3/MeOH, NH_2OSO_3H (2.58 g, 22.81 mol) in 40 mL of MeOH was added dropwise and purified as described above. To residue of the diaziridine, 30 mL MeOH, 5 mL of TEA, and iodine were added and processed as above, yielding 1.31g **13** in 47% yield as a light orange liquid. ^{1}H-NMR (300 MHz, $CDCl_3$): δ 1.02 (3H, s), 1.43 (2H, m), 1.51 (2H, m), 2.35 (2H, t, *J* = 7.2 Hz). ESI-MS for $C_6O_2N_2H_{10}$ $[M-H]^-$, calcd. for 141.07, found 141.07. Representative ^{1}H-NMR spectrum is shown in Supplemental Figure S11.

Synthesis of 6,6-azo-septanoic acid (15)

To 6-oxoheptanoic acid (**14**, 0.5 g , 3.47 mmol) and 30 mL of 7 M NH_3/MeOH, NH_2OSO_3H (0.451 g, 4.0 mmol) in 20 mL of MeOH was added dropwise and purified as described above. To residue of the diaziridine, 25 mL MeOH, 10 mL of TEA, and iodine were added and processed as above, yielding 0.51g, **15** in 54% yield as a light orange liquid. ^{1}H-NMR (300 MHz, $CDCl_3$): δ 1.00 (3H, s), 1.23 (2H, m), 1.38 (2H, m), 1.61 (2H, q, *J* = 7.5 Hz), 2.33 (2H, t, *J* = 7.5 Hz). ESI-MS for $C_7O_2N_2H_{12}$ $[M-H]^-$, calcd. for 155.08, found 155.08. Representative ^{1}H-NMR spectrum is shown in Supplemental Figure S12.

Synthesis of Ac_4ManNAz (2)

Synthesis of Ac_4ManNAz was based on a literature procedure (Scheme S1B).[4] Briefly, to a solution of azido acetic acid (**9**, 120 mg, 1.0 mmol) in 5.0 mL MeOH, D-(+)-mannosamine hydrochloride (216 mg, 1.00 mmol), TEA (280 μL), EDC (383 mg, 2.00 mmol), and HOBt (136 mg, 1.01 mmol) were added as described above. Purification was also described above and yielded a crude product as a pale yellow gum. The crude product was immediately acetylated by the same procedure described in the synthesis of Ac_4ManNAc to afford Ac_4ManNAz, **2**. The reaction was treated as above and purification afforded 134 mg as a colorless gum in 31% yield in two steps as a mixture of anomers. ^{1}H-NMR (500 MHz, $CDCl_3$): δ 1.96 (3H, s), 2.03 (3H, s), 2.08 (3H, s), 2.15 (3H, s), 4.02 (2H, s), 4.09 (1H, ddd, *J* = 2.0, 8.0, 14.4 Hz), 4.20 (1H, d, *J* = 1.8 Hz), 4.58 (1H, ddd, *J* = 4.2, 9.3, 13.5 Hz), 5.04 (1h, d, *J* = 3.9 Hz), 5.19 (1H, t, *J* = 10.1 Hz), 5.20 (1H, d, *J* = 4.3 Hz), 6.01 (1H, s), 6.65 (1H, d, *J* = 18.1 Hz). ^{13}C-NMR (125 MHz, $CDCl_3$): δ 20.80, 20.84, 20.87, 20.91, 20.95, 20.98, 21.06, 49.44, 49.90, 52.55, 52.74, 61.84, 61.93, 65.08, 65.27, 69.02, 70.41, 71.62, 73.55, 90.42, 91.47, 166.94, 167.52, 168.30, 168.54, 169.76, 170.30, 170.35, 170.73. ESI-MS for $C_{16}H_{22}N_4O_{10}$ $[M-H]^-$, calculated for 429.13, found 429.14.

Synthesis of 1,3,4,6-tetra-O-acetyl-2-acetyl-N-4,4-azo-pentamido-2-deoxy-α,β-D-mannopyranose (Ac_4ManNDAz(2me), 4)

As described previously (and see Scheme S1C), to a solution of 4,4-azo-pentanoic acid (**11**, 270 mg, 2.1 mmol) in 6 mL of methanol, D-(+)-mannosamine hydrochloride (160 mg, 0.72 mol) and TEA (350 mL) were added. The mixture was cooled to 4 ºC for the addition of EDC (475 mg, 2.5 mol) and HOBt (167 mg, 1.2 mmol). The reaction mixture was stirred for 20 h at RT. The solvent was evaporated *in vacuo*, leaving a yellow oil. The residue was purified with flash column chromatography (CH_2Cl_2 / MeOH = 1/0, 10/1, 4/1) yielding the unacetylated product as an oil. For 69 mg of the unacetylated product, acetylation was performed by the same procedure described in the synthesis of Ac_4ManNAc to afford Ac_4ManNDAz(2me), **4**. The reaction mixture was diluted with EtOAc and washed successively with 1 M HCl, saturated sodium bicarbonate, water, and brine. The organic layer was dried over anhydrous sodium sulfate and evaporated *in vacuo*. The residue was purified by flash column chromatography (hexanes/EtOAc = 1/1, 1/2). Rotary evaporation afforded 68 mg of **4** as a colorless gum in 56% yield as a mixture of anomers over two steps. ^{1}H-NMR (400 MHz, $CDCl_3$, major anomer): δ 1.06 (3H, s), 1.73- 1.85 (2H, m), 2.00-2.16 (2H, m), 2.02 (3H, s), 2.07 (3H, s), 2.11 (3H, s), 2.19 (3H, s), 4.03-4.08 (2H, m), 4.29 (1H, dd, *J* = 5.6, 12.8 Hz), 4.65 (1H, ddd, *J* = 1.2, 4.4, 9.2 Hz), 5.20 (1H, t, *J* = 10.0 Hz), 5.34 (1H, dd, *J* = 4.4, 10.4 Hz), 5.95 (1H, d, *J* = 9.2 Hz), 6.03 (1H, d, *J* = 2.0 Hz). ^{13}C-NMR (400 MHz, $CDCl_3$, major anomer): δ 19.9, 20.6, 20.7, 20.7, 20.8, 25.3, 29.7, 30.4, 49.2, 62.0, 65.3, 68.8, 70.1, 91.5, 168.1, 169.6, 170.0, 170.6, 171.5. ESI-MS for $C_{19}O_{10}N_3H_{27}$ $[M-H]^-$, calcd. for 456.16, found 456.17. Representative ^{1}H-NMR spectrum, ^{13}C-

NMR spectrum, and HPLC trace are shown in Supplemental Figures S14, S18, and S22, respectively.

Synthesis of 1,3,4,6-tetra-O-acetyl-2-acetyl-N-5,5-azo-hexamido-2-deoxy-α,β-D-mannopyranose (Ac$_4$ManNDAz(3me), 5)

To a solution of 5,5-azo-hexanoic acid (**13**, 147 g, 1.03 mmol) in 4 mL MeOH, D-(+)-mannosamine hydrochloride (218 mg, 1.01 mol), TEA (278 μL), EDC (383 mg, 2.0 mol), and HOBt (132 mg, 0.97 mol) were added as described above (and see Scheme S1D). Purification was also as described above and yielded crude product as a pale yellow gum. The crude product was immediately acetylated by the same procedure described in the synthesis of Ac$_4$ManNAc to afford Ac$_4$ManNDAz(3me), **5**. The reaction was treated as above and purification afforded 319 mg as a colorless gum in 67% yield over two steps as a mixture of anomers. ^{1}H-NMR (300 MHz, $CDCl_3$, major anomer): δ 1.03 (3H, s), 1.35-1.55 (2H, m), 1.54-1.64 (2H, m), 1.99 (3H, s), 2.06 (3H, s), 2.11 (3H, s), 2.18 (3H, s), 2.27 (2H, m), 4.01-4.12 (2H, m), 4.29 (1H, dd, *J* = 5.4, 13.5 Hz), 4.63 (1H, ddd, *J* = 1.8, 4.5, 9.6 Hz), 5.17 (1H, t, *J* = 9.6 Hz), 5.32 (1H, dd, *J* = 4.5, 10.5 Hz), 5.80 (1H, d, *J* = 9.3 Hz), 6.02 (1H, d, *J* = 1.8 Hz). ^{13}C-NMR (500 MHz, $CDCl_3$, major anomer): δ 19.54, 20.15, 20.62, 20.73, 20.86, 25.48, 33.30, 35.41, 49.15, 61.94, 65.29, 68.89, 70.11, 71.37, 73.44, 91.64, 168.13, 169.59, 169.93, 170.55, 172.17. ESI-MS for $C_{20}O_{10}N_3H_{29}$ $[M-H]^-$, calcd. for 470.18, found 470.19. Representative ^{1}H-NMR spectrum, ^{13}C-NMR spectrum, and HPLC trace are shown in Supplemental Figures S15, S19, and S23, respectively.

Synthesis of 1,3,4,6-tetra-O-acetyl-2-acetyl-N-6,6-azo-septamido-2-deoxy-α,β-D-mannopyranose (Ac$_4$ManNDAz(4me), 6)

To a solution of 6,6-azo-heptanoic acid (**15**, 530 mg, 3.39 mmol) in 30 mL MeOH, D-(+)-mannosamine hydrochloride (25 mg, 1.00 mol), TEA (279 μL), EDC (383 mg, 2.0 mol), and HOBt (135 mg, 0.99 mol) were added as described above (and see Scheme S1E). Purification was also as described above and yielded crude product as a pale yellow gum. The crude product was immediately acetylated by the same procedure described in the synthesis of Ac$_4$ManNAc to afford Ac$_4$ManNDAz(4me), **6**. The reaction was treated as above and purification afforded 320 mg as a colorless gum in 72% yield over two steps as a mixture of anomers. ^{1}H-NMR (300 MHz, $CDCl_3$, major anomer): δ 1.00 (3H, s), 1.1641.27 (2H, m), 1.35-1.42 (2H, m), 1.57-1.66 (2H, m), 2.00 (3H, s), 2.06 (3H, s), 2.10 (3H, s), 2.18 (3H, s), 2.23 (2H, t, *J* = 7.5 Hz), 4.01-4.12 (2H, m), 4.29 (1H, ddd, *J* = 2.4, 8.1, 15.6 Hz), 4.65 (1H, ddd, *J* = 1.8, 6.0, 11.1), 5.16 (1H, t, *J* = 9.6 Hz), 5.79 (1H, t, *J* = 9.3 Hz), 6.02 (1H, d, *J* = 1.8 Hz). ^{13}C-NMR (500 MHz, $CDCl_3$, major anomer): δ 19.79, 20.64, 20.74, 20.78, 20.86, 23.57, 25.0, 25.66, 33.97, 36.18, 49.11, 61.97, 65.33, 68.85, 70.08, 91.68, 168.15, 169.65, 169.99, 170.52, 172.58. ESI-MS for $C_{21}O_{10}N_3H_{31}$ $[M-H]^-$, calcd. for 484.19, found 485.20. Representative ^{1}H-NMR spectrum, ^{13}C-NMR spectrum, and HPLC trace are shown in Supplemental Figures S16, S20, and S24, respectively.

Synthesis of standards SiaDAz(2me) and SiaDAz(3me) (19)

SiaDAz(2me) was prepared as described.[3] Synthesis of SiaDAz(3me) (**19**) followed a similar protocol (Scheme S2) and is described briefly. A NaOMe solution (20 μL, 1 M in anhydrous MeOH) was added to a solution of Ac$_4$ManNDAz(3me) (**5**) (1 μmol) in anhydrous MeOH (100 μL) at 0 °C. The solution was stirred at room temperature for 3 h. MeOH was removed by SpeedVac before the solid was redissolved in water and moved to a 1.5 mL centrifuge tube containing sodium pyruvate (100 mM), Tris-HCl buffer (100 mM, pH 7.5) and $MgCl_2$ (20 mM).

Finally *N*-acetylneuraminic acid aldolase (22.5 μL of 11.05U/mL, Cat# NAL-301, Toyobo CO., LTD) was added to bring the final volume of the reaction mixture to 50 μL. The reaction mixture was incubated with agitation at 125 rpm in a 37 °C incubator overnight. The reaction was terminated by addition of 50 μL of ice-cold EtOH followed by incubation at 4 °C for 30 min. The resulting suspension was then filtered in 10 kDa MWCO filter by centrifugation and the resulting flow-through was evaporated to yield a white powder. ESI-MS for $C_{15}H_{25}N_3O_9$ $[M-H]^-$, calcd. 390.15, found 390.14.

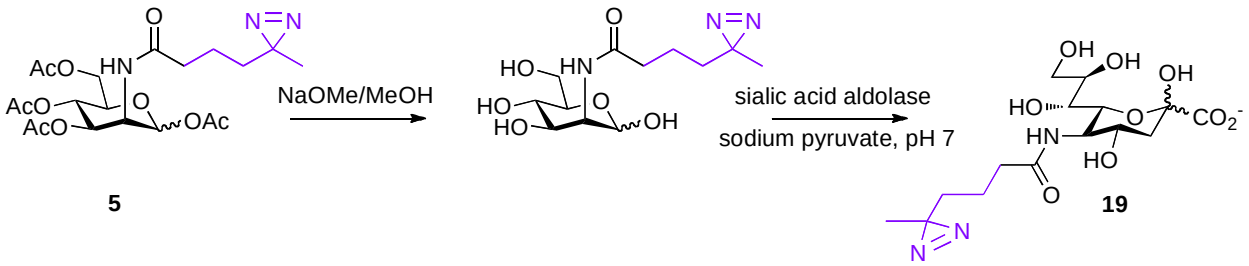

Scheme S2. **Synthesis of SiaDAz(3me) standard.** SiaDAz(3me) (**19**) was prepared from Ac_4ManNDAz(3me) for use as a standard in DMB derivatization experiments.

*Synthesis of 1,3,4,6-tetra-O-acetyl-2-acetyl-N-4,4-azo-pentamido-2-deoxy-α,β-D-glucopyranose (Ac_4GlcNDAz(2me), **3**)*

The synthesis of Ac_4GlcNDAz follows published procedures (Scheme S1C).[1, 3] Briefly, to a solution of 4,4-azo-pentanoic acid (**11**, 420 mg, 3.27 mmol) in 20 mL of methanol, D-(+)-glucosamine hydrocholride (640 mg, 2.89 mol) and TEA (1.25 mL) were added. The mixture was cooled to 4 ºC for the addition of EDC (1.09 g, 5.7 mol) and HOBt (440 mg, 3.3 mmol). Solvent was removed *in vacuo* and the sample triturated with 100% ice-cold ethanol and methylene chloride and the resulting solid filtered. The solid was dried to obtain a white, crystalline solid GlcNDAz, which was acetylated. For 107 mg (0.35 mmol) of GlcNDAz, the acetylation was performed by the same procedure described in the synthesis of Ac_4ManNAc to afford Ac_4GlcNDAz(2me), **3**. The reaction was treated as above and purification afforded 150 mg of a pale yellow oil in 40.0% yield as a mixture of anomers over two steps. ^{1}H NMR (400 MHz, $CDCl_3$, major anomer): δ 1.01 (3H, s), 1.74-1.79 (2H, m), 1.83-1.93 (2H, m), 2.05 (3H, s), 2.07 (3H, s), 2.10 (3H, s), 2.20 (3H, s), 3.98-4.02 (1H, m), 4.07 (1H, dd, *J* = 2.4, 12.4 Hz), 4.25-4.30 (2H, m), 5.19-5.28 (2H, m), 5.59 (1H, d, *J* = 8.8 Hz), 6.19 (1H, d, *J* = 3.6 Hz). ^{13}C NMR (100 MHz, $CDCl_3$, major anomer): δ 20.0, 20.5, 20.7, 20.8, 20.9, 25.3, 29.2, 30.3, 51.1, 61.5, 67.4, 69.6, 70.5, 90.4, 168.6, 169.1, 171.2, 171.2, 171.8. HRMS (ES-TOF) for $C_{19}H_{27}N_3O_{10}Na$ $[M+Na]^+$, calcd. for 480.1594, found 480.1597.

*Synthesis of UDP-GlcNDAz(2me) (**18**)*

UDP-GlcNDAz(2me) (**18**) was prepared from Ac_4GlcNDAz (**3**), as described below (Scheme S3).

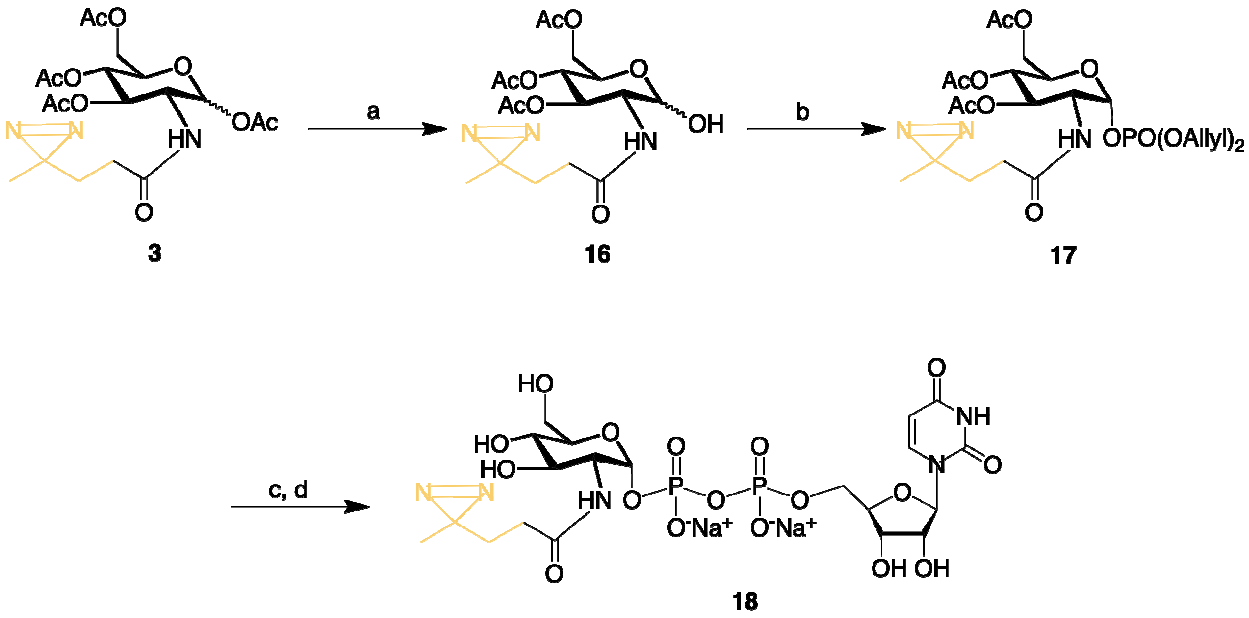

Scheme S3. **Synthesis of UDP-GlcNDAz(2me) (18).** a) $BnNH_2$, tetrahydrofuran, 72%. b) i) diallyl *N*,*N*-diisopropylphosphoramidite, tetrazole, AcCN, ii) mCPBA, 59%. c) Sodium *p*-toluenesulfinate, $Pd(PPh_3)_4$, tetrahydrofuran-MeOH (1:1). d) i) UMP salt, tetrazole, pyridine, ii) Dowex 50WX8-100 (Na^+ form), 60 %.

*Synthesis of Ac_3GlcNDAz(2me)-1-OH (**16**)*

To the solution of Ac_4GlcNDAz(2me) (**3**, 457 mg, 1.0 mmol) in THF (4.0 ml), benzylamine (164 µl, 1.5 mmol) was added and the resulting solution was stirred overnight. After removing the solvent by evaporation, the crude mixture was purified by flash silica gel chromatography (EtOAc) to give Ac_3GlcNDAz(2me)-1-OH (**16**) a colorless foam (300 mg, 72.2%). ^{1}H NMR (300 MHz, $CDCl_3$, α anomer, α: β = 6 : 1): δ 1.01 (3H, s), 1.74 (2H, m), 1.93-1.99 (2H, m), 2.03 (3H, s), 2.04 (3H, s), 2.10 (3H, s), 3.23(1H, bs , *J* = 2.7 Hz, -OH), 4.10-4.23 (2H, m, H5, H6a, H6b), 4.29(1H, td, *J* = 3.0, 9.6 Hz, H2), 5.13 (1H, t, *J* = 9.9 Hz), 5.25-5.32 (2H, m), 5.78 (1H, d, *J* = 9.6 Hz), 6.19 (1H, d, *J* = 3.6 Hz). ^{13}C NMR (125 MHz, $CDCl_3$, major anomer): δ 19.8, 20.6, 20.8, 25.4, 30.5, 52.2, 62.0, 67.5, 68.2, 70.7, 91.5, 169.4, 171.0, 171.5, 171.6, ESI MS for $C_{17}H_{26}N3O_9$ $[M+H]^+$, calcd. for 416.17, found 416.17.

*Synthesis of Ac_3GlcNDAz(2me)-1-O-P(=O)(OAllyl)$_2$ (**17**)*

To the solution of **16** (300 mg, 0.72 mmol) in acetonitrile (AcCN) (2 mL) at 0 °C, were added diallyl *N*,*N*-diisopropylphosphoramidite (228 µl, 0.864 mmol) and 1*H*-tetrazole (2.88 mL, 0.45M in AcCN, 1.3 mmol). After stirring for 1 h at RT, meta-chloroperoxybenzoic acid (290 mg, 77% mCPBA, 1.3 mmol) was added at 0 °C. After 30 min, the reaction mixture was partitioned between EtOAc (30 mL) and 10% aqueous Na_2SO_3 and the organic layer was washed with saturated aq. $NaHCO_3$ and brine. The organic layer was dried (Na_2SO_4), concentrated and purified by silica gel chromatography (CH_2Cl_2:MeOH=40:1) and then re-crystallized in EtOAc-hexane to provide **17** as white solid (245mg, 0.425 mmol, 59%). ^{1}H NMR (500 MHz, $CDCl_3$, α anomer): δ 1.00 (3H, s), 1.64-1.79 (2H, m), 1.86-2.00 (2H, m), 2.02 (6H, s), 2.07 (3H, s), 4.07(1H, bd , *J* = 12.0 Hz), 4.19 (1H, m), 4.24(1H, dd, *J* = 4.0, 12.5 Hz), 4.41(1H, m), 4.55-

4.61(m, 4H), 5.17 (1H, t, *J* = 10.0 Hz), 5.22(1H, t, *J* = 10.0), 5.28-5.42 (4H, m), 5.66 (1H, dd, *J* = 3.0, 5.5 Hz), 5.88-6.00 (2H, m), 6.03(1H, bd, *J* = 9.0 Hz). ^{13}C NMR (125 MHz, $CDCl_3$): δ 19.9, 20.6, 20.7 (2s), 25.3, 29.4, 30.27, 51.8(2s), 51.84, 61.3, 67.3, 68.7(2s), 68.8(2s), 69.7, 69.9, 96.0, 119.1(2s), 131.8, 131.9, 132.0, 132,1, 169.1, 170.5, 171.3, 171.4; ^{31}P NMR (200MHz, $CDCl_3$): δ -2.376 (s); ESI-MS for $C_{23}H_{35}N_3O_{12}P$ $[M+H]^+$, calcd. for 576.20, found 576.20, $C_{23}H_{34}N_3NaO_{12}P$ $[M+Na]^+$, calcd. for 598.18, found 598.18.

*Synthesis of UDP-GlcNDAz(2me) **(18)***

To the solution of Ac_3GlcNDAz(2me)-1-O-diallylphosphate (**17**, 200 mg, 0.347 mmol) in THF-MeOH (1:1, 4ml) at RT, were added sodium *p*-toluenesulfinate (124 mg, 0.695 mmol) and $Pd(PPh_3)_4$ (20 mg, 17.3 μmol). After stirring for 1 h at RT, the resulting mixture was concentrated and then co-evaporated with dry pyridine (2 mL) three times and then used for the next step without purification. To the crude mixture (Ac_3GlcNDAz(2me)-1-OPO_3^{2-} $2Na^+$) was added UMP salt (uridine 5'-monophosphomorpholidate 4-morpholine-*N*,*N*′-dicyclohexylcarboxamidine salt, 537 mg, 0.832 mmol) and the mixture was co-evaporated in pyridine (2 mL, three times). To the residue, 1H-tetrazole (2.31 mL, 0.45M in AcCN, 1.04 mmol) was added and the resulting mixture was evaporated to remove AcCN. The resulting mixture was co-evaporated with pyridine (2mL) and 4 mL of pyridine was added and then concentrated until ~2 mL of pyridine was left, and then the resulting mixture was stirred for at RT. After 5 days, the reaction mixture was concentrated thoroughly to remove pyridine and the residue was re-dissolved in MeOH:water:TEA (8 mL, 5:2:1) and then stirred for 24 h. The resulting mixture was concentrated by evaporation and then partitioned between CH_2Cl_2 (12 mL × 3) and water (12 mL × 3). The aqueous layer was lyophilized and the residue was purified by Bio-gel P2 (2.6 cm × 60 cm) column by elution with 0.1% aq. NH_4HCO_3. The pure compound containing fractions were collected and lyophilized. The dried residue was re-dissolved in 3 mL of water and then passed through Dowex 5WX8-100 (Na^+ form) and then lyophilized to give UDP-GlcNDAz(2me) disodium salt (**18**, 149 mg, 0.207 mmol, 60% from **17**). ^{1}H NMR (500 MHz, D_2O, α anomer): δ 1.00 (3H, s), 1.60-1.70 (2H, m), 2.21-2.32 (2H, m), 3.53(1H, t, *J* = 9.5 Hz), 3.76-3.86(3H, m), 3.91(1H, m), 3.98(1H, m), 4.15-4.26(3H, m), 4.34 (2H, m), 5.50(1H, dd, *J* = 3.5, 7.0 Hz), 5.95(2H, m), 7.93(1H, d, *J* = 8 Hz). ^{13}C NMR (125 MHz, D_2O): δ 18.6, 26.4, 29.9, 30.25, 53.5, 53.7, 53.8, 60.4, 65.1, 69.6, 69.7, 71.0, 73.1, 73.9, 83.2(2s), 88.7, 94.7, 102.8, 141.6, 153.0, 167.9, 176.1. ^{31}P-NMR (200 MHz, D_2O): δ -11.28 (d, *J* = 20.6Hz), -13.04 (d, *J* = 20.6 Hz). ESI-MS for $C_{20}H_{30}N_5Na_2O_{17}P_2$ $[M+H]^+$, calcd. 720.09, found 720.10, $C_{20}H_{29}N_5Na_3O_{17}P_2$ $[M+Na]^+$, calcd. 742.07, found 742.08.

Reverse-phase HPLC analysis of compound purity

Acetylated sugars **1**-**6** were evaporated to near dryness and resuspended in a 2:1 ddH_2O:acetonitrile solution. Generally, a GRACE analytical Vydac 218TP c18 5u column was used with 250 mm length and an internal diameter of 4.6 mm. Sugars were separated by reverse phase HPLC with a gradient of 5-40% acetonitrile (ddH_2O) with 0.1% trifluoroacetic acid (TFA) and detected by absorbance at 210 nm. All compounds were to be at least 95% pure prior to use in experiments. In the case of sugar purification by preparatory column, a similar method was used, but no TFA was present in the solvents.

Effects of compounds on cell growth and viability

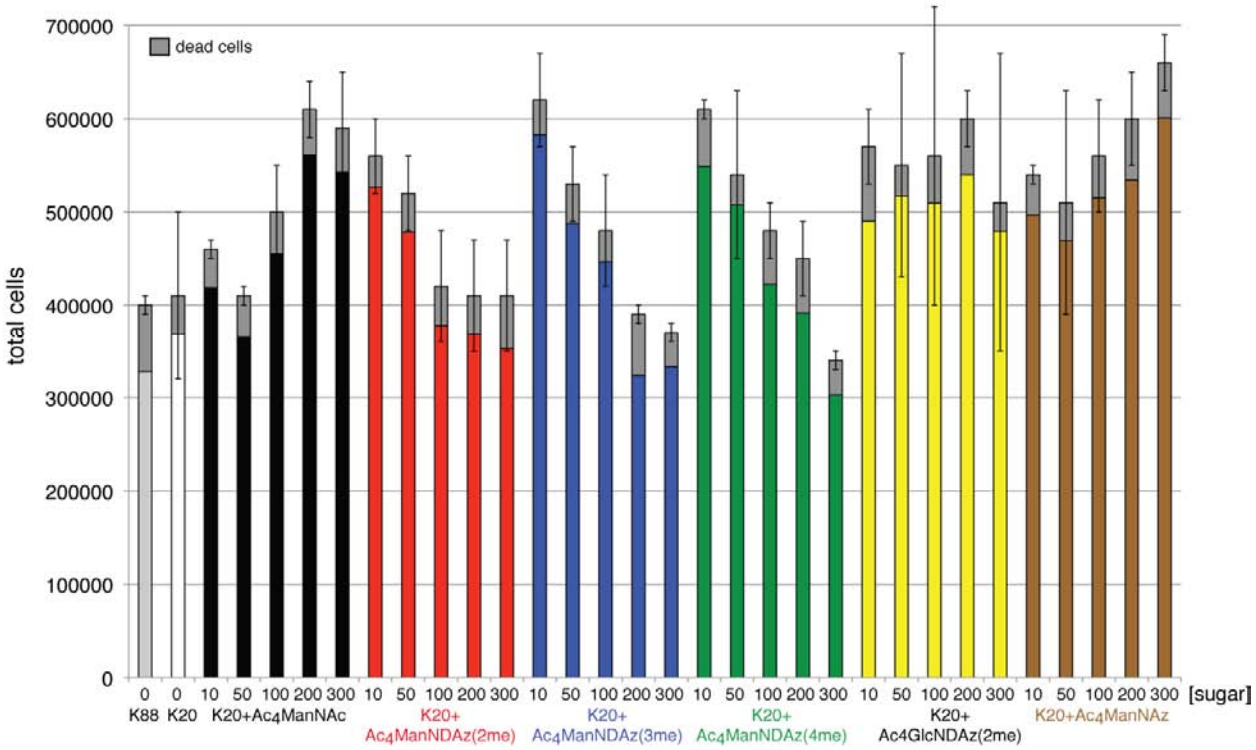

Figure S1. **Cell growth and viability of BJA-B cells grown in serum free media with photocrosslinking sugar analogs.** Cells (5 x 10^6 per sample) were treated with increasing concentrations (10, 50, 100, 200, and 300 μM) of Ac_4ManNAc, Ac_4ManNAc analogs, or Ac_4GlcNDAz(2me). With photocrosslinking sugar analogs, higher concentrations yielded less cell growth. The total number of live cells was determined by Trypan blue staining. No significant variation in the percentage of live cells was observed.

Cell culture, flow cytometry, and immunoblotting

Materials

RPMI 1640 with 2 mM L-glutamine, fetal calf serum, heat-inactivated fetal bovine serum (FBS), penicillin/streptomycin, DPBS, PBS (pH 7.4), FITC-streptavidin, DTAF-streptavidin, *N*-(aminooxyacetyl)-*N*'-(D-biotinoyl) hydrazine trifluoroacetic acid salt (ARP), and propidium iodide were purchased from Invitrogen (Carlsbad, CA). Nutridoma SP and bovine serum albumin (BSA) Fraction V were purchased from Roche Applied Science (Indianapolis, IN). Aniline was purchased from Sigma-Aldrich (St. Louis, MO). Glycerol was purchased from Fisher Scientific (Waltham, MA). Complete™ Protease Inhibitor Cocktail Tablet, EDTA-free were purchased from Santa Cruz Biotechnology (Santa Cruz, CA). The Invitrogen Countess Automated Cell Counter and Trypan Blue exclusion were used for cell counting. BD Biosciences FACSCalibur Flow Cytometer was used for flow cytometry experiments. Antibodies and proteins were obtained from the following vendors: goat anti-rabbit-HRP (Invitrogen), anti β-actin (Abcam, Cambridge, MA), rabbit anti-CD22 (Abcam), streptavidin-DTAF (Jackson Immunoresearch; West Grove, PA), goat anti-LaminB (Santa Cruz Biotechnology, Santa Cruz, CA) and rabbit anti-calnexin (Santa Cruz Biotechnology). Cholera toxin B (CTxB) subunit from *Vibrio cholerae* was purchased from Sigma Aldrich (St. Louis, MO). The antibody against the CTxB subunit was purchased from Abcam, rabbit anti-CTxB. CTxB-HRP and CTxB-488 were purchased from Invitrogen. Lectins were purchased from the following vendors: SNA-FITC (EY Laboratories, San Mateo, CA), ECA-FITC (EY Laboratories), MAL-II-biotin (Vector Labs; Burlingame, CA; B-1265), and HPA-FITC (EY Laboratories). PVDF membranes were purchased from Millipore, Immobiolon (Billerica, CA). For chemiluminescent visualization, SuperSignal WestPico Chemiluminescent Substrate (ECL reagent) was purchased from Pierce (Rockford, IL). The bicinchoninic acid (BCA) Protein Assay Kit from Pierce was used to assess protein concentration. All other reagents, chemicals, and general supplies were purchased and used as received from Fisher Scientific or Sigma-Aldrich unless otherwise noted.

The mild stripping buffer used was composed of 200 mmol glycine, 3.5 mmol SDS, 1% v/v Tween20 at pH 2.2. Tris-buffered saline Tween-20 was used in blocking solutions (TBST, 10 mM Tris base, 150 mM NaCl, 0.1% v/v Tween 20, pH 8.0).

Detection of total cell surface sialic acid by flow cytometry

We used the PAL method, as previously described.[5] Cells were resuspended in PBS (pH = 7.4) and aliquoted in a v-bottom 96 well plate to approximately 4.0 x 10^5 cells per well. Cells were pelleted by centrifugation (650*g* for 4 min at 4 °C) and the supernatant removed by inverting the plate over the sink. Cells were washed a total of three times in the same manner with PBS (pH = 7.4). Next, cells were resuspended in 200 µl 1.0 mM $NaIO_4$ in PBS (pH = 7.4) and incubated for 30 min on ice. To the sodium periodate solution, 50 µl of 5.0 mM glycerol in PBS (pH = 7.4) was added and incubated for 10 min on ice to quench the oxidation reaction. Cells were pelleted by centrifugation (650*g* for 4 min at 4 °C) and washed twice with 5.0% FBS in DPBS (pH = 6.7). Cells were resuspended in 200 µl of 0.1 mM aminooxy-biotin, 10.0 mM aniline in 5.0 % FBS in DPBS (pH = 6.7) and incubated for 90 min on ice. Following three washes with 5.0% FBS in DPBS (pH = 6.7), cells were resuspended in 200 µl of 3.2 µg/ml DTAF-streptavidin in 5.0% FBS in DPBS for 30 min on ice. Finally, cells were washed three more times with 5.0% FBS in DPBS (pH = 6.7) and resuspended in 400 µl of 5.0% FBS in PBS (pH = 6.7). Cells were

analyzed with a FACSCalibur Flow Cytometer. Live cells (10,000 cells/sample) were identified by their forward scatter versus side scatter and DTAF fluororescence was measured on the FL-1 channel of the instrument. Data were analyzed with FlowJo (Tree Star, Inc.; Ashland, OR). Representative data are shown.

Detection of α2-3-linked and α2-6-linked cell surface sialic acid by flow cytometry
Cells were resuspended in 0.1% BSA in DPBS and aliquoted in a v-bottom 96 well plate to approximately 4.0 x 10^5 cells per well. Cells were pelleted by centrifugation (650*g* for 4 min at 4 °C) and the supernatant removed by inverting the plate over the sink. Cells were washed a total of three times in the same manner with DPBS.

For the SNA binding experiment, cells were incubated with 150 μL of 10 μg/ml SNA-FITC (specific for Siaα2-6Gal) in 0.1% BSA in DPBS for 30 min on ice. After being washed twice with 0.1% BSA in DPBS, the cells were resuspended in 400 μl of 0.1% BSA in DPBS. To distinguish the difference between live and dead cells, propidium iodide (PI) was added into each tube before analysis. Using a FACSCalibur Flow Cytometer, the cells were analyzed and live cells (10,000 cells/sample) were identified by their forward scatter versus side scatter. In addition, all PI positive cells (dead cells) were excluded from analysis. FITC fluorescence was measured on the FL-1 channel of the instrument and PI was measured on the FL-2 channel of the instrument.

For the MAL-II binding experiment, after the three wash steps, cells were incubated with 150 μL of 10 μg/ml MAL-II-biotin (specific for Siaα2-3Gal)[6] in 0.1% BSA/PBS for 30 min on ice. Cells were then washed twice with 0.1% BSA in DPBS and incubated with 10 μg/ml of streptavidin-FITC for 30 min on ice. Cells were washed two final times with 0.1% BSA in DPBS and resuspended in 400 μl of 0.1% BSA in DPBS for flow cytometry analysis. Cells were treated with PI and analyzed as described above for SNA-FITC binding. Data were analyzed with FlowJo (Tree Star, Inc.). Representative data are shown.

Detection of core glycan structures by flow cytometry
Cells were resuspended in 0.1% BSA in DPBS and aliquoted in a v-bottom 96 well plate to approximately 4.0 x 10^5 cells per well. Cells were pelleted by centrifugation (650*g* for 4 min at 4 °C) and the supernatant removed by inverting the plate over the sink. Cells were washed a total of three times in the same manner with DPBS.

For ECA and HPA binding experiments, cells were incubated with 150 μL of 5 μg/ml ECA-FITC (specific for LacNAc)[7] or 10 μg/ml HPA-FITC (specific for GalNAc)[8] in 0.1% BSA in DPBS for 30 min on ice. After being washed twice with 0.1% BSA in DPBS, the cells were resuspended in 400 μl of 0.1% BSA/DPBS. To distinguish the difference between live and dead cells, PI was added to each tube before analysis. Using a FACSCalibur Flow Cytometer, the cells were analyzed and live cells (10,000 cells/sample) were first identified by their forward scatter versus side scatter. In addition, all PI positive cells (dead cells) were excluded from analysis. FITC fluorescence was measured on the FL-1 channel of the instrument and PI was measured on the FL-2 channel of the instrument. Data were analyzed with FlowJo (Tree Star, Inc.). Representative data are shown.

CD22 photocrosslinking in BJA-B cells

For crosslinking study, BJA-B K88 and K20 cells (3.0×10^5 cells/mL) or Daudi cells (0.25×10^5 cells/mL) were cultivated with or without per-*O*-acetylated sugars in serum free media (or normal media for Daudi cells) as described above. Cells were harvested and washed twice with DPBS. Cells were resuspended in an appropriate volume of DPBS to achieve a final density of 1.0×10^6 cells/mL. 1.0 mL of each cell suspension was added to two identical 12-well plates which where were placed on ice. One plate was photoirradiated by 365 nm UV light (Black Ray Lamp, XX-20BLB, UVP) on ice for 10 min while the other remained covered with aluminum foil. Cells were then transferred to microcentrifuge tubes and the wells of the plate washed and added to the respective tube. Cell suspensions were centrifuged at 650*g* for 5 min at RT followed by aspiration of the supernatant.

Cells were washed twice with DPBS before lysis buffer (200 μL) was added. After incubation in lysis buffer (300 mM NaCl, 50 mM Tris (pH = 8.0), 1% Triton X-100 and 1 mM EDTA and protease inhibitors) at 4 ºC for 1 h in the dark, lysates were centrifuged at 17,000*g* for 4 min at RT. Supernatants were transferred to new microcentrifuge tubes and stored at 4 ºC until used.

Cell lysates were resolved on BioRad 7.5% Tris HCl gels and transferred to PVDF membranes overnight at 4 ºC. The PVDF membrane was pre-hydrated in methanol for 2 min. The membranes were blocked with 5% milk in TBST for 5 h and then probed with anti-CD22 antibody (1:1000 dilution) in 5% milk in TBST at 4 ºC overnight followed by three washes in TBST. After being probed with HRP conjugated goat anti-rabbit antibody (1:5000 dilution) for 1 h, the membranes were then washed three times with TBST followed by incubation with ECL reagent and exposure to film. Finally, the membrane was probed by a β-actin antibody to confirm similar loading in every lane. The membrane was first stripped with a mild stripping buffer for 1 h at 37 °C, then washed twice with TBST. The PVDF was blocked with 5% milk in TBST for 1 h followed by incubation with rabbit anti-β-actin antibody (1:10,000 dilution) overnight at 4 °C in 5% milk in TBST. The membrane was then washed three times with TBST followed by incubation with goat anti-rabbit-HRP conjugate (1:5000 dilution) for 1 h at RT. The membrane was then washed three times with TBST followed by incubation with ECL reagent and exposure to film.

CTxB-GM1a photocrosslinking in Jurkat cells

Prior to the addition of cells to a 12 well plate, EtOH, Ac_4ManNAc, Ac_4ManNDAz(2me), Ac_4ManNDAz(3me), Ac_4ManNDAz(4me), Ac_4GlcNDAz(2me), or Ac_4ManNAz in EtOH were added to achieve a final concentration of 100 μM and the EtOH pre-evaporated at ambient temperature and pressure. Jurkat cells were then seeded at a density of 2.5×10^5 cells/mL and incubated in the presence of the monosaccharides. After culturing cells with compounds for 70 h, cells were pelleted at 650*g* followed by resuspension in RPMI 1640 media containing 2 mM L-glutamine and supplemented with 10% heat-inactivated FBS to 5.0×10^6 cells/mL. Cells (1.0×10^6 cells in 200 μL) were then aliquoted to the wells of a 24 well tissue culture plate. To each well, 0.5 mL of 1 mg/mL cholera toxin beta subunit (CTxB) was added and the plate swirled. Plates were then incubated at 4 °C for 45 min. After pre-incubation with CTxB, plates were placed on ice and those designated as +UV were exposed to 365 nm light for 45 min on ice – approximately 2 cm away from bulb. Those plates designated as –UV were stored under aluminum foil, on ice during this 45 min time period.

After photoirradiation, cells were transferred to a 1.5 mL microcentrifuge tube and centrifuged for 5 min at 650*g*. The supernatant was removed by aspiration. Cell pellets were washed twice with 200 μL of DPBS and then lysed in 100 μL of 300 mM NaCl, 1 mM EDTA, 1% Triton X-100, and protease inhibitors at 4 °C for 60 min. Insoluble material was removed by centrifugation at 17,000*g* for 10 min and the supernatant was analyzed by immunoblot analysis. Cell lysates were mixed in a 1:1 ratio with 2X SDS loading dye containing DTT (100 mM final concentration). Samples were heated at 90 °C for 5 min prior to loading. Cell lysates were resolved on BioRad 12% Tris HCl gels and transferred to PVDF membranes (pre-hydrated in MeOH) overnight at 4 ºC. Membranes were probed twice, first for the presence of CTxB or GM1a and second for β-actin.

One membrane was probed for the presence of CTxB. The PVDF was blocked with 5% milk in TBST for 1 h followed by incubation with a rabbit anti-CTxB antibody (1:10000 dilution) for 1 h at RT in 5% milk in TBST. The membrane was washed three times with TBST followed by incubation with goat-anti-rabbit-HRP conjugate (1:5000 dilution) for 1 h at RT. The membrane was then washed three times with TBST followed by incubation with ECL reagent and exposure to film.

A second membrane was probed for the presence of GM1a using HRP-conjugated CTxB. The membrane was blocked with 5% milk in TBST followed by incubation with CTxB-HRP (1:10,000 dilution) in 5% milk in TBST for 5 h at RT. The membranes were then washed three times with TBST followed by incubation with an ECL reagent and exposure to film.

All membranes were subsequently probed with a β-actin antibody to confirm that equal amounts of samples were loaded in each lane. The membrane was first stripped with a mild stripping buffer for 1 h at 37 °C, then washed twice with TBST. The PVDF was blocked with 5% milk in TBST for 1 h followed by incubation with a rabbit anti-β-actin antibody (1:10,000 dilution) overnight at 4 °C in 5% milk in TBST. The membrane was washed three times with TBST followed by incubation with goat anti-rabbit-HRP conjugate (1:5000 dilution) for 1 h at RT. The membrane was then washed three times with TBST followed by incubation with ECL reagent and exposure to film.

Diazirine-containing sugars are stable to periodate oxidation conditions

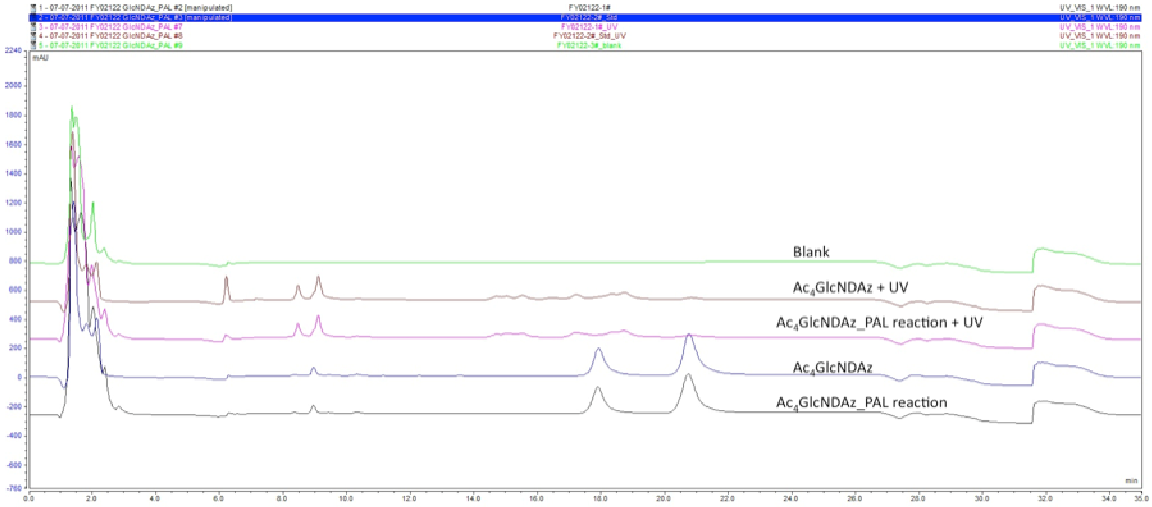

Figure S2. **PAL oxidation reaction does not affect diazirine functionality *in vitro*.** A diazirine-containing sugar subjected to periodate oxidation conditions and its integrity was analyzed by HPLC. Ac_4GlcNDAz (10 μM, 50 μL) was incubated with or without sodium periodate (10 mM in PBS buffer pH 7.4, 100 μL) for 30 min on ice. The reactions were quenched with glycerol (5 mM in PBS buffer pH 7.4, 250 μL) and incubated for 10 min on ice. Half of each sample (+ $NaIO_4$, - $NaIO_4$) was irradiated with UV (365nm, XX-20BLB, UVP) for 30 min on ice. The reaction mixtures were injected on Symmetry®C18 column (Waters, 5μm, 4.6 x 150 mm). The analysis was performed using Dionex Ultimate 3000 pump equipped with an Ultimate 3000RS variable wavelength detector. Sugars were separated using a gradient of 5-40% acetonitrile in water and monitored at 190 nm.

Sialic acid concentration determination using resorcinol/periodate assay

The following procedure is based on literature protocols.[9, 10] BJA-B cells (3.0 x 10^5 cells/mL) were cultivated with and without sugar supplementation to achieve a final concentration of 100 μM. The cells were incubated at 37 ºC for 72 h and then harvested and aliquoted with 10 million cells/sample. Cells were washed three times with 0.5 mL of Dulbecco's phosphate buffered saline (DPBS), centrifuged at 650*g* for 5 min at RT, and the supernatant aspirated. Cells were then resuspended in 250 μL of DPBS and lysed in 4 freeze/thaw cycles. All samples were oxidized with periodic acid (8 mM final concentration) on ice (for total cell sialic acid concentration) or at 37 ºC (for glycoconjugate-bound sialic acid) for 1.5 h. After adding 500 μL resorcinol solution (6.0% (w/v) resorcinol, 2.5 mM $CuSO_4$, 44% (v/v) HCl), samples were boiled at 100 ºC for 15 min. Samples were cooled on ice and 500 μL of t-butanol was added to quench the reaction. Samples were centrifuged at 13300*g* for 5 min to pellet insoluble cell debris. Immediately after centrifugation, 1 mL of samples aliquoted into cuvettes. Absorbance readings of samples were then taken at 630 nM and absorbance intensities were compared to a standard curve of known concentrations – 250, 125, 62.5, 31.3, 15.63, 7.81, 3.91, 1.95, 0 μM sialic acid – (which were treated in the same fashion as described above). Absorbance was measured on Ultrospec 2100 Pro UV/Visible spectrophotometer from Amersham Biosciences. The results are shown in Figure S3.

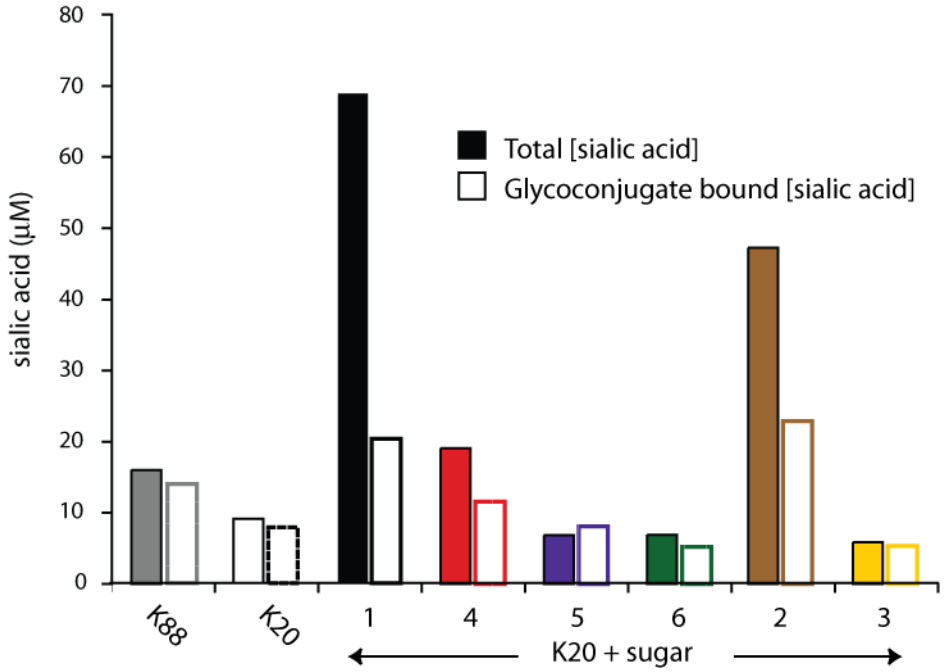

Figure S3. **Resorcinol assay to determine total and glycoconjugate bound sialic acid concentrations.** Cells treated with and without unnatural sugar analogs yield differing amounts of total cell and glycoconjugate bound sialic acids. The largest increases in absorbance were seen for Ac_4ManNAc-, Ac_4ManNAz-, and Ac_4ManNDAz(2me)-treated BJA-B K20 cells cultured in serum-starved conditions. The large differences in total and glycoconjugate bound sialic acids suggest that cells cultured with Ac_4ManNAc, Ac_4ManNAz, and Ac_4ManNDAz(2me) have a significant pool of free sialic acid present. These data represent one biological replicate and are representative of two separate experiments.

HPLC analysis of DMB derivatization

For HPLC, standards for DMB-Neu5Ac, DMB-SiaDAz(2me), and DMB-SiaDAz(3me) were used. Derivatized sugars (10 μL each) were diluted with 90 μL ddH_2O and separated on a Waters Symmetry c18, 5 μm, 4.6 x 150 mm column using a gradient of ddH_2O/acetonitrile gradient, as specified in the supplementary material. A Shimadzu SCL-10A VP HPLC with the RF-10AXL detector and Class-VP 7.4 software was used. The fluorophore was excited at 373 nm and the emission detected at 448 nm. Peaks were manually defined and the area under the curve integrated.

HPLC traces (Figures S4-S6) show raw data used to derive the percentages shown in Table 1. The identities of DMB-SiaDAz(2me) and DMB-SiaDAz(3me) were confirmed by LC-MS analysis. LC-MS for DMB-SiaDAz(2me), $C_{21}H_{27}N_5O_9$ [M], calcd. 493.18, found 493.91. LC-MS for DMB-SiaDAz(3me), $C_{22}H_{30}N_5O_9$ $[M+H]^+$, calcd. 508.20, found 508.21.

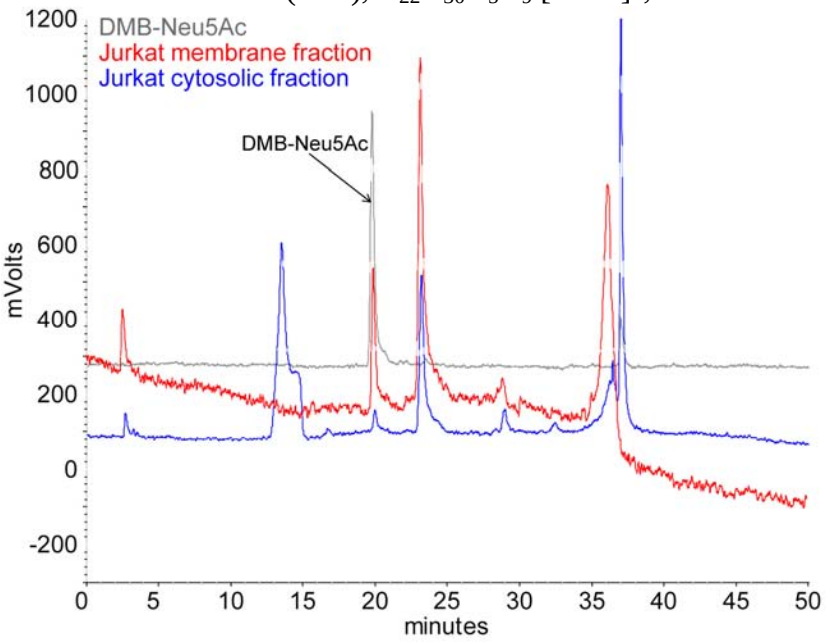

Figure S4. **HPLC traces of DMB-derivatized sialic acids from Jurkat cells.** Fluorescent molecules were excited with 373 nm light and emission detected at 448 nm. The elution gradient used the following percentages of CH_3CN in H_2O: T(0 min) 2%; T(2 min) 2%; T(30 min) 15%; T(35 min) 90%; T(40 min) 90%; T(45 min) 2%; T(50 min) 2%.

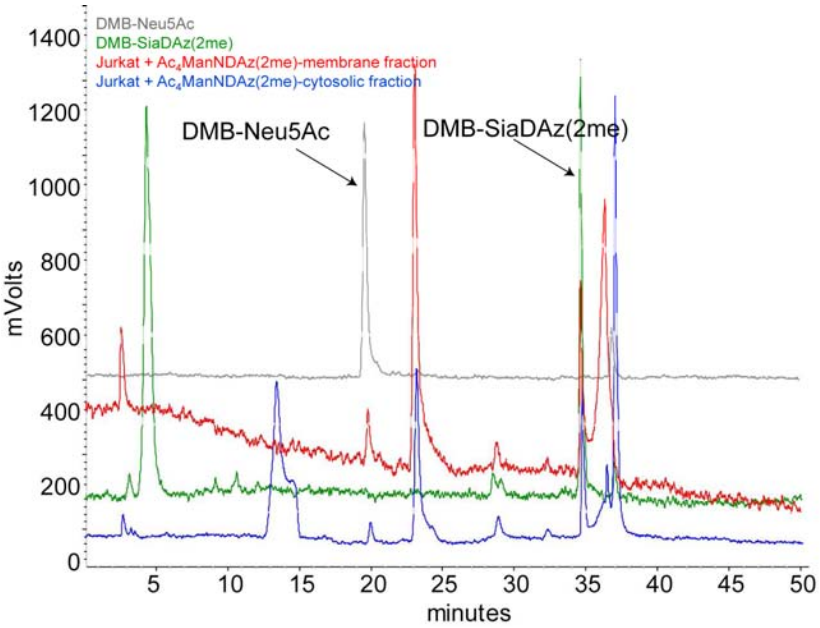

Figure S5. **HPLC traces of DMB-derivatized sialic acids from Jurkat cells cultured with Ac_4ManNDAz(2me).** Fluorescent molecules were excited with 373 nm light and emission detected at 448 nm. The peak labeled as DMB-SiaDAz(2me) displays the same retention time as the standard molecule and is observed only in samples from cells cultured with Ac_4ManNDAz(2me). The elution gradient used the following percentages of CH_3CN in H_2O: T(0 min) 2%; T(2 min) 2%; T(30 min) 15%; T(35 min) 90%; T(40 min) 90%; T(45 min) 2%; T(50 min) 2%.

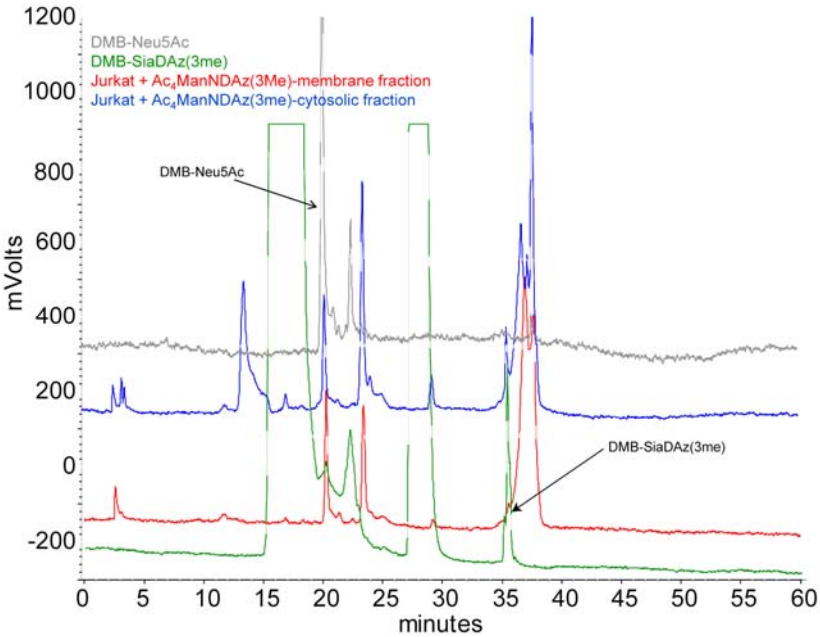

Figure S6. **HPLC traces of DMB-derivatized sialic acids from Jurkat cells cultured with Ac_4ManNDAz(3me).** Fluorescent molecules were excited with 373 nm light and emission detected at 448 nm. The peak labeled as DMB-SiaDAz(3me) displays the same retention time as the standard molecule and is observed only in samples from cells cultured with Ac_4ManNDAz(3me). A modified elution gradient was used with the following percentages of CH_3CN in H_2O: T(0 min) 2%; T(2 min) 2%; T(30 min) 15%; T(35 min) 70%; T(40 min) 70%; T(45 min) 90%; T(50 min) 90%; T(55 min) 2%; T(60 min) 2%.

Analysis of CMP-SiaDAz(2me) and UDP-GlcNDAz(2me) in Jurkat cells by HPAEC

Jurkat cells were seeded at a density of 2.5 x 10^5 cells/mL in 10 cm dishes and DMSO, 25 mM Ac_4ManNDAz(2me), or 25 mM Ac_4GlcNDAz(2me) in DMSO were added to a final concentration of 100 μM and then incubated at 37 ºC and 5% CO_2. After 72 h, cells were harvested, counted, and centrifuged at 200*g* for 4 min in 15 mL conical tubes and the cell pellet was washed two times with DPBS. The resulting pellet was lysed in 75% ethanol (700 μL) by sonication (VirSonic 100, VirTis, Gardiner, NY) and then was centrifuged at 20,000*g* for 10 min at 4 ºC. The resulting supernatant was collected and concentrated in a Savant SpeedVac in the dark. The concentrated residue was resuspended in 40 mM sodium phosphate buffer (pH 7.0, 10 μL/million cells) and then directly filtered through an Amicon Ultra centrifugal filter unit (Millipore, 10,000 MWCO). HPAEC analysis was performed by injecting 20 μL of the resulting filtrate.

HPAEC analysis was performed by injecting 20 μL of the each sample in CarboPac PA1 column (Dionex, 4 x 250 mm) through a 20 μL sample loading loop and a guard column (Dionex, CarboPac PA1, 4 x 50 mm). Elution was performed using buffers E1 (1 mM NaOH) and E2 (1 mM NaOH, 1.0 M NaOAc). For the analysis of CMP, CMP-NeuAc and CMP-SiaDAz(2me), HPAEC analysis was performed by using Dynamax SD-200, with electrochemical detector (Dionex), flow rate = 1 ml/min, gradient of T_{0min} = 2% E2, T_{2min} = 2% E2, T_{30min} = 30% E2, T_{40min} = 30% E2, T_{41min} = 55% E2, T_{60min} = 55% E2, T_{63min} = 100% E2, T_{72min} = 100% E2, T_{75min} = 2% E2, T_{81min} = 2% E2. For the analysis of UDP-GalNAc, UDP-GlcNAc and UDP-GlcNDAz(2me), HPAEC analysis was performed by using Dionex ICS-3000, PAD (UV-C, Dynamax), flow rate = 1 ml/min, gradient of T_{0min} = 2% E2, T_{2min} = 2% E2, T_{30min} = 30% E2, T_{40min} = 30% E2, T_{41min} = 55% E2, T_{60min} = 55% E2, T_{63min} = 100% E2, T_{72min} = 100% E2, T_{75min} = 2% E2, T_{81min} = 2% E2. The results are shown in Figures S7 and S8.

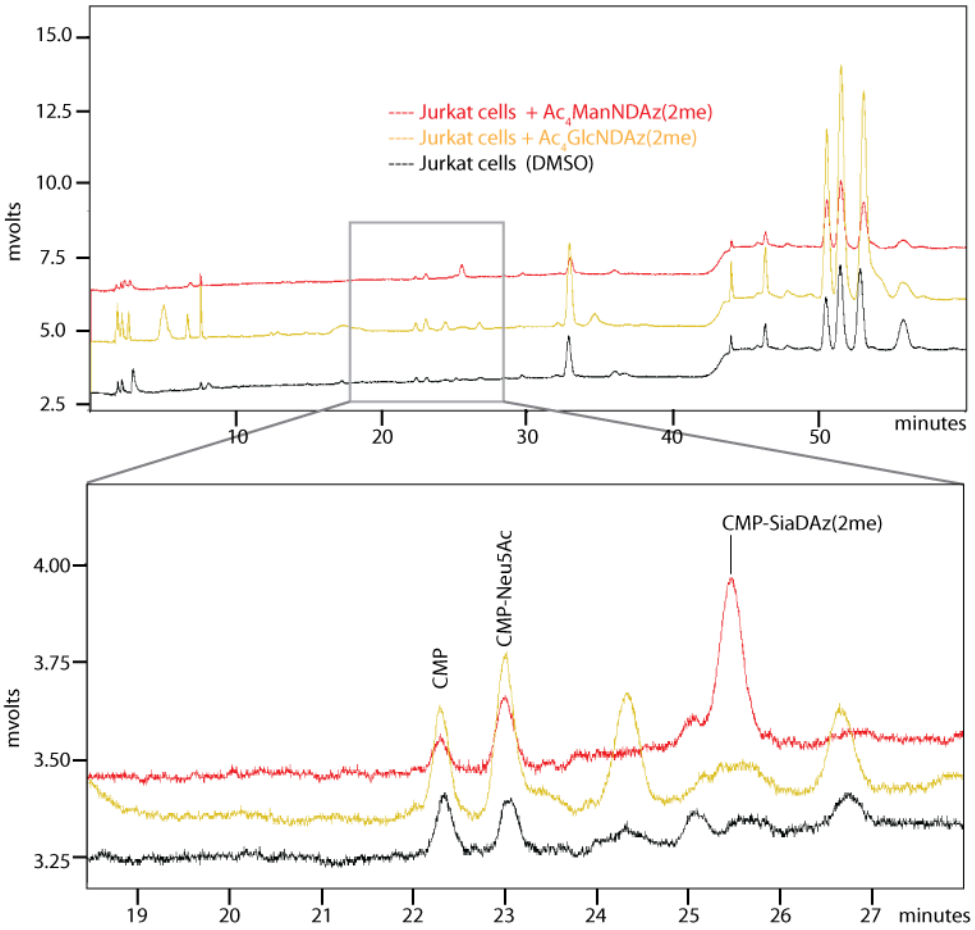

Figure S7. HPAEC analysis of Jurkat cell lysate after culturing 72 h with DMSO, Ac_4ManNDAz(2me), or Ac_4GlcNDAz(2me). UV absorbance was monitored at 260 nm with UV-C detector and CarboPac PA1 analytical column (Dionex) with Dynamax SD-2000 HPLC system. CMP and CMP-NeuAc were identified based on comparison to standards.

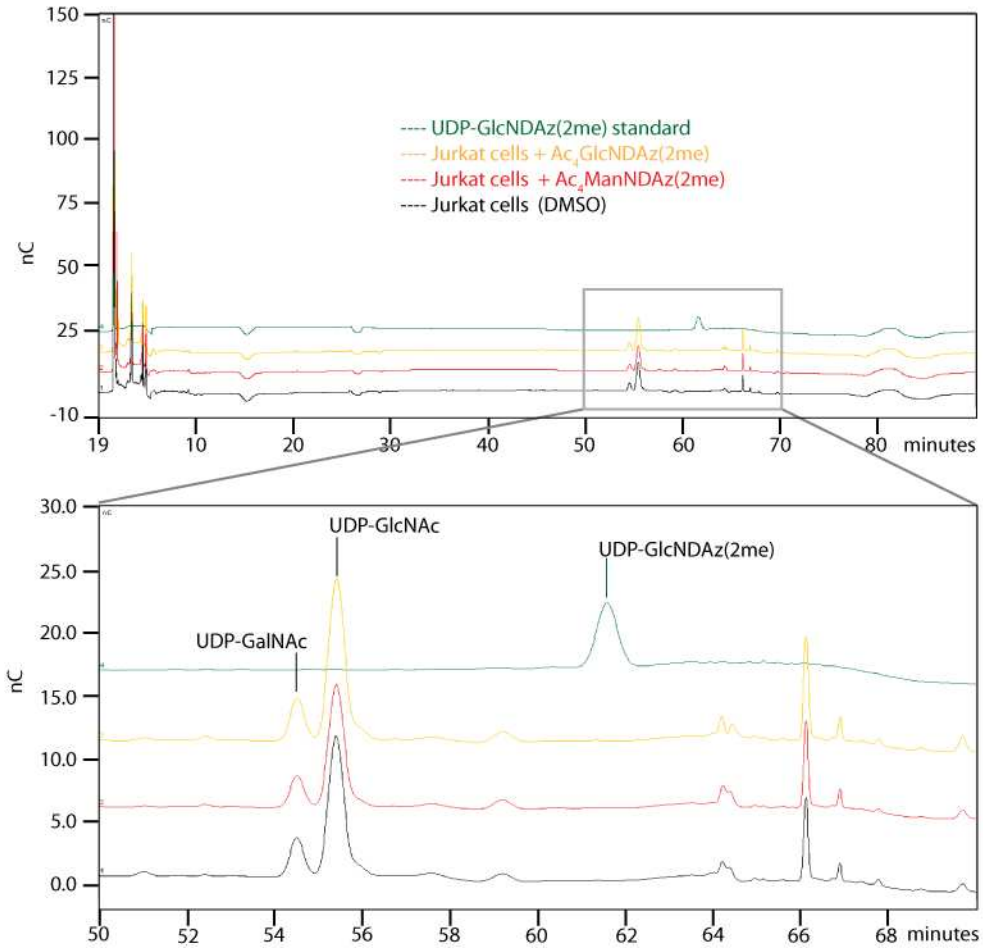

Figure S8. HPAEC analysis of Jurkat cell lysate after culturing 72 h with DMSO, Ac_4ManNDAz(2me), or Ac_4GlcNDAz(2me). UDP sugars were monitored by pulse amperometry detection (PAD) and identified based on comparison of retention times with those of known standards.

HPTLC staining with CTxB-488 is more sensitive than resorcinol staining

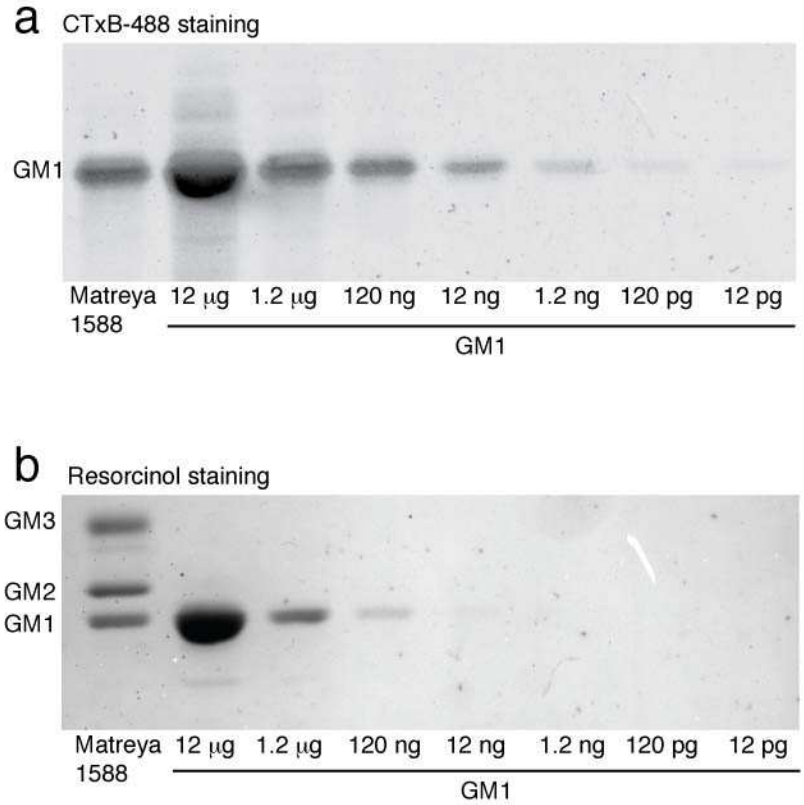

Figure S9. **Alexa Fluor 488 conjugated cholera toxin subunit B (CTxB-488) staining of HPTLC-resolved ganglioside GM1a is 1000 times more sensitive than resorcinol staining.** Pure ganglioside GM1a was spotted at decreasing concentrations and resolved on an HPTLC plate next to a ganglioside standard from Matreya. Bands corresponding to 120 pg GM1a are visible with CTxB-488 detection, whereas 120 ng GM1a is required for resorcinol detection.

Mass spectrometry analysis of CTxB-GM1a-SiaDAz(2me)

All reagents, chemicals, and general supplies were purchased and used as received from Fisher Scientific (Waltham, MA) or Sigma-Aldrich (St. Louis, MO) unless otherwise noted. The MALDI matrix, CHCA, was purchased from Fluka (Sigma-Aldrich). All solvents used for mass spectrometry were of HPLC grade. EtOH to store and wash SAM plates was absolute anhydrous 200 proof. Water was purified using a Millipore purification system to resistance of 18 MΩ. His_6-tagged protein G was purchased from Biovision Inc. (Mountain View, CA). Microscope cover glasses (24 x 50 mm size with 0.16 mm thick) were purchased from Fisher Scientific (Pittsburgh, PA). Myoglobin from equine skeletal muscle and ubiquitin from bovine erythrocytes were purchased from Sigma Aldrich.

Prior to the addition of cells to a 12 well plate, Ac_4ManNAc or Ac_4ManNDAz(2me) in EtOH were added to a final concentration of 100 μM and the EtOH pre-evaporated at ambient temperature and pressure. Jurkat cells were then seeded at a density of 2.5 x 10^5 cells/mL and incubated in the presence of the monosaccharides for 72 h at 37 °C and 5% CO_2 as described above. After growth with the appropriate compounds for 70 h, cells were pelleted at 650*g* followed by resuspension in original media to 5.0 x 10^6 cells/mL. Then 200 μL of cells (1.0 x 10^6 cells) were aliquoted to the wells of a 24 well tissue culture plate. To each well, 0.5 μL of 1 mg/mL CTxB was added and the plate swirled. Plates were then incubated at 4 °C for 45 min. After pre-incubation with CTxB, plates were placed on ice and exposed to 365 nm light approximately 2 cm away from bulb for 45 min. After photoirradiation, cells were transferred to a 1.5 mL microcentrifuge tube and centrifuged for 5 min at 650*g*. The supernatant was then removed by aspiration. Cell pellets were washed twice with 200 μL of DPBS and then lysed in 50 μL of 300 mM NaCl, 1 mM EDTA, 1% Triton X-100, and protease inhibitor cocktail at 4 °C for 1 h. Cell debris was removed by centrifugation at 17,000*g* for 10 min.

Briefly, 30 Å of chromium followed by 290 Å of gold were evaporated by electron beam onto a microscope cover glass. Self-assembled monolayers were generated by immersion of the metallized slides in an ethanolic solution containing tri(ethylene glycol)-terminated (EG3) and nitrilotriacetic acid (NTA)-terminated alkanethiolates. An 85:15 solution ratio of EG3 to NTA alkanethiolates was used and monolayers were generated for 3 days at 4 °C. The SAM slides were washed with EtOH and stored in EtOH at -20 °C prior to use.

The NTA-based monolayers on the gold-coated glass slides were treated with an aqueous solution of $NiSO_4$ for 30 min to generate the NTA/Ni^{2+} complex (10 mM, PBS, pH 7.2). They were then were cut into square pieces measuring 4 mm^2 and treated for 1 h with His_6-tagged protein G (3.84 μM in PBS pH 7.2). The resulting monolayers were treated with rabbit anti-CTxB (100 μM in PBS, pH 7.2) for 1 h. Lastly, cell lysates were diluted in equal volume of the same lysis buffer and incubated on the chips for 3 h. Chips were washed under a stream of water. Chips were dried with a stream of nitrogen after each step. α-Cyano-4-hydroxycinnamic acid (CHCA) matrix solution (0.3 μL, 10 mg/mL in acetone) was applied to each chip and dried before the MALDI-TOF-MS analysis.

The SAM chips were placed onto a MALDI sample plate (AB Sciex, V700668) that accommodates very thin SAM gold-coated glass slides (0.16 ~ 0.19 mm thickness). SAM chips

are applied directly onto the MALDI plate with vacuum grease. Mass analysis was carried out using a Voyager DE-PRO MALDI-TOF mass spectrometer (Applied Biosystems; Framingham, MA) equipped with a dual microchannel plate (MCP) detector for linear and reflectron mode (1.3 m effective flight path length) of detection with a delayed ion extraction. The instrument parameters were set such as accelerating voltage (AV) at 20 or 25 kV, grid voltage at 93% of AV, guide wire at 0.1%, and extraction delay time at 510 or 575 ns. A 337 nm nitrogen UV laser (pulse width: 3 ns, pulse energy: 120 μJ at 10 Hz) was used at a repetition rate of 3 Hz for sample ionization. The mass spectra obtained were an accumulation of 100 laser shots.

Obtained mass spectra were externally calibrated with myoglobin from equine skeletal muscle and ubiquitin from bovine erythrocytes. Raw data were baseline subtracted and Gaussian smoothed (11 points) in the DataExplorer software (Applied Biosystems; Framingham, MA). The accuracy of the external calibration for the instrument is approximately 1000 ppm. With broad peaks for both the monomeric CTxB and the CTxB-GM1a-SiaDAz(2me) complex, error propagation was handled as follows: the full width of both peaks were determined at half the maximal height. The resulting widths were divided by the median peak value corresponding to the peak's centroid. The resulting values were squared and summed. Finally, the square root was taken and multiplied by 1555 (the difference between the peaks' centroids) yielding the calculated error of ± 38 Da. Mass spectra were processed for publication with OriginPro 7.5G Software (OriginLab; Northampton, MA).

NMR spectra of purified compounds

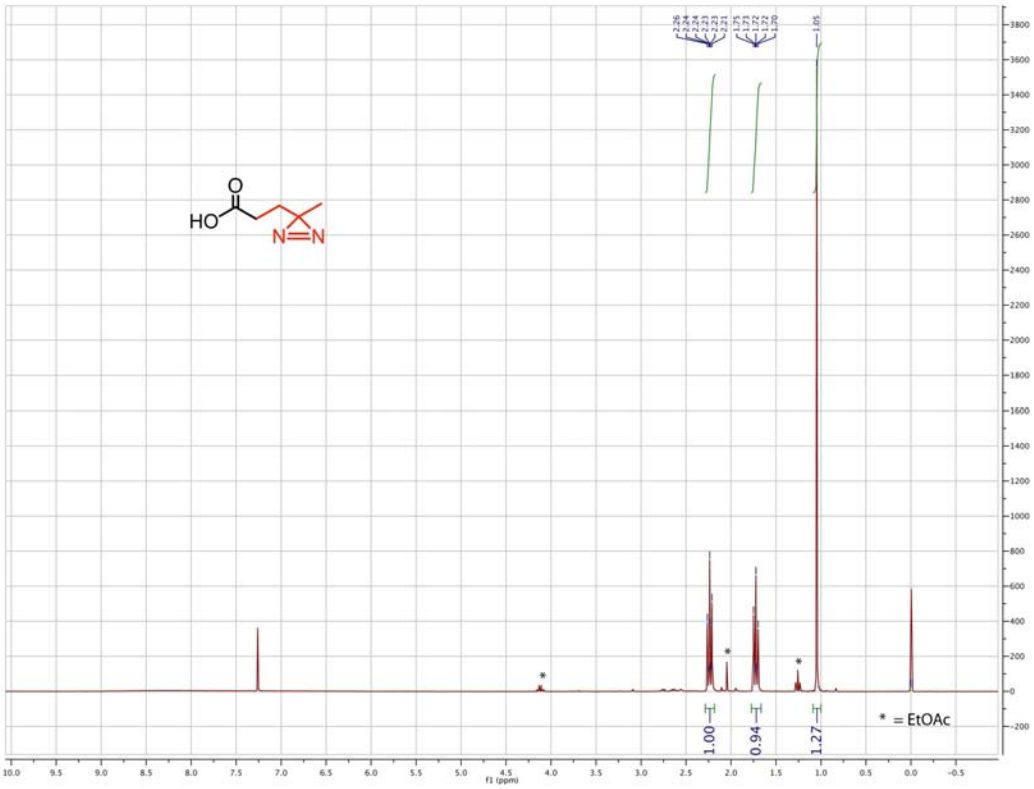

Figure S10. **^{1}H-NMR spectrum of 4,4-azo-pentanoic acid (11).**

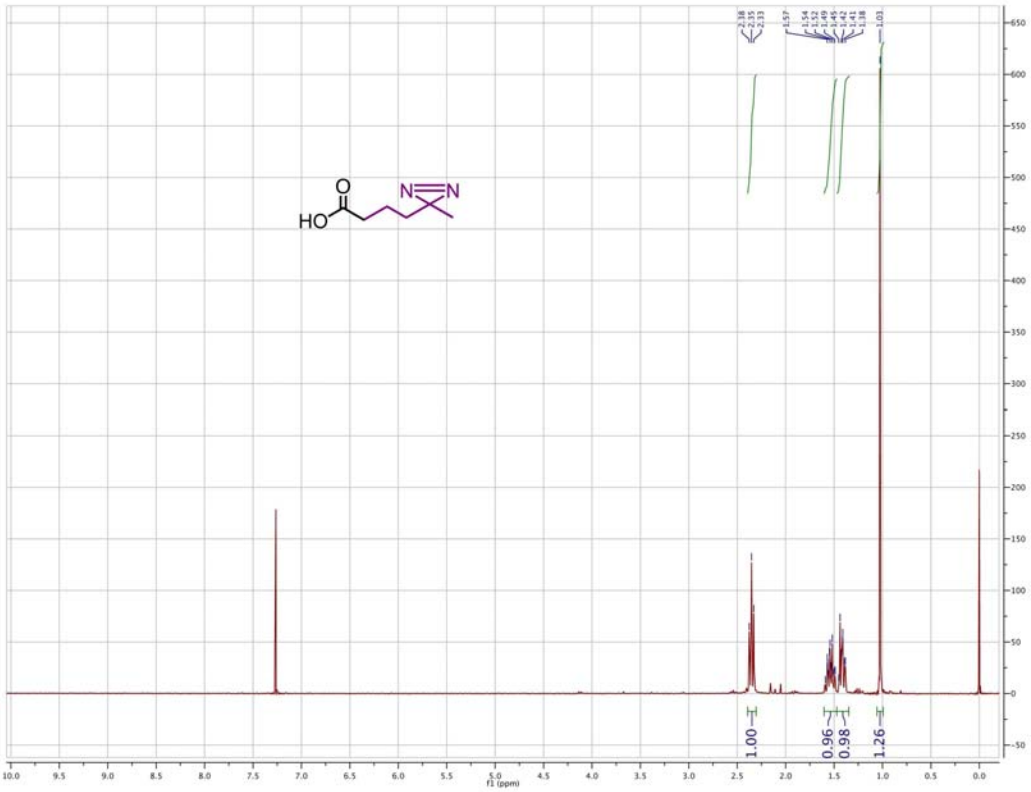

Figure S11. **^{1}H-NMR spectrum of 5,5-azo-hexanoic acid (13).**

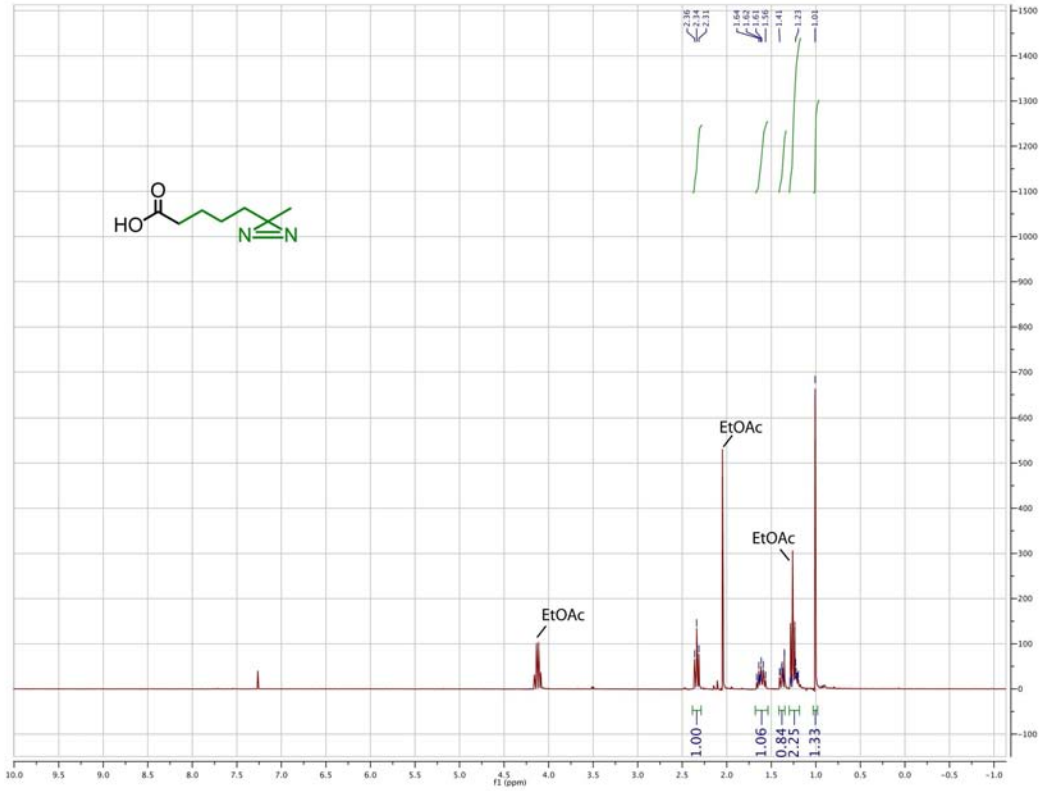

Figure S12. **^{1}H-NMR spectrum of 6,6-azo-septanoic acid (15).**

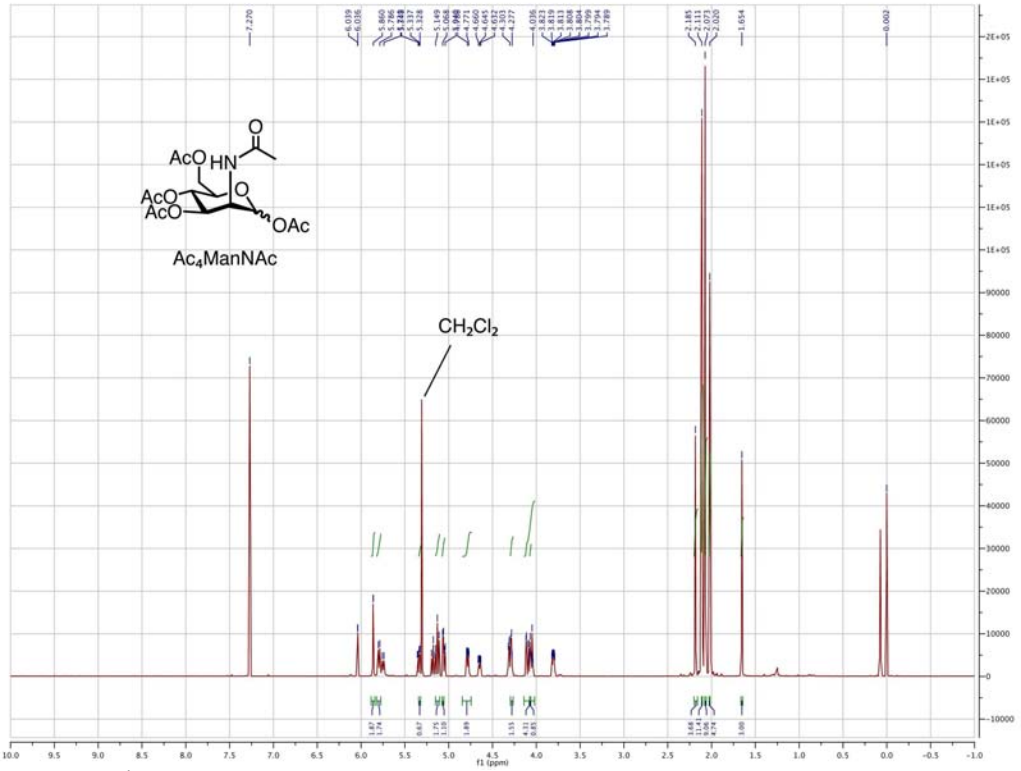

Figure S13. **^{1}H-NMR spectrum of Ac_4ManNAc (1).**

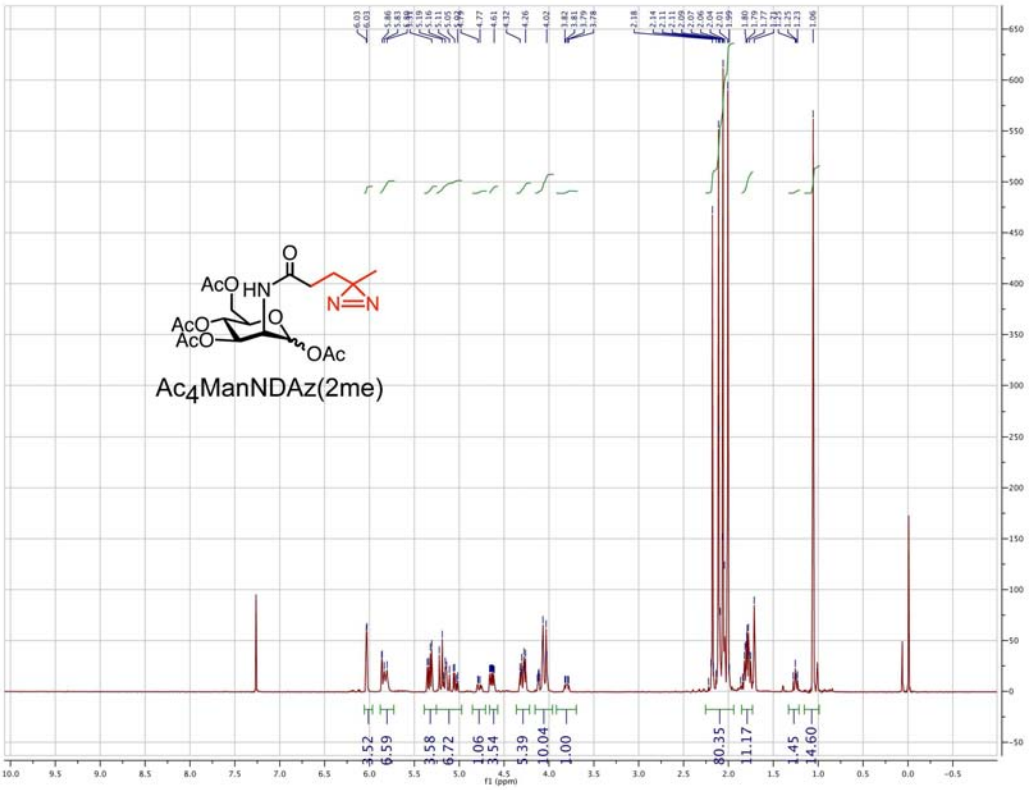

Figure S14. **^{1}H-NMR spectrum of Ac_4ManNDAz(2me) (4).**

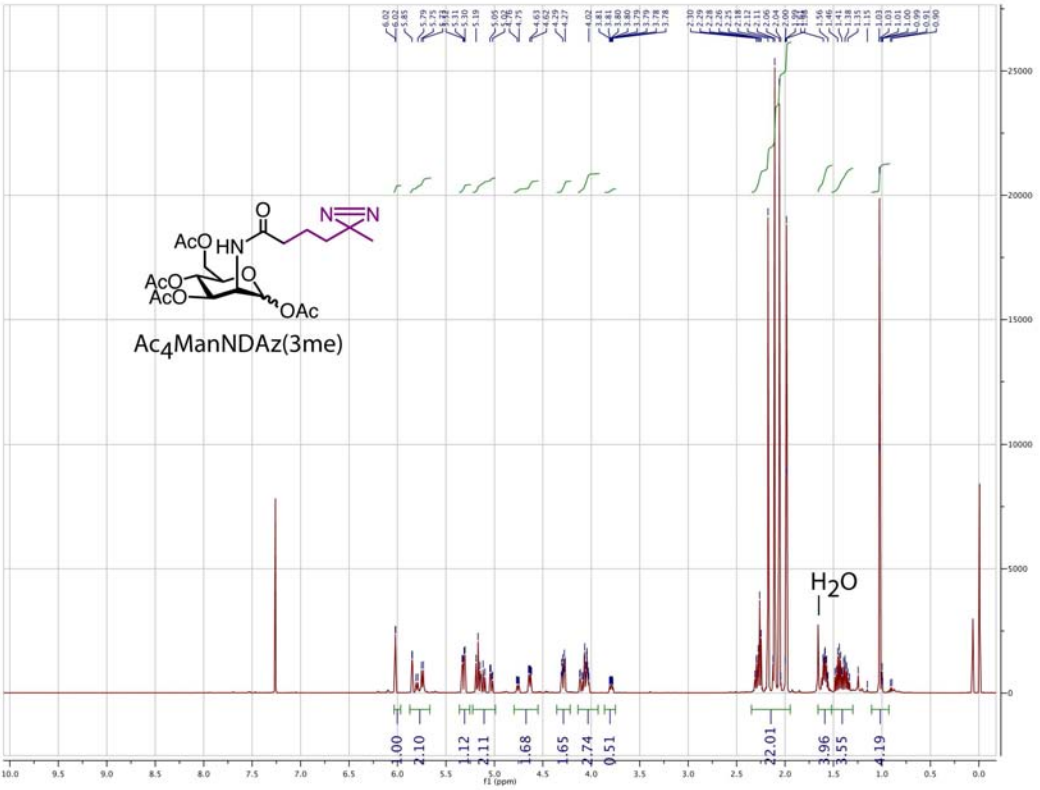

Figure S15. **^{1}H-NMR spectrum of Ac_4ManNDAz(3me) (5).**

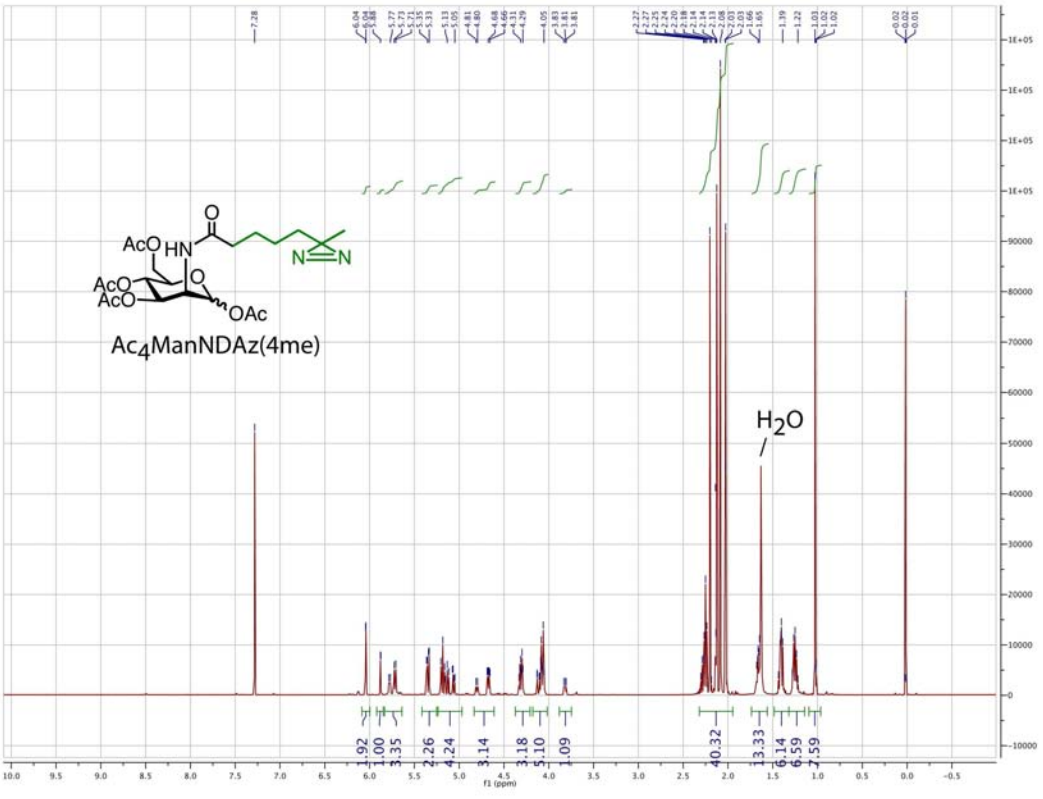

Figure S16. **^{1}H-NMR spectrum of Ac_4ManNDAz(4me) (6).**

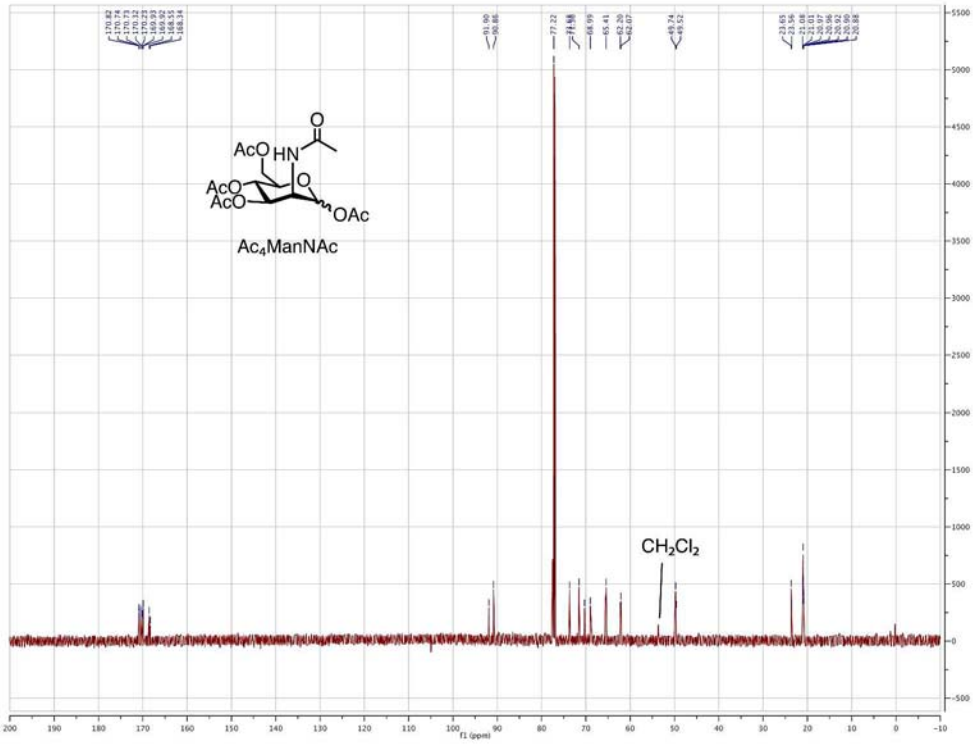

Figure S17. **^{13}C-NMR spectrum of Ac_4ManNAc (1).**

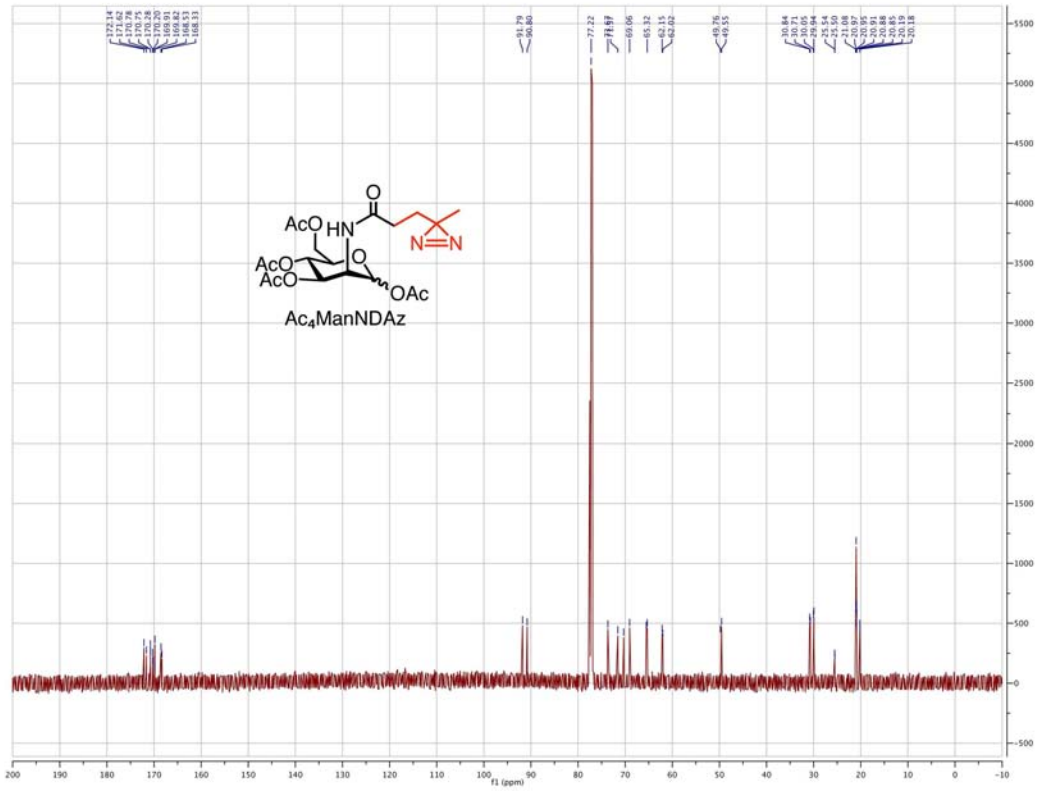

Figure S18. **^{13}C-NMR spectrum of Ac_4ManNDAz(2me) (4).**

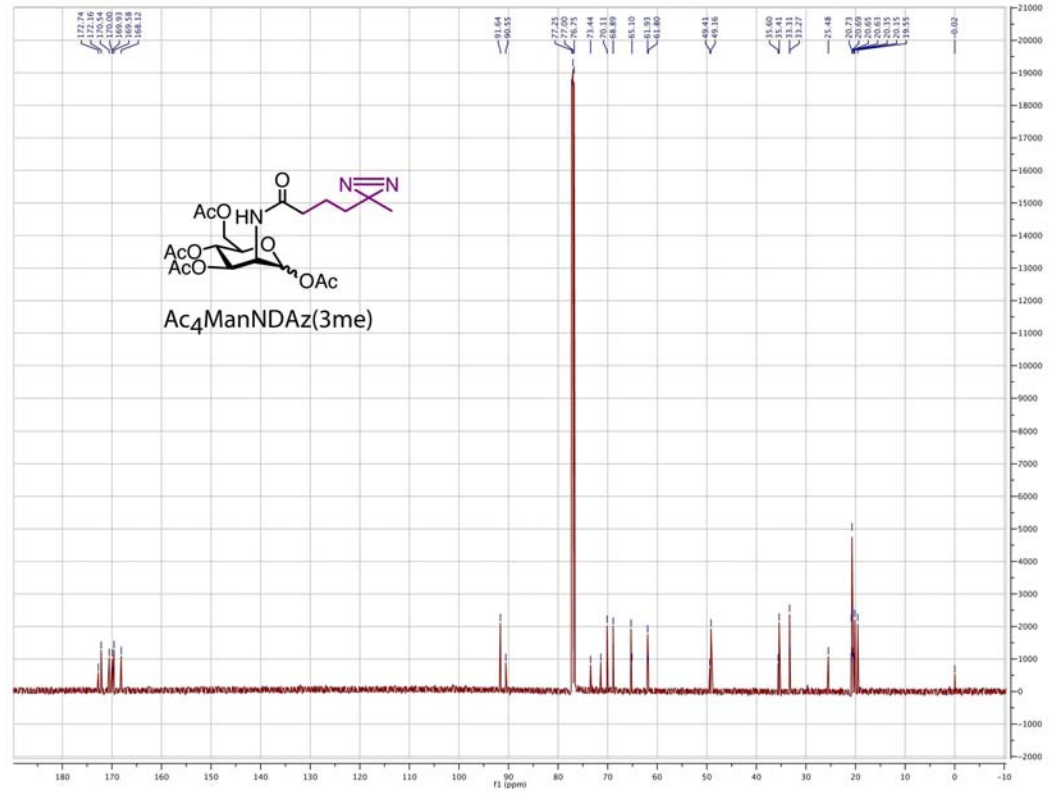

Figure S19. **^{13}C-NMR spectrum of Ac_4ManNDAz(3me) (5).**

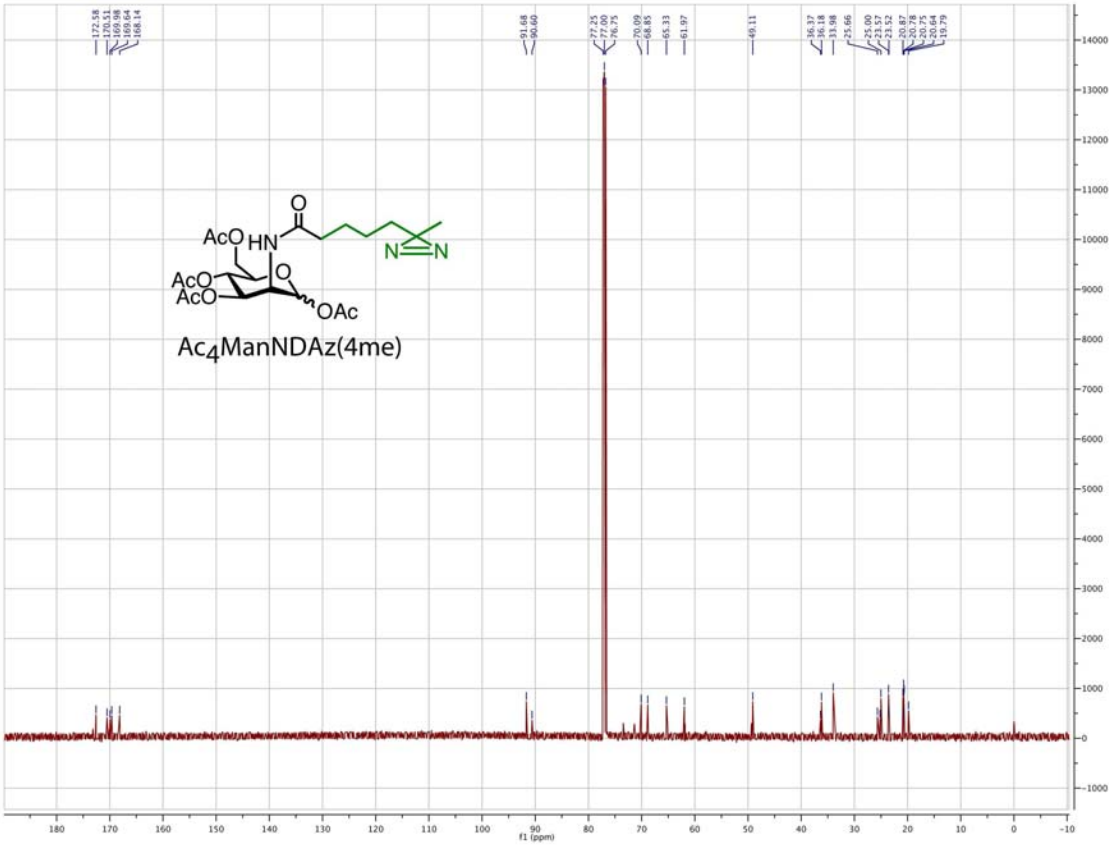

Figure S20. **^{13}C-NMR spectrum of Ac_4ManNDAz(4me) (6).**

HPLC evaluation of compound purity

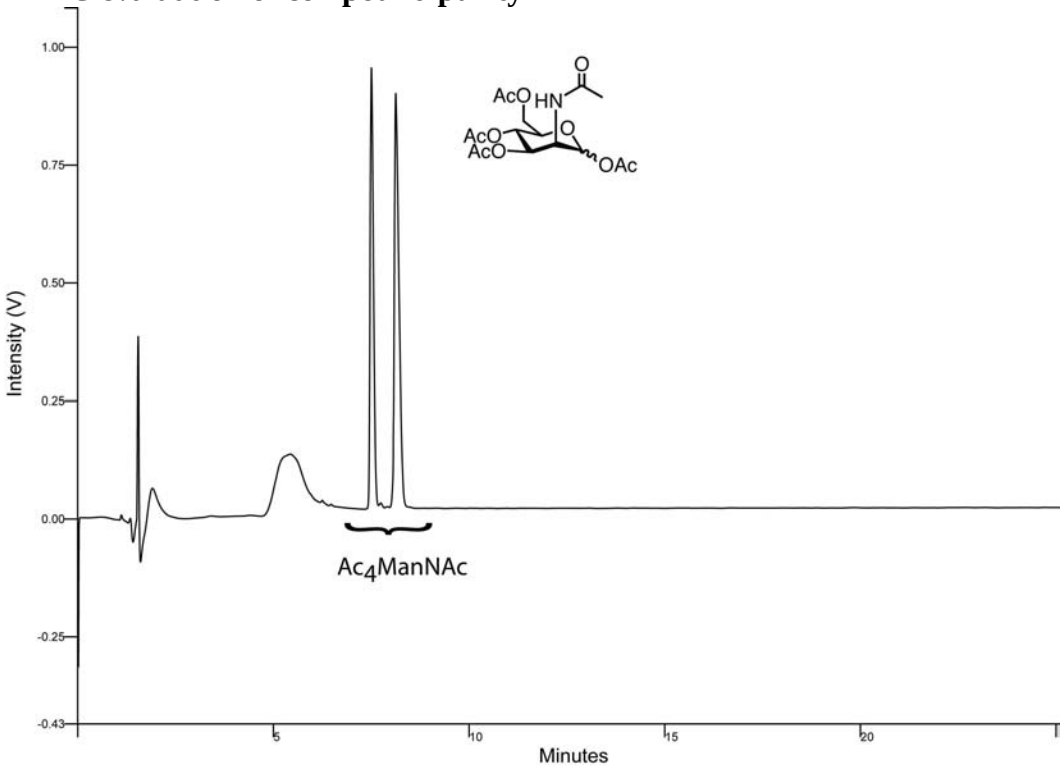

Figure S21. **HPLC trace of Ac_4ManNAc (1).** HPLC elution of acetylated sugars was monitored at 210 nm.

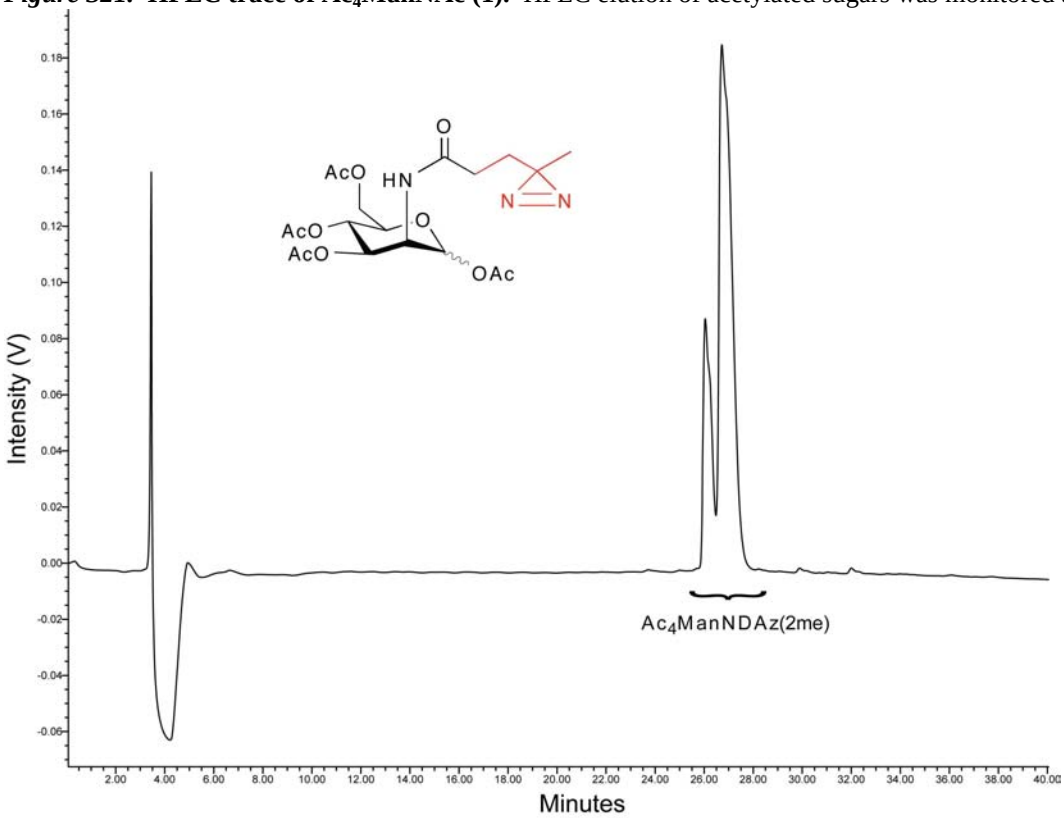

Figure S22. **HPLC trace of Ac_4ManNDAz(2me) (4).** HPLC elution of acetylated sugars was monitored at 210 nm.

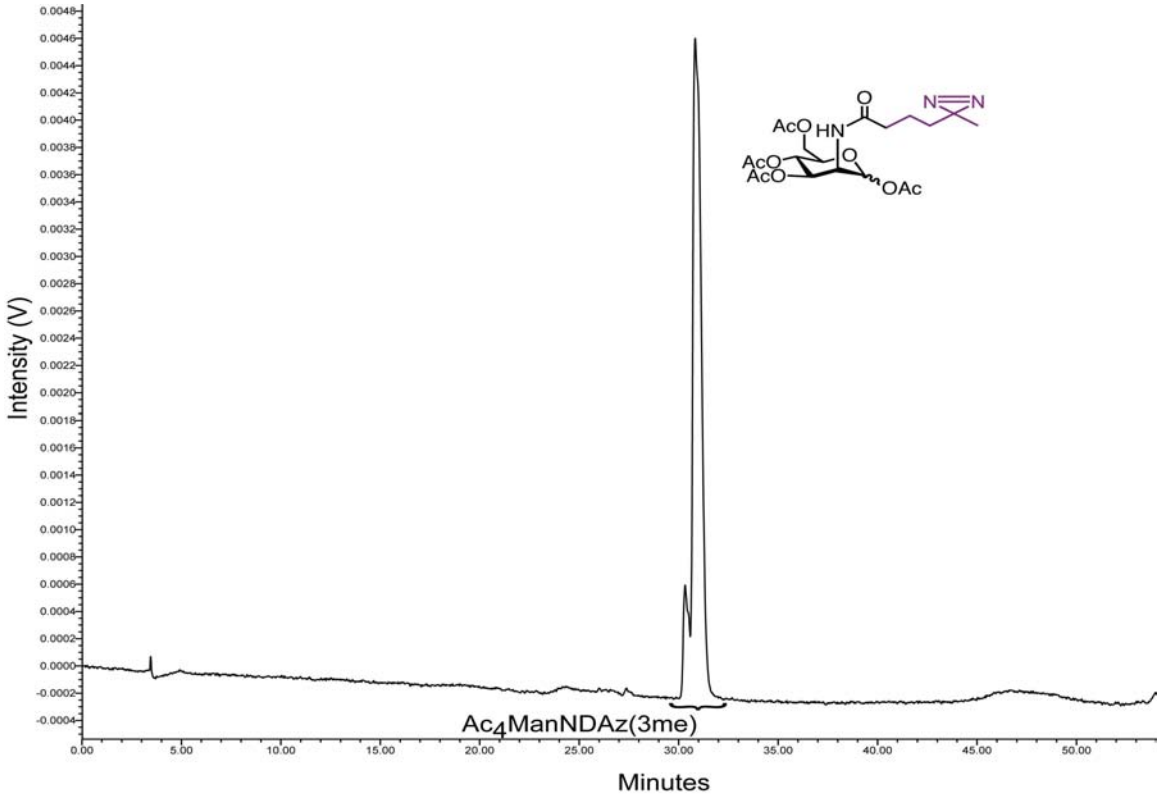

Figure S23. **HPLC trace of Ac_4ManNDAz(3me) (5).** HPLC elution of acetylated sugars was monitored at 210 nm.

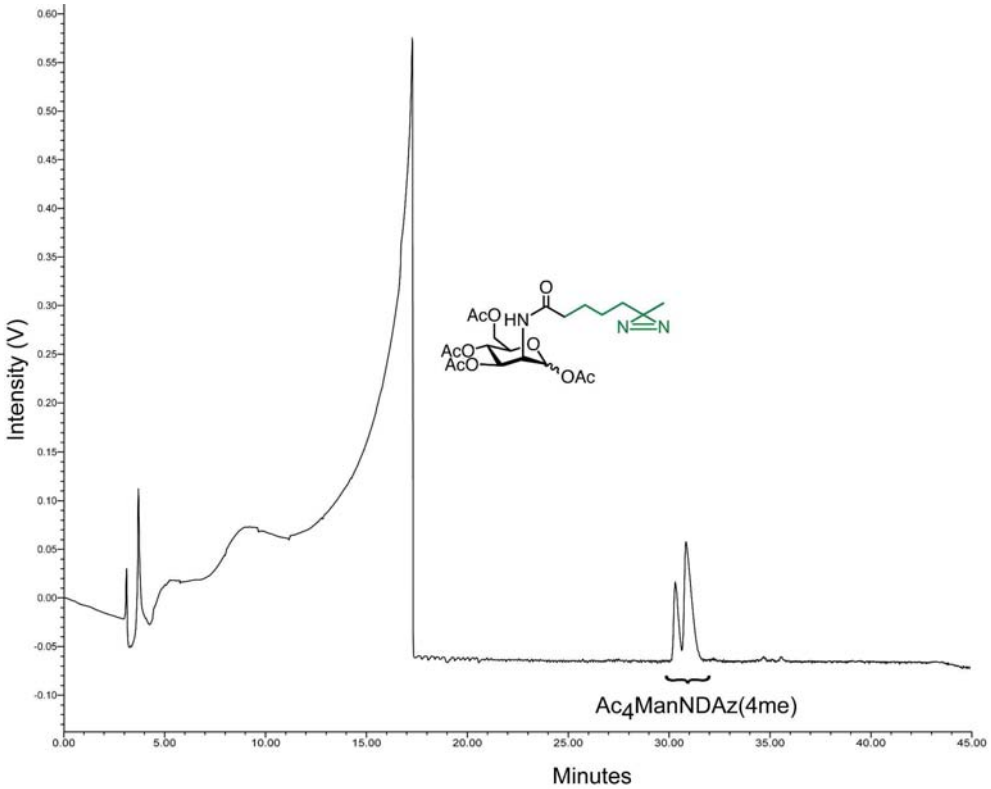

Figure S24. **HPLC trace of Ac_4ManNDAz(4me) (6).** HPLC elution of acetylated sugars was monitored at 210 nm.

References

1. Bond, M. R., Zhang, H., Vu, P. D., and Kohler, J. J. (2009) Photocrosslinking of glycoconjugates using metabolically incorporated diazirine-containing sugars, ***Nat. Prot. 4***, 1044-1063.
2. Luchansky, S. J., Hang, H. C., Saxon, E., Grunwell, J. R., Yu, C., Dube, D. H., and Bertozzi, C. R. (2003) Constructing azide-labeled cell surfaces using polysaccharide biosynthetic pathways, ***Methods Enz. 362***, 249-272.
3. Tanaka, Y., and Kohler, J. J. (2008) Photoactivatable crosslinking sugars for capturing glycoprotein interactions, ***J. Am. Chem. Soc. 130***, 3278-3279.
4. Laughlin, S. T., and Bertozzi, C. R. (2007) Metabolic labeling of glycans with azido sugars and subsequent glycan-profiling and visualization via Staudinger ligation, ***Nat. Protocols 2***, 2930-2944.
5. Zeng, Y., Ramya, T. N. C., Dirksen, A., Dawson, P. E., and Paulson, J. C. (2009) High-efficiency labeling of sialylated glycoproteins on living cells, ***Nat. Meth. 6***, 207-209.
6. Brinkman-Van der Linden, E. C. M., Sonnenburg, J. L., and Varki, A. (2002) Effects of sialic acid substitutions on recognition by ***Sambucus nigra*** agglutinin and ***Maackia amurensis*** hemagglutinin, ***Anal. Biochem. 303***, 98-104.
7. Iglesias, J. L., Lis, H., and Sharon, N. (1982) Purification and properties of a D-galactose/N-acetyl-D-galactosamine-specific lectin from ***Erythrina cristagalli***, ***Eur. J. Biochem. 123***, 247-252.
8. Sanchez, J. F., Lescar, J., Chazalet, V., Audfray, A., Gagnon, J., Alvarez, R., Breton, C., Imberty, A., and Mitchell, E. P. (2006) Biochemical and structural analysis of ***Helix pomatia*** agglutinin. A hexameric lectin with a novel fold, ***J. Biol. Chem. 281***, 20171-20180.
9. Wang, Z., Sun, Z., Li, A. V., and Yarema, K. J. (2006) Roles for UDP-GlcNAc 2-epimerase/ManNAc 6-kinase outside of sialic acid biosynthesis: Modulation of sialyltransferase and BiP expression, GM3 and GD3 biosynthesis, proliferation, and apoptosis, and ERK1/2 phosphorylation, ***J. Biol. Chem. 281***, 27016-27028.
10. Jourdian, G. W., Dean, L., and Roseman, S. (1971) The Sialic Acids. XI. A periodate-resorcinol method for the quantitative estimation of free sialic acids and their glycosides, ***J. Biol. Chem. 246***, 430-435.

Bioconjugate Chemistry

ARTICLE

pubs.acs.org/bc

Self-Assembly Properties and Dynamics of Synthetic Proteo−Nucleic Building Blocks in Solution and on Surfaces

Aude Laisne,[†] Maxime Ewald,[‡] Toshio Ando,[§] Eric Lesniewska,[‡] and Denis Pompon*[,†]

[†]Centre de Génétique Moléculaire, CNRS, UPR3404, Avenue de la Terrasse, F91190 Gif-sur-Yvette, France

[‡]Institut Carnot Bourgogne, UMR CNRS 5209, University of Bourgogne, F21078 Dijon, France

[§]Department of Physics, Kanazawa University, Kakuma-machi, Kanazawa 920-1192, Japan

Supporting Information

ABSTRACT: Synthetic proteo−nucleic structures (PDNAs) encompassing a single-stranded DNA sequence covalently attached to a redox protein domain able to interact with surface or matrix were designed and characterized. They constitute versatile building blocks alternative to regular DNA for creating scaffolds with optical, electrical, or catalytic properties. PDNAs self-assemble in the presence of complementary oligonucleotides, to form a network of protein domains linked by double-stranded DNA segments. Electrophoretic and hydrodynamic behaviors of PDNAs and corresponding DNA were compared under electrophoresis and gel filtration conditions. Hybridization rates between small and large assemblies were characterized by rapid-mixing experiments. Results showed that the protein part significantly contributes to hydrodynamic behaviors of structures but marginally affects the conformation and hybridization properties of the nucleic domain. PDNA metal-mediated complexes with nitriloacetate-modified phospholipids can diffuse and interact at the surface of vesicles or supported membranes. Surface plasmon resonance analysis of membrane−PDNA interactions indicated that two protein units are required to allow stable surface association and that surface occupancy constrains assembly sizes. High-speed atomic force microscopy illustrated rapid lateral diffusion of assemblies on mica, revealing transient association between noncomplementary PDNA extremities and frequent trapping by surface defects. Regularly organized protein domains were visualized using a larger DNA framework.

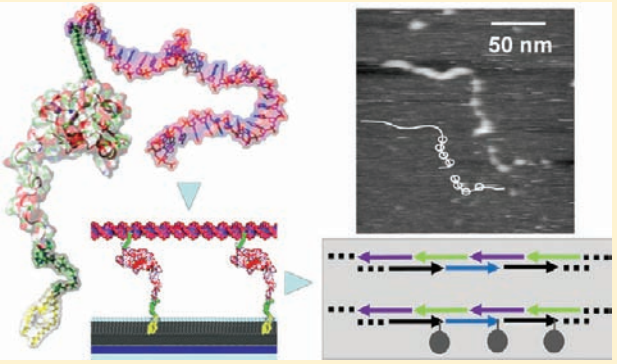

INTRODUCTION

The use of a synthetic DNA scaffold to build mono- or multidimensional nano-objects with fully predictable shapes rapidly developed as an important field of synthetic biology.[1−7] However, the limited range of functionalities that can be assembled using only nucleic acid tiles raised the question of the position specific incorporation of protein block in such scaffolds.[8] One way involved the DNA binding domain or the recognition of modified bases (for example biotin) by specific protein domains (avidin, antibodies, etc.).[8−11] Reciprocally, alternate approaches profit from the recognition of specific protein domains by aptamer structures embedded into the DNA scaffold.[12] However, these two methods suffer strong limitations because they require fusion of a large protein recognition domain to functional parts of interest or restrict the approach to structures for which suitable aptamers can be created. Protein−DNA recognition based on chemically mediated approaches (such as NTA−metal complexes) can also be considered, but either gives rise to reversible association or lacks specificity.[13,14]

PDNAs (protein−DNA structure), which are artificial structures that consist of a protein domain covalently linked to a single-stranded DNA (ssDNA) part through synthetic structures, constitute an attractive alternative.[15,16] The protein part of PDNA can be chosen to carry various types of functions such as surface interaction, binding, enzymatic, optical, or electrical properties, potentially creating nanostructures that can be used as biosensors[17,18] or active molecular devices. PDNA tiles can self-assemble in solution or be attached to a matrix in the presence of complementary ssDNA.[19] However, little is known about the stability and physicochemical and structural features of such objects or the ways they interact together compared to regular DNA tiles. This is particularly critical for defining methods adapted for specifically incorporating these building blocks into DNA scaffolds like origami[6] or other DNA-based supramolecular assemblies.[20]

This paper extends synthesis approaches for such PDNA building blocks and analyzes their physicochemical and assembly properties in comparison to their corresponding pure nucleotidic parts, at both global and single-molecule levels.

Received: May 2, 2011
Revised: July 8, 2011
Published: August 19, 2011

ACS Publications © 2011 American Chemical Society

EXPERIMENTAL PROCEDURES

Synthesis of the PDNA Building Block. Oligonucleotides (Eurogentec) presented in section 1 of the Supporting Information were purified by ion-pairing reverse phase chromatography as previously described.[21] PDNAs were prepared by hemisynthesis from engineered human cytochrome b_5 (b_5) as described in sections 2 and 3 of the Supporting Information and previous work.[16,17,19] Briefly, a 3′- or internally amino linker-modified oligonucleotide was covalently attached through a disulfide bond to a modified b_5 containing a unique Cys residue and a His_4 C-terminal tag. During the synthesis, the amino linker of the ssDNA was coupled to a second linker terminated by a thiopyridine-protected thiol using NHS chemistry. A disulfide bond was finally formed by reacting the activated linker end with the unique Cys residue of the protein. The resulting products were purified to homogeneity by a combination of ion exchange and affinity chromatography, taking advantage of the protein His tag.

PDNA Thermal Stability. Experiments were performed in 20 mM Na/K phosphate buffer (pH 7.4) using PDNA or b_5 concentrations in the 10 μM range. Thermal denaturation was monitored on a Lambda 2 (Perkin-Elmer) spectrophotometer using increasing temperature steps of 4 °C. Spectra were recorded between 260 and 600 nm immediately after each temperature stabilization at a rate of 120 nm/min. Denaturation curves for native, engineered b_5, and PDNA were calculated from the changes in the 413 nm absorbance.

Phospholipid Vesicle Preparation. 1,2-Dimyristoyl-*rac*-glycero-3-phosphocholine (DMPC) was purchased from Sigma-Aldrich and 1,2-dioleoyl-*sn*-glycero-3-{[*N*-(5-amino-1-carboxypentyl)iminodiacetic acid]succinyl} (nickel salted) (DOGS-NTA) from Avanti Polar Lipids. A chloroform solution containing 1 mg of a DMPC/nickel DOGS-NTA mixture (90:10 molar ratio) was evaporated into a glass vial under a nitrogen flow, and the residue was dried under vacuum for 2 h. Phospholipids were hydrated overnight at 4 °C with 1.4 mL of 1× PBS buffer (Sigma-Aldrich), and the mixture was sonicated until a clear solution containing a total phospholipid concentration of 1 mM was obtained. The vesicles were extruded 19 times through polycarbonate membranes with 100 nm pores (Liposofast, Avestin).

Synthesis of Defined PDNA Assemblies. A detailed description is given in section 8 of the Supporting Information. Briefly, hybridizations of DNA and PDNA tiles were performed at 24 °C in 1× PBS buffer using a slight molar excess of DNA compared to PDNA. The constructs were purified from excess DNA either by association of IMAC and Sephadex G25/G50 chromatography or by HPLC size exclusion chromatography. The first method involved binding to an IMAC column (0.5 cm × 1.5 cm) and elution with a buffer supplemented with 30 mM histidine. EDTA (final concentration of 10 mM) was added to the eluate prior it being loaded onto a Sephadex G25 gel filtration column (0.5 cm × 1.5 cm) equilibrated with 1× PBS buffer. Alternatively, purification was performed by size exclusion chromatography (BioSuite 250, 4 μm UHR SEC, 4.6 mm × 300 mm, Waters) at a rate of 0.3 mL/min with 0.25 M NaCl and 0.15 M $NaKPO_4$ buffer (pH 6.8). DNA Ladders N3233 (Biolabs) were used for calibration.

Analysis of DNA and PDNA Hybridization Kinetics by Rapid-Mixing Experiments. Hybridization of simple DNA and PDNA tiles and preformed dimers was analyzed in rapid-mixing experiments by monitoring the hypochromic effect associated with the formation of double-stranded structures. Kinetic constants were calculated by fitting of the traces as described previously.[21]

Gel Filtration and Electrophoresis Methods. HPLC gel filtration analysis was performed on a Waters BioSuite 250 column (4 μm UHR SEC, 4.6 mm × 300 mm) at a rate of 0.3 mL/min with 0.25 M NaCl and 0.15 M $NaKPO_4$ buffer (pH 6.8). Sodium dodecyl sulfate−polyacrylamide gel electrophoresis (SDS−PAGE) analysis was performed using 4 to 12% NuPAGE Novex Bis-Tris polyacrylamide gels run at 24 °C and 120 V. Protein parts of PDNA were revealed by fast Coomassie blue staining and calibrated using the Mark12 Unstained standard from Invitrogen. Agarose gel analysis was performed using 3.5% NuSieve GTG Agarose from Tebu-bio in 1× TBE run at 50 V and 4 °C. DNA Ladders N3233 (Biolabs) were used for calibration. Agarose gel electrophoresis patterns were deconvoluted using an optimized expansion factor of 1.5 and band quantified as described previously for the analysis of regular DNA polymers.[21]

Surface Plasmon Resonance (SPR) Methods. SPR experiments were performed on a SPRi-Lab$^+$ array system (Genoptics) using 1× PBS as running buffer at a flow rate of 230 μL/min and 24 °C. Gold layer-covered prisms were cleaned by gentle sonication in a hot acid Pyranha solution (equal volume of 30% hydrogen peroxide and pure sulfuric acid), abundantly rinsed with Milli-Q water, and stored in pure HPLC grade acetonitrile until they were used. Experiments were performed following phospholipid vesicle fusion either on bare gold (lipid bilayer) or on a self-assembly monolayer of alkyl chains (lipid hemilayer). For that, the Pyranha-cleaned prism was immersed in a freshly prepared 1 mM solution of 1-octadecanethiol in ethanol (Sigma Aldrich) for 18 h and then rinsed with ethanol and water. Freshly extruded phospholipid vesicles (1 mM into 1× PBS buffer) were fused onto the treated substrate by circulation in the SPR cell at a flow rate of 50 μL/min for 30 min at 24 °C. An excess of adsorbed vesicles was removed by washing for 10 min with pure water (hypo-osmotic choc) followed by equilibration with 1× PBS buffer.

High-Speed Atomic Force Microscopy (HS-AFM). A laboratory-built high-speed atomic force microscope described previously was used to visualize the structure.[22−24] All observations were performed in oscillating contact mode in liquid. Small cantilevers designed for HS-AFM with a spring constant of 0.1−0.2 N/m, a resonant frequency of 0.8−1.2 MHz, and a quality factor of ∼2 in buffer solution were used.[25] The cantilever tips were grown by electron beam deposition (SEM Jeol 6500) and further sharpened by oxygen plasma etching (Plasma cleaner Harrick). The cantilever's free oscillation peak-to-peak amplitude (A_0) was set to 4−5 nm, while the feedback set point during imaging was set to ∼0.9 A_0. The samples were diluted (2−10-fold) in an observation buffer (OB) containing 10 mM $MgCl_2$. A drop (∼2 μL) was deposited on freshly cleaved green muscovite mica, and the mica was incubated at room temperature for 5 min. Subsequently, the mica surface was immersed in a liquid chamber filled with 60−100 μL of OB and subjected to HS-AFM. Diluted samples were used within a day (storage at 4 °C).

RESULTS

Three types of PDNAs including an engineered cytochrome b_5 redox domain and differing by the sequence of their nucleotidic parts and by the grafting position on the sequence of the

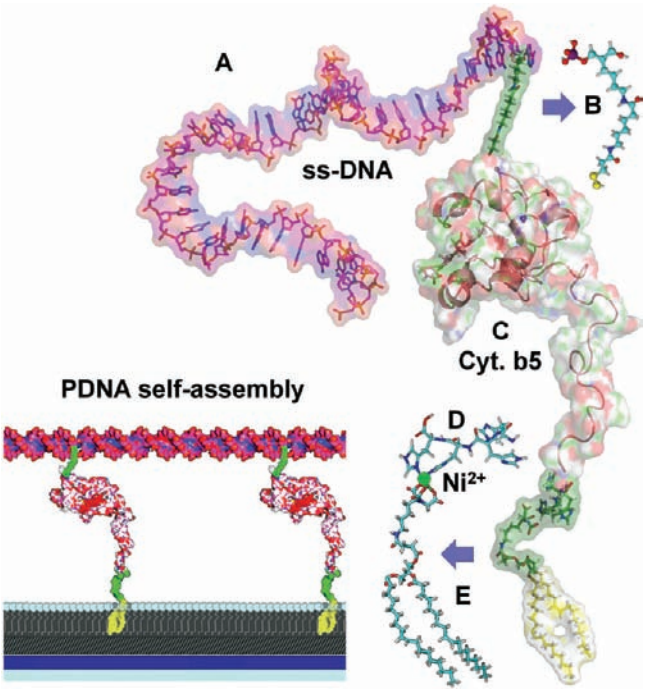

Figure 1. Structures of the PDNA building block, including a b_5 core. The structure is composed of a 39-base ssDNA part (A) attached either by its 3′-end (as illustrated) or by an internal amino C6 thymidine (not shown) to a synthetic linker (B) coupled to cytochrome b_5 (C) by the thiolate extremity of a cysteine at position 24. The His_4 C-terminal end (D) of the protein interacts with the nickel ion of an 18:1 DOGS-NTA-modified lipid (E). The structure at the bottom left shows PDNA blocks inserted into a dsDNA structure. The structure is floating on a supported membrane composed of a phospholipid monolayer covering a self-assembled octadecanethiol monolayer on gold.

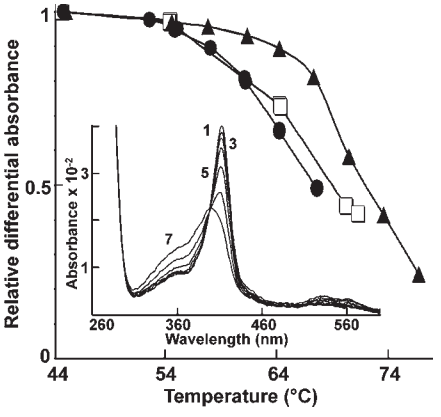

Figure 2. Thermal stabilities of b_5 folding in wild-type, Cys-modified, and corresponding PDNA structures. Protein denaturation was monitored by observation of the spectral changes of the bound heme cofactor at 413 nm. Denaturation curves were compared for native (▲), Cys-modified b_5 (□), and PDNA (●) forms. Typical spectral changes following incubation of a PDNA at temperatures increasing from 44 to 68 °C in steps of 4 °C are illustrated in inset curves 1 (44 °C) to 7 (68 °C).

protein domain (Figure 1, right) were prepared by hemisynthesis and purified to homogeneity (sections 2 and 3 of the Supporting Information). In these structures, the protein C-terminal His tag

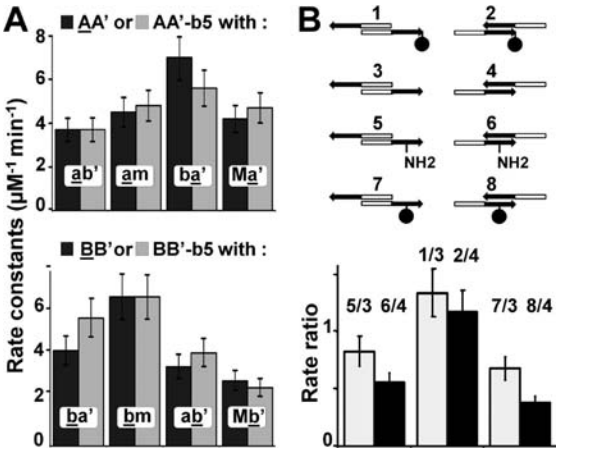

Figure 3. Comparative rate constants for DNA and PDNA hybridizations. (A) Hybridizing oligonucleotides are indicated inside bars (matching segments underlined). Dark and light gray boxes refer to hybridization of DNA and corresponding PDNA to half-cDNA, respectively. Second-order rate constants were deduced from measurements of the hypochromic effect in rapid-mixing experiments. (B) Ratios among hybridization rates for normal, base-modified, and protein-coupled oligonucleotides. These ratios are defined by a scheme in which the circle stands for the protein domain and the NH2 label for the internal base modification. White and black bars correspond to hybridizations involving the distal and proximal segments of oligonucleotides, respectively.

plays an important role in permitting the formation of a metal chelate linkage between the PDNAs and Ni-NTA groups attached to either a polymer matrix, modified phospholipids, or functionalized surfaces. Lateral diffusion of anchored PDNAs remains possible either by stepwise release and rebinding of the metal chelate or, in the case of vesicles or a supported membrane, through lipid diffusion. Hybridization of the PDNA single-stranded part to complementary nucleic acid generates a more rigid double-stranded DNA (dsDNA) structure (Figure 1, left) that, depending on sequences, could self-organize into a wide range of nucleo−proteic networks. Such structures can alternatively be made by substituting the cytochrome b_5 domain with any other protein of interest provided that a single grafting point can be engineered at the surface.

Stability and Hybridization Properties of the PDNA Building Block in Solution. The termal stability of the PDNA protein domain under conditions required for hybridization reactions is critical for the maintenance of the functional integrity and particularly redox properties. This was analyzed in solution by monitoring the temperature-dependent disruption of the cytochrome b_5 absorption spectra, which tightly depend on the iron coordination by two histidine residues of the protein. Results indicated that the reversible denaturation of the protein part of the PDNA is observed only above 55 ± 2 °C, a value identical to that found for the DNA-free engineered protein and slightly lower (2−3 °C) than that for the native protein (Figure 2). Oxidoreduction properties of the cytochrome b_5 domain in PDNA structures were found to be conserved. An identical transition in the absorption spectra, which is characteristic of the redox change of the histidine-coordinated iron porphyrin, was observed upon electron transfer in the native protein and on PDNA structures. Thus, the presence of the ssDNA part has no significant effect on the stability and redox properties of the protein domain. The thermal stability of the protein is sufficiently

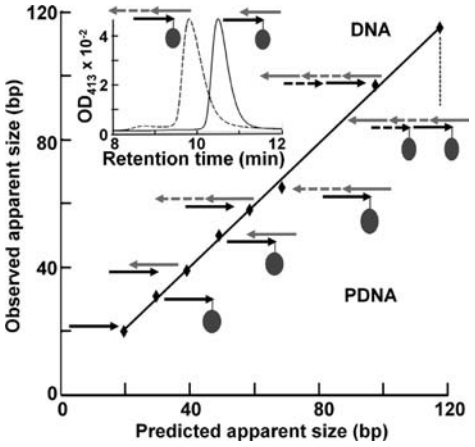

Figure 4. Size exclusion chromatography characterization of short PDNA assemblies. Structures depicted were analyzed on a HPLC gel filtration column (detection at 413 and 254 nm) and apparent molecular masses calculated using dsDNA as molecular mass standards. Apparent molecular masses (expressed in base pairs) were predicted using the formula molecular mass (base pairs) = $10P + 0.5S + D$, where P, S, and D stand for the number of protein unit(s) (●) and ss- and dsDNA bases (arrows), respectively. The inset shows experimental peak shapes for illustrated constructs.

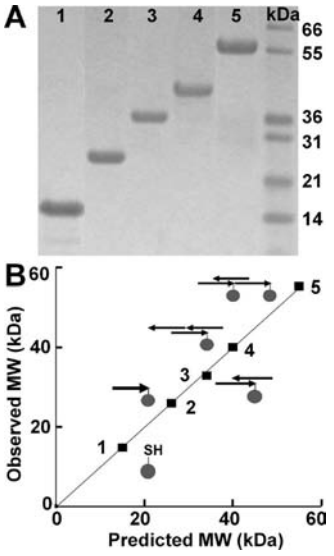

Figure 5. SDS−PAGE analysis of short PDNA assemblies. (A) Experimental gel, in which the numbering of lanes corresponds to the structure depicted in the bottom panel. (B) Relation between the observed molecular mass (calculated on the basis of a protein standard) and those predicted using the formula molecular mass (kilodaltons) = $15P + 0.282S + 0.359D$, where P, S, and D stand for the number of protein unit(s) (●) and ss- and dsDNA bases (arrows), respectively. Structures 2−4 are derived from AA′-b5 PDNAs, and structure 5 combines AA′-b5 and BB′-b5 PDNAs.

high to allow hybridization to proceed under classical conditions (55 °C) for oligonucleotides.

Reciprocally, the effect of the protein domain on the hybridization properties of the DNA domain was investigated for structures in which covalent grafting was performed either internally or at the 3′-end of the oligonucleotidic part. Monitoring of hypochromic effects was used to analyze the relative rates of hybridization of the different PDNAs with complementary ssDNA sequences. To discriminate between hydrodynamic and protein-related microenvironment effects, hybridization properties were analyzed on both the proximal and the distal sides (3′- and 5′-halves, respectively) of the nucleic part of PDNAs. In addition, the potential influence of the nature (ds- vs ssDNA) of the region flanking the hybridization site was investigated.

During hybridization of PDNAs, protein absorption at 260 nm represents less than 10% of the nucleic acid absorbance and does not contribute to spectral changes. Second-order hybridization rate constants ranging from 1.9 to 7 μM^{-1} min^{-1} were observed (Figure 3), while the lengths of the hybridizing segments were almost identical (19−20 bases) in all experiments. Comparison of hybridization rates for DNA and 3′-end-grafted PDNA with an identical sequence indicated that protein-dependent modulation of rates is limited with regard to the effects related to the sequence of hybridizing segments (Figure 3A). Moreover, analysis of the relative rates of hybridization events occurring in the distal and proximal parts of PDNA confirmed a hardly significant influence of the protein domain when grafted at the 3′-end of the nucleic part (labels 1/3 and 2/4 in Figure 3B). In contrast, when the grafting was performed internally in the nucleic part, a more significant effect on rates was observed, which resulted both from the presence of a modified base in the hybridizing segment (labels 5/3 and 6/4 in Figure 3B) and the attachment of the protein domain (labels 7/3 and 8/4). In both cases, distal grafting has a limited influence compared to proximal grafting, suggesting that the effect relates more directly to protein−DNA interaction rather than to changes in the global hydrodynamic properties in solution.

Electrophoretic and Chromatographic Properties of PDNA Assemblies of Increasing Sizes. To further investigate the relations between hydrodynamic behaviors and structures, different types of PDNA assemblies were built. The relative contributions of protein and nucleic domains were analyzed using a series of constructs built from hybridization-driven assembly of two PDNA tiles (or corresponding DNA controls), namely, AA′-b5 and BB′-b5 (section 1 of the Supporting Information). The AA′ PDNA building block was designed to hybridize with the 5′-half of ab′ and the 3′-half of ba′ cDNA, matching their a and a′ parts, respectively. Similarly, the BB′ PDNA block can hybridize to ba′ and ab′ DNA tiles by matching their b and b′ parts, respectively. The complementary tiles were assembled by single-step or sequential (purification of intermediates) hybridizations at low (25−45 °C) temperatures followed by final purification to homogeneity by combinations of Ni-NTA affinity and gel filtration chromatography to resolve PDNA assemblies from excess DNA. Corresponding structures and HPLC gel filtration profiles are illustrated in Figure 4. Individual constructs migrate during gel filtration as Gaussian-shaped bands, allowing easy determination of their relative mobility under the high-salt buffer conditions required to prevent interaction with the silica matrix of columns. Interestingly, DNA and protein structural elements contributed in a perfect additive way to the apparent size calculated on the basis of dsDNA standards. The individual contributions of the ssDNA (0.5 bp/base), dsDNA (1 bp/bp), and protein (equivalent to 10 bp/unit) parts appeared to be independent of the assemblies considered. Consequently, the plot of the apparent sizes versus calculated values for eight different constructs is linear. The 10 bp/unit equivalent contribution of the protein part corresponds to an apparent molecular mass of 6.6 kDa, a value significantly

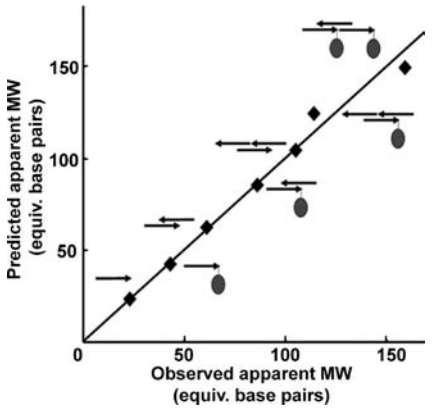

Figure 6. Agarose gel analysis of the apparent molecular mass of PDNA and DNA assemblies. Structures depicted on the figure were resolved by 3.5% agarose gel electrophoresis in 1× TBE. Calibration was performed with dsDNA standards. Molecular masses were predicted using the formula molecular mass (base pairs) = $2S + 0.6S + D$ for DNA−DNA constructs and the formula molecular mass (base pairs) = $2S + 1.55S + D$ for PDNA−DNA constructs, where P, S, and D stand for the number of protein units, ssDNA bases, and dsDNA base pairs, respectively.

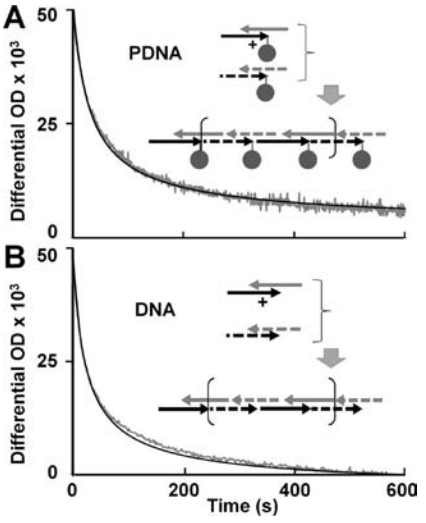

Figure 7. Rapid-mixing analysis of the formation of tile concatemers. (A) Experimental (gray line) and simulated (black line) kinetic courses for the copolymerization of the depicted preformed PDNA−DNA hybrids. (B) Same data for the hybridization of corresponding DNA−DNA hybrids. Simulations were performed using rate constants from Figure 3A and parameters from section 6 of the Supporting Information.

smaller than its actual size of 13 kDa, which would correspond to smaller hydrodynamic radii for proteins compared to those of dsDNA standards with identical masses. However, this is not consistent with predicted hydrodynamic radii[26,27] that are similar (1.9−2 nm) for a dsDNA of 13 kDa (20 bp) and for the b_5 core (13 kDa). The difference can be related to the flux-dependent hydrodynamic stretching that is expected to occur and affect differentially globular and linear structures in the tightly packed HPLC gel filtration column.

To gain additional insight, the electrophoretic mobility of the different constructs was evaluated under SDS−PAGE conditions (Figure 5). Analysis illustrated that coupling of the DNA parts to the protein induces a strong shift in mobility. The apparent molecular mass increases from ∼15 kDa for the b_5 core alone to 27 kDa for the corresponding single-stranded PDNA, the difference of 12 kDa being consistent with the molecular mass (∼13 kDa) of the DNA part. This result contrasts with gel filtration data and could appear surprising as the protein and DNA parts exhibit very different permanent charges. However, protein in SDS−PAGE is expected to be denatured into an extended and rather rigid form and negatively charged by the interacting SDS.[28] SDS-denatured protein and dsDNA have thus some common conformational features that de facto result in identical electrophoretic mobilities for similar masses. In contrast, the contribution to the apparent molecular mass of the ssDNA part was consistently found to be ∼50% larger than that of the dsDNA part for equivalent masses with a lower persistence length of ssDNA compared to that of dsDNA.

The conformation of PDNA-based structures in solution was analyzed using nondenaturing agarose gel electrophoresis (Figure 6). An additive contribution to the apparent size (expressed as base pair equivalents) of PDNA assembly components was observed as described previously with ssDNA, dsDNA, and protein parts contributing to ∼0.6, 1, and 25 bp equivalents, respectively (section 4 of the Supporting Information). The 16.5 kDa protein contribution is close to the 15 kDa value determined by SDS−PAGE, while calibration was performed using dsDNA standards. This feature is the reciprocal of the situation found for DNA calibrated on a protein standard using SDS−PAGE. It suggests that the folded b_5 core has electrophoretic mobility similar to that of dsDNA with the same mass in agarose gels. Likewise, the relative apparent masses of ss- and dsDNA are similar in the two electrophoretic systems. However, analysis of the electrophoretic mobilities of DNA and PDNA polymers evidenced that the contribution of ssDNA to the apparent molecular mass differs in PDNA (1.55−1.78 bp/base) and DNA (0.60−0.69 bp/base) assemblies (section 4 of the Supporting Information). The effect is identical with one or several protein units per construct and suggests that the presence of protein affects the contribution to mobility of linked ssDNA but not of dsDNA (section 4 of the Supporting Information). This phenomenon was not observed during gel filtration where the protein is folded but an electrical field is absent or during SDS−PAGE where the protein domain is unfolded.

Hybridization Properties of Large PDNA-Based Structures. While hybridization properties of defined small PDNA and corresponding DNA structures appeared to be very similar, we questioned the behavior of larger assemblies in which protein content could significantly impact geometry and steric hindrance causing topological restriction to base pairing. The model used was the formation of block copolymers involving regular repeats of two types of PDNAs. When AA′ and BB′ PDNA were mixed with half-complementary tiles (ab′ and ba′), a polymer featuring AA′-BB′ PDNA repeats can be formed. The reaction was first monitored using the hypochromic effect resulting from the hybridization of single-stranded sticky ends. Panels A and B of Figure 7 compare the reaction courses for PDNA−DNA and DNA−DNA polymerization, respectively. Individual rate constants described in Figure 3 were used to simulate the reaction courses using the same modeling approaches[21] for PDNA and DNA assemblies. This model assumes that hybridization rates of large polymer fragments decrease with a power of −0.57 of species length for DNA.[21,29] For PDNA, an equivalent length was

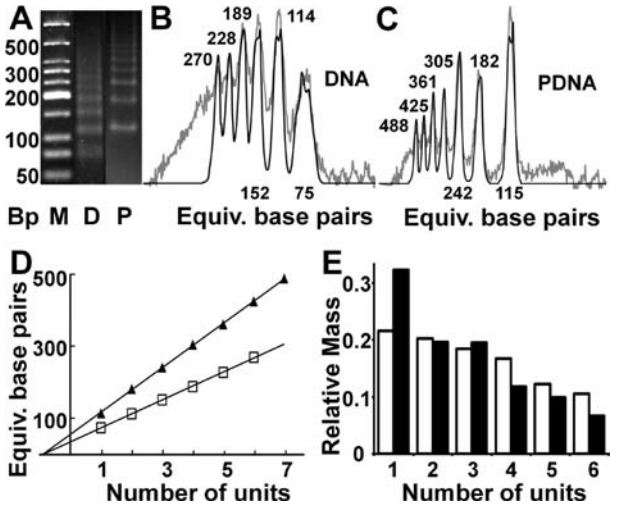

Figure 8. Size distribution of DNA and PDNA copolymers. (A) Agarose gel electrophoresis of DNA and PDNA polymer distribution after polymerization for 10 min of the four reactant tiles at ~1 μM each and quenching with ~1.5 μM terminator tiles (section 6 of the Supporting Information). (B and C) Scans of the experimental gel profiles (gray lines) and their deconvolution (black lines) for DNA and PDNA, respectively. (D) Plot of the dsDNA equivalent size of PDNA (▲) and DNA (□) polymers vs the number of units. Slopes correspond to 67 and 40.5 bp/unit for PDNA and DNA, respectively. (E) Quantification as equivalent masses of bands from panels B (white bars) and C (black bars) as a function of polymer size. The error in band quantification depends on methods but does not exceed a relative error of 10−15%.

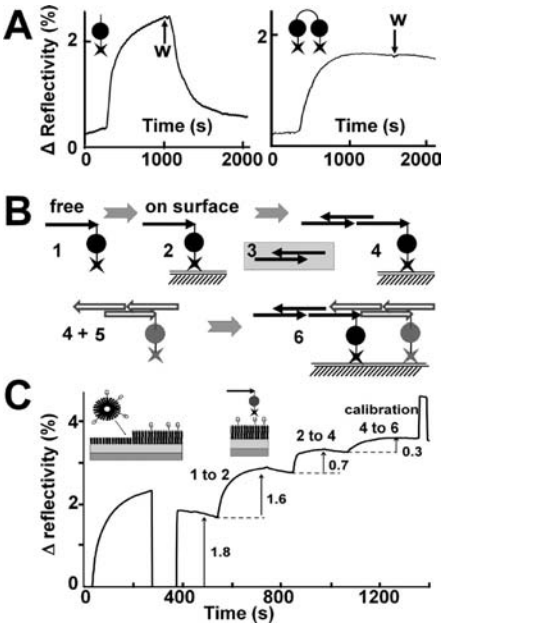

Figure 9. SPR analysis of the interaction of PDNA assemblies and of their b_5 component with phospholipids. (A) Binding kinetics of the b_5 component of PDNAs in the monomeric state (left) or following protein dimerization through a disulfide bond (right). The W label denotes the start of the washing phase. (B) Step by step self-assembly of PDNAs on a membrane surface. Free PDNA (1), supported membrane-bound PDNA (2), free DNA−tile dimer (3), coupling product of steps 2 and 3 (4), free hybrid (5) between one PDNA and two DNA tiles, and coupling product of steps 4 and 5 (6). (C) SPR sensorgram corresponding to panel B. The numbers correspond to steps depicted in panel B. The differential reflectivity for each step is indicated by the arrows.

calculated as the sum of the real size of the nucleic part and of a contribution of the protein equivalent to 10 dsDNA bases per protein unit. This value was set to be identical to the protein contribution evidenced in gel filtration experiments. The figure illustrates that experimental courses were well-simulated with this same model for DNA- and PDNA-based experiments. This indicates that, for large linear assemblies, no significant additional factor, which could differentiate PDNA from DNA, needs to be taken into account to describe the global behavior.

For further comparison, the size distribution of polymer species was analyzed by gel electrophoresis and profiles were deconvoluted as previously described[21] to calculate the electrophoretic mobility and for quantification (Figure 8A−C). However, in this case, terminator tiles (namely, am, Ma′, bm, and Mb′) able to cap the free ssDNA parts (A, A′, B, and B′, respectively) of polymer extremities have to be added to quench the polymerization and allow gel electrophoresis analysis. The quenching process was incorporated into the simulation model (sections 5 and 6 of the Supporting Information).[21] For DNA and PDNA polymers, the apparent size was found to be proportional to the number of repeats with an additional contribution of single-stranded quencher ends (Figure 8D). As expected, the size step between bands appeared to be significantly larger for PDNA (~65 bp equivalent) than for DNA (40 bp equivalent) because of the contribution of protein domains to PDNA. However, relative distributions of polymer concentration obtained in DNA−DNA and PDNA−DNA experiments were found to be similar (Figure 8E) and consistent with simulations. At this point, we can conclude that DNA and PDNA recognition in solution is fully driven by the nucleic acid part with almost undetectable interference of the protein domain, except for hydrodynamic effects associated with size differences.

Self-Assembly of PDNAs on Vesicles and Supported Membranes. The protein domain of PDNA carries a C-terminal His_4 tag that can form a complex with nickel, cobalt, or copper divalent ions, mediating association through a surface and thus constraining self-assembly mechanisms. While the affinity of short His tag sequences for the nickel-nitriloacetate linker is sufficient for tight binding on affinity columns, the lifetime of such a complex is fairly short, generally a few seconds.[14,30−32] Binding of the PDNA protein part to the phospholipid bilayer supplemented with DOGS-Ni was evaluated using 100 nm calibrated liposomes. The protein and phospholipid saturation curves are illustrated in section 7 of the Supporting Information. Half-saturation for the monomeric b_5 domain used in PDNA construction was found to be ~5 μM, and the binding capacity was clearly proportional to the total phospholipid concentration, leading to an average binding surface of ~50 nm^2 for a single b_5 unit.

Assembly of PDNA on a membrane was further investigated using a DOGS-NTA-Ni-doped hemimembrane supported on gold, which allows monitoring of assembly by surface plasmon resonance (SPR). Figure 9A illustrates that the binding of the protein part of PDNA to the supported membrane is efficient but rapidly reversible with an affinity in the micromolar range, confirming the previous observation with vesicles. However, when the protein parts form a dimeric structure, a stable association is observed with a dissociation rate hardly measurable (hour

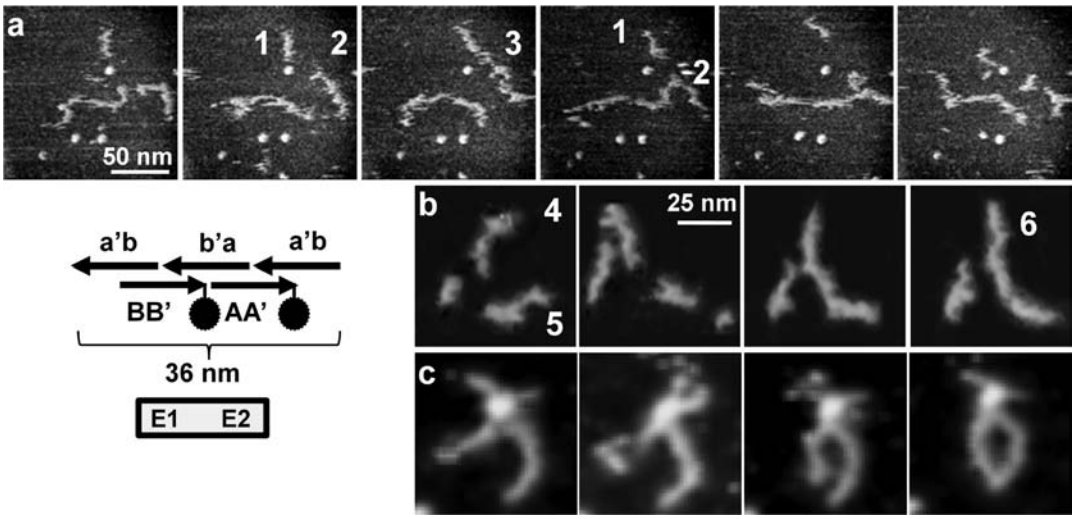

Figure 10. High-speed AFM analysis of the dynamics of PDNA structures. (a and b) Dynamic AFM imaging (10 frames/s) evidencing the formation of transient concatemers (species 1 and 2 giving 3 and 4 and 5 giving 6) of the construct described in the scheme. (c) Dynamics of two constructs anchored onto a nanoparticle. Images from lane a were untreated, while nonrelevant background noise was removed for the sake of readability in lanes b and c.

range). This is due to a rebinding process in the diffusion limit layer immediately surrounding the surface when at least two linkages exist between the object and the surface. Such a situation typically occurs when two PDNA tiles become linked through hybridization with a cDNA tile. This principle is used in the experiment described in Figure 9B and is illustrated by the SPR sensorgram in Figure 9C. Formation of a supported membrane hemilayer is evidenced by the fusion of DOGS-Ni-supplemented phospholipid vesicles onto alkane thiol-modified gold. Binding of PDNA to the Ni-NTA lipid head (steps 1 and 2) appeared to be efficient, and the trace clearly illustrates that the bound PDNA can be easily hybridized (steps 2−4) with the complementary extremity of a DNA−DNA half-hybrid that acts as a linker between two PDNAs (steps 4−6) finally stabilizing the whole construct on the surface. However, the addition of mass following hybridization appeared to be significantly below the expected stoichiometry, and the defect increased with a larger number of assembly steps. This could be explained by the fact that binding of additional PDNA tiles to the surface is sterically impaired by tiles already associated on the surface. Reducing the effect would need careful control of surface saturation during assembly initiation. However, this would suppose working under conditions far from surface saturation, which would in turn dramatically reduce the magnitude of the SPR signal, making multiple-step assemblies difficult to monitor.

AFM Analysis of the Dynamics and Interactions of Short PDNA Assemblies. A construct encompassing two PDNA tiles (scheme in Figure 10) was prepared and adsorbed onto freshly cleaved mica in the presence of magnesium. High-speed AFM imaging evidenced lateral mobility with large changes in position (tens of a nanometer) and shapes of objects within the 100 ms time lapse between two scans (Figure 10a). An overlay of consecutive images separated by a 100 ms time lapse on a 300 nm × 300 nm scale illustrates the presence in the population of lower-mobility segments, while other regions of the molecules were rapidly laterally diffusing (image sequence available in section 9 of the Supporting Information). Surface defects, such as nanoparticles a few nanometers in diameter, can very efficiently trap diffusing PDNA structures, anchoring them onto a specific point of the surface when the remaining parts are still stochastically moving around leading to tweezerslike structures (Figure 10a, lane 3). Interestingly, two or more constructs can frequently interact together, resulting in the apparent fusion of objects to give unstable longer species (Figure 10a, lane 2). The events appeared to be mostly conservative with respect to length

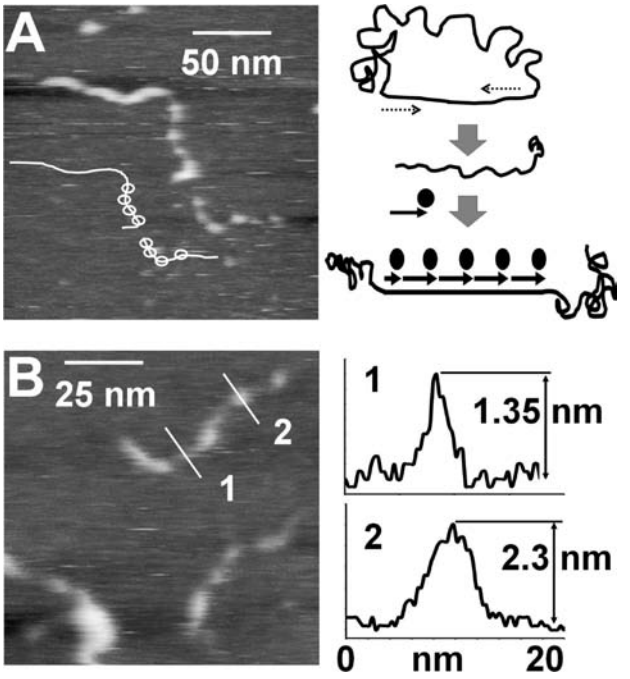

Figure 11. Structures of immobilized PDNA assemblies. (A) High-speed AFM imaging (raw data) of two assemblies and a schematic description of the image. (B) Three other objects are illustrated at a higher resolution (raw data), and section profiles of the DNA (1) and protein (2) parts are given. Constructs encompassing five PDNA units hybridized to a large single-stranded DNA were prepared as outlined in the right part of the scheme (see section 8 of the Supporting Information for details).

(daughter species has a length close to the sum of the parents), a feature expected for classical base pairing. However, the construct exhibits single-stranded extremities that are not complementary and cannot give rise to a stable duplex. Consistently, the species appeared to be monodisperse in gel electrophoresis. However, formation during gel filtration of shoulder peaks with molecular masses greater than that of the main species suggested weak interactions of construct extremities, consistently with predicted ΔG values of −7.8 (b/b), −7.5 (a′/a′), and −3.6 kcal/mol (b/a′) for the formation of intermolecular hydrogen bonds in a salty solution (section 10 of the Supporting Information). Such energies are sufficient to create short life (few seconds) but easily observable concatemers under dynamic AFM conditions. Statistical analysis of the length distribution of the concatemer (one to eight repeats) was performed on 106 objects, and the resulting profiles were found to be consistent with a model in which single-stranded extremities of the species interact together on the surface with ΔG values of −1.8 and −0.8 kcal/mol, respectively (section 11 of the Supporting Information). The observation was found to be dentical upon imaging of DNA and PDNA of identical nucleotidic structures. As a control, concatenation events were never observed with a dsDNA (513 bp) that does not include single-stranded extremities.

Structural Analysis of Large PDNA Structures. It could appear surprising that the protein domains were hardly visible under previously used experimental conditions. However, the linker attaching DNA and protein domains in PDNA is sufficiently flexible to allow fairly different dynamics for the two components. Under previously used conditions, the scanning rate probably remained too slow compared to the dynamics of the protein domain to capture the 2 nm globular structural details. To limit the overall dynamics, larger objects were designed, including a 513-base single-stranded DNA scaffold on the middle of which up to five PDNA tiles can be hybridized (Figure 11A). As previously reported,[33] ssDNA segments generate tightly folded regions strongly interacting with the substrate. Under such conditions, a string of protein domains (thickness of 2.3 nm) regularly placed (10−15 nm) along the DNA filament (thickness of 1.35 nm) can clearly be imaged by high-speed AFM. Control involving dsDNA with same sequence illustrates a filament with a homogeneous thickness of ∼1.3 nm (not shown). This illustrates that PDNA building blocks can be easily used to decorate a DNA scaffold.

DISCUSSION

Covalent coupling of protein and DNA domains into a single building block is a versatile alternative to noncovalent complexes for building proteo−nucleic structures.[34−37] Different PDNAs encompassing a cytochrome b_5 protein domain linked to a ssDNA were designed, synthesized, and purified to homogeneity. The C-terminal His tag on the protein part offers a way to create more specific and localized interactions with substrates than DNA alone that nonspecifically interacts with ion-doped material like Ni^{2+}-treated mica.[33] The requirement to build PDNAs is the availability of a unique grafting position in the protein sequence. Use of a surface cysteine residue is a method of choice, but alternate solutions include the use of a rare or non-natural amino acid like a selenocysteine or an *N*-acetylphenylalanine,[38] which can be selectively grafted using adapted chemistry. A generic approach could also involve grafting of the surface cysteine opposite the CDR3 binding region onto small (14 kDa) VHH single-chain antibodies. Such antibodies could be used in turn to form a noncovalent high-affinity complex with any protein of interest.[39]

This work specifically aimed to compare the physicochemical and self-assembly properties of DNA and PDNA in different environments. Defining and controlling parameters implied in self-assembly mechanisms of such hybrid synthetic structures will permit us not only to use them as modular building blocks for multifunctional nanostructures but also to improve our understanding of properties of natural nucleo−proteic complexes. A contribution of the protein domain to the hydrodynamic properties of PDNAs was clearly evidenced by gel filtration and electrophoresis in SDS−PAGE and nondenaturing agarose gels. In all cases, the protein contribution appeared to be additive with respect to the one of the nucleic acid parts provided to use an equivalent DNA length that differs depending on the analysis method considered. During gel filtration, the 13 kDa protein domain migrates like a solvated dsDNA of 6.6 kDa. This contrasts with an equivalent mass of 16−17 kDa observed in nondenaturing agarose gel electrophoresis calibrated using dsDNA. This last value is consistent with a mass of 15 kDa for the protein domain in SDS−PAGE following calibration with proteins. This is in agreement with a common extended conformation of the reference molecules (DNA and protein) used for calibration in an agarose gel and during SDS−PAGE, respectively. During HPLC gel filtration, hydrodynamic constraints resulting from flow are expected to favor a rather extended conformation of the DNA used for size calibration. In contrast, the protein domain remains globular, which tends to decrease its relative apparent size. Reciprocally, during agarose gel electrophoresis, the much lower charge of the protein domain compared to that of DNA decreases the relative protein mobility, thus compensating for the more compact structure of the protein domain. The strictly additive contributions of double-stranded nucleic and protein domains to hydrodynamic behaviors for a variety of PDNA assemblies suggested that conformational interactions between the two components are likely weak under all tested conditions and do not affect their individual shapes.

In contrast to pure nucleic structures that are generally assembled under conditions close to the melting temperature to avoid formation of dead-end parasitic hybrids,[6,20] proteo−nucleic structures must be preferentially assembled in a kinetically controlled manner,[40−42] far below the melting temperature to prevent thermal denaturation of protein domains. Hybridization rates are thus critical parameters of PDNAs that were analyzed by monitoring hypochromic effects associated with hybridization in rapid-mixing experiments. While the length of hybridizing segments is homogeneous for all considered tiles, observed hybridization rates significantly differ over a 4-fold range. This dispersion does not simply correlate with obvious sequence features and for the same hybridizing segment depends on the nature of flanking regions. The reason is likely related to the formation of possible secondary structures of ssDNA parts, some of them having predicted stability sufficiently large (8−14 kcal/mol) to significantly interfere. In contrast, comparison of the hybridization rates of DNA and corresponding PDNA does not evidence a significant effect of the protein domain when grafted on the oligonucleotide 3′-end. However, a moderate decrease in hybridization rates was observed for internal grafting proximal to the hybridizing segment. In this case, base modification by the linker and protein presence exhibited cumulative effects. When hybridization between larger polymers was considered, no additional effect

was observed compared to the situation with short building blocks, suggesting the absence of long-range interaction between PDNAs when formation of linear polymer was considered.

Altogether, our results indicate that DNA and PDNA tiles are mostly equivalent at the level of their hybridization properties and that PDNA can easily substitute for DNA in most DNA-based supramolecular assemblies, provided that the folding can sterically accommodate the protein parts. A potential limitation remains the thermal stability of the protein domain under the fairly high-temperature conditions required to prevent formation of a dead-end product by spurious hybridization.[6,43] However, analysis of the thermal stability of our constructs evidenced that linkage to the nucleic acid part has no significant detrimental influence on protein stability leading, in our case, to constructs stable up to 55 °C, a value that is compatible with current hybridization procedures. Thus, any reasonably stable protein can be substituted for our cytochrome b_5 domain, including recognition protein-like single-chain antibodies of the VHH family. In the case of very unstable protein domains, an alternative assembly procedure under kinetic control remains possible using, for example, DNA hairpin or loop motifs as programmable units.[41,44] A combination of kinetic and thermodynamic control can also be used to direct self-assembly processes by engineering intra- and interparticle DNA hybridization.[5,45]

PDNAs potentially offer many advantages when self-assemblies on surfaces are targeted. The protein domain can be used, for example, for the recognition of surface chemical or physical features using material specific affinity domains.[46] This also applies to redox active proteins (like cytochrome b_5), for which electron transfer properties at surface interfaces can be modulated by the conformation of the DNA scaffold, thus constituting biosensors. Analysis by rapid-scan AFM clearly evidenced lateral diffusion properties of PDNA assemblies on surfaces. SPR experiments demonstrated that such structures can be sequentially built by stepwise extension from a matrix-bound primer[19] or by self-organization of tiles attached to membranes (this work). However, the progressive yield decrease during constructions resulted either from surface saturation or, as shown by HS-AFM, from the presence of surface defects able to anchor laterally diffusing PDNA molecules. A possible turnaround to build defect-free surfaces would be the use of phospholipid vesicles as assembly frame. This work illustrates that the fairly limited stability of the attachment of PDNA to NTA-modified phospholipids is a limitation, which could be somewhat overcome when several protein modules are bound to the same vesicles. Alternatively, multiple-head NTA constructs can be used to increase affinity.[13,14,30−32] However, the fairly rigid structure of large PDNA−DNA supramolecular assemblies was found to conflict with the strong curvature of small (50−100 nm) vesicles and more importantly can reciprocally induce an unwanted phase transition of the support phospholipid structures, leading to uncontrolled organization.

Formation of transient end-to-end concatemers was evidenced by HS-AFM upon lateral diffusion of PDNA assemblies on the surface. Similar behavior was observed when DNA was substituted with PDNA under the same experimental conditions. The phenomenon was clearly related to the presence of ssDNA extensions on constructs that can form short stretches of paired bases (four to six bases) and was not observed with fully dsDNA. Interaction energies deduced from modeling of the concatemer distribution appeared to be ∼4-fold smaller than calculated values in solution, which is consistent with the much lower salt concentration used under AFM imaging conditions. Formation of these transient structures while they are reversible competes with true hybrid formation during assemblies slowing the process on surfaces. The phenomena could be enhanced by the presence of surface defects that efficiently trap diffusing PDNA assemblies and by the observed topological cluttering on the surface (AFM and SPR experiments). These three effects combine in reducing the self-assembly efficiency of surface-bound objects.

While high-speed AFM opens a new dimension for the analysis at the single-molecule level of nucleic acid assemblies, difficulties could arise from the relative values of scan rate and object dynamics. Our data evidence that the small b_5 domain (13 kDa) was not visible when attached to highly dynamic structures, whereas it was clearly imaged when bound to much larger DNA exhibiting a lower mobility. Thus, it seems that some compromise has to be found between resolution and dynamic analyses, particularly when very small objects are involved. While dynamic AFM observation of a fairly small protein (calmodulin, 17 kDa) bound to a streptavidin crystal was recently reported,[47] our results go further than previous reports[48] by visualizing for the first time a small protein domain (13 kDa) linked to isolated DNA molecules in solution.

■ ASSOCIATED CONTENT

Supporting Information. DNA tile sequences and matches (section 1), schematic for the synthesis of protein−DNA (PDNA) structures (section 2), synthesis of PDNA structures (section 3), contribution of building blocks to the apparent size in gel filtration and electrophoresis (section 4), experimental and simulated profiles for PDNA copolymers (section 5), parameter sets for simulations (section 6), cytochrome b_5 and phospholipid concentration dependence for the formation of protein−lipid complexes (section 7), purification of the DNA and PDNA assemblies described here (section 8), high-speed AFM image sequences (section 9), thermodynamic parameters (section 10), and statistical analysis of the formation of concatemers (section 11). This material is available free of charge via the Internet at http://pubs.acs.org.

■ AUTHOR INFORMATION

Corresponding Author

*Telephone: +33 567048806. Fax: +33 561559400. E-mail: denis.pompon@insa-toulouse.fr. Present address: LISBP/INSA, UMR INSA/CNRS 5504, 135 Avenue de Rangueil, 31077 Toulouse cedex 4, France.

Funding Sources

We acknowledge the financial support of this work by Grants ANR-05-NANO-021-04, ANR-08-NANO-010-01, and ANR-08-PCV08_343399 from the Programme Nanosciences et Nanotechnologies (PNANO) and Programme interdisciplinaire en physique et chimie du vivant (PCV) actions of the National Research Agency (ANR), France.

■ ACKNOWLEDGMENT

We thank Dr. Takayuki Uchihashi (Physics Laboratory, Kanazawa University), Drs. Ignacio Casuso and Simon Sheuring (Institute Curie, Paris, France), Dr. Pierre-Emmanuel Milhiet

(CBS, Montpellier, France) for technical support, and Dr. Gilles Truan for proofreading the manuscript.

REFERENCES

(1) Brucale, M., Zuccheri, G., and Samori, B. (2006) Mastering the complexity of DNA nanostructures. *Trends Biotechnol. 24*, 235–243.

(2) He, Y., Tian, Y., Chen, Y., Deng, Z., Ribbe, A. E., and Mao, C. (2005) Sequence Symmetry as a Tool for Designing DNA Nanostructures. *Angew. Chem., Int. Ed. 44*, 6694–6696.

(3) Ke, Y., Liu, Y., Zhang, J., and Yan, H. (2006) A study of DNA tube formation mechanisms using 4-, 8-, and 12-helix DNA nanostructures. *J. Am. Chem. Soc. 128*, 4414–4421.

(4) Liu, Y., Ke, Y., and Yan, H. (2005) Self-assembly of symmetric finite-size DNA nanoarrays. *J. Am. Chem. Soc. 127*, 17140–17141.

(5) Rotello, V. M. (2009) DNA nanotechnology: Hot and sticky or cold and aloof. *Nat. Mater. 8*, 539–540.

(6) Rothemund, P. W. (2006) Folding DNA to create nanoscale shapes and patterns. *Nature 440*, 297–302.

(7) Seeman, N. C. (1998) DNA nanotechnology: Novel DNA constructions. *Annu. Rev. Biophys. Biomol. Struct. 27*, 225–248.

(8) Teller, C., and Willner, I. (2010) Organizing protein-DNA hybrids as nanostructures with programmed functionalities. *Trends Biotechnol. 28*, 619–628.

(9) Yan, H., Park, S. H., Finkelstein, G., Reif, J. H., and LaBean, T. H. (2003) DNA-templated self-assembly of protein arrays and highly conductive nanowires. *Science 301*, 1882–1884.

(10) Park, S. H., Pistol, C., Ahn, S. J., Reif, J. H., Lebeck, A. R., Dwyer, C., and LaBean, T. H. (2005) Finite-Size, Fully Addressable DNA Tile Lattices Formed by Hierarchical Assembly Procedures. *Angew. Chem., Int. Ed. 45*, 735–739.

(11) Beyer, S., Nickels, P., and Simmel, F. C. (2005) Periodic DNA nanotemplates synthesized by rolling circle amplification. *Nano Lett. 5*, 719–722.

(12) Liu, Y., Lin, C., Li, H., and Yan, H. (2005) Aptamer-directed self-assembly of protein arrays on a DNA nanostructure. *Angew. Chem., Int. Ed. 44*, 4333–4338.

(13) Conti, M., Falini, G., and Samori, B. (2000) How Strong Is the Coordination Bond between a Histidine Tag and Ni - Nitrilotriacetate? An Experiment of Mechanochemistry on Single Molecules. *Angew. Chem., Int. Ed. 39*, 215–218.

(14) Lata, S., Reichel, A., Brock, R., Tampe, R., and Piehler, J. (2005) High-affinity adaptors for switchable recognition of histidine-tagged proteins. *J. Am. Chem. Soc. 127*, 10205–10215.

(15) Boireau, W., Bombard, S., Sari, M. A., and Pompon, D. (2002) Bioengineering and characterization of DNA-protein assemblies floating on supported membranes. *Biotechnol. Bioeng. 77*, 225–231.

(16) Boireau, W., Duncan, A. C., and Pompon, D. (2005) Bioengineering and characterization of DNA-protein assemblies floating on supported membranes. *Methods Mol. Biol. 300*, 349–368.

(17) Boireau, W., Zeeh, J. C., Puig, P. E., and Pompon, D. (2005) Unique supramolecular assembly of a redox protein with nucleic acids onto hybrid bilayer: Towards a dynamic DNA chip. *Biosens. Bioelectron. 20*, 1631–1637.

(18) Berthier, A., Elie-Caille, C., Lesniewska, E., Delage-Mourroux, R., and Boireau, W. (2008) Nanobioengineering and Characterization of a Novel Estrogen Receptor Biosensor. *Sensors 8*, 4413–4428.

(19) Pompon, D., and Laisne, A. (2007) PDNA as building blocks for membrane-guided self-assemblies. *Biochem. Soc. Trans. 35*, 495–497.

(20) Rothemund, P. W., Papadakis, N., and Winfree, E. (2004) Algorithmic self-assembly of DNA Sierpinski triangles. *PLoS Biol. 2*, e424.

(21) Laisne, A., Lesniewska, E., and Pompon, D. (2011) Design and experimental validation of a generic model for combinatorial assembly of DNA tiles into 1D-structures. *Biochim. Biophys. Acta 1810*, 603–611.

(22) Ando, T., Kodera, N., Takai, E., Maruyama, D., Saito, K., and Toda, A. (2001) A high-speed atomic force microscope for studying biological macromolecules. *Proc. Natl. Acad. Sci. U.S.A. 98*, 12468–12472.

(23) Ando, T., Uchihashi, T., Kodera, N., Yamamoto, D., Miyagi, A., Taniguchi, M., and Yamashita, H. (2008) High-speed AFM and nano-visualization of biomolecular processes. *Pfluegers Arch. 456*, 211–225.

(24) Ando, T., Uchihashi, T., Kodera, N., Yamamoto, D., Taniguchi, M., Miyagi, A., and Yamashita, H. (2007) High-speed atomic force microscopy for observing dynamic biomolecular processes. *J. Mol. Recognit. 20*, 448–458.

(25) Kitazawa, M., Shiotani, K., and Toda, A. (2003) Batch Fabrication of Sharpened Silicon Nitride Tips. *Jpn. J. Appl. Phys. 42*, 4844–4847.

(26) Garcia De La Torre, J., Huertas, M. L., and Carrasco, B. (2000) Calculation of hydrodynamic properties of globular proteins from their atomic-level structure. *Biophys. J. 78*, 719–730.

(27) Robert, C. H. (1995) Estimating friction coefficients of mixed globular/chain molecules, such as protein/DNA complexes. *Biophys. J. 69*, 840–848.

(28) Reynolds, J. A., and Tanford, C. (1970) The gross conformation of protein-sodium dodecyl sulfate complexes. *J. Biol. Chem. 245*, 5161–5165.

(29) Sorlie, S. S., and Pecora, R. (1990) A dynamic light scattering study of four DNA restriction fragments. *Macromolecules 23*, 487–497.

(30) Huang, Z., Hwang, P., Watson, D. S., Cao, L., and Szoka, F. C., Jr. (2009) Tris-nitrilotriacetic acids of subnanomolar affinity toward hexahistidine tagged molecules. *Bioconjugate Chem. 20*, 1667–1672.

(31) Huang, Z., Park, J. I., Watson, D. S., Hwang, P., and Szoka, F. C., Jr. (2006) Facile synthesis of multivalent nitrilotriacetic acid (NTA) and NTA conjugates for analytical and drug delivery applications. *Bioconjugate Chem. 17*, 1592–1600.

(32) van Broekhoven, C. L., and Altin, J. G. (2005) The novel chelator lipid 3-(nitrilotriacetic acid)-ditetradecylamine (NTA(3)-DTDA) promotes stable binding of His-tagged proteins to liposomal membranes: Potent anti-tumor responses induced by simultaneously targeting antigen, cytokine and costimulatory signals to T cells. *Biochim. Biophys. Acta 1716*, 104–116.

(33) Maeda, Y., Matsumoto, T., and Kawai, T. (1999) Observation of single- and double-stranded DNA using non-contact atomic force microscopy. *Appl. Surf. Sci. 140*, 400–405.

(34) Endo, M., and Sugiyama, H. (2009) Chemical approaches to DNA nanotechnology. *ChemBioChem 10*, 2420–2443.

(35) Niemeyer, C. M. (2001) Semi-synthetic nucleic acid-protein conjugates: Applications in life sciences and nanobiotechnology. *J. Biotechnol. 82*, 47–66.

(36) Niemeyer, C. M. (2007) Functional devices from DNA and proteins. *Nano Today 2*, 42–52.

(37) Niemeyer, C. M. (2010) Semisynthetic DNA-protein conjugates for biosensing and nanofabrication. *Angew. Chem., Int. Ed. 49*, 1200–1216.

(38) Liu, C. C., and Schultz, P. G. (2010) Adding new chemistries to the genetic code. *Annu. Rev. Biochem. 79*, 413–444.

(39) Kastelic, D., Frkovic-Grazio, S., Baty, D., Truan, G., Komel, R., and Pompon, D. (2009) A single-step procedure of recombinant library construction for the selection of efficiently produced llama VH binders directed against cancer markers. *J. Immunol. Methods 350*, 54–62.

(40) Lubrich, D., Green, S. J., and Turberfield, A. J. (2009) Kinetically controlled self-assembly of DNA oligomers. *J. Am. Chem. Soc. 131*, 2422–2423.

(41) Shih, W. (2008) Biomolecular assembly: Dynamic DNA. *Nat. Mater. 7*, 98–100.

(42) Wieland, M., Benz, A., Haar, J., Halder, K., and Hartig, J. S. (2010) Small molecule-triggered assembly of DNA nanoarchitectures. *Chem. Commun. 46*, 1866–1868.

(43) Winfree, E., Liu, F., Wenzler, L. A., and Seeman, N. C. (1998) Design and self-assembly of two-dimensional DNA crystals. *Nature 394*, 539–544.

(44) Yin, P., Choi, H. M., Calvert, C. R., and Pierce, N. A. (2008) Programming biomolecular self-assembly pathways. *Nature 451*, 318–322.

(45) Leunissen, M. E., Dreyfus, R., Cheong, F. C., Grier, D. G., Sha, R., Seeman, N. C., and Chaikin, P. M. (2009) Switchable self-protected attractions in DNA-functionalized colloids. *Nat. Mater. 8*, 590–595.

(46) Seeman, N. C. (2002) Key experimental approaches in DNA nanotechnology. *Current Protocols in Nucleic Acid Chemistry*, Chapter 12, Unit 12, p 1, Wiley, New York.

(47) Yamamoto, D., Nagura, N., Omote, S., Taniguchi, M., and Ando, T. (2009) Streptavidin 2D crystal substrates for visualizing biomolecular processes by atomic force microscopy. *Biophys. J. 97*, 2358–2367.

(48) Lyubchenko, Y. L., and Shlyakhtenko, L. S. (2009) AFM for analysis of structure and dynamics of DNA and protein-DNA complexes. *Methods 47*, 206–213.

Supporting Information for:

Self-assembly properties and dynamic of synthetic proteo-nucleic building blocks in solution and on surfaces

Aude LAISNE[†], Maxime EWALD[‡], Toshio ANDO[§], Eric LESNIEWSKA[‡], and Denis POMPON[†*]

[†] Centre de Génétique Moléculaire. CNRS.UPR3404, Avenue de la Terrasse, F91190 Gif-sur-Yvette, France.

[‡] Institut Carnot Bourgogne UMR CNRS 5209, University of Bourgogne, F-21078 Dijon, France.

[§] Department of Physics, Kanazawa University, Kakuma-machi, Kanazawa 920-1192, Japan.

***Corresponding Author**: Denis POMPON

*To whom correspondence should be addressed. Tel: +33 567048806; Fax: +33 561559400; Email: denis.pompon@insa-toulouse.fr

Present address:

LISBP/INSA, UMR INSA/CNRS 5504, 135 Avenue de Rangueil, 31077 Toulouse cedex 4, France.

Section 1. DNA tile sequences and matches.

Tiles	Sequence (5'- - 3')	Bases
A---A'	CCGTAGGGTCTCCATTTTGA---AGCGAAGTCACACTGTACA	39
B---B'	GTCCATATGCAAGTCAGCGT---CAGTGTACAGTCACGTCAG	39
a---b'	TCAAAATGGAGACCCTACGG---CTGACGTGACTGTACACTG	39
b---a'	ACGCTGACTTGCATATGGAC---TGTACAGTGTGACTTCGCT	39
a---m	TCAAAATGGAGACCCTACGG---GTAAAACGACGGCCAG	36
b---m	ACGCTGACTTGCATATGGAC---GTAAAACGACGGCCAG	36
M---a'	CAGGAAACAGCTATGAC---TGTACAGTGTGACTTCGCT	36
M---b'	CAGGAAACAGCTATGAC---CTGACGTGACTGTACACTG	36

Matching tile moieties are 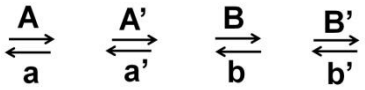

BB' sequence was synthetized in three versions: without, with a 3' amino-linker and with an internally amino-linker coupled thymidine base (underlined). In the case of the AA' sequence, only the unmodified and 3' amino-linker versions were used. The amino-linker modifications were used for protein derivatization in PDNAs.

Section 2. Schematic for the synthesis of protein-DNA (PDNA) structures.

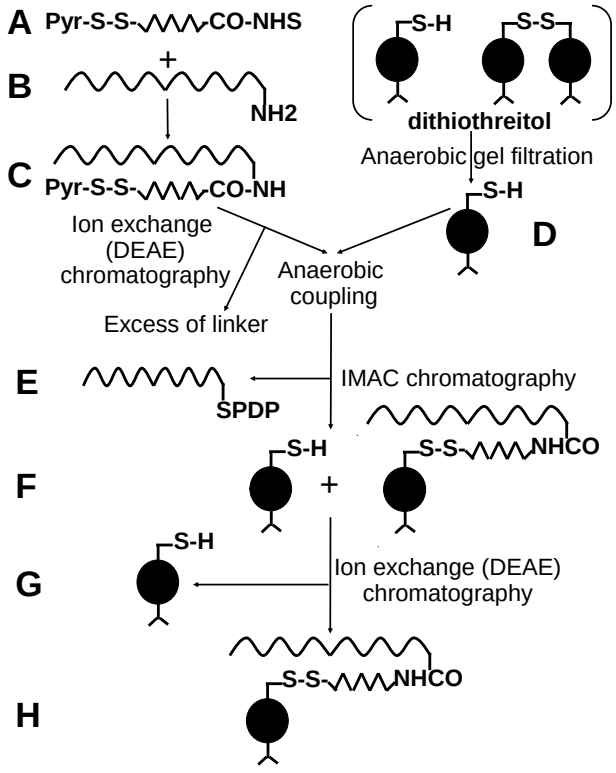

Section 3. Synthesis of protein-DNA (PDNA) structures.

Genetic Engineering of Cytochrome b5: A human microsomal cytochrome b5 cDNA (GenBank accession number L39792) has been previously engineered to substitute the 26 C-terminal residues constituting the hydrophobic membrane anchor tail by the -NGHHHH-COOH sequence (16) encoding an His-tag. Engineered cDNA was subcloned into pCR®2.1-TOPO® cloning (Invitrogen) and the *Sph*I-*Bam*H1 fragment was ligated into the corresponding sites o*f* digested pUHE25-2 expression vector giving pUHE-[Hb5-(HIS_4)C-term]. This construction includes an additional Leu codon inserted immediately after the normal Met initiation codon. Site directed mutagenesis of plasmid was performed with QuickChange II XL Site-Directed Mutagenesis kit (Stratagene) to introduce a Ser-24-Cys aa-sequence change. This brought a unique solvent accessible thiol-containing residue at the surface of the b5 globular domain. Mutation has been checked by sequencing resulting in the pUHE-[Hb5-24C-(HIS_4) C-term] expression plasmid.

Protein expression and purification: XL1-Blue E. *coli* cells transformed by pUHE-[Hb5-24C-(HIS_4)C-term] were transferred in 50 mL liquid Luria-Bertani containing 100 µg/mL ampicillin and grown over-night at 37°C, 160 rpm. 45 mL of this culture were transferred into 1 L of Terrific Broth (TB) containing 100 µg/mL ampicillin and bacteria were grown at 28°C for 24 hrs. 1 mL aliquotes of the culture were stored at -80°C in 1X Hogness. Protein expression was induced with 0.5 mM IPTG and 0.5 mM δ-ALA added with 500 mL of TB and occured at 28°C for 24 hrs with shaking at 160 rpm. Cells were harvested after 10 minutes 8500 x g centrifugation at 4°C, washed 2 times with 50 mL 20 mM Na/K phosphate, 0.5 M NaCl, pH 6.5 in the presence of 1 mM PMSF, and suspended into the same buffer with anti-protease cocktail. Cells lysis was performed by repeated sonication following treatment with 1.25 g/L lysozyme , 50 mg/L ribonuclease A and 50 mg/L DNAse I. After removal of cell debris by centrifugation at 18500 g for 10 min, the supernatant was applied onto a 1.5 x 6 cm column of imminodiacetate immobilised on agarose (Sigma) equilibrated successively with 0.05 M $NiCl_2$ in 0.1 M KAc, 0.4 M KCl adjusted to pH4.5, with HCl, washed with the same buffer without $NiCl_2$ and finally equilibrated with 50 mM Na/K phosphate buffer pH 7.4 (buffer A). For elution, column was washed with buffer A containing increasing NaCl concentrations (0.1 M to 0.5 M) until OD_{280} of the eluate was lower than 0.3. The protein was eluted with 30 mM L-histidine solution in buffer A containing 1 mM PMSF. 5 mM EDTA was added to fractions containing the protein before loading onto a DEAE-Sephacel column (1.5 x 9 cm) equilibrated with buffer A. The column was washed with buffer A supplemented

with 0.1 M NaCl. The protein was eluted with buffer A containing 0.35 M NaCl. Fractions were pooled and dialysed against 1 L of 20 mM Na/K phosphate, 1 mM DTT pH 6.5. Eluate was concentrated using a Vivaspin 10000 MWCO device (Vivascience) before loading on a gel filtration column (Superdex 75 prep grade Amersham Biosciences) 1.6 x 50 cm equilibrated with 20 mM Na/K phosphate pH 6.5 and eluted at 2 ml/min. Concentration of the purified protein was determined by spectrophotometry using ε_{412nm}=118 $mM^{-1}.cm^{-1}$.

Linker coupling to ss-DNA: the SPDP reagents (Pierce) are heterobifunctionnal cross-linkers (SI Section 2A). Succinimidyl 6-[3'-(2-pyridyldithio) propionamido]hexanoate (LC-SPDP) is a 15.6 Å long spacer arm which can form, on one side an amid bond with the 3'-amino-modified oligonucleotide and, on the other side a disulfide bond with the engineered protein : Hb5-24C-(His_4)Cterm. Poorly soluble in aqueous buffers, LC-SPDP was first dissolved in DMSO (90 mM) before all dilution. The 39 mers 3'-amino-modified ss-DNA (SI Section 2B) were coupled to the bifunctional linker in 50 mM Na/K phosphate buffer pH 8, using 15 mM LC-SPDP for a DNA concentration ranging between 50 µM to 100 µM. The reaction occurred at room temperature. The coupling efficiency was checked by ion-pairing reverse phase chromatography on a Waters XTerra MS C18 column (3.5 µM, 4.6 x 100 mm) equilibrated with 0.1 M triethylamonium acetate pH 7.4 in water and eluted at 1 mL/min using a linear gradient between the aqueous buffer and acetonitrile (0 to 21.4% by vol. in 10 min). Coupled ssDNA (SI Section 2C) were purified from excess of reagent and of hydrolysis subproducts by chloroform extractions prior loading onto an 0.6 x 2 cm anion exchange column (DEAE Sephacel) equilibrated with 50 mM Na/K phosphate pH 7.4 (buffer A). After washing with 0.25 M NaCl in buffer A, DNA was eluted with 1 M NaCl in buffer A. DNAs were desalted against water using Float-A-Lyzer (Fisher) ∅5 mm, MWCO 3,5 K and concentrated by speed vacuum without heating (concentrator 5301, Eppendorf). Concentrations of coupled oligonucleotides were calculated from their absorption spectra and were stored at -20 °C.

Hb5-24C($HIS)_4$ coupling with LC-SPDP-DNA: To prevent a high level of spontaneous dimerisation of Hb5-24C($HIS)_4$, the protein was reduced and the monomer separated from DTT excess by gel filtration on G25 sephadex column equilibrated in 10 mM Tris-HCl pH 8 1mM EDTA under anaerobic conditions (SI Section 2D). LC-SPDP-oligonucleotides were coupled for 24 h at room temperature with 1.5 molar excess of reduced engineered b5 in a hermetic flask filled with argon. Coupling products were analyzed by ion pairing reverse phase HPLC.

Protein-DNA complex purification: Combined chromatographies were used to separate the complex from non-coupled DNA and non-coupled engineered b5. The reaction mixtures were loaded separately onto a 0.5 x 1.5 cm nickel chelate column equilibrated with buffer A. Column was washed with buffer A to remove uncoupled oligonucleotides (SI Section 2E) and pyridine-thiol subproducts until A_{260} absorbance was no more detectable. The his-tagged proteins were eluted by a solution of 30 mM histidine in buffer A. DNA-coupled and non-coupled protein fractions (SI Section 2F) were pooled based on the 413 nm absorption spectra and were treated with 5 mM EDTA in order to disrupt potential nickel-proteine complexes. Fractions were applied onto a 0.5 x 3 cm DE52 anion exchange column equilibrated with buffer A. Following a wash step with 0.35 M NaCl in buffer A to elute protein which is not coupled to oligonucleotide (SI Section 2G), the PDNA complex (H) was finally eluted with 1 M NaCl in Buffer A. The concentrations of PDNA complexes were determined by spectrophotometry at 260 and 413 nm and the purity checked by reverse phase HPLC for chemical contaminants and by reducing and non-reducing SDS-PAGE gels for protein contaminants. Both controls demonstrated the absence of any detectable DNA, protein or chemical contamination.

Section 4. Contribution of building blocks to apparent size in gel filtration and electrophoresis.

Methods	Unit	ss-DNA[1] (base)	ss-DNA[2] (base)	ds-DNA (bp)	Prot (unit)
Gel filtration[a]	kDa (bp)	0.30 (0.50)	0.30 (0.50)	0.70 (1.00)	6.6 (10)
SDS-PAGE[b]	kDa (bp)	0.28 (0.46)	0.28 (0.46)	0.36 (0.51)	15.0 (25)
Agarose gel[a,c]	kDa (bp)	0.36 (0.60)	0.94 (1.55)	0.70 (1.00)	16.5 (25)
Agarose gel[a,d]	kDa (bp)	0.42 (0.69)	1.08 (1.78)	0.73 (1.04)	17.5 (26.5)

Coefficients were calculated from the least square adjustment of calculated to experimental values.

[1]Contribution per base for m and M ss-DNA extensions in protein free constructs

[2]Contribution per base for m and M ss-DNA extensions in protein containing constructs

[a]Calibrated with ds-DNA standards standards assuming an average of 330 Daltons per base.[b]Calibrated with protein standards. [c]Simple assemblies of PDNA and DNA from Figure 6. [d]Data from Figure 8.

Section 5. Experimental and simulated profiles for PDNA copolymers.

Scan (line 1 on the next Figure) of the experimental PDNA gel profile from Figure 8A and its deconvolution using an optimized expansion factor of 1.5 (line 2) and regular resolution for ds-DNA (line 3). Simulations using parameters defined in SI Section 6 with (line 4) or without (line 5) taking into account the SIC value. Regular ds-DNA gel resolution was used for reconstruction.

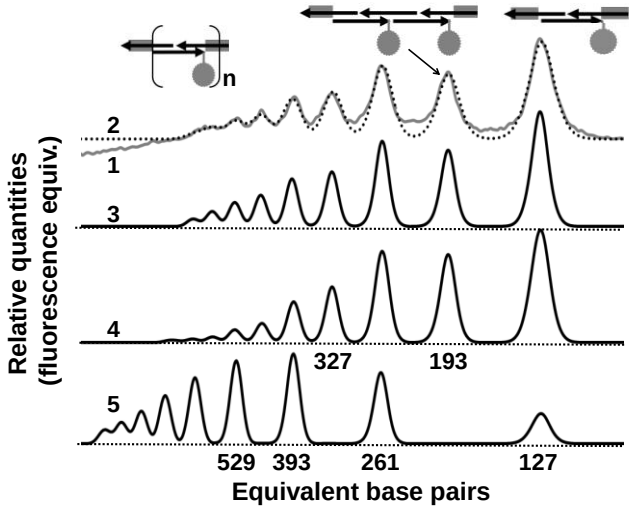

Section 6. Parameter sets for simulations.

All simulations were performed and parameters defined as described in (21) and take into account the environment and length modulation of rate constants (with RL =19 bases), and the J-Factor table PT2 of the same paper. For rapid–mixing experiments (Figure 7) final concentrations used were 0.28 µM of [AA'PDNA-ba'DNA] and [BB'PDNA-ab'DNA] hybrids (panel A) and 0.35µM of [AA'-ba'DNA] and [BB'-ab'DNA] hybrids (panel B). For simulation of agarose gel profile in SI Section 5, concentrations were AA'b5 (0.7), BB'b5 (1.1), ab' (0.95), ba' (0.85), Ma' (1.54), Mb' (1.5), am (1.74), bm (1.38) µM. Rate constants used for simulation are given in the following table. Others parameters, for rapid-mixing experiments simulation, were hypochromic factors (Hf) of 11.3 and 10.4 % for PDNA and DNA, respectively. For the simulation of agarose gel profiles visualization parameters were SSEH = 0.5, DSEQ: yes, DSSS =1, DSDS =1.05 and DSCS =1. A value of 0.09 µM for SIC parameter was only used for curve 4 in SI Section 5.

Rate constants ($\mu M^{-1}. min^{-1}$)	PDNA	DNA	PDNA	DNA
	Type 1		Type 2	
A'/a'	5.6	7.0	8.8	11.1
A/a	3.7	3.7	5.8	5.8
B'/b'	4	3.4	6.3	5.4
B/b	5.5	4.1	8.7	6.5

Type 1 corresponds to the hybridization of ss-regions flanked by ss-regions. Type 2 refers to the hybridization of the ss-regions flanked by ds-regions.

Section 7. Cytochrome b5 and phospholipid concentration dependence for the formation of protein-lipid complexes.

A, saturation curve for the association of cytochrome b5 to liposomes using a total phospholipid concentration of 700 μM and variable b5 concentrations. B, same experiment using a constant b5 concentration of 10 μM and variable phospholipid concentrations. Freshly extruded (DOPC, DMPC, DOGS, 45: 45: 10, by mol.) phospholipids (0.7 mM) were incubated for 10 min at 24°C with different concentrations of cysteine-containing protein (1.2, 2.3, 4.6, 9.2, 18.5 and 37 μM). The mix (70 μL) was diluted to 400 μL with 1 x PBS buffer, before loading onto a nickel-charged IMAC column (0.5 x 1 cm). The column was washed with 2 x 400 μL buffer. Spectra were recorded on each eluted fraction and the amount of unbound material calculated by deconvolution of the cytochrome b5 spectra. The procedure was repeated using variable concentrations of phospholipids and a fixed concentration of cytochrome b5.

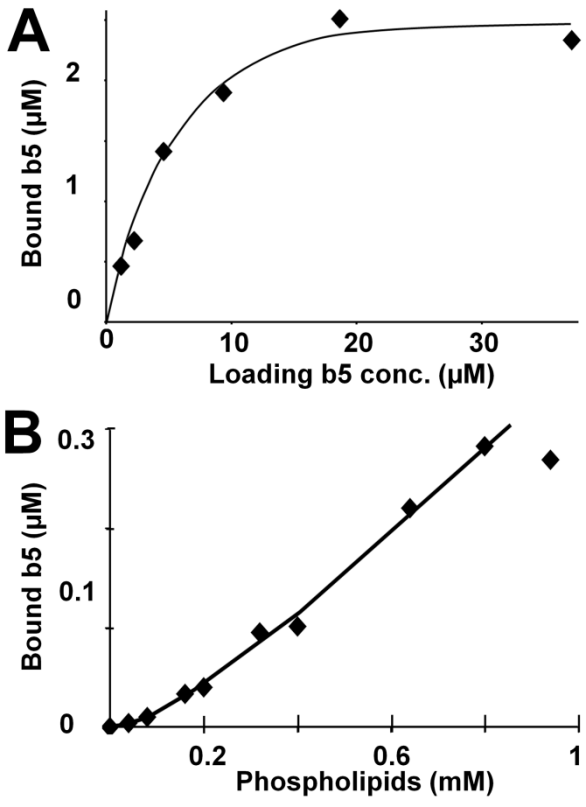

Section 8. Purification of the DNA and PDNA assemblies described in the paper

Bi-block construction (AA'/ba', BB'/ab', AA'-b5/ba', BB'-b5/ab'). Corresponding tiles (PDNA or/and DNA) 1-20 µM (depending on experiment) were hybridized in 1x PBS buffer for 1h at 42°C, then centrifugated prior purification by HPLC gel filtration performed at 0.3 ml/ min in 0.25 M NaCl, 0.15 M NaKPO4 buffer at pH 6.8 using a 4µm UHR SEC, 4.6 x 300 mm column (Waters). When PDNA and DNA were hybridized together a slight molar excess (1.2 x) of the DNA tile was used to improve yield.

Tri-block construction (AA'/ba'/ab', BB'/ba'/ab', AA'/BB'/ab', AA'-b5/ba'/ab', BB'-b5/ba'/ab', AA'-b5/BB'-b5/ab'). The procedure was formally the same than for diblock synthesis except that three tiles were used.

Penta-block construction (AA'/BB'/ba'/ab'/ba', AA'-b5/BB'-b5/ba'/ab'/ba'): suitable HPLC purified di-block and tri-block (see previously) were mixed and let to hybridize at 42°C for 60 minutes prior purification by HPLC gel filtration.

Framework bound PDNA (Figure 11): The [Mb'-ba'-ab'-ba'-ab'-reverse of m] sequence block was cloned on the M13 minus strand orientation (see SI Section 1 for letter codes) in the PCR cloning site of pCR2.1 (Invitrogen) using standard molecular biology techniques. A 513 bp fragment of the plasmid was amplified by 30 cycles of unsymmetrical PCR using a 10:1 molar ratio of primers 5'-CTGTTGGGAAGGGCGATCG-3' and 5'-ACAGCTATGACCATGATTACGCC-3', respectively. The PCR product was purified from protein by phenol-chloroform extraction and ethanol precipitation. Following quantification, the PCR product was heated for 3 min at 100°C and frozen in liquid nitrogen. 1.5-stoichiometry of 3'-end grafted AA'-b5 and internally grafted BB'-b5 PDNAs (taking into account the presence of 2 binding sites for AA' and 3 for BB' on the matrix) were added to the frozen tube and let to warm to room temperature. Following incubation for 30 min at 42°C, resulting hybrids were purified by HPLC size exclusion chromatography. While asymmetric PCR mostly generates ss-matrix, the construct might contain small amount of re-hybridized double stranded matrix contaminating the expected PDNA-framework hybrid due to the impossibility to discriminate large DNA structures by gel filtration.

Section 9. HS-AFM image sequence.

Section 10. Thermodynamic parameters calculation

ΔG (kcal/mol) for formation of partial base pairing between ss-extension of the PDNA construct analyzed on Figure 10 was found to be -7.8 for (b/b), -7.5 for (a'/a') and -3.6 for (b/a') extension couples. Calculation was performed assuming a solution including 150 mM NaCl and 1 µM DNA using the online calculator (http://eu.idtdna.com/analyzer/ Applications/ OligoAnalyzer). The energy of the stronger possible interaction was taken in each case.

For calculation of interaction energies of ss-extension in the dynamic AFM conditions, the experimental distribution of concatemer lengths determined from AFM images was first simulated using as model a monomer block bordered by two sticky extensions, considering only the two stronger classes (b/b and a'/a') of interactions. The model was simulated with different affinities of sticky ends until the global shape of simulated length distribution (SD figure 11 B) optimally fit experimental distribution. Finally, affinities were converted to free energies using standard thermodynamic formula.

Section 11. Size distribution of concatemers observed in AFM imaging (main text Figure 10)

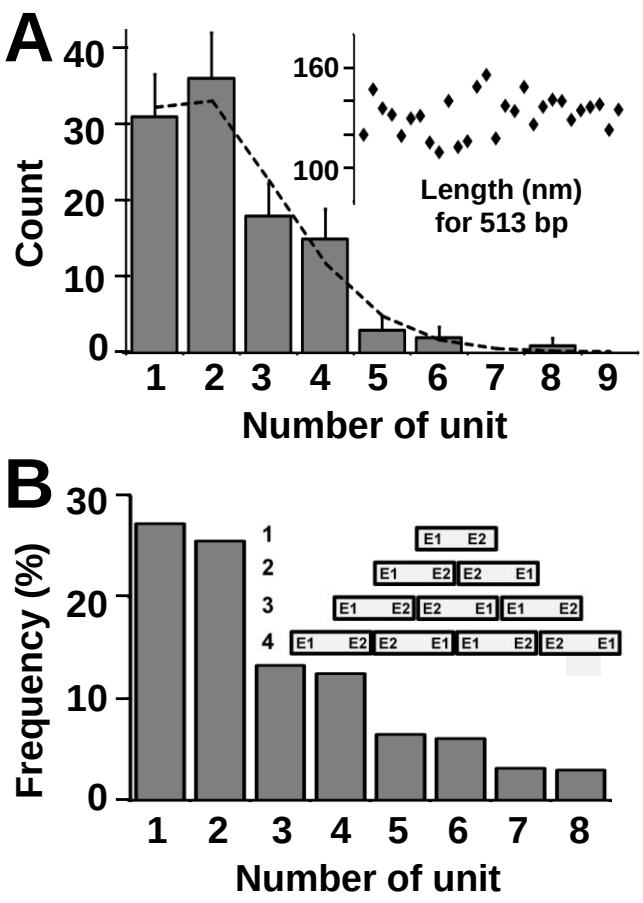

Panel A, the contour length distribution of concatemers was characterized using several sets of images (time range of ~3 min). Figure insert, contour length distribution for a 513 bp DNA.

Panel B, simulation of the concatemer formation assuming end-to-end interactions and ratios between rates of dissociation and formation of 0.05 and 0.25 for E1-E1 and E2-E2 interactions, respectively. No E1-E2 interaction was considered.

Method: Statistical analysis of the formation of concatemers was performed on a large set (several tenths of images, 106 objects) resulting in determining the size distribution of species. Calibration was performed using a 513 bp DNA, leading in high speed imaging conditions to apparent contour length of 0.26 nm/bp. The observed PDNA assemblies indeed correspond to structures including one to eight repeats (2-16 PDNAs) of the 36 nm long construct.

Bioconjugate Chemistry

ARTICLE

pubs.acs.org/bc

A Bioluminescent Probe for Salivary Cortisol

Sung Bae Kim,*,† Yasuhiro Takenaka,‡ and Masaki Torimura†

†Research Institute for Environmental Management Technology, National Institute of Advanced Industrial Science and Technology (AIST), 16-1 Onogawa, Tsukuba 305-8569, Japan

‡Department of Endocrinology and Diabetes, Saitama Medical University, 38 Morohongo Moroyama-machi, Iruma-gun, Saitama 350-0495, Japan

Supporting Information

ABSTRACT: Cortisol is a classical biomarker for the stress levels of human beings. We fabricated highly sensitive bioluminescent probes for salivary cortisol. The following strategies were contrived in the molecular design. *Gaussia princeps* luciferase (GLuc) was dissected into two fragments, between which an N-terminal-extended ligand binding domain of glucocorticoid receptor (GR HLBD), named Simgr4, was inserted. First, this unique single-chain probe was then situated downstream of a glucocorticoid response element (GRE) promoter in a reporter-gene system for constructing two ON−OFF switches for cortisol. Second, a circularly permutated (CP) variant of Simgr4 was formulated. The reporter-gene system exerted an improved signal-to-background (S/B) ratio of 8.5 to cortisol. Furthermore, a circularly permutated (CP) variant of Simgr4 exerted a 10× enhanced detection limit to cortisol and a long dynamic range from 10^{-9} to 10^{-6} M cortisol, covering all of the normal clinical ranges of serum, urine, and saliva. This optimized probe successfully determined daily fluctuations of salivary cortisol and the correlations with those by ELISA. This study is the first to investigate the contribution of the HLBD of a nuclear receptor and multiple ON−OFF switches for molecular probes and salivary cortisols.

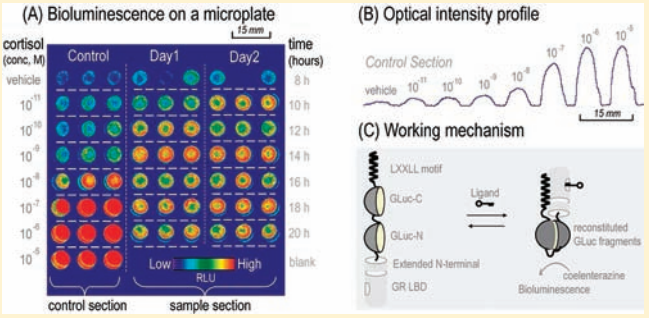

INTRODUCTION

Glucocorticoids, called the "stress" hormones, ubiquitously affect almost every cellular, molecular, and physiologic network of the living subjects.[1] The levels of glucocorticoids in physiological samples are elevated by various stimulators, including psychological stress and even by 2-deoxy-D-glucose (2DG),[2] and direct the signs and symptoms of diseases, such as Cushing's Syndrome and Addison's Disease.[3] An acute elevation of glucocorticoids impairs the retrieval of long-term memory.[4]

Among glucocorticoids, cortisol has been classically targeted as a "biomarker" of the stress levels of human beings, and is related directly or indirectly with inflammation, autoimmune disease, and cancers.[5] The normal clinical levels of cortisol range from 0.8 to 6.4 × 10^{-7} M in serum, from 0.6 to 7.5 × 10^{-7} M in urine, and from 0.2 to 2.8 × 10^{-8} M in saliva.[3] This clinical level of salivary cortisol is approximately 10 times less than those of urine and serum, and thus requires improved sensitivity for salivary cortisol. The low levels of salivary cortisol were conventionally estimated with an enzyme-linked immunosorbent assay (ELISA) and radio immunoassay (RIA).[6] However, these approaches carry intrinsic demerits of time consumption, labor intensity, cost, a long protocol starting from sample dilution, and a narrow linear range.

We recently introduced a smart single-chain probe illuminating intracellular molecular events.[7,8] The unique molecular design for an intracellular complementation of split-luciferase was proven to be effective for determining steroids, second messengers, and protein phosphorylation in living mammalian cells.[8−10] We also represented a single-chain bioluminescent probe for stress hormones using split-*Gaussia princeps* luciferase (GLuc), where appropriate consensus motifs of coactivators and corepressors were intensively examined in a circularly permutated (CP) probe backbone.[11] However, these approaches are still insufficient even for a direct determination of the low levels of salivary cortisol, and are poorly demonstrated in real samples.

To address the conventional limitations, we first formulated a new single-chain probe. Upon design of the single-chain probe, the N-terminal end of the ligand binding domain of glucocorticoid receptor (GR HLBD) was extended from 527 to 777 to 486−777 AA. The GR HLBD was sandwiched between the two fragments of GLuc, named "Simgr4". Through this molecular design, we intended (i) to approximate the N- and C-terminal ends within 8 Å according to the previous consideration on protein fragment reconstitution[12] and (ii) to exert a weak transcriptional effect on the host probe as observed previously in a GR truncation study.[13,14]

On the basis of the molecular design, we first fabricated a new bioluminescent probe system, where the system carries two ON−OFF switches exerting multiple recognitions of salivary cortisol, i.e., the glucocorticoid-response element (GRE) promoter for determining

Received: May 4, 2011
Revised: July 13, 2011
Published: August 13, 2011

ACS Publications © 2011 American Chemical Society

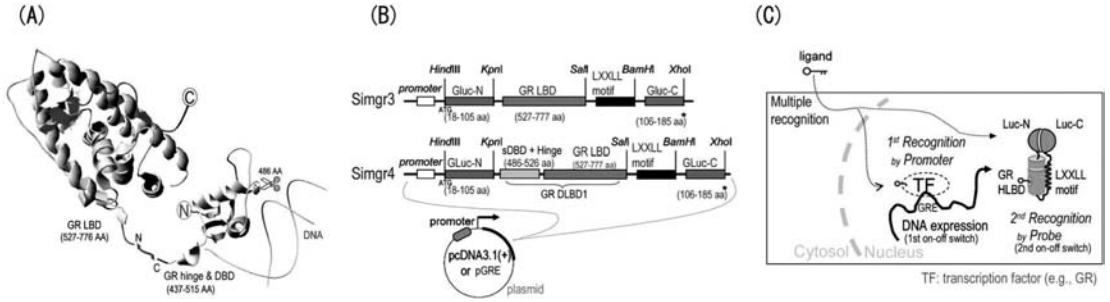

Figure 1. (A) X-ray crystallographic structure of GR LBD and GR DBD in the complex with cDNA comprising a glucocorticoid response element (GRE). The mark of scissors indicates the N-terminal end of GR HLBD (486−777 AA). (B) Schematic structures of cDNA constructs encoding Simgr3 and Simgr4. Abbreviations: GLuc-N, the N-terminal fragment of GLuc; GLuc-C, the C-terminal fragment of GLuc; GR LBD, the ligand-binding domain of glucocorticoid receptor; sDBD, the shortened DNA binding domain; Hinge, the hinge region of GR; LXXLL motif, a LXXLL motif originated from GRIP1 ID3. (C) The working mechanism of the probe with multiple recognizing ligands. An exogenous ligand first activates expression of a bioluminescent probe at the downstream of the GRE promoter (first ON−OFF switch). The ligand is recognized again by the expressed probe (second ON−OFF switch).

transcriptional activity (first switch) and a glucocorticoid-sensitive single-chain probe downstream of the GRE promoter (second switch; Figure 1).

A CP modification of Simgr4 was second made for improving the signal-to-background (S/B) ratio, named "cSimgr4". This molecular design was surprisingly effective to determine very low levels ($<10^{-8}$ M) of salivary cortisol. The advantage of this probe was finally demonstrated with the determination of daily fluctuation of cortisol levels in human saliva. The cortisol levels were found to correspond with those by ELISA. The plausible molecular mechanism of the probe system for cortisol recognition has been correspondingly discussed with references.

This study has introduced a unique bioassay for salivary cortisol with improved sensitivity. These approaches direct new strategies for illuminating low levels of ligands in real, physiological samples.

EXPERIMENTAL SECTION

Plasmid Construction. A reporter expression vector carrying a minimal GRE promoter, pTransLucent (LR0033; named pGRE), was purchased from Panomics. The cDNA encoding firefly luciferase (FLuc) in the vector was replaced with humanized *G. princeps* Luciferase (GLuc) for a control vector (named *pGRE-GLuc*). A mammalian expression vector, pcDNA 3.1(+), was bought from Invitrogen. cDNA templates encoding GLuc and human GR were obtained from Nanolights and Invitrogen, respectively.

The cDNA constructs encoding the single-chain probes, Simgr3 and Simgr4, were synthesized as follows: The cDNAs of N- and C-terminal fragments (GLuc-N [18−105 AA]; GLuc-C [106−185 AA]) were generated by PCR to introduce unique restriction sites, *Hin*dIII/ *Kpn*I for GLuc-N and *BamH*I/ *Xho*I for GLuc-C. In addition, the cDNAs encoding GR LBD and the N-terminal extended GR LBD (named GR HLBD [486−777 AA], GR DLBD1 [407−777 AA], and GR DLBD2 [361−777 AA], according to the length) were synthesized by PCR to introduce adequate restriction sites, *Kpn*I/ *Sal*I, at both the ends. The cDNA oligomers encoding an α-helical LXXLL motif originated from GR Interacting Protein 1 Interaction Domain 3 (GRIP1 ID3: ^{742}NALLRYLLDKD^{753}) were order-synthesized by Exigen (Tokyo, Japan).

The above cDNA segments were tandemly ligated via appropriate oligomers encoding a GS linker to complete the constructs, as shown in Figure 1B. The constructs were subcloned into pGRE vector. They were named *pGRE-Simgr3* and *pGRE-Simgr4*. Similarly, the same constructs subcloned into pcDNA 3.1(+) were correspondingly named *pSimgr3* and *pSimgr4*. The probes expressed from the plasmids were named Simgr3 and Simgr4, respectively.

A CP version of Simgr4 was designed as follows (also illustrated in Figure 3): The cDNA encoding GLuc was first fragmented into two segments at the point encoding Q105 for creating artificial 5′ and 3′ terminals in the middle of GLuc, whereas the original 5′ and 3′ ends were genetically fused with an oligomer encoding a GS linker. The new 5′ and 3′ terminals were connected with cDNAs encoding the LXXLL motif from GRIP1 ID3 and varying sizes of GR LBD, respectively, i.e., GR HLBD (486−777 AA), GR DLBD1 (407−777 AA), and GR DLBD2 (361−777 AA). The constructs were then subcloned into pcDNA3.1(+) or pGRE vector. The plasmids were named as *pcSimgr4*, *pGRE-cSimgr4*, *pGRE-cSimgr5*, and *pGRE-cSimgr6*, respectively, where the lower case "*c*" indicates a circular permutation. The probes expressed from the plasmids were named as cSimgr4, cSimgr5, and cSimgr6, respectively.

All the plasmids were sequenced to ensure fidelity with a BigDye Terminator Cycle sequencing kit and a genetic analyzer ABI Prism310 (Applied Biosystems).

Comparison of Cortisol Sensitivity of Simgr3 and Simgr4. The ligand sensitivity of Simgr3 and Simgr4 was examined in the presence or absence of 10^{-6} M cortisol (Figure 2A). As a mammalian culture cell line, COS-7 cells derived from the kidney of the African Green Monkey were raised in a 24-well plate (Nunc). The COS-7 cells in the plate were transiently transfected with the plasmids, pGRE-GLuc, pSimgr4, or pGRE-Simgr4, using a lipofection reagent, TransIT-LT1 (Mirus). Three hours after transfection, the cells in the plate followed two different protocols: (i) the COS-7 cells carrying pGRE-GLuc or pGRE-Simgr4 were stimulated with 10^{-6} M cortisol or vehicle (0.1% DMSO), and incubated for 16 h, and (ii) the COS-7 cells carrying pSimgr4 were initially incubated for 16 h, and then stimulated with 10^{-6} M cortisol for 20 min. The cells were finally harvested, lysed, and mixed with a native coelenterazine (CTZ, Promega) for quantifying the recovered luciferase activities using a luminometer (MiniLumat LB9506, Berthold). The ligand selectivity of Simgr3 and Simgr4 was similarly examined in the presence or absence of various steroids and chemicals (Figure 2C). The dynamic increase in the bioluminescence intensities was also recorded for a few seconds before and after the substrate injection (Figure 2C, inset). The values were normalized to cellular protein contents (per μg) unless otherwise designated.

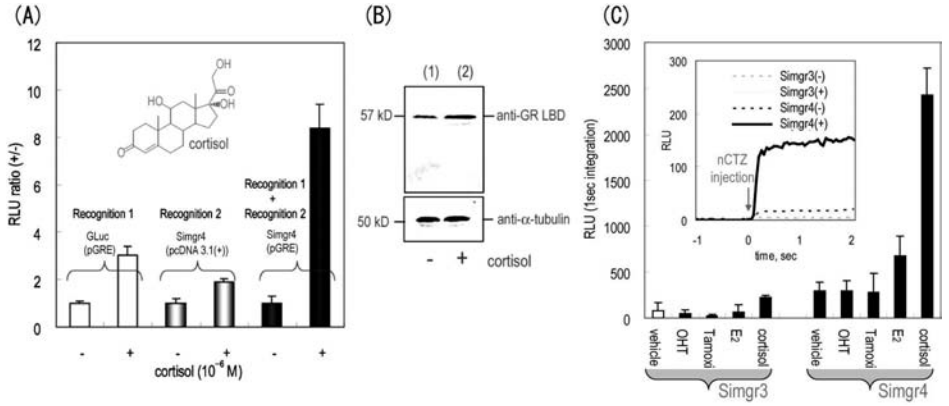

Figure 2. (A) Comparison of ligand sensitivities of Simgr4 expressed from pGRE vector with those of the control probes ($n = 3$). Simgr4 from pGRE secondarily senses of 10^{-6} M of cortisol and exhibited a better signal-to-background (S/B) ratio. The luminescence intensities were normalized as a relative luminescence unit ratio (RLU (±)), where RLU (+) and RLU (−) represent the luminescence intensities from a 1 μg protein of cell lysates from COS-7 cells stimulated with and without ligand, respectively. (B) Western blot analysis. The relative expression levels of Simgr4 from pGRE were examined in the presence or absence of 10^{-6} M of cortisol. The expression levels of α-tubulin as a housekeeping protein were simultaneously determined for control. (C) Ligand selectivity of Simgr3 and Simgr4 from pGRE vector ($n = 3$). Simgr4 exhibited better S/B ratios and optical intensities. Inset compares the dynamic increases of the bioluminescence intensities by Simgr3 and Simgr4 in the presence (+) or absence (−) of 10^{-6} M of cortisol. Abbreviations: OHT, 4-hydroxytamoxifen; Tamoxi, tamoxifen; E_2, 17β-estradiol.

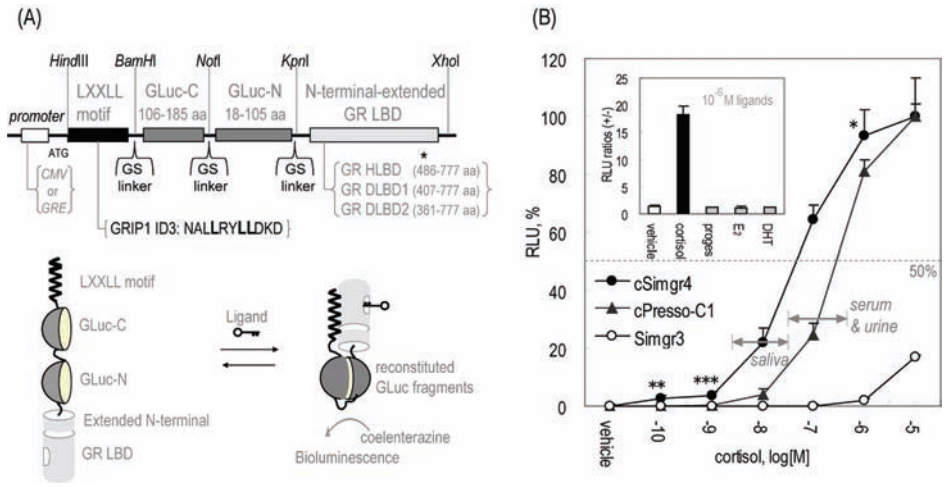

Figure 3. (A) Schematic structure of a cDNA construct encoding circularly permutated indicators (upper panel). After expression, GR HLBD or GR DLBDs in the ligand-activated probe initiate a conformation change provoking reconstitution of the fragmented luciferase. The restored bioluminescence intensities index the original ligand activities (lower panel). (B) Dose−response curves showing the detection limits and dynamic ranges of cSimgr4, Simgr3, and cPresso-C1 ($n = 3$). The dose−response curves of Simgr3 and cPresso-C1 were adapted from ref 11. The inset shows the ligand selectivity of cSimgr4. The arrows indicate approximate normal clinical ranges of physiological samples. The statistical significance (p values; two-tail) of data groups at the borders was specified with asterisks, * ($p < 0.5$; between 10^{-6} and 10^{-5} M), ** ($p < 0.01$; between vehicle and 10^{-10} M), or *** ($p < 0.001$; between vehicle and 10^{-9} M).

Western Blot Analysis. The relative expression levels of Simgr4 in COS-7 cells according to cortisol were examined with a Western blot analysis (Figure 2B). The experimental steps are based on a standard protocol for Western blotting shown in our previous paper.[11]

Dose−Response Curves of cSimgr4 and Conventional Probes. A CP variant of Simgr4 was synthesized according to the "Plasmid construction" section and named *pcSimgr4* (Figure 3A).

The dose−response curve of cSimgr4 to cortisol was compared with those of cPresso-C1 and Simgr3[11] for demonstrating the detection limits and dynamic linear ranges (Figure 3B). The detection limit and upper plateau were briefly estimated by an extrapolation of the dose−response curves. The p value (two-tail) between the vehicle and 10^{-9} M groups was 0.001 ($p < 0.05$), indicating significance in the variances between the two groups. The COS-7 cells carrying pcSimgr4 were prepared with the same protocol as that for Figure 2A and C, and stimulated with varying concentrations of steroid hormones for 20 min. The obtained dose−response curve was finally compared with those of conventional probes shown in previous papers.[8,11] The inset shows the relative intensities of cSimgr4 in response to 10^{-6} M of the indicated steroid hormones, i.e., cortisol, 5α-dihydroxytestosterone (DHT), and E_2.

Daytime Fluctuation of Salivary Cortisol Levels. Daytime fluctuation of salivary cortisol levels was monitored every 2 h over

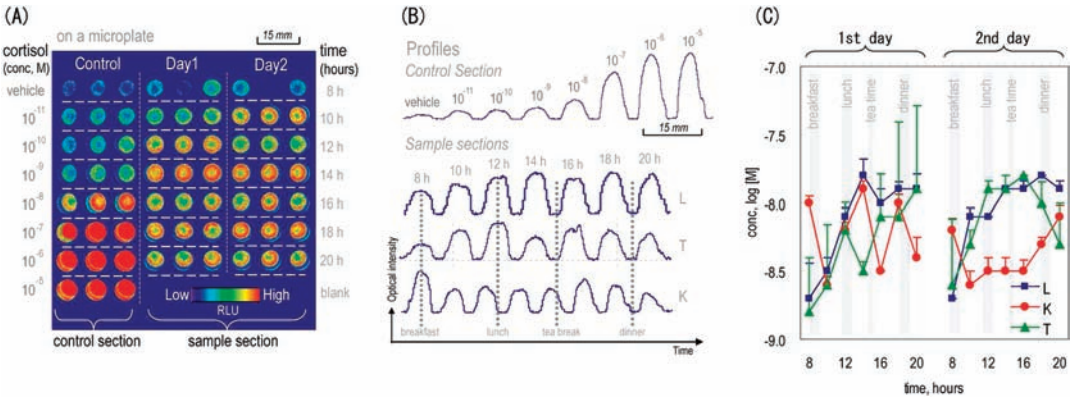

Figure 4. Bioluminescent imaging of salivary cortisol levels. (A) Optical image of a microplate after stimulation by salivary cortisol. The wells were divided into Control and Sample sections. Twenty minutes were adequate to determine salivary cortisol using the microplate with cSimgr4. (B) The profiles of the bioluminescence intensities in the columns were aligned. The vertical and horizontal arrows exhibit optical intensities and sampling times, respectively. (C) Daily fluctuations of salivary cortisol levels. The cortisol levels in the saliva were monitored over 2 consecutive days. The letters L, K, and T are the initials of the volunteers' names.

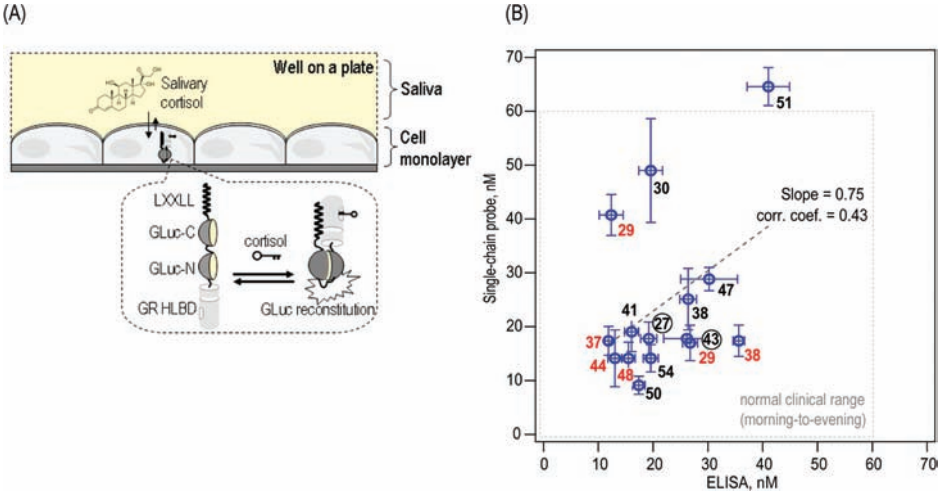

Figure 5. Determination of salivary cortisols in saliva donated by 15 volunteers. (A) The working mechanism of the present bioluminescent probe. Salivary cortisol is extracted into living cells on a culture dish. The active cortisol is recognized by the bioluminescent probe, pre-expressed in the cells beforehand. The consequent conformation change of the probe is visualized in the presence of the specific substrate, coelenterazine. (B) The correlation of the cortisol levels represented by the present probe and ELISA. The volunteers consist of 9 males and 6 females. Two of the 9 males are smokers. The ages are distributed from 29 to 54, while the body weights range 42−88 kg. We determined that all of the volunteers are healthy and mentally stable. Among 15 samples, 12 samples were collected in a narrow region, whereas 3 of the total samples were hit in a higher region. The digits and circles indicate ages and smokers. Red digits mean female.

2 consecutive days (Figure 4). During the 2 days, ca. 500 μL of salivary samples every 2 h were kindly donated by three healthy volunteers. The samples were overnight-stocked in a 4 °C refrigerator before experiment.

At the same time, COS-7 cells raised in a 96-well black-frame plate (Nunc) were transfected with pcSimgr4, and incubated for 16 h. The cell culture media in the plate were carefully removed before the following steps: (i) The cells in a section on the plate were immersed for 20 min in 50 μL of the supernatants of the saliva samples and (ii) the cells in the other section were also stimulated with 50 μL of standard cortisol samples ranging from 10^{-5} to 10^{-11} M for 20 min. After decantation of the solutions from the wells, the cells in the plate were washed once in PBS and lysed. The reconstituted bioluminescence intensities were determined using LAS-4000 in an automatic detection mode after multichannel injection of 40 μL of CTZ into the wells.

Correlation between the Salivary Cortisols by cSimgr4 and by ELISA. The levels of salivary cortisol in human samples were estimated with both COS-7 cells carrying cSimgr4 and an enzyme-linked immunosorbent assay (ELISA) kit (Cortisol Saliva, IMMUNOSPEC Co.) (Figure 5).

The salivary samples for this comparison were donated from 15 volunteers affiliated with AIST. The sampling time and date were 2 p.m. of April 13, respectively. The samples were collected using a saliva collection tube (SARSTEDT) for volunteer's convenience, centrifuged, stocked in a 4 °C refrigerator before use, and used up in 48 h.

First of all, COS-7 cells raised in 96-well plates were transfected with pcSimgr4 and incubated for 16 h. The cells were washed once with PBS, and some of the cells in the Sample section directly exposed for 20 min to 50 μL of saliva samples donated from 15 volunteers affiliated with AIST. Meanwhile,

some of the cells in the Control section were stimulated with varying concentrations of controlled cortisol (10^{-7}−10^{-9} M) for 20 min for calibration curves. The reconstituted bioluminescence intensities from the cells were finally estimated in the presence of coelenterazine with the microplate reader (Mithras LB940; Berthold).

In parallel, the salivary cortisols in the same human samples were determined with the ELISA assay kit according to manufacturer's instructions, the results of which were compared with those of cSimgr4 (Figure 5B). The determined levels of salivary cortisol were categorized into male and female groups (Supporting Information Figure 1C).

RESULTS

S/B Ratio by pGRE-Simgr4 is Superior. pGRE-Simgr4 is designed to multiply sense cortisol (Figure 1B,C). With this unique design, we intended to construct a unique bioluminescent system carrying two "ON−OFF switches." The first remarkable outcome of this probing system appeared in the enhanced S/B ratios 16 h after cortisol stimulation (Figure 2A). The S/B ratio was ca. 9, whereas those of pGRE-GLuc (a control for Switch #2) and pSimgr4 (a control for Switch #1) were ca. 3 and 2, respectively, according to the same protocol.

The expression levels of Simgr4 in COS-7 cells were comparatively increased in the presence of 10^{-6} M of cortisol, according to a Western blot analysis (Figure 2B), while the expression levels of α-tubulin as a housekeeping protein were almost invariant.

The results indicate that the enhanced S/B ratio presented in Figure 2A is contributed by the synergistic effect of the two "switches," i.e., the GRE promoter and the single-chain probe.

pGRE-Simgr4 Exhibits a Better Optical Intensity and Sensitivity to Cortisol. The sensitivity of pGRE-Simgr4 to cortisol in COS-7 cells were compared with those of pGRE-Simgr3 (Figure 2C). The comparison revealed that the living COS-7 cells carrying pGRE-Simgr4 score 11 times stronger absolute intensity than those carrying pGRE-Simgr3 (Figure 2C). The S/B ratio with pGRE-Simgr4 was ca. 8.4 ± 1.0, whereas that with pGRE-Simgr3 was ca. 2.9 ± 0.4. The detection limit by pGRE-Simgr4 was also improved up to nearly $10^{-8.5}$ M of cortisol (Supporting Information Figure 1A). These results indicate that the N-terminal extension of GR LBD can be an effective strategy to modify the sensorial properties of single-chain probes.

Circular Permutational Modification of Simgr4 Enhances the Detection Limit and Selectivity to Cortisol. The two GLuc segments in Simgr4 carrying GR HLBD were circularly permutated with the speculation of improving the sensorial properties of cortisol (Figure 3). The circular permutation and GR HLBD raised the cortisol sensitivity of cSimgr4 up to 10 times upon determination with the luminometer (MiniLumat LB9506, Berthold). The detection limit was found at ca. 10^{-9} M of cortisol (Figure 3B). The optical intensities reached the plateau at 10^{-6} M of cortisol. The half maximal effective concentration (EC_{50}) was 5.0 × 10^{-8} M of cortisol. This cortisol sensitivity was approximately 10 times better than that of the conventional cPresso-C1. cPresso-C1 comprises a consensus motif (LXXIIXXXL) of corepressors and the ligand binding domain of the glucocorticoid receptor (GR LBD; 527−777 aa) as the key components. The corepressor motif in cPresso-C1 was designed to block the basal, nonspecific reconstitution between the two fragmented active sites of GLuc, and to stabilize the probe backbone. An additional ligand selectivity study exhibited a high selectivity only to cortisol, and was completely insensitive to 10^{-6} M of progesterone, E_2, and DHT (Figure 3B, inset). A further extension of the N-terminal of GR LBD in cSimgr4 did not improve the sensitivity to cortisol (Supporting Information Figure 1B).

Daytime Fluctuation of Salivary Cortisol Levels Is Efficiently Monitored. Daytime variation of salivary cortisol levels was carefully estimated using living COS-7 cells carrying pcSimgr4 (Figure 4). On the plate, the pseudocolor image in the control section exhibited extremely high S/B ratios (Figure 4A,B). In the sample section, the wells stimulated by saliva samples (n = 3) reported reasonable levels of optical intensities, from $10^{-8.8}$ to $10^{-7.8}$ M of cortisol. The concentration levels agreed well with those in the literature.[15]

The intensity profile in the control section using LAS-4000 shows that the maximal variance in the intensities is found at the concentration range from 10^{-9} to 10^{-6} M of cortisol. This result is in agreement with the calibration curve obtained by the luminometer (MiniLumat LB9506; see Figure 3B). The intensity profiles in the sample section demonstrate that daytime cortisol levels in saliva fluctuate differently according to the subjects. The salivary cortisol levels of two subjects (L and T) exhibited a similar pattern and gradually increased before noon and reached a plateau at noon. On the other hand, the cortisol levels of the other subject (K) were unstable the first day, and were stabilized the second day. A quick increase or decrease in the salivary cortisol levels of the subjects were occasionally observed right after breakfast, tea break, and dinner times.

Levels of Salivary Cortisols by cSimgr4 Correspond with Those by ELISA. The cortisol levels in saliva samples donated from 15 volunteers affiliated with AIST were determined using COS-7 cells carrying cSimgr4, and compared with those from an ELISA assay (Figure 5).

The correlation coefficient (a) and the slope by least-squares analysis between the cortisol levels by cSimgr4 and ELISA were 0.43 and 0.75, respectively. The cortisol levels of 12 samples among the 15 samples well agreed each other in a narrow concentration range, whereas the levels of the other 3 samples did not correlate with each other. The 3 samples declined the correlation coefficient.

The cortisol levels in saliva of the 15 volunteers were (2.4 ± 1.5) × 10^{-8} M (the present probe) and (2.2 ± 0.9) × 10^{-8} M (ELISA). The contribution of age, sex, smoking, and body weight to the levels of salivary cortisol were not apparent.

DISCUSSION

The measurement of cortisol in saliva provides several advantages over its measurement in serum or plasma. Saliva is not harmful to mammalian cell lines and exactly reflects the cortisol levels in blood.[16] Furthermore, saliva provides a convenient, stress-free sample to collect. Saliva testing is a more accurate way to measure the bioavailable levels of cortisol delivered topically through the skin, different from testing plasma carrying the majority of cortisol with high-affinity corticosteroid-binding globulin.[16,17]

Despite the physiological importance of stress hormones, extremely low and variable features of salivary cortisol levels generally hamper the rapid, efficient bioanalysis. To date, the conventional determinations of stress hormones have heavily depended on ELISA, which is less competent in time, labor, and cost.

Here, we have introduced unique single-chain probes emitting bioluminescence for rapidly determining broad ranges of cortisol in physiological samples with appropriate ligand sensitivity.

Generally, cell-based bioassays are categorized into two groups, i.e., (i) genetic, transcriptional and (ii) nontranscriptional assays. A genetic, transcriptional assay, such as a reporter-gene assay, requires a long ligand-stimulation time until sufficient accumulation of a reporter protein is reached. A nontranscriptional assay, such as a protein fragment complementation assay (PCA), expresses and prelocalizes the probe in adequate intracellular compartments of interest beforehand. The luminescence intensity is ready to be developed upon the host cell being stimulated by a signal. One of the present assay systems carrying two ON−OFF switches comprises both characteristics and thus is characteristically classified into an interface region between the two categories.

It is interesting to consider the optimal truncation of full-length GR, which may retain the transcriptional activity and ligand-binding ability. Shorter is better to relieve the burden of host cells upon design of a single-chain probe. However, an excessive truncation may lose the expected molecular functions. Here, we examined the optimal length of GR for a single-chain probe in Supporting Information Figure 1B. Our overall studies, including the Western blot analysis, conclude that the GR HLBD (486−777 AA) has an appropriate length for retaining the ligand-binding property without collapsing the probe balance.

It has been a great issue for a long time to extend a narrow dynamic range in bioimaging studies using fluorescent proteins.[18,19] Here, the optimal bioluminescent probe, cSimgr4, recognizes a thousand-fold variance in the cortisol levels, from 10^{-9} to 10^{-6} M. This wide dynamic range covers all of the normal clinical ranges of cortisol in saliva, serum, and urine. We assume that this dynamic range is contributed by the optimization of the probe structure in addition to the intrinsic merit of the bioluminescent probes, i.e., low background intensity and absence of external light source. With regard to the selectivity issue, cSimgr4 is highly selective only to cortisol and not disrupted even by equivalent concentrations of other steroids, such as DHT, E_2, and progesterone (Figure 3).

Daytime fluctuation of salivary cortisol was examined over two consecutive days with samples donated by three healthy volunteers (Figure 4). The overall cortisol levels were consistent with the known clinical ranges of salivary cortisol, i.e., $(0.2-2.8) \times 10^{-8}$ M, although the diurnal cortisol rhythms of the three volunteers were diverse. Previously known diurnal cortisol patterns were different according to references, e.g., a highest level in the morning and consistent decline thereafter,[15] and a peak at noon or evening.[20] Further, we should note that the cortisol levels are elevated by two categorized stressors: interoceptive (systemic, physiological, or homeostatic) and exteroceptive (neurogenic, psychological, or emotional) stressors.[21] Thus, our results may be concluded as follows: (i) we visualized the extent of the daytime stress levels sensed by three volunteers in the form of bioluminescence on a plate; (ii) considering that the cortisol levels reflect psychological and physical stresses of individuals, the daytime fluctuations in salivary cortisol reflect human activities and appear natural.

It is interesting to consider the kinetics of the cortisol-induced GR LBD−LXXLL motif binding inside the single-chain probe. Furthermore, the two main driving forces should be discussed, i.e., (i) the hydrogen bonds between the side chains of the components and (ii) the hydrophobic interaction as discussed previously.[22,23] The cortisol recognition process of cSimgr4 in COS-7 cells is divided into three steps: first, the free cortisol in saliva is extracted into the plasma membrane. The consequent cortisol−GR DLBD binding in the cytosol (second step) initiates the intramolecular conformational change of cSimgr4 (third step). The rate-determining step should be the membrane penetration step, considering that other molecular actions are inter- or intramolecular binding.

In the experimental setup, the substrate, CTZ, is saturated in the host cells beforehand. All the other experimental parameters were equivalent. Nevertheless, the ligand sensitivities of Simgr4 and cSimgr4 to cortisol significantly differ (Supporting Information Figure 1B).

This comparison reveals that the molecular structural variances between the Simgr4 and cSimgr4 dominate the apparent ligand sensitivities. The structural advantages of cSimgr4 include (i) decreasing background intensities by a circular permutation (i.e., rare encountering chance between the GLuc fragments) and (ii) optimizing the N-terminal end of GR LBD for the efficient binding between LXXLL motif and GR LBD.

As mentioned earlier, the intrinsic signal-transduction steps of GR were taken as the optical index to reconstitute bioluminescence, whereas conventional ELISA and EIA were based on an antigen−antibody reaction to develop chemiluminescence. The present probe was characterized to sense the active cortisol extracted into the cytosol of living COS-7 cells within 20 min. The present bioluminescent probe is thus optimal to duly reflect ligand-activated molecular actions of GR. On the other hand, the ELISA assay reflects cortisol levels recognized by the specific antibody. In spite of the intrinsic differences in the approaches, the results agreed well. Both the methods are valuable to determine salivary cortisols.

Normal clinical ranges of salivary cortisol differ according to references: e.g., $(0.2-2.8) \times 10^{-8}$ M in saliva,[3] $(1.4-6.0) \times 10^{-8}$ M in saliva (morning; a technical bulletin of IMMUNOSPEC co., cat #: E18188), $(8-77) \times 10^{-8}$ M in saliva (radioimmunoassay).[24] The indicated levels of salivary cortisols, ca. 2.4×10^{-8} M, using the present probe correspond with the referenced values in the clinical ranges.

■ ASSOCIATED CONTENT

Supporting Information. Supplemental experimental data providing further information on the (i) cortisol-derived dynamic increases of the bioluminescence intensities, (ii) the signal-to-background (S/B) ratios of various probes, (iii) the comparison of the male and female data by the present probe and ELISA. This material is available free of charge via the Internet at http://pubs.acs.org.

■ AUTHOR INFORMATION

Corresponding Author
*kimu-sb@aist.go.jp.

■ ACKNOWLEDGMENT

This work was supported by a Grant-in-Aid for Young Scientists (B) from Japan Society for the Promotion of Science (JSPS).

■ REFERENCES

(1) Nicolaides, N. C., Galata, Z., Kino, T., Chrousos, G. P., and Charmandari, E. (2010) The human glucocorticoid receptor: Molecular basis of biologic function. *Steroids 75*, 1–12.

(2) Edmonds, B. K., and Edwards, G. L. (1998) Dorsomedial hindbrain participation in glucoprivic feeding response to 2DG but

not 2DG-induced hyperglycemia or activation of the HPA axis. *Brain Res. 801*, 21–28.

(3) Burtis, C. A., Ashwood, E. R., and Tietz, N. W. (1999) *Tietz textbook of clinical chemistry*, 3rd ed., W.B. Saunders, Philadelphia.

(4) de Quervain, D. J. F., Aerni, A., Schelling, G., and Roozendaal, B. (2009) Glucocorticoids and the regulation of memory in health and disease. *Front. Neuroendocrinol. 30*, 358–370.

(5) Oakley, R. H., and Cidlowski, J. A. (2011) Cellular processing of the glucocorticoid receptor gene and protein: New mechanisms for generating tissue-specific actions of glucocorticoids. *J. Biol. Chem. 286*, 3177–3184.

(6) Raff, H., Homar, P. J., and Burns, E. A. (2002) Comparison of two methods for measuring salivary cortisol. *Clin. Chem. 48*, 207–208.

(7) Kim, S. B., Awais, M., Sato, M., Umezawa, Y., and Tao, H. (2007) Integrated molecule-format bioluminescent probe for visualizing androgenicity of ligands based on the intramolecular association of androgen receptor with its recognition peptide. *Anal. Chem. 79*, 1874–1880.

(8) Kim, S. B., Otani, Y., Umezawa, Y., and Tao, H. (2007) Bioluminescent indicator for determining protein-protein interactions using intramolecular complementation of split click beetle luciferase. *Anal. Chem. 79*, 4820–4826.

(9) Kim, S. B., Umezawa, Y., Kanno, K. A., and Tao, H. (2008) An integrated-molecule-format multicolor probe for monitoring multiple activities of a bioactive small molecule. *ACS Chem. Biol. 3*, 359–372.

(10) Kim, S. B., Sato, M., and Tao, H. (2009) Split Gaussia luciferase-based bioluminescence template for tracing protein dynamics in living cells. *Anal. Chem. 81*, 67–74.

(11) Kim, S. B., Sato, M., and Tao, H. (2009) Genetically encoded bioluminescent indicators for stress hormones. *Anal. Chem. 81*, 3760–3768.

(12) Michnick, S. W. (2001) Exploring protein interactions by interaction-induced folding of proteins from complementary peptide fragments. *Curr. Opin. Struct. Biol. 11*, 472–477.

(13) He, B., Bowen, N. T., Minges, J. T., and Wilson, E. M. (2001) Androgen-induced NH_2- and COOH-terminal Interaction Inhibits p160 coactivator recruitment by activation function 2. *J. Biol. Chem. 276*, 42293–42301.

(14) Wang, D. Q., Wang, Q., Awasthi, S., and Simons, S. S. (2007) Amino-terminal domain of TIF2 is involved in competing for corepressor binding to glucocorticoid and progesterone receptors. *Biochemistry 46*, 8036–8049.

(15) den Hartog, H. M., Nicolson, N. A., Derix, M. M. A., van Bemmel, A. L., Kremer, B., and Jolles, J. (2003) Salivary cortisol patterns and cognitive speed in major depression: a comparison with allergic rhinitis and healthy control subjects. *Biol. Psychol. 63*, 1–14.

(16) Laudat, M. H., Cerdas, S., Fournier, C., Guiban, D., Guilhaume, B., and Luton, J. P. (1988) Salivary cortisol measurement - a practical approach to assess pituitary-adrenal-function. *J. Clin. Endocr. Metab. 66*, 343–348.

(17) Aardal-Eriksson, E., Karlberg, B. E., and Holm, A. C. (1998) Salivary cortisol - an alternative to serum cortisol determinations in dynamic function tests. *Clin. Chem. Lab. Med. 36*, 215–222.

(18) Nagai, T., Yamada, S., Tominaga, T., Ichikawa, M., and Miyawaki, A. (2004) Expanded dynamic range of fluorescent indicators for Ca^{2+} by circularly permuted yellow fluorescent proteins. *Proc. Natl. Acad. Sci. U. S. A. 101*, 10554–10559.

(19) Okada, S., Ota, K., and Ito, T. (2009) Circular permutation of ligand-binding module improves dynamic range of genetically encoded FRET-based nanosensor. *Protein Sci. 18*, 2518–2527.

(20) Sephton, S. E., Sapolsky, R. M., Kraemer, H. C., and Spiegel, D. (2000) Diurnal cortisol rhythm as a predictor of breast cancer survival. *J. Natl. Cancer Inst. 92*, 994–1000.

(21) Ritter, S., Watts, A. G., Dinh, T. T., Sanchez-Watts, G., and Pedrow, C. (2003) Immunotoxin lesion of hypothalamically projecting norepinephrine and epinephrine neurons differentially affects circadian and stressor-stimulated corticosterone secretion. *Endocrinology 144*, 1357–1367.

(22) Dubbink, H. J., Hersmus, R., Verma, C. S., van der Korput, H. A., Berrevoets, C. A., van Tol, J., Ziel-van der Made, A. C., Brinkmann, A. O., Pike, A. C., and Trapman, J. (2004) Distinct recognition modes of FXXLF and LXXLL motifs by the androgen receptor. *Mol. Endocrinol. 18*, 2132–2150.

(23) He, B., Gampe, R. T., Jr., Kole, A. J., Hnat, A. T., Stanley, T. B., An, G., Stewart, E. L., Kalman, R. I., Minges, J. T., and Wilson, E. M. (2004) Structural basis for androgen receptor interdomain and coactivator interactions suggests a transition in nuclear receptor activation function dominance. *Mol. Cell 16*, 425–438.

(24) Brock, P., Eldred, E. W., Woiszwillo, J. E., Doran, M., and Schoemaker, H. J. (1978) Direct solid-phase I125 radioimmunoassay of serum cortisol. *Clin. Chem. 24*, 1595–1598.

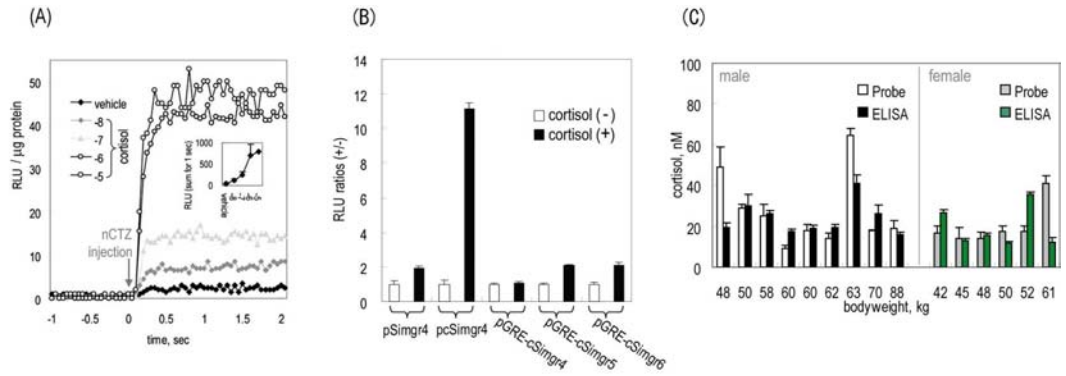

Suppl. Figure 1. (A) Dynamic increases of the bioluminescence intensities by COS-7 cells carrying pGRE-Simgr4 in response to varying concentrations of cortisol, ranging from the vehicle (0.1% DMSO) to 10^{-5} M of cortisol (0.05-s integration). The dynamic increase in the bioluminescence intensities were recorded for a few seconds before and after the substrate injection using the microplate reader. The dynamic intensities were the average of triplicate determination. Inset shows the dynamic response curve to varying concentrations of cortisol (1-s integration). (B) Comparison of the ligand selectivity of the present probes. The COS-7 cells carrying pSimgr4, pcSimgr4, pGRE-cSimgr4, pGRE-cSimgr5, or pGRE-cSimgr6 were stimulated with 10^{-6} M of cortisol for 20 min. Meanwhile, the cells carrying pGRE-cSimgr4, pGRE-cSimgr5, or pGRE-cSimgr6 were initially stimulated with 10^{-6} M of cortisol for 16 h until enough probe accumulation 3 h after the transfection. The recovered bioluminescence intensities were determined soon after a programmed, automatic injection of 40 μL of the specific substrate, CTZ (Promega). In response to 10^{-6} M of cortisol, cSimgr4 exhibited an S/B ratio superior to the other probing systems (n=3). (C) Comparison of the cortisol levels determined by the probe (white and gray bars) and ELISA (black and green bars). The salivary cortisols from male and female are listed in left and right sections, respectively. The digits at the X-axis indicate the bodyweight of volunteers.

Bioconjugate Chemistry

ARTICLE

pubs.acs.org/bc

PCL Film Surfaces Conjugated with P(DMAEMA)/Gelatin Complexes for Improving Cell Immobilization and Gene Transfection

C. Y. Li,[‡,†] W. Yuan,[§,†] H. Jiang,[‡] J. S. Li,[∥] F. J. Xu,[*,‡] W. T. Yang,[‡] and J. Ma[*,§]

[‡]State Key Laboratory of Chemical Resource Engineering, Key Laboratory of Carbon Fiber and Functional Polymers, Ministry of Education, College of Materials Science & Engineering, Beijing University of Chemical Technology, Beijing 100029 China

[§]State Key Laboratory of Molecular Oncology, Cancer Institute & Hospital, Chinese Academy of Medical Sciences, Beijing 100021 China

[∥]College of Polymer Science and Engineering, Sichuan University, Chengdu 610065 China

ABSTRACT: Successful gene transfection on a tissue scaffold is of crucial importance in facilitating tissue repair and regeneration by enabling the localized production of therapeutic drugs. Polycaprolactone (PCL) has been widely adopted as a scaffold biomaterial, but its unfavorable cell-adhesion property needs to be improved. In this work, the PCL film surface was conjugated with poly((2-dimethyl amino)ethyl methacrylate) (P(DMAEMA))/gelatin complexes via surface-initiated atom transfer radical polymerization (ATRP) for improving cell immobilization and subsequent gene transfection. A simple aminolysis-based method was first used for the covalent immobilization of ATRP initiators on the PCL film. Well-defined P(DMAEMA) brushes were subsequently prepared via surface-initiated ATRP from the initiator-functionalized PCL surfaces. The P(DMAEMA) chains with a pK_a of 7.0−7.3 were used for conjugating gelatin with a pI of 4.7 via electrostatic interaction. The amount of complexed gelatin increased as that of the grafted P(DMAEMA) layer. The cell-adhesion property on the functionalized PCL surface could be controlled by adjusting the ratio of P(DMAEMA)/gelatin. It was found that the gene transfection property on the immobilized cells was dependent on the density of the immobilized cells on the functionalized PCL film. With the good cell-adhesive nature of gelatin and the efficient gene transfection on the dense immobilized cells, the incorporating the suitable of P(DMAEMA)/gelatin complexes onto PCL surfaces could endow the PCL substrates new and interesting properties for potential tissue engineering applications.

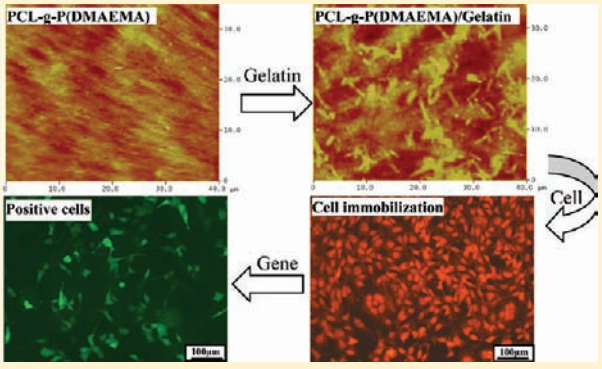

INTRODUCTION

Polycaprolactone (PCL) has been widely adopted for biomaterials and biomedical applications because of its slow degradability and good biocompatibility, as well as its good mechanical and thermoplastic characteristics.[1,2] The application of synthetic biomaterials depends upon their interfacial properties and resultant interactions with cells and biological fluids *in vivo*. The ability to manipulate and control the surface properties of a biomaterial without altering its bulk properties is of crucial importance in the designing of biomedical materials.[3,4] Covalent tethering of well-defined polymer brushes on a solid substrate is an effective method for modifying the surface properties.[5−7] Surface-initiated atom transfer radical polymerization (ATRP) allows the preparation of well-defined dense polymer brushes and hence provides the high capacity for conjugating functional molecules.[7−9] Recently, we explored surface-initiated ATRP of glycidyl methacrylate (GMA) to tailor the functionality of polycaprolactone (PCL) film surfaces.[10] The well-defined PGMA brushes were used for conjugating cell-adhesive collagen and RGDS to improve the cell-adhesion properties of the PCL film surface.

The immobilization of ATRP initiators on PCL surfaces was based on the hydroxyl groups from the surface hydrolysis of PCL.[10] However, such hydrolysis process of polyester also produced the corresponding −COOH groups, which could hamper the immobilization efficiency of the ATRP initiators. Further improvement in cell adhesion properties of the PCL film surface will facilitate its biomedical applications. In addition, the expanded research about the possibility to combine the immobilized cells with other functionalities such as local gene delivery is also very important to the development of multifunctional PCL-based tissue scaffolds. It was reported that successful gene transfection on a biomaterial could enable the localized production of therapeutic drugs to facilitate tissue repair and regeneration.[11,12]

In this work, a simple aminolysis-based method was first used for the covalent immobilization of ATRP initiators on the PCL surfaces (Figure 1). It was well-known that the aminolysis process of polyester film surfaces with 1,6-hexanediamine can

Received: May 10, 2011
Revised: August 10, 2011
Published: August 18, 2011

ACS Publications © 2011 American Chemical Society

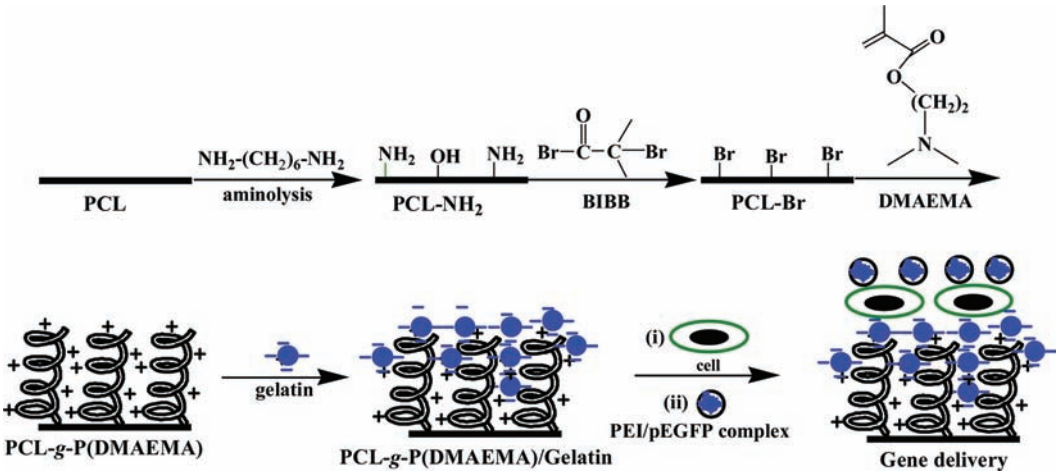

Figure 1. Schematic diagram illustrating the reaction of free amine and hydroxyl groups on the aminolyzed PCL film surface with 2-bromoisobutyrate bromide (BIBB) to produce the PCL-Br surface, surface-initiated ATRP of DMAEMA from the PCL-Br surface to produce the PCL-*g*-P(DMAEMA) surface, and physical immobilization of gelatin to produce the PCL-*g*-P(DMAEMA)/gelatin surface for biomedical applications.

introduce the free amino and hydroxyl groups.[13−15] Both reactive groups are ready to react with 2-bromoisobutyryl bromide to produce the ATRP initiator-coupled surfaces (the PCL-Br surfaces). Instead of P(GMA) brushes,[10] well-defined poly((2-dimethyl amino)ethyl methacrylate) (P(DMAEMA)) brushes (the PCL-*g*-P(DMAEMA) surfaces) were subsequently prepared via surface-initiated ATRP of DMAEMA from the PCL-Br surfaces. The P(DMAEMA) chains with a pK_a of 7.0−7.3[16,17] were used for conjugation of gelatin with a pI of 4.7[18] (derived from naturally extracellular matrix collagen) via electrostatic interaction for improving the cell-adhesion properties of the PCL surfaces. The subsequent gene transfection in the immobilized cells was further investigated to develop multifunctional PCL-based scaffolds. The chemical compositions, topography, cell adhesion, and gene delivery characteristics of the modified PCL film surfaces were characterized by X-ray photoelectron spectroscopy (XPS), atomic force spectroscopy (AFM), fluorescent microscopy, and fluorescence-activated cell sorting analysis (FACS), respectively.

EXPERIMENTAL PROCEDURES

Materials. Polycaprolactone pellets (PCL, M_n = 42 500), 1,6-hexanediamine, branched polyethylenimine (PEI, M_w ~25 000 Da), gelatin powder from porcine skin, 2-bromoisobutyryl bromide (98%), (2-dimethylamino)ethyl methacrylate (DMAEMA, >98%), copper(I) bromide (CuBr, 99%), copper(II) bromide ($CuBr_2$, >98%), and 2,2′-byridine (Bpy, 98%), were obtained from Sigma-Aldrich Chemical Co., St. Louis, MO. DMAEMA was used after removal of the inhibitors in a ready-to-use disposable inhibitor-removal column (Sigma-Aldrich). HEK293 cell lines were purchased from the American Type Culture Collection (ATCC, Rockville, MD).

Aminolysis of PCL Films. The polycaprolactone (PCL) film was prepared by dissolving 4 g of PCL pellets in 40 mL of methylene chloride. The polymer solution was then cast onto a glass substrate and the solvent was removed by controlled evaporation at room temperature over a period of 24 h. The so-obtained pristine PCL film with a thickness of 40−100 μm was washed with copious amounts of an alcohol/water (1/1, v/v) mixture.[10] The dried PCL films were cut into specimen size of 2 cm × 2 cm for the subsequent surface reactions. The cleaned PCL films were subsequently immersed in 1,6-hexanediamine/2-propanol solution of 60 mg/mL for 2 h at room temperature. The aminolysis process produced the PCL-NH_2 films.

Surface-Initiated ATRP of DMAEMA and Gelatin Immobilization. As shown schematically in Figure 1, the immobilization of ATRP initiator on the PCL-NH_2 film surface was accomplished via the reaction of the amino and hydroxyl groups with 2-bromoisobutyrate bromide (BIBB). The PCL-NH_2 films were introduced into 10 mL of dried hexane, followed by addition of 0.5 mL of 2-bromoisobutyryl bromide and 0.2 mL of dry pyridine. The reaction mixture was kept for 2 h at 0 °C, and then at room temperature for 22 h to produce the 2-bromoisobutyryl-immobilized PCL surface (the PCL-Br surface). The PCL-Br substrate was washed repeatedly with a methanol/water (1/2, v/v) mixture and dried by pumping under reduced pressure. In order to estimate the ATRP initiator (alkyl bromide) density of the PCL-Br surface, the initiator density was first set at an unknown value, ρ^* (Brs/nm^2). On the basis of the initiator density (ρ^*), mass density (ρ_1) of the 2-bromoisobutyrate (BIB) layer (1.0 g/cm^3), and molecular weight (M_1) of BIB (165.5 g/mol), the thickness (h) of the initiator layer was estimated to be about 0.27ρ^* ($h = \rho^* \cdot M_1/\rho_1$). From the mass density (ρ_2) of the PCL film (1.0 g/cm^3), the molecular weight (M_2) of the caprolactone (CL) repeat unit (114 g/mol), the stoichiometry ($C_6H_{10}O_2$) of the CL repeat unit, and the sampling depth (about 7.5 nm in an organic matrix) of the XPS technique, the number (n) of the total C atoms per unit volume of the XPS probing depth (V = 7.5 nm^3) is about ($237.8 - 4.6\rho^*$) ($n = 4\rho^* + 6[(7.5 - h)\rho_2/M_2]$).[10] On the basis of the [Br]/[C] ratio (r) (determined from the sensitivity factor-corrected Br 3d and C 1s core-level spectral area ratio of the PCL-Br surface), the initiator density (ρ^*) could be calculated by $r = \rho^*/n$.

For the preparation of P(DMAEMA) brushes on the PCL-Br surface, the reaction was carried out using a [DMAEMA (5 mL)]/[CuBr]/[$CuBr_2$]/[2,2′-byridine, Bpy] molar feed ratio of 100:1:0.2:2 in 10 mL of methanol/water mixed solvent (1/4, v/v) at room temperature in a Pyrex tube. The mixture was stirred and degassed with argon for 20 min. The PCL−Br substrate was then introduced into the reaction mixture. The reaction was allowed to proceed for 5 to 120 min to produce the

Table 1. Reaction Time, Grafting Yield (GY), Chemical Composition, and Static Water Contact Angle of the Functionalized PCL Surfaces

sample	reaction time	GY[d] (μg/cm^2)	water contact angle (±3°)
Pristine PCL	--	--	70
PCL-NH_2[a]	24 h		65
PCL-Br	24 h	--	82
PCL-*g*-P(DMAEMA)1 [b]	5 min	0.66 (±0.2)	58
PCL-*g*-P(DMAEMA)2 [b]	30 min	3.7 (±0.6)	49
PCL-*g*-P(DMAEMA)3 [b]	60 min	7.7 (±0.5)	43
PCL-*g*-P(DMAEMA)1/Gelatin [c]	48 h	0.7 (±0.1)	49
PCL-*g*-P(DMAEMA)2/Gelatin [c]	48 h	3.2 (±0.3)	46
PCL-*g*-P(DMAEMA)3/Gelatin [c]	48 h	6.1 (±0.7)	42

[a] Obtained by immersing the pristine PCL film in 1,6-hexanediamine/2-propanol solution of 60 mg/mL for 24 h at room temperature. [b] Reaction conditions: [DMAEMA]/[CuBr]/[$CuBr_2$]/[Bpy] = 100:1:0.2:1.2 in methanol/water mixture (1/4, v/v) at room temperature. [c] Obtained by immersing the corresponding PCL-*g*-P(DMAEMA) surfaces in PBS solution containing the gelatin at a concentration of 10 mg/mL at 37 °C. [d] Grafting yield (GY) is defined as GY = $(W_a - W_b)/A$, where W_a and W_b represent the weight of the dry films after and before grafting, respectively, and A is the film area (about 28 cm^2). Data are presented as means ± standard deviation (n = 3).

PCL-*g*-P(DMAEMA) surface. After the reaction, the PCL-*g*-P(DMAEMA) surface was washed thoroughly with methanol and water to ensure the complete removal of the physically adsorbed reactants, prior to being dried under reduced pressure. Details on the surface-initiated ATRP had been described earlier.[19]

In this work, gelatin was immobilized onto the PCL-*g*-P(DMAEMA) surface via electrostatic interaction to improve the cell-adhesion properties of the PCL film surface. The PCL-*g*-P(DMAEMA) surfaces were immersed into PBS solution (pH 7.4) containing the gelatin at a concentration of 10 mg/mL at 37 °C. The electrostatical interaction was allowed to proceed for 48 h to produce the PCL-*g*-P(DMAEMA)/Gelatin surface. After the immobilization reaction, the films were washed sequentially with doubly distilled water at 40 °C to desorb the reversibly bound gelatin. These functionalized PCL surfaces were finally washed with sterilized PBS for further biological experiments. It is very difficult to estimate the fractional surface coverage with gelatin. In this work, the surface concentration of immobilized gelatin was instead expressed as the [N]/[C] ratio (determined from the sensitivity factors-corrected N 1s and C 1s core-level spectral area ratio of the PCL-*g*-P(DMAEMA)/Gelatin surfaces.

Surface Characterization. The chemical compositions of the modified PCL film surfaces were characterized by X-ray photoelectron spectroscopy (XPS). The XPS measurements were performed on a Kratos AXIS HSi spectrometer using a monochromatized Al K_α X-ray source (1486.6 eV photons) and procedures similar to those described earlier.[19] The static water contact angles of the pristine and functionalized PCL film surfaces were measured at 25 °C and 60% relative humidity, using the sessile drop method with 3 μL water droplets, in a telescopic goniometer (Rame-Hart model 100-00-(230), manufactured by Rame-Hart, Inc., Mountain Lakes, NJ). The topography of the modified PCL surfaces was studied by atomic force microscopy (AFM), using a Dimension 3100 AFM from the Veeco-Digital Instruments (Santa Barbara, CA, USA). In each case, an area of 40 μm × 40 μm square was scanned using the tapping mode. The drive frequency of the equipment, with the voltage between 3.0 and 4.0 V, was 330 ± 50 kHz. The drive amplitude was about 300 mV and the scan rate was 0.5−1.0 Hz. The arithmetic mean of the surface roughness (R_a) reported was calculated from the roughness profile determined by AFM.

Cell Culture. The cell-adhesion and gene transfection characteristics of the functionalized PCL surfaces were assessed by HEK293 cell lines. Cells were cultured in Dulbecco's modified eagle medium (DMEM) supplemented with 10% fetal bovine serum. All media contained 100 U/mL of penicillin and 100 μg/mL of streptomycin. Cells were incubated at 37 °C and supplemented with 5% CO_2 in the humidified chamber. For assaying the cell-adhesion characteristics of the functionalized PCL films, the surface-modified PCL films were washed twice with PBS, prior to being placed into the wells of a 24-well culture plate. HEK293 cells at a density of 8 × 10^4 cells/well in culture media were seeded and cultured on the functionalized PCL films for 24 h. The surfaces after incubation were washed twice with PBS solution to remove the dead and loosely attached cells. The cultured cells on the film surfaces were fixed with cold 70% ethanol at 4 °C for 2 h and then stained for 15 min with 50 μg/mL propidium iodide (PI) for fluorescent imaging (BX51, Olympus; Japan). For cell number on each type of surface, the surfaces prewashed with PBS solution were incubated with trypsin−EDTA solution (0.25% trypsin, 1 mM EDTA) for 10 min at 37 °C to detach the cells. The detached cells were collected and counted using a hemocytometer.

For assaying the gene transfection in the immobilized HEK293 cell lines, the plasmid (encoding enhanced green fluorescent protein (EGFP)) used in this work was pEGFP-C1. HEK293 cells at a density of 8 × 10^4 cells/well were seeded and cultured on the functionalized PCL films for 24 h. The PEI/pEGFP-C1 complexes (20 μL/well containing 0.8 μg of pDNA) at the optimal N/P ratio of 10 were prepared by mixing the equal volumes of PEI and pEGFP solutions, followed by vortexing and incubation for 30 min at room temperature. At the time of transfection, the medium in each well was replaced with 300 μL of fresh normal medium (supplemented with 10% FBS). The complexes were added into the transfection medium and incubated with the cells for 6 h under standard incubator conditions. Then, the medium was replaced with 800 μL of the fresh normal medium. The cells were further incubated until a total transfection time of 48 h. The transfected cells were imaged by using an Olympus fluorescence microscope (BX51, Olympus; Japan). EGFP was excited at 488 nm and measured at 525 nm. The percentage of the EGFP positive cells was determined using fluorescence-activated cell sorting analysis (FACS). Briefly, transfected cells were washed twice with PBS and incubated with trypsin−EDTA solution (0.25% trypsin, 1 mM EDTA) until cells detached from the surface. Then, 1 mL of complete medium was added to inhibit trypsin, followed by centrifugation at 1000 rpm for 3 min. The supernatant was removed and the cells were washed with PBS and resuspended in 0.8 mL PBS solution. Flow cytometry (FCM) analysis was conducted using Epics Elite ESP with excitation wavelength of 488 nm (Beckman Coulter, USA). The percentage of transfected cells was obtained by determining the statistics of cells fluorescing above the control level, where nontransfected cells were used as the control. For each sample, 10 000 cells were counted.

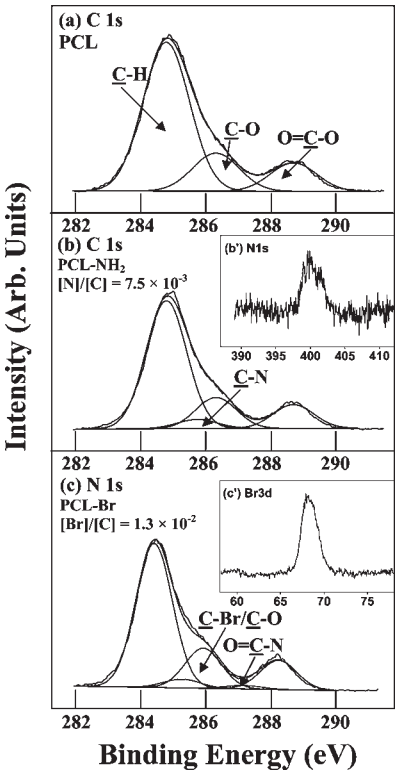

Figure 2. C 1s core-level spectra of the (a) pristine PCL, (b) PCL-NH_2, and (c) PCL-Br, surfaces, (b′) N 1s core-level spectrum of the PCL-NH_2 surface, and (c′) Br 3d core-level spectrum of the PCL-Br surface.

RESULTS AND DISCUSSION

Immobilization of the ATRP Initiators. For the preparation of polymer brushes, the initiator immobilization on the PCL film surface is indispensable. It was reported that the immobilization of ATRP initiators on PCL surfaces could be based on the hydroxyl groups from the surface hydrolysis of PCL.[10] However, the accompanying −COOH groups from the hydrolysis process could hamper the immobilization efficiency of the ATRP initiators. In this work, an alternative aminolysis-based method was developed for the covalent immobilization of ATRP initiators on the PCL surfaces. It is possible to introduce free amino and hydroxyl groups on PCL film surfaces through the aminolysis reaction with 1,6-hexanediamine.[13,14] One amine group can react the with −COO− species to produce the covalent bond, −CONH−, and the other $-NH_2$ group remains free. In addition, this aminolysis process also produces the hydroxyl-terminated chains. Both the resultant $-NH_2$ and −OH groups are ready to react with 2-bromoisobutyryl bromide (BIBB) to produce the ATRP initiator species (Figure 1). The pristine PCL film was immersed in 1,6-hexanediamine/2-propanol solution to induce the surface aminolysis processes for 24 h, producing the aminolyzed PCL-NH_2 film (Table 1). The resultant amino and hydroxyl groups on the PCL-NH_2 film surfaces were used to react with BIBB to produce the corresponding ATRP initiator-coupled surfaces (the PCL-Br surfaces).

The chemical compositions of the PCL film surfaces at various stages of surface modification were determined by X-ray photoelectron spectroscopy (XPS). Figure 2 shows the C 1s core-level spectra of the (a) pristine PCL, (b) PCL-NH_2, and (c) PCL-Br surfaces. The C 1s core-level spectrum of the PCL surface can be curve-fitted into three peak components with binding energies (BEs) at about 284.6, 286.4, and 288.7 eV, attributable to the C−H, C−O, and O=C−O species, respectively.[21] After aminolysis, the C 1s core-level spectrum of the PCL-NH_2 surface possesses an additional peak at about 285.7 eV, attributable to the C−N species,[21] which is associated with the aminolysis process. The corresponding N 1s core-level spectrum of the PCL-NH_2 surface was shown in Figure 2b′. In this work, further prolonging the aminolysis time after 24 h at the present conditions did not lead enhancement in the intensities of the resultant N 1s signals. After the immobilization of alkyl bromide, the weak O=C−N peak component with BE at about 287.5 eV, associated with the linkages between the PCL film surface and ATRP initiators, can be observed in the C 1s core-level spectrum of the PCL-Br surface. The corresponding Br 3d signal at BE of about 69 eV, characteristic of covalently bonded bromine[21] was shown in Figure 2c′. The above results confirmed that the ATRP initiators had been successfully introduced onto the PCL-Br film surface.

On the basis of the [Br]/[C] ratio (r) of 1.3×10^{-2} (Figure 2c′), the initiator density (ρ^*) was finally estimated to be about 2.9 initiators/nm^2, higher than that (1.9 initiators/nm^2) from the surface hydrolysis method.[10] In addition, the static water contact angle has increased from about 70° for the pristine surface to about 82° for the PCL-Br surface (Table 1). The variation in static water contact angles for the PCL-Br surface also suggests that the alkyl halide initiators had been successfully introduced onto the PCL film surface.

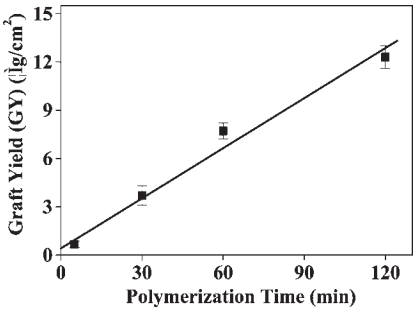

Figure 3. Dependence of the graft yield (GY) of the P(DMAEMA) chains of the PCL-*g*-P(DMAEMA) surfaces from the PCL-Br surfaces on the surface-initiated ATRP time.

Surface-Initiated ATRP of DMAEMA. The physicochemical properties of PCL surfaces can be tuned by the choice of functional vinyl monomers. Instead of P(GMA) brushes,[10] well-defined poly((2-dimethyl amino)ethyl methacrylate) (P(DMAEMA)) brushes (the PCL-*g*-P(DMAEMA) surfaces) were subsequently prepared in this work via surface-initiated ATRP of DMAEMA from the PCL-Br surfaces for immobilizing biomolecules. For surface-initiated ATRP, an excess amount of deactivating Cu(II) complex ($CuBr_2$) was added.[10] The reaction conditions and the definition of grafting yield (GY) were described in Table 1. The kinetics of P(DMAEMA) growth from the PCL-Br surfaces via surface-initiated ATRP was investigated in Figure 3. An approximately linear increase in GY of the grafted P(DMAEMA) chains with polymerization time was observed, indicating that the chain growth from the PCL-Br surface was consistent with a "controlled" and well-defined process.

Figure 4 shows the C 1s core-level spectra of the (a) PCL-*g*-P(DMAEMA)1 (from 5 min of ATRP), (b) PCL-*g*-P(DMAEMA)2 (from 30 min of ATRP), and (c) PCL-*g*-P(DMAEMA)3 (from

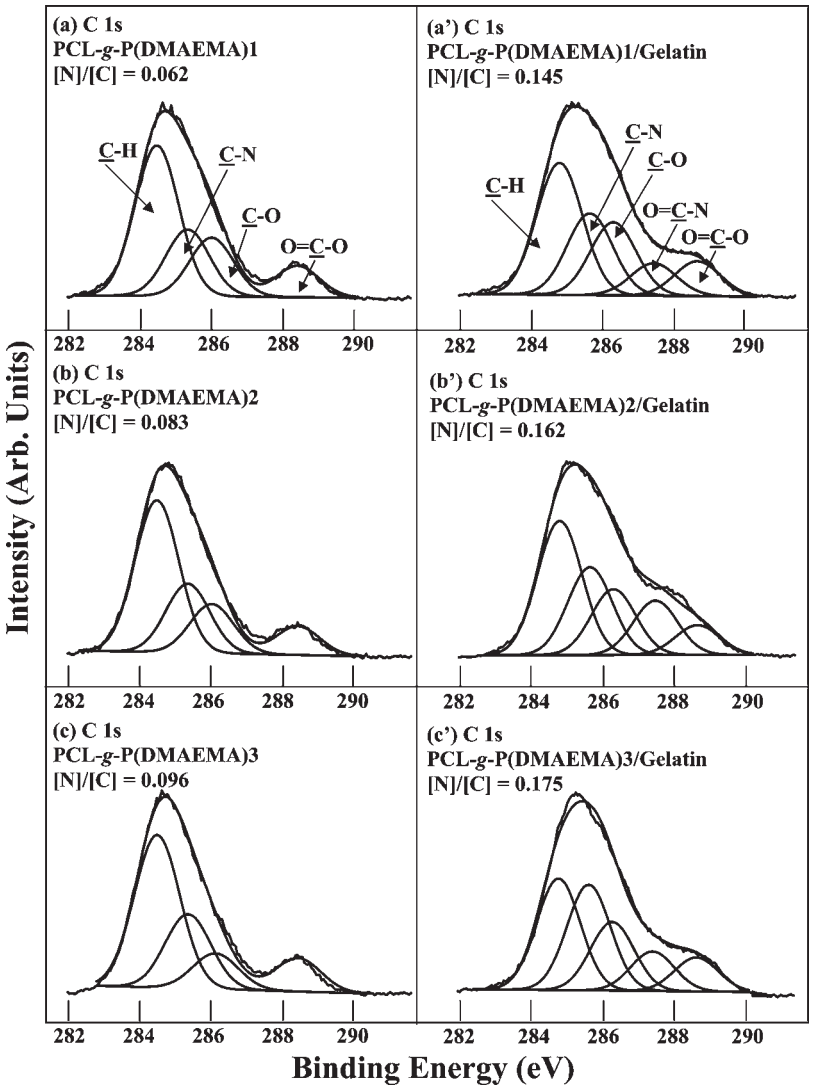

Figure 4. C 1s core-level spectra of the (a) PCL-*g*-P(DMAEMA)1, (b) PCL-*g*-P(DMAEMA)2, (c) PCL-*g*-P(DMAEMA)3, (a′) PCL-*g*-P(DMAEMA)1/Gelatin, (b′) PCL-*g*-P(DMAEMA)2/Gelatin, and (c′) PCL-*g*-P(DMAEMA)3/Gelatin surfaces.

60 min of ATRP) (Table 1). The C 1s core-level spectra were composed of four peak components with BEs at about 284.6, 285.5, 286.2, and 288.4 eV, attributable to the C−H, C−N, C−O, and O═C−O species, respectively.[21] In comparison with the C 1s core-level spectrum (Figure 2c) of PCL-Br, the significant increase in intensities of the C−N species is consistent with the presence of P(DMAEMA) brushes on the PCL-*g*-P(DMAEMA) surfaces. With the increase in ATRP time, the surface coverage of P(DMAEMA) brushes is expected to increase. For the PCL-*g*-P(DMAEMA)1, PCL-*g*-P(DMAEMA)2, and PCL-*g*-P(DMAEMA)3 surfaces, their corresponding [N]/[C] ratios (or GY values) are about 0.062 (or 0.66 μg/cm^2), 0.083 (or 3.7 μg/cm^2), and 0.096 (or 7.7 μg/cm^2), respectively (Figure 4 and Table 1). The above results were consistent with the fact that the increased GY of the P(DMAEMA) brushes from longer ATRP time would produce a more complete surface coverage. The average static water contact angles of the PCL-*g*-P(DMAEMA)3 surfaces decreased to 43° from 82° (for the starting PCL-Br surface) (Table 1), indicating that P(DMAEMA) has been successfully graft copolymerized onto the PCL-Br surface via surface-initiated ATRP. The molecular weight and molecular weight distribution of the surface-grafted polymer cannot be determined with sufficient accuracy without the cleavage of the grafted chains. It is very difficult, if not impossible, to precisely cleave the grafted P(DMAEMA) chains from the PCL chains.

Gelatin Immobilization. Gelatin has been widely used in tissue engineering, because of its excellent cell adhesion, biodegradability, and superior biocompatibility in tissue replacement and wound healing.[13,16,20,22,23] It has been demonstrated that gelatin immobilization on biomaterial surfaces can improve cell-adhesion properties.[15,20,23] The isoelectric point of ampholytic gelatin is about 4.7.[18] When pH > 4.7, the net charge of gelatin is negative, and the electrostatic interaction will occur between cationic species and carboxylate groups of gelatin. It was reported that gelatin can form polyelectrolyte complexes with polycations, such as chitosan with a pK_a of 6.5.[18,22,23] P(DMAEMA) is a cationic polymer and its pK_a is 7.0−7.3.[16,17] Similar to chitosan, P(DMAEMA) can also form stable polyelectrolyte complexes with gelatin. In this work, the P(DMAEMA) brushes were used for immobilization of gelatin via electrostatic interaction for improving the cell-adhesion properties of the PCL surfaces.

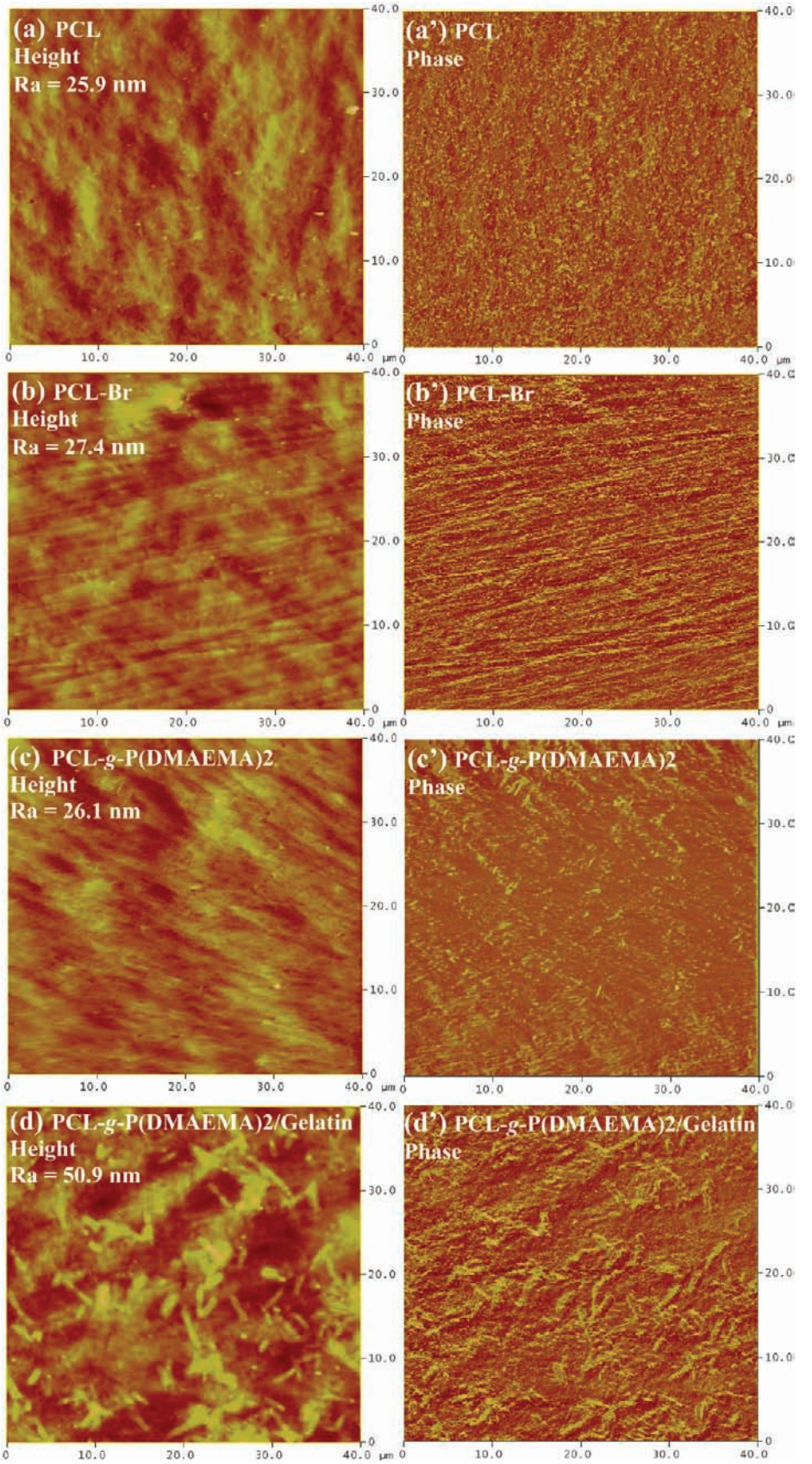

Figure 5. AFM height and phase images of the (a,a′) pristine PCL, (b,b′) PCL-Br, (c,c′) PCL-*g*-P(DMAEMA)2, and (d,d′) PCL-*g*-P(DMAEMA)2/Gelatin surfaces.

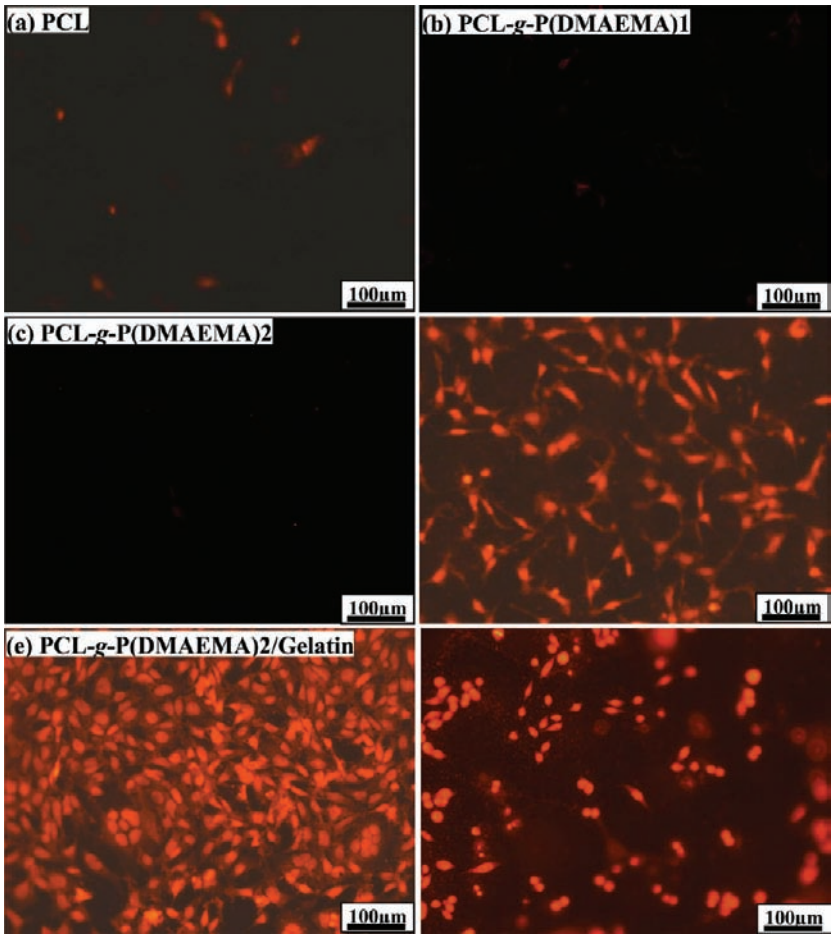

Figure 6. Optical images of HEK293 cells cultured for 24 h on the (a) pristine PCL, (b) PCL-*g*-P(DMAEMA)1, (c) PCL-*g*-P(DMAEMA)2, (d) PCL-*g*-P(DMAEMA)1/Gelatin, (e) PCL-*g*-P(DMAEMA)2/Gelatin, and (f) PCL-*g*-P(DMAEMA)3/Gelatin surfaces.

The PCL-*g*-P(DMAEMA) surfaces were immersed into gelatin solution (pH 7.4) at 37 °C for 48 h to produce the PCL-*g*-P(DMAEMA)/Gelatin surface.

After the vigorous extraction of the reversibly and loosely bound gelatin, the C 1s core-level spectra of the PCL-*g*-P(DMAEMA)/Gelatin surfaces are shown in Figure 4a′,b′,c′. In comparison with the PCL-*g*-P(DMAEMA) surfaces (Figure 4a,b, c, the C 1s core-level spectra of the PCL-*g*-P(DMAEMA)/Gelatin surfaces possess an additional peak at about 287.4 eV, attributable to the O═C−N species,[21] which is associated with the peptide bonds in gelatin. The amount of grafted P(DMAEMA) played a dominant role in the immobilization of gelatin. With the increase in the amount of the grafted P(DMAEMA) layer, the concentration of complexed gelatin is expected to increase. For the PCL-*g*-P(DMAEMA)1/Gelatin, PCL-*g*-P(DMAEMA)2/Gelatin and PCL-*g*-P(DMAEMA)3/Gelatin surfaces, the [N]/[C] ratios are about 0.145, 0.162, and 0.175, respectively (Figure 4). Their corresponding immobilized amounts of gelatin are 0.7, 3.2, and 6.1 μg/cm^2, respectively. In addition, the water contact angles of the PCL-*g*-P(DMAEMA)/Gelatin surfaces were also summarized in Table 1.

The changes in surface topography of the PCL film after modification were investigated by atomic force microscopy (AFM). Figure 5 shows the representative AFM height and phase images of the (a,a′) pristine PCL, (b,b′) PCL-Br, (c,c′) PCL-*g*-P(DMAEMA)2, and (d,d′) PCL-*g*-P(DMAEMA)2/Gelatin surfaces. The freshly prepared PCL film surface is rather uniform with a root-mean-square surface roughness value (R_a) of about 25.9 nm. After modification, the R_a values of the PCL-Br and PCL-*g*-P(DMAEMA)2 surfaces were 27.4 and 26.1 nm, respectively. No obvious changes in the surface roughness indicated that the ATRP initiator immobilization and subsequent

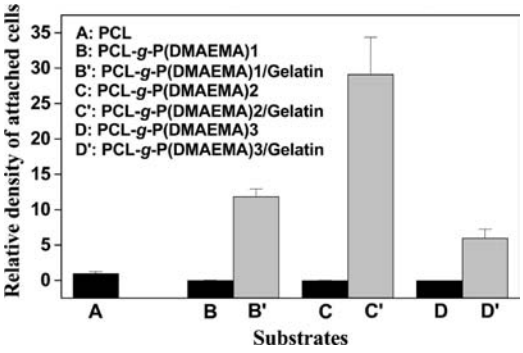

Figure 7. Relative cell-adhesion density of HEK293 cells cultured for 24 h on the pristine PCL, PCL-*g*-P(DMAEMA), and PCL-*g*-P(DMAEMA)/Gelatin surfaces, where the cell density cultured for 24 h on the pristine PCL was used as the reference. Data are presented as means ± standard deviation (n = 3).

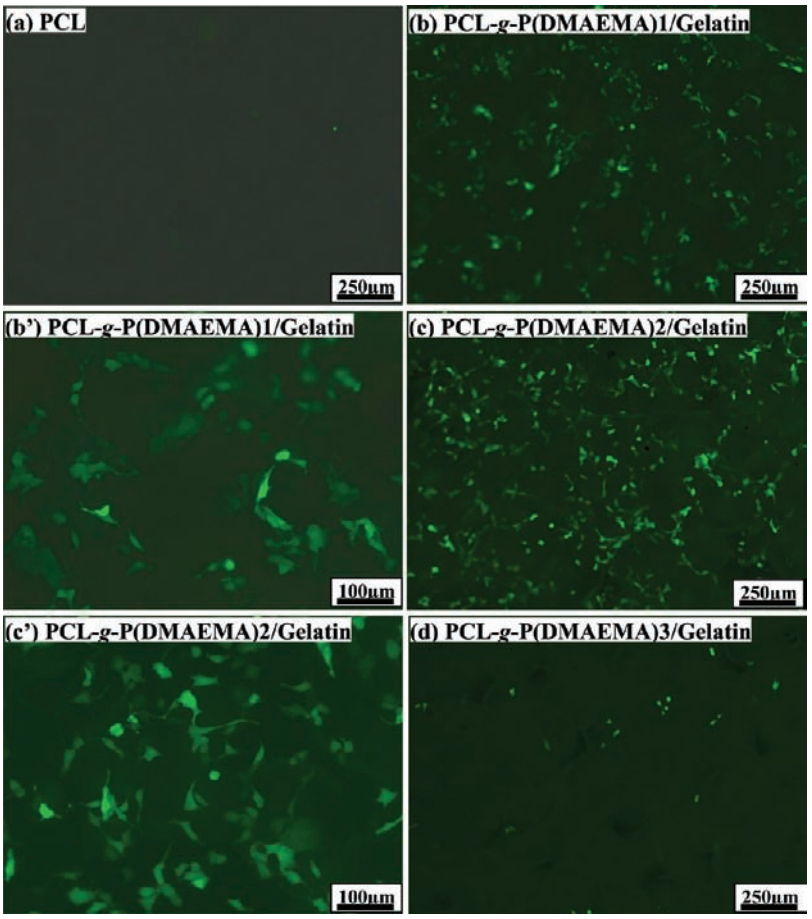

Figure 8. Representative images of pEGFP-positive HEK293 cells after 48 h post transfection with PEI/pEGFP complexes at the optimal N/P ratio of 10 on the (a) pristine PCL, (b,b′) PCL-*g*-P(DMAEMA)1/Gelatin, (c,c′) PCL-*g*-P(DMAEMA)2/Gelatin, and (d) PCL-*g*-P(DMAEMA)3/Gelatin surfaces.

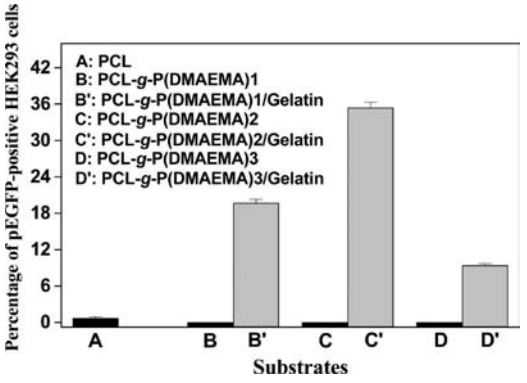

Figure 9. Gene transfection efficiency of PEI/pEGFP complexes at the optimal N/P ratio of 10 in HEK293 cell lines on the pristine PCL, PCL-*g*-P(DMAEMA), and PCL-*g*-P(DMAEMA)/Gelatin surfaces. Data are presented as means ± standard deviation (n = 3).

graft polymerization have proceeded uniformly on the PCL surfaces. After complexing with gelatin, the PCL-*g*-P(DMAEMA)2/Gelatin surface became much rougher and the R_a value increased to about 50.9 nm. The substantial increase in surface roughness was caused by the formation of the rod-like P(DMAEMA)/gelatin complexes (as shown in Figures 5(d,d′)).

Cell Adhesion. The cell-adhesion property of the functionalized PCL film surfaces was evaluated by culturing HEK293 cells. After 24 h of incubation, the surfaces were washed twice with the PBS solution to remove the dead and loosely attached cells. Figure 6 shows the representative optical images of PI-stained HEK293 cells cultured on the pristine PCL, PCL-*g*-P(DMAEMA), and PCL-*g*-P(DMAEMA)/Gelatin surfaces. The cells adhered and grew to some extent on the pristine PCL film surfaces. In comparison with the gelatin-immobilized PCL surfaces, the pristine PCL surfaces exhibited very poor cell attachment, due to its poor ability to interact with cells.[10] After grafting P(DMAEMA) brushes, almost no attached cells were observed on the PCL-*g*-P(DMAEMA) surface, probably because the cationic properties of P(DMAEMA) are unfavorable to cell adhesion. It was reported that the cationic P(DMAEMA) exhibits some cytotoxicity effects on cells.[24] After the gelatin immobilization, the attached cells on the PCL-*g*-P(DMAEMA)/Gelatin surfaces were enhanced substantially, arising from the bioactive components of gelatin.[15,20] As mentioned above, with the increase in the amount of the grafted P(DMAEMA) layer, the concentration of complexed gelatin also increased (Table 1). The higher content of the immobilized gelatin produced a higher surface coverage. The cell proliferation on the PCL-*g*-P(DMAEMA)/Gelatin surface should have a positive correlation with the proportion of immobilized gelatin. Unexpectedly,

among the PCL-*g*-P(DMAEMA)/Gelatin surfaces, the PCL-*g*-P(DMAEMA)2/Gelatin surface (with 3.2 μg/cm^2 of the immobilized gelatin) exhibited the highest level of cell attachments. The density of cell attachment on the PCL-*g*-P(DMAEMA)3/Gelatin surface (with 6.1 μg/cm^2 of the immobilized gelatin) decreased substantially, even lower than that on the PCL-*g*-P(DMAEMA)1/Gelatin surface (with 0.7 μg/cm^2 of the immobilized gelatin). In comparison with the roughness (R_a = 50.9 nm) of the PCL-*g*-P(DMAEMA)2/Gelatin surface, the PCL-*g*-P(DMAEMA)3/Gelatin surface was much rougher and its R_a value was about 81.2 nm. With such a rough surface and the excess amount of grafted P(DMAEMA), it is very difficult for the complexed gelatin on the PCL-*g*-P(DMAEMA)3/Gelatin surface (with about 6.1 μg/cm^2 of grafted P(DMAEMA), Table 1) to produce efficient surface coverage. In addition, zeta potential measurements of cut segments of the PCL-*g*-P(DMAEMA)3/Gelatin films confirmed that the PCL-*g*-P(DMAEMA)3/Gelatin film surface still possessed relatively strong positive surface charges. The above results indicated that more intact cationic groups of P(DMAEMA) on PCL-*g*-P(DMAEMA)3/Gelatin film surface remain and hamper the cell adhesion.

The relative cell-adhesion density on the different functionalized PCL film surfaces was also investigated in Figure 7. The PCL and PCL-*g*-P(DMAEMA) surfaces are unfavorable to cell attachment and growth. The surfaces of the gelatin-functionalized PCL films are favorable to cell growth and survival, and the PCL-*g*-P(DMAEMA)2/Gelatin surface with suitable graft amount of P(DMAEMA) is more favorable to cell attachment. These results are consistent with those of Figure 6. The above results indicated that the cell-adhesion process on the functionalized PCL surface can be controlled by adjusting the ratio of P(DMAEMA)/gelatin.

Gene Transfection. Successful gene transfection on a tissue scaffold could enable the localized production of therapeutic drugs to facilitate tissue repair and regeneration.[11,12] Thus, it is very meaningful to investigate the gene transfection in the immobilized cells on the functionalized PCL films. In this work, the subsequent gene transfection in the immobilized HEK 293 cells was investigated using the branched PEI(25KDa)/pEGFP-C1 complexes in the presence of serum at the optimal N/P ratio of 10.[24] Figure 8 shows the typical photos of pEGFP-positive HEK293 cells on (a) pristine PCL, (b,b′) PCL-*g*-P(DMAEMA)1/Gelatin, (c,c′) PCL-*g*-P(DMAEMA)2/Gelatin, and (d) PCL-*g*-P(DMAEMA)3/Gelatin surfaces, which were taken at 48 h after transfection. The densities of the transfected cells on the functionalized surfaces corresponded to those of the immobilized cells on their corresponding surfaces as shown in Figure 6. Almost no transfected cells were observed on the pristine PCL film. The PCL-*g*-P(DMAEMA)2/Gelatin surface exhibited the densest transfected cells, while only a few transfected cells scattered on the PCL-*g*-P(DMAEMA)3/Gelatin surface.

The transfection efficiency (as reflected by the percentage of the EGFP positive cells) on the functionalized PCL surface was qualitatively determined using fluorescence-activated cell sorting analysis (FACS) (as shown in Figure 9). The percentages of the EGFP positive cells mediated by the PEI(25KDa)/pEGFP-C1 complexes (at the N/P ratio of 10) on the PCL-*g*-P(DMAEMA)1/Gelatin, PCL-*g*-P(DMAEMA)2/Gelatin, and PCL-*g*-P(DMAEMA)3/Gelatin surfaces were 19.8 (±0.6), 35.5 (±0.85), and 9.4 (±0.3)%, respectively. The transfection efficiency on the pristine PCL was only 0.7 (±0.2)%. The ctytotoxicity induced by the PEI(25KDa)/pEGFP complexes was dependent on the cell-adhesion density on the different functionalized PCL film surfaces. After the transfection, the cell viabilities on the PCL-*g*-P(DMAEMA)1/Gelatin, PCL-*g*-P(DMAEMA)2/Gelatin, and PCL-*g*-P(DMAEMA)3/Gelatin surfaces were 61%, 75%, and 40%, respectively. The higher cytotoxicity on the functionalized film surfaces with lower cell-adhesion density may result in a reduction in the transfection efficiency.[24] The transfection efficiency on the control tissue culture polystyrene (TCPS) surface without the PCL films was 44.1(±2.2)%. After the addition of the PEI(25KDa)/pEGFP complexes, the cell viability on the TCPS surface was 82%. The above results indicated that the density of the immobilized cells on the surfaces played a dominated role in the transfection efficiency of the PEI(25KDa)/pEGFP-C1 complexes, which is of crucial importance in guiding the design of multifunctional tissue scaffolds.

CONCLUSIONS

The PCL film surfaces were successfully modified via surface-initiated ATRP of DMAEMA, followed by the conjugation of gelatin on the P(DMAEMA) brushes via electrostatic interaction for enhancing the cell adhesion and gene transfection properties. Kinetics study revealed an approximately linear increase in graft yield of the functional P(DMAEMA) brushes with polymerization time. The amount of complexed gelatin increases as that of the grafted P(DMAEMA) layer. The cell-adhesion process on the functionalized PCL surface can be controlled by adjusting the ratio of P(DMAEMA)/gelatin. More interestingly, the gene transfection efficiency on the immobilized cells is dependent on the density of the immobilized cells on the functionalized PCL film. With the inherent advantages of the good cell-adhesive nature of gelatin and the subsequent efficient gene transfection on the dense immobilized cells, the functionalized PCL films are potentially useful for the design of multifunctional tissue scaffolds.

AUTHOR INFORMATION

Corresponding Author

*E-mail: xufj@mail.buct.edu.cn (FJ Xu); majie2004@yahoo.com.cn (J Ma).

Author Contributions

†Both authors contributed equally to this work.

ACKNOWLEDGMENT

This work was supported in part by National Natural Science Foundation of China (grant numbers 50903007 and 21074007), Fok Ying Tung Education Foundation (Project no. 121048), Program for New Century Excellent Talents in University (NCET-10-0203), National Novel Drug Development Foundation of China (Grant no. 2009ZX09303-008), National Basic Research Program of China (Grant no. 2011CB911004), and Beijing Natural Science Foundation of China (Grant no. 7092086).

REFERENCES

(1) Kweon, H. Y., Yoo, M. K., Park, I. Y., Kim, T. H., Lee, H. C., Lee, H. S., Oh, J. S., Akaike, T., and Cho, C. S. (2003) A novel degradable polycaprolactone networks for tissue engineering. *Biomaterials 24*, 801–808.

(2) Cheng, Z., and Teoh, S. H. (2004) Surface modification of ultra thin poly(ε-caprolactone) films using acrylic acid and collagen. *Biomaterials 25*, 1991–2001.

(3) Teramura, Y., and Iwata, H. (2008) Islets surface modification prevents blood-mediated inflammatory responses. *Bioconjugate Chem 19*, 1389–1395.

(4) Oyane, A., Uchida, M., Choong, C., Triffitt, J., Jones, J., and Ito., A. (2005) Simple surface modification of poly(ε-caprolactone) for apatite deposition from simulated body fluid. *Biomaterials 26*, 2407–2413.

(5) Fu, L., Chen, X., He, J., Xiong, C., and Ma, H. W. (2008) Study viscoelasticity of ultrathin poly(oligo(ethylene glycol) methacrylate) brushes by a quatrz crystal microbalance with dissipation. *Langmuir 24*, 6100–6106.

(6) Gabriel, M., Nazmi, K., Veerman, E. C., Nieuw Amerongen, A. V., and Zentner, A. (2006) Preparation of LL-37-grafted titanium surfaces with bactericidal activity. *Bioconjugate Chem 17*, 548–550.

(7) Glinel, K., Jonas, A. M., Jouenne, T., Leprince, J., Galas, L., and Huck, W. T. S. (2009) Antibacterial and antifouling polymer brushes incorporating antimicrobial peptide. *Bioconjugate Chem 20*, 71–77.

(8) Matyjaszewski, K., and Xia, J. H. (2001) Atom transfer radical polymerization. *Chem. Rev. 101*, 2921–2990.

(9) Xu, F. J., Neoh, K. G., and Kang, E. T. (2009) Bioactive surfaces and biomaterials *via* atom transfer radical polymerization. *Prog. Polym. Sci. 34*, 719–761.

(10) Xu, F. J., Wang, Z. H., and Yang, W. T. (2010) Surface functionalization of polycaprolactone films via surface-initiated atom transfer radical polymerization for covalently coupling cell-adhesive biomolecules. *Biomaterials 31*, 3139–3147.

(11) De laporte, L., and Shea, L. D. (2007) Matrices and scaffolds for protein delivery in tissue engineering. *Adv. Drug Delivery Rev. 59*, 292–307.

(12) Blocker, K. M., Kiick, K. L., and Sullivan, M. O. (2011) Surface immobilization of plasmid DNA with a cell-responsive tether for substrate-mediated gene delivery. *Langmuir 27*, 2739–2746.

(13) Zhu, Y., Gao, C., Liu, X., and Shen, J. (2002) Surface modification of polycaprolacton membrane via aminolysis and biomacromolecule immobilization for promoting cytocompatibility of human endothelial cells. *Biomacromolecules 3*, 1312–1319.

(14) Zhu, Y., Gao, C., Liu, X., He, T., and Shen, J. (2004) Immobilization of biomacromolecules onto aminolyzed poly(L-lactic acid) toward acceleration of endothelium regeneration. *Tissue Eng. 10*, 53–61.

(15) Xu, F. J., Yang, X. C., Li, C. Y., and Yang, W. T. (2011) Functionalized polylactide flim surfaces via surface-initiated ATRP. *Macromolecules 44*, 2371–2377.

(16) Liu, S., and Armes, S. P. (2001) The facile one-pot synthesis of shell cross-linked micelles in aqueous solution at high solids. *J. Am. Chem. Soc. 123*, 9910–9911.

(17) Xu, F. J., Kang, E. T., and Neoh, K. G. (2006) pH- and temperature-responsive hydrogels from crosslinked triblock copolymers prepared via consecutive atom transfer radical polymerizations. *Biomaterials 27*, 2787–2797.

(18) Yin, Y. J., Li, Z. Y., Sun, Y. B., and Yao, K. D. (2005) A preliminary study on chitosan/gelatin polyelectrolyte complex formation. *J. Mater. Sci. 40*, 4649–4652.

(19) Xu, F. J., Li, Y. L., Kang, E. T., and Neoh., K. G. (2005) Heparin-coupled poly(poly(ethylene glycol) monomethacrylate)-Si(111) hybrids and their blood compatible surfaces. *Biomacromolecules 6*, 1759–1768.

(20) Bratt-Leal, A. M., Carpenedo, R. L., Ungrin, M. D., Zandstra, P. W., and McDevitt, T. C. (2011) Incorporation of biomaterials in multicellular aggregates modulates pluripote stem cell differentiation. *Biomaterials 32*, 48–56.

(21) Moulder, J. F., Stickle, W. F., Sobol, P. E., Bomben, K. D. (1992) In *X-ray Photoelectron Spectroscopy*; Chastain, J., Ed.; Perkin-Elmer: Eden Prairie, MN.

(22) Mao, J. S., Cui, Y. L., Wang, X. H., Sun, Y., Yin, Y. J., Zhao, H. M., and Yao, K. D. (2004) A preliminary study on chitosan and gelatin polyelectrolyte complex cytocompativility by cell cycle and apoptosis analysis. *Biomaterials 25*, 3973–3981.

(23) Jiang, T., Zhang, Z., Zhou, Y., Liu, Y., Wang, Z., Tong, H., Shen, X., and Wang, Y. (2010) Surface functionalization of titanium with chitosan/gelatin via electrophoretic deposition:charaterization and cell behavior. *Biomacromolecules 11*, 1254–1260.

(24) Wang, Z. H., Li, W. B., Ma, J., Tang, G. P., Yang, W. T., and Xu, F. J. (2011) Functionalized nonionic dextran backbones by atom transfer radical polymerization for efficient gene delivery. *Macromolecule 44*, 230–239.

Bioconjugate Chemistry

ARTICLE

pubs.acs.org/bc

Novel Three-Color FRET Tool Box for Advanced Protein and DNA Analysis

Andrea Kienzler,[‡] Roman Flehr,[†] Rolf A. Kramer,[‡] Sören Gehne,[†] Michael U. Kumke,[†] and Willi Bannwarth*[,‡]

[†]University of Potsdam, Institute of Chemistry (Physical Chemistry), Karl-Liebknecht-Str. 24-25, 14476 Potsdam-Golm, Germany

[‡]Albert-Ludwigs University of Freiburg, Institute of Organic Chemistry and Biochemistry, Albertstr. 21, 79104 Freiburg, Germany

Supporting Information

ABSTRACT: We report on a new three-color FRET system which we were able to verify in peptides as well as in synthetic DNA. All three chromophores could be introduced by a building block approach avoiding postsynthetic labeling. Additional features are robustness, matching spectroscopic properties, high-energy transfer, and sensitivity. The system was investigated in detail on a set of peptides as well as an array of tailored oligonucleotides. The detailed analysis of the experimental data and comparison with theoretical considerations were in excellent agreement. It is shown that in the case of polypeptides specific interaction with the fluorescence probes has to be considered. In contrast with DNA, the fluorescence probes did not show any indications of such interactions. The novel three-color FRET toolbox revealed the potential for applications studying fundamental processes of three interacting molecules in life science applications.

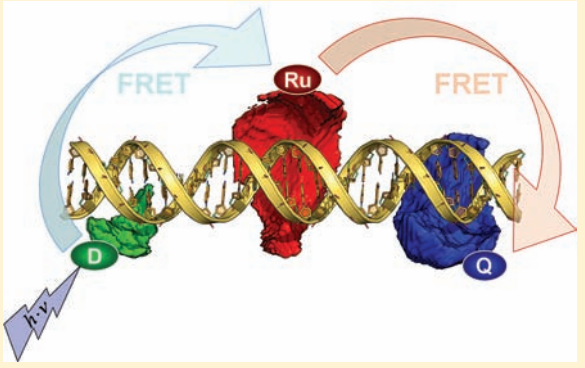

INTRODUCTION

Molecular systems based on Förster resonance energy transfer (FRET) have emerged as powerful tools for the elucidation of distance-dependent interactions on the molecular level. Such systems allow us to monitor adjustments in distances on a nanometer scale and in real-time mode, and they are therefore especially well-suited for the characterization of biochemical events both in vitro and in vivo.[1,2] The FRET technique is based on the resonant transfer of energy between a donor fluorophore (D) and an acceptor fluorophore (A) via dipole−dipole interactions. In order to achieve a powerful FRET, the spectroscopic properties of D and A need to be matched. Key variables for obtaining high FRET efficiencies are the spectral overlap of the two dyes as well as their distance from, and orientation to, each other.[3] A conventional FRET system can be used as a spectroscopic ruler for the measurement of molecular distances r in the range of 10 Å to 100 Å. Distances of interest in many of the current research topics involving protein interactions and large supramolecular complexes exceed this limit.

Applying a third dye leads to so-called three color or triple FRET (tc-FRET) systems. They consist of two coupled D/A pairs, sharing one chromophore (A) that acts as a relay station for the energy transfers as depicted in Figure 1.

Such tc-FRET systems offer a number of advantages. They yield information about the relative position of the three chromophores relative to each other in real time which is not possible with other methods. Moreover, tc-FRET systems offer additional flexibility with respect to the working range of r, which is normally given by $0.5 \cdot R_0 < r < 2 \cdot R_0$. Here, R_0 represents the so-called Förster radius, which is a specific property of the D/A pair and equals the distance between D and A at which the energy transfer efficiency is 50%. On the basis of the choice of the pairs D/A and A/Q, short as well as longer distances become accessible with equal sensitivity. They are ideal for the study of interactions between three different biomolecules and the positional changes resulting thereof, e.g., in the formation of supramolecular structures out of three proteins. In addition to this, they show a very large spectral shift between the excitation of D and the emission of Q, and require fewer labeled sample molecules to measure relative distances.[4,5] In an ideal system acceptor 2, (Q) in the FRET-chain (D→A→Q) should be excited only by the emission from the second chromophore (A) but not by that emitted from the first chromophore (D), nor should it be excited directly at the excitation wavelength of D.

Despite the obvious advantages of tc-FRETs, relatively few systems have been hitherto reported, particularly for investigations of interactions concerning biomolecules. The main reason for this is the difficulty (i) to identify three chromophores with well matching spectroscopic properties and (ii) to meet the synthetic challenges of labeling procedures for three different dyes.

In proteins, the establishment of tc-FRET systems was reported for mutants of the green fluorescent protein. These systems were successfully applied to analyze interactions of three

Received: May 26, 2011
Revised: August 3, 2011
Published: August 15, 2011

ACS Publications © 2011 American Chemical Society

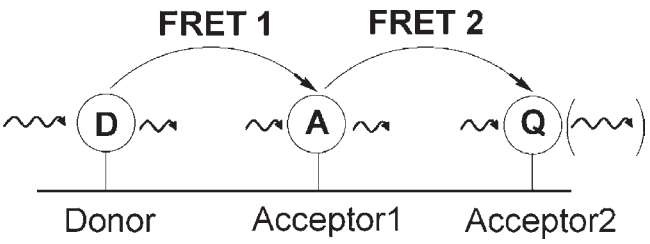

Figure 1. Principle of a three color FRET-system.

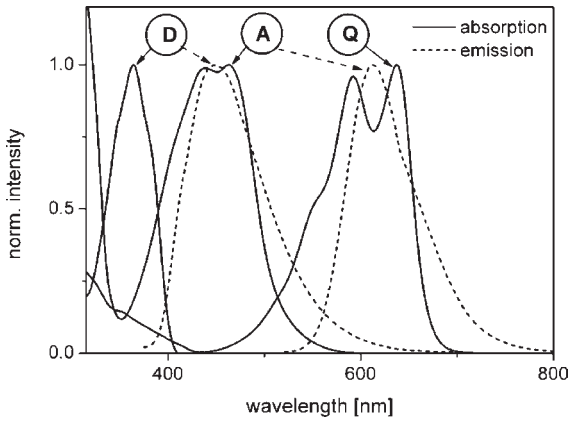

Figure 2. Absorption (solid lines) and emission (dashed lines) spectra of the three dyes for the envisaged tc-FRET system.

proteins in single endosomal compartments and to detect the TRAF2 homotrimerization in living cells.[6,7]

Most applications for tc-FRET systems have been reported for DNA.[8−15] One reason for this preference is the fact that uracil and adenine can be modified easily for postsynthetic attachments of dyes without hampering the Watson−Crick base pairing. Some dyes even allow for their incorporation during synthesis of the oligonucleotide chain via chromophore-modified phosphoramidites. Furthermore, short and medium-sized double-stranded (ds) DNA is considered a stiff rod and distances in ds-DNA can be estimated roughly from the length of a helical turn (approximately 3.4 nm for a full turn). In addition, multilabeling of a particular single strand can be avoided by assembling individually labeled oligonucleotide fragments to the desired double-stranded arrangement.

A very impressive example for multistep energy transfers in DNA was recently published by *Tinnefeld* and *Sauer* in the construction of molecular photonic wires involving five different dyes and by *Tinnefeld* for DNA-Origami.[16,17]

Recently, we have reported on two different alternative FRET systems of which the first one was based on a carbostyril donor and a Ru(II)-bathophenanthroline complex as acceptor.[18] We were able to establish the FRET system in peptides as well as in oligonucleotides and it was used for a new assay format for the transcription factor NF-κB.[19−21] The second system consisted of the Ru-complex as donor in combination with an anthraquinone as acceptor.[22] During the insertion into peptides and DNA-fragments, the spectroscopic properties of the three different chromophores used in these systems remained largely unaffected by the labeling to peptides or oligonucleotides, and both systems turned out to be very robust, efficient, and sensitive. Due to the matching spectral properties, we surmised that a combination of the two FRET-systems should result in an efficient tc-FRET assembly (see Figure 2). A comparison of the absorption and the emission spectra of the components reveal a strong overlap of the emission of the carbostyril donor with the absorption of the Ru-complex. This is also true for the emission of the Ru-complex with the absorption of the anthraquinone quencher. These facts should guarantee efficient energy transfer steps within the two pairs. Since the absorption of the Ru-complex (A) shows a minimum at the wavelength for the excitation of the carbostyril donor (D), the direct excitation of the Ru-complex at this wavelength should be largely prevented. Since the anthraquinone quencher (Q) shows also a minimum at λ = 440 nm direct quenching of the emission of D should also be of negligible importance. From these considerations, one should expect an efficient tc-FRET arrangement.

In the aspired system, the Ru(II)-bathophenanthroline complex would act as a relay chromophore (A). The complex shows high thermodynamic stability and chemical inertness, and it is accessible by straightforward synthesis.[23] A characteristic property is the long-lived metal-to-ligand charge transfer (MLCT) exited triplet state. An energy transfer from this state to a singlet state of an acceptor chromophore is generally spin forbidden, but this can be compensated for by the long emission lifetime still leading to high FRET efficiencies.[24] The long emission lifetimes in the low microsecond range allow also for time-gated detection schemes eliminating background fluorescence.[25,26]

In principle, there exist two different strategies for the insertion of dyes into peptides and DNA fragments. The attachment can be achieved either by postsynthetic labeling or by a building block approach, in which the insertion of the dye is achieved during the synthesis of the peptide or the oligonucleotide. In general, the postsynthetic labeling requires orthogonal functionalities so to allow for a specific coupling of dyes. To incorporate these functionalities, special precursor compounds are required or protecting group strategies have to be worked out. Furthermore, the yields for the coupling steps are at times modest, and the final compounds have to be purified extensively. These drawbacks can be prevented by insertion of dye-labeled building blocks during the stepwise assembly of peptides or oligonucleotides on solid support. This requires the stability of these building blocks against the reaction conditions applied, especially the deprotection steps in peptide (TFA) and in DNA synthesis (conc. NH_3).

The first goal of this work was to establish the novel tc-FRET system in peptides, being aware of the fact that, due to their conformational flexibility and the possibility of short-range electronic interactions which can compete with the energy transfer, they are less ideal tools for quantitative studies using FRET approaches. Nevertheless, peptides are often used as mimics of proteins in binding studies of which the concomitant structural changes during binding events can be followed by FRET-measurements in real time. Hence, a prime focus of this study was to demonstrate the efficient and straightforward incorporation of the three dyes into peptides during their assembly on solid support. In a further step, we demonstrate the attachment of the three dyes to synthetic DNA strands via the same synthetic strategy. Due to the highly defined structure of ds-DNA, this will allow us to work out specific qualitative and quantitative aspects of the novel tc-FRET system, despite of the fact that due to the helical staircase effect the spatial distance between the chromophores is not linear.[27]

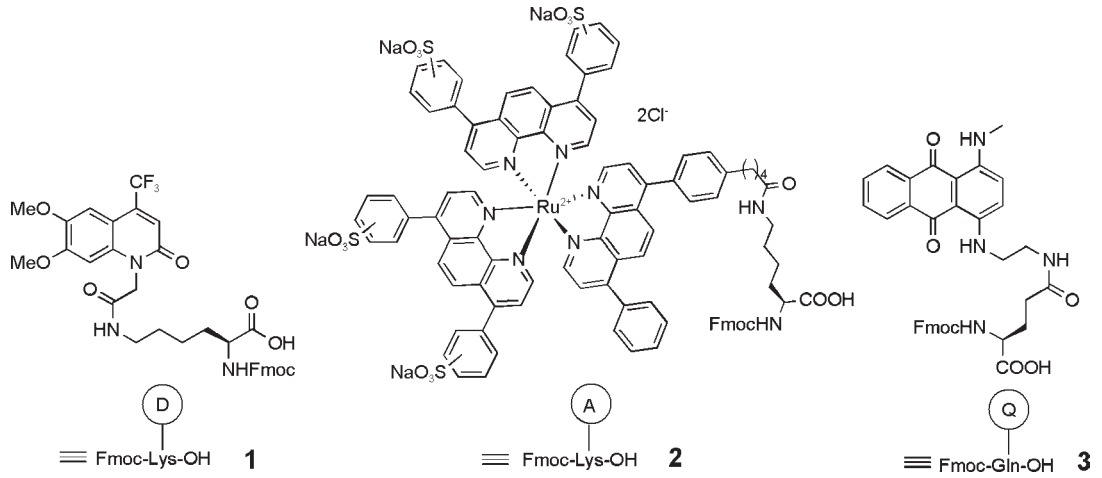

Figure 3. Amino acid building blocks for the insertion of the three dyes into peptides.

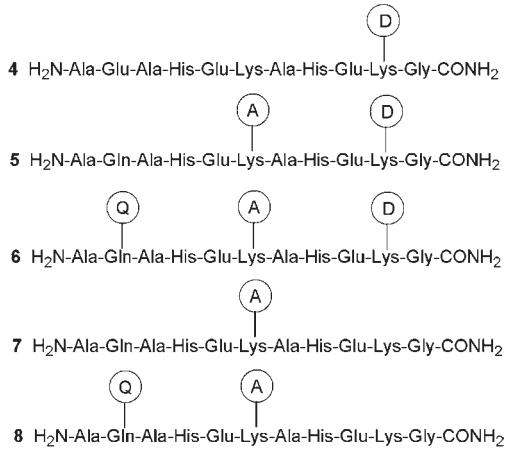

Figure 4. Synthesized peptides with inserted dyes.

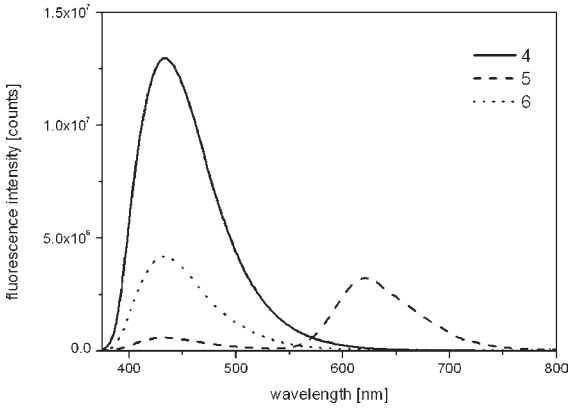

Figure 5. Fluorescence emission spectra of peptides **4**, **5**, and **6** (λ_{ex} = 355 nm).

MATERIALS AND METHODS

A detailed description of the compounds synthesized and their basic characterization by NMR and mass spectrometry is given in the Supporting Information (SI) section.

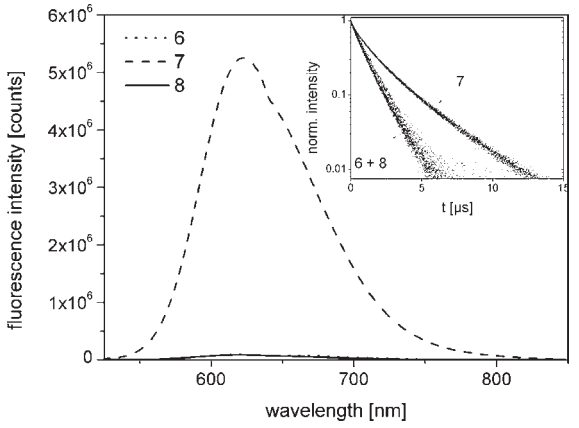

Figure 6. Steady-state and time-resolved (inset) fluorescence emission of **6**, **7**, and **8** after excitation at 430 nm.

Photophysical Characterization. The absorption and fluorescence spectra were recorded on a Cary 500 UV/vis spectrometer (Varian) and a Fluoromax3 spectrometer (Jobin Yvon). In the time-resolved emission measurements, the frequency-doubled output (second harmonic generation, SHG) with a vertical polarization plane of a Titan sapphire laser (Tsunami 3960; Spectra Physics; λ_{TiSa} = 720−860 nm, λ_{SHG} = 360−430 nm, pulse width (fwhm) 120 fs) was used for excitation. The repetition rate of 80.2 MHz was reduced to 4 MHz−50 kHz or 50−4000 kHz with a Pulse Picker (Pulse Select; APE). The luminescence was detected in a right-angle configuration to the incoming beam. For the detection, a multichannel plate (ELDI EM1−132/300; Europhoton GmbH) coupled to a FL920 fluorescence lifetime spectrophotometer (Edinburgh Instruments) was used. The time-resolved emission was recorded in the time-correlated single photon counting mode. Fluorescence decays were deconvoluted and modeled with single or double exponential decays based on Levenberg−Marquardt algorithm.[28]

The fluorescence quantum yields were measured on a PL Quantum Yield Measurement System C9920−02 with an integrating sphere (Hamamatsu, Japan).

Data Analysis. The energy transfer efficiency E strongly depends on the distance r between D and A. This relationship

dx.doi.org/10.1021/bc2002659 |*Bioconjugate Chem.* 2011, 22, 1852–1863

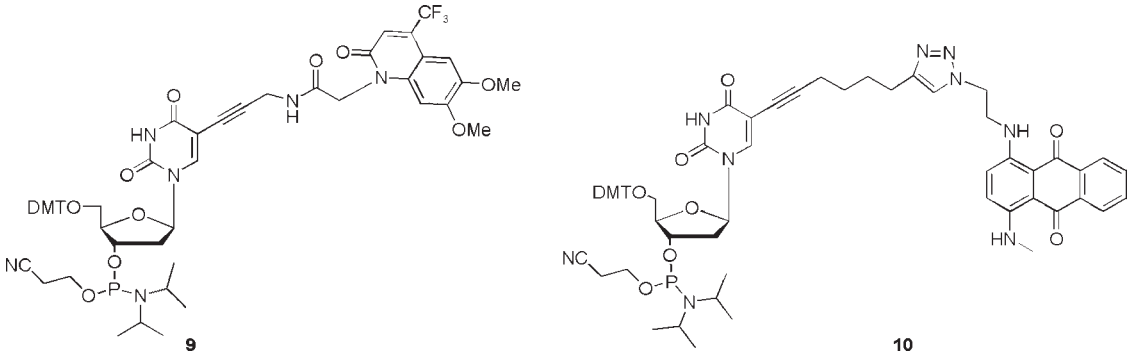

Figure 7. Building blocks **9** and **10** used for the incorporation of the donor and the quencher chromophore into DNA.

Scheme 1. Synthesis of Building Block 9[a]

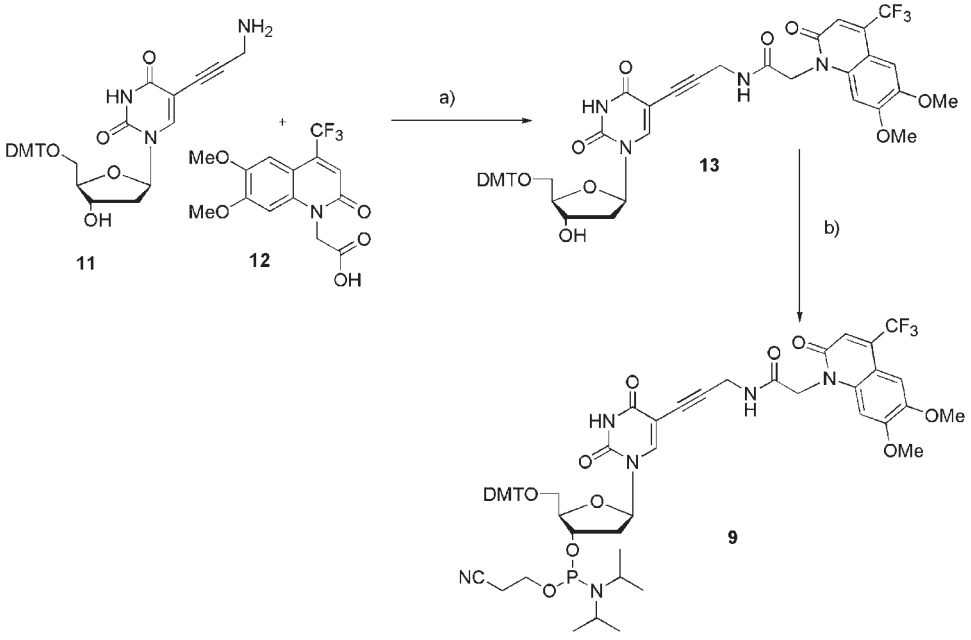

[a] (a) TBTU, Hünig's base, DMF, rt, overnight, 82%; (b) $(i\text{-}Pr_2N)_2POCH_2CH_2CN$, diisopropylammonium tetrazolide, DCM, 2.5 h, r.t., quant.

can be seen in eq 1.

$$E = \left[1 + \left(\frac{r}{R_0}\right)^6\right]^{-1} \quad \text{and} \quad r = R_0\left[\left(\frac{1}{E}\right) - 1\right]^{1/6} \qquad (1)$$

The FRET efficiencies were calculated using eq 2, where I and I_0 are the donor luminescence intensities in the presence and absence of an acceptor.

$$E = 1 - \frac{I}{I_0} = 1 - \frac{\tau}{\tau_0} \qquad (2)$$

In the case of two coupled FRET pairs sharing a dye as relay chromophore, the overall energy transfer efficiency E_{tot} is determined by the energy transfer efficiencies related to the single pairs according to eq 3:

$$E_{tot} = E_1 \cdot E_2 \qquad (3)$$

The efficiency E_1 ist related to the energy transfer between D and A and E_2 to the energy transfer between A and Q, respectively.[13]

Theoretical interdye distance calculation was done by accessible volume (AV) simulations based on "Model Satellite Prior" algorithm using the "*FRETnpsTools*" program as described here.[29,30] The needed pdb-files of ds-DNA were constructed with *Nucleic Acid Builder* (NAB) software, provided by AmberTools.[31]

RESULTS AND DISCUSSION

Labeling of Biomolecules: Polypeptides. For the labeling of the peptides, we have employed the building blocks outlined in Figure 3.

Building block **1** was used in this study instead of our previously applied carbostyril compound.[27] In a comparative study of different carbostyril derivatives, the chromophore in **1** showed the highest quantum efficiency Φ_F. Therefore, **1** yielded an improved FRET performance in combination with the Ru (II) bathophenanthroline complex as acceptor due to a larger R_0.[32] In addition to that, **1** was accessible in just five synthetic steps in a straightforward manner starting from 3,4-dimethoxy aniline.[32]

dx.doi.org/10.1021/bc2002659 |*Bioconjugate Chem.* 2011, 22, 1852–1863

Scheme 2. Preparation of building block 10[a]

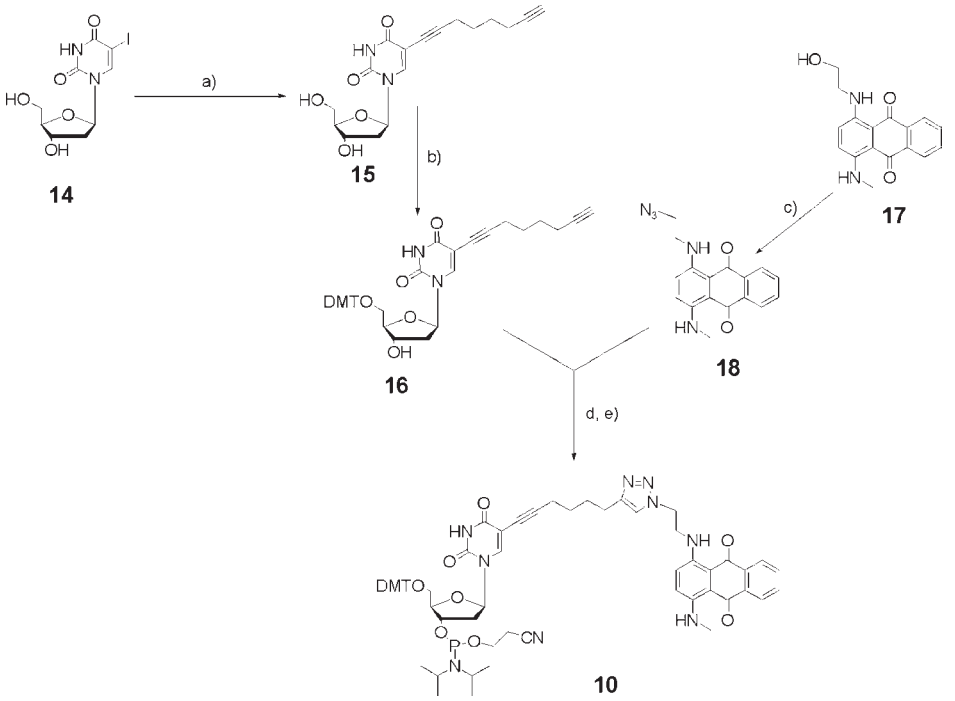

[a] (a) Octadiyne, Pd/C, CuI, Amberlite IRA-67, DMF, 50 °C, overnight, 78%; (b) DMT-Cl, DMAP, TEA, pyridine, r.t., 5 h, 70%; (c) NaN_3, CBr_4, PPh_3, dry DMF, rt, overnight, quant.; (d) $CuSO_4$, ascorbic acid, Hünigs base, DMF, H_2O, overnight, r.t., 77%; (e) $(i\text{-}Pr_2N)_2\text{-}POCH_2CH_2CN$, diisopropylammonium tetrazolide, DCM, 2.5 h, r.t., 96%.

19 5′GAA TAG TAG AGA ATT TAC ATA GAT AAT AGT 3′

20 5′ACT ATT ATC TAT GTA AAT TCT CTA CTA TTC 3′

21 5′ACT AT^{Q}T ATC TAT GTA AAT TCT^{D} CTA CTA TTC 3′

22 5′ACT ATT ATC T^{Q}AT GTA AAT TCT^{D} CTA CTA TTC 3′

23 5′ACT AT^{Q}T ATC TAT GTA AAT TCT CTA CT^{D}A TTC 3′

24 5′ACT ATT ATC T^{Q}AT GTA AAT TCT CTA CT^{D}A TTC 3′

25 5′ACT ATT ATC TAT GTA AAT TCT CTA CT^{D}A TTC 3′

26 5′ACT ATT ATC TAT GTA AAT TCT^{D} CTA CTA TTC 3′

27 5′ACT AT^{Q}T ATC TAT GTA AAT TCT CTA CTA TTC 3′

28 5′ACT ATT ATC T^{Q}AT GTA AAT TCT CTA CTA TTC 3′

29 5′AAT TCT^{D} CTA CTA TTC 3′

30 5′ACT ATT ATC T^{Q}AT GTA ·3

31-1/2 5′GAA TAG TAG AGA ATT^{R} TAC ATA GAT AAT AGT 3′

Figure 8. Oligonucleotides **19**−**31**.

The preparation of building blocks **2** and **3** was reported in refs 22,33.

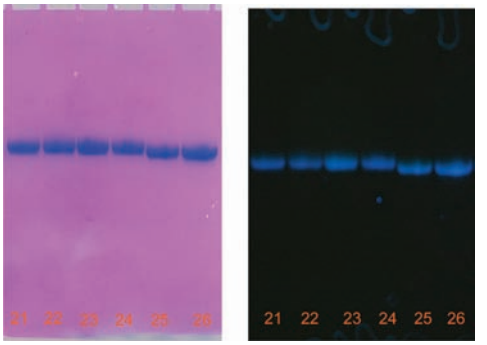

Figure 9. Analytical PAGE of purified oligonucleotides **21**−**26**. Left: excitation with visible light; right: excitation at 366 nm.

In order to demonstrate the efficient incorporation of the three chromophore-modified building blocks **1**−**3**, we have synthesized peptides **4**−**8** (Figure 4) using standard Fmoc-building blocks for the natural amino acids. All three building blocks were inserted with high efficiency during solid-phase assembly by using an excess of 1.2 equiv of the amino acids and TBTU as coupling reagent.[34] The deprotection and removal from the support by TFA caused no harm to the chromophores. The peptides were obtained in pure form after semipreparative reversed-phase HPLC. A leading idea in the design of the different polypeptides was to guarantee a good energy transfer efficiency E to proof the principle of the novel tc-FRET dye combination. Hence, only a small number of separating amino acids between D, A, and Q, respectively, was implemented.

Photophysical Characterization: Peptides. Peptide sequence **6** contains the novel tc-FRET system and peptide sequences **5** and **8** represent the single FRET pairs, respectively.

dx.doi.org/10.1021/bc2002659 |*Bioconjugate Chem.* 2011, 22, 1852–1863

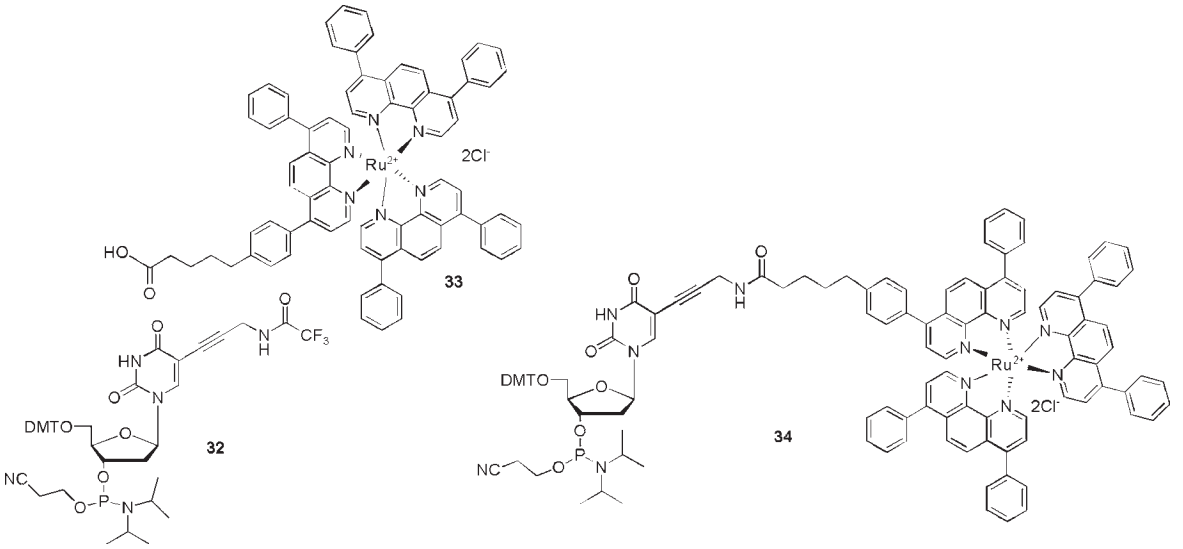

Figure 10. Building blocks (**32**/**33** and **34**) for post- or presynthetic incorporation of the Ru-complex during DNA assembly.

Scheme 3. Synthesis of building block 34[a]

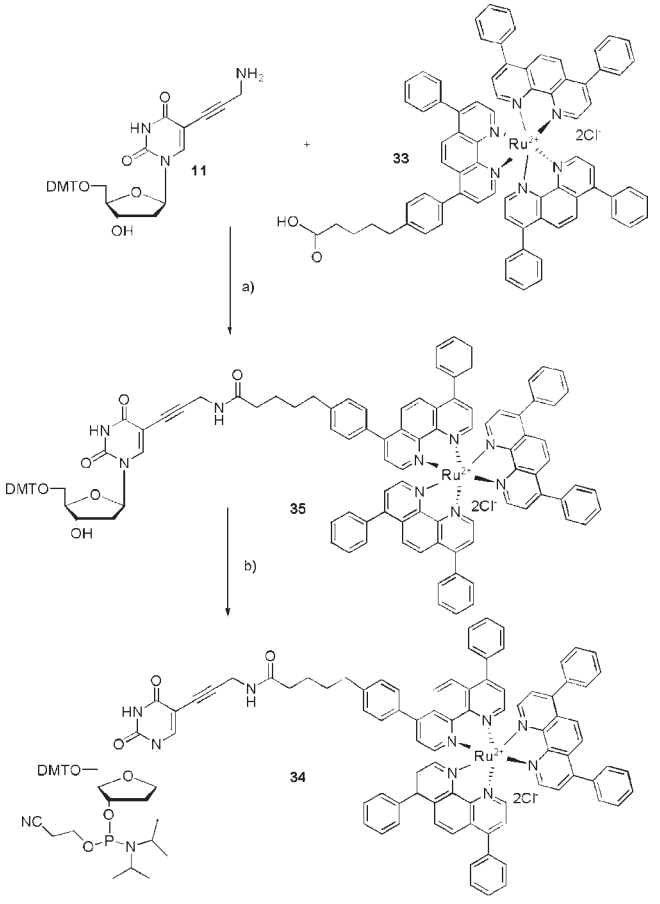

[a] (a) TBTU, Hünig's base, DMF, r.t., overnight; (b) $(i\text{-}Pr_2N)_2POCH_2CH_2CN$, diisopropylammonium tetrazolide, DCM, 2.5 h, r.t.

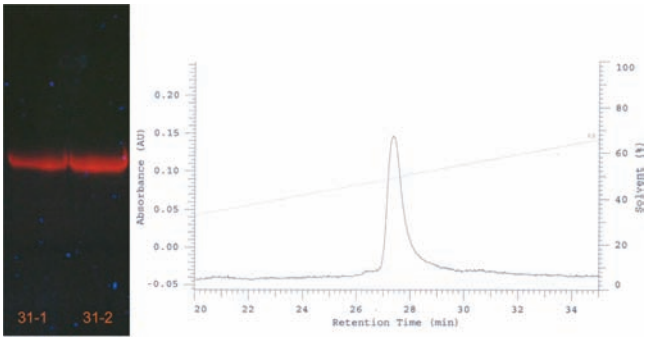

Figure 11. Left: Analytical PAGE of oligonucleotides **31-1** and **31-2** (366 nm). Right: Analytical HPLC of coinjection (oligonucleotides **31-1** and **31-2**).

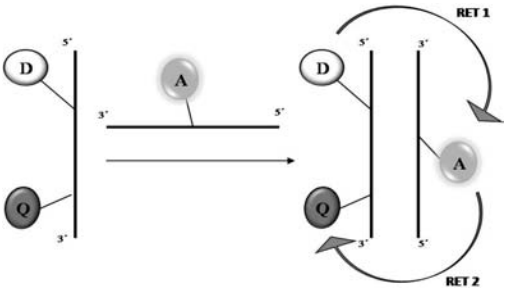

Figure 12. Principle of the formation of the triple FRET-system in double-stranded DNA and visualization of the different resonance energy transfer (RET) steps.

Sequences **4** and **7** serve as references to obtain the unquenched fluorescence data of D and A. First, the three peptide sequences **4**−**6** were investigated by steady-state fluorescence measurements with excitation at λ_{ex} = 355 nm, which corresponds to the absorption maximum of D with only minimal direct excitation of A and Q (Figure 2 and Figure 5, respectively). In peptide **4**, this resulted in the bright emission of the donor entity with $\lambda_{em,max}$ = 440 nm. The emission of D was significantly reduced in peptide **5** due to the energy transfer to the Ru(II)-bathophenanthroline complex. As a consequence of the successful energy transfer, an intense emission of the Ru(II)-bathophenanthroline complex with $\lambda_{em,max}$ = 620 nm was observed. Due to the high quenching

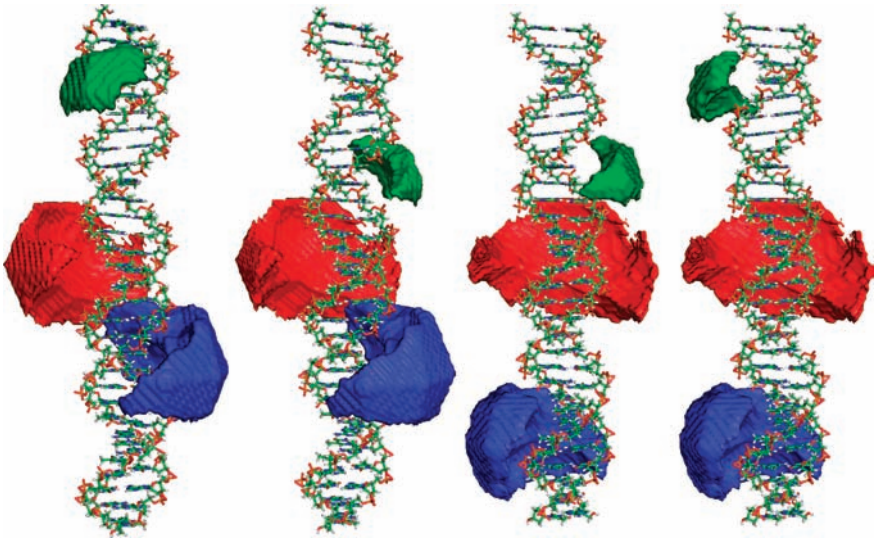

Figure 13. **24/31** "D2-A-Q1" (left), **22/31** "D1-A-Q1"(left-middle), **21/31** "D1-A-Q2" (right-middle), and **23/31** "D2-A-Q2" (right) with D (green), A (red), and Q (blue).

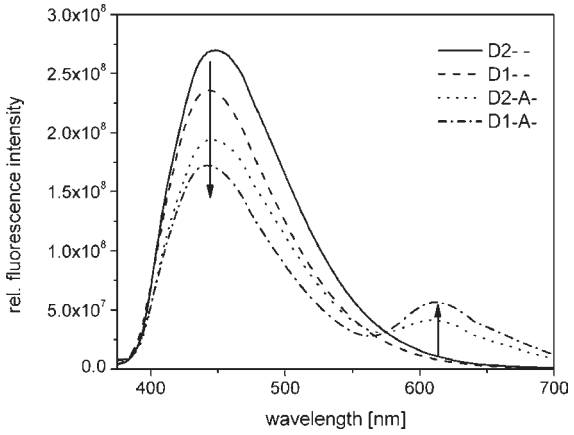

Figure 14. Fluorescence emission spectra of sample D2 - (**25/19** solid line), D1- (**26/19** dashed line), D2-A - (**25/31** dotted line), and D1-A - (**26/31** dotted−dashed line) (λ_{ex} = 360 nm).

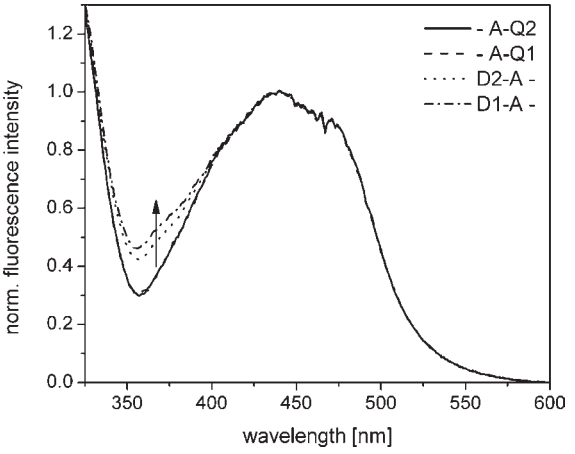

Figure 15. Fluorescence excitation spectra of sample - A-Q2 (**27/31** solid line), - A-Q1 (**28/31** dashed line), D2-A - (**25/31** dotted line), and D1-A - (**26/31** dotted−dashed line) (λ_{em} = 620 nm).

efficiency of the anthraquinone chromophore (Q), this emission of A was no longer present in peptide **6** and demonstrates as proof of principle the successful implementation of the tc-FRET system in polypeptides.

In order to prove the high quenching efficiency of A by Q in peptide **6**, the fluorescence spectra of the three peptides **6**−**8** under direct excitation of A with λ_{ex}= 430 nm were measured as well (see Figure 6). A comparison of the emission intensity data shows a high transfer efficiency E of about 98% to Q. For sequences **6** and **8**, the luminescence decay time τ of the Ru-complex was determined. From the data analysis, a decrease from τ = 1.9 μs (peptide **7**) to τ = 1.1 μs (see inset Figure 6) was found, which corresponds to a transfer efficiency of only E = 42%. The differences in the results of steady-state and time-resolved measurements indicate that, in addition to the resonance energy transfer, which changes the luminescence decay time as well as the luminescence intensity of A, in the peptides an additional molecular interaction is present causing an additional quenching of the luminescence intensity. In the UV/vis absorption spectra of the peptides, a slight bathochromic shift as well as a spectral broadening in the absorption band of Q is found (see SI Figure 1SI). This strongly points toward an electronic interaction between Q and A which is already present in the electronic ground state of the molecules. Such interactions can induce a static luminescence quenching. In contrast to intensity measurements, time-resolved luminescence measurements are not prone to contributions from static quenching, and therefore, only the quenching directly related to energy transfer is observed.

Labeling of Biomolecules: Oligonucleotides. In order to minimize any influence based on ground-state interactions of the chromophores, double-stranded DNA fragments were designed as a rigid spacer with better control of intermolecular distances between the dye molecules for further systematic characterization of the novel tc-FRET system. For perfect tailoring of dye-labeled DNA strands via dye-labeled building blocks, the latter were designed, synthesized, and implemented during assembly of the DNA strands.

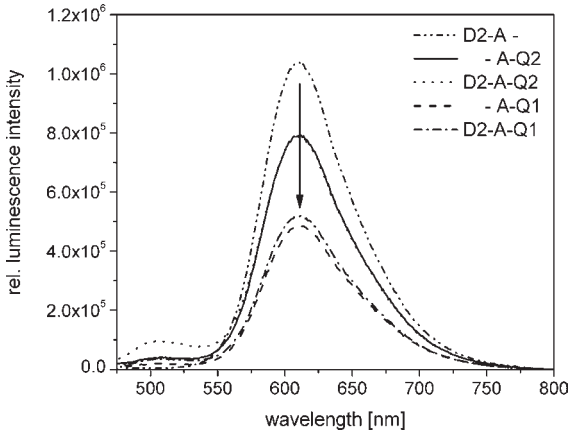

Figure 16. Fluorescence emission spectra of samples D2-A - (**25**/**31** dotted-dashed line), - A-Q2 (**27**/**31** solid line), D2-A-Q2 (**23**/**31** dotted line), - A-Q1 (**28**/**31** dashed line), and D2-A-Q1 (**24**/**31** dash−dash−dot line) (λ_{ex} = 450 nm).

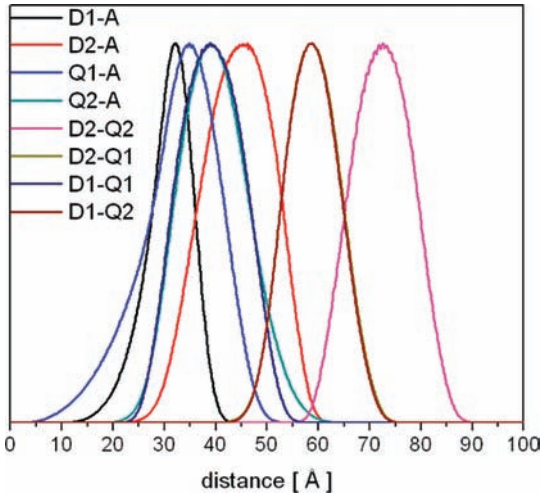

Figure 17. Distance distribution of the D/A and A/Q couples derived from theoretical calculations of the accessible space of the dye molecules, respectively (see also Figure 13).

The building blocks used for the incorporation of the donor and the quencher chromophore into synthetic DNA are outlined in Figure 7.

Phosphoramidites **9** and **10** were synthesized according to reaction Schemes 1 and 2, and they were obtained in pure form as diastereoisomers after short column chromatography.

After having determined via testing that the quinolinone-derivative **12** was completely stable toward all conditions applied to DNA synthesis including deprotection with concentrated ammonia, this entity was coupled to the amino-modified nucleoside **11** using TBTU as coupling reagent to yield derivative **13**. Phosphinylation with (2-cyanoethoxy)-bis-(*N*,*N*-diisopropylamino) phosphine in the presence of diisopropylammonium tetrazolide yielded the phosphoramidite **9** which was obtained after short column chromatography in pure form as a mixture of diastereoisomers.

Brown had already reported on the incorporation of the anthraquinone quencher into synthetic DNA.[35] A drawback of the described derivative was the lability of the linker between the nucleoside and the anthraquinone toward concentrated ammonia in the deprotection step. We prevented this lability by connecting both entities via a Huisgen 1,3-dipolar cycloaddition between an azide and alkyne, now commonly dubbed Click reaction (Scheme 2).[36]

The preparation started with 2′-deoxy-5-iodouridine (**14**) which was coupled in a Sonogashira reaction to octadiyne with Pd/C as catalyst in the presence of Amberlite-IRA-6 which was followed by regioselective introduction of the 4,4′-dimethoxytrityl group into the 5′-position.[38] The anthraquinone derivative **17** was transferred via a Mukaiyama reduction followed by an azide substitution to the azide-modified derivative **18**.[39] This compound was coupled via a click reaction to the alkyne-modified nucleoside. The resulting intermediate was transformed to the desired phosphoramidite **10**. Test reactions revealed that both phosphoramidites could be coupled with high efficiency in standard DNA synthesis. After synthesis of the oligonucleotide sequences **19** and **20**, which are complementary but are not containing a chromophore of the FRET system, building blocks **9** and **10** were then applied to the synthesis of the dye-modified sequences **21**−**30** (Figure 8). After deprotection and removal from the support, they were purified by preparative PAGE (Figure 9).

For the synthesis of sequence **31** carrying the Ru-complex as relay chromophore, we have used two different approaches. In the first one, we have carried out a postsynthetic labeling using building blocks **32** and **33** (Figure 10). Phosphoramidite **32** was coupled with high efficiency and yielded after deprotection of the trifluoroacetyl group a primary aminofunction, to which the Ru-complex **33** was coupled after activation with TSTU (DNA **31**−**1**).[34]

The overall approach for this postsynthetic modification procedure turned out to be rather cumbersome. As an alternative, we have therefore synthesized the Ru-complex-phosphoramidite **34**, which can be directly incorporated in the course of the assembly of oligonucleotide **31**. The synthesis of this building block is depicted in Scheme 3.

In the first step, the Ru-complex was coupled to the amino-modified nucleoside **11** using TBTU as coupling reagent to yield derivative **35**. This intermediate was then converted into the corresponding phosphoramidite **34** using (2-cyanoethoxy)-bis-(*N*,*N*-diisopropylamino)phosphine in the presence of diisopropylammonium tetrazolide. With phosphoramidite **34**, it was possible to incorporate the Ru-complex directly during DNA synthesis (DNA **31**-**2**).

DNA strands **31**-**1** and **31**-**2** obtained by applying the two different approaches were purified via preparative PAGE. Their purity was verified by analytical PAGE and HPLC (Figure 11).

The tc-FRET-system was then established by hybridizing the Ru-complex-modified oligonucleotide fragment **31** to the complementary strands equipped with the donor and the quencher chromophore as depicted in Figure 12. The different hybrids were then investigated by photophysical measurements.

Photophysical Characterization: Oligonucleotides. Two sets of tc-FRET ds-DNA samples with different relative distances between D, A, and Q, respectively, were characterized in detail. Here, the position of the relay dye A was fixed on the ds-DNA and the relative position of D and Q were altered (see Figures 8 and 12). As an extension of the tests performed with the peptide based tc-FRET system, the distances between D and A as well as between A and Q were systematically varied, in order to specifically address and distinguish the two consecutive energy transfer steps. In addition to the standard reference samples, which contain only one of the dyes, samples without the relay dye

Table 1. FRET-Efficiencies and Inter-Dye Distances

sample no.	sample	E_{DA}	E_{AQ}	R_{theo}[a] $_{DA}$ [nm]	R_{theo}[a] $_{AQ}$ [nm]	R_{spec}[b] $_{DA}$ [nm]	R_{spec}[c] $_{AQ}$ [nm]
21/31	D1-A-Q2	0.42	0.33	3.2 ± 0.5	3.9 ± 0.7	4.0 ± 0.3	4.5 ± 0.4
22/31	D1-A-Q1	0.38	0.55	3.2 ± 0.5	3.4 ± 0.7	4.1 ± 0.3	3.9 ± 0.3
23/31	D2-A-Q2	0.29	0.28	4.5 ± 0.7	3.9 ± 0.7	4.4 ± 0.3	4.7 ± 0.4
24/31	D2-A-Q1	0.27	0.54	4.5 ± 0.7	3.4 ± 0.7	4.5 ± 0.3	3.8 ± 0.3
29 + 30/31	D1-A-Q1	0.31	0.43	3.2 ± 0.5	3.4 ± 0.7	4.3 ± 0.4	4.2 ± 0.4
25/31	D2-A -	0.27	-	4.5 ± 0.7	-	4.5 ± 0.3	-
26/31	D1-A -	0.36	-	3.2 ± 0.5	-	4.2 ± 0.3	-
27/31	- A-Q2	-	0.30	-	3.9 ± 0.7	-	4.6 ± 0.4
28/31	- A-Q1	-	0.54	-	3.4 ± 0.7	-	3.8 ± 0.3

sample no.	sample	E_{DQ}	R_{theo}[a] [nm]	R_{spec}[d] [nm]
21/19	D1- -Q2	0.06	5.9 ± 0.7	5.5 ± 0.4
22/19	D1- -Q1	0.14	3.9 ± 0.5	4.6 ± 0.3
23/19	D2- -Q2	-	7.2 ± 0.5	-
24/19	D2- -Q1	0.06	5.9 ± 0.6	5.5 ± 0.4
29 + 30/31	D1-A-Q1	0.15	3.9 ± 0.5	4.6 ± 0.4

[a] Calculated from AV-simulations. [b] With $R_{0(D/A)}$ = 38.2 Å. [c] With $R_{0(A/Q)}$ = 40.5 Å. [d] With $R_{0(D/Q)}$ = 34.4 Å.

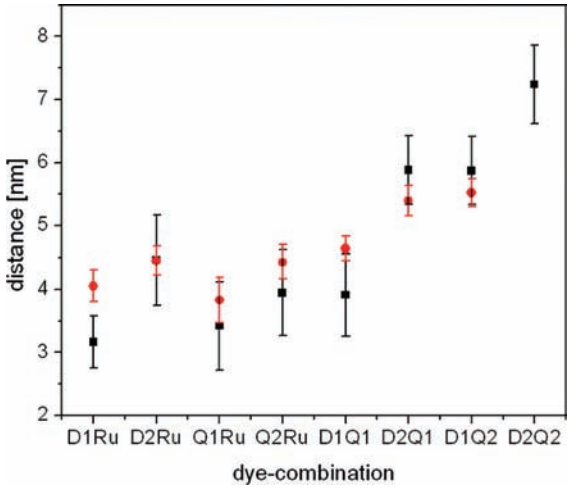

Figure 18. Comparison of theoretical (black squares) and spectroscopically derived (red circles) inter-dye distances.

(A) were designed. The latter samples were used to investigate the possible contribution of a direct interaction between D and Q. Moreover, the D/A FRET couple as such has already been extensively investigated with A attached to the end of the ds-DNAs before.[22]

In the absorption spectra of the anthraquinone quencher (Q), a small bathochromic shift due to coupling to DNA was observed relative to the reference sample of free Q, but no further alteration due to the presence of D or A was found. This finding indicates the absence of a significant ground-state interaction between the different dye pairs as was the case for the investigated peptides.

In Figure 13, the tentative spatial distribution of the different probes based on a force field approach is shown for the various ds-DNA investigated. It can be seen that even for the shortest distances only a minor - if any - possibility of a direct electronic interaction between the probes, e.g., due to orbital overlap, is expected. This is in good agreement with the results obtained from UV/vis absorption and underlines the specific benefits (the rigid character as well as the turn of the helix) of ds-DNA as spacer.

In order to control any direct influence of the DNA base or the DNA sequence on the fluorescence properties of the probes, single-labeled ds-DNA (**19/25**, **19/26**, and **20/31**), fluorescence probes (D or A) attached to the DNA base, and the free dyes were investigated under comparable experimental conditions as well. The attachment of the DNA base to D and A, respectively, only slightly changed their photophysical characteristics.

The influence of the incorporation into the ds-DNA was investigated only for D (because in the samples the relative position of A in the ds-DNA was fixed, so no additional differences between the samples due to different chemical environments of A originating for the DNA strand were expected). In the standard reference samples with only D attached to the DNA strand, the fluorescence intensity and the fluorescence decay time were dependent on the relative position within the DNA strand. Two different positions corresponding to five or ten separating base pairs (Δbp) between D/A in the tc-FRET system were investigated with D-only labeled ds-DNA as control. The subscripts "1" and "2" correspond to a Δbp of five and ten separating base pairs, respectively. Depending on the position of D in the ds-DNA sequence, the fluorescence intensity as well as the fluorescence decay time of D was reduced. The average fluorescence decay time of D in position 2 changed from τ_{D2} = 3.9 ns to τ_{D1} = 3.4 ns in position 1, which corresponds to a relative alteration of about 15%. The comparison of the fluorescence intensities showed a reduction of the fluorescence intensity by about 14%, which is in good agreement with the time-resolved data. Here, the presence of the nucleic acid base guanine in the next neighborhood of D (on the cDNA strand) might be responsible for the observed fluorescence quenching (see SI Figure SI2).[37]

For characterization of the consecutive energy transfer steps, two distances between the D/A and A/Q couple (and their permutations) were investigated together with the respective reference compounds containing only one of the D/A pairs (D2-A - (**25/31**), D1-A - (**26/31**), -A-Q2 (**27/31**) and -A-Q1 (**28/31**)).

From the decrease of the fluorescence emission intensity of D (see Figure 14) and from the fluorescence excitation spectra (with λ_{em} = 620 nm corresponding to the emission of A; see Figure 15), the successful energy transfer between D and A can be concluded for both of the investigated relative positions (Δbp = 5 and 10 base pairs, respectively).

Similarly, the second energy transfer step between A and Q can be shown by the decrease in the emission intensity of the relay dye A. The overall decrease was dependent on the distance to Q as can be seen from the comparison of the fluorescence intensities (see Figure 16).

Using the fluorescence intensity data, the energy transfer efficiencies $E_{D/A}$ and $E_{A/Q}$ were calculated (see Table 1). On the basis of model calculations for the distance distribution between D and A, an average distance of 4.9 nm (position 2, Δbp = 10) and of 3.5 nm (position 1, Δbp = 5) was expected (see Figures 13 and 17). From the experimental data, an energy transfer efficiency E_{DA} of about 30% for Δbp = 10 and of about 40% for Δbp = 5 were found, which corresponds to (4.5 ± 0.3) nm and (4.0 ± 0.3) nm, respectively, and is in good agreement with the predicted distances calculated based on R_0 as well as with the mean distances found in the distance distribution derived from theoretical calculations of the accessible space of the dye molecules (see Table 1 as well as Figures 17 and 18). A similar approach was pursued for the second energy transfer step of the A/Q couple. Using an excitation wavelength selective for A, in tc-FRET systems specifically the energy transfer between A and Q could be addressed and compared to the corresponding reference compounds.

In addition, $E_{D/Q}$ was determined from the control measurement of compounds D1- -Q2 (**21/19**), D1- -Q1 (**22/19**), D2- -Q2 (**23/19**), D2- -Q1 (**24/19**) and D1 - - (**26/19**), D2 - - (**25/19**), respectively (see Table 1). The comparison of the energy transfer efficiencies for the reference samples with only one FRET pair with the respective tc-FRET systems is in good agreement. The overall energy transfer efficiencies E_{tot} can be calculated according to eq 3. It can be seen that E_{tot} ranges from 8% to 35% depending on the overall separation of D and Q. The overall Δbp of D and Q is the main factor which can be seen from the samples **21/31** and **24/31**. For those samples, the same E_{tot} = 20% was determined.

Moreover, it was found that especially for the shorter distances a direct energy transfer between D and Q has to be taken into account. For the shortest distance (Δbp = 10) between D and Q, an energy transfer efficiency of $E_{D/Q}$ = 14% was found. For distances with Δbp = 15 between D and Q, the measured $E_{D/Q}$ = 6% and for Δbp > 15 no direct energy transfer (sample **23/19**) could be observed, and in this case, $E_{D/Q}$ can be neglected in subsequent calculations of the overall energy transfer, in which contributions from the direct transfer between D and Q have to be considered according to eq 4

$$E_{tot} = E_{D/A} \cdot E_{A/Q} + E_{D/Q} \quad (4)$$

In Table 2, the calculated overall energy transfer efficiencies E_{tot} are summarized. In final control experiments, the short DNA sequences **29** and **30** were used with the DNA strand **31**, which should show comparable results to the sample **22/31**. It was found that the measured energy transfer efficiencies were slightly smaller, which can be attributed to the fact that such small DNA sequences have a much lower melting point and thus the hybridization is less perfect compared to longer stands.

Table 2. Overall FRET Efficiency E_{tot}

sample no.	sample	E_{tot}
21/31	D1-A-Q2	0.20
22/31	D1-A-Q1	0.35
23/31	D2-A-Q2	0.08
24/31	D2-A-Q1	0.21
29 + 30/31	D1-A-Q1	0.28

The novel FRET tool box combines robustness in synthesis with excellent spectroscopic parameters. The very stable building blocks allow the highly specific inclusion of fluorescence probes in peptides as well as DNA strands. The fluorescence probes perfectly match in their spectroscopic properties yielding an excellent tc-FRET system, in which each probe (especially, the donor D and the relay dye A) can be selectively excited. This novel FRET tool box was characterized in a proof-of-principle approach for polypeptides as well as for DNA strands. Our first results for polypeptides nicely show the feasibility of the experimental approach using peptide building blocks to implement a tc-FRET system and prove the proposed working hypothesis. However, the experimental data also underline the challenges in working with peptide constructs due to their chain flexibility and folding. A contribution from additional static quenching related to ground-state interaction between A and Q can be attributed to the small separation between D and A as well as A and Q, which is further enhanced by the flexibility of the polypeptide chain. The results underline the call for a case-by-case study when using fluorescence probes in general and FRET as detection in particular for the investigation of proteins. With the novel tool box, the building of tailored peptide sequences addressing such issues in detail can now be easily envisaged. For the ds-DNA samples, the distance dependence of the two possible FRET steps was systematically investigated. In control experiments, the presence of the nucleic acid base guanine in the next neighborhood of D (on the cDNA strand) a sequence dependent quenching (by the DNA stand) was found. This result underlines the necessity of appropriate ds-DNA reference samples in order to quantify any direct influence of the DNA sequence on the fluorescence probe due to specific interactions and also calls for a case-by-case study for the DNA samples of interest. Nevertheless, the different possible energy transfer steps of the tc-FRET system were characterized for ds-DNA and compared to theoretical considerations. With the novel FRET tool box, the investigation of large but also small distances within a macromolecular system is now in hand. Especially in life science investigations, in which the interaction of three partners is of interest, the introduced tc-FRET system will be very valuable, especially because the tool box provided allows the tailored design of many biomolecules involving polypeptides and DNA (e.g., investigation of triple helix formation).

■ ASSOCIATED CONTENT

Supporting Information. Absorption spectra of peptide sequences, with varying quencher behavior; steady-state and time-resolved fluorescence emission spectra of D-only labeled DNA (D2 - - **27/19** and D1 - - **28/19**); detailed information on synthesis of building blocks and the fundamental analysis such as NMR and mass spectrometry data. This material is available free of charge via the Internet at http://pubs.acs.org.

AUTHOR INFORMATION

Corresponding Author

*E-mail: willi.bannwarth@organik.chemie.uni-freiburg.de. Tel.: +497612036073. Fax: +4976112038705.

ACKNOWLEDGMENT

Parts of this work were funded by the German Federal Department for Science and Education BMBF (IP 03/517).

REFERENCES

(1) Sapsford, K. E., Berti, L., and Menditz, I. L. (2006) Materials for fluorescence resonance energy transfer analysis: beyond traditional donor-acceptor combinations. *Angew. Chem., Int. Ed. 45*, 4562–4589.

(2) Tinnefeld, P., and Sauer, M. (2005) Branching out of single-molecule fluorescence spectroscopy: challenges for chemistry and influence on biology. *Angew. Chem., Int. Ed. 44*, 2642–2671.

(3) Förster, T. (1948) Zwischenmolekulare Energiewanderung und Fluoreszenz. *Ann. Phys. 2*, 55–75.

(4) Watrob, H. M., Pan, C.-P., and Barkley, M. D. (2003) Two-Step FRET as a structural tool. *J. Am. Chem. Soc. 125*, 7336–7343.

(5) Jiang, Z.-J., and Goedel, W. A. (2008) Fluorescence properties of systems with multiple Förster transfer pairs. *PhysChemPhys 10*, 4584–4593.

(6) Galperin, E., Verkhusha, V. V., and Sorkin, A. (2004) Three-chromophore FRET microscopy to analyze multiprotein interactions in living cells. *Nat. Methods 3*, 209–217.

(7) He, L., Wu, X., Simone, J., Hewgill, D., and Lipsky, P. E. (2005) Determination of tumor necrosis factor receptor-associated factor trimerization in living cells by CFP -> YFP -> mRFP FRET detected by flow cytometry. *Nucleic Acids Res. 33*, e61.

(8) Kawahara, S., Uchimaru, T., and Murata, S. (1999) Sequential multistep energy transfer: enhancement of efficiency of long-range fluorescence resonance energy transfer. *Chem. Commun. 6*, 563–564.

(9) Tong, A. K., Jockusch, S., Li, Z., Zhu, H.-R., Akins, D. L., Turro, N. J., and Ju, J. (2001) Triple fluorescence energy transfer in covalently trichromophore-labeled DNA. *J. Am. Chem. Soc. 123*, 12923–12924.

(10) Tong, A. K., Li, Z., Jones, G. S., Russo, J. J., and Ju, J. (2001) Combinatorial fluorescence energy transfer tags for multiplex biological assays. *Nat. Biotechnol. 19*, 756–759.

(11) Liu, J., and Lu, Y. (2002) FRET study of a trifluorophore-labeled DNAzyme. *J. Am. Chem. Soc. 124*, 15208–15216.

(12) Ohya, Y., Yabuki, K., Hashimoto, M., Nakajima, A., and Ouchi, T. (2003) Multistep fluorescence resonance energy transfer in sequential chromophore array constructed on oligo-DNA assemblies. *Bioconjugate Chem. 14*, 1057–1066.

(13) Haustein, E., Jahnz, M., and Schwille, P. (2003) Triple FRET: A tool for studying long-range molecular interactions. *ChemPhysChem 4*, 745–748.

(14) Hohng, S., Joo, C., and Ha, T. (2004) Single-molecule three-color FRET. *Biophys. J. 87*, 1328–1337.

(15) Clamme, J.-P., and Deniz, A. A. (2005) Three-color single-molecule fluorescence resonance energy transfer. *ChemPhysChem 6*, 74–77.

(16) Tinnefeld, P., Heilemann, M., and Sauer, M. (2005) Design of molecular photonic wires based on multistep electronic excitation transfer. *ChemPhysChem 6*, 217–222.

(17) Stein, I. H., Schüller, V., Böhm, P., Tinnefeld, P., and Liedl, T. (2011) Single-Molecule FRET ruler based on rigid DNA origami blocks. *ChemPhysChem 12*, 689–695.

(18) (a) Kainmüller, E. K., Ollé, E. P., and Bannwarth, W. (2005) Synthesis of a new pair of fluorescence resonance energy transfer donor and acceptor dyes and its use in a protease assay. *Chem. Commun. 43*, 5459–5461. (b) Kainmüller, E. K., and Bannwarth, W. (2006) A new robust and highly sensitive FRET donor-acceptor pair: Synthesis, characterization, and application in a thrombin assay. *Helv. Chim. Acta 89*, 3056–3070.

(19) Clima, L., Hirtz-Haag, C., Kienzler, A., and Bannwarth, W. (2007) Application of a highly robust and efficient fluorescence-resonance-energy-transfer (FRET) system in DNA. *Helv. Chim. Acta 90*, 1082–1098.

(20) Clima, L., and Bannwarth, W. (2008) Building-block approach for the straightforward incorporation of a new FRET (fluorescence-resonance-energy transfer) system into synthetic DNA. *Helv. Chim. Acta 91*, 165–175.

(21) Altevogt, D., Hrenn, A., Kern, C., Clima, L., Bannwarth, W., and Merfort, I. (2009) A new assay format for NF-kappaB based on a DNA triple helix and a fluorescence resonance energy transfer. *Org. Biomol. Chem 7*, 3934–3939.

(22) Kramer, R. A., Kainmüller, E. K., Flehr, R., Kumke, M. U., and Bannwarth, W. (2008) Quenching of the long-lived Ru(II) bathophenanthroline luminescence for the detection of supramolecular interactions. *Org. Biomol. Chem. 6*, 2355–2360.

(23) Kramer, R. A., Rumi, L., and Bannwarth, W. (2009) Optimized batchwise and continuous microreactor synthesis of a (bathophenanthroline)-ruthenium(II) complex carrying different ligands. *Helv. Chim. Acta 92*, 267–272.

(24) Marti, A. A., Puckett, C. A., Dyer, J., Stevens, N., Jockusch, S., Ju, J., Barton, J. K., and Turro, N. J. (2007) Inorganic-organic hybrid luminescent binary probe for DNA detection based on spin-forbidden resonance energy transfer. *J. Am. Chem. Soc. 129*, 8680–868.

(25) Bannwarth, W., Schmidt, D., Stallard, R. L., Hornung, C., Knorr, R., and Müller, F. (1988) Bathophenanthroline-ruthenium(II) complexes as non-radioactive labels for oligonucleotides which can be measured by time-resolved fluorescence techniques. *Helv. Chim. Acta 71*, 2085–2099.

(26) Lakowicz, J. R. (2006) In *Principles of fluorescence spectroscopy*, 3rd ed., Kluwer Academic, Plenum Publishers, New York.

(27) Flehr, R., Kienzler, A., Bannwarth, W., and Kumke, M. U. (2010) Photophysical characterization of a FRET system using tailor-made DNA oligonucleotide sequences. *Bioconjugate Chem. 21*, 2347–2354.

(28) O'Connor, D. V., and Phillips, D. (1984) In *Time-correlated single photon counting*, Academic Press Harcourt Brace Jovanovich Publishers, London.

(29) (a) Muschielok, A., Andrecka, J., Brückner, F., Jawhari, A., Cramer, P., and Michaelis, J. (2008) A nano-positioning system for macromolecular structural analysis. *Nature Methods 5*, 965–971. (b) Muschielok, A. Michaelis, J. (2008) *FRETnps Tool 2.6*, Ludwig-Maximilians-Universität Munich.

(30) Sindbert, S., Kalinin, S., Nguyen, H., Kienzler, A., Clima, L., Bannwarth, W., Appel, B., Müller, S., and Seidel, C. A. M. (2010) Accurate distance determination of nucleic acids via Förster resonance energy transfer: implications of dye linker length and rigidity. *J. Am. Chem. Soc. 133*, 2463–2480.

(31) Case, D. A. et al. ; (2010), *AmberTools Version 1.4*, University of California, San Francisco.

(32) Kramer, R. A., Flehr, R., Lay, M., Kumke, M. U., and Bannwarth, W. (2009) Comparative studies of different quinolinone derivatives as donors in fluorescence-resonance-energy transfer (FRET) - systems in combination with a (bathophenanthroline)ruthenium(II) complex as acceptor. *Helv. Chim. Acta 92*, 1933–1943.

(33) Kramer, R. A., and Bannwarth, W. (2009) Alternative solid-phase strategies for the efficient labelling of peptides with (bathophenanthroline)ruthenium(II) complexes. *Helv. Chim. Acta 92*, 1046–1055.

(34) Knorr, R., Trzeciak, A., Bannwarth, W., and Gillessen, D. (1989) New coupling reagents in peptide chemistry. *Tetrahedron Lett. 30*, 1927–1930.

(35) May, J. P., Brown, L. J., v.Delft, I., Thelwell, N., Harley, K., and Brown, T. (2005) Synthesis and evaluation of a new non-fluorescent quencher in fluorogenic oligonucleotide probes for real-time PCR. *Org. Biomol. Chem. 3*, 2534–2542.

(36) Kolb, H. C., Finn, M. G., and Sharpless, K. B. (2001) Click chemistry: Diverse chemical function from a few good reactions. *Angew. Chem., Int. Ed. 40*, 2004–2021.

(37) Seidel, C. A. M., Schulz, A, and Sauer, M. H. M. (1996) Nucleobase-specific quenching of fluorescent dyes. 1. Nucleobase one-electron redox potentials and their correlation with static and dynamic quenching efficiencies. *J. Phys. Chem. 100*, 5541–5553.

(38) Garg, N. K., Woodroofe, C. C., Lacenere, C. J., Quake, S. R., and Stoltz, B. M. (2005) A ligand-free solid-supported system for Sonogashira couplings: applications in nucleoside chemistry. *Chem. Commun. 36*, 4551–4553.

(39) Mukaiyama, T. (1976) Oxidation-reduction condensation. *Angew. Chem., Int. Ed. 15*, 94–103.

SUPPORTING INFORMATION

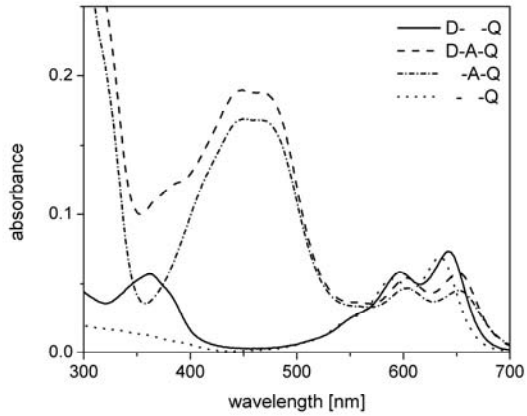

Figure 1SI. Absorption spectra of peptide sequences, with varying quencher behaviour

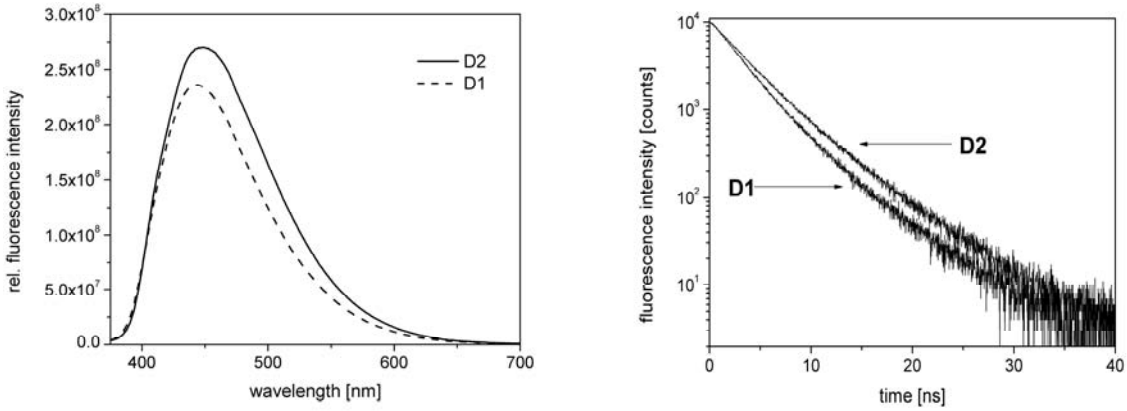

Figure SI2. steady-state (left) and time-resolved (right) fluorescence emission spectra of D-only labelled DNA (D2 - - **26/19** and D1 - - **25/19**)

Synthesis and general characterization:

Oligonucleotide syntheses were carried out on an Expedite™ 8909 Nucleic Acid Synthesis system on a 1 µmol scale using phosphoramidite chemistry and standard protocols. Phosphoramidites as well as nucleosides coupled to solid support (CPG) were obtained from Proligo/Sigma Aldrich. Cleavage of the modified and unmodified oligonucleotides from the solid support and concomitant deprotection was performed by adding a 25% NH_3-solution

followed by vortexing over night at room temperature. After exchanging the counter ion NH_4^+ by K^+, the oligonucleotide samples were desalted by size exclusion chromatography using NAP-10 columns. Purification of the modified oligonucleotides was performed by preparative polyacrylamide-gel electrophoresis (PAGE). Pre-electrophoresis was performed over night at 400 V with tris-borate buffer. Oligonucleotide (5 µL, 1 OD/µL in H_2O) and bromophenol-blue/xylenecyanol- solution (5 µL) were heated to 90°C for 2 min and rapidly cooled to 0°C before being loaded onto the gel. Electrophoretic separation was performed for 18 h at 400 V. The gel was visualized at 366 nm and the bands containing the desired DNA were isolated and cut into small slices. Together with twice the volume of MilliQ water they were extracted over night. After centrifugation, the supernatant was collected and concentrated. Resulting oligonucleotide samples were desalted by size exclusion chromatography on NAP-10 columns.

All oligonucleotides were analyzed by electrophoresis on polyacrylamide gels (20 %) of 0.4 mm thickness. Pre-electrophoresis was performed for 2 h at 500 V with tris-borate running buffer. Oligonucleotide (1 µL, 0.1 OD/µL in H_2O) and bromophenol-blue/xylenecyanol-solution (2 µL) were heated to 90°C for 2 min and rapidly cooled to 0°C before being loaded on the gel. Electrophoretic separations were performed for 2 h at 500 V. Oligonucleotide bands were stained with a solution of 3,3'-diethyl-9-methyl-4,5,4',5'-dibenzothiacarbocyanine bromide (Stains-All, Fluka).

HPLC runs were performed on a Merck/Hitachi system using an EC-125/4-Nucleosil-100-5-C18 (analytical) column. The mobile phase was a gradient of solvent A = 0.1 M $Et_3NH(OAc)$ buffer at pH 7.0 and solvent B = CH_3CN.

Quantification was done by UV-measurements on a Perkin-Elmer-Lambda-35-

UV/VIS spectrometer. ^1H-, ^{13}C- and ^{31}P-NMR-spectra were measured on AC 250, AM 400 and DRX 500 from Bruker as well as a Mercury VX 300 from Varian using $CDCl_3$, CD_3OD

CD_3CN or d-DMSO as solvent. Column chromatography was performed on silica gel type 60 ACC 35-70 µmol.

5'-O-[Bis(4-methoxyphenyl)phenylmethyl]-2'-deoxy-5-{3-{2-[6'',7''-dimethoxy-4''-(trifluoromethyl)-2''-oxoquinolin-1''(2H)-yl]acetamido}prop-1-yn-1-yl}uridine (13)

6,7-Dimethoxy-4-(trifluoromethyl)-2-oxoquinoline-1(2H)-acetic acid (**12**) (174.8 mg, 0.528 mmol, 1.0 equiv.) was dissolved in DMF (10 mL), TBTU [29] (169.8 mg, 0.528 mmol, 1.0 equiv.) and Hünigs base (287.0 mg, 377.6 µL, 2.112 mmol, 4 equiv.) were added and the mixture was stirred for 10 min at room temperature.

5'-O-[Bis(4-methoxyphenyl)phenylmethyl]-2'-deoxy-5-{3-{amino}prop-1-yn-1-yl}uridine (**11**) (400.0 mg, 0.685 mmol, 1.3 equiv.), which was had been dried three times azeotropically with 10 mL anhydrous acetonitrile each was dissolved in 10 mL of DMF and then added to the reaction mixture. The mixture was stirred over night at rt. After removal of DMF under reduced pressure, the residue was purified by short CC (silica gel, 0 - 5% (V/V) MeOH in CH_2Cl_2) yielding 400 mg of the desired compound **13** (82%, 0.446 mmol).

^{1}H-NMR ($CDCl_3$,400 MHz): δ = 2.22-2.58 (m, 2 H, 2'-H), 3.29-3.40 (m, 2 H, 5'-H), 3.74 (m, 6 H, 2× DMT-OMe), 3.87-3.94 (m, 5 H,6''-OMe, N-$\underline{CH_2}$), 3.95 (s, 3 H, 7''-OMe), 4.07-4.13 (m, 1 H, 4'-H), 4.50- 4.56 (m, 1 H, 3'-H), 4.91 (s, 2 H, $\underline{CH_2}$-Carbostyril), 6.30 (t, 1H, 1'-H), 6.78-6.87 (m, 4H, arom. DMT) 6.93 (s, 1 H, 3''-H), 7.03 (s, 1 H, 8''-H), 7.13-7.42 (m, 10H, 9H arom. DMT, 1H 5''-H), 8.03 (s, 1 H, 6-H) ppm.

^{13}C-NMR (CD_3OD, 100 MHz): δ = 30.15, 41.60, 47.35, 55.33, 56.24, 56.45, 63.73, 72.43, 74.29, 86.00, 86.81, 87.11, 89.19, 98.60, 99.39, 106.22, 108.83, 113.43, 117.25, 127.08,

127.96, 128.12, 130.04, 130.09, 135.52, 135.58, 136.50, 143.18, 144.62, 146.07, 149.37, 153.39, 158.69, 158.71, 161.07, 162.07, 166.77 ppm.

MS (EI): m/z (%) = 1790.8 (15) $[2\ M]^+$, 931.0 (33) $[M+35]^+$, 895.2 (100) $[M]^+$.

5'-O-[Bis(4-methoxyphenyl)phenylmethyl]-2'-deoxy-5-{3-{{2-[6'',7''-dimethoxy-4''-(trifluoromethyl)-2''-oxoquinolin-1''(2H)-yl] acetamido}prop-1-yn-1-yl}uridine 3'-[2-cyanoethyl-bis(1-methylethyl)phosphoramidite] (9)

5'-O-[Bis(4-methoxyphenyl)phenylmethyl]-2'-deoxy-5-{3-{2-[6'',7''-dimethoxy-4''-(trifluoromethyl)-2''-oxoquinolin-1''(2H)-yl]acetamido}prop-1-yn-1-yl}uridine (**13**) (160 mg, 0.18 mmol) and diisopropylammonium tetrazolide (23.0 mg, 0.14 mmol, 0.8 equiv.) were dried three times azeotropically with 5 mL of anhydrous acetonitrile each. Under argon, anhydrous CH_2Cl_2 (10 mL) and (2-cyanoethoxy)-bis-(*N*,*N*-diisopropylamino)phosphine (141 mg, 148 µl, 0.47 mmol) were added and stirred for 2.5 h at rt. The reaction was quenched with 10 mL of degassed saturated $NaHCO_3$ solution. The aqueous phase was extracted three times with 10 mL of degassed CH_2Cl_2 each. The combined organic phases were dried over $MgSO_4$ and the solvent was removed under reduced pressure.

The residue was purified by CC (silica gel, 5% (V/V) MeOH in CH_2Cl_2) yielding 196 mg of the desired compound **9** (quantitative, 0.18 mmol).

^{1}H-NMR (CD_3CN, 300 MHz): δ = 1.02-1.30 (m, 12H, 2x CH($\underline{CH_3}$)$_2$), 2.36-2.72 (m, 4H, 2'-H, CH_2CN), 3.22-3.69 (m, 6H, O-$\underline{CH_2}$, 2× C$\underline{H}$(CH_3)$_2$, 5'-H), 3.75 (s, 6 H, 2× DMT-OMe), 3.85-3.93 (m, 8H, 6''-OMe, 7''-OMe, N-$\underline{CH_2}$), 4.09-4.19 (m, 1H, 4'-H), 4.57-4.71 (m, 1H, 3'-H), 4.97 (s, 2 H, CH_2-Carbostyril), 6.10-6.19 (m, 1H, 1'-H), 6.81 (s, 1H, 3''-H), 6.84-6.92

(m, 4H, arom. DMT) 6.95 (s, 1H, 8’’-H), 6.98-7.05 (m, 1H, 5’’-H), 7.18-7.51 (m, 9H, arom. DMT), 7.89-7.95 (m, 1H, 6-H) ppm.

^{31}P-NMR (CD_3CN, 120 MHz): δ = 149.19 ppm.

2’-Deoxy-5-(octadiynyl)-uridine (15)

A two neck flask was charged with 2’-deoxy-5-iodouridine (**14**) (1.00 g, 2.82 mmol), Pd/C (150 mg, 0.14 mmol, 0.05 equiv.), CuI (110 mg, 0.58 mmol, 0.20 equiv.) and Amberlite IRA-67 (3.00 g). The compounds were dried under high vacuum and afterwards kept under argon. Octadiyne (2.96 g, 27.9 mmol, 10 equiv.) and DMF (28 mL) were added. Through this suspension anhydrous argon was bubbled for 15 minutes and then it was kept under argon. The reaction mixture was stirred at 50°C for 17 h and afterwards cooled to rt. The cooled reaction mixture was filtered over celite and the celite was washed with 50 mL of a mixture of CH_2Cl_2/MeOH (1:1). The solvent of the combined organic phases was removed under reduced pressure and the residue was purified by CC (silica gel, 0-10% (V/V) MeOH in CH_2Cl_2) yielding 730 mg of the desired product **15** (78%, 2.20 mmol).

^{1}H-NMR (CD_3OD, 400 MHz): δ = 1.62-1.78 (m, 4H, 4’’-H, 5’’-H), 2.22-2.38 (m, 5H, 8’’-H, 6’’-H, 2’-H), 2.45(t, $J_{3'',4''}$= 6.8, 2H, 3’’-H), AB-signal ($\delta_{5'a}$ = 3.77, $\delta_{5'b}$ = 3.85, $J_{A,B}$ = $J_{B,A}$ = 12, additional coupling $J_{5'a,4'}$= 3.6, $J_{5'b,4'}$= 3.2, 2H, 5’-H) 3.95-3.99 (m, 1H, 4’-H), 4.42-4.46 (m, 1H, 3’-H), 6.28 (t, $J_{1',2'}$ = 6.6, 1H, 1’-H), 8.23 (s, 1H, 6-H) ppm.

^{13}C-NMR (100 MHz, inCD_3OD): δ = 18.55, 19.67, 28.62, 28.77, 41.60, 62.61, 69.69, 72.04, 72.82, 84.72, 86.87, 89.06, 94.73, 101.21, 144.23, 151.25, 164.69 ppm.

CHN analysis found (theoretical): C: 61.69 (61.62), H: 5.86 (5.78), N: 8.25 (8.45).

MS [APCI]: m/z (%) = 438.8 (7), 373.8 (5), 332.7 (100) $[M]^+$, 217.0 (25), 96.5(8).

5'-O-[Bis(4-methoxyphenyl)phenylmethyl]-2'-deoxy-5-(octadiynyl)uridine (16)

2'-Deoxy-5-(octadiynyl)-uridine (**15**) (80.0 mg, 0.26 mmol) was dried three times azeotropically with 3 mL of anhydrous pyridine each. Afterwards, it was dissolved in 2 mL of anhydrous pyridine. DMAP (7.33 mg, 0.06 mmol, 0.25 equiv.), NEt_3 (48.7 mg, 0.48 mmol, 2.0 equiv.) and DMT-Cl (97.6 mg, 0.29 mmol, 1.2 equiv.) were added and the reaction mixture was allowed to stir over night at rt. The reaction was quenched with 3 mL of MeOH and the resulting mixture was allowed to stir for an additional 30 min. The solvents were removed under reduced pressure and the residue was purified by CC (silica gel 0-4% (V/V) MeOH in CH_2Cl_2) yielding in 105 mg of the desired compound **16** (65%, 0.17 mmol).

^{1}H-NMR ($CDCl_3$, 400 MHz): δ = 1.30-1.44 (m, 4H, 4''-H, 5''-H), 1.88 (t, $^3J_{8'', 6''}$ = 2.6, 1H, 8''-H), 2.01(td, $J_{6'', 5''}$= 6.8, $J_{6'', 8''}$= 2.6, 2H, 6''-H), 2.08-2.12 (m, 2H, 3''-H), 2.22-2.50 (m, 2H, 2'-H), AB-signal ($\delta_{5'a}$ = 3.31, $\delta_{5'b}$ = 3.42, $J_{A,B}$ = $J_{B,A}$ = 10.7, additional coupling $J_{5'a,4'}$= 3.5, $J_{5'b,4'}$= 3.2, 2H, 5´-H), 3.78 (s, 6H, 2× OMe), 4.05-4.08 (m, 1H, 4'-H), 4.48-4.52 (m, 1H, 3'-H), 6.31 (dd, $J_{1', 2'a,}$= 5.8, $J_{1', 2'b}$= 7.6, 1H, 1'-H), 6.81-6.86 (m, 4H, arom. DMT), 7.18-7.45 (m, 9H, arom DMT), 8.00 (s, 1H, 6-H) ppm.

^{13}C-NMR ($CDCl_3$, 100 MHz): δ =17.85, 19.03, 27.25, 27.59, 41.49, 55.34, 63.53, 68.52, 71.02, 72.39, 84.23, 85.59, 86.52, 87.10, 94.87, 101.15, 113.40, 127.03, 128.00, 128.11, 130.06, 135.59, 135.64, 141.63, 144.57, 149.33, 158.71, 161.79 ppm.

MS (ESI): m/z (%) = 1941.7 (11), 1394.4 (8), 1290.4 (45) $[2\ M+Na]^+$, 761.1 (23), 657.1 (80) $[M+Na]^+$, 303.2 (100) $[DMT]^+$.

CHN analysis found (theoretical): C: 71.79 (71.91), H: 6.25 (6.03), N: 4.32 (4.41).

1-((2-Azidoethyl)amino)-4-(methylamino)anthraquinone (18)

1-((2-Hydroxyethyl)amino)-4-(methylamino)anthraquinone (Disperse Blue 3) (**17**) (500 mg, 1.69 mmol, 1.0 equiv.) was dissolved in DMF (25 mL) and CBr_4 (559 mg, 1.69 mmol, 1 equiv.), PPh_3 (443 mg, 1.69 mmol, 1.0 equiv.) and NaN_3 (504 mg, 7.77 mmol, 4.6 equiv.) were added and the reaction mixture was stirred over night at rt. Thereafter MeOH (6 mL) was added and the mixture was stirred for additional 15 min. The solvent was evaporated and the residue was purified by CC (silica gel, 0-5% (V/V) MeOH in CH_2Cl_2) yielding in 440 mg of the desired product **18** (81%, 1.37 mmol).

^{1}H-NMR ($CDCl_3$, 400 MH): δ = 3,07 (d, $J_{N\text{-}CH3,\ NH}$ = 5.2, 3H, N-$\underline{CH_3}$), 3.60-3.65 (m, 4H, $\underline{CH_2}$-$\underline{CH_2}$-N_3), 7.20-7.25(m, 2H, 2-H, 3-H), 7.67-7.72(m, 2H, 5-H, 8-H), 8.31-8.36 (m, 2H, 6-H, 7-H), 10.50-10.57 (m, 1H, $\underline{NH}$-CH_3), 10.75-10.83 (m, 1H, $\underline{NH}$-CH_2) ppm.

^{13}C-NMR ($CDCl_3$, 100 MHz): δ = 29.61, 42.07, 51.12, 110.26, 110.89, 122.97, 123.05, 126.15, 126.28, 132.24, 132.42, 134.39, 134.60, 145.27, 147.14, 182.76, 183.38 ppm.

MS ($CI(NH_3)$): m/z (%) 322.1 (100) $[M]^+$, 294.1 (35), 265 (36).

CHN analysis found (theoretical): C: 63.34 (63.54), H: 4.90 (4.71), N: 21.74 (21.79).

5’-O-[Bis(4-methoxyphenyl)phenylmethyl]-2’-deoxy-5-(6-{1-(1-((2-ethyl)amino)-4-(methylamino)anthraquinone)-[1,2,3]-triazol-4-yl]hex-1-yn-1-yl} uridine (36)

Nucleoside **16** (106 mg, 0.17 mmol) was dissolved in a mixture of DMF (4 mL) and H_2O (1.5 mL) Then Hünigs base (279 mg, 367 µL, 2.15 mmol, 13.0 equiv.), quencher **18** (53.6 mg, 0.17 mmol, 1.0 equiv.), $CuSO_4$ (41.7 mg, 0.17 mmol, 1.0 equiv.) and ascorbic acid (294 mg, 1.67 mmol, 10.0 equiv.) were added and the mixture was allowed to stir over night at rt. Afterwards the solvents were removed under reduced pressure. The residue was adsorbed on silica gel and purified by CC (silica gel, 2-10% (V/V) MeOH in CH_2Cl_2) yielding 123 mg of the desired compound **36** (76%, 0.13 mmol).

^{1}H-NMR ($CDCl_3$, 400 MHz): δ = 1.32-1.42 (m, 2H, 4’’-H), 1.59-1.72 (m, 2H, 5’’-H), 2.04-2.10 (m, 2H, 3’’-H), 2.26-2.51 (m, 2H, 2’-H), 2.65(t, $J_{6'', 5''}$= 6.9, 2H, 6’’-H), 3.07 (d, $J_{\text{N-CH3, NH}}$ = 5.2, 3H, NH-$\underline{CH_3}$), 3.35-3.39 (m, 2H, 5’-H), 3.76 (s, 6H, 2× OMe), 3.87-3.94 (m, 2H, NH-$\underline{CH_2}$-CH_2), 4.05-4.08 (m, 1H, 4’-H), 4.51-4.56 (m, 1H, 3’-H), 4.58-4.63 (m, 2H, NH-CH_2-$\underline{CH_2}$), 6.30-6.35 (m, 1H, 1’-H), 6.78-6.84 (m, 4H, arom. DMT), 7.18-7.45 (m, 11H, 9 H arom. DMT, 2’’’-H, 3’’’-H), 7.64-7.71 (m, 2H, 5’’’-H, 8’’’-H), 7.77 (s, 1H, 8’’-H), 7.94 (s, 1H, 6-H), 8.26-8.44 (m, 2H,6’’’-H, 7’’’-H), 10.54-10.63 (m, 1H, $\underline{NH}$-CH_3), 10.92-11.00 (m, 1H, $\underline{NH}$) ppm.

^{13}C-NMR ($CDCl_3$, 100 MHz): δ = 19.24, 24.78, 25.13, 27.11, 27.28, 29.53, 37.85, 41.47, 43.02, 45.93, 50.11, 50.25, 55.29, 63.64, 67.49, 70.04, 71.52, 72.26, 76.03, 85.60, 86.30, 86.46, 87.03, 87.08, 88.00, 94.74, 100.87, 109.78, 110.41, 113.34, 113.42, 122.29, 122.46, 122.61, 122.77, 123.48, 126.07, 126.38, 126.98, 127.17, 128.00, 128.05, 128.16, 130.05, 130.07, 130.12, 130.15, 132.22, 132.43, 132.53, 134.19, 134.47, 134.52, 135.60, 135.66,

141.76, 144.40, 144.58, 145.44, 147.22, 148.28, 149.47, 158.65, 158.75, 159.09, 162.39, 176.13, 182.22, 182.38, 182.92 ppm.

MS (ESI): m/z (%) 1931.2 (9) $[2\ M+Na]^+$, 977.7 (100) $[M+Na]^+$, 303.2 (7) $[DMT]^+$.

5'-O-[Bis(4-methoxyphenyl)phenylmethyl]-2´-deoxy-5-{6-[1-(1-((2-ethyl)amino)-4-(methylamino)anthraquinone)-[1,2,3]-triazol-4-yl]hex-1-yn-1-yl}uridine 3'-[2-cyanoethyl-bis(1-methylethyl)phosphoramidite] (10)

Compound **36** (150 mg, 0.16 mmol) and diisopropylammonium tetrazolide (20.0 mg, 0.12 mmol, 0.8 equiv.) were dried three times azeotropically with 5 mL anhydrous acetonitrile each. Under argon, anhydrous CH_2Cl_2 (11 mL) and (2-cyanoethoxy)-bis-(*N*,*N*-diisopropylamino)phosphine (123 mg, 117 µL, 0.4 mmol, 2.6 equiv.) were added and stirred for 2.5 h at rt. The reaction was quenched with 10 mL of degassed saturated $NaHCO_3$ solution. The aqueous phase was extracted three times with 10 mL degassed CH_2Cl_2 each. The combined organic phases were dried over Na_2SO_4 and the solvent was removed under reduced pressure.

The residue was purified by CC (silica gel, 2% (V/V) MeOH in CH_2Cl_2) yielding in 175 mg of the desired compound **10** (96%, 0.15 mmol).

^{1}H-NMR (CD_3CN, 400 MHz): δ = 1.03-1.19 (m, 12 H, 2× CH($\underline{CH_3}$)$_2$), 1.24-1.29 (m, 2H, 4''-H), 1.46-1.57 (m, 2H, 5''-H), 1.96-2.02 (m, 2H, 3''-H), 2.27-2.55 (m, 4H, 2'-H, CH_2CN), 2.60-2.65 (m, 2H, 6''-H), 3.00-3.03 (m, 3H, N-$\underline{CH_3}$), 3.20-3.30 (m, 2H, 5'-H), 3.52-3.61 (m, 2H, 2× $\underline{CH}(CH_3)_2$), 3.69-3.82 (m, 8H, 2× DMT-OMe, O$\underline{CH_2}$), 3.86-3.93 (m, 2H, NH-$\underline{CH_2}$-CH_2), 4.05-4.08 (m, 1H, 4'-H), 4.51-4.56 (m, 1H, 3'-H), 4.58-4.63 (m, 2H, NH-CH_2-$\underline{CH_2}$), 6.08-6.20 (m, 1H, 1'-H), 6.78-6.84 (m, 4H, arom. DMT), 7.13-7.33 (m, 9H, arom. DMT),

7.37-7.42 (m, 2H, 2’’’-H, 3’’’-H), 7.50-7.51 (m, 1H, 8’’-H), 7.63-7.68 (m, 2H, 5’’’-H, 8’’’-H), 7.76 (s, 1H, 6-H), 8.15-8.24 (m, 2H, 6’’’-H, 7’’’-H), 10.43-10.49 (m, 1H, NH-CH_3), 10.63-10.69 (m, 1H, NH-CH_2) ppm.

^{31}P-NMR (400 MHz, CD_3CN): δ = 153.30 ppm.

MS (ESI): m/z (%) 1178.2 (100) $[M+Na]^+$, 1155.3 (24), 1109.2 (9), 1095.2 (16), 401.2 (27), 303.3 (28) $[DMT]^+$.

5’-O-[Bis(4-methoxyphenyl)phenylmethyl]-2’-deoxy-5-{3{5-[bis[1,10-phenanthrolin-4,7-diylκN, κN´)bis phenyl][4-(7phenyl-1,10-phenanthrolin-4-yl-κN, κN’)]ruthenium(II)chlorid]pentanamid}prop-1-yn-1-yl}uridine (35)

Bis (4,7-diphenyl-1,10-phenanthroline-kN^1,kN^{10})[4-(7-phenyl-1,10-phenanthrolin-4-ylkN^1, kN^{10})benzenepentanoic acid]ruthenium (II) (**33**) (168 mg, 0.13 mmol, 1.0 equiv.) was dissolved in DMF (4 mL). TBTU[29] (43.4 mg, 0.13 mmol, 1.0 equiv.) and Hünigs base (68.4 mg, 90.8 µl, 0.53 mmol, 4.0 equiv.) were added and the mixture stirred for 10 min at rt.

5’-O-[Bis(4-methoxyphenyl)phenylmethyl]-2’-deoxy-5-{3-{{2-acetyl}amino}prop-1-yn-1-yl}uridine **13** (100 mg, 0.17 mmol, 1.3 equiv.) which had been dried three times azeotropically with 5 mL of anhydrous acetonitrile each, was dissolved in 10 mL of DMF and then added to the reaction mixture. The mixture was stirred over night at rt. Thereafter, DMF was removed under reduced pressure. The crude product was dissolved in 10 mL DCM and extracted four times with 10 mL saturated $NaHCO_3$ solution each. The combined organic layers were dried over Na_2SO_4 and the solvent was removed under reduced pressure. The crude product was used without further purification in the next step.

MS (ESI): m/z (%) 882.0 (100) $[M\text{-}2Cl^{-}\text{-}2H^{+}]^{2+}$, 673.1 (20).

5'-O-[Bis(4-methoxyphenyl)phenylmethyl]-2'-deoxy-5-{3{5-[bis[1,10-phenanthrolin-4,7-diylκN, κN')bis phenyl][4-(7phenyl-1,10-phenanthrolin-4-yl-κN, κN')]ruthenium(II)chlorid]pentanamid}prop-1-yn-1-yl}uridine 3'-[2-cyanoethyl-bis(1-methylethyl)phosphoramidite] (34)

Compound **35** (123 mg, 66.0 µmol) and diisopropylammonium tetrazolide (7.0 mg, 39.0 µmol, 0.6 equiv.) were dried three times azeotropically with 5 mL anhydrous acetonitrile each. Under argon, anhydrous CH_2Cl_2 (8 mL) and (2-cyanoethoxy)-bis-(*N*,*N*-diisopropylamino)phosphine (22.1 mg, 23.0 µl, 70.0 µmol. 1.1 eqiuv.) were added and it was stirred for 2.5 h at rt. Afterwards, the reaction was quenched with 10 mL of degassed saturated $NaHCO_3$ solution and the aqueous phase was extracted three times with 10 mL degassed CH_2Cl_2 each. The combined organic layers were dried over Na_2SO_4 and the solvent was removed under reduced pressure. The residue was dried azeotropically with 5 mL of acetonitrile. The product **34** was used directly in the DNA synthesis.

MS (ESI): m/z (%) 1062 (13.29), 990 (100) $[M+O\text{-}2Cl^{-}\text{-}2H^{+}]^{2+}$, 981 (9) $[M\text{-}2Cl^{-}\text{-}2H^{+}]^{2+}$, 898 (20), 672 (32), 417 (13) 303 (12) $[DMT]^{+}$.

Syntheses of the oligonucleotides **19-31**: The modified building blocks (**9**, **10**, **32**) (67 µmol/mL in MeCN) were incorporated into the corresponding oligonucleotide sequences during the automated synthesis using standard DNA synthesis cycles.

The coupling of the hydroxysuccinimide ester of the Ru-complex **33** to the free amino function was carried out in solution. To a solution of the oligo (108 OD, 285 nmol) in a mixture of DMF, 1,4-dioxane and H_2O 1:1:1 (983 µL), Hünigs base (11.2 µL, 65.5 µmol) and

(bathophenanthroline)ruthenium(II) complex hydroxysuccinimide ester (11.2 mg, 8.2 µmol) were added. The mixture was incubated at 25°C in the dark for 24 h. After removal of the solvents, the residue was washed with $CHCl_3$ (3 x 500 µL) to remove excess of Ru-complex (**31-1**).

The modified building block **34** (130 mg, 0.06 mmol) was incorporated manually into the oligonucleotide sequence using 0.7 mL of 0.3 M BMT as activation reagent (**31-2**).

Hybridization: To the DNA strands 20-30 (0.1 OD in 1 µl H_2O) 1.0 eq. of the corresponding complementary DNA-strand 19 or 31 (0.1 OD in 1 µl H_2O) were added and the solvent removed in vacuum. The precipitate was dissolved in phosphate buffer (5 mM, pH 7) and thermal hybridization was performed by heating the sample to 90°C for 2 minutes and then cooling it slowly to room temperature.

Bioconjugate Chemistry

ARTICLE

pubs.acs.org/bc

Zinc-Chelated Poly(1-vinylimidazole) and a Carbohydrate Ligand Polycation Form DNA Ternary Complexes for Gene Delivery

Shoichiro Asayama,* Satoshi Nishinohara, and Hiroyoshi Kawakami

Department of Applied Chemistry, Tokyo Metropolitan University, 1-1 minami-Osawa, Hachioji, Tokyo 192-0397, Japan

Supporting Information

ABSTRACT: Zinc-chelated poly(1-vinylimidazole) (PVIm-Zn) and a carbohydrate ligand polycation, a poly(L-lysine) conjugated with lactose molecules (PLL-Lac), have formed DNA ternary complexes for gene delivery. The particle size of the PVIm-Zn/DNA complexes with negative zeta potential was decreased by the addition of the PLL-Lac. The resulting PLL-Lac/PVIm-Zn/DNA ternary complexes, which exhibited the pH-dependent dissociation of the PLL-Lac, mediated more gene expression than the PVIm/DNA binary complexes. The PLL-Lac/PVIm-Zn/DNA complexes with the specific recognition of cell surface receptors mediated the highest gene expression without cytotoxicity at a relatively lower charge ratio (positive/negative = 2.5). These results suggest that the pH-dependent dissociation of the carbohydrate ligands after the recognition of cell surface receptors, including the physicochemical and biochemical function of PVIm-Zn, played an important role in gene expression.

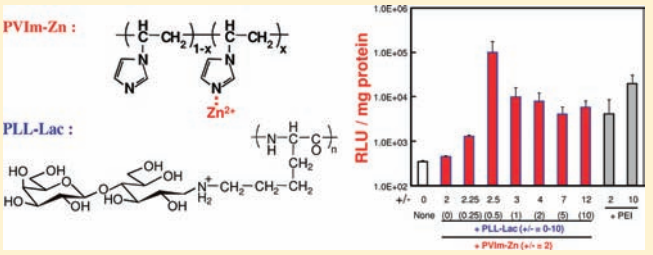

INTRODUCTION

In gene delivery systems, the formation of DNA−carrier polyion complexes is a key factor for new design of efficient delivery vehicles.[1−3] The self-assembly of DNA and polycation forming polyion complexes has been an attractive approach to introduce genes into mammalian cells.[4−7] Inside the cell, DNA routes via acidic vesicles (endosomes) where it must escape to reach the cytosol and then the nucleus for gene expression. For the achievement of the above intracellular events, a large number of polyion complexes such as pH-sensitive ternary complexes[8,9] or complexes with nucleus-targeting molecules[10,11] have been demonstrated.

A nucleus-targeting molecule, nuclear localization signal (NLS), exists in the zinc family protein (ZIC3) within the zinc finger domain, which is considered to be a transcriptional regulator, based on its ability to bind DNA and activate transcription. Zinc is a structural constituent of a great number of proteins, including enzymes for cellular signaling pathways and transcription factors, and it is essential for their biological activity.[12,13] In these cases, zinc binds tightly to proteins containing the zinc finger motif and maintains their structure. Recently, zinc is reported to be a novel intracellular second messenger/signaling ion.[14] Zinc ion has the potential to influence many aspects of cellular signaling through its effect on zinc-binding proteins because there are many transcription factors and enzymes containing zinc-binding sites.

We have already reported pH-sensitive binary or ternary complexes containing imidazole groups for efficient gene delivery.[15,16] Especially, gene expression depends on our new concept that DNA ternary complexes dissociate carbohydrate ligand polycations in response to endosomal pH.[17,18] However, the charge ratio of polycation to DNA is relatively higher, that is, 5. Furthermore, we have proven that the pH-dependent chelation of Zn^{2+} ions with the imidazole groups of poly(1-vinylimidazole) (PVIm) and that the zinc-chelated PVIm (PVIm-Zn) formed the DNA polyion complex via chelated Zn^{2+} ions. The resulting PVIm-Zn/DNA complexes have exhibited no significant cytotoxicity and led to outstanding gene expression at relatively low charge ratio, that is, around 3.[19] However, the PVIm-Zn/DNA complex exhibits a large particle size with negative zeta potential.

These backgrounds have inspired us to establish our strategy that zinc-chelated PVIm and carbohydrate ligand polycation, lactosylated poly(L-lysine) (PLL-Lac), form ternary complexes for gene delivery with biological functions of zinc ions. This paper communicates the physicochemical properties of the PLL-Lac/PVIm-Zn/DNA ternary complexes, the cytotoxicity of the resulting polyion complexes, and the gene expression mediated by the resulting PLL-Lac/PVIm-Zn/DNA complexes; detailed studies on the mechanism of the gene expression by the biological effect of the zinc ions are outside the scope of the present study.

EXPERIMENTAL PROCEDURES

Materials. 1-Vinylimidazole (VIm) was purchased from Aldrich Chemical Co. (Milwaukee, WI). The VIm was distilled under reduced pressure. 2,2′-Azobis(2,4-dimethyl-valeronitrile) (V-65) was purchased from Wako Pure Chemical Industries, Ltd. (Osaka, Japan), and the V-65 was recrystallized from ethanol.

Received: June 25, 2011
Revised: August 8, 2011
Published: August 15, 2011

ACS Publications © 2011 American Chemical Society

Zinc chloride was from Kanto Chemical Co., Inc. (Tokyo, Japan). Poly(L-lysine) (PLL) hydrobromide (M_v = 4000−15 000), poly(ethylenimine) (PEI) solution (M_n = ∼60 000) and fluorescein isothiocyanate (FITC) isomer I were from Sigma Chemical Co. (St. Louis, MO). All other chemicals of a special grade were used without further purification.

Preparation of PVIm-Zn. VIm (300 μL) and V-65 (15.8 mg) as an initiator were dissolved in 2.7 mL *N*,*N*-dimethylformamide (DMF). Radical polymerization reaction was carried out at 45 °C for 1 day. After the reaction, the content was poured into a large excess of acetone, and the precipitate was dried in vacuo. The resulting polymer PVIm (50 mg) and zinc chloride (181.28 mg) were dissolved in 100 mL of H_2O and incubated at room temperature for 1 day. The supernatant was dialyzed against distilled water using a Spectra/Por 7 membrane (molecular weight cutoff = 10^3), followed by the centrifugation (30 min, 5000 rpm). The resulting supernatant was used as a stock solution. The zinc in the stock solution was determined by atomic absorption spectrometry at 213.9 nm using a Varian SpectrAA-640 (Varian Australia Pty., Ltd., Australia).

Synthesis of PLL-Lac. PLL (50 mg) and lactose monohydrate (288 mg) were preincubated at 37 °C for 3 days in 7.5 mL of sodium borate buffer (0.1 M, pH 8.5).[20] Then, a reducing agent, $NaBH_3CN$, was added to the mixture of PLL and lactose in 10 mL of the sodium borate buffer at a final concentration of 0.3 M. The reaction mixture was incubated at 37 °C for 3 days. The degree of amino group modification (approximately 100 mol %) was examined by the primary amino group determination with fluorescamine.[21] The reaction mixture was dialyzed against distilled water using a Spectra/Por 7 membrane (molecular weight cutoff = 10^3) to remove unreacted lactose, followed by freeze−drying. For fluorescent labeling, the resulting PLL-Lac (10 mg) and FITC isomer I (1 mg) were dissolved in 1.1 mL of 10 mM K_2CO_3. The reaction mixture was incubated at room temperature for 2 h, followed by dialysis against distilled water using a Spectra/Por 7 membrane (molecular weight cutoff of 10^3) to remove unreacted FITC. The resulting polypeptide was obtained by freeze−drying.

Agarose Gel Retardation Assay. Plasmid DNA (pGL3-Control Vector; from Promega Co.) was dissolved in TE buffer, and the solution was diluted with 50 mM sodium phosphate buffer (pH 7.4 or 5.0). To the resulting plasmid DNA solution was added the PVIm-Zn solutions in the 50 mM sodium phosphate buffer at a PVIm-Zn/DNA ratio (positive/negative) of 2. To the resulting DNA/PVIm-Zn mixture was then added the PLL-Lac solutions in the 50 mM sodium phosphate buffer at various PLL-Lac/DNA ratios (positive/negative = 0−10). After 30 min of incubation at room temperature, each sample (corresponding to 200 ng of DNA) was mixed with a loading buffer and loaded onto a 1% agarose gel containing 1 μg/mL of ethidium bromide. Gel electrophoresis was run at room temperature in 50 mM sodium phosphate buffer (pH 7.4 or 5.0) at 50 V for 15 min. The DNA bands were visualized under UV irradiation.

Size and Zeta Potential Measurement. The size of the complexes was measured by a dynamic light scattering (DLS) method using an electrophoresis light scattering spectrophotometer (ELS-Z2, Otsuka Electronics Co., Ltd., Tokyo, Japan) and the zeta potential was measured by ELS with electrodes. The size and zeta potential of the complexes of DNA (20 μg) and PVIm-Zn (positive/negative = 2) with PLL-Lac (positive/negative = 0−10) were measured in 3 mL of 10 mM sodium phosphate buffer (pH 7.4) containing 130 mM NaCl.

Cell Viability Assay. HepG2 cells (a gift from the Japan Health Sciences Foundation), human hepatoma cell line, were cultured in tissue culture flasks containing Dulbecco's modified Eagle's medium supplemented with 10% heat-inactivated FBS (FBS was heated for 30 min at 56 °C to inactivate the complement system). The cells were seeded at 1×10^4 cells/well in a 96-well plate and incubated overnight at 37 °C in a 5% CO_2 incubator. The cells were incubated in the presence of the PVIm-Zn/DNA (positive/negative = 2) with PLL-Lac (positive/negative = 0−10) or PEI/DNA (positive/negative = 2, 10) complexes under the same conditions for the transfection procedure (as below) and incubated for 48 h at 37 °C. By further incubation for 4 h, the cell viability was measured using the Alamar Blue assay[22] in triplicate.

Transfection Procedure. In a typical 96-well plate experiment, 1×10^4 cells/well HepG2 cells were transfected in Dulbecco's modified Eagle's medium supplemented with 10% heat-inactivated FBS by the addition of 15 μL of PBS (-) containing 200 ng of plasmid DNA encoding the modified firefly luciferase (pGL3-Control Vector) and complexed with PVIm-Zn (positive/negative = 2) plus PLL-Lac (positive/negative = 0−10), or PEI (positive/negative = 2, 10). After 1 day of incubation, the medium was removed and the cells were further incubated for 2 days in the Dulbecco's modified Eagle's medium supplemented with 10% FBS. For the competition assay, the DNA complexes were incubated for 24 h at 37 °C in the presence of lactose or maltose (4 mM or 40 mM). Then, the cells were subjected to the luciferase assay (Promega kit) according to the manufacturer instruction. Luciferase activities were normalized by protein concentrations and are presented as relative light units (RLU). Protein concentrations were determined by BCA protein assay kit (Pierce) according to the manufacturer instruction.

RESULTS AND DISCUSSION

Physicochemical Properties of PLL-Lac/PVIm-Zn/DNA Complexes. To prepare the zinc-chelated PVIm (PVIm-Zn), as shown in Figure 1, we mixed PVIm with $ZnCl_2$ in an aqueous solution, according to ref 19. The resulting PVIm-Zn with an imidazole/Zn ratio of 50 was then mixed with DNA at positive/negative ratio of 2. As shown in Figure 2, it should be noted that the resulting PVIm-Zn/DNA binary complexes exhibited a large particle size (around 7000 nm) and negative zeta potential (around −30 mV) in spite of a cation excess charge ratio (positive/negative = 2). In this study, therefore, the lactosylated poly(L-lysine) (PLL-Lac),[20] as shown in Figure 1, was added to the resulting PVIm-Zn/DNA binary complexes. Figure 2 also shows the particle size and zeta potential of the resulting PLL-Lac/PVIm-Zn/DNA ternary complexes at various mixing ratios. The particle size drastically decreased around 300 nm by mixing with PLL-Lac at any mixing ratios (positive/negative = 0.25−2) (Figure 2A). Although the size of complexes generally decreases and the zeta potential of the complexes generally increases when positive/negative ratio increases, as shown in Figure 2A, the size of the resulting complexes became smaller and larger as the positive/negative ratio is increased. This is probably due to the wide range of zeta potential from negative (−15 mV) to positive (+6 mV) by mixing with PLL-Lac up to positive/negative ratio of 2, as shown in Figure 2B, as well as the effect of the PLL-Lac as dispersing agent. Thus, we have succeeded the ternary complex formation among PLL-Lac, PVIm-Zn, and DNA.

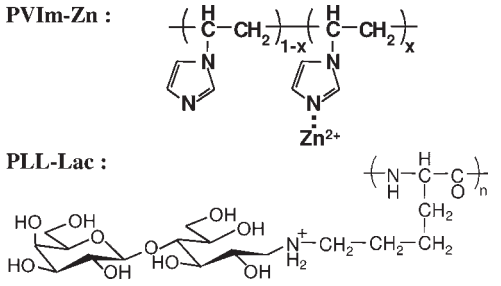

Figure 1. Chemical structure of zinc-chelated poly(1-vinylimidazole) (PVIm-Zn) and lactosylated poly(L-lysine) (PLL-Lac).

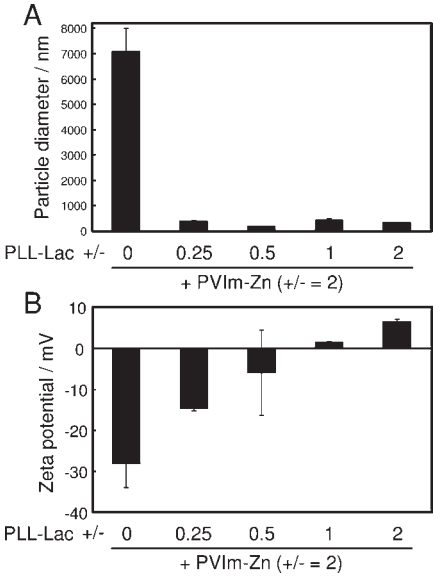

Figure 2. Particle size (A) and zeta potential (B) of PVIm-Zn/DNA, and PLL-Lac/PVIm-Zn/DNA complexes. The size and zeta potential of the complexes of DNA (20 μg) and PVIm-Zn (positive/negative = 2) with PLL-Lac (positive/negative = 0−10) were measured in 3 mL of 10 mM sodium phosphate buffer (pH 7.4) containing 130 mM NaCl.

We have already reported the concept that DNA ternary complexes dissociate ligand polycations in response to endosomal pH.[17,18] In this study, as shown in Figure 3, we examined the pH-dependent dissociation of PLL-Lac from the DNA ternary complexes with the PLL-Lac and the PVIm-Zn by agarose gel electrophoresis. It should be noted that free DNA was observed in spite of the mixing at a positive/negative ratio of 2 in case of PVIm-Zn/DNA binary complexes at pH 7.4. These results suggest that the polyion complex formation between PVIm-Zn and DNA is considered to be difficult, although the details are unclear, due to less accessibility between chelated Zn^{2+} ions and phosphate groups. Taking the result of the negative zeta potential of the PVIm/Zn binary complexes at a positive/negative charge ratio of 2 (Figure 2B) into account, the rigid chelated structure between Zn^{2+} ions and imidazole groups is considered to be surrounded by DNA macromolecules. As PLL-Lac was mixed with the PVIm-Zn/DNA binary complexes, on the other hand, free DNA disappeared. This is consistent with the zeta potential increase by mixing the PLL-Lac (Figure 2B). At pH 5.0, in the case of all samples, no free DNA was observed and the band appeared at the origin. These results suggest that the imidazole

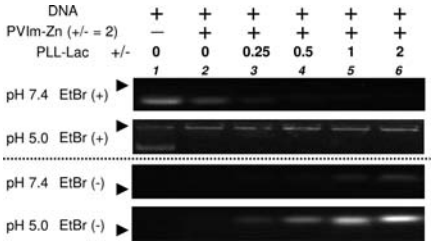

Figure 3. Analysis of the pH-dependent formation of PLL-Lac/PVIm-Zn/DNA ternary complexes in the presence [EtBr(+)] or absence [EtBr(-); where PLL-Lac was labeled with FITC] of ethidium bromide. The DNA complexes of PVIm-Zn (positive/negative = 2) with PLL-Lac (positive/negative = 0, 0.25, 0.5, 1, 2) were loaded at pH 7.4 or pH 5.0: lane 1, DNA alone; lane 2, PVIm-Zn/DNA alone; lane 3, PVIm-Zn/DNA with PLL-Lac (positive/negative = 0.25); lane 4, with PLL-Lac (positive/negative = 0.5); lane 5, with PLL-Lac (positive/negative = 1); lane 6, with PLL-Lac (positive/negative = 2). Solid arrowhead indicates the well where each sample was loaded.

groups of the PVIm-Zn were protonated to induce DNA structural change.[23,24] Taking these results into account, the pH-dependent control of chelation[19] is considered to slacken the ycross-linked structure of the PVIm-Zn and to decrease the density of cationic charges via acidic conditions.

To examine further the PLL-Lac/PVIm-Zn/DNA ternary complex formation, we labeled PLL-Lac with FITC and performed agarose gel electrophoresis in the absence of ethidium bromide (EtBr). At pH 7.4, although no band at origin was observed, presumably due to the reduced excitation of FITC by the light scattering of the resulting complexes, free PLL-Lac migrated into the negative pole of the gel, as the mixing ratio of the PLL-Lac increased (above positive/negative = 0.5) . At pH 5.0, it should be noted that the fluorescence of the free PLL-Lac increased. The increased migration into the negative pole suggests that the PLL-Lac was dissociated from the PLL-Lac/PVIm-Zn/DNA ternary complexes by the protonation of the imidazole groups of PVIm-Zn at pH 5.0. Subsequently, it is therefore expected that the release of Zn^{2+} from the PVIm backbone[19] induces the dissociation of the DNA polyion complexes for transcription.

Biochemical Properties of PLL-Lac/PVIm-Zn/DNA Complexes. Cytotoxicity of a gene carrier is an important factor for clinical applications. As shown in Figure 4, we examine the effect of the PLL-Lac/PVIm-Zn/DNA complexes on cell viability. The viability of HepG2 hepatoma cells did not significantly decrease when the PLL-Lac/PVIm-Zn/DNA complexes were added up to the positive/negative ratio of 12. On the other hand, a little cytotoxicity was observed when the control PEI was added up to the positive/negative ratio of 10. The noncytotoxic property may be attributed to the partial shielding of surface charge, as well as lactose molecules, by unmodified imidazole groups of PVIm backbone as poly(ethylene glycol).[19,25]

As a result of no apparent cytotoxicity of the PLL-Lac/PVIm-Zn/DNA complexes, we finally examined the gene expression mediated by the resulting complexes. As shown in Figure 5, the resulting gene expression depended on the positive/negative ratio. The gene expression mediated by the PLL-Lac/PVIm-Zn/DNA ternary complexes was higher than that mediated by the PVIm-Zn/DNA binary complexes. It should be noted that the PLL-Lac/PVIm-Zn/DNA complexes at the positive/negative charge ratio of 2.5 mediated the highest gene expression under

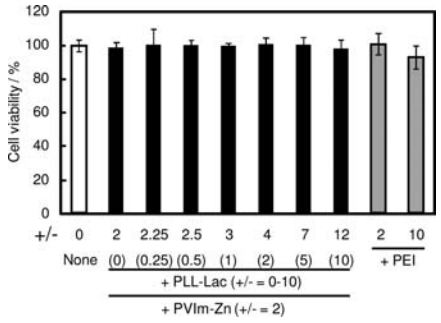

Figure 4. Effect of PLL-Lac/PVIm-Zn/DNA ternary complexes on the viability of HepG2 cells during transfection procedures. The DNA complexes of PVIm-Zn (positive/negative = 2) with PLL-Lac (positive/negative = 0−10) were used, so that total positive/negative ratios are indicated (positive/negative = 2−12). Symbols and error bars represent the mean and standard deviation of the measurements made in triplicate wells.

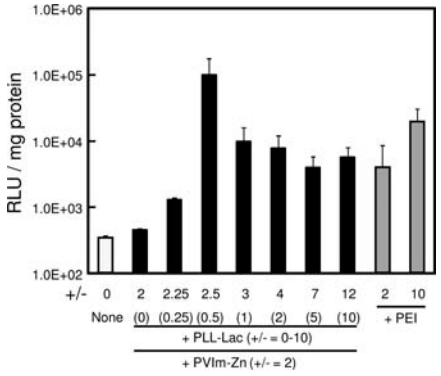

Figure 5. Transfection of luciferase gene to HepG2 cells by the PLL-Lac/PVIm-Zn/DNA ternary complexes. The DNA complexes of PVIm-Zn (positive/negative = 2) with PLL-Lac (positive/negative = 0−10) were used, so that total positive/negative ratios are indicated (positive/negative = 2−12). Gene expression was determined as RLU normalized by protein concentrations. Symbols and error bars represent the mean and standard deviation of the measurements made in triplicate wells.

these experimental conditions (in spite of using the PEI/DNA complexes at the positive/negative ratio of 10). This is consistent with no free PLL-Lac in the PLL-Lac/PVIm-Zn/DNA ternary complexes at the positive/negative ratio of 2.5 (Figure 3, EtBr(-) at pH 7.4). The gene expression mediated by the PLL-Lac/PVIm-Zn/DNA complexes was decreased by the treatment of the HepG2 cells with lactose but not maltose molecules (Figure S1, Supporting Information). These results suggest that the PLL-Lac/PVIm-Zn/DNA ternary complexes with β-galactose residues recognized the HepG2 cells via asialoglycoprotein receptors on the cell surface. Furthermore, after the internalization of the ternary complexes, the resulting PVIm-Zn/DNA binary complexes, by the pH-dependent dissociation of the PLL-Lac, are considered to release Zn^{2+} ions from the PVIm backbone, resulting active release of DNA from the PVIm-Zn/DNA complexes in the cytoplasm to lead efficient gene expression. From these results, the delivery system by using PLL-Lac/PVIm-Zn/DNA ternary complexes in this study is expected to be applied for a new design of gene carriers.

In this study, we also focus on Zn(II) as biological active ions. Zinc affects the regulation of transcription factors. Zinc can induce the expression of some genes, including those coding for molecules involved in zinc homeostasis, like zinc transporters and metallothioneins.[26] The gene expression of metallothioneins by zinc is regulated by metal response element-binding transcription factor-1.[27] Furthermore, the nuclear localization of the transcription factor *Snail* is dependent on the zinc transporter *Zip6*, suggesting that zinc plays a role in the nuclear localization of *Snail* and may act as an intracellular signaling molecule.[28] Therefore, we consider that Zn^{2+} ions lead the possible enhancement of transcription for efficient gene expression.

As another biological viewpoint, moreover, we also have to consider membrane fusion activity because traditional endosomal escape is necessary for efficient gene expression, which we have been focusing on.[15−18] Divalent cations such as Zn^{2+} are known to induce membrane fusion which can be increased in the presence of polyamines.[29−32] It has also been reported that Zn^{2+} induced an efficient fusion of liposomes in the presence of peptides containing several histidine residues such as the antimicrobial salivary peptide Histatin-5 (DSHAKRHHGY-KRKFHE- KHHSHRGY).[33] Of these bases, we also consider that Zn^{2+} ions help to enhance endosome membrane destabilization for the escape of DNA to the cytosol.

CONCLUSION

In this study, we have prepared the PLL-Lac/PVIm-Zn/DNA ternary complexes for gene delivery. The PLL-Lac decreased the particle size of the PVIm-Zn/DNA complexes with negative zeta potential. The resulting PLL-Lac/PVIm-Zn/DNA ternary complexes mediated more gene expression than the PVIm/DNA binary complexes. At positive/negative ratio of 2.5, a relatively lower charge ratio, the PLL-Lac/PVIm-Zn/DNA complexes mediated the highest gene expression without cytotoxicity, by the pH-dependent dissociation of the PLL-Lac after the recognition of cell surface receptors. Including the physicochemical and biochemical function of PVIm-Zn, the PLL-Lac/PVIm-Zn/DNA ternary complexes are expected to offer unique design for gene delivery systems.

ASSOCIATED CONTENT

Supporting Information. Additional figure. This material is available free of charge via the Internet at http://pubs.acs.org.

AUTHOR INFORMATION

Corresponding Author

*Telephone: +81-42-677-1111 (ext.) 4976. Fax: +81-42-677-2821. E-mail: asayama-shoichiro@tmu.ac.jp.

ABBREVIATIONS

PVIm, poly(1-vinylimidazole); PVIm-Zn, zinc-chelated poly(1-vinylimidazole); PLL-Lac, lactosylated poly(L-lysine); VIm, 1-vinylimidazole; PEI, poly(ethylenimine); FBS, fetal bovine serum; RLU, relative light unit

REFERENCES

(1) Fukushima, S., Miyata, K., Nishiyama, N., Yamasaki, Y., and Kataoka, K. (2005) PEGylated polyplex micelles from triblock cationers with spatially ordered layering of condensed pDNA and buffering units for enhanced intracellular gene delivery. *J. Am. Chem. Soc. 127*, 2810–2811.

(2) Zugates, G. T., Anderson, D. G., Little, S. R., Lowhorn, I. E. B., and Ranger, R. (2006) Synthesis of poly(β-amino ester)s with thiol-reactive side chains for DNA delivery. *J. Am. Chem. Soc. 128*, 12726–12734.

(3) Liu, Y., and Reineke, T. M. (2007) Poly(glycoamidoamine)s for gene delivery. Structural effects on cellular internalization, buffering capacity, and gene expression. *Bioconjugate Chem. 18*, 19–30.

(4) Zauner, W., Ogris, M., and Wagner, E. (1998) Polylysine-based transfection systems utilizing receptor-mediated delivery. *Adv. Drug Delivery Rev. 30*, 97–113.

(5) Mahato, R. I., Monera, O. D., Smith, L. C., and Rolland, A. (1999) Peptide-based gene delivery. *Curr. Opin. Mol. Ther. 1*, 226–243.

(6) Garnett, M. C. (1999) Gene-delivery systems using cationic polymers. *Crit. Rev. Ther. Drug Carrier Syst. 16*, 147–207.

(7) Godbey, W. T., Wu, K. K., and Mikos, A. G. (1999) Poly-(ethyleneimine) and its role in gene delivery. *J. Controlled Release 60*, 149–160.

(8) Trubetskoy, V. S., Wong, S. C., Subbotin, V., Budker, V. G., Loomis, A., Hagstrom, J. E., and Wolff, J. A. (2003) Recharging cationic DNA complexes with highly charged polyanions for in vitro and in vivo gene delivery. *Gene Ther. 10*, 261–271.

(9) Ito, T., Iida-Tanaka, N., Niidome, T., Kawano, T., Kubo, K., Yoshikawa, K., Sato, T., Yang, Z., and Koyama, Y. (2006) Hyaluronic acid and its derivative as a multi-functional gene expression enhancer: Protection from non-specific interactions, adhesion to targeted cells, and transcriptional activation. *J. Controlled Release 112*, 382–388.

(10) Nagasaki, T., Kawazu, T., Tachibana, T., Tamagaki, S., and Shinkai, S. (2005) Enhanced nuclear import and transfection efficiency of plasmid DNA using streptavidin-fused importin-β. *J. Controlled Release 103*, 199–207.

(11) Shiraishi, T., Hamzavi, R., and Nielsen, P. E. (2005) Targeted delivery of plasmid DNA into the nucleus of cells via nuclear localization signal peptide conjugated to DNA intercalating bis- and trisacridines. *Bioconjugate Chem. 16*, 1112–1116.

(12) Vallee, B. L., and Auld, D. S. (1993) Cocatalytic zinc motifs in enzyme catalysis. *Proc. Natl. Acad. Sci. U.S.A. 90*, 2715–2718.

(13) Prasad, A. S. (1995) Zinc: an overview. *Nutrition 11*, 93–99.

(14) Yamasaki, S., Sakata-Sogawa, K., Hasegawa, A., Suzuki, T., Kabu, K., Sato, E., Kurosaki, T., Yamashita, S., Tokunaga, M., Nishida, K., and Hirano, T. (2007) Zinc is a novel intracellular second messenger. *J. Cell Biol. 177*, 637–645.

(15) Asayama, S., Hakamatani, T., and Kawakami, H. (2010) Synthesis and characterization of alkylated poly(1-vinylimidazole) to control the stability of its DNA polyion complexes for gene delivery. *Bioconjugate Chem. 21*, 646–652.

(16) Asayama, S., Sudo, M., Nagaoka, S., and Kawakami, H. (2008) Carboxymethyl poly(L-histidine) as a new pH-sensitive polypeptide to enhance polyplex gene delivery. *Mol. Pharmaceutics 5*, 898–901.

(17) Asayama, S., Sekine, T., Kawakami, H., and Nagaoka, S. (2006) pH-Dependent dissociation of carbohydrate ligand polycations from DNA ternary complexes. *Chem. Lett. 35*, 100–101.

(18) Asayama, S., Sekine, T., Kawakami, H., and Nagaoka, S. (2007) Design of aminated poly(1-vinylimidazole) for a new pH-sensitive polycation to enhance cell-specific gene delivery. *Bioconjugate Chem. 18*, 1662–1667.

(19) Asayama, S., Nishinohara, S., and Kawakami, H. (2011) Zinc-chelated imidazole groups for DNA polyion complex formation. *Metallomics 3*, 680–682.

(20) Martinez-Fong, D., Mullersman, J. E., Purchio, A. F., Armendariz-Borunda, J., and Martinez-Hernandez, A. (1994) Nonenzymatic glycosylation of poly-L-lysine: A new tool for targeted gene delivery. *Hepatology 20*, 1602–1608.

(21) Udenfriend, S., Stein, S., Bohlen, P., Dairman, W., Leimgruber, W., and Weigele, M. (1972) Fluorescamine: a reagent for assay of amino acids, peptides, proteins, and primary amines in the picomole range. *Science 24*, 871–872.

(22) Unsworth, J. M., Rose, F. R. A. J., Wright, E., Scotchford, C. A., and Shakesheff, K. M. (2003) Seeding cells into needled felt scaffolds for tissue engineering applications. *J. Biomed. Mater. Res. 53*, 617–620.

(23) Shuai, X., Merdan, T., Unger, F., and Kissel, T. (2005) Supramolecular gene delivery vectors showing enhanced transgene expression and good biocompatibility. *Bioconjugate Chem. 16*, 322–329.

(24) Pouton, C. W., Lucas, P., Thomas, B. J., Uduehi, A. N., Milroy, D. A., and Moss, S. H. (1998) Polycation-DNA complexes for gene delivery: a comparison of the biopharmaceutical properties of cationic polypeptides and cationic lipids. *J. Controlled Release 53*, 289–299.

(25) Ahn, C. H., Chae, S. Y., Bae, Y. H., and Kim, S. W. (2004) Synthesis of biodegradable multi-block copolymers of poly(L-lysine) and poly(ethylene glycol) as a non-viral gene carrier. *J. Controlled Release 97*, 567–574.

(26) Palmiter, R. D. (2004) Protection against zinc toxicity by metallothionein and zinc transporter 1. *Proc. Natl. Acad. Sci. U.S.A. 101*, 4918–4923.

(27) Lichtlen, P., and Schaffner, W. (2001) Putting its fingers on stressful situations: the heavy metal-regulatory transcription factor MTF-1. *Bioessays 23*, 1010–1017.

(28) Yamashita, S., Miyagi, C., Fukuda, T., Kagara, N., Che, Y. S., and Hirano, T. (2004) Zinc transporter LIVI controls epithelial-mesenchymal transition in zebrafish gastrula organizer. *Nature 429*, 298–302.

(29) Gad, A. E., Silver, B. L., and Eytan, G. D. (1982) Polycation-induced fusion of negatively charged vesicles. *Biochim. Biophys. Acta 690*, 124–132.

(30) Ohki, S., and Duax, J. (1986) Effects of cations and polyamines on the aggregation and fusion of phosphatidylserine membranes. *Biochim. Biophys. Acta 861*, 177–186.

(31) Binder, H., Arnold, K., Ulrich, A. S., and Zschornig, O. (2001) Interaction of Zn^{2+} with phospholipid membranes. *Biophys. Chem. 90*, 57–74.

(32) Pichon, C., Guérin, B., Réfrégiers, M., Gonçalves, C., Vigny, P., and Midoux, P. (2002) Zinc improves gene transfer mediated by DNA/cationic polymer complexes. *J. Gene Med. 4*, 548–559.

(33) Melino, S., Rufini, S., Sette, M., Morero, R., Grottesi, A., Paci, M., and Petruzzelli, R. (1999) Zn^{2+} ions selectively induce antimicrobial salivary peptide Histatin-5 to fuse negatively charged vesicles. Identification and characterization of a zinc-binding motif present in the functional domain. *Biochemistry 38*, 9626–9633.

(Supporting Information for an Article to the Editor of *Bioconjugate Chemistry*)

Zinc-Chelated Poly(1-vinylimidazole) and a Carbohydrate Ligand Polycation Form DNA Ternary Complexes for Gene Delivery

Shoichiro Asayama,* Satoshi Nishinohara, and Hiroyoshi Kawakami

Department of Applied Chemistry, Tokyo Metropolitan University,
1-1 Minami-Osawa, Hachioji, Tokyo 192-0397, Japan

*To whom correspondence should be addressed.
E-mail: asayama-shoichiro@tmu.ac.jp.

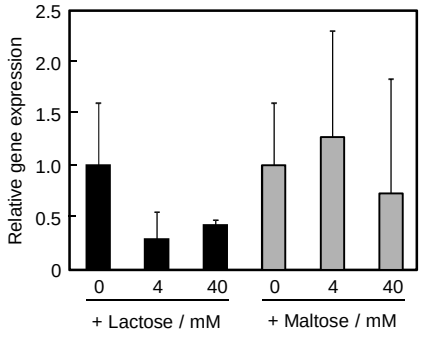

Figure S-1. Cellular recognition of PLL-Lac/PVIm-Zn/DNA ternary complexes by HepG2 cells. The PLL-Lac/PVIm-Zn/DNA complexes were incubated in the presence of lactose (4 or 40 mM) or maltose (4 or 40 mM). Gene expression was represented as relative gene expression compared with the sample in the absence of lactose and maltose. Symbols and error bars represent the mean and standard deviation of the measurements made in triplicate wells.

Bioconjugate Chemistry

ARTICLE

pubs.acs.org/bc

Improved Templated Fluorogenic Probes Enhance the Analysis of Closely Related Pathogenic Bacteria by Microscopy and Flow Cytometry

Raphael M. Franzini and Eric T. Kool*

Department of Chemistry, Stanford University, Stanford, California 94305-5080, United States

Supporting Information

ABSTRACT: Templated fluorescence activation has recently emerged as a promising molecular approach to detect and differentiate nucleic acid sequences *in vitro* and in cells. Here, we describe the application of a reductive quencher release strategy to the taxonomic analysis of Gram-negative bacteria by targeting a single nucleotide difference in their 16S rRNA in a two-color assay. For this purpose, it was necessary to develop a release linker containing a quencher suitable for red and near-infrared fluorophores, and to improve methods for the delivery of probes into cells. A cyanine-dye labeled oligonucleotide probe containing the new quencher-release linker showed unprecedentedly low background signal and high fluorescence turn-on ratios. The combination of a fluorescein-containing and a near-IR emitting probe discriminated *E. coli* from *S. enterica* despite nearly identical ribosomal target sequences. Two-color analysis by microscopy and the first successful discrimination of bacteria by two-color flow cytometry with templated reactive probes are described.

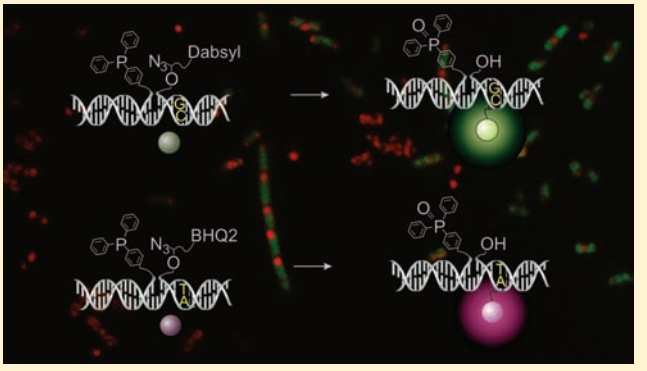

INTRODUCTION

The development of methods for rapid detection and identification of human pathogenic bacteria is widely regarded as important both in medical diagnostics and in monitoring food safety. The standard analytical approach for most bacteria involves growing cultures followed by microbiological assessment, which is time-consuming and labor-intensive and requires expert personnel. Consequently, there is significant interest in developing methods to identify microbes directly from clinical samples with a straightforward readout. Of particular appeal in this respect are fluorescence in situ hybridization (FISH) methods,[1,2] which target specific RNA or DNA sequences with labeled hybridization probes followed by microscopic analysis or flow cytometry.[3] Bacterial FISH assays frequently target rRNAs (rRNAs) because these markers are highly expressed and the target accessibility is well-established.[4,5] However, it is challenging to distinguish closely related pathogens with standard-length hybridization probes, because rRNAs are evolutionarily conserved and a difference of only one or two nucleotides in a target sequence has an insignificant influence on the binding of a standard-length probe of 25 nucleotides or more.[6] Furthermore, standard FISH assays involve cell fixation and washing steps, extending the time and care required for analysis.

One possible approach to avoid these limitations of standard FISH probes involves the use of quenched probes that report the presence of a target with a fluorescence turn-on signal.[7] Prominent examples of fluorescence turn-on probes include molecular beacon (MB) probes,[8] forced intercalation (FIT) probes,[9] and templated reactive probes.[10] Because such probes are nonfluorescent before binding their target, they can (at least in principle) be used without washing steps, thus simplifying the genetic analysis considerably. Indeed, MB probes have been employed in the analysis of bacterial RNAs.[11,12] In a different molecular strategy, templated reactive probes allow the identification and analysis of bacteria in a single step requiring as little as 45 min incubation time.[13] In this approach, two modified oligonucleotide probes bind at adjacent sites on a nucleic acid target sequence, bringing two chemically reactive groups together to generate a fluorescence signal.[10] The possibility to use short probes provides this strategy with excellent mismatch selectivity on highly expressed, conserved RNA sequences such as rRNAs.[13−17] This high degree of sequence specificity is a major advantage over standard FISH probes for which single base specificity is possible[18] but is often challenging. Two-color sets of templated quenched autoligation (QUAL) probes enabled discrimination of bacteria by a simple fluorescence color-call.[19] In preliminary experiments, this technique has been applied to distinguish *Escherichia coli* from *Salmonella enterica*[13−17] and *Shigella*[19] pathogens by fluorescence microscopy and single-color flow cytometry.[15] Several laboratories have recently reported advances in templated reactive

Received: July 5, 2011
Revised: August 8, 2011
Published: August 26, 2011

ACS Publications © 2011 American Chemical Society

dx.doi.org/10.1021/bc2003567 | *Bioconjugate Chem.* 2011, 22, 1869–1877

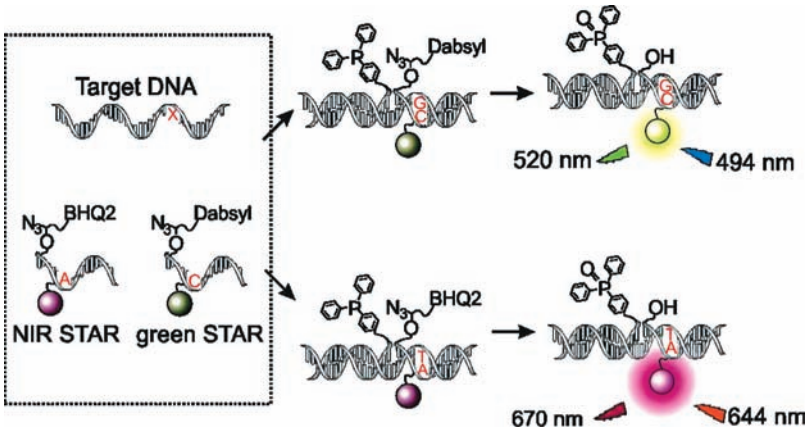

Figure 1. Schematic illustration of two-color discrimination of DNA targets with single nucleotide specificity. A cyanine dye-labeled quencher release probe (NIR STAR) hybridizes specifically to one target strand, providing a near-IR fluorescence signal after templated reaction with a TPP-DNA probe, while a green STAR probe specific for the other target strand provides a green fluorescence signal.

oligonucleotide designs;[20−25] examples included probes that are based on templated Staudinger reactions.[26−30] Among these, we have described quenched Staudinger reaction triggered α-azidoether release (Q-STAR) probes, which release a quencher after an azide reduction reaction on a linker carrying it.[31−33]

Despite the promise of early experiments, challenges remain for the general application of templated probes in bacteria, including spectral limitations and problems with probe delivery into cells. Previous two-color reactive probe systems for the detection of bacterial rRNAs relied on a FRET-reporter strategy, in which one probe contained fluorescein and the second one fluorescein combined with a TAMRA FRET-acceptor.[17,19,31] This strategy offers direct visual readout under a fluorescence microscope with single-wavelength excitation. However, low emission quantum yield and poor spectral resolution render such FRET-based probes unsuitable for quantitative analytical methods such as flow cytometry, which may benefit from probes with fluorophores that are excited at separate wavelengths. Multicolor QUAL probes have been described and applied to imaging of bacteria;[34] however, the Dabsyl group intrinsic to the QUAL design quenches red and near-IR emitting dyes inefficiently. Other examples of two-color reactive probes based on two distinct profluorophores have been described but their potential for cellular RNA probing remains untested.[35,36] Delivery of oligonucleotide probes into bacteria is another challenge for the direct detection of genetic markers in microbes. Cell fixation is one possible solution; however, this adds extra time and effort to the experimental protocol, renders bacteria less amenable to separation by flow cytometry, and excludes the possibility of isolating live cells for further analysis. One report described the use of a detergent to aid in delivery of FISH probes into bacteria, offering a simple alternative to fixation.[15] However, it is unknown to what extent various detergents might aid probe uptake into bacteria and how such reagents affect bacterial viability.

Here, we describe the preparation and evaluation of quencher release probes suitable for red and near-IR emitting fluorophores and their potential for pathogen analysis in a two-color assay with fluorescein-labeled probes (Figure 1).[31] We found that these probes enable the discrimination of *E. coli* and *S. enterica* with improved signal contrast by fluorescence microscopy and by flow cytometry. Moreover, we investigated the use of various detergents and delivery agents on probe uptake, probe background signals, and bacterial viability. Furthermore, we outline and discuss the remaining challenges for development of practical whole-cell microbial detection assays based on templated reactive probes and light-up probes in general.

EXPERIMENTAL SECTION

Preparation of Reactive Oligonucleotide Probes. Probes were prepared by solid-phase conjugation of the quencher release linker (synthesis described in Supporting Information) to the protected, fluorophore labeled (Quasar 670-dT, Biosearch Technologies) NIR STAR probes and (Fluorescein-dT, Glen Research)) green STAR probes oligonucleotides containing a 5′-terminal amino modifier (5′-amino-modifier 5, Glen Research). NIR STAR probes were synthesized with UltraMILD deprotection phosphoramidites (Glen Research); labeling of these oligonucleotides with **3** provided the NIR STAR probes in lower yield than green STAR probes. The major side product had a mass corresponding to the amine-modified DNA plus a Pac group, possibly resulting from a transfer of a Pac protecting group from nucleobases to the terminal amine under the quencher conjugation conditions. For the introduction of the 2,6-diaminopurine (DAP) DNA monomer, we used 2-Amino-dA-CE phosphoramidite (Glen Research). The trityl protecting group of the terminal amine was removed by repetitive cycles of 2% trichloroacetic acid in DCM on the DNA synthesizer. Controlled pore glass (CPG) containing the oligonucleotides was incubated with a solution of the quencher release linker (25 mM), PyBOP (25 mM), and DIEA (50 mM) in DMF (250 μL) and gently shaken at room temperature for 5 h, protected from light. The supernatant was removed and the beads washed with DMF (2×) and MeCN (3×) until the solution was colorless. For cleavage from the solid support and deprotection of green STAR probes, the CPG were incubated for 90 min with concentrated aqueous ammonia/methylamine at 55 °C; for NIR STAR probes, beads were incubated in 0.5 M potassium carbonate solution in methanol for 4 h at room temperature. The purity of the probes was assessed by analytical HPLC chromatography (the probes were found to be >95% pure) and the molecular structure was verified by MALDI-TOF mass spectrometry analysis. The triphenylphosphine (TPP)-DNA probe was prepared as previously described.[31]

Chart 1. Structures of Releasable Quencher Linkers Designed for Green STAR and NIR-STAR Probes

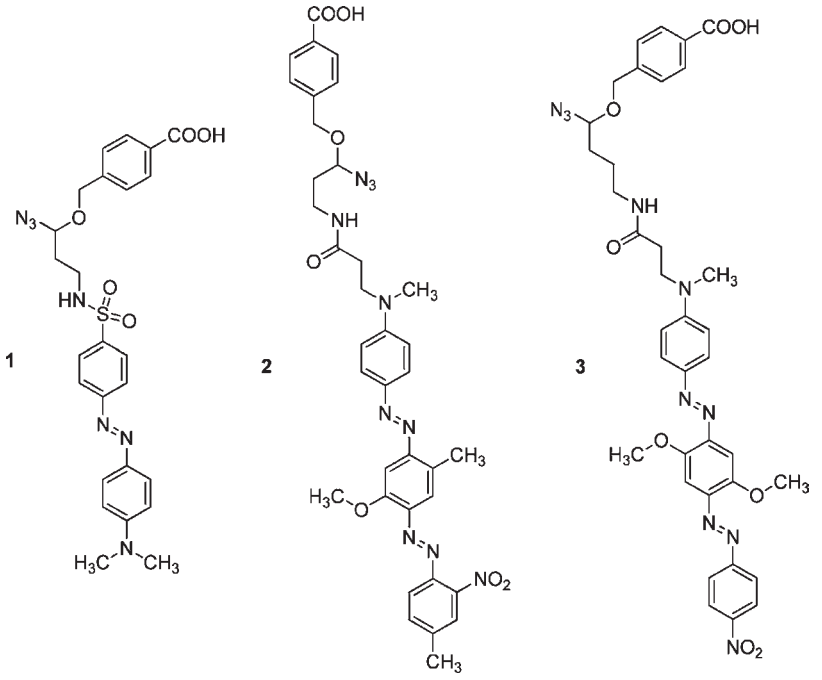

Unmodified template and helper DNAs were obtained from the Stanford Protein and Nucleic Acid Facility.

Kinetic Measurements. Quenched probes (200 nM) and the corresponding template (200 nM) were incubated at 37 °C in Tris-borate buffer (70 mM, pH 7.55) containing $MgCl_2$ (10 mM). TPP-DNA (600 nM) was added and the fluorescence emission (λ_{ex} = 494 nM; λ_{em} = 521 nm for green STAR; λ_{ex} = 644 nm and λ_{em} = 670 nm for NIR STAR) was measured as a function of time on a Fluorolog 3 Jobin Yvon spectrometer equipped with an external temperature controller.

Fluorescence Microscopy. *E. coli* K12 and *S. enterica* were grown to midlog phase (OD_{600} = 0.4) in Luria−Bertani (LB) media with rapid shaking at 37 °C. Aliquots of the media (100−200 μL) were carefully centrifuged and the supernatant decanted. Pellets were washed with 1× PBS buffer (pH 7.4) and resuspended in 6× saline sodium citrate (SSC) buffer (pH 7.4) containing 0.05% SDS. Green STAR (200 nM), NIR STAR (200 nM), TPP-DNA (2 μM), and helper DNAs (3 μM) were added and the samples incubated at 37 °C for 3 h without shaking and protected from light. Aliquots of incubated bacteria suspensions were mixed with 2% agarose solution and spotted on cover slides without washing or fixation. Imaging was performed on a Nikon Eclipse E800 epifluorescence microscope equipped with a Nikon Plan AP 100×/1.40 oil immersion objective and a SPOT RT digital camera; filter sets were B-2A (excitation 450−490 nm, dichroic mirror 500 nm, emission >500 nm) for green STAR and Cy5 HYQ (excitation 590−650 nm, dichroic mirror 660 nm, emission 663−738 nm) for NIR STAR probes.

Flow Cytometry Analysis. Bacteria were grown and treated with reactive probes as described for fluorescence microscopy experiments. Bacteria were diluted 10-fold in 6× SSC and the cell suspension immediately analyzed using an LSR I flow cytometer (BD Biosciences). Side angle light scattering was used as the triggering event. Forward angle light scattering and side angle light scattering were recorded as well as fluorescein (λ_{ex} = 488 nm laser; λ_{em} = 530−560 nm) and Q670 (λ_{ex} = 640 nm laser; λ_{em} = 666−690 nm) fluorescence emission. Flow cytometry data were analyzed with *FlowJo* software (Tree Star).

Bactericidal Activity of Surfactants. Bacteria cells were grown to midlog phase (OD_{600} = 0.4), concentrated 10-fold by mild centrifugation and dispersed in SSC buffer (pH 7.0). Bacteria were incubated with different additives for 4 h at 37 °C without shaking. Aliquots of the bacteria samples were spread over solid LB-agar medium in Petri dishes and the dishes incubated at 37 °C overnight. The degree of bacteria growth was assessed visually.

Surfactant-Mediated Effects on Probe Signals. A mixture of Q-STAR (green STAR SE, 200 nM) and TPP-DNA (2.0 μM) probes was incubated in SSC buffer (1×, pH 7.0) containing different additives (1.0% w/v) at 37 °C for 4 h. The fluorescence intensity was measured with a Flexstation II microplate reader (Molecular Devices) in a 96-well quartz microplate (λ_{ex} = 494 nm, λ_{em} = 525 nm). The fluorescence intensity was normalized by dividing by the fluorescence intensity of a sample containing the probes in SSC buffer only.

RESULTS

Design, Preparation, and Evaluation of Quenched Near-IR Probes. We aimed to develop a quenched probe with a red-light emitting fluorophore that could be used in combination with fluorescein-labeled green STAR probes[31] for two-color instrumental analyses. The choice of a new long-wavelength dye required pairing it with a compatible quencher, since the original Dabsyl quencher (see **1** in Chart 1) is limited to shorter-wavelength fluorophores (λ_{em} < 550 nm). Thus, we designed the new quencher-linker **2** containing a Black Hole Quencher 1 (BHQ-1) and the same α-azidoether linker structure as the preceding Dabsyl-probe **1**. The synthesis of **2** was identical to that of **1** except for the quencher attachment step, which involved HBTU-mediated amide bond formation (Supporting Information). To test the templated cleavage kinetics, the linker **2** was

Table 1. Sequences of Reactive Probes, Templates, and Helper Oligonucleotides Used in This Study

probe[a]	sequence[b]
green STAR EC	5′-**1**-AGT$_{Fl}$CGACA-3′
green STAR SE	5′-**1**-AGT$_{Fl}$AGACA-3′
green STAR SE DAP	5′-**1**-AGT$_{Fl}$DGACA-3
green STAR EC BHQ-1	5′-**2**-AGT$_{Fl}$CGACA-3′
NIR STAR EC	5′-**3**-AGT$_{Q670}$CGACA-3′
NIR STAR SE	5′-**3**-AGT$_{Q670}$AGACA-3′
TPP-DNA	5′-CAACCTCCA-TPP-3′
TPP-DNA*	5′-AGGGCACAACCTCCA-TPP-3′
EC DNA	5′-GATGTCGACTTGGAGGTTGTG-3′
SE DNA	5′-GATGTCTACTTGGAGGTTGTG-3′
Helper 1	5′-TCGTTTACGGCGTGGACT-3′
Helper 2	5′-GCTCCGGAAGCCACGCCT-3′

[a] TPP-DNA is used for in vitro experiments; TPP-DNA* is used for experiments with bacteria. [b] Fl: fluorescein. Q670: Quasar 670. TPP: Triphenylphosphine. D: 2,6-diaminopurine. For the chemical structures of **1**, **2**, and **3**, see Chart 1.

incorporated at the 5′-terminus of a labeled Q-STAR probe specific to a target sequence of 16S rRNA of *E. coli* (green STAR EC BHQ-1, Table 1).

Evaluation of the quencher-linker **2** showed that the DNA-templated reaction was rapid but that background quencher release is elevated compared with other probes. The presence of the EC DNA template induced a rapid reaction between green STAR EC BHQ-1 and TPP-DNA, eliciting a strong fluorescence turn-on signal (Figure 2a). The reaction kinetics were similar to those observed previously for probes containing linker **1**.[31] Control experiments (mismatch template SE DNA, no template, no TPP-DNA) confirmed the target-specificity of the probes (Figure 2a). Interestingly, the fluorescence activation was similar for all control experiments, indicating significant phosphine-independent breakdown of probes containing the BHQ-1 release linker **2**. Mass spectrometry analysis revealed cleavage of the α-azidoether group upon incubation of probe alone at room temperature in buffer.

We hypothesized that the carboxamide moiety of linker **2** is responsible for the significant spontaneous decomposition of these probes, possibly by stabilizing the transition state of α-azidoether hydrolysis[37] via an unidentified cyclic intermediate. On the basis of this assumption, we synthesized linker **3** (Chart 1) with an additional methylene group to disfavor a possible intramolecular interaction. Concomitantly, we changed the quencher to Black Hole Quencher 2 (BHQ-2) because this dye quenches red and near-IR fluorophores more efficiently than BHQ-1.[38] The synthesis of BHQ-2 release linker **3** is similar to that of **1** and **2**, affording the product in 6 steps (Supporting Information).

Using the new quencher-linker **3**, we prepared NIR STAR probes containing a Cy5-derivative (Quasar 670, Q670) as the fluorophore (Table 1). Probes were complementary to a target site on 16S rRNA containing a single site difference between *E. coli* (EC) and *S. enterica* (SE).[15]

Fluorescence Activation and Sequence-Specificity. Incubation of NIR STAR EC with TPP-DNA and the matched template EC DNA rapidly elicited a strong increase of fluorescence (λ_{ex} = 644 nm, λ_{em} = 670 nm) with a kinetic trace similar to that of green STAR EC BHQ-1 (Figure 2b). The measured

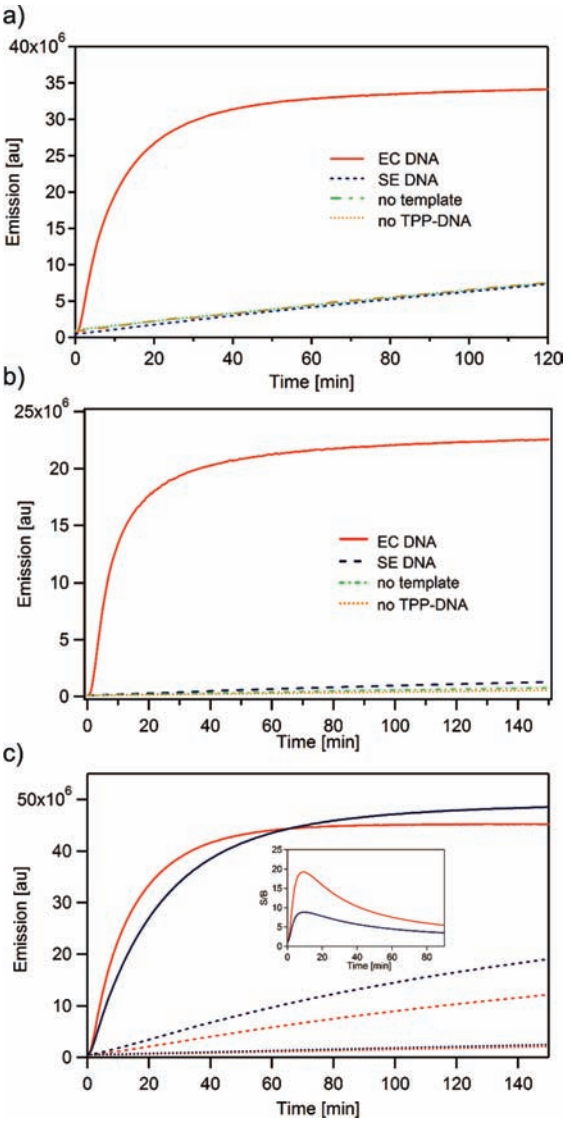

Figure 2. In vitro DNA-templated fluorescence activation of several green- and NIR-STAR probes by TPP-DNA. (a) Green STAR EC BHQ-1 containing linker **2**. (b) NIR STAR EC containing linker **3**. (c) Comparison of probes with either 2,6-diaminopurine (green STAR SE DAP, red traces) or adenine (green STAR SE, blue) in the presence of the matched template (SE DNA, solid traces), singly mismatched template (EC DNA, dashed traces), and without template (dotted traces). Inset shows mismatch selectivity (ratio of matched/mismatched signal) for the probes as a function of time.

fluorescence turn-on ratio (fluorescence intensity after quencher release, divided by fluorescence intensity before addition of TPP-DNA) exceeded 200-fold, establishing that the fluorophore is quenched with >99.5% efficiency. This quenching effect compares favorably with probes containing a Dabsyl/fluorescein pair (67-fold fluorescence activation)[31] and is presumably caused by the high quenching efficiency of BHQ-2.[38] Importantly, the generation of background fluorescence for NIR STAR EC was distinctly slower in the absence of TPP-DNA than for green STAR EC BHQ-1 and was below the rate of the reaction in the absence of the template or in the presence of the singly mismatched template SE DNA (Figure 2b). A second NIR STAR probe complementary to the sequence corresponding to *S. enterica*

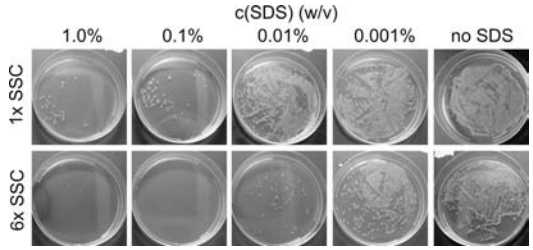

Figure 3. Effect of delivery protocols (buffer salinity (saline sodium citrate, SSC) and concentration of sodium dodecyl sulfate (SDS)) on the viability of *Escherichia coli* K12. Bacteria were incubated with the indicated buffers for 4 h before spreading on the culture plates; cultures are shown 12 h post-treatment at 37 °C.

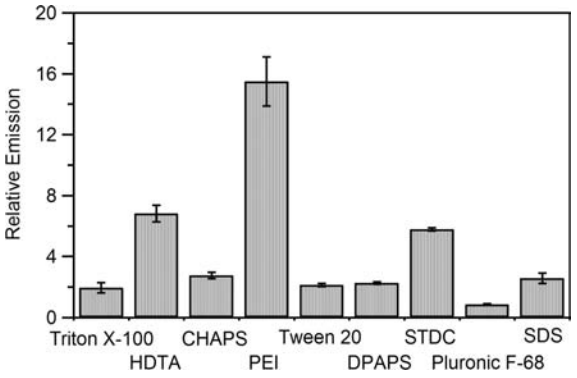

Figure 4. Template-independent fluorescence activation of green STAR SE probes by TPP-DNA mediated by selected additives in solution (in the absence of bacteria). Data are taken after 4 h at 37 °C with TPP (2.0 μM) and green STAR SE (200 nm). Values are fluorescence signals normalized to controls with probes in 1× SSC buffer alone. Error bars are standard deviations from triplicate experiments. (For full name of additives and molecular structures, see Supporting Information).

(NIR STAR SE, Table 1) also exhibited sequence-selective fluorescence activation of similar rate and magnitude (Figure S2, Supporting Information) although with significantly lower single-mismatch specificity because of the small energetic difference between the A-T match and the A-G mismatch, one of the most challenging mismatches to discriminate.[39]

To enhance sequence discrimination of SE DNA at this target site, we investigated the use of the 2,6-diaminopurine (DAP) base surrogate, which reportedly enhances single nucleotide discrimination over canonical adenine.[40] We prepared a DAP-containing green STAR probe (green STAR SE DAP, Table 1) and compared its sequence-specificity to a probe with an adenine at this position (green STAR SE, Table 1). (Note: Quasar 670 is incompatible with the stringent deprotection condition of commercial 2-amino-dA-CE phosphoramidite.) The SE DNA-mediated reaction was faster with green STAR SE DAP than with green STAR SE, and the reaction mediated by the mismatch-containing EC DNA target was reduced for green STAR SE DAP relative to green STAR EC (Figure 2c). These two favorable effects synergistically yielded a 2-fold enhancement of mismatch selectivity for the DAP probe; after 9.5 min incubation, the sequence-specificity reached a maximum of 19.2 for green STAR SE DAP and only 8.8 for green STAR SE (Figure 2c inset).

Effect of Probe Delivery Protocols on Bacteria Growth. Protocols that enable cellular probe delivery without complex and time-consuming fixation steps would be advantageous to harness the simplicity of fluorogenic probes in bacteria. Previous studies described the introduction of oligonucleotide probes into Gram-negative bacteria by incubating the prokaryotes in hyperosomotic buffer (6× saline-sodium citrate buffer, SSC) containing the detergent SDS (sodium dodecyl sulfate).[15,34] Although early studies suggested that bacteria remain viable under these conditions,[15,41] this conclusion remains uncertain.[42] The survival of the bacteria is unnecessary for many diagnostic applications; however, it would be useful, for example, for culturing colonies from genetically sorted bacteria.

We tested the toxicity of SDS on the bacteria and compared it with the bactericidal effect of a small array of selected surfactants also to be tested for probe delivery. We examined cationic (HDTA), anionic (SDS, STDC), neutral (Triton X-100; Tween 20), and zwitterionic (CHAPS; DPAPS) detergents and selected polymers previously used for cell delivery purposes (polyethylene imine, PEI;[43] Pluronic F-68[44]) (for full names and molecular structures, see Table S1, Supporting Information). As anticipated, different additives exhibited widely varying toxicities (Figure 3 and Figure S1, Supporting Information). HDTA was highly toxic at all tested concentrations, in agreement with the bactericidal activity of cationic lipids.[45] The neutral surfactants exhibited low toxicity in the investigated concentration range. Zwitterionic and anionic detergents, including SDS, exhibited a dose-dependent toxicity. SDS significantly inhibited colony formation in 6× SSC buffer; colonies formed only for the sampled with 0.01% to 0.001% SDS but were absent in samples for 1.0% and 0.1% SDS (Figure 3). The data reveal that the previously employed delivery protocol (0.05% SDS in 6× SSC) is toxic to *E. coli*, leaving only a few colonies. The hyperosmotic medium partially accounts for this bactericidal effect; bacteria treated with 1× SSC solutions formed significantly more colonies than those treated with 6× SSC.

Effect of Delivery Agents on Probe Background. For assessment of probe delivery agents, it was important to evaluate whether the reagents engender background signals, for example, by sequence-independent aggregation of probes with polymers or lipids. To test this possibility, we incubated Q-STAR (green STAR SE) and TPP-DNA probes for 4 h in the presence of the additives (1% w/v) without template DNA and compared the fluorescence level to a control sample of probes without TPP-DNA. All additives with the exception of Pluronic F-68 generated higher fluorescence levels than the control (Figure 4). For SDS and several other detergents (Triton X-100, Tween 20, CHAPS, DPAPS), the level was approximately 2-fold higher than the control; this level of background fluorescence is acceptable for RNA detection in bacteria. In contrast, background fluorescence for PEI (15.5-fold), HDTA (6.8-fold), and STDC (5.8-fold) substantially exceeded the level of the control sample, ruling out these reagents for use with templated probes. The template-independent background fluorescence may arise from condensation of the polyanionic DNA reactive probes with cationic or zwitterionic surfactants.

Effect of Detergents and Polymers on Probe Uptake. We next tested whether milder SDS conditions (1× SSC buffer, low SDS concentrations) or alternative delivery agents promote the uptake of oligonucleotide probes into Gram-negative bacteria (Figure S3, Supporting Information). For this purpose, we incubated *E. coli* with the reactive probes (green STAR EC and TPP-DNA*) and unlabeled helper oligonucleotides (Helper 1 and 2, Table 1; helper oligonucleotides enhance target accessibility by hybridizing adjacent to the probe binding sites and

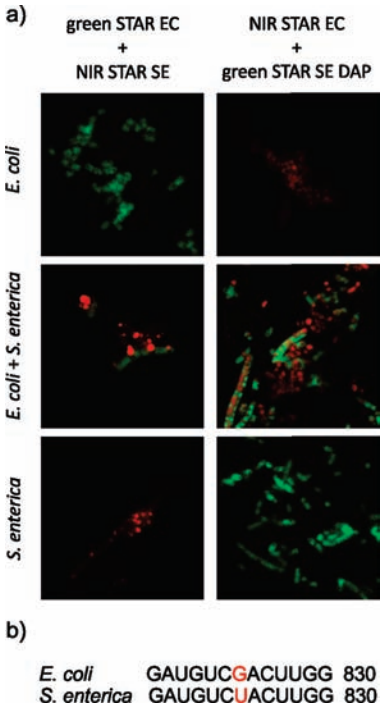

Figure 5. (a) Discrimination of *E. coli* and *S. enterica* by two-color excitation/emission fluorescence microscopy with a combination of green STAR and NIR STAR probes targeted to a single nucleotide difference in 16S rRNA. Signals are shown after 3 h incubation. (b) 16S RNA sequences of the two bacteria at the target site (ref 15).

unwinding the local secondary structure[5,15]) in the presence of varying concentrations of the additives (for structures, see Table S1, Supporting Information). From the tested surfactants, only SDS provided detectable probe uptake as judged by fluorescence signal associated with cells (HTDC and PEI were not tested because of high toxicity and nonspecific fluorescence background, respectively). We then evaluated the effect of SDS and SSC buffer concentration on the bacterial staining (Figure S3, Supporting Information). Samples with 6× SSC buffer showed the characteristic green fluorescence staining of *E. coli* at 0.5% and 0.05% SDS and to a lesser degree at 0.005% SDS. Fluorescence was also observable for the 1× SSC sample with 0.5% SDS but the signal faded considerably with decreasing SDS concentration. Therefore, the nontoxic conditions deliver oligonucleotide probes with only low efficiency into *E. coli*. For further experiments with Q-STAR probes in bacteria, we used the previously described protocol (6× SSC with 0.05% SDS) with the knowledge that the viability is significantly affected for the majority of the cells.

Two-Color Discrimination of Bacteria by Fluorescence Microscopy. We tested species-specific Q670-containing NIR STAR probes in combination with fluorescein-containing green STAR probes for two-color discrimination of *E. coli* and *S. enterica* (Figure 5). Bacteria were incubated with the Q-STAR and TPP-DNA probes and the helper oligonucleotide probes in hybridization buffer (6× SSC, 0.05% SDS) for 3 h and analyzed by fluorescence microscopy with two filter sets (see Experimental Section). A mixture of NIR STAR SE and green STAR EC probes resulted in a strong and exclusive Q670-fluorescence staining of *S. enterica*, while *E. coli* exhibited strong fluorescein signal without detectable Q670-emission (Figure 5a). The inverse staining pattern was present when we reversed the dye labeling of the probe sequences (green STAR SE DAP and NIR STAR EC). Co-incubation of mixed microbes with NIR STAR and green STAR probes provided images of bacteria stained either red or green, enabling the discrimination of single bacterial cells by a fluorescence color call.

Interestingly, while fluorescein staining for the combined bacteria was selective for the assumed *E. coli* in the mixture, all bacteria exhibited some degree of Q670-emission (Figure 5a, middle row). Possibly under the given conditions, NIR STAR probes after being activated in a sequence-specific manner (after release of the BHQ-2 quencher) can exit the host bacteria and reenter another bacterium.

Two-Color Analysis of Bacteria Cultures by Flow Cytometry. Next, we evaluated the optimized two-color probes for use in flow cytometry. Previously, we described the application of a single monocolor probe using simple fluorescence intensity as the flow cytometry readout.[15] However, a variety of experimental parameters influence the fluorescence intensity besides the presence and the sequence of the target rRNA, for example, efficiency of probe uptake or bacteria aggregation. Thus, a ratiometric two-color analysis is desirable and is expected to provide more reliable results.

To this end, we employed fluorescein- and Q670-labeled probes (green STAR SE DAP and NIR STAR EC) as described for the microscopy experiments. The bacteria were incubated with the reactive probes and helper oligonucleotides in the delivery buffer (6× SSC, 0.05% SDS) and analyzed by two-color flow cytometry. The signal measured in the fluorescein channel was distinctively higher for *S. enterica* than for *E. coli* (3.7 ± 0.5-fold) for green STAR SE DAP (Figures 6 and 7). Inversely, the NIR STAR EC probe produced a stronger Q670-fluorescence signal in *E. coli* relative to *S. enterica* (6.7 ± 1.6-fold difference). Neither of the probes generated a significant fluorescence signal in the nonspecific detection channel, as expected because of the high spectral resolution of the chosen fluorophore labels. When incubated with a mixture of green STAR SE DAP and NIR STAR EC, bacteria colonies developed distinct fluorescence patterns. *E. coli* exhibited strong Q670-fluorescence, whereas for *S. enterica*, fluorescein emission was predominant (Figures 6 and 7). The combination of the probes also provided a better discrimination signal than single probe measurements; taking the ratio of Q670 and fluorescein emission provided a 15.7 ± 3.4-fold difference between the two bacterial strains.

E. coli treated with NIR STAR EC separated into two major subpopulations in flow cytometric analysis, one having approximately 10-fold higher Q670-emission than the other (distinguishable as a shoulder on the histogram in Figure 6, right panel). The fraction of the low-emission population increased with incubation time, and such an effect was absent for green STAR SE DAP. This result agrees with the observation of a small population of doubly stained bacteria in mixtures of *E. coli* and *S. enterica* and points toward incomplete retention of the NIR STAR probes after quencher release.

■ DISCUSSION

The present data demonstrate improved methods for identification of two bacterial pathogens with a two-color pair of templated reductive quencher release probes targeting the 16S rRNA. The results show that bacteria can be successfully discriminated with fluorescence microscopy by a simple fluorescence

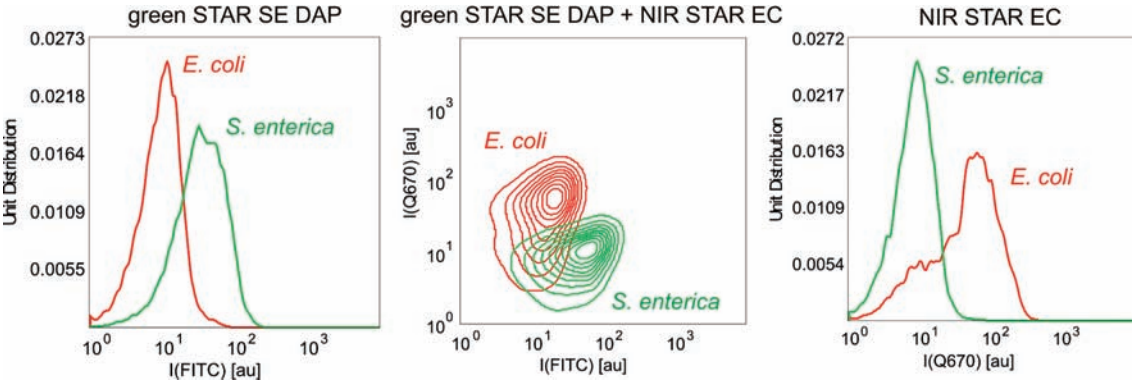

Figure 6. Flow cytometric analysis of *E. coli* (red) and *S. enterica* (green) populations stained with Q-STAR probes. Histograms of cell fluorescence intensity for single probe experiments with either green STAR SE DAP (left graph) or NIR STAR EC (right graph). The center graph shows a two-color plot of the fluorescence intensities of either bacteria in an experiment containing both probes. (FITC: λ_{ex} = 488 nm laser; λ_{em} = 530−560 nm; Q670: λ_{ex} = 640 nm laser; λ_{em} = 666−690 nm).

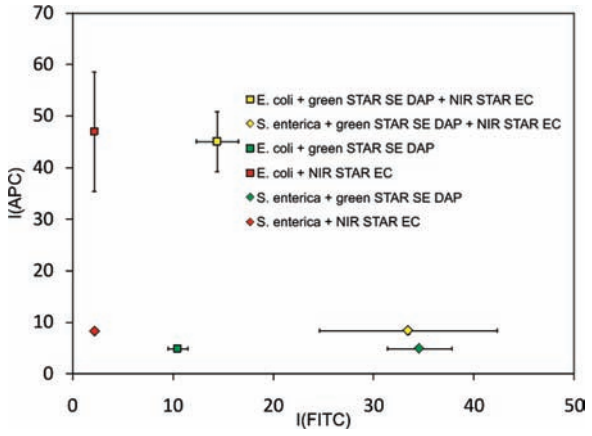

Figure 7. Quantitative analysis of flow cytometric results of bacteria incubated with Q-STAR probes. Values indicate mean fluorescence intensity; error bars are standard deviations of three independent experiments. *I*(FITC) = Intensity in FITC channel; *I*(APC) = Intensity in Cy5 channel.

color-call and, for the first time, by two-color flow cytometry. The performed experiments constitute a significant advance over previous assays targeting rRNAs. Standard FISH probes are simple label-containing oligonucleotide hybridization probes, requiring cell fixation and extensive washing steps. However, the necessity for cell fixation makes the protocol more cumbersome, can produce artifacts, and is incompatible with the long-term goal of culturing bacteria obtained from fluorescence-activated cell sorting. Light-up probes provide a powerful tool to overcome these limitations; for example, MB probes have been applied to the analysis of bacteria RNA with FISH and flow cytometry.[11,12] However, those reports used fixed cells and their value for the analysis of intact cells remains to be evaluated. In addition, background fluorescence from nonspecific interactions of MB probes with cellular macromolecules or degradation of the probes complicates analysis.[46] Templated reactive probes in general and the described two-color set of probes in particular offer several possible advantages in bacterial RNA targeting. First, the dual probe design minimizes nonspecific activation of reactive probes, as demonstrated here by the minimal fluorescence background observed in microscopy and flow cytometry experiments. Second, the short length of the probes enables excellent sequence specificity, demonstrated by the ability to discriminate two bacteria by a single nucleotide difference. Finally, templated reactive probes can yield isothermally amplified signals, while MB and FIT are stoichiometric at best.

The current probe set with two distinct fluorophores also offers several advantages over previous templated probe designs that employed either a single color or a FRET pair. Two-color approaches allow for ratiometric analysis of the readout, which in this study provides significantly better discrimination than a single probe. The two-color ratio further reduces the uncertainty deriving from experimental parameters, such as variations in bacteria size, copy number of rRNAs, and probe delivery efficiency, obviating the necessity of an external standard. During this study, we also noted that, under the given experimental conditions, the bacteria tend to aggregate and the *E. coli* more strongly so than *S. enterica*, but again the use of a two-color ratio alleviates problems associated with this effect.

The use of two spectrally separated dyes can be advantageous relative to FRET-based probes when using sophisticated equipment such as modern flow cytometers. The current fluorescein and Q670 dyes are bright fluorophores, while FRET-based probes can suffer from low emission quantum yields[47] and suboptimal spectral resolution. Previous attempts to analyze bacteria by flow cytometry were hampered by low fluorescence intensity. Nevertheless, the earlier FRET probes may remain advantageous for certain applications with simpler equipment, such as in cases where there is only a single excitation wavelength and a single filter set available.

A major challenge for in situ hybridization-based experiments with live bacteria remains the difficulty of delivering oligonucleotides into cells. The current protocols enable bacterial analysis by microscopy and flow cytometry without fixation; however, our results show that cells are rendered largely nonviable by the studied delivery agents. While many diagnostic applications require no live bacteria, it may be useful for applications such as sorting and selecting bacteria genetically. On the basis of the present experiments, it seems possible that conditions for probe delivery and cell viability are orthogonal, likely because the pores induced in the cell wall to allow for probe delivery are also lethal to the cells. In this light, it has been reported that the conjugation of cationic peptides to some oligonucleotide analogues (such as

PNAs[48] or morpholino DNAs)[49] enhances bacterial uptake. Whether such an approach is effective with light-up probes in general or with template reactive probes in particular remains to be determined.

Finally, the development of the new quencher-linker **3** expands the utility of templated quencher release (Q-STAR) probes. In combination with the previously established Dabsyl release linker, the newly developed BHQ-2 (NIR STAR) probes are highly versatile allowing straightforward design of quenched probes with fluorophores emitting in colors ranging from blue to near-infrared. Furthermore, because of the efficiency of the new quencher, NIR STAR probes reach turn-on values exceeding 200-fold, which is significantly better than previous quencher release probes and rivals the highest turn-on ratios reported to date for any template reactive probes.[21,30] Such multicolor probes may find applications in multiplex detection of nucleic acids in complex samples.

■ ASSOCIATED CONTENT

Supporting Information. Synthesis of quencher release linkers, ^{1}H- and ^{13}C NMR analysis of synthetic intermediates and products, MALDI-TOF and analytical HPLC analysis of reactive probes, and additional experiments. This material is available free of charge via the Internet at http://pubs.acs.org.

■ AUTHOR INFORMATION

Corresponding Author

*E-mail: kool@stanford.edu, Tel.: 650-724-4741, Fax: 650-725-0295.

■ ACKNOWLEDGMENT

This project was supported by the National Institutes of Health (GM068122) and a Gerhard Casper Fellowship to RMF from Stanford University. Fluorescence experiments were performed on a fluorescence spectrometer in the Department of Chemistry supported by the National Science Foundation (CHE-0639053).

■ REFERENCES

(1) Moter, A., and Göbel, U. B. (2000) Fluorescence *in situ* hybridization (FISH) for direct visualization of microorganisms. *J. Microbiol. Methods 41*, 85–112.

(2) Wagner, M., Horn, M., and Daims, H. (2003) Fluorescence *in situ* hybridisation for the identification and characterisation of prokaryotes. *Curr. Opin. Microbiol. 6*, 302–9.

(3) Czechowska, K., Johnson, D. R., and van der Meer, J. R. (2008) Use of flow cytometric methods for single-cell analysis in environmental microbiology. *Curr. Opin. Microbiol. 11*, 205–212.

(4) Fuchs, B. M., Wallner, G., Beisker, W., Schwippl, I., Ludwig, W., and Amann, R. (1998) Flow cytometric analysis of the *in situ* accessibility of *Escherichia coli* 16S rRNA for fluorescently labeled oligonucleotide probes. *Appl. Environ. Microbiol. 64*, 4973–82.

(5) Fuchs, B. M., Syutsubo, K., Ludwig, W., and Amann, R. (2001) *In situ* accessibility of *Escherichia coli* 23S rRNA to fluorescently labeled oligonucleotide probes. *Appl. Environ. Microbiol. 67*, 961–8.

(6) Demidov, V. V., and Frank-Kamenetskii, M. D. (2004) Two sides of the coin: affinity and specificity of nucleic acid interactions. *Trends Biochem. Sci. 29*, 62–71.

(7) Silverman, A. P., and Kool, E. T. (2005) Quenched probes for highly specific detection of cellular RNAs. *Trends Biotechnol. 23*, 225–30.

(8) Tyagi, S., and Kramer, F. R. (1996) Molecular beacons: probes that fluoresce upon hybridization. *Nat. Biotechnol. 14*, 303–8.

(9) Svanvik, N., Westman, G., Wang, D., and Kubista, M. (2000) Light-up probes: thiazole orange-conjugated peptide nucleic acid for detection of target nucleic acid in homogeneous solution. *Anal. Biochem. 281*, 26–35.

(10) Silverman, A. P., and Kool, E. T. (2006) Detecting RNA and DNA with templated chemical reactions. *Chem. Rev. 106*, 3775–89.

(11) Xi, C., Balberg, M., Boppart, S. A., and Raskin, L. (2003) Use of DNA and peptide nucleic acid molecular beacons for detection and quantification of rRNA in solution and in whole cells. *Appl. Environ. Microbiol. 69*, 5673–8.

(12) Lenaerts, J., Lappin-Scott, H. M., and Porter, J. (2007) Improved fluorescence *in situ* hybridization method for detection of bacteria from activated sludge and river water by using DNA molecular beacons and flow cytometry. *Appl. Environ. Microbiol. 73*, 2020–3.

(13) Miller, G. P., Silverman, A. P., and Kool, E. T. (2008) New, stronger nucleophiles for nucleic acid-templated chemistry: synthesis and application in fluorescence detection of cellular RNA. *Bioorg. Med. Chem. 16*, 56–64.

(14) Sando, S., and Kool, E. T. (2002) Imaging of RNA in bacteria with self-ligating quenched probes. *J. Am. Chem. Soc. 124*, 9686–7.

(15) Silverman, A. P., and Kool, E. T. (2005) Quenched autoligation probes allow discrimination of live bacterial species by single nucleotide differences in rRNA. *Nucleic Acids Res. 33*, 4978–86.

(16) Abe, H., Wang, J., Furukawa, K., Oki, K., Uda, M., Tsuneda, S., and Ito, Y. (2008) A reduction-triggered fluorescence probe for sensing nucleic acids. *Bioconjugate Chem. 19*, 1219–26.

(17) Kleinbaum, D. J., Miller, G. P., and Kool, E. T. (2010) Double displacement: an improved bioorthogonal reaction strategy for templated nucleic acid detection. *Bioconjugate Chem. 21*, 1115–20.

(18) Splettstoesser, W. D., Seibold, E., Zeman, E., Trebesius, K., and Podbielski, A. (2010) Rapid differentiation of *Francisella* species and subspecies by fluorescent in situ hybridization targeting the 23S rRNA. *BMC Microbiol. 10*, 72–85.

(19) Silverman, A. P., Baron, E. J., and Kool, E. T. (2006) RNA-templated chemistry in cells: discrimination of *Escherichia*, *Shigella* and *Salmonella* bacterial strains with a new two-color FRET strategy. *ChemBioChem 7*, 1890–4.

(20) Grossmann, T. N., and Seitz, O. (2006) DNA-catalyzed transfer of a reporter group. *J. Am. Chem. Soc. 128*, 15596–7.

(21) Huang, Y., and Coull, J. M. (2008) Diamine catalyzed hemicyanine dye formation from nonfluorescent precursors through DNA programmed chemistry. *J. Am. Chem. Soc. 130*, 3238–9.

(22) Shibata, A., Abe, H., Ito, M., Kondo, Y., Shimizu, S., Aikawa, K., and Ito, Y. (2009) DNA templated nucleophilic aromatic substitution reactions for fluorogenic sensing of oligonucleotides. *Chem. Commun. (Camb.)* 6586–8.

(23) Prusty, D. K., and Herrmann, A. (2010) A fluorogenic reaction based on heavy-atom removal for ultrasensitive DNA detection. *J. Am. Chem. Soc. 132*, 12197–9.

(24) Jentzsch, E., and Mokhir, A. (2009) A fluorogenic, nucleic acid directed "click" reaction. *Inorg. Chem. 48*, 9593–5.

(25) Meguellati, K., Koripelly, G., and Ladame, S. (2010) DNA-templated synthesis of trimethine cyanine dyes: A versatile fluorogenic reaction for sensing G-quadruplex formation. *Angew. Chem., Int. Ed. 49*, 2738–42.

(26) Cai, J., Li, X., Yue, X., and Taylor, J. S. (2004) Nucleic acid-triggered fluorescent probe activation by the Staudinger reaction. *J. Am. Chem. Soc. 126*, 16324–5.

(27) Pianowski, Z. L., and Winssinger, N. (2007) Fluorescence-based detection of single nucleotide permutation in DNA via catalytically templated reaction. *Chem. Commun. (Camb.)* 3820–2.

(28) Franzini, R. M., and Kool, E. T. (2008) 7-Azidomethoxycoumarins as profluorophores for templated nucleic acid detection. *ChemBioChem 9*, 2981–8.

(29) Pianowski, Z., Gorska, K., Oswald, L., Merten, C. A., and Winssinger, N. (2009) Imaging of mRNA in live cells using nucleic acid-templated reduction of azidorhodamine probes. *J. Am. Chem. Soc. 131*, 6492–7.

(30) Furukawa, K., Abe, H., Hibino, K., Sako, Y., Tsuneda, S., and Ito, Y. (2009) Reduction-triggered fluorescent amplification probe for the detection of endogenous RNAs in living human cells. *Bioconjugate Chem. 20*, 1026–36.

(31) Franzini, R. M., and Kool, E. T. (2009) Efficient nucleic acid detection by templated reductive quencher release. *J. Am. Chem. Soc. 131*, 16021–3.

(32) Li, H., Franzini, R. M., Bruner, C., and Kool, E. T. (2010) Templated chemistry for sequence-specific fluorogenic detection of duplex DNA. *ChemBioChem 11*, 2132–7.

(33) Franzini, R. M., and Kool, E. T. (2011) Two successive reactions on a DNA template: a strategy for improving background fluorescence and specificity in nucleic acid detection. *Chem.—Eur. J. 17*, 2168–75.

(34) Sando, S., Abe, H., and Kool, E. T. (2004) Quenched autoligating DNAs: multicolor identification of nucleic acids at single nucleotide resolution. *J. Am. Chem. Soc. 126*, 1081–7.

(35) Furukawa, K., Abe, H., Wang, J., Uda, M., Koshino, H., Tsuneda, S., and Ito, Y. (2009) Reduction-triggered red fluorescent probes for dual-color detection of oligonucelotide sequences. *Org. Biomol. Chem. 7*, 671–7.

(36) Koripelly, G., Meguellati, K., and Ladame, S. (2010) Dual sensing of hairpin and quadruplex DNA structures using multicolored peptide nucleic acid fluorescent probes. *Bioconjugate Chem. 21*, 2103–9.

(37) Amyes, T. L., and Jencks, W. P. (1989) Lifetimes of oxocarbenium ions in aqueous solution from common ion inhibition of the solvolysis of α-azido ethers by added azide ion. *J. Am. Chem. Soc. 111*, 7888–900.

(38) Johansson, M. K. (2006) Choosing reporter-quencher pairs for efficient quenching through formation of intramolecular dimers. *Methods Mol. Biol. 335*, 17–29.

(39) Ke, S.-H., and Wartell, R. M. (1993) Influence of nearest neighbor sequence on the stability of base pair mismatches in long DNA: determination by temperature-gradient gel electrophoresis. *Nucleic Acids Res. 21*, 5137–43.

(40) Cheong, C., Tinoco, I., and Chollet, A. (1988) Thermodynamic studies of base pairing involving 2,6-diaminopurine. *Nucleic Acids Res. 16*, 5115–22.

(41) Comas, J., and Vives-Rego, J. (1997) Assessment of the effects of gramicidin, formaldehyde, and surfactants on *Escherichia coli* by flow cytometry using nucleic acid and membrane potential dyes. *Cytometry 29*, 58–64.

(42) Amann, R., and Fuchs, B. M. (2008) Single-cell identification in microbial communities by improved fluorescence *in situ* hybridization techniques. *Nat. Rev. Microbiol. 6*, 339–48.

(43) Dheur, S., and Saison-Behmoaras, T. E. (2000) Polyethyleneimine-mediated transfection to improve antisense activity of 3′-capped phosphodiester oligonucleotides. *Methods Enzymol. 313*, 56–73.

(44) Berlatzky, I. A., Rouvinski, A., and Ben-Yehuda, S. (2008) Spatial organization of a replicating bacterial chromosome. *Proc. Natl. Acad. Sci. U.S.A. 105*, 14136–40.

(45) Baker, Z., Harrison, R. W., Miller, B. F., and Wexler, R. (1941) The bactericidal action of synthetic detergents. *J. Exp. Med. 74*, 611–20.

(46) Molenaar, C., Marras, S. A., Slats, J. C. M., Truffert, J.-C., Lemaître, M., Raap, A. K., Dirks, R. W., and Tanke, H. J. (2001) Linear 2′ O-methyl RNA probes for the visualization of RNA in living cells. *Nucleic Acids Res. 29*, e89.

(47) Ju, J., Ruan, C., Fuller, C. W., Glazer, A. N., and Mathies, R. A. (1995) Fluorescence energy transfer dye-labeled primers for DNA sequencing and analysis. *Proc. Natl. Acad. Sci. 92*, 4347–51.

(48) Nikravesh, A., Dryselius, R., Faridani, O. R., Goh, S., Sadeghizadeh, M., Behmanesh, M., Ganyu, A., Klok, E. J., Zain, R., and Good, L. (2007) Antisense PNA accumulates in *Escherichia coli* and mediates a long post-antibiotic effect. *Mol. Ther. 15*, 1537–42.

(49) Geller, B. L., Deere, J., Tilley, L., and Iversen, P. L. (2005) Antisense phosphorodiamidate morpholino oligomer inhibits viability of *Escherichia coli* in pure culture and in mouse peritonitis. *J. Antimicrob. Chemother. 55*, 983–8.

Supporting Information

Improved Templated Fluorogenic Probes Enhance the Analysis of Closely Related Pathogenic Bacteria by Microscopy and Flow Cytometry

Raphael M. Franzini and Eric T. Kool*

Department of Chemistry, Stanford University

Stanford, California, 94305-5080

kool@stanford.edu

Table of contents

General information	p. S1-S2
Synthetic procedures	p. S3-S8
Detergents as Delivery Agents	p. S9
Supplementary experiments	p. S10-S11
MALDI-TOF mass spectra	p. S12-S14
^{1}H – NMR spectra	p. S15-S22
^{13}C-NMR spectra	p. S23-S27
References	p. S28

General Information

Chemicals and reagents

Anhydrous solvents were purchased from Fisher Scientific and used without further purification. Chemicals were purchased from either Sigma-Aldrich or Acros and used without further purification. Chemicals used for the solid-phase synthesis of oligonucleotides such as

phosphoramidites, solid-supports, amino-modifiers, and synthesizer reagent-solutions were acquired from Glen Research. Bioreagents were purchased from VWR, and bacteria cultures from ATCC.

Instrumentation

All ^{1}H- and ^{13}C-NMR spectra were recorded on a Varian Innova 500 MHz NMR spectrometer. ^{1}H- and ^{13}C-NMR Spectra were internally referenced to the residual solvent signal. High-resolution mass spectrometry analysis was performed by the UC Riverside Mass Spectrometry Facility. Analytical and semi-preparative high performance liquid chromatography was performed on a LC-CAD Shimadzu liquid chromatograph, equipped with a SPD-M10A VD diode array detector and a SCL 10A VP system controller and using reverse phase C18 columns. Fluorescence measurements were performed on a Fluorolog 3 Jobin Yvon fluorophotospectrometer equipped with an external temperature controller. Oligonucleotide masses were determined by the Stanford University Protein and Nucleic Acid Facility using a Perspective Voyager-DE RP Biospectrometry MALDI-TOF mass-spectrometry instrument using a 3-Hydroxypicolinic acid/di-ammonium hydrogen citrate matrix. Bacterial imaging was performed on a Nikon Eclipse E800 epifluorescence microscope equipped with a Nikon Plan AP 100x/1.40 oil immersion objective and a SPOT RT digital camera.

Bacteria culture

Growth medium (Lauria-Bertain), and glass containers were sterilized by autoclaving at 120˚C for 20 min. ***E. coli K12*** and ***Salmonella enterica*** were acquired from ATCC (catalog numbers 10798 and 700720 for ***E.coli*** and ***Salmonella enteric,*** respectively). Bacteria cultures were grown to mid-log phase in Luria-Bertani medium at 37˚C.

Synthetic procedures

Scheme S1. Synthesis of the α-azidoether BHQ-1 release linker **2**.

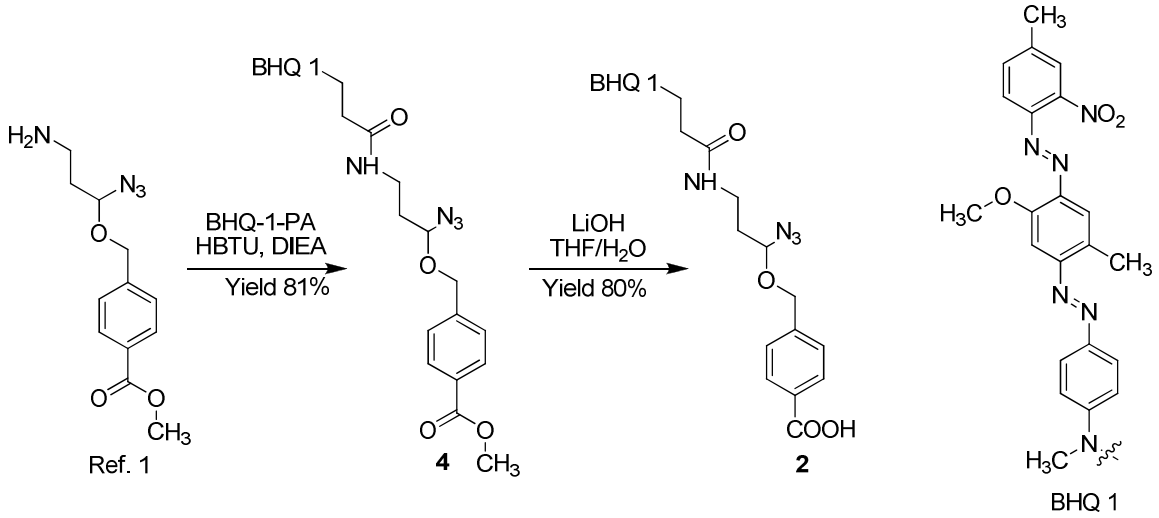

Methyl 4-[(1-azido-3-(3-(BHQ-1)-propionamido)propoxy)methyl]benzoate (**4**)

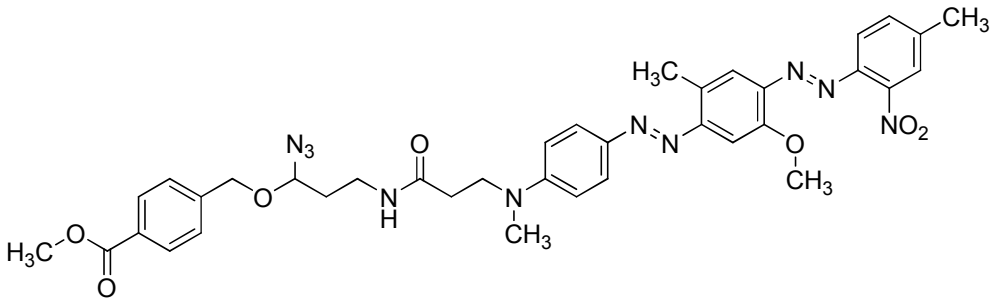

A solution of BHQ-1-propionic acid (220 mg; 0.46 mmol), HBTU (175 mg; 0.46 mmol) and DIEA (60 mg; 0.46 mmol) in DMF (5 mL) was kept at room temperature for 5 min and then added to a solution of methyl 4-(3-amino-1-azidopropoxymethyl)benzoate[1] (98 mg; 0.37 mmol) in DMF (1 mL). The solution was kept at room temperature for 30 min and volatiles evaporated. The residue was dissolved in DCM, washed with brine, dried over $MgSO_4$, filtrated and evaporated. The residue was purified by column chromatography (DCM: MeCN 9:1 + 2% MeOH) to give the product as a black solid in a yield of 220 mg (81%).
^{1}H-NMR (CDCl3, 500MHZ): 1.90-2.00 ppm (m, 2H), 2.38 ppm (t, J^3(H,H) = 6.75 Hz, 2H), 2.48 ppm (s, 3H), 2.68 ppm (s, 3H), 3.02 ppm (s, 3H), 3.26-3.36 ppm (m, 1H), 3.36-3.44 ppm (m, 1H), 3.75 ppm (t, J^3(H,H) = 6.75 Hz, 2H), 3.88 ppm (s, 3H), 3.99 ppm (s, 3H), 4.51 ppm (dd, J^3(H,H) = 5.75 Hz, 1H), 4.55 ppm (d, J^3(H,H) = 12.0 Hz, 1H), 4.82 ppm (d, J^3(H,H) = 12.0 Hz, 1H), 6.01 ppm (dd, J^3(H,H) = 5.75 Hz, 1H), 6.71 ppm (d, J^3(H,H) = 9.5 Hz, 2H), 7.37 ppm (d, J^3(H,H) = 8.0 Hz, 2H), 7.37 ppm (s, 1H), 7.44 ppm (d, J^3(H,H) = 8.5 Hz, 1H), 7.55 ppm (s, 1H), 7.63 ppm (d, J^3(H,H) = 8.5 Hz, 1H), 7.67 ppm (s, 1H), 7.88 ppm (d, J^3(H,H) = 9.0 Hz, 2H), 7.99 ppm (d, J^3(H,H) = 8.0 Hz, 2H). ^{13}C-NMR ($CDCl_3$, 500 MHz): 16.75, 21.30, 34.10, 34.15, 35.55, 38.94, 48.86, 52.22, 56.28, 70.33, 90.45, 99.34, 111.52, 118.95, 119.07, 124.32, 125.84, 127.61, 129.90, 132.99, 133.55, 141.66, 141.83, 143.40, 144.71, 145.15, 147.44, 151.08, 151.17, 154.81, 166.72, 170.93 ppm.

4-[(1-azido-3-(3-(BHQ-1)-propionamido)propoxy)methyl]benzoic acid (**2**)

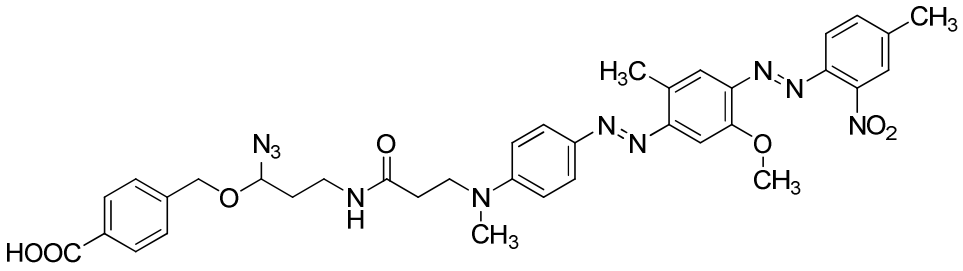

To a solution of **4** (180 mg; 0.24 mmol) in THF (3 mL) was added a solution of lithium hydroxide monohydrate (180 mg; 4.3 mmol) in water (1 mL) was added and the mixture stirred vigorously at 40˚C for 6 h. The mixture was diluted with water, acidified with little acetic acid and extracted with EtOAc. The organic layer was dried over $MgSO_4$, filtrated and volatiles evaporated. The resiude was dissolved in little DCM and precipitation with hexanes provided the product as a fine black powder in a yield of 142 mg (80%).

^{1}H-NMR (DMSO, 500MHz): 1.76-1.90 ppm (m, 2H), 2.37 (t, J^3(H,H) = 6.75 Hz, 1H), 2.47 ppm (s, 3H), 2.60 ppm (s, 3H), 3.01 ppm (s, 3H), 3.12-3.20 ppm (m, 2H), 3.70 ppm (t, J^3(H,H) = 7.0 Hz, 2H), 3.90 ppm (s, 3H), 4.64 ppm (d, J^3(H,H) = 12.5 Hz, 1H), 4.74 ppm (dd, J^3(H,H) = 6.0 Hz, 1H), 4.79 ppm (d, J^3(H,H) = 12.5 Hz, 1H), 6.84 ppm (d, J^3(H,H) = 9.5 Hz, 2H), 7.26 ppm (s, 1H), 7.45 ppm (d, J^3(H,H) = 8.5 Hz, 2H), 7.472 ppm (s, 1H), 7.73 ppm (d, J^3(H,H) = 8.0 Hz, 1H), 9.0 Hz), 7.91 ppm (s, 1H), 7.93 ppm (d, J^3(H,H) = 8.0 Hz, 2H), 8.07 ppm (dd, J^3(H,H) = 5.5 Hz, 1H),
HRMS [+ Scan]; calculated m/z for C36G39N10O7 723.2998; observed mass 723.3002.

Scheme S2. Synthesis of the α-azidoether BHQ-2 release linker **3**.

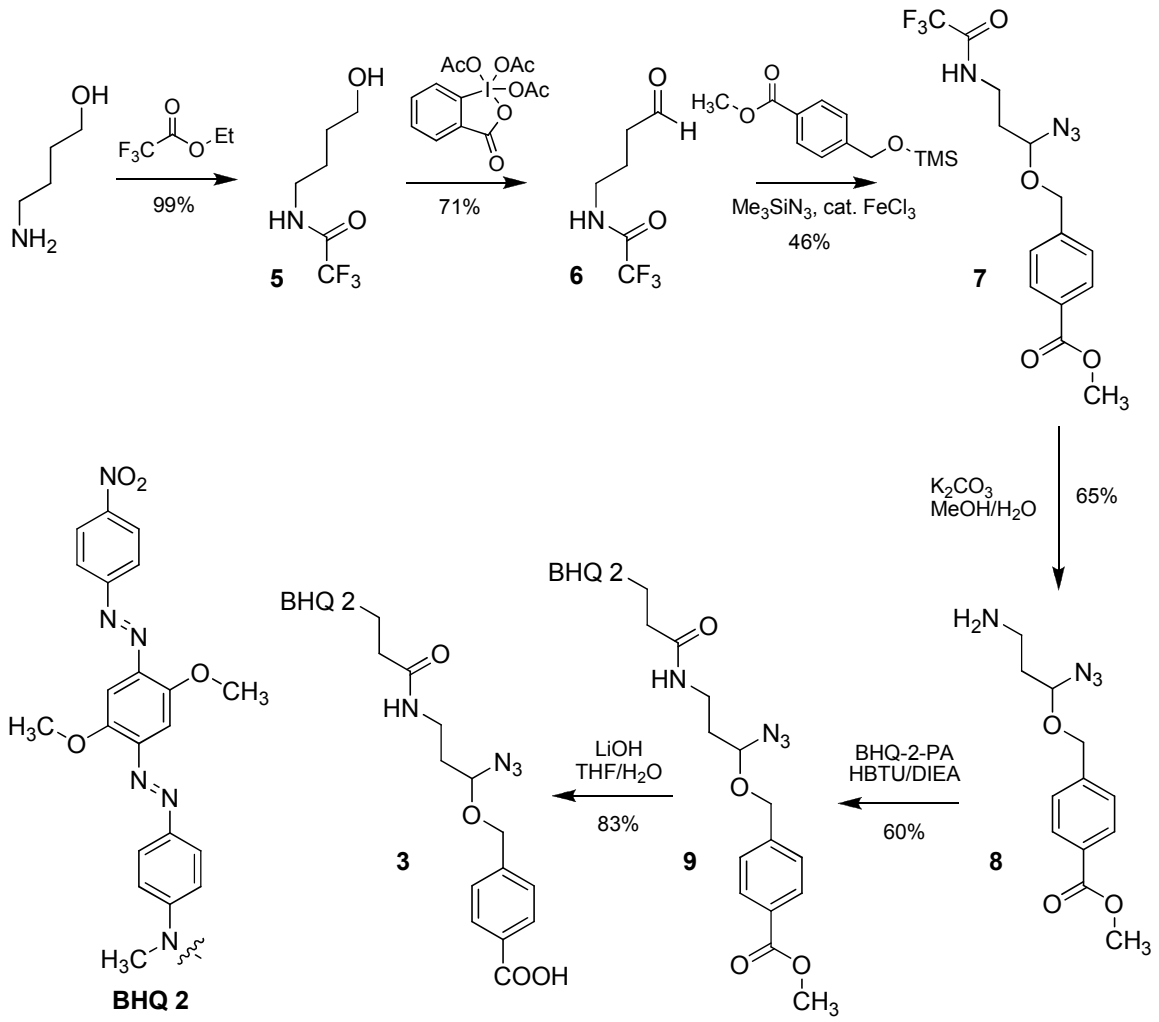

N-(4-hydroxybutyl)trifluoroacetamide (**5**)

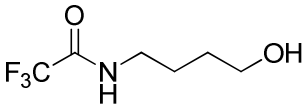

Ethyl trifluoroacetate (3.3 mL; 28 mmol) was added dropwise to cooled (0˚C) 4-amino-1-butanol (2.0 g; 22.4 mmol). The mixture was stirred for 2 h at 0˚C and evaporated. The clear liquid was dried on the high vacuum. The product was obtained in a yield of 4.1 g (99%).
^{1}H-NMR (500 MHz, $CDCl_3$): δ = 1.61-1.67 ppm (m, 2H), 1.68-1.74 ppm (m, 2H), 2.31 (bs, 1H), 3.38 ppm (dt, 2H), 3.72 ppm (t, 2H), 7.40 ppm (bs, 1H).
^{13}C-NMR (500 MHz, $CDCl_3$): δ = 26.02, 29.70, 40.01, 62.48, 116.20 ppm (q, ***J*** = 1144.0 Hz), 157.66 ppm (q, ***J*** = 146.5 Hz).
HRMS [+ Scan]; calculated m/z for C6H11NO2F3 186.0747; observed mass: 186.0741.

N-(4-oxobutyl)trifluoroacetamide (**6**)

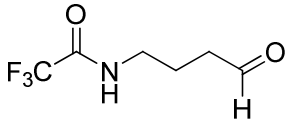

N-(4-hydroxybutyl)trifluoroacetamide (1.65 g; 8.9 mmol) was dissolved in anhydrous DCM (9 mL) and cooled to 0˚C. A solution of Dess-Martin periodinane (15% in DCM; 30 mL; 14.0 mmol) was added to the cooled solution and stirred first at 0˚C for 10 min and then at room temperature for 2.5 h. The reaction was quenched with 1:1 10% sodium thiosulfate and saturated $NaHCO_3$ and the biphasic mixture vigorously stirred for 30 min. The layers were separated and the aqueous layer extracted with DCM. The combined organic layers were dried over $MgSO_4$, filtrated and evaporated. The residue was purified by column chromatography (Hex:EtOAc 2:1 + 1% MeOH) providing ***N-***(4-oxobutyl)trifluoroacetamide in a yield of 1.15 mg (71%).
^{1}H-NMR (400 MHz, $CDCl_3$): δ = 1.85-1.95 ppm (m, 2H), 2.61 ppm (t, ***J*** = 5.2 Hz, 2H), 3.35-3.40 (m, 2H), 6.95 ppm (bs, 1H), 9.79 ppm (s, 1H). The ^{1}H-NMR spectrum confirms with literature reports.[2]

Methyl 4-[(1-azido-4-trifluoroacetamidobutoxy)methyl]benzoate (**7**)

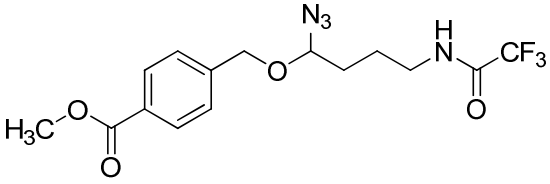

A solution of ***N***-(4-oxobutyl)trifluoroacetamide (1.0 g; 5.5 mmol) and a catalytic amount of anhydrous ferric chloride (44 mg; 0.27 mmol) in anhydrous MeCN (6 mL) was cooled to -40˚C. A solution of methyl 4-[(trimethylsilyloxy)methyl]benzoate[1] (1.56 g; 6.6 mmol) and azidotrimethylsilane (0.94 g; 8.2 mmol) in MeCN (5 mL) was added dropwise to the cooled solution. The reaction mixture was stirred at -40˚C for 60 min and quenched with buffered phosphate saline (pH 7.2). The aqueous solution was extracted with Et_2O. The organic layer was washed with brine, dried over $MgSO_4$, filtrated and evaporated. The residue was purified by column chromatography (Hex:DCM:EtOAc 7:2:1) to provide methyl 4-[(1-azido-4-trifluoroacetamidobutoxy)methyl]benzoate in a yield of 0.95 g (46%).
^{1}H-NMR (500 MHz, $CDCl_3$): δ = 1.72-1.78 ppm (m, 2H), 1.83-1.90 ppm (m, 2H), 3.36-3.44 (m, 2H), 3.92 ppm (s, 3H), 4.51 ppm (t, ***J*** = 6.0 Hz, 1H), 4.62 ppm (d, ***J*** = 12.5 Hz, 1H), 4.88 ppm (d, ***J*** = 12.0 Hz, 1H), 6.50 ppm (bs, 1H), 7.41 ppm (d, ***J*** = 8.0 Hz, 2H), 8.04 ppm (d, ***J*** = 8.0 Hz, 2H).
^{13}C-NMR (500 MHz, $CDCl_3$): δ = 21.14, 31.71, 39.42, 52.27, 70.35, 91.70, 115.85 ppm (q, ***J*** = 1146.5 Hz), 127.69, 129.96, 141.80, 157.40 ppm (q, ***J*** = 146.5 Hz), 166.86 ppm.
HRMS [+ Scan]; calculated m/z for C15H21N5O4F3 392.1540; observed mass: 392.1543.

Methyl 4-[(4-amino-1-azidobutoxy)methyl]benzoate (**8**)

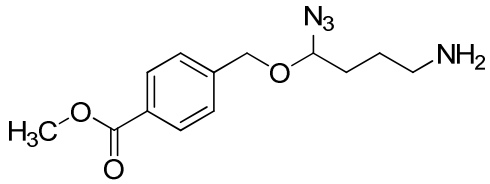

To a solution of methyl 4-[(1-azido-4-trifluoroacetamidobutoxy)methyl]benzoate (0.4g; 1.1 mmol) in MeOH (4.6 mL) was added a solution of potassium carbonate (0.4 g; 2.9 mmol) in water (2.4

mL) and the mixture stirred at room temperature for 4 h. The mixture was diluted with water and extracted with EtOAc. The organic layers were combined, dried over $MgSO_4$, filtrated and evaporated. The residue was purified by column chromatography (MeCN + 5% MeOH) to provide methyl 4-[(4-amino-1-azidobutoxy)methyl]benzoate in 0.19 g yield (65%).
^{1}H-NMR (500 MHz, $CDCl_3$): δ = 1.51-1.69 ppm (m, 2H), 1.77-1.91 ppm (m, 2H), 2.70 ppm (bs, 2H), 2.74 ppm (t, ***J*** = 7.0 Hz, 2H), 3.90 ppm (s, 3H), 4.45 ppm (t, ***J*** = 6.0 ppm, 1H), 4.60 ppm (d, ***J*** = 12.5 Hz, 1H), 4.86 ppm (d, ***J*** = 12.5 Hz, 1H), 7.41 ppm (d, ***J*** = 8.5 Hz, 2H), 8.02 ppm (d, ***J*** = 8.0 Hz, 2H).
^{13}C-NMR (500 MHz, $CDCl_3$): δ = 27.95, 31.90, 41.34, 52.21, 70.12, 91.77, 127.55, 129.76, 129.87, 142.19, 166.87 ppm.

Methyl 4-[(1-azido-4-(3-(BHQ-2)-propionamido)butoxy)methyl]benzoate (**9**)

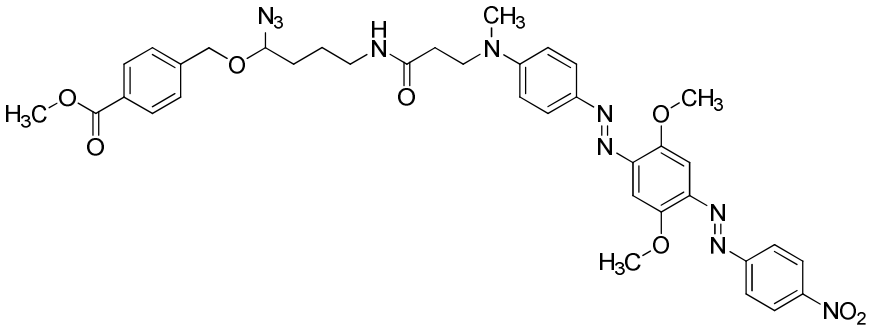

A solution of BHQ-2 propionic acid (255 mg; 0.52 mmol), ***O***-(Benzotriazol-1-yl)-***N,N,N',N'***-tetramethyluronium hexafluorophosphate (HBTU, 196 mg; 0.52 mmol) and DIEA (134 mg; 1.03 mmol) in anhydrous DMF (7 mL) was added to methyl 4-[(4-amino-1-azidobutoxy)methyl]benzoate (0.12 g; 0.43 mmol). The mixture was stirred at room temperature for 30 min. The solvent was evaporated and the residue dissolved in DCM and washed twice with brine. The organic layer was dried over $MgSO_4$, filtrated and evaporated. The residue was purified by silica column chromatography (DCM:MeCN 9:1 + 1% MeOH) to provide (**9**) in a yield of 195 mg (60%).
^{1}H-NMR (500 MHz, $CDCl_3$): δ = 1.51-1.69 ppm (m, 2H), 1.77-1.91 ppm (m, 2H), 2.70 ppm (bs, 2H), 2.74 ppm (t, ***J*** = 7.0 Hz, 2H), 3.90 ppm (s, 3H), 4.45 ppm (t, ***J*** = 6.0 ppm, 1H), 4.60 ppm (d, ***J*** = 12.5 Hz, 1H), 4.86 ppm (d, ***J*** = 12.5 Hz, 1H), 7.41 ppm (d, ***J*** = 8.5 Hz, 2H), 8.02 ppm (d, ***J*** = 8.0 Hz, 2H).
^{13}C-NMR (500 MHz, $CDCl_3$): δ = 27.95, 31.90, 41.34, 52.21, 70.12, 91.77, 127.55, 129.76, 129.87, 142.19, 166.87 ppm.
HRMS [+ Scan]; calculated m/z for C37H41N10O8 753.3103; observed mass: 753.3111.

4-[(1-azido-4-(3-(BHQ-2)-propionamido)butoxy)methyl]benzoaic acid (**3**)

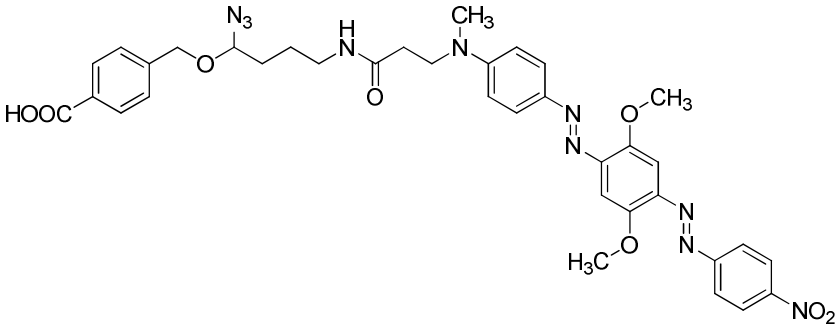

To a solution of **9** in THF (5 mL) was added a solution of lithium hydroxide monohydrate (320 mg; 7.6 mmol) in water (4 mL). The biphasic mixture was vigorously stirred at 40°C for 5 h. The mixture was diluted with water, acidified with citric acid and extracted with DCM. The organic

layer was washed with brine, dried over $MgSO_4$, filtrated and evaporated. **13** was obtained in a yield of 129 mg (83%).
^{1}H-NMR (500 MHz, [D6]DMSO): δ = 1.43-1.50 ppm (m, 2H), 1.62-2.1.75 ppm (m, 2H), 2.38 ppm (t, ***J*** = 8.5 Hz, 2H), 3.03 ppm (s, 3H), 3.06 ppm (q, 8.0 Hz, 2H), 3.715 ppm (t, 8.5 Hz, 2H), 3.94 ppm (s, 3H), 3.99 ppm (s, 3H), 4.66 ppm (d, ***J*** = 16.0 Hz, 1H), 4.73 ppm (t, ***J*** = 7.5 Hz, 1H), 4.81 ppm (d, ***J*** = 15.5 Hz, 1H), 6.86 ppm (d, ***J*** = 11.5 Hz, 2H), 7.37 ppm (s, 1H), 7.44 ppm (s, 1H), 7.44 ppm (d, ***J*** = 10.0 Hz, 2H), 7.81 ppm (d, ***J*** = 12.0 Hz, 2H), 7.92 ppm (d, ***J*** = 10.0 Hz, 2H), 8.01 ppm (t, 1H), 8.06 ppm (d, ***J*** = 11.5 Hz, 2H), 8.46 ppm (d, ***J*** = 11.5 Hz, 2H).
HRMS [+ Scan]; calculated m/z for C36H39N10O8 739.2947; observed mass: 739.2953.

Table S1. Molecular structures of additives investigated in this study.

Pluronic F-68	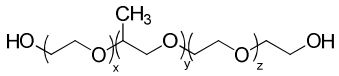	Neutral polymer
Triton X-100	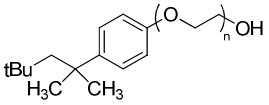	Neutral detergent
Tween 20	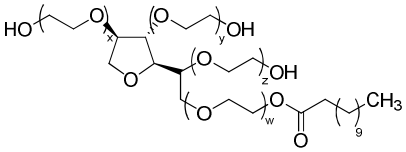	Neutral detergent
DPAPS[a]	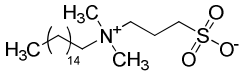	Zwitterionic detergent
CHAPS[b]	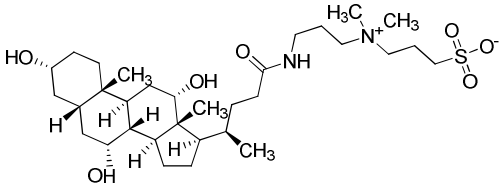	Zwitterionic detergent
STDC[c]	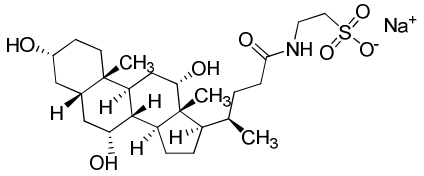	Anionic detergent
SDS[d]	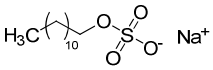	Anionic detergent
PEI[e]	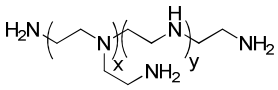	Cationic polymer
HDTA[f]	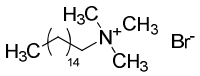	Cationic detergent

[a]DPAPS = 3-(***N,N***-Dimethylpalmitylammonio)propane sulfonate; [b]CHAPS = 3-[(3-Cholamidopropyl)dimethylammonio]-1-propanesulfonate; [c]STDC = Sodium taurodeoxycholate; [d]SDS = Sodium dodecyl sulfate; [f]PEI = Polyethyleneimine; [f]HDTA = Hexadecyltrimethylammonium bromide.

Supplementary Experiments

Figure missing.

Figure S1. Effect of increasing concentrations of selected delivery additives on the growth of ***E. coli*** in a Petri dish assay. Conditions as described in experimental section.

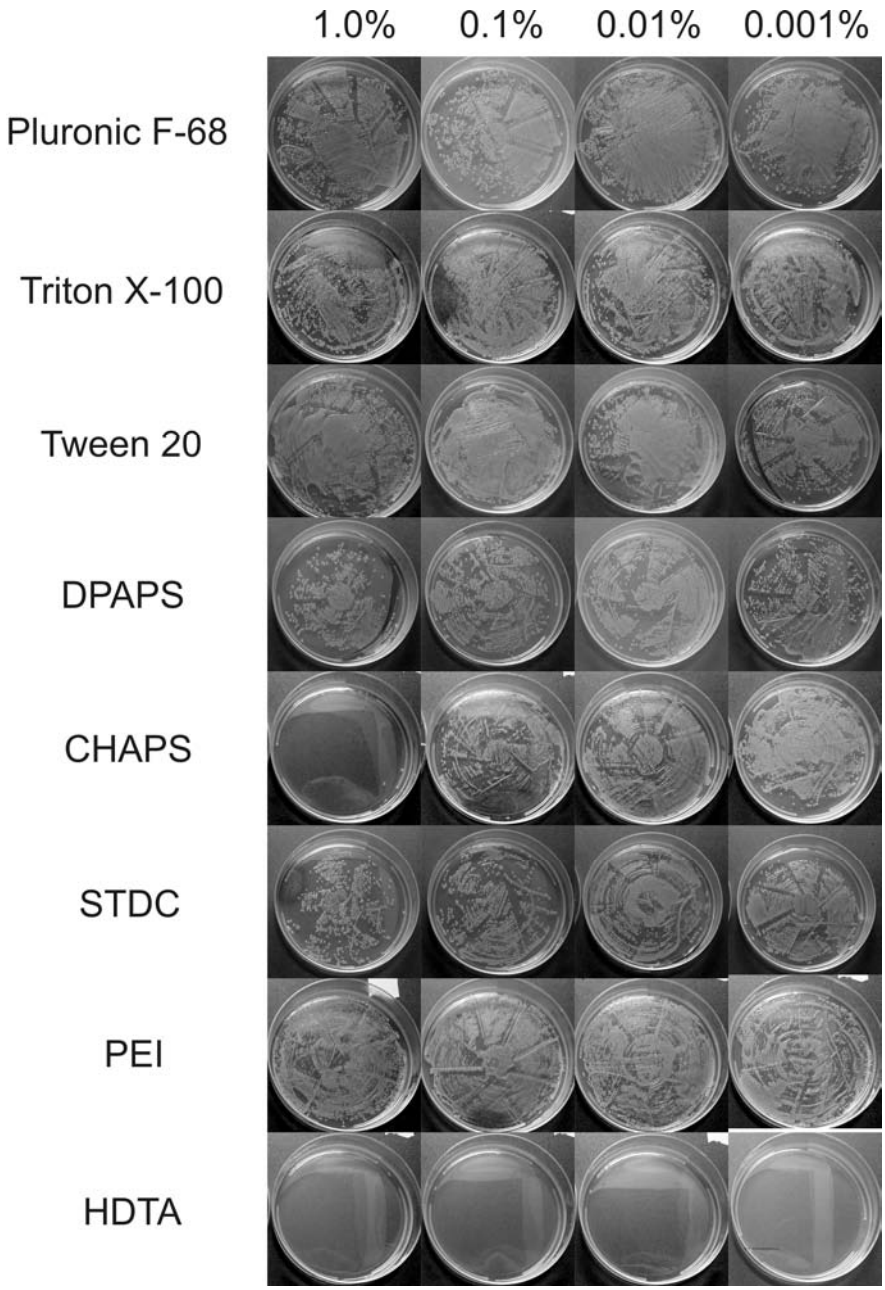

Figure S2. Reaction kinetics and mismatch discrimination of templated fluorescence activation of NIR STAR SE by TPP-DNA.

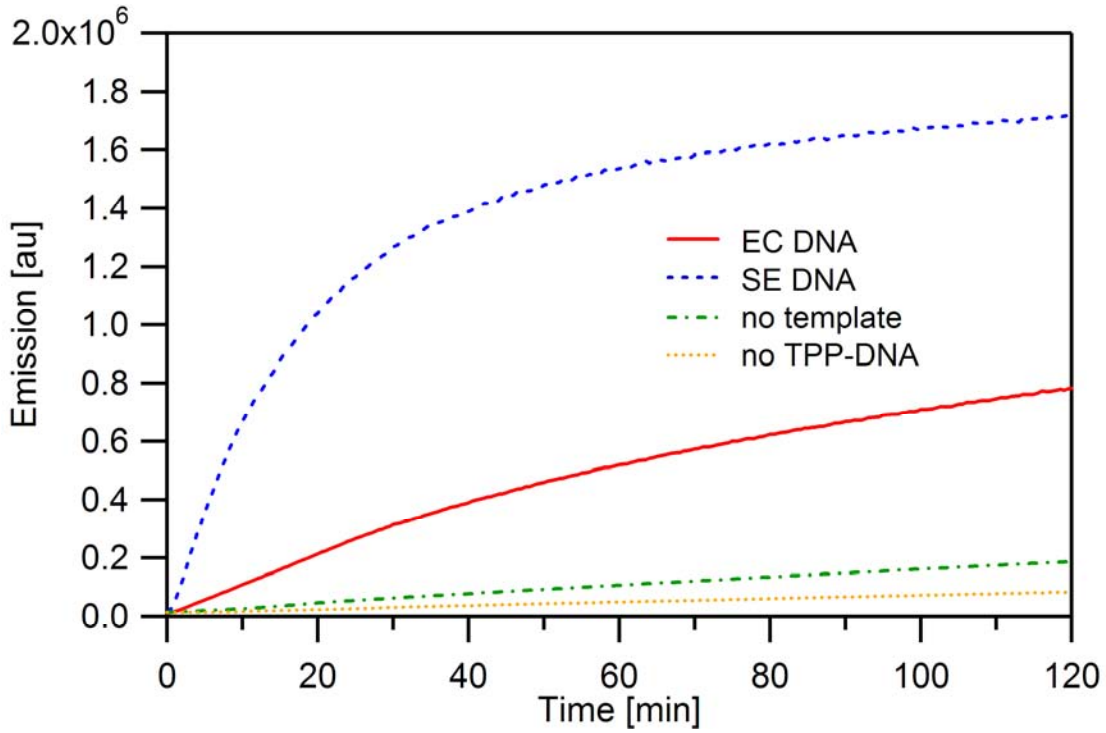

Figure S3. Delivery of template probes into ***Escherichia coli*** K12 under varied salinity and SDS detergent concentrations. Signal is generated by green STAR EC probes after 4 h incubation.

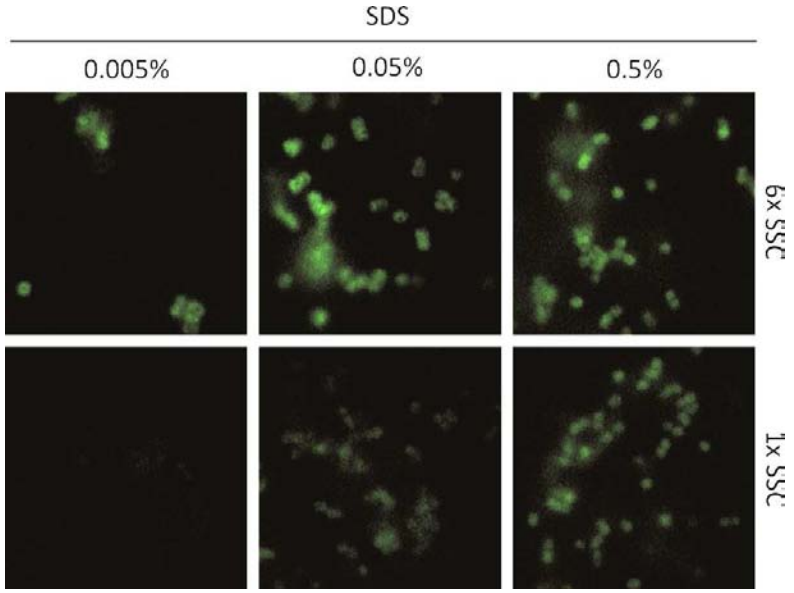

Table S2. Summary of MALDI-TOF mass spectrometry data.

Strand	Calculated mass[a]	Observed mass
green STAR EC	3616 m/z	3616 m/z
green STAR SE	3640 m/z	3640 m/z
green STAR SE DAP	3655 m/z	3655 m/z
green STAR EC BHQ1	3802 m/z	3804 m/z
NIR STAR EC	3938 m/z	3938 m/z
NIR STAR SE	3962 m/z	3966 m/z
EC DNA	6544 m/z	6540 m/z
SE DNA	6519 m/z	6515 m/z
Helper 1	5519 m/z	5521 m/z
Helper 2	5443 m/z	5541 m/z
TPP-DNA	3082 m/z	3080 m/z

[a] The molecular peak of TPP-DNA is accompanied by a major peak + 16 m/z which was assigned to oxidation of the triphenylphosphine moiety during mass-spec sample preparation and measurement.

Figure S4. Analytical HPLC of Purified NIR STAR EC.

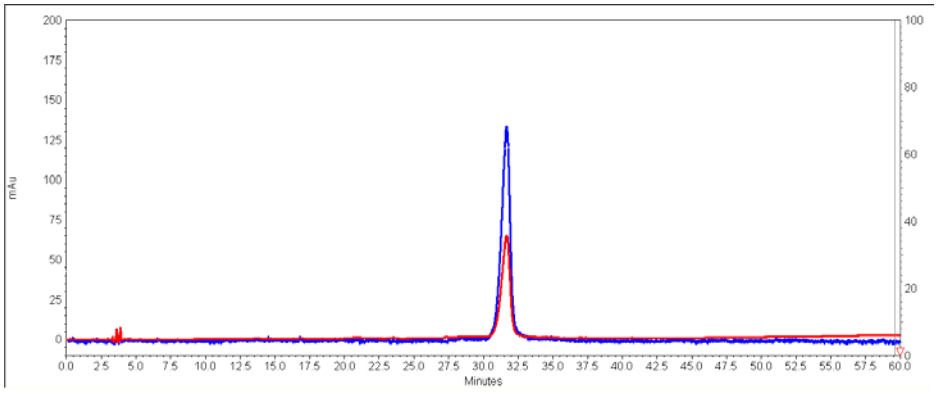

HPLC gradient: 50 mM TEAA buffer + 25 – 90 % MeCN in 60 minutes.
Blue trace: λ_{abs} = 644 nm; red trace: λ_{abs} = 260 nm.

Figure S5. Analytical HPLC of Purified NIR STAR SE.

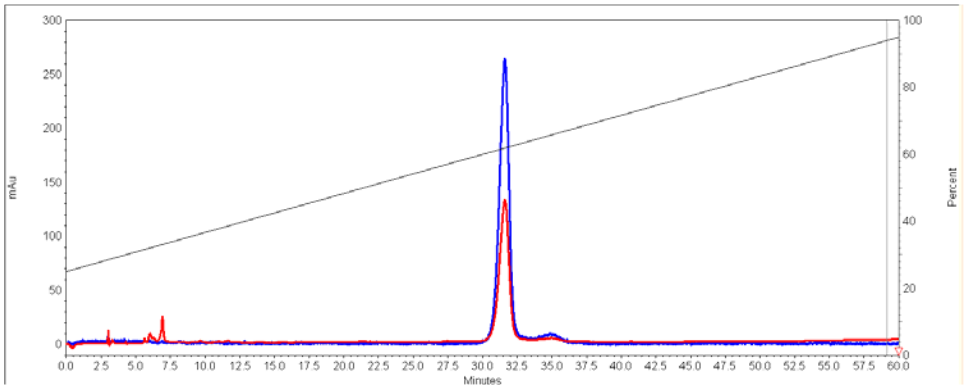

HPLC gradient: 50 mM TEAA (triethylammonium acetate, pH 8.5) buffer + 25 – 90 % MeCN in 60 minutes. Blue trace: λ_{abs} = 644 nm; red trace: λ_{abs} = 260 nm.

Figure S6. Analytical HPLC of Purified green STAR SE DAP.

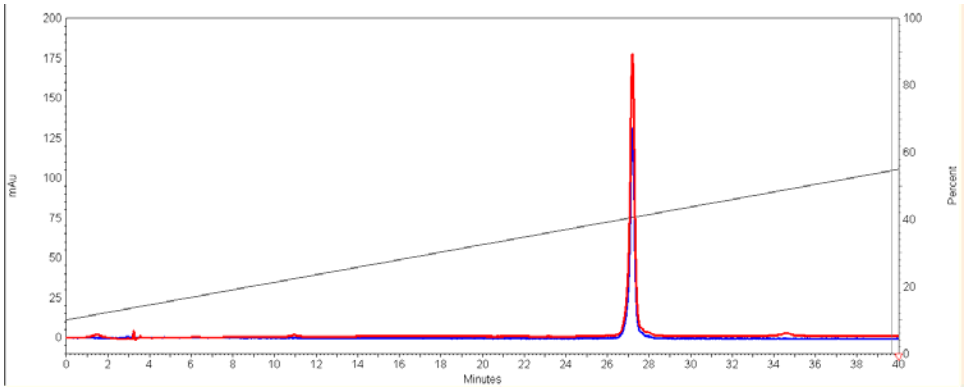

HPLC gradient: 50 mM TEAA buffer + 10 – 55 % MeCN in 40 minutes.
Blue trace: λ_{abs} = 494 nm; red trace: λ_{abs} = 260 nm.

Figure S7. Analytical HPLC of Purified green STAR EC

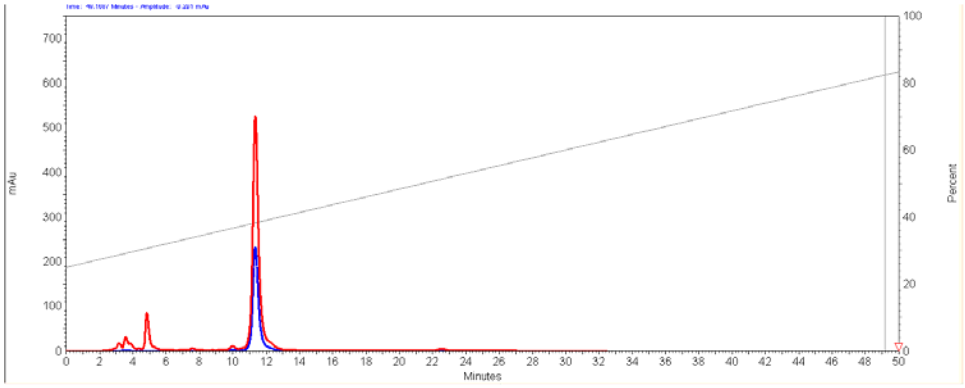

HPLC gradient: 50 mM TEAA buffer + 25 - 60 % MeCN in 60 minutes.
Blue trace: λ_{abs} = 494 nm; red trace: λ_{abs} = 260 nm.

Figure S8. Analytical HPLC of Purified green STAR SE.

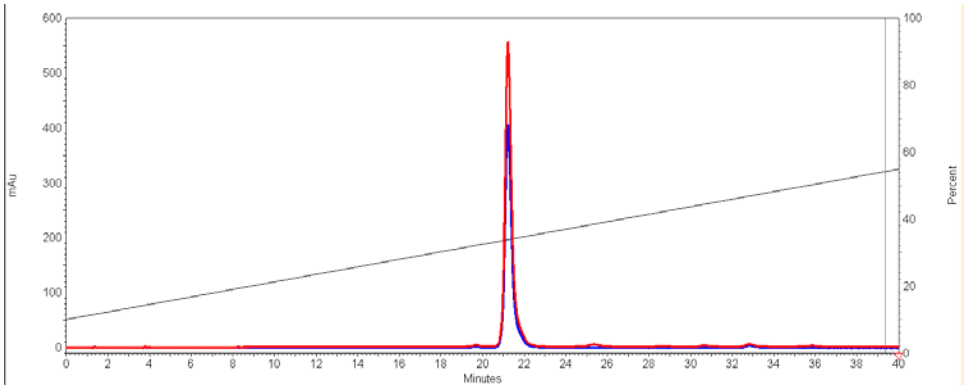

HPLC gradient: 50 mM TEAA buffer + 10 – 55 % MeCN in 40 minutes.
Blue trace: λ_{abs} = 494 nm; red trace: λ_{abs} = 260 nm.

Figure S9. Analytical HPLC of Purified green STAR BHQ1 EC.

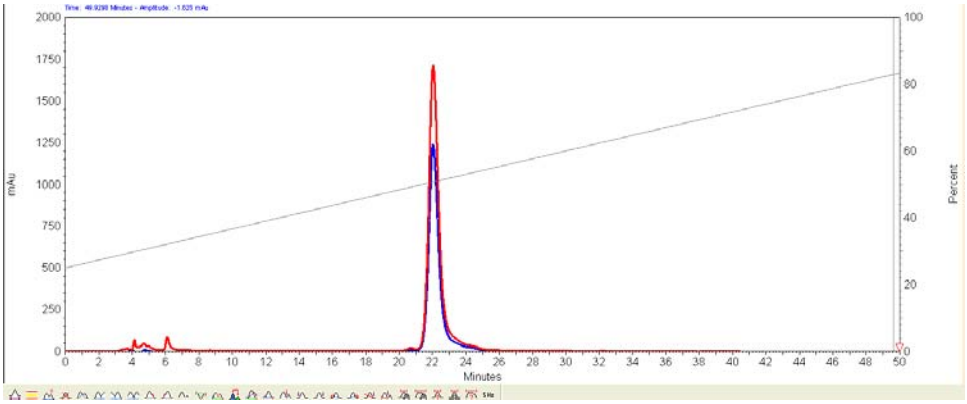

HPLC gradient: 50 mM TEAA buffer + 25 – 90 % MeCN in 60 minutes.
Blue trace: λ_{abs} = 494 nm; red trace: λ_{abs} = 260 nm.

^{1}H-NMR Spectra

Figure S10. ^{1}H-NMR spectrum of Methyl 4-[(1-azido-3-(3-(BHQ-1)-propionamido)propoxy)-methyl]benzoate (**4**); 500 MHz, $CDCl_3$.

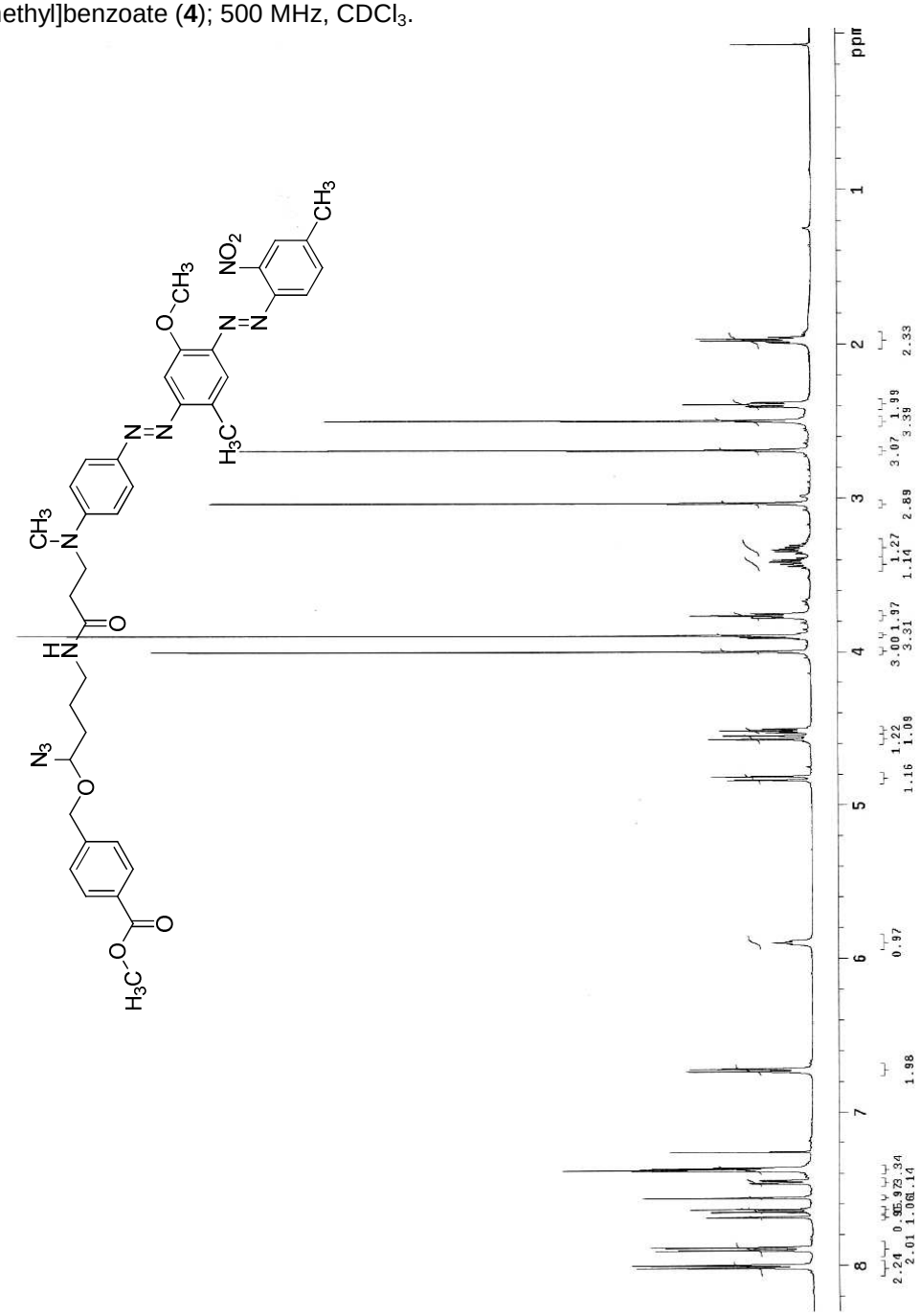

Figure S11. ^{1}H-NMR spectrum of 4-[(1-azido-3-(3-(BHQ-1)-propionamido)propoxy)-methyl]benzoaic acid (**2**). 500 MHz, [D_6]DMSO.

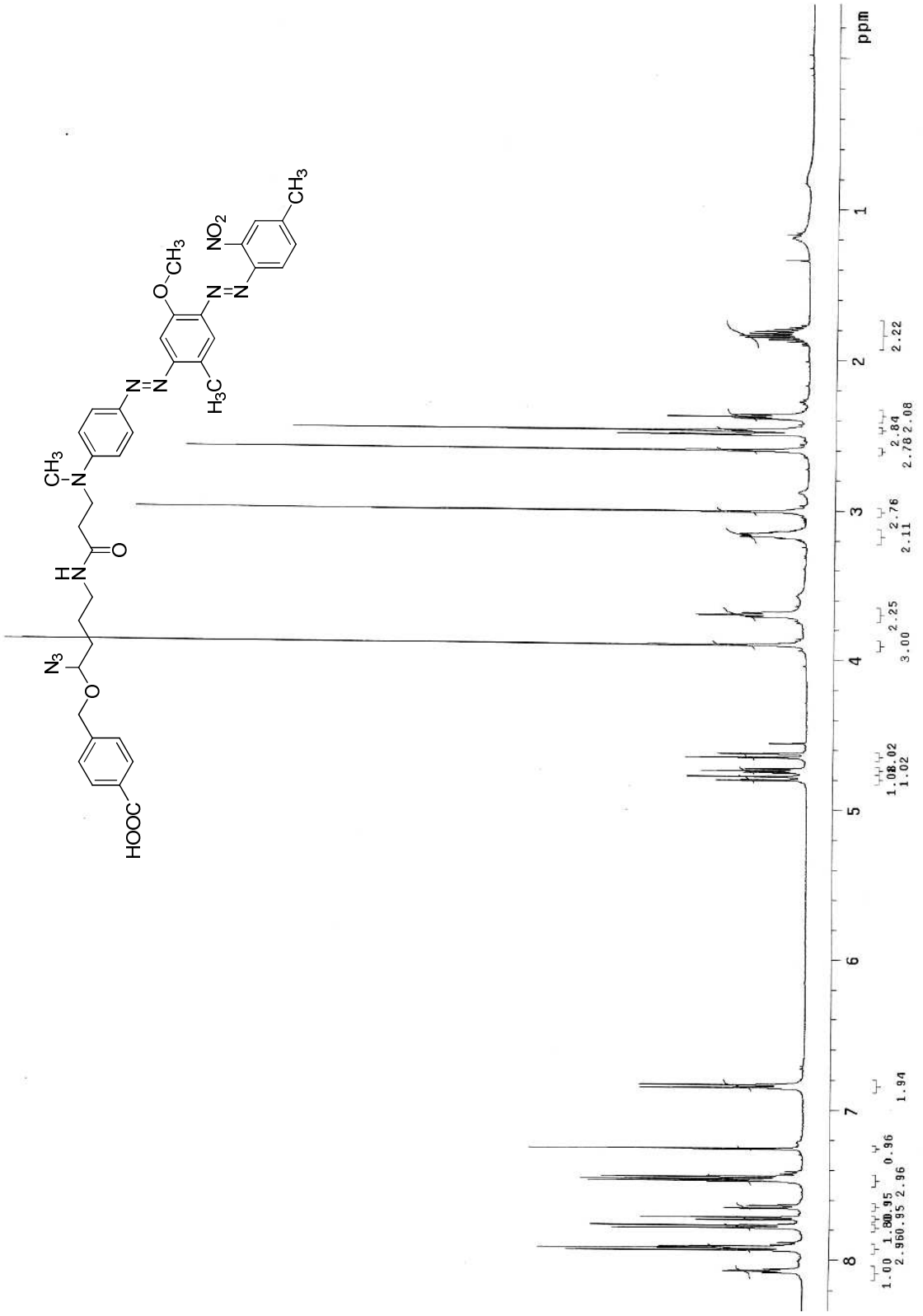

Figure S12. ^{1}H-NMR spectrum of ***N***-(4-hydroxybutyl)trifluoroacetamide ***(5)***; 500 MHz, [D_6]DMSO.

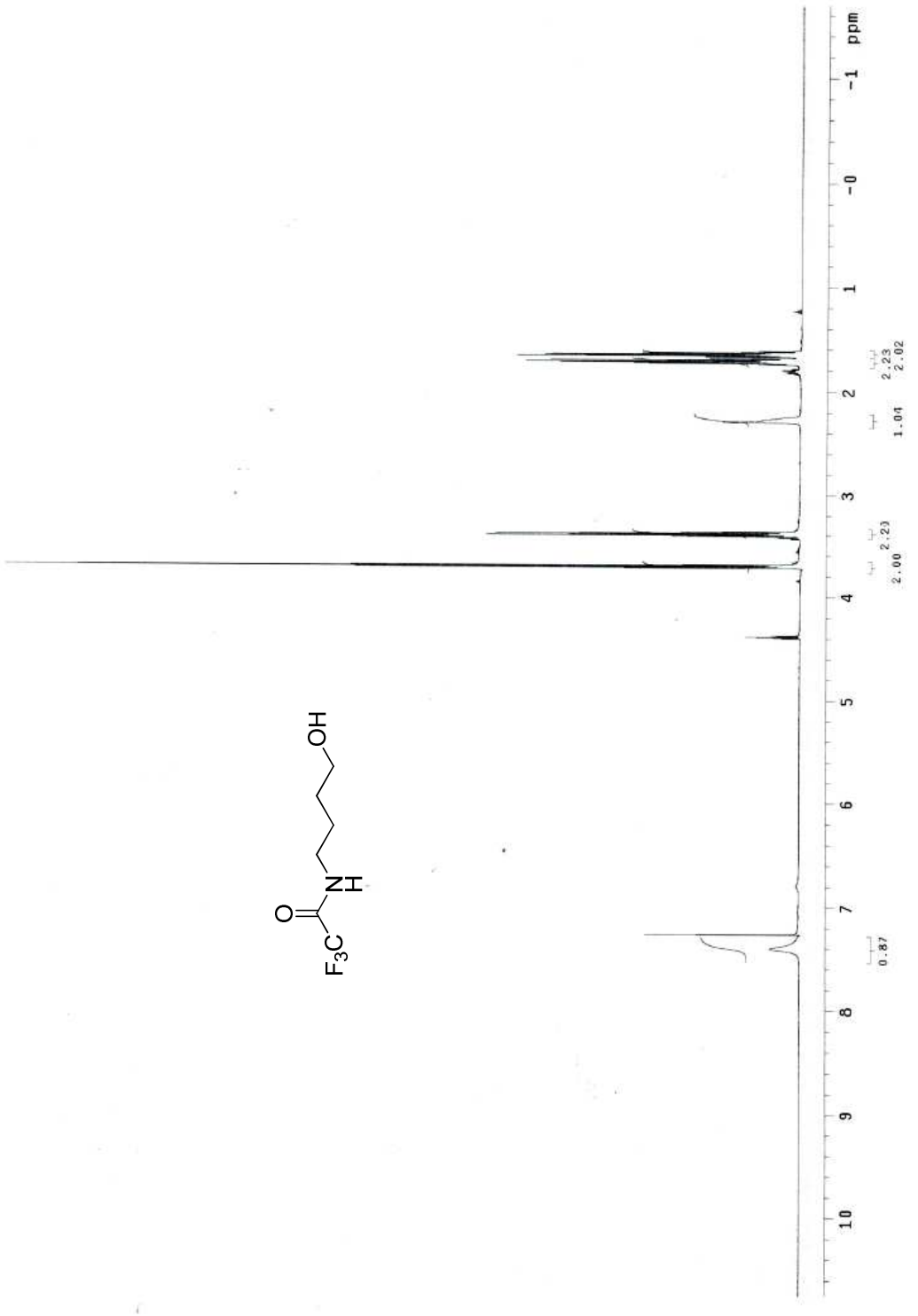

Figure S13. ^{1}H-NMR spectrum of ***N***-(4-oxobutyl)trifluoroacetamide ***(6)*** ; 400 MHz, $CDCl_3$.

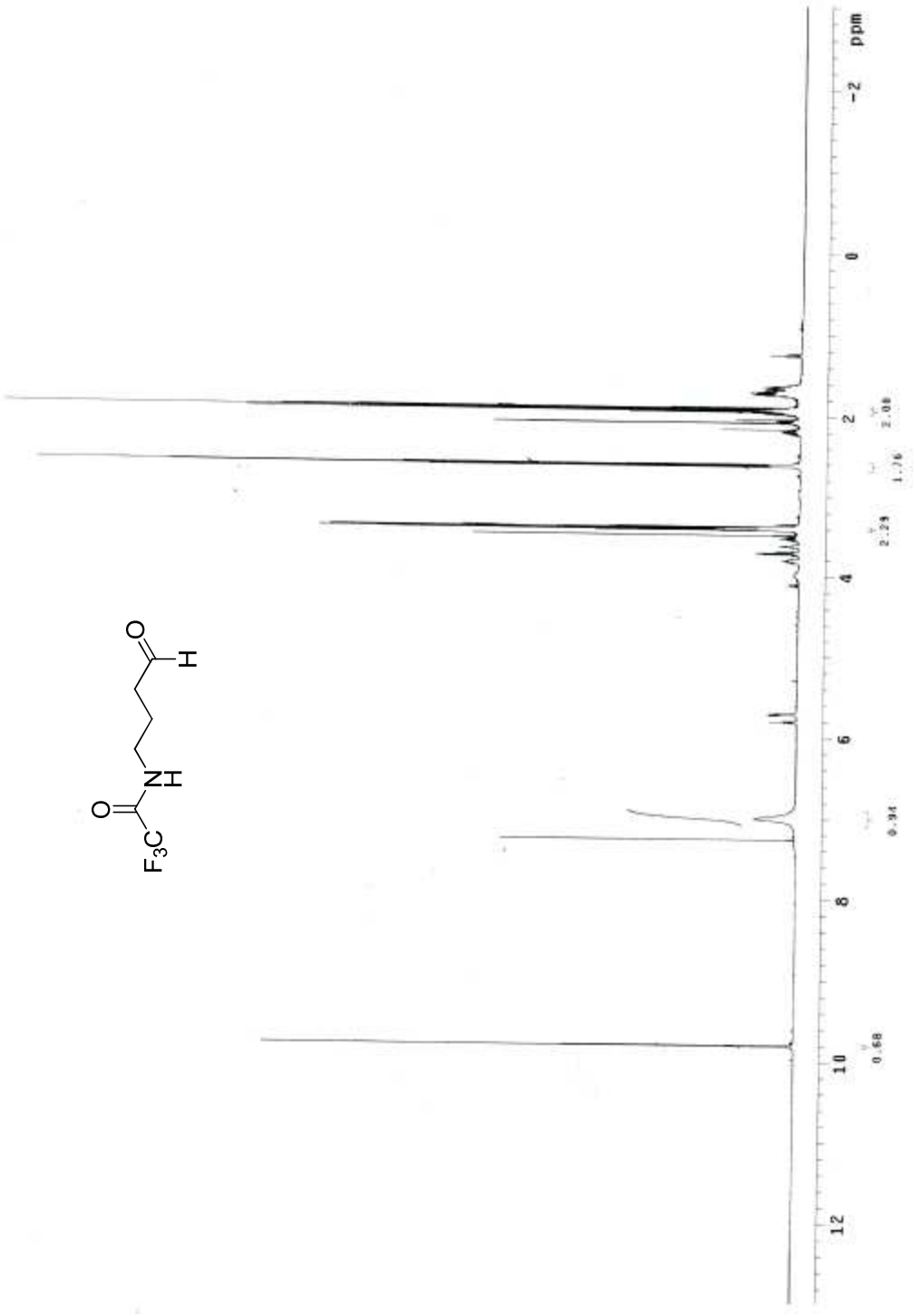

Figure S14. ^{1}H-NMR spectrum of Methyl 4-[(1-azido-4-trifluoroacetamidobutoxy)methyl]-benzoate ***(7)***; 500 MHz, $CDCl_3$.

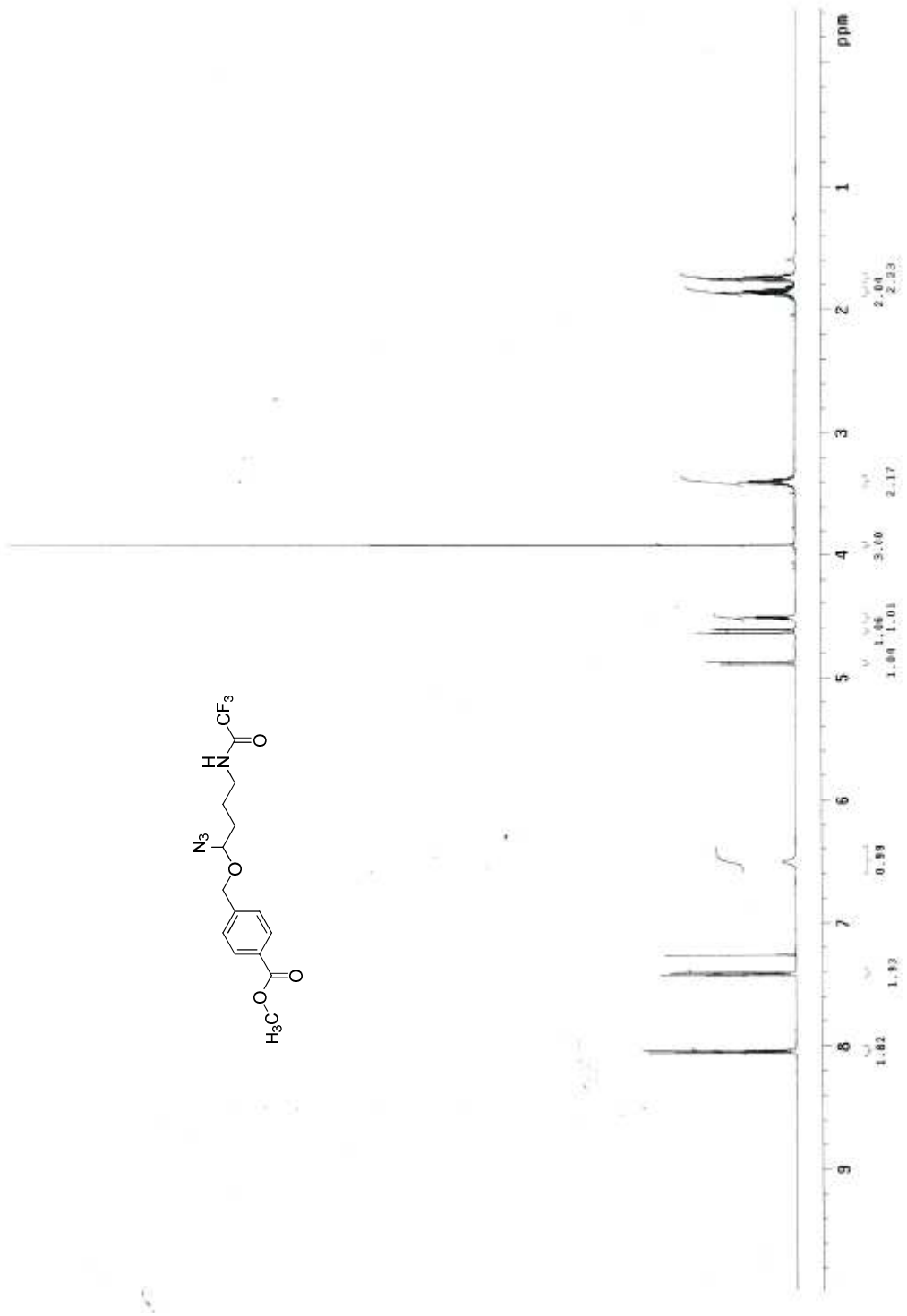

Figure S15. ^{1}H-NMR spectrum of Methyl 4-[(4-amino-1-azidobutoxy)methyl]benzoate ***(8)***; 500 MHz, $CDCl_3$.

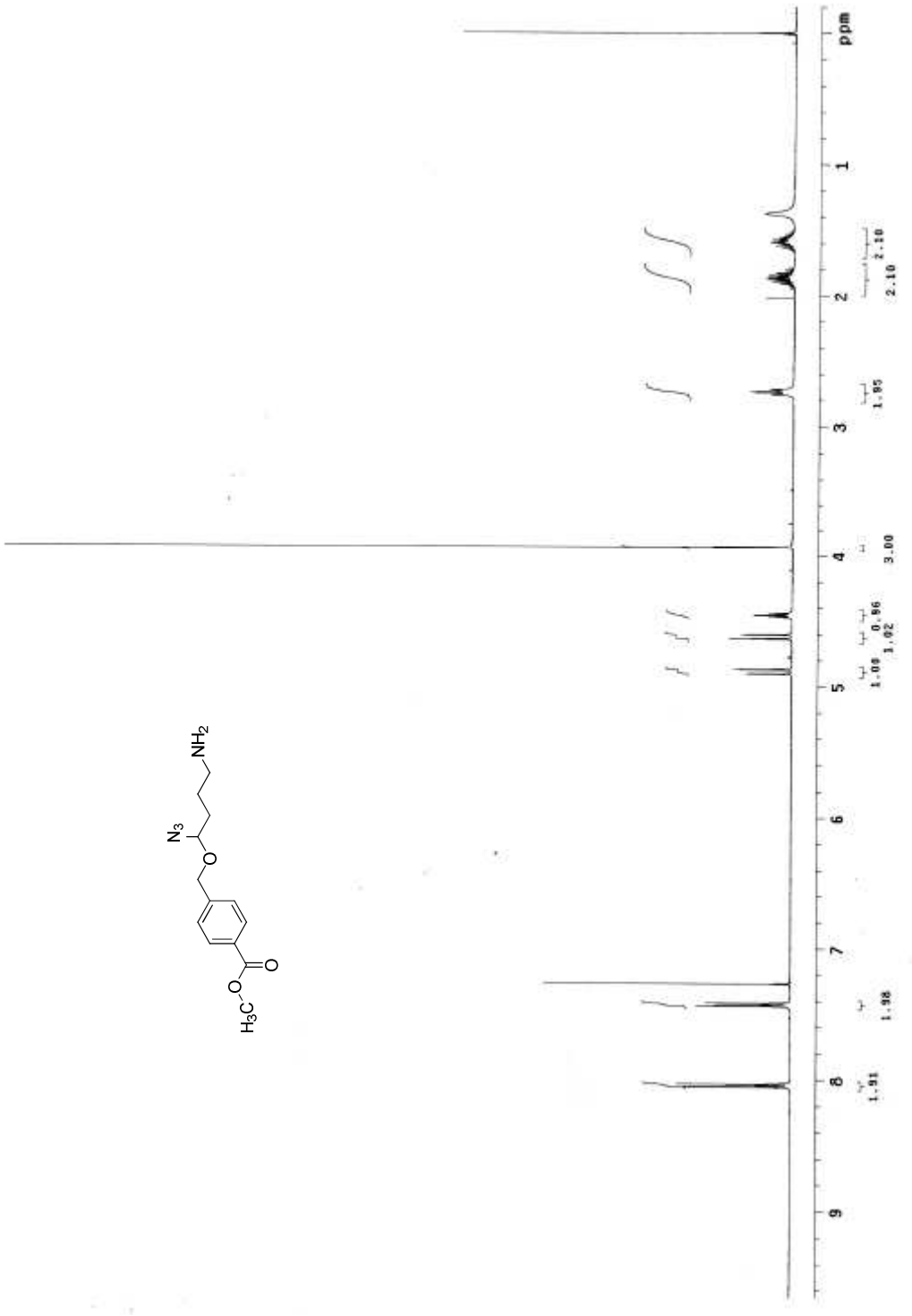

Figure S16. ^{1}H-NMR spectrum of Methyl 4-[(1-azido-4-(3-(BHQ-2)-propionamido)butoxy)methyl]-benzoate ***(9)***; 500 MHz, $CDCl_3$.

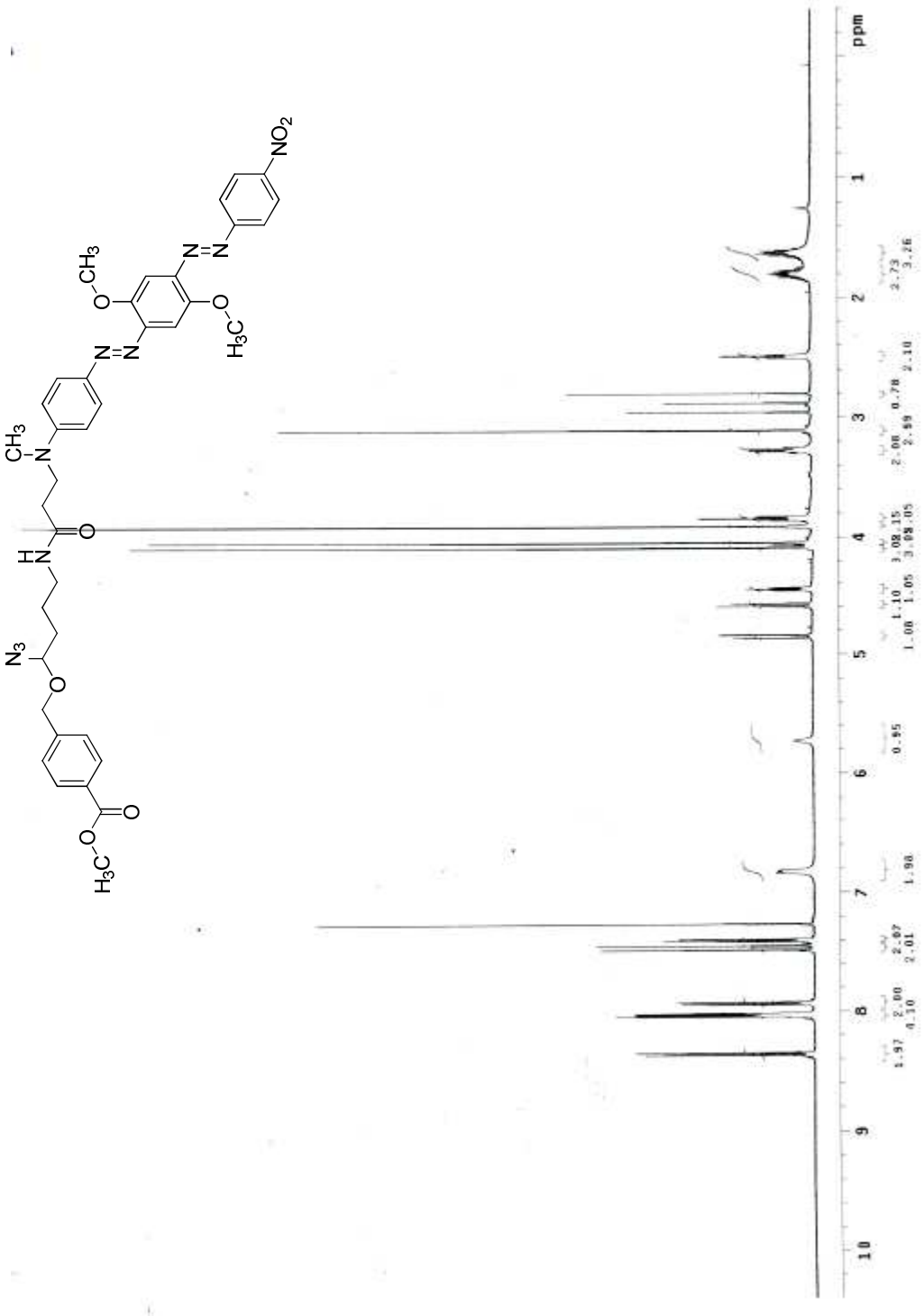

Figure S17. ^{1}H-NMR spectrum of 4-[(1-azido-4-(3-(BHQ-2)-propionamido)butoxy)methyl]-benzoaic acid (**3**); 500 MHz, [D_6]DMSO.

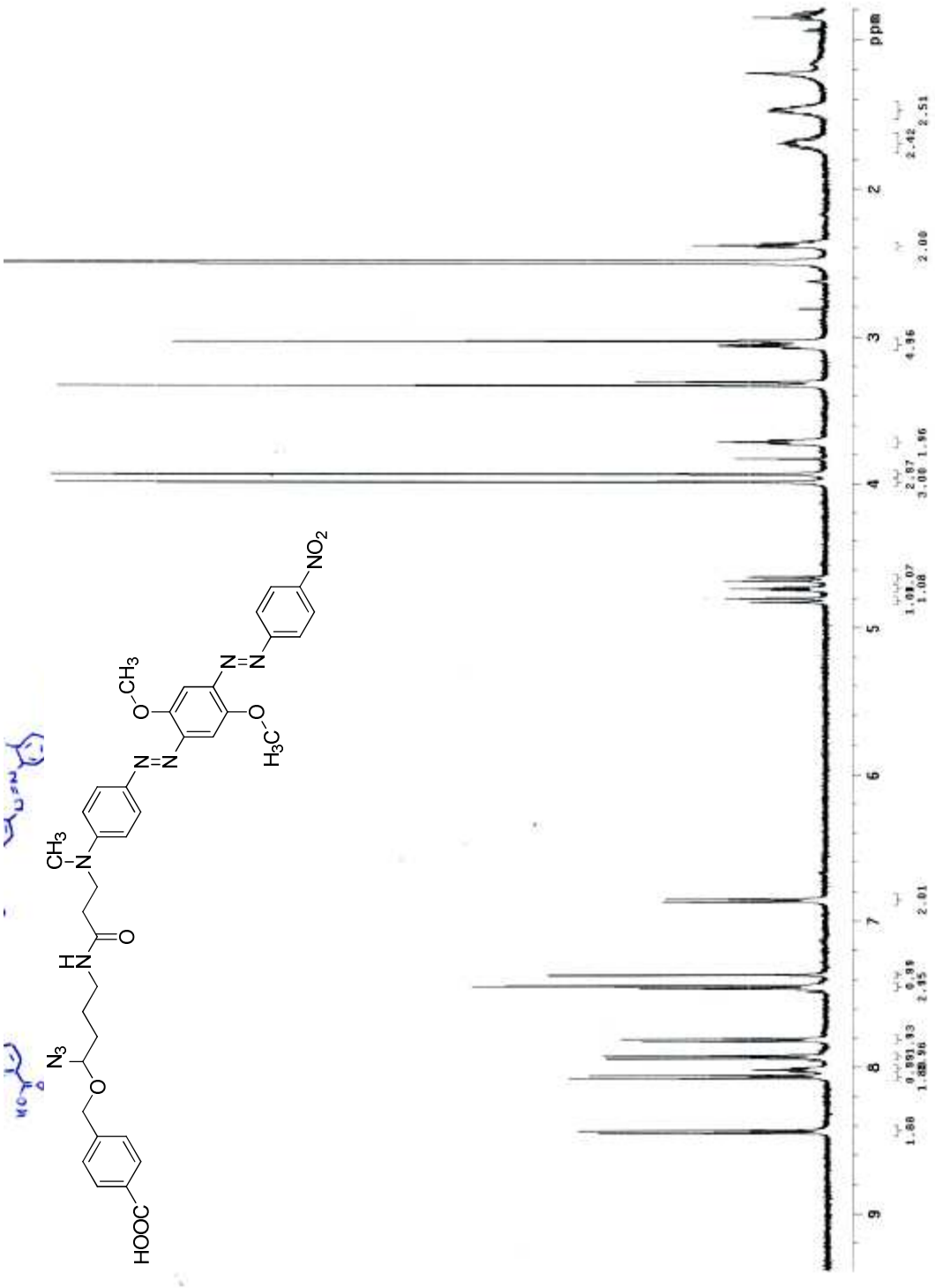

^{13}C-NMR Spectra

Figure S18. ^{13}C-NMR spectrum of Methyl 4-[(1-azido-3-(3-(BHQ-1)-propionamido)propoxy)-methyl]benzoate (**4**); 500 MHz, $CDCl_3$.

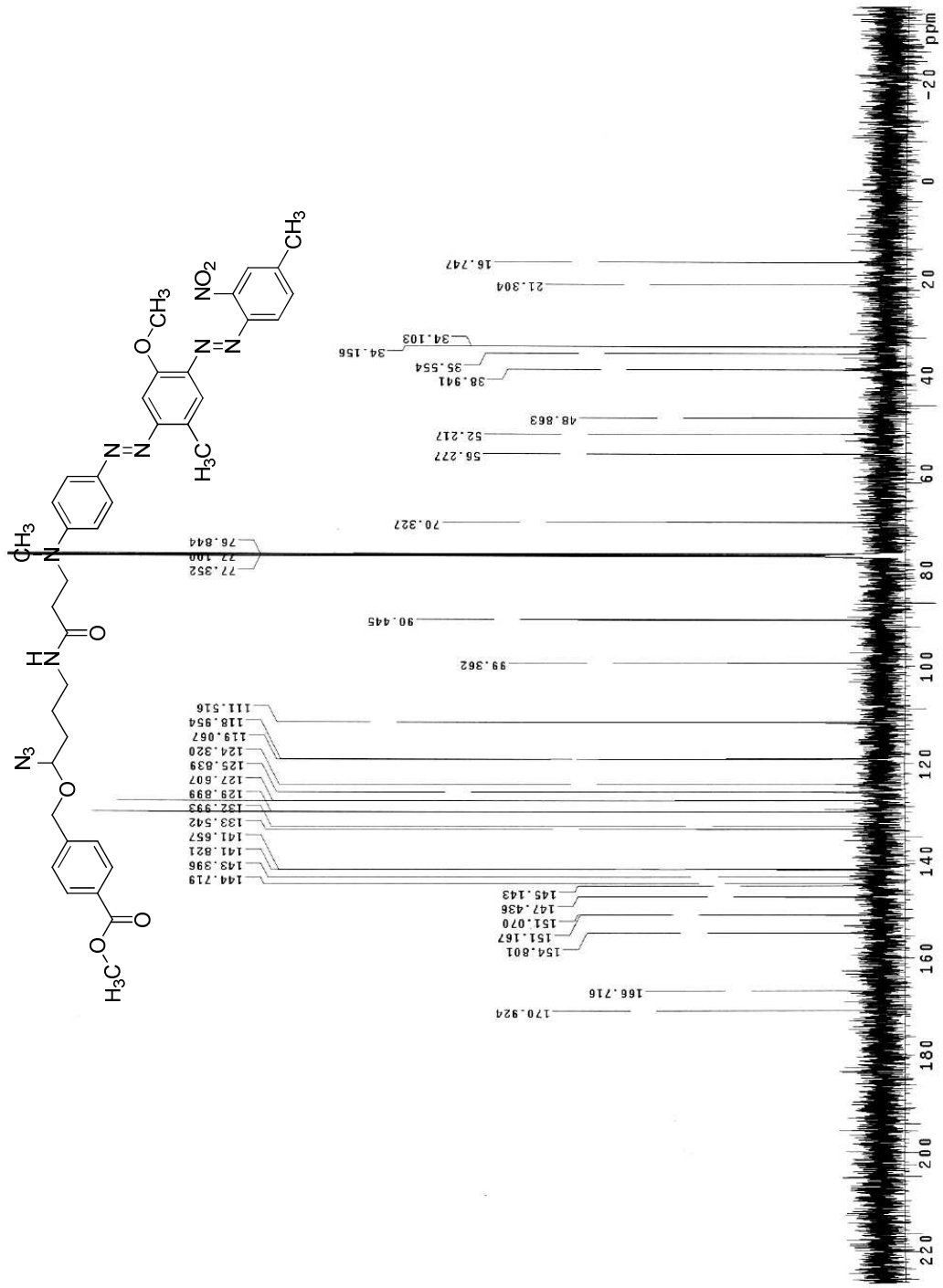

Figure S19. ^{13}C-NMR spectrum of ***N***-(4-hydroxybutyl)trifluoroacetamide ***(5)***; 500 MHz, $CDCl_3$.

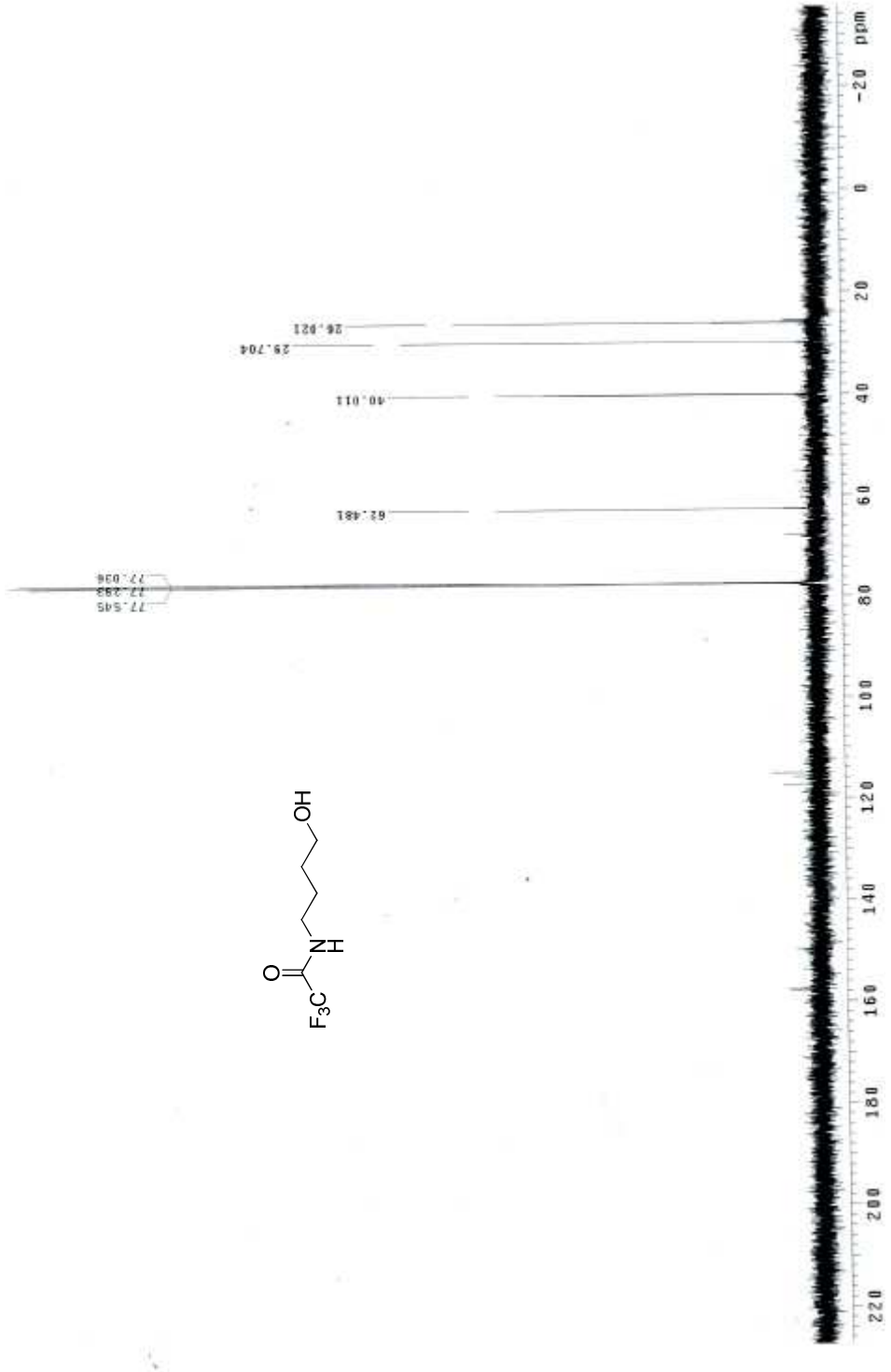

Figure S20. ^{13}C-NMR spectrum of Methyl 4-[(1-azido-4-trifluoroacetamidobutoxy)methyl]-benzoate ***(7)***; 500 MHz, $CDCl_3$.

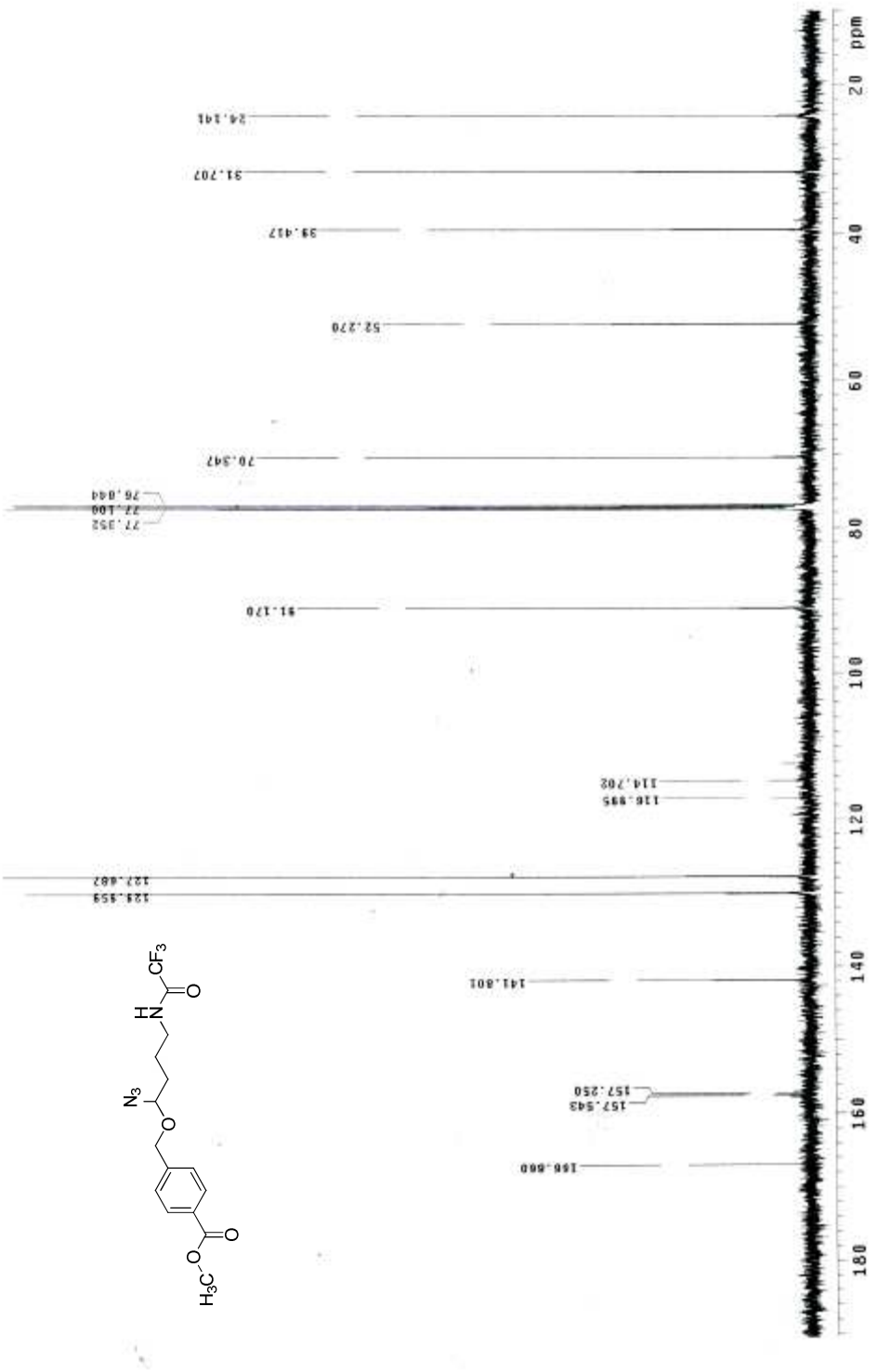

Figure 21. ^{13}C-NMR spectrum of Methyl 4-[(4-amino-1-azidobutoxy)methyl]benzoate ***(8)***; 500 MHz, $CDCl_3$.

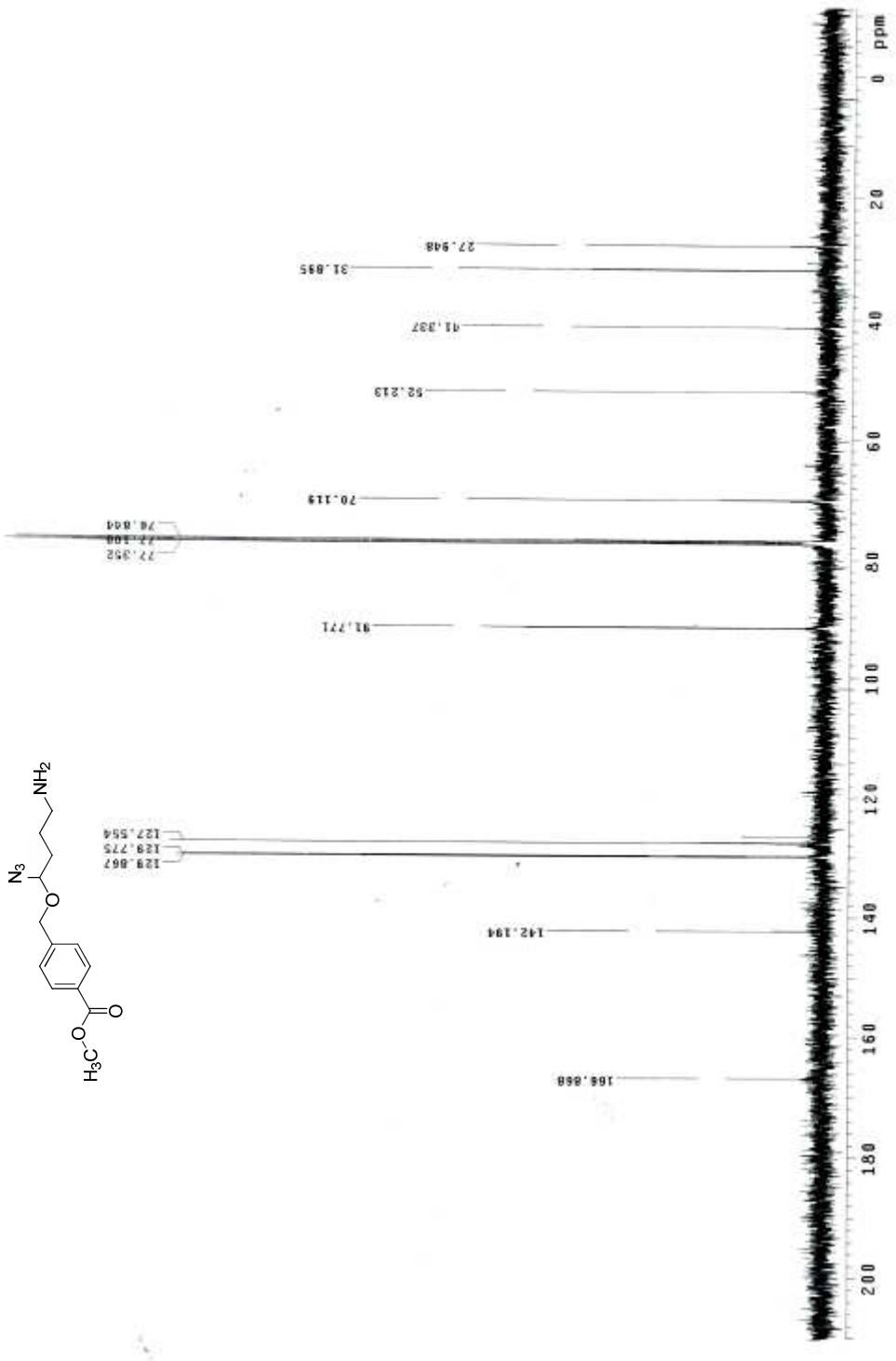

Figure S22. ^{13}C-NMR spectrum of Methyl 4-[(1-azido-4-(3-(BHQ-2)-propionamido)butoxy)methyl]-benzoate ***(9)***; 500 MHz, $CDCl_3$.

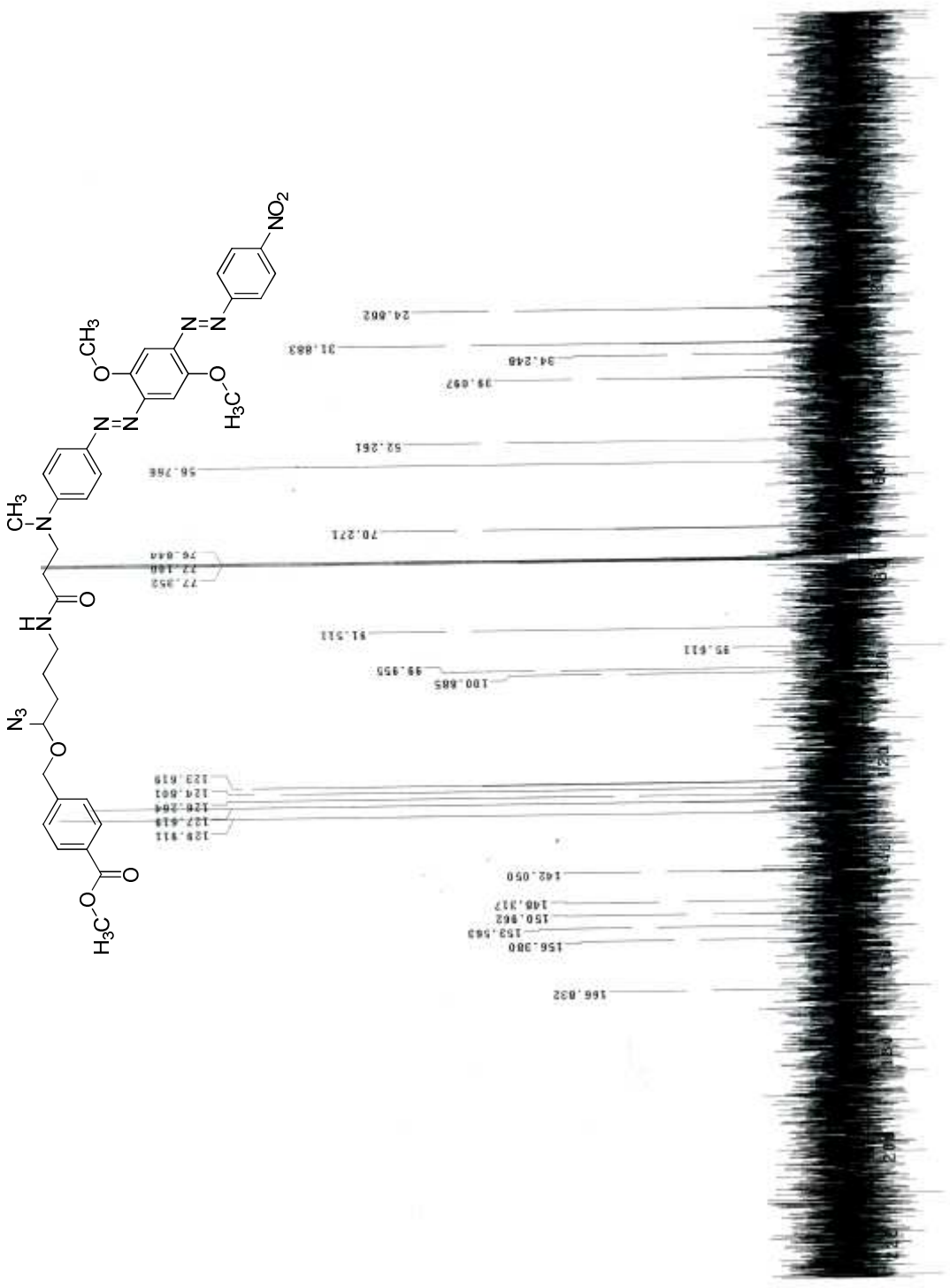

References

[1] R. M. Franzini, E. T. Kool ***J. Am. Chem. Soc.*** **2009**, ***J. Am. Chem. Soc. 131***, 16021.

[2] C. Quinet, L. Sampoux, I. E. Marko ***Eur. J. Org. Chem.*** **2009**, ***2009***, 1806-1811.